

# Principles of Fluorescence Spectroscopy

Third Edition

# Principles of Fluorescence Spectroscopy

Third Edition

Joseph R. Lakowicz

*University of Maryland School of Medicine  
Baltimore, Maryland, USA*



Joseph R. Lakowicz  
Center for Fluorescence Spectroscopy  
University of Maryland School of Medicine  
Baltimore, MD 21201  
USA

Library of Congress Control Number: 2006920796

ISBN-10: 0-387-31278-1  
ISBN-13: 978-0387-31278-1

Printed on acid-free paper.

© 2006, 1999, 1983 Springer Science+Business Media, LLC

All rights reserved. This work may not be translated or copied in whole or in part without the written permission of the publisher (Springer Science+Business Media, LLC, 233 Spring Street, New York, NY 10013, USA), except for brief excerpts in connection with reviews or scholarly analysis. Use in connection with any form of information storage and retrieval, electronic adaptation, computer software, or by similar or dissimilar methodology now known or hereafter developed is forbidden.

The use in this publication of trade names, trademarks, service marks, and similar terms, even if they are not identified as such, is not to be taken as an expression of opinion as to whether or not they are subject to proprietary rights.

Printed in Singapore. (KYO)

9 8 7 6 5 4 3 2 1

[springer.com](http://springer.com)

*Dedicated to Mary,  
for her continuous support and encouragement,  
without whom this book would not have been written*

# Preface

The first edition of *Principles* was published in 1983, and the second edition 16 years later in 1999. At that time I thought the third edition would not be written until 2010 or later. However, the technology of fluorescence has advanced at an accelerating pace. Single-molecule detection and fluorescence-correlation spectroscopy are becoming almost routine. New classes of probes have appeared, such as the semiconductor nanoparticles, or QDots, and genetically engineered green fluorescent probes. Additionally, it is now becoming possible to control the excited states of fluorophores, rather than relying only on spontaneous emission. These developments are changing the par-

adigm of fluorescence, from a reliance on organic fluorophores, to the use of genetic engineering, nanotechnology, and near-field optics.

I wish to express my appreciation and special thanks to the individuals who have assisted me in the preparation of the book. These include Ignacy Gryczynski for assistance with the figures, Krystyna Gryczynski for drawing the figures, Joanna Malicka for proofreading the chapters, Kazik Nowaczyk for the cover design and color digitizing of all figures, Tim Oliver for typesetting, and the NIH for their support of my laboratory. And finally, Mary, for her endless hours of typing, correspondence and support.

*Joseph R. Lakowicz*

# Glossary of Acronyms

A	acceptor	C102	coumarin 102
AA	anthranilic acid	C152	coumarin 152
2-AA	2-acetylanthracene	C153	coumarin 153
Ac	acetonitrile	9-CA	9-cyanoanthracene
Ac	acetone or acridine	CaM	calmodulin
ACF	acriflavine	cAMP	cyclic AMP
AcH	acridinium cation	CFD	constant fraction discriminator
ACTH	adrenocorticotropin hormone	CG	calcium green
Alexa-Bz	Alexa-labeled benzodiazepine	CHO	Chinese hamster ovary
ADC	analog-to-digital converter	CC	closed circular
Adx	adrenodoxin	CCDs	charged-coupled devices
I-AEDANS	5(((2-iodoacetyl)amino)ethyl)amino)-naphthalene-1-sulfonic acid	CH	cyclohexane
AFA	aminofluoranthene	Chol	cholesterol
AN	anthracene	CLSM	confocal laser scanning microscopy
2-AN	2-anilinonaphthalene	CNF	carboxynaphthofluorescein
2,6-ANS	6-(anilino)naphthalene-2-sulfonic acid	ConA	concanavalin A
AO	acridine orange or acoustooptic	CRABPI	cellular retinoic acid binding protein I
2-AP	2-aminopurine	CSR	continuous spectral relaxation
4-AP	4-aminophthalimide	CT	charge transfer
APC	allophycocyanin	CW	continuous wave
APDs	avalanche photodiodes	D	donor
9-AS	9-anthroyloxy stearic acid	Dansyl	5-dimethylaminonaphthalene-1-sulfonic acid
ASEs	asymptotic standard errors	DAPI	4',6-diamidino-2-phenylindole
AT	antithrombin	DAS	decay-associated spectra
B	benzene	DBS	4-dimethylamino-4'-bromostilbene
BABAPH	2-(sulfonatobutyl)-7-(dibutylamino)-2-aza-phenanthrene	DC	deoxycytosine
BABP	sulfonatobutyl)-4-[4'-(dibutylamino)-phenyl]pyridine	DDQ	distance-dependent quenching
BCECF	7'-bis(2-carboxyethyl)-5(6)-carboxyfluorescein	DEA	diethylaniline
BSA	bovine serum albumin	DEE	diethyl ether
BODIPY	refers to a family of dyes based on 1,3,5,7,8-pentamethyl pyrromethene-BF <sub>2</sub> , or 4,4-difluoro-4-bora-3a,4a-diaza-s-indacene; BODIPY is a trademark of Molecular Probes Inc.	DHE	dihydroequilenin
β-PE	β-phycoerythrin	DHP	dihexadecyl phosphate
BPTI	bovine pancreatic trypsin inhibitor	DiI or DiIC <sub>12</sub>	1,1'-didodecyl-3,3,3',3'-tetramethyl lindocarbocyanine
Bromo-PCs	brominated phosphatidylcholines	DM	dodecylmaltoside
Bu	butanol	DMA	dimethylaniline
		DMAS	N-dimethylaniline sulfonate
		DMF	dimethylformamide
		DMPC	dimyristoyl-L-α-phosphatidylcholine
		DMP	dimethyldiazaperopyrenium
		DMSO	dimethyl sulfoxide
		DMQ	2,2'-dimethyl-p-quaterphenyl
		10-DN	10-doxylnonadecane

## GLOSSARY OF ACRONYMS

DNS	dansyl or 4-dimethylamino-4'-nitrostilbene	GPD	glyceraldehyde-3-phosphate dehydrogenase
DNS-Cl	dansyl chloride	GPI	glycosylphosphatidylinositol
DOS	trans-4-dimethylamino-4'-(1-oxobutyl)stilbene	GuHCl	guanidine hydrochloride
DPA	9,10-diphenylanthracene	GUVs	giant unilamellar vesicles
DPA	dipicolinic acid	H	n-hexane
DPE	dansyl-labeled phosphatidylethanolamine	HDL	high-density lipoprotein
DPH	1,6-diphenyl-1,3,5-hexatriene	HeCd	helium–cadmium
DPO	2,5-diphenyloxazole	HG	harmonic generator
DPPC	dipalmitoyl-L- $\alpha$ -phosphatidylcholine	HITCI	hexamethylindotricarbocyanine iodide
DPPC	dipalmitoylphosphatidylcholine	HLH	human luteinizing hormone
DP(M,O)PC(E)	dipalmitoyl(myristoyl, oleoyl)-L- $\alpha$ -phosphatidylcholine (ethanolamine)	HO	highest occupied
DTAC	dodecyltrimethylammonium chloride	HpRz	hairpin ribozyme
EA	ethyl acetate	HPTS	1-hydroxypyrene-3,6,8-trisulfonate
EA	ethanol	hIFN- $\gamma$	human recombinant interferon $\gamma$
EAN	ethylaniline	HSA	human serum albumin
EB	ethidium bromide	17 $\beta$ -HSD	17 $\beta$ -hydroxysteroid dehydrogenase
EC	ethylcellulose	hw	half-width
ECFP	enhanced cyan fluorescent protein	IAEDANS	5(((2-iodoacetyl)amino)ethyl)amino)-naphthalene-1-sulfonic acid
EDT	1,2-ethanedithiol	IAF	5-iodoacetamidofluorescein
EG	ethylene glycol	ICT	internal charge transfer
ELISA	enzyme-linked immunoassay	IM	insertion mutant
eosin-PE	eosin-phosphatidylethanolamine	Indo-1-C <sub>18</sub>	indo-1 with a C <sub>18</sub> chain
EP	1-ethylpyrene	IRF	instrument response function
EPE	eosin-labeled phosphatidylethanolamine	IXP	isoxanthopterin
ESIPT	excited-state intramolecular proton transfer	KF	Klenow fragment
ESR	excited-state reaction	KSI	3-ketosteroid isomerase
EO	electrooptic	LADH	liver alcohol dehydrogenase
EYFP	enhanced yellow fluorescent protein	LCAT	lecithin:cholesterol acyltransferase
F	single-letter code for phenylalanine	LDs	laser diodes
Fl	fluorescein	LE	locally excited
Fl-C	fluorescein-labeled catalytic subunit	LEDs	light-emitting diodes
FABPs	fatty acid binding proteins	LU	lowest unoccupied
FAD	flavin adenine dinucleotide	M	monomer
FC	fura-2 with calcium	MAI	N-methylquinolinium iodide
FCS	fluorescence correlation spectroscopy	MBP	maltose-binding protein
FD	frequency domain	MCA	multichannel analyzer
Fn	fibronectin	MCP	microchannel plate
Fs	femtosecond	Me	methanol
FITC	fluorescein-5-isothiocyanate	MEM	method-of-moments
FLIM	fluorescence-lifetime imaging microscopy	met RS	methionyl-tRNA synthetase
FMN	flavin mononucleotide	3-MI	3-methyl indole
FR	folate receptor	MLC	metal-ligand complex, usually of a transition metal, Ru, Rh or Os
FRET	fluorescence-resonance energy transfer	MLCK	myosin light chain kinase
FWHM	full width of half-maximum intensity	MLCT	metal-ligand charge transfer (state)
4FW	4-fluorotryptophan	MLE	maximum likelihood estimates
GADPH	glyceraldehyde-3-phosphate dehydrogenase	MPE	multiphoton excitation
GFP	green fluorescent protein	MPM	multiphoton microscopy
GGBP	glucose-galactose binding protein	MQAE	6-methoxy-quinolyl acetoethyl ester
GM	Goppert-Mayer	MRI	magnetic resonance imaging
GOI	gated optical image intensifier		
GP	generalized polarization		

NADH	reduced nicotinamide adenine dinucleotide	QDs	quantum dots
NATA	N-acetyl-L-tryptophanamide	QTH	quartz–tungsten halogen
NATyrA	N-acetyl-L-tyrosinamide	RBC	radiation boundary condition
NB	Nile blue	RBL	rat basophilic leukemia
NBD	N-(7-nitrobenz-2-oxa-1,3-diazol-4-yl)	R-PE	R-phycerythrin
NBD-DG	1-oleoyl-2-hexanoyl-NBD-glycerol	REES	red-edge excitation shifts
Nd:YAG	neodymium:YAG	Re I	rhenum
NIR	near infrared	RET	resonance energy transfer
NLLS	nonlinear least squares	RF	radio frequency
NMA	N-methylantraniloyl amide	RFP	red fluorescent protein
NO	nitric oxide	Rh	rhodamine
NPN	N-phenyl-1-naphthylamine	RhB	rhodamine B
NR	neutral red	RhG	rhodamine green
NRP	neuronal receptor peptide	R6G	rhodamine 6G
5-NS	5-doxylstearate	RNase T <sub>1</sub>	ribonuclease T <sub>1</sub>
OG	Oregon green	RR	rhodamine red
OPO	optical parameter oscillator	Ru	ruthenium
ORB	octadecyl rhodamine B	SAS	species-associated spectra
Os	osmium	SBFI	sodium-binding benzofuran isophthalate
PBFI	potassium-binding benzofuran isophthalate	SBP	steroid-binding protein
PC	phosphatidylcholine	SBS	substrate-binding strand
PCSC	photon-counting streak camera	SC	subtilisin Carlsberg
PDA	pyrene dodecanoic acid	SDS	sodium dodecylsulfate
PDs	photodiodes	SEDA	dapoxyl sulfonyl ethylenediamine
PE	phycoerythrin	SMD	single-molecule detection
PE	phosphatidylethanolamine	SNAFLs	seminophthofluorescins
1PE	one-photon	SNARFs	seminaphthorhodafluors
2PE	two-photon	SP	short-pass
3PE	three-photon	SPQ	6-methoxy-N-[3-sulfonypropyl]quinoline
PET	photoinduced electron transfer	T	tetramer
PeCN	3-cyanoperylene	TAC	time-to-amplitude converter
PG	propylene glycol	TCE	trichloroethanol
PGK	phosphoglycerate kinase	t-COPA	16-octadecapentaenoic acid
Phe(F)	phenylalanine	TCSPC	time-correlated single photon counting
PK	protein kinase	TD	time-domain
PKI	protein kinase inhibitor	TEOS	tetraethylorthosilicate
PMMA	poly(methylmethacrylate)	TFA	trifluoroacetamide
PMT	photomultiplier tube	TFE	trifluoroethanol
POPC	1-palmitoyl-2-oleoylphosphatidylcholine	THF	tetrahydrofuran
POPOP	1,4-bis(5-phenyloxazol-2-yl)benzene	TICT	twisted internal charge transfer
PP	pulse picker	TK	thymidine kinase
PPD	2,5-diphenyl-1,3,4-oxadizole	TL	tear lipocalin
PPi	pyrophosphate	TMA	donor alone
PPO	2,5-diphenyloxazole	TMR	tetramethylrhodamine
PRODAN	6-propionyl-2-(dimethylamino)-naphthalene	TnC	troponin C
ps	picosecond	TNS	6-(p-toluidinyl)naphthalene-2-sulfonic acid
PSDF	phase-sensitive detection of fluorescence	TOAH	tetraoctylammonium hydroxide
PTP	phosphoryl-transfer protein	TOE	tryptophan octyl ester
Py2	pyridine 2	TPI	triosephosphate isomerase

TRES	time-resolved emission spectra	w	single-letter code for tryptophan
TrpNH <sub>2</sub>	tryptophanamide	W	water
TRITC	tetramethylrhodamine-5-(and-6)-isothiocyanate	WT	wild type
tRNA <sup>fMet</sup>	methionine tRNA	WD	window discriminator
trp(w)	tryptophan	Xe	xenon
TTS	transit time spread	y	single-letter code for tryptophan
TU2D	donor–acceptor pair		
tyr(y)	tyrosine	YFP	yellow fluorescent protein
U	uridine		
7-Ump	7-umbelliferyl phosphate		

# Glossary of Mathematical Terms

$A$	acceptor or absorption	$pK_a$	acid dissociation constant, negative logarithm
$B_i$	brightness of a fluorophore	$q$	efficiency for detection of emitted photons, typically for FCS
$c$	speed of light	$Q$	quantum yield
$C_0$	characteristic acceptor concentration in RET	$r$	anisotropy (sometimes distance in a distance distribution)
$C(t)$	correlation function for spectral relaxation	$\bar{r}$	average distance in a distance distribution
$D$	donor, or diffusion coefficient, or rotational diffusion coefficient	$r(0)$	time-zero anisotropy
$D_{\parallel}$ or $D_{\perp}$	rate of rotation diffusion around or (displacing) the symmetry axis of an ellipsoid of revolution	$r(t)$	anisotropy decay
$D(\tau)$	part of the autocorrelation function for diffusion containing the diffusion-dependent terms	$r_c$	distance of closest approach between donors and acceptors in resonance energy transfer, or fluorophores and quenchers
$E$	efficiency of energy transfer	$r_{0i}$ or $r_0 g_i$	fractional amplitudes in a multi-exponential anisotropy decay
$F$	steady-state intensity or fluorescence	$r_0$	fundamental anisotropy in the absence of rotational diffusion
$F\chi$	ratio of $\chi_R^2$ values, used to calculate parameter confidence intervals	$r_{0i}$	anisotropy amplitudes in a multi-exponential anisotropy decay
$F(\lambda)$	emission spectrum	$r_{\infty}$	long-time anisotropy in an anisotropy decay
$f_i$	fractional steady-state intensities in a multi-exponential intensity decay	$r_{\omega}$	modulated anisotropy
$f_Q$	efficiency of collisional quenching	$R_0$	Förster distance in resonance energy transfer
$G$	correction factor for anisotropy measurements	$T$	temperature
$G(\tau)$	autocorrelation function of fluorescence fluctuations	$T_p$	phase transition temperature for a membrane
$hw$	half-width in a distance or lifetime distribution	$\alpha_i$	pre-exponential factors in a multi-exponential intensity decay
$I(t)$	intensity decay, typically the impulse response function	$\beta$	angle between absorption and emission transition moments
$k_{nr}$	non-radiative decay rate	$\gamma$	inverse of the decay time, $\gamma = 1/\tau$
$k_s$	solvent relaxation rate	$\Gamma$	radiative decay rate
$k_T$	transfer rate in resonance energy transfer	$\varepsilon$	dielectric constant or extinction coefficient
$k_{st}$	rate of singlet to triplet intersystem crossing	$\varepsilon_A$ or $\varepsilon$	molar extinction coefficient for absorption
$k_{ts}$	rate of return to the singlet ground state from the triplet state	$\theta$	rotational correlation time
$m_o$	modulation at a light modulation frequency $\omega$	$\theta_c$	critical angle for total internal reflection
$n$	refractive index, when used in consideration of solvent effects	$\kappa^2$	orientation factor in resonance energy transfer
$N$	number of observed molecules in FCS	$\lambda$	wavelength
$N(t_k)$	number of counts per channel, in time-correlation single-photon counting	$\lambda_{em}$	emission wavelength
$P(r)$	probability function for a distance ( $r$ ) distribution	$\lambda_{em}^{max}$	maximum emission wavelength
		$\lambda_{ex}$	excitation wavelength

**GLOSSARY OF MATHEMATICAL TERMS**

$\lambda_{\text{ex}}^{\text{max}}$	maximum excitation or absorption wavelength for the lowest $S_0 \rightarrow S_1$ transition	$\bar{v}$	specific gravity or wavelength in $\text{cm}^{-1}$
$\lambda_{\text{max}}$	emission maxima	$\bar{v}_{\text{cg}}$	center of gravity of an emission spectrum in $\text{cm}^{-1}$
$\Lambda?$	ratio of the modulated amplitudes of the polarized components of the emission	$\sigma$ or $\sigma_A$	optical cross-section for absorption
$\eta$	viscosity	$\sigma_S$	optical cross-section for scattering
$\mu_E$	excited-state dipole moment	$\tau$	lifetime or time-delay in FCS
$\mu_G$	ground-state dipole moment	$\tau_D$	diffusion time in FCS
$\mu\text{m}$	micron	$\tau_s$	solvent or spectral relaxation time

# Contents

## I. Introduction to Fluorescence

1.1. Phenomena of Fluorescence.....	1
1.2. Jablonski Diagram.....	3
1.3. Characteristics of Fluorescence Emission.....	6
1.3.1. The Stokes Shift .....	6
1.3.2. Emission Spectra Are Typically Independent of the Excitation Wavelength .....	7
1.3.3. Exceptions to the Mirror-Image Rule .....	8
1.4. Fluorescence Lifetimes and Quantum Yields.....	9
1.4.1. Fluorescence Quenching .....	11
1.4.2. Timescale of Molecular Processes in Solution .....	12
1.5. Fluorescence Anisotropy .....	12
1.6. Resonance Energy Transfer.....	13
1.7. Steady-State and Time-Resolved Fluorescence .....	14
1.7.1. Why Time-Resolved Measurements?.....	15
1.8. Biochemical Fluorophores .....	15
1.8.1. Fluorescent Indicators .....	16
1.9. Molecular Information from Fluorescence .....	17
1.9.1. Emission Spectra and the Stokes Shift .....	17
1.9.2. Quenching of Fluorescence.....	18
1.9.3. Fluorescence Polarization or Anisotropy .....	19
1.9.4. Resonance Energy Transfer.....	19
1.10. Biochemical Examples of Basic Phenomena.....	20
1.11. New Fluorescence Technologies .....	21
1.11.1. Multiphoton Excitation .....	21
1.11.2. Fluorescence Correlation Spectroscopy.....	22
1.11.3. Single-Molecule Detection.....	23
1.12. Overview of Fluorescence Spectroscopy .....	24
References .....	25
Problems.....	25

## 2. Instrumentation for Fluorescence Spectroscopy

2.1. Spectrofluorometers .....	27
2.1.1. Spectrofluorometers for Spectroscopy Research .....	27
2.1.2. Spectrofluorometers for High Throughput ...	29
2.1.3. An Ideal Spectrofluorometer .....	30
2.1.4. Distortions in Excitation and Emission Spectra.....	30

2.2. Light Sources .....	31
2.2.1. Arc Lamps and Incandescent Xenon Lamps .....	31
2.2.2. Pulsed Xenon Lamps .....	32
2.2.3. High-Pressure Mercury (Hg) Lamps .....	33
2.2.4. Xe–Hg Arc Lamps .....	33
2.2.5. Quartz–Tungsten Halogen (QTH) Lamps.....	33
2.2.6. Low-Pressure Hg and Hg–Ar Lamps.....	33
2.2.7. LED Light Sources.....	33
2.2.8. Laser Diodes.....	34
2.3. Monochromators .....	34
2.3.1. Wavelength Resolution and Emission Spectra .....	35
2.3.2. Polarization Characteristics of Monochromators .....	36
2.3.3. Stray Light in Monochromators.....	36
2.3.4. Second-Order Transmission in Monochromators .....	37
2.3.5. Calibration of Monochromators.....	38
2.4. Optical Filters .....	38
2.4.1. Colored Filters.....	38
2.4.2. Thin-Film Filters .....	39
2.4.3. Filter Combinations.....	40
2.4.4. Neutral-Density Filters.....	40
2.4.5. Filters for Fluorescence Microscopy.....	41
2.5. Optical Filters and Signal Purity .....	41
2.5.1. Emission Spectra Taken through Filters .....	43
2.6. Photomultiplier Tubes .....	44
2.6.1. Spectral Response of PMTs .....	45
2.6.2. PMT Designs and Dynode Chains .....	46
2.6.3. Time Response of Photomultiplier Tubes .....	47
2.6.4. Photon Counting versus Analog Detection of Fluorescence .....	48
2.6.5. Symptoms of PMT Failure .....	49
2.6.6. CCD Detectors .....	49
2.7. Polarizers .....	49
2.8. Corrected Excitation Spectra.....	51
2.8.1. Corrected Excitation Spectra Using a Quantum Counter .....	51
2.9. Corrected Emission Spectra .....	52
2.9.1. Comparison with Known Emission Spectra .....	52
2.9.2. Corrections Using a Standard Lamp .....	53
2.9.3. Correction Factors Using a Quantum Counter and Scatterer .....	53

2.9.4. Conversion between Wavelength and Wavenumber.....	53	4.1.3. Examples of Time-Domain and Frequency-Domain Lifetimes .....	100
2.10. Quantum Yield Standards.....	54	4.2. Biopolymers Display Multi-Exponential or Heterogeneous Decays .....	101
2.11. Effects of Sample Geometry .....	55	4.2.1. Resolution of Multi-Exponential Decays Is Difficult .....	103
2.12. Common Errors in Sample Preparation .....	57	4.3. Time-Correlated Single-Photon Counting .....	103
2.13. Absorption of Light and Deviation from the Beer-Lambert Law.....	58	4.3.1. Principles of TCSPC .....	104
2.13.1. Deviations from Beer's Law.....	59	4.3.2. Example of TCSPC Data .....	105
2.14. Conclusions .....	59	4.3.3. Convolution Integral.....	106
References .....	59	4.4. Light Sources for TCSPC .....	107
Problems.....	60	4.4.1. Laser Diodes and Light-Emitting Diodes ....	107
<b>3. Fluorophores</b>		4.4.2. Femtosecond Titanium Sapphire Lasers .....	108
3.1. Intrinsic or Natural Fluorophores.....	63	4.4.3. Picosecond Dye Lasers .....	110
3.1.1. Fluorescence Enzyme Cofactors .....	63	4.4.4. Flashlamps.....	112
3.1.2. Binding of NADH to a Protein .....	65	4.4.5. Synchrotron Radiation .....	114
3.2. Extrinsic Fluorophores .....	67	4.5. Electronics for TCSPC .....	114
3.2.1. Protein-Labeling Reagents .....	67	4.5.1. Constant Fraction Discriminators .....	114
3.2.2. Role of the Stokes Shift in Protein Labeling.....	69	4.5.2. Amplifiers .....	115
3.2.3. Photostability of Fluorophores.....	70	4.5.3. Time-to-Amplitude Converter (TAC) and Analyte-to-Digital Converter (ADC)....	115
3.2.4. Non-Covalent Protein-Labeling Probes .....	71	4.5.4. Multichannel Analyzer .....	116
3.2.5. Membrane Probes.....	72	4.5.5. Delay Lines .....	116
3.2.6. Membrane Potential Probes .....	72	4.5.6. Pulse Pile-Up.....	116
3.3. Red and Near-Infrared (NIR) Dyes.....	74	4.6. Detectors for TCSPC.....	117
3.4. DNA Probes .....	75	4.6.1. Microchannel Plate PMTs.....	117
3.4.1. DNA Base Analogues .....	75	4.6.2. Dynode Chain PMTs.....	118
3.5. Chemical Sensing Probes.....	78	4.6.3. Compact PMTs.....	118
3.6. Special Probes .....	79	4.6.4. Photodiodes as Detectors .....	118
3.6.1. Fluorogenic Probes.....	79	4.6.5. Color Effects in Detectors .....	119
3.6.2. Structural Analogues of Biomolecules.....	80	4.6.6. Timing Effects of Monochromators .....	121
3.6.3. Viscosity Probes .....	80	4.7. Multi-Detector and Multidimensional TCSPC .....	121
3.7. Green Fluorescent Proteins .....	81	4.7.1. Multidimensional TCSPC and DNA Sequencing .....	123
3.8. Other Fluorescent Proteins.....	83	4.7.2. Dead Times, Repetition Rates, and Photon Counting Rates.....	124
3.8.1. Phytofluors: A New Class of Fluorescent Probes .....	83	4.8. Alternative Methods for Time-Resolved Measurements.....	124
3.8.2. Phycobiliproteins.....	84	4.8.1. Transient Recording .....	124
3.8.3. Specific Labeling of Intracellular Proteins.....	86	4.8.2. Streak Cameras.....	125
3.9. Long-Lifetime Probes .....	86	4.8.3. Upconversion Methods.....	128
3.9.1. Lanthanides .....	87	4.8.4. Microsecond Luminescence Decays .....	129
3.9.2. Transition Metal–Ligand Complexes.....	88	4.9. Data Analysis: Nonlinear Least Squares.....	129
3.10. Proteins as Sensors .....	88	4.9.1. Assumptions of Nonlinear Least Squares .....	130
3.11. Conclusion.....	89	4.9.2. Overview of Least-Squares Analysis .....	130
References .....	90	4.9.3. Meaning of the Goodness-of-Fit .....	131
Problems.....	94	4.9.4. Autocorrelation Function .....	132
<b>4. Time-Domain Lifetime Measurements</b>		4.10. Analysis of Multi-Exponential Decays .....	133
4.1. Overview of Time-Domain and Frequency-Domain Measurements.....	98	4.10.1. p-Terphenyl and Indole: Two Widely Spaced Lifetimes .....	133
4.1.1. Meaning of the Lifetime or Decay Time .....	99	4.10.2. Comparison of $\chi^2_R$ Values: F Statistic .....	133
4.1.2. Phase and Modulation Lifetimes .....	99	4.10.3. Parameter Uncertainty: Confidence Intervals .....	134
		4.10.4. Effect of the Number of Photon Counts .....	135
		4.10.5. Anthranilic Acid and 2-Aminopurine: Two Closely Spaced Lifetimes.....	137

4.10.6. Global Analysis: Multi-Wavelength Measurements.....	138	5.5. Simple Frequency-Domain Instruments .....	173
4.10.7. Resolution of Three Closely Spaced Lifetimes.....	138	5.5.1. Laser Diode Excitation.....	174
4.11. Intensity Decay Laws .....	141	5.5.2. LED Excitation.....	174
4.11.1. Multi-Exponential Decays .....	141	5.6. Gigahertz Frequency-Domain Fluorometry .....	175
4.11.2. Lifetime Distributions .....	143	5.6.1. Gigahertz FD Measurements .....	177
4.11.3. Stretched Exponentials.....	144	5.6.2. Biochemical Examples of Gigahertz FD Data .....	177
4.11.4. Transient Effects.....	144	5.7. Analysis of Frequency-Domain Data .....	178
4.12. Global Analysis .....	144	5.7.1. Resolution of Two Widely Spaced Lifetimes.....	178
4.13. Applications of TCSPC .....	145	5.7.2. Resolution of Two Closely Spaced Lifetimes.....	180
4.13.1. Intensity Decay for a Single Tryptophan Protein .....	145	5.7.3. Global Analysis of a Two-Component Mixture .....	182
4.13.2. Green Fluorescent Protein: Systematic Errors in the Data .....	145	5.7.4. Analysis of a Three-Component Mixture: Limits of Resolution.....	183
4.13.3. Picosecond Decay Time .....	146	5.7.5. Resolution of a Three-Component Mixture with a Tenfold Range of Decay Times .....	185
4.13.4. Chlorophyll Aggregates in Hexane .....	146	5.7.6. Maximum Entropy Analysis of FD Data .....	185
4.13.5. Intensity Decay of Flavin Adenine Dinucleotide (FAD).....	147	5.8. Biochemical Examples of Frequency-Domain Intensity Decays .....	186
4.14. Data Analysis: Maximum Entropy Method .....	148	5.8.1. DNA Labeled with DAPI .....	186
References .....	149	5.8.2. Mag-Quin-2: A Lifetime-Based Sensor for Magnesium .....	187
Problems .....	154	5.8.3. Recovery of Lifetime Distributions from Frequency-Domain Data .....	188
		5.8.4. Cross-Fitting of Models: Lifetime Distributions of Melittin.....	188
		5.8.5. Frequency-Domain Fluorescence Microscopy with an LED Light Source.....	189
		5.9. Phase-Angle and Modulation Spectra.....	189
		5.10. Apparent Phase and Modulation Lifetimes .....	191
		5.11. Derivation of the Equations for Phase-Modulation Fluorescence .....	192
		5.11.1. Relationship of the Lifetime to the Phase Angle and Modulation .....	192
		5.11.2. Cross-Correlation Detection.....	194
		5.12. Phase-Sensitive Emission Spectra .....	194
		5.12.1. Theory of Phase-Sensitive Detection of Fluorescence .....	195
		5.12.2. Examples of PSDF and Phase Suppression .....	196
		5.12.3. High-Frequency or Low-Frequency Phase-Sensitive Detection .....	197
		5.13. Phase-Modulation Resolution of Emission Spectra .....	197
		5.13.1. Resolution Based on Phase or Modulation Lifetimes.....	198
		5.13.2. Resolution Based on Phase Angles and Modulations .....	198
		5.13.3. Resolution of Emission Spectra from Phase and Modulation Spectra.....	198
		References .....	199
		Problems .....	203

## 5. Frequency-Domain Lifetime Measurements

5.1. Theory of Frequency-Domain Fluorometry .....	158
5.1.1. Least-Squares Analysis of Frequency-Domain Intensity Decays .....	161
5.1.2. Global Analysis of Frequency-Domain Data .....	162
5.2. Frequency-Domain Instrumentation .....	163
5.2.1. History of Phase-Modulation Fluorometers.....	163
5.2.2. An MHz Frequency-Domain Fluorometer....	164
5.2.3. Light Modulators.....	165
5.2.4. Cross-Correlation Detection.....	166
5.2.5. Frequency Synthesizers.....	167
5.2.6. Radio Frequency Amplifiers .....	167
5.2.7. Photomultiplier Tubes .....	167
5.2.8. Frequency-Domain Measurements .....	168
5.3. Color Effects and Background Fluorescence.....	168
5.3.1. Color Effects in Frequency-Domain Measurements.....	168
5.3.2. Background Correction in Frequency-Domain Measurements.....	169
5.4. Representative Frequency-Domain Intensity Decays .....	170
5.4.1. Exponential Decays.....	170
5.4.2. Multi-Exponential Decays of Staphylococcal Nuclease and Melittin.....	171
5.4.3. Green Fluorescent Protein: One- and Two-Photon Excitation.....	171
5.4.4. SPQ: Collisional Quenching of a Chloride Sensor.....	171
5.4.5. Intensity Decay of NADH.....	172
5.4.6. Effect of Scattered Light .....	172

## 6. Solvent and Environmental Effects

6.1. Overview of Solvent Polarity Effects.....	205
6.1.1. Effects of Solvent Polarity .....	205
6.1.2. Polarity Surrounding a Membrane-Bound Fluorophore .....	206
6.1.3. Other Mechanisms for Spectral Shifts .....	207
6.2. General Solvent Effects: The Lippert-Mataga Equation .....	208
6.2.1. Derivation of the Lippert Equation .....	210
6.2.2. Application of the Lippert Equation .....	212
6.3. Specific Solvent Effects .....	213
6.3.1. Specific Solvent Effects and Lippert Plots ..	215
6.4. Temperature Effects .....	216
6.5. Phase Transitions in Membranes .....	217
6.6. Additional Factors that Affect Emission Spectra .....	219
6.6.1. Locally Excited and Internal Charge-Transfer States .....	219
6.6.2. Excited-State Intramolecular Proton Transfer (ESIPT) .....	221
6.6.3. Changes in the Non-Radiative Decay Rates.....	222
6.6.4. Changes in the Rate of Radiative Decay .....	223
6.7. Effects of Viscosity .....	223
6.7.1. Effect of Shear Stress on Membrane Viscosity .....	225
6.8. Probe-Probe Interactions .....	225
6.9. Biochemical Applications of Environment-Sensitive Fluorophores .....	226
6.9.1. Fatty-Acid-Binding Proteins .....	226
6.9.2. Exposure of a Hydrophobic Surface on Calmodulin .....	226
6.9.3. Binding to Cyclodextrin Using a Dansyl Probe .....	227
6.10. Advanced Solvent-Sensitive Probes .....	228
6.11. Effects of Solvent Mixtures.....	229
6.12. Summary of Solvent Effects.....	231
References .....	232
Problems .....	235

## 7. Dynamics of Solvent and Spectral Relaxation

7.1. Overview of Excited-State Processes.....	237
7.1.1. Time-Resolved Emission Spectra .....	239
7.2. Measurement of Time-Resolved Emission Spectra (TRES) .....	240
7.2.1. Direct Recording of TRES .....	240
7.2.2. TRES from Wavelength-Dependent Decays .....	241
7.3. Spectral Relaxation in Proteins .....	242
7.3.1. Spectral Relaxation of Labeled Apomyoglobin.....	243
7.3.2. Protein Spectral Relaxation around a Synthetic Fluorescent Amino Acid .....	244
7.4. Spectral Relaxation in Membranes .....	245
7.4.1. Analysis of Time-Resolved Emission Spectra.....	246
7.4.2. Spectral Relaxation of Membrane-Bound Anthroyloxy Fatty Acids .....	248

7.5. Picosecond Relaxation in Solvents .....	249
7.5.1. Theory for Time-Dependent Solvent Relaxation.....	250
7.5.2. Multi-Exponential Relaxation in Water .....	251
7.6. Measurement of Multi-Exponential Spectral Relaxation.....	252
7.7. Distinction between Solvent Relaxation and Formation of Rotational Isomers .....	253
7.8. Comparison of TRES and Decay-Associated Spectra.....	255
7.9. Lifetime-Resolved Emission Spectra .....	255
7.10. Red-Edge Excitation Shifts .....	257
7.10.1. Membranes and Red-Edge Excitation Shifts .....	258
7.10.2. Red-Edge Excitation Shifts and Energy Transfer .....	259
7.11. Excited-State Reactions.....	259
7.11.1. Excited-State Ionization of Naphthol.....	260
7.12. Theory for a Reversible Two-State Reaction .....	262
7.12.1. Steady-State Fluorescence of a Two-State Reaction .....	262
7.12.2. Time-Resolved Decays for the Two-State Model .....	263
7.12.3. Differential Wavelength Methods .....	264
7.13. Time-Domain Studies of Naphthol Dissociation .....	264
7.14. Analysis of Excited-State Reactions by Phase-Modulation Fluorometry.....	265
7.14.1. Effect of an Excited-State Reaction on the Apparent Phase and Modulation Lifetimes.....	266
7.14.2. Wavelength-Dependent Phase and Modulation Values for an Excited-State Reaction.....	267
7.14.3. Frequency-Domain Measurement of Excimer Formation.....	269
7.15. Biochemical Examples of Excited-State Reactions .....	270
7.15.1. Exposure of a Membrane-Bound Cholesterol Analogue .....	270
References .....	270
Problems .....	275

## 8. Quenching of Fluorescence

8.1. Quenchers of Fluorescence .....	278
8.2. Theory of Collisional Quenching.....	278
8.2.1. Derivation of the Stern-Volmer Equation .....	280
8.2.2. Interpretation of the Bimolecular Quenching Constant .....	281
8.3. Theory of Static Quenching .....	282
8.4. Combined Dynamic and Static Quenching.....	282
8.5. Examples of Static and Dynamic Quenching .....	283
8.6. Deviations from the Stern-Volmer Equation: Quenching Sphere of Action .....	284
8.6.1. Derivation of the Quenching Sphere of Action.....	285

8.7. Effects of Steric Shielding and Charge on Quenching .....	286	8.16.2. Molecular Beacons Based on Quenching by a Gold Surface.....	314
8.7.1. Accessibility of DNA-Bound Probes to Quenchers.....	286	8.17. Intramolecular Quenching.....	314
8.7.2. Quenching of Ethenoadenine Derivatives.....	287	8.17.1. DNA Dynamics by Intramolecular Quenching .....	314
8.8. Fractional Accessibility to Quenchers.....	288	8.17.2. Electron-Transfer Quenching in a Flavoprotein.....	315
8.8.1. Modified Stern-Volmer Plots .....	288	8.17.3. Sensors Based on Intramolecular PET Quenching .....	316
8.8.2. Experimental Considerations in Quenching .....	289	8.18. Quenching of Phosphorescence .....	317
8.9. Applications of Quenching to Proteins .....	290	References .....	318
8.9.1. Fractional Accessibility of Tryptophan Residues in Endonuclease III.....	290	Problems .....	327
8.9.2. Effect of Conformational Changes on Tryptophan Accessibility.....	291		
8.9.3. Quenching of the Multiple Decay Times of Proteins .....	291		
8.9.4. Effects of Quenchers on Proteins.....	292		
8.9.5. Correlation of Emission Wavelength and Accessibility: Protein Folding of Colicin E1.....	292		
8.10. Application of Quenching to Membranes .....	293		
8.10.1. Oxygen Diffusion in Membranes.....	293		
8.10.2. Localization of Membrane-Bound Tryptophan Residues by Quenching .....	294		
8.10.3. Quenching of Membrane Probes Using Localized Quenchers .....	295		
8.10.4. Parallax and Depth-Dependent Quenching in Membranes .....	296		
8.10.5. Boundary Lipid Quenching.....	298		
8.10.6. Effect of Lipid-Water Partitioning on Quenching .....	298		
8.10.7. Quenching in Micelles .....	300		
8.11. Lateral Diffusion in Membranes .....	300		
8.12. Quenching-Resolved Emission Spectra .....	301		
8.12.1. Fluorophore Mixtures.....	301		
8.12.2. Quenching-Resolved Emission Spectra of the <i>E. Coli</i> Tet Repressor.....	302		
8.13. Quenching and Association Reactions .....	304		
8.13.1. Quenching Due to Specific Binding Interactions .....	304		
8.14. Sensing Applications of Quenching .....	305		
8.14.1. Chloride-Sensitive Fluorophores.....	306		
8.14.2. Intracellular Chloride Imaging.....	306		
8.14.3. Chloride-Sensitive GFP.....	307		
8.14.4. Amplified Quenching .....	309		
8.15. Applications of Quenching to Molecular Biology .....	310		
8.15.1. Release of Quenching upon Hybridization.....	310		
8.15.2. Molecular Beacons in Quenching by Guanine .....	311		
8.15.3. Binding of Substrates to Ribozymes.....	311		
8.15.4. Association Reactions and Accessibility to Quenchers.....	312		
8.16. Quenching on Gold Surfaces.....	313		
8.16.1. Molecular Beacons Based on Quenching by Gold Colloids .....	313		
8.16.2. Molecular Beacons Based on Quenching by a Gold Surface.....	314		
8.17. Intramolecular Quenching.....	314		
8.17.1. DNA Dynamics by Intramolecular Quenching .....	314		
8.17.2. Electron-Transfer Quenching in a Flavoprotein.....	315		
8.17.3. Sensors Based on Intramolecular PET Quenching .....	316		
8.18. Quenching of Phosphorescence .....	317		
References .....	318		
Problems .....	327		

## 9. Mechanisms and Dynamics of Fluorescence Quenching

9.1. Comparison of Quenching and Resonance Energy Transfer .....	331
9.1.1. Distance Dependence of RET and Quenching .....	332
9.1.2. Encounter Complexes and Quenching Efficiency .....	333
9.2. Mechanisms of Quenching.....	334
9.2.1. Intersystem Crossing .....	334
9.2.2. Electron-Exchange Quenching.....	335
9.2.3. Photoinduced Electron Transfer.....	335
9.3. Energetics of Photoinduced Electron Transfer .....	336
9.3.1. Examples of PET Quenching.....	338
9.3.2. PET in Linked Donor–Acceptor Pairs .....	340
9.4. PET Quenching in Biomolecules.....	341
9.4.1. Quenching of Indole by Imidazolium.....	341
9.4.2. Quenching by DNA Bases and Nucleotides .....	341
9.5. Single-Molecule PET .....	342
9.6. Transient Effects in Quenching.....	343
9.6.1. Experimental Studies of Transient Effects .....	346
9.6.2. Distance-Dependent Quenching in Proteins.....	348
References .....	348
Problems .....	351

## 10. Fluorescence Anisotropy

10.1. Definition of Fluorescence Anisotropy .....	353
10.1.1. Origin of the Definitions of Polarization and Anisotropy .....	355
10.2. Theory for Anisotropy .....	355
10.2.1. Excitation Photoselection of Fluorophores .....	357
10.3. Excitation Anisotropy Spectra.....	358
10.3.1. Resolution of Electronic States from Polarization Spectra .....	360
10.4. Measurement of Fluorescence Anisotropies .....	361
10.4.1. L-Format or Single-Channel Method.....	361
10.4.2. T-Format or Two-Channel Anisotropies.....	363
10.4.3. Comparison of T-Format and L-Format Measurements .....	363

10.4.4. Alignment of Polarizers.....	364	11.4.6. Example Anisotropy Decays of Rhodamine Green and Rhodamine Green-Dextran.....	394
10.4.5. Magic-Angle Polarizer Conditions .....	364	11.5. Time-Domain Anisotropy Decays of Proteins .....	394
10.4.6. Why is the Total Intensity Equal to $I_{\parallel} + 2I_{\perp}$ .....	364	11.5.1. Intrinsic Tryptophan Anisotropy Decay of Liver Alcohol Dehydrogenase .....	395
10.4.7. Effect of Resonance Energy Transfer on the Anisotropy .....	364	11.5.2. Phospholipase A <sub>2</sub> .....	395
10.4.8. Trivial Causes of Depolarization.....	365	11.5.3. Subtilisin Carlsberg .....	395
10.4.9. Factors Affecting the Anisotropy .....	366	11.5.4. Domain Motions of Immunoglobulins.....	396
<b>10.5. Effects of Rotational Diffusion on Fluorescence Anisotropies: The Perrin Equation.....</b>	<b>366</b>	11.5.5. Effects of Free Probe on Anisotropy Decays .....	397
10.5.1. The Perrin Equation: Rotational Motions of Proteins .....	367	<b>11.6. Frequency-Domain Anisotropy Decays of Proteins.....</b>	397
10.5.2. Examples of a Perrin Plot .....	369	11.6.1. Apomyoglobin: A Rigid Rotor .....	397
<b>10.6. Perrin Plots of Proteins.....</b>	<b>370</b>	11.6.2. Melittin Self-Association and Anisotropy Decays .....	398
10.6.1. Binding of tRNA to tRNA Synthetase .....	370	11.6.3. Picosecond Rotational Diffusion of Oxytocin.....	399
10.6.2. Molecular Chaperonin cpn60 (GroEL) .....	371	<b>11.7. Hindered Rotational Diffusion in Membranes.....</b>	399
10.6.3. Perrin Plots of an F <sub>ab</sub> Immunoglobulin Fragment.....	371	11.7.1. Characterization of a New Membrane Probe .....	401
<b>10.7. Biochemical Applications of Steady-State Anisotropies.....</b>	<b>372</b>	<b>11.8. Anisotropy Decays of Nucleic Acids .....</b>	402
10.7.1. Peptide Binding to Calmodulin.....	372	11.8.1. Hydrodynamics of DNA Oligomers .....	403
10.7.2. Binding of the Trp Repressor to DNA .....	373	11.8.2. Dynamics of Intracellular DNA .....	403
10.7.3. Helicase-Catalyzed DNA Unwinding .....	373	11.8.3. DNA Binding to HIV Integrase Using Correlation Time Distributions .....	404
10.7.4. Melittin Association Detected from Homotransfer.....	374	<b>11.9. Correlation Time Imaging .....</b>	406
<b>10.8. Anisotropy of Membranes and Membrane-Bound Proteins .....</b>	<b>374</b>	<b>11.10. Microsecond Anisotropy Decays.....</b>	408
10.8.1. Membrane Microviscosity.....	374	11.10.1. Phosphorescence Anisotropy Decays.....	408
10.8.2. Distribution of Membrane-Bound Proteins .....	375	11.10.2. Long-Lifetime Metal-Ligand Complexes .....	408
<b>10.9. Transition Moments.....</b>	<b>377</b>	References .....	409
References .....	378	Problems .....	412
Additional Reading on the Application of Anisotropy .....	380		
Problems .....	381		

## 11. Time-Dependent Anisotropy Decays

<b>11.1. Time-Domain and Frequency-Domain Anisotropy Decays .....</b>	<b>383</b>
<b>11.2. Anisotropy Decay Analysis .....</b>	<b>387</b>
11.2.1. Early Methods for Analysis of TD Anisotropy Data .....	387
11.2.2. Preferred Analysis of TD Anisotropy Data .....	388
11.2.3. Value of $r_0$ .....	389
<b>11.3. Analysis of Frequency-Domain Anisotropy Decays .....</b>	<b>390</b>
<b>11.4. Anisotropy Decay Laws .....</b>	<b>390</b>
11.4.1. Non-Spherical Fluorophores .....	391
11.4.2. Hindered Rotors .....	391
11.4.3. Segmental Mobility of a Biopolymer-Bound Fluorophore .....	392
11.4.4. Correlation Time Distributions .....	393
11.4.5. Associated Anisotropy Decays.....	393

## 12. Advanced Anisotropy Concepts

<b>12.1. Associated Anisotropy Decay .....</b>	<b>413</b>
12.1.1. Theory for Associated Anisotropy Decay .....	414
12.1.2. Time-Domain Measurements of Associated Anisotropy Decays .....	415
<b>12.2. Biochemical Examples of Associated Anisotropy Decays .....</b>	<b>417</b>
12.2.1. Time-Domain Studies of DNA Binding to the Klenow Fragment of DNA Polymerase .....	417
12.2.2. Frequency-Domain Measurements of Associated Anisotropy Decays .....	417
<b>12.3. Rotational Diffusion of Non-Spherical Molecules: An Overview .....</b>	<b>418</b>
12.3.1. Anisotropy Decays of Ellipsoids .....	419
<b>12.4. Ellipsoids of Revolution .....</b>	<b>420</b>
12.4.1. Simplified Ellipsoids of Revolution .....	421
12.4.2. Intuitive Description of Rotational Diffusion of an Oblate Ellipsoid .....	422

12.4.3. Rotational Correlation Times for Ellipsoids of Revolution .....	423	13.5.2. RET Imaging of Intracellular Protein Phosphorylation.....	459
12.4.4. Stick-versus-Slip Rotational Diffusion .....	425	13.5.3. Imaging of Rac Activation in Cells.....	459
12.5. Complete Theory for Rotational Diffusion of Ellipsoids.....	425	13.6. RET and Nucleic Acids .....	459
12.6. Anisotropic Rotational Diffusion .....	426	13.6.1. Imaging of Intracellular RNA .....	460
12.6.1. Time-Domain Studies.....	426	13.7. Energy-Transfer Efficiency from Enhanced Acceptor Fluorescence.....	461
12.6.2. Frequency-Domain Studies of Anisotropic Rotational Diffusion .....	427	13.8. Energy Transfer in Membranes .....	462
12.7. Global Anisotropy Decay Analysis .....	429	13.8.1. Lipid Distributions around Gramicidin.....	463
12.7.1. Global Analysis with Multi-Wavelength Excitation .....	429	13.8.2. Membrane Fusion and Lipid Exchange .....	465
12.7.2. Global Anisotropy Decay Analysis with Collisional Quenching.....	430	13.9. Effect of $\tau^2$ on RET .....	465
12.7.3. Application of Quenching to Protein Anisotropy Decays .....	431	13.10. Energy Transfer in Solution .....	466
12.8. Intercalated Fluorophores in DNA .....	432	13.10.1. Diffusion-Enhanced Energy Transfer.....	467
12.9. Transition Moments.....	433	13.11. Representative $R_0$ Values .....	467
12.9.1. Anisotropy of Planar Fluorophores with High Symmetry .....	435	References .....	468
12.10. Lifetime-Resolved Anisotropies.....	435	Additional References on Resonance Energy Transfer.....	471
12.10.1. Effect of Segmental Motion on the Perrin Plots .....	436	Problems .....	472
12.11. Soleillet's Rule: Multiplication of Depolarized Factors .....	436		
12.12. Anisotropies Can Depend on Emission Wavelength .....	437		
References .....	438		
Problems .....	441		
<b>13. Energy Transfer</b>			
13.1. Characteristics of Resonance Energy Transfer .....	443	14.1. Distance Distributions .....	477
13.2. Theory of Energy Transfer for a Donor-Acceptor Pair.....	445	14.2. Distance Distributions in Peptides .....	479
13.2.1. Orientation Factor $\kappa^2$ .....	448	14.2.1. Comparison for a Rigid and Flexible Hexapeptide.....	479
13.2.2. Dependence of the Transfer Rate on Distance ( $r$ ), the Overlap Integral ( $J$ ), and $\tau^2$ .....	449	14.2.2. Crossfitting Data to Exclude Alternative Models .....	481
13.2.3. Homotransfer and Heterotransfer.....	450	14.2.3. Donor Decay without Acceptor .....	482
13.3. Distance Measurements Using RET .....	451	14.2.4. Effect of Concentration of the D-A Pairs .....	482
13.3.1. Distance Measurements in $\alpha$ -Helical Melittin .....	451	14.3. Distance Distributions in Peptides .....	482
13.3.2. Effects of Incomplete Labeling .....	452	14.3.1. Distance Distributions in Melittin.....	483
13.3.3. Effect of $\kappa^2$ on the Possible Range of Distances .....	452	14.4. Distance-Distribution Data Analysis .....	485
13.4. Biochemical Applications of RET .....	453	14.4.1. Frequency-Domain Distance-Distribution Analysis .....	485
13.4.1. Protein Folding Measured by RET .....	453	14.4.2. Time-Domain Distance-Distribution Analysis .....	487
13.4.2. Intracellular Protein Folding .....	454	14.4.3. Distance-Distribution Functions .....	487
13.4.3. RET and Association Reactions.....	455	14.4.4. Effects of Incomplete Labeling.....	487
13.4.4. Orientation of a Protein-Bound Peptide.....	456	14.4.5. Effect of the Orientation Factor $\kappa^2$ .....	489
13.4.5. Protein Binding to Semiconductor Nanoparticles.....	457	14.4.6. Acceptor Decays.....	489
13.5. RET Sensors .....	458	14.5. Biochemical Applications of Distance Distributions .....	490
13.5.1. Intracellular RET Indicator for Estrogens .....	458	14.5.1. Calcium-Induced Changes in the Conformation of Troponin C .....	490
		14.5.2. Hairpin Ribozyme .....	493
		14.5.3. Four-Way Holliday Junction in DNA .....	493
		14.5.4. Distance Distributions and Unfolding of Yeast Phosphoglycerate Kinase .....	494
		14.5.5. Distance Distributions in a Glycopeptide .....	495
		14.5.6. Single-Protein-Molecule Distance Distribution.....	496
		14.6. Time-Resolved RET Imaging.....	497
		14.7. Effect of Diffusion for Linked D-A Pairs.....	498

14.7.1. Simulations of FRET for a Flexible D-A Pair.....	499	16.3. Tryptophan Emission in an Apolar Protein Environment.....	538
14.7.2. Experimental Measurement of D-A Diffusion for a Linked D-A Pair .....	500	16.3.1. Site-Directed Mutagenesis of a Single-Tryptophan Azurin.....	538
14.7.3. FRET and Diffusive Motions in Biopolymers .....	501	16.3.2. Emission Spectra of Azurins with One or Two Tryptophan Residues.....	539
14.8. Conclusion .....	501	16.4. Energy Transfer and Intrinsic Protein Fluorescence .....	539
References .....	501	16.4.1. Tyrosine-to-Tryptophan Energy Transfer in Interferon- $\gamma$ .....	540
Representative Publications on Measurement of Distance Distributions .....	504	16.4.2. Quantitation of RET Efficiencies in Proteins.....	541
Problems .....	505	16.4.3. Tyrosine-to-Tryptophan RET in a Membrane-Bound Protein .....	543
<b>15. Energy Transfer to Multiple Acceptors in One, Two, or Three Dimensions</b>		16.4.4. Phenylalanine-to-Tyrosine Energy Transfer .....	543
15.1. RET in Three Dimensions.....	507	16.5. Calcium Binding to Calmodulin Using Phenylalanine and Tyrosine Emission .....	545
15.1.1. Effect of Diffusion on FRET with Unlinked Donors and Acceptors .....	508	16.6. Quenching of Tryptophan Residues in Proteins.....	546
15.1.2. Experimental Studies of RET in Three Dimensions .....	509	16.6.1. Effect of Emission Maximum on Quenching .....	547
15.2. Effect of Dimensionality on RET .....	511	16.6.2. Fractional Accessibility to Quenching in Multi-Tryptophan Proteins.....	549
15.2.1. Experimental FRET in Two Dimensions ....	512	16.6.3. Resolution of Emission Spectra by Quenching .....	550
15.2.2. Experimental FRET in One Dimension.....	514	16.7. Association Reaction of Proteins .....	551
15.3. Biochemical Applications of RET with Multiple Acceptors .....	515	16.7.1. Binding of Calmodulin to a Target Protein .....	551
15.3.1. Aggregation of $\beta$ -Amyloid Peptides .....	515	16.7.2. Calmodulin: Resolution of the Four Calcium-Binding Sites Using Tryptophan-Containing Mutants .....	552
15.3.2. RET Imaging of Fibronectin.....	516	16.7.3. Interactions of DNA with Proteins.....	552
15.4. Energy Transfer in Restricted Geometries .....	516	16.8. Spectral Properties of Genetically Engineered Proteins .....	554
15.4.1. Effect of Excluded Area on Energy Transfer in Two Dimensions .....	518	16.8.1. Single-Tryptophan Mutants of Triosephosphate Isomerase .....	555
15.5. RET in the Presence of Diffusion .....	519	16.8.2. Barnase: A Three-Tryptophan Protein .....	556
15.6. RET in the Rapid Diffusion Limit .....	520	16.8.3. Site-Directed Mutagenesis of Tyrosine Proteins.....	557
15.6.1. Location of an Acceptor in Lipid Vesicles .....	521	16.9. Protein Folding .....	557
15.6.2. Location of Retinal in Rhodopsin Disc Membranes.....	522	16.9.1. Protein Engineering of Mutant Ribonuclease for Folding Experiments.....	558
15.7. Conclusions .....	524	16.9.2. Folding of Lactate Dehydrogenase .....	559
References .....	524	16.9.3. Folding Pathway of CRABPI.....	560
Additional References on RET between Unlinked Donor and Acceptor .....	526	16.10. Protein Structure and Tryptophan Emission .....	560
Problems .....	527	16.10.1. Tryptophan Spectral Properties and Structural Motifs.....	561
<b>16. Protein Fluorescence</b>		16.11. Tryptophan Analogues.....	562
16.1. Spectral Properties of the Aromatic Amino Acids ...	530	16.11.1. Tryptophan Analogues.....	564
16.1.1. Excitation Polarization Spectra of Tyrosine and Tryptophan.....	531	16.11.2. Genetically Inserted Amino-Acid Analogues.....	565
16.1.2. Solvent Effects on Tryptophan Emission Spectra.....	533	16.12. The Challenge of Protein Fluorescence .....	566
16.1.3. Excited-State Ionization of Tyrosine.....	534	References .....	567
16.1.4. Tyrosinate Emission from Proteins .....	535	Problems .....	573
16.2. General Features of Protein Fluorescence.....	535		

## 17. Time-Resolved Protein Fluorescence

17.1. Intensity Decays of Tryptophan: The Rotamer Model .....	578
17.2. Time-Resolved Intensity Decays of Tryptophan and Tyrosine .....	580
17.2.1. Decay-Associated Emission Spectra of Tryptophan .....	581
17.2.2. Intensity Decays of Neutral Tryptophan Derivatives .....	581
17.2.3. Intensity Decays of Tyrosine and Its Neutral Derivatives .....	582
17.3. Intensity and Anisotropy Decays of Proteins .....	583
17.3.1. Single-Exponential Intensity and Anisotropy Decay of Ribonuclease T <sub>1</sub> .....	584
17.3.2. Annexin V: A Calcium-Sensitive Single-Tryptophan Protein .....	585
17.3.3. Anisotropy Decay of a Protein with Two Tryptophans .....	587
17.4. Protein Unfolding Exposes the Tryptophan Residue to Water .....	588
17.4.1. Conformational Heterogeneity Can Result in Complex Intensity and Anisotropy Decays .....	588
17.5. Anisotropy Decays of Proteins .....	589
17.5.1. Effects of Association Reactions on Anisotropy Decays: Melittin .....	590
17.6. Biochemical Examples Using Time-Resolved Protein Fluorescence .....	591
17.6.1. Decay-Associated Spectra of Barnase .....	591
17.6.2. Disulfide Oxidoreductase DsbA .....	591
17.6.3. Immunophilin FKBP59-I: Quenching of Tryptophan Fluorescence by Phenylalanine .....	592
17.6.4. Trp Repressor: Resolution of the Two Interacting Tryptophans .....	593
17.6.5. Thermophilic β-Glycosidase: A Multi-Tryptophan Protein .....	594
17.6.6. Heme Proteins Display Useful Intrinsic Fluorescence .....	594
17.7. Time-Dependent Spectral Relaxation of Tryptophan .....	596
17.8. Phosphorescence of Proteins .....	598
17.9. Perspectives on Protein Fluorescence .....	600
References .....	600
Problems .....	605

## 18. Multiphoton Excitation and Microscopy

18.1. Introduction to Multiphoton Excitation .....	607
18.2. Cross-Sections for Multiphoton Absorption .....	609
18.3. Two-Photon Absorption Spectra .....	609
18.4. Two-Photon Excitation of a DNA-Bound Fluorophore .....	610
18.5. Anisotropies with Multiphoton Excitation .....	612

18.5.1. Excitation Photoselection for Two-Photon Excitation .....	612
18.5.2. Two-Photon Anisotropy of DPH .....	612
18.6. MPE for a Membrane-Bound Fluorophore .....	613
18.7. MPE of Intrinsic Protein Fluorescence .....	613
18.8. Multiphoton Microscopy .....	616
18.8.1. Calcium Imaging .....	616
18.8.2. Imaging of NAD(P)H and FAD .....	617
18.8.3. Excitation of Multiple Fluorophores .....	618
18.8.4. Three-Dimensional Imaging of Cells .....	618
References .....	619
Problems .....	621

## 19. Fluorescence Sensing

19.1. Optical Clinical Chemistry and Spectral Observables .....	623
19.2. Spectral Observables for Fluorescence Sensing .....	624
19.2.1. Optical Properties of Tissues .....	625
19.2.2. Lifetime-Based Sensing .....	626
19.3. Mechanisms of Sensing .....	626
19.4. Sensing by Collisional Quenching .....	627
19.4.1. Oxygen Sensing .....	627
19.4.2. Lifetime-Based Sensing of Oxygen .....	628
19.4.3. Mechanism of Oxygen Selectivity .....	629
19.4.4. Other Oxygen Sensors .....	629
19.4.5. Lifetime Imaging of Oxygen .....	630
19.4.6. Chloride Sensors .....	631
19.4.7. Lifetime Imaging of Chloride Concentrations .....	632
19.4.8. Other Collisional Quenchers .....	632
19.5. Energy-Transfer Sensing .....	633
19.5.1. pH and pCO <sub>2</sub> Sensing by Energy Transfer .....	633
19.5.2. Glucose Sensing by Energy Transfer .....	634
19.5.3. Ion Sensing by Energy Transfer .....	635
19.5.4. Theory for Energy-Transfer Sensing .....	636
19.6. Two-State pH Sensors .....	637
19.6.1. Optical Detection of Blood Gases .....	637
19.6.2. pH Sensors .....	637
19.7. Photoinduced Electron Transfer (PET) Probes for Metal Ions and Anion Sensors .....	641
19.8. Probes of Analyte Recognition .....	643
19.8.1. Specificity of Cation Probes .....	644
19.8.2. Theory of Analyte Recognition Sensing .....	644
19.8.3. Sodium and Potassium Probes .....	645
19.8.4. Calcium and Magnesium Probes .....	647
19.8.5. Probes for Intracellular Zinc .....	650
19.9. Glucose-Sensitive Fluorophores .....	650
19.10. Protein Sensors .....	651
19.10.1. Protein Sensors Based on RET .....	652
19.11. GFP Sensors .....	654
19.11.1. GFP Sensors Using RET .....	654
19.11.2. Intrinsic GFP Sensors .....	655

19.12. New Approaches to Sensing .....	655	21.2.3. DNA Fragment Sizing by Flow Cytometry .....	715
19.12.1. Pebble Sensors and Lipobeads .....	655	21.3. DNA Hybridization .....	715
19.13. In-Vivo Imaging .....	656	21.3.1. DNA Hybridization Measured with One-Donor- and Acceptor-Labeled DNA Probe .....	717
19.14. Immunoassays .....	658	21.3.2. DNA Hybridization Measured by Excimer Formation .....	718
19.14.1. Enzyme-Linked Immunosorbent Assays (ELISA) .....	659	21.3.3. Polarization Hybridization Arrays .....	719
19.14.2. Time-Resolved Immunoassays .....	659	21.3.4. Polymerase Chain Reaction .....	720
19.14.3. Energy-Transfer Immunoassays .....	660	21.4. Molecular Beacons .....	720
19.14.4. Fluorescence Polarization Immunoassays .....	661	21.4.1. Molecular Beacons with Nonfluorescent Acceptors .....	720
References .....	663	21.4.2. Molecular Beacons with Fluorescent Acceptors .....	722
Problems .....	672	21.4.3. Hybridization Proximity Beacons .....	722
<b>20. Novel Fluorophores</b>		21.4.4. Molecular Beacons Based on Quenching by Gold .....	723
20.1. Semiconductor Nanoparticles .....	675	21.4.5. Intracellular Detection of mRNA Using Molecular Beacons .....	724
20.1.1. Spectral Properties of QDots .....	676	21.5. Aptamers .....	724
20.1.2. Labeling Cells with QDots .....	677	21.5.1. DNAzymes .....	726
20.1.3. QDots and Resonance Energy Transfer .....	678	21.6. Multiplexed Microbead Arrays: Suspension Arrays .....	726
20.2. Lanthanides .....	679	21.7. Fluorescence In-Situ Hybridization .....	727
20.2.1. RET with Lanthanides .....	680	21.7.1. Preparation of FISH Probe DNA .....	728
20.2.2. Lanthanide Sensors .....	681	21.7.2. Applications of FISH .....	729
20.2.3. Lanthanide Nanoparticles .....	682	21.8. Multicolor FISH and Spectral Karyotyping .....	730
20.2.4. Near-Infrared Emitting Lanthanides .....	682	21.9. DNA Arrays .....	732
20.2.5. Lanthanides and Fingerprint Detection .....	683	21.9.1. Spotted DNA Microarrays .....	732
20.3. Long-Lifetime Metal–Ligand Complexes .....	683	21.9.2. Light-Generated DNA Arrays .....	734
20.3.1. Introduction to Metal–Ligand Probes .....	683	References .....	734
20.3.2. Anisotropy Properties of Metal–Ligand Complexes .....	685	Problems .....	740
20.3.3. Spectral Properties of MLC Probes .....	686		
20.3.4. The Energy Gap Law .....	687		
20.3.5. Biophysical Applications of Metal–Ligand Probes .....	688		
20.3.6. MLC Immunoassays .....	691		
20.3.7. Metal–Ligand Complex Sensors .....	694		
20.4. Long-Wavelength Long-Lifetime Fluorophores .....	695		
References .....	697		
Problems .....	702		
<b>21. DNA Technology</b>			
21.1. DNA Sequencing .....	705		
21.1.1. Principle of DNA Sequencing .....	705		
21.1.2. Examples of DNA Sequencing .....	706		
21.1.3. Nucleotide Labeling Methods .....	707		
21.1.4. Example of DNA Sequencing .....	708		
21.1.5. Energy-Transfer Dyes for DNA Sequencing .....	709		
21.1.6. DNA Sequencing with NIR Probes .....	710		
21.1.7. DNA Sequencing Based on Lifetimes .....	712		
21.2. High-Sensitivity DNA Stains .....	712		
21.2.1. High-Affinity Bis DNA Stains .....	713		
21.2.2. Energy-Transfer DNA Stains .....	715		
<b>22. Fluorescence-Lifetime Imaging Microscopy</b>			
22.1. Early Methods for Fluorescence-Lifetime Imaging .....	743		
22.1.1. FLIM Using Known Fluorophores .....	744		
22.2. Lifetime Imaging of Calcium Using Quin-2 .....	744		
22.2.1. Determination of Calcium Concentration from Lifetime .....	744		
22.2.2. Lifetime Images of Cos Cells .....	745		
22.3. Examples of Wide-Field Frequency-Domain FLIM .....	746		
22.3.1. Resonance Energy-Transfer FLIM of Protein Kinase C Activation .....	746		
22.3.2. Lifetime Imaging of Cells Containing Two GFPs .....	747		
22.4. Wide-Field FLIM Using a Gated-Image Intensifier .....	747		
22.5. Laser Scanning TCSPC FLIM .....	748		
22.5.1. Lifetime Imaging of Cellular Biomolecules .....	750		
22.5.2. Lifetime Images of Amyloid Plaques .....	750		

**PRINCIPLES OF FLUORESCENCE SPECTROSCOPY**

xxv

22.6. Frequency-Domain Laser Scanning Microscopy .....	750	24.2. Theory of FCS .....	800
22.7. Conclusions .....	752	24.2.1. Translational Diffusion and FCS.....	802
References .....	752	24.2.2. Occupation Numbers and Volumes in FCS.....	804
Additional Reading on Fluorescence-Lifetime Imaging Microscopy .....	753	24.2.3. FCS for Multiple Diffusing Species .....	804
Problem.....	755	24.3. Examples of FCS Experiments .....	805
		24.3.1. Effect of Fluorophore Concentration .....	805
		24.3.2. Effect of Molecular Weight on Diffusion Coefficients .....	806
		24.4. Applications of FCS to Bioaffinity Reactions.....	807
		24.4.1. Protein Binding to the Chaperonin GroEL .....	807
		24.4.2. Association of Tubulin Subunits .....	807
		24.4.3. DNA Applications of FCS .....	808
		24.5. FCS in Two Dimensions: Membranes .....	810
		24.5.1. Biophysical Studies of Lateral Diffusion in Membranes .....	812
		24.5.2. Binding to Membrane-Bound Receptors .....	813
		24.6. Effects of Intersystem Crossing .....	815
		24.6.1. Theory for FCS and Intersystem Crossing.....	816
		24.7. Effects of Chemical Reactions .....	816
		24.8. Fluorescence Intensity Distribution Analysis.....	817
		24.9. Time-Resolved FCS .....	819
		24.10. Detection of Conformational Dynamics in Macromolecules .....	820
		24.11. FCS with Total Internal Reflection .....	821
		24.12. FCS with Two-Photon Excitation.....	822
		24.12.1. Diffusion of an Intracellular Kinase Using FCS with Two-Photon Excitation.....	823
		24.13. Dual-Color Fluorescence Cross-Correlation Spectroscopy .....	823
		24.13.1. Instrumentation for Dual-Color FCCS .....	824
		24.13.2. Theory of Dual-Color FCCS .....	824
		24.13.3. DNA Cleavage by a Restriction Enzyme .....	826
		24.13.4. Applications of Dual-Color FCCS .....	826
		24.14. Rotational Diffusion and Photo Antibunching .....	828
		24.15. Flow Measurements Using FCS .....	830
		24.16. Additional References on FCS .....	832
		References .....	832
		Additional References to FCS and Its Applications .....	837
		Problems .....	840

**23. Single-Molecule Detection**

23.1. Detectability of Single Molecules.....	759		
23.2. Total Internal Reflection and Confocal Optics.....	760		
23.2.1. Total Internal Reflection.....	760		
23.2.2. Confocal Detection Optics .....	761		
23.3. Optical Configurations for SMD .....	762		
23.4. Instrumentation for SMD .....	764		
23.4.1. Detectors for Single-Molecule Detection .....	765		
23.4.2. Optical Filters for SMD .....	766		
23.5. Single-Molecule Photophysics .....	768		
23.6. Biochemical Applications of SMD .....	770		
23.6.1. Single-Molecule Enzyme Kinetics.....	770		
23.6.2. Single-Molecule ATPase Activity .....	770		
23.6.3. Single-Molecule Studies of a Chaperonin Protein.....	771		
23.7. Single-Molecule Resonance Energy Transfer .....	773		
23.8. Single-Molecule Orientation and Rotational Motions.....	775		
23.8.1. Orientation Imaging of R6G and GFP .....	777		
23.8.2. Imaging of Dipole Radiation Patterns.....	778		
23.9. Time-Resolved Studies of Single Molecules .....	779		
23.10. Biochemical Applications.....	780		
23.10.1. Turnover of Single Enzyme Molecules...	780		
23.10.2. Single-Molecule Molecular Beacons .....	782		
23.10.3. Conformational Dynamics of a Holliday Junction .....	782		
23.10.4. Single-Molecule Calcium Sensor.....	784		
23.10.5. Motions of Molecular Motors .....	784		
23.11. Advanced Topics in SMD .....	784		
23.11.1. Signal-to-Noise Ratio in Single-Molecule Detection.....	784		
23.11.2. Polarization of Single Immobilized Fluorophores.....	786		
23.11.3. Polarization Measurements and Mobility of Surface-Bound Fluorophores.....	786		
23.11.4. Single-Molecule Lifetime Estimation .....	787		
23.12. Additional Literature on SMD .....	788		
References .....	788		
Additional References on Single-Molecule Detection .....	791		
Problem.....	795		

**24. Fluorescence Correlation Spectroscopy**

24.1. Principles of Fluorescence Correlation Spectroscopy .....	798
--	-----

**25. Radiative Decay Engineering:  
Metal-Enhanced Fluorescence**

25.1. Radiative Decay Engineering .....	841
25.1.1. Introduction to RDE.....	841
25.1.2. Jablonski Diagram for Metal- Enhanced Fluorescence .....	842
25.2. Review of Metal Effects on Fluorescence.....	843

25.3. Optical Properties of Metal Colloids .....	845
25.4. Theory for Fluorophore–Colloid Interactions .....	846
25.5. Experimental Results on Metal-Enhanced Fluorescence .....	848
25.5.1. Application of MEF to DNA Analysis.....	848
25.6. Distance-Dependence of Metal-Enhanced Fluorescence .....	851
25.7. Applications of Metal-Enhanced Fluorescence.....	851
25.7.1. DNA Hybridization Using MEF .....	853
25.7.2. Release of Self-Quenching.....	853
25.7.3. Effect of Silver Particles on RET.....	854
25.8. Mechanism of MEF.....	855
25.9. Perspective on RET .....	856
References .....	856
Problem.....	859

## 26. Radiative Decay Engineering: Surface Plasmon-Coupled Emission

26.1. Phenomenon of SPCE .....	861
26.2. Surface-Plasmon Resonance .....	861
26.2.1. Theory for Surface-Plasmon Resonance.....	863
26.3. Expected Properties of SPCE.....	865
26.4. Experimental Demonstration of SPCE.....	865
26.5. Applications of SPCE.....	867
26.6. Future Developments in SPCE.....	868
References .....	870

## Appendix I. Corrected Emission Spectra

1. Emission Spectra Standards from 300 to 800 nm.....	873
2. $\beta$ -Carboline Derivatives as Fluorescence Standards .....	873
3. Corrected Emission Spectra of 9,10-Diphenyl- anthracene, Quinine, and Fluorescein .....	877
4. Long-Wavelength Standards.....	877
5. Ultraviolet Standards .....	878
6. Additional Corrected Emission Spectra .....	881
References .....	881

## Appendix II. Fluorescent Lifetime Standards

1. Nanosecond Lifetime Standards.....	883
2. Picosecond Lifetime Standards .....	884
3. Representative Frequency-Domain Intensity Decays .....	885
4. Time-Domain Lifetime Standards.....	886

## Appendix III. Additional Reading

1. Time-Resolved Measurements .....	889
2. Spectra Properties of Fluorophores.....	889
3. Theory of Fluorescence and Photophysics.....	889
4. Reviews of Fluorescence Spectroscopy .....	889
5. Biochemical Fluorescence .....	890
6. Protein Fluorescence .....	890
7. Data Analysis and Nonlinear Least Squares .....	890
8. Photochemistry.....	890
9. Flow Cytometry.....	890
10. Phosphorescence.....	890
11. Fluorescence Sensing .....	890
12. Immunoassays .....	891
13. Applications of Fluorescence .....	891
14. Multiphoton Excitation.....	891
15. Infrared and NIR Fluorescence .....	891
16. Lasers.....	891
17. Fluorescence Microscopy .....	891
18. Metal–Ligand Complexes and Unusual Lumophores .....	891
19. Single-Molecule Detection.....	891
20. Fluorescence Correlation Spectroscopy .....	892
21. Biophotonics .....	892
22. Nanoparticles .....	892
23. Metallic Particles .....	892
24. Books on Fluorescence.....	892
<b>Answers to Problems .....</b>	893
<b>Index .....</b>	923

# 1

# Introduction to Fluorescence

During the past 20 years there has been a remarkable growth in the use of fluorescence in the biological sciences. Fluorescence spectroscopy and time-resolved fluorescence are considered to be primarily research tools in biochemistry and biophysics. This emphasis has changed, and the use of fluorescence has expanded. Fluorescence is now a dominant methodology used extensively in biotechnology, flow cytometry, medical diagnostics, DNA sequencing, forensics, and genetic analysis, to name a few. Fluorescence detection is highly sensitive, and there is no longer the need for the expense and difficulties of handling radioactive tracers for most biochemical measurements. There has been dramatic growth in the use of fluorescence for cellular and molecular imaging. Fluorescence imaging can reveal the localization and measurements of intracellular molecules, sometimes at the level of single-molecule detection.

Fluorescence technology is used by scientists from many disciplines. This volume describes the principles of fluorescence that underlie its uses in the biological and chemical sciences. Throughout the book we have included examples that illustrate how the principles are used in different applications.

## I.I. PHENOMENA OF FLUORESCENCE

Luminescence is the emission of light from any substance, and occurs from electronically excited states. Luminescence is formally divided into two categories—fluorescence and phosphorescence—depending on the nature of the excited state. In excited singlet states, the electron in the excited orbital is paired (by opposite spin) to the second electron in the ground-state orbital. Consequently, return to the ground state is spin allowed and occurs rapidly by emission of a photon. The emission rates of fluorescence are typically  $10^8 \text{ s}^{-1}$ , so that a typical fluorescence lifetime is near 10 ns ( $10 \times 10^{-9} \text{ s}$ ). As will be described in Chapter 4, the lifetime ( $\tau$ ) of a fluorophore is the average time between its excitation and return to the ground state. It is valuable to consider a 1-ns lifetime within the context of the speed of

light. Light travels 30 cm, or about one foot, in one nanosecond. Many fluorophores display subnanosecond lifetimes. Because of the short timescale of fluorescence, measurement of the time-resolved emission requires sophisticated optics and electronics. In spite of the added complexity, time-resolved fluorescence is widely used because of the increased information available from the data, as compared with stationary or steady-state measurements. Additionally, advances in technology have made time-resolved measurements easier, even when using microscopes.

Phosphorescence is emission of light from triplet excited states, in which the electron in the excited orbital has the same spin orientation as the ground-state electron. Transitions to the ground state are forbidden and the emission rates are slow ( $10^3$  to  $10^0 \text{ s}^{-1}$ ), so that phosphorescence lifetimes are typically milliseconds to seconds. Even longer lifetimes are possible, as is seen from "glow-in-the-dark" toys. Following exposure to light, the phosphorescence substances glow for several minutes while the excited phosphors slowly return to the ground state. Phosphorescence is usually not seen in fluid solutions at room temperature. This is because there exist many deactivation processes that compete with emission, such as non-radiative decay and quenching processes. It should be noted that the distinction between fluorescence and phosphorescence is not always clear. Transition metal-ligand complexes (MLCs), which contain a metal and one or more organic ligands, display mixed singlet-triplet states. These MLCs display intermediate lifetimes of hundreds of nanoseconds to several microseconds. In this book we will concentrate mainly on the more rapid phenomenon of fluorescence.

Fluorescence typically occurs from aromatic molecules. Some typical fluorescent substances (fluorophores) are shown in Figure 1.1. One widely encountered fluorophore is quinine, which is present in tonic water. If one observes a glass of tonic water that is exposed to sunlight, a faint blue glow is frequently visible at the surface. This glow is most apparent when the glass is observed at a right

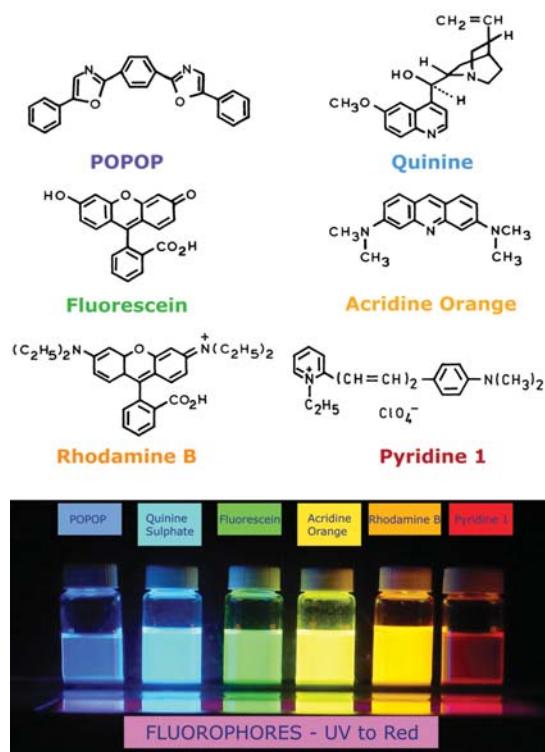


**Figure 1.1.** Structures of typical fluorescent substances.

angle relative to the direction of the sunlight, and when the dielectric constant is decreased by adding less polar solvents like alcohols. The quinine in tonic water is excited by the ultraviolet light from the sun. Upon return to the ground state the quinine emits blue light with a wavelength near 450 nm. The first observation of fluorescence from a quinine solution in sunlight was reported by Sir John Frederick William Herschel (Figure 1.2) in 1845.<sup>1</sup> The following is an excerpt from this early report:

*On a case of superficial colour presented by a homogeneous liquid internally colourless. By Sir John Frederick William Herschel, Philosophical Translation of the Royal Society of London (1845) 135:143–145.  
Received January 28, 1845 — Read February 13, 1845.*

"The sulphate of quinine is well known to be of extremely sparing solubility in water. It is however easily and copiously soluble in tartaric acid. Equal weights of the sulphate and of crystallised tartaric acid, rubbed up together with addition of a very little water, dissolve entirely and immediately. It is this solution, largely diluted, which exhibits the optical phenomenon in question. Though perfectly transparent and colourless when held between the eye and the

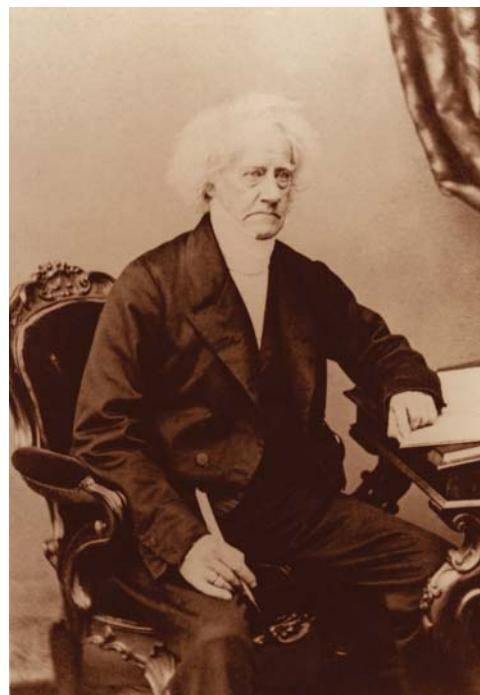


**Figure 1.2.** Sir John Frederick William Herschel, March 7, 1792 to May 11, 1871. Reproduced courtesy of the Library and Information Centre, Royal Society of Chemistry.

light, or a white object, it yet exhibits in certain aspects, and under certain incidences of the light, an extremely vivid and beautiful celestial blue colour, which, from the circumstances of its occurrence, would seem to originate in those strata which the light first penetrates in entering the liquid, and which, if not strictly superficial, at least exert their peculiar power of analysing the incident rays and dispersing those which compose the tint in question, only through a very small depth within the medium.

To see the colour in question to advantage, all that is requisite is to dissolve the two ingredients above mentioned in equal proportions, in about a hundred times their joint weight of water, and having filtered the solution, pour it into a tall narrow cylindrical glass vessel or test tube, which is to be set upright on a dark coloured substance before an open window exposed to strong daylight or sunshine, but with no cross lights, or any strong reflected light from behind. If we look down perpendicularly into the vessel so that the visual ray shall graze the internal surface of the glass through a great part of its depth, the whole of that surface of the liquid on which the light first strikes will appear of a lively blue, ...

If the liquid be poured out into another vessel, the descending stream gleams internally from all

its undulating inequalities, with the same lively yet delicate blue colour, ... thus clearly demonstrating that contact with a denser medium has no share in producing this singular phenomenon.

The thinnest film of the liquid seems quite as effective in producing this superficial colour as a considerable thickness. For instance, if in pouring it from one glass into another, ... the end of the funnel be made to touch the internal surface of the vessel well moistened, so as to spread the descending stream over an extensive surface, the intensity of the colour is such that it is almost impossible to avoid supposing that we have a highly coloured liquid under our view."

It is evident from this early description that Sir Herschel recognized the presence of an unusual phenomenon that could not be explained by the scientific knowledge of the time. To this day the fluorescence of quinine remains one of the most used and most beautiful examples of fluorescence. Herschel was from a distinguished family of scientists who lived in England but had their roots in Germany.<sup>2</sup> For most of his life Sir Herschel did research in astronomy, publishing only a few papers on fluorescence.

It is interesting to notice that the first known fluorophore, quinine, was responsible for stimulating the development of the first spectrofluorometers that appeared in the 1950s. During World War II, the Department of War was interested in monitoring antimalaria drugs, including quinine. This early drug assay resulted in a subsequent program at the National Institutes of Health to develop the first practical spectrofluorometer.<sup>3</sup>

Many other fluorophores are encountered in daily life. The green or red-orange glow sometimes seen in antifreeze is due to trace quantities of fluorescein or rhodamine, respectively (Figure 1.1). Polynuclear aromatic hydrocarbons, such as anthracene and perylene, are also fluorescent, and the emission from such species is used for environmental monitoring of oil pollution. Some substituted organic compounds are also fluorescent. For example 1,4-bis(5-phenyloxazol-2-yl)benzene (POPOP) is used in scintillation counting and acridine orange is often used as a DNA stain. Pyridine 1 and rhodamine are frequently used in dye lasers.

Numerous additional examples of probes could be presented. Instead of listing them here, examples will appear throughout the book, with a description of the spectral properties of the individual fluorophores. An overview of fluorophores used for research and fluorescence sensing is presented in Chapter 3. In contrast to aromatic organic mol-

ecules, atoms are generally nonfluorescent in condensed phases. One notable exception is the group of elements commonly known as the lanthanides.<sup>4</sup> The fluorescence from europium and terbium ions results from electronic transitions between *f* orbitals. These orbitals are shielded from the solvent by higher filled orbitals. The lanthanides display long decay times because of this shielding and low emission rates because of their small extinction coefficients.

Fluorescence spectral data are generally presented as emission spectra. A fluorescence emission spectrum is a plot of the fluorescence intensity versus wavelength (nanometers) or wavenumber ( $\text{cm}^{-1}$ ). Two typical fluorescence emission spectra are shown in Figure 1.3. Emission spectra vary widely and are dependent upon the chemical structure of the fluorophore and the solvent in which it is dissolved. The spectra of some compounds, such as perylene, show significant structure due to the individual vibrational energy levels of the ground and excited states. Other compounds, such as quinine, show spectra devoid of vibrational structure.

An important feature of fluorescence is high sensitivity detection. The sensitivity of fluorescence was used in 1877 to demonstrate that the rivers Danube and Rhine were connected by underground streams.<sup>5</sup> This connection was demonstrated by placing fluorescein (Figure 1.1) into the Danube. Some sixty hours later its characteristic green fluorescence appeared in a small river that led to the Rhine. Today fluorescein is still used as an emergency marker for locating individuals at sea, as has been seen on the landing of space capsules in the Atlantic Ocean. Readers interested in the history of fluorescence are referred to the excellent summary by Berlman.<sup>5</sup>

## 1.2. JABLONSKI DIAGRAM

The processes that occur between the absorption and emission of light are usually illustrated by the Jablonski<sup>6</sup> diagram. Jablonski diagrams are often used as the starting point for discussing light absorption and emission. Jablonski diagrams are used in a variety of forms, to illustrate various molecular processes that can occur in excited states. These diagrams are named after Professor Alexander Jablonski (Figure 1.4), who is regarded as the father of fluorescence spectroscopy because of his many accomplishments, including descriptions of concentration depolarization and defining the term "anisotropy" to describe the polarized emission from solutions.<sup>7,8</sup>

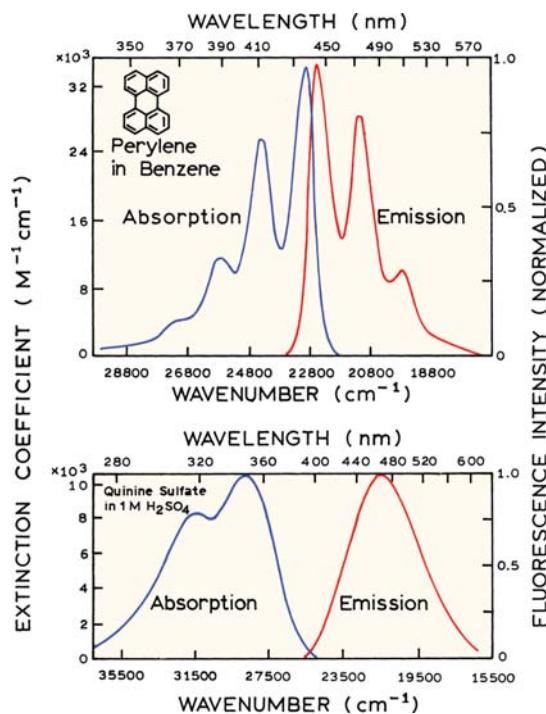


**Figure 1.3.** Absorption and fluorescence emission spectra of perylene and quinine. Emission spectra cannot be correctly presented on both the wavelength and wavenumber scales. The wavenumber presentation is correct in this instance. Wavelengths are shown for convenience. See Chapter 3. Revised from [5].

#### *Brief History of Alexander Jablonski*

Professor Jablonski was born February 26, 1898 in Voskresenovka, Ukraine. In 1916 he began his study of atomic physics at the University of Kharkov, which was interrupted by military service first in the Russian Army and later in the newly organized Polish Army during World War I. At the end of 1918, when an independent Poland was re-created after more than 120 years of occupation by neighboring powers, Jablonski left Kharkov and arrived in Warsaw, where he entered the University of Warsaw to continue his study of physics. His study in Warsaw was again interrupted in 1920 by military service during the Polish-Bolshevik war.

An enthusiastic musician, Jablonski played first violin at the Warsaw Opera from 1921 to 1926 while studying at the university under Stefan Pienkowski. He received his doctorate in 1930 for work "On the influence of the change of wavelengths of excitation light on the fluorescence spectra." Although Jablonski left the opera in 1926 and devoted himself entirely to scientific work, music remained his great passion until the last days of his life.



**Figure 1.4.** Professor Alexander Jablonski (1898–1980), circa 1935. Courtesy of his daughter, Professor Danuta Frackowiak.

Throughout the 1920s and 30s the Department of Experimental Physics at Warsaw University was an active center for studies on luminescence under S. Pienkowski. During most of this period Jablonski worked both theoretically and experimentally on the fundamental problems of photoluminescence of liquid solutions as well as on the pressure effects on atomic spectral lines in gases. A problem that intrigued Jablonski for many years was the polarization of photoluminescence of solutions. To explain the experimental facts he distinguished the transition moments in absorption and in emission and analyzed various factors responsible for the depolarization of luminescence.

Jablonski's work was interrupted once again by a world war. From 1939 to 1945 Jablonski served in the Polish Army, and spent time as a prisoner of first the German Army and then the Soviet Army. In 1946 he returned to Poland to chair a new Department of Physics in the new Nicholas Copernicus University in Torun. This beginning occurred in the very difficult postwar years in a country totally destroyed by World War II. Despite all these difficulties, Jablonski with great energy organized the Department of Physics at the university, which became a scientific center for studies in atomic and molecular physics.

His work continued beyond his retirement in 1968. Professor Jablonski created a spectroscopic school of thought that persists today through his numerous students, who now occupy positions at universities in Poland and elsewhere. Professor Jablonski died on September 9, 1980. More complete accounts of his accomplishments are given in [7] and [8].

A typical Jablonski diagram is shown in Figure 1.5. The singlet ground, first, and second electronic states are depicted by  $S_0$ ,  $S_1$ , and  $S_2$ , respectively. At each of these electronic energy levels the fluorophores can exist in a number of vibrational energy levels, depicted by 0, 1, 2, etc. In this Jablonski diagram we excluded a number of interactions that will be discussed in subsequent chapters, such as quenching, energy transfer, and solvent interactions. The transitions between states are depicted as vertical lines to illustrate the instantaneous nature of light absorption. Transitions occur in about  $10^{-15}$  s, a time too short for significant displacement of nuclei. This is the Franck-Condon principle.

The energy spacing between the various vibrational energy levels is illustrated by the emission spectrum of perylene (Figure 1.3). The individual emission maxima (and hence vibrational energy levels) are about  $1500\text{ cm}^{-1}$  apart. At room temperature thermal energy is not adequate to significantly populate the excited vibrational states. Absorption and emission occur mostly from molecules with the lowest vibrational energy. The larger energy difference between the  $S_0$  and  $S_1$  excited states is too large for thermal population of  $S_1$ . For this reason we use light and not heat to induce fluorescence.

Following light absorption, several processes usually occur. A fluorophore is usually excited to some higher vibrational level of either  $S_1$  or  $S_2$ . With a few rare exceptions, molecules in condensed phases rapidly relax to the lowest vibrational level of  $S_1$ . This process is called internal conversion and generally occurs within  $10^{-12}$  s or less. Since fluorescence lifetimes are typically near  $10^{-8}$  s, internal conversion is generally complete prior to emission. Hence, fluorescence emission generally results from a thermally equilibrated excited state, that is, the lowest energy vibrational state of  $S_1$ .

Return to the ground state typically occurs to a higher excited vibrational ground state level, which then quickly ( $10^{-12}$  s) reaches thermal equilibrium (Figure 1.5). Return to an excited vibrational state at the level of the  $S_0$  state is the reason for the vibrational structure in the emission spectrum of perylene. An interesting consequence of emission to higher vibrational ground states is that the emission spec-

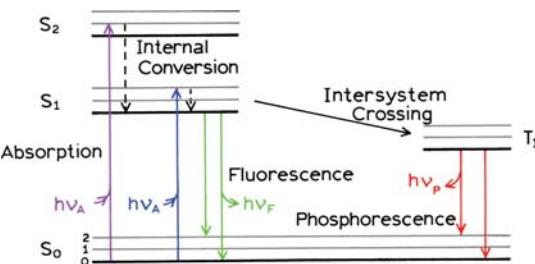


Figure 1.5. One form of a Jablonski diagram.

trum is typically a mirror image of the absorption spectrum of the  $S_0 \rightarrow S_1$  transition. This similarity occurs because electronic excitation does not greatly alter the nuclear geometry. Hence the spacing of the vibrational energy levels of the excited states is similar to that of the ground state. As a result, the vibrational structures seen in the absorption and the emission spectra are similar.

Molecules in the  $S_1$  state can also undergo a spin conversion to the first triplet state  $T_1$ . Emission from  $T_1$  is termed phosphorescence, and is generally shifted to longer wavelengths (lower energy) relative to the fluorescence. Conversion of  $S_1$  to  $T_1$  is called intersystem crossing. Transition from  $T_1$  to the singlet ground state is forbidden, and as a result the rate constants for triplet emission are several orders of magnitude smaller than those for fluorescence. Molecules containing heavy atoms such as bromine and iodine are frequently phosphorescent. The heavy atoms facilitate intersystem crossing and thus enhance phosphorescence quantum yields.

### 1.3. CHARACTERISTICS OF FLUORESCENCE EMISSION

The phenomenon of fluorescence displays a number of general characteristics. Exceptions are known, but these are infrequent. Generally, if any of the characteristics described in the following sections are not displayed by a given fluorophore, one may infer some special behavior for this compound.

#### 1.3.1. The Stokes Shift

Examination of the Jablonski diagram (Figure 1.5) reveals that the energy of the emission is typically less than that of absorption. Fluorescence typically occurs at lower energies or longer wavelengths. This phenomenon was first observed by Sir. G. G. Stokes in 1852 at the University of Cambridge.<sup>9</sup> These early experiments used relatively simple

instrumentation (Figure 1.6). The source of ultraviolet excitation was provided by sunlight and a blue glass filter, which was part of a stained glass window. This filter selectively transmitted light below 400 nm, which was absorbed by quinine (Figure 1.6). The incident light was prevented from reaching the detector (eye) by a yellow glass (of wine) filter. Quinine fluorescence occurs near 450 nm and is therefore easily visible.

It is interesting to read Sir George's description of the observation. The following is from his report published in 1852:<sup>9</sup>

*On the Change of Refrangibility of Light. By G. G. Stokes, M.A., F.R.S., Fellow of Pembroke College, and Lucasian Professor of Mathematics in the University of Cambridge. Phil. Trans. Royal Society of London (1852) pp. 463-562.*  
Received May 11, — Read May 27, 1852.

"The following researches originated in a consideration of the very remarkable phenomenon discovered by Sir John Herschel in a solution of sulphate of quinine, and described by him in two papers printed in the Philosophical Transactions for 1845, entitled "On a Case of Superficial Colour presented by a Homogeneous Liquid internally colourless," and "On the Epipolic Dispersion of Light." The solution of quinine, though it appears to be perfectly transparent and colourless, like water, when viewed by transmitted light, exhibits nevertheless in certain aspects, and under certain incidences of the light, a beautiful celestial blue colour. It appears from the experiments of Sir John Herschel that the blue colour comes only from a stratum of fluid of small but finite thickness adjacent to the surface by which the light enters. After passing through this stratum, the incident light, though not sensibly enfeebled nor coloured, has lost the power of producing the same effect, and therefore may be con-

sidered as in some way or other qualitatively different from the original light."

Careful reading of this paragraph reveals several important characteristics of fluorescent solutions. The quinine solution is colorless because it absorbs in the ultraviolet, which we cannot see. The blue color comes only from a region near the surface. This is because the quinine solution was relatively concentrated and absorbed all of the UV in the first several millimeters. Hence Stokes observed the inner filter effect. After passing through the solution the light was "enfeebled" and no longer capable of causing the blue glow. This occurred because the UV was removed and the "enfeebled" light could no longer excite quinine. However, had Sir George used a second solution of fluorescein, rather than quinine, it would have still been excited because of the longer absorption wavelength of fluorescein.

Energy losses between excitation and emission are observed universally for fluorescent molecules in solution. One common cause of the Stokes shift is the rapid decay to the lowest vibrational level of  $S_1$ . Furthermore, fluorophores generally decay to higher vibrational levels of  $S_0$  (Figure 1.5), resulting in further loss of excitation energy by thermalization of the excess vibrational energy. In addition to these effects, fluorophores can display further Stokes shifts due to solvent effects, excited-state reactions, complex formation, and/or energy transfer.

#### Brief History of Sir. G. G. Stokes:

Professor Stokes was born in Ireland, August 3, 1819 (Figure 1.7). He entered Pembroke College, Cambridge, in 1837, and was elected as a fellow of Pembroke immediately upon his graduation in 1841. In 1849 Stokes became Lucasian Professor at Cambridge, a chair once held by Newton. Because of poor endowment for the chair, he also worked in the Government School of Mines.

Stokes was involved with a wide range of scientific problems, including hydrodynamics, elasticity of solids, and diffraction of light. The wave theory of light was already known when he entered Cambridge. In his classic paper on quinine, he understood that light of a higher "refrangibility" or frequency was responsible for the blue glow of lower refrangibility or frequency. Thus invisible ultraviolet rays were absorbed to produce the blue light at the surface. Stokes later suggested using optical properties such as absorption, colored reflection, and fluorescence, to identify organic substances.

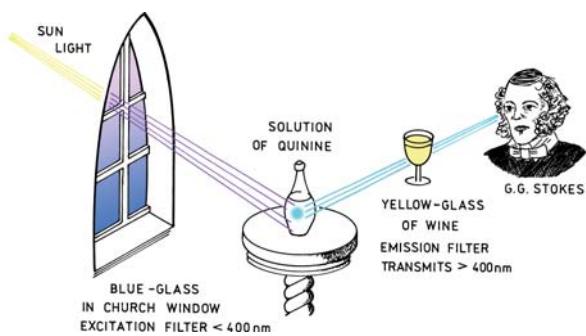


Figure 1.6. Experimental schematic for detection of the Stokes shift.

Later in life Stokes was universally honored with degrees and medals. He was knighted in 1889 and became Master of Pembroke College in 1902. After the 1850s, Stokes became involved in administrative matters, and his scientific productivity decreased. Some things never change. Professor Stokes died February 1, 1903.

### 1.3.2. Emission Spectra Are Typically Independent of the Excitation Wavelength

Another general property of fluorescence is that the same fluorescence emission spectrum is generally observed irrespective of the excitation wavelength. This is known as Kasha's rule,<sup>10</sup> although Vavilov reported in 1926 that quantum yields were generally independent of excitation wavelength.<sup>5</sup> Upon excitation into higher electronic and vibrational levels, the excess energy is quickly dissipated, leaving the fluorophore in the lowest vibrational level of  $S_1$ . This relaxation occurs in about  $10^{-12}$  s, and is presumably a result of a strong overlap among numerous states of nearly equal energy. Because of this rapid relaxation, emission spectra are usually independent of the excitation wavelength. Exceptions exist, such as fluorophores that exist in two ionization states, each of which displays distinct absorption and emission spectra. Also, some molecules are known to emit from the  $S_2$  level, but such emission is rare and generally not observed in biological molecules.

It is interesting to ask why perylene follows the mirror-image rule, but quinine emission lacks the two peaks seen in its excitation spectrum at 315 and 340 nm (Figure 1.3). In the case of quinine, the shorter wavelength absorption peak is due to excitation to the second excited state ( $S_2$ ), which relaxes rapidly to  $S_1$ . Emission occurs predominantly from the lowest singlet state ( $S_1$ ), so emission from  $S_2$  is not observed. The emission spectrum of quinine is the mirror image of the  $S_0 \rightarrow S_1$  absorption of quinine, not of its total absorption spectrum. This is true for most fluorophores: the emission is the mirror image of  $S_0 \rightarrow S_1$  absorption, not of the total absorption spectrum.

The generally symmetric nature of these spectra is a result of the same transitions being involved in both absorption and emission, and the similar vibrational energy levels of  $S_0$  and  $S_1$ . In most fluorophores these energy levels are not significantly altered by the different electronic distributions of  $S_0$  and  $S_1$ . Suppose the absorption spectrum of a fluorophore shows distinct peaks due to the vibrational energy levels. Such peaks are seen for anthracene in Figure



**Figure 1.7.** Sir George Gabriel Stokes, 1819–1903, Lucasian Professor at Cambridge. Reproduced courtesy of the Library and Information Centre, Royal Society of Chemistry.

1.8. These peaks are due to transitions from the lowest vibrational level of the  $S_0$  state to higher vibrational levels of the  $S_1$  state. Upon return to the  $S_0$  state the fluorophore can return to any of the ground state vibrational levels. These vibrational energy levels have similar spacing to those in the  $S_1$  state. The emission spectrum shows the same vibrational energy spacing as the absorption spectrum. According to the Franck-Condon principle, all electronic transitions are vertical, that is, they occur without change in the position of the nuclei. As a result, if a particular transition probability (Franck-Condon factor) between the 0th and 1st vibrational levels is largest in absorption, the reciprocal transition is also most probable in emission (Figure 1.8).

A rigorous test of the mirror-image rule requires that the absorption and emission spectra be presented in appropriate units.<sup>12</sup> The closest symmetry should exist between the modified spectra  $\epsilon(\bar{v})/\bar{v}$  and  $F(\bar{v})/\bar{v}^3$ , where  $\epsilon(\bar{v})$  is the extinction coefficient at wavenumber  $(\bar{v})$ , and  $F(\bar{v})$  is the relative photon flux over a wavenumber increment  $\Delta\bar{v}$ . Agreement between these spectra is generally found for polynuclear aromatic hydrocarbons.

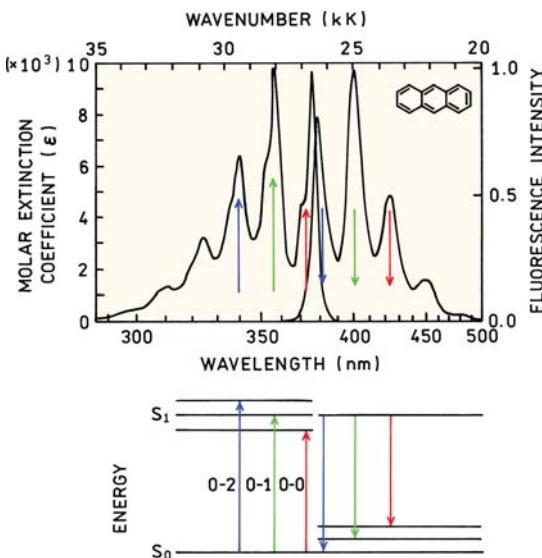


**Figure 1.8.** Mirror-image rule and Franck-Condon factors. The absorption and emission spectra are for anthracene. The numbers 0, 1, and 2 refer to vibrational energy levels. From [11].

### 1.3.3. Exceptions to the Mirror-Image Rule

Although often true, many exceptions to the mirror-image rule occur. This is illustrated for the pH-sensitive fluorophore 1-hydroxypyrene-3,6,8-trisulfonate (HPTS) in Figure 1.9. At low pH the hydroxyl group is protonated. The absorption spectrum at low pH shows vibrational structure typical of an aromatic hydrocarbon. The emission spectrum shows a large Stokes shift and none of the vibrational structure seen in the absorption spectrum. The difference between the absorption emission spectra is due to ionization of the hydroxyl group. The dissociation constant ( $pK_a$ ) of the hydroxyl group decreases in the excited state, and this group becomes ionized. The emission occurs from a different molecular species, and this ionized species displays a broad spectrum. This form of HPTS with an ionized hydroxyl group can be formed at pH 13. The emission spectrum is a mirror image of the absorption of the high pH form of HPTS.

Changes in  $pK_a$  in the excited state also occur for biochemical fluorophores. For example, phenol and tyrosine each show two emissions, the long-wavelength emission being favored by a high concentration of proton acceptors. The  $pK_a$  of the phenolic hydroxyl group decreases from 11 in the ground state to 4 in the excited state. Following excitation, the phenolic proton is lost to proton acceptors in the solution. Depending upon the concentration of these acceptors, either the phenol or the phenolate emission may dominate the emission spectrum.

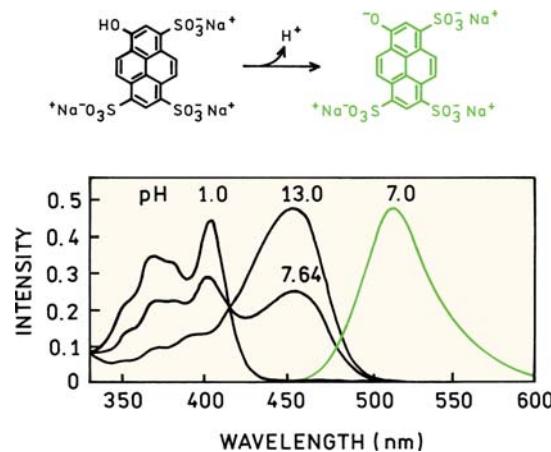


**Figure 1.9.** Absorption (pH 1, 7.64, and 13) and emission spectra (pH 7) of 1-hydroxypyrene-3,6,8-trisulfonate in water. From [11].

Excited-state reactions other than proton dissociation can also result in deviations from the mirror symmetry rule. One example is shown in Figure 1.10, which shows the emission spectrum of anthracene in the presence of diethylaniline.<sup>13</sup> The structured emission at shorter wavelengths is a mirror image of the absorption spectrum of anthracene. The unstructured emission at longer wavelengths is due to formation of a charge-transfer complex between the excited state of anthracene and diethylaniline. The unstructured emission is from this complex. Many polynuclear aromatic hydrocarbons, such as pyrene and perylene, also form charge-transfer complexes with amines. These excited-state complexes are referred to as exciplexes.

Some fluorophores can also form complexes with themselves. The best known example is pyrene. At low concentrations pyrene displays a highly structured emission (Figure 1.11). At higher concentrations the previously invisible UV emission of pyrene becomes visible at 470 nm. This long-wavelength emission is due to excimer formation. The term "excimer" is an abbreviation for an excited-state dimer.

### 1.4. FLUORESCENCE LIFETIMES AND QUANTUM YIELDS

The fluorescence lifetime and quantum yield are perhaps the most important characteristics of a fluorophore. Quantum yield is the number of emitted photons relative to the number of absorbed photons. Substances with the largest quantum yields, approaching unity, such as rhodamines, display the brightest emissions. The lifetime is also important, as it determines the time available for the fluorophore

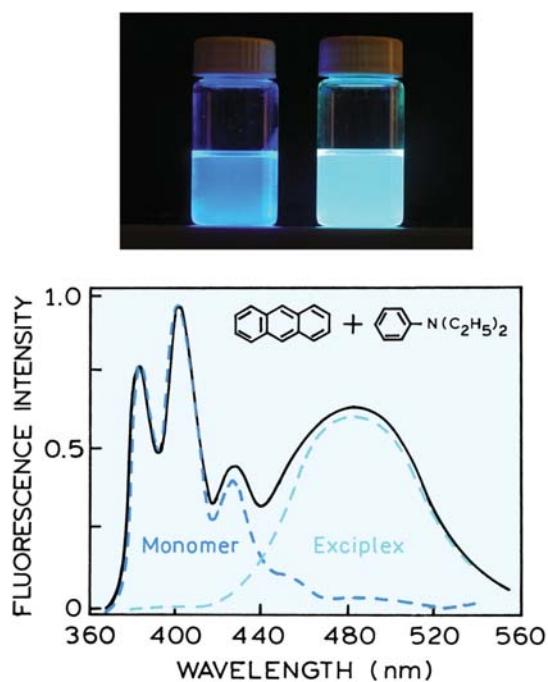


**Figure 1.10.** Emission spectrum of anthracene in toluene containing 0.2 M diethylaniline. The dashed lines show the emission spectra of anthracene or its exciplex with diethylaniline. Figure revised from [13], photo from [14].

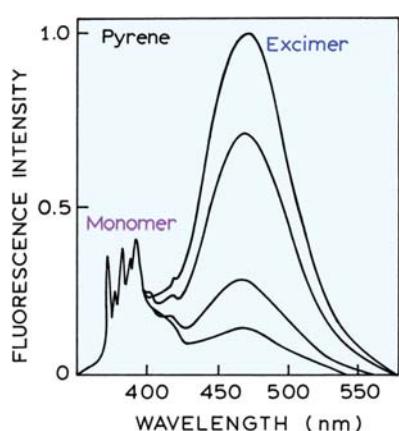


**Figure 1.11.** Emission spectra of pyrene and its excimer. The relative intensity of the excimer peak (470 nm) decreases as the total concentration of pyrene is decreased from  $6 \times 10^{-3}$  M (top) to  $0.9 \times 10^{-4}$  M (bottom). Reproduced with permission from John Wiley and Sons Inc. From [12].

to interact with or diffuse in its environment, and hence the information available from its emission.

The meanings of quantum yield and lifetime are best represented by a simplified Jablonski diagram (Figure 1.12). In this diagram we do not explicitly illustrate the

individual relaxation processes leading to the relaxed  $S_1$  state. Instead, we focus on those processes responsible for return to the ground state. In particular, we are interested in the emissive rate of the fluorophore ( $\Gamma$ ) and its rate of non-radiative decay to  $S_0$  ( $k_{nr}$ ).

The fluorescence quantum yield is the ratio of the number of photons emitted to the number absorbed. The rate constants  $\Gamma$  and  $k_{nr}$  both depopulate the excited state. The fraction of fluorophores that decay through emission, and hence the quantum yield, is given by

$$Q = \frac{\Gamma}{\Gamma + k_{nr}} \quad (1.1)$$

The quantum yield can be close to unity if the radiationless decay rate is much smaller than the rate of radiative decay, that is  $k_{nr} < \Gamma$ . We note that the energy yield of fluorescence is always less than unity because of Stokes losses. For convenience we have grouped all possible non-radiative decay processes with the single rate constant  $k_{nr}$ .

The lifetime of the excited state is defined by the average time the molecule spends in the excited state prior to return to the ground state. Generally, fluorescence lifetimes are near 10 ns. For the fluorophore illustrated in Figure 1.12 the lifetime is

$$\tau = \frac{1}{\Gamma + k_{nr}} \quad (1.2)$$

Fluorescence emission is a random process, and few molecules emit their photons at precisely  $t = \tau$ . The lifetime is an average value of the time spent in the excited state. For a single exponential decay (eq. 1.13) 63% of the molecules have decayed prior to  $t = \tau$  and 37% decay at  $t > \tau$ .

An example of two similar molecules with different lifetimes and quantum yields is shown in Figure 1.13. The differences in lifetime and quantum yield for eosin and erythrosin B are due to differences in non-radiative decay rates. Eosin and erythrosin B have essentially the same extinction coefficient and the same radiative decay rate (see eq. 1.4). Heavy atoms such as iodine typically result in shorter lifetimes and lower quantum yields.

The lifetime of the fluorophore in the absence of non-radiative processes is called the intrinsic or natural lifetime, and is given by

$$\tau_n = \frac{1}{\Gamma} \quad (1.3)$$

In principle, the natural lifetime  $\tau_n$  can be calculated from the absorption spectra, extinction coefficient, and

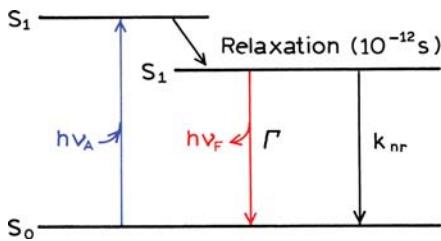


**Figure 1.12.** A simplified Jablonski diagram to illustrate the meaning of quantum yields and lifetimes.

emission spectra of the fluorophore. The radiative decay rate  $\Gamma$  can be calculated using<sup>15,16</sup>

$$\begin{aligned} \Gamma &\approx 2.88 \times 10^9 n^2 \frac{\int F(\bar{v}) d\bar{v}}{\int F(\bar{v}) d\bar{v}/\bar{v}^3} \int \frac{\varepsilon(\bar{v})}{\bar{v}} d\bar{v} \\ &= 2.88 \times 10^9 n^2 \langle \bar{v}^{-3} \rangle^{-1} \int \frac{\varepsilon(\bar{v})}{\bar{v}} d\bar{v} \end{aligned} \quad (1.4)$$

where  $F(\bar{v})$  is the emission spectrum plotted on the wavenumber ( $\text{cm}^{-1}$ ) scale,  $\varepsilon(\bar{v})$  is the absorption spectrum, and  $n$  is the refractive index of the medium. The integrals are calculated over the  $S_0 \leftrightarrow S_1$  absorption and emission spectra. In many cases this expression works rather well, particularly for solutions of polynuclear aromatic hydrocarbons. For instance, the calculated value<sup>15</sup> of  $\Gamma$  for perylene is  $1.8 \times 10^8 \text{ s}^{-1}$ , which yields a natural lifetime of 5.5 ns. This value is close to that observed for perylene, which displays a quantum yield near unity. However, there are numerous reasons why eq. 1.4 can fail. This expression assumes no interaction with the solvent, does not consider changes in the refractive index ( $n$ ) between the absorption

and emission wavelength, and assumes no change in excited-state geometry. A more complete form of eq. 1.4 (not shown) includes a factor  $G = g_l/g_u$  on the right-hand side, where  $g_l$  and  $g_u$  are the degeneracies of the lower and upper states, respectively. For fluorescence transitions  $G = 1$ , for phosphorescence transitions  $G = 1/3$ .

The natural lifetime can be calculated from the measured lifetime ( $\tau$ ) and quantum yield

$$\tau_n = \tau / Q \quad (1.5)$$

which can be derived from eqs. 1.2 and 1.3. Many biochemical fluorophores do not behave as predictably as unsubstituted aromatic compounds. Hence, there is often poor agreement between the value of  $\tau_n$  calculated from eq. 1.5 and that calculated from its absorption and emission spectra (eq. 1.4). These discrepancies occur for a variety of unknown and known reasons, such as a fraction of the fluorophores located next to quenching groups, which sometimes occurs for tryptophan residues in proteins.

The quantum yield and lifetime can be modified by factors that affect either of the rate constants ( $\Gamma$  or  $k_{nr}$ ). For example, a molecule may be nonfluorescent as a result of a large rate of internal conversion or a slow rate of emission. Scintillators are generally chosen for their high quantum yields. These high yields are a result of large  $\Gamma$  values. Hence, the lifetimes are generally short: near 1 ns. The fluorescence emission of aromatic substances containing  $-NO_2$  groups are generally weak, primarily as a result of large  $k_{nr}$  values. The quantum yields of phosphorescence are extremely small in fluid solutions at room temperature. The triplet-to-singlet transition is forbidden by symmetry, and the rates of spontaneous emission are about  $10^3 \text{ s}^{-1}$  or smaller. Since  $k_{nr}$  values are near  $10^9 \text{ s}^{-1}$ , the quantum yields of phosphorescence are small at room temperature. From eq. 1.1 one can predict phosphorescence quantum yields of  $10^{-6}$ .

Comparison of the natural lifetime, measured lifetime, and quantum yield can be informative. For example, in the case of the widely used membrane probe 1,6-diphenyl-1,3,5-hexatriene (DPH) the measured lifetime near 10 ns is much longer than that calculated from eq. 1.4, which is near 1.5 ns.<sup>17</sup> In this case the calculation based on the absorption spectrum of DPH is incorrect because the absorption transition is to a state of different electronic symmetry than the emissive state. Such quantum-mechanical effects are rarely seen in more complex fluorophores with heterocyclic atoms.

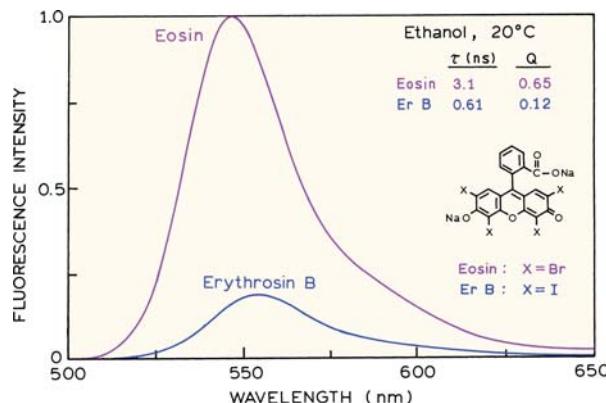


**Figure 1.13.** Emission spectra of eosin and erythrosin B (ErB).

### 1.4.1. Fluorescence Quenching

The intensity of fluorescence can be decreased by a wide variety of processes. Such decreases in intensity are called quenching. Quenching can occur by different mechanisms. Collisional quenching occurs when the excited-state fluorophore is deactivated upon contact with some other molecule in solution, which is called the quencher. Collisional quenching is illustrated on the modified Jablonski diagram in Figure 1.14. In this case the fluorophore is returned to the ground state during a diffusive encounter with the quencher. The molecules are not chemically altered in the process. For collisional quenching the decrease in intensity is described by the well-known Stern-Volmer equation:

$$\frac{F_0}{F} = 1 + K[Q] = 1 + k_q \tau_0 [Q] \quad (1.6)$$

In this expression  $K$  is the Stern-Volmer quenching constant,  $k_q$  is the bimolecular quenching constant,  $\tau_0$  is the unquenched lifetime, and  $[Q]$  is the quencher concentration. The Stern-Volmer quenching constant  $K$  indicates the sensitivity of the fluorophore to a quencher. A fluorophore buried in a macromolecule is usually inaccessible to water-soluble quenchers, so that the value of  $K$  is low. Larger values of  $K$  are found if the fluorophore is free in solution or on the surface of a biomolecule.

A wide variety of molecules can act as collisional quenchers. Examples include oxygen, halogens, amines, and electron-deficient molecules like acrylamide. The mechanism of quenching varies with the fluorophore-quencher pair. For instance, quenching of indole by acrylamide is probably due to electron transfer from indole to acrylamide, which does not occur in the ground state. Quenching by halogen and heavy atoms occurs due to spin-orbit coupling and intersystem crossing to the triplet state (Figure 1.5).

Aside from collisional quenching, fluorescence quenching can occur by a variety of other processes. Fluorophores can form nonfluorescent complexes with quenchers. This process is referred to as static quenching since it occurs in the ground state and does not rely on diffusion or molecular collisions. Quenching can also occur by a variety of trivial, i.e., non-molecular mechanisms, such as attenuation of the incident light by the fluorophore itself or other absorbing species.

### 1.4.2. Timescale of Molecular Processes in Solution

The phenomenon of quenching provides a valuable context for understanding the role of the excited-state lifetime in

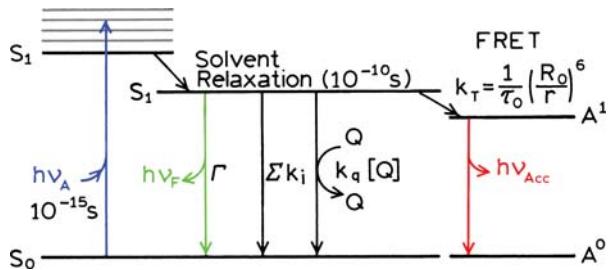


**Figure 1.14.** Jablonski diagram with collisional quenching and fluorescence resonance energy transfer (FRET). The term  $\Sigma k_i$  is used to represent non-radiative paths to the ground state aside from quenching and FRET.

allowing fluorescence measurements to detect dynamic processes in solution or in macromolecules. The basic idea is that absorption is an instantaneous event. According to the Franck-Condon principle, absorption occurs so fast that there is no time for molecular motion during the absorption process. Absorption occurs in the time it takes a photon to travel the length of a photon: in less than  $10^{-15}$  s. As a result, absorption spectroscopy can only yield information on the average ground state of the molecules that absorb light. Only solvent molecules that are immediately adjacent to the absorbing species will affect its absorption spectrum. Absorption spectra are not sensitive to molecular dynamics and can only provide information on the average solvent shell adjacent to the chromophore.

In contrast to absorption, emission occurs over a longer period of time. The length of time fluorescent molecules remain in the excited state provides an opportunity for interactions with other molecules in solution. Collisional quenching of fluorescence by molecular oxygen is an excellent example of the expansion of time and distance provided by the fluorescence lifetime. If a fluorophore in the excited state collides with an oxygen molecule, then the fluorophore returns to the ground state without emission of a photon. The diffusion coefficient ( $D$ ) of oxygen in water at  $25^\circ\text{C}$  is  $2.5 \times 10^{-5} \text{ cm}^2/\text{s}$ . Suppose a fluorophore has a lifetime of 10 ns. Although 10 ns may appear to be a brief time span, it is in fact quite long relative to the motions of small molecules in fluid solution. The average distance ( $\Delta x^2$ ) $^{1/2}$  an oxygen molecule can diffuse in  $10^{-8}$  s or 10 ns is given by the Einstein equation:

$$\Delta x^2 = 2D\tau \quad (1.7)$$

The distance is about 70 Å, which is comparable to the thickness of a biological membrane or the diameter of a protein. Some fluorophores have lifetimes as long as 400

ns, and hence diffusion of oxygen molecules may be observed over distances of 450 Å. Absorption measurements are only sensitive to the immediate environment around the fluorophore, and then only sensitive to the instantaneously averaged environment.

Other examples of dynamic processes in solution involve fluorophore–solvent interactions and rotational diffusion. As was observed by Stokes, most fluorophores display emission at lower energies than their absorption. Most fluorophores have larger dipole moments in the excited state than in the ground state. Rotational motions of small molecules in fluid solution are rapid, typically occurring on a timescale of 40 ps or less. The relatively long timescale of fluorescence allows ample time for the solvent molecules to reorient around the excited-state dipole, which lowers its energy and shifts the emission to longer wavelengths. This process is called solvent relaxation and occurs within  $10^{-10}$  s in fluid solution (Figure 1.14). It is these differences between absorption and emission that result in the high sensitivity of emission spectra to solvent polarity, and the smaller spectral changes seen in absorption spectra. Solvent relaxation can result in substantial Stokes shifts. In proteins, tryptophan residues absorb light at 280 nm, and their fluorescence emission occurs near 350 nm.

## 1.5. FLUORESCENCE ANISOTROPY

Anisotropy measurements are commonly used in the biochemical applications of fluorescence. Anisotropy measurements provide information on the size and shape of proteins or the rigidity of various molecular environments. Anisotropy measurements have been used to measure protein–protein associations, fluidity of membranes, and for immunoassays of numerous substances.

Anisotropy measurements are based on the principle of photoselective excitation of fluorophores by polarized light. Fluorophores preferentially absorb photons whose electric vectors are aligned parallel to the transition moment of the fluorophore. The transition moment has a defined orientation with respect to the molecular axis. In an isotropic solution, the fluorophores are oriented randomly. Upon excitation with polarized light, one selectively excites those fluorophore molecules whose absorption transition dipole is parallel to the electric vector of the excitation (Figure 1.15). This selective excitation results in a partially oriented population of fluorophores (photoselection), and in partially polarized fluorescence emission. Emission also occurs with the light polarized along a fixed axis in the fluorophore. The

relative angle between these moments determines the maximum measured anisotropy [ $r_0$ , see eq. 10.19]. The fluorescence anisotropy ( $r$ ) and polarization ( $P$ ) are defined by

$$r = \frac{I_{\parallel} - I_{\perp}}{I_{\parallel} + 2I_{\perp}} \quad (1.8)$$

$$P = \frac{I_{\parallel} - I_{\perp}}{I_{\parallel} + I_{\perp}} \quad (1.9)$$

where  $I_{\parallel}$  and  $I_{\perp}$  are the fluorescence intensities of the vertically ( $\parallel$ ) and horizontally ( $\perp$ ) polarized emission, when the sample is excited with vertically polarized light. Anisotropy and polarization are both expressions for the same phenomenon, and these values can be interchanged using eqs. 10.3 and 10.4.

Several phenomena can decrease the measured anisotropy to values lower than the maximum theoretical values. The most common cause is rotational diffusion (Figure 1.15). Such diffusion occurs during the lifetime of the excited state and displaces the emission dipole of the fluorophore. Measurement of this parameter provides information about the relative angular displacement of the fluorophore between the times of absorption and emission. In fluid solution most fluorophores rotate extensively in 50 to 100 ps. Hence, the molecules can rotate many times during the 1–10 ns excited-state lifetime, and the orientation of the polarized emission is randomized. For this reason fluorophores in non-viscous solution typically display anisotropies near zero. Transfer of excitation between fluorophores also results in decreased anisotropies.

The effects of rotational diffusion can be decreased if the fluorophore is bound to a macromolecule. For instance, it is known that the rotational correlation time for the protein human serum albumin (HSA) is near 50 ns. Suppose HSA is covalently labeled with a fluorophore whose lifetime is 50 ns. Assuming no other processes result in loss of anisotropy, the expected anisotropy is given by the Perrin equation:<sup>18</sup>

$$r = \frac{r_0}{1 + (\tau/\theta)} \quad (1.10)$$

where  $r_0$  is the anisotropy that would be measured in the absence of rotational diffusion, and  $\theta$  is the rotational correlation time for the diffusion process. In this case binding of the fluorophore to the protein has slowed the probe's rate of rotational motion. Assuming  $r_0 = 0.4$ , the anisotropy is expected to be 0.20. Smaller proteins have shorter correla-

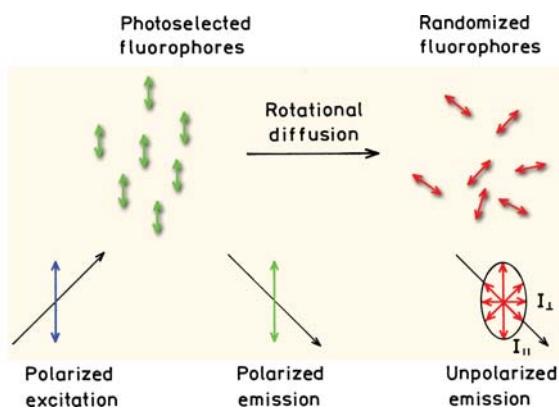


**Figure 1.15.** Effects of polarized excitation and rotational diffusion on the polarization or anisotropy of the emission.

tion times and are expected to yield lower anisotropies. The anisotropies of larger proteins can also be low if they are labeled with long-lifetime fluorophores. The essential point is that the rotational correlation times for most proteins are comparable to typical fluorescence lifetimes. As a result, measurements of fluorescence anisotropy will be sensitive to any factor that affects the rate of rotational diffusion. The rotational rates of fluorophores in cell membranes also occur on the nanoscale timescale, and the anisotropy values are thus sensitive to membrane composition. For these reasons, measurements of fluorescence polarization are widely used to study the interactions of biological macromolecules.

## 1.6. RESONANCE ENERGY TRANSFER

Another important process that occurs in the excited state is resonance energy transfer (RET). This process occurs whenever the emission spectrum of a fluorophore, called the donor, overlaps with the absorption spectrum of another molecule, called the acceptor.<sup>19</sup> Such overlap is illustrated in Figure 1.16. The acceptor does not need to be fluorescent. It is important to understand that RET does not involve emission of light by the donor. RET is not the result of emission from the donor being absorbed by the acceptor. Such reabsorption processes are dependent on the overall concentration of the acceptor, and on non-molecular factors such as sample size, and thus are of less interest. There is no intermediate photon in RET. The donor and acceptor are coupled by a dipole–dipole interaction. For these reasons the term RET is preferred over the term fluorescence resonance energy transfer (FRET), which is also in common use.

The extent of energy transfer is determined by the distance between the donor and acceptor, and the extent of spectral overlap. For convenience the spectral overlap (Figure 1.16) is described in terms of the Förster distance ( $R_0$ ). The rate of energy transfer  $k_T(r)$  is given by

$$k_T(r) = \frac{1}{\tau_D} \left( \frac{R_0}{r} \right)^6 \quad (1.11)$$

where  $r$  is the distance between the donor ( $D$ ) and acceptor ( $A$ ) and  $\tau_D$  is the lifetime of the donor in the absence of energy transfer. The efficiency of energy transfer for a single donor–acceptor pair at a fixed distance is

$$E = \frac{R_0^6}{R_0^6 + r^6} \quad (1.12)$$

Hence the extent of transfer depends on distance ( $r$ ). Fortunately, the Förster distances are comparable in size to biological macromolecules: 30 to 60 Å. For this reason energy transfer has been used as a "spectroscopic ruler" for measurements of distance between sites on proteins.<sup>20</sup> The value of  $R_0$  for energy transfer should not be confused with the fundamental anisotropies ( $r_0$ ).

The field of RET is large and complex. The theory is different for donors and acceptors that are covalently linked, free in solution, or contained in the restricted geometries of membranes or DNA. Additionally, depending on donor lifetime, diffusion can increase the extent of energy transfer beyond that predicted by eq. 1.12.

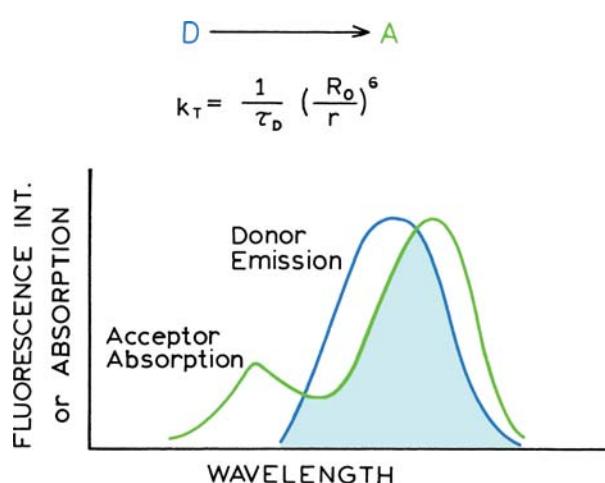


**Figure 1.16.** Spectral overlap for fluorescence resonance energy transfer (RET).

## 1.7. STEADY-STATE AND TIME-RESOLVED FLUORESCENCE

Fluorescence measurements can be broadly classified into two types of measurements: steady-state and time-resolved. Steady-state measurements, the most common type, are those performed with constant illumination and observation. The sample is illuminated with a continuous beam of light, and the intensity or emission spectrum is recorded (Figure 1.17). Because of the ns timescale of fluorescence, most measurements are steady-state measurements. When the sample is first exposed to light, steady state is reached almost immediately.

The second type of measurement is time-resolved, which is used for measuring intensity decays or anisotropy decays. For these measurements the sample is exposed to a pulse of light, where the pulse width is typically shorter than the decay time of the sample (Figure 1.17). This intensity decay is recorded with a high-speed detection system that permits the intensity or anisotropy to be measured on the ns timescale.

It is important to understand the relationship between steady-state and time-resolved measurements. A steady-state observation is simply an average of the time-resolved phenomena over the intensity decay of the sample. For instance, consider a fluorophore that displays a single decay time ( $\tau$ ) and a single rotational correlation time ( $\theta$ ). The intensity and anisotropy decays are given by

$$I(t) = I_0 e^{-t/\tau} \quad (1.13)$$

$$r(t) = r_0 e^{-t/\theta} \quad (1.14)$$

where  $I_0$  and  $r_0$  are the intensities and anisotropies at  $t = 0$ , immediately following the excitation pulse, respectively.

Equations 1.13 and 1.14 can be used to illustrate how the decay time determines what can be observed using fluorescence. The steady-state anisotropy ( $r$ ) is given by the average of  $r(t)$  weighted by  $I(t)$ :

$$r = \frac{\int_0^\infty r(t)I(t)dt}{\int_0^\infty I(t)dt} \quad (1.15)$$

In this equation the denominator is present to normalize the anisotropy to be independent of total intensity. In the numerator the anisotropy at any time  $t$  contributes to the steady-state anisotropy according to the intensity at time  $t$ .

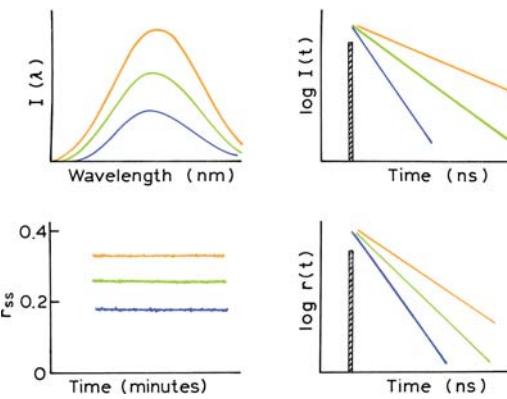


**Figure 1.17.** Comparison of steady-state and time-resolved fluorescence spectroscopy.

Substitution of eqs. 1.13 and 1.14 into 1.15 yields the Perrin equation, 1.10.

Perhaps a simpler example is how the steady-state intensity ( $I_{ss}$ ) is related to the decay time. The steady-state intensity is given by

$$I_{ss} = \int_0^\infty I_0 e^{-t/\tau} dt = I_0 \tau \quad (1.16)$$

The value of  $I_0$  can be considered to be a parameter that depends on the fluorophore concentration and a number of instrumental parameters. Hence, in molecular terms, the steady-state intensity is proportional to the lifetime. This makes sense in consideration of eqs. 1.1 and 1.2, which showed that the quantum yield is proportional to the lifetime.

### 1.7.1. Why Time-Resolved Measurements?

While steady-state fluorescence measurements are simple, nanosecond time-resolved measurements typically require complex and expensive instrumentation. Given the relationship between steady-state and time-resolved measurements, what is the value of these more complex measurements? It turns out that much of the molecular information available from fluorescence is lost during the time averaging process. For example, anisotropy decays of fluorescent macromolecules are frequently more complex than a single exponential (eq. 1.14). The precise shape of the anisotropy decay contains information about the shape of the macromolecule and its flexibility. Unfortunately, this shape information is lost during averaging of the anisotropy over the decay time (eq. 1.15). Irrespective of the form of  $r(t)$ , eq. 1.15 yields a

single steady-state anisotropy. In principle, the value of  $r$  still reflects the anisotropy decay and shape of the molecule. In practice, the information from  $r$  alone is not sufficient to reveal the form of  $r(t)$  or the shape of the molecule.

The intensity decays also contain information that is lost during the averaging process. Frequently, macromolecules can exist in more than a single conformation, and the decay time of a bound probe may depend on conformation. The intensity decay could reveal two decay times, and thus the presence of more than one conformational state. The steady-state intensity will only reveal an average intensity dependent on a weighted averaged of the two decay times.

There are numerous additional reasons for measuring time-resolved fluorescence. In the presence of energy transfer, the intensity decays reveal how acceptors are distributed in space around the donors. Time-resolved measurements reveal whether quenching is due to diffusion or to complex formation with the ground-state fluorophores. In fluorescence, much of the molecular information content is available only by time-resolved measurements.

## 1.8. BIOCHEMICAL FLUOROPHORES

Fluorophores are divided into two general classes—*intrinsic* and *extrinsic*. Intrinsic fluorophores are those that occur naturally. Extrinsic fluorophores are those added to a sample that does not display the desired spectral properties. In proteins, the dominant fluorophore is the indole group of tryptophan (Figure 1.18). Indole absorbs near 280 nm, and emits near 340 nm. The emission spectrum of indole is highly sensitive to solvent polarity. The emission of indole may be blue shifted if the group is buried within a native protein (N), and its emission may shift to longer wavelengths (red shift) when the protein is unfolded (U).

Membranes typically do not display intrinsic fluorescence. For this reason it is common to label membranes with probes which spontaneously partition into the nonpolar side chain region of the membranes. One of the most commonly used membrane probes is diphenylhexatriene (DPH). Because of its low solubility and quenched emission in water, DPH emission is only seen from membrane-bound DPH (Figure 1.18). Other lipid probes include fluorophores attached to lipid or fatty acid chains.

While DNA contains nitrogenous bases that look like fluorophores, DNA is weakly or nonfluorescent. However, a wide variety of dyes bind spontaneously to DNA—such as acridines, ethidium bromide, and other planar cationic species. For this reason staining of cells with dyes that bind to DNA is widely used to visualize and identify chromosomes. One example of a commonly used DNA probe is

4',6-diamidino-2-phenolindole (DAPI). There is a wide variety of fluorophores that spontaneously bind to DNA.

A great variety of other substances display significant fluorescence. Among biological molecules, one can observe fluorescence from reduced nicotinamide adenine dinucleotide (NADH), from oxidized flavins (FAD, the adenine dinucleotide, and FMN, the mononucleotide), and pyridoxyl phosphate, as well as from chlorophyll. Occasionally, a species of interest is not fluorescent, or is not fluorescent in a convenient region of the UV visible spectrum. A wide variety of extrinsic probes have been developed for labeling the macromolecules in such cases. Two of the most widely used probes, dansyl chloride DNS-Cl, which stands for 1-dimethylamino-5-naphthylsulfonyl chloride, and fluorescein isothiocyanate (FITC), are shown in Figure 1.19. These probes react with the free amino groups of proteins, resulting in proteins that fluoresce at blue (DNS) or green (FITC) wavelengths.

Proteins can also be labeled on free sulphydryl groups using maleimide reagents such as Bodipy 499/508 maleimide. It is frequently useful to use longer-wavelength probes such as the rhodamine dye Texas Red. Cyanine dyes are frequently used for labeling nucleic acids, as shown for the labeled nucleotide Cy3-4-dUTP. A useful fluorescent probe is one that displays a high intensity, is stable during continued illumination, and does not substantially perturb the biomolecule or process being studied.

### 1.8.1. Fluorescent Indicators

Another class of fluorophores consists of the fluorescent indicators. These are fluorophores whose spectral properties are sensitive to a substance of interest. One example is Sodium Green, which is shown in Figure 1.20. This fluorophore contains a central azacrown ether, which binds  $\text{Na}^+$ . Upon binding of sodium the emission intensity of Sodium Green increases, allowing the amount of  $\text{Na}^+$  to be determined. Fluorescent indicators are presently available for a variety of substances, including  $\text{Ca}^{2+}$ ,  $\text{Mg}^{2+}$ ,  $\text{Na}^+$ ,  $\text{Cl}^-$ , and  $\text{O}_2$ , as well as pH. The applications of fluorescence to chemical sensing is described in Chapter 19.

## 1.9. MOLECULAR INFORMATION FROM FLUORESCENCE

### 1.9.1. Emission Spectra and the Stokes Shift

The most dramatic aspect of fluorescence is its occurrence at wavelengths longer than those at which absorption occurs. These Stokes shifts, which are most dramatic for

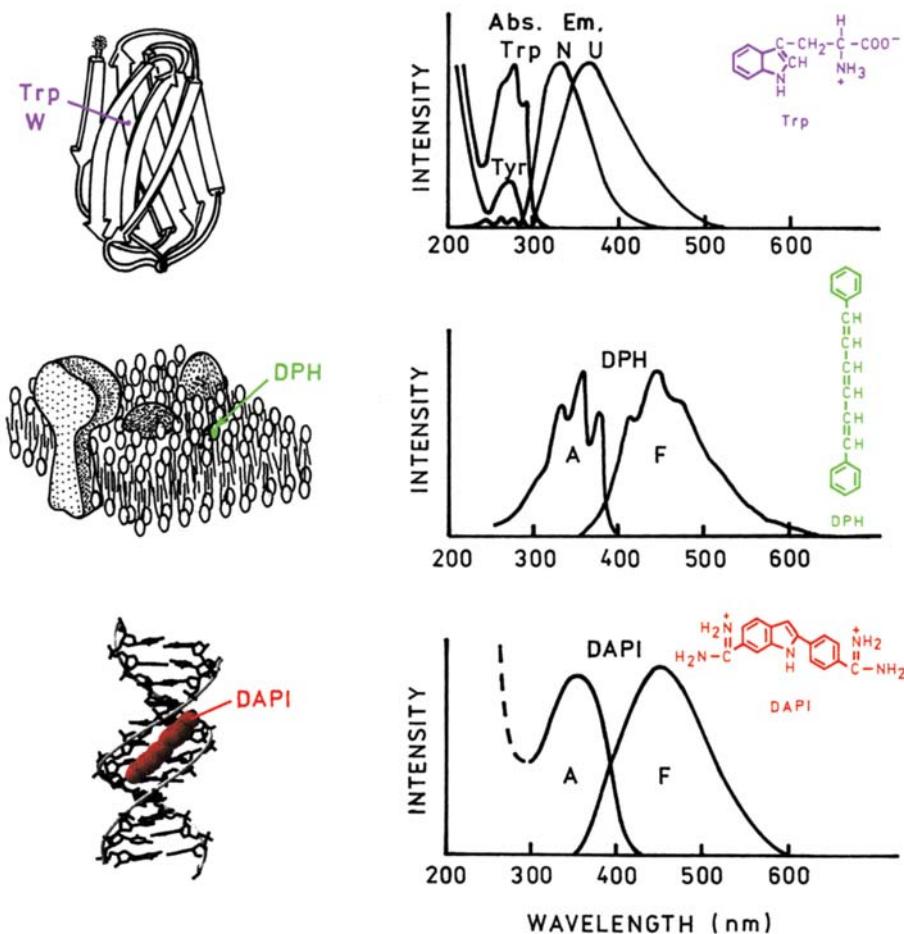


**Figure 1.18.** Absorption and emission spectra of biomolecules. Top, tryptophan emission from proteins. Middle, spectra of extrinsic membrane probe DPH. Bottom, spectra of the DAPI bound to DNA (—). DNA itself displays very weak emission. Reprinted with permission by Wiley-VCH, STM. From [21].

polar fluorophores in polar solvents, are due to interactions between the fluorophore and its immediate environment. The indole group of tryptophan residues in proteins is one such solvent-sensitive fluorophore, and the emission spectra of indole can reveal the location of tryptophan residues in proteins. The emission from an exposed surface residue will occur at longer wavelengths than that from a tryptophan residue in the protein's interior. This phenomenon was illustrated in the top part of Figure 1.18, which shows a shift in the spectrum of a tryptophan residue upon unfolding of a protein and the subsequent exposure of the tryptophan residue to the aqueous phase. Prior to unfolding, the residue is shielded from the solvent by the folded protein.

A valuable property of many fluorophores is their sensitivity to the surrounding environment. The emission spectra and intensities of extrinsic probes are often used to determine a probe's location on a macromolecule. For example, one of the widely used probes for such studies is

6-(*p*-toluidinyl)naphthalene-2-sulfonate (TNS), which displays the favorable property of being very weakly fluorescent in water (Figure 1.21). The green emission of TNS in the absence of protein is barely visible in the photographs. Weak fluorescence in water and strong fluorescence when bound to a biomolecule is a convenient property shared by other widely used probes, including many DNA stains. The protein apomyoglobin contains a hydrophobic pocket that binds the heme group. This pocket can also bind other non-polar molecules. Upon the addition of apomyoglobin to a solution of TNS, there is a large increase in fluorescence intensity, as well as a shift of the emission spectrum to shorter wavelengths. This increase in TNS fluorescence reflects the nonpolar character of the heme-binding site of apomyoglobin. TNS also binds to membranes (Figure 1.21). The emission spectrum of TNS when bound to model membranes of dimyristoyl-L- $\alpha$ -phosphatidylcholine (DMPC) is somewhat weaker and at longer wavelengths

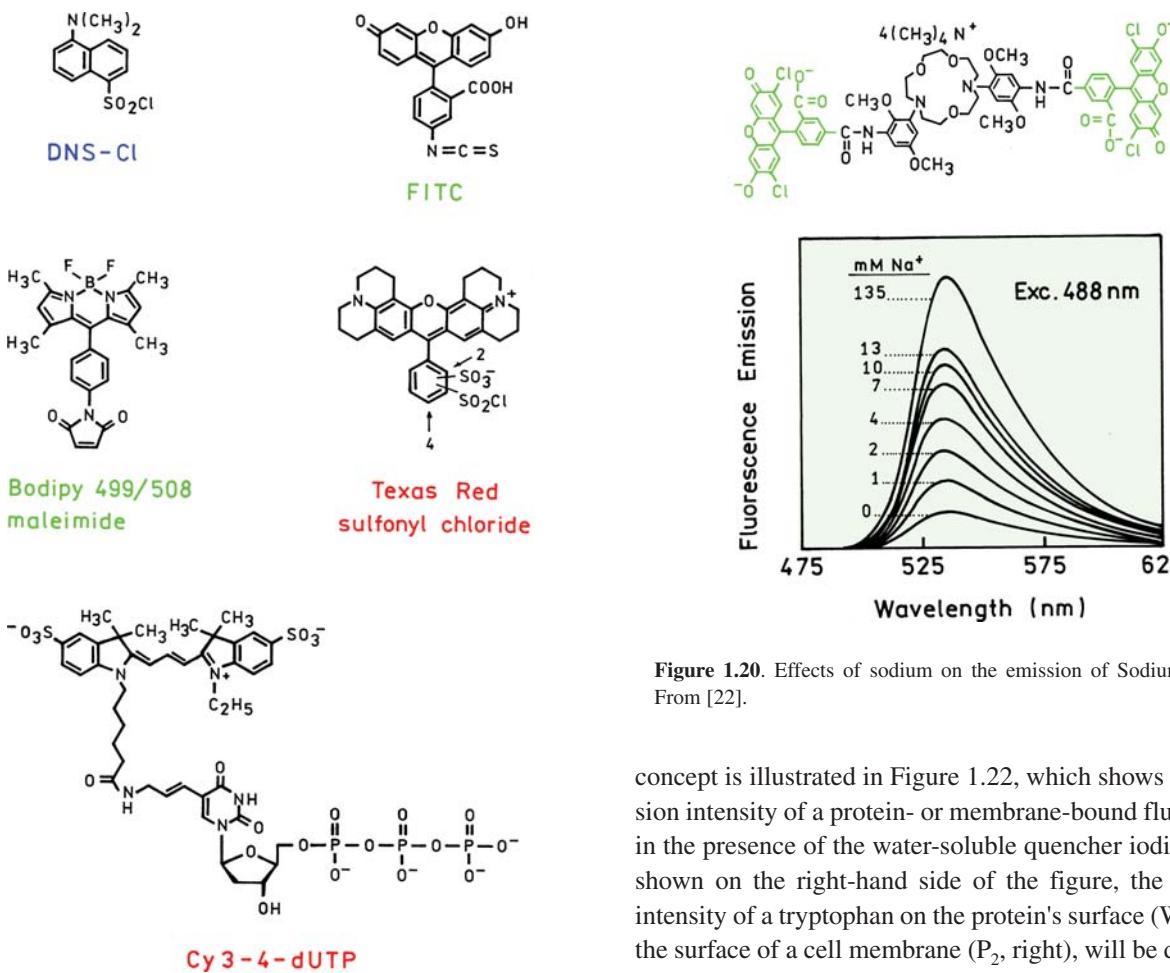


Figure 1.19. Fluorophores for covalent labeling of biomolecules.

compared to that of apomyoglobin. This indicates that the TNS binding sites on the surface of the membrane are more polar. From the emission spectrum it appears that TNS binds to the polar head group region of the membranes, rather than to the nonpolar acyl side chain region. Hence, the emission spectra of solvent-sensitive fluorophores provide information on the location of the binding sites on the macromolecules.

### 1.9.2. Quenching of Fluorescence

As described in Section 1.4.1, a wide variety of small molecules or ions can act as quenchers of fluorescence, that is, they decrease the intensity of the emission. These substances include iodide (I<sup>-</sup>), oxygen, and acrylamide. The accessibility of fluorophores to such quenchers can be used to determine the location of probes on macromolecules, or the porosity of proteins and membranes to quenchers. This

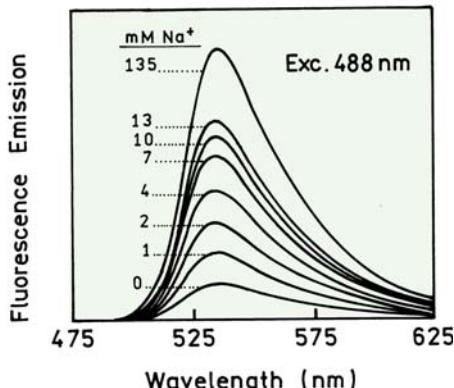
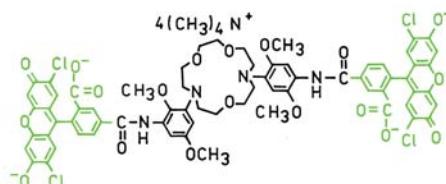


Figure 1.20. Effects of sodium on the emission of Sodium Green. From [22].

concept is illustrated in Figure 1.22, which shows the emission intensity of a protein- or membrane-bound fluorophore in the presence of the water-soluble quencher iodide, I<sup>-</sup>. As shown on the right-hand side of the figure, the emission intensity of a tryptophan on the protein's surface (W<sub>2</sub>), or on the surface of a cell membrane (P<sub>2</sub>, right), will be decreased in the presence of a water-soluble quencher. The intensity of a buried tryptophan residue (W<sub>1</sub>) or of a probe in the membrane interior (P<sub>1</sub>) will be less affected by the dissolved iodide (left). The iodide Stern-Volmer quenching constant  $K$  in eq. 1.6 will be larger for the exposed fluorophores than for the buried fluorophores. Alternatively, one can add lipid-soluble quenchers, such as brominated fatty acids, to study the interior acyl side chain region of membranes, by measurement from the extent of quenching by the lipid-soluble quencher.

### 1.9.3. Fluorescence Polarization or Anisotropy

As described in Section 1.5, fluorophores absorb light along a particular direction with respect to the molecular axes. For example, DPH only absorbs light polarized along its long axis (Figure 1.18). The extent to which a fluorophore rotates during the excited-state lifetime determines its polarization or anisotropy. The phenomenon of fluorescence polarization can be used to measure the apparent vol-

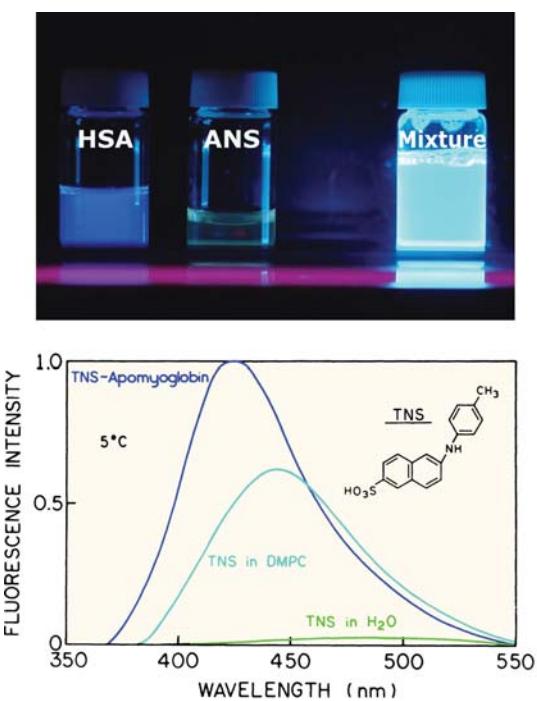


Figure 1.21. Emission spectra of TNS in water, bound to apomyoglobin, and bound to lipid vesicles.

ume (or molecular weight) of proteins. This measurement is possible because larger proteins rotate more slowly. Hence, if a protein binds to another protein, the rotational rate decreases, and the anisotropy(s) increases (Figure 1.23). The rotational rate of a molecule is often described by its rotational correlation time  $\theta$ , which is related to

$$\theta = \frac{\eta V}{RT} \quad (1.17)$$

where  $\eta$  is the viscosity,  $V$  is the molecular volume,  $R$  is the gas constant, and  $T$  is the temperature in °K. Suppose a protein is labeled with DNS-Cl (Figure 1.23). If the protein associates with another protein, the volume increases and so does the rotational correlation time. This causes the anisotropy to increase because of the relationship between the steady-state anisotropy  $r$  to the rotational correlation time  $\theta$  (eq. 1.10).

Fluorescence polarization measurements have also been used to determine the apparent viscosity of the side chain region (center) of membranes. Such measurements of microviscosity are typically performed using a hydrophobic probe like DPH (Figure 1.23), which partitions into the membrane. The viscosity of membranes is known to decrease in the presence of unsaturated fatty acid side

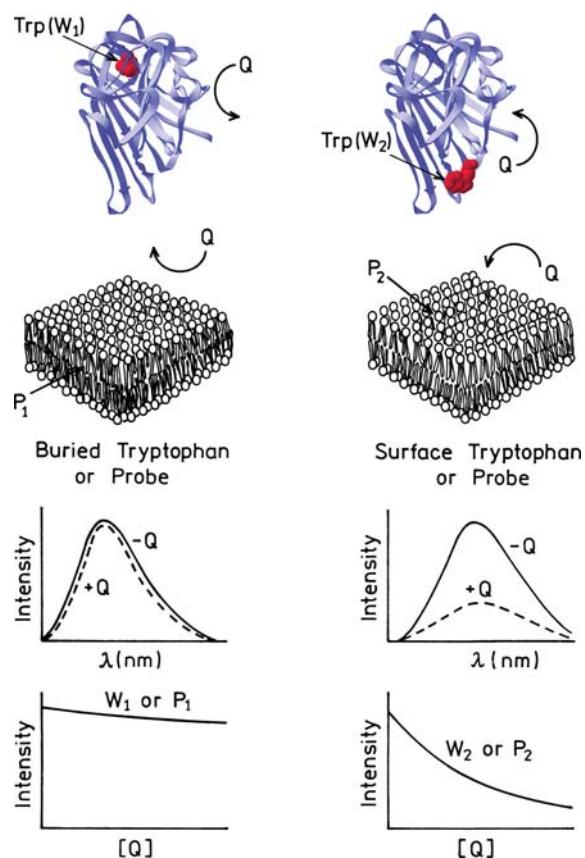


Figure 1.22. Accessibility of fluorophores to the quencher (Q). Reprinted with permission by Wiley-VCH, STM. From [21].

chains. Hence, an increase in the amount of unsaturated fatty acid is expected to decrease the anisotropy. The apparent microviscosity of the membrane is determined by comparing the polarization of the probe measured in the membrane with that observed in solutions of known viscosity.

Anisotropy measurements are widely used in biochemistry, and are even used for clinical immunoassays. One reason for this usage is the ease with which these absolute values can be measured and compared between laboratories.

#### 1.9.4. Resonance Energy Transfer

Resonance energy transfer (RET), sometimes called fluorescence resonance energy transfer (FRET), provides an opportunity to measure the distances between sites on macromolecules. Förster distances are typically in the range of 15 to 60 Å, which is comparable to the diameter of many proteins and to the thickness of membranes. According to eq. 1.12, the distance between a donor and acceptor can be calculated from the transfer efficiency.

The use of RET to measure protein association and distance is shown in Figure 1.24 for two monomers that associate to form a dimer. Suppose one monomer contains a tryptophan residue, and the other a dansyl group. The Förster distance is determined by the spectral overlap of the trp donor emission with the dansyl acceptor absorption. Upon association RET will occur, which decreases the intensity of the donor emission (Figure 1.24). The extent of donor quenching can be used to calculate the donor-to-acceptor distance in the dimer (eq. 1.12). It is also important to notice that RET provides a method to measure protein association because it occurs whenever the donor and acceptor are within the Förster distance.

### 1.10. BIOCHEMICAL EXAMPLES OF BASIC PHENOMENA

The uses of fluorescence in biochemistry can be illustrated by several simple examples. The emission spectra of proteins are often sensitive to protein structure. This sensitivity is illustrated by melittin,<sup>23</sup> which is a 26-amino-acid peptide containing a single tryptophan residue. Depending upon the solution conditions, melittin can exist as a monomer or self-associate to form a tetramer. When this occurs the tryptophan emission maximum shifts to shorter wavelengths (Figure 1.25). These spectra show that a protein association reaction can be followed in dilute solution using simple measurements of the emission spectra.

Association reactions can also be followed by anisotropy measurements. Figure 1.26 shows anisotropy measurements of melittin upon addition of calmodulin.<sup>24</sup> Calmodulin does not contain any tryptophan, so the total tryptophan emission is only due to melittin. Upon addition of calmodulin the melittin anisotropy increases about twofold. This effect is due to slower rotational diffusion of the melittin–calmodulin complex as compared to melittin alone. The emission spectra of melittin show that the tryptophan residue becomes shielded from the solvent upon binding to calmodulin. The tryptophan residue is probably located at the interface between the two proteins.

Resonance energy transfer can also be used to study DNA hybridization.<sup>25</sup> Figure 1.27 shows complementary DNA oligomers labeled with either fluorescein (Fl) or rhodamine (Rh). Hybridization results in increased RET from fluorescein to rhodamine, and decreased fluorescein intensities (lower panel). Disassociation of the oligomers results in less RET and increased fluorescein intensities. The extent of hybridization can be followed by simple intensity measurements.

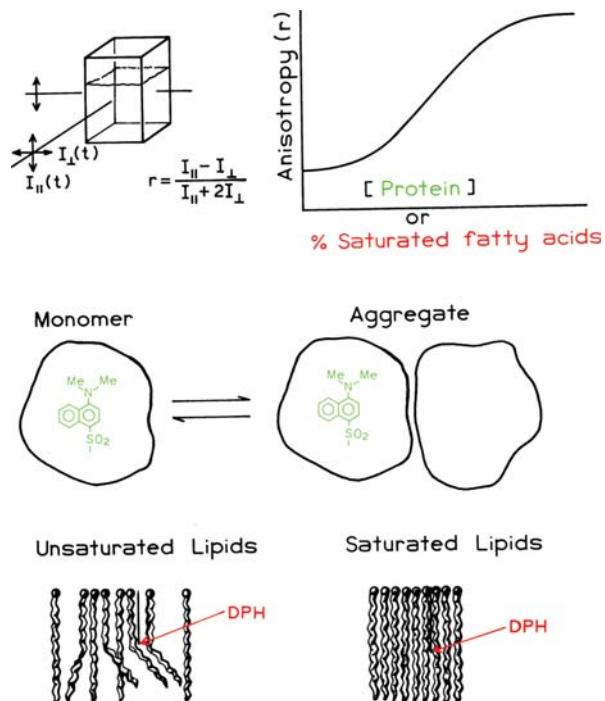


**Figure 1.23.** Effect of protein association and membrane microviscosity on the fluorescence anisotropy. From [21].

RET can also be used to study gene expression. One approach is to use donor- and acceptor-labeled DNA oligomers (Figure 1.28). If a complementary mRNA is present, the oligomers can bind close to each other.<sup>26</sup> The RET will result in increased emission intensity from the acceptor. The lower panels show fluorescence microscopy images of human dermal fibroblasts. The cells on the left were not stimulated and did not produce the K-ras gene product. The cells on the right were stimulated to cause expression of the K-ras oncogene. Mutations in the gene are associated with human colorectal cancer.<sup>27</sup> The images show the emission intensity of the acceptor. Significant acceptor intensity is only found in the stimulated cells where the mRNA for K-ras is present. RET is now widely used in cellular imaging to detect many types of gene expression and the intracellular proximity of biomolecules.

### 1.11. NEW FLUORESCENCE TECHNOLOGIES

#### 1.11.1. Multiphoton Excitation

During the past several years technological advances have provided new uses of fluorescence. These technologies have been quickly adopted and are becoming mainstream methods. One of these technologies is two-photon or multi-

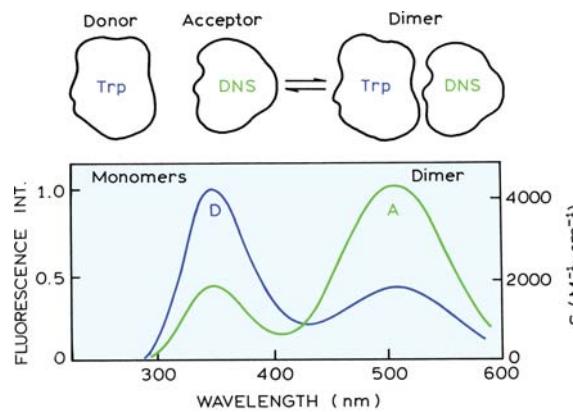


**Figure 1.24.** Energy transfer between donor- (D) and acceptor- (A) labeled monomers, which associate to form a dimer. In this case the donor is tryptophan and the acceptor DNS.

photon excitation and multiphoton microscopy.<sup>28–30</sup> Fluorescence is usually excited by absorption of a single photon with a wavelength within the absorption band of the fluorophore. Pulse lasers with femtosecond pulse widths can excite fluorophores by two-photon absorption. Such lasers have become easy to use and available with microscopes. If the laser intensity is high, a fluorophore can simultaneously absorb two long-wavelength photons to reach the first singlet state (Figure 1.29). This process depends strongly on the light intensity and occurs only at the focal point of the laser beam. This can be seen in the photo, where emission is occurring only from a single spot within the sample. Fluorophores outside the focal volume are not excited.

Localized excitation from two-photon excitation has found widespread use in fluorescence microscopy. Multiphoton excitations allow imaging from only the focal plane of a microscope. This is an advantage because fluorescence

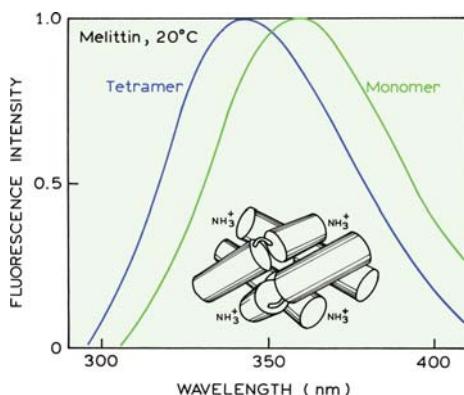


**Figure 1.25.** Emission spectra of melittin monomer and tetramer. Excitation was at 295 nm. In the schematic structure, the tryptophans are located in the center between the four helices. From [23].

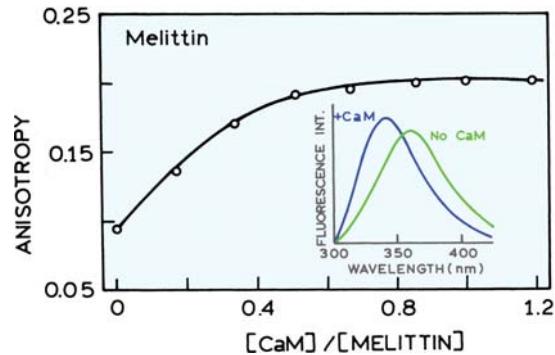


**Figure 1.26.** Effect of melittin–calmodulin association on the anisotropy of melittin. **Inset:** Emission spectra of melittin in the presence and absence of calmodulin (CaM). Modified from [24].

images are otherwise distorted from fluorescence from above and below the focal plane. Figure 1.30 shows an example of the remarkably sharp images obtainable with multiphoton excitation. The cells were labeled with three probes: DAPI for DNA, Patman for membranes, and tetramethylrhodamine for mitochondria. A single excitation wavelength of 780 nm was used. This wavelength does not excite any of the fluorophores by one-photon absorption, but 780 nm is absorbed by all these fluorophores through a multiphoton process. The images are sharp because there is no actual phase fluorescence that decreases the contrast in non-confocal fluorescence microscopy. Such images are now being obtained in many laboratories.

### 1.11.2. Fluorescence Correlation Spectroscopy

Fluorescence correlation spectroscopy (FCS) has rapidly become a widely used tool to study a wide range of association reactions.<sup>31</sup> FCS is based on the temporal fluctuations occurring in a small observed volume. Femtoliter volumes can be obtained with localized multiphoton excitation or using confocal optics (Figure 1.31, top). Bursts of photons are seen as single fluorophores diffuse in and out of the laser beam. The method is highly sensitive since only a few fluorophores are observed at one time. In fact, FCS cannot be performed if the solution is too concentrated and there are many fluorophores in the observed volume. Less fluorophores result in more fluctuations, and more fluorophores result in smaller fluctuations and a more constant average signal.

FCS is performed by observing the intensity fluctuations with time (Figure 1.31, middle panel). The rate of fluctuation depends on the rate of fluorophore diffusion. The intensity increases and decreases more rapidly if the

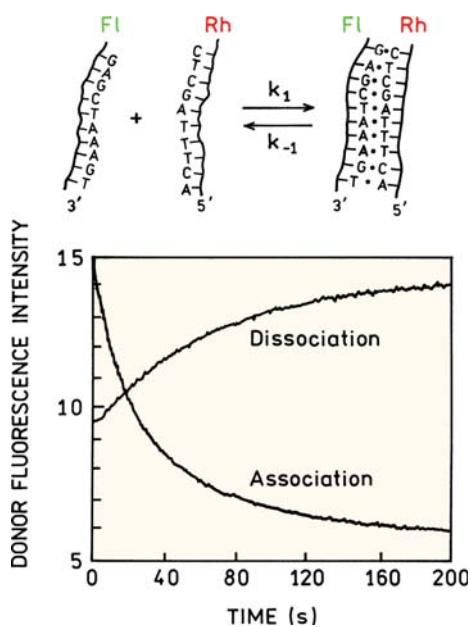


**Figure 1.27.** DNA hybridization measured by RET between fluorescein (Fl) and rhodamine (Rh). The lower panel shows the fluorescein donor intensities. Revised from [25].

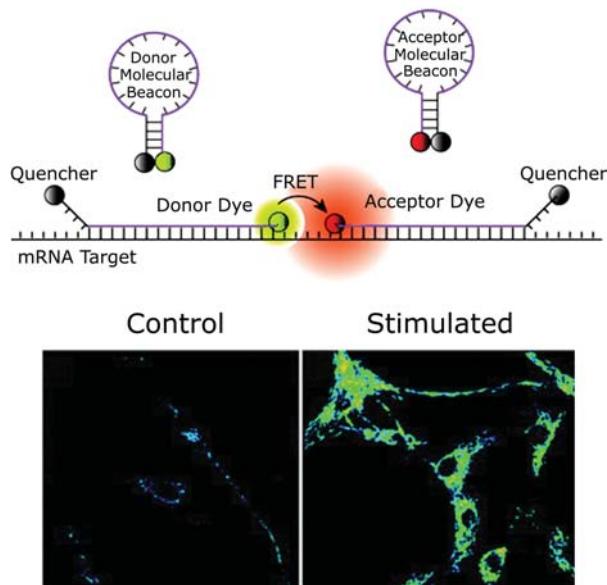


**Figure 1.28.** Detection of mRNA with RET and molecular beacons. The lower panels show acceptor intensity images of control cells and stimulated fibroblasts expressing the K-ras gene. Revised from [26].

fluorophores diffuse rapidly. If the fluorophores diffuse slowly they remain in the observed volume for a longer period of time and the intensity fluctuations occur more slowly. The amplitude and speed of the fluctuations are used to calculate the correlation function (lower panel). The height of the curve is inversely proportional to the average

number of fluorophores being observed. The position of the curve on the time axis indicates the fluorophore's diffusion coefficient.

Figure 1.32 shows how FCS can be used to study ligand and bindings to a single neuronal cell. The ligand was an Alexa-labeled benzodiazepine.<sup>32</sup> Benzodiazepines are used to treat anxiety and other disorders. FCS curves are shown for Alexa-Bz in solution and when bound to its receptor. The receptors were present on the membrane of a single neuronal cell where the laser beam was focused. The FCS curve clearly shows binding of Alexa-Bz to the receptor by a 50-fold increase in the diffusion time. Such measurements can be performed rapidly with high sensitivity. FCS will be used increasingly in drug discovery and biotechnology, as well as biochemistry and biophysics.

### 1.11.3. Single-Molecule Detection

Observations on single molecules represent the highest obtainable sensitivity. Single-molecule detection (SMD) is now being performed in many laboratories.<sup>33–34</sup> At present

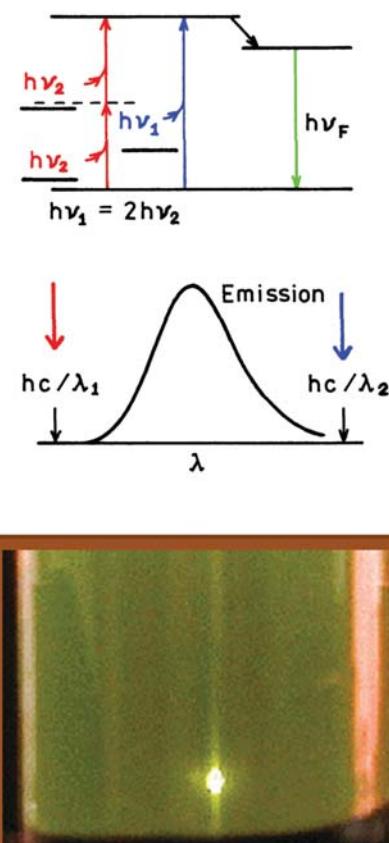


**Figure 1.29.** Jablonski diagram for two-photon excitation. The photo shows localized excitation at the focal point of the laser beam.

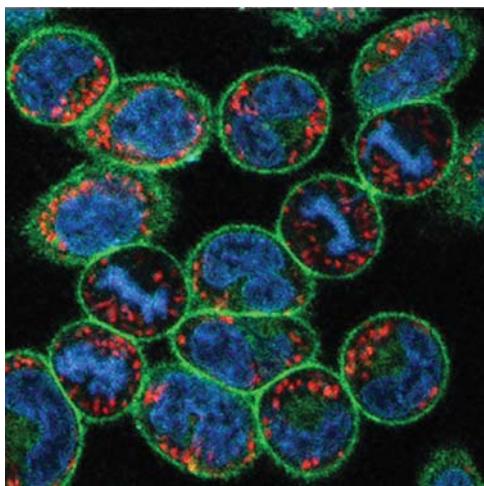


**Figure 1.30.** Fluorescence image of RBL-3H3 cells stained with DAPI (blue), Patman (green), and tetramethylrhodamine (red). Courtesy of Dr. W. Zipfel and Dr. W. Webb, Cornell University. Reprinted with permission from [30].

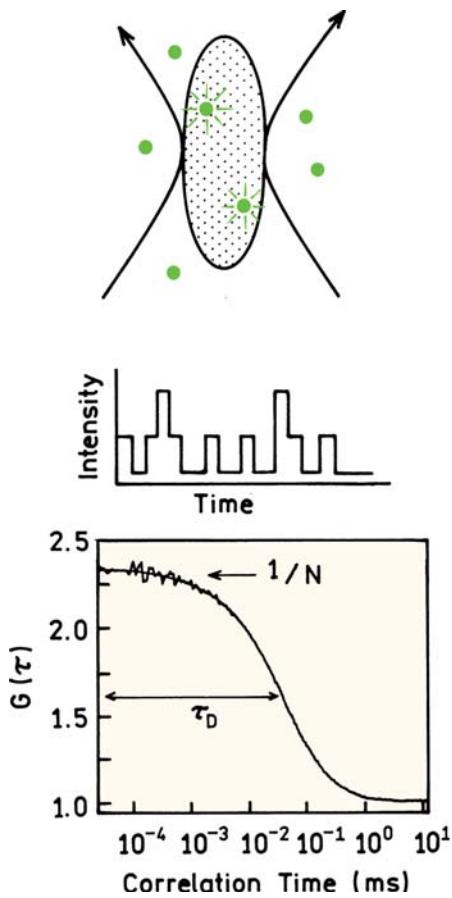


**Figure 1.31.** Fluorescence correlation spectroscopy. **Top:** observed volume shown as a shaded area. **Middle:** intensity fluctuations. **Bottom:** correlation function.

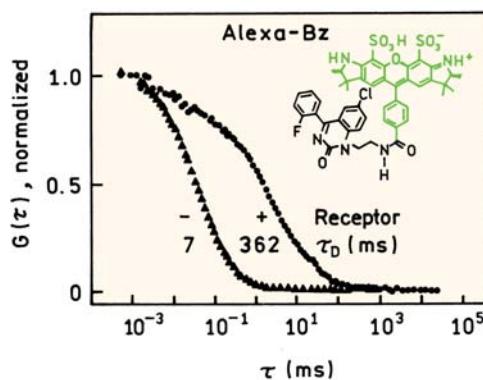


**Figure 1.32.** FCS of an Alexa-labeled benzodiazepine (Alexa-Bz) in solution and on a single neuronal cell. Revised from [32].

most single-molecule experiments are performed on immobilized fluorophores, with fluorophores chosen for their high quantum yields and photostability (Chapter 23). A typical instrument for SMD consists of laser excitation through microscope objective, a scanning stage to move the sample and confocal optics to reject unwanted signals. SMD is now being extended to include UV-absorbing fluorophores, which was considered unlikely just a short time ago. The probe 2,2'-dimethyl-p-querterphenyl (DMQ) has an absorption maximum of 275 nm and an emission maximum of 350 nm. Figure 1.33 (left) shows intensity images of DMQ on a quartz cover slip.<sup>35</sup> The spots represent the individual DMQ molecules, which can yield signals as high as 70,000 photons per second. The technology for SMD has advanced so rapidly that the lifetimes of single molecules can also be measured at the same time the intensity images are being collected (right). The individual DMQ molecules all display lifetimes near 1.1 ns.

Without the use of SMD, almost all experiments observe a large number of molecules. These measurements reveal the ensemble average of the measured properties. When observing a single molecule there is no ensemble averaging, allowing for the behavior of a single molecule to be studied. Such an experiment is shown in Figure 1.34 for a hairpin ribozyme labeled with a donor and acceptor. Steady-state measurements on a solution of the labeled ribozyme would yield the average amount of energy transfer, but would not reveal the presence of subpopulations showing different amounts of energy transfer. Single-molecule experiments show that an individual ribozyme molecule fluctuates between conformations with lower or higher amounts of energy transfer.<sup>36</sup> These conformational changes are seen from simultaneous increases and decreases

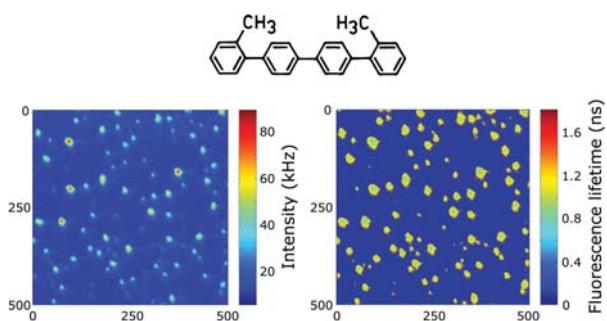


**Figure 1.33.** Single-molecule intensities and lifetimes of DMQ in a quartz slide. Excitation at 266 nm. Figure courtesy of Dr. S. Seeger, University of Zürich. Reprinted with permission from [35].

es in donor and acceptor emission. The single-molecule experiments also reveal the rate of the conformational changes. Such detailed information is not available from ensemble measurements.

At present single-molecule experiments are mostly performed using cleaned surfaces to minimize background. However, SMD can be extended to intracellular molecules if they are not diffusing too rapidly. One such experiment is detection of single molecules of the oncogen product Ras within cells.<sup>37</sup> Ras was labeled with yellow fluorescent pro-

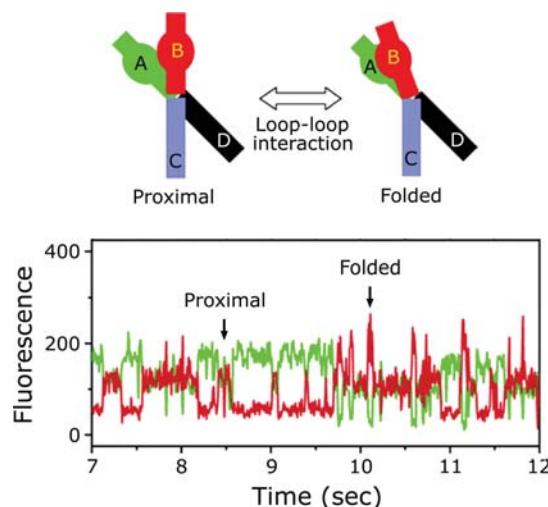


**Figure 1.34.** Single-molecule RET between a donor (green) and acceptor (red) on a hairpin ribozyme. Revised from [36].

tein (YFP). Upon activation Ras binds GTP (Figure 1.35). In this experiment activated Ras binds GTP labeled with a fluorophore called Bodipy TR. Single molecules of YFP-Ras were imaged on a plasma membrane (lower left). Upon activation of Ras, fluorescent red spots appeared that were

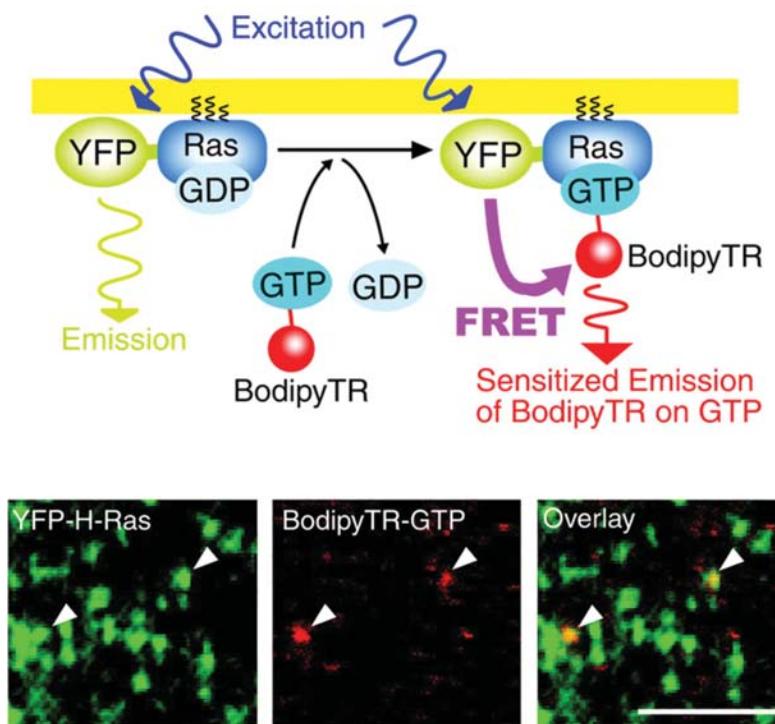


**Figure 1.35.** Binding of Bodipy TR-labeled GTP to activated YFP-Ras. The lower panels show single-molecule images of YFP-Ras and Bodipy TR-labeled GTP. The overlay of both images shows the location of activated Ras from the plasma membrane of KB cells. Bar = 5 μm. Revised from [37].

due to binding of Bodipy TR-GTP. The regions where emission from both YFP and Bodipy TR is observed corresponds to single copies of the activated Ras protein.

## 1.12. OVERVIEW OF FLUORESCENCE SPECTROSCOPY

Fluorescence spectroscopy can be applied to a wide range of problems in the chemical and biological sciences. The measurements can provide information on a wide range of molecular processes, including the interactions of solvent molecules with fluorophores, rotational diffusion of biomolecules, distances between sites on biomolecules, conformational changes, and binding interactions. The usefulness of fluorescence is being expanded by advances in technology for cellular imaging and single-molecule detection. These advances in fluorescence technology are decreasing the cost and complexity of previously complex instruments. Fluorescence spectroscopy will continue to contribute to rapid advances in biology, biotechnology and nanotechnology.

## REFERENCES

- Herschel, Sir JFW. 1845. On a case of superficial colour presented by a homogeneous liquid internally colourless. *Phil Trans Roy Soc (London)* **135**:143–145.
- Gillispie CC, ed. 1972. John Frederick William Herschel. In *Dictionary of scientific biography*, Vol. 6, pp. 323–328. Charles Scribner's Sons, New York.
- Undenfriend S. 1995. Development of the spectrophotofluorometer and its commercialization. *Protein Sci* **4**:542–551.
- Martin BR, Richardson F. 1979. Lanthanides as probes for calcium in biological systems. *Quart Rev Biophys* **12**:181–203.
- Berlman IB. 1971. *Handbook of fluorescence spectra of aromatic molecules*, 2nd ed. Academic Press, New York.
- Jablonski A. 1935. Über den Mechanismus des Photolumineszenz von Farbstoffphosphoren, *Z Phys* **94**:38–46.
- Szudy J, ed. 1998. *Born 100 years ago: Aleksander Jablonski (1898–1980)*, Uniwersytet Mikołaja Kopernika, Toruń, Poland.
- Acta Physica Polonica. 1978. Polska Akademia Nauk Instytut Fizyki. *Europhys J*, Vol. A65(6).
- Stokes GG. 1852. On the change of refrangibility of light. *Phil Trans R Soc (London)* **142**:463–562.
- Kasha M. 1950. Characterization of electronic transitions in complex molecules. *Disc Faraday Soc* **9**:14–19.
- Courtesy of Dr. Ignacy Gryczynski.
- Birks JB. 1970. *Photophysics of aromatic molecules*. John Wiley & Sons, New York.
- Lakowicz JR, Balter A. 1982. Analysis of excited state processes by phase-modulation fluorescence spectroscopy. *Biophys Chem* **16**:117–132.
- Photo courtesy of Dr. Ignacy Gryczynski and Dr. Zygmunt Gryczynski.
- Birks JB. 1973. *Organic molecular photophysics*. John Wiley & Sons, New York.
- Strickler SJ, Berg RA. 1962. Relationship between absorption intensity and fluorescence lifetime of molecules. *J Chem Phys* **37**(4):814–822.
- See [12], p. 120.
- Berberan-Santos MN. 2001. Pioneering contributions of Jean and Francis Perrin to molecular luminescence. In *New trends in fluorescence spectroscopy: applications to chemical and life sciences*, Vol. 18, pp. 7–33. Ed B Valeur, J-C Brochon. Springer, New York.
- Förster Th. 1948. Intermolecular energy migration and fluorescence (Transl RS Knox). *Ann Phys (Leipzig)* **2**:55–75.
- Stryer L. 1978. Fluorescence energy transfer as a spectroscopic ruler. *Annu Rev Biochem* **47**:819–846.
- Lakowicz JR. 1995. Fluorescence spectroscopy of biomolecules. In *Encyclopedia of molecular biology and molecular medicine*, pp. 294–306. Ed RA Meyers. VCH Publishers, New York.
- Haugland RP. 2002. LIVE/DEAD BacLight bacterial viability kits. In *Handbook of fluorescent probes and research products*, 9th ed., pp. 626–628. Ed J Gregory. Molecular Probes, Eugene, OR.
- Gryczynski I, Lakowicz JR. Unpublished observations.
- Lakowicz JR, Gryczynski I, Laczkó G, Wiczko W, Johnson ML. 1994. Distribution of distances between the tryptophan and the N-terminal residue of melittin in its complex with calmodulin, troponin, C, and phospholipids. *Protein Sci* **3**:628–637.
- Morrison LE, Stols LM. 1993. Sensitive fluorescence-based thermodynamic and kinetic measurements of DNA hybridization in solution. *Biochemistry* **32**:3095–3104.
- Santangelo PJ, Nix B, Tsourkas A, Bao G. 2004. Dual FRET molecular beacons for mRNA detection in living cells. *Nucleic Acids Res* **32**(6):e57.
- Alberts B, Johnson A, Lewis J, Raff M, Roberts K, Walter P. 2002. *Molecular biology of the cell*, 4th ed. Garland Science, New York.
- Diaspro A, ed. 2002. *Confocal and two-photon microscopy, foundations, applications, and advances*. Wiley-Liss, New York.
- Masters BR, Thompson BJ, eds. 2003. *Selected papers on multiphoton excitation microscopy*. SPIE Optical Engineering Press, Bellingham, Washington.
- Zipfel WR, Williams RM, Webb WW. 2003. Nonlinear magic: multiphoton microscopy in the biosciences. *Nature Biotechnol* **21**(11):1369–1377.
- Rigler R, Elson ES. 2001. *Fluorescence correlation spectroscopy*. Springer, Berlin.
- Hegener O, Jordan R, Häberlein H. 2004. Dye-labeled benzodiazepines: development of small ligands for receptor binding studies using fluorescence correlation spectroscopy. *J Med Chem* **47**:3600–3605.
- Rigler R, Orrit M, Basché T. 2001. *Single molecule spectroscopy*. Springer, Berlin.
- Zander Ch, Enderlein J, Keller RA, eds. 2002. *Single molecule detection in solution, methods and applications*. Wiley-VCH, Darmstadt, Germany.
- Li Q, Ruckstuhl T, Seeger S. 2004. Deep-UV laser-based fluorescence lifetime imaging microscopy of single molecules. *J Phys Chem B* **108**:8324–8329.
- Ha T. 2004. Structural dynamics and processing of nucleic acids revealed by single-molecule spectroscopy. *Biochemistry* **43**(14):4055–4063.
- Murakoshi H, Iino R, Kobayashi T, Fujiwara T, Ohshima C, Yoshimura A, Kusumi A. 2004. Single-molecule imaging analysis of Ras activation in living cells. *Proc Natl Acad Sci USA* **101**(19):7317–7322.
- Kasha M. 1960. Paths of molecular excitation. *Radiation Res* **2**:243–275.
- Hagag N, Birnbaum ER, Darnall DW. 1983. Resonance energy transfer between cysteine-34, tryptophan-214, and tyrosine-411 of human serum albumin. *Biochemistry* **22**:2420–2427.
- O'Neil KT, Wolfe HR, Erickson-Viitanen S, DeGrado WF. 1987. Fluorescence properties of calmodulin-binding peptides reflect alpha-helical periodicity. *Science* **236**:1454–1456.
- Johnson DA, Leathers VL, Martinez A-M, Walsh DA, Fletcher WH. 1993. Fluorescence resonance energy transfer within a heterochromatic cAMP-dependent protein kinase holoenzyme under equilibri-

um conditions: new insights into the conformational changes that result in cAMP-dependent activation. *Biochemistry* **32**:6402–6410.

*A glossary of mathematical terms and commonly used acronyms is located at the end of this volume.*

## PROBLEMS

- P1.1. *Estimation of Fluorescence and Phosphorescence Quantum Yields:* The quantum yield for fluorescence is determined by the radiative and non-radiative decay rates. The non-radiative rates are typically similar for fluorescence and phosphorescence states, but the emissive rates ( $\Gamma$ ) vary greatly. Emission spectra, lifetimes ( $\tau$ ) and quantum yields ( $Q$ ) for eosin and erythrosin B (ErB) are shown in Figure 1.13.
- Calculate the natural lifetime ( $\tau_n$ ) and the radiative and non-radiative decay rates of eosin and ErB. What rate accounts for the lower quantum yield of ErB?
  - Phosphorescence lifetimes are typically near 1–10 ms. Assume that the natural lifetime for phosphorescence emission of these compounds is 10 ms, and that the non-radiative decay rates of the two compounds are the same for the triplet state as for the singlet state. Estimate the phosphorescence quantum yields of eosin and ErB at room temperature.
- P1.2. *Estimation of Emission from the  $S_2$  State:* When excited to the second singlet state ( $S_2$ ) fluorophores typically relax to the first singlet state within  $10^{-13}$  s.<sup>38</sup> Using the radiative decay rate calculated for eosin (problem 1.1), estimate the quantum yield of the  $S_2$  state.
- P1.3. *Thermal Population of Vibrational Levels:* The emission spectrum of perylene (Figure 1.3) shows equally spaced peaks that are due to various vibrational states, as illustrated. Use the Boltzmann distribution to estimate the fraction of the ground-state molecules that are in the first vibrationally excited state at room temperature.
- P1.4. *Anisotropy of a Labeled Protein:* Naphthylamine sulfonic acids are widely used as extrinsic labels of proteins. A number of derivatives are available. One little known but particularly useful derivative is 2-diethylamino-5-naphthalenesulfonic acid (DENS), which displays a lifetime near 30 ns, longer than that of most similar molecules. Absorption and emission spectra of DENS are shown in Figure 1.36.
- Suppose the fundamental anisotropy of DENS is 0.30 and that DENS is bound to a protein with a rotational correlation time of 30 ns. What is the anisotropy?
  - Assume now that the protein is bound to an antibody with a molecular weight of 160,000 and a rotational correlation time of 100 ns. What is the anisotropy of the DENS-labeled protein?
- P1.5. *Effective Distance on the Efficiency of FRET:* Assume the presence of a single donor and acceptor and that the distance between them ( $r$ ) can be varied.

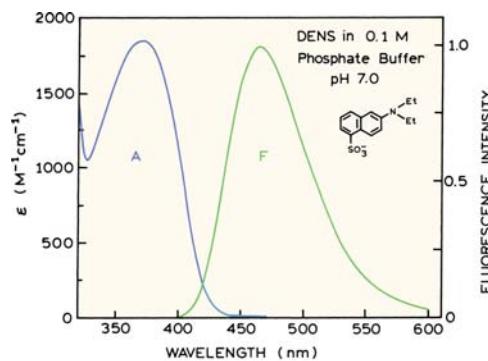


**Figure 1.36.** Absorption and emission spectra of DENS. The quantum yield relative to quinine sulfate is 0.84, and its lifetime is near 30 ns.

- Plot the dependence of the energy transfer efficiency on the distance between the donor and the acceptor.
  - What is the transfer efficiency when the donor and the acceptor are separated by  $0.5R_0$ ,  $R_0$ , and  $2R_0$ ?
- P1.6. *Calculation of a Distance from FRET Data:* The protein human serum albumin (HSA) has a single tryptophan residue at position 214. HSA was labeled with an anthraniloyl group placed covalently on cysteine-34.<sup>39</sup> Emission spectra of the labeled and unlabeled HSA are shown in Figure 1.37. The Förster distance for Trp to anthraniloyl transfer is 30.3 Å. Use the emission spectra in Figure 1.37 to calculate the Trp to anthraniloyl distance.
- P1.7. *Interpretation of Tryptophan Fluorescence from a Peptide:* Figure 1.38 shows a summary of spectral data for a peptide from myosin light-chain kinase (MLCK). This peptide contained a single tryptophan residue, which was placed at positions 1 through 16 in the peptide. This peptide binds to the hydrophobic patch of calmodulin. Explain the changes in emission maxima, Stern-Volmer quenching constant for acrylamide ( $K$ ), and anisotropy ( $r$ ).

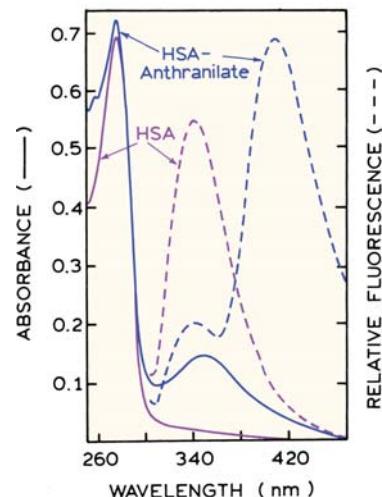


**Figure 1.37.** Absorption and fluorescence spectra of human serum albumin (HSA) and anthraniloyl-HSA. From [39].

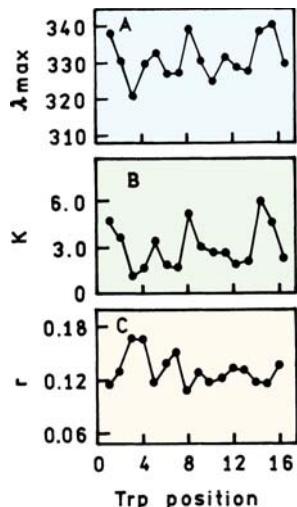


**Figure 1.38.** Dependence of the emission maxima (A), acrylamide quenching constants (B), and steady-state anisotropies (C) of MLCK peptides bound to calmodulin on the position of tryptophan residue. Reprinted, with permission, from [40]. (O'Neil KT, Wolfe HR, Erickson-Vitanen S, DeGrado WF. 1987. Fluorescence properties of calmodulin-binding peptides reflect alpha-helical periodicity. *Science* **236**:1454–1456, Copyright © 1987, American Association for the Advancement of Science.)

P1.8. *Interpretation of Resonance Energy Transfer Between Protein Subunits:* Figure 1.39 shows emission spectra of fluorescein (Fl) and rhodamine (Rh) when covalently attached to the catalytic (C) or regulator (R) subunit of a cAMP-dependent protein kinase (PK).<sup>41</sup> When the subunits are associated, RET occurs from Fl to Rh. The associated form is C<sub>2</sub>R<sub>2</sub>. Figure 1.40 shows emission spectra of both subunits without any additives, in the presence of cAMP, and in the presence of protein kinase inhibitor (PKI). Suggest an interpretation of these spectra. Your interpretation should be consistent with the data, but it may not be the only possible interpretation.

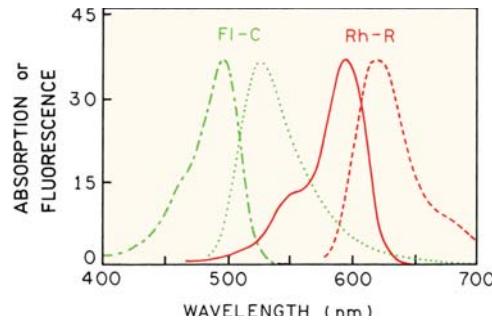


**Figure 1.39.** Spectral overlap of the fluorescein-labeled catalytic subunit (Fl-C) and the Texas red-labeled regulator subunit (Rh-R) of a cAMP-dependent protein kinase. Revised and reprinted with permission from [41]. (Copyright © 1993, American Chemical Society.)

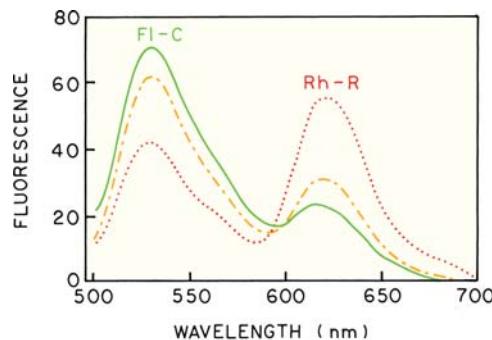


**Figure 1.40.** Effect of cAMP and the protein kinase inhibitor on the emission spectra of the donor and acceptor labeled holoenzyme. Emission spectra are shown without cAMP or PK (●●●●), and the following addition of cAMP (—●—●—), and PKI (—). Revised and reprinted with permission from [41]. (Copyright © 1993, American Chemical Society.)

# 2

# Instrumentation for Fluorescence Spectroscopy

The success of fluorescence experiments requires attention to experimental details and an understanding of the instrumentation. There are also many potential artifacts that can distort the data. Light can be detected with high sensitivity. As a result, the gain or amplification of instruments can usually be increased to obtain observable signals, even if the sample is nearly nonfluorescent. These signals seen at high amplification may not originate with the fluorophore of interest. Instead, the interference can be due to background fluorescence from the solvents, light leaks in the instrumentation, emission from the optical components, stray light passing through the optics, light scattered by turbid solutions, and Rayleigh and/or Raman scatter, to name a few interference sources.

An additional complication is that there is no ideal spectrofluorometer. The available instruments do not yield true excitation or emission spectra. This is because of the nonuniform spectral output of the light sources and the wavelength-dependent efficiency of the monochromators and detector tubes. The polarization or anisotropy of the emitted light can also affect the measured fluorescence intensities because the efficiency of gratings depends on polarization. It is important to understand and control these numerous factors. In this chapter we will discuss the properties of the individual components in a spectrofluorometer, and how these properties affect the observed spectral data. These instrumental factors can affect the excitation and emission spectra, as well as the measurement of fluorescence lifetimes and anisotropies. Additionally, the optical properties of the samples—such as optical density and turbidity—can also affect the spectral data. Specific examples are given to clarify these effects and the means to avoid them.

## 2.1. SPECTROFLUOROMETERS

### 2.1.1. Spectrofluorometers for Spectroscopy Research

With most spectrofluorometers it is possible to record both excitation and emission spectra. An emission spectrum is the wavelength distribution of an emission measured at a single constant excitation wavelength. Conversely, an excitation spectrum is the dependence of emission intensity, measured at a single emission wavelength, upon scanning the excitation wavelength. Such spectra can be presented on either a wavelength scale or a wavenumber scale. Light of a given energy can be described in terms of its wavelength  $\lambda$ , frequency  $v$ , or wavenumber. The usual units for wavelength are nanometers, and wavenumbers are given in units of  $\text{cm}^{-1}$ . Wavelengths and wavenumbers are easily interconverted by taking the reciprocal of each value. For example, 400 nm corresponds to  $(400 \times 10^{-7} \text{ cm})^{-1} = 25,000 \text{ cm}^{-1}$ . The presentation of fluorescence spectra on the wavelength or wavenumber scale has been a subject of debate. Admittedly, the wavenumber scale is linear in energy. However, most commercially available instrumentation yields spectra on the wavelength scale, and such spectra are more familiar and thus easier to interpret visually. Since corrected spectra are not needed on a routine basis, and since accurately corrected spectra are difficult to obtain, we prefer to use the directly recorded technical or uncorrected spectra on the wavelength scale.

For an ideal instrument, the directly recorded emission spectra would represent the photon emission rate or power emitted at each wavelength, over a wavelength interval determined by the slit widths and dispersion of the emission

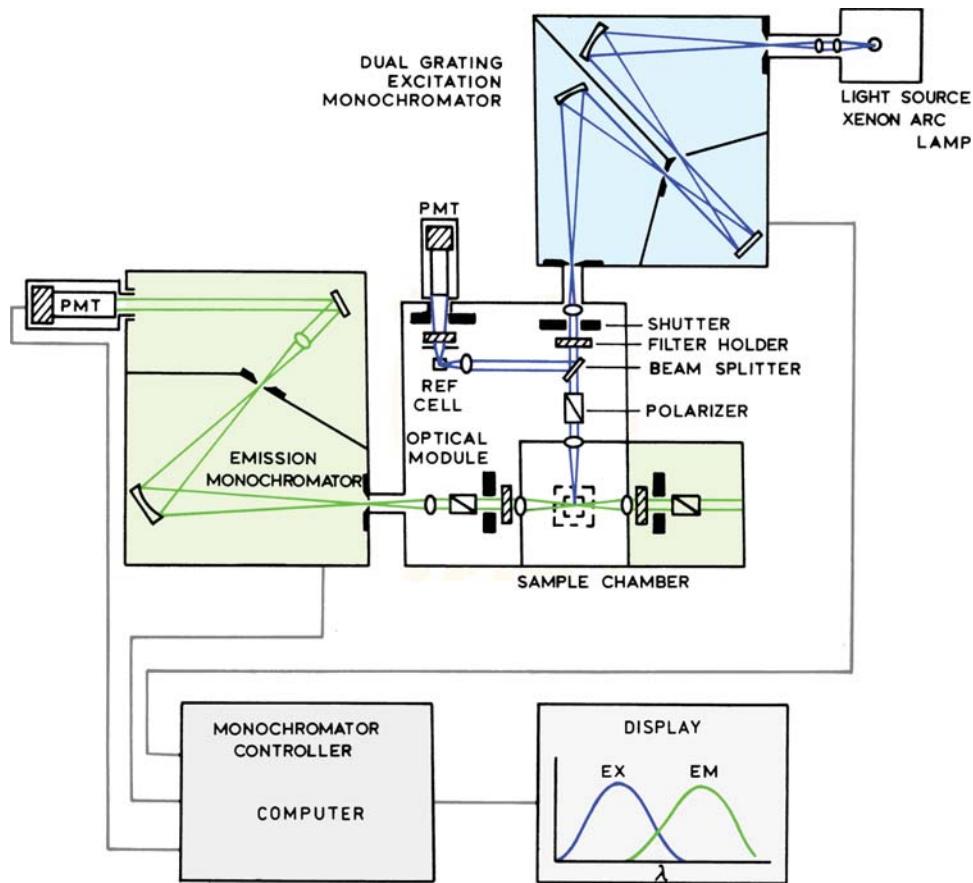


Figure 2.1. Schematic diagram of a spectrofluorometer [1].

monochromator. Similarly, the excitation spectrum would represent the relative emission of the fluorophore at each excitation wavelength. For most fluorophores the quantum yields and emission spectra are independent of excitation wavelength. As a result, the excitation spectrum of a fluorophore can be superimposable on its absorption spectrum. However, such identical absorption and excitation spectra are rarely observed because the excitation intensity is different at each wavelength. Even under ideal circumstances such correspondence of the excitation and absorption spectra requires the presence of only a single type of fluorophore, and the absence of other complicating factors, such as a nonlinear response resulting from a high optical density of the sample or the presence of other chromophores in the sample. Emission spectra recorded on different instruments can be different because of the wavelength-dependent sensitivities of the instruments.

Figure 2.1 shows a schematic diagram of a general-purpose spectrofluorometer: this instrument has a xenon

lamp as a source of exciting light. Such lamps are generally useful because of their high intensity at all wavelengths ranging upward from 250 nm. The instrument shown is equipped with monochromators to select both the excitation and emission wavelengths. The excitation monochromator in this schematic contains two gratings, which decreases stray light, that is, light with wavelengths different from the chosen one. In addition, these monochromators use concave gratings, produced by holographic means to further decrease stray light. In subsequent sections of this chapter we will discuss light sources, detectors and the importance of spectral purity to minimize interference due to stray light. Both monochromators are motorized to allow automatic scanning of wavelength. The fluorescence is detected with photomultiplier tubes and quantified with the appropriate electronic devices. The output is usually presented in graphical form and stored digitally.

The instrument schematic also shows the components of the optical module that surrounds the sample holder. Ver-

satile and stable optical components are indispensable for a research spectrofluorometer. The module shown in Figure 2.1 contains a number of convenient features that are useful on a research instrument. Shutters are provided to eliminate the exciting light or to close off the emission channel. A beam splitter is provided in the excitation light path. This splitter reflects part of the excitation light to a reference cell, which generally contains a stable reference fluorophore. The beam splitter consists of a thin piece of clear quartz, which reflects about 4% of the incident light. This amount is generally adequate for a reference channel that frequently contains a highly fluorescent quantum counter (Section 2.8.1). The intensity from the standard solution is typically isolated with a bandpass filter, and is proportional to the intensity of the exciting light. Changes in the intensity of the arc lamp may be corrected for by division of the intensity from the sample by that of the reference fluorophore.

Polarizers are present in both the excitation and emission light paths. Generally, the polarizers are removable so that they can be inserted only for measurements of fluorescence anisotropy, or when it is necessary to select for particular polarized components of the emission and/or excitation. Accurate measurement of fluorescence anisotropies requires accurate angular positioning of the polarizers. The polarizer mounts must be accurately indexed to determine the angular orientation. The optical module shown in Figure 2.1 has an additional optical path on the right side of the sample holder. This path allows measurement of fluorescence anisotropy by the T-format method (Chapter 10). There are many occasions where the additional light path is necessary or convenient for experiments, but with modern electronics it is usually not necessary to use the T-format for anisotropy measurements.

The present trend is toward small compact spectrofluorometers, with all the optical components in a single enclosure. Such instruments are easy to maintain because there is little opportunity to alter the configuration. A modular instrument has some advantages in a spectroscopy laboratory. For instance, if the xenon lamp and monochromator are removable, a laser source can be used in place of the arc lamp. On some occasions it is desirable to bypass the emission monochromator and use bandpass filters to collect as much of the emission as possible. Such experiments are possible if the emission monochromator is removable. If the monochromator cannot be removed the gratings can act like mirrors if set at the zero-order diffraction or a wavelength of zero. If the wavelength is set to zero the monochromator

typically transmits all wavelengths. Filters can be used to isolate the desired range of wavelengths.

It is convenient if the instrument has a versatile sample holder. If the research involves anisotropy measurements it will often be necessary to measure the fundamental anisotropy ( $r_0$ ) in the absence of rotational diffusion. This is accomplished at low temperature, typically  $-50^\circ\text{C}$  in glycerol. Low temperature can only be achieved if the sample holder is adequately sized for a high rate of coolant flow, has good thermal contact with the cuvette, and is insulated from the rest of the instrument. Many cuvette holders can maintain a temperature near room temperature, but may not be able to maintain a temperature much above or below that.

Another useful feature is the ability to place optical filters into the excitation or emission light path. Filters are often needed, in addition to monochromators, to remove unwanted wavelengths in the excitation beam, or to remove scattered light from the emission channel.

### 2.1.2. Spectrofluorometers for High Throughput

At present the design of fluorescence experiments is changing toward a multi-sample approach. Instead of detailed experiments on a single sample, the experiments are designed to include many samples. Such experiments can include binding studies, quenching, and cell-based assays. High-throughput screening assays are used in drug discovery, often using numerous microplates, each with 384 or more wells. Such measurements are typically performed using microplate readers (Figure 2.2). The samples are contained in the wells of the microplates, which are taken inside the instrument for the measurements. Such an instrument may not provide the detailed information available using an instrument designed for spectroscopy (Figure 2.1) but can rapidly provide measurements on numerous samples.

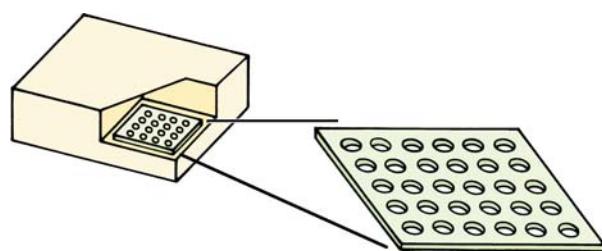


**Figure 2.2.** Fluorescence microplate reader.

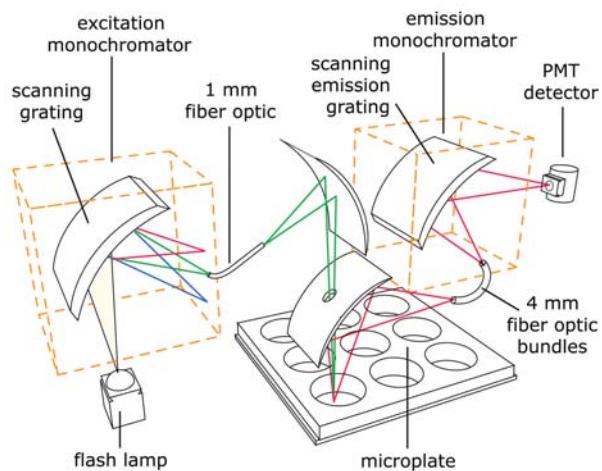


**Figure 2.3.** Optical path for a microplate reader [2].

The optics used in microplate readers are different than in an instrument designed for use with a cuvette. Microwell plates must remain horizontal, and it is not possible to use right-angle observation as can be used with a cuvette. Figure 2.3 shows a typical optical path for microplate readers. The light source is a xenon flash lamp, which is becoming more common in fluorescence instruments. The desired excitation wavelength is selected using a monochromator. A unique feature is the mirror with a hole to transmit the excitation. The fluorescence, which occurs in all directions, is directed toward the detector optics by the same mirror. Typically, the microplate is moved to position each well in the observation path by an  $x$ - $y$  scanning stage. Some microplate readers include a second mirror under the microplate to facilitate cell-based assays or absorption measurements. Microplate readers are typically used for intensity measurements on a large number of samples. Microplate readers have become available for research spectrofluorometers allowing collection of spectra, anisotropies, and lifetimes.

### 2.1.3. An Ideal Spectrofluorometer

In an ideal case the recorded excitation and emission spectra would represent the relative photon intensity per wavelength interval. To obtain such "corrected" emission spectra the individual components must have the following characteristics:

1. the light source must yield a constant photon output at all wavelengths;
2. the monochromator must pass photons of all wavelengths with equal efficiency;

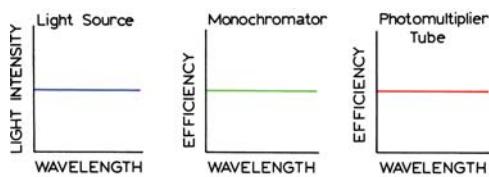


**Figure 2.4.** Properties of the ideal components of a spectrofluorometer.

3. the monochromator efficiency must be independent of polarization; and
4. the detector (photomultiplier tube) must detect photons of all wavelengths with equal efficiency.

These characteristics for ideal optical components are illustrated in Figure 2.4. Unfortunately, light sources, monochromators, and photomultiplier tubes with such ideal characteristics are not available. As a result, one is forced to compromise on the selection of components and to correct for the nonideal response of the instrument.

An absorption spectrophotometer contains these same components, so why is it possible to record correct absorption spectra? In recording an absorption spectrum the intensity of light transmitted by the sample is measured relative to that transmitted by the blank. Comparative measurements are performed with the same components, at the same wavelengths. The nonideal behavior of the components cancels in the comparative measurements. In contrast to absorption measurements, fluorescence intensity measurements are absolute, not relative. Comparison of the sample fluorescence with a blank is not useful because the blank, in principle, displays no signal. Also, the weak background signal has an unknown spectral distribution, and thus cannot be used for correction of the wavelength dependence of the optical components. Hence, the opportunity for internal compensation is limited. As will be described below, a limited number of standard spectra are available for correction purposes. Corrected emission spectra are provided in Appendix I.

### 2.1.4. Distortions in Excitation and Emission Spectra

To record an excitation spectrum, the emission monochromator is set at the desired wavelength, generally the emission maximum. The excitation monochromator is then scanned through the absorption bands of the fluorophore. The observed signal is distorted for several reasons:

1. The light intensity from the excitation source is a function of wavelength. Even if the intensity of the exciting light is monitored via the beam splitter shown in Figure 2.1, and corrected by division, the response of the reference solution or detector may be dependent upon wavelength.
2. The transmission efficiency of the excitation monochromators is a function of wavelength.
3. The optical density of the sample may exceed the linear range, which is about 0.1 absorbance units, depending upon sample geometry.

Emission spectra are recorded by choosing an appropriate excitation wavelength and scanning wavelength with the emission monochromator. In addition to the factors discussed above, the emission spectrum is further distorted by the wavelength-dependent efficiency of the emission monochromator and photomultiplier. The emission spectrum can also be distorted by absorption of the sample.

## 2.2. LIGHT SOURCES

We now describe the individual components of a spectrofluorometer. The general characteristics of these components are considered along with the reason for choosing specific components. Understanding the characteristics of these components allows one to understand the capabilities and limitations of spectrofluorometers. We will first consider light sources.

### 2.2.1. Arc and Incandescent Xenon Lamps

At present the most versatile light source for a steady-state spectrofluorometer is a high-pressure xenon (Xe) arc lamp. These lamps provide a relatively continuous light output from 250 to 700 nm (Figure 2.5), with a number of sharp lines occurring near 450 nm and above 800 nm. Xenon arc lamps emit a continuum of light as a result of recombination of electrons with ionized Xe atoms. These ions are generated by collisions of Xe atoms with the electrons that flow across the arc. Complete separation of the electrons from the atoms yields the continuous emission. Xe atoms that are in excited states but not ionized yield lines rather than broad emission bands. The peaks near 450 nm are due to these excited states. The output intensity drops rapidly below 280 nm. Furthermore, many Xe lamps are classified as being ozone-free, meaning that their operation does not generate

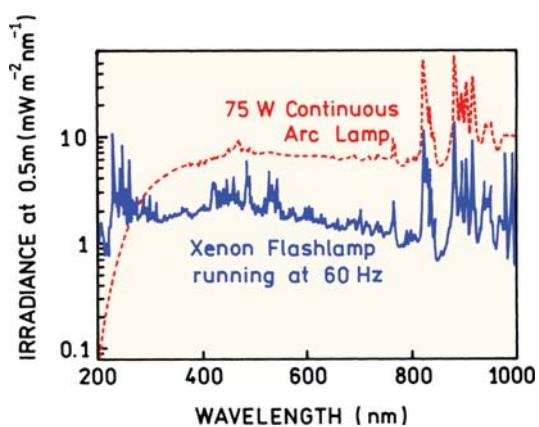


**Figure 2.5.** Spectral output of a continuous xenon arc lamp and a xenon flash lamp. Revised from [3]. Courtesy of Newport Corp.

ozone in the surrounding air. The quartz envelope used in such ozone-free lamps does not transmit light with wavelengths shorter than 250 nm, and the output of such lamps decreases rapidly with decreasing wavelength.

The wavelength-dependent output of Xe lamps is a major reason for distortion of the excitation spectra of compounds that absorb in the visible and ultraviolet. To illustrate this effect Figure 2.6 shows corrected and uncorrected excitation fluorescein spectra. The uncorrected spectra are recorded emission intensities with no correction for wavelength-dependent excitation intensity. The uncorrected excitation spectrum displays a number of peaks near 450 nm. These peaks are due to the output of the Xe lamp, which also displays peaks near 450 nm (Figure 2.5). Also shown in Figure 2.6 is the excitation spectrum, corrected for the wavelength-dependent output of the Xe arc lamp. A

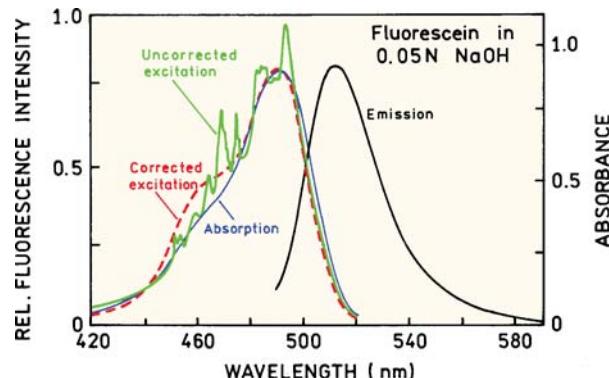


**Figure 2.6.** Corrected and uncorrected excitation spectra of fluorescein. From [4].

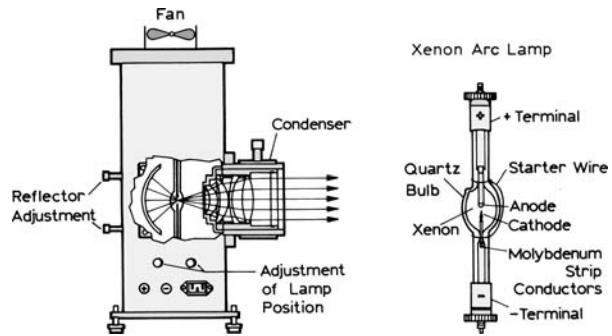


**Figure 2.7.** Xenon air lamp and a typical lamp housing. Revised from [5]. Courtesy of Newport Corp.

quantum counter was used in the reference channel to provide a signal proportional to the lamp intensity, and the intensity of the sample was divided by this reference intensity (Section 2.8.1). The peaks are no longer apparent in the corrected excitation spectrum, and this spectrum corresponds more closely with the absorption spectrum of fluorescein. The marked difference between the corrected and uncorrected spectra illustrates how the spectral output of the lamp influences the shape of the excitation spectra.

Xenon lamps are usually contained within specially designed housings. The arc lamp housing serves several important functions (Figure 2.7). The gas in xenon lamps is under high pressure (about 10 atmospheres), and explosion is always a danger. The housing protects the user from the lamp and also from its intense optical output. The housing also directs air over the lamp and removes excess heat and ozone. A xenon lamp that is on should never be observed directly. The extreme brightness will damage the retina, and the ultraviolet light can damage the cornea.

Another important role of the housing is for collecting and collimating lamp output, which is then focused into the entrance slit of the monochromator. Some lamp houses have mirrors behind the lamp to direct additional energy toward the output. Most of the light output originates from the small central region between the electrodes, and this spot needs to be focused on the optical entrance slit of the excitation monochromator.

Because of the heat and high intensity of a running xenon lamp, it is not practical to adjust the position of an uncovered lamp. Hence the lamp housing should have external provisions for position adjustment and focusing. The useful life of a xenon lamp is about 2000 hours. Safety glasses should be worn when handling these lamps. The

quartz envelope should not be touched, and if touched should be cleaned with a solvent such as ethanol. The fingerprint residues will char, resulting in hot spots on the quartz envelope and possible lamp failure. To protect the next person handling the disposed lamp, one should wrap the lamp in heavy paper and break the quartz envelope. It is important to pay close attention to mounting lamps in the proper orientation, which can be different for different types of lamps.

The power supplies of arc lamps are extremely dangerous, generating 25 amps at 20 volts, for a typical 450-watt lamp. Starting the lamps requires high-voltage pulses of 20 to 40 kV. This voltage can penetrate the skin, and the following high current could be lethal. Starting of xenon lamps can damage nearby sensitive electronics. The high-voltage starting pulse can destroy sensitive amplifiers or confuse computers. If possible, it is preferable to start a lamp first, and then turn on other electronic devices.

Xenon arc lamps have become more compact (Figure 2.8). These lamps typically have the arc within a parabolic reflector, which collects a large solid angle and provides a collimated output.<sup>6</sup> In addition to improved light collection efficiency, these lamps are compact, and as a result are found in commercial spectrofluorometers.

When using a xenon arc lamp it is important to remember the lamps emit a large amount of infrared radiation, extending beyond the wavelength range of Figure 2.5. Because of the infrared output, the lamp output cannot be passed directly through most optical filters. The filter will heat and/or crack, and the samples will be heated. When passed through a monochromator the optical components and housing serve as a heat sink. If the xenon lamp output is to be used directly, one should use a heat filter made of heat-resistant glass, which absorbs the infrared.

## 2.2.2. Pulsed Xenon Lamps

At present compact fluorometers and plate readers often use xenon flash lamps. The output of a xenon flash lamp is more structured than a continuous lamp (Figure 2.5). The output of a flash lamp is higher in the UV. The output intensities in Figure 2.5 are the time-averaged output of the lamp. The peak intensity of the pulses is usually higher than that of the continuous arcs. The flash lamps consume less power and generate less heat. In some cases the lack of continuous excitation can minimize photodamage to the sample.

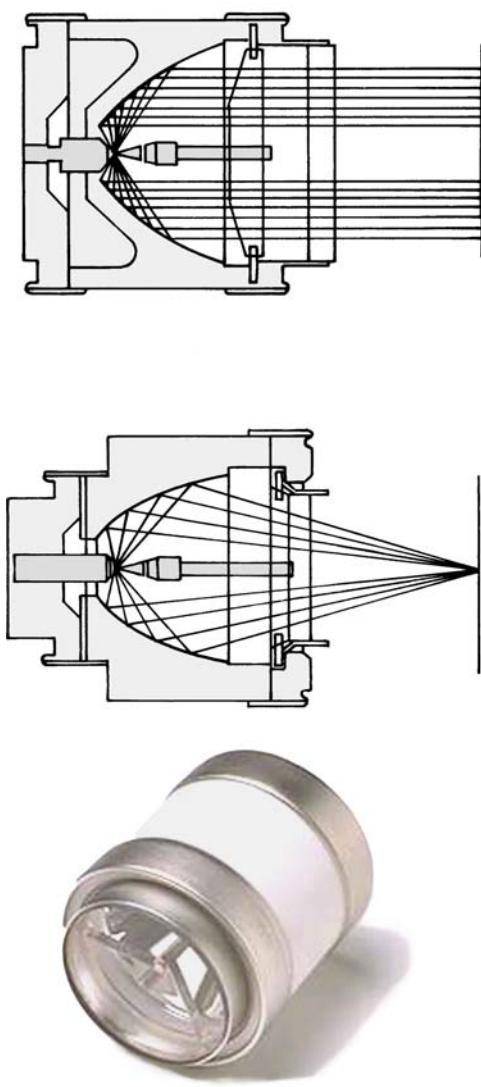


**Figure 2.8.** Compact xenon arc lamps. Reprinted from Cermax lamp engineering guide.

### 2.2.3. High-Pressure Mercury (Hg) Lamps

In general Hg lamps have higher intensities than Xe lamps, but the intensity is concentrated in lines. It is usually better to choose the excitation wavelengths to suit the fluorophore, rather than vice versa. These lamps are only useful if the Hg lines are at suitable wavelengths for excitation.

### 2.2.4. Xe–Hg Arc Lamps

High-pressure mercury–xenon lamps are also available. These have higher intensities in the ultraviolet than Xe lamps, and the presence of Xe tends to broaden the spectral

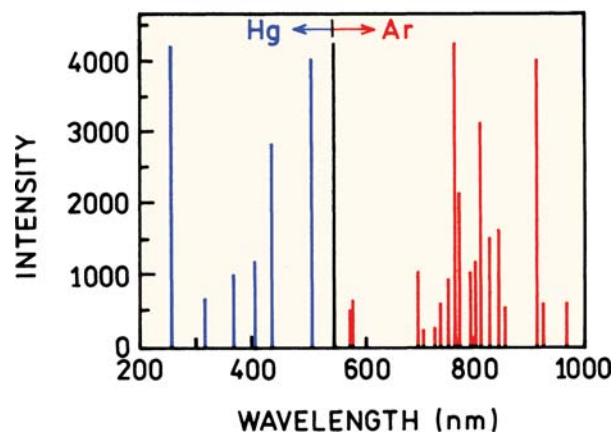


**Figure 2.9.** Spectral output of a low pressure mercury–argon lamp. Revised from [7]. Courtesy of Ocean Optics Inc.

output. The output of these lamps is dominated by the Hg lines. The Hg–Xe lamp has slightly more output between the Hg lines. When first started the Hg–Xe lamp output is due mostly to Xe. As the lamp reaches operating temperature all the Hg becomes vaporized, and the Hg output increases.

### 2.2.5. Quartz–Tungsten Halogen (QTH) Lamps

These lamps provide continuous output in the visible and IR regions of the spectrum. Previously such lamps were not useful for fluorescence because they have low output below 400 nm, and are thus not useful for excitation of UV absorbing fluorophores. However, there is presently increasing interest in fluorophores absorbing in the red and near infrared (NIR), where the output of a QTH lamp is significant.

### 2.2.6. Low-Pressure Hg and Hg–Ar Lamps

These lamps yield very sharp line spectra that are useful primarily for calibration purposes (Figure 2.9). Previously the lamps contained only mercury. Some lamps now contain both mercury and argon. The mercury lines are below 600 nm and the argon lines are above 600 nm (Table 2.1). The use of these lamps for wavelength calibration is described in Section 2.3.5.

### 2.2.7. LED Light Sources

LEDs are just beginning to be used as light sources in spectrofluorometers.<sup>8–9</sup> A wide range of wavelengths are available with LEDs (Figure 2.10, see also Figure 4.13). In order

**Table 2.1.** Strong Emission Lines from a Mercury–Argon Calibration Source<sup>a</sup>

Mercury lines (nm)			Argon lines (nm)	
253.7	404.7	696.5	763.5	842.5
296.7	407.8	706.7	772.4	852.1
302.2	435.8	710.7	794.8	866.8
313.2	546.1	727.3	800.6	912.3
334.1	577.0	738.0	811.5	922.6
365.0	579.1	750.4	826.5	

<sup>a</sup>Data from [7].

to obtain a wide range of wavelengths an array of LEDs can be used.<sup>8</sup> LEDs can be placed close to the samples, and if needed the excitation wavelength can be defined better by the use of an excitation filter. Unlike a xenon lamp, LEDs do not generate significant infrared, so that an additional heat filter is not needed. There are ongoing efforts to develop white LEDs, which are already found in LED flashlights. These LEDs contain phosphors to provide a wider range of wavelengths.<sup>9</sup> LEDs have the advantage of long life and low power consumption. The use of LEDs as an excitation source is likely to broaden in the near future.

### 2.2.8. Laser Diodes

Another light source is the laser diode. In contrast to LEDs, laser diodes emit monochromatic radiation. Laser diodes are available with wavelengths ranging from about 405 to 1500 nm. Laser diodes are convenient because the output is easily focused and manipulated. In contrast to arc lamps or incandescent lamps, the output of LEDs and laser diodes can be pulsed or modulated. LEDs can be amplitude modulated up to about 100 MHz, and laser diodes can be modulated to several GHz. The use of these light sources

for time-resolved measurements is described in Chapters 4 and 5.

### 2.3. MONOCHROMATORS

Monochromators are used to disperse polychromatic or white light into the various colors or wavelengths. This dispersion can be accomplished using prisms or diffraction gratings. The monochromators in most spectrofluorometers use diffraction gratings rather than prisms. The performance specifications of a monochromator include dispersion, efficiency, and stray light levels. Dispersion is usually given in nm/mm. The slit width is sometimes expressed in mm, which requires knowledge of the dispersion. A monochromator for fluorescence spectroscopy should have low stray light levels to avoid problems due to scattered or stray light. By stray light we mean light transmitted by the monochromator at wavelengths outside the chosen wavelength and bandpass. Monochromators are also chosen for high efficiency to maximize the ability to detect low light levels. Resolution is usually of secondary importance since emission spectra rarely have peaks with line widths less than 5 nm. The slit widths are generally variable, and a typical monochromator will have both an entrance and exit slit. The light intensity that passes through a monochromator is approximately proportional to the square of the slit width. Larger slit widths yield increased signal levels, and therefore higher signal-to-noise ratios. Smaller slit widths yield higher resolution, but at the expense of light intensity. If the entrance slit of the excitation monochromator is already wide enough to accept the focused image of the arc, then the intensity will not be increased significantly with a wider slit width. If photobleaching of the sample is a problem, this factor can sometimes be minimized by decreasing the excitation intensity. Gentle stirring of the sample can also minimize photobleaching. This is because only a fraction of the sample is illuminated and the bleached portion of the sample is continuously replaced by fresh solution.

Monochromators can have planar or concave gratings (Figure 2.11). Planar gratings are usually produced mechanically. Concave gratings are usually produced by holographic and photoresist methods. Imperfections of the gratings are a source of stray light transmission by the monochromators, and of ghost images from the grating. Ghost images can sometimes be seen within an open monochromator as diffuse spots of white light on the inside surfaces. Monochromators sometimes contain light blocks to intercept these ghost images. Monochromators based on

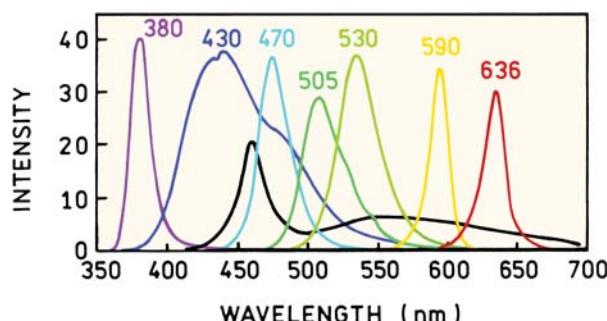


**Figure 2.10.** Spectral output of light-emitting diodes [8]. The black line shows the output of a white LED [7].

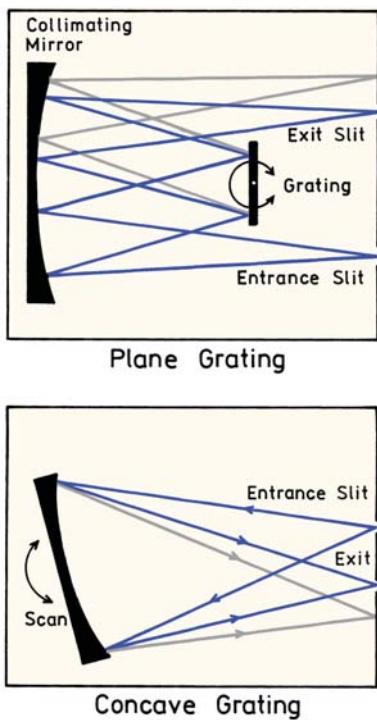


**Figure 2.11.** Monochromators based on a plane (top) or concave (bottom) grating. Revised from [7].

concave gratings can have fewer reflecting surfaces, lower stray light, and can be more efficient. A concave grating can serve as both the diffraction and focusing element, resulting on one instead of three reflecting surfaces. For these reasons the holographic gratings are usually preferable for fluorescence spectroscopy.

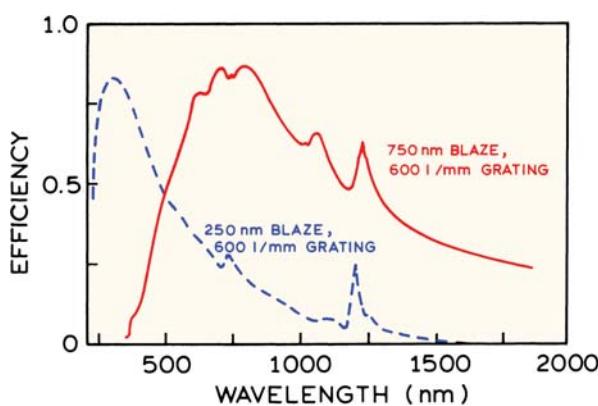


**Figure 2.12.** Efficiency of two RULED grating blazed for different wavelengths. Redrawn from [5]. Courtesy of Newport Corp.

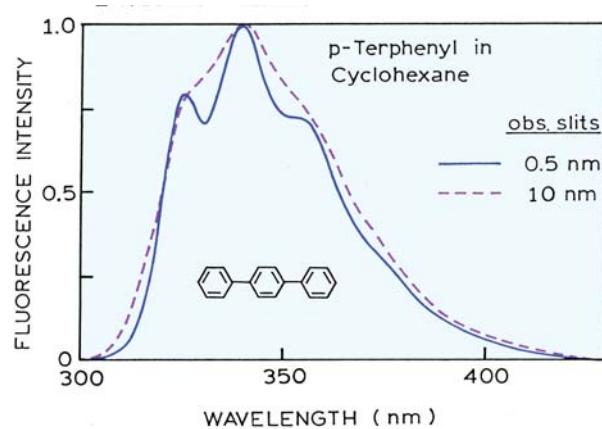


**Figure 2.13.** Emission spectra of p-terphenyl collected with a spectral resolution of 0.5 and 10 nm. From [10].

The transmission efficiency of a grating and monochromator is dependent on wavelength and on the design of the grating. Examples are shown in Figures 2.12 and 2.13. For a mechanically produced plane grating the efficiency at any given wavelength can be maximized by choice of blaze angle, which is determined by the shape and angle of the tool used to produce the grating. By choice of this angle one may obtain maximum diffraction efficiency for a given wavelength region, but the efficiency is less at other wavelengths. For the examples shown in Figure 2.12 the efficiency was optimized for 250 or 750 nm. Generally, the excitation monochromator is chosen for high efficiency in the ultraviolet and an emission monochromator for high efficiency at visible wavelengths.

### 2.3.1. Wavelength Resolution and Emission Spectra

The emission spectra of most fluorophores are rather broad and devoid of structure. Hence, the observed emission spectra are typically independent of spectral resolution. For fluorophores that display structured emission, it is important to maintain adequate wavelength resolution, which is adjusted by the slit widths on the monochromator. Emission spectra of p-terphenyl are shown in Figure 2.13. They display vibrational structure when recorded with a resolution of 0.5 nm. However, this structure is nearly lost when the resolution is 10 nm. Although not important for steady-state measurements, the transit time through a monochromator can depend on wavelength (Section 4.6.5).

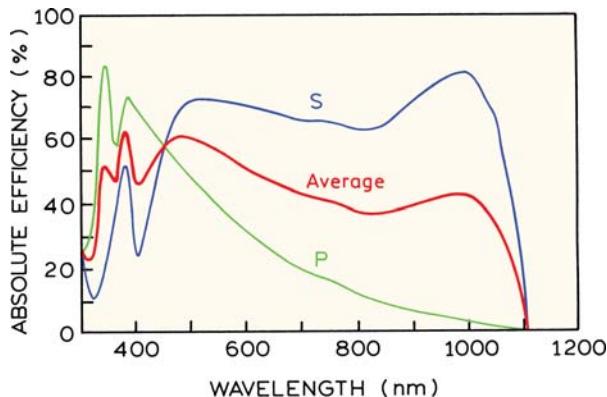


**Figure 2.14.** Grating efficiency for a 1800 line/mm holographic grating, optimized for the UV. The bold line is the average, and the other lines are for differently (S and P) polarized light, defined in Figure 2.39. Redrawn from [11].

### 2.3.2. Polarization Characteristics of Monochromators

For a grating monochromator the transmission efficiency depends upon the polarization of the light. This is illustrated in Figure 2.14 for a concave grating. For this reason, the observed fluorescence intensities can be dependent upon the polarization displayed by the fluorescence emission. The emission spectrum can be shifted in wavelength and altered in shape, depending upon the polarization conditions chosen to record the emission spectrum. For example, consider an emission spectrum recorded with the grating shown in Figure 2.14, and through a polarizer oriented vertically ( $\parallel$ ) or horizontally ( $\perp$ ). Assume that the dotted transmission curve corresponds to vertically polarized light. The spectrum recorded through the vertically oriented polarizer would appear shifted to shorter wavelengths relative to that recorded with the polarizer in the horizontal position. This is because the transmission efficiency for vertically polarized light is higher at shorter wavelengths. This spectral shift would be observed irrespective of whether its emission was polarized or not polarized.

The polarization properties of concave gratings can have a dramatic effect on the appearance of emission spectra. This is shown in Figure 2.15 for a probe bound to DNA. The emission spectrum shows a dramatic decrease near 630 nm when the emission polarizer is in the horizontal position. This drop is not seen when the emission polarizer is in a vertical orientation. In addition to this unusual dip in the spectrum, the emission maximum appears to be different for each polarizer orientation. These effects are due to the polarization properties of this particular grating, which dis-

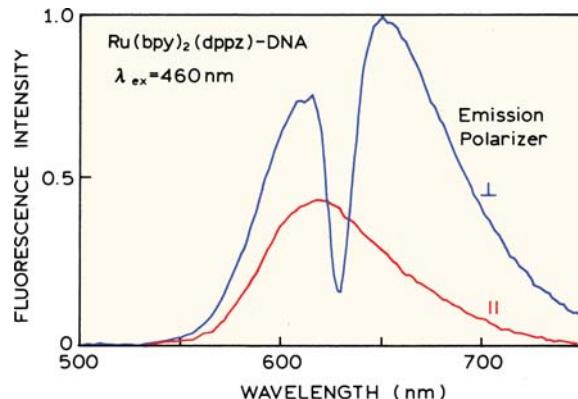


**Figure 2.15.** Emission spectra of  $[\text{Ru}(\text{bpy})_2(\text{dppz})]^{2+}$  bound to DNA. This probe is described in chapter 20. Excitation at 460 nm. Except for intensity, the same spectral distributions was observed for vertically as horizontally polarized excitation. From [12].

plays a minimum in efficiency at 630 nm for horizontally polarized light. Such effects are due to the emission monochromator, and are independent of the polarization of the excitation beam.

The polarization characteristics of monochromators have important consequences in the measurement of fluorescence anisotropy. Such measurements must be corrected for the varying efficiencies of each optical component. This correction is expressed as the G factor (Section 10.4). However, the extreme properties of the concave gratings (Figure 2.14) can cause difficulties in the measurement of fluorescence polarization. For example, assume that the polarization is to be measured at an excitation wavelength of 450 nm. The excitation intensities will be nearly equal with the excitation polarizers in each orientation, which makes it easier to compare the relative emission intensities. If the emission is unpolarized the relative intensities with parallel ( $\parallel$ ) and perpendicular ( $\perp$ ) excitation intensities will be nearly equal. However, suppose the excitation is at 340 nm, in which case the intensities of the polarized excitation will be very different. In this case it is more difficult to accurately measure the relative emission intensities because of the larger difference in the excitation intensities. Measurement of the G factor is generally performed using horizontally polarized light, and the intensity of this component would be low.

### 2.3.3. Stray Light in Monochromators

The stray light level of the monochromator is a critical parameter for fluorescence measurements. Stray light is

defined as any light that passes through the monochromator besides the desired wavelength. Consider the excitation monochromator. The entire output from the light source enters the monochromator. Ultraviolet wavelengths are frequently used for excitation, and the ultraviolet intensity may be 100-fold less than the visible output of the Xe lamp. Stray light at longer wavelengths can be passed by the excitation monochromator, and can easily be as intense as the fluorescence itself. Fluorescence intensities are frequently low, and many biological samples possess significant turbidity. The incident stray light at the emission wavelength can be scattered, and can interfere with measurements of the fluorescence intensity. For these reasons, double-grating monochromators are frequently used, especially for excitation. Stray light levels for such monochromators are frequently  $10^{-8}$  to  $10^{-12}$  of the peak intensities. However, double-grating monochromators are less efficient, and sensitivity must be sacrificed.

The stray light properties of the emission monochromator are also important. Generally, only a low percentage of the exciting light is absorbed by the fluorophores, and fluorescence quantum yields can be small. It is not unusual for the fluorescence signal to be 1000-fold less intense than the exciting light. Now consider a turbid suspension of membranes, from which we wish to observe the fluorescence of membrane-bound proteins. The excitation and emission wavelengths would be near 280 and 340 nm, respectively. Since the emission monochromator is imperfect, some of the scattered light at 280 nm can pass through the emission monochromator set at 340 nm. Assume that the emission monochromator, when set at 340 nm, discriminates against 280 nm by a factor of  $10^{-4}$ . The intensity of scattered light at 280 nm can easily be  $10^3$ -fold more intense than the fluorescence at 340 nm. Hence 10% of the "fluorescence" at 340 nm may actually be due to scattered exciting light at 280 nm. It is also important to recognize that scattered light is highly polarized, typically 100%. This means that the scattered light will contribute to the vertical intensity but not to the horizontal intensity. Stray scattered light can easily invalidate measurements of fluorescence anisotropy.

The stray light rejection of holographic gratings is superior to that of the mechanically produced ruled gratings. It appears that the passage of stray light depends upon imperfections in the gratings, resulting in ghost images which can escape from the monochromators. Fewer such images are present with the holographic gratings because

they are produced optically and have fewer imperfections. In addition, monochromators with holographic gratings generally have fewer reflecting surfaces within the monochromators (Figure 2.11). This is because the concave grating can also act as an imaging device, and thus additional concave mirrors are not required for focusing. With fewer reflecting surfaces there is a decreased probability of stray light escaping from the monochromator.

### 2.3.4. Second-Order Transmission in Monochromators

Another source of unwanted light is higher-order light diffraction by the monochromator. Light diffraction at the grating can occur as a first, second- or higher-order process. These diffraction orders frequently overlap (Figure 2.16). Suppose the excitation monochromator is set at 600 nm. The xenon light source contains output of both 300 and 600 nm. When the monochromator is set at 600 nm, some 300-nm light can be present at the exit slit due to second-order diffraction.

Transmission of second-order diffraction can also result in extraneous light passing through the emission monochromators. Suppose the excitation is at 300 nm and the emission monochromator is scanned through 600 nm. If the sample is strongly scattering, then some of the scattered light at 300 nm can appear as second-order diffraction when the emission monochromator is set to 600 nm. The emission spectrum from a turbid solution can have a peak at twice the excitation wavelength due to 2nd-order transmission through the emission monochromator. Bandpass excitation filters can be used to remove unwanted wavelengths from the excitation beam.

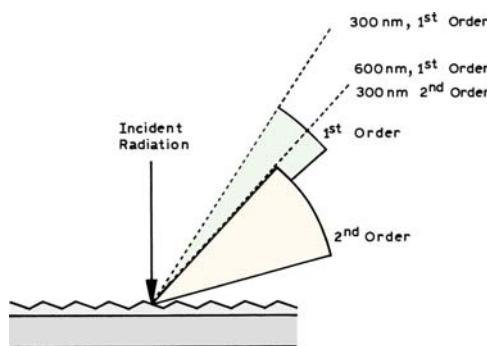


**Figure 2.16.** First- and second-order diffraction off a diffraction grating. The region where there is no overlap of the 1st- and 2nd-order diffraction is called the free spectral range.

### 2.3.5. Calibration of Monochromators

The wavelength calibration of monochromators should be checked periodically. Calibration can be performed using a low pressure mercury or mercury–argon lamp. These lamps are shaped like a cylinder, about 5 mm in diameter, and conveniently fit into the cuvette holder. These lamps provide a number of sharp lines that can be used for calibration (Figure 2.9). The lamp can be held stationary with a block of metal in which the lamp fits snugly. This holder is the same size as a cuvette. A pinhole on the side of this holder allows a small amount of the light to enter the emission monochromator. A small slit width is used to increase the precision of wavelength determination and to decrease light intensity. It is important to attenuate the light so that the photomultiplier tube and/or amplifiers are not damaged. Following these precautions, the dominant Hg lines are located using the emission monochromator. The measured wavelengths are compared with the known values, which are listed in Table 2.1. Since there are multiple Hg lines, it is necessary to observe three or more lines to be certain a line is assigned the correct wavelength. If the observed wavelengths differ from the known values by a constant amount, one recalibrates the monochromator to obtain coincidence. A more serious problem is encountered if the wavelength scale is nonlinear.

After calibration of the emission monochromator, the excitation monochromator can be calibrated against this new standard. The slits on both monochromators should be set to the same small value, consistent with the available light intensity. A dilute suspension of glycogen or Ludox is placed in the cuvette holder to scatter the exciting light. The emission monochromator is set to some arbitrary wavelength. If the excitation monochromator is properly calibrated, then the maximum intensity of the scattered light is seen when the indicated wavelengths are identical. The linearity of the wavelength scale can be determined by setting the emission monochromator at various wavelengths. One advantage of this procedure is that there is no need to remove the light source. The mercury light can be used in place of the xenon lamp to calibrate the excitation monochromator, but then the xenon lamp must be removed.

## 2.4. OPTICAL FILTERS

### 2.4.1. Colored Filters

While spectrofluorometers have monochromators for wavelength selection, it is often important to use optical filters in

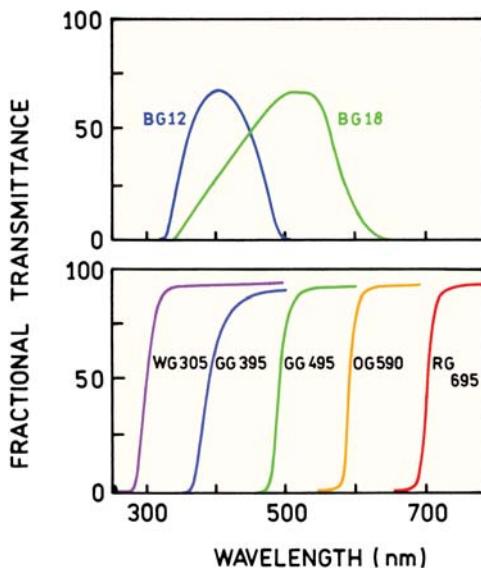


**Figure 2.17.** Transmission spectra of some typical colored glass filters. From [13].

addition to monochromators. Optical filters are used to compensate for the less-than-ideal behavior of monochromators. Also, when the spectral properties of a fluorophore are known, maximum sensitivity is often obtained using filters rather than monochromators. A large range of filters are available. The manufacturers typically provide the transmission spectra of the filters. Before the advances in thin film technology, most filters were colored-glass filters. Colored-glass filters can transmit a range of wavelengths (Figure 2.17, top). Some color filters are called long-pass filters and transmit all wavelengths above some particular wavelength (bottom). The names of the filters divide them into classes according to their colors (BG, blue glass, GG, green glass, etc.).

The transmission spectra shown in Figure 2.17 are visually pleasing but may not provide all the needed information. In turbid or dilute samples the scattered light can be orders of magnitude more intense than the fluorescence. This is also true for two-photon excitation when the excitation wavelength is longer than the emission wavelength. For these reasons transmission curves are often presented on a logarithm scale, which makes it possible to determine if the filter transmits 1% or much less than 1% of the light at any given wavelength (Figure 2.18). These curves also show transmission at longer wavelengths, where there may be interference from scattered light from the higher-order transmission of monochromators.

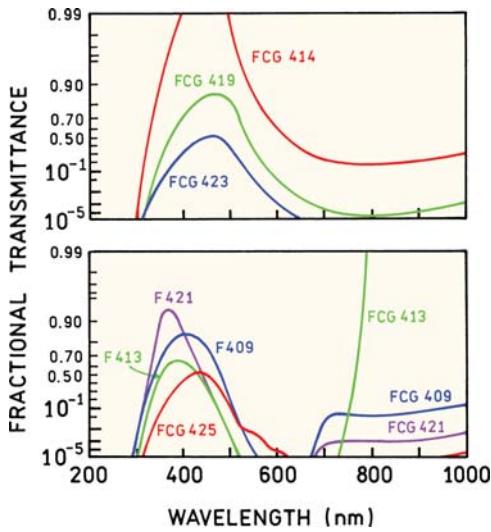


**Figure 2.18.** Transmission spectra of colored-glass filters. Top: in order of increasing wavelength FCG 414, 419, and 423. Bottom: FCG 409, 413, 421, and 425. From [13].

An important consideration in the use of bandpass filters is the possibility of emission from the filter itself. Many filters are luminescent when illuminated with UV light, which can be scattered from the sample. For this reason it is usually preferable to locate the filter further away from the sample, rather than directly against the sample. Glass filters of the type shown in Figures 2.17 and 2.18 are highly versatile, effective, and inexpensive, and a wide selection is needed in any fluorescence laboratory. Excitation and emission filters can be used in all experiments, even those using monochromators, to reduce the possibility of undesired wavelengths corrupting the data.

#### 2.4.2. Thin-Film Filters

A wide variety of colored-glass filters are available, but the transmission curves are not customized for any given application. During the past ten years there have been significant advances in the design of thin-film optical filters.<sup>14</sup> Almost any desired transmission curve can be obtained. Filters are now being designed for specific applications, rather than choosing the colored-glass filter that best suits an application. Long-pass filters are an example of this type filter (Figure 2.19). These filters have a sharp cut on the transmission above 325 nm or 488 nm, which are wavelengths available from a helium–cadmium or argon ion laser, respectively. The transmission above the cut-on wavelength is close to 100% to provide maximum sensitivity.

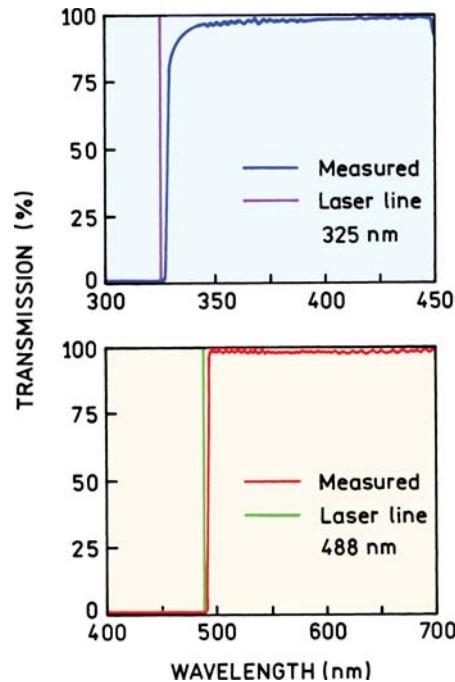


**Figure 2.19.** Long-pass filters designed to reject light from a helium–cadmium laser at 325 nm or an argon ion laser at 488 nm. Revised from [15].

Thin-film filters are also available to specifically transmit or reject laser lines. Laser light can contain additional wavelengths in addition to the main laser line. This emission is referred to as the plasma emission, which typically occurs over a range of wavelengths and is not strongly directional. The light can be made more monochromatic by passing the laser beam through a laser line filter, such as the one shown for a helium–neon laser at 633 nm (Figure 2.20). Alternatively, it may be necessary to eliminate scattered light at the laser wavelength. This can be accomplished with a notch filter which transmits all wavelengths except the laser wavelengths. These filters are sometimes called Raman notch filters because of their use in Raman spectroscopy.

Emission can usually be selected using a long-pass filter. However, there may be additional emission at longer wavelengths, such as the acceptor emission in an energy transfer experiment. In these cases it is useful to have a filter that transmits a selected range of wavelengths or auto-fluorescence from the sample. Figure 2.21 shows examples of bandpass filters that transmit from 460 to 490 nm or from 610 to 700 nm. The width of transmission can be made narrower or wider. Such filters are often referred to as interference filters.

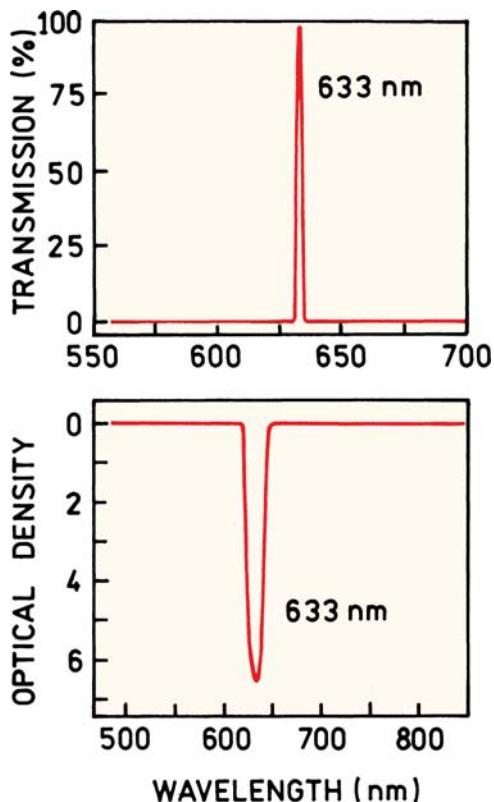


**Figure 2.20.** Laser line filter to transmit only the laser wavelength (top) and a notch filter to reject the laser wavelength. From [15].

#### 2.4.3. Filter Combinations

While one can obtain almost any desired filter with modern coating technology, the design of custom filters for each experiment is usually not practical. If a single filter is not

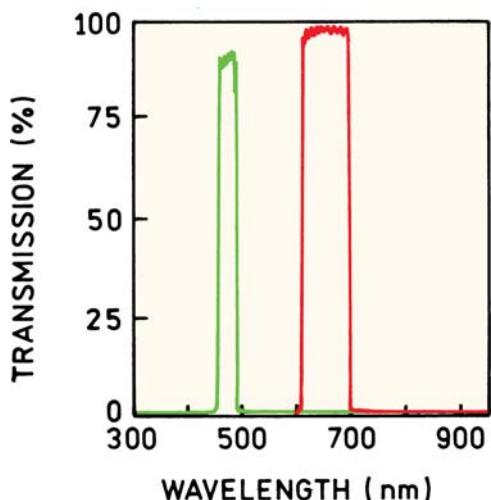


**Figure 2.21.** Interference filter to transmit selected wavelengths. From [15].

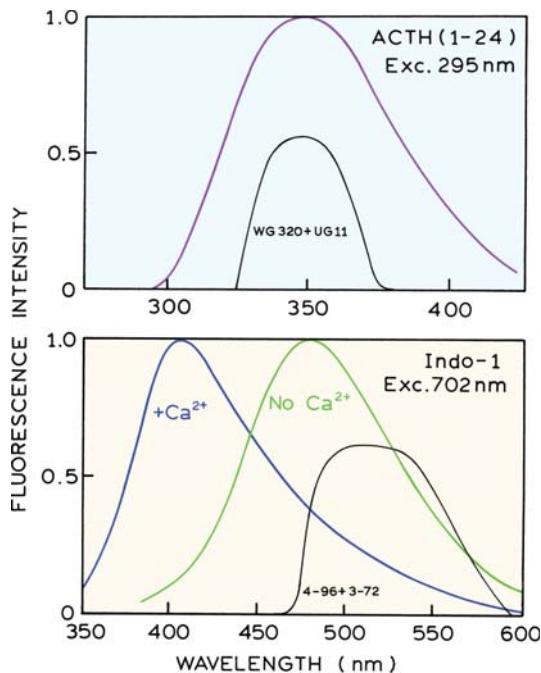


**Figure 2.22.** Transmission profile of a combination of Corning and Schott filters used to isolate protein fluorescence (top) and Indo-1 fluorescence (bottom). Lower panel from [17].

adequate for a given experiment, it is often possible to combine two or more bandpass filters to obtain the desired spectral properties. This possibility is shown in Figure 2.22. The UG-11 and WG-320 filters are often used in our laboratory to isolate protein fluorescence.<sup>16</sup> For probes emitting near 450 nm, we often use a combination of Corning 4-96 and 3-72 filters.<sup>17</sup> In this example the filter was selected to reject 702 nm, which was the excitation wavelength for two-photon excitation of Indo-1.<sup>17</sup> This example illustrates an important aspect in selecting filters. Filters should be selected not only for their ability to transmit the desired wavelength, but perhaps more importantly for their ability to reject possible interfering wavelengths.

#### 2.4.4. Neutral-Density Filters

Neutral-density filters are used to attenuate light equally at all wavelengths. They are typically composed of sheets of glass or quartz coated with a metal to obtain the desired optical density. Quartz transmits in the UV and is preferred unless no experiments will be done using wavelengths below 360 nm. Neutral-density filters are described by their optical density, and can typically be obtained in increments of 0.1, up to optical densities of 4. It is often necessary to adjust or match the intensity of two signals, which is conveniently accomplished using neutral-density filters.

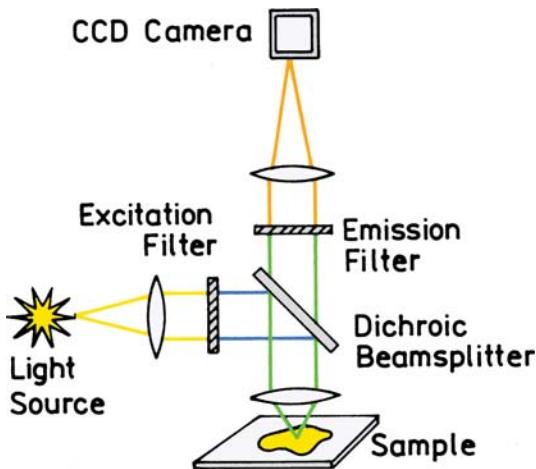


Figure 2.23. Filter geometry used for epifluorescence microscopy.

#### 2.4.5. Filters for Fluorescence Microscopy

Fluorescence microscopy relies on optical filters rather than monochromators for wavelength selection. Most fluorescence microscopy is performed using the epifluorescence configuration. The term epifluorescence refers to excitation and emission passing through the same objective (Figure 2.23). This configuration has the advantage of most of the excitation traveling away from the detector. Additionally, the excitation can be observed for the same location. Even though most of the excitation passes through the sample, a substantial fraction of the excitation is reflected or scattered back into the objective.

Observation of the fluorescence image requires specially designed sets of filters. A set contains an excitation filter, an emission filter, and a dichroic beam splitter. The function of such filters can be understood by examination of their transmission spectra (Figure 2.24). The excitation filter selects a range of wavelengths from a broadband source to excite the sample. The emission filter transmits the emission and rejects the excitation wavelengths. The unusual component is the dichroic beam splitter, which serves a dual function. It reflects the excitation wavelengths into the objective, and transmits the emission and allows it to reach the eyepiece or detector. Filter sets for microscopy are now often named for use with specific fluorophores rather than wavelengths.

Fluorescence microscopy is often performed using multiple fluorophores to label different regions of the cell, allowing the region to be identified by the emission wavelength. Emission filters have been designed to pass the emission from multiple fluorophores. Figure 2.25 shows

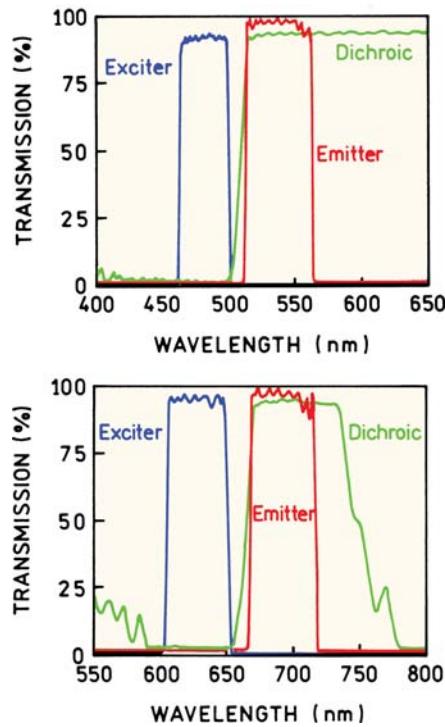


Figure 2.24. Epifluorescence filter sets for fluorescein or Cy5. From [15].

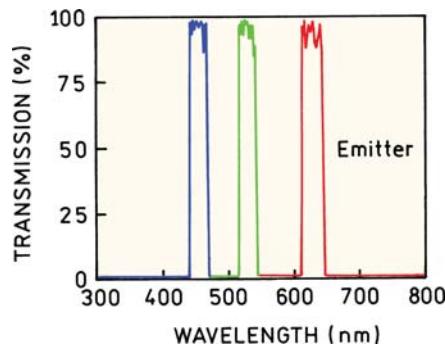
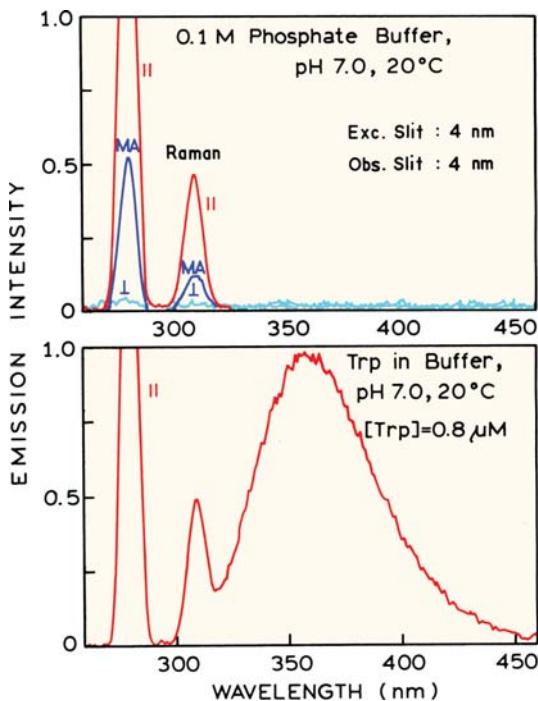


Figure 2.25. Multi-bandpass filter designed to transmit the emission of DAPI, fluorescein and Texas Red. Note that this is a single filter with three bandpasses. From [15].

the transmission curve of a filter designed to pass the emission from DAPI near 460 nm, fluorescein near 530 nm, and Texas Red at 630 nm. The availability of such filters has greatly expanded the capabilities of fluorescence microscopy.

#### 2.5. OPTICAL FILTERS AND SIGNAL PURITY

A major sources of errors in all fluorescence measurements is interference due to scattered light, stray light, or sample



**Figure 2.26.** Emission spectrum of a  $0.8\text{-}\mu\text{M}$  solution of tryptophan (bottom) in  $0.1\text{ M}$  phosphate buffer, pH 7.0. The observation polarizer was vertically oriented. Top: emission spectrum of a blank buffer solution under the same optical conditions. The emission polarizer was vertical (||), horizontal (⊥) or at the  $54.7^\circ$  magic angle (MA) position. From [10].

impurities. These problems can be minimized by careful selection of the emission filter, the use of optical filters in addition to the excitation and emission monochromators, and by control experiments designed to reveal the presence of unwanted components. The use of optical filters and control experiments to avoid such artifacts is best illustrated by specific examples.

Figure 2.26 (bottom) shows the emission spectrum of a dilute solution of tryptophan in aqueous buffer. The large sharp peak on the left is due to scattered excitation, the broad peak at 360 nm is the tryptophan fluorescence, and the small sharp peak at 310 nm is the Raman scatter. Raman scatter will occur from all solvents. For water, the Raman peak appears at a wavenumber  $3600\text{ cm}^{-1}$  lower than the incident wavenumber. For excitation at 280 nm, the Raman peak from water occurs at 311 nm. Highly fluorescent samples generally overwhelm the Raman peak. However, if the gain of the instrument is increased to compensate for a dilute solution or a low quantum yield, the Raman scatter may become significant and distort the emission spectrum. Raman scatter always occurs at a constant wavenumber dif-

ference from the incident light, and can be identified by changing the excitation wavelength. Also, the spectral width of the Raman peak will be determined by the resolution of the monochromators.

In microscopy and in assays the fluorescence may be observed without a monochromator. The emission can be observed through a filter that is presumed to remove the scattered light. Observation through a filter rather than a monochromator increases the sensitivity because the bandpass of the observation is increased and the attenuation due to the monochromator is removed. The signal level can often be 50-fold higher when observed through filters rather than a monochromator. Lifetime measurements are usually performed using long-pass filters to observe the entire emission. Under these conditions it is important to choose an emission filter that eliminates both the scattered incident light and the Raman scatter.

In any fluorescence experiment it is essential to examine blank samples, which are otherwise identical to the sample but do not contain the fluorophore. These control samples allow the presence of Rayleigh and Raman scatter to be determined. Control samples can also reveal the presence of fluorescent impurities. An emission spectrum of the buffer blank for the dilute tryptophan solution is shown in Figure 2.26 (top). The gain of the instrument should be the same when recording the emission spectrum of the sample and that of the blank. These control spectra are recorded under the same conditions, because the only meaningful consideration is whether the blank contributes to the emission under the conditions of a given experiment. In this case the blank spectrum above 320 nm is essentially zero, showing that the peak at 360 nm (bottom) is in fact due to the sample. While this may seem like a trivial result, the presence of background fluorescence and/or scattered light is the most common error in fluorescence measurements. Examination of the blank sample also allows identification of the peak at 310 nm as due to the buffer and not to the sample.

The most appropriate blank solution is one that is identical to the sample, but does not contain the fluorophore. This can be difficult to accomplish with protein or membrane solutions, where the macromolecules themselves are the source of the signal. Such solutions will typically be more strongly scattering than the buffer blanks. In these cases it is useful to add glycogen or colloidal silica (Ludox) to the buffer blank, to mimic the amount of scattering from the sample. This allows selection of filters that are adequate to reject scattered light from the sample.

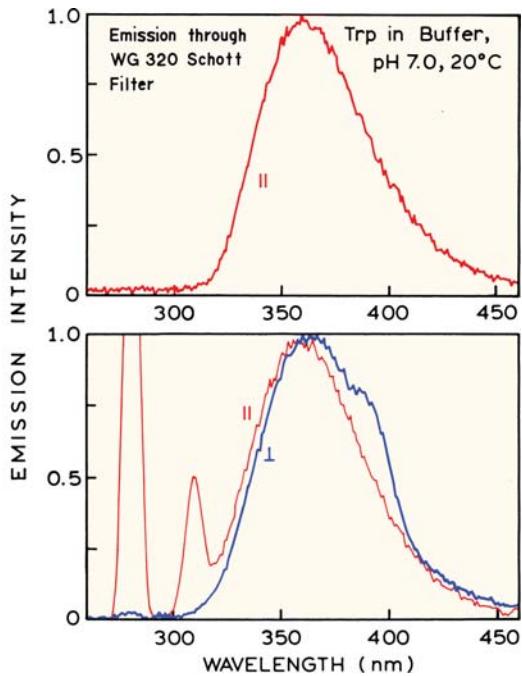


**Figure 2.27.** Rejection of scattered light from the 0.8- $\mu\text{M}$  tryptophan solution using a bandpass filter (top) or a polarizer but no bandpass filter (bottom). The emission polarizer was oriented vertically (||) or horizontally (⊥). From [10].

### 2.5.1. Emission Spectra Taken through Filters

Suppose you wanted to measure the lifetime of the tryptophan sample in Figure 2.26 (bottom) and the measurements are to be performed using a bandpass filter to isolate the emission. How can one know the scattered light has been rejected by the emission filter? This control is performed by collecting an emission spectrum through the filter used to measure the lifetime (Figure 2.27, top). In this case the Schott WG320 filter rejected both the scattered light and the Raman scatter, as seen by the zero intensity from 280 to 310 nm. In some cases the filter itself can be a source of background emission. The use of an equivalent scattering solution is preferred, as this provides the most rigorous test of the filter for rejecting scattered light and for displaying minimal fluorescence.

It is important to remember that scattered light is usually 100% polarized ( $p = r = 1.0$ ). This is the reason the emission polarizer was vertical in Figure 2.27 (top), which is the worst-case situation. If the emission spectrum was recorded with the polarizer in the horizontal position, then the scattered light would be rejected by the polarizer (Figure 2.27, bottom). If the sample is then measured with a vertical polarizer, scattered light may be detected. When

examining spectra for the presence of scattered light, it is preferable to keep both polarizers in the vertical position, and thereby maximize the probability that the interfering signal will be observed. Conversely, a horizontal emission polarizer can be used to minimize the scattered light if only the emission spectrum needs to be recorded.

The emission spectra in Figure 2.27 (bottom) illustrate how the polarization-dependent transmission properties of the monochromator can distort the emission spectra. For these spectra the excitation was polarized vertically, and the emission spectra were recorded through a polarizer oriented vertically (||) or horizontally (⊥). These spectra are clearly distinct. The spectrum observed through the vertically oriented polarizer is blue shifted relative to the spectrum observed when the emission polarizer is in the horizontal orientation. The extra shoulder observed at 390 nm is due to the transmission properties of the monochromator. These results illustrate the need for comparing only those spectra that were recorded under identical conditions, including the orientation of the polarizers. The emission spectra for the same fluorophore can differ slightly if the emission is polarized or unpolarized.

One way to avoid these difficulties is to use a defined orientation of the polarizers when recording emission spectra. One preferred method is to use the so-called "magic angle" conditions. This is vertically polarized excitation and an emission polarizer oriented  $54.7^\circ$  from the vertical. In effect, the use of this condition results in a signal proportional to the total fluorescence intensity ( $I_\perp$ ) which is given by  $I_{||} + 2I_\perp$ , where  $I_{||}$  and  $I_\perp$  are the intensities of vertically and horizontally polarized emission. Such precautions are generally taken only when necessary. If the excitation source is unpolarized, the presence of polarizers in both the excitation and emission light paths results in an approximate fourfold decrease in signal level.

Polarization or anisotropy measurements are frequently performed using filters rather than monochromators. Scattered light is 100% polarized ( $r = 1.0$ ). Hence, a small percentage of scatter can result in serious errors. For example, assume 10% of the observed intensity is due to Raman scatter. Furthermore, assume that the actual anisotropy of a sample, in the absence of scatter, is 0.10. The observed anisotropy is then given by

$$r_{\text{obs}} = f_s r_s + f_F r_F \quad (2.1)$$

where the  $f_s$  value represents the fractional contribution of the scattered light,  $f_F$  is the fractional contribution of the flu-

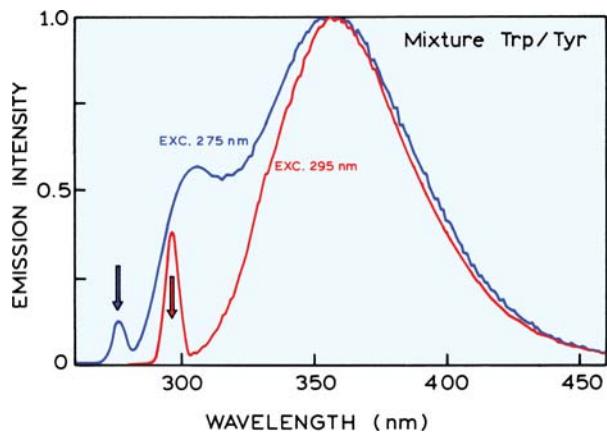


**Figure 2.28.** Emission spectra of tryptophan with a trace impurity of tyrosine, for excitation at 275 and 295 nm. From [10].

orescence,  $r_F$  is the anisotropy of the fluorescence, and  $r_s$  is the anisotropy of the scattered light. Substitution into eq. 2.1 yields  $r_{\text{obs}} = 0.19$ . Hence, a 10% contribution from scattered light can result in an almost twofold error in the measured anisotropy. The relative error would be still larger if  $r_F$  was smaller. These considerations apply to both Raman and Rayleigh scattering.

When measuring tryptophan or protein emission it is important to recognize that Raman scatter can be mistaken for tyrosine emission. This possibility is shown in Figure 2.28, which shows the emission spectrum of a tryptophan solution that contains a minor amount of tyrosine. Upon excitation at 275 nm the tyrosine results in a peak near 300 nm. The fact that this peak is due to tyrosine is shown by the spectrum obtained for 295-nm excitation, which shows only the tryptophan emission. If the emission spectrum of tryptophan alone was recorded at lower resolution, one can readily imagine how the broadened Raman line would become visually similar to tyrosine emission (Figure 2.28).

## 2.6. PHOTOMULTIPLIER TUBES

Almost all fluorometers use photomultiplier tubes (PMTs) as detectors, and it is important to understand their capabilities and limitations. A PMT is best regarded as a current source. The current is proportional to the light intensity. A PMT responds to individual photons, and the pulses can be detected as an average signal or counted as individual photons.

A PMT vacuum tube consists of a photocathode and a series of dynodes which are the amplification stages (Figure

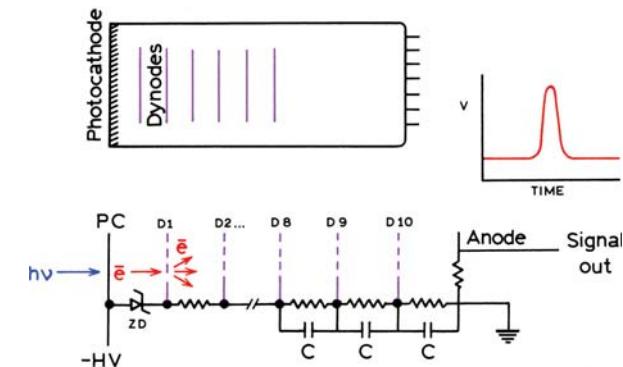


**Figure 2.29.** Schematic diagram of a photomultiplier tube and its dynode chain.

2.29). The photocathode is a thin film of metal on the inside of the window. Incident photons cause electrons to be ejected from this surface. The generation efficiency of photoelectrons is dependent upon the incident wavelength. The photocathode is held at a high negative potential, typically  $-1000$  to  $-2000$  volts. The dynodes are also held at negative potentials, but these potentials decrease toward zero along the dynode chain. The potential difference between the photocathode and the first dynode is generally fixed at a constant voltage by a Zener diode, at values ranging from  $-50$  to  $-200$  volts. This potential difference causes an ejected photoelectron to be accelerated toward the first dynode. Upon collision with the first dynode the photoelectron causes 5 to 20 additional electrons to be ejected, depending on the voltage difference to this dynode. This process continues down the dynode chain until a current pulse arrives at the anode. The size of this pulse depends upon the overall voltage applied to the PMT. Higher voltages result in an increased number of electrons ejected from each dynode, and hence higher amplification. PMTs are useful for low-level light detection because they are low-noise amplifiers. Little additional noise is created as the electrons pass through the PMT. Amplification outside of the PMT generally results in more noise being added to the signal.

For quantitative measurements, the anode current must be proportional to the light intensity. A nonlinear response can result from an excessive current being drawn from the photocathode. Under high-intensity illumination the electrical potential of the photocathode can be decreased because of its limited current-carrying capacity. This decreases the voltage difference between the photocathode and the first dynode, and also decreases the gain. Excessive photocurrents can damage the light-sensitive photocathodes, result-

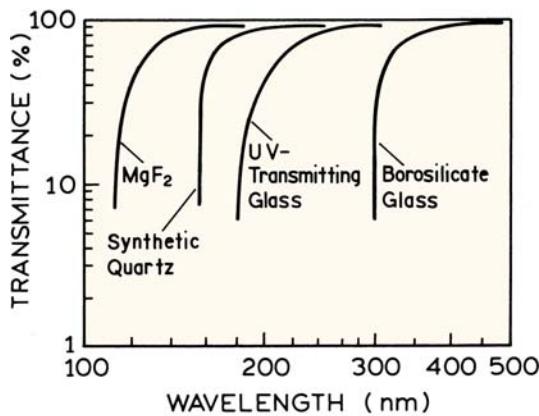


Figure 2.30. Typical transmittance of PMT window materials.

ing in loss of gain and excessive dark currents. The dark current from a PMT is the current in the absence of incident light.

A linear response also requires that the dynode voltages remain constant, irrespective of the incident light level and anode current. Dynode chains are designed so that the total current through the chain is at least 100-fold greater than the maximum anode current. Consider the 10-stage tube shown in Figure 2.29. Using resistors with  $R = 100 \text{ k}\Omega$ , the dynode current would be  $1.0 \text{ mA}$  at 1000 volts total voltage across the PMT. Hence  $10 \mu\text{A}$  should be the maximum anode current. There are often capacitors placed between the higher-numbered dynodes to provide a source of current during a single photoelectron pulse or periods of high illumination. Constant amplification by a PMT requires careful control of the high voltage. A typical PMT will yield a threefold increase in gain for each 100 volts. Hence, a small change in voltage can result in a significant change in the signal. The high voltage supply needs to provide a constant, ripple-free voltage that is stable for long periods of time. Photomultiplier tubes are available in a wide variety of types. They can be classified in various ways, such as according to the design of the dynode chain, size, and shape, spectral response, or temporal response.

### 2.6.1. Spectral Response of PMTs

The sensitivity of a PMT depends upon the incident wavelength. The spectral response is determined by the type of transparent material used for the window, and the chemical composition of the photocathode. Only light that enters the PMT can generate photocurrent. The input windows must be transparent to the desired wavelengths. The transmission

curves of typical windows material are shown in Figure 2.30. UV transmitting glass is frequently used and transmits all wavelengths above 200 nm. Synthetic quartz can be used for detection deeper into the UV.  $\text{MgF}_2$  windows are only selected for work in the vacuum ultraviolet. Since atmospheric oxygen absorbs strongly below 200 nm, there is little reason for selecting  $\text{MgF}_2$  unless the apparatus is used in an oxygen-free environment. For this reason the spectral region below 200 nm is called the vacuum ultraviolet.

The second important factor is the material used for the photocathode. Numerous types of photocathodes are available, and the spectral responses of just a few are shown in Figure 2.31. The quantum efficiency is not constant over any reasonable range of wavelengths. This is one origin of the nonideal wavelength response of spectrofluorometers. Most photocathodes are sensitive in the UV, blue and green (300–500 nm) regions of the spectrum. The differences in photocathode material are important mostly for wavelengths above 600 nm. One of the most commonly used is the bialkali photocathode (Figure 2.31), which provides high sensitivity and low dark current. One disadvantage of the bialkali photocathode is the rapid decrease in sensitivity above 600 nm. Given the current emphasis on red and

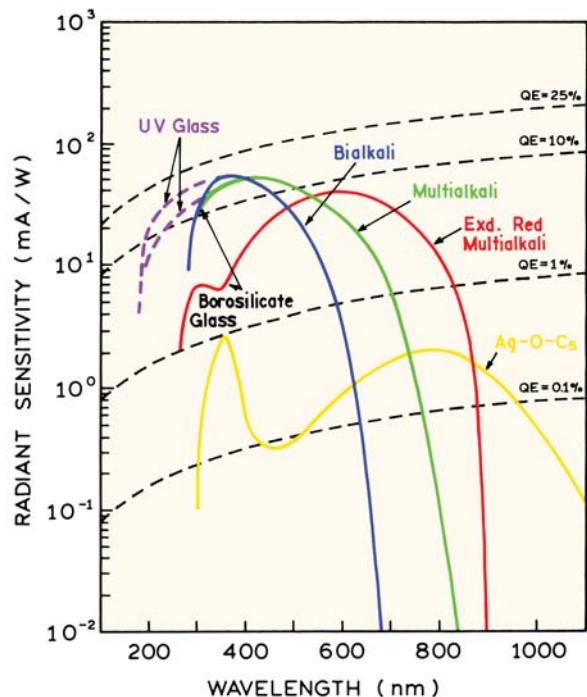


Figure 2.31. Spectral response curves of typical photocathodes. From [18].

**Table 2.2.** Characteristics of Typical Photomultiplier Tubes<sup>a</sup>

Type	R446 Side window	R2560 Head-on	R3809 Head-on	R3811 Subminiature
Dynode chain	Circular cage	Linear plate	Microchannel cage	Circular cage
Photocathode	Multi-alkali	Bialkali	Multi-alkali S-20	Multi-alkali
Wavelength range (nm)	185–870	300–650	160–185	185–850
Amplification	$5 \times 10^6$	$6 \times 10^6$	$2 \times 10^5$	$1.3 \times 10^6$
Rise time (ns)	2.2	2.2	0.15	1.4
Transit time (ns)	22	26	0.55	15
Bandwidth (MHz) (estimate)	200	200	2000	300

<sup>a</sup> The number refers to types provided by Hamamatsu Inc.<sup>18</sup>

NIR fluorescence, the bialkali photocathode is becoming less useful.

The sensitivity above 500 nm has been increased by the introduction of multi-alkali and extended red multi-alkali photocathodes, which provide good sensitivity to 700 or 800 nm (Figure 2.31). Red-sensitive PMTs typically have higher dark current, but for most multi-alkali photocathodes the dark current is not a problem. Sensitivity to still longer wavelengths can be obtained using Ag-O-Cs or S-1 photocathodes. However, their quantum efficiency is uniformly poor, and it is often difficult to detect the signal above the dark current with an S-1 PMT. In fact, these PMTs are rarely used without cooling to reduce the dark current.

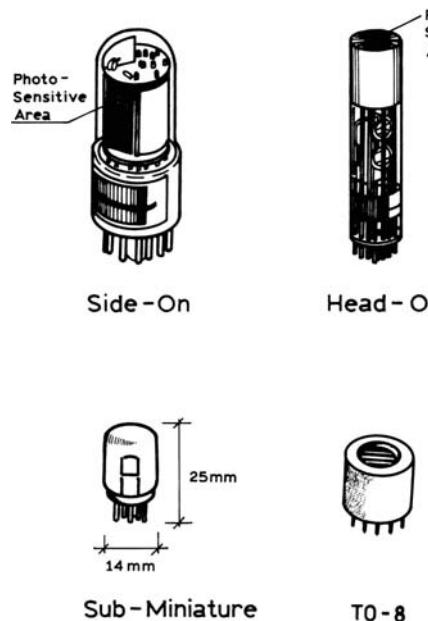


Figure 2.32. Types of photomultiplier tubes.

## 2.6.2. PMT Designs and Dynode Chains

The major types of PMTs and dynode chains used in fluorescence are shown in Figures 2.32 and 2.33. A commonly used PMT is the side-window or side-on tube. A large number of variants are available, and all are descendants of one of the earliest PMTs, the 1P-28. These side-on tubes used a circular cage dynode chain, sometimes referred to as a squirrel cage (Figure 2.33). The specifications of one side-on tube are listed in Table 2.2. The multi-alkali photocathode of the R446 is sensitive from 185 to 870 nm. This type of circular cage PMT has evolved into the subminiature PMTs. Because of their compact design the time response is excellent (Table 2.2). PMTs are also available in the compact TO-8 format, which is 16 nm in diameter. Small PMTs are available complete with a high voltage supply and dynode chain, all in a compact package. These compact high-sensitivity detectors have appeared in many research and clinical instruments.

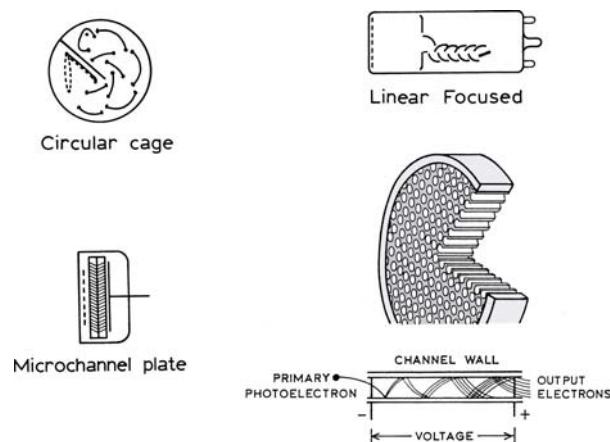


Figure 2.33. Types of PMT dynode chains. From [14].

Another type of PMT is the head-on design (Figure 2.32). This design is used with various types of dynode chains, such as the box and grid, blind and mesh design. For time-resolved fluorescence the head-on PMTs typically use a linear-focused dynode chain (Figure 2.33). The purpose of this design is to minimize the transit time spread and thus improve the time response of the PMT. The use of a head-on design allows the dynode chain to be extended as long as desired, so that the highest amplification is usually available with this type of PMT.

The final type of PMT is the microchannel plate PMT (MCP-PMT). In place of a dynode chain the MCP-PMT has plates that contain numerous small holes (Figure 2.33). The holes in these plates are the microchannels, which are lined with a secondary emissive dynode material. The electrons are amplified as they drop down the voltage gradient across the microchannel plate. Because of the short distances for electron travel, and the restricted range of electron paths, this type of PMT shows the fastest time response and is used in the most demanding time-resolved measurements. MCP-PMTs are available with one, two, or three stages of microchannel plates. The amplification is generally lower than for PMTs with discrete dynode chains. Also, the maximum photocurrent is typically 100 nA, as compared with 10 to 100  $\mu$ A for a dynode PMT.

### 2.6.3. Time Response of Photomultiplier Tubes

For steady-state measurements the time response of a PMT is not important. The PMT time response is important for lifetime measurements. There are three main timing characteristics of PMT—the transit time, the rise time, and the transit time spread (Figure 2.34). The transit time of a PMT is the time interval between the arrival of a photon at the cathode and the arrival of the amplified pulse at the anode. Typical transit times range from 20 to 50 ns. The rise time is the time required for the PMT anode signal to rise from 10 to 90% of its final level. The rise time is determined primarily by the transit time variation in the PMT, that is, the scatter around the average transit time.

The transit time spread is the most important specification for time-resolved measurements. These timing variations result from the different geometric paths that the electrons can take from the photocathode to the anode. The photoelectrons can originate from different parts of the photocathode, or can have different trajectories from the same region of the photocathode. The electrons subsequently ejected from the dynodes can take slightly different geo-

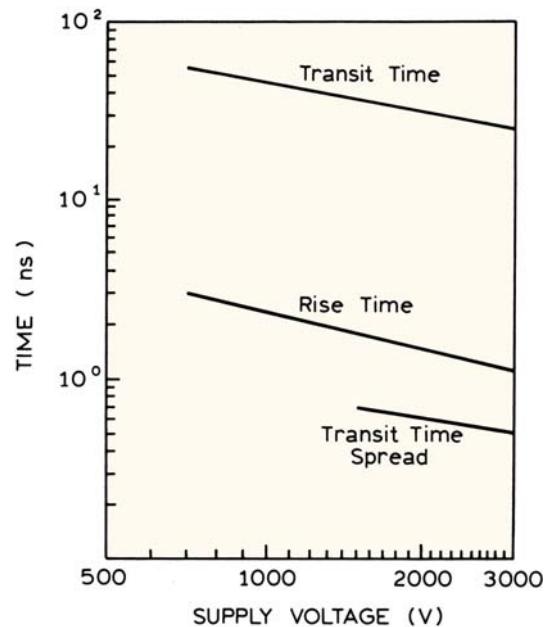


**Figure 2.34.** Time response of a typical PMT. The data are for a R2059, head on, 12-stage linear focused PMT. Revised from [18].

metric paths through the PMT. This can be seen in Figure 2.29 from the various ejection angles of electrons coming off the first dynode. Transit time spread can be decreased by using photocathode and dynode geometries which minimize the number of different trajectories. This can be accomplished by the use of small illuminated areas, or a dynode designed to direct the flight of the electrons along a defined trajectory.

The most dramatic advance in high-speed PMTs has been the introduction of the MCP-PMT. In this case the photoelectrons are proximity focused into the MCP (Figure 2.33). There is very little variation in terms of electron trajectory within the MCP. For this reason MCP-PMTs have transit time spreads tenfold smaller than those of standard PMTs (Table 2.2).

A second source of the time dependence of a PMT results from the photocathode itself. Typically, its time response is dependent upon the wavelength incident on the photocathode. This property is called the color effect. The energy of the ejected electrons is dependent upon the incident wavelength, and the energy affects the path an electron takes through the phototube. Color effects are not important for steady-state measurements. Color effects were a significant source of error in lifetime measurements, but color effects seem to be smaller in the current generation of fast PMTs.

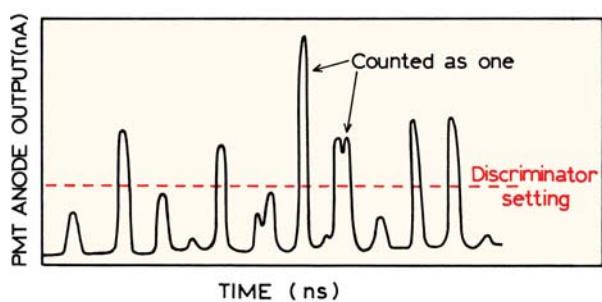


Figure 2.35. Photon-counting detection using a PMT. From [19].

#### 2.6.4. Photon Counting versus Analog Detection of Fluorescence

A PMT is capable of detecting individual photons. Each photoelectron results in a burst of  $10^5$  to  $10^6$  electrons, which can be detected as individual pulses at the anode (Figure 2.35). Hence, PMTs can be operated as photon counters, or can be used in the analog mode in which the average photocurrent is measured. Note that we are considering steady-state measurements. Time-correlated photon counting for lifetime measurements will be discussed in Chapter 4. In photon-counting mode, the individual anode pulses due to each photon detected and counted. As a result, the detection system is operating at the theoretical limits of sensitivity. Noise or dark current in the PMT frequently results from electrons that do not originate at the photocathode, but from further down the dynode chain. Such anode pulses from these electrons are smaller, and can be ignored by setting the detection threshold high enough to count only fully amplified primary photoelectrons. Besides increased sensitivity, the stability of the detection system can be increased. Because the PMT is operated at a constant high voltage, small drifts in the voltage do not result in significant changes in the efficiency with which each photon is counted. Photon-counting detection is frequently used when signal levels are low, and when it is necessary to average repetitive wavelength scans to increase the signal-to-noise ratio.

There can be disadvantages to photon counting for steady-state measurements. The gain of the PMT cannot be varied by changing the applied voltage. Photon-counting detection can be inconvenient when signal levels are high. To stay within the linear range, one must adjust the slit widths or the fluorescence intensities (using neutral-density filters). Another disadvantage of photon counting is the limited range of intensity over which the count rate is linear. If

two pulses arrive at the anode closely spaced in time, they will be counted as a single pulse. Anode pulses resulting from a single photon are typically 5 ns wide. This limits the response of the PMT to 200 MHz, or  $2 \times 10^8$  Hz for a periodic signal. For random events, the count rates need to be about 100-fold less to avoid the simultaneous arrival of two photons. Hence, count rates are limited to several MHz. Manufacturers often specify count rates of 50 MHz or higher. However, these count rates apply to uniformly spaced pulses, and the pulse widths of the detector may be too wide to distinguish pulses which occur too close together. In practice, the count rates often become sublinear before the theoretical upper limit is reached (Figure 2.36). Higher count rates can be obtained with PMTs which show shorter pulse widths. Additionally, the signal-to-noise ratio becomes unsatisfactory at count rates below 10,000 photons per second. The linear dynamic range can be as small as 3 log units (Figure 2.36).<sup>20</sup> This limited intensity range is a drawback of photon-counting detection for steady-state measurements of fluorescence, unless the highest sensitivity is required.

In analog mode the individual pulses are averaged. Since the current from each pulse contributes to the average anode current, the simultaneous arrival of pulses is not a problem. When using analog detection the gain of the detection system can be varied by changing either the amplifier gain or the voltage on the photomultiplier tube. As a result, a wider range of signal levels can be detected without concerns about a nonlinear response. The precision of the individual measurements can be higher than for photon counting measurements, because of the higher overall sig-

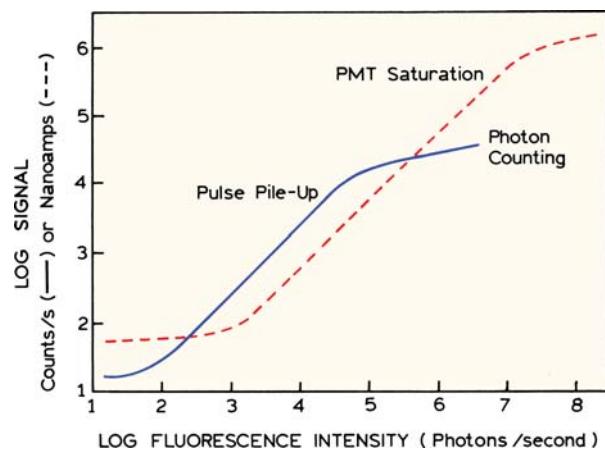


Figure 2.36. Dynamic range available with photon counting and analogue detection. From [19].

nal levels. However, even the analog measurements have a limited range because all PMTs display saturation above a certain light level if one exceeds the capacity of the photocathode to carry the photocurrent, or an ability of the dynode chain to maintain a constant voltage.

### 2.6.5. Symptoms of PMT Failure

Photomultiplier tubes should be handled with care. Their outer surfaces should be free of dust and fingerprints, and should not be touched with bare hands. The photocathode is light sensitive, and it is best to perform all manipulations in dim light. It is convenient to know the common signs of PMT failure. One may observe pulses of current when the applied voltage is high. At lower voltages this symptom may appear as signal instability. For instance, the gain may change 20% to several-fold over a period of 2–20 seconds. The origin of this behavior is frequently, but not always, a leakage of gas into the tube. The tube cannot be fixed and replacement is necessary. In some instances the tube may perform satisfactory at lower voltages.

A second symptom is high dark current. This appears as an excessive amount of signal when no light is incident on the PMT. The origin of high dark currents is usually excessive exposure of the tube to light. Such exposure is especially damaging if voltage is applied to the tube at the same time. Again, there is no remedy except replacement or the use of lower voltages.

Signal levels can be unstable for reasons other than a failure of the photomultiplier tube. If unstable signals are observed one should determine that there are no light leaks in the instrument, and that the high voltage supplies and amplifiers are functioning properly. In addition, the pins and socket connections of the PMT should be checked, cleaned, and tightened, as necessary. Over a period of years, oxide accumulation can result in decreased electrical contact. Photobleaching of a sample may give the appearance of an instrument malfunction. For example, the fluorescence intensity may show a time-dependent decrease due to bleaching, and then an increase in intensity due to convection currents which replenish the bleached portion of the sample.

### 2.6.6. CCD Detectors

There is a growing usefulness of charge-coupled devices (CCDs) in fluorescence spectroscopy.<sup>21–22</sup> CCDs are imaging detectors with remarkable sensitivity and linear dynam-

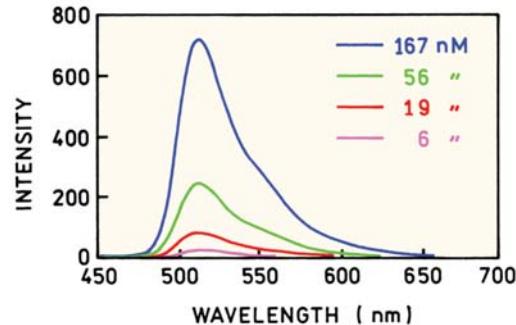
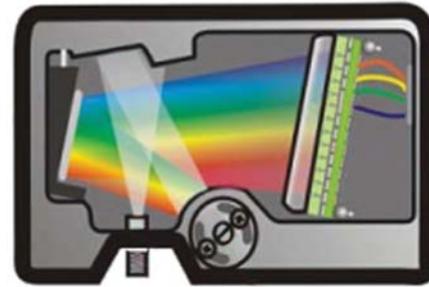


**Figure 2.37.** CCD spectrofluorometer and emission spectra of fluorescein. The light source for the fluorescein spectra was a 450 nm blue LED. From [25]. Image courtesy of Ocean Optics Inc.

ic range. CCDs typically contain  $10^6$  or more pixels. Each pixel acts as an accumulating detector where charge accumulates in proportion to total light exposure. The charge at each pixel point can be read out when desired, to obtain a two-dimensional image. CCDs are used widely in fluorescence microscopy.<sup>23–24</sup>

Small spectrofluorometers using CCDs are commercially available.<sup>25</sup> These devices are conveniently interfaced via a USB cable and have no moving parts. The sensitivity can be rather good, as seen from the fluorescein emission spectra (Figure 2.37). The signal is easily brought to the device using a fiber-optic cable. When combined with an LED light source the entire instrument becomes a solid-state device. These spectrofluorometers are convenient for bringing the instrument to the experiment, rather than vice versa.

## 2.7. POLARIZERS

When discussing polarizers it is useful to recall a few conventional definitions. The laboratory vertical-axis is typically referred to as the *z*-axis. Light can be described as

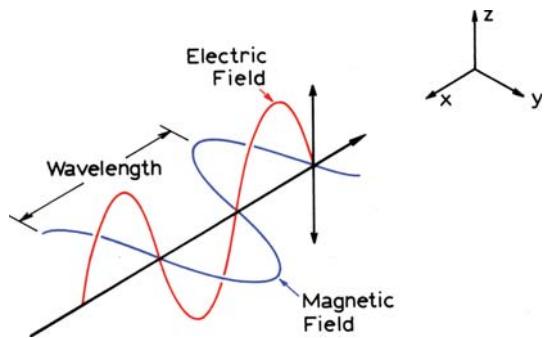


Figure 2.38. Vertically polarized light.

having a direction for its electrical component. Unpolarized light, of the type from incandescent or arc lamp sources, has equal amplitudes of the electric vector normal to the direction of light propagation. Polarized light has greater amplitude in one of the directions. Light with its electrical vector directed along the  $z$ -axis is said to be vertically polarized (Figure 2.38). Light with its electrical vector at right angles to the  $z$ -axis is said to be horizontally polarized.

In a discussion of polarization, the terms "S" and "P" polarization are often used. These terms are defined relative to the normal to the plane of incidence of the light on the optical interface. The plane of incidence is the plane defined by the light ray and the axis normal to the surface. If the electrical vector is in the plane of incidence the ray is said to be "P" polarized (Figure 2.39). If the electrical vector is perpendicular to the plane of incidence this ray is said to be "S" polarized.

Polarizers transmit light when the electric vector is aligned with the polarization axis, and block light when the

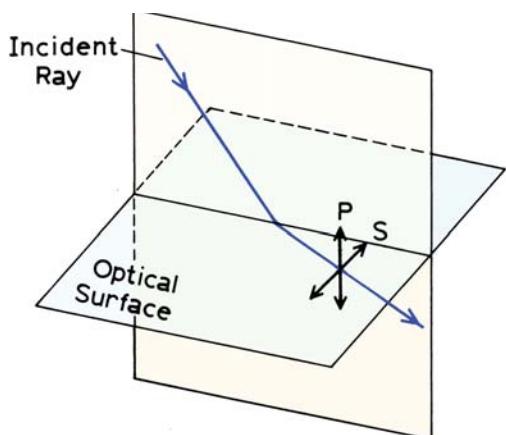


Figure 2.39. Definition of S and P polarization. P-polarized light has the electric field parallel to the plane of incidence. S-polarized light has the electric field polarized perpendicular to the plane of incidence.

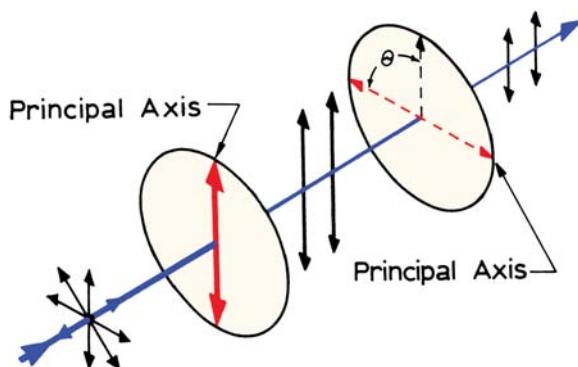


Figure 2.40. Transmission of light through polarizers. The incident beam is unpolarized. Only vertically polarized light passes through the first polarizer. Transmission through the second polarizer is proportional to  $\cos^2 \theta$ .

electric vector is rotated  $90^\circ$ . These principles are shown in Figure 2.40. The incident light is unpolarized. About 50% of the light is transmitted by the first polarizer, and this beam is polarized along the principal axis of the polarizer. If the second polarizer is oriented in the same direction, then all the light is transmitted except for reflection losses. If the second polarizer is rotated through an angle  $\theta$  the intensity is given by

$$I = I_{\max} \cos^2 \theta \quad (2.2)$$

where  $I_{\max}$  corresponds to  $\theta = 0^\circ$ . Polarizers are frequently characterized by their extinction ratios. If the first polarizer is illuminated with linearly polarized light along the principal axis, the extinction ratio is the ratio of intensities for parallel ( $\theta = 0^\circ$ ) and crossed polarizers ( $\theta = 90^\circ$ ). A slightly different definition is used if the first polarizer is illuminated with unpolarized light. Extinction ratios range from  $10^3$  to  $10^6$ .

For general use in fluorescence spectroscopy a UV-transmitting Glan-Thompson polarizer has the best all-around properties (Figure 2.41). These polarizers consist of calcite prisms, which are birefringent, meaning the refractive index is different along each optical axis of the crystal. The angle of the crystal is cut so that one polarized component undergoes total internal reflection at the interface, and the other continues along its optical path. The reflected beam is absorbed by the black material surrounding the calcite. The purpose of the second prism is to ensure that the desired beam exits the polarizer in the same direction as the entering beam. For high-power laser applications an exit port is provided to allow the reflected beam to escape.

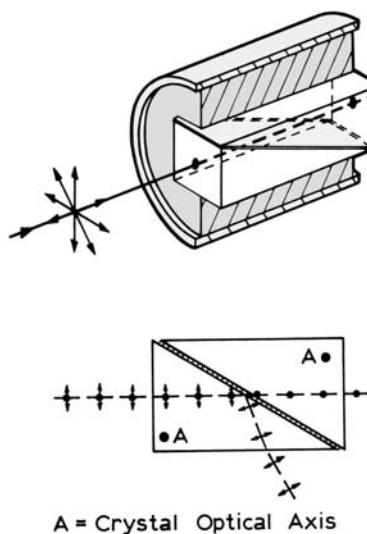


Figure 2.41. Glan-Thompson polarizer (top) and light paths (bottom).

Calcite transmits well into the UV, and the transmission properties of the polarizer are determined by the material between the two prisms, which can be air or some type of cement. An air space is usually used for UV transmission. The polarizers are typically mounted in 1 inch diameter cylinders for ease of handling. Glan-Thompson polarizers provide high extinction coefficients near  $10^6$ , but that is not the reason they are used in fluorescence. Glan-Thompson polarizers have a high acceptance angle,  $10\text{--}15^\circ$ , allowing them to be used where the beams are not well collimated. Another advantage is the low UV and visible absorbance of calcite, providing high transmission efficiency.

Another type of polarizer used in fluorescence are film polarizers, the same type used in polaroid glasses. These are thin films of a stretched polymer that transmit the light polarized in one direction and absorb the light polarized in another direction (Figure 2.40). Because the light is absorbed they are easily damaged by intense laser beams. They have a wide acceptance angle, but overall transmission is poor, especially in the ultraviolet. A wide variety of other polarizers are available. Most of the others, such as Wallaston polarizers and Rachon prism polarizers, split the unpolarized light into two beams, which must then be spatially selected.

## 2.8. CORRECTED EXCITATION SPECTRA

The development of methods to obtain excitation and emission spectra, corrected for wavelength-dependent effects,

has been the subject of numerous investigations. None of these methods are completely satisfactory, especially if the corrected spectra are needed on a regular basis. Prior to correcting spectra, the researcher should determine if such corrections are necessary. Frequently, it is only necessary to compare emission spectra with other spectra collected on the same instrument. Such comparisons are usually made between the technical (or uncorrected) spectra. Furthermore, the response of many spectrofluorometers is similar because of the similar components, and comparison with spectra in the literature can frequently be made. Of course, the spectral distributions and emission maxima will differ slightly, but rigorous overlap of spectra obtained in different laboratories is rarely a necessity.

Modern instruments with red-sensitive PMTs and with gratings comparable to that shown in Figure 2.41 can provide spectra that are not very distorted, particularly in the visible to red region of the spectrum. Corrected spectra are needed for calculation of quantum yields and overlap integrals (Chapter 13). We briefly describe the methods judged to be most useful.

### 2.8.1. Corrected Excitation Spectra Using a Quantum Counter

Excitation spectra are distorted primarily by the wavelength dependence of the intensity of the exciting light. This intensity can be converted to a signal proportional to the number of incident photons by the use of a quantum counter. Rhodamine B (RhB) in ethylene glycol (3 g/l) is the best-known quantum counter,<sup>26</sup> and to this day remains the most generally reliable and convenient quantum counter. This concentrated solution absorbs virtually all incident light from 220 to 600 nm. The quantum yield and emission maximum ( $\approx 630$  nm) of rhodamine B are essentially independent of excitation wavelength from 220 to 600 nm.

The principle of a quantum counter is illustrated in Figure 2.42, which shows the ratio of the intensities observed from the RhB quantum counter and a thermopile. It is seen that the ratio remains constant at varying wavelengths. Since the emission spectrum of rhodamine B is independent of excitation wavelength, the quantum counter circumvents the wavelength-dependent sensitivity of the reference phototube. Hence, this solution provides a signal of constant emission wavelength and this signal, which is proportional to the photon flux of the exciting light. Quantum counters can also be made using moderately concentrated solutions of quinine sulfate or fluorescein. Quinine sulfate (4 g/l in 1

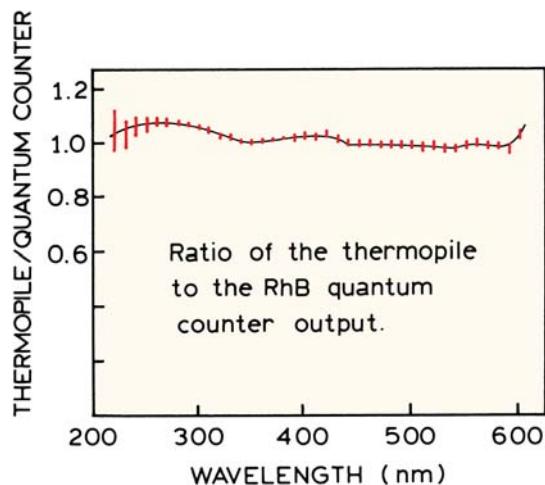


**Figure 2.42.** Comparison of the thermopile and the rhodamine B quantum counter as radiation detectors. Redrawn from [26].

$\text{N H}_2\text{SO}_4$ ) is useful at excitation wavelengths ranging from 220 to 340 nm and fluorescein (2 g/l in 0.1 N NaOH) is useful over this same range, but is less reliable from 340 to 360 nm,<sup>26</sup> where absorption of fluorescein is weaker.

To record corrected excitation spectra, the quantum counter is placed in the reference channel of the spectrofluorometer (Figure 2.1). Because of the high optical density, the reference cell holder is modified so that the emission is observed from the same surface of the quantum counter that is being illuminated. Alternatively, quantum counters can be used in a transmission mode by observing the fluorescent light exiting the back surface of the illuminated cuvette.<sup>27</sup> In either case an optical filter is placed between the quantum counter and the PMT, which eliminates incident light but transmits the fluorescence. With a quantum counter in place, a corrected excitation spectrum may be obtained by scanning the excitation monochromator and measuring the ratio of the fluorescence intensity from the sample to that from the quantum counter. The wavelength-dependent response of the emission monochromator and phototube are not important because the emission wavelength is unchanged during a scan of the excitation wavelength. This procedure was used to record the corrected excitation spectrum of fluorescein shown in Figure 2.6.

Other quantum counters have been described, and are summarized in Table 2.3. The long wavelength dye HITC extends the range to 800 nm, but its response is not as flat as RhB. Unfortunately, there is no perfect quantum counter, and for most applications RhB appears to be the best choice.

**Table 2.3.** Quantum Counters

Solution	Range (nm)	Flatness	Reference
3 g/l Rhodamine B in ethylene glycol	220–580	$\pm 5\%$	26
8 g/l Rhodamine B in ethylene glycol <sup>a</sup>	250–600	$\pm 4\%$	27
2 g/l Fluorescein in 0.1 N NaOH	240–400 <sup>b</sup>	$\pm 5\%$	26
4 g/l quinine sulfate in 1 N $\text{H}_2\text{SO}_4$	220–340	$\pm 5\%$	26
Rhodamine in polyvinyl alcohol (PVA) films	360–600	$\pm 3\%$	28 <sup>c</sup>
Coumarins in PVA films	360–480	$\pm 3\%$	28 <sup>c</sup>
5 g/l $\text{Ru}(\text{bpy})_3^{2+}$ in methanol	360–540	1.1%	29
$\text{Ru}(\text{bpy})_3^{2+}$ in PVA films	360–530	1%	29 <sup>d</sup>
8 g/l HITC <sup>e</sup> in acetonitrile	320–800 <sup>f</sup>	$\pm 10\%$	30

<sup>a</sup>A higher concentration of RhB is claimed to be preferred for use in transmission mode. See [27].

<sup>b</sup>Response may be 15% lower from 340 to 360 nm.

<sup>c</sup>See [28] for details on the rhodamines, coumarins, and PVA film preparations.

<sup>d</sup>See [29] for details.

<sup>e</sup>HITC, 1,1',3,3,3',3'-hexamethylindotricarbocyanine.

<sup>f</sup>Deviation up to 20% occurs near 470 nm.

## 2.9. CORRECTED EMISSION SPECTRA

### 2.9.1. Comparison with Known Emission Spectra

It is necessary to know the wavelength-dependent efficiency of the detection system to calculate the corrected emission spectra. It is difficult and time consuming to measure the correction factors for any given spectrofluorometer. Even after careful corrections are made the results are only accurate to  $\pm 10\%$ . For this reason the observed technical spectra are usually reported. If corrected spectra are necessary, one simple and reliable method of obtaining the necessary correction factors is to compare the observed emission spectrum of a standard substance with the known corrected spectrum for this same substance. Such spectra have been published for a variety of readily available fluorophores including quinine sulfate,  $\beta$ -naphthol, 3-aminophthalimide, 4-dimethylamino-4'-nitrostilbene, and N,N-dimethylamino-m-nitrobenzene.<sup>31–36</sup> The emission wavelengths of these compounds cover the range from 300 to 800 nm and the data are presented in graphical and numerical form. Corrected spectra have been published for a series of harmine derivatives, covering the range 400–600

nm.<sup>37</sup> For convenience some of these corrected spectra are given in Appendix I, Corrected Emission Spectra.

To obtain correction factors the emission spectrum of a standard compound is recorded and compared to the data for a standard compound. This simple comparative method avoids the difficulties inherent in the more rigorous procedures described below.  $\beta$ -Naphthol should probably not be used as a standard because, under the conditions described, both naphthol and naphthalate emission are observed. The dual emission is a result of an excited state reaction, the extent of which is difficult to control. Quinine sulfate has been questioned as a standard, because its intensity decay may not be a single exponential and its quantum yield may be somewhat dependent on excitation wavelength.<sup>38</sup> However, it seems to be an acceptable standard for most circumstances. One should remember that quinine sulfate is collisionally quenched by chloride,<sup>39</sup> so solutions of quinine used as a quantum yield standard should not contain chloride. A potentially superior standard is  $\beta$ -carboline, whose spectral characteristics are similar to quinine sulfate and which displays a single exponential decay time.<sup>40</sup> The emission spectra of quinine sulfate and  $\beta$ -carboline are similar.

### 2.9.2. Corrections Using a Standard Lamp

The correction factors can also be obtained by observing the wavelength-dependent output from a calibrated light source. The wavelength distribution of the light from a tungsten filament lamp can be approximated by that of a black body of equivalent temperature. Standard lamps of known color temperature are available from the National Bureau of Standards and other secondary sources. Generally one uses the spectral output data provided with the lamp ( $L(\lambda)$ ) because the black-body equation is not strictly valid for a tungsten lamp. The detection system is then calibrated as follows:

1. The intensity of the standard lamp versus wavelength  $I(\lambda)$  is measured using the detection system of the spectrofluorometer.
2. The sensitivity of the detection system  $S(\lambda)$  is calculated using

$$S(\lambda) = I(\lambda)/L(\lambda) \quad (2.3)$$

where  $L(\lambda)$  is the known output of the lamp.

3. The corrected spectra are then obtained by dividing the measured spectra by these sensitivity factors.

It is important to recognize that the operation of a standard lamp requires precise control of the color temperature. In addition, the spectral output of the lamp can vary with age and usage of the lamp.

### 2.9.3. Correction Factors Using a Quantum Counter and Scatterer

Another method to obtain the correction factors for the emission monochromator and PMT is to calibrate the xenon lamp in the spectrofluorometer for its spectral output.<sup>26</sup> The relative photon output ( $L(\lambda)$ ) can be obtained by placing a quantum counter in the sample compartment. Once this intensity distribution is known, the xenon lamp output is directed onto the detector using a magnesium oxide scatterer. MgO is assumed to scatter all wavelengths with equal efficiency. Correction factors are obtained as follows:

1. The excitation wavelength is scanned with the quantum counter in the sample holder. The output yields the lamp output  $L(\lambda)$ .
2. The scatterer is placed in the sample compartment and the excitation and emission monochromators are scanned in unison. This procedure yields the product  $L(\lambda) S(\lambda)$ , where  $S(\lambda)$  is the sensitivity of the detector system.
3. Division of  $S(\lambda) \cdot L(\lambda)$  by  $L(\lambda)$  yields the sensitivity factors  $S(\lambda)$ .

A critical aspect of this procedure is obtaining a reliable scatterer. The MgO must be freshly prepared and be free of impurities. Although this procedure seems simple, it is difficult to obtain reliable correction factors. It is known that the reflectivity of MgO changes over time, and with exposure to UV light, particularly below 400 nm.<sup>41</sup> In addition to changes in reflectivity, it seems probable that the angular distribution of the scattered light and/or collection efficiency changes with wavelength, and one should probably use an integrating sphere at the sample location to avoid spatial effects. Given the complications and difficulties of this procedure, the use of emission spectrum standards is the preferred method when corrected emission spectra are needed.

### 2.9.4. Conversion Between Wavelength and Wavenumber

Occasionally, it is preferable to present spectra on the wavenumber scale ( $\bar{\gamma}$ ) rather than on the wavelength scale

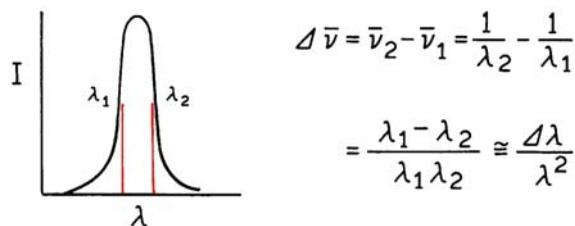


**Figure 2.43.** Relationship between spectral resolution in wavelength ( $\lambda$ ) or wavenumber ( $\bar{\nu}$ ).

( $\lambda$ ). Wavelengths are easily converted to wavenumbers ( $\text{cm}^{-1}$ ) simply by taking the reciprocal. However, the bandpass in wavenumbers is not constant when the spectrum is recorded with constant wavelength resolution, as is usual with grating monochromators. For example, consider a constant bandpass  $\Delta\lambda = \lambda_2 - \lambda_1$ , where  $\lambda_1$  and  $\lambda_2$  are wavelengths on either side of the transmission maximum (Figure 2.43). At 300 nm a bandpass ( $\Delta\lambda$ ) of 2 nm is equivalent to 222  $\text{cm}^{-1}$ . At 600 nm, this same bandpass is equivalent to a resolution ( $\Delta$ ) of 55  $\text{cm}^{-1}$ . As the wavelength is increased, the bandpass (in  $\text{cm}^{-1}$ ) decreases as the square of the exciting wavelength. From  $\bar{\nu} = 1/\lambda$ , it follows that  $|\Delta\nu| = |\Delta\lambda|/\lambda^2$ . Therefore, if spectra are obtained in the usual form of intensity per wavelength interval  $I(\lambda, \lambda + \Delta\lambda)/\Delta\lambda$  and  $I(\bar{\nu}) = I(\bar{\nu}, \bar{\nu} + \Delta\bar{\nu})$ , then conversion to the wavenumber scale requires<sup>38–40</sup> that each intensity be multiplied by  $\lambda^2$ :

$$I(\bar{\nu}) = \lambda^2 I(\lambda) \quad (2.4)$$

The effect of this wavelength-to-wavenumber conversion is illustrated in Appendix I. Multiplication by  $\lambda^2$  results in selective enhancement of the long-wavelength side of the emission, and there is a shift in the apparent emission maximum. It should be noted that even after this correction is performed the resolution of the spectrum still varies with wavenumber.

## 2.10. QUANTUM YIELD STANDARDS

The easiest way to estimate the quantum yield of a fluorophore is by comparison with standards of known quantum yield. Some of the most used standards are listed in Table 2.4. The quantum yields of these compounds are mostly independent of excitation wavelength, so the standards can be used wherever they display useful absorption.

Determination of the quantum yield is generally accomplished by comparison of the wavelength integrated intensity of the unknown to that of the standard. The optical density is kept below 0.05 to avoid inner filter effects, or the optical densities of the sample and reference ( $r$ ) are matched at the excitation wavelength. The quantum yield of the unknown is calculated using

$$Q = Q_R \frac{I}{I_R} \frac{OD_R}{OD} \frac{n^2}{n_R^2} \quad (2.5)$$

**Table 2.4.** Quantum Yield Standards

Compound	Solvent	$\lambda_{\text{ex}}$ (nm)	°C	$Q$	Reference
Quinine sulfate	0.1 M H <sub>2</sub> SO <sub>4</sub>	350	22	0.577	45
		366	—	0.53 ± 0.023	46
β-Carboline <sup>a</sup>	1 N H <sub>2</sub> SO <sub>4</sub>	350	25	0.60	40
Fluorescein	0.1 M NaOH	496	22	0.95 ± 0.03	47
9,10-DPA <sup>b</sup>	cyclohexane	—	—	0.95	48
9,10-DPA	"	366	—	1.00 ± 0.05	49–50
POPOP <sup>c</sup>	cyclohexane	—	—	0.97	48
2-Aminopyridine	0.1 N H <sub>2</sub> SO <sub>4</sub>	285	—	0.60 ± 0.05	50–51
Tryptophan	water	280	—	0.13 ± 0.01	52
Tyrosine	water	275	23	0.14 ± 0.01	52
Phenylalanine	water	260	23	0.024	52
Phenol	water	275	23	0.14 ± 0.01	52
Rhodamine 6G	ethanol	488	—	0.94	53
Rhodamine 101	ethanol	450–465	25	1.0	54
Cresyl Violet	methanol	540–640	22	0.54	55

<sup>a</sup>β-carboline is 9H-pyrido[3,4-β]-indole.

<sup>b</sup>9,10-DPA, 9,10-diphenylanthracene.

<sup>c</sup>POPOP, 2,2'-(1,4-phenylene)bis[5-phenyloxazole].

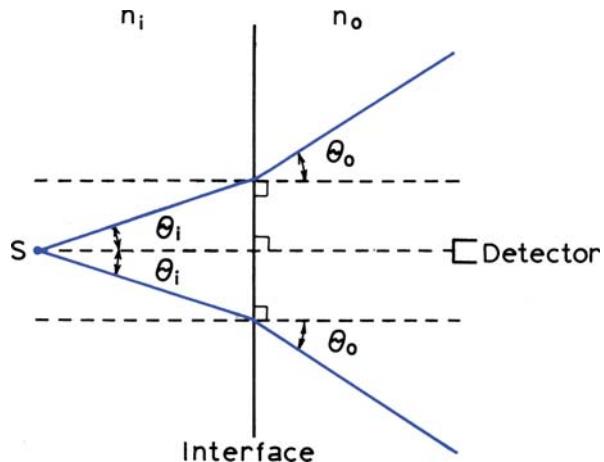


**Figure 2.44.** Refractive index effects in quantum yield measurements. The point source, S, is in a medium of refractive index  $n_i$ , the detector in a medium of refractive index  $n_0$ .  $n_0 < n_i$ . Reprinted with permission from [42], copyright © 1971, American Chemical Society.

where  $Q$  is the quantum yield,  $I$  is the integrated intensity,  $OD$  is the optical density, and  $n$  is the refractive index. The subscript  $R$  refers to the reference fluorophore of known quantum yield. In this expression it is assumed that the sample and reference are excited at the same wavelength, so that it is not necessary to correct for the different excitation intensities of different wavelengths.

This expression is mostly intuitive, except for the use of the ratio of refractive indices of the sample ( $n$ ) and reference ( $n_R$ ). This ratio has its origin in consideration of the intensity observed from a point source in a medium of refractive index  $n_i$ , by a detector in a medium of refractive index  $n_0$  (Figure 2.44). The observed intensity is modified<sup>42–43</sup> by the ratio  $(n_i/n_0)^2$ . While the derivation was for a point source, the use of the ratio was found to be valid for many detector geometries.<sup>44</sup>

## 2.11. EFFECTS OF SAMPLE GEOMETRY

The apparent fluorescence intensity and spectral distribution can be dependent upon the optical density of the sample, and the precise geometry of sample illumination. The most common geometry used for fluorescence is right-angle observation of the center of a centrally illuminated cuvette (Figure 2.45, top left). Other geometric arrangements include front-face and off-center illumination. Off-center illumination decreases the path length, which can also be accomplished by using cuvettes with path lengths less than 1 cm. These methods are generally used to

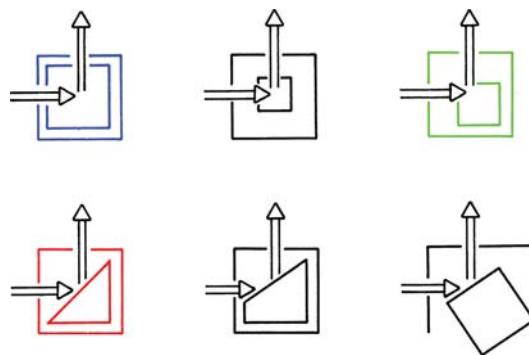


**Figure 2.45.** Various geometric arrangements for observation of fluorescence.

decrease the inner filtering effects due to high optical densities or to sample turbidity.

Frequently, front-face illumination is performed using either triangular cuvettes or square cuvettes oriented at 30 to 60° relative to the incident beam (Figure 2.45). In our opinion, an angle of 45° should be discouraged. A large amount of light is reflected directly into the emission monochromator, increasing the chance that stray light will interfere with the measurements. With front-face illumination we prefer to orient the illuminated surface about 30° from the incident beam. This procedure has two advantages. First, less reflected light enters the emission monochromator. Second, the incident light is distributed over a larger surface area, decreasing the sensitivity of the measurement to the precise placement of the cuvette within its holder. One disadvantage of this orientation is a decreased sensitivity because a larger fraction of the incident light is reflected off the surface of the cuvette.

It is important to recognize that fluorescence intensities are proportional to the concentration over only a limited range of optical densities. Consider a 1 x 1 cm cuvette that is illuminated centrally and observed at a right angle (Figure 2.45, top left). Assume further that the optical density at the excitation wavelength is 0.1. Using the definition of optical density ( $\log I_0/I = OD$ ), the light intensity at the center of the cuvette ( $I$ ) is  $0.88I_0$ , where  $I_0$  is the intensity of the light incident to the cuvette. Since the observed fluorescence intensity is proportional to the intensity of the exciting light, the apparent quantum yield will be about 10% less than that observed for an infinitely dilute solution. This is called an inner filter effect. These effects may decrease the intensity of the excitation at the point of observation, or decrease the observed fluorescence by absorption of the fluorescence. The relative importance of each process depends

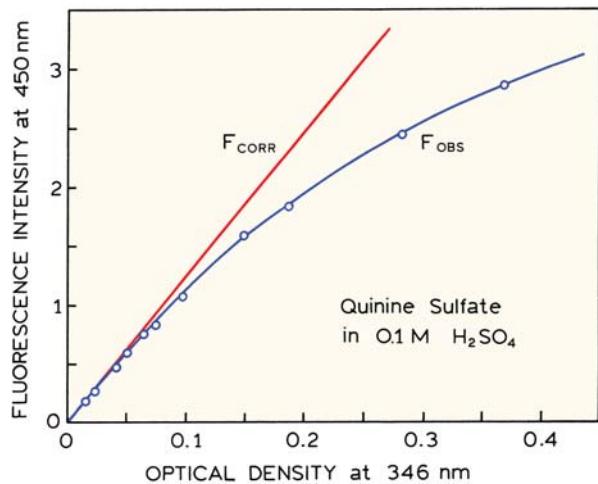


**Figure 2.46.** Effects of optical density on the fluorescence intensity of quinine sulfate. The solid line (—) shows the measured intensities, and the dashed line (---) indicates the corrected intensities, according to equation (2.6) with  $OD_{em} = 0$ . These data were obtained in a 1- $\text{cm}^2$  cuvette that was centrally illuminated.

upon the optical densities of the sample at the excitation and emission wavelengths.

The data for quinine sulfate in Figure 2.46 illustrates the effect of optical density on fluorescence intensity. The measured intensity is proportional to optical density only to an optical density of 0.05. The linear range of the fluorescence intensities could be expanded by using off-center illumination, which reduces the effective light path. These intensities can be approximately corrected for the inner filter effects as follows. Suppose the sample has a significant optical density at both the excitation and emission wavelengths,  $OD_{ex}$  and  $OD_{em}$ , respectively. These optical densities attenuate the excitation and emission by  $10^{-0.5OD_{ex}}$  and  $10^{-0.5OD_{em}}$ , respectively. Attenuation due to absorption of the incident light or absorption of the emitted light are sometimes called the primary and secondary inner filter effects, respectively.<sup>56–57</sup> The corrected fluorescence intensity is given approximately by

$$F_{corr} = F_{obs} \text{ antilog} \left( \frac{OD_{ex} + OD_{em}}{2} \right) \quad (2.6)$$

The corrected intensities for quinine sulfate are shown in Figure 2.46, and these calculated values are seen to match the initial linear portion of the curve. For precise corrections it is preferable to prepare calibration curves using the precise compounds and conditions that will be used for the actual experimentation. Empirical corrections are typi-

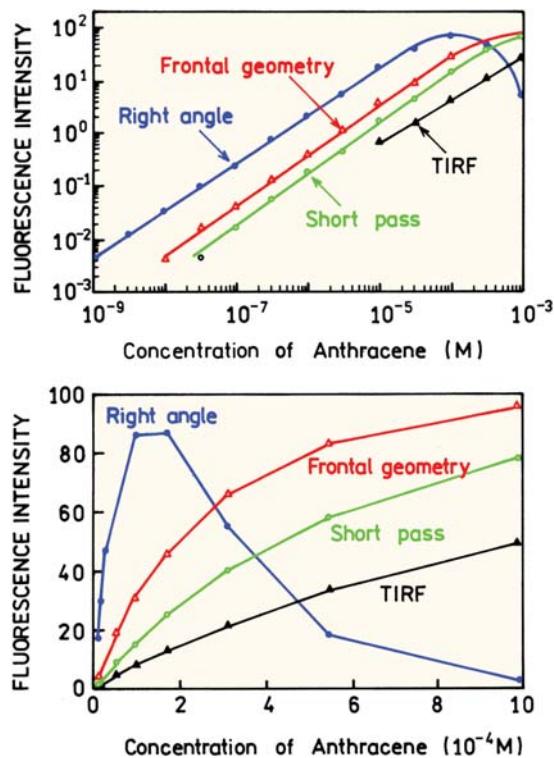


**Figure 2.47.** Effect of concentrations on the intensity of anthracene. Short pass refers to a 1 mm x 10 mm cuvette. Revised from [61].

cally used in most procedures to correct for sample absorbance.<sup>56–60</sup>

Figure 2.47 shows the effect of anthracene concentration on its emission intensity as observed for several geometries. TIRF refers to total internal reflection, which is described in Chapter 23. Short pass refers to a cuvette, 1 by 10 mm in dimension. The highest signal levels were obtained with the standard right-angle geometry. The linear range can be somewhat extended by using other geometries. Intuitively we may expect that with the front-face geometry the intensity will become independent of fluorophore concentration at high concentrations.<sup>60,62</sup> Under these conditions all the incident light is absorbed near the surface of the cuvette. Front-face illumination is also useful for studies of optically dense samples such as whole blood, or a highly scattering solution. The intensity is expected to be proportional to the ratio of the optical density of the fluorophore to that of the sample.<sup>63</sup> When front-face illumination is used the total optical density can be very large (20 or larger). However, high fluorophore concentrations can result in quenching due to a variety of interactions, such as radiative and non-radiative transfer and excimer formation. Fluor-

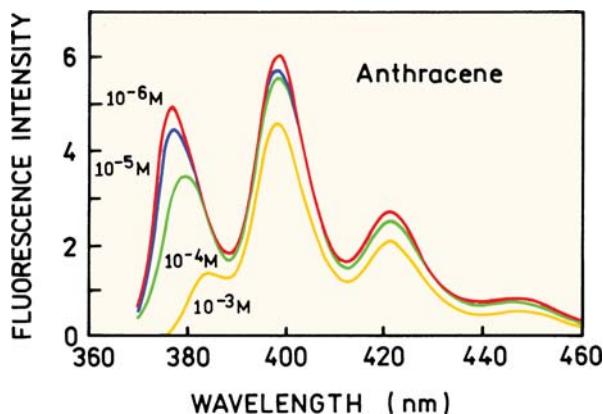


**Figure 2.48.** Effects of self-absorption of anthracene on its emission spectrum. A 1-cm<sup>2</sup> cuvette was used with right-angle observation. Revised from [61].

rophores like fluorescein with a small Stokes shift are particularly sensitive to concentration quenching.

High optical densities can distort the emission spectra as well as the apparent intensities. For example, when right-angle observation is used, the short-wavelength emission bands of anthracene are selectively attenuated (Figure 2.48). This occurs because these shorter wavelengths are absorbed by anthracene. Attenuation of the blue edge of the emission is most pronounced for fluorophores that have significant overlap of the absorption and emission spectra. Fluorophores that display a large Stokes shift are less sensitive to this phenomenon.

A dramatic effect of concentration can be seen with fluorophores that display a small Stokes shift. Figure 2.49 shows a photograph of three bottles of rhodamine 6G on a light box, with the concentration increasing from left to right. The color changes from green to orange. This effect is due to reabsorption of the shorter wavelength part of the emission. The emission spectra shift dramatically to longer wavelengths at higher concentrations.

## 2.12. COMMON ERRORS IN SAMPLE PREPARATION

It is valuable to summarize some of the difficulties that can be encountered with any given sample (Figure 2.50). The sample can be too concentrated, in which case all the light is absorbed at the surface facing the light source. In fact, this is one of the more common errors. With highly absorbing solutions and right-angle observations the signal levels can be very low. Other problems are when the sample contains a fluorescent impurity, or the detected light is contam-

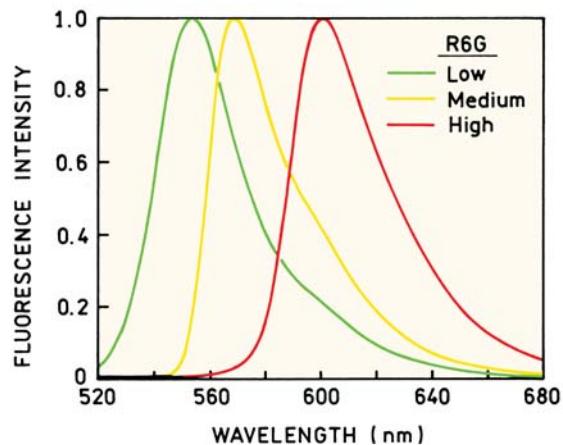
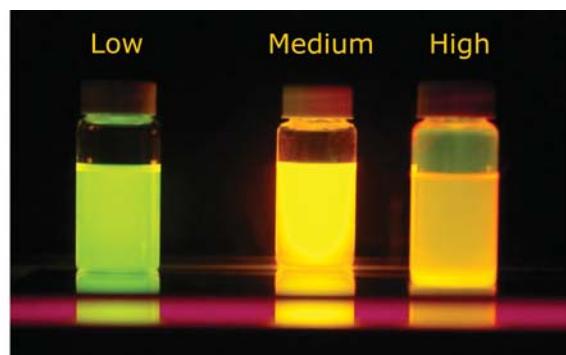


**Figure 2.49.** Effect of concentrations on the color and emission spectra of rhodamine 6G. The concentrations of R6G are  $5 \times 10^{-6}$ ,  $1.6 \times 10^{-4}$ , and  $5.7 \times 10^{-3}$  M. From [64].

inated by Rayleigh or Raman scatter. Sometimes the signal may seem too noisy given the signal level. Intensity fluctuations can be due to particles that drift through the laser beam, and fluoresce or scatter the incident light.

Even if the fluorescence is strong, it is important to consider the possibility of two or more fluorophores, that is, an impure sample. Emission spectra are usually independent of excitation wavelength.<sup>65</sup> Hence it is useful to determine if the emission spectrum remains the same at different excitation wavelengths.

One example of a mixture of fluorophores is shown in Figure 2.51, which contains a mixture of coumarin 102 (C102) and coumarin 153 (C153). For a pure solution of C102 the same emission spectrum is observed for excitation at 360 and 420 nm (top). For a mixture of C102 and C153, one finds an increased intensity above 500 nm for excitation at 420 (bottom, dashed). This peak at 520 nm is due to C153, which can be seen from its emission spectrum (dot-

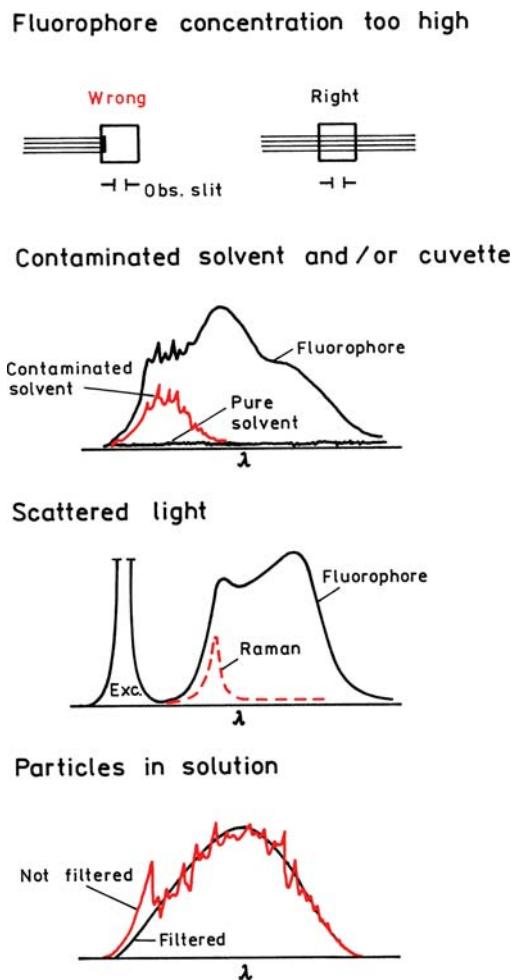


Figure 2.50. Common errors in sample preparation.

ted). Whenever the emission spectrum changes with excitation wavelength one should suspect an impurity.

It is interesting to note the significant change in the emission spectra of these two coumarin derivatives for a small change in structure. The fluorine-substituted coumarin (C153) appears to be more sensitive to solvent polarity. This effect is probably due to an increased charge separation in C153, due to movement of these amino electrons toward the  $-CF_3$  group in the excited state. These effects are described in Chapter 6.

### 2.13. ABSORPTION OF LIGHT AND DEVIATION FROM THE BEER-LAMBERT LAW

A fundamental aspect of fluorescence spectroscopy is the measurement of light absorption. While the theory of light absorption is well known, a number of factors can result in

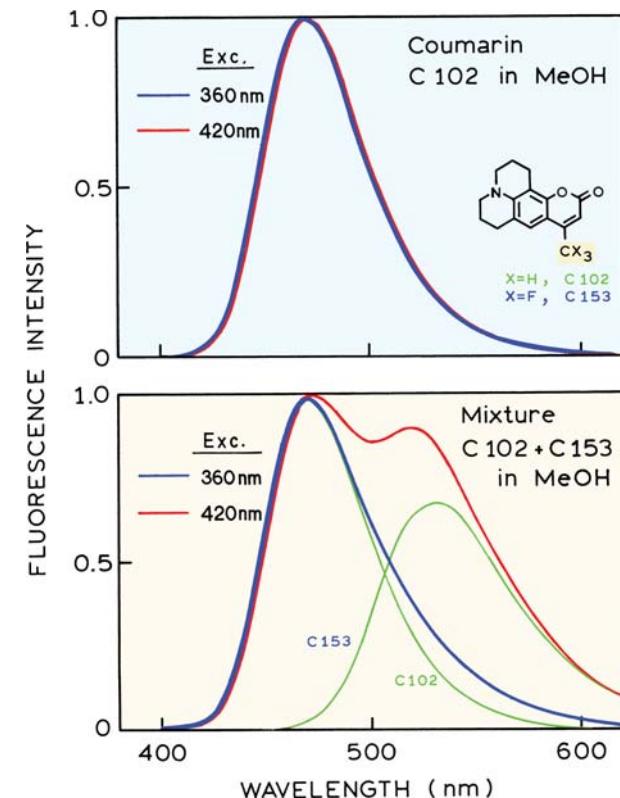


Figure 2.51. Emission spectra of C102 (top) and a mixture of C102 and C153 (bottom) excited at 360 and 420 nm. From [66].

misleading measurements of light absorption. We will first derive the Beer-Lambert Law, and then describe reasons for deviations from this law.

Consider a thin slab of solution of thickness  $dx$  that contains  $n$  light-absorbing molecules/cm<sup>3</sup> (Figure 2.52). Let  $\sigma$  be the effective cross-section for absorption in cm<sup>2</sup>. The light intensity  $dI$  absorbed per thickness  $dx$  is proportional to the intensity of the incident light  $I$  and to both  $\sigma$  and  $n$ , where  $n$  is the number of molecules per cm<sup>3</sup>:

$$\frac{dI}{dx} = -I\sigma n \quad (2.7)$$

Rearrangement and integration, subject to the boundary condition  $I = I_0$  at  $x = 0$ , yields

$$\ln \frac{I_0}{I} = \sigma n d \quad (2.8)$$

where  $d$  is the thickness of the sample. This is the Beer-Lambert equation, which is generally used in an alternative form:

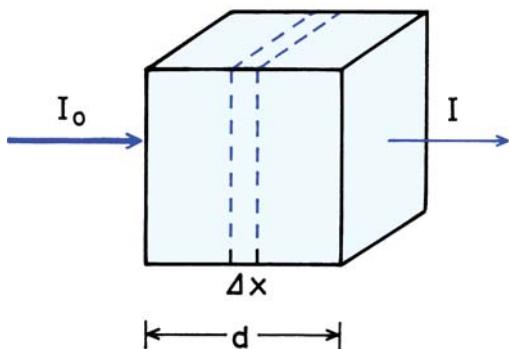


Figure 2.52. Light absorption.

$$\log \frac{I_0}{I} = \epsilon cd = \text{optical density} \quad (2.9)$$

where  $\epsilon$  is the decadic molar extinction coefficient (in  $M^{-1} \text{cm}^{-1}$ ) and  $c$  is the concentration in moles/liter. Combination of eqs. 2.8 and 2.9 yields the relationship between the extinction coefficient and the cross-section for light absorption:

$$\sigma = 2.303 \frac{\epsilon c}{n} \quad (2.10)$$

Since  $n = Nc/10^3$  (where  $N$  is Avogadro's number), we obtain

$$\sigma = 3.82 \times 10^{-21} \epsilon \quad (\text{in } \text{cm}^2) \quad (2.11)$$

It is interesting to calculate the absorption cross-section for typical aromatic compounds. The extinction coefficients of anthracene are 160,000 and  $6,300 \text{ M}^{-1} \text{ cm}^{-1}$  at 253 and 375 nm, respectively. These values correspond to cross-sections of 6.1 and  $0.24 \text{ \AA}^2$ , respectively. Assuming the molecular cross-section of anthracene to be  $12 \text{ \AA}^2$ , we see that anthracene absorbs about 50% of the photons it encounters at 253 nm and 2% of the photons at 375 nm.

Occasionally one encounters the term "oscillator strength." This term represents the strength of absorption relative to a completely allowed transition. The oscillator strength ( $f$ ) is related to the integrated absorption of a transition by

$$f = \frac{4.39 \times 10^{-9}}{n} \int \epsilon(\bar{v}) d\bar{v} \quad (2.12)$$

where  $n$  is the refractive index.

### 2.13.1. Deviations from Beer's Law

Beer's Law predicts that the optical density is directly proportional to the concentration of the absorbing species. Deviations from Beer's law can result from both instrumental and intrinsic causes. Biological samples are frequently turbid because of macromolecules or other large aggregates that scatter light. The optical density resulting from scatter will be proportional to  $1/\lambda^4$  (Rayleigh scattering), and may thus be easily recognized as a background absorption that increases rapidly with decreasing wavelength.

If the optical density of the sample is high, and if the absorbing species is fluorescent, the emitted light cannot reach the detector. This effect yields deviations from Beer's law that are concave toward the concentration axis. The fluorescence is omnidirectional, whereas the incident light is collimated along an axis. Hence, this effect can be minimized by keeping the detector distant from the sample, and thereby decreasing the efficiency with which the fluorescence emission is collected.

If the absorbing species is only partially soluble, it may aggregate in solutions at high concentrations. The absorption spectra of the aggregates may be distinct from the monomers. An example is the common dye bromophenol blue. At concentrations around 10 mg/ml it appears as a red solution, whereas at lower concentrations it appears blue. Depending upon the wavelength chosen for observation, the deviations from Beer's law may be positive or negative.

The factors described above were due to intrinsic properties of the sample. Instrumental artifacts can also yield optical densities that are nonlinear with concentration. This is particularly true at high optical densities. For example, consider a solution of indole with an optical density of 5 at 280 nm. In order to accurately measure this optical density, the spectrophotometer needs to accurately quantify the intensity of  $I_0$  and  $I$ , the latter of which is  $10^{-5}$  less intense than the incident light  $I_0$ . Generally, the stray light passed by the monochromator, at wavelengths where the compound does not absorb, are larger than this value. As a result, one cannot reliably measure such high optical densities unless considerable precautions are taken to minimize stray light.

---

### 2.14. CONCLUSIONS

At first glance it seems easy to perform fluorescence experiments. However, there are numerous factors that can compromise the data and invalidate the results. One needs to be constantly aware of the possibility of sample contamina-

tion, or contamination of the signal from scattered or stray light. Collection of emission spectra, and examination of blank samples, is essential for all experiments. One cannot reliably interpret intensity values, anisotropy, or lifetimes without careful examination of the emission spectra.

## REFERENCES

1. Revised from commercial literature provided by SLM Instruments.
2. Revised from commercial literature provided by Molecular Devices, <http://www.moleculardevices.com/pages/instruments/gemini.html>.
3. Revised from commercial literature from Spectra Physics, [www.spectra-physics.com](http://www.spectra-physics.com).
4. Laczko G, Lakowicz JR, unpublished observations.
5. Oriel Corporation, 250 Long Beach Blvd., PO Box 872, Stratford, CT 06497: Light Sources, Monochromators and Spectrographs, Detectors and Detection Systems, Fiber Optics.
6. ILC Technology Inc. 399 West Joan Drive, Sunnyvale, CA 94089: Cermax Product Specifications for collimated and focused xenon lamps.
7. Ocean Optics product literature, <http://www.oceanoptics.com/products/>
8. Hart SJ, JiJi RD. 2002. Light emitting diode excitation emission matrix fluorescence spectroscopy. *Analyst* **127**:1643–1699.
9. Landgraf S. 2004. Use of ultrabright LEDs for the determination of static and time-resolved fluorescence information of liquid and solid crude oil samples. *J Biochem Biophys Methods* **61**:125–134.
10. Gryczynski I, Lakowicz JR, unpublished observations.
11. Optometrics USA Inc., Nemco Way, Stony Brook Industrial Park, Ayer, MA 01432: 1996 Catalog Optical Components and Instruments.
12. Castellano P, Lakowicz JR, unpublished observations.
13. Melles Griot product literature, <http://shop.mellesgriot.com/products/optics/>
14. Macleod HA. 2001. *Thin-film optical filters*, 3rd ed. Institute of Physics, Philadelphia.
15. Semrock Inc., Rochester, NY, [www.semrock.com](http://www.semrock.com).
16. Gryczynski I, Malak H, Lakowicz JR, Cheung HC, Robinson J, Umeda PK. 1996. Fluorescence spectral properties of troponin C mutant F22W with one-, two- and three-photon excitation. *Biophys J* **71**:3448–3453.
17. Szmacinski H, Gryczynski I, Lakowicz JR. 1993. Calcium-dependent fluorescence lifetimes of Indo-1 for one- and two-photon excitation of fluorescence. *Photochem Photobiol* **58**:341–345.
18. Hamamatsu Photonics K.K., Electron Tube Center, (1994), 314-5, Shimokanzo, Toyooka-village, Iwata-gun, Shizuoka-ken, 438-01 Japan: Photomultiplier Tubes.
19. Provided by Dr. R. B. Thompson
20. Leback DH. 1997. Extended theory, and improved practice for the quantitative measurement of fluorescence. *J Fluoresc* **7**(1):55S–57S.
21. Epperson PM, Denton MB. 1989. Binding spectral images in a charge-coupled device. *Anal Chem* **61**:1513–1519.
22. Bilhorn RB, Sweedler JV, Epperson PM, Denton MB. 1987. Charge-transfer device detectors for analytical optical spectroscopy—operation and characteristics. *Appl Spectrosc* **41**:1114–1124.
23. Hiraoka Y, Sedat JW, Agard DA. 1987. The use of a charge-coupled device for quantitative optical microscopy of biological structures. *Science* **238**:36–41.
24. Aikens RS, Agard DA, Sedat JW. 1989. Solid-state imagers for microscopy. *Methods Cell Biol* **29**:291–313.
25. Ocean Optics Inc., [http://www.oceanoptics.com/products/usb2000\\_flg.asp](http://www.oceanoptics.com/products/usb2000_flg.asp).
26. Melhuish WH. 1962. Calibration of spectrofluorometers for measuring corrected emission spectra. *J Opt Soc Am* **52**:1256–1258.
27. Yguerabide J. 1968. Fast and accurate method for measuring photon flux in the range 2500–6000 Å. *Rev Sci Instrum* **39**(7):1048–1052.
28. Mandal K, Pearson TDL, Demas JN. 1980. Luminescent quantum counters based on organic dyes in polymer matrices. *Anal Chem* **52**:2184–2189.
29. Mandal K, Pearson TDL, Demas NJ. 1981. New luminescent quantum counter systems based on a transition-metal complex. *Inorg Chem* **20**:786–789.
30. Nothnagel EA. 1987. Quantum counter for correcting fluorescence excitation spectra at 320- and 800-nm wavelengths. *Anal Biochem* **163**:224–237.
31. Lippert E, Nagelle W, Siebold-Blakenstein I, Staiger U, Voss W. 1959. Messung von fluoreszenzspektren mit hilfe von spektralphotometern und vergleichsstandards. *Zeitschr Anal Chem* **17**:1–18.
32. Schmillen A, Legler R. 1967. *Landolt-Bornstein*. Vol 3: Lumineszenz Organischer Substanzen. Springer-Verlag, New York.
33. Argauer RJ, White CE. 1964. Fluorescent compounds for calibration of excitation and emission units of spectrofluorometer. *Anal Chem* **36**:368–371.
34. Melhuish WH. 1960. A standard fluorescence spectrum for calibrating spectrofluorometers. *J Phys Chem* **64**:762–764.
35. Parker CA. 1962. Spectrofluorometer calibration in the ultraviolet region. *Anal Chem* **34**:502–505.
36. Velapoldi RA. 1973. Considerations on organic compounds in solution and inorganic ions in glasses as fluorescent standard reference materials. *Proc Natl Bur Stand* **37B**:231–244.
37. Pardo A, Reyman D, Poyato JML, Medina F. 1992. Some β-carboline derivatives as fluorescence standards. *J Lumines* **51**:269–274.
38. Chen RF. 1967. Some characteristics of the fluorescence of quinine. *Anal Biochem* **19**:374–387.
39. Verity B, Bigger SW. 1996. The dependence of quinine fluorescence quenching on ionic strength. *Int J Chem Kinet* **28**(12):919–923.
40. Ghiggino KP, Skilton PF, Thistletonwaite PJ. 1985. β-Carboline as a fluorescence standard. *J Photochem* **31**:113–121.
41. Middleton WEK, Sanders CL. 1951. The absolute spectral diffuse reflectance of magnesium oxide. *J Opt Soc Am* **41**(6):419–424.
42. Demas JN, Crosby GA. 1971. The measurement of photoluminescence quantum yields: a review. *J Phys Chem* **75**(8):991–1025.
43. Birks JB. 1970. *Photophysics of aromatic molecules*. Wiley-Interscience, New York.
44. Hermans JJ, Levinson S. 1951. Some geometrical factors in light-scattering apparatus. *J Opt Soc Am* **41**(7):460–465.
45. Eastman JW. 1967. Quantitative spectrofluorimetry—the fluorescence quantum yield of quinine sulfate. *Photochem Photobiol* **6**:55–72.
46. Adams MJ, Highfield JG, Kirkbright GF. 1977. Determination of absolute fluorescence quantum efficiency of quinine bisulfate in aqueous medium by optoacoustic spectrometry. *Anal Chem* **49**:1850–1852.
47. Brannon JH, Magde D. 1978. Absolute quantum yield determination by thermal blooming: fluorescein. *J Phys Chem* **82**(6):705–709.
48. Mardelli M, Olmsted J. 1977. Calorimetric determination of the 9,10-diphenyl-anthracene fluorescence quantum yield. *J Photochem* **7**:277–285.
49. Ware WR, Rothman W. 1976. Relative fluorescence quantum yields using an integrating sphere: the quantum yield of 9,10-diphenylanthracene in cyclohexane. *Chem Phys Lett* **39**(3):449–453.
50. Testa AC. 1969. Fluorescence quantum yields and standards. *Fluoresc News* **4**(4):1–3.

51. Rusakowicz R, Testa AC. 1968. 2-aminopyridine as a standard for low-wavelength spectrofluorometry. *J Phys Chem* **72**:2680–2681.
52. Chen RF. 1967. Fluorescence quantum yields of tryptophan and tyrosine. *Anal Lett* **1**:35–42.
53. Fischer M, Georges J. 1996. Fluorescence quantum yield of rhodamine 6G in ethanol as a function of concentration using thermal lens spectrometry. *Chem Phys Lett* **260**:115–118.
54. Karstens T, Kobe K. 1980. Rhodamine B and Rhodamine 101 as reference substances for fluorescence quantum yield measurements. *J Phys Chem* **84**:1871–1872.
55. Magde D, Brannon JH, Cremers TL, Olmsted J. 1979. Absolute luminescence yield of cresyl violet: a standard for the red. *J Phys Chem* **83**(6):696–699.
56. Kubista M, Sjöback R, Eriksson S, Albinsson B. 1994. Experimental correction for the inner-filter effect in fluorescence spectra. *Analyst* **119**:417–419.
57. Yappert MC, Ingle JD. 1989. Correction of polychromatic luminescence signals for inner-filter effects. *Appl Spectrosc* **43**(5):759–767.
58. Wiechelman KJ. 1986. Empirical correction equation for the fluorescence inner filter effect. *Am Lab* **18**:49–53.
59. Puchalski MM, Morra MJ, von Wandruszka R. 1991. Assessment of inner filter effect corrections in fluorimetry. *Fresenius J Anal Chem* **340**:341–344.
60. Guilbault GG, ed. 1990. *Practical fluorescence*. Marcel Dekker, New York.
61. Kao S, Asanov AN, Oldham PB. 1998. A comparison of fluorescence inner-filter effects for different cell configurations. *Instrum Sci Tech* **26**(4):375–387.
62. Eisinger J. 1969. A variable temperature, UV luminescence spectrophotograph for small samples. *Photochem Photobiol* **9**:247–258.
63. Eisinger J, Flores J. 1979. Front-face fluorometry of liquid samples. *Anal Biochem* **94**:15–21.
64. Courtesy of Drs. Joanna Lukomska and Ignacy Gryczynski.
65. Kasha M. 1960. Paths of molecular excitation. *Radiat Res* **2**:243–275.
66. Gryczynski I, unpublished observations.

---

## PROBLEMS

- P2.1. *Measurement of High Optical Densities:* Suppose you wish to determine the concentration of a  $10^{-4}$  M solution of rhodamine B, which has an extinction coefficient near  $100,000 \text{ M}^{-1} \text{ cm}^{-1}$  at 590 nm. The monochromator in your spectrophotometer is imperfect, and the incident light at 590 nm contains 0.01% of light at longer wavelengths, not absorbed by rhodamine B. What is the true optical density of the solution? Which is the apparent optical density measured with your spectrophotometer? Assume the path length is 1 cm.
- P2.2. *Calculation of Concentrations by Absorbance:* Suppose a molecule displays an extinction coefficient of  $30,000 \text{ M}^{-1} \text{ cm}^{-1}$ , and that you wish to determine its concentration from the absorbance. You have two solutions, with actual optical densities of 0.3 and 0.003 in a 1-cm cuvette. What are the concentrations of the two solutions? Assume the measurement error in percent transmission is 1%. How does the 1% error affect determination of the concentrations?

# 3

# Fluorophores

Fluorescence probes represent the most important area of fluorescence spectroscopy. The wavelength and time resolution required of the instruments is determined by the spectral properties of the fluorophores. Furthermore, the information available from the experiments is determined by the properties of the probes. Only probes with non-zero anisotropies can be used to measure rotational diffusion, and the lifetime of the fluorophore must be comparable to the timescale of interest in the experiment. Only probes that are sensitive to pH can be used to measure pH. And only probes with reasonably long excitation and emission wavelengths can be used in tissues, which display autofluorescence at short excitation wavelengths.

Thousands of fluorescent probes are known, and it is not practical to describe them all. This chapter contains an overview of the various types of fluorophores, their spectral properties, and applications. Fluorophores can be broadly divided into two main classes—*intrinsic* and *extrinsic*. Intrinsic fluorophores are those that occur naturally. These include the aromatic amino acids, NADH, flavins, derivatives of pyridoxyl, and chlorophyll. Extrinsic fluorophores are added to the sample to provide fluorescence when none exists, or to change the spectral properties of the sample. Extrinsic fluorophores include dansyl, fluorescein, rhodamine, and numerous other substances.

## 3.1. INTRINSIC OR NATURAL FLUOROPHORES

Intrinsic protein fluorescence originates with the aromatic amino acids<sup>1–3</sup> tryptophan (trp), tyrosine (tyr), and phenylalanine (phe) (Figure 3.1). The indole groups of tryptophan residues are the dominant source of UV absorbance and emission in proteins. Tyrosine has a quantum yield similar to tryptophan (Table 3.1), but its emission spectrum is more narrowly distributed on the wavelength scale (Figure 3.2). This gives the impression of a higher quantum yield for tyrosine. In native proteins the emission of tyrosine is often

quenched, which may be due to its interaction with the peptide chain or energy transfer to tryptophan. Denaturation of proteins frequently results in increased tyrosine emission. Like phenol, the  $Pk_A$  of tyrosine decreases dramatically upon excitation, and excited state ionization can occur. Emission from phenylalanine is observed only when the sample protein lacks both tyrosine and tryptophan residues, which is a rare occurrence (Chapter 16).

The emission of tryptophan is highly sensitive to its local environment, and is thus often used as a reporter group for protein conformational changes. Spectral shifts of protein emission have been observed as a result of several phenomena, including binding of ligands, protein–protein association, and protein unfolding. The emission maxima of proteins reflect the average exposure of their tryptophan residues to the aqueous phase. Fluorescence lifetimes of tryptophan residues range from 1 to 6 ns. Tryptophan fluorescence is subject to quenching by iodide, acrylamide, and nearby disulfide groups. Tryptophan residues can be quenched by nearby electron-deficient groups like  $-NH_3^+$ ,  $-CO_2H$ , and protonated histidine residues. The presence of multiple tryptophan residues in proteins, each in a different environment, is one reason for the multi-exponential intensity decays of proteins.

### 3.1.1. Fluorescence Enzyme Cofactors

Enzyme cofactors are frequently fluorescent (Figure 3.1). NADH is highly fluorescent, with absorption and emission maxima at 340 and 460 nm, respectively (Figure 3.3). The oxidized form,  $NAD^+$ , is nonfluorescent. The fluorescent group is the reduced nicotinamide ring. The lifetime of NADH in aqueous buffer is near 0.4 ns. In solution its fluorescence is partially quenched by collisions or stacking with the adenine moiety. Upon binding of NADH to proteins, the quantum yield of the NADH generally increases fourfold,<sup>4</sup> and the lifetime increases to about 1.2 ns. How-

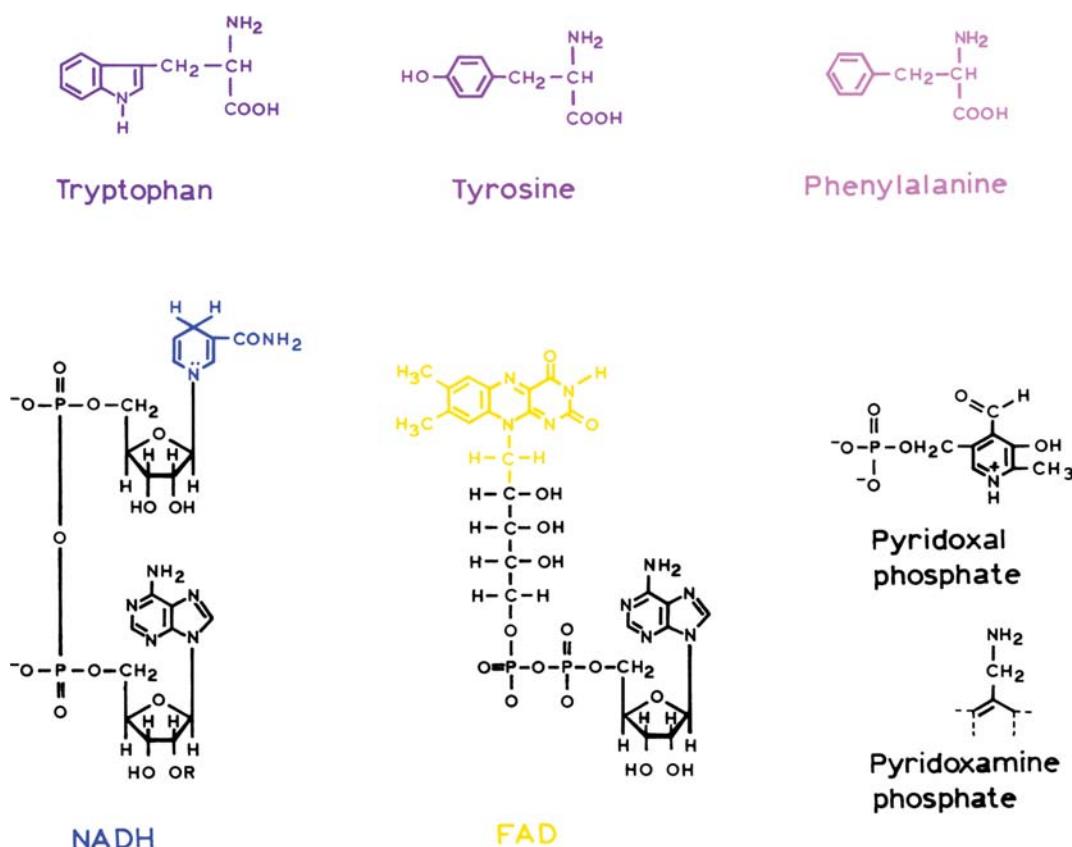


Figure 3.1. Intrinsic biochemical fluorophores. R is a hydrogen in NADH, and a phosphate group in NADPH.

ever, depending on the protein, NADH fluorescence can increase or decrease upon protein binding. The increased yield is generally interpreted as binding of the NADH in an elongated fashion, which prevents contact between adenine and the fluorescent-reduced nicotinamide group. Lifetimes as long as 5 ns have been reported for NADH bound to horse liver alcohol dehydrogenase<sup>5</sup> and octopine dehydrogenase.<sup>6</sup> The lifetimes of protein-bound NADH are typically different in the presence and absence of bound enzyme substrate.

The cofactor pyridoxyl phosphate is also fluorescent (Figure 3.4).<sup>7–14</sup> Its absorption and emission spectra are dependent upon its chemical structure in the protein, where pyridoxyl groups are often coupled to lysine residues by the

aldehyde groups. The emission spectrum of pyridoxamine is at shorter wavelengths than that of pyridoxyl phosphate. The emission spectrum of pyridoxamine is dependent on pH (not shown), and the emission spectrum of the pyridoxyl group depends on its interaction with proteins. The spectroscopy of pyridoxyl groups is complex, and it seems that this cofactor can exist in a variety of forms.

Riboflavin, FMN (Flavin mononucleotide), and FAD (Flavin adenine dinucleotide) absorb light in the visible range ( $\approx 450$  nm) and emit around 525 nm (Figure 3.3). In contrast to NADH, the oxidized forms of flavins are fluorescent, not the reduced forms. Typical lifetimes for FMN and FAD are 4.7 and 2.3 ns, respectively. As for NADH, the flavin fluorescence is quenched by the adenine. This

Table 3.1. Fluorescence Parameters of Aromatic Amino Acids in Water at Neutral pH

Species <sup>a</sup>	$\lambda_{\text{ex}}$ (nm)	$\lambda_{\text{em}}$ (nm)	Bandwidth (nm)	Quantum yield	Lifetime (ns)
Phenylalanine	260	282	—	0.02	6.8
Tyrosine	275	304	34	0.14	3.6
Tryptophan	295	353	60	0.13	3.1 (mean)

<sup>a</sup>From [1].

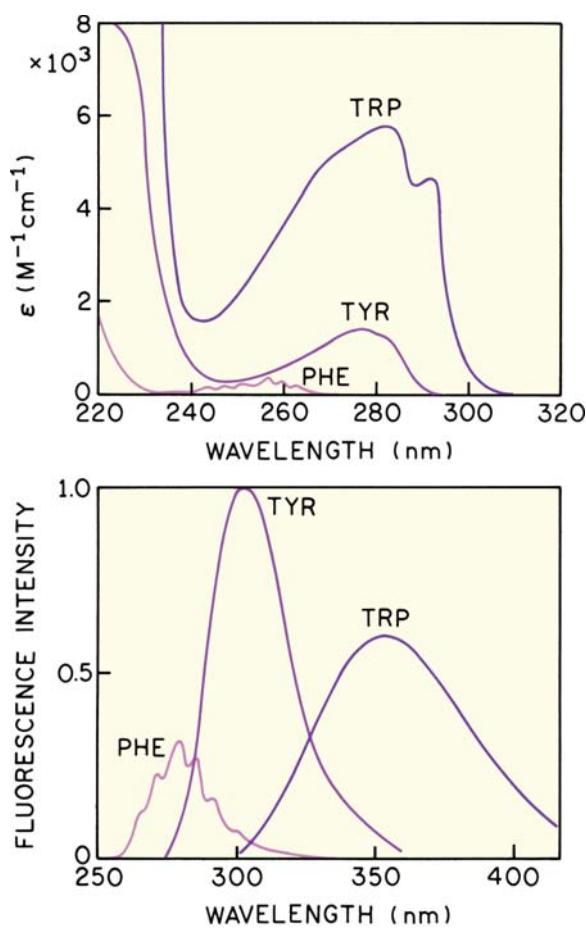


**Figure 3.2.** Absorption and emission spectra of the fluorescent amino acids in water of pH 7.0.

quenching is due to complex formation between the flavin and the adenine.<sup>15</sup> The latter process is referred to as static quenching. There may also be a dynamic component to the quenching due to collisions between adenine and the reduced nicotinamide moiety. In contrast to NADH, which is highly fluorescent when bound to proteins, flavoproteins are generally weakly fluorescent<sup>16–17</sup> or nonfluorescent, but exceptions exist. Intensity decays of protein-bound flavins are typically complex, with multi-exponential decay times ranging from 0.1 to 5 ns, and mean decay times from 0.3 to 1 ns.<sup>18</sup>

Nucleotides and nucleic acids are generally nonfluorescent. However, some exceptions exist. Yeast tRNA<sup>PHE</sup> contains a highly fluorescent base, known as the Y-base, which has an emission maximum near 470 nm and a lifetime near 6 ns. The molecules described above represent the dominant fluorophores in animal tissues. Many additional

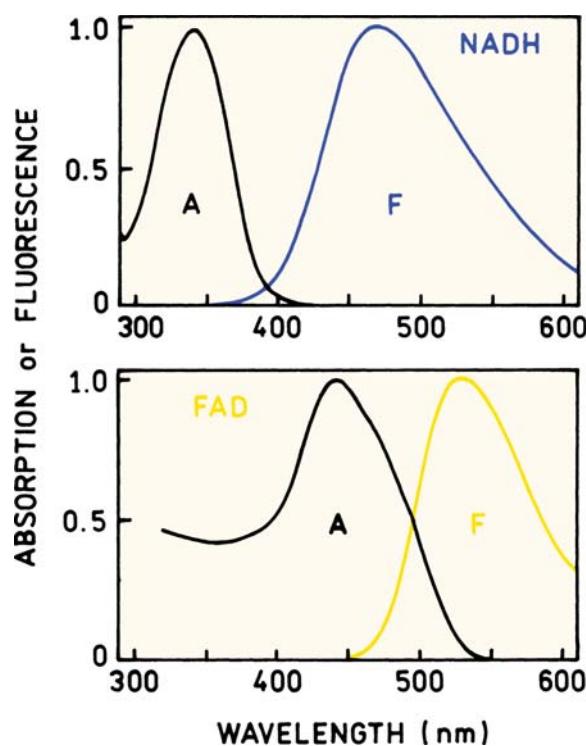


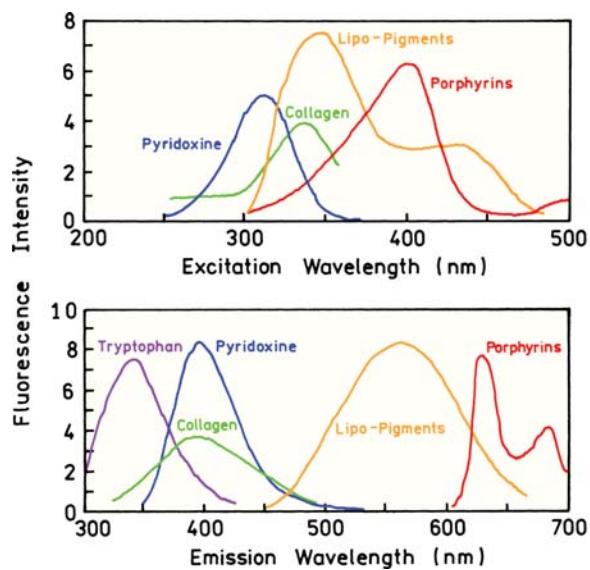
**Figure 3.3.** Absorption and emission spectra of the enzyme cofactors NADH and FAD.

naturally occurring fluorescence substances are known and have been summarized.<sup>19</sup>

There is presently interest in the emission from intrinsic fluorophores from tissues, from fluorophores that are not enzyme cofactors.<sup>20–25</sup> Much of the fluorescence from cells is due to NADH and flavins.<sup>26–27</sup> Other fluorophores are seen in intact tissues, such as collagen, elastin lipo-pigments and porphyrins (Figure 3.4). In these cases the emission is not due to a single molecular species, but represents all the emitting structures present in a particular tissue. The emitting species are thought to be due to crosslinks between oxidized lysine residues that ultimately result in hydroxypyridinium groups. Different emission spectra are observed with different excitation wavelengths. Much of the work is intrinsic tissue fluorescence, to identify spectral features that can be used to identify normal versus cancerous tissues, and other disease states.

### 3.1.2. Binding of NADH to a Protein

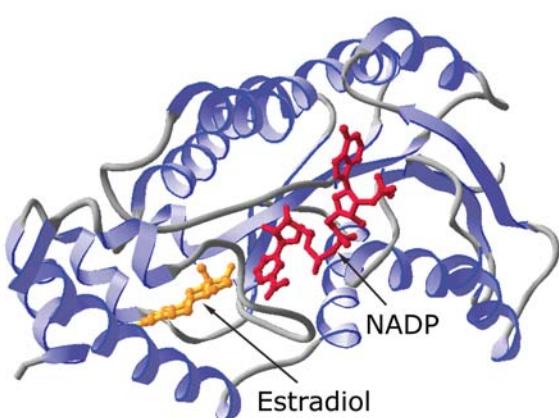
Fluorescence from NADH and FAD has been widely used to study their binding to proteins. When bound to protein NADH is usually in the extended conformation, as shown in



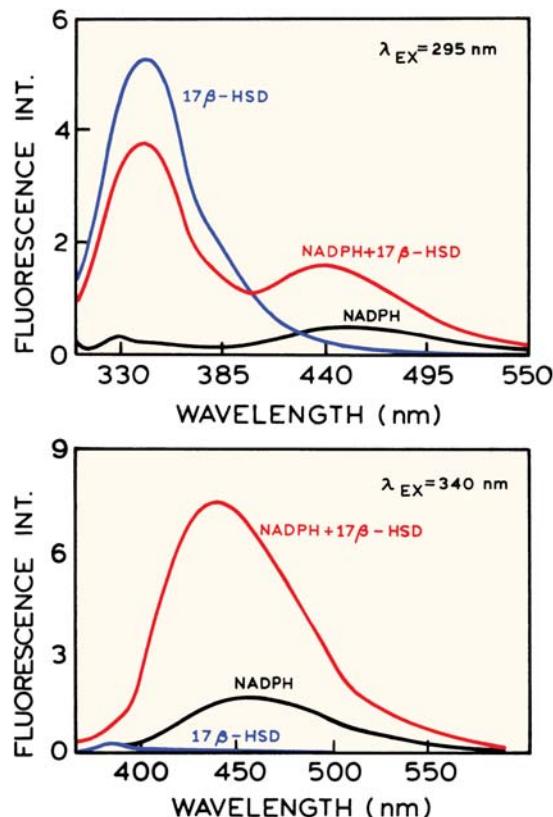
**Figure 3.4.** Emission spectra from intrinsic tissue fluorophores. Revised from [25].

Figure 3.5. This is shown for the enzyme  $17\beta$ -hydroxysteroid dehydrogenase ( $17\beta$ -HSD), which catalyzes the last step in the biosynthesis of estradiol from estrogen.<sup>28</sup> The protein consists of two identical subunits, each containing a single tryptophan residue.  $17\beta$ -HSD binds NADPH as a cofactor. Binding prevents quenching of the reduced nicotinamide by the adenine group. As a result the emission intensity of NADPH is usually higher when bound to protein than when free in solution.

Emission spectra of  $17\beta$ -HSD and of NADPH are shown in Figure 3.6. NADPH is identical to NADH (Figure



**Figure 3.5.** Structure of  $17\beta$ -hydroxysteroid hydrogenase ( $\beta$ -HSD) with bound NADPH. From [28].



**Figure 3.6.** Emission spectra  $17\beta$ -hydroxysteroid dehydrogenase ( $\beta$ -HSD) in the presence and absence of NADPH. Revised from [29].

3.1) except for a phosphate group on the 2'-position of the ribose. For excitation at 295 nm both the protein and NADPH are excited (top). Addition of NADPH to the protein results in 30% quenching of protein fluorescence, and an enhancement of the NADPH fluorescence.<sup>29</sup> The Förster distance for trp $\rightarrow$ NADPH energy transfer in this system is 23.4 Å. Using eq. 1.12 one can readily calculate a distance of 26.9 Å from the single tryptophan residue to the NADPH.

For illumination at 340 nm only the NADPH absorbs, and not the protein. For excitation at 340 nm the emission spectrum of NADPH is more intense in the presence of protein (Figure 3.6, lower panel). An increase in intensity at 450 nm is also seen for excitation at 295 nm (top panel), but in this case it is not clear if the increased intensity is due to a higher quantum yield for NADPH or to energy transfer from the tryptophan residues. For excitation at 340 nm the emission intensity increases about fourfold. This increase is due to less quenching by the adenine group when NADPH is bound to the protein. The increased quantum yield can be

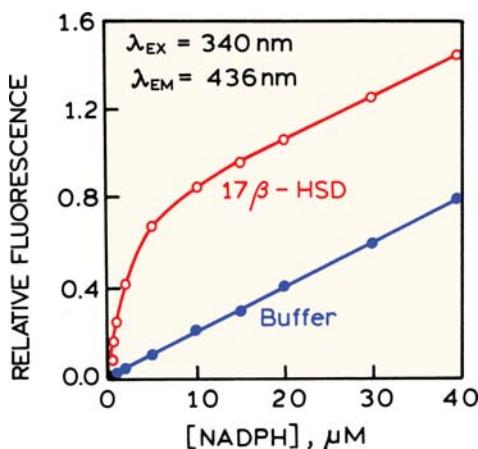


**Figure 3.7.** Fluorescence intensity of NADPH titrated into buffer (●) or a solution of 17 $\beta$ -HSD (○). Revised from [29].

used to study binding of NADPH to proteins (Figure 3.7). In the absence of protein the emission increases linearly with NADPH concentration. In the presence of protein the intensity initially increases more rapidly, and then increases as in the absence of protein. The initial increase in the intensity of NADPH is due to binding of NADPH to 17 $\beta$ -HSD, which occurs with a fourfold increase in the quantum yield of NADPH. Once the binding sites on 17 $\beta$ -HSD are saturated, the intensity increases in proportion to the concentration of unbound NADPH. In contrast to NADH,

emission from FAD and flavins is usually quenched upon binding to proteins.

### 3.2. EXTRINSIC FLUOROPHORES

Frequently the molecules of interest are nonfluorescent, or the intrinsic fluorescence is not adequate for the desired experiment. For instance, DNA and lipids are essentially devoid of intrinsic fluorescence (Figure 1.18). In these cases useful fluorescence is obtained by labeling the molecule with extrinsic probes. For proteins it is frequently desirable to label them with chromophores with longer excitation and emission wavelengths than the aromatic amino acids. Then the labeled protein can be studied in the presence of other unlabeled proteins. The number of fluorophores has increased dramatically during the past decade. Useful information on a wide range of fluorophores can be found in the Molecular Probes catalogue.<sup>30</sup>

#### 3.2.1. Protein-Labeling Reagents

Numerous fluorophores are available for covalent and non-covalent labeling of proteins. The covalent probes can have a variety of reactive groups, for coupling with amines and sulfhydryl or histidine side chains in proteins. Some of the more widely used probes are shown in Figure 3.8. Dansyl chloride (DNS-Cl) was originally described by Weber,<sup>31</sup>

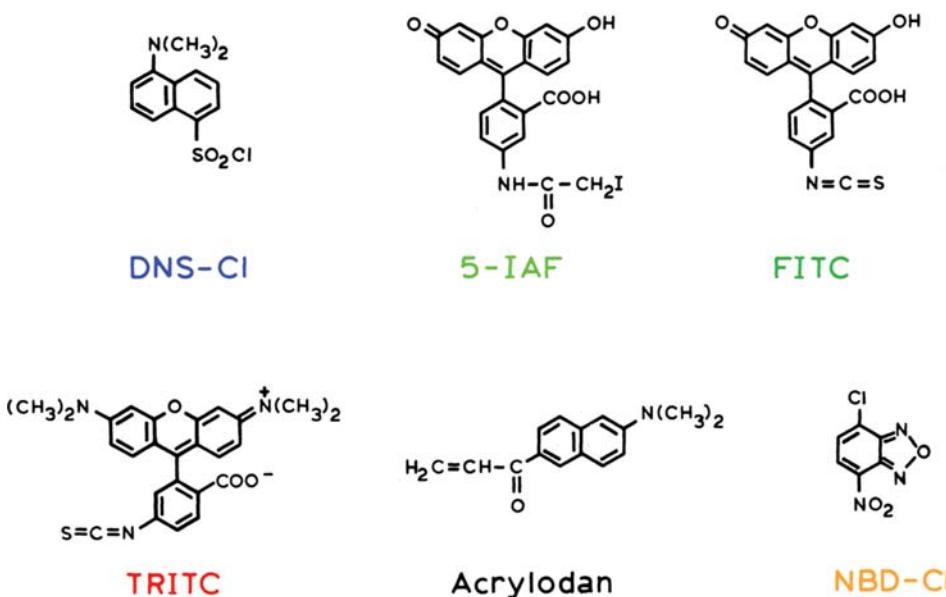


**Figure 3.8.** Reactive probes for conjugation with macromolecules.

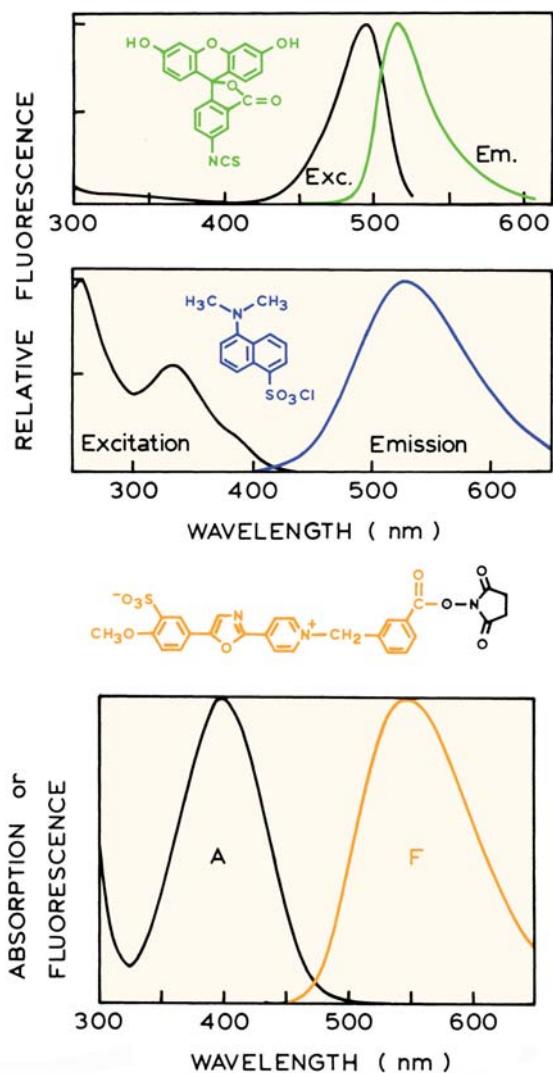


**Figure 3.9.** Excitation and emission spectra of FITC (top) and DNS-Cl (middle) labeled antibodies. Also shown in the excitation and emission spectra of Cascade Yellow in methanol (bottom).

and this early report described the advantages of extrinsic probes in biochemical research. Dansyl chloride is widely used to label proteins, especially where polarization measurements are anticipated. This wide use is a result of its early introduction in the literature and its favorable lifetime ( $\approx 10$  ns). Dansyl groups can be excited at 350 nm, where proteins do not absorb. Since dansyl groups absorb near 350 nm they can serve as acceptors of protein fluorescence. The emission spectrum of the dansyl moiety is also highly sensitive to solvent polarity, and the emission maxima are typically near 520 nm (Figure 3.9).

#### Brief History of Gregorio Weber 1916–1997

The Professor, as he is referred to by those who knew him, was born in Buenos Aires, Argentina in 1916. He received an M.D. degree from the University of Buenos Aires in 1942 and went on to graduate studies at Cambridge University. Dr. Weber's talents were recognized by Sir Hans Krebs, who recruited him to the University of Sheffield in 1953. During his years at Sheffield, Professor Weber developed the foundations of modern fluorescence spectroscopy. While at Sheffield, the Professor developed the use of fluorescence polarization for studying macromolecular dynamics. In 1962 Professor Weber joined the University of Illinois at Urbana-Champaign, remaining active until his death in 1997. Dr. Weber's laboratory at the University of Illinois was responsible for the first widely used phase modulation fluorometer, a design that went on to successful commercialization. Professor Weber stressed that fluorescence spectroscopy depends on the probes first and instrumentation second.

While dansyl chloride today seems like a common fluorophore, its introduction by Professor Weber represented a fundamental change in the paradigm of fluorescence spectroscopy. Professor Weber introduced molecular considerations into fluorescence spectroscopy. The dansyl group is solvent sensitive, and one is thus forced to consider its interactions with its local environment. Professor Weber (Figure 3.10) recognized that proteins could be labeled with fluorophores, which in turn reveal information about the proteins and their interactions with other molecules. The probes that the Professor developed are still in widespread use, including dansyl chloride, 1-anilinonaphthalene-6-sulfonic acid (ANS), 2-(*p*-toluidinyl)naphthalene-6-sulfonic acid (TNS), and Prodan derivatives.

Fluoresceins and rhodamines are also widely used as extrinsic labels (Figure 3.11). These dyes have favorably long absorption maxima near 480 and 600 nm and emission wavelengths from 510 to 615 nm, respectively. In contrast to the dansyl group, rhodamines and fluoresceins are not sensitive to solvent polarity. An additional reason for their widespread use is the high molar extinction coefficients near  $80,000\text{ M}^{-1}\text{ cm}^{-1}$ . A wide variety of reactive derivatives are available, including iodoacetamides, isothiocyanates, and maleimides. Iodoacetamides and maleimides are typically used for labeling sulphydryl groups, whereas isothiocyanates, N-hydroxysuccinimide, and sulfonyl chlorides are used for labeling amines.<sup>32</sup> Frequently, commercial labeling reagents are a mixture of isomers.



Figure 3.10. Professor Gregorio Weber with the author, circa 1992.

One common use of fluorescein and rhodamine is for labeling of antibodies. A wide variety of fluorescein- and rhodamine-labeled immunoglobulins are commercially available, and these proteins are frequently used in fluorescence microscopy and in immunoassays. The reasons for selecting these probes include high quantum yields and the long wavelengths of absorption and emission, which minimize the problems of background fluorescence from biological samples and eliminate the need for quartz optics. The lifetimes of these dyes are near 4 ns and their emission spectra are not significantly sensitive to solvent polarity. These dyes are suitable for quantifying the associations of small labeled molecules with proteins via changes in fluorescence polarization.

The BODIPY dyes have been introduced as replacements for fluorescein and rhodamines. These dyes are based on an unusual boron-containing fluorophore (Figure 3.12). Depending on the precise structure, a wide range of emission wavelengths can be obtained, from 510 to 675 nm. The BODIPY dyes have the additional advantage of displaying high quantum yields approaching unity, extinction coefficients near  $80,000 \text{ M}^{-1} \text{ cm}^{-1}$ , and insensitivity to solvent polarity and pH. The emission spectra are narrower than those of fluorescein and rhodamines, so that more of the light is emitted at the peak wavelength, possibly allowing more individual dyes to be resolved. A disadvantage of the BODIPY dyes is a very small Stokes shift.<sup>33</sup> As a result the

dyes transfer to each other with a Förster distance near 57 Å.

### 3.2.2. Role of the Stokes Shift in Protein Labeling

One problem with fluoresceins and rhodamines is their tendency to self-quench. It is well known that the brightness of fluorescein-labeled proteins does not increase linearly with the extent of labeling. In fact, the intensity can decrease as the extent of labeling increases. This effect can be understood by examination of the excitation and emission spectra (Figure 3.9). Fluorescein displays a small Stokes shift. When more than a single fluorescein group is bound to a protein there can be energy transfer between these groups. This can be understood by realizing that two fluorescein groups attached to the same protein are likely to be within 40 Å of each other, which is within the Förster distance for fluorescein-to-fluorescein transfer. Stated differently, multiple fluorescein groups attached to a protein result in a high local fluorescein concentration.

Examples of self-quenching are shown in Figure 3.13 for labeled antibodies.<sup>30,34</sup> Fluorescein and Texas-Red both show substantial self-quenching. The two Alexa Fluor dyes show much less self-quenching, which allows the individually labeled antibodies to be more highly fluorescent. It is not clear why the Alexa Fluor dyes showed less self-quenching since their Stokes shift is similar to that of fluo-

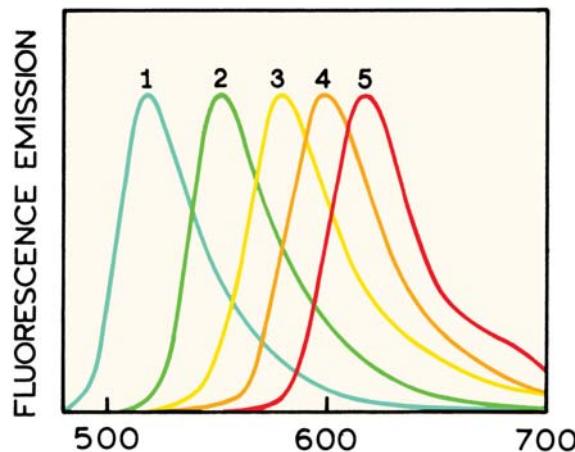
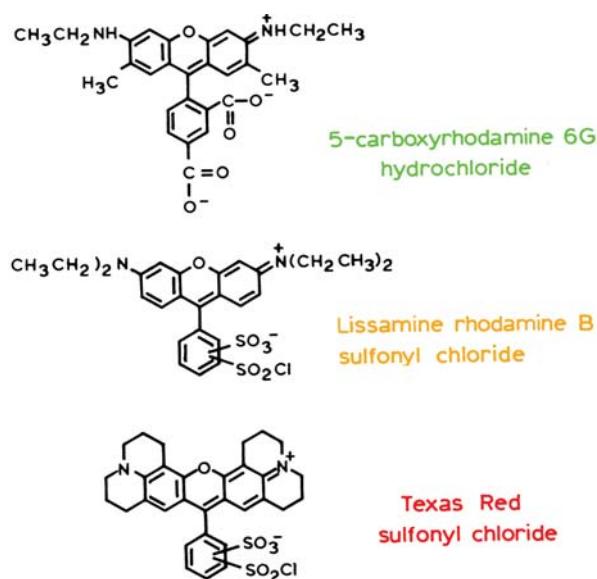
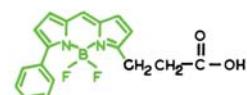


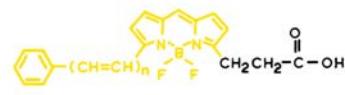
**Figure 3.11.** Structures and normalized fluorescence emission spectra of goat anti-mouse IgG conjugates of (1) fluorescein, (2) rhodamine 6G, (3) tetramethylrhodamine, (4) Lissamine rhodamine B, and (5) Texas Red dyes. Revised from [30].

rescein and rhodamine. The BODIPY dyes have a small Stokes shift and usually display self-quenching. New dyes are being developed that show both a large Stokes shift and good water solubility. One such dye is Cascade Yellow, which displays excitation and emission maximum near 409 and 558 nm, respectively (Figure 3.9). The large Stokes shift minimizes the tendency for homotransfer, and the charges on the aromatic rings aid solubility.

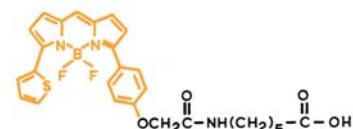
In contrast to fluorescein, rhodamines, and BODIPYs, there are fluorophores that display high sensitivity to the polarity of the local environment. One example is Prodan<sup>35</sup> (Figure 3.8), which is available in the reactive form—called



**BODIPY-R6G**



**BODIPY-581/591**



**BODIPY-Texas Red**

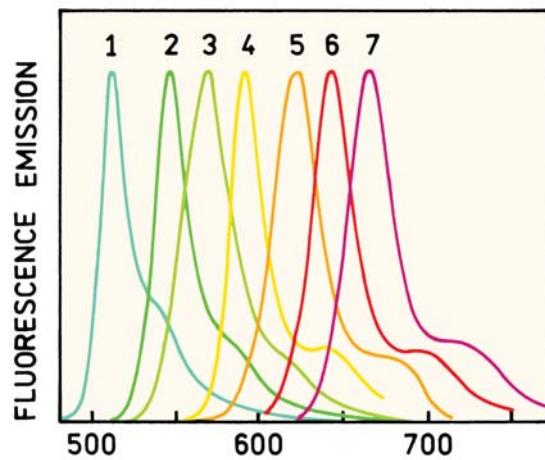


**Figure 3.12.** Normalized fluorescence emission spectra of BODIPY fluorophores in methanol. Revised from [30].

acrylodan.<sup>36</sup> In the excited state there is a charge separation from the amino to the carbonyl groups. When bound to membranes, Prodan and its derivatives display large spectral shifts at the membrane phase-transition temperature.

### 3.2.3. Photostability of Fluorophores

One of the most important properties of a probe is its photostability. Almost all fluorophores are photobleached upon continuous illumination, especially in fluorescence microscopy where the light intensities are high. Fluorescein is one of the least photostable dyes (Figure 3.14). The Alexa

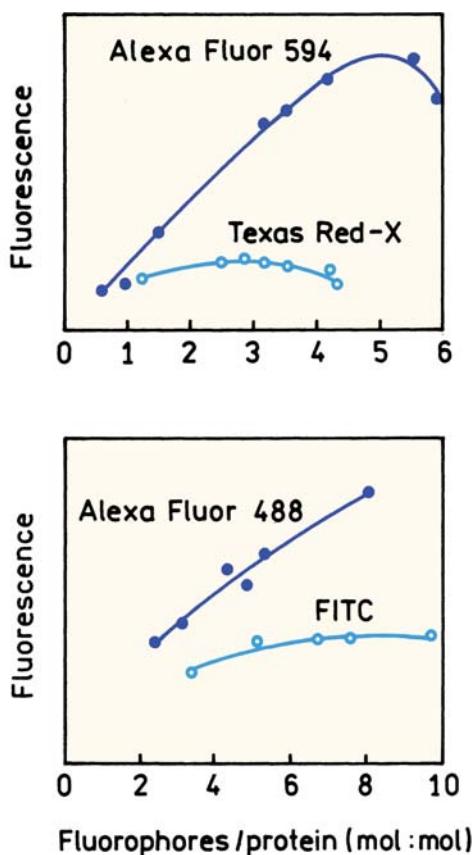


**Figure 3.13.** Effect of the fluorophore-to-protein ratio on the intensity of covalently labeled antibodies. Revised from [30].

Fluor dyes are more photostable and appear to have been developed for this reason. The chemical structures of Alexa Fluor dyes are not available. The emission maximum of Alexa Fluor dyes ranges from 442 to 775 nm. The photostability of a dye can be affected by its local environment. In

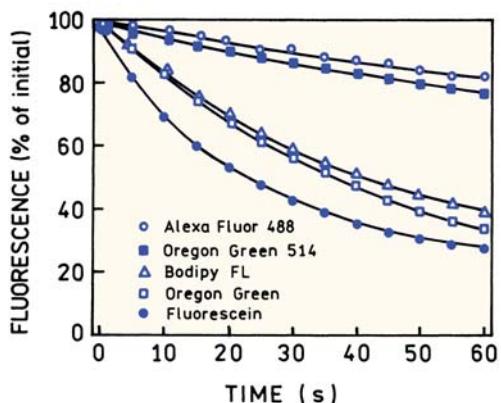


**Figure 3.14.** Comparison of the photostability of labeled antibodies in cells on fixed slides. The intensities were measured using a fluorescence microscope. Revised from [30].

some cases photostability is increased by removal of oxygen, and in other cases oxygen has no effect. There appears to be no general principles that can be used to predict photostability.

### 3.2.4. Non-Covalent Protein-Labeling Probes

There are a number of dyes that can be used to non-covalently label proteins. These are typically naphthylamine sulfonic acids, of which 1-anilinonaphthalene-6-sulfonic acid (ANS) and 2-(*p*-toluidinyl)naphthalene-6-sulfonic acid (TNS) are most commonly used.<sup>37</sup> Dyes of this class are frequently weakly or nonfluorescent in water, but fluoresce strongly when bound to proteins<sup>38</sup> or membranes. Figure 3.15 shows the emission spectra of BSA excited at 280 nm as the sample is titrated with ANS. In the absence of BSA

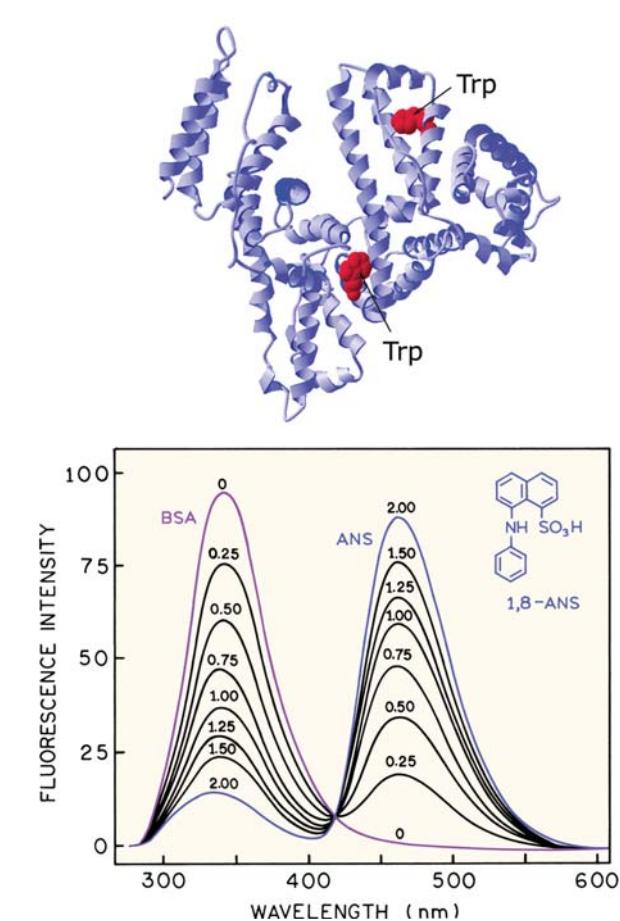


**Figure 3.15.** Fluorescence emission spectra of bovine serum albumin (BSA) in the presence of increasing ANS concentration. The numbers indicate the average number of ANS molecules bound per BSA molecule. Excitation at 280 nm. The structure shows the crystal structure of HSA modified to contain two tryptophanes. Revised from [38].



**Figure 3.16.** Color photograph of solutions of HSA, ANS and a mixture when illuminated with a UV hand lamp. From [39].

the emission from the ANS dissolved in buffer would be insignificant (not shown). Tryptophan emission from BSA is quenched upon addition of ANS, and the ANS emission increases as the BSA emission decreases. There is no observable emission from ANS alone, which shows an emission maximum above 500 nm in water. ANS-type dyes are amphipathic, so that the nonpolar region prefers to adsorb onto nonpolar regions of macromolecules. Since the water-phase dye does not contribute to the emission, the observed signal is due to the area of interest, the probe binding site on the macromolecule.

Binding of ANS to BSA or human serum albumin (HSA) can be used as a visible demonstration. Take an aqueous solution of ANS (about  $10^{-5}$  M) and BSA (about 10 mg/ml) and observe them under a UV hand lamp. Little emission will be seen from either sample. Any emission seen from the ANS solution will be weak and greenish. Then mix the two solutions while illuminating with the UV hand lamp. There will be an immediate increase in fluorescence intensity and a shift of the ANS emission to the blue (Figure 3.16). We frequently use this demonstration to illustrate fluorescence to students.

### 3.2.5. Membrane Probes

Labeling of membranes is often accomplished by simple partitioning of water-insoluble probes into the nonpolar regions of membranes. DPH, 1,6-diphenyl-1,3,5-hexatriene, is one of the most commonly used membrane probes. Addition of DPH to a membrane suspension results in complete binding, with no significant emission from DPH in the aqueous phase. All the emission from DPH is

then due to DPH in the membrane environment. The tasks of labeling membranes have been made easier by the availability of a wide variety of lipid probes. A few examples are shown in Figure 3.17. Lipid probes can be attached to the fatty acid chains or to the phospholipids themselves. The depth of this probe in the bilayer can be adjusted by the length of the various chains, as shown for the anthroyl fatty acid. DPH, often used as a partitioning probe, can be localized near the membrane–water interface by attachment of a trimethylammonium group to one of the phenyl rings (TMA-DPH).<sup>40</sup> Unsaturated fatty acids can also be fluorescent if the double bonds are conjugated as in parinaric acid.<sup>41</sup>

Membranes can also be labeled by covalent attachment of probes to the lipids. This is useful with more water-soluble probes like fluorescein or rhodamine. The probes can be forced to localize in the membrane by attachment to long acyl chains or to the phospholipids themselves (Figure 3.17). Depending on chemical structure, the fluorescent group can be positioned either on the fatty acid side chains (Fluorenyl-PC) or at the membrane–water interface (Texas Red-PE). The fluorophore Texas Red is often used for long-wavelength absorption and high photostability. Pyrene has been attached to lipids (pyrenyl lipid) to estimate diffusive processes in membranes by the extent of excimer formation. The pyrenyl PC probe displays unusual spectral properties. The emission spectra of pyrenyl-PC liposomes are highly dependent on temperature (Figure 3.18). The unstructured emission at higher temperatures is due to excimer formation between the pyrene groups.<sup>42</sup> If the pyrenyl-PC is present at a lower mole fraction the amount of excimer emission decreases. The relative amounts of monomers and excimer emission can be used to estimate the rate of lateral diffusion of lipids in the membranes.

### 3.2.6. Membrane Potential Probes

There are membrane probes that are sensitive to the electrical potential across the membrane. Typical membrane potential probes are shown in Figure 3.19. A number of mechanisms are thought to be responsible, including partitioning of the dye from the water to the membrane phase, reorientation of the dyes in the membrane, aggregation of dyes in the membrane, and the inherent sensitivity of the dyes to the electric field.<sup>43–48</sup> The carbocyanine dyes typically respond to potential by partitioning and/or aggregation in the membranes,<sup>49–50</sup> whereas the stryryl dyes seem to respond directly to the electric field.<sup>51</sup> The merocyanine

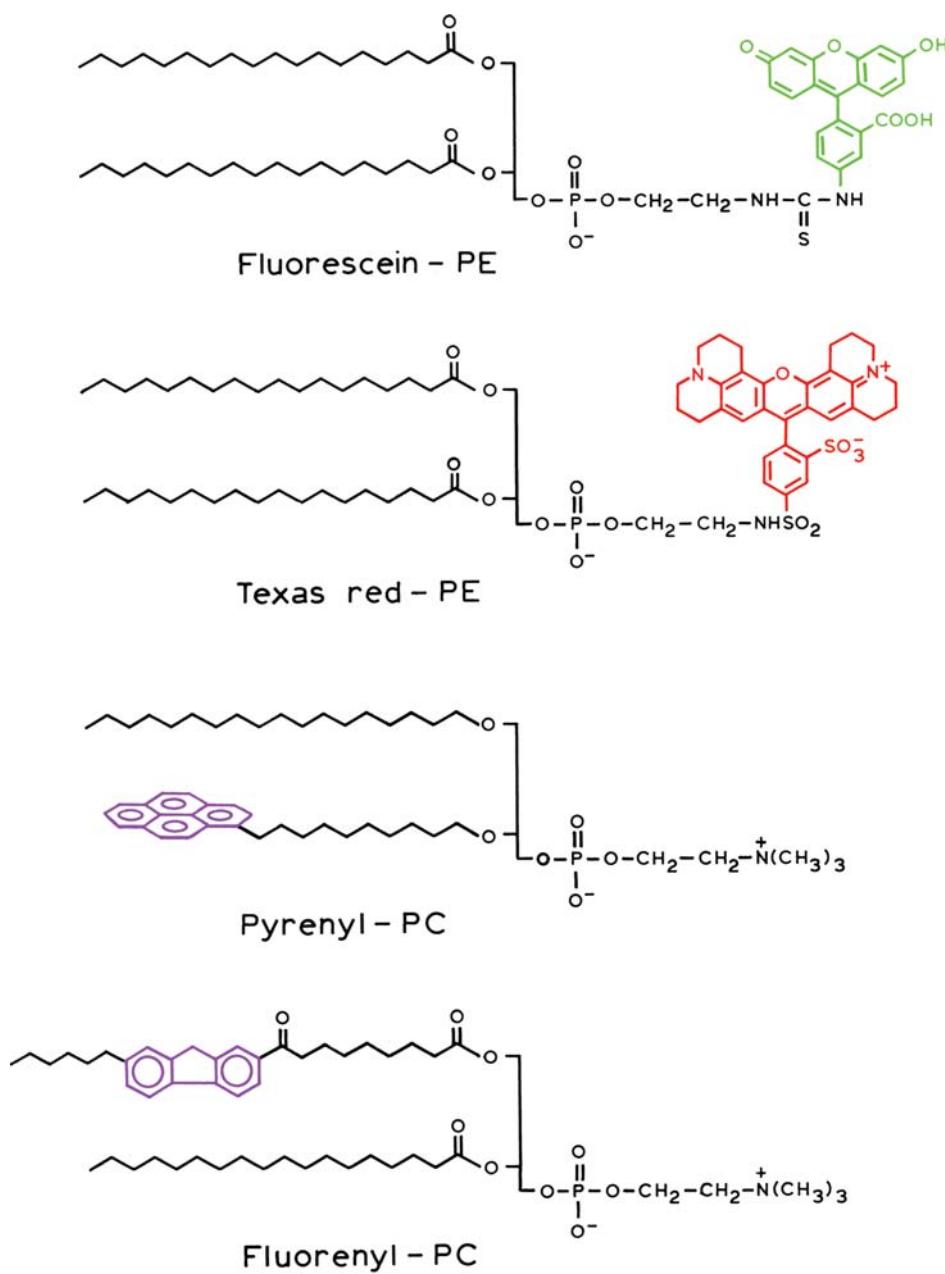


**Figure 3.17.** Fluorescent phospholipid analogues. PC = phosphatidylcholine; PE = phosphatidylethanolamine.

dyes probably respond to membrane potential by both mechanisms.<sup>51–53</sup> There are continuing efforts to develop improved dyes.<sup>54–55</sup> With all these probes the effect of potential is small, typically a few percent, so that intensity ratios are often used to provide more stable signals.<sup>56–57</sup>

Because of the small size of fluorophores it is difficult to obtain a significant change in voltage across the fluorophore. The sensitivity to voltage can be improved by

using RET and a dye that translocates across the membrane in response to voltage.<sup>58–59</sup> This is accomplished by positioning a fluorophore (coumarin-lipid) on one side of the membrane and allowing a second dye (oxonal) to partition into the membrane (Figure 3.20). The oxonal is an acceptor for coumarin. There was minimal absorption by oxonal at the coumarin excitation wavelength so that RET was the dominant origin of the oxonal emission. Changes in voltage

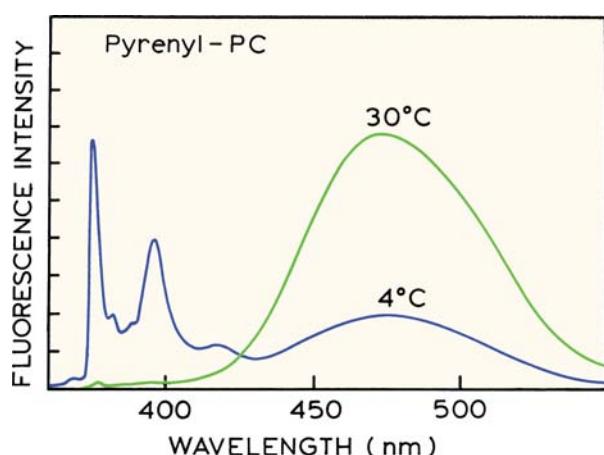


**Figure 3.18.** Fluorescence emission spectra for pyrenyl-PC measured at 4 and 30°C. The lipid probe was dispersed in water. From [42] and reprinted with permission from Springer-Verlag Inc.

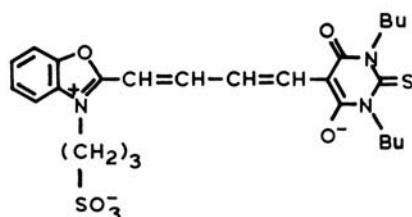
result in changes in oxonal concentration near the coumarin and hence change in intensity of the oxonal emission. This system is about fivefold more sensitive to voltage than the ASP class of dyes.

### 3.3. RED AND NEAR-INFRARED (NIR) DYES

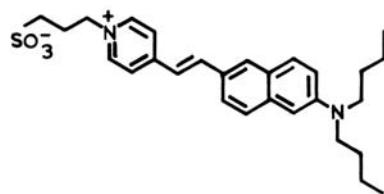
The cyanine dyes were initially used as membrane potential probes and evolved into some of the more commonly used

long-wavelength dyes. Long-wavelength probes are of current interest for several reasons. The sensitivity of fluorescence detection is often limited by the autofluorescence of biological samples. As the excitation wavelength becomes longer, the autofluorescence decreases, and hence detectability over background increases.<sup>60</sup> Long-wavelength dyes can be excited with laser diodes. The most familiar long-wavelength dyes are the cyanine dyes, such as the Cy-3, Cy-5 and Cy-7 in Figure 3.21. Such dyes have absorption and emission wavelengths above 550 nm.<sup>61–63</sup> The cyanine dyes typically display small Stokes shift, with the absorption maxima about 30 nm blue shifted from the emission maxima, as shown for Cy3. A wide variety of conjugatable cyanine dyes are available. Charged side chains are used for improved water solubility or to prevent self-association, which is a common cause of self-quenching in these dyes. Lipid side-chains are used to bind these dyes to membranes.

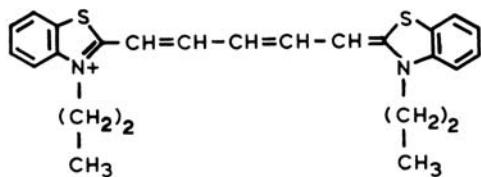
Additional long-wavelength dyes are shown in Figure 3.22. Some rhodamine derivatives display long absorption and emission spectra, as seen for Rhodamine 800.<sup>64</sup> The oxazine dyes display surprising long absorption and emission maxima given their small size.<sup>65</sup> Extended conjugated systems result in long absorption and emission wavelengths, as shown for IR-125 and thiazole orange. Dyes of this class have been extensively characterized for use as long-wavelength probes and in DNA sequencing.<sup>66</sup> The dye



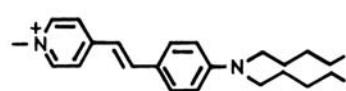
Merocyanine 540



Naphthyl Styryl



diS-C<sub>3</sub>-(5)



di-5-ASP

**Figure 3.19.** Membrane potential probes.

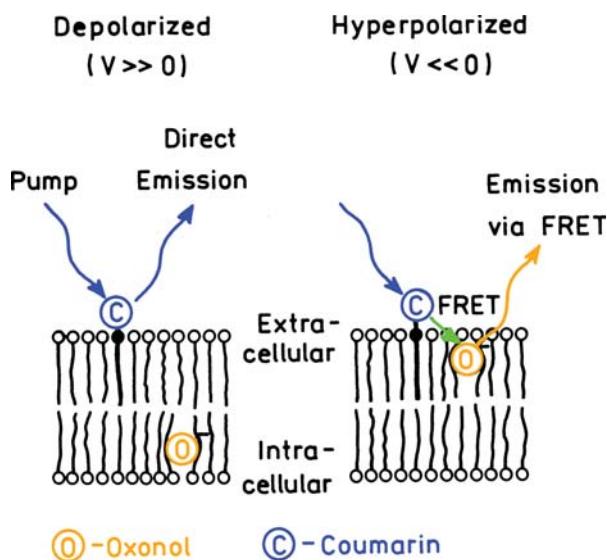


**Figure 3.20.** Measurement of membrane potential using RET and a mobile dye. The donor is a coumarin lipid and the acceptor is oxonol. Revised from [59].

thiazole orange can be excited at 735 nm and binds strongly to DNA. Dyes of this type are also used for staining DNA restriction fragments during capillary electrophoresis. Another class of long-wavelength dyes are the phthalocyanines and naphthalocyanines (Figure 3.22). At present these dyes are used less in biochemistry due to a lack of water solubility and a tendency to aggregate.<sup>67</sup> There is ongoing work to improve the phthalocyanines<sup>68</sup> and to develop other red-NIR dyes.<sup>69–72</sup>

### 3.4. DNA PROBES

While very weak intrinsic emission has been observed from unlabeled DNA, this emission is too weak and too far in the UV for practical applications. Fortunately, there are numerous probes that spontaneously bind to DNA and display enhanced emission.<sup>73–75</sup> Several representative DNA probes are shown in Figure 3.23. One of the most widely used dyes is ethidium bromide (EB). EB is weakly fluorescent in water, and its intensity increases about 30-fold upon binding to DNA. The lifetime of ethidium bromide is about 1.7 ns in water, and increases to about 20 ns upon binding to double-helical DNA. The mode of binding appears to be due to intercalation of the planar aromatic ring between the base pairs of double helical DNA. Many DNA probes such as acridine orange also bind by intercalation. Other types of probes bind into the minor groove of DNA, such as DAPI

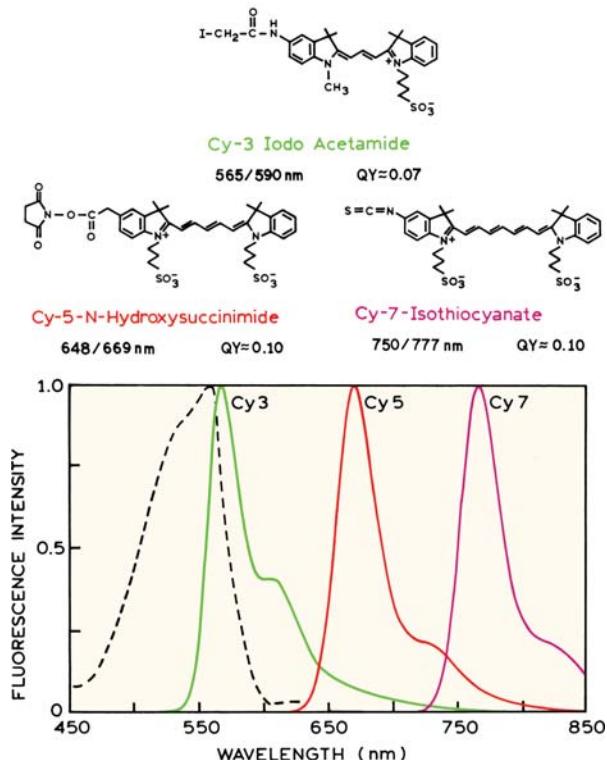


**Figure 3.21.** Chemically reactive cyanine dyes. The dashed line shows the absorption spectrum of Cy3.

and Hoechst 33342. The fluorescence of DAPI appears to be most enhanced when adjacent to AT-rich regions of DNA.<sup>76</sup> Hoechst 33358 binds with some specificity to certain base-pair sequences.<sup>77–79</sup> In recent years improved DNA dyes have been developed that bind to DNA with high affinity. Typical high-affinity dyes are dimers of known DNA probes, such as the ethidium homodimer<sup>80</sup> and elongated positively charged dyes like TOTO-1.<sup>81</sup> Such dyes remain bound to DNA during gel electrophoresis and allow DNA detection with high sensitivity.

#### 3.4.1. DNA Base Analogues

The native bases of DNA are not useful as fluorescent probes, and thus the use of extrinsic DNA probes is necessary. However, DNA can be made fluorescent by the use of DNA base analogues. 2-amino purine (2-AP) is an analogue of adenine, and isoxanthopterin (IXP) is an analogue of guanine (Figure 3.24). In solution, 2-amino purine has a high quantum yield and a single exponential decay time near 10 ns. Upon incorporation into double-stranded DNA

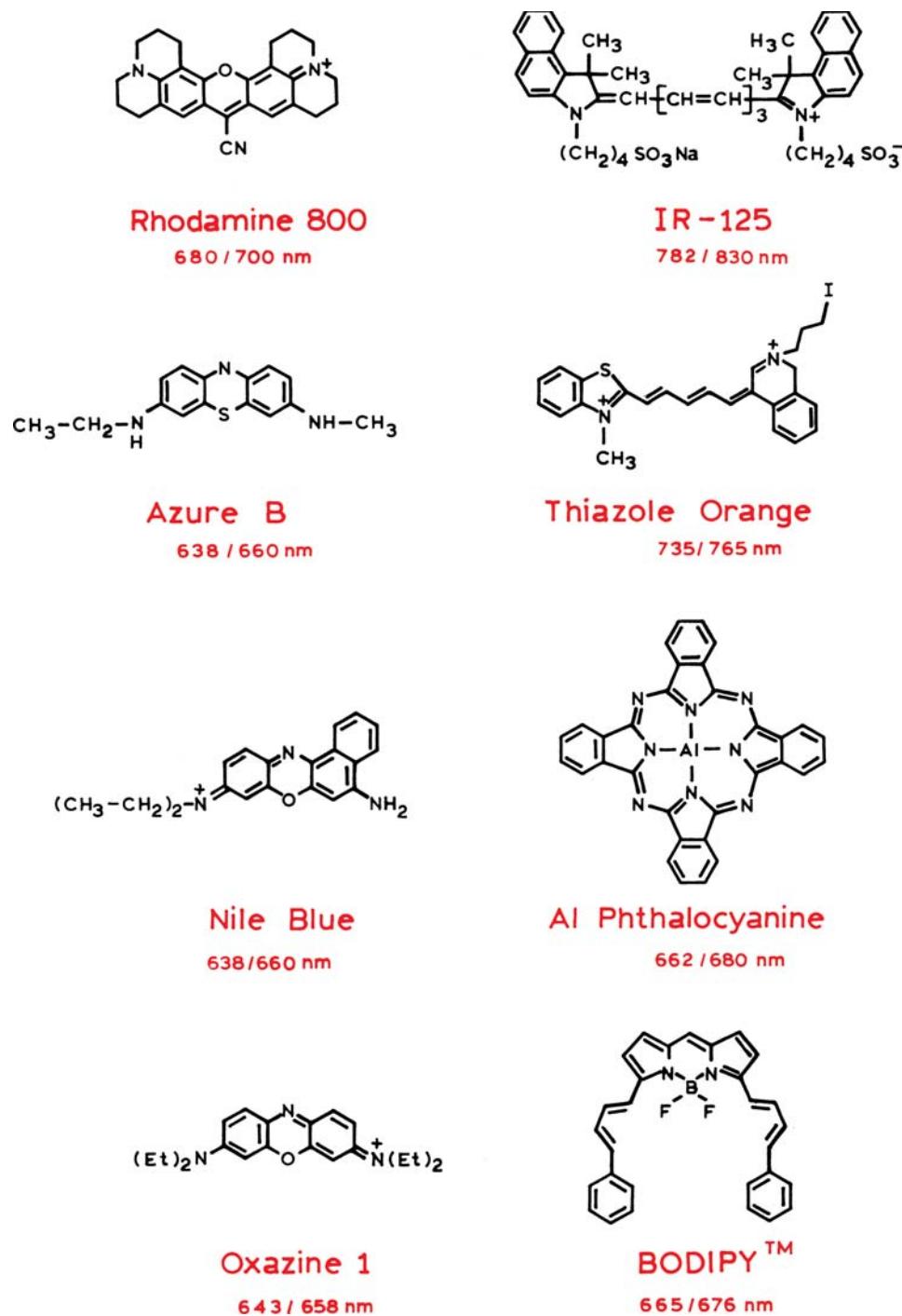


Figure 3.22. Representative NIR dyes.

oligomers, its fluorescence is partially quenched and its decay becomes complex.<sup>82</sup> The sensitivity of 2-AP to its environment makes it a useful probe for studies of DNA conformation and dynamics.<sup>83–86</sup>

Figure 3.24 shows emission spectra of isoanthopterin (IXP). Like 2-AP, IXP is partially quenched when in double-helical DNA (Figure 3.25), but more fluorescent when present in a dinucleotide.<sup>87–88</sup> The dependence of the IXP

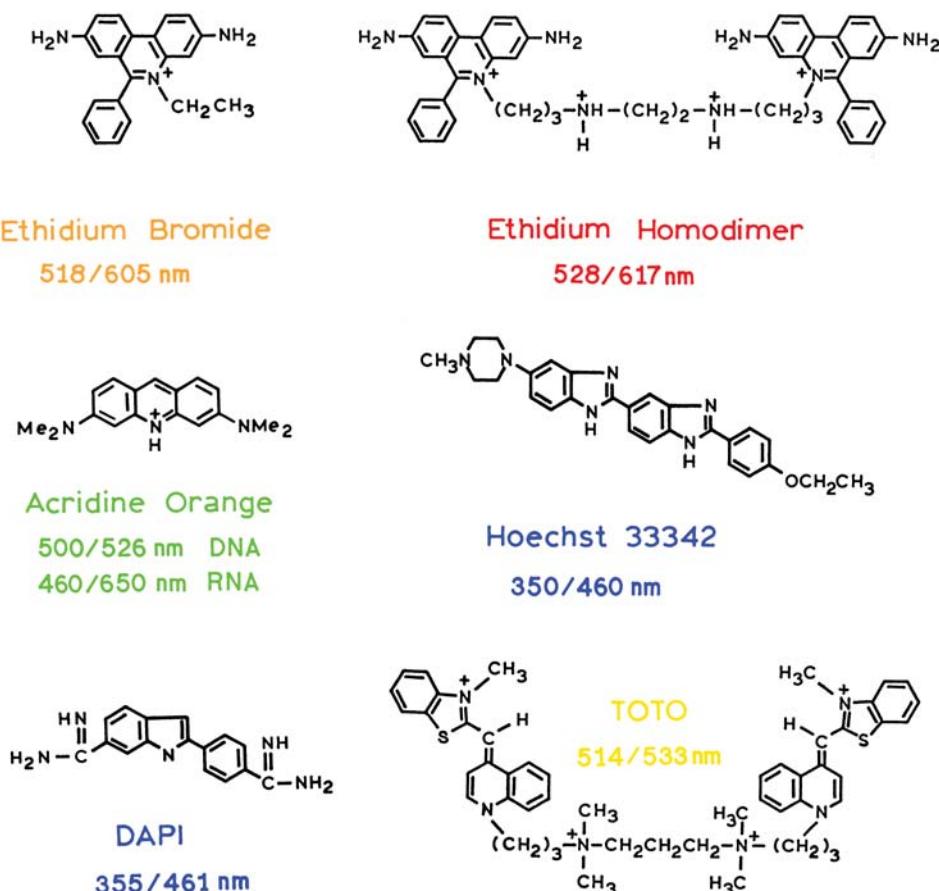


Figure 3.23. Representative DNA probes. Excitation and emission wavelengths refer to DNA-bound dye.

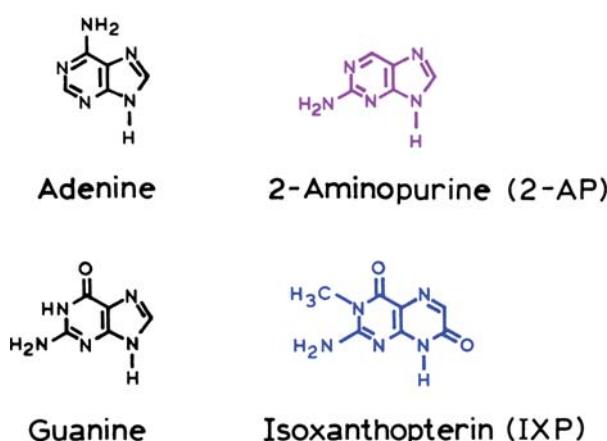


Figure 3.24. DNA purine bases (left) and fluorescent base analogues (right).

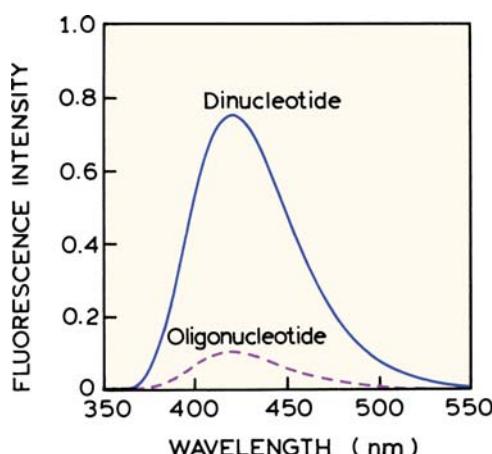
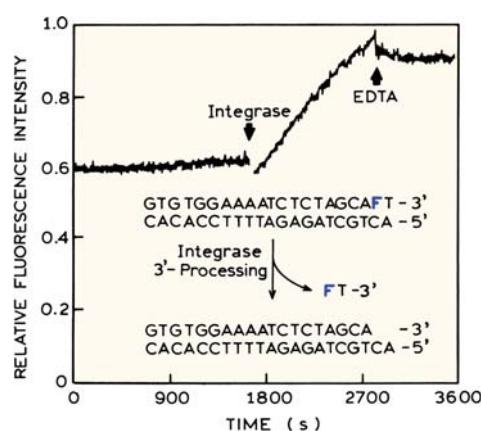


Figure 3.25. Emission spectra of the isoxanthopterin nucleotide in a dinucleotide and an oligonucleotide. From [87].



**Figure 3.26.** HIV integrase assay based on release of the isoxanthopterin-containing nucleotide (F). Revised from [87], and reprinted with permission of Oxford University Press.

on DNA structure was used as an assay for the HIV integrase protein. This protein is responsible for integration of HIV DNA into the host cell's genome.<sup>89-90</sup> The assay was based on a DNA oligonucleotide that has the sequence specific for HIV integrase (Figure 3.26). The enzyme mechanism involves cleavage of a dinucleotide from the 3'-end of HIV DNA, followed by ligation to the 5'-end of the host DNA. The IXP nucleotide was positioned near the 3'-end of the synthetic substrate. Incubation with HIV integrase resulted in release of the dinucleotide, which was detected by an increase in IXP fluorescence.

### 3.5. CHEMICAL SENSING PROBES

It is often desirable to detect spectroscopically silent substances such as Cl<sup>-</sup>, Na<sup>+</sup>, or Ca<sup>2+</sup>. This is possible using

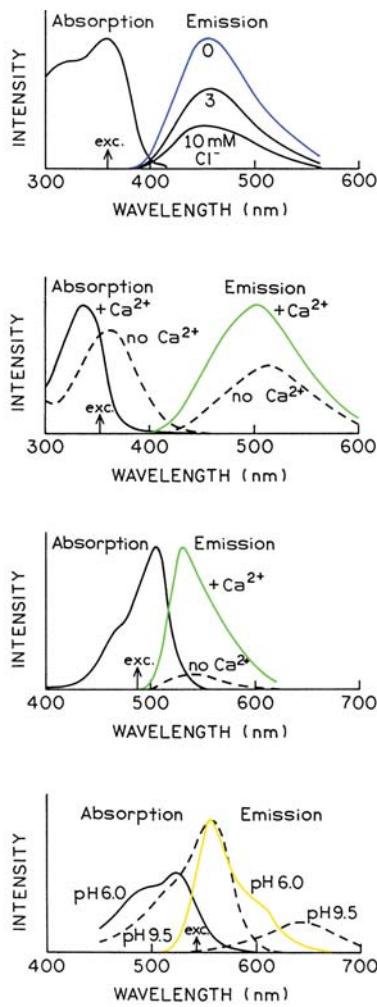
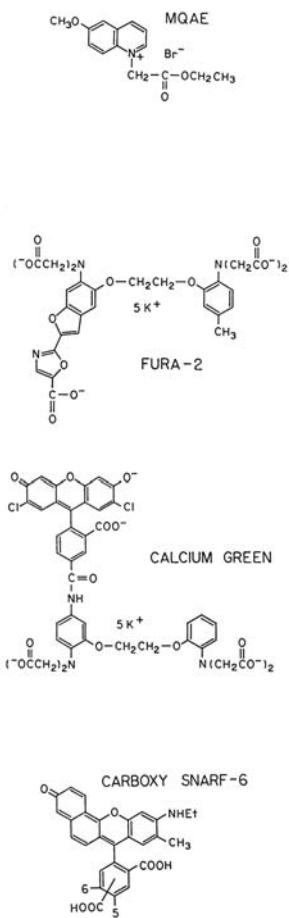


**Figure 3.27.** Chemical sensing probes (left) and thus spectra (right).

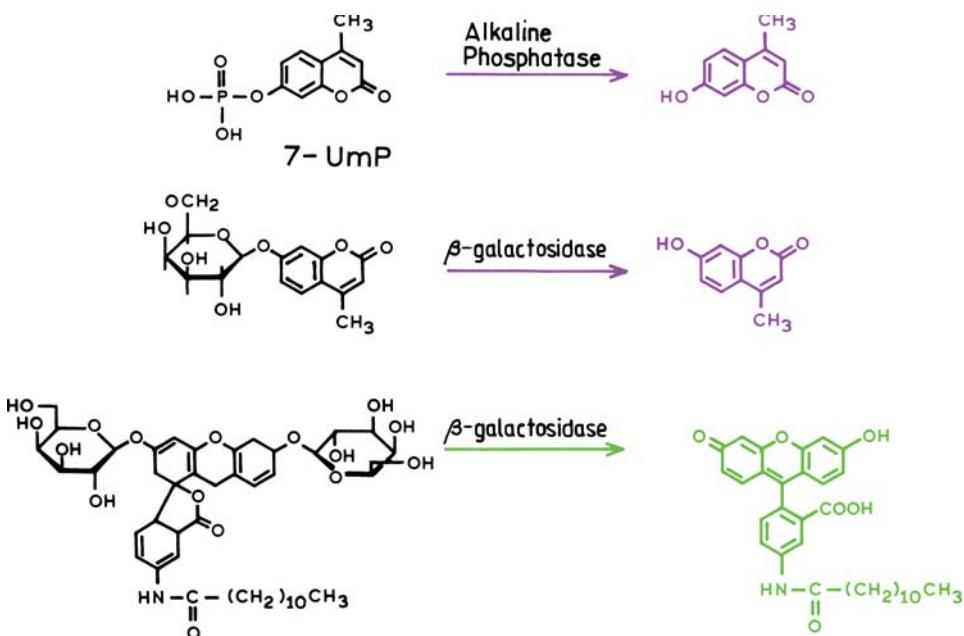


Figure 3.28. Fluorogenic probes.

sensing probes, some of which are shown in Figure 3.27. The probe MQAE is collisionally quenched by chloride according to the Stern-Volmer equation (eq. 1.6), allowing the chloride concentration to be estimated from the extent of quenching.<sup>91</sup> Other probes allow measurement of free Ca<sup>2+</sup>. Probes such as Fura-2 display Ca<sup>2+</sup>-dependent spectral shifts. Such probes are called wavelength-ratiometric probes because the analyte (Ca<sup>2+</sup>) concentration can be determined from a ratio of intensities at different excitation or emission wavelengths. Other probes such as Calcium Green display a Ca<sup>2+</sup>-dependent increase in intensity but no spectral shift. Wavelength-ratiometric and non-ratiometric probes are known for many species,<sup>92</sup> including H<sup>+</sup>, Na<sup>+</sup>, K<sup>+</sup>, and Mg<sup>2+</sup>, amines, and phosphate.<sup>93–96</sup> These dyes typically consist of a fluorophore and a region for analyte recognition, such as an azacrown ether for Na<sup>+</sup> or K<sup>+</sup>, or a BAPTA group for Ca<sup>2+</sup>. Such dyes are most often used in fluorescence microscopy and cellular imaging, and are trapped in cells either by hydrolysis of cell-permeable esters or by microinjection.

### 3.6. SPECIAL PROBES

#### 3.6.1. Fluorogenic Probes

Another class of probes is the fluorogenic probes.<sup>97–99</sup> These are dyes that are non- or weakly fluorescent until

some event occurs, such as enzymatic cleavage. Typical fluorogenic probes are shown in Figure 3.28. 7-Umbelliferyl phosphate (7-UmP) is nonfluorescent as the phosphate ester, but becomes highly fluorescent upon hydrolysis. 7-UmP is used to measure the activity of alkaline phosphatase. This enzyme is often used as the basis of enzyme-linked immunoadsorbent (ELISA) assays, and is also used in enzyme-amplified DNA assays.

It is often important to measure β-galactosidase activity in cells. This enzyme is often used as a gene marker in cells. Its activity can be detected by a galactoside of umbelliferone or 7-hydroxy-4-methylcoumarin (Figure 3.28, middle). An improved probe is shown in the lower panel. This fluorescein derivative contains a fatty acid chain that serves to retain the probe at the site of hydrolysis. This allows the cells with β-galactosidase activity to be identified under a microscope.

Another class of fluorogenic reagents are those that are initially nonfluorescent, and become fluorescent upon reacting with amines (Figure 3.29). While they have been used for labeling proteins, they are more commonly used in protein sequencing, determination of protein concentration, or for detection of low molecular weight amines in chromatography.

Fluorogenic probes can also be based on energy transfer.<sup>100–102</sup> One example is shown in Figure 3.30, in which a peptide is labeled with a donor and acceptor. The sequence

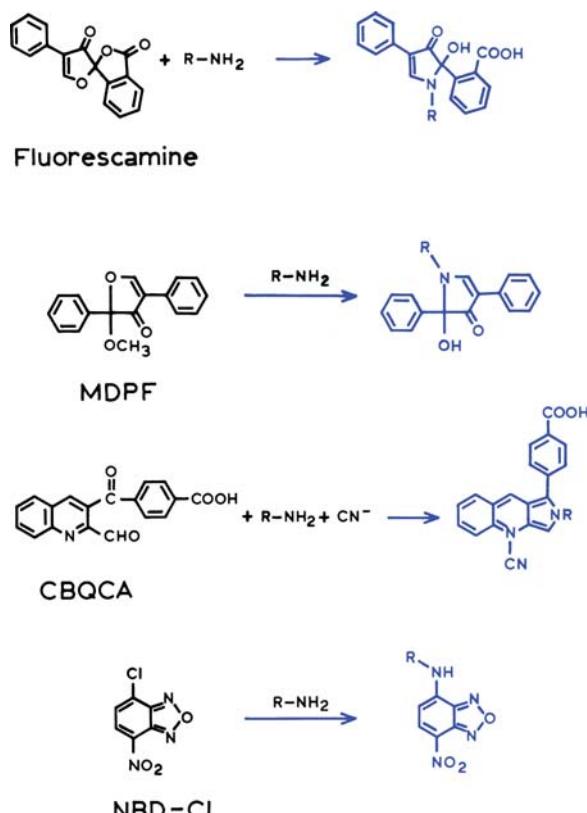


Figure 3.29. Fluorogenic reagents for amines.

of amino acids was selected to be specific for a protease found in HIV. Cleavage of the peptide results in a greater distance between the donor and acceptor and increased donor intensity. This concept of a decrease in energy transfer upon cleavage has also been applied to lipases that hydrolyze phospholipids.

### 3.6.2. Structural Analogues of Biomolecules

One approach to designing fluorophores is to make the shape similar to the parent biomolecule. This approach was used to make fluorescent analogues of steroids. Two examples are shown in Figure 3.31. Cholesterol is an essential component of cell membranes, and estradiol is important for the expression of female sexual characteristics. Both molecules are nonfluorescent, but structurally similar molecules have been synthesized which display useful fluorescence. Dehydroergosterol is a fluorescent analogue of cholesterol that displays absorption and emission maxima near 325 and 390 nm, respectively. Dehydroergosterol has been used as a probe for the interactions of steroids with membranes.<sup>103–106</sup> Ligand analogues have also been reported for the estrogen receptor.<sup>107–108</sup>

### 3.6.3. Viscosity Probes

Fluorescent quantum yields are often dependent on viscosity, but there are relatively few fluorophores characterized

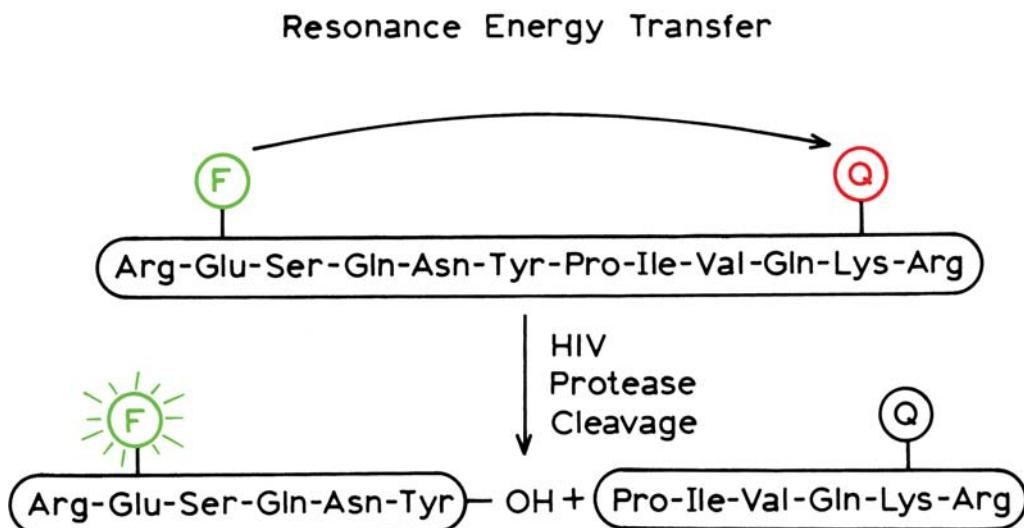
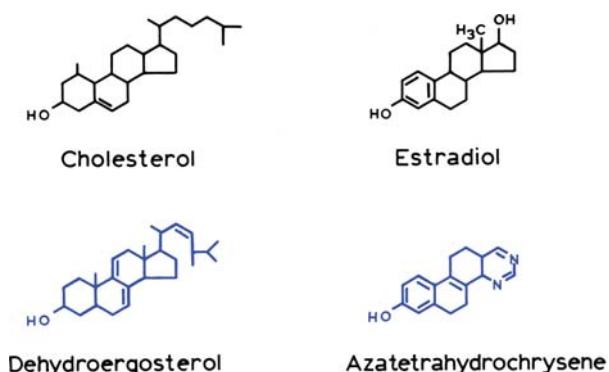


Figure 3.30. Fluorogenic probes for HIV protease. The fluorescence signal is generated when HIV protease releases the fluorophore (F) from the quenching effects of the nearby acceptor chromophore (Q).



**Figure 3.31.** Nonfluorescent steroid cholesterol and estradiol, and fluorescent analogues dehydroergosterol and 1,3-diaza-9-hydroxy-5,6,11,12-tetrahydrochrysene. Revised from [103].

as viscosity probes. One such probe is shown in Figure 3.32. These probes display charge transfer in the excited state, presumably from the amine to the vinyl or cyano group. In a highly viscous environment the molecule cannot distort as needed for charge transfer, and the decay is radiative.<sup>109–111</sup> In a less viscous environment the molecule displays internal rotation and charge transfer, which results in radiationless decay. As a result the quantum yield depends on solvent viscosity. These probes have been used to study the viscosities of membranes, and the rigidity of binding sites on proteins. These viscosity probes can be regarded as a subclass of the TICT probes, which are probes that distort in the excited state to form twisted intramolecular charge transfer states.<sup>112</sup> For probes like DPH the quantum yield is only weakly dependent on the viscosity. For DPH the viscosity is determined from the anisotropy.

### 3.7. GREEN FLUORESCENT PROTEINS

An important addition to the library of probes has been the green fluorescent protein (GFP) from the bioluminescent jellyfish *Aequorea victoria*. The bioluminescence of the primary photoprotein aequorin is blue. The bioluminescence from the jellyfish is green due to a closely associated green fluorescent protein. GFP contains a highly fluorescent group within a highly constrained and protected region of the protein. The chromophore is contained within a barrel of  $\beta$ -sheet protein<sup>113</sup> (Figure 3.33). The remarkable feature of the GFP is that the chromophore forms spontaneously upon folding of the polypeptide chain<sup>114–115</sup> without the need for enzymatic synthesis (Figure 3.34). As a result, it is possible to express the gene for GFP into cells, and to obtain proteins which are synthesized with attached

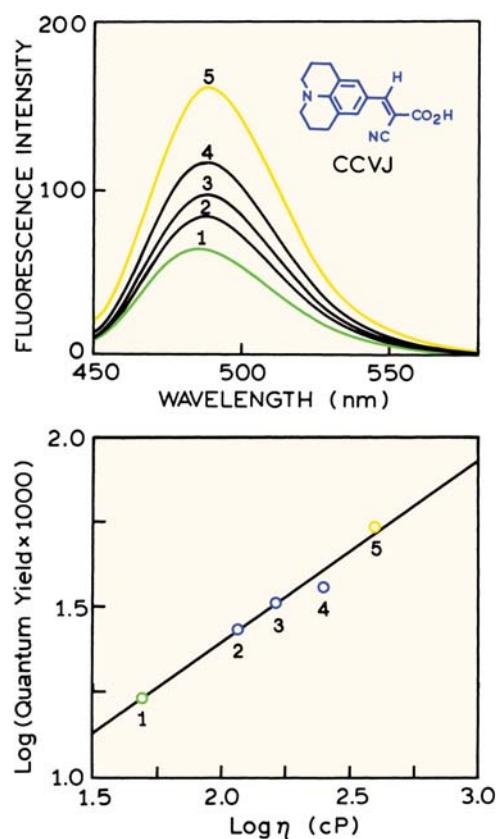


**Figure 3.32.** Fluorescence emission spectra and relative quantum yields of CCVJ in ethylene glycol/glycol mixtures of varying viscosity. Reprinted with permission from [111]. Copyright © 1993, American Chemical Society.

GFP.<sup>116–118</sup> It is even possible to express GFP in entire organisms.<sup>119–121</sup>

GFPs with different spectral properties have been created by introducing mutations into the amino-acid sequence. Mutants are known that display longer absorption and emission wavelengths (Figure 3.35) and have higher photostability.<sup>122–124</sup> In general GFPs have good photostability and display high quantum yields, which is probably because the  $\beta$ -barrel structure shields the chromophore from the local environment.

For a time it was thought that GFP was only present in *Aequorea victoria*. It is known that similar naturally fluorescent proteins are present in a number of Anthrozoa species, in corals.<sup>125–129</sup> As a result, a large number of fluorescent proteins are now available with emission maxima ranging from 448 to 600 nm (Figure 3.35). Because of the variety of fluorescent proteins the terminology has become confusing. The fluorescent proteins from coral are often referred to as yellow (YFPs) or red (RFPs) fluorescent pro-

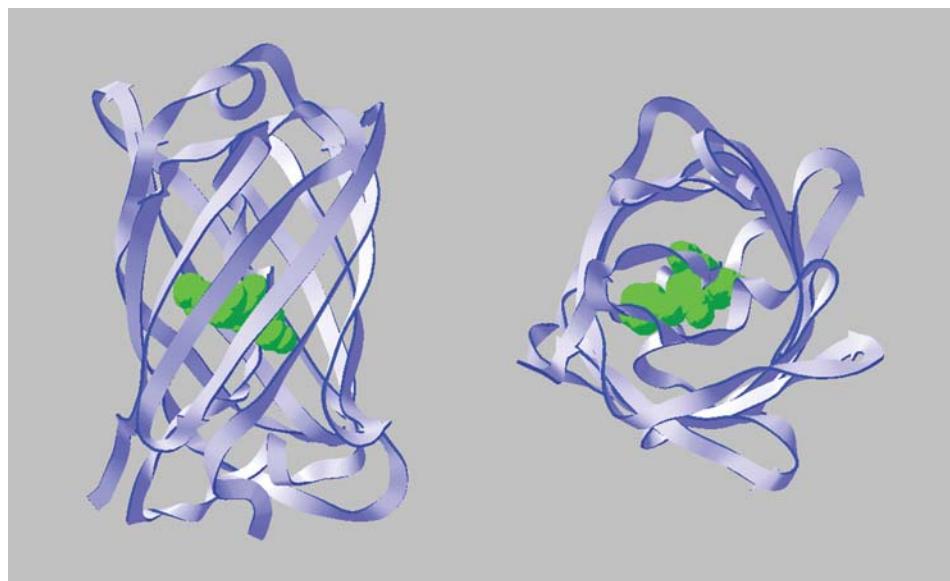


**Figure 3.33.**  $\beta$ -Barrel structure of GFP. Side and top view. The chromophore is linked covalently to the protein.

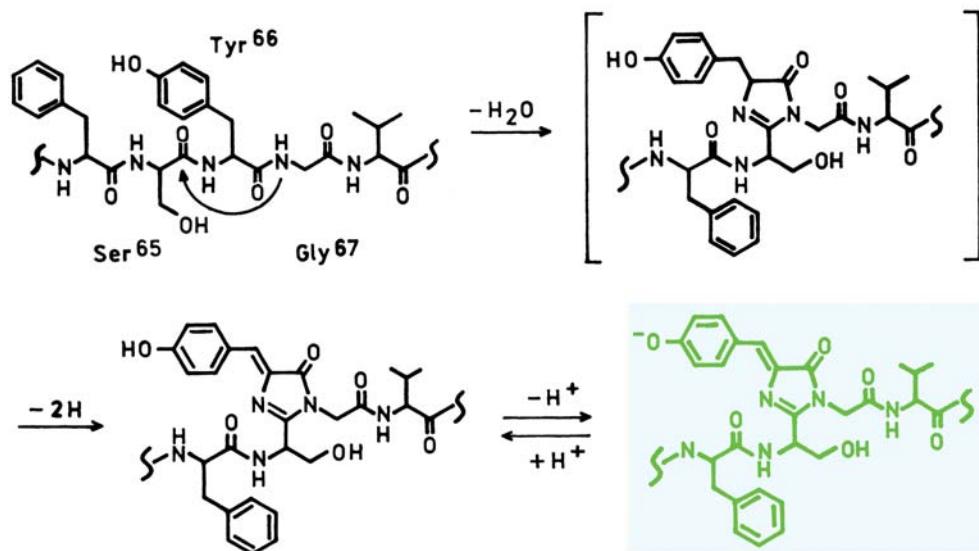


**Figure 3.34.** Spontaneous formation of the fluorophore in GFP by the serine–tyrosine–glycine residues. From [115].

teins. However, this is a misnomer because green fluorescent proteins can also come from coral.<sup>127</sup> It has been suggested that proteins derived from *Aequores victoria* be called AFPs to indicate their origin with this jellyfish.<sup>130</sup> For simplicity we will refer to all these proteins as GFPs.

An unfavorable property of all these fluorescent proteins is their tendency to self-associate. AFPs tend to form weakly bound dimers. The proteins from coral form strongly bound tetramers.<sup>130–132</sup> This self-association makes them

less useful as intracellular probes, particularly with fusion proteins where the nonfluorescent proteins will be artificially brought into close proximity to each other. Another difficulty with the most widely used red fluorescent proteins, DsRed, is that the fluorescence develops too slowly and can take 30 hours to become fluorescent. These problems have been mostly solved by mutating the sequence to disrupt the self-association and to obtain proteins that mature more rapidly.<sup>132–136</sup>

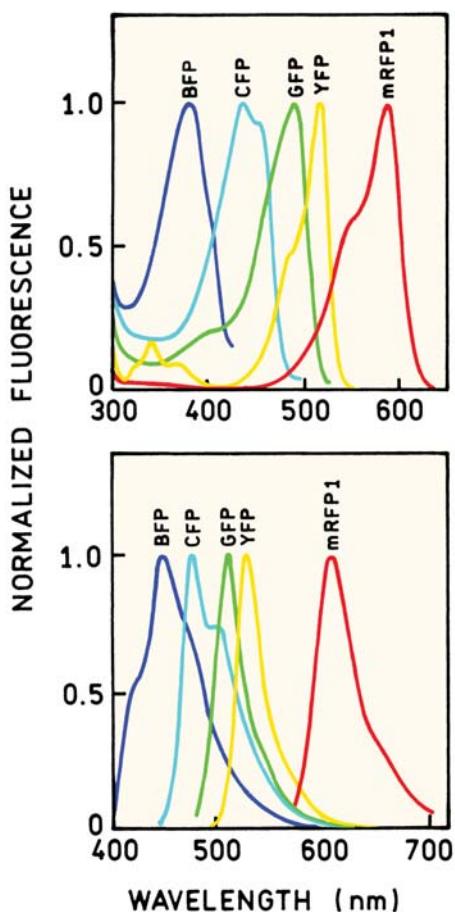


**Figure 3.35.** Excitation (top) and emission spectra (bottom) of GFP mutants. Revised from [129].

The fluorophores in GFPs are formed autocatalytically, and it is not necessary to add a fluorophore or enzymes to synthesize the fluorophore. All that is needed is the gene or mRNA that codes for the amino-acid sequence. As a result organisms that contain the gene or mRNA can express the fluorescent protein. This possibility is shown in Figure 3.36 for a *Xenopus* embryo. While in the blastomer stage the right and left blastomeres were injected with mRNA for a green or red fluorescent coral protein, respectively. One week later the descendants of the injected blastomer showed fluorescence from the fluorescent proteins coded by the mRNAs.

### 3.8. OTHER FLUORESCENT PROTEINS

#### 3.8.1. Phytofluors: A New Class of Fluorescent Probes

A new type of fluorescent probe is the so-called "phytofluors." These fluorescent probes are derived from the phytochromes, which are light-sensitive proteins present in photosynthetic organisms. These proteins allow the organisms to adjust to external light conditions, and are important in seed germination, flowering, and regulation of plant growth. Phytochromes typically contain a nonfluorescent chromophore that interconverts between two stable forms. Some phytochromes spontaneously form covalent adducts<sup>137–139</sup> with phycoerythrobilin. The absorption and

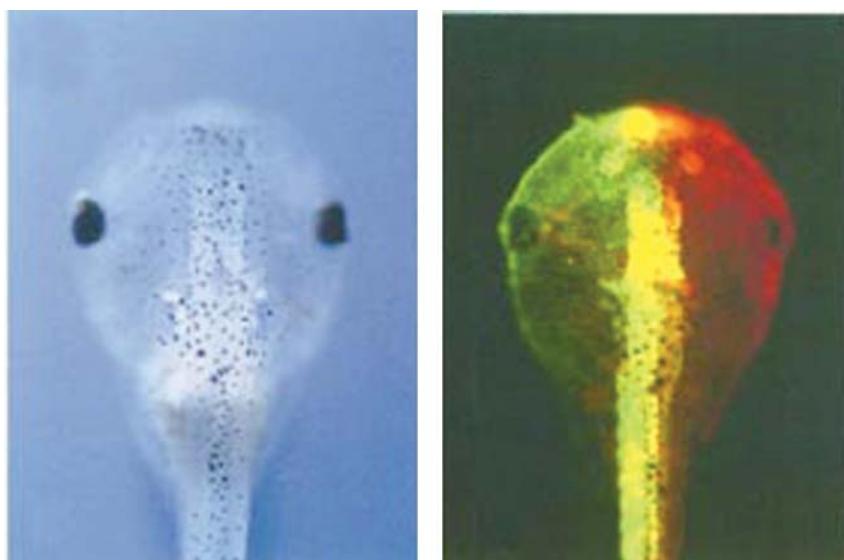


**Figure 3.36.** Color photograph (right) of a *Xenopus* embryo injected with the mRNA from a green fluorescent coral protein (right side) and a red fluorescent coral protein (left side). The left side shows a white light photograph. Reprinted from [125].

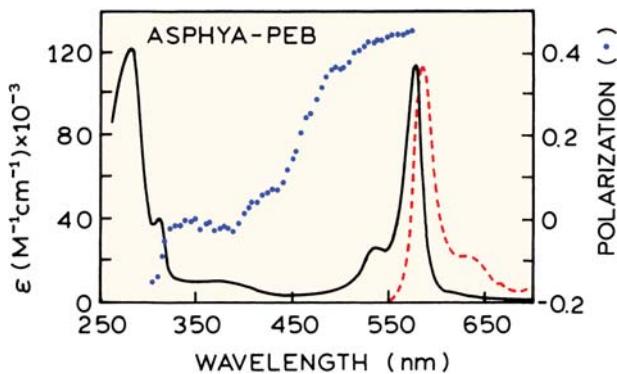


**Figure 3.37.** Absorption, emission, and excitation polarization spectra of a phytochrome from the plant *Avena sativa*, which contains bound phycoerythrobilin (PEB). Revised and reprinted with permission from [139]. Copyright © 1997, Current Biology Ltd.

emission spectra of one phytofluor protein are shown in Figure 3.37. The spectra are at favorably long wavelengths, and the quantum yield is near 0.70. A favorable property of these proteins is their high anisotropy, which occurs because, in contrast to the phycobiliproteins, there is only a single chromophore.

The phytochrome apoproteins can be expressed as recombinant proteins. Phycoerythrobilin binds spontaneously to these phytochromes and becomes fluorescent. These proteins may become useful as probes for gene expression. In contrast to GFP, it is necessary to add the phycoerythrobilin pigment, which needs to be transported into the cells. A recent report has shown that the genes for the apophytochrome, and the two genes needed to synthesize a nonfluorescent pigment from hemes, can be inserted into *E. coli*.<sup>140</sup> It has been shown recently that the photochromes themselves can be made highly fluorescent.<sup>141</sup> This was accomplished by a tyrosine-to-histidine mutation. This mutation interferes with the light-sensory function of the phytochrome, but causes the protein with its native chromophore to become fluorescent in solution and when expressed in *E. coli* (Figure 3.38). The fluorescent photochromes may provide another approach to the synthesis of fluorescent proteins within cells or animals of interest.

### 3.8.2. Phycobiliproteins

The phycobiliproteins are intensely fluorescent proteins from blue-green and red algae.<sup>142–146</sup> These proteins are contained in phycobilisomes, which harvest light and transfer the energy to chlorophyll. The phycobilisomes absorb strongly from 470 to 650 nm (Figure 3.39), in the gap

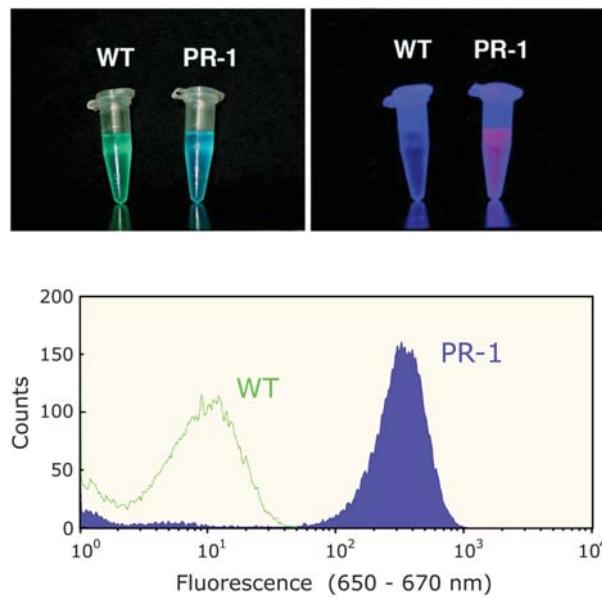


**Figure 3.38.** White light- and UV-illuminated images of wild type (WT) phytochrome and the fluorescent mutant (PR-1). The lower panel shows flow cytometry data of *E. coli* cells expressing the WT or PR-1 protein. From [141].

between the blue and far-red absorption of chlorophyll. In algae the phycobiliproteins exist as large assemblies that contain phycoerythrin (PE), phycocyanine (PC), and allophycocyanin (APC) (Figure 3.39). Light absorbed by PE is transferred to PC and then to APC, and finally to the photosynthetic reaction center. In intact phycobilisomes the phycobiliproteins are very weakly fluorescent due to efficient energy transfer to photosynthetic reaction centers. However, upon removal from the phycobilisomes the phycobiliproteins become highly fluorescent.

The chromophores in the phycobiliprotein are open-chain tetrapyrrol groups called bilins. These chromophores are covalently bound to the phycobiliprotein subunit. Each phycobiliprotein displays different spectral properties, depending on the type of bound bilins. Representative emission spectra are shown in Figure 3.39. Each phycobiliprotein is made up of a number of subunits, with molecular weights ranging from 100,000 to 240,000 daltons (Table 3.2). A remarkable feature of the phycobiliproteins is the high density of chromophores. The 34 bilins in phycoerythrin correspond to a bilin concentration near 80 mM. Also, the large number of chromophores results in high extinction coefficients of  $2.4 \times 10^6 \text{ M}^{-1} \text{ cm}^{-1}$ , or about 30 times that of fluorescein.

These spectral properties of the bilin groups result in the favorable fluorescence properties of the phycobilipro-

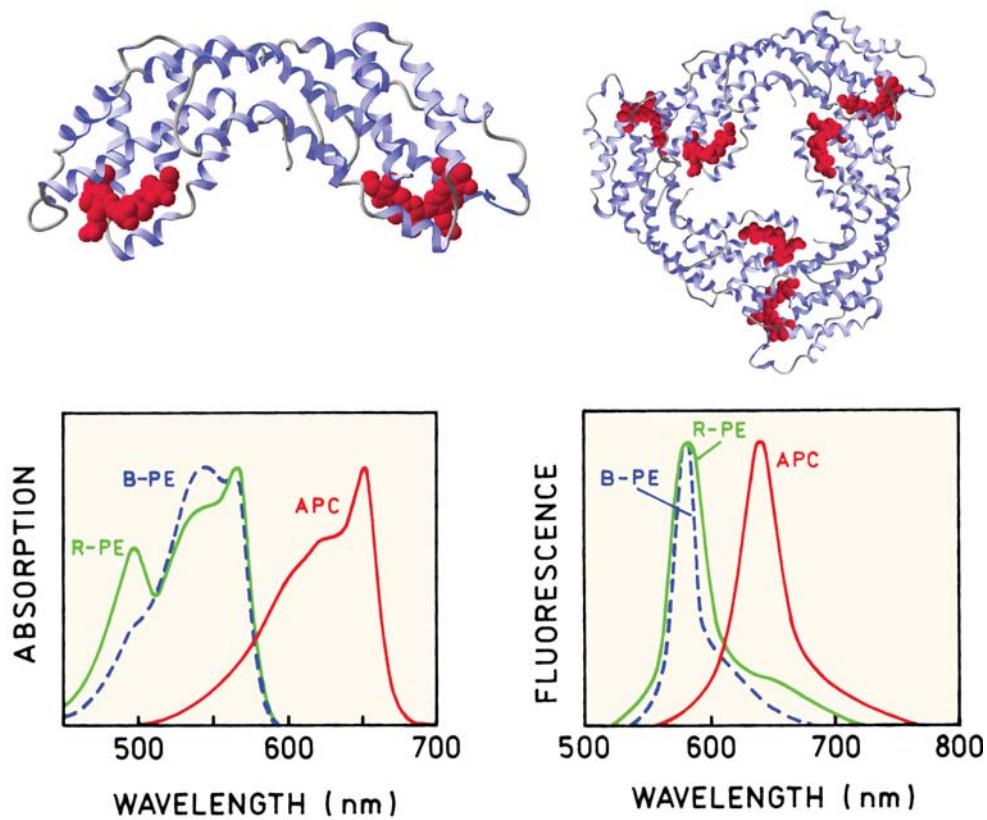


**Figure 3.39.** Absorption (middle) and fluorescence emission spectra (bottom) of three representative phycobiliproteins. The allophycocyanin is from the filamentous cyanobacterium *Anabaena variabilis*, B-phycoerythrin (B-PE) is from the unicellular red alga *Prophyridium cruentum*, and R-phycoerythrin (R-PE) from the higher red alga *Gastroclonium coulteri*. The structures shown on the top are the  $\alpha\beta$  monomer of APC and the  $\alpha\beta$  trimer ( $(\alpha\beta)_3$ ). Revised from [142].

teins. They display high quantum yields and are up to 20-fold brighter than fluorescein. They are highly water soluble and stable proteins, which can be stored for long periods of time. They are about 10-fold more photostable than fluorescein.<sup>148</sup> They contain a large number of surface lysine groups and are readily conjugatable to other proteins.<sup>147–149</sup> The long-wavelength absorption and emission make them useful where autofluorescence is a problem. And finally, they display good a Stokes shift. This is not

evident from Figure 3.39 unless one realizes that they can be excited at wavelengths below the excitation maxima. Phycobiliproteins have been successfully used for immunoassays,<sup>150–151</sup> for marking of cell-surface antigens in flow cytometry,<sup>152–153</sup> and in single-particle detection.<sup>154</sup>

A minor drawback of the phycobiliproteins is their sensitivity to illumination. This is not due to photobleaching, but to the possibility of exciting more than one chromophore per protein. This results in annihilation of the

**Table 3.2.** Properties of Some Major Phycobiliproteins

Protein	Subunit composition	Approx. mol. wt.	$\epsilon(M^{-1} cm^{-1})$	Total bilins per protein	$\lambda_{ab}^{max}$ (nm)	$\lambda_{ab}^{max}$ (nm)	Quantum yield
Allophycocyanin	$(\alpha\beta)_3$	100,000	700,000	6	650	660	0.68
B-Phycoerythrin	$(\alpha\beta)_6\gamma$	240,000	2,400,000	34	543,562	576	0.98
R-Phycoerythrin	$(\alpha\beta)_6\gamma$	240,000	2,200,000	34	495,536,565	576	0.84

<sup>a</sup>From [143] and [144]. C-phycocyanine (620/642 nm) and C-phycoerythrin (562/576 nm) have a subunit structure  $(\alpha\beta)_n$ ,  $n = 1–6$ , with molecular weights from 36,500 to 240,000.

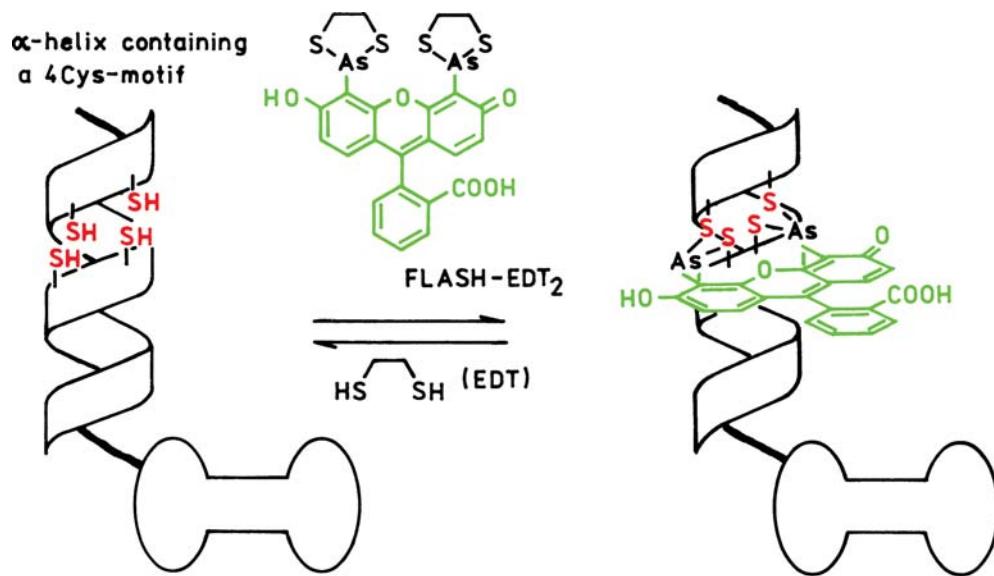


**Figure 3.40.** Schematic of the reaction of Flash-EDT<sub>2</sub> with a recombinant protein containing four cysteine residues at positions *i*, *i* + 1, *i* + 4, and *i* + 5.

excited state, and a decreased quantum yield and lifetime. The intensity decays are complex, with up to four exponential components ranging from 10 ps to 1.8 ns.<sup>155</sup>

### 3.8.3. Specific Labeling of Intracellular Proteins

Fusion proteins containing GFP provide a way to specifically label intracellular proteins. GFP is a relatively larger probe and can interfere with the function of the attached protein. A new method for specific labeling of intracellular proteins has recently been reported (Figure 3.40). This method relies on expressing recombinant proteins that contain four cysteine residues in an α-helix.<sup>156–157</sup> These residues are located at positions *i*, *i* + 1, *i* + 4 and *i* + 5, which positions the SH groups on the same side of the α-helix. This grouping of SH groups does not appear to occur naturally. Proteins containing this motif react specifically with fluorescein analogues containing two trivalent arsenic atoms. Fortunately, the arsenic-containing compounds are not fluorescent, but the reaction product has a quantum yield near 0.49. The reaction can be reversed by addition of excess 1,2-ethanedithiol (EDT). Specific labeling of the intracellular recombinant proteins can be accomplished by exposure of the cells to the bis-arsenic fluorophore, which can passively diffuse into cells.

The fluorophore used for labeling the four-cysteine motif is called Flash-EDT<sub>2</sub>, meaning fluorescein arsenical helix binder, bis-EDT adduct. This approach is being used

in several laboratories<sup>158–159</sup> and is used with other fluorophores to create labeled proteins that are sensitive to their environment.<sup>160–161</sup>

### 3.9. LONG-LIFETIME PROBES

The probes described above were organic fluorophores with a wide variety of spectral properties, reactivities, and environmental sensitivities. While there are numerous organic fluorophores, almost all display lifetimes from 1 to 10 ns, which limit the dynamic information content of fluorescence. There are several exceptions to the short lifetimes of organic fluorophores. Pyrene displays a lifetime near 400 ns in degassed organic solvents. Pyrene has been derivatized by adding fatty acid chains, which typically results in decay times near 100 ns. In labeled macromolecules the intensity decays of pyrene and its derivatives are usually multi-exponential. Pyrene seems to display photochemical changes.

Another long-lived organic fluorophore is coronene, which displays a lifetime near 200 ns. In membranes the intensity decay of coronene is multi-exponential.<sup>162</sup> Coronene has also been conjugated to lipids.<sup>163</sup> Both pyrene and coronene display low initial anisotropies and are only moderately useful for anisotropy experiments. However, there are two types of organometallic fluorophores which display long lifetimes and other unique features which allow new types of experiments.

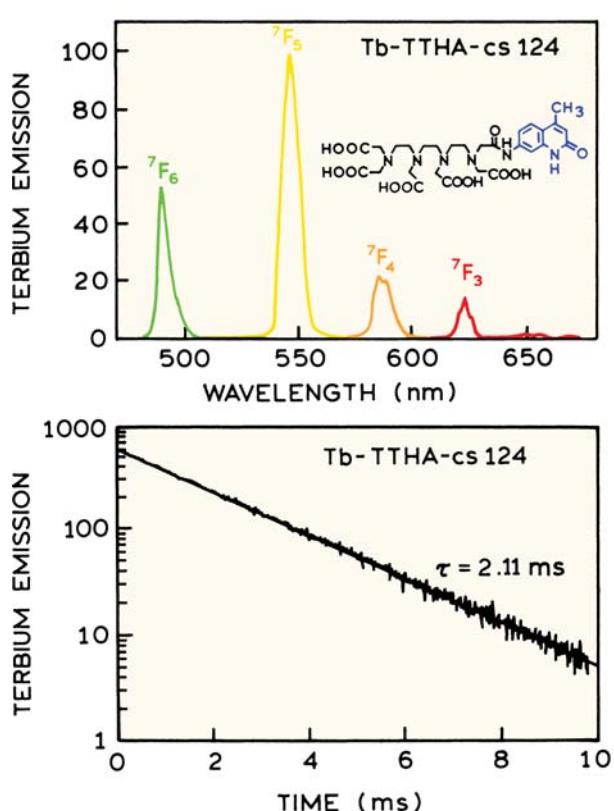


**Figure 3.41.** Emission spectrum and intensity decay of the lanthanide terbium. Revised and reprinted from [167]. Copyright © 1995, American Chemical Society.

### 3.9.1. Lanthanides

The lanthanides are uniquely fluorescent metals that display emission in aqueous solution and decay times of 0.5 to 3 ms.<sup>164–167</sup> Emission results from transitions involving  $4f$  orbitals, which are forbidden transitions. As a result, the absorption coefficients are very low, less than  $10 \text{ M}^{-1} \text{ cm}^{-1}$ , and the emissive rates are slow, resulting in long lifetimes. The lanthanides behave like atoms and display line spectra<sup>164</sup> (Figure 3.41). Because of the weak absorption, lanthanides are usually not directly excited, but rather excited through chelated organic ligands (Figures 3.41 and 3.42). Hence, the excitation spectrum of the complex shown in Figure 3.41 reflects the absorption spectrum of the ligand and not the lanthanide itself.

Lanthanides possess some favorable properties as biochemical probes. They can substitute chemically for calcium in many calcium-dependent proteins.<sup>168–170</sup> A main route of non-radiative decay is via coupling to vibrations of water. For both  $\text{Eu}^{3+}$  and  $\text{Tb}^{3+}$  the lifetime in  $\text{H}_2\text{O}$  and  $\text{D}_2\text{O}$

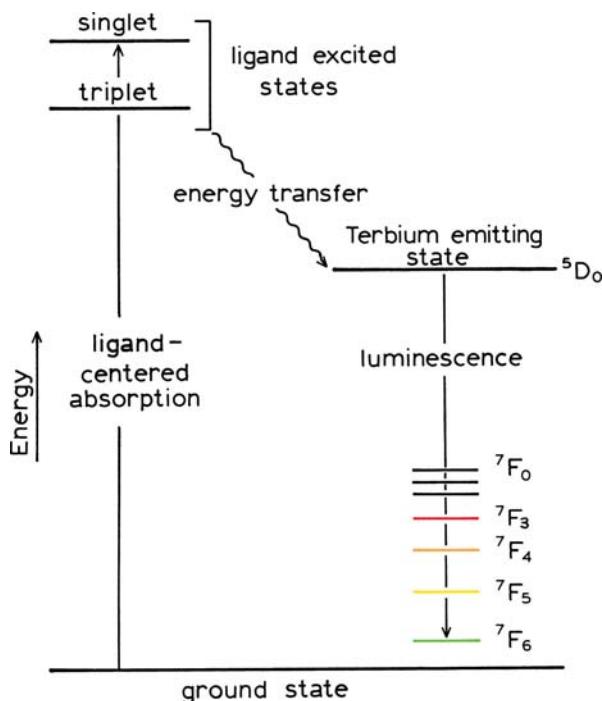


**Figure 3.42.** Jablonski diagram for excitation of terbium by energy transfer. Modified and redrawn from [165]. Copyright © 1993, with permission from Elsevier Science.

can be used to calculate the number of bound water molecules ( $n$ )

$$n = q \left( \frac{1}{\tau_{\text{H}_2\text{O}}} - \frac{1}{\tau_{\text{D}_2\text{O}}} \right) \quad (3.1)$$

where  $q$  is a constant different for each metal.<sup>165</sup> Hence, the decay times of the lanthanides when bound to proteins can be used to calculate the number of bound water molecules in a calcium binding site. Lanthanides can also be used with proteins that do not have intrinsic binding sites. Reagents have been developed that can be coupled to proteins and chelate lanthanides.<sup>171–172</sup> Because of their sensitivity to water, lanthanide complexes designed as labels generally have most sites occupied by the ligand.

Lanthanides have found widespread use in high sensitivity detection, particularly for immunoassays.<sup>173–174</sup> The basic idea is shown in Figure 3.43. All biological samples display autofluorescence, which is usually the limiting factor in high sensitivity detection. The autofluorescence usually decays on the nanosecond timescale, as do most fluorophores. Because of their long decay times, the lanthanides continue to emit following disappearance of the autofluorescence. The detector is turned on after the excitation flash

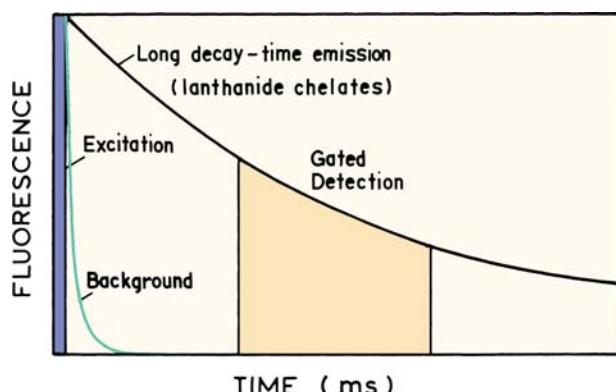


**Figure 3.43.** Principle of "time-resolved" detection in lanthanide immunoassays. Revised from [174].

to integrate the intensity from the lanthanide. The term "time-resolved" is somewhat of a misnomer, and does not refer to measurement of the decay time. These time-gated immunoassays are essentially steady-state intensity measurements in which the intensity is measured over a period of time following pulsed excitation.

The lanthanides do suffer several limitations. One is the need to chelate the lanthanide in order to obtain significant excitation. The requirement often results in multi-step assays, the last step being addition of the chelator. Another difficulty is the absence of polarized emission, so that the lanthanides cannot be used for anisotropy measurements.

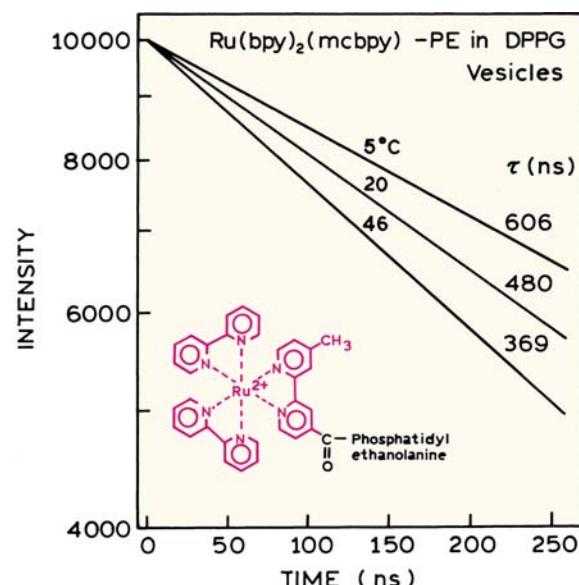


**Figure 3.44.** Intensity decay of  $\text{Ru}(\text{bpy})_2(\text{mcbpy})\text{-PE}$  in DPPG vesicles. Modified From [176].

### 3.9.2. Transition Metal–Ligand Complexes

Another class of probes with long lifetimes are the transition metal complexes. These are typically complexes of ruthenium (Ru II), rhenium (Re I), or osmium (Os II) with one or more diimine ligands (Figure 3.44). In contrast to the lanthanides, these compounds display molecular fluorescence from a metal-to-ligand charge-transfer state. The transition is partially forbidden, so that the decay times are long. These complexes are highly stable, like covalent bonds, so there is no significant dissociation of the metal and ligands. Transition metal complexes display lifetimes ranging from 10 ns to 10  $\mu\text{s}$ .<sup>175</sup> For example,  $\text{Ru}(\text{bpy})_2(\text{mcbpy})$  in Figure 3.44 displayed a decay time near 400 ns when conjugated to proteins and lipids.<sup>177</sup> The MLC probes are highly photostable, and display large Stokes shifts, so that probe–probe interactions are not expected. These molecules are known to display polarized emission (Chapter 20) and are thus useful for measurement of dynamic processes on the microsecond timescale.

### 3.10. PROTEINS AS SENSORS

The use of fluorescence for chemical sensing requires highly specific probes. One approach to obtaining the needed specificity is to rely on proteins that are known to bind the desired analyte. This approach has been used to develop sensing proteins for a variety of analytes.<sup>178–179</sup> One example is a sensor for zinc based on a zinc finger peptide. Zinc fingers are part of transcription factors. These proteins bind zinc with high affinity and specificity, typically to histidine and/or cysteine residues. To make a zinc sensor, the zinc finger amino-acid sequence was modified to contain a covalently linked dansyl group near the middle of the peptide (Figure 3.45).<sup>180</sup> Upon addition of zinc the emission intensity increases, and the emission maxima shift to shorter wavelengths (Figure 3.46). In the absence of zinc the peptide is unfolded, and the dansyl group is exposed to the water. In the presence of zinc the peptide adopts a folded structure that was anticipated to result in shielding the dansyl group from water.

Another example of a protein sensor is shown in Figure 3.47. In this case the protein is calmodulin that was genetically modified to contain a cysteine residue at position 109. This residue was labeled with an environmentally sensitive fluorophore.<sup>181</sup> This labeled protein was sensitive to the antipsychotic drug trifluoperazine. The fluorescence of the coumarin label was almost completely quenched upon addition of this drug.

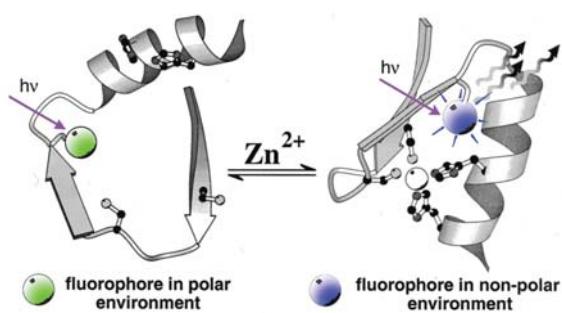


**Figure 3.45.** A zinc-sensitive peptide based on the dansyl fluorophore. Reprinted with permission from [180]. Copyright © 1996, American Chemical Society.

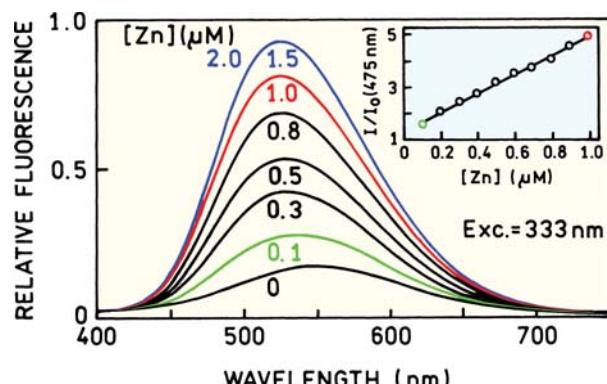


**Figure 3.46.** Zinc-dependent emission spectra of the dansyl-labeled zinc finger peptide. From [180].

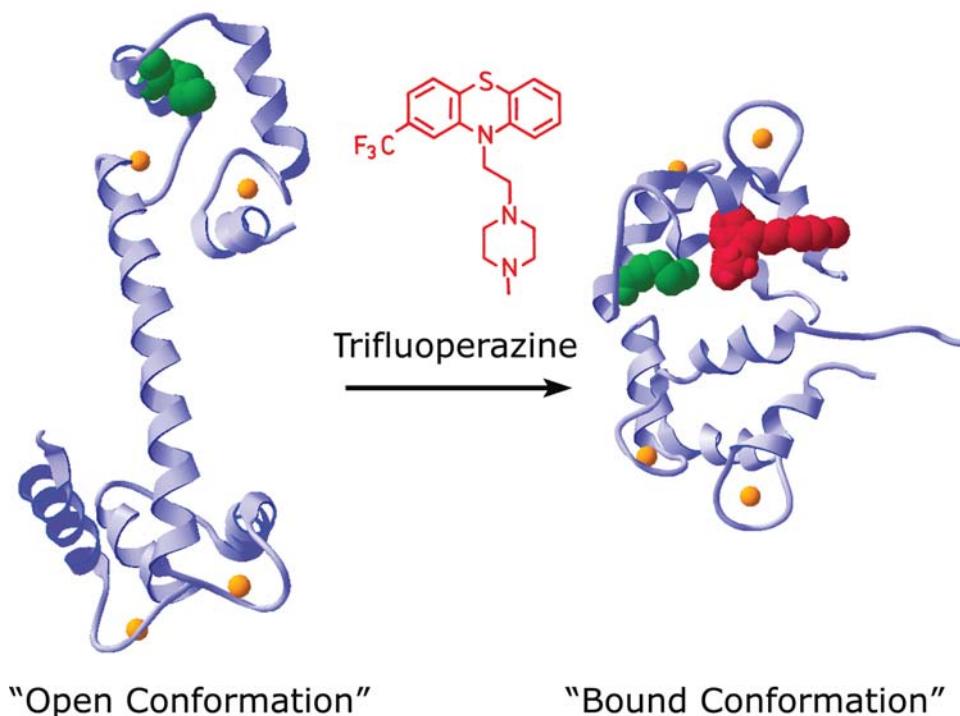


**Figure 3.47.** Protein sensor for the antipsychotic drug trifluoperazine. The protein is calmodulin labeled with a fluorophore at a genetically inserted cysteine residue at position 109. From [181].

### 3.11. CONCLUSION

A diversity of molecules display fluorescence, and numerous interactions and processes can alter the spectral properties. Fluorophores can be covalently attached to macromolecules, or designed to interact with specific ions. Emission

can occur from the UV to the NIR, and probes are available with short (ns) and long ( $\mu\text{s}$  to ms) lifetimes. The technology of probe chemistry is rapidly changing, and new probes are allowing previously impossible experiments to be performed.

## REFERENCES

1. Demchenko AP. 1981. *Ultraviolet spectroscopy of proteins*. Springer-Verlag, New York.
2. Longworth JW. 1971. Luminescence of polypeptides and proteins. In *Excited states of proteins and nucleic acids*, pp. 319–484. Ed RF Steiner, I Welnryb, Plenum, New York.
3. Permyakov EA. 1993. *Luminescent spectroscopy of proteins*. CRC Press, London.
4. Velick SF. 1958. Fluorescence spectra and polarization of glyceraldehyde-3-phosphate and lactic dehydrogenase coenzyme complexes. *J Biol Chem* **233**:1455–1467.
5. Gafni A, Brand L. 1976. Fluorescence decay studies of reduced nicotinamide adenine dinucleotide in solution and bound to liver alcohol dehydrogenase. *Biochemistry* **15**(15):3165–3171.
6. Brochon J-C, Wahl P, Monneuse-Douillet M-O, Olomucki A. 1977. Pulse fluorimetry study of octopine dehydrogenase-reduced nicotinamide adenine dinucleotide complexes. *Biochemistry* **16**(21):4594–4599.
7. Churchich JE. 1965. Fluorescence properties of pyridoxamine 5-phosphate. *Biochim Biophys Acta* **102**:280–288.
8. Hull RV, Conger PS, Hoobler RJ. 2001. Conformation of NADH studied by fluorescence excitation transfer spectroscopy. *Biophys Chem* **90**:9–16.
9. Vaccari S, Bencì S, Peracchi A, Mozzarelli A. 1997. Time-resolved fluorescence of pyridoxal 5'-phosphate-containing enzymes: tryptophan synthetase and O-acetylserine sulfhydrylase. *J Fluoresc* **7**(1):135S–137S.
10. Kwon O-S, Blazquez M, Churchich JE. 1994. Luminescence spectroscopy of pyridoxic acid and pyridoxic acid bound to proteins. *Eur J Biochem* **219**:807–812.
11. Xiao G-S, Zhou J-M. 1996. Conformational changes at the active site of bovine pancreatic RNase A at low concentrations of guanidine hydrochloride probed by pyridoxal 5'-phosphate. *Biochim Biophys Acta* **1294**:1–7.
12. Churchich JE. 1986. Fluorescence properties of free and bound pyridoxal phosphate and derivatives. *Pyridoxal Phosphate: Chem Biochem Med Asp A*, **1A**:545–567.
13. Churchich JE. 1976. Fluorescent probe studies of binding sites in proteins and enzymes. *Mod Fluoresc Spectrosc* **2**:217–237.
14. Vaccari S, Bencì S, Peracchi A, Mozzarelli A. 1996. Time-resolved fluorescence of tryptophan synthase. *Biophys Chem* **61**:9–22.
15. Visser AJWG. 1984. Kinetics of stacking interactions in flavin adenine dinucleotide from time-resolved flavin fluorescence. *Photochem Photobiol* **40**(6):703–706.
16. Mataga N, Chosrowjan H, Taniguchi S, Tanaka F, Kido N, Kitamura M. 2002. Femtosecond fluorescence dynamics of flavoproteins: comparative studies on flavodoxin, its site-directed mutants, and riboflavin binding protein regarding ultrafast electron transfer in protein nanospaces. *J Phys Chem B* **106**:8917–8920.
17. Albani JR, Sillen A, Engelborghs Y, Gervais M. 1999. Dynamics of flavin in flavocytochrome b<sub>2</sub>: a fluorescence study. *Photochem Photobiol* **69**(1):22–26.
18. Leenders R, Kooijman M, van Hoek A, Veeger C, Visser AJWG. 1993. Flavin dynamics in reduced flavodoxins. *Eur J Biochem* **211**:37–45.
19. Wolfbeis OS. 1985. The fluorescence of organic natural products. In *Molecular luminescence spectroscopy*, Part 1, pp. 167–370. Ed SG Schulman. John Wiley & Sons, New York.
20. Wagnieres GA, Star WM, Wilson BC. 1998. In vivo fluorescence spectroscopy and imaging for oncological applications. *Photochem Photobiol* **68**(5):603–632.
21. Richards-Kortum R, Sevick-Muraca E. 1996. Quantitative optical spectroscopy for tissue diagnosis. *Annu Rev Phys Chem* **47**:555–606.
22. DaCosta RS, Andersson H, Wilson BC. 2003. Molecular fluorescence excitation-emission matrices relevant to tissue spectroscopy. *Photochem Photobiol* **78**(4):384–392.
23. Madhuri S, Vengadesan N, Aruna P, Koteeswaran D, Venkatesan P, Ganesan S. 2003. Native fluorescence spectroscopy of blood plasma in the characterization of oral malignancy. *Photochem Photobiol* **78**(2):197–204.
24. Palmer GM, Keely PJ, Breslin TM, Ramanujam N. 2003. Autofluorescence spectroscopy of normal and malignant human breast cell lines. *Photochem Photobiol* **78**(5):462–469.
25. Mizeret J. 1998. Cancer detection by endoscopic frequency-domain fluorescence lifetime imaging. Thesis presented at École Polytechnique Federale de Lausanne, 177 pp.
26. Benson RC, Meyer RA, Zaruba ME, McKhann GM. 1979. Cellular autofluorescence: is it due to flavins? *J Histochem Cytochem* **27**(1):44–48.
27. Huang S, Heikal AA, Webb WW. 2002. Two-photon fluorescence spectroscopy and microscopy of NAD(P)H and flavoprotein. *Biophys J* **82**:2811–2825.
28. Breton R, Housset D, Mazza C, Fontecilla-Camps JC. 1996. The structure of a complex of human 17-β-hydroxysteroid dehydrogenase with estradiol and NADP<sup>+</sup> identifies two principal targets for the design of inhibitors. *Structure* **4**:905–915.
29. Li B, Lin S-X. 1996. Fluorescence-energy transfer in human estradiol 17-β-dehydrogenase–NADH complex and studies on the coenzyme binding. *Eur J Biochem* **235**:180–186.
30. Haugland RP. 1996. *Handbook of fluorescent probes and research chemicals*, 9th ed. Molecular Probes Inc, Eugene, OR.
31. Weber G. 1951. Polarization of the fluorescence of macromolecules. *Biochem J* **51**:155–167.
32. Waggoner A. 1995. Covalent labeling of proteins and nucleic acids with fluorophores. *Methods Enzymol* **246**:362–373.
33. Johnson ID, Kang HC, Haugland RP. 1991. Fluorescent membrane probes incorporating dipyrrometheneboron difluoride fluorophores. *Anal Biochem* **198**:228–237.
34. Berlier JE, Rothe A, Buller G, Bradford J, Gray DR, Filanowski BJ, Telford WG, Yue S, Liu J, Cheung C-Y, Chang W, Hirsch JD, Beechem JM, Haugland RP, Haugland RP. 2003. Quantitative comparison of long-wavelength Alexa fluor dyes to Cy dyes: fluorescence of the dyes and their bioconjugates. *J Histochem Cytochem* **51**(12):1699–1712.
35. Weber G, Farris FJ. 1979. Synthesis and spectral properties of a hydrophobic fluorescent probe: 6-propionyl-2-(dimethylamino)-naphthalene. *Biochemistry* **18**:3075–3078.
36. Prendergast FG, Meyer M, Carlson GL, Iida S, Potter JD. 1983. Synthesis, spectral properties, and use of 6-acryloyl-2-dimethylaminonaphthalene (Acrylodan). *J Biol Chem* **258**(12):7541–7544.
37. Slavik J. 1982. Anilinonaphthalene sulfonate as a probe of membrane composition and function. *Biochim Biophys Acta* **694**:1–25.
38. Daniel E, Weber G. 1966. Cooperative effects in binding by bovine serum albumin, I: the binding of 1-anilino-8-naphthalenesulfonate. Fluorimetric titrations. *Coop Effects Binding Albumin* **5**:1893–1900.
39. Courtesy of Drs. I. Gryczynski and Z. Gryczynski
40. Prendergast FG, Haugland RP, Callahan PJ. 1981. 1-[4-(trimethylamino)phenyl]-6-phenylhexa-1,3,5 triene: synthesis, fluorescence properties, and use as a fluorescence probe of lipid bilayers. *Biochemistry* **20**:7333–7338.
41. Sklar LA, Hudson BS, Petersen M, Diamond J. 1977. Conjugated polyene fatty acids on fluorescent probes: Spectroscopic characterization. *Biochemistry* **16**(5):813–818.

42. Kinnunen PKJ, Koiv A, Mustonen P. 1993. Pyrene-labeled lipids as fluorescent probes in studies on biomembranes and membrane models. In *Fluorescence spectroscopy: new methods and applications*, pp. 159–171. Ed OS Wolfbeis. Springer-Verlag, New York.
43. Plásek J, Sigler K. 1996. Slow fluorescent indicators of membrane potential: survey of different approaches to probe response analysis. *J Photochem Photobiol B: Biol* **33**:101–124.
44. Clarke RJ, Kane DJ. 1997. Optical detection of membrane dipole potential: avoidance of fluidity and dye-induced effects. *Biochim Biophys Acta* **1323**:223–239.
45. Dragsten PR, Webb WW. 1978. Mechanism of the membrane potential sensitivity of the fluorescent membrane probe merocyanine 540. *Biochemistry* **17**:5228–5240.
46. Loew LM. 1994. Characterization of potentiometric membrane dyes. *Adv Chem Ser* **235**:151–173.
47. Waggoner AS. 1979. Dye indicators of membrane potential. *Annu Rev Biophys Biophys Methods* **8**:47–68.
48. Loew LM. 1982. Design and characterization of electrochromic membrane probes. *J Biochem Biophys Methods* **6**:243–260.
49. Smiley ST, Reers M, Mottola-Hartshorn C, Lin M, Chen A, Smith TW, Steele GD, Chen LB. 1991. Intracellular heterogeneity in mitochondrial membrane potentials revealed by a J-aggregate-forming lipophilic cation JC-1. *Proc Natl Acad Sci USA* **88**:3671–3675.
50. Sims PJ, Waggoner AS, Wang C-H, Hoffman JF. 1974. Studies on the mechanism by which cyanine dyes measure membrane potential in red blood cells and phosphatidylcholine vesicles. *Biochemistry* **13**(16):3315–3336.
51. Gross E, Bedlack RS, Loew LM. 1994. Dual-wavelength ratiometric fluorescence measurement of the membrane dipole potential. *Biophys J* **67**:208–216.
52. Zhang J, Davidson RM, Wei M, Loew LM. 1998. Membrane electric properties by combined patch clamp and fluorescence ratio imaging in single neurons. *Biophys J* **74**:48–53.
53. Loew LM. 1996. Potentiometric dyes: imaging electrical activity of cell membranes. *Pure Appl Chem* **68**(7):1405–1409.
54. Klymchenko AS, Dupontail G, Mély Y, Demchenko AP. 2003. Ultrasensitive two-color fluorescence probes for dipole potential in phospholipid membranes. *Proc Natl Acad Sci USA* **100**(20):11219–11224.
55. Chang PY, Jackson MB. 2003. Interpretation and optimization of absorbance and fluorescence signals from voltage-sensitive dyes. *J Membr Biol* **196**:105–116.
56. Kao WY, Davis CE, Kim YI, Beach JM. 2001. Fluorescence emission spectral shift measurements of membrane potential in single cells. *Biophys J* **81**:1163–1170.
57. Shapovalov VL, Kotova EA, Rokitskaya TI, Antonenko YN. 1999. Effect of Gramicidin A on the dipole potential of phospholipid membranes. *Biophys J* **77**:299–305.
58. Gonzalez JE, Tsien RY. 1995. Voltage sensing by fluorescence resonance energy transfer in single cells. *Biophys J* **69**:1272–1280.
59. Cacciatore TW, Brodfuehrer PD, Gonzalez JE, Jiang T, Adams SR, Tsien RY, Kristan Jr WB, Kleinfield D. 1999. Identification of neural circuits by imaging coherent electrical activity with FRET-based dyes. *Neuron* **23**:449–459.
60. Thompson RB. 1994. Red and near-infrared fluorometry. In *Topics in fluorescence spectroscopy*, Vol 4: *Probe design and chemical sensing*, pp. 151–152. Ed JR Lakowicz. Plenum Press, New York.
61. Southwick PL, Ernst LA, Tauriello EW, Parker SR, Mujumdar RB, Mujumdar SW, Clever HA, Waggoner AS. 1990. Cyanine dye labeling reagents-carboxymethylindocyanine succinimidyl esters. *Cytometry* **11**:418–430.
62. Buschmann V, Weston KD, Sauer M. 2003. Spectroscopic study and evaluation of red-absorbing fluorescent dyes. *Bioconjugate Chem* **14**:195–204.
63. Lin Y, Weissleder R, Tung CH. 2003. Synthesis and properties of sulphydryl-reactive near-infrared cyanine fluorochromes for fluorescence imaging. *Mol Imaging* **2**(2):87–92.
64. Rahavendran SV, Karnes HT. 1996. Application of rhodamine 800 for reversed phase liquid chromatographic detection using visible diode laser induced fluorescence. *Anal Chem* **68**:3763–3768.
65. Rahavendran SV, Karnes HT. 1996. An oxazine reagent for derivatization of carboxylic acid analytes suitable for liquid chromatographic detection using visible diode laser-induced fluorescence. *J Pharmacol Biomed Anal* **15**:83–98.
66. Flanagan JH, Romero SE, Legendre BL, Hammer RP, Soper A. 1997. Heavy-atom modified near-IR fluorescent dyes for DNA sequencing applications: synthesis and photophysical characterization. *SPIE Proc* **2980**:328–337.
67. Leznoff CC, Lever ABP. 1989. *Phthalocyanines properties and applications*. VCH Publishers, New York.
68. Hammer RP, Owens CV, Hwang SH, Sayes CM, Soper SA. 2002. Asymmetrical, water-soluble phthalocyanine dyes for covalent labeling of oligonucleotides. *Bioconjugate Chem* **13**:1244–1252.
69. Adachi M, Nagao Y. 2001. Design of near-infrared dyes based on II-conjugation system extension, 2: theoretical elucidation of framework extended derivatives of perylene chromophore. *Chem Mater* **13**:662–669.
70. Arden-Jacob J, Frantzeskos J, Kemnitzer NU, Zilles A, Drexlage KH. 2001. New fluorescent markers for the red region. *Spectrochim Acta A* **57**:2271–2283.
71. Oswald B, Gruber M, Bohmer M, Lehmann F, Probst M, Wolfbeis OS. 2001. Novel diode laser-compatible fluorophores and their application to single molecule detection, protein labeling and fluorescence resonance energy transfer immunoassay. *Photochem Photobiol* **74**(2):237–245.
72. Klonis N, Wang H, Quazi NH, Casey JL, Neumann GM, Hewish DR, Hughes AB, Deady LW, Tilley L. 2001. Characterization of a series of far red absorbing perylene diones: a new class of fluorescent probes for biological applications. *J Fluoresc* **11**(1):1–11.
73. Steiner RF, Kubota Y. 1983. Fluorescent dye-nucleic acid complexes. In *Excited states of biopolymers*. Ed RF Steiner. Plenum Press, New York.
74. Georghiou S. 1977. Interaction of acridine drugs with DNA and nucleotides. *Photochem Photobiol* **26**:59–68.
75. Suh D, Chaires JB. 1995. Criteria for the mode of binding of DNA binding agents. *Bioorg Med Chem* **3**(6):723–728.
76. Eriksson S, Kim SK, Kubista M, Norden B. 1993. Binding of 4',6-diamidino-2-phenylindole (DAPI) to AT regions of DNA: evidence for an allosteric conformational change. *Biochemistry* **32**:2987–2998.
77. Parkinson JA, Barber J, Douglas KT, Rosamond J, Sharples D. 1990. Minor-groove recognition of the self-complementary duplex d(CGCGAATTCGCG)<sub>2</sub> by Hoechst 33258: a high-field NMR study. *Biochemistry* **29**:10181–10190.
78. Loontjens FG, McLaughlin LW, Diekmann S, Clegg RM. 1991. Binding of Hoechst 33258 and 4',6-diamidino-2-phenylindole to self-complementary decadeoxynucleotides with modified exocyclic base substituents. *Biochemistry* **30**:182–189.
79. Haq I, Ladbury JE, Chowdhry BZ, Jenkins TC, Chaires JB. 1997. Specific binding of Hoechst 33258 to the d(CGCAAATTTGCG)<sub>2</sub> duplex: calorimetric and spectroscopic studies. *J Mol Biol* **271**:244–257.

80. Glazer AN, Peck K, Matheis RA. 1990. A stable double-stranded DNA ethidium homodimer complex: application to picogram fluorescence detection of DNA in agarose gels. *Proc Natl Acad Sci USA* **87**:3851–3855.
81. Rye HS, Yue S, Wemmer DE, Quesada MA, Haugland RP, Mathies RA, Glazer AN. 1992. Stable fluorescent complexes of double-stranded DNA with bis-intercalating asymmetric cyanine dyes: properties and applications. *Nucleic Acids Res* **20**(11):2803–2812.
82. Wu P, Li H, Nordlund TM, Rigler R. 1990. Multistate modeling of the time and temperature dependence of fluorescence from 2-aminopurine in a DNA decamer. *SPIE Proc* **204**:262–269.
83. Nordlund TM, Wu P, Anderson S, Nilsson L, Rigler R, Graslund A, McLaughlin LW, Gildea B. 1990. Structural dynamics of DNA sensed by fluorescence from chemically modified bases. *SPIE Proc* **1204**:344–353.
84. Jean JM, Hall KB. 2001. 2-aminopurine fluorescence quenching and lifetimes: role of base stacking. *Proc Natl Acad Sci USA* **98**(1):37–41.
85. Kawai M, Lee MJ, Evans KO, Nordlund TM. 2001. Temperature and base sequence dependence of 2-aminopurine fluorescence bands in single- and double-stranded oligodeoxynucleotides. *J Fluoresc* **11**(1):23–32.
86. Jean JM, Hall KB. 2002. 2-aminopurine electronic structure and fluorescence properties in DNA. *Biochemistry* **41**:13152–13161.
87. Hawkins ME, Pfleiderer W, Mazumder A, Pommier YG, Balis FM. 1995. Incorporation of a fluorescent guanosine analog into oligonucleotides and its application to a real time assay for the HIV-1 integrase 3'-processing reaction. *Nucleic Acids Res* **23**(15):2872–2880.
88. Hawkins ME. 2001. Fluorescent pteridine nucleoside analogues. *Cell Biochem Biophys* **34**:257–281.
89. Kulkosky J, Skalka AM. 1990. HIV DNA integration: observations and inferences. *J Acquired Immune Def Synd* **3**:839–851.
90. Brown PO. 1990. Integration of retroviral DNA. *Curr Top Microbiol Immunol* **157**:19–48.
91. Biwersi J, Tulk B, Verkman AS. 1994. Long-wavelength chloride-sensitive fluorescent indicators. *Anal Biochem* **219**:139–143.
92. Geddes CD, Lakowicz JR, eds. 2005. Advanced concepts in fluorescence sensing: small molecule sensing. *Top Fluoresc Spectrosc* **9**, forthcoming.
93. Valeur B. 1994. Principles of fluorescent probe design for ion recognition. In *Topics in fluorescence spectroscopy*, Vol. 4: *Probe design and chemical sensing*, pp. 21–48. Ed JR Lakowicz. Plenum Press, New York.
94. Poenie M, Chen C-S. 1993. New fluorescent probes for cell biology. In *Optical microscopy*, pp. 1–25. Ed B Herman, JJ Lemasters. Academic Press, New York.
95. Szymanski H, Lakowicz JR. 1994. Lifetime-based sensing. In *Topics in fluorescence spectroscopy*, Vol. 4: *Probe design and chemical sensing*, pp. 295–334. Ed JR Lakowicz. Plenum Press, New York.
96. Czarnik AW. 1994. Fluorescent chemosensors for cations, anions, and neutral analytes. In *Topics in fluorescence spectroscopy*, Vol. 4: *probe design and chemical sensing*, pp. 49–70. Ed JR Lakowicz. Plenum Press, New York.
97. Haugland RP, Johnson ID. 1993. Detecting enzymes in living cells using fluorogenic substrates. *J Fluoresc* **3**(3):119–127.
98. Wang Q, Scheijetz J, Gilbert M, Snider J, Ramachandran C. 1999. Fluorescein monophosphates as fluorogenic substrates for protein tyrosine phosphatases. *Biochim Biophys Acta* **1431**:14–23.
99. Zhou M, Upson RH, Diwu Z, Haugland RP. 1996. A fluorogenic substrate for  $\beta$ -glucuronidase: applications in fluorometric, polyacrylamide gel and histochemical assays. *J Biochem Biophys Methods* **33**:197–205.
100. Gershkovich AA, Kholodovych VV. 1996. Fluorogenic substrates for proteases based on intramolecular fluorescence energy transfer (IFETS). *J Biochem Biophys Methods* **33**:135–162.
101. Geoghegan KF. 1996. Improved method for converting an unmodified peptide to an energy-transfer substrate for a proteinase. *Bioconjugate Chem* **7**(3):385–391.
102. Matayoshi ED, Wang GT, Krafft GA, Erickson J. 1990. Novel fluorogenic substrates for assaying retroviral proteases by resonance energy transfer. *Science* **247**:954–957.
103. Hale JE, Schroeder F. 1982. Asymmetric transbilayer distribution of sterol across plasma membranes determined by fluorescence quenching of dehydroergosterol. *Eur J Biochem* **122**:649–661.
104. Fischer RT, Cowlen MS, Dempsey ME, Schroeder F. 1985. Fluorescence of  $\Delta^{5,7,9(11),22}$ -ergostatetraen-3 $\beta$ -ol in micelles, sterol carrier protein complexes, and plasma membranes. *Biochemistry* **24**:3322–3331.
105. Schroeder F, Barenholz Y, Gratton E, Thompson TE. 1987. A fluorescence study of dehydroergosterol in phosphatidylcholine bilayer vesicles. *Biochemistry* **26**:2441–2448.
106. Loura LMS, Prieto M. 1997. Aggregation state of dehydroergosterol in water and in a model system of membranes. *J Fluoresc* **7**(1):173S–175S.
107. Hwang K-J, O'Neil JP, Katzenellenbogen JA. 1992. 5,6,11,12-Tetrahydrochrysene: synthesis of rigid stilbene systems designed to be fluorescent ligands for the estrogen receptor. *J Org Chem* **57**:1262–1271.
108. Bowen CM, Katzenellenbogen JA. 1997. Synthesis and spectroscopic characterization of two aza-tetrahydrochrysene as potential fluorescent ligands for the estrogen receptor. *J Org Chem* **62**:7650–7657.
109. Akers W, Haidekker MA. 2004. A molecular rotor as viscosity sensor in aqueous colloid solutions. *Trans ASME* **126**:340–345.
110. Kung CE, Reed JK. 1986. Microviscosity measurements of phospholipid bilayers using fluorescent dyes that undergo torsional relaxation. *Biochemistry* **25**:6114–6121. See also *Biochemistry* (1989) **28**:6678–6686.
111. Iwaki T, Torigoe C, Noji M, Nakanishi M. 1993. Antibodies for fluorescent molecular rotors. *Biochemistry* **32**:7589–7592.
112. Rettig W, Lapouyade R. 1994. Fluorescence probes based on twisted intramolecular charge transfer (TICT) states and other adiabatic photoreactions. In *Topics in fluorescence spectroscopy*, Vol. 4: *Probe design and chemical sensing*, pp. 109–149. Ed JR Lakowicz. Plenum Press, New York.
113. Ormo M, Cubitt AB, Kallio K, Gross LA, Tsien RY, Remington SJ. 1996. Crystal structure of the *Aequorea victoria* green fluorescent protein. *Science* **273**:1392–1395.
114. Chalfie M, Tu Y, Euskirchen G, Ward WW, Prasher DC. 1994. Green fluorescent protein as a marker for gene expression. *Science* **263**:802–805.
115. Niwa H, Inouye S, Hirano T, Matsuno T, Kojima S, Kubota M, Ohashi M, Tsuji FI. 1996. Chemical nature of the light emitter of the *Aequorea* green fluorescent protein. *Proc Natl Acad Sci USA* **93**:13617–13622.
116. Tsien RY. 1998. The green fluorescent protein. *Annu Rev Biochem* **67**:509–544.
117. Zimmer M. 2002. Green fluorescent protein (GFP): applications, structure, and related photophysical behavior. *Chem Rev* **102**:759–781.
118. Billinton N, Knight AW. 2001. Seeing the wood through the trees: a review of techniques for distinguishing green fluorescent protein from endogenous autofluorescence. *Anal Biochem* **291**:175–197.
119. Yang M, Baranov E, Jiang P, Sun FX, Li XM, Li L, Hasegawa S, Bouvet M, Al-tuwaijri M, Chishima T, Shimada H, Moossa AR, Penman S, Hoffman RM. 2000. Whole-body optical imaging of

- green fluorescent protein-expressing tumors and metastases. *Proc Natl Acad Sci USA* **97**(3):1206–1211.
120. Kwon MS, Koo BC, Choi BR, Lee HT, Kim YH, Ryu WS, Shim H, Kim JH, Kim NH, Kim T. 2004. Development of transgenic chickens expressing enhanced green fluorescent protein. *Biochem Biophys Res Commun* **320**:442–448.
  121. Diegelmam S, Fiala A, Leibold C, Spall T, Buchner E. 2002. Transgenic flies expressing the fluorescence calcium sensor cameleon 2.1 under UAS control. *Genesis* **34**:95–98.
  122. Ehrig T, O'Kane DJ, Prendergast FG. 1995. Green fluorescent protein mutants with altered fluorescence excitation spectra. *FEBS Lett* **367**:163–166.
  123. Cubitt AB, Heim R, Adams SR, Boyd AE, Gross LA, Tsien RY. 1995. Understanding, improving and using green fluorescent proteins. *Trends Biochem Sci* **20**:448–455.
  124. Heim R, Tsien RY. 1996. Engineering green fluorescent protein for improved brightness, longer wavelengths and fluorescence resonance energy transfer. *Curr Biol* **6**:178–182.
  125. Matz MV, Fradkov AF, Labas YA, Savitsky AP, Zaraisky AG, Markelov ML, Lukyanov SA. 1999. Fluorescent proteins from non-bioluminescent Anthozoa species. *Nature Biotechnol* **17**:969–973.
  126. Fradkov AF, Chen Y, Ding L, Barsova EV, Matz MV, Lukyanov SA. 2000. Novel fluorescent protein from *discosoma* coral and its mutants possesses a unique far-red fluorescence. *FEBS Lett* **479**:127–130.
  127. Karasawa S, Araki T, Yamamoto-Hino M, Miyawaki A. 2003. A green-emitting fluorescent protein from *Galaxeidae* coral and its monomeric version for use in fluorescent labeling. *J Biol Chem* **278**(36):34167–34171.
  128. Lukyanov KA, Fradkov AF, Gurskaya NG, Matz MV, Labas YA, Savitsky AP, Markelov ML, Zaraisky AG, Zhao X, Fang Y, Tan W, Lukyanov SA. 2000. Natural animal coloration can be determined by a nonfluorescent green fluorescent protein homolog. *J Biol Chem* **275**(34):25879–25882.
  129. Lippincott-Schwartz J, Patterson GH. 2003. Development and use of fluorescent protein markers in living cells. *Science* **300**:87–91.
  130. Zhang J, Campbell RE, Ting AY, Tsien RY. 2002. Creating new fluorescent probes for cell biology. *Nature* **3**:906–918.
  131. Mizuno H, Sawano A, Eli P, Hama H, Miyawaki A. 2001. Red fluorescent protein from *discosoma* as a fusion tag and a partner for fluorescence resonance energy transfer. *Biochemistry* **40**:2502–2510.
  132. Baird GS, Zacharias DA, Tsien RY. 2000. Biochemistry, mutagenesis, and oligomerization of DsRed, a red fluorescent protein from coral. *Proc Natl Acad Sci USA* **97**(22):11984–11989.
  133. Campbell RE, Tour O, Palmer AE, Steinbach PA, Baird GS, Zacharias DA, Tsien RY. 2002. A monomeric red fluorescent protein. *Proc Natl Acad Sci USA* **99**(12):7877–7882.
  134. Wiedenmann J, Schenk A, Rocker C, Girod A, Spindler KD. 2002. A far-red fluorescent protein with fast maturation and reduced oligomerization tendency from *Entacmaea quadricolor* (anthozoa, actinaria). *Proc Natl Acad Sci USA* **99**(18):11646–11651.
  135. Bevis BJ, Glick BS. 2002. Rapidly maturing variants of the *discosoma* red fluorescent protein (DsRed). *Nature Biol* **20**:83–87.
  136. Remington SJ. 2002. Negotiating the speed bumps to fluorescence. *Nature Biotechnol* **20**:28–29.
  137. Li L, Murphy JT, Lagarias JC. 1995. Continuous fluorescence assay of phytochrome assembly in vitro. *Biochemistry* **34**:7923–7930.
  138. Murphys JT, Lagarias JC. 1997. Purification and characterization of recombinant affinity peptide-tagged oat phytochrome A. *Photochem Photobiol* **65**(4):750–758.
  139. Murphy JT, Lagarias JC. 1997. The phytofluors: a new class of fluorescent protein probes. *Curr Biol* **7**:870–876.
  140. Gambetta GA, Lagarias JC. 2001. Genetic engineering of phytochrome biosynthesis in bacteria. *Proc Natl Acad Sci USA* **98**(19):10566–10571.
  141. Fischer AJ, Lagarias JC. 2004. Harnessing phytochrome's glowing potential. *Proc Natl Acad Sci USA (Early Ed.)* **101**:17334–17339.
  142. Loos D, Cotlet M, De Schryver F, Habuchi S, Jofkens J. 2004. Single-molecule spectroscopy selectively probes donor and acceptor chromophore in the phycobiliprotein allophycocyanin. *Biophys J* **87**:2598–2608.
  143. Glazer AN. 1985. Light harvesting by phycobilisomes. *Annu Rev Biophys Biophys Chem* **14**:47–77.
  144. MacColl R, Guard-Friar D. 1987. *Phycobiliproteins*. CRC Press, Boca Raton, FL.
  145. Glazer AN, Stryer L. 1984. Phycofluor probes. *Trends Biochem Sci* **423**:423–427.
  146. Adir N, Lerner N. 2003. The crystal structure of a novel unmethylated form of C-phycocyanin, a possible connector between cores and rods in phycobilisomes. *J Biol Chem* **278**(28):25926–25932.
  147. White JC, Stryer L. 1987. Photostability studies of phycobiliprotein fluorescent labels. *Anal Biochem* **161**:442–452.
  148. Oi VT, Glazer AN, Stryer L. 1982. Fluorescent phycobiliprotein conjugates for analyses of cells and molecules. *J Cell Biol* **93**:981–986.
  149. Trinquet E, Maurin F, Préaudat M, Mathis G. 2001. Allphycocyanin 1 as a near-infrared fluorescent tracer: isolation, characterization, chemical modification, and use in a homogeneous fluorescence resonance energy transfer system. *Anal Biochem* **296**:232–244.
  150. Graefe KA, Tang Z, Karnes HT. 2000. High-performance liquid chromatography with on-line post-column immunoreaction detection of digoxin and its metabolites based on fluorescence energy transfer in the far-red spectral region. *J Chromatogr B* **745**:305–314.
  151. Tjioe I, Legerton T, Wegstein J, Herzenberg LA, Roederer M. 2001. Phycoerythrin-allophycocyanin: a resonance energy transfer fluorochrome for immunofluorescence. *Cytometry* **44**:24–29.
  152. Telford WG, Moss MW, Morseman JP, Allnutt FCT. 2001. Cyanobacterial stabilized phycobilisomes as fluorochromes for extracellular antigen detection by flow cytometry. *J Immunol Methods* **254**:13–30.
  153. Telford WG, Moss MW, Morseman JP, Allnutt FCT. 2001. Cryptomonad algal phycobiliproteins as fluorochromes for extracellular and intracellular antigen detection by flow cytometry. *Cytometry* **44**:16–23.
  154. Triantafilou K, Triantafilou M, Wilson KM. 2000. Phycobiliprotein-fab conjugates as probes for single particle fluorescence imaging. *Cytometry* **41**:226–234.
  155. Holzwarth AR, Wendler J, Suter GW. 1987. Studies on chromophore coupling in isolated phycobiliproteins. *Biophys J* **51**:1–12.
  156. Griffin BA, Adams SR, Tsien RY. 1998. Specific covalent labeling of recombinant protein molecules inside live cells. *Science* **281**:269–272.
  157. Adams SR, Campbell RE, Gross LA, Martin BR, Walkup GK, Yao Y, Llopis J, Tsien RY. 2002. New biarsenical ligands and tetracycysteine motifs for protein labeling in vitro and in vivo: synthesis and biological applications. *J Am Chem Soc* **124**:6063–6076.
  158. Ignatova Z, Giersch LM. 2004. Monitoring protein stability and aggregation in vivo by real-time fluorescent labeling. *Proc Natl Acad Sci USA* **101**:523–528.
  159. Andresen M, Schmitz-Salue R, Jakobs S. 2004. Short tetracycysteine tags to  $\beta$ -tubulin demonstrate the significance of small labels for live cell imaging. *Mol Biol Cell* **15**:5616–5622.
  160. Nakanishi J, Maeda M, Umezawa Y. 2004. A new protein conformation indicator based on biarsenical fluorescein with an extended benzoic acid moiety. *Anal Sci* **20**:273–278.

161. Nakanishi J, Nakajima T, Sato M, Ozawa T, Tohda K, Umezawa Y. 2001. Imaging of conformational changes of proteins with a new environment-sensitive fluorescent probe designed for site-specific labeling of recombinant proteins in live cells. *Anal Chem* **73**: 2920–2928.
162. Davenport L, Targowski P. 1996. Submicrosecond phospholipid dynamics using a long lived fluorescence emission anisotropy probe. *Biophys J* **71**:1837–1852.
163. Davenport L, Shen B, Joseph TW, Straher MP. 2001. A novel fluorescent coronenyl-phospholipid analogue for investigations of submicrosecond lipid fluctuations. *Chem Phys Lipids* **109**:145–156.
164. Richardson FS. 1982. Terbium(III) and europium(III) ions as luminescent probes and stains for biomolecular systems. *Chem Rev* **82**:541–552.
165. Sabbatini N, Guardigli M. 1993. Luminescent lanthanide complexes as photochemical supramolecular devices. *Coord Chem Rev* **123**:201–228.
166. Balzani V, Ballardini R. 1990. New trends in the design of luminescent metal complexes. *Photochem Photobiol* **52**(2):409–416.
167. Li M, Selvin PR. 1995. Luminescent polyaminocarboxylate chelates of terbium and europium: the effect of chelate structure. *J Am Chem Soc* **117**:8132–8138.
168. Martin RB, Richardson FS. 1979. Lanthanides as probes for calcium in biological systems. *Quart Rev Biophys* **12**(2):181–209.
169. Bruno J, Horrocks WDeW, Zauhar RJ. 1992. Europium(III) luminescence and tyrosine to terbium(III) energy transfer studies of invertebrate (octopus) calmodulin. *Biochemistry* **31**:7016–7026.
170. Horrocks WDeW, Sudnick DR. 1981. Lanthanide ion luminescence probes of the structure of biological macromolecules. *Acc Chem Res* **14**:384–392.
171. Lamture JB, Wensel TG. 1993. A novel reagent for labelling macromolecules with intensity luminescent lanthanide complexes. *Tetrahedron Lett* **34**(26):4141–4144.
172. Lamture JB, Wensel TG. 1995. Intensely luminescent immunoconjugate conjugates of proteins and dipicolinate-based polymeric Tb(III) chelates. *Bioconjugate Chem* **6**:88–92.
173. Lövgren T, Pettersson K. 1990. Time-resolved fluoroimmunoassay, advantages and limitations. In *Luminescence immunoassay and molecular applications*, pp. 233–253. Ed K Van Dyke, R Van Dyke. CRC Press, Boca Raton, FL.
174. Hemmila I. 1993. Progress in delayed fluorescence immunoassay. In *Fluorescence spectroscopy, new methods and applications*, pp. 259–266. Ed OS Wolfbeis. Springer-Verlag, New York.
175. Demas JN, DeGraff BA. 1992. Applications of highly luminescent transition metal complexes in polymer systems. *Macromol Chem Macromol Symp* **59**:35–51.
176. Li L, Szmacinski H, Lakowicz JR. 1997. Long-lifetime lipid probe containing a luminescent metal-ligand complex. *Biospectroscopy* **3**:155–159.
177. Terpetschnig E, Szmacinski H, Lakowicz JR. 1997. Long lifetime metal-ligand complexes as probes in biophysics and clinical chemistry. *Methods Enzymol* **278**:295–321.
178. Giuliano KA, Taylor DL. 1998. Fluorescent-protein biosensors: new tools for drug discovery. *Tibtech* **16**:135–140.
179. Hellenga HW, Marvin JS. 1998. Protein engineering and the development of generic biosensors. *Tibtech* **16**:183–189.
180. Walkup GK, Imperiali B. 1996. Design and evaluation of a peptidyl fluorescent chemosensor for divalent zinc. *J Am Chem Soc* **118**:3053–3054.
181. Douglass PM, Salins LLE, Dikici E, Daunert S. 2002. Class-selective drug detection: fluorescently labeled calmodulin as the biorecognition element for phenothiazines and tricyclic antidepressants. *Bioconjugate Chem* **13**:1186–1192.
182. Illsley NP, Verkman AS. 1987. Membrane chloride transport measured using a chloride-sensitive fluorescent probe. *Biochemistry* **26**:1215–1219.
183. Kao JPY. 1994. Practical aspects of measuring  $[Ca^{2+}]$  with fluorescent indicators. In *Methods in Cell Biology*, Vol. 40, pp. 155–181. Ed R Nuccitelli. Academic Press, New York.

## PROBLEMS

### P3.1. Binding of Proteins to Membranes or Nucleic Acids:

Suppose you have a protein that displays tryptophan fluorescence, and you wish to determine if the protein binds to DNA or lipid bilayers. Describe how you could use the tryptophan fluorescence to detect binding. Be specific regarding the spectral observables and expected results, including the use of intrinsic fluorescence, anisotropy and resonance energy transfer.

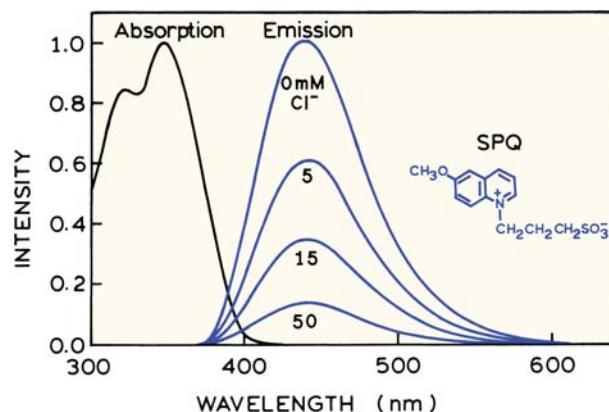


**Figure 3.48.** Absorption and emission spectra of 6-methoxy-N-(3-sulfopropyl) quinolinium (SPQ) in water with increasing amounts of  $Cl^-$ . From [182].

### P3.2. Chloride Quenching of SPQ:

Figure 3.48 shows the absorption and emission spectra of the chloride sensitive probe 6-methoxy-N-(3-sulfopropyl) quinolinium (SPQ) in the presence of increasing amounts of  $Cl^-$ . SPQ is collisionally quenched by  $Cl^-$ . The unquenched lifetime is 26.3 ns.<sup>182</sup>

- Use the data in Figure 3.48 to determine the Stern-Volmer quenching constant for chloride.
- The average concentration of intracellular chloride in blood serum is 103 mM. What is the lifetime and relative intensity of SPQ in blood serum?

- C. Suppose the concentration of  $\text{Cl}^-$  decreases to 75 mM. What is the expected lifetime and relative intensity of SPQ?
- D. What factors would complicate interpretation of the SPQ intensities and lifetimes as a measure of  $\text{Cl}^-$  in blood serum?
- P3.3. *Calcium Concentrations Using Calcium Green and Fura-2:* The probes Calcium Green and Fura-2 display spectral changes in the presence of bound  $\text{Ca}^{2+}$ . Calcium Green shows changes in fluorescence intensity but not in spectra shape. Fura-2 displays a large shift in its absorption spectrum, but little change in the shape of its emission spectrum. Calcium Green and Fura-2 display  $\text{Ca}^{2+}$  dissociation constants ( $K_D$ ) near 200 nM.
- A. Derive an expression for the fluorescence intensity of Calcium Green relating its intensity to the  $[\text{Ca}^{2+}]$ . For your answer let  $F_{\min}$  and  $F_{\max}$  be the fluorescent intensities of Calcium Green in the absence and presence of saturating  $\text{Ca}^{2+}$ , respectively, and let  $K_D$  be the dissociation constant.
- B. Derive an expression for the use of Fura-2 as an excitation wavelength-ratiometric probe of  $[\text{Ca}^{2+}]$ . This is a somewhat difficult problem to solve, and the exact form of the answer depends on how one defines the various terms. Let the subscripts 1 and 2 represent the two excitation wavelengths. Let  $R_{\min}$  and  $R_{\max}$  be the ratio of intensities of the free ( $f$ ) and calcium-bound ( $b$ ) form of Fura-2.

# 4

# Time-Domain Lifetime Measurements

Time-resolved measurements are widely used in fluorescence spectroscopy, particularly for studies of biological macromolecules and increasingly for cellular imaging. Time-resolved measurements contain more information than is available from the steady-state data. For instance, consider a protein that contains two tryptophan residues, each with a distinct lifetime. Because of spectral overlap of the absorption and emission, it is not usually possible to resolve the emission from the two residues from the steady-state data.

However, the time-resolved data may reveal two decay times, which can be used to resolve the emission spectra and relative intensities of the two tryptophan residues. The time-resolved measurements can reveal how each of the tryptophan residues in the protein is affected by the interactions with its substrate or other macromolecules. Is one of the tryptophan residues close to the binding site? Is a tryptophan residue in a distal domain affected by substrate binding to another domain? Such questions can be answered if one measures the decay times associated with each of the tryptophan residues.

There are many other examples where the time-resolved data provide information not available from the steady-state data. One can distinguish static and dynamic quenching using lifetime measurements. Formation of static ground-state complexes do not decrease the decay time of the uncomplexed fluorophores because only the unquenched fluorophores are observed. Dynamic quenching is a rate process acting on the entire excited-state population, and thus decreases the mean decay time of the entire excited-state population. Resonance energy transfer is also best studied using time-resolved measurements. Suppose a protein contains a donor and acceptor, and the steady-state measurements indicate the donor is 50% quenched by the acceptor. The result of 50% donor quenching can be due to 100% quenching for half of the donors, or 50% quenching

of all the donors, or some combination of these two limiting possibilities. The steady-state data cannot distinguish between these extreme cases. In contrast, very different donor intensity decays would be observed for each case. If all the donors are 50% quenched by the acceptors, and the acceptors are at a single distance, then the donor decay will be a single exponential with a lifetime of half the unquenched lifetime. If 50% of the donors are completely quenched and 50% are not quenched, then the donor lifetime will be the same as the unquenched lifetime. A multi-exponential decay would be observed if the donor is partially quenched by the acceptor and some of the donors do not have a nearby acceptor. The time-resolved donor decays are highly informative about the purity of the sample as well as the donor-to-acceptor distance.

There are many other instances where lifetime measurements are advantageous over steady-state measurements. One important application is cellular imaging using fluorescence microscopy. When labeled cells are observed in a fluorescence microscope, the local concentration of the probe in each part of the cell is not known. Additionally, the probe concentration can change during the measurement due to washout or photobleaching. As a result it is difficult to make quantitative use of the local intensities. In contrast, if the probe emission is well above the background signal, fluorescence lifetimes are typically independent of the probe concentration. Many fluorescence sensors such as the calcium probes display changes in lifetime in response to analytes. Also, resonance energy transfer (RET) reveals the proximity of donors and acceptors by changes in the donor lifetime. Because of advances in technology for time-resolved measurements, it is now possible to create lifetime images, where the image contrast is based on the lifetime in each region of the sample. Fluorescence lifetime imaging microscopy, or FLIM, has now become an accessible and increasingly used tool in cell biology (Chapter 22). An

understanding of FLIM must be based on an understanding of the technology used for time-resolved fluorescence measurements.

Prior to describing the technology for time-resolved measurements we present an overview of the two dominant methods for time-resolved measurements: the time-domain (TD) and frequency-domain (FD) methods. There are also several variations to each approach. Since the previous edition of this book there have been advances in both methods. The time-domain technology has become smaller, less expensive, and more reliable. We will also describe some of the earlier approaches, which clarify why specific procedures have been selected. We also discuss the important topic of data analysis, which is essential for using the extensive data from modern instruments, and avoiding misuse of the results by over-interpretation of the data.

#### 4.1. OVERVIEW OF TIME-DOMAIN AND FREQUENCY-DOMAIN MEASUREMENTS

Two methods of measuring time-resolved fluorescence are in widespread use: the time-domain and frequency-domain methods. In time-domain or pulse fluorometry, the sample is excited with a pulse of light (Figure 4.1). The width of the pulse is made as short as possible, and is preferably much shorter than the decay time  $\tau$  of the sample. The time-dependent intensity is measured following the excitation pulse, and the decay time  $\tau$  is calculated from the slope of a plot of  $\log I(t)$  versus  $t$ , or from the time at which the intensity decreases to  $1/e$  of the intensity at  $t = 0$ . The intensity decays are often measured through a polarizer oriented

at  $54.7^\circ$  from the vertical  $z$ -axis. This condition is used to avoid the effects of rotational diffusion and/or anisotropy on the intensity decay (Chapter 11).

The alternative method of measuring the decay time is the frequency-domain or phase-modulation method. In this case the sample is excited with intensity-modulated light, typically sine-wave modulation (Figure 4.2). The amplitude-modulated excitation should not be confused with the electrical component of an electromagnetic wave. The intensity of the incident light is varied at a high frequency typically near 100 MHz, so its reciprocal frequency is comparable to the reciprocal of decay time  $\tau$ . When a fluorescent sample is excited in this manner the emission is forced to respond at the same modulation frequency. The lifetime of the fluorophore causes the emission to be delayed in time relative to the excitation, shown as the shift to the right in Figure 4.2. This delay is measured as a phase shift ( $\phi$ ), which can be used to calculate the decay time. Magic-angle polarizer conditions are also used in frequency-domain measurements.

The lifetime of the fluorophore also causes a decrease in the peak-to-peak height of the emission relative to that of the modulated excitation. The modulation decreases because some of the fluorophores excited at the peak of the excitation continue to emit when the excitation is at a minimum. The extent to which this occurs depends on the decay time and light modulation frequency. This effect is called demodulation, and can also be used to calculate the decay time. FD measurements typically use both the phase and modulation information. At present, both

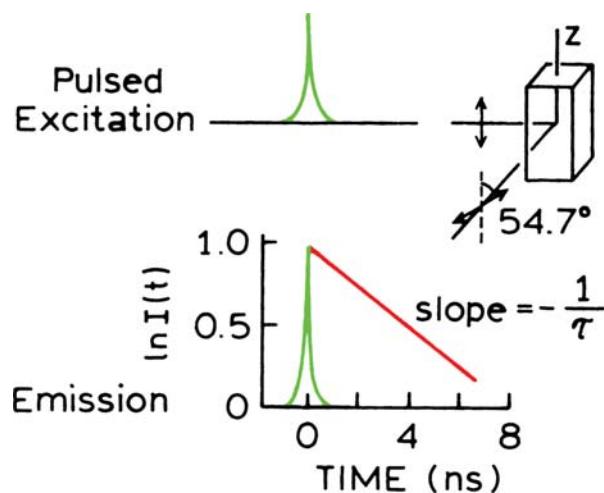


Figure 4.1. Pulse or time-domain lifetime measurements.

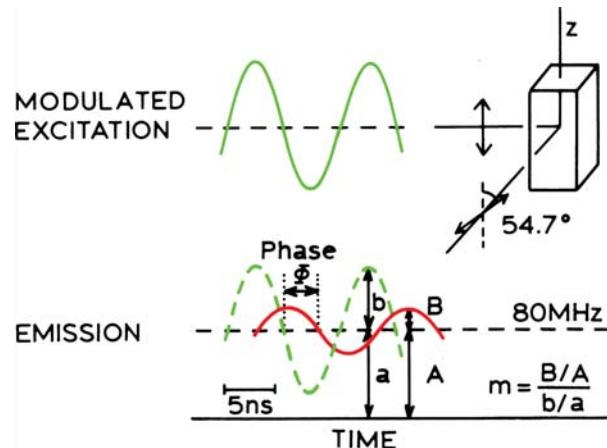


Figure 4.2. Phase-modulation or frequency-domain lifetime measurements. The ratios  $B/A$  and  $b/a$  represent the modulation of the emission and excitation, respectively.

time-domain and frequency-domain measurements are in widespread use.

#### 4.1.1. Meaning of the Lifetime or Decay Time

Prior to further discussion of lifetime measurements, it is important to have an understanding of the meaning of the lifetime  $\tau$ . Suppose a sample containing the fluorophore is excited with an infinitely sharp ( $\delta$ -function) pulse of light. This results in an initial population ( $n_0$ ) of fluorophores in the excited state. The excited-state population decays with a rate  $\Gamma + k_{\text{nr}}$  according to

$$\frac{dn(t)}{dt} = (\Gamma + k_{\text{nr}}) n(t) \quad (4.1)$$

where  $n(t)$  is the number of excited molecules at time  $t$  following excitation,  $\Gamma$  is the emissive rate, and  $k_{\text{nr}}$  is the non-radiative decay rate. Emission is a random event, and each excited fluorophore has the same probability of emitting in a given period of time. This results in an exponential decay of the excited state population,  $n(t) = n_0 \exp(-t/\tau)$ .

In a fluorescence experiment we do not observe the number of excited molecules, but rather fluorescence intensity, which is proportional to  $n(t)$ . Hence, eq. 4.1 can also be written in terms of the time-dependent intensity  $I(t)$ . Integration of eq. 4.1 with the intensity substituted for the number of molecules yields the usual expression for a single exponential decay:

$$I(t) = I_0 \exp(-t/\tau) \quad (4.2)$$

where  $I_0$  is the intensity at time 0. The lifetime  $\tau$  is the inverse of the total decay rate,  $\tau = (\Gamma + k_{\text{nr}})^{-1}$ . In general, the inverse of the lifetime is the sum of the rates which depopulate the excited state. The fluorescence lifetime can be determined from the slope of a plot of  $\log I(t)$  versus  $t$  (Figure 4.1), but more commonly by fitting the data to assumed decay models.

The lifetime is the average amount of time a fluorophore remains in the excited state following excitation. This can be seen by calculating the average time in the excited state  $\langle t \rangle$ . This value is obtained by averaging  $t$  over the intensity decay of the fluorophore:

$$\langle t \rangle = \frac{\int_0^\infty t I(t) dt}{\int_0^\infty I(t) dt} = \frac{\int_0^\infty t \exp(-t/\tau) dt}{\int_0^\infty \exp(-t/\tau) dt} \quad (4.3)$$

The denominator is equal to  $\tau$ . Following integration by parts, one finds the numerator is equal to  $\tau^2$ . Hence for a single exponential decay the average time a fluorophore remains in the excited state is equal to the lifetime:

$$\langle t \rangle = \tau \quad (4.4)$$

It is important to note that eq. 4.4 is not true for more complex decay laws, such as multi- or non-exponential decays. Using an assumed decay law, an average lifetime can always be calculated using eq. 4.3. However, this average lifetime can be a complex function of the parameters describing the actual intensity decay (Section 17.2.1). For this reason, caution is necessary in interpreting the average lifetime.

Another important concept is that the lifetime is a statistical average, and fluorophores emit randomly throughout the decay. The fluorophores do not all emit at a time delay equal to the lifetime. For a large number of fluorophores some will emit quickly following the excitation, and some will emit at times longer than the lifetime. This time distribution of emitted photons is the intensity decay.

#### 4.1.2. Phase and Modulation Lifetimes

The frequency-domain method will be described in more detail in Chapter 5, but it is valuable to understand the basic equations relating lifetimes to phase and modulation. The modulation of the excitation is given by  $b/a$ , where  $a$  is the average intensity and  $b$  is the peak-to-peak height of the incident light (Figure 4.2). The modulation of the emission is defined similarly,  $B/A$ , except using the intensities of the emission (Figure 4.2). The modulation of the emission is measured relative to the excitation,  $m = (B/A)/(b/a)$ . While  $m$  is actually a demodulation factor, it is usually called the modulation. The other experimental observable is the phase delay, called the phase angle ( $\phi$ ), which is usually measured from the zero-crossing times of the modulated components. The phase angle ( $\phi$ ) and the modulation ( $m$ ) can be employed to calculate the lifetime using

$$\tan \phi = \omega \tau_\phi, \quad \tau_\phi = \omega^{-1} \tan \phi \quad (4.5)$$

$$m = \frac{1}{\sqrt{1 + \omega^2 \tau_m^2}}, \quad \tau_m = \frac{1}{\omega} \left[ \frac{1}{m^2} - 1 \right]^{1/2} \quad (4.6)$$

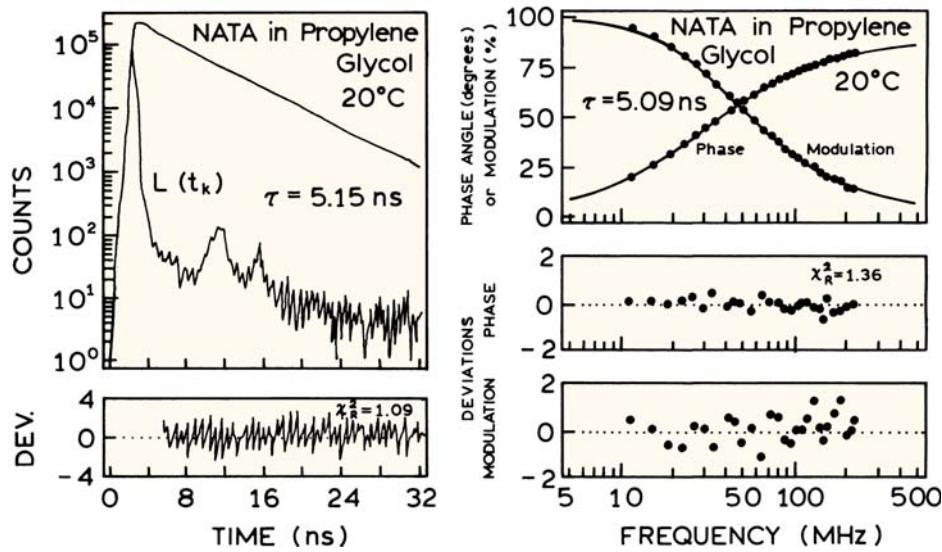


**Figure 4.3.** Comparison of time-domain (left) and frequency-domain (right) decay time measurements of N-acetyl-L-tryptophanamide (NATA).  $L(t_k)$  is the instrument response function.

These expressions can be used to calculate the phase ( $\tau_\phi$ ) and modulation ( $\tau_m$ ) lifetimes for the curves shown in Figure 4.2 (Problem 4.1). If the intensity decay is a single exponential, then eqs. 4.5 and 4.6 yield the correct lifetime. If the intensity decay is multi- or non-exponential, then eqs. 4.5 and 4.6 yield apparent lifetimes that represent a complex weighted average of the decay components.

#### 4.1.3. Examples of Time-Domain and Frequency-Domain Lifetimes

It is useful to understand the appearance of the time-domain (TD) and the frequency-domain (FD) data. TD and FD data are shown for the tryptophan derivative N-acetyl-L-tryptophanamide (Figure 4.3). This tryptophan derivative (NATA) is known to display a single exponential decay (Chapter 17). In the time domain (left) the data are presented as log counts versus time. The data are presented as photon counts because most such measurements are performed by single-photon counting. The plot of the log intensity versus time for NATA is linear, which indicates the decay is a single exponential. The noisy curve marked  $L(t_k)$  is the instrument response function (IRF), which depends on the shape of the excitation pulse and how this pulse is detected by the instrument. This IRF is clearly not a  $\delta$ -function, and much of the art of lifetime measurements is accounting for this nonideal response in analyzing the data.

Analysis of the time domain is accomplished mostly by nonlinear least squares.<sup>1–2</sup> In this method one finds the lifetime that results in the best fit between the measured data and the data calculated for the assumed lifetime. Although not separately visible in Figure 4.3 (left), the calculated intensity decay for  $\tau = 5.15$  ns overlaps precisely with the number of photons counted in each channel. The lower panel of Figure 4.3 (left) shows the deviations between the measured and calculated data, weighted by the standard deviations of each measurement. For a good fit the deviations are random, indicating the only source of difference is the random error in the data.

Frequency-domain data for the same NATA sample are shown in Figure 4.3 (right). The phase and modulation are measured over a range of light modulation frequencies. As the modulation frequency is increased the phase angle increases from 0 to 90°, and the modulation decreases from 1 (100%) to 0 (0%). As for the time-domain data, the frequency-domain data are also analyzed by nonlinear least squares. The dots represent the data, and the solid line represents the best fit with a single lifetime of 5.09 ns. As for the TD data, the goodness-of-fit is judged by the differences (deviations) between the data and the calculated curves. For the FD data there are two observables—phase and modulation—so there are two sets of deviations (lower panel). The randomness of the deviations indicates that a single lifetime is adequate to explain the data.

## 4.2. BIOPOLYMERS DISPLAY MULTI-EXPONENTIAL OR HETEROGENEOUS DECAYS

At first glance the measurement of decay times seems straightforward (Figure 4.3), so why do these measurements receive so much attention? Interpretation of the data in Figure 4.3 was relatively simple because the decays were single exponentials. However, most samples display more than one decay time. This situation is illustrated by a protein with two tryptophan residues (Figure 4.4). Suppose that both residues display lifetimes of 5 ns. Then the decay would be a simple single exponential decay. The decay would be simple to analyze, but one could not distinguish between the two tryptophan residues. Now suppose a collisional quencher is added and that only the residue on the surface of the protein is accessible to quenching. Assume that the added quencher reduces the lifetime of the exposed residue to 1 ns. The intensity decay is now a double exponential:

$$I(t) = \alpha_1 e^{-t/5.0} + \alpha_2 e^{-t/1.0} \quad (4.7)$$

In this expression the  $\alpha_i$  values are called the pre-exponential factors. For the same fluorophore in different environments, which usually display the same radiative decay rates, the values of  $\alpha_i$  represent the fractional amount of fluorophore in each environment. Hence, for the protein shown in Figure 4.4 one expects  $\alpha_1 = \alpha_2 = 0.5$ . The presence of two decay times results in curvature in the plot of  $\log I(t)$  versus time (dashed). The goal of the intensity decay measurements is to recover the decay times ( $\tau_i$ ) and amplitudes ( $\alpha_i$ ) from the  $I(t)$  measurements.

The presence of two decay times can also be detected using the frequency-domain method. In this case one examines the frequency response of the sample, which consists of a plot of phase and modulation on a logarithmic frequency axis. The longer lifetime tryptophan ( $\tau_1 = 5$  ns, solid) and the shorter lifetime tryptophan ( $\tau_2 = 1$  ns, dotted) each display the curves characteristic of a single decay time. In the presence of both decay times ( $\tau_1 = 5$  ns and  $\tau_2 = 1$  ns, dashed), the frequency response displays a more complex shape that is characteristic of the heterogeneous or multi-exponential intensity decay. The FD data are used to recover the individual decay times ( $\tau_i$ ) and amplitudes ( $\alpha_i$ ) associated with each tryptophan residue.

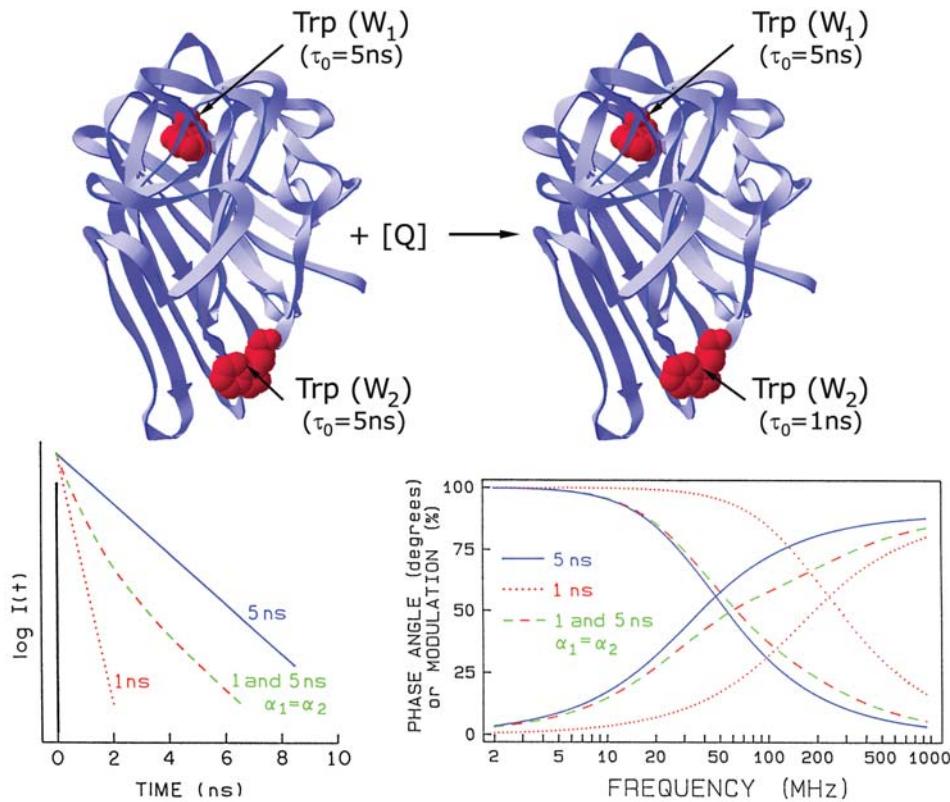


**Figure 4.4.** Simulated intensity decays of buried ( $W_1$ ) and exposed ( $W_2$ ) tryptophan residues in the absence and presence of a collisional quencher.

ciated with each decay time, typically using fitting by non-linear least squares.

Examination of Figure 4.4 shows that the  $I(t)$  values start at the same initial value. At first this is confusing because the intensity of one of the residues was decreased 80% by quenching. The intercept remains the same because the  $\alpha_i$  values are proportional to the fractional population. For the protein model shown the time-zero intensities of each component are shown to be the same. In general the time-zero intensities of the components in a multi-exponential decay are not equal because the absorption spectra of the residues may not be the same, or some residues may be completely unobservable. An important point about lifetime measurements is that the intensity decay, or phase and modulation values, are typically measured without concern about the actual intensity. Intensity decays are typically fit to the multi-exponential model:

$$I(t) = \sum_i \alpha_i \exp(-t/\tau_i) \quad (4.8)$$

where  $\sum \alpha_i$  is normalized to unity.

Time-resolved measurements are also used to measure rotational diffusion and association reactions. This information is available from the time-resolved anisotropy decays. Consider a protein that self-associates into a tetramer (Figure 4.5). For a spherical molecule one expects a single decay time for the anisotropy, which is called the rotational correlation time ( $\theta$ ):

$$r(t) = r_0 \exp(-t/\theta) \quad (4.9)$$

In this expression  $r_0$  is the anisotropy at  $t = 0$ , which is a characteristic spectral property of the fluorophore. The rotational correlation time  $\theta$  is the time at which the initial anisotropy has decayed to  $1/e$  of its original value. The correlation time is longer for larger proteins. If the protein monomers associate to a larger tetramer, the rotational correlation time will become longer and the anisotropy will decay more slowly. The situation for biomolecules is usually more complex, and the protein can be present in both the monomeric and tetrameric states. In this case the anisotropy decay will be a double exponential:

$$r(t) = r_0 f_M \exp(-t/\theta_M) + r_0 f_T \exp(-t/\theta_T) \quad (4.10)$$

where  $f_i$  represents the fraction of the fluorescence from the monomeric and tetrameric proteins,  $f_M + f_T = 1.0$ . The

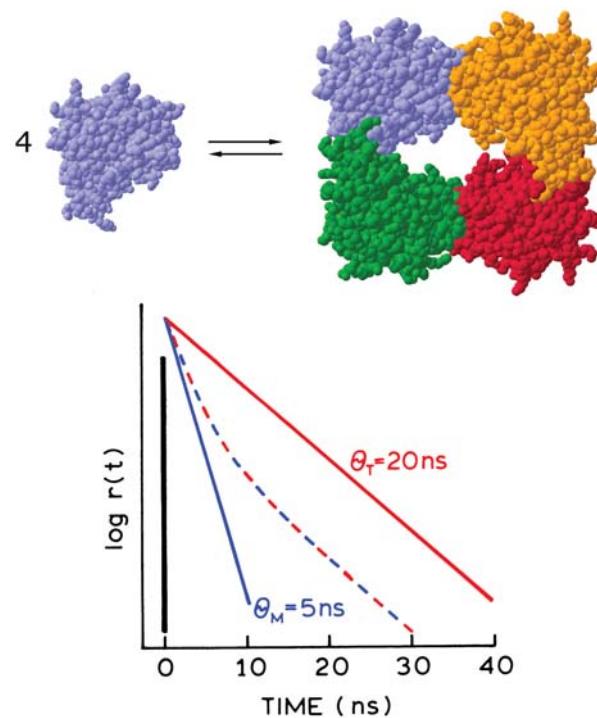


**Figure 4.5.** Anisotropy decay of a protein monomer (M) that self-associates into a tetramer (T). The dashed line shows the anisotropy decay expected for partially associated monomers.

anisotropy decay will be a double exponential because both monomers and tetramers are present, each with different correlation times. The fractional fluorescence from the monomers and tetramers can be used to calculate the concentrations of each species if their quantum yields are known.

Anisotropy decays can be more complex than eqs. 4.9–4.10. The decays are typically presented as a sum of exponentials:

$$r(t) = \sum_j r_{0j} \exp(-t/\theta_j) \quad (4.11)$$

The meaning of the amplitudes ( $r_{0j}$ ) and correlation times ( $\theta_j$ ) can depend on the chosen molecular model. The goal of many time-resolved measurements is to determine the form of complex anisotropy decay. In general, it is more difficult to resolve a multi-exponential anisotropy decay (eq. 4.11) than a multi-exponential intensity decay (eq. 4.8).

The intensity decay and anisotropy decay have similar mathematical forms, but there is no direct linkage between the decay times and rotational correlation times. The decay times are determined by the spectral properties of the fluo-

rophore. The rotational correlation times are determined by the size, shape, and flexibility of the macromolecules. Both the decay times and the rotational correlation times are often on the nanosecond timescale. These conditions result in anisotropies that are sensitive to the size of the protein and its interactions with other macromolecules.

#### 4.2.1. Resolution of Multi-Exponential Decays Is Difficult

Why is so much attention given to data analysis and obtaining high signal-to-noise in the time-resolved data? The need for high signal-to-noise is due to the inherent difficulty in recovering the amplitudes and lifetimes for a multi-exponential process. This difficulty was well known to mathematicians, and was pointed out to fluorescence spectroscopists when time-resolved measurements were first being applied to biochemical systems.<sup>3</sup> This paper defined a method for analyzing time-resolved fluorescence data that is still in use today. This paper illustrated how apparently different multi-exponential decays can yield similar  $I(t)$  values. Consider the following two double exponential decays:

$$I_1(t) = 7500 \exp(-t/5.5) + 2500 \exp(-t/8.0) \quad (4.12)$$

$$I_2(t) = 2500 \exp(-t/4.5) + 7500 \exp(-t/6.7) \quad (4.13)$$

The pre-exponential factor sum of 10,000 corresponds to 10,000 photons in the highest intensity channel, which is typical of data for time-correlated single-photon counting (TCSPC). From examination of these equations one would think that the intensity decays would be distinct. However, a plot of the intensity decays on a linear scale shows that they are indistinguishable at all times (Figure 4.6). On a logarithmic scale one notices some minor differences at 30–50 ns. However, at 50 ns there are only about 3 photons per channel with a 1-ns width. The difference between the two decays at long times is just 1–2 photons. If one adds the Poisson noise, which is unavoidable in photon-counting data, the differences between the curves is seven-fold less than the uncertainties due to the Poisson noise.<sup>4</sup> This illustrates that it is difficult to distinguish between some multi-exponential functions, and that it is difficult to recover the actual values of  $\alpha_i$  and  $\tau_i$  for a multi-exponential decay. A similar result can be obtained from simulations of the frequency-domain data. The simulated frequency responses are visually indistinguishable for these two decay laws.

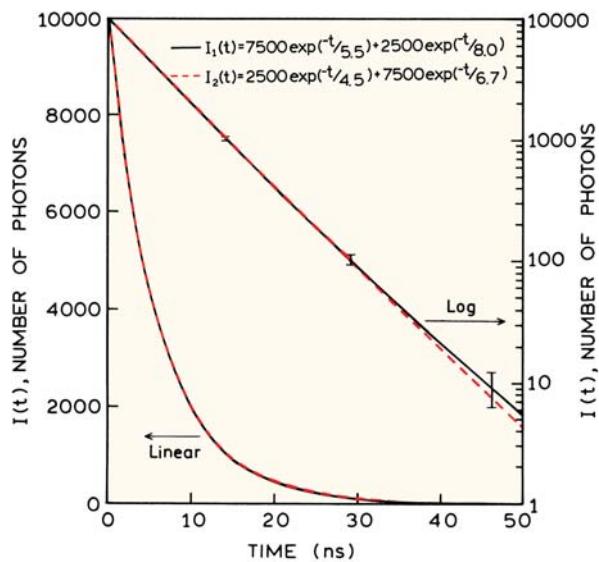


**Figure 4.6.** Comparison of two intensity decays: on a linear (left) and logarithmic scale (right). The error bars represent Poisson noise on the photon counts. The decay functions were described in [3].

Why is it difficult to resolve multi-exponential decays? In  $I_1(t)$  and  $I_2(t)$  the lifetimes and amplitudes are different for each decay law. In fact, this is the problem. For a multi-exponential decay one can vary the lifetime to compensate for the amplitude, or vice versa, and obtain similar intensity decays with different values of  $\alpha_i$  and  $\tau_i$ . In mathematical terms the values of  $\alpha_i$  and  $\tau_i$  are said to be correlated. The problem of correlated parameters is well known within the framework of general least-squares fitting.<sup>5–7</sup> The unfortunate result is that the ability to determine the precise values of  $\alpha_i$  and  $\tau_i$  is greatly hindered by parameter correlation. There is no way to avoid this problem, except by careful experimentation and conservative interpretation of data.

#### 4.3. TIME-CORRELATED SINGLE-PHOTON COUNTING

At present most of the time-domain measurements are performed using time-correlated single-photon counting, but other methods can be used when rapid measurements are needed. Many publications on TCSPC have appeared.<sup>4,8–13</sup> One book is completely devoted to TCSPC and provides numerous valuable details.<sup>8</sup> Rather than present a history of the method, we will start by describing current state-of-the-art instrumentation. These instruments use high repetition rate mode-locked picosecond (ps) or femtosecond (fs) laser light sources, and high-speed microchannel plate (MCP)

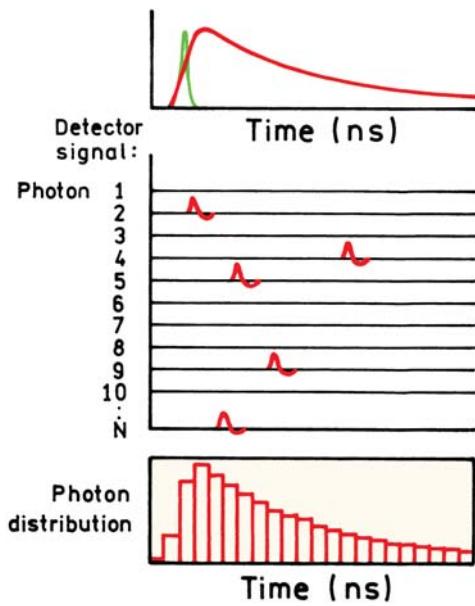


**Figure 4.7.** Principle of TCSPC. The pulses in the middle panel represent the output from a constant fraction discriminator (see Figure 4.22). Revised from [11].

photomultiplier tubes (PMTs). For many applications, these expensive systems are being rapidly replaced by systems using pulsed-laser diodes (LDs), light-emitting diodes (LEDs), and small, fast PMTs.

#### 4.3.1. Principles of TCSPC

The principle of TCSPC is somewhat unique (Figure 4.7). The sample is excited with a pulse of light, resulting in the waveform shown at the top of the figure. This is the wave-

form that would be observed when many fluorophores are excited and numerous photons are observed. However, for TCSPC the conditions are adjusted so that less than one photon is detected per laser pulse. In fact, the detection rate is typically 1 photon per 100 excitation pulses. The time is measured between the excitation pulse and the observed photon and stored in a histogram. The  $x$ -axis is the time difference and the  $y$ -axis the number of photons detected for this time difference. When much less than 1 photon is detected per excitation pulse, the histogram represents the waveform of the decay. If the count rate is higher the histogram is biased to shorter times. This is because with TCSPC only the first photon can be observed. At present the electronics are not fast enough to measure multiple photons per pulse when the lifetimes are in the nanosecond range. Multiple photons per pulse can be measured for decay times near a microsecond or longer. Specialized electronics are used for measuring the time delay between the excitation and emission (Figure 4.8). The experiment starts with the excitation pulse that excites the samples and sends a signal to the electronics. This signal is passed through a constant function discriminator (CFD), which accurately measures the arrival time of the pulse. This signal is passed to a time-to-amplitude converter (TAC), which generates a voltage ramp that is a voltage that increases linearly with time on the nanosecond timescale. A second channel detects the pulse from the single detected photon. The arrival time of the signal is accurately determined using a CFD, which sends a signal to stop the voltage ramp. The TAC now contains a voltage proportional to the time delay ( $\Delta t$ ) between the excitation and emission signals. As needed the voltage is amplified by a programmable gain amplifier (PGA) and sent to an analog-to-digital converter (ADC).

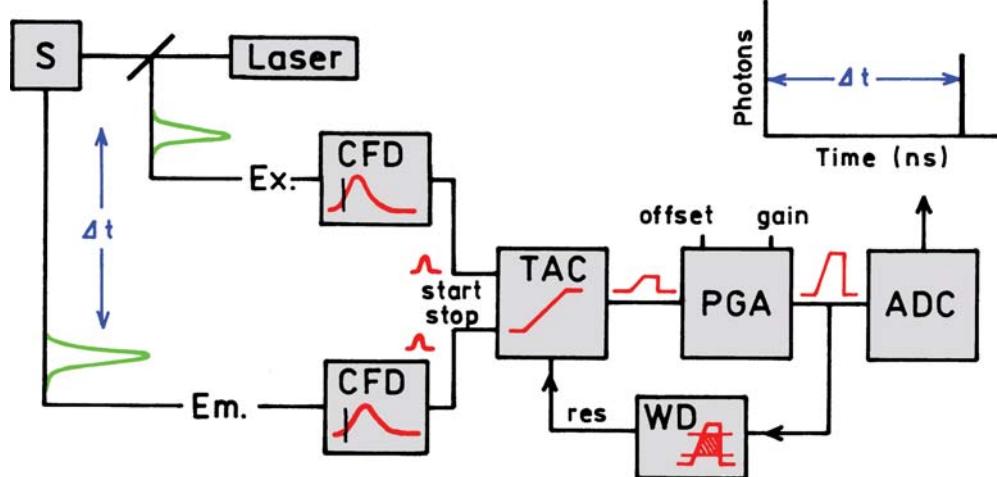


**Figure 4.8.** Electronic schematic for TCSPC. Revised from [14].

fier (PGA) and converted to a numerical value by the analog-to-digital converter (ADC). To minimize false readings the signal is restricted to given range of voltages. If the signal is not within this range the event is suppressed by a window discriminator (WD). The voltage is converted to a digital value that is stored as a single event with the measured time delay. A histogram of the decay is measured by repeating this process numerous times with a pulsed-light source.

The principle of TCSPC can be understood from the preceding description. However, at present almost all TCSPC measurements are performed in the "reverse mode." The process is the same as described above except that the emission pulse is used to start the TAC and the excitation pulse is used to stop the TAC. This procedure is used because of the high repetition rate of modern pulsed-light sources. The TAC has to be reset and set to zero before each start pulse, which takes a finite amount of time. The TAC can be constantly in reset mode if the start signals arrive too rapidly. The emission signals occur about 1 per 100 excitation pulses, and thus much less frequently than the excitation pulses. These emission pulses are used to start the TAC, and the next laser pulse is used to stop the TAC.

There are many subtleties in TCSPC that are not obvious at first examination. Why is the photon counting rate limited to 1 photon per 100 laser pulses? Present electronics for TCSPC only allow detection of the first arriving photon. The dead times range from 10 microseconds in older systems to about 120 ns with modern TCSPC electronics. These times are much longer than the fluorescence decay. The dead time in the electronics prevents detection of another photon resulting from the same excitation pulse. Recall that emission is a random event. Following the excitation pulse, more photons are emitted at early times than at late times. If all these photons could be measured, then the histogram of arrival times would represent the intensity decay. However, if many arrive, and only the first is counted, then the intensity decay is distorted to shorter times. This effect is described in more detail in Section 4.5.6.

Another important feature of TCSPC is the use of the rising edge of the photoelectron pulse for timing. This allows phototubes with ns pulse widths to provide subnanosecond resolution. This is possible because the rising edge of the single-photon pulses is usually steeper than one would expect from the time response of the PMT. Also, the use of a constant fraction discriminator provides improved time resolution by removing the variability due to the amplitude of each pulse.

#### 4.3.2. Example of TCSPC Data

Prior to examining these electronic components in more detail it is valuable to examine the actual data. Intensity decay for the scintillator 2,5-diphenyl-1,3,4-oxadiazole (PPD) is shown in Figure 4.9. These data were obtained with a cavity-dumped R6G dye laser that was cavity-dumped at 1 MHz and frequency-doubled to 300 nm. The detector was an MCP PMT. There are typically three curves associated with an intensity decay. These are the measured data  $N(t_k)$ , the instrument response function  $L(t_k)$ , and the calculated decay  $N_c(t_k)$ . These functions are in terms of discrete times ( $t_k$ ) because the counted photons are collected into channels each with a known time ( $t_k$ ) and width ( $\Delta t$ ). The instrument response function (IRF) is the response of the instrument to a zero lifetime sample. This curve is typically collected using a dilute scattering solution such as colloidal silica (Ludox) and no emission filter. This decay represents the shortest time profile that can be measured by

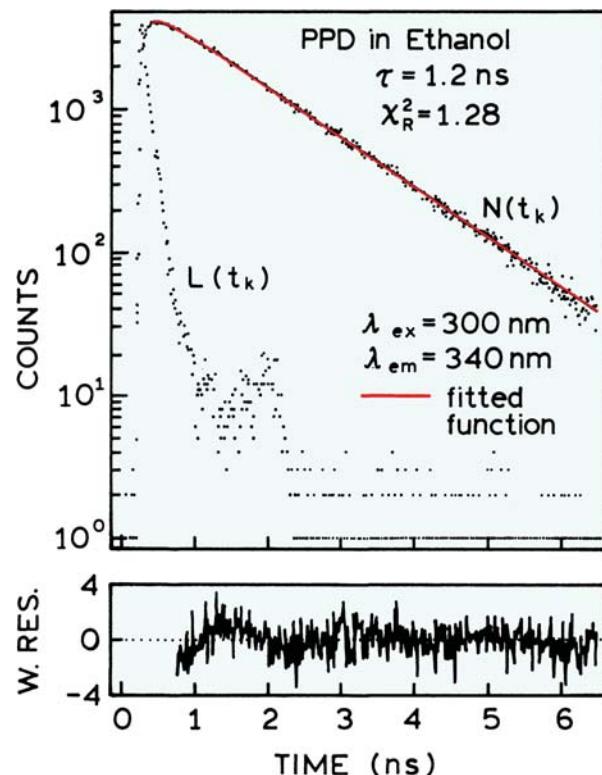


**Figure 4.9.** TCSPC data for 2,5-diphenyl-1,3,4-oxadiazole (PPD) in ethanol. The light source was an R6G dye laser, cavity dumped at 1 MHz. The detector was an R2809 MCP PMT (Hamamatsu). The left side of the residuals (lower panel) show some minor systematic error. From [15].

the instrument. The width of the IRF is due to both the characteristics of the detector and the timing electronics. The IRF in Figure 4.9 is quite narrow, about 60 ps wide, measured as the full width of the half maximum intensity (FWHM). The use of a logarithmic intensity scale exaggerates the low-intensity regions of the profile. There is an afterpulse about 2 ns after the main peak. Afterpulses are observed with many PMTs. The instrument response function shown in Figure 4.9 is rather good, and some PMTs give far less ideal profiles. For instance, the profile in Figure 4.3 was measured with an end-on linear-focused PMT, for which the afterpulses and long time tail are more significant. However, even in this case (Figure 4.3) the number of photons in the peak of the afterpulse is only about 0.05% of the counts in the peak channel.

The measured intensity decay  $N(t_k)$  is shown as a histogram of dots. The height of the dots on the y-axis represents the number of photons that were detected within the timing interval  $t_k$  to  $t_k + \Delta t$ , where  $\Delta t$  is the width of the timing channel. In this case the peak channel, with the largest number of counts, has recorded approximately 3000 photons. On the log scale the decay is seen to be a straight line suggesting a single decay time.

The last curve is the calculated data  $N_c(t_k)$ , which is usually called the fitted function. This curve (solid) represents a convolution of the IRF with the impulse response function, which is the intensity decay law. The fitted function is the time profile expected for a given intensity decay when one considers the form of the IRF. The details of calculating the convolution are described in the next section. For a single exponential decay the lifetime is the value of  $\tau$  that provides the best match between the measured data  $N(t_k)$  and the calculated time-dependent intensities  $N_c(t_k)$ . For a multi-exponential decay (eq. 4.2) the analysis yields the values of  $\alpha_i$  and  $\tau_i$  that are most consistent with the data.

### 4.3.3. Convolution Integral

It is important to understand why the measured intensity decay is a convolution with the lamp function. The intensity decay law or impulse response function  $I(t)$  is what would be observed with  $\delta$ -function excitation and a  $\delta$ -function for the instrument response. Equations 4.2, 4.12, and 4.13 are examples of impulse-response functions. Unfortunately, it is not possible to directly measure the impulse response function. Most instrument response functions are 0.5 to 2 ns wide. However, we can imagine the excitation pulse to be a series of  $\delta$ -functions with different amplitudes.

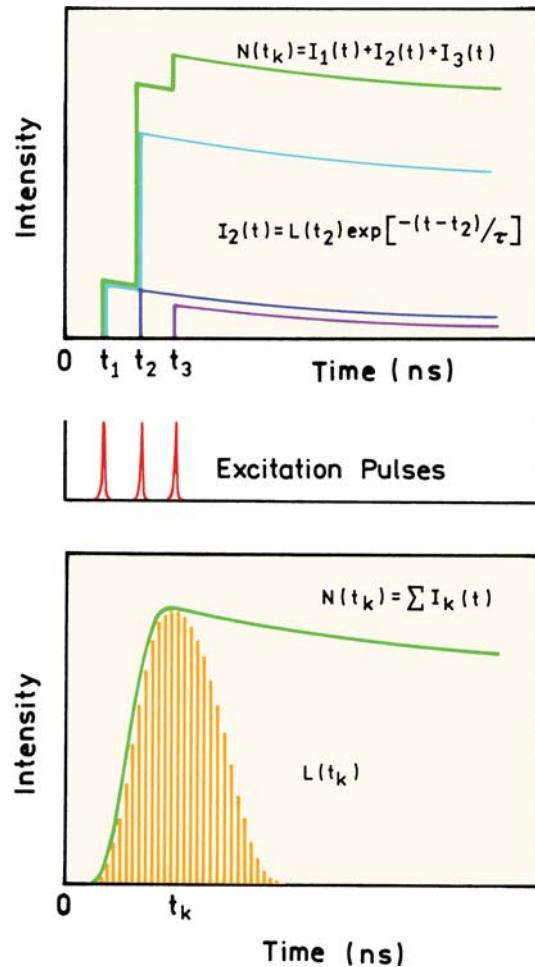


**Figure 4.10.** Convolution of an impulse response function  $I(t)$  with three excitation pulses (top) or with a lamp profile  $L(t_k)$  to yield the measured function  $N(t_k)$ .

Each of these  $\delta$ -functions excites an impulse response from the sample, with an intensity proportional to the height of the  $\delta$ -function (Figure 4.10, top). The measured function  $N(t_k)$  is the sum of all these exponential decays, starting with different amplitudes and different times.

Mathematically, the concept of convolution can be expressed as follows.<sup>16</sup> Each  $\delta$ -function excitation is assumed to excite an impulse response at time  $t_k$ :

$$I_k(t) = L(t_k) I(t - t_k) \Delta t(t > t_k) \quad (4.14)$$

The amplitude of the impulse response function excited at time  $t_k$  is proportional to the excitation intensity  $L(t_k)$  occurring at the same time. The term  $(t - t_k)$  appears because the impulse response is started at  $t = t_k$ , and it is understood that

there is no emission from  $I(t_k)$  before excitation ( $t < t_k$ ). The measured decay  $N(t_k)$  is the sum of the impulse responses created by all the individual  $\delta$ -function excitation pulses occurring until  $t_k$ :

$$N(t_k) = \sum_{t=0}^{t=t_k} L(t_k)I(t - t_k)\Delta t \quad (4.15)$$

For small values of  $\Delta t$  this equation can be expressed as an integral:

$$N(t) = \int_0^t L(t')I(t - t')dt' \quad (4.16)$$

This expression says that the experimentally measured intensity at time  $t$  is given by the sum of the intensities expected for all the  $\delta$ -function excitation pulses that occur until time  $t$ . It is important to notice that new intensity decays are created in the sample as long as there is nonzero intensity in  $L(t_k)$ . This is why the intensity decay takes on the shape of the IRF. For convenience the dummy variable of integration is changed using  $t' = t - \mu$ , so that the convolution integral is expressed as

$$N(t) = \int_0^t L(t - \mu)I(\mu)d\mu \quad (4.17)$$

The task is to determine the impulse response function  $I(\mu)$  that best matches the experimental data. Since the data are digital (counts per channel), eq. 4.15 is perhaps the more convenient form. It is important to notice that  $time = 0$  is not defined in a TCSPC experiment. There is no zero time because there is no single  $\delta$ -function initiating the decay. For convenience the excitation pulse is positioned close to zero on the time axis so that one can consider the values of  $N(t_k)$  relative to the decay time of the sample. The impulse response function recovered from the analysis does have a defined  $t = 0$ .

#### 4.4. LIGHT SOURCES FOR TCSPC

##### 4.4.1. Laser Diodes and Light-Emitting Diodes

The instrumentation for TCSPC is moderately complex, and effective use of this method requires understanding of the various components. Measurement of intensity decays requires a pulsed-light source. Prior to 2000 the dominant light sources for TCSPC were picosecond dye lasers or

flashlamps. At present the ps dye lasers are being replaced by Ti:sapphire lasers that are still expensive but can be simpler to operate. Perhaps the most important development for TCSPC since 2000 is the introduction of pulsed-laser diodes (LDs) and pulsed light-emitting diodes (LEDs) as simple solid-state sources. These devices consume little power, are easy to operate, and require almost no maintenance. LDs and LEDs make TCSPC measurements more readily available to a wide range of researchers. LDs and LEDs will soon become the dominant light sources for TCSPC of extrinsic fluorophores absorbing above 350 nm. While this chapter was being written, the first report appeared on excitation of intrinsic protein fluorescence using a pulsed LED.<sup>17</sup> It appears likely that the pulsed 280 nm LEDs will soon be generally available and the larger lasers will be less needed for most biochemical applications of fluorescence.

The simplicity of a pulsed LD is shown in Figure 4.11. The output at 405 nm can be used to excite a variety of fluorophores. The pulse width near 70 ps is more than adequate for measuring ns decay times. The repetition rate up to 40 MHz allows rapid data acquisition. If 1% of the puls-

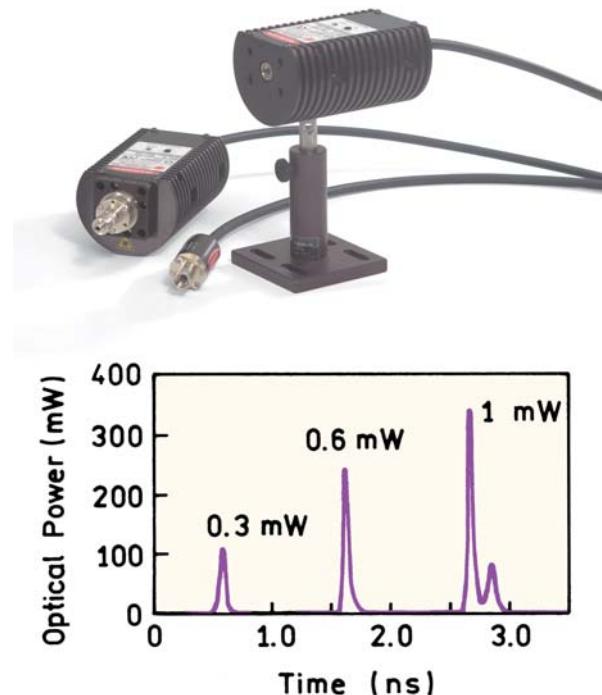


**Figure 4.11.** Pulsed picosecond laser diode emitting at 370 nm. The FWHM is less than 70 ps with a maximum repetition rate of 40 MHz. From [18].

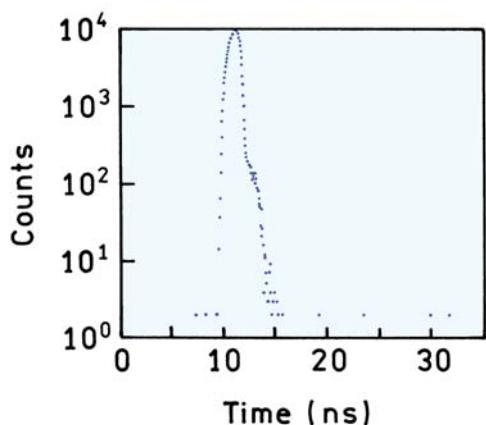


**Figure 4.12.** Pulsed light-emitting diode at 405 nm. FWHM = 1.4 ns. From [19].

es result in a detectable photon, then up to 400,000 photons per second can be measured. Single exponential decays can be determined with less than 4000 photons, so data acquisition times can be as short as a microsecond. The output is

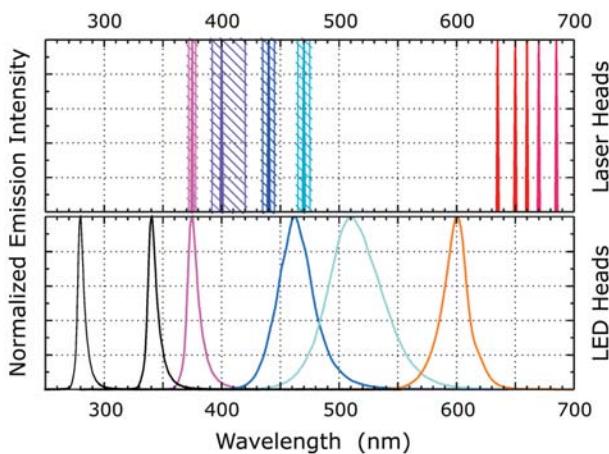


**Figure 4.13.** Wavelengths available from pulsed LEDs and LDs. Courtesy of Dr. Rainer Erdmann, PicoQuant GmbH.

driven directly by the electrical input, so that the repetition rate can be easily varied. This is in contrast to argon, Nd:YAG, or Ti:sapphire lasers, where the repetition rate is determined by the length of the cavity.

An even simpler pulsed-light source is shown in Figure 4.12, in this case a light-emitting diode at 370 nm.<sup>19</sup> In this case the pulse width is about 1.4 ns with an upper repetition rate of 1 MHz. Pulsed LEDs are available with repetition rates up to 40 MHz. A wide range of wavelengths is available for both LEDs and LDs (Figure 4.13).<sup>17–23</sup> Laser diodes have a single-wavelength output and LEDs typically have a wider spectral output. In the near future we can expect LEDs and LDs emitting near 340 and 285 nm.

In addition to simple pulsed-light sources there have also been advances in the electronics for TCSPC (Section 4.5). All the components can be placed on a single computer board,<sup>20</sup> and compact PMT modules are available for photon counting<sup>21</sup> (Section 4.6). As a result it is now possible to obtain compact and reliable instruments for TCSPC (Figure 4.14). Such simple instruments can provide excellent data with short data acquisition times. Figure 4.15 (top) shows the intensity decay of Coumarin 152 obtained with a pulsed LD. The IRF had an FWHM of 50 ps. The absence of systematic errors is seen from the value of  $\chi_R^2 = 1.03$  for the single-decay-time fit. Another example is seen in Figure 4.16 (bottom), in this case for fluorescein with pulsed LED excitation at 450 nm. The IRF is about 1 ns due to the wider pulses obtained with LEDs as compared to LDs. These results show that high-quality TCSPC data can now be obtained for many fluorophores without the need for more complex laser systems.

#### 4.4.2. Femtosecond Titanium Sapphire Lasers

Titanium sapphire lasers are now in widespread use for TCSPC. Ti:sapphire lasers are simpler to operate than

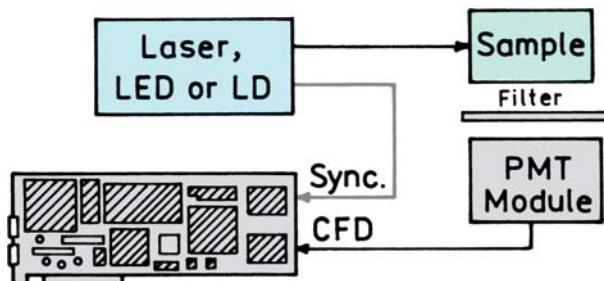


**Figure 4.14.** Schematic for TCSPC with a pulsed LED or LD.

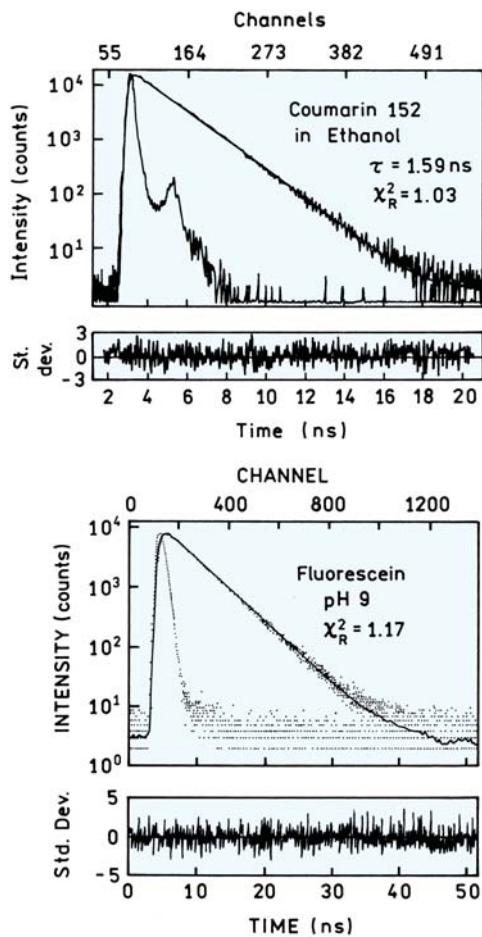


**Figure 4.15.** Top: Intensity decay of Coumarin 152 in ethanol. The light source was a 400-nm laser diode with a 50-ps FWHM and a 20-MHz repetition rate [23]. Bottom: Intensity decay of fluorescein in water at pH 9. Excitation at 450 nm with a pulsed LED with a 20-MHz repetition rate and a 1-ns FWHM [22].

mode-locked cavity-dumped dye lasers (Section 4.4.3) but are considerably more complex than LD and LED light sources. These lasers provide pulse widths near 100 fs with high output power; they are widely used for multi-photon excitation and for laser scanning microscopy.

The pump source for a Ti:sapphire laser is a continuous, not mode-locked, argon ion laser (Figure 4.16). Mode-locked lasers are sensitive and somewhat difficult to maintain. In addition to being simpler, the continuous output of an argon ion laser is typically 10–15-fold larger than the mode-locked output. Typically, 15 watts or more are available from an argon ion laser. Ti:sapphire lasers are pumped with up to 7 watts at 514 nm. This allows a Ti:sapphire laser to be pumped with a small frame argon ion laser. At present Ti:sapphire lasers are routinely pumped with solid-state diode-pumped lasers, which are similar to Nd:YAG lasers.

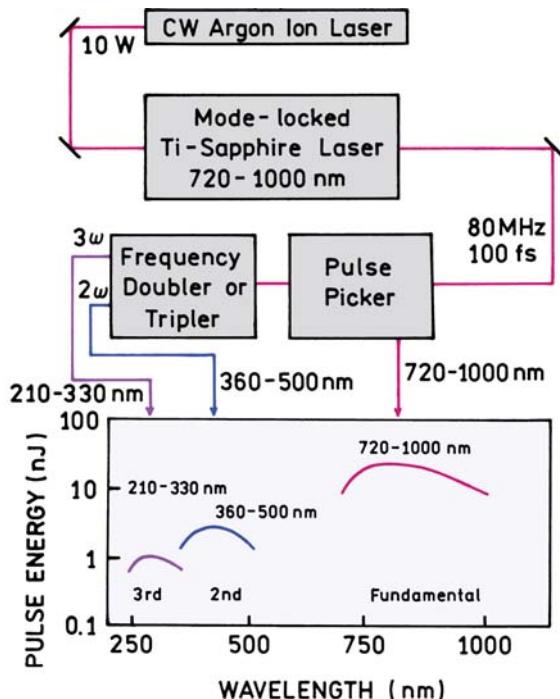


**Figure 4.16.** Mode-locked femtosecond Ti:sapphire laser.

A favorable feature of the Ti:sapphire lasers are that they are self-mode locking. If one taps a Ti:sapphire when operating in continuous mode, it can switch to mode-locked operation with 100-fs pulses. This phenomenon is due to a Kerr lens effect within the Ti:sapphire crystal. The high-intensity pulses create a transient refractive index gradient in the Ti:sapphire crystal that acts like an acoustooptic mode locker. In fact, the phenomenon is referred to as Kerr lens mode locking. While the laser can operate in this free running mode-locked state, an active mode locker can be placed in the cavity to stabilize the mode-locked frequency and provide synchronization for other parts of the apparatus. However, since it is not necessary to actively maintain the mode-locked condition, the fs Ti:sapphire lasers are stable and reasonably simple to operate.

An advantage of the Ti:sapphire laser is that it is a solid-state device. There are no flowing dyes to be replaced, and the Ti:sapphire crystal seems to have an indefinitely long operational life. Self-mode locking circumvents the need for matching cavity lengths with the pump laser, as must be done with a synchronously pumped dye laser. A disadvantage of the Ti:sapphire laser is that the output is at long wavelengths from 720 to 1000 nm. After frequency doubling the wavelengths from 350 to 1000 nm are ideal for exciting a wide range of extrinsic fluorophores. However, after frequency doubling the wavelengths are too long for

excitation of intrinsic protein fluorescence. This problem can be solved by frequency tripling or third harmonic generation. This is somewhat more complex because one has to double the fundamental output in one crystal and then overlap the second harmonic and fundamental beams in a second crystal. The beams need to be overlapped in time and space, which is difficult with fs pulses. A minor disadvantage of the Ti:sapphire lasers for TCSPC is the use of a pulse picker, instead of a cavity dumper, to decrease the repetition rate. Since mode locking occurs with the laser cavity, rather than being accomplished by synchronous pumping of an external dye laser (Section 4.4.3), a cavity dumper cannot be used with a Ti:sapphire laser. After the 80-MHz pulses exit the laser, the desired pulses are selected with an AO deflector, called a pulse picker. The energy in the other pulses is discarded, and there is no increase in peak power as occurs with cavity dumping. In fact, there is a significant decrease in average power when using a pulse picker. For example, a 100-mW output with an FWHM repetition rate will be decreased to 10 mW if the repetition rate is decreased to 8 MHz with a pulse picker. However, since many fluorophores have lifetimes near a nanosecond, and since TCSPC electronics now allow high repetition rates, nearly the full 80-MHz output can be used in many experiments.

Because of the fs pulse widths and high peak intensities, Ti:sapphire lasers are widely used for two- and multi-photon excitation, particularly in laser scanning microscopy. With this laser one can use the intense fundamental output to excite fluorophores by simultaneous absorption of two or more photons. The use of multiphoton excitation is particularly valuable in microscopy because localized excitation occurs only at the focal point of the excitation beam.

#### 4.4.3. Picosecond Dye Lasers

Before the introduction of pulsed LEDs and LDs the synchronously pumped cavity-dumped dye lasers were the dominant light source for TCSPC. Such lasers provide pulses about 5 ps wide, and the repetition rate is easily chosen from kHz rates up to 80 MHz.

A dye laser is a passive device that requires an optical pump source. The primary light source is usually a mode-locked argon ion laser. Mode-locked neodymium:YAG (Nd:YAG) lasers are also used as the primary source, but they are generally less stable than a mode-locked argon ion laser. Nd:YAG lasers have their fundamental output of 1064 nm. This fundamental output is frequency doubled to 532

nm or frequency tripled to 355 nm in order to pump the dye lasers. The need for frequency doubling is one reason for the lower stability of the Nd:YAG lasers, but heating effects in the Nd:YAG laser rod also contribute to the instability. The argon ion laser has a fundamental output at 514 nm, which is used directly for pumping most laser dyes.

It is not practical to provide a complete description of laser physics, and the reader is referred to the many books on this topic,<sup>24–26</sup> or to a description of laser principles written for chemists.<sup>27</sup> The argon ion mode-locked laser provides pulses at 514 nm, about 70 ps wide, with a repetition rate near 80 MHz. The precise repetition rate is determined by the round-trip time for light pulses within the laser cavity (Figure 4.17). Without active mode locking the argon ion laser would provide a continuous output. This output is changed to an 80-MHz pulse train by a mode-locking crystal within the laser cavity. This crystal is an acoustooptic device that deflects light out of the cavity based on light diffraction by sound waves in the crystal.<sup>28–29</sup>

In order to obtain mode locking there is a delicate balance between the length of the argon ion laser cavity, the resonance frequency at the acoustooptic (AO) crystal, and the driving frequency to the AO crystal. The resonance frequency of the AO crystal and the driving frequency must be matched in order to obtain stable operation. This can be difficult because the resonances of the AO crystal are temperature dependent. For this reason the mode locking crystal is usually thermostatted above room temperature. Once the AO crystal is at a stable temperature and resonance, the cavity length of the argon ion laser must be adjusted so that the round-trip time for photons (near 12 ns for a typical large-frame laser) coincides with the nulls in the AO crystal deflection. Since there are two nulls per cycle, the AO crystal operates near 40 MHz. The laser pulses at 80 MHz exit one end of the laser through a partially transmitting mirror. The presence of the AO modulator within the laser cavity causes the loss of energy at times other than the round-trip time for the photons and the nulls in the AO crystal. If the cavity length matches the AO crystal frequency, then the photons accumulate in a single bunch and bounce back and forth together within laser cavity. This is the mode-locked condition.

One may wonder why the argon lasers are usually mode locked at 514 nm, and not at 488 nm which is the most intense output. Several reasons have been given for the absence of mode locking at 488 nm. It has been stated that the 488-nm line has more gain, so that one obtains modulated but not mode-locked output. Also, there appear

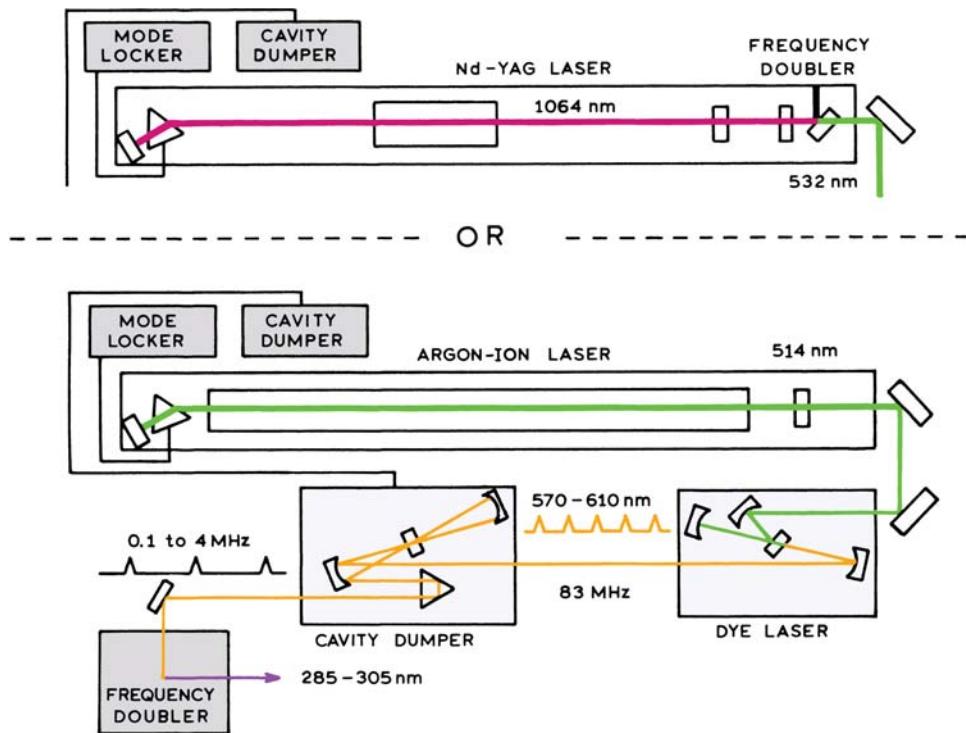


**Figure 4.17.** Picosecond light sources for TCSPC. The primary pump can be an argon ion or a Nd:YAG laser.

to be two closely spaced lines at 488 nm, which cannot be simultaneously mode locked. In any event, the 514-nm output is convenient for pumping a rhodamine 6G dye laser (R6G), which is perhaps the most stable dye and easiest-to-adjust dye laser for day-to-day use.

Mode-locked argon ion lasers found use in TCSPC starting in the late 1970s and early 1980s.<sup>30-35</sup> However, this light source was not particularly useful for biochemistry unless one had a fluorophore that could be excited at 514 nm. This problem was solved by the introduction of picosecond dye lasers for TCSPC.<sup>36-41</sup> The mode-locked argon (or Nd:YAG) laser is used as the pumping source for a dye laser, typically R6G. The cavity length of the dye laser is adjusted to be exactly the same as that of the argon laser, so that the round-trip time for the photon bunch in the dye laser cavity is the same as in the argon laser. When the cavity lengths are matched, the incoming 514-nm pulses reinforce a single bunch of photons that oscillates at 80 MHz within the dye laser cavity. When this occurs the dye laser is said to be synchronously pumped. To conserve space and to have a stable cavity length, the dye laser cavity is often folded. However, this makes these dye lasers difficult to align because a number of mirrors have to be perfectly aligned, not just two as with a linear cavity.

Because of the wide emission curve of R6G, this dye laser has intrinsically narrow pulses, so that a typical pulse width is near 5 ps. This pulse width is narrower than any available detector response, so that for all practical purposes the dye lasers provide  $\delta$ -function excitation. When using a ps dye laser source the width of the instrument response function is due primarily to the detection electronics and photomultiplier tube.

There are two difficulties with the output of the R6G dye laser. Its wavelength is too long for excitation of most fluorophores, and the repetition rate of 80 MHz is too high for measurement of fluorophores with decay times over 3 ns. At 80 MHz the pulses occur every 12.5 ns, which is too soon for many intensity decays. One typically measures the intensity decay to about four times the mean decay time, so that decay times longer than 3 ns are too long for an 80-MHz pulse rate. This problem is solved using a cavity dumper, which is an acoustooptic device placed within the dye laser cavity. The cavity dumper is synchronized with the argon ion laser and hence also the dye laser. At the desired time when an optical pulse is about to enter the AO crystal, a burst of radio frequency (RF) signal (typically near 400 MHz) is put on the AO crystal. This causes the laser beam to be deflected by a small angle, typically 1–3°.

The deflected beam is captured by a prism, which deflects the beam out of the laser cavity (Figure 4.17). This procedure is called cavity dumping.

For cavity dumping, the AO crystal is pulsed at the desired repetition rate. For instance, for a 1-MHz repetition rate, the RF pulses are sent to the cavity dumping crystal at 1 MHz, which selects one pulse in 80 to be dumped from the dye laser cavity. The RF pulse width is narrow enough to extract a single optical pulse from the dye laser. The arrival times of the acoustooptic and laser pulses have to be matched. The timing of a cavity dumper is typically obtained by dividing the frequency of the mode locker by factors of two, to obtain progressively lower repetition rates. A somewhat confusing terminology is the use of "continuous wave" (CW) to describe the 80-MHz output of a dye laser. This term refers to continuous operation of the cavity dumper, resulting in a continuous train of pulses at 80 MHz.

A valuable aspect of cavity dumping is that it does not typically decrease the average power from the dye laser, at least within the 1–4-MHz range typical of TCSPC. To be specific, if the 80-MHz output of the dye laser is 100 mW, the output of 4 MHz will also be close to 100 mW. When optical power is not being dumped from the dye laser, the power builds up within the cavity. The individual cavity-dumped pulses become more intense, which turns out to be valuable for frequency doubling the output of the dye laser.

A final problem with the R6G dye laser output is its long wavelength from 570 to 610 nm. While shorter wavelength dyes are available, these will typically require a shorter wavelength pump laser. Argon ion lasers have been mode locked at shorter wavelengths, but this is generally difficult. For instance, there are only a few reports of using a mode-locked argon ion laser at 351 nm as an excitation source for TCSPC.<sup>41</sup> Even after this is accomplished, the wavelength is too long for excitation of protein fluorescence. Fortunately, there is a relatively easy way to convert the long-wavelength pulses to shorter wavelength pulses, which is frequency doubling or second harmonic generation. The cavity-dumped dye laser pulses are quite intense. When focused into an appropriate crystal one obtains photons of twice the energy, or half the wavelength. This process is inefficient, so only a small fraction of the 600-nm light is converted to 300 nm. Hence careful separation of the long-wavelength fundamental and short-wavelength second harmonic is needed. The important point is that frequency doubling provides ps pulses, at any desired repetition rate, with output from 285 to 305 nm when using an

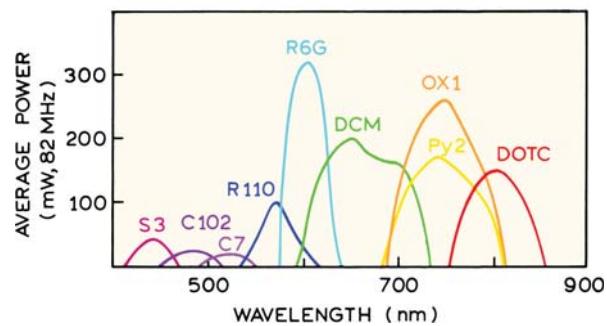


Figure 4.18. Output power of commonly used laser dyes.

R6G dye laser. These wavelengths are ideal for excitation of intrinsic protein fluorescence.

A convenient feature of dye lasers is the tunable wavelength. The range of useful wavelengths is typically near the emission maximum of the laser dye. Tuning curves of typical dyes are shown in Figure 4.18. Most of these dye lasers are used after frequency doubling. We use R6G for excitation of intrinsic protein fluorescence, and 4-(dicyanomethylene)-2-methyl-6-(4-dimethylaminostyryl)-4H-pyran (DCM) and Pyridine 2 (Py2) for excitation of extrinsic probes. Excitation of tyrosine requires output of shorter wavelengths than what is available from R6G. Rhodamine 560 and rhodamine 575 were found suitable for tyrosine excitation using an argon ion or Nd:YAG laser pump source, respectively.<sup>42</sup>

#### 4.4.4. Flashlamps

Prior to the introduction of ps lasers, most TCSPC systems used coaxial flashlamps. A wide range of wavelengths is available, depending on the gas within the flashlamp. These devices typically provide excitation pulses near 2 ns wide, with much less power than that available from a laser source. Flashlamp sources became available in the 1960s,<sup>43–45</sup> but their use in TCSPC did not become widespread until the mid-1970s.<sup>46–49</sup> Because of the lower repetition rate and intensity of the flashlamps, long data acquisition times were necessary. This often resulted in difficulties when fitting the data because the time profile of the lamps changed during data acquisition.<sup>50–51</sup> While these problems still occur, the present lamps are more stable, provide higher repetition rates to 50 kHz, and can provide pulse widths near 1 ns.<sup>52–55</sup>

Figure 4.19 shows a typical coaxial flashlamp. Earlier flashlamps were free running, meaning that the spark

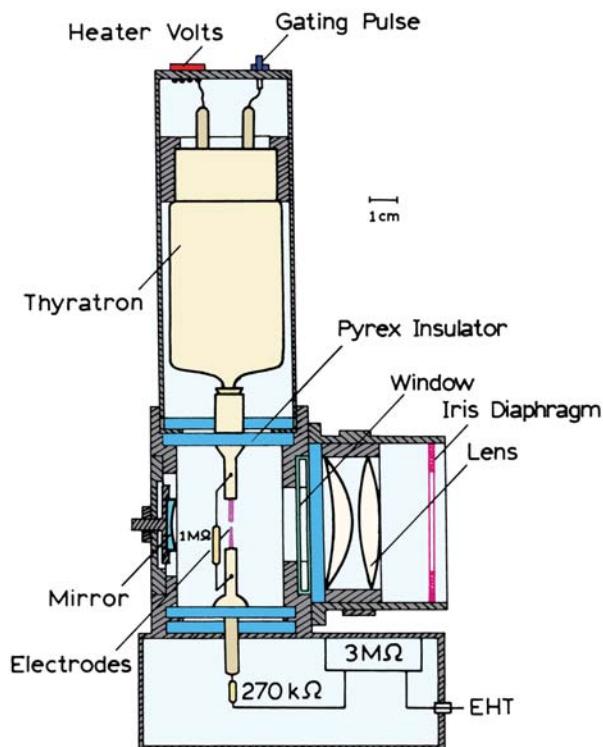


**Figure 4.19.** Coaxial nanosecond flashlamp. Revised and reprinted with permission from [52]. Copyright © 1981, American Institute of Physics.

occurred whenever the voltage across the electrodes reached the breakdown value. Almost all presently used lamps are gated. The electrodes are charged to high voltage.

At the desired time the thyratron is gated on to rapidly discharge the top electrode to ground potential. A spark discharge occurs across the electrodes, which results in a flash of light. These pulses are rather weak, and one frequently has to block the room light to see the flash with the naked eye.

Compared to ion or Ti:sapphire laser sources, flashlamps are simple and inexpensive. Hence, there have been considerable efforts to obtain the shortest pulse widths and highest repetition rates. Despite these efforts, the flashes are much wider than that available with a laser source. One of the shortest time profiles is shown in Figure 4.20 (left), where the full width at half maximum is 730 ps FWHM. More typical is the 1.2-ns FWHM for a flashlamp in which the gas is an argon–hydrogen mixture. Also typical of flashlamps is the long tail that persists after the initial pulse. The spectral output of the pulse lamps depends on the gas, and the pulse width typically depends on both the type of gas and the pressure. Hydrogen or deuterium (Figure 4.21) provides a wide range of wavelengths in the UV, but at low intensity. Nitrogen provides higher intensity at its peak wavelengths, but little output between these wavelengths. In recognition of the growing interest in red and near-infrared (NIR) fluorescence, flashlamps have been developed with red and NIR outputs.<sup>53–54</sup> Given the availability of pulsed LEDs and laser diodes in the red and NIR, there is less motivation to develop red and NIR flashlamps.

The most significant drawback of using a flashlamp is the low repetition rate. The fastest flashlamps have repeti-

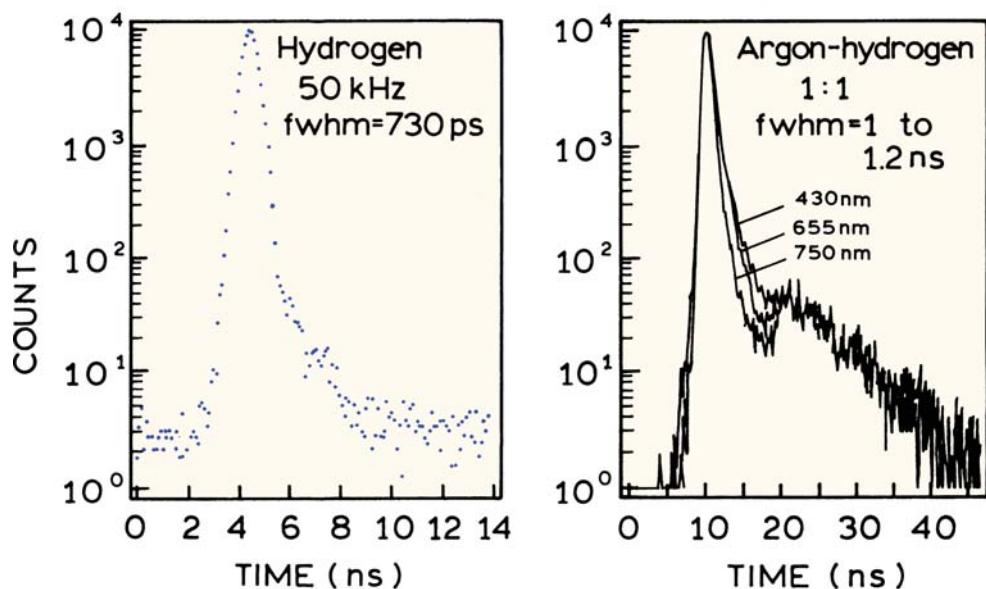


**Figure 4.20.** Time-profiles of coaxial flashlamps. Revised and reprinted from [9] and [53]. Copyright © 1991, American Institute of Physics.

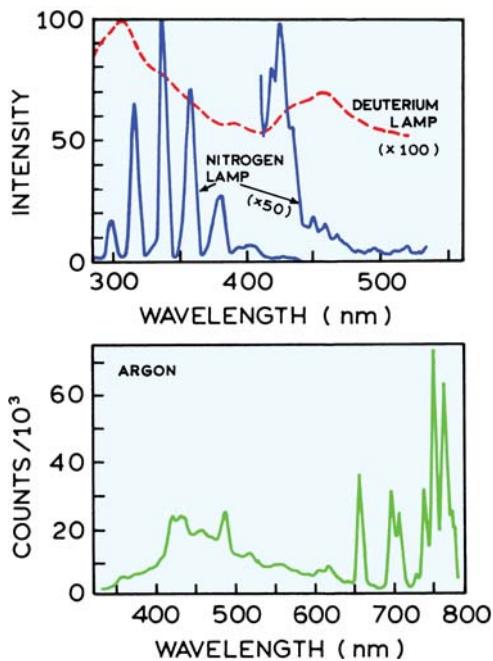


**Figure 4.21.** Spectral output of flashlamps. The output of the deuterium lamp is 100-fold less than of the nitrogen lamp. It is possible that emission below 600 nm for argon is due to impurities. Revised from [16] and [53].

tion rates up to 100 kHz, with 20 kHz being more common. Recall that one can only collect about one photon per 50 to 100 light pulses, so that the maximum photon count rate is near 200 Hz. Hence, a decay curve with 500,000 counts can take up to 40 minutes to accumulate. The data acquisition time can be decreased using a higher repetition rate and a ratio of stop-to-start pulses above 1%. However, even with the high sensitivity of single-photon counting, the low optical output of the flashlamps can limit sensitivity. For these reasons the higher optical power and faster repetition rates of laser systems makes them the preferred light source for TCSPC.

#### 4.4.5. Synchrotron Radiation

Another light source for TCSPC is synchrotron radiation. If electrons are circulated at relativistic speeds they radiate energy over a wide range of wavelengths. These pulses have clean Gaussian shapes and can be very intense. Instruments for TCSPC have been installed at a number of synchrotron sites.<sup>56–61</sup> Unfortunately, it is rather inconvenient to use these light sources. The experimental apparatus must be located at the synchrotron site, and one has to use the beam

when it is available. An advantage of the synchrotron source is that a wide range of wavelengths are available, and all wavelengths appear with the same time distribution.

---

#### 4.5. ELECTRONICS FOR TCSPC Advanced Material

Prior to 2000, most electronics for TCSPC were based on separate components installed in NIM bins (where NIM stands for Nuclear Instruments Module). At present all the necessary electronic components can be contained on a single or small number of computer boards. Electronics to identify the single photoelectron pulses are often contained within the PMT module. However, it is still valuable to understand the operation of the individual components.

##### 4.5.1. Constant Fraction Discriminators

The first component encountered by the single photoelectron pulses are the constant fraction discriminators (Figure 4.22). The goal is to measure the arrival time of the photoelectron pulse with the highest possible time resolution. This goal is compromised because the pulses due to single photoelectrons have a distribution of pulse lights. If one measures the arrival of the pulses by the time when the signal exceeds a threshold, there is a spread,  $\Delta t$ , in the measured times due to pulse height variations (top panel). While this effect may seem minor, it can be the dominant factor in an instrument response function. Leading-edge discriminators can be used for pulses that all have the same height, which may be true for the trigger (start) channel if the laser system is stable.

The contribution of the pulse height distribution can be minimized by the use of constant fraction discriminators.<sup>62–64</sup> The basic idea of a CFD is to split the signal into two parts, one part of which is delayed by about half the pulse width. The other part of the signal is inverted. When these two parts are recombined, the zero crossing point is mostly independent of the pulse height. The difference between leading-edge and constant-fraction discrimination is remarkable, the timing jitter being 1 ns and 50 ps, respectively.<sup>9</sup> It is important to note that the requirements of a CFD are different for pulses from standard PMTs and MCP PMTs. The shorter pulse width from an MCP PMT means that the time delay in the CFD needs to be smaller in order to properly mix the split signals.<sup>65–67</sup>

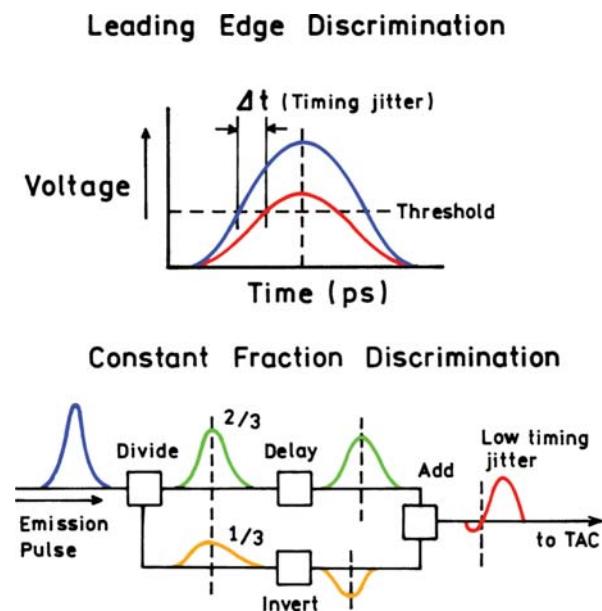


**Figure 4.22.** Constant fraction discrimination in TCSPC. **Top:** Timing error due to pulse height variations using leading edge discrimination. **Bottom:** Operation of a constant fraction discriminator.

#### 4.5.2. Amplifiers

Amplifiers can be used after the start and stop detectors in order to obtain adequate signal levels for timing. The present trend is to avoid such amplifiers,<sup>65</sup> which can result in additional difficulties. In general, the most noise-free amplification can be obtained within the detector (PMT or photodiode). The cable connecting the detector and amplifier can act as an antenna, resulting in amplification of the RF noise. The use of amplifiers was necessary when MCP PMTs first appeared because the pulses were too short for the CFDs available at that time. Amplifiers were used to broaden the pulses sent to the CFD.<sup>40</sup> This is no longer necessary with newer CFDs. If amplifiers must be used, they should be positioned as close as possible to the detector.

#### 4.5.3. Time-to-Amplitude Converter (TAC) and Analyte-to-Digital Converter (ADC)

The role of the TAC in Figure 4.8 is to generate a voltage proportional to the time between the excitation pulse and the first arriving emitted photon, which are the start and stop pulses, respectively. This is accomplished by charging a capacitor during the time interval between the pulses. Typically the capacitor is charged from 0 to 10 volts over a nanosecond to microsecond time range. For instance, if the

chosen range is 50 ns, the capacitor is fully charged at 50 ns. If a stop pulse is received at 25 ns, the charging is stopped at 5 volts. The voltages are calibrated to time delays using delay lines or optical pulses with known time separation. If a stop pulse is not received, the TAC is reset to zero. After the start and stop pulses are received the voltage is connected to a digital value by the ADC. This method of measuring time delays is indirect but provides higher time resolution. At present, inert measurements of time delays cannot be performed accurately enough for nanosecond timescale delays.

In general, the TAC is a rate-limiting component in TCSPC. A certain amount of time is needed to discharge the capacitor and reset the TAC. Prior to about the year 2000, the reset time for most TACs was about 2 ms. This was not a problem with flashlamps where a 50-kHz rate results in start pulses every 20  $\mu$ s. However, with a high-repetition-rate laser source at 1 MHz, the TAC will be overloaded due to continuous start pulses. The TAC will be instructed to reset before it has completed the previous reset.

The solution to this problem is relatively simple, which is to operate the TAC in reverse mode.<sup>68–70</sup> In this mode of operation the first photon detected from the sample serves as the start pulse, and the signal from the excitation pulse is the stop signal. In this way the TAC is only activated if the emitted photon is detected. The decay curves can appear reversed on the screen of the multichannel analyzer (MCA), but this is corrected by software. The reverse mode of TAC operation is not needed with flashlamps because of their lower repetition rates.

The reset time of a TAC is also called the dead time. A TAC with a 2- $\mu$ s dead time has a saturated count rate of 0.5 MHz. Photons arriving within the dead time cannot be counted, so the counting efficiency drops. The photon count rate for 50% counting efficiency is sometimes called the maximum useful count rate, which for a 2- $\mu$ s dead time is 250 kHz. Modern TCSPC electronics have dead times near 125 ns and a saturated count rate of 8 MHz. These electronics can efficiently process and count photons at MHz rates.

An important characteristic of a TAC is its linearity. If the voltage is not linear with time, then the data will contain systematic errors, resulting in difficulties with data analysis. One way to test the linearity of a TAC is by exposure of the detector to a low level of room light, and still use the pulsed-light source to trigger the TAC start signal. Since the photons from the room lights are not correlated with the start pulses, the stop pulses should be randomly distributed across the time range, which is a horizontal line in the mul-

tichannel analyzer (MCA). There were some initial concerns about the linearity of the TAC on the computer boards as compared to the NIM bin systems. However, the problem has been solved and there is no longer a need for NIM bin electronics for TCSPC.

#### 4.5.4. Multichannel Analyzer

In the older systems for TCSPC with separate components there was a multichannel analyzer (MCA). When a separate MCA is present its function is to measure the voltages from the TAC and sort the values according to counts at each particular voltage (time). The MCA first performs an analog-to-digital conversion (ADC), which typically takes about 1–10  $\mu$ s, during which time the MCA is unable to read another voltage from the TAC. The histogram of the number of counts at each voltage (time) is displayed on a screen. This histogram represents the measured intensity decay. MCAs typically have 2048 to 8192 channels, which can be subdivided into smaller segments. This allows several experiments to be stored in the MCA prior to data transfer and analysis. This ability to store several histograms is particularly important for measurement of anisotropy decays. In this case one needs to measure the two polarized intensity decays, as well as one or two lamp profiles. In the modern systems the MCA is replaced by the ADC with direct transfer of the data into computer memory.

#### 4.5.5. Delay Lines

Delay lines, or a way to introduce time delays, are incorporated into all TCSPC instruments. The need for delay lines is easily understood by recognizing that there are significant time delays in all components of the instrument. A photoelectron pulse may take 20 ns to exit a PMT. Electrical signals in a cable travel a foot in about 1 ns. It would be difficult to match all these delays within a couple of nanoseconds in the start and stop detector channels without a way to adjust the delays. The need for matching delays through the components is avoided by the use of calibrated delay lines. Such delays are part of the NIM bin electronics. However, lengths of coaxial cable are prone to picking up RF interference.

Calibrated delay lines are also useful for calibration of the time axis of the MCA. This is accomplished by providing the same input signal to the start and stop channels of the TAC. The preferred approach is to split an electrical signal, typically from the start detector, and direct this signal

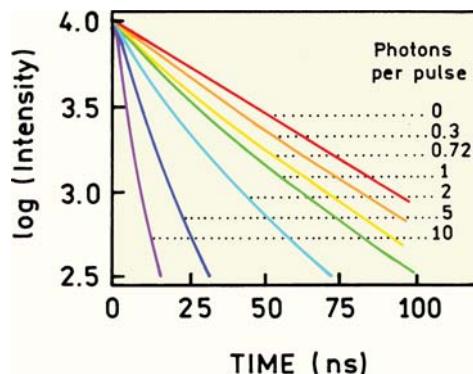


**Figure 4.23.** Effect of the pulse count rate on a single exponential decay. The numbers are the number of arriving photons per excitation pulse. For a rate of 0.01 or 1% the curve overlaps the actual decay (0). From [4].

to both inputs of the TAC. Since the pulses arrive with a constant time difference, one observes a single peak in the MCA. One then switches the time delay in the start or stop channel by a known amount, and finds the peak shift on the MCA display. By repeating this process for several delay times, the TAC and MCA can be calibrated.

#### 4.5.6. Pulse Pile-Up

In TCSPC only one photon from the sample is counted for every 50 to 100 excitation pulses. What errors occur if the average number of detected photons is larger? If more than one photon arrives, how does this affect the measured intensity decay? These questions cannot be answered directly because the electronics limit the experiment to detecting the first arriving photon. Simulations are shown in Figure 4.23 for a single exponential decay with larger numbers of arriving photons. The numbers in the figure refer to the number of observed photons per excitation pulse, not the percentage. The apparent decay time becomes shorter and the decay becomes non-exponential as the number of arriving photons increases. The apparent decay is more rapid because the TAC is stopped by the first arriving photon. Since emission is a random event, the first photon arrives at earlier times for a larger number of arriving photons. Methods to correct for pulse pileup have been proposed,<sup>71–72</sup> but most laboratories avoid pulse pileup by using a low counting rate, typically near 1%. However, this is probably being overcautious,<sup>9</sup> as the measured lifetimes decrease by less than 1% with count rates up to 10%. The intensity decay is only changed by a modest amount for a 30% count rate (Figure 4.23). At present the concerns about pulse pileups

are decreasing because the higher-repetition-rate lasers provide high data rates even with a 1% count rate. Additionally, multichannel systems with multiplexing have become available for TCSPC (Section 4.7).

## 4.6. DETECTORS FOR TCSPC

### 4.6.1. Microchannel Plate PMTs

Perhaps the most critical component for timing is the detector. The timing characteristics of various PMTs have been reviewed for their use in TCSPC.<sup>22,27,73–74</sup> At present the detector of choice for TCSPC is the microchannel plate PMT. An MCP PMT provides a tenfold shorter pulse width than any other PMT, and displays lower intensity afterpulses. Also, the effects of wavelength and spatial location of the light seem to be much smaller with MCP PMTs than with linear-focused or side-window tubes. While good time resolution can be obtained with linear-focused and side-window PMTs, the high-speed performance and absence of timing artifacts with an MCP PMT make them the preferred detector for TCSPC.

Development of MCP PMTs began in the late 1970s,<sup>75–78</sup> with the first useful devices appearing in the early to mid-1980s,<sup>79</sup> and their use for TCSPC beginning at the same time.<sup>80–88</sup> The design of an MCP PMT is completely different from that of a dynode chain PMT (Figure 4.24). The factor that limits the time response of a PMT is

its transit time spread (TTS), which is the distribution of transit times through the detector. The overall transit time of the electrons through a PMT is not important, as this is just a time delay corrected for in the measurements. However, the distribution of transit times or TTS is important because this spread limits the time resolution of a PMT. One cannot do timing measurements more accurately than the uncertainty in the time it takes a signal to pass through the detector. In a linear-focused PMT the TTS is minimized by designing the dynodes so all the electrons tend to travel along the same path. The TTS of most phototubes is near 2 ns, and it can be less than 1 ns with carefully designed PMTs (Table 4.1).

The design of an MCP is completely different because it does not have dynodes. Instead, the photoelectrons are amplified along narrow channels lined with the dynode material (Figure 4.24). Because these channels are very narrow, typically 4 to 12 microns in diameter, the electrons all travel the same path and hence have the same transit time. Smaller channels result in less transit time spread. There are a few additional features in the MCP PMT design that provide improved time response. The channels are angled relative to each other, which prevents feedback between the channels and broadening of the time response.<sup>77–78</sup> Also, the first MCP surface is typically covered with aluminum, which prevents secondary electrons emitted from the top of the MCP from entering adjacent channels.

MCP PMTs provide very low TTS. Figure 4.25 shows the response of an R3809U to femtosecond pulses from a Ti:sapphire laser. The R3809U is now widely used for TCSPC. The FWHM is only 28 ps and the afterpulse a factor of 100 smaller than the primary response. MCP PMTs do have some disadvantages. The photocurrent available from an MCP PMT is typically 100 nA (R2908), as compared to 0.1 mA (R928) for a dynode PMT. This means that the MCP PMT responds linearly to light intensity over a smaller range of incident intensities than does a dynode PMT. The current carrying capacity of an MCP PMT is less because the electrical conductance of the MCPs is low. It is known that the pulse widths from an MCP PMT can depend on the count rate,<sup>88–89</sup> presumably because of voltage changes resulting from the photocurrent. Another disadvantage of the MCP PMTs is their presumed limited useful lifetime which depends on the photocurrent drawn from the tube. In our hands this has not been a problem, and it is difficult to know if an MCP PMT has lost gain due to the total current drawn or due to the inevitable overexposure to light that occurs during the lifetime of a PMT. MCP PMT are

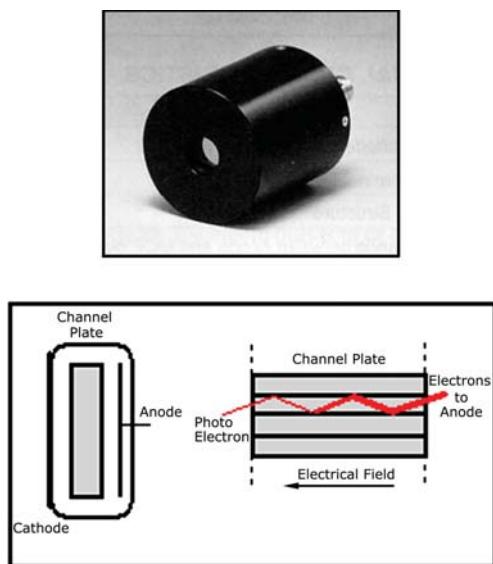


**Figure 4.24.** Photograph and schematic of an MCP PMT. The diameter of the housing is about 45 mm. Revised from [90–91].

**Table 4.1.** Transient Time Spreads of Conventional and MCP PMTs<sup>a</sup>

Photomultiplier		Configuration (upper frequency)	TTS (ns)	Dynode
Hamamatsu	R928	Side-on (300 MHz) <sup>b</sup>	0.9	9 stage
	R1450	Side-on	0.76	10 stage
	R1394	Head-on	0.65	10 stage
	R7400	Compact PMT, TO-8 (900 MHz)	300 ps	—
	H5023	Head-on (1 GHz)	0.16	10 stage
RCA	C31000M	Head-on	0.49	12 stage
	8852	Head-on	0.70	12 stage
Philips	XP2020Q	Head-on	0.30	12 stage
Hamamatsu	R1294U	Nonproximity MCP-PMT	0.14	2 MCP
	R1564U	Proximity focused MCP-PMT, 6 micron (1.6–2 GHz)	0.06	2 MCP
	R2809U	Proximity MCP-PMT, 6 micron	0.03 <sup>d</sup>	2 MCP
	R3809U	Proximity MCP-PMT Compact size, 6 micron	0.025 <sup>d</sup>	2 MCP
	R2566	Proximity MCP-PMT with a grid, 6 micron (5 GHz) <sup>c</sup>	—	2 MCP

<sup>a</sup>Revised from [81].<sup>b</sup>Numbers in parentheses are the approximate frequencies where the response is 10% of the low-frequency response. The H5023 has already been used to 1 GHz.<sup>c</sup>From [86].<sup>d</sup>From [87].

considerably more expensive than dynode PMTs. In general the expense of an MCP PMT is justified only if used with a ps light source.

#### 4.6.2. Dynode Chain PMTs

Dynode PMTs cost less than MCP PMTs and are adequate for many TCSPC experiments, especially if the excitation source is a flashlamp. Two types of dynode PMTs are used for TCSPC: side-window and linear-focused PMTs. Their performance is comparable, but there are minor differences. The side-window tubes are less expensive but can still provide good time resolution. Pulse widths from 112 to 700 ps have been obtained using side-window tubes,<sup>36,92–95</sup> but pulse widths of 1–2 ns are more common. A disadvantage of a side-window PMT is that the time response can depend on the region of the photocathode that is illuminated. Linear-focused PMTs are somewhat more expensive but provide slightly shorter transit time spreads (Table 4.1) and are less sensitive to which region of the photocathode is illuminated. Linear-focused PMTs are probably still the most widely used detectors in TCSPC, but there is a continual shift towards the MCP PMTs and compact PMTs.

#### 4.6.3. Compact PMTs

The expense of TCSPC has been decreased significantly by the introduction of compact PMTs (Figure 4.26). These PMTs are built into standard TO-8 packages.<sup>96–97</sup> Typically these PMTs come in modules that include the dynode chain, a high-voltage power supply, and sometimes the circuits to transform the pulses into TTL level signals. The TTS of these compact PMTs can be short: just 300 ps (Figure 4.25). The compact PMTs appear to be rugged and long-lived and do not have the current limitations of an MCP PMT. These compact PMTs are becoming the detector of choice for most TCSPC instruments.

#### 4.6.4. Photodiodes as Detectors

Photodiodes (PDs) are inexpensive and can respond faster than an MCP PMT. Why are phototubes still the detector of choice? Photodiodes are not usually used for photon counting because of the lack of gain. However, avalanche photodiodes (APDs) have adequate gain and can be as fast as MCP PMTs. The main problem is the small active area. In a PMT or MCP PMT, the area of the photocathode is typically 1 cm × 1 cm, and frequently larger. Photons arriving

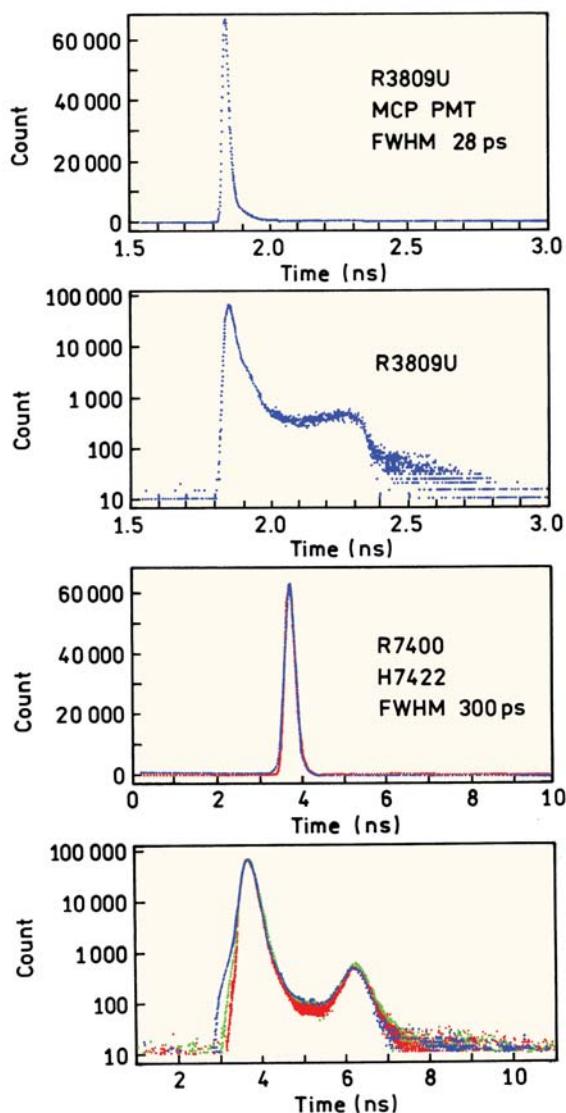


**Figure 4.25.** Transit time spread for an MCP PMT (R3809U) and a miniature PMT (R7400 series in a H7422 module). Revised from [90].

anywhere on the photocathode are detected. In contrast, the active area of an avalanche photodiode is usually less than  $1\text{ mm}^2$ , and less than  $10\text{ }\mu\text{m} \times 10\text{ }\mu\text{m}$  for a high-speed APD. It is therefore difficult to focus the fluorescence onto the APD, so the sensitivity is too low for most measurements. Another disadvantage is the relatively long tail following each pulse, the extent of which depends on wavelength. The presence of a wavelength-dependent tail can create problems in data analysis since the instrument response function will depend on wavelength. Methods have been developed to actively quench the tail. Values of the full width at half



**Figure 4.26.** Compact PMTs and modules containing the PMTs. The diameter of the PMT is 16 mm. The width of the PMT modules is 25 nm. Courtesy of William Cieslik, Hamamatsu Photonics Systems.

maxima have been reported from 20 to 400 ps, and APDs have been successfully used in TCSPC.<sup>98–105</sup>

APDs are now routinely used for TCSPC, especially in applications where the emission can be tightly focused, such as single-molecule detection (SMD) and fluorescence-correlation spectroscopy (FCS). TCSPC measurements can be performed at the same time as SMD and FCS experiments. APDs have high quantum efficiencies at real wavelengths, and are the detector of choice for these applications.

#### 4.6.5. Color Effects in Detectors

When performing lifetime measurements, one generally compares the response of a fluorescent sample with that of a zero decay time scattering sample. Because of the Stokes shift of the sample, the wavelengths are different when measuring the sample and the impulse response function. The timing characteristics of a PMT can depend on wavelength. Color effects were significant with the older-style tubes, such as the linear-focused 56 DVVP and the side-window tubes.<sup>106–111</sup> The time response of PMTs can also depend on which region of the photocathode is illuminated. Color effects are almost nonexistent in MCP PMTs<sup>80</sup> and do not appear to be a problem with the compact PMTs.

Methods are available to correct for such color effects. There are two general approaches, one of which is to use a standard with a very short lifetime.<sup>112–113</sup> The standard should emit at the wavelength used to measure the sample. Because of the short decay time one assumes that the measured response is the instrument response function. Because

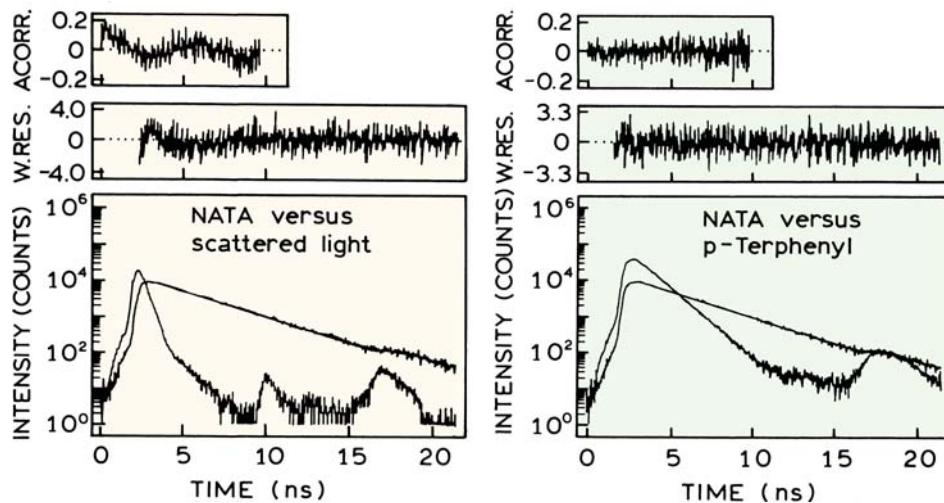


**Figure 4.27.** Intensity decay of N-acetyl-L-tryptophanamide as measured versus scattered light (left) and using a p-terphenyl lifetime reference (right). Revised from [118].

the wavelengths are matched, one assumes that the color effects are eliminated.

The more common method is to use a standard fluorophore that is known to display a single exponential decay.<sup>114–124</sup> One measures the intensity decay of the sample and the reference fluorophore at the same wavelength. The intensity decays of the reference fluorophore with the known decay time  $\tau_R$  and of the sample are analyzed simultaneously. In order to correct for the reference lifetime a different functional form is used for  $I(t)$ :

$$I(t) = \sum_{i=1}^n \alpha_i \left[ \delta(t) + \left( \frac{1}{\tau_R} - \frac{1}{\tau_i} \right) \exp(-t/\tau_i) \right] \quad (4.18)$$

where  $\delta(t)$  is the Dirac delta-function. In this expression the values of  $\alpha_i$  and  $\tau_i$  have their usual meaning (eq. 4.8). This method is best performed when the decay time of the standard is precisely known. However, some groups vary the assumed decay time of the standard to obtain the best fit.

Figure 4.27 shows how the TCSPC data can be improved using a lifetime standard.<sup>118</sup> N-acetyl-L-tryptophanamide (NATA) is known to display a single exponential decay in water. Its intensity decay was measured with 295 nm excitation from a cavity-dumped frequency-doubled R6G dye laser.<sup>39</sup> The emission was detected with a Philips PM 2254 PMT, which is a linear-focused dynode PMT. When NATA was measured relative to scattered light the fit was fair. However, there were some non-random deviations, which are most easily seen in the autocorrela-

tion trace (Figure 4.27, top left). Also, the goodness-of-fit parameter  $\chi_R^2 = 1.2$  is somewhat elevated. The fit was improved when measured relative to a standard, p-terphenyl in ethanol,  $\tau_R = 1.06$  ns at 20°C. One can see the contribution of the reference lifetime to the instrument response function as an increased intensity from 5 to 15 ns in the instrument response function (right). The use of the p-terphenyl reference resulted in more random deviations and a flatter autocorrelation plot (top right). Also, the value  $\chi_R^2$  was decreased to 1.1. Comparison of the two sides of Figure 4.27 illustrates the difficulties in judging the quality of the data from any single experiment. It would be difficult to know if the minor deviations seen on the left were due to NATA or to the instrument. Some of the earlier reports overestimated the extent of color effects due to low voltage between the photocathode and first dynode. At present, most PMTs for TCSPC use the highest practical voltage between the photocathode and first dynode to minimize these effects. Also, most programs for analysis of TCSPC allow for a time shift of the lamp function relative to the measured decay. This time shift serves to correct for any residual color effects in the PMT. While one needs to be aware of the possibility of color effects, the problem appears to be minor with MCP PMTs and compact PMTs.

Prior to performing any TCSPC measurements it is desirable to test the performance of the instrument. This is best accomplished using molecules known to display single exponential decays.<sup>113</sup> Assuming the sample is pure and decays are a single exponential, deviations from the expected decay can reveal the presence of systematic errors in the

measurements. A number of known single exponential lifetimes are summarized in Appendix II.

As described in Chapter 2, it is also important to test for background fluorescence from blank solutions. Autofluorescence from the sample can result in errors in the intensity decay, which results in confusion and/or erroneous conclusions. There is a tendency to collect the time-resolved data prior to measuring the steady-state spectra of the sample and controls. This is particularly dangerous for time-resolved measurements because the data are often collected through filters, without examining the emission spectra. Measurements may be performed on an impure sample, resulting in a corrupted data set. Since the emission spectra were not recorded the impurity may go undetected. Subsequent analysis of the data is then unsatisfactory, and the source of the problem is not known. In our experience, more time is wasted by not having the spectra than the time needed to record blank spectra prior to time-resolved data collection.

Background correction in TCSPC is straightforward. Data are collected from the blank sample at the same time and conditions as used for the sample. As a result, the background can then be subtracted from the sample data. The source intensity, repetition rate, and other conditions must be the same. Inner filter effects in the samples can attenuate the background signal. If the control samples have a lower optical density, the measured background can be an overestimation of the actual background. If the number of background counts is small, there is no need to consider the additional Poisson noise in the difference data file. However, if the background level is large, it is necessary to consider the increased Poisson noise level in the difference data file.

#### 4.6.6. Timing Effects of Monochromators

As the time resolution of the instrumentation increases one needs to consider the effects of the various optical components. Monochromators can introduce wavelength-dependent time delays and/or broaden the light pulses.<sup>125–126</sup> This effect is shown in Figure 4.28, which shows the path length difference for an optical grating with  $N$  facets. Monochromators are usually designed to illuminate the entire grating. The maximum time delay is given by<sup>127</sup>

$$t_d = \frac{Nm\lambda}{c} \quad (4.19)$$

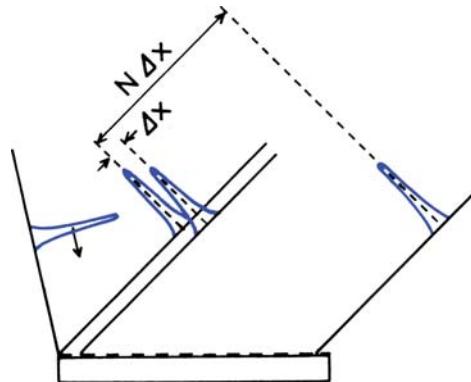


**Figure 4.28.** Path length difference across a monochromator grating.  $N$  is the total number of facets in the grating and  $\Delta x$  is the path length difference between adjacent reflections. From [126].

where  $N$  is the number of facets,  $m$  is the diffraction order (typically 1),  $\lambda$  is the wavelength, and  $c$  is the speed of light. A typical grating may have 1200 lines/mm and be 60 mm across. The maximum time delay at 350 nm is thus 84 ps. While ps and fs laser pulses are not usually passed through a monochromator, this can be expected to broaden the pulse. Alternatively, the apparent intensity decay of a short-lived fluorophore may be broadened by the use of a monochromator to isolate the emission. These effects can be avoided by the use of subtractive dispersion monochromators.<sup>128–129</sup>

---

#### 4.7. MULTI-DETECTOR AND MULTI-DIMENSIONAL TCSPC

In all the preceding examples TCSPC was performed using a single detector. However, there are many instances where it would be useful to collect data simultaneously with more than one detector. This method is called multidimensional or multichannel TCSPC. These measurements can be accomplished in several ways. One approach is to use a number of completely separate electronics for each channel,<sup>130</sup> which unfortunately results in high complexity and costs. Another approach is to use a single TAC and MCA and to multiply the input from several detectors.<sup>131–135</sup> Recall that TCSPC is limited to detection of about 1 photon per 100 excitation pulses. By using several detectors the overall rate of photon counting can be increased several fold. The maximum counting rate does not increase in direct proportion to the number of detectors because of interference between simultaneously arriving signals, but

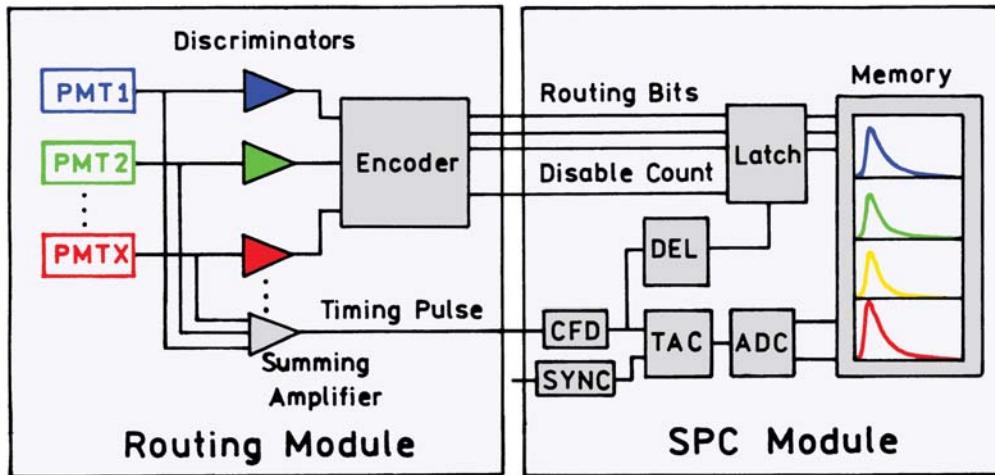


Figure 4.29. Electronic schematic for TCSPC with multiple detectors. Revised from [134].

this is a minor problem compared to the advantages of multidimensional measurements.

Advances in electronics for TCSPC have made multidimensional measurements rather simple, reliable, and relatively inexpensive. Multiple intensity decays can be collected simultaneously at different emission wavelengths or at different locations in a sample. There are numerous potential applications for such measurements in analytical chemistry and cellular imaging. In the future we can expect many if not most TCSPC experiments to be performed with multiple detectors.

Multidimensional capabilities are now easily accessible and are standard in some of the TCSPC electronics. A typical circuit is shown in Figure 4.29. The pulses from 4 to 16 separate detectors are sent to a rotating module that keeps track of their origins and sends them to the TAC and ADC. A single TAC and ADC are used because these are the most expensive, complex, and power-consuming parts of the electronics. After conversion the data are sent to separate blocks of memory as directed by the routing module. If two photons are detected in different channels at the same time, the routing module discards their pulses.

The power and simplicity of multidimensional TCSPC is shown in Figure 4.30 for a mixture of fluorescein and rhodamine 6G. The light source was a ps diode laser. The emission wavelengths were separated and focused onto a multi-anode PMT (Figure 4.31). Such PMTs have a single photocathode and dynodes that maintain the position of the electrons so they arrive at the appropriate anode. The transit time spreads of these PMTs are 0.3 to 0.6 ns, so that nanosecond decay times can be measured. The output from

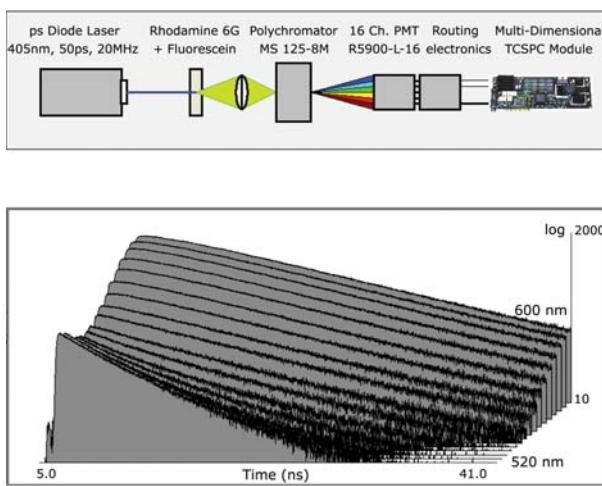


Figure 4.30. Multidimensional TCSPC of a mixture of fluorescein and rhodamine 6G. Excitation was a 405-ns pulse with a ps diode laser, 20 MHz repetition rate. The detector was an R5900-L16, which has 16 separate anodes in a linear geometry. Revised from [134].

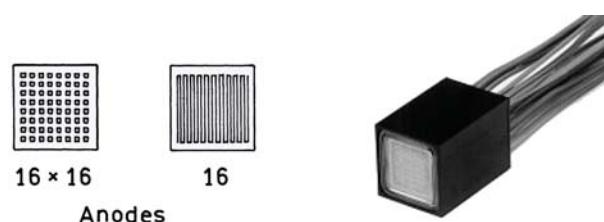
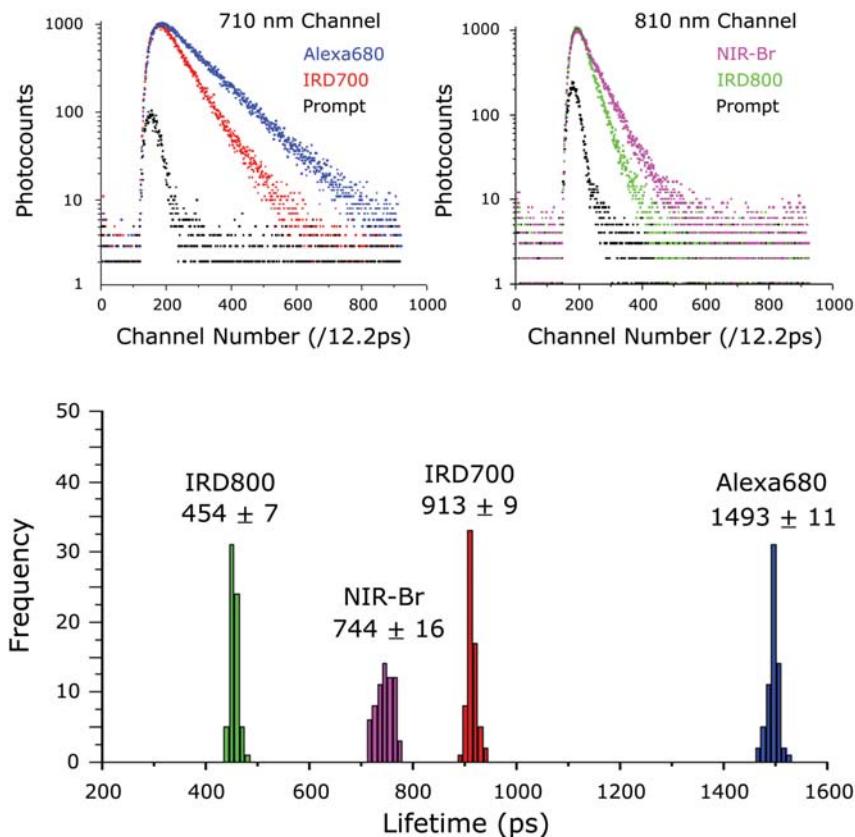


Figure 4.31. Multi-anode PMT for Hamamatsu, R5900. Reprinted with permission from [11,136].



**Figure 4.32.** Intensity decays and recovered lifetimes of four labeled nucleotides used for DNA sequencing. Revised from [142].

the 16 anodes is sent to a multiplexing TCSPC board that measures the time delays between the start and stop pulses. The system keeps track of the anode that sent the signal, so the counts can be loaded into different regions of memory, which correspond to different wavelengths.

Sixteen decay curves were measured simultaneously for the fluorescein–rhodamine 6G mixture (Figure 4.30). The different decay times are seen from the slopes, which change with emission wavelength. In this case the lifetime of fluorescein was probably decreased by resonance energy transfer to R6G. It is easy to imagine such measurements being extended to time-dependent processes such as resonance energy transfer or solvent relaxation.

#### 4.7.1. Multidimensional TCSPC and DNA Sequencing

An important application of multichannel detection will be DNA sequencing. Because of the large number of bases the sequencing must be performed as inexpensively as possible.

Sequencing was initially done using four lanes, one for each base. It would be an advantage to identify the four bases in a single lane. Because of the limited range of available wavelengths and overlap of emission spectra, there is ongoing research to perform sequencing using the decay times of the labeled bases.<sup>137–142</sup> Using four detectors the intensity decays are at four different excitation, and/or emission wavelengths could be measured in a single lane of a sequencing gel. If the decay times of the labeled bases were different, the decay times could be used to identify the bases.

The possibility of DNA sequencing based on lifetime is shown in Figure 4.32. TCSPC data are shown for four probes attached to DNA. These dyes are typical of those used for sequencing. They can be excited with two NIR laser diodes, which can easily occur at different times by turning the laser diodes on and off. The four probes show different lifetimes, and can be identified based on the lifetimes recovered from a reasonable number of counts. Each of the decays in Figure 4.32 were collected in about 7.5 s.

It is easy to imagine how the four fluorophores in Figure 4.32 could be measured simultaneously using multi-detector TCSPC.

TCSPC data are usually analyzed using nonlinear least squares (NLLS) or the method of moments. Both these methods rely on a large number of photon counts, so that the uncertainties in the data have a Gaussian distribution. In applications such as DNA sequencing (Figure 4.32) the goal is not to resolve a multi-exponential decay, but rather to obtain an estimate of a single lifetime. When the number of counts is small the data have a Poissonian distribution rather than a Gaussian distribution. For such data NLLS does not provide the best estimate of the lifetime. The lifetime that is most likely the correct lifetime can be calculated from the maximum likelihood estimates (MLE):<sup>143–144</sup>

$$1 + (e^{T/\tau} - 1)^{-1} - m(e^{mT/\tau} - 1)^{-1} = N_t^{-1} \sum_{i=1}^m iN_i \quad (4.20)$$

In this expression  $m$  is the number of time bins within the decay profile,  $N_t$  is the number of photocounts in the decay spectrum,  $N_i$  is the number of photocounts in time bin  $i$ ,  $T$  is the width of each time bin, and  $\tau$  is the lifetime. This expression allows rapid estimation of the lifetime, which is essential with the high throughput of DNA sequences.

#### 4.7.2. Dead Times, Repetition Rates, and Photon Counting Rates

When examining the specifications for TCSPC electronics it is easy to become confused. The maximum count rates are determined by several factors that affect the rate in different ways depending upon the sample. It is easier to understand these limitations if they are considered separately.

The maximum pulse repetition rate is determined by the decay times of the sample. The time between the pulses is usually at least four times the longest decay time in the sample. If the longest decay time is 12.5 ns then the excitation pulses must be at least 50 ns apart, which corresponds to a repetition rate of 20 MHz. It will not matter if the laser can pulse at a higher frequency, or if the electronics can synchronize to a higher repetition rate laser. For this sample the pulse repetition rate should not exceed 20 MHz.

The maximum photon counting rate is determined by the repetition rate of the laser. For the 20-MHz rate the maximum photon counting rate is 200 kHz, using the 1% rule. The electronics may be able to count photons faster,

but the 1% rule and the laser repetition rate limit the maximum photon count rate.

Depending upon the sample the maximum counting rate can be limited by either the sample or the electronics. Suppose the TCSPC electronics are modern with a 125 ns dead time. The maximum count rate is usually listed as the inverse of the dead time, or 8 MHz. However, photons cannot be counted at 8 MHz because the electronics would be busy most of the time and unable to accept start pulses. Detection becomes inefficient because photons arriving within the dead time are not counted. An upper effective count rate is when the counting efficiency decreases to 50% or 4 MHz. It is important to recognize that this is an electronic limitation that is independent of the sample. It would be difficult to obtain a 4-MHz count rate when using the 1% rule. This would require a pulse repetition rate of 400 MHz or 2.5 ns between pulses. This pulse rate could only be used if the lifetime were shorter than 0.625 ns.

The considerations in the previous paragraph indicate the usefulness of multi-detector TCSPC. The count rate of the electronics exceeds the count rate determined by the sample lifetime, so the electronics can process more photons. Input from the multiple detectors is sent to the electronics by the routing module. This module has its own dead time near 70 ns. Hence the saturated count rate from all the detectors is about 14 MHz, but for a 50% counting efficiency is limited to 7 MHz. The dead time of the electronics would not allow efficient photon counting at 7 MHz. The overall count rate can be increased by using multiple independent sets of TCSPC electronics.

In summary, the timing considerations of TCSPC can appear complex. It is easier to consider the problem from first principles than to work backwards from the specifications.

---

#### 4.8. ALTERNATIVE METHODS FOR TIME-RESOLVED MEASUREMENTS Advanced Material

##### 4.8.1. Transient Recording

While TCSPC and frequency-domain fluorometry are the dominant methods used by biochemists, there are alternative methods for measuring intensity decays. Prior to the introduction of TCSPC, intensity decays were measured using stroboscopic or pulse sampling methods. The basic idea is to repetitively sample the intensity decay during pulsed excitation (Figure 4.33). The detection gate is displaced across the intensity decay until the entire decay is

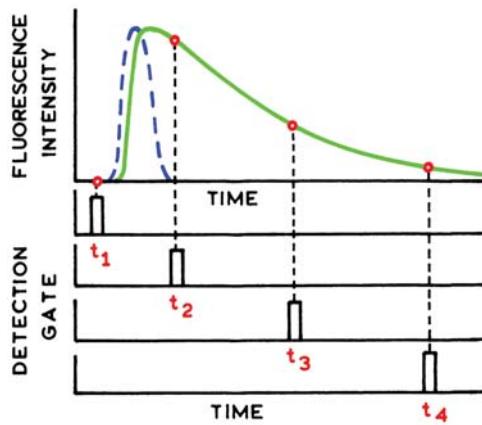


**Figure 4.33.** Decay time measurements using gated detection in the pulse sampling method. Revised from [10].

measured. In fact, the first time-domain lifetime instruments used gated detection to sample the intensity decay.<sup>44</sup>

Gated detection can be accomplished in two ways. One method is to turn on or gate the gain of the detector for a short period during the intensity decay.<sup>145–146</sup> Surprisingly, this can be accomplished on a timescale adequate for measurement of nanosecond lifetimes. Alternatively, the detector can be on during the entire decay, and the electrical pulse measured with a sampling oscilloscope.<sup>147–148</sup> Such devices can sample electrical signals with a resolution of tens of picoseconds.

While such methods seem direct, they have been mostly abandoned due to difficulties with systematic errors. The flashlamps and N<sub>2</sub> lasers generate RF signals that can be picked up by the detection electronics. This difficulty is avoided in TCSPC because low-amplitude noise pulses are rejected, and only the higher-amplitude pulses due to primary photoelectrons are counted. Also, in TCSPC the standard deviation of each channel can be estimated from Poisson statistics. There are no methods to directly estimate the uncertainties with stroboscopic measurements. Hence, TCSPC became the method of choice due to its high sensitivity and low degree of systematic errors, when the goal of the experiments was resolution of complex intensity decays.

Recent years have witnessed reintroduction of gated detection methods.<sup>149–150</sup> The time resolution can be good but not comparable to a laser source and an MCP PMT. Typical instrument response functions are close to 3 ns wide. An advantage of this method is that one can detect many photons per lamp pulse, which can be an advantage in clinical applications when the decays must be collected rap-

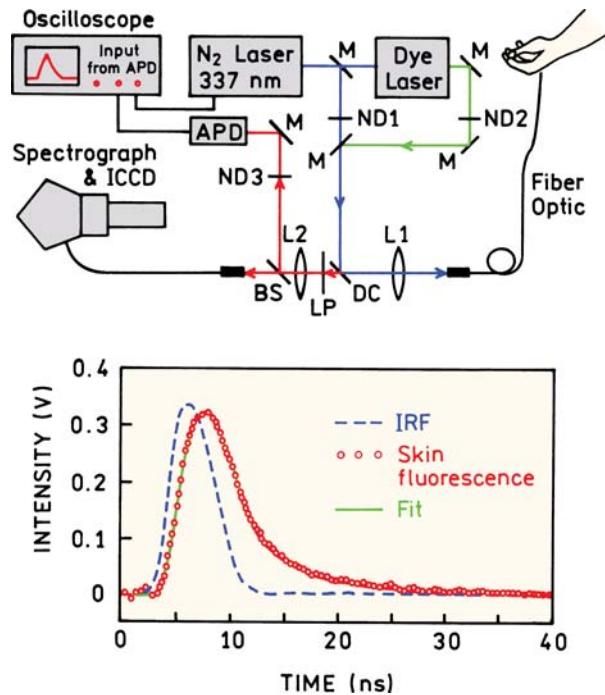


**Figure 4.34.** Time-resolved instrument using a high-speed oscilloscope for measuring of time-resolved decays of skin of human skin. Revised from [150].

idly. Gated detection can be used with low-repetition-rate nitrogen lasers, which can also be used to pump dye lasers. An example of directly recorded intensity decay is shown in Figure 4.34. The instrument was designed for studies of skin and tissue using this autofluorescence, so the excitation light was delivered to the sample via an optical fiber.<sup>150</sup> The excitation source was a nitrogen laser excitation source with a repetition rate near 10 Hz. The emission was detected with an APD and digitized on a high-speed oscilloscope. The intensity decay of human skin was collected in about 1 s by averaging of several transients. The IRF is about 5 ns wide but the intensity decay of skin autofluorescence could be recorded. The wide IRF shows why TCSPC is used rather than direct transient recording. At this time it is not possible to directly record nanosecond decays with the accuracy needed for most biochemical studies.

#### 4.8.2. Streak Cameras

Streak cameras can provide time resolution of several ps,<sup>151–160</sup> and some streak cameras have instrument response functions of 400 fs, considerably faster than TCSPC with an MCP PMT. Streak cameras operate by dispersing the photoelectrons across an imaging screen. This can be accom-

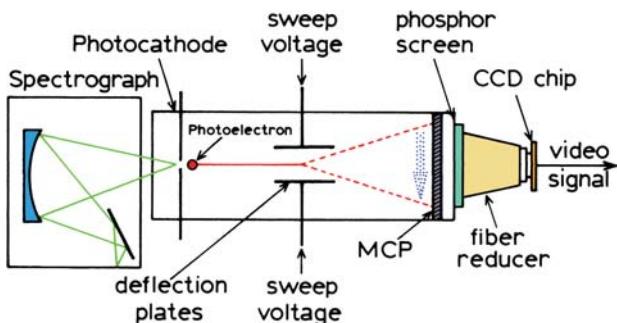


**Figure 4.35.** Schematic of a streak camera with wavelength resolution. From [152].

plished at high speed using deflection plates within the detector (Figure 4.35). In the example shown, the light is dispersed by wavelength in a line across the front of the photocathode. Hence, streak cameras can provide simultaneous measurements of both wavelength and time-resolved decays. Such data are valuable when studying time-dependent spectral relaxation or samples which contain fluorophores emitting at different wavelengths.

The time resolution obtainable with a streak camera is illustrated in Figure 4.36. The instrument response function is superior to that found with the fastest MCP PMTs. Earlier-generation streak camera were delicate, and difficult to use and synchronize with laser pulses. This situation has changed, and streak cameras have become more widely used, especially for simultaneous measurement of sub-nanosecond decays over a range of emission wavelength. One example is the decay of PyDMA (Figure 4.37), which decays rapidly due to exciplex formation and solvent relaxation around the charge-transfer (CT) complex.<sup>161</sup> Pyrene in

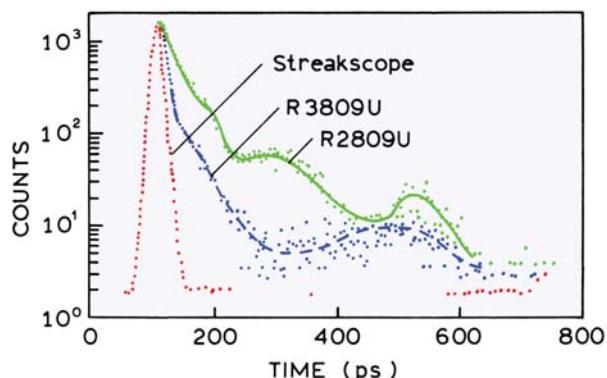


**Figure 4.36.** Comparison of the instrument response functions of a streak camera and two MCP PMTs (R3809U and R2809U). The 600 nm dye laser pulse width was 2 ps. Revised from [158].

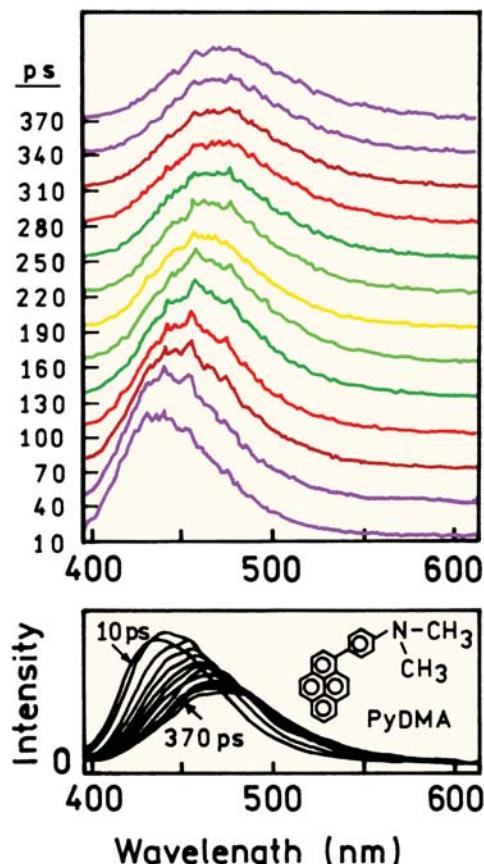


**Figure 4.37.** Time and wavelength-dependent intensity decays of dimethyl-(4-pyren-1-yl-phenyl)amine (PyDMA) measured with a streak camera. Revised from [161].

the excited state forms a charge-transfer complex, an exciplex, with the linked dimethylphenyl group. The charge-transfer complex is polar and shows a time-dependent spectral shift to longer wavelengths. This shift occurs rapidly and is complete in less than 500 ps. The time-dependent shift to longer wavelength is due to reorientation of the solvent around the CT state. The high temporal resolution of the streak camera allows recording of the complete emission spectra over intervals as short as 10 ps. The data can also be displayed in a format where the axes are time and wavelength and the color reveals the intensity (Figure 4.38).

An important development in streak camera technology is the introduction of the photon-counting streak camera (PCSC).<sup>162</sup> These devices provide single-photon detection with high time resolution (14 ps) and simultaneous wavelength resolution. The photon counts can be collected at high rates because pulse pileup and dead time are not problems with these instruments. A PCSC functions the same as

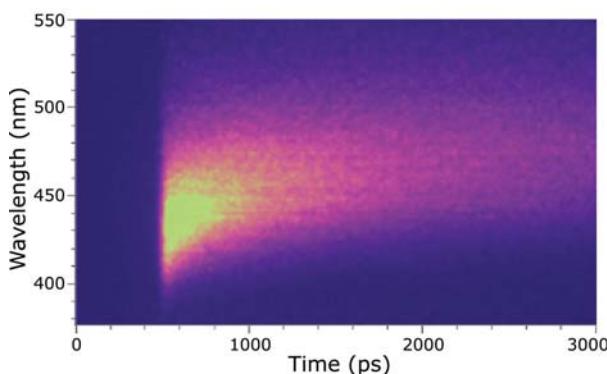


**Figure 4.38.** Time- and wavelength-dependent intensity decay of PyDMA. Figure courtesy of Professor Hubert Staerk, Max-Planck Institute for Biophysical Chemie, Göttingen, Germany.

the camera shown in Figure 4.35 except for the mode of detection. Instead of digitizing an analog signal, the PCSC counts the pulses on the phosphor screen due to single photoelectrons. The pulses are recorded with a CCD camera. The software examines the size of the pulse and only accepts pulses above a defined threshold, analogous to the discriminator in TCSPC (Figure 4.39). The instrument

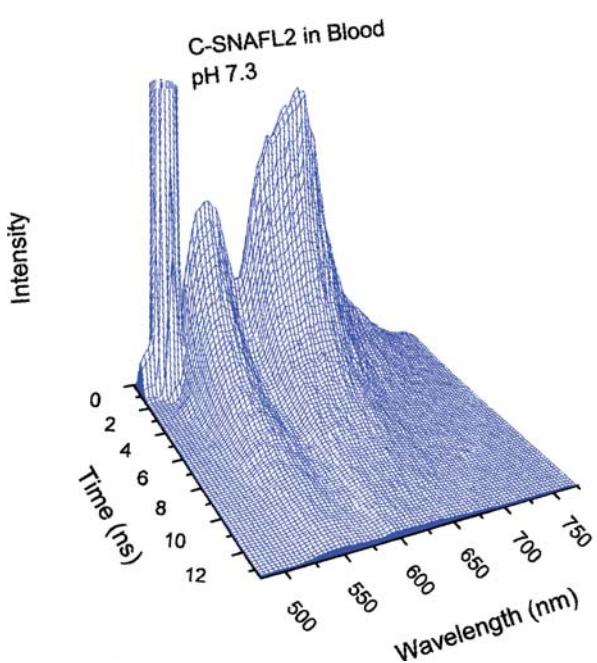


**Figure 4.40.** Intensity decay of C-SnafL2 in blood at pH 7.3 measured with a photon counting streak camera. From [163].

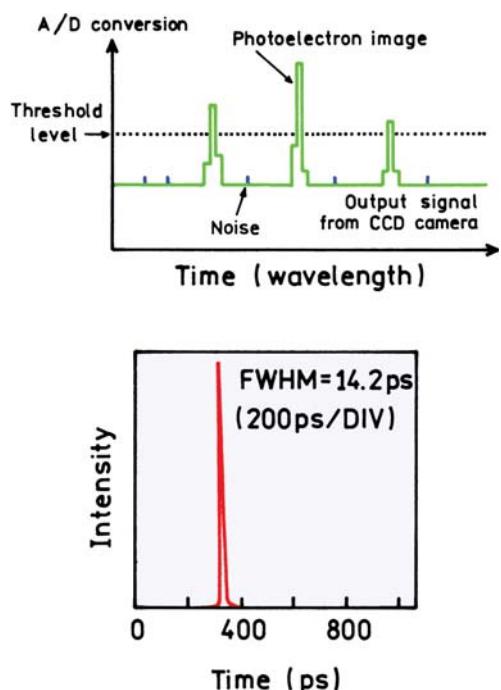


**Figure 4.39.** Single photoelectron detection and time resolution of a photon counting streak camera. Revised from [162].

response function is the width of a single photoelectron image, which is about 14 ps. There is no dead time because the photons are distributed in space across the photocathode, so more than a single photon can be collected at each wavelength for each laser pulse. Of course the photons cannot be accurately counted if they overlap in time and space on the phosphor screen. Data can be collected at all wavelengths simultaneously because the wavelengths are at different locations on the photocathode.

The high sensitivity of a PCSC allows measurements that would be difficult with more conventional instruments. Figure 4.40 shows intensity decays of a pH probe C-SnafL2 in blood, which has high absorbance at the excitation wavelength. The decays at all wavelengths were obtained simultaneously. It was not possible to suppress all the scattered light using filters, but the scattered light appears at a different position (wavelength) on the photocathode that minimized its effect on emission of C-SnafL2. The data from a PCSC can be presented as emission spectra or as intensity decays (Figure 4.41). By seeing the position and intensity of the scattered light it is possible to judge the contributions of the scatter at longer wavelengths. Hence, considerable information about a sample can be obtained in a single measurement.

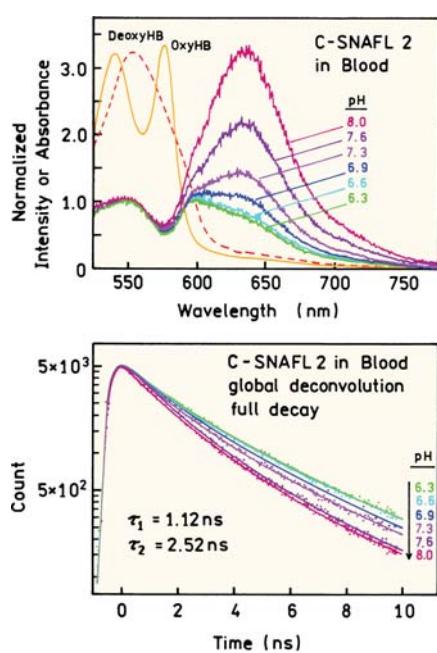


**Figure 4.41.** Emission spectra and intensity decays of C-Snafl 2 in blood measured with a photon counting streak camera. From [163].

#### 4.8.3. Upconversion Methods

The ultimate time resolution is provided by methods that bypass the limited time-resolution of the detectors, and rely on the ps and fs pulse widths available with modern

lasers.<sup>164–166</sup> The basic idea is to pass the fluorescence signal through an upconversion crystal, and to gate the crystal with another ps or fs light pulse (Figure 4.42). One observes the shorter wavelength harmonic generated by the combined effects of the laser pulse and the emission. In this schematic the sample is excited with the second harmonic of a Ti:sapphire laser. The emission is focused on the upconversion crystal. The fundamental output of the Ti:sapphire is focused on the crystal in the same region where the fluorescence is focused. An upconversion signal is generated that is proportional to the emission at the moment the gating pulse arrives. The time resolution is determined by the width of the laser pulse. The time-resolved decay is obtained by measuring the intensity of the upconverted signal as the optical delay time is varied. The signals are typically weak, so that an optical chopper and lock-in detectors sometimes are needed to measure the upconverted signal in the presence of considerable background.

Upconversion provides impressive time resolution; however, the instrumentation is rather complex. For instance, even a seemingly minor change of the emission wavelength can require a major readjustment of the apparatus since the orientation of the upconversion crystal has to be adjusted according to the wavelength. Decay times of more than 1–2 ns are difficult to measure because of the use of a delay line ( $\approx 1$  ns/foot). Alignment of the delay line can be quite difficult to maintain as the time delay is altered.

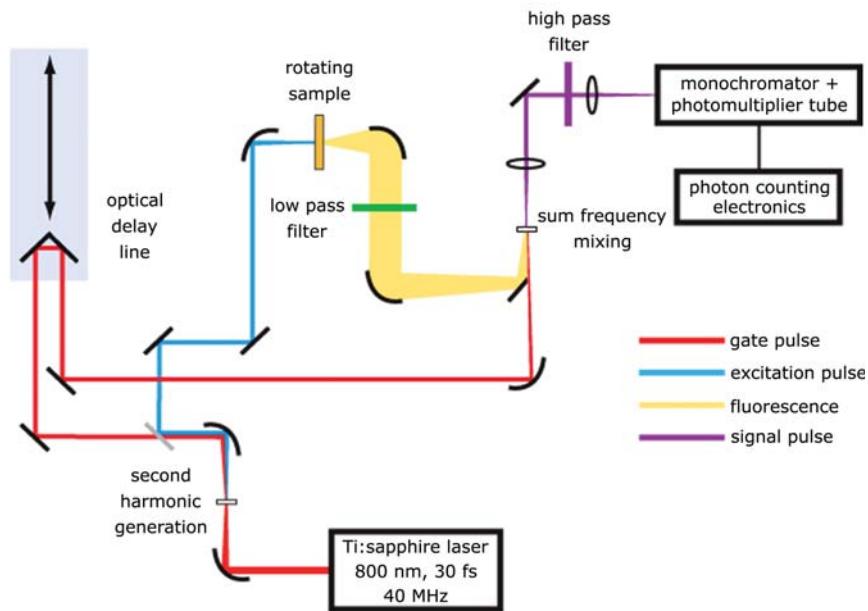


**Figure 4.42.** Schematic for fluorescence upconversion measurements. Courtesy of Professor Eric Vauthery, University of Geneva, Switzerland.

The high time resolution of upconversion measurements can be illustrated by quenching and exciplex formation of 3-cyanoperylene (PeCN) in neat diethylaniline (DEA).<sup>167–168</sup> The cyano group makes perylene a good electron acceptor, and DEA is a good electron donor. PeCN in the excited state undergoes photoinduced electron transfer (PET) with DEA (Chapter 9). This reaction is very rapid because in DEA the PeCN molecules are surrounded by potential electron donors. Emission spectra of PeCN show that it is highly quenched in DEA as compared to a non-electron-donating solvent (Figure 4.43). The lower panel shows the wavelength-dependent decays of PeCN. The time resolution is limited by the pulse width of the pump lasers, which is near 100 fs. The decay time is about 1 ps for the PeCN emission near 500 nm and about 20 ps for the exciplex emission.

#### 4.8.4. Microsecond Luminescence Decays

For decay times that become longer than about 20 ns, the complexity of TCSPC is no longer necessary. In fact, TCSPC is slow and inefficient for long decay times because of the need to use a low pulse repetitive rate and to wait a long time to detect each photon. In the past such decays

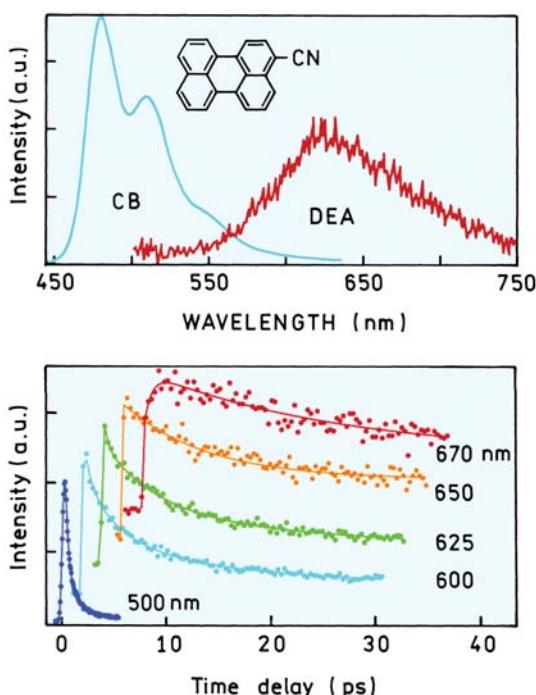


**Figure 4.43.** Emission spectra and time-resolved decays of 3-cyanoperylene in chlorobenzene (CB) and diethylaniline (DEA). Revised from [168].

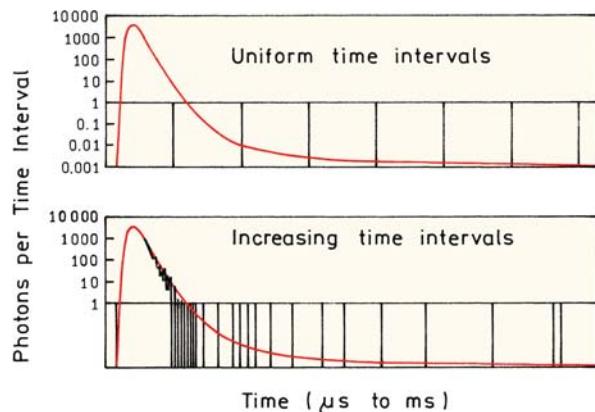


**Figure 4.44.** Time-resolved intensities measured with a photon counting multiscalar. Revised from [169].

would be measured using a sampling oscilloscope. At present the preferred method is to use a multiscalar card. These devices function as photon-counting detectors that sum the number of photons occurring within a time interval. Figure 4.44 shows the operating principle. Following the excitation pulse, photons arriving within a defined time interval are counted. The arrival times within the interval are not recorded. The time intervals can be uniform, but this becomes inefficient at long times because many of the intervals will contain no counts. A more efficient approach is to use intervals that increase with time. The count rates for multiscares can be high: up to about 1 GHz. At present the minimum width of a time interval is about 1 ns, with 5 ns being more typical. Hence, the multiscares are not yet practical for measuring ns decays.

An example of a decay measured with a multiscalar is shown in Figure 4.45. The fluorophore was  $[\text{Ru}(\text{bpy})_3]^{2+}$ , which has a lifetime of several hundred nanoseconds. A large number of counts were obtained even with the long lifetimes. However, the count rate is not as high as one may expect: about 1 photon per 2 laser pulses. The data acquisition time would be much longer using traditional TCSPC with a 1% count rate (Problem 4.6).

#### 4.9. DATA ANALYSIS: NONLINEAR LEAST SQUARES

Time-resolved fluorescence data are moderately complex, and in general cannot be analyzed using graphical methods. Since the mid-1970s many methods have been proposed for analysis of TCSPC data. These include nonlinear least squares (NLLS),<sup>3,16,170</sup> the method-of-moments,<sup>171–173</sup> Laplace transformation,<sup>174–177</sup> the maximum entropy

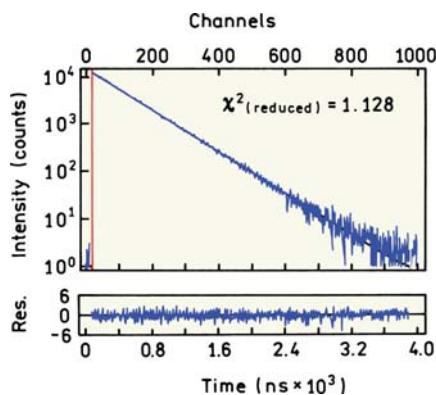


**Figure 4.45.** Intensity decay of  $[\text{Ru}(\text{bpy})_3]^{2+}$  measured with a photon counting multiscalar. Excitation was accomplished using a 440 nm laser diode with a repetition rate of 200 kHz. The lifetime was 373 ns. Revised from [169].

method,<sup>178–179</sup> Prony's method,<sup>180</sup> sine transforms,<sup>181</sup> and phase-plane methods.<sup>182–183</sup> These various techniques have been compared.<sup>184</sup> The method-of-moments (MEM) and the Laplace methods are not widely used at the current time. The maximum entropy method is newer, and is being used in a number of laboratories. The MEM is typically used to recover lifetime distributions since these can be recovered without assumptions about the shape of the distributions.

During the 1990s most studies using TCSPC made extensive use of NLLS and to a somewhat lesser extent the MEM. This emphasis was due to the biochemical and biophysical applications of TCSPC and the need to resolve complex decays. At present TCSPC is being used in analytical chemistry, cellular imaging, single molecule detection, and fluorescence correlation spectroscopy. In these applications the lifetimes are used to distinguish different fluorophores on different environments, and the number of observed photons is small. A rapid estimation of a mean lifetime is needed with the least possible observed photons. In these cases maximum likelihood methods are used (eq. 4.20). In the following sections we describe NLLS and the resolution of multi-exponential decay.

#### 4.9.1. Assumptions of Nonlinear Least Squares

Prior to describing NLLS analysis, it is important to understand its principles and underlying assumptions. It is often stated that the goal of NLLS is to fit the data, which is only partially true. With a large enough number of variable parameters, any set of data can be fit using many different mathematical models. The goal of least squares is to test whether a given mathematical model is consistent with the

data, and to determine the parameter values for that model which have the highest probability of being correct. Least squares provides the best estimate for parameter values if the data satisfy a reasonable set of assumptions, which are as follows:<sup>185–186</sup>

1. All the experimental uncertainty is in the dependent variable (y-axis).
2. The uncertainties in the dependent variable (measured values) have a Gaussian distribution, centered on the correct value.
3. There are no systematic errors in either the dependent (y-axis) or independent (x-axis) variables.
4. The assumed fitting function is the correct mathematical description of the system. Incorrect models yield incorrect parameters.
5. The datapoints are each independent observations.
6. There is a sufficient number of datapoints so that the parameters are overdetermined.

These assumptions are generally true for TCSPC, and least squares is an appropriate method of analysis. In many other instances the data are in a form that does not satisfy these assumptions, in which case least squares may not be the preferred method of analysis. This can occur when the variables are transformed to yield linear plots, the errors are no longer a Gaussian and/or there are also errors in the x-axis. NLLS may not be the best method of analysis when there is a small number of photon counts, such as TCSPC measurements on single molecules (Section 4.7.1). The data for TCSPC usually satisfy the assumptions of least-squares analysis.

#### 4.9.2. Overview of Least-Squares Analysis

A least-squares analysis starts with a model that is assumed to describe the data. The goal is to test whether the model is consistent with the data and to obtain the parameter values for the model that provide the best match between the measured data,  $N(t_k)$ , and the calculated decay,  $N_c(t_k)$ , using assumed parameter values. This is accomplished by minimizing the goodness-of-fit parameter, which is given by

$$\begin{aligned}\chi^2 &= \sum_{k=1}^n \frac{1}{\sigma_k^2} [N(t_k) - N_c(t_k)]^2 \\ &= \sum_{k=1}^n \frac{[N(t_k) - N_c(t_k)]^2}{N(t_k)}\end{aligned}\quad (4.21)$$

In this expression the sum extends over the number ( $n$ ) of channels or datapoints used for a particular analysis and  $\sigma_k$  in the standard deviation of each datapoint.

In TCSPC it is straightforward to assign the standard deviations ( $\sigma_k$ ). From Poisson statistics the standard deviation is known to be the square root of the number of photon counts:  $\sigma_k = \sqrt{N(t_k)}$ . Hence, for a channel with 10,000 counts,  $\sigma_k = 100$ , and for  $10^6$  counts,  $\sigma_k = 1000$ . This relationship between the standard deviation and the number of photons is only true if there are no systematic errors and counting statistics are the only source of uncertainty in the data. If the data contains only Poisson noise then the relative uncertainty in the data decreases as the number of photons increases. The value of  $\chi^2$  is the sum of the squares deviations between the measured  $N(t_k)$  and expected values  $N_c(t_k)$ , each divided by squared deviations expected for the number of detected photons.

It is informative to compare the numerator and denominator in eq. 4.21 for a single datapoint. Assume a channel contains  $10^4$  counts. Then the expected deviation for this measurement is 100 counts. If the assumed model accounts for the data, then the numerator and denominator of eq. 4.21 are both  $(10^2)^2$ , and this datapoint contributes 1.0 to the value of  $\chi^2$ . In TCSPC, and also for frequency-domain measurements, the number of datapoints is typically much larger than the number of parameters. For random errors and the correct model,  $\chi^2$  is expected to be approximately equal to the number of datapoints (channels).

Suppose the data are analyzed in terms of the multi-exponential model (eq. 4.8). During NLLS analysis the values of  $\alpha_i$  and  $\tau_i$  are varied until  $\chi^2$  is a minimum, which occurs when  $N(t_k)$  and  $N_c(t_k)$  are most closely matched. Several mathematical methods are available for selecting how  $\alpha_i$  and  $\tau_i$  are changed after each iteration during NLLS fitting. Some procedures work more efficiently than others, but all seem to perform adequately.<sup>185–186</sup> These methods include the Gauss-Newton, modified Gauss-Newton, and Nelder-Mead algorithms. This procedure of fitting the data according to eq. 4.21 is frequently referred to as deconvolution, which is inaccurate. During analysis an assumed decay law  $I(t)$  is convoluted with  $L(t_k)$ , and the results are compared with  $N(t_k)$ . This procedure is more correctly called iterative reconvolution.

It is not convenient to interpret the values of  $\chi^2$  because  $\chi^2$  depends on the number of datapoints.<sup>1</sup> The value of  $\chi^2$  will be larger for data sets with more datapoints. For this reason one uses the value of reduced  $\chi^2$ :

$$\chi_R^2 = \frac{\chi^2}{n - p} = \frac{\chi^2}{v} \quad (4.22)$$

where  $n$  is the number of datapoints,  $p$  is the number of floating parameters, and  $v = n - p$  is the number of degrees of freedom. For TCSPC the number of datapoints is typically much larger than the number of parameters so that  $(n - p)$  is approximately equal to  $n$ . If only random errors contribute to  $\chi_R^2$ , then this value is expected to be near unity. This is because the average  $\chi^2$  per datapoint should be about one, and typically the number of datapoints ( $n$ ) is much larger than the number of parameters. If the model does not fit, the individual values of  $\chi^2$  and  $\chi_R^2$  are both larger than expected for random errors.

The value of  $\chi_R^2$  can be used to judge the goodness-of-fit. When the experimental uncertainties  $\sigma_k$  are known, then the value of  $\chi_R^2$  is expected to be close to unity. This is because each datapoint is expected to contribute  $\sigma_k^{-2}$  to  $\chi^2$ , the value of which is in turn normalized by the  $\sum \sigma_k^{-2}$ , so the ratio is expected to be near unity. If the model does not fit the data, then  $\chi_R^2$  will be significantly larger than unity. Even though the values of  $\chi_R^2$  are used to judge the fit, the first step should be a visual comparison of the data and the fitted function, and a visual examination of the residuals. The residuals are the differences between the measured data and the fitted function. If the data and fitted function are grossly mismatched there may be a flaw in the program, the program may be trapped in a local minimum far from the correct parameter values, or the model may be incorrect. When the data and fitted functions are closely but not perfectly matched, it is tempting to accept a more complex model when a simpler one is adequate. A small amount of systematic error in the data can give the appearance that the more complex model is needed. In this laboratory we rely heavily on visual comparisons. If we cannot visually see a fit is improved, then we are hesitant to accept the more complex model.

#### 4.9.3. Meaning of the Goodness-of-Fit

During analysis of the TCSPC data there are frequently two or more fits to the data, each with a value of  $\chi_R^2$ . The value of  $\chi_R^2$  will usually decrease for the model with more adjustable parameters. What elevation of  $\chi_R^2$  is adequate to reject a model? What decrease in  $\chi_R^2$  is adequate to justify accepting the model with more parameters? These questions can be answered in two ways, based on experience and based on mathematics. In mathematical terms one can

**Table 4.2.**  $\chi_R^2$  Distribution<sup>a</sup>

Probability ( $P$ )/ degrees of freedom	0.2	0.1	0.05	0.02	0.01	0.001
10	1.344	1.599	1.831	2.116	2.321	2.959
20	1.252	1.421	1.571	1.751	1.878	2.266
50	1.163	1.263	1.350	1.452	1.523	1.733
100	1.117	1.185	1.243	1.311	1.358	1.494
200	1.083 <sup>b</sup>	1.131	1.170	1.216	1.247	1.338

<sup>a</sup>From [1, Table C-4].<sup>b</sup>Mentioned in text.

predict the probability for obtaining a value of  $\chi_R^2$  because of random errors. These values can be found in standard mathematical tables of the  $\chi_R^2$  distribution. Selected values are shown in Table 4.2 for various probabilities and numbers of degrees of freedom. Suppose you have over 200 datapoints and the value of  $\chi_R^2 = 1.25$ . There is only a 1% chance ( $P = 0.01$ ) that random errors could result in this value. Then the model yielding  $\chi_R^2 = 1.25$  can be rejected, assuming the data are free of systematic errors. If the value of  $\chi_R^2$  is 1.08, then there is a 20% chance that this value is due to random deviations in the data. While this may seem like a small probability, it is not advisable to reject a model if the probability exceeds 5%, which corresponds to  $\chi_R^2 = 1.17$  (Table 4.2). In our experience, systematic errors in the data can easily result in a 10–20% elevation in  $\chi_R^2$ . For example, suppose the data does contain systematic errors and a two-component fit returns a value of  $\chi_R^2 = 1.17$ . The data are then fit to three components, which results in a decreased  $\chi_R^2$ . If the three-component model is accepted as the correct model, then an incorrect conclusion is reached. The systematic errors in the data will have resulted in addition of a third component that does not exist in the experimental system.

While we stated that assumptions 1 through 6 (above) are generally true for TCSPC, we are not convinced that number 5 is true. Based on our experience we have the impression that the TCSPC data have fewer independent observations (degrees of freedom) in the TCSPC data than the number of actual observations (channels). This is not a criticism of NLLS analysis or TCSPC. However, if the effective number of independent datapoints is less than the number of datapoints, then small changes in  $\chi_R^2$  may not be as significant as understood from the mathematical tables.

Complete reliance on mathematical tables can lead to overinterpretation of the data. The absolute value of  $\chi_R^2$  is often of less significance than its relative values. Systematic errors in the data can easily result in  $\chi_R^2$  values in excess

of 1.5. This small elevation in  $\chi_R^2$  does not mean the model is incorrect. We find that for systematic errors the  $\chi_R^2$  value is not significantly decreased using the next more complex model. Hence, if the value of  $\chi_R^2$  does not decrease significantly when the data are analyzed with a more complex model, the value of  $\chi_R^2$  probably reflects the poor quality of the data. In general we consider decreases in  $\chi_R^2$  significant if the ratio decreases by twofold or more. Smaller changes in  $\chi_R^2$  are interpreted with caution, typically based on some prior understanding of the system.

#### 4.9.4. Autocorrelation Function Advanced Topic

Another diagnostic for the goodness of fit is the autocorrelation function.<sup>3</sup> For a correct model, and the absence of systematic errors, the deviations are expected to be randomly distributed around zero. The randomness of the deviations can be judged from the autocorrelation function. Calculation of the correlation function is moderately complex, and does not need to be understood in detail to interpret these plots. The autocorrelation function  $C(t_j)$  is the extent of correlation between deviations in the  $k$  and  $k+j$ th channel. The values of  $C(t_j)$  are calculated using

$$C(t_j) = \left( \frac{1}{m} \sum_{k=1}^m D_k D_{k+j} \right) / \left( \frac{1}{n} \sum_{k=1}^n D_k^2 \right) \quad (4.23)$$

where  $D_k$  is the deviation in the  $k$ th datapoint and  $D_{k+j}$  is the deviation in the  $k+j$ th datapoint (eq. 4.23). This function measures whether a deviation at one datapoint (time channel) predicts that the deviation in the  $j$ th higher channel will have the same or opposite sign. For example, the probability is higher that channels 50 and 51 have the same sign than channels 50 and 251. The calculation is usually extended to test for correlations across half of the data channels ( $m = n/2$ ) because the order of multiplication in

the numerator does not matter. The autocorrelation plots have half as many datapoints as the original data set.

One example of an autocorrelation plot was seen in Figure 4.27, where data for NATA were presented for measurements versus scattered light and versus a lifetime reference. This instrument showed a minor color effect, which resulted in some systematic deviations between  $N_c(t_k)$  and  $N(t_k)$ . The systematic differences are barely visible in the direct plot of the deviations (middle left). The autocorrelation plot (upper left) allowed the deviations to be visualized as positive and negative correlations in adjacent or distant channels, respectively. For closely spaced channels the deviations are likely to both be the same sign. For more distant channels the deviations are likely to be of opposite signs. These systematic errors were eliminated by the use of a lifetime reference, as seen by the flat autocorrelation plot (upper right panel).

#### 4.10. ANALYSIS OF MULTI-EXPONENTIAL DECAYS

##### 4.10.1. p-Terphenyl and Indole: Two Widely Spaced Lifetimes

An understanding of time-domain data analysis is facilitated by examination of representative data. As an example we chose a mixture of p-terphenyl and indole, which individually display single exponential decays of 0.93 and 3.58 ns, respectively. For the time-domain measurements a mixture of p-terphenyl and indole was observed at 330 nm, where both species emit (Figure 4.46). TCSPC data for this mix-

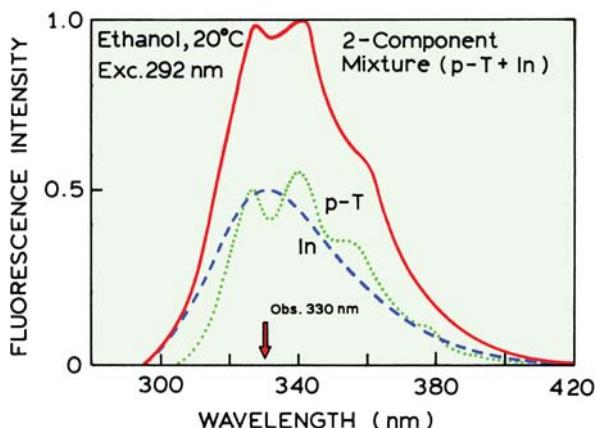


**Figure 4.46.** Emission spectra of p-terphenyl (p-T), indole (In) and of the mixture. Excitation was at 292 nm, from a frequency-doubled R6G dye laser. The emission at 330 nm was isolated with a monochromator. From [187].

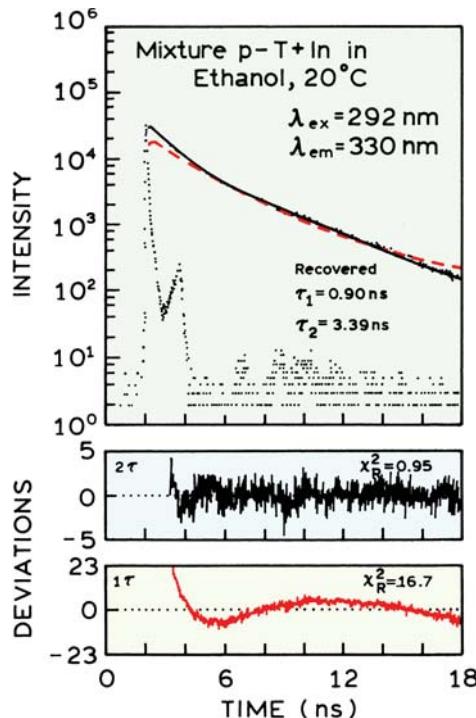


**Figure 4.47.** Time-domain intensity decay of a two-component mixture of indole and p-terphenyl. The dashed line shows the one-decay-time fit, and the solid line the two-decay-time fit. From [187].

ture are shown in Figure 4.47. The presence of two decay times is evident from curvature in the plot of  $\log N(t)$  versus time. The time-dependent data could not be fit to a single decay time, as seen by the mismatch of the calculated convolution integral (dashed) with the data (dots).

The lower panels show the deviations ( $D_k$ ) or differences between the measured and calculated data:

$$D_k = \frac{I(t_k) - I_c(t_k)}{\sqrt{I(t_k)}} \quad (4.24)$$

The weighted residual (W.Res.) or deviations plots are used because it is easier to see the differences between  $I(t_k)$  and  $I_c(t_k)$  in these plots than in a plot of  $\log I(t_k)$  versus  $t_k$ . Also, the residuals are weighted according to the standard deviation of each datapoint. For a good fit these values are expected to randomly distribute around zero, with a mean value near unity.

##### 4.10.2. Comparison of $\chi^2_R$ Values: F Statistic

How can one compare the values of  $\chi^2_R$  for two fits? This can be done using the *F* statistic, which is a ratio of  $\chi^2_R$  val-

**Table 4.3.** *F* Statistic for Comparison of  $\chi_R^2$  Values<sup>a</sup>

Degrees of freedom (v)	Probability ( <i>P</i> )					
	0.32	0.25	0.10	0.05	0.025	0.01
10	1.36	1.55	2.32	2.98	3.96	4.85
15	1.28	1.43	1.97	2.40	2.86	3.52
20	1.24	1.36	1.79	2.12	2.46	2.94
40	1.16	1.24	1.51	1.69	1.88	2.11
60	1.13	1.19	1.40	1.53	1.67	1.84
120	1.09	1.13	1.26	1.35	1.43	1.53
$\infty$	1.00	1.00	1.00	1.00	1.00	1.00

<sup>a</sup>From [188, Table A-4]. In general, the *F* values are computed for different degrees of freedom for each  $\chi_R^2$  value. For TCSPC data and for FD data, the degrees of freedom are usually similar in the numerator and in the denominator. Hence, *F* values are listed for only one value of *v*. Additional *F* values can be found in [1, Tables C-6 and C-7].

ues. This ratio depends on the number of degrees of freedom (*v*) for each fit, and this number will depend on the model. The values of the  $\chi_R^2$  ratios that are statistically significant at various levels of probability are available in statistical tables, of which a few values are listed in Table 4.3. In practice, there are usually many more datapoints than parameters, so that *v* is almost the same for both fits. For this reason we did not consider the slightly different number of degrees of freedom in the numerator and denominator.

For the mixture of p-terphenyl and indole the residuals of the single-decay-time fit oscillate across the time axis, which is characteristic of an incorrect model. The value of  $\chi_R^2 = 16.7$  is obviously much greater than unity, and according to Table 4.2 there is a less than 0.1% chance that random error could result in such an elevated value of  $\chi_R^2$ . Additionally, the  $\chi_R^2$  ratio of 17.6 is much larger than the values of the *F* statistic in Table 4.3. Hence, the single-decay-time model is easily rejected for this sample. There is a potential problem with the use of an *F* statistic to compare two  $\chi_R^2$  values originating from different mathematical models and the same data set.<sup>189</sup> The use of the *F* statistic requires that the residuals for each analysis be independent from each other. It is not clear if this assumption is correct when analyzing the same set of data with different mathematical models.

#### 4.10.3. Parameter Uncertainty: Confidence Intervals

The NLLS analysis using the multi-exponential model returns a set of  $\alpha_i$  and  $\tau_i$  values. It is important to recognize that there can be considerable uncertainty in these values, particularly for closely spaced decay times. Estimation of

the uncertainties in the recovered parameters is an important but often-ignored problem. With nonlinear least-squares analysis there are no general methods for estimating the range of parameter values that are consistent with the data. Uncertainties are reported by almost all the data analysis programs, but these estimates are invariably smaller than the actual uncertainties. Most software for nonlinear least-square analysis reports uncertainties that are based on the assumption of no correlation between parameters. These are called the asymptotic standard errors (ASEs).<sup>185</sup> As shown below for a mixture having more closely spaced lifetimes (Section 4.10.5), the errors in the recovered parameters often exceed the ASEs. The ASEs usually underestimate the actual uncertainties in the parameter values.

In our opinion the best way to determine the range of parameters consistent with the data is to examine the  $\chi_R^2$  surfaces, which is also called a support plane analysis.<sup>186</sup> The procedure is to change one parameter value from its value where  $\chi_R^2$  is a minimum, and then rerun the least-squares fit, keeping this parameter value constant at the selected value. By rerunning the fit, the other parameters can adjust to again minimize  $\chi_R^2$ . If  $\chi_R^2$  can be reduced to an acceptable value, then the offset parameter value is said to be consistent with the data. The parameter value is changed again by a larger amount until the  $\chi_R^2$  value exceeds an acceptable value, as judged by the  $F_\chi$  statistic (eq. 4.25) appropriate for *p* and *v* degrees of freedom.<sup>190</sup> This procedure is then repeated for the other parameter values.

The range of parameter values consistent with the data can be obtained using  $P = 0.32$ , where *P* is the probability that the value of  $F_\chi$  is due to random errors in the data. When the value of *P* exceeds 0.32 there is less than a 32%

chance that the parameter value is consistent with the data. When the value of  $P$  is less than 0.32 there is a 68% chance that the parameter value is consistent with the data, which is the usual definition of a standard deviation.

To determine the confidence interval, the value of  $\chi_R^2$  with a fixed parameter value,  $\chi_R^2(\text{par})$ , is compared with the minimum value of  $\chi_R^2$  with all parameter variables,  $\chi_R^2(\text{min})$ .<sup>190-191</sup> The range of parameter values is expanded until  $\chi_R^2(\text{par})$  exceeds the  $F_\chi$  value for the number of parameters ( $p$ ) and the degrees of freedom ( $v$ ) and the chosen probability, typically  $P = 0.32$ :

$$F_\chi = \frac{\chi_R^2(\text{par})}{\chi_R^2(\text{min})} = 1 + \frac{p}{v} F(p, v, P) \quad (4.25)$$

In this expression<sup>192</sup>  $F(p, v, P)$  is the  $F$  statistic with  $p$  parameters and  $v$  degrees of freedom with a probability of  $P$ . The  $F$  statistics needed to calculate  $F_\chi$  are listed in Table 4.4. It is important to realize that, in general, the uncertainty range will not be symmetrical around the best fit value of the parameter. For a two-decay-time model ( $p = 4$ ) and 400 degrees of freedom ( $v = 400$ ), the  $F_\chi$  value is 1.012 for  $p = 0.32$ . Calculation of the  $\chi_R^2$  surfaces is a time-consuming process, and has not yet been automated within most data-analysis software. However, these calculations provide a realistic judgment of what one actually knows from the data.

There appears to be no general agreement that the procedure described above represents the correct method to estimate confidence intervals. This is a topic that requires further research. There is some disagreement in the statistics literature about the proper form of  $F_\chi$  for estimating the parameter uncertainty.<sup>189</sup> Some reports<sup>193</sup> argue that, since one parameter is being varied, the number of degrees of freedom in the numerator should be one. In this case  $F_\chi$  is calculated using

$$F_\chi = \frac{\chi^2(\text{par})}{\chi^2(\text{min})} = 1 + \frac{1}{v} F(p, v, P) \quad (4.26)$$

Since we are varying  $p$  parameters to calculate the  $\chi_R^2$  surface, we chose to use eq. 4.25. Irrespective of whether the  $F_\chi$  values accurately define the confidence interval, examination of the  $\chi_R^2$  surfaces provides valuable insight into the resolution of parameters provided by a given experiment. If the  $\chi_R^2$  surfaces do not show well-defined minima, then the data are not adequate to determine the parameters.

A confidence interval analysis is shown in Figure 4.48 for the mixture of p-terphenyl and indole. The confidence intervals are given by the intercept of the  $\chi_R^2$  surfaces (solid) with the appropriate  $F_\chi$  values (dashed). For comparison we have also shown the ASEs as solid bars. The ASEs are about twofold smaller than the confidence intervals. This is a serious underestimation, but a factor of two is small compared to what is found for more closely spaced lifetimes. Also, in our opinion, the  $F_\chi$  value near 1.005 for about 950 degrees of freedom is an underestimation because the time-resolved decay may not have completely independent datapoints. Suppose the actual number of independent datapoints was 200. In this case the  $F_\chi$  value would be near 1.02, which may provide a more realistic range of the uncertainties. For instance, the confidence interval of  $\alpha_2$  would become  $0.305 \pm 0.015$  instead of  $0.305 \pm 0.005$ . The uncertainty in the latter value appears to be unrealistically small.

Another way to estimate parameter uncertainty is by Monte Carlo simulations.<sup>194</sup> The basic idea is to simulate data based on the recovered decay law using the known level of random noise present in a given experiment. Newly generated random noise is added to each simulated data set, which is then analyzed as if it were actual data. New random noise is added and the process repeated. This results in a histogram of parameter values. These parameter values are examined for the range that results from the randomly added noise. It is important that the simulations use a model that correctly describes the system. The Monte Carlo method is time consuming and thus seldom used. However, with the rapid advances in computer speed, one can expect Monte Carlo simulations to become more widely utilized for estimation of confidence intervals.

#### 4.10.4. Effect of the Number of Photon Counts

For a single-exponential decay, the decay time can usually be determined with adequate accuracy even for a small number of observed photons. However, for multi-exponential decays it is important to measure as many photons as possible to obtain the highest resolution of the parameter values. This is illustrated in Figure 4.49 for the same two-component mixture of p-terphenyl and indole. For these data the number of counts in the peak channel was tenfold less than in Figure 4.47, 3,000 counts versus 30,000 counts. The correct values for the two decay times were still recovered. However, the relative decrease in  $\chi_R^2$  for the two decay time models was only 1.9-fold, as compared to 17-

**Table 4.4.** *F* Statistic for Calculation of Confidence Intervals<sup>a</sup>

Degrees of freedom ( <i>v</i> )	Probability ( <i>P</i> )						
	0.32 <sup>d</sup>	0.25	One parameter ( <i>p</i> ) <sup>b</sup>	0.10	0.05	0.025	0.01
10	1.09	1.49	3.29	4.96	6.94	10.0	
30	1.02	1.38	2.88	4.17	5.57	7.56	
60	1.01	1.35	2.79	4.00	5.29	7.08	
120	1.00	1.34	2.75	3.92	5.15	6.85	
$\infty$	1.00	1.32	2.71 <sup>c</sup>	3.84	5.02	6.63	
Two Parameters <sup>b</sup>							
10	1.28	1.60	2.92	4.10	5.46	7.56	
30	1.18	1.45	2.49	3.32	4.18	5.39	
60	1.16	1.42	2.39	3.15	3.93	4.98	
120	1.15	1.40	2.35	3.07	3.80	4.79	
$\infty$	1.14	1.39	2.30	3.00	3.69	4.61	
Three Parameters							
10	1.33	1.60	2.73	3.71	4.83	6.55	
30	1.22	1.44	2.28	2.92	3.59	4.51	
60	1.19	1.41	2.18	2.76	3.34	4.13	
120	1.18	1.39	2.13	2.68	3.23	3.95	
$\infty$	1.17	1.37	2.08	2.60	3.12	3.78	
Four Parameters							
10	1.34	1.59	2.61	3.48	4.47	5.99	
30	1.23	1.42	2.14	2.64	3.25	4.02	
60	1.20	1.38	2.04	2.53	3.01	3.65	
120	1.19	1.37	1.99	2.45	2.89	3.48	
$\infty$	1.18	1.35	1.94	2.37	2.79	3.32	
Five Parameters							
10	1.35	1.59	2.52	3.33	4.24	5.64	
30	1.23	1.41	2.05	2.53	3.03	3.70	
60	1.20	1.37	1.95	2.37	2.79	3.34	
120	1.19	1.35	1.90	2.29	2.67	3.17	
$\infty$	1.17	1.33	1.85	2.21	2.57	3.02	
Eight Parameters							
10	1.36	1.56	2.34	3.07	3.85	5.06	
30	1.22	1.37	1.88	2.27	2.65	3.17	
60	1.19	1.32	1.77	2.10	2.41	2.82	
120	1.17	1.30	1.72	2.02	2.30	2.66	
$\infty$	1.16	1.28	1.67	1.94	2.19	2.51	
Ten Parameters							
10	1.35	1.55	2.32	2.98	3.72	4.85	
30	1.22	1.35	1.82	2.16	2.51	2.98	
60	1.18	1.30	1.71	1.99	2.27	2.63	
120	1.17	1.28	1.65	1.91	2.16	2.47	
$\infty$	1.15	1.25	1.59	1.83	2.05	2.32	

<sup>a</sup>From [188]. In the ratio of  $\chi^2_R$  values, the degrees of freedom refer to that for the denominator. The degrees of freedom in the numerator are one, two, or three, for one, two or three additional parameters.

<sup>b</sup>These values refer to the degrees of freedom in the numerator (*p*).

<sup>c</sup>This value appears to be incorrect in [188], and was taken from [1].

<sup>d</sup>The values for 0.32 were calculated with a program (F-stat) provided by Dr. M. L. Johnson, University of Virginia.

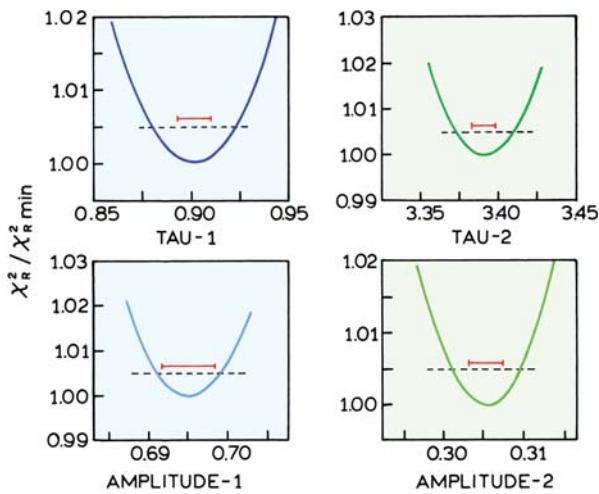


**Figure 4.48.** Confidence interval for the two component mixture of indole and p-terphenyl. The solid bars show the asymptotic standard errors. From [187].

fold for the higher number of counts. Also, the  $\chi_r^2$  surfaces rise more slowly as the lifetimes are varied (Figure 4.49, right), so that the lifetimes are determined with less precision.

#### 4.10.5. Anthranilic Acid and 2-Aminopurine: Two Closely Spaced Lifetimes

The resolution of two decay times becomes more difficult if the decay times are more closely spaced. This is illustrated by a mixture of anthranilic acid (AA) and 2-amino purine

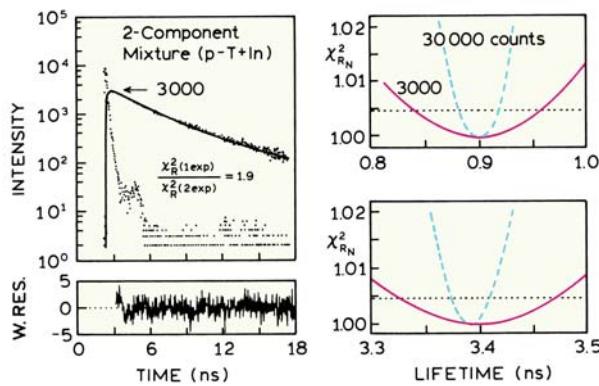


**Figure 4.49.** Effect of the number of photons counts on the resolution of the lifetimes for the mixture of p-terphenyl (p-T) and indole (In) in Figure 4.47. **Left:** Two-decay-time fit of the intensity decay measured with 3000 counts in the peak channel. The corresponding plot for the data obtained with 30,000 counts in the peak channel is shown in Figure 4.31. **Right:** Comparison of the  $\chi_r^2$  surfaces for the data obtained with 3000 (—) and 30,000 counts (---). From [187].

(2-AP), which individually display single exponential decays of 8.53 and 11.27 ns, respectively (shown in Figure 4.54 below). Emission spectra for the mixture are shown in Problem 4.5. The time-dependent data for the mixture of AA and 2-AP are shown in Figure 4.50. At 380 nm, where both fluorophores emit, it is difficult to visually detect the presence of two decay times. The single-decay-time model (dashes) shows only small differences from the data (dots). However, the residual plot shows systematic deviations (lower panel), which are easier to see on the linear scale used for the deviations than on the logarithmic plot. The 4.5-fold decrease in  $\chi_r^2$  for the two-decay-time model is adequate to reject the single-decay-time model.

While the data support acceptance of two decay times, these values of  $\alpha_i$  and  $\tau_i$  are not well determined. This is illustrated in Figure 4.51, which shows the  $\chi_r^2$  surfaces for the mixture of AA and 2-AP. This mixture was measured at five emission wavelengths. The data were analyzed individually at each wavelength. Each of the  $\chi_r^2$  surfaces shows distinct minima, which leads one to accept the recovered lifetimes. However, one should notice that different life-

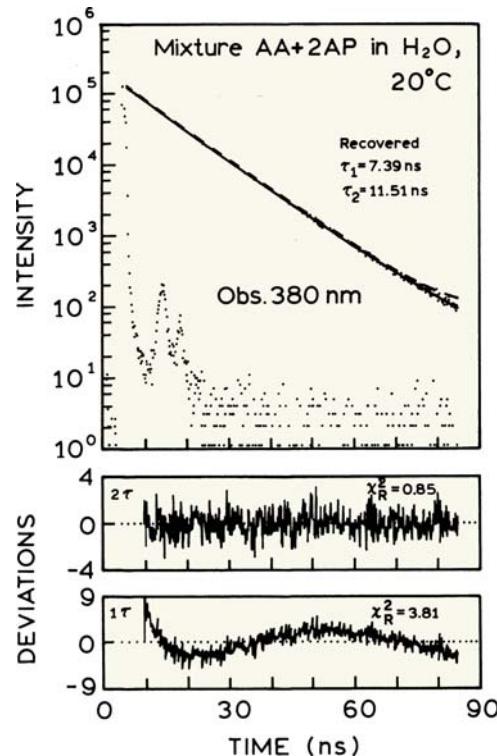


**Figure 4.50.** Time-dependent intensity decay of a two-component mixture of anthranilic acid (AA) and 2-amino-purine (2-AP). The dashed line shows the one-decay-time fit, and the solid line the two-decay-time fit to the data (dots). From [187].

**Table 4.5.** Resolution of a Two-Component Mixture of Anthranilic Acid and 2-Aminopurine, Observed at a Single Wavelength, Using Time-Domain Data

Observation wavelength (nm)	Lifetimes (ns)		Pre-exponential factors		Fractional intensities		$\chi_R^2$	
	$\tau_1$	$\tau_2$	$\alpha_1$	$\alpha_2$	$f_1$	$f_2$	2 <sup>a</sup>	1 <sup>a</sup>
360	6.72	11.58	0.223	0.777	0.143	0.857	1.01	2.77
380	7.51	11.51	0.404	0.596	0.306	0.694	0.85	3.81
400	7.22	11.08	0.448	0.552	0.347	0.653	0.91	4.51
420	7.99	11.22	0.595	0.405	0.511	0.489	0.93	2.95
440	8.38	11.91	0.763	0.237	0.692	0.308	0.89	2.72

<sup>a</sup>Refers to a two- or one-component fit.

times were recovered at each emission wavelength. This suggests that the actual uncertainties in the recovered lifetimes are larger than expected from the ASEs, and then seem to be even larger than calculated from the  $\chi_R^2$  surfaces. Furthermore, the differences in the lifetimes recovered at each emission wavelength seem to be larger than expected even from the  $\chi_R^2$  surfaces. This illustrates the difficulties in recovering accurate lifetimes if the values differ by less than twofold.

Another difficulty is that the recovered amplitudes do not follow the emission spectra expected for each component (Table 4.5 and Problem 4.5). As the lifetimes become closer together, the parameter values become more highly

correlated, and it is difficult to know the true uncertainties. This is not intended to be a criticism of the TD measurements, but rather is meant to illustrate the difficulties inherent in the analysis of multi-exponential decays.

#### 4.10.6. Global Analysis: Multi-Wavelength Measurements

One way to improve the resolution of closely spaced lifetimes is to perform measurements at additional wavelengths, and to do a global analysis (Section 4.12). The concept of global analysis is based on the assumption that decay times are independent of wavelength. The decay times are global parameters because they are the same in all data sets. The amplitudes are non-global because they are different in each data set. Global analysis of the multi-wavelength data results in much steeper  $\chi_R^2$  surfaces (Figure 4.52), and presumably a higher probability of recovery of the correct lifetimes. The lifetimes are determined with higher certainty from the global analysis because of the steeper  $\chi_R^2$  surfaces and the lower value of  $F_\chi$  with more degrees of freedom (more data). As shown in Problem 4.5, the amplitudes (Table 4.6) recovered from the global analysis more closely reflect the individual emission spectra than the amplitudes recovered from the single wavelength data.

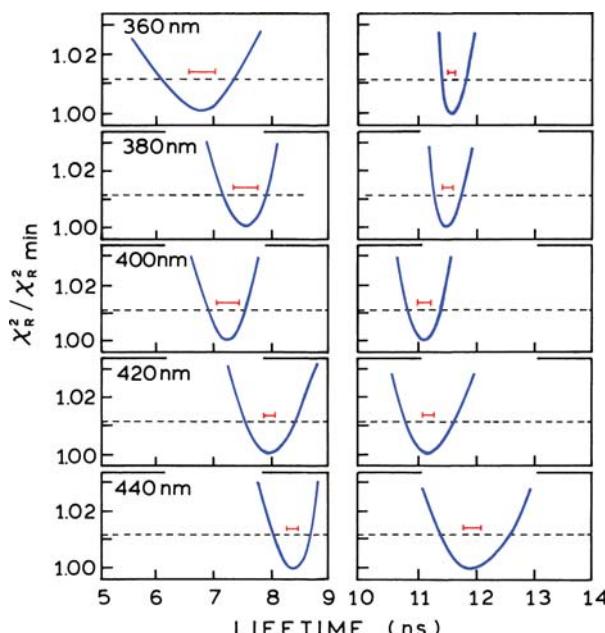


**Figure 4.51.** Lifetime  $\chi_R^2$  surfaces for the two-component mixture of AA and 2-AP (Figure 4.50). The horizontal bars show the asymptotic standard errors. From [187].

#### 4.10.7. Resolution of Three Closely Spaced Lifetimes

The resolution of multi-exponential decays becomes more difficult as the number of decay times increases. This difficulty is illustrated by a mixture of indole (In), anthranilic acid (AA), and 2-amino purine (2-AP) (Figure 4.53). At 380 nm all three fluorophores emit, and the decay is expected to be a sum of three exponentials.

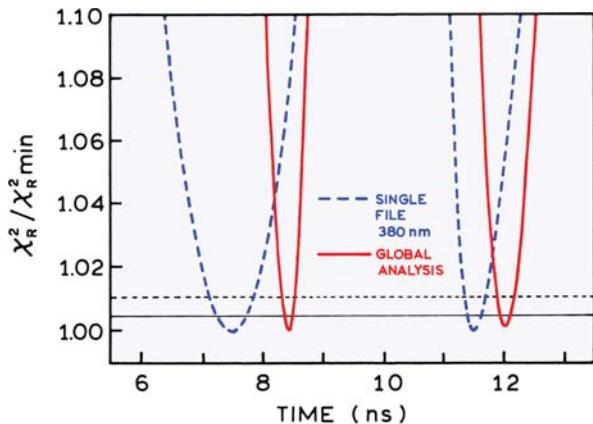


**Figure 4.52.** Lifetime  $\chi^2$  surface for the global analysis of the two component mixture of AA and 2-AP (—). Also shown for comparison is the  $\chi^2$  surface at 380 nm (dashed). The horizontal lines represent the  $F_\chi$  values. From [187].

TCSPC data for the three individual fluorophores are shown in Figure 4.54. Excitation was with the frequency-doubled output of an R6G dye laser, and the emission detected with an R2809 MCP PMT. The excitation was polarized vertically and the emission detected  $54.7^\circ$  from vertical to avoid the effects of rotational diffusion on the measured intensity decays. The points represent the data  $I(t_k)$  or number of counts measured at each time interval  $t_k$ . The solid lines are the fitted functions or calculated data  $I_c(t_k)$  using a single decay time.  $I(t_k)$  and  $I_c(t_k)$  are well matched, which indicates that each individual fluorophore decays as a single exponential with decay times of 4.41, 8.53, and 11.27 ns, respectively. As expected for a good fit,

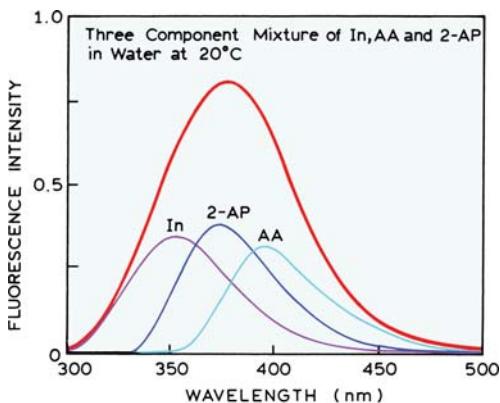


**Figure 4.53.** Emission spectra of Indole (In), 2-aminopurine (2-AP), and anthranilic acid (AA), and of the three-component mixture. From [187].

**Table 4.6.** Global Analysis of a Two-Component Mixture of Anthranilic Acid and 2-Aminopurine Measured at Five Emission Wavelengths: Time Domain Data

Observation wavelength (nm)	AA <sup>a</sup>		2-AP	
	$\alpha_1$	$f_1$	$\alpha_2$	$f_2$
360	0.117	0.089	0.883	0.911
380	0.431	0.357	0.569	0.643
400	0.604	0.528	0.396	0.472
420	0.708	0.640	0.292	0.360
440	0.810	0.758	0.190	0.242

<sup>a</sup>For the two-component fit  $\chi^2 = 0.92$ , and for the one-component fit  $\chi^2 = 22.3$ .

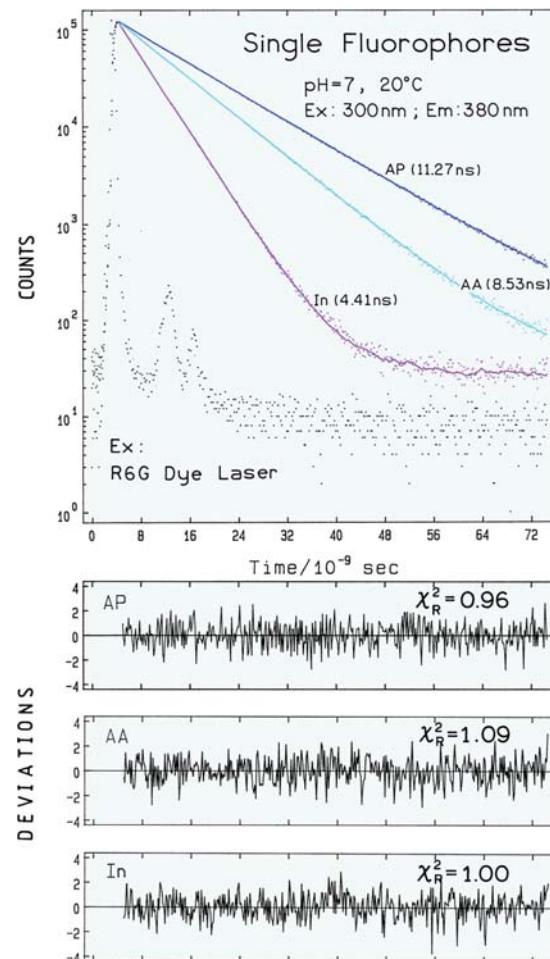


**Figure 4.54.** TCSPC data for indole (In), anthranilic acid (AA), and 2-aminopurine (AP). From [187].

the deviations are randomly distributed around zero and the values of  $\chi_R^2$  are near unity.

The intensity decay for indole in Figure 4.54 illustrates the need to consider the convolution integral when using an MCP PMT, even with a 4.41-ns decay time. At long times the plot of  $\log I(t_k)$  versus time becomes nonlinear even though there is only a single lifetime. This effect is most visible for indole, with the shortest lifetime of 4.41 ns. This long tail on the intensity decay is due to continued excitation from the tail of the impulse response function and possibly some background emission. If one did not consider convolution, and calculated the decay times only from the slopes, then one would reach the erroneous conclusion that the indole sample displayed a second long decay time.

Now consider similar data for a mixture of the three fluorophores. The decay times range threefold from 4 to 12 ns, but this is a difficult resolution. Examination of Figure 4.55 shows that the single exponential fit (dashes) appears to provide a reasonable fit to the data. However, the failure of this model is easily seen in the deviations, which are much larger than unity and not randomly distributed on the time axis (lowest panel). The failure of the single exponential model can also be seen from the value of  $\chi_R^2 = 26.45$ , which according to Table 4.2 allows the single exponential model to be rejected with high certainty. To be more specific, there is a less than a 0.1% chance ( $P < 0.001$ ) that this value of  $\chi_R^2$  could be the result of random error in the data.

The situation is less clear with a double exponential fit. In this case the fitted curve overlaps the data (not shown),  $\chi_R^2 = 1.22$ , and the deviations are nearly random. According to the  $\chi_R^2$  data (Table 4.2), there is only a 2% chance that  $\chi_R^2 = 1.22$  could result from statistical uncertainties in the data. In practice, such values of  $\chi_R^2$  are often encountered owing to systematic errors in the data. For comparison, the systematic errors in Figure 4.27 resulted in an elevation of  $\chi_R^2$  to a similar value. In an actual experiment we do not know beforehand if the decay is a double, triple, or non-exponential decay. One should always accept the simplest model that accounts for the data, so we would be tempted to accept the double exponential model because of the weak evidence for the third decay time.

An improved fit was obtained using the triple exponential model,  $\chi_R^2 = 0.93$ , and the deviations are slightly more random than the two-decay-time fit. It is important to understand that such a result indicates the data are consistent with three decay times, but does not prove the decay is a triple exponential. By least-squares analysis one cannot exclude other more complex models, and can only state that

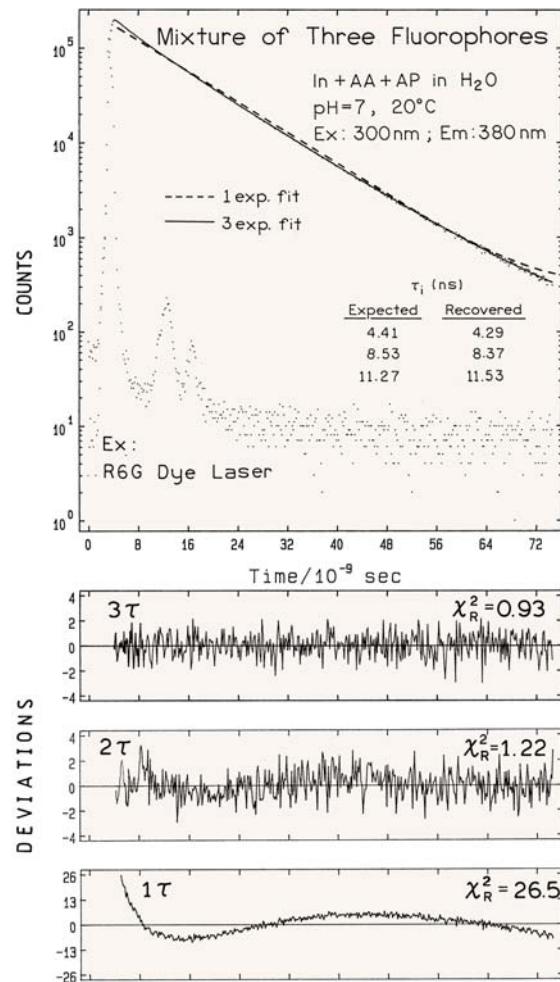


Figure 4.55. TCSPC data for a mixture of indole (In), anthranilic acid (AA), and 2-aminopurine (AP). From [187].

a particular model is adequate to explain the data. In this case, the data are consistent with the three-exponential model, but the analysis does not exclude the presence of a fourth decay time.

The two- and three-decay-time fits can also be compared using the ratio of  $\chi_R^2$  values. For this mixture the ratio of  $\chi_R^2$  values was 1.31. This value can be compared with the probability of this ratio occurring due to random deviations in the data, which is between 5 and 10% (Table 4.3). Hence, there is a relatively low probability of finding this reduction in  $\chi_R^2$  (1.22 to 0.93) unless the data actually contained three decay times, or was described by some model other than a two-decay-time model. Stated alternatively, there is a 90 to 95% probability that the two-decay-time model is not an adequate description of the sample.

**Table 4.7.** Multi-Exponential Analysis of the Three-Component Mixture of Indole, 2-Aminopurine, and Anthranilic Acid

Observation wavelength (nm)	Lifetimes (ns)			Pre-exponential factors			Fractional intensities <sup>a</sup>			$\chi_R^2$ , number of exponents		
	$\tau_1$	$\tau_2$	$\tau_3$	$\alpha_1$	$\alpha_2$	$\alpha_3$	$f_1$	$f_2$	$f_3$	3	2	1
360	4.79 (0.10) <sup>b</sup>	7.51 (1.66)	11.43 (0.02)	0.314	0.004	0.682	0.161 (0.001)	0.003 (0.001)	0.836	1.10	1.10	17.67
380	4.29 (0.33)	8.37 (0.05)	11.53 (0.02)	0.155	0.622	0.223	0.079 (0.001)	0.617 (0.001)	0.304	0.93	1.22	26.45
400	4.99 (0.16)	9.50 (0.13)	13.48 (0.25)	0.180	0.722	0.098	0.099 (0.001)	0.755 (0.001)	0.146	0.96	0.97	7.88
420	4.32 (0.47)	8.54 (0.25)	11.68 (0.09)	0.072	0.658	0.270	0.034 (0.001)	0.618 (0.001)	0.348	0.93	0.34	4.97
440	1.70 (0.61)	7.94 (0.24)	11.07 (0.06)	0.037	0.580	0.383	0.007 (0.001)	0.517 (0.001)	0.476	1.02	1.04	4.14

<sup>a</sup> $f_i = \alpha_i \tau_i / \sum \alpha_j \tau_j$ .<sup>b</sup>Asymptotic standard errors.

One may question why there are two tests for goodness of fit: based on  $\chi_R^2$  itself and based on the  $F$  statistic. The values of  $\chi_R^2$  are useful when the experimental errors can be accurately estimated, which is usually the case with TCSPC data. In this case the value of  $\chi_R^2$  provides a test of both the agreement of the measured and calculated  $N(t_k)$  values, and whether the only source of noise is Poisson photon statistics. In contrast to  $\chi_R^2$ , the  $F$  statistic can be used when the experimental uncertainties ( $\sigma_k$  values) are not precisely known. This is usually the case with stroboscopic, gated detection, and streak camera measurements, in which photon counting is not used. This situation also occurs in frequency-domain fluorometry, where the uncertainties in the phase and modulation values can only be estimated. The calculated values of  $\chi_R^2$  can be very different from unity even for a good fit, because the  $\sigma_k^2$  values may not be equal to the values of  $[N(t_k) - N_c(t_k)]^2$ . This is not a problem as long as the relative values of  $\chi_R^2$  are known. In these cases one uses the  $F$  statistic, or relative decrease in  $\chi_R^2$ , to determine the goodness of fit.

For closely spaced lifetimes, the ASEs will greatly underestimate the uncertainties in the parameters. This underestimation of errors is also illustrated in Table 4.7, which lists the analysis of the three-component mixture when measured at various emission wavelengths. It is clear from these analyses that the recovered lifetimes differ by amounts considerably larger than the asymptotic standard errors. This is particularly true for the fractional intensities, for which the asymptotic standard errors are  $\pm 0.001$ . Simi-

lar results can be expected for any decay with closely spaced lifetimes.

#### 4.11. INTENSITY DECAY LAWS

So far we have considered methods to measure intensity decays, but we have not considered the forms that are possible. Many examples will be seen in the remainder of this book. A few examples are given here to illustrate the range of possibilities.

##### 4.11.1. Multi-Exponential Decays

In the multi-exponential model the intensity is assumed to decay as the sum of individual single exponential decays:

$$I(t) = \sum_{i=1}^n \alpha_i \exp(-t/\tau_i) \quad (4.27)$$

In this expression  $\tau_i$  are the decay times,  $\alpha_i$  represent the amplitudes of the components at  $t = 0$ , and  $n$  is the number of decay times. This is the most commonly used model, but the meaning of the parameters ( $\alpha_i$  and  $\tau_i$ ) depends on the system being studied. The most obvious application is to a mixture of fluorophores, each displaying one of the decay times  $\tau_i$ . In a multi-tryptophan protein the decay times may be assigned to each of the tryptophan residue, but this usually requires examination of mutant protein with some of the tryptophan residues deleted. Many samples that contain

only a single fluorophore display decays more complex than a single exponential. These data are usually interpreted in terms of eq. 4.27, which then requires explanation of the multiple decay times. If the probe can exist in two environments, such as exposed and shielded from water, then a decay time can be assigned to each of these states. Hence, single-tryptophan proteins that exist in multiple conformational states may display a decay time for each state. Papers on protein fluorescence sometimes interpret the multi-exponential decays in terms of conformational distributions.<sup>195–196</sup>

The meaning of the pre-exponential factors  $\alpha_i$  are different for a mixture of fluorophores and for one fluorophore displaying a complex decay. For the latter case, it is generally safe to assume that the fluorophore has the same radiative decay rate in each environment. In this case the  $\alpha_i$  values represent the fraction of the molecules in each conformation at  $t = 0$ , which represents the ground-state equilibrium. However, the meaning of the  $\alpha_i$  values is more complex for a mixture of fluorophores. In this case the relative  $\alpha_i$  values depend on the concentrations, absorption, quantum yields, and intensities of each fluorophore at the observation wavelength.

Irrespective of whether the multi-exponential decay originates with a single fluorophore or multiple fluorophores, the value of  $\alpha_i$  and  $\tau_i$  can be used to determine the fractional contribution ( $f_i$ ) of each decay time to the steady-state intensity. These values are given by

$$f_i = \frac{\alpha_i \tau_i}{\sum_j \alpha_j \tau_j} \quad (4.28)$$

The terms  $\alpha_i \tau_i$  are proportional to the area under the decay curve for each decay time. In a steady-state measurement one measures all the emissions irrespective of when the photon is emitted. This is why the intensity is usually weaker for a short decay time and the  $\alpha_i \tau_i$  product is smaller. For a mixture of fluorophores, the values of  $f_i$  represent the fractional intensity of each fluorophore at each observation wavelength (Tables 4.5 and 4.6). However, the recovered values of  $f_i$  may not correlate well with the expected intensities due to the difficulties of resolving a multi-exponential decay.

What are the variable parameters in a multi-exponential analysis? Typically these are the  $n$  lifetimes, and  $n$  or  $n - 1$  amplitudes. In most intensity decay analyses the total intensity is not measured, and the  $\Sigma \alpha_i$  is normalized to unity. Also,  $\Sigma f_i$  is normalized to unity. Hence for a three-

decay-time fit there are typically five independently variable parameters, three lifetimes, and two amplitudes. However, most programs require that all the amplitudes remain variable during the fitting procedure, and the  $\alpha_i$  values are normalized at the end of the analysis. In these cases one is fitting to the total intensity, and there are three variable-amplitude parameters.

And, finally, it is important to remember that the multi-exponential model (eq. 4.27) is perhaps the most powerful model. Almost any intensity decay, irrespective of its complexity, can be fit using eq. 4.27. This means that one can say the data are consistent with eq. 4.27, but the data can also be consistent with many other decay laws.

When using the multi-exponential decay law it is often useful to determine the average lifetime ( $\bar{\tau}$ ). The average lifetime is given by eq. 4.3. For a two-exponential decay it is given by

$$\bar{\tau} = \frac{\alpha_1 \tau_1^2 + \alpha_2 \tau_2^2}{\alpha_1 \tau_1 + \alpha_2 \tau_2} = f_1 \tau_1 + f_2 \tau_2 \quad (4.29)$$

Occasionally one finds the "average lifetime" given by

$$\langle \tau \rangle = \sum_i \alpha_i \tau_i \quad (4.30)$$

which is not correct. The value of  $\langle \tau \rangle$  is proportional to the area under the decay curve, and for a double-exponential decay becomes

$$\int_0^\infty I(t) dt = \alpha_1 \tau_1 + \alpha_2 \tau_2 \quad (4.31)$$

This value should perhaps be called a lifetime-weighted quantum yield or an amplitude-weighted lifetime. There are occasions where the value of  $\langle \tau \rangle$  is useful. For instance, the efficiency of energy transfer is given by

$$E = 1 - \frac{F_{DA}}{F_D} = 1 - \frac{\int I_{DA}(t) dt}{\int I_D(t) dt} \quad (4.32)$$

where  $I_{DA}(t)$  and  $I_D(t)$  are the intensity decays of the donor in the presence and absence of energy transfer, respectively. The integrals in eq. 4.32 are proportional to the steady-state intensities in the presence ( $F_{DA}$ ) and absence ( $F_D$ ) of

acceptor, which is given by eq. 4.31. When using the results of a multi-exponential analysis, the transfer efficiency should be calculated using  $\langle \tau \rangle$  values, since these are proportional to the steady-state intensity.

#### 4.11.2. Lifetime Distributions

There are many situations where one does not expect a limited number of discrete decay times, but rather a distribution of decay times. Such behavior may be expected for a fluorophore in a mixture of solvents, so that a range of environments exists. One can imagine a fluorophore being surrounded by one, two, three, or more polar molecules, each resulting in a different intensity decay. Another possibility is a protein with many tryptophan residues, so that it is not practical to consider individual decay times.

In such cases the intensity decays are typically analyzed in terms of a lifetime distribution. In this case the  $\alpha_i$  values are replaced by distribution functions  $\alpha(\tau)$ . The component with each individual  $\tau$  value is given by

$$I(\tau, t) = \alpha(\tau) e^{-t/\tau} \quad (4.33)$$

However, one cannot observe these individual components with lifetime  $\tau$ , but only the entire decay. The total decay law is the sum of the individual decays weighted by the amplitudes:

$$I(t) = \int_{\tau=0}^{\infty} \alpha(\tau) e^{-t/\tau} d\tau \quad (4.34)$$

where  $\int \alpha(\tau) d\tau = 1.0$ .

Lifetime distributions are usually used without a theoretical basis for the  $\alpha(\tau)$  distribution. One typically uses arbitrarily selected Gaussian (G) and Lorentzian (L) lifetime distributions. For these functions the  $\alpha(\tau)$  values are

$$\alpha_G(\tau) = \frac{1}{\sigma\sqrt{2\pi}} \exp\left\{-\frac{1}{2}\left(\frac{\tau - \bar{\tau}}{\sigma}\right)^2\right\} \quad (4.35)$$

$$\alpha_L(\tau) = \frac{1}{\pi} \frac{\Gamma/2}{(\tau - \bar{\tau})^2 + (\Gamma/2)^2} \quad (4.36)$$

where  $(\bar{\tau})$  is the central value of the distribution,  $\sigma$  the standard deviation of the Gaussian, and  $\Gamma$  the full width at half

maximum (FWHM) for the Lorentzian. For a Gaussian the full width at half maximum is given by  $2.345\sigma$ . For ease of interpretation we prefer to describe both distributions by the full width at half maxima. An alternative approach would be to use  $\alpha(\tau)$  distributions that are not described by any particular function. This approach may be superior in that it makes no assumptions about the shape of the distribution. However, the use of functional forms for  $\alpha(\tau)$  minimizes the number of floating parameters in the fitting algorithms. Without an assumed function form it may be necessary to place restraints on the adjacent values of  $\alpha(\tau)$ .

By analogy with the multi-exponential model, it is possible that  $\alpha(\tau)$  is multimodal. Then

$$\alpha(\tau) = \sum_i g_i \alpha_i^0(\tau) = \sum_i \alpha_i(\tau) \quad (4.37)$$

where  $i$  refers to the  $i$ th component of the distribution centered at  $\alpha_i$ , and  $g_i$  represents the amplitude of this component. The  $g_i$  values are amplitude factors and  $\alpha_i^0(\tau)$  the shape factors describing the distribution. If part of the distribution exists below  $\tau = 0$ , then the  $\alpha_i(\tau)$  values need additional normalization. For any distribution, including those cut off at the origin, the amplitude associated with the  $i$ th mode of the distribution is given by

$$\alpha_i = \frac{\int_0^{\infty} \alpha_i(\tau) d\tau}{\int_0^{\infty} \sum_i \alpha_i(\tau) d\tau} \quad (4.38)$$

The fractional contribution of the  $i$ th component to the total emission is given by

$$f_i = \frac{\int_0^{\infty} \alpha_i(\tau) \tau d\tau}{\int_0^{\infty} \sum_i \alpha_i(\tau) \tau d\tau} \quad (4.39)$$

In the use of lifetime distributions each decay time component is associated with three variables,  $\alpha_i$ ,  $f_i$  and the half width ( $\sigma$  or  $\Gamma$ ). Consequently, one can fit a complex decay with fewer exponential components. For instance, data that can be fit to three discrete decay times can typically be fit to a bimodal distribution model. In general, it is not possible to distinguish between the discrete multi-exponential model (eq. 4.27) or the lifetime distribution model (eq. 4.34), so the model selection must be based on one's knowledge of the system.<sup>197–199</sup>

### 4.11.3. Stretched Exponentials

A function similar to the lifetime distributions is the stretched exponential

$$I(t) = I_0 \exp[(-t/\tau)^\beta] \quad (4.40)$$

In this expression  $\beta$  is related to the distribution of decay times. The function is not used frequently in biophysics but is often found in studies of polymers when one expects a distribution of relaxation times. In a least-squares fit,  $\beta$  and  $\tau$  would be the variable parameters.

### 4.11.4. Transient Effects

In many samples the intensity decay can be non-exponential due to phenomena which occur immediately following excitation. This occurs in collisional quenching and in resonance energy transfer. In the presence of a quencher, a fluorophore that displays an unquenched single-exponential lifetime will decay according to

$$I(t) = I_0 \exp(-t/\tau - 2bt^{1/2}) \quad (4.41)$$

In this expression  $b$  depends on the quencher concentration and diffusion coefficient. One can fit such decays to the multi-exponential model, but one would then erroneously conclude that there are two fluorophore populations. In this case a single fluorophore population gives a non-exponential decay due to rapid quenching of closely spaced fluorophore-quencher pairs.

Resonance energy transfer (RET) can also result in decays that have various powers of time in the exponent. Depending on whether RET occurs in one, two, or three dimensions,  $t$  can appear with powers of 1/6, 1/3, or 2 respectively. Hence we see that intensity decays can take a number of forms depending on the underlying molecular phenomenon. In our opinion it is essential to analyze each decay with the model that correctly describes the samples. Use of an incorrect model, such as the multi-exponential model, to describe transient effects, results in apparent parameter values ( $\alpha_i$  and  $\tau_i$ ) that cannot be easily related to the quantities of interest (quencher concentration and diffusion coefficient).

---

## 4.12. GLOBAL ANALYSIS

In Section 4.10 we indicated the difficulties of resolving the decay times and amplitudes in a multi-exponential decay.

The parameters in the various decay functions are correlated and difficult to resolve. The resolution of correlated parameters can be improved by the use of global analysis.<sup>200–205</sup> The procedure is to combine two or more experiments in which some of the parameters are the same in all measurements, and some are different. This can be illustrated by the emission spectra in Figure 4.53. A non-global experiment would be to recover the values of  $\alpha_i$  and  $\tau_i$  from the intensity decay collected at 380 nm, where all three fluorophores emit. A global experiment would be to measure the intensity decays at several wavelengths, say 360, 380, 400, and 420 nm. The multiple intensity decay curves are then analyzed simultaneously to recover the  $\tau_i$  values and the  $\alpha_i(\lambda)$  values. The  $\tau_i$  values are assumed to be independent of emission wavelength. In the case of global analysis the calculation of  $\chi_R^2$  extends over several data sets. The global value of  $\chi_R^2$  is given by

$$\chi_R^2 = \frac{1}{v} \sum_{\lambda} \sum_{k=1}^n \frac{[I_c^\lambda(t_k) - I^\lambda(t_k)]^2}{I^\lambda(t_k)} \quad (4.42)$$

where the additional sum extends over the files measured at each wavelength ( $\lambda$ ). For the fitted functions the  $\alpha_i$  values are different at each wavelength  $\alpha_i(\lambda)$  because of the different relative contributions of the three fluorophores. The values of  $\tau_i$  are assumed to be independent of emission wavelength since each fluorophore is assumed to display a single exponential decay.

It is easy to see how global analysis can improve resolution. Suppose one of the intensity decays was measured at 320 nm. This decay would be almost completely due to indole (Figure 4.53), and thus would determine its lifetime without contribution from the other fluorophores. Since there is only one decay time, there would be no parameter correlation, and  $\tau_1$  would be determined with good certainty. The data at 320 nm will constrain the lifetime of indole in data measured at longer wavelengths and in effect decrease the number of variable parameters at this wavelength. Even if the choice of wavelengths only partially selects for a given fluorophore, the data serve to determine its decay time and reduce the uncertainty in the remaining parameters.

Global analysis was used to recover the lifetimes across the emission spectrum of the three-component mixture, using the decays measured from 360 to 440 nm. The lifetime  $\chi_R^2$  surface for the three decay times is shown in Figure 4.56. The expected decay time was recovered for each of the components. However, even with a multi-wave-

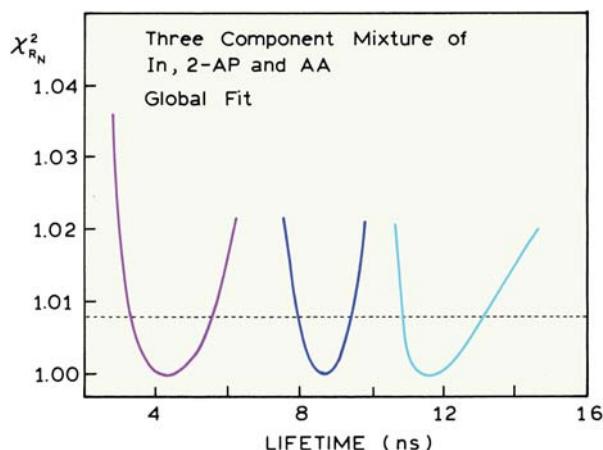


**Figure 4.56.** Global lifetime  $\chi^2_{RN}$  surface for the three-component mixture of In, AA, and 2-AP. From [187].

length global analysis the uncertainties are significant. For instance, the value of the 4.1-ns lifetime can range from about 3.2 to 5.5 ns and still be consistent with the data.

#### 4.13. APPLICATIONS OF TCSPC

The concepts described in the preceding sections can be made more understandable by examination of some specific examples.

##### 4.13.1. Intensity Decay for a Single Tryptophan Protein

The tet repressor controls the gene in Gram-negative bacteria that provides resistance to the antibiotic tetracycline.<sup>206</sup> This protein usually contains two tryptophans, but a mutant protein was engineered that contains a single tryptophan residue at position 43. Intensity decays are shown in Figure 4.57. The light source was a frequency-doubled R6G dye laser at 590 nm, frequency doubled to 295 nm. The dye laser was cavity dumped at 80 kHz. The excitation was vertically polarized and the emission detected through a polarizer set  $54.7^\circ$  from the vertical. The use of magic-angle polarization conditions is essential in this case because the protein can be expected to rotate on a timescale comparable to the intensity decay. A Schott WG 320 filter was used in front of the monochromator to prevent scattered light from entering the monochromator, which was set at 360 nm.

The emission was detected with an XP-2020 PMT. This PMT shows a wavelength-dependent time response and an afterpulse. To avoid color effects the authors used a

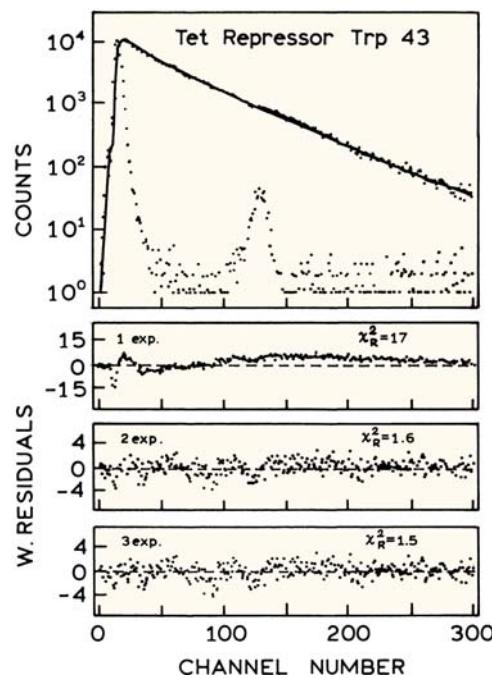


**Figure 4.57.** Intensity decay of trp-43 in the tet repressor protein F75 TetR at 360 nm. The calibration is 108 ps/channel. Revised and reprinted with permission from [206]. Copyright © 1992, American Chemical Society.

short-lifetime reference that shifted the wavelength to the measurement wavelength with minimal time delay.<sup>112</sup> This was accomplished with a solution of p-terphenyl highly quenched by  $\text{CCl}_4$ . The fact that the measurements were performed with a dynode PMT is evident from the width of the impulse response function, which appears to be near 500 ps. Some of this width may be contributed from the short lifetime standard.

The intensity decay was fit to the one, two, and three exponential models, resulting in  $\chi^2_{RN}$  values of 17, 1.6, and 1.5, respectively. Rejection of the single-exponential model is clearly justified by the data. However, it is less clear that three decay times are needed. The ratio of the  $\chi^2_{RN}$  values is 1.07, which is attributed to random error with a probability of over 20% (Table 4.3). The fractional amplitude of the third component was less than 1%, and the authors accepted the double exponential fit as descriptive of their protein.

##### 4.13.2. Green Fluorescent Protein: Systematic Errors in the Data

Green fluorescent protein (GFP) spontaneously becomes fluorescent following synthesis of its amino-acid chain.

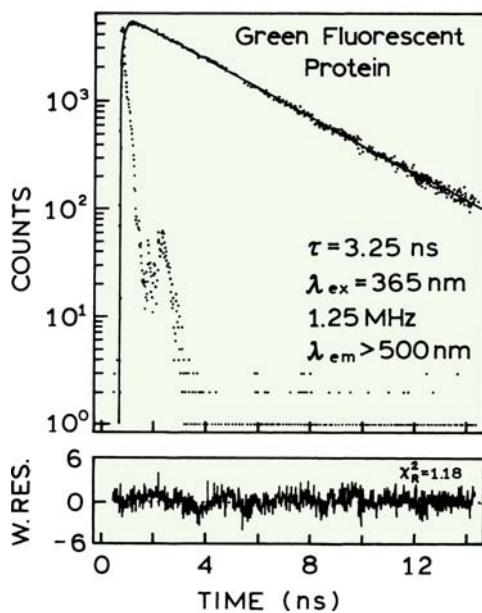


**Figure 4.58.** Intensity decay of green fluorescence protein. From [207].

GFPs are widely used as a tag to follow gene expression. The intensity decay of GFP was measured with 365-nm excitation, a 1.25-MHz repetition rate, and magic-angle polarizer conditions.<sup>207</sup> The emission was detected above 500 nm, using an MCP PMT.

The intensity decay of GFP could be well fit to a single exponential (Figure 4.58). The value of  $\chi_R^2$  is slightly elevated, and not consistent with a single exponential model. However, the value of  $\chi_R^2$  was not decreased by including a second decay time ( $\chi_R^2 = 1.18$ ). Examination of the deviations (lower panel) reveals the presence of systematic oscillations for which a second decay time does not improve the fit. The failure of  $\chi_R^2$  to decrease is typically an indication of systematic error as the origin of the elevated value of  $\chi_R^2$ .

#### 4.13.3. Picosecond Decay Time

The measurement of picosecond decay times remains challenging even with the most modern instruments for TCSPC. Figure 4.59 shows a schematic for a state-of-the-art instrument.<sup>208</sup> The primary source of excitation is a Ti:sapphire laser, which is pumped by a continuous argon ion laser. The repetition rate is decreased as needed by a pulse picker (PP). Additional excitation wavelengths are obtained using a harmonic generator (HG) for frequency doubling or tripling, or an optical parameter oscillator (OPO). The pulse

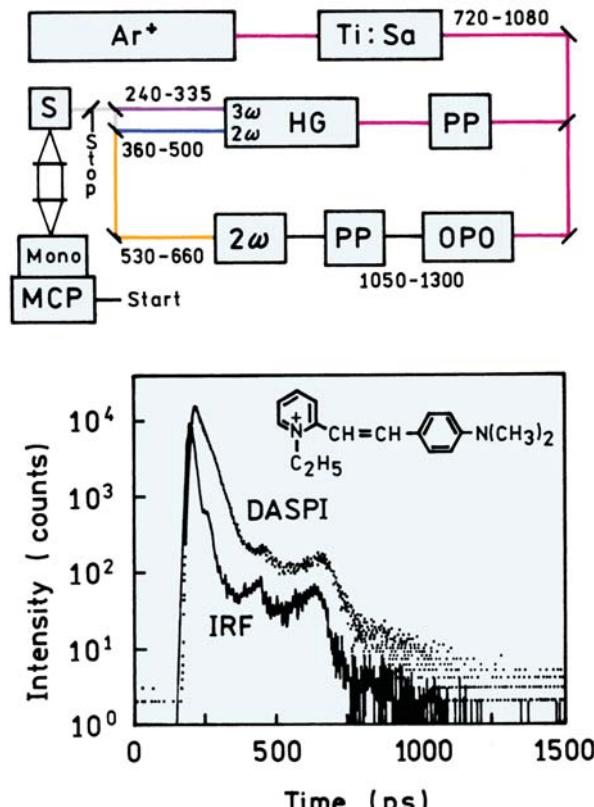


**Figure 4.59.** Intensity decay of DASPI in methanol. The upper panel shows a schematic of the instrument with a Ti:sapphire-OPO pump source at 543 nm and an R3809U MPC PMT. DASPI is 2-[2-[3-dimethylamino]phenyl]-ethyl-N-methyl pyridinium iodide (DASPI). Revised from [208].

widths were near 1 ps. This instrument has an R3809U MCP PMT that has one of the smallest available transient time spreads.

The lower panel in Figure 4.59 shows the intensity decay of DASPI in methanol. DASPI has a very short decay time in this solvent. The intensity decay is not much wider than the IRF, which has an FWHM below 28 ps. The decay time recovered for DASPI is 27.5 ps. Comparison of the IRF and intensity decay of DASPI shows the need for deconvolution. In spite of the complex profile of these curves, they are consistent with a single-exponential decay of DASPI with a 27.5 ps lifetime.

#### 4.13.4. Chlorophyll Aggregates in Hexane

The intensity decay for the tryptophan residues in the tet repressor was relatively close to a single exponential. Intensity decays can be much more heterogeneous. One example

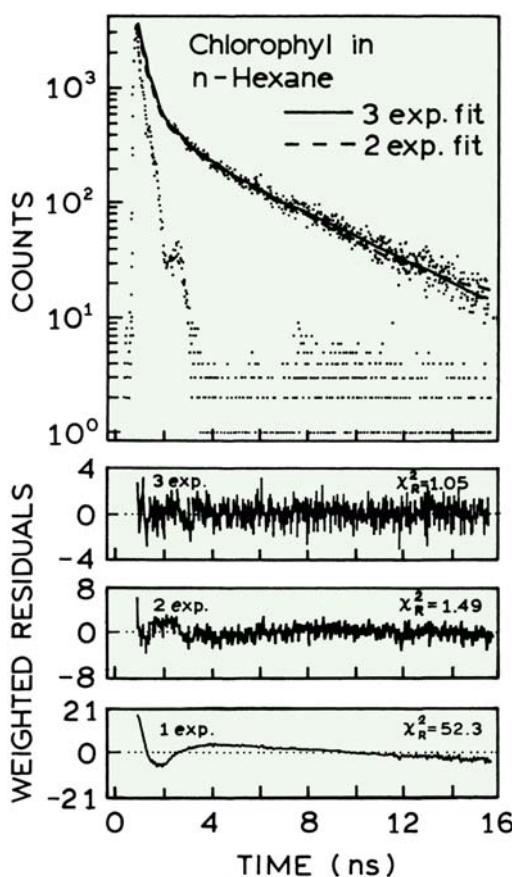


**Figure 4.60.** Intensity decay of chlorophyll in wet n-hexane [209].

is the intensity decay of chlorophyll in wet hexane solvents, in which chlorophyll exists in a variety of aggregated states.<sup>209</sup> Data were obtained using a Pyridine dye laser at 760 nm, which was cavity dumped at 1 MHz and frequency doubled to 380 nm. The emission was detected at 715 nm through an interference filter. The detector was an R2809 MCP PMT, with 6 micron channels. Even though the excitation and emission wavelengths were far apart (380 and 715 nm), color effect corrections did not seem necessary with this MCP PMT. Magic-angle polarizer conditions were used.

The intensity decay of chlorophyll was strongly heterogeneous (Figure 4.60). The decay could not even be approximated by a single decay time. The fit with two decay times was much improved, reducing  $\chi^2_R$  from 52.3 to 1.49. A further reduction of 40% in  $\chi^2_R$  occurred for the three-decay-time fit. The two-decay-time model can be rejected because this  $\chi^2_R$  ratio of 1.41 would only occur between 1 and 5% of the time due to statistical errors in the data (Table 4.3).

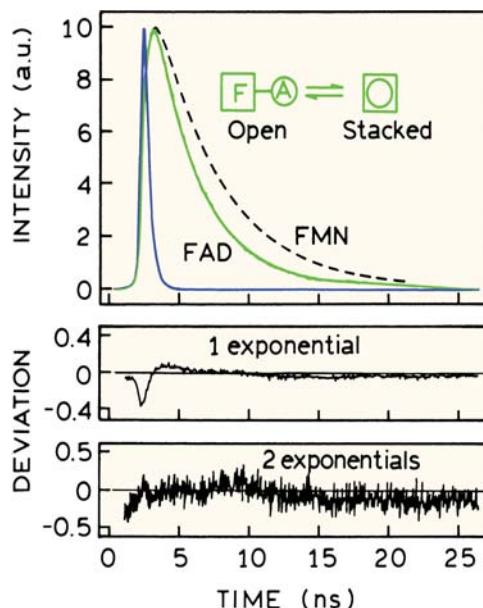


**Figure 4.61.** Intensity decays of FAD and FMN at pH 7.5, 3°C. Also shown is the laser pulse profile. The deviations are for fits to the FAD intensity decay. Data from [212].

Complex intensity decays with up to four lifetimes have been reported for photosynthetic systems.<sup>210–211</sup>

#### 4.13.5. Intensity Decay of Flavin Adenine Dinucleotide (FAD)

Flavin adenine dinucleotide (FAD) is a cofactor in many enzymatic reactions. The fluorescent moiety is the flavin, which can be quenched on contact with the adenine. In solution FAD can exist in an open or stacked configuration. It is known that a significant amount of quenching occurs because cleavage of FAD with phosphodiesterase results in a several-fold increase in fluorescence intensity.

The nature of the flavin quenching by the adenine was studied by TCSPC.<sup>212</sup> Data were obtained using the output of a mode-locked argon ion laser at 457.9 nm. The detector was an XP 2020 linear-focused PMT, resulting in a relatively wide instrument response function (Figure 4.61). The intensity decay of the flavin alone (FMN) was found to be a single exponential with a decay time of 4.89 ns. FAD displayed a double-exponential decay with a component of 3.38 ns ( $\alpha_1 = 0.46$ ) and of 0.12 ns ( $\alpha_2 = 0.54$ ). The short decay time component was assigned to the stacked forms, allowing calculation of the fraction of FAD present in the stacked and open conformations. The lifetime of 3.38 ns is thought to be due to dynamic quenching of the flavin by the adenine moiety.

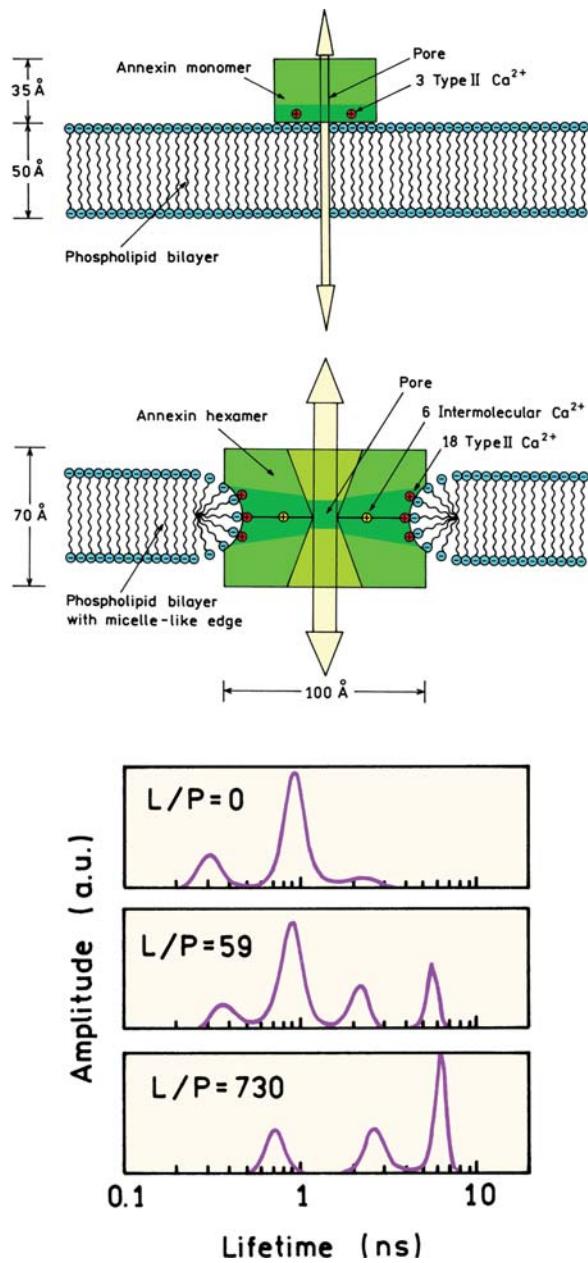


**Figure 4.62.** Lifetime distribution of Annexin V Domain III in the presence of phospholipid at various lipid-to-protein molar ratios ( $L/P$ ). The lipid was an 80/20 molar ratio of DOPC and DOPS, where S indicates serine. Revised from [214]. The upper panel shows a schematic of Annexin insertion into membranes. Reprinted with permission from [218].

#### 4.14. DATA ANALYSIS: MAXIMUM ENTROPY METHOD

Intensity decays of biomolecules are usually multi-exponential or non-exponential. The decays can be fitted using the multi-exponential model. However, it is difficult to

obtain an intuitive understanding of the results by examining table of  $\alpha_i$  and  $\tau_i$  values. Analysis of the decays in terms of lifetime distribution (Section 4.11.2) is often useful for visualizing the decay. However, when using NLLS the lifetime distribution analysis is usually performed in terms of assumed shape functions (eqs. 4.35 and 4.36). Analysis using the maximum entropy method (MEM) allows recovery of lifetime distributions without assumptions about the shape of the components.

The MEM is mathematically complex<sup>213–216</sup> and the fitting criteria somewhat subjective. Most of the published analyses were performed using commercial algorithms which are not completely explained. Nonetheless, the MEM is now widely utilized and provides insight into complex intensity decays.

The MEM is based on maximizing a function called the Skilling-Jaynes entropy function:

$$S = \int_0^{\infty} \alpha(\tau) - m(\tau) - \alpha(\tau) \log \frac{\alpha(\tau)}{m(\tau)} d\tau \quad (4.43)$$

In this expression  $\alpha(\tau)$  is the recovered distribution and  $m(\tau)$  is an assumed starting model that is flat in  $\log \tau$  space. The MEM method is not used alone, but the fits are performed while calculating  $\chi^2_R$  according to eq. 4.22 to ensure that the recovered distribution is consistent with the data. In contrast to NLLS there does not appear to be a well-defined stopping point for the MEM analysis. The analysis is stopped when  $\chi^2_R$  does not decrease more than 2% for 20 interactions. The MEM is advantageous because it provides smooth  $\alpha(\tau)$  spectra that have enough detail to reveal the shape of the distribution. The MEM method is claimed to not introduce  $\alpha(\tau)$  components unless they are needed to fit the data.

An example of an MEM analysis is shown in Figure 4.62 for domain III of Annexin V. Annexins are peripheral membrane proteins that interact with negatively charged phospholipids. Annexins can become inserted into membranes (Figure 4.62), so the tryptophan intensity decays are expected to be dependent on the presence of phospholipids. This domain of Annexin V contains a single tryptophan residue at position 187 (W187). The intensity decays of W187 were measured by TCSPC. The excitation source was synchrotron radiation that appeared as pulses at 13.6 MHz with a pulse width of 1.4 ns.<sup>215</sup> The maximum entropy analysis shows a shift from a dominant component near 0.9 ns in the absence of membrane to a longer-lived component

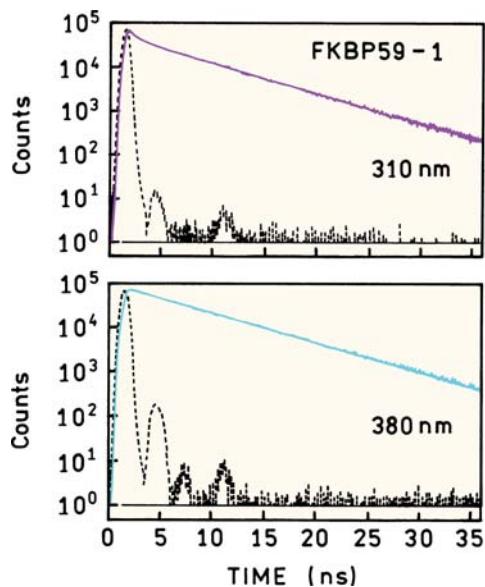


**Figure 4.63.** Tryptophan intensity decays of FKBP59-1 excited by synchrotron radiation at 295 nm and observed at 310 and 380 nm. Revised from [219].

near 6 ns in the presence of lipid. It is easier to visualize the effects of lipid from the distributions than from a table of parameter values.

Lifetime distributions and the MEM are also useful in visualizing the effects of observation wavelength on intensity decays.<sup>219</sup> The immunophilin FKBP59-1 contains two tryptophan residues, one buried and one exposed to the solvent (Chapter 16 and 17). The intensity decays are visually similar on the short (310 nm) and long (380 nm) sides of the emission spectrum (Figure 4.63). The difference between the decays are much more apparent in lifetime distributions recovered from the maximum entropy analysis (Figure 4.64). An excellent monograph has recently been published on TCSPC [220]. Readers are encouraged to see this book for additional details on TCSPC.

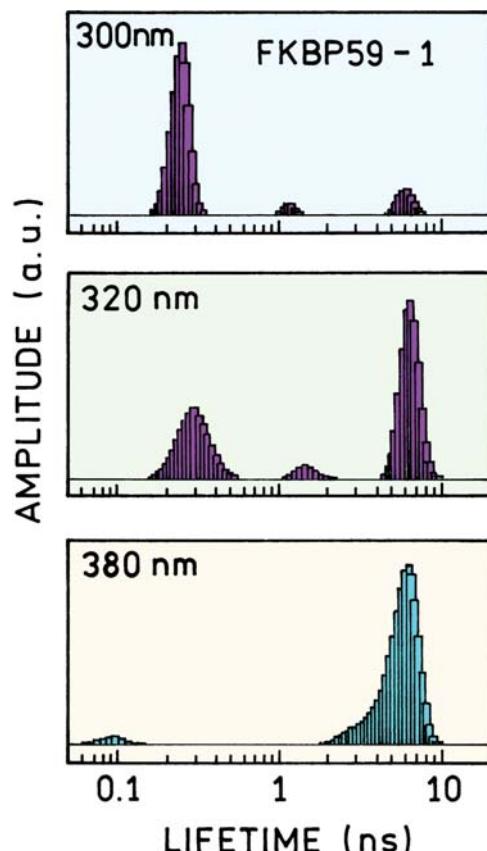


**Figure 4.64.** Lifetime distribution of the immunophilin FKBP59-1 recovered by the MEM. Revised from [219].

5. Johnson ML. 1985. The analysis of ligand binding data with experimental uncertainties in the independent variables. *Anal Biochem* **148**:471–478.
6. Bard J. 1974. *Nonlinear parameter estimation*. Academic Press, New York.
7. Johnson ML. 1983. Evaluation and propagation of confidence intervals in nonlinear, asymmetrical variance spaces: analysis of ligand binding data. *Biophys J* **44**:101–106.
8. O'Connor DV, Phillips D. 1984. *Time-correlated single-photon counting*. Academic Press, New York.
9. Birch DJS, Imhof RE. 1991. Time-domain fluorescence spectroscopy using time-correlated single-photon counting. In *Topics in fluorescence spectroscopy*, Vol. 1: *Techniques*, pp. 1–95. Ed JR Lakowicz, Plenum Press, New York.
10. Ware WR. 1971. Transient luminescence measurements. In *Creation and detection of the excited state*, Vol. 1A, pp. 213–302. Ed AA Lamola. Marcel Dekker, New York.
11. Becker W, Bergmann A. 2005. Multidimensional time-correlated single-photon counting. In *Reviews in fluorescence*, Vol. 2, pp. 77–108. Ed CD Geddes, JR Lakowicz. Kluwer Academic/Plenum Publishers, New York.
12. Bassi A, Swartling J, D'Andrea C, Pifferi A, Torricelli A, Cubeddu R. 2004. Time-resolved spectrophotometer for a turbid media based on supercontinuum generation in a photonic crystal fiber. *Opt Lett* **29**(20):2405–2407.

## REFERENCES

1. Bevington PR, Robinson DK. 1992. *Data reduction and error analysis for the physical sciences*, 2nd ed. McGraw-Hill, New York.
2. Taylor JR. 1982. *An introduction to error analysis: the study of uncertainties in physical measurements*. University Science Books, Sausalito, CA.
3. Grinvald A, Steinberg IZ. 1974. On the analysis of fluorescence decay kinetics by the method of least-squares. *Anal Biochem* **59**:583–593.
4. Demas JN. 1983. *Excited state lifetime measurements*. Academic Press, New York.

13. Karolczak J, Komar D, Kubicki J, Wrozowa T, Dobek K, Ciesielska B, Maciejewski A. 2001. The measurements of picosecond fluorescence lifetimes with high accuracy and subpicosecond precision. *Chem Phys Lett* **344**:154–164.
14. Becker W, Hickl H, Zander C, Drexhage KH, Sauer M, Siebert S, Wolfrum J. 1999. Time-resolved detection and identification of single analyte molecules in microcapillaries by time-correlated single-photon counting (TCSPC). *Rev Sci Instrum* **70**(3):1835–1841.
15. Malak H. Unpublished observations.
16. Badea MG, Brand L. 1971. Time-resolved fluorescence measurements. *Methods Enzymol* **61**:378–425.
17. McGuinness CD, Sagoo K, McLoskey D, Birch DJS. 2004. A new sub-nanosecond LED at 280 nm: application to protein fluorescence. *Meas Sci Technol* **15**:L1–L4.
18. Pico Quant GmbH, Berlin, Germany [http://www.picoquant.com/products\\_products.htm](http://www.picoquant.com/products_products.htm).
19. IBH Jobin Yvon, Glasgow, United Kingdom <http://www.issainc.com/usadivisions/Fluorescence/IBH/nanoled.htm>.
20. Becker and Hickl GmbH, Berlin, Germany, <http://www.becker-heckl.de>.
21. Hamamatsu Photonics, KK, Hamamatsu City, Japan, <http://usa.hamamatsu.com>.
22. <http://www.picoquant.com/products/ledhead.htm>.
23. O'Hagan WJ, McKenna M, Sherrington DC, Rolinski OJ, Birch DJS. 2002. MHz LED source for nanosecond fluorescence sensing. *Meas Sci Technol* **13**:84–91.
24. Svelto O. 1998. *Principles of lasers*, 4th ed. Transl DC Hanna. Plenum Press, New York.
25. Yariv A. 1989. *Quantum electronics*, 3rd ed. John Wiley & Sons, New York.
26. Iga, K. 1994. *Fundamentals of laser optics*. Plenum Press, New York.
27. Small EW. 1991. Laser sources and microchannel plate detectors for pulse fluorometry. In *Topics in fluorescence spectroscopy*, Vol. 1: *Techniques*, pp. 97–182. Ed JR Lakowicz. Plenum Press, New York.
28. Wilson J, Hawkes JFB. 1983. *Optoelectronics: an introduction*. Prentice Hall, Englewood Cliffs, NJ.
29. Berg NJ, Lee JN, eds. 1983. *Acoustooptic signal processing*. Marcel Dekker, Inc., New York.
30. Visser AJWG, Van Hoek A. 1979. The measurement of subnanosecond fluorescence decay of flavins using time-correlated photon counting and a mode-locked Ar ion laser. *J Biochem Biophys Methods* **1**:195–208.
31. Spears KG, Cramer LE, Hoffland LD. 1978. Subnanosecond time-correlated photon counting with tunable lasers. *Rev Sci Instrum* **49**:255–262.
32. Lytle E, Kelsey MS. 1974. Cavity-dumped argon-ion laser as an excitable source on time-resolved fluorimetry. *Anal Chem* **46**:855–860.
33. Wild UP, Holzwarth AR, Good HP. 1977. Measurement and analysis of fluorescence decay curves. *Rev Sci Instrum* **48**(12):1621–1627.
34. Turko BT, Nairn JA, Sauer K. 1983. Single photon timing system for picosecond fluorescence lifetime measurements. *Rev Sci Instrum* **54**(1):118–120.
35. Alfano AJ, Fong FK, Lytle FE. 1983. High repetition rate subnanosecond gated photon counting. *Rev Sci Instrum* **54**(8):967–972.
36. Kinoshita S, Ohta H, Kushida T. 1981. Subnanosecond fluorescence lifetime measuring system using single photon counting method with mode-locked laser excitation. *Rev Sci Instrum* **52**(4):572–575.
37. Koester VJ, Dowben RM. 1978. Subnanosecond single photon counting fluorescence spectroscopy using synchronously pumped tunable dye laser excitation. *Rev Sci Instrum* **49**(8):1186–1191.
38. Zimmerman HE, Penn JH, Carpenter CW. 1982. Evaluation of single-photon counting measurements of excited-state lifetimes. *Proc Natl Acad Sci USA* **79**:2128–2132.
39. van Hoek A, Vervoort J, Visser AJWG. 1983. A subnanosecond resolving spectrophotometer for the analysis of protein fluorescence kinetics. *J Biochem Biophys Methods* **7**:243–254.
40. Small EW, Libertini LJ, Isenberg I. 1984. Construction and tuning of a monophoton decay fluorometer with high-resolution capabilities. *Rev Sci Instrum* **55**(6):879–885.
41. Visser AJWG, van Hoek A. 1981. The fluorescence decay of reduced nicotinamides in aqueous solution after excitation with a UV-mode locked Ar Ion laser. *Photochem Photobiol* **33**:35–40.
42. Libertini LJ, Small EW. 1987. On the choice of laser dyes for use in exciting tyrosine fluorescence decays. *Anal Biochem* **163**:500–505.
43. Malmberg JH. 1957. Millimicrosecond duration of light source. *Rev Sci Instrum* **28**(12):1027–1029.
44. Bennett RG. 1960. Instrument to measure fluorescence lifetimes in the millimicrosecond region. *Rev Sci Instrum* **31**(12):1275–1279.
45. Yguerabide J. 1965. Generation and detection of subnanosecond light pulses: application to luminescence studies. *Rev Sci Instrum* **36**(12):1734–1742.
46. Birch DJS, Imhof RE. 1977. A single photon counting fluorescence decay-time spectrometer. *J Phys E: Sci Instrum* **10**:1044–1049.
47. Lewis C, Ware WR, Doemny LJ, Nemzek TL. 1973. The measurement of short lived fluorescence decay using the single photon counting method. *Rev Sci Instrum* **44**:107–114.
48. Leskovar B, Lo CC, Hartig PR, Sauer K. 1976. Photon counting system for subnanosecond fluorescence lifetime measurements. *Rev Sci Instrum* **47**(9):1113–1121.
49. Bollinger LM, Thomas GE. 1961. Measurement of the time dependence of scintillation intensity by a delayed-coincidence method. *Rev Sci Instrum* **32**(9):1044–1050.
50. Hazan G, Grinvald A, Maytal M, Steinberg IZ. 1974. An improvement of nanosecond fluorimeters to overcome drift problems. *Rev Sci Instrum* **45**(12):1602–1604.
51. Dreeskamp H, Salthammer T, Laufer AGE. 1989. Time-correlated single-photon counting with alternate recording of excitation and emission. *J Lumin* **44**:161–165.
52. Birch DJS, Imhof RE. 1981. Coaxial nanosecond flashlamp. *Rev Sci Instrum* **52**:1206–1212.
53. Birch DJS, Hungerford G, Imhof RE. 1991. Near-infrared spark source excitation for fluorescence lifetime measurements. *Rev Sci Instrum* **62**(10):2405–2408.
54. Birch DJS, Hungerford G, Nadolski B, Imhof RE, Dutch A. 1988. Time-correlated single-photon counting fluorescence decay studies at 930 nm using spark source excitation. *J Phys E: Sci Instrum* **21**:857–862.
55. <http://www.ibh.co.uk/products/lightsources/5000f.htm>.
56. Laws WR, Sutherland JC. 1986. The time-resolved photon-counting fluorometer at the national synchrotron light source. *Photochem Photobiol* **44**(3):343–348.
57. Munro IH, Martin MM. 1991. Time-resolved fluorescence spectroscopy using synchrotron radiation. In *Topics in fluorescence spectroscopy*, Vol. 1: *Techniques*, pp. 261–291. Ed JR Lakowicz. Plenum Press, New York.
58. Munro IH, Schwentner N. 1983. Time-resolved spectroscopy using synchrotron radiation. *Nucl Instrum Methods* **208**:819–834.
59. Lopez-Delgado R. 1978. Comments on the application of synchrotron radiation to time-resolved spectrophotofluorometry. *Nucl Instrum Methods* **152**:247–253.
60. Rehn V. 1980. Time-resolved spectroscopy in synchrotron radiation. *Nucl Instrum Methods* **177**:193–205.

61. van Der Oord CJR, Gerritsen HC, Rommerts FFG, Shaw DA, Munro IH, Levine YK. 1995. Micro-volume time-resolved fluorescence spectroscopy using a confocal synchrotron radiation microscope. *Appl Spec* **49**(10):1469–1473.
62. Gedcke DA, McDonald WJ. 1967. A constant fraction of pulse height trigger for optimum time resolution. *Nucl Instrum Methods* **55**:377–380.
63. Gedcke DA, McDonald WJ. 1966. Design of the constant fraction of pulse height trigger for optimum time resolution. *Nucl Instrum Methods* **58**:253–260.
64. Arbel A, Klein I, Yarom A. 1974. Snap-off constant fraction timing discriminators. *IEEE Trans Nucl Sci* **NS-21**:3–8.
65. Becker & Hickl GmbH, Berlin, Germany. *How (and why not) to amplify PMT signals*. <http://www.becker-hickl.de>.
66. Cova S, Ghioni M, Zappa F, Lacaita A. 1993. Constant-fraction circuits for picosecond photon timing with microchannel plate photomultipliers. *Rev Sci Instrum* **64**(1):118–124.
67. Cova S, Ripamonti G. 1990. Improving the performance of ultrafast microchannel plate photomultipliers in time-correlated photon counting by pulse pre-shaping. *Rev Sci Instrum* **61**(3):1072–1075.
68. Haugen GR, Wallin BW, Lytle FE. 1979. Optimization of data-acquisition rates in time-correlated single-photon fluorimetry. *Rev Sci Instrum* **50**(1):64–72.
69. Bowman LE, Berglund KA, Nocera DG. 1993. A single photon timing instrument that covers a broad temporal range in the reversed timing configuration. *Rev Sci Instrum* **64**(2):338–341.
70. Baumier W, Schmalzl AX, Göhl G, Penzkofer A. 1992. Fluorescence decay studies applying a cw femtosecond dye laser pumped ungated inverse time-correlated single photon counting system. *Meas Sci Technol* **3**:384–393.
71. Harris CM, Selinger BK. 1979. Single-photon decay spectroscopy, II: the pileup problem. *Aust J Chem* **32**:2111–2129.
72. Williamson JA, Kendall-Tobias MW, Buhl M, Seibert M. 1988. Statistical evaluation of dead time effects and pulse pileup in fast photon counting: introduction of the sequential model. *Anal Chem* **60**:2198–2203.
73. Candy BH. 1985. Photomultiplier characteristics and practice relevant to photon counting. *Rev Sci Instrum* **56**(2):183–193.
74. Hungerford G, Birch DJS. 1996. Single-photon timing detectors for fluorescence lifetime spectroscopy. *Meas Sci Technol* **7**:121–135.
75. Leskovar B. 1977. Microchannel plates. *Phys Today* **30**:42–49.
76. Boutot JP, Delmotte JC, Miehé JA, Sipp B. 1977. Impulse response of curved microchannel plate photomultipliers. *Rev Sci Instrum* **48**(11):1405–1407.
77. Timothy JG, Bybee RL. 1977. Preliminary results with microchannel array plates employing curved microchannels to inhibit ion feedback. *Rev Sci Instrum* **48**(3):292–299.
78. Lo CC, Leskovar B. 1981. Performance studies of high gain photomultiplier having z-configuration of microchannel plates. *IEEE Trans Nucl Sci* **NS-28**(1):698–704.
79. Ito M, Kume H, Oba K. 1984. Computer analysis of the timing properties in micro channel plate photomultiplier tubes. *IEEE Trans Nucl Sci* **NS-31**(1):408–412.
80. Bebelaar D. 1986. Time response of various types of photomultipliers and its wavelength dependence in time-correlated single photon counting with an ultimate resolution of 47 ps FWHM. *Rev Sci Instrum* **57**(6):1116–1125.
81. Yamazaki I, Tamai N, Kume H, Tsuchiya H, Oba K. 1985. Microchannel plate photomultiplier applicability to the time-correlated photon-counting method. *Rev Sci Instrum* **56**(6):1187–1194.
82. Uyttenhoeve J, Demuynck J, Deruytter A. 1978. Application of a microchannel plate photomultiplier in subnanosecond lifetime measurements. *IEEE Trans Nucl Sci* **NS-25**(1):566–567.
83. Murao T, Yamazaki I, Shindo Y, Yoshihara K. 1982. A subnanosecond time-resolved spectrophotometric system by using synchronously pumped, mode-locked dye laser. *J Spectrosc Soc Jpn*, pp. 96–103.
84. Murao T, Yamazaki I, Yoshihara K. 1982. Applicability of a microchannel plate photomultiplier to the time-correlated photon counting technique. *Appl Opt* **21**(13):2297–2298.
85. Hamamatsu Photonics KK. 1997. *Microchannel plate-photomultiplier tube (MCP-PMTs) R38097-50 series*.
86. Koyama K, Fatlowitz D. 1987. Application of MCP-PMTs to time correlated single photon counting and related procedures. *Hamamatsu Tech Inf* **ET-03**:1–18.
87. Kume H, Taguchi T, Nakatsugawa K, Ozawa K, Suzuki S, Samuel R, Nishimura Y, Yamazaki I. 1992. Compact ultrafast microchannel plate photomultiplier tube. *SPIE Proc* **1640**:440–447.
88. Boens N, Tamai N, Yamazaki I, Yamazaki T. 1990. Picosecond single photon timing measurements with a proximity type microchannel plate photomultiplier and global analysis with reference convolution. *Photochem Photobiol* **52**(4):911–917.
89. Lo CC, Leskovar B. 1979. Studies of prototype high-gain microchannel plate photomultipliers. *IEEE Trans Nucl Sci* **NS-26**(1):388–394.
90. Becker & Hickl GmbH, Berlin, Germany. *AMPTM1.doc*.
91. Becker W, Bergmann A., Becker & Hickl GmbH. *Detectors for high-speed photon counting*.
92. Beck G. 1976. Operation of a 1P28 photomultiplier with sub-nanosecond response time. *Rev Sci Instrum* **47**:537–541.
93. Kinoshita S, Kushida T. 1982. High-performance, time-correlated single photon counting apparatus using a side-on type photomultiplier. *Rev Sci Instrum* **53**(4):469–472.
94. Canonica S, Forrer J, Wild UP. 1985. Improved timing resolution using small side-on photomultipliers in single photon counting. *Rev Sci Instrum* **56**(9):1754–1758.
95. Ware WR, Pratinidhi M, Bauer RK. 1983. Performance characteristics of a small side-window photomultiplier in laser single-photon fluorescence decay measurements. *Rev Sci Instrum* **54**:1148–1156.
96. Hamamatsu Photonics KK. 2001. *Metal package photomultiplier tube R7400U series*.
97. Hamamatsu Photonics KK. 2000. *Photosensor modules H5773/H5783/H6779/H6780/H5784 series*.
98. Cova S, Longoni A, Andreoni A, Cubeddu R. 1983. A semiconductor detector for measuring ultraweak fluorescence decays with 70ps FWHM resolution. *IEEE J Quantum Electron* **QE-19**:630–634.
99. Buller GS, Massa JS, Walker AC. 1992. All solid-state microscope-based system for picosecond time-resolved photoluminescence measurements on II-VI semiconductors. *Rev Sci Instrum* **63**(5):2994–2998.
100. Louis TA, Ripamonti G, Lacaita A. 1990. Photoluminescence lifetime microscope spectrometer based on time-correlated single-photon counting with an avalanche diode detector. *Rev Sci Instrum* **61**(1):11–22.
101. Cova S, Ripamonti G, Lacaita A. 1987. Avalanche semiconductor detector for single optical photons with a time resolution of 60 ps. *Nucl Instrum Methods Phys Res* **A253**:482–487.
102. Cova S, Lacaita A, Ghioni M, Ripamonti G, Louis TA. 1989. 20-ps timing resolution with single-photon avalanche diodes. *Rev Sci Instrum* **60**(6):1104–1110.
103. Cova S, Longoni A, Andreoni A. 1981. Towards picosecond resolution with single-photon avalanche diodes. *Rev Sci Instrum* **52**(3):408–412.
104. Louis T, Schatz GH, Klein-Böltig P, Holzwarth AR, Ripamonti G, Cova S. 1988. Performance comparison of a single-photon avalanche diode with a microchannel plate photomultiplier in time-correlated single-photon counting. *Rev Sci Instrum* **59**(7):1148–1152.

105. Lacaita A, Cova S, Ghioni M. 1988. Four-hundred picosecond single-photon timing with commercially available avalanche photodiodes. *Rev Sci Instrum* **59**(7):1115–1121.
106. Wahl P, Auchet JC, Donzel B. 1974. The wavelength dependence of the response of a pulse fluorometer using the single photoelectron counting method. *Rev Sci Instrum* **45**(1):28–32.
107. Sipp B, Miehe JA, Lopez-Delgado R. 1976. Wavelength dependence of the time resolution of high-speed photomultipliers used in single-photon timing experiments. *Opt Commun* **16**(1):202–204.
108. Rayner DM, McKinnon AF, Szabo AG. 1978. Confidence in fluorescence lifetime determinations: a ratio correction for the photomultiplier time response variation with wavelength. *Can J Chem* **54**:3246–3259.
109. Thompson RB, Gratton E. 1988. Phase fluorometric method for determination of standard lifetimes. *Anal Chem* **60**:670–674.
110. Meister EC, Wild UP, Klein-Böltig P, Holzwarth AR. 1988. Time response of small side-on photomultiplier tubes in time-correlated single-photon counting measurements. *Rev Sci Instrum* **59**(3):499–501.
111. Bauer RK, Balter A. 1979. A method of avoiding wavelength-dependent errors in decay-time measurements. *Opt Commun* **28**(1):91–96.
112. Kolber ZS, Barkley MD. 1986. Comparison of approaches to the instrumental response function in fluorescence decay measurements. *Anal Biochem* **152**:6–21.
113. Vecer J, Kowalczyk AA, Davenport L, Dale RE. 1993. Reconvolution analysis in time-resolved fluorescence experiments, an alternative approach: reference-to-excitation-to-fluorescence reconvolution. *Rev Sci Instrum* **64**(12):3413–3424.
114. Van Den Zegel M, Boens N, Daems D, De Schryver FC. 1986. Possibilities and limitations of the time-correlated single photon counting technique: a comparative study of correction methods for the wavelength dependence of the instrument response function. *Chem Phys* **101**:311–335.
115. James DR, Demmer DRM, Verrall RE, Steer RP. 1983. Excitation pulse-shape mimic technique for improving picosecond-laser excited time-correlated single-photon counting deconvolutions. *Rev Sci Instrum* **54**(9):1121–1130.
116. Zuker M, Szabo AG, Bramall L, Krajcelski DT, Selinger B. 1985. Delta function convolution method (DFCM) for fluorescence decay experiments. *Rev Sci Instrum* **56**(1):14–22.
117. Castelli F. 1985. Determination of correct reference fluorescence lifetimes by self-consistent internal calibration. *Rev Sci Instrum* **56**(4):538–542.
118. Vos K, van Hoek A, Visser AJWG. 1987. Application of a reference convolution method to tryptophan fluorescence in proteins. *Eur J Biochem* **165**:55–63.
119. Martinho JMG, Egan LS, Winnik MA. 1987. Analysis of the scattered light component in distorted fluorescence decay profiles using a modified delta function convolution method. *Anal Chem* **59**:861–864.
120. Ricka J. 1981. Evaluation of nanosecond pulse-fluorometry measurements: no need for the excitation function. *Rev Sci Instrum* **52**(2):195–199.
121. Visser AJWG, Kulinski T, van Hoek A. 1988. Fluorescence lifetime measurements of pseudoazulenes using picosecond-resolved single photon counting. *J Mol Struct* **175**:111–116.
122. Holtom GR. 1990. Artifacts and diagnostics in fast fluorescence measurements. *SPIE Proc* **1204**:2–12.
123. Grinvald A. 1976. The use of standards in the analysis of fluorescence decay data. *Anal Biochem* **75**:260–280.
124. Lampert RA, Chewter LA, Phillips D, O'Connor DV, Roberts AJ, Meech SR. 1983. Standards for nanosecond fluorescence decay time measurements. *Anal Chem* **55**:68–73.
125. Schiller NH, Alfano RR. 1980. Picosecond characteristics of a spectrograph measured by a streak camera/video readout system. *Opt Commun* **35**(3):451–454.
126. Rubin B, Herman RM. 1981. Monochromators as light stretchers. *Am J Phys* **49**(9):868–871.
127. Imhof RE, Birch DJS. 1982. Distortion of gaussian pulses by a diffraction grating. *Opt Commun* **42**(2):83–86.
128. Saari P, Aaviksoo J, Freiberg A, Timpmann K. 1981. Elimination of excess pulse broadening at high spectral resolution of picosecond duration light emission. *Opt Commun* **39**(1,2):94–98.
129. Bebelaar D. 1986. Compensator for the time dispersion in a monochromator. *Rev Sci Instrum* **57**:1686–1687.
130. Beechem JM. 1992. Multi-emission wavelength picosecond time-resolved fluorescence decay data obtained on the millisecond time scale: application to protein: DNA interactions and protein folding reactions. *SPIE Proc* **1640**:676–680.
131. Birch DJS, McLoskey D, Sanderson A, Suhling K, Holmes AS. 1994. Multiplexed time-correlated single-photon counting. *J Fluoresc* **4**(1):91–102.
132. McLoskey D, Birch DJS, Sanderson A, Suhling K, Welch E, Hicks PJ. 1996. Multiplexed single-photon counting, I: a time-correlated fluorescence lifetime camera. *Rev Sci Instrum* **67**(6):2228–2237.
133. Suhling K, McLoskey D, Birch DJS. 1996. Multiplexed single-photon counting, II: the statistical theory of time-correlated measurements. *Rev Sci Instrum* **67**(6):2238–2246.
134. Becker W, Bergmann A, Giscotti G, Rück A. 2004. Advanced time-correlated photon counting technique for spectroscopy and imaging in biomedical systems. *Proc SPIE* **5340**:104–112.
135. Becker W, Bergmann A, Wabnitz H, Grosenick D, Liebert A. 2001. High count rate multichannel TCSPC for optical tomography. *Eur Conf Biomed Opt: Proc SPIE* **4431**:249–254.
136. Hamamatsu Photonics KK. Phototube Manual
137. Zhu L, Stryjewski WJ, Soper SA. 2004. Multiplexed fluorescence detection in microfabricated devices with both time-resolved and spectral-discrimination capabilities using near-infrared fluorescence. *Anal Biochem* **330**:206–218.
138. Lassiter SJ, Stryjewski W, Legendre BL, Erdmann R, Wahl M, Wurm J, Peterson R, Middendorf L, Soper SA. 2000. Time-resolved fluorescence imaging of slab gels for lifetime base-calling in DNA sequencing applications. *Anal Chem* **72**:5373–5382.
139. He H, McGown LB. 2000. DNA sequencing by capillary electrophoresis with four-decay fluorescence detection. *Anal Chem* **72**:5865–5873.
140. Sauer M, Arden-Jacob J, Drexhage KH, Gobel F, Lieberwirth U, Muhlegger K, Muller R, Wolfrum J, Zander C. 1998. Time-resolved identification of individual mononucleotide molecules in aqueous solution with pulsed semiconductor lasers. *Bioimaging* **6**:14–24.
141. Waddell E, Wang Y, Stryjewski W, McWhorter S, Henry AC, Evans D, McCarley RL, Soper SA. 2000. High-resolution near-infrared imaging of DNA microarrays with time-resolved acquisition of fluorescence lifetimes. *Anal Chem* **72**:5907–5917.
142. Zhu L, Stryjewski W, Lassiter S, Soper SA. 2003. Fluorescence multiplexing with time-resolved and spectral discrimination using a near-IR detector. *Anal Chem* **75**:2280–2291.
143. Hall P, Sellinger B. 1981. Better estimates of exponential decay parameters. *J Phys Chem* **85**:2941–2946.
144. Tellinghuisen J, Wilkerson CW. 1993. Bias and precision in the estimation of exponential decay parameters from sparse data. *Anal Chem* **65**:1240–1246.

145. Bhaumik ML, Clark GL, Snell J, Ferder L. 1965. Stroboscopic time-resolved spectroscopy. *Rev Sci Instrum* **36**(1):37–40.
146. Barisas BG, Leuther MD. 1980. Grid-gated photomultiplier photometer with subnanosecond time response. *Rev Sci Instrum* **51**(1):74–78.
147. Steingraber OJ, Berlman IB. 1963. Versatile technique for measuring fluorescence decay times in the nanosecond region. *Rev Sci Instrum* **34**(5):524–529.
148. Hundley L, Coburn T, Garwin E, Stryer L. 1967. Nanosecond fluorimeter. *Rev Sci Instrum* **38**(4):488–492.
149. James DR, Siemarczuk A, Ware WR. 1992. Stroboscopic optical boxcar technique for the determination of fluorescence lifetimes. *Rev Sci Instrum* **63**(2):1710–1716.
150. Pitts JD, Mycek M-A. 2001. Design and development of a rapid acquisition laser-based fluorometer with simultaneous spectral and temporal resolution. *Rev Sci Instrum* **72**(7):3061–3072.
151. Nordlund TM. 1991. Streak camera for time-domain fluorescence. In *Topics in fluorescence spectroscopy*, Vol. 1: *Techniques*, pp. 183–260. Ed JR Lakowicz. Plenum Press, New York.
152. Schiller NH. 1984. Picosecond streak camera photonics. In *Semiconductors probed by ultrafast laser spectroscopy*, Vol. 2, pp. 441–458. Academic Press, New York.
153. Campillo AJ, Shapiro SL. 1983. Picosecond streak camera fluorometry: a review. *IEEE J Quantum Electron* **QE-19**:585–603.
154. Knox W, Mourou G. 1981. A simple jitter-free picosecond streak camera. *Opt Commun* **37**(3):203–206.
155. Ho PP, Katz A, Alfano RR, Schiller NH. 1985. Time response of ultrafast streak camera system using femtosecond laser pulses. *Opt Commun* **54**(1):57–62.
156. Tsuchiya Y, Shinoda Y. 1985. Recent developments of streak cameras. *Proc SPIE* **533**:110–116.
157. Kinoshita K, Ito M, Suzuki Y. 1987. Femtosecond streak tube. *Rev Sci Instrum* **58**(6):932–938.
158. Watanabe M, Koishi M, Roehrenbeck PW. 1993. Development and characteristics of a new picosecond fluorescence lifetime system. *SPIE Proc* **1885**:155–164.
159. Wiessner A, Staerk H. 1993. Optical design considerations and performance of a spectro-streak apparatus for time-resolved fluorescence spectroscopy. *Rev Sci Instrum* **64**(12):3430–3439.
160. Graf U, Bühl C, Betz M, Zuber H, Anliker M. 1994. Optimized streak-camera system: Wide excitation range and extended time scale for fluorescence lifetime measurement. *SPIE Proc* **2137**:204–210.
161. Techert S, Wiessner A, Schmatz S, Staerk H. 2001. Time-resolved fluorescence and solvatochromy of directly linked pyrene-DMA derivatives in alcoholic solution. *J Phys Chem B* **105**:7579–7587.
162. Hamamatsu Photonics KK. *Picosecond fluorescence lifetime measurement system C4780*.
163. Herman P, Lakowicz JR. Unpublished observations.
164. Porter G, Reid ES, Tredwell CJ. 1974. Time-resolved fluorescence in the picosecond region. *Chem Phys Lett* **29**(3):469–472.
165. Beddar GS, Doust T, Porter G. 1981. Picosecond fluorescence depolarisation measured by frequency conversion. *Chem Phys* **61**:17–23.
166. Kahlow MA, Jarzeba W, DuBruil TP, Barbara PF. 1988. Ultrafast emission spectroscopy in the ultraviolet by time-gated upconversion. *Rev Sci Instrum* **59**(7):1098–1109.
167. Morandeira A, Fürstenberg A, Gumi J-C, Vauthey E. 2003. Fluorescence quenching in electron-donating solvents, 1: influence of the solute-solvent interactions on the dynamics. *J Phys Chem A* **107**:5375–5383.
168. Morandeira A, Fürstenberg A, Vauthey E. 2004. Fluorescence quenching in electron-donating solvents, 2: solvent dependence and product dynamics. *J Phys Chem A* **108**:8190–8200.
169. PicoQuant GmbH, NanoHarp 250 Multiscaler Board, [http://picquant.com/products/spec\\_nano'harp.html](http://picquant.com/products/spec_nano'harp.html).
170. Ware WR, Doemery LJ, Nemzek TL. 1973. Deconvolution of fluorescence and phosphorescence decay curves: a least-squares method. *J Phys Chem* **77**(17):2038–2048.
171. Isenberg I, Dyson RD, Hanson R. 1973. Studies on the analysis of fluorescence decay data by the method of moments. *Biophys J* **13**:1090–1115.
172. Small EW, Isenberg I. 1977. On moment index displacement. *J Chem Physiol* **66**:3347–3351.
173. Small EW. 1992. Method of moments and treatment of nonrandom error. *Methods Enzymol* **210**:237–279.
174. Gafni A, Modlin RL, Brand L. 1975. Analysis of fluorescence decay curves by means of the Laplace transformation. *Biophys J* **15**:263–280.
175. Almgren M. 1973. Analysis of pulse fluorometry data of complex systems. *Chem Scr* **3**:145–148.
176. Ameloot M. 1992. Laplace deconvolution of fluorescence decay surfaces. *Methods Enzymol* **210**:237–279.
177. Ameloot M, Hendrickx H. 1983. Extension of the performance of laplace deconvolution in the analysis of fluorescence decay curves. *Biophys J* **44**:27–38.
178. Livesey AK, Brochon JC. 1987. Analyzing the distribution of decay constants in pulse-fluorimetry using the maximum entropy method. *Biophys J* **52**:693–706.
179. Brochon J-C. 1994. Maximum entropy method of data analysis in time-resolved spectroscopy. *Methods Enzymol* **240**:262–311.
180. Zhang Z, Grattan KTV, Hu Y, Palmer AW, Meggitt BT. 1996. Prony's method for exponential lifetime estimations in fluorescence based thermometers. *Rev Sci Instrum* **67**(7):2590–2594.
181. López RJ, González F, Moreno F. 1992. Application of a sine transform method to experiments of single-photon decay spectroscopy: single exponential decay signals. *Rev Sci Instrum* **63**(6):3268–3273.
182. Carraway ER, Hauenstein BL, Demas JN, DeGraff BA. 1985. Luminescence lifetime measurements: elimination of phototube time shifts with the phase plane method. *Anal Chem* **57**:2304–2308.
183. Novikov EG. 1998. Reference reconvolution analysis by phase plane method. *Rev Sci Instrum* **69**(7):2603–2610.
184. O'Connor DVO, Ware WR, Andre JC. 1979. Deconvolution of fluorescence decay curves: a critical comparison of techniques. *J Phys Chem* **83**:1333–1343.
185. Johnson ML. 1994. Use of least-squares techniques in biochemistry. *Methods Enzymol* **240**:1–22.
186. Straume M, Frasier-Cadoret SG, Johnson ML. 1991. Least-squares analysis of fluorescence data. In *Topics in fluorescence spectroscopy*, Vol. 2: *Principles*, pp. 177–239. Ed JR Lakowicz. Plenum Press, New York.
187. Gryczynski I. Unpublished observations.
188. Montgomery DC, Peck EA. 1982. *Introduction to linear regression analysis*. John Wiley & Sons, New York.
189. Johnson ML. Personal communication.
190. Johnson ML, Faunt LM. 1992. Parameter estimation by least-squares methods. *Methods Enzymol* **210**:1–37.
191. Johnson ML, Frasier SG. 1985. Nonlinear least-squares analysis. *Methods Enzymol* **117**:301–342.
192. Box GEP. 1960. Fitting empirical data. *Ann NY Acad Sci* **86**:792–816.
193. Bates DM, Watts DG. 1988. *Nonlinear regression analysis and its applications*. John Wiley, New York.
194. Straume M, Johnson ML. 1992. Monte Carlo method for determining complete confidence probability distributions of estimated model parameters. *Methods Enzymol* **210**:117–129.

195. Alcalá JR. 1994. The effect of harmonic conformational trajectories on protein fluorescence and lifetime distributions. *J Chem Phys* **101**(6):4578–4584.
196. Alcalá JR, Gratton E, Prendergast FG. 1987. Fluorescence lifetime distributions in proteins. *Biophys J* **51**:597–604.
197. James DR, Ware WR. 1985. A fallacy in the interpretation of fluorescence decay parameters. *Chem Phys Lett* **120**(4,5):455–459.
198. Vix A, Lami H. 1995. Protein fluorescence decay: discrete components or distribution of lifetimes? Really no way out of the dilemma? *Biophys J* **68**:1145–1151.
199. Lakowicz JR, Cherek H, Gryczynski I, Joshi N, Johnson ML. 1987. Analysis of fluorescence decay kinetics measured in the frequency-domain using distribution of decay times. *Biophys Chem* **28**: 35–50.
200. Beechem JM, Knutson JR, Ross JBA, Turner BW, Brand L. 1983. Global resolution of heterogeneous decay by phase/modulation fluorometry: mixtures and proteins. *Biochemistry* **22**:6054–6058.
201. Beechem JM, Ameloot M, Brand L. 1985. Global analysis of fluorescence decay surfaces: excited-state reactions. *Chem Phys Lett* **120**(4,5):466–472.
202. Knutson JR, Beechem JM, Brand L. 1983. Simultaneous analysis of multiple fluorescence decay curves: a global approach. *Chem Phys Lett* **102**(6):501–507.
203. Beechem JM. 1989. A second generation global analysis program for the recovery of complex inhomogeneous fluorescence decay kinetics. *Chem Phys Lipids* **50**:237–251.
204. Beechem JM, Gratton E, Ameloot M, Knutson JR, Brand L. 1991. The global analysis of fluorescence intensity and anisotropy decay data: second-generation theory and programs. In *Topics in fluorescence spectroscopy*, Vol. 2: *Principles*, pp. 241–305. Ed JR Lakowicz. Plenum Press, New York.
205. Beechem JM. 1992. Global analysis of biochemical and biophysical data. *Methods Enzymol* **210**:37–55.
206. Chabbert M, Hillen W, Hansen D, Takahashi M, Bousquet J-A. 1992. Structural analysis of the operator binding domain of Tn10-Encoded tet repressor: a time-resolved fluorescence and anisotropy study. *Biochemistry* **31**:1951–1960.
207. Dattelbaum JD, Castellano FN. Unpublished observations.
208. Maus M, Rousseau E, Cotlet M, Schweitzer G, Hofkens J, Van der Auweraer M, De Schryver FC, Krueger A. 2001. New picosecond laser system for easy tunability over the whole ultraviolet/visible/near infrared wavelength range based on flexible harmonic generation and optical parametric oscillation. *Rev Sci Instrum* **72**(1):36–40.
209. Frackowiak D, Zelent B, Malak H, Planner A, Cegielski R, Munger G, Leblanc RM. 1994. Fluorescence of aggregated forms of CHI $\alpha$  in various media. *J Photochem Photobiol A: Chem* **78**:49–55.
210. Werst M, Jia Y, Mets L, Fleming GR. 1992. Energy transfer and trapping in the photosystem I core antenna. *Biophys J* **61**:868–878.
211. Gulotty RJ, Mets L, Alberte RS, Fleming GR. 1986. Picosecond fluorescence studies of excitation dynamics in photosynthetic light-harvesting arrays. In *applications of fluorescence in the biomedical sciences*, pp. 91–104. Ed DL Taylor, AS Waggoner, F Lanni, RF Murphy, RR Birge. Alan R. Liss, New York.
212. Visser AJWG. 1984. Kinetics of stacking interactions in flavin adenine dinucleotide from time-resolved flavin fluorescence. *Photochem Photobiol* **40**(6):703–706.
213. Dudewicz EJ, Van Der Meulen EC. 1981. Entropy-based tests of uniformity. *J Am Stat Assoc* **76**(376):967–974.
214. Livesey AK, Brochon JC. 1987. Analyzing the distribution of decay constants in pulse-fluorimetry using the maximum entropy method. *Biophys J* **52**:693–706.
215. Vincent M, Brochon J-C, Merola F, Jordi W, Gallay J. 1988. Nanosecond dynamics of horse heart apocytochrome c in aqueous solution as studied by time-resolved fluorescence of the single tryptophan residue (Trp-59). *Biochemistry* **27**:8752–8761.
216. Merola F, Rigler R, Holmgren A, Brochon J-C. 1989. Picosecond tryptophan fluorescence of thioredoxin: Evidence for discrete species in slow exchange. *Biochemistry* **28**:3383–3398.
217. Sopkova J, Vincent M, Takahashi M, Lewit-Bentley A, Gallay J. 1999. Conformational flexibility of domain III of Annexin V at membrane/water interfaces. *Biochemistry* **38**:5447–5458.
218. Luecke H, Chang BT, Mailliard WS, Schlaepfer DD, Harry H. 1995. Crystal structure of the annexin XII hexamer and implications for bilayer insertion. *Nature* **378**(6556):512–515.
219. Rouvière N, Gallay J. 2000. Wavelength-resolved fluorescence emission of proteins using the synchrotron radiation as pulsed-light source: Cross-correlations between lifetimes, rotational correlation times and tryptophan heterogeneity in FKBP59 immunophilin. *Cell Mol Biol* **46**(5):1113–1131.
220. Becker W. 2005. *Advanced time-correlated single photon counting techniques*. Springer, New York.

## PROBLEMS

- P4.1. *Calculation of Lifetimes:* Use the data in Figures 4.1 and 4.2 to estimate the lifetime from the time-domain data, and from the phase and modulation.
- P4.2. *Fractional Intensity of Components in the Tryptophan Intensity Decay:* At pH 7, tryptophan displays a double-exponential intensity decay. At 320 nm the intensity decay low is  $I(t) = 0.19 \exp(-t/0.62 \text{ ns}) + 0.81 \exp(-t/3.33 \text{ ns})$ . What is the fractional contribution of the 0.62-ns component to the steady-state intensity at 320 nm?
- P4.3. *Stacking Equilibrium in Flavin Adenine Dinucleotide:* Use the intensity decays and lifetimes in Figure 4.61 to calculate the collisional rate between the flavin and adenine groups in FAD.
- P4.4. *Average Lifetime:* Suppose that a protein contains two tryptophan residues with identical lifetimes ( $\tau_1 = \tau_2 = 5 \text{ ns}$ ) and pre-exponential factors ( $\alpha_1 = \alpha_2 = 0.5$ ). Now suppose that a quencher is added such that the first tryptophan is quenched tenfold in both lifetime and steady-state intensity. What is the intensity decay law in the presence of quencher? What is the average lifetime ( $\bar{\tau}$ ) and the lifetime-weighted quantum yield ( $\langle \tau \rangle$ )? Explain the relative values.
- P4.5. *Decay Associated Spectra:* Tables 4.5 and 4.6 list the results of the multi-exponential analysis of the two-component mixture of anthranilic acid (AA) and 2-aminopurine (2-AP). Use these data to construct the decay associated spectra. Explain the results for the DAS recovered from the non-global (Table 4.5) and global (Table 4.6) analysis.

- P4.6. *Data Acquisition Times Using TCSPC With Microsecond Decay Times:* Calculate the time needed to acquire the data in Figure 4.45. Assume the lifetime of  $[\text{Ru}(\text{bpy})_3]^{2+}$  is 400 ns and that one photon is detected for each excitation pulse. Calculate the data acquisition time to obtain the same data using TCSPC with the same pulse repetition rate and a 1% count rate.
- P4.7. *Data Acquisition Times Using TCSPC With Nanosecond Decay Times:* Suppose the lifetime of a fluorophore is 4 ns. Determine the conditions needed for TCSPC. Calcu-

late the time required to count  $4 \times 10^6$  photons with 1 photon counted per 100 excitation pulses. Consider dead times of 2  $\mu\text{s}$  and 120 ns.

- P4.8. *Calculation of Fractional Intensities and Pre-Exponential Factors:* Suppose two compounds have equal quantum yields but different lifetimes of  $\tau_1 = 1 \mu\text{s}$  and  $\tau_2 = 1$  ns. If a solution contains an equimolar amount of both fluorophores, what is the fractional intensity of each fluorophore?

# 5

# Frequency-Domain Lifetime Measurements

In the preceding chapter we described the theory and instrumentation for measuring fluorescence intensity decays using time-domain measurements. In the present chapter we continue this discussion, but describe frequency-domain fluorometry. In this method the sample is excited with light that is intensity modulated at a high frequency comparable to the reciprocal of the lifetime. When this is done, the emission is intensity modulated at the same frequency. However, the emission does not precisely follow the excitation, but rather shows time delays and amplitude changes that are determined by the intensity decay law of the sample. The time delay is measured as a phase angle shift between the excitation and emission, as was shown in Figure 4.2. The peak-to-peak height of the modulated emission is decreased relative to the modulated excitation, and provides another independent measure of the lifetime.

Time-resolved measurements, whether performed in the time domain or in the frequency domain, provides information about intensity decay of the sample. Samples with multiple fluorophores typically display multi-exponential decays. Even samples with a single fluorophore can display complex intensity decays due to conformational heterogeneity, resonance energy transfer, and transient effects in diffusive quenching or fluorophore–solvent interactions, to name just the most common origins. The goal of the time-resolved measurement is to determine the form of the intensity decay law, and to interpret the decay in terms of molecular features of the sample.

Intensity decays can be single-exponential, multi-exponential, or non-exponential. Irrespective of the complexity of the decay, one can always define a mean or apparent decay time. For a single exponential decay in the time domain the actual lifetime is given by this the time when the intensity decays to  $1/e$  of its initial value. For a multi-exponential decay, the  $1/e$  time is typically not equal to any of the decay times. In the frequency domain an apparent lifetime ( $\tau_\phi$ ) determined from the phase angle ( $\phi_\omega$ ) or the appa-

ent lifetime ( $\tau_m$ ) determined from the modulation ( $m_\omega$ , eqs. 4.5 and 4.6). The apparent lifetimes are characteristic of the sample, but do not provide a complete description of the complex intensity decay. The values of  $\tau_\phi$  and  $\tau_m$  need not be equal, and each value represents a different weighted average of the decay times displayed by the sample. In general, the apparent lifetime depends on the method of measurement. The earlier literature on time-resolved fluorescence often describes apparent lifetimes. At present, there are relatively few reports of only the mean decay times. This is because the mean lifetimes represent complex weighted averages of the multi-exponential decay. Quantitative interpretation of mean decay times is usually difficult and the results are often ambiguous.

Prior to 1983, frequency-domain fluorometry allowed determination of mean lifetime, but was not able to resolve complex intensity decays. This limitation was the result of phase-modulation fluorometers, which only operated at one, two, or three fixed light modulation frequencies. The resolution of a complex decay requires measurements at a number of modulation frequencies that span the frequency response of the sample. While several variable-frequency instruments were described prior to 1983, these were not generally useful and were limited by systematic errors. The first generally useful variable frequency instrument was described in the mid 1980s.<sup>1–2</sup> These instruments allowed phase and modulation measurements from 1 to 200 MHz. These designs are the basis of currently available instruments. Frequency-domain fluorometry is now in widespread use,<sup>3–9</sup> and instruments are commercially available. Frequency-domain fluorometers are now routinely used to study multi-exponential intensity decays, and non-exponential decays resulting from resonance energy transfer, time-dependent solvent relaxation, and collisional quenching.

In this chapter we describe the instrumentation for FD measurements and the theory used to interpret the experimental data. We will describe examples that illustrate the

applications of the FD method for the resolution of complex decay kinetics. We describe the present state-of-the-art instrumentation, which allows FD data to be obtained to 10 GHz, depending upon the photodetector and associated electronics. We will describe the newer simple FD instrumentation based on laser diodes (LD) or light-emitting diodes (LED) as the excitation source.

The objective of both the time- and frequency-domain measurements is to recover the parameters describing the time-dependent decay. Assume that the sample is excited with a  $\delta$ -function pulse of light. The resulting time-dependent emission is called the impulse response function, which is often represented by the multi-exponential model:

$$I(t) = \sum_i \alpha_i e^{-t/\tau_i} \quad (5.1)$$

In this expression the values of  $\alpha_i$  are the pre-exponential factors and the  $\tau_i$  values the decay times.

If the emission decays with a single decay time (Figure 5.1), it is rather easy to measure the decay time with good accuracy. If the single decay time is long relative to the excitation pulse, then  $\log I(t)$  decays linearly versus time, and the decay time is easily obtained from the slope. The more difficult task is recovery of multiple decay times, which is illustrated for two widely spaced decay times in Figure 5.1 (5 and 20 ns). In this case,  $\log I(t)$  does not decay linearly with time. Unfortunately, decay times of the emission from macromolecules are often more closely spaced than the fivefold difference shown in Figure 5.1, and resolution of the decay times becomes increasingly difficult as

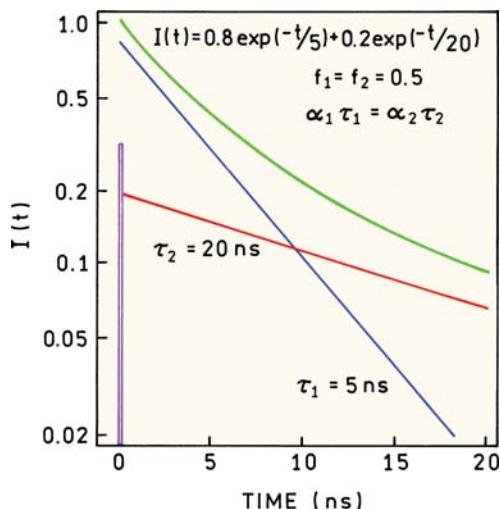


**Figure 5.1.** Impulse response function for decay times of 5 and 20 ns, and for a multi-exponential decay with the same decay times.

the decay times become more closely spaced. If the decay times are spaced by 20% (e.g., 5 and 6 ns or 10 and 12 ns), it is difficult to visually distinguish a single-exponential decay from a double-exponential decay. In fact, such closely spaced decay times cannot usually be resolved using TD or FD measurements. It is generally difficult to resolve sums of exponentials because the parameters describing the decay are highly correlated. Hence, one requires a high signal-to-noise ratio, or equivalently a large number of photons, to recover the multiple decay times with reasonable confidence.

It is valuable to understand how a multi-exponential decay is related to the steady-state intensity of the same sample. The fraction of the intensity observed in the usual steady-state measurement due to each component in the multi-exponential decay is

$$f_i = \frac{\alpha_i \tau_i}{\sum_j \alpha_j \tau_j} \quad (5.2)$$

The contribution of any decay component to the steady-state intensity is proportional to the  $\alpha\tau$  product for this component. This can be understood by visualizing the area under an intensity decay, which is proportional to the  $\alpha\tau$  product (Figure 5.1).

Intensity decays are routinely analyzed in terms of the multi-exponential model. However this does not mean that the values of  $\alpha_i$  and  $\tau_i$  have any physical meaning. The multi-exponential model is very powerful and able to account for almost any decay law. Depending upon the sample, the values of  $\alpha_i$  and  $\tau_i$  may have direct or indirect molecular significance. For a mixture of two fluorophores, each of which displays a single decay time,  $\tau_i$  are the decay times of the two fluorophores, and  $f_i$  are the fractional contributions of each fluorophore to the total emission. In many circumstances there is no obvious linkage between the  $\alpha_i$  and  $\tau_i$  values and the molecular features of the sample. For instance, non-exponential decays occur due to transient effects in quenching, or due to distributions of donor-acceptor distances. These intensity decays can usually be satisfactorily fit by the multi-exponential model, for such decays it is difficult to relate the values of  $\alpha_i$  and  $\tau_i$  to the molecular parameters of the sample.

## 5.1. THEORY OF FREQUENCY-DOMAIN FLUOROMETRY

In frequency-domain fluorometry the excitation source and measurements are rather different than for time-domain

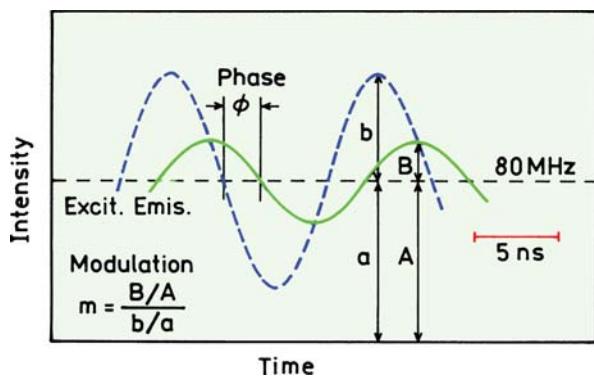


**Figure 5.2.** Definitions of the phase angle and modulation of emission. The assumed decay time is 5 ns and the light modulation frequency is 80 MHz.

measurements. In time-domain measurements the excitation source is a pulsed light source. In frequency-domain measurements the excitation is an intensity-modulated light source.<sup>3</sup> Because of the time lag between absorption and emission, the emission is delayed in time relative to the modulated excitation (Figure 5.2). The delay is measured as a phase shift  $\phi_\omega$  between the excitation and emission, where  $\omega$  is the modulation frequency in radians/s. The finite time response of the sample also results in demodulation of the emission by a factor  $m_\omega$ . The finite lifetime of the excited

state prevents the emission from precisely following the excitation. This results in a decrease in the peak-to-peak amplitude of the modulated emission, which is measured relative to the modulated excitation (Figure 5.2).

The phase shift and modulation of the emission depend on the relative values of the lifetime and the light modulation frequency. This is shown in Figure 5.3 for a decay time of 5 ns and modulation frequencies of 2.5, 25, and 250 MHz. As the light modulation frequency increases, the phase shift of the emission increases and the modulation of the emission decreases. The dependence of the phase angle  $\phi$  and modulation  $m$  on the light modulation frequency is used to recover the intensity decay of the sample.

The origin of the phase shift and demodulation can be understood by considering the time-dependent excitation intensity and the time of intensity decay of the fluorophore. Figure 5.4 shows a 10-ns intensity decay superimposed on the modulated excitation. Consider the fluorophores that are excited when the intensity is at its maximum ( $t = 0$ ). If the modulation frequency is 2.5 MHz, a full cycle is 400 ns long. On this timescale the intensity decay is barely visible. For this reason the emission closely follows the excitation with a minimal phase shift and nearly complete modulation. Now consider modulation at 250 MHz, where a cycle is 4

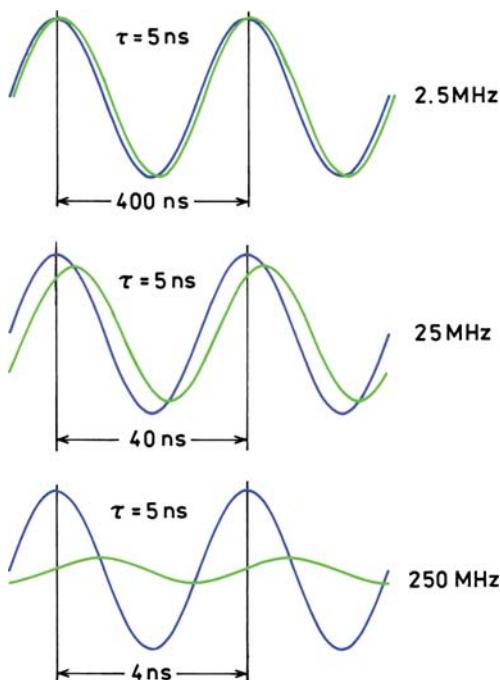


**Figure 5.3.** Emission of a 5-ns decay time fluorophore in response to sinusoidally modulated excitation at 2.5, 25, and 250 MHz.

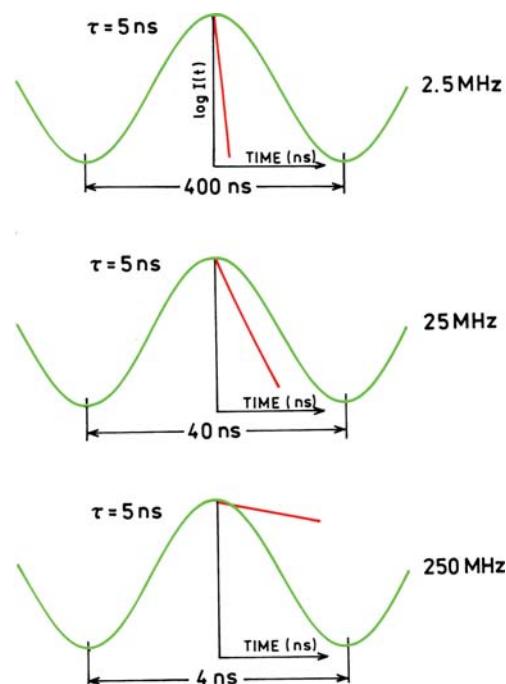


**Figure 5.4.** Comparison of a 5-ns intensity decay with light modulation frequencies of 2.5, 25, and 250 MHz. The time axis of the inserts are the same as for the modulated intensity.

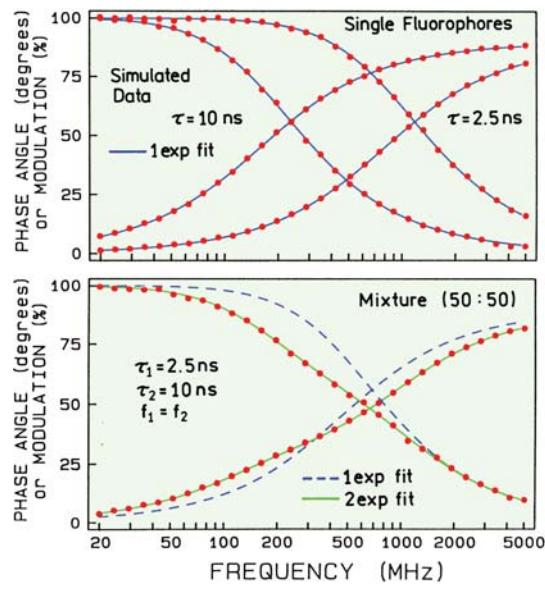


**Figure 5.5.** Simulated frequency-domain data for single- (top) and double- (bottom) exponential decays. The phase angle increases and the modulation decreases with increasing modulation frequency. The datapoints indicate the simulated data. **Top:** The solid lines show the best fits to a single decay time. **Bottom:** The dashed and solid lines show the best single- and double-exponential fits, respectively.

ns long. In this case the molecules excited at the peak of the intensity continue to emit during the entire modulation cycle. This results in an averaging of the decay across the peaks and valleys of the excitation. This averaging results in the phase shift and decrease in modulation of the emission. At an intermediate modulation frequency of 25 MHz some averaging occurs, but to a lesser extent than at 250 MHz.

In FD measurements the phase angle and modulation are measured over a wide range of frequencies. These data are called the frequency response of the sample. The characteristic features of the frequency response of a sample are illustrated in Figure 5.5 (top) for a single exponential decay. As the light modulation frequency is increased the phase angle increases from 0 to 90°. At first glance the 90° phase angle limit is counterintuitive. For a time delay of the type available from an optical delay line, the phase shift can exceed 90° and reach any arbitrary value. For a single exponential or multi-exponential decay, the maximum phase angle is 90°. Hence the phase angle displayed by any sample is some fraction of 90°, independent of the modulation frequency. Only under special circumstances can the phase angle exceed 90° (Chapter 17).

The modulation of the emission also depends on the modulation frequency of the incident light. As the frequency increases the modulation decreases from 1.0 to 0. The

modulation of the emission is zero when the frequency is much larger than the emission rate. In presenting frequency-domain data, the modulation frequency on the *x*-axis (Figure 5.5) is usually described in cycles/s (Hz or MHz). The circular modulation frequency ( $\omega = 2\pi \times \text{Hz}$ ) in radians/s is used for calculations.

The shape of the frequency response is determined by the number of decay times displayed by the sample. If the decay is a single exponential (Figure 5.5, top), the frequency response is simple. One can use the phase angle or modulation at any frequency to calculate the lifetime. For a single-exponential decay, the phase and modulation are related to the decay time ( $\tau$ ) by

$$\tan \phi_\omega = \omega \tau \quad (5.3)$$

and

$$m_\omega = (1 + \omega^2 \tau^2)^{-1/2} \quad (5.4)$$

The derivation of eqs. 5.3 and 5.4 is given in Section 5.11. For the 10-ns decay time, the phase shift at 20 MHz is 51.5°, and the emission is demodulated by a factor of 0.62 relative to the excitation. At a modulation frequency of 100 MHz the phase angle increases to 81°, and the modulation decreases to 0.16. Most samples of interest display more than one decay time. In this case the lifetimes calculated from the value of  $\phi_\omega$  or  $m_\omega$ , measured at a particular frequency, are only apparent values and are the result of a complex weighting of various components in the emission (Section 5.10). For such samples it is necessary to measure the phase and modulation values over the widest possible range of modulation frequencies.

The frequency response has a different shape for a multi-exponential decay (Figure 5.5, bottom). In this simulation the assumed decay times are 2.5 and 10 ns. The shape of the frequency response is used to determine the form of the intensity decay. This is generally accomplished using nonlinear least-squares procedures.<sup>10-13</sup> The fitting procedure is illustrated by the solid and dashed lines in Figure 5.5. For the single-exponential decays shown in the top half of the figure, it is possible to obtain a good match between the data (●) and the curves calculated using the single-exponential model (solid line). For a double-exponential decay, as shown in the bottom half of the figure, the data cannot be matched using a single-decay time fit, represented by the dashed lines. However, the complex frequency response is accounted for by the double-exponential model,

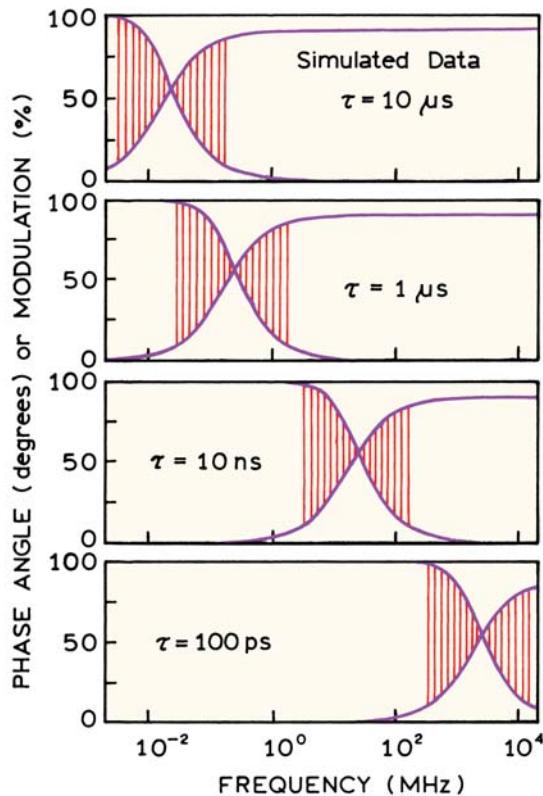


**Figure 5.6.** Relationship between the decay time and the useful range of light modulation frequencies.

represented by the solid lines, with the expected decay times (2.5 and 10 ns) and fractional intensities ( $f_1 = f_2 = 0.5$ ) being recovered from the least-squares analysis.

The range of modulation frequencies needed to recover the intensity decay depends on the lifetimes. The useful modulation frequencies are those where the phase angle is frequency dependent, and there is still measurable modulation (Figure 5.6). Most fluorophores display lifetimes near 10 ns, so that modulation frequencies are typically near 2–200 MHz. If the decay time is near 100 ps, higher modulation frequencies near 2 GHz are needed. For longer decay times of 1 to 10  $\mu$ s the modulation frequencies can range from 10 kHz to 1 MHz. As the modulation frequency increases, the modulation of the emission decreases. Hence it becomes more difficult to measure the phase angles as they approach 90°.

### 5.1.1. Least-Squares Analysis of Frequency-Domain Intensity Decays

The procedures used to analyze the frequency-domain data are analogous to those used for TCSPC. The frequency-

domain data are usually analyzed by the method of nonlinear least squares.<sup>10–13</sup> The measured data are compared with values predicted from a model, and the parameters of the model are varied to yield the minimum deviations from the data. The phase and modulation values can be predicted for any decay law. This is accomplished using sine and cosine transforms of the intensity decay  $I(t)$ :

$$N_{\omega} = \frac{\int_0^{\infty} I(t) \sin \omega t dt}{\int_0^{\infty} I(t) dt} \quad (5.5)$$

$$D_{\omega} = \frac{\int_0^{\infty} I(t) \cos \omega t dt}{\int_0^{\infty} I(t) dt} \quad (5.6)$$

where  $\omega$  is the circular modulation frequency ( $2\pi$  times the modulation frequency in Hz). The denominator  $J = \int_0^{\infty} I(t) dt$  normalizes the expression for the total intensity of the sample. These expressions are valued for any intensity decay law, whether the decay is multi-exponential or non-exponential. Non-exponential decay laws can be transformed numerically. For a sum of exponentials the transforms are<sup>12–13</sup>

$$N_{\omega} = \sum_i \frac{\alpha_i \omega \tau_i^2}{(1 + \omega^2 \tau_i^2)} / \sum_i \alpha_i \tau_i \quad (5.7)$$

$$D_{\omega} = \sum_i \frac{\alpha_i \tau_i}{(1 + \omega^2 \tau_i^2)} / \sum_i \alpha_i \tau_i \quad (5.8)$$

For a multi-exponential decay  $J = \sum \alpha_i \tau_i$ , which is proportional to the steady-state intensity of the sample. Because of this normalization factor one can always fix one of the amplitudes ( $\alpha_i$  or  $f_i$ ) in the analysis of frequency-domain data. The calculated frequency-dependent values of the phase angle ( $\phi_{c\omega}$ ) and the demodulation ( $m_{c\omega}$ ) are given by

$$\tan \phi_{c\omega} = N_{\omega} / D_{\omega} \quad (5.9)$$

$$m_{c\omega} = (N_{\omega}^2 + D_{\omega}^2)^{1/2} \quad (5.10)$$

In the least-squares analysis the parameters ( $\alpha_i$  and  $\tau_i$ ) are varied to yield the best fit between the data and the calcu-

lated values, as indicated by a minimum value for the goodness-of-fit parameters  $\chi_R^2$ :

$$\chi_R^2 = \frac{1}{v} \sum_{\omega} \left[ \frac{\phi_{\omega} - \phi_{c\omega}}{\delta\phi} \right]^2 + \frac{1}{v} \sum_{\omega} \left[ \frac{m_{\omega} - m_{c\omega}}{\delta m} \right]^2 \quad (5.11)$$

where  $v$  is the number of degrees of freedom. The value of  $v$  is given by the number of measurements, which is typically twice the number of frequencies minus the number of variable parameters. The subscript c is used to indicate calculated values for assumed values of  $\alpha_i$  and  $\tau_i$ , and  $\delta\phi$  and  $\delta m$  are the uncertainties in the phase and modulation values, respectively. Unlike the errors in the photon-counting experiments (Chapter 4), these errors cannot be estimated directly from Poisson statistics.

The correctness of a model is judged based on the values of  $\chi_R^2$ . For an appropriate model and random noise,  $\chi_R^2$  is expected to be near unity. If  $\chi_R^2$  is sufficiently greater than unity, then it may be correct to reject the model. Rejection is judged from the probability that random noise could be the origin of the value of  $\chi_R^2$ .<sup>10,11</sup> For instance, a typical frequency-domain measurement from this laboratory contains phase and modulation data at 25 frequencies. A double-exponential model contains three floating parameters (two  $\tau_i$  and one  $\alpha_i$ ), resulting in 47 degrees of freedom. A value of  $\chi_R^2$  equal to 2 is adequate to reject the model with a certainty of 99.9% or higher (Table 4.2).

In practice, the values of  $\chi_R^2$  change depending upon the values of the uncertainties ( $\delta\phi$  and  $\delta m$ ) used in its calculation. The effects of selecting different values of  $\delta\phi$  and  $\delta m$  has been considered in detail.<sup>12–13</sup> The fortunate result is that the recovered parameter values ( $\alpha_i$  and  $\tau_i$ ) do not depend strongly on the chosen values of  $\delta\phi$  and  $\delta m$ . The parameter values can be expected to be sensitive to  $\delta\phi$  and  $\delta m$  if the data are just adequate to determine the parameter values, that is, at the limits of resolution.

For consistency and ease of day-to-day data interpretation we use constant values of  $\delta\phi = 0.2^\circ$  and  $\delta m = 0.005$ . While the precise values may vary between experiments, the  $\chi_R^2$  values calculated in this way indicate to us the degree of error in a particular data set. For instance, if a particular data set has poor signal-to-noise, or systematic errors, the value of  $\chi_R^2$  is elevated even for the best fit. The use of fixed values of  $\delta\phi$  and  $\delta m$  does not introduce any ambiguity in the analysis, as it is the relative values of  $\chi_R^2$  that are used in accepting or rejecting a model. We typically compare  $\chi_R^2$  for the one-, two-, and three-exponential fits. If  $\chi_R^2$  decreases twofold or more as the model is incre-

mented, then the data probably justify inclusion of the additional decay time. According to Table 4.3, a ratio of  $\chi_R^2$  values of 2 is adequate to reject the simpler model with a 99% certainty. It should be remembered that the values of  $\delta\phi$  and  $\delta m$  might depend upon frequency, either as a gradual increase in random error with frequency, or as higher-than-average uncertainties at discrete frequencies due to interference or other instrumental effects. In most cases the recovered parameter values are independent of the chosen values of  $\delta\phi$  and  $\delta m$ . However, caution is needed as one approaches the resolution limits of the measurements. In these cases the values of the recovered parameters might depend upon the values chosen for  $\delta\phi$  and  $\delta m$ .

The values of  $\delta\phi$  and  $\delta m$  can be adjusted as appropriate for a particular instrument. For instance, the phase data may become noisier with increasing modulation frequency because the phase angle is being measured from a smaller signal. One can use values of  $\delta\phi$  and  $\delta m$  which increase with frequency to account for this effect. In adjusting the values of  $\delta\phi$  and  $\delta m$ , we try to give equal weight to the phase and modulation data. This is accomplished by adjusting the relative values of  $\delta\phi$  and  $\delta m$  so that the sum of the squared deviations (eq. 5.11) is approximately equal for the phase and modulation data.

Another way to estimate the values of  $\delta\phi$  and  $\delta m$  is from the data itself. The phase and modulation values at each frequency are typically an average of 10 to 100 individual measurements. In principle, the values of  $\delta\phi$  and  $\delta m$  are given by the standard deviation of the mean of the phase and modulation, respectively. In practice we find that the standard deviation of the mean underestimates the values of  $\delta\phi$  and  $\delta m$ . This probably occurs because the individual phase and modulation measurements are not independent of each other. For simplicity and consistency, the use of constant values of  $\delta\phi$  and  $\delta m$  is recommended.

In analyzing frequency-domain data it is advisable to avoid use of the apparent ( $\tau_{\phi}$ ) or modulation ( $\tau_m$ ) lifetimes. These values are the lifetimes calculated from the measured phase and modulation values at a given frequency. These values can be misleading, and are best avoided. The characteristics of  $\tau_{\phi}$  and  $\tau_m$  are discussed in Section 5.10.

### 5.1.2. Global Analysis of Frequency-Domain Data

Resolution of closely spaced parameters can be improved by global analysis. This applies to the frequency-domain data as well as the time-domain data. The use of global analysis is easiest to visualize for a mixture of fluorophores

each displaying a different emission spectrum. In this case the intensity decay at each wavelength ( $\lambda$ ) is given by

$$I(\lambda, t) = \sum_{i=1} \alpha_i(\lambda) e^{-t/\tau_i} \quad (5.12)$$

where the values of  $\alpha_i(\lambda)$  represent the relative contribution of the  $i$ th fluorophore at wavelength  $\lambda$ . The frequency response is typically measured at several wavelengths resulting in wavelength-dependent values of the phase angle  $\phi_\omega(\lambda)$  and the modulation  $m_\omega(\lambda)$ . In this case the values of  $N_\omega^\lambda$  and  $D_\omega^\lambda$  depend on the observation wavelength, and are given by

$$N_\omega^\lambda = \sum_i \frac{\alpha_i(\lambda)\omega\tau_i^2}{1 + \omega^2\tau_i^2} / \sum_i \alpha_i(\lambda)\tau_i \quad (5.13)$$

$$D_\omega^\lambda = \sum_i \frac{\alpha_i(\lambda)\omega\tau_i}{1 + \omega^2\tau_i^2} / \sum_i \alpha_i(\lambda)\tau_i \quad (5.14)$$

The wavelength-dependent data sets can be used in a global minimization of  $\chi_R^2$ :

$$\begin{aligned} \chi_R^2 = & \frac{1}{v} \sum_{\lambda, \omega} \left[ \frac{\phi_\omega(\lambda) - \phi_{co}(\lambda)}{\delta\phi} \right]^2 \\ & + \frac{1}{v} \sum_{\lambda, \omega} \left[ \frac{m_\omega(\lambda) - m_{co}(\lambda)}{\delta m} \right]^2 \end{aligned} \quad (5.15)$$

where the sum now extends over the frequencies ( $\omega$ ) and wavelengths ( $\lambda$ ). Typically the values of  $\tau_i$  are assumed to be independent of wavelength and are thus the global parameters. The values of  $\alpha_i(\lambda)$  are usually different for each data set, that is, are non-global parameters. The data are normalized at each wavelength, allowing one of the amplitudes at each wavelength to be fixed in the analysis.

It is important to estimate the range of parameter values that are consistent with the data. As for TCSPC, the asymptotic standard errors (ASEs) recovered from least-square analysis do not provide a true estimate of the uncertainty, but provide a significant underestimation of the range of parameter values which is consistent with the data. This effect is due to correlation between the parameters, which is not considered in calculation of the asymptotic standard errors. Algorithms are available to estimate the upper and lower bounds of a parameter based on the extent

of correlation.<sup>14–16</sup> If the analysis is at the limits of resolution we prefer to examine the  $\chi_R^2$  surfaces. This is accomplished just as for the time-domain data. Each parameter value is varied around its best fit value, and the value of  $\chi_R^2$  is minimized by adjustment of the remaining parameters. The upper and lower limits for a parameter are taken as those which result in an elevation of the  $F_\chi$  value expected for one standard deviation ( $P = 0.32$ ) and the number of degrees of freedom (Section 5.7.1).

## 5.2. FREQUENCY-DOMAIN INSTRUMENTATION

### 5.2.1. History of Phase-Modulation Fluorometers

The use of phase-modulation methods for measurements of fluorescence lifetimes has a long history.<sup>17</sup> The first lifetime measurements were performed by Gaviola in 1926 using a phase fluorometer.<sup>18</sup> The first suggestion that phase angle measurements could be used for measuring fluorescence lifetimes appears to have been made even earlier in 1921.<sup>19</sup> The use of phase delays to measure short time intervals appears to have been suggested even earlier, in 1899.<sup>20</sup> Hence, the use of phase shifts for timing of rapid processes has been recognized for 100 years. Since the pioneering measurements by Gaviola<sup>18</sup> a large number of phase-modulation instruments have been described. These include an instrument by Duschinsky in 1933,<sup>21</sup> and an instrument of somewhat more advanced design described by Szymonowski<sup>22</sup>, on which many of Jablonski's early measurements were performed. Phase fluorometers have been described by many research groups.<sup>23–53</sup> The first generally useful design appeared in 1969.<sup>41</sup> This instrument used a Debye-Sears ultrasonic modulator<sup>42–43</sup> to obtain intensity-modulated light from an arc lamp light source. The use of the Debye-Sears modulator has been replaced by electrooptic modulators in current FD instruments. However, an important feature of this instrument<sup>41</sup> is the use of cross-correlation detection (Section 5.11.2). The use of this radio frequency mixing method simplified measurement of the phase angles and modulation values at high frequencies, and allowed measurement of the phase angle and modulation with relatively slow timing electronics.

The primary technical factor limiting the development of frequency-domain fluorometers was the inability to obtain intensity-modulated light over a range of modulation frequencies. Debye-Sears modulators are limited to operating at the frequency of the crystal, or multiples thereof.

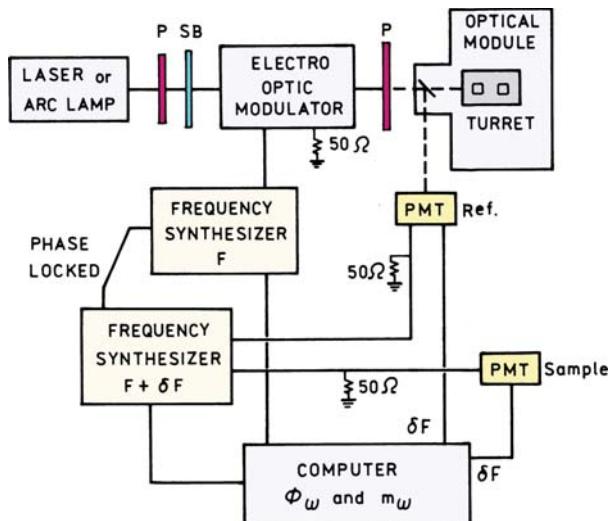


**Figure 5.7.** Schematic representation of the variable-frequency phase-modulation fluorometer. P, polarizer; SB, Soliel-Babinet compensator; F, frequency;  $\delta F$ , cross-correlation frequency; PMT, photomultiplier tube.

Consequently, the early phase-modulation fluorometers operated at only one to three fixed modulation frequencies. The limited data these instruments provided were adequate for measuring mean decay times, or for detecting the presence of a complex decay. However, the data at a limited number of modulation frequencies were not generally useful for resolution of the parameters describing multi- or non-exponential decays.

As has occurred for TCSPC, pulsed-laser diodes (LDs), and light-emitting diodes (LEDs) are becoming the preferred excitation source. The output of the LDs and LEDs can be modulated directly by the electrical input. This eliminates the need for the electrooptic modulator, which adds cost and complexity to the FD instruments.

### 5.2.2. An MHz Frequency-Domain Fluorometer

Frequency-domain fluorometers are now in widespread use. Most designs are similar to that shown in Figure 5.7. The main differences are the laser light source, the light modulator, and the associated radio-frequency electronics. Without the use of LDs or LEDs it is difficult to obtain light modulation over a wide range of frequencies. Amplitude modulation of laser sources over a continuous range of frequencies to 200 MHz is possible with electrooptic modulators. Light can also be modulated with acoustooptic modulators. However, acoustooptic modulators provide modulation at discrete resonances over a limited range of frequencies.<sup>54-56</sup>

Most electrooptic modulators have long narrow optical apertures, and electrooptic modulators are not easily used with arc lamp sources. Initially, only laser sources seemed practical for use with electrooptic modulators. Surprisingly, it is now possible to use electrooptic devices to modulate arc lamps to 200 MHz, which is done in commercial FD instruments. The operational principles of the modulators and the electronic parts needed to construct such an FD instrument are discussed below, along with the rationale for selecting the various components.

The light source for an FD instrument can be almost any continuous-wave (cw) light source or a high-repetition-rate pulse laser. The choice of source is based on the needed wavelengths and power levels. The He-Cd laser is a convenient cw source, providing cw output at 325 and 442 nm. Unfortunately, these wavelengths are not suitable for excitation of protein fluorescence. A very versatile source is the Ar ion laser, which can now provide deep UV lines (~275 nm) for intrinsic fluorescent probes. However, only a limited number of UV wavelengths are available. Studies of protein fluorescence usually require 290 to 300 nm to avoid excitation of tyrosine and to obtain high fundamental anisotropies. These wavelengths are not available from an argon ion laser. The argon ion laser at 514 nm is an ideal source for pumping dye lasers. The 514 nm line can be mode-locked to synchronously pump a picosecond dye laser system (Section 4.4). An Nd:YAG laser can also be the primary source, particularly for pumping dye lasers.

Appropriate electronics are needed to measure the phase angle and modulation at high frequencies. The measurements appear difficult because the resolution of multi-exponential decays requires accuracy near  $0.2^\circ$  in phase and 0.5% (0.005) in modulation, and that this accuracy needs to be maintained from 1 to 200 MHz. In fact, the measurements are surprisingly easy and free of interference because of cross-correlation detection. In cross-correlation detection the gain of the detector is modulated at a frequency offset ( $F + \delta F$ ) from that of the modulated excitation ( $F$ ). The difference frequency ( $\delta F$ ) is typically in the range of 10 to 100 Hz. This results in a low-frequency signal at  $\delta F$  that contains the phase and modulation information in the original high-frequency signal (Section 5.11.2). At all modulation frequencies, the phase and modulation are measured at the same low cross-correlation frequency ( $\delta F$ ). The use of cross-correlation detection results in the rejection of harmonics and other sources of noise. The newer FD instruments use signal processing boards that extract the values from the digitized low-frequency signal.

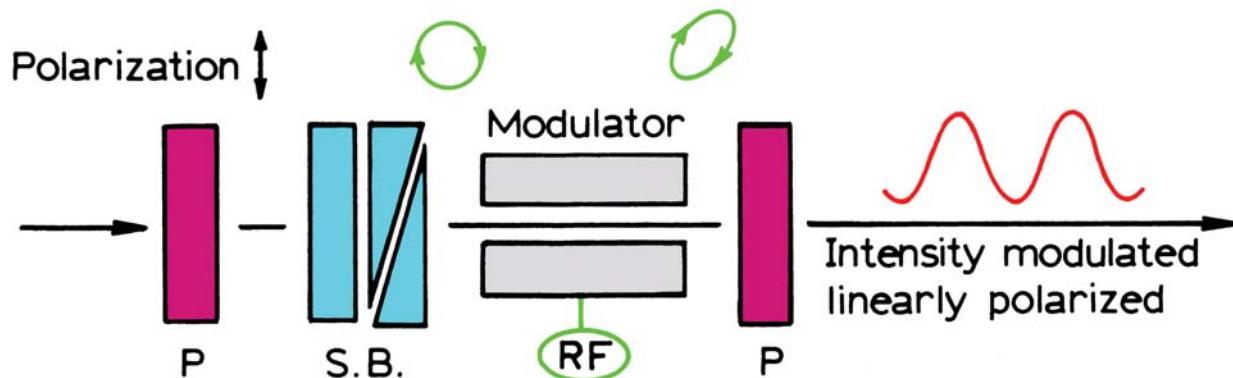


**Figure 5.8.** Optical arrangement for an electrooptic modulator. P, polarizer; SB, Soliel-Babinet compensator; RF, radio frequency signal. The SB compensator is replaced by an electrical DC voltage in some commercial FD instruments.

The cross-correlation method is surprisingly robust. The harmonic content (frequency components) of almost any excitation profile can be used if it contains frequency components that are synchronized with the detector. Both pulsed lasers and synchrotron radiation have been used as modulated light sources. Pulse lasers provide harmonic content to many gigahertz, so the bandwidth of the frequency-domain instruments is then limited by the detector and not the light modulator (Section 5.6).

### 5.2.3. Light Modulators

Adjustment of the frequency-domain instruments is aided by understanding the operating principles of light modulators. Light can be modulated with high efficiency using acoustooptic modulators, which diffract light based on a periodic density gradient caused by sound waves. Acoustooptic (AO) modulators are typically resonant devices that operate at only certain frequencies. While broadband or variable frequency AO modulators are known, the active area is usually small, limiting their use to focused laser sources.

A general procedure to modulate light is provided by the use of electrooptic (EO) modulators (Figure 5.8). EO modulators are constructed of materials that rotate polarized light when the material is exposed to an electrical field.<sup>54–56</sup> The modulator is placed between crossed polarizers. In the absence of any voltage there is no effect on the incident light, and no light is transmitted. If a voltage is applied to the modulator, the electric vector of the light is rotated and some light passes through the second polarizer. A voltage is applied to the modulator at the desired modulation frequency.

When an EO modulator is used as just described, without a bias, it provides modulated light at twice the frequency of the electric field applied to the modulator. This occurs because the optical system becomes transmissive whether the voltage is positive or negative (Figure 5.9). However, the amount of light transmitted is rather small. Hence, EO modulators are usually operated with an optical or elec-

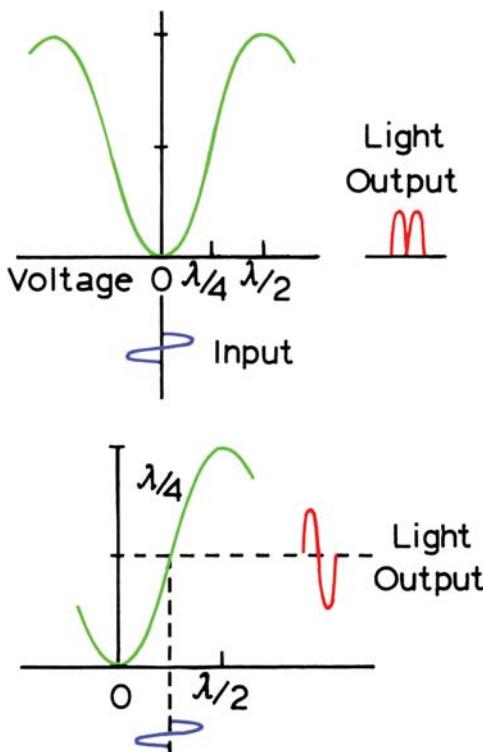


**Figure 5.9.** Modulated intensity from an electrooptic modulator. The upper drawing shows the modulated intensity without an electrical or optical bias, the lower drawing includes a  $\lambda/4$  bias.

cal bias, which results in some light transmission when the voltage applied to the modulation is zero. This can be accomplished by the use of an optical bias (Soliel-Babinet compensator) or an electrical bias (DC voltage). This bias converts the linearly polarized light to circular or elliptically polarized light even if no AC voltage is applied to the modulator. This results in partial transmission of the laser beam in the absence of the RF voltage. Application of an RF voltage now results in amplitude modulation of the laser beam at the applied RF frequency (Figure 5.9). The modulated light is polarized according to the orientation of the second polarizer.

The usefulness of the EO modulator results from the ability to rapidly change the electric field across the EO crystal. In practice, adequate RF voltage can be applied up to about 200 MHz, which is also the upper frequency limit of most dynode PMTs. The EO modulators are not resonant devices, and perform equally well at any frequency below the upper frequency limit. However, there are several features of EO modulators that are not ideal for use in a frequency domain fluorometer. Perhaps the most serious limitation is the high half-wave voltage. The half-wave voltage is the voltage needed to rotate the electrical vector by 90° and allow all the light to pass through the second polarizer. Half-wave voltages for commonly used EO modulators are 1 to 7 kV, whereas the maximum practical RF peak-to-peak voltages are near 100 volts. For this reason one can only obtain a relatively small amount of modulation.

In frequency-domain fluorometers the extent of modulation is usually increased by adjusting the optical or electrical bias close to the zero transmission point. This decreases both the AC and DC intensities, but the DC intensity can be decreased to a greater extent, resulting in a larger AC/DC ratio. Because of the large half-wave voltage, crossed polarizers, and a modulator biased near zero transmission, the overall efficiency of light transmission rarely exceeds 10%.

Another disadvantage of the EO modulators is that they generally require collimated light. They are easier to use with lasers than with arc lamp sources. It is possible to obtain useful amounts of modulation with an arc lamp, but the transmission is typically less than 5%. Unfortunately, there does not seem to be any general solution to this problem. As shown in Section 5.6, the limitations of using a light modulator can be avoided by using intrinsically modulated light sources. These include pulsed lasers, laser diodes, and LEDs. LEDs and LDs are now available for FD measurements with output from 370 to 830 nm<sup>56</sup> that can be

used to excite many extrinsic fluorophores. A pulsed sub-nanosecond LED at 280 nm has recently been described for TCSPC,<sup>57</sup> so that modulated LEDs for excitation of intrinsic protein fluorescence should be available in the near future.

Modulators are known that have lower half-wave voltages and higher frequency limits above 1 GHz.<sup>54</sup> These include the longitudinal field and traveling wave modulators. These devices typically have long narrow light paths and are only suitable for use with lasers. Also, they are sensitive to temperature and RF power. This instability limits their use in frequency-domain instruments.

#### 5.2.4. Cross-Correlation Detection

The use of cross-correlation detection is an essential feature of the frequency-domain measurements. The basic idea is to modulate the gain of the PMT at a frequency offset ( $\delta F$ ) from the light modulation frequency. The result is a low-frequency signal from the PMT at frequency  $\delta F$  that contains the phase and modulation information. The phase shift and modulation of the low-frequency signal is the same as one would have observed at high frequency. The phase and modulation of the low-frequency signal is easily measured using either analog or digital methods. Some FD instruments use zero crossing detectors and a ratio voltmeter (DVM) to measure these values, as was done in the early instruments.<sup>41</sup> In newer FD instruments the low-frequency signal is digitized and analyzed by a fast Fourier transform.<sup>58–60</sup> It seems that digital data acquisition of the low-frequency signal decreases the noise in the phase and modulation data by about twofold compared to the analog circuits. The equations describing cross-correlation detection are provided in Section 5.11.2.

Cross-correlation detection provides a significant advantage in addition to allowing low-frequency measurements. The process of cross-correlation suppresses harmonic or other frequencies, so that the modulation of the light or PMT gain need not be a pure sine wave. In fact, the excitation waveform can be almost any repetitive waveform, even a laser pulse train. After cross-correlation, the phase and modulation values are the values that would have been observed if the modulation were perfectly sinusoidal. This feature of harmonic suppression makes the frequency-domain instruments easy to use. One need not be concerned about the shape of the modulated signals, as this will be corrected by cross-correlation.

### 5.2.5. Frequency Synthesizers

The use of cross-correlation distributions requires two frequencies that are synchronized but different by a small frequency  $\delta F$ . The cross-correlation frequency  $\delta F$  can be any value, and is generally selected to be between 10 and 100 Hz. The synthesizer must provide frequencies to 200 MHz or higher, with 1 or 0.1 Hz resolution, which is not difficult with modern electronics. The requirements for frequency resolution in the synthesizer can be relaxed if one uses higher cross-correlation frequencies,<sup>61</sup> and schemes are being developed that use only one high-stability frequency source.<sup>62</sup> It seems clear that the cost of frequency-domain instrumentation will continue to decrease.

### 5.2.6. Radio Frequency Amplifiers

The electrooptic modulator requires the highest reasonable voltage, preferably 1500 volts peak-to-peak over a wide frequency range. Unfortunately, this is not practical. In order to obtain variable frequency operation the circuit is usually terminated with a 50- $\Omega$  power resistor. A 25-watt amplifier provides only about 100 volts into 50  $\Omega$ , which is why overall light transmission is low. One can usually remove the 50- $\Omega$  terminating resistor, which results in a twofold increase in voltage. The RF amplifier should be protected from reflected power. It is important to avoid standing waves in the amplifier to modulator cable, which should be less than 30 cm long.

In contrast to the high power required by the light modulator, relatively little power is needed to modulate the gain of the PMT. This amplifier is typically near 1 watt, and can be less. In fact, we often directly use the output of the frequency synthesizer without amplification for gain modulation of the PMT.

### 5.2.7. Photomultiplier Tubes

The detector of choice for FD measurements is a PMT. The upper frequency limit of a PMT is determined by its transient time spread, so that the same detectors that are useful in TCSPC are useful in FD fluorometry. There is a slight difference in that the most important feature for TCSPC is the rise time of the pulse. For FD measurements the PMTs with the highest frequency limits are those with the narrowest pulses for each photoelectron. While fast rise times usually imply narrow photoelectron pulse widths, some detectors can have fast rise times with long tails.

The approximate upper frequency limits of commonly used PMTs are listed in Table 4.1. These values are estimated based on our experience and product literature. The upper frequency limit of the side window R928 is near 200 MHz. Much higher-frequency measurements are possible with MCP PMTs (Section 5.7), but special circuits are needed for cross-correlation outside of the PMT.

It is informative to examine the PMT electronics used in a frequency-domain fluorometer (Figure 5.10), in this case for an R928 PMT. The circuit starts with a high negative voltage of the photocathode. There is a Zener diode ( $Z_1$ ) between the photocathode and first dynode. This diode maintains a constant high 250-volt potential. With the use of a constant high potential, the wavelength- and position-dependent time response of the PMT is minimized. The next dynodes are all linked by simple resistors. This allows the gain of the PMT to be varied by changes in applied voltage. Capacitors are included to maintain the voltage difference during periods of transiently high illumination.

Cross-correlation is accomplished by injection of a small RF signal at dynode 9 ( $D_9$ ). The voltage between  $D_8$  and  $D_9$  is held constant by the Zener diode ( $Z_2$ ). The average voltage between  $D_9$  and ground is adjusted by bias

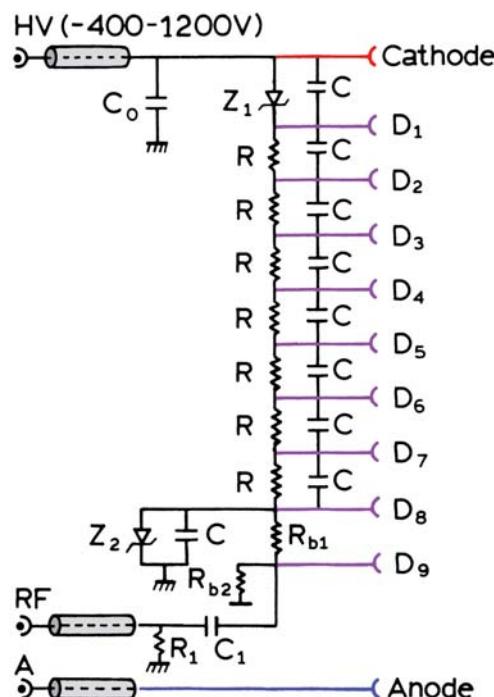


**Figure 5.10.** Dynode chain for an R928 photomultiplier tube used in a frequency-domain fluorometer. Revised from [1] and reprinted with permission from the Biophysical Society.

resistors  $R_{b1}$  and  $R_{b2}$ . A few volts of RF signal are adequate to obtain nearly 100% gain modulation of the PMT.

### 5.2.8. Frequency-Domain Measurements

When performing frequency-domain measurements it is valuable to understand what is being measured. One performs a comparison of the sample emission and scattered light, similar to the comparison in TCSPC. The FD instruments typically contain two detectors, one for the sample and one that serves as a timing reference (Figure 5.7). The reference PMT typically observes reflected light, scattered light, or the emission from a short-lifetime standard. The sample PMT is exposed alternately to the emission from either the sample or to scattered light. The sample and scattering solutions are usually in a rotating sample holder (turret) that precisely positions each solution in the same location. Since everything else in the measurement remains the same, any change in relative phase or modulation is due to the intensity decay of the sample.

Because the scatterer and sample are not observed at the same time, the phase difference and relative modulation cannot be measured at the same time. Instead, all measurements are performed relative to the reference PMT (Figure 5.11). First, the phase shift between the scatterer and reference PMT is measured. These signals are shifted by an arbitrary phase angle ( $\phi_1$ ) due to the inevitable time delays in the cables and electronic circuits. The second measurement is the phase of the sample relative to the reference PMT. This phase angle ( $\phi_2$ ) contains both the arbitrary phase shift  $\phi_1$  and the value of interest,  $\phi_\omega$ . The actual phase shift is then calculated from  $\phi_\omega = \phi_2 - \phi_1$ .

The modulation is measured in a similar way, except that one typically does not measure the modulation of the reference PMT is not measured. The modulation is determined from the AC and DC components of the sample ( $B/A$ ) and scatterer ( $b/a$ ), as shown in Figure 5.2. For measurement of the modulation it does not matter if one measures the peak-to-peak or RMS voltage of the modulated signal, as the method of measurement cancels in the ratio. The modulation at the reference PMT can be used as a correction for modulation drifts in the instrument. In this case all measured modulation values are divided by the value at the reference PMT during each particular measurement. This procedure is useful if the extent of modulation is changing during the measurement due to instabilities in the modulator or light source.

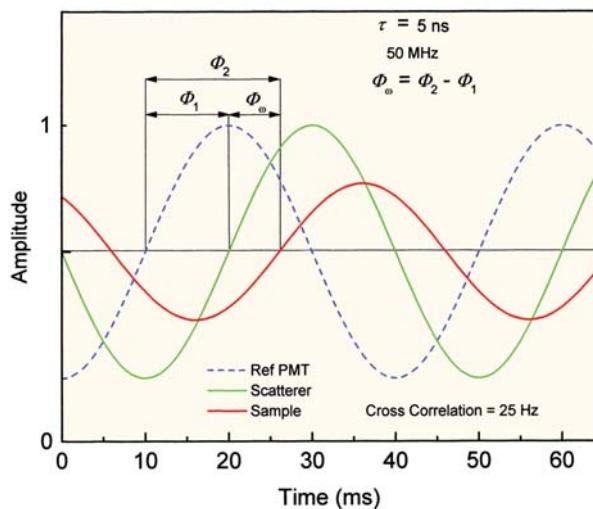


**Figure 5.11.** Measurement of phase shift and modulation for a modulation frequency of 50 MHz, a lifetime of 5 ns, and a cross-correlation frequency of 25 Hz. The phase angle is  $57.5^\circ$  and the modulation 0.54.

As described in Chapter 4 for time-domain measurements, it is important to consider the effects of rotational diffusion on the measured intensity decays. Rotational diffusion can also affect the frequency-domain measurements (Chapter 11). The use of an excitation and/or emission monochromator results in either partially polarized excitation or selective observation of one of the polarized components of the emission. If the decay rate is comparable to the rate of rotational diffusion, which is a situation frequently encountered for fluorophores bound to biological macromolecules, then the decay of the individual polarized components of the emission is multi-exponential. This effect is unimportant if the rate of rotational diffusion is either much slower or faster than the decay rate. These effects can be canceled by use of vertically polarized excitation and an emission polarizer oriented at  $54.7^\circ$  to the vertical.

## 5.3. COLOR EFFECTS AND BACKGROUND FLUORESCENCE

### 5.3.1. Color Effects in Frequency-Domain Measurements

Photomultiplier tubes can display a wavelength-dependent time response (Section 4.6.4), which can affect the frequency-domain measurements.<sup>63–68</sup> In frequency-domain measurements the effects are somewhat more difficult to under-

stand. There can be systematic errors in the phase or modulation values, and the direction of the errors is not always intuitively obvious. Fortunately, the color effects are minor with presently used side-window dynode PMTs, and the effect appears to be negligible with microchannel plate PMTs. Although no reports have appeared, it is likely that color effects are minimal with the TO-8 compact PMTs (Section 4.6.3.). Systematic errors due to the wavelength-dependent time response are easily corrected using lifetime standards.

In order to correct for a wavelength-dependent response one uses a lifetime standard in place of the scatterer in the sample turret (Figure 5.7). The standard should display a single-exponential decay of known lifetime  $\tau_R$ . The lifetime of the standard should be as short as possible, typically near 1 ns, to avoid demodulation that results in decreased precision of the phase-angle measurements. Another advantage of short-lifetime standards is the minimal effect of dissolved oxygen on the lifetimes. Short lifetimes can be obtained with collisional quenching, but this is not recommended because such samples display non-exponential decays. Lifetime standards are summarized in Appendix II. The chosen standard should absorb and emit at wavelengths comparable to the sample, so that the sample and reference can be observed with the same emission filter and/or monochromator setting. Under these conditions the PMT observes essentially the same wavelength for both sample and reference measurements, so the color effects are eliminated.

The decay time of the reference results in a phase delay ( $\phi_R$ ) and demodulation ( $m_R$ ) of the reference emission compared to that which would have been observed using a scatterer with a lifetime of zero. Of course,  $\phi_R$  and  $m_R$  depend on the modulation frequency. The measured values ( $\phi_\omega^{\text{obs}}$  and  $m_\omega^{\text{obs}}$ ) need to be corrected for this effect. The corrected values are given by

$$\phi_\omega = \phi_\omega^{\text{obs}} + \phi_R \quad (5.16)$$

$$m_\omega = m_\omega^{\text{obs}} \cdot m_R = m_\omega^{\text{obs}} / \sqrt{1 + \omega^2 \tau_R^2} \quad (5.17)$$

where  $\phi_\omega^{\text{obs}}$  and  $m_\omega^{\text{obs}}$  are the observed values measured relative to the lifetime standard. These equations can be understood by noting that the observed phase angle is smaller than the actual phase angle due to the phase angle of the reference ( $\phi_\omega^{\text{obs}} = \phi_\omega - \phi_R$ ). Similarly, the observed modulation is the ratio of the modulation of the sample relative to the

reference ( $m_\omega^{\text{obs}} = m_\omega / m_R$ ). We find this simple approach adequate for all samples we have encountered. Somewhat different methods have also been proposed.<sup>67–68</sup>

### 5.3.2. Background Correction in Frequency-Domain Measurements

Correction for background fluorescence from the sample is somewhat complex when using the FD method.<sup>69–70</sup> In time-domain measurements, correction for autofluorescence can be accomplished by a relatively straightforward subtraction of the data file measured for the blank from that measured for the sample, with error propagation of Poisson noise if the background level is high. In the frequency domain it is not possible to perform a simple subtraction of the background signal. The background may be due to scattered light with a zero decay time, due to impurities with finite lifetimes, or a combination of scattered light and autofluorescence. The phase ( $\phi_{\omega B}$ ) and modulation ( $m_{\omega B}$ ) of the background can be measured at each light modulation frequency. However, the measured values  $\phi_{\omega B}$  and  $m_{\omega B}$  cannot be subtracted from the sample data unless the intensities are known and the correction is properly weighted.

Background correction of the FD data is possible, but the procedure is somewhat complex and degrades the resolution of the measurements. It is preferable to perform the FD measurements under conditions where background correction is not necessary. If needed, the correction is performed by measuring the frequency response of the background, and its fractional contribution ( $f_B$ ) to the steady-state intensity of the sample. If the background level is low, then the values of  $\phi_{\omega B}$  and  $m_{\omega B}$  have large uncertainties due to the weak signals. However, this is not usually a problem because if the background is low its weighted contribution to the sample data is small, so that minimal additional uncertainty is added to the data. If the background is larger, its significance is greater, but it can also be measured with higher precision.

A data file corrected for background is created by the following procedure.<sup>66</sup> Let

$$N_{\omega B} = m_{\omega B} \sin \phi_{\omega B} \quad (5.18)$$

$$D_{\omega B} = m_{\omega B} \cos \phi_{\omega B} \quad (5.19)$$

represent the sine and cosine transforms. In these equations  $\phi_{\omega B}$  and  $m_{\omega B}$  represent the measured values for the phase

and modulation of the background. A least-squares fit of the phase and modulation data for the background is performed and for the parameter values to calculate  $\phi_{\omega B}$  and  $m_{\omega B}$ . This latter procedure is useful if the background file is not measured at the same modulation frequencies as the sample. In the presence of background the observed values of  $N_{\omega}^{\text{obs}}$  and  $D_{\omega}^{\text{obs}}$  are given by

$$N_{\omega}^{\text{obs}} = (1 - f_B)m_{\omega} \sin \phi_{\omega} + f_B m_{\omega B} \sin \phi_{\omega B} \quad (5.20)$$

$$D_{\omega}^{\text{obs}} = (1 - f_B)m_{\omega} \cos \phi_{\omega} + f_B m_{\omega B} \sin \phi_{\omega B} \quad (5.21)$$

In these equations  $f_B$  is the fraction of the total signal due to the background, and  $\phi_{\omega}$  and  $m_{\omega}$  are the correct phase and modulation values in the absence of background. The corrected values of  $N_{\omega}$  and  $D_{\omega}$  are given by

$$N_{\omega} = \frac{N_{\omega}^{\text{obs}} - f_B N_{\omega B}}{1 - f_B} \quad (5.22)$$

$$D_{\omega} = \frac{D_{\omega}^{\text{obs}} - f_B D_{\omega B}}{1 - f_B} \quad (5.23)$$

In using these expressions the values of  $\phi_{\omega B}$  and  $m_{\omega B}$  are known from the measured frequency response of the background. The value of  $f_B$  is found from the relative steady-state intensity of the blank measured under the same instrumental conditions and gain as the sample. Except for adjusting the gain and/or intensity, the values of  $\phi_{\omega B}$  and  $m_{\omega B}$  should be measured under the same conditions as the sample. The corrected values of  $N_{\omega}$  and  $D_{\omega}$  can be used in eqs. 5.9 and 5.10 to calculate the corrected phase and modulation values. An important part of this procedure is propagation of errors into the corrected data file. Error propagation is straightforward but complex to describe in detail.<sup>69</sup>

#### 5.4. REPRESENTATIVE FREQUENCY-DOMAIN INTENSITY DECAYS

##### 5.4.1. Exponential Decays

It is informative to examine some typical frequency-domain measurements.<sup>71</sup> Frequency-domain intensity decays for anthracene (AN) and 9-cyanoanthracene (9-CA) are shown in Figure 5.12. The samples were in equilibrium with atmospheric oxygen. The emission was observed through a

long pass filter to reject scattered light. Magic-angle polarizer conditions were used, but this is unnecessary for such samples where the emission is completely depolarized. The excitation at 295 nm was obtained from the frequency-doubled output of a rhodamine 6G dye laser, cavity dumped at 3.8 MHz. This pulse train provides intrinsically modulated excitation over a wide range of frequencies (Section 5.6).

Experimental FD data are shown in Figure 5.12 (upper panel). The increasing values are the frequency-dependent phase angles ( $\phi_{\omega}$ ) and the decreasing values are the modulation values ( $m_{\omega}$ ). The solid lines are calculated curves for the best single-decay-time fits. In the single-exponential model the decay time is the only variable parameter. The shape of a single-decay-time frequency response is always the same, except that the response is shifted to higher frequencies for shorter decay times.

The lower panels show the deviations between the data ( $\bullet$ ,  $\circ$ ) and the fitted curve (solid line). In this case the deviations are presented in units of degrees and percentage modulation. For calculation of  $\chi_R^2$  the standard errors were taken as  $\delta\phi = 0.2$  and  $\delta m = 0.005$ . The fact that the values of  $\chi_R^2$  are close to unity reflects an appropriate choice for the values of  $\delta\phi$  and  $\delta m$ . In analysis of the FD data the absolute values of  $\chi_R^2$  are variable due to the unknown

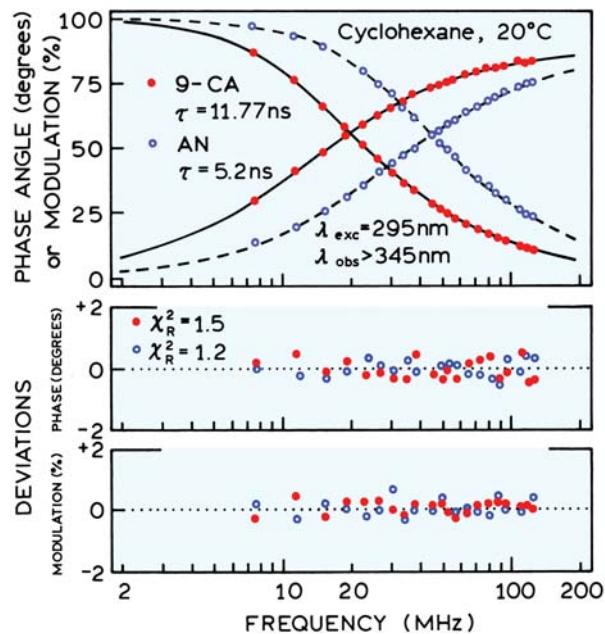


**Figure 5.12.** Single-exponential decays of anthracene (AN) and 9-cyanoanthracene (9-CA). Samples were equilibrated with atmospheric oxygen.  $\delta\phi = 0.2$  and  $\delta m = 0.005$ . From [71].

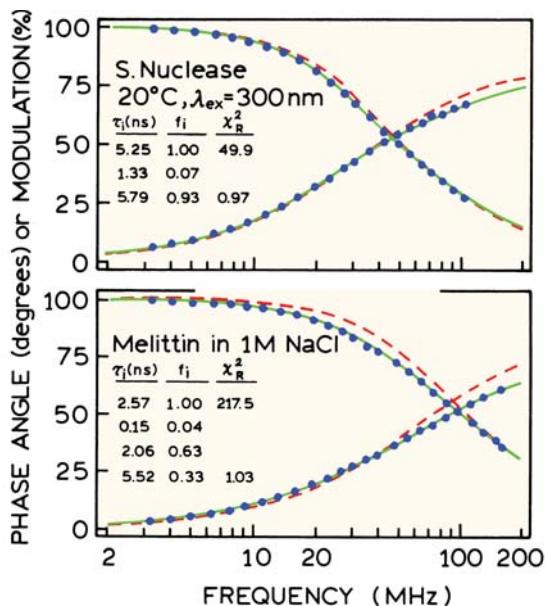


**Figure 5.13.** Frequency responses of staph nuclease and melittin. The data are the solid dots. The best single- (dashed) and double- or triple-exponential fits (solid) are shown.

amounts of noise. The ratio of the  $\chi_R^2$  is used for testing various models. For anthracene and 9-cyanoanthracene, the values of  $\chi_R^2$  did not decrease for the two-decay-time model, so the single-exponential model was accepted.

#### 5.4.2. Multi-Exponential Decays of Staphylococcal Nuclease and Melittin

Most single-tryptophan proteins display multi-exponential intensity decays. This is illustrated for two proteins in Figure 5.13.<sup>70</sup> The intensity decay of trp-140 in staph nuclease is at least a double exponential. The intensity decay of trp-19 in melittin is at least a triple-exponential decay. Under these experimental conditions (1 M NaCl) melittin is a tetramer, with the monomers each in the  $\alpha$ -helical state. The frequency responses and recovered lifetimes in Figure 5.13 are typical of many single- and multi-tryptophan proteins.

#### 5.4.3. Green Fluorescent Protein: One- and Two-Photon Excitation

Green fluorescent protein (GFP) is of wide interest because it can be used to follow gene expression. GFP spontaneously forms a highly fluorescent fluorophore after the amino-acid backbone is synthesized. GFP is widely used in optical microscopy and cellular imaging. In these applications GFP

is frequently excited by two-photon absorption (Chapter 18). In this process a fluorophore simultaneously absorbs two or more long-wavelength photons to reach the first singlet excited state. Two-photon excitation occurs when there is reasonable probability of two photons being in the same place at the same time, and thus the power density must be rather high. Multi-photon excitation requires locally intense excitation, and there is often concern about the stability of the fluorophores. The stability of GFP under these conditions was investigated by measuring the intensity decays with one- and two-photon excitation.

Since GFP is a modest-sized protein ( $\approx 28$  kDa) the emission is expected to be polarized. For this reason the intensity decays were measured with magic-angle polarizer conditions. Excitation was obtained using fs pulses from a Ti:sapphire laser.<sup>72</sup> A pulse picker was used to reduce the repetition rate to near 4 MHz. For one-photon excitation the laser pulses were frequency doubled to 400 nm. For two-photon excitation the 800-nm output from the Ti:sapphire laser was used directly to excite the sample. These measurements used the harmonic content of the pulse train (Section 5.6). It is essential to select emission filters that reject scattered light at both 400 and 800 nm. The emission was observed through a 510-nm interference filter and a Corning 4-96 colored glass filter.

Intensity decays of proteins and labeled macromolecules are typically dependent on the conformation, and any perturbation of the structure is expected to alter the decay times. The intensity decays of GFP were found to be essentially identical for one- and two-photon excitation (Figure 5.14). This indicated that GFP was not perturbed by the intense illumination at 800 nm. The values of  $\chi_R^2$  are somewhat high, but did not decrease when using the two-decay-time model. The single-decay-time model was thus accepted for GFP, in agreement with one-photon excitation results from other laboratories.<sup>73</sup>

#### 5.4.4. SPQ: Collisional Quenching of a Chloride Sensor

Collisional quenching decreases the lifetime of the quenched fluorophore (Chapter 8). This suggests that the lifetimes can be used to determine the concentration of quenchers. The probe SPQ (6-methoxy-N-[3-sulfopropyl]quinoline) is sensitive to quenching by chloride,<sup>74–76</sup> probably by photoinduced electron transfer (Chapter 9).

Absorption and emission spectra of SPQ were shown in Chapter 3. Frequency responses of SPQ are shown in

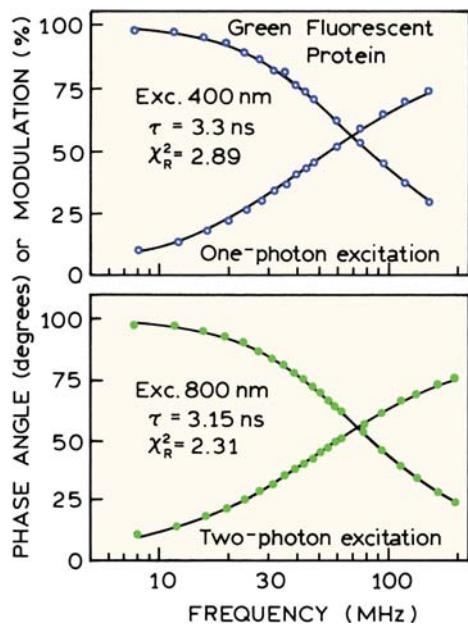


**Figure 5.14.** Frequency-domain intensity decay data for GFPuv in 0.05 M phosphate buffer, pH = 7, for one-photon excitation at 400 nm, and for two-photon excitation at 800 nm. From [72].

Figure 5.15. The frequency responses shift to higher frequencies with increasing amounts of chloride, indicating a decrease in lifetime. One can use the data to calculate the decay times at each chloride concentration. These lifetimes are 25.5, 11.3, 5.3, and 2.7 ns, for 0, 10, 30, and 70 mM chloride, respectively (Problem 5.1).

#### 5.4.5. Intensity Decay of NADH

Reduced nicotinamide adenine dinucleotide (NADH) is known to display a subnanosecond decay time near 0.4 ns.

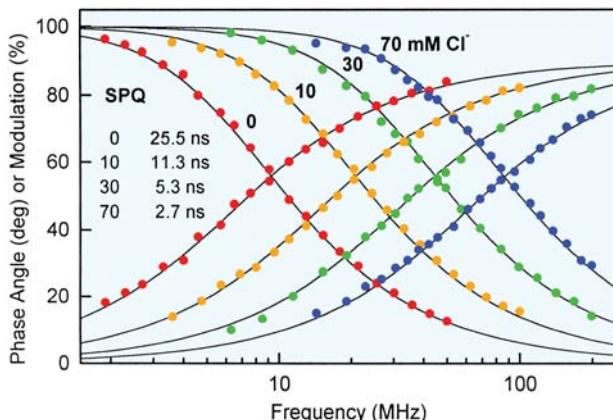


**Figure 5.15.** Frequency-domain intensity decays of SPQ in the presence of 0, 10, 40, and 70 mM chloride.

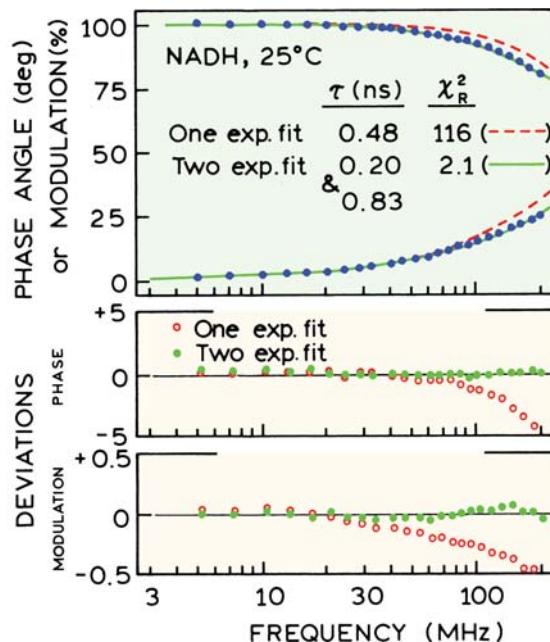


**Figure 5.16.** Frequency response of NADH dissolved in 0.02 M Tris (pH 8) 25°C. The excitation wavelength was 325 nm from an HeCd laser, which was modulated with an electrooptic modulator. The emission filter was a Corning 0-52. For the two-component analysis  $f_1 = 0.57$  and  $f_2 = 0.43$ . Revised and reprinted from [2], Copyright © 1985, with permission from Elsevier Science.

Its intensity decay is complex, with decay times near 0.3 and 0.8 ns.<sup>77</sup> Frequency-domain data for NADH are shown in Figure 5.16. The presence of more than one lifetime is immediately evident from the failure of the single exponential fit (—) and the systematic deviations (○). Use of the two decay time model resulted in a 50-fold decrease of  $\chi^2_R$ . The frequency-domain data for NADH illustrate a limitation of the commercially available instruments. An upper frequency of 200 MHz is too low to determine the entire frequency response of NADH or other subnanosecond intensity decays. For this reason FD instruments were developed to allow measurements at higher modulation frequencies.

#### 5.4.6. Effect of Scattered Light

A critical component of any frequency-domain or time-domain experiment should be collection of emission spectra. One possible artifact is illustrated in Figure 5.17, which shows the emission spectrum of 9,10-diphenylanthracene (DPA) in a solution that also scattered light.<sup>69</sup> 9,10-Diphenylanthracene was dissolved in ethanol that contained a small amount of Ludox scatterer. When the emission is

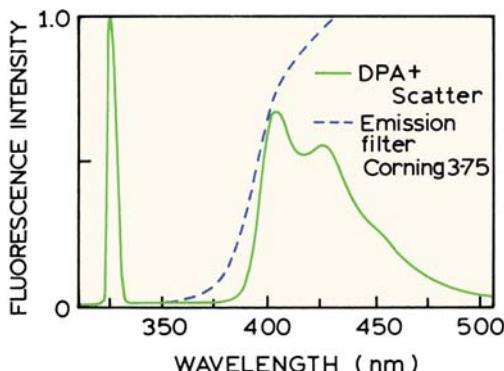


**Figure 5.17.** Emission spectra of 9,10-diphenylanthracene (DPA) in ethanol for excitation at 325 nm from a helium–cadmium laser. The solvent contained a small amount of Ludox colloidal silica as the scatterer. The dashed line is the transmission of the Corning 3-75 filter. Revised from [69].

observed without an emission filter (solid) there is a large peak due to scattered light at the excitation wavelength of 325 nm. The presence of this scattered component would not be recognized without measurement of the emission spectrum, and would result in an incorrect intensity decay.

Scattered light is typically rejected from the detector by using emission filters. In this case we used a Corning 3-75 filter, which transmits above 360 nm (dashed). As a control measurement one should always record the emission spectrum of the blank sample through the emission filter to ensure scattered light is rejected. Alternatively, one can measure the intensity of the blank through the filter to determine that the blank contribution is negligible. In such control measurements it is important that the blank scatters light to the same extent as the sample. Frequently, buffer blanks do not scatter as strongly as the sample containing the macromolecules because of the inner filter effect present in the sample.

It is useful to understand how scattered light can corrupt the frequency-domain data. Frequency responses for the DPA solution are shown in Figure 5.18. For these measurements the excitation source was a helium–cadmium (HeCd) laser at 325 nm. The cw output of this laser was modulated with an electrooptic modulator, as shown in Figure 5.8. The effect of scattered light is visually evident in the frequency-domain data. When measured without an emission filter, the phase angles ( $\circ$ ) are considerably smaller than expected for the single exponential decay of DPA ( $\bullet$ ). The phase angle error becomes larger at higher frequencies. It should be noted that the fractional intensity of the background is only 15% ( $f_B = 0.15$ ), so that significant

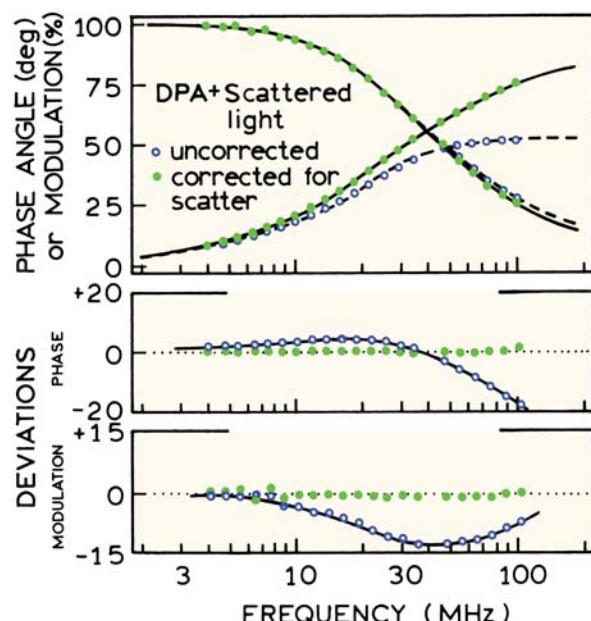


**Figure 5.18.** Frequency-domain intensity decay of 9,10-diphenylanthracene in ethanol with a scatterer. The sample was in equilibrium with dissolved oxygen. Data were measured without an emission filter ( $\circ$ ) and then corrected ( $\bullet$ ) for the scattered light using eqs. 5.18–5.23. Bottom panels: deviations from the best single exponential fits for the data with ( $\circ$ ), and corrected for ( $\bullet$ ) scattered light. Revised from [69].

errors in phase angle are expected for even small amounts of scattered light.

It is possible to correct for background from the sample. The solid dots represent the data corrected according to eqs. 5.18–5.23. The corrected data can be fit to a single decay time with  $\tau = 6.01$  ns. An alternative approach is to fit the data with scattered light to include a second component with a lifetime near zero. This also results in a good fit to the data, with a decay time near zero associated with  $f_B = 0.15$ . However, this procedure is only appropriate if the background is only due to scattered light. In general auto-fluorescence will display nonzero lifetimes and nonzero phase angles.

## 5.5. SIMPLE FREQUENCY-DOMAIN INSTRUMENTS

A large fraction of the cost of a frequency-domain instrument is the light source and/or modulation optics. In TCSPC these expensive light sources are being replaced by LEDs. This substitution is also occurring with frequency-domain instruments. For most experiments the

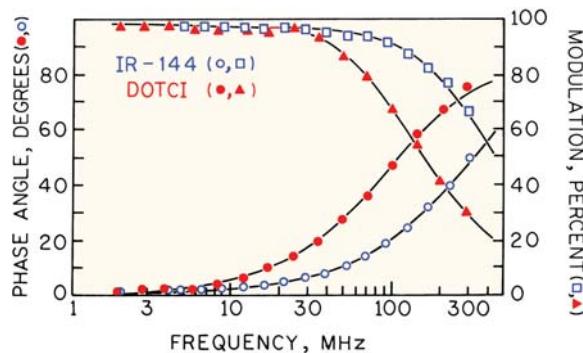


**Figure 5.19.** Frequency response for IR-144 in ethanol (open symbols) and DOTCI in ethanol (filled symbols). Best one-component fits to each data are indicated by the lines. IR-144 and DOTCI were excited with laser diodes at 790 and 670 nm, respectively. Revised and reprinted with permission from [79], Copyright © 1992, American Chemical Society.

complex laser source can be replaced with laser diodes,<sup>78–79</sup> and light-emitting diodes.<sup>80–86</sup> Frequency-domain measurements have also been accomplished with electroluminescent devices,<sup>87</sup> and even a modulated deuterium lamp.<sup>88</sup> Given the rapid advances with pulsed LDs and LEDs these devices are likely to be the dominant excitation source for FD measurements in the near future.

### 5.5.1. Laser Diode Excitation

The output of laser diodes can be modulated up to several GHz. Hence, laser diodes can be used for FD excitation without the use of a modulator. Data are shown in Figure 5.19 for two laser dyes—IR-144 and DOTCI—which were excited with 791- or 670-nm laser diodes, respectively (Figure 5.19). Frequency-doubled laser diodes have also been used to obtain shorter excitation wavelengths near 400 nm.<sup>89</sup> However, the need for frequency-doubled LDs has diminished given the availability of LDs and LEDs with fundamental outputs ranging from 280 to 820 nm.

### 5.5.2. LED Excitation

It is now known that LEDs can be modulated to several hundred MHz.<sup>85–86</sup> Hence, LEDs are becoming an alternative to modulated arc lamps. The modulated output of a 390-nm LED output was used to measure the 3.2-ns decay time of green fluorescent protein (not shown) and the 11.8-ns lifetime of 9-cyanoanthracene<sup>85</sup> (Figure 5.20).

The use of a simple light source such as an LED is likely to find use in analytical chemistry and clinical chemistry.<sup>84–85</sup> This is illustrated in Figure 5.21 for the potassium

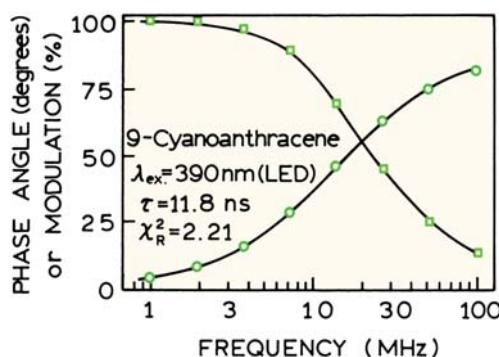


**Figure 5.20.** Intensity decay of 9-cyanoanthracene in ethanol using the 390-nm output of a UV LED as the excitation source. Revised from [85].

um-sensitive probe CD 222. This probe has a lifetime of 0.15 ns in the absence of potassium and 0.67 ns in the presence of bound potassium. The frequency response could be measured up to 300 MHz using a modulated UV LED at 373 nm. The possibility of measuring nanosecond decay times using modulated LEDs, and the availability of a wide range of wavelengths, suggests these light sources will be used for low-cost FD instruments in the near future.

Another application of LEDs will be for excitation of the longer-lived metal–ligand complexes (Chapter 20). The LEDs are ideal because the 450-nm output is centered on the 450-nm charge-transfer absorption of the ruthenium complexes. The shorter wavelengths are suitable for excitation of the higher-quantum-yield rhenium complexes (Figure 5.22). In this case the entire frequency response of  $[\text{Re}(\text{dpphen})(\text{CO})_3]^-$  (4-COOHPy)<sup>+</sup> was measured in the absence (10.24  $\mu$ s) or presence of oxygen (598 ns).<sup>84</sup>

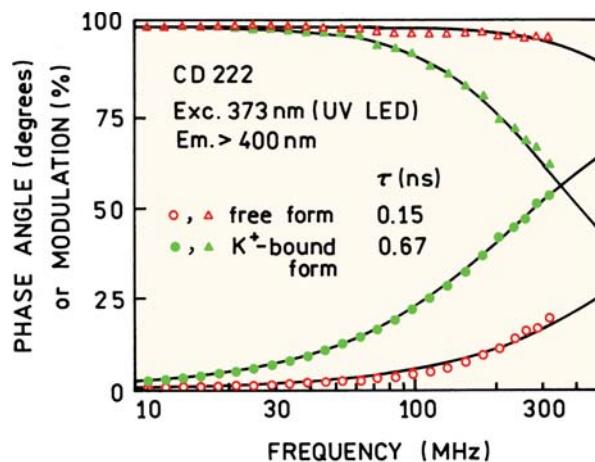


**Figure 5.21.** Frequency response of the potassium probe CD 222 measured with a 373-nm LED (○). From [84].

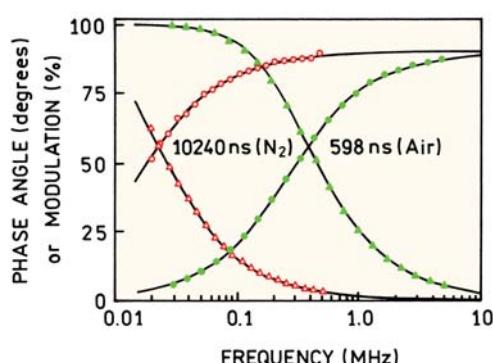


**Figure 5.22.** Frequency-domain intensity decays of  $[\text{Re}(\text{dpphen})-(\text{CO})_3(4-\text{COOHPy})]^+$  in methanol; dpphen is 4,7-diphenyl-1,10-phenanthroline, Py is pyridine. Excitation was 373 nm from the UV LED. From [84].

Given the simplicity of such light sources, one can imagine the frequency-domain fluorometer built on a card in a personal computer. pH can be measured using lifetimes either in standard cuvette measurements,<sup>90</sup> or through optical fibers.<sup>91</sup> LEDs have been used in phase fluorometric sensors for oxygen<sup>92–93</sup> and carbon dioxide.<sup>94</sup> Phase-modu-

lation lifetimes have been used in HPLC to assist in the identification and quantitation of polynuclear aromatic hydrocarbons.<sup>95–97</sup> Phase-modulation lifetime measurements have already been used to quantify a wide variety of clinically important analytes.<sup>98</sup> Several companies are already designing simple phase-modulation instruments for use in analytical applications. Frequency-domain fluorometry can now be accomplished with components no more complex than consumer electronics.

## 5.6. GIGAHERTZ FREQUENCY-DOMAIN FLUOROMETRY

In frequency-domain measurements it is desirable to measure over the widest possible range of frequencies, so as to examine the entire frequency response of the sample. Most FD instruments are limited to an upper frequency near 200 MHz. This limitation arises from two components. First, it is difficult to obtain light modulation above 200 MHz. This limitation is due in part to the large half-wave voltages of most electrooptic modulators. Second, many PMTs have an upper frequency limit near 200 MHz.

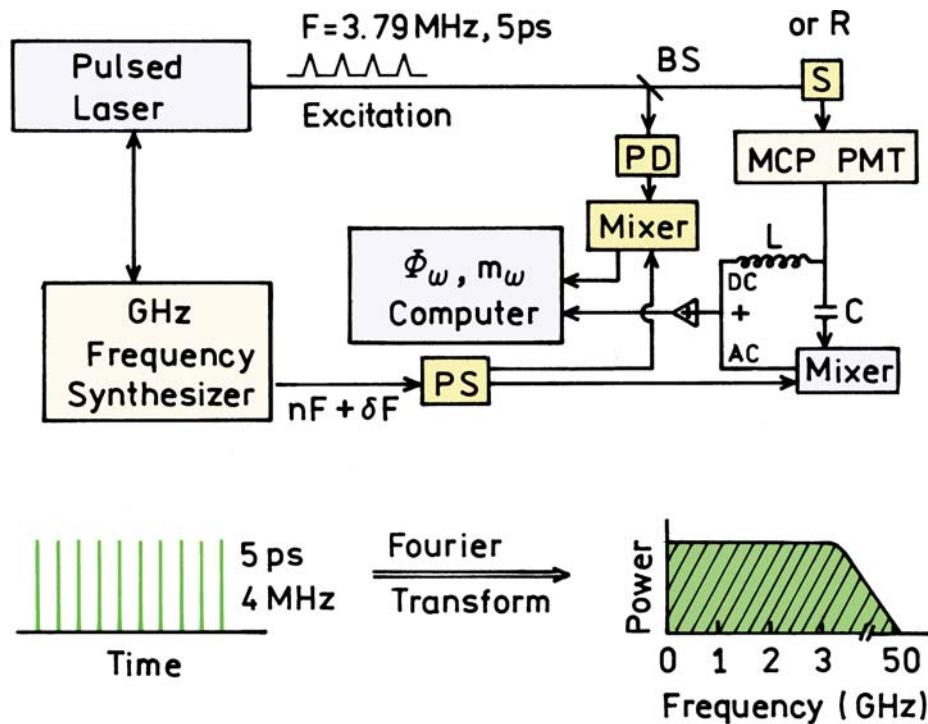


**Figure 5.23.** Harmonic content frequency-domain fluorometer. PD, high speed photodiode; PS, power splitter; MCP PMT, microchannel plate photomultiplier tube; BS, beam splitter; F, pulse repetition rate of the cavity dumped dye laser;  $\delta F$ , cross-correlation frequency; n, number of the harmonic; S, sample; R, reference or scatterer. The lower panel shows a laser pulse train and its Fourier transform. Revised from [106].

Alternative technologies are available to obtain FD measurements at frequencies above 200 MHz. The need for a light modulator can be eliminated by using the harmonic frequency content of a laser pulse train. Suppose the light source consists of a mode-locked argon ion laser and a cavity-dumped ps dye laser. This source provides 5-ps pulses with a repetition rate near 4 MHz. In the frequency domain this source is intrinsically modulated to many gigahertz, as shown by the schematic Fourier transform in Figure 5.23 (lower panel). The idea of using the harmonic content of a pulse train was originally proposed for pulsed lasers<sup>99</sup> and later for synchrotron radiation.<sup>100–102</sup> Pulse sources provide intrinsically modulated excitation at each integer multiple of the repetition rate, up to about the reciprocal of the pulse width.<sup>103–104</sup> For a ps dye laser the 4-MHz pulse train can be used for frequency domain measurements at 4, 8, 12, 16 MHz, etc. These harmonics extend to GHz frequencies, which are higher than the upper frequency limit of most detectors.

There are significant advantages in using the pulses from a ps laser. The cavity-dumped output of dye lasers is rather easy to frequency double because of the high peak power. Frequency doubling provides wavelengths for excitation of proteins and other extrinsic probes absorbing in the UV. Importantly, when using a ps dye laser source it is no longer necessary to use an electrooptic modulator and nearly crossed polarizers, which results in a significant attenuation of the incident light. There appears to be no detectable increase in noise up to 10 GHz, suggesting that there is no multiplication of phase noise at the higher harmonics.

The second obstacle to higher frequency measurements was the detector. The PMT in the 200-MHz instrument (Figure 5.7) is replaced with a microchannel plate (MCP) PMT.<sup>105–108</sup> These devices are 10- to 20-fold faster than a standard PMT, and hence a multi-gigahertz bandwidth was expected. As presently designed, the MCP PMTs do not allow internal cross-correlation, which is essential for an adequate signal-to-noise ratio. This problem was circumvented by designing an external mixing circuit,<sup>105–106</sup> which allows cross-correlation and preserves both the phase and the modulation data. The basic idea is analogous to Figure 5.10, except that mixing with the low-frequency signal is accomplished after the signal exits the MCP PMT. External cross-correlation was found to perform well without any noticeable increase in noise.

What range of frequencies can be expected with a pulsed-laser light source and an MCP PMT detector? For

Lorentzian-shaped pulses the harmonic content decreases to half the low-frequency intensity at a frequency  $\omega_2 = 2 \ln 2 / \Delta t$ , where  $\Delta t$  is the pulse width.<sup>104</sup> For 5-ps pulses the harmonics extend to 280 GHz, higher than the upper frequency limit of any available detector. Hence for the foreseeable future the measurements will be limited by the detector.

The upper frequency of a detector is limited by the pulse width due to a single photoelectron, or equivalently the transit time spread. Hence, one expects the highest modulation frequencies to be measurable with MCP PMTs that have the smallest transit time spread (Table 4.1). The relative power at various frequencies can be measured with a spectrum analyzer. This was done for several PMTs using a ps pulse train with its high harmonic content as the light source. These results show that the side-window R928 is most useful below 200 MHz (Figure 5.24), and cannot be used for measurements much above about 400 MHz. The R-1564U is a 6-micron MCP PMT, and shows a useful response to 2 GHz. This PMT was used in the first 2-GHz instrument.<sup>105</sup>

To obtain frequencies above 2 GHz it was necessary to use a specially designed MCP PMT, the R-2566. The data in Figure 5.25 are for the 6-micron version of the R-2566, which provides measurable power to 10 GHz, and allowed construction of a 10-GHz FD instrument.<sup>106</sup> This MCP PMT possesses a grid between the microchannel plates and the anode, which serves to decrease the width of the photo-electron pulses. In the frequency domain the upper limit of the detector is determined by the reciprocal of the pulse width. In TCSPC the time resolution is determined by the rise time of the PMT, and the overall pulse width is less important.

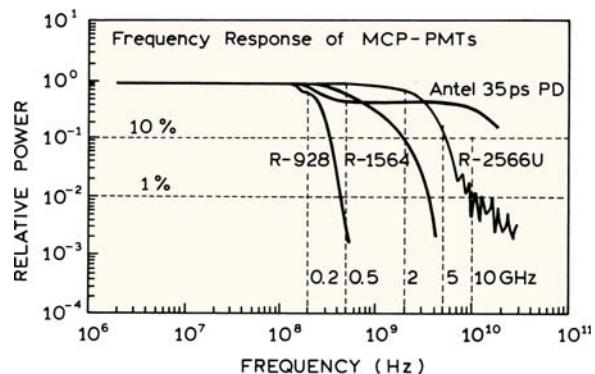


**Figure 5.24.** Measured frequency-response of several PMTs, and a fast photodiode (PD). Data from [107] and [108], and technical literature from Hamamatsu Inc.

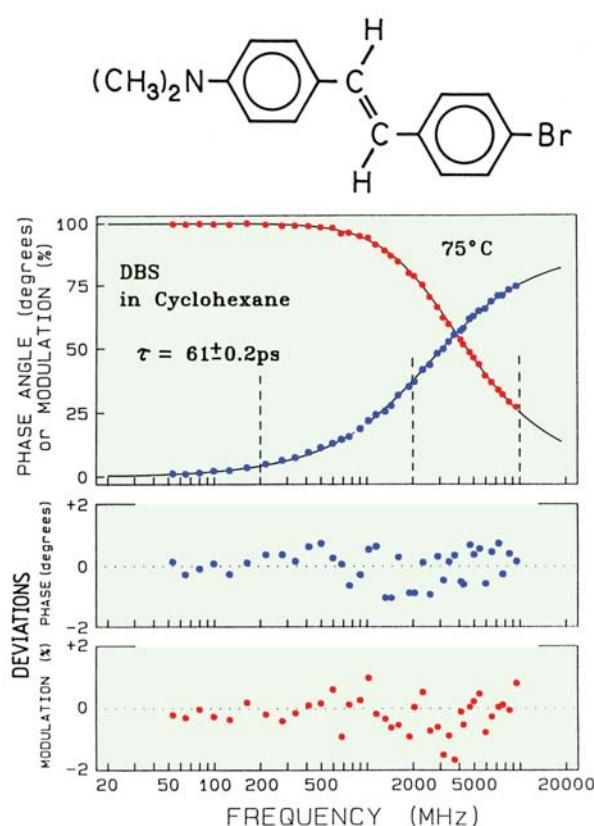


**Figure 5.25.** Frequency response of 4-dimethylamino-4'-bromostilbene (DBS) up to 10 GHz. The vertical dashed lines are at 200 MHz, 2 GHz, and 10 GHz. From [3].

Figure 5.24 shows that the photodiode provides a higher bandwidth than does any of the MCP PMTs. In fact, photodiode detectors were used in several phase fluorometers for measurements at high frequencies.<sup>109–112</sup> Unfortunately, the small active area of photodiodes results in low sensitivity, so that photodiodes are rarely used for fluorescence spectroscopy.

The schematic for the 10-GHz instrument shown in Figure 5.23 incorporates a ps laser as an intrinsically modulated light source, and an MCP PMT as the detector. A photodiode (PD) is adequate as the reference detector because the laser beam can be focused on its small active area. The use of cross-correlation allows measurement over the entire frequency range from 1 MHz to 10 GHz without any noticeable increase in noise. Cross-correlation allows measurements at any modulation frequency at the same low cross-correlation frequency, and avoids the need to measure phase angles and modulation at high frequencies. A valuable feature of cross-correlation is that the entire signal

appears at the measured frequency. Contrary to intuition, one is not selecting one harmonic component out of many, which would result in low signal levels. The use of cross-correlation provides absolute phase and modulation values as if the excitation and detector were both modulated as sine waves. A final favorable feature of this instrument is that the modulation can be higher than 1.0, which is the limit for sine wave modulation. At low frequencies where the detector is fully responsive, the modulation can be as high as 2.0. To understand this unusual result one needs to examine the Fourier components for a pulse train.

### 5.6.1. Gigahertz FD Measurements

Several examples of gigahertz FD measurements will illustrate the value of a wide range of frequencies. Short decay times are needed to utilize the high-frequency capabilities.<sup>113</sup> Otherwise, the emission is demodulated prior to reaching the upper frequency limit. A short decay time was obtained using 4-dimethylamino-4'-bromostilbene (DBS) in cyclohexane at 75°C (Figure 5.25). Because of the short 61-ps lifetime the phase and modulation data could be measured to 10 GHz. The intensity decay was found to be a single exponential.<sup>3</sup> The vertical dashed lines illustrate how only a fraction of the frequency response could be explored if the upper limit was 200 MHz, or even 2 GHz. It would be difficult to detect additional components in the intensity decay if the data stopped at 200 MHz, which would display a maximum phase angle of 4.4°. An important aspect of these measurements is that no measurable color effect has been observed in the 10 GHz measurements.<sup>106</sup>

### 5.6.2. Biochemical Examples of Gigahertz FD Data

GHz measurements may seem exotic, but such data are often needed for studies of routine biochemical samples. One example is NADH. At 200 MHz the data only sampled part of the frequency response (Figure 5.16). When measured to higher frequencies one can more dramatically see the difference between the one and two decay time model (Figure 5.26). The decrease in  $\chi_R^2$  for the two decay time model is 400-fold. While we have not performed a support plane analysis on these data, the  $\alpha_i$  and  $\tau_i$  values will be more closely determined using the data extending above 200 MHz.

Another biochemical example is provided by the peptide hormone vasopressin, which acts as an antidiuretic and

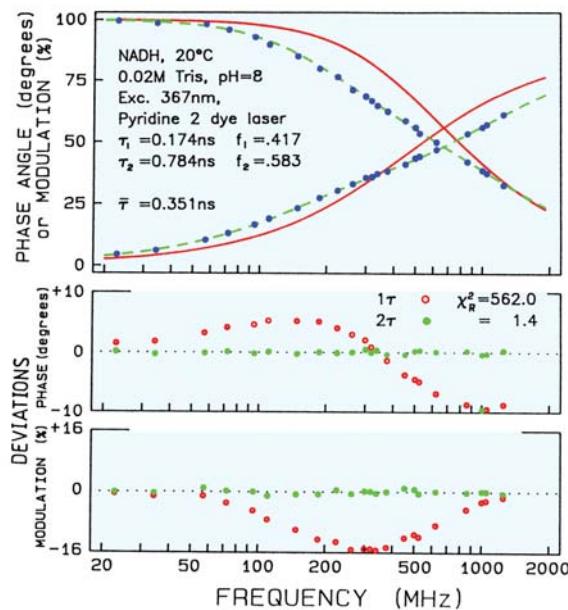


**Figure 5.26.** Frequency-domain measurements of the intensity decay of NADH up to 2-GHz. From [3].

a vasoconstrictor. Vasopressin is a cyclic polypeptide that contains 9 amino acids including a single tyrosine residue at position 2. Oxytocin has a similar structure, but has a distinct physiological activity of stimulating smooth muscle contraction. Hence there have been many efforts to use the tyrosine emission to learn about the solution conformation of these peptide hormones. The frequency-domain data for vasopressin reveal a complex intensity decay (Figure 5.27).<sup>114</sup> The decay is not even closely approximated by the single exponential model (dashed). Fitting the data requires three decay times of 0.17, 0.75, and 1.60 ns. These multiple decay times could probably not be recovered if the data were limited to 200 MHz.

MCP PMTs are moderately expensive, and their use in FD measurements requires special circuits for cross-correlation. However, the advantages of high-frequency FD data may become available without the use of MCP PMTs. Examination of Figures 5.26 and 5.27 indicates that considerable data can be obtained if the data were available to just 1 GHz. This frequency limit can probably be reached with the new compact PMTs, which show short transit time spreads (Table 4.1). A dynode PMT (H5023) has already been used up to 1 GHz.<sup>115</sup> It seems likely that a compact PMT such as the R74000 will be useful up to 900 MHz. Laser diodes with 30-ps pulse widths will provide useful harmonics up to 40 GHz.

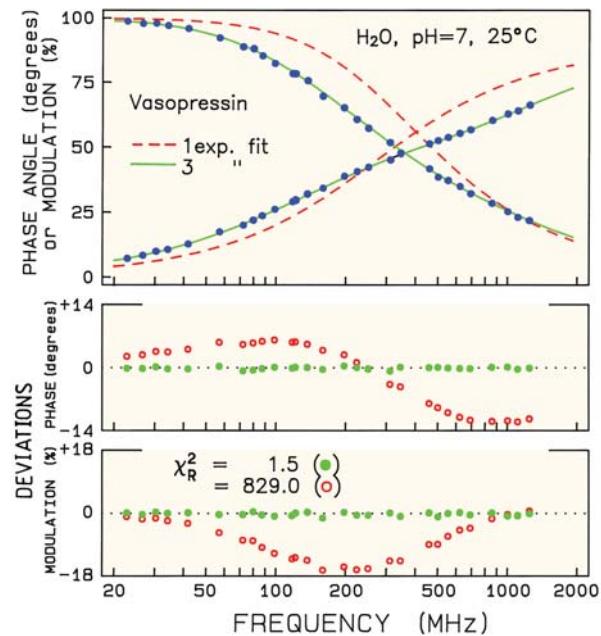


**Figure 5.27.** Phase and modulation data for the vasopressin tyrosine fluorescence intensity decay. The dashed line is the best single-exponential fit, and the solid line is the best three-exponential fit. From [114].

In the near future gigahertz FD instruments will be available based on pulsed-laser diodes and compact PMTs.

## 5.7. ANALYSIS OF FREQUENCY-DOMAIN DATA

Frequency-domain data is often analyzed in terms of the multi-exponential model. As described in Chapter 4, the amplitudes ( $\alpha_i$ ) and decay times ( $\tau_i$ ) are usually strongly correlated, so that there can be considerable uncertainty in the values of the recovered parameters. In this section we describe examples that show correlation between the parameter values.

### 5.7.1. Resolution of Two Widely Spaced Lifetimes

The analysis of frequency-domain data can be illustrated using a mixture of p-terphenyl and indole. This same mixture was used in Chapter 4 for TCSPC data (Figures 4.46–4.49). The same 292-nm excitation and 330-nm emission wavelengths were used for the frequency-domain measurements as for the time-domain measurements. The decay times of the individual fluorophores are 0.93 and 3.58 ns for p-terphenyl and indole, respectively. For this mixture the decay times are spaced 3.8-fold, making this a moderately

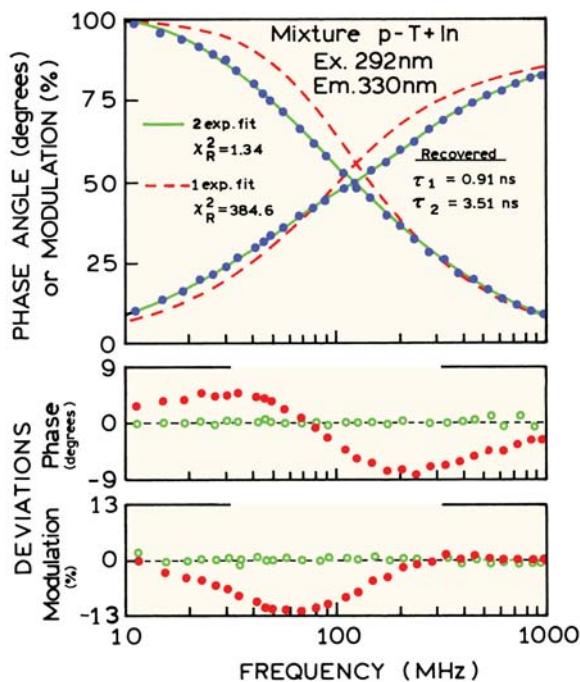


**Figure 5.28.** Frequency-domain intensity decay data of a two-component mixture of p-terphenyl (p-T) and indole (In) in ethanol, 20°C. Magic-angle polarization conditions were used. The sample was in equilibrium with air. The repetition rate was 1.9 MHz from a frequency-doubled rhodamine 6G dye laser. Emission at 330 nm was isolated with a monochromator. The dashed line (top panel) and closed circles (lower panels) show the best fit with one decay time. The solid curves (top) and open circles (bottom) show the best fit with two decay times. From [116].

easy resolution. Frequency-domain intensity decay data are shown in Figure 5.28. The presence of more than a single decay time is evident from the shape of the frequency response, which appears to be stretched out along the frequency axis. The fact that the decay is more complex than a single exponential is immediately evident from the attempt to fit the data to a single decay time. The best single decay time fit (dashed) is very poor and the deviations

are large and systematic (●, lower panels). Also, the value of  $\chi^2_R = 384.6$  is easily rejected as being too large.

Use of a two-decay-time model results in a good fit of the calculated frequency response (Figure 5.28, solid) to the measured phase and modulation values (●). Also, the value of  $\chi^2_R$  decreases to 1.34. Use of the three-decay-time model results in a modest reduction of  $\chi^2_R$  to 1.24, so that the two-decay-time model is accepted. For this mixture the recovered decay times of 0.91 and 3.51 ns closely match the lifetimes measured for the individual fluorophores. The recovered amplitudes and fractional intensities suggest that about 64% of the emission at 330 nm is from the indole with a decay time of 3.51 ns (Table 5.1).

An important part of data analysis is estimating this confidence intervals for each parameter. Most computer programs report the asymptotic standard errors (ASEs), which are the uncertainties calculated under the assumption that the parameters are not correlated. The range of possible parameters are usually 2- to 10-fold larger than that estimated from the ASEs. For this reason, examination of the  $\chi^2_R$  surfaces is preferred. The upper and lower limits of each parameter are determined from the  $\chi^2_R$  ratio as the parameter value is held fixed around the optimal value. The least-squares analysis is then run again to obtain the lowest value of  $\chi^2_R$  consistent with the fixed parameter value. This allows calculation of the  $\chi^2$  ratios:

$$F_\chi = \frac{\chi^2_R(\text{par})}{\chi^2_R(\text{min})} = 1 + \frac{p}{m-p} F(p, v, P) \quad (5.24)$$

where  $\chi^2_R(\text{par})$  is the value of  $\chi^2_R$  with a parameter value held fixed at a value different from that yielding the minimum value of  $\chi^2_R(\text{min})$ . The upper and lower bounds of each parameter are selected as those where the  $\chi^2_R$  ratio intercepts with the  $F_\chi$  value for one standard deviation ( $P = 0.32$ ) and the number of parameters ( $p$ ) and degrees of free-

**Table 5.1.** Multi-Exponential Analysis of a Two-Component Mixture of p-Terphenyl and Indole

Sample	Lifetime (ns)		Pre-exponential factors		Fractional intensity		$\chi^2_R$	
	$\tau_1$	$\tau_2$	$\alpha_1$	$\alpha_2$	$f_1$	$f_2$	1 <sup>a</sup>	2 <sup>a</sup>
p-Terphenyl	0.93	—	1.0	—	1.0	—	1.38	1.42
Indole	—	3.58	—	1.0	—	1.0	1.10	1.13
Mixture	0.91	3.51	0.686	0.314	0.36	0.64	384.6	1.34 <sup>b</sup>

<sup>a</sup>Refers to a two- or one-component fit.  $\delta\phi = 0.2$  and  $\delta m = 0.005$ . From [116].

<sup>b</sup>The value of  $\chi^2_R$  for the three-decay-time fit for the mixture was 1.24.

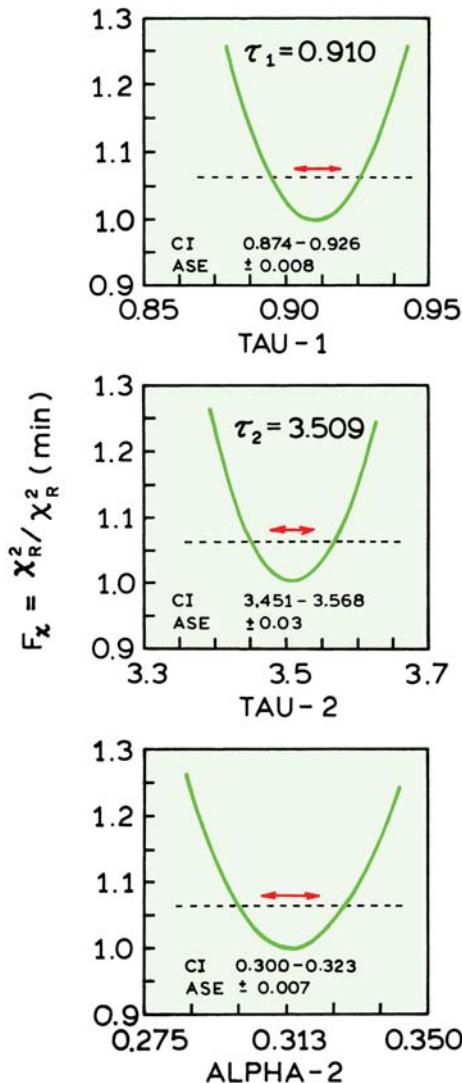


**Figure 5.29.**  $\chi^2$  surfaces for the two-component mixture of p-terphenyl and indole. The horizontal arrows show the asymptotic standard errors (ASE), and the dashed lines are at the appropriate  $F_\chi$  values. From [116].

dom ( $v = m - p$ ). It is useful to consider some representative values for the ratio of  $\chi^2$  values. For the two-component mixture of p-terphenyl and indole there are 29 frequencies and 58 datapoints. The two-decay-time model has three variable parameters. The  $F$  statistic for  $p = 3$  and  $m = 60$  can be found from Table 4.4 and is 1.19. Hence, the  $F_\chi$  value used for the confidence interval of each parameter is 1.06. As described in Section 4.10.3, there is some disagreement in the statistics literature as to the exact equation for finding the confidence intervals. We will use eq. 5.24, but its correctness has not yet been proven.

The  $\chi^2$  surfaces for the two-component mixture are shown in Figure 5.29. The confidence intervals (CI) are determined from the intercept of the  $\chi^2$  surfaces with the  $\chi^2$  ratio appropriate for the number of parameters and degrees of freedom. The arrows in Figure 5.29 show the asymptotic standard errors. The ASEs are about twofold smaller than the confidence intervals. The decay times in this mixture are widely spaced. For more closely spaced decay times it becomes even more important to consider parameter correlation in the calculation of confidence intervals, and the ASEs can grossly underestimate the true confidence intervals.

### 5.7.2. Resolution of Two Closely Spaced Lifetimes

The resolution of multi-exponential decays becomes more difficult as the decay times become more closely spaced. It was previously noted that two decay times spaced by a factor of 1.4 represents the practical resolution limit for double exponential decay.<sup>12</sup> It is instructive to examine data for such a mixture because the analysis illustrates the difficulties encountered at the limits of resolution.

To illustrate a sample with two closely spaced decay times we have chosen the mixture of anthranilic acid (AA,  $\tau = 8.5$  ns) and 2-aminopurine (2-AP,  $\tau = 11.3$  ns). This may seem to be an easy resolution, but it is difficult to resolve decay times which are less than two-fold different. Emission spectra are shown in Figure 5.30. Frequency-domain data for the individual fluorophores and for the mixture are

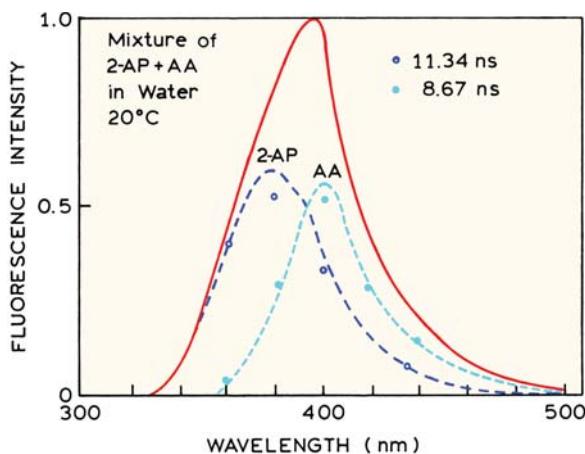


**Figure 5.30.** Emission spectra of a two-component mixture of anthranilic acid (AA) and 2-aminopurine (2-AP). Also shown are the amplitudes recovered from the global analysis (Figure 5.33). From [116].

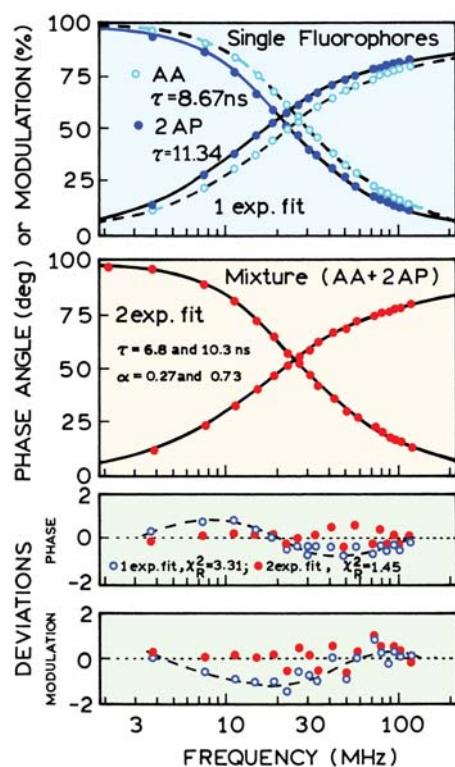


**Figure 5.31.** Frequency-domain intensity decays for 2-aminopurine (2-AP) and anthranilic acid (AA). Top: single fluorophore data at 400 nm. Middle: the two component mixture measured at 400 nm. Bottom: deviations for fits to the two component mixture. The value of  $\chi_R^2$  for the one- and two-component fits are 3.31 and 1.45, respectively. From [116].

shown in Figure 5.31. Each of the single fluorophores displays a frequency response characteristic of a single decay time. The values of  $\chi_R^2$  for the single-decay-time fits were acceptably low, and were not improved by using a two-decay-time model. The 40% difference in decay time

results in only a modest shift on the frequency axis. Figure 5.31 (middle panel) also shows the frequency-domain data for the two component mixture of AA and 2-AP. Frequency-domain data were measured through a 400-nm interference filter. At this wavelength both fluorophores contribute almost equally to the measured intensities. For these two closely spaced lifetimes, it is difficult to see a difference between the calculated curves for the one and two decay time fits. The deviation plots (lower panels) show larger and systematic deviations for the one component fit. Also,  $\chi_R^2$  decreases from 3.3 for the one-decay-time fit to 1.45 for the one- and two-decay-time fits. For these measurements we have approximately 40 degrees of freedom. The  $F$  value of 2.3 is seen to be significant at the 1% level (Table 4.3), and there is less than a 0.1% probability that random noise is the origin of the elevated  $\chi_R^2$  value for the one-decay-time fit (Table 4.2).

In general we accept the more complex model if  $\chi_R^2$  decreases by at least 50%, preferably twofold. Occasionally, the value of  $\chi_R^2$  is larger than expected, but  $\chi_R^2$  does not decrease for the next more complex model. In these cases the elevated  $\chi_R^2$  is usually due to systematic errors in the measurements. It is fortunate that in many cases systematic errors cannot be accounted for by another decay time component in the model.

The twofold reduction in  $\chi_R^2$  for the two-decay-time mixture seems reasonable, but the recovered parameter values have considerable uncertainty. At 400 nm the two-component analysis returns a fractional intensity of 80% for the longer lifetime, and decay times of 6.82 and 10.29 ns (Table 5.2). These values are considerably different from the expected fractional intensity near 40% for the longer decay time component. Also, the recovered decay times of 6.82 and 10.29 ns are different from the expected decay times of

**Table 5.2.** Resolution of a Two-Component Mixture of Anthranilic Acid and 2-Aminopurine, Observed at a Single Wavelength

Observation wavelength (nm)	Lifetimes (ns)		Pre-exponential factors		Fractional intensity		$\chi_R^2$	
	$\tau_1$	$\tau_2$	$\alpha_1$	$\alpha_2$	$f_1$	$f_2$	$2^a$	$1^a$
360	6.18	11.00	0.037	0.963	0.021	0.979	0.95	1.07
380	8.99	12.26	0.725	0.275	0.659	0.341	1.24	2.06
400	6.82	10.29	0.268	0.732	0.195	0.805	1.54	3.44
420	8.44	12.15	0.832	0.168	0.775	0.225	1.36	2.22
440	7.69	9.73	0.479	0.521	0.421	0.579	1.69	2.01

<sup>a</sup>Refers to a two- or one-component fit.  $\delta\phi = 0.2$  and  $\delta m = 0.005$ . From [116].

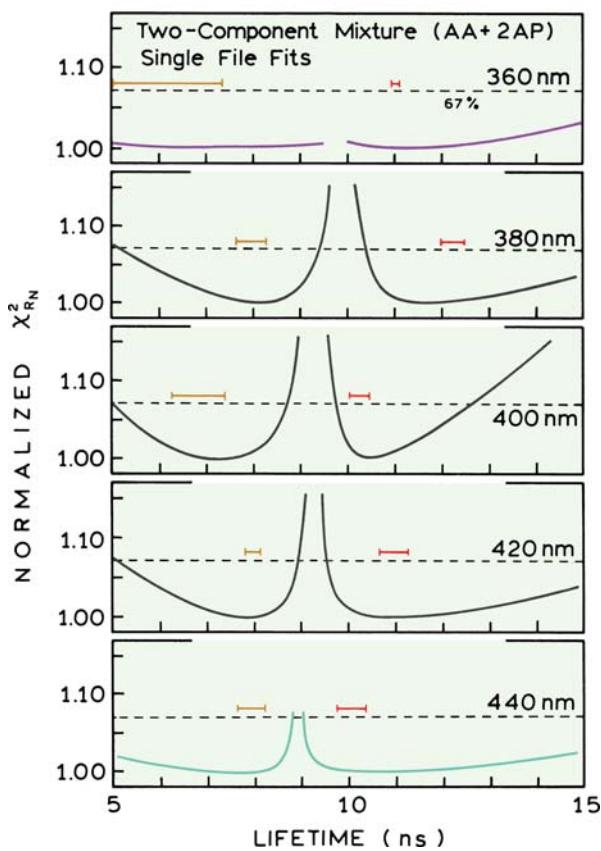


**Figure 5.32.** Lifetime  $\chi_R^2$  surfaces for the mixture of anthranilic acid (AA) and 2-aminopurine (2-AP) for single observation wavelengths. The solid bars (—) show the asymptotic standard errors. From [116].

8.5 and 11.3 ns. Analysis of the intensity decays at other wavelengths reveals considerable variability in the recovered lifetimes and fractional intensities. This can be seen in Figure 5.32 from the range of lifetimes consistent with the data from the  $\chi_R^2$  surfaces. At different emission wavelengths the lifetime of the shorter decay time ranges from 6.18 to 8.99 ns, and the lifetime of the longer component ranges from 9.73 to 12.26 ns (Table 5.2). The amplitudes and fractional intensities recovered from the measurements at different wavelengths do not accurately represent the emission spectra of the two fluorophores. This is seen at 400 nm, where the amplitude of AA is expected to be dominant, but a low value was recovered (0.195, Table 5.2). Such variability is typical in the analysis of closely spaced decay times, whether the measurements are performed in the frequency domain or in the time domain.

The uncertainties in the recovered lifetimes is best determined from the  $\chi_R^2$  surfaces (Figure 5.32). These surfaces for the mixture of AA and 2-AP are wide due to the

closely spaced lifetimes and correlation between the lifetimes and amplitudes. The lack of resolution is especially apparent for observation at 360 nm. In this case the emission is due primarily to just one of the fluorophores (AA). The lifetime of one component can be fixed near 12 ns without an elevation in  $\chi_R^2$ , even when the dominant lifetime is near 8 ns. This probably occurs because the amplitude of the 12-ns component can be decreased as the new  $\chi_R^2$  values are calculated. At observation wavelengths where both AA and 2-AP emit there are modest minima in the  $\chi_R^2$  surfaces (Figure 5.32). However, the confidence intervals are large, and in some cases the desired  $\chi_R^2$  increase is not reached for any reasonable value of the decay times. The confidence intervals, which are the range of parameter values consistent with the data, are not symmetrical about the best-fit values.

### 5.7.3. Global Analysis of a Two-Component Mixture

The resolution of complex intensity decays can be dramatically enhanced by global analysis, which is the simultaneous analysis of multiple data sets measured under slightly different conditions. For the two-component mixture of AA and 2-AP, data were measured for five emission wavelengths (Figure 5.33, 360 to 440 nm). The decay time of each fluorophore is expected to be independent of emission

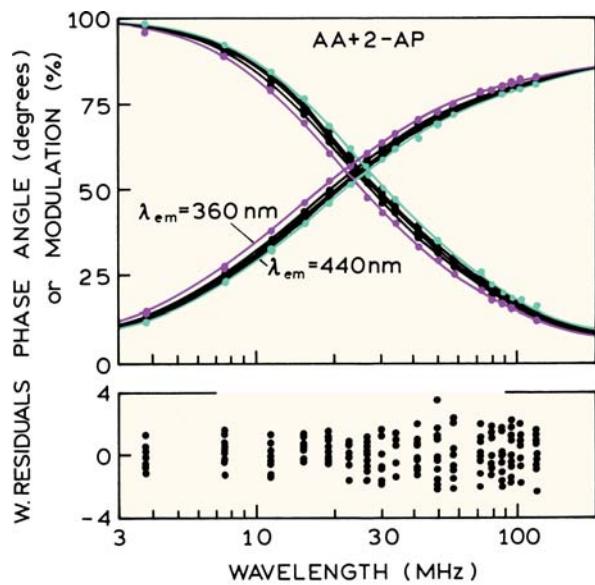


**Figure 5.33.** Global analysis of the two-component mixtures of AA and 2-AP. From left to right, the data are for 360, 380, 400, 420, and 440 nm. The values of  $\chi_R^2$  for the global one- and two-component fits are 37.4 and 1.33, respectively. From [116].

**Table 5.3.** Global Analysis of a Two-Component Mixture of Anthranilic Acid and 2-Aminopurine Measured at Five Emission Wavelengths<sup>a,b</sup>

Observation wavelength (nm)	2-AP		AA <sup>c</sup>	
	$\tau_1 = 8.19$ ns	$f_1$	$\tau_2 = 11.18$ ns	$f_2$
360	0.117	0.089	0.883	0.911
380	0.431	0.357	0.569	0.643
400	0.604	0.528	0.396	0.472
420	0.708	0.640	0.292	0.360
440	0.810	0.758	0.190	0.242

<sup>a</sup>Analysis of the data in Figure 5.33.  $f = 0.2$  and  $\delta m = 0.005$ . From [116].

<sup>b</sup>For the one-component fit  $\chi_R^2 = 37.4$ , for the two-component fit  $\chi_R^2 = 1.33$ .

<sup>c</sup>Lifetimes assigned to these fluorophores based on measurements of the individual fluorophores (Figure 5.31).

wavelength. Hence the global analysis is performed as described in eqs. 5.13 to 5.15, where the  $\alpha_i(\lambda)$  values are assumed to be different at each wavelength, but the  $\tau_i$  values were assumed to be independent of wavelength.

Results of the global analysis are shown in Figure 5.33 and Table 5.3. The value of  $\chi_R^2 = 37.4$  for the one-component fit is easily rejected. Use of the two-component model results in a decrease of  $\chi_R^2$  to 1.33. For the global analysis, the frequency responses at each emission wavelength are in good agreement with the calculated curves when using two wavelength-independent decay times. Use of three decay times does not improve  $\chi_R^2$ , so the two-decay-times model is accepted.

Global analysis results in less uncertainty in the recovered parameters. The lifetime  $\chi_R^2$  surfaces from the global

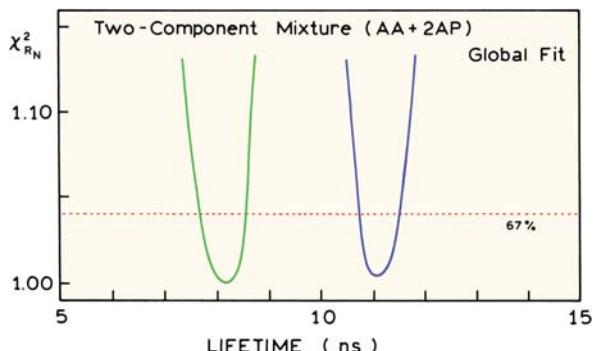


**Figure 5.34.** Lifetime  $\chi_R^2$  surfaces for the mixture of anthranilic acid (AA) and 2-aminopurine (2-AP). The 67% line refers to the  $F_\chi$  values for global analysis. From [116].

analysis are much steeper when calculated using the data at six emission wavelengths (Figure 5.34, —). The elevated values of  $\chi_R^2$  are more significant because of the larger degrees of freedom. For this global analysis there are approximately 200 datapoints, and seven variable parameters. Hence the  $F$  statistic is 1.16 (Table 4.4), and the  $F_\xi$  value is 1.04 (eq. 5.24). Global analysis also results in improved estimates of the amplitudes. The fractional intensities ( $f_i$ ) and decay times ( $\tau_i$ ) recovered from the global analysis closely match those expected from the spectral properties of the individual fluorophores (Figure 5.30).

#### 5.7.4. Analysis of a Three Component Mixture: Limits of Resolution

A three-component mixture with less than a threefold range in lifetime represents the practical limit of resolution for both time and frequency domain measurements. Analysis of the data from such a sample illustrates important considerations in data analysis at the limits of resolution. Frequency-domain intensity decay data for the mixture of indole (IN, 4.41 ns), anthranilic acid (AA, 8.53 ns) and 2-aminopurine (2-AP, 11.27 ns) are shown in Figure 5.35. The data cannot be fit to a single decay time, resulting in  $\chi_R^2 = 54.2$ , so this model is easily rejected. The situation is less clear for the two- and three-decay-time fits, for which the values

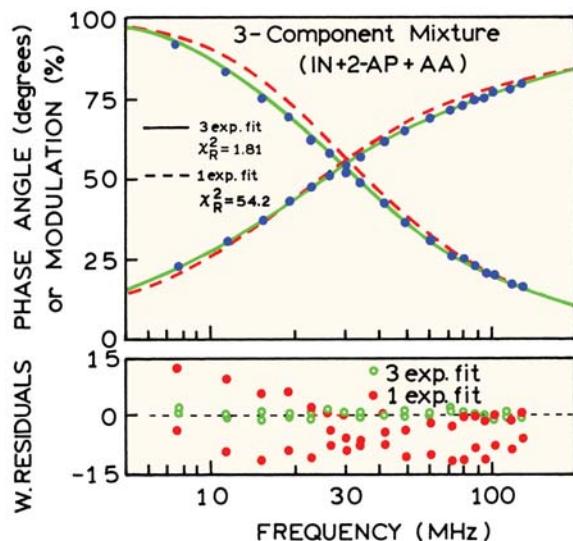


**Figure 5.35.** Frequency-domain intensity decay for a three-component mixture of indole (IN), 2-aminopurine (2-AP), and anthranilic acid (AA) in water, 20°C, pH 7, observed at 380 nm. The  $\chi_R^2$  values for one-, two-, and three-decay-time fits are 54.2, 1.71, and 1.81, respectively. From [116].

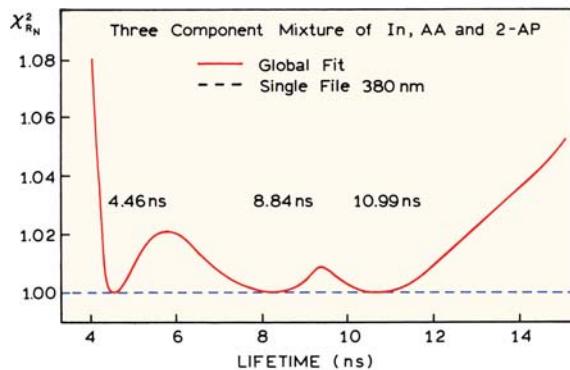


**Figure 5.36.** Lifetime  $\chi^2_R$  surfaces for the three component mixtures of In, AA, and 2-AP; dashed, 380 nm; solid, global fit at 360, 380, 400, 420, and 440 nm. From [116].

of  $\chi^2_R$  are 1.71 and 1.81, respectively. At first glance it seems that  $\chi^2_R$  has increased for the three-exponential fit. However, the increase in  $\chi^2_R$  for the three-decay-time model is a result of the larger number of variable parameters and the smaller number of degrees of freedom. The value of  $\chi^2$ , which is the sum of the squared deviations, for these three fits is 2006, 59.7, and 59.6, for the one-, two-, and three-decay-time fits. Hence, the fit is not worse for the three-decay-time fit, but is essentially equivalent to the two-decay-time model.

Samples such as this three-component mixture are difficult to analyze. In this case we know there are three decay times, and the three decay times are correctly determined by the analysis. However, obtaining the correct values required that the starting parameter values are close to the correct values. Otherwise, the program stopped at incorrect values, apparently trapped in local  $\chi^2_R$  minima. Additionally, the  $\chi^2_R$  surface is almost independent of lifetime, as shown in Figure 5.36 for the data measured at 380 nm (dashed). Without prior knowledge of the presence of three decay times, it would be difficult to know whether to accept the two or three decay time fit.

At this point in the analysis there is little reason for proceeding further. If the information is not present in the data, no amount of analysis will create new information. One can either add new experimental data, or add information by restricting parameters based on separate knowledge about the sample. If one or more of the lifetimes are known, these can be held constant during the least-square fit. Similarly, one of the amplitudes could be fixed. However, the best approach is to add new data and perform a global analysis.

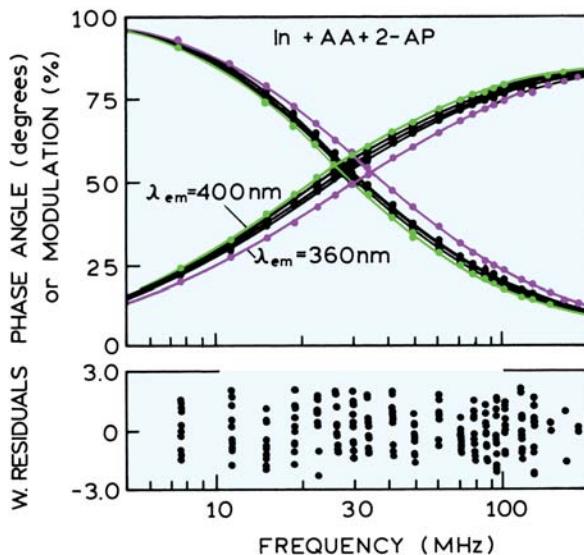


**Figure 5.37.** Frequency-domain intensity decays of the three-component mixture observed at 360, 380, 400, 420, and 440 nm. The lines are for the best fit to three global decay times and non-global amplitudes. The values of  $\chi^2_R$  for the one-, two-, and three-decay-time fit are 109.8, 2.3, and 1.1, respectively. From [116].

The emission from the three-component mixture was measured at five wavelengths: 360, 380, 400, 420 and 440 nm (Figure 5.37). At each wavelength each fluorophore displays the same decay time, but a different fractional amplitude based on its emission spectrum (Figure 5.38). Because of the different amplitudes at each wavelength, the frequency responses are wavelength dependent (Figure 5.37). The

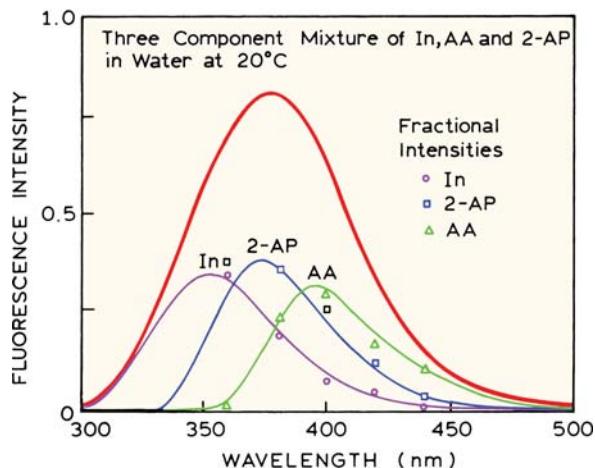


**Figure 5.38.** Emission spectra of the three-component mixture of indole, anthranilic acid, and 2-aminopurine. Also shown are the fractional intensities recovered from global analysis of the frequency-domain data. From [116].

**Table 5.4.** Global Analysis of the Frequency-Domain Data for a Three-Component Mixture of Indole, Anthranilic Acid, and 2-Aminopurine<sup>a</sup>

Observation wavelength (nm)	$\tau_1 = 4.46$ ns		$\tau_2 = 8.84$ ns		$\tau_3 = 10.99$ ns	
	$\alpha_1$	$f_1$	$\alpha_2$	$f_2$	$\alpha_3$	$f_3$
360	0.700	0.488	0.008	0.011	0.292	0.501
380	0.434	0.254	0.244	0.282	0.322	0.464
400	0.235	0.123	0.429	0.444	0.336	0.433
420	0.306	0.169	0.430	0.471	0.264	0.360
440	0.219	0.121	0.687	0.752	0.094	0.127

<sup>a</sup> $\delta\phi = 0.2$  and  $\delta m = 0.005$ . From [116].  $\chi_R^2 = 1.19$ , 2.30, and 109.8 for the three-, two-, and one-component fits, respectively.

relative position of these curves can be understood by recognizing that indole (4.41 ns) displays the shortest lifetime and emits towards shorter wavelengths. The mean lifetime is expected to be largest near 380 nm, which is the emission maximum of 2-AP (11.27 ns). The mean lifetime decreases at longer wavelengths as the emission becomes dominated by AA (8.53 ns).

Figure 5.38 and Table 5.4 show the results of global analysis of the wavelength-dependent data. The one- and two-component fits are easily rejected on the basis of the  $\chi_R^2$  values of 109.8 and 2.3, respectively, which are both significantly larger than  $\chi_R^2 = 1.2$  for the three-decay-time fit. The uncertainties in the parameter values can be found by examining  $\chi_R^2$  surfaces (Figure 5.36). For the single-wavelength data at 380 nm the value of  $\chi_R^2$  was insensitive to fixing any of the three decay times. When this occurs, recovery of the correct decay times should be regarded as a fortunate coincidence rather than evidence for the resolution obtainable from the data. For the global data the  $\chi_R^2$  surfaces display distinct minima at the correct lifetimes, providing good estimates of the values and range consistent with the data. Also, the recovered amplitudes now closely match those expected from the known emission spectra of the fluorophores (Figure 5.38). By performing additional measurements at different wavelengths, and global analysis, a sample that had been unresolvable became a readily resolvable mixture. The magnitude of the  $\chi_R^2$  ratio is larger for the more widely spaced decay times. The ratio increases to 1.02 between the 4.46- and 8.84-ns lifetimes, and to only 1.01 between the 8.84 and 10.99-ns lifetimes. This effect illustrates why it is more difficult to resolve more closely spaced lifetimes. Finally, it is interesting to consider the  $F_\chi$  value appropriate for this analysis. There are

approximately 200 datapoints and 13 parameters. The  $\chi_R^2$  ratio is 1.15, so  $F_\chi = 1.08$ . Hence, the confidence intervals overlap for the three lifetimes.

### 5.7.5. Resolution of a Three-Component Mixture with a Tenfold Range of Decay Times

The ability to resolve a three-component mixture increases rapidly if the decay times are more widely spaced. A mixture with a tenfold range of lifetimes is provided by POPOP (1.32 ns), 9-methylanthracene (4.44 ns), and 9-cyanoanthracene (12.12 ns). The relative value of  $\chi_R^2$  decreased 20-fold for the three-decay-time fit relative to the two-decay-time fit (Figure 5.39). For this mixture the calculated phase and modulation values for the two-decay-time model ( $\circ$ ) differ systematically from the data, whereas the deviations from the three-decay-time model ( $\bullet$ ) are randomly distributed (Figure 5.39). In this analysis the value of  $\chi_R^2 = 0.26$  for the three-decay-time fit seems too small. This is not an error, but indicates the assumed values of  $\delta\phi = 0.3$  and  $\delta m = 0.003$  are too large, and that the actual uncertainties are smaller. From these results we see that three decay times with a tenfold range are easily recovered, but three lifetimes with a threefold range are difficult to resolve.

### 5.7.6. Maximum Entropy Analysis of FD Data

The maximum entropy method (MEM) has also been used to analyze frequency-domain data. However, there are relatively few papers on this topic,<sup>117–121</sup> so it is difficult to judge the usefulness of the MEM for FD data. The published results give the impression that the MEM is less robust with FD data than with TD data, but a detailed comparison has not been published.

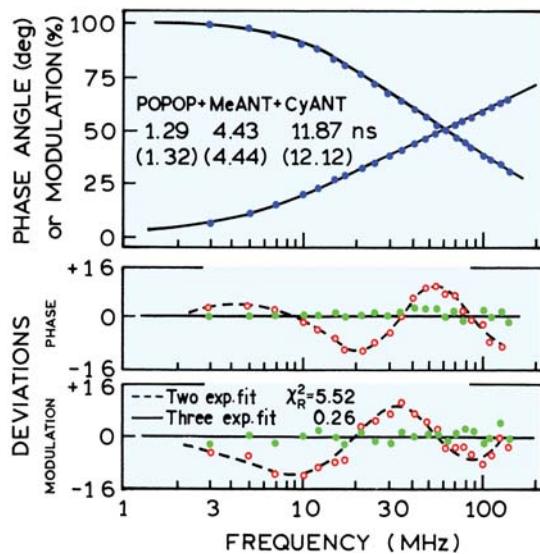


**Figure 5.39.** Phase and modulation data for a three-component mixture of POPOP, 9-methylanthracene (MeANT), and 9-cyanoanthracene (CyANT) in ethanol at 20°C, in equilibrium with air. The values shown are recovered from the three-component fit, and the values in parentheses are from separate measurement of the pure compounds. The fractional intensities of the three components were equal ( $f_1 = f_2 = f_3 = 1/3$ ). The excitation wavelength was 325 nm and the emission filter a Corning 0-52. The measurements were performed relative to a POPOP reference solution with a reference lifetime of 1.32 ns.  $\delta\phi = 0.3^\circ$  and  $\delta m = 0.003$ . Revised from [13] and reprinted with permission from the Biophysical Society.

## 5.8. BIOCHEMICAL EXAMPLES OF FREQUENCY-DOMAIN INTENSITY DECAYS

### 5.8.1. DNA Labeled with DAPI

The probe DAPI (4',6-diamidino-2-phenylindole) is widely used to study DNA.<sup>122–126</sup> DAPI binds to the minor groove of DNA and shows preferential binding to AT-rich regions of DNA. DAPI is only weakly fluorescent in water (Figure 5.40), and displays an increase in quantum yield upon binding to DNA.<sup>126</sup> The increase in quantum yield is minimal for binding to poly d(GC). A more significant enhancement in DAPI fluorescence is found upon binding to DNA containing both GC and AT pairs (circular and linear DNA in Figure 5.40). The largest enhancement of DAPI fluorescence is found for binding of DAPI to poly d(A)-poly d(T) or to poly d(AT). The dependence of DAPI fluorescence on the base composition of DNA suggests that DAPI will display complex decay kinetics when bound to DNA because the DAPI will be near both AT and GC base pairs.

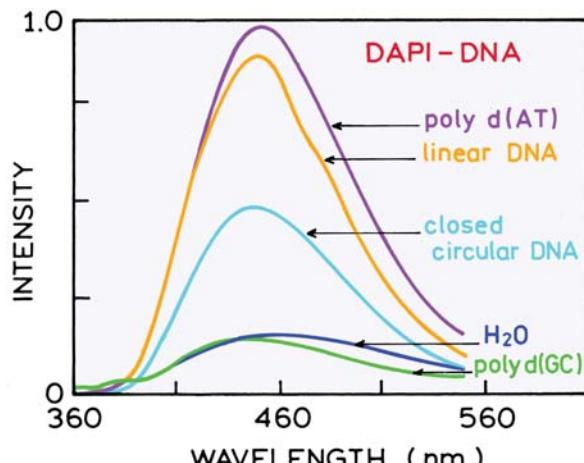


**Figure 5.40.** Top: Structure of a DAPI-DNA complex. Bottom: Emission spectra (x20) of DAPI in water at pH 7.1, and complexed with poly d(GC) (x20), closed circular DNA (x10), linear DNA and to polyd (AT). Excitation at 340 nm. Lower panel revised from [126].

Frequency-domain intensity decays of DAPI are shown in Figure 5.41. Excitation was at 325 nm from an HeCd laser. For the intensity decay measurements the entire emission was observed using an RG370 longpass filter. Measurements were performed using POPOP in ethanol as a reference, with a lifetime of 1.35 ns. The frequency responses are visually heterogeneous for DAPI bound to poly d(GC) and to linear DNA, indicating that DAPI is bound in more than one environment with different decay times. The average lifetime is longest when DAPI is bound to poly d(A)-poly d(T), as seen from the frequency response shifted to the lowest frequencies.

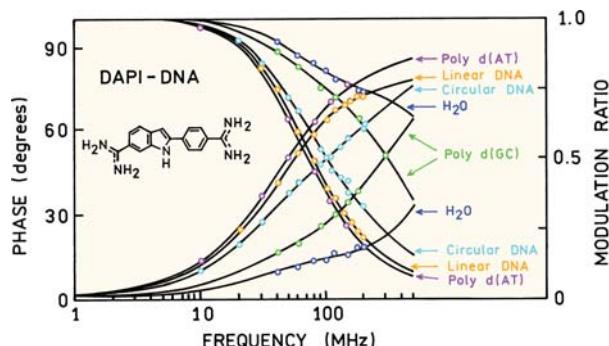


**Figure 5.41.** Frequency-domain intensity decays of various DNAs labeled with DAPI. DAPI in water at pH 7.1, and complexed with polyd(GC), linear DNA, circular DNA, and AT polymers. The solid lines correspond to the best fits using a double-exponential model. Revised from [126].

The intensity decays could be fit to the two decay time model (Table 5.5). In the absence of DNA, the intensity is dominated by a 0.19-ns component. The decay is nearly unchanged by the presence of poly d(GC), except for an increase in the decay time of the short component to 0.6 ns. Substantial changes in the intensity decay are found upon binding to the other DNAs, where the decays are dominated by a 3.8–3.9-ns component. Linear and closed circular (CC) DNA has both AT and GC base pairs. In these cases the intensity decay is heterogeneous due to the presence of DAPI bound to both types of base pairs. Binding of DAPI to a homogeneous DNA, either poly d(AT) or poly d(A)-poly d(T), results in a homogeneous decay. These results show how the time-resolved decays can be used to learn about the presence of more than one type of binding site for a fluorophore.

As discussed in Section 5.10, the lifetimes calculated from the phase and modulation at a single frequency are only apparent values. The heterogeneous decay of DAPI in water illustrates this effect.<sup>126</sup> For an observation wave-

length of 470 nm, and a modulation frequency of 100 MHz, the apparent phase and modulation lifetimes are  $\tau_{\phi}^{\text{app}} = 0.47$  ns and  $\tau_m^{\text{app}} = 1.24$  ns. The fact that  $\tau_{\phi} < \tau_m$  indicates that the decay is heterogeneous.

### 5.8.2. Mag-Quin-2: A Lifetime-Based Sensor for Magnesium

Ion-sensitive fluorophores are widely used in cell biology to measure intracellular calcium concentrations. While most calcium and magnesium measurements are based on intensity or wavelength-ratiometric measurements, one can also use intensity decay measurements. Lifetime measurements offer the advantage of being independent of the total fluorescence intensity, and can thus be used in fluorescence microscopy where quantitative intensity measurements are difficult. Probes that display changes in lifetime can be used for fluorescence-lifetime imaging microscopy (Chapter 22).

The use of a magnesium probe as lifetime-based sensors requires an understanding of how the decay times change in response to Mg<sup>2+</sup>. One example is shown in Figure 5.42 for Mag-Quin-2.<sup>127</sup> The mean decay time of Mag-Quin-2 increases from 0.84 ns in the absence of Mg<sup>2+</sup> to 8.16 ns in the presence of Mg<sup>2+</sup>. This increase in lifetime results in a dramatic shift of the frequency response to lower frequencies. At intermediate Mg<sup>2+</sup> concentrations, where Mag-Quin-2 is partially saturated with Mg<sup>2+</sup>, one can visually see that the frequency response is heterogeneous and one can see the contributions of the short and long decay times of Mag-Quin-2.

Data of the type shown in Figure 5.42 are ideal for a global analysis. The two decay times are expected to be constant at all Mg<sup>2+</sup> concentrations, and the amplitudes are expected to depend on magnesium. An alternative approach to improving the resolution is to fix the decay times. In this case the lifetimes in the absence and presence of saturating

**Table 5.5.** Intensity Decays of DAPI Bound to Various DNAs<sup>a</sup>

DNA <sup>b</sup>	$\tau_1$ (ns)	$\tau_2$ (ns)	$f_1$	$f_2$
None, in water at pH 7.1 <sup>c</sup>	0.19	2.80	0.73	0.27
Poly d(GC) <sup>b</sup>	0.6	2.9	0.71	0.29
CC-DNA <sup>d</sup>	0.4	3.8	0.05	0.95
Linear DNA	0.5	3.8	0.20	0.80
Poly d(AT)	—	3.9	—	1.00
Poly d(A)-poly d(T)	—	3.9	—	1.00

<sup>a</sup>From [126]. The DNA phosphate:DAPI ratio was 60.

<sup>b</sup>The measurements with DNA were at pH 7.2 in 0.1 M tris with 0.1 M NaCl.

<sup>c</sup>DAPI in water at pH 7.1.

<sup>d</sup>Closed circular DNA-CoEl plasmid DNA.

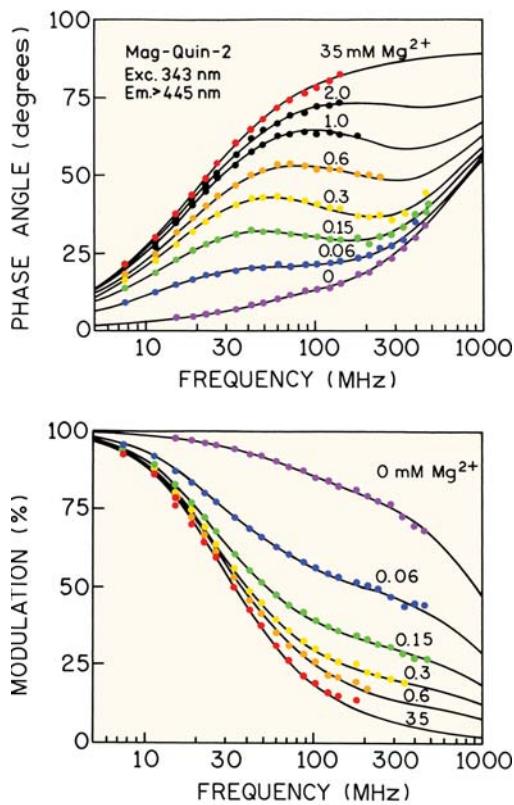


**Figure 5.42.** Frequency response of the magnesium indicator Mag-Quin-2 with increasing amounts of magnesium. Revised from [127].

$Mg^{2+}$  can be used as known values. Analysis of the frequency-domain data at one  $Mg^{2+}$  concentration can then be used to recover the amplitudes with less uncertainty than if the lifetimes were variable parameters.

### 5.8.3. Recovery of Lifetime Distributions from Frequency-Domain Data

Frequency-domain data can be used to recover lifetime distributions. For a distribution of lifetimes the intensity decay is given by

$$I(t) = \int_0^\infty \alpha(\tau) \exp(-t/\tau) \quad (5.25)$$

where the lifetime distribution  $\alpha(\tau)$  can be a unimodal or multimodal distribution:

$$\alpha(\tau) = \sum_i \alpha_i(\tau) \quad (5.26)$$

For a lifetime distribution the transforms are given by

$$N_\omega J = \int_{t=0}^{\infty} \int_{\tau=0}^{\infty} \alpha(\tau) e^{-t/\tau} d\tau \sin \omega t dt \quad (5.27)$$

$$D_\omega J = \int_{t=0}^{\infty} \int_{\tau=0}^{\infty} \alpha(\tau) e^{-t/\tau} d\tau \cos \omega t dt \quad (5.28)$$

where

$$J = \int_{\tau=0}^{\infty} \alpha(\tau) \tau d\tau \quad (5.29)$$

It is not easy to write analytical expressions for the sine and cosine transforms. Hence, the sine and cosine transforms are calculated numerically. This is not a problem with modern computers, which can rapidly do the required numerical integrations. It is important to recognize that it is difficult to recover all the parameters of a multimodal lifetime distribution, and that in general a lifetime distribution cannot be distinguished from a multi-exponential distribution.<sup>128–129</sup>

### 5.8.4. Cross-Fitting of Models: Lifetime Distributions of Melittin

When analyzing data in terms of lifetime distribution it is difficult to know if the results are unique. In such cases we suggest cross-fitting of models to determine whether the recovered distributions are statistically different. This procedure is illustrated by the intensity decay of melittin. Frequency-domain data for the single tryptophan protein melittin are shown in Figure 5.43. In a mixture of 20% water and 80% methanol, melittin exists as  $\alpha$ -helical monomers. The data could be fit to a bimodal Lorentzian,<sup>130</sup> which is shown in the lower panel of Figure 5.44. The lifetime distributions found for melittin are consistent with the notion of protein structure being an origin of the complex intensity decays of proteins. When dissolved in 6 M guanidine hydrochloride (GuHCl), which eliminates all structure, the intensity decay becomes equivalent to a double exponential decay (Figure 5.44, top). In water, melittin is known to have a small amount of residual structure. Under these conditions one

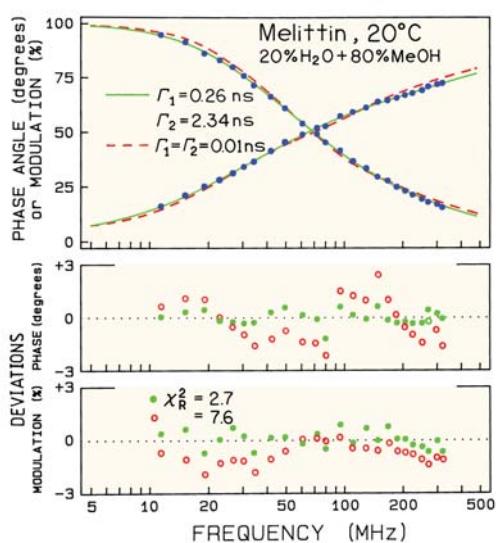


**Figure 5.43.** Phase and modulation data for synthetic melittin in 20% H<sub>2</sub>O + 80% MeOH. The solid line and filled circles show the best fit to a bimodal Lorentzian. The dashed line and open circles show the best fit when the widths of the distribution  $\Gamma_1$  and  $\Gamma_2$  were held constant at the narrow value of 0.01 ns. From [130].

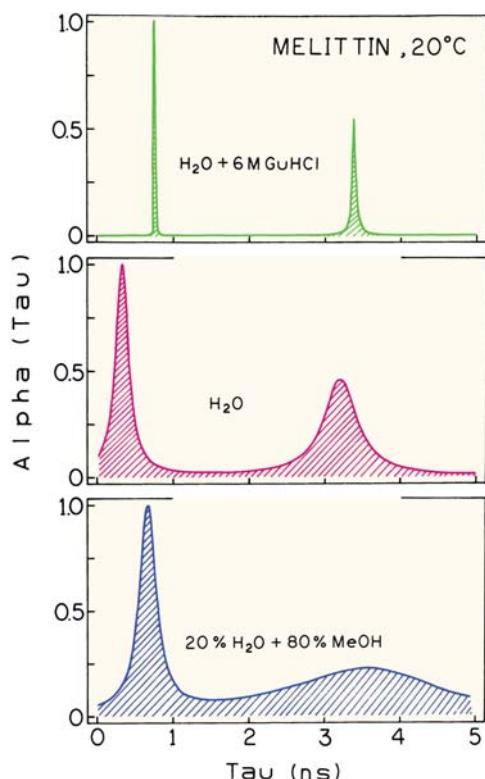


**Figure 5.44.** Lifetime distributions for synthetic melittin in H<sub>2</sub>O with 6 M GuHCl (top), H<sub>2</sub>O (middle), and a mixture of 20% H<sub>2</sub>O + 80% MeOH (bottom). From [130].

notices that the lifetime distributions become broader (Figure 5.44, middle and lower panels).

While lifetime distributions can be recovered from the FD data, it is important to ask whether the various distributions are distinct within the resolution limits of the data, or cannot be distinguished from the data. We answer this question by fitting the data with some of the fixed parameter values. In this case we asked whether the data for melittin in 80% methanol (broad distribution) could be fit with narrow Lorentzian half widths ( $\Gamma_1 = \Gamma_2 = 0.01$  ns). The mean lifetimes and amplitudes of the Lorentzian were still variable parameters. The forced fit results in an approximate three-fold elevation of  $\chi^2_R$ , indicating that the intensity decay of melittin in 80% methanol is not consistent with two lifetimes and narrow distributions. A less rigorous test would be to cross-fit the data with all the parameters fixed, which results in easier rejection of the alternate decay law. The cross-fitting procedure is recommended whenever one is trying to distinguish between two similar models.

### 5.8.5. Frequency-Domain Fluorescence Microscopy with an LED Light Source

Frequency-domain measurements are finding use in fluorescence microscopy, for both single point measurements<sup>131–135</sup> and for imaging (Chapter 22). Figure 5.45 shows fluorescence images of mouse 3T3 fibroblasts stained with three different fluorophores, with widely varying lifetimes.<sup>134</sup> The images show that an LED can be used as the excitation source for steady-state fluorescence microscopy. Coum-Eu is a europium chelate with a submillisecond decay time. Ru(bpy)<sub>2</sub>phe-C<sub>12</sub> is a lipophilic ruthenium metal-ligand complex and Syto 14 is a nuclear stain. The mean lifetimes of these probes when bound to the fibroblasts were 1.01 ms, 0.95 μs, and 2.57 ns, respectively. These results show that a wide range of decay times can be readily measured using the FD method. In contrast to TCSPC, the FD measurements are not restricted to a small number of photons per time interval, allowing short and long decay times to be measured using the same apparatus.

### 5.9. PHASE-ANGLE AND MODULATION SPECTRA

#### Advanced Topic

In all the preceding sections we emphasized FD measurements at a single emission wavelength. When using phase-modulation methods it is also possible to record the phase and modulation data as the emission wavelength is

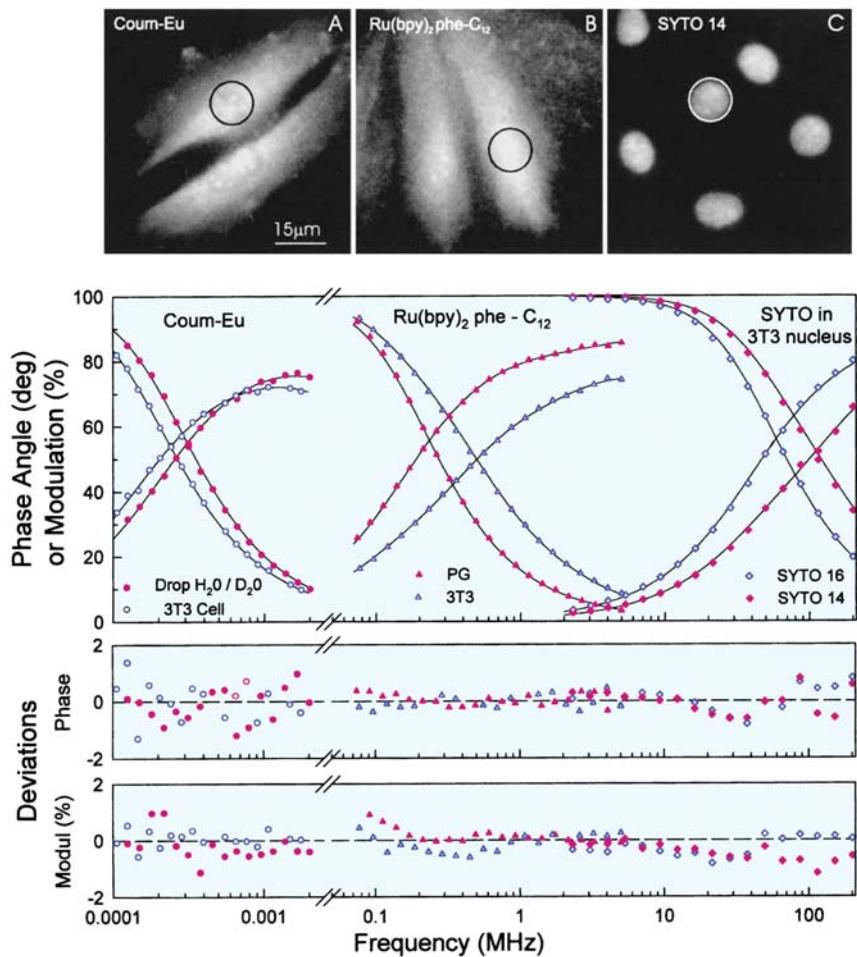


**Figure 5.45.** Fluorescence images of mouse 3T3 fibroblasts labeled with a europium chelate, a ruthenium metal–ligand complex and syto 14. The lower panels show the frequency responses obtained using a modulated 460 nm LED as the excitation source, in solvents and in cells. Revised from [134].

scanned.<sup>135–136</sup> Such data can be referred to as phase-angle or modulation spectra. Given the stability of modern FD instruments, this procedure is quite reliable. For very short decay times one may need to correct for the wavelength-dependent transit time through the monochromator and/or PMT. For ns-timescale measurements such corrections are not necessary.

The use of phase-modulation spectra can be illustrated by a mixture of fluorophores, acriflavine (ACF, 4.0 ns), and 3-aminofluoranthene (AFA, 11.7 ns) (Figure 5.46). Phase-angle and modulation spectra were recorded using the 325-nm output of an HeCd laser modulated by the Lasermetrics 1024 modulator, and detected through a monochromator with an R928 PMT. Phase and modulation spectra were collected at various modulation frequencies (Figure 5.47). The phase angles increase with wavelength (top) and the modulation decreases (bottom). These effects are due to the

increase in mean lifetime as the relative contribution of the 11.7-ns decay time of AFA increases at longer wavelengths.

The phase-modulation spectra can be used to recover the emission spectra and lifetime of each component in the mixture. This is accomplished by a global analysis of the phase-modulation spectra measured at various frequencies. Except for a change in the nature of the data files, the analysis is performed according to eqs. 5.12 to 5.15. The emission spectra associated with each fluorophore can be calculated from the recovered values of  $\alpha_i(\lambda)$  and the steady-state spectrum of the mixture  $I(\lambda)$ . The fractional intensity of each fluorophore at wavelength  $\lambda$  is given by

$$f_i(\lambda) = \frac{\alpha_i(\lambda) \tau_i}{\sum_j \alpha_j(\lambda) \tau_j} \quad (5.30)$$

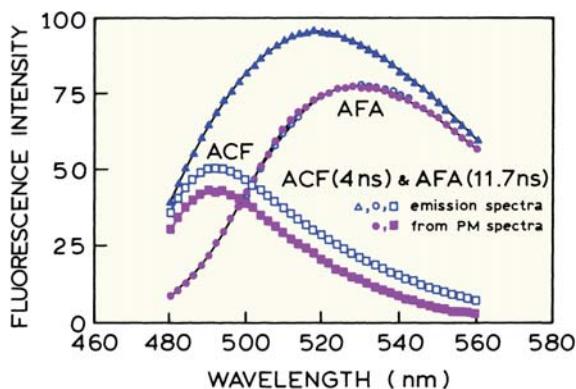


**Figure 5.46.** Emission spectra and recovered spectra for a mixture of ACF and AFA in propylene glycol at 20°C. Emission spectra are shown for the mixture (closed inverted triangles), of the individual components (open squares, open circles), and recovered from the phase-modulation spectra (closed squares, closed circles).  $[ACF] = 5 \times 10^{-7} M$ ,  $[AFA] = 2 \times 10^{-5} M$ . Revised and reprinted with permission from [135], Copyright © 1990, American Chemical Society.

and the emission spectrum of each component is given by

$$I_i(\lambda) = f_i(\lambda)I(\lambda) \quad (5.31)$$

The fractional contribution of each fluorophore to the total intensity of the sample is given by

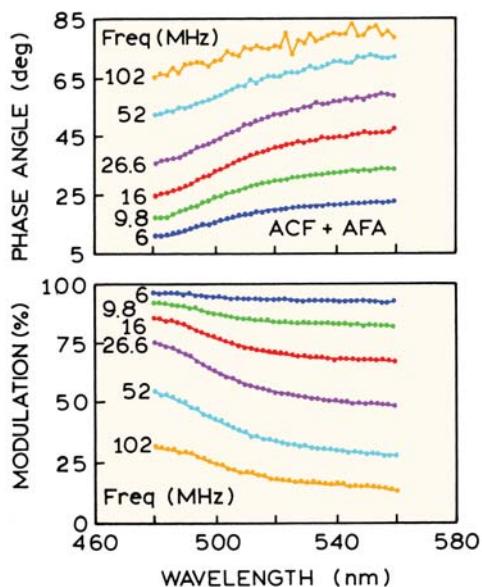


**Figure 5.47.** Representative phase-angle (top) and modulation spectra (bottom) for a mixture of ACF and AFA. The complete data set consisted of spectra at 20 modulation frequencies. Revised and reprinted with permission from [135], Copyright © 1990, American Chemical Society.

$$F_i = \frac{1}{N} \sum_{\lambda} f_i(\lambda) \quad (5.32)$$

where  $N$  is the number of emission wavelengths. The emission spectra recovered from the analysis were in good agreement with those known from the sample preparation (Figure 5.46). For samples such as ACF and AFA there is little advantage in using phase and modulation spectra, as compared with frequency-swept measurements at a single wavelength followed by changing the wavelength. However, phase and modulation spectra can be more convenient if the fluorophores show highly structured emission spectra. In these cases it may be easier to scan wavelength than to measure at discrete wavelengths adequate to determine the individual emission spectra.

## 5.10. APPARENT PHASE AND MODULATION LIFETIMES

Prior to the availability of variable-frequency instruments most phase-modulation fluorometers operated at one or a few fixed modulation frequencies. During this time it became standard practice to report the apparent phase and modulation lifetimes, which are the values calculated from the data at a single modulation frequency. These values are given by

$$\tau_{\phi}^{\text{app}} = \frac{1}{\omega} \tan \phi_{\omega} \quad (5.33)$$

$$\tau_m^{\text{app}} = \frac{1}{\omega} \left[ \frac{1}{m_{\omega}^2} - 1 \right]^{1/2} \quad (5.34)$$

where we have dropped the indicator of wavelength for simplicity.

There are several characteristics of the phase and modulation lifetimes that are valuable to know.<sup>41,137</sup> The apparent values are equal only if the intensity decay is a single exponential, for which case

$$\tau_{\phi}^{\text{app}} = \tau_m^{\text{app}} = \tau \quad (5.35)$$

For multi-exponential or non-exponential decays the apparent phase lifetimes are shorter than the apparent modulation lifetimes ( $\tau_{\phi}^{\text{app}} < \tau_m^{\text{app}}$ ). Also,  $\tau_{\phi}^{\text{app}}$  and  $\tau_m^{\text{app}}$  generally decrease at higher modulation frequencies. Hence, their

apparent lifetimes depend on the method of measurement, and are not true molecular parameters.

The relationship of  $\tau_{\phi}^{\text{app}}$  and  $\tau_m^{\text{app}}$  are most easily seen by consideration of a double exponential decay. Using eqs. 5.7 and 5.8 one obtains

$$N_{\omega}(\alpha_1\tau_1 + \alpha_2\tau_2) = \frac{\alpha_1\omega\tau_1^2}{1 + \omega^2\tau_1^2} + \frac{\alpha_2\omega\tau_2^2}{1 + \omega^2\tau_2^2} \quad (5.36)$$

$$D_{\omega}(\alpha_1\tau_1 + \alpha_2\tau_2) = \frac{\alpha_1\tau_1}{1 + \omega^2\tau_1^2} + \frac{\alpha_2\tau_2}{1 + \omega^2\tau_2^2} \quad (5.37)$$

Using eqs. 5.9 and 5.33, the apparent phase lifetime is given by

$$\tau_{\phi}^{\text{app}} = \frac{\sum_i \alpha_i \tau_i^2 / (1 + \omega^2 \tau_i^2)}{\sum_i \alpha_i \tau_i / (1 + \omega^2 \tau_i^2)} \quad (5.38)$$

Recall that the average lifetime is given by

$$\bar{\tau} = \frac{\sum_i \alpha_i \tau_i^2}{\sum_i \alpha_i \tau_i} = \sum_i f_i \tau_i = \frac{\alpha_1 \tau_1^2 + \alpha_2 \tau_2^2}{\alpha_1 \tau_1 + \alpha_2 \tau_2} \quad (5.39)$$

Comparison of eqs. 5.38 and 5.39 shows that in  $\tau_{\phi}^{\text{app}}$  each decay time is weighted by a factor  $\alpha_i \tau_i / (1 + \omega^2 \tau_i^2)$  rather than a factor  $\alpha_i \tau_i = f_i$ . For this reason the components with shorter decay times are weighted more strongly in  $\tau_{\phi}^{\text{app}}$  than in  $\bar{\tau}$ . Increasing the modulation frequency increases the relative contribution of the short-lived component and hence decreases the value of  $\tau_{\phi}^{\text{app}}$ . Using similar reasoning but more complex equations,<sup>41</sup> one can demonstrate that the apparent modulation lifetime is longer than the average lifetime.

An example of the use of apparent phase and modulation lifetimes is given in Figure 5.48, for the mixture of ACF and AFA. This figure shows the phase-angle and modulation spectra in terms of  $\tau_{\phi}^{\text{app}}$  and  $\tau_m^{\text{app}}$ . The fact that  $\tau_{\phi}^{\text{app}} < \tau_m^{\text{app}}$  for a heterogeneous decay is evident by comparison of the upper and lower panels. Also, one immediately notices that the apparent lifetime by phase or modulation depends on modulation frequency, and that higher frequencies result in shorter apparent lifetimes. Hence, the apparent lifetimes depend on the method of measurement (phase or modulation) and on the frequency, and it is difficult to interpret these values in terms of molecular features of the sample.

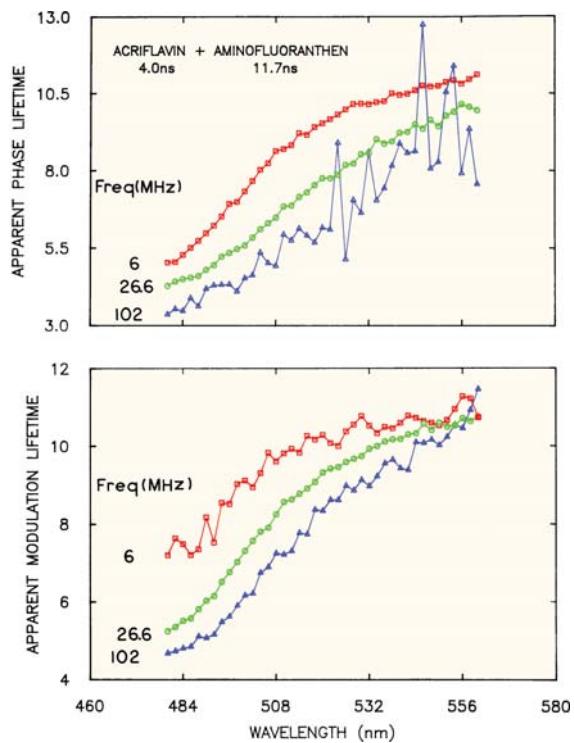


**Figure 5.48.** Apparent phase (top) and modulation (bottom) lifetimes for a mixture of ACF and AFA. Revised and reprinted with permission from [135], Copyright © 1990, American Chemical Society.

It is always possible to interpret the phase and modulation values in terms of the apparent lifetimes. However, the use of apparent phase and modulation lifetimes is no longer recommended. These are only apparent values that are the result of a complex weighting of the individual decay times and amplitudes, which depend on the experimental conditions. Also, one does not actually measure apparent lifetimes. These values are interpretations of the measurable quantities, which are the phase and modulation values.

## Supplemental Material

### 5.11. DERIVATION OF THE EQUATIONS FOR PHASE-MODULATION FLUORESCENCE

#### 5.11.1. Relationship of the Lifetime to the Phase Angle and Modulation

The equations relating the phase and modulation values to the apparent lifetimes (eqs. 5.3 and 5.4) are widely known,

but the derivation is rarely given. These expressions have been derived by several routes.<sup>41,138–139</sup> The simplest approach uses the kinetic equations and algebraic manipulation.<sup>41,138</sup> The excitation is assumed to be sinusoidally modulated light

$$L(t) = a + b \sin \omega t \quad (5.40)$$

so that  $b/a = m_L$  is the modulation of the incident light. The fluorescence emission is forced to respond with the same frequency, but the phase shift and modulation will be different. One can assume the excited-state population is given as follows:

$$N(t) = A + B \sin(\omega t - \phi) \quad (5.41)$$

and determine the relationship between fluorescence lifetime and the phase shift ( $\phi$ ) and the demodulation ( $m$ ). The intensity  $I(t)$  at any time is proportional to the number of molecules in the excited state  $N(t)$ .

Suppose the intensity decay following  $\delta$ -function excitation is a single exponential:

$$I(t) = I_0 \exp(-t/\tau) \quad (5.42)$$

For a single-exponential decay the differential equation describing the time-dependent excited-state population is

$$\frac{dI(t)}{dt} = -\frac{1}{\tau} I(t) + L(t) \quad (5.43)$$

Substitution of 5.41 into eq. 5.43 yields

$$\begin{aligned} & \omega B \cos(\omega t - \phi) = \\ & -\frac{1}{\tau} [A + B \sin(\omega t - \phi)] + a + b \sin \omega t \end{aligned} \quad (5.44)$$

This equation must be valid for all times. The relationship between the values of  $a$ ,  $b$ ,  $A$ , and  $B$  and the fluorescence lifetime  $\tau$  can be obtained by expansion of the sine and cosine functions, followed by equating of the constant terms and terms in  $\sin \omega t$  and  $\cos \omega t$ . This yields

$$a - (1/\tau) A = 0 \quad (5.45)$$

$$\omega \cos \phi - (1/\tau) \sin \phi = 0 \quad (5.46)$$

$$\omega \sin \phi + (1/\tau) \cos \phi = b/B \quad (5.47)$$

From eq. 5.46 one obtains the familiar relationship

$$\frac{\sin \phi}{\cos \phi} = \tan \phi = \omega \tau_\phi \quad (5.48)$$

Squaring eqs. 5.46 and 5.47, followed by addition, yields

$$[\omega^2 + (1/\tau)^2] = (b/B)^2 \quad (5.49)$$

Recalling that  $A = a\tau$  [eq. 5.45], one obtains

$$m = \frac{B/A}{b/a} = [1 + \omega^2 \tau_m^2]^{-1/2} \quad (5.50)$$

which is the usual relationship between the lifetime and the demodulation factor.

An alternative derivation is by the convolution integral.<sup>134</sup> The time-dependent intensity  $I(t)$  is given by the convolution of excitation function (eq. 5.40) with the impulse response function (eq. 5.42):

$$I(t) = \int_0^\infty L(t') I(t - t') dt' \quad (5.51)$$

Substitution of eqs. 5.40 and 5.42 yields

$$I(t) = I_0 \int_0^\infty \exp(-t'/\tau) [a + b \cos(\omega t - \omega t')] dt' \quad (5.52)$$

These integrals can be calculated by recalling the identities

$$\cos(x - y) = \cos x \cos y + \sin x \sin y \quad (5.53)$$

$$\int_0^\infty \exp(-kx) \sin mx dx = \frac{m}{k^2 + m^2} \quad (5.54)$$

$$\int_0^\infty \exp(-kx) \cos mx dx = \frac{a}{k^2 + m^2} \quad (5.55)$$

Using these identities yields

$$\int_0^\infty \exp(-t'/\tau) \cos\omega(t-t') dt' = \quad (5.56)$$

$$= \frac{\tau}{\sqrt{1 + \omega^2 \tau^2}} \left\{ \frac{\cos\omega t}{\sqrt{1 + \omega^2 \tau^2}} + \frac{\omega t \sin\omega t}{\sqrt{1 + \omega^2 \tau^2}} \right\} \quad (5.57)$$

$$= \frac{\tau}{\sqrt{1 + \omega^2 \tau^2}} \cos(\omega t - \phi) \quad (5.58)$$

Equation 5.58 was obtained using

$$\cos\phi = (1 + \omega^2 \tau^2)^{-1/2} \quad (5.59)$$

$$\tan\phi = \frac{\sin\phi}{\cos\phi} \quad (5.60)$$

Hence, the time dependent intensity is given by

$$I(t) = I_0 \tau \left\{ a + \frac{b}{\sqrt{1 + \omega^2 \tau^2}} \cos(\omega t - \phi) \right\} \quad (5.61)$$

This expression shows that the emission is demodulated by a factor  $(1 + \omega^2 \tau^2)^{-1/2}$  relative to the excitation and that the emission is delayed by an angle  $\phi$  relative to the excitation.

### 5.11.2. Cross-Correlation Detection

The use of cross-correlation detection transforms the high-frequency emission to a low-frequency signal while preserving the meaning of the phase and modulation values. This can be seen by considering the nature of the signals. The high-frequency time-dependent intensity is given by

$$I(t) = I_0 [1 + m \cos(\omega t - \phi)] \quad (5.62)$$

This signal is multiplied by the sinusoidal gain modulation of the detector:<sup>138</sup>

$$G(t) = G_0 [1 + m_c \cos(\omega_c t + \phi_c)] \quad (5.63)$$

where  $G_0$  is the average value of the function, and  $m_c$ ,  $\omega_c$ , and  $\phi_c$  are the modulation, frequency, and phase of the cross-correlation signal. Multiplication of eqs. 5.62 to 5.63 yields

$$S(t) = N_0 G_0 [1 + m \cos(\omega t + \phi) + m_c \cos(\omega_c t + \phi_c) + m m_c \cos(\omega t + \phi) \cos(\omega_c t + \phi_c)] \quad (5.64)$$

Using trigonometric identities the last term becomes

$$\frac{m m_c}{2} [\cos(\Delta\omega t + \Delta\phi) + \cos(\omega_c t + \omega t + \Delta\phi)] \quad (5.65)$$

where  $\Delta\omega = \omega_c - \omega$  and  $\Delta\phi = \phi_c - \phi$ . The frequencies  $\omega_c$  and  $\omega$  typically differ by only a small amount. Hence eq. 5.64 contains a constant term plus terms with frequencies,  $\omega$ ,  $\omega_c$ ,  $\omega + \omega_c$ , and  $\Delta\omega$ . The  $\Delta\omega$  term contains the phase and modulation information. In the electronic filtering process the constant term and terms in  $\omega$ ,  $\omega_c$ , and  $\omega + \omega_c$  all contribute to average intensity, and the term  $\Delta\omega$  determines the phase and amplitude of the low-frequency modulated emission. The presence of the phase and modulation information in the low-frequency signal can also be seen by integration of eqs. 5.62 and 5.63 over one measurement cycle.<sup>41</sup>

---

### 5.12. PHASE-SENSITIVE EMISSION SPECTRA

The frequency-domain method also allows several other types of measurement that can be useful in special circumstances. One method is measurement of phase-sensitive intensities and/or emission spectra.<sup>140-143</sup> In phase-sensitive detection of fluorescence (PSDF) the measurements are somewhat different than in frequency-domain fluorometers. In PSDF the emission from the sample is analyzed with a phase-sensitive detector, typically a lock-in amplifier. This measurement procedure selectively attenuates the signal from individual fluorophores on the basis of their fluorescence lifetimes, or more precisely, their phase angles relative to the phase of the detector. PSDF allows the emission from any one species to be suppressed, or, more precisely, the emission with any desired angle to be suppressed. Phase suppression is accomplished when the phase of the detector is  $90^\circ$  shifted from the phase angle of the emission. Then, the resulting phase-sensitive emission spectrum represents only the emission from the remaining fluorophores. For a two-component mixture, suppression of the emission from

one component allows the emission spectrum of the second component to be directly recorded. This procedure is experimentally simple and can be used to record the emission spectra of fluorophores with closely spaced lifetimes. PSDF is frequently used in fluorescence lifetime imaging microscopy (Chapter 22).

### 5.12.1. Theory of Phase-Sensitive Detection of Fluorescence

A phase fluorometer, when coupled with phase-sensitive detection of fluorescence, can be used in a simple manner to resolve heterogeneous fluorescence. Consider a sample containing a single fluorescent species with a lifetime  $\tau$ . When excited with sinusoidally modulated light the emission is given by

$$F(t) = 1 + m_L m \sin(\omega t - \phi) \quad (5.66)$$

where  $m_L$  is the modulation of the exciting light. In this equation,  $m$  and  $\phi$  are related to the lifetime by eqs. 5.3 and 5.4. Since phase-sensitive spectra are typically measured at a single modulation frequency the subscript  $\omega$  has been dropped for simplicity. If the sample contains more than one fluorophore then the modulated emission at each wavelength ( $\lambda$ ) is given by

$$F(\lambda, t) = \sum_i I_i(\lambda) f_i m_i \sin(\omega t - \phi_i) \quad (5.67)$$

In this expression  $I_i(\lambda)$  are the individual emission spectra,  $f_i$  are the fractional intensities to the total steady-state intensity,  $\sum f_i = 1.0$ ,  $m_i$  is the modulation of the  $i$ th component, and  $\phi_i$  is its phase angle. Depending upon the needs of the experiment, the steady-state spectra of each species  $I_i(\lambda)$  can be replaced by the steady-state spectra of the sample  $I(\lambda)$  and the wavelength-dependent fractional intensities:

$$F(\lambda, t) = I(\lambda) \sum_i f_i(\lambda) m_i \sin(\omega t - \phi_i) \quad (5.68)$$

In eqs. 5.67 and 5.68 we have assumed that the sample contains discrete lifetimes characterized by  $m_i$  and  $\phi_i$ , rather than a non-exponential decay or a lifetime distribution.

Phase-sensitive detection is accomplished by multiplying the emission  $F(\lambda, t)$  by a square wave, and integrating the result over time to yield a steady-state intensity.<sup>1-9</sup> The

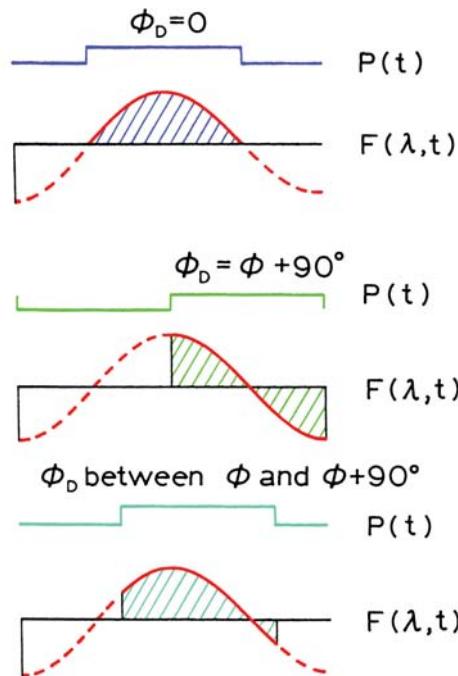


**Figure 5.49.** Phase-sensitive detection of fluorescence. The detector phase ( $\phi_D$ ) can be in phase with the emission  $\phi_D = \phi$  (top), out of phase with the emission ( $\phi_D = \phi + 90^\circ$ , middle), or at some intermediate value (bottom).

square wave is usually regarded as having a value of 0 or 1 depending on the angle within a single period of  $2\pi$  (Figure 5.49):

$$\left\{ \begin{array}{l} = 0 \text{ from } 0 \text{ to } \phi_D \\ = 1 \text{ from } \phi_D \text{ to } \phi_D + \pi \\ = 0 \text{ from } \phi_D \text{ to } \phi_D + 2\pi \end{array} \right. \quad (5.69)$$

Typically the phase angle of the detector ( $\phi_D$ ) is varied to integrate the emission over various portions of the 0 to  $2\pi$  cycle.

The phase-sensitive detector yields a direct current signal proportional to the modulated amplitude and to the cosine of the phase difference between the detector phase  $\phi_D$  and the phase of the sample. If an emission spectrum of a sample containing a single fluorophore (lifetime) is scanned using phase-sensitive detection, one observes a steady-state spectrum whose amplitude depends on the detector phase angle  $\phi_D$  and the phase angle of the fluorophore  $\phi_1$ :

$$F(\lambda, \phi_D) = k F(\lambda) m \cos(\phi_D - \phi_1) \quad (5.70)$$

where  $F(\lambda)$  is the steady-state emission spectrum,  $\lambda$  is the wavelength, and  $k$  is a constant that contains the usual sample and instrumental factors and the constant factor  $m_L$ . From eq. 5.70 one can predict the appearance of the phase-sensitive spectrum of a single component solution at various detector phase angles. One expects the intensity of the spectra to vary as  $\cos(\phi_D - \phi)$ , and the spectral distribution to remain unchanged.

The principle and usefulness of phase-sensitive detection is best understood by considering a mixture of two fluorophores,  $A$  and  $B$ , whose lifetimes ( $\tau_A$  and  $\tau_B$ ) are each independent of emission wavelength (Figure 5.50). To resolve the spectra of  $A$  and  $B$  by PSDF the phase angles ( $\phi_A$  and  $\phi_B$ ) or lifetimes must be different. We will assume  $\tau_A < \tau_B$ . The time-dependent emission is given by

$$\begin{aligned} F(\lambda,t) = & F_A(\lambda)m_A \sin(\omega t - \phi_A) \\ & + F_B(\lambda)m_B \sin(\omega t - \phi_B) \end{aligned} \quad (5.71)$$

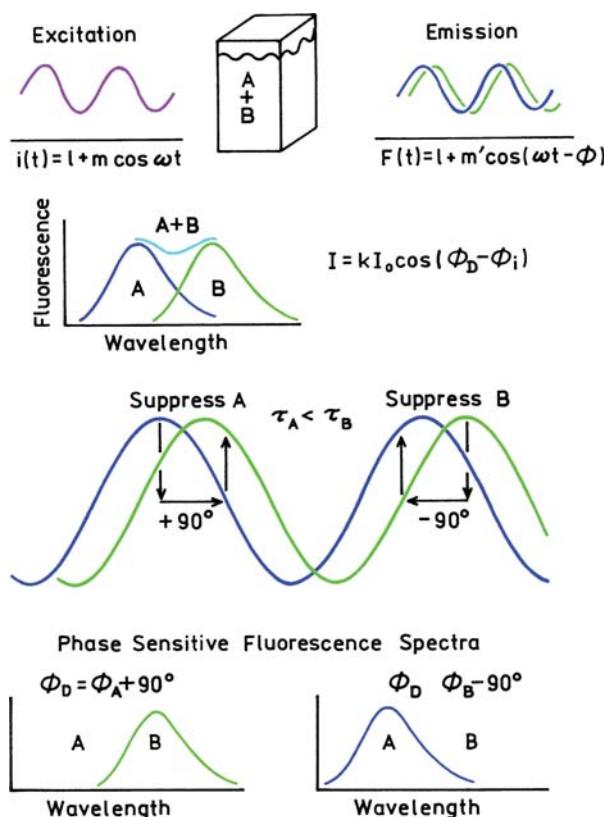


Figure 5.50. Intuitive description of phase-sensitive detection of fluorescence. Reprinted from [140], Copyright © 1981, with permission from Elsevier Science.

where  $F_A(\lambda)$  and  $F_B(\lambda)$  are the intensities of components  $A$  and  $B$  at wavelength  $\lambda$  in the steady-state spectrum. An important characteristic of the modulated emission is that it is a superimposition of sine waves of the same frequency but differing phases, each resulting from one of the fluorophores (Figure 5.50). The modulated emission can be conveniently examined with a phase-sensitive detector or lock-in amplifier. The resulting unmodulated signal is given by

$$\begin{aligned} F(\lambda, \phi_D) = & F_A(\lambda)m_A \cos(\phi_D - \phi_A) \\ & + F_B(\lambda)m_B \cos(\phi_D - \phi_B) \end{aligned} \quad (5.72)$$

For a mixture of two fluorophores one expects the phase-sensitive spectra to contain contributions from both fluorophores, with a fractional contribution dependent on the relative intensities ( $F_i(\lambda)$ ), the modulations ( $m_i$ ), and, most important, the values of  $\phi_D - \phi_i$ . The relative contribution of each fluorophore to the phase-sensitive intensity depends on the value of  $\cos(\phi_D - \phi_i)$ . By selection of  $\phi_D - \phi_i = 90^\circ$ , the detector can be out of phase with one component in the sample. Then the phase-sensitive spectrum represents the emission spectrum of the other component.

### 5.12.2. Examples of PSDF and Phase Suppression

Since the initial reports on PSDF, this method has been applied to a variety of samples. These applications are illustrated by two examples: suppression of scattered light and resolution of an excited-state reaction. Scattered light has a zero lifetime, and is thus always out of phase to some extent with the emission. Several laboratories have suggested the use of phase-sensitive detection to suppress scattered light or sample autofluorescence.<sup>145–150</sup> This application is illustrated in Figure 5.51 for a dilute solution of quinine sulfate excited at 355 nm. There is a large peak due to Rayleigh scatter below 370 nm, and a Raman scatter peak at 410 nm. The scattered light could be suppressed by phase-sensitive detection, allowing the emission spectrum of quinine sulfate to be directly recorded.

PSDF can be used to study excited-state reactions, as well as ground state multi-exponential decays.<sup>151–153</sup> This application is illustrated in Figure 5.52 for exciplex formation between anthracene and diethylaniline. In this case the long-wavelength emission forms subsequent to excitation of anthracene, and displays the features of an excited-state reaction. In PSDF it does not matter if the pre-exponential

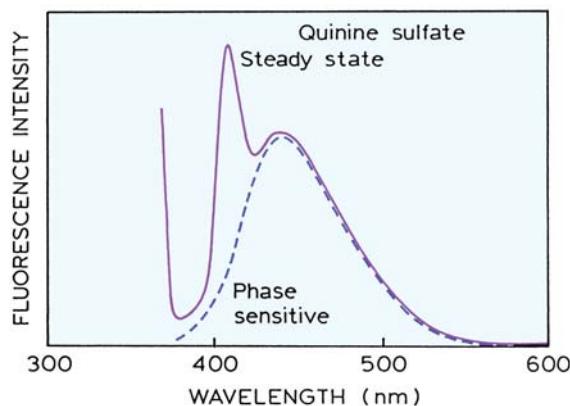


**Figure 5.51.** Steady-state emission spectrum of quinine sulfate (solid) and the phase-sensitive spectrum with nulling of the scattered light (dashed). Revised from [145].

factors are positive or negative, or if the phase angle exceeds  $90^\circ$ . Adjustment of the detector phase angle to be out of phase with either anthracene or its exciplex allows the emission spectrum of the other species to be recorded (lower panel).

Phase-sensitive spectra of relaxing systems can be informative. PSDF has been used to resolve mixtures of four or more fluorophores<sup>154–159</sup> and to suppress background fluorescence.<sup>160</sup> Phase-sensitive detection has also been used to resolve the emission of fluorophores free in solution and bound to macromolecules,<sup>161–162</sup> and to study binding between antigens and antibodies.<sup>163–165</sup>

### 5.12.3. High-Frequency or Low-Frequency Phase-Sensitive Detection

To this point we have not described the technical details associated with recording phase-sensitive emission spectra. Do the phase-sensitive spectra need to be recorded using the high-frequency signal prior to cross-correlation,<sup>166</sup> or can phase-sensitive detection be performed using the low-frequency cross-correlation signals? Fortunately, it is not necessary to perform phase-sensitive detection at high frequency. It was found that the modulated emission from individual fluorophores could still be resolved using the low-frequency cross-correlation signals. Such low-frequency detection is easy to perform, and one need not be concerned with the possible perturbation of tuned high-frequency circuits. The reference signal for the phase-sensitive detector is provided by the reference phototube, which observes the emission from a reference fluorophore or scatterer (Figure

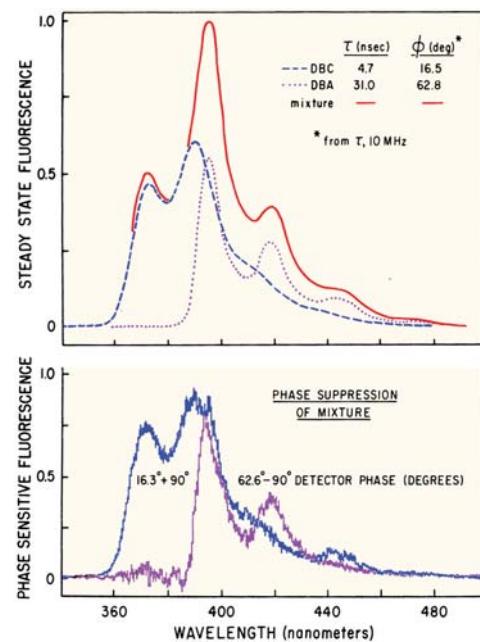


**Figure 5.52.** Emission spectra of anthracene and its exciplex with diethylaniline. Normalized steady-state spectra are shown in the upper panel. Phase-sensitive fluorescence spectra of anthracene in the presence of diethylaniline are shown in the lower panel. The excitation wavelength was 357 nm, and the excitation and emission bandpasses were 8 nm. The solution was not purged with inert gas. Reprinted from [140], Copyright © 1981, with permission from Elsevier Science.

5.7). Following selection of the detector phase angle, the phase-sensitive spectra are collected in the usual manner by scanning the emission monochromator.

### 5.13. PHASE-MODULATION RESOLUTION OF EMISSION SPECTRA

In recent years the use of phase-sensitive detection has diminished, except for its use in lifetime imaging. The phase-sensitive spectra contain less information than the phase angle and modulation spectra. In the time it takes to record the phase-sensitive spectra, one can now record the phase angle and/or modulation across the emission spectra. From these phase-modulation spectra one can compute the phase-resolved spectra.<sup>167–169</sup> Calculation of individual spectra from the phase and modulation spectra has a long history, dating to the early reports by Veselova and co-workers.<sup>170–171</sup> The equations to accomplish these resolutions have been presented in several different forms, which are useful under different circumstances.

### 5.13.1. Resolution Based on Phase or Modulation Lifetimes

One approach to calculating this phase resolved spectra is based on use of the apparent phase ( $\tau_\phi(\lambda)$ ) or modulation ( $\tau_m(\lambda)$ ) lifetimes at each wavelength.<sup>167</sup> Suppose that the sample contains two species, with fractional steady-state intensities of  $f_1(\lambda)$  and  $f_2(\lambda)$ , and that the two decay times  $\tau_1$  and  $\tau_2$  are known and are independent of wavelength. Then the ratio of fractional intensities can be calculated from<sup>167</sup>

$$\frac{f_1(\lambda)}{f_2(\lambda)} = \frac{\tau_2 - \tau_\phi(\lambda)}{\tau_\phi(\lambda) - \tau_1} \frac{(1 + \omega^2\tau_1^2)}{(1 + \omega^2\tau_2^2)} \quad (5.73)$$

A similar calculation can be performed using the apparent modulation lifetime:

$$\frac{f_1(\lambda)}{f_2(\lambda)} = \frac{\omega\tau_1 - [(1 + \omega^2\tau_1^2)(1 + \omega^2\tau_2^2)/(1 + (\omega\tau_m(\lambda))^2) - 1]^{1/2}}{[(1 + \omega^2\tau_1^2)(1 + \omega^2\tau_2^2)/(1 + (\tau_m(\lambda))^2) - 1]^{1/2} - \omega\tau_1} \quad (5.74)$$

An advantage of this direct calculation procedure is that one can change the assumed values of  $\tau_1$  and  $\tau_2$  to see how these values affect the calculated spectra. Such further calculations are not possible using the phase-sensitive spectra.

### 5.13.2. Resolution Based on Phase Angles and Modulations

The equations for spectral resolution based on phase and modulation data can be presented in several ways. For simplicity, we will present these equations for a system with two emitting species. For any decay law the values of  $N(\lambda)$  and  $D(\lambda)$  are given by<sup>168–169</sup>

$$\begin{aligned} N(\lambda) &= m(\lambda) \sin \phi(\lambda) \\ &= f_1(\lambda) m_1 \sin \phi_1 + f_2(\lambda) m_2 \sin \phi_2 \quad (5.75) \\ D(\lambda) &= m(\lambda) \cos \phi(\lambda) \\ &= f_1(\lambda) m_1 \cos \phi_1 + f_2(\lambda) m_2 \cos \phi_2 \quad (5.76) \end{aligned}$$

It is important to understand the meaning of the terms in eqs. 5.74 and 5.75. The values of  $m(\lambda)$  and  $\phi(\lambda)$  are the experimentally determined data. The values of  $m_i$  and  $\phi_i$  are constant terms that will somehow be known or separately measured. If the intensity decay is due to a mixture of fluorophores, each of which displays a single exponential decay, then  $m_1 = \cos \phi_1$  and  $m_2 = \cos \phi_2$  and

$$N(\lambda) = f_1(\lambda) \sin \phi_1 \cos \phi_1 + f_2(\lambda) \sin \phi_2 \cos \phi_2 \quad (5.77)$$

$$D(\lambda) = f_1(\lambda) \cos^2 \phi_1 + f_2(\lambda) \cos^2 \phi_2 \quad (5.78)$$

However, if the decay is non-exponential, then  $m_i \neq \cos \phi_i$ .

Applications of Cramer's rule to eqs. 5.75 and 5.76, followed by the law for the sine of a difference between two angles, yield

$$f_1(\lambda) = \frac{m(\lambda) \sin(\phi(\lambda) - \phi_2)}{m_1 \sin(\phi_1 - \phi_2)} \quad (5.79)$$

$$f_2(\lambda) = \frac{m(\lambda) \sin(\phi_1 - \phi(\lambda))}{m_2 \sin(\phi_1 - \phi_2)} \quad (5.80)$$

These expressions were first used by Veselova et al.<sup>170</sup> to calculate the emission spectra of relaxed and unrelaxed fluorophores during spectral relaxation. Alternative forms of eqs. 5.79 and 5.80 can be found by noting that  $f_1(\lambda) + f_2(\lambda) = 1.0$ :

$$f_1(\lambda) = \frac{m(\lambda) \cos \phi(\lambda) - m_2 \cos \phi_2}{m_1 \cos \phi_1 - m_2 \cos \phi_2} \quad (5.81)$$

$$f_2(\lambda) = \frac{m(\lambda) \cos \phi(\lambda) - m_1 \cos \phi_1}{m_2 \cos \phi_2 - m_1 \cos \phi_1} \quad (5.82)$$

Employing either form of these equations requires knowledge of  $\phi_1$ ,  $\phi_2$ ,  $m_1$ , and  $m_2$ , or for a mixture of fluorophores  $\tau_1$  and  $\tau_2$ .

### 5.13.3. Resolution of Emission Spectra from Phase and Modulation Spectra

Resolution of spectra from the phase and modulation data is illustrated in Figure 5.53. The dashed line shows the emis-

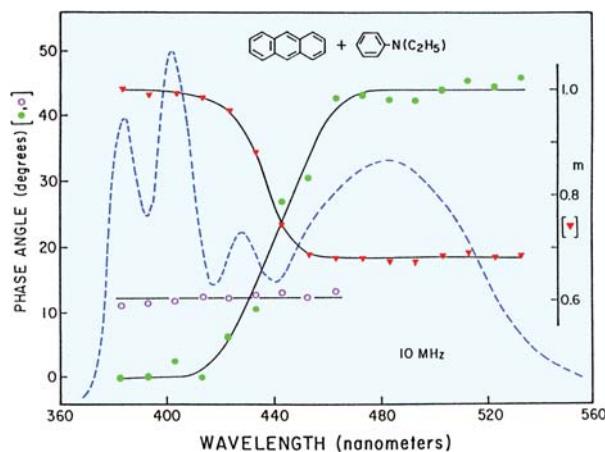


**Figure 5.53.** Phase angles and demodulation factors for anthracene and its exciplex with diethylaniline. Anthracene was dissolved in toluene and the concentration of diethylaniline was 0.2 M. The excitation was at 357 nm. The solution was not purged with inert gas. Reprinted from [169], Copyright © 1982, with permission from Elsevier Science.

sion spectrum of anthracene in the presence of diethylaniline (DEA). The structured emission is due to anthracene, and the broad long wavelength emission is due to the exciplex formed with DEA. The presence of DEA results in a decrease in the phase angle (●) of anthracene seen near 400 nm and an increased phase angle at long wavelengths where the exciplex emits. The modulation decreases at wavelengths where the exciplex emission contributes to the intensity.

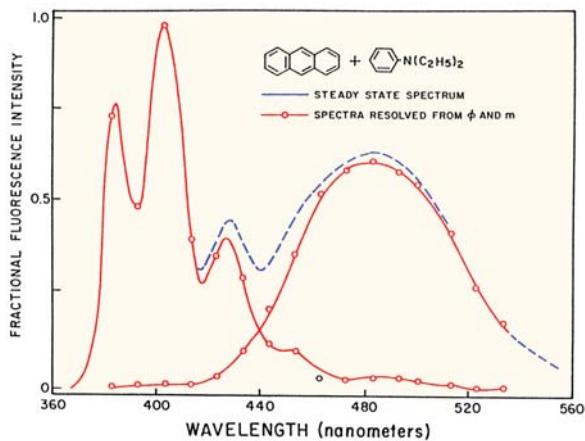


**Figure 5.54.** Resolution of the monomer and exciplex emission of anthracene. The spectra were calculated using eqs. 5.81 and 5.82 and the data shown in Figure 5.53. Reprinted from [169], Copyright © 1982, with permission from Elsevier Science.

At long and short wavelengths the phase and modulation values are constant, allowing assignment of  $\phi_1$ ,  $\phi_2$ ,  $m_1$  and  $m_2$ . The constant phase angles and modulations indicate the excited-state reaction in a two-state process, rather than a continuous process. In this case of an excited-state reaction it may not be possible to use eqs. 5.73 and 5.74 because the phase angles can exceed 90° and the value of the modulation is not due to a single modulation lifetime. One can use eqs. 5.81 and 5.82 to calculate the fractional intensity at each wavelength. When the  $f_i(\lambda)$  values are multiplexed by the steady-state spectrum one can calculate the emission spectra of anthracene and its exciplex (Figure 5.54).

This procedure can also be used when the phase and modulation values do not display constant values on the blue and red sides of the emission. In this case one obtains apparent spectra, whose molecular significance can only be understood with additional information about the sample.<sup>170</sup>

## REFERENCES

1. Gratton E, Limkeman M. 1983. A continuously variable frequency cross-correlation phase fluorometer with picosecond resolution. *Biophys J* **44**:315–324.
2. Lakowicz JR, Maliwal BP. 1985. Construction and performance of a variable-frequency phase-modulation fluorometer. *Biophys Chem* **21**:61–78.
3. Lakowicz JR, Gryczynski I. 1991. Frequency-domain fluorescence spectroscopy. In *Topics in fluorescence spectroscopy*. Vol 1: *Techniques*, pp. 293–355. Ed JR Lakowicz. Plenum Press, New York.
4. Gratton E. 1984. The measurement and analysis of heterogeneous emissions by multifrequency phase and modulation fluorometry. *Appl Spectrosc Rev* **20**(1):55–106.
5. Gratton E, Jameson DM, Hall RD. 1984. Multifrequency phase and modulation fluorometry. *Ann Rev Biophys Bioeng* **13**:105–124.
6. Lakowicz JR. 1986. Biochemical applications of frequency-domain fluorometry. In *Applications of fluorescence in the biomedical sciences*, pp. 225–244. Ed D Lansing, AS Waggoner, F Lanni, RF Murphy, RR Birge. Alan R. Liss, New York.
7. Bright FV, Betts TA, Litwiler KS. 1990. Advances in multifrequency phase and modulation fluorescence analysis. *Anal Chem* **21**:389–405.
8. Lakowicz JR. 1985. Frequency-domain fluorometry for resolution of time-dependent fluorescence emission. *Spectroscopy* **1**:28–37.
9. Rabinovich EM, O'Brien M, Srinivasan B, Elliott S, Long X-C, Ravinder KJ. 1998. A compact, LED-based phase fluorimeter-detection system for chemical and biosensor arrays, *SPIE Proc* **3258**:2–10.
10. Bevington PR, Robinson DK. 1992. *Data reduction and error analysis for the physical sciences*. McGraw-Hill, New York.
11. Taylor JR. 1982. *An introduction to error analysis, the study of uncertainties in physical measurements*. University Science Books, Mill Valley, CA.
12. Lakowicz JR, Laczko G, Cherek H, Gratton E, Limkeman M. 1984. Analysis of fluorescence decay kinetics from variable-frequency phase shift and modulation data. *Biophys J* **46**:463–477.

13. Gratton E, Limkeman M, Lakowicz JR, Maliwal B, Cherek H, Laczko G. 1984. Resolution of mixtures of fluorophores using variable-frequency phase and modulation data. *Biophys J* **46**:479–486.
14. Straume M, Frasier-Cadoret SG, Johnson ML. 1991. Least-squares analysis of fluorescence data. In *Topics in fluorescence spectroscopy*. Vol. 2: *Principles*, pp. 177–239. Plenum Press, New York.
15. Johnson ML. 1994. Use of least-squares techniques in biochemistry. *Methods Enzymol* **240**:1–22.
16. Johnson ML, Faunt LM. 1992. Parameter estimation by least-squares methods. *Methods Enzymol* **210**:1–37.
17. Klein UKA. 1984. Picosecond fluorescence decay studied by phase fluorometry and its application to the measurement of rotational diffusion in liquids. *Arabian J Sci Eng* **9**(4):327–344.
18. Gaviola Z. 1926. Ein Fluorometer, apparat zur messung von fluo-reszenzabklingungszeiten. *Z Phys* **42**:853–861.
19. Wood RW. 1921. The time interval between absorption and emission of light in fluorescence. *Proc Roy Soc London A* **99**:362–371.
20. Abraham H, Lemoine T. 1899. *C R Hebd Seances Acad Sci* **129**:206–208. As cited in reference [23].
21. Duschinsky VF. 1933. Der zeitliche intensitätsverlauf von intermit-tierend angeregter resonanzstrahlung. *Z Phys* **81**:7–22.
22. Szymanowski W. 1935. Verbesserte fluorometermethode zur mes-sung der abklingzeiten der fluoreszensstrahlung. *Z Phys* **95**:440–449.
23. Tumerman LA. 1941. On the law of decay of luminescence of com-plex molecules. *J Phys (USSR)* **4**:151–166.
24. Maercks VO. 1938. Neuartige fluorometer. *Z Phys* **109**:685–699.
25. Hupfeld VH-H. 1929. Die nachleuchtdauern der  $J_2^-$ ,  $K_2^-$ ,  $Na_2^-$  und  $Na$ -resonanzstrahlung. *Z Phys* **54**:484–497.
26. Schmillen A. 1953. Abklingzeitmessungen an flüssigen und festen losungen mit einem neuen fluorometer. *Z Phys* **135**:294–308.
27. Galanin MD. 1950. Duration of the excited state of a molecule and the properties of fluorescent solutions. *Trudy Fiz Inst, Akad Nauk SSSR* **5**:339–386.
28. Birks JB, Little WA. 1953. Photo-fluorescence decay times of organic phosphors. *Proc Phys Soc A* **66**:921–928.
29. Resewitz VE-P, Lippert E. 1974. Ein neuartiges phasenfluorometer. *Ber Bunsenges* **78**:1227–1229.
30. Labhart VH. 1964. Eine experimentelle methode zur ermittlung der singulett-triplett-konversionswahrscheinlichkeit und der triplett-spektren von gelosten organischen molekülen messungen an 1,2-ben-zanthracen. *Fasciculus S* **252**:2279–2288.
31. Bailey EA, Rollefson GK. 1953. The determination of the fluores-cence lifetimes of dissolved substances by a phase shift method. *J Chem Phys* **21**:1315–1326.
32. Bonch-Breuvich AM, Kazarin IM, Molchanov VA, Shirokov IV. 1959. An experimental model of a phase fluorometer. *Instrum Exp Technol (USSR)* **2**:231–236.
33. Bauer RK, Rozwadowski M. 1959. A new type of fluorometer: mea-surements of decay periods of fluorescence of acridine yellow solu-tions as a function of concentration. *Bull Acad Pol Sci Ser Sci Math Astr Phys* **8**:365–368.
34. Birks JB, Dyson DJ. 1961. Phase and modulation fluorometer. *J Sci Instrum* **38**:282–285.
35. Muller A, Lumry R, Kokubun H. 1965. High-performance phase flu-orometer constructed from commercial subunits. *Rev Sci Instrum* **36**:1214–1226.
36. Michelbacher E. 1969. Decay time measurements on pseudo-isocya-nine by a phase-fluorometer of 200 Mc modulation frequency. *Z Naturforsch A* **24**:790–796.
37. Demtroder W. 1962. Bestimmung von oszillatorenstärken durch lebensdauermessungen der ersten angeregten niveaus für die ele-mente Ga, Al, Mg, Tl und Na. *Z Phys* **42**:42–55.
38. Schlag EW, Wessenhoff HV. 1969. Direct timing of the relaxation from selected excited states; beta-naphthylamine. *J Chem Phys* **51**(6):2508–2514.
39. Venetta BD. 1959. Microscope phase fluorometer for determining the fluorescence lifetimes of fluorochromes. *Rev Sci Instrum* **30**(6):450–457.
40. Schaefer VW. 1956. Bestimmung der schwingungsrelaxationszeit in  $CO/N_2$ -gasgemischen aus der analyse des frequenzganges eines ultrarot-gasanalysators. *Z Ang Physik* **19**:55–61.
41. Spencer RD, Weber G. 1969. Measurement of subnanosecond fluo-rescence lifetimes with a cross-correlation phase fluorometer. *Ann NY Acad Sci* **158**:361–376.
42. Debye P, Sears FW. 1932. On the scattering of light by supersonic waves. *Proc Natl Acad Sci USA* **18**:409–414.
43. Lakowicz JR. 1983. *Principles of Fluorescence Spectroscopy*, pp. 76–78. Plenum Press, New York.
44. Hauser M, Heidt G. 1975. Phase fluorometer with a continuously variable frequency. *Rev Sci Instrum* **46**(4):470–471.
45. Salmeen I, Rimal L. 1977. A phase-shift fluorometer using a laser and a transverse electrooptic modulator for subnanosecond lifetime measurements. *Biophys J* **20**:335–342.
46. Menzel ER, Popovic ZD. 1978. Picosecond-resolution fluorescence lifetime measuring system with a cw laser and a radio. *Rev Sci Instrum* **49**(1):39–44.
47. Haar H-P, Hauser M. 1978. Phase fluorometer for measurement of picosecond processes. *Rev Sci Instrum* **49**(5):632–633.
48. Gugger H, Calzaferri G. 1979. Picosecond time resolution by a con-tinuous wave laser amplitude modulation technique, I: a critical investi-gation. *J Photochem* **13**:21–33.
49. Gugger H, Calzaferri G. 1980. Picosecond time resolution by a con-tinuous wave laser amplitude modulation technique, II: experimental basis. *J Photochem* **13**:295–307.
50. Gugger H, Calzaferri G. 1981. Picosecond time resolution by a con-tinuous wave laser amplitude modulation technique, III: dual-beam luminescence experiment. *J Photochem* **16**:31–41.
51. Baumann J, Calzaferri G. 1983. Development of picosecond time-resolved techniques by continuous-wave laser amplitude modulation, IV: systematic errors. *J Photochem* **22**:297–312.
52. Baumann J, Calzaferri G. 1983. Development of picosecond time-resolved techniques by continuous-wave, V: elimination of r.f. inter-fERENCE problems. *J Photochem* **23**:387–390.
53. Ide G, Engelborghs Y, Persoons A. 1983. Fluorescence lifetime resolu-tion with phase fluorometry. *Rev Sci Instrum* **54**(7):841–844.
54. Kaminov IP. 1984. *An introduction to electrooptic devices*. Academic Press, New York.
55. Wilson J, Hawkes JFB. 1983. *Optoelectronics: an introduction*. Prentice/Hall, London.
56. ISS Inc., Urbana, IL. <http://www.ISS.com>.
57. McGuinness CD, Sagoo K, McLoskey D, Birch DJS. 2004. A new sub-nanosecond LED at 280 nm: application to protein fluorescence. *Meas Sci Technol* **15**:L1–L4.
58. Fedderson BA, Piston DW, Gratton E. 1989. Digital parallel acqui-sition in frequency domain fluorimetry. *Rev Sci Instrum* **60**(9):2929–2936.
59. Watkins AN, Ingersoll CM, Baker GA, Bright FV. 1998. A parallel multiharmonic frequency-domain fluorometer for measuring excit-ed-state decay kinetics following one-, two-, or three-photon excita-tion. *Anal Chem* **70**:3384–3396.
60. Alcalá JR. 1991. Comment on "Digital parallel acquisition in fre-quency domain fluorometry." *Rev Sci Instrum* **62**(6):1672–1673.
61. Barbieri B, De Piccoli F, Gratton E. 1989. Synthesizers' phase noise in frequency-domain fluorometry. *Rev Sci Instrum* **60**(10): 3201–3206.

62. Levy R, Guignon EF, Cobane S, St. Louis E, Fernandez SM. 1997. Compact, rugged and inexpensive frequency-domain fluorometer. *SPIE Proc* **2980**:81–89.
63. Lakowicz JR, Cherek H, Balter A. 1981. Correction of timing errors in photomultiplier tubes used in phase-modulation fluorometry. *J Biochem Biophys Methods* **5**:131–146.
64. Berndt K, Dürr H, Palme D. 1983. Picosecond phase fluorometry and color delay error. *Opt Commun* **47**(5):321–323.
65. Baumann J, Calzaferri G, Forss L, Hungentobler Th. 1985. Wavelength-dependent fluorescence decay: an investigation by multiple-frequency picosecond phase fluorometry. *J Photochem* **28**: 457–473.
66. Pouget J, Mugnier J, Valeur B. 1989. Correction of systematic phase errors in frequency-domain fluorometry. *J Phys E: Sci Instrum* **22**:855–862.
67. Barrow DA, Lentz BR. 1983. The use of isochronal reference standards in phase and modulation fluorescence lifetime measurements. *J Biochem Biophys Methods* **7**:217–234.
68. Thompson RB, Gratton E. 1988. Phase fluorometric method for determination of standard lifetimes. *Anal Chem* **60**:670–674.
69. Lakowicz JR, Jayaweera R, Joshi N, Gryczynski I. 1987. Correction for contaminant fluorescence in frequency-domain fluorometry. *Anal Biochem* **160**:471–479.
70. Reinhart GD, Marzola P, Jameson DM, Gratton E. 1991. A method for on-line background subtraction in frequency domain fluorometry. *J Fluoresc* **1**(3):153–162.
71. Gryczynski I, Malak H. Unpublished observations.
72. Dattelbaum JD, Castellano FN, Gryczynski I, Lakowicz JR. 1998. *Two-photon spectroscopic properties of a mutant green fluorescent protein*. Manuscript in preparation. Biophysical Society Meeting, March 1998. Kansas City, MO, Tu-pos 369.
73. Swaminathan R, Hoang CP, Verkman AS. 1997. Photobleaching recovery and anisotropy decay of green fluorescent protein GFP-S65T in solution and cells: cytoplasmic viscosity probed by green fluorescent protein translational and rotational diffusion. *Biophys J* **72**:1900–1907.
74. Illsley NP, Verkman AS. 1987. Membrane chloride transport measured using a chloride-sensitive fluorescent probe. *Biochemistry* **26**:1215–1219.
75. Verkman AS. 1990. Development and biological applications of chloride-sensitive fluorescent indicators. *Am J Physiol* **253**:C375–C388.
76. Verkman AS, Sellers MC, Chao AC, Leung T, Ketcham R. 1989. Synthesis and characterization of improved chloride-sensitive fluorescent indicators for biological applications. *Anal Biochem* **178**: 355–361.
77. Visser AJWG, van Hoek A. 1981. The fluorescence decay of reduced nicotinamides in aqueous solution after excitation with a UV-mode locked Ar ion laser. *Photochem Photobiol* **33**:35–40.
78. Berndt KW, Gryczynski I, Lakowicz JR. 1990. Phase-modulation fluorometry using a frequency-doubled pulsed laser diode light source. *Rev Sci Instrum* **61**(7):1816–1820.
79. Thompson RB, Frisoli JK, Lakowicz JR. 1992. Phase fluorometry using a continuously modulated laser diode. *Anal Chem* **64**:2075–2078.
80. Sipior J, Carter GM, Lakowicz JR, Rao G. 1996. Single quantum well light-emitting diodes demonstrated as excitation sources for nanosecond phase-modulation fluorescence lifetime measurements. *Rev Sci Instrum* **67**(11):3795–3798.
81. Landgraf S. 2001. Application of semiconductor light sources for investigations of photochemical reactions. *Spectrosc Acta A* **57**:2029–2048.
82. Landgraf S, Grampp G. 1998. Application of laser diodes and ultrabright light-emitting diodes for the determination of fluorescence lifetimes in the nano- and subnanosecond region. *J Inf Rec Mater* **24**:141–148.
83. Landgraf S, Grampp G. 1996. Application of cw-laser diodes for the determination of fluorescence lifetimes. *J Inf Rec Mater* **23**:203–207.
84. Szmacinski H, Chang Q. 2000. Micro- and sub-nanosecond lifetime measurements using a UV light-emitting diode. *Appl Spectrosc* **54**:106–109.
85. Sipior J, Carter GM, Lakowicz JR, Rao G. 1997. Blue light-emitting diode demonstrated as an ultraviolet excitation source for nanosecond phase-modulation fluorescence lifetime measurements. *Rev Sci Instrum* **68**(7):2666–2670.
86. Fantini S, Franceschini MA, Fishkin JB, Barbieri B, Gratton E. 1994. Quantitative determination of the absorption spectra of chromophores in strongly scattering media: a light-emitting diode based technique. *Appl Opt* **33**(22):5204–5213.
87. Berndt KW, Lakowicz JR. 1992. Electroluminescent lamp-based phase fluorometer and oxygen sensor. *Anal Biochem* **201**:319–325.
88. Morgan CG, Hua Y, Mitchell AC, Murray JG, Boardman AD. 1996. A compact frequency domain fluorometer with a directly modulated deuterium light source. *Rev Sci Instrum* **67**(1):41–47.
89. Holavanahali R, Romano MG, Carter GM, Rao G, Sipior J, Lakowicz JR, Bierlein JD. 1996. Directly modulated diode laser frequency doubled in a KTP waveguide as an excitation source for CO<sub>2</sub> and O<sub>2</sub> phase fluorometric sensors. *J Biomed Opt* **1**(1):124–130.
90. Szmacinski H, Lakowicz JR. 1993. Optical measurements of pH using fluorescence lifetimes and phase-modulation fluorometry. *Anal Chem* **65**:1668–1674.
91. Thompson RB, Lakowicz JR. 1993. Fiber optic pH sensor based on phase fluorescence lifetimes. *Anal Chem* **65**:853–856.
92. O'Keefe G, MacCraith BD, McEvoy AK, McDonagh CM, McGilp JF. 1995. Development of an LED-based phase fluorimetric oxygen sensor using evanescent wave excitation of a sol-gel immobilized gel. *Sens Actuators* **29**:226–230.
93. Lippitsch ME, Pasterhofer J, Leiner MJP, Wolfbeis OS. 1988. Fibre-optic oxygen sensor with the fluorescence decay time as the information carrier. *Anal Chim Acta* **205**:1–6.
94. Sipior J, Randers-Eichhorn L, Lakowicz JR, Carter GM, Rao G. 1996. Phase fluorometric optical carbon dioxide gas sensor for fermentation off-gas monitoring. *Biotechnol Prog* **12**:266–271.
95. Cobb WT, McGown LB. 1987. Phase-modulation fluorometry for on-line liquid chromatographic detection and analysis of mixtures of benzo(k)fluoranthene and benzo(b)fluoranthene. *Appl Spectrosc* **41**(8):1275–1279.
96. Cobb WT, McGown LB. 1989. Multifrequency phase-modulation fluorescence lifetime determinations on-the-fly in HPLC. *Appl Spectrosc* **43**(8):1363–1367.
97. Cobb WT, Nithipatikom K, McGown LB. 1988. Multicomponent detection and determination of polycyclic aromatic hydrocarbons using HPLC and a phase-modulation spectrophotofluorometer. Special Technical Publication, American Society for Testing and Materials, Vol. 1009, pp. 12–25.
98. Szmacinski H, Lakowicz JR. 1994. Lifetime-based sensing. In *Topics in fluorescence spectroscopy*, Vol. 4: *Probe Design and Chemical Sensors*, pp. 295–334. Ed JR Lakowicz. Plenum Press, New York.
99. Merkelo HS, Hartman SR, Mar T, Singhal GS, Govindjee GS. 1969. Mode-locked lasers: measurements of very fast radiative decay in fluorescent systems. *Science* **164**:301–303.
100. Gratton E, Lopez-Delgado R. 1980. Measuring fluorescence decay times by phase-shift and modulation techniques using the high

- harmonic content of pulsed light sources. *Nuovo Cimento B* **56**:110–124.
101. Gratton E, Jameson DM, Rosato N, Weber G. 1984. Multifrequency cross-correlation phase fluorometer using synchrotron radiation. *Rev Sci Instrum* **55**:486–494.
  102. Gratton E, Delgado RL. 1979. Use of synchrotron radiation for the measurement of fluorescence lifetimes with subpicosecond resolution. *Rev Sci Instrum* **50**(6):789–790.
  103. Berndt K, Duerr H, Palme D. 1982. Picosecond phase fluorometry by mode-locked CW lasers. *Opt Commun* **42**:419–422.
  104. Gratton E, Barbieri B. 1986. Multifrequency phase fluorometry using pulsed sources: theory and applications. *Spectroscopy* **1**(6): 28–36.
  105. Lakowicz JR, Laczko G, Gryczynski I. 1986. 2-GHz frequency-domain fluorometer. *Rev Sci Instrum* **57**(10):2499–2506.
  106. Laczko G, Gryczynski I, Gryczynski Z, Wiczk W, Malak H, Lakowicz JR. 1990. A 10-GHz frequency-domain fluorometer. *Rev Sci Instrum* **61**(9):2331–2337.
  107. Lakowicz JR, Laczko G, Gryczynski I, Szmacinski H, Wiczk W. 1989. Frequency-domain fluorescence spectroscopy: principles, biochemical applications and future developments. *Ber Bunsenges Phys Chem* **93**:316–327.
  108. Lakowicz JR, Laczko G, Gryczynski I, Szmacinski H, Wiczk W. 1988. Gigahertz frequency domain fluorometry: resolution of complex decays, picosecond processes and future developments. *J Photochem Photobiol B: Biol* **2**:295–311.
  109. Berndt K, Durr H, Palme D. 1985. Picosecond fluorescence lifetime detector. *Opt Commun* **55**(4):271–276.
  110. Berndt K. 1987. Opto-electronic high-frequency cross-correlation using avalanche photodiodes. *Measurement* **5**(4):159–166.
  111. Berndt K, Klose E, Schwarz P, Feller K-H, Fassler D. 1984. Time-resolved fluorescence spectroscopy of cyanine dyes. *Z Phys Chem* **265**:1079–1086.
  112. Berndt K, Durr H, Feller K-H. 1987. Time resolved fluorescence spectroscopy of cyanine dyes. *Z Phys Chem* **268**:250–256.
  113. Lakowicz JR, Gryczynski I, Laczko G, Gloyna D. 1991. Picosecond fluorescence lifetime standards for frequency- and time-domain fluorescence. *J Fluoresc* **1**(2):87–93.
  114. Gryczynski I, Szmacinski H, Laczko G, Wiczk W, Johnson ML, Kusba J, Lakowicz JR. 1991. Conformational differences of oxytocin and vasopressin as observed by fluorescence anisotropy decays and transient effects in collisional quenching of tyrosine fluorescence. *J Fluoresc* **1**(3):163–176.
  115. Vos R, Strobbe R, Engelborghs Y. 1997. Gigahertz phase fluorometry using a fast high-gain photomultiplier. *J Fluoresc* **7**(1):33S–35S.
  116. Gryczynski I. Unpublished observations.
  117. Brochon JC, Livesey AK, Pouget J, Valeur B. 1990. Data analysis in frequency-domain fluorometry by the maximum entropy method: recovery of fluorescence lifetime distributions. *Chem Phys Lett* **174**(5):517–522.
  118. Shaver JM, McGown LB. 1996. Maximum entropy method for frequency domain fluorescence lifetime analysis, 1: effects of frequency range and random noise. *Anal Chem* **68**:9–17.
  119. Shaver JM, McGown LB. 1996. Maximum entropy method for frequency-domain fluorescence lifetime analysis, 2: timing, mismatched intensity, and reference lifetime errors. *Anal Chem* **68**:611–620.
  120. He Y, Geng L. 2001. Analysis of heterogeneous fluorescence decays: distribution of pyrene derivatives in an octadecylsilane layer in capillary electrochromatography. *Anal Chem* **73**:5564–5575.
  121. Vinogradov SA, Wilson DF. 2000. Recursive maximum entropy algorithm and its application to the luminescence lifetime distribution recovery. *Appl Spectrosc* **54**(6):849–855.
  122. Manzini G, Barcellona ML, Avitabile M, Quadrifoglio F. 1983. Interaction of diamidino-2 phenylindole (DAPI) with natural and synthetic nucleic acids. *Nucleic Acids Res* **11**(24):8861–8876.
  123. Cavatorta P, Masotti L, Szabo AG. 1985. A time-resolved fluorescence study of 4',6-diamidino-2-phenylindole dihydrochloride binding to polynucleotides. *Biophys Chem* **22**:11–16.
  124. Tanious FA, Veal JM, Buczak H, Ratmeyer LS, Wilson WD. 1992. DAPI (4',6-diamidino-2-phenylindole) binds differently to DNA and RNA: minor-groove binding at AT sites and intercalation at AU sites. *Biochemistry* **31**:3103–3112.
  125. Barcellona ML, Gratton E. 1989. Fluorescence lifetime distributions of DNA-4',6-diamidino-2-phenylindole complex. *Biochim Biophys Acta* **993**:174–178.
  126. Barcellona ML, Gratton E. 1990. The fluorescence properties of a DNA probe. *Eur Biophys J* **17**:315–323.
  127. Szmacinski H, Lakowicz JR. 1996. Fluorescence lifetime characterization of magnesium probes: improvement of Mg<sup>2+</sup> dynamic range and sensitivity using phase-modulation fluorometry. *J Fluoresc* **6**:83–95.
  128. Lakowicz JR, Cherek H, Gryczynski I, Joshi N, Johnson ML. 1987. Analysis of fluorescence decay kinetics measured in the frequency domain using distributions of decay times. *Biophys Chem* **28**:35–50.
  129. Alcala JR, Gratton E, Prendergast FG. 1987. Resolvability of fluorescence lifetime distributions using phase fluorometry. *Biophys J* **51**:587–596.
  130. Lakowicz JR, Gryczynski I, Wiczk W, Johnson ML. 1994. Distributions of fluorescence decay times for synthetic melittin in water–methanol mixtures and complexed with calmodulin, troponin C, and phospholipids. *J Fluoresc* **4**(2):169–177.
  131. Collini M, D'Alfonso L, Baldini G, Oldani A, Cellai L, Giordano C, Barone F, Mazzei F, Chirico G. 2004. Fluorescence anisotropy in the frequency domain by an optical microscope. *Appl Spectrosc* **58**(2):160–165.
  132. Despa S, Vecer J, Steels P, Ameloot M. 2000. Fluorescence lifetime microscopy of the Na<sup>+</sup> indicator sodium green in HeLa cells. *Anal Biochem* **281**:159–175.
  133. Booth MJ, Wilson T. 2004. Low-cost, frequency-domain, fluorescence lifetime confocal microscopy. *J Microsc* **214**(1):36–42.
  134. Herman P, Maliwal BP, Lin H-J, Lakowicz JR. 2001. Frequency-domain fluorescence microscopy with the LED as a light source. *J Microsc* **203**(2):176–181.
  135. Lakowicz JR, Jayaweera R, Szmacinski H, Wiczk W. 1990. Resolution of multicomponent fluorescence emission using frequency-dependent phase angle and modulation spectra. *Anal Chem* **62**:2005–2012.
  136. Lakowicz JR, Jayaweera R, Szmacinski H, Wiczk W. 1989. Resolution of two emission spectra for tryptophan using frequency-domain phase-modulation spectra. *Photochem Photobiol* **50**(4):541–546.
  137. Kilin SF. 1962. The duration of photo- and radioluminescence of organic compounds. *Opt Spectrosc* **12**:414–416.
  138. Jameson DM, Gratton E, Hall RD. 1984. The measurement and analysis of heterogeneous emissions by multifrequency phase and modulation fluorometry. *Appl Spectrosc Rev* **20**(1):55–106.
  139. Ware WR. 1971. Transient luminescence measurements. In *Creation and detection of the excited state*, pp. 213–302. Ed AA Lamola. Marcel Dekker, New York.

140. Lakowicz JR, Cherek H. 1981. Phase-sensitive fluorescence spectroscopy: a new method to resolve fluorescence lifetimes or emission spectra of components in a mixture of fluorophores. *J Biochem Biophys Methods* **5**:19–35.
141. Lakowicz JR, Cherek H. 1981. Resolution of heterogeneous fluorescence from proteins and aromatic amino acids by phase-sensitive detection of fluorescence. *J Biol Chem* **256**:6348–6353.
142. Lakowicz JR, Cherek H. 1982. Resolution of heterogeneous fluorescence by phase-sensitive fluorescence spectroscopy. *Biophys J* **37**:148–150.
143. Jameson DM, Gratton E, Hall RD. 1984. The measurement and analysis of heterogeneous emissions by multifrequency phase and modulation fluorometry. *Appl Spectrosc Rev* **20**(1):55–106.
144. McGown L, Bright F. 1984. Phase-resolved fluorescence spectroscopy. *Anal Chem* **56**(13):1400–1415.
145. Fugate RD, Bartlett JD, Mattheis JR. 1984. Phase-resolution in spectrofluorometric measurements: applications to biochemical systems. *BioTechniques* **2**(3):174–180.
146. Demas JN, Keller RA. 1985. Enhancement of luminescence and Raman spectroscopy by phase-resolved background suppression. *Anal Chem* **57**:538–545.
147. Nithipatikom K, McGown LB. 1987. Phase-resolved suppression of scattered light in total luminescence spectra. *Appl Spectrosc* **41**(6):1080–1082.
148. Wirth MJ, Chou S-H. 1988. Comparison of time and frequency domain methods for rejecting fluorescence from raman spectra. *Anal Chem* **60**:1882–1886.
149. Nithipatikom K, McGown LB. 1986. Elimination of scatter background in synchronous excitation spectrofluorometry by the use of phase-resolved fluorescence spectroscopy. *Anal Chem* **58**:3145–3147.
150. Crowell E, Geng L. 2001. Reduction of multiexponential background in fluorescence with phase-sensitive detection. *Appl Spectrosc* **55**(12):1709–1716.
151. Lakowicz JR, Balter A. 1982. Direct recording of the initially excited and the solvent relaxed fluorescence emission spectra of tryptophan by phase-sensitive detection of fluorescence. *Photochem Photobiol* **36**:125–132.
152. Lakowicz JR, Balter A. 1982. Detection of the reversibility of an excited-state reaction by phase-modulation fluorometry. *Chem Phys Lett* **92**(2):117–121.
153. Lakowicz JR, Thompson RB, Cherek H. 1983. Phase fluorometric studies of spectral relaxation at the lipid-water interface of phospholipid vesicles. *Biochim Biophys Acta* **734**:295–308.
154. Nithipatikom K, McGown LB. 1987. Five- and six-component determinations using phase-resolved fluorescence spectroscopy and synchronous excitation. *Appl Spectrosc* **41**(3):395–398.
155. Bright FV, McGown LB. 1986. Three-component determinations using fluorescence anisotropy measurements and wavelength selectivity. *Anal Chem* **58**:1424–1427.
156. Bright FV, McGown LB. 1985. Phase-resolved fluorometric determinations of four-component systems using two modulation frequencies. *Anal Chem* **57**:2877–2880.
157. Bright FV, McGown LB. 1985. Four-component determinations using phase-resolved fluorescence spectroscopy. *Anal Chem* **57**:55–59.
158. Vitense KR, McGown LB. 1987. Simultaneous determination of metals in two-component mixtures with 5-sulfo-8-quinolinol by using phase-resolved fluorimetry. *Anal Chim Acta* **193**:119–125.
159. Nithipatikom K, McGown LB. 1986. Multidimensional data formats for phase-resolved fluorometric multicomponent determinations using synchronous excitation and emission spectra. *Anal Chem* **58**:2469–2473.
160. Bright FV, McGown LB. 1984. Elimination of bilirubin interference in fluorometric determination of fluorescein by phase-resolved fluorescence spectrometry. *Anal Chim Acta* **162**:275–283.
161. Lakowicz JR, Keating S. 1983. Binding of an indole derivative to micelles as quantified by phase-sensitive detection of fluorescence. *J Biol Chem* **258**(9):5519–5524.
162. McGown LB. 1984. Phase-resolved fluorometric determination of two albumin-bound fluorescein species. *Anal Chim Acta* **157**:327–332.
163. Nithipatikom K, McGown LB. 1989. Studies of the homogeneous immunochemical determination of insulin by using a fluorescent label. *Talanta* **36**(1/2):305–309.
164. Nithipatikom K, McGown LB. 1987. Homogeneous immunochemical technique for determination of human lactoferrin using excitation transfer and phase-resolved fluorometry. *Anal Chem* **59**:423–427.
165. Tahboub YR, McGown LB. 1986. Phase-resolved fluoroimmunoassay of human serum albumin. *Anal Chim Acta* **182**:185–191.
166. Veselova TV, Cherkasov AS, Shirokov VI. 1970. Fluorometric method for individual recording of spectra in systems containing two types of luminescent centers. *Opt Spectrosc* **29**:617–618.
167. Gratton E, Jameson DM. 1985. New approach to phase and modulation resolved spectra. *Anal Chem* **57**:1694–1697.
168. Lakowicz JR, Balter A. 1982. Theory of phase-modulation fluorescence spectroscopy for excited state processes. *Biophys Chem* **16**:99–115.
169. Lakowicz JR, Balter A. 1982. Analysis of excited-state processes by phase-modulation fluorescence spectroscopy. *Biophys Chem* **16**:117–132.
170. Veselova TV, Limareva LA, Cherkasov AS, Shirokov VI. 1965. Fluorometric study of the effect of solvent on the fluorescence spectrum of 3-amino-N-methylphthalimide. *Opt Spectrosc* **19**:39–43.
171. Limareva LA, Cherkasov AS, Shirokov VI. 1968. Evidence of the radiating-centers inhomogeneity of crystalline anthracene in fluorometric phase spectra. *Opt Spectrosc* **25**:132–134.

## PROBLEMS

- P5.1. *Calculation of the Decay Time of SPQ from Phase and Modulation Data:* Use the data in Figure 5.15 to calculate the decay times of SPQ at each chloride concentration. For convenience, selected phase and modulation values are listed in Table 5.6. Data can also be read from Figure 5.15.
- P5.2. *Determination of Chloride Concentrations with SPQ:* Chloride quenches the fluorescence of SPQ, and this intensity can be used to measure chloride concentrations. Suppose one is measuring SPQ fluorescence in a fluorescence microscope, and that the SPQ concentration is not known. Under these conditions it is difficult to use the intensity values to measure the chloride concentrations. Suggest how the phase or modulation data of SPQ (Figure 5.15) could be used to measure chloride concentrations. Assume that the uncertainties in the phase and modulation values are  $\pm 0.2^\circ$  and  $\pm 0.5\%$ , respectively. What is

**Table 5.6.** Selected Phase and Modulation Values for the Chloride Probe SPQ<sup>a</sup>

Chloride concentration	Frequency (MHz)	Phase angle (degrees)	Modulation
0	10	57.4	0.538
	100	86.3	0.060
10 mM	10	35.1	0.821
	100	82.2	0.141
30 mM	10	18.0	0.954
	100	73.1	0.286
70 mM	10	9.4	0.988
	100	59.1	0.505

<sup>a</sup>The listed values were interpolated using the measured frequency responses (Figure 5.15).

the expected accuracy in the measured chloride concentrations?

**P5.3. Effect of Heterogeneity on Apparent Phase and Modulation Lifetimes:** Suppose you have samples that display a double-exponential-decay law, with lifetimes of 0.5 and 5.0 ns. In one sample the pre-exponential factors are equal ( $\alpha_1 = \alpha_2 = 0.5$ ), and in the other sample the fractional intensities are equal ( $f_1 = f_2 = 0.5$ ). Calculate the apparent phase and modulation lifetimes for these two decay laws at modulation frequencies of 50 and 100 MHz. Explain the relative values of the apparent lifetimes.

**P5.4. Determination of the Excitation Wavelength:** The steady-state emission spectrum of quinine sulfate shows a Raman scatter peak at 410 nm (Figure 5.51). What is the excitation wavelength?

**P5.5. Attenuation of Phase-Sensitive Spectra:** Assume that the lifetime of quinine sulfate is 20 ns, and the light modulation frequency is 10 MHz (Figure 5.51). What detector phase angle was used to suppress the scattered light? What detector phase angle would yield the highest signal for quinine sulfate? What are the relative values of the quinine sulfate intensity for the maximum intensity and when the scattered light is suppressed?

**P5.6. Resolution of a Free and Protein-Bound Fluorophore:** Assume the fluorescent probe 5-dimethylamino-1-naphthalene sulfonic acid (DNS) binds to bovine serum albumin. Assume further that the yield

of DNS increases twofold upon binding, and that the lifetime of the free and bound forms are 5 and 10 ns, respectively. Use the following data to calculate the percentage of DNS free in solution and the percentage bound to BSA in the solution containing equimolar concentrations of DNS and BSA. The modulation frequency is 10 MHz. Also, explain the intensity changes between the first two solutions.

Sample	Phase-sensitive intensity at $\phi_D = 17.4 + 90^\circ$	Phase-sensitive intensity at $\phi_D = 3.21 - 90^\circ$
DNS ( $10^{-5}$ M)	0	1.0
DNS ( $10^{-5}$ M) plus excess BSA	1.776	0
DNS ( $10^{-5}$ M) plus $10^{-5}$ M BSA	0.886	0.50

**P5.7. Phase-Sensitive Spectra and Spectral Relaxation:** Phase-sensitive emission spectra were obtained for N-acetyl-L-tryptophanamide in propylene glycol at various temperatures (Figure 5.55). These spectra were recorded following adjustment of the detector to suppress the emission on the blue or the red side of the emission. Explain the phase-sensitive spectra in Figure 5.55 in terms of the rates of spectral relaxation.

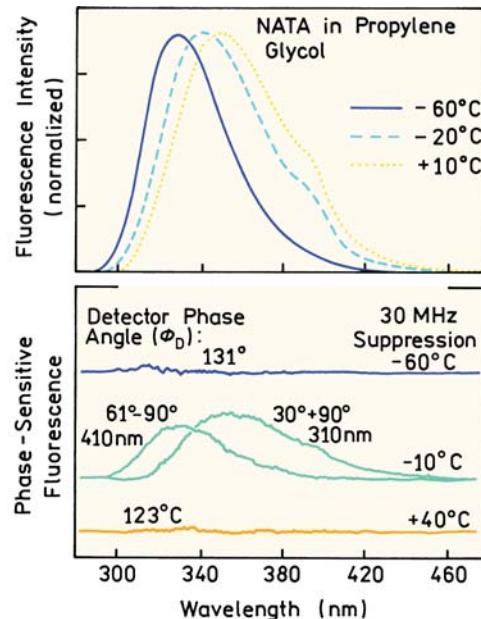


**Figure 5.55.** Resolution of the initially excited and relaxed states of N-acetyl-L-tryptophanamide by phase-sensitive detection of fluorescence. Excitation was at 280 nm. Emission was observed through a monochromator with a bandpass of 8 nm. Reprinted from [169], Copyright © 1982, with permission from Elsevier Science.

# 6

# Solvent and Environmental Effects

Solvent polarity and the local environment have profound effects on the emission spectral properties of fluorophores. The effects of solvent polarity are one origin of the Stokes shift, which is one of the earliest observations in fluorescence. Emission spectra are easily measured, resulting in numerous publications on emission spectra of fluorophores in different solvents, and when bound to proteins, membranes, and nucleic acids. One common use of solvent effects is to determine the polarity of the probe binding site on the macromolecule. This is accomplished by comparison of the emission spectra and/or quantum yields when the fluorophore is bound to the macromolecule or dissolved in solvents of different polarity. However, there are many additional instances where solvent effects are used. Suppose a fluorescent ligand binds to a protein or membrane. Binding is usually accompanied by spectral shift or change in quantum yield due to the different environment for the bound ligand. Alternatively, the ligand may induce a spectral shift in the intrinsic or extrinsic protein fluorescence. In either case the spectral changes can be used to measure the extent of binding.

The effects of solvent and environment on fluorescence spectra are complex, and are due to several factors in addition to solvent polarity. The factors that affect fluorescence emission spectra and quantum yields include:

- Solvent polarity and viscosity
- Rate of solvent relaxation
- Probe conformational changes
- Rigidity of the local environment
- Internal charge transfer
- Proton transfer and excited state reactions
- Probe–probe interactions
- Changes in radiative and non-radiative decay rates

These multiple effects provide many opportunities to probe the local environment surrounding a fluorophore. However, it can be difficult to know which effect is domi-

nant in a particular experimental system, and typically more than one effect will simultaneously affect the fluorophore.

When considering environmental effects, solvent polarity is usually the first topic. However, environmental effects as complex and even solvent polarity cannot be described using a single theory. The Lippert equation partially explains the effect of solvent polarity, but does not account for other effects such as hydrogen bonding to the fluorophore or internal charge transfer that depends on solvent polarity. In this chapter we will start with a description of general solvent effects, and then describe the other mechanisms that affect emission maxima and quantum yields.

---

## 6.1. OVERVIEW OF SOLVENT POLARITY EFFECTS

### 6.1.1. Effects of Solvent Polarity

Emission from fluorophores generally occurs at wavelengths that are longer than those at which absorption occurs. This loss of energy is due to a variety of dynamic processes that occur following light absorption (Figure 6.1). The fluorophore is typically excited to the first singlet state ( $S_1$ ), usually to an excited vibrational level within  $S_1$ . The excess vibrational energy is rapidly lost to the solvent. If the fluorophore is excited to the second singlet state ( $S_2$ ), it rapidly decays to the  $S_1$  state in  $10^{-12}$  s due to internal conversion. Solvent effects shift the emission to still lower energy due to stabilization of the excited state by the polar solvent molecules. Typically, the fluorophore has a larger dipole moment in the excited state ( $\mu_E$ ) than in the ground state ( $\mu_G$ ). Following excitation the solvent dipoles can reorient or relax around  $\mu_E$ , which lowers the energy of the excited state. As the solvent polarity is increased, this effect becomes larger, resulting in emission at lower energies or longer wavelengths. In general, only fluorophores that are themselves polar display a large sensitivity to solvent polar-

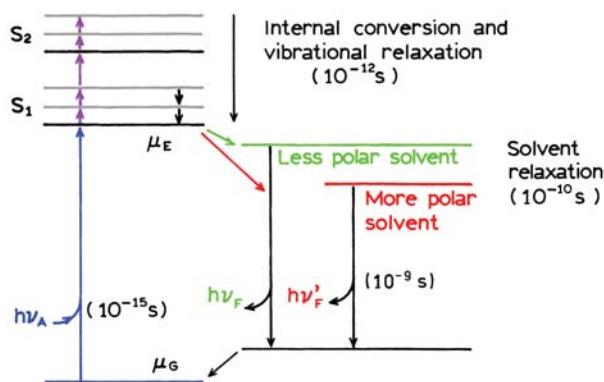


**Figure 6.1.** Jablonski diagram for fluorescence with solvent relaxation.

ity. Nonpolar molecules, such as unsubstituted aromatic hydrocarbons, are much less sensitive to solvent polarity.

Fluorescence lifetimes (1–10 ns) are usually much longer than the time required for solvent relaxation. For fluid solvents at room temperature, solvent relaxation occurs in 10–100 ps. For this reason, the emission spectra of fluorophores are representative of the solvent relaxed state. Examination of Figure 6.1 reveals why absorption spectra are less sensitive to solvent polarity than emission spectra. Absorption of light occurs in about  $10^{-15}$  s, a time too short for motion of the fluorophore or solvent. Absorption spectra are less sensitive to solvent polarity because the molecule is exposed to the same local environment in the ground and excited states. In contrast, the emitting fluorophore is exposed to the relaxed environment, which contains solvent molecules oriented around the dipole moment of the excited state.

Solvent polarity can have a dramatic effect on emission spectra. Figure 6.2 shows a photograph of the emission from 4-dimethylamino-4'-nitrostilbene (DNS) in solvents of increasing polarity. The emission spectra are shown in the lower panel. The color shifts from deep blue ( $\lambda_{\max} = 450$  nm) in hexane to orange in ethyl acetate ( $\lambda_{\max} = 600$  nm), and red in n-butanol ( $\lambda_{\max} = 700$  nm).

### 6.1.2. Polarity Surrounding a Membrane-Bound Fluorophore

Prior to describing the theory of solvent effects it is helpful to see an example. Emission spectra of trans-4-dimethylamino-4'-(1-oxobutyl) stilbene (DOS) are shown in Figure 6.3.<sup>1</sup> The emission spectra are seen to shift dramatically to longer wavelengths as the solvent polarity is increased from cyclohexane to butanol. The sensitivity to solvent polarity is

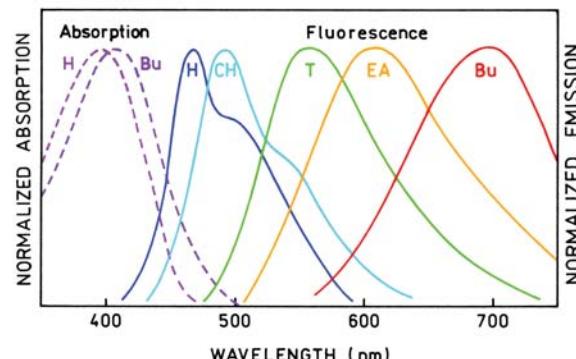


**Figure 6.2.** Photograph and emission spectra of DNS in solvents of increasing polarity. H, hexane; CH, cyclohexane; T, toluene; EA, ethyl acetate; Bu, n-butanol.

similar to DNS because of the similar electron-donating and -accepting groups on the fluorophore. The dimethyl amino group is the electron donor. The nitro group and carbonyl groups are both electron acceptors. The high sensitivity to solvent is due to a charge shift away from the amino groups in the excited state, towards the electron acceptor. This results in a large dipole moment in the excited state. This dipole moment interacts with the polar solvent molecules to reduce the energy of the excited state.

A typical use of spectral shifts is to estimate the polarity which surrounds the fluorophore. In Figure 6.3 the goal

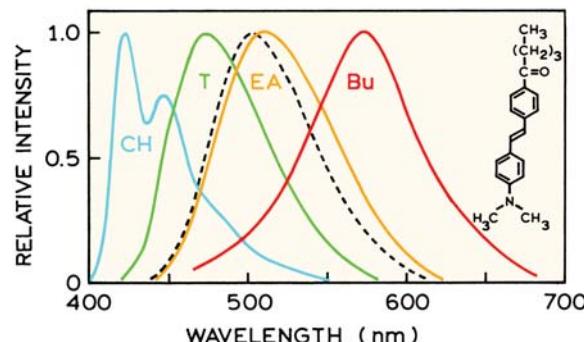


**Figure 6.3.** Corrected fluorescence emission spectra of DOS in cyclohexane (CH), toluene (T), ethyl acetate (EA), and butanol (Bu). The dashed line shows the emission of DOS from DPPC vesicles. Revised from [1].

was to determine the polarity of the DOS binding site on a model membrane that was composed of dipalmitoyl-L- $\alpha$ -phosphatidylcholine (DPPC). The emission spectrum of DOS bound to DPPC vesicles (dashed line) was found to be similar to that of DOS in ethyl acetate, which has a dielectric constant ( $\epsilon$ ) near 5.8. The polarity of the DOS binding site on DPPC vesicles is obviously greater than hexane ( $\epsilon = 1.9$ ) and less than butanol ( $\epsilon = 17.8$  at 20°C). Hence, the emission spectra of DOS indicate an environment of intermediate polarity for DOS when bound to DPPC vesicles.

### 6.1.3. Other Mechanisms for Spectral Shifts

While interpretation of solvent-dependent emission spectra appears simple, this is a very complex topic. The complexity is due to the variety of interactions that can result in spectral shifts. At the simplest level, solvent-dependent emission spectra are interpreted in terms of the Lippert equation (eq. 6.1, below), which describes the Stokes shift in terms of the changes in dipole moment which occur upon excitation, and the energy of a dipole in solvents of various dielectric constant ( $\epsilon$ ) or refractive index ( $n$ ).<sup>2-3</sup> These general solvent effects occur whenever a fluorophore is dissolved in any solvent, and are independent of the chemical properties of the fluorophore and the solvent.

The theory for general solvent effects is often inadequate for explaining the detailed behavior of fluorophores in a variety of environments. This is because fluorophores often display multiple interactions with their local environment, which can shift the spectra by amounts comparable to general solvent effects. For instance, indole displays a structured emission in the nonpolar solvent cyclohexane (see Figure 16.5). This spectrum is a mirror image of its

absorption spectrum. Addition of a small amount of ethanol (1 to 5%) results in a loss of the structured emission. This amount of ethanol is too small to significantly change solvent polarity and cause a spectral shift due to general solvent effects. The spectral shift seen in the presence of small amounts of ethanol is due to hydrogen bonding of ethanol to the imino nitrogen on the indole ring. Such specific solvent effects occur for many fluorophores, and should be considered while interpreting the emission spectra. Hence, the Jablonski diagram for solvent effects should also reflect the possibility of specific solvent–fluorophore interactions that can lower the energy of the excited state (Figure 6.4).

In addition to specific solvent–fluorophore interactions, many fluorophores can form an internal charge transfer (ICT) state, or a twisted internal charge transfer (TICT) state.<sup>4</sup> For instance, suppose the fluorophore contains both an electron-donating and an electron-accepting group. Such groups could be amino and carbonyl groups, respectively, but numerous other groups are known. Following excitation there can be an increase in charge separation within the fluorophore. If the solvent is polar, then a species with charge separation (the ICT state) may become the lowest energy state (Figure 6.4). In a nonpolar solvent the species without charge separation, the so-called locally excited (LE) state, may have the lowest energy. Hence, the role of solvent polarity is not only to lower the energy of the excited state due to general solvent effects, but also to govern which state has the lowest energy. In some cases formation of the ICT state requires rotation of groups on the fluorophore to form the TICT state. Formation of ICT states is not contained within the theory of general solvent effects. Additionally, a fluorophore may display a large spectral shift due to excimer or exciplex formation. The fluorophores may be

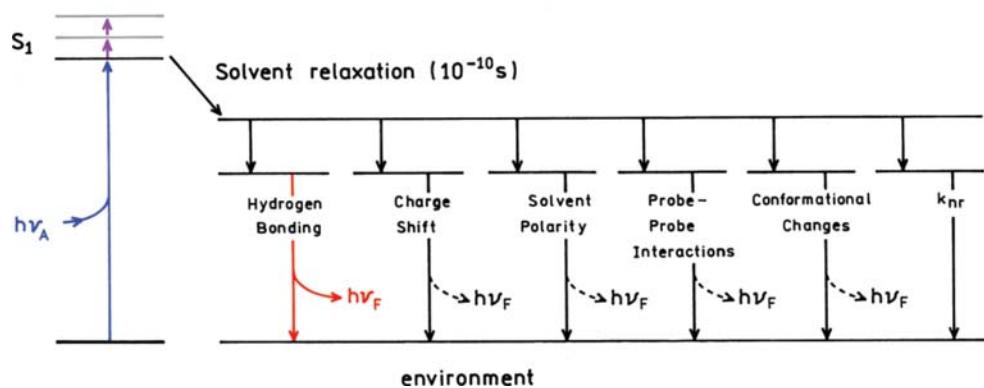


**Figure 6.4.** Effects of environment on the energy of the excited state. The dashed arrows indicate the fluorophore can be fluorescent or nonfluorescent in the different states.

fluorescent or nonfluorescent in these different states. The quantum yield can change due to change in the rate of non-radiative decay ( $k_{nr}$ ) or due to a conformational change in the fluorophore.

In summary, no single theory can be used for a quantitative interpretation of the effects of environment on fluorescence. Interpretation of these effects relies not only on polarity considerations, but also on the structure of the fluorophore and the types of chemical interactions it can undergo with other nearby molecules. The trends observed with solvent polarity follow the theory for general solvent effects, which may give the impression that solvent polarity is the only factor to consider. In reality, multiple factors affect the emission of any given fluorophore.

## 6.2. GENERAL SOLVENT EFFECTS: THE LIPPERT-MATAGA EQUATION

The theory of general solvent effects provides a useful framework for consideration of solvent-dependent spectral shifts. In the description of general solvent effects the fluorophore is considered to be a dipole in a continuous medium of uniform dielectric constant (Figure 6.5). This model does not contain any chemical interactions, and hence cannot be used to explain the other interactions which affect the emission. These other interactions, such as hydrogen bonding or formation of charge transfer states, are sometimes detected as deviations from the general theory.

The interactions between the solvent and fluorophore affect the energy difference between the ground and exci-

ed states. To a first approximation this energy difference (in  $\text{cm}^{-1}$ ) is a property of the refractive index ( $n$ ) and dielectric constant ( $\epsilon$ ) of the solvent, and is described by the Lippert-Mataga equation:<sup>2-3</sup>

$$\bar{v}_A - \bar{v}_F = \frac{2}{hc} \left( \frac{\epsilon - 1}{2\epsilon + 1} - \frac{n^2 - 1}{2n^2 + 1} \right) \frac{(\mu_E - \mu_G)^2}{a^3} + \text{constant} \quad (6.1)$$

In this equation  $h$  ( $= 6.6256 \times 10^{-27}$  ergs) is Planck's constant,  $c$  ( $= 2.9979 \times 10^{10}$  cm/s) is the speed of light, and  $a$  is the radius of the cavity in which the fluorophore resides.  $\bar{v}_A$  and  $\bar{v}_F$  are the wavenumbers ( $\text{cm}^{-1}$ ) of the absorption and emission, respectively. Equation 6.1 is only an approximation, but there is reasonable correlation between the observed and calculated energy losses in non-protic solvents. By non-protic solvents we mean those not having hydroxyl groups, or other groups capable of hydrogen bonding. The Lippert equation is an approximation in which the polarizability of the fluorophore and higher-order terms are neglected. These terms would account for second-order effects, such as the dipole moments induced in the solvent molecules resulting by the excited fluorophore, and vice versa.

It is instructive to examine the opposite effects of  $\epsilon$  and  $n$  on the Stokes shift. An increase in  $n$  will decrease this energy loss, whereas an increase in  $\epsilon$  results in a larger difference between  $\bar{v}_A$  and  $\bar{v}_F$ . The refractive index ( $n$ ) is a high-frequency response and depends on the motion of electrons within the solvent molecules, which is essentially instantaneous and can occur during light absorption. In contrast, the dielectric constant ( $\epsilon$ ) is a static property, which depends on both electronic and molecular motions, the latter being solvent reorganization around the excited state. The different effects of  $\epsilon$  and  $n$  on the Stokes shift will be explained in detail in Section 6.2.1. Briefly, an increase in refractive index allows both the ground and excited states to be instantaneously stabilized by movements of electrons within the solvent molecules. This electron redistribution results in a decrease in the energy difference between the ground and excited states (Figure 6.6). For this reason most chromophores display a red shift of the absorption spectrum in solvents relative to the vapor phase.<sup>5-7</sup> An increase in  $\epsilon$  will also result in stabilization of the ground and excited states. However, the energy decrease of the excited state due to the dielectric constant occurs only after reorientation of the solvent dipoles. This process requires movement of

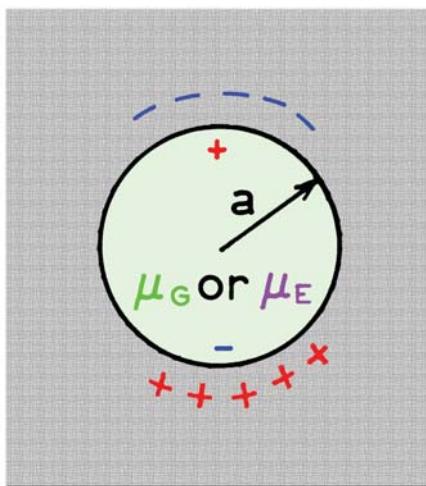


**Figure 6.5.** Dipole in a dielectric medium.

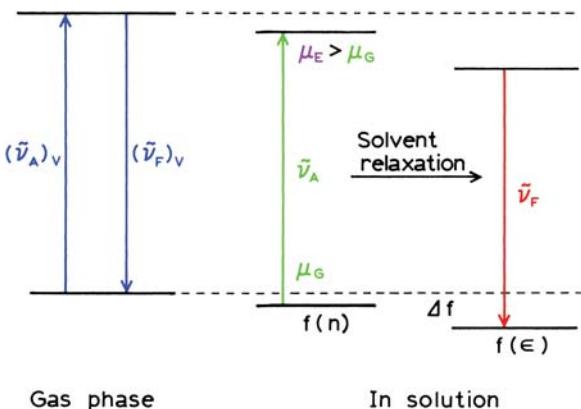


**Figure 6.6.** Effects of the refractive index ( $n$ ) and dielectric constant ( $\epsilon$ ) on the absorption and emission energies.

the entire solvent molecule, not just its electrons. As a result, stabilization of the ground and excited states of the fluorophore depends on the dielectric constant ( $\epsilon$ ) and is time dependent. The rate of solvent relaxation depends on the temperature and viscosity of the solvent (Chapter 7). The excited state shifts to lower energy on a timescale comparable to the solvent reorientation time. In the derivation of the Lippert equation (Section 6.2.1), and throughout this chapter, it is assumed that solvent relaxation is complete prior to emission.

The term inside the large parentheses in eq. 6.1 is called the orientation polarizability ( $\Delta f$ ). The first term  $(\epsilon - 1)/(2\epsilon + 1)$  accounts for the spectral shifts due to both the reorientation of the solvent dipoles and to the redistribution of the electrons in the solvent molecules (Figure 6.6, center). The second term  $(n^2 - 1)/(2n^2 + 1)$  accounts for only the redistribution of electrons. The difference of these two terms accounts for the spectral shifts due to reorientation of the solvent molecules (Figure 6.6, right), and hence the term orientation polarizability. According to this simple model, only solvent reorientation is expected to result in substantial Stokes shifts. The redistribution of electrons occurs instantaneously, and both the ground and excited states are approximately equally stabilized by this process. As a result, the refractive index and electronic redistribution has a comparatively minor effect on the Stokes shift.

It is instructive to calculate the magnitude of the spectral shifts that are expected for general solvent effects. Most fluorophores have nonzero dipole moments in the ground and excited states. As an example we will assume that the ground-state dipole moment is  $\mu_G = 6D$ , and the excited-

state dipole moment is  $\mu_E = 20D$ , so that  $\mu_E - \mu_G = 14D$ . We will also assume the cavity radius is  $4 \text{ \AA}$ , which is comparable to the radius of a typical aromatic fluorophore. One Debye unit (1D) is  $1.0 \times 10^{-18} \text{ esu cm}$ .  $4.8D$  is the dipole moment that results from a charge separation of one unit charge ( $4.8 \times 10^{-10} \text{ esu}$ ) by  $1 \text{ \AA}$  ( $10^{-8} \text{ cm}$ ). An excited-state dipole moment of  $20D$  is thus comparable to a unit charge separation of  $4.2 \text{ \AA}$ , which is a distance comparable to the size of a fluorophore. These assumed values of  $\mu_E$  and  $\mu_G$  are similar to those observed for fluorophores which are frequently used as polarity probes in biochemical research.

For the model calculation of Stokes losses we compare the nonpolar solvent hexane with several polar solvents. Nonpolar solvents such as hexane do not have a dipole moment. Hence, there are no dipoles to reorient around the excited state of the fluorophore. This physical property of hexane is reflected by  $\epsilon \approx n^2$  (Table 6.1). From eq. 6.1 one calculates a small value for the orientation polarizability ( $\Delta f$ ), and  $\bar{\nu}_A$  and  $\bar{\nu}_F$  are expected to be small or zero. For example, if we assume that our model fluorophore absorbs at 350 nm, the emission in hexane is calculated to also be at 350 nm (Table 6.2). However, even in nonpolar solvents, absorption and emission maxima do not coincide this closely. Excitation generally occurs to higher vibrational levels, and this energy is rapidly dissipated in fluid solvents ( $10^{-12} \text{ s}$ ). Emission generally occurs to an excited vibrational level of the ground state. As a result, absorption and emission are generally shifted by an amount at least equal to the vibrational energy, or about  $1500 \text{ cm}^{-1}$ . These energy losses are accounted for by the constant term in eq. 6.1, and would shift emission of our model fluorophore to 370 nm.

In polar solvents such as methanol, substantially larger Stokes losses are expected. For example, our model fluorophore is expected to emit at 526 nm in this polar solvent (Table 6.2). This shift is due to the larger orientation polarizability of methanol, which is a result of its dipole moment. This sensitivity of the Stokes shift to solvent polarity is the reason why fluorescence emission spectra are frequently used to estimate the polarity of the environment surrounding the fluorophore.

**Table 6.1.** Polarizability Properties of Some Common Solvents

	Water	Ethanol	Ether	Hexane
$\epsilon$	78.3	24.3	4.35	1.89
$n$	1.33	1.35	1.35	1.37
$\Delta f$	0.32	0.30	0.17	0.001

**Table 6.2.** Stokes Shifts Expected from General Solvent Effects

Solvent	$\epsilon$	$n$	$\Delta f^a$	$\bar{v}_A - \bar{v}_F$ (cm <sup>-1</sup> ) <sup>b</sup>	$\lambda_{\max}^c$ (nm)
Hexane	1.874	1.372	-0.0011 <sup>d</sup>	35	350 <sup>d</sup>
Chloroform	4.98	1.447	0.1523	4697	418.9
Ethyl Acetate	6.09	1.372	0.201	6200	447.0
1-Octanol	10.3	1.427	0.2263	6979	463.1
1-Butanol	17.85	1.399	0.2644	8154	489.8
n-Propanol	21.65	1.385	0.2763	8522	498.8
Methanol	33.1	1.326	0.3098	9554	525.8

<sup>a</sup> $\Delta f = [(\epsilon - 1)/(2\epsilon + 1)] - [(n^2 - 1)/(2n^2 + 1)]$ .

<sup>b</sup>From eq. 6.1, assuming  $\mu_G = 6D$ ,  $\mu_E = 20D$ ,  $\mu_E - \mu_G = 14D$ , and a cavity radius of 4 Å. 4.8D is the dipole moment that results from a charge separation of 1 unit of charge ( $4.8 \times 10^{-10}$  esu) by 1 Å ( $10^{-8}$  cm).  $1 \times 10^{-18}$  esu cm is 1 Debye unit (1.0D).

<sup>c</sup>Assuming an absorption maximum of 350 nm.

<sup>d</sup>The small negative value of  $\Delta f$  was ignored.

### 6.2.1. Derivation of the Lippert Equation

The interactions responsible for general solvent effects are best understood by derivation of the Lippert equation. This equation can be written as

$$hc\Delta\bar{v} = hc(\bar{v}_A - \bar{v}_F) = \frac{2\Delta f}{a^3} (\mu_E - \mu_G)^2 + \text{const} \quad (6.2)$$

where  $\Delta\bar{v}$  is the frequency shift (in cm<sup>-1</sup>) between absorption and emission,  $\Delta f$  is the orientation polarizability, and  $\mu_E$  and  $\mu_G$  are the excited- and ground-state dipole moments, respectively. The Lippert equation is derived by consideration of the interaction of a fluorophore with the solvent, and the timescale of these interactions. We need to recall the Franck-Condon principle, which states that nuclei do not move during an electronic transition ( $10^{-15}$  s). In contrast, the electrons of the solvent molecules can redistribute around the new excited state dipole during this time span. In addition, because of the relatively long lifetime of the excited state ( $\sim 10^{-8}$  s), the solvent molecules can orientate to their equilibrium position around the excited state of the fluorophore prior to emission.

Derivation of the Lippert equation starts with the consideration of a point dipole in a continuous dielectric medium (Figure 6.4). The energy of the dipole in an electric field given by

$$E_{\text{dipole}} = -\mu R \quad (6.3)$$

where  $R$  is the electric field.<sup>8</sup> In our case the electric field is the relative reactive field in the dielectric induced by the dipole. The reactive field is parallel and opposite to the

direction of the dipole, and is proportional to the magnitude of the dipole moment,

$$R = \frac{2\mu}{a^3} f \quad (6.4)$$

In this equation  $f$  is the polarizability of the solvent and  $a$  is the cavity radius. The polarizability of the solvent is a result of both the mobility of electrons in the solvent and the dipole moment of the solvent molecules. Each of these components has a different time dependence. Reorientation of the electrons in the solvent is essentially instantaneous. The high frequency polarizability  $f(n)$  is a function of the refractive index:

$$f(n) = \frac{n^2 - 1}{2n^2 + 1} \quad (6.5)$$

The polarizability of the solvent also depends on the dielectric constant, which includes the effect of molecular orientation of the solvent molecules. Because of the slower timescale of molecular reorientation, this component is called the low frequency polarizability of the solvent, and is given by

$$f(\epsilon) = \frac{\epsilon - 1}{2\epsilon + 1} \quad (6.6)$$

The difference between these two terms is

$$\Delta f = \frac{\epsilon - 1}{2\epsilon + 1} - \frac{n^2 - 1}{2n^2 + 1} \quad (6.7)$$

and is called the orientation polarizability. If the solvent has no permanent dipole moment,  $\epsilon = n^2$  and  $\Delta f \sim 0$ . Table 6.1 lists representative values of  $\epsilon$ ,  $n$  and  $\Delta f$ . From the magnitudes of  $\Delta f$  one may judge that spectral shifts  $\Delta\bar{v}$  will be considerably larger in water than in hexane.

The interactions of a fluorophore with solvent can be described in terms of its ground- ( $\mu_G$ ) and excited-state ( $\mu_E$ ) dipole moments, and the reactive fields around these dipoles. These fields may be divided into those due to electronic motions ( $R_{el}^G$  and  $R_{el}^E$ ) and those due to solvent reorientation ( $R_{or}^G$  and  $R_{or}^E$ ). Assuming equilibrium around the dipole moments of the ground and excited states, these reactive fields are

$$\begin{aligned} R_{el}^G &= \frac{2\mu_G}{a^3}f(n) & R_{el}^E &= \frac{2\mu_E}{a^3}f(n) \\ R_{or}^G &= \frac{2\mu_G}{a^3}\Delta f & R_{el}^E &= \frac{2\mu_E}{a^3}\Delta f \end{aligned} \quad (6.8)$$

Consider Figure 6.7, which describes these fields during the processes of excitation and emission. For light absorption the energies of the ground ( $E^G$ ) and nonequilibrium excited ( $E^E$ ) states are

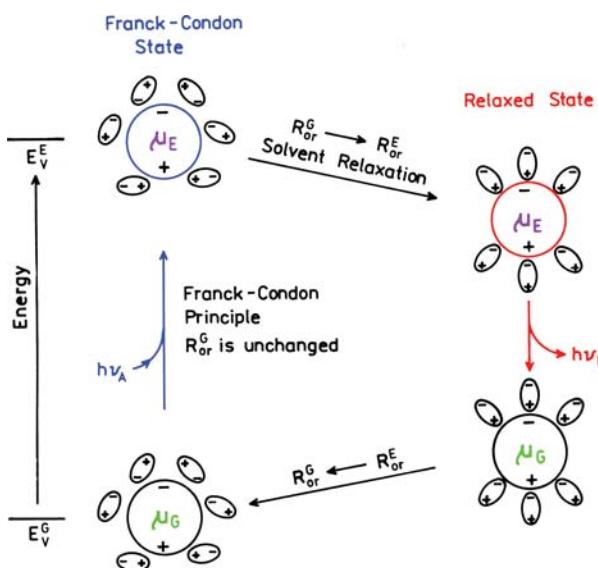


**Figure 6.7.** Effects of the electronic and orientation reaction fields on the energy of a dipole in a dielectric medium,  $\mu_E > \mu_G$ . The smaller circles represent the solvent molecules and their dipole moments.

$$\text{Energy}^E(\text{absorption}) = E_V^E - \mu_E R_{or}^G - \mu_E R_{el}^E \quad (6.9)$$

$$\text{Energy}^G(\text{absorption}) = E_V^G - \mu_G R_{or}^G - \mu_G R_{el}^E \quad (6.10)$$

where  $E_V$  represents the energy levels of the fluorophore in the vapor state, unperturbed by solvent. The absorption transition energy is decreased by the electronic reaction field induced by the excited state dipole. This occurs because the electrons in the solvent can follow the rapid change in electron distribution within the fluorophore. In contrast, the orientation of the solvent molecules does not change during the absorption of light. Therefore, the effect of the orientation polarizability, given by  $\mu_G R_{or}^G$  and  $\mu_E R_{or}^G$ , contains only the ground-state orientational reaction field. This separation of effects is due to the Franck-Condon principle. Recalling that energy is related to the wavelength by  $\bar{v} = \Delta E/hc$ , subtraction of eq. 6.10 from 6.9 yields the energy of absorption:

$$hc\bar{v}_A = hc(\bar{v}_A)_V - (\mu_E - \mu_G)(R_{or}^G)$$

$$- \mu_E R_{el}^E + \mu_G R_{el}^G \quad (6.11)$$

where  $hc(\bar{v}_A)_V$  is the energy difference in a vapor where solvent effects are not present. By a similar consideration one can obtain the energy of the two electronic levels for emission. These are

$$\text{Energy}^E(\text{emission}) = E_V^E - \mu_E R_{or}^E - \mu_E R_{el}^E \quad (6.12)$$

$$\text{Energy}^G(\text{emission}) = E_V^G - \mu_G R_{or}^E - \mu_G R_{el}^E \quad (6.13)$$

To derive these expressions we assumed that the solvent relaxed quickly in comparison to the lifetime of the excited state, so that the initial orientation field ( $R_{or}^G$ ) changed to  $R_{or}^E$  prior to emission. The electronic field changed during emission, but the orientation field remained unchanged. The energy of the emission is given by

$$hc\bar{v}_F = hc(\bar{v}_F)_V - (\mu_E - \mu_G)R_{or}^E - \mu_E R_{el}^E + \mu_G R_{el}^G \quad (6.14)$$

In the absence of environmental effects one may expect  $\bar{v}_A - \bar{v}_F$  to be a constant for complex molecules that undergo vibrational relaxation. Hence, subtracting eq. 6.14 from 6.11 yields

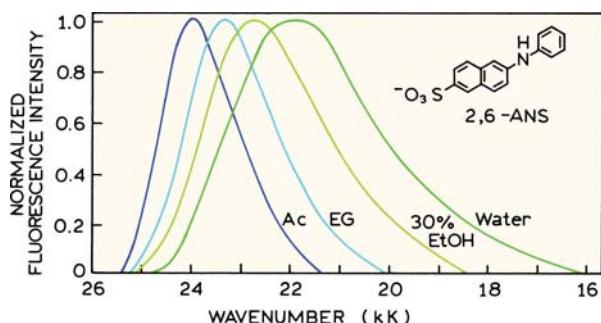


**Figure 6.8.** Normalized emission spectra for 6-anilino-2-naphthalene sulfonic acid (ANS). The solvents are acetonitrile (Ac), ethylene glycol (EG), 30% ethanol/70% water (30% EtOH), and water.  $1\text{ K} = 1000 \text{ cm}^{-1}$ . Revised from [19].

$$\bar{v}_A - \bar{v}_F = -\frac{1}{hc}(\mu_E - \mu_G)(R_{\text{or}}^G - R_{\text{or}}^E) + \text{const} \quad (6.15)$$

Substitution from eq. 6.8 yields the Lippert equation:

$$\bar{v}_A - \bar{v}_F = \frac{-2}{hca^3}(\mu_E - \mu_G)(\mu_G\Delta f - \mu_E\Delta f) + \text{const} \quad (6.16)$$

$$\bar{v}_A - \bar{v}_F = \frac{2\Delta f}{hca^3}(\mu_E - \mu_G)^2 + \text{const} \quad (6.17)$$

It is important to remember that the Lippert equation is only an approximation, and contains many assumptions. The fluorophore is assumed to be spherical, and there is no consideration of specific interactions with the solvent. Other more complex equations have been presented, and the interested reader is referred to extensive publications on this subject.<sup>9–14</sup> In all these treatments the solvent is regarded as a continuum. The Lippert equation ignores the polarizability of the fluorophore and assumes that the ground and excited states dipole moments point in the same direction. If one assumes the polarizability of the fluorophore is the same as the solvent, and that  $\mu_G$  and  $\mu_E$  point in different directions, then if these directions are different, the Lippert equation becomes<sup>13–14</sup>

$$hc\Delta\bar{v} = \Delta b \left[ \frac{\varepsilon - 1}{\varepsilon + 2} - \frac{n^2 - 1}{n^2 + 2} \right] \frac{(2n^2 + 1)}{(n^2 + 2)} + \text{const} \quad (6.18)$$

where

$$\Delta b = \frac{2}{hca^3} (\mu_G^2 - \mu_E^2 - \mu_G\mu_E \cos\alpha) \quad (6.19)$$

and  $\alpha$  is the angle between  $\mu_G$  and  $\mu_E$ . It seems reasonable that general solvent effects would depend on the angle between  $\mu_E$  and  $\mu_G$ . However, it seems that the directions of the dipole moments are similar for many fluorophores in the ground and excited state. Given the fact that the spectral shifts due to specific solvent effects and formation of ICT states are often substantial, it seems preferable to use the simplest form of the Lippert equation to interpret the spectral data. Deviations from the predicted behavior can be used to indicate the presence of additional interactions.

To avoid confusion we note that eq. 6.18 was incorrect in the second edition of this book, as was pointed out in [15]. This equation was also incorrect on the original reports.<sup>13–14</sup>

### 6.2.2. Application of the Lippert Equation

The emission spectra of many fluorophores used to label macromolecules are known to be sensitive to solvent polarity. One of the best-known examples is the probe ANS. This class of probes has become widespread since its introduction in 1954.<sup>16</sup> ANS and similar molecules are essentially nonfluorescent when in aqueous solution, but become highly fluorescent in nonpolar solvents or when bound to proteins and membranes. These probes are highly sensitive to solvent polarity and can potentially reveal the polarity of their immediate environments.<sup>17–19</sup> For example, the emission maximum of 2,6-ANS shifts from 416 nm in acetonitrile to about 460 nm in water (Figure 6.8), and the emission maximum could be used to estimate the polarity of the binding site of ANS on the macromolecules.<sup>20</sup> Another reason for the widespread use of these probes is their low fluorescence in water. For example, the quantum yield of 1-anilinonaphthalene-8-sulfonate (1,8-ANS) is about 0.002 in aqueous buffer, but near 0.4 when bound to serum albumin. This 200-fold enhancement of the quantum yield is useful because the fluorescence of a dye–protein or dye–membrane mixture results almost exclusively from the dye that is bound to the biopolymers, with almost no contribution from the unbound probe. As a result, the spectral properties of the bound fraction may be investigated without interference from free dye.

The solvent sensitivity of a fluorophore can be estimated by a Lippert plot. This is a plot of  $(\bar{v}_A - \bar{v}_F)$  versus the orientation polarizability ( $\Delta f$ ). The most sensitive fluorophores are those with the largest change in dipole moment upon excitation. Representative Lippert plots for two naphthylamine derivatives are shown in Figure 6.9. The

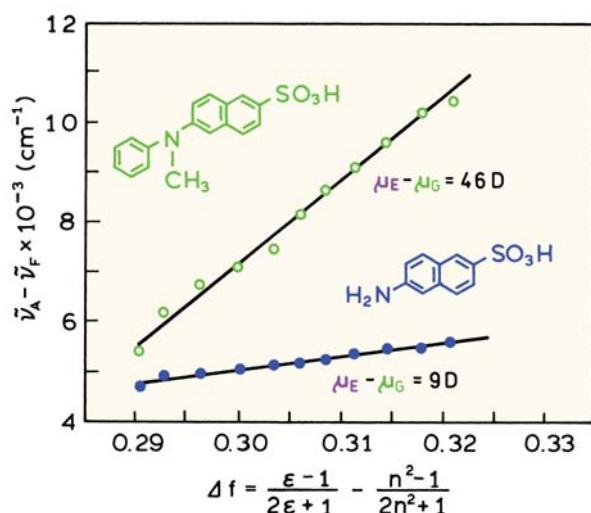


**Figure 6.9.** Lippert plots for two naphthylamine derivatives in ethanol–water mixtures. Data are shown for N-phenyl-N-methyl-6-aminonaphthalene-2-sulfonate ( $\circ$ ) and 6-aminonaphthalene-2-sulfonate ( $\bullet$ ). Revised and reprinted with permission from [10]. Copyright © 1971, American Chemical Society.

sensitivity of these fluorophores to solvent polarity is probably due to a charge shift from the amino group towards the electronegative sulfonic acid group. The N-phenyl-N-methyl derivative of 6-aminonaphthalene-2-sulfonic acid is more sensitive to solvent polarity than the unsubstituted amino derivatives.<sup>10</sup> This higher sensitivity to solvent polarity is probably because the phenyl ring allows for a larger charge separation than the unsubstituted amino group.

The linearity of these plots is often regarded as evidence for the dominant importance of general solvent effects in the spectral shifts. Specific solvent effects lead to

nonlinear Lippert plots (Section 6.3). The data in Figure 6.9 are for a limited range of similar solvents. Specifically, these were ethanol–water mixtures, so the same specific effects due to hydrogen bonding were present in all mixtures. In general, the attachment of side chains to the amino group, especially aromatic groups, enhances the sensitivity to solvent polarity. This general trend can be seen from Figure 6.10, in which we show values of  $(\mu_E - \mu_G)$  for several naphthylamine derivatives as determined from the Lippert plots. The change in dipole moment is large when electron-donating alkyl groups are attached to the nitrogen. Attachment of a toluyl group further increases the charge separation in the excited state.

### 6.3. SPECIFIC SOLVENT EFFECTS

In the preceding sections we described the general interactions between fluorophores and solvents, as modeled by the Lippert equation. These general effects are determined by the electronic polarizability of the solvent (which is described by the refractive index  $n$ ) and the molecular polarizability (which results from reorientation of solvent dipoles). The latter property is a function of the static dielectric constant,  $\epsilon$ . In contrast, specific interactions are produced by one or a few neighboring molecules, and are determined by the specific chemical properties of both the fluorophore and solvent.<sup>21–22</sup> Specific effects can be due to hydrogen bonding, preferential solvation, acid–base chemistry, or charge-transfer interactions, to name a few.<sup>23–30</sup> The spectral shifts due to such specific interactions can be substantial, and if not recognized, limit the detailed interpretation of fluorescence emission spectra.

Specific solvent–fluorophore interactions can often be identified by examining emission spectra in a variety of solvents. Typical data for 2-anilinonaphthalene (2-AN) in cyclohexane are shown in Figure 6.11. Addition of low concentrations of ethanol, which are too small to alter the bulk properties of the solvent, result in substantial spectral shifts.<sup>19</sup> Less than 3% ethanol causes a shift in the emission maximum from 372 to 400 nm. Increasing the ethanol concentration from 3 to 100% caused an additional shift to only 430 nm. A small percentage of ethanol (3%) caused 50% of the total spectral shift. Upon addition of the trace quantities of ethanol one sees that the intensity of the initial spectrum is decreased, and a new red-shifted spectrum appears. The appearance of a new spectral component is a characteristic of specific solvent effects. It is important to recognize that solvent-sensitive fluorophores can yield misleading infor-



**Figure 6.10.** Chemical structure and change in dipole moment  $\Delta\mu = \mu_E - \mu_G$  for naphthylamine derivatives.

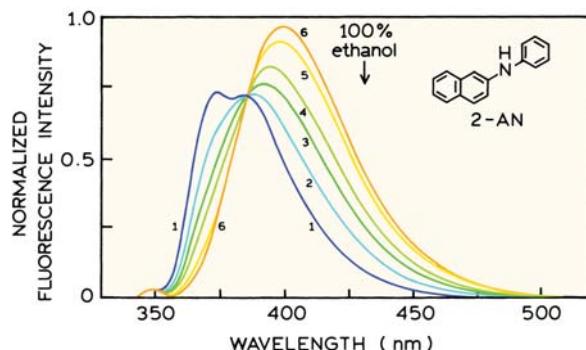


**Figure 6.11.** Fluorescence emission spectra of 2-anilinonaphthalene in cyclohexane, to which ethanol was added. These quantities were 0% (1), 0.2% (2), 0.4%, (3), 0.7% (4), 1.7% (5), and 2.7% (6). The arrow indicates the emission maximum in 100% ethanol. Revised and reprinted with permission from [19]. Copyright © 1971, Academic Press Inc.

mation on the polarity of their environments if specific interactions occur, or if solvent relaxation is not complete. Because the specific spectral shift occurs at low ethanol concentrations, this effect is probably due to hydrogen bonding of ethanol to the amino groups, rather than general solvent effects.

Another example of specific solvent effects is provided by 2-acetylanthracene (2-AA) and its derivatives.<sup>31–33</sup> Emission spectra of 2-AA in hexane containing small amounts of methanol are shown in Figure 6.12. These low concentrations of ethanol result in a loss of the structured emission, which is replaced by a longer-wavelength unstructured emission. As the solvent polarity is increased further, the

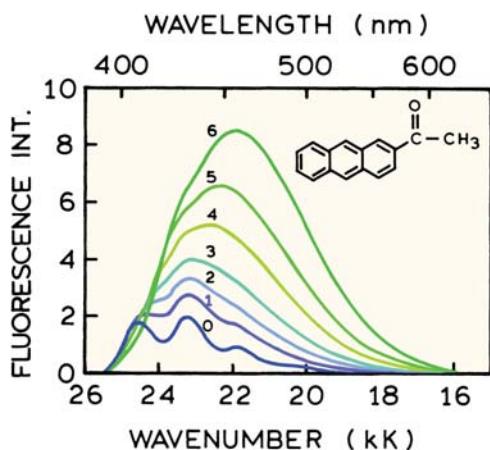


**Figure 6.12.** Fluorescence spectra of 2-acetylanthracene in methanol-hexane mixtures at 20°C. Concentrations of methanol in mol dm<sup>-3</sup>: (0) 0, (1) 0.03, (2) 0.05, (3) 0.075, (4) 0.12, (5) 0.2, and (6) 0.34. Revised from [32].

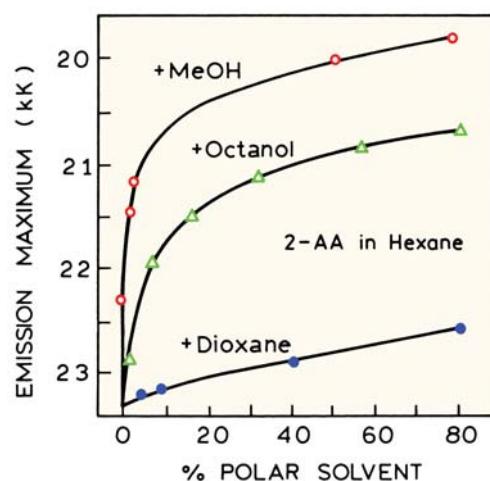


**Figure 6.13.** Effect of solvent composition on the emission maximum of 2-acetylanthracene. 1 kK = 1000 cm<sup>-1</sup>. Revised from [32].

emission spectra continue a more gradual shift to longer wavelengths. These spectra suggest that the emission of 2-AA is sensitive to both specific solvent effects, and general solvent effects in more polar solvents.

The presence of specific solvent effects can be seen in the dependence of the emission maxima on the percentage of polar solvent (Figure 6.13). In hexane the emission maximum of 2-AA shifted gradually as the percentage of dioxane was increased to 100%. These shifts induced by dioxane are probably a result of general solvent effects. In contrast, most of the shift expected for methanol was produced by only about 1–2% methanol. This amount of alcohol is too small to affect the refractive index or dielectric constant of the solvent, and hence this shift is a result of specific solvent effects.

Specific solvent–fluorophore interactions can occur in either the ground state or the excited state. If the interaction only occurred in the excited state, then the polar additive would not affect the absorption spectra. If the interaction occurs in the ground state, then some change in the absorption spectrum is expected. In the case of 2-AA the absorption spectra showed loss of vibrational structure and a red shift upon adding methanol (Figure 6.14). This suggests that 2-AA and alcohol are already hydrogen bonded in the ground state. An absence of changes in the absorption spectra would indicate that no ground-state interaction occurs. Alternatively, weak hydrogen bonding may occur in the ground state, and the strength of this interaction may increase following excitation. If specific effects are present for a fluorophore bound to a macromolecule, interpretation

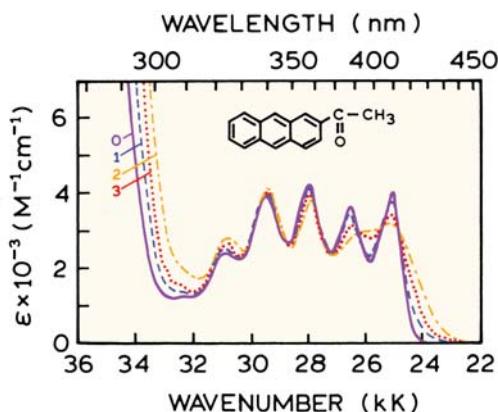


**Figure 6.14.** Absorption spectra of 2-acetylanthracene in pure hexane (0) and mixtures of methanol and hexane. The concentrations of methanol in mol dm<sup>-3</sup> are 0.2 (1) and pure methanol (2). Spectrum 3 (dotted) refers to the H-bonded complex. Revised from [32].

of the emission spectrum is complex. For example, a molecule like 2-acetylanthracene, when bound in a hydrophobic site on a protein, may display an emission spectrum comparable to that seen in water if only a single water molecule is near the carbonyl group.

The presence of specific interactions in the ground state or only in the excited state determines the timescale of these interactions. If the fluorophore and polar solvent are already associated in the ground state, then one expects an immediate spectral shift upon excitation. If the fluorophore and polar solvent only associate in the excited state, then the appearance of the specific solvent effect will depend on the rates of diffusion of the fluorophore and polar solvent. In this case the dependence on the concentration of polar solvent will be similar to quenching reactions.

### 6.3.1. Specific Solvent Effects and Lippert Plots

Evidence for specific solvent–fluorophore interactions can be seen in the Lippert plots. One example is a long-chain fatty acid derivative of 2-AA. The compound was synthesized for use as a membrane probe.<sup>34–35</sup> One notices that the Stokes shift is generally larger in hydrogen bonding solvents (water, methanol, and ethanol) than in solvents that less readily form hydrogen bonds (Figure 6.15). Such behavior of larger Stokes shifts in protic solvents is typical of specific solvent–fluorophore interactions, and have been seen for other fluorophores.<sup>36–38</sup>

The sensitivity of fluorophores to specific interactions with solvents may be regarded as a problem, or a favorable

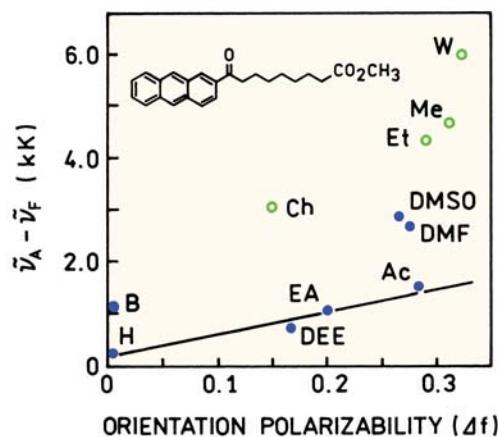


**Figure 6.15.** Stokes shifts of methyl 8-(2-anthroyl) octanoate in organic solvents and water. The solvents are benzene (B), n-hexane (H), diethyl ether (DEE), ethyl acetate (EA), acetone (Ac), N,N-dimethylformamide (DMF), chlorophorm (Ch), dimethyl sulfoxide (DMSO), ethanol (EA), methanol (Me), and water (W). Revised from [35]. Copyright © 1991, with permission from Elsevier Science.

circumstance. It is problematic because these effects can prevent a quantitative interpretation of the emission spectra in terms of the orientation polarizability of the macromolecule. The situation is favorable because the specific effects of protic solvents could reveal the accessibility of the macromolecule-bound probe to the aqueous phase. Also, specific solvent effects can cause larger and hence more easily observed spectral shifts.

In view of the magnitude of specific solvent effects, how can one reliably use fluorescence spectral data to indicate the polarity of binding sites? At present there seems to be no completely reliable method. However, by careful examination of the solvent sensitivity of a fluorophore, reasonable estimates can be made. Consider the following hypothetical experiment. Assume that 2-acetylanthracene (2-AA) binds strongly to lipid bilayers so that essentially all the 2-AA is bound to the membrane. It seems likely that, irrespective of the location of 2-AA in the bilayer, adequate water will be present, either in the ground state or during the excited-state lifetime, to result in saturation of the specific interactions shown in Figures 6.12 to 6.14. Under these conditions the solvent sensitivity of this fluorophore will be best represented by that region of Figure 6.13 where the concentration of the protic solvent is greater than 10–20%. Note that essentially equivalent slopes are found within this region for methanol, octanol and dioxane. These similar slopes indicate a similar mechanism, which is the general solvent effect.

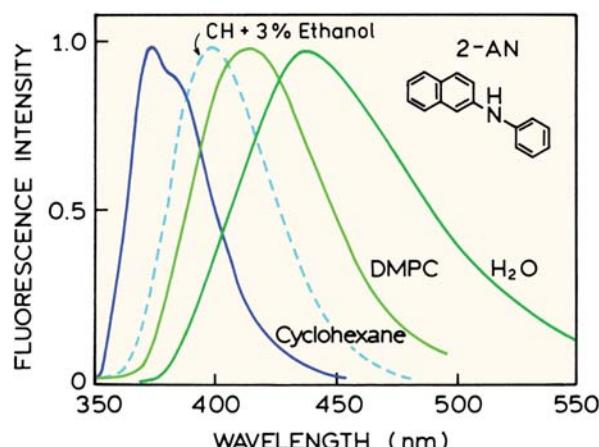


**Figure 6.16.** Normalized fluorescence emission spectra of 2-anilinonaphthalene in solvents and bound to vesicles of dimyristoyl-L- $\alpha$ -phosphatidylcholine (DMPC). The dashed line indicates the spectrum in cyclohexane (CH), which contains 3% ethanol. Revised from [39].

An understanding of specific and general solvent effects can provide a basis for interpreting the emission spectra of fluorophores that are bound to macromolecules. Consider the emission spectra of 2-anilinonaphthalene bound to membranes composed of dimyristoyl-L- $\alpha$ -phosphatidylcholine (DMPC).<sup>39</sup> The emission spectrum of 2-AN in DMPC is considerably red shifted relative to the emission in cyclohexane, but it is blue shifted relative to water (Figure 6.16). What is the polarity of the environment of 2-AN in the membranes? Interpretation of the emission maxima of these labeled membranes is also complicated by the time-dependent spectral shifts, a complication we will

ignore for the moment. We noted earlier (Figure 6.11) that 2-AN is highly sensitive to small concentrations of ethanol. It seems likely that cyclohexane containing more than 3% ethanol is the preferable reference solvent for a low polarity environment. This spectrum is indicated by the dashed line in Figure 6.16. In this solvent the specific effects are saturated. With this adjustment in mind, one may conclude that the environment in which the 2-AN is localized is mostly nonpolar, but that this site is accessible to water. Without consideration of specific solvent effects one might conclude that the 2-AN is in a more polar environment.

The fact that the hydrogen bonding interactions of 2-AN are saturated in membranes is supported by time-resolved data. The measurement and interpretation of such data will be described in Chapter 7. Figure 6.17 shows the time-dependent emission maxima of 2-AN bound to DMPC vesicles, and in glycerol and cyclohexane. Even at the shortest observable time of one nanosecond, the emission maximum of 2-AN-labeled membranes is similar to that found in the protic solvent glycerol. This initial value for the emission maximum is also comparable to the completely relaxed value found for 2-AN in cyclohexane which contains 0.1 M methanol. This final value can be regarded as that expected when the specific solvent effects are saturated. This result indicates that in membranes the specific interactions with water or other polar hydrogen bonding groups are saturated. These interactions may have occurred in the ground state, or on a subnanosecond timescale that is too rapid to be resolved in this particular experiment. In either event, it seems clear that the emission spectra of 2-AN bound to model membranes can be interpreted more reasonably when compared to reference solvents in which the specific solvent effects are saturated.

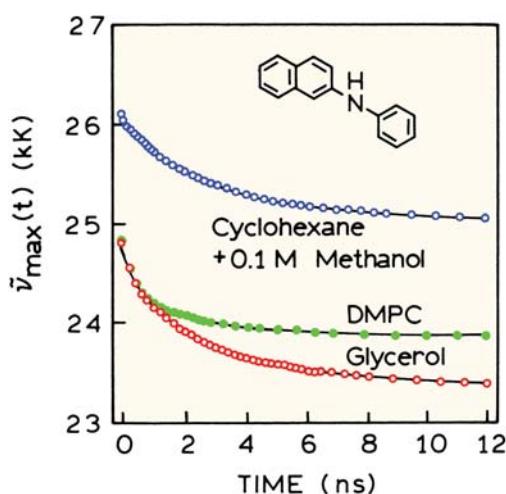


**Figure 6.17.** Time-resolved emission maxima of 2-anilinonaphthalene in DMPC vesicles and in solvents. Revised from [39].

#### 6.4. TEMPERATURE EFFECTS

In the preceding sections we assumed that solvent relaxation was complete prior to emission, which is true for fluid solvents. At low temperatures the solvent can become more viscous, and the time for solvent reorientation increases. This is illustrated schematically in Figure 6.18, which shows a simplified description of solvent relaxation. Upon excitation the fluorophore is assumed to be initially in the Franck-Condon state (F). Solvent relaxation proceeds with a rate  $k_S$ . If this rate is much slower than the decay rate ( $\gamma = 1/\tau$ ), then one expects to observe the emission spectrum of the unrelaxed F state. If solvent relaxation is much faster than the emission rate ( $k_S \gg \gamma$ ), then emission from the

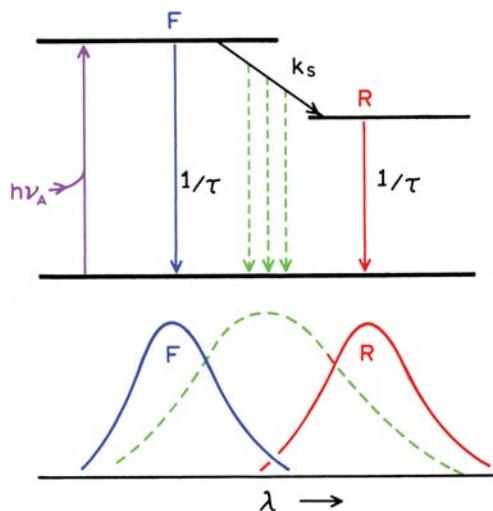


Figure 6.18. Jablonski diagram for solvent relaxation.

relaxed state (R) will be observed. At intermediate temperatures, where  $k_s \approx \gamma$ , emission and relaxation will occur simultaneously. Under these conditions an intermediate emission spectrum will be observed. Frequently this intermediate spectrum (—) is broader on the wavelength scale because of contributions from both the F and R states. Time-dependent spectral relaxation is described in more detail in Chapter 7.

Examples of temperature-dependent emission spectra are shown in Figure 6.19 for the neutral tryptophan derivative N-acetyl-L-tryptophanamide (NATA) in propylene glycol. Solvents such as propylene glycol, ethylene glycol, and glycerol are frequently used to study fluorescence at low temperature. These solvents are chosen because their viscosity increases gradually with decreasing temperature, and they do not crystallize. Instead they form a clear highly vis-

cous glass in which the fluorophores are immobilized. The presence of hydroxyl groups and alkyl chains makes these compounds good solvents for most fluorophores.

As the temperature of NATA in propylene glycol is decreased the emission spectrum shifts to shorter wavelengths<sup>40</sup> (Figure 6.19). This shift occurs because the decay rate of fluorophores is not very dependent on temperature, but the relaxation rate is strongly dependent on temperature. Hence, at low temperature, emission is observed from the unrelaxed F state. It is important to notice that the structured  $^1L_b$  (Chapter 16) emission of NATA is not seen even at the lowest temperature ( $-68^\circ\text{C}$ ). This is because the hydrogen bonding properties of propylene glycol persist at low temperature. It is clear that the temperature-dependent spectral shifts for NATA are due to the temperature dependence of the orientation polarizability  $\Delta f$ .

Another example of temperature-dependent spectra is provided by Patman (Figure 6.20).<sup>42</sup> This fluorophore is a lipid-like analogue of Prodan, which was developed to be a probe highly sensitive to solvent polarity.<sup>42</sup> The basic idea is that the amino and carbonyl groups serve as the electron donor and acceptor, respectively. In the excited state one expects a large dipole moment due to charge transfer (Figure 6.21), and thus a high sensitivity to solvent polarity. As the temperature of propylene glycol is decreased, the emission spectra of Patman shift dramatically to shorter wavelengths (Figure 6.20). The effects of low temperature are similar to those of low-polarity solvents. Because of the decreased rate of solvent motion, emission occurs from the unrelaxed state at low temperature.

## 6.5. PHASE TRANSITIONS IN MEMBRANES

Since its introduction as a solvent-sensitive probe, Prodan and its derivative have become widely used to label biomolecules.<sup>43–46</sup> Alkyl or fatty acid chains have been added to Prodan so that it localizes in membranes (Figure 6.22). Acrylodan is a derivative of Prodan that can be used to label sulphydryl groups in proteins. Prodan is highly sensitive to solvent polarity. Its emission maximum shifts from 410 nm in cyclohexane to 520 nm in polar solvents (Figure 6.23).<sup>47</sup> Prodan and its derivatives have been especially useful for studies of cell membranes and model membranes because of its high sensitivity to the phase state of the membranes.<sup>48–52</sup> DPPC vesicles have a phase transition temperature near  $37^\circ\text{C}$ . When Prodan is bound to DPPC vesicles the emission maximum shifts from 425 to 485 nm (Figure 6.24).

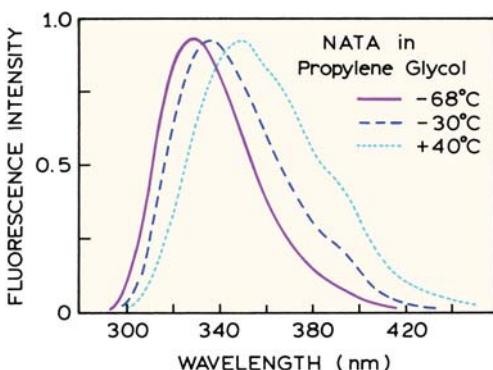
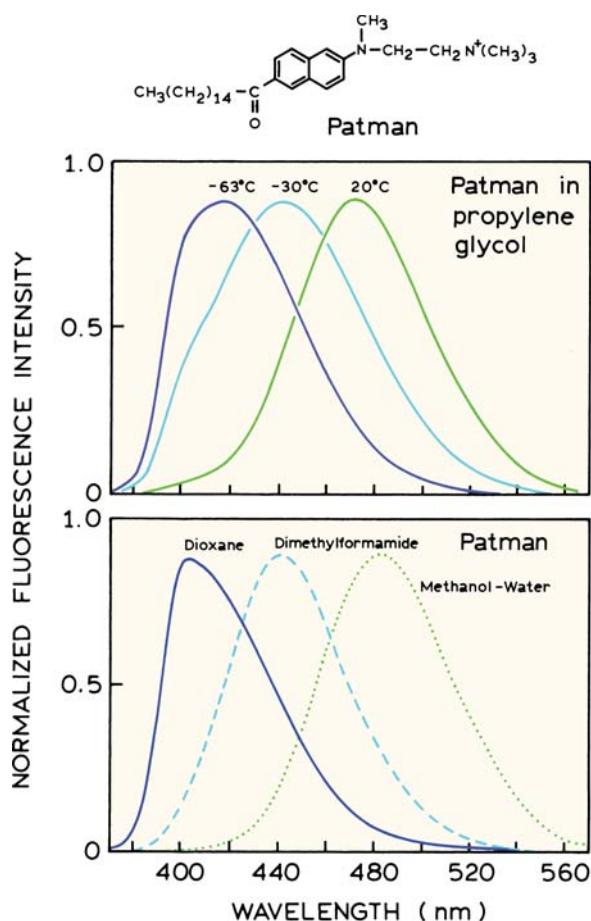
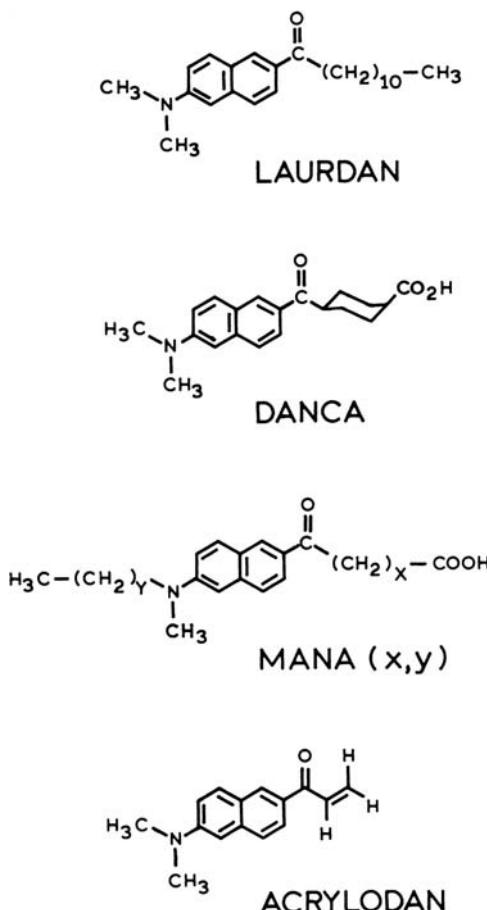


Figure 6.19. Emission spectra of N-acetyl-L-tryptophanamide (NATA) in propylene glycol. From [40].



**Figure 6.20.** Emission spectra of the lipid-like Prodan derivative Patman at various temperatures in propylene glycol (top) and in solvents of different polarities (bottom). Revised and reprinted from [41]. Copyright © 1983, American Chemical Society.

The large spectral shifts displayed by Prodan allowed its use in imaging the phase state of membranes.<sup>53–54</sup> When using fluorescence microscopy it is difficult to record the entire emission spectrum for each point in the image. The need for emission spectra was avoided by defining a wavelength-ratiometric parameter that represented the emission spectrum. This parameter is defined analogously to fluores-



**Figure 6.22.** Derivatives of Prodan.

cence polarization. This parameter was named the generalized polarization (GP) and is given by

$$GP = \frac{I_B - I_R}{I_B + I_R} \quad (6.20)$$

where  $I_B$  and  $I_R$  are the steady state intensities at a shorter blue (B) wavelength and a longer red (R) wavelength, respectively.

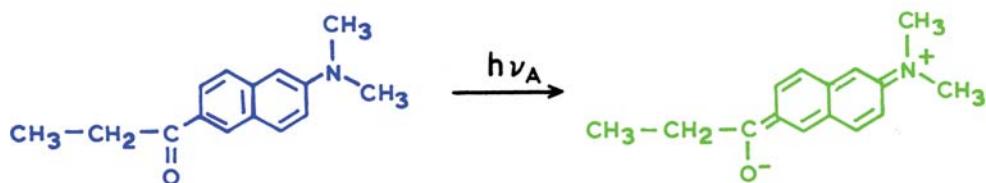


**Figure 6.21.** Charge separation in the excited state of Prodan (6-propionyl-2-(dimethylamino) naphthalene).

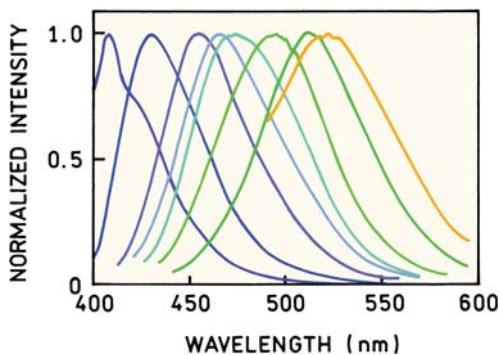


**Figure 6.23.** Emission spectra of Prodan in various solvents. From left to right the solvents are cyclohexane, toluene,  $\text{CH}_2\text{Cl}_2$ ,  $\text{CH}_3\text{CN}$ , DMSO, isopropanol, methanol, and  $\text{CF}_3\text{CH}_2\text{COOH}$ . Revised and reprinted with permission from [47]. Copyright © 2003, American Chemical Society.

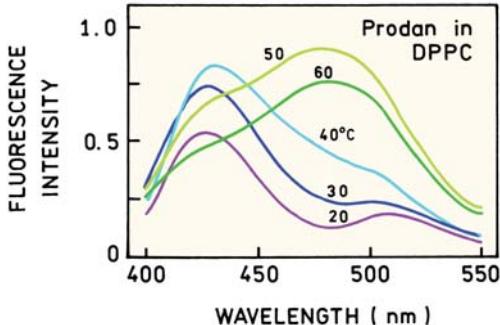


**Figure 6.24.** Emission spectra of Prodan in DPPC vesicles as a function of temperature. Revised from [50].

Giant unilamellar vesicles (GUVs) were formed from a mixture of DPPE and DPPC attached to Pt wires to hold them in position. The vesicles were labeled with the lipophilic probe Laurdan. Excitation was accomplished using a two-photon process, which eliminates out-of-focus fluorescence. Figure 6.25 shows the GP images of the vesicles at several temperatures. At  $40^\circ\text{C}$  the GP values are high (near 0.5) because the membrane is in the solid phase with more intense emission at short wavelengths. As the temperature is increased GP decreases and even becomes slightly negative due to the increased intensity at longer wavelengths.

In Figure 6.25 the phase state and GP values were rather constant throughout the GUV. However, real membranes are expected to be less homogeneous and to display rafts or domains that are either in the fluid or solid state. The sensitivity of Laurdan to the phase of the membrane allowed its use for imaging of domains in living cells. Fig-

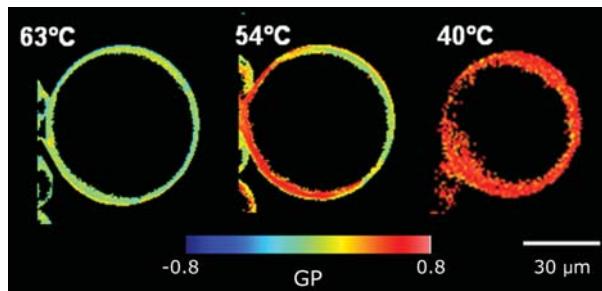


**Figure 6.25.** Generalized polarization of Laurdan in GUV of DPPE/DPPC 7:3 obtained with two-photon excitation at 780 nm. The blue and red intensities needed to calculate GP were measured through 46 nm wide bandpass filters centered at 446 and 499 nm, respectively. Reprinted from [53]. Courtesy of Dr. Luis Bagatolli.

ure 6.26 shows GP images of fibroblasts that were taken off the top of the cell (left) and from the region of the cell in contact with the glass slide (right). These images show regions of high GP, typically at protrusions of the membrane or points of contact with the glass slide. These results show how the spectroscopic studies of polarity effects can now be used for cellular imaging.

## 6.6. ADDITIONAL FACTORS THAT AFFECT EMISSION SPECTRA

### 6.6.1. Locally Excited and Internal Charge-Transfer States

Depending upon solvent polarity some fluorophores can display emission before or after charge separation. One example is shown in Figure 6.27. The initially excited state is called the locally excited (LE) state. In low-polarity solvents FPP emits at short wavelengths from the LE state (top

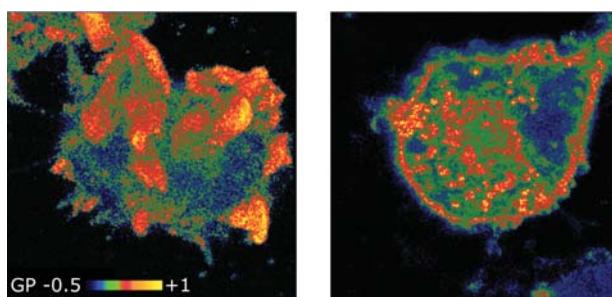


**Figure 6.26.** Generalized polarization of Laurdan in fibroblasts observed with two-photon excitation. The images were taken from above (left) and below (right) the glass slide. Reprinted from [54]. Courtesy of Dr. Katharina Gaus from the University of New South Wales, Australia.

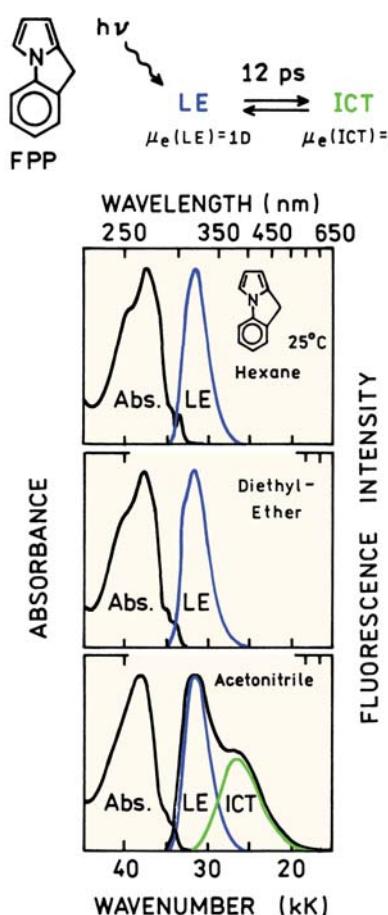


**Figure 6.27.** Emission spectra of FPP in several solvents. Revised and reprinted with permission from [55]. Copyright © 2004, American Chemical Society.

two panels). As the solvent polarity increases a new longer wavelength emission appears. This longer-wavelength emission (lower panel) is due to an internal charge-transfer (ICT) state, which forms rapidly following excitation. In this case the two ends of the fluorophore are held rigidly by the methylene bridge, so that formation of the ICT state does not depend on the twisting. There have been a large number of papers on conformational changes in the excited-state fluorophore to form a twisted internal charge transfer (TICT) state in a variety of molecules. There seems to be a lack of agreement on the need for twisting. To avoid stating an opinion on this topic, we will simply refer to such states as ICT states.

Another example of LE and ICT emission is given by Laurdan.<sup>56</sup> Part of the large spectral shift displayed by Laurdan is due to emission from the locally excited state (LE), which occurs near 400 nm, as well as from an ICT state emitting at longer wavelengths. A hint of this behavior was seen in Figure 6.20 (top), where at -30°C a shoulder appeared on the short-wavelength side of the Patman emission. Such changes in spectral shape often indicate the presence of another state. This new blue-emitting state was more easily seen in ethanol at low temperatures (Figure 6.28). As the temperature is decreased the emission maximum shifts from about 490 to 455 nm. As the temperature is lowered to -190°C a new emission appears with a maximum near 420 nm.

Although solvent relaxation usually proceeds faster at higher temperatures, high temperature can also prevent the alignment of solvent dipoles. This effect can also prevent

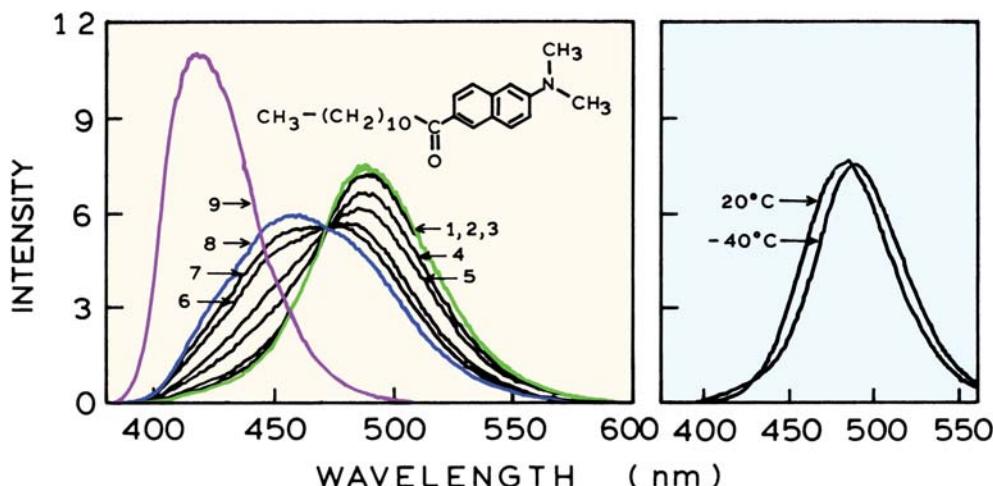


**Figure 6.28.** Emission spectra of Laurdan in ethanol at -50°C (1), -60°C (2), -70°C (3), -80°C (4), -85°C (5), -90°C (6), -100°C (7), -110°C (8), and -190°C (9). The panel on the right compares the emission spectra of Laurdan at -40 and 20°C. Revised from [56].

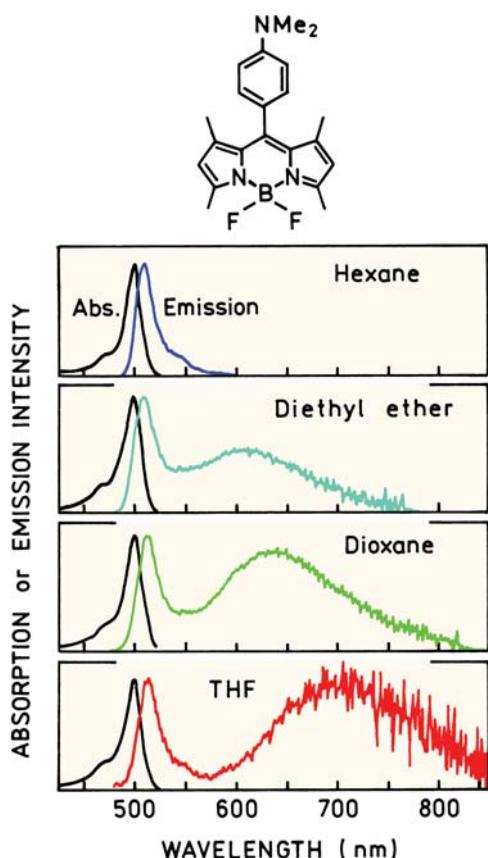


**Figure 6.29.** Emission spectra of a dimethylamino-substituted Bodipy probe. Tetrahydrofuran (THF). Revised and reprinted with permission from [67]. Copyright © 1998, American Chemical Society.

the alignment of solvent dipoles. This effect is seen for Laurdan in ethanol at 20°C (Figure 6.28, right). This emission spectrum is blue-shifted relative to the emission spectrum in ethanol at -40°C. In general, the most pronounced red shifts occur at temperatures at which the solvent is fluid enough to reorient prior to fluorescence emission but thermal energy is not so great as to disrupt these orientations.

The unusual temperature-dependent spectra displayed by Laurdan were explained by the presence of emission from the locally excited (LE) state and from the internal charge-transfer (ICT) state. In the LE state the excitation is localized on the naphthalene ring, so that the molecule is not very polar. In this LE state the amino and carbonyl groups are not part of the delocalized electron system. At higher temperature the ICT state forms, with complete charge transfer from the amino group to the carbonyl group. Some authors propose that twisting of the dimethyl amino group is required to allow the nitrogen electrons to be in

conjugation with the naphthalene ring.<sup>57–58</sup> Hence, the large spectral shift displayed by Prodan-like molecules is somewhat misleading. Part of the shift from 420 to 455 nm is due to formation of the TICT state. The remaining shift from 455 to 490 nm is due to the orientation polarizability ( $\Delta f$ ) of the solvent. Prodan is just one example of a large number of molecules that display ICT emission.<sup>59–66</sup>

Formation of ICT states can also occur with some of the more recently developed fluorophores. Figure 6.29 shows the emission spectra of a Bodipy fluorophore that has been substituted with a dimethylamino group.<sup>67</sup> In a low-polarity solvent the usual narrow Bodipy emission is seen with a small Stokes shift. In slightly more polar solvents a new longer wavelength emission is seen that is due to an ICT state. The important point from these examples is that the spectral shifts due to formation of ICT states are not explained by the Lippert equation. Instead of polarity, the appearance of the ICT emission depends on the electron-donating and -accepting properties of groups within or attached to the fluorophore.

### 6.6.2. Excited-State Intramolecular Proton Transfer (ESIPT)

The formation of ICT states indicates that the electron distribution can be different for a fluorophore in the ground or excited states. This can result in changes of ionization in the excited state. One example is intramolecular proton transfer in the excited state, which is referred to as ESIPT. This is shown in the top schematic in Figure 6.30, for the probe FA.<sup>70</sup> This probe can exist in the normal form (N) or as a tautomer (T). The process of ESIPT can be very rapid because the transferring proton is already next to the proton acceptor at the moment of excitation.

Figure 6.30 shows the emission spectra of FA when dissolved in two nonpolar solvents and when in aqueous solution but bound to BSA. The emission near 525 nm is the N\* form, and the emission near 625 nm is the T\* form. FA exhibits very low fluorescence in water, but it is highly fluorescent when bound to BSA. This high intensity and the similar intensities of the N\* and T\* forms indicate that FA is in a highly nonpolar environment when bound to BSA. The relative intensities of the N\* and T\* emission can be expected to be dependent on the detailed charge and polarity surrounding the fluorophore, as well as its extent of exposure to the aqueous phase. ESIPT occurs in a variety of other fluorophores.<sup>68–77</sup>

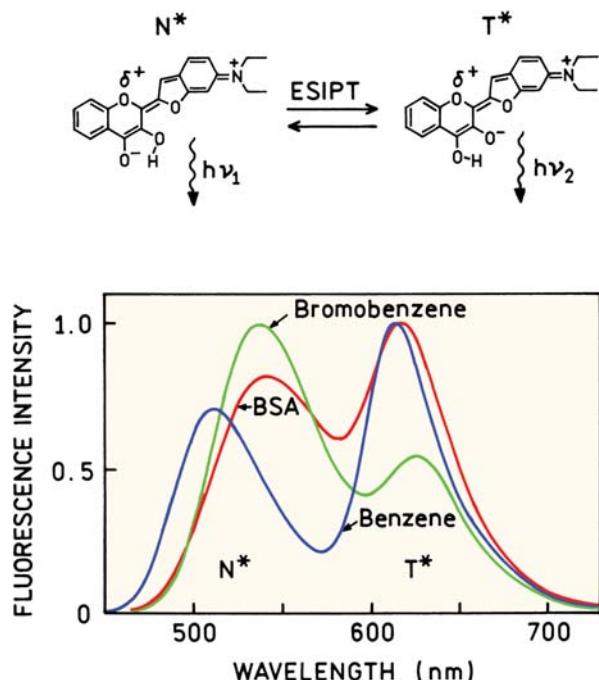


**Figure 6.30.** Emission spectra of FA that undergoes ESIPT. Revised from [70].

### 6.6.3. Changes in the Non-Radiative Decay Rates

In the previous example the probe FA displayed a very low quantum yield in water but a high quantum yield when bound to BSA. Increases in quantum yield are frequently observed when fluorophores bind to biomolecules. These changes are due to solvent or environmental effects, but these changes are not explained by the Lippert equation. It seems reasonable to suggest that changes in quantum yield are due to changes in the rates of non-radiative decay ( $k_{nr}$ ). This suggestion is correct, and changes in  $k_{nr}$  have been observed for a variety of fluorophores. One example is coumarin-151 (C151), which is highly sensitive to solvent polarity.<sup>78</sup> Figure 6.31 shows the Stokes shift and quantum yields for C151 in solvents ranging from 2-methylpentane ( $\Delta f = 0$ ) to methanol ( $\Delta f = 0.309$ ). The Stokes shift increases in a stepwise manner upon addition of the polar solvent dioxane, even though the value of  $\Delta f$  is almost unchanged. The quantum yield is low in nonpolar solvents and also increases stepwise when the solvent contains a polar additive. Since the excitation coefficient and radiative decay rates are usually not very sensitive to solvent polarity, the decrease in quantum yield suggests an increase in  $k_{nr}$  in nonpolar solvents. The values of the radiative ( $\Gamma$ ) and non-

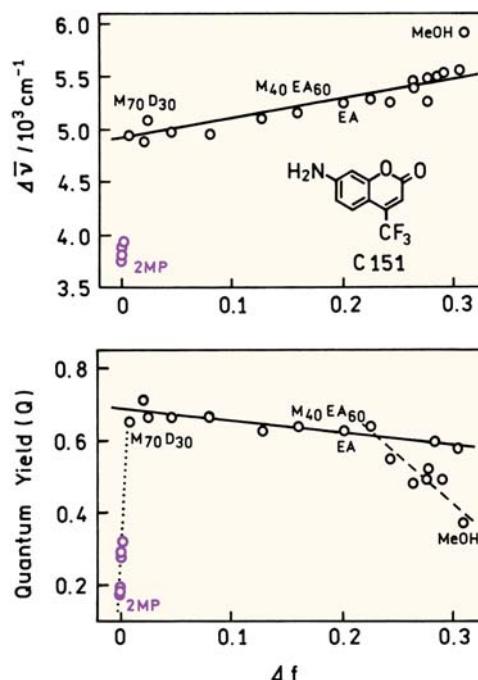


**Figure 6.31.** Stokes shifts and quantum yields for Coumarin-151 in various solvents. 2-MP, 2-methylpentane; M<sub>70</sub>D<sub>30</sub>, 70% 2-MP and 30% dioxane (D); M<sub>60</sub>EA<sub>40</sub>, 60%, 2 MP and 40% EA, ethyl acetate; MeOH, methanol. The composition of the solvents is only listed for several of the mixtures. Revised and reprinted with permission from [78]. Copyright © 2001, American Chemical Society.

radiative ( $k_{nr}$ ) decay rates can be calculated using the measured quantum yields ( $Q$ ) and lifetimes ( $\tau$ ). These rate constants are given by

$$k_{nr} = (1 - Q)/\Gamma \quad (6.21)$$

$$G = Q/\Gamma \quad (6.22)$$

Figure 6.32 shows the lifetimes of C151 and the calculated rate constants. As expected  $\Gamma$  (○) is mostly independent of solvent polarity. The value of  $k_{nr}$  (●) increases dramatically in low-polarity solvents. The authors attribute the increased value of  $k_{nr}$  in nonpolar solvents to rotation of the amino group, which provides a rapid deactivation pathway to the ground state. In more polar solvents an ICT state is formed, which causes the larger Stokes shift. In this ICT state, rotation of the amino group is restricted and  $k_{nr}$  is smaller. The purpose of this example is not to explain the detailed photophysics of C151, but rather to show how the chemical structures of the fluorophore and the solvent can

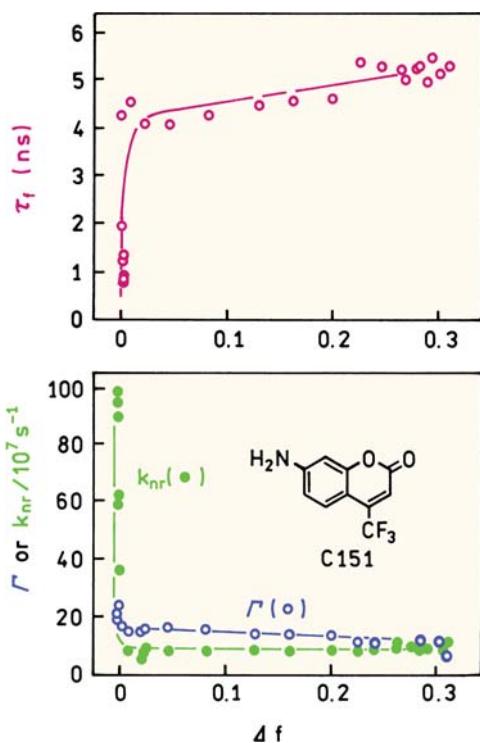


**Figure 6.32.** Lifetimes, radiative, and non-radiative decay rates for C151 in various solvents. Revised and reprinted with permission from [78]. Copyright © 2001, American Chemical Society.

result in specific interactions that affect the emission maxima and quantum yields of fluorophores.

#### 6.6.4. Changes in the Rate of Radiative Decay

In the previous example the quantum yield of C151 decreases in low-polarity solvents. A more typical situation is an increase in quantum yield in low-polarity solvents, which is illustrated by the probe neutral red (NR).<sup>79</sup> For this probe the Lippert plot is biphasic and shows a larger slope for high-polarity solvents ( $\Delta f > 0.35$  in Figure 6.33). This behavior is explained by formation of an ICT state in high-polarity solvents, and emission from an LE state in lower-polarity solvents. The slopes of the Lippert plots for NR are consistent with excited-state dipole moments of 4.8D for the LE state and 17.5D for the ICT state. There appears to be a decrease in the radiative decay rate in the higher-polarity solvents. Such a decrease in  $\Gamma$  is possible because the ICT emission is from a different electronic state than the LE emission.

The spectral properties of NR can be understood by considering the energy of the LE and ICT states in solvents

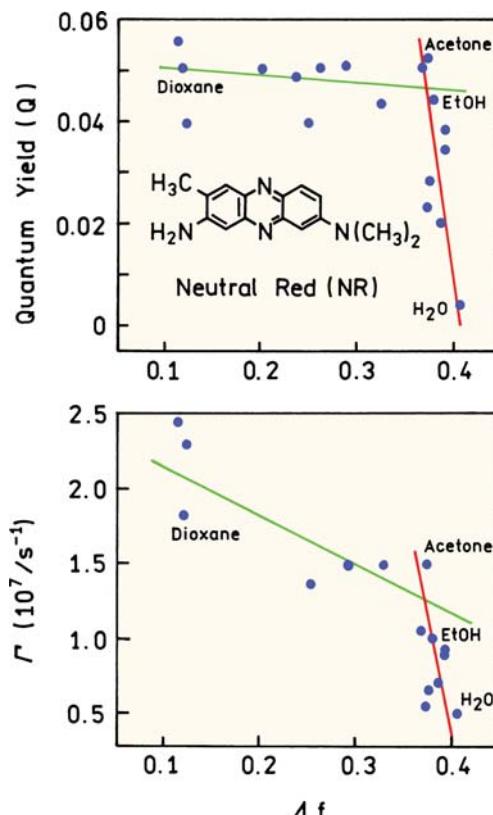


**Figure 6.33.** Quantum yields and radiative decay rates of Neutral Red in various solvents. Revised from [79].

of different polarity (Figure 6.34). In low-polarity solvents the LE state has a lower energy. In higher-polarity solvents the ICT state is stabilized by interaction with the solvent and thus becomes the emitting species. These examples of C151 and NR show that no single model or interaction can explain the diverse spectral properties displayed by fluorophores in various environments.

#### 6.7. EFFECTS OF VISCOSITY

Viscosity can have a dramatic effect on the emission intensity of fluorophores. Perhaps the best-known example is trans-stilbene. The intensity decays of stilbene (Figure 6.35) are strongly dependent on temperature.<sup>80</sup> This effect has been interpreted as due to rotation about the central ethylene double bond in the excited state (Figure 6.36).<sup>81–82</sup> In the ground state there is a large energy barrier to rotation about this bond. The energy barrier is much smaller in the excited state. Rotation about this bond occurs in about 70 ps, providing a return path to the ground state. Rotation of

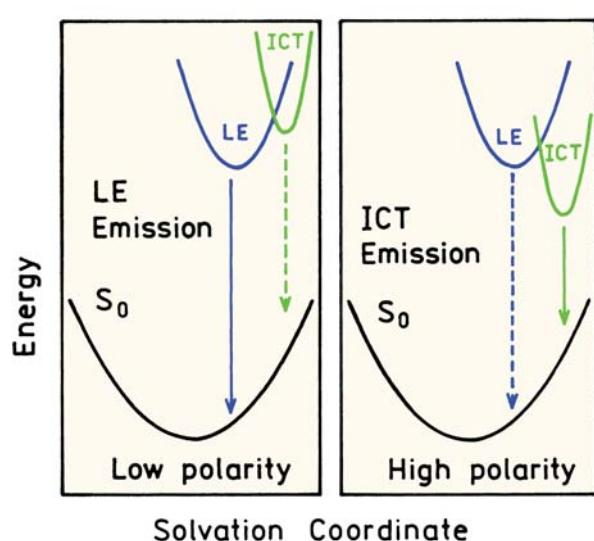


**Figure 6.34.** Effect of solvent polarity on the energies of LE and ICT states. Revised from [79].

cis-stilbene is even more rapid, resulting in very short fluorescence lifetime. Such rotations in the excited state are thought to affect the emission of many other fluorophores.<sup>83</sup>

Increase in local viscosity contributes to the increased intensities displayed by many fluorophores when bound to biomolecules. In Chapter 1 we mentioned the viscosity probe CCVJ, which displayed increases in quantum yield with increases in viscosity. Figure 6.37 shows the emission intensities of this probe when bound to an antibody directed against this probe.<sup>84</sup> Binding of CCVJ to the antibody prevents rotation around the ethylene bond and increases the quantum yield.

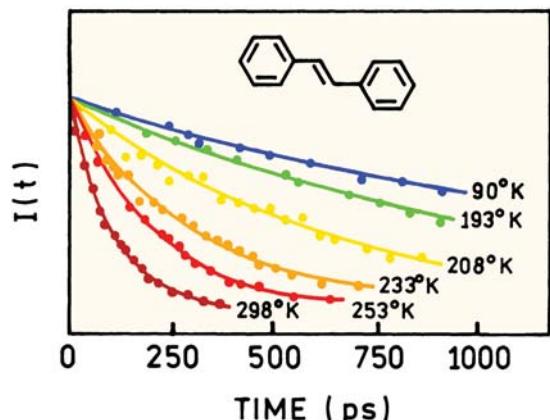


**Figure 6.35.** Intensity decays of trans-stilbene in methylcyclohexane: isooctane (3:2). Revised from [80].

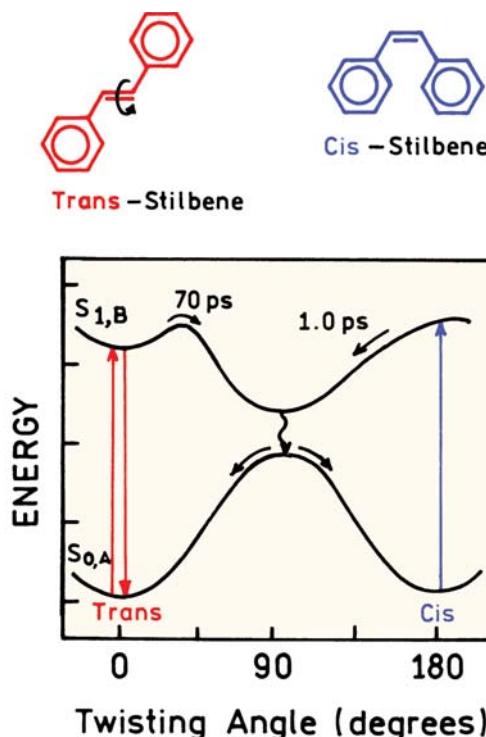


**Figure 6.36.** Excited-state isomerization of stilbene. From [81].

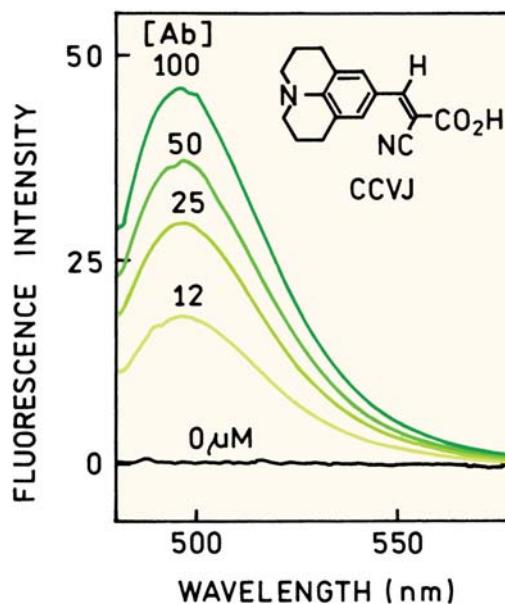


**Figure 6.37.** Effect of anti-CCVJ antibody on the emission of CCVJ. Antibody concentrations are shown in  $\mu\text{M}$ . Revised and reprinted with permission from [84]. Copyright © 1993, American Chemical Society.

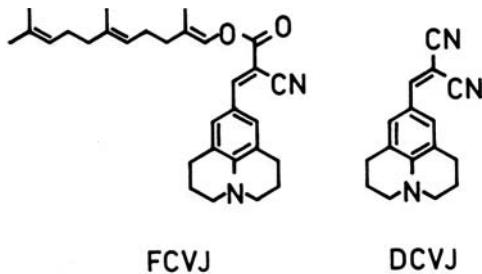
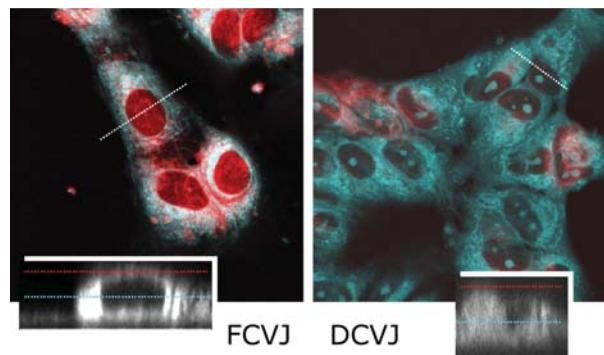


**Figure 6.38.** Chemical structures of viscosity-sensitive fluorophores. The carbon chain on the left is a farnesol group. Revised from [86].



### 6.7.1. Effect of Shear Stress on Membrane Viscosity

The viscosity of some membranes are thought to be sensitive to the shear stresses created by fluid flow.<sup>85</sup> This possibility was tested using the viscosity probes shown in Figure 6.38. DCVJ was expected to be more water soluble and FCVJ was expected to label cell membranes. The locations of these probes in human epidermal cells were determined by recording images at various heights in the cells (*z*-axis sectioning). Figure 6.39 shows pseudocolor images of the labeled cells. Blue indicates images recorded in a plane passing through the center of the cells and thus staining of the cytoplasm. Red indicates images recorded in a plane across the top of the cells, and thus staining of the plasma membrane. These images show that FCVJ localizes primarily in the plasma membrane (left) and that DCVJ localizes primarily in the cytoplasm.

The fluorescence intensities of DCVJ and FCVJ were examined as the epidermal cells were subjected to shear stress. For DCVJ, which was localized in the cytoplasm, there was no change in intensity (Figure 6.39, lower panel). For FCVJ, which bound to the plasma membrane, there was a large drop in intensity in response to shear stress. The reversibility of the changes with elimination of fluid flow showed that the probes were not being washed out of the cells, indicating a decrease in viscosity. These viscosity-dependent probes thus provide an optical means to follow changes in the microviscosity of cell membranes in response to stimuli.

### 6.8. PROBE-PROBE INTERACTIONS

In addition to interacting with solvents, fluorophores can interact with each other. One example is excimer formation due to an excited-state complex of two identical fluorophores. Excimer formation is a short-range interaction

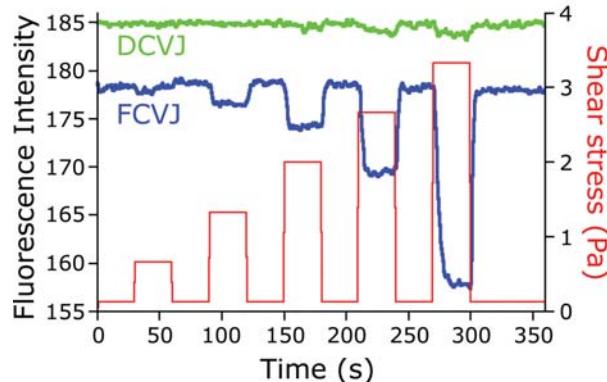


**Figure 6.39.** Pseudocolor images of human epidermal cells stained with FCVJ or DCVJ. In the images red indicates labeling of the cell membrane and blue indicates labeling of the cytoplasm. The red and blue lines on the inserts indicate the *z*-level of the images. The lower panel shows the effect of shear stress on the intensities of cells labeled with FCVJ or DCVJ. Revised from [86]. Courtesy of Dr. Emmanuel Theodorakis from the University of California, San Diego.

that requires molecular contact between the fluorophore. In Chapter 1 we described excimer formation by pyrene as a means to measure diffusion in membranes.

Excimer formation is beginning to find use in biotechnology. Figure 6.40 shows the use of excimer formation to detect an insertion mutation in DNA.<sup>87-88</sup> A DNA oligomer was synthesized that contained two nearby pyrene residues. The sequence of this probe was mostly complementary to the target sequence, except for the region near the pyrene groups. When bound to the wild-type (WT) sequence, one of the pyrenes intercalated into the double helix and the second remained outside the double helix. Since the pyrenes were not in contact there was no excimer emission. This probe DNA was then hybridized with a insertion mutant (IM) sequence that contained an extra base. This base prevented the pyrene from intercalating into the double helix, resulting in a blue emission from the excimer.

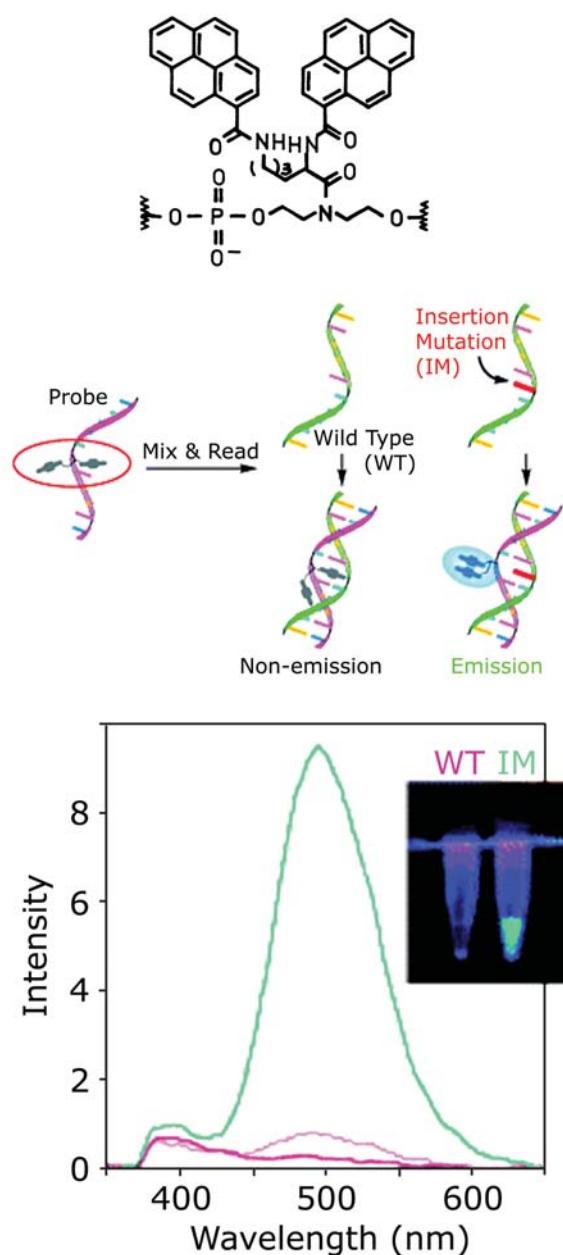


**Figure 6.40.** Use of excimer formation for detection of a DNA insertion mutation. Top: structure of the probe oligonucleotide. Middle: schematic of the hybridization reaction. Bottom: emission spectra of the probe bound to the wild-type (WT) sequence or the insertion mutation (IM) sequence. Revised and reprinted with permission from [87]. Copyright © 2004, American Chemical Society.

Excimer formation is also finding use in nanotechnology, in particular for following self-assembly processes. Derivatives of perylene were found to self-associate.<sup>89</sup> The extent of self-association depends on the solvent and the starting concentrations of the fluorophore (Figure 6.41,

top). Different starting concentrations could be used to obtain a wide range of emission colors (bottom). One can imagine such complexes being used for organic multicolor displays using just a single type of fluorophore.

## 6.9. BIOCHEMICAL APPLICATIONS OF ENVIRONMENT-SENSITIVE FLUOROPHORES

The use of probes sensitive to this local environment has a long history in biochemical research. We now describe a few examples to illustrate the diversity of these applications.

### 6.9.1. Fatty-Acid-Binding Proteins

Fatty acids are a significant source of energy. In blood the fatty acids are usually transported bound to serum albumin. In cells the fatty acids are transported by fatty-acid-binding proteins (FABPs), which are a family of small proteins ( $\approx 15$  kDa) with a variety of amino-acid sequences. Since fatty acids are spectroscopically silent, their association with FABPs is not easily measured.

The problem of detecting fatty acid binding was solved using FABP labeled with acrylodan.<sup>90–94</sup> The structure of acrylodan is shown in Figure 6.22. In the absence of added fatty acid the emission spectrum of acrylodan is blue shifted, indicating a nonpolar environment. Titration of the labeled FABP with fatty acid resulted in a progressive red shift of the emission spectrum (Figure 6.42). Apparently, bound fatty acid displaces this probe from its hydrophobic binding site into the aqueous phase. Displacement of the acrylodan residue from the hydrophobic pocket was supported by a decrease in anisotropy from 0.32 to 0.15 in the presence of bound fatty acid. The spectral shifts were also used to provide a method to measure the concentration of free fatty acids in clinical samples.<sup>95–96</sup>

### 6.9.2. Exposure of a Hydrophobic Surface on Calmodulin

Calmodulin is involved in calcium signaling and the activation of intracellular enzymes. In the presence of calcium calmodulin exposes a hydrophobic surface, which can interact with other proteins. This surface can also bind hydrophobic probes. Calmodulin was mixed with one of three different probes: 9-anthroxycholine (9-AC), 8-anilino-1-naphthalenesulfonate (ANS), or N-phenyl-1-naphthylamine (NPN).<sup>97</sup> In aqueous solution, these probes are all

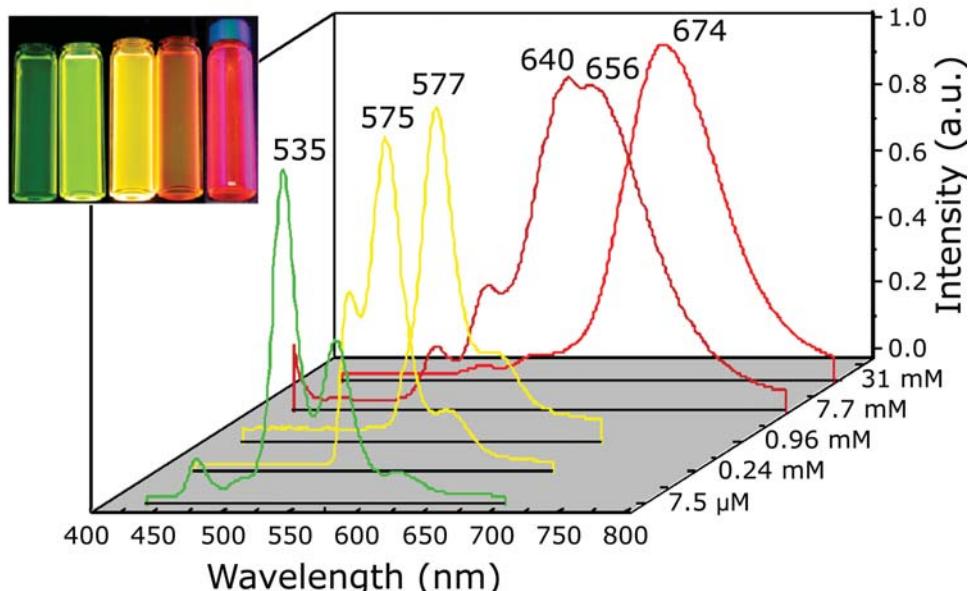
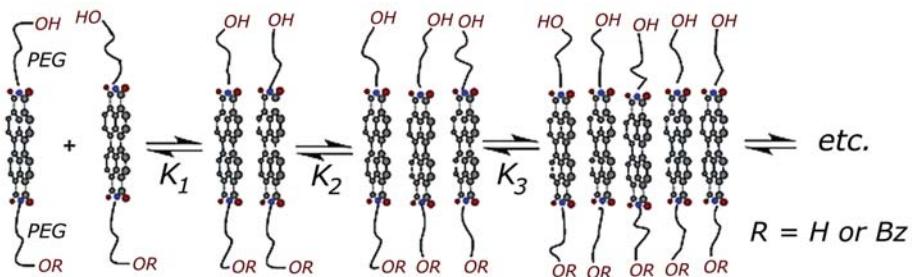


**Figure 6.41.** Excimer formation by a self-assembled perylene diimide derivative. Revised and reprinted with permission from [89]. Copyright © 2003, American Chemical Society. Courtesy of Dr. Alex D. Q. Li from the Washington State University.

weakly fluorescent in the absence of protein (Figure 6.43). Addition of calmodulin, without calcium, had only a minor effect on the emission. Addition of calcium to calmodulin resulted in a dramatic increase in the intensity of the three probes. Since the effect was seen with neutral (NPN), negatively charged (ANS), and partially charged (9-AC) probes, the binding was interpreted as due to hydrophobic rather than electrostatic interactions between the probe and calmodulin.

### 6.9.3. Binding to Cyclodextrin Using a Dansyl Probe

While there are numerous examples of proteins labeled with fluorescent probes, relatively few studies are available using labeled carbohydrates.<sup>98–99</sup> The solvent sensitivity of

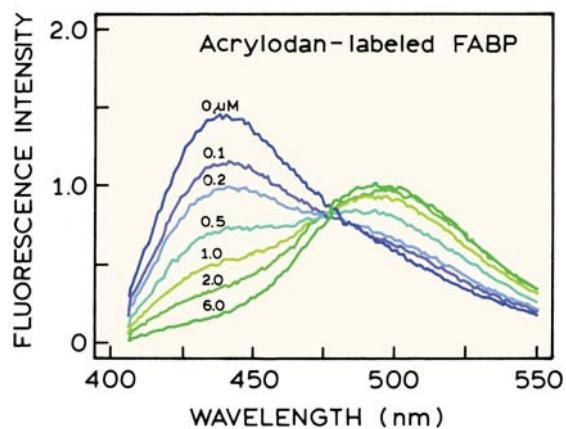


**Figure 6.42.** Emission spectra of acrylodan-labeled fatty acid binding protein (FABP). The numbers refer to the concentration in  $\mu\text{M}$  of fatty acid (oleate) added to  $0.2\text{-}\mu\text{M}$  FABP. Revised from [90].

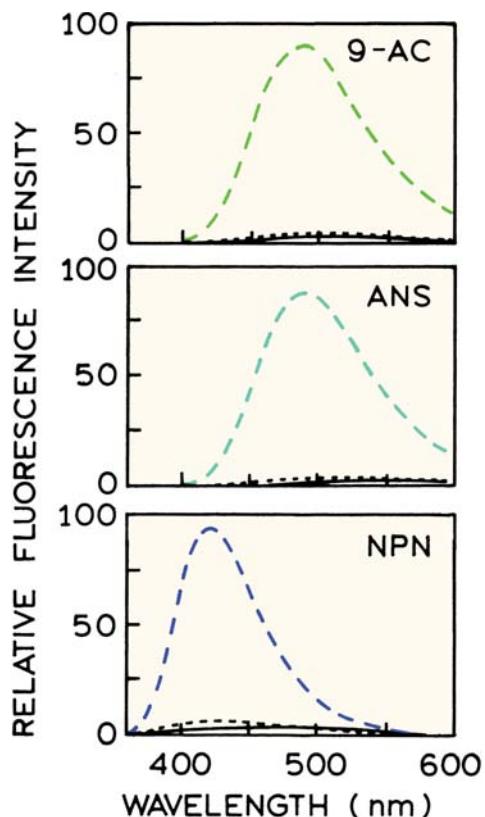


**Figure 6.43.** Emission spectra of 9-AC, ANS and NPN in aqueous buffer (—), in the presence of calmodulin (---), and in the presence of calmodulin plus calcium (— · —). Revised and reprinted with permission from [97]. Copyright © 1980, American Chemical Society.

the dansyl probes have been used to study the binding of organic molecules to cyclodextrins.<sup>98</sup> Cyclodextrins are cyclic sugars. The interior surface of cyclodextrin is hydrophobic, and can bind appropriately sized molecules.

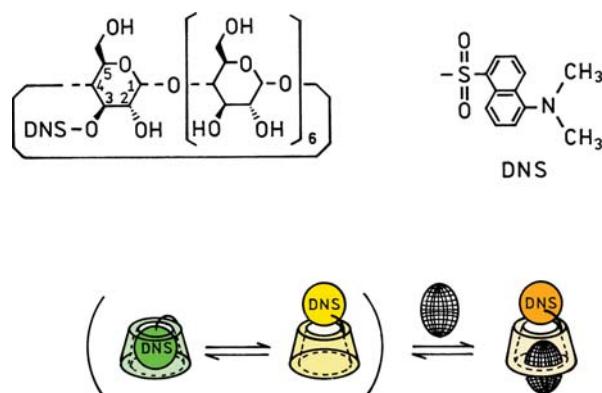


**Figure 6.44.** Dansyl-labeled cyclodextrin. Also shown is a schematic of the effects of 1-adamantanol (black balls) on the location of the DNS group. Revised from [98].

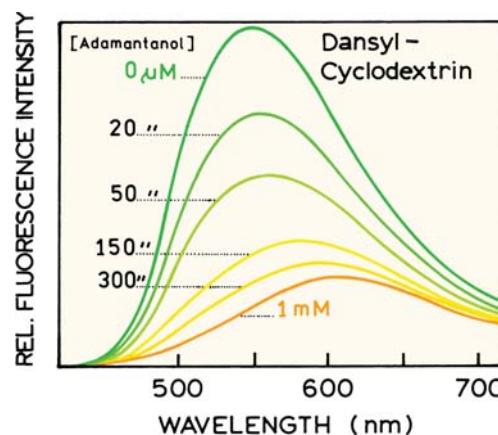


**Figure 6.45.** Emission spectra of dansyl-cyclodextrin with increasing concentrations of 1-adamantanol. Probe concentrations = 10 M. Revised from [98].

Carbohydrates are not fluorescent. In order to obtain a signal cyclodextrin was labeled with the dansyl group (Figure 6.44). The labeled cyclodextrin was titrated with 1-adamantanone, which resulted in a decrease in fluorescence intensity and a red shift in the emission spectra (Figure 6.45). In the absence of 1-adamantanone the dansyl group binds in the cyclodextrin cavity, resulting in a blue-shifted and enhanced emission. Addition of 1-adamantanone displaces the dansyl group, resulting in greater exposure to the aqueous phase and a red shift in the emission spectra.

## 6.10. ADVANCED SOLVENT SENSITIVE PROBES

The increased understanding of solvent effects and formation of ICT states has resulted in the development of additional fluorophores that are highly sensitive to solvent polarity.<sup>100–102</sup> These probes are based on 2,5-diphenyloxazole (DPO), which is a well-known scintillator. DPO is soluble mostly in organic solvents, where it displays a high quantum yield. By itself, DPO would not be very sensitive to solvent polarity. Solvent sensitivity was engineered into DPO by the addition of electron donor and acceptor groups (Figure 6.46). The top compound is DPO. In the lower structures the DPO is modified to contain an electron donor, acceptor, or both groups.

Absorption and emission spectra of these four DPO derivatives are shown in Figures 6.47 and 6.48. In methanol, DPO displays structured absorption and emission spectra, with only a small Stokes shift. Addition of the sulfonylic acid group alone results in a modest red shift. A larger red shift is observed upon addition of the dimethylamino



**Figure 6.46.** Derivatives of 2,5-diphenyloxazole (DPO, A) with donor and acceptor groups (B–D). Revised from [101].

group. The most dramatic shift was found when both electron-donating and -accepting groups were present on the DPO. By addition of both groups the absorption maxima is shifted to more convenient wavelengths near 380 nm, and the emission is shifted to 600 nm. The absence of vibronic structure suggests that the long-wavelength emission is due to an ICT state.

Based on these model compounds, reactive forms of dyes have been prepared, and are called Dapoxyl probes.<sup>102</sup> These probes are highly sensitive to solvent polarity (Figure 6.49). A structured emission is seen in hexane, which disappears in more polar solvents, suggesting that these dyes form ICT states. These dyes are more sensitive to solvent

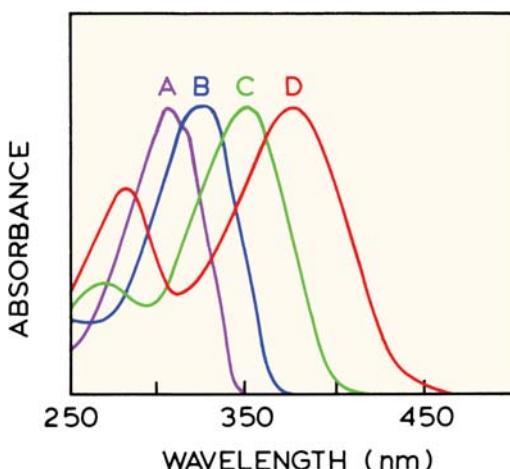


**Figure 6.47.** Absorption spectra of the DPO derivatives shown in Figure 6.46. The absorption spectra are normalized. From [101].

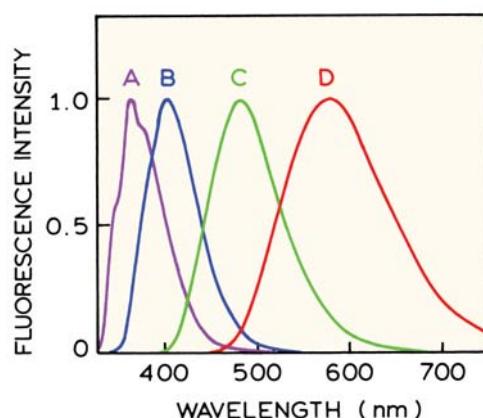


**Figure 6.48.** Emission spectra of the DPO derivatives shown in Figure 6.46 in methanol. The spectra were normalized. From [101].

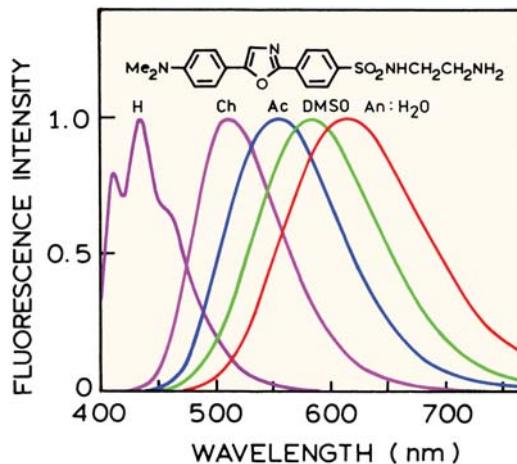


**Figure 6.49.** Emission spectra of the Dapoxyl SEDA (dapoxyl sulfonyl ethylenediamine) in solvents of increasing polarity, from left to right, hexane (H), chloroform (Ch), acetone (Ac), 1 dimethylsulfoxide (DMSO), and acetonitrile–water (Ac:H<sub>2</sub>O, 1:1, vol/vol). From [101].

than other presently used fluorophores (Table 6.3), and they also display usefully high extinction coefficients. In future years one can expect to see increased use of such dyes designed to display large Stokes shifts.

## 6.11. EFFECTS OF SOLVENT MIXTURES

**Advanced Topic**

In Section 6.3 we described the phenomena of specific solvent effects, in which small amounts of a polar solvent result in dramatic shifts of the emission spectra. The presence of such effects suggests the presence of a distribution of fluorophores, each with a somewhat different solvent

**Table 6.3.** Spectral Properties of Well-Known Solvent Sensitive Probes

Probe <sup>a</sup>	$\lambda_{\text{abs}}$ (nm) ( $\epsilon$ , M <sup>-1</sup> cm <sup>-1</sup> )	$\lambda_{\text{F}}$ (nm) in MeOH	$\lambda_{\text{F}}$ (nm) in CHCl <sub>3</sub>	$\Delta\lambda_{\text{F}}$ (nm)
Dapoxyl SEDA	373 (28 000)	584	509	75 <sup>b</sup>
Dansyl EDA	335 (4600)	526	499	27
ADMAN	360 (15 000)	499	440	59
Prodan	361 (16 000)	498	440	58
1,8-ANS	372 (7800)	480	490	-10
2,6-ANS	319 (27 000)	422	410	12
7-Ethoxycoumarin	324 (11 000)	399	385	14 <sup>b</sup>

<sup>a</sup>Dapoxyl SEDA, dapoxyl sulfonyl ethylenediamine; Dansyl EDA, dansyl ethylenediamine; ADMAN, 6-acetyl-2-dimethylaminonaphthalene; Prodan, 6-propionyl-2-dimethylaminonaphthalene; 1,8-ANS, 8-anilinonaphthalene-1-sulfonic acid; 2,6-ANS, 6-anilinonaphthalene-2-sulfonic acid. From [101].

<sup>b</sup>This value was calculated from  $\lambda_{\text{F}}$  (in MeOH) –  $\lambda_{\text{F}}$  (in CHCl<sub>3</sub>), which may have been listed incorrectly in [101].

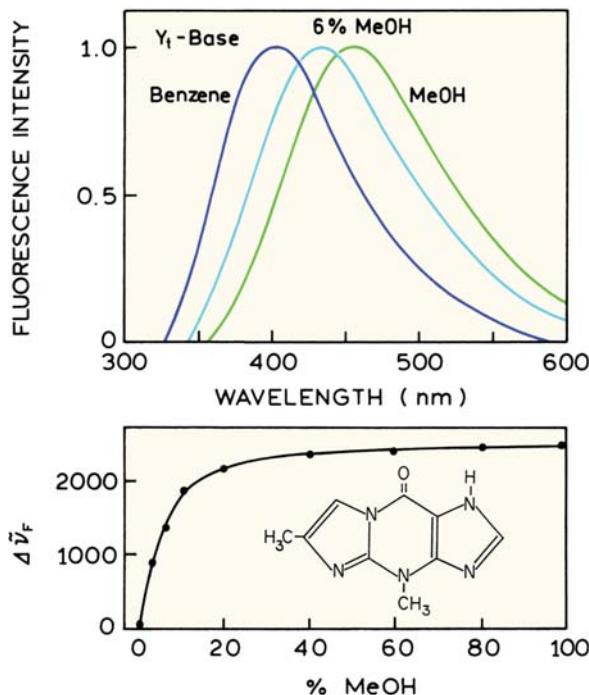


**Figure 6.50.** Emission spectra of Yt-base in benzene, benzene with 6% methanol, and in methanol. Lower panel, dependence of the spectral shift on the percentage of methanol in benzene. From [105].

shell. Such a distribution of environments can result in complex intensity decays.

The effect of a solvent mixture on an intensity decay is illustrated by Yt-base, which is highly sensitive to solvent polarity.<sup>103–105</sup> The emission maximum of Yt-base shifts from 405 nm in benzene to 455 nm in methanol (Figure 6.50). Addition of only 6% methanol, which does not dramatically change the orientation polarizability  $\Delta f$ , results in a large shift of the emission maximum to 430 nm. A large

spectral shift for a small change in the composition of the solvent usually indicates specific solvent effects.

Solvent mixtures provide a natural situation where one can expect a complex intensity decay, or a distribution of lifetimes. The intensity decay of Yt-base in pure benzene or methanol is mostly a single exponential (Table 6.4). However, the decay times are different in each solvent, so that one can expect a more complex decay in a benzene–methanol mixture. In fact, a more heterogeneous intensity decay was observed in benzene with 6% methanol than in either pure solvent. This can be seen by the elevated value of  $\chi_R^2$  for the single-decay-time fit for the intensity decay of Yt-base with 6% methanol (Table 6.4). Use of the double-exponential model reduces  $\chi_R^2$  from 8.9 to 1.2.

While the intensity decays of Yt-base could be fit using a two-decay-time model, it seems unlikely that there would be only two decay times in a solvent mixture. Since the solvent mixture provides a distribution of environments for the fluorophores, one expects the intensity decay to display a distribution of lifetimes. The frequency response of Yt-base in the solvent mixture could not be fit to a single decay time (Figure 6.51). However, the data also could be fit to a distribution of lifetimes (Figure 6.52). In 100% benzene or 100% methanol the intensity decays were described by narrow lifetime distributions, which are essentially the same as a single decay time. In benzene–methanol mixtures, wide lifetime distributions were needed to fit the intensity decay (Figure 6.52). Lifetime distributions can be expected for any macromolecule in which there exists a distribution of fluorophore environments.

It is interesting to notice that the  $\chi_R^2$  values are the same for the multi-exponential and for the lifetime distribution fits for Yt-base with 6% methanol. This illustrates a frequently encountered situation where different models yield

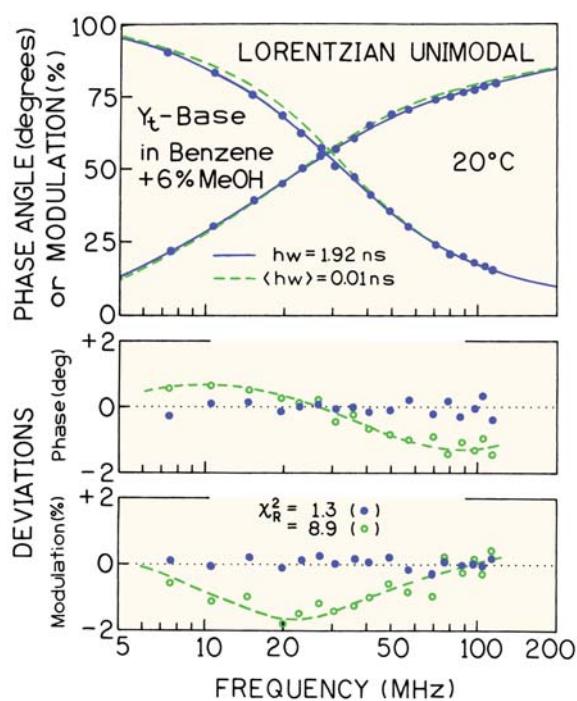


Figure 6.51. Frequency-domain intensity decay of Yt-base in benzene with 6% methanol. From [103].

equivalent fits. In such cases one must rely on other information to select the more appropriate model. In this case the lifetime distribution model seems preferable because there is no reason to expect two unique decay times in a solvent mixture.

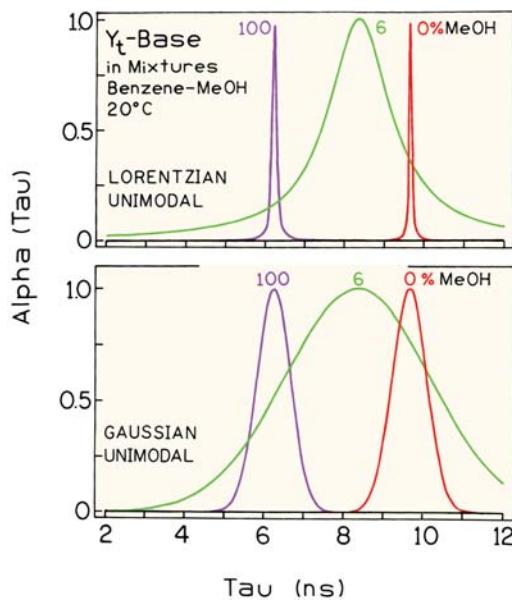


Figure 6.52. Lifetime distribution analysis of the intensity decay of Yt-base in pure methanol, pure benzene, and benzene with 6% methanol. Revised from [103].

## 6.12. SUMMARY OF SOLVENT EFFECTS

A quantitative description of the effects of environment on fluorescence emission spectra is perhaps the most challenging topic in fluorescence spectroscopy. No single theory or type of interactions can be used in all circumstances. A number of factors affect the emission including:

Table 6.4. Multi-Exponential Analysis of the Intensity Decays of Yt-Base in Benzene/Methanol Mixtures<sup>a</sup>

% Methanol	Number of decay times	$\tau_i$ (ns)	$\alpha_i$	$f_i$	$\chi_2^R$
0		9.67	1.0	1.0	1.3
4	1	8.80	1.0	1.0	3.2
	2	3.67 9.10	0.061 0.939	0.026 0.974	1.2
6	1	8.36	1.0	1.0	8.9
	2	3.50 8.92	0.113 0.887	0.048 0.952	1.2
	1	7.23	1.0	1.0	4.9
10	2	2.99 7.56	0.082 0.918	0.034 0.966	1.0
	1	6.25	1.0	1.0	1.9

<sup>a</sup>From [103].

1. General solvent effects due to the interactions of the dipole of the fluorophore with its environment
2. Specific solvent effects due to fluorophore–solvent interactions
3. Formation of ICT or TICT states depending on the probe structure and the surrounding solvent
4. Viscosity and changes in the radiative and non-radiative decay rates
5. Probe-probe interactions

Even if only one type of interaction were present, the effects would still be complex and beyond the limits of most models. For instance, the Lippert equation is only an approximation, and ignores higher-order terms. Also, this equation only applies to a spherical dipole in a spherical cavity. More complex expressions are needed for non-spherical molecules, but one cannot generally describe the fluorophore shape in adequate detail. With regard to specific effects, there is no general theory to predict the shift in emission spectra due to hydrogen bond formation. And, finally, for fluorophores bound to macromolecules or in viscous solvents, spectral relaxation can occur during emission, so that the emission spectrum represents some weighted average of the unrelaxed and relaxed emission.

Given all these complexities, how can one hope to use the data from solvent sensitive probes? In our opinion, the best approach is to consider the fluorophore structure rather than to rely completely on theory. Observed effects should be considered within the framework of the interactions listed above. Unusual behavior may be due to the presence of more than one type of interaction. Use the theory as an aid to interpreting plausible molecular interactions, and not as a substitute for careful consideration probe structure and its likely chemical interactions.

## REFERENCES

1. Safarzadeh-Amiri A, Thompson M, Krull UJ. 1989. Trans-4-dimethylamino-4'-(1-oxobutyl)stilbene: a new fluorescent probe of the bilayer lipid membrane. *J Photochem Photobiol A: Chem* **47**:299–308.
2. Lippert Von E. 1957. Spektroskopische bestimmung des dipolmomentes aromatischer verbindungen im ersten angeregten singulettzustand. *Z Electrochem* **61**:962–975.
3. Mataga N, Kaifu Y, Koizumi M. 1956. Solvent effects upon fluorescence spectra and the dipole moments of excited molecules. *Bull Chem Soc Jpn* **29**:465–470.
4. Rettig W. 1986. Charge separation in excited states of decoupled systems: TICT compounds and implications regarding the development of new laser dyes and the primary processes of vision and photosynthesis. *Angew Chem, Int Ed* **25**:971–988.
5. Bayliss NS. 1950. The effect of the electrostatic polarization of the solvent on electronic absorption spectra in solution. *J Chem Phy* **18**(3):292–296.
6. Bayliss NS, McRae EG. 1954. Solvent effects in organic spectra: dipole forces and the Franck-Condon principle. *J Phys Chem* **58**:1002–1006.
7. McRae EG. 1956. Theory of solvent effects of molecular electronic spectra: frequency shifts. *J Phys Chem* **61**:562–572.
8. Griffiths DJ. 1999. *Introduction to electrodynamics*. Prentice-Hall, Englewood Cliffs, NJ.
9. Kawski A. 1992. Solvent-shift effect of electronic spectra and excited state dipole moments. In *Progress in photochemistry and photophysics*, pp. 1–47. Ed JF Rabek, CRC Press, New York.
10. Seliskar CJ, Brand L. 1971. Electronic spectra of 2-aminonaphthalene-6-sulfonate and related molecules, II: effects of solvent medium on the absorption and fluorescence spectra. *J Am Chem Soc* **93**:5414–5420.
11. Suppan P. 1990. Solvatochromic shifts: the influence of the medium on the energy of electronic states. *J Photochem Photobiol A: Chem* **50**:293–330.
12. Bakhshiev NG. 1961. Universal molecular interactions and their effect on the position of the electronic spectra of molecules in two component solutions, I: theory (liquid solutions). *Opt Spectrosc* **10**:379–384.
13. Bakhshiev NG. 1962. Universal molecular interactions and their effects on the position of electronic spectra of molecules in two-component solutions, IV: dependence on the magnitude of the Stokes shift in the solvent luminescence spectrum (liquid solutions). *Opt Spectrosc* **12**:309–313.
14. Bakhshiev NG. 1962. Universal intermolecular interactions and their effect on the position of the electronic spectra of molecules in two-component solutions. *Opt Spectrosc* **13**:24–29.
15. Kawski A. 2002. On the estimation of excited-state dipole moments from solvatochromic shifts of absorption and fluorescence spectra. *Z Naturforsch A* **57**:255–262.
16. Weber G, Laurence DJR. 1954. Fluorescent indicators of absorption in aqueous solution and on the solid phase. *Biochem J* **56**:XXXI.
17. Slavik J. 1982. Anilinonaphthalene sulfonate as a probe of membrane composition and function. *Biochim Biophys Acta* **694**:1–15.
18. McClure WO, Edelman GM. 1954. Fluorescent probes for conformational states of proteins, I: mechanism of fluorescence of 2-p-toluidinylnaphthalene-6-sulfonate, a hydrophobic probe. *Biochemistry* **5**:1908–1919.
19. Brand L, Seliskar CJ, Turner DC. 1971. The effects of chemical environment on fluorescence probes. In *Probes of structure and function of macromolecules and membranes*, pp. 17–39. Ed B Chance, CP Lee, J-K Blaisie. Academic Press, New York.
20. Turner DC, Brand L. 1968. Quantitative estimation of protein binding site polarity: fluorescence of N-arylamino naphthalenesulfonates. *Biochemistry* **7**(10):3381–3390.
21. Perov AN. 1980. Energy of intermediate pair interactions as a characteristic of their nature: theory of the solvato (fluoro) chromism of three-component solutions. *Opt Spectrosc* **49**:371–374.
22. Neporen BS, Bakhshiev NG. 1960. On the role of universal and specific intermolecular interactions in the influence of the solvent on the electronic spectra of molecules. *Opt Spectrosc* **8**:408–413.
23. Petrov NK, Markov DE, Gulakov MN, Al'fimov MV, Staerk H. 2002. Study of preferential solvation in binary mixtures by means of frequency-domain fluorescence spectroscopy. *J Fluoresc* **12**(1):19–24.
24. Petrov NK, Wiessner A, Staerk H. 2001. A simple kinetic model of preferential solvation in binary mixtures. *Chem Phys Lett* **349**:517–520.

25. Schulman SG, Townsend RW, Baeyens WRG. 1995. Proton-transfer kinetics of photoexcited 2-hydroxybiphenyl in aqueous methanol solutions. *Anal Chim Acta* **303**:25–29.
26. Kim S, Chang DW, Park SY, Kawai H, Nagamura T. 2002. Excited-state intramolecular proton transfer in a dendritic macromolecular system: poly(aryl ether) dendrimers with phototautomerizable quinoline core. *Macromolecules* **35**:2748–2753.
27. Carmona C, Balón M, Galán M, Guardado P, Muñoz MA. 2002. Dynamic Study of excited state hydrogen-bonded complexes of harmane in cyclohexane-toluene mixtures. *Photochem Photobiol* **76**(3):239–246.
28. Molotsky T, Huppert D. 2002. Solvation statics and dynamics of coumarin 153 in hexane-propionitrile solvent mixtures. *J Phys Chem A* **106**:8525–8530.
29. Fery-Forgues S, Fayet J-P, Lopez A. 1993. Drastic changes in the fluorescence properties of NBD probes with the polarity of the medium: involvement of a TICT state. *J Photochem Photobiol A: Chem* **70**: 229–243.
30. Mazères S, Schram V, Tocanne J-F, Lopez A. 1996. 7-nitrobenz-2-oxa-1,3-diazole-4-yl-labeled phospholipids in lipid membranes: differences in fluorescence behavior. *Biophys J* **71**:327–335.
31. Cherkasov AS. 1960. Influence of the solvent on the fluorescence spectra of acetylanthracenes. *Akad Nauk SSSR Bull Phys Sci* **24**:597–601.
32. Tamaki T. 1982. The photoassociation of 1- and 2-acetylanthracene with methanol. *Bull Chem Soc Jpn* **55**:1761–1767.
33. Tamaki T. 1980. Polar fluorescent state of 1- and 2-acylanthenacenes, II: The perturbation of protic solvents. *Bull Chem Soc Jpn* **53**: 577–582.
34. Perochon E, Tocanne J-F. 1991. Synthesis and phase properties of phosphatidylcholine labeled with 8-(2-anthroyl)-octanoic acid, a solvatochromic fluorescent probe. *Chem Phys Lipids* **58**:7–17.
35. Perochon E, Lopez A, Tocanne JF. 1991. Fluorescence properties of methyl 8-(2-anthroyl) octanoate, a solvatochromic lipophilic probe. *Chem Phys Lipids* **59**:17–28.
36. Rosenberg HM, Eimutis E. 1966. Solvent shifts in electronic spectra, I: Stokes shift in a series of homologous aromatic amines. *Spectrochim Acta* **22**:1751–1757.
37. Werner TC, Hercules DM. 1969. The fluorescence of 9-anthroic acid and its esters: environmental effects on excited-state behavior. *J Phys Chem* **73**:2005–2011.
38. Werner TC, Hoffman RM. 1973. Relation between an excited state geometry change and the solvent dependence of 9-methyl anthroate fluorescence. *J Phys Chem* **77**:1611–1615.
39. Badea MG, De Toma RP, Brand L. 1978. Nanosecond relaxation processes in liposomes. *Biophys J* **24**:197–212.
40. Lakowicz JR, Balter A. 1982. Direct recording of the initially excited and the solvent relaxed fluorescence emission of a tryptophan derivative in viscous solution by phase-sensitive detection of fluorescence. *Photochem Photobiol* **36**:125–132.
41. Lakowicz JR, Bevan DR, Maliwal BP, Cherek H, Balter A. 1983. Synthesis and characterization of a fluorescence probe of the phase transition and dynamic properties of membranes. *Biochemistry* **22**:5714–5722.
42. Weber G, Farris FJ. 1979. Synthesis and spectral properties of a hydrophobic fluorescent probe: 6-propionyl-2-(dimethylamino)-naphthalene. *Biochemistry* **18**:3075–3078.
43. Sire O, Alpert B, Royer CA. 1996. Probing pH and pressure effects of the apomyoglobin heme pocket with the 2'-(N,N-dimethylamino)-6-naphthoyl-4-trans-cyclohexanoic acid fluorophore. *Biophys J* **70**:2903–2914.
44. Prendergast FG, Meyer M, Carlson GL, Iida S, Potter JD. 1983. Synthesis, spectral properties, and use of 6-acryloyl-2-dimethylaminonaphthalene (acrylodan). *J Biol Chem* **258**:7541–7544.
45. Hendrickson HS, Dumdei EJ, Batchelder AG, Carlson GL. 1987. Synthesis of prodan-phosphatidylcholine, a new fluorescent probe, and its interactions with pancreatic and snake venom phospholipases A<sub>2</sub>. *Biochemistry* **26**:3697–3703.
46. Sandez MI, Suarez A, Rios MA, Balo MC, Fernandez F, Lopez C. 1996. Spectroscopic study of new fluorescent probes. *Photochem Photobiol* **64**(3):486–491.
47. Lobo BC, Abelt CJ. 2003. Does PRODAN possess a planar or twisted charge-transfer excited state? Photophysical properties of two PRODAN derivatives. *J Phys Chem A* **107**:10938–10943.
48. Hutterer R, Hof M. 2002. Probing ethanol-induced phospholipid phase transitions by the polarity sensitive fluorescence probes prodan and patman. *Z Phys Chem* **216**:333–346.
49. Parasassi T, Gratton E, Yu WM, Wilson P, Levi M. 1997. Two-photon fluorescence microscopy of laurdan generalized polarization domains in model and natural membranes. *Biophys J* **72**:2413–2429.
50. Parasassi T, Krasnowska EK, Bagatolli LA, Gratton E. 1998. Laurdan and prodan as polarity-sensitive fluorescent membrane probes. *J Fluoresc* **8**(4):365–373.
51. Bagatolli LA, Gratton E, Khan TK, Chong PLG. 2000. Two-photon fluorescence microscopy studies of bipolar tetraether giant liposomes from thermoacidophilic archaeabacteria *sulfolobus acidocaldarius*. *Biophys J* **79**:416–425.
52. Bondar OP, Rowe ES. 1999. Preferential interactions of fluorescent probe prodan with cholesterol. *Biophys J* **76**:956–962.
53. Bagatolli LA, Gratton E. 2000. Two-photon fluorescence microscopy of coexisting lipid domains in giant unilamellar vesicles of binary phospholipid mixtures. *Biophys J* **78**:290–305.
54. Gaus K, Gratton E, Kable EPW, Jones AS, Gelissen I, Kritharides L, Jessup W. 2003. Visualizing lipid structure and raft domains in living cells with two-photon microscopy. *Proc Natl Acad Sci USA* **100**(26):15554–15559.
55. Yoshihara T, Druzhinin SI, Zachariasse KA. 2004. Fast intramolecular charge transfer with a planar rigidized electron donor/acceptor molecule. *J Am Chem Soc* **126**:8535–8539.
56. Viard M, Gallay J, Vincent M, Meyer O, Robert B, Paternostre M. 1997. Laurdan solvatochromism: solvent dielectric relaxation and intramolecular excited-state reaction. *Biophys J* **73**:2221–2234.
57. Nowak W, Sygula A, Adamczak P, Balter A. 1986. On the possibility of fluorescence from twisted intramolecular charge transfer states of 2-dimethylamino-6-acylnaphthalenes: a quantum-chemical study. *J Mol Struct* **139**:13–23.
58. Balter A, Nowak W, Pawelkiewicz W, Kowalczyk A. 1988. Some remarks on the interpretation of the spectral properties of prodan. *Chem Phys Lett* **143**:565–570.
59. Rettig W, Lapouyade R. 1994. Fluorescence probes based on twisted intramolecular charge transfer (TICT) states and other adiabatic photoreactions. In *Topics in fluorescence spectroscopy*, Vol. 4: *Probe design and chemical sensors*, pp. 109–149. Ed JR Lakowicz. Plenum Press, New York.
60. Cornelissen C, Rettig W. 1994. Unusual fluorescence red shifts in TICT-forming boranes. *J Fluoresc* **4**(1):71–74.
61. Vollmer F, Rettig W, Birckner E. 1994. Photochemical mechanisms producing large fluorescence Stokes shifts. *J Fluoresc* **4**(1):65–69.
62. Rotkiewicz K, Grellmann KH, Grabowski ZR. 1973. Reinterpretation of the anomalous fluorescence of P-N,N-dimethylamino-benzonitrile. *Chem Phys Lett* **19**:315–318.

63. Grabowski ZR, Rotkiewicz K, Siemarczuk A. 1979. Dual fluorescence of donor-acceptor molecules and the twisted intramolecular charge transfer TICT states. *J Lumin* **18**:420–424.
64. Belletête M, Durocher G. 1989. Conformational changes upon excitation of dimethylamino para-substituted 3H-indoles: viscosity and solvent effects. *J Phys Chem* **93**:1793–1799.
65. Jones G, Jackson WR, Choi C-Y, Bergmark WR. 1985. Solvent effects on emission yield and lifetime for coumarin laser dyes: requirements for a rotatory decay mechanism. *J Phys Chem* **89**: 294–300.
66. Ayuk AA, Rettig W, Lippert E. 1981. Temperature and viscosity effects on an excited state equilibrium as revealed from the dual fluorescence of very dilute solutions of 1-dimethylamino-4-cyanonaphthalene. *Ber Bunsenges Phys Chem* **85**:553–555.
67. Kollmannsberger M, Rurack K, Resch-Genger U, Daub J. 1998. Ultrafast charge transfer in amino-substituted boron dipyrromethene dyes and its inhibition by cation complexation: a new design concept for highly sensitive fluorescent probes. *J Phys Chem A* **102**:10211–10220.
68. Klymchenko AS, Duportail G, Mely Y, Demchenko AP. 2003. Ultrasensitive two-color fluorescence probes for dipole potential in phospholipid membranes. *Proc Natl Acad Sci USA* **100**(20):11219–11224.
69. Klymchenko AS, Duportail G, Ozturk T, Pivovarenko VG, Mely Y, Demchenko AP. 2002. Novel two-band ratiometric fluorescence probes with different location and orientation in phospholipid membranes. *Chem Biol* **9**:1199–1208.
70. Ercelen S, Klymchenko AS, Demchenko AP. 2003. Novel two-color fluorescence probe with extreme specificity to bovine serum albumin. *FEBS Lett* **538**:25–28.
71. Fahrni CJ, Henary MM, VanDerveer DG. 2002. Excited-state intramolecular proton transfer in 2-(2'-tosylaminophenyl)benzimidazole. *J Phys Chem A* **106**:7655–7663.
72. Dennison SM, Guharay J, Sengupta PK. 1999. Intramolecular excited-state proton transfer and charge transfer fluorescence of a 3-hydroxyflavone derivative in micellar media. *Spectrochim Acta Part A* **55**:903–909.
73. Do Cabo JL, Faria HB, Portugal SGM, Silva MAA, Brinn IM. 1999. Excited-state acidity of bifunctional compounds, 7: long distance, solvent-assisted excited-state proton transfer in olivacine. *Photochem Photobiol* **69**(6):664–670.
74. Rampey ME, Halkyard CE, Williams AR, Angel AJ, Hurst DR, Townsend JD, Finefrock AE, Beam CF, Studer-Martinez SL. 1999. A new series of proton/charge transfer molecules: synthesis and spectral studies of 2-(5-aryl-1-carbomethoxy-1*H*-pyrazol-3-yl)phenols. *Photochem Photobiol* **70**(2):176–183.
75. Del Valle JC, Dominguez E, Kasha M. 1999. Competition between dipolar relaxation and double proton transfer in the electronic spectroscopy of pyrroloquinolines. *J Phys Chem A* **103**:2467–2475.
76. Chou PT, Chen YC, Yu WS, Chou YH, Wei CY, Cheng YM. 2001. Excited-state intramolecular proton transfer in 10-hydroxybenzo[*h*]quinoline. *J Phys Chem A* **105**:1731–1740.
77. Nagaoka S, Nakamura A, Nagashima U. 2002. Nodal-plane model in excited-state intramolecular proton transfer of o-hydroxybenzaldehyde: substituent effect. *J Photochem Photobiol A: Chem* **154**(1): 23–32.
78. Nad S, Pal H. 2001. Unusual photophysical properties of coumarin-151. *J Phys Chem A* **105**(7):1097–1106.
79. Singh MK, Pal H, Bhasikuttan AC, Sapre AV. 1998. Dual solvatochromism of neutral red. *Photochem Photobiol* **68**(1):32–38.
80. Sumitani M, Nakashima N, Yoshihara K, Nagakura S. 1977. Temperature dependence of fluorescence lifetimes of *trans*-stilbene. *Chem Phys Lett* **51**(1):183–185.
81. Todd DC, Jean JM, Rosenthal SJ, Ruggiero AJ, Yang D, Fleming GR. 1990. Fluorescence upconversion study of *cis*-stilbene isomerization. *J Chem Phys* **93**(12):8658–8668.
82. Meier H. 2001. Blue fluorescent exciplexes consisting of *trans*-stilbene and antibodies. *Angew Chem, Int Ed* **40**(10):1851–1853.
83. Rettig W, Lapouyade R. 1994. Fluorescence probes based on twisted intramolecular charge transfer (TICT) states and other adiabatic photoreactions. In *Topics in fluorescence spectroscopy*, Vol. 4: *Probe design and chemical sensing*, pp. 109–149. Ed JR Lakowicz. Plenum Press, New York.
84. Iwaki T, Torigoe C, Noji M, Nakanishi M. 1993. Antibodies for fluorescent molecular rotors. *Biochemistry* **32**:7589–7592.
85. Haidekker MA, L'Heureux N, Frangos JA. 2000. Fluid shear stress increases membrane fluidity in endothelial cells: a study with DCVJ fluorescence. *Am J Physiol Heart Circ Physiol* **278**:H1401–H1406.
86. Haidekker MA, Ling T, Anglo M, Stevens HY, Frangos JA, Theodorakis EA. 2001. New fluorescent probes for the measurement of cell membrane viscosity. *Chem Biol* **8**:123–131.
87. Okamoto A, Ichiba T, Saito I. 2004. Pyrene-labeled oligodeoxynucleotide probe for detecting base insertion by excimer fluorescence emission. *J Am Chem Soc* **126**:8364–8365.
88. Yamana K, Iwai T, Ohtani Y, Sato S, Nakamura M, Nakano H. 2002. Bis-pyrene-labeled oligonucleotides: sequence specificity of excimer and monomer fluorescence changes upon hybridization with DNA. *Bioconjugate Chem* **13**:1266–1273.
89. Wang W, Han JJ, Wang LQ, Li LS, Shaw WJ, Li ADQ. 2003. Dynamic π–π stacked molecular assemblies emit from green to red colors. *Nano Lett* **3**(4):455–458.
90. Richieri GV, Ogata RT, Kleinfeld AM. 1992. A fluorescently labeled intestinal fatty acid binding protein. *J Biol Chem* **267**(33):23495–23501.
91. Richieri GV, Anel A, Kleinfeld AM. 1993. Interactions of long-chain fatty acids and albumin: determination of free fatty acid levels using the fluorescent probe ADIFAB. *Biochemistry* **32**:7574–7580.
92. Richieri GV, Ogata RT, Kleinfeld AM. 1996. Kinetics of fatty acid interactions with fatty acid binding proteins from adipocyte, heart, and intestine. *J Biol Chem* **271**(19):11291–11300.
93. Richieri GV, Ogata RT, Kleinfeld AM. 1996. Thermodynamic and kinetic properties of fatty acid interactions with rat liver fatty acid-binding protein. *J Biol Chem* **271**(49):31068–31074.
94. Richieri GV, Ogata RT, Kleinfeld AM. 1994. Equilibrium constants for the binding of fatty acids with fatty acid-binding proteins from adipocyte, intestine, heart and liver measured with the fluorescent probe ADIFAB. *J Biol Chem* **269**(39):23918–23930.
95. Richieri GV, Kleinfeld AM. 1995. Unbound free fatty acid levels in human serum. *J Lipid Res* **36**:229–240.
96. Kleinfeld AM, Prothro D, Brown DL, Davis RC, Richieri GV, DeMaria A. 1996. Increases in serum unbound free fatty acid levels following coronary angioplasty. *Am J Cardiol* **78**:1350–1354.
97. LaPorte DC, Wierman BM, Storm DR. 1980. Calcium-induced exposure of a hydrophobic surface on calmodulin. *Biochemistry* **19**:3814–3819.
98. Wang Y, Ikeda T, Ikeda H, Ueno A, Toda F. 1994. Dansyl-β-cyclodextrins as fluorescent sensors responsive to organic compounds. *Chem Soc Jpn* **67**:1598–1607.
99. Nagata K, Furuike T, Nishimura S-I. 1995. Fluorescence-labeled synthetic glycopolymers: a new type of sugar ligands of lectins. *J Biochem* **118**:278–284.

100. *BioProbes 25: New Products and Applications*. 1997. Molecular Probes Inc. Eugene, OR. May 1997.
101. Diwu Z, Lu Y, Zhang C, Kalubert DH, Haugland RP. 1997. Fluorescent molecular probes, II: the synthesis, spectral properties and use of fluorescent solvatochromic dapoxyl™ dyes. *Photochem Photobiol* **66**:424–431.
102. Dapoxyl is a trademark of Molecular Probes Inc.
103. Gryczynski I, Wiczk W, Lakowicz JR, Johnson ML. 1989. Decay time distribution analysis of Yt-base in benzene-methanol mixtures. *J Photochem Photobiol B: Biol* **4**:159–170.
104. Gryczynski I, Wiczk W, Johnson ML, Lakowicz JR. 1988. Lifetime distributions and anisotropy decays of indole fluorescence in cyclohexane/ethanol mixtures by frequency-domain fluorometry. *Biophys Chem* **32**:173–185.
105. Gryczynski I. Unpublished observations.

## PROBLEMS

- P6.1. *Calculation of a Stokes Shift:* Calculate the spectral shift of a fluorophore in methanol with  $\mu_E - \mu_G = 14\text{D}$  and a cavity radius of  $4\text{\AA}$ . That is, confirm the values in Table 6.2. Show that the answer is calculated in  $\text{cm}^{-1}$ . Note,  $\text{esu} = \text{g}^{1/2} \text{cm}^{3/2}/\text{s}$  and  $\text{erg} = \text{g cm}^2/\text{s}^2$ .
- P6.2. *Calculation of the Excited State Dipole Moment:* Use the data in Table 6.5 to calculate the change in dipole moment ( $\Delta\mu$ ) of Prodan excited state. Calculate the change in dipole moment  $\Delta\mu$  for both the locally excited (LE) and the internal charge-transfer (ICT) state. Assume the cavity radius is  $4.2\text{\AA}$ .

**Table 6.5.** Spectral Properties of PRODAN in Various Solvents<sup>a</sup>

No.	Solvent	Absorption maximum (nm)	Emission maximum (nm)	Stokes shift ( $\text{cm}^{-1}$ )	$\Delta f$
1	Cyclohexane	342	401	4302	0.001
2	Benzene	355	421	4416	0.002
3	Triethylamine	343	406	4523	0.102
4	Chlorobenzene	354	430	4992	0.143
5	Chloroform	357	440	5284	0.185
6	Acetone	350	452	6448	0.287
7	Dimethylformamide	355	461	6477	0.276
8	Acetonitrile	350	462	6926	0.304
9	Ethylene glycol	375	515	7249	0.274
10	Propylene glycol	370	510	7419	0.270
11	Ethanol	360	496	7616	0.298
12	Methanol	362	505	8206	0.308
13	Water	364	531	8646	0.302

<sup>a</sup>Data from [42].

# 7

# Dynamics of Solvent and Spectral Relaxation

In the preceding chapter we described the effects of solvent and local environment on emission spectra, and how spectral changes could be used to determine the properties of the environment surrounding a fluorophore. We showed that emission spectra could be affected by solvent polarity and specific solvent effects. We also showed that fluorophores could display charge separation and/or conformational changes while in the excited state. During these descriptions we did not consider the rate constants for these processes, but mostly assumed the lifetime of a fluorophore was in equilibrium with its environment prior to emission. More specifically, we assumed the decay rates of the fluorophores were slow compared to the rate constants for solvent reorientation, charge separation, or conformational changes in the fluorophore. The assumption of emission from equilibrated states was reasonable because fluid solvents reorient around excited fluorophores in 0.1 to 10 ps, and the decay times are typically 1 ns or longer.

There are many situations where the fluorophore can emit prior to or during other dynamic processes. For example, in viscous solvents the rate of solvent relaxation around the fluorophore may be comparable to or slower than the decay rate. In this case the emission occurs during solvent relaxation, and the emission spectrum represents an average of the partially relaxed emission. Under these conditions the emission spectra display time-dependent changes. These time-dependent effects are not observed in the steady-state emission spectra, but can be seen in the time-resolved data or the intensity decays measured at various emission wavelengths. Many fluorophores undergo reactions in the excited state, such as the loss or gain of a proton. Depending on the chemical properties of the fluorophore, its exposure to the solvent, and/or the concentration of proton donors or acceptors in the solution, the excited-state reaction may be occurring during emission. In this case the steady-state spectrum will contain contributions from each form of the fluorophore, assuming that both forms are fluorescent.

As was true for solvent effects, there is no universal theory that provides a quantitative description of all the observed phenomena. Time-dependent shifts occur as the result of general solvent effects, specific solvent-fluorophore interactions, formation of internal charge-transfer states, and excited-state reactions. All of these processes affect the time-dependent decays. Interpretation of the time-resolved data should be based on a molecular understanding of the fluorophore and the nature of its environment. In some cases the effects are often similar and not immediately assignable to a particular molecular event. Hence, it can be challenging to select a model for interpretation of the time-dependent spectra.

## 7.1. OVERVIEW OF EXCITED-STATE PROCESSES

Prior to consideration of specific mechanisms, it is useful to understand how emission spectra are affected by processes occurring during the excited-state lifetime. We can divide the time-dependent spectral changes into two categories: a continuous spectral shift or a two-state model. In the continuous model the emission spectrum shifts with time but does not change the spectral shape.<sup>1–3</sup> The continuous model is usually appropriate for general solvent effects. In the two-state model there are distinct emission spectral from two forms of the fluorophore. The two-state model is usually appropriate for excited-state reactions or formation of internal charge-transfer (ICT) states.

Excited-state processes are usually studied by measurement of the time-resolved emission spectra (TRES). The TRES are the emission spectra that would be observed if measured at some instant in time following pulsed excitation. Figure 7.1 shows a schematic for the continuous spectral relaxation (CR) model. The fluorophore is excited to the Franck-Condon ( $F$ ) or unrelaxed state. Following excitation the solvent reorients around the excited-state dipole moment, which occurs with a solvent relaxation rate  $k_s$ ,

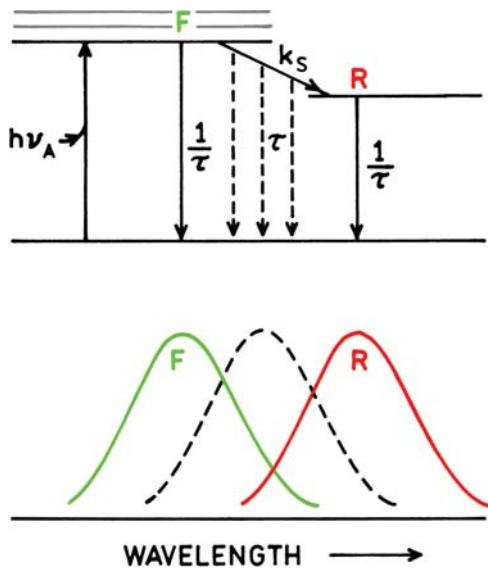


Figure 7.1. Jablonski diagram for continuous spectral relaxation.

which can also be described by a solvent relaxation time  $\tau_s = k_s^{-1}$ . If the solvent is fluid the solvent relaxation time will be less than the lifetime ( $\tau_s \ll \tau$ ) and emission occurs from the relaxed ( $R$ ) state. At low temperature, solvent relaxation can be slower than emission ( $\tau_s \gg \tau$ ) so that emission is observed from the  $F$  state. At intermediate temperature emission where  $\tau_s = \tau$  emission will be occurring during the relaxation process. Hence a spectrum intermediate between  $F$  and  $R$  will be observed (dashed curve in Figure 7.1), which represents some weighted average of the emission spectra at each point in time during the relaxation process. In rigorous terms the intermediate spectrum would have the same shape and half width as the  $F$ - and  $R$ -state emission spectra. In practice the intermediate spectrum can be wider due to contributions from fluorophores with varying extents of relaxation. In Figure 7.1 we show the same lifetime  $\tau$  for the fluorophore in the  $F$  and  $R$  state because the fluorophore is emitting from the same electronic state. In practice these decay times can be different.

Spectral relaxation can also occur in a stepwise manner, which we will call the excited-state reaction (ESR) model. In this case there are two distinct emitting species: the initially excited state  $F$  and the species  $R$  resulting from the excited-state reaction. The lifetime of the  $F$  and  $R$  states ( $\tau_F$  and  $\tau_R$ ) are different because emission is occurring from a different molecular species (Figure 7.2). In the case of excited-state ionization the emission would be from the initially excited and the ionized species. The  $F$  and  $R$  states

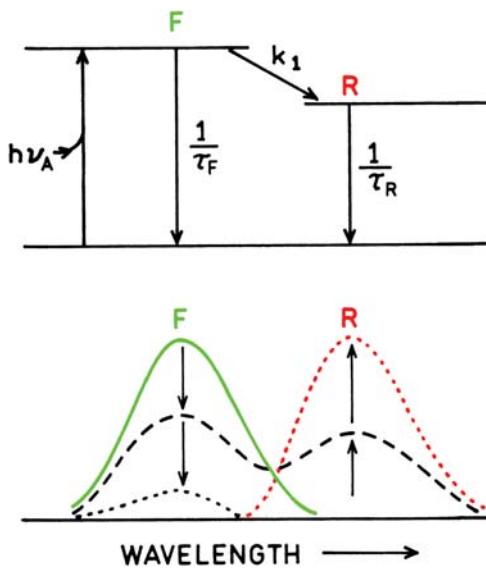
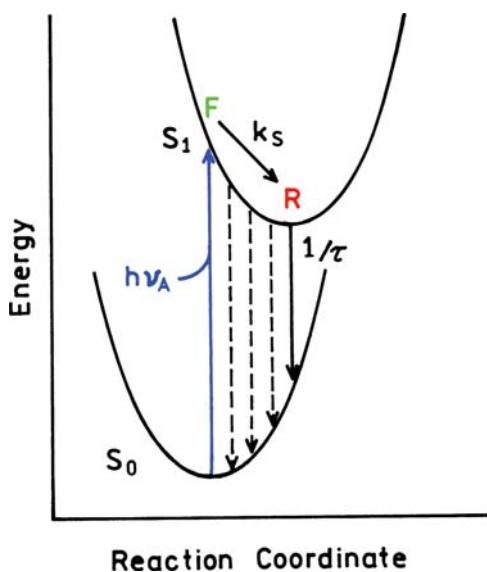


Figure 7.2. Jablonski diagram for an excited-state reaction.

can also have different emission spectra because the electronic states or chemical structures are different.

For the ESR model the  $F$  and  $R$  states are linked by a rate constant  $k_1$ . The reaction can be reversible, but for simplicity is shown as an irreversible reaction. The rate constant  $k_1$  is now a chemical rate constant that is determined by the chemical structures and solvent composition. If the rate constant is small relative to the decay rate of the  $F$  state ( $k_1 < \tau_F^{-1}$ ) the emission occurs mostly from the  $F$  state. If the reaction rate is greater than the decay rate of the  $F$  state ( $k_1 > \tau_F^{-1}$ ) then emission occurs primarily from the  $R$  state. If the reaction rate and decay rates are comparable then emission occurs from both species. If the emission spectra of the  $F$  and  $R$  states are well separated then two distinct components will be seen in the emission spectrum. If the emission spectra of the  $F$  and  $R$  states overlap, the intermediate emission spectra may show a shoulder or be wider than the individual emission spectra.

The continuous relaxation and ESR models can also be described in terms of reaction coordinates. In the CR model emission is occurring from the same state (Figure 7.3), except for a displacement due to solvent reorientation. The rate constant  $k_s$  describes the rate at which the excited-state energy slides towards the equilibrium  $R$  state. Emission occurs at all positions along the reaction coordinate. For the ESR model there are two excited-state species, typically separated by an energy barrier (Figure 7.4). Emission can occur from either state, but the states are distinct. The rate



**Figure 7.3.** Energy schematic for continuous spectral relaxation.

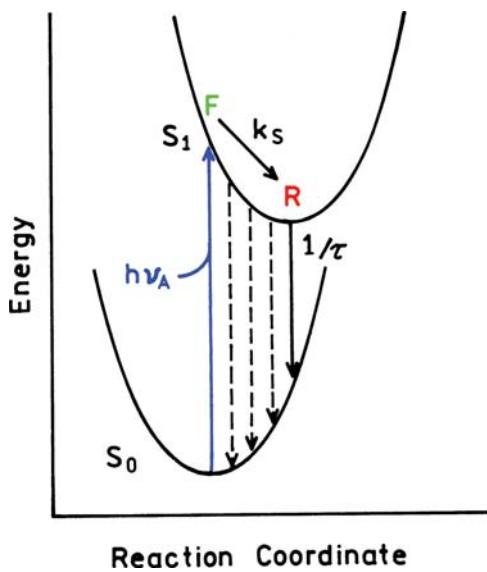


**Figure 7.4.** Energy schematic for an excited-state reaction.

constant  $k_1$  describes the rate at which the  $F$  state is transformed into the  $R$  state.

#### 7.1.1. Time-Resolved Emission Spectra

Excited-state processes result in complex time-dependent decays. The intensity decays depend on the observation wavelength because of the time needed for the  $F$  state to

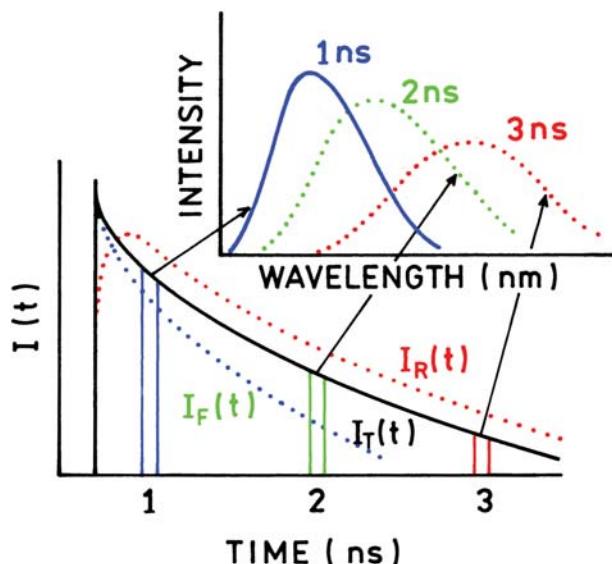


**Figure 7.5.** Schematic of time-resolved emission spectra.  $I_T(t)$  represents the decay of the total emission.  $I_F(t)$  and  $I_R(t)$  are the intensity decays on blue and red sides of the emission spectrum, respectively. The upper insert shows the emission spectra at  $t = 1, 2$ , or  $3$  ns.

become an  $R$  state or some intermediate state. This situation is illustrated in Figure 7.5. In this figure the solid line shows the intensity decay of the total emission, or the decay that would be observed in the absence of excited-state processes. Now suppose the intensity decay is measured on the short-wavelength side of the total emission. This decay,  $I_F(t)$ , is more rapid than the decay of the total emission,  $I_T(t)$ , because the short-wavelength emission is decaying by both emission and relaxation, which is removing excited fluorophores from the observation wavelength. On the long-wavelength side of the emission the emitting fluorophores are those that have relaxed.

Time is needed for the  $F$ -state molecules to reach the  $R$  state. Even if the  $F$  and  $R$  states have the same intrinsic decay time, the long-wavelength decay will appear to be slower. Also, at the moment of excitation all the molecules are assumed to be in the  $F$  state. No molecules are in the  $R$  state until some relaxation has occurred. For this reason one typically observes a rise in the intensity at long wavelengths representing formation of the relaxed state. The rise time is frequently associated with a negative pre-exponential factor that is recovered from the multi-exponential analysis. Following the rise in intensity, the decay  $I_R(t)$  typically follows the total emission. Another way of understanding the wavelength-dependent decays is to recall that emission is a random event. Some fluorophores emit at earlier times, and

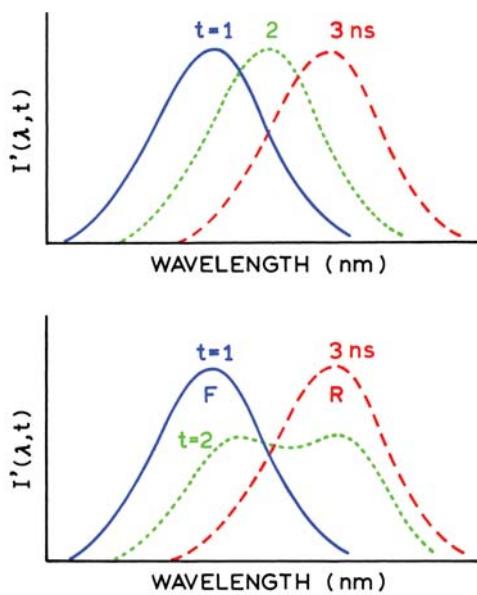


**Figure 7.6.** Normalized time-resolved emission spectra for continuous relaxation (top) and for a two-state process (bottom).

some at later times. The decay rate represents the ensemble average. The fluorophores that emit at earlier times tend to have shorter wavelength emission, and those that emit at later times have longer wavelength emission.

Suppose that emission spectra could be recorded at any desired instant following the excitation pulse (Figure 7.6) and that the spectra are normalized. First consider a continuous relaxation process (top panel). If the emission spectrum was observed immediately after excitation ( $t = 1$  ns), then a blue-shifted or unrelaxed emission will be observed. If the time of observation is later, then more of the molecules will have relaxed to longer wavelengths, resulting in emission spectra that are progressively shifted to longer wavelengths at longer times. For continuous spectral relaxation the shape of the emission spectra are expected to remain the same. Now consider the ESR model (Figure 7.6, lower panel). At short times the blue-shifted emission would be observed. At long times the emission would be from the reacted fluorophore. At intermediate times emission from both species would be observed. Typically the emission spectrum would be wider at intermediate times due to emission from both forms of the fluorophore. These emission spectra, representing discrete times following excitation, are called the time-resolved emission spectra (TRES). It is technically challenging to determine the TRES, and the molecular interpretation can be equally difficult.

## 7.2. MEASUREMENT OF TIME-RESOLVED EMISSION SPECTRA (TRES)

### 7.2.1. Direct Recording of TRES

The measurement of TRES is most easily understood using pulse sampling or time-gated detection (Chapter 4). In fact, the first reported TRES were obtained using this method,<sup>4–6</sup> but this method is rarely used at the present time. The sample was 4-aminophthalimide (4-AP) in propanol at  $-70^{\circ}\text{C}$ . At this temperature the rate of solvent relaxation is comparable to the decay time. The sample is excited with a brief pulse of light, and the detector was gated on for a brief period (typically  $<0.5$  ns) at various times following the excitation pulse. The emission spectrum is then scanned as usual. For short time delays a blue-shifted emission was observed (Figure 7.7). As the delay time was increased, the emission spectrum shifted to longer wavelength. At these longer times the solvent has relaxed around the excited-state dipole.

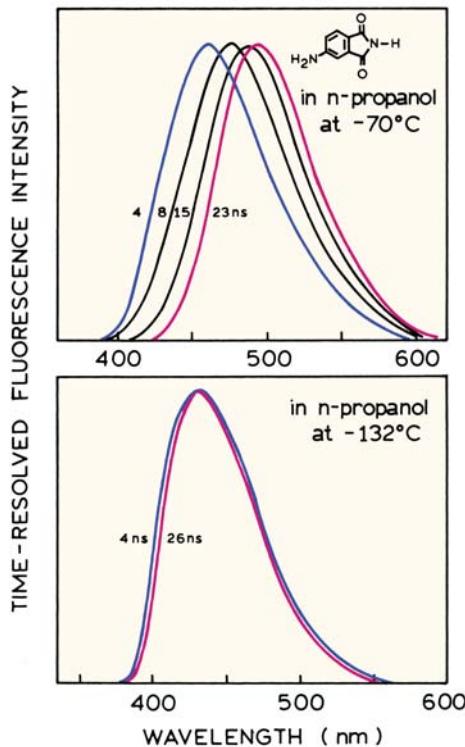


**Figure 7.7.** Time-resolved fluorescence spectra of 4-aminophthalimide in n-propanol at  $-70$  and  $-132^{\circ}\text{C}$  recording using the pulse sampling method (Chapter 4). The times between excitation and gated sampling of the emission intensity are listed on the figures. Revised from [4].

Examination of Figure 7.7 reveals that the shape and/or width of the emission spectrum is not changed during spectral relaxation. This suggests that relaxation of 4-aminophthalimide in n-propanol proceeds as a continuous process. When the temperature was lowered to  $-132^{\circ}\text{C}$  the emission spectra were similar for time delays of 4 and 26 ns. This is because at lower temperatures the relaxation time of the solvent is longer than the decay time of 4-aminophthalimide, which is near 10 ns.

TRES have also been obtained using TCSPC. When using TCSPC one can record photons arriving within a small time interval. In this instance one selects the output pulses from the TAC to be within a limited range of voltage values. The range of accepted voltages determines the time window that is observed. The emission spectrum is then recorded with a monochromator. While intuitively simple, this method is rather inefficient and has not been widely utilized.

Direct recording of TRES is easy to understand, but this procedure has a serious limitation. The directly recorded TRES do not provide for deconvolution using the instrument response function. Hence the recorded TRES are apparent spectra containing distortions due to the instrument response function. One exception is use of the pump-probe or upconversion methods, when the time resolution can be fast compared to the rates of spectral relaxation.

### 7.2.2. TRES from Wavelength-Dependent Decays

At present, time-resolved emission spectra are usually obtained indirectly. The procedure starts with measurement of the time-resolved decays at a number of wavelengths across the emission spectrum,  $I(\lambda,t)$ .<sup>7-9</sup> The intensity decays are wavelength dependent. The short wavelengths decay more rapidly than the longer wavelengths. This occurs because the emission on the short-wavelength side of the spectrum is decaying by both emission and by relaxation to longer wavelengths. In contrast, the emission at long wavelengths requires that the fluorophores relax prior to emission, and is thus delayed by the relaxation time.

For calculation of the TRES the intensity decays are usually analyzed in terms of the multi-exponential model

$$I(\lambda,t) = \sum_{i=1}^n \alpha_i(\lambda) \exp[-t/\tau_i(\lambda)] \quad (7.1)$$

where  $I(\lambda,t)$  are the intensity decays at each wavelength,  $\alpha_i(\lambda)$  are the pre-exponential factors,  $\tau_i(\lambda)$  are the decay

times, with  $\sum \alpha_i(\lambda) = 1.0$ . In this analysis the decay times can be variables at each wavelength  $\tau_i(\lambda)$ , or assumed to be independent of wavelength,  $\tau_i$ . Wavelength-dependent decay times are expected for the continuous model, and wavelength-independent lifetimes are expected for the two-state model. However, because of limited resolution and parameter correlation, the data can usually be fit with either wavelength-dependent  $\tau_i(\lambda)$  or wavelength-independent  $\tau_i$  lifetimes, irrespective of whether relaxation is a continuous or two-state process. For purposes of calculating the TRES the choice does not matter as long as good fits are obtained. The goal is to obtain a parametrized form of the intensity decays, which are then used to reconstruct the TRES. Typically, no molecular significance is assigned to the intensity decay parameters.

In order to calculate the TRES one computes a new set of intensity decays, which are normalized so that the time-integrated intensity at each wavelength is equal to the steady-state intensity at that wavelength. Suppose  $F(\lambda)$  is the steady-state emission spectrum. One calculates a set of  $H(\lambda)$  values using

$$H(\lambda) = \frac{F(\lambda)}{\int_0^\infty I(\lambda,t) dt} \quad (7.2)$$

which for the multi-exponential analysis becomes

$$H(\lambda) = \frac{F(\lambda)}{\sum_i \alpha_i(\lambda) \tau_i(\lambda)} \quad (7.3)$$

These equations can be understood as follows. The term  $H(\lambda)$  is the volume that, when multiplied by the time-integrated intensity at the same wavelength, is equal to the steady-state intensity at that wavelength. Then, the appropriately normalized intensity decay functions, which are used to calculate the TRES, are given by

$$I'(\lambda,t) = H(\lambda) I(\lambda,t) = \sum_i \alpha'_i(\lambda) \exp[-t/\tau_i(\lambda)] \quad (7.4)$$

where  $\alpha'_i(\lambda) = H(\lambda) \alpha_i(\lambda)$ .

The values of  $I'(\lambda,t)$  can be used to calculate the intensity at any wavelength and time, and thus the TRES. The TRES can be shown with the actual intensities, as in Figure 7.5, or peak normalized, as shown in Figures 7.6 (top) and 7.7 (lower panel). Assuming the intensity decays have been measured at an adequate number of wavelengths, this procedure (eqs. 7.1–7.4) yields the actual TRES independent of

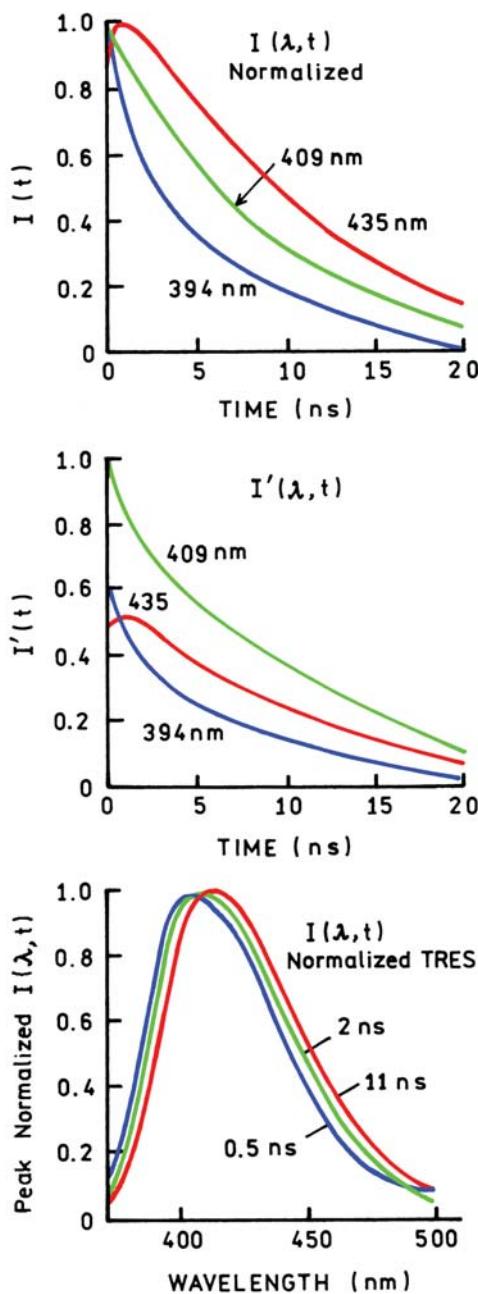


**Figure 7.8.** Calculation of time-resolved emission spectra. Revised from [9].

the nature of the relaxation process. The advantage of this procedure is that the values of  $I'(\lambda, t)$  are the actual impulse response functions, corrected for distortions due to convolution with the instrument response function. The time dependence of the spectral shifts, and the shape of the TRES, are then used to determine the rates of relaxation and the nature of the relaxation process.

The calculation of TRES from the measured intensity decays is best understood by a specific example (Figure 7.8). This example is for the probe 2-anilinonaphthalene (2-AN) bound to phospholipid vesicles,<sup>9–10</sup> but the procedure is the same for any sample. The time-resolved decays are measured at appropriate wavelengths across the entire emission spectrum. Typical decays at 394, 409, and 435 nm are shown in the upper panel. The time-resolved decays are used to derive the impulse response functions at each emission wavelength,  $I(\lambda, t)$ . These decays were obtained using an unusual deconvolution calculation (Figure 7.8, top panel). A multi-exponential fit is used, but no physical significance is attached to the values of  $\alpha_i(\lambda)$  and  $\tau_i(\lambda)$ . These are simply used to obtain an accurate representation for the observed intensity decays. One may interpret these results as follows. At shorter wavelengths the intensity decay is faster due to spectral relaxation. At longer wavelengths one selectively observes those fluorophores that have relaxed, and hence those that have emitted at later times following excitation. Thus the overall decay is slower at longer wavelengths.

The decays at each wavelength are then normalized so the time-integrated areas for each wavelength are equal to the steady-state intensity at that wavelength (middle panel). These decays are then used to calculate the emission spectra for any desired time following the excitation pulse. The TRES are usually peak normalized to allow easy visualization of the time-dependent spectral shifts. For 2-AN bound to vesicles one notices that the spectra shift to longer wavelengths at longer times (bottom panel).

Examination of Figure 7.8 (top and middle panels) shows a characteristic feature of solvent relaxation, which is a rise in intensity at long wavelengths (435 nm). This rise occurs because at  $t = 0$  no fluorophores are in the relaxed state. The population of the relaxed state increases prior to decreasing due to the total intensity decay. Observation of such a term provides proof that an excited-state process has occurred. If the sample displayed only ground-state heterogeneity, then the decays would be dependent upon wavelength. However, no rise in intensity would be observed for ground state heterogeneity because all the pre-exponential factors would be positive (Section 7.11).

### 7.3. SPECTRAL RELAXATION IN PROTEINS

Time-resolved emission spectra have been used to study the dynamics of proteins and membranes. The basic idea is that excitation provides an instantaneous perturbation because

of the increased dipole moment of the excited state. If the biomolecule is rigid, there will be no relaxation, as was seen for 4-AP in propanol at  $-132^{\circ}\text{C}$  (Figure 7.7). If the biomolecule is flexible, then the TRES should relax on a timescale characteristic of the macromolecule. Time-dependent spectral shifts have been observed for probes bound to proteins,<sup>11–21</sup> membranes,<sup>22–33</sup> micelles,<sup>34–39</sup> and polymers,<sup>40–41</sup> and has recently been reviewed.<sup>42</sup> Spectral relaxation of intrinsic tryptophan fluorescence in proteins will be described in Chapter 17.

### 7.3.1. Spectral Relaxation of Labeled Apomyoglobin

One example of TRES of a protein is provided by labeled myoglobin. Myoglobin is a muscle protein that binds oxygen from the blood and releases oxygen as needed to the muscles. Myoglobin thus acts as an oxygen reservoir. In myoglobin the oxygen molecule is bound to the heme group, which is near the center of the protein. The heme group can be removed from the protein, leaving a hydrophobic pocket that is known to bind a number of fluorophores.<sup>43–44</sup> Myoglobin without the heme group is called apomyoglobin. The dynamics of myoglobin are of interest because myoglobin cannot bind and release oxygen without undergoing structural fluctuations to allow diffusion of oxygen through the protein. If the protein is flexible on the nanosecond timescale for oxygen penetration, then it seems likely the protein can be flexible during the nanosecond decay times of bound fluorophores.

In the previous chapter we described Prodan and its derivatives as being highly sensitive to solvent polarity. The dynamics of the heme binding site was studied using the probe Danca, which is an analogue of Prodan (Figure 7.9). The carboxy cyclohexyl side chain serves to increase the affinity of Danca for apomyoglobin, and to ensure it binds to the protein in a single orientation. A single mode of binding simplifies interpretation of the data by providing a homogeneous probe population. Excitation of Danca results in the instantaneous creation of a new dipole within the apomyoglobin molecule. If myoglobin is flexible on the ns timescale, one expects time-dependent shifts in its emission spectrum as the protein rearranges around the new dipole moment.

Intensity decays were measured at various wavelengths across the emission spectrum (Figure 7.9). The amplitudes of these decays were adjusted according to eq. 7.3. The decays are somewhat faster at shorter emission wave-

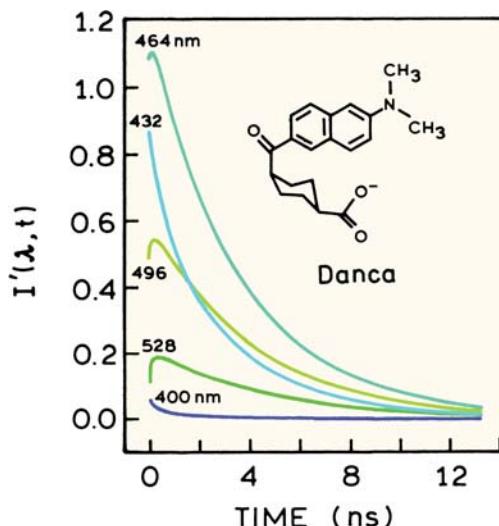


**Figure 7.9.** Deconvolved fluorescence decays of Danca-apomyoglobin complex from 400 to 528 nm at  $298^{\circ}\text{K}$ . The area under each trace has been scaled to the steady-state intensity at that wavelength. Note the intensity decays show a rise time at longer wavelengths. Revised and reprinted with permission from [17]. Copyright © 1992, American Chemical Society.

lengths. Importantly, there is evidence of a rise time at longer wavelengths, which is characteristic of an excited-state process. A rise time can only be observed if the emission is not directly excited, but rather forms from a previously excited state. In this case the initially excited state does not contribute at 496 and 528 nm, so that the decays at these wavelengths show an initial rise in intensity. The emission at these wavelengths is due to relaxation of the initially excited state.

The time-dependent decays were used to construct the time-resolved emission spectra (Figure 7.10). These spectra shift progressively to longer wavelength at longer times. Even at the earliest times (20 ps) the TRES are well shifted from the steady-state spectrum observed at  $77^{\circ}\text{K}$ . At this low temperature solvent relaxation does not occur. As was described in Chapter 6 (Figure 6.28), Prodan-like molecules can emit from locally excited (LE) and internal charge-transfer (ICT) states. The short-wavelength emission at  $77^{\circ}\text{K}$  is probably due to the LE state. Hence, the emission of DANCA-apomyoglobin is from the ICT state, which has undergone nearly complete charge separation.

The TRES can be used to calculate the rates of spectral relaxation. These data are usually presented as the average energy of the emission versus time (Figure 7.11). Alternatively, one can calculate the time-dependent change in the emission maximum. In the case of Danca-apomyoglobin

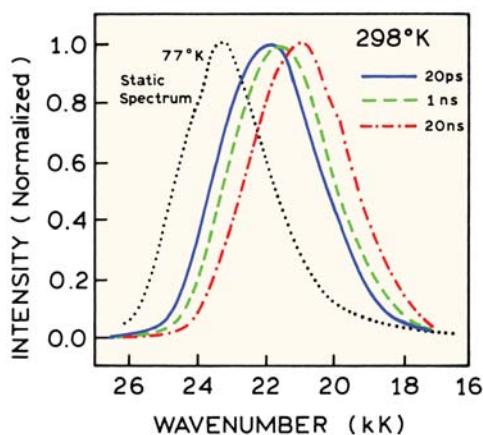


**Figure 7.10.** Time-resolved emission spectra of Danca bound to apomyoglobin. Also shown is the steady-state spectrum at 77°K. Revised and reprinted with permission from [17]. Copyright © 1992, American Chemical Society.

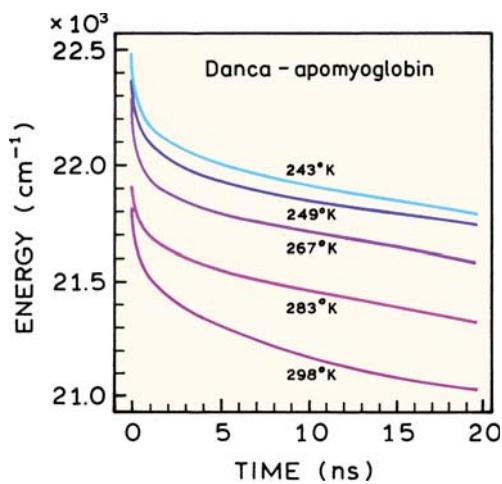


**Figure 7.11.** Decay of the mean energy of the emission (in  $\text{cm}^{-1}$ ) of Danca-apomyoglobin at various temperatures in water and glycerol-water mixtures. Revised and reprinted with permission from [17]. Copyright © 1992, American Chemical Society.

the decay of the average energy was highly non-exponential, and with relaxation times ranging from 20 ps to 20 ns. Spectral relaxation is typically a multi- or non-exponential process for probes in solvents or when bound to macromolecules. Methods used to determine the relaxation times are described below.

### 7.3.2. Protein Spectral Relaxation Around a Synthetic Fluorescent Amino Acid

The previous example showed relaxation of apomyoglobin around a Prodan analogue, which occurred in

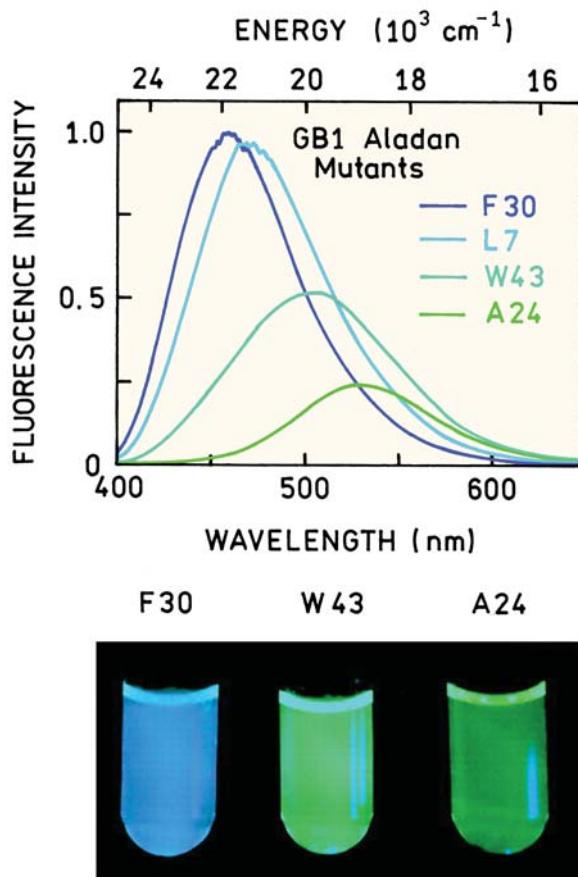
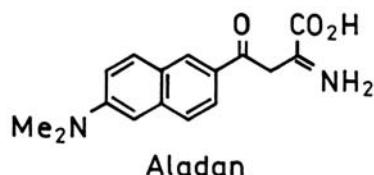


**Figure 7.12.** Emission spectra and color photographs of GB1 mutants containing Aladan in the sequence. Revised from [45].

about 10 ns. It was not clear if a 10 ns relaxation time was typical of proteins or a consequence of the artificial probe in the heme binding site. Hence it was of interest to measure spectral relaxation in an unperturbed protein. Tryptophan is one choice as a probe, but it is usually more difficult to perform high time-resolution experiments with UV excitation and emission wavelengths. To minimize the effects of labeling a synthetic amino acid was synthesized that was analogous to Prodan (Aladan in Figure 7.12).<sup>46</sup> This amino-acid analogue was incorporated into the B1 domain of streptococcal protein G (GB1). This protein binds to IgG and is frequently used as a model for protein

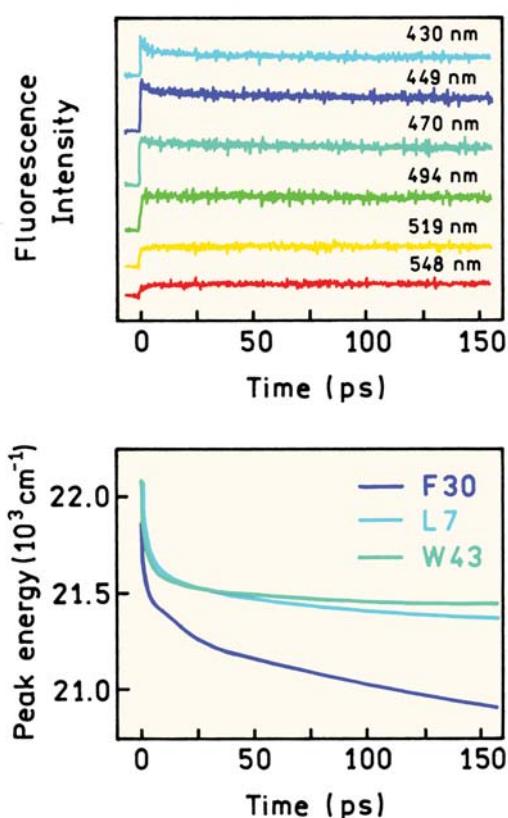


**Figure 7.13.** Time-dependent intensity decays and time-dependent peak emission energy of the F30 Aladan mutant of GB1 measured using fluorescence upconversion. The lower panel shows the time-dependent peak energy for three mutants of GB1. Revised from [45].

folding.<sup>47</sup> Figure 7.12 shows the emission spectra of Aladan-GB1 when Aladan is incorporated into four different sites. The emission maxima are different for each mutant, showing that the Aladan residue can be shielded, partially exposed, or exposed to the aqueous phase.

Time-dependent decays are needed to calculate the TRES (Figure 7.13). For Aladan-GB1 the wavelength-dependent parts of the decays were complete in about 20 ps, much faster than for Danca-labeled apomyoglobin. The 20-ps timescale is too fast for reliable TCSPC measurements, so these decays were recorded using fluorescence upconversion. The intensity decays were used to calculate the TRES (Figure 7.14). The time-dependent shifts were found to occur over a range of timescales. There is a rapid component that occurs in less than 20 ps (Figure 7.13, lower panel) and a slower shift occurring over several nanoseconds. Presumably, these slower components will result in the emission spectra becoming similar to the steady-state spectra (thick lines in Figure 7.14).

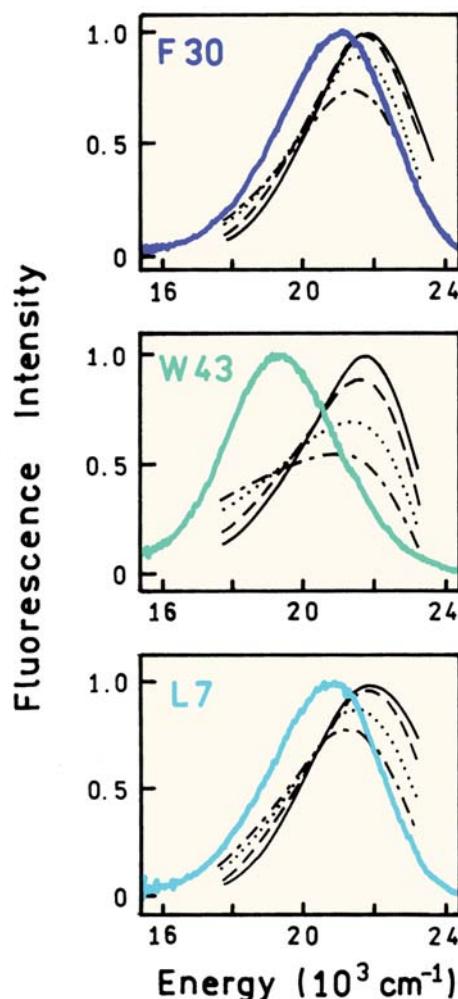


**Figure 7.14.** Time-resolved and steady-state emission spectra for GB1 mutants with Aladan in the sequence. The thick lines are the steady-state emission spectra. The time-resolved spectra are at 200 fs (solid lines), 1 ps (dashed line), 10 ps (dotted lines) and 150 ps (dot dashed lines). Revised from [45].

#### 7.4. SPECTRAL RELAXATION IN MEMBRANES

Time-resolved emission spectra have been extensively used to study membrane dynamics.<sup>24–33</sup> While not intuitively obvious, frequency-domain data can also be used to determine TRES, as will be shown for Patman-labeled DPPC vesicles. Patman is also a Prodan derivative, in this case designed to bind to membranes (Chapter 6, Figure 6.20). As for the time-domain measurements, the frequency-domain data are measured for various wavelengths across the emission spectrum (Figure 7.15). The phase and modulation values are strongly dependent on emission wavelength. At 46°C on the blue side of the emission, the phase angles are

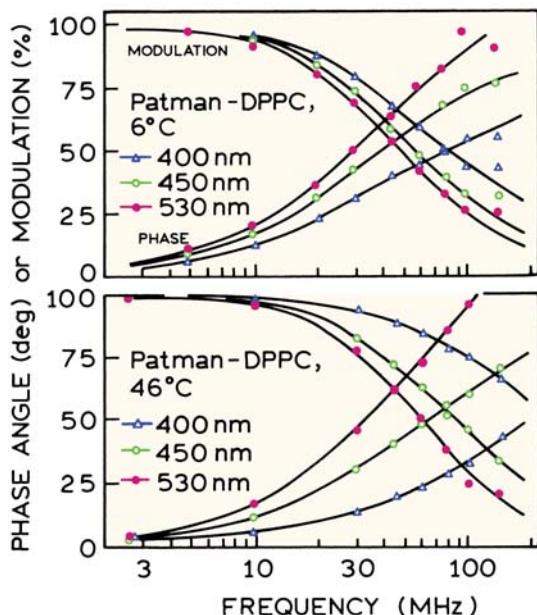


**Figure 7.15.** Frequency-dependent phase and modulation values for Patman-labeled DPPC vesicles. Top, 6°C; bottom, 46°C. For both temperatures, data are shown for 400 ( $\Delta$ , 450 ( $\circ$ ) and 530 nm ( $\bullet$ ). Revised from [26]. Copyright © 1984, with permission from Elsevier Science.

shorter and the modulation values higher than on the red side of the emission. The phase angles on the red side of the emission exceed 90°, which is proof of an excited-state reaction. The data at low temperature (6°C) are also characteristic of an excited-state process, larger phase angles, and lower modulation on the long-wavelength side of the emission. However, the long-wavelength phase angles are less obviously in excess of 90°. An absence of phase angles over 90° does not prove relaxation has not occurred, only that the conditions were not suited to result in very large phase angles.

The phase and modulation data can be used to derive the wavelength-dependent impulse response functions. In this case the data at all wavelengths could be fit to a set of three wavelength-independent lifetimes (Table 7.1). The three decay times are similar at both 8 and 46°C. The main distinction between the high- and low-temperature data is the larger contribution of terms with negative pre-exponential factors at the higher temperature. Phase angles in excess of 90° in the frequency-domain data are similar to negative pre-exponential factors in the time-domain. At the longest emission wavelength these positive and negative terms are nearly equal in magnitude and opposite in sign. This is characteristic of emission from a relaxed state that can be

**Table 7.1.** Intensity Decays of Patman-Labeled DPPC Vesicles<sup>a</sup>

Wavelength	6°C ( $\tau$ , ns)		
	(0.98 ns) $\alpha_1(\lambda)^b$	(3.74 ns) $\alpha_2(\lambda)$	(5.52 ns) $\alpha_3(\lambda)$
400	1.15	0.60	0.25
430	0.21	1.02	0.77
450	-0.13	0.95	0.92
470	-0.40	0.73	0.87
490	-0.50	0.57	0.93
510	-0.61	0.33	1.06
530	-0.74	0.18	1.08
Wavelength	46°C ( $\tau$ , ns)		
	(0.95 ns) $\alpha_1(\lambda)$	(1.48 ns) $\alpha_2(\lambda)$	(3.94 ns) $\alpha_3(\lambda)$
400	1.84	—	0.16
430	0.52	1.16	0.32
450	-0.56	0.91	0.53
470	-0.77	0.45	0.78
490	-0.85	0.14	1.01
510	-0.71	-0.20	1.09
530	-0.50	-0.42	1.08

<sup>a</sup>From [26].

<sup>b</sup>The sum of the absolute values of  $\alpha_i(\lambda)$  are set to 2.0 at each wavelength.

observed without a substantial contribution from the initially excited state.<sup>48</sup>

The recovered impulse response functions (Table 7.1) can be used to calculate the time-resolved emission spectra (Figure 7.16). To facilitate comparison of these spectra we chose to display normalized time-resolved spectra at 0.2, 2, and 20 ns. For DPPC, below its transition temperature near 37° there is only a modest red shift of 15 nm at 20 ns. At 46°C a dramatic spectral shift is seen to occur between 0.2 and 20 ns, about 50 nm. These TRES indicate that the extent and/or rate of spectral relaxation are greater at the higher temperature. At 2 ns and 46°C, the time-resolved emission spectrum of Patman appears wider than at 0.2 or 20 ns. This suggests a two-state model for spectra relaxation. Specifically, at 46°C and 2 ns emission is observed from both the unrelaxed and relaxed states of Patman.

#### 7.4.1. Analysis of Time-Resolved Emission Spectra

The time-dependent spectral shifts can be characterized by the time-dependent center of gravity, in wavenumbers ( $\text{cm}^{-1}$  or  $\text{kK}$ ). The center of gravity is proportional to the average energy of the emission. The center of gravity of the emission is defined by

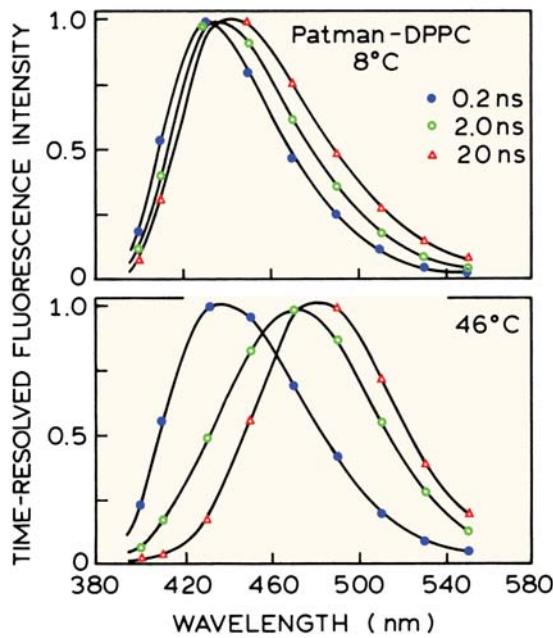


**Figure 7.16.** Time-resolved emission spectra of Patman-labeled DPPC vesicles. Top, 8°C; bottom, 46°C. Time-resolved spectra are shown at 0.2 (●), 2 (○\$), and 20 ns (D\$). Revised from [26]. Copyright © 1984, with permission from Elsevier Science.

$$\bar{v}_{cg}(t) = \frac{\int_0^{\infty} I(\bar{v}, t) \bar{v} d\bar{v}}{\int_0^{\infty} I(\bar{v}, t) d\bar{v}} \quad (7.5)$$

where  $I(\bar{v}, t)$  represents the number of photons per wavenumber interval. These are the intensity decays as normalized in eq. 7.4, but on the wavenumber scale. The data are typically collected for selected wavelengths, and the center of gravity in kK ( $= 10^3 \text{ cm}^{-1}$ ) is calculated using

$$\bar{v}_{cg}(t) = 10,000 \frac{\sum_{\lambda} I(\lambda, t) \lambda^{-1}}{\sum_{\lambda} I(\lambda, t)} \quad (7.6)$$

Note that the integral in eq. 7.5 is over the emission spectrum ( $\bar{v}$ ), and not over time. The TRES at any instant in time are used to calculate  $\bar{v}_{cg}(t)$  at the chosen time. The calculated center of gravity is typically an approximation since the time-resolved data are not collected at all wavelengths. Also, a vigorous calculation of the center of gravity requires use of the corrected emission spectra on the wavenumber scale. Equation 7.6 is simply an expression which uses the available data ( $I(\lambda, t)$ ) to obtain an approximate value of  $\bar{v}_{cg}(t)$ .

The time-dependent emission centers of gravity are shown in Figure 7.17 (top panel). It is apparent that the extent of relaxation is greater at 46°C than at 8°C. The rate of relaxation is somewhat faster at the higher temperature. If desired, the values of  $\bar{v}_{cg}(t)$  versus time can be fit to multi-exponential (eq. 7.15, below) or other non-exponential decay laws for  $\bar{v}_{cg}(t)$ .

The time-dependent spectral half width  $\Delta\bar{v}(t)$  ( $\text{cm}^{-1}$ ) can be used to reveal whether the spectral relaxation is best described by a continuous or two-step model. This half width can be defined in various ways. One method is to use a function comparable to a standard deviation. In this case  $\Delta\bar{v}(t)$  can be defined as

$$[\Delta\bar{v}(t)]^2 = \frac{\int_0^{\infty} (\bar{v} - \bar{v}_{cg}(t))^2 I(\bar{v}, t) d\bar{v}}{\int_0^{\infty} I(\bar{v}, t) d\bar{v}} \quad (7.7)$$

For calculation of  $\Delta\bar{v}(t)$  one uses the TRES calculated for a chosen time  $t$  and integrates eq. 7.7 across the emission spectrum. For data collected at various wavelengths in nanometers the value of  $\Delta\bar{v}(t)$  in kK is given by

$$[\Delta\bar{v}(t)]^2 = \frac{\sum_{\lambda} [10,000/\lambda - \bar{v}_{cg}(t)]^2 I(\lambda, t)}{\sum_{\lambda} I(\lambda, t)} \quad (7.8)$$

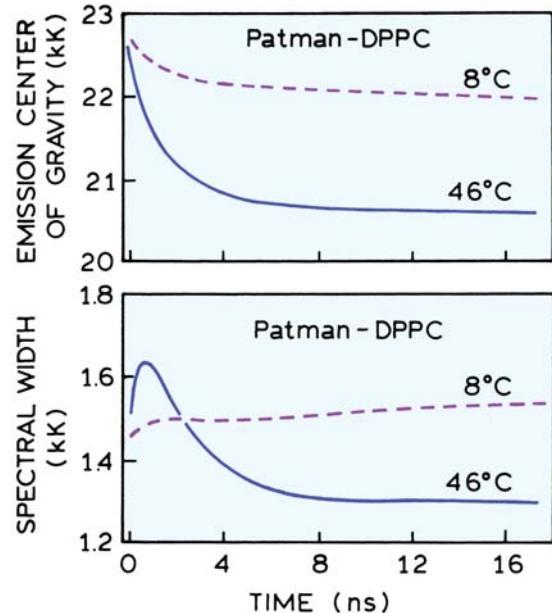


**Figure 7.17.** Time-resolved emission center of gravity (top) and spectral half width (bottom) of Patman-labeled DPPC vesicles. Revised from [26]. Copyright © 1984, with permission from Elsevier Science.

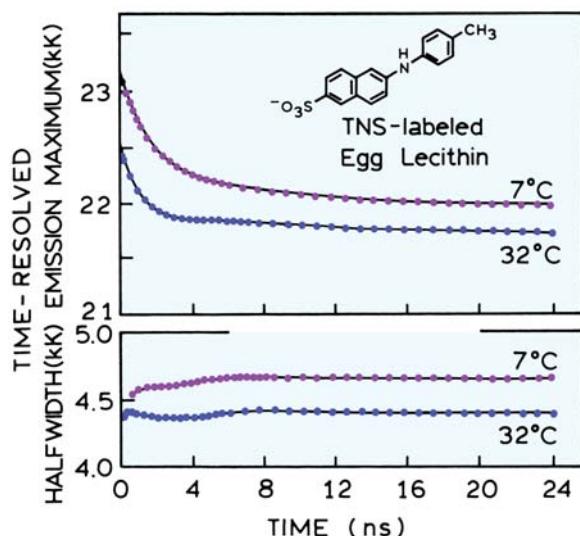


**Figure 7.18.** Time-resolved emission maxima and spectral half widths for TNS-labeled egg lecithin. Redrawn from [48].

Examination of the time-dependent value of  $\Delta\bar{v}(t)$  can reveal the nature of the relaxation process. For Patman in DPPC vesicles at 46°C there is an increase in half width at intermediate times. This suggests that spectral relaxation around Patman is best described as a two-state process. Such behavior is not seen for all probes. For TNS-labeled vesicles<sup>26,48</sup> the half-width remains constant during spectral relaxation (Figure 7.18). This suggests that relaxation around TNS is best described by a continuous process in which an emission spectrum of constant shape slides to longer wavelengths.

#### 7.4.2. Spectral Relaxation of Membrane-Bound Anthroyloxy Fatty Acids

Another example of spectral relaxation in membranes is the anthroyloxy fatty acids, which have been extensively used as membrane probes. One advantage of these probes is that the fluorophore can be localized at the desired depth in the membrane by its point of attachment to the fatty acid. The localized anthroyloxy groups have been used to study the dynamics of spectral relaxation at various depths in membranes. The time-resolved emission spectra of these probes are sensitive to the location of the probe in these membranes.<sup>29</sup> This is seen by the larger time-dependent shifts for 2-AS than for 16-AP (Figure 7.19). At first glance this difference seems easy to interpret, with larger spectral shifts for the probe located closer to the polar membrane-water

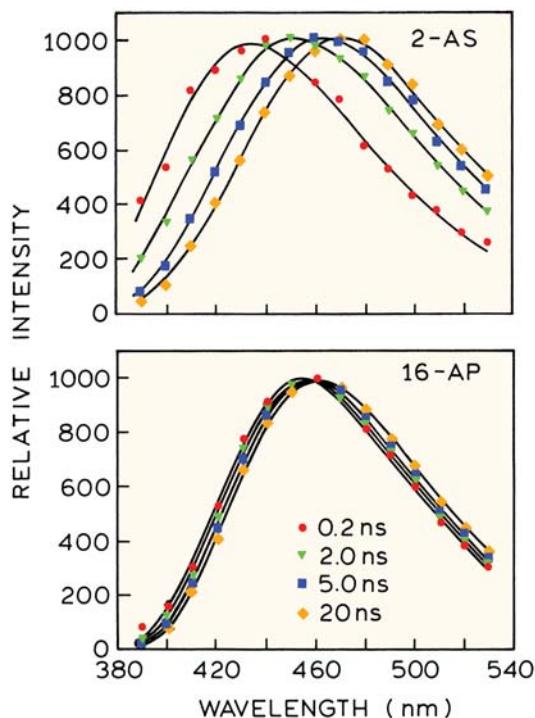


**Figure 7.19.** Time-resolved emission spectra of anthroyloxy fatty acids (2-AS and 16-AP) in egg phosphatidylcholine vesicles. Revised from [29].

interface. However, closer inspection reveals that the emission spectra of 16-AP are more shifted to the red at early times following excitation. This is evident from the time-dependent emission maxima (Figure 7.20). It seems that the probes located deeper in the bilayer should display a more blue-shifted emission. The reason for the larger red shift of 16-AP is not understood at this time. However, it is thought that the anthroyloxy probes near the ends of acyl chains can fold back to the lipid–water interface. The data in Figure 7.20 are consistent with the fluorophores in both 12-AS and 16-AP being localized near the lipid–water interface.

The rates of spectral relaxation for the anthroyloxy probes also seem to be unusual. The fluidity of lipid bilayers is thought to increase towards the center of the bilayer. Examination of the time-dependent emission maxima (Figure 7.20) suggests that the relaxation becomes slower for probes localized deeper in the membranes. This is seen more clearly in the correlation functions (eq. 7.12, below), which display the relaxation behavior on a normalized scale (Figure 7.21). The apparent relaxation times increase from 2.7 to 5.9 ns as the anthroyloxy moiety is attached more distant from the carboxy group. These results can be understood by the membrane becoming more fluid near the cen-

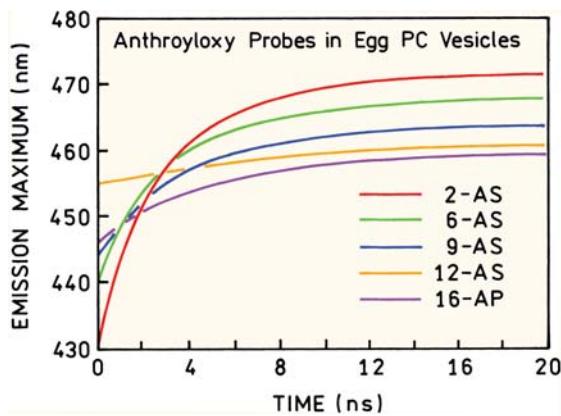


**Figure 7.20.** Time-dependent emission maxima of anthroyloxy fatty acids in egg PC vesicles. Dots: 2-AS; triangles: 6-AS; boxes: 9-AS; circles: 12-AS; asterisks: 16-AP. Revised from [29].

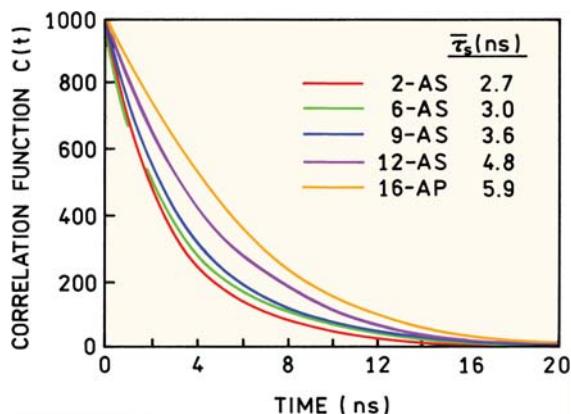


**Figure 7.21.** Correlation functions for spectral relaxation of the anthroyloxy fatty acids in egg PC vesicles. Revised from [29].

ter, if the 12-AS and 16-AP probes are located near the surface. Irrespective of the interpretation, the data demonstrated that membranes relax on the ns timescale, but the details are not completely understood.

## 7.5. PICOSECOND RELAXATION IN SOLVENTS

Advanced Topic

In fluid solvents at room temperature spectral relaxation is usually complete within about 10 ps, which is prior to the emission of most fluorophores. This rapid process is too rapid to be resolved with the usual instrumentation for time-domain or frequency-domain fluorescence. However, advances in laser technology and methods for ultrafast spectroscopy have resulted in an increasing interest in ps

and fs solvent dynamics.<sup>49–61</sup> Because of the rapid timescale the data on solvent dynamic are usually obtained using fluorescence upconversion. This method is described in Chapter 4. Typical data are shown in Figure 7.22 for coumarin 152 (C152). The intensity decays very quickly on the blue side of the emission, and displays a rise on the long-wavelength side of the emission. The total intensity decay of coumarin 152 with a lifetime of 0.9 ns is not visible on the ps timescale of these measurements, as is seen as the nearly horizontal line after 1 ps in the lower panel. The wavelength-dependent upconversion data were used to reconstruct the time-resolved emission spectra, which are shown in Figure 7.23 at 0.1 and 5.0 ps. By 5 ps the relaxation is essentially complete, which is why time-dependent effects are usually not considered for fluorophores in fluid solution.

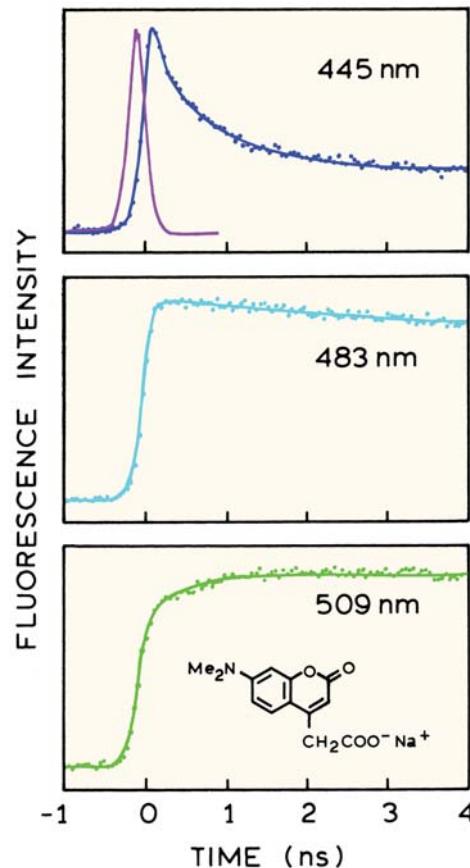


**Figure 7.22.** Fluorescence upconversion intensity decays of 7-(dimethylamino)coumarin-4-acetate (C152) in water. The solid line through the points is a multi-exponential fit to the intensity decay at each wavelength. The peak near zero time in the upper panel is the instrument response function (280 fs FWHM). Revised and reprinted with permission from [61]. Copyright © 1988, American Chemical Society.

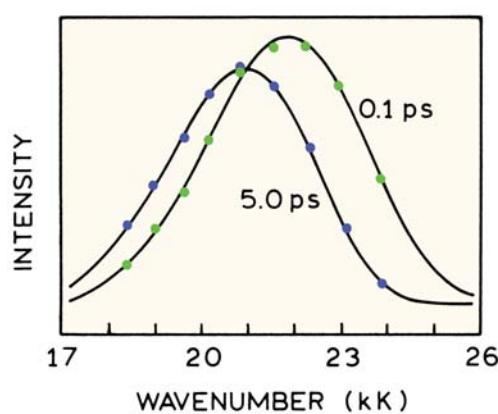


**Figure 7.23.** Time-resolved emission spectra of 7-(dimethylamino)-coumarin-4-acetate in water at 0.1 and 5.0 ps after excitation. Revised and reprinted with permission from [61]. Copyright © 1988, American Chemical Society.

### 7.5.1. Theory for Time-Dependent Solvent Relaxation

There is no comprehensive theory that can be used to explain all time-dependent spectral shifts. This is because the spectral shifts can have their molecular origin in general solvent effects, specific solvent effects, or other excited-state processes. However, it is possible to predict the time dependence of spectral shifts due to general solvent effects. The basic idea is that the reaction field around the excited molecule relaxes in a manner predictable from the dielectric relaxation times ( $\tau_D$ ).<sup>62–65</sup> The dielectric relaxation time is a measure of the time needed for solvent molecules to reorient in response to an electric field. However, the spectral relaxation time ( $\tau_S$ ) is not expected to be equal to  $\tau_D$ , but to be equal to the longitudinal relaxation time ( $\tau_L$ ). The value of  $\tau_L$  is related to the dielectric relaxation time ( $\tau_D$ ) by

$$\tau_S \approx \tau_L = \tau_D \frac{2\epsilon_\infty + \epsilon_c}{2\epsilon_0 + \epsilon_c} \quad (7.9)$$

where  $\epsilon_\infty$  is the infinite frequency dielectric constant, and  $\epsilon_0$  is the low-frequency dielectric constant. The value of  $\epsilon_c$  is the dielectric constant of the cavity containing the fluorophore and is usually set equal to 1, which is near the dielectric constant of organic molecules. The values of  $\tau_L$  are often estimated using various approximations. The value of  $\epsilon_\infty$  is often taken as  $n^2$ , where  $n$  is the refractive index, and the value of  $\epsilon_0$  is taken as the static dielectric constant  $\epsilon$ . Expressions used for  $\tau_L$  include<sup>66–69</sup>

$$\tau_S \approx \tau_L = \frac{2n^2 + 1}{2\epsilon + 1} \tau_D \approx \frac{\epsilon_\infty}{\epsilon_0} \tau_D \approx \frac{n^2}{\epsilon} \tau_D \quad (7.10)$$

Values of  $\tau_D$  and  $\tau_L$  for typical solvents are given in Table 7.2. For polar solvents the spectral relaxation times are expected to be five- to tenfold smaller than the value of  $\tau_D$ . Hence the rate of spectral relaxation is expected to be faster than the rate of dielectric relaxation.

At first glance it seems that the spectral relaxation time should be equal to the dielectric relaxation time, which depends on the rotational rate of the fluorophore. It appears that the difference between  $\tau_D$  and  $\tau_S$  can be explained by classical electrodynamics.<sup>62</sup> The value of  $\tau_D$  refers to the rate of reorientation of the fluorophores to a fixed voltage. Experimentally a fixed voltage is placed on a capacitor at  $t = 0$ , and this voltage is maintained while the system relaxes. The solvent relaxation time is more consistent with creation of a fixed charge on the capacitor at  $t = 0$ , with no additional current flow during relaxation. This second type of experiment predicts the relationship between  $\tau_S$  and  $\tau_D$  in eq. 7.9.

Unfortunately, solvent relaxation even in simple solvents is expected to be complex. This is because most solvents are known to display multiple dielectric relaxation times. For instance, propanol is known to display three dielectric relaxation times. Typical values are listed in Table 7.3. The largest value ( $\tau_{D1}$ ) is too large for overall rotation

**Table 7.2.** Dielectric Properties of Solvents

Solvent	°C	$\epsilon_0$	$\epsilon_\infty$	$n$	$\tau_D$ (ps)	$\tau_L$ (ps)	Ref.
Water	25	78.3	5.2	1.33	8.3	0.4	70
Methanol	19	31.8	2.0	1.33	60	8.2	71
Ethanol	19	26.0	1.9	1.36	90	12.4	71
n-Propanol	19	21.3	1.9	1.38	320	59 ps	71
	-20	27	5.6	-	1.3 ns	0.34 ns	72–74
Glycerol	12	46.8	4.0	-	39 ps	-	75
	-70	74	4.2	-	0.11 ns	-	73

**Table 7.3.** Dielectric Relaxation Times of Alcohols<sup>76-77</sup>

	°C	$\tau_{D1}$ (ps)	$\tau_{D2}$ (ps)	$\tau_{D3}$ (ps)
Methanol	20	52	13	1.4
Ethanol	20	191	16	1.6
n-Propanol	20	430	22	2
	40	286	17	2
n-Butanol	20	670	27	2.4
n-Octanol	20	1780	38	3
	40	668	29	3

of the alcohol molecules, and is attributed to rotation of the alcohol following breakage of a hydrogen bond. The second dielectric relaxation time ( $\tau_{D2}$ ) is assigned to rotational diffusion of the free alcohol molecule. The shortest time ( $\tau_{D3}$ ) is assigned to rotation of the hydroxyl group around the carbon-oxygen bond. Based on this behavior, the center of gravity of the emission spectrum of a fluorophore in n-propanol is expected to decay as

$$\bar{v}_{cg}(t) = \bar{v}_\infty + (\bar{v}_0 - \bar{v}_\infty) \sum_i \beta_i \exp(t/\tau_{si}) \quad (7.11)$$

where  $\beta_i$  are the amplitudes associated with each relaxation time ( $\tau_{si}$ ). Hence, the time-dependent values of  $\bar{v}_{cg}(t)$  can show complex multi-exponential decays even in simple solvents. Complex decays of  $\bar{v}_{cg}(t)$  were already seen for a labeled protein in Figure 7.11.

Spectral relaxation data are frequently presented as the correlation function

$$C(t) = \frac{\bar{v}_{cg}(t) - \bar{v}_\infty}{\bar{v}_0 - \bar{v}_\infty} \quad (7.12)$$

This expression has the advantage of normalizing the extent of relaxation to unity, allowing different experiments to be compared. However, when using eq. 7.12, one loses the information on the emission spectra at  $t = 0$  and  $t = \infty$ . If some portion of the relaxation occurs more rapidly than the time resolution of the measurement, this portion of the energy will be missed and possibly not noticed.

### 7.5.2. Multi-Exponential Relaxation in Water

It is of interest to understand the relaxation times expected for probes in water. Such experiments have become possible because of the availability of femtosecond lasers. One such study examined 7-(dimethylamino)coumarin-4-acetate

tate in water (Figure 7.22).<sup>61</sup> The excitation source was a styryl 8 dye laser, with a 1,1',3,3,3',3'-hexamethylindotri-carbocyanine iodide (HITCI) saturable absorber, which provided 70-fs pulses at 792 nm. These pulses were frequency doubled for excitation at 396 nm.

The emission was detected using sum frequency upconversion with a potassium dehydrogen phosphate (KDP) crystal and the residual 792-nm light for gating the crystal. The instrument response function with an FWHM of 280 fs allowed the intensity decay to be directly recorded (Figure 7.22). These decays showed a rapid component on the short-wavelength side of the emission (top panel), a nearly single-exponential decay near the middle of the emission spectrum (middle panel), and a rise time on the low-energy side of the emission (bottom panel).

These upconversion data allowed construction of the TRES. The time-dependent shifts all occur within 5 ps (Figure 7.24). In this case it was necessary to use two correlation times of 0.16 and 1.2 ps to account for the time-dependent shifts. Both values are smaller than the dielectric relaxation time of water, which is near 8.3 ps (Table 7.2). Similar results have been observed for other fluorophores in other solvents. In general, spectral relaxation times are shorter than the  $\tau_D$  values, but the values of  $\tau_S$  can be smaller or larger than the calculated values of  $\tau_L$ . This is illustrated by Yt-base in n-propanol at  $-20^\circ\text{C}$ .<sup>78</sup> At least two relax-

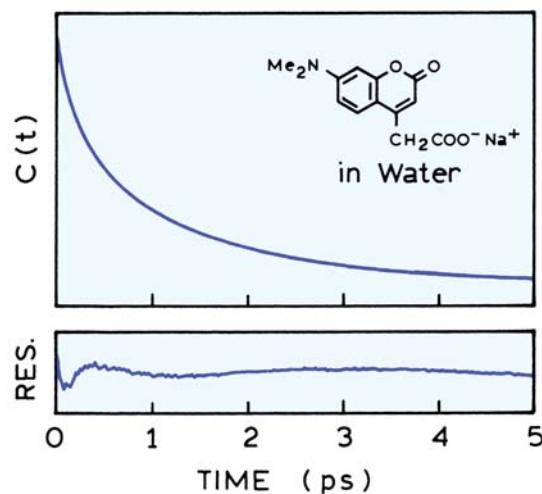


**Figure 7.24.** Correlation function for spectral relaxation of 7-(dimethylamino)coumarin-4-acetate in water. The upper section of the figure is a superposition of an experimentally determined  $C(t)$  function for the water and a biexponential function with relaxation time of 0.16 and 1.2 ps. The lower panel shows the residuals for this fit expanded threefold. Revised and reprinted with permission from [61]. Copyright © 1988, American Chemical Society.

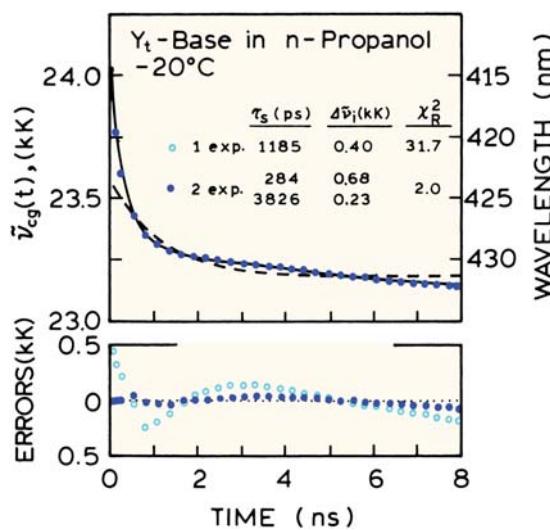


**Figure 7.25.** Time-resolved emission center of gravity of Yt-base in n-propanol at  $-20^{\circ}\text{C}$ . From [78].

ation times are required to explain the time-dependent shifts (Figure 7.25). One can use the correlation functions  $C(t)$  to compare the measured and expected relaxation times (Figure 7.26). For Yt-base in propanol the decay of  $C(t)$  is faster than predicted from the dielectric relaxation time  $\tau_D$ , and slower than predicted from the longitudinal relaxation time

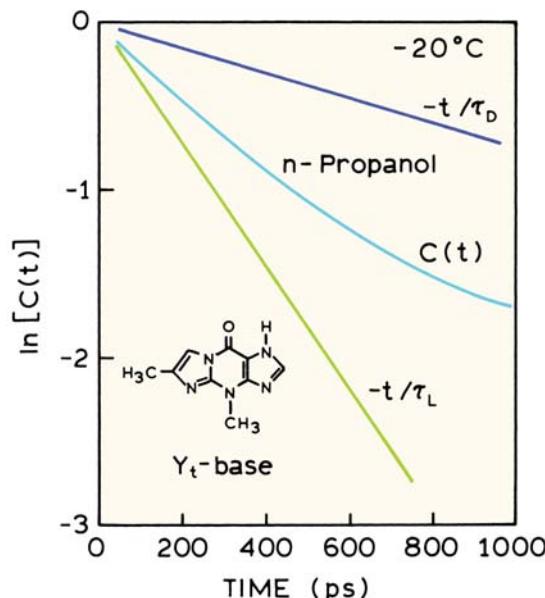


**Figure 7.26.** Extent of spectral relaxation for Yt-base [ $C(t)$ ], compared to the dielectric ( $\tau_D$ ) and longitudinal ( $\tau_L$ ) relaxation times of n-propanol at  $-20^{\circ}\text{C}$ . Revised from [78].

$\tau_L$ . This result is typical of that observed for many fluorophores in polar solvents.<sup>79</sup>

## 7.6. MEASUREMENT OF MULTI-EXPONENTIAL SPECTRAL RELAXATION

Measurement of the complete process of spectral relaxation is a technological challenge. Such measurements are difficult because relaxation occurs over a wide range of timescales. For instance, the dielectric relaxation times for a simple solvent like n-octanol range from 3 to 1780 ps (Table 7.3). Hence the apparatus needs to have resolution of both ps and ns processes. As discussed in Chapter 4,

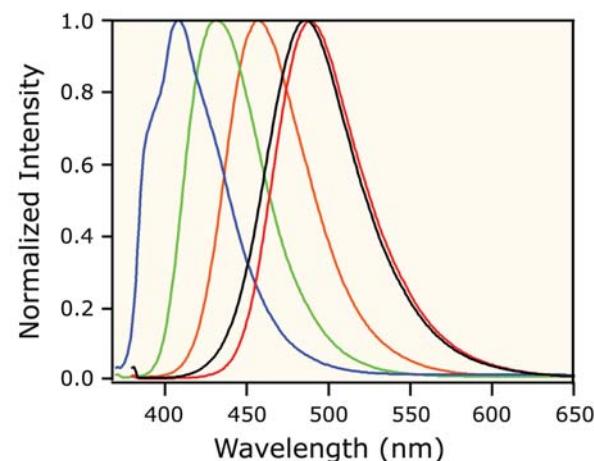
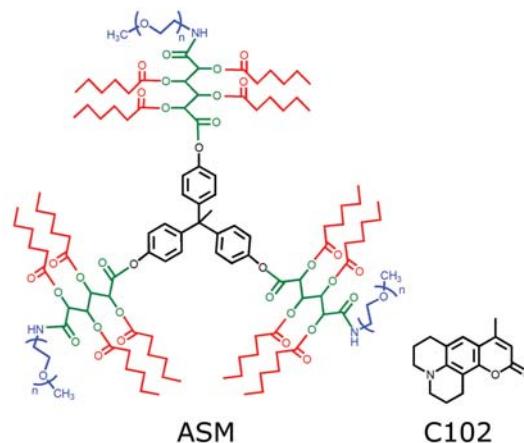


**Figure 7.27.** Chemical structures of an amphiphilic starlike macromolecule (ASM) and coumarin 102 (C102). The lower panel shows the emission spectra of C102 in cyclohexane (blue), ethyl acetate (green), octanol (orange), water (red) and bound to the ASM in water (black). Reprinted with permission from [80]. Copyright © 2002, American Chemical Society. Courtesy of Dr. Edward W. Castner, Jr. from the Rutgers University, NJ.

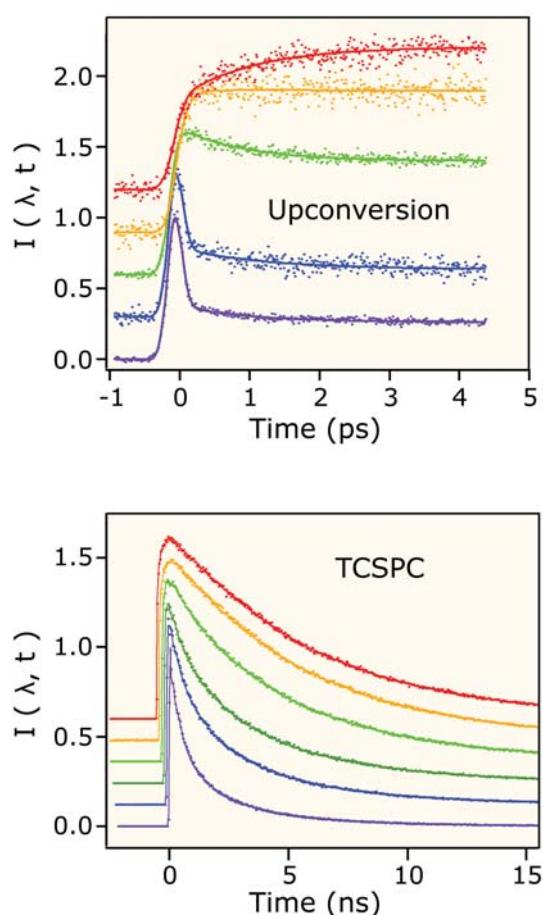


**Figure 7.28.** Wavelength-dependent intensity decays of C102 bound to the ASM. Top, fluorescence upconversion. Bottom, TCSPC. Revised and reprinted with permission from [80]. Copyright © 2002, American Chemical Society. Courtesy of Dr. Edward W. Castner, Jr. from the Rutgers University, NJ.

TCSPC can measure decay time down to about 50 ps. Fluorescence upconversion can be used to measure subpicosecond decay times but is generally less useful for decay times above 100 ps. Hence it would be difficult to measure spectral resolution in a solvent like n-octanol using either type of instrument.

An instructive approach to measuring multi-exponential spectra relaxation is provided for coumarin 102 (C102) bound to an amphiphilic starlike macromolecules (ASM). Such molecules are being developed for use as nanoscale drug carriers. A typical ASM contains a lipophilic core to bind nonpolar drugs and a hydrophilic outer shell for water solubility (Figure 7.27). Such molecules are more stable than other carriers such as micelles or liposomes. The emission spectra of C102 is highly sensitive to solvent polarity.

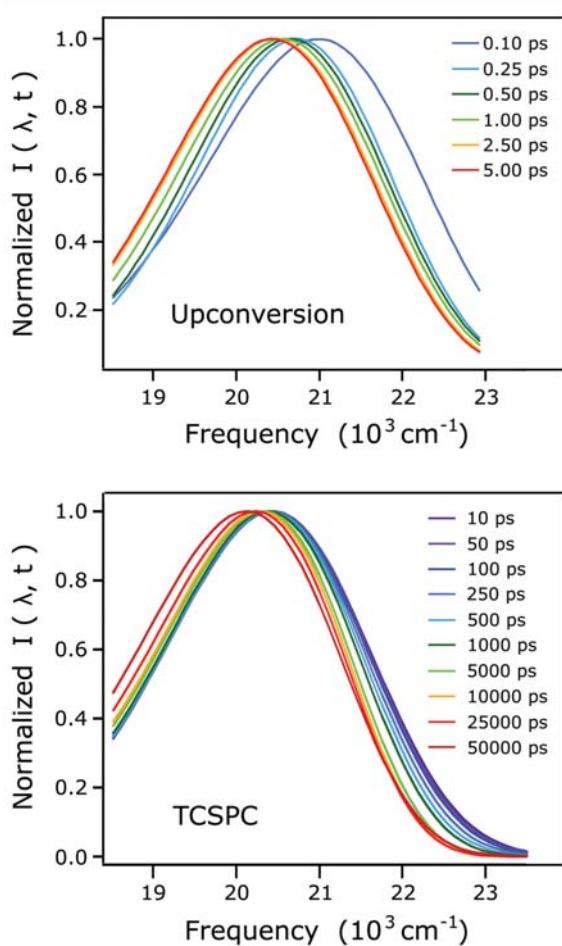
The emission spectrum of C102 bound to the ASM shows that C102 is highly sensitive to solvent polarity, and that C102 is located in a polar water-like environment.<sup>80</sup> The similarity of the emission spectra of C102 in water and in the ASM solution suggests that C102 is in the aqueous phase. However, the anisotropy decays (not shown) demonstrated that C102 was mostly bound to the ASM.

Figure 7.28 shows the wavelength-dependent intensity decays of C102 bound to the ASM. The top panel shows decays measured using fluorescence upconversion for times from 0 to 5 ps. The lower panel shows decays measured by TCSPC for times up to 15 ns. As expected for spectral relaxation, the intensity decayed more rapidly on the short-wavelength side of the emission. These decays were used to calculate the time-relaxed emission spectra (Figure 7.29). Relaxation is occurring both on a subpicosecond timescale, and on a timescale near 500 ps. Using TCSPC measurements alone would have probably not detected the subpicosecond component.

## 7.7. DISTINCTION BETWEEN SOLVENT RELAXATION AND FORMATION OF ROTATIONAL ISOMERS

The shape of the TRES can yield insights into the molecular origin of the time-dependent spectral changes.<sup>81</sup> This concept is illustrated by studies of two closely related fluorophores (BABAPH and BABP, Figure 7.30). These dyes have been used as probes of membrane potential, but an understanding of their excited-state properties was not available. These dyes are known to be solvent dependent, but there was also the possibility that BABP formed rotational isomers in the excited state. In order to separate the solvent-dependent spectral shifts from formation of a polar twisted rotamer, two closely related molecules were examined. The BABAPH derivative contains an ethylene bridge that prevents rotation of the dibutylamino group in the ground or excited state.

Time-resolved decays were recorded at single wavelengths and the decays analyzed in terms of the multi-exponential model. These decays were then used to calculate the time-resolved emission spectra. The normalized TRES show that BABP displays a larger time-dependent shift than does the restrained analogue BABAPH (Figure 7.31). Importantly, the shape of the TRES were time dependent for BABP, but were independent of time for BABAPH. This result was interpreted in terms of formation of a polar twisted state for BABP. Formation of the twisted state was also



**Figure 7.29.** Time-resolved emission spectra of ASM encapsulated C102. Top, fluorescence upconversion. Bottom, TCSPC. Revised and reprinted with permission from [80]. Copyright © 2002, American Chemical Society. Courtesy of Dr. Edward W. Castner, Jr. from the Rutgers University, NJ.

an additional rate of deactivation, resulting in more rapid intensity decays for BABP than for BABAPH (Figure 7.32, lower panel).

The TRES were also used to determine the time-dependent center of gravity ( $\bar{V}_{cg}(t)$ ) and the time-dependent half width ( $\Delta V_{cg}(t)$ ). The results of least-squares fitting of the TRES line shapes are shown in Figure 7.32. The dramatic difference in spectral shape between BABP and BABAPH is seen in the middle panel. The spectral width of the restrained analogue BABP is independent of time, whereas BABAPH shows an increase in spectral width. The data are consistent with rotation of the dibutylamino group in BABP to allow a larger charge separation than in BABAPH. The larger charge separation results in a new

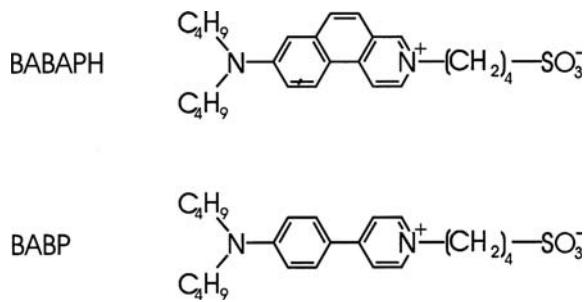


**Figure 7.30.** Hemicyanine dyes 2-(sulfonatobutyl)-7-(dibutylamino)-2-azaphenanthrene (BABAPH) and 1-(sulfonatobutyl)-4-[4'-(dibutylamino)phenyl]pyridine (BABP). Reprinted with permission from [81]. Copyright © 1996, American Chemical Society.

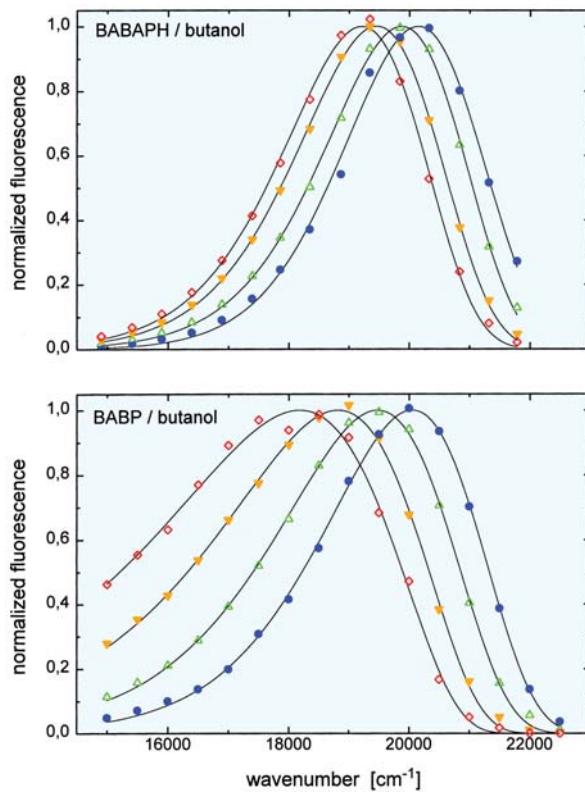


**Figure 7.31.** Normalized time-resolved emission fluorescence spectra of BABAPH and BAPH in butanol, 25°C, at time delays of 20, 50, 150, and 2000 ps after excitation (from right to left). The data are fitted by the log-normal spectral-shape functions. Reprinted with permission from [81]. Copyright © 1996, American Chemical Society.

species emitting at longer wavelengths, and thus the increase in spectral half width of BABAPH. In this case the TRES provided an explanation for the different spectral shifts displayed by these similar molecules.

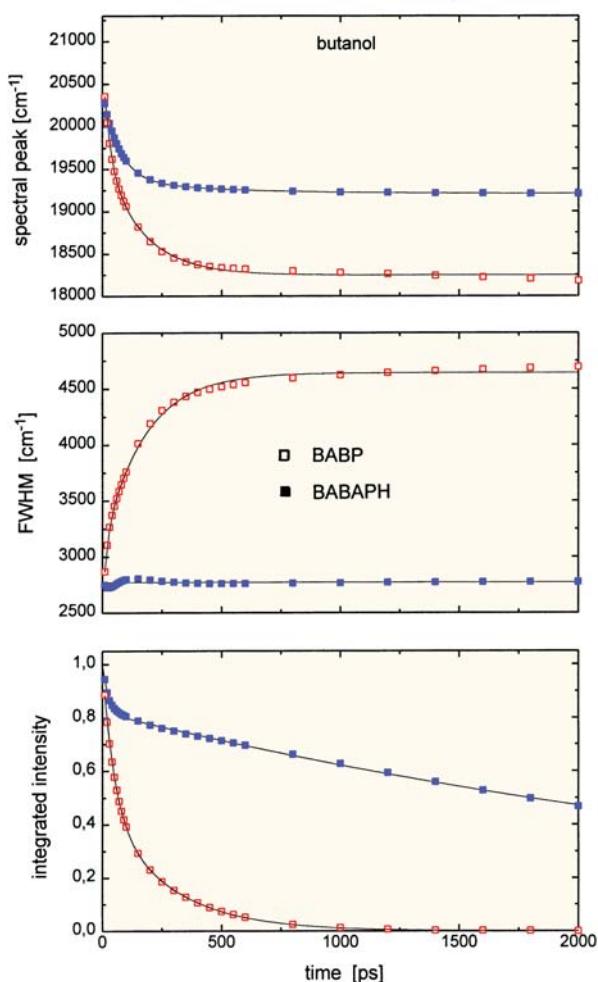


**Figure 7.32.** Fluorescence dynamics of BABAPH (full symbols) and BABP (open symbols) in butanol at 25°C. Top: Position of spectral maximum. Middle: Spectral width (full width at half maximum). Bottom: Integral intensity normalized to its initial value. Reprinted with permission from [81]. Copyright © 1996, American Chemical Society.

## 7.8. COMPARISON OF TRES AND DECAY-ASSOCIATED SPECTRA

In Chapters 4 and 5 we described the use of time-resolved data to calculate the decay-associated spectra (DAS). One may ask how the DAS are related to the TRES. There is no direct relationship between these two types of calculated spectra. This can be seen by examination of the TRES and DAS for a mixture of fluorophores (Figure 7.33, top). This mixture contained anthracene ( $\tau = 4.1$  ns) and 9-cyanoanthracene (9-CA,  $\tau = 11.7$  ns).<sup>82</sup> The TRES show contributions from anthracene and 9-CA at all times. At shorter

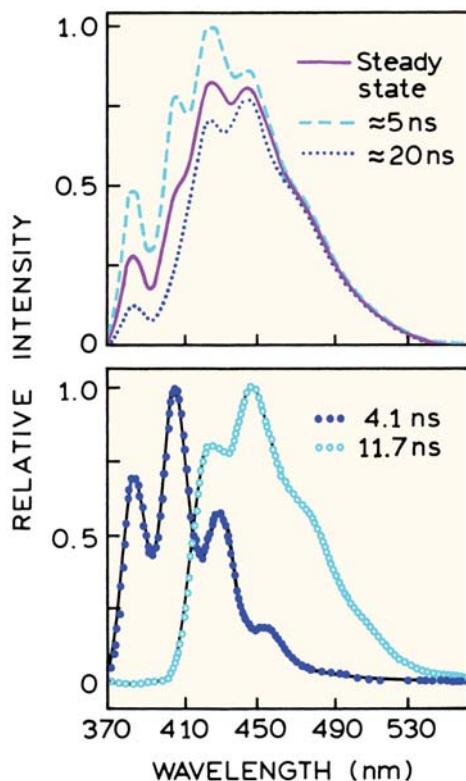


**Figure 7.33.** Top: Steady-state (solid curve) and time-resolved emission spectra of a mixture of anthracene and 9-cyano-anthracene. The TRES are shown for an early time window near 5 ns and a late time window near 20 ns. Bottom: Decay-associated spectra: 4.1 ns (dotted) and 11.7 ns (○). components. Revised and reprinted with permission from [82]. Copyright © 1982, American Chemical Society.

times (approximately 5 ns) the contribution from anthracene is larger than in the steady-state spectrum. At longer times (approximately 20 ns) the relative contribution of the shorter-lived anthracene becomes smaller.

The DAS for this mixture have a completely different meaning (Figure 7.33, bottom). These calculated spectra correspond to the emission spectra of the individual components. Also, the DAS are not dependent on time. Interpretation of the DAS is straightforward for a mixture of fluorophores. However, for time-dependent spectral relaxation the DAS can be positive or negative, and hence do not correspond to the emission spectra of any particular component.

## 7.9. LIFETIME-RESOLVED EMISSION SPECTRA

Advanced Topic

In the preceding sections we described the relatively complex experiments needed to calculate time-resolved emis-

sion spectra. In some circumstances it is possible to obtain information about the rate of relaxation using only steady-state measurements. The basic idea is to use collisional quenching to decrease the lifetime of the excited state ( $\tau$ ) to a value comparable to the relaxation time ( $\tau_s$ ). As described in Section 7.5, the center of gravity of the emission can be expected to decay exponentially from  $\bar{v}_0$  at  $t = 0$  to  $v_\infty$  at  $t = \infty$  according to

$$\bar{v}_{cg}(t) = \bar{v}_\infty + (\bar{v}_0 - \bar{v}_\infty) \exp(-t/\tau_s) \quad (7.13)$$

Suppose the total intensity decays with a single decay time  $\tau$ . The center of gravity observed in a steady-state emission spectra is given by the integral average of  $\bar{v}_{cg}(t)$  over the intensity decay:

$$\bar{v}_{cg} = \frac{\int_0^\infty \bar{v}_{cg}(t) \exp(-t/\tau) dt}{\int_0^\infty \bar{v}_{cg}(t) dt} \quad (7.14)$$

Substitution of eq. 7.13 into 7.15 yields

$$\bar{v}_{cg} = \bar{v}_\infty + (\bar{v}_0 - \bar{v}_\infty) \frac{\tau_s}{\tau_s + \tau} \quad (7.15)$$

This expression connects the center-of-gravity observed in a steady-state experiment, with the relative values of the decay time  $\tau$  and the spectral relaxation time  $\tau_s$ . From this expression one can also understand the spectral shifts observed at low and high temperatures. At low temperature,  $\tau_s \gg \tau$ , and the center of gravity is  $\bar{v}_0$ . At high temperature,  $\tau_s \ll \tau$ , and the relaxed emission is observed. The center of gravity and/or emission spectrum is sensitive to temperature or lifetime when  $\tau_s \approx \tau$ .

Examination of eq. 7.15 suggests an alternative way to measure spectral relaxation.<sup>83-85</sup> Suppose the lifetime  $\tau$  can be changed. Then  $\bar{v}_{cg}$  will vary depending on the relative values of  $\tau$  and  $\tau_s$ . One way to vary the lifetime is by collisional quenching. In the presence of a quenching agent the fluorescence lifetime is decreased according to

$$\tau = \tau_0 / (1 + K_D [Q]) \quad (7.16)$$

where  $\tau_0$  is the lifetime in absence of quenching,  $K_D$  is the collisional quenching constant, and  $[Q]$  is the concentration of quencher. Strictly speaking, calculation of  $\tau$  in the presence of quencher requires the separation of the static and dynamic quenching constants. Hence, the dynamic quench-

ing constant ( $K_D$ , Chapter 8) should be used when calculating the lifetime. For significant quenching one requires solutions of relatively low viscosity to permit rapid diffusion of the quencher. The quenching procedure is particularly useful for biological macromolecules. This is because it permits the relaxation rates to be measured without variation of the temperature. For proteins and membranes, such temperature changes can themselves alter the relaxation rates. An additional advantage of lifetime-resolved measurements is that only steady-state measurements are required, assuming  $\tau_0$  and  $K_D$  are known.

Lifetime-resolved emission spectra of TNS-labeled vesicles are illustrated in Figure 7.34. In this case oxygen was used to decrease the lifetime of TNS. As the average lifetime is decreased from 6.7 to 0.53 ns, the steady-state spectra are seen to shift almost 20 nm to shorter wavelengths. Quenching of fluorescence is a random collisional encounter between TNS and the oxygen molecule. Those fluorophores that remain in the excited state for a longer period of time are more likely to be quenched. The longer-lived fluorophores are also those for which relaxation is more complete. Quenching selectively prevents observation of the emission from these more relaxed fluorophores, and thus results in shifts of the average emission to shorter wavelengths. The lack of change in spectral shape is consistent with the continuous relaxation process shown in Figure 7.6.

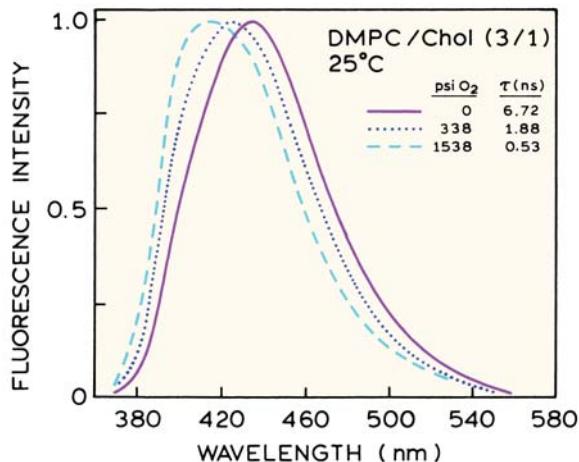


**Figure 7.34.** Effects of oxygen quenching on the fluorescence emission spectrum of TNS-labeled DMPC/cholesterol (3:1) vesicles. Reprinted with permission from the American Chemical Society. Revised and reprinted with permission from [85]. Copyright © 1981, American Chemical Society.

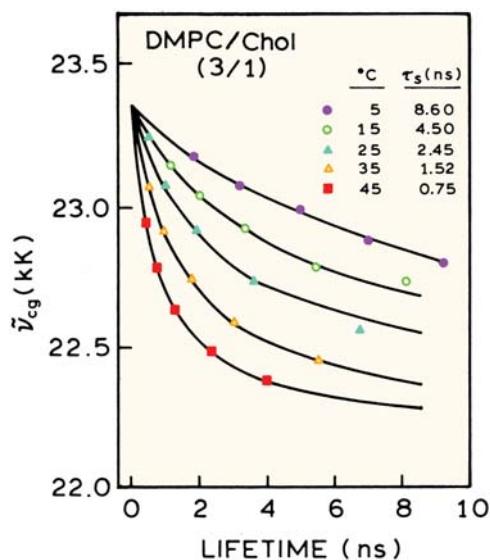


**Figure 7.35.** Lifetime-resolved centers of gravity for TNS-labeled DMPC/cholesterol vesicles. Revised and reprinted with permission from [85]. Copyright © 1981, American Chemical Society.

These lifetime-dependent spectra can be used to measure the spectral relaxation times at the DMPC/cholesterol membranes over a range of temperatures (Figure 7.35). The solid lines through the datapoints represent the best fit using eq. 7.15. It is interesting to note that all these relaxation times fall into a narrow range from 8.6 to 0.75 ns, and do not show evidence for a phase transition. This is probably because the TNS is localized at the lipid–water interface, when the dynamic properties are similar irrespective of the phase state of the acyl side chains.

Oxygen quenching of fluorescence is particularly useful for lifetime-resolved studies of solvent relaxation. Oxygen quenching can provide a wide range of lifetimes with little change in solvent composition. This is because oxygen diffuses rapidly in most solvents, and it is a small nonpolar molecule. In addition, oxygen is highly soluble in organic solvents and is an efficient collisional quencher. These properties result in a large accessible range of lifetimes. However, oxygen quenching requires specialized pressure cells,<sup>83</sup> and of course there are dangers when using high pressures and/or organic solvents.

## 7.10. RED-EDGE EXCITATION SHIFTS

### Advanced Material

In all the preceding discussions we assumed that the emission spectra were independent of the excitation wavelength.

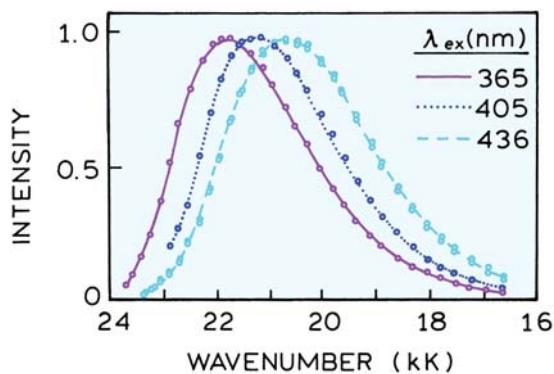


**Figure 7.36.** Emission spectra of 3-amino-N-methylphthalimide in isobutanol at  $-100^{\circ}\text{C}$ . The sample was excited at 365 nm (solid), 405 nm (dotted), and 436 nm (dashed). At  $20^{\circ}\text{C}$  all excitation wavelengths yielded the same emission spectrum (dashed). Revised from [91].

This is a good assumption for fluorophores in fluid solvents. However, this assumption is no longer true in viscous and moderately viscous solvents. For polar fluorophores under conditions where solvent relaxation is not complete, emission spectra shift to longer wavelengths when the excitation is on the long-wavelength edge of the absorption spectrum. This effect can be quite substantial, as is shown for 3-amino-N-methylphthalimide in Figure 7.36. This is known as a red-edge excitation shift, which has been observed in a number of laboratories for a variety of fluorophores.<sup>86–97</sup>

What is the origin of this unusual behavior? The behavior of polar molecules with red-edge excitation can be understood by examining a Jablonski diagram that includes spectral relaxation (Figure 7.37). Suppose the fluorophore is in a frozen solvent, and that the sample is excited in the center of the last absorption band ( $\lambda_{\text{C}}$ ) or on the red edge ( $\lambda_{\text{R}}$ ). For excitation at  $\lambda_{\text{C}}$  the usual emission from the  $F$  state is observed; however, excitation at  $\lambda_{\text{R}}$  selects for those fluorophores that have absorption at lower energy. In any population of molecules in frozen solution there are some fluorophores that have a solvent configuration similar to that of the relaxed state. These fluorophores are typically more tightly hydrogen bonded to the solvent, and thus display a red-shifted emission. In frozen solution the fluorophore-solvent configuration persists during the intensity decay, so that the emission is red shifted.

Knowing the molecular origin of the red-edge shifts, it is easy to understand the effects of increasing temperature. It is known that the red-edge shift disappears in fluid solvents. This is because there is rapid reorientation of the solvent. Hence, even if red-emitting fluorophores are initially

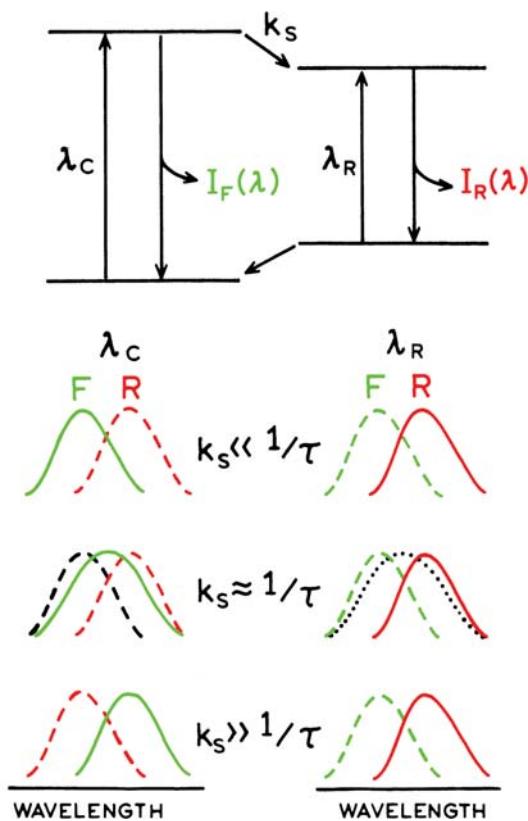


**Figure 7.37.** Effects of red-edge excitation on emission spectra. The term  $\lambda_C$  indicates excitation in the center of the last absorption band of the fluorophore. The term  $\lambda_R$  indicates excitation on the red edge of the absorption band. The solid lines represent the observed spectra. To allow comparison the dashed lines represent the emission spectra of either the F or R state. The dotted line (middle panel) represents a possible consequence of reverse relaxation. Revised and reprinted with permission from [98]. Copyright © 1984, American Chemical Society.

excited, the emission spectra reach equilibrium prior to emission. This implies that there may be some reverse relaxation from the red-shifted emission to the equilibrium condition, as is shown in the middle panel for  $k_s = \tau^{-1}$  (Figure 7.37). In fact, relaxation to higher energies has been observed with red-edge excitation.

Red-edge excitation has been applied to biochemically relevant fluorophores. The widely used probe 1,8-ANS displays a substantial red shift (Figure 7.38). As the excitation wavelength is increased, the emission maxima converge to the same value typical of the relaxed emission (Figure 7.39). This suggests that excitation red shift can be used to estimate biopolymer dynamics.<sup>98–100</sup> Excitation red shifts should only be observed if relaxation is not complete. Also, the magnitude of the red shifts will depend on the rate of

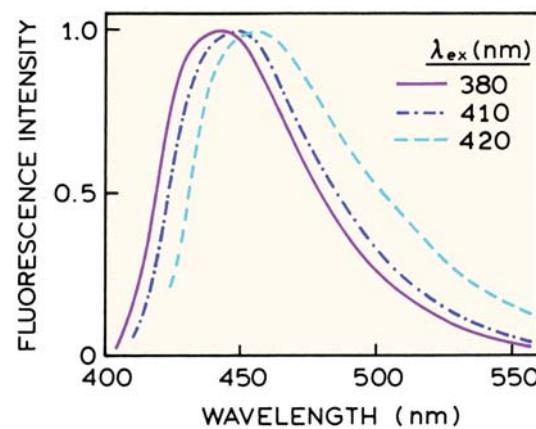


**Figure 7.38.** Fluorescence emission spectra 8-anilinonaphthalene-1-sulfonic acid in 1-propanol at 77 K. Excitation and emission bandpass are both 5 nm. Revised from [95].

spectral relaxation. Excitation red shifts have been observed for labeled proteins, labeled membranes,<sup>101–104</sup> and for the intrinsic tryptophan fluorescence of proteins.<sup>105–109</sup>

### 7.10.1. Membranes and Red-Edge Excitation Shifts

Red-edge excitation shifts (REES) are displayed by solvent sensitive fluorophores in polar environments. This suggests the use of REES to study fluorophores that localize in the headgroup region of lipid bilayers. One example is shown in Figure 7.40 for adducts of NBD. Two NBD derivatives were used: NBD-PE and NBD-Cholesterol. It seemed likely that the polar NBD groups would localize at the lipid–water interface, especially below the phase transition temperature of the DPPC vesicles where the acyl side

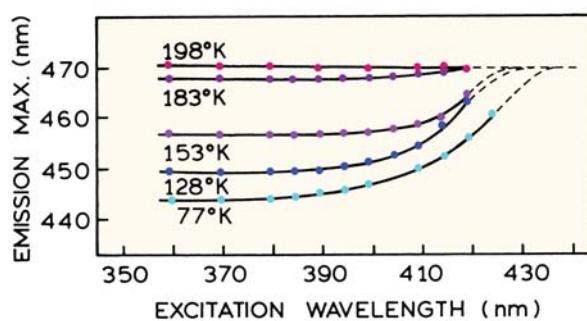


**Figure 7.39.** Temperature dependence of fluorescence excitation red shift for 8-anilinonaphthalene-1-sulfonic acid in 1-propanol. Revised from [95].

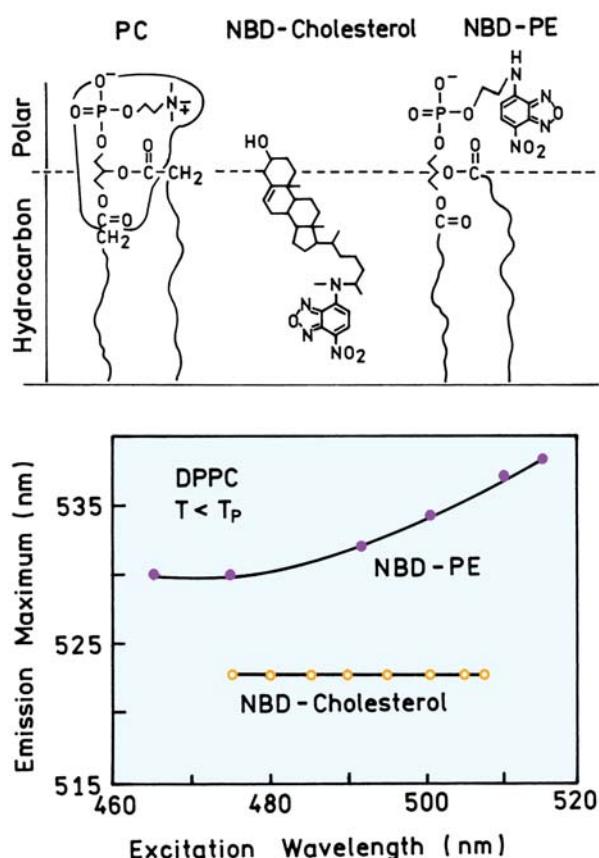


**Figure 7.40.** Red-edge excitation shifts for NBD-PE and NBD-cholesterol in gel phase DPPC vesicles. Revised from [102].

chains are in an ordered conformation. The lower panel in Figure 7.40 shows the dependence of the emission maximum on the excitation wavelengths. For NBD-PE the emission maxima shift about 8 nm with red-edge excitation. In contrast, the emission maxima of NBD cholesterol remain constant regardless of the excitation wavelength. The absence of an REES and the short-wavelength emission maxima of NBD-cholesterol indicate that the NBD group is localized in the acyl side chain region of the membrane, as shown in Figure 7.40. Apparently, the forces that orient the cholesterol moiety are large enough to overcome the tendency of the polar NBD group to localize at the lipid–water interface.

### 7.10.2. Red-Edge Excitation Shifts and Energy Transfer

Red-edge excitation shifts can explain some unusual observations. There are early reports that suggested the failure of

homoresonance energy transfer on red-edge excitation.<sup>110–112</sup> These studies also reported a decrease in the rate of rotational diffusion upon red-edge excitation. The smaller rate of rotational diffusion was explained as being due to excitation of an out-of-plane transition that was not capable of RET. In retrospect, these data are all understandable in terms of the red-edge effect shown in Figure 7.37. The decrease in homotransfer was probably due to the spectral shifts that decreased the overlap integral for homotransfer. The decrease in the rate of rotation can be explained as due to increased hydrogen bonding to the solvent. It is known that the rate of rotational diffusion decreases with increasing numbers of fluorophore-solvent hydrogen bonds.<sup>113</sup> Hence, shifts in the emission spectra can explain the failure of RET with red-edge excitation.

### 7.11. EXCITED-STATE REACTIONS

In the preceding sections of this chapter we considered the interactions of fluorophores with their surrounding environment. These interactions did not involve chemical reactions of the fluorophores. However, fluorophores can undergo chemical reactions while in the excited state. Such reactions occur because light absorption frequently changes the electron distribution within a fluorophore, which in turn changes its chemical or physical properties. The best-known example of a fluorophore that undergoes an excited-state reaction is phenol. In neutral solution phenol and naphthols can lose the phenolic proton in the excited state. Deprotonation occurs more readily in the excited state because the electrons on the hydroxyl groups are shifted into the aromatic ring, making this hydroxyl group more acidic. Excited-state reactions are not restricted to ionization. Many dynamic processes that affect fluorescence can be interpreted in terms of excited-state reactions. These processes include resonance energy transfer and excimer formation (Table 7.4). Excited-state processes display characteristic time-dependent decays that can be unambiguously assigned to the presence of an excited-state process.

Perhaps the most dominant type of an excited-state reaction is the loss or gain of protons.<sup>114–124</sup> Whether a fluorophore loses or gains a photon in the excited-state reaction is determined from the direction of the change in  $pK_A$  in the excited state. If the  $pK_A$  decreases ( $pK_A^* < pK_A$ ), where the asterisk denotes the excited state, then the fluorophore will tend to lose a proton in the excited state. If the  $pK_A$  increases ( $pK_A^* > pK_A$ ), then the fluorophore may pick up a proton in the excited state. The best known examples

**Table 7.4.** Known Excited-State Ionization Reactions

Reaction	Compound	pK <sub>A</sub>	pK <sub>A</sub> <sup>*</sup>	D or P <sup>a</sup>
ROH ⇌ RO <sup>-</sup> + H <sup>+</sup>	Phenol	10.0	4.1	D
	1-Naphthol	9.2	2.0	D
	2-Naphthol	9.5	2.8	D
	HPTS <sup>b</sup>	7.3	1.0	D
RNH <sub>2</sub> ⇌ RNH <sup>-</sup> + H <sup>+</sup>	2-Naphthylamine	>14	12.2	D
RNH <sub>3</sub> <sup>+</sup> ⇌ RNH <sub>2</sub> + H <sup>+</sup>	2-Naphthylamine H <sup>+</sup>	4.1	-1.5	D
ArN + H <sup>+</sup> ⇌ ArNH <sup>+</sup>	Acridine	5.1	10.6	P
RCO <sub>2</sub> <sup>-</sup> + H <sup>+</sup> ⇌ RCO <sub>2</sub> H	Benzoic acid	4.2	9.5	P
	1-Naphthoic acid	3.7	7.7	P
	Anthracene-9-carboxylic acid	3.7	6.9	P

<sup>a</sup>Deprotonation (D) or protonation (P).<sup>b</sup>HPTS, 8-hydroxypyrene-1,3,6-trisulfonate.

are phenols and acridines. In general, phenols undergo excited-state deprotonation, and acridine undergoes excited-state protonation. Electron donors such as  $-\text{OH}$ ,  $-\text{SH}$ ,  $-\text{NH}_2$  have a lone pair of electrons, and these electrons tend to become more conjugated to the aromatic ring system in the excited state, resulting in  $\text{pK}_{\text{A}}^* < \text{pK}_{\text{A}}$ . Electron acceptors such as  $-\text{CO}_2^-$  and  $-\text{CO}_2\text{H}$  have vacant  $\pi$  orbitals into which electrons can be transferred in the excited state. This increased electron density results in weaker dissociation in the excited state:  $\text{pK}_{\text{A}}^* > \text{pK}_{\text{A}}$ . Representative ground-state and excited-state pK<sub>A</sub>s are given in Table 7.4.

### 7.11.1. Excited-State Ionization of Naphthol

Perhaps the most widely studied excited-state reaction is the ionization of aromatic alcohols.<sup>125–131</sup> In the case of 2-naphthol the pK<sub>A</sub> decreases from 9.2 in the ground state to 2.0 in the excited state.<sup>130</sup> In acid solution the emission is from naphthol with an emission maximum of 357 nm (Figure 7.41). In basic solution the emission is from the naphtholate anion, and is centered near 409 nm. At intermediate pH values emission from both species is observed (dashed). Depending on pH, the excited-state dissociation of 2-naphthol can be either reversible or irreversible. At pH values near 3 the reaction is reversible, but at pH values above 6 the reaction is irreversible.<sup>129–130</sup> Hence, this system illustrates the characteristics of both reversible and irreversible excited-state reactions.

The spectra shown in Figure 7.41 illustrate another feature of an excited-state process, which is the appearance of the reaction product under conditions where no product is present in the ground state. At low or high pH, the ground-state fluorophore is present in only one ionization state and only the emission from this state is observed. The absorption spectra of these low- and high-pH solutions are characteristic of naphthol and naphtholate, respectively (Figure 7.42). However, at pH = 3 about 50% of the total emission is from each species. Because the ground state pK<sub>A</sub> of 2-naphthol is 9.2, only the unionized form is present at pH = 3, and the absorption spectrum is that of unionized naphthol. Whereas only unionized naphthol is present in the ground state at pH 3, the emission spectrum at pH 3 shows emission from both naphthol and naphtholate. At pH 3 the naphtholate emission results from molecules that have

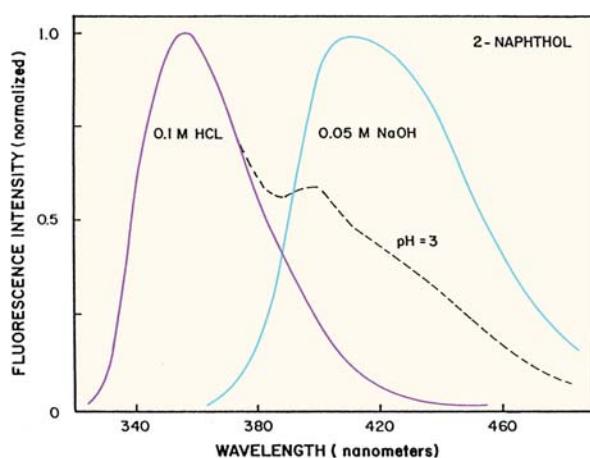


**Figure 7.41.** Steady-state emission spectra of 2-naphthol. Spectra at 24°C are shown in 0.1 M HCl, 0.05 M NaOH and in water at pH = 3.0 (dashed). Reprinted from [139]. Copyright © 1982, with permission from Elsevier Science.

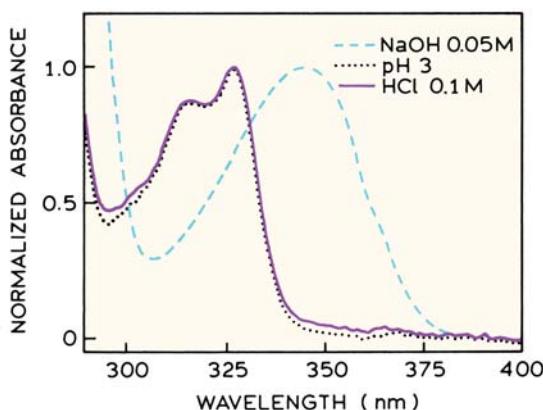


**Figure 7.42.** Absorption spectra of 2-naphthol in 0.1 M HCl, 0.05 M NaOH, and at pH 3.

undergone dissociation during the duration of the excited state. The invariance of the absorption spectrum, under conditions where the emission spectrum of a reacted state is observed, is a characteristic feature of an excited-state reaction.

This characteristic of an excited-state reaction is shown in Figure 7.43. Suppose one measured the fraction of the signal, absorption or emission, from unionized 2-naphthol. The absorption measurement would show a decrease in this fraction at pH 9.2, which is near the ground state  $pK_A$ . The fluorescence measurements would show a change near pH 2, near the  $pK_A^*$  value of the excited state. The difference is due to ionization that occurs during the excited-state lifetime. Depending on the fluorophore and solvent, the excited-state reaction can be complete or only partially complete during the excited-state lifetime. It is also important to note that the extent of dissociation depends on the buffer concen-

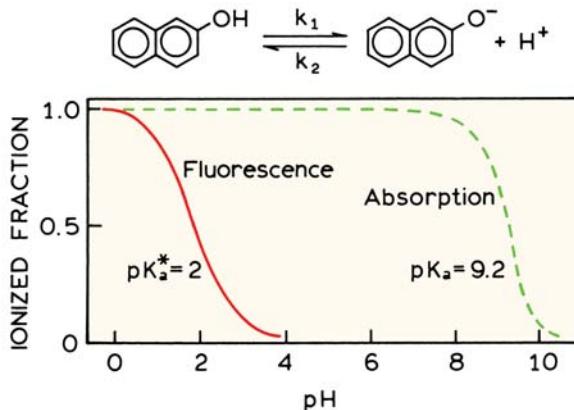


**Figure 7.43.** Comparison of ground state (dashed) and excited-state (solid) ionization of 2-naphthol.

tration. For instance, suppose that 2-naphthol is dissolved in buffer solutions of the same pH, but with an increasing concentration of the buffer. The extent of ionization will increase with increasing buffer concentration owing to reaction of excited 2-naphthol with the weak base form of the buffer.

The spectral shifts that occur upon dissociation in the excited state can be used to calculate the change in  $pK_A$  that occurs upon excitation. This is known as the Förster cycle<sup>132–135</sup> (Figure 7.44). The energies of the ground and excited states depend on ionization. Because the dissociation constants are small, the dissociated form of the fluorophore is shown at higher energy. If the  $pK_A$  value is lower in the excited state ( $pK_A^* < pK_A$ ), then there is a smaller increase in energy upon dissociation of the excited state ( $\Delta H^* < \Delta H$ ). If one assumes that the entropy change for dissociation is the same for the ground and excited states, then the difference in energy between the ground and excited states of AH and  $A^-$  can be related to the change in  $pK_A$  values by

$$\Delta pK_A = pK_A - pK_A^* = \frac{E_{HA} - E_{A^-}}{2.3RT} \quad (7.17)$$

where  $R$  is the gas constant and  $T$  is the temperature (°K). The energies of the protonated form ( $E_{HA}$ ) and of the dissociated form ( $E_{A^-}$ ) are usually estimated from the average of the absorption  $\bar{v}_A$  and emission  $\bar{v}_F$  maxima of each species:

$$E_i = Nhc \frac{\bar{v}_A + \bar{v}_F}{2} \quad (7.18)$$

where  $\bar{v}_A$  and  $\bar{v}_F$  are in  $\text{cm}^{-1}$ ,  $h$  is the Planck constant,  $N$  is Avogadro's number, and  $c$  is the speed of light.

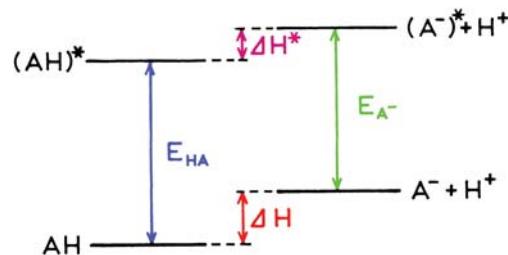


**Figure 7.44.** Electronic energy levels of an acid AH and its conjugate base  $A^-$  in the ground and excited states (the Förster cycle). Reprinted with permission from [131], the *Journal of Chemical Education*, Vol. 69, No. 3, 1992, pp. 247–249. Copyright © 1992, Division of Chemical Education Inc.

While the Förster cycle calculation is useful for understanding the excited-state ionization of fluorophores, the calculated values of  $\Delta pK_A$  should be used with caution. This is because at 300 nm an error of 4 nm corresponds to a shift of one  $pK_A$  unit. Hence the Förster cycle is useful for determining the direction of the change in  $pK_A$  but is less reliable in estimating the precise value of  $pK_A^*$ .

## 7.12. THEORY FOR A REVERSIBLE TWO-STATE REACTION

The features of an excited-state reaction are illustrated by the Jablonski diagram for the reversible two-state model (Figure 7.45). The terms and subscripts F and R refer to the initially excited and the reacted states, respectively. The decay rates of these species are given by  $\gamma_F = \Gamma_F + k_1 + k_{nr}^F$  and  $\gamma_R = \Gamma_R + k_2 + k_{nr}^R$ , where  $\Gamma_F$  and  $\Gamma_R$  are the radiative decay rates, and  $k_{nr}^R$  are the rates of non-radiative decay. The rate of the forward reaction is given by  $k_1$  and the rate of the reverse reaction by  $k_2$ . For simplicity we have not included the rates of intersystem crossing to the triplet state, nor the rates of solvent relaxation. Depending upon the specific process under consideration,  $k_1$  and  $k_2$  can each be more complex than a simple rate constant. For example, in the case of a reversible loss of a proton, the reverse rate would be  $k_2 = k_2' [H^+]$ . In the case of exciplex formation the forward rate would include the concentration of the species ( $Q$ ) forming the exciplex:  $k_1 = k_1'[Q]$ . If the reaction is irreversible,  $k_2 = 0$ . It is simpler to interpret the decay kinetics for irreversible reactions than for reversible reactions. Because there are only two states with well-defined rate constants, it is practical to derive analytical expressions for the steady-state and time-resolved behavior.

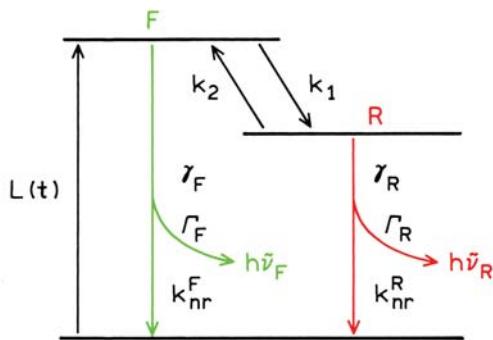


**Figure 7.45.** Jablonski diagram for a reversible excited-state reaction.  $L(t)$  is the excitation function, which can be a pulsed or amplitude-modulated light beam.

### 7.12.1. Steady-State Fluorescence of a Two-State Reaction

Prior to discussing the time-resolved properties of an excited-state reaction, it is useful to describe the spectral properties observed using steady-state methods. Assume that unique wavelengths can be selected where emission occurs only from the unreacted ( $F$ ) or the reacted ( $R$ ) states, and assume initially that the reaction is irreversible, that is,  $k_2 = 0$  (Figure 7.45). The relative quantum yield of the  $F$  state is given by the ratio of the emissive rate to the total rate of depopulation of the  $F$  state. Thus,

$$F_0 = \Gamma_F / (\Gamma_F + k_{nr}^F) \quad (7.19)$$

$$F = \Gamma_F / (\Gamma_F + k_{nr}^F + k_1) \quad (7.20)$$

where  $F_0$  and  $F$  are the fluorescence intensities observed in the absence and presence of the reaction, respectively. Division of eq. 7.20 by 7.21 yields

$$\frac{F}{F_0} = \frac{1}{1 + k_1 \tau_{0F}} \quad (7.21)$$

where  $\tau_{0F} = \gamma_F^{-1} = (\Gamma_F + k_{nr}^F)^{-1}$  is the lifetime of the  $F$  state in the absence of the reaction. Recall that for a bimolecular rate process  $k_1$  would be replaced by  $k_1[Q]$ , where  $Q$  is the species reacting with the fluorophore. Hence, for some circumstances, the initially excited state can be quenched by a Stern-Volmer dependence.

The yield of the reaction product  $R$  is the fraction of  $F$  molecules that have reacted. This yield is given by

$$\frac{R}{R_0} = 1 - \frac{F}{F_0} = \frac{k_1 \tau_{0F}}{1 + k_1 \tau_{0F}} \quad (7.22)$$

where  $R$  and  $R_0$  are the intensities of the reacted species when the reaction is incomplete and complete, respectively. In the case of excimer formation,  $R_0$  would be observed at high concentrations of the monomer. It is important to note the distinctly different dependence of the  $F$ - and  $R$ -state intensities on the extent of the reaction. The intensity of the  $F$  state is decreased monotonically to zero as the reaction rate becomes greater than the reciprocal lifetime. In contrast, the intensity of the  $R$  state is zero when the forward rate constant is much less than the decay rate of the  $F$  state:  $k_1 < \gamma_F$  or  $k_1 \tau_{0F} \ll 1$ . The intensity of the  $R$  state increases

to a constant value when  $k_1 \tau_{0F} \gg 1$ . The reason for this limiting behavior is that essentially all the  $F$  state is converted to the  $R$  state. In practice, the fluorescence of the reacted species may not reach a limiting value, but may rather decrease as the rate of the forward reaction is increased. This can occur because the conditions needed to drive the reaction to completion may result in other interactions that quench the  $R$  state.

### 7.12.2. Time-Resolved Decays for the Two-State Model

The model described in Figure 7.45 is described by the following kinetic equations:

$$-\frac{d[F]}{dt} = \gamma_F [F] - k_2[R] - L(t) \quad (7.23)$$

$$-\frac{d[R]}{dt} = \gamma_R [R] - k_1[F] \quad (7.24)$$

where  $[F]$  and  $[R]$  are the concentrations of these states and  $L(t)$  is the time profile of the excitation. The solution to these kinetic equations has been described previously with the boundary conditions  $[F] = [F_0]$  and  $[R] = 0$  at  $t = 0$ .<sup>129–130,136–137</sup> Following  $\delta$ -pulse excitation the fluorescence decays of the  $F$  and  $R$  states are given by expressions of the form

$$I_F(t) = \alpha_1 \exp(-\gamma_1 t) + \alpha_2 \exp(-\gamma_2 t) \quad (7.25)$$

$$I_R(t) = \beta_1 \exp(-\gamma_1 t) - \beta_2 \exp(-\gamma_2 t) \quad (7.26)$$

where the  $\alpha_i$ ,  $\beta_i$ , and  $\tau_i$  values are moderately complex functions of the various rate constants. The values of  $\gamma_1 = \tau_1^{-1}$  and  $\gamma_2 = \tau_2^{-1}$  are given by

$$\gamma_1, \gamma_2 = \frac{1}{2} \{ (x + y) \mp [(x + y)^2 + 4k_1 k_2]^{1/2} \} \quad (7.27)$$

where

$$x = \Gamma_F + k_{nr}^F + k_1 = \gamma_F + k_1 \quad (7.28)$$

$$y = \Gamma_R + k_{nr}^R + k_2 = \gamma_R + k_2 \quad (7.29)$$

The important point from these equations is that both species display the same decay times, and that the decays of both states is a double exponential decay. Hence, the consequence of a reversible excited-state reaction is that the  $F$  and  $R$  states both display a double-exponential decay, and that the decay times are the same for both species.

Another important characteristic of an excited-state reaction is seen from the pre-exponential factors for the  $R$  state. If only the  $R$  state is observed, then the pre-exponential factors ( $\beta_i$ ) for the two lifetimes are expected to be equal and opposite (eq. 7.26). The negative pre-exponential factor results in a rise in intensity, which is characteristic of excited-state reactions.

For many molecules that display excited-state reactions there is spectral overlap of the  $F$  and  $R$  states. If one measures the wavelength-dependent intensity decays this will be described by

$$I(\lambda, t) = \alpha_1(\lambda) \exp(-t/\tau_1) + \alpha_2(\lambda) \exp(-t/\tau_2) \quad (7.30)$$

where the same two decay times will be present at all wavelengths. In this case one can perform a global analysis with two wavelength-independent lifetimes. The meaning of the  $\alpha_i(\lambda)$  values is complex, and has been described in detail.<sup>130</sup> As the observation wavelength is increased one observes an increasing fraction of the  $R$  state. The  $\alpha_i(\lambda)$  values thus shift from those characteristic of the  $F$  state (eq. 7.25) to those characteristic of the  $R$  state (eq. 7.26). On the long-wavelength side of the emission one expects to observe a negative pre-exponential factor, unless the spectral shift is small so that the  $F$  and  $R$  states overlap at all wavelengths. The values of  $\alpha_i(\lambda)$  can be used to calculate decay-associated spectra (DAS), which shows positive and negative amplitudes. The DAS do not correspond to the emission spectra of either of the species. The  $I(\lambda, t)$  data can also be used to calculate the species-associated spectra (SAS), which are the spectra of each of the states (Section 7.14.3).

The theory for an excited-state reaction is considerably simplified if the reaction is irreversible ( $k_2 = 0$ ). In this case eq. 7.27 yields  $\gamma_1 = \gamma_F + k_1$  and  $\gamma_2 = \gamma_R$ . Also, one of the pre-exponential factors in eq. 7.25 becomes zero, so that

$$I_F(t) = \alpha_1 \exp(-\gamma_1 t) \quad (7.31)$$

$$I_R(t) = \beta_1 \exp(-\gamma_1 t) - \beta_2 \exp(-\gamma_2 t) \quad (7.32)$$

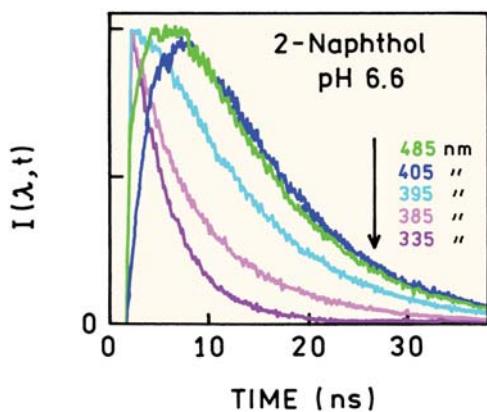


**Figure 7.46.** Time- and wavelength-dependent intensity decays of 2-naphthol in 10 mM sodium phosphate buffer, pH = 6.6. Revised and reprinted with permission from [141]. Copyright © 2001, American Chemical Society.

Hence, the decay of the initially excited state becomes a single exponential. This prediction has been verified in experimental studies of reversible and irreversible reactions. We note that the negative pre-exponential factor may be associated with either of the decay times ( $\tau_1$  or  $\tau_2$ ) depending on the values of the kinetic constants. The negative pre-exponential factor is always associated with the shorter decay time.<sup>138</sup>

### 7.12.3. Differential Wavelength Methods

In considering excited-state reactions there is a general principle that clarifies the complex decay kinetics and results in simplified methods of analysis.<sup>139–140</sup> This principle is that the population of the *R* state can be regarded as a convolution integral with the *F* state. That is, the *F*-state population is the excitation pumping function of the *R* state. Consider a measurement of the *R* state, made relative to the *F* state. The *F* state effectively becomes the lamp function, so that measurements relative to the *F* state directly reveal the decay kinetics of the *R* state. The application of this procedure requires a spectral region where the emission from the *F* state can be observed, without overlap from the *R* state. Since non-overlap of states is frequently found on the short-wavelength side of the emission, the time profile of the *F* state can generally be measured directly. Deconvolving the *R*-state emission with the *F*-state emission yields the lifetime of the *R* state that would be observed if the *R* state could be directly excited.

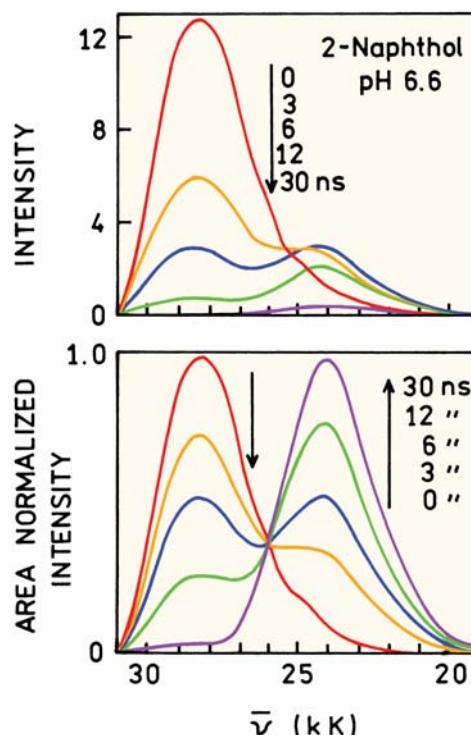


**Figure 7.47.** Time-resolved emission spectra of 2-naphthol in 10 mM sodium phosphate, pH 6.6. The top panel shows the actual time-resolved intensities. The lower panel shows the area-normalized intensities. Revised and reprinted with permission from [1041]. Copyright © 2001, American Chemical Society.

### 7.13. TIME-DOMAIN STUDIES OF NAPHTHOL DISSOCIATION

The properties of excited-state reactions can be effectively studied using time-domain methods. Typical data for the excited-state ionization of 2-naphthol are shown in Figure 7.46. The time-dependent data were collected at wavelengths across the emission spectrum ranging from 335 to 485 nm.<sup>141</sup> Examination of Figure 7.41 shows the emission at 335 nm is from the unionized form of 2-naphthol and the emission at 485 nm is due to the ionized naphtholate form. The naphtholate emission starts at zero and shows a rise time during which the ionized species is formed.

Time-resolved data collected across the emission spectra can be used to calculate the time-resolved emission spectra (Figure 7.47). The top panel shows the actual time-resolved intensities, not the peak or area-normalized values. As time proceeds the emission from both species decays to zero. At  $\tau = 0$  the emission is dominantly due to unionized

2-naphthol. The ionized form shows a transient increase in intensity at time from 3 to 12 ns. These TRES show two distinct emission spectra, which is different from the gradual spectral shifts seen for solvent relaxation. The lower panel in Figure 7.47 shows the TRES that are normalized to the same total area. These spectra show an isoemissive point at 389 nm. Observation of an isoemissive point in the area-normalized TRES proves that there are only two emitting species.<sup>139</sup> An isoemissive point is not expected for continuous spectral relaxation or if there are more than two emitting species.

#### 7.14. ANALYSIS OF EXCITED-STATE REACTIONS BY PHASE-MODULATION FLUOROMETRY

Frequency-domain fluorometry provides a number of interesting opportunities for the analysis of excited-state reactions. One measures the frequency responses across the emission spectra. These data can be used to construct the TRES. However, the data can also be analyzed in terms of the kinetic constants, which leads to insights into the meaning of the measured phase and modulation values. Additional detail can be found elsewhere.<sup>142–144</sup>

For simplicity we consider the irreversible reaction ( $k_2 = 0$ ). Assume that by appropriate optical filtering the emission from the  $F$  and  $R$  states can be individually observed. Then, relative to the phase and modulation of the excitation, the phase and modulation of the  $F$  and  $R$  state are given by

$$\tan \phi_F = \omega / (\gamma_F + k_1) = \omega \tau_F \quad (7.33)$$

$$m_F = \frac{\gamma_F + k_1}{\sqrt{(\gamma_F + k_1)^2 + \omega^2}} = \frac{1}{\sqrt{1 + \omega^2 \tau_F^2}} \quad (7.34)$$

Several aspects of these equations are worthy of mention. Since we have initially assumed that  $F$  and  $R$  are separately observable, and the reverse reaction does not occur, the decay of  $F$  is a single exponential. Hence, for the  $F$  state we find the usual expressions for calculation of lifetimes from phase and modulation data. In the absence of any reaction ( $k_1 = 0$ ) the lifetime is  $\tau_{0F} = \gamma_F^{-1}$ . In the presence of a reaction, the lifetime of  $F$  is shortened to  $\tau_F = (\gamma_F + k_1)^{-1}$ . Thus, for an irreversible reaction, the observed values of  $\phi_F$  and  $m_F$  can be used to calculate the true lifetime of the unreacted state.

The phase and modulation of the  $R$  state, when measured relative to the excitation, are complex functions of the various kinetics constants. These values are given by

$$\tan \phi_R = \frac{\omega(\gamma_F + \gamma_R + k_1)}{\gamma_R(\gamma_F + k_1) - \omega^2} \quad (7.35)$$

$$m_R = m_F \frac{\gamma_R}{\sqrt{\gamma_R^2 + \omega^2}} = m_F m_{0R} \quad (7.36)$$

In contrast to the  $F$  state, the measured values for the  $R$  state cannot be directly used to calculate the  $R$  state fluorescence lifetime. The complexity of the measured values ( $\phi_R$  and  $m_R$ ) shows why it is not advisable to use the apparent phase ( $\tau^\phi$ ) and modulation ( $\tau^m$ ) lifetimes of the relaxed state.

Closer examination of eqs. 7.33–7.36 reveals important relationships between the phase and modulation values of the  $F$  and  $R$  states. For an excited-state process, the phase angles of the  $F$  and  $R$  states are additive, and the modulations multiply. Once this is understood, the complex expressions (eqs. 7.35–7.36) become easier to understand. Let  $\phi_{0R}$  be the phase angle of the  $R$  state that would be observed if this state could be excited directly. Of course, this is related to the lifetime of the directly excited  $R$  state by  $\tan \phi_{0R} = \omega \tau_{0R}$ . Using eq. 7.36, the law for the tangent of a sum, and  $\tan(\phi_F + \phi_{0R}) = \tan \phi_R$ , one finds

$$\phi_R = \phi_F + \phi_{0R} \quad (7.37)$$

Hence, the phase angle of the reacted state, measured relative to the excitation, is the sum of the phase angle of the unreacted state ( $\phi_F$ ) and the phase angle of the reacted state, if this state could be directly excited ( $\phi_{0R}$ ). This relationship (Figure 7.48) may be understood intuitively by recognizing that the  $F$  state is populating the  $R$  state. Of course, these are the same considerations used to describe differential-wavelength deconvolution. For the irreversible reaction, measurement of  $\Delta\phi = \phi_R - \phi_F = \phi_{0R}$  reveals directly the intrinsic lifetime of the reacted fluorophore, unaffected by its population through the  $F$  state.

The demodulation factors of the two states display similar properties. From eq. 7.36 one finds that the demodulation of the relaxed state ( $m_R$ ) is the product of the demodulation of the unrelaxed state ( $m_F$ ) and that demodulation due to the intrinsic decay of the  $R$  state alone ( $m_{0R}$ ). That is,

$$m_R = m_F \frac{1}{\sqrt{1 + \omega^2 \tau_R^2}} = m_F m_{0R} \quad (7.38)$$

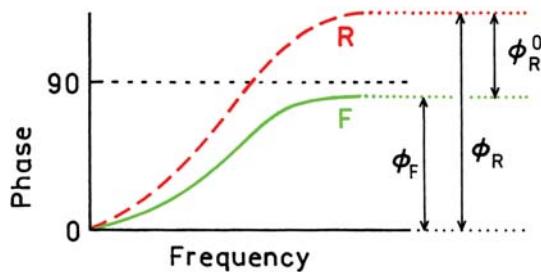


Figure 7.48. Relationship of the phase angles of the  $F$  and  $R$  states.

A further interesting aspect of the phase difference or the demodulation between  $F$  and  $R$  is the potential of measuring the reverse reaction rate  $k_2$ . This reverse rate can be obtained from the phase-angle difference between the  $R$  and  $F$  states, or from the modulation of the  $R$  state relative to the  $F$  state. For a reversible reaction these expressions are

$$\tan(\phi_R - \phi_F) = \frac{\omega}{(\gamma_R + k_2)} = \omega\tau_R \quad (7.39)$$

$$\frac{m_R}{m_F} = \frac{\gamma_R + k_2}{\sqrt{(\gamma_R + k_2)^2\omega^2}} = \frac{1}{\sqrt{1 + \omega^2\tau_R^2}} \quad (7.40)$$

These expressions are similar to the usual expressions for the dependence of phase shift and demodulation on the decay rates of an excited state, except that the decay rate is that of the reacted species ( $\gamma_R + k_2$ ). The initially excited state populates the relaxed state and the reverse reaction repopulates the  $F$  state. Nonetheless, the kinetic constants of the  $F$  state do not affect the measurement of  $\tan(\phi_R - \phi_F)$  or  $m_R/m_F$ . Measurement of either the phase or modulation of the reacted state, relative to the unrelaxed state, yields a lifetime of the reacted state. This lifetime is decreased by the reverse reaction rate in a manner analogous to the decrease in the lifetime of the  $F$  state by  $k_1$ . If the decay rate ( $\gamma_R$ ) is known,  $k_2$  may be calculated. If the emission results from a single species that displays one lifetime, and  $\phi$  and  $m$  are constant across the emission, then  $\phi_R - \phi_F = 0$  and  $m_R/m_F = 1$ .

Returning to the irreversible model, we note an interesting feature of  $\phi_R$  (eq. 7.35). This phase angle can exceed  $90^\circ$ . Specifically, if  $\omega^2$  exceeds  $\gamma_R(\gamma_F + k_1)$ , then  $\tan \phi_R < 0$  or  $\phi_R > 90^\circ$ . In contrast, the phase angles of directly excited species, or the phase angles resulting from a heterogeneous population of fluorophores, cannot exceed  $90^\circ$ . Therefore, observation of a phase angle in excess of  $90^\circ$  constitutes proof of an excited-state reaction.

### 7.14.1. Effect of an Excited-State Reaction on the Apparent Phase and Modulation Lifetimes

The multiplicative property of the demodulation factors and the additive property of the individual phase angles are the origin of a reversed frequency dependence of the apparent phase shift and demodulation lifetimes, and the inversion of apparent phase and modulation lifetimes when compared to a heterogeneous sample. The apparent phase lifetime ( $\tau_R^\phi$ ) calculated from the measured phase ( $\phi_R$ ) of the relaxed state is

$$\tan \phi_R = \omega\tau_R^\phi = \tan(\phi_F + \phi_{0R}) \quad (7.41)$$

Recalling the law for the tangent of a sum one obtains

$$\tau_R^\phi = \frac{\tau_F + \tau_{0R}}{1 - \omega^2\tau_F\tau_{0R}} \quad (7.42)$$

Because of the term  $\omega^2\tau_F\tau_{0R}$ , an increase in the modulation frequency can result in an increase in the apparent phase lifetime. This result is opposite to that found for a heterogeneous emitting population where the individual species are excited directly. For a heterogeneous sample an increase in modulation frequency yields a decrease in the apparent phase lifetime.<sup>145</sup> Therefore, the frequency dependence of the apparent phase lifetimes can be used to differentiate a heterogeneous sample from a sample that undergoes an excited-state reactions. Similarly, the apparent modulation lifetime is given by

$$\tau_R^m = \left( \frac{1}{m_R^2} - 1 \right)^{-1/2} \quad (7.43)$$

Recalling eq. 7.36, one obtains

$$\tau_R^m = (\tau_F^2 + \tau_{0R}^2 + \omega^2\tau_F^2\tau_{0R}^2)^{1/2} \quad (7.44)$$

Again, increasing  $\omega$  yields an increased apparent modulation lifetime. This frequency dependence is also opposite to that expected from a heterogeneous sample, and is useful in proving that emission results from an excited-state process. In practice, however, the dependence of  $\tau_R^m$  upon modulation frequency is less dramatic than that of  $\tau_R^\phi$ . We again stress that the calculated lifetimes are apparent values and not true lifetimes.

The information derived from phase-modulation fluorometry is best presented in terms of the observed quantities

$\phi$  and  $m$ . For a single-exponential decay, and for the unrelaxed state if relaxation is irreversible,  $m_F = \cos \phi_F$ . Also  $m_{0R} = \cos \phi_{0R}$ , irrespective of the reversibility of the reaction. A convenient indicator of an excited-state process is the ratio  $m/\cos \phi$ , where  $m$  and  $\phi$  are the experimentally measured demodulation factor and phase angle, respectively. This ratio is unity for a single-exponential decay, and is less than one for a heterogeneous emission. In contrast,  $m/\cos \phi > 1$  if the emitting species forms subsequent to excitation.<sup>146</sup> Using eqs. 7.37 and 7.38, and the law for the cosine of a sum, we obtain

$$\begin{aligned}\frac{m_R}{\cos \phi_R} &= \frac{\cos \phi_{0R} \cos \phi_F}{\cos(\phi_{0R} + \phi_F)} \\ &= \frac{\cos \phi_{0R} \cos \phi_F}{\cos \phi_{0R} \cos \phi_F - \sin \phi_{0R} \sin \phi_F} \quad (7.45)\end{aligned}$$

Dividing numerator and demodulator by  $\cos \phi_{0R} \cos \phi_F$  we obtain

$$\frac{m_R}{\cos \phi_R} = \frac{1}{1 - \tan \phi_{0R} \tan \phi_F} = \frac{1}{1 - \omega^2 \tau_{0R} \tau_F} \quad (7.46)$$

If relaxation is much slower than emission, significant relaxation does not occur. The  $R$  state cannot be observed and eq. 7.46 cannot be applied. If relaxation is much faster than emission,  $\phi_F = 0$  and  $m_R/\cos \phi_R = 1$ . Importantly, if relaxation and emission occur on comparable timescales, ratio  $m_R/\cos \phi_R$  exceeds unity. Observation of  $m/\cos \phi > 1$  proves the occurrence of an excited-state reaction. However, failure to observe  $m/\cos \phi > 1$  does not prove a reaction has not occurred. Heterogeneity, spectral overlap or the reverse reaction can prevent observation of  $m/\cos \phi > 1$ .

#### 7.14.2. Wavelength-Dependent Phase and Modulation Values for an Excited-State Reaction

The general features of phase-shift and demodulation data for a sample that undergoes an irreversible excited-state reaction is illustrated by the excited-state protonation of acridine by ammonium ion.<sup>143</sup> In basic solution an emission maximum of 430 nm is observed (Figure 7.49). Upon acidification this spectrum is replaced by a red-shifted spectrum with an emission maximum of 475 nm. The former spec-

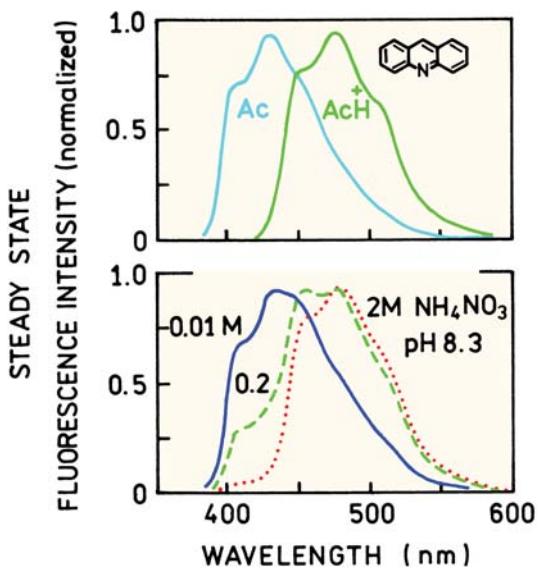


**Figure 7.49.** Fluorescence emission spectra of acridine. Spectra are shown for the neutral and protonated forms of acridine (top) and of acridine at pH 8.3 with various concentrations of ammonium ion (bottom). Reprinted from [143]. Copyright © 1982, with permission from Elsevier Science.

trum is due to neutral acridine (Ac) and the latter is due to the acridinium cation ( $\text{AcH}^+$ ). Since the ground-state  $pK_A$  of acridine is 5.45, only the neutral species is present at pH = 8.3. Nonetheless, increasing concentrations of ammonium ion, at pH = 8.3, yield a progressive quenching of the short-wavelength emission, with a concomitant appearance of the emission from the acridinium ion (Figure 7.49). These spectral shifts are the result of protonation of the excited neutral acridine molecules by ammonium ions. In the excited state the  $pK_A$  of neutral acridine increases from the ground state value of 5.45 to 10.7.

This excited-state reaction illustrates the phase-modulation theory just described. It is a two-state process that is essentially irreversible. Time-resolved studies demonstrated that at 410 nm the decay is a single exponential.<sup>124</sup> At 560 nm the fluorescence decay can be described with two lifetimes, one of which has the same as the decay time observed at 410 nm. The two lifetimes were independent of emission wavelength, but the pre-exponential factors were dependent on emission wavelength. These data imply that the lifetime of each species (Ac and  $\text{AcH}^+$ ) is constant across its emission spectrum, and that the irreversible two-state theory is appropriate to describe this excited-state process. Examination of the emission spectra (Figure 7.49) reveals a region where only the neutral species emits

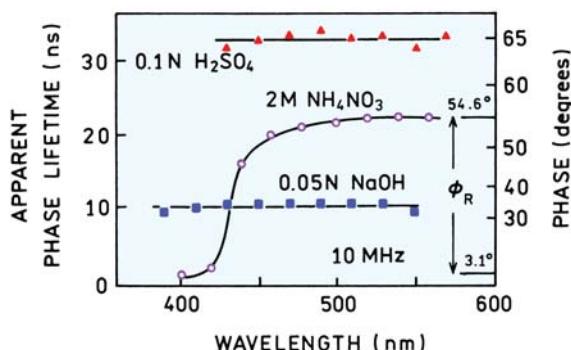


**Figure 7.50.** Apparent phase lifetimes of acridine. The inserted axis on the right-hand side indicates the phase angles relative to the exciting light. The phase angle difference between the red ( $\phi_R = 54.6^\circ$ ) and blue ( $\phi_F = 3.1^\circ$ ) regions of the emission reveals the lifetime of the acridinium cation that would be observed if this species could be directly excited. The phase angles of acridinium, relative to the exciting light, do not yield true lifetimes for the directly excited acridinium cation. Reprinted from [143]. Copyright © 1982, with permission from Elsevier Science.

(390–410 nm), a region of strong overlap (440–500 nm), and a region of moderate overlap where the spectrum is dominated by the  $\text{AcH}^+$  emission (>500 nm).

The apparent phase lifetimes ( $\tau^\phi$ ) for acridine in 0.05 N NaOH, 0.1 N  $\text{H}_2\text{SO}_4$ , and 2 M  $\text{NH}_4\text{NO}_3$  are shown in Figure 7.50. In acidic or basic solution, one species is present in both the ground and excited states, and the lifetimes (or phase angles) are independent of emission wavelength. In contrast, the lifetimes in 2 M  $\text{NH}_4\text{NO}_3$  are highly dependent upon wavelength because of protonation of acridine subsequent to excitation. At short wavelengths (410 nm), where neutral acridine emits, the lifetime is decreased in the presence of ammonium ion. A decreased phase angle (or lifetime) of the initially excited state is a characteristic feature of an excited-state reaction. At longer wavelengths the apparent lifetime increases until a nearly constant value is reached for wavelengths longer than 500 nm. In this wavelength range the emission is dominated by the acridinium ion. The constant lifetime, or more correctly phase angle, on the red and blue sides of the emission may be regarded as evidence for the two-state model. If the overall emission were shifting to longer wavelengths according to the continuous Bakhshiev model,<sup>1</sup> such regions of constant phase angle are not expected. Overall, the phase data for acridine may be regarded as typical for a two-state reaction with moderate spectral overlap. These characteristics include a decrease in lifetime on the blue side of the emission, an increase in apparent lifetime with emission wavelength, and

nearly constant lifetimes on the blue and red sides of the emission.

An interesting potential of phase fluorometry is the ability to measure directly the intrinsic lifetime of the reacted species. By "intrinsic" we mean the lifetime that would be observed if this species were formed by direct excitation, rather than by an excited-state reaction. The intrinsic lifetime of the reacted species is revealed by the phase difference ( $\Delta\phi$ ) between the blue and red sides of the emission ( $\Delta\phi = \phi_R - \phi_F$ ). Consider the phase difference between 400 and 560 nm shown in Figure 7.50. This phase angle difference ( $\Delta\phi = 51.5^\circ$ ) yields the lifetime of the acridine cation ( $\tau(\text{AcH}^+)$ ) according to

$$\tan \Delta\phi = \omega \tau(\text{AcH}^+) \quad (7.47)$$

which is found to be 20 ns in 2 M  $\text{NH}_4\text{NO}_3$ . Recall that the origin of this simple result is that the excited neutral acridine population is the pumping function for the excited-state acridinium molecules.

Phase measurements alone, at a single modulation frequency, cannot be used to distinguish between ground-state heterogeneity and an excited-state reaction. The increase in phase angle shown in Figure 7.50 could also be attributed to a second directly excited fluorophore with a longer lifetime. Of course, the decrease in the phase lifetime at short wavelengths indicates a quenching process. A rigorous proof of the presence of an excited-state process is obtainable by comparison of the phase shift and demodulation data from the same sample. Figure 7.51 shows apparent phase and modulation lifetimes and the ratio  $m/\cos \phi$  for acridine in 0.2 M  $\text{NH}_4\text{NO}_3$ . On the blue edge  $\tau^\phi \approx \tau^m$  and  $m/\cos \phi \approx$

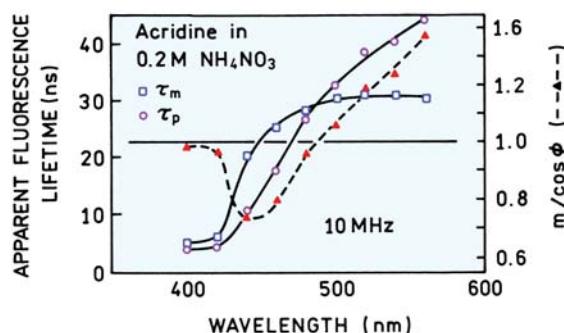


**Figure 7.51.** Apparent phase (open circle) and modulation (open square) lifetimes of acridine at pH 8.3, 0.2 M  $\text{NH}_4\text{NO}_3$ . Also shown is the wavelength dependence of  $m/\cos \phi$  (triangle). Reprinted from [143]. Copyright © 1982, with permission from Elsevier Science.

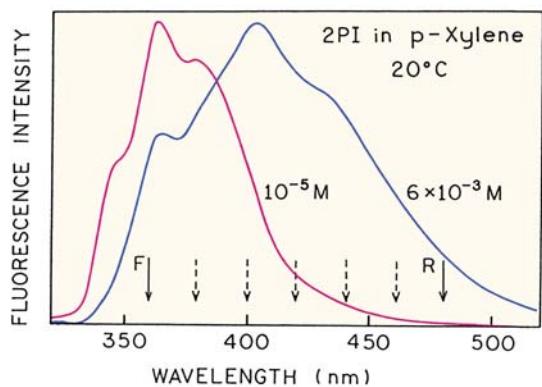


**Figure 7.52.** Emission spectra of 2-phenylindole in p-xylene at  $10^{-5}$  and  $6 \times 10^{-3}$  M. The emission at long wavelengths is due to excimer formation. From [147].

1, indicative of a single-exponential decay and therefore an irreversible reaction. In the central overlap region,  $\tau^\phi < \tau^m$  and  $m/\cos \phi < 1$ , which is indicative of emission from more than one state. At longer wavelengths,  $\tau^\phi > \tau^m$  and  $m/\cos \phi > 1$ . These last results are impossible for a multi-exponential decay with any degree of heterogeneity. This observation proves that the emission at these longer wavelengths was not a result of direct excitation, but rather is the result of an excited-state reaction.

#### 7.14.3. Frequency-Domain Measurement of Excimer Formation

In the preceding section we described how the phase and modulation values, when measured at a single modulation frequency, were affected by an excited-state reaction. When using a variable-frequency instrument, the intensity decay

can be recovered without a detailed interpretation of the individual phase and modulation values. This is illustrated for excimer formation by 2-phenylindole (2-PI).<sup>147</sup> At higher concentrations of 2-PI there is increased intensity on the long-wavelength sides of the emission (Figure 7.52), which is thought to be due to formation of excimers. However, the long-wavelength emission could also be the result of ground state complexes of 2-PI. These possibilities were distinguished by measurement of the frequency response at various emission wavelengths (arrows in Figure 7.52). The data for observation at 360 nm ( $F$ ) and 480 nm ( $R$ ) are shown in Figure 7.53. At 360 nm (●) a typical frequency response was observed. At 480 nm (○) the phase angles increase rapidly with frequency and exceed  $90^\circ$ , which proves the emission at 480 nm is not directly excited.

The frequency responses at each wavelength were used to recover the intensity decays (Table 7.5). It was possible to fit the data globally with two wavelength-independent lifetimes. As the observation wavelength increases, the amplitude of the 0.86-ns component becomes negative. At 480 nm the amplitudes are nearly equal and opposite, suggesting that there is minimal contribution of the  $F$  state at this wavelength. If desired, the decay times and amplitudes in Table 7.5 can be used to construct the time-resolved emission spectra (TRES), or the decay-associated spectra (DAS). The decay-associated spectra of the shorter-lifetime component show regions of positive and negative amplitudes (Figure 7.54). This occurs because there is a negative pre-exponential factor associated with this decay time at longer wavelengths.

Another type of calculated spectra are the species-associated spectra (SAS).<sup>148–150</sup> The species-associated spectra are the emission spectra of the individual species if these could be observed individually. The difference between

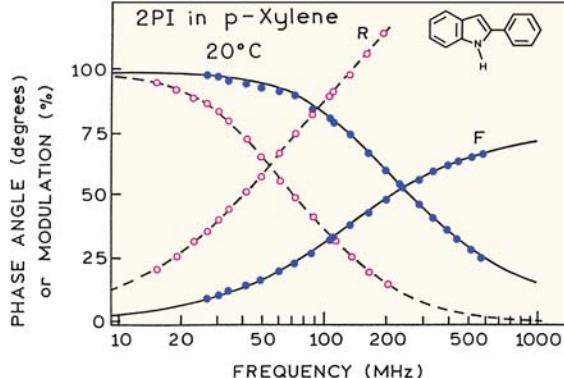


**Figure 7.53.** Frequency-domain intensity decays of 2-phenylindole ( $6 \times 10^{-3}$  M) observed at 360 ( $F$ ) and 480 nm ( $R$ ). From [147].

**Table 7.5.** Wavelength-Dependent Intensity Decays of 2-Phenylindole ( $6 \times 10^{-3}$  M) in p-Xylene at 20°C

$\lambda_{\text{em}}$ (nm)	$\tau_1 = 0.86 \text{ ns}^a$		$\tau_2 = 3.42 \text{ ns}$	
	$\alpha_1$	$f_1$	$\alpha_2$	$f_2$
360	0.967	0.879	0.033	0.121
380	0.951	0.831	0.049	0.069
400	0.731	0.405	0.269	0.595
420	-0.047	-0.012	0.953	0.988
440	-0.326	-0.108	0.674	0.892
460	-0.407	-0.147	0.593	0.853
480	-0.453	-0.172	0.547	0.828

<sup>a</sup>The intensity decays measured for each emission wavelength ( $\lambda_{\text{em}}$ ) were fit with  $\tau_1$  and  $\tau_2$  as a global parameters. The  $\chi^2_R$  of this global fit is 3.9. From [147].

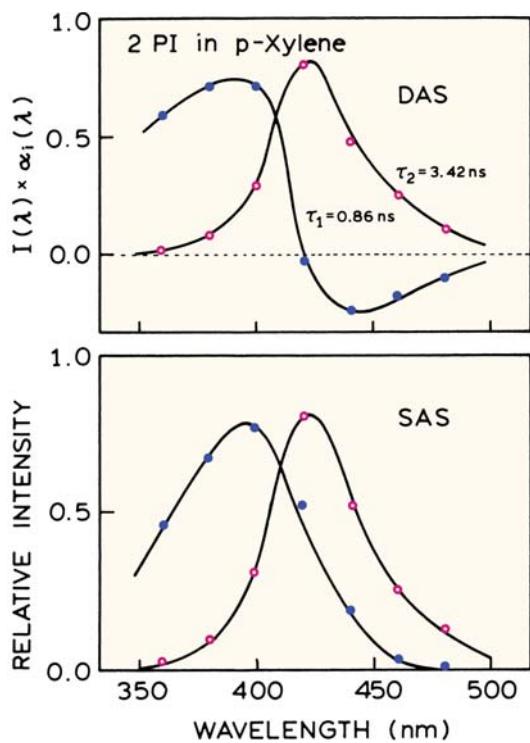


**Figure 7.54.** Decay-associated spectra (DAS, top) and species-associated spectra (SAS, bottom) for 2-PI ( $6 \times 10^{-3}$  M) in p-xylene. From [147].

DAS and SAS can be confusing. For ground-state heterogeneity or a mixture of fluorophores, the DAS and SAS are the same because each lifetime is associated with a separate fluorophore. For an excited-state reaction the SAS are more

complex. Recall from Section 7.12.2 that for a reversible excited-state reaction both the decays of the *F* and *R* states are both double exponentials. Hence, the DAS are not the emission spectra of each species, but contain contributions from both the *F* and *R* states. The SAS are the emission spectra of the *F* and *R* states, not of a lifetime component. The theory describing the relationship between DAS and SAS is moderately complex and best explained in the papers on this topic.<sup>148–150</sup> For the case of 2-PI, the SAS indicate that the monomer emission of 2-PI is centered near 390 nm, and the excimer emission is only moderately red shifted to 420 nm (Figure 7.54).

## 7.15. BIOCHEMICAL EXAMPLES OF EXCITED-STATE REACTIONS

### 7.15.1. Exposure of a Membrane-Bound Cholesterol Analogue

Excited-state reactions have been used to determine the water accessibility of fluorophores when bound to biomolecules. This is illustrated by the examples of the cholesterol analogue dihydroequilenin (DHE), which can lose a proton in the excited state (Figure 7.55). The emission spectra of DHE were examined when bound to DMPC vesicles without or with 10 mole% cholesterol.<sup>138</sup> The long-wavelength emission from the ionized DHE was more intense in the vesicles which also contained cholesterol. This result indicates that cholesterol displaces DHE towards the surface of the bilayers, allowing deprotonation and thus results in a more intense long-wavelength emission. The concept of an excited-state reaction was also used to study diffusion of lipids in membranes. Similarly, pyrene-labeled lipids were used to determine the extent to which excimer emission was formed by diffusion, or due to preexisting ground state complexes.<sup>151–152</sup> Excimer formation has also been used to study end-to-end motions in polymers.<sup>153–155</sup>

Additional information is available in detailed reports that describe methods to determine the kinetics parameters.<sup>155–161</sup>

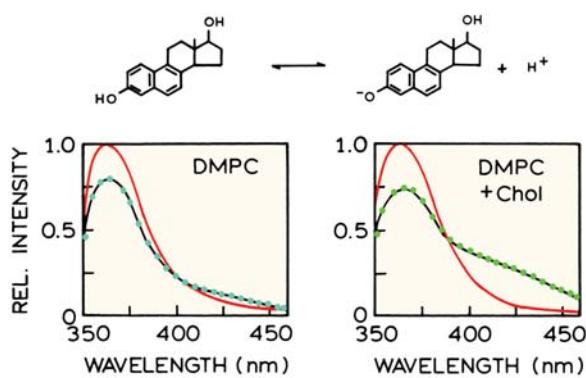


**Figure 7.55.** Top: Excited-state ionization of dihydroequilenin (DHE). Bottom: Emission spectra of DHE bound to DMPC vesicles (left) or DMPC vesicles containing 10 mole% cholesterol. Revised and reprinted with permission from [138]. Copyright © 1986, American Chemical Society.

## REFERENCES

1. Bakshiev NG, Mazurenko YuT, Piterskaya IV. 1966. Luminescence decay in different portions of the luminescence spectrum of molecules in viscous solution. *Opt Spectrosc* **21**:307–309.
2. Mazurenko YuT, Bakshiev NK. 1970. Effect of orientation dipole relaxation on spectral, time, and polarization characteristics of the luminescence of solutions. *Opt Spectrosc* **28**:490–494.

3. Bakhshiev NK, Mazurenko YuT, Piterskaya IV. 1969. Relaxation effects in the luminescence characteristics of viscous solutions. *Akad Nauk SSSR Bull Phys Sci* **32**:1262–1266.
4. Ware WR, Lee SK, Brant GJ, Chow PP. 1970. Nanosecond time-resolved emission spectroscopy: spectral shifts due to solvent-excited solute relaxation. *J Chem Phys* **54**:4729–4737.
5. Ware WR, Chow P, Lee SK. 1968. Time-resolved nanosecond emission spectroscopy: spectral shifts due to solvent-solute relaxation. *Chem Phys Lett* **2**(6):356–358.
6. Chakrabarti SK, Ware WR. 1971. Nanosecond time-resolved emission spectroscopy of 1-anilino-8-naphthalene sulfonate. *J Chem Phys* **55**(12):5494–5498.
7. Easter JH, DeToma RP, Brand L. 1976. Nanosecond time-resolved emission spectroscopy of a fluorescence probe adsorbed to L- $\alpha$ -egg lecithin vesicles. *Biophys J* **16**:571–583.
8. O'Connor DV, Phillips D. 1984. *Time-correlated single photon counting*, pp. 211–251. Academic Press, New York.
9. Badea MG, Brand L. 1979. Time-resolved fluorescence measurements. *Methods Enzymol* **61**:378–425.
10. Badea MG, De Toma RP, Brand L. 1978. Nanosecond relaxation processes in liposomes. *Biophys J* **24**:197–212.
11. Buzády A, Erostýák J, Somogyi B. 2001. Phase-fluorometry study on dielectric relaxation of acrylodan-labeled human serum albumin. *Biophys Chem* **94**:75–85.
12. Mandal D, Sen S, Sukul D, Bhattacharyya K, Mandal AK, Banerjee R, Roy S. 2002. Solvation dynamics of a probe covalently bound to a protein and in an AOT microemulsion: 4(N-bromoacetylamino)phthalimide. *J Phys Chem B* **106**:10741–10747.
13. Halder A, Sen P, Das Burman A, Bhattacharyya K. 2004. Solvation dynamics of DCM in a polypeptide-surfactant aggregate: gelatin-sodium dodecyl sulfate. *Langmuir* **20**:653–657.
14. Gafni A, De Toma RP, Manrow RE, Brand L. 1977. Nanosecond decay studies of a fluorescence probe bound to apomyoglobin. *Biophys J* **17**:155–168.
15. Lakowicz JR, Cherek H. 1981. Proof of nanosecond timescale relaxation in apomyoglobin by phase fluorometry. *Biochim Biophys Res Commun* **99**:1173–1178.
16. Lakowicz JR, Gratton E, Cherek H, Maliwal BP, Laczkó G. 1984. Determination of time-resolved fluorescence emission spectra and anisotropies of a fluorophore-protein complex using frequency-domain phase-modulation fluorometry. *J Biol Chem* **259**(17):10967–10972.
17. Pierce DW, Boxer SG. 1992. Dielectric relaxation in a protein matrix. *J Phys Chem* **96**:5560–5566.
18. Wang R, Sun S, Bekos EJ, Bright FV. 1995. Dynamics surrounding Cys-34 in native, chemically denatured, and silica-adsorbed bovine serum albumin. *Anal Chem* **67**:149–159.
19. Demchenko AP, Apell H-J, Stürmer W, Feddersen B. 1993. Fluorescence spectroscopic studies on equilibrium dipole-relaxational dynamics of Na,K-ATPase. *Biophys Chem* **48**:135–147.
20. Pal SK, Mandal D, Sukul D, Sen S, Bhattacharyya K. 2001. Solvation dynamics of DCM in human serum albumin. *J Phys Chem B* **105**:1438–1441.
21. Sen P, Mukherjee S, Dutta P, Halder A, Mandal D, Banerjee R, Roy S, Bhattacharyya K. 2003. Solvation dynamics in the molten globule state of a protein. *J Phys Chem B* **107**:14563–14568.
22. Hutterer R, Hof M. 2001. Dynamics in diether lipid bilayers and interdigitated bilayer structures studied by time-resolved emission spectra, decay time and anisotropy profiles. *J Fluoresc* **11**(3):227–236.
23. Hutterer R, Hof M. 2002. Probing ethanol-induced phospholipid phase transitions by the polarity sensitive fluorescence probes prodan and patman. *Z Phys Chem* **216**:333–346.
24. Easter JH, Detoma RP, Brand L. 1978. Fluorescence measurements of environmental relaxation at the lipid–water interface region of bilayer membranes. *Biochim Biophys Acta* **508**:27–38.
25. DeToma RP, Easter JH, Brand L. 1976. Dynamic interactions of fluorescence probes with the solvent environment. *J Am Chem Soc* **98**:5001–5007.
26. Lakowicz JR, Cherek H, Laczkó G, Gratton E. 1984. Time-resolved fluorescence emission spectra of labeled phospholipid vesicles, as observed using multi-frequency phase-modulation fluorometry. *Biochim Biophys Acta* **777**:183–193.
27. Parasassi T, Conti F, Gratton E. 1986. Time-resolved fluorescence emission spectra of laurdan in phospholipid vesicles by multifrequency phase and modulation fluorometry. *Cell Mol Biol* **32**(1):103–108.
28. Sommer A, Paltauf F, Hermetter A. 1990. Dipolar solvent relaxation on a nanosecond timescale in ether phospholipid membranes as determined by multifrequency phase and modulation fluorometry. *Biochemistry* **29**:11134–11140.
29. Hutterer R, Schneider FW, Lanig H, Hof M. 1997. Solvent relaxation behaviour of n-anthroyloxy fatty acids in PC-vesicles and paraffin oil: a time-resolved emission spectra study. *Biochim Biophys Acta* **1323**:195–207.
30. Hof M, Hutterer R. 1998. Solvent relaxation of fluorescent labels as a new tool for the detection of polarity and rigidity changes in membranes. *Czech J Phys* **48**(4):435–441.
31. Sykora J, Mudogo V, Hutterer R, Nepras M, Vanerka J, Kapusta P, Fidler V, Hof M. 2002. ABA-C<sub>15</sub>: a new dye for probing solvent relaxation in phospholipid bilayers. *Langmuir* **18**:9276–9282.
32. Pal SK, Sukul D, Mandal D, Bhattacharyya K. 2000. Solvation dynamics of DCM in lipid. *J Phys Chem B* **104**:4529–4531.
33. Dutta P, Sen P, Mukherjee S, Bhattacharyya K. 2003. Solvation dynamics in DMPC vesicle in the presence of a protein. *Chem Phys Lett* **382**:426–433.
34. Chakrabarty D, Hazra P, Chakraborty A, Sarkar N. 2003. Solvation dynamics of coumarin 480 in bile salt–cetyltrimethylammonium bromide (CTAB) and bile salt–tween 80 mixed micells. *J Phys Chem B* **107**:13543–13648.
35. Hara K, Kuwabara H, Kajimoto O. 2001. Pressure effect on solvation dynamics in micellar environment. *J Phys Chem B* **105**:7174–7179.
36. Balasubramanian S, Bagchi B. 2001. Slow solvation dynamics near an aqueous micellar surface. *J Phys Chem B* **105**:12529–12533.
37. Maciejewski A, Kubicki J, Dobek K. 2003. The origin of time-resolved emission spectra (TRES) changes of 4-aminophthalimide (4-AP) in SDS micelles: the role of the hydrogen bond between 4-AP and water present in micelles. *J Phys Chem B* **107**:13986–13999.
38. Corbeil EM, Levinger NE. 2003. Dynamics of polar solvation in quaternary microemulsions. *Langmuir* **19**:7264–7270.
39. Sarkar R, Ghosh M, Pal SK. 2005. Ultrafast relaxation dynamics of a biologically relevant probe dansyl at the micellar surface. *J Photochem Photobiol B* **78**(2):93–98.

40. Egelhaaf H-J, Lehr B, Hof M, Häfner A, Fritz H, Schneider FW, Bayer E, Oelkrug D. 2000. Solvation and solvent relaxation in swellable copolymers as studied by time-resolved fluorescence spectroscopy. *J Fluoresc* **10**(4):383–392.
41. Shirota H, Segawa H. 2003. Time-resolved fluorescence study on liquid oligo(ethylene oxide)s: coumarin 153 in poly(ethylene glycol)s and crown ethers. *J Phys Chem A* **107**:3719–3727.
42. Bhattacharyya K. 2005. Organized assemblies probed by fluorescence spectroscopy. In *Reviews in fluorescence*, pp. 1–19. Ed C Geddes, JR Lakowicz. Springer Verlag, New York.
43. Stryer L. 1965. The interactions of a naphthalene dye with apomyoglobin and apohemoglobin: a fluorescent probe of non-polar binding sites. *J Mol Biol* **13**:482–495.
44. Murakami H, Kushida T. 1994. Fluorescence properties of Zn-substituted myoglobin. *J Luminesc* **58**:172–175.
45. Cohen BE, McAnaney TB, Park ES, Jan YN, Boxer SG, Jan LY. 2002. Probing protein electrostatics with a synthetic fluorescent amino acid. *Science* **296**:1700–1703.
46. Kobayashi N, Honda S, Yoshii H, Munekata E. 2000. Role of side-chains in the cooperative β-hairpin folding of the short c-terminal fragment derived from streptococcal protein G. *Biochemistry* **39**: 6564–6571.
47. Park SH, Shastry MCR, Roder H. 1999. Folding dynamics of the B1 domain of protein G explored by ultrarapid mixing. *Nat Struct Mol Biol*. **6**(10):943–947.
48. Easter JH, Brand L. 1973. Nanosecond time-resolved emission spectroscopy of a fluorescence probe bound to L-α-egg lecithin vesicles. *Biochem Biophys Res Comm* **52**(3):1086–1092.
49. Molotsky T, Huppert D. 2003. Site specific solvation statics and dynamics of coumarin dyes in hexane-methanol mixture. *J Phys Chem A* **107**(16):2769–2780.
50. Pal SK, Zhao L, Zewail AH. 2003. Water at DNA surfaces: ultrafast dynamics in minor groove recognition. *Proc Natl Acad Sci USA* **100**(14):8113–8118.
51. Fleming GR, Cho M. 1996. Chromophore-solvent dynamics. *Annu Rev Phys Chem* **47**:109–134.
52. Simon JD. 1988. Time-resolved studies of solvation in polar media. *Acc Chem Res* **21**:128–134.
53. Chapman CF, Fee RS, Maroncelli M. 1995. Measurements of the solute dependence of solvation dynamics in 1-propanol: the role of specific hydrogen-bonding interactions. *J Phys Chem* **99**:4811–4819.
54. Glasbeek M, Zhang H. 2004. Femtosecond studies of solvation and intramolecular configurational dynamics of fluorophores in liquid solution. *Chem Rev* **104**:1929–1954.
55. Bhattacharyya K. 2003. Solvation dynamics and proton transfer in supramolecular assemblies. *Acc Chem Res* **36**(2):95–101.
56. Bhattacharyya K, Bagchi B. 2000. Slow dynamics of constrained water in complex geometries. *J Phys Chem A* **104**:10603–10613.
57. Smith NA, Meech SR, Rubtsov IV, Yoshihara K. 1999. LDS-750 as a probe of solvation dynamics: a femosecond time-resolved fluorescence study in liquid aniline. *Chem Phys Lett* **303**:209–217.
58. Murakami H. 2000. Femtosecond time-resolved fluorescence spectra of a coumarin dye in glycerol. *J Mol Liq* **89**:33–45.
59. Benderskii AV, Eisenthal KB. 2000. Effect of organic surfactant on femosecond solvation dynamics at the air–water interface. *J Phys Chem B* **104**:11723–11728.
60. Liu J-Y, Fan W-H, Han K-L, Xu D-L, Lou N-Q. 2003. Ultrafast dynamics of dye molecules in solution as a function of temperature. *J Phys Chem A* **107**:1914–1917.
61. Jarzeba W, Walker GC, Johnson AE, Kahlow MA, Barbara PF. 1988. Femtosecond microscopic solvation dynamics of aqueous solutions. *J Phys Chem* **92**:7039–7041.
62. Friedman HL. 1983. Fast response of a dielectric to the motion of a charge. *J Chem Soc Faraday Trans* **79**:1465–1467.
63. Bagchi B, Oxtoby DW, Fleming GR. 1984. Theory of the time development of the Stokes shift in polar media. *Chem Phys* **86**:257–267.
64. Castner EW, Fleming GR, Bagchi B. 1988. Influence of non-Debye relaxation and of molecular shape on the time dependence of the Stokes shift polar media. *Chem Phys Lett* **143**(3):270–276.
65. Castner EW, Bagchi B, Maroncelli M, Webb SP, Ruggiero AJ, Fleming GR. 1988. The dynamics of polar solvation. *Ber Bunsenges Phys Chem* **92**:363–372.
66. Bakhshiev NG. 1964. Universal intermolecular interactions and their effect on the position of the electronic spectra of molecules in two-component solutions, VII: theory (general case of an isotropic solution). *Opt Spectrosc* **16**:446–451.
67. Castner EW, Fleming GR, Bagchi B, Maroncelli M. 1988. The dynamics of polar solvation: inhomogeneous dielectric continuum models. *J Chem Phys* **89**:3519–3534.
68. Piterskaya IV, Bakhshiev NG. 1963. Quantitative investigation of the temperature dependence of the absorption and fluorescence spectra of complex molecules. *Akad Nauk SSSR Bull Phys Ser* **27**:625–629.
69. Bushuk BA, Rubinov AN. 1997. Effect of specific intermolecular interactions on the dynamics of fluorescence spectra of dye solutions. *Opt Spectrosc* **82**(4):530–533.
70. Kaatze U, Uhendorf V. 1981. The dielectric properties of water at microwave frequencies. *Z Phys Chem Neu Folge* **126**:151–165.
71. Cole KS, Cole RH. 1941. Dispersion and absorption in dielectrics. *J Chem Phys* **9**:341–351.
72. Fellner-Feldegg H. 1969. The measurement of dielectrics in the time domain. *J Phys Chem* **75**:616–623.
73. Davidson DW, Cole RH. 1951. Dielectric relaxation in glycerol, propylene glycol, and n-propanol. *J Chem Phys* **19**(12):1484–1490.
74. Denny DJ, Cole RH. 1955. Dielectric properties of methanol and methanol-1-propanol solutions. *J Chem Phys* **23**(10):1767–1772.
75. McDuffie GE, Litovitz TA. 1962. Dielectric relaxation in associated liquids. *J Chem Phys* **37**(8):1699–1705.
76. Gard SK, Smyth CP. 1965. Microwave absorption and molecular structure in liquids, LXII: the three dielectric dispersion regions of the normal primary alcohols. *J Phys Chem* **69**:1294–1301.
77. Bamford CH, Compton RG. 1985. *Chemical kinetics*. Elsevier, New York.
78. Szmacinski H, Gryczynski I, Lakowicz JR. 1996. Resolution of multi-exponential spectral relaxation of Yt-base by global analysis of collisionally quenched samples. *J Fluoresc* **6**(3):177–185.
79. Castner EW, Maroncelli M, Fleming GR. 1987. Subpicosecond resolution studies of solvation dynamics in polar aprotic and alcohol solvents. *J Chem Phys* **86**(3):1090–1097.
80. Frauchiger L, Shirota H, Uhrich KE, Castner EW. 2002. Dynamic fluorescence probing of the local environments within amphiphilic starlike macromolecules. *J Phys Chem B* **106**:7463–7468.

81. Röcker C, Heilemann A, Fromherz P. 1996. Time-resolved fluorescence of a hemicyanine dye: dynamics of rotamerism and resolution. *J Phys Chem* **100**:12172–12177.
82. Knutson JR, Walbridge DG, Brand L. 1982. Decay associated fluorescence spectra and the heterogeneous emission of alcohol dehydrogenase. *Biochemistry* **21**:4671–4679.
83. Weber G, Lakowicz JR. 1973. Subnanosecond solvent relaxation studies by oxygen quenching of fluorescence. *Chem Phys Lett* **22**:419–423.
84. Rotkiewicz K, Grabowski ZR, Jasny J. 1975. Picosecond isomerization kinetics of excited p-dimethylaminobenzonitriles studied by oxygen quenching of fluorescence. *Chem Phys Lett* **34**:55–100.
85. Lakowicz JR, Hogen D. 1981. Dynamic properties of the lipid–water interface of model membranes as revealed by lifetime-resolved fluorescence emission spectra. *Biochemistry* **20**:1366–1373.
86. Raghuraman H, Kelkar DA, Chattopadhyay A. 2005. Novel insights into protein structure and dynamics utilizing the red edge excitation shift approach. In *Reviews in fluorescence*, pp. 199–222. Ed C Geddes, JR Lakowicz. Springer Verlag, New York.
87. Demchenko AP. 2002. The red-edge effects: 30 years of exploration. *Luminescence* **19**:19–42.
88. Rawat SS, Chattopadhyay A. 1999. Structural transition in the micellar assembly: a fluorescence study. *J Fluoresc* **9**(3):233–243.
89. Mukherjee S, Chattopadhyay A. 1995. Wavelength-selective fluorescence as a novel tool to study organization and dynamics in complex biological systems. *J Fluoresc* **5**(3):237–246.
90. Rawat SS, Mukherjee S, Chattopadhyay A. 1997. Micellar organization and dynamics: a wavelength-selective fluorescence approach. *J Phys Chem B* **101**:1922–1929.
91. Rudik KI, Pikulik LG. 1971. Effect of the exciting light on the fluorescence spectra on phthalmide solutions. *Opt Spectrosc* **30**: 147–148.
92. Rubinov AN, Tomin VI. 1970. Bathochromic luminescence in solutions of organic dyes at low temperatures. *Opt Spectrosc* **29**: 578–580.
93. Galley WC, Purkey RM. 1970. Role of heterogeneity of the solvation site in electronic spectra in solution. *Proc Natl Acad Sci USA* **67**(3): 1116–1121.
94. Itoh K, Azumi T. 1973. Shift of emission band upon excitation at the long wavelength absorption edge. *Chem Phys Lett* **22**(2):395–399.
95. Azumi T, Itoh K, Shiraishi H. 1976. Shift of emission band upon the excitation at the long wavelength absorption edge, III: temperature dependence of the shift and correlation with the time dependent spectral shift. *J Chem Phys* **65**(7):2550–2555.
96. Itoh K, Azumi T. 1975. Shift of the emission band upon excitation at the long wavelength absorption edge, II: importance of the solute–solvent interaction and the solvent reorientation relaxation process. *J Chem Phys* **62**(9):3431–3438.
97. Kawski A, Ston M, Janic I. 1983. On the intensity distribution within photoluminescence bands in rigid and liquid solutions. *Z Naturforsch A* **38**:322–324.
98. Lakowicz JR, Keating-Nakamoto S. 1984. Red-edge excitation of fluorescence and dynamic properties of proteins and membranes. *Biochemistry* **23**:3013–3021.
99. Demchenko AP. 1982. On the nanosecond mobility in proteins, Edge excitation fluorescence red shift of protein-bound 2-(p-toluidinyl-naphthalene)-6-sulfonate. *Biophys Chem* **15**:101–109.
100. Shcherbatska NV, van Hoek A, Visser AJWG, Koziol J. 1994. Molecular relaxation spectroscopy of lumichrome. *J Photochem Photobiol A: Chem* **78**:241–246.
101. Chattopadhyay A, Mukherjee S. 1993. Fluorophore environments in membrane-bound probes: a red edge excitation shift study. *Biochemistry* **32**:3804–3811.
102. Chattopadhyay A, Mukherjee S. 1999. Red edge excitation shift of a deeply embedded membrane probe: implications in water penetration in the bilayer. *J Phys Chem B* **103**:8180–8185.
103. Demchenko AP, Shcherbatska NV. 1985. Nanosecond dynamics of charged fluorescent probes at the polar interface of a membrane phospholipid bilayer. *Biophys Chem* **22**:131–143.
104. Raudino A, Guerrera F, Asero A, Rizza V. 1983. Application of red-edge effect on the mobility of membrane lipid polar head groups. *FEBS Lett* **159**(1,2):43–46.
105. de Oliveira AHC, Giglio JR, Andrião-Escarso SH, Ward RJ. 2001. The effect of resonance energy homotransfer on the intrinsic tryptophan fluorescence emission of the bothropstoxin-I dimer. *Biochem Biophys Res Commun* **284**:1011–1015.
106. Chattopadhyay A, Rukmini R. 1993. Restricted mobility of the sole tryptophan in membrane-bound melittin. *Fed Eur Biochem Soc* **335**(3):341–344.
107. Ghosh AK, Rukmini R, Chattopadhyay A. 1997. Modulation of tryptophan environment in membrane-bound melittin by negatively charged phospholipids: implications in membrane organization and function. *Biochemistry* **36**:14291–14305.
108. Guha S, Rawat SS, Chattopadhyay A, Bhattacharyya B. 1996. Tubulin conformation and dynamics: a red edge excitation shift study. *Biochemistry* **35**:13426–13433.
109. Demchenko AP, Ladokhin AS. 1988. Temperature-dependent shift of fluorescence spectra without conformational changes in protein: studies of dipole relaxation in the melittin molecule. *Biochim Biophys Acta* **955**:352–360.
110. Weber G, Shinitzky M. 1970. Failure of energy transfer between identical aromatic molecules on excitation at the long wave edge of the absorption spectrum. *Proc Natl Acad Sci USA* **65**(4):823–830.
111. Valeur B, Weber G. 1977. Anisotropic rotations in 1-naphthylamine, existence of a red-edge transition moment normal to the ring plane. *Chem Phys Lett* **45**(1):140–144.
112. Valeur B, Weber G. 1978. A new red-edge effect in aromatic molecules: anomaly of apparent rotation revealed by fluorescence polarization. *J Phys Chem* **69**(6):2393–2400.
113. Mantulin WW, Weber G. 1977. Rotational anisotropy and solvent-fluorophore bonds: an investigation by differential polarized-phase fluorometry. *J Chem Phys* **66**(9):4092–4099.
114. Tolbert LM, Solntsev KM. 2002. Excited-state proton transfer: from constrained systems to "super" photoacids to superfast proton transfer. *Acc Chem Res* **35**:19–27.
115. Yang R, Schulman SG. 2001. Kinetics of excited-state proton transfer of doubly protonated 2-aminoacridine. *J Fluoresc* **11**(2):109–112.
116. Cohen B, Huppert D, Agmon N. 2001. Diffusion-limited acid–base nonexponential dynamics. *J Phys Chem A* **105**:7165–7173.
117. Leiderman P, Genosar L, Koifman N, Huppert D. 2004. Effect of pressure on the proton-transfer rate from a photoacid to a solvent, 2: 2-naphthol-6-sulfonate in water. *J Phys Chem A* **108**:2559–2566.
118. Mironczyk A, Jankowski A, Chyla A, Ozyhar A, Dobryszycki P. 2004. Investigation of excited-state proton transfer in 2-naphthol

- derivatives included in Langmuir-Blodgett films. *J Phys Chem A* **108**:5308–5314.
119. Cohen B, Huppert D. 2001. Excited state proton-transfer reactions of coumarin 4 in protic solvents. *J Phys Chem A* **105**:7157–7164.
  120. Ameer-Beg S, Ormson SM, Poteau X, Brown RG, Foggi P, Bussotti L, Neuwahl FVR. 2004. Ultrafast measurements of charge and excited-state intramolecular proton transfer in solutions of 4'-(N,N-dimethylamino) derivatives of 3-hydroxyflavone. *J Phys Chem A* **108**:6938–6943.
  121. Kleinman MH, Flory JH, Tomalia DA, Turro NJ. 2000. Effect of protonation and PAMAM dendrimer size on the complexation and dynamic mobility of 2-naphthol. *J Phys Chem B* **104**:11472–11479.
  122. Ireland JF, Wyatt PAH. 1976. Acid–base properties of electronically excited states of organic molecules. In *Advances in physical organic chemistry*, pp. 132–215. Ed V Gold, D Bethell. Academic Press, New York.
  123. Wan P, Shukla D. 1993. Utility of acid–base behavior of excited states of organic molecules. *Chem Rev* **93**:571–584.
  124. Gafni A, Brand L. 1978. Excited state proton transfer reactions of acridine studied by nanosecond fluorometry. *Chem Phys Lett* **58**:346–350.
  125. Harris CM, Sellinger BK. 1980. Acid–base properties of 1-naphthol: proton-induced fluorescence quenching. *J Phys Chem* **84**:1366–1371.
  126. Mandal D, Pal SK, Bhattacharyya B. 1998. Excited-state proton transfer of 1-naphthol in micelles. *J Phys Chem A* **102**:9710–9714.
  127. Boyer R, Deckey G, Marzzacco C, Mulvaney M, Schwab C, Halpern AM. 1985. The photophysical properties of 2-naphthol. *J Chem Educ* **62**:630–632.
  128. Bardez E, Monnier E, Valeur B. 1985. Dynamics of excited-state reactions in reversed micelles, 2: proton transfer involving various fluorescent probes according to their sites of solubilization. *J Phys Chem* **89**:5031–5036.
  129. Loken MR, Hayes JW, Gohlke JR, Brand L. 1972. Excited-state proton transfer as a biological probe: determination of rate constants by means of nanosecond fluorometry. *Biochemistry* **11**:4779–4786.
  130. Laws WR, Brand L. 1979. Analysis of two-state excited-state reactions: the fluorescence decay of 2-naphthol. *J Phys Chem* **83**(7):795–802.
  131. Marciak B, Kozubek H, Paszyc S. 1992. Estimation of pKa in the first excited single state. *J Chem Educ* **69**(3):247–249.
  132. Förster Th. 1950. Die pH-abhangigkeit der fluoreszenz von naphthalinderivaten. *Z Electrochem* **54**:531–553.
  133. Grabowski ZR, Grabowska A. 1976. The Förster cycle reconsidered. *Z Phys Chem Neu Folge* **104**:197–208.
  134. Grabowski ZR. 1981. Generalized Förster cycle applied to coordination compounds. *J Luminesc* **24/25**:559–562.
  135. Grabowski ZR, Rubaszewska W. 1977. Generalised Förster cycle. *J Chem Soc Faraday* **73**:11–28.
  136. Birks JB. 1970. *Photophysics of aromatic molecules*, pp. 300–309. Wiley-Interscience, New York.
  137. Brand L, Laws WR. 1983. Excited-state proton transfer. In *Time-resolved fluorescence spectroscopy in biochemistry and biology*, pp. 319–340. Ed RD Cundall, FE Dale. Plenum, New York.
  138. Davenport L, Knutson JR, Brand L. 1986. Excited-state proton transfer of equilenin and dihydroequilenin: interaction with bilayer vesicles. *Biochemistry* **25**:1186–1195.
  139. Lakowicz JR, Balter A. 1982. Differential wavelength deconvolution of time-resolved fluorescence intensities: a new method for the analysis of excited state processes. *Biophys Chem* **16**:223–240.
  140. Rumbles G, Smith TA, Brown AJ, Carey M, Soutar I. 1997. Autoreconvolution: an extension to the "reference convolution" procedure for the simultaneous analysis of two fluorescence decays from one sample. *J Fluoresc* **7**(3):217–229.
  141. Koti ASR, Krishna MMG, Periasamy N. 2001. Time-resolved area-normalized emission spectroscopy (TRANES): a novel method for confirming emission from two excited states. *J Phys Chem A* **105**:1767–1771.
  142. Lakowicz JR, Balter A. 1982. Theory of phase-modulation fluorescence spectroscopy for excited state processes. *Biophys Chem* **16**:99–115.
  143. Lakowicz JR, Balter A. 1982. Analysis of excited state processes by phase-modulation fluorescence spectroscopy. *Biophys Chem* **16**:117–132.
  144. Lakowicz JR, Balter A. 1982. Detection of the reversibility of an excited state reaction by phase modulation fluorometry. *Chem Phys Lett* **92**(2):117–121.
  145. Spencer RD, Weber G. 1969. Measurement of subnanosecond fluorescence lifetimes with a cross-correlation phase fluorometer. *Ann NY Acad Sci* **158**:361–376.
  146. Veselova TV, Limareva LA, Cherkasov AS, Shirokov VI. 1965. Fluorometric study of the effect of solvent on the fluorescence spectrum of 3-amino-N-methylphthalimide. *Opt Spectrosc* **19**:39–43.
  147. Gryczynski I. Unpublished observations.
  148. Löfroth J-E. 1985. Recent developments in the analysis of fluorescence intensity and anisotropy data. In *Analytical instrumentation*, pp. 403–431. Ed JWG Visser. Marcel Dekker, New York.
  149. Krishna MMG. 1999. Excited-state kinetics of the hydrophobic probe nile red in membranes and micelles. *J Phys Chem A* **103**(19):3589–3595.
  150. Lofroth JE. 1986. Time-resolved emission spectra, decay-associated spectra, and species-associated spectra. *J Phys Chem* **90**:1160–1168.
  151. Hresko RC, Sugar IP, Barenholz Y, Thompson TE. 1986. Lateral distribution of a pyrene-labeled phosphatidylcholine in phosphatidylcholine bilayers: fluorescence phase and modulation study. *Biochemistry* **25**:3813–3823.
  152. Novikov EG, Visser JWG. 2001. Inter- and intramolecular dynamics of pyrenyl lipids in bilayer membranes from time-resolved fluorescence spectroscopy. *J Fluoresc* **11**(4):297–305.
  153. Farinha JPS, Picarra S, Miesel K, Martinho JMG. 2001. Fluorescence study of the coil-globule transition of a PEO chain in toluene. *J Phys Chem B* **105**:10536–10545.
  154. Mathew AK, Siu H, Duhamel J. 1999. A blob model to study chain folding by fluorescence. *Macromolecules* **32**:7100–7108.
  155. Boens N, Kowalczyk A. 1996. Identifiability of competitive intermolecular three-state excited-state processes. *Chem Phys Lett* **260**:326–330.
  156. Beechem JM, Ameloot M, Brand L. 1985. Global analysis of fluorescence decay surfaces: excited-state reactions. *Chem Phys Lett* **120**(4,5):466–472.
  157. Ameloot M, Boens N, Andriessen R, Van den Bergh V, De Schryver FC. 1991. Non a priori analysis of fluorescence decay surfaces of excited-state processes, 1: theory. *J Phys Chem* **95**:2041–2047.

158. Andriessen R, Boens N, Ameloot M, De Schryver FC. 1991. Non a priori analysis of fluorescence decay surfaces of excited-state processes, 2: intermolecular excimer formation of pyrene. *J Phys Chem* **95**:2047–2058.
159. Boens N, Andriessen R, Ameloot M, Van Dommelen L, De Schryver FC. 1992. Kinetics and identifiability of intramolecular two-state excited state processes: global compartmental analysis of the fluorescence decay surface. *J Phys Chem* **96**:6331–6342.
160. Van Dommelen L, Boens N, Ameloot M, De Schryver FC, Kowalczyk A. 1993. Species-associated spectra and upper and lower bounds on the rate constants of reversible intramolecular two-state excited state processes with added quencher: global compartmental analysis of the fluorescence decay surface. *J Phys Chem* **97**: 11738–11753.
161. Van Dommelen L, Boens N, De Schryver FC, Ameloot M. 1995. Distinction between different competing kinetic models of irreversible intramolecular two-state excited-state processes with added quencher: global compartmental analysis of the fluorescence decay surface. *J Phys Chem* **99**:8959–8971.
162. Brand L, Seliskar CJ, Turner DC. 1971. The effects of chemical environment on fluorescence probes. In *Probes of structure and function of macromolecules and membranes*, pp. 17–39. Ed B Chance, CP Lee, JK Blaisie. Academic Press, New York.
163. Gakamsky DM, Demchenko AP, Nemkovich NA, Rubinov AN, Tomin VI, Shcherbatska NV. 1992. Selective laser spectroscopy of 1-phenylnaphthylamine in phospholipid membranes. *Biophys Chem* **42**:49–61.

## PROBLEMS

- P7.1. *Estimation of the Spectral Relaxation Time:* Figure 7.56 shows time-dependent intensity decays of TNS bound to

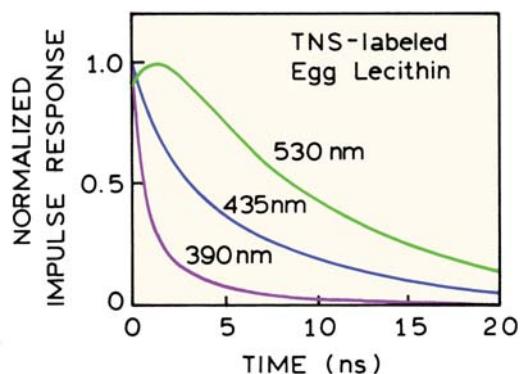


**Figure 7.56.** Fluorescence impulse response functions of TNS-labeled egg lecithin vesicles. Time-dependent intensities are shown for 390, 435, and 530 nm. From [162].

egg lecithin vesicles.<sup>162</sup> The wavelengths of 390, 435, and 530 nm are on the blue, center, and red regions of the emission spectrum. Use the data in Figure 7.56 to calculate the spectral relaxation time for the TNS-labeled residue. Assume that the emission at 390 nm is dominated by the initially excited states ( $F$ ) and that the emission at 435 nm represents the TNS, unaffected by relaxation.

- P7.2. *Interpretation of Wavelength-Dependent Lifetimes:* TNS was dissolved in various solvents or bound to vesicles of dialeoyl-L- $\alpha$ -phosphatidylcholine (DOPC). Apparent phase and modulation lifetimes were measured across the emission spectra of these samples. Explain these data in Figure 7.57.

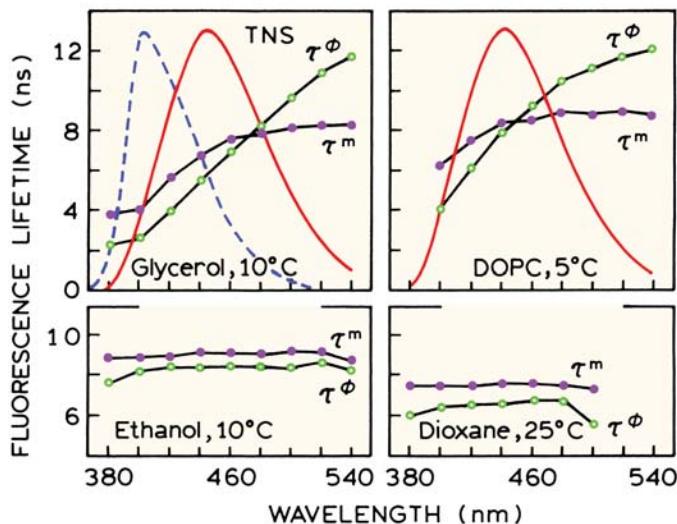


**Figure 7.57.** Fluorescence lifetimes and spectra of TNS, dissolved in various solvents and TNS bound to DOPC vesicles. Apparent phase shift (○) and modulation (●) lifetimes were measured at 30 MHz. Normalized emission spectra are shown for TNS in glycerol and bound in DOPC vesicles (solid), and for TNS in dioxane at 25°C (dashed).

P7.3. *Lifetime of the R State:* Use the data in Figure 7.53 to calculate the decay time of the 2-PI excimer emission, assuming this state could be excited directly.

P7.4. *Interpretation of Time-Resolved Decays of Acridine:* The excited-state protonation of acridine was examined by time-resolved measurements of the fluorescence decays.<sup>139</sup> Neutral acridine is protonated in the excited state by ammonium ions. The impulse response functions for acridine in 0.2 M NH<sub>4</sub>NO<sub>3</sub>, pH = 8.3 (Figure 7.49), are listed in Table 7.6.

- A. If available, how would you use the absorption spectra of acridine in 0.05 M NaOH, 0.05 M H<sub>2</sub>SO<sub>4</sub>, and 0.2 M NH<sub>4</sub>NO<sub>3</sub> to distinguish between ground-state and excited-state protonation of acridine?
- B. What characteristics of the data in Table 7.6 most clearly illustrate that an excited-state reaction is present? Do these data indicate a two-state reaction or some more complex process? Is the reaction reversible or irreversible?

P7.5. *Interpretation of TRES:* Figure 7.58 shows time-resolved emission spectra of the solvent-sensitive probe 1-anilinonaphthalene (1-AN) in glycerol.<sup>163</sup> The TRES were obtained using excitation in the center of the absorption band (337 nm) and excitation on the red edge of the absorption (416 nm). Explain the difference between these TRES.

**Table 7.6.** Time-Resolved Decays of Acridine in 0.2 M NH<sub>4</sub> NO<sub>3</sub><sup>139</sup>

$\lambda$ (nm)	$\alpha_1^a$	$\tau_1$ (ns)	$\alpha_2$	$\tau_2$ (ns)
400	0.503	3.94	-0.001	33.96
410	0.220	4.00	—	—
420	0.491	3.88	0.002	25.20
450	0.067	3.90	0.028	30.05
500	-0.010	4.91	0.082	29.13
540	-0.036	3.76	.064	29.83
550	-0.036	3.56	.058	29.94
560	-0.029	3.86	.046	29.90

<sup>a</sup>The  $[\alpha_i \tau_i]$  products are normalized to the steady-state emission intensity at each wavelength.

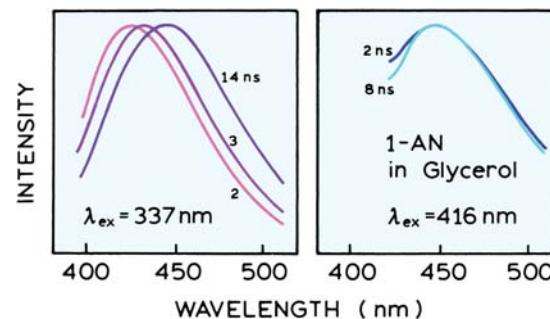


**Figure 7.58.** The time-resolved fluorescence spectra of 1-AN in glycerol at different excitation wavelengths. Left: 2 ns, 3 ns, and 14 ns after excitation. Right: 2 and 8 ns after excitation. Revised from [163].

# 8

# Quenching of Fluorescence

Fluorescence quenching refers to any process that decreases the fluorescence intensity of a sample. A variety of molecular interactions can result in quenching. These include excited-state reactions, molecular rearrangements, energy transfer, ground-state complex formation, and collisional quenching. In this chapter we will be concerned primarily with quenching resulting from collisional encounters between the fluorophore and quencher, which is called collisional or dynamic quenching. We will also discuss static quenching, which can be a valuable source of information about binding between the fluorescent sample and the quencher. Static quenching can also be a complicating factor in the data analysis. In addition to the processes described above, apparent quenching can occur due to the optical properties of the sample. High optical densities or turbidity can result in decreased fluorescence intensities. This trivial type of quenching contains little molecular information. Throughout this chapter we will assume that such trivial effects are not the cause of the decreases in fluorescence intensity.

Fluorescence quenching has been widely studied both as a fundamental phenomenon, and as a source of information about biochemical systems. These biochemical applications of quenching are due to the molecular interactions that result in quenching. Both static and dynamic quenching require molecular contact between the fluorophore and quencher. In the case of collisional quenching, the quencher must diffuse to the fluorophore during the lifetime of the excited state. Upon contact, the fluorophore returns to the ground state, without emission of a photon. In general, quenching occurs without any permanent change in the molecules, that is, without a photochemical reaction. In static quenching a complex is formed between the fluorophore and the quencher, and this complex is nonfluorescent. For either static or dynamic quenching to occur the fluorophore and quencher must be in contact. The require-

ment of molecular contact for quenching results in the numerous applications of quenching. For example, quenching measurements can reveal the accessibility of fluorophores to quenchers. Consider a fluorophore bound either to a protein or a membrane. If the protein or membrane is impermeable to the quencher, and the fluorophore is located in the interior of the macromolecule, then neither collisional nor static quenching can occur. For this reason quenching studies can be used to reveal the localization of fluorophores in proteins and membranes, and their permeabilities to quenchers. Additionally, the rate of collisional quenching can be used to determine the diffusion coefficient of the quencher.

It is important to recognize that the phenomenon of collisional quenching results in the expansion of the volume and distance within the solution which affects the fluorophore. The root-mean-square distance  $\sqrt{\Delta x^2}$  that a quencher can diffuse during the lifetime of the excited state ( $\tau$ ) is given by  $\sqrt{\Delta x^2} = \sqrt{2D\tau}$ , where  $D$  is the diffusion coefficient. Consider an oxygen molecule in water at 25°C. Its diffusion coefficient is  $2.5 \times 10^{-5} \text{ cm}^2/\text{s}$ . During a typical fluorescence lifetime of 4 ns the oxygen molecule can diffuse 45 Å. If the lifetime is longer, diffusion over still larger distances can be observed. For example, for lifetimes of 20 and 100 ns the average distances for oxygen diffusion are 100 and 224 Å, respectively. With the use of longer-lived probes with microsecond lifetimes (Chapter 20), diffusion over still larger distances can be observed. Hence, fluorescence quenching can reveal the diffusion of quenchers over moderately large distances comparable to the size of proteins and membranes. This situation is different from solvent relaxation. Spectral shifts resulting from reorientation of the solvent molecules are due primarily to the solvent shell immediately adjacent to the fluorophore.

## 8.1. QUENCHERS OF FLUORESCENCE

A wide variety of substances act as quenchers of fluorescence. One of the best-known collisional quenchers is molecular oxygen,<sup>1</sup> which quenches almost all known fluorophores. Depending upon the sample under investigation, it is frequently necessary to remove dissolved oxygen to obtain reliable measurements of the fluorescence yields or lifetimes. The mechanism by which oxygen quenches has been a subject of debate. The most likely mechanism is that the paramagnetic oxygen causes the fluorophore to undergo intersystem crossing to the triplet state. In fluid solutions the long-lived triplets are completely quenched, so that phosphorescence is not observed. Aromatic and aliphatic amines are also efficient quenchers of most unsubstituted aromatic hydrocarbons. For example, anthracene fluorescence is effectively quenched by diethylaniline.<sup>2</sup> For anthracene and diethylaniline the mechanism of quenching is the formation of an excited charge-transfer complex. The excited-state fluorophore accepts an electron from the amine. In nonpolar solvents fluorescence from the excited charge-transfer complex (exciplex) is frequently observed, and one may regard this process as an excited state reaction rather than quenching. In polar solvents the exciplex emission is often quenched, so that the fluorophore–amine interaction appears to be that of simple quenching. While it is now known that there is a modest through-space component to almost all quenching reactions, this component is short range (<2 Å), so that molecular contact is a requirement for quenching.

Another type of quenching is due to heavy atoms such as iodide and bromide. Halogenated compounds such as trichloroethanol and bromobenzene also act as collisional quenchers. Quenching by the larger halogens such as bromide and iodide may be a result of intersystem crossing to an excited triplet state, promoted by spin-orbit coupling of the excited (singlet) fluorophore and the halogen.<sup>3</sup> Since emission from the triplet state is slow, the triplet emission is highly quenched by other processes. The quenching mechanism is probably different for chlorine-containing substances. Indole, carbazole, and their derivatives are uniquely sensitive to quenching by chlorinated hydrocarbons and by electron scavengers<sup>4</sup> such as protons, histidine, cysteine,  $\text{NO}_3^-$ , fumarate,  $\text{Cu}^{2+}$ ,  $\text{Pb}^{2+}$ ,  $\text{Cd}^{2+}$ , and  $\text{Mn}^{2+}$ . Quenching by these substances probably involves a donation of an electron from the fluorophore to the quencher. Additionally, indole, tryptophan, and its derivatives are quenched by acrylamide, succinimide, dichloroacetamide, dimethylfor-

mamide, pyridinium hydrochloride, imidazolium hydrochloride, methionine,  $\text{Eu}^{3+}$ ,  $\text{Ag}^+$ , and  $\text{Cs}^+$ . Quenchers of protein fluorescence have been summarized in several insightful reviews.<sup>5–7</sup> Hence a variety of quenchers are available for studies of protein fluorescence, especially to determine the surface accessibility of tryptophan residues and the permeation of proteins by the quenchers.

Additional quenchers include purines, pyrimidines, N-methylnicotinamide and N-alkyl pyridinium, and picolinium salts.<sup>8–9</sup> For example, the fluorescence of flavin adenine dinucleotide (FAD) and reduced nicotinamide adenine dinucleotide (NADH) are both quenched by the adenine moiety. Flavin fluorescence is quenched by both static and dynamic interactions with adenine,<sup>10</sup> whereas the quenching of dihydronicotinamide appears to be primarily dynamic.<sup>11</sup> These aromatic substances appear to quench by formation of charge-transfer complexes. Depending upon the precise structure involved, the ground-state complex can be reasonably stable. As a result, both static and dynamic quenching are frequently observed. A variety of other quenchers are known. These are summarized in Table 8.1, which is intended to be an overview and not a complete list. Known collisional quenchers include hydrogen peroxide, nitric oxide (NO), nitroxides,  $\text{BrO}_4^-$ , and even some olefins.

Because of the variety of substances that act as quenchers, one can frequently identify fluorophore–quencher combinations for a desired purpose. It is important to note that not all fluorophores are quenched by all the substances listed above. This fact occasionally allows selective quenching of a given fluorophore. The occurrence of quenching depends upon the mechanism, which in turn depends upon the chemical properties of the individual molecules. Detailed analysis of the mechanism of quenching is complex. In this chapter we will be concerned primarily with the type of quenching, that is, whether quenching depends on diffusive collisions or formation of ground-state complexes. Later in this chapter we describe biochemical applications of quenching. The mechanisms of quenching will be discussed in the following chapter.

## 8.2. THEORY OF COLLISIONAL QUENCHING

Collisional quenching of fluorescence is described by the Stern-Volmer equation:

$$\frac{F_0}{F} = 1 + k_q \tau_0 [Q] = 1 + K_D [Q] \quad (8.1)$$

**Table 8.1.** Quenchers of Fluorescence

Quenchers	Typical fluorophore	References
Acrylamide	Tryptophan, pyrene, and other fluorophores	5–7, 176–180
Amines	Anthracene, perylene	2, 124, 181–186
Amines	Carbazole	187
Amine anesthetics	Perylene, anthroyloxy probes	188–190
Bromate	—	191
Bromobenzene	Many fluorophores	192
Carbon disulfide	Laser dyes, perylene	193
Carboxy groups	Indole	194
Cesium ( $\text{Cs}^+$ )	Indole	195
Chlorinated compounds	Indoles and carbazoles	196–199
Chloride	Quinolinium, SPQ	200–203
Cobalt ( $\text{Co}^{2+}$ )	NBD, PPO, Perylene (Energy transfer for some probes)	204–210
Dimethylformamide	Indole	211
Disulfides	Tyrosine	212
Ethers	9-Arylxanthyl cations	213
Halogens	Anthracene, naphthalene, carbazole	214–229
Halogen anesthetics	Pyrene, tryptophan	230–232
Hydrogen peroxide	Tryptophan	233
Iodide	Anthracene	234–237
Imidazole, histidine	Tryptophan	238
Indole	Anthracene, pyrene, cyanoanthracene	239–241
Methylmercuric chloride	Carbazole, pyrene	242
Nickel ( $\text{Ni}^{2+}$ )	Perylene	243–244
Nitromethane and nitro compounds	Polycyclic aromatic hydrocarbon	245–256
Nitroxides	Naphthalene, PAH, $\text{Tb}^{3+}$ , anthroyloxy probes	257–266
NO (nitric oxide)	Naphthalene, pyrene	267–270
Olefins	Cyanonaphthalene, 2,3-dimethylnaphthalene, pyrene	271–273
Oxygen	Most fluorophores	274–290
Peroxides	Dimethylnaphthalene	291
Picolinium nicotinamide	Tryptophan, PAH	292–296
Pyridine	Carbazole	297
Silver ( $\text{Ag}^+$ )	Perylene	298
Succinimide	Tryptophan	299–300
Sulfur dioxide	Rhodamine B	301
Thallium ( $\text{Ti}^{+}$ )	Naphthylamine sulfonic acid	302
Thiocyanate	Anthracene, 5,6-benzoquinoline	303–304
Xenon		305

In this equation  $F_0$  and  $F$  are the fluorescence intensities in the absence and presence of quencher, respectively;  $k_q$  is the bimolecular quenching constant;  $\tau_0$  is the lifetime of the fluorophore in the absence of quencher, and  $Q$  is the concentration of quencher. The Stern-Volmer quenching constant is given by  $K_D = k_q\tau_0$ . If the quenching is known to be dynamic, the Stern-Volmer constant will be represented by  $K_D$ . Otherwise this constant will be described as  $K_{SV}$ .

Quenching data are usually presented as plots of  $F_0/F$  versus  $[Q]$ . This is because  $F_0/F$  is expected to be linearly

dependent upon the concentration of quencher. A plot of  $F_0/F$  versus  $[Q]$  yields an intercept of one on the  $y$ -axis and a slope equal to  $K_D$  (Figure 8.1). Intuitively, it is useful to note that  $K_D^{-1}$  is the quencher concentration at which  $F_0/F = 2$  or 50% of the intensity is quenched. A linear Stern-Volmer plot is generally indicative of a single class of fluorophores, all equally accessible to quencher. If two fluorophore populations are present, and one class is not accessible to quencher, then the Stern-Volmer plots deviate from linearity toward the  $x$ -axis. This result is frequently found

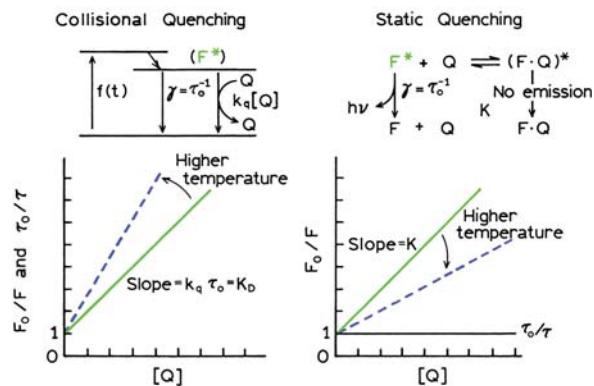


Figure 8.1. Comparison of dynamic and static quenching.

for the quenching of tryptophan fluorescence in proteins by polar or charged quenchers. These molecules do not readily penetrate the hydrophobic interior of proteins, and only those tryptophan residues on the surface of the protein are quenched.

It is important to recognize that observation of a linear Stern-Volmer plot does not prove that collisional quenching of fluorescence has occurred. In Section 8.3 we will see that static quenching also results in linear Stern-Volmer plots. Static and dynamic quenching can be distinguished by their differing dependence on temperature and viscosity, or preferably by lifetime measurements. Higher temperatures result in faster diffusion and hence larger amounts of collisional quenching (Figure 8.1). Higher temperature will typically result in the dissociation of weakly bound complexes, and hence smaller amounts of static quenching.

### 8.2.1. Derivation of the Stern-Volmer Equation

The Stern-Volmer equation can be derived by consideration of the fluorescence intensities observed in the absence and presence of quencher. The fluorescence intensity observed for a fluorophore is proportional to its concentration in the excited state,  $[F^*]$ . Under continuous illumination a constant population of excited fluorophores is established, and therefore  $d[F^*]/dt = 0$ . In the absence and presence of quencher the differential equations describing  $[F^*]$  are

$$\frac{d[F^*]}{dt} = f(t) - \gamma[F^*]_0 = 0 \quad (8.2)$$

$$\frac{d[F^*]}{dt} = f(t) - (\gamma + k_q[Q])[F^*] = 0 \quad (8.3)$$

where  $f(t)$  is the constant excitation function, and  $\tilde{\alpha} = \tau_0^{-1}$  is the decay rate of the fluorophore in the absence of quencher. In the absence of quenching the excited-state population decays with a rate  $\tilde{\alpha} = (\Gamma + k_{nr})$ , where  $\Gamma$  is the radiative rate and  $k_{nr}$  is the non-radiative decay rate. In the presence of quencher there is an additional decay rate  $k_q[Q]$ . With continuous excitation the excited-state population is constant, so the derivatives in these equations can be set to zero. Division of eq. 8.3 by 8.2 yields

$$\frac{F_0}{F} = \frac{\gamma + k_q[Q]}{\gamma} = 1 + k_q\tau_0[Q] \quad (8.4)$$

which is the Stern-Volmer equation.

The Stern-Volmer equation may also be obtained by considering the fraction of excited fluorophores, relative to the total, which decay by emission. This fraction ( $F/F_0$ ) is given by the ratio of the decay rate in the absence of quencher ( $\gamma$ ) to the total decay rate in the presence of quencher ( $\gamma + k_q[Q]$ ):

$$\frac{F}{F_0} = \frac{\gamma}{\gamma + k_q[Q]} = \frac{1}{1 + K_D[Q]} \quad (8.5)$$

which is again the Stern-Volmer equation. Since collisional quenching is a rate process that depopulates the excited state, the lifetimes in the absence ( $\tau_0$ ) and presence ( $\tau$ ) of quencher are given by

$$\tau_0 = \gamma^{-1} \quad (8.6)$$

$$\tau = (\gamma + k_q[Q])^{-1} \quad (8.7)$$

and therefore

$$\frac{\tau_0}{\tau} = 1 + k_q\tau_0[Q] \quad (8.8)$$

This equation illustrates an important characteristic of collisional quenching, which is an equivalent decrease in fluorescence intensity and lifetime (Figure 8.1, left). For collisional quenching

$$\frac{F_0}{F} = \frac{\tau_0}{\tau} \quad (8.9)$$

The decrease in lifetime occurs because quenching is an additional rate process that depopulates the excited state.

The decrease in yield occurs because quenching depopulates the excited state without fluorescence emission. Static quenching does not decrease the lifetime because only the fluorescent molecules are observed, and the uncomplexed fluorophores have the unquenched lifetime  $\tau_0$ .

### 8.2.2. Interpretation of the Bimolecular Quenching Constant

In papers on quenching one frequently encounters the bimolecular quenching constant ( $k_q$ ), which reflects the efficiency of quenching or the accessibility of the fluorophores to the quencher. As shown below, diffusion-controlled quenching typically results in values of  $k_q$  near  $1 \times 10^{10} \text{ M}^{-1} \text{ s}^{-1}$ . Values of  $k_q$  smaller than the diffusion-controlled value can result from steric shielding of the fluorophore or a low quenching efficiency. Apparent values of  $k_q$  larger than the diffusion-controlled limit usually indicate some type of binding interaction.

The meaning of the bimolecular quenching constant can be understood in terms of the collisional frequency between freely diffusing molecules. The collisional frequency ( $Z$ ) of a fluorophore with a quencher is given by

$$Z = k_0[Q] \quad (8.10)$$

where  $k_0$  is the diffusion-controlled bimolecular rate constant. This constant may be calculated using the Smoluchowski equation:

$$k_0 = \frac{4\pi N}{1000} (R_f + R_q)(D_f + D_q) \quad (8.11)$$

where  $R$  is the collision radius,  $D$  is the sum of the diffusion coefficients of the fluorophore ( $D_f$ ) and quencher ( $D_q$ ), and  $N$  is Avogadro's number. The collision radius is generally assumed to be the sum of the molecular radii of the fluorophore ( $R_f$ ) and quencher ( $R_q$ ). This equation describes the diffusive flux of a molecule with a diffusion coefficient  $D$  through the surface of a sphere of radius  $R$ . The factor of 1000 is necessary to keep the units correct when the concentration is expressed in terms of molarity. The term  $N/1000$  converts molarity to molecules/cm<sup>3</sup>.

The collisional frequency is related to the bimolecular quenching constant by the quenching efficiency  $f_Q$ :

$$k_q = f_Q k_0 \quad (8.12)$$

For example, if  $f_Q = 0.5$  then 50% of the collisional encounters are effective in quenching and  $k_q$  will be half the diffusion-controlled value  $k_0$ . Since  $k_0$  can be estimated with moderate precision, the observed value of  $k_q$  can be used to judge the efficiency of quenching. Quenchers like oxygen, acrylamide, and  $I^-$  generally have efficiencies near unity, but the quenching efficiency of weak quenchers like succinimide depends on the solvent and/or viscosity. The efficiency is generally less with the lighter halogens. The quenching efficiency depends upon the reduction potentials of the fluorophore and amine quencher, as expected for a charge-transfer reaction (Chapter 9).

The efficiency of quenching can be calculated from the observed value of  $k_q$ , if the diffusion coefficients and molecular radii are known. The radii can be obtained from molecular models, or from the molecular weights and densities of the quencher in question. Diffusion coefficients may be obtained from the Stokes-Einstein equation:

$$D = kT/6\pi\eta R \quad (8.13)$$

where  $k$  is Boltzmann's constant,  $\eta$  is the solvent viscosity, and  $R$  is the molecular radius. Frequently, the Stokes-Einstein equation underestimates the diffusion coefficients of small molecules. For example, quenching efficiencies of 2–3 were calculated for oxygen quenching of fluorophores dissolved in various alcohols.<sup>12</sup> These impossibly large efficiencies were obtained because the diffusion coefficient of oxygen in organic solvents is several fold larger than predicted by eq. 8.13. This equation describes the diffusion of molecules that are larger than the solvent molecules, which is not the case for oxygen in ethanol. As an alternative method, diffusion coefficients can be obtained from nomograms based upon the physical properties of the system.<sup>13</sup> Once the diffusion coefficients are known, the bimolecular quenching constant for  $f_Q = 1$  can be predicted using Smoluchowski eq. 8.11.

It is instructive to consider typical values for  $k_q$  and the concentrations of quencher required for significant quenching. For example, consider the quenching of tryptophan by oxygen.<sup>14</sup> At 25 °C the diffusion coefficient of oxygen in water is  $2.5 \times 10^{-5} \text{ cm}^2/\text{s}$  and that of tryptophan is  $0.66 \times 10^{-5} \text{ cm}^2/\text{s}$ . Assuming a collision radius of 5 Å, substitution into eq. 8.11 yields  $k_0 = 1.2 \times 10^{10} \text{ M}^{-1} \text{ s}^{-1}$ . The observed value of the oxygen Stern-Volmer quenching constant was 32.5 M<sup>-1</sup>. The unquenched lifetime of tryptophan is 2.7 ns, so that  $k_q = 1.2 \times 10^{10} \text{ M}^{-1} \text{ s}^{-1}$ , which is in excellent agreement with the predicted value. This indicates that essential-

ly every collision of oxygen with tryptophan is effective in quenching, that is  $f_Q = 1.0$ . A bimolecular quenching constant near  $1 \times 10^{10} \text{ M}^{-1} \text{ s}^{-1}$  may be considered as the largest possible value in aqueous solution. Many quenchers are larger than oxygen. Smaller diffusion-limited quenching constants are expected because the larger molecules have smaller diffusion coefficients. For example, the acrylamide quenching efficiency of tryptophan fluorescence is also near unity,<sup>15</sup> but  $k_q = 5.9 \times 10^9 \text{ M}^{-1} \text{ s}^{-1}$ . This somewhat smaller value of  $k_q$  is a result of the smaller diffusion coefficient of acrylamide relative to oxygen. Frequently data are obtained for fluorophores that are bound to macromolecules. In this case the fluorophore is not diffusing as rapidly. Also, the quenchers can probably only approach the fluorophores from a particular direction. In such cases the maximum bimolecular quenching constant is expected to be about 50% of the diffusion-controlled value.<sup>16</sup>

### 8.3. THEORY OF STATIC QUENCHING

In the previous section we described quenching that resulted from diffusive encounters between the fluorophore and quencher during the lifetime of the excited state. This is a time-dependent process. Quenching can also occur as a result of the formation of a nonfluorescent ground-state complex between the fluorophore and quencher. When this complex absorbs light it immediately returns to the ground state without emission of a photon (Figure 8.1).

For static quenching the dependence of the fluorescence intensity upon quencher concentration is easily derived by consideration of the association constant for complex formation. This constant is given by

$$K_s = \frac{[F - Q]}{[F][Q]} \quad (8.14)$$

where  $[F - Q]$  is the concentration of the complex,  $[F]$  is the concentration of uncomplexed fluorophore, and  $[Q]$  is the concentration of quencher. If the complexed species is nonfluorescent then the fraction of the fluorescence that remains ( $F/F_0$ ) is given by the fraction of the total fluorophores that are not complexed:  $f = F/F_0$ . Recalling that the total concentration of fluorophore  $[F]_0$  is given by

$$[F]_0 = [F] + [F - Q] \quad (8.15)$$

substitution into eq. 8.14 yields

$$K_s = \frac{[F]_0 - [F]}{[F][Q]} = \frac{[F_0]}{[F][Q]} - \frac{1}{[Q]} \quad (8.16)$$

We can substitute the fluorophore concentration for fluorescence intensities, and rearrangement of eq. 8.16 yields

$$\frac{F_0}{F} = 1 + K_s[Q] \quad (8.17)$$

Note that the dependence of  $F_0/F$  on  $[Q]$  is linear, which is identical to that observed for dynamic quenching, except that the quenching constant is now the association constant. Unless additional information is provided, fluorescence quenching data obtained by intensity measurements alone can be explained by either dynamic or static processes. As will be shown below, the magnitude of  $K_s$  can sometimes be used to demonstrate that dynamic quenching cannot account for the decrease in intensity. The measurement of fluorescence lifetimes is the most definitive method to distinguish static and dynamic quenching. Static quenching removes a fraction of the fluorophores from observation. The complexed fluorophores are nonfluorescent, and the only observed fluorescence is from the uncomplexed fluorophores. The uncomplexed fraction is unperturbed, and hence the lifetime is  $\tau_0$ . Therefore, for static quenching  $\tau_0/\tau = 1$  (Figure 8.1, right). In contrast, for dynamic quenching  $F_0/F = \tau_0/\tau$ .

One additional method to distinguish static and dynamic quenching is by careful examination of the absorption spectra of the fluorophore. Collisional quenching only affects the excited states of the fluorophores, and thus no changes in the absorption spectra are expected. In contrast, ground-state complex formation will frequently result in perturbation of the absorption spectrum of the fluorophore. In fact, a more complete form of eq. 8.17 would include the possibility of different extinction coefficients for the free and complexed forms of the fluorophore.

### 8.4. COMBINED DYNAMIC AND STATIC QUENCHING

In many instances the fluorophore can be quenched both by collisions and by complex formation with the same quencher. The characteristic feature of the Stern-Volmer

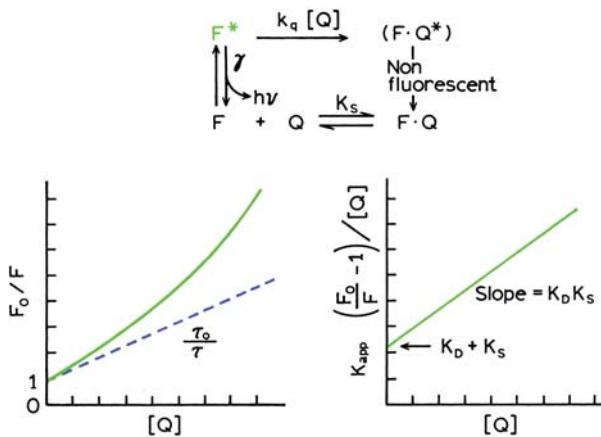


**Figure 8.2.** Dynamic and static quenching of the same population of fluorophores.

plots in such circumstances is an upward curvature, concave towards the  $y$ -axis (Figure 8.2). Then the fractional fluorescence remaining ( $F/F_0$ ) is given by the product of the fraction not complexed ( $f$ ) and the fraction not quenched by collisional encounters. Hence

$$\frac{F}{F_0} = f \frac{\gamma}{\gamma + k_q[Q]} \quad (8.18)$$

In the previous section we found that  $f^{-1} = 1 + K_s[Q]$ . Inversion of eq. 8.18 and rearrangement of the last term on the right yields

$$\frac{F_0}{F} = (1 + K_d[Q])(1 + K_s[Q]) \quad (8.19)$$

This modified form of the Stern-Volmer equation is second order in  $[Q]$ , which accounts for the upward curvature observed when both static and dynamic quenching occur for the same fluorophore.

The dynamic portion of the observed quenching can be determined by lifetime measurements. That is,  $\tau_0/\tau = 1 + K_d[Q]$ —the dashed line in Figure 8.2. If lifetime measurements are not available, then eq. 8.19 can be modified to allow a graphical separation of  $K_s$  and  $K_d$ . Multiplication of the terms in parentheses yields

$$\frac{F_0}{F} = 1 + (K_d + K_s)[Q] + K_d K_s [Q]^2 \quad (8.20)$$

$$\frac{F_0}{F} = 1 + K_{\text{app}}[Q] \quad (8.21)$$

where

$$K_{\text{app}} = \left[ \frac{F_0}{F} - 1 \right] \frac{1}{[Q]} = (K_d + K_s) + K_d K_s [Q] \quad (8.22)$$

The apparent quenching constant is calculated at each quencher concentration. A plot of  $K_{\text{app}}$  versus  $[Q]$  yields a straight line with an intercept of  $K_d + K_s$  and a slope of  $K_s K_d$  (Figure 8.2). The individual values can be obtained from the two solutions of the quadratic equation (see eq. 8.23 below). The dynamic component can generally be selected to be the solution comparable in magnitude to the expected diffusion-controlled value, by the temperature or viscosity dependence of the values, or from other available information about the sample.

## 8.5. EXAMPLES OF STATIC AND DYNAMIC QUENCHING

Before proceeding with additional theories and examples of quenching it seems valuable to present some examples which illustrate both static and dynamic quenching. Data for oxygen quenching of tryptophan are shown in Figure 8.3.<sup>14</sup> The Stern-Volmer plot is linear, which indicates that only one type of quenching occurs. The proportional decrease in the fluorescence lifetime and yields proves that the observed quenching is due to a diffusive process. From the

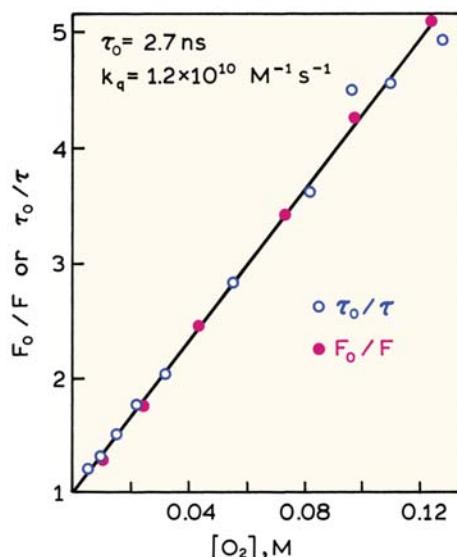


**Figure 8.3.** Oxygen quenching of tryptophan as observed by fluorescence lifetimes and yields. Revised and reprinted with permission from [14]. Copyright © 1973, American Chemical Society.

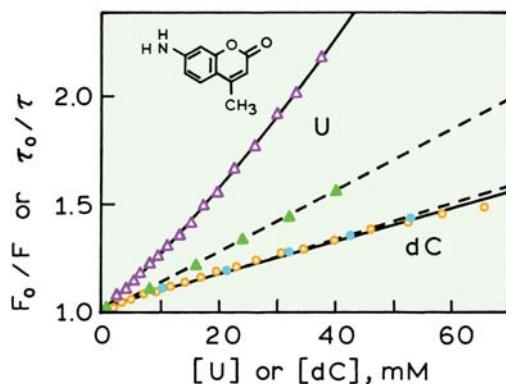


**Figure 8.4.** Quenching of coumarin C-120 by the nucleotides uridine ( $F_0/F$ , open triangle;  $\tau_0/\tau$ , solid triangle) or deoxycytosine ( $F_0/F$ , ○;  $\tau_0/\tau$ , ●). The sample was excited at the isoelectric point at 360 nm. Revised and reprinted with permission from [19]. Copyright © 1996, American Chemical Society.

slope of the Stern-Volmer plot one can calculate that  $K_D = 32.5 \text{ M}^{-1}$ , or that 50% of the fluorescence is quenched at an oxygen concentration of 0.031 M. The value of  $K_D$  and the fluorescence lifetime are adequate to calculate the bimolecular quenching constant,  $k_q = 1.2 \times 10^{10} \text{ M}^{-1} \text{ s}^{-1}$ . This is the value expected for the diffusion-controlled bimolecular rate constant between oxygen and tryptophan (eq. 8.11), which indicates efficient quenching by molecular oxygen.

Static quenching is often observed if the fluorophore and quencher can have a stacking interaction. Such interactions often occur between purine and pyrimidine nucleotides and a number of fluorophores.<sup>17–19</sup> One example is quenching of the coumarin derivative C-120 by the nucleotides uridine (U) and deoxycytosine (dC). The intensity Stern-Volmer plot for quenching by U (open triangles) shows clear upward curvature (Figure 8.4). The lifetime Stern-Volmer plot (solid triangles) is linear and shows less quenching than the intensity data. The larger amount of quenching seen from the intensity as compared to the lifetime indicates that C-120 is being decreased by both complex formation with uridine as well as collisional quenching by uridine. Contrasting data were obtained for quenching of C-120 by cytosine (dC). In this case the Stern-Volmer plots are linear for both intensities and lifetimes, and  $F_0/F = \tau_0/\tau$ . Hence quenching of C-120 by dC is purely dynamic.

For quenching of C-120 by uridine, the static and dynamic quenching constants can be determined by a plot of  $K_{app}$  versus [nucleotide] (see Figure 8.5). The slope ( $S$ ) and intercept ( $I$ ) were found to be  $158 \text{ M}^{-2}$  and  $25.6 \text{ M}^{-1}$ , respectively. Recalling  $I = K_D + K_S$  and  $S = K_D K_S$ , rearrangements yields

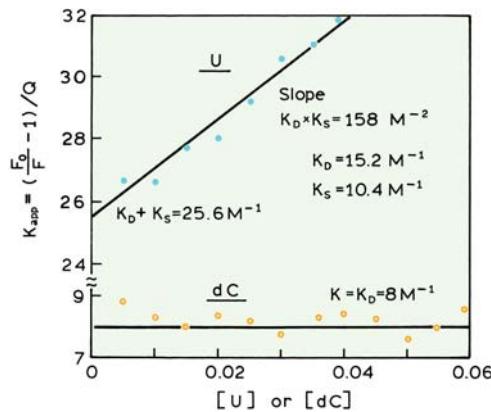


**Figure 8.5.** Separation of the dynamic and static quenching constants for quenching of C-120 by U or dC. Data from [19].

$$K_S^2 - K_S I + S = 0 \quad (8.23)$$

The solutions for this quadratic equation are  $K_S = 15.2$  or  $10.4 \text{ M}^{-1}$ . From the lifetime data we know  $K_D$  is near  $13.5 \text{ M}^{-1}$ . The lower value of  $10.4 \text{ M}^{-1}$  was assigned as the static quenching constant. At a uridine concentration of 96 mM, 50% of the ground-state C-120 is complexed and thus nonfluorescent.

It is interesting to mention why the interactions of nucleotides and C-120 were studied. The goal was to develop a method for DNA sequencing using a single electrophoretic lane for all four nucleotides.<sup>19</sup> This would be possible if coumarin derivatives could be identified that display different lifetimes when adjacent to each nucleotide. In this case the DNA sequence would be determined from the lifetimes observed for each band on the sequencing gel. For this fluorophore-quencher pair the quenching mechanism is a charge-transfer interaction. This mechanism is well understood, which could facilitate a rational approach to selection of the fluorophore for lifetime-based sequencing. The use of lifetime measurements in fluorescence sensing is Chapter 19 and DNA sequencing is described in Chapter 21.

## 8.6. DEVIATIONS FROM THE STERN-VOLMER EQUATION: QUENCHING SPHERE OF ACTION

Positive deviations from the Stern-Volmer equation are frequently observed when the extent of quenching is large. Two examples of upward-curving Stern-Volmer plots are shown for acrylamide quenching of NATA (Figure 8.6) and of the fluorescent steroid dihydroequilenin (DHE) (Figure

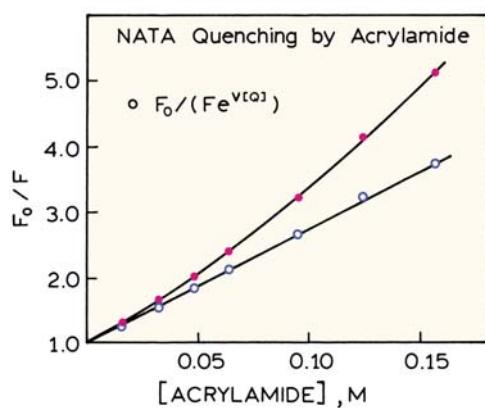


**Figure 8.6.** Acrylamide quenching of NATA in water (●). The open circles show the values of  $F_0/(F e^{V[Q]})$  where  $V = 2.0 \text{ M}^{-1}$ . Revised from [20].

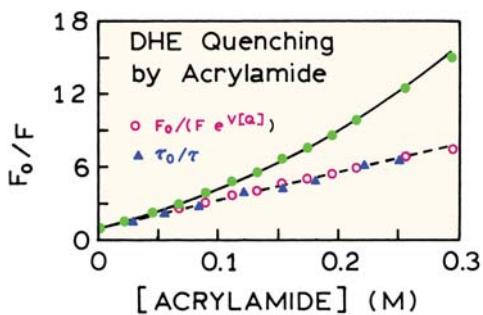


**Figure 8.7.** Acrylamide quenching of dihydroequilenin (DHE) in buffer containing 10% sucrose at 11°C. The value of  $V$  was  $2.4 \text{ M}^{-1}$ . Revised and reprinted with permission from [21]. Copyright © 1990, American Chemical Society.

8.7). The upward-curving Stern-Volmer plots could be analyzed in terms of the static and dynamic quenching constants (eq. 8.19). This analysis yields  $K_s$  values near 2.8 and  $5.2 \text{ M}^{-1}$  for acrylamide quenching of NATA and DHE, respectively. These values imply that quencher concentrations near 0.3 M are required to quench half of the fluorophores by a static process. Such a weak association suggests that the fluorophores and quenchers do not actually form a ground-state complex. Instead it seems that the apparent static component is due to the quencher being adjacent to the fluorophore at the moment of excitation. These closely spaced fluorophore–quencher pairs are immediately quenched, and thus appear to be dark complexes.

This type of apparent static quenching is usually interpreted in terms of a "sphere of action" within which the

probability of quenching is unity. The modified form of the Stern-Volmer equation that describes this situation is

$$\frac{F_0}{F} = (1 + K_D[Q]) \exp([Q]VN/1000) \quad (8.24)$$

where  $V$  is the volume of the sphere.<sup>22</sup> The data in Figures 8.6 and 8.7 are consistent with a sphere radius near 10 Å, which is only slightly larger than the sum of the radii of the fluorophore and quencher. When the fluorophore and quencher are this close, there exists a high probability that quenching will occur before these molecules diffuse apart. As the quencher concentration increases, the probability increases that a quencher is within the first solvent shell of the fluorophore at the moment of excitation.

### 8.6.1. Derivation of the Quenching Sphere of Action

Assume the existence of a sphere of volume  $V$  within which the probability of immediate quenching is unity. Intuitively, if a fluorophore is excited when a quencher is immediately adjacent, then this fluorophore is quenched and is therefore unobservable. The only observable fluorophores are those for which there are no adjacent quenchers. The modified form of Stern-Volmer eq. 8.24 is derived by calculating the fraction of fluorophores that does not contain a quencher within its surrounding sphere of action.<sup>22</sup>

The probability of finding a number ( $n$ ) of quenchers molecules in a given volume can be calculated from the Poisson distribution:

$$P(n) = \frac{\lambda^n}{n!} e^{-\lambda} \quad (8.25)$$

where  $\lambda$  is the mean number of quenchers per volume  $V$ . The average concentration in molecules/cm<sup>3</sup> is given by  $[Q]N/1000$ , so the average number of molecules in the sphere is  $\lambda = V[Q]N/1000$ . Only those fluorophores without nearby quenchers are fluorescent. The probability that no quenchers are nearby is

$$P(0) = e^{-\lambda} \quad (8.26)$$

Thus, the existence of the sphere of action reduces the proportion of observable fluorophores by the factor  $\exp(-V[Q]N/1000)$ , which in turn yields eq. 8.24. Division

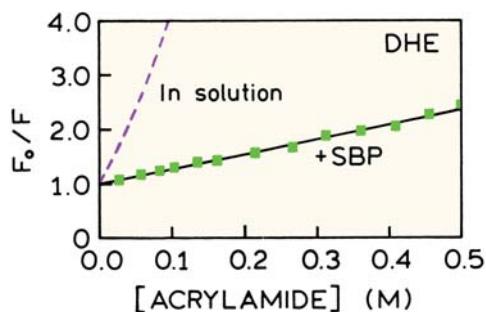


**Figure 8.8.** Acrylamide quenching of DHE when free in solution (dashed), and when bound to steroid-binding protein (SBP, — ■ —). Revised and reprinted with permission from [21]. Copyright © 1990, American Chemical Society.

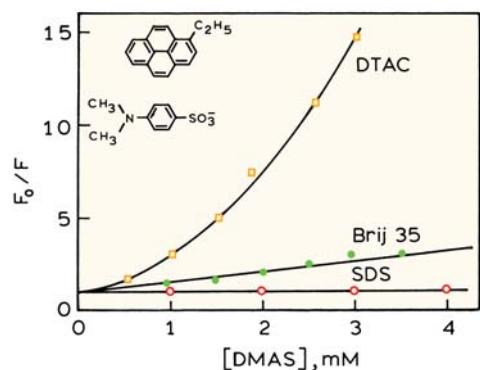


**Figure 8.9.** Quenching of 1-ethylpyrene (EP) by dimethylaniline sulfonate (DMAS) in positively charged micelles of dodecyltrimethylammonium chloride (DTAC), neutral micelles of Brij 35, or negatively charged micelles of sodium dodecylsulfate (SDS). Revised from [27].

of the values of  $F_0/F$  by  $\exp(V[Q]N/1000)$  corrects the steady-state intensities for this effect and reveals the dynamic portion of the observed quenching (Figures 8.6 and 8.7). For simplicity, the static term is often expressed in terms of reciprocal concentration.

## 8.7. EFFECTS OF STERIC SHIELDING AND CHARGE ON QUENCHING

The extent of quenching can be affected by the environment surrounding the fluorophore. One example is the quenching of the steroid dihydroequilenin (DHE) by acrylamide. When free in solution, DHE is readily quenched by acrylamide. However, when bound to a steroid-binding protein (SBP) much less quenching occurs (Figure 8.8). In fact, the modest amount of quenching was attributed to dissociation

of DHE from the protein.<sup>21</sup> Protection against quenching is frequently observed for probes bound to macromolecules,<sup>23–24</sup> and even cyclodextrins.<sup>25</sup> In fact, binding of probes to cyclodextrin has been used as a means to obtain room temperature phosphorescence.<sup>26</sup> The macromolecules or cyclodextrins provide protection from the solvent, but usually not complete protection from diffusing quenchers. Such solutions are usually purged to remove dissolved oxygen in order to observe phosphorescence.

The electronic charge on the quenchers can have a dramatic effect on the extent of quenching (Figure 8.9). This is illustrated by quenching of 1-ethylpyrene (EP) in micelles, where the detergent molecules have different charges.<sup>27</sup> The quencher was p-N,N-dimethylaniline sulfonate (DMAS) which is negatively charged. The micelles were positively charged (DTAC), neutral (Brij35), or negatively charged (SDS). There is extensive quenching of EP in the positively charged DTAC micelles, and essentially no quenching in the negatively charged SDS micelles. In general, one can expect charge effects to be present with charged quenchers such as iodide, and to be absent for neutral quenching like oxygen and acrylamide.

### 8.7.1. Accessibility of DNA-Bound Probes to Quenchers

The most dramatic effects of charge and shielding on quenching have been observed for fluorophores bound to DNA. The extent of quenching is decreased by intercalation of probes into the DNA double helix. For instance, ethidium bromide (EB) bound to DNA was found to be protected from oxygen quenching by a factor of 30 as compared to EB in solution.<sup>14</sup> Given the high negative charge density of DNA, one can expect the quenching to be sensitive to the charge of the quencher, the ionic strength of the solution, and the rate of quencher diffusion near the DNA helix.<sup>28–29</sup>

Collisional quenching by oxygen was used to study quenching of several DNA-bound probes.<sup>30–31</sup> Oxygen was chosen as the quencher because it is neutral, and should thus be unaffected by the charge on the DNA. The probes were selected to have different sizes and different modes of binding to DNA (Figure 8.10). Proflavin intercalates into double-helical DNA, and was expected to be protected from quenching. The bimolecular quenching constant for intercalated proflavin was less than 10% of the diffusion-controlled rate (Table 8.2). The  $k_q$  value for proflavin may be smaller than shown, as there was little quenching under these experimental conditions. Hoechst 33258 is known to

**Table 8.2.** Decay Times and Oxygen Quenching Constants of Probes Bound to DNA<sup>31</sup>

Fluorophore	Type of complex	$\tau_0$ (ns)	$k_q$ ( $M^{-1} \text{ sec}^{-1}$ )
Proflavine	Intercalation	6.3	$<0.1 \times 10^{10}$
Coronene	Partial intercalation	225	$0.17 \times 10^{10}$
Hoechst 33258	Minor groove	3.5	$1.1 \times 10^{10}$

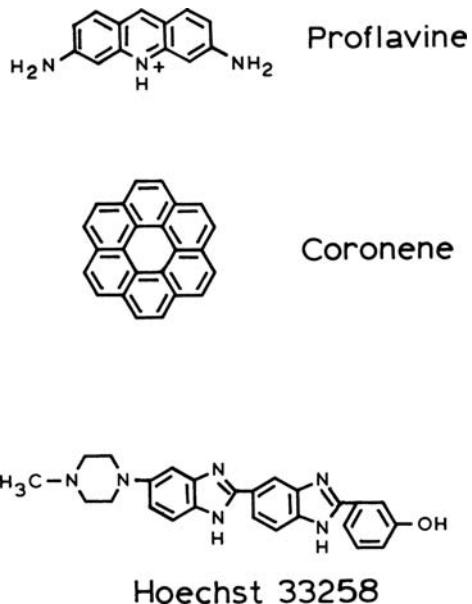


**Figure 8.10.** Structure of three probes bound to DNA (Table 8.2). Reprinted with permission from [31]. Copyright © 1988, American Society for Photobiology.

bind to the minor groove of DNA. Surprisingly, the  $k_q$  values for Hoechst DNA is near the diffusion-controlled limit, suggesting complex accessibility by oxygen. The behavior of coronene was intermediate. Coronene is rather large, and not able to fully fit into a DNA helix. The intermediate value of  $k_q$  was explained as due to partial intercalation of coronene, with the value of  $k_q$  reflecting partial exposure to water. These results illustrate how the extent of probe exposure can be correlated with the bimolecular quenching constant. The values of the unquenched fluorescence lifetimes were needed to calculate the values of  $k_q$  from the Stern-Volmer quenching constants.

The extent of quenching can also be affected by the charge on the quenchers. This is illustrated by iodide quenching of Hoechst 33258 when free in solution and

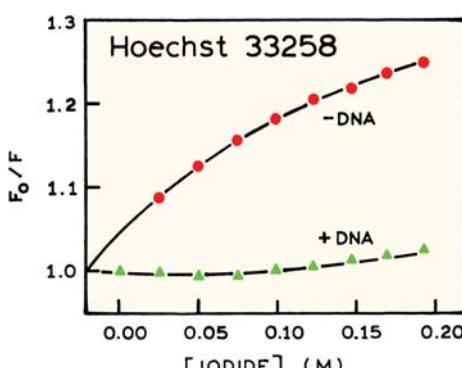


**Figure 8.11.** Iodide quenching of Hoechst 33258 in the absence and presence of calf thymus DNA. The ionic strength was kept constant using KCl. Revised from [32].

when bound to DNA (Figure 8.11). Hoechst 33258 is readily quenched by iodide when free in solution, but is not quenched when bound to DNA. In the previous paragraph we saw that Hoechst 33258 bound to DNA was completely accessible to the neutral quencher oxygen. Apparently, the negative charges on DNA prevent iodide from coming into contact with Hoechst 33258 when bound to the minor groove of DNA.

### 8.7.2. Quenching of Ethenoadenine Derivatives

The nucleotide bases of DNA are mostly nonfluorescent. A fluorescent analogue of adenine has been created by addition of an etheno bridge, the so called  $\varepsilon$ -ATP derivatives (Chapter 3). Depending on the pH and extent of phosphorylation, the charge on the ethenoadenine nucleotides ranges from -3 for  $\varepsilon$ -ATP to 0 for ethenoadenosine. Hence one expects the extent of quenching to depend on the charge of the quencher.

Stern-Volmer plots for the various  $\varepsilon$ -Ad nucleotides are shown in Figure 8.12. For the neutral quencher acrylamide there is no effect of charge (right). For the positively charged quencher  $Tl^+$  the largest Stern-Volmer constant was observed for  $\varepsilon$ -ATP, with progressively smaller values as the number of negatively charged phosphates decreased (left). The opposite trend was observed for iodide quenching where the extent of quenching was lowest for  $\varepsilon$ -ATP with three negative charges (middle). Such effects of charge on quenching can be used to determine the local charge around fluorophores on proteins based on quenching by positive, neutral, and negatively charged quenchers.<sup>33-35</sup>

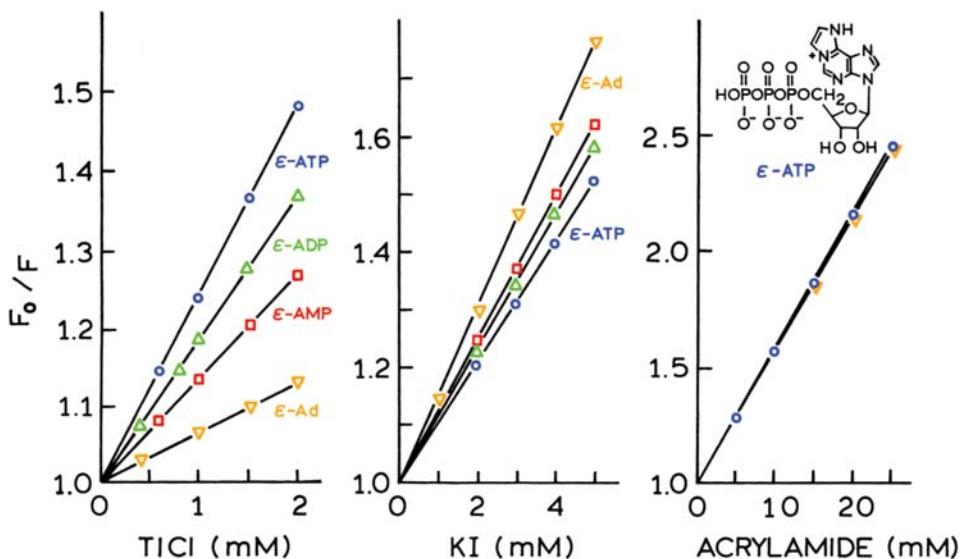


**Figure 8.12.** Quenching of etheno-ATP ( $\epsilon$ -ATP,  $\circ$ ),  $\epsilon$ -ADP ( $\Delta$ ),  $\epsilon$ -AMP ( $\square$ ) and  $\epsilon$ -Ad ( $\nabla$ ) by thallium, iodide, and acrylamide in 10 mM phosphate buffer, 0.1 M KCl, 20°C, pH 7.0. Revised from [33].

### 8.8. FRACTIONAL ACCESSIBILITY TO QUENCHERS

Proteins usually contain several tryptophan residues that are in distinct environments. Each residue can be differently accessible to quencher. Hence one can expect complex Stern-Volmer plots, and even spectral shifts due to selective quenching of exposed versus buried tryptophan residues. One example is quenching of lysozyme. This protein from egg white has six tryptophan residues, several of which are known to be near the action site. Lysozyme fluorescence was observed with increasing concentrations of trifluoroacetamide (TFA), which was found to be a collisional quencher of tryptophan fluorescence.<sup>36</sup> The Stern-Volmer plot curves downward towards the  $x$ -axis. As will be described below, this is a characteristic feature of two fluorophore populations, one of which is not accessible to the quencher. In the case of lysozyme the emission spectrum shifts progressively to shorter wavelengths with increasing TFA concentrations (Figure 8.13, right). This indicates that those tryptophan residues emitting at larger wavelengths are quenched more readily than the shorter wavelength tryptophans.

The emission spectrum of the quenched residues can be calculated from taking the difference between the unquenched and quenched emission spectra. This spectrum shows that the quenched residues display an emission maxima at 348 nm. The protected residues display an emission

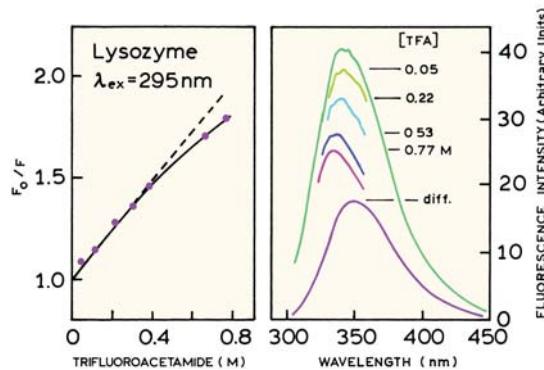


**Figure 8.13.** Quenching of lysozyme by trifluoroacetamide (TFA). **Left:** Stern-Volmer plot. **Right:** Emission spectra with increasing concentrations of TFA. Also shown is the difference spectrum (diff.), 0.0–0.77 M TFA. Revised and reprinted from [36]. Copyright © 1984, with permission from Elsevier Science.

maxima at 333 nm. Similar results were obtained for quenching of lysozyme by iodide.<sup>37</sup>

#### 8.8.1. Modified Stern-Volmer Plots

The differing accessibilities of tryptophan residues in proteins has resulted in the frequent use of quenching to resolve the accessible and inaccessible residues.<sup>37</sup> Suppose there are two populations of fluorophores, one of which is accessible ( $a$ ) to quenchers and the other being inaccessible or buried ( $b$ ). In this case the Stern-Volmer plot will display

downward curvature (Figure 8.13). The total fluorescence in the absence of quencher ( $F_0$ ) is given by

$$F_0 = F_{0a} + F_{0b} \quad (8.27)$$

where the subscript 0 once again refers to the fluorescence intensity in the absence of quencher. In the presence of quencher the intensity of the accessible fraction ( $f_a$ ) is decreased according to the Stern-Volmer equation, whereas the buried fraction is not quenched. Therefore, the observed intensity is given by

$$F = \frac{F_{0a}}{1 + K_a[Q]} + F_{0b} \quad (8.28)$$

where  $K_a$  is the Stern-Volmer quenching constant of the accessible fraction, and  $[Q]$  is the concentration of quencher. Subtraction of eq. 8.28 from eq. 8.27 yields

$$\Delta F = F_0 - F = F_{0a} \left( \frac{K_a[Q]}{1 + K_a[Q]} \right) \quad (8.29)$$

Inversion of eq. 8.29 followed by division into eq. 8.27 yields

$$\frac{F_0}{\Delta F} = \frac{1}{f_a K_a [Q]} + \frac{1}{f_a} \quad (8.30)$$

where  $f_a$  is the fraction of the initial fluorescence that is accessible to quencher:

$$f_a = \frac{F_{0a}}{F_{0b} + F_{0a}} \quad (8.31)$$

This modified form of the Stern-Volmer equation allows  $f_a$  and  $K_a$  to be determined graphically (Figure 8.14). A plot of  $F_0/\Delta F$  versus  $1/[Q]$  yields  $f_a^{-1}$  as the intercept and  $(f_a K_a)^{-1}$  as the slope. A y-intercept of  $f_a^{-1}$  may be understood intuitively. The intercept represents the extrapolation to infinite quencher concentration ( $1/[Q] = 0$ ). The value of  $F_0/(F_0 - F)$  at this quencher concentration represents the reciprocal of the fluorescence that was quenched. At high quencher concentration only the inaccessible residues will be fluorescent.

In separation of the accessible and inaccessible fractions of the total fluorescence it should be realized that there may be more than two classes of tryptophan residues.

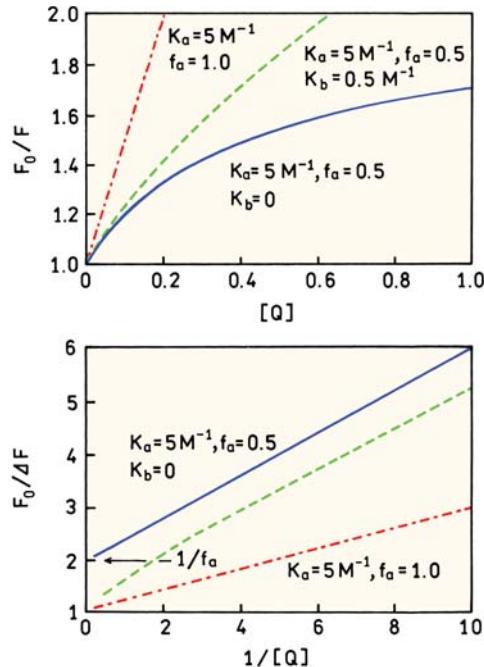


**Figure 8.14.** Stern-Volmer and modified Stern-Volmer plots for two populations of fluorophores, an accessible fraction with  $K_a = 5 \text{ M}^{-1}$  and  $f_a = 0.5$ , and an inaccessible fraction with  $K_b = 0$ . The dashed line shows the effect of the "inaccessible" population being quenched with a  $K$  value one-tenth of the accessible population,  $K_b = 0.5 \text{ M}^{-1}$ .

Also, even the presumed "inaccessible" fraction may be partially accessible to quencher. This possibility is illustrated by the dashed lines in Figure 8.14, which show the expected result if the Stern-Volmer constant for the buried fraction ( $K_b$ ) is one-tenth that of the accessible fraction ( $K_b = 0.1 K_a$ ). For a limited range of quencher concentrations, the modified Stern-Volmer plot can still appear to be linear. The extrapolated value of  $f_a$  would be larger than seen with  $K_b = 0$ . Hence, the modified Stern-Volmer plots provide a useful but arbitrary resolution of two assumed classes of tryptophan residues.

### 8.8.2. Experimental Considerations in Quenching

While quenching experiments are straightforward, there are several potential problems. One should always examine the emission spectra under conditions of maximum quenching. As the intensity is decreased the contribution from background fluorescence may begin to be significant. Quenchers are often used at high concentrations, and the quenchers themselves may contain fluorescent impurities. Also, the intensity of the Raman and Rayleigh scatter peaks from water is independent of quencher concentration. Hence the

relative contribution of scattered light always increases with quenching.

It is also important to consider the absorption spectra of the quenchers. Iodide and acrylamide absorb light below 290 nm. The inner filter effect due to absorption can decrease the apparent fluorescence intensity, and thereby distort the quenching data.<sup>38–39</sup> Regardless of the quencher being used, it is important to determine if the inner filter effects are significant. If inner filter effects are present the observed fluorescence intensities must be corrected. The lifetime measurements are mostly independent of inner filter effects because the lifetime measurements are relatively independent of total intensity.

When using iodide or other ionic quenchers it is important to maintain a constant ionic strength. This is usually accomplished by addition of KCl. When using iodide it is also necessary to add a reducing agent such as  $\text{Na}_2\text{S}_2\text{O}_3$ . Otherwise,  $\text{I}_2$  is formed, which is reactive and can partition into the nonpolar regions of proteins and membranes.

## 8.9. APPLICATIONS OF QUENCHING TO PROTEINS

### 8.9.1. Fractional Accessibility of Tryptophan Residues in Endonuclease III

There have been numerous publications on determining the fraction of protein fluorescence accessible to quenchers.<sup>40–47</sup> In Section 13.5 we show that proteins in the native state often display a fraction of the emission that is not accessible to water-soluble quenchers, and that denaturation of the proteins usually results in accessibility of all the tryptophan residues to quenchers. The possibility of buried and exposed residues in an apurinic single protein is illustrated by endonuclease III. Endo III is a DNA repair enzyme that displays both N-glycosylase and apurinic/apyrimidinic lyase activities. The structure of Endo III shows two domains, with the DNA binding site in the cleft region. Endo III contains two tryptophan residues.<sup>42</sup> Trp 132 is exposed to the solvent, and trp 178 is buried in one of the domains (Figure 8.15). Hence one expects these residues to be differently accessible to water-soluble quenchers.

The Stern-Volmer plot for iodide quenching of Endo III shows clear downward curvature (Figure 8.16, top). The modified iodide Stern-Volmer plot for Endo III shows clear evidence for a shielded fraction (bottom). Extrapolation to high iodide concentrations yields an intercept near 2, indicating that only half of the emission can be quenched by

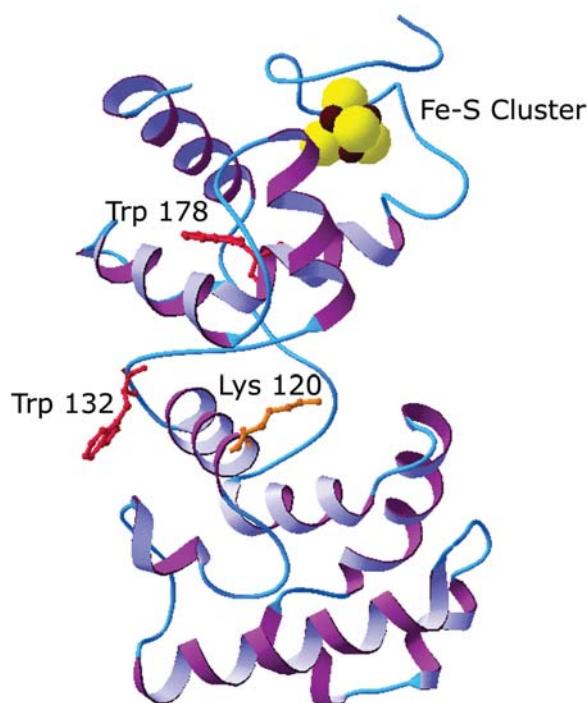


**Figure 8.15.** Structure of Endo III showing the exposed residue trp 132 and the buried residue trp 178 near the iron-sulfur cluster.

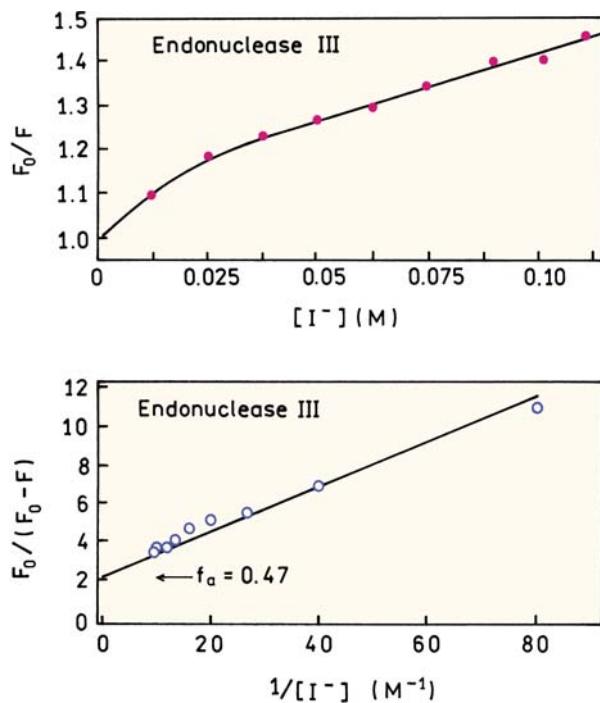


**Figure 8.16.** Stern-Volmer plot and modified Stern-Volmer plot for iodide quenching of Endo III showing evidence for two types of tryptophan residues. The inaccessible fraction is  $f_a = 0.47$ . Revised and reprinted with permission from [42]. Copyright © 1995, American Chemical Society.

iodide. This suggests that both trp residues in Endo III are equally fluorescent, and that only one residue (trp 132) can be quenched by iodide. Similar results have been obtained for a large number of proteins, and the extent of quenching is known to depend on the size and polarity of the quenchers.<sup>6,7</sup> Quenching of solvent-exposed residues in proteins is now a standard tool in the characterization of proteins.

### 8.9.2. Effect of Conformational Changes on Tryptophan Accessibility

The conformational state of a protein can have an influence on the exposure of its tryptophan residues to solvent. This is illustrated by the cyclic AMP (cAMP) receptor protein (CRP) from *E. coli*.<sup>44</sup> This protein regulates the expression of more than 20 genes in *E. coli*. CRP consists of two identical polypeptide chains, each containing 209 amino acids. CRP contains two nonidentical trp residues at positions 13 and 85.

Acrylamide Stern-Volmer plots for CRP are shown in Figure 8.17, in the absence and presence of bound cAMP. In the absence of cAMP the Stern-Volmer plot shows obvious downward curvature, indicating that one of the trp residues is inaccessible or only slightly accessible to acrylamide. Binding of cAMP results in a dramatic change in the Stern-Volmer plot, which becomes more linear and even displays some upward curvature. Apparently, binding of cAMP to the CRP causes a dramatic conformational change that results in exposure of the previously shielded trp residue. Changes in accessibility due to conformational changes have been reported for other proteins.<sup>48–49</sup> Binding of substrates to proteins can also result in shielding of tryptophan, as has been observed for lysozyme<sup>37</sup> and for wheat-germ agglutinin.<sup>36</sup>

### 8.9.3. Quenching of the Multiple Decay Times of Proteins

The intensity decays of proteins are typically multi-exponential. Hence, it is natural to follow the individual decay times as the protein is exposed to increasing concentrations of quencher. One example is the CRP protein we just described.<sup>44</sup> Frequency-domain data of its intrinsic tryptophan emission yield decay times near 1.5 and 6.8 ns. Similar decay times were observed in the absence and presence of bound cAMP. For the protein without bound cAMP, the shorter decay time did not change with increasing iodide

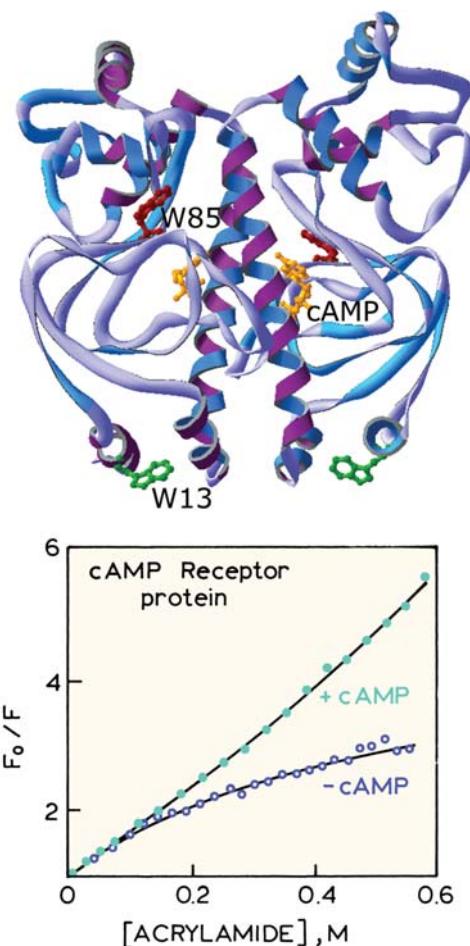


**Figure 8.17.** Acrylamide Stern-Volmer plot for cAMP receptor protein in the absence and presence of cAMP. Revised from [44].

concentration (Figure 8.18, top), whereas the long lifetime decreased. This decrease in lifetime indicates that the 6.8-ns component is due to the exposed trp residue. The 1.5-ns component is not quenched by iodide and is assigned to the buried trp residue. In the presence of bound cAMP both decay times are seen to decrease in the presence of iodide, indicating both are quenched (bottom). These results agree with the linear Stern-Volmer plot found for CRP with bound cAMP (Figure 8.17).

While the results shown in Figure 8.18 show a clear separation of decay times, caution is needed when interpreting decay times in the presence of quenchers. For many proteins the decay times will be closer than 1.5 and 6.8 ns, and the decay time for each trp residue can depend on emission wavelength. Hence, it may not be possible to assign a unique decay time to each tryptophan residue. Additionally, collisional quenching results in non-exponential decays,

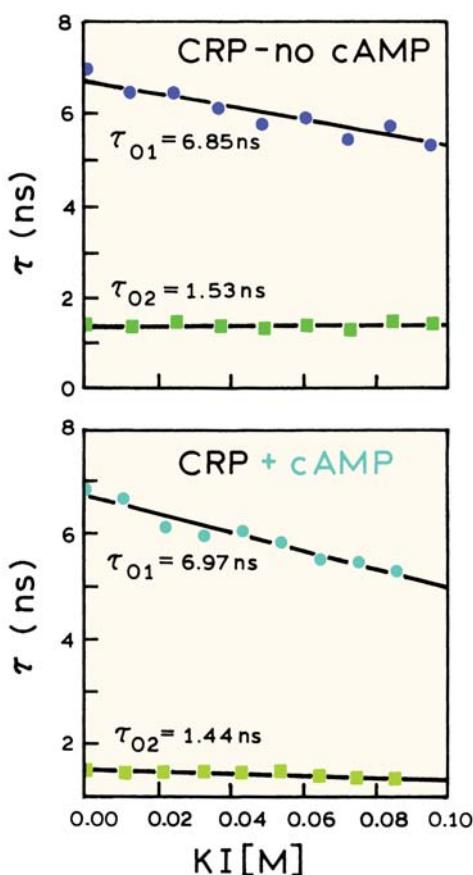


**Figure 8.18.** Iodide-dependent decay times of cAMP receptor protein (CRP) in the absence (top) and presence (bottom) of bound cAMP. Revised from [44].

even if the fluorophore shows a single decay time in the absence of quencher. This change in the intensity decay is due to transient effects in quenching, which are due to the rapid quenching of closely spaced  $F-Q$  pairs, followed by a slower quenching rate due to quencher diffusion. The presence of transient effects results in additional ns decay time components, which, depending on the method of measurement, can affect the apparent lifetimes for each residue. The assignment of decay times to trp residues in the presence of quenching can be ambiguous. Transient effects in quenching are described in the following chapter.

#### 8.9.4. Effects of Quenchers on Proteins

When performing quenching experiments it is important to consider whether the quencher has an adverse effect on the protein. Some quenchers such as 2,2,2-trichloroethanol are known to bind to proteins and induce conformational

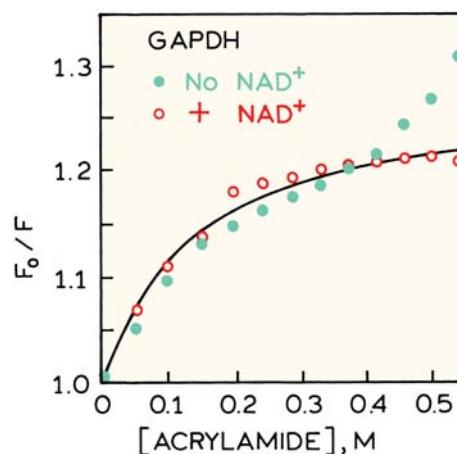


**Figure 8.19.** Acrylamide quenching of GAPDH in the absence (●) and presence (○) of the cofactor NAD<sup>+</sup>. Revised and reprinted with permission from [54]. Copyright © 1992, American Society for Photobiology.

changes.<sup>50</sup> For a time it was thought that acrylamide bound to proteins, but it is now accepted that such binding does not occur outside of several specific cases.<sup>51–53</sup> However, even the non-perturbing quencher acrylamide can affect certain proteins, as was found for glyceraldehyde-3-phosphate dehydrogenase (GAPDH).<sup>54</sup> This protein contains three tryptophan residues in each subunit of the tetrameric enzyme. For the apoenzyme, which lacks NAD<sup>+</sup>, the acrylamide Stern-Volmer plot is highly unusual. The extent of quenching increases rapidly above 0.4 M acrylamide (Figure 8.19). This effect is not seen for the holoenzyme that contains bound NAD<sup>+</sup>. Acrylamide also caused a slow loss of activity and reduction in the number of thiol groups. Acrylamide appears to bind to GAPDH, to react with the protein and destroy its activity, while at the same time increasing the exposure of the tryptophan residues to the aqueous phase.

#### 8.9.5. Correlation of Emission Wavelength and Accessibility: Protein Folding of Colicin E1

Colicin E1 is a 522 residue polypeptide that is lethal to *E. coli* strains that do not contain the resistance plasmid. Colicin E1 exerts its toxic effects by forming a channel in the cytoplasmic membrane that depolarizes and deenergizes the cell. The active channel-forming domain consists of about 200 residues from the carboxy terminus, which form ten  $\alpha$ -helices spanning the membrane.

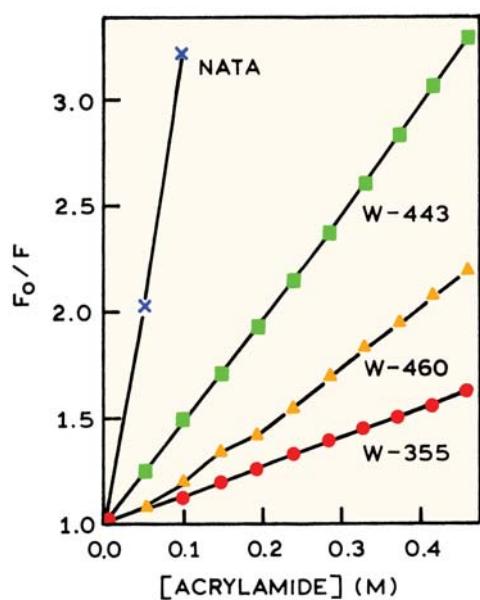


**Figure 8.20.** Acrylamide Stern-Volmer plot for NATA (x), and three single-tryptophan mutants of the channel-forming peptide of Colicin E1 at pH 3.5, W-355 (●), W-460 (▼), and W-443 (■). Revised and reprinted with permission from [55]. Copyright © 1993, American Chemical Society.

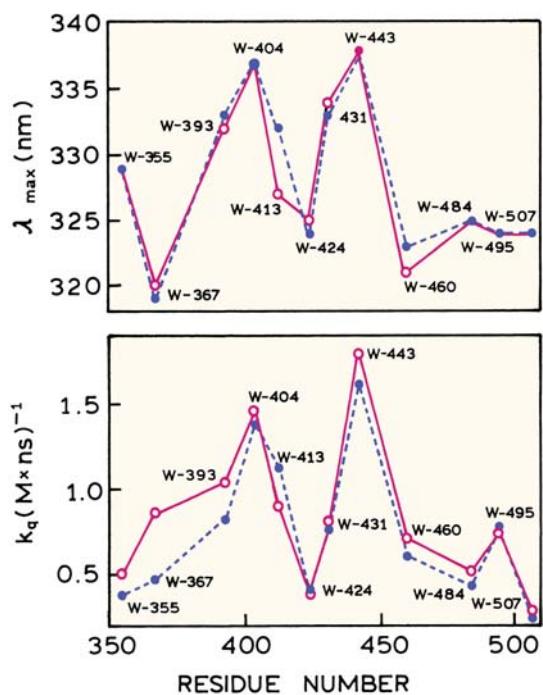


**Figure 8.21.** Emission maxima (top) and bimolecular quenching constants (bottom) of the twelve single-tryptophan mutants of the channel-forming peptide of Colicin E1 at pH 3.5. Revised and reprinted with permission from [55]. Copyright © 1993, American Chemical Society.

The conformation of the membrane-bound form of the colicin E1 channel peptide was studied by acrylamide quenching.<sup>55</sup> Twelve single tryptophan mutants were formed by site-directed mutagenesis. The tryptophan residues were mostly conservative replacements, meaning the trp residues were placed in positions previously containing phenylalanine or tyrosine. Acrylamide Stern-Volmer plots of three of these mutant proteins are shown in Figure 8.20. The accessibility to acrylamide quenching is strongly dependent on the location of the residue, and all residues are shielded relative to NATA. Depending on position, the trp residues also showed different emission maxima (Figure 8.21, top). The acrylamide bimolecular quenching constants were found to closely follow the emission maxima, with lower values of  $k_q$  for the shorter-wavelength tryptophans (bottom). Such data can be used to suggest a folding pattern for the channel-forming peptide, and to reveal conformational changes that occur upon pH activation of colicin E1.

## 8.10. APPLICATION OF QUENCHING TO MEMBRANES

### 8.10.1. Oxygen Diffusion in Membranes

Quenching by oxygen has been used to determine the apparent diffusion coefficient of oxygen in membranes. This can be accomplished using probes that partition into the lipid bilayers or are covalently bound to the lipids. Figure 8.22 shows oxygen Stern-Volmer plots for 2-methylanthracene in vesicles of DMPC and DPPC, which have phase-transition temperatures ( $T_c$ ) near 24 and 37°C, respectively.<sup>56</sup> At the experimental temperature near 31°C the DPPC bilayers are below the phase transition, and the DMPC bilayers are above the phase transition. While anisotropy measurement on such a bilayer suggests a large change in viscosity at the transition temperature (Chapter 10), the effect on oxygen diffusion is only modest: near twofold. This surprisingly small change in the oxygen diffusion coefficient has been confirmed by other fluorescence<sup>57–59</sup> and ESR experiments.<sup>60</sup> These experiments even suggest that cholesterol, which generally makes membranes more rigid, results in increased rates of oxygen transport. This can be seen by quenching of pyrene dodecanoic acid (PDA) in erythrocyte ghost membranes (Figure 8.23). In this case, the ghost membranes were modified by addition of endogenous cholesterol. The apparent bimolecular quenching constant increases with increasing amounts of cholesterol, except for the highest membrane concentration

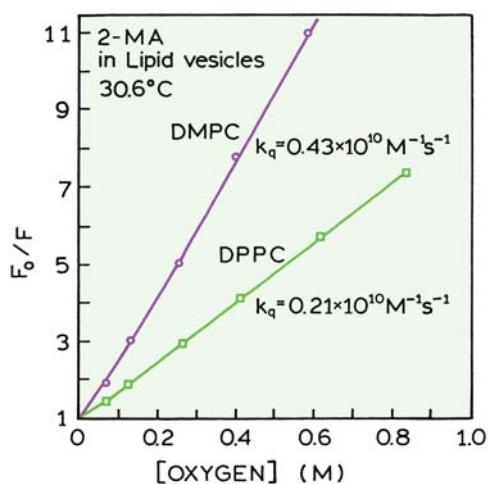


**Figure 8.22.** Oxygen quenching of 2-methylanthracene (2-MA) at 30.6°C, in DMPC ( $T_c = 24^\circ\text{C}$ ) and DPPC ( $T_c = 37^\circ\text{C}$ ) bilayers.

of cholesterol where the amount of quenching decreases (Figure 8.23, ●).

In order to calculate the bimolecular quenching constants it is necessary to know the oxygen concentration in the membranes. Unfortunately, precise values are not known, particularly for membranes with different lipid compositions. The oxygen solubility in membranes is usually taken as equal to that in nonpolar solvents, and thus

approximately fourfold larger than in water. Assuming a lifetime of PDA near 120 ns, one can use the data in Figure 8.23 to calculate  $k_q = 0.22 \times 10^{10} \text{ M}^{-1} \text{ s}^{-1}$ . The permeability ( $P$ ) of a membrane can be approximated by  $P = k_q D / \Delta x$ , where  $D$  is the oxygen diffusion coefficient and  $\Delta x$  is the membrane thickness. Given that the diffusion coefficient of oxygen is about 1/5 of that in water, and the lipid–water partition coefficient is near 5, this equation suggests that biological membranes do not pose a significant diffusive barrier to oxygen.

### 8.10.2. Localization of Membrane-Bound Tryptophan Residues by Quenching

Collisional quenching is a short-range interaction, so that the extent of quenching can be used to indicate the amount of molecular contact between the fluorophore and quencher. This concept has been used to study the location of tryptophan residues in membrane-spanning peptides.<sup>61</sup> A series of peptides were synthesized that contained a single tryptophan residue. These peptides were roughly of the form  $K_q L_k WL_m K_m$ , where  $K$  is a charged amino acid lysine,  $L$  is a nonpolar amino acid leucine, and  $W$  is tryptophan. The number of nonpolar residues on each side of the tryptophan was varied to position the trp at various distances from the center of the DOPC bilayers. Figure 8.24 shows acrylamide quenching of the peptides when bound to DOPC vesicles. The extent of quenching depends strongly

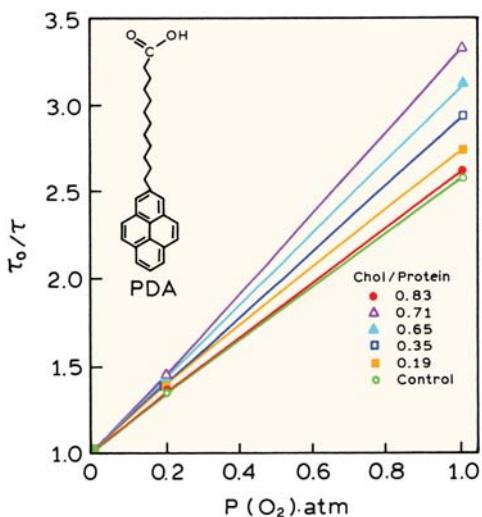


**Figure 8.23.** Oxygen quenching of pyrene dodecanoic acid in erythrocyte ghost membranes with various cholesterol/protein ratios: ○, control, no added cholesterol; Chol/Protein ratios: ■, 0.19; □, 0.35; ▲, 0.65; △, 0.71; ●, 0.83. Revised from [59].

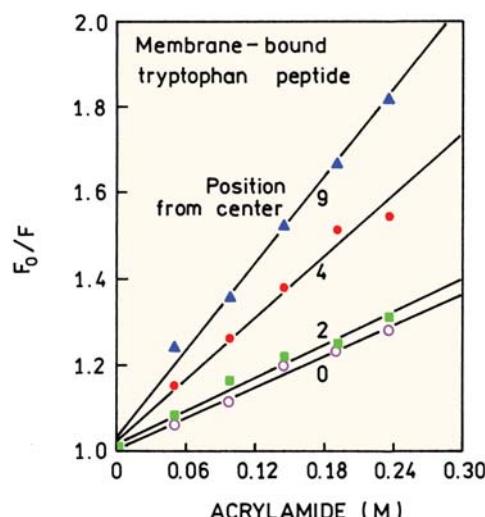


**Figure 8.24.** Acrylamide quenching of tryptophan residues in a membrane-spanning peptide. Revised and reprinted with permission from [61]. Copyright © 2003, American Chemical Society.

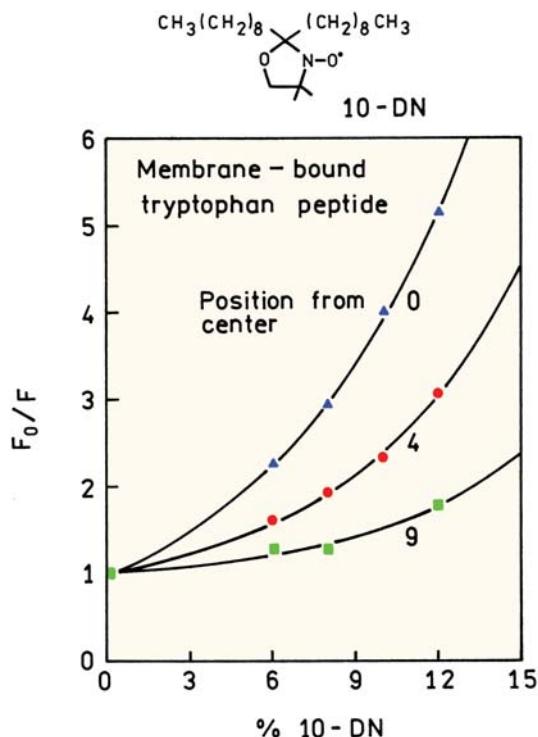


**Figure 8.25.** Quenching of tryptophan residues in a membrane-spanning peptide by a hydrophobic nitroxide. Revised and reprinted with permission from [61]. Copyright © 2003, American Chemical Society.

on the position of the trp residue relative to the center of the bilayer. The most accessible trp residue is located 9 positions from the center, and is the most protected residue in the center of the bilayer.

These membrane-bound peptides were also studied with hydrophobic quencher 10-doxylnonadecane (10-DN). This quencher (19 carbons in total length) should be able to bind to the DOPC bilayer without folding back on itself. The alkyl chains on each side of the doxyl group are equivalent in length. Hence the doxyl group was expected to localize at the center of the bilayer. Figure 8.25 shows quenching of the trp peptides in DOPC bilayers by 10-DN. 10-DN is not significantly soluble in water and the Stern-Volmer plot is presented in terms of the mole% of 10-DN in the bilayers. The Stern-Volmer plots curve upward but it is still clear that the trp residue at the center of the bilayer is most strongly quenched, and the extent of quenching by 10-DN decreases as the trp residue is displaced from the center of the bilayer. The effect of trp position on quenching is summarized in Figure 8.26. The extent of quenching by acrylamide, which is water soluble, decreases as the trp residue is displaced from the center of the bilayer. The extent of trp quenching by 10-DN shows the opposite dependence. Such experiments can be used to determine the location of tryptophan or other fluorophores in membranes when the structures are not known.

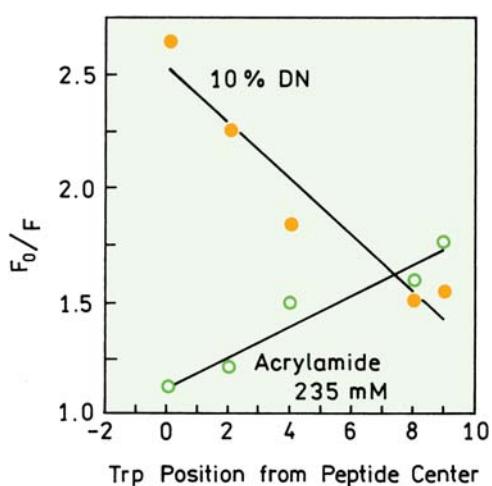


**Figure 8.26.** Comparison of acrylamide and nitroxide quenching of tryptophan residues in a membrane-spanning peptide. Revised and reprinted with permission from [61]. Copyright © 2003, American Chemical Society.

### 8.10.3. Quenching of Membrane Probes Using Localized Quenchers

The previous example showed that accessibility of a fluorophore to a quencher can be used to roughly indicate its position in a membrane. However, this approach did not provide an estimate of its actual location. A somewhat more advanced approach is to use quenchers that are covalently linked to the phospholipids and thus restricted to particular depths in the lipid bilayers. Typical lipid quenchers are the brominated phosphatidylcholines (bromo-PCs) and nitroxide-labeled PCs or fatty acids (Figure 8.27). This approach was used to determine the locations of the fluorenyl groups in a series of fluorenyl fatty acids when bound to erythrocyte ghosts (Figure 8.28). The term "ghosts" refers to the red-blood-cell membranes following removal of hemoglobin by cell lysis. The fluorenyl probes were quenched by 9,10-dibromostearate that partitioned into the membrane.<sup>62</sup> Since the bromine atoms are rather small, they are expected to be localized according to their position on the fatty-acid chain. The bromine atoms are located near the center

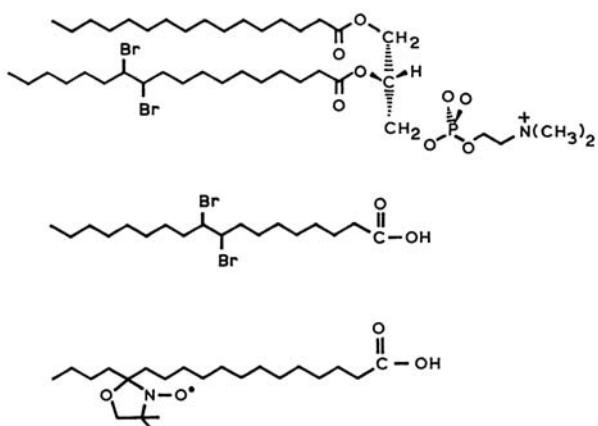


**Figure 8.27.** Structures of a bromo-PC (top), 9,10-dibromostearic acid (middle), and a nitroxide labeled fatty acid (bottom), which act as localized quenchers in membranes.

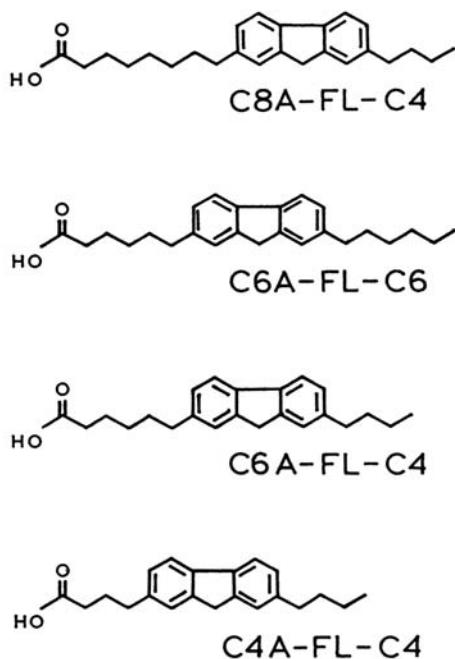


**Figure 8.28.** Structures of the fluorenyl fatty acids. Revised from [62].

of the fatty acid (Figure 8.27, middle), so one expects maximal quenching for those fluorenyl groups located as deep as the bromine atoms. The quenching data reveal larger amounts of quenching when the fluorenyl groups are placed more deeply in the bilayer by a longer methylene chain between the fluorenyl and carboxyl groups (Figure 8.29). Hence, the fluorenyl probes are located as expected from

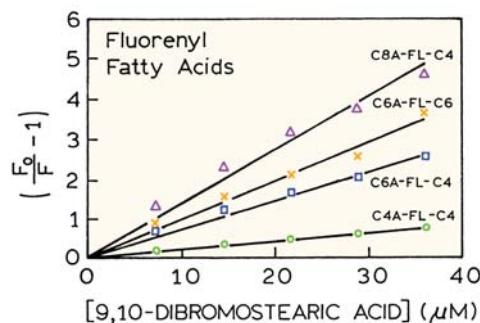


**Figure 8.29.** Quenching of fluorenyl fatty acids (Figure 8.28) by 9,10-dibromostearic acid in erythrocyte ghost membranes. Revised and reprinted with permission from [62]. Copyright © 1992, American Chemical Society.

their structure. For these fluorenyl fatty acids a continuing alkyl chain beyond the fluorenyl group was important for probe localization.

Another example of using localized quenchers is provided by studies of pyrene-labeled lipids.<sup>63</sup> A number of pyrene PCs were used that had a different number of methylene groups ( $n$ ) between the glycerol backbone and the pyrene. This localizes the pyrene groups at different depths in the bilayers (Figure 8.30). Three different bromo-PCs with the bromides at position 6 and 7, 9 and 10, or 11 and 12 were used as quenchers. The apparent Stern-Volmer quenching constants were measured for each pyrene PC and each quencher (Figure 8.31). The largest quenching constant was observed for the smallest number of methylene groups in the pyrene PC ( $n$ ) when using  $\text{Br}_{6,7}\text{PC}$ , in which the bromides are located just beneath the membrane surface. For larger values of  $n$ , maximum quenching was observed for  $\text{Br}_{11,12}\text{PC}$ , where the bromides are located more deeply in the membrane. In this case the fluorophores were localized in bilayer as would be predicted from their structure. Bromo-PCs are known to quench the fluorescence of membrane-bound proteins,<sup>64–66</sup> and have been used to study lateral phase separations in membranes.<sup>67–68</sup>

#### 8.10.4. Parallax and Depth-Dependent Quenching in Membranes

##### Advanced Topic

The use of quenching to determine the location of fluorophores in membranes has been formalized using two similar methods: parallax quenching<sup>69–75</sup> and depth-dependent quenching.<sup>76–78</sup> The basic idea is to compare the amount of quenching observed for quenchers that are located at two

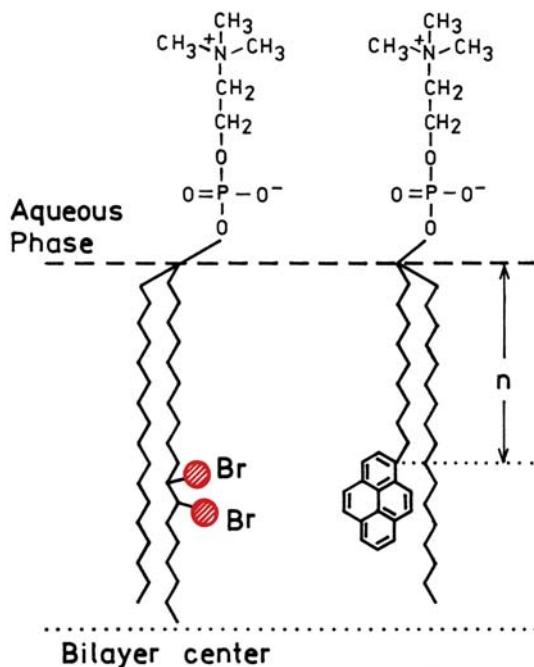


**Figure 8.30.** Schematic representation of the structures of Pyr<sub>n</sub>PC and Br<sub>x,y</sub>PC species used to study depth-dependent quenching of the pyrene moiety. Revised and reprinted with permission from [63]. Copyright © 1995, American Chemical Society.

different depths in the bilayer. The distance of the fluorophore from the center of the bilayer ( $Z_{CF}$ ) is then calculated from<sup>79</sup>

$$Z_{CF} = L_{cl} + \{ [-\ln(F_1/F_2)/\pi C] - L_{21} \} / 2L_{21} \quad (8.32)$$

where  $L_{21}$  is the difference in depth between the shallow and deep quenchers. The shallow quencher is located at a distance  $L_{cl}$  from the center of the bilayer.  $C$  is the concentration of quenchers in molecules per unit area.  $F_1$  and  $F_2$  are the relative intensities of the fluorophore in the presence of the shallow and deep quencher, respectively. This model was derived by assuming complete quenching within a critical distance of the quencher, and that quenching does not occur across the bilayer. This model also assumes there is no diffusion in the membrane. In principle the location of the fluorophore can be determined using two quenchers. This analysis yields a single distance and will not reveal a distribution of fluorophore depths if such a distribution is present.

An alternative method is depth-dependent quenching.<sup>79</sup> In this case the fluorophore is assumed to be present at a

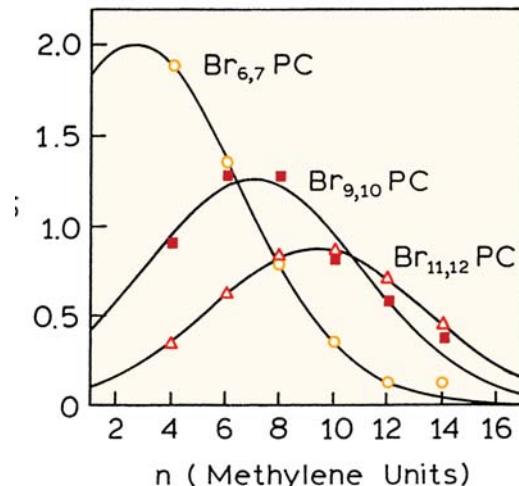
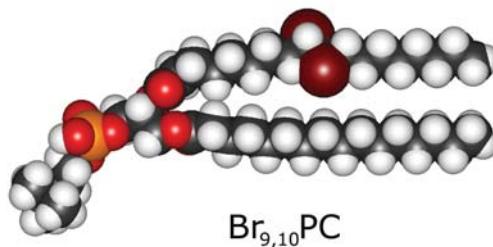


**Figure 8.31.** Dependence of  $K_{SV}^{app}$ , the apparent Stern-Volmer quenching constant, on  $n$ , the number of methylene units in the pyrenylacyl chains, for bilayers with different Br<sub>x,y</sub>PC quenchers. The subscripts x and y indicate the location of the bromine atoms. The bilayers consisted of 1-palmitoyl-2-oleoylphosphatidylcholine (POPC) with 50 mole% cholesterol. Revised and reprinted with permission from [63]. Copyright © 1995, American Chemical Society. Structure courtesy of Dr. Alexey S. Ladokhin from University of Kansas.

distribution of depths. For a quencher at a depth  $h$  the extent of quenching is given by

$$\frac{F_0}{F(h)} = G(h) + G(-h) \quad (8.33)$$

$$G(h) = \frac{S}{\sigma \sqrt{2\pi}} \exp \left[ -\frac{(h - h_m)^2}{2\sigma^2} \right] \quad (8.34)$$

where in this expression  $h_m$  is the most probable depth for the fluorophore, and  $\sigma$  is the width of the distribution of fluorophore depth. Two distributions are used to account for both sides of bilayers. If more than two quenchers are used the distribution is overdetermined and the values of  $h_m$  and

$\sigma$  are found by least-squares or other filtering procedures. Depth-dependent quenching was used for the analysis shown in Figure 8.31.

### 8.10.5. Boundary Lipid Quenching

#### Advanced Topic

Quenching in membranes can also be used to study boundary lipids, which are the lipid molecules surrounding a fluorophore or a membrane-bound protein.<sup>80–86</sup> Suppose a protein is surrounded by a discrete number of lipid molecules, and that the tryptophan fluorescence is accessible to quenchers in the membrane phase. Then the number of boundary lipid molecules can be estimated from

$$\frac{F - F_{\min}}{F_0 - F_{\min}} = (1 - [Q])^n \quad (8.35)$$

where  $F_0$  is the intensity in the absence of quencher and  $F_{\min}$  is the intensity when the probe is in pure quencher lipid.  $F$  is the intensity at a given mole fraction of quencher lipid.

This model was tested using small probes in membranes, and for Ca<sup>2+</sup>-ATPase, which is a large membrane-bound protein containing 11 to 13 tryptophan residues. For tryptophan octyl ester, the intensity decreased according to  $n = 6$ , indicating that each tryptophan was surrounded by 6 lipid molecules (Figure 8.32). For the Ca<sup>2+</sup>-ATPase, the intensity decreased with  $n = 2$ . This does not indicate that only two lipid molecules surrounded this protein, but that only two lipid molecules are in contact with tryptophan residues in the Ca<sup>2+</sup>-ATPase. Similar results of two boundary quenchers were found for the Ca<sup>2+</sup>-ATPase using 1,2-bis(9,10-dibromooleoyl)phosphatidylcholine.<sup>82</sup>

### 8.10.6. Effect of Lipid-Water Partitioning on Quenching

In the preceding examples of quenching in membranes the quenchers were not soluble in water. Hence, the quencher concentrations in the membrane were known from the amount of added quencher. However, there are many instances where the quencher partitions into the membranes, but some fraction of the quencher remains in the aqueous phase. Consequently, the quencher concentration in the membrane is not simply determined by the amount of

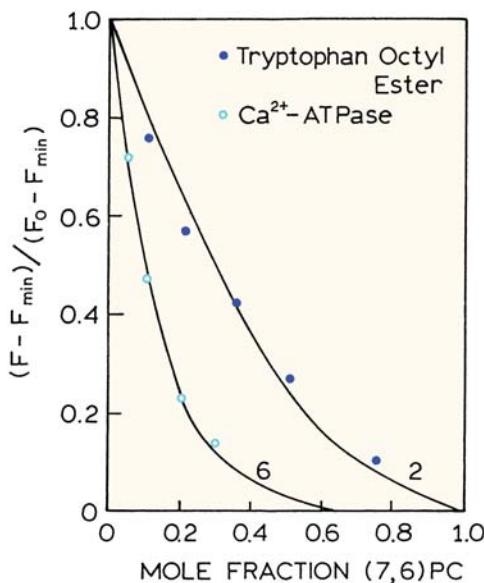


**Figure 8.32.** Quenching of tryptophan octyl ester ( $\circ$ ) and the Ca<sup>2+</sup>-ATPase ( $\bullet$ ) by a spin labeled (7,6)PC in egg PC vesicles. (7,6)-PC in a phosphatidylcholine in which the spin label is located on the 8th carbon atom chain of the 2-position fatty acyl group. The structure of the nitroxide spin label is shown in Figure 8.27. The solid lines are for the indicated values of  $n$  (eq. 8.35). The dashed lines show the theoretical curves for  $n = 10$  or 2 in (eq. 8.35). Revised and reprinted with permission from [80]. Copyright © 1981, American Chemical Society.

quencher added, but also by the total lipid concentration in the sample. In these cases it is necessary to determine the lipid–water partition coefficient in order to interpret the observed quenching.

Consider a quencher that distributes between the membrane and aqueous phases. At non-saturating concentrations of quencher the concentrations in the water ( $w$ ) and membrane ( $m$ ) phases are related by the partition coefficient

$$P = [Q]_m / [Q]_w \quad (8.36)$$

The total ( $T$ ) concentration of quencher added ( $[Q]_T$ ) partitions between the water and membrane phases according to

$$[Q]_T V_T = [Q]_m V_m + [Q]_w V_w \quad (8.37)$$

where  $V_m$  and  $V_w$  represent the volume of the membrane and water phases, respectively. By defining

$$\alpha_m = V_m / V_T \quad (8.38)$$

to be the volume fraction of membrane phase, one obtains<sup>87</sup>

$$[Q]_m = \frac{P[Q]_T}{P\alpha_m + (1 - \alpha_m)} \quad (8.39)$$

Substitution of this expression for the membrane concentration of quencher into the Stern-Volmer equation yields

$$\frac{1}{\tau} = \frac{1}{\tau_0} + \frac{k_m P [Q]_T}{P\alpha_m + (1 - \alpha_m)} = \frac{1}{\tau_0} + k_{app} [Q]_T \quad (8.40)$$

where  $k_m$  is the bimolecular quenching constant for the membrane-bound fluorophore. The apparent quenching constant is given by

$$\frac{1}{k_{app}} = \alpha_m \left( \frac{1}{k_m} - \frac{1}{k_m P} \right) + \frac{1}{k_m P} \quad (8.41)$$

When the fluorophore is present in the membrane phase, the apparent quenching constant is dependent upon  $P$ ,  $\alpha_m$  and  $k_m$ . A plot of  $k_{app}^{-1}$  vs.  $\alpha_m$  allows  $P$  and  $k_m$  to be determined. Thus, the quenching method allows simultaneous quantitation of both the extent to which a quencher partitions into a bilayer and its diffusion rate ( $D_q$ ) in this bilayer. The successful determination of the quencher diffusion and partition coefficients requires that the range of lipid concentrations results in a range of fractional partitioning of the quencher. The fraction of the quencher partitioned in the membrane ( $f_m$ ) is given by

$$f_m = \frac{P\alpha_m}{P\alpha_m + (1 - \alpha_m)} \quad (8.42)$$

To calculate the volume fraction of the lipid, the usual assumption is equal densities for the water and membrane phases. In this case a 10-mg/ml membrane suspension corresponds to  $\alpha_m = 0.01$ . The above method of determining the lipid–water partition coefficient only applies when the quencher molecules are present in the bilayer at the moment of excitation. If the diffusional encounters involve molecules in the aqueous phase, which diffuse into the lipid phase during the lifetime of the excited state, then no dependence of the apparent quenching on lipid concentration is expected. The situation is more complex when the quenching results from quenchers in both the lipid phase and in the water phase.

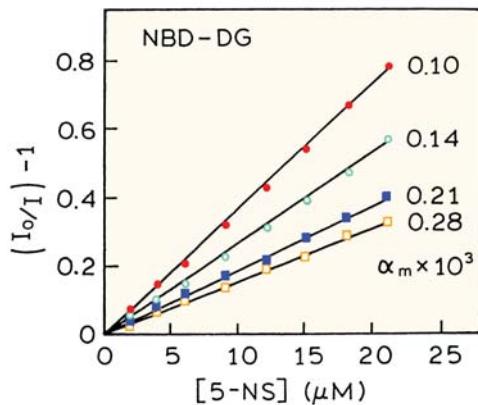


**Figure 8.33.** Quenching of 1-oleoyl-2-hexanoyl-NBD-glycerol (NBD-DG) by 5-doxylstearate (5-NS).  $\alpha_m$  refers to the volume fraction of the egg PC phase. Revised from [92]. Copyright © 1994, with permission from Elsevier Science.

A number of publications have appeared on the effect of partitioning and quenching.<sup>87–92</sup> One example is quenching of a NBD-labeled lipid by the nitroxide fatty acid 5-doxylstearate (5-NS). In contrast to the nitroxide-labeled PCs, the fatty acids have a low but significant solubility in water. When NBD-labeled vesicles are titrated with 5-NS the Stern-Volmer plots are dependent on lipid concentration (Figure 8.33). At lower lipid concentrations addition of the same total amount of 5-NS results in larger amounts of quenching than observed at higher lipid concentrations. At low lipid concentrations, the added quencher results in a higher quencher concentration in the membrane. This is because there is less lipid into which the quencher can partition. It is this dependence of the apparent quenching constant on lipid concentration that allows the partition coefficient to be determined. This is done by a plot of  $k_{app}^{-1}$  vs.  $\alpha_m$  (Figure 8.34). The data indicate that 5-NS partitions almost 10,000-fold into the lipid phase, and that the bimolecular quenching constant is  $1.1 \times 10^9 \text{ M}^{-1} \text{ s}^{-1}$ . Use of the Smoluchowski equation yields a mutual diffusion coefficient for the probe and quencher near  $3 \times 10^{-6} \text{ cm}^2/\text{s}$ . This value is larger than expected for a quencher in a membrane, and 100-fold larger than the diffusion coefficient of lipid in membranes determined by fluorescence recovery after photobleaching (FRAP). This difference is probably the result of different diffusion coefficients for short- and long-range diffusion in membranes, the so-called anomalous sub-diffusion (Chapter 24).

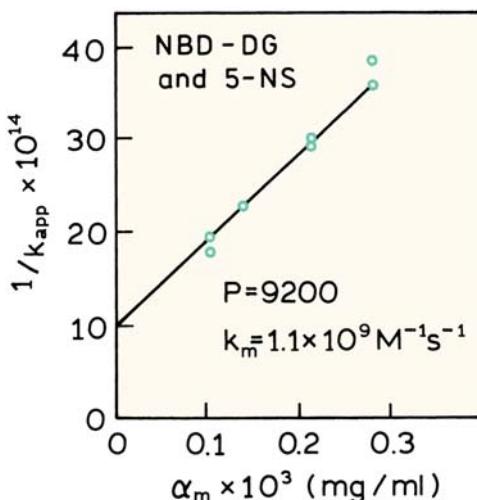


**Figure 8.34.** Dependence of the apparent quenching (NBD-DG and 5-NS) on lipid concentration ( $\alpha_m$ ). Revised from [92].

### 8.10.7. Quenching in Micelles

Quenching of fluorescence in micelles can also be complex (Figure 8.35). The top panel shows quenching of pyrene in methanol by a lipid-soluble pyridinium derivative, which probably quenches by a charge-transfer mechanism (Chapter 9). When the quencher  $C_{16}PC$  is added to a methanol solution of pyrene the lifetimes decrease but remain a single exponential. When pyrene is bound to micelles, and lipid solubles quenchers are added, the decays become strongly multi-exponential. These decays are not typical of collisional quenchers in solution, as seen from the decay at long times above 200 ns. The decay time of this component is the same as pyrene in micelles without quenchers.

The complex pyrene intensity decays seen in Figure 8.35 are due to Poisson statistics in quencher binding to the micelles. Under the conditions of these experiments there was an average of less than one quencher per micelle. Hence some of the micelles contained a quencher, and some did not. The micelles without bound quencher display the lifetime of unquenched pyrene. The micelles with quenchers display a shorter lifetime. For such a system the intensity decay is given by<sup>93–96</sup>

$$I(t) = I_0 \exp(-t/\tau_0 + \bar{n}[\exp(-k_q t) - 1]) \quad (8.43)$$

where  $\tau_0$  is the unquenched lifetime,  $\bar{n}$  is the mean number of quenchers per micelle, and  $k_q$  is the decay rate due to a single quencher molecule in the micelle.

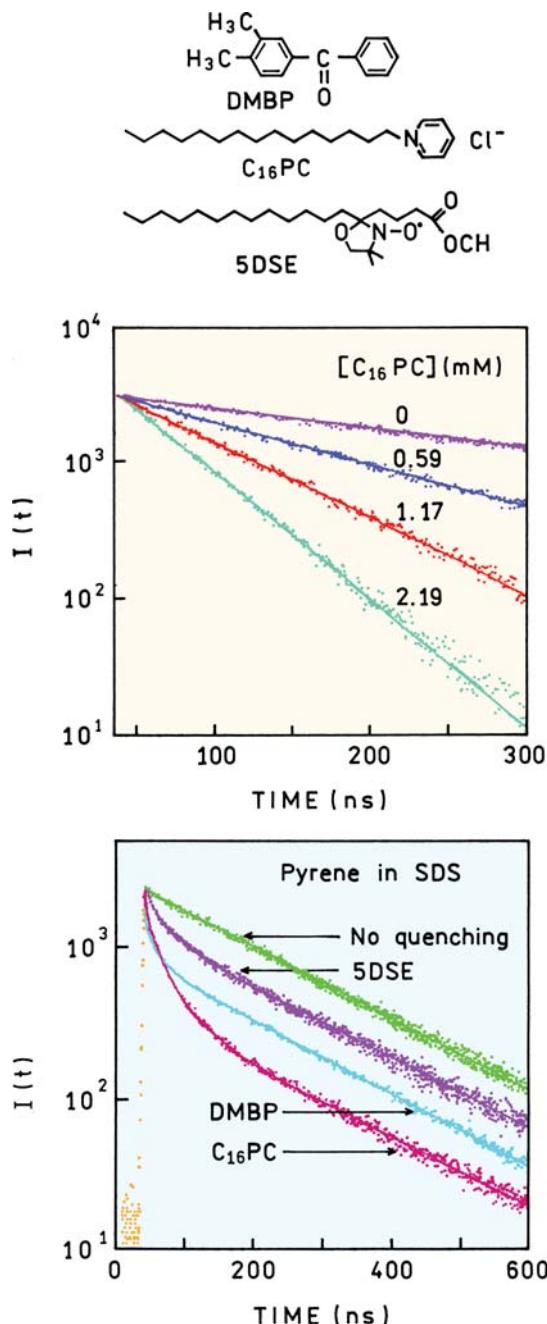


**Figure 8.35.** Quenching of pyrene in methanol solution (top) and in SDS micelles (bottom). Revised and reprinted with permission from [93]. Copyright © 2003, American Chemical Society.

### 8.11. LATERAL DIFFUSION IN MEMBRANES

#### Advanced Topic

In the preceding section on localization (except for oxygen) of probes in membranes, we did not consider diffusion of

the quenchers in the membranes. Diffusion in membranes is a complex topic, and the appropriate model depends on the chemical structure of the quencher. For small nonpolar quenchers, the membrane can be considered to be a three-dimensional system with the quencher diffusing freely. The situation changes if the quencher is a lipid, such as the bromo-PCs (Figure 8.27). In this case the quencher will be limited to lateral diffusion within a plane, which requires a different theory.

The theory for two-dimensional diffusion in membranes is complex. Analytical expressions are now available for the time-dependent decays of fluorophores in membranes, with the quenchers constrained to lateral diffusion in two dimensions.<sup>97–102</sup> The time-dependent decays expected for Smoluchowski quenching in two dimensions, and for the radiation model, have been reported.<sup>97–100</sup> For the usual assumption of instantaneous quenching on fluorophore-quencher contact, the intensity decay is given by

$$\ln \frac{I(t)}{I_0(t)} = -\gamma t - \frac{1}{2} R^2 [Q] Q(t/\tau_q) \quad (8.44)$$

where

$$Q(t/\tau_q) = \frac{16}{\pi} \int_0^\infty \frac{1 - \exp(-(t/\tau_q)x^2)}{J_0^2(x) + Y_0^2(x)} \frac{dx}{x^3} \quad (8.45)$$

In these expressions  $\gamma$  is the reciprocal of the unquenched decay time,  $[Q]$  is the quencher concentration in molecules/ $\text{\AA}^2$ ,  $R$  is the interaction radius, and  $\tau_q = R^2/D$ , where  $D$  is the mutual diffusion coefficient.  $J_0(x)$  and  $Y_0(x)$  are zero-order Bessel functions of the first and second kinds, respectively. Even more complex expressions are needed for the radiation model. Because of the difficulties in evaluating eqs. 8.44–8.45, several approximate analytical expressions have been proposed.<sup>98–99</sup>

## 8.12. QUENCHING-RESOLVED EMISSION SPECTRA

### 8.12.1. Fluorophore Mixtures

The emission spectra of proteins often shift in the presence of quenching. This effect occurs because the various trp residues are differently exposed to the aqueous phase and thus differently accessible to quenchers. Alternatively, if a solution contains two fluorophores with different Stern-

Volmer quenching constants, it will show different amounts of quenching at each wavelength depending on the relative amplitudes of the emission spectra. This concept of wavelength-dependent quenching has been extended to calculation of the underlying emission spectra from the quenching constant at each wavelength.<sup>103–106</sup> This is accomplished by measuring a Stern-Volmer plot of each emission wavelength ( $\lambda$ ). For more than one fluorophore the wavelength-dependent data can be described by

$$\frac{F(\lambda)}{F_0(\lambda)} = \sum_i \frac{f_i(\lambda)}{1 + K_i(\lambda)[Q]} \quad (8.46)$$

where  $f_i(\lambda)$  is the fractional contribution of the  $i$ th fluorophore to the steady-state intensity at wavelength  $\lambda$  to the unquenched emission spectrum, and  $K_i(\lambda)$  is the Stern-Volmer quencher constant of the  $i$ th species at  $\lambda$ . For a single fluorophore the quenching constant is usually independent of emission wavelength,  $K_i(\lambda) = K_i$ .

In order to resolve the individual emission spectra the data are analyzed by nonlinear least squares. Typically one performs a global analysis in which the  $K_i$  values are global, and the  $f_i(\lambda)$  values are variable at each wavelength. By global we mean that the quenching constant is the same for each fluorophore irrespective of the emission wavelength. The result of the analysis is a set of  $K_i$  values, one for each component, and the fractional intensities  $f_i(\lambda)$  at each wavelength with  $\sum f_i(\lambda) = 1.0$ . The values of  $f_i(\lambda)$  are used to calculate the emission spectrum of each component:

$$F_i(\lambda) = f_i(\lambda) F(\lambda) \quad (8.47)$$

where  $F(\lambda)$  is the steady-state emission spectrum of the sample.

The use of quenching to resolve emission spectra is illustrated by a sample containing both 1,6-diphenyl-1,3,5-hexatriene (DPH) and 5-(((2-iodoacetyl)amino)ethyl)-amino)naphthalene-1-sulfonic acid (I-AEDANS). DPH is not soluble in water, so the DPH is expected to be dissolved in the SDS micelles (Figure 8.36). I-AEDANS is water soluble and negatively charged, so it is not expected to bind to the negatively charged SDS micelles. Hence, I-AEDANS is expected to be quenched by the water soluble quencher acrylamide, and DPH is not expected to be accessible to acrylamide quenching.

Acrylamide Stern-Volmer plots for the separate solution of DPH-SDS and I-AEDANS are shown in Figure 8.37. As predicted from the low solubility of DPH in water

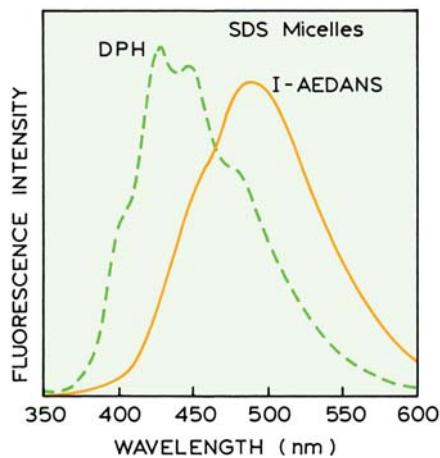


**Figure 8.36.** Steady-state emission spectra of (dashed) diphenylhexatriene (DPH) and (solid) I-AEDANS in 1.2 mM SDS micelles at 23°C. The concentration of diphenylhexatriene was 2  $\mu$ M, that of I-AEDANS 170  $\mu$ M. The excitation wavelength was 337 nm. Revised from [103].

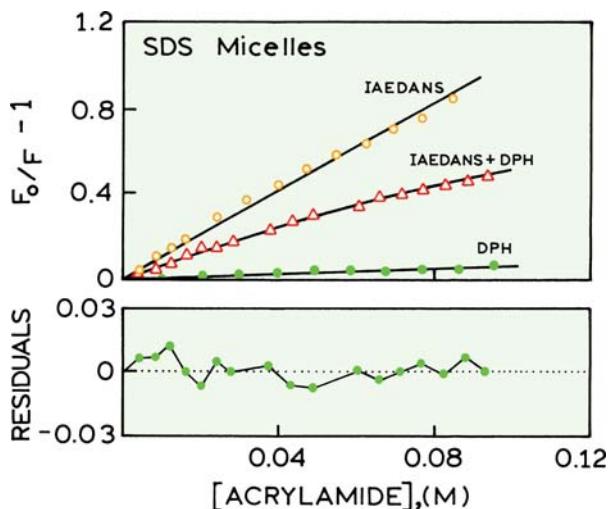


**Figure 8.37.** Stern-Volmer plots for acrylamide quenching of I-AEDANS, DPH, or I-AEDANS and DPH, in SDS micelles. For the mixture the solid line represents the fit with calculated parameters  $K_1 = 9.9 \text{ M}^{-1}$ ,  $K_2 = 0 \text{ M}^{-1}$ ,  $f_1 = 0.69$ ,  $f_2 = 0.31$ . The lower panel shows the residuals for these values. Revised from [103].

and the high solubility of acrylamide in water, DPH is weakly quenched by acrylamide. In contrast, I-AEDANS is strongly quenched. The extent of quenching for the mixture is intermediate between that observed for each probe alone. As expected for a mixture of fluorophores, the Stern-Volmer plots curve downward due to the increasing fractional contribution of the more weakly quenched species at higher quencher concentrations.

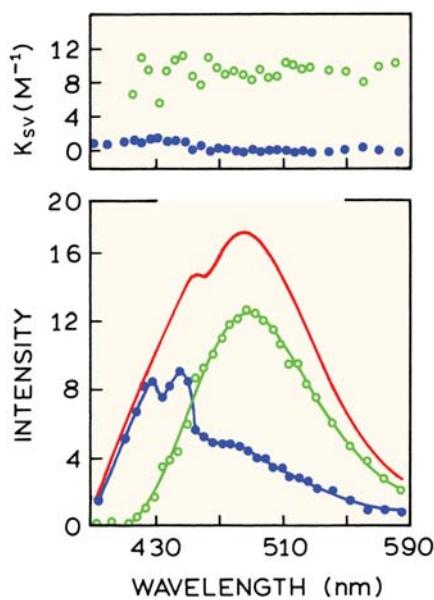


**Figure 8.38.** Quenching resolved emission spectra of the DPH-I-AEDANS mixture (bottom). The solid line shows the emission spectrum of the mixture. The upper panel shows the wavelength-dependent quenching constant, with average values of  $K_1 = 9.6 \text{ M}^{-1}$  and  $K_2 = 0.47 \text{ M}^{-1}$ . Revised from [103].

The curvature in the Stern-Volmer plots are used to recover the values of  $K_i(\lambda)$  and  $f_i(\lambda)$  at each wavelength. In this case the  $K_i(\lambda)$  values were not used as global parameters, so that  $K_1(\lambda)$  and  $K_2(\lambda)$  were obtained for each wavelength. At wavelengths above 420 nm there were two values of 0.47 and 9.6 M<sup>-1</sup>, representing the quenching constants of DPH and I-AEDANS, respectively. At the shortest wavelength below 420 nm there is only one  $K_i(\lambda)$  value because only DPH emits. The recovered values of  $f_i(\lambda)$  were used to calculate the individual spectra from the mixture (Figure 8.38). In Chapters 4 and 5 we showed how the component spectra for heterogeneous samples could be resolved using the time-domain or the frequency-domain data. The use of wavelength-dependent quenching provides similar results, without the use of complex instrumentation. Of course, the method depends on the probes being differently sensitive to collisional quenching, which requires that the decay times and/or accessibility to quenchers be different.

### 8.12.2. Quenching-Resolved Emission Spectra of the *E. coli* Tet Repressor

The tet repressor from *E. coli* is a DNA-binding protein that controls the expression of genes that confer resistance to

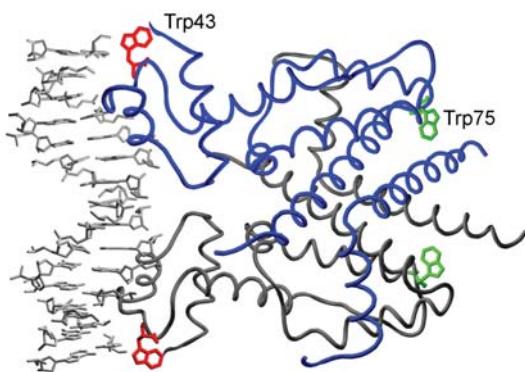


**Figure 8.39.** Three-dimensional structure of the *E. coli* tet repressor. The position of a bound DNA oligomer is shown for Problem 8.10. Figure courtesy of Dr. Oliver Scholz from the Friedrich-Alexander University of Erlangen-Nuremberg, Germany.

tetracycline. This protein is a symmetrical dimer that contains two tryptophan residues in each subunit at positions 43 and 75 (Figure 8.39). W43 is thought to be an exposed residue, and W75 is thought to be buried in the protein matrix.<sup>107</sup> Earlier studies of single-tryptophan mutants of the tet repressor confirmed the accessibility of W43 to iodide and the shielding of W75 from iodide quenching.<sup>108</sup> Hence, this protein provided an ideal model protein to attempt quenching resolution of the individual emission spectra of two tryptophan residues in a protein.

Iodide Stern-Volmer plots for the tet repressor were measured for various emission wavelengths<sup>107</sup> (Figure 8.40). A larger amount of quenching was observed at longer wavelengths. When analyzed in terms of two components, one of these components was found to be almost inaccessi-

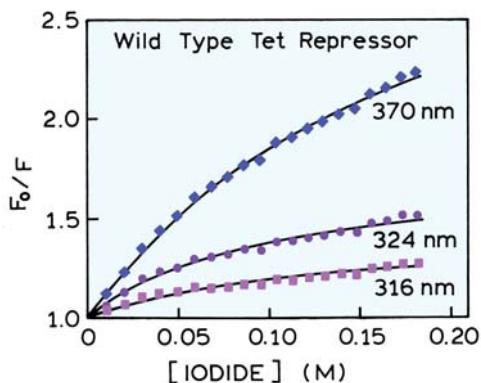


**Figure 8.40.** Iodide Stern-Volmer plots for the wild type tet repressor. The solution contained 1 mM sodium thiosulfate to prevent formation of  $I_2$ . From [107].

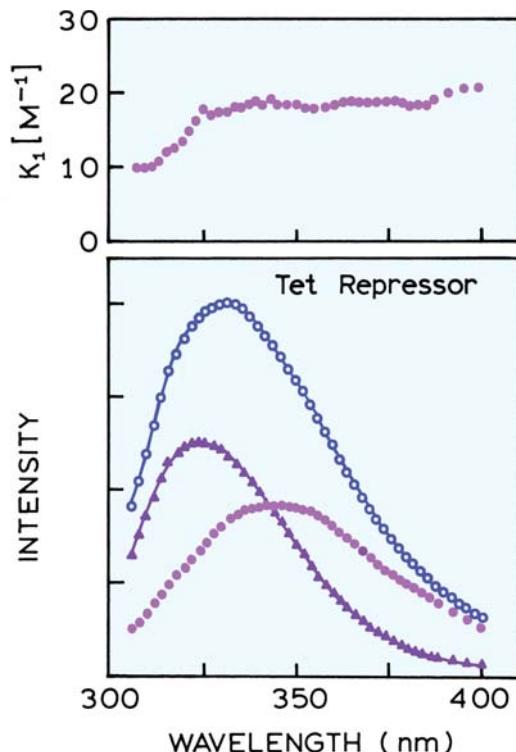


**Figure 8.41.** Fluorescence quenching-resolved spectra of wild-type tet repressor using potassium iodide as the quencher. The solid line is the unquenched emission spectrum. Top: wavelength-dependent values of  $K_1$ . From [107].

ble to iodide. At 324 nm the recovered values for the more accessible fraction are  $f_1 = 0.34$  and  $K_1 = 16.2 \text{ M}^{-1}$ . For the inaccessible fraction the values are  $f_2 = 0.66$  and  $K_2 = 0$ . The wavelength-dependent data were used to calculate the individual spectra (Figure 8.41). The blue-shifted emission with a maximum of 324 nm corresponds to the inaccessible fraction, and the red-shifted spectrum at 349 nm is the fraction accessible to iodide quenching. These emission spectra are assigned to W75 and W43, respectively. The results in Figure 8.41 (top) illustrate one difficulty often encountered in determination of quenching-resolved spectra. The quenching constant for a single species can be dependent on emission wavelength. In this case the quenching constant of the accessible tryptophan changed about twofold across its emission spectrum. When this occurs the values of  $K_i(\lambda)$  cannot be treated as global parameters.

Single-tryptophan mutants of the tet repressor were used to study the accessibility of each trp residue to iodide quenching (Figure 8.42). Little if any quenching was observed for the protein containing only tryptophan 75, and tryptophan 43 was readily quenched by iodide.<sup>109</sup> Iodide

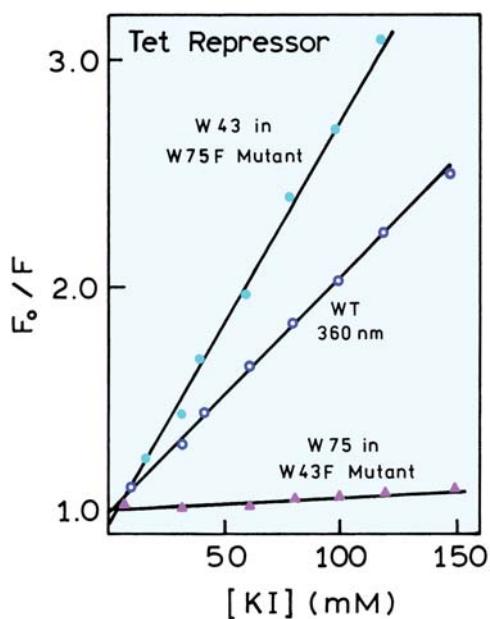


**Figure 8.42.** Stern-Volmer plots for the iodide quenching of *E. coli* tet repressor (wild type, WT) and its mutants (W75F and W43F). Revised from [108].

quenching of the wild-type protein is intermediate between the two single-tryptophan mutants. These results are consistent with those obtained from the quenching-resolved emission spectra. While the same information is available from the mutant proteins, the use of quenching provided the resolved spectra using only the wild-type protein.

It is valuable to notice a difference in the method of data analysis for the modified Stern-Volmer plots (Section

8.8.1) and for the quenching-resolved emission spectra. In a modified Stern-Volmer plot one assumes that a fraction of the fluorescence is totally inaccessible to quenchers. This may not be completely true because one component can be more weakly quenched, but still quenched to some extent. If possible, it is preferable to analyze the Stern-Volmer plots by nonlinear least squares, when the  $f_i$  and  $K_i$  values are variable. This approach allows each component to contribute to the data according to its fractional accessibility, instead of forcing one to be an inaccessible fraction. Of course, such an analysis is more complex, and the data may not be adequate to recover the values of  $f_i$  and  $K_i$  at each wavelength.

### 8.13. QUENCHING AND ASSOCIATION REACTIONS

#### 8.13.1. Quenching Due to Specific Binding Interactions

In the preceding sections we considered quenchers that were in solution with the macromolecule but did not display any specific interactions. Such interactions can occur, and often appear to be of static quenching.<sup>110–115</sup> One example is provided by a synthetic peptide which spontaneously forms a four  $\alpha$ -helical bundle in aqueous solution (Figure 8.43). The bundle consists of two peptide chains. Each peptide chain contains two  $\alpha$ -helical regions and a single tryptophan residue.<sup>114</sup> The general anesthetics are nonpolar and were expected to bind to the central nonpolar region of the four helix bundles.

The effects of halothane on the emission intensity of the four-helix bundle are shown in Figure 8.43. The emission is strongly quenched by even low concentrations of halothane. Quenching of the trp residues was also examined in the presence of 50% trifluoroethanol (TFE). Halothane quenching is much less efficient in this solvent (Figure 8.44). TFE is known to disrupt hydrophobic interactions but to enhance helix formation in peptides. In 50% TFE the peptide is expected to exist as two separate  $\alpha$ -helical peptides that are not bound to each other. These results show that the trp residues are buried in a nonpolar region in the four-helix bundle and become exposed to the solvent phase when the two peptides dissociate.

How can one determine whether the quenching seen for the helix bundle in water is due to halothane binding, or to collisional quenching? One method is to calculate the apparent bimolecular quenching constant ( $k_q^{\text{app}}$ ). Assume the decay time of trp residues in the bundle is near 5 ns. The

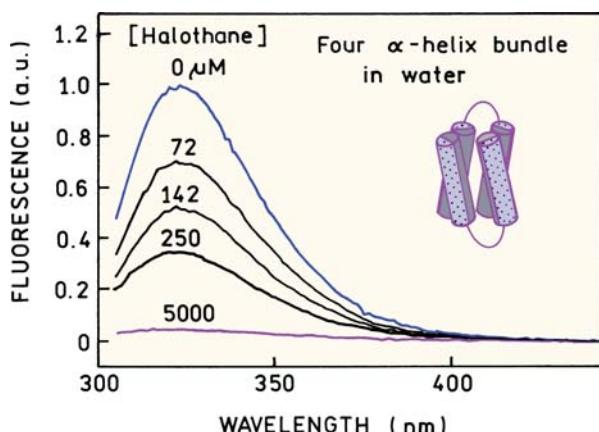


**Figure 8.43.** Emission spectra of a four  $\alpha$ -helix bundle in water in the presence of halothane. Each peptide chain contains one tryptophan residue. Revised from [114].

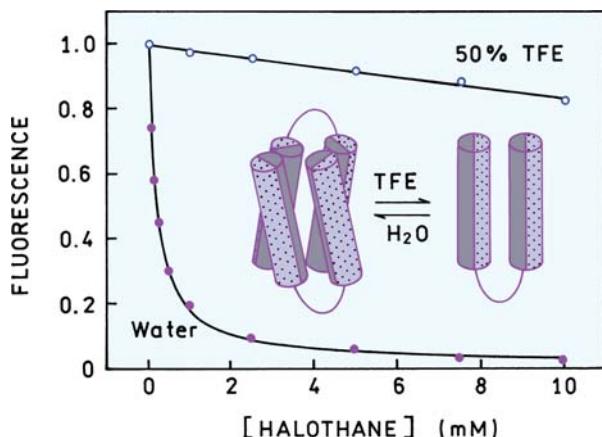


**Figure 8.44.** Tryptophan fluorescence intensities of the four  $\alpha$ -helix bundle in the presence of halothane. Revised from [114].

data in Figure 8.43 indicate that the trp residues are about 50% quenched at 142  $\mu\text{M}$  halothane. This corresponds to a Stern-Volmer quenching constant of  $K_{\text{SV}} = 7042 \text{ M}^{-1}$ , which is two to three orders of magnitude larger than possible for diffusion-limited quenching in water. These results show that hydrophobic interactions of halothane result in the appearance of static quenching of the trp residues. These interactions result in an increase in the local concentration of halothane near the trp residues, as shown in the molecular dynamics snapshot of this system (Figure 8.45).

At a more microscopic level there may still be a dynamic component to the quenching. There is no reason to expect the formation of ground-state complexes between the trp and halothane. Hence the quenching may be dynamic but due to diffusion motions of halothane with-

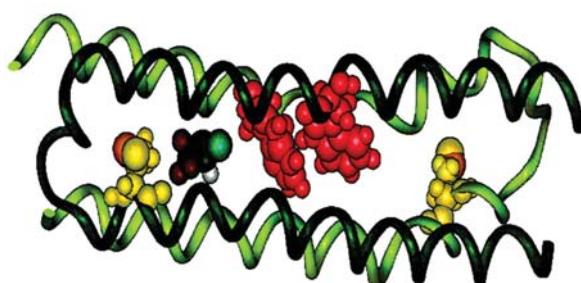


**Figure 8.45.** Molecular dynamic snapshot of the four  $\alpha$ -helix bundle with one bound halothane molecule. The two peptides are shown in light and dark green, the tryptophans are red and the methionines are yellow-orange. The halothane molecule contains the multicolor spheres. Reprinted from [114]. Courtesy of Dr. Jonas Johansson from the University of Pennsylvania, USA.

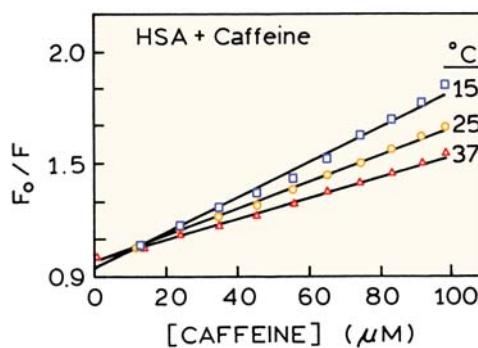


**Figure 8.46.** Quenching of HSA by caffeine. Revised from [113].

in the hydrophobic region of the bundle. There is not always a clear distinction between static and dynamic quenching. Actual and apparent complex formation may be distinguished from the absorption spectra, which is only expected to change for actual formation of ground-state complexes.

Another example of quenching due to a specific binding interaction is shown for binding of caffeine to HSA, an experiment most of us start each morning (Figure 8.46). The Stern-Volmer plots show a value of  $K_{\text{SV}} = 7150 \text{ M}^{-1}$ . This value is obviously too large to be due to collisional quenching, especially for a lifetime near 5 ns. The apparent value of  $k_q^{\text{app}}$  is  $1.4 \times 10^{12}$ , over 100-fold larger than the maximum diffusion limited rate. Hence, the caffeine must be bound to the HSA. Caffeine is an electron-deficient molecule, and may form ground-state complexes with indole. This possibility could be tested by examination of the absorption spectra of HSA in the absence and presence of caffeine. If ground-state association with indole occurs, then the trp absorption spectrum is expected to change. Another indicator of complex formation is the temperature dependence of the Stern-Volmer plots. For diffusive quenching one expects more quenching at higher temperatures. In the case of HSA and caffeine there is less quenching at higher temperatures (Figure 8.46), which suggests the complex is less stable at higher temperatures.

#### 8.14. SENSING APPLICATIONS OF QUENCHING

Fluorescence quenching has been used for sensing of a wide variety of analytes including oxygen, NO, and heavy metals. Fluorescence sensing is discussed in more detail in Chapter 19. The use of collisional quenching for sensing is illustrated by chloride-sensitive fluorophores.

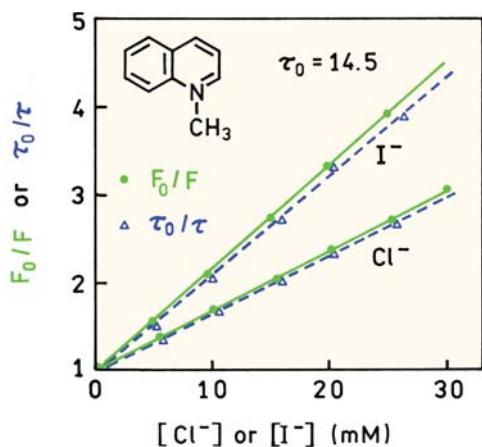


**Figure 8.47.** Chloride and iodide quenching of N-methylquinolinium iodide. The amount of iodide from the fluorophore is not significant. Revised from [123].

### 8.14.1. Chloride-Sensitive Fluorophores

Chloride is an important biological anion that plays a role in fluid adsorption, neuronal processes, and cellular pH. There has been extensive development of chloride-sensitive fluorophores for analytical and biochemical applications.<sup>116–122</sup> These chloride-sensitive fluorophores are usually based on a quinolinium or acridinium structure, with additional groups to modify the solubility or sensitivity of the fluorophore to quenching. Chloride quenching is usually collisional, as can be seen in Figure 8.47. This figure shows Stern-Volmer plots for quenching of N-methylquinolinium iodide (MAI) by chloride or iodide.<sup>123</sup> The equivalent decrease in intensity and lifetime shows that the quenching is collisional and complex formation does not occur.

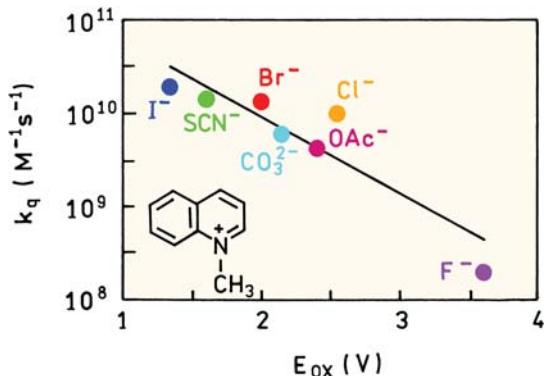


**Figure 8.48.** Bimolecular quenching constants for N-methylquinolinium iodide. Revised from [123].

Iodide appears to quench more strongly than chloride. Since the diffusion coefficients of chloride and iodide are similar, this result indicates that iodide is a more efficient quencher. The mechanism of quenching is most probably electron transfer from the anion to the fluorophore, which suggests the quenching efficiency should depend on the oxidation potential of the quencher. Figure 8.48 shows bimolecular quenching constants for MAI and several quenchers. The quenching efficiency is highest for iodide, which is easily oxidized. Quenching by fluoride is much less efficient because it is more difficult to remove an electron from the highly electronegative fluoride ion.

The quenching efficiencies for a charge-transfer mechanism is expected to depend on the free energy change for the reaction (Chapter 9). For a charge-transfer process the free energy change is given by<sup>124</sup>

$$\Delta G \text{ (eV)} = E_{\text{ox}}(D^+/D) - E_{\text{red}}(A/A^-) - E_{00} + C \quad (8.48)$$

where  $E_{\text{ox}}$  is the oxidation potential of the electron donor, which in this case is the quencher.  $E_{\text{red}}$  is the reduction potential of the electron acceptor, which is the fluorophore.  $E_{00}$  is the singlet energy of the fluorophore, and  $C$  is a constant that accounts for the energy release due to the charge separation interaction of the charges with the solvent. As the oxidation potential increases, the value of  $\Delta G$  becomes less negative and quenching becomes less efficient. The quenching efficiencies do not correlate precisely with eq. 8.48, because electron exchange and heavy atom effects are also present, but for this class of probes charge-transfer is the dominant mechanism for quenching by halides. Knowledge of the quenching mechanism is valuable because it allows rational design of fluorophores with the desired sensitivity to halides. For instance, substitutions on the quinolinium ring that decrease the affinity for electrons are likely to decrease the quenching efficiency.

### 8.14.2. Intracellular Chloride Imaging

Chloride-sensitive fluorophores have found use for measurements of intracellular chloride and for imaging the local chloride concentrations.<sup>125–126</sup> When using fluorescence microscopy for imaging it is difficult to use the local intensity values because of photobleaching and the unknown probe concentrations at each position in the cells. In contrast to probes for pH, calcium, and other cations (Chapter 14), collisionally quenched probes do not show spectral shifts. Direct wavelength-ratiometric probes for chloride are not available.

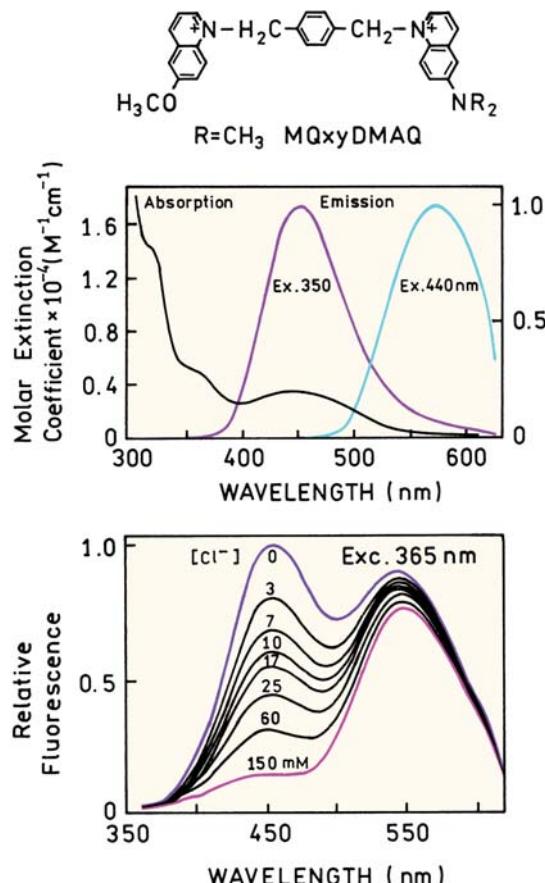


**Figure 8.49.** Structure and spectra of a wavelength-ratiometric chloride probe. Revised from [129].

Knowledge of the mechanism of chloride quenching has allowed the design of wavelength-ratiometric chloride probes.<sup>127–129</sup> This was accomplished by linking two fluorophores, one which is quenched by chloride and one which is not sensitive to chloride (Figure 8.49). This probe contains two quinoline rings. The methoxy-substituted ring on the left readily accepts electrons and is quenched by chloride. The ring on the right, with the amino group, does not accept electrons from chloride and is not quenched. The lower panel shows the emission spectra of MQxyDMAQ in the presence of increasing chloride concentrations. The shorter-wavelength emission is quenched, but the longer-wavelength emission is not sensitive to chloride. Examination of the spectra in Figure 8.49 suggests that there will be RET from the MQ to the DMAQ ring. In this probe some energy transfer occurs, which reduces the lifetime of the MQ ring and makes it less sensitive to quenching by chloride. However, the RET efficiency is modest, so that the MQ ring remains sensitive to chloride.

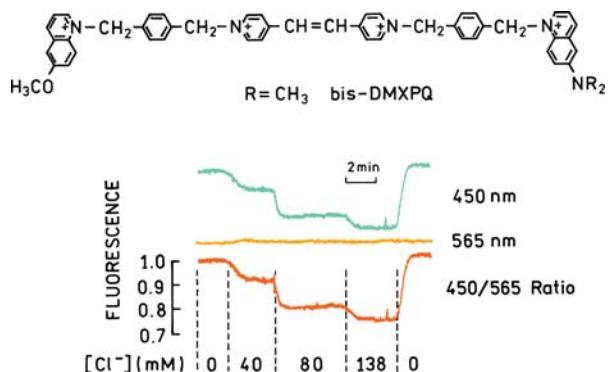


**Figure 8.50.** Structure and intracellular calibration of the chloride probe bis-DMXPQ. Revised from [129].

When used in an intracellular environment, the sensitivity of a probe can change from its sensitivity in a pure solution. For this reason the chloride-sensitive probes were calibrated in cells by changing the intracellular chloride concentration. This is accomplished by exposing the membrane permeability of the 3T3 fibroblast cells using valinomycin and other similar compounds, followed by exposing the cells to different chloride concentrations (Figure 8.50). The intensity of the short-wavelength MQ emission at 450 nm is decreased as the chloride concentration increases. The intensity of the long-wavelength emission at 565 nm is not affected.

The wavelength-ratiometric chloride probes were used to measure local chloride concentrations in CHO cells (Figure 8.51). This was accomplished by collecting the intensity images at 450 and 565 nm. The intensity at 450 nm will be sensitive to the local chloride concentration.<sup>129</sup> However, the image at 450 nm alone does not allow the chloride concentrations to be determined because the concentration of the probe can be different in each region of the cell. The concentration of chloride can be determined from the ratio of the emission intensities. These images show that the chloride concentrations in these cells is rather uniform, with a somewhat lower chloride concentration in the nuclei.

### 8.14.3. Chloride-Sensitive GFP

Green fluorescent protein (GFP) and its mutants are widely used to study gene expression and as sensors.<sup>130–131</sup> A yellow variant of GFP (YFP) is known to be sensitive to chloride.<sup>132–133</sup> The intensity of YFP-H148Q decreases progressively in response to added chloride in a manner and concentration range that suggests collisional quenching (Figure

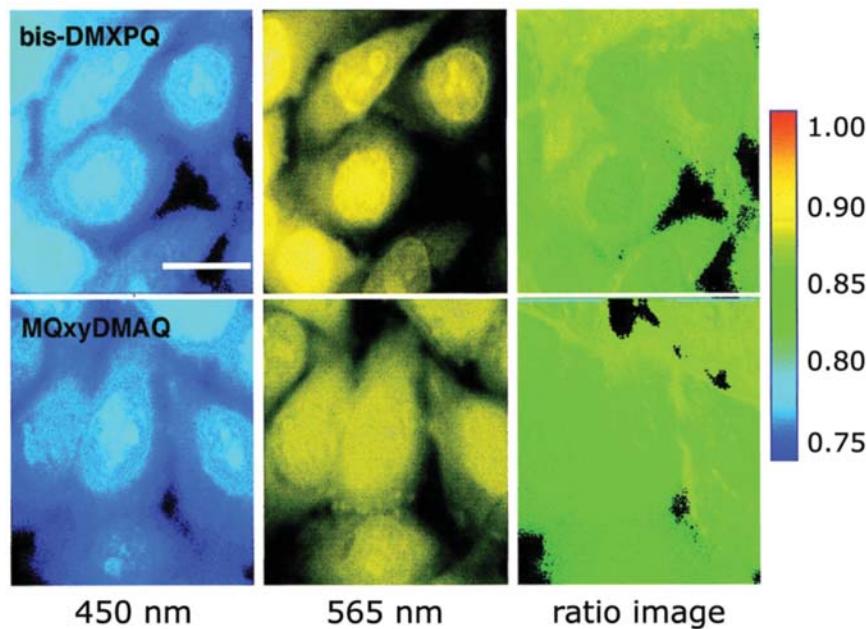


**Figure 8.51.** Fluorescence microscopy images of CHO cells labeled with the chloride probes. The intensities of 450 and 565 nm were color coded for clarity. The images on the right are the chloride concentrations calculated from the intensity ratios. Reprinted with permission from [129].

8.52). The extent of quenching depends on pH, which is not expected for collisional quenching. Additionally, the chromophore in GFP is known to be buried in a  $\beta$ -barrel structure (Figure 8.53) and not expected to be accessible to freely diffusing chloride. These considerations suggest that the chloride sensitivity of this YFP is not due to collisional quenching.

Figure 8.54 shows the absorption spectra of YFP-H148Q in the presence of chloride. As  $[Cl^-]$  increases the absorption at the excitation wavelength 514 nm decreases, and the short-wavelength absorption increases. There appears to be an isoelectric point near 430 nm, which indicates the presence of two species. It appears that chloride changes the structures or conformation of the protein or chromophore, decreasing the absorbance and giving the appearance of quenching. The x-ray structure has been solved with bound iodide ions (Figure 8.53), one of which is next to the chromophore. An iodide or chloride next to the chromophore might result in static quenching. However, static quenching by chloride is not the reason for the chloride sensitivity of YFP. For YFP the apparent quenching by chloride is due to a change in the structure of the chromophore. It is now thought that chloride binds near the chromophore in contact with the imidizolinone oxygen atom. This binding probably forces the equilibrium to the left side in Figure 8.54. The larger amount of chloride quenching at lower pH (Figure 8.52) is consistent with protonation of the phenolic oxygen upon binding of chloride. Hence the apparent quenching of YFP by chloride in Figure 8.52 is not due to collisional or static quenching, but instead due to a specific binding interaction which changes the structure of the chromophore.

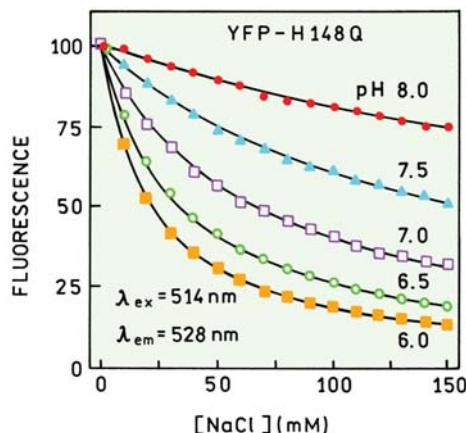


**Figure 8.52.** Fluorescence intensity of YFP-H148Q in the presence of NaCl. Revised from [132].

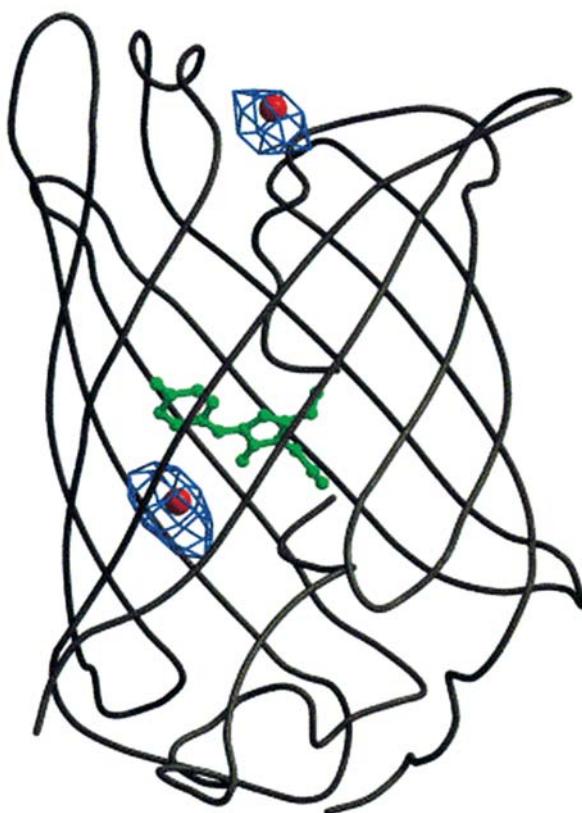


**Figure 8.53.** Three-dimensional structure of yellow fluorescent protein YFP-H148Q. The solid line is the peptide backbone, and the green structure is the native chromophore. The red and blue surfaces show the location of bound iodide ions. Reprinted with permission from [132].

As discussed in Chapter 19, a wide variety of fluorophores are available that can be used for intracellular sensing. It is difficult to use these probes in an intracellular environment because they are likely to bind to macromolecules that can shift the analyte calibration curves. GFP and its variants are promising intracellular sensors because the chromophore is buried in the  $\beta$ -barrel and unable to interact directly with biomolecules. With this consideration in mind, YFP-H148Q was used to measure the intracellular pH of Swiss 3T3 fibroblasts.<sup>133</sup> An advantage of GFP is that the probe is synthesized by the cell itself, and not added to the cells. The fibroblast were transfected with the gene for YFP-H148Q, which appeared as a bright green fluorescence in the epifluorescence microscope (Figure 8.55). The response of the protein to pH and chloride was tested using ionophores to modify the internal ion concentrations.<sup>133</sup> When excited at 480 nm the emission intensity decreased with increasing pH and decreased with increasing chloride

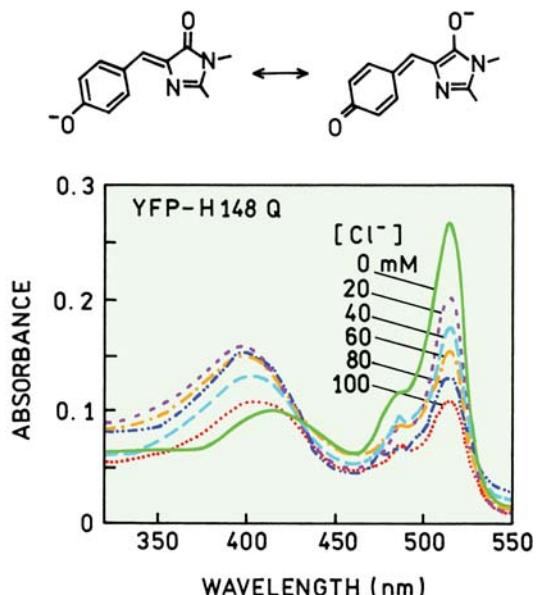


**Figure 8.54.** Absorption spectra of YFP-H148Q in the presence of NaCl, pH 6.4. Binding of chloride is thought to stabilize the right side structure in the upper panel. Revised from [133].

concentrations. These remarkable results show that it is now possible to insert genes that cause the cells to synthesize their own fluorophores, and the genetically engineered protein-fluorophore can be designed to have sensitivity to a desired analyte.

#### 8.14.4. Amplified Quenching

Collisional quenching was useful for sensing and imaging of chloride because of its high physiological concentration. However, quenching does not usually provide high sensitivity detection.<sup>134</sup> However, it is now possible to amplify quenching to obtain higher sensitivity detection.<sup>135</sup> Amplification is accomplished in two ways. The fluorophore is bound to a fluorescent conjugated polymer (Figure 8.56). In this case the polymer contained conjugated stilbene residues. This polymer was found to be highly sensitive to quenching by the PET acceptor methylviologen ( $MV^{2+}$ ). The Stern-Volmer quenching constant is near  $10^7\text{ M}^{-1}$ , which is clearly too large for collisional quenching.

There are two reasons for the large quenching constant. The positively charged  $MV^{2+}$  binds electrostatically to the polymer. Secondly, the excited state migrates rapidly between the stilbene residues. If any one residue is excited this energy migrates until it encounters the bound  $MV^{2+}$ . One  $MV^{2+}$  quenches the emission from about 1000 stil-

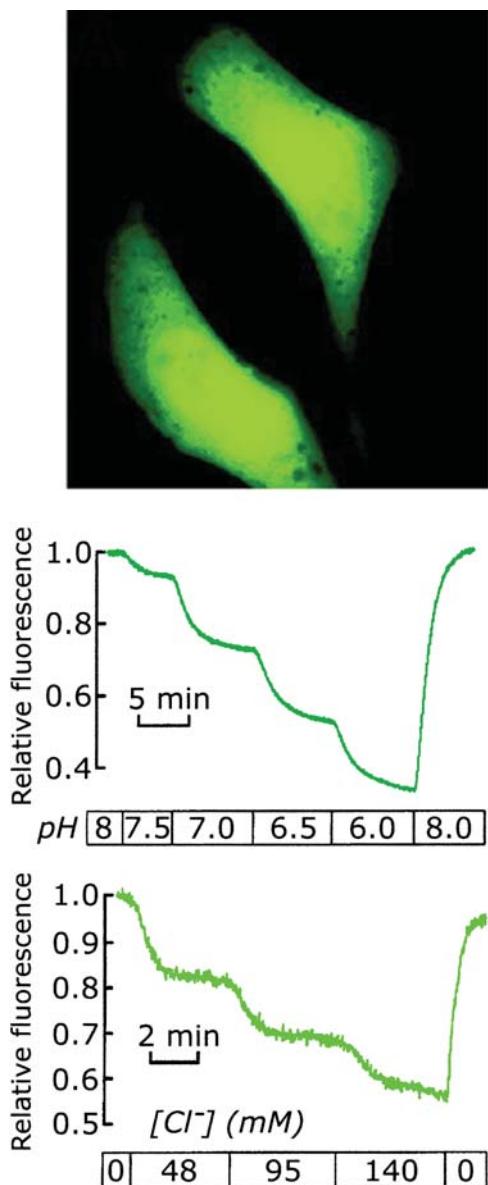


**Figure 8.55.** pH and chloride sensing using YFP-H148Q in Swiss 3T3 fibroblasts. Reprinted with permission from [133].

benes, resulting in nearly complete quenching at low  $MV^{2+}$  concentrations.

Amplified quenching can be applied to sensing by the addition of specific binding partners. This was accomplished by covalent linkage of  $MV^{2+}$  to biotin ( $B-MV^{2+}$ ). Protein-bound  $MV^{2+}$  also quenched the polymer with high sensitivity (Figure 8.57). The polymer fluorescence returned when  $B-MV^{2+}$  was removed from the polymer by avidin. One can imagine this approach being used in protein or nucleic acid binding assays.

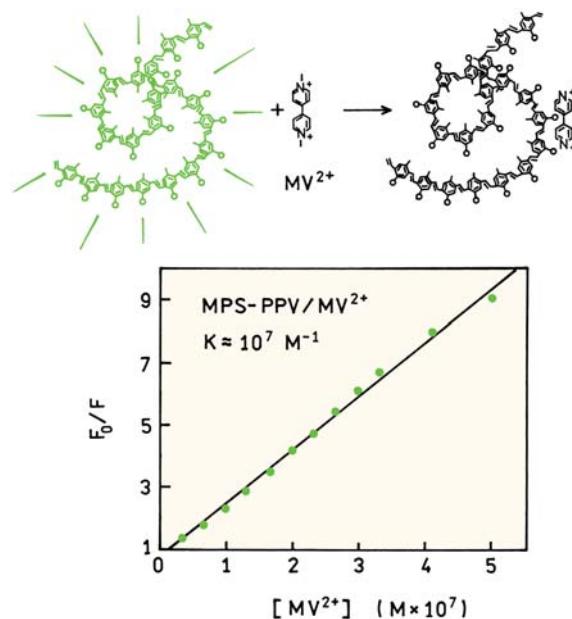


**Figure 8.56.** Quenching of a conjugated stilbene polymer by methylviologen. Revised from [135].

## 8.15. APPLICATIONS OF QUENCHING TO MOLECULAR BIOLOGY

During the past decade there have been many advances in the use of sensing for DNA analysis (Chapter 21). Many of these applications depend on RET, but some make use of quenching. A typical situation is the need to detect a target oligomer of known sequence in a sample containing many sequences. Detection of the target oligomer is usually accomplished by synthesis of a probe oligomer with the complementary sequence. The probe oligomer also contains bound fluorophores that display spectral changes upon hybridization with the target oligomers. The spectral changes can be due to RET, intercalation or quenching.

### 8.15.1. Release of Quenching Upon Hybridization

One approach to target detection is to change the extent of quenching upon hybridization. One example is shown in Figure 8.58.<sup>136</sup> In this case the fluorescein label is quenched by a nearby pyrene residue. In the absence of target DNA the fluorescence is quenched by the pyrene. Upon binding to the target sequence the pyrene intercalates into the double helical DNA, resulting in a several-fold increase in the fluorescein emission. This approach is general and could be used with a variety of fluorophore-quencher pairs.

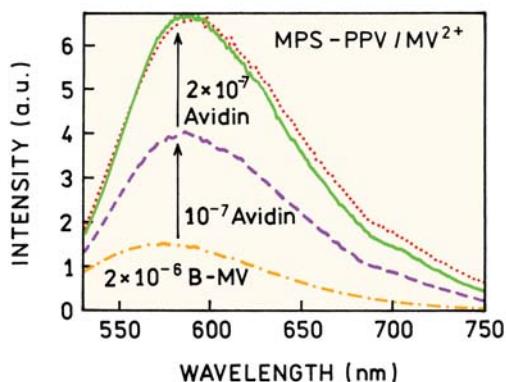
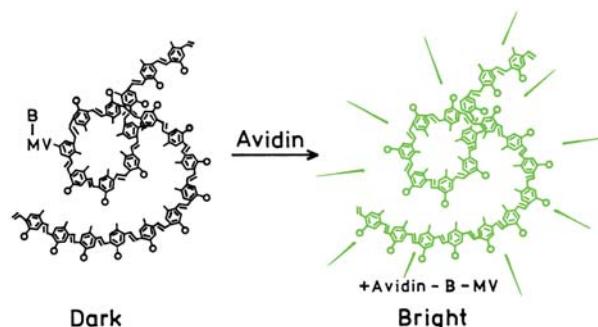


**Figure 8.57.** Reversal of biotin–methylviologen quenching by avidin. Revised from [135].

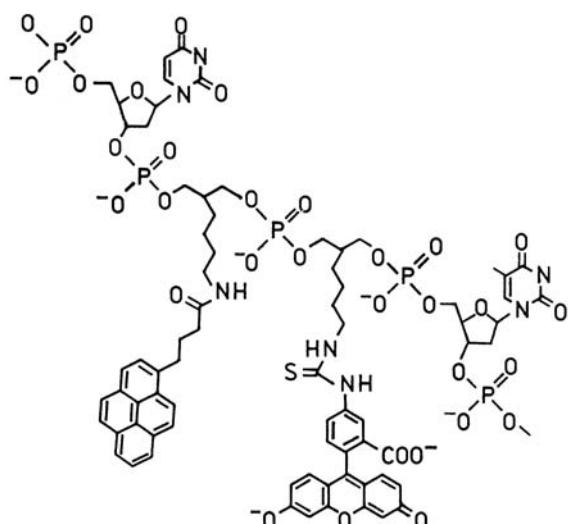
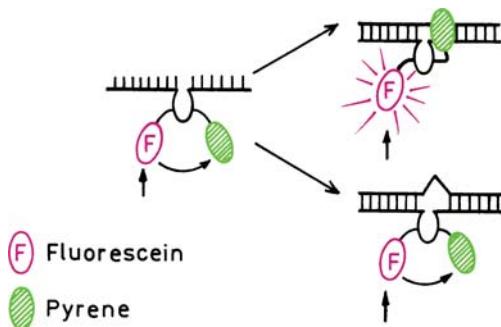


**Figure 8.58.** Molecular beacon based on release of quenching upon hybridization. Revised from [136].

### 8.15.2. Molecular Beacons in Quenching by Guanine

Among the nucleic acid bases guanine shows efficient quenching of many fluorophores. This quenching is probably due to photoinduced electron transfer.<sup>137–139</sup> The other bases can also act as quenchers, but are usually much less efficient. Figure 8.59 shows Stern–Volmer plots for four fluorophores with dGMP as the quencher. This result shows that quenching by guanine is not limited to a single fluorophore but can occur with many fluorophores. Among these four probes MR121 is the most sensitive to quenching by dGMP. Among the four nucleotide manophosphates, dGMP is the most efficient quencher, with the others having no quenching effect on MR121.

Quenching by guanine was used to design a molecular beacon.<sup>140</sup> The fluorophore JA242 was positioned at one end of the beacon, and the other end was terminated with several guanine residues. The residues quench the fluorophore when in the folded state (Figure 8.60). The emission intensity increases about fivefold when the beacon is unfolded and hybridized with the target sequence.

### 8.15.3. Binding of Substrates to Ribozymes

Quenching by guanine has also been applied to structural studies of RNA. In contrast to DNA, RNA is rather flexible and frequently forms base-paired regions within a single strand of RNA. Single strands of RNA can adopt well-defined three-dimensional structures in solution, similar to the folding behavior of peptide chains. One type of structural RNAs are the ribozymes, which display catalytic enzyme-like behavior.

The catalytic properties of these highly structured RNAs was first reported in 1982, showing that certain RNAs displayed autocatalytic activity. Since that time there have been numerous studies of ribozymes and their catalytic behavior. One example is the hairpin ribozyme that cleaves single-stranded RNA (Figure 8.61). The observations of quenching by quanosine nucleotides<sup>17–18</sup> (Section 8.5) suggested the use of guanine quenching to study substrate binding to ribozymes. The substrate contained a fluo-

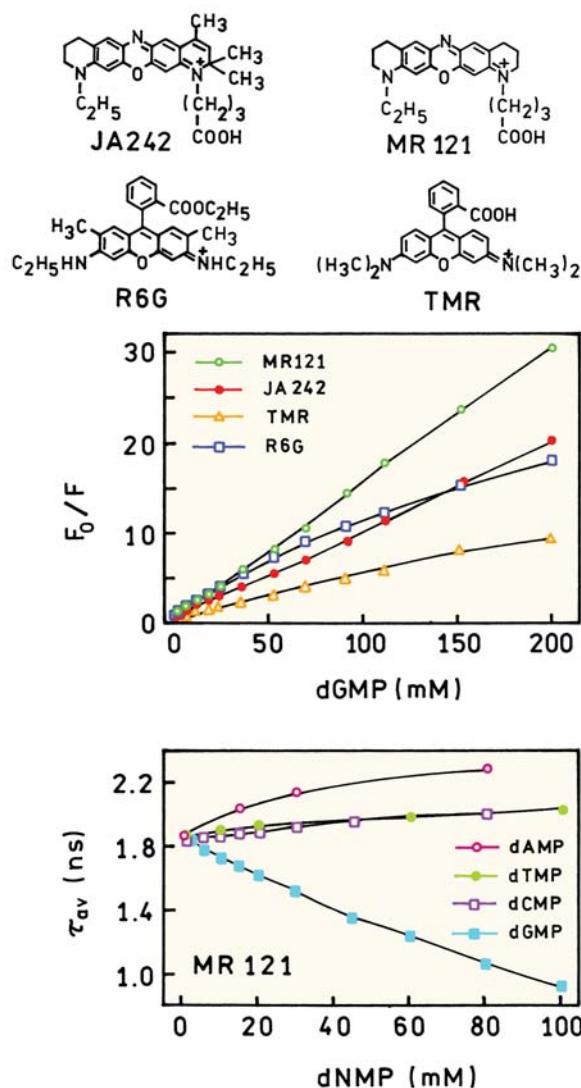


**Figure 8.59.** Quenching of four fluorophores by dGMP (top). Quenching of MR121 by four nucleotide monophosphates (bottom). Revised from [139].

rescein residue covalently linked at the 3' end (Figure 8.61). The hairpin ribozyme contains a guanosine residue at the 5N end. Upon binding of substrate nucleotide to the ribozyme, the fluorescein emission is quenched (Figure 8.62). Quenching also occurs when the fluorescein-labeled substrate binds to the substrate-binding strand (SBS) that contains a 5N-guanosine residue (G-SBS). The guanosine residue is needed for quenching, and the emission of fluorescein is unchanged in the presence of the substrate-binding strand without a 5' terminal guanosine residue (not shown). The example shows how fundamental studies of

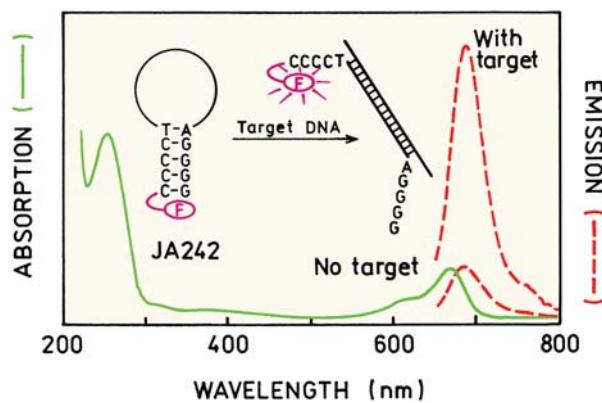


**Figure 8.60.** Absorption and emission spectra of a molecular beacon based on guanine quenching of JA242. Revised and reprinted with permission from [140]. Copyright © 2000, American Chemical Society.

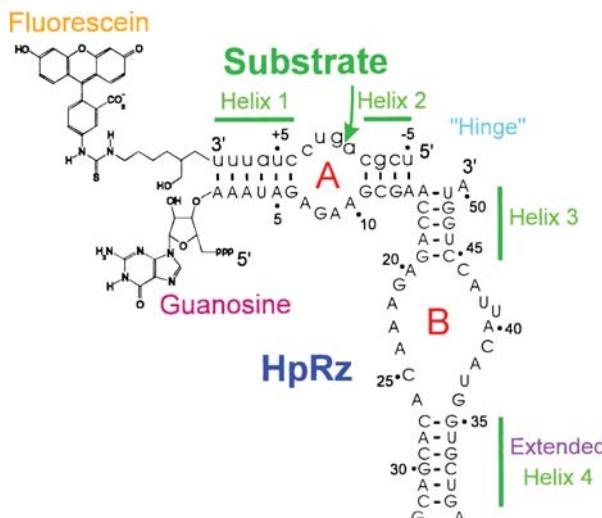


**Figure 8.61.** Structure of the hairpin ribozyme (HpRz) and the fluorescein-labeled substrate. The substrate-binding strand is the region adjacent to the substrate. Reprinted with permission from [141]. Copyright © 1997, Cambridge University Press.

nucleotide quenching have found useful applications in modern biochemistry.

#### 8.15.4. Association Reactions and Accessibility to Quenchers

In the previous examples the association reactions were detected by the spectral changes which occurred upon binding. However, a useful spectral change may not occur for

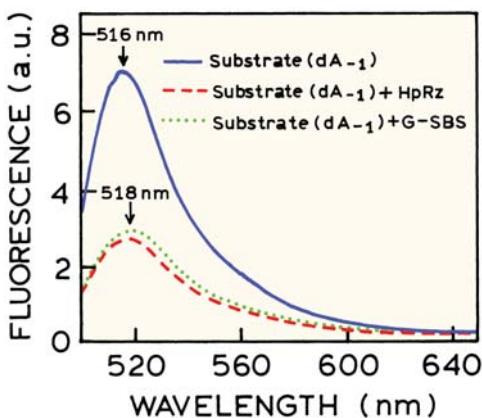


**Figure 8.62.** Emission spectra of the fluorescein-labeled substrate analogue ( $dA_{-1}$ ) in solution, and when bound to the hairpin ribozyme (HpRz) or the guanine-containing substrate binding strand. From [141].

the reaction of interest. One example is the binding of  $\epsilon$ -ADP to the DNA  $\beta$  helicase hexamer. The fluorescence of  $\epsilon$ -ADP displayed only a small increase upon binding to the protein. The change in intensity was too small to be used to measure binding. Collisional quenching was used to induce a larger change in fluorescence on binding.<sup>142</sup> Acrylamide is an efficient quencher of  $\epsilon$ -ADP, which should be quenched more strongly in solution than when bound to the helicase. Hence, if the binding is studied in a solution which contains a high concentration of acrylamide, there should be an increase in  $\epsilon$ -ADP fluorescence on binding to the helicase.

Solutions of  $\epsilon$ -ADP were titrated with the helicase (Figure 8.63). In the absence of acrylamide there was little

change in the  $\epsilon$ -ADP fluorescence. The titrations were performed again, in solutions with increasing amounts of acrylamide. Under these conditions  $\epsilon$ -ADP showed an increase in fluorescence upon binding. This increase occurred because the  $\epsilon$ -ADP became shielded from acrylamide upon binding to helicase. The authors also showed that acrylamide had no effect in the affinity of  $\epsilon$ -ADP for helicase.<sup>142</sup> In this system the use of a quencher allowed measurement of a binding reaction when there was no change in intensity due to the binding reaction alone.

## 8.16. QUENCHING ON GOLD SURFACES

During the past several years there has been increased interest in the interactions of fluorophores with metallic surfaces or particles.<sup>143–145</sup> Gold and silver colloids display intense colors due to their strong interactions with light.<sup>143–145</sup> The intensity of fluorophores near silver particles is usually increased,<sup>146</sup> and fluorophores near gold particles are usually quenched. The interactions of fluorophores with metallic surfaces is described in Chapter 25. We now describe DNA molecular beacons that are based on the strong quenching by gold colloids and surfaces.

### 8.16.1. Molecular Beacon Based on Quenching by Gold Colloids

During the past several years there have been developments in the use of gold colloids and surfaces for DNA analysis. Many of these reports make use of the high extinction coefficients and light scattering cross-sections of gold particles.<sup>147–151</sup> It is also possible to create molecular beacons based on the strong quenching of fluorophores near gold surfaces.<sup>152–153</sup> One example is shown in Figure 8.64. In this case the DNA oligomer contained a tetramethylrhodamine (TMR) on the 5' end. The 3' end contained a thiol group that spontaneously binds to gold surfaces. The beacon was made by incubating the thiolated oligomers with gold colloids. When bound to the colloids the TMR adsorbed to the gold surface and was completely quenched. The mechanism of quenching by gold is probably RET to the absorption bands of gold. Addition of a complementary oligomer results in a dramatic increase in intensity. Apparently, the stiffness of double-stranded DNA overcomes the attraction between the gold surface and the TMR. If the added oligomer has a single-base mismatch then the increase in fluorescence is less dramatic. This is probably due to the less-rigid or bent structures of the hybridized DNA with the single-base mis-

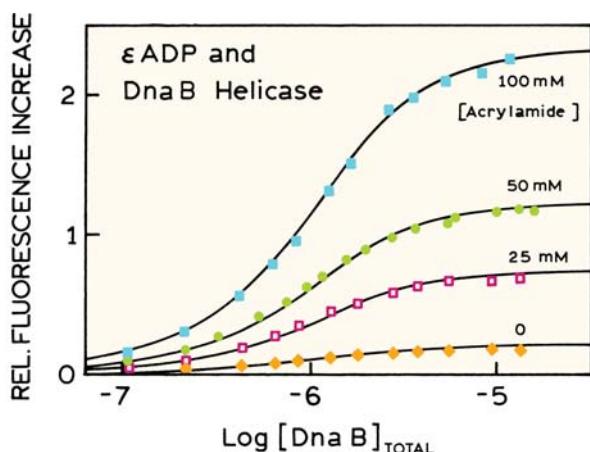


**Figure 8.63.** Fluorescence titration of  $\epsilon$ -ADP, at the same concentration of nucleotide, with the DNA  $\beta$  helicase in buffer containing different concentrations of acrylamide. Revised and reprinted from [142]. Copyright © 1997, with permission from Elsevier Science.

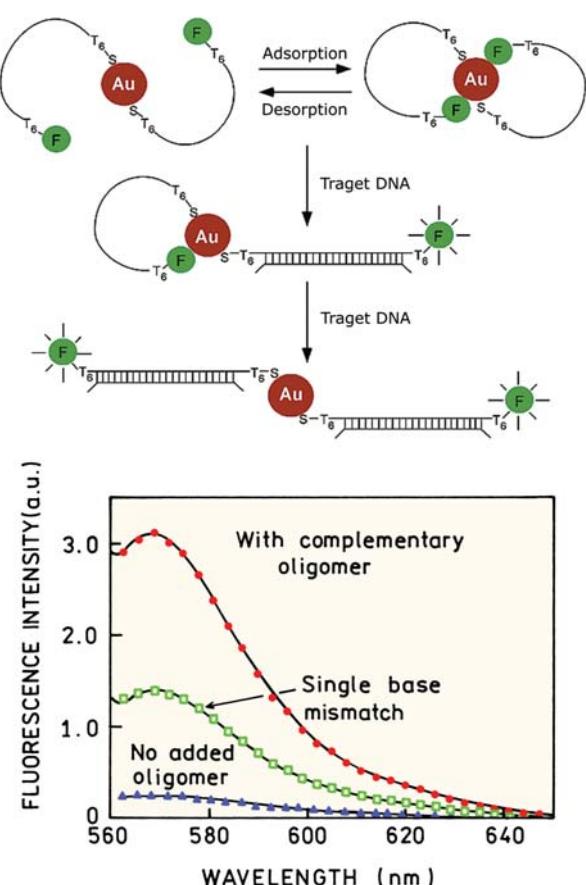


**Figure 8.64.** Schematic and emission spectra for a TMR-labeled oligo bound to gold colloids. Revised and reprinted with permission from [152]. Copyright © 2002, American Chemical Society.

match. Molecular beacons are most useful if they display a high contrast ratio, that is, a large difference in intensity between the unhybridized and hybridized states. The strong quenching by gold resulted in a high contrast ratio for this gold colloid-based beacon.

### 8.16.2. Molecular Beacons Based on Quenching by a Gold Surface

Another approach to a molecular beacon is shown in Figure 8.65.<sup>153</sup> In this case the rhodamine-labeled and thiolated beacon was bound to a continuous gold surface. In the absence of a complementary oligomer the fluorophore was held close to the gold surface by the folded beacon and was quenched. Addition of the complementary oligomer was expected to move the rhodamine away from the gold sur-

face and to decrease the extent of quenching. Figure 8.65 shows real color photographs of this beacon on the gold surface. In the absence of complementary oligomers no emission is seen (top). The rhodamine emission is easily seen when the beacon is hybridized with the target sequences (middle). A lower intensity is seen with an excess of non-specific DNA (bottom). An advantage of this approach is that only a single fluorophore is needed. One can readily imagine the use of gold surfaces with the DNA arrays used to monitor gene expression (Chapter 21).

### 8.17. INTRAMOLECULAR QUENCHING

In the previous sections the fluorophores and quenchers were not covalently linked. Quenching can also occur between covalently linked fluorophore-quencher pairs.<sup>154–155</sup> One common example is the formation of exciplexes by covalently linked aromatic hydrocarbon and amines. Another example are covalent adducts of indole and acrylamide (Figure 8.66). The lifetime of N-acetyl tryptamine is near 5.1 ns. When the acetyl group is replaced by an acryloyl group the lifetime is reduced to 31 ps. Similarly, covalent attachment of spin labels to a naphthalene derivative reduced its lifetime from 33.7 to 1.1 ns.

#### 8.17.1. DNA Dynamics by Intramolecular Quenching

Intramolecular quenching has recently been used to measure end-to-end motions of single-stranded DNA.<sup>156</sup> Most fluorophores have nanosecond lifetimes, which are too short for significant end-to-end motions of most biopolymers. A novel fluorophore with a long lifetime was used to allow time for end-to-end collisions. This diazo compound DBO (Figure 8.67) displays an unquenched lifetime near 215 ns when not quenched by a DNA base. DBO was quenched strongly by guanine (G), and less strongly by the other DNA bases. The data analysis is complicated by the presence of some quenching by the bases aside from guanine, but the presence of a guanine residue on the end opposite from DBO clearly reduces the lifetime (Figure 8.67). The rate of quenching can be calculated from a modified form of the Stern-Volmer equation. For a covalently attached quencher the Stern-Volmer equation becomes

$$\frac{\tau_0}{\tau} = 1 + k_q \tau_0 \quad (8.49)$$

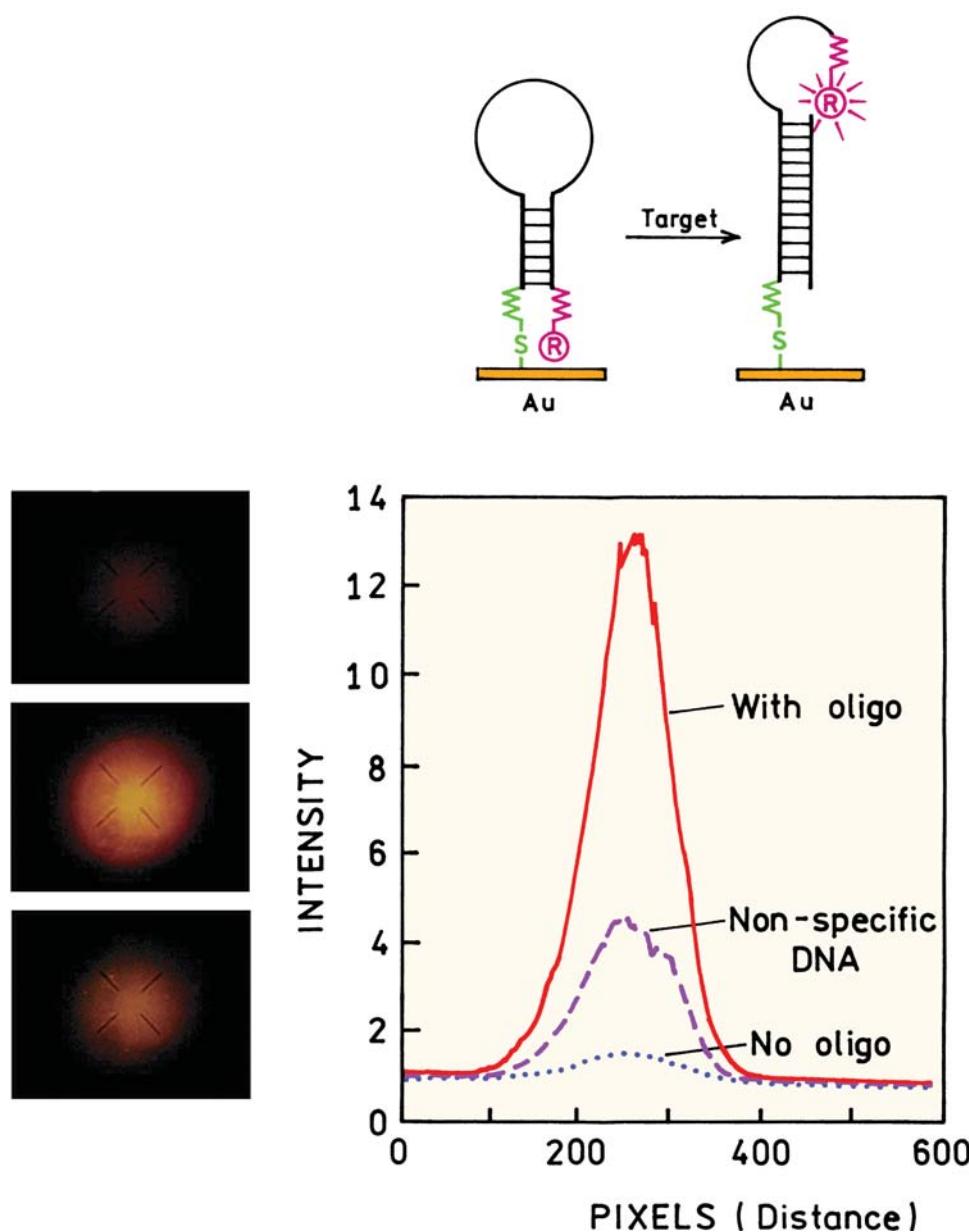


**Figure 8.65.** Rhodamine-labeled molecular beacon on a gold surface. Photos on the left show the beam without complementary oligo (top), with the complementary oligo (middle), and with an excess of nonspecific salmon sperm DNA. Also shown are the spatial intensity profiles from the CCD camera. Revised and reprinted with permission from [153]. Copyright © 2003, American Chemical Society.

where  $k_q$  is the unimolecular rate constant for quenching. Rearrangement of eq. 8.49 yields

$$k_q = \frac{1}{\tau} - \frac{1}{\tau_0} \quad (8.50)$$

The lifetime of the oligonucleotides containing two uridine residues in Figure 8.67 are  $\tau_0 = 120$  ns without guanine and

$\tau = 58$  ns with a terminal guanine residues. Hence the collision rate is  $9 \times 10^6 \text{ s}^{-1}$ .

### 8.17.2. Electron-Transfer Quenching in a Flavoprotein

In solution flavins are highly fluorescent. However, the flavin emission from flavoproteins is usually highly

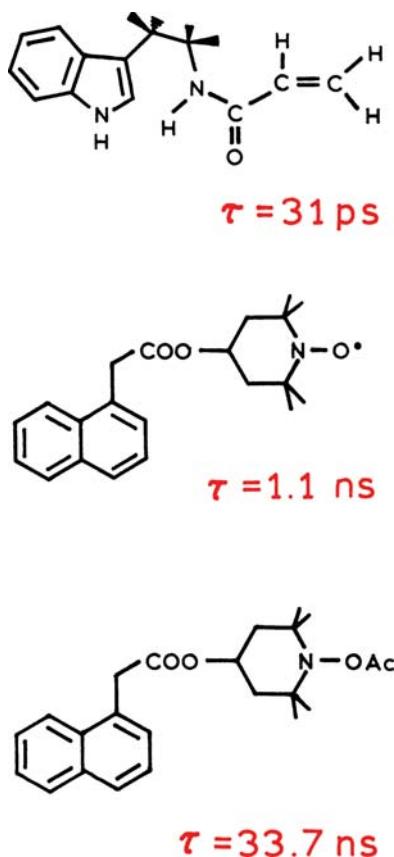


**Figure 8.66.** Fluorophore-quencher conjugates that display intramolecular quenching. Revised and reprinted with permission from [154–155]. Copyright © 1990, American Chemical Society.

quenched. It is now known that this quenching is due to electron transfer.<sup>157–158</sup> The amino-acid residues responsible for flavin quenching were identified using site-directed mutagenesis. Figure 8.68 shows the intensity decays of FMN free in solution and when bound to flavin reductase from *Escherichia coli*. The lifetime of FMN bound to the wild-type (WT) protein is much shorter than for FMN in solution. This flavin reductase contains three tyrosine (Y) residues at position 35, 72, and 116. Mutant proteins were prepared that contained only two of these residues. The flavin lifetime was still short for the mutants without tyr 72 or tyr 116, indicating that these tyrosines were not responsible for quenching. The lifetime of FMN increased dramatically when tyr 35 was removed, demonstrating that this residue is responsible for quenching. The quenching mechanism is electron transfer from try 35 to FMN. Tyr 35 is 4.5D away from FMN (upper panel). The other two residues are further away from the flavin: 9.6D and 7.0D for tyr 72 and tyr 116, respectively. Electron-transfer reactions

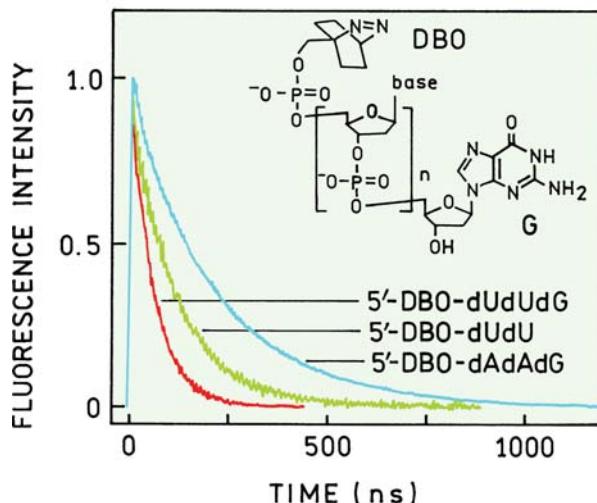
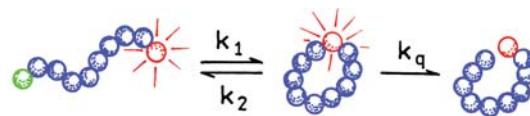


**Figure 8.67.** Intramolecular quenching of a DBO-labeled oligomer by a terminal guanine residue. Revised and reprinted with permission from [156]. Copyright © 2004, American Chemical Society.

only occur over short distances, which explains the lack of quenching by tyr 72 and tyr 116.

### 8.17.3. Sensors Based on Intramolecular PET Quenching

Intramolecular photoinduced electron transfer (PET) often results in quenching. The phenomenon of PET has been widely used to develop fluorescent sensors.<sup>159–163</sup> In a typical PET sensor an aromatic fluorophore such as anthracene is covalently linked to an aliphatic amine, typically by a short methylene chain. If the amine is not protonated it quenches the fluorophore. Protonation of the amine decreases its ability to donate an electron, so the fluorescence intensity increases.

Figure 8.69 shows the structure of a typical PET sensor.<sup>163</sup> The anthracene group is quenched by the amino groups. Addition of pyrophosphate (PPi) resulted in an increase in fluorescence because of protonation of some of the linked amino groups. The increased fluorescence may have also been due in part to less motion of the side chain during the excited-state lifetime, and thus less quenching.

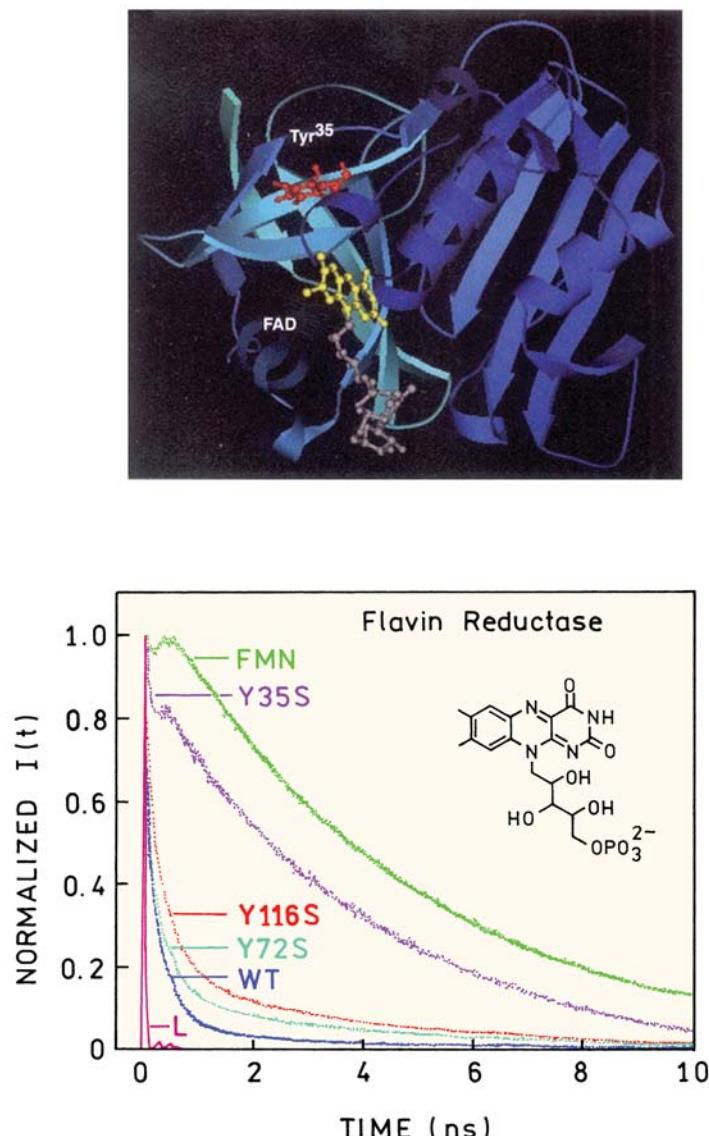


**Figure 8.68.** Intensity decays of FMN bound to flavin reductase. Intensity decays are shown for free FMN, and for FMN bound to the mutants and wild type protein. L is the lamp profile. The upper panel shows the crystal structure of flavin reductase with bound FMN. Reprinted from [158].

### 8.18. QUENCHING OF PHOSPHORESCENCE

Phosphorescence is not usually observed in fluid solutions near room temperature. One reason for the absence of phosphorescence is the long phosphorescence lifetimes and the presence of dissolved oxygen and other quenchers. For instance, the phosphorescent lifetime of tryptophan in water has been reported to be 1.2 ms in the absence of oxygen.<sup>164</sup> Suppose the oxygen bimolecular quenching constant is  $1 \times 10^{10} \text{ M}^{-1} \text{ s}^{-1}$ , and that the aqueous sample is in equilibrium with dissolved oxygen from the air ( $0.255 \text{ mM O}_2$ ). Using

eq. 8.1 the intensity is expected to be quenched 3000-fold. For this reason, methods have been developed to remove dissolved oxygen from samples used to study phosphorescence.<sup>165–166</sup> In practice, other dissolved quenchers and non-radiative decay rates result in vanishingly small phosphorescence quantum yields in room-temperature solutions. Some exceptions are known, such as when fluorophores are located in highly protected environments within proteins.<sup>167–170</sup> Phosphorescence has also been observed at room temperature for probes bound to cyclodextrins, even in the presence of oxygen.<sup>171</sup> Other small molecules such as

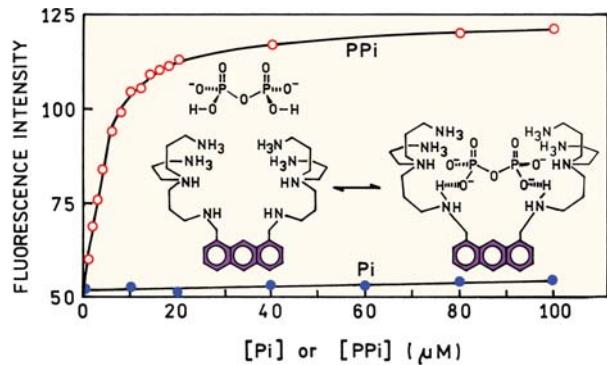


**Figure 8.69.** Fluorescence sensor for pyrophosphate based on intramolecular PET. The nitrogens are positively charged, which is not shown for clarity. Revised from [163].

amino acids,  $\text{H}_2\text{O}$ , and  $\text{CS}_2$  can also quench protein phosphorescence.<sup>172–173</sup> For these reasons, phosphorescence is not commonly observed near room temperature.

Protein phosphorescence can be quenched by oxygen. An example of the dramatic quenching of phosphorescence by even low concentration of oxygen is shown for alkaline phosphatase<sup>174</sup> (Figure 8.70). It is now known that the phosphorescence from alkaline phosphatase results from one of its three nonidentical tryptophan residues: trp-109. This residue is located in a highly shielded environment near the dimer interface. In the presence of  $7.8 \mu\text{M}$  oxygen the phosphorescence lifetime is reduced from  $1.57 \text{ s}$  to  $0.1 \text{ ns}$ . Note that an oxygen concentration of  $7.8 \mu\text{M}$  would have an insignificant effect on ns fluorescence. It is also important to notice that trp-109 in alkaline phosphatase is one of the most shielded residues identified to date in a protein. The lifetimes in the absence and presence of  $7.8 \mu\text{M}$  oxygen can be used to calculate the bimolecular quenching constant  $k_q = 1.2 \times 10^6 \text{ M}^{-1} \text{ s}^{-1}$ . If the residue were more typical, with a  $k_q$  value of  $0.1 \times 10^9 \text{ M}^{-1} \text{ s}^{-1}$ , one could calculate that the decay time in  $7.8 \mu\text{M}$  oxygen would have been reduced to  $1.28 \text{ ms}$ , and thus quenched by over 1000-fold for a micromolar quencher concentration.

## REFERENCES

- Kautsky H. 1939. Quenching of luminescence by oxygen. *Trans Faraday Soc* **35**:216–219.
- Knibbe H, Rehm D, Weller A. 1968. Intermediates and kinetics of fluorescence quenching by electron transfer. *Ber Bunsenges Phys Chem* **72**:257–263.
- Kasha M. 1952. Collisional perturbation of spin-orbital coupling and the mechanism of fluorescence quenching: a visual demonstration of the perturbation. *J Chem Phys* **20**:71–74.

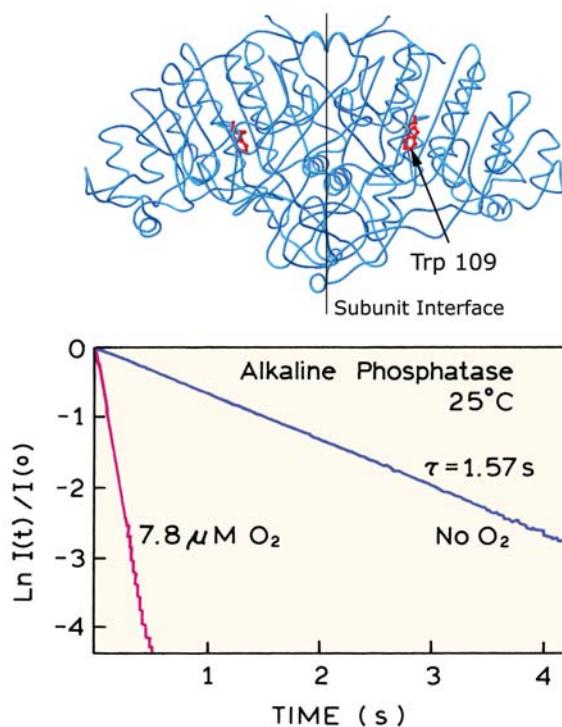


**Figure 8.70.** Phosphorescence decay of alkaline phosphatase,  $25^\circ\text{C}$ , in the absence of oxygen and in the presence of  $7.8 \mu\text{M}$  oxygen. Revised and reprinted with permission from [174]. Copyright © 1987, Biophysical Society.

- Steiner RF, Kirby EP. 1969. The interaction of the ground and excited states of indole derivatives with electron scavengers. *J Phys Chem* **73**:4130–4135.
- Eftink MR, Ghiron C. 1981. Fluorescence quenching studies with proteins. *Anal Biochem* **114**:199–227.
- Eftink MR. 1991. Fluorescence quenching reactions: probing biological macromolecular structures. In *Biophysical and biochemical aspects of fluorescence spectroscopy*, pp. 1–41. Ed TG Dewey. Plenum Press, New York.
- Eftink MR. 1991. Fluorescence quenching: theory and applications. In *Topics in fluorescence spectroscopy*, Vol. 2: *Principles*, pp. 53–126. Ed JR Lakowicz. Plenum Press, New York.
- Davis GA. 1973. Quenching of aromatic hydrocarbons by alkylpyridinium halides. *JCS Chem Comm*, 728–729.
- Shinitzky M, Rivnay B. 1977. Degree of exposure of membrane proteins determined by fluorescence quenching. *Biochemistry* **16**:982–986.
- Spencer RD, Weber G. 1972. Thermodynamics and kinetics of the intramolecular complex in flavin-adenine dinucleotide. In *Structure and function of oxidation reduction enzymes*, pp. 393–399. Ed A Akeson, A Ehrenberg. Pergamon Press, New York.
- Scott TG, Spencer RD, Leonard NJ, Weber G. 1970. Emission properties of NADH: studies of fluorescence lifetimes and quantum efficiencies of NADH, AcPyADH, and simplified synthetic models. *J Am Chem Soc* **92**:687–695.

12. Ware WR. 1962. Oxygen quenching of fluorescence in solution: An experimental study of the diffusion process. *J Phys Chem* **66**:455–458.
13. Othmer DF, Thakar MS. 1953. Correlating diffusion coefficients in liquids. *Ind Eng Chem Res* **45**:589–593.
14. Lakowicz JR, Weber G. 1973. Quenching of fluorescence by oxygen: a probe for structural fluctuation in macromolecule. *Biochemistry* **12**:4161–4170.
15. Eftink MR, Ghiron CA. 1977. Exposure of tryptophanyl residues and protein dynamics. *Biochemistry* **16**:5546–5551.
16. Johnson DA, Yguerabide J. 1985. Solute accessibility to N'-fluorescein isothiocyanate-lysine-23: cobra  $\alpha$ -toxin bound to the acetylcholine receptor. *Biophys J* **48**:949–955.
17. Kubota Y, Nakamura H, Morishita M, Fujisaki Y. 1978. Interaction of 9-aminoacridine with 7-methylguanosine and 1,N<sup>6</sup>-ethenoadenosine monophosphate. *Photochem Photobiol* **27**:479–481.
18. Kubota Y, Motoda Y, Shigemune Y, Fujisaki Y. 1979. Fluorescence quenching of 10-methylacridinium chloride by nucleotides. *Photochem Photobiol* **29**:1099–1106.
19. Seidel CAM, Schulz A, Sauer MHM. 1996. Nucleobase-specific quenching of fluorescent dyes, I: nucleobase one-electron redox potentials and their correlation with static and dynamic quenching efficiencies. *J Phys Chem* **100**:5541–5553.
20. Eftink MR, Ghiron CA. 1976. Fluorescence quenching of indole and model micelle systems. *J Phys Chem* **80**:486–493.
21. Casali E, Petra PH, Ross JBA. 1990. Fluorescence investigation of the sex steroid binding protein of rabbit serum: steroid binding and subunit dissociation. *Biochemistry* **29**:9334–9343.
22. Frank IM, Vavilov SI. 1931. Über die wirkungssphäre der auslöschrungs-vargänge in den flureszierenden flüssigkeiten. *Z Phys* **69**:100–110.
23. Maniara G, Vanderkooi JM, Bloomgarden DC, Koloczek H. 1988. Phosphorescence from 2-(p-toluidinyl)naphthalene-6-sulfonate and 1-anilinonaphthalene-8-sulfonate, commonly used fluorescence probes of biological structures. *Photochem Photobiol* **47**(2): 207–208.
24. Kim H, Crouch SR, Zabik MJ. 1989. Room-temperature phosphorescence of compounds in mixed organized media: synthetic enzyme model-surfactant system. *Anal Chem* **61**:2475–2478.
25. Encinas MV, Lissi EA, Rufas AM. 1993. Inclusion and fluorescence quenching of 2,3-dimethylnaphthalene in  $\beta$ -cyclodextrin cavities. *Photochem Photobiol* **57**(4):603–608.
26. Turro NJ, Bolt JD, Kuroda Y, Tabushi I. 1982. A study of the kinetics of inclusion of halonaphthalenes with  $\beta$ -cyclodextrin via time correlated phosphorescence. *Photochem Photobiol* **35**:69–72.
27. Waka Y, Hamamoto K, Mataga N. 1980. Heteroexcimer systems in aqueous micellar solutions. *Photochem Photobiol* **32**:27–35.
28. Atherton SJ, Beaumont PC. 1986. Quenching of the fluorescence of DNA-intercalated ethidium bromide by some transition metal ions. *J Phys Chem* **90**:2252–2259.
29. Pasternack RF, Caccam M, Keogh B, Stephenson TA, Williams AP, Gibbs EJ. 1991. Long-range fluorescence quenching of ethidium ion by cationic porphyrins in the presence of DNA. *J Am Chem Soc* **113**: 6835–6840.
30. Poulos AT, Kuzmin V, Geacintov NE. 1982. Probing the microenvironment of benzo[a]pyrene diol epoxide-DNA adducts by triplet excited state quenching methods. *J Biochem Biophys Methods* **6**:269–281.
31. Zinger D, Geacintov NF. 1988. Acrylamide and molecular oxygen fluorescence quenching as a probe of solvent-accessibility of aromatic fluorophores complexed with DNA in relation to their conformations: coronene-DNA and other complexes. *Photochem Photobiol* **47**:181–188.
32. Suh D, Chaires JB. 1995. Criteria for the mode of binding of DNA binding agents. *Bioorgan Med Chem* **3**(6):723–728.
33. Ando T, Asai H. 1980. Charge effects on the dynamic quenching of fluorescence of fluorescence of 1,N<sup>6</sup>-ethenoadenosine oligophosphates by iodide, thallium (I) and acrylamide. *J Biochem* **88**: 255–264.
34. Ando T, Fujisaki H, Asai H. 1980. Electric potential at regions near the two specific thiols of heavy meromyosin determined by the fluorescence quenching technique. *J Biochem* **88**:265–276.
35. Miyata H, Asai H. 1981. Amphoteric charge distribution at the enzymatic site of 1,N<sup>6</sup>-ethenoadenosine triphosphate-binding heavy meromyosin determined by dynamic fluorescence quenching. *J Biochem* **90**:133–139.
36. Midoux P, Wahl P, Auchet J-C, Monsigny M. 1984. Fluorescence quenching of tryptophan by trifluoroacetamide. *Biochim Biophys Acta* **801**:16–25.
37. Lehrer SS. 1971. Solute perturbation of protein fluorescence: the quenching of the tryptophan fluorescence of model compounds and of lysozyme by iodide ion. *Biochemistry* **10**:3254–3263.
38. Kao S, Asanov AN, Oldham PB. 1998. A comparison of fluorescence inner-filter effects for different cell configurations. *Instrum Sci Technol* **26**(4):375–387.
39. Fanget B, Devos O. 2003. Correction of inner filter effect in mirror coating cells for trace level fluorescence measurements. *Anal Chem* **75**:2790–2795.
40. Eftink MR, Selvidge LA. 1982. Fluorescence quenching of liver alcohol dehydrogenase by acrylamide. *Biochemistry* **21**:117–125.
41. Eftink M, Hagaman KA. 1986. Fluorescence lifetime and anisotropy studies with liver alcohol dehydrogenase and its complexes. *Biochemistry* **25**:6631–6637.
42. Xing D, Dorr R, Cunningham RP, Scholes CP. 1995. Endonuclease III interactions with DNA substrates, 2: the DNA repair enzyme endonuclease III binds differently to intact DNA and to apurimidinic/apurinic DNA substrates as shown by tryptophan fluorescence quenching. *Biochemistry* **34**:2537–2544.
43. Sontag B, Reboud A-M, Divita G, Di Pietro A, Guillot D, Reboud JP. 1993. Intrinsic tryptophan fluorescence of rat liver elongation factor eEF-2 to monitor the interaction with guanylic and adenylic nucleotides and related conformational changes. *Biochemistry* **32**: 1976–1980.
44. Wasylewski M, Malecki J, Wasylewski Z. 1995. Fluorescence study of Escherichia coli cyclic AMP receptor protein. *J Protein Chem* **14**(5):299–308.
45. Hannemann F, Bera AK, Fischer B, Lisurek M, Teuchner K, Bernhardt R. 2002. Unfolding and conformational studies on bovine adrenodoxin probed by engineered intrinsic tryptophan fluorescence. *Biochemistry* **41**:11008–11016.
46. Soulages JL, Arrese EL. 2000. Fluorescence spectroscopy of single tryptophan mutants of apolipoporphin-III in discoidal lipoproteins of dimyristoylphosphatidylcholine. *Biochemistry* **39**:10574–10580.

47. Raja SM, Rawat SS, Chattopadhyay A, Lala AK. 1999. Localization and environment of tryptophans in soluble and membrane-bound states of a pore-forming toxin from *Staphylococcus aureus*. *Bioophys J* **76**:1469–1479.
48. Weber J, Senior AE. 2000. Features of F<sub>1</sub>-ATPase catalytic and non-catalytic sites revealed by fluorescence lifetimes and acrylamide quenching of specifically inserted tryptophan residues. *Biochemistry* **39**:5287–5294.
49. Wells TA, Nakazawa M, Manabe K, Song P-S. 1994. A conformational change associated with the phototransformation of *Pisum* phytochrome A as probed by fluorescence quenching. *Biochemistry* **33**:708–712.
50. Eftink MR, Zajicek JL, Ghiron CA. 1977. A hydrophobic quencher of protein fluorescence: 2,2,2-trichloroethanol. *Biochim Biophys Acta* **491**:473–481.
51. Blatt E, Husain A, Sawyer WH. 1986. The association of acrylamide with proteins: the interpretation of fluorescence quenching experiments. *Biochim Biophys Acta* **871**:6–13.
52. Eftink MR, Ghiron CA. 1987. Does the fluorescence quencher acrylamide bind to proteins? *Biochim Biophys Acta* **916**:343–349.
53. Punyiczki M, Norman JA, Rosenberg A. 1993. Interaction of acrylamide with proteins in the concentration range used for fluorescence quenching studies. *Biophys Chem* **47**:9–19.
54. Bastyns K, Engelborghs Y. 1992. Acrylamide quenching of the fluorescence of glyceraldehyde-3-phosphate dehydrogenase: reversible and irreversible effects. *Photochem Photobiol* **55**:9–16.
55. Merrill AR, Palmer LR, Szabo AG. 1993. Acrylamide quenching of the intrinsic fluorescence of tryptophan residues genetically engineered into the soluble colicin E1 channel peptide: structural characterization of the insertion-competent state. *Biochemistry* **32**:6974–6981.
56. Lakowicz JR. 1980. Fluorescence spectroscopic investigations of the dynamic properties of proteins, membranes, and nucleic acids. *J Biochem Biophys Methods* **2**:90–119.
57. Subczynski WK, Hyde JS, Kusumi A. 1989. Oxygen permeability of phosphatidylcholine-cholesterol membranes. *Proc Natl Acad Sci USA* **86**:4474–4478.
58. Fischkoff S, Vanderkooi JM. 1975. Oxygen diffusion in biological and artificial membranes determined by the fluorochrome pyrene. *J Gen Physiol* **65**:663–676.
59. Dumas D, Muller S, Gouin F, Baros F, Viriot M-L, Stoltz J-F. 1997. Membrane fluidity and oxygen diffusion in cholesterol-enriched erythrocyte membrane. *Arch Biochem Biophys* **341**(1):34–39.
60. Subczynski WK, Hyde JS, Kusumi A. 1991. Effect of alkyl chain unsaturation and cholesterol intercalation on oxygen transport in membranes: a pulse ESR spin labeling study. *Biochemistry* **30**:8578–8590.
61. Caputo GA, London E. 2003. Using a novel dual fluorescence quenching assay for measurement of tryptophan depth within lipid bilayers to determine hydrophobic  $\alpha$ -helix locations within membranes. *Biochemistry* **42**:3265–3274.
62. Lala AK, Koppaka V. 1992. Fluorenyl fatty acids as fluorescent probes for depth-dependent analysis of artificial and natural membranes. *Biochemistry* **31**:5586–5593.
63. Sassaroli M, Ruonala M, Virtanen J, Vauhkonen M, Somerharju P. 1995. Transversal distribution of acyl-linked pyrene moieties in liquid-crystalline phosphatidylcholine bilayers. A fluorescence quenching study. *Biochemistry* **34**:8843–8851.
64. Ladokhin A, Wang L, Steggles AW, Holloway PW. 1991. Fluorescence study of a mutant cytochrome  $b_5$  with a single tryptophan in the membrane-binding domain. *Biochemistry* **30**:10200–10206.
65. Everett J, Zlotnick A, Tennyson J, Holloway PW. 1986. Fluorescence quenching of cytochrome  $b_5$  in vesicles with an asymmetric transbilayer distribution of brominated phosphatidylcholine. *J Biol Chem* **261**(15):6725–6729.
66. Gonzalez-Manas JM, Lakey JH, Pattus F. 1992. Brominated phospholipids as a tool for monitoring the membrane insertion of colicin A. *Biochemistry* **31**:7294–7300.
67. Silvius JR. 1990. Calcium-induced lipid phase separations and interactions of phosphatidylcholine/anionic phospholipid vesicles: fluorescence studies using carbazole-labeled and brominated phospholipids. *Biochemistry* **29**:2930–2938.
68. Silvius JR. 1992. Cholesterol modulation of lipid intermixing in phospholipid and glycosphingolipid mixtures: evaluation using fluorescent lipid probes and brominated lipid quenchers. *Biochemistry* **31**:3398–3403.
69. Chattopadhyay A, London E. 1987. Parallax method for direct measurement of membrane penetration depth utilizing fluorescence quenching by spin-labeled phospholipids. *Biochemistry* **26**:39–45.
70. Abrams FS, London E. 1992. Calibration of the parallax fluorescence quenching method for determination of membrane penetration depth: refinement and comparison of quenching by spin-labeled and brominated lipids. *Biochemistry* **31**:5312–5322.
71. Abrams FS, Chattopadhyay A, London E. 1992. Determination of the location of fluorescent probes attached to fatty acids using parallax analysis of fluorescence quenching: effect of carboxyl ionization state and environment on depth. *Biochemistry* **31**:5322–5327.
72. Abrams FS, London E. 1993. Extension of the parallax analysis of membrane penetration depth to the polar region of model membranes: use of fluorescence quenching by a spin-label attached to the phospholipid polar headgroup. *Biochemistry* **32**:10826–10831.
73. Asuncion-Punzalan E, London E. 1995. Control of the depth of molecules within membranes by polar groups: determination of the location of anthracene-labeled probes in model membranes by parallax analysis of nitroxide-labeled phospholipid induced fluorescence quenching. *Biochemistry* **34**:11460–11466.
74. Kachel K, Asuncion-Punzalan E, London E. 1995. Anchoring of tryptophan and tyrosine analogs at the hydrocarbon-polar boundary in model membrane vesicles: parallax analysis of fluorescence quenching induced by nitroxide-labeled phospholipids. *Biochemistry* **34**:15475–15479.
75. Ren J, Lew S, Wang Z, London E. 1997. Transmembrane orientation of hydrophobic  $\alpha$ -helices is regulated both by the relationship of helix length to bilayer thickness and by the cholesterol concentration. *Biochemistry* **36**:10213–10220.
76. Ladokhin AS. 1999. Analysis of protein and peptide penetration into membranes by depth-dependent fluorescence quenching: theoretical considerations. *Biophys J* **76**:946–955.
77. Ladokhin AS. 1999. Evaluation of lipid exposure of tryptophan residues in membrane peptides and proteins. *Anal Biochem* **276**:65–71.

78. Ladokhin AS. 1997. Distribution analysis of depth-dependent fluorescence quenching in membranes: a practical guide. *Methods Enzymol* **278**:462–473.
79. London E, Ladokhin AS. 2002. Measuring the depth of amino acid residues in membrane-inserted peptides by fluorescence quenching. *Current Top Membr* **52**:89–111.
80. London E, Feigenson GW. 1981. Fluorescence quenching in model membranes, 1: characterization of quenching caused by a spin-labeled phospholipid. *Biochemistry* **20**:1932–1938.
81. London E, Feigenson GW. 1981. Fluorescence quenching in model membranes, 2: determination of the local lipid environment of the calcium adenosinetriphosphatase from sarcoplasmic reticulum. *Biochemistry* **20**:1939–1948.
82. East JM, Lee AG. 1982. Lipid selectivity of the calcium and magnesium ion dependent adenosinetriphosphatase, studied with fluorescence quenching by a brominated phospholipid. *Biochemistry* **21**:4144–4151.
83. Caffrey M, Feigenson GW. 1981. Fluorescence quenching in model membranes, 3: relationship between calcium adenosinetriphosphatase enzyme activity and the affinity of the protein for phosphatidylcholines with different acyl chain characteristics. *Biochemistry* **20**:1949–1961.
84. Markello T, Zlotnick A, Everett J, Tennyson J, Holloway PW. 1985. Determination of the topography of cytochrome  $b_5$  in lipid vesicles by fluorescence quenching. *Biochemistry* **24**:2895–2901.
85. Froud RJ, East JM, Rooney EK, Lee AG. 1986. Binding of long-chain alkyl derivatives to lipid bilayers and to ( $\text{Ca}^{2+}$ - $\text{Mg}^{2+}$ )-ATPase. *Biochemistry* **25**:7535–7544.
86. Yeager MD, Feigenson GW. 1990. Fluorescence quenching in model membranes: phospholipid acyl chain distributions around small fluorophores. *Biochemistry* **29**:4380–4392.
87. Lakowicz JR, Hogen D, Omann G. 1977. Diffusion and partitioning of a pesticide, lindane, into phosphatidylcholine bilayers: a new fluorescence quenching method to study chlorinated hydrocarbon-membrane interactions. *Biochim Biophys Acta* **471**:401–411.
88. Omann GM, Glaser M. 1985. Dynamic quenchers in fluorescently labeled membranes. *Biophys J* **47**:623–627.
89. Fato R, Battino M, Esposti MD, Castelli GP, Lenaz G. 1986. Determination of partition of lateral diffusion coefficients of ubiquinones by fluorescence quenching of n-(9-anthroyloxy)stearic acids in phospholipid vesicles and mitochondrial membranes. *Biochemistry* **25**:3378–3390.
90. Vermeir M, Boens N. 1992. Partitioning of  $(\pm)$ -5,6-dihydro-6-phenyl-2-n-alkyl-imidazo-[2,1-b]thiazoles into large unilamellar liposomes: a steady-state fluorescence quenching study. *Biochim Biophys Acta* **1104**:63–72.
91. Lakos Z, Szarka A, Somogyi B. 1995. Fluorescence quenching in membrane phase. *Biochem Biophys Res Commun* **208**(1):111–117.
92. Prieto MJE, Castanho M, Coutinho A, Ortiz A, Aranda FJ, Gomez-Fernandez JC. 1994. Fluorescence study of a derivatized diacylglycerol incorporated in model membranes. *Chem Phys Lipids* **69**:75–85.
93. Ranganathan R, Vautier-Giongo C, Bales BL. 2003. Toward a hydrodynamic description of biomolecular collisions in micelles: an experimental test of the effect of the nature of the quencher on the fluorescence quenching of pyrene in SDS micelles and in bulk liquids. *J Phys Chem B* **107**:10312–10318.
94. Infelta PP. 1979. Fluorescence quenching in micellar solutions and its application to the determination of aggregation numbers. *Chem Phys Lett* **61**(1):88–91.
95. Waka Y, Hamamoto K, Mataga N. 1980. Heteroexcimer systems in aqueous micellar solutions. *Photochem Photobiol* **32**:27–35.
96. Tachiya M. 1982. Kinetics of quenching of luminescent probes in micellar systems, II. *J Chem Phys* **76**(1):343–348.
97. Naqvi KR. 1974. Diffusion-controlled reactions in two-dimensional fluids: discussion of measurements of lateral diffusion of lipids in biological membranes. *Chem Phys Lett* **28**(2):280–284.
98. Owen CS. 1975. Two-dimensional diffusion theory: cylindrical diffusion model applied to fluorescence quenching. *J Chem Phys* **62**(8):3204–3207.
99. Medhage B, Almgren M. 1992. Diffusion-influenced fluorescence quenching: dynamics in one to three dimensions. *J Fluoresc* **2**(1):7–21.
100. Caruso F, Grieser F, Thistlthwaite PJ. 1993. Lateral diffusion of amphiphiles in fatty acid monolayers at the air–water interface: a steady-state and time-resolved fluorescence quenching study. *Langmuir* **9**:3142–3148.
101. Blackwell MF, Gounaris K, Zara SJ, Barber J. 1987. A method for estimating lateral diffusion coefficients in membranes from steady-state fluorescence quenching studies. *Biophys J* **51**:735–744.
102. Caruso F, Grieser F, Thistlthwaite PJ, Almgren M. 1993. Two-dimensional diffusion of amphiphiles in phospholipid monolayers at the air–water interface. *Biophys J* **65**:2493–2503.
103. Wasylewski Z, Kaszycki P, Guz A, Stryjewski W. 1988. Fluorescence quenching resolved spectra of fluorophores in mixtures and micellar solutions. *Eur J Biochem* **178**:471–476.
104. Wasylewski Z, Koloczek H, Wasniowska A. 1988. Fluorescence quenching resolved spectroscopy of proteins. *Eur J Biochem* **172**:719–724.
105. Laws WR, Shore JD. 1978. The mechanism of quenching of liver alcohol dehydrogenase fluorescence due to ternary complex formation. *J Biol Chem* **23**:8593–8597.
106. Stryjewski W, Wasylewski Z. 1986. The resolution of heterogeneous fluorescence of multityptophan-containing proteins studied by a fluorescence quenching method. *Eur J Biochem* **158**:547–553.
107. Blicharska Z, Wasylewski Z. 1995. Fluorescence quenching studies of Trp repressor using single-tryptophan mutants. *J Protein Chem* **14**(8):739–746.
108. Wasylewski Z, Kaszycki P, Drwiega M. 1996. A fluorescence study of Tn10-encoded tet repressor. *J Protein Chem* **15**(1):45–52.
109. Hansen D, Altschmid L, Hillen W. 1987. Engineered tet repressor mutants with single tryptophan residues as fluorescent probes. *J Biol Chem* **29**:14030–14035.
110. Lange R, Anzenbacher P, Müller S, Maurin L, Balny C. 1994. Interaction of tryptophan residues of cytochrome P450cc with a highly specific fluorescence quencher, a substrate analogue, compared to acrylamide and iodide. *Eur J Biochem* **226**:963–970.
111. Johansson JS, Eckenhoff RG, Dutton L. 1995. Binding of halothane to serum albumin demonstrated using tryptophan fluorescence. *Anesthesiology* **83**:316–324.
112. Johansson JS. 1997. Binding of the volatile anesthetic chloroform to albumin demonstrated using tryptophan fluorescence quenching. *J Biol Chem* **272**:17961–17965.

113. Gonzalez-Jimenez J, Frutos G, Cayre I. 1992. Fluorescence quenching of human serum albumin by xanthines. *Biochem Pharmacol* **44**(4):824–826.
114. Johansson JS, Scharf D, Davies LA, Reddy KS, Eckenhoff RG. 2000. A designed four- $\alpha$ -helix bundle that binds the volatile general anesthetic halothane with high affinity. *Biophys J* **78**:982–993.
115. Johansson JS, Solt K, Reddy KS. 2003. Binding of the general anesthetics chloroform and 2,2,2-trichloroethanol to the hydrophobic core of a four- $\alpha$ -helix bundle protein. *Photochem Photobiol* **77**(1):89–95.
116. Geddes CG. 2001. Optical halide sensing using fluorescence quenching: theory, simulations and applications—a review. *Meas Sci Technol* **12**:R53–R88.
117. Geddes CG. 2000. Optical thin film polymeric sensors for the determination of aqueous chloride, bromide and iodide ions at high pH, based on the quenching of fluorescence of two acridinium dyes. *Dyes Pigm* **45**:243–251.
118. Geddes CG, Apperson K, Birch DJS. 2000. New fluorescent quinolinium dyes—applications in nanometre particle sizing. *Dyes Pigm* **44**:69–74.
119. Huber C, Werner T, Krause C, Wolfbeis OS. 1999. Novel chloride-selective optode based on polymer-stabilised emulsions doped with a lipophilic fluorescent polarity-sensitive dye. *Analyst* **124**:1617–1622.
120. Huber C, Fähnrich K, Krause C, Werner T. 1999. Synthesis and characterization of new chloride-sensitive indicator dyes based on dynamic fluorescence quenching. *J Photochem Photobiol A: Chem* **128**:111–120.
121. Geddes CG, Apperson K, Karolin J, Birch JDS. 2001. Chloride-sensitive fluorescent indicators. *Anal Biochem* **293**:60–66.
122. Geddes CG. 2001. Halide sensing using the SPQ molecule. *Sens Actuators B* **72**:188–195.
123. Jayaraman S, Verkman AS. 2000. Quenching mechanism of quinolinium-type chloride-sensitive fluorescent indicators. *Biophys Chem* **85**:45–57.
124. Rehm D, Weller A. 1970. Kinetics of fluorescence quenching by electron and H-atom transfer. *Isr J Chem* **8**:259–271.
125. Jayaraman S, Song Y, Vetrivel L, Shankar L, Verkman AS. 2001. Noninvasive in vivo fluorescence measurement of airway-surface liquid depth, salt concentration, and pH. *J Clin Invest* **107**(3):317–324.
126. Inglefield JR, Schwartz-Bloom RD. 1999. Fluorescence imaging of changes in intracellular chloride in living brain slices. *Methods: A Companion to Methods in Enzymology* **18**:197–203.
127. Sonawane ND, Thiagarajah JR, Verkman AS. 2002. Chloride concentration in endosomes measured using a ratioable fluorescent Cl<sup>-</sup> indicator. *J Biol Chem* **277**(7):5506–5513.
128. Jayaraman S, Teitler L, Skalski B, Verkman AS. 1999. Long-wavelength iodide-sensitive fluorescent indicators for measurement of functional CFTR expression in cells. *Am J Physiol* **277**:C1008–C1018.
129. Jayaraman S, Biwersi J, Verkman AS. 1999. Synthesis and characterization of dual-wavelength Cl<sup>-</sup> sensitive fluorescent indicators for ratio imaging. *Am J Physiol* **276**:C747–C757.
130. Zhang J, Campbell RE, Ting AY, Tsien R. 2002. Creating new fluorescent probes for cell biology. *Nature Rev Mol Cell Biol* **3**(12):906–918.
131. Zimmer M. 2002. Green fluorescent protein (GFP): applications, structure, and related photophysical behavior. *Chem Rev* **102**:759–781.
132. Wachter RM, Yarbrough D, Kallio K, Remington SJ. 2000. Crystallographic and energetic analysis of binding of selected anions to the yellow variants of green fluorescent protein. *J Mol Biol* **301**:157–171.
133. Jayaraman S, Haggie P, Wachter RM, Remington SJ, Verkman AS. 2000. Mechanism and cellular applications of a green fluorescent protein-based halide sensor. *J Biol Chem* **275**(9):6047–6050.
134. Rakicioglu Y, Young MM, Schulman SG. 1998. Limitations of quenching as a method of fluorometric analysis of non-fluorescent analytes. *Anal Chim Acta* **359**:269–273.
135. Chen L, McBranch DW, Wang H-L, Helgeson R, Wudi F, Whitten DG. 1999. Highly sensitive biological and chemical sensors based on reversible fluorescence quenching in a conjugated polymer. *Proc Natl Acad Sci USA* **96**(22):12287–12292.
136. Yamane A. 2002. MagiProbe: a novel fluorescence quenching-based oligonucleotide probe carrying a fluorophore and an intercalator. *Nucleic Acids Res* **30**(19):e97.
137. Sauer M, Drexlage KH, Lieberwirth U, Müller R, Nord S, Zander C. 1998. Dynamics of the electron transfer reaction between an oxazine dye and DNA oligonucleotides monitored on the single-molecule level. *Chem Phys Lett* **284**:153–163.
138. Torimura M, Kurata S, Yamada K, Yokomaku T, Kamagata Y, Kanagawa T, Kurane R. 2001. Fluorescence-quenching phenomenon by photoinduced electron transfer between a fluorescent dye and a nucleotide base. *Anal Sci* **17**:155–160.
139. Heinlein T, Knemeyer J-P, Piestert O, Sauer M. 2003. Photoinduced electron transfer between fluorescent dyes and guanosine residues in DNA-hairpins. *J Phys Chem* **107**:7957–7964.
140. Knemeyer J-P, Marmé N, Sauer M. 2000. Probes for detection of specific DNA sequences at the single-molecule level. *Anal Chem* **72**:3717–3724.
141. Walter NG, Burke JM. 1997. Real-time monitoring of hairpin ribozyme kinetics through base-specific quenching of fluorescein-labeled substrates. *RNA* **3**:392–404.
142. Jezewska MJ, Bujalowski W. 1997. Quantitative analysis of ligand-macromolecule interactions using differential dynamic quenching of the ligand fluorescence to monitor the binding. *Biophys Chem* **64**:253–269.
143. Thomas KG, Kamat PV. 2003. Chromophore-functionalized gold nanoparticles. *Acc Chem Res* **36**(12):888–898.
144. Kerker M. 1985. The optics of colloidal silver: something old and something new. *J Colloid Interface Sci* **105**(2):297–314.
145. Link S, El-Sayed M. 1999. Spectral properties and relaxation dynamics of surface plasmon electronic oscillations in gold and silver nanodots and nanorods. *J Phys Chem B* **103**:8410–8426.
146. Lakowicz JR. 2001. Radiative decay engineering: Biophysical and biomedical applications. *Anal Biochem* **298**:1–24.
147. Storhoff JJ, Lucas AD, Garimella V, Bao YP, Müller UR. 2004. Homogeneous detection of unamplified genomic DNA sequences based on colorimetric scatter of gold nanoparticles probes. *Nature Biotechnol* **22**:883–887.
148. Storhoff JJ, Elghanian R, Mucic RC, Mirkin CA, Letsinger RL. 1998. One-pot colorimetric differentiation of polynucleotides with

- single base imperfections using gold nanoparticle probes. *J Am Chem Soc* **120**:1959–1964.
- 149. He L, Musick MD, Nicewarner SR, Salinas FG, Benkovic SJ, Natan MJ, Keating CD. 2000. Colloidal Au-enhanced surface plasmon resonance for ultrasensitive detection of DNA hybridization. *J Am Chem Soc* **122**:9071–9077.
  - 150. Taton TA, Mirkin CA, Letsinger RL. 2000. Scanometric DNA array detection with nanoparticle probes. *Science* **289**:1757–1760.
  - 151. Dubertret B, Calame M, Libchaber AJ. 2001. Single-mismatch detection using gold-quenched fluorescent oligonucleotides. *Nature Biotechnol* **19**:365–370.
  - 152. Maxwell DJ, Taylor JR, Nie S. 2002. Self-assembled nanoparticle probes for recognition and detection of biomolecules. *J Am Chem Soc* **124**:9606–9612.
  - 153. Du H, Disney MD, Miller BL, Krauss TD. 2003. Hybridization-based unquenching of DNA hairpins on Au surfaces: prototypical "molecular beacon" biosensors. *J Am Chem Soc* **125**:4012–4013.
  - 154. Eftink MR, Jia Y-W, Graves DE, Wiczek W, Gryczynski I, Lakowicz JR. 1989. Intramolecular fluorescence quenching in covalent acrylamide-indole adducts. *Photochem Photobiol* **49**(6):725–729.
  - 155. Green SA, Simpson DJ, Zhou G, Ho PS, Blough NV. 1990. Intramolecular quenching of excited singlet states by stable nitroxyl radicals. *J Am Chem Soc* **112**:7337–7346.
  - 156. Wang X, Nau WM. 2004. Kinetics of end-to-end collision in short single-stranded nucleic acids. *J Am Chem Soc* **126**:808–813.
  - 157. van den Berg PAW, van Hoek A, Walentas CD, Perham RN, Visser AJWG. 1998. Flavin fluorescence dynamics and photoinduced electron transfer in *Escherichia coli* glutathione reductase. *Biophys J* **74**:2046–2058.
  - 158. Yang H, Luo G, Karnchanaphanurach P, Louie T-M, Rech I, Cova S, Xun L, Xie XS. 2003. Protein conformational dynamics probed by single-molecule electron transfer. *Science* **302**:262–266.
  - 159. Kavarnos GJ. 1993. *Fundamentals of photoinduced electron transfer*. VCH Publishers, New York.
  - 160. Pina F, Bernando MA, García-España E. 2000. Fluorescent chemosensors containing polyamine receptors. *Eur J Inorg Chem* 2143–2157.
  - 161. de Silva AP, Fox DB, Moody TS, Weir SM. 2001. The development of molecular fluorescent switches. *Trends Biotechnol* **19**(1):29–34.
  - 162. de Silva AP, Gunaratne HQN, Gunnlaugsson T, Huxley AJM, McCoy CP, Rademacher JT, Rice TE. 1997. Signaling recognition events with fluorescent sensors and switches. *Chem Rev* **97**:1515–1566.
  - 163. Czarnik AW. 1994. Fluorescent chemosensors of ion and molecule recognition. *Interfacial Des Chem Sens* **561**:314–323.
  - 164. Strambini GB, Gonnelli M. 1995. Tryptophan phosphorescence in fluid solution. *J Am Chem Soc* **117**:7646–7651.
  - 165. Englander SW, Calhoun DB, Englander JJ. 1987. Biochemistry without oxygen. *Anal Biochem* **161**:300–306.
  - 166. Zhang HR, Zhang J, Wei YS, Jin EJ, Liu CS. 1997. Study of new facile deoxygenation methods in cyclodextrin induced room temperature phosphorescence. *Anal Chim Acta* **357**:119–125.
  - 167. Cioni P, Puntoni A, Strambini GB. 1993. Tryptophan phosphorescence as a monitor of the solution structure of phosphoglycerate kinase from yeast. *Biophys Chem* **46**:47–55.
  - 168. Gonnelli M, Strambini GB. 1993. Glycerol effects on protein flexibility: a tryptophan phosphorescence study. *Biophys J* **65**:131–137.
  - 169. Strambini GB, Gabellieri E. 1996. Proteins in frozen solutions: evidence of ice-induced partial unfolding. *Biophys J* **70**:971–976.
  - 170. Vanderkooi JM, Calhoun DB, Englander SW. 1987. On the prevalence of room-temperature protein phosphorescence. *Science* **236**:568–569.
  - 171. Turro NJ, Cox GS, Li X. 1983. Remarkable inhibition of oxygen quenching of phosphorescence by complexation with cyclodextrins. *Photochem Photobiol* **37**(2):149–153.
  - 172. Gonnelli M, Strambini GB. 1995. Phosphorescence lifetime of tryptophan in proteins. *Biochemistry* **34**:13847–13857.
  - 173. Wright WW, Owen CS, Vanderkooi JM. 1992. Penetration of analogues of  $H_2O$  and  $CO_2$  in proteins studied by room temperature phosphorescence of tryptophan. *Biochemistry* **31**:6538–6544.
  - 174. Strambini GB. 1987. Quenching of alkaline phosphatase phosphorescence by  $O_2$  and NO. *Biophys J* **52**:23–28.
  - 175. Courtesy of Dr. Ari Gafni, University of Michigan.
  - 176. Boaz H, Rollefson GK. 1950. The quenching of fluorescence: deviations from the Stern-Volmer law. *J Am Chem Soc* **72**:3425–3443.
  - 177. Harrison M, Powell B, Finbow ME, Findlay JBC. 2000. Identification of lipid-accessible sites on the *Nephrops* 16-kDa proteolipid incorporated into a hybrid vacuolar  $H^+$ -ATPase: site-directed labeling with N-(1-pyrenyl)cyclohexylcarbodiimide and fluorescence quenching analysis. *Biochemistry* **39**:7531–7537.
  - 178. Moro A, Gatti C, Delorenzi N. 2001. Hydrophobicity of whey protein concentrates measured by fluorescence quenching and its relation with surface functional properties. *J Agric Food Chem* **49**:4784–4789.
  - 179. Galletto R, Bujalowski W. 2002. Kinetics of the *E. coli* replication factor DnaC protein–nucleotide interactions, II: fluorescence anisotropy and transient, dynamic quenching stopped-flow studies of the reaction intermediates. *Biochemistry* **41**:8921–8934.
  - 180. Eftink MR, Ghiron CA. 1976. Exposure of tryptophanyl residues in proteins: quantitative determination by fluorescence quenching studies. *Biochemistry* **15**(3):672–680.
  - 181. Saik VO, Goun AA, Fayer MD. 2004. Photoinduced electron transfer and geminate recombination for photoexcited acceptors in a pure donor solvent. *J Chem Phys* **120**(20):9601–9611.
  - 182. Schneider S, Stammle W, Bierl R, Jager W. 1994. Ultrafast photoinduced charge separation and recombination in weakly bound complexes between oxazine dyes and N,N-dimethylaniline. *Chem Phys Lett* **219**:433–439.
  - 183. Yoshihara K, Yartsev A, Nagasawa Y, Kandori H, Douhal A, Kemnitz K. 1993. Femtosecond intermolecular electron transfer between dyes and electron-donating solvents. *Pure Appl Chem* **65**(8):1671–1675.
  - 184. Pischel U, Abad S, Miranda MA. 2003. Stereoselective fluorescence quenching by photoinduced electron transfer in naphthalene-amine dyads. *Chem Commun* **9**:1088–1089.
  - 185. Morandeira A, Fürstenberg A, Gumy JC, Vauthey E. 2003. Fluorescence quenching in electron-donating solvents, 1: influence of the solute-solvent interactions on the dynamics. *J Phys Chem* **107**:5375–5383.
  - 186. Goodpaster JV, McGuffin VL. 2000. Selective fluorescence quenching of polycyclic aromatic hydrocarbons by aliphatic amines. *Anal Chem* **72**:1072–1077.
  - 187. Bisht PB, Tripathi HB. 1993. Fluorescence quenching of carbazole by triethylamine: exciplex formation in polar and nonpolar solvents. *J Luminesc* **55**:153–158.

188. Sikaris KA, Sawyer WH. 1982. The interaction of local anaesthetics with synthetic phospholipid bilayers. *Biochem Pharmacol* **31**(16): 2625–2631.
189. Fernandez MS, Calderon E. 1990. The local anaesthetic tetracaine as a quencher of perylene fluorescence in micelles. *J Photochem Photobiol B: Biol* **7**:75–86.
190. Hutterer R, Krämer K, Schneider FW, Hof M. 1997. The localization of the local anesthetic tetracaine in phospholipid vesicles: a fluorescence quenching and resonance energy transfer study. *Chem Phys Lipids* **90**:11–23.
191. Winkler MH. 1969. A fluorescence quenching technique for the investigation of the configurations of binding sites for small molecules. *Biochemistry* **8**:2586–2590.
192. Berlman IB. 1973. Empirical study of heavy-atom collisional quenching of the fluorescence state of aromatic compounds in solution. *J Phys Chem* **77**(4):562–567.
193. Groenzin H, Mullins OC, Mullins WW. 1999. Resonant fluorescence quenching of aromatic hydrocarbons by carbon disulfide. *J Phys Chem A* **103**:1504–1508.
194. James DR, Ware WR. 1985. Multiexponential fluorescence decay of indole-3-alkanoic acids. *J Phys Chem* **89**:5450–5458.
195. Fonseca MM, Scifano HM, Carvalho-Alves PC, Barrabin H, Mignaco JA. 2002. Conformational changes of the nucleotide site of the plasma membrane  $\text{Ca}^{2+}$ -ATPase probed by fluorescence quenching. *Biochemistry* **41**:7483–7489.
196. Daems D, Boens N, Schryver FC. 1989. Fluorescence quenching with lindane in small unilamellar L, $\alpha$ -dimyristoylphosphatidylcholine vesicles. *Eur Biophys J* **17**:25–36.
197. Namiki A, Nakashima N, Yoshihara K. 1979. Fluorescence quenching due to the electron transfer: indole-chloromethanes in rigid ethanol glass. *J Chem Phys* **71**(2):925–930.
198. Johnson GE. 1980. Fluorescence quenching of carbazoles. *J Phys Chem* **84**:2940–2946.
199. Jones OT, Lee AG. 1985. Interactions of hexachlorocyclohexanes with lipid bilayers. *Biochim Biophys Acta* **812**:731–739.
200. Chao AC, Dix JA, Sellers MC, Verkman AS. 1989. Fluorescence measurement of chloride transport in monolayer cultured cells. *Biophys J* **56**:1071–1081.
201. Verkman AS. 1990. Development and biological applications of chloride-sensitive fluorescent indicators. *Am J Phys* **253**:C375–C388.
202. Martin A, Narayanaswamy R. 1997. Studies on quenching of fluorescence of reagents in aqueous solution leading to an optical chloride-ion sensor. *Sens Actuators B* **38–39**:330–333.
203. Bigger SW, Watkins PI, Verity B. 2000. Quinine fluorescence quenching at low ionic strength. *Int J Chem Kinet* **32**(8):473–477.
204. Hariharan C, Vijaysree V, Mishra AK. 1997. Quenching of 2,5-diphenyloxazole (PPO) fluorescence by metal ions. *J Luminesc* **75**: 205–211.
205. Morris SJ, Bradley D, Blumenthal R. 1985. The use of cobalt ions as a collisional quencher to probe surface charge and stability of fluorescently labeled bilayer vesicles. *Biochim Biophys Acta* **818**: 365–372.
206. Homan R, Eisenberg M. 1985. A fluorescence quenching technique for the measurement of paramagnetic ion concentrations at the membrane/water interface: intrinsic and X537A-mediated cobalt fluxes across lipid bilayer membranes. *Biochim Biophys Acta* **812**:485–492.
207. Salthammer T, Dreeskamp H, Birch DJS, Imhof RE. 1990. Fluorescence quenching of perylene by  $\text{Co}^{2+}$  ions via energy transfer in viscous and non-viscous media. *J Photochem Photobiol A: Chem.* **55**:53–62.
208. Holmes AS, Birch DJS, Suhling K, Imhof RE, Salthammer T, Dreeskamp H. 1991. Evidence for donor–donor energy transfer in lipid bilayers: perylene fluorescence quenching by  $\text{Co}^{2+}$  ions. *Chem Phys Lett* **186**(2,3):189–194.
209. Birch DJS, Suhling K, Holmes AS, Salthammer T, Imhof RE. 1992. Fluorescence energy transfer to metal ions in lipid bilayers. *SPIE* **1640**:707–718.
210. Perochon E, Tocanne J-F. 1991. Synthesis and phase properties of phosphatidylcholine labeled with 8-(2-anthroyl)octanoic acid, a solvatochromic fluorescent probe. *Chem Phys Lipids* **58**:7–17.
211. Fucaloro AF, Forster LS, Campbell MK. 1984. Fluorescence quenching of indole by dimethylformamide. *Photochem Photobiol* **39**:503–506.
212. Swadesh JK, Mui PW, Scheraga HA. 1987. Thermodynamics of the quenching of tyrosyl fluorescence by dithiothreitol. *Biochemistry* **26**:5761–5769.
213. Valentino MR, Boyd MK. 1995. Ether quenching of singlet excited 9-aryl-xanthyl cations. *J Photochem Photobiol* **89**:7–12.
214. Medinger T, Wilkinson F. 1965. Mechanism of fluorescence quenching in solution, I: quenching of bromobenzene. *Trans Faraday Soc* **61**:620–630.
215. Ahmad A, Durocher G. 1981. How hydrogen bonding of carbazole to ethanol affects its fluorescence quenching rate by electron acceptor quencher molecules. *Photochem Photobiol* **34**:573–578.
216. Bowen EJ, Metcalf WS. 1951. The quenching of anthracene fluorescence. *Proc Roy Soc London* **206A**:437–447.
217. Schmidt R, Janssen W, Brauer H-D. 1989. Pressure effect on quenching of perylene fluorescence by halonaphthalenes. *J Phys Chem* **93**:466–468.
218. Encinas MV, Rubio MA, Lissi E. 1983. Quenching and photobleaching of excited polycyclic aromatic hydrocarbons by carbon tetrachloride and chloroform in micellar systems. *Photochem Photobiol* **37**(2):125–130.
219. Behera PK, Mukherjee T, Mishra AK. 1995. Quenching of substituted naphthalenes fluorescence by chloromethanes. *J Luminesc* **65**: 137–142.
220. Behera PK, Mishra AK. 1993. Static and dynamic model for 1-naphthol fluorescence quenching by carbon tetrachloride in dioxane-acetonitrile mixtures. *J Photochem Photobiol A: Chem* **71**:115–118.
221. Behera PK, Mukherjee T, Mishra AK. 1995. Simultaneous presence of static and dynamic component in the fluorescence quenching for substituted naphthalene- $\text{CCl}_4$  system. *J Luminesc* **65**:131–136.
222. Zhang J, Roek DP, Chateauneuf JE, Brennecke JF. 1997. A steady-state and time-resolved fluorescence study of quenching reactions of anthracene and 1,2-benzanthracene by carbon tetrabromide and bromoethane in supercritical carbon dioxide. *J Amer Chem Soc* **119**:9980–9991.
223. Tucker SA, Cretella LE, Waris R, Street KW, Acree WE, Fetzer JC. 1990. Polycyclic aromatic hydrocarbon solute probes, VI: effect of

- dissolved oxygen and halogenated solvents on the emission spectra of select probe molecules. *Appl Spectrosc* **44**(2):269–273.
224. Wiczek WM, Latowski T. 1992. The effect of temperature on the fluorescence quenching of perylene by tetrachloromethane in mixtures with cyclohexane and benzene. *Z Naturforsch A* **47**:533–535.
225. Wiczek WM, Latowski T. 1986. Photophysical and photochemical studies of polycyclic aromatic hydrocarbons in solutions containing tetrachloromethane, I: fluorescence quenching of anthracene by tetrachloromethane and its complexes with benzene, p-xylene and mesitylene. *Z Naturforsch A* **41**:761–766.
226. Goswami D, Sarpal RS, Dogra SK. 1991. Fluorescence quenching of few aromatic amines by chlorinated methanes. *Bull Chem Soc Jpn* **64**:3137–3141.
227. Takahashi T, Kikuchi K, Kokubun H. 1980. Quenching of excited 2,5-diphenyloxazole by  $\text{CCl}_4$ . *J Photochem* **14**:67–76.
228. Bonesi SM, Erra-Balsells R. 2000. Outer-sphere electron transfer from carbazoles to halomethanes: reduction potentials of halomethanes measured by fluorescence quenching experiments. *J Chem Soc Perkin Trans 2*:1583–1595.
229. Canuel C, Badre S, Groenin H, Berheide M, Mullins OC. 2003. Diffusional fluorescence quenching of aromatic hydrocarbons. *Appl Spectrosc* **57**(5):538–544.
230. Alford PC, Cureton CG, Lampert RA, Phillips D. 1983. Fluorescence quenching of tertiary amines by halocarbons. *Chem Phys* **76**:103–109.
231. Lopez MM, Kosk-Kosicka D. 1998. Spectroscopic analysis of halothane binding to the plasma membrane  $\text{Ca}^{2+}$ -ATPase. *Biophys J* **74**: 974–980.
232. Eckenhoff RG, Tanner JW. 1998. Differential halothane binding and effects on serum albumin and myoglobin. *Biophys J* **75**:477–483.
233. Cavatorta P, Favilla R, Mazzini A. 1979. Fluorescence quenching of tryptophan and related compounds by hydrogen peroxide. *Biochim Biophys Acta* **578**:541–546.
234. Khwaja HA, Semeluk GP, Unger I. 1984. Quenching of the singlet and triplet state of benzene in condensed phase. *Can J Chem* **62**:1487–1491.
235. Washington K, Sarasua MM, Koehler LS, Koehler KA, Schultz JA, Pedersen LG, Hiskey RG. 1984. Utilization of heavy-atom effect quenching of pyrene fluorescence to determine the intramembrane distribution of halothane. *Photochem Photobiol* **40**(6):693–701.
236. Mae M, Wach A, Najbar J. 1991. Solvent effects on the fluorescence quenching of anthracene by iodide ions. *Chem Phys Lett* **176**(2): 167–172.
237. Frajji LK, Hayes DM, Werner TC. 1992. Static and dynamic fluorescence quenching experiments for the physical chemistry laboratory. *J Chem Educ* **69**:424–428.
238. Vos R, Engelborghs Y. 1994. A fluorescence study of tryptophan–histidine interactions in the peptide alantin and in solution. *Photochem Photobiol* **60**(1):24–32.
239. Nakashima K, Tanida S, Miyamoto T, Hashimoto S. 1998. Photoinduced electron transfer from indolic compounds to 1-pyrenemethanol in polystyrene latex dispersions. *J Photochem Photobiol A: Chem* **117**:111–117.
240. Novaira AI, Avila V, Montich GG, Previtali CM. 2001. Fluorescence quenching of anthracene by indole derivatives in phospholipid bilayers. *J Photochem Photobiol B: Biol* **60**:25–31.
241. Marmé N, Knemeyer J-P, Sauer M, Wolfrum J. 2003. Inter- and Intramolecular fluorescence quenching of organic dyes by tryptophan. *Bioconjugate Chem* **14**:1122–1139.
242. Lakowicz JR, Anderson CJ. 1980. Permeability of lipid bilayers to methylmercuric chloride: quantification by fluorescence quenching of a carbazole-labeled phospholipid. *Chem–Biol Interact* **30**:309–323.
243. Holmes AS, Suhling K, Birch DJS. 1993. Fluorescence quenching by metal ions in lipid bilayers. *Biophys Chem* **48**:193–204.
244. Birch DJS, Suhling K, Holmes AS, Salthammer T, Imhof RE. 1993. Metal ion quenching of perylene fluorescence in lipid bilayers. *Pure Appl Chem* **65**(8):1687–1692.
245. Sawicki E, Stanley TW, Elbert WC. 1964. Quenchofluorometric analysis for fluoranthenic hydrocarbons in the presence of other types of aromatic hydrocarbon. *Talanta* **11**:1433–1441.
246. Dreeskamp H, Koch E, Zander M. 1975. On the fluorescence quenching of polycyclic aromatic hydrocarbons by nitromethane. *Z Naturforsch A* **30**:1311–1314.
247. Pandey S, Fletcher KA, Powell JR, McHale MER, Kauppila A-SM, Acree WE, Fetzer JC, Dai W, Harvey RG. 1997. Spectrochemical investigations of fluorescence quenching agents, 5: effect of surfactants on the ability of nitromethane to selectively quench fluorescence emission of alternant PAHs. *Spectrosc Acta Part A* **53**:165–172.
248. Pandey S, Acree WE, Cho BP, Fetzer JC. 1997. Spectroscopic properties of polycyclic aromatic compounds, 6: the nitromethane selective quenching rule revisited in aqueous micellar zwitterionic surfactant solvent media. *Talanta* **44**:413–421.
249. Acree WE, Pandey S, Tucker SA. 1997. Solvent-modulated fluorescence behavior and photophysical properties of polycyclic aromatic hydrocarbons dissolved in fluid solution. *Curr Top Solution Chem* **2**:1–27.
250. Tucker SA, Acree WE, Tanga MJ, Tokita S, Hiruta K, Langhals H. 1992. Spectroscopic properties of polycyclic aromatic compounds: examination of nitromethane as a selective fluorescence quenching agent for alternant polycyclic aromatic nitrogen hetero-atom derivatives. *Appl Spectrosc* **46**(2):229–235.
251. Yang RH, Wang KM, Xiao D, Luo K, Yang XH. 2000. A renewable liquid drop sensor for di- or trinitrophenol based on fluorescence quenching of 3,3',5,5'-tetramethylbenzidine dihydrochloride. *Analyst* **125**: 877–882.
252. Wentzell PD, Nair SS, Guy RD. 2001. Three-way analysis of fluorescence spectra of polycyclic aromatic hydrocarbons with quenching by nitromethane. *Anal Chem* **73**:1408–1415.
253. Patra D, Mishra AK. 2001. Fluorescence quenching of benzo[k]fluoranthene in poly(vinyl alcohol) film: a possible optical sensor for nitro aromatic compounds. *Sens Actuators B* **80**:278–282.
254. Goodpaster JV, McGuffin VL. 2001. Fluorescence quenching as an indirect detection method for nitrated explosives. *Anal Chem* **73**: 2004–2011.
255. Ellison EH, Thomas JK. 2001. Enhanced quenching of anthracene fluorescence by nitroalkanes in zeolite X and Y. *Langmuir* **17**:2446–2454.
256. Goodpaster JV, Harrison JF, McGuffin VL. 2002. Ab initio study of selective fluorescence quenching of polycyclic aromatic hydrocarbons. *J Phys Chem A* **106**:10645–10654.

257. Koivusalo M, Alvesalo J, Virtanen JA, Somerharju P. 2004. Partitioning of pyrene-labeled phosphor- and sphingolipids between ordered and disordered bilayer domains. *Biophys J* **86**:923–935.
258. Bieri VG, Wallach DFH. 1975. Fluorescence quenching in lecithin: cholesterol liposomes by paramagnetic lipid analogues: introduction of new probe approach. *Biochim Biophys Acta* **389**:413–427.
259. Encinas MV, Lissi EA, Alvarez J. 1994. Fluorescence quenching of pyrene derivatives by nitroxides microheterogeneous systems. *Photochem Photobiol* **59**(1):30–34.
260. Matko J, Ohki K, Edidin M. 1992. Luminescence quenching by nitroxide spin labels in aqueous solution: studies on the mechanism of quenching. *Biochemistry* **31**:703–711.
261. Fayed TA, Grampp G, Landgraf M. 1999. Fluorescence quenching of aromatic hydrocarbons by nitroxide radicals: a mechanistic study. *Int J Photoenergy* **1**:1–4.
262. Green JA, Singer LA, Parks JH. 1973. Fluorescence quenching by the stable free radical di-t-butylnitroxide. *J Chem Phys* **58**(7):2690–2659.
263. Lozinsky E, Martin VV, Berezina TA, Shames AI, Weis AL, Likhtenshtein GI. 1999. Dual fluorophore-nitroxide probes for analysis of vitamin C in biological liquids. *J Biochem Biophys Methods* **38**:29–42.
264. Kalai T, Hideg E, Jeko J, Hideg K. 2003. Synthesis of paramagnetic BODIPY dyes as new double (spin and fluorescence) sensors. *Tetrahedron Lett* **44**:8497–8499.
265. Grenier S, Dutta AK, Salesse C. 1998. Evaluation of membrane penetration depth utilizing fluorescence quenching by doxylated fatty acids. *Langmuir* **14**:4643–4649.
266. Szajdzinska-Pietek E, Wolszczak M. 1998. Quenching of excited states or pyrene derivatives by amphiphilic nitroxide radicals in cationic micellar solutions: dynamics and location of the guest molecules in the aggregates. *J Photochem Photobiol A: Chem* **112**:245–249.
267. Jones PF, Siegel S. 1971. Quenching of naphthalene luminescence by oxygen and nitric oxide. *J Chem Phys* **54**(8):3360–3366.
268. Denicola A, Batthyány C, Lissi E, Freeman BA, Rubbo H, Radi R. 2002. Diffusion of nitric oxide into low-density lipoprotein. *J Biol Chem* **277**(2):932–936.
269. Harper J, Sailor MJ. 1996. Detection of nitric oxide and nitrogen dioxide with photoluminescent porous silicon. *Anal Chem* **68**:3713–3717.
270. Denicola A, Souza JM, Radi R, Lissi E. 1996. Nitric oxide diffusion in membranes determined by fluorescence quenching. *Arch Biochem Biophys* **328**(1):208–212.
271. Ware WR, Holmes JD, Arnold DR. 1974. Exciplex photophysics, II: fluorescence quenching of substituted anthracenes by substituted 1,1-diphenylethylenes. *J Am Chem Soc* **96**:7861–7864.
272. Labianca DA, Taylor GN, Hammond GS. 1972. Structure-reactivity factors in the quenching of fluorescence from naphthalenes by conjugated dienes. *J Am Chem Soc* **94**(11):3679–3683.
273. Encinas MV, Guzman E, Lissi EA. 1983. Intramicellar aromatic hydrocarbon fluorescence quenching by olefins. *J Phys Chem* **87**: 4770–4772.
274. Abuin EB, Lissi EA. 1993. Quenching rate constants in aqueous solution: influence of the hydrophobic effect. *J Photochem Photobiol* **71**:263–267.
275. Chang SLP, Schuster DI. 1987. Fluorescence quenching of 9,10-dicyanoanthracene by dienes and alkenes. *J Phys Chem* **91**:3644–3649.
276. Eriksen J, Foote CS. 1978. Electron-transfer fluorescence quenching and exciplexes of cyano-substituted anthracenes. *J Phys Chem* **82**: 2659–2662.
277. Cioni P. 2000. Oxygen and acrylamide quenching of protein phosphorescence: correlation with protein dynamics. *Biophys Chem* **87**: 15–24.
278. Jameson DM, Gratton E, Weber G, Alpert B. 1984. Oxygen distribution and migration within MB<sup>DES FE</sup> and HB<sup>DES FE</sup>. *Biophys J* **45**: 795–803.
279. Canuel C, Badre S, Groenzin H, Berheide M, Mullins OC. 2003. Diffusional fluorescence quenching of aromatic hydrocarbons. *Appl Spectrosc* **57**(5):538–544.
280. Gouterman M. 1997. Oxygen quenching of luminescence of pressure sensitive paint for wind tunnel research. *J Chem Educ* **74**(6): 697–702.
281. Camyshan SV, Gritsan NP, Korolev VV, Bazhin NM. 1990. Quenching of the luminescence of organic compounds by oxygen in glassy matrices. *Chem Phys* **142**:59–68.
282. Kikuchi K, Sato C, Watabe M, Ikeda H, Takahashi Y, Miyashi T. 1993. New aspects on fluorescence quenching by molecular oxygen. *J Am Chem Soc* **115**:5180–5184.
283. Vaughan WM, Weber G. 1970. Oxygen quenching of pyrenebutyric acid fluorescence in water: a dynamic probe of the microenvironment. *Biochemistry* **9**:464–473.
284. Abuin EB, Lissi EA. 1991. Diffusion and concentration of oxygen in microheterogeneous systems: evaluation from luminescence quenching data. *Prog React Kinet* **16**:1–33.
285. Parasassi T, Gratton E. 1992. Packing of phospholipid vesicles studies by oxygen quenching of laurdan fluorescence. *J Fluoresc* **2**(3): 167–174.
286. Lu X, Winnik MA. 2001. Luminescence quenching in polymer/filler nanocomposite films using in oxygen sensors. *Chem Mater* **13**: 3449–3463.
287. Okamoto M. 2001. Temperature dependence of the nearly diffusion-controlled fluorescence quenching by oxygen of 9,10-dimethylanthracene in liquid solution. *Phys Chem Chem Phys* **3**:3696–3700.
288. Okamoto M, Wada O, Tanaka F, Hirayama S. 2001. Fluorescence quenching by oxygen of 9,10-dimethylanthracene in liquid and supercritical carbon dioxide. *J Phys Chem* **105**:566–572.
289. Poulsen L, Zebger I, Klinger M, Eldrup M, Sommer-Larsen P, Ogilby PR. 2003. Oxygen diffusion in copolymers of ethylene and norbornene. *Macromolecules* **36**:7189–7198.
290. Brunori M, Cutruzzolà F, Savino C, Travagliini-Allocatelli C, Vallone B, Gibson QH. 1999. Structural dynamics of ligand diffusion in the protein matrix: a study on a new myoglobin mutant Y(B10) Q(E7) R(E10). *Biophys J* **76**:1259–1269.
291. Encinas MV, Lissi EA. 1983. Intramicellar quenching of 2,3-dimethylnaphthalene fluorescence by peroxides and hydroperoxides. *Photochem Photobiol* **37**(3):251–255.
292. Holmes LG, Robbins FM. 1974. Quenching of tryptophyl fluorescence in proteins by N'-methylnicotinamide chloride. *Photochem Photobiol* **19**:361–366.

293. Mao C, Tucker SA. 2002. High-performance liquid chromatographic separation of polycyclic aromatic hydrocarbons using pyridinium chloride as a selective fluorescence quencher to aid detection. *J Chromatogr A* **966**:53–61.
294. Diaz X, Abuin E, Lissi E. 2003. Quenching of BSA intrinsic fluorescence by alkylpyridinium cations its relationship to surfactant-protein association. *J Photochem Photobiol A: Chem* **155**:157–162.
295. Strom C, Hansson P, Jonsson B, Soderman O. 2000. Size of cationic surfactant micelles at the silica–water interface: a fluorescent probe study. *Langmuir* **16**:2469–2474.
296. Saha SK, Krishnamoorthy G, Dogra SK. 1999. Fluorescence quenching of 2-aminofluorene by cetylpyridinium chloride, iodide ion and acrylamide in non-ionic micelles: tweens. *J Photochem Photobiol A: Chem* **121**:191–198.
297. Martin MM, Ware WR. 1978. Fluorescence quenching of carbazole by pyridine and substituted pyridines: radiationless processes in the carbazole-amine hydrogen bonded complex. *J Phys Chem* **82**(26): 2770–2776.
298. Dreeskamp H, Laufer A, Zander M. 1983. Lösung der perylen-fluoreszenz durch  $\text{Ag}^+$ -ionen. *Z Naturforsch A* **38**:698–700.
299. Badley RA. 1975. The location of protein in serum lipoproteins: a fluorescence quenching study. *Biochim Biophys Acta* **379**:517–528.
300. Eftink MR, Ghiron CA. 1984. Indole fluorescence quenching studies on proteins and model systems: use of the inefficient quencher succinimide. *Biochemistry* **23**:3891–3899.
301. Razek TMA, Miller MJ, Hassan SSM, Arnold MA. 1999. Optical sensor for sulfur dioxide based on fluorescence quenching. *Talanta* **50**:491–498.
302. Moore H-PH, Raftery MA. 1980. Direct spectroscopic studies of cation translocation by *Torpedo* acetylcholine receptor on a time scale of physiological relevance. *Proc Natl Acad Sci USA* **77**(8): 4509–4513.
303. Mac M, Najbar J, Phillips D, Smith TA. 1992. Solvent dielectric relaxation properties and the external heavy atom effect in the time-resolved fluorescence quenching of anthracene by potassium iodide and potassium thiocyanate in methanol and ethanol. *J Chem Soc Faraday Trans* **88**(20):3001–3005.
304. Carrigan S, Doucette S, Jones C, Marzzacco CJ, Halpern AM. 1996. The fluorescence quenching of 5,6-benzoquinoline and its conjugate acid by  $\text{Cl}^-$ ,  $\text{Br}^-$ ,  $\text{SCN}^-$  and  $\text{I}^-$  ions. *J Photochem Photobiol A: Chem* **99**:29–35.
305. Horrochs AR, Kearvell A, Tickle K, Wilkinson F. 1966. Mechanism of fluorescence quenching in solution, II: quenching by xenon and intersystem crossing efficiencies. *Trans Faraday Soc* **62**:3393–3399.
306. Thulborn KR, Sawyer WH. 1978. Properties and the locations of a set of fluorescent probes sensitive to the fluidity gradient of the lipid bilayer. *Biochim Biophys Acta* **511**:125–140.
307. Ware WR, Andre JC. 1980. The influence of diffusion fluorescence quenching. In *Time-resolved fluorescence spectroscopy in biochemistry and biology*, pp. 363–392. Ed RB Cundall, R Dale. Plenum Press, New York.
308. Nelson G, Warner IM. 1990. Fluorescence quenching studies of cyclodextrin complexes of pyrene and naphthalene in the presence of alcohols. *J Phys Chem* **94**:576–581.
309. Peviani C, Hillen W, Ettner N, Lami H, Doglia SM, Piemont E, Ellouze C, Chabbert M. 1995. Spectroscopic investigation of tet

repressor tryptophan-43 upon specific and nonspecific DNA binding. *Biochemistry* **34**:13007–13015.

## PROBLEMS

- P8.1. *Interpretation of Apparent Bimolecular Quenching Constants:* Calculate the apparent bimolecular quenching constant of 2-anthroyloxypalmitate (2-AP) for quenching by copper or dimethylaniline (Figure 8.71). Assume the unquenched lifetime is 10 ns. Interpret these values with respect to the maximum value of  $k_q$  possible in aqueous solution.

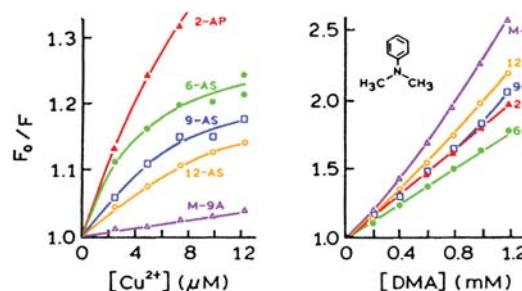


**Figure 8.71.** Quenching of the anthroyloxy probes by a water-soluble quencher,  $\text{Cu}^{2+}$ , and by a lipid-soluble quencher, dimethylaniline (DMA). Revised and reprinted from [306]. Copyright © 1978, Elsevier Science.

- P8.2. *Oxygen Bimolecular Quenching Constant in a Membrane:* Use the data in Figure 8.72 to calculate  $k_q$  for oxygen quenching of pyrene in DMPC vesicles.

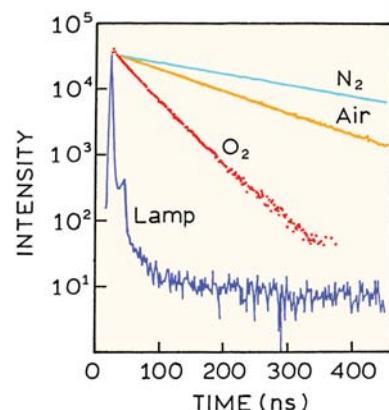


**Figure 8.72.** Intensity decays of pyrene in dimyristoyl phosphatidylcholine (DMPC) vesicles at 25°C, equilibrated with various partial pressure of oxygen. Revised and reprinted with permission from [58]. Copyright © 1975, Rockefeller University Press.

P8.3. *Quenching in the Presence of Cyclodextrins:* Figure 8.73 shows iodide quenching of naphthalene with 3 mM  $\beta$ -cyclodextrin. Figure 8.74 shows iodide quenching of naphthalene with 1% v/v benzyl alcohol with increasing amounts of  $\beta$ -CD. Assume the unquenched lifetime of naphthalene is 45 ns. Explain the results.

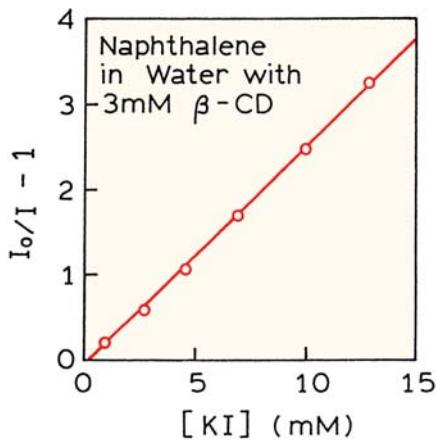


**Figure 8.73.** Quenching of naphthalene by iodide in the presence of 3.00 mM  $\beta$ -cyclodextrin. Revised and reprinted with permission from [308]. Copyright © 1990, American Chemical Society.

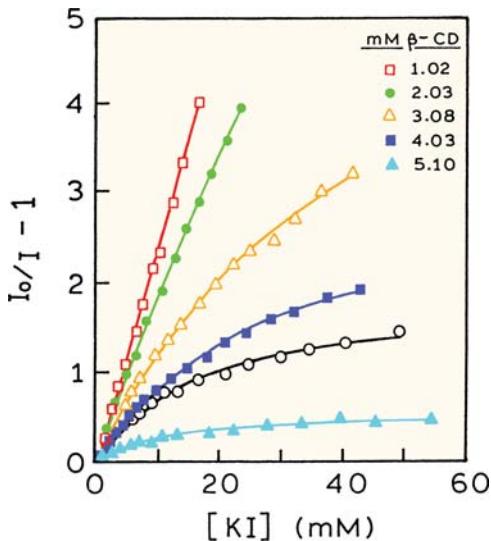


**Figure 8.74.** Quenching of naphthalene by iodide in the presence of benzyl alcohol (1% V/V) at various  $\eta$ -CD concentrations. Revised and reprinted with permission from [308]. Copyright © 1990, American Chemical Society.

P8.4. *Separation of Static and Dynamic Quenching of Acridone by Iodide:*<sup>176</sup> The following data were obtained for quenching of acridone in water at 26°C.  $\text{KNO}_2$  is used

to maintain a constant ionic strength, and does not quench the fluorescence of acridone.

M KI	M $\text{KNO}_2$	$F_0/F$
0.0	1.10	1.0
0.04	1.06	4.64
0.10	1.00	10.59
0.20	0.90	23.0
0.30	0.80	37.2
0.50	0.60	68.6
0.80	0.30	137.0

- A. Construct a Stern-Volmer plot.
- B. Determine the dynamic ( $K_D$ ) and static ( $K_S$ ) quenching constants. Use the quadratic equation to obtain  $K_D$  and  $K_S$  from the slope and intercept of a plot of  $K_{app}$  versus  $[Q]$ .
- C. Calculate the observed bimolecular quenching constant. The unquenched lifetime  $\tau_0 = 17.6$  ns.
- D. Calculate the diffusion limited bimolecular quenching constant, and the quenching efficiency. The diffusion constant of KI in water is  $2.065 \times 10^{-5} \text{ cm}^2/\text{s}$  for 1 M KI (*Handbook of Chemistry and Physics*, 55th Edition).
- E. Comment on the magnitude of the sphere of action and the static quenching constant, with regard to the nature of the complex.

P8.5. *Separation of Static and Dynamic Quenching:* The following table lists the fluorescence lifetimes and relative quantum yield of 10-methylacridinium chloride (MAC) in the presence of adenosine monophosphate (AMP).<sup>18</sup>

[AMP] (mM)	$\tau$ (ns)	Intensity
0	32.9	1.0
1.75	26.0	0.714
3.50	21.9	0.556
5.25	18.9	0.426
7.00	17.0	0.333

- A. Is the quenching dynamic, static, or both?
- B. What is (are) the quenching constant(s)?
- C. What is the association constant for MAC-AMP complex?
- D. Comment on the magnitude of the static quenching constant.
- E. Assume the MAC-AMP complex is completely nonfluorescent, and complex formation shifts the absorption spectrum of MAC. Will the corrected excitation spectrum of MAC, in the presence of non-saturating amounts of AMP, be comparable to the absorption spectrum of MAC or the MAC-AMP complex?

**P8.6. Effects of Dissolved Oxygen on Fluorescence Intensities and Lifetimes:** Oxygen is known to dissolve in aqueous and organic solutions, and is a collisional quencher of fluorescence. Assume your measurements are accurate to 3%. What are the lifetimes above which dissolved oxygen from the atmosphere will result in changes in the fluorescence intensities or lifetimes that are outside your accuracy limits? Indicate these lifetimes for both aqueous and ethanolic solutions. The oxygen solubility in water is 0.001275 M for a partial pressure of one atmosphere. Oxygen is fivefold more soluble in ethanol than in water. The following information is needed to answer this question:

$$k_q \text{ (in water)} = 1 \times 10^{10} \text{ M}^{-1} \text{ s}^{-1}$$

$$k_q \text{ (in ethanol)} = 2 \times 10^{10} \text{ M}^{-1} \text{ s}^{-1}$$

**P8.7. Intramolecular Complex Formation by Flavin-Adenine Dinucleotide (FAD):** FAD fluorescence is quenched by both static complex formation between the flavin and adenine rings, and by collisions between these two moieties. Flavin mononucleotide (FMN) is similar to FAD except that it lacks the adenine ring. Use the following data for FAD and FMN to calculate the fraction complexed ( $f$ ) and the collisional deactivation rate ( $k$ ) of the flavin by the adenine ring.  $Q$  is the relative quantum yield. Note that the deactivation rate is in  $\text{s}^{-1}$ :

$$\tau (\text{FMN}) = 4.6 \text{ ns}$$

$$\tau (\text{FAD}) = 2.4 \text{ ns}$$

$$Q (\text{FMN}) = 1.0 \text{ (assumed unity)}$$

$$Q (\text{FAD}) = 0.09$$

**P8.8. Quenching of Protein Fluorescence: Determination of the Fraction of the Total Fluorescence Accessible to Iodide:** Assume a protein contains four identical subunits, each containing two tryptophan residues. The following data are obtained in the presence of iodide.

[I <sup>-</sup> ] M	Fluorescence intensity
0.00	1.0
0.01	0.926
0.03	0.828
0.05	0.767
0.10	0.682
0.20	0.611
0.40	0.563

- A. What fraction of the total tryptophan fluorescence is accessible to quenching? Which property of the

Stern-Volmer plots does indicate an inaccessible fraction?

- B. Assume all the tryptophans have equal quantum yields and lifetimes (5 ns). How many tryptophan residues are accessible to quenching?
- C. What are the bimolecular quenching constants for the accessible and inaccessible residues?
- D. Assume you could selectively excite the accessible tryptophans by excitation at 300 nm. Draw the predicted Stern-Volmer and modified Stern-Volmer plots for the accessible and the inaccessible residues.

**P8.9. Quenching of Endonuclease III:** Figure 8.75 shows the effect of a 19-mer of poly(dAdT) on the intrinsic tryptophan emission of Endo III. Explain the data in terms of the structure of Endo III (Figure 8.15). Is it the quenching collisional or static? Assume the unquenched decay time is 5 ns. The concentration of Endo III is 0.8 μM.

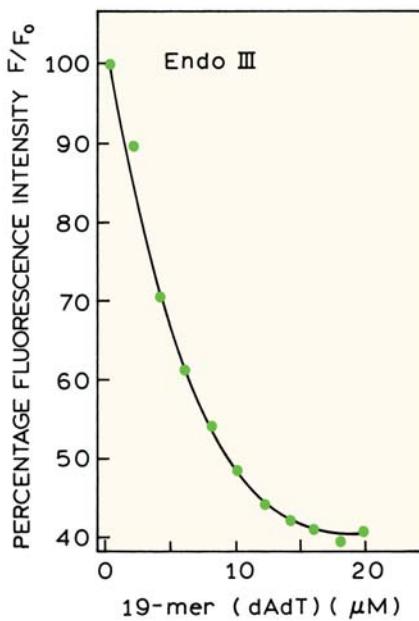


**Figure 8.75.** Fluorescence intensity of Endo III with increasing concentrations of a 19-mer of poly(dAdT). Revised and reprinted with permission from [42]. Copyright © 1995, American Chemical Society.

**P8.10. Quenching of the Tet Repressor F75:** Figure 8.76 shows the emission spectra of the W75F mutant of the tet repressor in the absence and presence of bound operator. Explain the extent of quenching. Predict the extent of quenching for the wild-type protein.

- P8.11. *Intramolecular Quenching*: Figure 8.67 showed intensity decay data for DBO with a quencher collision rate of  $9 \times 10^6 \text{ s}^{-1}$ . Calculate the decrease in DBO intensity

due to guanine quenching. Also calculate the relative intensity ( $F/F_0$ ) expected for a fluorophore with a lifetime of 2 ns or 2 ms.

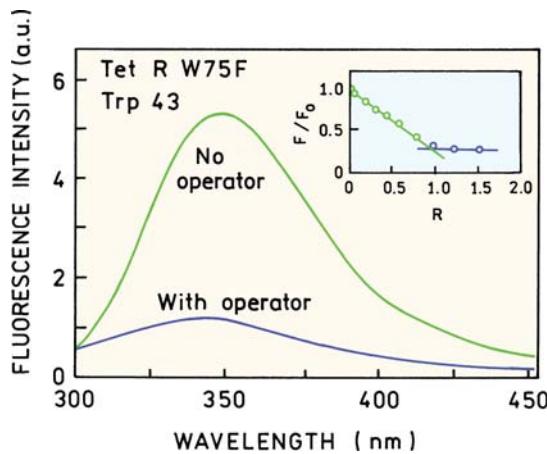


**Figure 8.76.** Emission spectra of Trp 43 in tet repressor W75F in the absence and presence of a 76-bp operator. In the insert the concentration of Tet R dimer is  $1 \mu\text{M}$  and the ratio refers to the molar ratio of operator to dimer. Revised and reprinted with permission from [309]. Copyright © 1995, American Chemical Society.

# 9

# Mechanisms and Dynamics of Fluorescence Quenching

In the previous chapter we described the basic principles and biochemical applications of quenching. Quenching requires molecular contact between the fluorophore and quencher. This contact can be due to diffusive encounters, which is dynamic quenching, or due to complex formation, which is static quenching. Because of the close distance interaction required for quenching, the extent of quenching is sensitive to molecular factors that affect the rate and probability of contact, including steric shielding and charge–charge interactions. In contrast, resonance energy transfer is a through-space interaction that occurs over longer distances and is insensitive to these factors.

In this chapter we describe quenching in more detail. Initially we compare quenching with resonance energy transfer, which illustrates the different types of interactions for these two processes. We then describe the different types of chemical and/or electronic interactions that cause quenching. These interactions include intersystem crossing, electron exchange, and photoinduced electron transfer. Since quenching occurs over short distances, diffusion is needed for efficient quenching. This results in transient effects, which cause the intensity decays to become non-exponential. This effect can complicate interpretation of the time-resolved data, but also provide additional information about the distances and dynamics of quenching.

## 9.1. COMPARISON OF QUENCHING AND RESONANCE ENERGY TRANSFER

Any process that causes a decrease in intensity can be considered to be quenching. Quenching results in dissipation of the fluorophore's electronic energy as heat. Resonance energy transfer (RET) decreases the intensity of the donor and transfers the energy to an acceptor. The acceptor can be

fluorescent or nonfluorescent, but in both cases the fluorescence intensity of the initially excited molecule is decreased. Comparison of RET and quenching clarifies the nature of both processes. Figure 9.1 shows a molecular orbital schematic for RET. The fluorophore initially has two electrons in the highest-occupied (HO) molecular orbital. Absorption of light results in elevation of one electron to the lowest-unoccupied (LU) orbital. When RET occurs the electron in the excited donor ( $D_R^*$ ) returns to the ground state. Simultaneously an electron in the acceptor ( $A_R$ ) goes into a higher excited-state orbital. If the acceptor is fluorescent it may then emit. If the acceptor is nonfluorescent the energy is dissipated as heat. The mechanism of RET is the same whether the acceptor is fluorescent or nonfluorescent: simultaneous electron transitions in  $D_R$  and  $A_R$ . The subscript R refers to RET and will be used to distinguish RET from other mechanisms of quenching discussed in this chapter.

It is informative to consider the size of the fluorophores as compared to the distances for RET.<sup>1–3</sup> The donor and acceptor molecules in Figure 9.1 are drawn roughly to scale relative to the Förster distance  $R_0$ , which is the distance at which RET is 50% efficient. From comparison of the distance for RET with the size of the molecules, one can see that RET is a through-space interaction. The assumed Förster distance of 30 Å is too large for direct interaction between the electron clouds in the molecules. This schematic also shows that RET does not require molecular contact between  $D_R$  and  $A_R$ . For this reason RET is not sensitive to steric factors or electrostatic interactions.

Figure 9.2 shows a schematic for quenching, again drawn to scale. For quenching to occur the fluorophore (F) and quencher (Q) have to come into molecular contact, allowing the electron clouds of both molecules to interact.

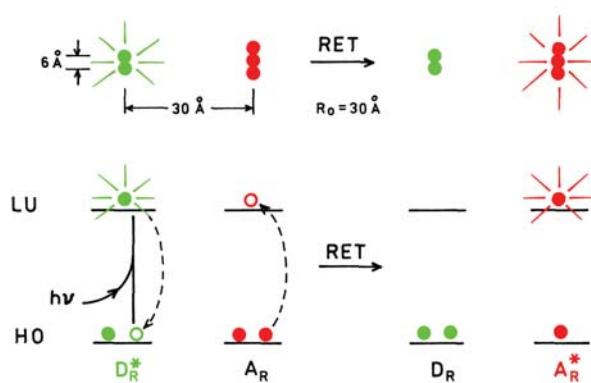


**Figure 9.1.** Molecular orbital schematic for resonance energy transfer. The top row shows the size of fluorophores relative to the Förster distance  $R_0$ . The bottom row shows the LU orbital of the donor emitting light and the HO orbital of the acceptor.

The electron density falls off very rapidly with distance from the surface of the molecules, typically decreasing as  $\exp[-\beta(r - r_c)]$  where  $1/\beta$  is near  $1 \text{ \AA}$ ,  $r$  is the center-to-center distance, and  $r_c$  is the center-to-center distance upon molecular contact. This interaction becomes insignificant for distances  $r$  larger than several angstroms.

Because the electron clouds are strongly localized, quenching requires molecular contact at the van der Waals radii. When the quencher comes in contact with the excited fluorophore its excited electron in the LU orbital returns to the ground state. The fluorophore cannot emit, and the energy is dissipated as heat. In Figure 9.2 the quencher is shown as remaining in the ground state. Depending on the mechanism, this may occur or the quencher can also go to an excited state, which then returns to the ground state. The important point is that quenching is due to short-range interactions between F and Q, and RET is due to long-range interactions between F and Q.

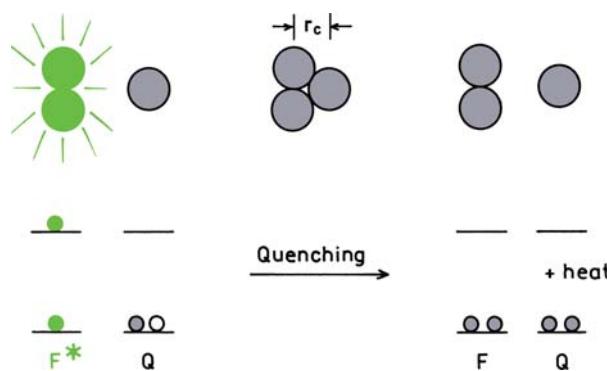


**Figure 9.2.** Schematic of fluorescence quenching.

dipolar interactions through  $D_R^*$  and  $A_R$ . The different distance dependence of quenching and RET results in different molecular information being available from each phenomenon. The description of quenching in Figure 9.2 is purely phenomenological and does not consider the nature of the interaction between  $F^*$  and  $Q$ .

### 9.1.1. Distance Dependence of RET and Quenching

It is informative to examine simulations on the distance dependence of RET and quenching between the molecules. The rate of energy transfer is given by

$$k_T(r) = \frac{1}{\tau_D} \left( \frac{R_0}{r} \right)^6 \quad (9.1)$$

where  $\tau_D$  is the donor lifetime in the absence of acceptor,  $r$  is the center-to-center distance between  $D_R$  and  $A_R$ , and  $R_0$  is the Förster distance.

The rate of quenching depends on the extent of interaction between the electron clouds in F and Q. Since the electron density decreases exponentially with distance from the nuclei, the rate of quenching depends on the distance according to

$$k_E(r) = A \exp[-\beta(r - r_c)] \quad (9.2)$$

where  $r$  is the center-to-center distance between F and Q, and  $r_c$  is the distance of closest approach at molecular contact. For interactions between orbitals,  $A$  is expected to have a value near  $10^{13} \text{ s}^{-1}$ . The values of  $\beta$  are typically near  $1 \text{ \AA}^{-1}$ . These interactions between orbitals are usually called electron exchange ( $E$ ) or exchange interactions because electrons can move between the molecules at these short distances. Equation 9.2 describes the quenching rate for a fluorophore and quencher at a distance  $r$ . This equation does not include the effect of diffusion on quenching.

Equations 9.1 and 9.2 can be used to show how RET and quenching depends on distance. Figure 9.3 shows simulated values for  $k_T(r)$  and  $k_E(r)$ . For RET we assumed  $\tau_D = 1 \text{ ns}$  and  $R_0 = 30 \text{ \AA}$ . The rate of energy transfer remains high for distances of  $20 \text{ \AA}$  or longer. The right-side axis shows the rate constant as the frequency of transfer events. For  $D_R$  and  $A_R$  at a distance of  $20 \text{ \AA}$ , the frequency of events is about tenfold larger than the reciprocal lifetime or emission frequency. This shows that at  $20 \text{ \AA}$  RET can occur about

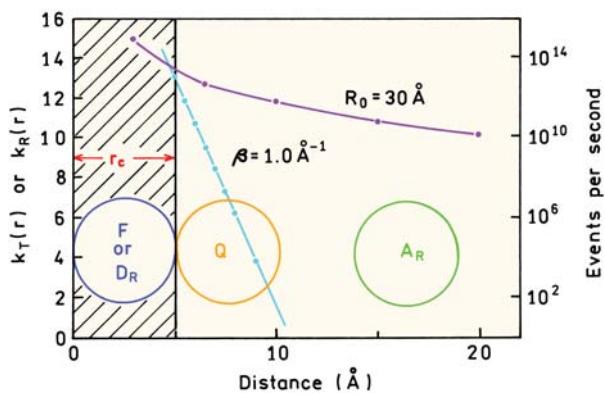


**Figure 9.3.** Distance-dependent rate constants for RET and exchange interactions. For these simulations  $\tau_D = 1 \text{ ns}$ ,  $R_0 = 30 \text{ \AA}$ ,  $\beta = \text{\AA}^{-1}$ , and  $r_c = 5 \text{ \AA}$ .

tenfold faster than emission, and will thus be about 90% efficient.

The dependence on distance is remarkably different for electron exchange. The value of  $k_E(r)$  drops rapidly with distance. When the nuclei are 10 Å apart, with  $r_c = 5 \text{ \AA}$ , the electron clouds are 5 Å apart. At this short distance, the exchange rate of  $10^4$  is much smaller than the emission rate of  $10^9$ , so that essentially no exchange will occur during the 1 ns lifetime. When the distance between the electron clouds is less than 2 Å and  $r_c = 7 \text{ \AA}$ , the exchange rate has already decreased to less than the emission rate, so that the quenching is less than 100% efficient. This result shows that close molecular contact is needed for quenching.

Another way to compare RET and quenching is to consider the RET transfer efficiency  $E_T$  or the quenching efficiency  $Q_E$  (Figure 9.4). These efficiencies were calculated using the same parameter values as used in Figure 9.3. The RET efficiency can be calculated using

$$E_T = \frac{k_T(r)}{\gamma + k_T(r)} \quad (9.3)$$

where  $\gamma = \tau_D^{-1}$  is the donor decay rate in the absence of acceptor. The quenching efficiency can be calculated using

$$Q_E = \frac{k_E(r)}{\gamma + k_E(r)} \quad (9.4)$$

These calculations show that RET is efficient over long distances, but quenching is efficient only at very short distances, when the electron clouds are within 2 Å. While eqs.

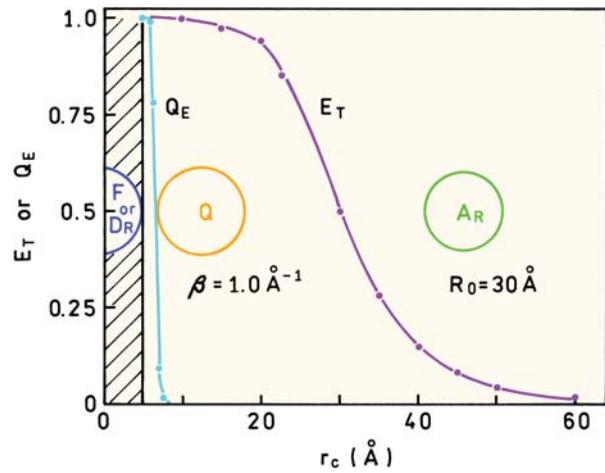


**Figure 9.4.** Calculated efficiencies for resonance energy transfer  $E_T$  and for quenching  $Q_E$ . The parameter values are the same as used in Figure 9.3.

9.3 and 9.4 appear similar, there is an important difference. In eq. 9.3 the rate  $k_T(r)$  contains a factor  $\gamma = \tau_D^{-1}$ , so that the RET efficiency is independent of the donor decay time. In eq. 9.4 the exchange rate  $k_E(r)$  is independent of the fluorophore decay time. For this reason the quenching occurs over longer distances for longer decay time fluorophores. However, this effect is modest and very long lifetimes are needed to substantially increase the transfer distance.

### 9.1.2. Encounter Complexes and Quenching Efficiency

Unless the quencher concentrations are very high, significant quenching requires diffusion to bring the molecules into contact. Figure 9.5 shows a kinetic scheme for quenching. The molecules come in contact by the bimolecular rate constant  $k_0$ . Upon collision the molecules form an encounter complex. This complex can proceed to quenching with a rate constant  $k(r)$ , or break apart with a rate constant  $k_2$ . The efficiency of quenching is given by

$$E_Q = \frac{k(r)}{k_2 + k(r)} \quad (9.5)$$

Typically,  $k(r)$  is much larger than  $k_2$ , so that each encounter results in quenching. Some authors consider the possibility of emission from the encounter complex, in which case an additional term,  $\gamma = \tau_D^{-1}$ , appears in the denominator of eq. 9.5.<sup>4-5</sup>

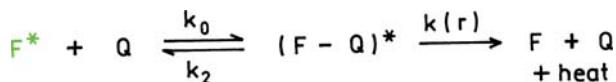


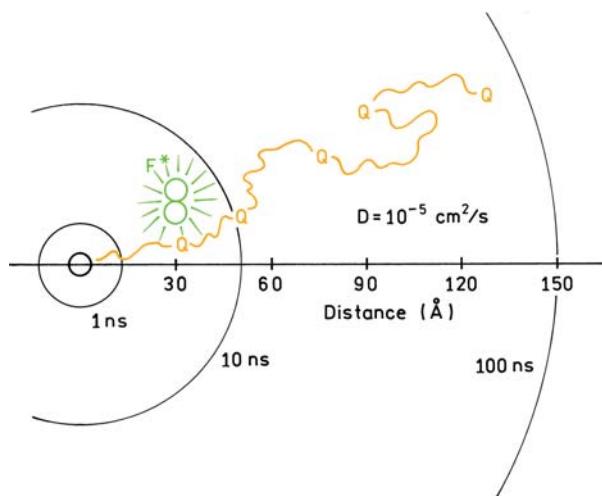
Figure 9.5. Kinetic scheme for quenching.

The concept of an encounter complex is clarified by considering the distances a quencher can diffuse during the excited state lifetime. The mean square distance is given by

$$\Delta x^2 = 2D\tau \quad (9.6)$$

where  $D$  is the diffusion coefficient and  $\tau$  is the lifetime. Figure 9.6 illustrates how a quencher can diffuse over long distances. During 1 ns the quencher diffuses an average of 15 Å. During 100 ns the quencher diffuses an average of 150 Å. Since the quencher moves randomly one can see that a quencher will usually undergo many collisions with a fluorophore prior to diffusing away from the fluorophore. An encounter complex is thus a fluorophore and quencher in close proximity, probably with one or no intervening solvent molecules.

The concept of an encounter complex shows how the quenching efficiency can depend on viscosity. If quenching is efficient, each encounter results in quenching. However, if quenching is inefficient then the pair may diffuse apart prior to quenching. In this case the quenching efficiency will be higher at higher viscosities because  $F^*$  and  $Q$  remain close together for a longer period of time, allowing more time for quenching to occur.

Figure 9.6. Distances for diffusion for various times.  $D = 10^{-5} \text{ cm}^2/\text{s}$ .

## 9.2. MECHANISMS OF QUENCHING

Equation 9.2 describes the effect of distance on quenching, but does not reveal the mechanism of quenching. There are at least three mechanisms for quenching:

1. Intersystem crossing or the heavy atom effect
2. Electron exchange or Dexter interactions
3. Photoinduced electron transfer

All of these mechanisms are expected to have the same distance dependence described by eq. 9.2. It is often difficult to know the mechanism of quenching. The mechanisms are not mutually exclusive, and many reports indicate that quenching occurs by a combination of these mechanisms. We will use these three mechanisms as limiting cases to provide a framework of discussion.

### 9.2.1. Intersystem Crossing

Quenching by heavy atoms halogens<sup>6–14</sup> and oxygen<sup>15</sup> is thought to occur by intersystem crossing. An encounter with a heavy atom or a triplet oxygen molecule is thought to cause the excited singlet state to become an excited triplet (Figure 9.7). Since the triplet states are usually long lived and also quenched by oxygen,<sup>16–17</sup> they are likely to be quenched to the ground state by the same quencher, or return to the ground state by non-radiative decay. It is not always clear which mechanism is dominant. Various reports have suggested oxygen quenching occurs by mixed mechanisms that include intersystem crossing, charge transfer, and electron exchange.<sup>18–20</sup> Depending upon the structure of the fluorophore, quenching by halogens has also been

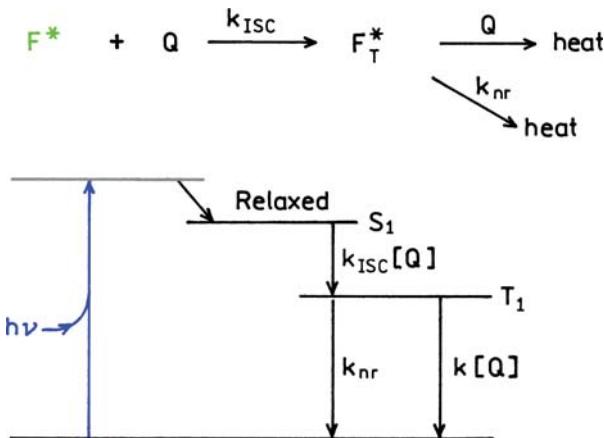


Figure 9.7. Quenching by intersystem crossing.

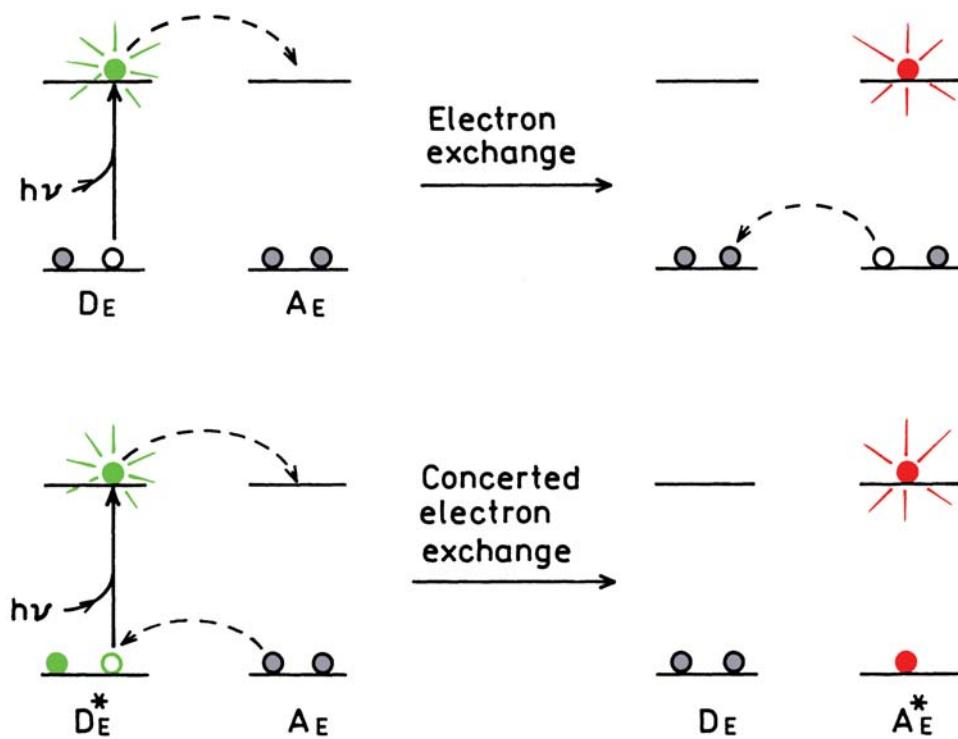


Figure 9.8. Schematic for stepwise (top) or concerted (bottom) electron exchange.

attributed to charge transfer, intersystem crossing, and/or electron exchange.<sup>21–30</sup> In general it seems that halocarbons quench by intersystem crossing and halides quench by charge transfer. Additionally, many fluorophores undergo photodestruction in the presence of halocarbons.<sup>31–33</sup>

### 9.2.2. Electron-Exchange Quenching

Figure 9.8 shows a schematic for the electron exchange or Dexter interaction.<sup>34–37</sup> This interaction occurs between a donor  $D_E$  and an acceptor  $A_E$ , where  $E$  indicates electron exchange. The excited donor has an electron in the LU orbital. This electron is transferred to the acceptor. The acceptor then transfers an electron back to the donor. This electron comes from the HO orbital of the acceptor, so the acceptor is left in an excited state. Electron exchange is similar to RET because energy is transferred to an acceptor. This mode of energy transfer also depends on spectral overlap of the donor and acceptor, just like RET. In contrast to RET, the Dexter interaction is a quantum mechanical effect that does not have an analogy in classical electrodynamics.

RET is well known to result in an excited acceptor. In contrast, the Dexter interaction is usually associated with quenching. This association occurs because RET occurs

over large distances, so if there is spectral overlap the transfer occurs by RET before Dexter transfer can occur. Dexter transfer may occur at short donor–acceptor distances, but the donor will be completely quenched by RET or Dexter transfer, and thus non-observable. Dexter transfer can be observed if the spectral overlap is small, so that the large rates of exchange become significant. Additionally, high concentrations are needed for significant Dexter transfer, whereas RET occurs at much lower concentrations. For an unlinked donor and acceptor the bulk concentration of the acceptor needs to be about  $10^{-2}$  M to have an average distance of 30 Å. For a fluorophore and quencher the bulk quencher concentration needs to be near 1 M to obtain an average distance of 6.5 Å.

### 9.2.3. Photoinduced Electron Transfer

The third mechanism for quenching is photoinduced electron transfer (PET). In PET a complex is formed between the electron donor  $D_P$  and the electron acceptor  $A_P$ , yielding  $D_P^+A_P^-$  (Figure 9.9). The subscript P is used to identify the quenching as due to a PET mechanism. This charge transfer complex can return to the ground state without emission of a photon, but in some cases exciplex emission is

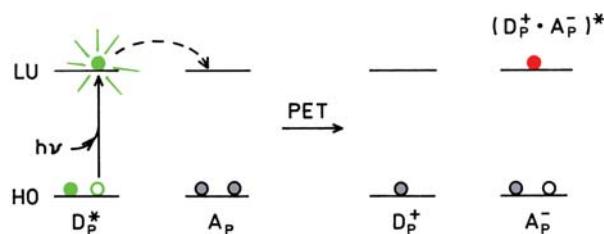


**Figure 9.9.** Molecular orbital schematic for photoinduced electron transfer.

observed. Finally, the extra electron on the acceptor is returned to the electron donor.

The terminology for PET can be confusing because the excited fluorophore can be either the electron donor or acceptor. The direction of electron transfer in the excited state is determined by the oxidation and reduction potential of the ground and excited states. When discussing PET the term donor refers to the species that donates an electron to an acceptor. In PET the terms donor and acceptor do not identify which species is initially in the excited state. This is different from RET, where a fluorophore is always the donor.

The nature of PET quenching is clarified by examining several examples. The more common situation is when the excited state of a fluorophore acts as an electron acceptor (Table 9.1). One typical example is an electron-rich species such as dimethylaniline (DMA), which can donate electrons to a wide range of polynuclear aromatic hydrocarbons, which act as electron acceptors. Electron transfer is even more favorable to electron-deficient species like cyanonaphthalenes. There are some unusual PET pairs, such as indole donating to pyrene and dienes donating to

**Table 9.1.** PET Quenching Where the Fluorophore Is the Electron Acceptor

F <sup>*</sup> – Q → (F <sup>-</sup> · Q <sup>+</sup> ) <sup>*</sup> → heat or exciplex Fluorophore (PET acceptor)	Quencher (PET donor)
Polynuclear aromatic hydrocarbons	Amines, dimethylaniline
2-Cyanonaphthalenes	Dimethylaniline
7-Methoxycoumarin	Guanine monophosphate
Pyrene	Indole
9-Cyanoanthracene	Methyl indoles
9,10-Dicyanoanthracene	Dienes and alkenes, alkyl benzenes
Anthraquinones	Amines
Oxazine	Amines

These quenching reactions are described in [38–48].

**Table 9.2.** PET Quenching Where the Fluorophore Is the Electron Donor

F <sup>*</sup> – Q → (F <sup>+</sup> · Q <sup>-</sup> ) <sup>*</sup> → heat or exciplex Fluorophore (PET donor)	Quencher (PET acceptor)
Indole or NATA	Imidazole, protonated
Indole	RCO <sub>2</sub> H, but not RCO <sub>2</sub> <sup>-</sup>
Tryptophan	Acrylamide, pyridinium
Carbazole	Halocarbons; trichloroacetic acid
Indole	Halocarbons
[Ru(bpy) <sub>3</sub> ] <sup>2+</sup>	Methylviologen
Dimethoxynaphthalene	N-methylpyridinium

These quenching reactions are described in [49–57].

cyanoanthracene. This table is not exhaustive, but provides only examples of PET pairs.

PET quenching can also occur by electron transfer from the excited fluorophore to the quencher (Table 9.2). Examples include electron transfer from excited indoles to electron-deficient imidazolium or acrylamide quenchers. Quenching by halocarbons can also occur by electron transfer from the fluorophore to the electronegative halocarbon. Electron-rich dimethoxynaphthalene can donate electrons to pyridinium. And finally there is the well-known example of electron transfer from excited [Ru(bpy)<sub>3</sub>]<sup>2+</sup> to methylviologen.

### 9.3. ENERGETICS OF PHOTOINDUCED ELECTRON TRANSFER

Photoinduced electron transfer has been extensively studied to understand quenching and to develop photovoltaic devices. For quenching by intersystem crossing and electron exchange it is difficult to predict the efficiency of quenching. Hence the description of these quenching processes is mostly based on experience rather than calculation. In contrast PET is more predictable because the possibility of electron transfer can be predicted from the redox potentials of the fluorophore and quencher.

Most descriptions of PET derive the energy change due to electron transfer starting with the basic principles of electrochemistry. This can be confusing because of the sign conventions used in redox chemistry. Hence we will start with the final result and then explain its origin. Figure 9.10 shows an energy diagram for PET with the excited molecule being the electron donor. For clarity, this diagram does not include diffusion that may be needed to bring D<sub>P</sub> and A<sub>P</sub> into contact. We are assuming the molecules are already in contact. Upon excitation the electron donor transfers an

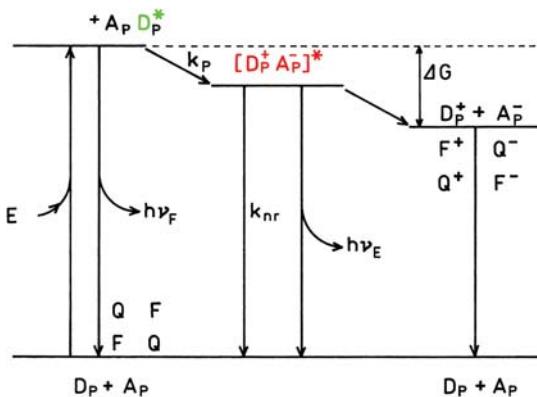


**Figure 9.10.** Energy diagram for photoinduced electron transfer. The excited molecule is assumed to be the electron donor.  $\nu_F$  and  $\nu_E$  are emission from the fluorophore and exciplex, respectively.

electron to the acceptor with a rate  $k_p(r)$ , forming the charge-transfer complex  $[D_p^+ A_p^-]^*$ . This complex may emit as an exciplex or be quenched and return to the ground state.

The important part of this process is the decrease in total energy of the charge transfer complex. The energy decreases because the ability to donate or accept electrons changes when a fluorophore is in the excited state. Excitation provides the energy to drive charge separation.  $D_p$  and  $A_p$  do not form a complex when both are in the ground state because this is energetically unfavorable. The energy released by electron transfer can also change if the ions become solvated and/or separated in a solvent with a high dielectric constant.

The energy change for PET is given by the Rehm-Weller equation:

$$\Delta G = E(D^+/D) - E(A/A^-) - \Delta G_{00} - \frac{e^2}{\epsilon d} \quad (9.7)$$

In this equation the reduction potential  $E(D^+/D)$  describes the process



and the reduction potential  $E(A/A^-)$  describes the process



$\Delta G_{00}$  is the energy of the  $S_0 \rightarrow S_1$  transition of the fluorophore, which can be either  $D_p$  or  $A_p$ . The last term on the

right is the coulombic attraction energy experienced by the ion pair following the electron transfer reaction;  $\epsilon$  is the dielectric constant of the solvent, and  $d$  is the distance between the charges.

The Rehm-Weller equation has its origin in the free energy change for moving charge in an electric potential. The energy released by a mole of electrons moving in a potential  $\Delta E$  is given by

$$\Delta G = -nF\Delta E \quad (9.10)$$

where  $n$  is the number of electrons in the reaction,  $\Delta E$  is the potential, and  $F$  is the Faraday constant, which is the charge on 1 mole of electrons. From this expression one can see that  $\Delta E$  is positive for a thermodynamically favored reaction. This convention is confusing because we normally associate a negative value with a favored reaction.

In describing the PET process we need to consider the redox potential of  $D_p$  and  $A_p$  and the energy of the incident light. Hence it is important to know the conversion factors. For a mole of electrons moving across a potential difference of  $\Delta E = 1$  V the energy is 1 eV = 23.06 kcal, so that

$$\Delta G \text{ (in kcal/mol)} = -23.06n\Delta E \quad (9.11)$$

We also need to convert a mole of absorbed photons into kcal/mole. The energy in a mole of photons is given by

$$\Delta E \text{ (kcal/mol)} = 28,600/\lambda \text{ (nm)} \quad (9.12)$$

A mole of 400-nm photons equals 71.5 kcal, and a mole of 600 nm photons equals 47.7 kcal.

Studies of PET are usually performed in polar solvents, frequently acetonitrile, which is a common solvent used when determining the reduction potentials. For complete separation of one electron charge in acetonitrile  $e^2/\epsilon d$  is equal to 1.3 kcal/mole = 0.06 eV. This term usually makes a small contribution to the overall energy change for PET.

The form of eq. 9.7 can now be understood intuitively. The terms  $\Delta G_{00}$  and  $e^2/\epsilon d$  appear with a negative sign because the energy will be lost when the light energy is dissipated and the ions experience coulombic attraction.  $E(D^+/D)$  and  $E(A/A^-)$  appear with opposite signs because these are both reduction potentials. However,  $D$  is oxidized to  $D^+$  and  $A$  is reduced to  $A^-$ . For the same reaction the oxidation potential is the negative of the reduction potential.

Why is the energy of the charge-transfer state lower than the energy before electron transfer? This can be under-

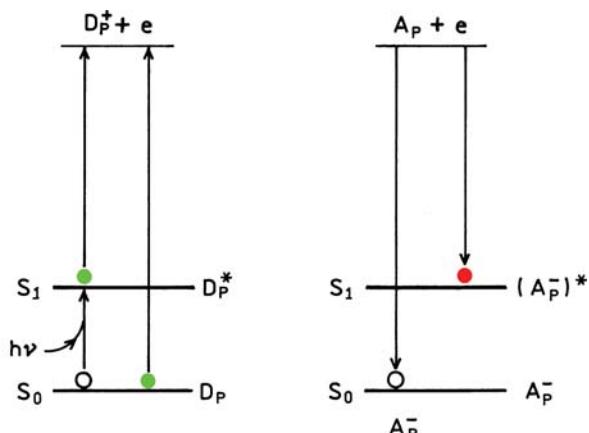


**Figure 9.11.** Changes in electron affinity between the  $S_0$  and  $S_1$  states.

stood by considering the energy required to remove an electron completely from the electron donor (Figure 9.11), which is the energy needed to ionize a donor fluorophore. When the fluorophore is in the excited state the electron is at a higher energy level than a ground-state electron. Hence it will require less energy to remove an electron from the  $S_1$  (LU) state than from the  $S_0$  (HO) state. This means the donor fluorophore in the  $S_1$  state has a higher propensity to donating an electron.

Now consider a quencher that is an electron acceptor (Figure 9.11). The energy released on binding the electron is larger if the electron returns to the  $S_0$  state than to the  $S_1$  state. The electron can return to the lowest orbital of the quencher because the donor–acceptor complex is momentarily an excited-state complex. When the electron acceptor is in the excited state there is a place for the electron to bind to the lowest orbital.

### 9.3.1. Examples of PET Quenching

The energetics of PET quenching is clarified by specific examples. Figure 9.12 shows lifetime Stern-Volmer plots for quenching of three coumarin derivatives by ethylaniline (EAN).<sup>58</sup> All three coumarins have a trifluoromethyl group, which increases their ability to accept electrons from EAN. Based on the chemical structures we expect EAN to be the electron donor and the coumarins to be the electron acceptors. The largest Stern-Volmer constant is for the amino derivative C151, with lesser amounts of quenching for the methylated C522 and C152. The methylated coumarins are less quenched than the amino coumarin, which is consistent with the well-known electron-donating properties of methyl

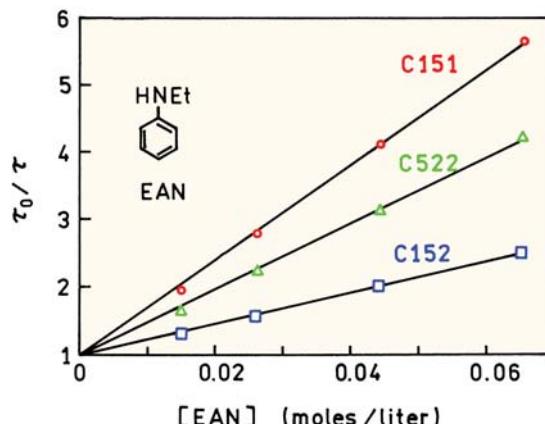
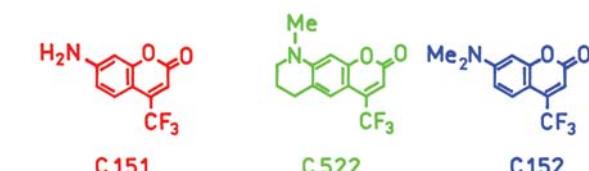


**Figure 9.12.** Quenching of coumarin derivatives by ethylaniline. Revised and reprinted with permission from [58]. Copyright © 2000, American Chemical Society.

groups. The additional methyl groups decrease the ability of the coumarin to accept electrons.

Figure 9.13 shows a similar PET quenching experiment, but one using a single fluorophore, Neutral Red (NR), and three different aromatic amine quenchers.<sup>58–59</sup> The

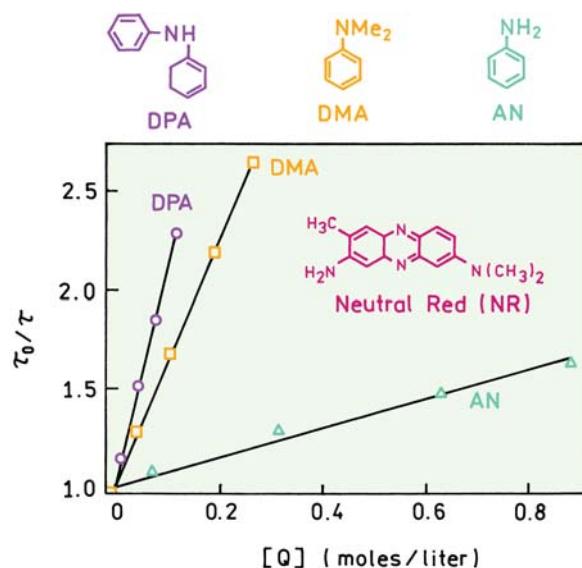


**Figure 9.13.** PET quenching of Neutral Red by aromatic amines. Revised from [59].

**Table 9.3.** Reduction Potentials and Quenching Constants for PET Quenching

Acceptor fluorophore	Donor quencher	$E_{00}$ (eV)	$E(A/A^-)$ (volts)	$E(D^+/D)$ (volts)	$\Delta G$ (eV)	$\Delta G$ (kcal/mole)	$\tau_0$ (ns)	$k_q$ ( $M^{-1} s^{-1}$ )
C151	EAN	2.98	-1.565	0.80	-0.67	-15.45	5.18	$10.9 \times 10^9$
C522	EAN	2.70	-1.653	0.80	-0.31	-7.15	5.48	$5.3 \times 10^9$
C152	EAN	2.76	-1.626	0.80	-0.39	-8.99	1.96	$9.1 \times 10^9$
Neutral Red	DPA	2.41	-1.51	0.64	-0.32	-7.38	4.15	$3.55 \times 10^9$
Neutral Red	DMA	2.41	-1.51	0.76	-0.20	-4.61	4.15	$1.49 \times 10^9$
Neutral Red	AN	2.41	-1.51	0.93	-0.03	-0.69	4.15	$0.24 \times 10^9$

$$\Delta G \text{ (eV)} = E(D^+/D) - E(A/A^-) - E_{00} - 0.06.$$

Data from [58–59].

amount of quenching increases when the quenchers have methyl or phenyl groups on the amino group, which increased the electron density and propensity of the quenchers to donate electrons.

It is instructive to examine calculations of the  $\Delta G$  values for PET (Table 9.3). The  $E_{00}$  values were obtained from the intersection of the normalized absorption and emission spectra of the fluorophores, and converted to eV using eqs. 9.11 and 9.12. These values, and the polarographic reduction potentials, can be used with eq. 9.7 to calculate which coumarin has a higher propensity to undergo PET. The  $\Delta G$  values for electron transfer for all three coumarins are negative, showing that PET is energetically possible. The larger value of  $E_{00}$  for C151 results in the largest value of  $\Delta G$  and the largest amount of PET quenching. Table 9.3 also contains Rehm-Weller calculation for quenching of NR.

The PET reaction releases more energy when the aniline contains the additional electron-donating groups. The largest bimolecular quenching constant was found for the PET reaction with the most negative  $\Delta G$  value. There is a strong correlation of larger bimolecular quenching constants with more negative  $\Delta G$  values.

Figure 9.14 shows a schematic of the energy changes upon PET to NR. Excitation at 514 nm adds 55.6 kcal/mole to NR. The amines that have the largest bimolecular constants also show the largest decrease in energy when the charge transfer complex is formed. Examination of this figure and Table 9.3 reveals why it is intuitively difficult to look at the reduction potential of  $D_p$  and  $A_p$  to predict the energy change for the reaction. The overall  $\Delta G$  is the difference of three large numbers that all contribute to  $\Delta G$  for the reaction.

Examination of the  $k_q$  values in Table 9.3 shows a strong dependence on  $\Delta G$  for quenching of NR, but a weaker dependence on  $\Delta G$  for quenching of the coumarins. It is easy to understand why the correlation is variable. Figure 9.15 shows  $k_q$  values for amine quenching of Neutral Red. From left to right the reduction potential  $E(D^+/D)$  of the amine increases. Using eq. 9.7 shows that  $\Delta G$  for the reaction is less negative for AN than for the other quenchers. This indicates that AN binds its electrons more tightly than the other two amines in Figure 9.15, which in turn results in less efficient PET and less efficient quenching. However, if  $\Delta G$  is more negative than  $-0.5$  eV, then PET formation and quenching is 100% efficient, so that small changes in  $\Delta G$  do not affect the efficiency. In Table 9.3 the  $\Delta G$  values for quenching of the coumarins were  $-0.31$  eV, or more negative, so that all three coumarins were efficiently quenched.

The rate of PET can be measured using time-resolved measurements. However, if quenching is almost 100% efficient then the unusual quenching experiment reveals the value of  $k_q$ . The rate of PET will not have a large effect on

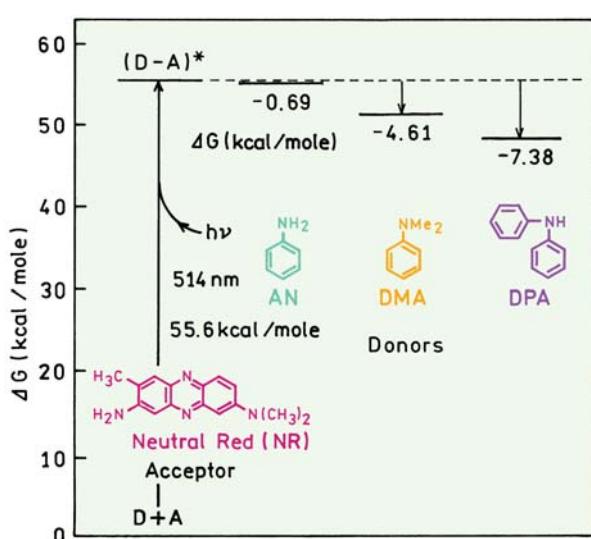


**Figure 9.14.** Energy diagram for quenching of Neutral Red with aromatic amines. Data from [59].

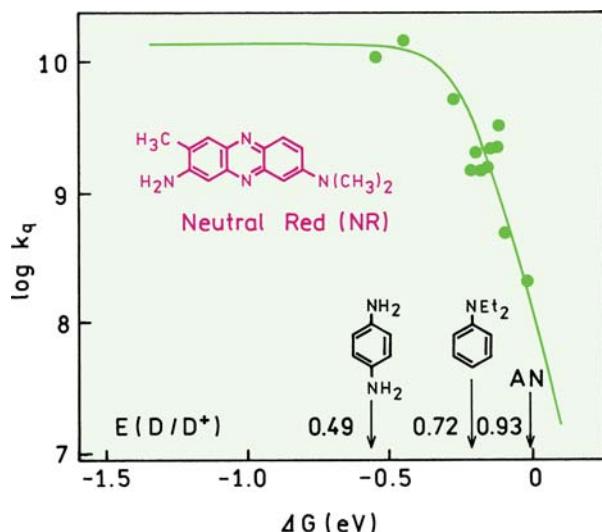


**Figure 9.15.** Correlation of  $k_q$  for PET quenching of Neutral Red with  $\Delta G$  for the reaction. Revised from [59].

$k_q$  because  $k_p(r)$  is much larger than  $k_q$  and PET is limited by the rates of diffusion. In order to study the electron-transfer rate it is necessary to eliminate the effect of diffusion. However, high quencher concentrations are required

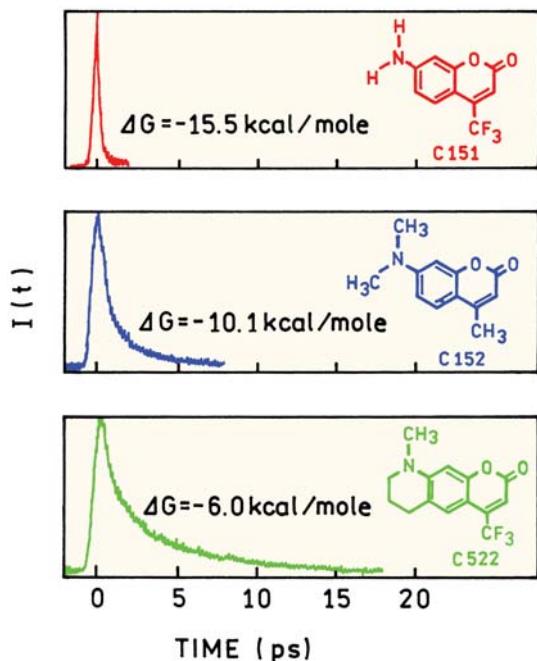


**Figure 9.16.** Time-dependent decays of coumarin derivatives in neat DMA. Revised and reprinted with permission from [60]. Copyright © 1993, American Chemical Society.

to obtain contact quenching without diffusion. The intensity decays of the three coumarin derivatives were examined in neat DMA (Figure 9.16).<sup>60</sup> In pure DMA the fluorophores are surrounded by electron donors so no diffusion is needed to bring  $D_p$  and  $A_p$  into contact. Hence the intensity decays should reflect the electron-transfer rate  $k_p(r)$  rather than the diffusion-controlled collision rate. The most rapid intensity decay was observed for C151 where  $\Delta G = -15.5$  kcal/mole. Slightly slower decays were observed for C152 and C522, where  $\Delta G$  is less negative.

### 9.3.2. PET in Linked Donor–Acceptor Pairs

The need for high quencher concentrations can be avoided using covalently linked D–A pairs. One example is shown in Figure 9.17, where the electron acceptor methylviologen ( $MV^{2+}$ ) is covalently linked to 1,8-naphthalimide. The spacer contained  $n = 2$  to 6 methylene groups.<sup>61</sup> In this case the naphthalimide fluorophore is the electron donor and  $MV^{2+}$

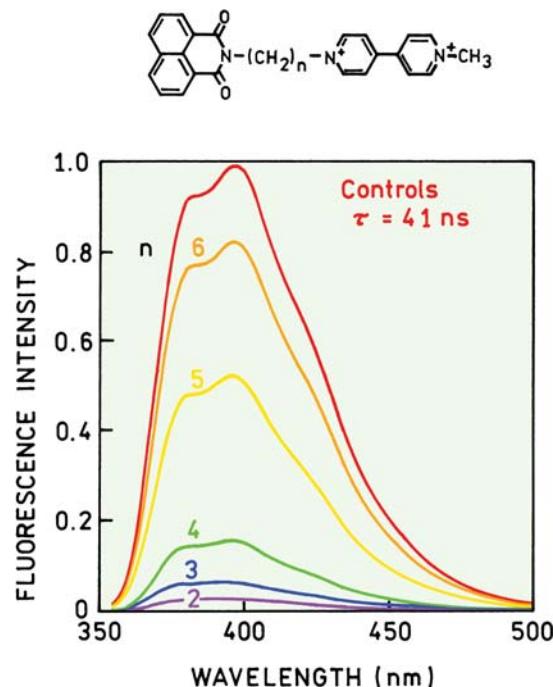


**Figure 9.17.** Emission spectra of covalently linked 1,8-naphthalimide and methylviologen.  $n$  is the number of methylene groups. The control compound lacked the methylviologen acceptor, and instead had a linked pyridine group with the same number of methylene groups. Revised and reprinted with permission from [61]. Copyright © 2000, American Chemical Society.

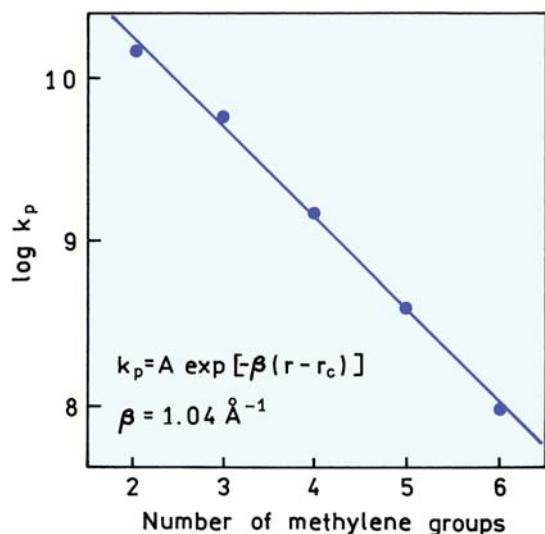


**Figure 9.18.** Distance dependence of the electron-transfer rate from 1,8-naphthalimide to covalently linked methylviologen.  $\beta = 1.32$  per methylene group (assuming 1.27 Å per methylene group). Revised and reprinted with permission from [61]. Copyright © 2000, American Chemical Society.

the electron acceptor. The intensity decreases as the number of methylene groups decreases. The D–A pair was examined in dilute aqueous solution. In highly dilute solution, collisions between D and A groups on different molecules is not significant. Hence the change in donor intensity reflects the effect of distance on the rate of electron transfer. There may also be a component due to flexing of the D–A pair during the excited-state lifetime.

The intensity data were used to calculate the rates of energy transfer. This was accomplished by using eq. 9.4, where  $Q$  is the relative intensity and  $\gamma = 41 \text{ ns}^{-1}$  (Figure 9.18). The rate of electron transfer decreases by a factor of 180 as  $n$  increases from 2 to 6, which is an increase in distance of about 5 Å. This result shows the dramatic decrease in  $k_p(r)$  with distance.

#### 9.4. PET QUENCHING IN BIOMOLECULES

##### 9.4.1. Quenching of Indole by Imidazolium

Intrinsic fluorescence from tryptophan residues is frequently used to study the properties of proteins. In order to interpret the tryptophan emission it is important to understand the effects of nearby amino acid side chains. The amino acid histidine has an imidazole group in its side chain. Since the  $pK_a$  of this group is near 6.5, it can be protonated or unprotonated depending on the pH and the charges on other

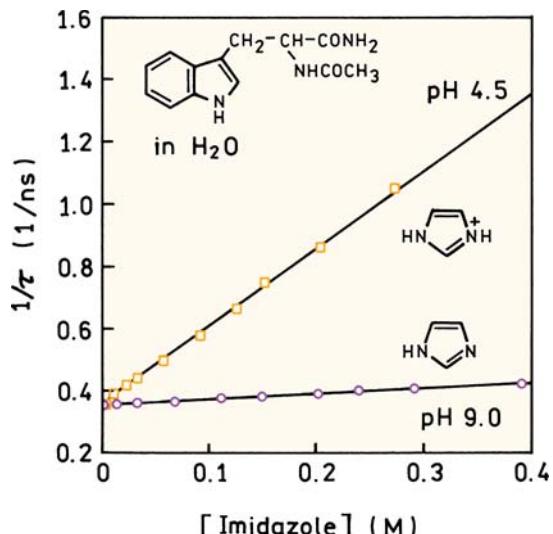


**Figure 9.19.** Quenching of NATA by imidazole (pH 9) and imidazolium (pH 4.5). Revised from [62].

nearby amino-acid side chains. Proteins frequently display pH-dependent changes in intensity near pH 7, suggesting an effect due to the imidazole–imidazolium equilibrium.

Figure 9.19 shows the inverse lifetime of NATA in an aqueous solution that contains imidazole.<sup>62</sup> At pH 4.5 there is strong quenching of NATA. At pH 9, at the same imidazole concentrations, there is little quenching. Since NATA is uncharged this difference is not due to electrostatic interactions. The indole ring in the excited state donates an electron to the imidazolium because PET is energetically favorable to this electron-deficient species. Uncharged imidazole does not accept the electron, so quenching does not occur at pH 9.

##### 9.4.2. Quenching by DNA Bases and Nucleotides

Fluorescently labeled oligomers are widely used in DNA analysis and biotechnology. Hence there is interest in understanding what factors influence the intensity of covalently bound fluorophores. The extent of quenching depends on the base and the structure of the fluorophore.<sup>43,63</sup> Among the bases guanine appears to be the most efficient quencher, probably because it has the highest tendency to donate an electron. Figure 9.20 shows the lifetime distributions for oligomers labeled with MR121.<sup>64</sup> If the oligomer does not contain guanine, the decay of MR121 is a single exponential with  $\tau = 2.72 \text{ ns}$ . The presence of a single guanine as the second base results in a short-lived component with  $\tau = 0.43 \text{ ns}$  that is due to PET quenching.

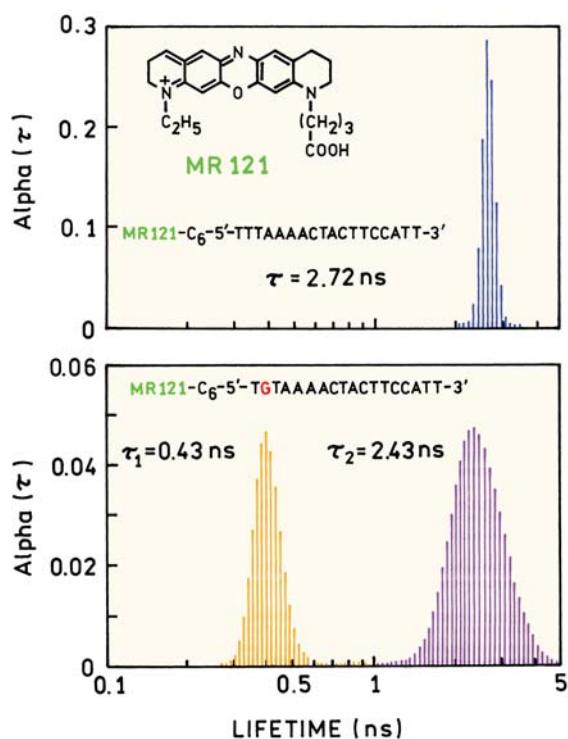


**Figure 9.20.** Lifetime distribution of MR121-labeled oligomers with T or G as the second base. Revised from [64].

One can expect the quantum yields and lifetimes of labeled oligomers to depend on the base sequence near the fluorophore.

PET has been used to study electron transfer along double-helical DNA.<sup>65</sup> Figure 9.21 shows a DNA hairpin that contains a covalently bound stilbene residue at the bending site. A single guanine residue was positioned next to the stilbene or spaced by several base pairs. The lifetimes decrease dramatically as the guanine approaches the stilbene residue with  $\beta = 0.64 \text{ \AA}^{-1}$ . One can imagine PET quenching being used to develop molecular beacons or DNA hybridization assays based on quenching by guanine residues.

## 9.5. SINGLE-MOLECULE PET

During the past 10 years fluorescence technology has advanced to allow studies of single molecules. This is usually accomplished using fluorophores immobilized on a surface and confocal optics to reject out-of-focus light. Single-molecule detection (SMD) has been extended to PET quenching.<sup>66–67</sup> Figure 9.22 shows the intensity versus time observed for single fluorophores on a glass surface dis-

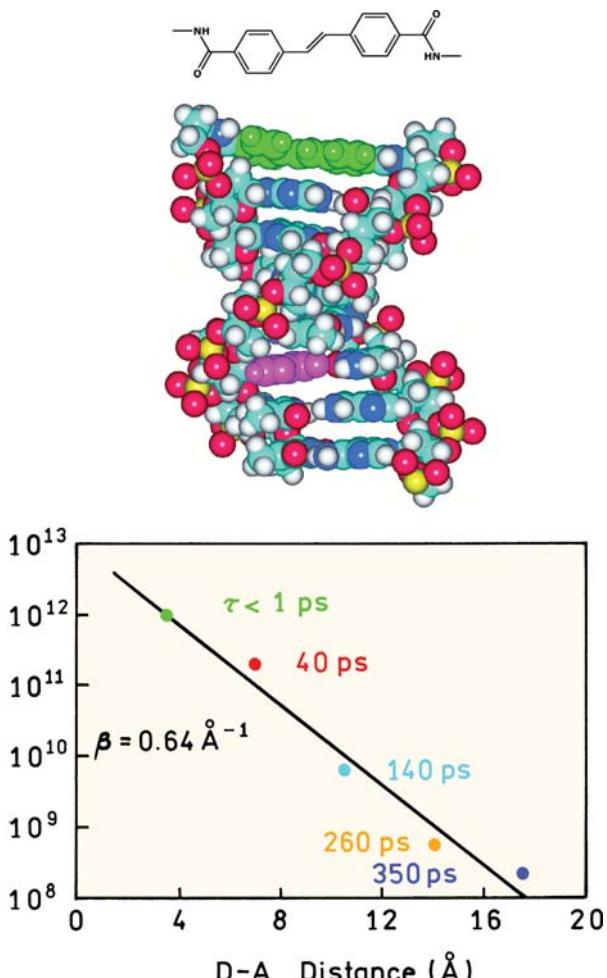


**Figure 9.21.** PET quenching of oligomers labeled with stilbene (green) and containing a single guanine residue (red base). From left to right in the lower panel this guanine is the 1st, 2nd, 3rd, 4th, or 5th base pair away from the stilbene. Revised from [65].

solved in a thin layer of a viscous polymer. The fluorophores are dimers of perylene connected directly or by three phenyl groups. The phenyl groups are thought to act as a nonconducting bridge. The intensities were found to blink on and off. Under the same experimental conditions the monomer control compound did not show blinking. The on and off blinking of these perylene dimers was assigned to fluctuations in the conformations of the molecule between one favorable for PET, when the molecules are dark, or a conformation unfavorable for PET, where the molecules are fluorescent. Single fluorophores of many types are known to display blinking due to transitions to the triplet state (Chapter 23). In Figure 9.22 the off times were claimed to be too long to be due to triplets, even in a rigid

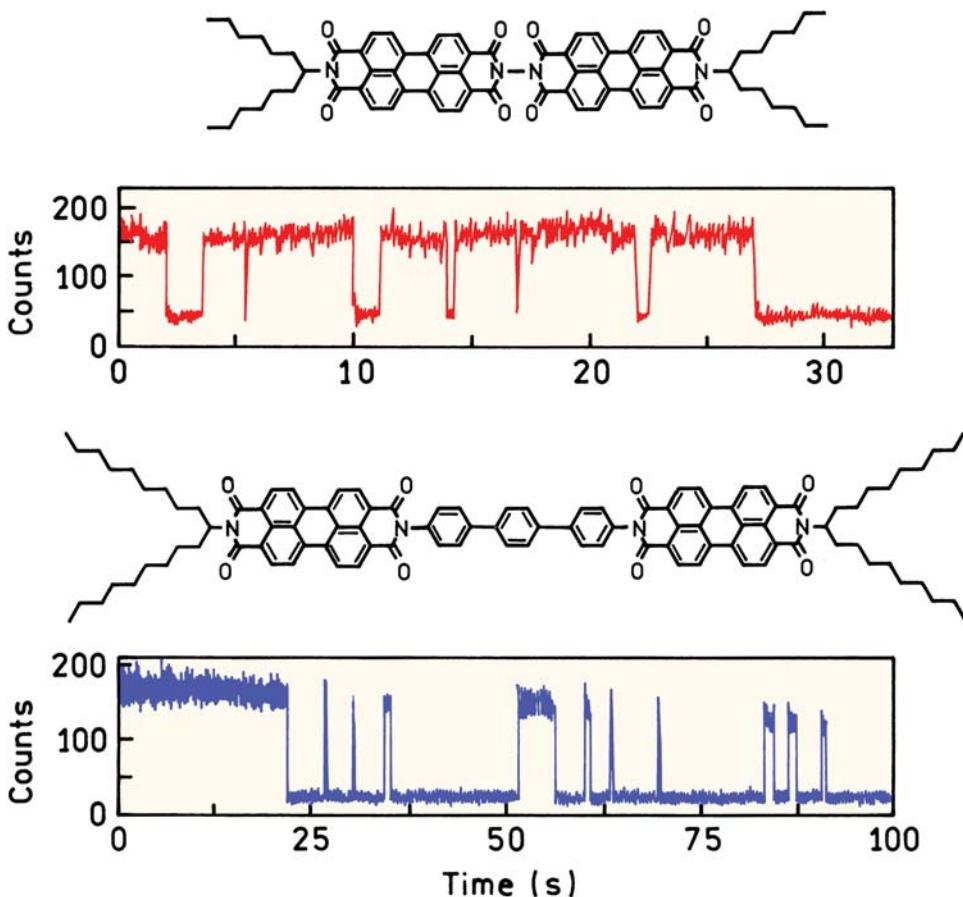


**Figure 9.22.** Single-molecule intensity traces for two bis-perylene compounds. The intensity axis is photons per 20 ms. Revised and reprinted with permission from [67]. Copyright © 2003, American Chemical Society.

polymer, so the blinking was assigned to conformational fluctuations which affected the rate of PET.

#### 9.6. TRANSIENT EFFECTS IN QUENCHING

We have now seen that collisional quenching occurs by several mechanisms. All these mechanisms have the same requirement for molecular contact between the fluorophore and quencher. As a result quenching requires diffusion to bring the molecules into contact. Without diffusion high concentrations of quencher near 1 M are necessary to statistically position a quencher adjacent to the fluorophore at the moment of excitation.

For diffusive or collisional quenching, we stated in Chapter 8 that the lifetime decreases in proportion to the decrease in fluorescence intensity. If the decay was a single exponential before quenching, we assumed the decay remained a single exponential in the presence of quencher. In reality, intensity decays become non-exponential in the

presence of collisional quenching. By non-exponential we mean not described by a sum of exponentials. This effect is due to the so-called transient effects in quenching.<sup>68</sup> For small amounts of quenching in fluid solvents, these effects are barely noticeable. For larger amounts of quenching, especially in moderately viscous solvents, the intensity decays become strongly non-exponential.

The theory for transient effects is complex and has been presented in a monograph on diffusion-controlled reactions.<sup>69</sup> This effect was first identified by Smoluchowski, who considered diffusion-controlled reactions between particles in solution.<sup>70</sup> The rate constant for reaction between the particles was shown to be time-dependent

$$k(t) = 4\pi RND[1 + R(\pi Dt)^{-1/2}] \quad (9.13)$$

where  $R$  is the interaction radii (sum of the radius of the fluorophore ( $F$ ) and quencher ( $Q$ )),  $N = 6.02 \times 10^{20}$ , and  $D$  is

the sum of the F and Q diffusion coefficients. The time dependence originates with the random distribution of fluorophores and quenchers at the moment of excitation. Some fluorophore–quencher pairs will be in close proximity, and others will be more widely spaced. The fluorophores with a closely located quencher are extinguished rapidly. With time following excitation, the ensemble of fluorophores evolves, and the fluorophores that remain in the excited state longest are those that were most distant from the closest quencher at the moment of excitation. The time-dependent rate constant decreases from an initially high value to the diffusion limited value ( $k_q = 4\pi R N' D$ ). The intensity decay in the presence of collisional quenching can be obtained by integration of the differential equation describing  $dI(t)/dt$  that includes the time-dependent rate constant. This yields

$$I(t) = I_0 \exp(-t/\tau - 2bt^{1/2}) \quad (9.14)$$

where  $\tau$  is given by

$$\frac{1}{\tau} = \frac{1}{\tau_0} + k_q [Q] \quad (9.15)$$

and

$$b = 4R^2 N (\pi D)^{1/2} [Q] \quad (9.16)$$

While these equations seem complex, the actual situation is still more complex. The Smoluchowski model assumes that the fluorophore is instantaneously deactivated upon contact with the quencher, which results in an infinite quencher concentration gradient around the fluorophore. Also, the Smoluchowski model assumes no quenching in the absence of molecular contact. These assumptions have been modified to allow more realistic modeling of the quenching process.<sup>71–72</sup> These quenching models are shown schematically in Figure 9.23. The radiation boundary condition (RBC) model assumes that quenching occurs with a finite rate constant  $k$  when F and Q are in contact (Figure 9.23). For the Smoluchowski model  $k(r) = 4$  when F and Q are in contact, and  $k(r) = 0$  otherwise.

Another model for quenching assumes that the quenching rate is dependent on the F–Q distance. In this model the quenching constant is assumed to depend on the distance between the fluorophore and quencher. In the previous sections we saw that the rates of electron exchange and electron transfer depend exponentially on distance. A similar

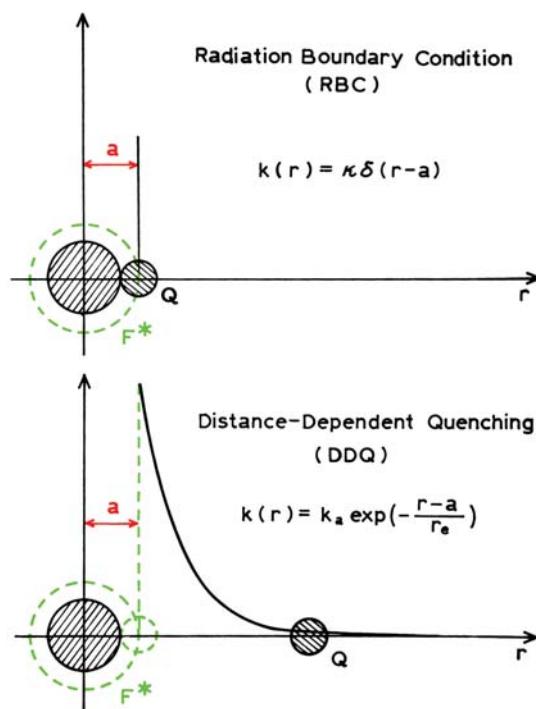


**Figure 9.23.** Comparison of the RBC and DDQ models for collisional quenching of fluorescence. Revised and reprinted with permission from [80]. Copyright © 1996, American Chemical Society.

dependence on distance has been reported for intersystem crossing.<sup>8</sup> This effect can be accounted for using the distance-dependent quenching (DDQ) model. For this model of distance-dependent interactions the rate of quenching at an F–Q distance  $r$  is given by

$$k(r) = k_a \exp\left(-\frac{r}{r_e}\right) \quad (9.17)$$

where  $r_e$  is the characteristic distance, and  $k_a$  is the rate of reaction at the distance of closest approach ( $a$ ), typically 5–7 Å. This expression has the same form as eq. 9.2. The time-dependent rate constant is given by

$$k(t) = \frac{4\pi}{C_q^0} \int_a^\infty r^2 k(r) C_q(r,t) dr \quad (9.18)$$

where  $C_q(r,t)$  is the concentration of the quencher molecules at distance  $r$  from the excited fluorophore at time instant  $t$  and  $C_q^0$  is the bulk quencher concentration. This expression says that the bimolecular quenching constant at any time is given by the values of  $k(r)$  averaged over the

concentration gradient around the fluorophore at some instant in time. The use of these quenching models requires rather complex theory and analysis. For the Smoluchowski, RBC, or DDQ models the intensity decay is given by

$$I(t) = I_0 \exp(-t/\tau_0) \exp\left[-[Q] \int_0^t k(t) dt\right] \quad (9.19)$$

where  $k(t)$  is the time-dependent rate constant. For the RBC model  $k(t)$  is given by<sup>73–76</sup>

$$k(t) = \frac{4\pi RDN}{1 + (D/\kappa R)} \left[ 1 + \frac{\kappa R}{D} \exp(X^2) \operatorname{erfc}(X) \right] \quad (9.20)$$

$$X = \frac{(Dt)^{1/2}}{R} \left[ 1 + \frac{\kappa R}{D} \right] \quad (9.21)$$

The function  $\operatorname{erfc}(X)$  is the complement of the error function:

$$\operatorname{erfc}(X) = \frac{2}{\pi^{1/2}} \int_X^\infty \exp(-z^2) dz \quad (9.22)$$

For the DDQ model analytical expressions for  $k(t)$  are not yet known, so numerical procedures are often used to calculate intensity decay  $I(t)$ .<sup>77–83</sup> Several reports have focused on the analysis of decays with transient effects.<sup>84–87</sup>

It is useful to visualize how the quenching constant depends on time. The values of  $k(t)$  are shown in Figure

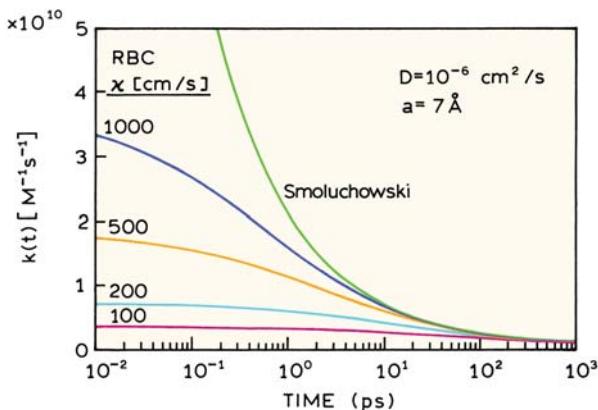


**Figure 9.24.** Time-dependent rate constants for the Smoluchowski and RBC models. From [88].

9.24 for the Smoluchowski model and for the RBC model with various values of  $\kappa$ . For a diffusion coefficient near  $10^{-6}$  cm<sup>2</sup>/s the transient effects are mostly complete in 10 ps, and are no longer present at 1 ns. For times over 1 ns the value of  $k(t)$  becomes equal to the usual bimolecular quenching constant (eq. 8.11). At short times the values of  $k(t)$  are initially larger than the calculated value of  $k_q$ . This effect is due to the rapid quenching of closely spaced F–Q pairs. In the Smoluchowski model the value of  $k(t)$  diverges to infinity at short times. This difficulty is avoided in the RBC model, where the maximal rate is limited by the value of  $\kappa$ . As  $\kappa$  increases, the RBC model becomes identical with the Smoluchowski model.

Equation 9.18 indicates that the concentration of quencher  $C_q(r,t)$  around the fluorophore changes with time and distance. This seems counterintuitive because the fluorophore is in equilibrium with the bulk concentration of quencher. This effect can be understood by considering the population of fluorophores being observed (Figure 9.25). The surfaces show the concentration of quencher around the fluorophore following pulsed excitation.<sup>83</sup> At  $t = 0$  there is a uniform quencher concentration around the fluorophore. As time increases the quencher concentration around the fluorophore decreases at short distances, with the effect being larger for the DDQ model than for the RBC model. Since the fluorophore and quencher are not destroyed upon quenching, it is not immediately obvious why  $C_q(r,t)$  changes.

In order to understand the changes in  $C_q(r,t)$  we need to recall that we are observing an ensemble of fluorophores. At short times following excitation there is rapid quenching of the closely spaced F–Q pairs, mostly without the need for diffusion. These pairs are quenched with the larger rate constant  $k(r)$ . At longer times all the closely spaced pairs have

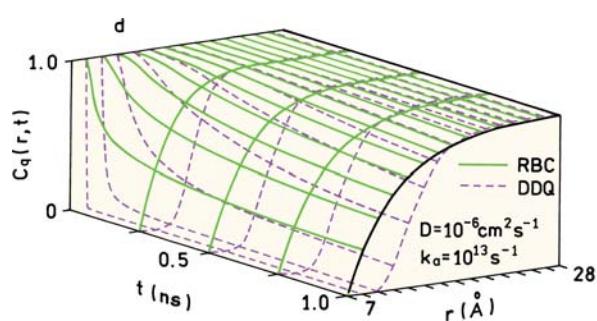


**Figure 9.25.** Simulations of the quencher concentration  $C_q(r,t)$  around the fluorophores for various times and distances. The solid and dashed lines are for the RBC and DDQ models, respectively. Reprinted from [83].

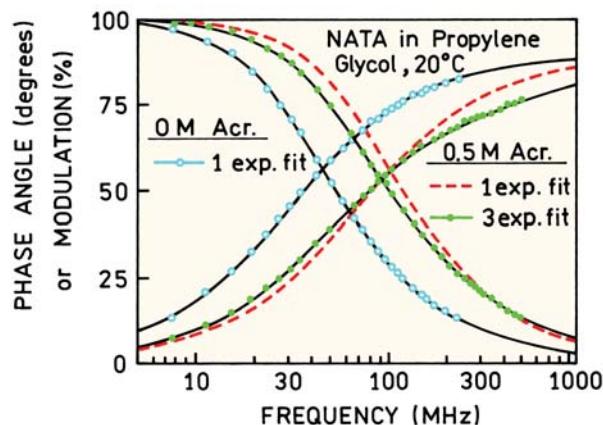


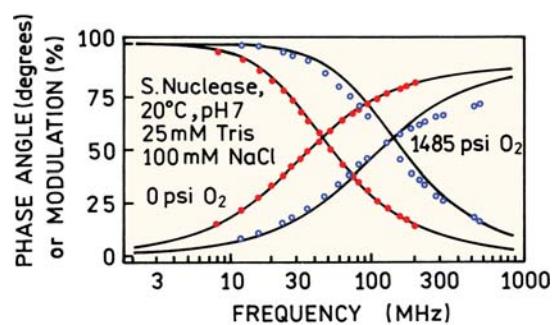
**Figure 9.26.** Frequency-domain intensity decays of NATA in propylene glycol in the absence and presence of 0.5 M acrylamide. Revised from [89].

decayed, and the rate of quenching becomes limited by diffusion with a bimolecular rate constant  $k_q$ .

As time proceeds the observed fluorophore population is changing from closely spaced to more distant F–Q pairs. The quencher concentration around the ground-state fluorophores is not changing. The excited fluorophore population is changing, so that the fluorophores remaining in the excited state were located further from a quencher at the moment of excitation.

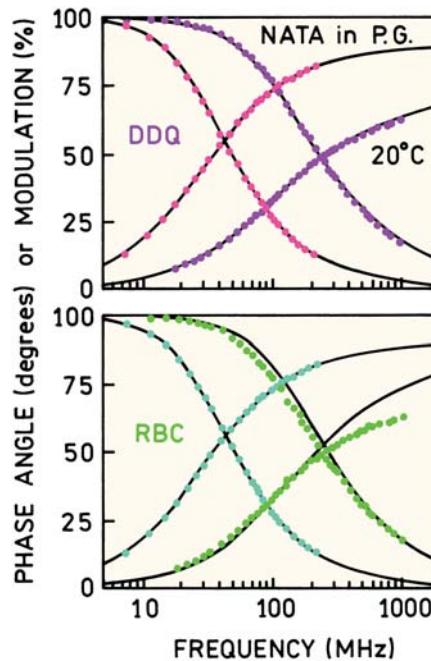
#### 9.6.1. Experimental Studies of Transient Effects

Figure 9.26 shows frequency-domain intensity decays for NATA in propylene glycol.<sup>89</sup> In the absence of quenching, the frequency-domain intensity decay reveals a single exponential decay. In the presence of 0.5 M acrylamide the decay becomes strongly heterogeneous, and cannot be fit by a single exponential decay law,  $\chi_R^2 = 240$ , but could be fit using a triple exponential decay. Transient effects can also be observed for proteins.<sup>90–91</sup> The single-tryptophan protein staphylococcal nuclease is known to display a dominant single exponential decay, as seen by the overlap with the single decay time model (Figure 9.27). When quenched by oxygen the intensity decay is no longer a single exponential. Oxygen diffusion is rapid, which minimizes the transient part of the rate constant (eq. 9.13). Larger effects can be expected if diffusion is slower or if the solution is somewhat viscous. These transient terms can be accounted for using the multi-exponential model. However, the decay components do not directly represent any molecular property of the sample.



**Figure 9.27.** Frequency response of staphylococcal nuclease in the absence (●) and presence (○) of 0.144 M oxygen. The solid lines show the best single exponential fits to the data. The values of  $P$  for the single exponential fits at 0 and 1485 psi  $O_2$  are 5.9 and 265, respectively. From [90].

The complex intensity decays observed in the presence of quenching can be explained by the transient models.<sup>92–93</sup> This is illustrated in Figure 9.28 for quenching of NATA by acrylamide.<sup>78</sup> The frequency-domain data could not be explained by the RBC model, but were consistent with the DDQ model. This indicates that the quenching rate displays



**Figure 9.28.** Frequency-domain intensity decays of NATA in propylene glycol at 20°C in the presence of increasing (left to right) concentrations of acrylamide (1.5 M). The solid lines (top) show the best fit to the DDQ model using  $a = 5 \text{ \AA}$  and  $r_e = 0.319 \text{ \AA}$ . The solid lines (bottom) show the best fit to the RBC model using  $a = 5 \text{ \AA}$ . Revised with permission from [78]. Copyright © 1994, American Society for Photobiology.

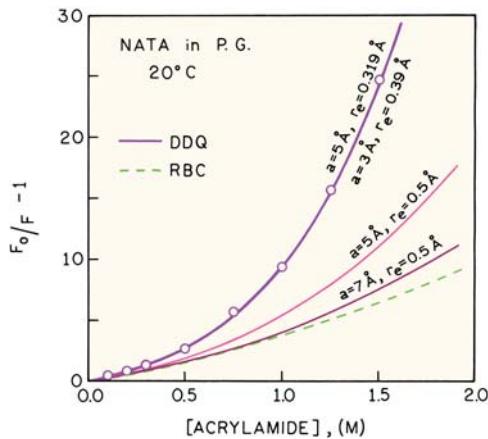


**Figure 9.29.** Stern-Volmer plots for NATA in propylene glycol at 20°C quenched by acrylamide ( $\circ$ ). The solid lines represent the calculated values of  $(F_0/F - 1)$  using the parameter values from the DDQ model for  $a = 7 \text{ \AA}$  and  $r_e = 0.5 \text{ \AA}$ ,  $a = 5 \text{ \AA}$  and  $r_e = 0.5 \text{ \AA}$ , and  $a = 5 \text{ \AA}$  and  $r_e = 0.319 \text{ \AA}$ . The dashed line represents the RBC model using  $a = 5 \text{ \AA}$ . Reprinted with permission from [78]. Copyright © 1994, American Society for Photobiology.

an exponential dependence on distance, and that quenching is not an all-or-none process that occurs only at the contact distance.

An important result from the transient analysis is an explanation for the upward curvature seen in many Stern-Volmer plots.<sup>78-79</sup> The acrylamide Stern-Volmer plot for NATA shows substantial upward curvature in the moderately viscous solvent propylene glycol (Figure 9.29). While the curvature could be explained by a weak static quenching constant, or by a sphere of action, the upward curvature is a natural consequence of distance dependent quenching. This

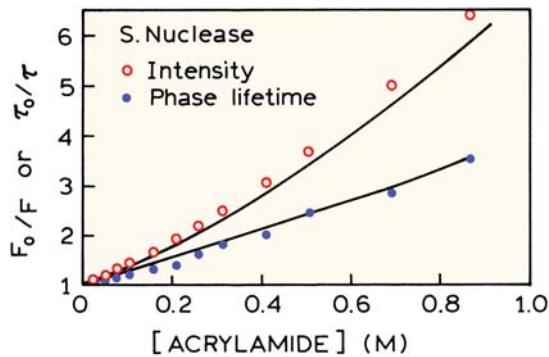


**Figure 9.30.** Intensity and phase-lifetime Stern-Volmer plots for the acrylamide quenching of staphylococcal nuclease A at 20°C, pH 7. Lifetimes were measured at 50 MHz. Solid lines are a simultaneous fit with  $R$  (fixed) = 7 Å,  $\tau_0$  = 4.60 ns, and  $D$  =  $0.058 \times 10^{-5} \text{ cm}^2/\text{s}$ . Revised from [91].

explanation of upward deviations in the Stern-Volmer plots is more satisfying because there is a single molecular interaction, the exponential distance dependence of quenching, which explains the time-dependent and steady-state data.

The transient model can also explain upward-curving Stern-Volmer plots in proteins. This is illustrated by the quenching of staphylococcal nuclease by acrylamide<sup>91</sup> (Figure 9.30). In this case the calculated curve for the intensity data was obtained using the Smoluchowski model (eq. 9.14). This equation can be integrated to obtain the Stern-Volmer equation with transient effects:<sup>68</sup>

$$\frac{F_0}{F} = \frac{1 + K_D[Q]}{Y} \quad (9.23)$$

where  $K_D = k_q \tau_D$  and

$$Y = 1 - \frac{b\sqrt{\pi}}{a} \exp(b^2/a) \operatorname{erfc}(b/\sqrt{a}) \quad (9.24)$$

$$a = \frac{1}{\tau_0} + k_q[Q] \quad (9.25)$$

with  $b$  as defined in eq. 9.16.

The validity of distance-dependent quenching is supported by an observation that cannot be explained by other models. In frozen solution, where diffusion does not occur, one still observes quenching of NATA by acrylamide (Figure 9.31). The magnitude of the effect cannot be explained

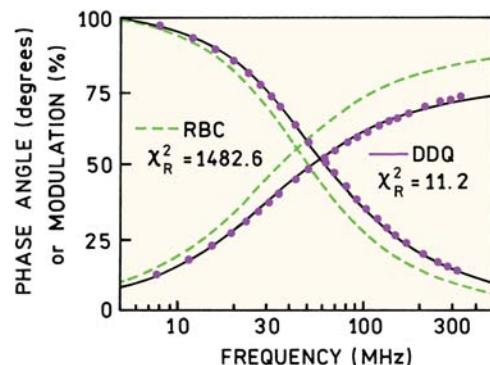


**Figure 9.31.** Frequency-response of the NATA intensity decay in propylene glycol at -60°C. The data ( $\bullet$ ) are for NATA with 1.048 M acrylamide at -60°C, and the solid line represents the best DDQ fit. The dashed line shows the RBC fit with  $D = 0$ . Reprinted with permission from [78]. Copyright © 1994, American Society for Photobiology.

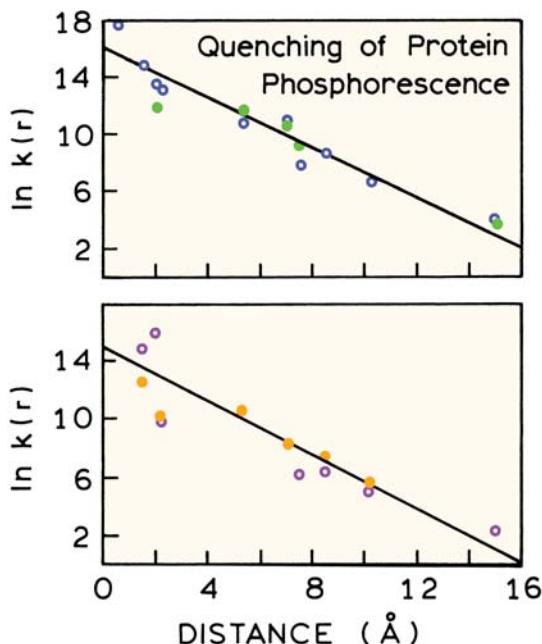


**Figure 9.32.** Relationship between Stern-Volmer quenching constants and distance from the protein surface. Top: quenching constants for nitrite (○) and azide (●). Bottom: quenching constants for ethanethiol (○) and nicotinamide (●). From [94].

by the RBC model. The data show a decrease in lifetime even in the absence of diffusion. This is not consistent with a sphere of action because the fluorophore–quencher pairs within the sphere are quenched and do not contribute to the intensity decay. Such data (Figure 9.31) can be explained by a short range exponential interaction.

### 9.6.2. Distance-Dependent Quenching in Proteins

The concept of distance-dependent quenching has been used to explain the quenching of protein phosphorescence by polar molecules (nitrite and azide), which were not expected to penetrate the proteins<sup>94</sup>. A number of single-tryptophan proteins were examined, for which the crystal structures were known. There was a strong correlation between the quenching constant and the distance of the tryptophan to the surface of the protein (Figure 9.32). The quenching constants were not sensitive to solution viscosity, suggesting that the rate of quenching was sensitive to the distance of closest approach. The exponential dependence of quenching constants on distance from the surface indicated that electron transfer or electron exchange governed the quenching process.

### REFERENCES

- Turro NJ. 1978. *Modern molecular photochemistry*. Benjamin/Cummings, Menlo Park, CA.
- Kavarnos GJ. 1993. *Fundamentals of photoinduced electron transfer*. VCH Publishers, New York.
- Kavarnos GJ, Turro NJ. 1986. Photosensitization by reversible electron transfer: theories, experimental evidence, and examples. *Chem Rev* **86**:401–449.
- Eftink MR, Selva TJ, Wasylewski Z. 1987. Studies of the efficiency and mechanism of fluorescence quenching reactions using acrylamide and succinimide as quenchers. *Photochem Photobiol* **46**: 3–30.
- Eftink MR. 1991. Fluorescence quenching: theory and applications. In *Topics in fluorescence spectroscopy*, Vol. 2: *Principles*, pp. 53–126. Ed JR Lakowicz. Plenum Press, New York.
- Zhang J, Roek DP, Chateauneuf JE, Brennecke JF. 1997. A steady-state and time-resolved fluorescence study of quenching reactions of anthracene and 1,2-benzanthracene by carbon tetrabromide and bromoethane in supercritical carbon dioxide. *J Am Chem Soc* **119**: 9980–9991.
- Lessard G, Durocher G. 1978. Singlet and triplet quenching of indole by heavy atom containing molecules in a low temperature glassy matrix, evidence for complexation in the triplet state. *J Phys Chem* **82**:2812–2819.
- Khwaja HA, Semeluk GP, Unger I. 1982. Quenching of the singlet and triplet state of benzene by halogenated alkanes in the vapor phase. *Can J Chem* **60**(13):1767–1774.
- Berlman IB. 1973. Empirical study of heavy-atom collisional quenching of the fluorescence state of aromatic compounds in solution. *J Phys Chem* **77**(4):562–567.
- Kasha M. 1952. Collisional perturbation of spin-orbital coupling and the mechanism of fluorescence quenching: a visual demonstration of the perturbations. *J Chem Phys* **20**(1):71–74.
- DeToma RP, Cowan DO. 1975. External heavy-atom perturbed inter-system crossing from the excited singlet and triplet states of anthracene and 9,10-dibromoanthracene in fluid solution. *J Am Chem Soc* **97**(12):3283–3291.
- Mac M. 1995. Fluorescence quenching of aromatic molecules by inorganic anions in polar solvents. *J Luminesc* **65**:143–151.
- Kropp JL, Burton M. 1962. Effect of added quenchers in organic scintillator solutions: organometallics. *J Chem Phys* **37**(8): 1752–1756.
- Dreeskamp H, Laufer A, Zander M. 1983. Quenching of the perylene fluorescence by Ag<sup>+</sup>-ions. *Z Naturforsch A* **38**:698–700.
- Evans DF. 1957. Perturbation of singlet-triplet transitions of aromatic molecules by oxygen under pressure. *J Chem Soc*, 1351–1357.
- Kawaoka K, Khan AU, Kearns DR. 1967. Role of singlet excited states of molecular oxygen in the quenching of organic triplet states. *J Chem Phys* **46**(5):1842–1853.
- Kearns DR, Stone AJ. 1971. Excited-state intermolecular interactions involving paramagnetic molecules: effect of spin–spin and spin–orbit interactions on the quenching of triplets. *J Chem Phys* **55**(7):3383–3389.
- Kikuchi K, Sato C, Watabe M, Ikeda H, Takahashi Y, Miyoshi T. 1993. New aspects on fluorescence quenching by molecular oxygen. *J Am Chem Soc* **115**:5180–5184.

19. Parmenter CS, Rau JD. 1969. Fluorescence quenching in aromatic hydrocarbons by oxygen. *J Chem Phys* **51**(5):2242–2246.
20. Camyshan SV, Gritsan NP, Korolev VV, Bazhin NM. 1990. Quenching of the luminescence of organic compounds by oxygen in glassy matrices. *Chem Phys* **142**:59–68.
21. Alford PC, Cureton CG, Lampert RA, Phillips D. 1983. Fluorescence quenching of tertiary amines by halocarbons. *Chem Phys* **76**:103–109.
22. Najbar J, Mac M. 1991. Mechanisms of fluorescence quenching of aromatic molecules by potassium iodide and potassium bromide in methanol-ethanol solutions. *J Chem Soc Faraday Trans* **87**(10): 1523–1529.
23. Goswami D, Sarpal RS, Dogra SK. 1991. Fluorescence quenching of few aromatic amines by chlorinated methanes. *Chem Soc Jpn* **64**:3137–3141.
24. Bortolus P, Bartocci G, Mazzucato U. 1975. Excited state reactivity ofaza aromatics, III: quenching of fluorescence and photoisomerization of azastilbenes by inorganic anions. *J Phys Chem* **79**:21–25.
25. Watkins AR. 1974. Kinetics of fluorescence quenching by inorganic anions. *J Phys Chem* **78**(25):2555–2558.
26. Carrigan S, Doucette S, Jones C, Marzzacco CJ, Halpern AM. 1996. The fluorescence quenching of 5,6-benzoquinoline and its conjugate acid by Cl<sup>-</sup>, Br<sup>-</sup>, SCN<sup>-</sup> and I<sup>-</sup> ions. *J Photochem Photobiol A: Chem* **99**:29–35.
27. Ahmad A, Durocher G. 1981. Fluorescence quenching of carbazole by halocarbons in 3-methylpentane solutions at room temperature. *Can J Spectrosc* **26**(1):19–24.
28. Ahmad A, Durocher G. 1981. How hydrogen bonding of carbazole to ethanol affects its fluorescence quenching rate by electron acceptor quencher molecules. *Photochem Photobiol* **34**:573–578.
29. Namiki A, Nakashima N, Yoshinara K. 1979. Fluorescence quenching due to the electron transfer: indole-chloromethanes in rigid ethanol glass. *J Chem Phys* **71**(2):925–932.
30. Tucker SA, Cretella LE, Waris R, Street KW, Acree WE, Fetzer JC. 1990. Polycyclic aromatic hydrocarbon solute probes, VI: effect of dissolved oxygen and halogenated solvents on the emission spectra of select probe molecules. *Appl Spectrosc* **44**:269–273.
31. Takahashi T, Kikuchi K, Kokubun H. 1980. Quenching of excited 2,5-diphenyloxazole by CCl<sub>4</sub>. *J Photochem* **14**:67–76.
32. Ellison EH, Thoms JK. 2001. Photoinduced reaction of arene singlets with carbon tetrachloride in zeolite Y. *Microporous Mesoporous Mater* **49**(1–3):15–24.
33. Encinas MV, Rubio MA, Lissi EA. 1982. Quenching and photo-bleaching of excited polycyclic aromatic hydrocarbons by carbon tetrachloride. *J Photochem* **18**:137–150.
34. Dexter DL. 1953. A theory of sensitized luminescence in solids. *J Chem Phys* **21**(5):836–850.
35. Inokuti M, Hirayama F. 1965. Influence of energy transfer by the exchange mechanism on donor luminescence. *J Chem Phys* **43**(6): 1978–1989.
36. Kobayashi H, Morita T. 1973. Influence of triplet-triplet excitation transfer on the decay function of donor luminescence. *Chem Phys Lett* **20**(4):376–378.
37. Hasson S, Lustig H, Rubin MB, Speiser S. 1984. The mechanism of short-range intramolecular electron energy transfer in bichromophoric molecules. *J Phys Chem* **88**:6367–6374.
38. Knibbe H, Rehm D, Weller A. 1968. Intermediates and kinetics of fluorescence quenching by electron transfer. *Ber Bunsenges* **72**(2): 257–263.
39. Kumbhakar M, Nath S, Rath MC, Mukherjee T, Pal H. 2004. Electron transfer interaction of dihydroxyquinones with amine quenchers: dependence of the quenching kinetics on the aliphatic and aromatic nature of the amine donors. *Photochem Photobiol* **74**(1): 1–10.
40. Rubstov IV, Shirota H, Yoshihara K. 1999. Ultrafast photoinduced solute–solvent electron transfer: configuration dependence. *J Phys Chem A* **103**:1801–1808.
41. Pal SK, Bhattacharya T, Misra T, Saini RD, Ganguly T. 2003. Photophysics of some disubstituted indoles and their involvements in photoinduced electron transfer reactions. *J Phys Chem A* **107**:10243–10249.
42. Jacques P, Haselbach E, Henseler A, Pilloud D, Suppan P. 1991. Multiple Rehm-Weller plots in the electron-transfer quenching of singlet excited 9,10-dicyanoanthracene. *J Chem Soc* **87**(24): 3811–3813.
43. Seidel CAM, Schulz A, Sauer MHM. 1996. Nucleobase-specific quenching of fluorescent dyes, 1: nucleobase one-electron redox potentials and their correlation with static and dynamic quenching efficiencies. *J Phys Chem* **100**:5541–5553.
44. Montejano HA, Cosa JJ, Garrera HA, Previtali CM, 1995. Solvent effects on the photoinduced electron transfer reaction between excited singlet pyrene and indole. *J Photochem Photobiol A: Chem* **86**:115–120.
45. Ghosh HN, Pal H, Palit DK, Mukherjee T, Mittal JP. 1993. Interaction of the excited singlet state of disubstituted anthraquinones with aliphatic and aromatic amines: a fluorescence quenching study. *J Photochem Photobiol A: Chem* **73**:17–22.
46. Cheung ST, Ware WR. 1983. Exciplex photophysics, 7: steric effects in exciplex photophysics. *J Phys Chem* **87**:466–473.
47. Zhou J, Shah RP, Findley BR, Braun CL. 2002. Long distance photoinduced electron transfer in solutions: a mechanism for producing large yields of free ions by electron transfer quenching. *J Phys Chem A* **106**:12–20.
48. Chang SLP, Schuster DI. 1987. Fluorescence quenching of 9,10-dicyanoanthracene by dienes and alkenes. *J Phys Chem* **91**:3644–3649.
49. Vos R, Engelborghs Y. 1994. A fluorescence study of tryptophan histidine interactions in the peptide anatin in solution. *Photochem Photobiol* **60**(1):24–32.
50. Ricci RW, Nesta JM. 1976. Inter- and intramolecular quenching of indole fluorescence by carbonyl compounds. *J Phys Chem* **80**(9): 974–980.
51. Evans RF, Kuntz RR, Volkert WA, Ghiron CA. 1978. Flash photolysis of N-acetyl-L-tryptophanamide: the relationship between radical yields and fluorescence quenching. *Photochem Photobiol* **27**: 511–515.
52. Suzuki M, Sano M, Kimura M, Hanabusa K, Shirai H. 1999. Enhancement of quenching of polymer-bound ruthenium (II) complexes with MV<sup>2+</sup> using L-tyrosine esters. *Eur Polym J* **35**:221–226.
53. Namiki A, Nakashima N, Yoshihara K. 1979. Fluorescence quenching due to the electron transfer: indole-chloromethanes in rigid ethanol glass. *J Chem Phys* **71**(2):925–930.

54. Nagai K, Tsukamoto J, Takamiya N, Kaneko M. 1995. Effect of amino acid residue model on the photoinduced long-distance electron transfer from the excited  $\text{Ru}(\text{bpy})_{3}^{2+}$  to methylviologen in a polymer film. *J Phys Chem* **99**:6648–6651.
55. Pownall HJ, Smith LC. 1974. Fluorescence quenching of anthracene in charged micelles by pyridium and iodide ions. *Biochemistry* **13**(12):2594–2597.
56. Clayton AHA, Ghiggino KP, Wilson GJ, Keyte PJ, Paddon-Row MN. 1992. Photoinduced electron transfer in rigidly linked dimethoxy-naphthalene-N-methylpyridinium donor–acceptor molecules. *Chem Phys Lett* **195**(2,3):249–254.
57. Johnson GE. 1980. Fluorescence quenching of carbazoles. *J Phys Chem* **84**:2940–2946.
58. Nad S, Pal H. 2000. Electron transfer from aromatic amines to excited coumarin dyes: fluorescence quenching and picosecond transient absorption studies. *J Phys Chem A* **104**:673–680.
59. Singh MK, Pal H, Sapre AV. 2000. Interaction of the excited singlet state of neutral red with aromatic amines. *Photochem Photobiol* **71**(3):300–306.
60. Nagasawa Y, Yartsev AP, Tominaga K, Johnson AE, Yoshibara K. 1993. Substituent effects on intermolecular electron transfer: coumarins in electron-donating solvents. *J Am Chem Soc* **115**:7922–7923.
61. Le TP, Rogers JE, Kelly LA. 2000. Photoinduced electron transfer in covalently linked 1,8-naphthalimide/viologen systems. *J Phys Chem A* **104**:6778–6785.
62. Vos R, Engelborghs Y. 1994. A fluorescence study of tryptophan-histidine interactions in the peptide anantin and in solution. *Photochem Photobiol* **60**(1):24–32.
63. Torimura M, Krata S, Yamada K, Yokomaku T, Kamagata Y, Kanagawa T, Kurane R. 2001. Fluorescence-quenching phenomenon by photoinduced electron transfer between a fluorescent dye and a nucleotide base. *Anal Sci* **17**:155–160.
64. Sauer M, Drexhage KH, Lieberwirth U, Muller R, Nord S, Zander C. 1998. Dynamics of the electron transfer reaction between an oxazine dye and DNA oligonucleotides monitored on the single-molecule level. *Chem Phys Lett* **284**:153–163.
65. Lewis FD, Wu T, Zhang Y, Letsinger RL, Greenfield SR, Wasielewski MR. 1997. Distance-dependent electron transfer in DNA hairpins. *Science* **277**:673–676.
66. Zang L, Liu R, Holman M, Nguyen KT, Adams DM. 2002. A single-molecule probe based on intramolecular electron transfer. *J Am Chem Soc* **124**:10640–10641.
67. Liu R, Holman M, Zang L, Adams DM. 2003. Single-molecule spectroscopy of intramolecular electron transfer in donor–bridge–acceptor systems. *J Phys Chem A* **107**:6522–6526.
68. Nemzek TL, Ware WR. 1975. Kinetics of diffusion-controlled reactions: transient effects in fluorescence quenching. *J Chem Phys* **62**(2):477–489.
69. Bamford CH, Tipper CFH, Compton RG. 1985 *Chemical kinetics*. Elsevier, New York.
70. Smoluchowski VM. 1916. Drei vortage über diffusion, brownsche molekularbewegung und koagulation von kolloidteilchen [Three lectures on diffusion, Brownian molecular motion and coagulation of colloids]. *Z Physik* **17**:557–571, 585–599. (An English translation is available in Chandrasekhar S, Kac M, Smoluchowski R. 1986. *Marian Smoluchowski, his life and scientific work*. Polish Scientific Publishers, Warsaw.)
71. Collins FC, Kimball GE. 1949. Diffusion-controlled reaction rates. *J Colloid Sci* **4**:425–437. (See also Collins FC. 1950. *J Colloid Sci* **5**:499–505 for correction.)
72. Yguerabide J, Dillon MA, Burton M. 1964. Kinetics of diffusion-controlled processes in liquids: theoretical consideration of luminescent systems—quenching and excitation transfer in collision. *J Chem Phys* **40**(10):3040–3052.
73. Ware WR, Novros JS. 1966. Kinetics of diffusion-controlled reactions: an experimental test of theory as applied to fluorescence quenching. *J Phys Chem* **70**:3246–3253.
74. Ware WR, Andre JC. 1980. The influence of diffusion on fluorescence quenching. In *Time-resolved fluorescence spectroscopy in biochemistry and biology*, pp. 363–392. Ed RB Cundall, RE Dale. Plenum Press, New York.
75. Lakowicz JR, Johnson ML, Gryczynski I, Joshi N, Laczkó G. 1987. Transient effects in fluorescence quenching measured by 2-GHz frequency-domain fluorometry. *J Phys Chem* **91**:3277–3285.
76. Periasamy N, Doraiswamy S, Venkataraman B, Fleming GR. 1988. Diffusion controlled reactions: experimental verification of the time-dependent rate equation. *J Chem Phys* **89**(8):4799–4806.
77. Lakowicz JR, Kusba, J., Szmacinski H, Johnson ML, Gryczynski I. 1993. Distance-dependent fluorescence quenching observed by frequency-domain fluorometry. *Chem Phys Lett* **206**(5,6):455–463.
78. Lakowicz JR, Zelent B, Gryczynski I, Kusba J, Johnson ML. 1994. Distance-dependent fluorescence quenching of tryptophan by acrylamide. *Photochem Photobiol* **60**(3):205–214.
79. Naumann W. 2000. Reversible fluorescence quenching: generalized Stern–Volmer equations on the basis of self-consistent quenching constant relations. *J Chem Phys* **112**(16):7152–7157.
80. Zelent B, Kusba J, Gryczynski I, Johnson ML, Lakowicz JR. 1996. Distance-dependent fluorescence quenching of p-bis[2-(5-phenyloxazolyl)]benzene by various quenchers. *J Phys Chem* **100**:18592–18602.
81. Lakowicz JR, Zelent B, Kusba J, Gryczynski I. 1996. Distance-dependent quenching of nile blue fluorescence by N,N-diethylaniline observed by frequency-domain fluorometry. *J Fluoresc* **6**(4):187–194.
82. Naqvi KR, Martins J, Melo E. 2000. Recipes for analyzing diffusion-controlled reactions in two dimensions: time-resolved and steady-state measurements. *J Phys Chem B* **104**:12035–12038.
83. Kusba J, Lakowicz JR. 1994. Diffusion-modulated energy transfer and quenching: analysis by numerical integration of diffusion equation in Laplace space. *Methods Enzymol* **240**:216–262.
84. Novikov E, Molski A, Boens N. 2000. Identifiability of a model for diffusion-mediated intramolecular excited-state quenching. *J Chem Phys* **112**(12):5348–5352.
85. Gladkikh VS, Burshtein AI, Tavernier HL, Fayer MD. 2002. Influence of diffusion on the kinetics of donor–acceptor electron transfer monitored by the quenching of donor fluorescence. *J Phys Chem A* **106**:6982–6990.
86. Owen CS, Vanderkooi JM. 1991. Diffusion-dependent and -independent collisional quenching of fluorescence and phosphorescence. *Comments Mol Cell Biophys* **7**(4):235–257.

87. Klos J, Molski A. 2004. Global analysis of kinetic and stationary diffusion-mediated fluorescence quenching data. *J Phys Chem A* **108**:2370–2374.
88. Kusba J. 1998. Personal communication.
89. Zelent B, Gryczynski I, Kusba J, Johnson ML, Lakowicz JR. 1992. Distance-dependent fluorescence quenching of N-acetyl-L-tryptophanamide by acrylamide and iodide. *Proc SPIE* **2137**:412–424.
90. Lakowicz JR, Joshi NB, Johnson ML, Szmacinski H, Gryczynski I. 1987. Diffusion coefficients of quenchers in proteins from transient effects in the intensity decays. *J Biol Chem* **262**(23):10907–10910.
91. Eftink MR. 1990. Transient effects in the solute quenching of tryptophan residues in proteins. *SPIE Proc* **1204**:406–414.
92. Lakowicz JR, Kusba J, Szmacinski H, Johnson ML, Gryczynski I. 1993. Distance-dependent fluorescence quenching observed by frequency-domain fluorometry. *Chem Phys Lett* **206**(5,6):455–463.
93. Zelent B, Kusba J, Gryczynski I, Lakowicz JR. 1995. Distance-dependent quenching of anthracene fluorescence by N,N-diethylaniline observed by frequency-domain fluorometry. *Appl Spectrosc* **49**(1):43–50.
94. Vanderkooi JM, Englander SW, Papp S, Wright WW, Owen CS. 1990. Long-range electron exchange measured in proteins by

quenching of tryptophan phosphorescence. *Proc Natl Acad Sci* **87**:5099–5103.

## PROBLEMS

P9.1. *Calculation of an Oxidation Potential for a Fluorophore:* Figures 9.17 and 9.18 show that PET occurs from 1,8-naphthalimide to methylviologen. Calculate the maximum value of the reduction potential  $E(D^+/D)$  for the fluorophore above which PET would not occur. The reduction potential of  $MV^{2+}$  is 0.4 V. The wavelength of the lowest electronic transition is 365 nm.

P9.2. Figure 9.33 shows emission spectra of two compounds. The short- and long-wavelength emissions are due to the fluorescence and phosphorescence of the dimethoxy-naphthalene moiety. Explain the different fluorescence intensities of the two compounds.

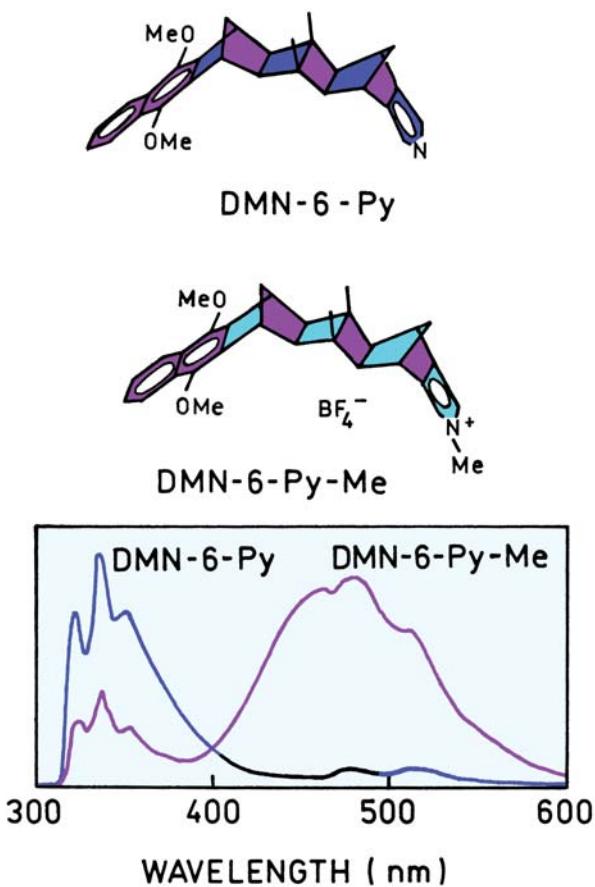


**Figure 9.33.** Emission spectra of DMN-6-Py and DMN-6-Py-Me in ethanol glass at 77°K. Revised from [56].

# 10

# Fluorescence Anisotropy

Measurements of fluorescence anisotropy are a powerful tool in biochemical research and medical testing. Upon excitation with polarized light the emission from many samples is also polarized. The extent of polarization of the emission is described in terms of the anisotropy ( $r$ ). Samples exhibiting nonzero anisotropies are said to display polarized emission. The origin of anisotropy is the existence of transition moments for absorption and emission that lie along specific directions within the fluorophore structure. In homogeneous solution the ground-state fluorophores are all randomly oriented. When exposed to polarized light, those fluorophores that have their absorption transition moments oriented along the electric vector of the incident light are preferentially excited. Hence the excited-state population is partially oriented. A significant fraction of the excited molecules have their transition moments oriented along the electric vector of the polarized exciting light.

The emission can become depolarized by a number of processes, the relative importance of which depends upon the sample under investigation. All chromophores have transition moments that occur along a specific direction in the molecular axis. Rotational diffusion changes the direction of the transition moments and is one common cause of depolarization. Anisotropy measurements reveal the average angular displacement of the fluorophore that occurs between absorption and subsequent emission of a photon. This angular displacement is dependent upon the rate and extent of rotational diffusion during the lifetime of the excited state. The rate of rotational diffusion depends on the viscosity of the solvent and the size and shape of the rotating molecule. The rotational rate of fluorophores in solution is dependent upon the viscous drag imposed by the solvent. A change in solvent viscosity will result in a change in fluorescence anisotropy. For small fluorophores in low-viscosity solutions the rate of rotational diffusion is typically faster than the rate of emission. Under these conditions the emission is depolarized and the anisotropy close to zero.

The dependence of fluorescence anisotropy upon fluorophore motions has resulted in numerous applications of this technique in biochemical research. This is because the timescale of rotational diffusion of biomolecules is comparable to the decay time of many fluorophores. For instance, a protein with a molecular weight of 25 kD can be expected to have a rotational correlation time near 10 ns. This is comparable to the lifetime of many fluorophores. Hence factors that alter the rotational correlation time will also alter the anisotropy. For biomolecules the anisotropy is decreased due to both rotational diffusion and internal flexibility. As examples we note that fluorescence anisotropy measurements have been used to quantify protein denaturation, which usually results in increased flexibility of the peptide backbone, and protein association with other macromolecules, which changes the overall rate of rotation. Anisotropy measurements can also be used to measure the dynamics of proteins. The anisotropies of membrane-bound fluorophores have been used to estimate the internal viscosities of membranes and the effects of lipid composition upon the membrane phase-transition temperature. In addition, anisotropy measurements are widely used in clinical chemistry in the form of fluorescence-polarization immunoassays.

In this chapter we describe the fundamental theory for steady-state measurements of fluorescence anisotropy. We also describe selected biochemical applications. In the subsequent chapters we will describe time-resolved anisotropy measurements and advanced applications.

## 10.1. DEFINITION OF FLUORESCENCE ANISOTROPY

The measurement of fluorescence anisotropy is illustrated in Figure 10.1. For most experiments the sample is excited with vertically polarized light. The electric vector of the excitation light is oriented parallel to the vertical or  $z$ -axis. The intensity of the emission is measured through a polar-

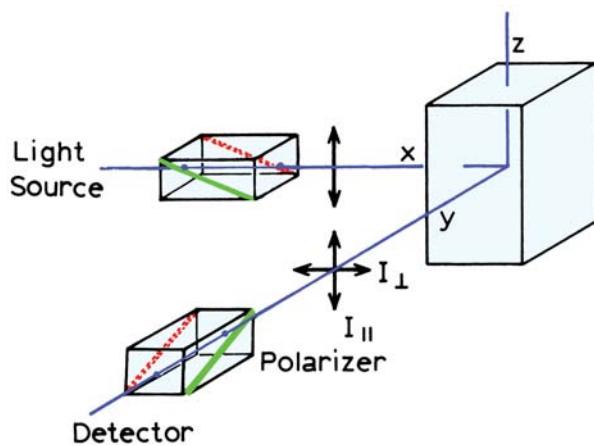


**Figure 10.1.** Schematic diagram for measurement of fluorescence anisotropies.

izer. When the emission polarizer is oriented parallel ( $\parallel$ ) to the direction of the polarized excitation the observed intensity is called  $I_{\parallel}$ . Likewise, when the polarizer is perpendicular ( $\perp$ ) to the excitation the intensity is called  $I_{\perp}$ . These intensity values are used to calculate the anisotropy:<sup>1</sup>

$$r = \frac{I_{\parallel} - I_{\perp}}{I_{\parallel} + 2I_{\perp}} \quad (10.1)$$

The anisotropy is a dimensionless quantity that is independent of the total intensity of the sample. This is because the difference  $(I_{\parallel} - I_{\perp})$  is normalized by the total intensity, which is  $I_T = I_{\parallel} + 2I_{\perp}$ . The anisotropy is an intensity ratio metric measurement. In the absence of artifacts the anisotropy is independent of the fluorophore concentration.

In earlier publications and in the clinical literature, the term polarization is frequently used. The polarization is given by

$$P = \frac{I_{\parallel} - I_{\perp}}{I_{\parallel} + I_{\perp}} \quad (10.2)$$

The polarization and anisotropy values can be interchanged using

$$P = \frac{3r}{2 + r} \quad (10.3)$$

$$r = \frac{2P}{3 - P} \quad (10.4)$$

The polarization and anisotropy contain the same information, but the use of polarization should be discouraged. Anisotropy is preferred because it is normalized by the total intensity  $I_T = I_{\parallel} + 2I_{\perp}$ , which results in simplification of the equations. Suppose the sample contains several emitting species with polarization values  $P_i$  and fractional intensities  $f_i$ . The polarization of this mixture ( $P$ ) is given by<sup>2</sup>

$$\left(\frac{1}{P} - \frac{1}{3}\right)^{-1} = \sum_i \frac{f_i}{\left(\frac{1}{P_i} - \frac{1}{3}\right)} \quad (10.5)$$

In contrast, the average anisotropy ( $\bar{r}$ ) is given by

$$\bar{r} = \sum_i f_i r_i \quad (10.6)$$

where  $r_i$  indicates the anisotropies of the individual species. The latter expression is clearly preferable. Furthermore, following pulsed excitation the fluorescence anisotropy decay  $r(t)$  of a sphere is given by

$$r(t) = r_0 e^{-t/\theta} \quad (10.7)$$

where  $r_0$  is the anisotropy at  $t = 0$ , and  $\theta$  is the rotational correlation time of the sphere. The decay of polarization is not a single exponential, even for a spherical molecule.

Suppose that the light observed through the emission polarizer is completely polarized along the transmission direction of the polarizer. Then  $I_{\perp} = 0$ , and  $P = r = 1.0$ . This value can be observed for scattered light from an optically dilute scatterer. Completely polarized emission is never observed for fluorescence from homogeneous unoriented samples. The measured values are smaller due to the angular dependence of photoselection (Section 10.2.1). Completely polarized emission can be observed for oriented samples.

Now suppose the emission is completely depolarized. In this case  $I_{\parallel} = I_{\perp}$  and  $P = r = 0$ . It is important to note that  $P$  and  $r$  are not equal for intermediate values. For the moment we have assumed these intensities could be measured without interference due to the polarizing properties of the optical components, especially the emission monochromator (Chapter 2). In Section 10.4 we will describe methods to correct for this effect.

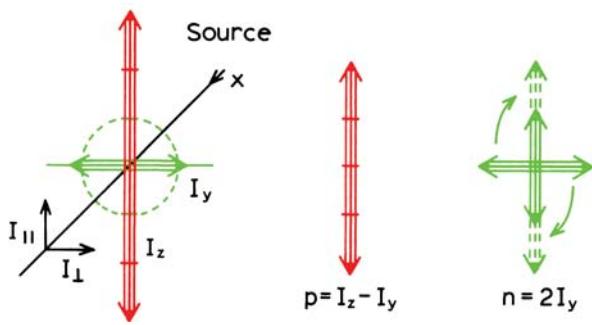


**Figure 10.2.** Polarization of a ray of light.

### 10.1.1. Origin of the Definitions of Polarization and Anisotropy

One may wonder why two widely used measures exist for the same phenomenon. Both  $P$  and  $r$  have a rational origin. Consider partially polarized light traveling along the  $x$  axis (Figure 10.2). The intensities  $I_z$  and  $I_y$  can be measured with a detector and polarizer positioned on the  $x$ -axis. The polarization of this light is defined as the fraction of the light that is linearly polarized. Specifically,

$$P = \frac{p}{p + n} \quad (10.8)$$

where  $p$  is the intensity of the polarized component and  $n$  the intensity of the natural component. The intensity of the natural component ( $n$ ) is given by  $n = 2I_y$ . The remaining intensity is the polarized component, which is  $p = I_z - I_y$ . For vertically polarized excitation  $I_z = I_{\parallel}$  and  $I_y = I_{\perp}$ . Substitution into eq. 10.8 yields eq. 10.2, which is the standard definition for polarization.

The anisotropy ( $r$ ) of a light source is defined as the ratio of the polarized component to the total intensity ( $I_T$ ):

$$r = \frac{I_z - I_y}{I_x + I_y + I_z} = \frac{I_z - I_y}{I_T} \quad (10.9)$$

When the excitation is polarized along the  $z$ -axis, emission from the fluorophores is symmetric around the  $z$ -axis (Figure 10.3). Hence  $I_x = I_y$ . Recalling  $I_y = I_{\perp}$  and  $I_z = I_{\parallel}$ , one obtains eq. 10.1.

The polarization is an appropriate parameter for describing a light source when a light ray is directed along a particular axis. In this case  $p + n$  is the total intensity and  $P$  the ratio of the excess intensity along the  $z$ -axis divided by the total intensity. This distribution of the emission is

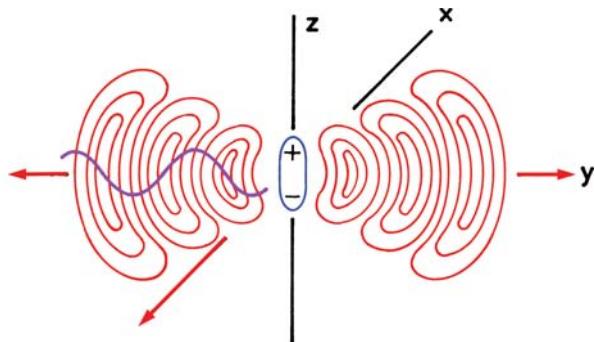


**Figure 10.3.** Electric field from a radiating dipole oriented along the  $z$ -axis. The thin arrows on the lines indicate the direction of the electric field  $E$ . The wide arrows indicate the direction of energy migration, which is symmetrical around the  $z$ -axis.

shown in Figure 10.3 for a dipole oriented along the  $z$ -axis. In contrast, the radiation emitted by a fluorophore is symmetrically distributed about the  $z$ -axis. The anisotropy is the ratio of the excess intensity that is parallel to the  $z$ -axis, divided by the total intensity. It is interesting to notice that a dipole oriented along the  $z$ -axis does not radiate along this axis, and cannot be observed with a detector on the  $z$ -axis.

### 10.2. THEORY FOR ANISOTROPY

The theory for fluorescence anisotropy can be derived by consideration of a single molecule.<sup>3</sup> Assume that the absorption and emission transition moments are parallel. This is nearly true for the membrane probe 1,6-diphenyl-1,3,5-hexatriene (DPH). Assume this single molecule is oriented with angles  $\theta$  relative to the  $z$ -axis and  $\phi$  relative to the  $y$ -axis (Figure 10.4). Of course, the ground-state DPH molecules will be randomly oriented in an isotropic solvent. If the excitation is polarized along the  $z$ -axis then there will be some preferential orientation of the excited-state population along this axis. It is known that emitting fluorophores behave like radiating dipoles.<sup>4</sup> Except for the quantized energy, the far-field radiation can be described completely by classical electrodynamics. Our goal is to calculate the anisotropy that would be observed for this oriented molecule in the absence of rotational diffusion. These assumptions of parallel dipoles, immobility, random ground-state orientation, and  $z$ -axis symmetry simplify the calculations.

Prior to deriving the expressions for anisotropy it is instructive to understand the origin of Figure 10.4. This figure shows  $I_{\parallel}$  and  $I_{\perp}$  being proportional to the projection of the transition moment onto the axes. This is true because the projection of the transition moment is the same as the

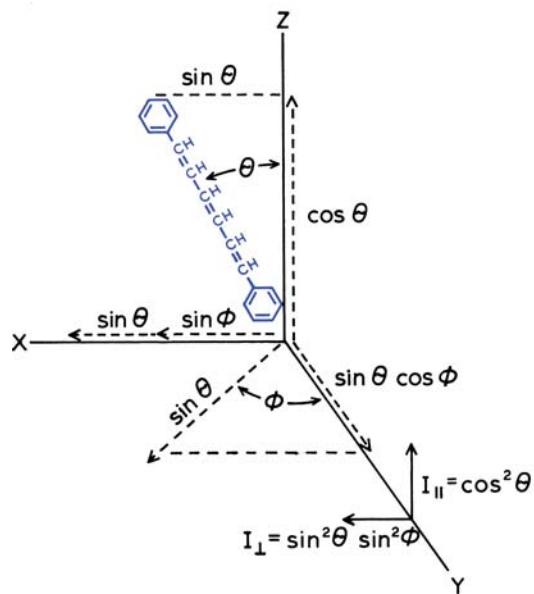


**Figure 10.4.** Emission intensities for a single fluorophore in a coordinate system.

projection of the electric field created by the fluorophore. The shape in Figure 10.3 shows the spatial distribution of light emitted by a dipole oriented along the  $z$ -axis. The electric field created by the fluorophore is described by<sup>5-6</sup>

$$E(\theta, \phi) = k \frac{\sin \theta}{r} \hat{\theta} \quad (10.10)$$

where  $k$  is a constant,  $r$  is the distance from the fluorophore and  $\hat{\theta}$  is a unit vector along the  $\theta$  coordinate. The intensity of emitted light is proportional to the square of the electric field and is given by

$$I(\theta, \phi) = k^2 \frac{\sin^2 \theta}{r^2} \quad (10.11)$$

where  $\hat{r}$  is a unit vector in the direction of propagation.

With this background we can understand the parallel and perpendicular intensities due to a dipole with some arbitrary orientation. Figure 10.5 shows the emission intensity for a dipole oriented the same as the previous DPH molecule. The electric field is always tangential to this surface. Around the equator of this surface the electric field points in the same direction as the emission transition moment. Hence the projection of the field onto the  $z$ -axis is proportional to  $\cos \theta$  and the intensity is proportional to

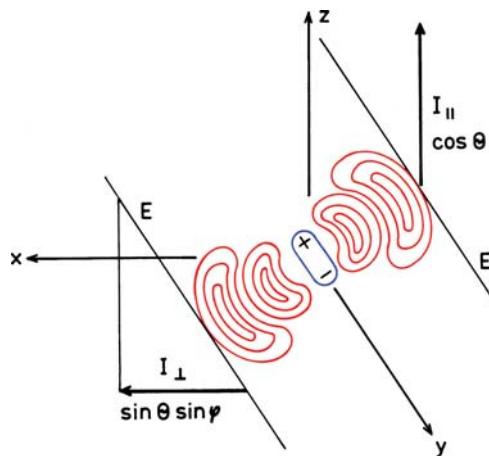


**Figure 10.5.** Radiating dipole in a coordinate system.

$\cos^2 \theta$ . Similarly, the field along the  $x$ -axis is proportional to  $\sin \theta \sin \phi$ . The polarized intensities are due to the projected electric fields, but it is usually easier to think in terms of molecular orientation rather than the radiated field. Hence we use diagrams such as Figure 10.4 to describe the anisotropy theory.

We now know the light polarized intensity along an axis is proportional to projection of the transition moments into this axis. Hence the parallel and perpendicular intensities for the molecule in Figure 10.4 are given by

$$I_{\parallel}(\theta, \phi) = \cos^2 \theta \quad (10.12)$$

$$I_{\perp}(\theta, \phi) = \sin^2 \theta \sin^2 \phi \quad (10.13)$$

We now need to consider randomly oriented fluorophores excited with polarized light. The anisotropy is calculated by performing the appropriate averaged intensities based on excitation photoselection and how the selected molecules contribute to the measured intensity. For excitation polarized along the  $z$ -axis all molecules at an angle  $\phi$  from the  $y$ -axis are excited with equal probability. That is, the population of excited fluorophore is symmetrically distributed around the  $z$ -axis. The population of excited molecules is oriented with values of  $\phi$  from 0 to  $2\pi$  with equal probability. Hence we can eliminate the  $\phi$  dependence in eq. 10.13. The average value of  $\sin^2 \phi$  is given by

$$\langle \sin^2 \phi \rangle = \frac{\int_0^{2\pi} \sin^2 \phi d\phi}{\int_0^{2\pi} d\phi} = \frac{1}{2} \quad (10.14)$$

and therefore

$$I_{\parallel}(\theta) = \cos^2 \theta \quad (10.15)$$

$$I_{\perp}(\theta) = \frac{1}{2} \sin^2 \theta \quad (10.16)$$

Now assume we are observing a collection of fluorophores that are oriented relative to the  $z$ -axis with a probability  $f(\theta)$ . In the following section we will consider the form of  $f(\theta)$  expected for excitation photoselection. The measured fluorescence intensities for this collection of molecules are

$$I_{\parallel} = \int_0^{\pi/2} f(\theta) \cos^2 \theta \, d\theta = k \langle \cos^2 \theta \rangle \quad (10.17)$$

$$I_{\perp} = \frac{1}{2} \int_0^{\pi/2} f(\theta) \sin^2 \theta \, d\theta = \frac{k}{2} \langle \sin^2 \theta \rangle \quad (10.18)$$

where  $f(\theta) d\theta$  is the probability that a fluorophore is oriented between  $\theta$  and  $\theta + d\theta$ , and  $k$  is an instrumental constant. Using eq. 10.1 and the identity  $\sin^2 \theta = 1 - \cos^2 \theta$ , one finds that

$$r = \frac{3 \langle \cos^2 \theta \rangle - 1}{2} \quad (10.19)$$

Hence the anisotropy is determined by the average value of  $\cos^2 \theta$ , where  $\theta$  is the angle of the emission dipole relative to the  $z$ -axis. This expression is only correct for samples that display  $z$ -axis symmetry. A different expression is needed to describe the anisotropy of a fluorophore oriented with unique angles  $\theta$  and  $\phi$ .

It is instructive to consider the relationship between  $r$  and  $\theta$ . For a single fluorophore oriented along the  $z$ -axis, with colinear transitions,  $\theta = 0$ , the use of eq. 10.19 shows that  $r = 1.0$ . However, it is not possible to obtain a perfectly oriented excited-state population with optical excitation of homogeneous solutions. Hence the anisotropies are always less than 1.0. Complete loss of anisotropy is equivalent to  $\theta = 54.7^\circ$ . This does not mean that each fluorophore is oriented at  $54.7^\circ$ , or that they have rotated through  $54.7^\circ$ . Rather, it means that the average value of  $\cos^2 \theta$  is  $1/3$ , where  $\theta$  is the angular displacement between the excitation and emission moments. In the derivation of eq. 10.19 we assumed that the transition moments were colinear. A slightly more complex expression is necessary for almost

all fluorophores because the transition moments are rarely colinear. In addition, we have not yet considered the effects of photoselection on the anisotropy values.

### 10.2.1. Excitation Photoselection of Fluorophores

When a sample is illuminated with polarized light, those molecules with absorption transitions aligned parallel to the electric vector of the polarized excitation have the highest probability of excitation. The electric dipole of a fluorophore need not be precisely aligned with the  $z$ -axis to absorb light polarized along this axis. The probability of absorption is proportional to the  $\cos^2 \theta$ , where  $\theta$  is the angle the absorption dipole makes with the  $z$ -axis.<sup>7</sup> Hence, excitation with polarized light results in a population of excited fluorophores that are partially oriented along the  $z$ -axis (Figure 10.6). This phenomenon is called photoselection. The excited-state population is symmetrical around the  $z$ -axis. Most of the excited fluorophores are aligned close to the  $z$ -axis, and very few fluorophores have their transition moments oriented in the  $x$ - $y$  plane. For the random ground-state distribution, which must exist in a disordered solution, the number of molecules at an angle between  $\theta$  and  $\theta + d\theta$  is proportional to  $\sin \theta \, d\theta$ . This quantity is proportional to the surface area on a sphere within the angles  $\theta$  and  $\theta + d\theta$ .

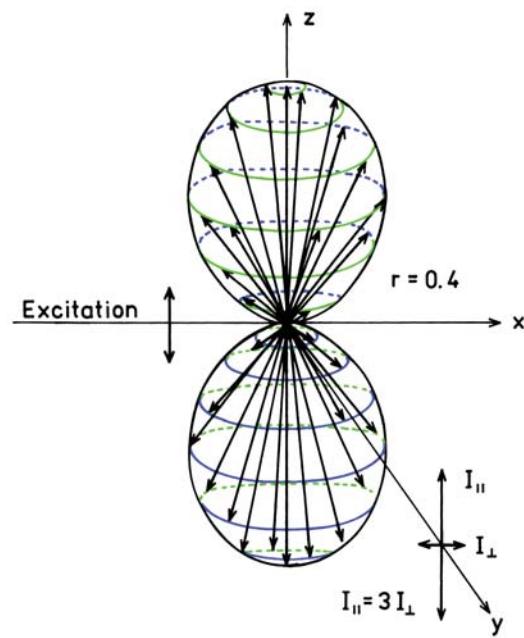


**Figure 10.6.** Excited-state distribution for immobile fluorophores with  $r_0 = 0.4$ .

Hence, the distribution of molecules excited by vertically polarized light is given by

$$f(\theta) d\theta = \cos^2 \theta \sin d\theta \quad (10.20)$$

The probability distribution given by eq. 10.20 determines the maximum photoselection that can be obtained using one-photon excitation of an isotropic solution. More highly oriented populations can be obtained using multiphoton excitation.<sup>7</sup>

The anisotropy is a function of  $\langle \cos^2 \theta \rangle$  (eq. 10.19). Hence, calculation of  $\langle \cos^2 \theta \rangle$  allows calculation of the anisotropy. For colinear absorption and emission dipoles the value of  $\langle \cos^2 \theta \rangle$  is given by

$$\langle \cos^2 \theta \rangle = \frac{\int_0^{\pi/2} \cos^2 \theta f(\theta) d\theta}{\int_0^{\pi/2} f(\theta) d\theta} \quad (10.21)$$

Substitution of 10.20 into 10.21 yields  $\langle \cos^2 \theta \rangle = 3/5$ . Equation 10.19 shows a maximum anisotropy of 0.4. This is the value that is observed when the absorption and emission dipoles are colinear, and when there are no processes which result in depolarization. Under these conditions the excited-state population is preferentially oriented along the  $z$ -axis (Figure 10.6) and the value of  $I_{\perp}$  is one-third the value of  $I_{\parallel}$  ( $I_{\parallel} = 3I_{\perp}$ ). This value of  $r = 0.4$  is considerably smaller than that possible for a single fluorophore oriented along the  $z$ -axis ( $r = 1.0$ ).

It is important to remember that there are other possible origins for polarized light. These include reflections and light scattered by the sample. For a dilute scattering solution, where there is a single scattering event, the anisotropy is close to 1.0. Scattered light can interfere with anisotropy measurements. If the measured anisotropy for a randomly oriented sample is greater than 0.4, one can confidently infer the presence of scattered light in addition to fluorescence. The maximum anisotropy of 0.4 for colinear absorption and emission dipoles is a consequence of the  $\cos^2 \theta$  probability of light absorption. Anisotropy values can exceed 0.4 for multiphoton excitation (Chapter 18).

### 10.3. EXCITATION ANISOTROPY SPECTRA

In the preceding section we assumed that the absorption and emission moments were colinear ( $r_0 = 0.4$ ). Few fluorophores display  $r_0 = 0.4$ . For most fluorophores the  $r_0$  values are less than 0.4, and in general the anisotropy values

depend on the excitation wavelength. This is explained by the transition moments being displaced by an angle  $\beta$  relative to each other. In the previous section (eqs. 10.12–10.19) we demonstrated that displacement of the emission dipole by an angle  $\theta$  from the  $z$ -axis resulted in a decrease in the anisotropy by a factor  $(3\cos^2 \theta - 1)/2$ . Similarly, the displacement of the absorption and emission dipoles by an angle  $\beta$  results in a further loss of anisotropy. The observed anisotropy in a vitrified dilute solution is a product of the loss of anisotropy due to photoselection (2/5), and that due to the angular displacement of the dipoles. The fundamental anisotropy of a fluorophore is given by

$$r_0 = \frac{2}{5} \left( \frac{3\cos^2 \beta - 1}{2} \right) \quad (10.22)$$

where  $\beta$  is the angle between the absorption and emission transitions.

The term  $r_0$  is used to refer to the anisotropy observed in the absence of other depolarizing processes such as rotational diffusion or energy transfer. For some molecules  $\beta$  is close to zero. For example,  $r_0$  values as high as 0.39 have been measured for DPH, although slightly lower values are frequently reported.<sup>8–10</sup> An anisotropy of 0.39 corresponds to an angle of 7.4° between the dipoles, whereas  $r_0 = 0.4$  corresponds to an angle of 0°. The fundamental anisotropy value is zero when  $\beta = 54.7^\circ$ . When  $\beta$  exceeds 54.7° the anisotropy becomes negative. The maximum negative value (−0.20) is found for  $\beta = 90^\circ$ . These values for both  $r_0$  and  $P_0$  are summarized in Table 10.1. For any fluorophore randomly distributed in solution, with one-photon excitation, the value of  $r_0$  must be within the range from −0.20 to 0.40 for single-photon excitation.

Measurement of the fundamental anisotropy requires special conditions. In order to avoid rotational diffusion the probes are usually examined in solvents that form a clear glass at low temperature, such as propylene glycol or glyc-

**Table 10.1.** Relationship between the Angular Displacement of Transition Moments ( $\beta$ ) and the Fundamental Anisotropy ( $r_0$ ) or Polarization ( $P_0$ )

$\beta$ (deg)	$r_0$	$P_0$
0	0.40	0.50 = 1/2
45	0.10	0.143 = 1/7
54.7	0.00	0.000
90	−0.20	−0.333 = −1/3

erol. Additionally, the solutions must be optically dilute to avoid depolarization due to radiative reabsorption and emission, or due to resonance energy transfer. One commonly used solvent for measuring fundamental anisotropies is propylene glycol at  $-60$  to  $-70^{\circ}\text{C}$ . Under these conditions the fluorophores remain immobile during the lifetime of the excited state. Glycerol also forms a rigid glass at low temperature. However, glycerol typically displays more auto-fluorescence than propylene glycol. At similar temperatures phosphorescence from the fluorophores seems to be more common in glycerol than in propylene glycol. In these rigid solutions the measured anisotropy values ( $r_0$ ) provide a measure of the angle between the absorption and emission dipoles (eq. 10.22). Since the orientation of the absorption dipole differs for each absorption band, the angle  $\beta$  varies with excitation wavelength. The changes in the fundamental anisotropy with excitation wavelength can be understood as a rotation of the absorption transition moment. A more precise explanation may be the changing contributions of two or more electronic transitions, each with a different value of  $\beta$ . As the excitation wavelength changes, so does the fraction of the light absorbed by each transition (Section 10.3.1).

The anisotropy spectrum is a plot of the anisotropy versus the excitation wavelength for a fluorophore in a dilute vitrified solution. The anisotropy is usually independent of the emission wavelength, so only excitation anisotropy spectra are reported. The lack of dependence on emission wavelength is expected since emission is almost always from the lowest singlet state. If emission occurs from more than one state, and if these states show different emission spectra, then the anisotropies can be dependent upon emission wavelength. Such dependence can also be observed in the presence of solvent relaxation (Chapter 7). In this case anisotropy decreases with increasing wavelength because the average lifetime is longer for longer wavelengths (Chapter 12). This effect is generally observed when the spectral relaxation time is comparable to the fluorescence lifetime. In completely vitrified solution, where solvent relaxation does not occur, the anisotropy is usually independent of emission wavelength.

The largest  $r_0$  values are usually observed for excitation into the longest wavelength absorption band.<sup>11</sup> This is because the lowest singlet state is generally responsible for the observed fluorescence, and this state is also responsible for the long-wavelength absorption band (Kasha's rule). Absorption and emission involving the same electronic transition have nearly colinear moments. Larger  $\beta$  values

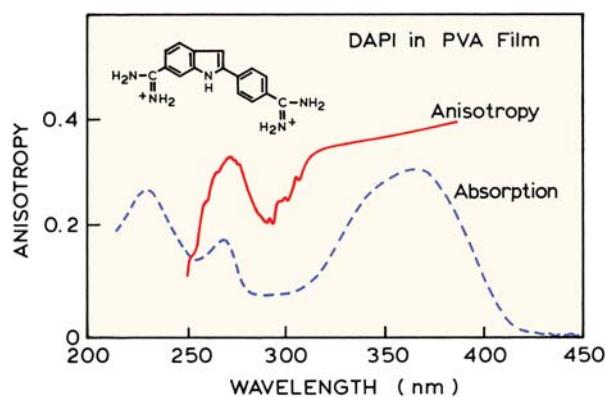


**Figure 10.7.** Excitation anisotropy spectra of DAPI in an unstretched polyvinyl alcohol film (solid). The dashed line is the absorption spectrum. Revised and reprinted with permission from [15]. Copyright © 1989, American Chemical Society.

(lower  $r_0$  values) are obtained upon excitation into higher electronic states, which are generally not the states responsible for fluorescence emission. Rather, the fluorophores relax very rapidly to the lowest singlet state. The excitation anisotropy spectrum reveals the angle between the absorption and emission transition moments. However, the direction of these moments within the molecule itself are not revealed. Such a determination requires studies with ordered systems, such as crystals or stretched films.<sup>12–14</sup>

These general features of an anisotropy spectrum are illustrated in Figure 10.7 for DAPI in an isotropic (unstretched) polyvinyl alcohol film.<sup>15</sup> This film is very viscous, so the fluorophores cannot rotate during the excited-state lifetime. The absorption and emission dipoles are in the plane of the rings. For excitation wavelengths longer than 330 nm the  $r_0$  value is relatively constant. The relatively constant  $r_0$  value across the  $S_0 \rightarrow S_1$  transition, and a gradual tendency towards higher  $r_0$  values at longer wavelengths, is typical of many fluorophores. As the excitation wavelength is decreased the anisotropy becomes more strongly dependent on wavelength. Different anisotropies are expected for the  $S_0 \rightarrow S_1$ ,  $S_0 \rightarrow S_2$  and higher transitions.

The excitation anisotropy spectrum of DAPI is rather ideal because  $r_0$  is relatively constant across the long wavelength absorption band. Many fluorophores show a gradual decrease in  $r_0$  as the excitation wavelength is decreased. This property is illustrated for 9-anthroyloxy stearic acid (9-AS) in Figure 10.8. When using such probes careful control of the excitation wavelength is needed if the experiments depend on knowledge of the  $r_0$  values.

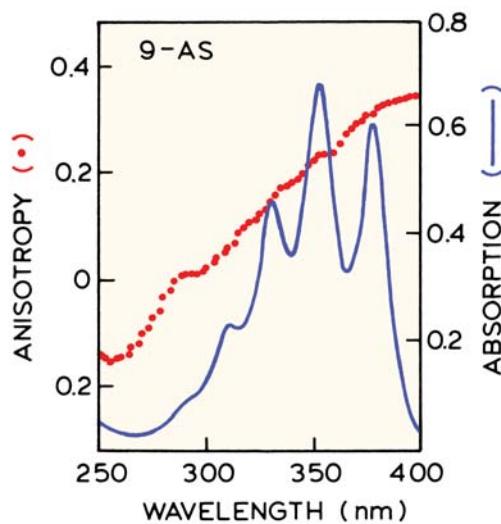


**Figure 10.8.** Excitation anisotropy spectrum of 9-anthroyloxy stearic acid (9-AS) in propylene glycol at  $-52^{\circ}\text{C}$ . The same excitation anisotropy spectrum was observed for 2-AS, 7-AS, 12-AS and 16-AP. Revised and reprinted with permission from [16]. Copyright © 1982, American Chemical Society.

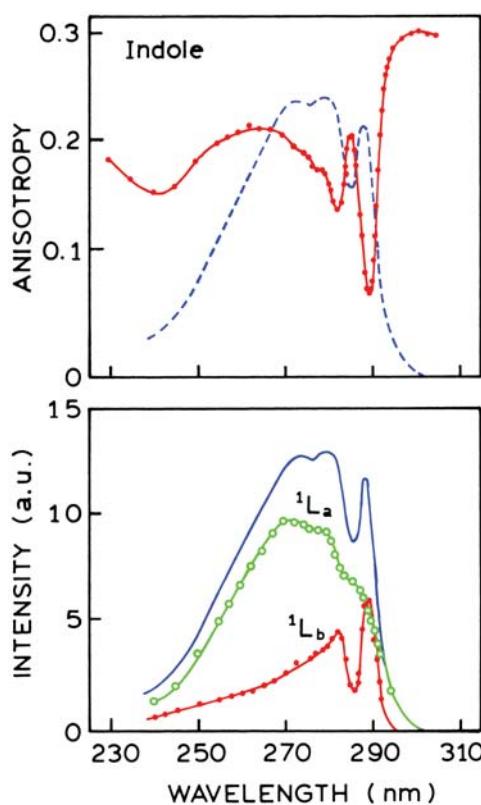


**Figure 10.10.** Excitation anisotropy spectrum of indole in vitrified propylene glycol. Also shown are the calculated absorption spectra of the  ${}^1\text{L}_a$  and  ${}^1\text{L}_b$  states. Revised from [19].

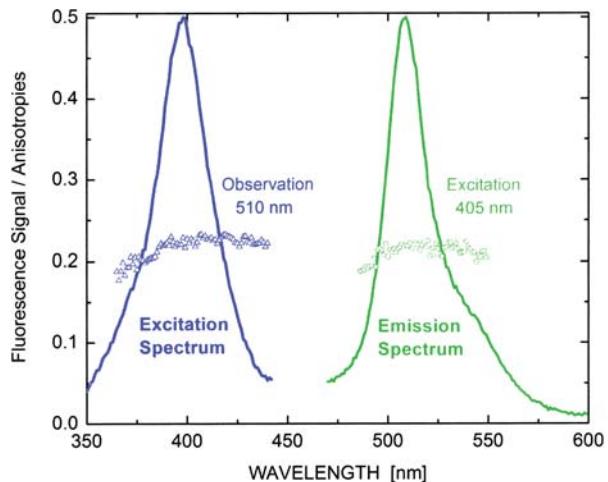


**Figure 10.9.** Excitation anisotropy spectrum of Green Fluorescent Protein. Figure courtesy of Drs. Z. Gryczynski, L. Black and R. B. Thompson.

Figure 10.9 shows excitation and emission anisotropy spectra for GFP that was packaged into the heads of T4 bacteriophage.<sup>17</sup> Each phage head contains about 90 GFP molecules. Given the size of the phage heads, the anisotropy is expected to be close to the fundamental anisotropy, which is near 0.38. Homotransfer between the concentrated GFP molecules was suggested as the reason for the lower

anisotropy. The anisotropy is constant across the emission spectrum, which is typical of emission anisotropy spectra.

### 10.3.1. Resolution of Electronic States from Polarization Spectra

Some fluorophores can display complex anisotropy spectra, even across the longest absorption band. One well-known example is indole.<sup>18–20</sup> The anisotropy varies abruptly with excitation wavelength across the long-wavelength absorption band (Figure 10.10, top). This dependence was attributed to the two excited states of indole ( ${}^1\text{L}_a$  and  ${}^1\text{L}_b$ ), which are responsible for the absorption from 250 to 300 nm.<sup>21–22</sup> The transition moments are thought to be at an angle of  $90^{\circ}$  relative to one another.<sup>23–24</sup> Emission of indole occurs mainly from the  ${}^1\text{L}_a$  state.

This complex anisotropy spectrum can be used to determine the absorption spectra corresponding to the  $\text{S}_0 \rightarrow {}^1\text{L}_a$  and  $\text{S}_0 \rightarrow {}^1\text{L}_b$  states.<sup>19</sup> This example illustrates the additivity of anisotropies (eq. 10.6). This example is also impor-

tant for an understanding of the fluorescence from tryptophan residues in proteins (Chapter 16). At any excitation wavelength  $\lambda$  the observed anisotropy is

$$r_0(\lambda) = f_a(\lambda)r_{0a} + f_b(\lambda)r_{0b} \quad (10.23)$$

where  $f_i(\lambda)$  represents the fractional contribution of the  $i$ th state to the total absorption at the wavelength  $\lambda$ , and  $r_{0i}$  represents the limiting anisotropy of this state. The assumption was made that  $r_{0a}$  and  $r_{0b}$  are independent of wavelength, that emission occurs only from the  ${}^1L_a$  state, and that the quantum yield is independent of excitation wavelength. The highest observed value of  $r_0$  was 0.3, and this value was assigned to  $r_{0a}$ . This means that absorption of the  ${}^1L_a$  state is assumed to be dominant at excitation wavelengths of 300 nm and greater. Selection of a value for  $r_{0b}$  is more difficult since there is no obvious wavelength where the absorption of  ${}^1L_b$  is dominant. The transition dipoles for  ${}^1L_a$  and  ${}^1L_b$  states are thought to be perpendicular. The anisotropy expected for  ${}^1L_b$  can be predicted using eq. 10.22, which describes the loss in anisotropy due to an angular displacement of two oscillators by a known angle. The maximum value of  $r_0$  (0.4) is replaced by  $r_{0a} = 0.3$ . Hence the anisotropy of the  ${}^1L_b$  state is given by

$$r_{0b} = 0.30 \left( \frac{3\cos^2\beta - 1}{2} \right) \quad (10.24)$$

Using  $\beta = 90^\circ$  one obtains  $r_{0b} = -0.15$ . These values of  $r_{0a}$  and  $r_{0b}$  are used in eq. 10.23, along with the restriction that the total fractional absorption is unity ( $f_a(\lambda) + f_b(\lambda) = 1$ ), to calculate the fractional absorption of each state as a function of wavelength. Rearrangement of eq. 10.23 yields

$$f_a(\lambda) = \frac{r_0(\lambda) - r_{0b}}{r_{0a} - r_{0b}} = \frac{r_0(\lambda) + 0.15}{0.45} \quad (10.25)$$

$$f_b(\lambda) = \frac{r_{0a} - r_0(\lambda)}{r_{0a} - r_{0b}} = \frac{0.3 - r_0(\lambda)}{0.45} \quad (10.26)$$

And finally, the absorption spectrum of each state is given by

$$A_a(\lambda) = f_a(\lambda) A(\lambda) \quad (10.27)$$

$$A_b(\lambda) = f_b(\lambda) A(\lambda) \quad (10.28)$$

where  $A(\lambda)$  is the total absorption spectrum. These resolved spectra are shown in the lower panel of Figure 10.10. The  ${}^1L_b$  absorption is structured, but this absorption is less intense than the  ${}^1L_a$  absorption. The peak at 290 nm in the absorption spectrum of indole is seen to be due to the  ${}^1L_b$  state, and this peak absorption corresponds to a minimum in the  $r_0$  value. Above 295 nm only the  ${}^1L_a$  state absorbs, and the anisotropy is relatively constant. This is one reason why 295–300 nm excitation is used when studying the intrinsic tryptophan emission of proteins. This example illustrates how polarization spectra reveal the electronic properties of fluorophores.

## 10.4. MEASUREMENT OF FLUORESCENCE ANISOTROPIES

Prior to describing the applications of anisotropy, it is useful to understand the methods used to measure the anisotropy or polarization. We describe steady-state measurements, but similar considerations apply to time-resolved measurements of anisotropies. Two methods are commonly used. These are the L-format method, in which a single emission channel is used, and the T-format method, in which the parallel and perpendicular components are observed simultaneously through separate channels. The procedures described below are intended to correct for the different efficiencies of the instrumentation for detection of the various polarized components of the emission (Chapter 2).

### 10.4.1. L-Format or Single-Channel Method

The L format is used most frequently because most fluorometers have only a single emission channel. Assume the sample is excited with vertically polarized light, and the emission is observed through a monochromator (Figure 10.11). The monochromator will usually have a different transmission efficiency for vertically and horizontally polarized light. Consequently, rotation of the emission polarizer changes the measured intensities even if the sample emits unpolarized light. The measured intensities are not the desired parallel and perpendicular intensities, but rather intensities that are also proportional to the transmission efficiencies of the monochromator for each polarized component. The objective is to measure these actual intensities,  $I_{||}$  and  $I_{\perp}$ , unbiased by the detection system.

We use two subscripts to indicate the orientation of the excitation and emission polarizers, respectively. For exam-

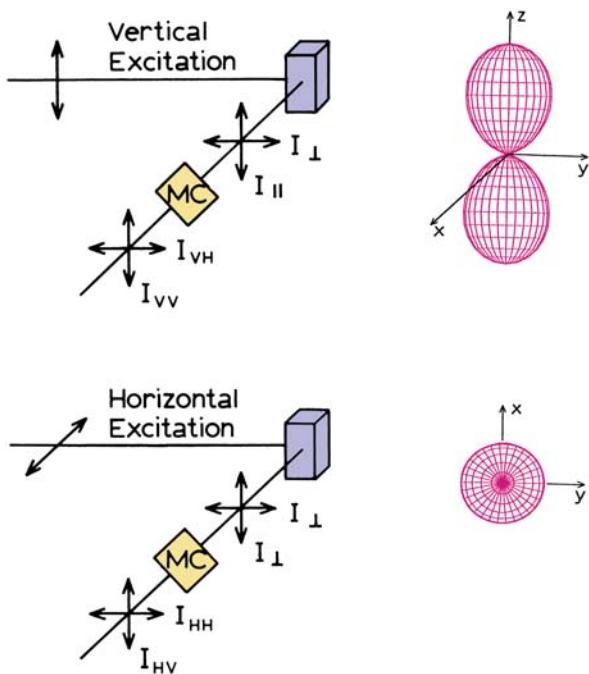


**Figure 10.11.** Schematic diagram for L-format measurements of fluorescence anisotropy. MC, monochromators. The shapes on the right are the excited-state distributions.

ple,  $I_{HV}$  corresponds to horizontally polarized excitation and vertically polarized emission. This notation is easy to recall since the order of the subscripts represents the order in which the light passes through the two polarizers. Let  $S_V$  and  $S_H$  be the sensitivities of the emission channel for the vertically and horizontally polarized components, respectively. For vertically polarized excitation the observed polarized intensities are

$$I_{VV} = kS_V I_{\parallel} \quad (10.29)$$

$$I_{VH} = kS_H I_{\perp} \quad (10.30)$$

where  $k$  is a proportionality factor to account for the quantum yield of the fluorophore and other instrumental factors aside from the polarization-dependent sensitivity. Division of 10.29 and 10.30 yields

$$\frac{I_{VV}}{I_{VH}} = \frac{S_V}{S_H} \frac{I_{\parallel}}{I_{\perp}} = G \frac{I_{\parallel}}{I_{\perp}} \quad (10.31)$$

The measured intensity ratio is different from the true value by a factor  $G$ . To calculate the actual intensity ratio ( $I_{\parallel}/I_{\perp}$ )

we need to determine the  $G$  factor, which is the ratio of the sensitivities of the detection system for vertically and horizontally polarized light:

$$G = \frac{S_V}{S_H} \quad (10.32)$$

If the measured intensities are not corrected for the  $G$  factor, the calculated anisotropy will be incorrect. For instance, assume  $G = 2.0$ . This means that the emission monochromator passes vertically polarized light, at the chosen emission wavelength, with twofold greater efficiency than horizontally polarized light. The  $G$  factor is dependent upon the emission wavelength, and to some extent the bandpass of the monochromator. Frequently, anisotropy measurements are performed using an emission filter rather than a monochromator. Filters generally do not have a significant polarizing effect, and hence one expects  $G = 1.0$ . Nonetheless, this factor should always be determined since rotation of the emission polarizer can cause the focused image of the fluorescence to change position, altering the effective sensitivity.

The  $G$  factor is easily measured using horizontally polarized excitation. With horizontally polarized excitation the excited-state distribution is rotated to lie along the observation axis. When this is done both the horizontally and vertically polarized components are equal and proportional to  $I_{\perp}$  (Figure 10.11). These components are equal because the electric field is equally distributed around the observation axis. Both polarizer orientations are perpendicular to the polarization of the excitation. Any measured difference in  $I_{HV}$  and  $I_{HH}$  must be due to the detection system. Specifically,

$$\frac{I_{HV}}{I_{HH}} = \frac{S_V}{S_H} \frac{I_{\perp}}{I_{\perp}} = \frac{S_V}{S_H} = G \quad (10.33)$$

Frequently the excitation intensity can change when the excitation polarizer is rotated. This change is a constant factor in the numerator and denominator of eq. 10.33, and hence cancels. When the  $G$  factor is known the ratio  $I_{\parallel}/I_{\perp}$  can be calculated using

$$\frac{I_{VV}}{I_{VH} G} = \frac{I_{VV} I_{HH}}{I_{VH} I_{HV}} = I_{\parallel}/I_{\perp} \quad (10.34)$$

The anisotropy is given by

$$r = \frac{I_{\parallel}/I_{\perp} - 1}{I_{\parallel}/I_{\perp} + 2} \quad (10.35)$$

which is frequently used in the alternative form:

$$r = \frac{I_{VV} - GI_{VH}}{I_{VV} + 2GI_{VH}} \quad (10.36)$$

#### 10.4.2. T-Format or Two-Channel Anisotropies

In the T-format method the intensities of the parallel and perpendicular components are measured simultaneously using two separate detection systems (Figure 10.12). The emission polarizers are left unchanged, so the sensitivity of each channel remains the same during the measurement. It is still necessary to measure the relative sensitivity of the two detection systems, which is accomplished using horizontally polarized excitation. The T-format measurements are performed as follows. The excitation polarizer is first placed in the vertical orientation to measure the ratio of the parallel and perpendicular signals ( $R_V$ ). This ratio is given by

$$R_V = \frac{G_{\parallel} I_{\parallel}}{G_{\perp} I_{\perp}} \quad (10.37)$$

where  $G_{\parallel}$  and  $G_{\perp}$  are the sensitivities of the parallel and perpendicular channels, respectively. This ratio can be adjusted to unity, but in practice it is easier to simply measure the ratio. This ratio is measured again using horizontally polarized excitation. Then both emission channels observe  $I_{\perp}$  (Figure 10.12). Hence the ratio of intensities is given by

$$R_H = G_{\parallel}/G_{\perp} \quad (10.38)$$

Division of 10.37 by 10.38 yields

$$\frac{R_V}{R_H} = \frac{I_{\parallel}}{I_{\perp}} \quad (10.39)$$

which can be used to calculate the anisotropy (eq. 10.35). The excitation intensity may vary upon rotation of the excitation polarizer. This factor cancels in taking the ratio. However, difficulties can arise if light from the excitation monochromator is completely polarized in either the verti-

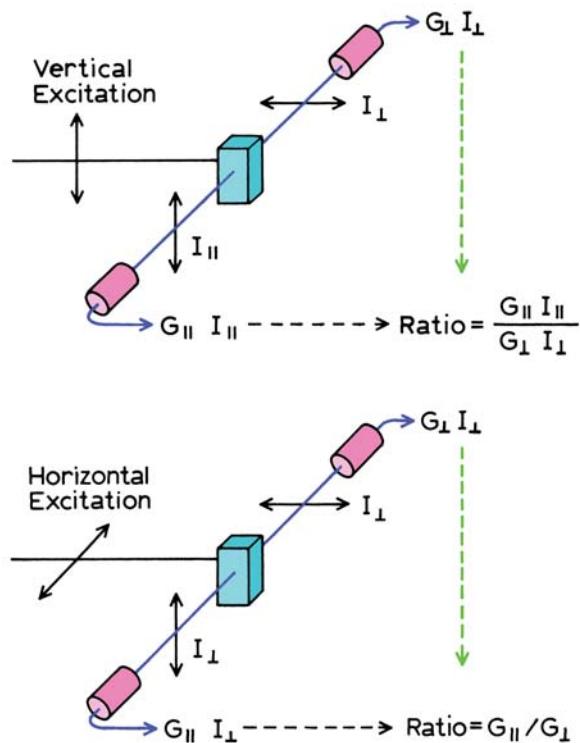


**Figure 10.12.** Schematic diagram for T-format measurements of fluorescence anisotropy.

cal or horizontal direction (Chapter 2). Then either  $R_H$  or  $R_V$  cannot be measured because of inadequate light intensity. This difficulty can be avoided by using a different excitation wavelength where adequate intensity is available for each polarization. This is acceptable because  $R_V$  and  $R_H$  are properties of the detection system, and are not dependent on the excitation wavelength or the degree of polarization displayed by the sample. The theoretical maximum for  $I_{\parallel}/I_{\perp}$  is 3 ( $r = 0.4$ ). Values of  $I_{\parallel}/I_{\perp}$  in excess of 3 generally indicate an artifact, typically scattered light. Scattered light is 100% polarized ( $I_{\parallel}/I_{\perp} = \infty$ ,  $r = 1.0$ ), and a small percentage of such light can seriously distort the anisotropy values.

#### 10.4.3. Comparison of T-Format and L-Format Measurements

For fluorometers with a single emission channel the L format must be used to measure anisotropies. This procedure requires four individual measurements:  $I_{VV}$ ,  $I_{VH}$ ,  $I_{HV}$ , and  $I_{HH}$ . The latter two determine the  $G$  factor, which does not need to be measured each time. The T-format method again requires four intensity measurements, which appear as two

ratios. Because of the simultaneous measurement, fluctuations in signal intensity are canceled in T-format measurements. In the early days of fluorescence spectroscopy T-format measurements were preferred. With modern instruments there no longer seems to be any significant advantage to T-format measurements, except possibly for a decreased time for data acquisition. L-format measurements are routinely used in this laboratory.

#### 10.4.4. Alignment of Polarizers

Accurate measurement of fluorescence anisotropies requires that the polarizers be precisely positioned in the vertical and horizontal orientations. The alignment can be easily checked and adjusted using a dilute suspension of glycogen or colloidal silica in water. The scattered light is 100% polarized, that is,  $r = 1.0$ . In this laboratory we consider the alignment to be adequate when the measured value is 0.97 or larger. It is essential to use dilute suspensions of scatterer. Otherwise multiple scattering events lead to decreased values of polarization.

Alignment can be accomplished as follows. The excitation polarizer is rotated to the approximate vertical position. Precise vertical alignment is not necessary since the scattered light is vertically polarized. The angular alignment of the emission polarizer is adjusted so that the minimum intensity is observed. This is the horizontal position. It is preferable to use this minimum intensity for alignment. The maximum intensity for the vertical component is less sharply defined. One should check that the vertical polarizer stop is also properly adjusted. Rotation of the emission polarizer should now yield the maximum and minimum intensities when the polarizer is at the vertical and horizontal stops, respectively. These adjustments should be performed with the emission monochromator removed, or its wavelength chosen for approximate equal transmission efficiencies for vertically and horizontally polarized light. Otherwise, the polarizing properties of the emission monochromator could interfere with the alignment. The wavelength selection for equal transmission efficiencies can be accomplished using either horizontally polarized excitation, to obtain  $I_{\parallel} = I_{\perp}$ , or a sample whose emission is not polarized. Examples of such solutions are 9-cyanoanthracene in the fluid solvent ethanol or  $[\text{Ru}(\text{bpy})_3]^{2+}$  in water.<sup>11</sup>

Alignment of the excitation polarizer is performed in a similar manner. The emission polarizer should be set in the vertical position. The minimum and maximum intensities of scattered light should be observed when the excitation

polarizer is at its horizontal and vertical stops, respectively. Once again one should consider the polarization properties of the excitation monochromator.

#### 10.4.5. Magic-Angle Polarizer Conditions

The goal of intensity measurements is usually to measure a signal proportional to the total intensity ( $I_T$ ), and not proportional to  $I_{\parallel}$  or  $I_{\perp}$ . However, since the transmission efficiency of the emission monochromator depends on polarization, the observed signal is not exactly proportional to  $I_{\parallel} + 2I_{\perp}$ , but rather to some other combination of  $I_{\parallel}$  and  $I_{\perp}$ . By the use of polarizers the measured intensity can be proportional to the total intensity,  $I_T = I_{\parallel} + 2I_{\perp}$ , irrespective of the degree of polarization of the sample. To accomplish this the excitation polarizer is oriented in the vertical position and the emission polarizer is oriented ( $54.7^\circ$ ) from the vertical. Since  $\cos^2 54.7^\circ = 0.333$  and  $\sin^2 54.7^\circ = 0.667$ , these polarizer settings result in  $I_{\perp}$  being selected twofold over  $I_{\parallel}$ , forming the correct sum for  $I_T = I_{\parallel} + 2I_{\perp}$ . The use of magic-angle conditions is especially important for intensity decay measurements. The intensity decays of the vertically and horizontally polarized components are usually distinct. If  $I_{\parallel}(t)$  and  $I_{\perp}(t)$  are not properly weighted, then incorrect decay times are recovered. If the anisotropy is zero, then the correct intensity and intensity decay times are recovered independent of polarizer orientation.

#### 10.4.6. Why is the Total Intensity Equal to $I_{\parallel} + 2I_{\perp}$ ?

It is widely known that the total intensity is given by  $I_{\parallel} + 2I_{\perp}$ , but the origin of this result is less widely understood. It is actually quite simple. For any fluorophore the total intensity is equal to the sum of the intensities along the three axes:  $I_T = I_x + I_y + I_z$ . Each intensity is given by the square of the transition moment projection on each axis. Using these terms from Figure 10.4, the sum of the three projections is unity. This is true for every fluorophore, so that if the three intensities are measured all fluorophores contribute equally to the total intensity, regardless of this orientation. Now suppose the sample has  $z$ -axis symmetry. Then  $I_z = I_{\parallel} + 2I_{\perp}$ .

#### 10.4.7. Effect of Resonance Energy Transfer on the Anisotropy

In Section 10.3 we discussed an intrinsic cause of depolarization, namely, angular displacement between the absorp-

tion and emission moments. The fluorophores were assumed to be immobile and the excited state was assumed to remain localized on the originally excited fluorophore. The anisotropy can also be decreased by extrinsic factors that act during the lifetime of the excited state. These include rotational diffusion of the fluorophore and the resonance energy transfer (RET) of energy among fluorophores (Chapter 13). Both processes result in additional angular displacement of the emission oscillator and hence lower anisotropies.

The effects of rotational diffusion and energy transfer are easily separated by selection of the experimental conditions. For example, Brownian rotations cause negligible depolarization when the rotational rate is much slower than the rate of fluorescence emission. Therefore, rotation diffusion can be decreased or eliminated using low temperatures and/or high viscosities. Radiationless energy transfer occurs only in concentrated solution where the average distance between the fluorophore molecules is comparable to a characteristic distance  $R_0$ , which is typically near 40 Å. Millimolar fluorophore concentrations are required to obtain this average distance (Chapter 13). This concentration is considerably larger than the usual concentrations required for fluorescence measurements, which are about  $10^{-6}$  M. Hence radiationless energy transfer is easily avoided by the use of dilute solutions. The solutions also need to be adequately diluted so that radiative transfer does not occur.

The effect of RET on the anisotropy is illustrated by the excitation anisotropy spectrum of fluorescein in dilute and concentrated solution.<sup>25</sup> Fluorescein is subject to radiative (emission and reabsorption) and non-radiative energy transfer because of the small Stokes shift. In this experiment (Figure 10.13) radiative transfer was avoided by using thin samples, and rotational diffusion was eliminated by using a vitrified sample. Under these experimental conditions RET is the only mechanism that can decrease the anisotropy. In dilute solution fluorescein displays its characteristic anisotropy spectrum, with high anisotropy for excitation above 380 nm. At high concentration the anisotropy is decreased. This effect is due to RET between fluorescein molecules. In random solution it is known that a single non-radiative transfer step reduces the anisotropy to 4% of the initial value.<sup>26-29</sup> Hence RET is an effective mechanism in depolarization. The presence or absence of RET can usually be predicted from the concentration in the sample and the spectral properties of the probes.

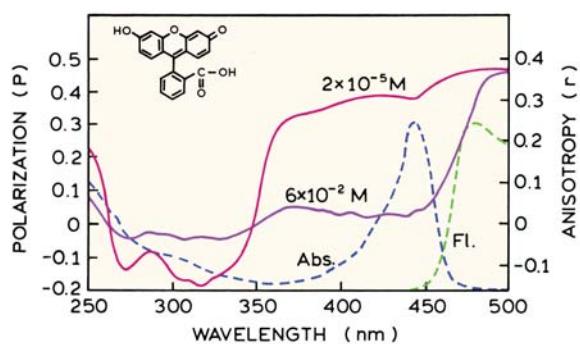


**Figure 10.13.** Excitation polarization spectra of fluorescein in propylene glycol at  $-50^{\circ}\text{C}$ . Radiative transfer was avoided by using thin samples, 30 to 50 microns thick. Revised and reprinted with permission from [25].

Examination of Figure 10.13 reveals that the anisotropy (polarization) of the concentrated sample increases for excitation wavelengths longer than 460 nm. This increase is due to the failure of energy transfer with red edge excitation (Chapter 7). The anisotropy increases because the red-edge excitation results in a shift of the emission spectrum to longer wavelength, decreased spectral overlap, and less energy transfer.

#### 10.4.8. Trivial Causes of Depolarization

The measured anisotropies can be lower than the actual values for several trivial reasons, including light scattering, reabsorption, and misalignment of the polarizers. While these are nontrivial experimental problems, they are dependent only on the optical conditions of the experiment and do not provide useful information on the molecular properties of the sample.

Biological samples, such as aqueous suspensions of membranes, are frequently turbid. This turbidity can cause scattering of both the incident light and the emitted photons. The scattered incident light can result in excitation, and the emitted photons can be scattered prior to observation. Each scattering event is thought to decrease the anisotropy of the scattered photon from 0.85 to 0.7 of the value in the absence of scatter.<sup>30-31</sup> The magnitude of the effect depends on the size of the scatterer. The observed anisotropy is expected to decrease linearly with the optical density due to turbidity. The actual proportionality constant will depend upon the sample under investigation.<sup>32</sup> It is therefore advisable to investigate the effect of turbidity for

any sample which displays visible turbidity. This can be accomplished by either actual dilution of the sample or using a cuvette with smaller dimensions. If dilution does not change in anisotropy, then there is unlikely to be significant depolarization due to scattering.

A more serious effect of scattering is the possibility that scattered light reaches the detector. This is particularly true for dilute solutions where the intensity is low, and scattering from the optics and sample can be significant. Since the scattered light will be highly polarized ( $r = 1.0$ ), a small percentage of scattered light can result in significant changes in the anisotropy (eq. 10.6, see also Problem 10.2). If scattered light reaches the detector, then the measured anisotropy will usually increase relative to its true value.

Another trivial cause of depolarization is radiative transfer, which is the reabsorption of emitted photons. It is more difficult to eliminate radiative transfer since it can occur at lower concentrations than RET. In fact, radiative transfer is a frequent cause of low anisotropy values for fluorescein. Because of their large spectral overlap, fluorescein solutions often show the effects of radiative transfer. Surprisingly, radiative transfer is less effective than RET in depolarization. A single radiative transfer step reduces the anisotropy to 28% of its initial value,<sup>33–34</sup> as compared to 4% of the initial value for a single RET step.

Measured anisotropy values can also be too low due to misalignment or inefficiency of the polarizers. Film polarizers become less ideal at short wavelengths. The polarizers can be tested by examination of a dilute scattering solution (Section 10.4.4.). And, finally, one should always examine a blank sample that scatters light approximately the same as the sample. Background signals can be especially problematic for anisotropy measurements. The background signal may be polarized if due to scattered light, or unpolarized if

due to low-molecular-weight impurities. Hence, background signals can either increase or decrease the anisotropy. In order to correct for background it is necessary to measure the four individual intensities from the blank sample, and subtract them from each respective intensity value in eq. 10.36.

#### 10.4.9. Factors Affecting the Anisotropy

The various factors that can affect the anisotropy were summarized in an insightful table,<sup>3</sup> which outlines the experimental conditions for various anisotropy measurements (Table 10.2). The fundamental anisotropy can be measured in dilute highly viscous solution, where rotational diffusion or RET do not occur. Information about the Förster distance ( $R_0$ ) for hetero- or homo-RET can be obtained from studies in concentrated viscous solution. The most interesting condition designated in Table 10.2 is that for dilute non-viscous solutions. In such solutions the anisotropy is primarily determined by rotational motion of the fluorophore. For labeled proteins these motions are dependent upon the size and shape of the protein, its extent of aggregation, and other factors. For membranes the anisotropy depends upon the chemical composition and phase state of the membranes. As a result, anisotropy measurements are frequently used to study the properties and interactions of biological macromolecules.

---

#### 10.5. EFFECTS OF ROTATIONAL DIFFUSION ON FLUORESCENCE ANISOTROPIES: THE PERRIN EQUATION

Rotational diffusion of fluorophores is a dominant cause of fluorescence depolarization, and most applications depend

**Table 10.2.** Extrinsic Causes of Depolarization<sup>a</sup>

Condition	Observable	Molecular property
Dilute viscous solution (propylene glycol, -70° C)	$r_0$ or $\cos \beta$ (eq. 10.22)	Angle between absorption and emission dipole as a function of excitation wavelength
Concentrated viscous solution	$0 <  r  <  r_0 $ Anisotropy decreased by energy migration	Distance dependence of radiationless energy transfer
Dilute non-viscous solution (H <sub>2</sub> O, EtOH, room temp.)	$0 <  r  <  r_0 $ Anisotropy decreased due to Brownian rotation	Size and shape of fluorophore or macromolecule

<sup>a</sup>From [3].

on changes in the rate of rotation. Depolarization by rotational diffusion of spherical rotors is described by the Perrin equation:<sup>35-37</sup>

$$\frac{r_0}{r} = 1 + \tau/\theta = 1 + 6D\tau \quad (10.40)$$

where  $\tau$  is the fluorescence lifetime,  $\theta$  is the rotational correlation time, and  $D$  is the rotational diffusion coefficient. If the correlation time is much larger than the lifetime ( $\theta \gg \tau$ ), then the measured anisotropy ( $r$ ) is equal to the fundamental anisotropy ( $r_0$ ). If the correlation time is much shorter than the lifetime ( $\theta \ll \tau$ ), then the anisotropy is zero.

The Perrin equation can be derived from first principles based on diffusional steps.<sup>3,38</sup> A simple derivation is possible using the time-resolved decay of anisotropy  $r(t)$  for a spherical molecule:

$$r(t) = r_0 e^{-t/\theta} = r_0 e^{-6Dt} \quad (10.41)$$

In this equation the rotational correlation time of the fluorophore ( $\theta$ ) is given by

$$\theta = \frac{\eta V}{RT} \quad (10.42)$$

where  $\eta$  is the viscosity,  $T$  is the temperature in °K,  $R$  is the gas constant, and  $V$  is the volume of the rotating unit. The rotational correlation time is related to the rotational diffusion coefficient by  $\theta = (6D)^{-1}$ . Only spherical molecules display a single exponential anisotropy decay. More complex expressions are predicted for nonsymmetric species or molecules (Chapter 12).

The steady-state anisotropy can be calculated from an average of the anisotropy decay,  $r(t)$ , over the intensity decay,  $I(t)$ :

$$r = \frac{\int_0^\infty I(t) r(t) dt}{\int_0^\infty I(t) dt} \quad (10.43)$$

For a single-exponential intensity decay, substitution into eq. 10.43 yields

$$r = \frac{r_0}{1 + \tau/\theta} \quad (10.44)$$

which is a form of the Perrin equation. Using this equation, it is possible to calculate the anisotropy expected for fluo-

rophores in solvents or for labeled macromolecules, assuming the molecules are spherical. For example, perylene has a lifetime of 6 ns and  $r_0 = 0.36$ . In ethanol rotational diffusion is expected to decrease the anisotropy to 0.005 (Problem 10.5).

### 10.5.1. The Perrin Equation: Rotational Motions of Proteins

Prior to the availability of time-resolved measurements the apparent molecular volumes of proteins were measured using the Perrin equation. This application can be seen by rearranging eq. 10.44:

$$\frac{1}{r} = \frac{1}{r_0} + \frac{\tau}{r_0 \theta} \quad (10.45)$$

For globular proteins the rotational correlation time is approximately related to the molecular weight ( $M$ ) of the protein by

$$\theta = \frac{\eta V}{RT} = \frac{\eta M}{RT} (\bar{v} + h) \quad (10.46)$$

where  $\bar{v}$  is the specific volume of the protein, and  $h$  is the hydration,  $T$  is the temperature in °K,  $R = 8.31 \times 10^7$  erg/mol°K, and the viscosity  $\eta$  is in poise (P). Values of  $h$  for proteins are typically near 0.73 ml/g, and the hydration is near 0.23 g H<sub>2</sub>O per gram of protein. This expression predicts that the correlation time of a hydrated protein is about 30% larger than that expected for an anhydrous sphere. Generally, the observed values of  $\theta$  are about twice that expected for an anhydrous sphere.<sup>39</sup> For example, for an anhydrous protein sphere with a 50 kD molecular weight, with  $h = 0.73$  ml/g and  $\eta = 0.94$  cP, the calculated rotational correlation time at 25°C is near 14 ns. The anisotropy decay of an immunoglobulin F<sub>ab</sub> fragment, labeled at the antigen binding site with dansyl-lysine, yielded a rotational correlation time of 33 ns. This larger correlation time was consistent with a hydration of 0.32 ml/g and an axial ratio near 2. This result is typical of that found for proteins (Table 10.3), and is probably a result of the non-spherical shape of most proteins and a larger effective solvent shell for rotational diffusion than for hydration. For convenience we have listed the calculated rotation correlation times for proteins with different molecular weights and different amounts of hydration in Table 10.4.

**Table 10.3.** Rotational Correlation Times for Proteins<sup>a</sup>

Protein	Molecular weight	Observed θ (ns)	$\theta_{\text{obs}}/\theta_{\text{calc}}$
Apomyoglobin	17,000	8.3	1.9
β-Lactoglobulin (monomer)	18,400	8.5	1.8
Trypsin	25,000	12.9	2.0
Chymotrypsin	25,000	15.1	2.3
Carbonic anhydrase	30,000	11.2	1.4
β-Lactoglobulin (dimer)	36,000	20.3	2.1
Apoperoxidase	40,000	25.2	2.4
Serum albumin	66,000	41.7	2.4

<sup>a</sup>θ<sub>obs</sub> is the observed rotational correlation time, adjusted to T/η corresponding to water at 25°C.

θ<sub>calc</sub> is the rotational correlation time calculated for a rigid unhydrated sphere with a molecular weight of the protein, assuming a partial specific volume of 0.73 ml/g. From [39].

**Table 10.4.** Calculated Rotational Correlation Times for Proteins<sup>a</sup>

T	Molecular weight (kD)	Correlation time θ (ns)		
		h = 0	h = 0.2	h = 0.4
2°C	10	5.5	6.9	8.4
	25	13.7	17.3	21.1
	50	27.4	34.6	42.0
	100	54.8	69.2	84.0
	500	274.0	346.0	420.0
20°C	10	3.1	3.9	4.7
	25	7.0	9.7	11.8
	50	15.4	19.5	23.6
	100	30.8	39.0	47.2
	500	154.0	195.0	236.0
37°C	10	2.0	2.5	3.1
	25	5.0	6.4	7.7
	50	10.0	12.7	15.4
	100	20.1	25.4	30.8
	500	100.5	127.0	154.0

<sup>a</sup>Calculated using  $\theta = \eta M (\bar{v} + h)/RT$  with  $\bar{v} = 0.75 \text{ ml/g}$ , and various degrees of hydration ( $h$ ). The viscosities are  $\eta$  (2°C) = 1.67 cP,  $\eta$  (20°C) = 1.00 cP,  $\eta$  (37°C) = 0.69 cP.

The apparent volume of a protein can be determined by measuring the anisotropy at various temperatures and/or viscosities. Substitution of eq. 10.42 into 10.45 yields a modified form of the Perrin equation:

$$\frac{1}{r} = \frac{1}{r_0} + \frac{\tau RT}{r_0 \eta V} \quad (10.47)$$

The use of eq. 10.47 was one of the earliest biochemical applications of fluorescence.<sup>40–42</sup> The general approach is to

covalently label the protein with an extrinsic fluorophore. The fluorophore is chosen primarily on the basis of its fluorescence lifetime. This lifetime should be comparable to the expected rotational correlation time of the protein. In this way the anisotropy will be sensitive to changes in the correlation time. Generally, the fluorescence anisotropies are measured over a range of  $T/\eta$  values. Temperature is varied in the usual manner, and viscosity is generally varied by addition of sucrose or glycerol. For biochemical samples only a limited range of  $T/\tau$  values are available. At high temperature the macromolecule may denature, and at low temperatures the solvent may freeze or the macromolecule may not be soluble. The apparent volume of the protein is obtained from a plot of  $1/r$  versus  $T/\eta$  (Figure 10.14). The intercept of the  $y$ -axis represents extrapolation to a very high viscosity, and should thus be  $1/r_0$ , where  $r_0$  is the fundamental anisotropy of the fluorophore. In practice fluorophores bound to protein often display segmental motions, which are independent of overall rotational diffusion. These motions are often much faster than rotational diffusion, and rather insensitive to the macroscopic viscosity. As shown in Chapter 12, such motions can be considered to be an independent factor which depolarizes the emission by a constant factor. The effect is to shift  $1/r$  to larger values, and shift the apparent  $r_0$  value to a smaller value (larger  $y$ -intercept). This does not mean that the  $r_0$  value is in fact smaller, but rather reflects the inability of the Perrin plot to resolve the faster motion.

What value of  $r_0$  should be used to calculate the volume of the protein? In general the extrapolated value of  $r_0$  ( $r_0^{\text{app}}$ ) will yield the best estimate of the volume because this value accounts for segmental motion of the probe and partially cancels the effects of this motion on the correlation time  $\theta$ .

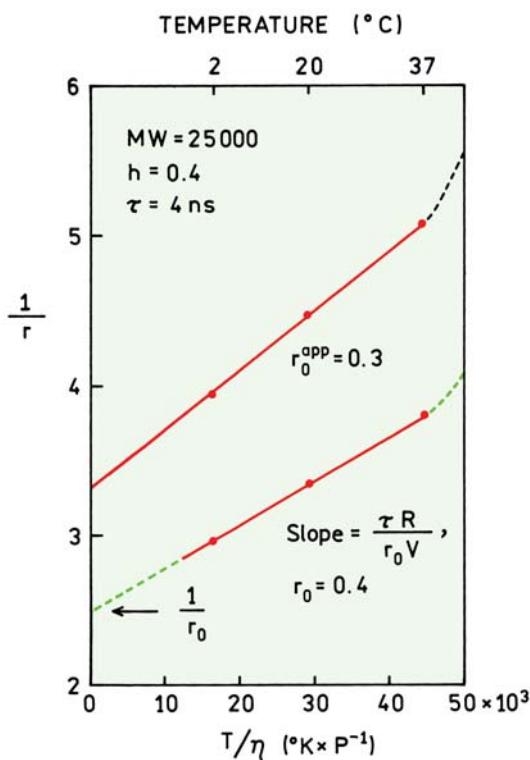


**Figure 10.14.** Perrin plots for determination of protein volume. The curves are drawn for a protein molecular weight of 25,000 daltons in water,  $h = 0.4$  and  $\tau = 4$  ns. The value of  $r_0 = 0.4$  represents a rigidly bound probe and  $r_0 = 0.3$  represents a probe with some segmented mobility. The upward curving dashed lines indicate the protein is denaturing at high temperature.

For example, assume the segmental motion of the fluorophore is much more rapid than the rotational diffusion of the protein. Then, the value of  $r_0$  is effectively reduced to

$$r_0^{\text{app}} = r_0 \left( \frac{<3 \cos^2 \alpha> - 1}{2} \right) \quad (10.48)$$

where  $\alpha$  is the angle through which the probe undergoes this segmental motion. The term  $(1/r_0^{\text{app}})$  cancels in the calculation of the molecular volume, and the apparent volume represents overall rotation diffusion of the protein. It is important to note that, if the short correlation time for segmental motion ( $\theta_s$ ) is not much faster than the overall correlation time ( $\theta_L$ ), then the apparent volume can be substantially decreased due to contributions from the more rapid motions (Section 10.9). Some information is available by comparison of the extrapolated and frozen solution values of  $r_0$ . If  $r_0^{\text{app}}$  is much smaller than  $r_0$  one may infer the existence of segmental motions of the probe on the macromol-

ecule, independent motions of domains of the protein, or possibly RET in multiply labeled proteins. Another behavior seen in Perrin plots is a rapid increase in  $1/r$  at high temperatures. Such an increase is usually the result of denaturation of the macromolecule, resulting in an increase in independent motion of the probe and a decrease in the anisotropy.

A different version of the Perrin equation is often found in the older literature:

$$\begin{aligned} \left( \frac{1}{P} - \frac{1}{3} \right) &= \left( \frac{1}{P_0} - \frac{1}{3} \right) \left( 1 + \frac{\tau RT}{\eta V} \right) \\ &= \left( \frac{1}{P_0} - \frac{1}{3} \right) \left( 1 + \frac{3\tau}{\rho} \right) \end{aligned} \quad (10.49)$$

This equation is equivalent to eq. 10.47, except for the use of polarization in place of anisotropy. When using the equation, a plot  $(1/P - 1/3)$  versus  $T/\eta$  is used to obtain the molecular volume. The intercept yields the apparent value of  $(1/P_0^{\text{app}} - 1/3)$ , which can be larger than the true value  $(1/P_0 - 1/3)$  if there is segmental motion of the probe. The term  $\rho$  is the rotational relaxation time ( $\rho = 30$ ). At present the use of anisotropy, the rotational correlation time, and eq. 10.44 is preferred.

### 10.5.2. Examples of a Perrin Plot

It is instructive to examine a representative Perrin plot (Figure 10.15).<sup>16</sup> These data are for 9-anthroyloxy stearic acid in a viscous paraffin oil, Primol 342. The anisotropies were measured at various excitation wavelengths, corresponding to different  $r_0$  values (Figure 10.8). The y-axis intercepts are different because of the different  $r_0$  values. Also, the slopes are larger for shorter excitation wavelengths because the value of  $r_0$  appears in the denominator of eq. 10.47. In spite of the very different values of  $1/r$  for different excitation wavelengths, the data are all consistent with a correlation time near 15 ns at 25°C (Table 10.5). For a spherical molecule, the correlation time is independent of  $r_0$ . In Chapter 12 we will see that the correlation times can depend on the value of  $r_0$  for non-spherical molecules. This effect may be the cause of the somewhat different correlation times found for different excitation wavelengths.

The y-axis intercepts yield the apparent values of  $r_0$  extrapolated to high viscosity, which can be compared with measured values in a glassy solvent (Table 10.5). The

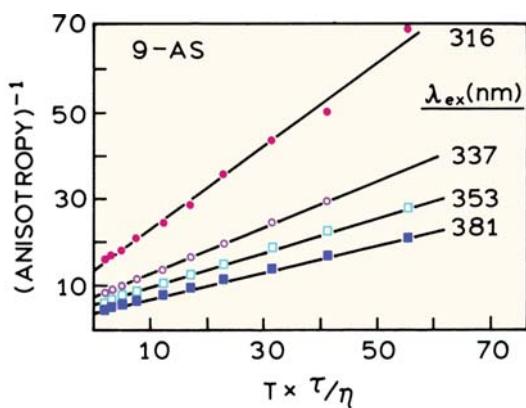


**Figure 10.15.** Perrin plots of 9-anthroyloxy stearic acid in Primol 342. The excitation wavelengths were 316 (●), 337 (○), 353 (□) and 381 nm (■). The lifetime, ranging from 10.5 to 9.7 ns, is incorporated into the  $x$ -axis. Revised and reprinted with permission from [16]. Copyright © 1982, American Chemical Society.

**Table 10.5.** Fundamental ( $r_0$ ) and Extrapolated ( $r_0^{\text{app}}$ ) Anisotropy Values and Rotational Correlation Times for Anthroyloxy Stearic Acid<sup>a</sup>

Excitation wavelength (nm)	$r_0$	$r_0^{\text{app}}$	$\theta$ (ns) <sup>b</sup>
316	0.090	0.075	13
337	0.178	0.136	14
353	0.231	0.179	14
381	0.323	0.242	18

<sup>a</sup>From [16].

<sup>b</sup>In Primol 342 at 6°C.

extrapolated values are about 25% lower than the measured  $r_0$  values. This is a typical result for Perrin plots. Fluorophores are often non-spherical, resulting in multi-exponential anisotropy decays. In such cases the Perrin plots are curved toward the  $x$ -axis, resulting in higher apparent intercepts on the  $y$ -axis.

## 10.6. PERRIN PLOTS OF PROTEINS

### 10.6.1. Binding of tRNA to tRNA Synthetase

Perrin plots of labeled macromolecules have been extensively used to determine the apparent hydrodynamic volumes. One example is the binding of methionine tRNA (tRNA<sup>fMet</sup>) with methionyl-tRNA synthetase (met-RS). The 3' end of the tRNA was labeled with fluorescein (Fl) by periodate oxidation of the tRNA followed by reaction with

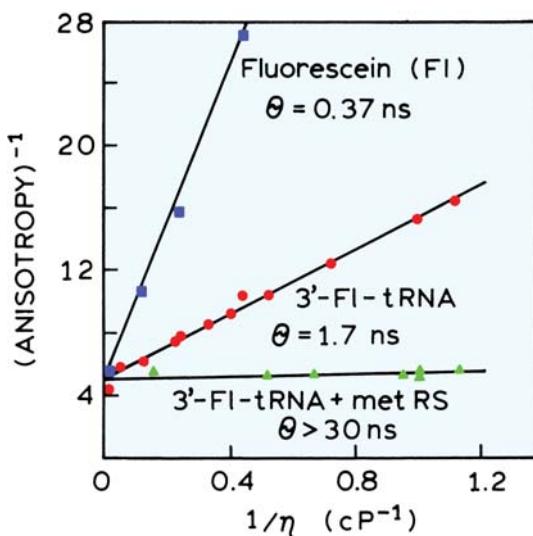


**Figure 10.16.** Perrin plot of fluorescein (Fl, ■) and tRNA<sup>fMet</sup> labeled at the 3' end with fluorescein (●). Also shown is the labeled tRNA when bound to methionyl-tRNA synthetase (met RS, ▲). The experiments were performed at 20°C. The viscosity  $\eta$  was varied by adding sucrose. Excitation at 480 nm and emission at 520 nm. Revised and reprinted with permission from [43]. Copyright © 1986, American Chemical Society.

fluorescein thiosemicarbazide.<sup>43</sup> The Perrin plots were obtained at a single temperature with the viscosity changed by adding sucrose. As expected, fluorescein free in solution displays a subnanosecond correlation time (Figure 10.16). More surprising is the apparent correlation time for 3'-Fl-tRNA, which is 1.7 ns. Based on the size and shape of tRNA, the rotational correlation time is expected to be near 25 ns. This result indicates that the 3'-fluorescein label displays significant segmental freedom independent of overall rotational diffusion of the tRNA and that these segmental motions are the dominant cause for depolarization.

Upon binding of 3'-Fl-tRNA to the synthetase the anisotropy increases dramatically from 0.062 to 0.197. The small slope of the Perrin plot indicates that the correlation time is larger than 30 ns. The synthetase consists of two identical subunits, 76 kD each, so that its rotational correlation time is expected to be 100 ns or longer. Apparently, the 3' end of the tRNA interacts with the synthetase, immobilizing the fluorescein residue. It should be noted that the lifetime of fluorescein, typically near 3 ns, is too short to accurately measure the rotational correlation time of the complex. Based on eq. 10.44 the anisotropy of a 3-ns fluorophore will be decreased by only 3% for a correlation time of 100 ns. For this reason the correlation time is only stated as over 30 ns in Figure 10.16.

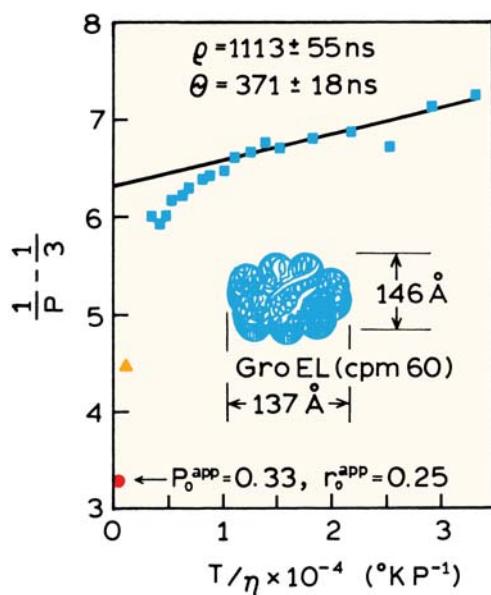


**Figure 10.17.** Perrin plot of chaperonin cpn60 labeled with 1-pyrene-sulfonyl chloride at 25°C. Viscosities were varied with sucrose. Two points ( $\bullet$  and  $\blacktriangledown$ ) were measured at 0°C. The pyrene lifetime was near 45 ns. Revised from [47].

The  $y$ -intercepts of the Perrin plots yield the apparent  $r_0$  values, which are near 0.2 for these three fluorescein samples. This value is less than that typical of fluorescein, which is near 0.35. Hence, there appears to be some unresolved motion of the fluorescein even when bound to the synthetase. It is difficult to determine the  $y$ -intercept for fluorescein itself due to the large extent of depolarization.

### 10.6.2. Molecular Chaperonin cpn60 (GroEL)

Molecular chaperonins are proteins that assist other proteins in folding.<sup>44–45</sup> The cpn60 chaperonin (GroEL) from *E. coli* is a large multi-subunit oligomer consisting of fourteen identical 60-kD subunits. These subunits are arranged in two stacked rings, each with seven subunits. Each subunit consists of three domains. The entire protein of 840 kD is a cylindrical oligomer, 146 Å tall, 137 Å wide, with a central channel 45 Å in diameter.<sup>46</sup>

Rotational diffusion of cpn60 was studied using a pyrene-labeled protein.<sup>47</sup> Pyrene was chosen for its long fluorescence lifetime, which can reach 200 ns. In this case the pyrenesulfonyl label displayed a lifetime near 45 ns. The Perrin plot for pyrene-labeled cpn60 shows significant curvature (Figure 10.17). In this figure the data are presented in the older style using polarization instead of anisot-

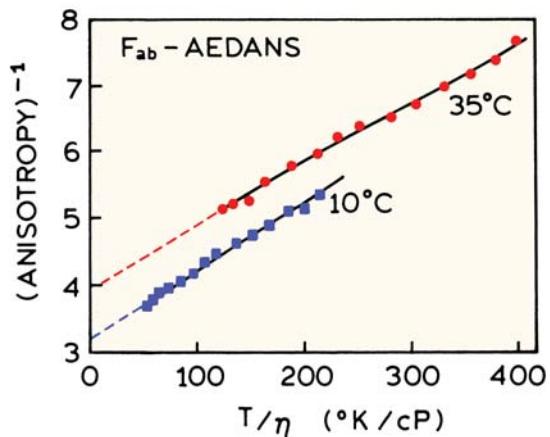


**Figure 10.18.** Perrin plots of immunoglobulin  $F_{ab}$  fragments labeled with AEDANS at the C terminus. Viscosity was varied by adding sucrose. Revised and reprinted with permission from [48]. Copyright © 1995, American Chemical Society.

ropy. The chaperonin displays considerable flexibility, as can be seen from the curvature in the Perrin plot. Different apparent correlation times can be obtained for different regions of the curve. At lower viscosities the faster motions are complete, so that the overall rotational correlation time can be estimated from the limiting slope. This calculation results in an apparent correlation time near 370 ns. Calculation of the correlation time using eq. 10.46, with 0.23 g H<sub>2</sub>O/g protein hydration, yields a correlation time near 347 ns. Hence, the slope from the Perrin plot observed for the lower viscosities provided a reasonable estimate of the overall size. The data at higher viscosity or lower temperature indicate the domain or subunits of cpn60 have significant independent mobility.

### 10.6.3. Perrin Plots of an $F_{ab}$ Immunoglobulin Fragment

A potentially confusing aspect of the Perrin plots is the use of  $T/\eta$  as the  $x$ -axis. This implies that the same result should be obtained independent of whether temperature or viscosity is varied. Unfortunately, this is not usually the case. In fact, it is common to observe different Perrin plots for variation in temperature as compared to variation in viscosity. This is illustrated by the Perrin plots of  $F_{ab}$  fragments labeled with IAEDANS. These  $F_{ab}$  fragments show segmental motions that depend on temperature.<sup>48</sup>  $F_{ab}$  fragments are the antibody-binding domains of immunoglobulins. Different Perrin plots are observed at 10 and 35°C (Figure 10.18). At the higher temperature there is more independent motion

of the probe and/or domains of the  $F_{ab}$  fragment. Hence, the  $y$ -intercepts are larger. Perrin plots that depend differently on temperature or viscosity should not be regarded as incorrect, but rather as reflecting the temperature-dependent dynamics of the protein.

## 10.7. BIOCHEMICAL APPLICATIONS OF STEADY-STATE ANISOTROPIES

Anisotropy measurements are ideally suited for measuring the association of proteins with other macromolecules. This is because the anisotropy almost always changes in response to a change in correlation time. Also, the experiments are simplified by the independence of the anisotropy from the overall protein concentration.

### 10.7.1. Peptide Binding to Calmodulin

The use of anisotropy to study protein binding is illustrated by calmodulin. This protein activates a number of intracellular enzymes in response to calcium. One example is myosin light-chain kinase (MLCK).<sup>49</sup> The amino-acid (RS20) sequence that binds to calmodulin contains a single tryptophan residue (Figure 10.19). Since calmodulin contains only tyrosine, the peptide (RS20) can be selectively observed by excitation at 295 nm (Chapter 16). Upon addition of calmodulin the emission intensity at RS20 increases and the emission shifts to shorter wavelengths. These changes indicate a shielded environment for the tryptophan

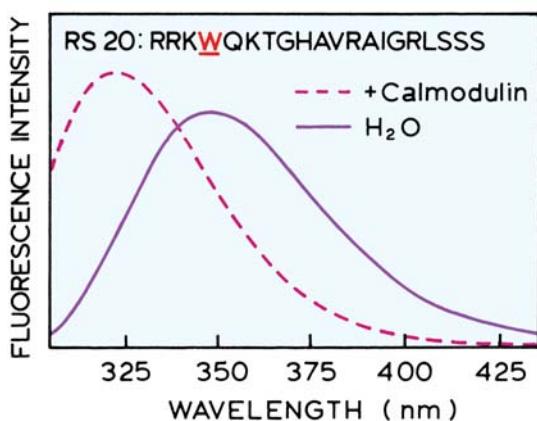


**Figure 10.19.** Emission spectra of the myosin light-chain kinase (MLCK) peptide RS20 in solution (solid) and bound to calmodulin in the presence of calcium (dashed). Excitation at 295 nm. Revised and reprinted with permission from [49]. Copyright © 1986, American Chemical Society.

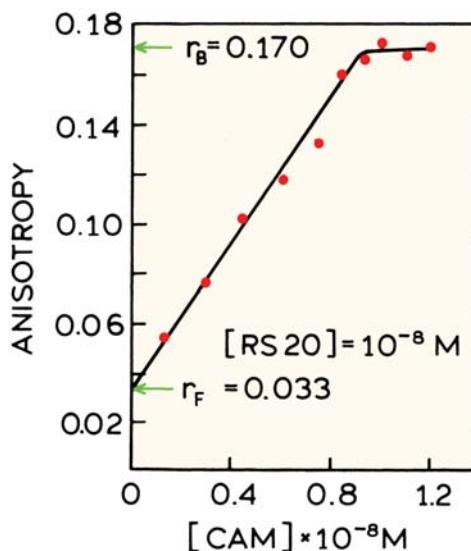


**Figure 10.20.** Titration of the MLCK peptide RS20 with calmodulin. Revised and reprinted with permission from [49]. Copyright © 1986, American Chemical Society.

residue in the complex. The anisotropy of RS20 increases dramatically on addition of calmodulin (Figure 10.20). These data can be used to determine that the stoichiometry of binding is 1:1. The sharp nature of the transition at  $10^{-8}$  M calmodulin implies that the binding constant is less than  $10^{-9}$  M.

How can such data be used to calculate the fraction of the peptide that is free in solution ( $f_F$ ) and the fraction bound to calmodulin ( $f_B$ )? The additivity law for anisotropies (eq. 10.6) is appropriate when  $f_i$  are the fractional intensities, not the fractional populations. Near 340 nm there is no change in intensity upon binding. If the polarized intensities are measured at this isoemissive point, the fraction of RS20 bound can be calculated using<sup>50–51</sup>

$$f_B = \frac{r - r_F}{r_B - r_F} \quad (10.50)$$

where  $r$  is the measured anisotropy, and  $r_F$  and  $r_B$  are the anisotropies of the free and bound peptides, respectively. The value of  $r_F$  is obtained by measuring the anisotropy of the free fluorophores, in this case the RS20 peptide prior to addition of calmodulin. The value of  $r_B$  is typically obtained from the limiting value observed when binding is thought to be complete. At different observation wavelengths the measured anisotropy can be weighted toward the free or bound forms. For instance, at 320 nm the bound peptide

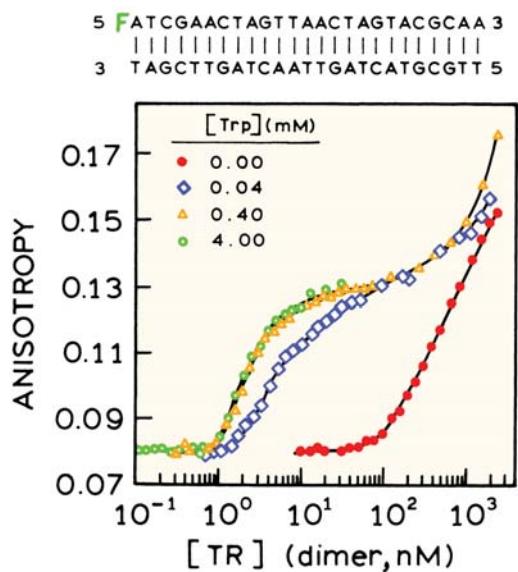


**Figure 10.21.** Anisotropy of the fluorescein (F)-labeled repressor DNA sequence upon titration with the Trp repressor (TR). Revised and reprinted with permission from [52]. Copyright © 1993, American Chemical Society.

contributes more strongly to the measured anisotropy. Under these conditions the fraction bound is given by

$$f_B = \frac{r - r_F}{(r - r_F) + R(r_B - r)} \quad (10.51)$$

where  $R = f_B/f_F$  is the ratio of intensities of the bound and free forms. Note that in eq. 10.51 the value of  $f_B$  represents the fractional concentration and not the fractional intensity. The fractional concentrations can be used to calculate the dissociation constant for the reaction.

### 10.7.2. Binding of the Trp Repressor to DNA

Studies of tryptophan repressor protein binding to DNA<sup>52</sup> are other examples of anisotropy measurements. In the

presence of tryptophan this protein binds to several regions of the *E. coli* genome, one of which controls tryptophan synthesis. Binding to this region of the genome suppresses the transcription of genes for proteins that are in the tryptophan synthesis pathway. The trp repressor binds to the DNA sequence shown in Figure 10.21. This double-stranded sequence was labeled with fluorescein on one of its 5' ends. Upon addition of the repressor protein the fluorescein anisotropy increases due to the decreased rotational rate of the DNA 25-mer when bound to the repressor. The concentration of repressor needed for binding was strongly dependent on the concentration of tryptophan in solution. The binding to DNA was much stronger in the presence of tryptophan, which can be seen from the anisotropy increasing at lower TR concentrations. This is consistent with the known function of the repressor, which is to turn off the genes responsible for tryptophan synthesis when tryptophan levels are adequate.

The titration curves shown in Figure 10.21 can be understood in terms of a model of Trp repressor binding to DNA (Figure 10.22). Binding of tryptophan to the repressor increases the repressor affinity for DNA. This model also explains another feature of the titration curves, which is the further increase in anisotropy at higher repressor concentrations (Figure 10.21). Apparently, the DNA 25-mer can bind more than a single repressor dimer, and this additional binding occurs at higher repressor concentrations.

### 10.7.3. Helicase-Catalyzed DNA Unwinding

Anisotropy measurements are rather simple and can be made rapidly. This allows anisotropies to be used to study reaction kinetics occurring in fractions of a second.<sup>53–55</sup> One example is unwinding of double-helical DNA by helicase.<sup>56</sup> Helicases are found in all species from humans to bacteria. Unwinding of DNA is necessary for DNA replication. Helicases move along DNA in a single direction and destabilize the DNA base pairs using energy derived from ATP. The helicases typically prefer to act on oligomers that have a single-stranded region.

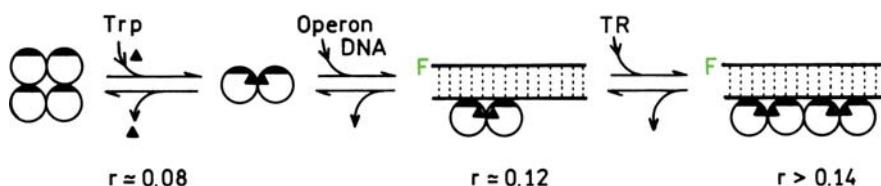


**Figure 10.22.** Binding of the Trp repressor to DNA. Revised and reprinted with permission from [52]. Copyright © 1993, American Chemical Society.

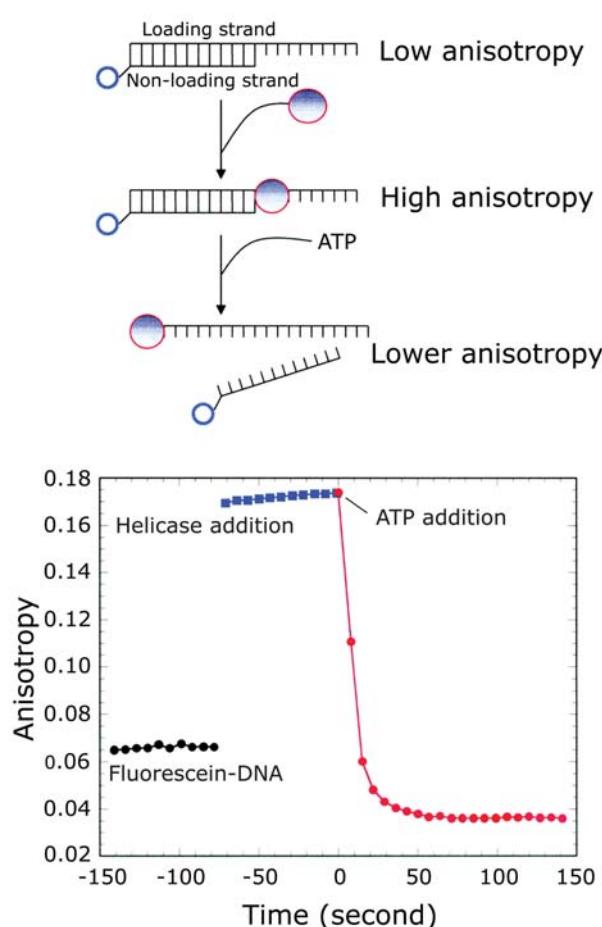


Figure 10.23. Effect of *E. coli* helicase on a fluorescein-labeled DNA oligomer. Revised from [56].

Figure 10.23 shows anisotropy measurements of a fluorescein-labeled oligomer in the presence of helicase. The anisotropy increases immediately upon addition of helicase to the DNA, showing that the binding reaction occurs rapidly. The anisotropy then remains constant because there is no source of energy to disrupt the hydrogen bonded base pairs. Upon addition of ATP the anisotropy drops rapidly to a value lower than the starting value. The final anisotropy is lower because the labeled DNA strand is no longer bound to the complementary strand. The single-stranded oligomer has a lower molecular weight and is more flexible than the double-stranded oligomer. In this experiment the DNA strands did not reassociate during the experiment. This helicase will not rebind to DNA shorter than a 20-mer. These results show that anisotropy measurements can be used to follow the kinetics of biochemical reactions on a rapid timescale.

#### 10.7.4. Melittin Association Detected from Homotransfer

In the preceding examples the binding reaction was detected from the increase in anisotropy resulting from the larger correlation time. Homo-resonance energy transfer can also be used to detect binding interactions. This is shown for melittin, which self-associates at high salt concentrations (Chapter 16). Melittin was randomly labeled with fluorescein isothiocyanate.<sup>57</sup> When the solution contained a small fraction of labeled melittin (1 of 25) the anisotropy increased at high salt concentrations (Figure 10.24). When all the melittin molecules were labeled, their anisotropy decreased markedly at high salt concentration. This decrease may be unexpected because melittin forms a tetramer in high salt solution, so its correlation time should increase fourfold. The decrease in anisotropy can be understood from the spectral properties of fluorescein (Chapter 3). The small Stokes shift and large overlap results in a Förster distance ( $R_0$ ) of 53 Å for homotransfer. The anisotropy decrease in Figure 10.24 is due to homotransfer between fluoresceins in the melittin tetramer.

### 10.8. ANISOTROPY OF MEMBRANES AND MEMBRANE-BOUND PROTEINS

#### 10.8.1. Membrane Microviscosity

Fluorescence anisotropy measurements can be used to study biological membranes. These studies have their origin

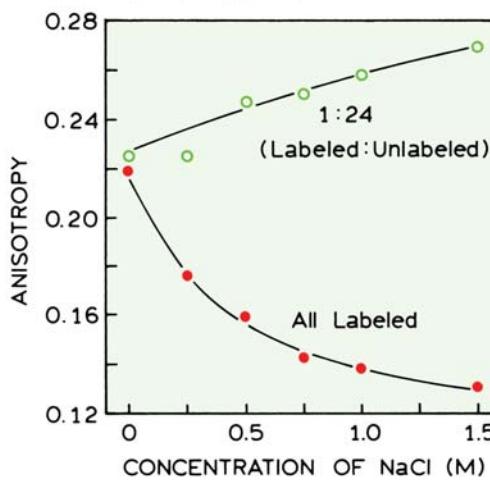
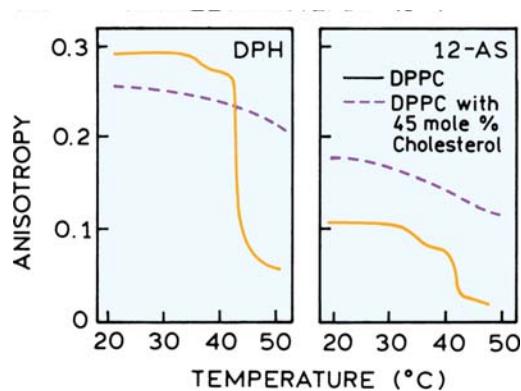


Figure 10.24. Self-association of melittin labeled with fluorescein in a 1:24 mixture with unlabeled melittin (○) or for all melittin labeled with fluorescein (●). Revised and reprinted with permission from [57]. Copyright © 1995, Biophysical Society.



**Figure 10.25.** Temperature-dependent polarization of 12-anthroyloxy stearate and DPH in DPPC vesicles (solid), and in DPPC vesicles with 45 mole% cholesterol (dashed). Revised and reprinted from [61]. Copyright © 1982, with permission from Elsevier Science.

in the early studies of microviscosity of micelles and membranes.<sup>58–60</sup> The basic idea is to measure the anisotropy of a fluorophore in a reference solvent of known viscosity, and then in the membrane. The microviscosity of the membrane is then estimated by comparison with the viscosity calibration curve.

At present there is less use of the term "microviscosity" because fluorophores in membranes display complex anisotropy decays, which prevents a straightforward comparison of the solvent and membrane data (Chapter 11). However, steady-state and time-resolved anisotropies are still widely used because of the dramatic changes which occur at the membrane phase transition temperature. This is illustrated by the steady-state polarization of 12-anthroyloxy stearate (12-AS) and DPH in DPPC vesicles (Figure 10.25). For both 12-AS and DPH the polarization decreases at 37°C, which is the phase-transition temperature of DPPC. The change is more dramatic for DPH than for 12-AS, which is one reason why DPH is so widely used. The polarization values are sensitive to the presence of cholesterol, which tends to make the membranes more rigid and to eliminate the sharp phase transition. In the following chapter we will see that the anisotropy values may not reflect the rate of probe rotation in the membranes, but rather the extent to which the probe motions are restricted by the anisotropic membrane environment.

### 10.8.2. Distribution of Membrane-Bound Proteins

In a cuvette experiment it is possible to control the fluorophore concentration, so that changes in quantum yield can be detected. In fluorescence microscopy this is usually

not possible because the local probe concentration is usually not known. Hence a high local intensity could be due to either a high probe concentration or a high quantum yield in this region of the cell. Anisotropy measurements are ratio-metric and, in the absence of other effects, independent of the probe concentration. Hence, when observing a cell, the anisotropy can provide useful information even if the local probe concentration is not known.

In Figure 10.24 we saw how homotransfer could decrease the anisotropy of nearby fluorophores. This effect was used to search for clusters of membrane-bound proteins in CHO cells.<sup>62</sup> The protein of interest was a folate receptor (FR). The FR is present in two forms: FR-GPI is a form that binds to glycosylphosphatidylinositol (GPI), and FR-TM is a transmembrane form not thought to bind to GPI. There are a number of GPI anchored proteins that are thought to be involved in lateral segregation of proteins in membranes. However, such clusters or domains could not be observed using fluorescence microscopy, suggesting that they were smaller than the resolution of an optical microscope.

Optical resolution is usually limited to structures over 300 nm in size. RET occurs over much smaller distances, and should thus be able to detect clustering even if the clusters are below optical resolution. The experimental concept is shown in Figure 10.26. Suppose the labeled proteins are distributed randomly in the membrane (top), at a concentration large enough for RET to occur. If the fluorophore concentration is decreased the anisotropy will increase because of less homo-RET.

Now suppose the fluorophores are contained in small clusters (Figure 10.26, bottom). The clusters are assumed to be too small to be seen in a microscope. If the fluorophore concentration in the membrane decreases there is no change in the anisotropy because the fluorophores are still in clusters with the same proximity to each other. This schematic suggests formation of protein clusters in membranes can be detected from the anisotropy measurements.

The CHO cells containing the labeled folate receptors were imaged using fluorescence microscopy (Figure 10.27). The images were recorded through a polarizer oriented at 0 or 90° relative to the polarized excitation. The polarized intensity images were used to calculate a total intensity image using  $I_{\parallel} + 2I_{\perp}$  (top panels). For both forms of the receptor there are regions of high and low intensity, suggesting variations in the receptor concentrations. However, domains were not detectable.

The intensity images were used to calculate the anisotropy images (Figure 10.27, lower panels). For FR-

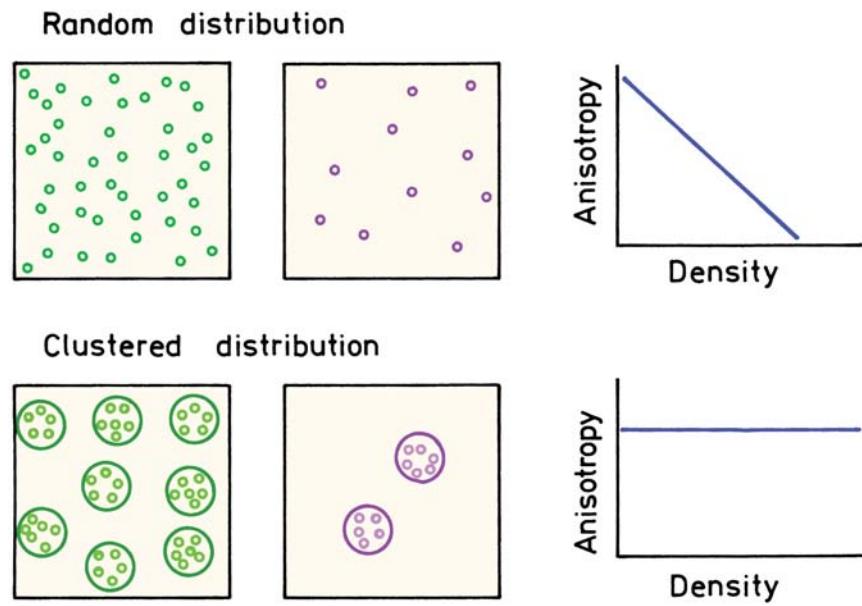


**Figure 10.26.** Effect of homotransfer on the anisotropy of a labeled membrane-bound protein for a random (top) and clustered (bottom) distribution. Revised from [62].

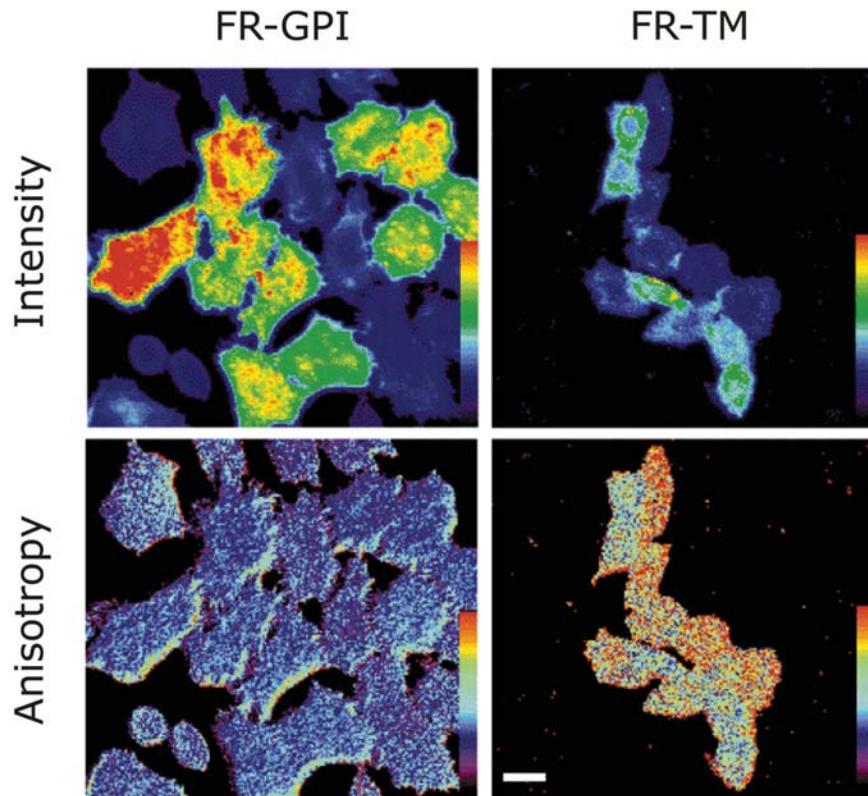


**Figure 10.27.** Intensity (top) and anisotropy (bottom) image of labeled folate receptors in CHO cells. Bar is 20  $\mu\text{m}$ . Revised from [62].

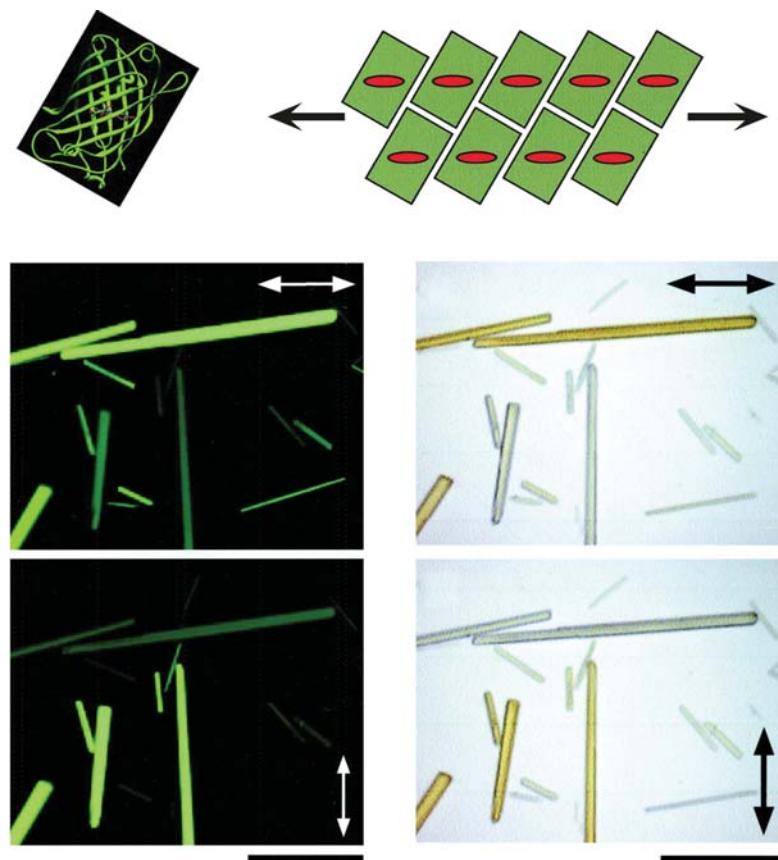


**Figure 10.28.** Transillumination fluorescence microscope image (left) and white light microscope image (right) of GFP crystals. The arrows indicate the direction of the direction of the incident polarization. The bars are  $30\text{ }\mu\text{m}$ . The upper schematic shows the orientation of GFP (green) and the red shapes the orientation of the chromophore transition moment of the crystals. Revised from [64].

GPI, the anisotropy appears to be independent of the total intensity. For FR-TM the anisotropy is lower where the intensities are higher. FR-TM was not expected to form clusters. The decrease in anisotropy with increasing intensity (density) is consistent with the top panel in Figure 10.26 for randomly distributed proteins. FR-GPI was expected to exist in small clusters. The constant anisotropy independent of intensity (density) is consistent with the cluster model in the lower panel of Figure 10.26. These results show how the principles of anisotropy and RET are being extended to cellular imaging.

### 10.9. TRANSITION MOMENTS

The concept of a transition moment is somewhat abstract. When fluorophores are observed in random solutions the nonzero anisotropy values prove that the transition moments exist, but the data do not indicate the direction of the moment in the molecular structure. However, the direc-

tion of the transition moment can be determined if the fluorophores are oriented. A dramatic example<sup>63–64</sup> is shown for GFP in Figure 10.28. The left panels show microscopic images of the emission from GFP crystals. Depending on the orientation of the incident polarization the crystals are either bright or dark. This result shows that the chromophore in GFP is aligned along the long axis of the crystals. The orientation of GFP and its chromophore in the crystals is shown in the upper schematic. The  $\beta$ -barrel of GFP is oriented at an angle to the long axis, but the transition moments are aligned along the long axis.

Also shown in Figure 10.28 (right) are color images of the crystals when transilluminated with polarized white light. The crystals aligned with the incident polarization are yellow. The crystals are clear or very pale blue when rotated  $90^\circ$  from the incident polarization. This phenomenon is called dichroism. The yellow color is the result of the blue-light absorption of GFP that occurs primarily when the transition moments are aligned with the incident polarization.

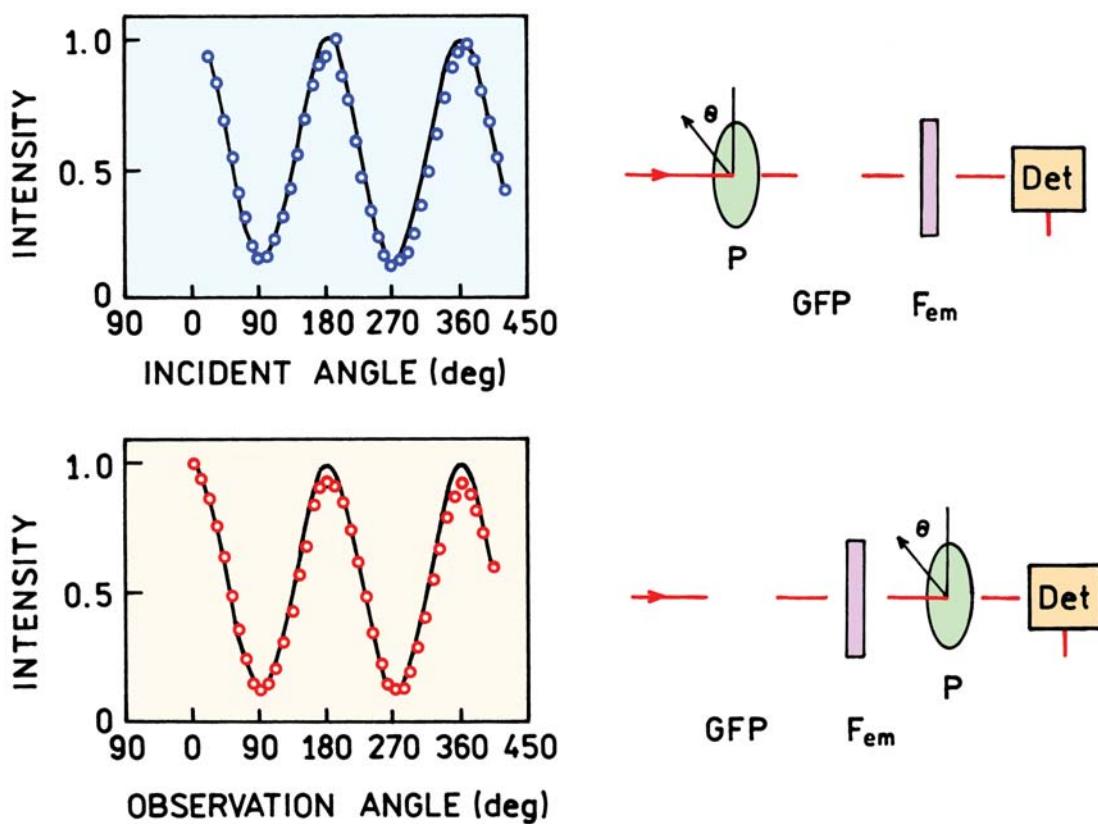


**Figure 10.29.** Fluorescence intensities of GFP crystals when illuminated with polarized light (top) or observed through a polarizer. For both traces only a single polarizer was used. Revised from [64].

Recall from Section 10.2 that for a random solution the maximum ratio of the polarized intensities was  $I_{\parallel}/I_{\perp} = 3$ . Much greater contrast can be obtained with an oriented system. Figure 10.29 shows the intensities of the GFP crystals using a single polarizer for the excitation and observation without an emission polarizer (top). The intensity changed by a factor close to 10. This result is due to the  $\cos^2 \theta$  photoselection of the absorption. The crystals only absorb when the transition moment is aligned with the incident polarization.

This experiment was repeated with unpolarized excitation and observation through an emission polarizer (Figure 10.29, bottom). A similar curve was observed, but for a different reason. In this case, the emission is almost completely polarized along the long axis of the crystal. The  $\cos^2 \theta$  dependence is due to the transmission efficiency as the emission polarizer is rotated. It was not necessary to use polarized excitation because the oriented chromophores emit light polarized along their transition moment irrespective of the polarization of the incident light. Another impor-

tant point from Figure 10.29 is that the absorption and emission transmission moments are nearly colinear. Otherwise there would be a shift in the phase of the two curves.

This example is instructive because it demonstrates several principles, in addition showing the existence and orientation of the transition moments. The chromophore in GFP is buried in the protein and held rigidly in a unique orientation. Otherwise the contrast ratio in Figure 10.29 would be smaller. Also, GFP shows a good Stokes shift and the protein separates the chromophores by a reasonable distance. If the chromophores were in direct contact there would probably be energy transfer, which could result in some depolarization.

## REFERENCES

1. Jablonski A. 1960. On the notion of emission anisotropy. *Bull l'Acad Pol Sci, Ser A* **8**:259–264.
2. Weber G. 1952. Polarization of the fluorescence of macromolecules, I: theory and experimental method. *Biochem J* **51**:145–155.

3. Weber G. 1966. Polarization of the fluorescence of solutions. In *Fluorescence and phosphorescence analysis*, pp. 217–240. Ed DM Hercules. John Wiley & Sons, New York.
4. Selényi P. 1939. Wide-angle interferences and the nature of the elementary light sources. *Phys Rev* **56**:477–479.
5. Griffiths DJ. 1999. *Introduction to electrodynamics*. Prentice Hall, Englewood Cliffs, NJ.
6. Born M, Wolf E. 1980. *Principles of optics electromagnetic theory of propagation, interference and diffraction of light*. Pergamon Press, New York.
7. Lakowicz JR, Gryczynski I. 1997. Multiphoton excitation of biochemical fluorophores. In *Topics in fluorescence spectroscopy*, Vol. 5: *Nonlinear and two-photon induced fluorescence*, pp. 87–144. Ed JR Lakowicz. Plenum Press, New York.
8. Faucon JF, Lakowicz JR. 1987. Anisotropy decay of diphenylhexatriene in melittin-phospholipid complexes by multifrequency phase-modulation fluorometry. *Arch Biochem Biophys* **252**(1):245–258.
9. Herman P, Konopásek I, Plásek J, Svobodová J. 1994. Time-resolved polarized fluorescence studies of the temperature adaptation in *Bacillus subtilis* using DPH and TMA-DPH fluorescent probes. *Biochim Biophys Acta* **1190**:1–8.
10. Shinitzky M, Barenholz Y. 1974. Dynamics of the hydrocarbon layer in liposomes of lecithin and sphingomyelin containing dicetylphosphate. *J Biol Chem* **249**:2652–2657.
11. Thompson RB, Gryczynski I, Malicka J. 2002. Fluorescence polarization standards for high-throughput screening and imaging. *Bio-technology* **32**:34–42.
12. Michl J, Thulstrup EW. 1986. *Spectroscopy with polarized light*. VCH Publishers, New York.
13. Albinsson B, Kubista M, Nordén B, Thulstrup EW. 1989. Near-ultra-violet electronic transitions of the tryptophan chromophore: linear dichroism, fluorescence anisotropy, and magnetic circular dichroism spectra of some indole derivatives. *J Phys Chem* **93**:6646–6655.
14. Albinsson B, Eriksson S, Lyng R, Kubista M. 1991. The electronically excited states of 2-phenylindole. *Chem Phys* **151**:149–157.
15. Kubista M, Åkerman B, Albinsson B. 1989. Characterization of the electronic structure of 4',6-diamidino-2-phenylindole. *J Am Chem Soc* **111**:7031–7035.
16. Vincent M, de Foresta B, Gallay J, Alfsen A. 1982. Nanosecond fluorescence anisotropy decays of n-(9-anthroyloxy) fatty acids in dipalmitoylphosphatidylcholine vesicles with regard to isotropic solvents. *Biochemistry* **21**:708–716.
17. Mullaney JM, Thompson RB, Gryczynski Z, Black LW. 2000. Green fluorescent protein as a probe of rotational mobility within bacteriophage T4. *J Virol Methods* **88**:35–40.
18. Weber G. 1960. Fluorescence-polarization spectrum and electronic-energy transfer in tyrosine, tryptophan and related compounds. *Biochem J* **75**:335–345.
19. Valeur B, Weber G. 1977. Resolution of the fluorescence excitation spectrum of indole into the  ${}^1L_a$  and  ${}^1L_b$  excitation bands. *Photochem Photobiol* **25**:441–444.
20. Eftink MR, Selvidge LA, Callis PR, Rehms AA. 1990. Photophysics of indole derivatives: Experimental resolution of  $L_a$  and  $L_b$  transitions and comparison of theory. *J Phys Chem* **94**:3469–3479.
21. Shen X, Knutson JR. 2001. Subpicosecond fluorescence spectra of tryptophan in water. *J Phys Chem B* **105**:6260–6265.
22. Short KW, Callis PR. 2002. One- and two-photon spectra of jet-cooled 2,3-dimethylindole:  ${}^1L_b$  and  ${}^1L_a$  assignments. *Chem Phys* **283**:269–278.
23. Yamamoto Y, Tanaka J. 1972. Polarized absorption spectra of crystals of indole and its related compounds. *Bull Chem Soc Jpn* **65**:1362–1366.
24. Suwaiyan A, Zwarich R. 1987. Absorption spectra of substituted indoles in stretched polyethylene films. *Spectrochim Acta* **43A**(5):605–609.
25. Weber G, Shinitzky M. 1970. Failure of energy transfer between identical aromatic molecules on excitation at the long wave edge of the absorption spectrum. *Proc Natl Acad Sci USA* **65**(4):823–830.
26. Kawski A. 1992. *Fotoluminescencja roztworów*. Wydawnictwo Naukowe PWN, Warsaw.
27. Van Der Meer BW, Coker III G, Chen S-YS. 1991. *Resonance energy transfer theory and data*. Wiley-VCH, New York.
28. Jablonski A. 1970. Anisotropy of fluorescence of molecules excited by excitation transfer. *Acta Phys Pol A* **38**:453–458.
29. Baumann J, Fayer MD. 1986. Excitation transfer in disordered two-dimensional and anisotropic three-dimensional systems: effects of spatial geometry on time-resolved observables. *J Chem Phys* **85**:4087–4107.
30. Teale FWJ. 1969. Fluorescence depolarization by light scattering in turbid solutions. *Photochem Photobiol* **10**:363–374.
31. Ghosh N, Majumder SK, Gupta PK. 2002. Fluorescence depolarization in a scattering medium: effect of size parameter of a scatterer. *Phys Rev E* **65**:026608-1–6.
32. Lenz BR. 1979. Light scattering effects in the measurement of membrane microviscosity with diphenylhexatriene. *Biophys J* **25**:489–494.
33. Berberan-Santos MN, Nunes Pereira EJ, Martinho JMG. 1995. Stochastic theory of molecular radiative transport. *J Chem Phys* **103**(8):3022–3028.
34. Nunes Pereira EJ, Berberan-Santos MN, Martinho JMG. 1996. Molecular radiative transport, II: Monte-Carlo simulation. *J Chem Phys* **104**(22):8950–8965.
35. Perrin F. 1929. La fluorescence des solutions: induction moléculaire. Polarisation et duree d'émission. *Photochimie. Ann Phys*, Ser 10 **12**:169–275.
36. Perrin F. 1926. Polarisation de la lumière de fluorescence: vie moyenne des molécules dans l'état excité. *J Phys Radium V*, Ser 6 **7**:390–401.
37. Perrin F. 1931. Fluorescence: durée élémentaire d'émission lumineuse. *Conférences D'Actualités Scientifiques et Industrielles* **22**:2–41.
38. Weber G. 1953. Rotational Brownian motion and polarization of the fluorescence of solutions. *Adv Protein Chem* **8**:415–459.
39. Yguerabide J, Epstein HF, Stryer L. 1970. Segmental flexibility in an antibody molecule. *J Mol Biol* **51**:573–590.
40. Weber G. 1952. Polarization of the fluorescence of macromolecules, II: fluorescence conjugates of ovalbumin and bovine serum albumin. *Biochem J* **51**:155–167.
41. Laurence DJR. 1952. A study of the absorption of dyes on bovine serum albumin by the method of polarization of fluorescence. *Biochem J* **51**:168–180.

42. Gottlieb YYa, Wahl Ph. 1963. Étude théorique de la polarisation de fluorescence des macromolécules portant un groupe émetteur mobile autour d'un axe de rotation. *J Chim Phys* **60**:849–856.
43. Ferguson BQ, Yang DCH. 1986. Methionyl-tRNA synthetase induced 3'-terminal and delocalized conformational transition in tRNA<sup>fMet</sup>: steady-state fluorescence of tRNA with a single fluorophore. *Biochemistry* **25**:529–539.
44. Buchner J. 1996. Supervising the fold: functional principals of molecular chaperones. *FASEB J* **10**:10–19.
45. Ellis RJ. 1996. *The chaperonins*. Academic Press, New York.
46. Braig K, Otwinowski Z, Hegde R, Bolsvert DC, Joachimiak A, Horwitz AL, Sigler PB. 1994. The crystal structure of the bacterial chaperonin GroEL at 2.8 Å. *Nature* **371**:578–586.
47. Gorovits BM, Horowitz PM. 1995. The molecular chaperonin cpn60 displays local flexibility that is reduced after binding with an unfolded protein. *J Biol Chem* **270**(22):13057–13062.
48. Lim K, Jameson DM, Gentry CA, Herron JN. 1995. Molecular dynamics of the anti-fluorescein 4-4-20 antigen-binding fragment, 2: time-resolved fluorescence spectroscopy. *Biochemistry* **34**:6975–6984.
49. Lukas TJ, Burgess WH, Prendergast FG, Lau W, Watterson DM. 1986. Calmodulin binding domains: characterization of a phosphorylation and calmodulin binding site from myosin light chain kinase. *Biochemistry* **25**:1458–1464.
50. Malencik DA, Anderson SR. 1984. Peptide binding by calmodulin and its proteolytic fragments and by troponin C. *Biochemistry* **23**: 2420–2428.
51. Eftink MR. 1994. The use of fluorescence methods to monitor unfolding transitions in proteins. *Biophys J* **66**:482–501.
52. LeTilly V, Royer CA. 1993. Fluorescence anisotropy assays implicate protein–protein interactions in regulating *trp* repressor DNA binding. *Biochemistry* **32**:7753–7758.
53. Banik U, Beechem JM, Klebanow E, Schroeder S, Weil PA. 2001. Fluorescence-based analyses of the effects of full-length recombinant TAF130p on the interaction of TATA box-binding protein with TATA box DNA. *J Biol Chem* **276**(52):49100–49109.
54. Hiller DA, Fogg JM, Martin AM, Beechem JM, Reich NO, Perona JJ. 2003. Simultaneous DNA binding and bending by ecoRV endonuclease observed by real-time fluorescence. *Biochemistry* **42**: 14375–14385.
55. Taniguchi M, Yoshimi T, Hongo K, Mizobata T, Kawata Y. 2004. Stopped-flow fluorescence analysis of the conformational changes in the GroEL apical domain. *J Biol Chem* **279**(16):16368–16376.
56. Xu HQ, Zhang AH, Auclair C, Xi XG. 2003. Simultaneously monitoring DNA binding and helicase-catalyzed DNA unwinding by fluorescence polarization. *Nucleic Acids Res* **31**(14):e70.
57. Runnels LW, Scarlata SF. 1995. Theory and application of fluorescence homotransfer to melittin oligomerization. *Biophys J* **69**:1569–1583.
58. Shinitzky M, Dianoux AC, Gitler C, Weber G. 1971. Microviscosity and order in the hydrocarbon region of micelles and membranes determined with fluorescence probes, I: synthetic micelles. *Biochemistry* **10**:2106–2113.
59. Cogen U, Shinitzky M, Weber G, Nishida T. 1973. Microviscosity and order in the hydrocarbon region of phospholipid and phospholipid–cholesterol dispersions determined with fluorescent probes. *Biochemistry* **12**:521–528.
60. Thulborn KR, Tilley LM, Sawyer WH, Treloar FE. 1979. The use of n-(9-anthroyloxy) fatty acids to determine fluidity and polarity gradients in phospholipids bilayers. *Biochim Biophys Acta* **558**: 166–178.
61. Thulborn KR, Beddard GS. 1982. The effects of cholesterol on the time-resolved emission anisotropy of 12-(9-anthroyloxy)stearic acid in dipalmitoylphosphatidylcholine bilayers. *Biochim Biophys Acta* **693**:246–252.
62. Varma R, Mayor S. 1998. GPI-anchored proteins are organized in submicron domains at the cell surface. *Nature* **394**:798–801.
63. Rosell FI, Boxer SG. 2003. Polarized absorption spectra of green fluorescent protein single crystals: transition dipole moment directions. *Biochemistry* **42**:177–183.
64. Inoué S, Shimomura O, Goda M, Shribak M, Tran PT. 2002. Fluorescence polarization of green fluorescence protein. *Proc Natl Acad Sci USA* **99**(7):4272–4277.

## ADDITIONAL READING ON THE APPLICATION OF ANISOTROPY

### Association Reactions

Hey T, Lipps G, Krauss G. 2001. Binding of XPA and RPA to damaged DNA investigated by fluorescence anisotropy. *Biochemistry* **40**: 2901–2910.

### Imaging

Lidke DS, Nagy P, Barisas BG, Heintzmann R, Post JN, Lidke KA, Clayton AHA, Arndt-Jovin DJ, Jovin TM. 2003. Imaging molecular interactions in cells by dynamic and static fluorescence anisotropy (rFLIM and emFRET). *Biochem Soc Trans* **31**(5):1020–1027.

### Membranes

Gidwani A, Holowka D, Baird B. 2001. Fluorescence anisotropy measurements of lipid order in plasma membranes and lipid rafts from RBL-2H3 mast cells. *Biochemistry* **40**:12422–12429.

Huertas ML, Cruz V, Cascales JJ, Acuña AU, Garcia de la Torre J. 1996. Distribution and diffusivity of a hydrophobic probe molecule in the interior of a membrane: theory and simulation. *Biophys J* **71**:1428–1439.

Sinha M, Mishra S, Joshi PG. 2003. Liquid-ordered microdomains in lipid rafts and plasma membrane of U-87 MG cells: a time-resolved fluorescence study. *Eur Biophys J* **32**:381–391.

### Oriented Systems

Fisz JJ, Buczkowski M. 2001. Excited-state orientation-dependent irreversible interconversion and fluorescence depolarization in organized molecular media, I: theory. *J Chem Phys* **115**(15):7051–7060.

Dale RE, Hopkins SC, an der Heide UA, Marszałek T, Irving M, Goldman YE. 1999. Model-independent analysis of the operation of fluorescent probes with restricted mobility in muscle fibers. *Biophys J* **76**:1606–1618.

### RET and Anisotropy

- Andrews DL, Juzeliunas G. 1991. The range dependence of fluorescence anisotropy in molecular energy transfer. *J Chem Phys* **95**(8): 5513–5518.
- Cohen-Kashi M, Moshkov S, Zurgil N, Deutsch M. 2002. Fluorescence resonance energy transfers measurements on cell surfaces via fluorescence polarization. *Biophys J* **83**:1395–1402.
- Gaab KM, Bardeen CJ. 2004. Wavelength and temperature dependence of the femtosecond pump-probe anisotropies in the conjugated polymer MEH-PPV: implications for energy-transfer dynamics. *J Phys Chem B* **108**:4619–4626.
- Kleima FJ, Hofmann E, Gobets B, van Stokkum IHM, van Grondelle R, Diederichs K, van Amerongen H. 2000. Förster excitation energy transfer in peridinin-chlorophyll-a-protein. *Biophys J* **78**:344–353.
- Tanaka F. 1998. Theory of time-resolved fluorescence under the interaction of energy transfer in bichromophoric system: effect of internal rotations of energy donor and acceptor. *J Chem Phys* **109**(3):1084–1092.
- Varnavski OP, Ostrowski J, Bazan GC, Goodson III T. 2002. Energy transfer and fluorescence depolarization in organic dendrimers and branched molecules. *Proc SPIE* **4464**:134–141.

### Surfaces

- Ishizaka S, Kinoshita S, Nishijima Y, Kitamura N. 2003. Direct observation of molecular recognition mediated by triple hydrogen bonds at a water/oil interface: time-resolved total internal reflection fluorometry study. *Anal Chem* **75**(22):6035–6042.

### Theory

- Bajzer Z, Moncrieffe MC, Penzar I, Prendergast FG. 2001. Complex homogeneous and heterogeneous fluorescence anisotropy decays: enhancing analysis accuracy. *Biophys J* **81**:1765–1775.
- Bialik CN, Wolf B, Rachofsky EL, Alexander Ross JB, Laws WR. 1998. Dynamics of biomolecules: assignment of local motions by fluorescence anisotropy decay. *Biophys J* **75**:2564–2573.
- Bryant J, Bain AJ. 1998. Controlled orientational photoselection via three-pulse excitation. *Chem Phys Lett* **286**:121–130.
- Fisz JJ. 1998. Flexible fluorophores as the probes for monitoring the structural and dynamical properties of organized molecular media. *Chem Phys Lett* **297**:409–418.
- Fisz JJ. 1996. Polarized fluorescence spectroscopy of two-ground- and two-excited-state systems in solutions. *Chem Phys Lett* **262**:495–506.
- Tanaka F. 2000. Effects of internal rotations on the time-resolved fluorescence in a bichromophoric protein system under the energy transfer interaction. *J Fluoresc* **10**(1):13–19.
- Tanaka F, Mataga N. 1998. Analytical theory of time-resolved fluorescence anisotropy and dynamic Stokes shift of polar solute molecules based on continuum model for solvent. *Chem Phys* **236**:277–289.

### PROBLEMS

- P10.1. Angles ( $\beta$ ) between Absorption and Emission Transition Moments: Figure 12.34 shows the excitation

anisotropy spectrum of perylene in propylene glycol at  $-60^{\circ}\text{C}$ . What is the angle between the transition moments for excitation at 430, 290, and 270 nm?

- P10.2. Effect of Scattered Light in the Anisotropy: Suppose a membrane-bound fluorophore displays a true anisotropy of 0.30. However, your emission filters allow 20% of the signal to be due to scattered light. What is the measured anisotropy?

- P10.3. Calculation of an Anisotropy: Using a T-format polarization instrument you obtain the following data for diphenylhexatriene (DPH). The first and second subscripts refer to the orientation of the excitation and emission polarizers, respectively. Calculate  $r_0$  and  $P_0$  for DPH. What is the angle  $\alpha$  between the absorption and emission oscillators?

Conditions	$I_{\text{HV}}$	$I_{\text{VV}}$
$-60^{\circ}\text{C}$ in propylene glycol	0.450	1.330

- P10.4. Derivation of the Perrin Equation: Derive the Perrin equation (eq. 10.44) for a single-exponential decay of the intensity and anisotropy.

- P10.5. Calculation of an Anisotropy in Fluid Solution: Calculate the expected anisotropy of perylene in ethanol at  $20^{\circ}\text{C}$ , and in propylene glycol at  $25^{\circ}\text{C}$ . The molecular weight of perylene is 252 g/mol, and the density can be taken as 1.35 g/ml. The viscosity of ethanol at  $20^{\circ}\text{C}$  is 1.194 cP, and that of propylene glycol at  $25^{\circ}\text{C}$  is 32 cP. Assume the lifetime is 6 ns, and  $r_0 = 0.36$ .

- P10.6. Binding Reactions by Anisotropy: Derive eqs. 10.50 and 10.51, which describe the fractional binding from the steady-state anisotropy and the change in intensity on binding.

- P10.7. Calculation of a Binding Constant From Anisotropies: Assume the probe 1-dimethylamino-5-naphthalene sulfonic acid (DNS) binds to bovine serum albumin (BSA). The DNS polarization values are given in Table 10.6. The dissociation constant ( $K_d$ ) for the binding is given by

$$K_d = \frac{[\text{DNS}][\text{BSA}]}{[\text{DNS} - \text{BSA}]} \quad (10.52)$$

- A. Calculate the dissociation constant assuming that the quantum yield of the probe is not altered upon binding.

- B. Now assume that the quantum yield of DNS increases twofold upon binding to BSA. What is  $K_d$ ?
- C. How would you determine whether the quantum yield of DNS changes upon binding to BSA?
- D. Predict the time-resolved anisotropies for each solution at 20°C. Assume  $P_0 = 0.3913$  for DNS and that

the rotational correlation times of DNS and BSA are well approximated by that predicted for an anhydrous sphere. The molecular weight of BSA is near 66,000 g/mol. The viscosity of water at 25°C is 0.894 cP (g cm<sup>-1</sup> sec<sup>-1</sup>). The density of BSA can be taken as 1.2 g/cm<sup>3</sup>.

**Table 10.6.** Polarization Values of DNS

[BSA]	[DNS]	<i>P</i>
0	1 x 10 <sup>-7</sup> M	0.0149
2 x 10 <sup>-5</sup> M	1 x 10 <sup>-7</sup> M	0.2727
>> $K_d$	1 x 10 <sup>-7</sup> M	0.3913

# 11

# Time-Dependent Anisotropy Decays

In the preceding chapter we described the measurement and interpretation of steady-state fluorescence anisotropies. These values are measured using continuous illumination, and represent an average of the anisotropy decay by the intensity decay. The measurement of steady-state anisotropies is simple. However, interpretation of the steady-state anisotropies usually depends on an assumed form for the anisotropy decay, which is not observed in the experiment. Additional information is available from measurements of the time-dependent anisotropy, that is, the values of  $r(t)$  following pulsed excitation. The form of the anisotropy decay depends on the size, shape, and flexibility of the labeled molecule. The measured decays can be compared with the decays calculated from various molecular models. Anisotropy decays can be measured using the time-domain (TD) or the frequency-domain (FD) method.

It is important to understand the factors which affect the anisotropy decays. For a spherical molecule the anisotropy is expected to decay with a single rotational correlation time ( $\theta$ ). Perhaps the most frequent interpretation of the correlation time is in terms of the overall rotational correlation time of a protein. The measured values of  $\theta$  can be compared with the values predicted for a hydrated sphere of equivalent molecular weight (eq. 10.46). However, anisotropy decays are usually multi-exponential, which can be the result of numerous factors. Multi-exponential anisotropy decays are expected for non-spherical fluorophores or proteins. The correlation times in the anisotropy decay are determined by the rates of rotation about the various molecular axes. By examination of the correlation time it is sometimes possible to estimate the shapes of proteins.

In addition to shape, anisotropy decays are affected by the segmental flexibility of the macromolecule. For instance, tryptophan anisotropy decays of proteins frequently display correlation times that are too short to be due to rotational diffusion of the whole protein. These compo-

nents are usually due to independent motions of the tryptophan residue within the protein or on the surface of the protein. The rates and amplitudes of tryptophan side-chain motions have been used to study the nanosecond dynamics of proteins. Anisotropy decays can also be affected by resonance energy transfer between the same type of fluorophore, that is, depolarization due to homotransfer.

Anisotropy decays of membrane-bound probes have been particularly informative. Membrane-bound probes often display unusual behavior in which the anisotropies do not decay to zero. This occurs because some probes do not rotate freely in membranes, at least not within the ns decay times of most fluorophores. The extent of rotation is often limited by the anisotropic environment of a membrane. The nonzero anisotropies at long times can be interpreted in terms of the order parameters of the membrane. In this chapter we present examples of simple and complex anisotropy decays to illustrate the information available from these measurements. In the following chapter we describe more advanced concepts in anisotropy decay analysis.

## 11.1. TIME-DOMAIN AND FREQUENCY-DOMAIN ANISOTROPY DECAYS

Suppose a fluorophore is excited with a pulse of vertically polarized light, and that it rotates with a single correlation time. The anisotropy decay is determined by measuring the decays of the vertically ( $\parallel$ ) and horizontally ( $\perp$ ) polarized emission. If the absorption and emission transition moments are colinear, the time-zero anisotropy is 0.4. In this case the initial intensity of the parallel component is threefold larger than that of the perpendicular component (Figure 11.1, left). If the fundamental anisotropy is greater than zero ( $r_0 > 0$ ), vertically polarized excitation pulse results in an initial population of fluorophores which is enriched in the parallel orientation.<sup>1</sup> The decay of the differ-

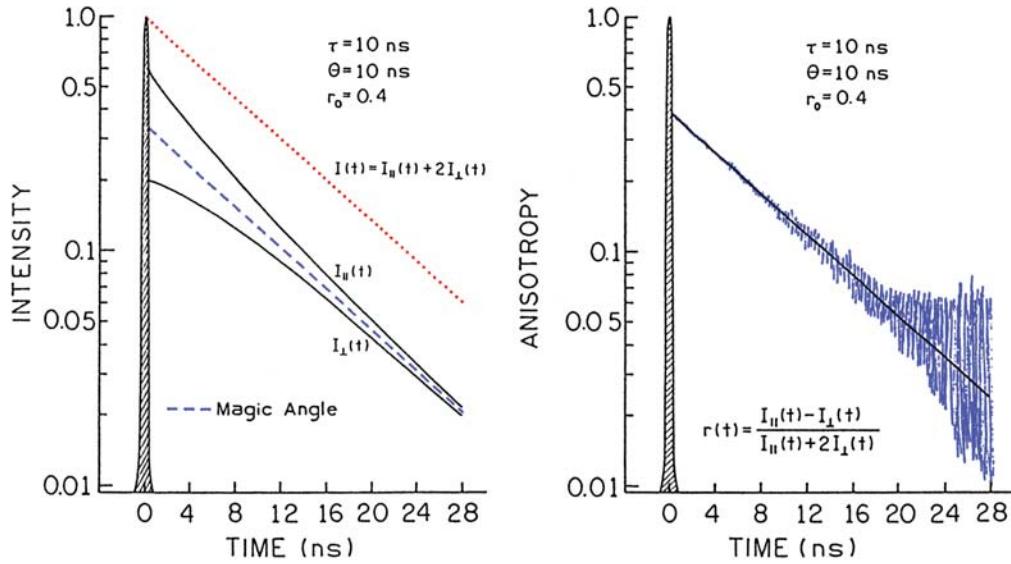


**Figure 11.1.** Time-dependent polarized decays (left) and the calculated anisotropy decay (right). From [1].

ence between  $I_{\parallel}(t)$  and  $I_{\perp}(t)$ , when properly normalized by the total intensity and corrected for the instrument response function, is the anisotropy decay (right).

The left panel of Figure 11.1 shows that the parallel component initially decays more rapidly than the horizontal component. This occurs because the vertically oriented fluorophores are decaying by two processes: the intensity decay with decay time  $\tau$ , and rotation out of the vertical orientation with correlation time  $\theta$ . The horizontal component initially decays more slowly because it is repopulated by rotation from the excess vertically oriented population.

Suppose the sample displays a single lifetime and a single correlation time. Even under these conditions the polarized intensity decays are multi-exponential. The decays of the parallel ( $\parallel$ ) and perpendicular ( $\perp$ ) components of the emission are given by

$$I_{\parallel}(t) = \frac{1}{3}I(t)[1 + 2r(t)] \quad (11.1)$$

$$I_{\perp}(t) = \frac{1}{3}I(t)[1 - r(t)] \quad (11.2)$$

where  $r(t)$  is the time-resolved anisotropy. Generally,  $r(t)$  can be described as a multi-exponential decay:

$$r(t) = r_0 \sum_j g_j \exp(-t/\theta_j) = \sum_j r_{0j} \exp(-t/\theta_j) \quad (11.3)$$

where  $r_0 = \sum r_{0j}$  is the limiting anisotropy in the absence of rotational diffusion, the  $\theta_j$  are the individual correlation times, and the  $g_j$  are the fractional amplitudes of each correlation time in the anisotropy decay ( $\sum g_j = 1.0$ ). Depending on the circumstances,  $r_0$  may be a known parameter, perhaps from a frozen solution measurement. Alternatively, all the amplitudes ( $r_{0j}$ ) can be considered to be experimental variables so that  $r_0 = \sum r_{0j}$  is a variable parameter. As shown in the previous chapter, the total intensity for a sample is given by  $I_T = I_{\parallel} + 2I_{\perp}$ . Similarly, the total (rotation-free) intensity decay is given by

$$I(t) = I_{\parallel}(t) + 2I_{\perp}(t) \quad (11.4)$$

Forming this sum eliminates the contributions of  $r(t)$  to the total decay. In the time domain one measures the time-dependent decays of the polarized components of the emission (eqs. 11.1 and 11.2). The polarized intensity decays can be used to calculate the time-dependent anisotropy

$$r(t) = \frac{I_{\parallel}(t) - I_{\perp}(t)}{I_{\parallel}(t) + 2I_{\perp}(t)} \quad (11.5)$$

The time-dependent anisotropy decay are then analyzed to determine which model is most consistent with the data. However, it is preferable to directly analyze the polarized intensity decays (Section 11.22) rather than the anisotropy values calculated from the polarized intensity decays.

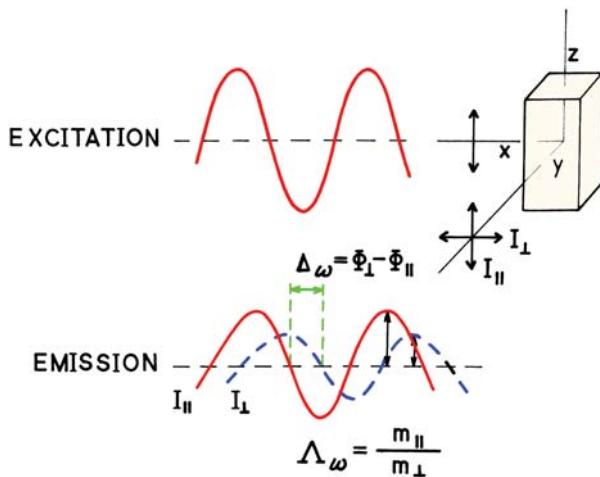


**Figure 11.2.** Frequency-domain measurements of anisotropy decays. For simplicity the average intensity is assumed equal for both polarized components. From [2].

The experimental procedures and the form of the data are different for frequency-domain of the anisotropy decay measurements.<sup>2</sup> The sample is excited with amplitude-modulated light, which is vertically polarized (Figure 11.2). The emission is observed through a polarizer that is rotated between the parallel and perpendicular orientations. In the frequency domain there are two observable quantities that characterize the anisotropy decay. These are the phase shift  $\Delta_{\omega}$ , at the modulation frequency  $\omega$ , between the perpendicular ( $\phi_{\perp}$ ) and parallel ( $\phi_{\parallel}$ ) components of the emission:

$$\Delta_{\omega} = \phi_{\perp} - \phi_{\parallel} \quad (11.6)$$

and the ratio

$$\Lambda_{\omega} = m_{\parallel}/m_{\perp} \quad (11.7)$$

of the parallel ( $m_{\parallel}$ ) and perpendicular ( $m_{\perp}$ ) components of the modulated emission. To avoid confusion, we stress that  $\Lambda_{\omega}$  is the ratio of the modulated amplitudes of the polarized components, not the ratio of the modulation of each polarized component. The ratio  $\Lambda_{\omega}$  is often presented as the frequency-dependent anisotropy ( $r_{\omega}$ ), which is defined by

$$r_{\omega} = \frac{\Lambda_{\omega} - 1}{\Lambda_{\omega} + 2} \quad (11.8)$$

The form of the frequency-domain anisotropy data is illustrated in Figures 11.3 and 11.4. Analogous to the time-domain measurements, one could measure the phase and modulation of the polarized components relative to scat-

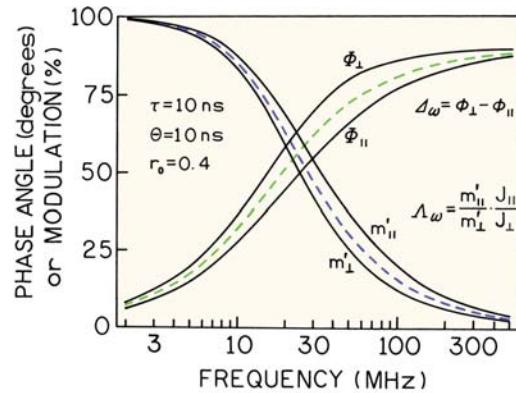


**Figure 11.3.** Simulated FD data for an anisotropy decay,  $\tau = 10$  ns and  $\theta = 10$  ns, showing the phase and actual modulation ( $m_{\parallel}'$  and  $m_{\perp}'$ ) of the polarized components of the emission, relative to the modulated excitation or scattered light. The dashed line shows the rotation-free phase and modulation values for the total emission. From [1].

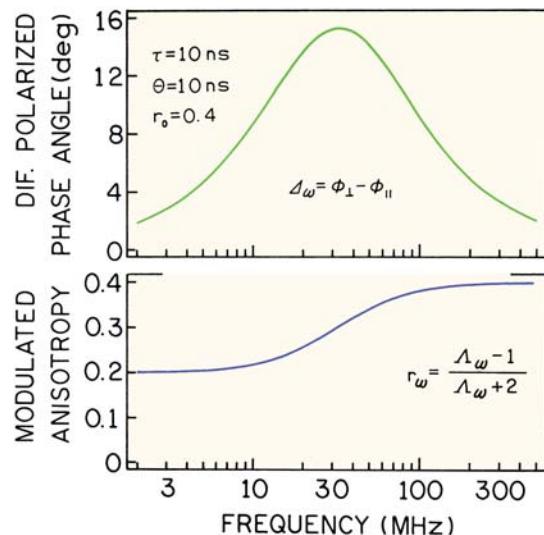


**Figure 11.4.** Differential phase ( $\Delta_{\omega}$ ) and modulated ( $\Lambda_{\omega}$ ) anisotropy for  $\tau = 10$  ns,  $\theta = 10$  ns, and  $r_0 = 0.4$ . From [1].

tered light (Figure 11.3, solid lines). The phase angle of the parallel component ( $\phi_{\parallel}$ ) will be smaller than the rotation-free phase angle for the total emission, and the modulation of the parallel component will be larger than that of the rotation-free modulation (dashed). These effects are the result of the shorter mean decay time of the vertically polarized decay (Figure 11.1). Similarly, the phase angle of the perpendicular component is larger, and the modulation smaller, because this component is being repopulated by the excess population in the parallel orientation, resulting in a longer mean decay time for the perpendicular component.

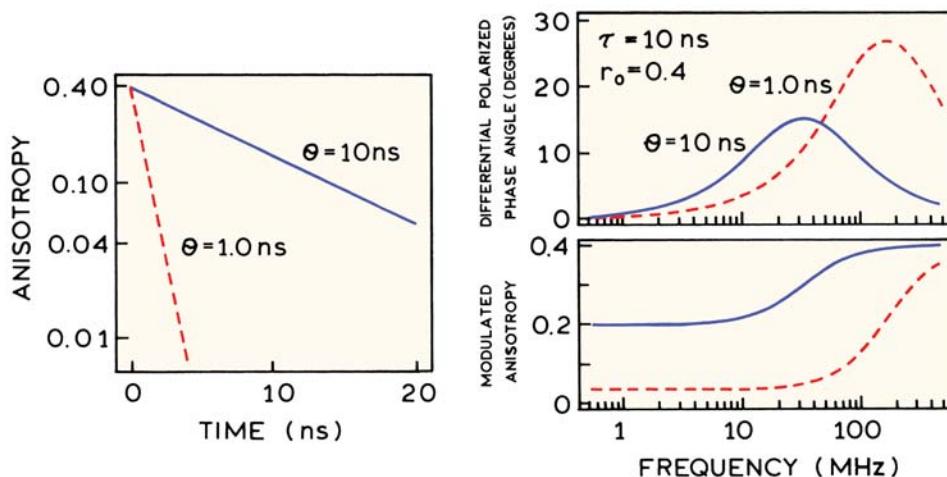


**Figure 11.5.** Comparison of TD and FD anisotropy decays with correlation times of 1.0 and 10.0 ns.

While the concept of a mean decay time is useful for understanding the relative behavior of the polarized intensity decays, the use of mean decay times to describe the decay times of the polarized components resulted in some confusion in the early literature.<sup>3–6</sup> For clarity we note that the modulations shown in Figure 11.3 ( $m_{\parallel}'$  and  $m_{\perp}'$ ), are the actual modulation of these components ( $I_{\parallel}(t)$  and  $I_{\perp}(t)$ ). For calculation of the anisotropy decay we use the non-normalized amplitudes of the modulated components of the polarized emission.

While one could measure  $\phi_{\parallel}$ ,  $\phi_{\perp}$ ,  $m_{\parallel}'$ , and  $m_{\perp}'$  to obtain the anisotropy decay, this is not the preferred method. Almost all FD anisotropy decays are measured by the differential method. The differential polarized phase angle ( $\Delta_{\omega}$ ) and modulation ratio ( $\Lambda_{\omega}$ ) is measured directly by rotation of the emission polarizer. It is more accurate to measure the difference and ratio directly, rather than calculating these values from two independently measured values.

The differential form of the FD anisotropy data measured by the differential method is illustrated in Figure 11.4. The differential phase angles appear to be approximately Lorentzian in shape on the log-frequency scale. The modulated anisotropy increases monotonically with frequency. The value of  $r_{\omega}$  at low frequency is equal to the steady-state anisotropy:

$$r = \frac{r_0}{1 + \tau/\theta} = \frac{r_0}{2} \quad (11.9)$$

The low-frequency anisotropy of  $r = 0.5 r_0$  is a result of  $\tau = \theta$  for the simulated curves. At high frequency,  $r_{\omega}$  approach-

es  $r_0$ . Longer correlation times shift the  $\Delta_{\omega}$  and  $r_{\omega}$  curves to lower modulation frequencies, and shorter correlation times shift these curves to higher frequencies.

It is valuable to visualize how changes in the anisotropy decay affect the TD and FD data. Suppose the correlation time decreases from 10 to 1.0 ns. In the TD data the anisotropy decays more rapidly (Figure 11.5). The changes in the FD data are somewhat more complex. The differential phase-angle distribution shifts to higher frequencies with shorter correlation times. The maximum differential phase angle increases or decreases depending on the relative values of  $\tau$  and  $\theta$ . A decrease in correlation time results in a decrease in the modulated anisotropy. The limiting value of  $r_{\omega}$  at low frequency is the steady-state anisotropy, and at high frequency the limit is still  $r_0$ .

Suppose the anisotropy decays with two correlation times. A typical anisotropy decay for a protein would be a 5-ns correlation time for overall rotational diffusion and a 50-ps correlation time due to segmental motion of the tryptophan residue (Figure 11.6). The TD anisotropy shows a rapid decay due to the 50-ps component, followed by a slower decay at longer times. Depending upon the resolution of the TD instrument, the fast component may or may not be resolved in the measurements. However, the presence of the fast component can be determined from a time-zero anisotropy ( $r(0)$ ), which is smaller than  $r_0$ .

The presence of two decay times also has an effect on the FD anisotropy data (Figure 11.7). Instead of a single Lorentzian distribution for  $\Delta_{\omega}$ , the differential phase angles show two such distributions, one for each correlation time (dashed lines). The presence of the rapid motion is evident

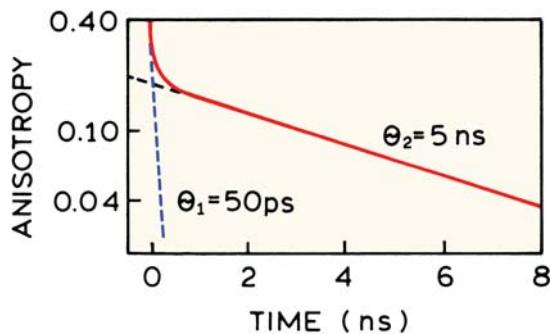


**Figure 11.6.** Simulated time anisotropy decay for a double-exponential decay with  $r_{01} = r_{02}$ ,  $\theta_1 = 50 \text{ ps}$ , and  $\theta_2 = 5 \text{ ns}$ .

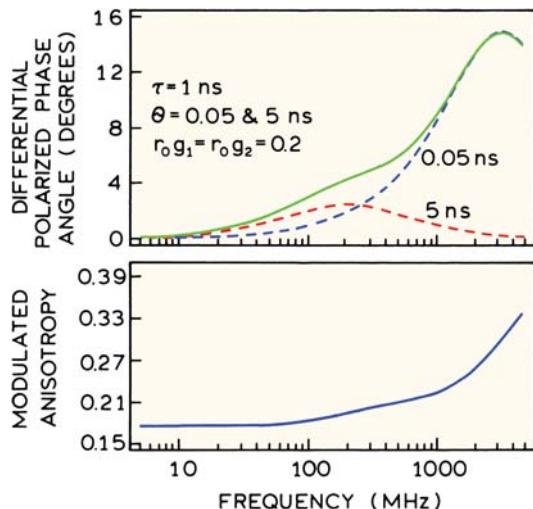


**Figure 11.7.** Frequency-domain anisotropy data for a double-exponential anisotropy decay. Revised from [2].

from the increasing phase angle at higher frequencies. If the amplitude of this rapid motion is increased, the phase angles become smaller at low frequencies and larger at the higher frequencies. If the rapid correlation time is very short, the frequency range of the instrument may not be adequate to detect this rapid motion. Then the increase in the differential phase angle at high frequency would not be observed. The emission may be highly demodulated due to the intensity decay, in which case the high-frequency limit of  $r_\omega$  cannot be measured even if the instrument can measure at the higher frequencies. The presence of an unresolved motion can be detected by a failure of  $r_\omega$  to approach the expected limiting value of  $r_0$ . This illustrates the advantage of using both the differential phase ( $\Delta_\omega$ ) and modulation ( $r_\omega$ ) data in any attempt to resolve a complex and/or rapid anisotropy decay. A failure of  $r_\omega$  to reach  $r_0$  in the frequency

domain is similar to finding  $r(0) < r_0$  in the time-domain data. As for the intensity decays, the parameters describing the anisotropy decay are recovered by comparison of the data with calculated values obtained using various models.

One may notice that the lifetime is included in the FD anisotropy simulations (Figure 11.7), but not in the TD simulations (Figure 11.6). The FD data depend on the intensity decay time. In the time domain the anisotropy decays do not depend on the lifetime. However, the lifetime determines the time range over which the intensities can be measured.

## 11.2. ANISOTROPY DECAY ANALYSIS

### 11.2.1. Early Methods for Analysis of TD Anisotropy Data

The most direct approach to analyzing the anisotropy data is to fit the measured  $r(t)$  values to an assumed anisotropy decay law. This approach is direct but partially incorrect. The measured values are calculated from the polarized intensity decays:

$$r_m(t_k) = \frac{N_{||}(t_k) - GN_{\perp}(t_k)}{N_{||}(t_k) + 2GN_{\perp}(t_k)} = \frac{D_m(t_k)}{S_m(t_k)} \quad (11.10)$$

where the  $N_{||}(t_k)$  and  $N_{\perp}(t_k)$  are the experimental data convolved with the instrument response function at time  $t_k$ ;  $D_m(t_k)$  is the difference between the polarized decays, and  $S_m(t_k)$  is the total decay, both corrected using the  $G$  factor. The calculated values  $r_m(t_k)$  are then compared with calculated values obtained from the convolution integral:

$$r_c(t_k) = \sum_{t=0}^{t=t_k} L(t_k)r(t - t_k)\Delta t \quad (11.11)$$

where  $L(t_k)$  is the instrument response function. The IRF is assumed to be independent of the orientation of the emission polarizer. The anisotropy decay is then determined by minimizing

$$\chi_R^2 = \frac{1}{v} \sum_{k=1}^n \frac{1}{\sigma_{Rk}^2} [r_m(t_k) - r_c(t_k)]^2 \quad (11.12)$$

In this equation  $r_c(t_k)$  is the anisotropy calculated using eq. 11.11 and the assumed anisotropy decay law, and  $v$  is the number of degrees of freedom. The noise in the measurements does not decrease when taking the differences in the intensity values. Instead, the calculated anisotropy values

contain all the noise present in the measured polarized decays, and it is important to correctly propagate the noise. In this case the weighting factor is a moderately complex function of the counts in each channel,<sup>7-8</sup> and is given by

$$\sigma_{Rk}^2 = r_m^2(t_k) \left( \frac{\sigma_{Sk}^2}{S_m^2(t_k)} + \frac{\sigma_{Dk}^2}{D_m^2(t_k)} - \frac{2\sigma_{SDk}^2}{S_m(t_k)D_m(t_k)} \right) \quad (11.13)$$

where

$$\sigma_{Dk}^2 = N_{||}(t_k) + G^2 N_{\perp}(t_k) \quad (11.14)$$

$$\sigma_{Sk}^2 = N_{||}(t_k) + 4G^2 N_{\perp}(t_k) \quad (11.15)$$

$$\sigma_{SDk}^2 = \sigma_{Sk}^2 - 2G^2 \sigma_{Dk}^2 \quad (11.16)$$

These expressions seem complex, but their origin is simple. These expressions are the result of propagating of the Poisson noise in each measured intensity into the anisotropy function. The origin of eq. 11.14 can be seen by considering the Poisson noise in the parallel and perpendicular components, which are given by  $[I_{||}(t_k)]^{1/2}$  and  $[I_{\perp}(t_k)]^{1/2}$ , respectively. The noise in the sum is given by the sum of the squares of the Poisson noise, with appropriate weighting by the  $G$  factor. The principles of error propagation can be found elsewhere.<sup>9</sup>

Anisotropy decays are sometimes analyzed by separate analysis of the sum and difference decays (eq. 11.10). In this method the sum  $S_m(t_k)$  is analyzed first to obtain the parameters describing the intensity decay, which are the  $\alpha_i$  and  $\tau_i$  values when using the multi-exponential model. For this analysis  $\chi_R^2$  is minimized using

$$\chi_R^2 = \frac{1}{V} \sum_{k=1}^n \frac{1}{\sigma_{Sk}^2} [S_m(t_k) - S_c(t_k)]^2 \quad (11.17)$$

where  $\sigma_{Sk}^2$  is given by eq. 11.15.

The intensity decay also appears in the difference data. The parameters ( $\alpha_i$  and  $\tau_i$ ) recovered from the sum analysis are held constant during analysis of  $D_m(t_k)$ . Once again,  $\chi_R^2$  is minimized using<sup>8,10</sup>

$$\chi_R^2 = \frac{1}{V} \sum_{k=1}^n \frac{1}{\sigma_{Dk}^2} [D_m(t_k) - D_c(t_k)]^2 \quad (11.18)$$

where  $\sigma_{Dk}^2$  is given by eq. 11.14. When this procedure is

used the different  $D(t)$  contain both the intensity decay and the anisotropy decay parameters. This can be seen by considering a single exponential decay of the intensity and the anisotropy. In this case

$$D(t) = S(t)r(t) = k \exp \left[ -t \left( \frac{1}{\tau} + \frac{1}{\theta} \right) \right] \quad (11.19)$$

where  $k$  is a constant. Hence the difference  $D(t)$  decays with an apparent decay time that is shorter than the lifetime ( $\tau$ ) and the correlation time ( $\theta$ ).

Of the two procedures described above, the second using separate analyses of  $S(t)$  and  $D(t)$  is preferable. This is because the use of eq. 11.10 to calculate the anisotropy is not correct, particularly when the correlation times are close to the width of the instrument response function. The operations of convolution and division do not commute, so that the measured values of  $r_m(t_k)$  are not a convolution of the impulse response  $r(t)$  with the lamp function. For instance, even if the anisotropy decay is a single exponential, the calculated values of  $r_m(t_k)$  can display unusual shapes, particularly near the rising edge of the curve. Also, the apparent time-zero anisotropies  $r(0)$  are often less than the true value of  $r_0$ .<sup>11</sup> The use of the calculated sum  $S_m(t_k)$  and difference ( $D_m(t_k)$ ) curves is more correct because the operations of addition and subtraction commute with convolution. However, this method still assumes that the lamp function is the same for the parallel and perpendicular components of the emission.

### 11.2.2. Preferred Analysis of TD Anisotropy Data

The preferred method of analysis is to directly analyze the polarized intensity decays without calculation of  $r_m(t_k)$  or  $D_m(t_k)$ .<sup>12-15</sup> This is a form of global analysis in which the parallel and perpendicular components (eqs. 11.1 and 11.2) are analyzed simultaneously to recover the intensity and anisotropy decay law. The polarized decay laws are used with the instrument response function to calculate

$$N_{||}^c(t_k) = \sum_{t=0}^{t=t_k} L_{||}(t_k) I_{||}(t - t_k) \Delta t \quad (11.20)$$

$$N_{\perp}^c(t_k) = \sum_{t=0}^{t=t_k} L_{\perp}(t_k) I_{\perp}(t - t_k) \Delta t \quad (11.21)$$

where  $L_{||}(t_k)$  and  $L_{\perp}(t_k)$  are the instrument response func-

tions measured for each polarized component. In contrast to the previous method, the instrument response functions are not assumed to be identical for each polarization, and can be rather different without affecting the validity of the procedure.

The calculated and measured polarized intensities are then used to minimize  $\chi_R^2$  based on the parameter values in the intensity ( $\alpha_i$  and  $\tau_i$ ) and anisotropy decays ( $r_{0i}$  and  $\theta_i$ ):

$$\begin{aligned}\chi_R^2 = & \frac{1}{v} \sum_{t=0}^n \frac{1}{\sigma_{||k}^2} [N_{||}(t_k) - N_{||}^c(t_k)]^2 \\ & + \frac{1}{v} \sum_{t=0}^n \frac{1}{\sigma_{\perp k}^2} [N_{\perp}(t_k) - N_{\perp}^c(t_k)]^2\end{aligned}\quad (11.22)$$

Since the polarized intensity decays are used directly, the weighting factors are given by

$$\sigma_{||k}^2 = N_{||}(t_k) \quad (11.23)$$

$$\sigma_{\perp k}^2 = N_{\perp}(t_k) \quad (11.24)$$

There is no need to propagate the weighting factors into the sum and difference data. All the parameters are varied simultaneously to obtain the best fit, so that the intensity and anisotropy decay parameters are all optimized to match the actual data.

Sometimes it is necessary to correct the polarized intensity decays for background signals. The counts measured for the blank sample with each polarizer position are subtracted from the measured data for the same polarizer position:

$$I_{||}(t_k) = I_{||}(t_k)_{\text{sample}} - I_{||}(t_k)_{\text{background}} \quad (11.25)$$

$$I_{\perp}(t_k) = I_{\perp}(t_k)_{\text{sample}} - I_{\perp}(t_k)_{\text{background}} \quad (11.26)$$

The weighting factor for the corrected data is given by the sum of the weighting factors for the sample and for the background. If the number of background counts is small, this correction to the weighting factor can be ignored. It is important to measure the background for both polarized components, because the background can be different for each component, particularly if scattered light reaches the detector.

It is necessary to know the  $G$  factor in order to calculate the intensity decay. The  $G$  factor can be obtained in the usual manner (Chapter 10), in which the intensities are measured with horizontally polarized excitation. The parallel and perpendicular intensities are then measured for the same period of time, assuming the excitation intensity is constant. Another method is to measure the steady-state anisotropy of the sample, which is then used to constrain the total intensities of the polarized decays. The steady-state anisotropy can be measured on a different instrument. The  $G$  factor can be calculated using<sup>10,12</sup>

$$G = \frac{1 - r}{1 + 2r} \frac{\sum N_{||}(t_k)}{\sum N_{\perp}(t_k)} \quad (11.27)$$

where the sums are the total number of counts in the polarized intensity decays. If the excitation intensity has changed, or the counting time is different, these values need to be corrected for the different experimental conditions.

### 11.2.3. Value of $r_0$

In the anisotropy decay analysis the value of  $r_0$  can be considered to be a known or unknown value. If the value of  $r_0$  is known, the anisotropy decay law can be written as

$$r(t) = r_0 \sum_j g_j \exp(-t/\theta_j) \quad (11.28)$$

where  $g_j$  are the fractional amplitudes that decay with the correlation times  $\theta_j$ . Since  $\sum g_j = 1.0$ , the use of a known  $r_0$  value reduces the number of variable parameters by one. In this type of analysis the time-zero anisotropy is forced to be equal to  $r_0$ .

Alternatively, the total or time-zero anisotropy can be a variable parameter. In this case,

$$r(t) = \sum_j r_{0j} \exp(-t/\theta_j) \quad (11.29)$$

where  $r_{0j}$  are the fractional anisotropies that decay with correlation times  $\theta_j$ . When using this type of analysis it is preferable to describe the time-zero anisotropy as  $r(0)$ , which is the recovered value of  $t = 0$ . If the anisotropy decay contains fast components that are not resolved by the instrument then the  $\sum r_{0j} = r(0)$  is less than the fundamental anisotropy  $r_0$ .

### 11.3. ANALYSIS OF FREQUENCY-DOMAIN ANISOTROPY DECAYS

Analysis of the FD anisotropy data is performed in a manner similar to the intensity decay analysis (Chapter 5). There is a somewhat more complex relationship between the data ( $\Delta_\omega$  and  $\Lambda_\omega$ ) and the transforms. The calculated values ( $\Delta_{co}$  and  $\Lambda_{co}$ ) can be obtained from the sine and cosine transforms of the individual polarized decays:<sup>3,16-17</sup>

$$N_k = \int_0^\infty I_k(t) \sin \omega t dt \quad (11.30)$$

$$D_k = \int_0^\infty I_k(t) \cos \omega t dt \quad (11.31)$$

where the subscript  $k$  indicates the orientation, parallel ( $\parallel$ ) or perpendicular ( $\perp$ ). For any assumed parameters the values  $\Delta_\omega$  ( $\Delta_{co}$ ) and  $\Lambda_\omega$  ( $\Lambda_{co}$ ) can be calculated (subscript  $c$ ) using the sine and cosine transforms of the polarized decays (eqs. 11.30 and 11.31). The calculated values of  $\Delta_\omega$  and  $\Lambda_\omega$  are given by

$$\Delta_{co} = \arctan \left( \frac{D_\parallel N_\perp - N_\parallel D_\perp}{N_\parallel N_\perp + D_\parallel D_\perp} \right) \quad (11.32)$$

$$\Lambda_{co} = \left( \frac{N_\parallel^2 + D_\parallel^2}{N_\perp^2 + D_\perp^2} \right)^{1/2} \quad (11.33)$$

where  $N_i$  and  $D_i$  are calculated at each frequency. The parameters describing the anisotropy decay are obtained by minimizing the squared deviations between measured and calculated values, using

$$\chi_R^2 = \frac{1}{v} \sum_\omega \left( \frac{\Delta_c - \Delta_{co}}{\delta \Delta} \right)^2 + \frac{1}{v} \sum_\omega \left( \frac{\Lambda_c - \Lambda_{co}}{\delta \Lambda} \right)^2 \quad (11.34)$$

where  $\delta \Delta$  and  $\delta \Lambda$  are the uncertainties in the differential phase and modulation ratio, respectively.

In the FD analysis the rotation-free intensity decay is measured in a separate experiment using magic-angle polarizer conditions. The parameter values, typically  $\alpha_i$  and  $\tau_i$  for the multi-exponential model, are held constant during the calculation of  $\chi_R^2$  for eq. 11.34. In principle, the phase and modulation of the polarized components could be measured relative to scattered light (Figure 11.4), and the values used to recover  $I(t)$  and  $r(t)$ . This would be analogous to the method used for TCSPC data. However, it

appears that the anisotropy decay is better determined by direct measurement of the difference ( $\Delta_\omega$ ) and ratio ( $\Lambda_\omega$ ) values.

There is no mention of the  $G$  factor in eqs. 11.30–11.33. This is because using the  $G$  factor is often unnecessary in analysis of the time-resolved data. This is because TD and FD measurements are typically performed using emission filters rather than a monochromator. The use of an emission monochromator in the steady-state anisotropy measurements is the dominant reason for the  $G$  factor being different from unity. For many time-resolved instruments, especially those using MCP-PMT detectors, the detection efficiency is the same for the parallel and perpendicular components, and hence  $G = 1.0$ .

In the frequency-domain measurements one checks for a sensitivity to polarization by excitation with horizontally polarized light. The measured values of the differential polarized phase angle ( $\Delta_\omega$ ) should be zero. Also, the measured value of the modulation ratio ( $\Lambda_\omega$ ) should be 1.0. If needed, FD anisotropy decays can be measured in a T format to avoid rotation of the emission polarizer.<sup>18</sup>

When the FD anisotropy data are analyzed using eq. 11.34, the weighting factors are the same as those used for directly measured phase and modulation values. We find values of  $\delta \Delta_\omega = 0.2$  and  $\delta \Lambda_\omega = 0.004$  to be appropriate for measurements. For separately measured the polarized phase ( $\phi_\parallel$  and  $\phi_\perp$ ) and modulation ratios ( $m_\parallel$  and  $m_\perp$ ) it would be necessary to propagate the uncertainties into the difference and ratio files, as was done for the time-domain analyses. A procedure to correct for background fluorescence has been described for the frequency-domain anisotropy measurements.<sup>19</sup> This procedure is somewhat more complex than the direct subtraction used for the time-domain data.

The values of  $r_0$  and  $r(0)$  are also treated the same way in the FD analysis as in the TD analysis. The value of  $r_0$  can be a fixed parameter (eq. 11.28), or the time-zero anisotropy ( $r(0)$ ) can be a variable in the analysis (eq. 11.29). Using a fixed value of  $r_0$  avoids the problem of missing a short correlation time present in the sample. However, use of an inappropriately large value of  $r_0$  will result in the appearance of a short correlation time in the calculated anisotropy decay which is not present in the sample.

### 11.4. ANISOTROPY DECAY LAWS

Depending upon the size and shape of the fluorophore, and its local environment, a wide variety of anisotropy decays

are possible. A spherical molecule displays a single rotational correlation time. Anisotropy decays can be more complex if the fluorophore is non-spherical, or if a non-spherical molecule is located in an anisotropic environment. Another origin of complex anisotropy decays is internal flexibility of a fluorophore within a larger macromolecule.

#### 11.4.1. Non-Spherical Fluorophores

One origin of multiple correlation times is a non-spherical shape. If a molecule is not spherical, there are different rotational rates around each axis. For instance, perylene is a disk-like molecule and the in-plane rotations are expected to be more rapid than the out-of-plane rotations. The out-of-plane motion requires displacement of solvent molecules. The in-plane rotations require less displacement of solvent and are expected to be more rapid. Such a molecule is referred to as an anisotropic rotor. Generally, macromolecules are nonsymmetric and one expects different rotational diffusion rates about each axis.

The theory for rotational diffusion of anisotropic rotors is complex. This topic is well understood, and is described in more detail in Chapter 12. Initially there was some disagreement about the predicted time-resolved decays for anisotropic molecules.<sup>20–25</sup> It is now agreed<sup>20</sup> that the anisotropy is expected to decay as a sum of exponentials:

$$r(t) = \sum_{j=1}^5 r_{0j} e^{-t/\theta_j} \quad (11.35)$$

There may be as many as five exponential terms for an asymmetric body, but in practice only three correlation times are expected to be distinguishable.<sup>25</sup> Ellipsoids of revolution are elongated (prolate) or flattened (oblate) molecules with two equal axes and one unique axis. The anisotropy decay of ellipsoids of revolution can display only three correlation times. The values of  $r_{0j}$  and  $\theta_j$  are complex functions of the rates of rotation around the molecular axes of the nonsymmetric body and the orientation of the absorption and emission dipoles relative to these axes. In practice, it is difficult to resolve more than two correlation times. It is important to remember that anisotropic rotations can result in multi-exponential decays of anisotropy. For small molecules in solution the rotational rates around the different axes are rarely different by more than a factor of ten. The resolution of such similar rates is difficult but has been accomplished using TD and FD measurements. The theory of anisotropic rotational diffusion is described

in Chapter 12, along with examples resolving multiple correlation times.

It is important to remember that the theory for rotation of non-spherical molecules assumes hydrodynamic behavior, in which the rates of rotation are determined by the viscous drag of the solvent. This theory fails for many small molecules in solution. This failure occurs because small molecules can slip within the solvent, particularly if the motion does not displace solvent or if the molecule is not hydrogen bonded to the solvent. In these cases one can recover a multi-exponential anisotropy decay, but the values of  $r_{0j}$  and  $\theta_j$  may not be understandable using eq. 11.35 with values or  $r_{0j}$  and  $\theta_j$  appropriate for hydrodynamic rotational diffusion (Chapter 12). It is useful to have a definition for the mean correlation time. The most commonly used average is the harmonic mean correlation time,  $\theta_H$ , which is given by

$$\frac{1}{\theta_H} = \frac{\sum_j r_{0j}/\theta_j}{\sum_j r_{0j}} = \frac{1}{r_0} \sum_j \frac{r_{0j}}{\theta_j} \quad (11.36)$$

This expression is sometimes used with  $r(0)$  in place of  $r_0$ . For a non-spherical molecule, the initial slope of the anisotropy decay is determined by the harmonic mean correlation time.<sup>26</sup>

#### 11.4.2. Hindered Rotors

Decays of fluorescence anisotropy can be complex even for isotropic rotors, if these molecules are contained in an anisotropic environment. For example, the emission dipole of DPH is oriented approximately along its long molecular axis. The rotations that displace this dipole are expected to be isotropic (Chapter 12) because the molecule is nearly symmetrical about this axis. Rotation about the long axes of the molecule is expected to be faster than the other rotational rates, but this fast rotation does not displace the emission dipole and hence does not depolarize the emission. Hence, only rotation that displaces the long axis of DPH is expected to depolarize the emission. In solvents only a single type of rotational motion displaces the emission dipole of DPH, and its anisotropy decay is a single exponential.

When DPH is in membranes the anisotropy decay is usually complex.<sup>27–30</sup> The rotational motions of DPH are hindered and the anisotropy does not decay to zero. By hindered we mean that the angular range of the rotational

motion is limited. In such cases a limiting anisotropy ( $r_\infty$ ) is observed at times which are long compared to the fluorescence lifetime. The anisotropy decay is described by

$$r(t) = (r_0 - r_\infty) \exp(-t/\theta) + r_\infty \quad (11.37)$$

This simple model for a hindered rotor assumes that the decay from  $r_0$  to  $r_\infty$  occurs exponentially. More complex expressions may be necessary for a rigorous analysis,<sup>31–33</sup> but the data are rarely adequate to resolve more than one correlation time for a hindered rotation. The constant term  $r_\infty$  has been interpreted as resulting from an energy barrier that prevents rotational diffusion of the fluorophore beyond a certain angle. Interpretation of the  $r_\infty$  values will be discussed in Section 11.7.

### 11.4.3. Segmental Mobility of a Biopolymer-Bound Fluorophore

Consider a fluorophore that is bound to a macromolecule, and assume that the fluorophore can undergo segmental motions with a fast correlation time  $\theta_F$ . Let  $\theta_P$  be the slow correlation time for overall rotation of the macromolecule. A number of theoretical treatments have appeared.<sup>34–36</sup> These rigorous treatments lead to various expressions for  $r(t)$ , most of which are well approximated by some simple expressions. Assume the segmental motions of the fluorophore occur independently of the rotational motion of the macromolecules. Then the anisotropy is given by

$$r(t) = r_0[\alpha e^{-t/\theta_F} + (1 - \alpha)]e^{-t/\theta_P} \quad (11.38)$$

The anisotropy at any time  $t$  depends on the extent of depolarization due to the internal motion with an amplitude  $r_0\alpha$  and the extent of depolarization due to overall protein rotation with an amplitude  $r_0(1 - \alpha)$ . Equation 11.38 may be regarded as a slightly more complex case of the hindered rotor in which the anisotropy decays rapidly to  $r_\infty = r_0(1 - \alpha)$  as a result of the segmental motion. However, the anisotropy continues to decay to zero as a result of the overall rotation of the macromolecule. The effect of segmental fluorophore motion within a macromolecule is the appearance of a multi-exponential anisotropy decay. This can be understood by multiplying the terms in eq. 11.38, resulting in two exponentially decaying terms. The faster motion must be hindered ( $\alpha < 1$ ) to observe a multi-exponential decay of  $r(t)$ . If the segmental motion were completely free, that is,  $\alpha = 1$ , then the anisotropy would decay with a single

apparent correlation time ( $\theta_A$ ). This apparent correlation time would be given by  $\theta_A = \theta_P\theta_F/(\theta_P + \theta_F)$ . The existence of the segmental motion would only be revealed by the small magnitude of  $\theta_A$ , relative to the correlation time expected for the macromolecule.

Time-resolved anisotropy decays are usually fit to a sum of exponential decays. Hence, a decay of the form shown by eq. 11.38 is generally fit to

$$r(t) = r_0(f_S e^{-t/\theta_S} + f_L e^{-t/\theta_L}) \quad (11.39)$$

where the subscripts S and L refer to the short and long correlation times. From comparison of eqs. 11.38 and 11.39 one can derive the following relationships between the parameters:

$$f_S = \alpha, \quad f_L = (1 - \alpha) \quad (11.40)$$

$$\frac{1}{\theta_S} = \frac{1}{\theta_F} + \frac{1}{\theta_P}, \quad \frac{1}{\theta_L} = \frac{1}{\theta_P} \quad (11.41)$$

Equation 11.41 indicates that it is acceptable to equate the longer correlation time with that of the overall rotational motion. However, the shorter observed correlation time is not strictly equal to the correlation time of the segmental motion. Only when  $\theta_F \ll \theta_P$  is  $\theta_S = \theta_F$ , the actual correlation time of the fast motion.

The effects of a fast segmental motion on the time-domain and frequency-domain data are shown in Figures 11.6 and 11.7, respectively. The presence of a 50-ps correlation time results in a rapid initial decrease in  $r(t)$ . The amplitude of this rapid component depends on the amplitude of the motion. In Figure 11.6 this amplitude is assumed to account for half of the total anisotropy ( $r_{01} = 0.2$ ). Following the rapid decrease, the anisotropy decays by the longer correlation time of 5 ns. This is the basis of estimating the overall correlation time of a protein from the correlation time observed at longer times. When the value of  $\theta_F$  is much less than  $\theta_P$ , and less than the instrumental resolution, the effect of the fast motion is to decrease the apparent value of  $r_0$ . The remaining anisotropy decays with  $\theta_P$ .

The presence of a short correlation time results in a complex appearance for the FD anisotropy data. The single bell-shaped  $\Delta_\omega$  curve is replaced by a more complex curve (Figure 11.7), which contains contributions from the two correlation times (dashed lines). Depending on the upper frequency limit of the FD instrument, it may not be possi-

ble to measure the maximum values of  $\Delta_\omega$  due to the faster motion. In these cases the observed value of  $\Delta_\omega$  increases up to the highest measured frequency. The presence of a rapid correlation time also results in complex behavior for the modulated anisotropy ( $r_\omega$ ). Depending on the upper frequency limit of the measurement the values of  $r_\omega$  may not reach the value of  $r_0$ .

#### 11.4.4. Correlation Time Distributions

Anisotropy decays can also be analyzed in terms of distributions of correlation times.<sup>37–39</sup> One approach is to describe the correlation time spread in terms of a Gaussian, Lorentzian, or other distribution. The Gaussian (G) and Lorentzian (L) distributions are given by

$$p_G(\theta) = \frac{1}{\sigma\sqrt{2\pi}} \exp\left[-\frac{1}{2}\left(\frac{\theta - \bar{\theta}}{\sigma}\right)^2\right] \quad (11.42)$$

$$p_L(\theta) = \frac{1}{\pi} \frac{\Gamma/2}{(\theta - \bar{\theta})^2 + (\Gamma/2)^2} \quad (11.43)$$

In these expressions  $\bar{\theta}$  are the central values,  $\sigma$  the standard deviation of the Gaussian, and  $\Gamma$  the full width at half maximum of the Lorentzian.

Suppose the anisotropy decay is described by a single modal distribution, with a single mean value ( $\bar{\theta}$ ). That part of the anisotropy that displays a correlation time  $\theta$  is given by

$$r(t, \theta) = r_0 p(\theta) \exp(-t/\theta) \quad (11.44)$$

where  $p(\theta)$  is the probability of a particular correlation time  $\theta$ . It is not possible to selectively observe the fraction of the anisotropy that decays with  $\theta$ . Hence, the observed anisotropy decay is given by the integral equation

$$r(t) = r_0 \int_0^\infty p(\theta) \exp(-t/\theta) d\theta \quad (11.45)$$

It is also possible to describe the anisotropy decay by a multimodal correlation time distribution. In this case the amplitude that decays with a correlation time  $\theta$  is given by

$$r(t, \theta) = \sum_j r_{0j} p_j(\theta) \exp(-t/\theta) \quad (11.46)$$

and the observed anisotropy decay is given by

$$r(t) = \sum_j r_{0j} \int_0^\infty p_j(\theta) \exp(-t/\theta) d\theta \quad (11.47)$$

In this formulation the distribution shape factors are normalized so that the integrated probability of each mode of the distribution is equal to unity. Equations 11.45 and 11.47 are properly normalized only if none of the probability occurs below zero.<sup>39</sup> Depending on the values of  $\theta$ ,  $\sigma$ , or  $\Gamma$ , part of the probability for the Gaussian or Lorentzian distributions (eqs. 11.42 and 11.43) can occur below zero, even if  $\theta$  is larger than zero. This component should be normalized by the integrated area of the distribution function above  $\theta = 0$ . The correlation time distributions can also be obtained using maximum entropy methods, typically without using assumed shapes for the distribution functions.<sup>37–38</sup>

#### 11.4.5. Associated Anisotropy Decays

Multi-exponential anisotropy decay can also occur for a mixture of independently rotating fluorophores. Such anisotropy decay can occur for a fluorophore when some of the fluorophores are bound to protein and some are free in solution. The anisotropy from the mixture is an intensity weighting average of the contribution from the probe in each environment:

$$r(t) = r_1(t)f_1(t) + r_2(t)f_2(t) \quad (11.48)$$

where  $r_1(t)$  and  $r_2(t)$  are the anisotropy decays in each environment. The fractional time-dependent intensities for each fluorophore are determined by the decay times in each environment. For single exponential decays these fractional contributions are given by

$$f_i(t) = \frac{\alpha_i \exp(-t/\tau_i)}{\alpha_1 \exp(-t/\tau_1) + \alpha_2 \exp(-t/\tau_2)} \quad (11.49)$$

Such systems can yield unusual anisotropy decays that show minima at short times and increase at long times.<sup>40–43</sup> Associated anisotropy decays are described in more detail in Chapter 12.

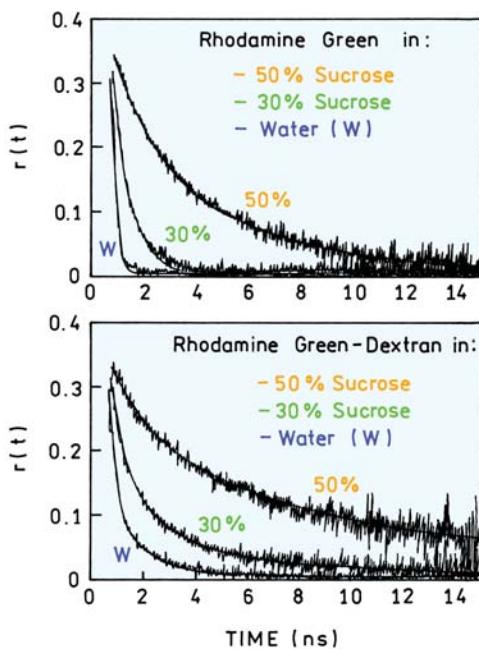


**Figure 11.8.** Anisotropy decays of Rhodamine Green in water, and 30 and 50% sucrose. Revised from [44].

#### 11.4.6. Example Anisotropy Decays of Rhodamine Green and Rhodamine Green-Dextran

It is instructive to examine several anisotropy decays. Figure 11.8 shows anisotropy decays for rhodamine green (RhG) in water and in water containing high concentrations of sucrose.<sup>44</sup> Water–sucrose mixtures are often used to increase the viscosity of a sample without denaturing the biomolecules. The top panel shows RhG that is not linked to dextran. The anisotropy in water decays in less than a nanosecond. As the viscosity is increased with sucrose the anisotropy decays for slowly, and is discernible from 0 till about 10 ns in 50% sucrose. The lifetimes and correlation

times are summarized in Table 11.1. The correlation time in water is 167 ps and increases to 3.44 ns in 50% sucrose. The correlation time increases roughly in proportion to the increase in viscosity. Only a single correlation time was needed to fit the data. The data were collected out to 15 ns, which is about fourfold longer than the RhG lifetime. The upper time limit for measuring the anisotropy data is determined by the intensity decay time of the fluorophore. If the lifetime were longer, then the anisotropy decay data could be collected at longer times.

The lower panel in Figure 11.8 shows the anisotropy decay of RhG when covalently linked to dextran, which had a molecular weight near 10 kDa. The anisotropy decays could not be fit using a single correlation time, but required two correlation times (Table 11.1). The shorter correlation times for RhG–dextran are similar to those found for RhG in water. This suggests the shorter correlation times are due to segmental motions of the covalently bound RhG, and that the motions are similar to the motion of RhG in water. The longer correlation times of RhG–dextran increase with viscosity, but less than expected from the increased in viscosity. For instance, the ratio of the longer correlation times in 50% and 0% sucrose is 6.0, but the ratio of viscosities is 15.4. This result suggests that the segmental motion in RhG–dextran contributed to the longer correlation time shown in eq. 11.38. That is, the longer measured correlation time is shorter than the correlation time for overall rotational diffusion of dextran because of contributions from the segmented motions.

#### 11.5. TIME-DOMAIN ANISOTROPY DECAYS OF PROTEINS

During the past 15 years there have been numerous anisotropy decay measurements on proteins, and it is not practi-

**Table 11.1.** Anisotropy Decay Parameters for Rhodamine Green and Rhodamine Green-Labeled Dextran<sup>a</sup>

Sample	$\tau$ (ns)	$r_{01}$	$\theta_1$ (ns)	$r_{02}$	$\theta_2$ (ns)	$\eta/\eta_{\text{w}}$
<b>Rhodamine Green</b>						
Water	3.94	—	—	0.317	0.167	1.0 <sup>b</sup>
30% sucrose	3.85	—	—	0.303	0.721	3.2
50% sucrose	3.70	0	—	0.328	3.44	15.4
<b>Rhodamine Green-dextran conjugate</b>						
Water	3.85	0.226	0.239	0.081	1.99	1.0
30% sucrose	3.68	0.201	0.698	0.114	4.50	3.2
50% sucrose	3.50	0.140	1.94	0.192	12.0	15.4

<sup>a</sup>Revised from [44].

<sup>b</sup>Viscosity ( $\eta$ ) relative to the viscosity of water ( $\eta_{\text{w}}$ ).

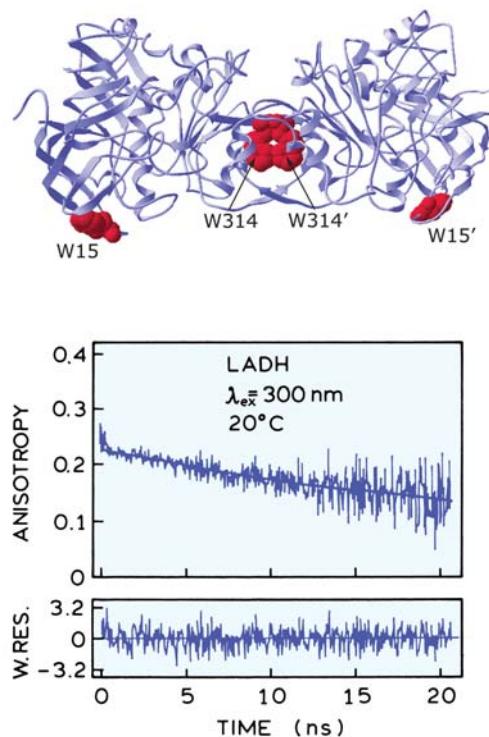


**Figure 11.9.** Anisotropy decay of LADH excited at 300 nm. The apparent time-zero anisotropy is  $r(0) = 0.22$ . Revised and reprinted with permission from [45]. Copyright © 1981, American Chemical Society.

cal to even cite the many references. We present examples that illustrate the range of behavior found for proteins.

#### 11.5.1. Intrinsic Tryptophan Anisotropy Decay of Liver Alcohol Dehydrogenase

Liver alcohol dehydrogenase (LADH) is a dimer with two tryptophan residues in each identical subunit and a total molecular weight of 80 kD. One of the residues is exposed to the solvent (trp-15), and one residue is buried (trp-314). This buried residue can be selectively excited on the red edge of the absorption spectrum at 300 nm.<sup>45</sup> The anisotropy decay of LADH excited at 300 nm is shown in Figure 11.9. The decay was found to be a single exponential with a correlation time of 33 ns. This single correlation time can be compared with that predicted for a hydrated sphere (0.2 g H<sub>2</sub>O/g of protein and eq. 10.46), which predicts a value of 31 ns at 20°C. Hence this tryptophan residue appears to be rigidly held within the protein matrix.

Trp-314 appears to rotate with the protein, but the data still suggest the presence of some segmental mobility. This is evident from the apparent time-zero anisotropy,  $r(0) =$

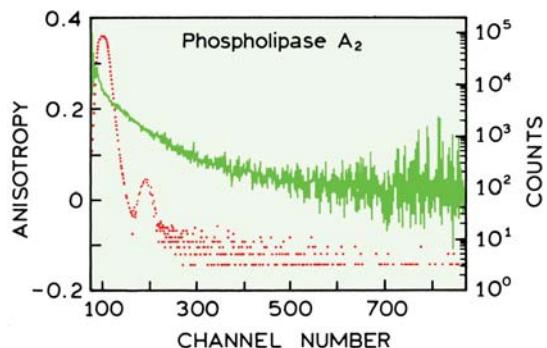


**Figure 11.10.** Anisotropy decay of trp-3 in phospholipase A<sub>2</sub> 30 ps per channel. The anisotropy decay parameters are  $r_{01} = 0.104$ ,  $r_{02} = 0.204$ ,  $\theta_1 < 50$  ps and  $\theta_2 = 6.5$  ns. Revised from [46].

0.22, which is less than the fundamental anisotropy of tryptophan at this excitation wavelength. The motions responsible for this loss of anisotropy may be on a timescale faster than the resolution of these measurements. Additionally, the studies have suggested that the apparent correlation times are different with excitation wavelengths. This cannot occur for a sphere, but can occur for non-spherical molecules if different excitation wavelengths change the orientation of the transition in the molecule. LADH is thought to be shaped like a prolate ellipsoid with semi-axes of 11 and 6 nm, and an axial ratio near 1.8.

#### 11.5.2. Phospholipase A<sub>2</sub>

A more typical protein anisotropy decay is shown by phospholipase A<sub>2</sub>. This enzyme catalyzes the hydrolysis of phospholipids and is most active when located at a lipid-water interface. Phospholipase A<sub>2</sub> has a single tryptophan residue (trp-3), which serves as the intrinsic probe. The anisotropy decay is clearly more complex than a single exponential.<sup>46</sup> At long times the correlation time is 6.5 ns, consistent with overall rotational diffusion. However, in comparison with LADH, there is a dramatic decrease in anisotropy at short times (Figure 11.10). The correlation time of the fast component is less than 50 ps, and this motion accounts for one-third of the total anisotropy.

#### 11.5.3. Subtilisin Carlsberg

The protease Subtilisin Carlsberg (SC) has a single tryptophan residue that is almost completely exposed to water, as seen from an emission maximum of 355 nm, accessibility to quenching by iodide, and the crystal structure (Figure 11.11). The anisotropy decays rapidly to zero with a corre-

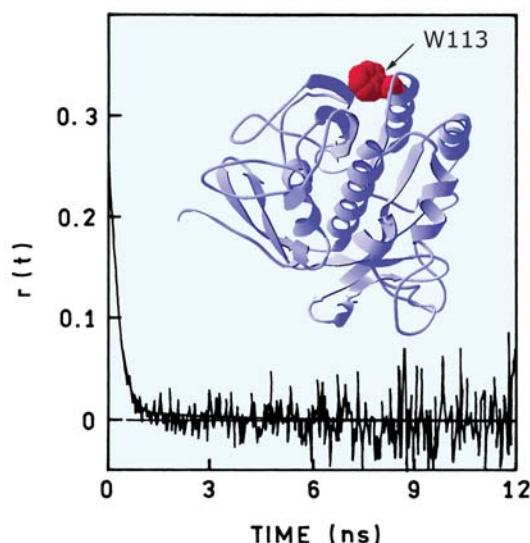


**Figure 11.11.** Anisotropy decay and structure (insert) of the single-tryptophan side chain in subtilisin Carlsberg. The anisotropy decay parameters are  $r(0) = 0.2$ ,  $g_1 = 0.9$ ,  $\theta_1 = 0.17$  ns,  $g_2 = 0.1$ , and  $\theta_2 = 3.5$  ns. Revised from [47].

lation time near 170 ps. There is only a 10% component of a 3.5-ns correlation time that is due to overall rotational diffusion. The correlation time of NATA in water is about 60 ps, so the tryptophan side chain rotates freely relative to the peptide backbone.

Independent tryptophan motions have been observed in a large number of proteins,<sup>48–50</sup> and have been predicted by molecular dynamic calculations.<sup>51</sup> Fast components in the anisotropy decay are also observed for labeled proteins.<sup>52–53</sup> Hence, segmental motions of intrinsic and extrinsic fluorophores appears to be a common feature of proteins.

#### 11.5.4. Domain Motions of Immunoglobulins

Anisotropy decay measurements have been used to examine the flexibility of immunoglobulins in solution.<sup>54–58</sup> Early studies of IgG suggested motions of the  $F_{ab}$  fragments that were independent of overall rotational motion. Many immunoglobulins are Y-shaped proteins. The two tops of the Y are the  $F_{ab}$  regions that bind to the antigen. In the case of IgE (Figure 11.12) the bottom of the Y is the  $F_c$  fragment, which binds to a receptor on the plasma membrane.

In order to study IgE dynamics the antigen dansyl-lysine was bound to the antigen-binding sites on the  $F_{ab}$  regions.<sup>59</sup> The anisotropy decays are dramatically different when the IgE is free in solution or when bound to the mem-

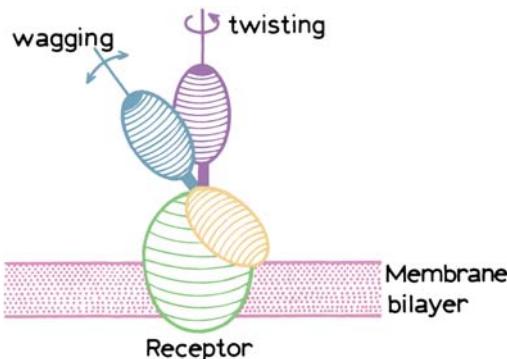


**Figure 11.12.** Model of IgE complexed with the plasma membrane receptor. The arrows suggest modes of segmental motion of the  $F_{ab}$  fragments. Reprinted with permission from [59]. Copyright © 1990, American Chemical Society.

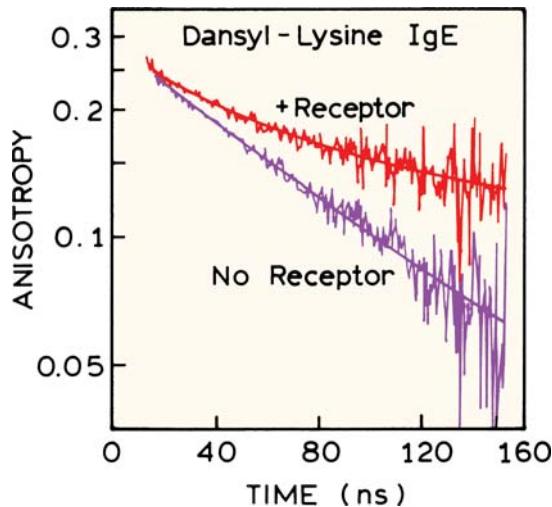


**Figure 11.13.** Anisotropy decay of dansyl-lysine bound to the antigen binding sites of IgE in the absence and presence of the membrane receptor. Revised and reprinted with permission from [59]. Copyright © 1990, American Chemical Society.

brane receptor (Figure 11.13). When bound to the receptor there is a long correlation time of 438 ns (Table 11.2). This correlation time is too long for overall rotational diffusion of the protein, and thus reflects the anisotropy decay of the membrane-bound form of IgE. The actual correlation time is probably longer, because 438 ns was the longest correlation time observable with the 27-ns intensity decay time of the dansyl-lysine.

Domain motions within the IgE molecule are evident from the multi-exponential fits to the anisotropy decays (Table 11.2). When free in solution, IgE displays two corre-

**Table 11.2.** Anisotropy Decays of Dansyl-Lysine Bound to IgE<sup>a</sup>

Sample	$g_1$ <sup>b</sup>	$\theta_1$ (ns)	$g_2$	$\theta_2$ (ns)
IgE in solution	0.30	48	0.70	125
IgE receptor	0.32	34	0.68	438

<sup>a</sup>From [59].<sup>b</sup>The  $g_j$  values represent the fraction of the total anisotropy that decay with the correlation time  $\theta_j$ .

lation times of 48 and 125 ns. The larger value is due to overall rotation of IgE, and the shorter value is due to independent motions of the  $F_{ab}$  fragments. Assignment of the 48-ns correlation time to  $F_{ab}$  motion is supported by a similar correlation time being present when the antibody bound to the receptor. These results indicate that IgE interacts with its receptor through the  $F_c$  region, and that this interaction does not inhibit motion of the  $F_{ab}$  domains (Figure 11.12).

### 11.5.5. Effects of Free Probe on Anisotropy Decays

Anisotropy decays of intrinsic and extrinsic probes frequently show subnanosecond components that are due to rapid segmental motions. However, such components should be interpreted with caution, and can be due to scattered light reaching the detector. Another origin of rapid anisotropy components is the presence of unbound probe in a sample thought to contain only the labeled macromolecule. A free probe will typically display a 50- to 100-ps correlation time, which can easily be mistaken for segmental motion.

The effect of free probe is illustrated by anisotropy decays of the yellow fluorescent protein (YFP) from *Vibrio fischeri*. This protein is from a bioluminescent bacterium, and the emitting fluorophore is flavin mononucleotide (FMN). The intensity decay time of FMN is 4.4 ns in solution and 7.6 ns when bound to YFP. The binding constant of FMN to YFP is only modest, so depending on YFP concentration, some of the FMN can dissociate from the protein.<sup>60</sup>

Anisotropy decays of YFP are shown in Figure 11.14. At higher protein concentration the decay is dominantly due to a 14.8-ns correlation time assigned to overall protein rotation. This correlation is longer than expected for a protein with a molecular weight of 22.7 kD (near 9 ns), which suggests an elongated shape for the protein. It appears the FMN is rigidly bound to YFP. As the protein is diluted, the anisotropy decay shows a fast component near 0.15 ns, which has been assigned to free FMN (Table 11.3). The fast

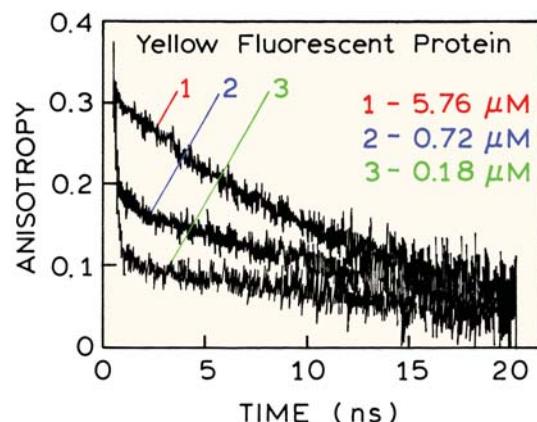


**Figure 11.14.** Anisotropy decays of yellow fluorescent protein at three concentrations. Revised and reprinted with permission from [60]. Copyright © 1997, American Society for Photobiology.

correlation time is probably beyond the time resolution of the measurements, so that the actual value may be smaller than 0.15 ns. As the protein concentration is decreased, the amplitude of the short decay time (4.4 ns) and the fast correlation time (0.15 ns) increases because a larger fraction of FMN is in the free form. Such data can be used to calculate the dissociation constant of FMN from the protein.

### 11.6. FREQUENCY-DOMAIN ANISOTROPY DECAYS OF PROTEINS

The frequency-domain method can also be used to resolve the complex anisotropy decays displayed by proteins.<sup>63–67</sup> Examples are provided in Chapter 17, so only a few examples will be presented here.

#### 11.6.1. Apomyoglobin: A Rigid Rotor

Apomyoglobin is known to bind a number of fluorescent probes in its hydrophobic heme binding site. One example is 2-p-toluidinyl-6-naphthalene sulfonate (TNS), which is essentially nonfluorescent in aqueous solution, and becomes highly fluorescent when bound to apomyoglobin. Differential polarized phase angles for TNS-labeled apomyoglobin are shown in Figure 11.15. These values are consistent with a correlation time of 20.5 ns, and an  $r(0)$  value of 0.331. Since the  $r_0$  values recovered from the FD data agree with the frozen solution value ( $r_0 = 0.32$ ), these data indicate that TNS-apomyoglobin rotates as a rigid body, without significant free rotation of the TNS group.<sup>67</sup>

**Table 11.3.** Flavin Mononucleotide Intensity and Anisotropy Decays in the Presence of Yellow Fluorescent Protein (YFP)<sup>a</sup>

[YFP]	$\alpha_1^b$	$\tau_1$ (ns)	$\tau_2$ (ns)	$r_{01}$	$\theta_1$ (ns)	$r_{02}$	$\theta_2$ (ns)	$r^c$
5.76 $\mu\text{M}$	0.08	4.4	7.6	0.02	0.15	0.29	14.8	0.157
0.72 $\mu\text{M}$	0.34	"	"	0.17	0.15	0.19	14.8	0.108
0.18 $\mu\text{M}$	0.69	"	"	0.26	0.14	0.11	14.8	0.071

<sup>a</sup>From [60].

<sup>b</sup> $\alpha_1 + \alpha_2 = 1.0$ .

<sup>c</sup>Steady-state anisotropy.

The insert shows the time-resolved anisotropy decay reconstructed from the FD data.

Also shown in Figure 11.15 are FD data for rotational diffusion of TNS in propylene glycol at 20°C. At this temperature the decay time of TNS in propylene glycol is 7.8 ns. The recovered correlation time was 9.5 ns, with  $r(0) = 0.351$ . As is typical for polar fluorophores in polar solvents, TNS appears to rotate like a spherical molecule.

### 11.6.2. Melittin Self-Association and Anisotropy Decays

Melittin is a small protein (26 amino acids) that self-associates into tetramers. Melittin was labeled with an anthraniloyl moiety (N-methylantraniloyl amide, NMA) to serve as an extrinsic probe.<sup>63</sup> Frequency-domain data for the monomeric and tetrameric forms of melittin are shown in Figure 11.16. Also shown are the FD data for the free probe (NMA) not bound to protein. The values of  $\Delta_\omega$  for the free probe are close to zero for all frequencies below 20 MHz, and increased to only several degrees near 150 MHz. Also the modulated anisotropies ( $r_\omega$ ) are near zero at all measurable frequencies. These low values are due to the rapid 73 ps correlation time of the free probe.

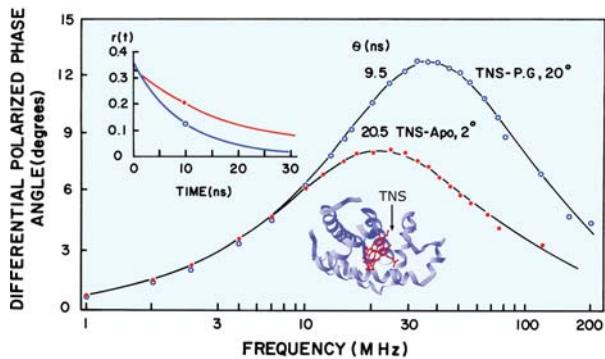


**Figure 11.15.** Frequency-domain anisotropy decays of 2-p-toluidinyl-6-naphthalene sulfonic acid in propylene glycol (PG) and bound to apomyoglobin (Apo). Insert: TD anisotropy decays. From [67].

The shape of the  $\Delta_\omega$  and  $r_\omega$  plots are different for the monomer (M) and tetramer (T) forms of melittin. In both cases the anisotropy decays are complex due to significant segmental mobility of the probe with a correlation time near 0.2 ns. Upon formation of a tetramer the shape of the  $\Delta_\omega$  curve shows evidence of overall rotational diffusion with a dominant correlation time near 3.7 ns. In the monomeric state overall rotational diffusion is not visible, but the data contain a substantial component near 1.6 ns, which is due to monomeric melittin. These changes in the overall rate of diffusion upon tetramer formation can be easily seen in the values of  $r_\omega$ , which are uniformly larger for the tetramer. The frequency-domain data at high frequencies are sensitive to rotational diffusion and local motions of proteins.

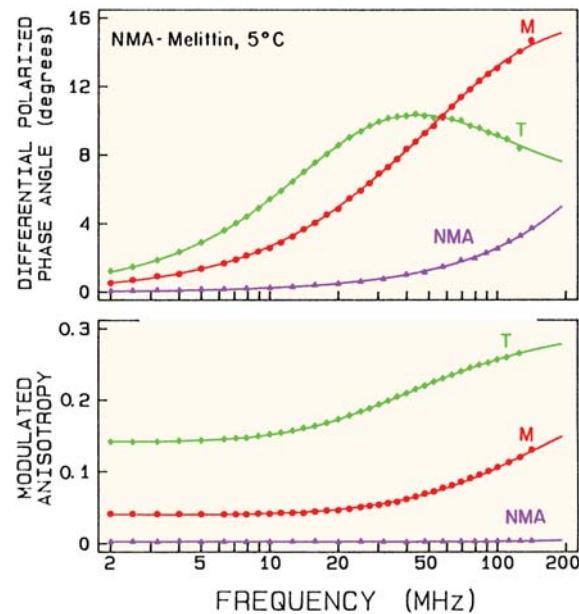


**Figure 11.16.** Differential phase angles and modulated anisotropies of N-methylantraniloyl (NMA)-melittin monomer (M) and tetramer (T). Also shown are data for the free probe N-methylantraniloyl-lamide (NMA) at 5°C. Reprinted from [63]. Copyright © 1986, with permission from Elsevier Science.

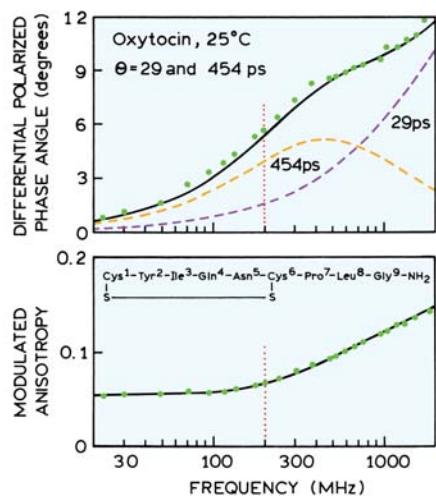


**Figure 11.17.** Frequency-domain anisotropy decay of the intrinsic tyrosine fluorescence of oxytocin. The dashed curves show the values expected for  $r_{01} = 0.208$ ,  $\theta_1 = 29$  ps,  $r_{02} = 0.112$ ,  $\theta_2 = 454$  ps. Revised and reprinted from [66]. Copyright © 1986, with permission from Elsevier Science.

### 11.6.3. Picosecond Rotational Diffusion of Oxytocin

If the correlation times are very short the fast motions can be missed in the measurements. In the time-domain the faster components are resolved by decreasing the width of the instrument response function. In the frequency-domain the resolution of faster components is accomplished by measuring at higher light modulation frequencies (Chapter 5). Measurements to 2 GHz can be used to resolve the picosecond anisotropy decays.

Oxytocin is a small cyclic polypeptide that contains 9 amino acids and a single tyrosine residue. The FD

anisotropy decay of the tyrosine fluorescence is shown in Figure 11.17. The FD data to 200 MHz (vertical dotted line) shows only increasing values of  $\Delta_\omega$  and little change in the modulated anisotropy.<sup>66</sup> Hence the data contain incomplete information on the anisotropy decay. This situation is improved by instrumentation which allowed measurements to 2 GHz. In this case there is detectable shape in the values of  $\Delta_\omega$ , and one can see that there are components due to two correlation times, 29 and 454 ps. The 29 ps correlation time is due to segmental motions of the tyrosyl residues, and the 454-ps correlation time is due to overall rotation of the peptide.

## 11.7. HINDERED ROTATIONAL DIFFUSION IN MEMBRANES

Anisotropy decays can be used to characterize model and real cell membranes. One of the most widely used probes is DPH, originally proposed as a probe to estimate the microviscosity of cell membranes.<sup>68</sup> The basic idea was to compare the anisotropy observed for the membrane-bound probe with that observed for the probe in solutions of known viscosity. By comparison, the microviscosity of the membrane could be calculated. This procedure assumes that the rotational motions are the same in the reference solvent and in the membranes.

A frequently used viscosity reference solvent for DPH is mineral oil. This solvent is used because the decay times of DPH in mineral oil are mostly independent of temperature, whereas the decay times in propylene glycol are dependent on temperature. Polarized intensity decays of DPH are shown in Figure 11.18. In mineral oil the differ-

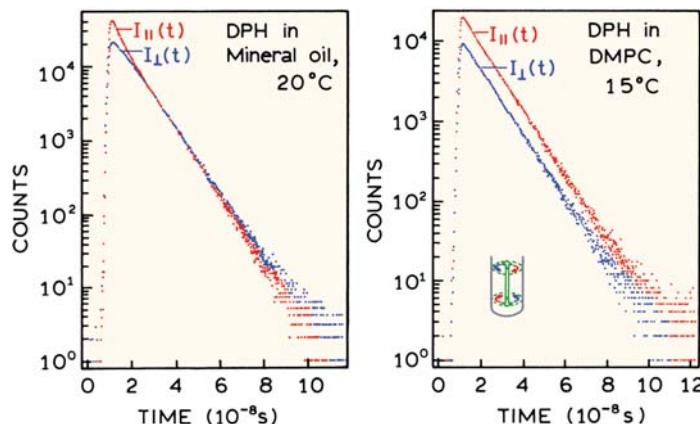


**Figure 11.18.** Polarized intensity decays of 1,6-diphenylhexatriene (DPH) in mineral oil at 20°C (left) and in DMPC vesicles at 15°C (right). Similar data have been reported from several laboratories.<sup>10,27,30</sup>

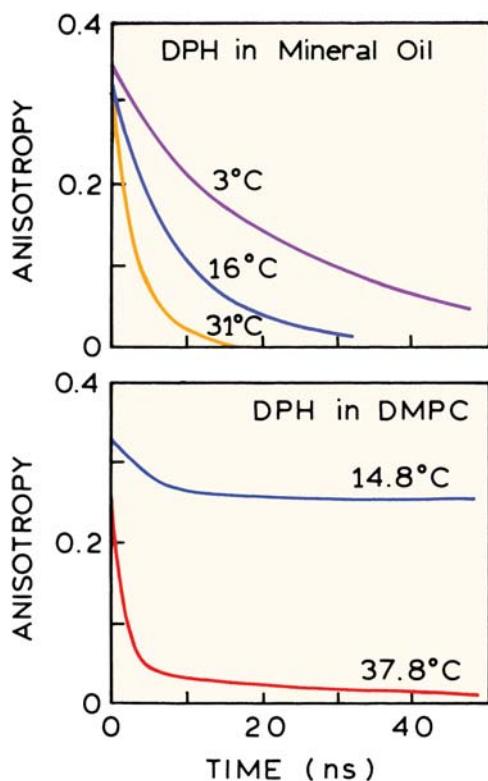


**Figure 11.19.** Anisotropy decays of DPH in mineral oil and in DMPC vesicles. Redrawn from [10] and [27].

ence decays to zero, indicating the anisotropy decays to zero (left). Contrasting results were found for DPH in vesicles of dimyristoyl-L- $\alpha$ -phosphatidylcholine (DMPC). In this case the polarized intensities remain different during the entire decay (right). This result indicates that the anisotropy does not decay to zero at long times (Figure 11.19). At higher temperature, above the membrane phase transition, the long time anisotropy becomes closer to zero, as shown for DMPC residues at 37.8°C (Figure 11.19).

Time-resolved anisotropies can be used to study the effects of cholesterol on membranes. A typical result is that the presence of cholesterol in the membranes results in more hindered rotational diffusion than in the absence of cholesterol. This can be seen in the experimental anisotropy decays of DPH in DPPC vesicles.<sup>69</sup> As the mole fraction of the cholesterol is increased the long time anisotropy increases (Figure 11.20). Such behavior is a general feature of the anisotropy decays of labeled membranes.<sup>70-76</sup>

Considerable attention has been given to the molecular interpretation of the limiting anisotropies ( $r_\infty$ ). The interest arises from a desire to understand the properties of the

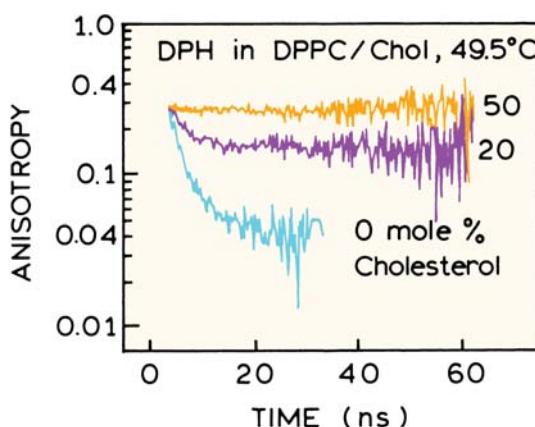


**Figure 11.20.** Anisotropy decays of DPH in DPPC vesicles at 49.5°C, containing 0, 20, and 50 mole% cholesterol. At 49.5°C the DPPC membranes are above their phase transition temperature, which is near 37°C. Revised and reprinted with permission from [69]. Copyright © 1978, American Chemical Society.

membranes that are responsible for the hindered rotation. In one analysis<sup>31,77</sup> the rod-like DPH molecule is assumed to exist in a square-well potential so that its rotation is unhindered until a certain angle ( $\theta_c$ ) is reached (see insert in Figure 11.18). Rotation beyond this angle is assumed to be energetically impossible. In this model the limiting anisotropy is related to the cone angle  $\theta_c$  by

$$\frac{r_\infty}{r_0} = S^2 = \left[ \frac{1}{2} \cos \theta_c (1 + \cos \theta_c) \right]^2 \quad (11.50)$$

This ratio is also equal to the square of the order parameter ( $S$ ). Completely unhindered motion is found for  $\theta_c = 90^\circ$ . The limiting anisotropies of DPH can be interpreted in terms of this model. As the cholesterol content of DPPC vesicles increases, the cone angle decreases (Figure 11.21), with the effect being much smaller at higher temperature. The cone angle of DPH in pure DPPC vesicles increases dramatically at the phase transition temperature near 37°C. The presence of cholesterol prevents free rotation of DPH at all temperatures.

This interpretation of the  $r_\infty$  values is intuitively pleasing, but the values of  $\theta_c$  should be interpreted with caution. One difficulty of this model is that the calculation of  $\theta_c$  from  $r_\infty/r_0$  depends upon the existence of a square-well potential in the membranes. The fact that a nonzero value of  $r_\infty$  is observed demonstrates the existence of a barrier to rotation, but does not demonstrate the barrier is an abrupt as a square-well potential. For this reason caution is advised in

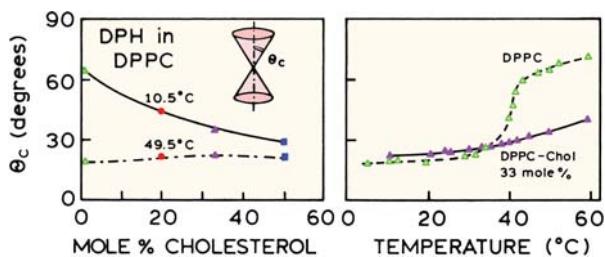


**Figure 11.21.** Cone angles (eq. 11.50) for rotational diffusion of DPH in DPPC vesicles as a function of the cholesterol content of the vesicles. Revised and reprinted with permission from [69]. Copyright © 1978, American Chemical Society.

the interpretation of derived  $\theta_c$  values from observed values of  $r_\infty$ . Alternatively, it has been shown that  $r_\infty$  is related to the order parameter describing the equilibrium orientation distribution of the probe at times much longer than the rotational correlation time.<sup>36,78–81</sup> Specifically,

$$S^2 = \frac{r_\infty}{r_0} = \left\langle \frac{3 \cos^2 \theta - 1}{2} \right\rangle^2 \quad (11.51)$$

where the brackets indicate an average over all fluorophores, and  $\theta$  is the angular rotation of DPH in the membrane. This result is claimed to be independent of any assumed model except for the assumption of cylindrical symmetry. In this case  $r_\infty = 0$  when the average value of  $\theta$  reaches  $54.7^\circ$ .

The presence of hindered rotations of DPH results in unusual frequency-domain data.<sup>82–84</sup> The effect of a nonzero value of  $r_\infty$  results in a uniform decrease in the differential phase angles (Figure 11.22). The values of  $\Delta_\omega$  are much smaller below the transition temperature of DPPC vesicles,

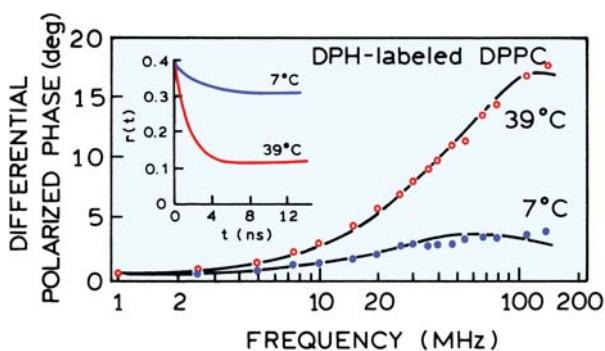


**Figure 11.22.** Frequency-dependent values of  $\Delta_\omega$  for DPH in DPPC vesicles. The insert shows the recovered anisotropy decay.

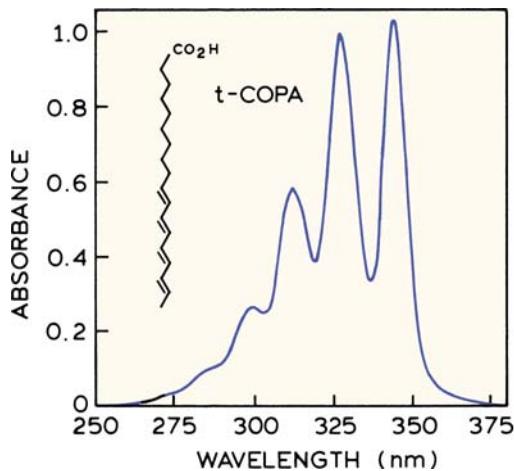


**Figure 11.23.** Absorption spectra of t-COPA  $10^{-6}$  M in ethanol at 20°C. Revised and reprinted from [85], from the Biophysical Society.

and increases dramatically above the transition temperature, when the DPH molecules can rotate freely. These data can be interpreted using eqs. 11.30–11.34 to recover the time-dependent anisotropy (Figure 11.22, insert).

### 11.7.1. Characterization of a New Membrane Probe

The concepts described for DPH allow us to understand the characteristics of newly developed probes. One example is the all-trans isomer of 8,10,12,14,16-octadecapentaenoic acid (t-COPA, Figure 11.23). This probe is insoluble and/or nonfluorescent in water, so that the only emission is from t-COPA bound to membranes.<sup>85</sup> The absorption spectrum of t-COPA is centered at 330 nm, making it an acceptor for the intrinsic tryptophan fluorescence of membrane-bound proteins. The effectiveness of t-COPA as an acceptor is due to its high extinction coefficient near  $105,000 \text{ M}^{-1} \text{ cm}^{-1}$ .

Localization of t-COPA in membranes was accomplished using the spin-labeled fatty acids as quenchers (Chapter 9). DMPC has a phase transition near 24°C, and quenching is more effective in the fluid phase at 30°C than in the gel phase at 17°C (Figure 11.24). The effect of temperature on quenching shows that there is a diffusive component to the quenching, which is in contrast to the usual assumptions of no diffusion in parallax quenching. Larger amounts of quenching by 16NS than by 5NS indicates that the chromophore is buried deeply in the bilayer, away from the lipid-water interface.

The intensity decay of t-COPA is multi-exponential in solvents and in lipid bilayers. In lipids the major component

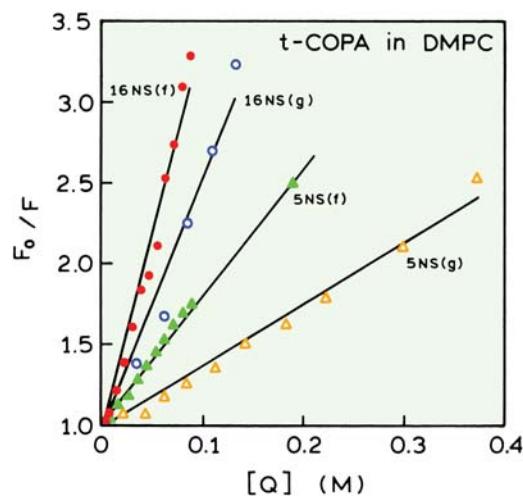


**Figure 11.24.** Stern-Volmer plot for the quenching of t-COPA by the spin probes 5NS and 16NS in unilamellar vesicles of DMPC at 17°C (gel phase) and 30°C (fluid phase). The concentration refers to the quencher concentration in the membrane phase. Revised and reprinted from [85], from the Biophysical Society.

in the intensity decay has a lifetime of about 20 ns. This means that the anisotropy decay of t-COPA can be measured to longer times than DPH, which has a typically lifetime in membranes near 9 ns. The time-zero anisotropy is near 0.385, making it a useful anisotropy probe. The anisotropy decays of t-COPA are multi-exponential in solvents and in lipid bilayers. In solvents the anisotropy decays to zero (not shown). In membranes t-COPA behaves like a highly hindered rotor. Below the phase transition the

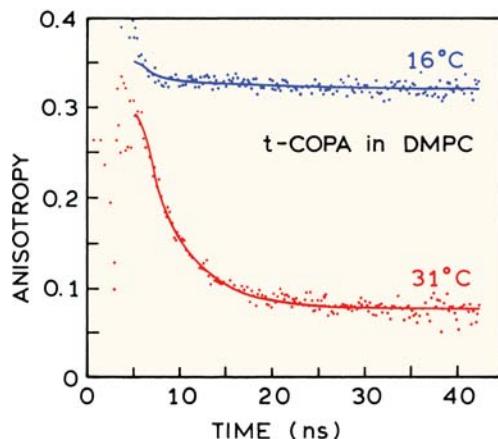


**Figure 11.25.** Time-resolved fluorescence anisotropy of t-COPA in unilamellar vesicles of DMPC in the gel (16°C) and fluid (31°C) phases. Revised and reprinted from [85], from the Biophysical Society.

anisotropy of t-COPA displays a high  $r_\infty$  value near 0.31. Above the phase transition the value of  $r_\infty$  decreases to 0.07 (Figure 11.25). In total, this polyene probe behaves similarly to DPH in model membranes.

### 11.8. ANISOTROPY DECAYS OF NUCLEIC ACIDS

Studies of DNA by fluorescence can be traced to the use of dyes to stain chromatin for fluorescence microscopy. The use of time-resolved fluorescence for DNA dynamics originated with the measurement of anisotropy decays of ethidium bromide (EB) bound to DNA.<sup>86-89</sup> These early studies showed the anisotropy at long times did not decay to zero (Figure 11.26), which is similar to that found for DPH in membranes. Initially the results were interpreted in terms of the angle through which the EB could rotate within the DNA helix. The anisotropy values in Figure 11.26 are lower than expected for ethidium bromide. This is because the experiments were performed with natural or unpolarized light for the excitation. When the excitation source is unpolarized, the emission is still polarized but the anisotropy values are half those observed with polarized excitation.

Since these early studies there has been theoretical progress in the use of fluorescence to study DNA dynam-

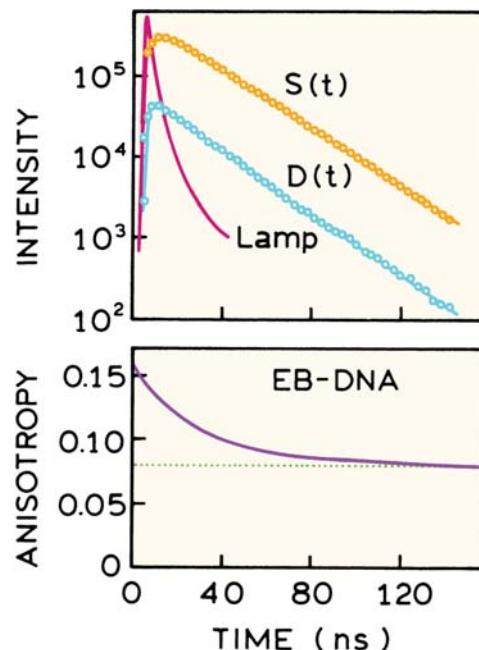


**Figure 11.26.** Anisotropy decay of ethidium bromide (EB) bound to calf thymus DNA. The excitation was with polarized or natural light. Revised from [86].

ics.<sup>90–92</sup> Unfortunately, the theory for DNA dynamics is rather complex, and not easily summarized. The basic result is that the anisotropy of DNA-bound probes can be depolarized by fast motions of the probes within the DNA helix by bending of DNA about the short axis, and by torsional motion of DNA about the long axis. The extent to which these motions contribute to the anisotropy decay depends on the orientation of the transition moments within the DNA helix. The different motions contribute at different times, and the anisotropy decays are expected to be highly non-exponential. Additional information on DNA anisotropy decays is presented in Chapter 12.

### 11.8.1. Hydrodynamics of DNA Oligomers

It is easier to interpret the anisotropy decays of short DNA oligomers. These molecules behave like rigid rods allowing the data to be interpreted in terms of the rotational correlation times.<sup>93</sup> The anisotropy of oligomers with up to 32 base pairs decays were found to be single exponentials. The correlation times increased linearly with the number of base pairs (Figure 11.27). Hence, DNA fragments of this size behave as rigid bodies. DNA can adopt shapes besides linear duplexes. One example is formation of bent helices (Figure 11.28). The linear structure (AO) is a DNA 50-mer. The second structure (A5) is bent due to the insertion of five unpaired adenines. This rather modest change in shape cannot be expected to result in a dramatic change in the

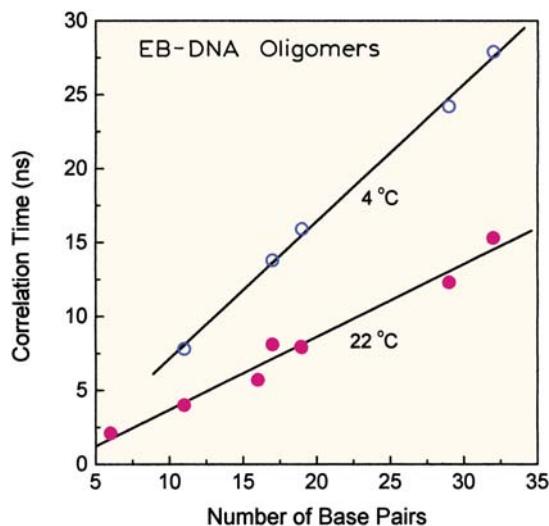


**Figure 11.27.** Rotational correlation time of EB bound to double helical DNA oligomers as a function of the size of the DNA fragments. Revised and reprinted with permission from [93]. Copyright © 1996, American Chemical Society.

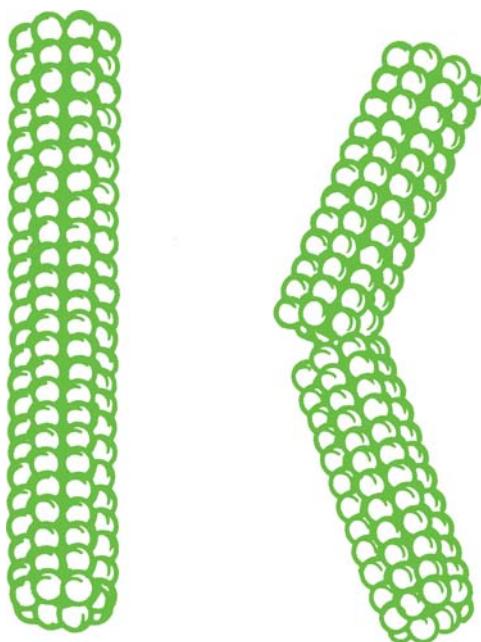


**Figure 11.28.** Structure of a DNA fragment with 50 base pairs (AO, left) and a bent DNA with five unpaired adenines (A5, right). Reprinted from [94]: Collini M, Chirico G, Baldini G, Bianchi ME, Conformation of short DNA fragments by modulated fluorescence polarization anisotropy, *Biopolymers* **36**:211–225. Copyright © 1995, by permission of John Wiley & Sons, Inc.

anisotropy decay. However, the different rotational properties of these two molecules could be seen in the frequency-domain anisotropy data (Figure 11.29). These data were analyzed in terms of a detailed hydrodynamic model, and found to be consistent with the known shapes. The different frequency responses can be understood intuitively by recognizing that the straight DNA molecule can rotate more rapidly around the long axis than the bent molecule. This explains the higher frequency of the maximum differential phase angle of AO (●) as compared to A5 (■). It was possible to detect this minor structural difference between the DNA oligomers from the frequency-domain data.

### 11.8.2. Dynamics of Intracellular DNA

During the past ten years there has been an increasing use of time-resolved measurements of a wide variety of intracellular fluorophores. One example is the use of ethidium bromide to study the rigidity of chromatin in Vero monkey kidney cells in the S2 phase.<sup>95</sup> Figure 10.30 (top) shows the intensity decays of EB bound to x-phage DNA as a control, and of EB bound to chromatin in the cells. The intensity

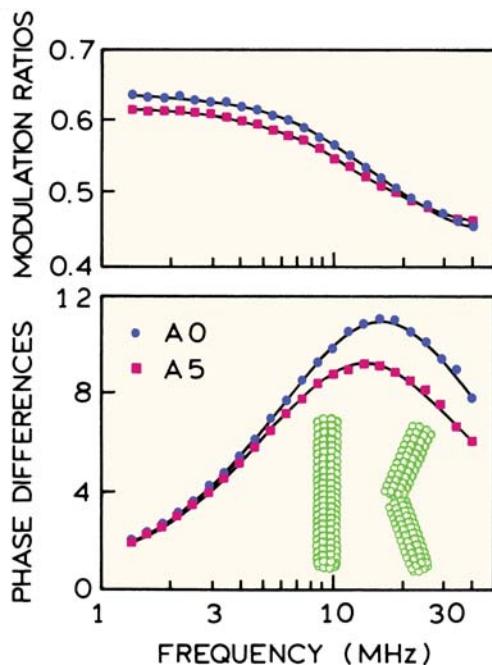


**Figure 11.29.** Frequency-domain anisotropy decay of the DNA 50mers shown in Figure 11.28 (AO, ●; A5, ■) labeled with EB. In this figure the modulation data is presented as the ratio of the polarized and modulated intensities, perpendicular divided by parallel. Reprinted from [94]: Collini M, Chirico G, Baldini G, Bianchi ME, Conformation of short DNA fragments by modulated fluorescence polarization anisotropy, *Biopolymers* 36:211–225. Copyright © 1995, by permission of John Wiley & Sons, Inc.

decay of EB bound to x-phage DNA is a single exponential. The intracellular EB shows a short ( $\tau_1 = 2$  ns) and a long component ( $\tau_2 = 21$  ns). These components were assigned to EB that was not bound or bound to chromatin, respectively. When performing measurements on intracellular probes it is important to determine the binding of the probe as well as the extent of autofluorescence.

The lower panel in Figure 11.30 shows the anisotropy decay of the intracellular EB. The intensity decay is almost flat, showing that the probe is essentially immobile for the 60 ns timescale of the measurements. There is a small dip in the anisotropy near 1–2 ns after excitation. This dip is due to the presence of unbound EB, which rotates rapidly and also decays rapidly. This is an example of an associated anisotropy decay (Section 11.4.5). An important consideration in using a microscope for anisotropy measurements is the numerical aperture of the objective. As the numerical aperture increases the apparent anisotropy (NA) decreases.<sup>96–97</sup> This occurs because light is collected which is not propagating directly along the observation axis. The effect

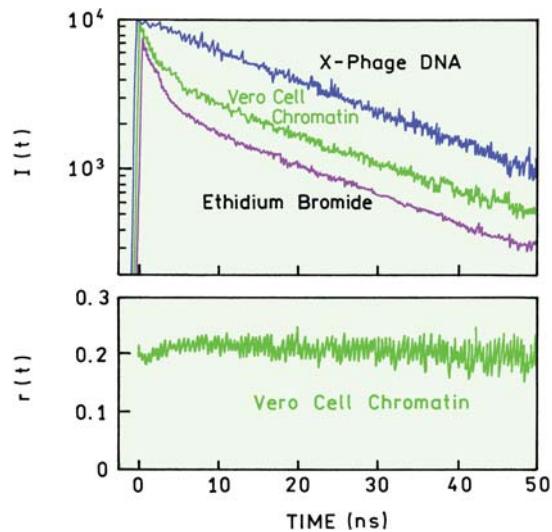


**Figure 11.30.** Intensity and anisotropy decays of EB-stained chromatin from S2 phase Vero cells. Also shown as a control is the intensity decay of EB bound to x-phage DNA. Revised from [95].

of NA probably contributed to the low apparent value of  $r(0)$  in Figure 11.30.

### 11.8.3. DNA Binding to HIV Integrase Using Correlation Time Distributions

Time-resolved anisotropy decays can be used to measure association reactions between biomolecules. The anisotropy decays in terms of multiple correlation times and the correlation times are assigned to the various species in the samples. It can be difficult to visualize the meaning of a table of correlation times and amplitudes. Part of the difficulty is the tendency to visualize a numerical value as a discrete number, rather than the range of numbers possible because of the limited resolution of the data. A more intuitive approach is to use distributions of correlation times to represent the data.

Correlation time distributions were used to study the interaction of HIV-1 integrase with a DNA substrate. Integrase plays a key role in inserting the viral DNA into the host, and is thus a target for drug therapies. Integrase was known to self-associate and occurs as monomers, dimers, and tetramers.<sup>98–102</sup> Each monomer in integrase has three domains: the N-terminal domain, the catalytic core domain, and the C-terminal domain. The association reactions of integrase and its interaction with DNA are of interest for the design of the anti-HIV drugs. Anisotropy decays of the intrinsic tryptophan emission of integrase were used to

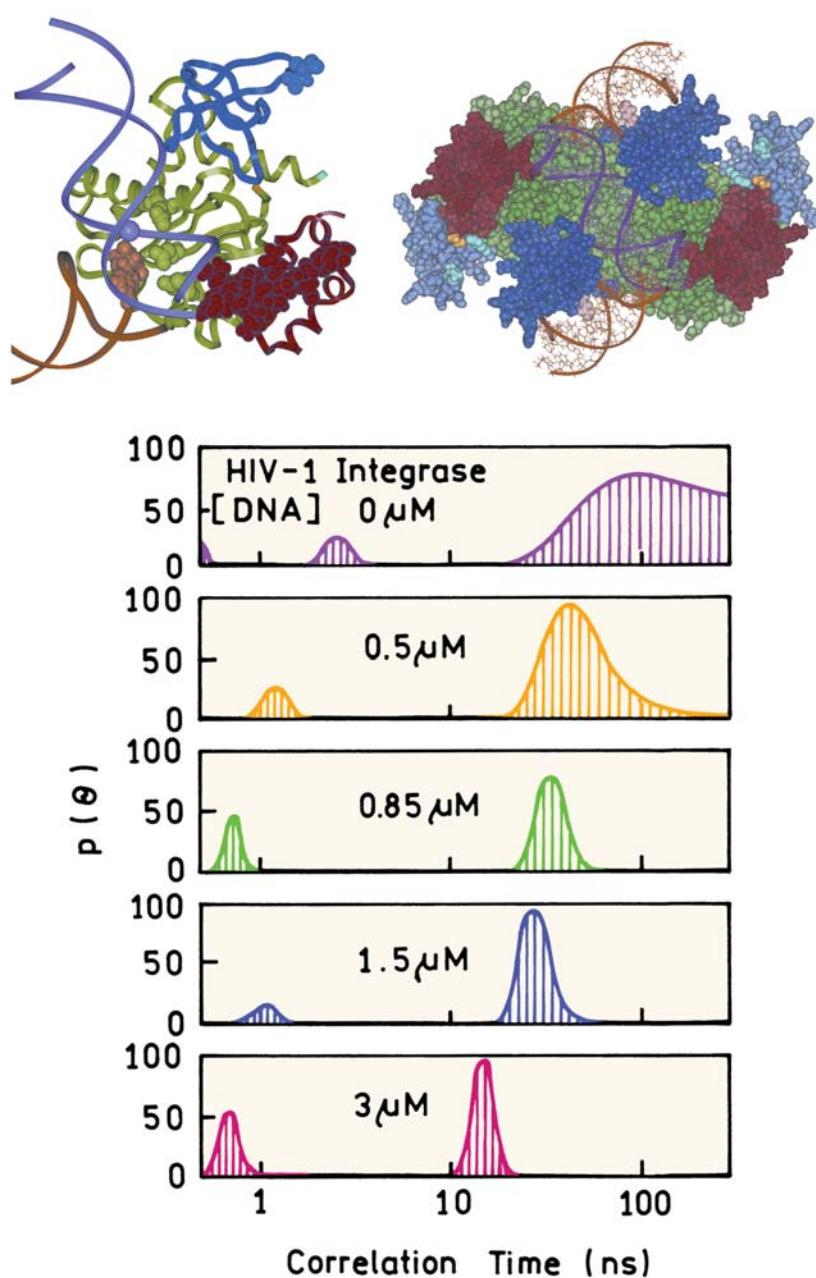


**Figure 11.31.** Tryptophan correlation time distributions for HIV-1 integrase in the presence of a 21-base-pair DNA oligomer [integrase] = 100 nM. Proposed structures are shown for the monomer and tetramer. N-terminal domain is red, catalytic core domain is green, and the C-terminal domain is blue. Revised from [98–99]. Structure courtesy of Dr. Alexei Podtelezhnikov from the University of California at San Diego.

study the self-association of integrase monomers.<sup>98</sup> Figure 11.31 shows the recovered correlation time distribution for integrase in the absence of DNA substrate. The correlation time near 2–3 ns was assigned to the local dynamics of integrase and not linked to its extent of association. The longer correlation times centered near 100 ns were interpreted as

due to the integrase tetramer. The distribution of the long correlation time is wide because this value is uncertain due to the short lifetime of tryptophan. The large difference between the lifetime and correlation time results in the wide amplitude at times above 80 ns which are not determined by the data.

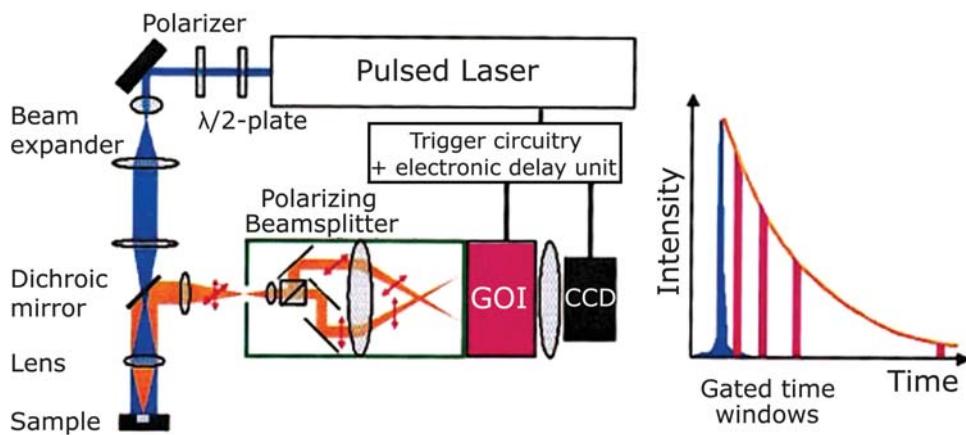


**Figure 11.32.** Instrument for correlation time imaging. Revised from [105].

Addition of DNA substrate results in a shift of the distribution to shorter time. The correlation time assigned to the monomer is sharply distributed between 10 and 20 ns. The better resolution of this correlation time is because the tryptophan lifetime is closer in magnitude to the correlation time. While the same information would be contained in tabular data, the use of distributions provides an intuitive understanding of both the correlation times themselves and the uncertainties associated with the central values.

### 11.9. CORRELATION TIME IMAGING

Magnetic resonance imaging (MRI) is a dominant medical imaging technology. The image contrast in MRI is not based on proton signal intensity, but rather on the  $T_1$  and  $T_2$  water or proton relaxation times. The relaxation times depend on the viscosity, elasticity, and other dynamic properties of the tissues, which is similar to the dependence of fluorophore rotational correlation time on solvent viscosity. Here it is natural to ask if cellular imaging can be accomplished based on the rotational correlation times of fluorophores. Such work is beginning to appear,<sup>103–105</sup> and is likely to become more widely used as technology makes these measurements more practical.

An instrument for correlation time imaging is shown in Figure 11.32. This instrument uses a pulsed laser and a gated optical image intensifier (GOI), similar to the instruments described in Chapter 4 for fluorescence lifetime imaging microscopy (FLIM). The instrument shown in Figure 11.32 allows simultaneous recording of the parallel and perpendicular images using a polarizing beam splitter. This optical element separates the image into two images with

orthogonal polarizations that are focused on different regions of the CCD camera. Thus a single gating pulse provides two images, one of each polarization, for the same time window.

The correlation time images were measured using rhodamine 6G in transparent microwell plates. The correlation time was varied by using solvents with different viscosities. Figure 11.33 shows the polarized time-dependent decays for R6G in two solvents (right). In methanol the correlation time is short and the polarized intensities are the same at the earliest available times. In ethylene glycol the parallel component has a higher intensity than the perpendicular compo-

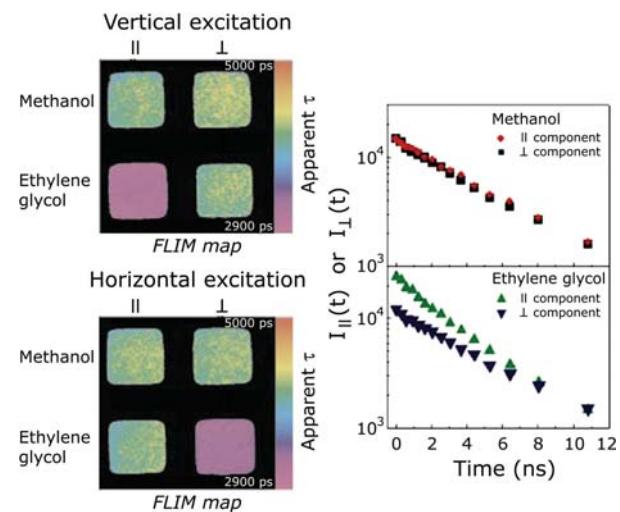


**Figure 11.33.** Apparent lifetime images (left) and polarized intensity decay (right) for rhodamine 6G in methanol and ethylene glycol. Revised from [105].

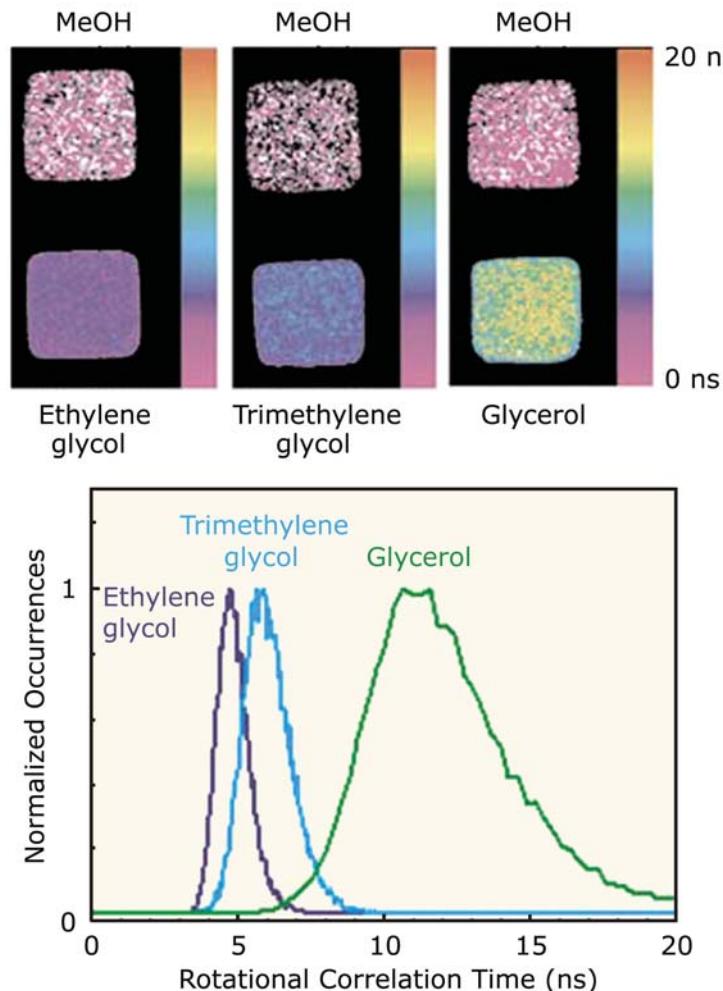


**Figure 11.34.** Correlation time images of R6G in various solvents (top) and histograms of the recovered correlation times (bottom). The upper three images are R6G in methanol. Revised from [105].

ment to about 6 ns. The polarized intensity decays are visually seen to be multi-exponential as predicted by eqs. 11.1 and 11.2.

The time-dependent decays were used to create FLIM images of the samples (Figure 11.33, left). The lifetimes at each pixel in the images are apparent lifetimes that are some weighted averages of the multi-exponential decays. In methanol the apparent lifetimes are the same regardless of the polarization, as expected based on the short correlation time. In ethylene glycol the apparent lifetime of the parallel component is shorter than the perpendicular component. The parallel component has a shorter apparent lifetime because the transition moments are rotating away from the orientation of the observation polarizer. These results show

that the gated polarized intensity images contain information in the correlation times of the samples.

There can be some confusion about the difference in apparent lifetime with horizontal excitation (Figure 11.33, lower left). With the usual right angle geometry horizontal excitation results in the same signals in the parallel and perpendicular channels (Section 10.4). The geometry is different for the instrument in Figure 11.32 where the emission is observed along the same axis as the excitation. For this geometry rotation of the excitation polarizer reverses the signals in the two polarized observation channels.

The polarized time-dependent intensities can be used to calculate the correlation times (Figure 11.34). The color of the images reveals the longer correlation times of R6G in

glycerol as compared to ethylene glycol. The lower panel shows histograms of the occurrence of each correlation time in the examples. While the distribution is wide in glycerol, the results demonstrate the possibility of imaging using correlation times. One can imagine such results being extended to intracellular fluorophores to obtain contrast based on the mobility of fluorophores in each region of a cell.

### 11.10. MICROSECOND ANISOTROPY DECAYS

#### 11.10.1. Phosphorescence Anisotropy Decays

The information available from an anisotropy decay is limited to times during which emission occurs. For this reason it is usually difficult to obtain reliable data at times longer than three intensity decay times. Even for probes having relatively long lifetimes such as dansyl-lysine (Section 11.5.4), this time window is too small to effectively study membrane-bound proteins.

Rotational motions at longer times can be measured using phosphorescence anisotropy decays.<sup>106–112</sup> These experiments are illustrated by studies of the sarcoplasmic reticulum  $\text{Ca}^{2+}$ -ATPase, which is a 110-kD transmembrane protein. Not many phosphorescence probes are available, and one of the most commonly used probes is erythrosin (Figure 11.35), which in deoxygenated solution displays a phosphorescence decay time near 100  $\mu\text{s}$ . Typical phosphorescence anisotropy decays are shown for erythrosin-labeled  $\text{Ca}^{2+}$ -ATPase. In this case the ATPase was aggregated in the membrane by melittin. The extent of aggregation

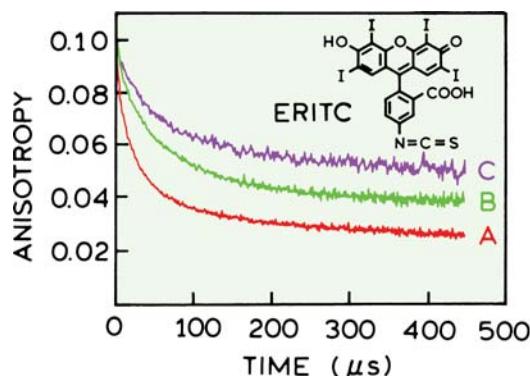


**Figure 11.35.** Phosphorescence decays of erythrosin-labeled  $\text{Ca}^{2+}$ -ATPase in sarcoplasmic reticulum vesicles. Anisotropy decays were obtained in the absence of melittin (A), in the presence of acetylated melittin (B), or native melittin (C). Revised and reprinted with permission from [110]. Copyright © 1995, American Chemical Society.

was greater for native melittin than for acetylated melittin, which neutralizes the positive charges on melittin and decreases its interactions with the  $\text{Ca}^{2+}$ -ATPase. Because the extent of crosslinking is less for acetylated melittin, so that the anisotropy decays more rapidly. There are several disadvantages to the use of erythrosin, eosin and other phosphorescent probes. The signals are usually weak due to the low phosphorescence quantum yields. Rigorous exclusion of oxygen is needed to prevent quenching. And, finally, fundamental anisotropies are usually low, near 0.1, resulting in decreased resolution of the anisotropy decays.

#### 11.10.2. Long-Lifetime Metal–Ligand Complexes

Another approach to measuring long correlation times is to use luminescent metal–ligand complexes (MLCs). These probes display lifetimes ranging from 100 ns to 10  $\mu\text{s}$ <sup>113–116</sup> (Chapter 20). These probes are typically complexes of transition metals with diimine ligands. A lipid MLC probe was made by covalently linking two phosphatidylethanolamine (PE) lipids to an Ru-MLC that contained two carboxyl groups. The MLC-lipid probe was then incorporated into DPPG vesicles (Figure 11.36). The maximum in the differential phase angle ( $\Delta_\omega$ ) is near 1 MHz, suggesting slow rotational diffusion. The lifetime of the Ru- $\text{PE}_2$  probe was near

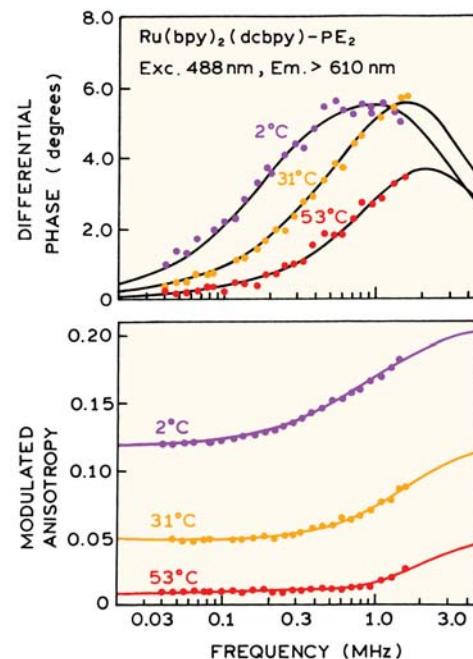


**Figure 11.36.** Frequency-domain anisotropy decays of  $\text{Ru}(\text{bpy})_2(\text{dcbpy})-\text{PE}_2$  in DPPG vesicles. Reprinted from [114], with permission from Academic Press, Inc.

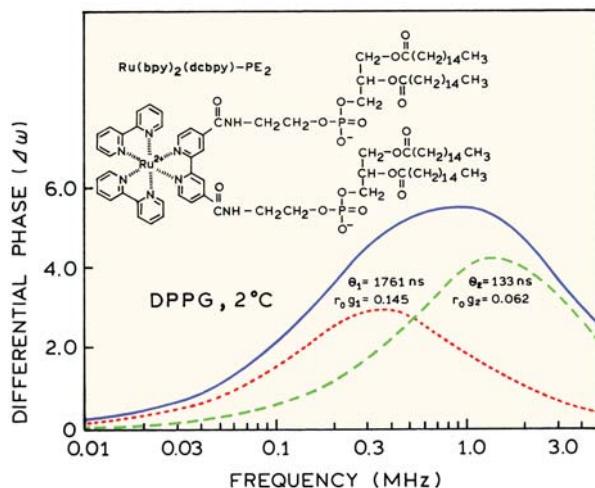


**Figure 11.37.** Differential phase angles of  $\text{Ru}(\text{bpy})_2(\text{dcbpy})-\text{PE}_2$  in DPPG vesicles at  $2^\circ\text{C}$ . The resolution of the  $\Delta_\omega$  values is based on the correlation times and amplitudes shown on the figure. Data from [114].

680 ns at  $2^\circ\text{C}$ , which allowed resolution of the slow correlation time.

The FD anisotropy data in Figure 11.37 were used to resolve a double exponential anisotropy decay, which showed correlation times of 133 and 1761 ns. It is useful to visualize how these correlation times contribute to the data, which is shown by the dashed lines in Figure 11.37. The correlation time of 1761 ns is consistent with that expected for rotational diffusion of phospholipid vesicles with a diameter of 250 Å. At this time the physical origin of the shorter correlation time is not clear, but presumably this correlation time is due to restricted motion of the probe within the membrane.

It is important to notice that the use of a long-lifetime probe allowed measurement of overall rotation of the phospholipid vesicles. Earlier in this chapter we saw that DPH displayed nonzero  $r_\infty$  values at long times. This occurred because the intensity decay times of DPH are short relative to the correlation times of the vesicles. Hence, the use of nanosecond decay time fluorophores provides no information on rotational motions of lipid vesicles.

The metal–ligand complexes have several advantages over the phosphorescent probes. In contrast to phosphorescence, the samples can be measured in the presence of dissolved oxygen. The MLCs are only partially quenched by ambient oxygen, whereas phosphorescence is usually completely quenched. Additionally, there are relatively few phosphorescent probes, but there are numerous metal–ligand complexes (Chapter 20).

## REFERENCES

- Lakowicz JR, Cherek H, Kusba J, Gryczynski I, Johnson ML. 1993. Review of fluorescence anisotropy decay analysis by frequency-domain fluorescence spectroscopy. *J Fluoresc* **3**(2):103–116.
- Lakowicz JR, Gryczynski I. 1991. Frequency-domain fluorescence spectroscopy. In *Topics in fluorescence spectroscopy*, Vol. 1: *Techniques*, pp. 293–355. Ed JR Lakowicz. Plenum Press, New York.
- Spencer RD, Weber G. 1970. Influence of Brownian rotations and energy transfer upon the measurement of fluorescence lifetimes. *J Chem Phys* **52**:1654–1663.
- Szymanowski W. 1935. Einfluss der Rotation der Moleküle auf die Messungen der Abklingzeit des Fluoreszenzstrahlung. *Z Phys* **95**: 466–473.
- Kudryashov PI, Sveshnikov BY, Shirokov VI. 1960. The kinetics of the concentration depolarization of luminescence and of the intermolecular transfer of excitation energy *Opt Spectrosc* **9**:177–181.
- Bauer RK. 1963. Polarization and decay of fluorescence of solutions. *Z Naturforsch A* **18**:718–724.
- Cross AJ, Fleming GR. 1984. Analysis of time-resolved fluorescence anisotropy decays. *Biophys J* **46**:45–56.
- Wahl Ph. 1979. Analysis of fluorescence anisotropy decays by the least squares method. *Biophys Chem* **10**:91–104.
- Taylor JR. 1982. *An introduction to error analysis*, Vol. 9, pp. 173–187. University Science Books, Mill Valley, CA.
- Dale RE, Chen LA, Brand L. 1977. Rotational relaxation of the "microviscosity" probe diphenylhexatriene in paraffin oil and egg lecithin vesicles. *J Am Chem Soc* **252**(21):7500–7510.
- Papenhuijzen J, Visser AJWG. 1983. Simulation of convoluted and exact emission anisotropy decay profiles. *Biophys Chem* **17**:57–65.
- Gilbert CW. 1983. A vector method for the non-linear least squares deconvolution-and-fitting analysis of polarized fluorescence decay data. In *Time-resolved fluorescence spectroscopy in biochemistry and biology*, pp. 605–605. Ed RB Cundall, RE Dale. Plenum Press, New York.
- Beechem JM, Brand L. 1986. Global analysis of fluorescence decay: applications to some unusual experimental and theoretical studies. *Photochem Photobiol* **44**:323–329.
- Crutzen M, Ameloot M, Boens N, Negri RM, De Schryver FC. 1993. Global analysis of unmatched polarized fluorescence decay curves. *J Phys Chem* **97**:8133–8145.
- Vos K, van Hoek A, Visser AJWG. 1987. Application of a reference convolution method to tryptophan fluorescence in proteins. *Eur J Biochem* **165**:55–63.
- Weber G. 1971. Theory of fluorescence depolarization by anisotropic Brownian rotations: discontinuous distribution approach. *J Chem Phys* **55**:2399–2407.
- Merkel H, Hammond JH, Hartman SR, Derzko ZI. 1970. Measurement of the temperature dependence of depolarization time of luminescence. *J Luminesc* **1,2**:502–512.
- Lakowicz JR, Prendergast FG, Hogen D. 1979. Differential polarized phase fluorometric investigations of diphenylhexatriene in lipid bilayers: quantitation of hindered depolarizing rotations. *Biochemistry* **18**:508–519.
- Reinhart GD, Marzola P, Jameson DM, Gratton E. 1991. A method for on-line background subtraction in frequency domain fluorometry. *J Fluoresc* **1**(3):153–162.

20. Belford GG, Belford RL, Weber G. 1972. Dynamics of fluorescence polarization in macromolecules. *Proc Natl Acad Sci USA* **69**:1392–1393.
21. Chuang TJ, Eisenthal KB. 1972. Theory of fluorescence depolarization by anisotropic rotational diffusion. *J Chem Phys* **57**:5094–5097.
22. Ehrenberg M, Rigler R. 1972. Polarized fluorescence and rotational Brownian diffusion. *Chem Phys Lett* **14**:539–544.
23. Tao T. 1969. Time-dependent fluorescence depolarization and Brownian rotational diffusion of macromolecules. *Biopolymers* **8**: 609–632.
24. Lombardi JR, Dafforn GA. 1966. Anisotropic rotational relaxation in rigid media by polarized photoselection. *J Chem Phys* **44**:3882–3887.
25. Small EW, Isenberg I. 1977. Hydrodynamic properties of a rigid molecule: rotational and linear diffusion and fluorescence anisotropy. *Biopolymers* **16**:1907–1928.
26. Steiner RF. 1991. Fluorescence anisotropy: theory and applications. in *Topics in fluorescence spectroscopy*, Vol. 2: *Principles*, pp. 1–52. Ed JR Lakowicz. Plenum Press, New York.
27. Veatch WR, Stryer L. 1977. Effect of cholesterol on the rotational mobility of diphenylhexatriene in liposomes: a nanosecond fluorescence anisotropy study. *J Mol Biol* **117**:1109–1113.
28. Chen LA, Dale RE, Roth S, Brand L. 1977. Nanosecond time-dependent fluorescence depolarization of diphenylhexatriene in dimyristoyllecithin vesicles and the determination of "microviscosity". *J Biol Chem* **252**(7):2163–2169.
29. Ameloot M, Hendrickx H, Herremans W, Pottel H, Van Cauwelaert F, van der Meer W. 1984. Effect of orientational order on the decay of fluorescence anisotropy in membrane suspensions. *Biophys J* **46**: 525–539.
30. Hildenbrand K, Nicolau C. 1979. Nanosecond fluorescence anisotropy decays of 1,6-diphenyl-1,3,5-hexatriene in membranes. *Biochim Biophys Acta* **553**:365–377.
31. Kinoshita K, Kawato S, Ikegami A. 1977. A theory of fluorescence polarization decay in membranes. *Biophys J* **20**:289–305.
32. Kinoshita K, Ikegami A, Kawato S. 1982. On the wobbling-in-cone analysis of fluorescence anisotropy decay. *Biophys J* **37**:461–464.
33. Komura S, Ohta Y, Kawato S. 1990. A theory of optical anisotropy decay in membranes. *J Phys Soc Jpn* **59**(7):2584–2595.
34. Wallach D. 1967. Effects of internal rotation on angular correlation functions. *J Chem Phys* **47**:5258–5268.
35. Gottlieb YYa, Wahl Ph. 1963. Étude théorique de la polarisation de fluorescence des macromolécules portant un groupe émetteur mobile autour d'un axe de rotation. *J Chim Phys* **60**:849–856.
36. Lapari G, Szabo A. 1980. Effect of librational motion on fluorescence depolarization and nuclear magnetic resonance relaxation in macromolecules and membranes. *Biophys J* **30**:489–506.
37. Vincent M, Gallay J. 1991. The interactions of horse heart apocytochrome c with phospholipid vesicles and surfactant micelles: time-resolved fluorescence study of the single tryptophan residue (Trp-59). *Eur Biophys J* **20**:183–191.
38. Pap EHW, Ter Horst JJ, Van Hoek A, Visser AJWG. 1994. Fluorescence dynamics of diphenyl-1,3,5-hexatriene-labeled phospholipids in bilayer membranes. *Biophys Chem* **48**:337–351.
39. Gryczynski I, Johnson ML, Lakowicz JR. 1994. Analysis of anisotropy decays in terms of correlation time distributions, measured by frequency-domain fluorometry. *Biophys Chem* **52**:1–13.
40. Peng K, Visser AJWG, van Hoek A, Wolfs CJAM, Sanders JC, Hemminga MA. 1990. Analysis of time-resolved fluorescence anisotropy in lipid-protein systems, I: application to the lipid probe octadecyl rhodamine B in interaction with bacteriophage M13 coat protein incorporated in phospholipid bilayers. *Eur Biophys J* **18**:277–283.
41. Visser AJWG, van Hoek A, van Paridon PA. 1987. Time-resolved fluorescence depolarization studies of parinaroyl phosphatidyl-choline in triton X-100 micelles and rat skeletal muscle membranes. *Membrane receptors, dynamics, and energetics*, pp. 353–361. Ed KWA Wirtz. Plenum Press, New York.
42. Brand L, Knutson JR, Davenport L, Beechem JM, Dale RE, Walbridge DG, Kowalczyk AA. 1985. Time-resolved fluorescence spectroscopy: some applications of associative behaviour to studies of proteins and membranes. In *Spectroscopy and the dynamics of molecular biological systems*, pp. 259–305. Ed P Bayley, RE Dale. Academic Press, London.
43. Ruggiero A, Hudson B. 1989. Analysis of the anisotropy decay of trans-parinaric acid in lipid bilayers. *Biophys J* **55**:1125–1135.
44. Visser NV, Hink MA, van Hoek A, Visser AJWG. 1999. Comparison between fluorescence correlation spectroscopy and time-resolved fluorescence anisotropy as illustrated with a fluorescent dextran conjugate. *J Fluoresc* **9**(3):251–255.
45. Ross JA, Schmidt CJ, Brand L. 1981. Time-resolved fluorescence of the two tryptophans in horse liver alcohol dehydrogenase. *Biochemistry* **20**:4369–4377.
46. Vincent M, Deveer A-M, De Haas GH, Verheij HM, Gallay J. 1993. Stereospecificity of the interaction of porcine pancreatic phospholipase A<sub>2</sub> with micellar and monomeric inhibitors. *Eur J Biochem* **215**(3):531–539.
47. Lakshminanth GS, Krishnamoorthy G. 1999. Solvent-exposed tryptophans probe the dynamics at protein surfaces. *Biophys J*, **77**:1100–1106.
48. Deprez E, Tauc P, Leh H, Mouscadot J-F, Auclair C, Brochon J-C. 2000. Oligomeric states of the HIV-1 integrase as measured by time-resolved fluorescence anisotropy. *Biochemistry* **39**:9275–9284.
49. Rami BR, Krishnamoorthy G, Udgaoarkar JB. 2003. Dynamics of the core tryptophan during the formation of productive molten globule intermediate of Barstar. *Biochemistry* **42**:7986–8000.
50. Tcherkasskaya O, Ptitsyn OB, Knutson JR. 2000. Nanosecond dynamics of tryptophans in different conformational states of apomyoglobin proteins. *Biochemistry* **39**:1879–1889.
51. Axelsen PH, Gratton E, Prendergast FG. 1991. Experimentally verifying molecular dynamics simulations through fluorescence anisotropy measurements. *Biochemistry* **30**:1173–1179.
52. Fa M, Karolin J, Aleshkov S, Strandberg L, Johansson LB-A, Ny T. 1995. Time-resolved polarized fluorescence spectroscopy studies of plasminogen activator inhibitor type I: conformational changes of the reactive center upon interactions with target proteases, vitronectin and heparin. *Biochemistry* **34**:13833–13840.
53. Broos J, Visser AJWG, Engbersen FJ, Verboom W, van Hoek A, Reinhoudt DN. 1995. Flexibility of enzymes suspended in organic solvents probed by time-resolved fluorescence anisotropy: evidence that enzyme activity and enantioselectivity are directly related to enzyme flexibility. *J Am Chem Soc* **117**(51):12657–12663.
54. Yguerabide J, Epstein HF, Stryer L. 1970. Segmental flexibility in an antibody molecules. *J Mol Biol* **51**:573–590.

55. Hanson DC, Yguerabide J, Schumaker VN. 1981. Segmental flexibility of immunoglobulin G antibody molecules in solution: a new interpretation. *Biochemistry* **20**:6842–6852.
56. Wahl Ph. 1969. Mesure de la décroissance de la fluorescence polarisée de la  $\gamma$ -globuline-1-sulfonyl-5-diméthylaminonaphthalène. *Biochim Biophys Acta* **175**:55–64.
57. Wahl Ph, Kasai M, Changex J-P. 1971. A study of the motion of proteins in excitable membrane fragments by nanosecond fluorescence polarization spectroscopy. *Eur J Biochem* **18**:332–341.
58. Brochon J-C, Wahl Ph. 1972. Mesures des déclins de l'anisotropie de fluorescence de la  $\gamma$ -globuline et de ses fragments Fab, Fc et F(ab)<sub>2</sub> marqués avec le 1-sulfonyl-5-diméthylaminonaphthalène. *Eur J Biochem* **25**:20–32.
59. Holowka D, Wensel T, Baird B. 1990. A nanosecond fluorescence depolarization study on the segmental flexibility of receptor-bound immunoglobulin E. *Biochemistry* **29**:4607–4612.
60. Visser AJG, van Hoek A, Visser NV, Lee Y, Ghisia S. 1997. Time-resolved fluorescence study of the dissociation of FMN from the yellow fluorescence protein from *Vibrio fischeri*. *Photochem Photobiol* **65**(3):570–575.
61. Lakowicz JR, Laczko G, Gryczynski I, Cherek H. 1986. Measurement of subnanosecond anisotropy decays of protein fluorescence using frequency-domain fluorometry. *J Biol Chem* **261**(5): 2240–2245.
62. Maliwal BP, Lakowicz JR. 1986. Resolution of complex anisotropy decays by variable frequency phase-modulation fluorometry: a simulation study. *Biochim Biophys Acta* **873**:161–172.
63. Maliwal BP, Hermetter A, Lakowicz JR. 1986. A study of protein dynamics from anisotropy decays obtained by variable frequency phase-modulation fluorometry: internal motions of N-methylantraniloyl melittin. *Biochim Biophys Acta* **873**:173–181.
64. Bayley P, Martin S, Browne P, Royer C. 2003. Time-resolved fluorescence anisotropy studies show domain-specific interactions of calmodulin with IQ target sequences of myosin V. *Eur Biophys J* **32**:122–127.
65. Lakowicz JR, Laczko G, Gryczynski I. 1987. Picosecond resolution of tyrosine fluorescence and anisotropy decays by 2-GHz frequency-domain fluorometry. *Biochemistry* **26**:82–90.
66. Lakowicz JR, Laczko G, Gryczynski I. 1986. Picosecond resolution of oxytocin tyrosyl fluorescence by 2-GHz frequency-domain fluorometry. *Biophys Chem* **24**:97–100.
67. Lakowicz JR, Gratton E, Cherek H, Maliwal BP, Laczko G. 1984. Determination of time-resolved fluorescence emission spectra and anisotropies of a fluorophore–protein complex using frequency-domain phase-modulation fluorometry. *J Biol Chem* **259**(17): 10967–10972.
68. Shinitzky M, Barenholz Y. 1978. Fluidity parameters of lipid regions determined by fluorescence polarization. *Biochim Biophys Acta* **515**:367–394.
69. Kawato S, Kinoshita K, Ikegami A. 1978. Effect of cholesterol on the molecular motion in the hydrocarbon region of lecithin bilayers studied by nanosecond fluorescence techniques. *Biochemistry* **17**:5026–5031.
70. Kawato S, Kinoshita K, Ikegami A. 1977. Dynamic structure of lipid bilayers studied by nanosecond fluorescence techniques. *Biochemistry* **16**:2319–2324.
71. Stubbs CD, Williams BW. 1992. Fluorescence in membranes. In *Topics in fluorescence spectroscopy*, Vol. 3: *Biochemical applications*, pp. 231–271. Ed JR Lakowicz. Plenum Press, New York.
72. Stubbs CD, Kouyama T, Kinoshita K, Ikegami A. 1981. Effect of double bonds on the dynamic properties of the hydrocarbon region of lecithin bilayers. *Biochemistry* **20**:4257–4262.
73. Vincent M, de Foresta B, Gallay J, Alfsen A. 1982. Nanosecond fluorescence anisotropy decays of n-(9-anthroyloxy) fatty acids in dipalmitoylphosphatidylcholine vesicles with regard to isotropic solvents. *Biochemistry* **21**:708–716.
74. Pal R, Petri WA, Ben-Yashar V, Wagner RR, Barenholz Y. 1985. Characterization of the fluorophore 4-heptadecyl-7-hydroxycoumarin: a probe for the head-group region of lipid bilayers and biological membranes. *Biochemistry* **24**:573–581.
75. Wolber PK, Hudson BS. 1981. Fluorescence lifetime and time-resolved polarization anisotropy studies of acyl chain order and dynamics in lipid bilayers. *Biochemistry* **20**:2800–2810.
76. Davenport L, Targowski P. 1996. Submicrosecond phospholipid dynamics using a long-lived fluorescence emission anisotropy probe. *Biophys J* **71**:1837–1852.
77. Kinoshita K, Kawato S, Ikegami A. 1984. Dynamic structure of biological and model membranes: analysis by optical anisotropy decay measurements. *Adv Biophys* **17**:147–203.
78. Jähnig F. 1979. Structural order of lipids and proteins in membranes: evaluation of fluorescence anisotropy data. *Proc Natl Acad Sci USA* **76**:6361–6365.
79. Heyn MP. 1979. Determination of lipid order parameters and rotational correlation times from fluorescence depolarization experiments. *FEBS Lett* **108**:359–364.
80. Van Blitterswijk WJ, Van Hoeven RP, Van Der Meer BW. 1981. Lipid structural order parameters (reciprocal of fluidity) in biomembranes derived from steady-state fluorescence polarization measurements. *Biochim Biophys Acta* **644**:323–332.
81. Best L, John E, Jähnig F. 1987. Order and fluidity of lipid membranes as determined by fluorescence anisotropy decay. *Eur Biophys J* **15**:87–102.
82. Lakowicz JR, Cherek H, Maliwal BP, Gratton E. 1985. Time-resolved fluorescence anisotropies of diphenylhexatriene and perylene in solvents and lipid bilayers obtained from multifrequency phase-modulation fluorometry. *Biochemistry* **24**:376–383.
83. Faucon JF, Lakowicz JR. 1987. Anisotropy decay of diphenylhexatriene in melittin-phospholipid complexes by multifrequency phase-modulation fluorometry. *Arch Biochem Biophys* **252**(1):245–258.
84. Lakowicz JR. 1985. Frequency-domain fluorometry for resolution of time-dependent fluorescence emission. *Spectroscopy* **1**:28–37.
85. Mateo CR, Souto AA, Amat-Guerri F, Acuña AU. 1996. New fluorescent octadecapentaenoic acids as probes of lipid membranes and protein-lipid interactions. *Biophys J* **71**:2177–2191.
86. Wahl Ph, Paoletti J, Le Pecq J-B. 1970. Decay of fluorescence emission anisotropy of the ethidium bromide–DNA complex evidence for an internal motion in DNA. *Proc Natl Acad Sci USA* **65**(2):417–421.
87. Millar DP, Robbins RJ, Zewail AH. 1981. Time-resolved spectroscopy of macromolecules: effect of helical structure on the torsional dynamics of DNA and RNA. *J Chem Phys* **74**(7):4200–4201.
88. Ashikawa I, Kinoshita K, Ikegami A, Nishimura Y, Tsuboi M, Watanabe K, Iso K, Nakano T. 1983. Internal motion of deoxyri-

- bonucleic acid in chromatin: nanosecond fluorescence studies of intercalated ethidium. *Biochemistry* **22**:6018–6026.
89. Wang J, Hogan M, Austin RH. 1982. DNA motions in the nucleosome core particle. *Proc Natl Acad Sci USA* **79**:5896–5900.
  90. Schurr JM, Fujimoto BS, Wu P, Song L. 1992. Fluorescence studies of nucleic acids: dynamics, rigidities, and structures. In *Topics in fluorescence spectroscopy*, vol. 3: *Biochemical applications*, pp. 137–229. Ed JR Lakowicz. Plenum Press, New York.
  91. Thomas JC, Allison SA, Appeloff CJ, Schurr JM. 1980. Torsion dynamics and depolarization of fluorescence of linear macromolecules, II: fluorescence polarization anisotropy measurements on a clean viral 29 DNA. *Biophys Chem* **12**:177–188.
  92. Barkley MD, Zimm BH. 1979. Theory of twisting and bending of chain macromolecules; analysis of the fluorescence depolarization of DNA. *J Chem Phys* **70**:2991–3007.
  93. Duhamel J, Kanyo J, Dinter-Gottlieb G, Lu P. 1996. Fluorescence emission of ethidium bromide intercalated in defined DNA duplexes: evaluation of hydrodynamics components. *Biochemistry* **35**:16687–16697.
  94. Collini M, Chirico G, Baldini G, Bianchi ME. 1995. Conformation of short DNA fragments by modulated fluorescence polarization anisotropy. *Biopolymers* **36**:211–225.
  95. Tramier M, Kemnitz K, Durleux C, Coppey J, Denjean P, Pansu RB, Coppey-Moisan M. 2000. Restrained torsional dynamics of nuclear DNA in living proliferative mammalian cells. *Biophys J* **78**: 2614–2627.
  96. Axelrod D. 1979. Carbocyanine dye orientation in red cell membrane studied by microscopic fluorescence polarization. *Biophys J* **26**:557–574.
  97. Axelrod D. 1989. Fluorescence polarization microscopy. *Methods Cell Biol* **30**:333–352.
  98. Deprez E, Tauc P, Leh H, Mouscadet J-F, Auclair C, Hawkins ME, Brochon J-C. 2001. DNA binding induces dissociation of the multi-meric form of HIV-1 integrase: a time-resolved fluorescence anisotropy study. *Proc Natl Acad Sci USA* **98**(18):10090–10095.
  99. Podtelezhnikov AA, Gao K, Bushman FD, McCammon JA. 2003. Modeling HIV-1 integrase complexes based on their hydrodynamic properties. *Biopolymers* **68**:110–120.
  100. De Luca L, Pedretti A, Vistoli G, Barreca ML, Villa L, Monforte P, Chimirri A. 2003. Analysis of the full-length integrase-DNA complex by a modified approach for DNA docking. *Biochem Biophys Res Commun* **310**:1083–1088.
  101. Leh H, Brodin P, Bischerour J, Deprez E, Tauc P, Brochon JC, LeCam E, Coulaud D, Auclair C, Mouscadet JF. 2000. Determinants of Mg<sup>2+</sup>-dependent activities of recombinant human immunodeficiency virus type 1 integrase. *Biochemistry* **39**:9285–9294.
  102. Deprez E, Tauc P, Leh H, Mouscadet JF, Auclair C, Brochon JC. 2000. Oligomeric states of the HIV-1 integrase as measured by time-resolved fluorescence anisotropy. *Biochemistry* **39**:9275–9284.
  103. Suhling K, Siegel J, Lanigan PMP, Lévéque-Fort S, Webb SED, Phillips D, Davis DM, French PMW. 2004. Time-resolved fluorescence anisotropy imaging applied to live cells. *Opt Lett* **29**(6):584–586.
  104. Clayton AHA, Hanley QS, Arndt-Jovin D, Subramaniam V, Jovin TM. 2002. Dynamic fluorescence anisotropy imaging microscopy in the frequency domain (rFLIM). *Biophys J*, **83**:1631–1649.
  105. Siegel J, Suhling K, Lévéque-Fort S, Webb SED, Davis DM, Phillips D, Sabharwal Y, French PMW. 2003. Wide-field time-resolved fluorescence anisotropy imaging (TR-FAIM): imaging the rotational mobility of a fluorophore. *Rev Sci Instrum* **74**(1):182–192.
  106. González-Rodríguez J, Acuña AU, Alvarez MV, Jovin TM. 1994. Rotational mobility of the fibrinogen receptor glycoprotein IIb/IIIa or integrin αIIbβ<sub>3</sub> in the plasma membrane of human platelets. *Biochemistry* **33**:266–274.
  107. Lavalette D, Téreau C, Tourbez M, Blouquit Y. 1999. Microscopic viscosity and rotational diffusion of proteins in a macromolecular environment. *Biophys J* **76**:2744–2751.
  108. Lettinga MP, van Kats CM, Philipse AP. 2000. Rotational diffusion of tracer spheres in packings and dispersions of colloidal spheres studied with time-resolved phosphorescence anisotropy. *Langmuir* **16**:6166–6172.
  109. Karon BS, Geddis LM, Kutchai H, Thomas DD. 1995. Anesthetics alter the physical and functional properties of the Ca-ATPase in cardiac sarcoplasmic reticulum. *Biophys J* **68**:936–945.
  110. Voss JC, Mahaney JE, Thomas DD. 1995. Mechanism of Ca-ATPase inhibition by melittin in skeletal sarcoplasmic reticulum. *Biochemistry* **34**:930–939.
  111. Brown LJ, Klonis N, Sawyer WH, Fajer PG, Hambly BD. 2001. Independent movement of the regulatory and catalytic domains of myosin heads revealed by phosphorescence anisotropy. *Biochemistry* **40**:8283–8291.
  112. Mueller B, Karim CB, Negrashov IV, Kutchai H, Thomas DD. 2004. Direct detection of phospholamban and sarcoplasmic reticulum Ca-ATPase interaction in membranes using fluorescence resonance energy transfer. *Biochemistry* **43**:8754–8765.
  113. Terpetschnig E, Szmacinski H, Lakowicz JR. 1997. Long-lifetime metal-ligand complexes as probes in biophysics and clinical chemistry. *Methods Enzymol* **278**:295–321.
  114. Li L, Szmacinski H, Lakowicz JR. 1997. Synthesis and luminescence spectral characterization of long-lifetime lipid metal-ligand probes. *Anal Biochem* **244**:80–85.
  115. Guo X-Q, Castellano FN, Li L, Szmacinski H, Lakowicz JR, Sipior J. 1997. A long-lived, highly luminescent Re(I) metal-ligand complex as a biomolecular probe. *Anal Biochem* **254**:179–186.
  116. DeGraff BA, Demas JN. 1994. Direct measurement of rotational correlation times of luminescent ruthenium (II) molecular probes by differential polarized phase fluorometry. *J Phys Chem* **98**:12478–12480.

## PROBLEMS

- P11.1. *Segmental Freedom in Proteins:* Use the data in Figure 11.9 for LADH to calculate the mean angle for the segmental motions of trp-314. Assume the fundamental anisotropy  $r_0 = 0.28$ .
- P11.2. *Binding Constant of FMN for YFP:* Use the intensity decay data in Table 11.3 to calculate the dissociation constant ( $K_d$ ) of FMN for YFP.

# 12

# Advanced Anisotropy Concepts

In the preceding two chapters we described steady-state and time-resolved anisotropy measurements, and presented a number of biochemical examples that illustrate the types of information available from these measurements. Throughout these chapters we stated that anisotropy decay depends on the size and shape of the rotating species. However, the theory that relates the form of anisotropy decay to the shape of the molecule is complex, and was not described in detail. In the present chapter we provide an overview of the rotational properties of non-spherical molecules, as well as representative examples.

For the initial topic in this chapter we describe associated anisotropy decays. Such decays occur when the solution contains more than one type of fluorophore, or the same fluorophore in different environments. Such systems can result in complex anisotropy decays, even if the individual species each display a single-exponential anisotropy decay.

## 12.1. ASSOCIATED ANISOTROPY DECAY

Biochemical samples frequently contain multiple fluorophores or a single fluorophore in more than one environment. Such a sample can be expected to display a multi-exponential anisotropy decay. For a mixture the origin of the multiple decay times is different from the preceding two chapters. In these chapters we described how a single fluorophore bound to a biomolecule could display multiple correlation times as the result of segmental motions in addition to rotational diffusion. Multiple correlation times can also occur for non-spherical molecules (Section 12.3) or for long flexible molecules like DNA. In these cases the multiple correlation times are due to a single fluorophore displaying complex motion.

There is another possible origin of complex anisotropy decays, which is a mixture of fluorophores or a single fluorophore in two different environments. This concept is illus-

trated in Figure 12.1, which shows tryptophan in two environments: free in solution and as the single-tryptophan residue in human serum albumin (HSA). Tryptophan has a lifetime near 3 ns, and a correlation time in water near 50 ps. The single-tryptophan residue in HSA has a longer lifetime near 8 ns and a correlation time near 40 ns. We have assumed that the intensity and anisotropy decay are all single exponentials.

A mixture of fluorophores with correlation times of 40 ns and 50 ps can result in an unusual anisotropy decay. In Section 11.5 we described how rapid segmental motions result in an initial rapid decrease in the anisotropy decay of a protein, followed by a slower anisotropy decay at longer times due to overall rotational diffusion. The resulting anisotropy decay can be quite different if the same two correlation times are present in the sample, but are due to a mixture of fluorophores rather than a single fluorophore. Such a mixture can display a different type of anisotropy decay in which the anisotropy decreases to a minimum and then increases at longer times (Figure 12.2).

The origin of the unusual behavior seen in Figure 12.2 can be understood by examining the intensity and anisotropy decays of the individual species (Figure 12.3). At any time following excitation the anisotropy is given by the additivity law:

$$r(t) = f_1(t)r_1(t) + f_2(t)r_2(t) \quad (12.1)$$

where  $f_1(t)$  is the fractional intensity of the tryptophan and  $f_2(t)$  is the fractional intensity of the HSA. The fractional intensity of each species can be calculated from the intensity decays. Assume that at  $t = 0$  both species contribute equally. Because of its shorter 3-ns lifetime the fractional intensity of the tryptophan decreases more rapidly with time than the emission from HSA with a lifetime of 8 ns. The fractional contribution of tryptophan becomes smaller at longer times. However, at intermediate times, the low

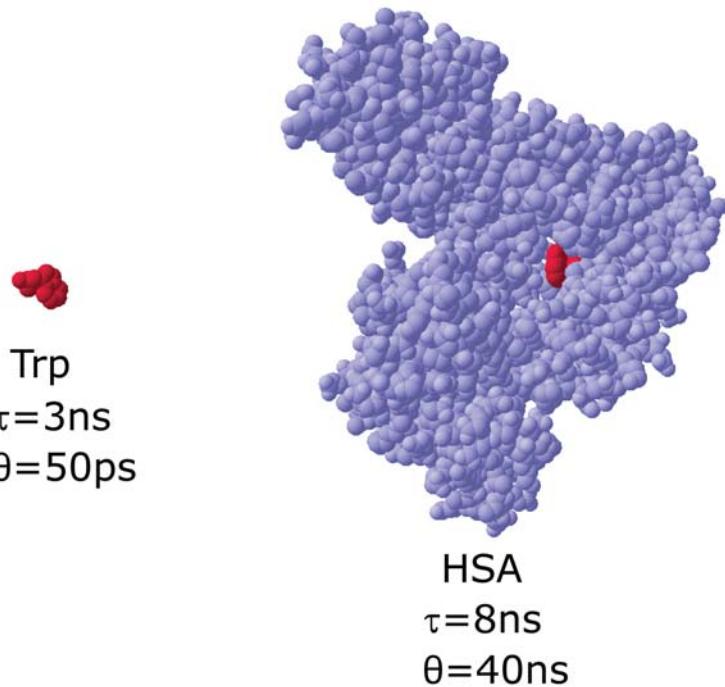


Figure 12.1. Model system for an associated anisotropy decay: a mixture of tryptophan in solution and in HSA.

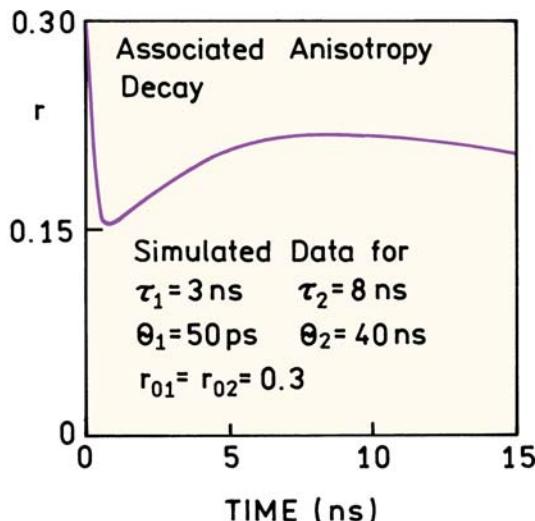


Figure 12.2. Simulated associated anisotropy decay simulated for a mixture of fluorophores,  $\tau_1 = 3$  ns,  $\theta_1 = 50$  ps,  $\tau_2 = 8$  ns,  $\theta_2 = 40$  ns,  $r_{01} = r_{02} = 0.30$ . The individual intensity and anisotropy decays are shown in Figure 12.3.

anisotropy of the tryptophan results in a transient decrease in the measured value of  $r(t)$ . At longer times, the emission becomes dominated by HSA with its larger anisotropy, resulting in an increase in  $r(t)$ .

### 12.1.1. Theory for Associated Anisotropy Decay

It is useful to compare the equations describing associated and non-associated anisotropy decays. For a single fluorophore that displays a multi-exponential intensity and anisotropy decay the parallel and perpendicular components of the emission are given by

$$I_{\parallel}(t) = \frac{1}{3} I(t)[1 + 2r(t)] \quad (12.2)$$

$$I_{\perp}(t) = \frac{1}{3} I(t)[1 - r(t)] \quad (12.3)$$

These expressions can be written in terms of the multiple exponential components in  $I(t)$  and  $r(t)$ :

$$I_{\parallel}(t) = \frac{1}{3} \sum_i \alpha_i \exp(-t/\tau_i) \left[ 1 + 2 \sum_j r_{0j} \exp(-t/\theta_j) \right] \quad (12.4)$$

$$I_{\perp}(t) = \frac{1}{3} \sum_i \alpha_i \exp(-t/\tau_i) \left[ 1 - \sum_j r_{0j} \exp(-t/\theta_j) \right] \quad (12.5)$$

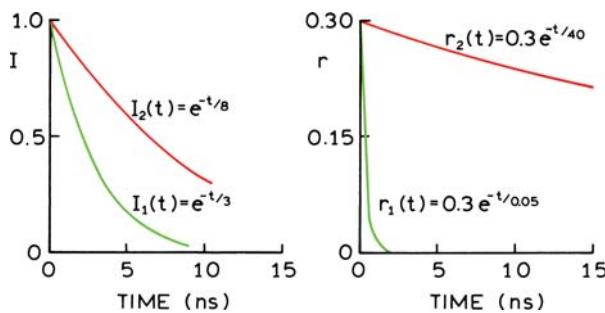


**Figure 12.3.** Intensity and anisotropy decays corresponding to the individual species shown in Figure 12.1.

For the non-associated decay there is a single intensity decay  $I(t)$  and a single anisotropy decay, even though both decays can be multi-exponential. A non-associated decay describes the motions of a single type of fluorophore in a single environment.

For an associated system each fluorophore population displays its own intensity and anisotropy decay. The polarized intensity decays are given by

$$I_{\parallel}(t) = \frac{1}{3} \sum_m I_m(t)[1 + 2r_m(t)] \quad (12.6)$$

$$I_{\perp}(t) = \frac{1}{3} \sum_m I_m(t)[1 - r_m(t)] \quad (12.7)$$

where the subscript m represents each fluorophore population, and not a component of a multi-exponential decay. Each fluorophore population is described by a different intensity decay  $I_m(t)$  and a different anisotropy decay  $r_m(t)$ .

The nature of an associated anisotropy decay can be understood by considering eqs. 12.6 and 12.7 for a two-component mixture. Assume each species displays a single lifetime ( $\tau_m$ ) and a single correlation time ( $\theta_m$ ). The amplitudes at  $t = 0$  can be represented by  $\alpha_m$ , which is the amplitude of the  $m$ th population at  $t = 0$ . The anisotropy decay for this mixture is then given by

$$r(t) = \frac{\sum_m \alpha_m \exp(-t/\tau_m) r_{0m} \exp(-t/\theta_m)}{\sum_m \alpha_m \exp(-t/\tau_m)} \quad (12.8)$$

The fractional intensity of the  $m$ th component at any time  $t$  is given by

$$f_m(t) = \frac{\alpha_m \exp(-t/\tau_m)}{\sum_m \alpha_m \exp(-t/\tau_m)} \quad (12.9)$$

and the time-dependent anisotropy is given by

$$r(t) = \sum_m f_m(t) r_m(t) \quad (12.10)$$

This equation states that the anisotropy at time  $t$  is given by the intensity-weighted average of the anisotropies of each species at the same time. Equation 12.10 is the additivity law for anisotropies at each time in the total decay. More detailed descriptions of the theory for associated anisotropy decays can be found elsewhere.<sup>1–8</sup>

### 12.1.2. Time-Domain Measurements of Associated Anisotropy Decays

Experimental studies of associated anisotropy decays started with early reports on cis- and trans-parinaric acid.<sup>9–11</sup> The anisotropy was observed to increase at long times (Figure 12.4). In this case the probe cis-parinaric acid was covalently linked to the second position on a phosphatidylcholine molecule (cis-parinaroyl-PC).<sup>12–13</sup> The increase in anisotropy at times longer than 10 ns was explained as the result of a population of fluorophores with a longer life-

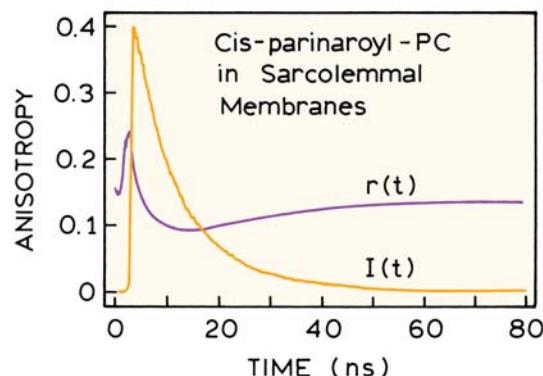


**Figure 12.4.** Intensity and anisotropy decay of cis-parinaroyl-PC in rat skeletal sarcolemmal membranes. From [12].

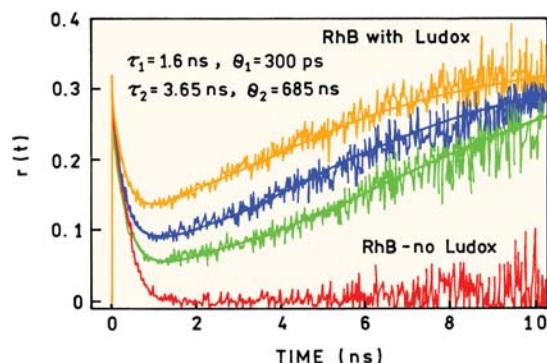


**Figure 12.5.** Anisotropy decay of rhodamine B in water and with 0.04, 0.08, and 0.27% Ludox (from bottom to top). For the highest silica concentration  $\alpha_1$  ( $H_2O$ ) = 0.70 and  $\alpha_2$  (silica) = 0.30 (eq. 12.8). Revised from [18].

time, which also displayed restricted motion. Associated anisotropy decays have also been observed for labeled oligonucleotides when bound to proteins<sup>14–15</sup> and for rhodamine and proteins in lipid–protein systems.<sup>16–17</sup>

A dramatic example of an associated anisotropy decay is shown in Figure 12.5. These anisotropy decays were observed for rhodamine B (RhB) in the presence of Ludox, which is colloidal silica. In the absence of silica the RhB anisotropy decays rapidly to zero. In the presence of increasing amounts of silica (bottom to top) the anisotropy initially decreases and then increases to nearly the time-zero value.<sup>18</sup> The initial rate of anisotropy decay is similar to that observed without silica. This suggests that in all samples, with and without silica, the anisotropy for times less than 1 ns is due to RhB that is not bound to silica. It seems logical to conclude that the anisotropy at long times is due to RhB bound to the silica particles. Since the long-time anisotropy is close to the time-zero anisotropy, the correlation time of RhB bound to silica must be long.

Associated anisotropy decays cannot always be distinguished from non-associated decays.<sup>1–3</sup> For instance, if the lifetimes of RhB were the same when in water and when bound to silica, the observed anisotropy decay would be a multi-exponential but the anisotropy would not increase at

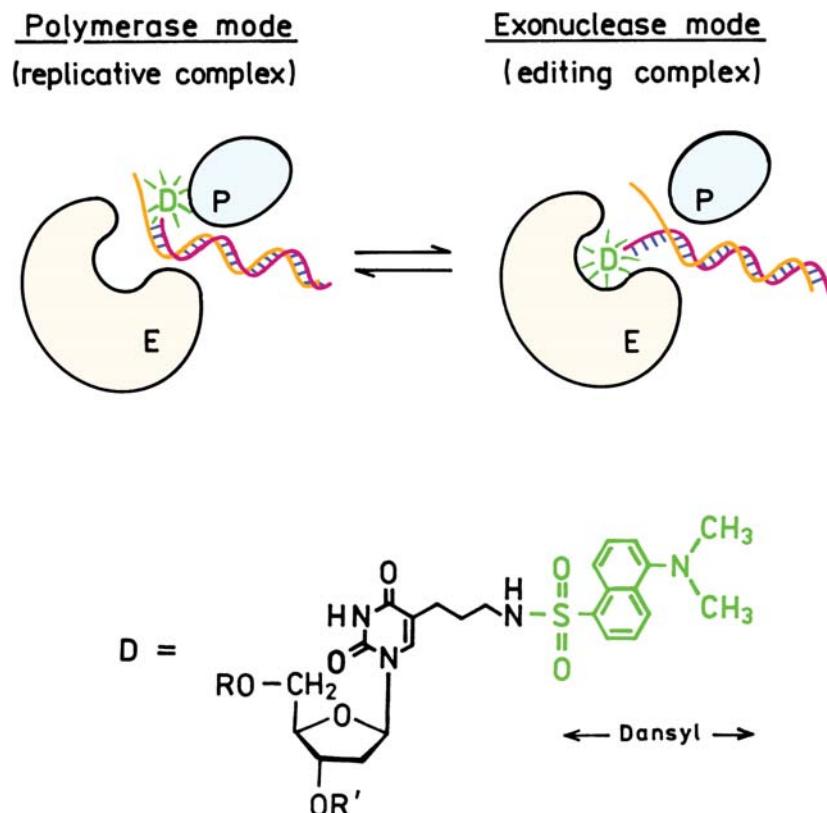


**Figure 12.6.** Klenow fragment of *E. coli* DNA polymerase with a bound DNA oligomer. The dansyl-labeled base (D) is located at the 10th residue from the 5' end of the 17-mer. Revised from [19].

long times (Problem 12.1). An increased anisotropy at long times requires that the species with a longer correlation time has a longer lifetime than the species with a short correlation time.

## 12.2. BIOCHEMICAL EXAMPLES OF ASSOCIATED ANISOTROPY DECAYS

### 12.2.1. Time-Domain Studies of DNA Binding to the Klenow Fragment of DNA Polymerase

DNA polymerase must replicate DNA with high accuracy. This requires that the polymerase be able to incorporate DNA bases into the nascent DNA primer strand and to remove incorrectly incorporated bases. The Klenow fragment (KF) from *E. coli* DNA polymerase is a single 68-kDa peptide that contains both the polymerase activity and the exonuclease activity (Figure 12.6). These activities are located at two different sites on the KF: the polymerase site and the exonuclease site. If a properly matched oligomer binds to the KF the shorter nascent chain is expected to bind to the polymerase site (left). If the DNA oligomer contains mismatched base pairs the nascent chain is expected to bind to the exonuclease site (right).

The mode of DNA binding to the KF was studied using dansyl-labeled DNA oligomers. These strands consisted of a 17-mer that contained the dansyl-labeled (D) base and a 27-mer that served as 7th template. These oligomers were either perfectly matched or contained 1 to 4 mismatched base pairs. Anisotropy decays of these oligomers bound to the KF are shown in Figure 12.7. When the oligomer is perfectly matched ( $x = 0$ ) there is an associated anisotropy

decay, as seen by the increasing anisotropy for times greater than 5 ns. As the number of mismatches increases from 1 to 4 the anisotropy decay loses the rising component and shows only the usual time-dependent decreases in anisotropy.

These anisotropy decays provide information about binding of the nascent strand for matched and mismatched oligomers. For the mismatched oligomers the non-associated anisotropy decay indicates the fluorophore is in a single type of environment. Since the anisotropy decay is slow the probe must be rigidly bound to the protein. Hence for mismatched oligomers, the 3' end of the nascent strand is firmly bound to the exonuclease site. For the matched oligomers some of the dansyl groups are freely rotating, resulting in a fast component in the anisotropy decay. The relative proportions of the 3' nascent strand end binding to each of the sites depends on the number of mismatched base pairs in the oligomer. The fractions of the dansyl probe bound to each site can be determined from the shape of the anisotropy decay.

The success of this experiment depended on the use of a dansyl-labeled oligomer, rather than fluorescein, rhodamine, or similar fluorophores. The lifetime of the dansyl group is sensitive to the surrounding polarity and/or rigidity. When the dansyl group was bound to the polymerase site it not only rotated more freely but also displayed a shorter lifetime than when bound rigidly to the exonuclease site. This shorter lifetime associated with the shorter correlation time is needed for unambiguous use of the associated model.

### 12.2.2. Frequency-Domain Measurements of Associated Anisotropy Decays

Associated anisotropy decays also result in unusual frequency-domain data.<sup>20–21</sup> This is shown by studies of ANS that is partially bound to apomyoglobin. Each apomyoglobin molecule binds only one ANS molecule, and the extent of binding is limited by using low concentrations of apomyoglobin. Frequency-domain anisotropy data for the system show differential phase angles which initially increase with frequency, and then decrease at higher frequencies (Figure 12.8). Surprisingly, the differential phase angles become negative even though the time-zero anisotropy is positive. This behavior is distinct from that observed for ANS when free in solution ( $\circ$ ) or when completely bound to apomyoglobin ( $\bullet$ , Figure 12.9). Data of the type shown in Figure 12.8 can be analyzed to recover

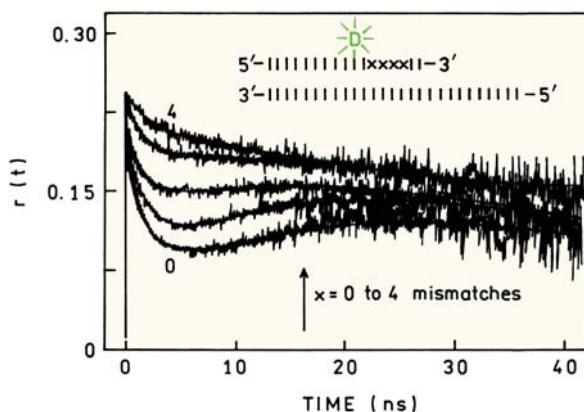


**Figure 12.7.** Anisotropy decay of the dansyl-labeled DNA oligomers when bound to the Klenow fragment. Revised from [19].

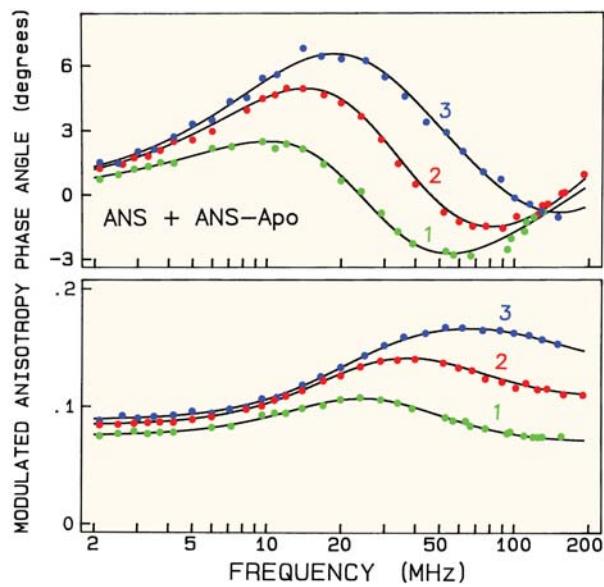


**Figure 12.8.** Frequency-domain anisotropy data for samples containing apomyoglobin ANS in molar ratios of 0.0087 (1), 0.0158 (2), and 0.079 (3). Reprinted from [20]. Copyright © 1987, with permission from Elsevier Science.

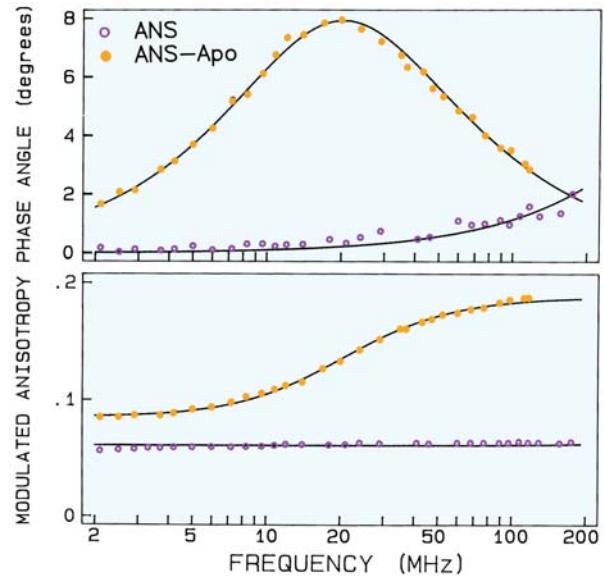


**Figure 12.9.** Frequency-domain anisotropy decays of apomyoglobin-ANS (●) and ANS alone (○). The correlation times are 13.2 ns for apomyoglobin-ANS and 97 ps for ANS alone. Reprinted from [20]. Copyright © 1987, with permission from Elsevier Science.

the time-zero anisotropies and correlation times of each fluorophore population.

To summarize, an anisotropy decay can be multi-exponential because a single population of fluorophores exhibits

complex motions, as due to more than one population of fluorophores with different rotational behavior. Associated anisotropy decays can sometimes be identified from unusual anisotropy decays. However, depending upon the lifetimes and correlation times it may or may not be possible to identify the decay as associated or non-associated.

### 12.3. ROTATIONAL DIFFUSION OF NON-SPHERICAL MOLECULES: AN OVERVIEW

Time-resolved anisotropy measurements can be used to determine the size and shape of the rotating fluorophore. A fluorophore that rotates at different rates around different axes is said to display anisotropic rotational diffusion. The theory for anisotropic rotational diffusion is rather complex. Prior to describing the complex equations for this topic it is valuable to have an overview of the results. A rotating fluorophore macromolecule need not be symmetric about any axis. A totally unsymmetric shape can only be described by the shape itself, and is thus not useful for a general theory. Hence non-spherical molecules are described as being a general ellipsoid or an ellipsoid of revolution (Figure 12.10). An ellipsoid is a shape whose plane sections are all ellipses or circles. A general ellipsoid has three unequal semi-axes,  $a \neq b \neq c$ , and an ellipsoid of revolution has two equal axes and one unique axis. The rotational properties of ellipsoids are described in terms of the rotational rates or rotational diffusion coefficients ( $D$ ) around each axis ( $D_1$ ,  $D_2$  and  $D_3$ ). The theory for rotational diffusion of non-spherical molecules predicts the anisotropy decays for ellipsoids and ellipsoids of revolution. A non-spherical molecule can display three or more rotational correlation times.

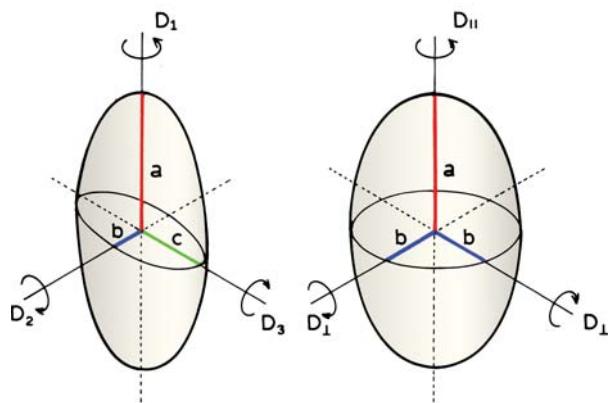


**Figure 12.10.** General ellipsoid with three unequal semi-axes  $a \neq b \neq c$ , and an ellipsoid of revolution ( $a = b = c$ ).

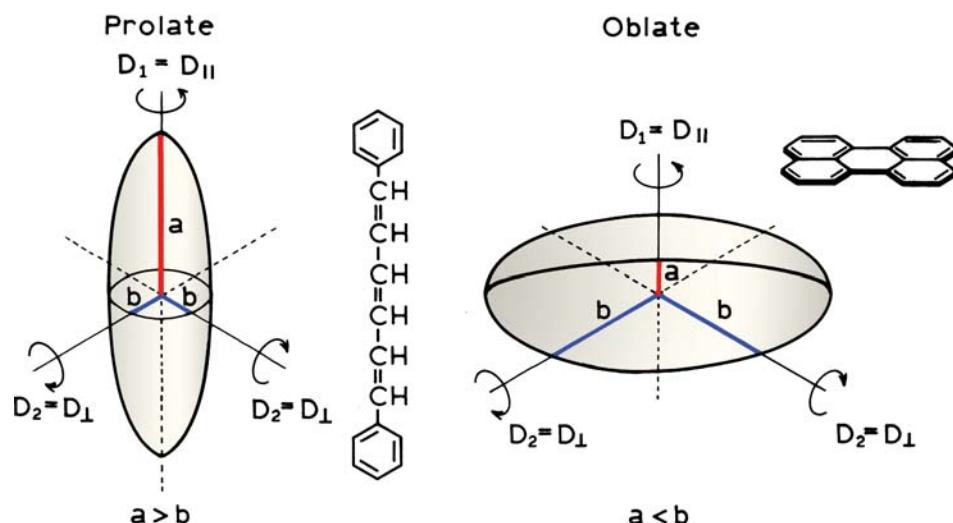


**Figure 12.11.** Prolate and oblate ellipsoids of revolution.

These correlation times are not simply equal to  $1/6D$  for each of the rotational diffusion coefficients. Instead, the rotational correlation times in the anisotropy decay are functions of the rotational diffusion coefficients. That is, each of the rotational diffusion coefficients can contribute to each of the correlation times.

Most experiments cannot reveal the shape of a general ellipsoid, so that most data are interpreted in terms of the ellipsoids of revolution. Two cases are possible: the prolate and oblate ellipsoids of revolution. These shapes are often referred to as prolate or oblate ellipsoids. In a prolate ellipsoid the unique axis is longer than the other two equal axes ( $a > b = c$ ). Prolate ellipsoids are elongated along the symmetry axis. A typical prolate ellipsoid would be DPH (Figure 12.11). For an oblate ellipsoid the unique axis is smaller than the other two equivalent axes ( $a < b = c$ ). Oblate ellipsoids are shaped like flattened spheres. Perylene is an oblate ellipsoid.

Because of the two equivalent axes in ellipsoids of revolution, their hydrodynamics can be described with only two diffusion coefficients (Figure 12.11), but recall that the anisotropy decay measurements reveal correlation times and not the individual rotational diffusion coefficients. Rotation about the unique axis in either a prolate or oblate ellipsoid is called  $D_{||}$ , and rotation about either of the other two equivalent axes is referred to as  $D_{\perp}$ . In general one can expect  $D_{||} > D_{\perp}$  for both prolate and oblate ellipsoids because rotation about the unique axis can occur with less displacement of solvent than rotation about the other two

axes. However, small molecules do not always rotate as hydrodynamic objects, and prolate or oblate-shaped fluorophores may display more than two correlation times.

### 12.3.1. Anisotropy Decays of Ellipsoids

The theory for rotational diffusion of ellipsoids as measured by fluorescence polarization can be traced to the classic reports by F. Perrin.<sup>22–25</sup> Since these reports, the theory has been modified to include a description of expected anisotropy decays for molecules free in solution and in constrained environments.<sup>26–37</sup> For a rigid ellipsoid with three unequal axes the anisotropy decays with five correlation times.<sup>28–30</sup> The correlation times depend on the three rotation diffusion coefficients, and the amplitudes depend on the orientation of the absorption and emission transition moments within the fluorophore and/or ellipsoid. The theory predicts five correlation times, but it is known that two pairs of correlation times are very close in magnitude. In practice only three correlation times are expected for a non-spherical molecule.<sup>31</sup>

The anisotropy decays of non-spherical molecules depend on the orientation of the transition moments relative to the principle axes. The absorption and emission moments can have any arbitrary direction relative to the major ( $a$ ) and minor ( $b$ ) axes of the ellipsoid (Figure 12.12). The transition moments are not necessarily aligned with an axis of the ellipsoid. The anisotropy decay of an ellipsoid of revolution can display up to three correlation times, which are func-

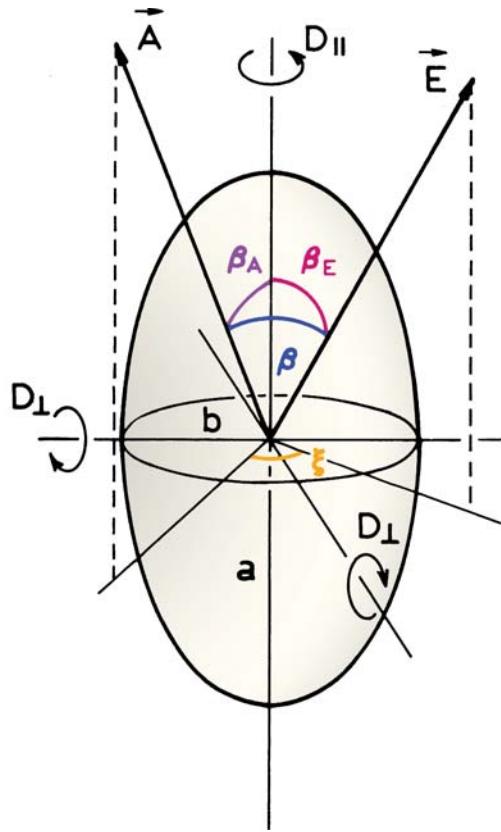


**Figure 12.12.** Prolate ellipsoid of revolution.  $\vec{A}$  and  $\vec{E}$  are the directions of the absorption and emission transition moments, respectively. Revised and reprinted with permission from [4]. Copyright © 1985, Academic Press, Inc.

tions of the two rotational rates ( $D_{\parallel}$  and  $D_{\perp}$ ). The amplitudes of the anisotropy decay depend on the orientation of the transition moments. If one of the transition moments is directed along any of the symmetry axes of the ellipsoid, then the anisotropy decay becomes a double exponential. Hence, one can expect double-exponential anisotropy decays for molecules like DPH or perylene, where the long-wavelength absorption and emission moments are directed along the long axis of the molecules.

#### 12.4. ELLIPSOIDS OF REVOLUTION

We now describe the theory for the anisotropy decays of ellipsoids of revolution. It is important to remember that this theory assumes the ellipsoid to be rigid. In the case of a labeled protein this assumption implies no independent motion of the fluorophore within the protein. For prolate or

oblate ellipsoids the anisotropy decay is expected to display three correlation times:

$$\begin{aligned} r(t) = & r_1 \exp(-t/\theta_1) + r_2 \exp(-t/\theta_2) \\ & + r_3 \exp(-t/\theta_3) \end{aligned} \quad (12.11)$$

The amplitudes decaying with each correlation time depend on the angles of the absorption ( $\beta_A$ ) and emission ( $\beta_E$ ) dipoles with the symmetry axis. Using the notation defined in Figure 12.12 these anisotropy amplitudes are

$$r_1 = 0.3 \sin 2\beta_A \sin 2\beta_E \cos \xi \quad (12.12)$$

$$r_2 = 0.3 \sin^2 \beta_A \sin^2 \beta_E \cos 2\xi \quad (12.13)$$

$$r_3 = 0.1(3 \cos^2 \beta_A - 1)(3 \cos^2 \beta_E - 1) \quad (12.14)$$

Occasionally one finds alternative forms<sup>37–38</sup> for  $r_1$  and  $r_2$ :

$$r_1 = 1.2 \sin \beta_A \cos \beta_A \sin \beta_E \cos \beta_E \cos \xi \quad (12.15)$$

$$r_2 = 0.3 \sin^2 \beta_A \sin^2 \beta_E \cos 2\xi \quad (12.16)$$

The fundamental anisotropy is given as usual by

$$r_0 = r_1 + r_2 + r_3 = 0.2(3 \cos^2 \beta - 1) \quad (12.17)$$

where  $\beta$  is the angle between the absorption and emission transition moments. The three correlation times are determined by the two different rotational rates:

$$\theta_1 = (D_{\parallel} + 5D_{\perp})^{-1} \quad (12.18)$$

$$\theta_2 = (4D_{\parallel} + 2D_{\perp})^{-1} \quad (12.19)$$

$$\theta_3 = (6D_{\perp})^{-1} \quad (12.20)$$

Depending upon the shape of the ellipsoid of rotation, and the orientation of the transition moments, a variety of complex anisotropy decays can be predicted.<sup>4,37</sup>

In the previous chapter we saw that one can calculate these rotational correlation times for a spherical molecule ( $\theta_S$ ) based on its volume and the solution viscosity. Similar-

ly one can calculate  $D_{\parallel}$  and  $D_{\perp}$  for ellipsoids of revolution. These relative values are given by

$$\frac{D_{\parallel}}{D} = \frac{3\rho(\rho - S)}{2(\rho^2 - 1)} \quad (12.21)$$

$$\frac{D_{\perp}}{D} = \frac{3\rho[(2\rho^2 - 1)S - \rho]}{2(\rho^4 - 1)} \quad (12.22)$$

where  $D = (6\theta_S)^{-1}$  is the rotational diffusion coefficient of a sphere of equivalent volume, and  $\rho = a/b$  is the axial ratio. The value of  $\rho$  is  $>1$  for a prolate ellipsoid and  $<1$  for an oblate ellipsoid:

$$S = (\rho^2 - 1)^{-1/2} \ln[\rho + (\rho^2 + 1)^{1/2}] \quad \rho > 1 \quad (12.23)$$

$$S = (1 - \rho^2)^{-1/2} \arctan[(1 - \rho^2)^{1/2}/\rho] \quad \rho < 1 \quad (12.24)$$

These expressions are somewhat complex, and can be used to predict a variety of anisotropy decays. It is important to recognize that one does not directly measure the rotational diffusion coefficients, but rather the correlation times that are functions of the rotational rates.

#### 12.4.1. Simplified Ellipsoids of Revolution

It is informative to describe the anisotropy decays when the absorption and/or emission transitions are directed along one of the axes. In these cases eqs. 12.11–12.24 reduce to simpler anisotropy decays, which can often be understood intuitively. Suppose the fluorophore is shaped like DPH, and both transition moments are aligned with the long axis (Figure 12.13, top). In this case  $r_1$  and  $r_2$  are zero (eqs. 12.12 and 12.13), and  $r_3 = 0.4$ . Hence the anisotropy decays as follows:

$$r(t) = 0.4 \exp(-6D_{\perp}t) \quad (12.25)$$

where the correlation time is  $\theta_3 = (6D_{\perp})^{-1}$ . This result supports the usual assumption that DPH behaves as an isotropic rotator. DPH is not actually an isotropic rotation. However, rotation of DPH around its long axis ( $D_{\parallel}$ ) does not displace the colinear transition moments, and thus does not decrease the anisotropy. Only the rotation that displaces the moments ( $D_{\perp}$ ) results in depolarization. For this reason the

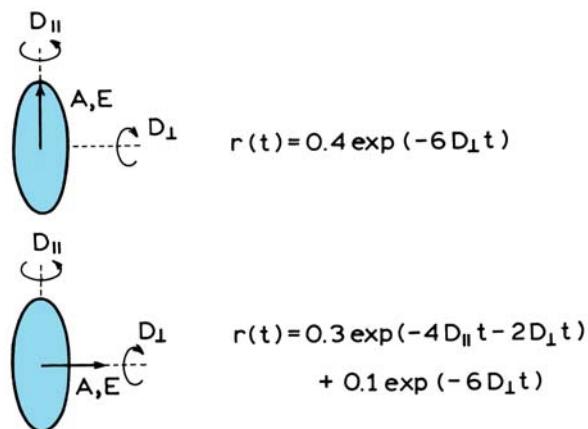


Figure 12.13. Anisotropy decays of prolate ellipsoids of revolution.

anisotropy of DPH in a homogeneous solution decays with a single correlation time.

The results will be different for the same prolate ellipsoid if both transition moments are perpendicular to the long axis. In this case the anisotropy decays with two correlation times (Figure 12.13, bottom). The anisotropy decay is more rapid than in the previous case because the faster rotation about the long axis ( $D_{\parallel}$ ) displaces the transition moments. This results in a rapid randomization about the long axis. At longer times the slower rotation ( $D_{\perp}$ ) will result in complete depolarization.

The theory can also be used to predict the anisotropy decays of disk-like oblate ellipsoids (Figure 12.14). For such molecules the transitions are almost always within the plane of the ring. For colinear transitions in an oblate ellip-

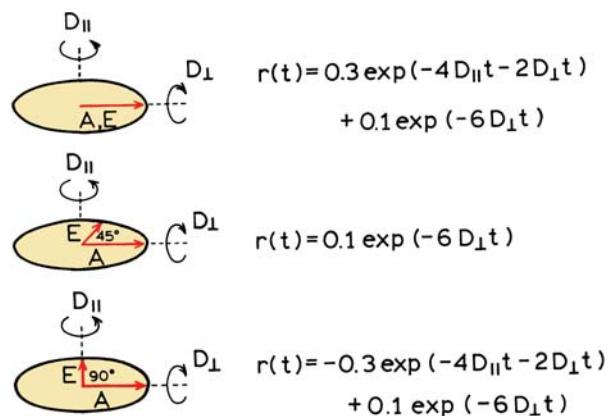


Figure 12.14. Anisotropy decays of oblate ellipsoids of revolution.

soid the anisotropy decay has the same form as that for a prolate ellipsoid with transitions normal to the long axis. The anisotropy decay is initially dominated by the faster in-plane rotation, and at later times by the slower out-of-plane rotation.

It is instructive to consider the anisotropy decays of oblate ellipsoids when the absorption and emission transitions moments are not colinear ( $\beta \neq 0$ ). Nonzero angles occur in many fluorophores, including indole and perylene. Suppose the transition moments are within the plane and displaced by  $90^\circ$  ( $\beta = 90^\circ$ ). To be more explicit,  $\beta_A = \beta_E = 90^\circ$  and  $\beta = \xi = 90^\circ$ . In this case the anisotropy decay displays positive and negative amplitudes:

$$\begin{aligned} r(t) = & -0.3 \exp(-4D_{\parallel}t - 2D_{\perp}t) \\ & + 0.1 \exp(-6D_{\perp}t) \end{aligned} \quad (12.26)$$

From this expression one can see that the faster in-plane rotation has a larger absolute amplitude and dominates the anisotropy decay at early times. In fact, the anisotropy can become positive prior to decaying to zero. Such behavior has been observed for perylene.

Now consider excitation when  $\beta = 45^\circ$ , with  $\beta_A = \beta_E = 90^\circ$ . In this case the anisotropy decay is given by

$$r(t) = 0.1 \exp(-6D_{\perp}t) \quad (12.27)$$

This means that excitation at a wavelength where  $r_0 = 0.1$  results in measurement of the out-of-plane rotation. When  $\beta = 45^\circ$  the excitation is randomized in the plane of the fluorophore, so the in-plane rotation has no further effects.

And finally, consider excitation with  $\beta = 54.7^\circ$ ,  $r_0 = 0$ . For this condition  $r(t)$  remains zero at all times if one of the transitions is aligned with one of the axes. However, if the transitions make nonzero angles with the axes, then  $r(t)$  can be nonzero at intermediate times, even with  $r_0 = 0$ .

An important aspect of these anisotropy decays (Figures 12.13 and 12.14) is that the correlation times are independent of  $r_0$ , but that the amplitudes ( $r_1$ ,  $r_2$ , and  $r_3$ ) depend on the excitation wavelength or the angles between the transition moments and the axes of the ellipsoid. This provides the opportunity for global analysis based on the anisotropy decays measured using multiple excitation wavelengths. At each excitation wavelength (or  $r_0$  value) there will be different relative contributions of each correlation time to the anisotropy decay. However, the correlation times will be

independent of excitation wavelength. By global analysis of the data, with the correlation times constrained to the same for all excitation wavelengths, one can obtain improved resolution of the multi-exponential anisotropy decay.

It is valuable to understand the origin of  $\beta$  values which are not equal to 0 or  $90^\circ$ . Individuals trained in molecular photophysics may expect the electronic transitions of perylene to be directed along the symmetry axes. For this reason the only expected values of  $\beta$  for perylene are 0 or  $90^\circ$  for the two in-plane transitions, corresponding to  $r_0$  values of 0.40 or  $-0.20$ , respectively. However, perylene and many other fluorophores display intermediate values of  $\beta$  and  $r_0$  between 0.40 and  $-0.20$ . Intermediate values of  $r_0$  probably represent a mixture of the two electronic transitions, the relative proportion of which depends on the excitation wavelength. We describe such mixed transitions as due to a single apparent value of  $\beta$  for a single transition.

#### 12.4.2. Intuitive Description of Rotational Diffusion of an Oblate Ellipsoid

The special cases described above can be understood intuitively by considering rotational diffusion of perylene. Assume perylene is excited in its long-wavelength absorption band where  $r_0$  is near 0.4. The excited-state population will initially be aligned along the vertical or  $z$ -axis (Figure 12.15). Rotation of perylene about its symmetry axis (normal to the plane) will displace the transition moments and result in depolarization. Similarly, one of the out-of-plane rotations will displace the transition moments. This intuitive result agrees with Figure 12.14 (middle panel), which indicates that for an oblate ellipsoid with  $r_0 = 0.4$  both  $D_{\parallel}$  and  $D_{\perp}$  contribute to the anisotropy decay.

Now consider excitation of perylene with  $r_0 = -0.2$ ,  $\beta = 90^\circ$ . Initially, neither out-of-plane rotation displaces the emission moment, so the only active depolarizing rotation is the in-plane rotation. (Recall the excited state population is symmetrical around the  $z$ -axis). Once the molecule has undergone in-plane rotation then the out-of-plane rotation displaces the emission moment. These motions result in the anisotropy decay described by eq. 12.26.

And, finally, consider excitation with  $\beta = 45^\circ$  or  $r_0 = 0.10$ . In this case the excited-state population is immediately randomized around the symmetry axis of the oblate ellipsoid. Hence only the out-of-plane rotations can further depolarize the emission, which is in agreement with eq. 12.27.

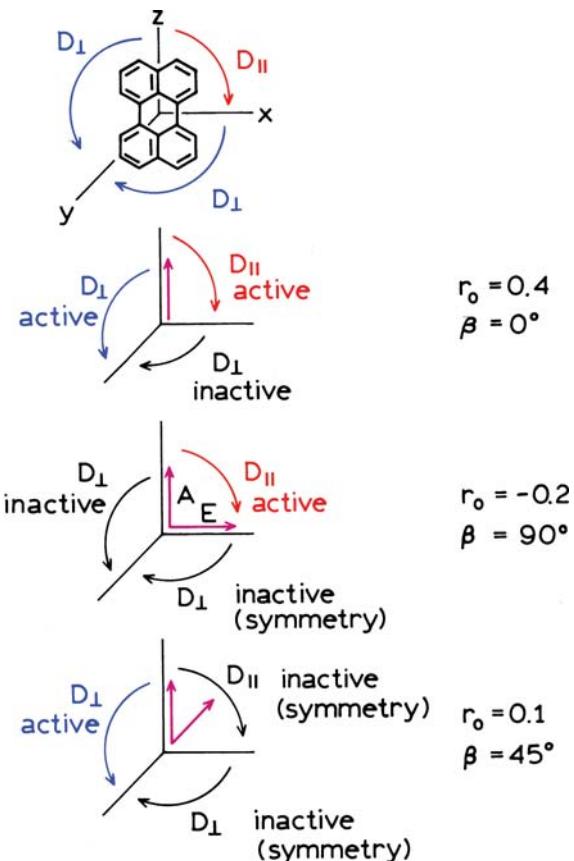


Figure 12.15. Rotational motions of an oblate ellipsoid.

### 12.4.3. Rotational Correlation Times for Ellipsoids of Revolution

It is interesting to see how the shape of an ellipsoid affects the correlation times. Some correlation times are summarized in Table 12.1. These values are shown as the ratio of the rotational correlation times for the ellipsoid to that expected for a sphere of equivalent volume.<sup>39</sup> The correlation times are quite different for prolate and oblate ellip-

soids. For prolate ellipsoids the three correlation times are all different in magnitude, and can be much larger than that for an equivalent sphere. For the prolate ellipsoids one correlation time ( $\theta_3$ ) increases dramatically as the axial ratio increases. This is understandable because a long rigid rod is expected to diffuse slowly in directions which displace the long axis. This correlation time ( $\theta_3 = (6D_{\perp})^{-1}$ ) is determined by the rotation that displaces the long axis of the prolate ellipsoid. For a prolate ellipsoid all three correlation times can be distinct for large axial ratios. The ability to detect these correlation times depends on the amplitudes, which depend on the angles with respect to the symmetry axis. For the oblate ellipsoids the three correlation times are all similar in magnitude. Hence it would be difficult to distinguish an oblate ellipsoid from a sphere, assuming that the oblate ellipsoid displayed hydrodynamic rotation. However, small oblate molecules often display slip diffusion, which results in faster in-plane rotations.

Some fluorophores display  $r_0$  values near 0.4, which indicates that the absorption and emission moments are colinear. In this case eqs. 12.12 and 12.13 can be simplified further. Using  $\beta_A = \beta_E = \beta_T$  and  $\xi = 0$  one finds

$$r_1 = 0.3 \sin^2 2\beta_T \quad (12.28)$$

$$r_2 = 0.3 \sin^4 \beta_T \quad (12.29)$$

$$r_3 = 0.1(3 \cos^2 \beta_T - 1)^2 \quad (12.30)$$

where  $\beta_T$  is the angle formed by the transition moments with the symmetry axis of the ellipsoid.

Because of the complexity of the equations relating shape to the anisotropy decays, it is useful to have some specific examples. Rotational correlation times for prolate ellipsoids are summarized in Table 12.2. These correlation times are calculated for proteins with  $\bar{v} = 0.75 \text{ ml/g}$  and for

Table 12.1. Rotational Correlation Times of Ellipsoid of Revolution<sup>a</sup>

Prolate				Oblate			
$\rho$	$\theta_1/\theta_S$	$\theta_2/\theta_S$	$\theta_3/\theta_S$	$\rho^{-1}$	$\theta_1/\theta_S$	$\theta_2/\theta_S$	$\theta_3/\theta_S$
1	1.0	1.0	1.0	1	1.0	1.0	1.0
2	1.32	0.95	1.50	2	1.17	1.49	1.13
5	2.41	0.98	4.64	5	2.30	2.51	2.24
10	3.25	0.99	13.37	10	4.38	4.61	4.30
20	3.73	0.99	41.82	20	8.60	8.85	8.52

<sup>a</sup>From [39].  $\theta_1 = (D_{\parallel} + 5D_{\perp})^{-1}$ ,  $\theta_2 = (4D_{\parallel} + 2D_{\perp})^{-1}$ ,  $\theta_3 = (6D_{\perp})^{-1}$ .

**Table 12.2.** Rotational Correlation Times for Prolate Ellipsoids of Revolution<sup>a</sup>

$\rho$	$\theta_1$ (ns)		$\theta_2$ (ns)		$\theta_3$ (ns)		$\theta_H$ (ns)	
	$h = 0$	$h = 0.2$						
MW = 10,000								
1.5	3.46	4.38	2.94	3.72	3.68	4.66	3.27	4.14
2	4.05	5.13	2.93	3.71	4.63	5.87	3.59	4.55
3	5.31	6.72	2.97	3.77	7.18	9.11	4.21	5.34
5	7.40	9.36	3.03	3.83	14.2	18.0	5.00	6.31
10	10.03	12.67	3.06	3.88	41.7	52.1	5.69	7.24
MW = 25,000								
1.5	8.66	10.96	7.34	9.31	9.21	11.65	8.16	10.37
2	10.11	12.79	7.33	9.29	11.57	14.62	8.96	11.36
3	13.2	16.8	7.43	9.42	17.9	22.8	10.54	13.25
5	18.4	23.4	7.56	9.60	35.4	45.0	12.36	15.96
10	25.1	31.6	7.65	9.71	104.2	128.2	14.23	23.19
MW = 50,000								
1.5	17.4	21.8	14.7	18.5	18.5	23.1	16.3	20.6
2	20.2	25.5	14.7	18.4	23.1	29.2	17.8	22.4
3	26.7	33.3	15.0	18.7	36.2	45.0	21.0	26.7
5	37.3	46.1	15.2	19.0	72.4	87.7	24.8	31.2
10	50.2	64.1	15.3	19.4	208.3	277.8	28.5	36.2
MW = 100,000								
1.5	34.7	43.4	29.3	36.7	37.0	46.3	32.6	41.8
2	40.5	50.2	29.4	36.5	46.3	57.4	36.9	44.5
3	53.4	65.3	29.9	37.0	72.4	87.7	42.2	52.1
5	73.0	94.3	30.1	38.1	138.9	185.2	49.5	63.3
10	100.0	128.2	30.4	38.7	416.7	555.5	56.6	72.3
MW = 500,000								
1.5	173.9	217.9	147.1	185.2	185.2	231.5	163.4	205.8
2	202.4	255.1	147.0	184.5	231.5	292.4	177.9	225.4
3	267.4	333.3	149.7	187.3	362.3	450.5	209.6	267.7
5	373.1	460.8	152.0	190.1	724.6	877.2	248.0	332.0
0	502.5	641.0	153.4	193.8	2083.3	2777.8	285.1	375.4

<sup>a</sup>  $\theta_1 = (D_{\parallel} + 5D_{\perp})^{-1}$ ,  $\theta_2 = (4D_{\parallel} + 2D_{\perp})^{-1}$ ,  $\theta_3 = (6D_{\perp})^{-1}$ .  $D_{\perp}/D$  from eq. 12.21 and  $D_{\parallel}/D$  from eq. 12.21,  $S$  from eq. 12.23,  $\bar{v} = 0.75$ .

a hydration of  $h = 0$  or  $h = 0.2$  ml/g. Values are not listed for oblate ellipsoids since most non-spherical proteins seem to be elongated rather than flattened. Of course, all the correlation times increase with increasing molecular weight. Two of the correlation times ( $\theta_1$  and  $\theta_3$ ) increase dramatically as the axial ratio increases. The other correlation time ( $\theta_2$ ) is relatively independent of shape.

It is useful to visualize how the three correlation times depend on the axial ratio. This dependence is shown in Figure 12.16 for a prolate ellipsoid of revolution. The chosen parameters MW = 10,000,  $\sqrt{v} = 0.75$ ,  $\bar{v} = 0.75$  ml/g, and  $h = 0.2$  ml/g were selected to represent a small protein. One of the correlation times ( $\theta_3$ ) increases progressively as the axial ratio increases. The other two correlation times ( $\theta_1$  and  $\theta_2$ ) reach limiting values at large axial ratios. This

occurs because these correlation times contain  $D_{\parallel}$ , which stays relatively constant as  $\rho$  increases. It is interesting to note that  $\theta_2$  actually decreases as  $\rho$  increases from 1 to 3.

Also shown in Table 12.2 are the harmonic mean correlation times ( $\theta_H$ ). Calculation of  $\theta_H$  is somewhat complicated because it depends on the value of  $r_0$  and the orientation of the transition moments relative to the ellipsoid axis. The values in Table 12.2 were calculated using

$$\frac{1}{\theta_H} = \frac{0.4}{\theta_1} + \frac{0.4}{\theta_2} + \frac{0.2}{\theta_3} \quad (12.31)$$

This definition of  $\theta_H$  is appropriate when the absorption and emission transition moments are randomly oriented with respect to the principal axes.<sup>36</sup>

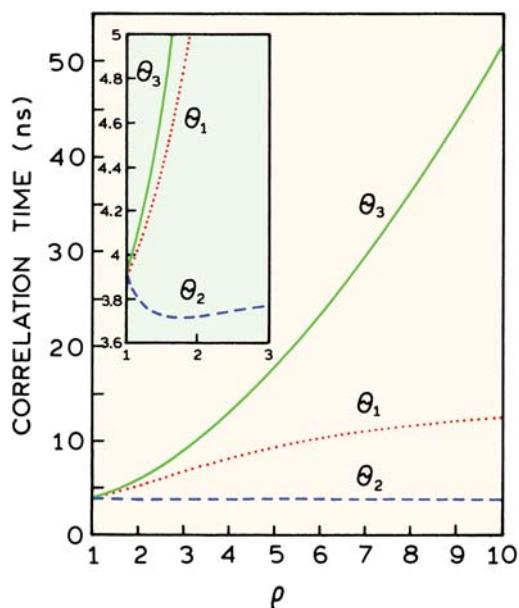


**Figure 12.16.** Correlation time for a prolate ellipsoid of revolution at various axial ratios ( $\rho$ ),  $\eta = 1 \text{ cP}$ ,  $\theta_1 = (D_{\parallel} + 5D_{\perp})^{-1}$ ,  $\theta_2 = (4D_{\parallel} + 2D_{\perp})^{-1}$ ,  $\theta_3 = (6D_{\perp})^{-1}$ . MW = 10,000,  $h = 0.2 \text{ ml/g}$  and  $\bar{v} = 0.75 \text{ ml/g}$ .

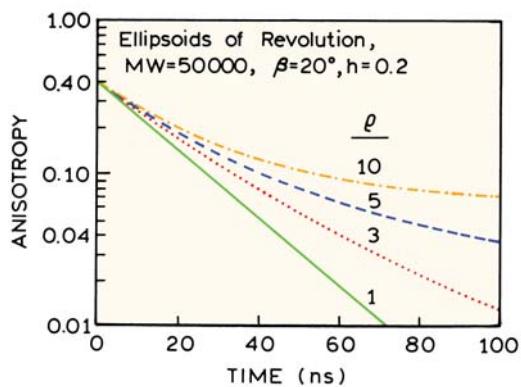


**Figure 12.17.** Simulated anisotropy decays for a protein (MW = 50 kD) shaped as a prolate ellipsoid of revolution with various axial ratios ( $\rho$ ). For these simulations we assumed  $\bar{v} = 0.75 \text{ ml/g}$ ,  $h = 0.2 \text{ ml/g}$ , and  $\beta = 20^\circ$ .

The form of an anisotropy decay depends on the axial ratio. The anisotropy decays were simulated using the assumption  $r_0 = 0.4$  (eqs. 12.28–12.30) and various axial ratios (Figure 12.17). For these decays the transition moments were assumed to make an angle of  $20^\circ$  relative to the symmetry axis of the prolate ellipsoid. The anisotropy

decays became visually different from a single exponential as the axial ratio exceeded 2. This change in the shape of an anisotropy decay is the basis for determining the shapes of proteins from the time-resolved anisotropies.

#### 12.4.4. Stick-versus-Slip Rotational Diffusion

The theory described above for rotation of ellipsoids applies only to the "stick" condition. The term "stick boundary conditions" refers to rotational diffusion in which the first solvent layer moves with the rotating species, so that rotation is governed by the viscosity of the solvent. Macromolecules and most fluorophores in polar solvents are well described by stick diffusion. However, small molecules in nonpolar solvents can often display slip-rotational diffusion.<sup>40–46</sup> As an example, perylene in a solvent like hexane can rotate in plane without significant displacement of solvent. When this occurs the molecule rotates as if it were in a vacuum, and not affected by solvent viscosity. The theory of slip-rotational diffusion is rather complex, and the results are often presented numerically.<sup>47–48</sup> The important point is that the possibility of slip diffusion results in a failure of the theory described above to predict the correlation times of non-spherical molecules. Stated alternatively, one can recover multiple correlation times for small non-spherical molecules, but these values cannot always be interpreted in terms of the correlation times predicted from the hydrodynamic theory (eqs. 12.11–12.24).

---

#### 12.5. COMPLETE THEORY FOR ROTATIONAL DIFFUSION OF ELLIPSOIDS

In the preceding sections we described the rotational behavior of ellipsoids with transitions directed along one of the symmetry axes. Although not frequently used, it is useful to have the complete expression for an ellipsoid with three nonequivalent axes and without restricting one of the transitions to be on an axis (Figure 12.10, left). In this case the anisotropy decays with five apparent correlation times;<sup>30,36,39</sup>

$$\begin{aligned}
 r(t) = & \frac{6}{5} \sum_{i=1}^3 C_i \exp(-t/\theta_i) \\
 & + [(F+G)/4] \exp[-(6D-2\Delta)t] \\
 & + [(F-G)/4] \exp[-(6D+2\Delta)t]
 \end{aligned} \quad (12.32)$$

In this expression  $D$  is the mean rotational diffusion coefficient:

$$D = \frac{1}{3}(D_1 + D_2 + D_3) \quad (12.33)$$

and

$$\Delta = (D_1^2 + D_2^2 + D_3^2 - D_1 D_2 - D_1 D_3 - D_2 D_3)^{1/2} \quad (12.34)$$

The directions of the transition moments in the ellipsoid (Figure 12.12) are defined by the cosine of the angles between the absorption transitions and the three axes ( $\alpha_1$ ,  $\alpha_2$  and  $\alpha_3$ ) and between the emission transitions ( $\varepsilon_1$ ,  $\varepsilon_2$ , and  $\varepsilon_3$ ) and the three axes. The values of  $C_i$  are given by

$$C_i = \alpha_i \alpha_k \varepsilon_j \varepsilon_k \quad (12.35)$$

with  $ijk = 123, 231$ , or  $312$ . The other quantities in eq. 12.32 are defined by

$$C_i = \alpha_i \alpha_k \varepsilon_j \varepsilon_k \quad (12.36)$$

$$F = \sum_{i=1}^3 \alpha_i^2 \varepsilon_i^2 - 1/3 \quad (12.37)$$

$$G\Delta = \sum_{i=1}^3 D_i (\alpha_i^2 \varepsilon_i^2 + \alpha_j^2 \varepsilon_k^2 + \alpha_k^2 \varepsilon_j^2) - D \quad (12.38)$$

where  $i \neq k$ .

In the limiting case of spherical symmetry, with  $D_1 = D_2 = D_3 = D$ , eq. 12.32 reduces to a single correlation time with  $\theta = (6D)^{-1}$ . For ellipsoids of revolution these equations (12.32 to 12.38) reduce to those given in Section 12.4.

## 12.6. ANISOTROPIC ROTATIONAL DIFFUSION

### 12.6.1. Time-Domain Studies

It is difficult to detect the presence of anisotropic rotation.<sup>49–53</sup> In one report<sup>53</sup> the anisotropy decay of 9,10-dimethylanthracene (DMA) was measured in a viscous non-polar solvent. The sample was excited at 401 nm using the 0.5-ns pulses available from a synchrotron. The solvent was glycerol tripropanoate, which at  $-38.7^\circ\text{C}$  had a viscosity of

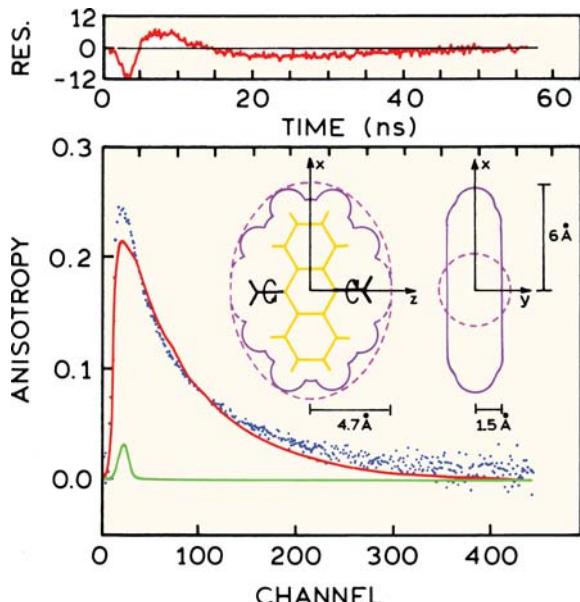


**Figure 12.18.** Time-domain anisotropy decay of 9,10-dimethylanthracene in glycerol tripropanoate (tripropionin) at  $-38.4^\circ\text{C}$ . Excitation at 401 nm was obtained as 0.5-ns pulse from the LURE-ACO synchrotron, Orsay, France. The solid line shows the single correlation time fit. Revised and reprinted with permission from [53]. Copyright © 1985, American Chemical Society.

11 poise. Under these conditions the mean correlation time was 10 ns. The experimental anisotropy decay could not be fit to a single correlation time (Figure 12.18), but the data were well fit using two correlation times (not shown). The presence of two correlation times is consistent with DMA being an ellipsoid of revolution, but the recovered diffusion coefficients did not agree with those predicted from the hydrodynamic theory for ellipsoids. This failure was assigned to the presence of partial slip diffusion. The overall behavior of DMA appeared to be intermediate between the slip and stick diffusion limits.

Perylene has been widely studied as an anisotropic rotation. When excited in its long-wavelength absorption band the anisotropy decay is a double exponential, but this can be difficult to detect from the time-resolved data. The use of a shorter excitation wavelength results in a definitive observation.<sup>49</sup> At this wavelength the absorption and emission transition moments are nearly perpendicular, and the time-zero anisotropy is  $-0.14$ . For a spherical molecule the anisotropy is expected to decay from  $-0.14$  to zero with a single correlation time. However, the anisotropy of perylene increases to values above zero and then decays to zero (Figure 12.19). This behavior can be understood in terms of the different rotational motions of perylene.

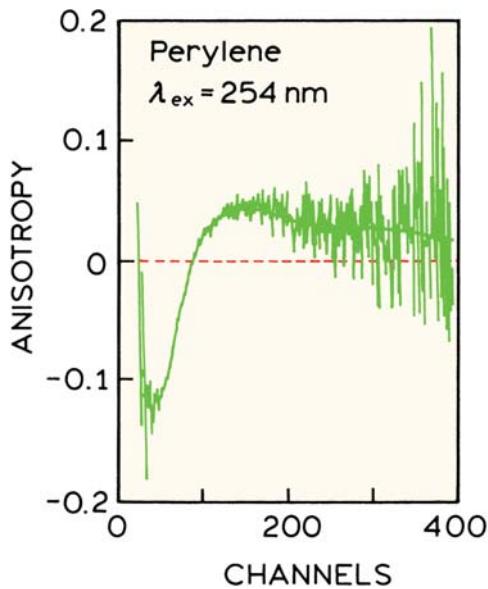


**Figure 12.19.** Anisotropy decay of perylene in glycerol at 30°C. Excitation at 254 nm where  $r_0 = -0.14$ . The data were fit as  $r(t) = 0.1 \exp(-t/17 \text{ ns}) - 0.24 \exp(-t/2.7 \text{ ns})$ . Revised and reprinted with permission from [49]. Copyright © 1981, American Institute of Physics.

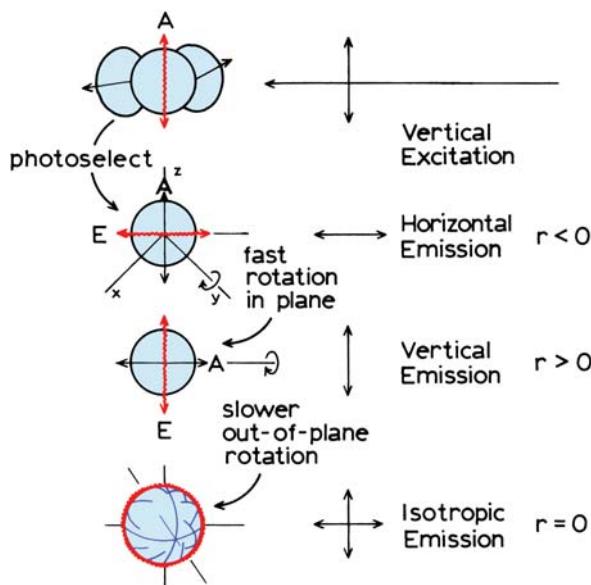


**Figure 12.20.** Effect of faster in-plane rotations on the anisotropy decay of perylene with  $r_0 = -0.2$ . Revised and reprinted with permission from [37], Academic Press Inc.

An intuitive description of the unusual perylene anisotropy decay is shown in Figure 12.20. When excited at a wavelength with  $r_0 = -0.2$  the emission moments are symmetrically distributed in the laboratory  $x$ - $y$  plane, and the

horizontal intensity is greater than the vertical intensity ( $r_0 < 0$ ). Because the in-plane rotation is more rapid than the out of plane rotation, the effect at short times is to rotate the emission dipoles out of the  $x$ - $y$  plane toward the vertical axis. This results in transient anisotropy values above zero (Figure 12.19). At longer times the slower out-of-plane motions contribute to depolarization, and the anisotropy decays to zero (Figure 12.20).

### 12.6.2. Frequency-Domain Studies of Anisotropic Rotational Diffusion

Anisotropic rotational diffusion can be studied using frequency-domain methods. In fact, the earliest reports on the anisotropic rotation of fluorophores were performed using fixed-frequency phase-modulation fluorometers.<sup>54–56</sup> At that time the phase-modulation instruments operated at only one or two fixed frequencies. Hence it was not possible to recover the anisotropy decay law. The experiments were performed by measuring the differential polarized phase angles ( $\Delta_\omega$ ) as the temperature was varied. It is relatively simple to predict the maximum value of  $\Delta_\omega$  for known values of the lifetime and fundamental anisotropy. For an isotropic rotator the predicted value of  $\Delta_\omega$  is given by

$$\tan \Delta_\omega \quad (12.39)$$

$$= \frac{(2D\tau)\omega\tau r_0}{\frac{1}{9}m_0(1 + \omega^2\tau^2) + [(2D\tau)/3](2 + r_0) + (2D\tau)^2}$$

where  $m_0 = (1 + 2r_0)(1 - r_0)$ . The value of  $\tan \Delta_\omega$  is a function of the rotational rate ( $D$ ),  $r_0$ ,  $\tau$ , and  $\omega$ . The maximum value of  $\tan \Delta_\omega$  is given by

$$\tan \Delta_\omega^{\max} = \frac{3\omega\tau r_0}{(2 + r_0) + 2[m_0(1 + \omega^2\tau^2)]^{1/2}} \quad (12.40)$$

and is independent of the rotational rate. We note that these expressions are only valid for an isotropic rotor with a single fluorescence lifetime. The maximum differential tangent depends only on  $\tau$ ,  $r_0$ , and  $\omega$ . If there is more than one rotational rate the maximum value of  $\tan \Delta$  is decreased.<sup>54</sup>

Anisotropic rotation of perylene was detected by measurements of the temperature-dependent values of  $\tan \Delta$ , measured at a single modulator-frequency.<sup>55</sup> The values of  $\tan \Delta$  are only nonzero in the temperature range where rotational diffusion is on a timescale comparable to the lifetime.

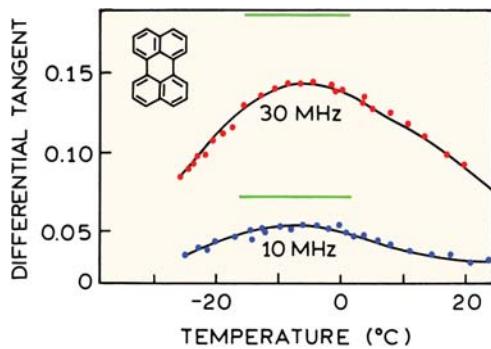


**Figure 12.21.** Differential polarized phase angles of perylene in propylene glycol. The horizontal solid bars show the theoretical maximum values for  $\tan \Delta_0$  with isotropic rotation. Revised and reprinted from [55]. Copyright © 1977, American Institute of Physics.

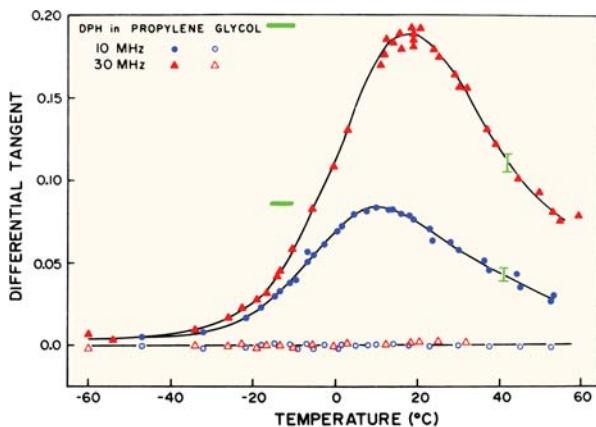


**Figure 12.22.** Temperature dependence of the differential polarized phase angles of DPH in propylene glycol. The solid bars show the maximum values of  $\tan \Delta_0$  for isotropic rotation. The open symbols are the values of  $\tan \Delta_0$  measured with horizontally polarized excitation. Reprinted with permission from [57]. Copyright © 1979, American Chemical Society.

At very high or low temperatures  $\tan \Delta = 0$ . Figure 12.21 shows the temperature-dependent data for perylene in propylene glycol. The maximum values of  $\tan \Delta$  are significantly smaller than the values predicted using eq. 12.40. Molecules like DPH, which are not spheres but do display a single rotational rate, display  $\tan \Delta_0^{\max}$  values that agree with the calculated values (Figure 12.22). The single-frequency data for perylene do not allow determination of the anisotropy decay parameters. The presence of anisotropic rotations in perylene were also detected by early studies with a variable frequency instruments, which indicated the correlation time for perylene was smaller than predicted based on its size.<sup>58</sup>

Frequency-domain measurements can be used to resolve complex anisotropy decays.<sup>59</sup> The resolution of the anisotropy decays is rather good, which is probably the result of direct measurement of the difference between the polarized components of the decay. In the frequency domain these differences are measured directly. In the time domain the anisotropy decay is calculated from the two independently measured quantities,  $I_{\parallel}(t)$  and  $I_{\perp}(t)$ . Additionally, there are two observable quantities in the frequency domain— $\Delta_0$  and  $\Lambda_0$ —which provides better resolution than the use of either quantity alone.

Resolution of anisotropic rotational diffusion using FD measurements is illustrated by data for two fluorophores: fluorescein and perylene. Frequency-domain anisotropy data for fluorescein are shown in Figure 12.23. This figure is visually similar to Figure 12.21, but the x-axis on Figure 12.23 is frequency and not temperature. These frequency-domain data are almost perfectly fit using a single correlation time, indicating that fluorescein behaves like an isotropic rotator.<sup>60</sup> Such behavior is expected for polar fluorophores in polar solvents. It appears that hydrogen bonding interactions decrease slip diffusion, and result in more isotropic rotations.

Rather different results were obtained for perylene (Figure 12.24). The frequency-domain data could not be fit

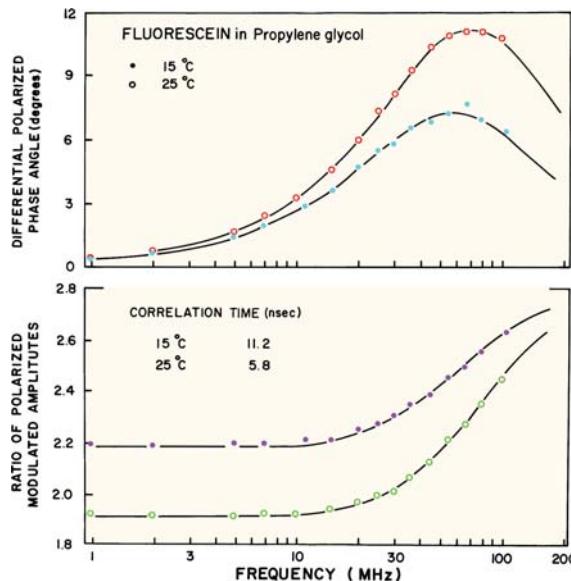


**Figure 12.23.** Frequency-domain anisotropy decay of fluorescein in propylene glycol. The solid lines show the best single correlation time fits. The lifetime of fluorescein was 3.7 ns at 15 and 25°C. Revised and reprinted with permission from [60]. Copyright © 1985, American Chemical Society.

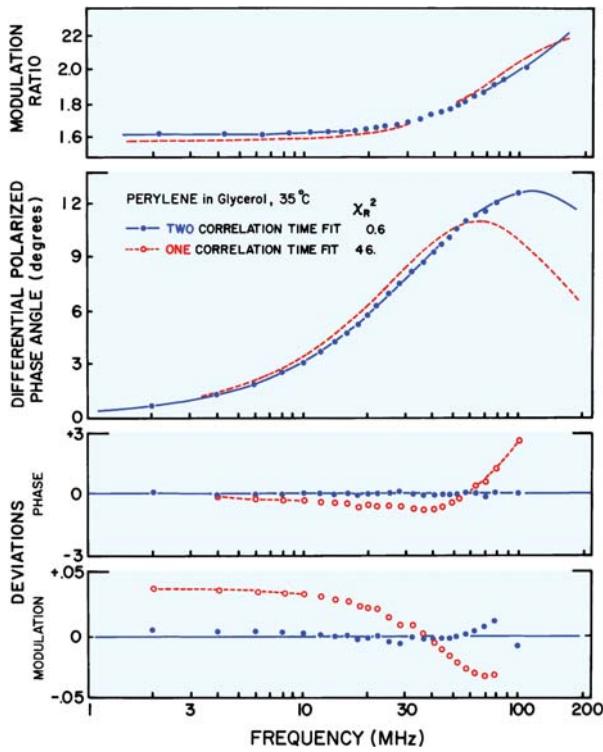


**Figure 12.24.** Frequency-domain anisotropy decay of perylene in glycerol at 35°C. The lifetime was 4.8 ns. Reprinted from [61]. Copyright © 1985, with permission from Elsevier Science.

to a single correlation time (dashed), but these data were well fit using two correlation times.<sup>61</sup> The multi-exponential anisotropy decay analysis yielded amplitudes of  $r_{01} = 0.17$  and  $r_{02} = 0.18$ , with correlation times of 1.5 and 10.8 ns. This ratio of correlation times is comparable to that recovered from the TD data.<sup>49</sup> The 80-fold decrease in  $\chi^2$  for the two-correlation time fit as compared to the one-correlation time fit, and the large and systematic deviation for the one-correlation time fit, indicate that complex anisotropy decays can be recovered from the FD data.

## 12.7. GLOBAL ANISOTROPY DECAY ANALYSIS

### 12.7.1. Global Analysis with Multi-Wavelength Excitation

The use of multiple excitation wavelengths provides a useful method for improving the resolution of closely spaced correlation times. For a rigid non-spherical molecule, different values of  $r_0$  are expected to yield different anisotropy amplitudes, but the same correlation times will remain the same. The contributions of diffusion coefficients are differ-

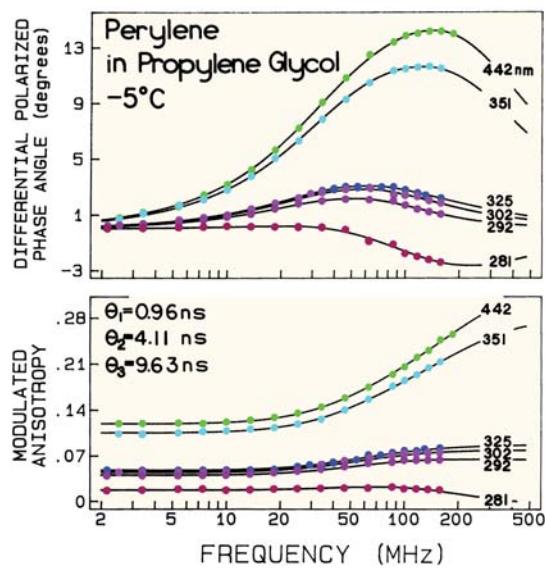


**Figure 12.25.** Frequency-domain anisotropy decays of perylene for various excitation wavelengths. From [65].

ent for different values of  $r_0$  (eqs. 12.11–12.20). The use of different excitation wavelengths allows each rotational rate to contribute differently to the data.<sup>62–64</sup>

The concept of using different  $r_0$  values is illustrated by perylene (Figure 12.25). A wide range of  $r_0$  values are available using perylene with different excitation wavelengths (Figure 12.34, below). For longer excitation wavelengths (351 and 442 nm) the fundamental anisotropy of perylene is near 0.35. For excitation between 292 and 325 nm the fundamental anisotropy is near 0.07, and for excitation at 281 the anisotropy is slightly below zero. Figure 12.25 shows that the frequency of the maximum differential phase angle depends on excitation wavelength. If there were a single rotational correlation time the curves would be proportional to  $r_0$ , but the shape would be unchanged. The shape changes because of the multiple rotational rates, and their different contributions at each excitation wavelength.

The wavelength-dependent shifts in the differential polarized phase curves can be understood in terms of the contribution of various rotations to the anisotropy decay. As reasoned in Figures 12.14 and 12.15, both the in-plane and out-of-plane rotations are expected to contribute where  $r_0 = 0.4$ . Hence the data for 351 and 442 nm excitation represent a weighted average of  $D_{\parallel}$  and  $D_{\perp}$ . For  $r_0$  values near –0.2 one expects the in-plane rotation to be dominant (Figure 12.20). This effect can be seen in the data for 281-nm excitation, for which the maximum value of  $\Delta_{\omega}$  (absolute value) is shifted toward higher modulation frequencies. And, final-

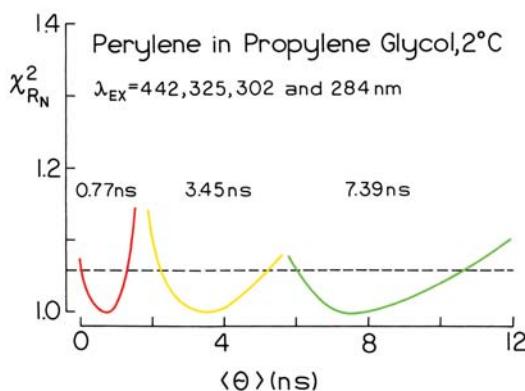


**Figure 12.26.**  $\chi_R^2$  surfaces for the three correlation times found for perylene. From [65].

ly, for  $r_0$  values near 0.1 one expects the out-of-plane rotation to dominate the anisotropy decay. These slower motions display a maximum value of  $\Delta_\omega$  of lower modulation frequencies.

Global analysis of the frequency-domain data is performed assuming the correlation times are independent of excitation wavelength, and that the amplitudes are dependent on wavelength. Under these assumptions the value of  $\chi_R^2$  is calculated using an expanded form of eq. 11.34, where the sum extends over the excitation wavelengths. The changes in shape of  $\Delta_\omega$  allow highly detailed resolution of an anisotropy decay using global analysis. In fact, the data

allowed recovery of three rotational correlation times. The fact that the three correlation times were needed to explain the data was demonstrated for the  $\chi_R^2$  surfaces (Figure 12.26). The presence of three correlation times for perylene is somewhat surprising because the transitions of perylene are along its long and short axes (Figure 12.35, below), and it is shaped like an oblate ellipsoid. Hence, only two correlation times are expected. The recovered correlation times and amplitudes do not seem to fit any reasonable hydrodynamic shape.<sup>65</sup> It appears that perylene displays partial slip diffusion and thus an anisotropy decay different from that predicted from the hydrodynamic model.

### 12.7.2. Global Anisotropy Decay Analysis with Collisional Quenching

As shown in Chapter 10 (eq. 10.43), the steady-state anisotropy is the average value of the anisotropy decay averaged over the intensity decay of the sample. If the sample displays several correlation times, eq. 10.49 indicates that their contributions to the anisotropy would be different if the lifetime was changed. This is possible using energy transfer or collisional quenching.<sup>66–68</sup> Consider a sample with a lifetime of 4 ns and a correlation time of 4.0 or 0.4 ns (Figure 12.27). The information about the anisotropy decay is contained in the difference between the parallel ( $I_{\parallel}$ ) and perpendicular ( $I_{\perp}$ ) components of the emission (Figure 12.27, left). For the 4-ns correlation time (dashed lines), the

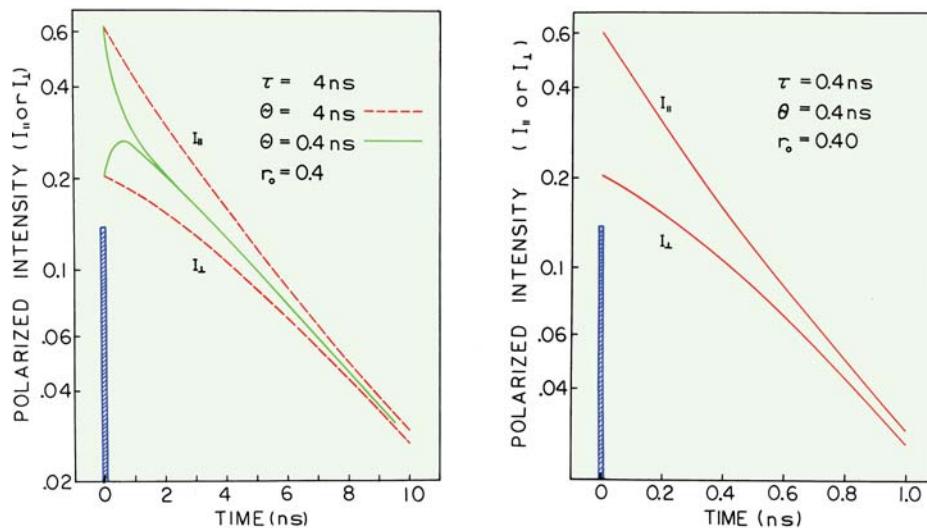


**Figure 12.27.** Simulated anisotropy decays for unquenched and quenched decays. Left: Unquenched decay with  $\tau = 4$  ns and  $\theta = 4$  (dashed lines), or  $0.4$  ns (solid lines). Right: Quenched decay with  $\tau = 0.4$  ns and  $\theta = 0.4$  ns.  $r_0$  is 0.4 for both decays. Reprinted with permission from [69]. Copyright © 1987, Biophysical Society.

difference persists throughout the duration of the emission, and all the emitted photons aid in recovering the anisotropy decay. Now suppose the correlation time is 400 ps (solid lines). The polarized components are essentially equal after 1 ns, and the photons detected after this time do not aid in recovering the anisotropy decay. However, the emitted photons all contributed to the emission and to the acquisition time. Because the acquisition times must be finite, it is difficult to collect data adequate to determine the picosecond correlation time because most of the observed photons will not contain information about the correlation time. Now consider the effect of decreasing the decay time to a sub-nanosecond value of 0.4 ns by quenching (Figure 12.27, right). Because of the shorter lifetime a larger fraction of the emission contains information on the 0.4-ns correlation time. Hence information on the faster process is increased by measurement of the quenched samples.

For determination of a single short correlation time, analysis of data from the most quenched sample is adequate. However, the usual goal is to improve resolution of the entire anisotropy decay. This can be accomplished by simultaneous analysis of data from the unquenched and several quenched samples. The data from the unquenched sample contributes most to determination of the longer correlation times, and the data from the quenched sample contributes to resolution of the faster motions.

### 12.7.3. Application of Quenching to Protein Anisotropy Decays

The use of global analysis with quenching is useful for studies of complex anisotropy decays from proteins. This is because the correlation times for segmental motions and overall rotations of a protein are usually quite different in magnitude. The correlation times of a rigid rotor are usually similar in magnitude, so that quenching is less useful.

The value of quenching can be seen from the simulated frequency-domain data (Figure 12.28). The unquenched lifetime was again assumed to be 4 ns. The correlation times were assumed to be 10 ns for overall rotation and 0.1 ns for the segmental motions. To be comparable with the data found for the proteins the fundamental anisotropy ( $r_0$ ) was 0.30, and the anisotropy amplitude of the segmental motion was taken as 0.07. Assume that the lifetime is reduced to 2.0 or 0.5 ns by quenching. In practice the decays may become more heterogeneous in the presence of quenching due to transient effects in diffusion, but this is not important for the simulations.

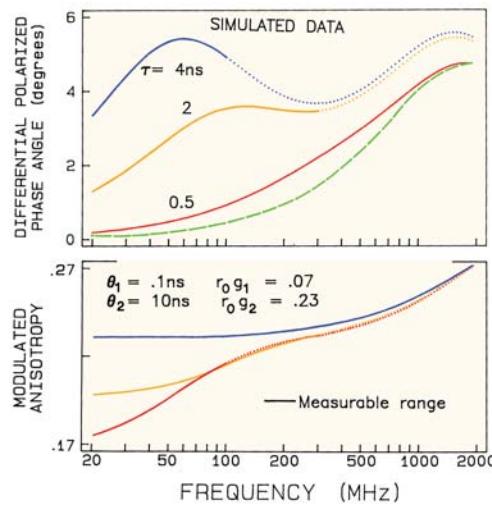


**Figure 12.28.** Simulated frequency-domain anisotropy data. The simulated correlation times were assumed to be 0.10 and 10.0 ns, with amplitudes of 0.07 and 0.23, respectively. Simulated data are shown for intensity decay times of 4, 2, and 0.5 ns. The solid regions of the curves indicate the measurable frequency range, where the modulation is 0.2 or larger for the intensity decay. The dashed line shows the phase values expected for the 0.1 ns correlation time, with the smaller amplitude (0.07). From [70].

The existence of two rotational motions is seen in the frequency response of the polarized emission. These motions are evident from the two peaks in the plots of differential phase angles. These peaks are due to the individual motions with correlation times of 10 and 0.1 ns. The 10-ns motion is responsible for the peak near 60 MHz. The 100-ps motion is responsible for the peak at higher frequencies (dashed line), with a maximum near 2 GHz. These are two features of the data from the quenched samples that provide increased resolution of the anisotropy decay. First, the frequency-domain data can be measured at higher frequencies for the samples with shorter decay times. This is because the emission is less demodulated with the shorter lifetimes. The solid regions of the curves show the measurable frequency range where the modulation of the emission is 20% or larger, relative to the modulation of the incident light. Based on this criterion the upper frequency limit in the absence of quenching ( $\tau_0 = 4$  ns) is only 100 MHz. If the lifetime is reduced to 0.5 ns, the upper frequency limit is 2 GHz, which provides more data at frequencies characteristic of the faster motion.

Quenching also increases the information content of the modulated anisotropies (lower panel, Figure 12.28). At low frequencies the value of the modulated anisotropy is equal to the steady-state anisotropy, which is increased by

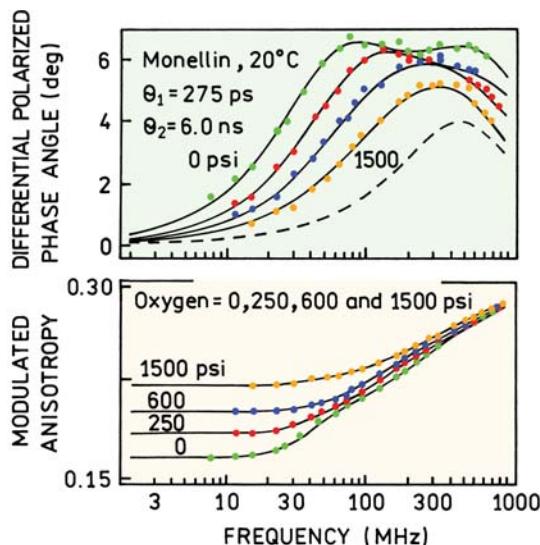


**Figure 12.29.** Frequency-domain anisotropy data for monellin with oxygen quenching. Data are shown for oxygen pressures of 0, 250, 600, and 1500 psi. The dashed line shows the values expected for a correlation time of 275 ps, with an amplitude of 0.075. From [70].

quenching. Once again the measurable range is extended to 2 GHz by collisional quenching. The values of  $r_\omega$  for the unquenched sample increase over the frequency range from 20 to 100 MHz, which is the portion of  $r_\omega$  that depends upon overall rotation of the protein. For the quenched sample the higher-frequency data begin to show a contribution from the faster motion.

An advantage of measuring a series of progressively quenched samples is that the data are differently sensitive to the two motions. The same motions determine the values of  $\Delta_\omega$  and  $\Lambda_\omega$  in the quenched and the unquenched samples. However, the proportions each motion contributes are different. As the decay time is decreased by quenching, the data is shifted towards higher frequencies and the contribution of overall diffusion is decreased (Figure 12.28). These effects provide increased resolution by simultaneous analy-

sis of the data from a series of progressively quenched samples.

The value of global anisotropy analysis using quenched samples is illustrated for monellin. This is a naturally sweet protein that contains a single-tryptophan residue. This residue is rather mobile, as seen from the two peaks in the differential phase angles near 70 and 500 MHz (Figure 12.29). As the sample is quenched by oxygen, the component due to overall rotation near 70 MHz decreases in amplitude. At the highest amounts of quenching the FD anisotropy data become dominated by the contribution of the shorter correlation time near 275 ps. Hence, one can visualize how global analysis of quenched and unquenched samples provides improved resolution of the two correlation times.

## 12.8. INTERCALATED FLUOROPHORES IN DNA

Many fluorophores intercalate into double-helical DNA. Some fluorophores, like ethidium bromide (EB), become more highly fluorescent when bound to DNA, allowing the emission for the DNA-bound probes to be easily detected. Consequently, there have been numerous studies of the anisotropy decays of DNA-bound probes. At first glance a DNA-bound probe seems relatively simple. Suppose the probe is located between the DNA base pairs, which is referred to as being intercalated. The anisotropy decay of such a probe is determined by its freedom within the DNA helix, and by the diffusive motions of DNA. These motions are characterized by the torsional motions around the  $z$ -axis of DNA (Figure 12.30), and by bending motions about the  $x$ -axis.

There have been theoretical reports on the anisotropy decay expected for DNA bound probes.<sup>71–73</sup> Unfortunately, the theory is complex in its complete form. The contribution of the torsional and bending motions of DNA depend on the orientation of the probe within the DNA helix, and

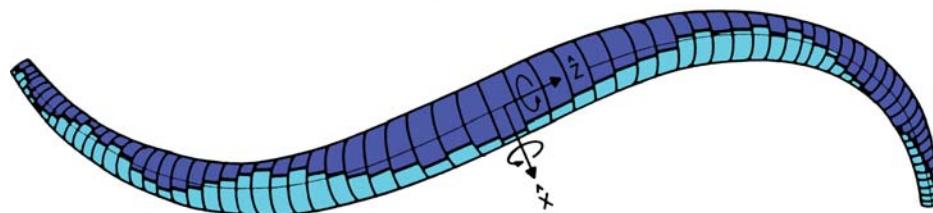


**Figure 12.30.** Torsional and bending motions of DNA. From [73].

the value of  $r_0$ . Also, the depolarization due to the torsional motions and bending motions occur on very different timescales. In fact, the bending motions do not make a significant contribution to the anisotropy decay of EB with its 23-ns lifetime, and  $r(t)$  is dominated by torsional motions around the  $z$ -axis.

Because of the complexity of the theory, one often encounters various simplified forms. When the absorption and emission transition moments are colinear, and perpendicular to the helix axis, the anisotropy decay is given by<sup>37</sup>

$$\begin{aligned} r(t) = & \{0.75 \exp[-\Gamma(t)] + 0.45 \exp[-\Delta(t) + \Gamma(t)] \\ & + 0.4 \exp[-\Delta(t)]\}/\{3 + \exp[-\Delta(t)]\} \end{aligned} \quad (12.41)$$

where the twisting decay function is given by

$$\Gamma(t) = 4kT(t/\pi C\rho)^{1/2} \quad (12.42)$$

and the bending decay function is

$$\Delta(t) = B(t)t^{1/4} \quad (12.43)$$

In these equations  $k$  is Boltzmann's constant,  $T$  is the temperature,  $C$  is the torsional stiffness of DNA, and  $\rho$  is a frictional coefficient per unit length for rotation about the helix axis.  $B(t)$  is a slowly varying function of time that is determined by the bending stiffness of DNA. Eqs. 12.41–12.43 shows that the anisotropy decay depends on  $t^{1/2}$  due to torsional or twisting motions, and  $t^{1/4}$  due to bending motions.

For ns decay times the bending motions have little effect on the anisotropy decay. Hence, one often encounters these equations in a more simplified form:<sup>74</sup>

$$r(t) = r_0[0.75 \exp(-t/\theta_1)^{1/2} + 0.25] \quad (12.44)$$

where

$$\theta_1 = \pi^2 b^2 \eta C / 4k^2 T \quad (12.45)$$

where  $b$  is the radius of DNA and  $\eta$  is viscosity.

Most of the anisotropy decays of EB bound to DNA are visually similar (Figure 12.31).<sup>74–78</sup> The anisotropy decays rapidly at early times, and tends towards a constant value at longer times. The early portion of the anisotropy decay is due to the torsional motions of DNA. The constant

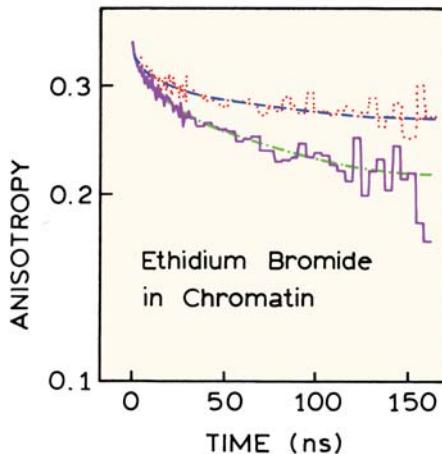


**Figure 12.31.** Fluorescence anisotropy decay curves of intercalated ethidium in chromatin DNA. Buffer conditions were 1 mM Tris and 0.2 mM EDTA, pH 7.5 (solid), and 50 mM NaCl, 1 mM Tris, and 0.2 mM EDTA, pH 7.5 (dotted). The temperature was 20°C. Revised and reprinted with permission from [78]. Copyright © 1983, American Chemical Society.

anisotropy at longer times is due to the bending motions, which are not significant on this timescale.

## 12.9. TRANSITION MOMENTS

Throughout this chapter we described the dependence of anisotropy on the direction of the transition moments. The existence of a discrete direction often seems somewhat mysterious because the experiments in isotropic solution do not reveal this direction in the molecule. The direction of transition moment can be determined if the fluorophores can be oriented. Molecules can be oriented in crystals, liquid crystals, oriented membranes, or stretched polymer films. Stretched films provide the easiest approach to obtaining oriented fluorophores, particularly if the molecules are elongated along one axis, and if uniaxial orientation is adequate.<sup>79–82</sup> The basic experiment is to dissolve the fluorophore and a polymer in a solvent. The polymer is typically polyvinyl alcohol. After removal of the solvent the polymer is then stretched about fivefold. For linear molecules like DPH and DAPI one can obtain nearly complete orientation along the stretching axis. Less asymmetric fluorophores are still aligned, but the orientation function can be more complex.<sup>83</sup>

An example of an oriented system is shown in Figure 12.32 for DPH in a stretched PVA film.<sup>84</sup> Prior to stretching

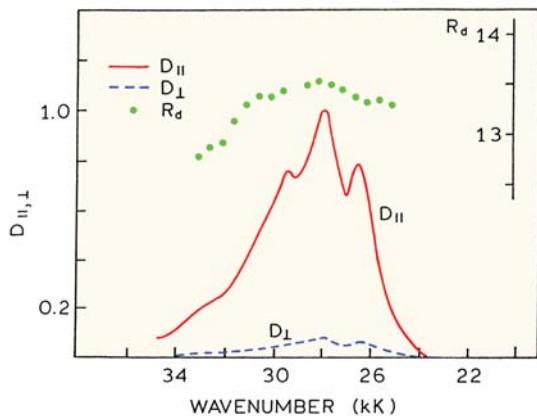


**Figure 12.32.** Absorption spectra of DPH parallel (||) and perpendicular (⊥) to the direction of stretching in a polyvinyl alcohol (PVA) film.  $R_d = D_{\parallel}/D_{\perp}$  is the dichroic ratio. Revised from [84].

the absorption spectra are independent of the orientation of the polarizer. After fivefold stretching, the sample absorbs strongly when the polarizer is oriented along the stretching axis, and the absorption is weak when the polarizer is perpendicular to this axis. Since the long axis of DPH orients parallel to the direction of stretching, these spectra provide an experimental demonstration that the transition moment of DPH is oriented along its long axis.

Recall from the theory of anisotropy (Section 10.2) that the highest anisotropy of 0.4 was a consequence of excitation photoselection, and that a single fluorophore oriented along the  $z$ -axis was predicted to have an anisotropy of 1.0. This prediction can be confirmed from experiments with

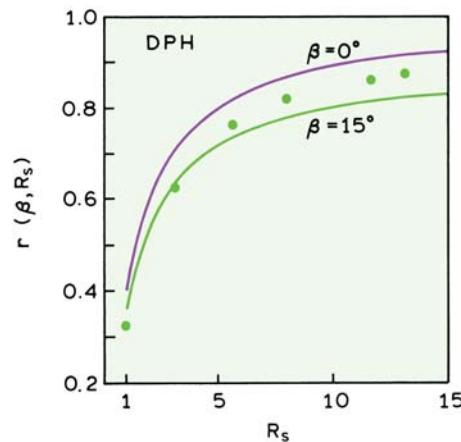


**Figure 12.34.** Absorption and excitation anisotropy spectra of perylene in propylene glycol.

stretched films (Figure 12.33). As the sample is stretched, the anisotropy of DPH increases well above 0.4, to about 0.82. The value is not 1.0 because the sample is not perfectly aligned, and the values of  $\beta$  for DPH obtained from  $\langle \cos^2 \beta \rangle$  seems to be about  $8^\circ$ . Such data have also been used to confirm the cosine-squared dependence of absorption.<sup>85</sup>

Perylene displays regions of high and low anisotropy (Figure 12.34). At wavelengths above 360 nm ( $S_0 \rightarrow S_1$ ) the anisotropy is positive and nearly constant. At wavelengths below 280 nm ( $S_0 \rightarrow S_2$ ) the anisotropy is negative. According to eq. 10.22 an anisotropy of -0.20 corresponds to an angle of  $90^\circ$  between the absorption and emission moments. This was demonstrated experimentally using the polarized absorption spectra of perylene (Figure 12.35).<sup>83</sup> The spectra are measured for light polarized parallel or perpendicular to the long axis of perylene. These spectra are calculated from the stretched film spectra. The long-wavelength absorption ( $S_0 > S_1$ ) is thus seen to be oriented along the long axis, and the short-wavelength absorption is oriented along the short axis.

As a final example, Figure 12.36 shows the polarized absorption spectra of 9-aminoacridine, again recovered from the experimental spectra in PVA films.<sup>86</sup> In 9-aminoacridine the long-wavelength transition displays positive anisotropy, which one tends to associate with transitions along the long axis. However, the long-wavelength ( $S_0 \rightarrow S_1$ ) transition is polarized along the short axis of the molecule. This result is counterintuitive because we generally assign the lowest energy transition to the longest axis. This result can be understood as the electronic charge moving between the two nitrogen atoms, each with a different elec-

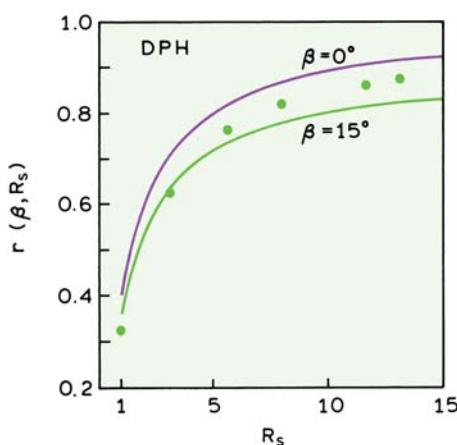


**Figure 12.33.** Steady-state anisotropy of DPH in polyvinyl alcohol (PVA). The lower axis shows the stretching ratio ( $R_s$ ). The solid lines are theoretical curves for  $\beta = 0$  and  $15^\circ$ . Revised from [84].

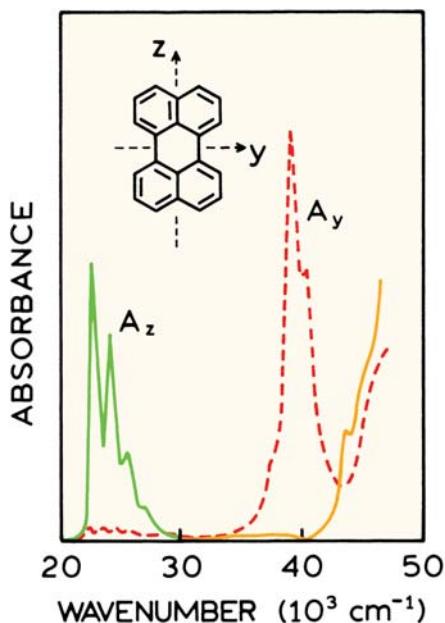


**Figure 12.35.** Absorption spectra of perylene along the long ( $z$ ) and short ( $y$ ) axes. Revised from [83].

tron density. Absorption spectra in stretched films have been used to determine the direction of transition moments in a number of fluorophores of biochemical interest, including adenine,<sup>87</sup> 2-aminopurine,<sup>88</sup> Yt-base<sup>89</sup>, DAPI,<sup>90</sup> Hoechst 33342,<sup>85</sup> and polynuclease aromatic hydrocarbons.<sup>91</sup>

### 12.9.1. Anisotropy of Planar Fluorophores with High Symmetry

The fundamental anisotropy can be determined in part by the symmetry of the molecule. This is illustrated by triphenylene, which has threefold symmetry and a fundamental

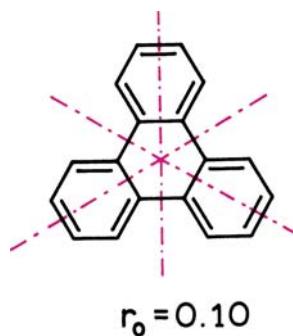


**Figure 12.37.** Structure and symmetry axes of triphenylene.

anisotropy of  $r_0 = 0.1$  (Figure 10.37).<sup>92</sup> This anisotropy value is found whenever the transition moments are randomized in a plane. The anisotropy value of 0.1 can be calculated from the additivity law of anisotropy (eq. 10.6). Following excitation along one of the axes the emission is randomized among the three identical axes. Since the axes are identical, a third of the emission originates from each transition, resulting in  $r_0 = 0.10$  (Problem 12.3).

## 12.10. LIFETIME-RESOLVED ANISOTROPIES

In Sections 10.5 and 10.6 we saw how the Perrin equation could be used to estimate the apparent volume of macromolecule. Examination of eq. 10.45 suggests an alternative method of estimating the rotational correlation time. Suppose the lifetime ( $\tau$ ) of the probe could be decreased by collisional quenching. Then a plot of  $1/r$  versus  $\tau$  would have a slope of  $(r_0/\theta)^{-1}$ , and thus allow measurement of the correlation time. These measurements are called lifetime-resolved anisotropies.<sup>93–98</sup> The first suggestion of lifetime-resolved anisotropies appeared early in the literature as a means to study polymers<sup>98–99</sup> as well as proteins.<sup>100</sup>

There are advantages to the use of lifetime-resolved measurements. The lifetime can typically be decreased with only a modest change in solution conditions. This is particularly true for oxygen quenching since oxygen diffuses rapidly and is an efficient quencher. The use of oxygen quenching is demonstrated in Figure 12.38, which shows anisotropy values of a peptide hormone when the single-tryptophan residue was quenched to various lifetimes.<sup>101</sup> The proteins were human luteinizing hormone (hLH) and its  $\beta$  subunit ( $\beta$ hLH). The intact hormone has a molecular weight of 28 kD, and the  $\beta$  subunit is 14 kD. The apparent correlation times were 6.0 and 4.9 ns, respectively. The calculated correlation times are 10.1 and 5.2 ns, respectively. The meas-

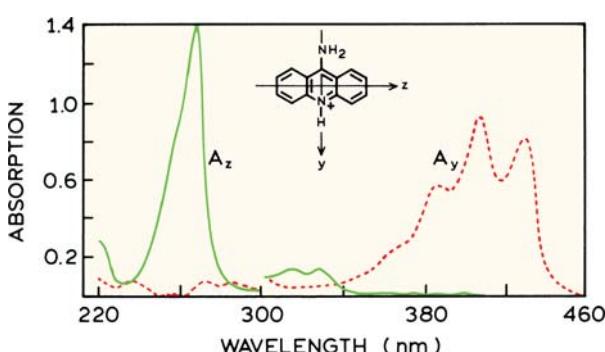


**Figure 12.36.** Polarized absorption spectra of 9-aminoacridinium in a stretched PVA film. Revised from [86].

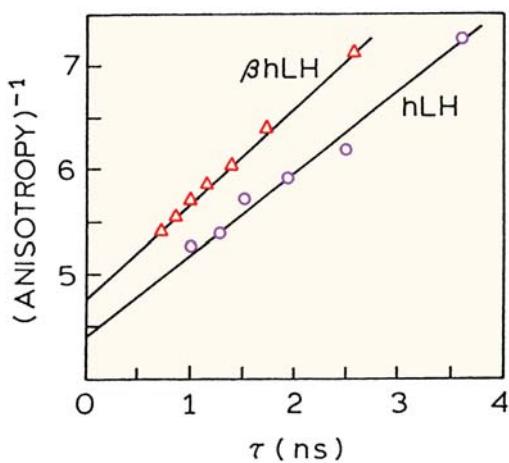


**Figure 12.38.** Lifetime-resolved anisotropies of human luteinizing hormone (hLH) and its  $\beta$  subunit. The lifetimes were varied by oxygen quenching, and calculated from the dynamic portion of the observed quenching. Revised and reprinted with permission from [101]. Copyright © 1987, American Chemical Society.

ured and calculated values are reasonably close, but the  $y$ -intercepts yield apparent  $r_0$  values smaller than the expected value of 0.27. This result is typical of other reports that suggest segmental freedom of tryptophan residue in many proteins.<sup>93–96</sup>

#### 12.10.1. Effect of Segmental Motion on the Perrin Plots

The effect of segmental motion on the Perrin plots can be seen by deriving the Perrin equation for the anisotropy decay expected in the presence of segmental motions. While the results are the same whether one measures anisotropy versus  $T/\eta$ , or versus lifetime, these effects are somewhat easier to understand in terms of the lifetime-resolved measurements. In addition, the experiments are easier to interpret because the temperature and solution conditions are not changed, so that changes in protein dynamics and conformation do not complicate the analysis.

Suppose a fraction  $\alpha$  of the total anisotropy is lost by the segmental motion, with a fast correlation time  $\theta_F$ , and the remainder of the anisotropy decays by overall rotational diffusion of the protein ( $\theta_P$ ). For independent segmental motions and rotational diffusion the anisotropy is given as the product of the depolarization factors, so that

$$r(t) = r_0[\alpha \exp(-t/\theta_F) + (1 - \alpha)] \exp(-t/\theta_P) \quad (12.46)$$

where  $f_F + f_P = 1.0$ . Use of eq. 10.43 with eq. 12.46 yields

$$r(\tau) = \frac{\alpha r_0}{1 + \left(\frac{1}{\theta_F} + \frac{1}{\theta_P}\right)\tau} + \frac{(1 - \alpha)r_0}{1 + \frac{\tau}{\theta_P}} \quad (12.47)$$

In this expression we used the notation  $r(\tau)$  as a reminder that the steady-state anisotropy depends on the lifetime  $\tau$ . In many cases the internal motions are more rapid than overall rotation ( $\theta_F \ll \theta_P$ ), simplifying eq. 12.47 to

$$r(\tau) = \frac{\alpha r_0}{1 + \tau/\theta_F} + \frac{r_0(1 - \alpha)}{1 + \tau/\theta_P} \quad (12.48)$$

This expression indicates that a fraction of the anisotropy ( $\alpha r_0$ ) is lost due to the rapid motion, and the remainder  $r_0(1 - \alpha)$  is lost due to overall rotational diffusion.

The effects of varying degrees of segmental motion are shown in Figure 12.39. The assumed correlation times were  $\theta_P = 20$  ns for overall rotational diffusion and  $\theta_F = 1.0$  or 0.1 ns for the rapid motion. As the amplitude of the fast motion increases the  $y$ -intercept increases. This shows how segmental motions in proteins result in low apparent  $r_0$  values. Perhaps more important is the observation that the apparent correlation times ( $\theta_A$ ), calculated from the limiting slope of the lifetime Perrin plots, decrease as  $\alpha$  increases. This illustrates how segmental freedom in a protein can result in apparent correlation times that are lower than the true values. These simulated data are for lifetime-resolved measurements, but similar effects can be seen in simulated  $T/\eta$  Perrin plots.

#### 12.11. SOLEILLET'S RULE: MULTIPLICATION OF DEPOLARIZATION FACTORS

In Chapter 10 we derived the value of  $r_0$  expected due to photoselection ( $r_0 = 0.4$ ), showed how  $r_0$  was decreased by a factor dependent on the angle  $\beta$  between the absorption and emission transition moments (eq. 10.22), and that the anisotropy was decreased further due to rotational diffusion (eq. 10.44). There is a simple relationship between these different causes of depolarization, which is known as Soleillet's rule.<sup>102–104</sup> The anisotropy is given by the product of the various depolarization factors that occur in a given sample:

$$r = r_0 \prod_i d_i \quad (12.49)$$

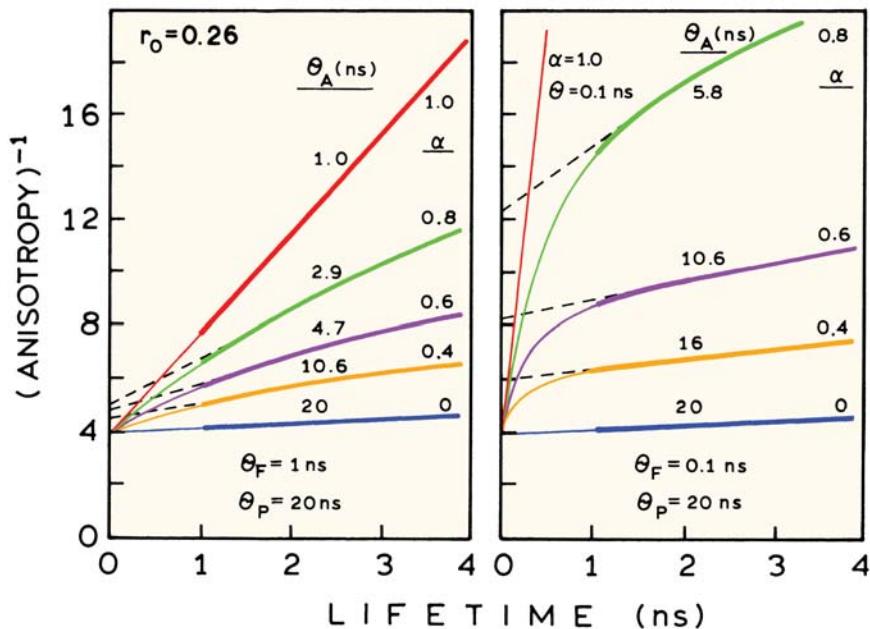


**Figure 12.39.** Simulated lifetime Perrin plots for a protein with an overall correlation time  $\theta_p = 20$  ns, and a fast segmental motion with  $\theta_F = 1.0$  or 0.1 ns. Revised and reprinted with permission from [94]. Copyright © 1983, American Chemical Society.

where  $d_i$  represents the extent to which anisotropy is decreased by each depolarization factor. This relationship can be clarified by a specific example. Suppose a fluorophore has an anisotropy less than 0.4 due to a displacement of the transition moment by an angle  $\beta$  and due to rotational diffusion. The steady-state anisotropy can be written as

$$r = d_1 d_2 d_3 = \frac{2}{5} \left( \frac{3\langle \cos^2 \beta \rangle - 1}{2} \right) \left( \frac{3\langle \cos^2 \omega \rangle - 1}{2} \right) \quad (12.50)$$

In this expression the first depolarization factor ( $d_1$ ) is 0.4, which accounts for excitation photoselection  $\langle \cos^2 \theta \rangle$  (eq. 10.20). The second term ( $d_2$ ) accounts for the angle between the transition moments  $\langle \cos^2 \beta \rangle$  (eq. 10.22). The third term ( $d_3$ ) is the average angular ( $\omega$ ) displacement of the fluorophore during the excited state lifetime  $\langle \cos^2 \omega \rangle$ . This factor is also given by  $d_3 = (1 + \tau/\theta)^{-1}$  (eq. 10.44). It is sometimes useful to be aware of Soleillet's rule when attempting to account for the overall loss of anisotropy.

## 12.12. ANISOTROPIES CAN DEPEND ON EMISSION WAVELENGTH

The anisotropy is generally independent of the emission wavelength. However, the presence of time-dependent spectral relaxation (Chapter 7) can result in a substantial decrease in anisotropy across the emission spectrum.<sup>105–108</sup> A biochemical example is shown in Figure 12.40 for egg PC vesicles labeled with 12-AS. Because of time-dependent reorientation of the local environment around the excited state of 12-AS, the emission spectra display a time-dependent shift to longer wavelengths.<sup>109</sup> Such relaxation is often analyzed in terms of the time-resolved emission spectra, but one can also determine the mean lifetime at various emission wavelengths (Figure 12.40, bottom). The mean lifetime increases with wavelength because the lifetime at short wavelengths is decreased by relaxation, and long-wavelength observation selects for the relaxed species.

Recall that the steady-state anisotropy is determined by  $r(t)$  averaged over  $I(t)$  (eq. 10.43), resulting in Perrin eq. 10.44. Because of the longer average lifetime at long wavelengths, the anisotropy decreases with increasing wave-

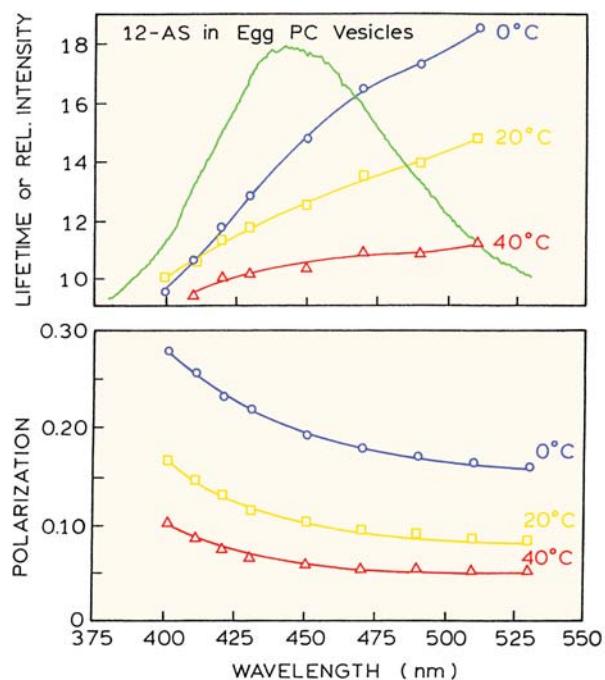


**Figure 12.40.** Average lifetime of 12-AS in egg PC vesicles (top) and the emission anisotropy (bottom). The average lifetimes were determined from the phase shift at 30 MHz. Revised from [109].

length (Figure 12.40). If the fluorophores were in a very fluid or glassy solvent, the lifetime and anisotropy would be constant across the emission spectrum.

## REFERENCES

- Bialik CN, Wolf B, Rachofsky EL, Ross JBA, Laws WR. 1998. Dynamics of biomolecules: assignment of local motions by fluorescence anisotropy decay. *Biophys J* **75**:2564–2573.
- Vyleta NP, Coley AL, Laws WR. 2004. Resolution of molecular dynamics by time-resolved fluorescence anisotropy: verification of two kinetic models. *J Phys Chem A* **108**:5156–5160.
- Rachofsky EL, Laws WR. 2000. Kinetic models and data analysis methods for fluorescence anisotropy decay. *Methods Enzymol* **321**:216–238.
- Brand L, Knutson JR, Davenport L, Beechem JM, Dale RE, Walbridge DG, Kowalczyk AA. 1985. Time-resolved fluorescence spectroscopy: Some applications of associative behaviour to studies of proteins and membranes. In *Spectroscopy and the dynamics of molecular biological systems*, pp. 259–305. Ed P Bayley, RE Dale. Academic Press London.
- Fisz JJ. 1996. Polarized fluorescence decay surface for a mixture of non-interacting species in solution. *Chem Phys Lett* **259**:579–587.
- Fisz JJ. 1996. Polarized fluorescence spectroscopy of two-ground and two-excited state systems in solutions. *Chem Phys Lett* **262**:495–506.
- Fisz JJ. 1996. Polarized fluorescence decay surface for many-ground- and many-excited-state species in solution. *Chem Phys Lett* **262**:507–518.
- Bialik CN, Wolf B, Rachofsky EL, Ross JBA, Laws WR. 1998. Fluorescence anisotropy decay: finding the correct physical model. *SPIE Proc* **3526**:60–67.
- Wolber PK, Hudson BS. 1981. Fluorescence lifetime and time-resolved polarization anisotropy studies of acyl chain order and dynamics in lipid bilayers. *Biochemistry* **20**:2800–2816.
- Wolber PK, Hudson BS. 1982. Bilayer acyl chain dynamics and lipid–protein interaction. *Biophys J* **37**:253–262.
- Ruggiero A, Hudson B. 1989. Analysis of the anisotropy decay of trans-parinaric acid in lipid bilayers. *Biophys J* **55**:1125–1135.
- van Paridon PA, Shute JK, Wirtz KWA, Visser AJWG. 1988. A fluorescence decay study of parinaroyl-phosphatidylinositol incorporated into artificial and natural membranes. *Eur Biophys J* **16**:53–63.
- Visser AJWG, van Hoek A, van Paridon PA. 1987. Time-resolved fluorescence depolarization studies of parinaroyl phosphatidylcholine in triton X-100 micelles and rat skeletal muscle membranes. In *Membrane receptors, dynamics, and energetics*, pp. 353–361. Ed KWA Wirtz. Plenum Publishing, New York.
- Millar DP, Allen DJ, Benkovic SJ. 1990. Structure and dynamics of a DNA: polymerase complex by time-resolved fluorescence spectroscopy. *SPIE Proc* **1204**:392–403.
- Guest CR, Hochstrasser RA, Dupuy CG, Allen DJ, Benkovic SJ, Millar DM. 1991. Interaction of DNA with the Klenow fragment of DNA polymerase I studied by time-resolved fluorescence spectroscopy. *Biochemistry* **30**:8759–8770.
- Peng K, Visser AJWG, van Hoek A, Wolfs CJAM, Sanders JC, Hemminga MA. 1990. Analysis of time-resolved fluorescence anisotropy in lipid–protein systems, I: application to the lipid probe octadecyl rhodamine B in interaction with bacteriophage M13 coat protein incorporated in phospholipid bilayers. *Eur Biophys J* **18**:277–283.
- Peng K, Visser AJWG, van Hoek A, Wolfs CJAM, Hemminga MA. 1990. Analysis of time-resolved fluorescence anisotropy in lipid–protein systems, II: application to tryptophan fluorescence of bacteriophage M13 coat protein incorporated in phospholipid bilayers. *Eur Biophys J* **18**:285–293.
- Smith TA, Irwanto M, Haines DJ, Ghiggino KP, Millar DP. 1998. Time-resolved fluorescence anisotropy measurements of the adsorption of Rhodamine-B and a labelled polyelectrolyte onto colloidal silica. *Colloid Polym Sci* **276**:1032–1037.
- Bailey MF, Thompson EHZ, Millar DP. 2001. Probing DNA polymerase fidelity mechanisms using time-resolved fluorescence anisotropy. *Methods* **25**:62–77.
- Szmacinski H, Jayaweera R, Cherek H, Lakowicz JR. 1987. Demonstration of an associated anisotropy decay by frequency-domain fluorometry. *Biophys Chem* **27**:233–241.
- Wang R, Bright FV. 1993. Rotational reorientation kinetics of dansylated bovine serum albumin. *J Phys Chem* **97**:4231–4238.
- Perrin F. 1929. Mouvement brownien d'un ellipsoïde (I): dispersion électrique pour des molécules ellipsoidales. *J Phys Radium* **7**(5): 497–511.
- Perrin F. 1936. Mouvement brownien d'un ellipsoïde (II): rotation libre et dépolarisation des fluorescences. Translation et diffusin de molécules ellipsoidales. *J Phys Radium* **7**(7):1–11.

24. Perrin F. 1936. Diminution de la polarisation de (I): fluorescence des solutions résultant du mouvement brownien de rotation. *Acta Phys Pol* **5**:335–345.
25. Perrin F. 1929. La fluorescence des solutions: induction moléculaire-polarisatron et duree d'émission-photochimie. *Ann Phys* **12**:169–275.
26. Lombardi JR, Dafforn GA. 1966. Anisotropic rotational relaxation in rigid media by polarized photoselection. *J Chem Phys* **44**:3882–3887.
27. Tao T. 1969. Time-dependent fluorescence depolarization and Brownian rotational diffusion of macromolecules. *Biopolymers* **8**: 609–632.
28. Ehrenberg M, Rigler R. 1972. Polarized fluorescence and rotational Brownian rotation. *Chem Phys Lett* **14**:539–544.
29. Chuang TJ, Eisenthal KB. 1972. Theory of fluorescence depolarization by anisotropic rotational diffusion. *J Chem Phys* **57**:5094–5097.
30. Belford GG, Belford RL, Weber G. 1972. Dynamics of fluorescence polarization in macromolecules. *Proc Natl Acad Sci USA* **69**:1392–1393.
31. Small EW, Isenberg I. 1977. Hydrodynamic properties of a rigid molecule: rotational and linear diffusion and fluorescence anisotropy. *Biopolymers* **16**:1907–1928.
32. Weber G. 1989. Perrin revisited: parametric theory of the motional depolarization of fluorescence. *J Phys Chem* **93**:6069–6073.
33. Piston DW, Bilash T, Gratton E. 1989. Compartmental analysis approach to fluorescence anisotropy: perylene in viscous solvents. *J Phys Chem* **93**:3963–3967.
34. Irving M. 1996. Steady-state polarization from cylindrically symmetric fluorophores undergoing rapid restricted motion. *Biophys J* **70**:1830–1835.
35. Feinstein E, Deikus G, Rusinova E, Rachofsky EL, Ross JBA, Laws WR. 2003. Constrained analysis of fluorescence anisotropy decay: application to experimental protein dynamics. *Biophys J* **84**:599–611.
36. Steiner RF. 1991. Fluorescence anisotropy: theory and applications. In *Topics in fluorescence spectroscopy*, Vol. 2: *Principles*, pp. 1–52. Ed JR Lakowicz. Plenum Press, New York.
37. Barkley MD, Kowalczyk AA, Brand L. 1981. Fluorescence decay studies of anisotropic rotations: Internal motions in DNA. In *Biomolecular stereodynamics*, Vol. 1, pp. 391–403. Ed RH Sarma. Adenine Press, New York.
38. Beechem JM, Knutson JR, Brand L. 1986. Global analysis of multiple dye fluorescence anisotropy experiments on proteins. *Biochem Soc Trans* **14**:832–835.
39. Kawasaki A. 1993. Fluorescence anisotropy: theory and applications of rotational depolarization. *Crit Rev Anal Chem* **23**(6):459–529.
40. Tan X, Gustafson TL. 2000. Solvent–solute interactions probed by picosecond time-resolved fluorescence spectroscopy: lifetime and anisotropy study of S<sub>1</sub> *trans*-4,4'-diphenylstilbene. *J Phys Chem A* **104**:4469–4474.
41. Dutt GB, Ghanty TK. 2003. Rotational dynamics of nondipolar probes in ethanol: how does the strength of the solute–solvent hydrogen bond impede molecular rotation? *J Chem Phys* **119**(9): 4768–4774.
42. Ito N, Kajimoto O, Hara K. 2002. High-pressure studies of rotational dynamics for coumarin 153 in alcohols and alkanes. *J Phys Chem A* **106**:6024–6029.
43. Singh MK. 2000. Rotational relaxation of neutral red in alkanes: effect of solvent size on probe rotation. *Photochem Photobiol* **72**(4):438–443.
44. Jas GS, Larson EJ, Johnson CK, Kuczera K. 2000. Microscopic details of rotational diffusion of perylene in organic solvents: molecular dynamics simulation and experiment vs Debye-Stokes-Einstein theory. *J Phys Chem A* **104**:9841–9852.
45. Brocklehurst B, Young RN. 1999. Rotation of aromatic hydrocarbons in viscous alkanes, 1: methylcyclohexane. *J Phys Chem A* **103**: 3809–3817.
46. Dutt GB. 2000. Rotational dynamics of nondipolar probes in alkane–alkanol mixtures: microscopic friction on hydrogen bonding and nonhydrogen bonding solute molecules. *J Chem Phys* **113**(24): 11154–11158.
47. Hu C-M, Zwanzig R. 1974. Rotational friction coefficients for spheroids with the slipping boundary condition. *J Chem Phys* **60**(11): 4354–4357.
48. Youngren GK, Acrivos A. 1975. Rotational friction coefficients for ellipsoids and chemical molecules with the slip boundary condition. *J Chem Phys* **63**:3846–3848.
49. Barkley MD, Kowalczyk AA, Brand L. 1981. Fluorescence decay studies of anisotropic rotations of small molecules. *J Chem Phys* **75**(7):3581–3593.
50. Brocklehurst B, Young RN. 1994. Fluorescence anisotropy decays and viscous behaviour of 2-methyltetrahydrofuran. *J Chem Soc Faraday Trans* **90**(2):271–278.
51. Brocklehurst B, Young RN. 1995. Rotation of perylene in alkanes: nonhydrodynamic behavior. *J Phys Chem* **99**:40–53.
52. Sasaki T, Hirota K, Yamamoto M, Nishijima K. 1987. Anisotropic rotation of perylene studied by fluorescence depolarization method. *Bull Chem Soc Jpn* **60**:1165–1167.
53. Viovy JL. 1985. Anisotropic rotation of 1,9-dimethylanthracene: a fluorescence anisotropy decay study. *J Phys Chem* **89**:5465–5472.
54. Weber G. 1977. Theory of differential phase fluorometry: detection of anisotropic molecular rotations. *J Chem Phys* **66**(9):4081–4091.
55. Mantulin WW, Weber G. 1977. Rotational anisotropy and solvent-fluorophore bond: an investigation by differential polarized phase fluorometry. *J Chem Phys* **66**(9):4092–4099.
56. Weber G, Mitchell GW. 1976. Demonstration of anisotropic molecular rotations by differential polarized phase fluorometry. In *Excited states of biological molecules*, pp. 72–76. Ed JB Birks. John Wiley & Sons, New York.
57. Lakowicz JR, Prendergast FG, Hogen D. 1979. Differential polarized phase fluorometric investigations of diphenylhexatriene in lipid bilayers: quantitation of hindered depolarizing rotations. *Biochemistry* **18**:508–519.
58. Klein UKA, Haas HP. 1979. Picosecond rotational diffusion of perylene. *Chem Phys Lett* **63**(1):40–42.
59. Lakowicz JR, Gryczynski I. 1991. Frequency-domain fluorescence spectroscopy. In *Topics in fluorescence spectroscopy*, Vol. 1: *Techniques*, pp. 293–355. Plenum Press, New York.
60. Lakowicz JR, Cherek H, Maliwal BP. 1985. Time-resolved fluorescence anisotropies of diphenylhexatriene and perylene in solvents and lipid bilayers obtained from multifrequency phase-modulation fluorometry. *Biochemistry* **24**:376–383.

61. Lakowicz JR, Maliwal BP. 1985. Construction and performance of a variable-frequency phase-modulation fluorometer. *Biophys Chem* **21**:61–78.
62. Lakowicz JR, Gryczynski I, Cherek H, Laczko G. 1991. Anisotropy decays of indole, melittin monomer and melittin tetramer by frequency-domain fluorometry and multi-wavelength global analysis. *Biophys Chem* **39**:241–251.
63. Gryczynski I, Cherek H, Laczko G, Lakowicz JR. 1987. Enhanced resolution of anisotropic rotational diffusion by multi-wavelength frequency-domain fluorometry and global analysis. *Chem Phys Lett* **135**(3):193–199.
64. Gryczynski I, Cherek H, Lakowicz JR. 1988. Detection of three rotational correlation times for a rigid asymmetric molecule using frequency-domain fluorometry. *SPIE Proc* **909**:285–292.
65. Gryczynski I, Danielson E, Lakowicz JR. Unpublished observations.
66. Lakowicz JR, Gryczynski I, Wiczk WM. 1988. Anisotropic rotational diffusion of indole in cyclohexane studied by 2 GHz frequency-domain fluorometry. *Chem Phys Lett* **149**(2):134–139.
67. Gryczynski I, Cherek H, Lakowicz JR. 1988. Detection of three rotational correlation times for a rigid asymmetric molecule using frequency-domain fluorometry. *Biophys Chem* **30**:271–277.
68. Gryczynski I, Wiczk W, Johnson ML, Lakowicz JR. 1988. Lifetime distributions and anisotropy decays of indole fluorescence in cyclohexane/ethanol mixtures by frequency-domain fluorometry. *Biophys Chem* **32**:173–185.
69. Lakowicz JR, Cherek H, Gryczynski I, Joshi N, Johnson ML. 1987. Enhanced resolution of fluorescence anisotropy decays by simultaneous analysis of progressively quenched samples. *Biophys J* **51**: 755–768.
70. Lakowicz JR, Gryczynski I, Szmacinski H, Cherek H, Joshi N. 1991. Anisotropy decays of single-tryptophan proteins measured by GHz frequency-domain fluorometry with collisional quenching. *Eur Biophys J* **19**:125–140.
71. Barkley MD, Zimm BH. 1979. Theory of twisting and bending of chain macromolecules; analysis of the fluorescence depolarization of DNA. *J Chem Phys* **70**(6):2991–3007.
72. Thomas JC, Allison SA, Appeloff CJ, Schurr JM. 1980. Torsion dynamics and depolarization of fluorescence of linear macromolecules, II: fluorescence polarization anisotropy measurements on a clean viral 29 DNA. *Biophys Chem* **12**:177–188.
73. Schurr JM, Fujimoto BS, Wu P, Song L. 1992. Fluorescence studies of nucleic acids: dynamics, rigidities, and structures. In *Topics in fluorescence spectroscopy*, Vol. 3: *Biochemical applications*, pp. 137–229. Ed JR Lakowicz. Plenum Press, New York.
74. Millar DP, Robbins RJ, Zewail AH. 1981. Time-resolved spectroscopy of macromolecules: effect of helical structure on the torsional dynamics of DNA and RNA. *J Chem Phys* **74**(7):4200–4201.
75. Ashikawa I, Furuno T, Kinoshita K, Ikegami A, Takahashi H, Akutsu H. 1983. Internal motion of DNA in bacteriophages. *J Biol Chem* **259**(13):8338–8344.
76. Ashikawa I, Kinoshita K, Ikegami A. 1984. Dynamics of z-form DNA. *Biochim Biophys Acta* **782**:87–93.
77. Genest D, Wahl Ph, Erard M, Champagne M, Daune M. 1982. Fluorescence anisotropy decay of ethidium bromide bound to nucleosomal core particles. *Biochim*. **64**:419–427.
78. Ashikawa, I., Kinoshita, K., Ikegami, A., Nishimura, Y., Tsuboi, M., Watanabe, K., Iso, K., and Nakano, T., 1983. Internal motion of deoxyribonucleic acid in chromatin. Nanosecond fluorescence studies of intercalated ethidium. *Biochemistry* **22**:6018–6026.
79. Thulstrup EW, Michl J. 1988. Polarized absorption spectroscopy of molecules aligned in stretched polymers. *Spectrochim Acta A* **44**:767–782.
80. Michl J, Thulstrup EW. 1987. Ultraviolet and infrared linear dichroism: polarized light as a probe of molecular and electronic structure. *Acc Chem Res* **20**:192–199.
81. Van Gurp M, Levine YK. 1989. Determination of transition moment directions in molecules of low symmetry using polarized fluorescence, I: theory. *J Chem Phys* **90**(8):4095–4100.
82. Matsuoka Y, Yamaoka K. 1980. Film dichroism, V: linear dichroism study of acridine dyes in films with emphasis on the electronic transitions involved in the long-wavelength band of the absorption spectrum. *Bull Chem Soc Jpn* **53**:2146–2151.
83. Michl J, Thulstrup EW. 1986. *Spectroscopy with polarized light*. VCH Publishers, New York.
84. Kawski A, Gryczynski Z. 1986. On the determination of transition-moment directions from emission anisotropy measurements. *Z Naturforsch A* **41**:1195–1199.
85. Kawski A, Gryczynski Z, Gryczynski I, Lakowicz JR, Piszczeck G. 1996. Photoselection of luminescent molecules in anisotropic media in the case of two-photon excitation, II: experimental studies of Hoechst 33342 in stretched poly(vinyl alcohol) films. *Z Naturforsch A* **51**:1037–1041.
86. Matsuoka Y, Norden B. 1982. Linear dichroism study of 9-substituted acridines in stretched poly(vinyl alcohol) film. *Chem Phys Lett* **85**(3):302–306.
87. Holmén A, Broo A, Albinsson B, Nordén B. 1997. Assignment of electronic transition moment directions of adenine from linear dichroism measurements. *J Am Chem Soc* **119**(50):12240–12250.
88. Holmén A, Nordén B, Albinsson B. 1997. Electronic transition moments of 2-aminopurine. *J Am Chem Soc* **119**(13):3114–3121.
89. Albinsson B, Kubista M, Sandros K, Nordén B. 1990. Electronic linear dichroism spectrum and transition moment directions of the hypermodified nucleic acid-base wye. *J Phys Chem* **94**:4006–4011.
90. Kubista M, Åkerman B, and Albinsson B. 1989. Characterization of the electronic structure of 4',6-diamidino-2-phenylindole. *J Am Chem Soc* **111**:7031–7035.
91. Andersen KB, Waluk J, Thulstrup EW. 1999. The electronic structure of carcinogenic dibenzopyrenes: linear dichroism, fluorescence polarization spectroscopy and quantum mechanical calculations. *Photochem Photobiol* **69**(2):158–166.
92. Hall RD, Valeur B, Weber G. 1985. Polarization of the fluorescence of triphenylene: a planar molecule with three-fold symmetry. *Chem Phys Lett* **116**(2,3):202–205.
93. Lakowicz JR, Weber G. 1980. Nanosecond segmental mobilities of tryptophan residues in proteins observed by lifetime-resolved fluorescence anisotropies. *Biophys J* **32**:591–601.
94. Lakowicz JR, Maliwal BP, Cherek H, Balter A. 1983. Rotational freedom of tryptophan residues in proteins and peptides. *Biochemistry* **22**:1741–1752.

95. Lakowicz JR, Maliwal BP. 1983. Oxygen quenching and fluorescence depolarization of tyrosine residues in proteins. *J Biol Chem* **258**(8):4794–4801.
96. Eftink M. 1983. Quenching-resolved emission anisotropy studies with single and multityptophan-containing proteins. *Biophys J* **43**: 323–334.
97. Lakos Z, Szarka Á, Koszorús L, Somogyi B. 1995. Quenching-resolved emission anisotropy: a steady state fluorescence method to study protein dynamics. *J Photochem Photobiol B: Biol* **27**:55–60.
98. Bentz JP, Beyl P, Beinert G, Weill G. 1973. Simultaneous measurements of fluorescence polarization and quenching: a specially designed instrument and an application to the micro-brownian motion of polymer chains. *Eur Polymer J* **11**:711–718.
99. Brown K, Soutar I. 1974. Fluorescence quenching and polarization studies of segmental motion in polystyrene. *Eur Polymer J* **10**: 433–437.
100. Chen RF. 1976. Quenching of the fluorescence of proteins by silver nitrate. *Arch Biochem Biophys* **168**:605–622.
101. Sanyal G, Charlesworth MC, Ryan RJ, Prendergast FG. 1987. Tryptophan fluorescence studies of subunit interaction and rotational dynamics of human luteinizing hormone. *Biochemistry* **26**: 1860–1866.
102. Soleillet P. 1929. Sur les paramètres caractérisant la polarisation partielle de la lumière dans les phénomènes de fluorescence. *Ann Phys Biol Med* **12**:23–97.
103. Kawski A. 1986. Fluorescence anisotropy as a source of information about different photophysical processes. In *Progress and trends in applied optical spectroscopy*, Vol. 13, pp. 6–34. Ed D Fassler, K-H Feller, B Wilhelm. Teubner Verlagsgesellschaft, Leipzig.
104. Weber G. 1966. Polarization of the fluorescence of solutions. In *Fluorescence and phosphorescence analysis*, pp. 217–240. Ed DM Hercules. John Wiley & Sons, New York.
105. Gurinovich GP, Sarzhevskii AM, Sevchenko AN. 1963. New data on the dependence of the degree of polarization on the wavelength of fluorescence. *Opt Spectrosc* **14**:428–432.
106. Mazurenko YT, Bakhshiev NG. 1970. Effect of orientation dipole relaxation on spectral, time, and polarization characteristics of the luminescence of solutions. *Opt Spectrosc* **28**:490–494.
107. Gakamskii DM, Nemkovich NA, Rubinov AN, Tomin VI. 1988. Light-induced rotation of dye molecules in solution. *Opt Spectrosc* **64**(3):406–407.
108. Chattopadhyay A, Mukherjee S. 1999. Depth-dependent solvent relaxation in membranes: wavelength-selective fluorescence as a membrane dipstick. *Langmuir* **15**:2142–2148.
109. Matayoshi ED, Kleinfeld AM. 1981. Emission wavelength-dependent decay of the 9-anthroyloxy-fatty acid membrane probes. *Biophys J* **35**:215–235.

## PROBLEMS

- P12.1. *Calculation of An Associated Anisotropy Decay:* Use the intensity and anisotropy decay in Figure 12.3 to calculate the anisotropy at  $t = 0, 1$ , and  $5$  ns. Also cal-

culate the anisotropy values of  $0, 1$  and  $5$  ns assuming a non-associated anisotropy decay. What feature of the calculated values indicates the presence of an associated anisotropy decay?

- P12.2. Figure 12.5 shows associated anisotropy decays for rhodamine B in water and bound to colloidal silica particles. Using the same parameter values, what is the form of the anisotropy decay for a non-associated model for the highest silica concentration? Describe the shape of the non-associated anisotropy decay.
- P12.3. *Anisotropy of a Planar Oscillator:* Calculate the anisotropy of triphenylene assuming the emission is randomized among three equivalent axes (Figure 12.37).
- P12.4. *Correlation Times from Lifetime-Resolved Anisotropies:* Figure 12.41 shows lifetime-resolved anisotropies of melittin. The lifetimes were varied by oxygen quenching. Calculate the correlation times and  $r(0)$  values in  $0$  and  $2.4$  M NaCl, where melittin exists as a monomer and tetramer, respectively. Assume that the  $r_0$  value for melittin is  $0.26$  and the monomeric molecular weight is  $3250$  daltons.

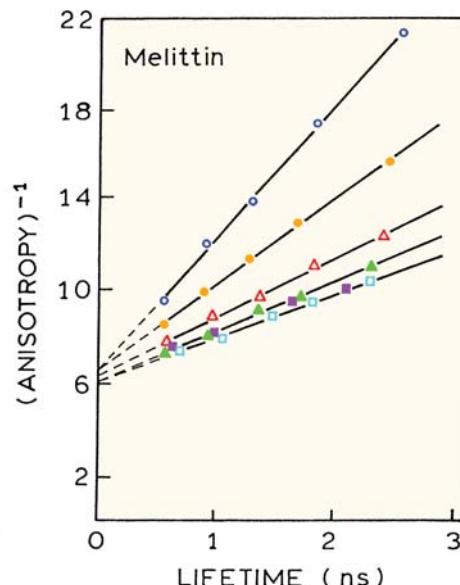


**Figure 12.41.** Lifetime-resolved anisotropy of melittin in aqueous buffer at  $25^\circ\text{C}$ . The concentrations of NaCl are  $0$  (open circles),  $0.15$  (solid circles),  $0.3$  (open triangles),  $0.6$  (solid triangles),  $1.5$  (solid squares), and  $2.4$  M (open squares). Revised and reprinted with permission from [94]. Copyright © 1983, American Chemical Society.

# 13

# Energy Transfer

Fluorescence resonance energy transfer (FRET) has become widely used in all applications of fluorescence, including medical diagnostics, DNA analysis, and optical imaging. The widespread use of FRET is due to the favorable distances for energy transfer, which are typically the size of a protein or the thickness of a membrane. Additionally, the extent of FRET is readily predictable from the spectral properties of the fluorophores. If the spectral properties of the fluorophores allow FRET, it will occur and will not be significantly affected by the biomolecules in the sample. These favorable properties allow for the design of experiments based on the known sizes and structural features of the sample.

FRET is an electrodynamic phenomenon that can be explained using classical physics. FRET occurs between a donor (D) molecule in the excited state and an acceptor (A) molecule in the ground state. The donor molecules typically emit at shorter wavelengths that overlap with the absorption spectrum of the acceptor. Energy transfer occurs without the appearance of a photon and is the result of long-range dipole–dipole interactions between the donor and acceptor. The term resonance energy transfer (RET) is preferred because the process does not involve the appearance of a photon. The rate of energy transfer depends upon the extent of spectral overlap of the emission spectrum of the donor with the absorption spectrum of the acceptor, the quantum yield of the donor, the relative orientation of the donor and acceptor transition dipoles, and the distance between the donor and acceptor molecules. The distance dependence of RET allows measurement of the distances between donors and acceptors.

The most common application of RET is to measure the distances between two sites on a macromolecule. Typically a protein is covalently labeled with a donor and an acceptor (Figure 13.1). In studies of protein structure the donor is often a tryptophan residue. However, extrinsic donors are often used because of the opportunity to position the donor in a desired location and to select the D–A pairs

that are most suitable for a particular application. If there is a single donor and acceptor, and if the D–A distance does not change during the excited-state lifetime, then the D–A distance can be determined from the efficiency of energy transfer. The transfer efficiency can be determined by steady-state measurements of the extent of donor quenching due to the acceptor.

RET is also used in studies in which the actual D–A distance is not being measured. Typical experiments of this type include DNA hybridization or any bioaffinity reactions. If the sample contains two types of macromolecules that are individually labeled with donor or acceptor, association of the molecules can usually be observed using RET. The observation of RET is sufficient to measure the extent of binding, even without calculation of the D–A distance. At present, steady-state measurements are often used to measure binding interactions. Distances are usually obtained from time-resolved measurements.

Resonance energy transfer is also used to study macromolecular systems when there is more than a single acceptor molecule near a donor molecule. This situation often occurs for larger assemblies of macromolecules, or when using membranes where the acceptor is a freely diffusing lipid analogue. Even with a single D–A pair, there can be more than a single D–A distance, such as for an unfolded protein. The extent of energy transfer can also be influenced by the presence of donor-to-acceptor diffusion during the donor lifetime. Although information can be obtained from the steady-state data, such systems are usually studied using time-resolved measurements. These more advanced applications of RET are presented in Chapters 14 and 15.

## 13.1. CHARACTERISTICS OF RESONANCE ENERGY TRANSFER

The distance at which RET is 50% efficient is called the Förster distance,<sup>1</sup> which is typically in the range of 20 to 60

$$k_T(r) = \frac{1}{\tau_D} \left( \frac{R_0}{r} \right)^6 = \text{TRANSFER RATE}$$

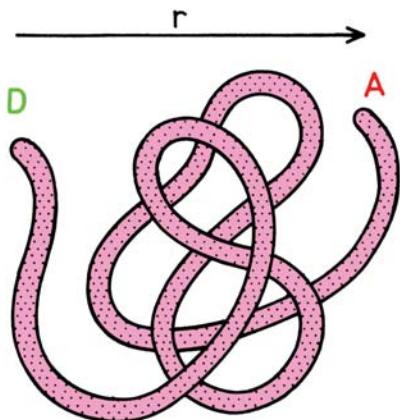


**Figure 13.1.** Fluorescence resonance energy transfer (FRET) for a protein with a single donor (D) and acceptor (A).

Å. The rate of energy transfer from a donor to an acceptor  $k_T(r)$  is given by

$$k_T(r) = \frac{1}{\tau_D} \left( \frac{R_0}{r} \right)^6 \quad (13.1)$$

where  $\tau_D$  is the decay time of the donor in the absence of acceptor,  $R_0$  is the Förster distance, and  $r$  is the donor-to-acceptor distance. Hence, the rate of transfer is equal to the decay rate of the donor ( $1/\tau_D$ ) when the D-to-A distance ( $r$ ) is equal to the Förster distance ( $R_0$ ), and the transfer efficiency is 50%. At this distance ( $r = R_0$ ) the donor emission would be decreased to half its intensity in the absence of acceptors. The rate of RET depends strongly on distance, and is proportional to  $r^{-6}$  (eq. 13.1).

Förster distances ranging from 20 to 90 Å are convenient for studies of biological macromolecules. These distances are comparable to the size of biomolecules and/or the distance between sites on multi-subunit proteins. Any condition that affects the D–A distance will affect the transfer rate, allowing the change in distance to be quantified. In this type of application, one uses the extent of energy transfer between a fixed donor and acceptor to calculate the D–A distance, and thus obtain structural information about the macromolecule (Figure 13.1). Such distance measurements have resulted in the description of RET as a "spectroscopic ruler."<sup>2,3</sup> For instance, energy transfer can be used to meas-

ure the distance from a tryptophan residue to a ligand binding site when the ligand serves as the acceptor.

In the case of multi-domain proteins, RET has been used to measure conformational changes that move the domains closer or further apart. Energy transfer can also be used to measure the distance between a site on a protein and a membrane surface, association between protein subunits, and lateral association of membrane-bound proteins. In the case of macromolecular association reactions one relies less on determination of a precise D–A distance, and more on the simple fact that energy transfer occurs whenever the donors and acceptors are in close proximity comparable to the Förster distance.

The use of energy transfer as a proximity indicator illustrates an important characteristic of energy transfer. Energy transfer can be reliably assumed to occur whenever the donors and acceptors are within the characteristic Förster distance, and whenever suitable spectral overlap occurs. The value of  $R_0$  can be reliably predicted from the spectral properties of the donors and acceptors. Energy transfer is a through-space interaction that is mostly independent of the intervening solvent and/or macromolecule. In principle, the orientation of the donors and acceptors can prevent energy transfer between a closely spaced D–A pair, but such a result is rare and possibly nonexistent in biomolecules. Hence one can assume that RET will occur if the spectral properties are suitable and the D–A distance is comparable to  $R_0$ . A wide variety of biochemical interactions result in changes in distance and are thus measurable using RET.

It is important to remember that resonance energy transfer is a process that does not involve emission and reabsorption of photons. The theory of energy transfer is based on the concept of a fluorophore as an oscillating dipole, which can exchange energy with another dipole with a similar resonance frequency.<sup>4</sup> Hence RET is similar to the behavior of coupled oscillators, like two swings on a common supporting beam. In contrast, radiative energy transfer is due to emission and reabsorption of photons, and is thus due to inner filter effects. Radiative transfer depends upon non-molecular optical properties of the sample, such as the size of the sample container, the path length, the optical densities of the sample at the excitation and emission wavelengths, and the geometric arrangement of the excitation and emission light paths. In contrast to these trivial factors, non-radiative energy transfer contains a wealth of structural information concerning the donor–acceptor pair.

Resonance energy transfer contains molecular information that is different from that revealed by solvent relaxation, excited-state reactions, fluorescence quenching, or fluorescence anisotropy. These other fluorescence phenomena depend on interactions of the fluorophore with other molecules in the surrounding solvent shell. These nearby interactions are less important for energy transfer, except for their effects on the spectral properties of the donor and acceptor. Non-radiative energy transfer is effective over much longer distances, and the intervening solvent or macromolecule has little effect on the efficiency of energy transfer, which depends primarily on the D–A distance. In this chapter we will describe the basic theory of non-radiative energy transfer and the applications of RET to biochemical systems. The biochemical applications of RET have been the subject of several reviews (additional references on RET and protein folding are listed near the end of this chapter). More complex formalisms are needed to describe other commonly encountered situations, such as distance distributions (Chapter 14) and the presence of multiple acceptors (Chapter 15).

### 13.2. THEORY OF ENERGY TRANSFER FOR A DONOR-ACCEPTOR PAIR

The theory for resonance energy transfer is moderately complex, and similar equations have been derived from classical and quantum mechanical considerations. We will describe only the final equations. Readers interested in the physical basis of RET are referred to the excellent review by Clegg.<sup>4</sup> RET is best understood by considering a single donor and acceptor separated by a distance ( $r$ ). The rate of transfer for a donor and acceptor separated by a distance  $r$  is given by

$$k_T(r) = \frac{Q_D \kappa^2}{\tau_D r^6} \left( \frac{9000(\ln 10)}{128\pi^5 N n^4} \right) \int_0^\infty F_D(\lambda) \varepsilon_A(\lambda) \lambda^4 d\lambda \quad (13.2)$$

where  $Q_D$  is the quantum yield of the donor in the absence of acceptor,  $n$  is the refractive index of the medium,  $N$  is Avogadro's number,  $r$  is the distance between the donor and acceptor, and  $\tau_D$  is the lifetime of the donor in the absence of acceptor. The refractive index ( $n$ ) is typically assumed to be 1.4 for biomolecules in aqueous solution.  $F_D(\lambda)$  is the corrected fluorescence intensity of the donor in the wavelength range  $\lambda$  to  $\lambda + \Delta\lambda$  with the total intensity (area under

the curve) normalized to unity.  $\varepsilon_A(\lambda)$  is the extinction coefficient of the acceptor at  $\lambda$ , which is typically in units of  $M^{-1} cm^{-1}$ . The term  $\kappa^2$  is a factor describing the relative orientation in space of the transition dipoles of the donor and acceptor.  $\kappa^2$  is usually assumed to be equal to 2/3, which is appropriate for dynamic random averaging of the donor and acceptor (Section 13.2.1, below). In eq. 13.2 the transfer rate is written as a function of  $r$ ,  $k_T(r)$ , to emphasize its dependence on distance.

The overlap integral ( $J(\lambda)$ ) expresses the degree of spectral overlap between the donor emission and the acceptor absorption:

$$J(\lambda) = \int_0^\infty F_D(\lambda) \varepsilon_A(\lambda) \lambda^4 d\lambda = \frac{\int_0^\infty F_D(\lambda) \varepsilon_A(\lambda) \lambda^4 d\lambda}{\int_0^\infty F_D(\lambda) d\lambda} \quad (13.3)$$

$F_D(\lambda)$  is dimensionless. If  $\varepsilon_A(\lambda)$  is expressed in units of  $M^{-1} cm^{-1}$  and  $\lambda$  is in nanometers, then  $J(\lambda)$  is in units of  $M^{-1} cm^{-1} nm^4$ . If  $\lambda$  is in centimeters then  $J(\lambda)$  is in units of  $M^{-1} cm^3$ . In calculating  $J(\lambda)$  one should use the corrected emission spectrum with its area normalized to unity (eq. 13.3, middle), or normalize the calculated value of  $J(\lambda)$  by the area (eq. 13.3, right). The overlap integral has been defined in several ways, each with different units. In our experience we find it is easy to get confused, so we recommend the units of nm or cm for the wavelength, and units of  $M^{-1} cm^{-1}$  for the extinction coefficient.

In designing a biochemical experiment it is usually easier to think about distances than transfer rates. For this reason eq. 13.2 is written in terms of the Förster distance  $R_0$ . At this distance, half the donor molecules decay by energy transfer and half decay by the usual radiative and non-radiative rates. From eqs. 13.1 and 13.2 with  $k_T(r) = \tau_D^{-1}$  one obtains

$$R_0^6 = \frac{9000(\ln 10)\kappa^2 Q_D}{128\pi^5 N n^4} \int_0^\infty F_D(\lambda) \varepsilon_A(\lambda) \lambda^4 d\lambda \quad (13.4)$$

This expression allows the Förster distance to be calculated from the spectral properties of the donor and the acceptor and the donor quantum yield. While eq. 13.4 looks complex, many of the terms are simple physical constants. It is convenient to have simpler expressions for  $R_0$  in terms of the experimentally known values, which is accomplished by combining the constant terms in equation 13.4. If the

wavelength is expressed in nm then  $F_D(\lambda)$  is in units of  $M^{-1} \text{ cm}^{-1} (\text{nm})^4$ , and the Förster distance in Å is given by

$$R_0 = 0.211(\kappa^2 n^{-4} Q_D J(\lambda))^{1/6} \text{ (in } \text{\AA}) \quad (13.5)$$

$$R_0^6 = 8.79 \times 10^{-5}(\kappa^2 n^{-4} Q_D J(\lambda)) \text{ (in } \text{\AA}^6) \quad (13.6)$$

If the wavelength is expressed in cm and  $J(\lambda)$  is in units of  $M^{-1} \text{ cm}^3$ , the Förster distance is given by

$$R_0^6 = 8.79 \times 10^{-25}(\kappa^2 n^{-4} Q_D J(\lambda)) \text{ (in cm}^6) \quad (13.7)$$

$$R_0 = 9.78 \times 10^3(\kappa^2 n^{-4} Q_D J(\lambda))^{1/6} \text{ (in } \text{\AA}) \quad (13.8)$$

$$R_0^6 = 8.79 \times 10^{23}(\kappa^2 n^{-4} Q_D J(\lambda)) \text{ (in } \text{\AA}^6) \quad (13.9)$$

It is important to recognize that the Förster distances are usually reported for an assumed value of  $\kappa^2$ , typically  $\kappa^2 = 2/3$ . Once the value of  $R_0$  is known the rate of energy transfer can be easily calculated using

$$k_T(r) = \frac{1}{\tau_D} \left( \frac{R_0}{r} \right)^6 \quad (13.10)$$

If the transfer rate is much faster than the decay rate, then energy transfer will be efficient. If the transfer rate is slower than the decay rate, then little transfer will occur during the excited-state lifetime, and RET will be inefficient.

The efficiency of energy transfer ( $E$ ) is the fraction of photons absorbed by the donor which are transferred to the acceptor. This fraction is given by

$$E = \frac{k_T(r)}{\tau_D^{-1} + k_T(r)} \quad (13.11)$$

which is the ratio of the transfer rate to the total decay rate of the donor in the presence of acceptor. Recalling that  $k_T(r) = \tau_D^{-1}(R_0/r)^6$ , one can easily rearrange eq. 13.11 to yield

$$E = \frac{R_0^6}{R_0^6 + r^6} \quad (13.12)$$

This equation shows that the transfer efficiency is strongly dependent on distance when the D–A distance is near  $R_0$  (Figure 13.2). The efficiency quickly increases to 1.0 as the

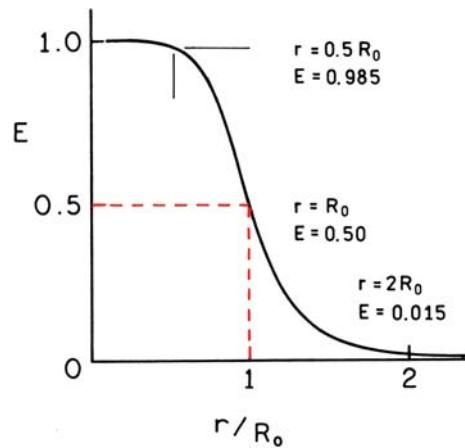


**Figure 13.2.** Dependence of the energy transfer efficiency ( $E$ ) on distance.  $R_0$  is the Förster distance.

D–A distance decreases below  $R_0$ . For instance, if  $r = 0.1R_0$  one can readily calculate that the transfer efficiency is 0.999999, indicating that the donor emission would not be observable. Conversely, the transfer efficiency quickly decreases to zero if  $r$  is greater than  $R_0$ . Because  $E$  depends so strongly on distance, measurements of the distance ( $r$ ) are only reliable when  $r$  is within a factor of 2 of  $R_0$ . If  $r$  is twice the Förster distance ( $r = 2R_0$ ) then the transfer efficiency is 1.54%, and if  $r = 0.5R_0$  then the efficiency is 98.5%. It is not practical to use RET to measure distances outside the range of  $r = 0.5R_0$  to  $r = 2R_0$ .

The transfer efficiency is typically measured using the relative fluorescence intensity of the donor, in the absence ( $F_D$ ) and presence ( $F_{DA}$ ) of acceptor:

$$E = 1 - \frac{F_{DA}}{F_D} \quad (13.13)$$

The transfer efficiency can also be calculated from the lifetimes under these respective conditions ( $\tau_{DA}$  and  $\tau_D$ ):

$$E = 1 - \frac{\tau_{DA}}{\tau_D} \quad (13.14)$$

It is important to remember the assumptions involved in using these equations. Equations 13.13 and 13.14 are only applicable to donor–acceptor pairs that are separated by a fixed distance, a situation frequently encountered for labeled proteins. However, a single fixed donor–acceptor distance is not found for a mixture of donors and acceptors in solution, nor for donors and acceptors dispersed random-

ly in membranes. More complex expressions are required in these cases, and such expressions are generally derived by averaging the transfer rate over the assumed spatial distribution of donor–acceptor pairs.<sup>5–7</sup>

The use of lifetimes in eq. 13.14 has been a source of confusion. In eq. 13.14 we have assumed that the decay of the donor is a single exponential in the absence ( $\tau_D$ ) and presence ( $\tau_{DA}$ ) of acceptor. Single-exponential decays are rare in biomolecules. If the intensity decays are multi-exponential then it is important to use an average decay time which is proportional to the steady-state intensity. These averages are given by the sum of the  $\alpha_i\tau_i$  products. The decay rate in the presence of acceptor will only remain a single exponential if there is a single D–A distance. If the donor decay is a single exponential, the presence of acceptors at more than one distance can result in more complex decays (Chapter 14).

In order to calculate the D–A distance it is necessary to know  $R_0$ , which in turn depends upon  $\kappa^2$ ,  $n$ ,  $Q_D$ , and  $J(\lambda)$ . These values must be known to calculate the distance. The refractive index is generally known from the solvent composition or is estimated for the macromolecule. The refractive index is often assumed to be near that of water ( $n = 1.33$ ) or small organic molecules ( $n = 1.39$ ). The quantum yield of the donor ( $Q_D$ ) is determined by comparison with standard fluorophores. Since  $Q_D$  is used as the sixth root in the calculation of  $R_0$ , small errors in  $Q_D$  do not have a large effect on  $R_0$ . For instance, if the quantum yield is increased by a factor of 2 the  $R_0$  value is still correct to within  $\pm 12\%$ . The overlap integral must be evaluated for each D–A pair. The greater the overlap of the emission spectrum of the donor with the absorption spectrum of the acceptor, the higher the value of  $R_0$ . Acceptors with larger extinction coefficients result in larger  $R_0$  values. In the equations presented above it was assumed that the lifetime of the donor was not altered by binding of the acceptor, other than by the rate of energy transfer. For labeled macromolecules this may not always be the case. Allosteric interactions between the donor and acceptor sites could alter the donor lifetime by enhancement of other decay processes, or by protection from these processes. Under these circumstances more complex analysis of the apparent transfer efficiency is required, typically a comparison of the apparent efficiency by donor quenching and enhanced acceptor emission.

The dependence of  $R_0$  on spectral overlap is illustrated in Figure 13.3 for transfer from structural isomers of dansyl-labeled phosphatidylethanolamine (DPE) to the eosin-labeled lipid (EPE). Each of the dansyl derivatives of DPE

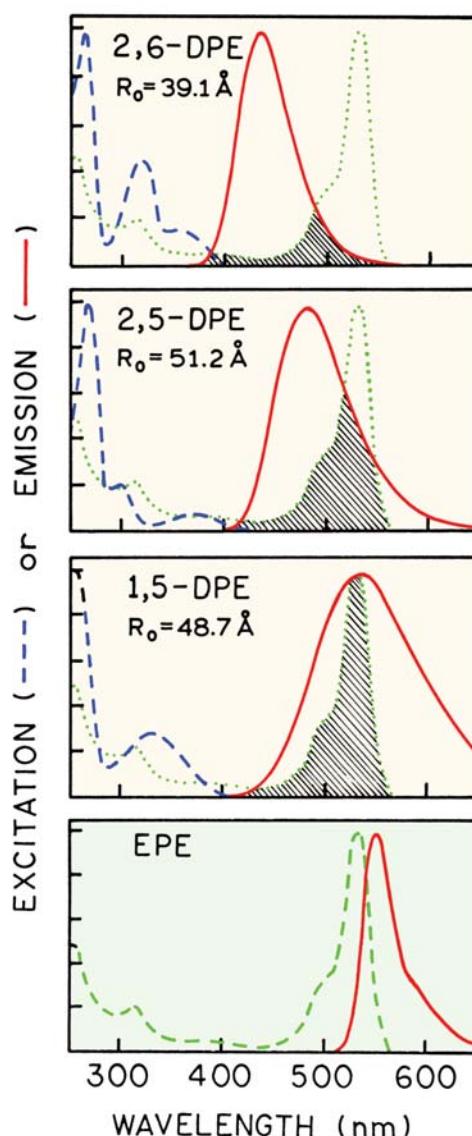


**Figure 13.3.** Excitation and emission spectra of dansyl-labeled lipids and an eosin-labeled lipid. The eosin- and dansyl-labeled compounds are N-derivatives of phosphatidylethanolamine (PE). The numbers refer to the location of the dimethylamino and the sulfonyl residues on the naphthalene ring. The extinction coefficient of EPE is  $85,000 \text{ M}^{-1} \text{ cm}^{-1}$  at 527 nm. In the top three panels the long wavelength absorption spectrum of eosin-PE is shown as a dotted line. Revised and reprinted with permission from [5]. Copyright © 1978, American Chemical Society.

displays a different emission spectrum.<sup>5</sup> As the spectra of the DPE isomers shift to longer wavelengths the overlap with the absorption spectrum of EPE increases and the  $R_0$  values increase (Table 13.1). One notices that  $R_0$  is not very dependent upon  $J(\lambda)$ . For instance, for two of the D–A pairs a 120-fold change in the overlap integral results in a 2.2-

**Table 13.1.** Calculated  $R_0$  Values for RET from Structural Isomers of Dansyl-Labeled Phosphatidylethanolamine (DPE) to Eosin-Labeled Phosphatidylethanolamine (EPE) and from 2,6-DPE to 2,5-DPE

Donor	Acceptor	$Q_D$	$J$ ( $M^{-1} \text{ cm}^3$ )	$J$ ( $M^{-1} \text{ cm}^3 (\text{nm})^4$ ) <sup>d</sup>	$R_0$ ( $\text{\AA}$ ) <sup>a</sup>
1,5-DPE <sup>b</sup>	EPE <sup>c</sup>	0.37	$2.36 \times 10^{-13}$	$2.36 \times 10^{15}$	48.7
2,5-DPE	EPE	0.76	$1.54 \times 10^{-13}$	$1.54 \times 10^{15}$	51.2
2,6-DPE	EPE	0.71	$3.31 \times 10^{-14}$	$3.31 \times 10^{14}$	39.1
2,6-DPE	2,5-DPE	0.71	$1.3 \times 10^{-15}$	$1.3 \times 10^{13}$	22.8

<sup>a</sup>From [5].  $R_0$  was calculated using  $n = 1.4$  and  $\kappa^2 = 2/3$ .

<sup>b</sup>Dansyl-labeled phosphatidylethanolamine.

<sup>c</sup>Eosin-labeled phosphatidylethanolamine.

<sup>d</sup>The factor of  $10^{28}$  between  $J(\lambda)$  in  $M^{-1} \text{ cm}^3$  and  $M^{-1} \text{ cm}^3 (\text{nm})^4$  arises from  $1 \text{ nm} = 10^{-7} \text{ cm}$ , raised to the fourth power.

fold change in the Förster distance. This is because of the sixth-root dependence in eq. 13.5. It should also be noted that the visual impression of overlap is somewhat misleading because the value of  $J(\lambda)$  depends on  $\lambda^4$  (eq. 13.3). Comparison of the spectral overlap for 2,5-DPE and 1,5-DPE suggests a larger Förster distance for 1,5-DPE, whereas the calculated value is smaller. The larger Förster distance for 2,5-DPE is due to its larger quantum yield. Because of the complexity in calculating overlap integrals and Förster distances it is convenient to have several examples. Values of the overlap integral corresponding to the spectra in Figure 13.3 are summarized in Table 13.1.

#### Brief History of Theodor Förster<sup>8-9</sup>

The theory for resonance energy transfer was developed by Professor Theodor Förster (Figure 13.4). He was born in Frankfurt, Germany in 1910. He received a PhD in 1933 for studies of the polarization of reflected electrons. He then became a Research Assistant in Leipzig, Germany, where he studied light absorption of organic compounds until 1942. In this phase of his work he applied the principles of quantum mechanics to chemistry. From 1942 to 1945 he held a Professorship in Poznan, Poland. In 1945 he joined the Max-Planck Institute for Physical Chemistry in Göttingen, where he wrote his classic book *Fluoreszenz Organischer Verbindungen*, which has been described as a "house bible" for the German community of spectroscopists. By 1946 Professor Förster had written his first paper on energy transfer, and pointed out the importance of energy transfer in photosynthesis systems. Professor Förster was also among the first scientists to observe excited-state proton transfer, which is now described by the Förster cycle. In 1954 he discovered excimer formation. Professor Förster died of a heart attack in his car on the way to work in 1974. For additional information see [8] and the introduction about Theodor Förster in [9].

#### 13.2.1. Orientation Factor $\kappa^2$

A final factor in the analysis of the energy transfer efficiencies is the orientation factor  $\kappa^2$  which is given by

$$\kappa^2 = (\cos \theta_T - 3 \cos \theta_D \cos \theta_A)^2 \quad (13.15)$$

$$\kappa^2 = (\sin \theta_D \sin \theta_A \cos \phi - 2 \cos \theta_D \cos \theta_A)^2 \quad (13.16)$$

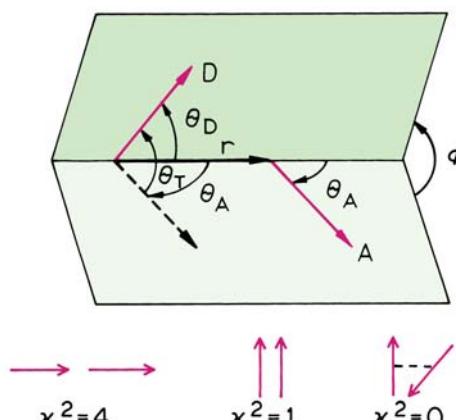
In these equations  $\theta_T$  is the angle between the emission transition dipole of the donor and the transition absorption dipole of the acceptor,  $\theta_D$  and  $\theta_A$  are the angles between these dipoles and the vector joining the donor and the acceptor, and  $\phi$  is the angle between the planes (Figure

### THEODOR FÖRSTER

15. 5. 1910 – 20. 5. 1974



**Figure 13.4.** Professor Theodor Förster. 15 May 1910–20 May 1974. Reprinted with permission from [8]. Copyright © 1974, Springer-Verlag.



$$\kappa^2 = (\cos \theta_T - 3 \cos \theta_D \cos \theta_A)^2$$

$$\kappa^2 = (\sin \theta_D \sin \theta_A \cos \phi - 2 \cos \theta_D \cos \theta_A)^2$$

**Figure 13.5.** Dependence of the orientation factor  $\kappa^2$  on the direction of the emission dipole of the donor and the absorption dipole of the acceptor.

13.5). Depending upon the relative orientation of donor and acceptor this factor can range from 0 to 4. For head-to-tail parallel transition dipoles  $\kappa^2 = 4$ , and for parallel dipoles  $\kappa^2 = 1$ . Since the sixth root is taken to calculate the distance, variation of  $\kappa^2$  from 1 to 4 results in only a 26% change in  $r$ . Compared to  $\kappa^2 = 2/3$ , the calculated distance can be in error by no more than 35%. However, if the dipoles are oriented perpendicular to one another,  $\kappa^2 = 0$ , which would result in serious errors in the calculated distance. This problem has been discussed in detail.<sup>10–12</sup> By measurements of the fluorescence anisotropy of the donor and the acceptor, one can set limits on  $\kappa^2$  and thereby minimize uncertainties in the calculated distance.<sup>11–13</sup> An example of calculating the range of possible values of  $\kappa^2$  is given below. In general, variation of  $\kappa^2$  does not seem to have resulted in major errors in the calculated distances.<sup>14–15</sup>  $\kappa^2$  is generally assumed equal to 2/3, which is the value for donors and acceptors that randomize by rotational diffusion prior to energy transfer. This value is generally assumed for calculation of  $R_0$ . Alternatively, one may assume that a range of static donor–acceptor orientations are present, and that these orientations do not change during the lifetime of the excited state. In this case  $\kappa^2 = 0.476$ .<sup>3</sup> For fluorophores bound to macromolecules, segmental motions of the donor and acceptor tend to randomize the orientations. Further, many donors and acceptors display fundamental anisotropies less than 0.4 due to overlapping electronic transi-

tions. In this case the range of possible  $\kappa^2$  values is more limited, and errors in distance are likely to be less than 10%.<sup>16</sup> Experimental results on the effect of  $\kappa^2$  are given in Section 13.9.

### 13.2.2. Dependence of the Transfer Rate on Distance ( $r$ ), the Overlap Integral ( $J$ ), and $\tau^2$

The theory of Förster predicts that  $k_T(r)$  depends on  $1/r^6$  (eq. 13.1) and linearly on the overlap integral (eq. 13.2). Given the complexity and assumptions of RET theory,<sup>4</sup> it was important to demonstrate experimentally that these dependencies were valid. The predicted  $1/r^6$  dependence on distance was confirmed experimentally.<sup>17–19</sup> One demonstration used oligomers of poly-L-proline, labeled on opposite ends with a naphthyl (donor) and a dansyl (acceptor) group.<sup>17–18</sup> Poly-L-proline forms a rigid helix of known atomic dimensions, providing fixed distances between the donor and acceptor moieties. By measuring the transfer efficiency with different numbers of proline residues, it was possible to demonstrate that the transfer efficiency in fact decreased as  $1/r^6$ . These data are described in detail in Problem 13.3.

The linear dependence of  $k_T(r)$  on the overlap integral  $J(\lambda)$  has also been experimentally proven.<sup>20</sup> This was accomplished using a D–A pair linked by a rigid steroid spacer. The extent of spectral overlap was altered by changing the solvent, which shifted the indole donor emission spectrum and the carbonyl acceptor absorption spectra. The rate of transfer was found to decrease linearly as the overlap integral decreased. These data are shown in Problem 13.4. To date there has not been experimental confirmation of the dependence of the transfer rate on  $\kappa^2$ .

Another important characteristic of RET is that the transfer rate is proportional to the decay rate of the fluorophore (eq. 13.2). This means that for a D–A pair spaced by the  $R_0$  value, the rate of transfer will be  $k_t(r) = \tau_D^{-1}$  whether the decay time is 10 ns or 10 ms. Hence, long-lived lanthanides are expected to display RET over distances comparable to those for nanosecond-decay-time fluorophores, as demonstrated by transfer from  $Tb^{3+}$  to acceptor.<sup>21–23</sup> This fortunate result occurs because the transfer rate is proportional to the emission rate of the donor. The proportionality to the emissive rate is due to the term  $Q_D/\tau_D$  in eq. 13.2. It is interesting to speculate what would happen if the transfer rate was independent of the decay rate. In this case a longer lived donor would allow more time for energy transfer. Then energy transfer would occur over longer

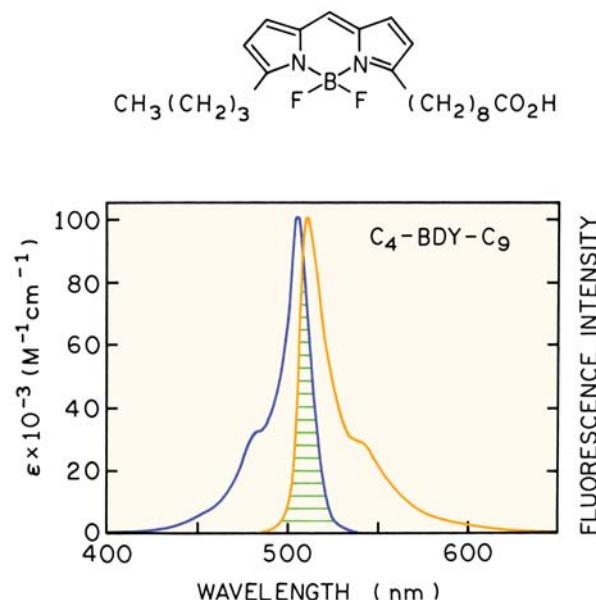


**Figure 13.6.** Absorption and corrected fluorescence emission (bandpass 2.5 nm) spectra of the Bodipy derivative  $\text{C}_4\text{-BDY-}\text{C}_9$  in methanol with shaded area representing spectral overlap. Revised and reprinted with permission from [25]. Copyright © 1991, Academic Press, Inc.

distances because a smaller rate of transfer will still be comparable to the donor decay rate.

### 13.2.3. Homotransfer and Heterotransfer

In the preceding sections we considered only energy transfer between chemically distinct donors and acceptors, which is called heterotransfer. Resonance energy transfer can also occur between chemically identical molecules. Such transfer, which is termed homotransfer, typically occurs for fluorophores which display small Stokes shifts. One example of homotransfer is provided by the Bodipy fluorophores.<sup>24</sup> The absorption and emission spectra of one Bodipy derivative are shown in Figure 13.6. Because of the small Stokes shift and high extinction coefficient of these probes, the Förster distance for homotransfer is near 57 Å.<sup>25</sup>

At first glance homotransfer may seem like an unlikely phenomenon, but its occurrence is rather common. For example, it is well known that biomolecules labeled with fluorescein do not become more highly fluorescent with higher degrees of labeling.<sup>26–28</sup> Antibodies are typically brightest with about four fluoresceins per antibody, after which the intensity starts to decrease. This effect is attributed to the small Stokes shift of fluorescence and homotransfer. In fact, homotransfer among fluorescent molecules

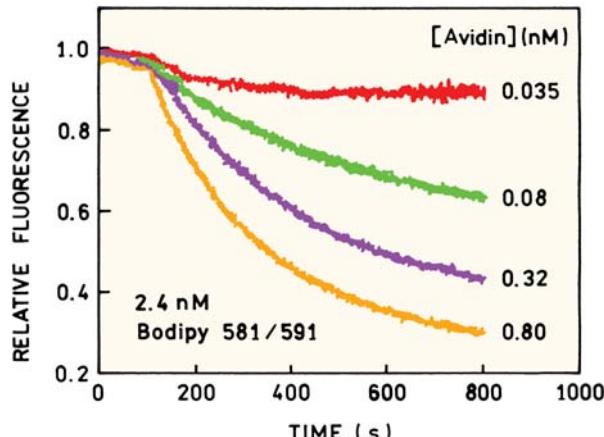
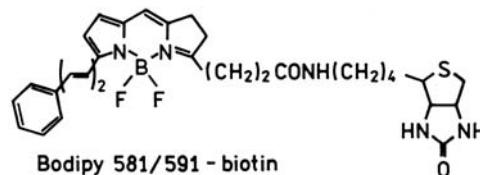


**Figure 13.7.** Self-quenching of Bodipy 581/591-biotin upon binding to avidin. Revised from [30].

was one of the earliest observations in fluorescence, and was detected by a decrease in the anisotropy of fluorophores at higher concentrations.<sup>29</sup> The possibility of homotransfer can be readily evaluated by examination of the absorption and emission spectra. For instance, perylene would be expected to display homotransfer but homotransfer is unlikely in quinine (Figure 1.3).

It is informative to see an example of self-quenching. Figure 13.7 shows the emission intensity of Bodipy 581/591-biotin upon the addition of avidin.<sup>30</sup> In the Bodipy probes the numbers refer to the excitation and emission wavelength, but these are only approximate values. Avidin is a tetramer with four binding sites for biotin. It is a relatively large protein about 50 Å in diameter. The biotin binding sites are about 30 Å apart. Before addition of avidin there is no self-quenching of Bodipy because the fluorophores are too far apart in this nM solution. Upon addition of avidin the Bodipy intensity decreases. There is little change in intensity when the avidin concentration is low: 0.035 mM. At this concentration there is not enough avidin to bind more than a small fraction of the Bodipy. At an avidin concentration of 0.8 nM there are about 3 Bodipy probes bound per avidin and the Bodipy is 70% quenched. The fact that Bodipy is quenched shows that the  $R_0$  value for

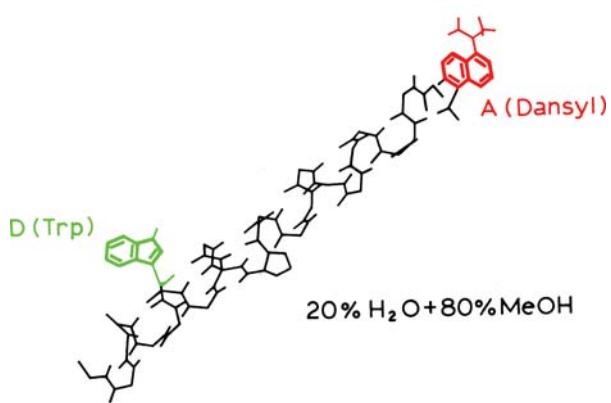


**Figure 13.8.** Chemical structure of melittin in the  $\alpha$ -helical state. The donor is tryptophan-19 and the acceptor is a N-terminal dansyl group. Revised from [31].

homotransfer is at least as large as the 30 Å distance between the binding sites.

### 13.3. DISTANCE MEASUREMENTS USING RET

#### 13.3.1. Distance Measurements in $\alpha$ -Helical Melittin

Since resonance energy transfer can be reliably assumed to depend on  $1/r^6$ , the transfer efficiency can be used to measure distances between sites in proteins. The use of RET in structural biochemistry is illustrated in Figure 13.8 for the peptide melittin.<sup>31</sup> This peptide has 26 amino acids. A single-tryptophan residue at position 19 serves as the donor. A single-dansyl acceptor was placed on the N-terminal amino group. The spectral properties of this D–A pair are shown in Figure 13.9. These spectral properties result in a Förster distance of 23.6 Å (Problem 13.5).

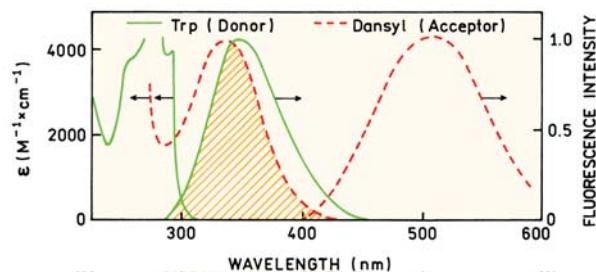


**Figure 13.9.** Overlap integral for energy transfer from a tryptophan donor to a dansyl acceptor on melittin  $R_0 = 23.6$  Å. Data from [31].

Depending on the solvent conditions melittin can exist in the monomer, tetramer,  $\alpha$ -helix, and/or random coil state.<sup>32–33</sup> In the methanol–water mixture specified on Figure 13.8 melittin is in the rigid  $\alpha$ -helical state and exists as a monomer. There is a single-dansyl acceptor adjacent to each tryptophan donor, and the helical structure ensures a single D–A distance, except for the range of distances allowed by the flexing side chains. Hence, we can use the theory described above, and in particular eqs. 13.12 and 13.13, to calculate the D–A distance.

In order to calculate the D–A distance it is necessary to determine the efficiency of energy transfer. This can be accomplished by comparing the intensity of the donor in the presence of acceptor ( $F_{DA}$ ), with the donor intensity from a control molecule which lacks the acceptor ( $F_D$ ). From Figure 13.10 one sees that the value of  $F_{DA}/F_D$  is near 0.55, so that the transfer efficiency is less than 50%:  $E = 0.45$ . Since  $E$  is less than 0.5 we know that the D-to-A distance must be larger than the  $R_0$  value. Using eq. 13.12 and an  $R_0$  value of 23.6 Å, one can readily calculate that the tryptophan-to-dansyl distance is 24.4 Å.

It is important to remember the assumptions used in calculating the distance. We assumed that the orientation factor  $\kappa^2$  was equal to the dynamic average of 2/3. In the case of melittin this is a good assumption because both the trp donor and dansyl acceptor are fully exposed to the liquid phase which is highly fluid. The rotational correlation times for such groups is typically near 100 ps, so that the dipoles can randomize during the excited-state lifetime.

Another assumption in calculating the trp to dansyl distance in melittin is that a single conformation exists, that there is a single D–A distance. This assumption is probably

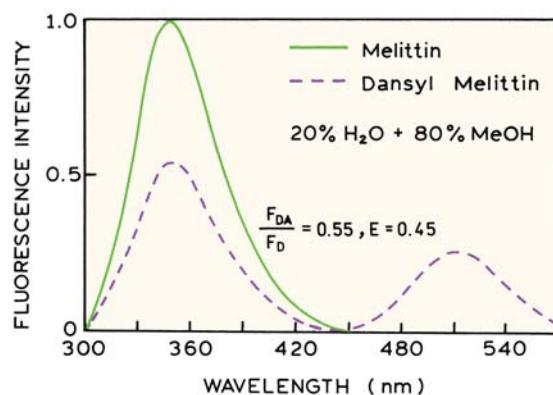


**Figure 13.10.** Emission spectra of the melittin donor (D) and acceptor-labeled melittin (D–A). Excitation at 282 nm. Revised from [31].

safe for many proteins in the native state, particularly for single-domain proteins. For unfolded peptides or multi-domain proteins a variety of conformations can exist, which results in a range of D–A distances. In this case calculation of a single distance using eq. 13.12 would result in an apparent distance, which would be weighted towards the shorter distances. Such systems are best analyzed in terms of a distance distribution using the time-resolved data (Chapter 14).

### 13.3.2. Effects of Incomplete Labeling

The largest source of error in calculating distance from the RET data is probably incomplete labeling with the acceptor. If melittin were incompletely labeled with acceptor, the measured value of  $F_{DA}$  would be larger than the true value, and the calculated distance too large. We are less concerned with underlabeling by the donor because the protein molecules that do not contain donors do not contribute to the donor intensity, assuming the extent of donor labeling is the same for the donor-alone and donor–acceptor pair.

If the fractional labeling with donor ( $f_a$ ) is known then the relative intensities can be used to calculate the transfer efficiency. In this case eq. 13.14 becomes<sup>13</sup>

$$E = 1 - \frac{F_{DA} - F_D(1 - f_A)}{F_D f_A} = \left(1 - \frac{F_{DA}}{F_D}\right) \frac{1}{f_A} \quad (13.17)$$

For a high degree of RET donor quenching, ( $F_{DA}/F_D \ll 1$ ), a small percentage of unlabeled acceptor can result in a

large change in the calculated transfer efficiency (Problem 13.9). The effect of  $f_a < 1.0$  is shown in Figure 13.11. Subfragment S-1 myosin, Myosin S-1, contains 42 thiol groups, two of which are highly reactive. These groups were labeled with 1,5-IAEDANS as the donor and IAF as the acceptor.<sup>34</sup> The transfer efficiency can be calculated from the relative intensities of the donor at 475 nm in the donor-alone or D–A pair. This yields a transfer efficiency of 30%. Since the Förster distance for this D–A pair is about 30 Å, the calculated distance between the D and A is 49 Å. However, the sample shown in Figure 13.11 was incompletely labeled with acceptor, so that  $f_a = 0.50$ . Using eq. 13.17 yields a transfer efficiency of 60% and a D–A distance of 40 Å. Hence it is essential to obtain complete labeling with the acceptor or to know the extent of acceptor labeling.

### 13.3.3. Effect of $\kappa^2$ on the Possible Range of Distances

**Advanced Topic**

In distance measurements using RET there is often concern about the effects of the orientation factor  $\kappa^2$ . At present there is no way to measure  $\kappa^2$ , except by determination of the x-ray crystal structure, or NMR structure, in which case the distance would be known and thus there would be no reason to use energy transfer. However, it is possible to set limits on  $\kappa^2$  that in turn set limits on the range of possible D–A distances. These limits are determined from the anisotropies of the donor and acceptor, which reflects the extent of orientational averaging toward the dynamic average of  $\kappa^2 = 2/3$ .

The problem of  $\kappa^2$  has been discussed in detail by Dale and coworkers<sup>10–12</sup> and summarized by Cheung.<sup>13</sup> The basic idea is that the donor and acceptor move freely within a cone and that energy transfer is rapidly averaged over all available D–A orientations. Interpretation of the formalism described by Dale and coworkers is not always straightforward, and we present the method preferred in this laboratory.<sup>35</sup> While it is not possible to calculate the values of  $\kappa^2$ , it is possible to set upper and lower limits. These values are given by

$$\kappa_{\min}^2 = \frac{2}{3} \left[ 1 - \frac{(d_D^x + d_A^x)}{2} \right] \quad (13.18)$$

$$\kappa_{\max}^2 = \frac{2}{3} (1 + d_D^x + d_A^x + 3d_D^x d_A^x) \quad (13.19)$$

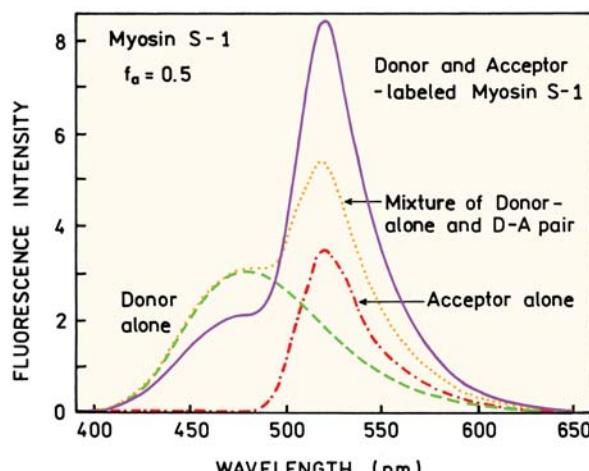


**Figure 13.11.** Emission spectra of labeled Myosin S-1. The donor is 1,5-IAEDANS and the acceptor is IAF. Revised from [34].

where

$$d_i^x = (r_i/r_0)^{1/2} \quad (13.20)$$

The value of  $d_i^x$  represents the depolarization factor due to segmental motion of the donor ( $d_D^x$ ) or acceptor ( $d_A^x$ ), but not the depolarization due to overall rotational diffusion of the protein. Overall rotational diffusion is not important because it does not change the D–A orientation. The values of  $r_i$  and  $r_0$  are often taken as the steady-state and fundamental anisotropies of the donor or acceptor. If the donor and acceptor do not rotate relative to each other during the excited-state lifetime, then  $d_D^x = d_A^x = 1.0$ , and  $\kappa_{\min}^2 = 0$  and  $\kappa_{\max}^2 = 4$ . If both D and A are independently and rapidly rotating over all space,  $\kappa_{\min}^2 = \kappa_{\max}^2 = 2/3$ .

There are several ways to obtain the values of  $d_D^x$  and  $d_A^x$ . The easiest method is to determine the anisotropy decays of the donor and acceptor, the latter when directly excited. This calculation of a range of  $\kappa^2$  values is illustrated by the anisotropy decays measured for the tryptophan donor and dansyl acceptor in  $\alpha$ -helical melittin (Table 13.2). Both the donor and the acceptor display two correlation times, one due to overall protein rotation near 2 ns, and a shorter correlation time near 0.3 ns due to segmental motions of the donor and the acceptor. It is these faster motions that randomize  $\kappa^2$ . The values of  $d_D^x$  and  $d_A^x$  are given by the ratio of the long correlation time amplitude to the total anisotropy. Hence, for melittin

$$d_D^x = \left( \frac{0.174}{0.294} \right)^{1/2} = 0.77 \quad (13.21)$$

$$d_A^x = \left( \frac{0.135}{0.300} \right)^{1/2} = 0.67 \quad (13.22)$$

Using these values and eqs. 13.18 and 13.19 one can calculate the limits on  $\kappa^2$ ,  $\kappa_{\min}^2 = 0.19$ , and  $\kappa_{\max}^2 = 2.66$ .

**Table 13.2.** Anisotropy Decays for  $\alpha$ -Helical Melittin<sup>a</sup>

Fluorophore	$r_{0i}$	$\theta_i$ (ns)
Tryptophan 19 <sup>b</sup>	0.120	0.23
	0.174	1.77
N-terminal dansyl	0.165	0.28
	0.135	2.18

<sup>a</sup>From [31].

<sup>b</sup>Determined for donor-only melittin. Similar amplitudes and correlation times were found for trp-19 in dansyl melittin.

Once the limiting values of  $\kappa^2$  are known one may use these values to calculate the maximum and minimum values of the distance which are consistent with the data. In calculating these distances one must remember that  $R_0$  was calculated with an assumed value of  $\kappa^2 = 2/3$ . Hence the minimum and maximum distances are given by

$$r_{\min} = \left( \frac{\kappa_{\min}^2}{2/3} \right)^{1/6} r \left( \kappa^2 = \frac{2}{3} \right) \quad (13.23)$$

$$r_{\max} = \left( \frac{\kappa_{\max}^2}{2/3} \right)^{1/6} r \left( \kappa^2 = \frac{2}{3} \right) \quad (13.24)$$

where  $r(\kappa^2 = 2/3)$  is the distance calculated assuming  $\kappa^2 = 2/3$ . Using the limiting values of  $\kappa^2$  one finds for the example given above that the distance can be from 0.81 to 1.26 of  $r(\kappa^2 = 2/3)$ . While this difference may seem large it should be remembered that there is an additional depolarization factor due to the transfer process itself, which will further randomize  $\kappa^2$  towards 2/3. Equations 13.18–13.20 provide a worst-case estimate, which usually overestimates the effects of  $\kappa^2$  on the calculated distance. For fluorophores with mixed polarization, where  $r_0 < 0.3$ , the error in distance is thought to be below 10%.<sup>16</sup>

There are two other ways to obtain the depolarization factors. One method is to construct a Perrin plot in which the steady-state polarization is measured for various viscosities. Upon extrapolation to the high-viscosity limit, the  $1/r_{app}$  intercept (Chapter 10) is typically larger than  $1/r_0$  in frozen solution. This difference is usually attributed to segmental probe motions, and can be used to estimate the depolarization factor,  $d_i^x = (r_{app}/r_0)^2$ . Another method is to estimate the expected steady-state anisotropy from the lifetime and correlation time of the protein, and to use these data to estimate  $d_D^x$  and  $d_A^x$  (Problem 13.8). The basic idea is to estimate  $d_A^x$  and  $d_D^x$  by correcting for the decrease in anisotropy resulting from rotational diffusion of the protein. Any loss in anisotropy, beyond that calculated for overall rotation, is assumed to be due to segmental motions of the donor or acceptor.

### 13.4. BIOCHEMICAL APPLICATIONS OF RET

#### 13.4.1. Protein Folding Measured by RET

In many experiments it is not necessary to calculate the distances because the biochemical question can be answered

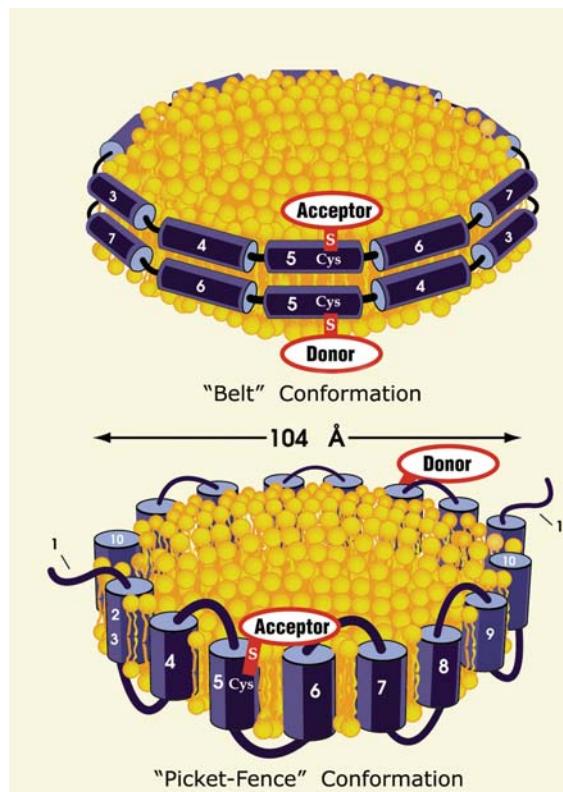


**Figure 13.12.** Possible conformations for apolipoprotein apoA-I when bound to lipids. Reprinted with permission from [36]. Figure courtesy of Dr. Mary G. Sorci-Thomas from the Wake Forest University, N.C.

from the presence or absence of RET. One example of this approach is determination of the conformation of an apolipoprotein when bound to lipids.<sup>36</sup> Apolipoproteins regulate cholesterol metabolism. ApoA-I is one of the most effective activators of lecithin:cholesterol acyltransferase (LCAT), which results in the formation of a discoidal form of high density lipoprotein (HDL). It is difficult to obtain x-ray structures from such proteins, and the conformation of the lipid-bound protein was uncertain. There were two possible structures (Figure 13.12). ApoA-I could form a belt around the lipid disk. Alternatively, apoA-I could fold as antiparallel  $\alpha$ -helices in a picket fence conformation.

The problem of the apoA-I conformation was addressed using RET. Recombinant apoA-I was made with a cysteine substituted for a glutamine at position 132, the Q132C mutant. It was known that the discoidal complex contained two molecules of apoA-I. One batch of apoA-I was labeled with the sulphydryl-reactive fluorescein 5-IAF, and the other batch labeled with a sulphydryl-reactive tetramethylrhodamine. Figure 13.13 shows emission spec-

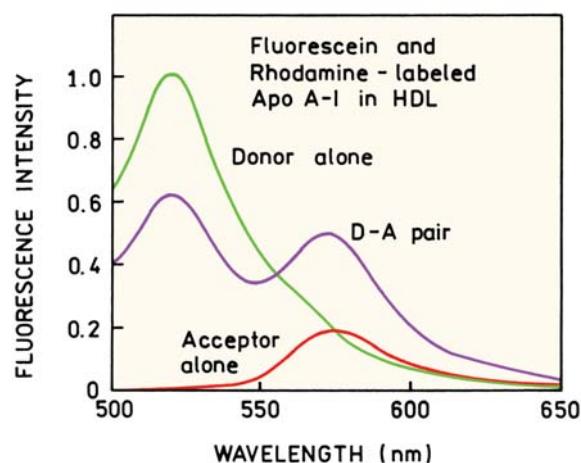


**Figure 13.13.** Emission spectra of labeled apoA-I in HDL. Revised from [36].

tra of labeled apoA-I in discoidal HDL. The spectrum of the D-A pair shows a decrease in donor intensity and an increase in acceptor intensity, consistent with about 40% energy transfer. The presence of RET proves that apoA-I is in the belt conformation (Figure 13.12) because RET would not occur for the picket-fence conformation where the donor and acceptor are 104D apart. Other groups agree with the belt structure, but believe the peptides are in a hairpin conformation.<sup>37</sup>

It is interesting to notice that the question was answered in spite of some complexity. Each discoidal particle could contain two donors, two acceptors, or one of each. The spectra in Figure 13.13 were obtained with a threefold excess of acceptor, so that most of the donors had a nearby acceptor. However, it was not necessary to resolve these populations to determine the confirmation of apoA-I in these particles. Additional references on RET and protein folding are listed near the end of the chapter.

### 13.4.2. Intracellular Protein Folding

RET with intensity ratio measurements have also been used to study protein folding in cells. Another apolipoprotein, apo E4, is associated with Alzheimer's disease. Apo E4, found in neurofibrillary tangles and amyloid plaques, is known to modulate plaque formation, and binds to very low density lipoproteins. Apo E3 has a similar amino acid sequence but binds to high-density lipoproteins and is not thought to be involved in amyloid protein deposition.

The different physiological effects of apo E4 and apo E3 are thought to be due to the different interactions

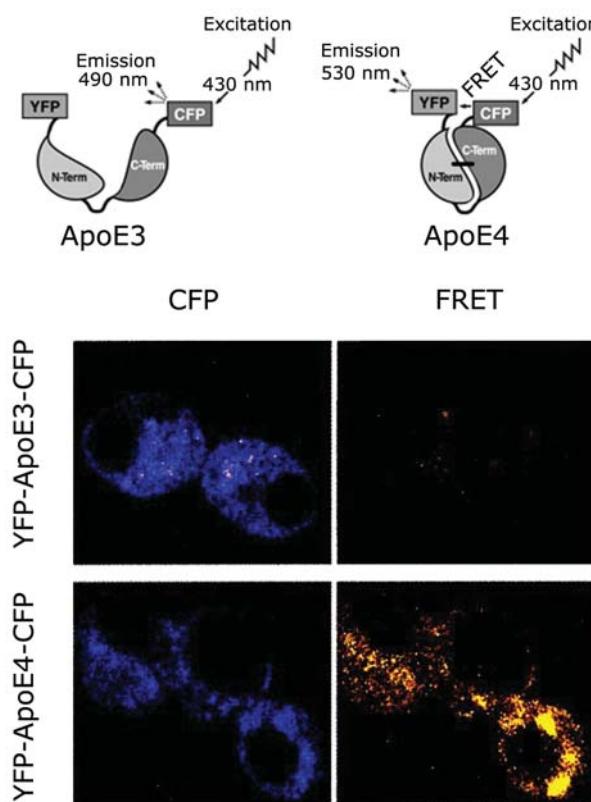


**Figure 13.14.** Schematic of labeled Apo E3 and Apo E4, and donor (CFP) and RET images in Neuro-2a cells. Reprinted with permission from [38].

between their two domains. Hence it was of interest to look for association of the domains in neuronal cells (Figure 13.14). The neuronal cells, Neuro-2a, were transfected with the constructs encoding for apo E4 or apo E3 that contained an energy-transfer pair of CFP (donor) and YFP (acceptor). The extent of RET was expected to depend on domain association. Donor images of the cells showed that the protein was expressed and was localized mostly in the cytoplasm. Taking ratios of the donor and acceptor images showed that RET occurred for intracellular apo E4 but not for intracellular apo E3. These results demonstrate how the applications of RET are being expanded to include in-vivo imaging.

### 13.4.3. RET and Association Reactions

RET can be used to measure binding interactions between molecules in solution<sup>39</sup> or in microscopy.<sup>40–41</sup> RET was used to detect association of the chaperonin proteins GroEL and GroES<sup>42</sup>. GroEL is a 798-kilodalton protein containing 57

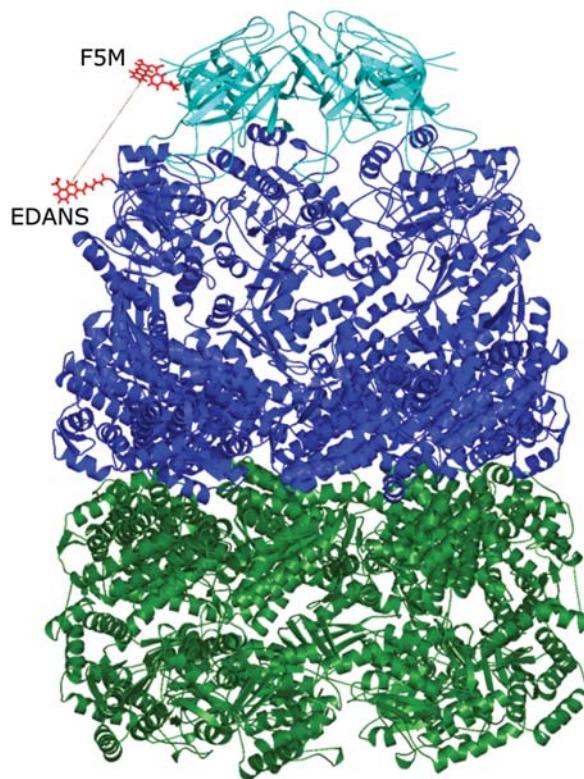


**Figure 13.15.** Structure of GroEL (green and blue) and GroES (light blue). The red structures are the donor and acceptor. Revised from [42]. Courtesy of Dr. Hays S. Kye from the Princeton University, N.J.

identical subunits. The subunits form a large barrel that facilitates refolding of proteins. This process requires binding of the 70-kilodalton CAP GroES (Figure 13.15). Binding of these two complexes depends on the presence of ATP.

Binding between GroEL and GroES was measured using RET. Mutant proteins were made with single-cysteine residues for labeling. GroEL was labeled with 2,5-IEDANS and GroES with a fluorescein derivative. Emission spectra of each protein and a mixture are shown in Figure 13.16. The spectrum from the mixture, in the absence of ATP (top), is the sum of the individual spectra. The result shows that GroEL and GroES are not bound together in the absence of ATP. Addition of ATP resulted in a decrease in the donor emission and an increase in the acceptor emission (bottom), which is due to formation of the GroEL–GroES complex.

RET was used to follow binding kinetics. Figure 13.17 shows the effect of adding unlabeled GroES to the complex. In the presence of ATP the complexes dissociate and reassociate, which may occur during refolding of proteins. As

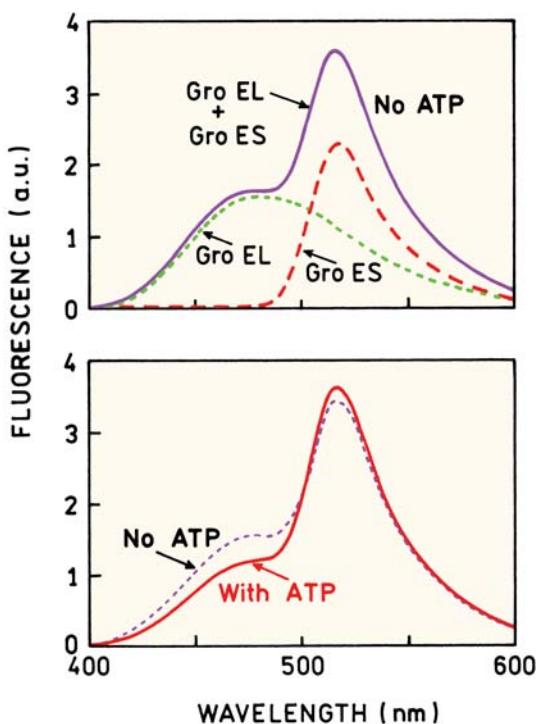


**Figure 13.16.** Emission spectra of IEDANS-labeled GroEL and fluorescein-labeled GroES without (top) and with (bottom) ATP. Revised from [42].

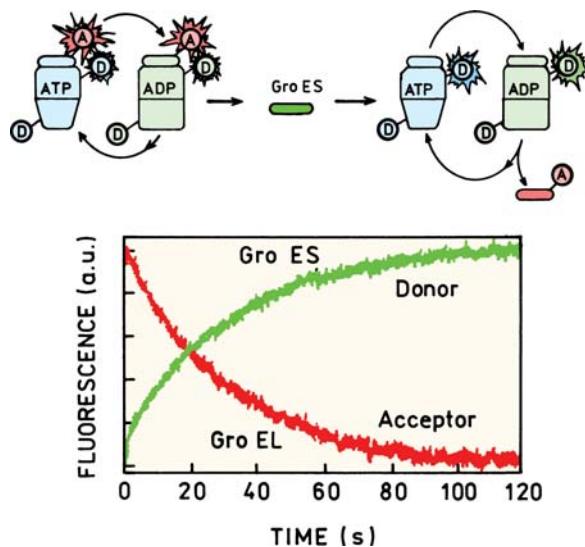


**Figure 13.17.** Dissociation of doubly labeled GroEL–GroES. Revised from [42].

unlabeled GroES associates with labeled GroEL the donor intensity increases and the acceptor intensity decreases. This result shows that information about binding can be obtained using either the donor or acceptor emission.

#### 13.4.4. Orientation of a Protein-Bound Peptide

In the presence of calcium, calmodulin is known to interact with a number of proteins and peptides. For example, a peptide from myosin light-chain kinase (MLCK) binds to calmodulin.<sup>43</sup> Such peptides are known to bind in the cleft between the two domains of calmodulin (Figure 13.18). When bound to calmodulin the MLCK peptide was known to adopt a  $\alpha$ -helical conformation. However, the direction of peptide binding to calmodulin was not known.

Information on the direction of binding was obtained by studying of four similar peptides, each containing a single-tryptophan residue that served as the donor (Figure 13.19). Calmodulin typically contains only tyrosine residues, so an intrinsic acceptor was not available. This problem was solved by using calmodulin from spinach, which contains a single-cysteine residue at position 26. This residue was labeled with 1,5-IAEDANS, which contains a thiol-reactive iodoacetyl group. The Förster distances for trp-to-AEDANS energy transfer ranged from 21 to 24 Å.

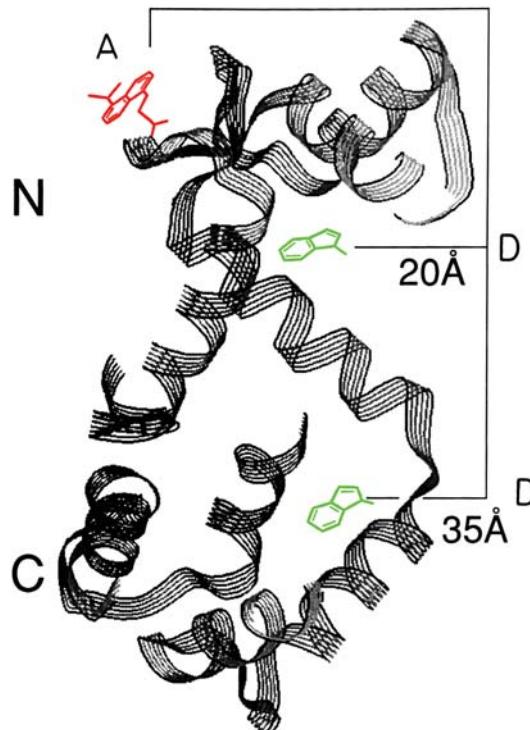


**Figure 13.18.** Structure of spinach calmodulin. The acceptor is AEDANS on cysteine-26 of calmodulin. The tryptophan donor is on the myosin light chain kinase peptides shown in Figure 13.19. Revised and reprinted with permission from [43]. Copyright © 1992, American Chemical Society.

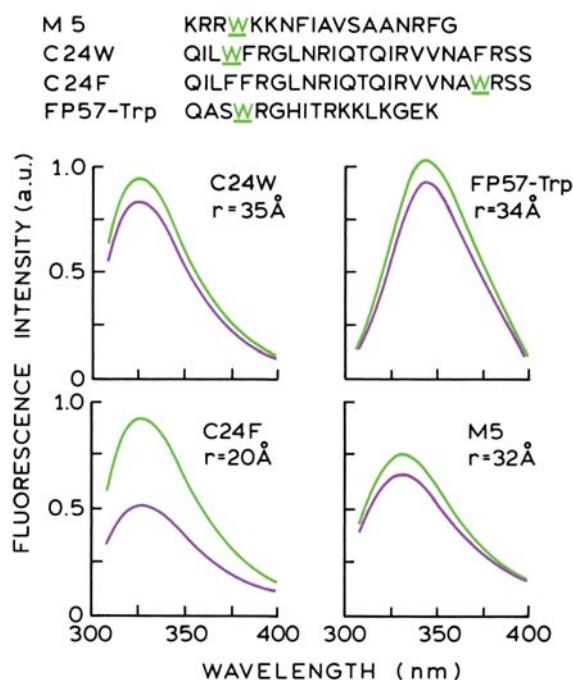


**Figure 13.19.** Emission spectra of the MLCK peptides when free in solution and when bound to AEDANS-calmodulin. The upper and lower spectra correspond to the peptide emission spectra in the absence and presence of AEDANS-calmodulin, respectively. The peptide sequences are shown in the top panel, and the calculated distance shown with the spectra. Excitation at 295 nm. Revised and reprinted with permission from [43]. Copyright © 1992, American Chemical Society.

Emission spectra of the tryptophan-containing peptides are shown in Figure 13.19. The excitation wavelength was 295 nm to avoid excitation of the tyrosine residues in calmodulin. Upon binding of AEDANS–calmodulin the tryptophan emission of each peptide is quenched. One of the peptides showed a transfer efficiency of 54%, and the remaining three peptides showed efficiencies ranging from 5 to 16%. These results demonstrated that the C-terminal region of the peptides bound closely to the N-terminal domain of calmodulin, and illustrate how structural information can be obtained by comparative studies of analogous structures.

#### 13.4.5. Protein Binding to Semiconductor Nanoparticles

Semiconductor nanoparticles, or Quantum Dots (QDs), have become widely used as fluorescent probes. They can have high quantum yields, narrow emission spectra, and

good photostability (Chapter 3). Understanding the interactions of Quantum Dots with proteins is important for their use as intracellular probes and for making the surfaces functional. RET has been used to determine the interaction of the *E. coli* maltose-binding protein (MBP) when bound to a QD.<sup>44</sup>

The orientation of MBP when bound to a QD was determined using six single-cysteine mutants of MBP. The individual proteins were labeled with Rhodamine Red (RR) at the sites shown in the top panel of Figure 13.20. The QDs were then titrated with the RR-labeled MBP. The donor was the QDs with a diameter near 60 Å and emitting at 555 nm. Binding of RR-MBP resulted in quenched QD emission and increased RR emission (middle panels). For some of the MBP mutants strong donor quenching was observed, for

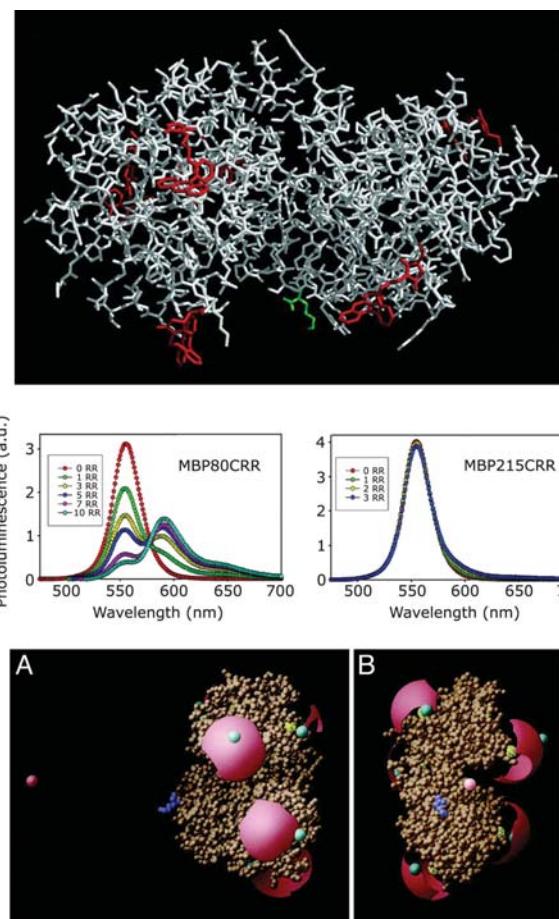


**Figure 13.20.** Top: *E. coli* maltose-binding protein shows six sites where Rhodamine Red was bound. Middle: Emission spectra of the QDs titrated with two RR-MBP. Bottom: Orientation of bound MBP relative to the center of the QD (pink dot). Revised from [44].

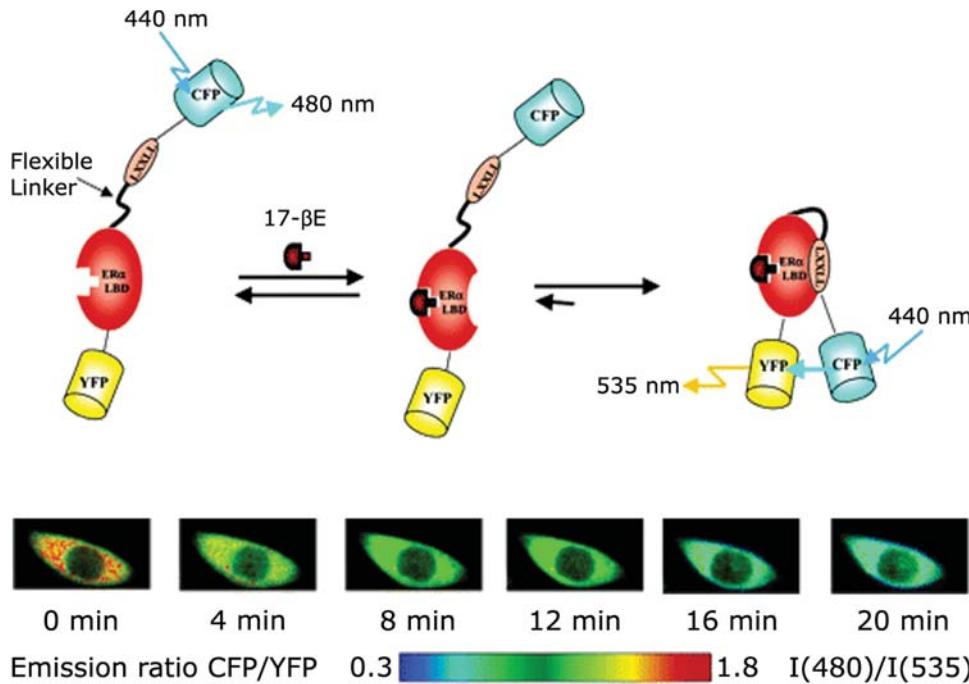


**Figure 13.21.** RET indicator for estrogens using the ligand-binding domain of estrogen receptor. The color scale shows the intensity at 480 nm divided by the intensity at 535 nm. Revised and reprinted with permission from [45]. Copyright © 2004, American Chemical Society.

other mutants there was almost no RET. By examination of the six mutant proteins the orientation of MBP on the surface of the a QD could be determined (Figure 13.20, lower panel). The center of the QD is shown as a pink dot, but the QD itself is not shown.

### 13.5. RET SENSORS

Resonance energy transfer has been used to develop a number of sensors. The use of donor-to-acceptor intensity ratios is valuable because the measurements become mostly independent of the overall intensity. This independence is especially important in fluorescence microscopy, where it is usually not possible to know or control the local fluorophore concentration.

#### 13.5.1. Intracellular RET Indicator for Estrogens

RET has been used with green fluorescent proteins (GFPs) and their variants to develop sensors for a variety of analytes. One example is an intracellular indicator for estrogens.<sup>45</sup> In this case cyan (CFP) and yellow (YFP) fluorescent proteins form the RET pair (Figure 13.21). These pro-

teins are linked by a peptide containing both the ligand-binding domain of estrogen receptor  $\alpha$  (ER) and an estrogen-dependent ER-interaction site. The latter domain is comprised of the sequence LXXLL, where L is leucine and X is any other amino acid. Upon binding the ER against 17- $\beta$  estradiol, the ER ligand-binding domain becomes competent to interact with the LXXLL motif. The resulting conformational change brings the tethered CFP and YFP moieties into close proximity, thus increasing the efficiency of energy transfer.

An advantage of using a GFP and its mutants is the potential to express the indicator in the cell rather than injecting or loading the indicator into the cell. A plasmid expression vector encoding the RET indicator was transfected into CHO cells, which then synthesized the indicator. The labeled cells were exposed to 17- $\beta$ E and imaged at the emission wavelength of CFP (480 nm) and YFP (535 nm). The ratio of intensities was used to create a false color image of the cells (Figure 13.21). After exposure to 17- $\beta$ E the intensity at 535 nm increased, while the intensity at 480 nm decreased. This approach allows cell-based assays for estrogen potency or the blocking effects of estrogen antagonists.

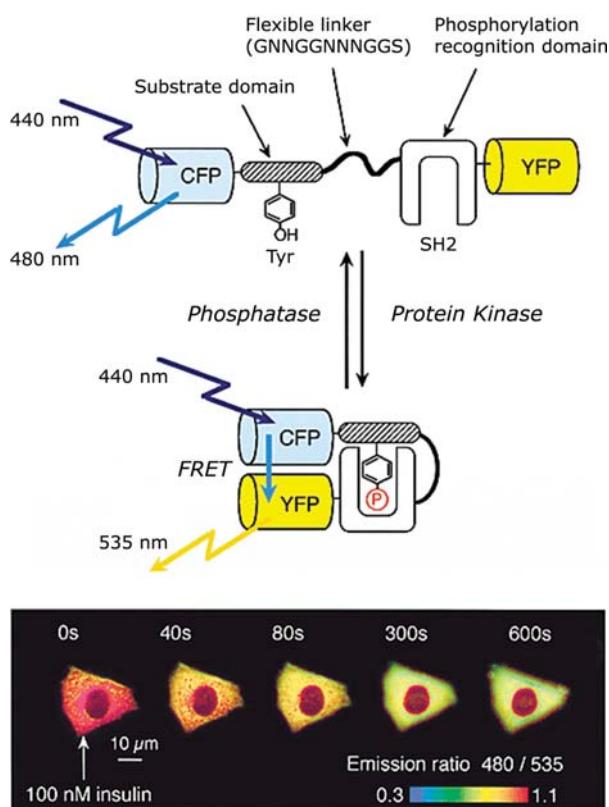


**Figure 13.22.** RET sensor for protein phosphorylation. Revised from [46].

### 13.5.2. RET Imaging of Intracellular Protein Phosphorylation

Protein phosphorylation by kinases is an important method of intracellular signaling. For example, the insulin receptor is a tyrosine kinase. The insulin receptor phosphorylates a tyrosine residue in a particular sequence, which then binds to a recognition domain (SH2) of another protein (Figure 13.22). This binding event brings CFP and YFP into closer proximity for increased RET. This protein was expressed in CHO-IR cells, which overexpress the insulin receptor. These transfected cells were then exposed to 100-nM insulin, which caused a time-dependent decrease in the donor-to-acceptor intensity ratio, which indicated an increase in RET. Ratiometric RET imaging can thus be used to study a wide variety of intracellular processes.

### 13.5.3. Imaging of Rac Activation in Cells

In the previous example the donor and acceptor proteins were covalently linked. Intracellular RET indicators can also be made when the donor and acceptor are not covalently

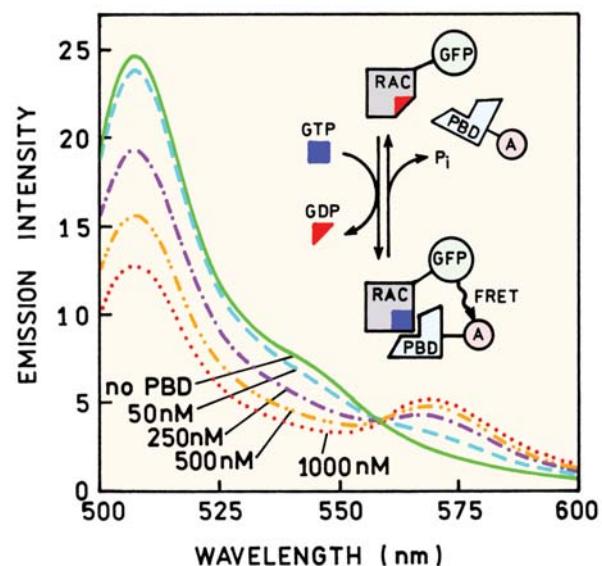


**Figure 13.23.** Emission spectra of Rac–GFP in the presence of GTP and an Alexa-546 labeled kinase (PBD) that binds to Rac. The value of  $R_0$  is 51D. Revised from [47].

linked but associate in the cell. The Rac is a GTPase that is involved in several processes, including actin dynamics and control of cell morphology. An approach for sensing Rac activation is shown in Figure 13.23. The donor was Rac–GFP. The acceptor was a kinase (PBD) labeled with Alexa-546. In the presence of GTP the labeled kinase PBD binds to Rac–GTP, as can be seen from the changes in the donor and acceptor intensities for these proteins in solution.<sup>47</sup> Assessment of this interaction in living cells was accomplished by transfection of the gene encoding Rac–GFP and microinjection of the labeled kinase. The confluent monolayer of cells was then scraped. This caused activation of Rac as the cells moved toward the open area and actin polymerization increases. The location-dependent concentrations of Rac–GFP are seen from the donor intensity images (Figure 13.24, right). An increase in RET, or binding of Rac–GFP to PBD, is seen as the shift from blue to green in the pseudocolor images (Figure 13.24, left). Comparison of the RET images with the GFP intensity images shows that the D–A intensity ratios are independent of the Rac–GFP concentration.

### 13.6. RET AND NUCLEIC ACIDS

RET is used extensively in DNA analysis,<sup>48–49</sup> which is discussed in Chapter 21. In contrast to DNA, RNA can adopt a variety of three-dimensional conformations owing to its

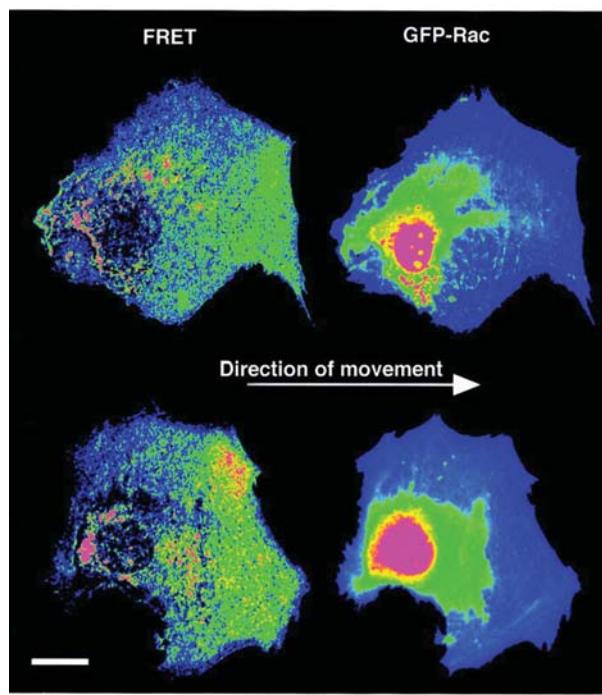


**Figure 13.24.** RET (left) and Rac–GFP intensity (near 510 nm) image (right) of motile 3T3 fibroblasts. Bar = 24  $\mu\text{m}$ . Reprinted from [47].

single-stranded structure. Some RNA molecules are catalytically active, which are called ribozymes. RET has found use in studies of ribozyme folding and dynamics.<sup>50–52</sup>

Figure 13.25 shows the donor, acceptor, sequence, and secondary structure of the labeled hairpin ribozyme containing the covalently linked donor and acceptor molecules.<sup>52</sup> After the substrate (S) binds it is cleaved by the ribozyme. Cleavage requires binding of the A and B loops to each other, a motion called docking. This motion is expected to bring the donor and acceptor closer together (lower panel). Upon addition of substrate there are changes in both the donor and acceptor intensities (Figure 13.26). The donor intensity decreases as expected for increased energy transfer. The behavior of the acceptor is more complicated. The acceptor intensity increases as expected, but only after an initial drop in intensity on substrate binding. This decrease is due to quenching of the acceptor by the nearby guanine residue (Chapter 8).

### 13.6.1. Imaging of Intracellular RNA

The localization and concentration of intracellular mRNA is an important factor in the control of protein synthesis.

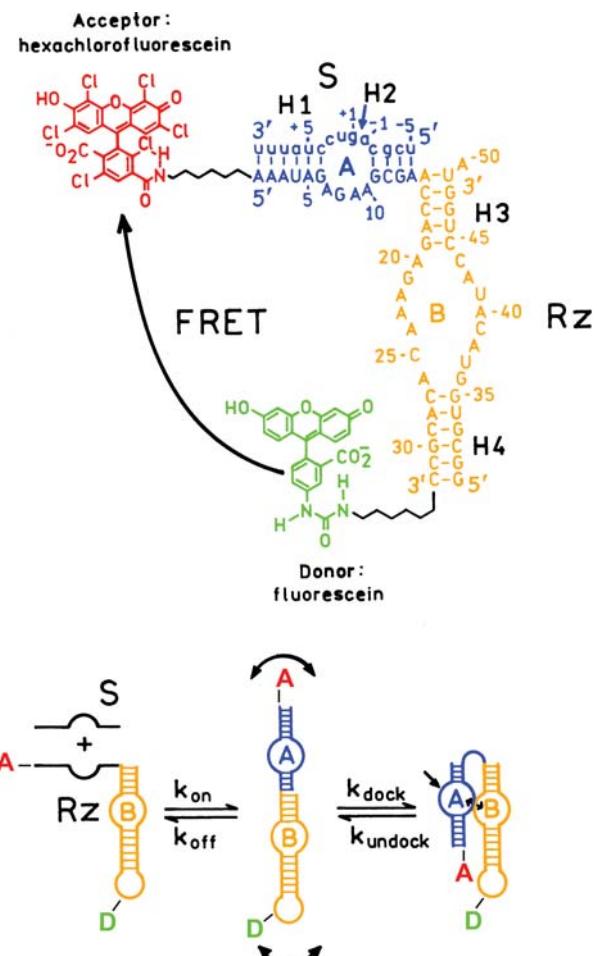


**Figure 13.25.** Structure of the hairpin ribozyme labeled with donor and acceptor. The lower panel shows the docking conformational change that occurs upon binding of the substrate. Revised from [52].

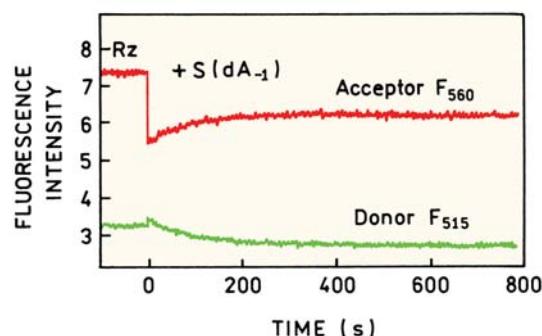


**Figure 13.26.** Intensity changes of the donor and acceptor on the hairpin ribozyme upon binding of substrate. Courtesy of Dr. Nils G. Walter, University of Michigan.

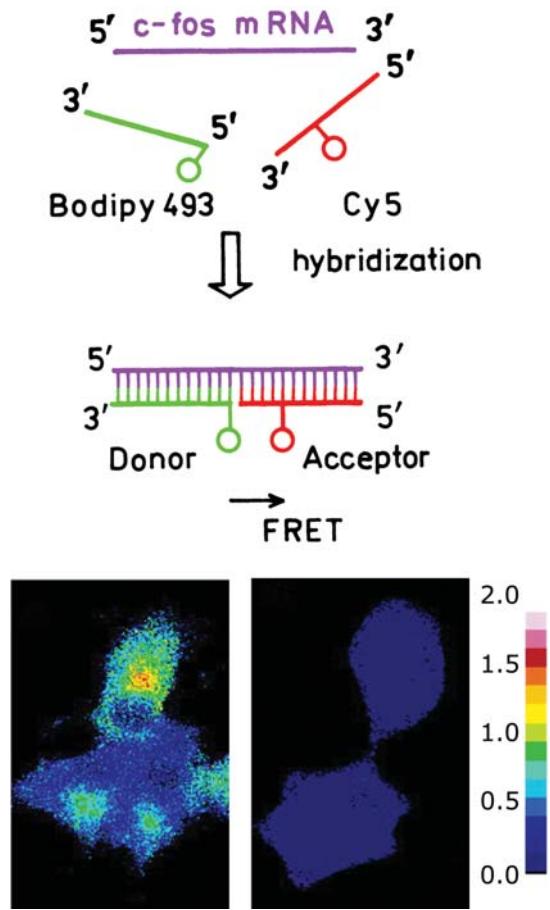


**Figure 13.27.** Intracellular detection of c-fos mRNA by RET ratio imaging. Revised from [53].

Control of c-fos mRNA is important because the c-fos protein is a transcription factor that participates in control of the cell cycle and differentiation. The presence of c-fos mRNA was studied using DNA oligomers that were expected to bind close to each other when hybridized with c-fos mRNA (Figure 13.27).<sup>53</sup> The level of c-fos mRNA could be controlled by stimulation of the Cos cells. The donor- and acceptor-labeled oligomers were added to the cells by microinjection. The presence of the mRNA was found in the stimulated (left) but not in the unstimulated cells. These results show that RET imaging can be used to study the difficult problem of the regulation of mRNA in cells.

### 13.7. ENERGY TRANSFER EFFICIENCY FROM ENHANCED ACCEPTOR FLUORESCENCE

In an RET experiment the acceptor absorption must overlap with the donor emission wavelengths, but the acceptor does

not need to be fluorescent. If the acceptor is fluorescent then light absorbed by the donor and transferred to the acceptor appears as enhanced acceptor emission. This enhanced acceptor emission can be seen in Figure 13.16 at 520 nm for the fluorescein-labeled GroES when bound to donor-labeled GroEL. By extrapolating the emission spectrum of the donors one can see that its emission extends to the acceptor wavelengths. Hence the intensity measured at the acceptor wavelength typically contains some contribution from the donor.

The use of acceptor intensities is further complicated by the need to account for directly excited acceptor emission, which is almost always present.<sup>13</sup> In the case of labeled apoA-I (Figure 13.13) the directly excited acceptor emission accounted for about half the total acceptor emission. The acceptor is almost always excited directly to some extent because the acceptor absorbs at the excitation wavelength used to excite the donor, resulting in acceptor emission without RET.

Calculation of the transfer efficiency from the enhanced acceptor emission requires careful consideration of all the interrelated intensities. Assuming that the donor does not emit at the acceptor wavelength, the efficiency of transfer is given by

$$E = \frac{\varepsilon_A(\lambda_D^{\text{ex}})}{\varepsilon_D(\lambda_D^{\text{ex}})} \left[ \frac{F_{AD}(\lambda_A^{\text{em}})}{F_A(\lambda_A^{\text{em}})} - 1 \right] \left( \frac{1}{f_D} \right) \quad (13.25)$$

In this expression  $\varepsilon_A(\lambda_D^{\text{ex}})$  and  $\varepsilon_D(\lambda_D^{\text{ex}})$  are the extinction coefficients (single D–A pairs) or absorbance (multiple acceptors) of the acceptor and donor at the donor excitation wavelength ( $\lambda_D^{\text{ex}}$ ), and  $f_D$  is the fractional labeling with the donor. The acceptor intensities are measured at an acceptor emission wavelength ( $\lambda_A^{\text{em}}$ ) in the absence  $F_A(\lambda_A^{\text{em}})$  and presence  $F_{AD}(\lambda_A^{\text{em}})$  of donor. This expression with  $f_D = 1.0$  can be readily obtained by noting that  $F_A(\lambda_A^{\text{em}})$  is proportional to  $\varepsilon_A(\lambda_D^{\text{ex}})$ , and  $F_{AD}(\lambda_A^{\text{em}})$  is proportional to  $\varepsilon_A(\lambda_D^{\text{ex}}) + E\varepsilon_D(\lambda_D^{\text{ex}})$ . The accuracy of the measured  $E$  value is typically less than when using the donor emission (eq. 13.13). When measuring the acceptor emission it is important to have complete donor labeling,  $f_D = 1.0$ .

It is also important to remember that it may be necessary to correct further for the donor emission at  $\lambda_A^{\text{em}}$ , which is not considered in eq. 13.25. The presence of donor emission at the acceptor wavelength, if not corrected for in measuring the acceptor intensities, will result in an apparent transfer efficiency larger than the actual value (see Problem 13.11). Equation 13.25 can also be applied when mul-

tiple acceptors are present, such as for unlinked donor and acceptor pairs (Chapter 15). In this case  $\varepsilon_D(\lambda_D^{ex})$  and  $\varepsilon_A(\lambda_D^{ex})$  are replaced by the optical densities of the donor,  $OD_D(\lambda_D^{ex})$ , and of the acceptor,  $OD_A(\lambda_D^{ex})$ , at the donor excitation wavelength.

Occasionally it is difficult to obtain the transfer efficiency from the sensitized acceptor emission. One difficulty is a precise comparison of the donor-alone and donor–acceptor pair at precisely the same concentration. The need for two samples at the same concentration can be avoided if the donor and acceptor-labeled sample can be enzymatically digested so as to eliminate energy transfer.<sup>54</sup> Additionally, methods have been developed which allow comparison of the donor-alone and donor–acceptor spectra without requiring the concentrations to be the same. This is accomplished using the shape of the donor emission and subtracting its contribution from the emission spectrum of the D–A pair. This method is best understood by reading the original descriptions.<sup>55–56</sup>

And, finally, one should be aware of the possibility that the presence of the acceptor affects the donor fluorescence by a mechanism other than RET. Such effects could occur due to allosteric interactions between the donor and acceptor sites. For example, the acceptor may block diffusion of a quencher to the donor, or it may cause a shift in protein conformation that exposes the donor to solvent. If binding of the acceptor results in quenching of the donor by some other mechanism, then the transfer efficiency determined from the donor will be larger than the true value. In such cases, the transfer efficiency determined from enhanced acceptor emission is thought to be the correct value. The possibility of non-RET donor quenching can be addressed by comparison of the transfer efficiencies observed from donor quenching and acceptor sensitization.<sup>57</sup> See Problem 13.11.

### 13.8. ENERGY TRANSFER IN MEMBRANES

In the examples of resonance energy transfer described above there was a single acceptor attached to each donor molecule. The situation becomes more complex for unlinked donors and acceptors.<sup>5</sup> In this case the bulk concentration of acceptors is important because the acceptor concentration determines the D–A proximity. Also, one needs to consider the presence of more than a single acceptor around each donor. In spite of the complexity, RET has considerable potential for studies of lateral organization in membranes. For example, consider a membrane that con-

tains regions that are in the liquid or solid phase. If the donor and acceptor both partition into the same region, one expects the extent of energy transfer to be increased relative to that expected for a random distribution of donors and acceptors between the phases. Conversely, if donor and acceptor partition into different phases, the extent of energy transfer will decrease relative to a random distribution, an effect that has been observed.<sup>58</sup> Alternatively, consider a membrane-bound protein. If acceptor-labeled lipids cluster around the protein, then the extent of energy transfer will be greater than expected for acceptor randomly dispersed in the membrane. Energy transfer to membrane-localized acceptors can be used to measure the distance of closest approach to a donor site on the protein, or the distance from the donor to the membrane surface.

RET in membranes is typically investigated by measuring the transfer efficiency as the membrane acceptor concentration is increased. Quantitative analysis of such data requires knowledge of the extent of energy transfer expected for fluorophores randomly distributed on the surface of a membrane. This is a complex problem that requires one to consider the geometric form of the bilayer (planar or spherical) and transfer between donors and acceptors which are on the same side of the bilayer as well as those on opposite sides. A variety of approaches have been used<sup>58–68</sup> and in general, numerical simulations and/or computer analyses are necessary. These theories are complex and not easily summarized. The complexity of the problem is illustrated by the fact that an analytical expression for the donor intensity for energy transfer in two dimensions only appeared in 1964,<sup>69</sup> and was extended to allow an excluded volume around the donor in 1979.<sup>59</sup> RET to multiple acceptors in one, two, and three dimensions is described in more detail in Chapter 15. Several of these results are present here to illustrate the general form of the expected data.

A general description of energy transfer on a two-dimensional surface has been given by Fung and Stryer.<sup>5</sup> Assuming no homotransfer between the donors, and no diffusion during the donor excited-state lifetime, the intensity decay of the donor is given by

$$I_D(t) = I_D^0 \exp(-t/\tau_D) \exp[-\sigma S(t)] \quad (13.26)$$

where

$$S(t) = \int_{r_c}^{\infty} \{ 1 - \exp[-(t/\tau_D)(R_0/r)^6] \} 2\pi r dr \quad (13.27)$$

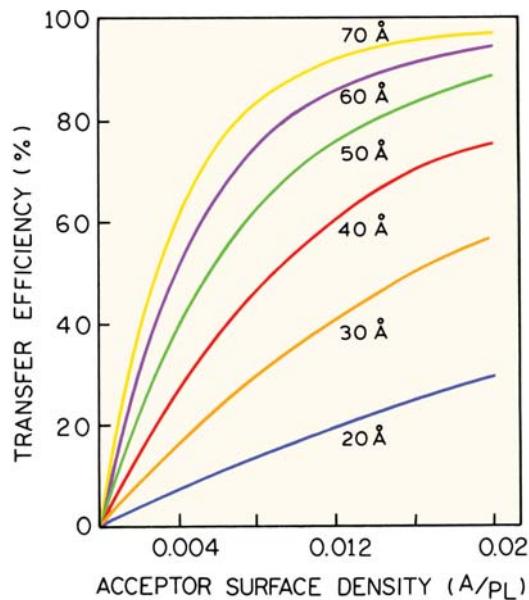


**Figure 13.28.** Calculated efficiencies of energy transfer for donor–acceptor pairs localized in a membrane. The distances are the  $R_0$  value for energy transfer and A/PL is the acceptor-to-phospholipid molar ratio. The area per phospholipid was assumed to be  $70 \text{ \AA}^2$ , so the distance of closest approach was  $8.4 \text{ \AA}$ . Revised and reprinted with permission from [5]. Copyright © 1978, American Chemical Society.

In these equations  $\exp[-\sigma S(t)]$  describes that portion of the donor decay due to RET,  $\sigma$  is the surface density of the acceptor, and  $r_c$  is the distance of closest approach between the donor and acceptors. The energy-transfer efficiency can be calculated by an equation analogous to eqs. 13.13 and 13.14, except that the intensities or lifetimes are calculated from integrals of the donor intensity decay:

$$E = 1 - \frac{1}{\tau_D} \int \frac{I_D(t)}{I_D^0} dt \quad (13.28)$$

Use of eqs. 13.26–13.28 is moderately complex and requires use of numerical integration. However, the approach is quite general, and can be applied to a wide variety of circumstances by using different expressions for  $S(t)$  that correspond to different geometric conditions. Figure 13.28 shows the calculated transfer efficiencies for a case in which the donor to acceptors are constrained to the lipid–water interface region of a bilayer. Several features of these predicted data are worthy of mention. The efficiency of transfer increases with  $R_0$  and the efficiency of energy transfer is independent of the concentration of donor. The absence of energy transfer between donors is generally a

safe assumption unless the donor displays a small Stokes shift or the donor concentration is high, conditions that favor homotransfer. Only small amounts of acceptor, 0.4 mole%, can result in easily measured quenching. For example, with  $R_0 = 40 \text{ \AA}$  the transfer efficiency is near 50% for just 0.8 mole% acceptor, or one acceptor per 125 phospholipid molecules.

One may readily visualize how energy quenching data could be used to determine whether the distributions of donor and acceptor were random. Using the calculated value of  $R_0$ , one compares the measured extent of donor quenching with the observed efficiency. If the measured quenching efficiency exceeds the calculated value then a preferential association of donors and acceptors within the membrane is indicated.<sup>70</sup> Less quenching would be observed if the donor and acceptor were localized in different regions of the membrane, or if the distance of closest approach were restricted due to steric factors. We note that these calculated values shown in Figure 13.28 are strictly true only for transfer between immobilized donor and acceptor on one side of a planar bilayer. However, this simple model is claimed to be a good approximation for a spherical bilayer.<sup>5</sup> For smaller values of  $R_0$  transfer across the bilayer is not significant.

### 13.8.1. Lipid Distributions Around Gramicidin

Gramicidin is a linear polypeptide antibiotic containing D- and L-amino acids and four tryptophan residues. Its mode of action involves increasing the permeability of membranes to cations and protons. In membranes this peptide forms a dimer (Figure 13.29),<sup>71</sup> which contains a 4-Å diameter aqueous channel that allows diffusion of cations. The nonpolar amino acids are present on the outside of the helix, and thus expected to be exposed to the acyl side chain region of the membrane. Hence, gramicidin provides an ideal model to examine energy transfer from a membrane-bound protein to membrane-bound acceptors.

It was of interest to determine if membrane-bound gramicidin was surrounded by specific types of phospholipids. This question was addressed by measurement of the transfer efficiencies from the tryptophan donor to dansyl-labeled phosphatidylcholine (PC). The lipid vesicles were composed of phosphatidylcholine (PC) and phosphatidic acid (PA).<sup>72</sup> Emission spectra of gramicidin bound to PC–PA membranes are shown in Figure 13.30. The tryptophan emission is progressively quenched as the dansyl-PC

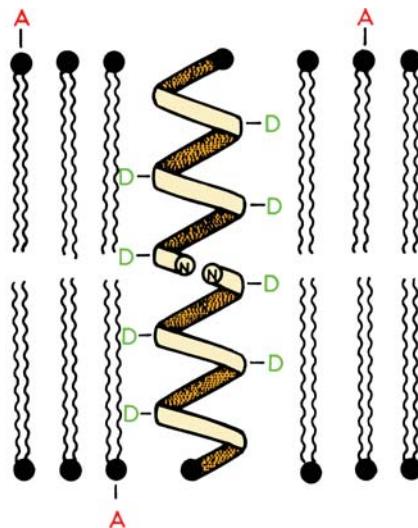
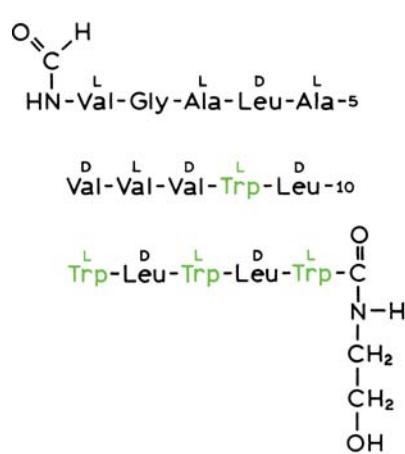


**Figure 13.29.** Amino-acid sequence (left) and structure of the membrane-bound dimer (right) of gramicidin A. The D and L (left) refer to the optical isomer of the amino acid. Revised from [71].

acceptor concentration is increased. The fact that the gramicidin emission is quenched by RET, rather than a collisional process, is supported by the enhanced emission of the dansyl-PC at 520 nm.

The decreasing intensities of the gramicidin emission can be used to determine the tryptophan to dansyl-PC transfer efficiencies (Figure 13.31). The transfer efficiencies are compared with the calculated efficiencies for a random

acceptor distribution in two dimensions. These curves were calculated using eqs. 13.26 and 13.28. The data match with the curve calculated for the known  $R_0$  of 24 Å, demonstrating that acceptor distribution of dansyl-PC around gramicidin is random. If the labeled lipid dansyl-PC was local-

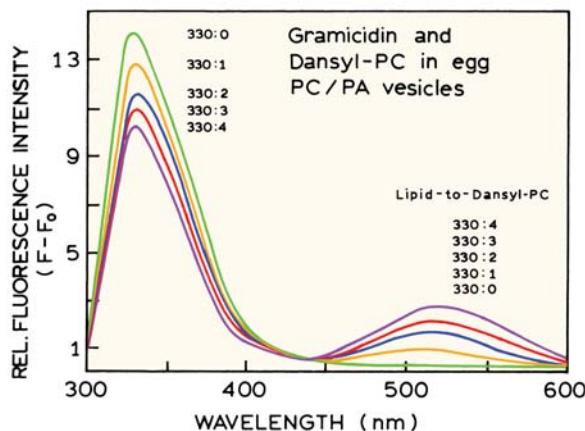


**Figure 13.30.** Emission spectra of gramicidin and dansyl-PC in vesicles composed of egg PC and egg PA.  $\lambda_{ex} = 282$  nm. Dansyl-PC is 1-acyl-2-[11-N-[5-dimethylamino naphthalene-1-sulfonyl]amino] undecanoyl phosphatidylcholine. The lipid-to-dansyl PC ratios are shown on the figure. Revised and reprinted with permission from [72]. Copyright © 1988, American Chemical Society.

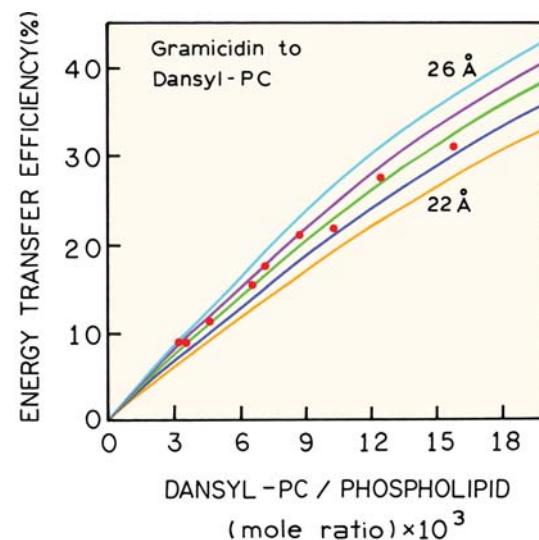


**Figure 13.31.** Efficiency of energy transfer from gramicidin to dansyl-PC as a function of dansyl-PC/phospholipid ratio. The experimental points (●) were calculated from the tryptophan quenching data, and the solid curves were calculated for a random array of donors and acceptors in two dimensions with  $R_0 = 22, 23, 24, 25$ , and 26 Å. A value of  $R_0 = 24 \pm 1$  Å gave the best fit to the experimental data. Revised and reprinted with permission from [72]. Copyright © 1988, American Chemical Society.

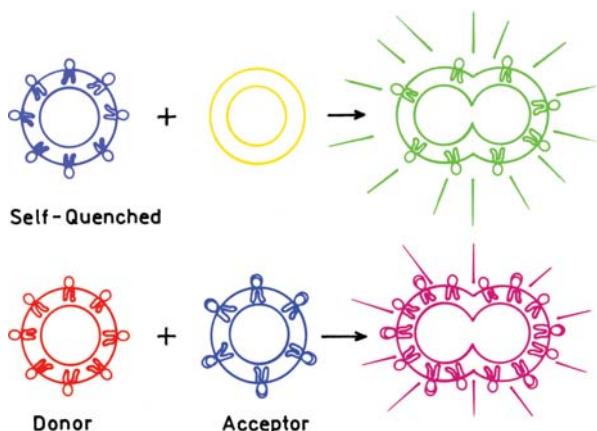


**Figure 13.32.** Membrane fusion detection by RET. **Top:** Homotransfer and self-quenching. **Bottom:** RET for a D–A pair.

ized around gramicidin then RET to the dansyl acceptor would exceed the calculated values.

### 13.8.2. Membrane Fusion and Lipid Exchange

Energy transfer has been widely used to study fusion and/or aggregation of membranes. These experiments are shown schematically in Figure 13.32. Suppose a lipid vesicle contains a high concentration of a fluorophore that undergoes homo-RET (Figure 13.32). Initially the membrane will be dimly fluorescent because of self-quenching (top). If this vesicle fuses with another unlabeled vesicle the extent of self-quenching will decrease and the emission intensity will increase. An alternative approach is to use RET between a donor and acceptor (bottom). In this case the vesicles labeled with each type of fluorophore will appear with different colors. Upon fusion the color will change. Depending upon the concentrations of donor and acceptor in the membranes, the extent of RET could be small, in which case the color of the fused vesicles would be a simple mixture of the two colors. If the probe concentration results in efficient RET then the fused vesicles will have the color of the acceptor.

As seen from Figure 13.28 the acceptor density does not need to be large. Any process that dilutes the donor and acceptors from the initially labeled vesicles will result in less energy transfer and increased donor emission. For example, if the D–A-labeled vesicles fuse with an unlabeled vesicle, the acceptor becomes more dilute and the donor intensity increases. Alternatively, the donor may display a modest water solubility adequate to allow exchange

between vesicles. Then some of the donors will migrate to the acceptor-free vesicles and again the donor fluorescence will increase. It is also possible to trap a water-soluble fluorophore–quencher pair inside the vesicles. Upon fusion the quencher can be diluted and/or released. A wide variety of different procedures have been proposed,<sup>73–79</sup> but most rely on these simple proximity considerations.

RET has been used to obtain images of membranes as they fuse together. Figure 13.33 shows images of giant unilamellar vesicles (GUVs) that were labeled either with a cyanine dye DiO (left, green) or a rhodamine dye Rh–PE (right, orange).<sup>80</sup> The two types of vesicles contained oppositely charged lipids, which resulted in rapid fusion. The GUVs were brought together by electrophoretic migration in a fluid channel. The images were obtained with a color CCD camera, so they are real color images. Prior to contact between the GUVs, the DiO-labeled vesicle is bright and the Rh–PE-labeled vesicle dark. Rh–PE is dark because it absorbs weakly at the excitation wavelength of near 450 nm. As the vesicles make contact and fuse, a bright orange signal appears, which is due to Rh–PE. Eventually the entire vesicle surface becomes orange. The green emission from DiO is mostly quenched due to RET to Rh–PE.

---

### 13.9. EFFECT OF $\tau^2$ ON RET

While the effect of  $\kappa^2$  in energy transfer is frequently discussed,<sup>81–82</sup> there are relatively few experimental results.<sup>83–86</sup> Most of the experimental results are measurements with a single  $\kappa^2$  value, rather than a systematic dependence of  $k_T(r)$  or  $\kappa^2$ . However, the experimental results show that the value of  $\kappa^2$  does affect the rate of energy transfer. Figure 13.34 shows the chemical structure of two donor–acceptor pairs. The anthracene donor was linked either in plane with the porphyrin acceptor ( $\kappa^2 = 4$ ) or in the axial position ( $\kappa^2 = 0$ ). The transition moment of the anthracene is along the short axis of the molecule. Emission spectra of these D–A pairs were compared to a donor control molecule. For the axial anthracene ( $\kappa^2 = 0$ ) there is almost no RET to the porphyrin. For the in-plane anthracene with  $\kappa^2 = 4$  there is almost no emission showing RET is rapid for these colinear transitions. These results show that orientation can have a dramatic effect on the RET efficiency. However, these D–A pairs are rather rigidly linked and a smaller effect is expected if the acceptor had more mobility relative to the porphyrin ring.

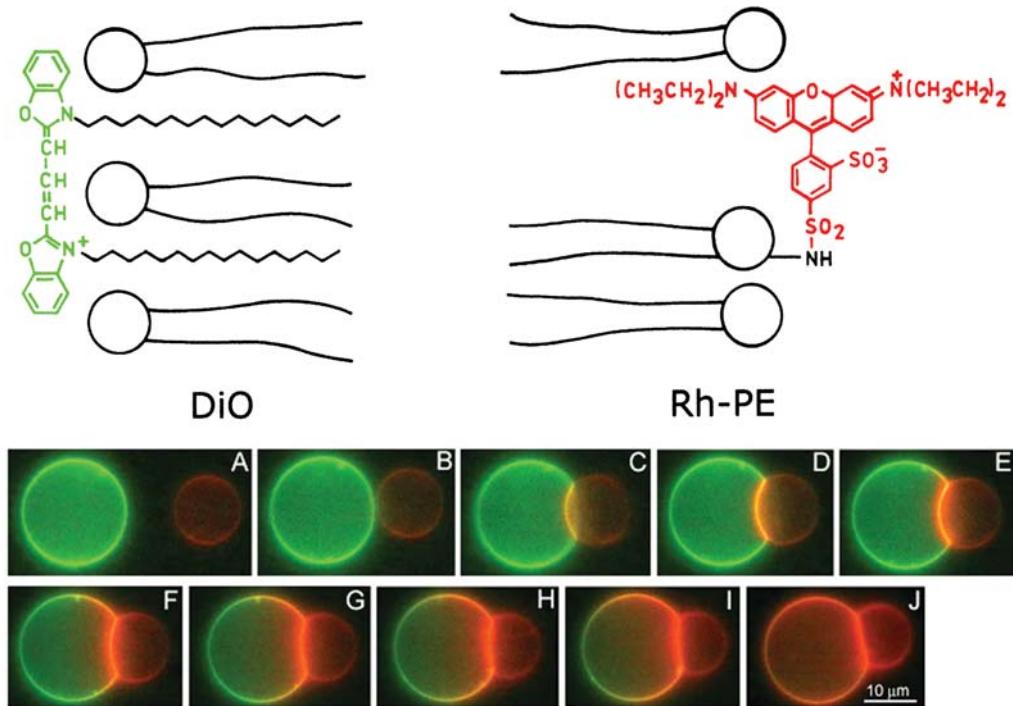


**Figure 13.33.** Fluorescence microscopy of lipid mixing between giant unilamellar vesicles. Reprinted from [80] and courtesy of Dr. Robert MacDonald, Northwestern University.

### 13.10. ENERGY TRANSFER IN SOLUTION

Energy transfer also occurs for donors and acceptors randomly distributed in three dimensional solutions. In this case the theory is relatively simple. Following  $\delta$ -function excitation the intensity decay of the donor is given by<sup>88-90</sup>

$$I_D(t) = I_D^0 \exp\left[-t/\tau_D - 2\gamma\left(\frac{t}{\tau_D}\right)^{1/2}\right] \quad (13.29)$$

with  $\gamma = A/A_0$ , where  $A$  is the acceptor concentration. If  $R_0$  is expressed in cm, the value of  $A_0$  in moles/liter is given by

$$A_0 = \frac{3000}{2\pi^{3/2} N R_0^3} \quad (13.30)$$

The relative steady-state quantum yield of the donor is given by

$$\frac{F_{DA}}{F_D} = 1 - \sqrt{\pi} \gamma \exp(\gamma^2)[1 - \text{erf}(\gamma)] \quad (13.31)$$

where

$$\text{erf}(\gamma) = \frac{2}{\sqrt{\pi}} \int_0^\gamma \exp(-x^2) dx \quad (13.32)$$

These expressions are valid for immobile donors and acceptors for which the orientation factor is randomized by rotational diffusion,  $\kappa^2 = 2/3$ . For randomly distributed acceptors,<sup>3</sup> where rotation is much slower than the donor decay,  $\kappa^2 = 0.476$ . Still more complex expressions are necessary if the donor and acceptor diffuse during the lifetime of the excited state (Chapters 14 and 15). The complex decay of donor fluorescence reflects the time-dependent population of D-A pairs. Those donors with nearby acceptors decay more rapidly, and donors more distant from acceptors decay more slowly.

The term  $A_0$  is called the critical concentration and represents the acceptor concentration that results in 76% energy transfer. This concentration in moles/liter (M) can be calculated from eq. 13.30, or from a simplified expression<sup>14</sup>

$$A_0 = 447/R_0^3 \quad (13.33)$$

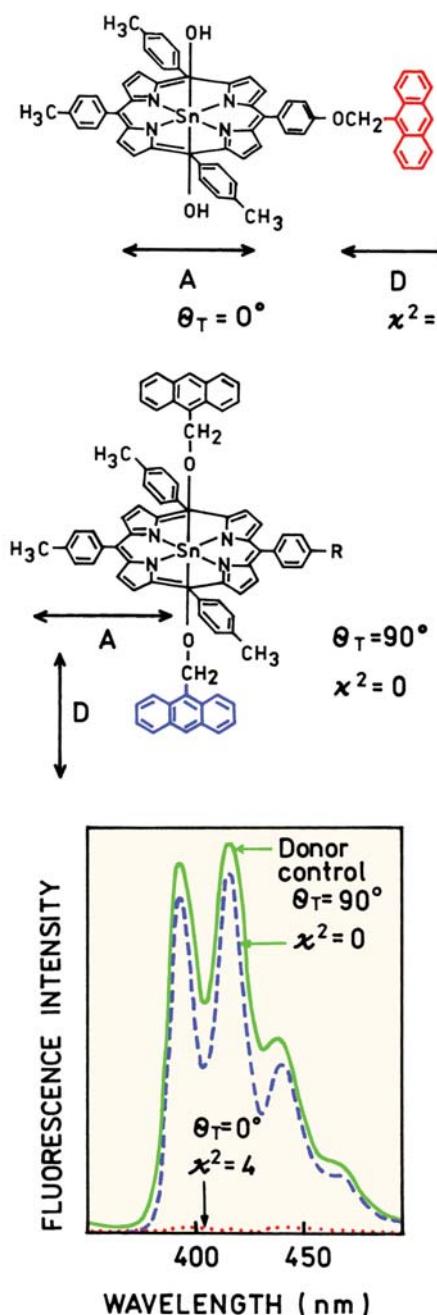


**Figure 13.34.** Chemical structures and emission spectra of covalently linked D-A pairs used to study the effect of  $\kappa^2$  on RET. Revised from [87].

where  $R_0$  is in units of Å. This reveals an important feature of energy transfer between unlinked donors and acceptors, which is that the acceptor concentrations need to be rather high for RET between unlinked donor and acceptors. For instance, if  $R_0 = 25 \text{ \AA}$ , then  $A_0 = 0.029 \text{ M} = 29 \text{ mM}$ . Because  $A_0$  is orders of magnitude larger than typical concentrations

in fluorescence experiments, we usually ignore energy transfer between donors and acceptors linked to different molecules. The high acceptor concentrations needed for RET in solution also make it difficult to measure RET between unlinked donors and acceptors. The high acceptor concentrations result in high optical densities, requiring front face observation and careful correction for inner filter effects. It is important to consider inner filter effects when comparing intensity values.

### 13.10.1. Diffusion-Enhanced Energy Transfer

To this point we have not considered the effects of diffusion on the extent of energy transfer. This is a complex topic that typically requires numerical methods for simulations and analysis of the data. However, there is one simple case in which the donor decay times are very long so that diffusive motions of the donors result in their sampling of the entire available space. This is called the rapid diffusion limit.<sup>91</sup> With fluorophores displaying ns decay times this limit is not obtainable. However, lanthanides are known to display much longer decay times near 0.6–2.5 ms for terbium and europium,<sup>92–93</sup> depending upon the ligands. In relatively fluid solution the long donor decay times allow the excited molecule to diffuse through all available space. The rate of transfer then becomes limited by the distance of closest approach between donors and acceptors. Suppose an acceptor is buried in a protein or a membrane. One can determine the depth of the acceptor from the extent of energy transfer to the acceptor from terbium or europium chelates in the aqueous phase. Another important feature of energy transfer in the rapid-diffusion limit is that it occurs at much lower acceptor concentrations.<sup>91</sup> For a homogeneous three-dimensional solution, energy transfer is 50% efficient at acceptor concentrations near 1 μM, which is 1000-fold lower than for energy transfer without diffusion.<sup>14</sup> This topic is described in detail in Chapter 15.

### 13.11. REPRESENTATIVE $R_0$ VALUES

It is often convenient to have an estimate of an  $R_0$  value prior to performing the complex calculation of the overlap integral or labeling of the macromolecule. Unfortunately, there is no general reference for the Förster distances. A larger number of  $R_0$  values are summarized in the book by Berlman,<sup>94</sup> but most of the listed fluorophores are not used in biochemistry. A large number of Förster distances have been summarized in reviews.<sup>14,95</sup> Some of these  $R_0$  values are

**Table 13.3.** Representative Förster Distances for Various Donor–Acceptor Pairs<sup>a</sup>

Donor	Acceptor	$R_0$ (Å)
Naphthalene <sup>14</sup>	Dansyl	22
Dansyl <sup>95</sup>	FITC	33–41
Dansyl <sup>114</sup>	ODR	43
$\epsilon$ -A <sup>14</sup>	NBD	38
IAF <sup>14</sup>	TMR	37–50
Pyrene <sup>14</sup>	Coumarin	39
FITC <sup>14</sup>	TMR	49–54
IAEDANS <sup>14</sup>	FITC	49
IAEDANS <sup>14</sup>	IAF	46–56
IAF <sup>14</sup>	EIA	46
CF	TR	51
Bodipy <sup>25</sup>	Bodipy	57
BPE <sup>14</sup>	Cy5	72
Terbium <sup>96</sup>	Rhodamine	65
Europium <sup>94</sup>	Cy5	70
Europium <sup>97</sup>	APC	90

<sup>a</sup>Dansyl, 5-dimethylamino-1-naphthalenesulfonic acid.  $\epsilon$ -A, 1-N<sup>6</sup>-ethenoadenosine; APC, allophycocyanin; Bodipy, 4,4-difluoro-4-bora-3a,4a-diaza-s-indacene; BPE, B-phycoerythrin; CF, carboxylfluorescein, succinimidyl ester; Cy5, carboxymethylindocyanine-N-hydroxysuccinimidyl ester; EIA, 5-(iodoacetamido) eosin; FITC, fluorescein-5-isothiocyanate; IAEDANS, 5-(2-O((iodocetyl)amino)ethyl)amino)naphthalene-1-sulfonic acid; IAF, 5-iodoacetamidoindole; NBD, 7-nitrobenz-2-oxa-1,3-diazol-4-yl; ODR, octadecylrhodamine; TMR, tetramethylrhodamine; TR, Texas Red.

summarized in Table 13.3 for a variety of D–A pairs, and in Table 13.4 for tryptophan donor–acceptor pairs. In the case of lanthanides in environments where the quantum yield is near unity, and for multi-chromophore acceptors,  $R_0$  values as large as 90 Å have been calculated.<sup>95</sup> This is the largest Förster distance reported to date.

## REFERENCES

1. Förster Th. 1948. Intermolecular energy migration and fluorescence. *Ann Phys* 2:55–75. [Translated by RS Knox, Department of Physics and Astronomy, University of Rochester, Rochester, NY 14627.]
2. Stryer L. 1978. Fluorescence energy transfer as a spectroscopic ruler. *Annu Rev Biochem* 47:819–846.
3. Steinberg IZ. 1971. Long-range nonradiative transfer of electronic excitation energy in proteins and polypeptides. *Annu Rev Biochem* 40:83–114.
4. Clegg RM. 1996. Fluorescence resonance energy transfer. In *Fluorescence imaging spectroscopy and microscopy*, pp. 179–252. Ed XF Wang, B Herman. John Wiley & Sons, New York.
5. Fung BKK, Stryer L. 1978. Surface density determination in membranes by fluorescence energy transfer. *Biochemistry* 17:5241–5248.
6. Yekta A, Duhamel J, Winnik MA. 1995. Dipole–dipole electronic energy transfer: fluorescence decay functions for arbitrary distributions of donors and acceptors—systems with planar geometry. *Chem Phys Lett* 235:119–125.
7. Rolinski OJ, Birch DJS. 2000. Determination of acceptor distribution from fluorescence resonance energy transfer: theory and simulation. *J Chem Phys* 112(20):8923–8933.
8. Weller A. 1974. Theodor Förster. *Ber Bunsenges Phys Chem* 78:969–971.
9. Gordon M, Ware WR., eds. 1975. *The exciplex*. Academic Press, New York. [See the Introduction about Theodor Förster.]
10. Dale RE, Eisinger J, Blumberg WE. 1979. The orientational freedom of molecular probes: the orientation factor in intramolecular energy transfer. *Biophys J* 26:161–194; *Errata* 30:365 (1980).
11. Dale RE, Eisinger J. 1975. Polarized excitation energy transfer. In *Biochemical fluorescence, concepts*, Vol. 1, pp. 115–284. Ed RF Chen, H Edelhoch. Marcel Dekker, New York.
12. Dale RE, Eisinger J. 1974. Intramolecular distances determined by energy transfer: dependence on orientational freedom of donor and acceptor. *Biopolymers* 13:1573–1605.
13. Cheung HC. 1991. Resonance energy transfer. In *Topics in fluorescence spectroscopy, Vol. 2: Principles*, pp. 127–176. Ed JR Lakowicz. Plenum Press, New York.
14. Wu P, Brand L. 1994. Resonance energy transfer: methods and applications [review]. *Anal Biochem* 218:1–13.
15. Dos Remedios CG, Moens PDJ. 1995. Fluorescence resonance energy transfer spectroscopy is a reliable "ruler" for measuring structural changes in proteins. *J Struct Biol* 115:175–185.

**Table 13.4.** Förster Distances for Tryptophan–Acceptor Pairs<sup>a</sup>

Donor	Acceptor <sup>b</sup>	$R_0$ (Å)
Trp	Nitrobenzoyl	16
Trp	Dansyl	21–24
Trp	IAEDANS	22
Trp	Anthroyloxy	24
Trp	TNB	24
Trp	Anthroyl	25
Trp	Tyr-NO <sub>2</sub>	26
Trp	Pyrene	28
Trp	Heme	29
Trp	NBS	30
Trp	DNBS	33
Trp	DPH	40

<sup>a</sup>From [14].

<sup>b</sup>ANS, 6-amlinonaphthalene-2-sulfonic acid; Dansyl, 5-dimethylamino-1-naphthalenesulfonic acid; DPH, 1,6-diphenyl-1,3,5-hexatriene; DNBS, dinitrobenzenesulfonyl; IAEDANS, 5-((2-iodocetyl)amino)ethyl)amino-naphthalene-1-sulfonic acid; NBS, nitrobenzenesulfonyl; TNB, trinitrophenyl; TNB, trinitrophenyl.

16. Haas E, Katchalski-Katzir E, Steinberg IZ. 1978. Effect of the orientation of donor and acceptor on the probability of energy transfer involving electronic transitions of mixed polarizations. *Biochemistry* **17**:5064–5070.
17. Latt SA, Cheung HC, Blout ER. 1965. Energy transfer: a system with relatively fixed donor-acceptor separation. *J Am Chem Soc* **87**(5): 996–1003.
18. Stryer L, Haugland RP. 1967. Energy transfer: a spectroscopic ruler. *Proc Natl Acad Sci USA* **58**:719–726.
19. Gabor G. 1968. Radiationless energy transfer through a polypeptide chain. *Biopolymers* **6**:809–816.
20. Haugland RP, Yguerabide J, Stryer L. 1969. Dependence of the kinetics of singlet-singlet energy transfer on spectral overlap. *Proc Natl Acad Sci USA* **63**:23–30.
21. Horrocks WDEW, Holmquist B, Vallee BL. 1975. Energy transfer between terbium(III) and cobalt(II) in thermolysin: a new class of metal–metal distance probes. *Proc Natl Acad Sci USA* **72**(12): 4764–4768.
22. Xiao M, Selvin PR. 2001. Quantum yields of luminescent lanthanide chelates and far-red dyes measured by resonance energy transfer. *J Am Chem Soc* **123**:7067–7073.
23. Chen J, Selvin PR. 2000. Lifetime- and color-tailored fluorophores in the micro- to millisecond time regime. *J Am Chem Soc* **122**: 657–660.
24. BODIPY, 4,4-difluoro-4-bora-3a,4a-diaza-s-indacene. BODIPY is a trademark of Molecular Probes Inc.
25. Johnson ID, Kang HC, Haugland RP. 1991. Fluorescent membrane probes incorporating dipyrrometheneboron difluoride fluorophores. *Anal Biochem* **198**:228–237.
26. Hemmila IA, ed. 1991. *Applications of fluorescence in immunoassays*. John Wiley & Sons, New York (see p. 113).
27. Malicka J, Gryczynski I, Lakowicz JR. 2003. Enhanced emission of highly labeled DNA oligomers near silver metallic surfaces. *Anal Chem* **75**:4408–4414.
28. Lakowicz JR, Malicka J, D'Auria S, Gryczynski I. 2003. Release of the self-quenching of fluorescence near silver metallic surfaces. *Anal Biochem* **320**:13–20.
29. Kawski A. 1983. Excitation energy transfer and its manifestation in isotropic media. *Photochem Photobiol* **38**(4):487–504.
30. Song X, Swanson BI. 2001. Rapid assay for avidin and biotin based on fluorescence quenching. *Anal Chim Acta* **442**:79–87.
31. Lakowicz JR, Gryczynski I, Wiczk W, Laczko G, Prendergast FC, Johnson ML. 1990. Conformational distributions of melittin in water/methanol mixtures from frequency-domain measurements of nonradiative energy transfer. *Biophys Chem* **36**:99–115.
32. Faucon JF, Dufourcq J, Lurson C. 1979. The self-association of melittin and its binding to lipids. *FEBS Lett* **102**:187–190.
33. Goto Y, Hagiwara Y. 1992. Mechanism of the conformational transition of melittin. *Biochemistry* **31**:732–738.
34. Cheung HC, Gonsoulin F, Garland F. 1983. Fluorescence energy transfer studies on the proximity of the two essential thiols of myosin subfragment-1. *J Biol Chem* **258**(9):5775–5786.
35. Lakowicz JR, Gryczynski I, Cheung HC, Wang C-K, Johnson ML, Joshi N. 1988. Distance distributions in proteins recovered by using frequency-domain fluorometry: applications to Troponin I and its complex with Troponin C. *Biochemistry* **27**:9149–9160.
36. Li HH, Lyles DS, Thomas MJ, Pan W, Sorci-Thomas MG. 2000. Structural determination of lipid-bound ApoA-I using fluorescence resonance energy transfer. *J Biol Chem* **275**(47):37048–37054.
37. Tricerri MA, Agree AKB, Sanchez SA, Bronski J, Jonas A. 2001. Arrangement of apolipoprotein A-I in reconstituted high-density lipoprotein disks: an alternative model based on fluorescence resonance energy transfer experiments. *Biochemistry* **40**:5065–5074.
38. Xu Q, Brecht WJ, Weisgraber KH, Mahley RW, Huang Y. 2004. Apolipoprotein E4 domain interaction occurs in living neuronal cells as determined by fluorescence resonance energy transfer. *J Biol Chem* **279**(24):25511–25516.
39. Berney C, Danuser G. 2003. FRET or no FRET: a quantitative comparison. *Biophys J* **84**:3992–4010.
40. Hoppe A, Christensen K, Swanson JA. 2002. Fluorescence resonance energy transfer-based stoichiometry in living cells. *Biophys J* **83**:3652–3664.
41. Gordon GW, Berry G, Liang XH, Levine B, Herman B. 1998. Quantitative fluorescence resonance energy transfer measurements using fluorescence microscopy. *Biophys J* **74**:2702–2713.
42. Rye HS. 2001. Application of fluorescence resonance energy transfer to the GroEL–GroES chaperonin reaction. *Methods* **24**:278–288.
43. Chapman ER, Alexander K, Vorherr T, Carafoli E, Storm DR. 1992. Fluorescence energy transfer analysis of calmodulin–peptide complexes. *Biochemistry* **31**:12819–12825.
44. Medintz IL, Konnert JH, Clapp AR, Stanish I, Twigg ME, Mattoussi H, Mauro JM, Deschamps JR. 2004. A fluorescence resonance energy transfer-derived structure of a quantum dot-protein bioconjugate nanoassembly. *Proc Natl Acad Sci USA* **101**(26):9612–9617.
45. Awais M, Sato M, Sasaki K, Umezawa Y. 2004. A genetically encoded fluorescent indicator capable of discriminating estrogen agonists from antagonists in living cells. *Anal Chem* **76**:2181–2186.
46. Sato M, Ozawa T, Inukai K, Asano T, Umezawa Y. 2002. Fluorescent indicators for imaging protein phosphorylation in single living cells. *Nature Biotechnol* **20**:287–294.
47. Kraynov VS, Chamberlain C, Bokoch GM, Schwartz MA, Slabaugh S, Hahn KM. 2000. Localized Rac activation dynamics visualized in living cells. *Science* **290**:333–337.
48. Parkhurst KM, Parkhurst LJ. 1996. Detection of point mutations in DNA by fluorescence energy transfer. *J Biomed Opt* **1**(4):435–441.
49. Morrison LE, Stols LM. 1993. Use of FRET to measure association of DNA oligomers. *Biochemistry* **32**:3095–3104.
50. Bassi GS, Murchie AIH, Walter F, Clegg RM, Lilley DMJ. 1997. Ion-induced folding of the hammerhead ribozyme: a fluorescence resonance energy transfer study. *EMBO J* **16**(24):7481–7489.
51. Walter NG. 2001. Structural dynamics of catalytic RNA highlighted by fluorescence resonance energy transfer. *Methods* **25**:19–30.
52. Walter NG, Hampel KJ, Brown KM, Burke JM. 1998. Tertiary structure formation in the hairpin ribozyme monitored by fluorescence resonance energy transfer. *EMBO J* **17**(8):2378–2391.
53. Tsuji A, Koshimoto H, Sato Y, Hirano M, Sei-Iida Y, Kondo S, Ishibashi K. 2000. Direct observation of specific messenger RNA in a single living cell under a fluorescence microscope. *Biophys J* **78**:3260–3274.
54. Epe B, Steinhauser KG, Woolley P. 1983. Theory of measurement of Förster-type energy transfer in macromolecules. *Proc Natl Acad Sci USA* **80**:2579–2583.

55. Clegg RM. 1992. Fluorescence resonance energy transfer and nucleic acids. *Methods Enzymol* **211**:353–388.
56. Clegg RM, Murchie AIH, Lilley DM. 1994. The solution structure of the four-way DNA junction at low-salt conditions: a fluorescence resonance energy transfer analysis. *Biophys J* **66**:99–109.
57. Berman HA, Yguerabide J, Taylor P. 1980. Fluorescence energy transfer on acetylcholinesterase: spatial relationships between peripheral site and active center. *Biochemistry* **19**:2226–2235.
58. Pedersen S, Jorgensen K, Baekmark TR, Mouritsen OG. 1996. Indirect evidence for lipid-domain formation in the transition region of phospholipid bilayers by two-probe fluorescence energy transfer. *Biophys J* **71**:554–560.
59. Estep TN, Thomson TE. 1979. Energy transfer in lipid bilayers. *Biophys J* **26**:195–207.
60. Wolber PK, Hudson BS. 1979. An analytical solution to the Förster energy transfer problem in two dimensions. *Biophys J* **28**:197–210.
61. Dewey TG, Hammes GG. 1980. Calculation of fluorescence resonance energy transfer on surfaces. *Biophys J* **32**:1023–1035.
62. Shaklai N, Yguerabide J, Ranney HM. 1977. Interaction of hemoglobin with red blood cell membranes as shown by a fluorescent chromophore. *Biochemistry* **16**:5585–5592.
63. Snyder B, Freire E. 1982. Fluorescence energy transfer in two dimensions. *Biophys J* **40**:137–148.
64. Yguerabide J. 1994. Theory for establishing proximity relations in biological membranes by excitation energy transfer measurements. *Biophys J* **66**:683–693.
65. Dewey TG. 1991. Fluorescence energy transfer in membrane biochemistry. In *Biophysical and biochemical aspects of fluorescence spectroscopy*, pp. 294–315. Ed TG Dewey. Plenum Press, New York.
66. Dobretsov GE, Kurek NK, Machov VN, Syrejshehikova TI, Yakimenko MN. 1989. Determination of fluorescent probes localization in membranes by nonradiative energy transfer. *J Biochem Biophys Meth* **19**:259–274.
67. Yekta A, Duhamel J, Winnik MA. 1995. Dipole–dipole electronic energy transfer: fluorescence decay functions for arbitrary distributions of donors and acceptors—systems with planar geometry. *Chem Phys Lett* **235**:119–125.
68. Tcherkasskaya O, Klushin L, Gronenborn AM. 2002. Effective lattice behavior of fluorescence energy transfer at lamellar macromolecular interfaces. *Biophys J* **82**:988–995.
69. Tweet AG, Bellamy WD, Gaines GL. 1964. Fluorescence quenching and energy transfer in monomolecular films containing chlorophyll. *J Chem Phys* **41**(1):2068–2077.
70. Loura LMS, Fedorov A, Prieto M. 1996. Resonance energy transfer in a model system of membranes: application to gel and liquid crystalline phases. *Biophys J* **71**:1823–1836.
71. Stryer L, ed. 1995. *Biochemistry*, 4th ed. W.H. Freeman, New York [see p. 274].
72. Wang S, Martin E, Cimino J, Omann G, Glaser M. 1988. Distribution of phospholipids around gramicidin and D- $\alpha$ -hydroxybutyrate dehydrogenase as measured by resonance energy transfer. *Biochemistry* **27**:2033–2039.
73. Ladokhin AS, Wimley WC, Hristova K, White SH. 1997. Mechanism of leakage of contents of membrane vesicles determined by fluorescence quenching. *Methods Enzymol* **278**:474–486.
74. Kok JW, Hoekstra D. 1993. Fluorescent lipid analogues applications in cell and membrane biology. In *Biological techniques: fluorescent and luminescent probes for biological activity*, pp. 101–119. Ed WT Mason. Academic Press, New York.
75. Pyror C, Bridge M, Loew LM. 1985. Aggregation, lipid exchange, and metastable phases of dimyristoylphosphatidylethanolamine vesicles. *Biochemistry* **24**:2203–2209.
76. Duzgunes N, Bentz J. 1988. Use of membrane-associated fluorescence probes to monitor fusion of bilayer vesicles. In *Spectroscopic membrane probes*, pp. 117–159. Ed LD Loew. CRC Press, Boca Raton, FL.
77. Silvius JR, Zuckermann MJ. 1993. Interbilayer transfer of phospholipid-anchored macromolecules via monomer diffusion. *Biochemistry* **32**:3153–3161.
78. El Jastimi R, Lafleur M. 1999. A dual-probe fluorescence method to examine selective perturbations of membrane permeability by melittin. *Biospectroscopy* **5**:133–140.
79. Malinin VS, Haque ME, Lentz BR. 2001. The rate of lipid transfer during fusion depends on the structure of fluorescent lipid probes: a new chain-labeled lipid transfer probe pair. *Biochemistry* **40**:8292–8299.
80. Lei G, MacDonald RC. 2003. Lipid bilayer vesicle fusion: intermediates captured by high-speed microfluorescence spectroscopy. *Biophys J* **85**:1585–1599.
81. Srinivas G, Bagchi B. 2001. Effect of orientational motion of mobile chromophores on the dynamics of Förster energy transfer in polymers. *J Phys Chem B* **105**:9370–9374.
82. Artyukhov VY, Mayer GV. 2001. Theoretical study of the effect of orientation and solvent on energy transfer on bichromophore systems. *Mol Spectrosc* **90**(5):664–668.
83. Ronova IA, Kovalevsky AY, Siling SA, Shamshin SV, Grachev AV, Tsyganova OY. 2001. Bifluorophores: molecular design and excitation energy transfer mechanism. *Chem Phys* **270**:99–108.
84. Zhong D, Pal SK, Zhang D, Chan SI, Zewail AH. 2002. Femtosecond dynamics of rubredoxin: tryptophan solvation and resonance energy transfer in the protein. *Proc Natl Acad Sci USA* **99**(1):13–18.
85. Wong KF, Bagchi B, Rossky PJ. 2004. Distance and orientation dependence of excitation transfer rates in conjugated systems: beyond the Förster theory. *J Phys Chem A* **108**:5752–5763.
86. Toniolo C, Formaggio F, Crisma M, Mazaleyrat JP, Wakselman GC, Deschamps JR, Flippin-Anderson JL, Pispisa B, Venanzi M, Palleschi A. 1999. First peptide-based system of rigid donor–rigid interchromophore spacer–rigid acceptor: a structural and photophysical study. *Chem-Eur J* **5**(8):2254–2264.
87. Giribabu L, Kumar AA, Neeraja V, Maiya BG. 2001. Orientation dependence of energy transfer in an anthracene–porphyrin donor–acceptor system. *Angew Chem Int Ed* **40**(19):3621–3624.
88. Bennett RG. 1964. Radiationless intermolecular energy transfer, I: singlet–singlet transfer. *J Chem Phys* **41**:3037–3041.
89. Eisenthal KB, Siegel S. 1964. Influence of resonance transfer on luminescence decay. *J Chem Phys* **41**:652–655.
90. Birks JB, Georghiou S. 1968. Energy transfer in organic systems, VII: effect of diffusion on fluorescence decay. *Proc Roy Soc (J Phys B)* **1**:958–965.
91. Thomas DD, Caslsen WF, Stryer L. 1978. Fluorescence energy transfer in the rapid diffusion limit. *Proc Natl Acad Sci USA* **75**:5746–5750.
92. Selvin PR, Rana TM, Hearst JE. 1994. Luminescence resonance energy transfer. *J Am Chem Soc* **116**:6029–6030.

93. Li M, Selvin PR. 1995. Luminescent polyaminocarboxylate chelates of terbium and europium: the effects of chelate structure. *J Am Chem Soc* **117**:8132–8138.
94. Berlman IB. 1973. *Energy transfer parameters of aromatic compounds*. Academic Press, New York.
95. Fairclough RH, Cantor CR. 1978. The use of singlet energy transfer to study macromolecular assemblies. *Methods Enzymol* **48**:347–379.
96. Selvin PR. 1995. Fluorescence resonance energy transfer. *Methods Enzymol* **246**:300–334.
97. Mathis G. 1993. Rare earth cryptates and homogeneous fluoroimmunoassays with human sera. *Clin Chem* **39**(9):1953–1959.
98. Lakowicz JR, Johnson ML, Wiczk W, Bhat A, Steiner RF. 1987. Resolution of a distribution of distances by fluorescence energy transfer and frequency-domain fluorometry. *Chem Phys Letts* **138**(6):587–593.
99. Johnson DA, Leathers VL, Martinez AM, Walsh DA, Fletcher WH. 1993. Fluorescence resonance energy transfer within a heterochromatic cAMP-dependent protein kinase holoenzyme under equilibrium conditions: new insights into the conformational changes that result in cAMP-dependent activation. *Biochemistry* **32**:6402–6410.

## ADDITIONAL REFERENCES ON RESONANCE ENERGY TRANSFER

### Association Reactions

- Amiri H, Schultz G, Schaefer M. 2003. FRET-based analysis of TRPC subunit stoichiometry. *Cell Calcium* **33**:463–470.
- Chatterjee SK, Laffray J, Patel P, Ravindra R, Qin Y, Kuehne ME, Bane SL. 2002. Interaction of tubulin with a new fluorescent analogue of vinblastine. *Biochemistry* **41**:14010–14018.
- Derdowski A, Ding L, Spearman P. 2004. A novel fluorescence resonance energy transfer assay demonstrates that the human immunodeficiency virus type 1 Pr55<sup>Gag</sup> I domain mediates Gag–Gag interactions. *J Virol* **78**(3):1230–1242.
- Li M, Reddy LG, Bennett R, Silva ND, Jones LR, Thomas DD. 1999. A fluorescence energy transfer method for analyzing protein oligomeric structure: application to phospholamban. *Biophys J* **76**:2587–2599.

### DNA

- Lee BW, Moon SJ, Youn MR, Kim JH, Jang HG, Kim SK. 2003. DNA mediated resonance energy transfer from 4',6-diamidino-2-phenylin-dole to [Ru(1,10-phenanthroline)<sub>2</sub>L]<sup>2+</sup>. *Biophys J* **85**:3865–3871.
- Norman DG, Grainger RJ, Uhrin D, Lilley DMJ. 2000. Location of cyanine-3 on double-stranded DNA: importance for fluorescence resonance energy transfer studies. *Biochemistry* **39**:6317–6324.
- Murchie AIH, Clegg RM, von Kitzing E, Duckett DR, Diekmann S, Lilley DMJ. 1989. Fluorescence energy transfer shows that the four-way DNA junction is a right-handed cross of antiparallel molecules. *Nature* **341**:763–766.
- Wang L, Gaigalas AK, Blasic J, Holden MJ, Gallagher DT, Pires R. 2003. Fluorescence resonance energy transfer between donor–acceptor pairs on two oligonucleotides hybridized adjacently to DNA template. *Biopolymers* **72**:401–412.

### Dendrimers

- Adronov A, Gilat SL, Fréchet JMJ, Ohta K, Neuwahl FVR, Fleming GR. 2000. Light harvesting and energy transfer in laser-dye-labeled poly(aryl ether) dendrimers. *J Am Chem Soc* **122**:1175–1185.
- Balzani V, Ceroni P, Gestermann S, Gorka M, Kauffmann C, Maestri M, Vögtle F. 2000. Eosin molecules hosted into a dendrimer which carries thirty-two dansyl units in the periphery: a photophysical study. *Chem Phys Chem* **4**:224–227.
- Brousmiche DW, Serin JM, Fréchet JMJ, He GS, Lin TC, Chung SJ, Prasad PN, Kannan R, Tan LS. 2004. Fluorescence resonance energy transfer in novel multiphoton absorbing dendritic structures. *J Phys Chem B* **108**:8592–9600.
- Maus M, De R, Lor M, Weil T, Mitra S, Wiesler UM, Herrmann A, Hofkens J, Vosch T, Müllen H, De Schryver FC. 2001. Intramolecular energy hopping and energy trapping in polyphenylene dendrimers with multiple peryleneimide donor chromophores and a terryleneimide acceptor trap chromophore. *J Am Chem Soc* **123**:7668–7676.

### Experimental Methods

- Guptasarma P, Raman B. 1995. Use of tandem cuvettes to determine whether radiative (Trivial) energy transfer can contaminate steady-state measurements of fluorescence resonance energy transfer. *Anal Biochem* **230**:187–191.

### Homo-Resonance Energy Transfer

- Hamann S, Kiilgaard JF, Litman T, Alvarez-Leefmans FJ, Winther BR, Zeuthen T. 2002. Measurement of cell volume changes by fluorescence self-quenching. *J Fluoresc* **12**(2):139–145.
- Kalinin S, Molotkovsky JG, Johansson LBA. 2003. Distance measurements using partial donor–donor energy migration within pairs of fluorescent groups in lipid bilayers. *J Phys Chem B* **107**:3318–3324.

### Membranes

- Pentcheva T, Edidin M. 2001. Clustering of peptide-loaded MHC Class I molecules for endoplasmic reticulum export imaged by fluorescence resonance energy transfer. *J Immunol* **166**:6625–6632.
- Polozov IV, Polozova AI, Molotkovsky JG, Epand RM. 1997. Amphiphatic peptide affects the lateral domain organization of lipid bilayers. *Biochim Biophys Acta* **1328**:125–139.

### Multiple-Step RET

- Galperin E, Verkhusha VV, Sorkin A. 2004. Three-chromophore FRET microscopy to analyze multiprotein interactions in living cells. *Nature Methods* **1**(3):209–217.
- Ohya Y, Yabuki K, Hashimoto M, Nakajima A, Ouchi T. 2003. Multistep fluorescence resonance energy transfer in sequential chromophore array constructed on oligo-DNA assemblies. *Bioconjugate Chem* **14**(6):1057–1066.

- Tong AK, Jockusch S, Li Z, Zhu HR, Akins DL, Turro NJ, Ju J. 2001. Triple fluorescence energy transfer in covalently trichromophore-labeled DNA. *J Am Chem Soc* **123**:12923–12924.
- Wang S, Gaylord BS, Bazan GC. 2004. Fluorescein provides a resonance gate for FRET from conjugated polymers to DNA intercalated dyes. *J Am Chem Soc* **126**:5446–5451.

### Orientation Factor

- Håkansson P, Isaksson M, Westlund P-O, Johansson LB-A. 2004. Extended Förster theory for determining intraprotein distances: I: the  $\kappa^2$ -dynamics and fluorophore reorientation. *J Phys Chem* **108**:17243–17250.
- Schartel B, Krüger S, Wachtendorf V, Hennecke M. 2000. Excitation energy transfer of a bichromophoric cross-shaped molecule investigated by polarized fluorescence spectroscopy. *J Chem Phys* **112**(22):9822–9827.

### Protein Folding

- Cai K, Schirch V. 1996. Structural studies on folding intermediates of serine hydroxymethyltransferase using fluorescence resonance energy transfer. *J Biol Chem* **271**(44):27311–27320.
- Fisher CA, Narayanaswami V, Ryan RO. 2000. The lipid-associated conformation of the low density lipoprotein receptor binding domain of human apolipoprotein E\*. *J Biol Chem* **275**(43):33601–33606.
- Hammarstrom P, Persson M, Carlsson U. 2001. Protein compactness measured by fluorescence resonance energy transfer. *J Biol Chem* **276**(24):21765–21775.
- Krishnakumar SS, Panda D. 2002. Spatial relationship between the prodan site, Trp-214, and Cys-34 residues in human serum albumin and loss of structure through incremental unfolding. *Biochemistry* **41**:7443–7452.
- Lakey JH, Duche D, Gonzalez-Manas JM, Baty D, Pattus F. 1993. Fluorescence energy transfer distance measurements: the hydrophobic helical hairpin of colicin A in the membrane bound state. *J Mol Biol* **230**:1055–1067.
- Lillo MP, Szpikowska BK, Mas MT, Sutin JD, Beechem JM. 1997. Real-time measurement of multiple intramolecular distances during protein folding reactions: a multisite stopped-flow fluorescence energy-transfer study of yeast phosphoglycerate kinase. *Biochemistry* **36**:11273–11281.

### Protein Motions

- Bilderback T, Fulmer T, Mantulin WW, Glaser M. 1996. Substrate binding causes movement in the ATP binding domain of *Escherichia coli* adenylate kinase. *Biochemistry* **35**:6100–6106.

### Reviews

- Chirio-Lebrun MC, Prats M. 1998. Fluorescence resonance energy transfer (FRET): theory and experiments. *Biochem Educ* **26**:320–323.
- Clegg RM. 2004. Nuts and bolts of excitation energy migration and energy transfer. In *Chlorophyll fluorescence: a signature of photosynthesis*. Ed GC Papageorgiou, Govindjee. Kluwer, Dordrecht.
- Clegg RM. 2004. The vital contributions of Perrin and Förster. *Biophotonics Int* **11**(9):42–45.
- De Angelis DA. 1999. Why FRET over genomics?. *Physiol Genomics* **1**:93–99.

- Lilley DMJ, Wilson TJ. 2000. Fluorescence resonance energy transfer as a structural tool for nucleic acids. *Curr Opin Chem Biol* **4**:507–517.
- Selvin PR. 1995. Fluorescence resonance energy transfer. *Methods Enzymol* **246**:300–334.
- Wemmer DA, Case DA, Millar DP, eds. 2002. Biopolymers nucleic acid sciences, fluorescence spectroscopy and nucleic acids. *Biopolymers* **61**(3):143–242.
- Wieb Van Der Meer B, Coker G, Simon Chen SY. 1991. *Resonance energy transfer theory and data*. Wiley-VCH, New York.

### Theory—Multiple Acceptors

- Jones GM, Wofsy C, Aurell C, Sklar LA. 1999. Analysis of vertical fluorescence resonance energy transfer from the surface of a small-diameter sphere. *Biophys J* **76**:517–527.
- Rolinski OJ, Birch DJS. 2002. Structural sensing using fluorescence nanotomography. *J Chem Phys* **116**(23):10411–10418.
- Uhlik F, Limpouchova Z, Matejicek P, Prochazka K, Tuzar Z, Webber S. 2002. Nonradiative excitation energy transfer in hydrophobically modified amphiphilic block copolymer micelles: theoretical model and Monte Carlo simulations. *Macromolecules* **35**:9497–9505.

### PROBLEMS

- P13.1. *Calculation of a Distance from the Transfer Efficiency:* Use the emission spectra in Figure 13.35 to calculate the distance from the indole donor to the dansyl acceptor. Assume that there is a single D–A distance, and that diffusion does not occur during the donor excited-state lifetime. The Förster distance  $R_0 = 25.9 \text{ \AA}$ , and the donor-alone lifetime is 6.8 ns. What is the D–A distance? What is the donor lifetime in the TUD D–A pair?

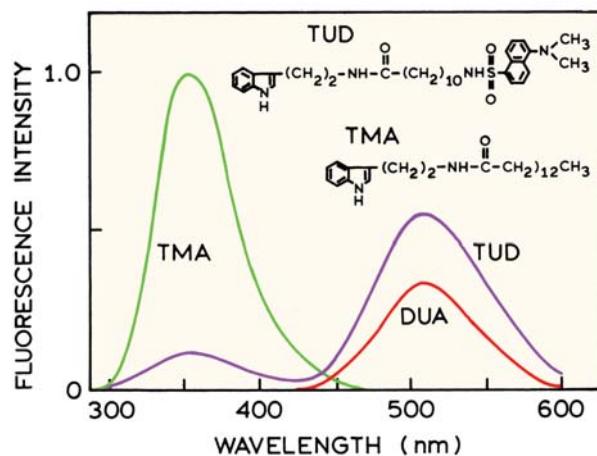


**Figure 13.35.** Emission spectra of a donor control (TMA) and a donor-acceptor pair (TUD) in propylene glycol at 20°C. DUA is an acceptor-only analogue. Revised from [98].

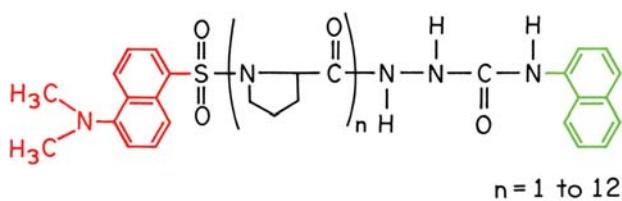


**Figure 13.36.** Structure of dansyl-(L-prolyl)<sub>n</sub>- $\alpha$ -naphthyl used for determining the effects of distance on energy transfer. Revised from [18].

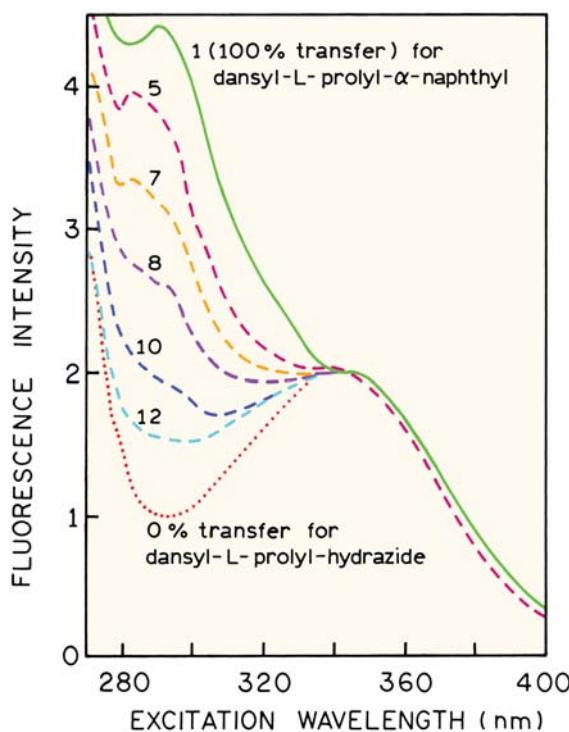


**Figure 13.37.** Excitation spectra of dansyl-(L-prolyl)<sub>n</sub>- $\alpha$ -naphthyl molecules. Spectra are shown for dansyl-L-prolyl-hydrazide (dotted), dansyl-L-prolyl- $\alpha$ -naphthyl (solid), and dansyl-(L-prolyl)<sub>n</sub>- $\alpha$ -naphthyl (dashed);  $n = 5, 7, 8, 10$ , and  $12$ . Emission was detected at the dansyl emission maximum near 450 nm. Revised from [18].

**P13.2. Measurement of FRET efficiencies ( $E$ ) from fluorescence intensities and lifetimes:** Use eq. 13.11 to derive the expressions for  $E$  based on intensities (eq. 13.13) or lifetimes (13.14).

**P13.3. Distance Dependence of Energy Transfer:** The theory of Förster states that the rate of energy transfer depends on  $1/r^6$ , where  $r$  is the donor-to-acceptor distance. This prediction was tested experimentally

using naphthyl donors and dansyl acceptors linked by rigid polyprolyl spacers (Figure 13.36). Figure 13.37 shows the excitation spectra for this series of D-A pairs. Assume that each prolyl spacer contributes 2.83 Å to the spacing, and that the distance ranges from 12 ( $n = 1$ ) to 43 Å ( $n = 12$ ).

Use the excitation spectra to demonstrate that  $k_T$  depends on  $1/r^6$ . Note that the dansyl acceptor absorbs maximally at 340 nm and the naphthyl donor has an absorption maximum at 290 nm. Excitation spectra were recorded with the emission monochromator centered on the dansyl emission near 450 nm. What is  $R_0$  for this D-A pair?

**P13.4. Effect of Spectral Overlap on the Rate of Energy Transfer:** Haugland et al.<sup>20</sup> investigated the effect of the magnitude of the spectral overlap integral on the rate of fluorescence energy transfer. For this study they used the steroids shown in Figure 13.38. They measured the fluorescence lifetimes of compounds I and II. The indole moiety is the donor that transfers energy to the ketone acceptor. Both the absorption spectrum of the ketone and the emission spectrum of the indole are solvent sensitive. Specifical-

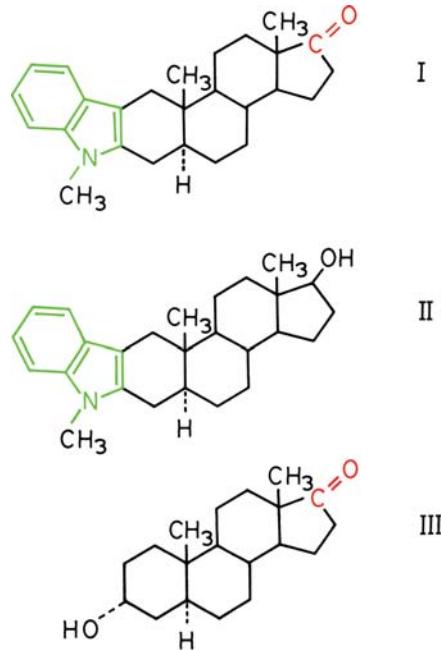


**Figure 13.38.** Structure of the rigid steroid donor–acceptor pair (I), the steroid containing the donor alone (II), and the steroid containing the acceptor alone (III). Indole is the donor and the carbonyl group is the acceptor. Revised from [20].

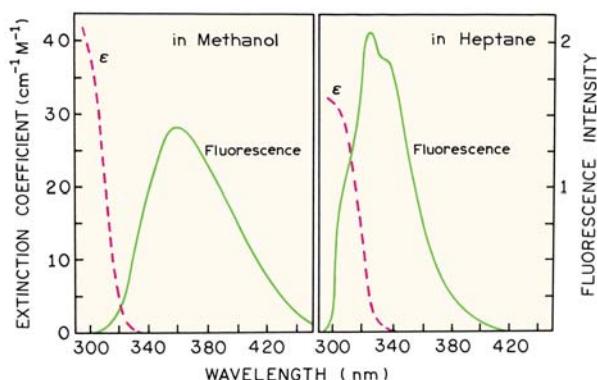


**Figure 13.39.** Overlap of emission spectrum of the indole donor (II) with the absorption spectrum of the carbonyl acceptor (III). Revised from [20].

ly, the emission spectrum of indole shifts to shorter wavelengths and the absorption spectrum of the ketone shifts to longer wavelengths as the solvent polarity decreases (Figure 13.39). These shifts result in increasing spectral overlap with decreasing solvent polarity.

Use the data in Table 13.5 to demonstrate that  $k_T$  is proportional to the first power of the extent of spectral overlap ( $J$ ).

- P13.5. *Calculation of a Förster Distance:* Calculate the Förster distance for the tryptophan-to-dansyl donor–acceptor pair shown in Figure 13.8. The quantum yield of the donor is 0.21.
- P13.6. *Optical Assay for cAMP:* Figure 13.40 shows the emission spectra of a protein kinase that changes conformation in the presence of cAMP, and dissociates completely in the presence of a protein kinase

**Table 13.5.** Fluorescence Spectral Properties of I and II in a Series of Solvents<sup>a</sup>

Solvent	$\tau$ (ns)		
	I	II	$J$ ( $\text{cm}^6/\text{m mole} \times 10^{19}$ )
Methanol	5.3	5.6	1.5
Ethanol	5.6	6.5	3.0
Dioxane	3.6	5.4	13.0
Ethyl acetate	3.3	4.7	12.8
Ethyl ether	2.1	4.5	30.0
Heptane	1.1	2.8	60.3

<sup>a</sup>From [20].

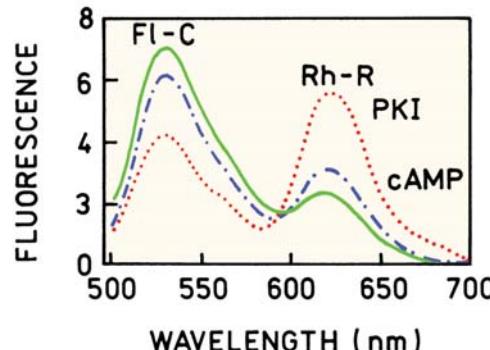
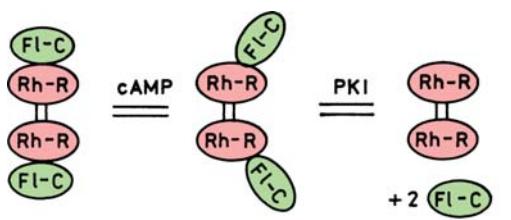


**Figure 13.40.** Emission spectra and schematic for the effect of cAMP and PKI on the emission spectra of the  $(\text{Rh}-\text{R})_2-(\text{Fl}-\text{C})_2$  complex. Revised and reprinted with permission from [99]. Copyright © 1993, American Chemical Society.

inhibitor (PKI). The catalytic subunit is labeled with fluorescein (Fl-C) and the regulatory subunit is labeled with rhodamine (Rh-R). Derive an expression relating the ratio of donor to acceptor intensities to the protein kinase–cAMP dissociation constant. Assume that the donor and acceptor quantum yields are unchanged upon binding cAMP, except for the change in energy transfer. Describe how the conformational change, and change in RET, can be used to measure the concentration of cAMP.

- P13.7. *Characteristics of a Closely Spaced D–A Pair:* Assume you have isolated a protein that contains a single-tryptophan residue, and binds dinitrophenol (DNP) in the active site. The absorption spectrum of DNP overlaps with the emission spectrum of the tryptophan residue. Assume  $R_0 = 50 \text{ \AA}$  and that DNP is not fluorescent. The fluorescence intensities of the tryptophan residue are 20.5 and 4.1 in the absence and presence of DNP, respectively, after correction for the inner filter effects due to the DNP absorption.

- a. What is the transfer efficiency

- b. Assume that the unquenched lifetime is 5 ns. What is the expected lifetime in the presence of DNP?
- c. What is the transfer rate?
- d. What is the distance between the tryptophan and the DNP?
- e. Assume that the solution conditions change so that the distance between the tryptophan and the DNP is 20 Å. What is the expected intensity for the tryptophan fluorescence?
- f. For this same solution ( $r = 20$  Å) what would be the effect on the fluorescence intensity of a 1% impurity of a second protein that did not bind DNP? Assume this second protein has the same lifetime and quantum yield.
- g. What lifetime would you expect for the sample that contains the impurity? Would this lifetime provide any indication of the presence of an impurity?

- P13.8. *Effect of  $\kappa^2$  on the Range of Possible Distances:* Suppose you have a donor- and acceptor-labeled protein that displays the following steady-state anisotropies.

Fluorophore	$\tau$ (ns)	$r_D$ or $r_A$	$r_0$
Donor-alone control	5 ns	0.1	0.4
Acceptor	15 ns	0.05	0.4

Using an assumed value of  $\tau^2 = 2/3$ , the D–A distance was calculated to be 25 Å, and  $R_0$  is also equal to 25 Å. Assume the protein displays a rotational correlation time of 5 ns. Use the data provided to calculate the range of distances possible for the D–A pair.

- P13.9. *Effect of Acceptor Underlabeling on the Calculated Transfer Efficiency:* Suppose you have a presumed

D–A pair. In the absence of acceptor the donor displays a steady-state intensity  $F_D = 1.0$ , and in the presence of acceptor  $F_{DA} = 0.5$ . Calculate the transfer efficiency assuming the fractional labeling with acceptor ( $f_A$ ) is 1.0 or 0.5. How does the change in  $f_A$  affect the calculated distance?

- P13.10. *FRET Efficiency from the Acceptor Intensities:* Derive eq. 13.25 for the case in which donor labeling is complete;  $f_D = 1.0$ . Also derive eq. 13.25 for the case when donor labeling is incomplete ( $f_D < 1$ ).

- P13.11. *Correction for Overlapping Donor and Acceptor Emission Spectra:* Equation 13.25 does not consider the possible contribution of the donor emission at the wavelength used to measure acceptor fluorescence ( $\lambda_A$ ). Derive an expression for the enhanced acceptor fluorescence when the donor emits at  $\lambda_A$ . Explain how the apparent transfer efficiency, calculated without consideration of the donor contribution, would be related to the true transfer efficiency.

- P13.12. Suppose that you have a protein with a single-trypotophan residue. Assume also that the protein non-covalently binds a ligand that serves as an RET acceptor for the tryptophan residue, and that the acceptor site is allosterically linked to the donor site such that acceptor binding induces an additional rate of donor quenching  $k_q$  in addition to  $k_T$ .

What is the apparent transfer efficiency upon acceptor binding in terms of  $\tau_D$ ,  $k_T$ , and  $k_q$ ? Is the apparent value ( $E_D$ ) smaller or larger than the true value ( $E$ )?

# 14

# Time-Resolved Energy Transfer and Conformational Distributions of Biopolymers

In the previous chapter we described the principles of resonance energy transfer (RET), and how the phenomenon could be used to measure distances between donor and acceptor sites on macromolecules or the association between donor-labeled and acceptor-labeled biomolecules. Energy transfer was described as a through-space interaction that occurred whenever the emission spectrum of the donor overlapped with the absorption spectrum of the acceptor. For a given donor–acceptor (D–A) pair, the efficiency of energy transfer decreases as  $r^{-6}$ , where  $r$  is the D–A distance. Each D–A pair has a characteristic distance: the Förster distance ( $R_0$ ) at which RET is 50% efficient. The extent of energy transfer, as seen from the steady-state data, can be used to measure the distance, to study protein folding, to determine the extent of association based on proximity, or to create images of associated intracellular proteins.

In this chapter we describe more advanced applications of RET, particularly those that rely on time-resolved measurements of covalently linked D–A pairs. For such pairs the time-resolved data can be used to recover the conformational distribution or distance distribution between the donor and acceptor. Donor-to-acceptor motions also influence the extent of energy transfer, which can be used to recover the mutual diffusion coefficient. In Chapter 15 we will consider RET between donors and acceptors that are not covalently linked. In this case the extent of RET depends on the dimensional geometry of the molecules, such as planar distributions in membranes and one-dimensional distributions in double-helical DNA.

While the phenomenon of energy transfer is the same in all these situations, each application of RET requires a different theory to interpret the steady-state or time-resolved data. RET depends on the geometry and dynamics of the system, and thus provides a powerful yet complex methodology for studies of donor–acceptor distributions in any dimensionality.

## 14.1. DISTANCE DISTRIBUTIONS

In the previous chapter we considered energy transfer between a single donor (D) and acceptor (A) positioned at a unique distance ( $r$ ). We now consider the case where a range of D–A distances is possible. This use of RET to study distance distributions was first reported by Haas, Steinberg, and coworkers using flexible polypeptides.<sup>1–3</sup> The concept of a distribution of donor-to-acceptor distances is shown in Figure 14.1. The protein is assumed to be labeled at unique sites by a single donor and single acceptor. In the native state one expects a single conformation and a single D–A distance. For the native state the distance is sharply localized at a particular value of  $r$ . This unique distance is expressed as a probability function  $P(r)$  that is narrowly distributed along the  $r$  axis.

Now suppose the protein is unfolded to the random-coil state by the addition of denaturant. Since the peptide is in a random state, there exists a range of D–A distances. This range of conformations results in a range of accessible D–A distances, or a wide  $P(r)$  distribution (Figure 14.1,

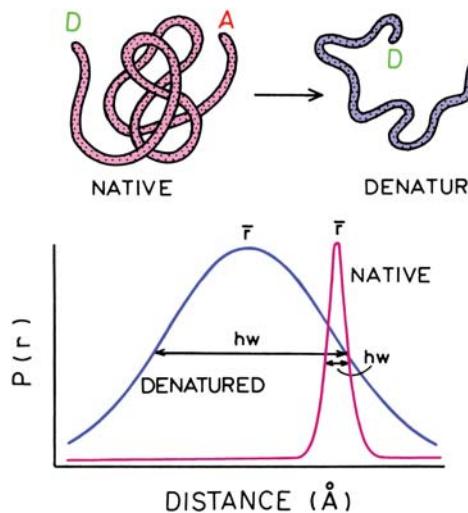


**Figure 14.1.** Distribution of D–A distance for a native and denatured protein. The probability functions  $P(r)$  are peak normalized. In both cases the integrate probability should be unity.

lower panel). For visual clarity, the  $P(r)$  distributions shown in Figure 14.1 are peak normalized, but the actual area under each curve should be normalized to unity to correspond to a single acceptor per donor.

The presence of a distribution of distances has a profound impact on the time-resolved decays of the donor. For the native protein the single D–A distance results in a single transfer rate for all the donors. Hence the decay time of the donor is shortened and is given by

$$I_{DA}(r,t) = I_D^0 \exp[-t/\tau_D - k_T(r)t] \quad (14.1)$$

where  $\tau_D$  is the decay time of the donor in the absence of acceptor,  $I_D^0$  is the donor intensity at  $t = 0$ , and  $k_T(r)$  is the D–A transfer rate, given by

$$k_T(r) = \frac{1}{\tau_D} \left( \frac{R_0}{r} \right)^6 \quad (14.2)$$

Since there is only one distance and only one transfer rate  $k_T(r) = k_T$ , the donor decay remains a single exponential (Figure 14.2, top), and

$$I_{DA}(r,t) = I_{DA}(t) = I_D^0 \exp[-t/\tau_{DA}] \quad (14.3)$$

where the lifetime in the presence of the acceptor,  $\tau_{DA}$ , is given by

$$\frac{1}{\tau_{DA}} = \frac{1}{\tau_D} + k_T(r) \quad (14.4)$$

It is this assumption of a single distance that allows calculation of the distance from the relative quantum yield of the donor (Chapter 13).

Now assume there is a range of D–A distances. For these simulated data we assumed a single-exponential

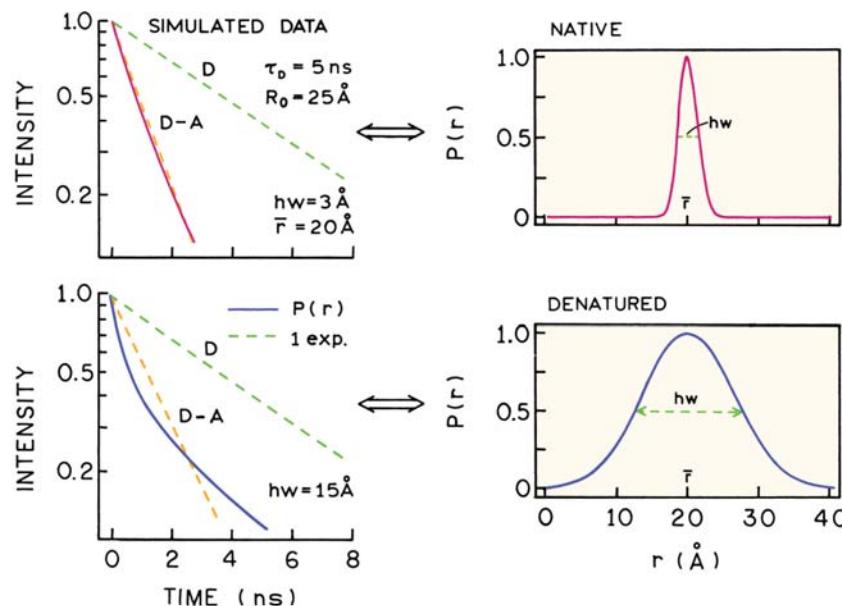


**Figure 14.2.** Effect of a distance distribution on the time-domain intensity decay of the donor.

decay time of 5 ns in the absence of acceptor, and  $R_0 = 25 \text{ \AA}$ . Some of the D–A pairs are closely spaced and display shorter decay times, and other D–A pairs are further apart and display longer decay times. The range of distances results in a range of decay times, so that the donor decay becomes more complex than a single exponential (Figure 14.2, bottom). Similar results are expected for frequency domain (FD) data. If there is a single D–A distance the frequency-domain intensity decay is well approximated by the single-exponential fit (Figure 14.3, top), which is shifted to higher frequencies by the presence of the acceptor. A range of D–A distances results in a frequency response that is spread out along the frequency axis, and one that is no longer a single exponential (Figure 14.3, bottom). The goal of most distance-distribution studies is to recover the D–A probability distribution from the non-exponential decays of the donor. This means that the shape of the intensity decays (Figure 14.2, left) are used to determine the D–A probability distribution (Figure 14.2, right). It is important to note the necessity of the time-resolved data to recover a distance distribution. For a distance distribution, measurement of the relative yield of the donor can be used to calculate an apparent distance, as was done in Problem 13.1. However, the steady-state data cannot be used to determine the distribution, and will not reveal the presence of a distribution. For the moment we have ignored donor-to-acceptor motions, which will be discussed in Section 14.7.

Irrespective of whether the donor intensity decays are measured in the time domain (TD) or frequency-domain (FD), the information content of the time-resolved data is limited. It is not practical to determine a distance distribution of arbitrary shape. For this reason it is common practice to describe the distribution using a limited number of parameters. The most appropriate and commonly used distribution is a Gaussian:

$$P(r) = \frac{1}{\sigma\sqrt{2\pi}} \exp\left[-\frac{1}{2}\left(\frac{\bar{r}-r}{\sigma}\right)^2\right] \quad (14.5)$$

In this equation  $\bar{r}$  is the mean of the Gaussian with a standard deviation of  $\sigma$ . Usually distance distributions are described by the full width at half maxima (Figure 14.2, lower right). This half width (nm) is given by  $hw = 2.354\sigma$ . Distance distributions have also been expressed as Lorentzian<sup>4</sup> and other functions,<sup>5–6</sup> but the principles remain the same. With presently available data, distance distributions can be resolved, but it is difficult to distinguish the precise shape of the distribution.

What equation describes the intensity decay for a distance distribution? Unfortunately, the donor decay can only be described by an integral equation. The intensity decay for those D–A pairs at a distance  $r$  is given by eq. 14.1. Unless a single molecule is observed in a rigid medium, the D–A pairs with a unique distance  $r$  cannot be individually observed. Rather, one observes a weighted average determined by  $P(r)$ . The donor intensity decay is a summation of the intensity decays for all accessible distances, and is usually written as

$$\begin{aligned} I_{\text{DA}}(t) &= \int_{r=0}^{\infty} P(r) I_{\text{DA}}(r, t) dr \\ &= I_{\text{D}}^0 \int_{r=0}^{\infty} P(r) \exp\left[-\frac{t}{\tau_{\text{D}}} - \frac{t}{\tau_{\text{D}}} \left(\frac{R_0}{r}\right)^6\right] dr \end{aligned} \quad (14.6)$$

This expression indicates that the intensity decay for an ensemble of flexible D–A pairs is given by the weighted average of the decays for each D–A distance.

Data analysis is performed by predicting the values of  $I_{\text{DA}}(t)$  for use with time-domain or frequency-domain measurements and the usual procedures of nonlinear least squares. Typically the decay time of the donor ( $\tau_{\text{D}}$ ) is known from measurements of the donor in the absence of acceptor. The variable parameters in the analysis are those describing the distance distribution:  $\bar{r}$  and  $hw$ .

This description of the intensity decay (eq. 14.6) illustrates the value of computer programs written in terms of the molecular features of the sample. The complex donor decays in the presence of acceptor (Figures 14.2 or 14.3) could be analyzed in terms of the multi-exponential model. While it would be possible to fit the data, the value of  $\alpha_i$  and  $\tau_i$  would only indirectly reflect the distance distribution. In contrast, programs based on eq. 14.6 provide direct information on  $P(r)$ .

## 14.2. DISTANCE DISTRIBUTIONS IN PEPTIDES

### 14.2.1. Comparison for a Rigid and Flexible Hexapeptide

The recovery of distance distributions from the time-resolved (TD or FD) data is best understood by examining a specific example. Consider the two hexapeptides each containing a tryptophanamide ( $\text{TrpNH}_2$ ) donor and a dansyl (DNS) acceptor (Figure 14.4).<sup>7</sup> One of the hexapeptides ( $\text{TrpNH}_2(\text{pro})_6\text{-DNS}$ ) consists of six rigid prolyl residues that sepa-

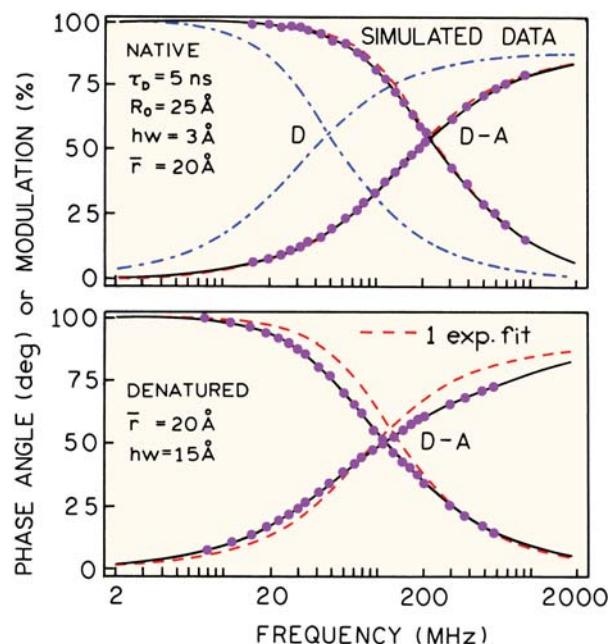


**Figure 14.3.** Effect of a distance distribution on the frequency-domain intensity decay of the donor. The dashed line shows the best single-exponential fit to the simulated data.

rate Trp and DNS by a single distance. The other donor–acceptor pair is linked by hexaglycine ( $\text{TrpNH}_2\text{--(gly)}_6\text{--DNS}$ ), which is highly flexible and expected to result in a range of Trp–DNS distances. The emission spectra of these peptides are shown in Figure 14.5. The donor is quenched in both D–A pairs, relative to the donor-alone control,  $\text{TrpNH}_2\text{--(gly)}_3\text{--Ac}$ . The donor is more highly quenched in the flexible  $(\text{gly})_6$  peptide relative to the rigid  $(\text{pro})_6$  peptide. One could use the relative amounts of donor quenching to calculate the D–A distance. This distance would be correct for the rigid peptide  $\text{TrpNH}_2\text{--(pro)}_6\text{--DNS}$ .

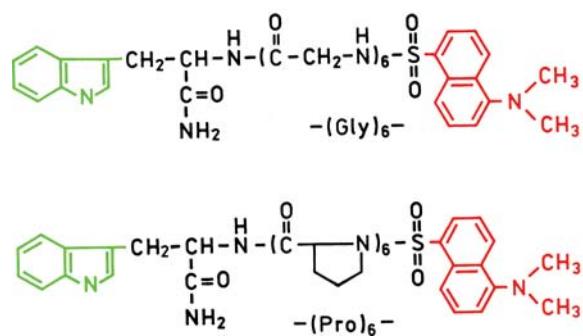


**Figure 14.4.** Flexible  $\text{TrpNH}_2\text{--(gly)}_6\text{--DNS}$  and rigid  $\text{TrpNH}_2\text{--(pro)}_6\text{--DNS}$  D–A pairs. Revised from [7].

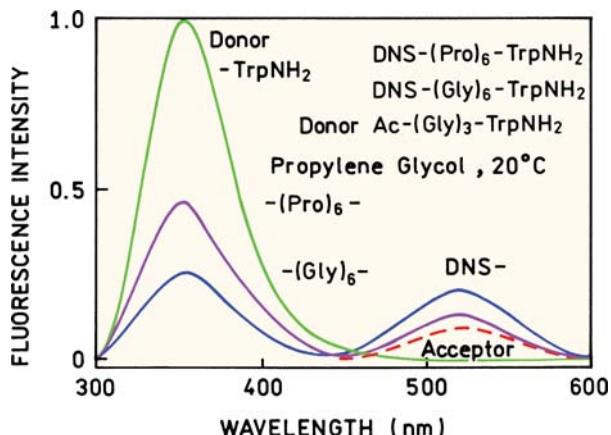


**Figure 14.5.** Emission spectra of  $\text{DNS--(Pro)}_6\text{--TrpNH}_2$  and  $\text{DNS--(Gly)}_6\text{--TrpNH}_2$  relative to the donor-alone control  $\text{Ac--(Gly)}_3\text{--TrpNH}_2$ . Ac refers to an N-acetyl group. Revised from [7].

DNA, but incorrect for the flexible  $\text{TrpNH}_2\text{--(gly)}_6\text{--DNS}$  peptide. For the  $(\text{gly})_6$  peptide one must use time-resolved measurements to obtain information beyond a weighted apparent distance.

Information about the distance distribution for flexible molecules can be recovered from the time-resolved decays of the donor. Frequency-domain data for the two D–A peptides (●) and the donor-alone control molecule (○) are shown in Figure 14.6. In the absence of acceptor the donor-alone control molecule displays a single-exponential decay with  $\tau_D = 5.27 \text{ ns}$ . For the rigid D–A pair (top) energy transfer decreases the donor decay time, as seen by the shift of the phase and modulation values to higher frequencies. However, the donor decay remains reasonably close to a single exponential, as seen by the visual similarity of the one- and two-exponential fits. As predicted in Figure 14.2, a single D–A distance results in a single-exponential decay of the donor. Close inspection of the FD-intensity decay does reveal some heterogeneity ( $\chi_R^2 = 8.1$ ), which is due to a narrow but finite D–A distance distribution.

A remarkably different donor decay is seen for the flexible D–A pair  $\text{DNS--(gly)}_6\text{--TrpNH}_2$ . For this case the donor decay cannot be approximated by a single exponential, as seen from the dashed line in Figure 14.6 (lower panel), and  $\chi_R^2 = 1254$  for the single-decay-time fit. A single-decay-time fit is equivalent to fitting the donor decay to a very narrow distance distribution (eqs. 14.1 and 14.2). For the flexible peptide, the presence of a range of D–A distances caused the donor decay to become highly non-exponential, the extent of which can be used to determine the distance distribution.

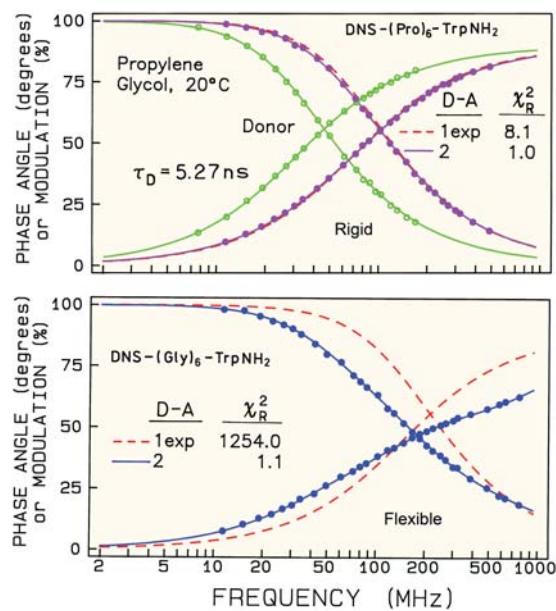


**Figure 14.6.** Frequency-domain donor intensity decays of  $\text{DNS-(pro)}_6\text{-TrpNH}_2$  (top) and  $\text{DNS-(Gly)}_6\text{-TrpNH}_2$  (bottom). For the D-A pairs the dashed and solid lines are the best single and double exponential fits, respectively.

The frequency-domain data can be analyzed to recover the distance distribution  $P(r)$ . This is accomplished by using eq. 14.6 to predict the phase and modulation values for assumed values of  $\bar{r}$  and  $hw$  using the general procedures described in Chapter 4 for time-domain data or Chapter 5 for frequency-domain data. These expressions are shown below (Section 14.4) for the case of single- and multi-exponential donor decays. Analyses of the FD data in terms of the distance-distribution model for both peptides are shown in Figure 14.7. These fits reveal wide and narrow distributions for the flexible and rigid peptides, respectively (Figure 14.8). In this analysis we used the complexity of the donor decays (Figure 14.2, left) to recover the distribution of D-A distances (Figure 14.2, right). The complexity in the donor decay caused by the acceptor (Figure 14.6) was used to determine the probability distribution of acceptors around the donor (Figure 14.8).

#### 14.2.2. Crossfitting Data to Exclude Alternative Models

In addition to obtaining the average distance  $\bar{r}$  and half width  $hw$ , it is important to consider whether the data exclude other distance distributions. This can be accomplished by the procedure of crossfitting the data. This

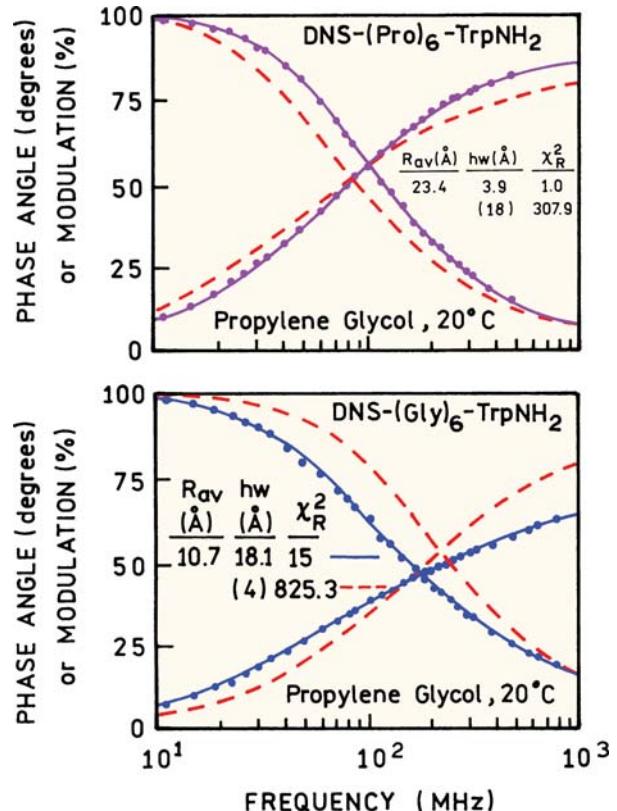


**Figure 14.7.** Distance-distribution fits to the frequency-domain donor decays for flexible (left) and rigid (right) peptides. The  $hw$  values in angular brackets (< >) indicate that this value was held constant in the analysis.

involves using one or more of the parameter values from a second competing model to see if they are consistent with the data. If a competing model also fits the data, then we cannot exclude that model from our consideration without

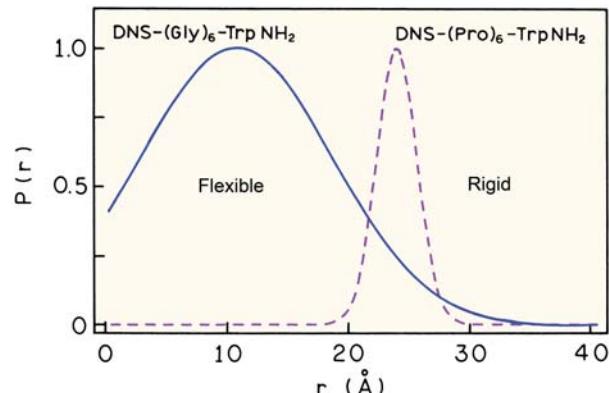


**Figure 14.8.** Distance-distribution fits for  $\text{DNS-(Gly)}_6\text{-TrpNH}_2$  (solid) and  $\text{DNS-(pro)}_6\text{-TrpNH}_2$  (dashed). Revised from [7].

additional data. During this fit the mean distance was a variable parameter. For the flexible peptide  $\text{TrpNH}_2\text{-(gly)}_6\text{-DNS}$  the alternative model was tested by attempting to fit the data using the half width of 4 Å found for the rigid peptide. The value of  $hw = 4 \text{ \AA}$  is held constant and the least-squares fit run again to minimize  $\chi^2_R$  using the flexible peptide data. The dashed line (Figure 14.7, left) shows the data for  $\text{TrpNH}_2\text{-(gly)}_6\text{-Gly}$  are not consistent with a narrow distance distribution. Similarly, the data for  $\text{TrpNH}_2\text{-(pro)}_6\text{-DNA}$  could not be fit with a wide distribution (dashed line, curves in right panel of Figure 14.7). In these cases the attempt to fit the data with different parameter values resulted in obviously unacceptable fits. However, for conformational changes of proteins one can expect the distance distributions to be more similar than for these two hexapeptides, so that the ability to reject similar distributions may be more questionable.

#### 14.2.3. Donor Decay without Acceptor

An important aspect of the distance-distribution analysis is knowledge of the donor decay time. This is typically measured using a control molecule that is comparable to the D–A pair except that it lacks the acceptor (donor-alone molecule). In the case of the two hexapeptides the donor control molecule was  $\text{TrpNH}_2\text{-(gly)}_3\text{-Ac}$ , in which the tryptophan donor was attached to a glycine tripeptide. The tripeptide was acetylated at the N terminus to be more like the D–A pairs and to avoid quenching by the terminal amino group. The amide group does not quench the nearby indole. The selection of a suitably designed donor-alone control molecule is a critical step in any energy transfer experiment. Typically the donor decay time (or decay times for a multi-exponential decay) is measured separately. The data (TD or FD) for the D–A pair are then analyzed while the value of  $\tau_D$  is held fixed. This is necessary because the donor intensity decays of the D–A pair only provides information when compared to the decay that would be observed without energy transfer.

Depending upon the available software the data for the donor-alone and D–A pairs can also be analyzed simultaneously. In this case the program needs to know that the value(s) of  $\tau_D$  is determined only by the donor-alone data, as there is no RET in the donor-alone decay. At first glance one may think that this simultaneous analysis is identical to fixing  $\tau_D$ , and analyzing the data for the D–A pair. In fact, these two methods are different and this second analysis is preferred. If the presence of the acceptor has no effect on

the donor decay besides that due to RET, both modes of analysis will yield the same value of  $\tau_D$ . However, if the presence of the acceptor somehow affects  $\tau_D$  other than by RET, then the second mode of analysis could reveal this effect. Alternatively, since energy transfer decreases the intensity of the donor, an increased contribution of impurity fluorescence to the data for the D–A pair could result in different values of  $\tau_D$  for each mode of analysis.

#### 14.2.4. Effect of Concentration of the D–A Pairs

In general, the extent of energy transfer depends on the concentration of the D–A pairs. However, for linked D–A pairs energy transfer is usually dominated by the linked acceptor. For unlinked D–A pairs the acceptor concentration needs to typically be in the millimolar range for significant energy transfer (Chapter 15). This is because mM concentrations are needed to result in one or more acceptor molecules to be within the Förster distance of the donor. Hence, we made no mention of the concentration of the linked D–A pairs in the preceding sections. Knowledge of the concentration was unnecessary because each donor sees an effective constant concentration of the acceptor determined by the length and flexibility of the linker to which the acceptor is attached. However, the concentration of linked D–A pairs should be low enough to avoid inner filter effects and transfer between donors and acceptors on unlinked D–A pairs. Under these conditions, the extent of energy transfer will be independent of the bulk concentration of the D–A pairs.

---

### 14.3. DISTANCE DISTRIBUTIONS IN PEPTIDES

The principles described above have been applied to a wide variety of proteins using time or frequency-domain measurements. Time-domain measurements have been used to recover distance distributions in native and unfolded staphylococcal nuclease,<sup>4</sup> troponin C,<sup>8</sup> and cardiac troponin I.<sup>9</sup> This approach was initially described by Haas and coworkers on bovine pancreatic trypsin inhibitor (BPTI). This protein was labeled with a naphthalene donor at the N-terminal amino group, and selectively labeled with a coumarin acceptor on each of its four lysine residues. The labeled BPTI was studied during folding and unfolding to determine the folding pathway. (See Representative Publications on Measurement of Distance Distributions near the end of this chapter for references). Frequency-domain measurements have also been used to measure distance distributions in proteins, including the ribonuclease S pep-

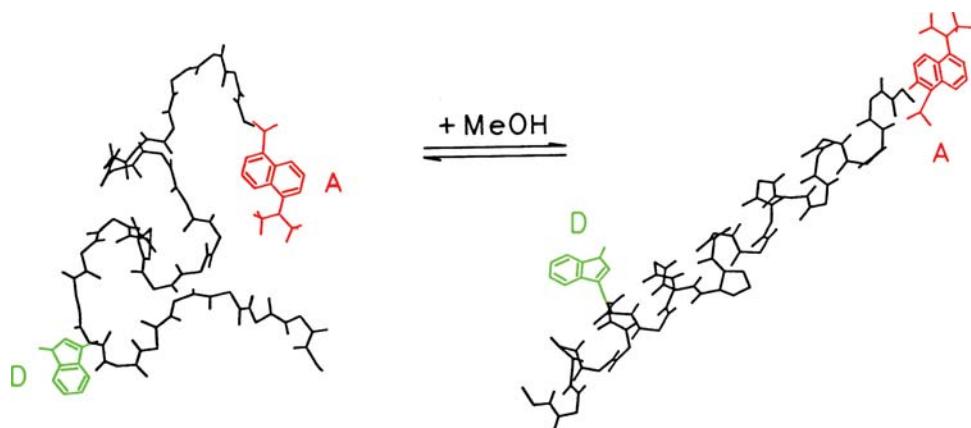


**Figure 14.9.** Dansyl (acceptor)-labeled melittin in the random-coil and  $\alpha$ -helical states. Revised from [23]. Copyright © 1990, with permission from Elsevier Science.

tide,<sup>10</sup> myosin subfragment-1<sup>11</sup>, troponin-I,<sup>12</sup> and other peptides and proteins.<sup>13–21</sup> The use of FRET with proteins has been reviewed by Cheung.<sup>22</sup>

#### 14.3.1. Distance Distributions in Melittin

For the purpose of illustrating distance distributions in proteins we have chosen to present data for melittin.<sup>23–24</sup> Melittin has a single intrinsic tryptophan residue as the donor, and was labeled on the N-terminal amino group with a dansyl acceptor. This 26-amino-acid peptide from bee venom was used in Chapter 13 to illustrate measurements of a single D–A distance when in the  $\alpha$ -helical state. We now consider melittin in the random-coil state, which folds into a monomeric  $\alpha$ -helical state upon addition of methanol (Figure

14.9). This simple peptide illustrates how a change in structure affects the Trp-19 to N-terminal distance.

Emission spectra of the donor-alone melittin and dansyl-melittin are shown in Figure 14.10. These spectra show the relative intensities of the D–A pairs relative to the donor without a nearby acceptor. The transfer efficiency can be calculated from these steady-state intensities. The overall efficiency of RET seems to be higher for  $\alpha$ -helical melittin in 80% methanol, where melittin is in the  $\alpha$ -helical state, than in aqueous buffer (5 mM MOPS), where melittin is in the random-coil state. This difference is seen as a weaker donor emission and stronger acceptor emission (dashed) in 80% methanol. If we calculated a single distance from these data we would conclude that the Trp-to-dansyl distance is smaller in the  $\alpha$ -helical state (dashed) than in the random-coil state (solid). However, the time-resolved data yield a different result.

Frequency-domain intensity decays are shown in Figure 14.11 for random-coil melittin, as the donor-alone control ( $\bullet$ ) and for dansyl-melittin ( $\circ$ ). The presence of the acceptor shortens the donor decay time, which is seen as a shift in the donor response to higher frequencies in the presence of acceptors. While we expect melittin to be in the random-coil state with a distribution of D–A distance, it is difficult to see increased heterogeneity in the tryptophan decay due to the presence of acceptor in the random-coil state. The similarity of the donor-alone and donor–acceptor frequency responses in Figure 14.11 illustrates the difficulty in determining distance distributions in proteins. Careful analysis is needed not only to recover the distance distributions, but also whether the data are consistent or not with competing models.

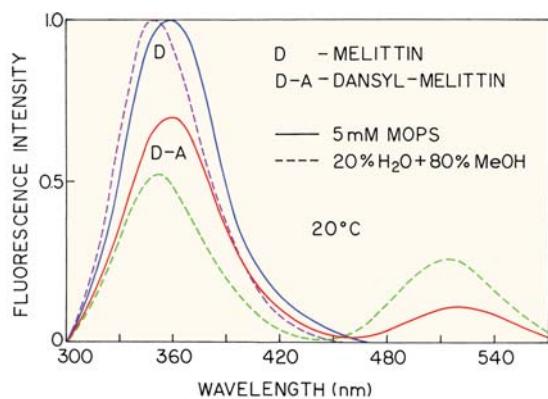


**Figure 14.10.** Emission spectra of dansyl-melittin in the  $\alpha$ -helical and random-coil state. The donor-alone (melittin) intensities are normalized. Reprinted from [23]. Copyright © 1990, with permission from Elsevier Science.

**Table 14.1.** Intensity Decays of Melittin and Dansyl-Melittin<sup>a</sup>

Sample	%MeOH	$\bar{\tau}$ (ns) <sup>b</sup>	$\gamma_i$ (ns)	$\alpha_i$	$f_i$	$\chi^2_R$		
						1 <sup>c</sup>	2	3
Melittin	0	3.29	0.32	0.408	0.065			
			2.49	0.401	0.440			
			4.64	0.191	0.400	548	5.7	1.4
Dansyl-melittin	0	2.41	0.14	0.500	0.064			
			1.12	0.287	0.297			
			3.24	0.213	0.639	733	7.4	2.5
Melittin	80	4.19	0.67	0.374	0.092			
			2.96	0.434	0.468			
			6.29	0.192	0.440	551	7.7	2.8
Dansyl-melittin	80	2.46	0.37	0.345	0.083			
			1.73	0.561	0.631			
			4.69	0.094	0.286	368	9.5	1.2

<sup>a</sup>From [23].<sup>b</sup> $\bar{\tau}$  is the mean decay time calculating using  $\bar{\tau} = f_1\gamma_1 + f_2\gamma_2 + f_3\gamma_3$ .<sup>c</sup>The numbers represent the number of decay times used in the analysis.

Another difficulty in measuring distance distributions in proteins is the presence of multi-exponential decays in the absence of acceptor. The intensity decay of melittin itself is a multi-exponential that requires at least three decay times for a suitable fit in either solvent (Table 14.1). Also shown in Table 14.1 are the multi-exponential analyses for dansyl-melittin in aqueous buffer (random coil) and in 80% methanol ( $\alpha$ -helical). The mean decay time ( $\bar{\tau}$ ) of the tryptophan donor is shortened by the presence of acceptor. However, it is difficult if not impossible to interpret these values of  $\alpha_i$  and  $\tau_i$  in terms of the melittin conformation.

The data are best analyzed in terms of a distance distribution (Figure 14.12). In the absence of methanol, the data are consistent with a wide distribution of Trp-to-dansyl distances ranging from 0 to 40 Å. The mean ( $\bar{\tau}$ ) and half width ( $hw$ ) were 17 and 25 Å, respectively. In the presence of

methanol the distance distribution becomes quite sharp, with  $(\bar{\tau}) = 25$  Å and  $hw = 3$  Å (Figure 14.13), which is interpreted as being due to the  $\alpha$ -helical structure shown in Figure 14.9.

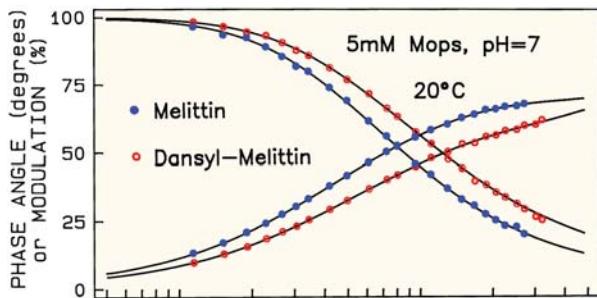


**Figure 14.11.** Frequency-domain donor decay of melittin (●) and dansyl-melittin (○). Revised from [23]. Copyright © 1990, with permission from Elsevier Science.

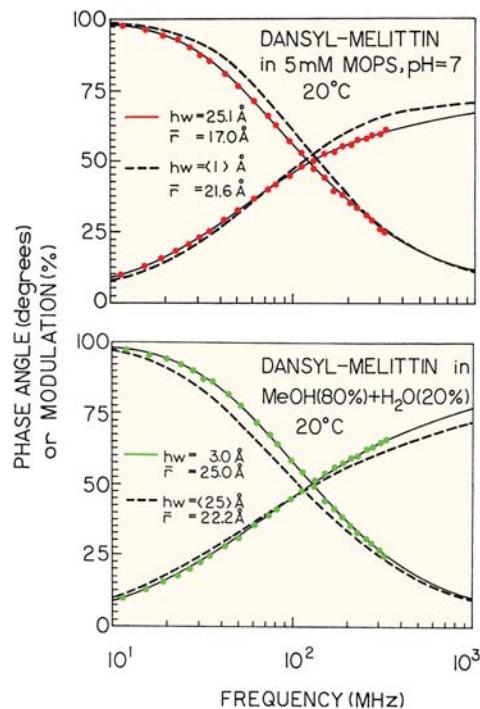


**Figure 14.12.** Frequency-domain tryptophan decays of dansyl-melittin in the random-coil (top) and  $\alpha$ -helical states (bottom). Revised from [23]. Copyright © 1990, with permission from Elsevier Science.

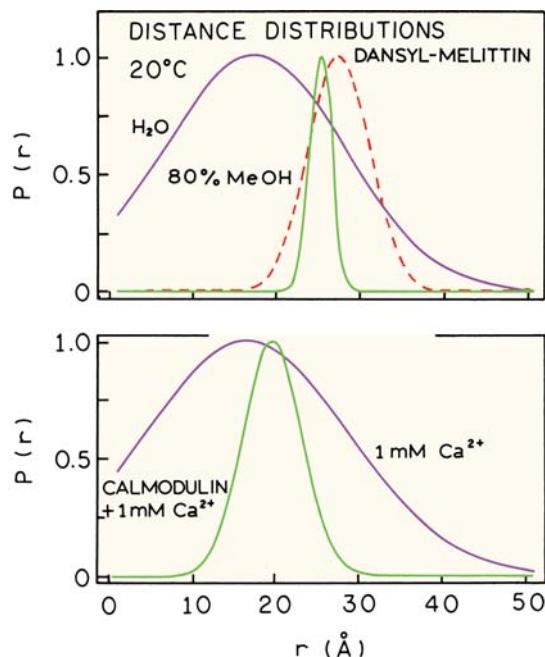


**Figure 14.13.** Distance distribution of dansyl-melittin in solution and when bound to calmodulin. Revised from [23]. The dashed line (top) shows the distance distribution obtained with consideration Trp-to-dansyl diffusion:  $D = 6.5 \times 10^{-6} \text{ cm}^2/\text{s}$ . Revised from [24].

Because of the limited resolution using the time-resolved data it is important to test the uniqueness of the result. This was accomplished by crossfitting the data with alternate parameter values. For instance, the data for the random-coil state are fit to a distribution with a variable mean value but a small half width, which is a fixed parameter. The data for the random-coil state (Figure 14.12, top) are clearly inconsistent with a narrow half width (dashed). The data for the  $\alpha$ -helical state (Figure 14.12, bottom) are clearly inconsistent with the half width of the random-coil state (dashed). The visual differences seen in the crossfits makes an important point. If you cannot visually see the difference between the fits of two different models to the data then it is risky to select one result as the correct model.

Distance-distribution analysis can be used to study the conformations of a protein when bound to other biomolecules. In the presence of calcium, calmodulin expresses a hydrophobic patch. When in the  $\alpha$ -helical state one side of the melittin helix contains hydrophobic amino-acid side chains that bind to calmodulin. A Trp-to-dansyl distance distribution for melittin was also obtained when bound to calmodulin<sup>24</sup> (Figure 14.13, lower panel). Melittin is expected to be in the  $\alpha$ -helical state. Calcium (1 mM) did not affect the melittin distance distribution. However, a rel-

atively narrow distribution was found with 1 mM  $\text{Ca}^{2+}$  and calmodulin, where binding is expected. It is interesting to notice that the mean distance is somewhat smaller than for the unbound  $\alpha$ -helix, suggesting that the hydrophobic patch of calmodulin has imposed some restrictions on the melittin structure. The distance distribution of melittin seems wider when bound to calmodulin than when in solution. There are two possible causes of this result. One is structural heterogeneity in the bound state. The second is the result of using an incorrect model. In Section 14.7 we describe the effects of donor-to-acceptor diffusion for melittin. In fact, the distribution shown for  $\alpha$ -helical melittin in Figure 14.13 is narrowed by diffusion, and consideration of this effect results in a somewhat wider distribution for melittin in 80% methanol (Figure 14.13, top, dashed). Donor-to-acceptor diffusion tends to narrow the apparent distance distribution if the analysis is performed without consideration of diffusion.

## 14.4. DISTANCE-DISTRIBUTION DATA ANALYSIS

### 14.4.1. Frequency-Domain Distance-Distribution Analysis

It is informative to describe in detail how the frequency domain data for dansyl-melittin were analyzed to recover the distance distribution. A similar approach can be used for analysis of the time-domain data. The first step in any distance-distribution analysis is determination of the intensity decay of the donor alone, followed by use of this decay law in the distance-distribution analysis. For any form of the decay law the phase ( $\phi_{c\omega}$ ) and modulation ( $m_{c\omega}$ ) at a given frequency can be calculated from

$$N_{\omega} = \frac{\int_0^{\infty} I(t) \sin \omega t dt}{\int_0^{\infty} I(t) dt} \quad (14.7)$$

$$D_{\omega} = \frac{\int_0^{\infty} I(t) \cos \omega t dt}{\int_0^{\infty} I(t) dt} \quad (14.8)$$

Using these transforms the phase and modulation values can be calculated from

$$\phi_{c\omega} = \arctan(N_{\omega}/D_{\omega}) \quad (14.9)$$

$$m_{c\omega} = (N_{\omega}^2 + D_{\omega}^2)^{1/2} \quad (14.10)$$

If the donor decay is a single exponential then the decay is given by eq. 14.6, and the transforms are

$$N_{\omega} = \frac{1}{J} \int_{r=0}^{\infty} \frac{P(r)\omega \tau_{DA}^2}{1 + \omega^2 \tau_{DA}^2} dr \quad (14.11)$$

$$D_{\omega} = \frac{1}{J} \int_{r=0}^{\infty} \frac{P(r)\tau_{DA}}{1 + \omega^2 \tau_{DA}^2} dr \quad (14.12)$$

where the normalization factor  $J$  is given by

$$J = [\int_0^{\infty} P(r) dr] [\int_0^{\infty} I_{DA}(t) dt] \quad (14.13)$$

In these equations the value of  $\tau_{DA}$  is given by

$$\frac{1}{\tau_{DA}} = \frac{1}{\tau_D} + \frac{1}{\tau_D} \left( \frac{R_0}{r} \right)^6 \quad (14.14)$$

Hence  $\tau_{DA}$  depends on distance  $r$ , as can be seen from eq. 14.6. The value of  $\tau_{DA}$  corresponds to the lifetime of the donor for a particular distance  $r$ . As was described above, these specific molecules cannot be observed. Only the entire population can be measured, and hence the integrals over  $r$  in eqs. 14.11 and 14.12. Analytical expressions for  $N_{\omega}$  and  $D_{\omega}$  are not available, so these values are calculated numerically. The parameter values describing the distance distribution are recovered from nonlinear least squares by minimization of  $\chi_R^2$ :

$$\chi_R^2 = \frac{1}{v} \sum_{\omega} \left( \frac{\phi_{\omega} - \phi_{c\omega}}{\delta\phi} \right)^2 + \frac{1}{v} \sum_{\omega} \left( \frac{m_{\omega} - m_{cw}}{\delta m} \right)^2 \quad (14.15)$$

In this expression  $\phi_{\omega}$  and  $m_{\omega}$  are the experimental values,  $v$  is the degrees of freedom, and the subscript  $c$  indicates calculated values for assumed values of  $\bar{r}$  and  $hw$ . The values  $\delta\phi$  and  $\delta m$  are the experimental uncertainties in phase and modulation, respectively.

For most proteins or macromolecules the donor-alone decays are not single exponentials. Hence we need to consider how to recover the distance distribution for multi-exponential donors. In this case the donor-alone decays are described by

$$I_D(t) = \sum_i \alpha_{Di} \exp(-t/\tau_{Di}) \quad (14.16)$$

where  $\alpha_{Di}$  are the pre-exponential factors and  $\tau_{Di}$  the decay times for the donor in the absence of any acceptor. This

expression was written with the factor  $I_D^0$  because this factor cancels in the frequency-domain analysis. At this point we need to make some assumptions. What are the transfer rates and/or Förster distances from each component in the donor decay? Equation 14.2 gives the decay rate for a fluorophore with a single decay time  $\tau_D$ . Hence it seems reasonable to assume that the transfer rate for each decay time component is given by

$$k_{Ti}(r) = \frac{1}{\tau_{Di}} \left( \frac{R_0}{r} \right)^6 \quad (14.17)$$

and that the distance-dependent donor decay times are given by

$$\frac{1}{\tau_{DAi}} = \frac{1}{\tau_{Di}} + \frac{1}{\tau_{Di}} \left( \frac{R_0}{r} \right)^6 \quad (14.18)$$

This assumption seems to yield reasonable results, but the assumption has not been proven to be correct. Other assumptions are possible,<sup>25</sup> but do not seem to alter the results. Assuming eq. 14.17 correctly describes the transfer rate from each component, the intensity decay of D–A pairs spaced at a distance  $r$  is given by

$$I_{DA}(r,t) = \sum_i \alpha_{Di} \exp \left[ -\frac{t}{\tau_{Di}} - \frac{t}{\tau_{Di}} \left( \frac{R_0}{r} \right)^6 \right] \quad (14.19)$$

and the intensity decay of the entire sample with many D–A pairs is given by

$$I_{DA}(t) = \int_0^{\infty} P(r) I_{DA}(r,t) dr \quad (14.20)$$

The sine and cosine transforms are

$$N_{\omega}^{DA} = \frac{1}{J} \int_0^{\infty} \sum_i \frac{P(r) \alpha_{Di} \omega^2 \tau_{DAi}^2}{1 + \omega^2 \tau_{DAi}^2} dr \quad (14.21)$$

$$D_{\omega}^{DA} = \frac{1}{J} \int_0^{\infty} \sum_i \frac{P(r) \alpha_{Di} \tau_{DAi}}{1 + \omega^2 \tau_{DAi}^2} dr \quad (14.22)$$

where  $J$  is given by eq. 14.13 using the multi-exponential decay law. It is important to notice that a multi-exponential decay for the donor does not introduce any additional parameters into the analysis. This is because the intrinsic decays of the donor are measured in a separate experiment,

using samples without acceptor. The data from the donor are fit to the multi-exponential model, and the parameters ( $\alpha_{D_i}$  and  $\tau_{D_i}$ ) are held constant in eqs. 14.21 and 14.22 during the least-squares analysis. It should be remembered that  $\tau_{DAi}$  depends on distance (eq. 14.18).

#### 14.4.2. Time-Domain Distance-Distribution Analysis

The procedure for the distance distribution from the time-domain data is analogous to that used for the frequency-domain data. The intensity at any time is described by eq. 14.6. This decay law is used with the convolution integral, and the measured instrument response function  $L(t)$ , to obtain calculated (*c*) values of  $I_{DA}(t)$  for any given time  $t_j$ :

$$I_{DA}^c(t_j) = \sum_{k=1}^j L(t_k) I_{DA}(t_j - t_k) \Delta t \quad (14.23)$$

where  $I_{DA}(t_j - t_k)$  is given by eq. 14.20. Equation 14.23 can be understood as the intensity at time  $t_j$ , being the sum of the intensities resulting from a series of  $\delta$ -function excitation pulses that in total represents the light pulse  $L(t)$ .

These calculated values are then compared to the measured (*m*) data  $I_{DA}^m(t)$  to minimize  $\chi_R^2$ . The experimental  $I_{DA}^m(t)$  data are a convolution of the impulse response function  $I_{DA}(t)$  with the instrument function  $L(t)$ . As for the FD measurements, a separate measurement of the donor decay is needed, and this decay law is held constant in the distance-distribution analysis.

Irrespective of the type of measurement, TD or FD, it should be noted that the limits of the integral (eqs. 14.11 to 14.13) can also be regarded as a variable parameter. Hence one can evaluate if there exists a distance of closest D–A approach ( $r_{\min}$ ) or a maximum D–A distance ( $r_{\max}$ ) that is allowed by the experimental data. If such  $r_{\min}$  and  $r_{\max}$  are used then one must be careful to normalize the integrated  $P(r)$  function to unity.

It is apparent from the above description (eqs. 14.11–14.22) that the distance-distribution analysis is moderately complex. A flow chart of the analysis may be easier to understand (Figure 14.14). The analysis starts with a model (Förster transfer) and measurements: time-domain or frequency-domain. For the FD data, measured and calculated values of  $\phi_\omega$  and  $m_\omega$  are compared and the parameters varied to minimize  $\chi_R^2$ . In the case of TD data the calculated values are obtained using eq. 14.23.

When the analysis is completed it is important to determine the uncertainties in the desired parameters. This can be accomplished by analyzing simulated data that contain an amount of noise similar to that in the experimental data, using values of  $\bar{r}$  and  $hw$  similar to the recovered values. Analysis of such simulated data allows one to determine whether it is possible to resolve the parameters. This is particularly important for similar distributions. We also recommend examination of the  $\chi_R^2$  surfaces, which reveal the sensitivity of the data to the described parameters, or the uncertainty range of the parameter values. The use of  $\chi_R^2$  surface was discussed in Chapters 4 and 5.

#### 14.4.3. Distance-Distribution Functions

Several different mathematical functions have been used to describe donor-to-acceptor distributions. The Gaussian distribution (eq. 14.5) has been most commonly used. This distribution has been multiplied by different elements,  $2\pi r$  and  $4\pi r^2$ , to presumably account for different volume elements available to the acceptor. Inverted parabolas and other functions have also been used.<sup>26</sup> These different functions result in different parameter values, but the overall distance-dependent probabilities look similar.<sup>26–27</sup> In general, there is only enough information to recover an estimate of the distribution, and finer details are not resolved. For most purposes the simple Gaussian (eq. 14.5) is adequate and best suited to describe D–A distribution in macromolecules. In some cases bimodal Gaussians have been used to describe a protein in multiple conformational states.<sup>28</sup>

The Lorentzian distribution has also been used,<sup>4</sup> but in our experience results in artificially narrow half widths. This is because the amplitude of a Lorentzian decreases slowly with distance from the  $\bar{r}$  value. As a result the half width is determined more by the ability of the time-resolved data to exclude these smaller and larger  $r$  values than by the actual width of the distribution. For this reason, half widths determined using a Lorentzian model are invariably smaller than those found using a Gaussian model.

#### 14.4.4. Effects of Incomplete Labeling

In studies of distance distributions, or in any study of energy transfer, it is critically important to consider the extent of labeling, particularly by the acceptors. Most often one will measure the donor decay, and paradoxically this means that it is most important to have complete labeling at the acceptor site. The importance of complete acceptor labeling can

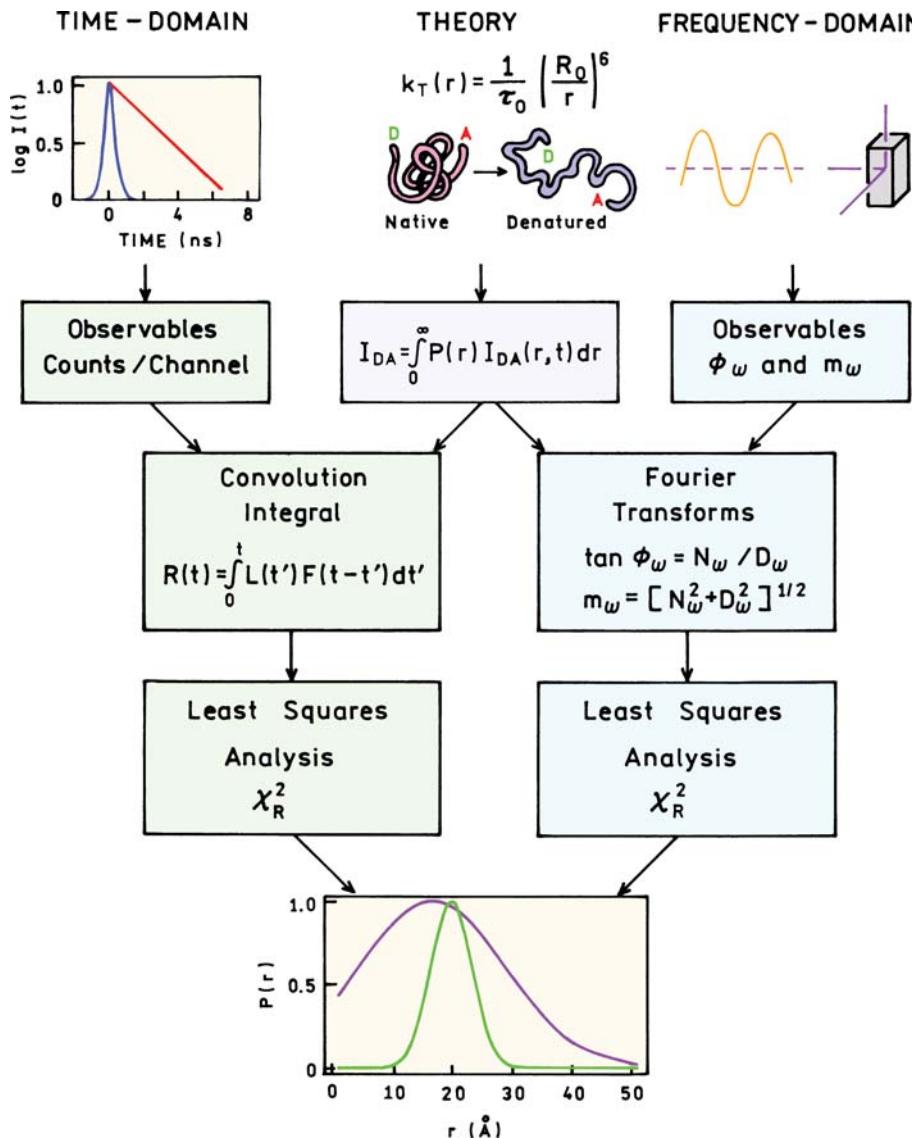


Figure 14.14. Flowchart for distance-distribution analysis.

be understood by considering the effects of incomplete acceptor labeling. This will result in the donor decay containing components due to both the D-A pairs, and from the donors that lack acceptors. The donor-alone molecules contribute to the measured emission greater than their mole fraction. For instance, suppose the donors are quenched tenfold by the linked acceptor, and that 10% of the donors lack acceptors. The donor-alone molecules will contribute tenfold more than their 10% mole fraction, so that the donor-alone signal will be equal to that of the D-A pairs. Hence, a small fraction of underlabeling by acceptors can result in

severe distortion of the donor decays. We have found that the presence of a small fraction of donor-alone molecules usually results in a failure of the Gaussian distance-distribution analysis to converge. This is a fortunate occurrence, and preferable to a convergent analysis that may be accepted as correct. We have less experience with the properties of the other distributions in the presence of a significant donor-alone population.

The presence of underlabeling by the acceptor can be accounted for in the least-squares analysis. The donor intensity decay is given by

$$I_{\text{DA}}(t) = (1 - f_A) I_{\text{D}}^0 \sum_i \alpha_{0i} \exp(-t/\tau_{\text{Di}}) + f_A I_{\text{D}}^0 \int_0^\infty P(r) \sum_i \alpha_{\text{Di}} \exp\left[-\frac{t}{\tau_{\text{Di}}} - \frac{t}{\tau_{\text{Di}}} \left(\frac{R_0}{r}\right)^6\right] \quad (14.24)$$

where  $f_A$  is the fraction of the molecules labeled with acceptors.<sup>29–30</sup> While it is possible to correct for acceptor underlabeling, its presence results in decreased information in the donor decay kinetics, and quickly results in loss of resolution about the distance distribution. There seems to be strong correlation between  $f_A$ ,  $\bar{r}$ , and  $hw$  during the least-squares analysis. If the value of  $f_A$  is not known, we regard 5% underlabeling by acceptors as the maximum consistent with reasonable confidence of the distance distribution. If  $f_A$  is known, and not a variable in the analysis, then a higher level of underlabeling can be tolerated. Surprisingly, the extent of donor underlabeling is not important in the distance-distribution analysis using the donor emission. Molecules lacking the donor (that is, labeled only with acceptor) do not contribute to the donor decay. The presence of acceptor-only molecules is not important since the solutions are typically too dilute for transfer to acceptors not covalently linked to donors.

#### 14.4.5. Effect of the Orientation Factor $\kappa^2$

As described in the previous chapter, the rate of energy transfer depends on the relative orientation of the donor emission dipole and the acceptor absorption dipole. Fortunately, for studies of distance distributions, the effect of  $\kappa^2$  is likely to be small and use of the dynamic average  $\kappa^2 = 2/3$  is reasonable.<sup>31–33</sup> This is because angular displacements of the donor and acceptor result in averaging the value of  $\kappa^2$  towards 2/3. For a native protein one can expect the donors and acceptors to be relatively immobile during the excited-state lifetime. This is less likely in the random-coil state, where the donor and acceptor, and the peptide itself, can be expected to rotate and diffuse. For molecules the size of fluorophores, the rotational correlation times are typically near 100 ps in water or when located on the surface of a macromolecule. The only mechanism by which  $\kappa^2$  could affect the distance distribution is if the average D–A orientation were in some way correlated with the D–A distance.<sup>31–32</sup> Given the multitude of conformations accessible to random-coil

peptides, this seems unlikely. In general, rotational probe motions occur more rapidly than translational diffusion, so that one can expect rotational averaging even when D–A translational diffusion is minimal. In general, it seems that distance distributions should be largely unaffected by  $\kappa^2$ , especially where the solution is fluid enough to allow segmental motions of the probes relative to the biomolecule.

#### 14.4.6. Acceptor Decays

Information about the distance distribution is also contained in the acceptor decays, so that one may ask why we have stressed measurements of the donor decays. Although in principle either the donors or acceptor decays could be used to recover the distance distribution,<sup>34–35</sup> in most circumstances there is less information in the acceptor decay than in the donor decay. This can be seen by examining the absorption spectra of tryptophan (indole) and dansyl (Figure 13.9). The acceptors typically absorb light at wavelengths used to excite the donors. As a result, the acceptor is excited by two routes: by direct excitation and by RET from the donor. Only the latter portion of the acceptor emission contains information on the distance distribution. Typically, this is the minor fraction of the acceptor intensity, so that most of the acceptor emission is due to the intrinsic decay of the directly excited acceptor. Because of this fact any analysis of the acceptor-decay kinetics must consider directly excited acceptors. Depending on the donor and acceptor emission spectra it may also be necessary to consider contributions of the donor emission at the wavelength chosen to observe the acceptor. In principle an analysis correcting for donor emission and a directly excited acceptor can be performed, but such analyses rarely appear in the literature.

If one can measure the acceptor-decay kinetics due only to RET it will display the unique properties of an excited-state reaction. In the time domain the characteristics of an excited-state reaction are a rise time in the time-dependent intensities, and a negative pre-exponential factor in the multi-exponential analysis. In the frequency domain the phase angles of the acceptor can exceed 90°. These characteristic features are the result of the acceptor being excited by the donor, rather than directly. These features can be hidden by spectral overlap of the donor and acceptor emission spectra and by a directly excited acceptor.

## 14.5. BIOCHEMICAL APPLICATIONS OF DISTANCE DISTRIBUTIONS

### 14.5.1. Calcium-Induced Changes in the Conformation of Troponin C

Troponin C (TnC) is one of several proteins involved in muscle contraction. The structure of troponin C in solution is known to be sensitive to calcium. The structure of troponin C consists of two domains linked by a helical peptide (Figure 14.15).

Troponin C typically lacks tryptophan residues. This is fortunate because it allows insertion of tryptophan donors at any desired location by site-directed mutagenesis. In the mutant shown in Figure 14.15 a single-tryptophan residue was placed at position 22 to serve as the donor. As is typical in the design of mutant proteins, the tryptophan (W) was a conservative replacement for phenylalanine (F). A uniquely reactive site for the acceptor was provided by replacing asparagine 52 with a cysteine residue (N52C). This site was labeled with IAEDANS.

The upper panel in Figure 14.16 shows the time-dependent donor decays of the donor-alone and the donor-acceptor protein in the absence of bound calcium.<sup>8</sup> Without acceptor the intensity decay of trp-22 is close to a single expo-

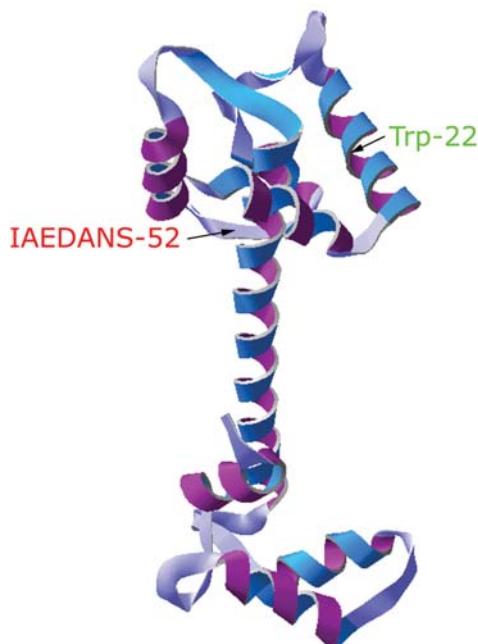


**Figure 14.15.** The crystal structure of turkey skeletal 2Ca-Troponin C.

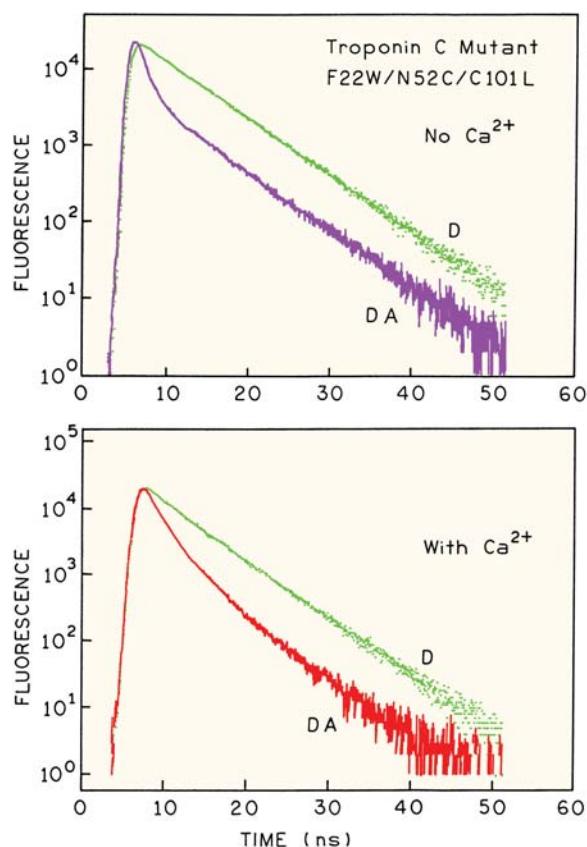


**Figure 14.16.** Tryptophan-22 intensity decays of Troponin C without (D) and with (DA) an IAEDANS on cysteine 52. Top, without  $\text{Ca}^{2+}$ . Bottom, with  $\text{Ca}^{2+}$ . From [8].

nential. The intensity decay of trp-22 becomes strongly heterogeneous in the presence of IAEDANS acceptor at position 52. This change in the donor decay was used to recover the trp-to-IAEDANS distance distribution, which is seen to be centered near 11 Å and to be about 10 Å wide (Figure 14.17). The close D–A distance and relatively wide distribution comprise one reason for the strongly heterogeneous intensity decay. Close inspection of Figure 14.16 shows that at longer times the intensity decay of the D–A pair is the same as the donor-only protein. This is due to less than 100% labeling by the acceptor. The extent of acceptor labeling is claimed to be about 95%. Because the donor is strongly quenched by the nearby acceptor, even 5% donor-alone protein contributes significantly to the measured intensity decay. The distance distribution shown in Figure 14.17 was corrected for acceptor underlabeling. The data in Figure 14.16 illustrates how only a small amount of donor-alone molecules can distort the data. Complete labeling by

**Table 14.2.** Tryptophan Intensity Decays in Troponin C F22W/N52C/C101L<sup>8</sup>

	$\tau_1$ (ns)	$\alpha_1(f_1)^a$	$\tau_2$ (ns)	$\alpha_2(f_2)$	$\tau_3$ (ns)	$\alpha_3(f_3)$	$\chi_R^2$
Donor-alone	5.74	1.00					1.4
	5.27	0.58	6.3	0.42			1.6
Donor-acceptor ( $R_0 = 22.1 \text{ \AA}$ )	1.81	1.0					192.3
	5.60	0.08	0.76	0.92			1.5
	5.74	0.07	1.28	0.26	0.50	0.67	1.3
		(0.39) <sup>a</sup>		(0.29)		(0.32)	
Donor-alone + Ca <sup>2+</sup>	4.81	1.0					2.7
	5.39	0.59	3.56	0.41			1.1
Donor-acceptor+Ca <sup>2+</sup> ( $R_0 = 23.9 \text{ \AA}$ )	2.29	1.0					31.8
	4.06	0.18	1.59	0.82			1.9
	5.16	0.06	2.18	0.57	0.79	0.37	1.2
		(0.17)		(0.67)		(0.16)	

<sup>a</sup>Values in parentheses are the fractional intensities calculated from  $f_i = \alpha_i \tau_i / \sum \alpha_j \tau_j$ .

acceptor is perhaps the most important step in measuring a distance distribution.

Binding of calcium to the troponin C mutant results in a substantial change in the intensity decay (Figure 14.16, bottom). When the protein contains bound calcium the decay of trp-22 appears to be mostly a single exponential in the absence of acceptors. The presence of acceptor results in a decrease in donor lifetime, and its decay is no longer a single exponential. The heterogeneity due to acceptor appears to be less than observed in the absence of Ca<sup>2+</sup>. Analysis of the data in terms of a distance distribution results in a calcium-dependent increase in the D–A distance, and a restriction to a narrow range of distances (Figure

14.17). These results suggest that troponin C adopts a more rigid and/or more unique structure in the presence of calcium.

It is informative to examine the multi-exponential analyses of the donor decays (Table 14.2). In the absence of acceptor the tryptophan decays are close to single exponentials, especially in the absence of Ca<sup>2+</sup>. In the presence of the IAEDANS acceptor the intensity decay becomes strongly heterogeneous. The extent of heterogeneity can be judged from the  $\chi_R^2$  value for the single-decay-time fits. The wider distribution in the absence of Ca<sup>2+</sup> results in a higher value of  $\chi_R^2 = 192$  than in the presence of Ca<sup>2+</sup> ( $\chi_R^2 = 32$ ), where the distribution is more narrow. The intensity decays in the absence and presence of Ca<sup>2+</sup> reveal components with decay times close to that of the donor alone. The  $\alpha_i$  values typically represent the molecular fraction of the molecules that display their respective decay time. This suggests that 6 to 7% of the TnC molecules lack a bound acceptor, in agreement with the known extent of labeling.<sup>8</sup>

The fractional intensities of each component ( $f_i$  values) represent the fractional contributions to the steady-state intensity or the time-integrated intensity decay. The fractional intensity of the component with the donor-alone decay time is nearly 39% in the absence of Ca<sup>2+</sup>, and 17% in the presence of Ca<sup>2+</sup>. The larger fractional contribution in the absence of Ca<sup>2+</sup> is due to the larger extent of energy transfer and a resulting increased contribution of the donor-alone molecules. This large contribution (39%) of the donor-alone molecules, when present at a molecular fraction of 7%, illustrates how the data from strongly quenched samples are easily corrupted by small impurity contributions or underlabeling by the acceptor.

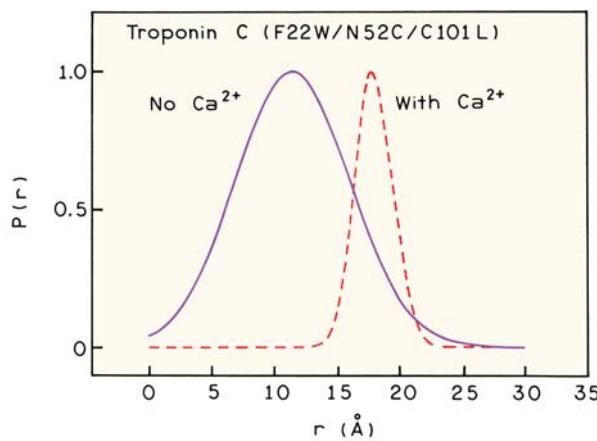


**Figure 14.17.** Trp-22 to IAEDANS-52 distribution in skeletal muscle TnC mutant (F22W/N52C/C101L) in the absence (solid) and presence (dashed) of bound calcium. From [8].

These results illustrate the usefulness of time-resolved measurements for detecting conformational heterogeneity in proteins. The short decay times of the tryptophan residues do not allow time for the conformation to be averaged during the excited-state lifetime, so that the individual conformations contribute to a complex donor decay. This is a somewhat unique feature of fluorescence, as most physical methods reveal an average conformation.

As a final point we wish to stress the importance of time-resolved data for measuring a single distance as well as for measuring distance distributions. If one measures only the steady-state intensities, then one cannot detect the presence of unlabeled or underlabeled molecules. It is easy to be misled by steady-state data that satisfy preconceived notions about the system. In contrast, the time-resolved donor decays contain more information, and will often

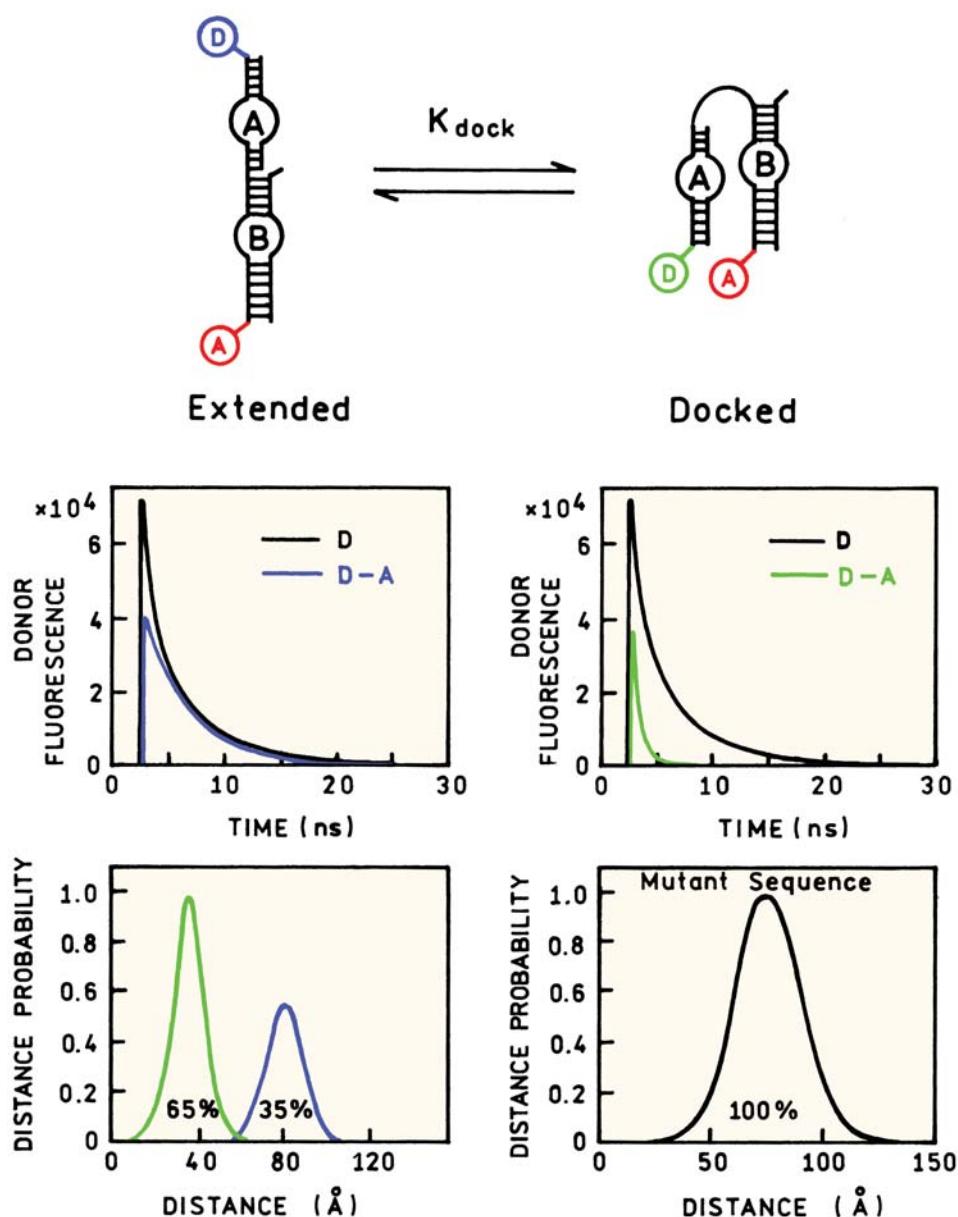


**Figure 14.18.** Time-resolved donor decays and D–A distance distribution for the hairpin ribozyme. In the lower panels the left side shows the D–A distributions for the native sequence, and the right side for a single G to A mutation. Revised from [36].

reveal inconsistencies due to incomplete labeling, multiple labeling or impurity fluorescence. For this reason measurement of the time-resolved donor decays is recommended for all distance measurements.

#### 14.5.2. Hairpin Ribozyme

In the previous chapter we saw how steady-state RET measurements could be used to study folding of the hairpin ribozyme. Time-resolved measurements provide additional detail on this conformational change.<sup>36–37</sup> Figure 14.18 shows a schematic of the docking motion of this ribozyme. Time-resolved measurements show that the donor decay is more rapid in the docked conformation than in the extended conformation. These decays were used with eqs. 14.18 and 14.20 to recover the distribution of D–A distances. These results confirm that the D–A distance is smaller in the docked conformation. However, in either the extended or docked conformation there is a distribution of D–A distances rather than a single distance. Time-resolved RET was also used to determine the effects of mutations in the hairpin sequence on its conformation. A single mutation near the junction site prevented the docking reaction and resulted in a single wide distribution apparently due to a

flexible extended conformation (lower right). See Representative Publications on Measurement of Distance Distributions (near the end of this chapter) for additional references related to RET studies of ribozyme structure.

#### 14.5.3. Four-Way Holliday Junction in DNA

Genetic recombination involves exchange of homologous strands between two duplex DNA molecules. This process occurs at a four-way branch point called a Holliday junction (Figure 14.19). This is a mobile structure that can propagate along the DNA strands. These sites are ultimately removed by cellular enzymes, yielding either the parental or recombinant DNA product. Time-resolved energy transfer has been used to study such junctions.<sup>38–41</sup>

The DNA sequence and sites of labeling of one Holliday junction are shown in Figure 14.19.<sup>39</sup> The strands were labeled on the 5' ends with either fluorescein or rhodamine to provide D–A pairs between sites I and IV. Examination of the oligonucleotide sequence suggests a rather symmetric structure. However, the time-resolved data reveal different rates of energy transfer when the donor (F) and acceptor (R) are on sites I and II or sites I and IV. The data suggest that sites I and II are further apart than sites I and IV

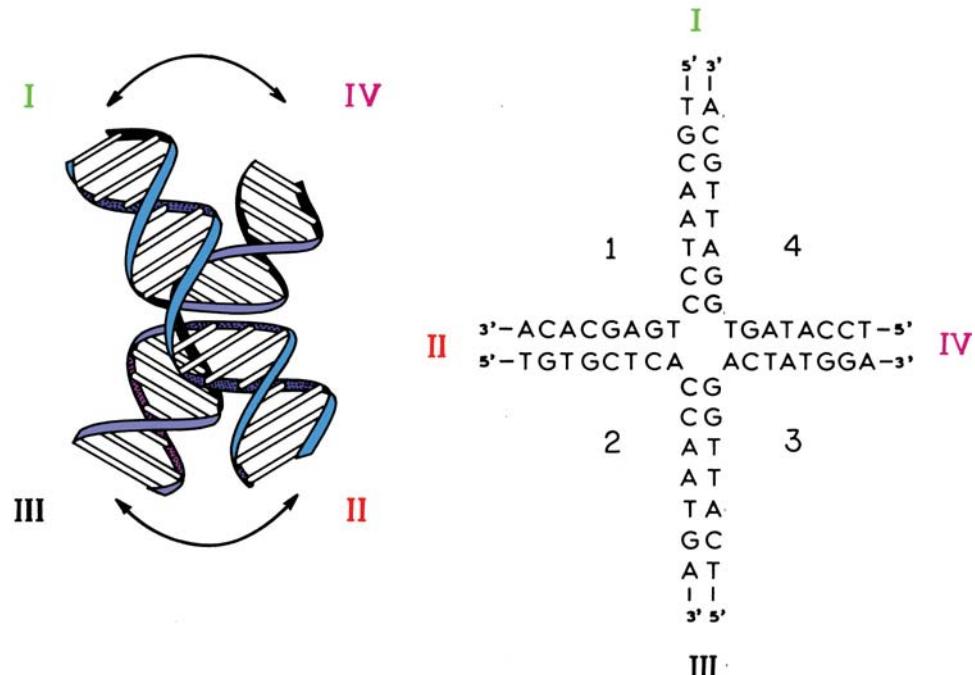


**Figure 14.19.** DNA Holliday junction. Right: nucleotide sequence; left: solution structure. The 5' ends of each strand contain an aminohexyl moiety for covalent attachment of donor and acceptor dyes. Revised and reprinted with permission from [39]. Copyright © 1993, American Chemical Society.

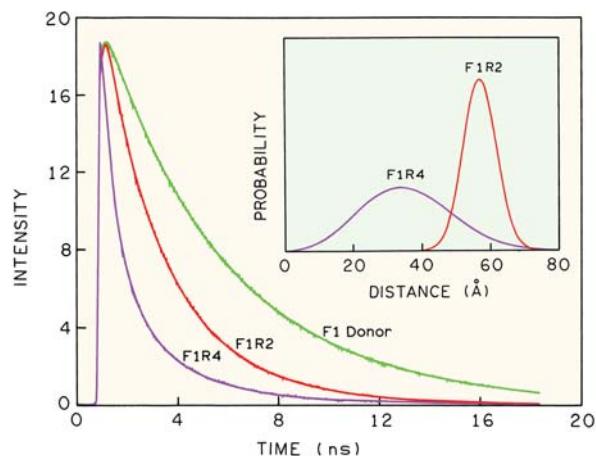


**Figure 14.20.** Intensity decays and distance distributions in a DNA Holliday junction. Data revised and reprinted with permission from [39]. Copyright © 1993, American Chemical Society.

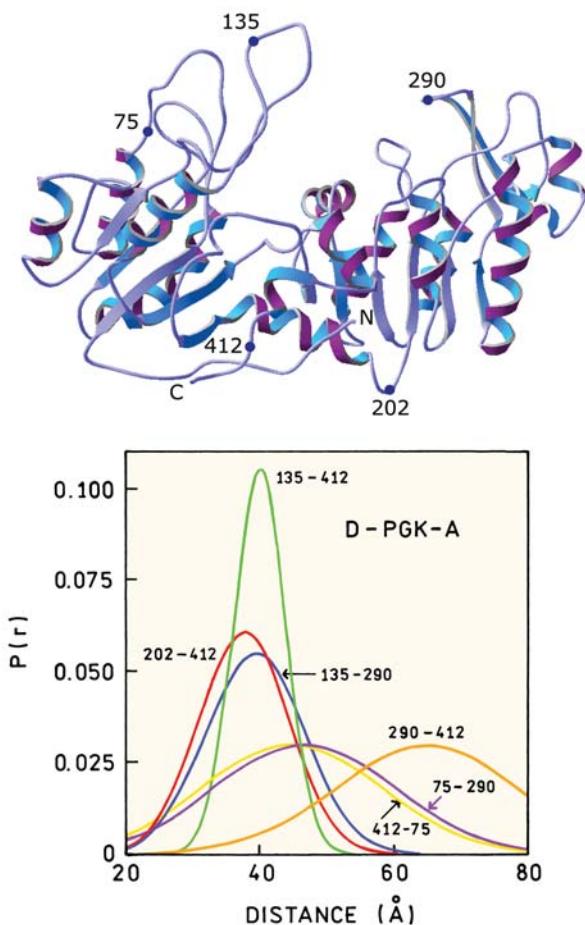


**Figure 14.21.** Top: Structure of PGK showing the sites of cysteine insertion. Bottom: Distance distributions recovered between various sites on PGK. Revised and reprinted with permission from [43]. Copyright © 1997, American Chemical Society.

(Figure 14.20). This expectation is confirmed from the recovered distance distributions. There is a narrow distance distribution between one pair of ends and a wide distribution between the other pair of ends (Figure 14.20). Results from other laboratories have suggested somewhat different structures.<sup>40</sup> Nonetheless, these data for a complex macromolecular assembly illustrate how resolution of distance distributions from the time-resolved energy transfer data has become a widely used tool in structural biology. These results on the ribozyme and Holliday junction represent just two examples of a number of studies of distance distribution in nucleic acids and DNA structure (see Representative Publications on Measurement of Distance Distributions).

#### 14.5.4. Distance Distributions and Unfolding of Yeast Phosphoglycerate Kinase

Time-resolved RET was used to measure the distance distributions between a number of sites on phosphoglycerate kinase (PGK), which consists of a single peptide chain with two domains (Figure 14.21).<sup>42–43</sup> A number of single- and double-cysteine mutants were made to provide sites for

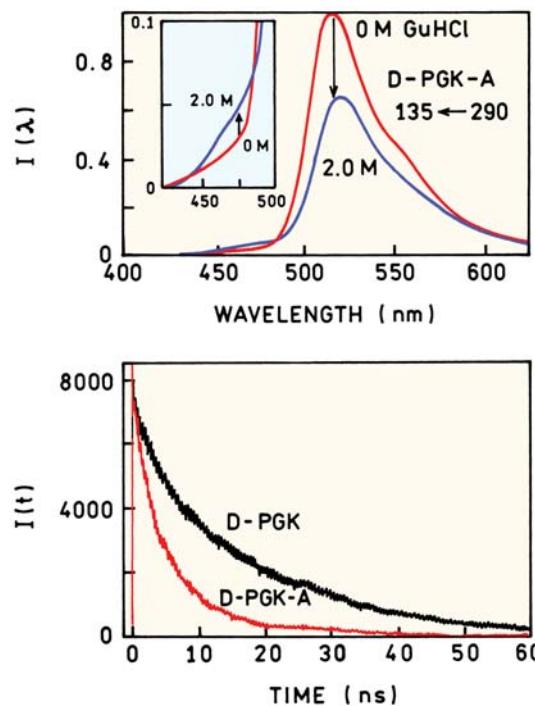


**Figure 14.22.** Top: Emission spectra of D-PGK-A, 135-290, in 0 and 2 M GuHCl. Bottom: Time-resolved decay of donor D-PGK and donor-acceptor D-PGK-A, 135-290. Revised and reprinted with permission from [43]. Copyright © 1997, American Chemical Society.

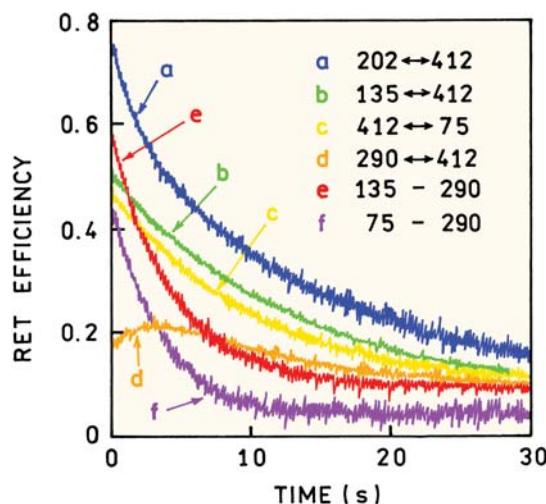


**Figure 14.23.** Unfolding of donor- and acceptor-labeled PGK in 1.23 M GuHCl. Revised and reprinted with permission from [42]. Copyright © 1997, American Chemical Society.

labeling with an IAEDANS donor and/or an IAF acceptor. The labeling and purification had to be performed carefully to obtain protein that was labeled with both the donor and acceptor, and not doubly labeled with the same fluorophore.<sup>44</sup> The emission spectra of the doubly labeled protein (Figure 14.22) shows a difficulty often encountered with RET measurements, which is observation of the donor or acceptor without contributions from the other fluorophore. In this case the fluorescein emission centered at 515 nm is more intense than the donor emission. Careful selection of emission filters was needed to isolate the relatively small intensity of the donor centered near 470 nm. For this mutant, energy transfer from the IAEDANS donor to the fluorescein acceptor decreases in the presence of 2 M guanidine hydrochloride (GuHCl).

The lower panel in Figure 14.22 shows the time-resolved decays of the donor alone and the D-A pairs for transfer between residues 135 and 290. These decays and other time-resolved donor decays were used to recover the distance distributions between the six sites on PGK (Figure 14.21, lower panel). In some cases the distribution is narrow, and for other D-A pairs the distribution much wider. It is not completely clear if the different distribution widths are due to regions of disorder in the native proteins or differences in the resolution of the time-resolved measurements. The mean distances between the D-A sites were consistent with the crystal structure of the protein.

Since the base-pair sequence of the human genome is known, the amino-acid sequences of many gene products

are also known. However, it is generally not possible to predict the three-dimensional structure of a protein from its amino-acid sequence. There is interest in learning the folding pathways of proteins to gain some predictive ability. The PGK mutants shown above were used to study the unfolding pathway of PGK (Figure 14.23).<sup>42</sup> These experiments were performed by mixing folded PGK with GuHCl in a stopped-flow apparatus. To calculate these RET efficiencies it was necessary to measure the donor intensity in the match pairs D-PGK and D-PGK-A (not shown). Examination of the time-dependent RET efficiencies shows that some D-A pairs separate more quickly than others, and that one D-A pair may move together slightly during the unfolding process. These data, and the known labeling sites, can be used to partially determine the pathway PGK takes during the unfolding process.

#### 14.5.5. Distance Distributions in a Glycopeptide

Whereas fluorescence is widely used to study proteins, membranes, and nucleic acids, there are relatively few studies of polysaccharides.<sup>45–48</sup> This is because it is difficult to obtain polysaccharides with a homogeneous structure, and even more difficult to obtain polysaccharides labeled with donor and acceptor fluorophores. Complex oligosaccharides are found in many glycoproteins, including antibodies, hormones, and receptors, yet little is known about their solution conformation. Time-resolved RET was used to resolve the complex conformational distributions of an oligosaccharide.<sup>45</sup> An oligosaccharide was labeled with a naphthyl-2-acetyl donor and a dansylethlenediamine acceptor at one of three locations (Figure 14.24). The authors used both time-resolved and steady-state measurements of RET. The steady-state data provide an important control in all energy transfer measurements. The transfer efficiency determine from the steady-state and time-resolved data should be the same. If not, something is wrong with the sample or analysis. Three donor and acceptor-labeled oligosaccharides were studied, and the data resulted in the resolution of the multiple conformations existing in aqueous solution (Figure 14.25). The Lorentzian model was used to describe the distance distributions. The distance distributions of two of the acceptor sites were bimodal, suggesting that the oligosaccharide branch could fold back toward the donor site. In contrast, the central branch existed in only one conformation and was unable to fold back towards the donor (Figure 14.25).

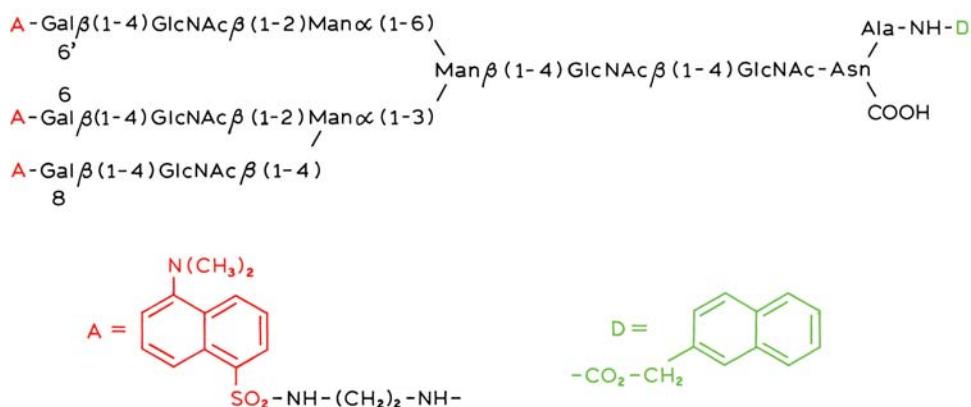


**Figure 14.24.** Structure of triantennary glycopeptide fluorescence energy-transfer probes. D, naphthyl-2-acetyl; A, dansylethylenediamine. GP-ADanNap glycopeptides all contain D and either A6', A6, or A8. Only one acceptor is present during RET measurements. Revised and reprinted with permission from [45]. Copyright © 1991, American Chemical Society.

#### 14.5.6. Single-Protein-Molecule Distance Distribution Advanced Topic

The observation of distance distributions in the ensemble measurements of proteins or nucleic acids implies that the

individual molecules have different D–A distances. If the individual molecules could be observed then it should be possible to detect differences in RET efficiencies. Single-molecule detection (SMD) is possible under favorable optical conditions for high-quantum-yield fluorophores (Chapter 23). Figure 14.26 shows the structure of a 64-amino-acid fragment of a chymotrypsin inhibitor labeled with a TMR donor and a Cy5 acceptor. A dilute solution of this peptide was observed using an instrument designed for SMD. The excitation was a focused laser beam. As the molecule diffused in and out of the laser beam there were bursts of photons from the donor and acceptor. The relative number of donor and acceptor photons was used to calculate RET efficiency. These bursts were counted to obtain a histogram of RET efficiencies (Figure 14.26). In 3 M GuHCl the inhibitor was in the native state with a high RET efficiency near 95%. In 6 M GuHCl there was a wide distribution of RET efficiencies indicating a longer average D–A distance and a range of D–A distances. At an intermediate concentration of 4 M GuHCl there is a bimodal distribution of RET efficiencies.

The RET efficiency histogram in Figure 14.26 shows that folding of the inhibitor is a two-state process. Otherwise there would be a unimodal distribution when the molecule was 50% unfolded. These data also show that the conformations did not interchange within the timescale of the observation, which was about 1 ms for each molecule. It should be noted that these are RET efficiency histograms and not D–A distance histograms, so that the D–A distance decreases along the x-axis as the RET efficiency increases.

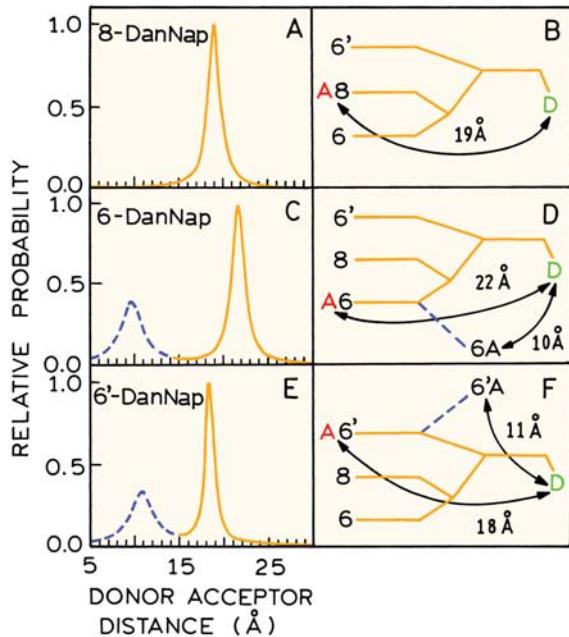


**Figure 14.25.** Donor/acceptor population distributions. Lorentzian fits of the donor decay curves are shown for GP-8-DanNap, GP-6-DanNap, and GP-6'-DanNap. The ratio of populations for GP-6-DanNap and GP-6'-DanNap were determined to be approximately 60% of the extended conformation and 40% of the folded form. Revised and reprinted with permission from [45]. Copyright © 1991, American Chemical Society.

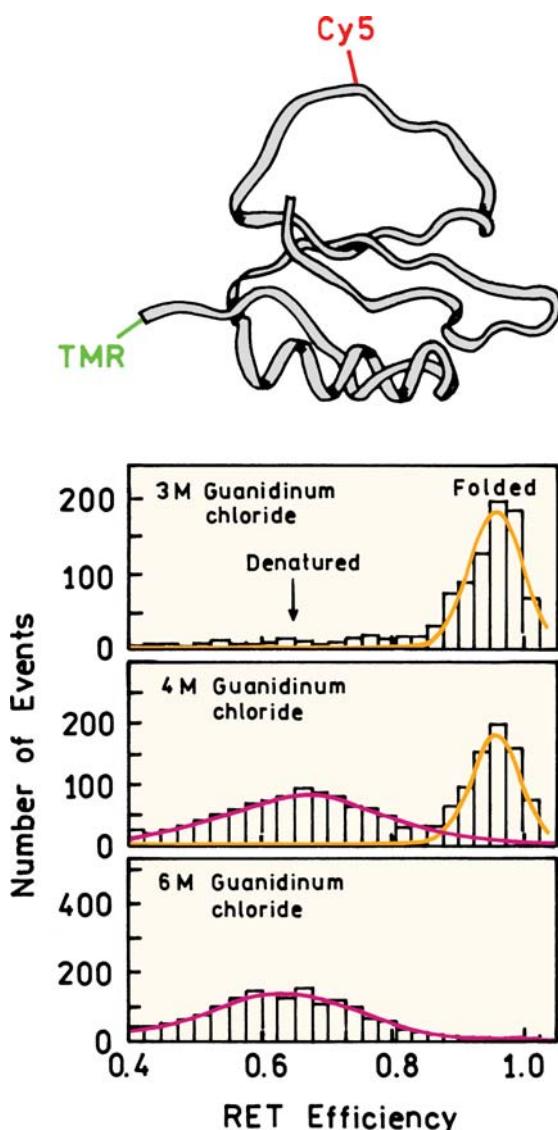


**Figure 14.26.** Structure of chymotrypsin inhibitor 2 and single-molecule RET efficiencies. Revised from [49].

#### 14.6. TIME-RESOLVED RET IMAGING

RET is beginning to be used with fluorescence-lifetime imaging microscopy (FLIM) to study association reactions in cells.<sup>50-56</sup> This is a promising approach because within reasonable limits the lifetimes can be independent of the local probe concentration. Such measurements require spatially resolved measurements of the donor intensity decays. One approach is to use a streak camera that provides spatial resolution along one axis and time resolution along another. Such measurements are shown for Vero cells in Figure 14.27. The genes for CFP or YFP were fused with the gene

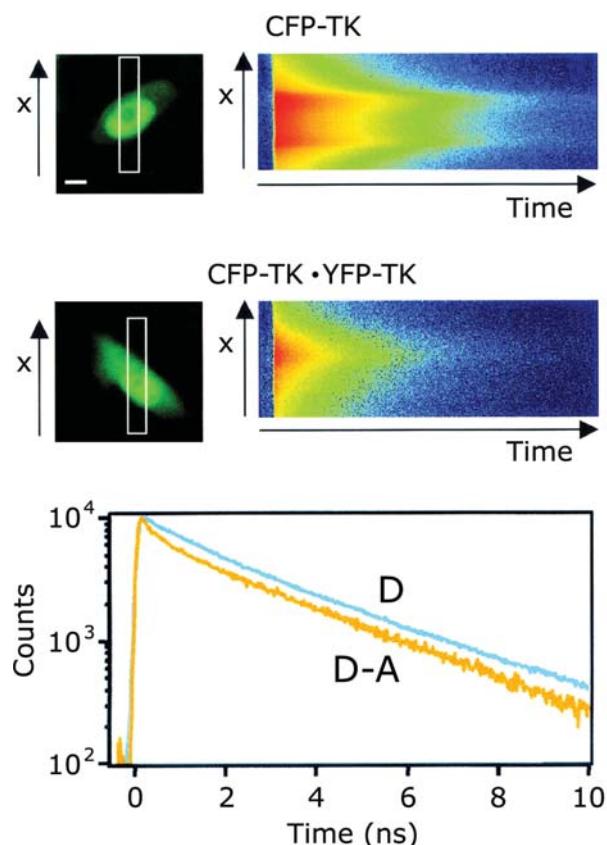


**Figure 14.27.** Intracellular CFP donor decays for RET between CFP and YFP in Vero cells. CFP and YFP were linked to monomers of thymidine kinase (TK). The transition from red to blue represents decreasing intensity. Revised from [55].

for thymidine kinase (TK) from herpes simplex virus.<sup>55</sup> These two constructs were expressed in Vero cells. The TK monomers form dimers in solution. The goal of the experiment was to detect intracellular dimers. Figure 14.27 shows streak-camera measurements of the CFP-TK donor in the cells. The *x*-axis represents the boxed region across the cells. The top panel shows the decay of the donor in the absence of acceptor, and the middle panel shows the donor decays for a cell transfected with the genes for both CFP-TK and YFP-TK. The CFP donor decays more rapidly in the cell transfected with CFP-TK and YFP-TK than in the cell transfected with only CFP-TK. The lower panel shows the total counts along the *x*-axis. The shape of the decay for the cell with both D and A suggests that a fraction of the CFP-TK is associated with acceptor and a fraction of CFP-TK probably does not have a nearby acceptor. This result is expected because TK forms a homodimer so the cell will contain D-D, A-A, as well as D-A pairs.

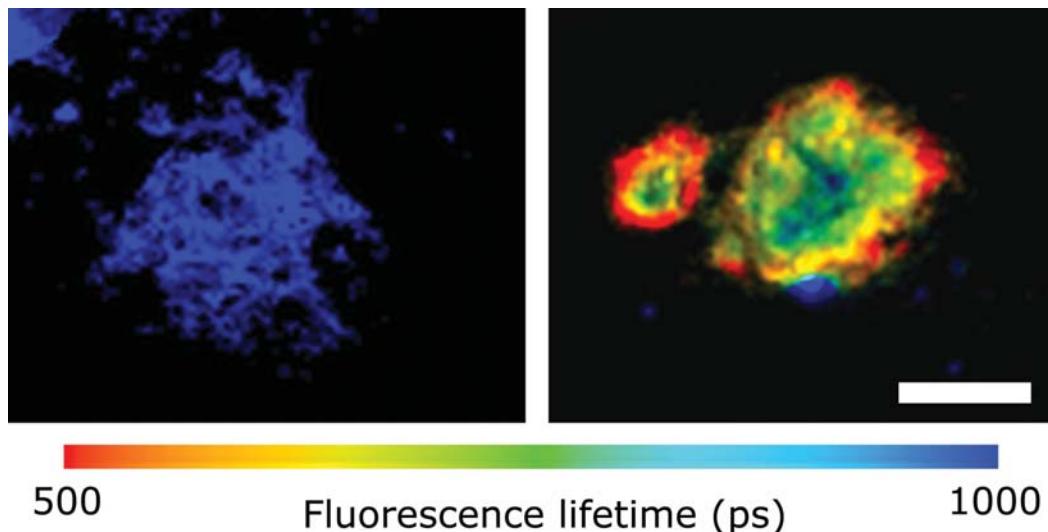


**Figure 14.28.** FLIM image of senile plaques from a mouse model stained with antibodies specific for the plaque. Left: stained with fluorescein-labeled antibody. Right: stained with both fluorescein-labeled and rhodamine-labeled antibody. Scale bar = 20  $\mu\text{m}$ . Courtesy of Dr. Brian J. Bocskai from Massachusetts General Hospital, Charlestown, MA.

Another example of time-resolved RET imaging is shown in Figure 14.28. The images are of senile plaques, from a mouse model, of the type found in Alzheimer's disease. These images were obtained by staining the plaque with specific antibodies.<sup>56</sup> On the left the plaque was stained with fluorescein-labeled antibody. The lifetime is constant across the plaque. For the image on the right the plaque was stained with two antibodies with the same specificity, one labeled with fluorescein and the other with rhodamine. The fluorescein lifetime is shorter, showing that RET has occurred and that the two types of antibodies are bound near each other on the plaque within the Förster distance. The fluorescein lifetime is not uniform across the plaque, indicating that the antigen density is variable across the plaque. Apparently the antigen density is higher around the edges of the plaque (shorter lifetime) than near the center of the plaque (longer lifetime).

#### 14.7. EFFECT OF DIFFUSION FOR LINKED D-A PAIRS

**Advanced Topic**

In the preceding sections we considered the donors and acceptors to be static in space and to remain at the same distance during the excited-state lifetime. However, depending on the donor lifetime, and the mutual diffusion coefficient,  $D = D_D + D_A$ , there can be changes in the D–A distance during the excited-state lifetime (Figure 14.29). For lifetimes

from 5 to 20 ns, displayed by most fluorophores, such as  $\text{TrpNH}_2-(\text{gly})_6-\text{DNS}$ , with  $\tau_D = 4.3$  ns (Section 14.2.1), there is little translational displacement, so that the data could be analyzed in terms of a static distance distribution. In more fluid solvents diffusion can influence the extent of energy transfer. The effects of diffusion are complex to calculate, and typically numerical methods are used. We will attempt to illustrate these effects with a minimum of mathematical detail.

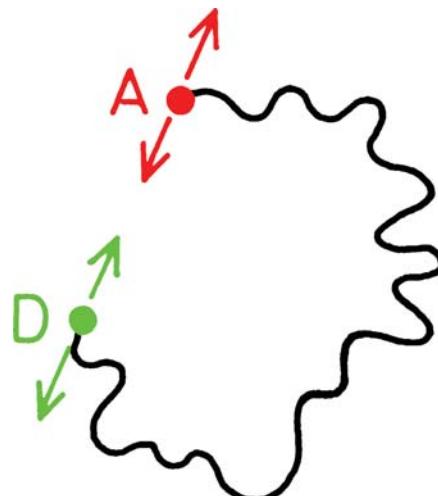


**Figure 14.29.** Donor–acceptor pair with diffusion.

### 14.7.1. Simulations of FRET for a Flexible D-A Pair

The effects of D-to-A diffusion on donor decay can be seen from the simulated data for a flexible D-A pair. The excited-state population is given by<sup>3,26</sup>

$$\frac{\partial \bar{N}^*(r,t)}{\partial t} = -\frac{1}{\tau_D} \left[ 1 + \left( \frac{R_0}{r} \right)^6 \right] \bar{N}^*(r,t) + \frac{1}{N_0(r)} \frac{\partial}{\partial r} \left( N_0(r) D \frac{\partial \bar{N}^*(r,t)}{\partial r} \right) \quad (14.25)$$

where  $\bar{N}^*(r,t)$  is the distribution of distances for the excited D-A pairs normalized by time-zero distribution  $N_0(r)$ . At  $t = 0$  the D-A distribution is the equilibrium distribution. However, the distribution changes following excitation due to more rapid energy transfer between the more closely

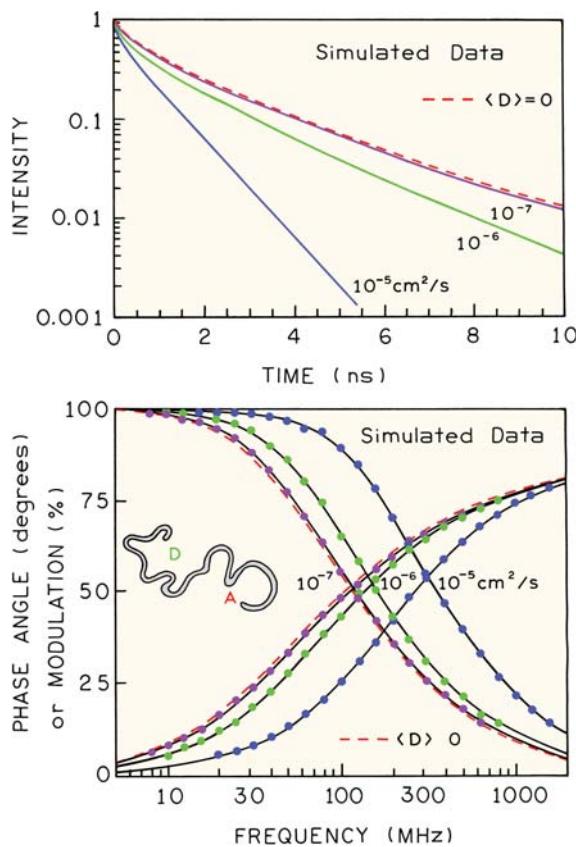


**Figure 14.30.** Effect of D-to-A diffusion in a linked D-A pair as seen in the time domain and the frequency domain. The dashed line shows the frequency response for  $D = 0$ . Revised from [58].

spaced D-A pairs as compared to the more widely spaced D-A pairs. Equation 14.25 is basically the diffusion equation with an added sink term to account for loss of the excited acceptor. The time-dependent intensity decay is given by

$$I_{DA}(t) = I_D^0 \int_{r_{min}}^{r_{max}} P(r) \bar{N}^*(r,t) dr \quad (14.26)$$

where  $r_{min}$  and  $r_{max}$  are chosen to include the accessible distances. Calculation of  $I_{DA}(t)$  in the presence of diffusion is moderately complex, and the details can be found elsewhere.<sup>57–61</sup>

To understand the expected effects of diffusion it is valuable to examine simulated data. Simulated time-domain and frequency-domain data for an assumed donor decay time of 5 ns are shown in Figure 14.30. The distribution of distances at time  $t = 0$  was assumed to be a Gaussian, with  $\bar{r} = 20 \text{ \AA}$ ,  $hw = 15 \text{ \AA}$ , and a Förster distance of 25 Å. If the value of  $D$  is  $10^{-7} \text{ cm}^2/\text{s}$  there is little time for motion during the excited-state lifetime. This can be seen from the near overlap of the simulated data with  $D = 0$  and  $D = 10^{-7} \text{ cm}^2/\text{s}$ . The mean D-to-A displacement ( $\Delta x^2$ )<sup>2</sup> can be calculated to be  $\sqrt{2D\tau_D} = 3.2 \text{ \AA}$ . While significant, this distance is about half the width of a donor or acceptor molecule, and small compared to the assumed  $\bar{r} = 20 \text{ \AA}$ . Because of the range of D-A distances the frequency-domain data are spread out along the frequency axis, and the intensity decay is complex (bottom). As the diffusion coefficient increases the intensity decay becomes more rapid, and the frequency response shifts to higher frequency. Both effects are indicative of an increasing amount of energy transfer. It is important to notice that the frequency response becomes more like a single exponential with increasing rates of diffusion. The same effect can be seen in the time-domain data (top). The donor decay becomes more rapid and more like a single exponential as the diffusion coefficient increases. These simulated data show that D-A diffusion increases the extent of energy transfer and alters the shape of the donor intensity decay. Either the FD or TD data can be used to recover the rate of D-A diffusion as well as the distribution of distances.

Why does D-A diffusion result in increased energy transfer? At first glance it seems that diffusion is just as likely to move the donor and acceptor further apart as it is likely to bring them closer together. A more in-depth understanding of diffusion and RET can be obtained by examining the distance distributions in the excited state. The excited-state distributions evolve with time following pulsed excitation. These time-dependent distributions are shown in

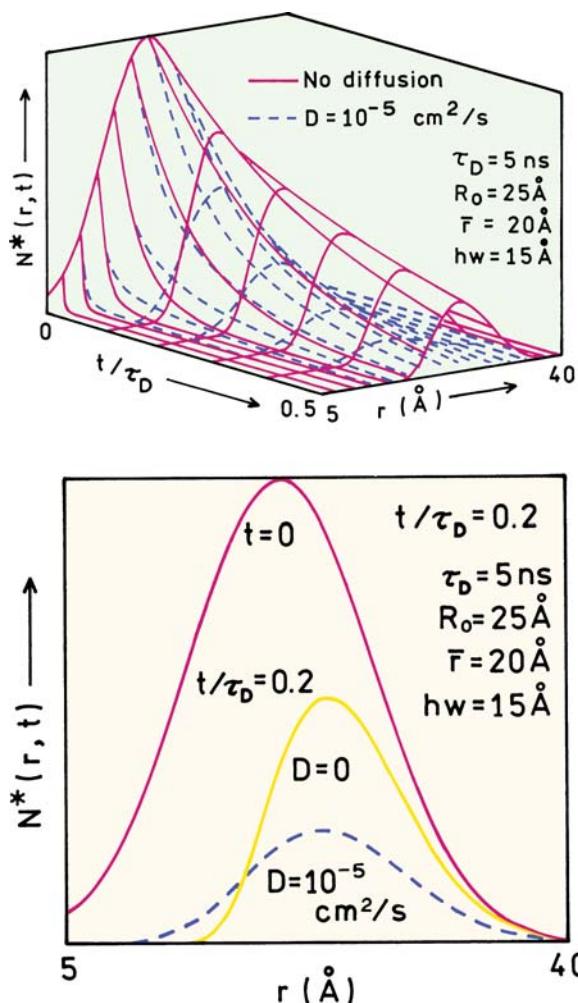


**Figure 14.31.** Simulated excited-state donor distributions in the absence and presence of diffusion. The assumed parameters values are shown on the figure. Reprinted with permission from [58]. Copyright © 1994, American Society for Photobiology.

Figure 14.31 for  $D = 10^{-5} \text{ cm}^2/\text{s}$  and the same donor lifetime and  $R_0$  as in Figure 14.30. The upper panel shows the entire excited-state population for both time and distance. The donor population decays more rapidly in the presence of diffusion (dashed). The lower panel in Figure 14.31 shows the  $P(r)$  distributions at  $t = 0$  and  $t = 1 \text{ ns}$ , with (dashed) and without diffusion (solid). In the absence of diffusion the excited-state population quickly shifts to longer distances, as shown for  $t = 1 \text{ ns}$ ,  $t/\tau_D = 0.2$ . This occurs because the distance dependence of  $k_T(r)$  causes the more closely spaced D–A pairs to transfer more rapidly. For rapid D–A diffusion the population of D–A pairs at shorter distances is replenished by diffusion (dashed), and the closely spaced D–A population displays more rapid transfer. This replen-

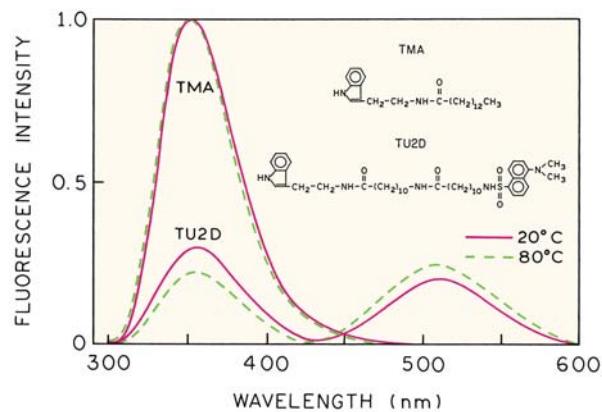


**Figure 14.32.** Emission spectra of the donor alone (TMA), and of the donor–acceptor pair (TU2D) in propylene glycol from 20 to 80°C. The emission spectra of TU2D are normalized to the intensity of TMA at each temperature.

ishment of the closely spaced D–A pairs by diffusion results in increased energy transfer with increasing rates of diffusion.

#### 14.7.2. Experimental Measurement of D–A Diffusion for a Linked D–A Pair

The role of diffusion in energy transfer is best understood by an example. Figure 14.32 shows the emission spectra for a linked indole–dansyl D–A pair TU2D.<sup>58</sup> The donor-alone control molecule is TMA. This flexible D–A pair was found to have the same distance distribution in propylene glycol irrespective of temperature. The donor is quenched to a greater extent at higher temperatures (dashed) due to D–A diffusion during the excited-state lifetime. During the 6-ns donor lifetime the expected D–A displacement is  $\sqrt{2D\tau} = 11 \text{ Å}$  for a diffusion coefficient near  $10^{-6} \text{ cm}^2/\text{s}$ , so there is time for donor and acceptor to approach each other while the donor is excited. This results in an increased rate of energy transfer for each D–A pair, and an overall higher transfer efficiency. The increased extent of energy transfer is also seen from the increased acceptor intensity.

Frequency-domain intensity decays of the donor are shown in Figure 14.33, along with the reconstructed time-dependent decays (top panel). A more rapid decay is seen at higher temperature, and the decay is more like a single exponential. The distance distributions recovered at each temperature are the same, so that the differences in the intensity decays are due to diffusion. Because the extent of diffusion in propylene glycol is minimal at 20°C, the differences in the frequency responses at these two temperatures

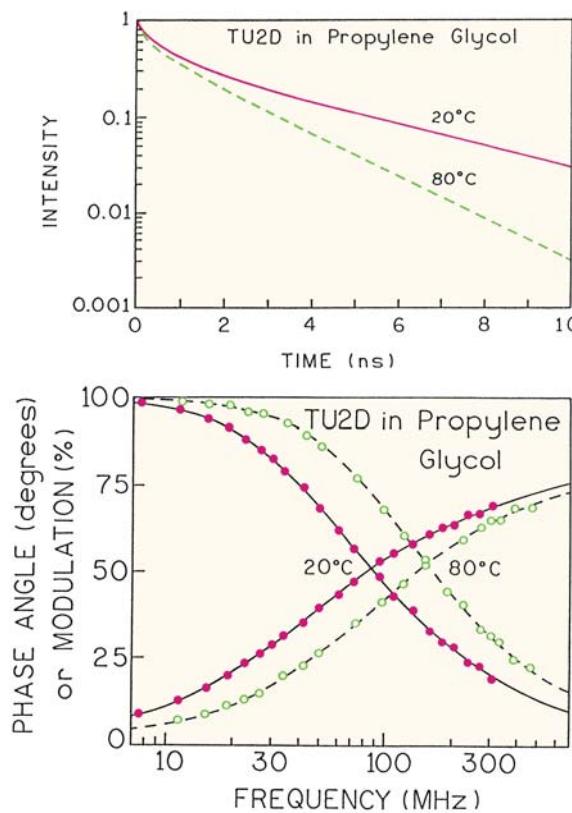


**Figure 14.33.** Frequency-domain donor decays of TU2D in propylene glycol at 20 and 80°C. The top panel shows the time-dependent decay reconstructed from the FD data. Reprinted with permission from [58]. Copyright © 1994, American Society for Photobiology.

can be regarded as the contribution of diffusion. Clearly D–A diffusion has a significant effect on the FD data.

#### 14.7.3. FRET and Diffusive Motions in Biopolymers

Time-resolved FRET has been proposed as a method to measure domain motions in proteins<sup>62–63</sup> and lateral diffusion in membranes. Motions between domains in proteins are known to occur in many proteins, and are thought to be essential for protein function.<sup>64</sup> Unfortunately, measurements of domain motions in proteins have been largely unsuccessful because of the short decay times of the donors. Diffusion in membranes has only been measured using pyrene derivatives that display decay times over 100 ns.<sup>65–66</sup> From the perspective of protein dynamics, the ns decay times of most fluorophores are too short for measurement of site-to-site motions. However, a few measurements have appeared. Ribonuclease A was studied in a partially unfolded state.<sup>67</sup> In this case the carboxyl terminus was

labeled with a naphthylalanine donor that displayed a donor decay time from 25 to 44 ns. The acceptor was a coumarin placed on one of three lysine residues. The time-domain donor decays yielded site-to-site diffusion coefficients of 2 Å<sup>2</sup>/ns in the denatured state, but the motions were mostly undetectable in the native state. Similar results were found for a zinc finger peptide, where site-to-site diffusion with  $D$  near 10 Å<sup>2</sup>/ns was found in the random state, but  $D$  decreased to unmeasurable values in the presence of zinc, which induced folding.<sup>15–16</sup> In the case of phosphoglycerate kinase the rate of domain flexing was too slow to allow estimation of the diffusion coefficient with a 20-ns donor lifetime.<sup>63</sup>

#### 14.8. CONCLUSION

In this chapter we have attempted to show the use of time-resolved measurements for determination of the solution conformations of macromolecules. The determination of conformational distributions appears to be a rather unique property of the time-resolved measurements. Most physical methods reveal only an average conformation. Additionally, the data contain information on the timescale of conformational changes. With the introduction of long-lived MLC and lanthanide probes, conformational dynamics will be measurable on timescales from nanoseconds to milliseconds.

As a final comment we want to emphasize that all the results described in this chapter were for covalently linked donor–acceptor pairs, with a single acceptor per donor. Different and somewhat more complex theory is needed to describe systems with multiple acceptors and unlinked probes. Such systems occur commonly in membranes and nucleic acids, which are described in the following chapter.

#### REFERENCES

1. Haas E, Wilchek M, Katchalski-Katzir E, Steinberg IA. 1975. Distribution of end-to-end distances of oligopeptides in solution as estimated by energy transfer. *Proc Natl Acad Sci USA* **72**:1807–1811.
2. Grinvald A, Haas E, Steinberg IZ. 1972. Evaluation of the distribution of distances between energy donors and acceptors by fluorescence decay. *Proc Natl Acad Sci USA* **69**:2273–2277.
3. Haas E, Katchalski-Katzir E, Steinberg IZ. 1978. Brownian motion of the ends of oligopeptide chains in solution as estimated by energy transfer between chain ends. *Biopolymers* **17**:11–31.
4. Wu P, Brand L. 1994. Conformational flexibility in a staphylococcal nuclease mutant K45C from time-resolved resonance energy transfer measurements. *Biochemistry* **33**:10457–10462.

5. Amir D, Krausz S, Haas E. 1992. Detection of local structures in reduced unfolded bovine pancreatic trypsin inhibitor. *Proteins* **13**: 162–173.
6. Amir D, Haas E. 1986. Determination of intramolecular distance distributions in a globular protein by nonradiative excitation energy transfer measurements. *Biopolymers* **25**:235–240.
7. Lakowicz JR, Wiczk W, Gryczynski I, Johnson ML. 1990. Influence of oligopeptide flexibility on donor–acceptor distance distribution by frequency-domain fluorescence spectroscopy. *Proc SPIE* **1204**:192–205.
8. She M, Xing J, Dong WJ, Umeda PK, Cheung HC. 1998. Calcium binding to the regulatory domain of skeletal muscle troponin C induces a highly constrained open conformation. *J Mol Biol* **281**: 445–452.
9. Dong W-J, Chandra M, Xing J, She M, Solaro RJ, Cheung HC. 1997. Phosphorylation induced distance change in a cardiac muscle troponin I mutant. *Biochemistry* **36**:6754–6761.
10. Maliwal BP, Lakowicz JR, Kuprysiewski G, Rekowski P. 1993. Fluorescence study of conformational flexibility of RNase S-peptide: distance-distribution, end-to-end diffusion, and anisotropy decays. *Biochemistry* **32**:12337–12345.
11. Cheung HC, Gryczynski I, Malak H, Wiczk W, Johnson ML, Lakowicz JR. 1991. Conformational flexibility of the Cys 697–Cys 707 segment of myosin subfragment, 1: distance distributions by frequency-domain fluorometry. *Biophys Chem* **40**:1–17.
12. Cheung HC, Wang C-K, Gryczynski I, Wiczk W, Laczko G, Johnson ML, Lakowicz JR. 1991. Distance distributions and anisotropy decays of troponin C and its complex with troponin I. *Biochemistry* **30**:5238–5247.
13. Lakowicz JR, Gryczynski I, Cheung HC, Wang C-K, Johnson ML, Joshi N. 1988. Distance distributions in proteins recovered by using frequency-domain fluorometry: applications to troponin I and its complex with troponin C. *Biochemistry* **27**:9149–9160.
14. Zhao X, Kobayashi T, Malak H, Gryczynski I, Lakowicz JR, Wade R, Collins JH. 1995. Calcium-induced troponin flexibility revealed by distance distribution measurements between engineered sites. *J Biol Chem* **270**(26):15507–15514.
15. Eis PS, Kusba J, Johnson ML, Lakowicz JR. 1993. Distance distributions and dynamics of a zinc finger peptide from fluorescence resonance energy transfer measurements. *J Fluoresc* **3**(1):23–31.
16. Eis PS, Lakowicz JR. 1993. Time-resolved energy transfer measurements of donor–acceptor distance distributions and intramolecular flexibility of a CCHH zinc finger peptide. *Biochemistry* **32**:7981–7993.
17. Bacchicocci C, Graceffa P, Lehrer SS. 2004. Myosin-induced movement of  $\alpha\alpha$ ,  $\alpha\beta$ , and  $\beta\beta$  smooth muscle tropomyosin on actin observed by multisite FRET. *Biophys J* **86**:2295–2307.
18. Miki M, Kouyama T. 1994. Domain motion in action observed by fluorescence resonance energy transfer. *Biochemistry* **33**:10171–10177.
19. Dong WJ, Chandra M, Xing J, She M, Solaro RJ, Cheung HC. 1997. Phosphorylation-induced distance change in a cardiac muscle troponin I mutant. *Biochemistry* **36**:6754–6761.
20. Navon A, Ittah V, Landsman P, Scheraga HA, Haas E. 2001. Distributions of intramolecular distances in the reduced and denatured states of bovine pancreatic ribonuclease A: folding initiation structures in the C-terminal portions of the reduced protein. *Biochemistry* **40**:105–118.
21. Szmacinski H, Wiczk W, Fishman MN, Eis PS, Lakowicz JR, Johnson ML. 1996. Distance distributions from the tyrosyl to disulfide residues in the oxytocin and [Arg<sup>8</sup>]-vasopressin measured using frequency-domain fluorescence resonance energy transfer. *Eur Biophys J* **24**:185–193.
22. Cheung HC. 1991. Resonance energy transfer. In *Topics in fluorescence spectroscopy*, Vol. 2: *Principles*, pp. 127–176. Ed JR Lakowicz. Plenum Press, New York.
23. Lakowicz JR, Gryczynski I, Wiczk W, Laczko G, Prendergast FC, Johnson ML. 1990. Conformational distributions of melittin in water/methanol mixtures from frequency-domain measurements of nonradiative energy transfer. *Biophys Chem* **36**:99–115.
24. Lakowicz JR, Gryczynski I, Laczko G, Wiczk W, Johnson ML. 1994. Distribution of distances between the tryptophan and the N-terminal residue of melittin in its complex with calmodulin, troponin C, and phospholipids. *Protein Sci* **3**:628–637.
25. Albaugh S, Steiner RF. 1989. Determination of distance distribution from time domain fluorometry. *J Phys Chem* **93**:8013–8016.
26. Katchalski-Katzir E, Haas E, Steinberg IA. 1981. Study of conformation and intramolecular motility of polypeptides in solution by a novel fluorescence method. *Ann NY Acad Sci* **36**:44–61.
27. Lakowicz JR, Johnson ML, Wiczk W, Bhat A, Steiner RF. 1987. Resolution of a distribution of distances by fluorescence energy transfer and frequency-domain fluorometry. *Chem Phys Letts* **138**(6): 587–593.
28. Kulinski T, Wennerberg ABA, Rigler R, Provencher SW, Pooga M, Langel U, Bartfai T. 1997. Conformational analysis of glanin using end to end distance distribution observed by Förster resonance energy transfer. *Eur Biophys J* **26**:145–154.
29. Lakowicz JR, Gryczynski I, Wiczk W, Kusba J, Johnson ML. 1991. Correction for incomplete labeling in the measurement of distance distributions by frequency-domain fluorometry. *Anal Biochem* **195**: 243–254.
30. Yang M, Millar DP. 1996. Conformational flexibility of three-way DNA junctions containing unpaired nucleotides. *Biochemistry* **35**: 7959–7967.
31. Englert A, Leclerc M. 1978. Intramolecular energy transfer in molecules with a large number of conformations. *Proc Natl Acad Sci USA* **75**(3):1050–1051.
32. Wu P, Brand L. 1992. Orientation factor in steady-state and time-resolved resonance energy transfer measurements. *Biochemistry* **31**:7939–7947.
33. Dos Remedios CG, Moens PDJ. 1995. Fluorescence resonance energy transfer spectroscopy is a reliable "ruler" for measuring structural changes in proteins. *J Struct Biol* **115**:175–185.
34. Beecham JM, Haas E. 1989. Simulations determination of intramolecular distance distributions and conformational dynamics by global analysis of energy transfer measurements. *Biophys J* **55**:1225–1236.
35. Ohmine I, Silbey R, Deutch JM. 1997. Energy transfer in labeled polymer chains in semidilute solutions. *Macromolecules* **10**:862–864.
36. Walter NG, Burke JM, Millar DP. 1999. Stability of hairpin ribozyme tertiary structure is governed by the interdomain junction. *Nature Struct Biol* **6**(6):544–549.

37. Walter NG, Harris DA, Pereira MJB, Rueda D. 2002. In the fluorescent spotlight: global and local conformational changes of small catalytic RNAs. *Biopolymers* **61**:224–241.
38. Yang M, Millar DP. 1997. Fluorescence resonance energy transfer as a probe of DNA structure and function. *Methods Enzymol* **278**: 417–444.
39. Eis PS, Millar DP. 1993. Conformational distributions of a four-way DNA junction revealed by time-resolved fluorescence resonance energy transfer. *Biochemistry* **32**:13852–13860.
40. Clegg RM, Murchie AIH, Lilley DM. 1994. The solution structure of the four-way DNA junction at low-salt conditions: a fluorescence resonance energy transfer analysis. *Biophys J* **66**:99–109.
41. Yang M, Millar DP. 1996. Conformational flexibility of three-way DNA junctions containing unpaired nucleotides. *Biochemistry* **35**: 7959–7967.
42. Lillo MP, Szpikowska BK, Mas MT, Sutin JD, Beechem JM. 1997. Real-time measurement of multiple intramolecular distances during protein folding reactions: a multisite stopped-flow fluorescence energy-transfer study of yeast phosphoglycerate kinase. *Biochemistry* **36**: 11273–11281.
43. Lillo MP, Beechem JM, Szpikowska BK, Sherman MA, Mas MT. 1997. Design and characterization of a multisite fluorescence energy-transfer system for protein folding studies: a steady-state and time-resolved study of yeast phosphoglycerate kinase. *Biochemistry* **36**:11261–11272.
44. Ratner V, Kahana E, Eichler M, Haas E. 2002. A general strategy for site-specific double labeling of globular proteins for kinetic FRET studies. *Bioconjugate Chem* **13**:1163–1170.
45. Rice KG, Wu P, Brand L, Lee YC. 1991. Interterminal distance and flexibility of a triantennary glycopeptide as measured by resonance energy transfer. *Biochemistry* **30**:6646–6655.
46. Brown MP, Toptygin D, Lee KB, Animashaun T, Hughes RC, Lee YC, Brand L. 1998. The tryptophan fluorescence of *tetracarbidium conophorum* agglutinin II and a solution-based assay for the binding of a biantennary glycopeptide. *J Protein Chem* **17**(2):149–159.
47. Rice KG. 2001. Application of fluorescence resonance energy transfer to analyze carbohydrates. *Anal Biochem* **297**:117–122.
48. Wu P, Lee KB, Lee YC, Brand L. 1996. Solution conformations of a biantennary glycopeptide and a series of its exoglycosidase products from sequential trimming of sugar residues. *J Biol Chem* **271**(3): 1470–1474.
49. Deniz AA, Laurence TA, Beligere GS, Dahan M, Martin AB, Chemla DS, Dawson PE, Schultz PG, Weiss S. 2000. Single-molecule protein folding: diffusion fluorescence resonance energy transfer studies of the denaturation of chymotrypsin inhibitor 2. *Proc Natl Acad Sci USA* **97**:5179–5184.
50. Elangovan M, Day RN, Periasamy A. 2002. Nanosecond fluorescence resonance energy transfer-fluorescence lifetime imaging microscopy to localize the protein interactions in a single living cell. *J Microsc* **205**:3–14.
51. Wouters FS, Bastiaens PIH. 1999. Fluorescence lifetime imaging of receptor tyrosine kinase activity in cells. *Curr Biol* **9**:1127–1130.
52. Wallrabe H, Stanley M, Periasamy A, Barroso M. 2003. One- and two-photon fluorescence resonance energy transfer microscopy to establish a clustered distribution of receptor-ligand complexes in endocytic membranes. *J Biomed Opt* **8**(3):339–346.
53. Krishnan RV, Masuda A, Centonze VE, Herman B. 2003. Quantitative imaging of protein-protein interactions by multiphoton fluorescence lifetime imaging microscopy using a streak camera. *J Biomed Opt* **8**(3):362–367.
54. Mills JD, Stone JR, Rubin DG, Melon DE, Okonkwo DO, Periasamy A, Helm GA. 2003. Illuminating protein interactions in tissue using confocal and two-photon excitation fluorescent resonance energy transfer microscopy. *J Biomed Opt* **8**(3):347–356.
55. Tramier M, Gautier I, Piolot T, Ravalet S, Kemnitz K, Coppey J, Durieux C, Mignotte V, Coppey-Moisan M. 2002. Picosecond-hetero-FRET microscopy to probe protein-protein interactions in live cells. *Biophys J* **83**:3570–3577.
56. Bacska BJ, Skoch J, Hickey GA, Allen R, Hyman BT. 2003. Fluorescence resonance energy transfer determinations using multiphoton fluorescence lifetime imaging microscopy to characterize amyloid-beta plaques. *J Biomed Opt* **8**(3):368–375.
57. Lakowicz JR, Kusba J, Wiczk W, Gryczynski I, Johnson ML. 1990. End-to-end diffusion of a flexible bichromophoric molecule observed by intramolecular energy transfer and frequency domain fluorometry. *Chem Phys Lett* **173**:319–326.
58. Lakowicz JR, Gryczynski I, Kusba J, Wiczk W, Szmacinski H, Johnson ML. 1994. Site-to-site diffusion in proteins as observed by energy transfer and frequency domain fluorometry. *Photochem Photobiol* **59**:16–29.
59. Kusba J, Lakowicz JR. 1994. Diffusion-modulated energy transfer and quenching: analysis by numerical integration of diffusion equation in Laplace space. *Methods Enzymol* **240**:216–262.
60. Lakowicz JR, Kusba J, Wiczk W, Gryczynski I, Szmacinski H, Johnson ML. 1991. Resolution of the conformational distribution and dynamics of a flexible molecule using frequency domain fluorometry. *Biophys Chem* **39**:79–84.
61. Lakowicz JR, Wiczk W, Gryczynski I, Szmacinski H, Johnson ML. 1990. Influence of end-to-end diffusion on intramolecular energy transfer as observed by frequency-domain fluorometry. *Biophys Chem* **38**:99–109.
62. Somogyi B, Matko J, Papp S, Hevessy J, Welch GR, Damjanovich S. 1984. Förster-type energy transfer as a probe for changes in local fluctuations of the protein matrix. *Biochemistry* **23**:3404–3411.
63. Haran G, Haas E, Szpikowska BK, Mas MT. 1992. Domain motions in phosphoglycerate kinase: determination of interdomain distance distributions by site-specific labeling and time-resolved fluorescence energy transfer. *Proc Natl Acad Sci USA* **89**:11764–11768.
64. Gerstein M, Lesk AM, Chothia C. 1994. Structural mechanisms for domain movements in proteins. *Biochemistry* **33**(22):6738–6749.
65. Blackwell MF, Gounaris K, Zara SJ, Barber J. 1987. A method for estimating lateral diffusion coefficients in membranes from steady state fluorescence quenching studies. *J Biophys Soc* **51**:735–744.
66. Ollmann M, Schwarzmann G, Sandhoff K, Galla H-J. 1987. Pyrene-labeled gangliosides: micelle formation in aqueous solution, lateral diffusion, and thermotropic behavior in phosphatidylcholine bilayers. *Biochemistry* **26**:5943–5952.
67. Buckler DR, Haas E, Scheraga HA. 1995. Analysis of the structure of ribonuclease A in native and partially denatured states by time-resolved nonradiative dynamic excitation energy transfer between site-specific extrinsic probes. *Biochemistry* **34**:15965–15978.

## REPRESENTATIVE PUBLICATIONS ON MEASUREMENT OF DISTANCE DISTRIBUTIONS

### Proteins—Distance Distributions

- Amir D, Haas E. 1987. Estimation of intramolecular distance distributions in bovine pancreatic trypsin inhibitor by site-specific labeling and nonradiative excitation energy-transfer measurements. *Biochemistry* **26**:2162–2175.
- Amir D, Haas E. 1988. Reduced bovine pancreatic trypsin inhibitor has a compact structure. *Biochemistry* **27**:8889–8893.
- Amir D, Levy DP, Levin Y, Haas E. 1986. Selective fluorescent labeling of amino groups of bovine pancreatic trypsin inhibitor by reductive alkylation. *Biopolymers* **25**:1645–1658.
- Amir D, Varshavski L, Haas E. 1985. Selective fluorescent labeling at the  $\alpha$ -amino group of bovine pancreatic trypsin inhibitor. *Biopolymers* **24**:623–638.
- Beals JM, Haas E, Krausz S, Scheraga HA. 1991. Conformational studies of a peptide corresponding to a region of the C-terminus of ribonuclease A: implications as a potential chain-folding initiation site. *Biochemistry* **30**:7680–7692.
- Haas E, McWherter CA, Scheraga HA. 1988. Conformational unfolding in the N-terminal region of ribonuclease A detected by nonradiative energy transfer: distribution of interresidue distances in the native, denatured, and reduced-denatured states. *Biopolymers* **27**:1–21.
- Haran G, Haas E, Szpikowska BK, Mas MT. 1992. Domain motions in phosphoglycerate kinase: determination of interdomain distance distributions by site-specific labeling and time-resolved fluorescence energy transfer. *Proc Natl Acad Sci USA* **89**:11764–11768.

### DNA Structures

- Clegg RM, Murchie AIH, Zechel A, Lilley DMJ. 1993. Observing the helical geometry of double-stranded DNA in solution by fluorescence resonance energy transfer. *Proc Natl Acad Sci USA* **90**:2994–2998.
- McKinney SA, Déclais AC, Lilley DMJ, Ha T. 2003. Structural dynamics of individual Holliday junctions. *Nature Struct Biol* **10**(2):93–97.
- Miick SM, Fee RS, Millar DP, Chazin WJ. 1997. Crossover isomer bias is the primary sequence-dependent property of immobilized Holliday junctions. *Proc Natl Acad Sci USA* **94**:9080–9084.
- Mizukoshi T, Kodama TS, Fujiwara Y, Furuno T, Nakanishi M, Iwai S. 2001. Structural study of DNA duplexes containing the (6-4) photoproduct by fluorescence resonance energy transfer. *Nucleic Acids Res* **29**(24):4948–4954.
- Murchie AIH, Clegg RM, von Kitzing E, Duckett DR, Diekmann S, Lilley DMJ. 1989. Fluorescence energy transfer shows that the four-way DNA junction is a right-handed cross of antiparallel molecules. *Nature* **341**:763–766.
- Norman DG, Grainger RJ, Uhrin D, Lilley DMJ. 2000. Location of cyanine-3 on double-stranded DNA: importance for fluorescence resonance energy transfer studies. *Biochemistry* **39**:6317–6324.
- Parkhurst KM, Parkhurst LJ. 1995. Donor–acceptor distributions in a double-labeled fluorescent oligonucleotide both as a single strand and in duplexes. *Biochemistry* **34**:293–300.

- Patel LR, Curran T, Kerppola TK. 1994. Energy transfer analysis of Fos-Jun dimerization and DNA binding. *Proc Natl Acad Sci USA* **91**:7360–7364.
- Ramirez-Carrozzi VR, Kerppola TK. 2001. Dynamics of Fos–Jun–NFAT1 complexes. *Proc Natl Acad Sci USA* **98**(9):4893–4898.
- Tsuji A, Sato Y, Hirano M, Suga T, Koshimoto H, Taguchi T, Ohsuka S. 2001. Development of a time-resolved fluorometric method for observing hybridization in living cells using fluorescence resonance energy transfer. *Biophys J* **81**:501–515.

### End-to-End Diffusion

- Bandyopadhyay T, Ghosh SK. 2003. Diffusion assisted end-to-end relaxation of a flexible Rouse polymer chain: fluorescence quenching through a model energy transfer. *J Chem Phys* **119**(1):572–584.
- Duus JØ, Meldal M, Winkler JR. 1998. Fluorescence energy-transfer probes of conformation in peptides: the 2-aminobenzamide/nitrotyrosine pair. *J Phys Chem B* **102**:6413–6418.
- Gryczynski I, Lakowicz JR, Kusba J. 1995. End-to-end diffusion coefficients and distance distributions from fluorescence energy transfer measurements: enhanced resolution by using multiple donors with different lifetimes. *J Fluoresc* **5**(2):195–203.
- Lakowicz JR, Kusba J, Gryczynski I, Wiczek W, Szmacinski H, Johnson M. 1991. End-to-end diffusion and distance distributions of flexible donor–acceptor systems observed by intramolecular energy transfer and frequency-domain fluorometry; enhanced resolution by global analysis of externally quenched and nonquenched samples. *J Phys Chem* **95**:9654–9660.
- Lakowicz JR, Nair R, Piszczeck G, Gryczynski I. 2000. End-to-end diffusion on the microsecond timescale measured with resonance energy transfer from a long-lifetime rhenium metal–ligand complex. *Photochem Photobiol* **71**(2):157–161.
- Maliwal BP, Lakowicz JR. 1993. Fluorescence study of conformational flexibility of RNase S-peptide: distance-distribution, end-to-end diffusion and anisotropy decays. *Biochemistry* **32**:12337–12345.
- Maliwal BP, Kusba J, Wiczek W, Johnson M, Lakowicz JR. 1993. End-to-end diffusion coefficients and distance distributions from fluorescence energy transfer measurements: enhanced resolution by using multiple acceptors with different Förster distances. *Biophys Chem* **46**:273–281.
- Neuweiler H, Schulz A, Böhmer M, Enderlein J, Sauer M. 2003. Measurement of submicrosecond intramolecular contact formation in peptides at the single-molecule level. *J Am Chem Soc* **125**:5324–5330.
- Nyitrai M, Hild G, Bódiz E, Lukács A, Somogyi B. 2000. Flexibility of myosin-subfragment-1 in its complex with actin as revealed by fluorescence resonance energy transfer. *Eur J Biochem* **267**:4334–4338.
- Talaga DS, Lau WL, Roder H, Tang J, Jia Y, DeGrado WF, Hochstrasser RM. 2000. Dynamics and folding of single two-stranded coiled-coil peptides studied by fluorescent energy transfer confocal microscopy. *Proc Natl Acad Sci USA* **97**(24):13021–13026.

### Reviews

- Wemmer DA, Case DA, Millar DP. 2002. Fluorescence spectroscopy and nucleic acids. *Biopolymers Nucleic Acid Sci* **61**(3):143–242.

### Ribozymes

- Lafontaine DA, Norman DG, Lilley DMJ. 2002. The global structure of the VS ribozyme. *EMBO J* **21**(10):2461–3471.
- Tan E, Wilson TJ, Nahas MK, Clegg RM, Lilley DMJ, Ha T. 2003. A four-way junction accelerates hairpin ribozyme folding via a discrete intermediate. *Proc Natl Acad Sci USA* **100**(16):9308–9313.
- Walter F, Murchie AIH, Duckett DR, Lilley DMJ. 1998. Global structure of four-way RNA junctions studied using fluorescence resonance energy transfer. *RNA* **4**:719–728.
- Walter F, Murchie AIH, Thomson JB, Lilley DMJ. 1998. Structure and activity of the hairpin ribozyme in its natural junction conformation: effect of metal ions. *Biochemistry* **37**:14195–14203.
- Wilson TJ, Lilley DMJ. 2002. Metal ion binding and the folding of the hairpin ribozyme. *RNA* **8**:587–600.

### Ribozomes

- Klostermeier D, Sears P, Wong CH, Millar DP, Williamson JR. 2004. A three-fluorophore FRET assay for high-throughput screening of small-molecule inhibitors of ribosome assembly. *Nucleic Acids Res* **32**(9):2707–2715.
- Melcher SE, Wilson TJ, Lilley DMJ. 2003. The dynamic nature of the four-way junction of the hepatitis C virus IRES. *RNA* **9**:809–820.

### Theory

- Farinha JPS, Spiro JG, Winnik MA. 2004. Dipole–dipole electronic energy transfer: fluorescence decay functions for arbitrary distributions of donors and acceptors in systems with cylindrical symmetry. *J Phys Chem B* **108**:16392–16400.
- Rolinski O, Birch DJS, McCartney LJ, Pickup JC. 2000. A method of determining donor acceptor distribution functions in Förster resonance energy transfer. *Chem Phys Lett* **324**:95–100.

- Rolinski O, Birch DJS, McCartney LJ, Pickup JC. 2001. Fluorescence nanotomography using resonance energy transfer: demonstration with a protein–sugar complex. *Phys Med Biol* **46**:N221–N226.
- Srinivas G, Yethiraj A, Bagchi B. 2001. FRET by FET and dynamics of polymer folding, 2001. *J Phys Chem* **105**(13):2475–2478.
- Valeur B, Mugnier J, Pouget J, Bourson J, Santi F. 1989. Calculation of the distribution of donor–acceptor distances in flexible bichromophoric molecules: application to intramolecular transfer of excitation energy. *J Phys Chem* **93**:6073–6079.

### PROBLEMS

**Intensity Decays for Various Donor–Acceptor Pairs:** Assume that you have three different solutions. All contain donors that display the same quantum yield, a single-exponential decay time of 5 ns in the absence of acceptor, and the same Förster distance of 20 Å. One sample (A) consists of a protein with a single donor and three acceptors at distances  $r_1 = 15$  Å,  $r_2 = 20$  Å, and  $r_3 = 25$  Å (Figure 14.34). The second sample (B) contains three equimolar proteins, each with a single donor and acceptor. However, in each protein there is a different D–A distance: 15, 20, or 25 Å. The third sample (C) is a protein with a single acceptor, but with three donors. Each donor displays the same donor-alone lifetime ( $\tau_D = 5$  ns), but a different distance (15, 20, or 25 Å) from the acceptor.

- P14.1. Describe the intensity decays of samples A, B, and C. Which samples display a single- or multi-exponential decay law?

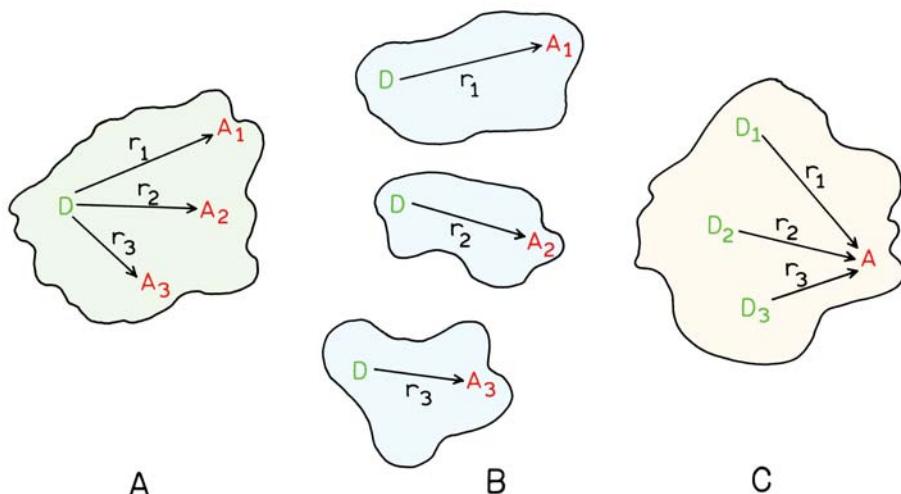


**Figure 14.34.** Schematic of a protein with three acceptors (A), three proteins each with a single acceptor (B), and a protein with three donors and one acceptor (C). The distances are  $r_1 = 15$  Å,  $r_2 = 20$  Å, and  $r_3 = 25$  Å. The Förster distance is 20 Å. See Problem 14.1.

- P14.2. Describe the intensity decay law of sample B, including the decay times, pre-exponential factors ( $\alpha_i$ ) and fractional intensity ( $f_i$ ) values. Assume each protein is present in equimolar amounts.
- P14.3. For the three-acceptor protein (sample A), could you detect the presence of three acceptors from the intensity decay?
- P14.4. For the three-acceptor protein what is the apparent D–A distance if you assumed the presence of a single acceptor?
- P14.5. *Acceptor Concentration for FRET for Unlinked D–A Pairs:*
- (a) Suppose you have a donor and acceptor that are not covalently linked, and that the Förster distance is 30 Å. Calculate the acceptor concentration needed to place, on average, one acceptor within a 60-Å cube containing a donor at the center. To a first approximation this concentration is comparable to that for 50% energy transfer. Compare this acceptor concentration with that calculated using eq. 13.33.
- (b) Consider a D–A pair covalently linked by a 30-Å linker. Calculate the effective concentration of acceptors around the donor.

# 16

# Protein Fluorescence

The biochemical applications of fluorescence often utilize intrinsic protein fluorescence. Among biopolymers, proteins are unique in displaying useful intrinsic fluorescence. Lipids, membranes, and saccharides are essentially nonfluorescent, and the intrinsic fluorescence of DNA is too weak to be useful. In proteins, the three aromatic amino acids—phenylalanine, tyrosine, and tryptophan—are all fluorescent. These three amino acids are relatively rare in proteins. Tryptophan, which is the dominant intrinsic fluorophore, is generally present at about 1 mole% in proteins. The small number of tryptophan residues is probably the result of the metabolic expense of its synthesis. A protein may possess just one or a few tryptophan residues, facilitating interpretation of the spectral data. If all twenty amino acids were fluorescent then protein emission would be more complex.

A valuable feature of intrinsic protein fluorescence is the high sensitivity of tryptophan to its local environment. Changes in the emission spectra of tryptophan often occur in response to conformational transitions, subunit association, substrate binding, or denaturation. These interactions can affect the local environment surrounding the indole ring. Tyrosine and tryptophan display high anisotropies that are often sensitive to protein conformation and the extent of motion during the excited-state lifetime. Also, tryptophan appears to be uniquely sensitive to collisional quenching, apparently due to a tendency of excited-state indole to donate electrons. Tryptophan can be quenched by externally added quenchers or by nearby groups within the proteins. There are numerous reports on the use of emission spectra, anisotropy, and quenching of tryptophan residues in proteins to study protein structure and function.

A complicating factor in the interpretation of protein fluorescence is the presence of multiple fluorescent amino acids in most proteins. The environment of each residue is distinct and the spectral properties of each residue are generally different. However, the absorption and emission spectra of tryptophan residues in proteins overlap at most

usable wavelengths, and it is difficult to separate the spectral contributions of each tryptophan in a multi-tryptophan protein. Complex time-resolved intensity decays are found even for proteins that contain a single-tryptophan residue. Most single-tryptophan proteins display multi-exponential intensity decays. For this reason one cannot simply interpret the multiple decay times of a multi-tryptophan protein in terms of the individual tryptophan residues in a protein.

As a further complicating factor, tryptophan displays complex spectral properties due to the presence of two nearly isoenergetic excited states,  ${}^1\text{L}_a$  and  ${}^1\text{L}_b$ . The electronic transitions display distinct absorption, emission, and anisotropy spectra, and are differently sensitive to solvent polarity. The complexity of indole photophysics has stimulated detailed studies of protein fluorescence, but has also inhibited interpretation of the data.

Protein fluorescence can be complex, but considerable progress has been made in the past decade. The origin of the multi-exponential decay of tryptophan in water is now largely understood as due to the presence of rotational conformational isomers (rotamers). These rotamers have different orientations of the amino and carboxyl groups relative to the indole ring. Studies of single-tryptophan proteins have provided information on the spectral properties of tryptophan in unique environments. Widely different spectral properties have been observed for single-tryptophan proteins. The highly variable tryptophan quantum yields of proteins appear to be the result of nearby quenchers in the protein, which include lysine and histidine residues. Under appropriate conditions it appears that even amide groups in the peptide backbone can act as quenchers. The use of site-directed mutagenesis has allowed creation of mutants that contain one instead of several tryptophan residues, insertion of tryptophan at desired locations in the protein, and modification of the environment around a tryptophan residue. Examination of single-tryptophan proteins and engineered proteins has provided a more detailed understanding of how

the local environment determines the spectral properties of tryptophan. It is also possible to insert tryptophan analogues into proteins. These analogues display unique spectral features, and are observable in the presence of other tryptophan residues.

In summary, a growing understanding of indole photo-physics, the ability to place the tryptophan residues at desired locations, and the availability of numerous protein structures has resulted in increased understanding of the general factors that govern protein fluorescence. The high

sensitivity of the emission from tryptophan to the details of its local environment have provided numerous opportunities for studies of protein functions, folding, and dynamics.

### 16.1. SPECTRAL PROPERTIES OF THE AROMATIC AMINO ACIDS

Several useful reviews and monographs have summarized the spectral properties of proteins.<sup>1–9</sup> Proteins contain three amino-acid residues that contribute to their ultraviolet flu-

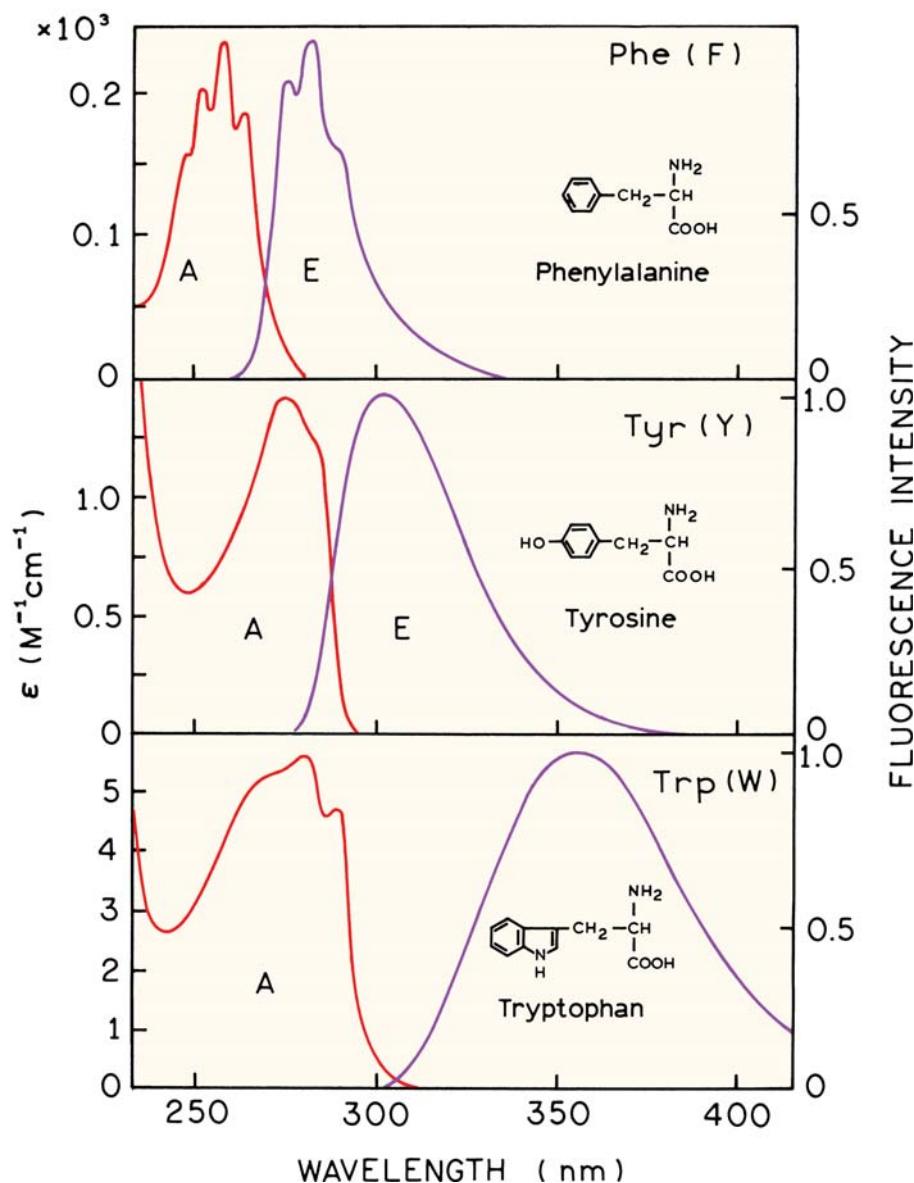


**Figure 16.1.** Absorption (A) and emission (E) spectra of the aromatic amino acids in pH 7 aqueous solution. Courtesy of Dr. I. Gryczynski, unpublished observations.

rescence which are usually described by their three- or one-letter abbreviations. These are tyrosine (tyr, Y), tryptophan (trp, W), and phenylalanine (phe, F). The absorption and emission spectra of these amino acids are shown in Figure 16.1. Emission of proteins is dominated by tryptophan, which absorbs at the longest wavelength and displays the largest extinction coefficient. Energy absorbed by phenylalanine and tyrosine is often transferred to the tryptophan residues in the same protein.

Phenylalanine displays the shortest absorption and emission wavelengths. Phenylalanine displays a structured emission with a maximum near 282 nm. The emission of tyrosine in water occurs at 303 nm and is relatively insensitive to solvent polarity. The emission maximum of tryptophan in water occurs near 350 nm and is highly dependent upon polarity and/or local environment. Indole is sensitive to both general solvent effects (Section 16.1.2). Indole displays a substantial spectral shift upon forming a hydrogen bond to the imino nitrogen, which is a specific solvent effect (Section 6.3). Additionally, indole can be quenched by several amino-acid side chains. As a result, the emission of each tryptophan residue in a protein depends on the details of its surrounding environment.

Protein fluorescence is generally excited at the absorption maximum near 280 nm or at longer wavelengths. Consequently, phenylalanine is not excited in most experiments. Furthermore, the quantum yield of phenylalanine in proteins is small—typically near 0.03—so emission from this residue is rarely observed for proteins. The absorption of proteins at 280 nm is due to both tyrosine and tryptophan residues. At 23°C in neutral aqueous solution the quantum yields of tyrosine and tryptophan are near 0.14 and 0.13, respectively,<sup>10</sup> the reported values being somewhat variable. At wavelengths longer than 295 nm, the absorption is due primarily to tryptophan. Tryptophan fluorescence can be selectively excited at 295–305 nm. This is why many papers report the use of 295-nm excitation, which is used to avoid excitation of tyrosine.

Tyrosine is often regarded as a rather simple fluorophore. However, under some circumstances tyrosine can also display complex spectral properties. Tyrosine can undergo excited-state ionization, resulting in the loss of the proton on the aromatic hydroxyl group. In the ground state the  $pK_A$  of this hydroxyl is about 10. In the excited state the  $pK_A$  decreases to about 4. In neutral solution the hydroxyl group can dissociate during the lifetime of the excited state, leading to quenching of the tyrosine fluorescence. Tyrosinate is weakly fluorescent at 350 nm, which can be con-

fused with tryptophan fluorescence. Tyrosinate emission is observable in some proteins, but it appears that excited-state ionization is not a major decay pathway for tyrosine in proteins.

Because of their spectral properties, resonance energy transfer can occur from phenylalanine to tyrosine to tryptophan. Energy transfer has been repeatedly observed in many proteins and is one reason for the minor contribution of phenylalanine and tyrosine to the emission of most proteins. Also, blue-shifted tryptophan residues can transfer the excitation to longer wavelength tryptophan residues. The anisotropies displayed by tyrosine and tryptophan are sensitive to both overall rotational diffusion of proteins, and the extent of segmental motion during the excited-state lifetimes. Hence, the intrinsic fluorescence of proteins can provide considerable information about protein structure and dynamics, and is often used to study protein folding and association reactions. We will present examples of protein fluorescence that illustrate the use of intrinsic fluorescence of proteins. In Chapter 17 we describe time-resolved studies of protein fluorescence.

### 16.1.1. Excitation Polarization Spectra of Tyrosine and Tryptophan

The emission maximum of tryptophan is highly sensitive to the local environment, but tyrosine emission maximum is rather insensitive to its local environment. What is the reason for this distinct behavior? Tryptophan is a uniquely complex fluorophore with two nearby isoenergetic transitions. In contrast, emission from tyrosine appears to occur from a single electronic state.

Information about overlapping electronic transitions can be obtained from the excitation anisotropy spectra (Chapter 10). The anisotropy spectrum is usually measured in frozen solution to prevent rotational diffusion during the excited-state lifetime. For a single electronic transition the anisotropy is expected to be constant across the absorption band. The anisotropy of tyrosine (Figure 16.2) is relatively constant across the long-wavelength absorption band (260–290 nm). Most fluorophores display some increase in anisotropy as the excitation wavelength increases across the  $S_0 \rightarrow S_1$  transition (260–290 nm), but such an anisotropy spectrum is usually regarded as the result of a single transition. The anisotropy data in Figure 16.2 are for N-acetyl-L-tyrosinamide (NATyrA) instead of tyrosine. Neutral derivatives of the aromatic amino acids are frequently used because the structures of these derivatives resemble those of

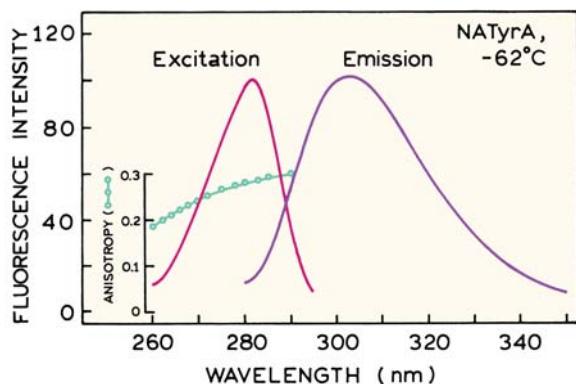


**Figure 16.2.** Excitation spectrum and excitation anisotropy spectra of N-acetyl-L-tyrosinamide (NATyrA). The fluorescence anisotropies ( $\text{O}$ ) were measured in a mixture of 70% propylene glycol with 30% buffer at  $-62^\circ\text{C}$ . The emission was observed at 302 nm. Data from [11–13].

the residues found in proteins. The quantum yield and lifetimes of tyrosine and tryptophan can be affected by the ionization state of the amino and carboxyl groups in tyrosine and tryptophan. These effects can be avoided by use of the

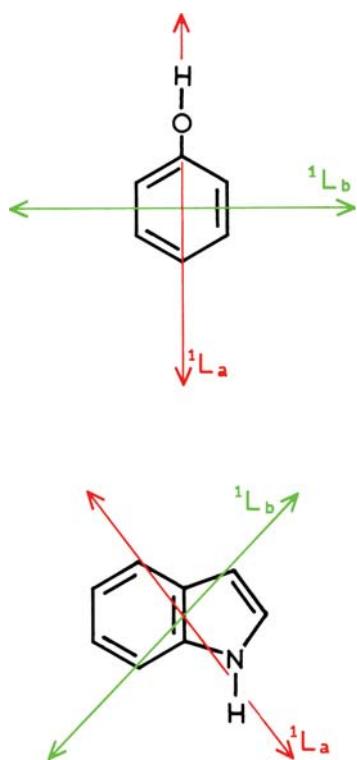


**Figure 16.3.** Electronic absorption transitions in tyrosine and tryptophan. Data from [16–17].

neutral analogues, but it is now known that amide groups can sometimes act as quenchers.<sup>14–15</sup>

Interpretation of the anisotropy or anisotropy decay is aided by knowledge of the direction of the electronic transition in the fluorophore. The lowest electronic transition of tyrosine, with absorption from 260 to 290 nm, is due to the  ${}^1\text{L}_b$  transition oriented across the phenol ring<sup>16</sup> (Figure 16.3). The  ${}^1\text{L}_a$  transition is the origin of the stronger absorption below 250 nm. The anisotropy of tyrosine decreases for shorter-wavelength excitation (Figure 16.2) and becomes negative below 240 nm (not shown). This indicates that the  ${}^1\text{L}_a$  transition is nearly perpendicular to the  ${}^1\text{L}_b$  emitting state. For longer-wavelength excitation, above 260 nm, the anisotropy is positive, indicating the absorption transition moment is mostly parallel to the  ${}^1\text{L}_b$  emission transition moment. For excitation above 260 nm the absorption and emission occur from the same  ${}^1\text{L}_b$  state.

In contrast to tyrosine, indole and tryptophan do not display constant anisotropy across the long-wavelength absorption band (Figure 16.4).<sup>17–18</sup> On the long-wavelength side of the absorption tryptophan displays a high value of  $r_0$  near 0.3. This indicates nearly collinear absorption and emission dipoles. The anisotropy decreases to a minimum at 290 nm, and increases at excitation wavelengths from 280 to 250 nm. This complex behavior is due to the presence of two electronic transitions to the  ${}^1\text{L}_a$  and  ${}^1\text{L}_b$  states in the last absorption band (Figure 16.3). These transition moments are oriented nearly perpendicular to each other,<sup>19–23</sup> so that the fundamental anisotropy ( $r_0$ ) is strongly dependent on the fractional contribution of each state to

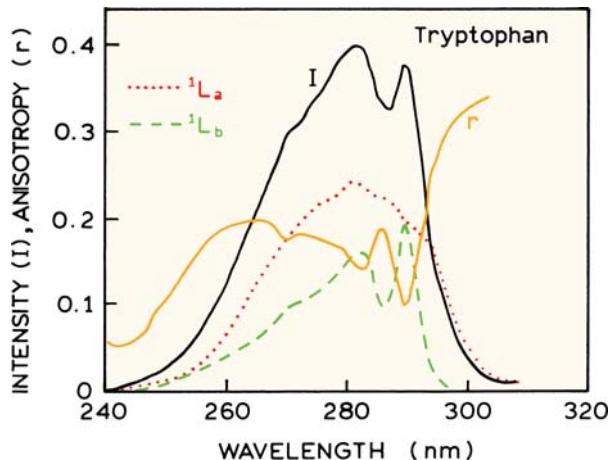


**Figure 16.4.** Excitation anisotropy spectra of tryptophan in propylene glycol at  $-50^\circ\text{C}$ . Also shown are the anisotropy-resolved spectra of the  ${}^1\text{L}_a$  (dotted) and  ${}^1\text{L}_b$  (dashed) transitions. Data from [18].

the absorption. The minimum anisotropy near 290 nm is due to a maximum in the absorption of the  ${}^1\text{L}_\text{b}$  state. The emission of tryptophan in solution and of most proteins is unstructured and due to the  ${}^1\text{L}_\text{a}$  state. The anisotropy is low with 290-nm excitation, because the emission is from a state ( ${}^1\text{L}_\text{a}$ ), which is rotated 90° from the absorbing state ( ${}^1\text{L}_\text{b}$ ). This is another reason why protein fluorescence is often excited at 295 to 300 nm. For these excitation wavelengths only the  ${}^1\text{L}_\text{a}$  state absorbs and the anisotropy is high. If emission occurs from the  ${}^1\text{L}_\text{b}$  state the emission spectrum frequently displays a structured emission spectrum.

The excitation anisotropy spectra can be used to resolve the absorption spectra of the  ${}^1\text{L}_\text{a}$  and  ${}^1\text{L}_\text{b}$  states.<sup>24</sup> This procedure is based on the additivity of anisotropies (Section 10.1). This resolution assumes that the maximal anisotropy is characteristic of absorption to and emission from a single state, the  ${}^1\text{L}_\text{a}$  state. A further assumption is that the transitions to the  ${}^1\text{L}_\text{a}$  and  ${}^1\text{L}_\text{b}$  states are oriented at 90°. Using these assumptions the  ${}^1\text{L}_\text{a}$  absorption is found to be unstructured and to extend to longer wavelengths than the structured  ${}^1\text{L}_\text{b}$  absorption (Figure 16.4). The dominance of  ${}^1\text{L}_\text{a}$  absorption at 300 nm, and emission from the same  ${}^1\text{L}_\text{a}$  state, is why proteins display high anisotropy with long-wavelength excitation.

The possible emission from two states can complicate the interpretation of time-resolved intensity decays. For example, the intensity decay of tryptophan at pH 7 is a double exponential, with decay times near 0.5 and 3.1 ns. At first it was thought that the two decay times were due to emission from the  ${}^1\text{L}_\text{a}$  and  ${}^1\text{L}_\text{b}$  states.<sup>25</sup> However, it is now thought<sup>26–27</sup> that the two decay times have their origin in the rotamer populations, and that tryptophan emits only from the  ${}^1\text{L}_\text{a}$  state unless the local environment is completely nonpolar. An early report of 2.1 and 5.4 ns for the two decay times of tryptophan<sup>28</sup> is an error due to photodecomposition of the sample. Time-resolved protein fluorescence will be discussed in more detail in Chapter 17.

### 16.1.2. Solvent Effects on Tryptophan Emission Spectra

In order to understand protein fluorescence it is important to understand how the emission from tryptophan is affected by its local environment.<sup>30–35</sup> One factor affecting tryptophan emission is the polarity of its surrounding environment. The emission spectrum of tryptophan is strongly dependent on solvent polarity. Depending upon the solvent, emission can occur from the  ${}^1\text{L}_\text{a}$  or  ${}^1\text{L}_\text{b}$  states, but emission

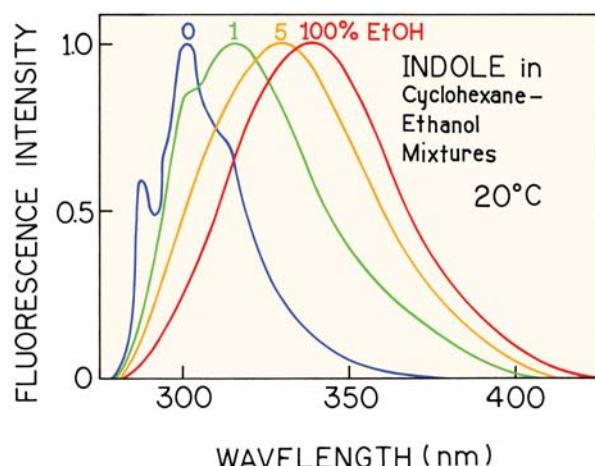


**Figure 16.5.** Emission spectra of indole in cyclohexane, ethanol and their mixtures at 20°C. From [29].

from the  ${}^1\text{L}_\text{b}$  state is infrequent. This is because the emission of tryptophan is sensitive to hydrogen bonding to the imino group. This sensitivity is shown by the emission spectra of indole in cyclohexane, which are sensitive to trace quantities of hydrogen bonding solvent (Figure 16.5). These spectra show the presence of specific and general solvent effects.<sup>29</sup> In pure cyclohexane, in the absence of hydrogen bonding, the emission is structured, and seems to be a mirror image of the absorption spectrum of the  ${}^1\text{L}_\text{b}$  transition (compare Figures 16.4 and 16.5). In the presence of a hydrogen-bonding solvent (ethanol) the structured emission is lost and the emission mirrors the  ${}^1\text{L}_\text{a}$  transition. These structured and unstructured emission spectra indicate the possibility of emission from either the  ${}^1\text{L}_\text{a}$  or  ${}^1\text{L}_\text{b}$  state. The  ${}^1\text{L}_\text{a}$  state is more solvent sensitive than the  ${}^1\text{L}_\text{b}$  state. The  ${}^1\text{L}_\text{a}$  transition shifts to lower energies in polar solvents. The higher solvent sensitivity for the  ${}^1\text{L}_\text{a}$  state seems reasonable since the  ${}^1\text{L}_\text{a}$  transition more directly involves the polar nitrogen atom of indole (Figure 16.3). Furthermore, the excited-state dipole moment of the  ${}^1\text{L}_\text{a}$  state is near 6 debye, but the excited-state dipole moment is smaller for the  ${}^1\text{L}_\text{b}$  state.<sup>36</sup> In a completely nonpolar environment the  ${}^1\text{L}_\text{b}$  state can have lower energy and dominate the emission. In a polar solvent the  ${}^1\text{L}_\text{a}$  state has the lower energy and dominates the emission. The electrical field due to the protein, or the solvent reaction field, may also influence the emission spectrum of indole.<sup>36–37</sup>

The different solvent sensitivities of the  ${}^1\text{L}_\text{a}$  and  ${}^1\text{L}_\text{b}$  states of indole can be seen in the absorption spectra of indole in the cyclohexane–ethanol mixtures (Figure 16.6).

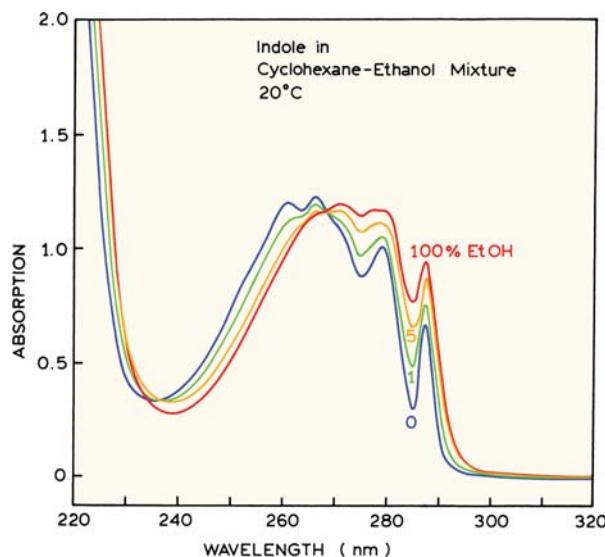


**Figure 16.6.** Absorption spectra of indole in cyclohexane with increasing amounts of ethanol. Data courtesy of Dr. Ignacy Grycynski.

As the ethanol concentration is increased the vibrational structure at 288 nm decreases. Similar results have been observed for indole derivatives.<sup>38–39</sup> These spectral changes can be understood as a red shift of the  ${}^1\text{L}_\text{a}$  absorption spectrum due to interaction of indole with the polar solvent. This energy shift is probably due to both hydrogen bonding interactions with the imino group and the general effects of solvent polarity. The  ${}^1\text{L}_\text{b}$  state is less sensitive to solvent, and its absorption is less affected by polar solvent.

The properties of the  ${}^1\text{L}_\text{a}$  and  ${}^1\text{L}_\text{b}$  states explain the complex emission spectra displayed by indole (Figure 16.5). In a completely nonpolar solvent the structured  ${}^1\text{L}_\text{b}$  state can be the lowest energy state, resulting in structured emission. The presence of polar solvent decreases the energy level of the  ${}^1\text{L}_\text{a}$  state, so that its unstructured emission dominates. At higher ethanol concentrations these specific solvent interactions are saturated, and indole displays a polarity-dependent red shift consistent with general solvent effects. Very few proteins display a structured emission, which suggests few tryptophan residues are in completely nonpolar environments.

### 16.1.3. Excited-State Ionization of Tyrosine

Tyrosine displays a simple anisotropy spectrum, but it is important to recognize the possibility of excited-state ionization. Excited-state ionization occurs because the  $\text{pK}_\text{A}$  of the phenolic hydroxyl group decreases from 10.3 in the

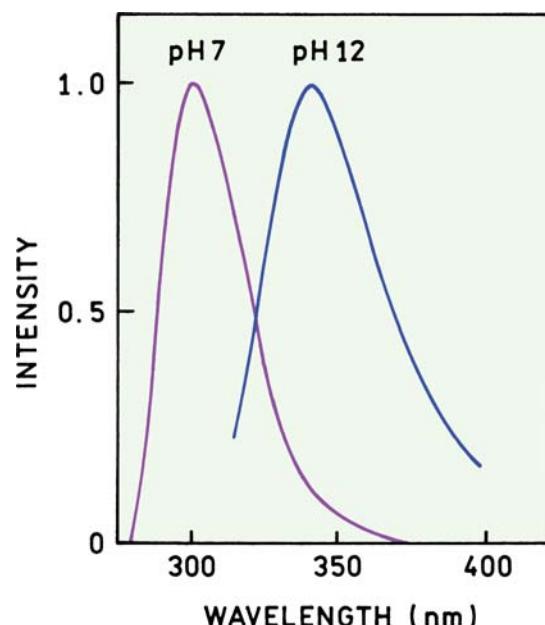


**Figure 16.7.** Normalized emission spectra of tyrosine at pH 7 and in 0.01 M NaOH (pH 12). Modified from [16].

ground state to about 4 in the excited state. Ionization can occur even at neutral pH, particularly if the solvent contains proton acceptors such as acetate. Tyrosinate emission is most easily observed at high pH, where the phenolic OH group is ionized in the ground state (Figure 16.7). In 0.01 M NaOH (pH 12) the emission of tyrosine is centered near 345 nm.<sup>6,40</sup> The emission from tyrosinate can be mistaken for tryptophan. The decay time of tyrosinate at pH 11 has been reported to be 30 ps.<sup>41</sup>

In Figure 16.7 the tyrosine hydroxyl group is ionized in the ground state. Tyrosinate emission can also be observed at neutral pH, particularly in the presence of a base that can interact with the excited state. One example is shown in Figure 16.8, which shows the emission spectra of tyrosine at the same pH, but with increasing concentrations of acetate buffer. The emission intensity decreases with increased acetate concentrations. This decrease occurs because the weakly basic acetate group can remove the phenolic proton, which has a  $\text{pK}_\text{A}$  of 4.2 to 5.3 in the first singlet state.<sup>40–43</sup> If the tyrosinate form does not emit, the acetate behaves like a collisional quencher, and the extent of excited-state ionization and quenching depends on the acetate concentration. Tyrosine can also form ground-state complexes with weak bases such as phosphate.<sup>44–45</sup>

Because of its low quantum yield the emission from tyrosinate is not easily seen in Figure 16.8. This emission is

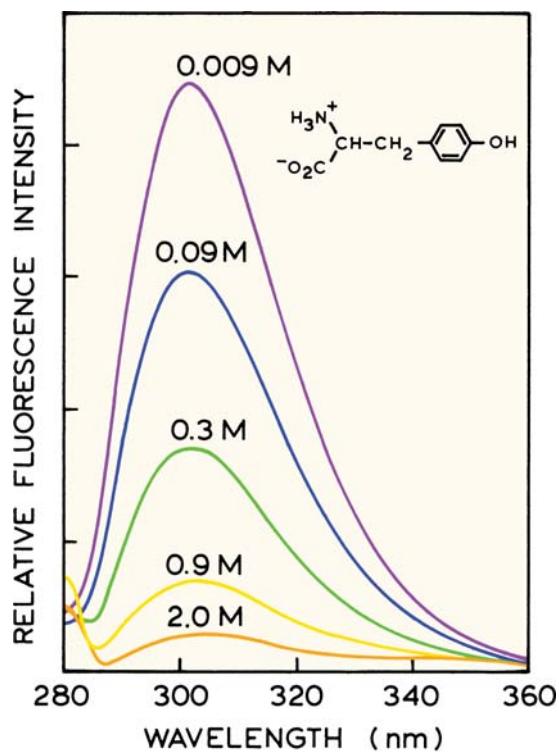


**Figure 16.8.** Corrected fluorescence emission spectra of tyrosine in acetate/acetic acid buffer solutions of differing ionic strength. pH = 6.05. Revised from [42].

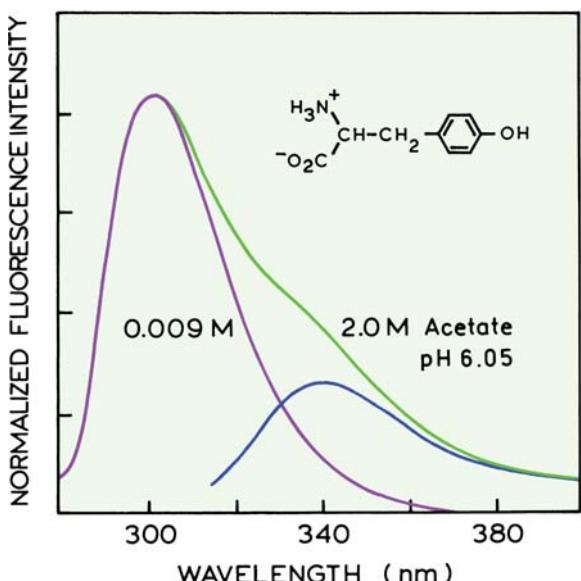


**Figure 16.9.** Corrected fluorescence emission spectra of tyrosine in 0.009 and 2 M acetate solutions at pH = 6.05. The difference spectrum with a maximum near 340 nm is due to tyrosinate. Revised from [42].

more easily seen in the peak-normalized emission spectra (Figure 16.9). In 2.0 M acetate tyrosine displays the usual emission maximum slightly above 300 nm. However, there is also increased intensity at 340 nm. This component is shown in the difference emission spectrum that displays a maximum near 345 nm. The important point is that the phenolic group of tyrosine can ionize even at neutral pH, and the extent to which this occurs depends on the base concentration and exposure of tyrosine to the aqueous phase.

In the example shown in Figure 16.9, tyrosinate was formed in the excited state, following excitation of un-ionized tyrosine. More complex behavior is also possible. The extent of excited-state ionization is limited by the short decay time of tyrosine and occurs to a limited extent under most conditions. Tyrosine can form a ground-state complex with weak bases.<sup>46–47</sup> In these complexes the hydroxyl group is not ionized, but is prepared to ionize immediately upon excitation. Quenching of tyrosine by phosphate and other bases can thus proceed by both static complex formation and by a collisional Stern-Volmer process.<sup>46–47</sup>

#### 16.1.4. Tyrosinate Emission from Proteins

Tyrosinate emission has been reported for a number of proteins that lack tryptophan residues.<sup>48–52</sup> Several examples are shown in Figure 16.10. Crambin contains two tyrosine residues that emit from the un-ionized state. Purothionines are toxic cationic proteins isolated from wheat.  $\alpha_1$ - and  $\beta$ -purothionin have molecular weights near 5000 daltons and do not contain tryptophan. The emission spectrum of  $\beta$ -purothionin is almost completely due to the ionized tyrosinate residue, and the emission from  $\alpha_1$ -purothionin shows emission from both tyrosine and tyrosinate. The emission from cytotoxin II, when excited at 275 nm, shows contributions from both the ionized and un-ionized forms of tyrosine. For three proteins the tyrosinate emission is thought to form in the excited state, but may be facilitated by nearby proton acceptor side chains. Examination of the emission spectra in Figure 16.10 shows that tyrosinate emission can appear similar to and be mistaken for tryptophan emission, or conversely that tryptophan contamination in a sample can be mistaken for tyrosinate emission.

#### 16.2. GENERAL FEATURES OF PROTEIN FLUORESCENCE

The general features of protein fluorescence have been described in several reviews.<sup>53–56</sup> Most proteins contain

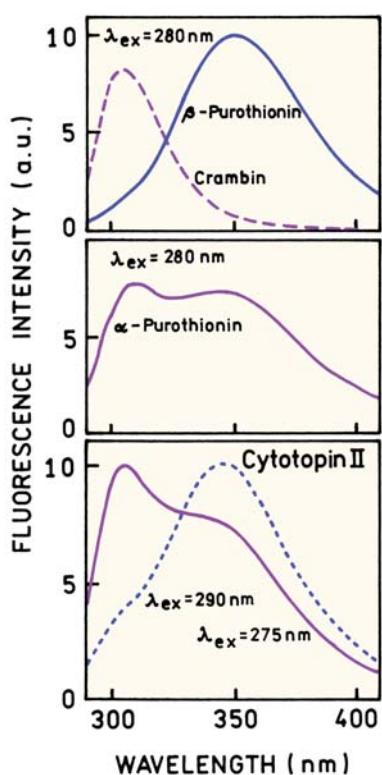


**Figure 16.10.** Emission spectra of proteins that lack tryptophan residues. Neutral pH. Revised from [48–49].

multiple tryptophan residues, and the residues contribute unequally to the total emission. There have been attempts to divide proteins into classes based on their emission spectra.<sup>56–59</sup> The basic idea is that the tryptophan emission spectrum should reflect the average environment of the tryptophan. For tryptophan in a completely apolar environment a blue-shifted structured emission characteristic of indole in cyclohexane can be observed. As the tryptophan residue becomes hydrogen bonded or exposed to water, the emission shifts to longer wavelengths (Figure 16.11). In fact, individual proteins are known that display this wide range of emission spectra.<sup>60–61</sup> For example, later in this chapter we will see that azurin displays an emission spectrum characteristic of a completely shielded tryptophan residue. The emission from adrenocorticotropin hormone (ACTH) is characteristic of a fully exposed tryptophan residue.

The emission maximum and quantum yield of tryptophan can vary greatly between proteins. Denaturation of proteins results in similar emission spectra and quantum yields for the unfolded proteins. Hence, the variations in tryptophan emission are due to the structure of the protein. We are not yet able to predict the spectral properties of proteins using the known structures, but some efforts are underway.<sup>61</sup> One might expect that proteins that display a blue-shifted emission spectrum will have higher quantum yields ( $Q$ ) or lifetimes ( $\tau$ ). Such behavior is expected from

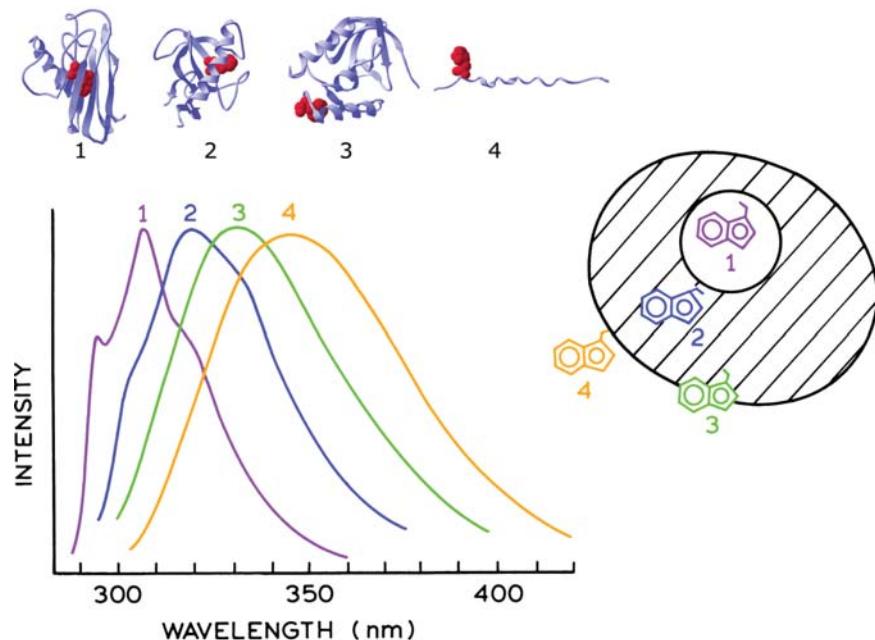


**Figure 16.11.** Effect of tryptophan environment on the emission spectra. The emission spectra are those of apoazurin Pfl, ribonuclease T<sub>1</sub>, staphylococcal nuclease, and glucagon, for 1 to 4, respectively. Revised from [59] and [60].

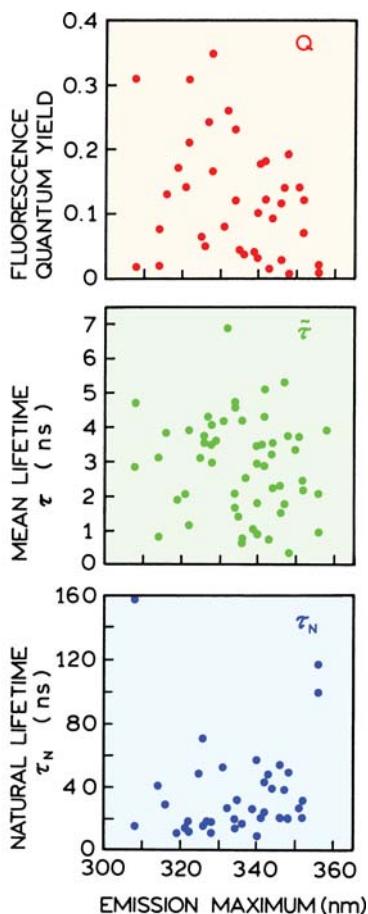


**Figure 16.12.** Relationship of the emission maximum of proteins to the quantum yield  $Q$  (top), mean lifetime  $\tau$  (middle), and natural lifetime  $\tau_N$  (bottom). Courtesy of Dr. Maurice Eftink, University of Mississippi.

the usual increase in quantum yield when a fluorophore is placed in a less polar solvent. For instance, the lifetime of indole decreases from 7.7 ns in cyclohexane to 4.1 ns in ethanol.<sup>29</sup> However, for single-tryptophan proteins there is no clear correlation between quantum yields and lifetimes (Figure 16.12). As described in Chapter 1, the natural lifetime ( $\tau_N$ ) of a fluorophore is the reciprocal of the radiative decay rate, which is typically independent of the fluorophore environment. The value of  $\tau_N$  can be calculated from the measured lifetime ( $\tau$ ) and quantum yield ( $Q$ ),  $\tau_N = \tau/Q$ . Surprisingly, the apparent values of  $\tau_N$  vary considerably for various proteins. Apparently, the complexity of the protein environment can override the general effects of polarity on the lifetime of tryptophan.

Why should the natural lifetimes of proteins be variable? One explanation is that some tryptophan residues are completely quenched in a multi-tryptophan protein, and

thus do not contribute to the measured lifetime and the emission maximum. For instance, indole is known to be partially quenched by benzene. Hence, indole may be quenched by nearby phenylalanine residues in proteins. The nonfluorescent residues still absorb light, and thus result in highly variable quantum yields for the different proteins. The residues that are completely quenched will not contribute to the measured lifetime. As a result the apparent value of the natural lifetime  $\tau_N$  will be larger than the true value. The lack of correlation between emission spectra and lifetimes of proteins is probably due to the effects of specific protein environments that quench particular tryptophan residues. One can imagine the proteins to be in slightly different conformations that bring the residue closer or further from a quenching group. Under these conditions only a fraction of the protein population would be fluorescent. This fluorescent fraction would display a longer lifetime than expected from the quantum yield.

The variability of the lifetimes and quantum yields of proteins has been a puzzle for the last several decades. The reasons for this variability are now becoming understood, but there is no single factor that explains the spectral properties summarized in Figure 16.12. There are several factors that determine the emission from tryptophan residues.<sup>62–70</sup> These are:

- quenching by proton transfer from nearby charged amino groups,
- quenching by electron acceptors such as protonated carboxyl groups,
- electron transfer quenching by disulfides and amides,
- electron transfer quenching by peptide bonds in the protein backbone, and
- resonance energy transfer among the tryptophan residues.

These interactions are strongly dependent on distance, especially the rate of electron transfer, which decreases exponentially with distance. The extent of electron transfer quenching can also depend on the location of nearby charged groups that can stabilize or destabilize the charge transfer state.<sup>64</sup> The rates of electron transfer and resonance energy transfer can be large, so that some tryptophan residues can be essentially nonfluorescent. Additionally, a protein may exist in more than a single conformation, with each displaying a different quantum yield. Proteins are known in which specific tryptophan residues are quenched, and examples where normally fluorescent tryptophan residues transfer energy to nonfluorescent tryptophan residues (Chapter 17). In summary, the variability in the quantum

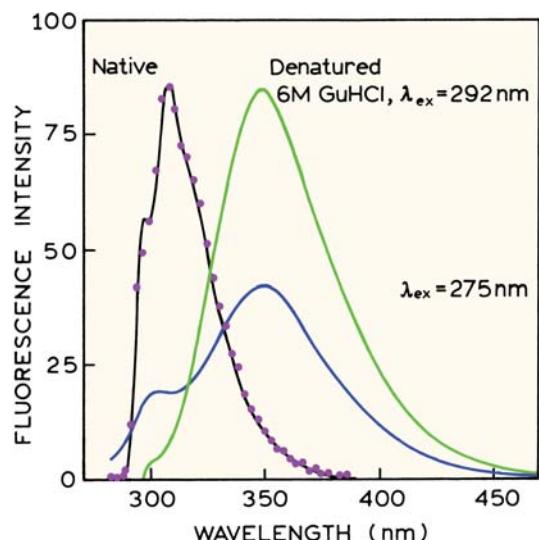


**Figure 16.13.** Emission spectra of *Pseudomonas fluorescens* (ATCC-13525-2) azurin Pfl. The solid lines show emission spectra for native (0.01 M cacodylate, pH 5.3) and denatured (6 M GuHCl) azurin Pfl for  $\lambda_{\text{ex}} = 292$ . Also shown is the emission spectrum of denatured azurin excited at 275 nm. The dots show the emission spectrum of 3-methyl-indole in methylcyclohexane. Data from [73].

yields and lifetimes of proteins is due to a number of interactions, all of which depend on the details of the protein structure.

### 16.3. TRYPTOPHAN EMISSION IN AN APOLAR PROTEIN ENVIRONMENT

Interpretation of protein fluorescence is hindered by the presence of multiple-tryptophan residues in most proteins. This has resulted in studies of single-tryptophan proteins. Fluorescence studies of azurins have been uniquely informative. These are small copper-containing proteins with molecular weights near 15,000 daltons. These proteins are involved in the electron transfer system of denitrifying bacteria. Some of the azurins contain a single-tryptophan residue that displays the most blue-shifted emission observed for a tryptophan residue in proteins.

Emission spectra of the single-tryptophan azurin Pfl from *Pseudomonas fluorescens* is shown in Figure 16.13. In contrast to the emission from most proteins, the emission spectrum of the wild-type (WT) protein shows structure characteristic of the  ${}^1\text{L}_\text{b}$  state.<sup>71-74</sup> In fact, the emission spectrum of native azurin is nearly identical with that of the tryptophan analogue 3-methyl-indole in the nonpolar solvent methylcyclohexane (●). This indicates that the indole

residue is located in a completely nonpolar region of the protein, most probably without a polar group for a hydrogen bond. These results agree with x-ray studies, which show the indole group is located in the hydrophobic core of the protein.<sup>75</sup>

If the structure of azurin is responsible for the tryptophan emission, then disruption of the protein structure should result in a more typical emission spectrum. In the presence of 6 M guanidine hydrochloride the tryptophan emission loses its structure and shifts to 351 nm, characteristic of a fully exposed tryptophan residue. The emission spectra of denatured azurin (Figure 16.13) illustrate another typical spectral property of proteins. The emission spectra are different for excitation at 275 and 292 nm. For 275-nm excitation a peak is observed near 300 nm, which is due to the tyrosine residue(s). The occurrence of tyrosine emission indicates that resonance energy transfer from tyrosine to tryptophan is not complete in denatured azurin. In the native conformation there is no tyrosine emission with 275-nm excitation. Either the tyrosines are quenched in the native structure or energy transfer to the tryptophan residue is highly efficient. For the denatured protein, excitation at 292 nm results in emission from only the tryptophan residue. These spectra demonstrate the wide range of tryptophan spectral properties that can be observed for proteins, and show that changes in the emission spectra can be used to follow protein unfolding.

#### 16.3.1. Site-Directed Mutagenesis of a Single-Tryptophan Azurin

Molecular biology provides a powerful tool for unraveling the complexities of protein fluorescence. Site-directed mutagenesis and expression of mutant proteins allow the amino-acid sequence of proteins to be altered.<sup>76-77</sup> Amino-acid residues in the wild-type sequence can be substituted with different amino acids. Site-directed mutagenesis was used to determine the effects of amino acids near the tryptophan 48 (W48) on the emission spectra of azurin Pae from *Pseudomonas aeruginosa*.<sup>78</sup> The three-dimensional structure of the protein consists of an  $\alpha$ -helix plus eight  $\beta$ -strands that form a hydrophobic core, the so called  $\beta$ -barrel (Figure 16.14). The single-tryptophan residue W48 is located in the hydrophobic region. The wild-type protein, with no changes in the amino-acid sequence, displays the structured emission characteristic of indole in a nonpolar solvent (Figure 16.15).

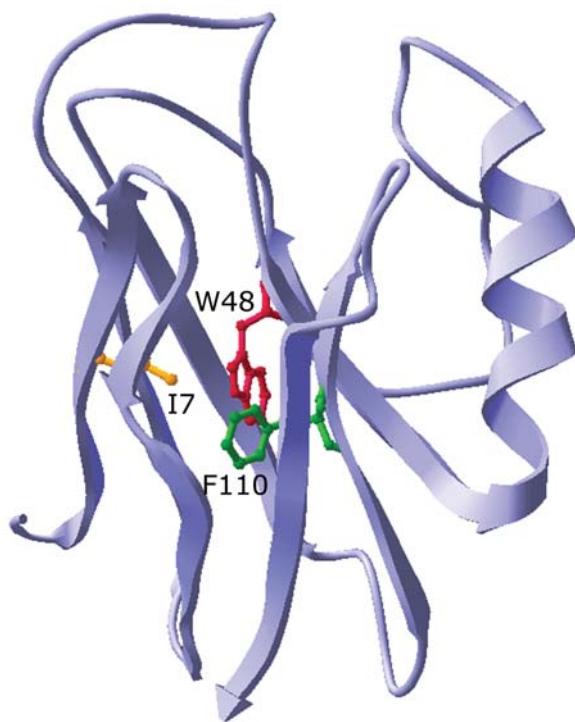


**Figure 16.14.**  $\alpha$ -Carbon backbone of wild-type azurin from *Pseudomonas aeruginosa*. The environment around the single-tryptophan residue (W48) was varied by mutating isoleucine (I7) or phenylalanine (F110).

Site-directed mutagenesis of azurin was used to change amino acids located near the tryptophan residue. A single amino acid substitution was found to eliminate the structured emission spectrum of tryptophan. In a mutant protein the nonpolar amino acid isoleucine (I) at position 7 was replaced with serine (S). This mutant protein is referred to as I7S. The amino acid serine contains a hydroxyl group, which might be expected to form a hydrogen bond to indole and thus mimic ethanol in cyclohexane (Figure 16.5). This single amino acid substitution resulted in a complete loss of the structured emission (Figure 16.15). The emission maximum is still rather blue shifted ( $\lambda_{\text{max}} = 313 \text{ nm}$ ), reflecting the predominantly nonpolar character of the indole environment. The emission of tryptophan 48 was also found to be sensitive to substitution of the phenylalanine residue at position 110 by serine (F110S, Figure 16.15). These studies demonstrate that just a single hydrogen bond can eliminate the structured emission of indole, and that the emission spectra of indole are sensitive to small changes in the local environment.

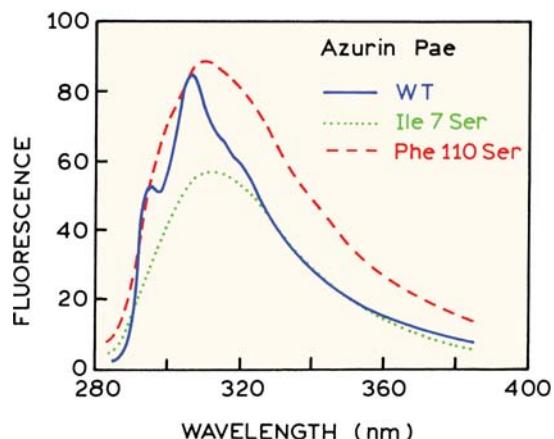


**Figure 16.15.** Corrected steady-state fluorescence spectra of holoazurin Pae: WT (solid), I7S (dotted), F110S (dashed). Data were collected at 298°K in 20 mM Hepes buffer at pH 8.0. The excitation wavelength was 285 nm. Reprinted with permission from [79]. Copyright © 1987, American Chemical Society.

### 16.3.2. Emission Spectra of Azurins with One or Two Tryptophan Residues

The azurins also provide examples of single-tryptophan proteins with the tryptophan residues located in different regions of the protein.<sup>79</sup> Azurins isolated from different microorganisms have somewhat different sequences. Azurin Pae has a single buried tryptophan residue at position 48. Azurin Afe has a single tryptophan on the surface at position 118, and azurin Ade has tryptophan residues at both positions 48 and 118. Each of these azurins displays distinct emission spectra (Figure 16.16). The emission of the buried residue W48 is blue shifted, and the emission of the exposed residue W118 displays a red-shifted featureless spectrum. The emission spectrum of azurin Ade with both residues is wider and shows emission from each type of tryptophan residue. Hence, a wide range of environments can exist within a single protein.

## 16.4. ENERGY TRANSFER AND INTRINSIC PROTEIN FLUORESCENCE

Resonance energy transfer can occur between the aromatic amino acids in proteins. Transfer is likely to occur because of spectral overlap of the absorption and emission spectra of phe, trp, and trp (Figure 16.1). The local concentrations of these residues in proteins can be quite large. Consider a typical globular protein with a molecular weight near

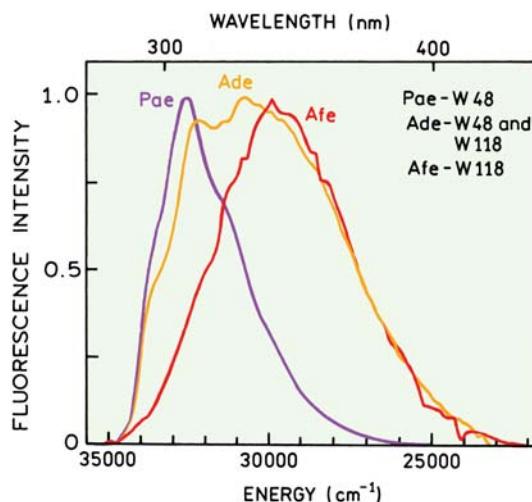


**Figure 16.16.** Fluorescence spectra of apo Pae azurin, apo Ade azurin, apo Afe azurin. The fluorescence spectra of the holoproteins only differ from that of the apoproteins in that they have a reduced intensity. Data reprinted with permission from [79]. Copyright © 1987, American Chemical Society.

50,000 daltons. Such a protein contains approximately 450 amino-acid residues (about 110 daltons per amino-acid residue), about 10 of which will be one of the aromatic amino acids. Using a typical density of proteins near 1.4 g/ml, one can calculate a protein radius near 24 Å. The concentration of aromatic amino acids in this protein is near 0.28 M = 280 mM.

Typical Förster distances ( $R_0$ ) and characteristic concentration values ( $A_0$ ) for energy transfer between the aromatic amino acids are listed in Table 16.1. These values illustrate the range of distances and concentrations typical of RET between the fluorescent amino acids. For any given donor–acceptor pair the actual distances will depend on the quantum yield and emission spectrum of the donor, which can vary in different protein environments. Absorption spectra are typically less sensitive to the environment, so the emission spectrum and quantum yield of the donor are the dominant origin of the range of  $R_0$  values. From the values in Table 16.1 it is evident that RET can be expected between the aromatic amino acids in proteins.

The Förster distance for tryptophan-to-tryptophan homotransfer is particularly variable. This is because the extent of spectral overlap is strongly dependent on solvent polarity. In polar solvents the emission spectrum of tryptophan is shifted away from the absorption spectrum and the Förster distances are smaller. For instance, for the fully exposed tryptophan residues in melittin the Förster distance was estimated to be just 4 Å.<sup>80–81</sup> At low temperature in vis-

**Table 16.1.** Förster Distances and Critical Concentrations for Resonance Energy Transfer in Proteins

Donor	Acceptor	$R_0$ (Å)	$A_0$ (M) <sup>a</sup>	Ref.
Phe	Tyr	11.5–13.5	0.29–0.18	82–84
Tyr	Tyr	9–16	0.61–0.11	12, 13
Tyr	Trp	9–18	0.61–0.08	12, 85–88
Trp	Trp	4–16	7.0–0.11	12, 89

<sup>a</sup>The critical concentration ( $A_0$ ) in moles/liter can be calculated from  $A_0 = 447/R_0^3$ , where  $R_0$  is in Å. See Chapter 13.

ous solvent, where the Stokes shift was smaller, the  $R_0$  value for tryptophan homotransfer<sup>12</sup> was found to be as large as 16 Å. Hence trp-to-trp transfer can be expected in proteins, particularly if some of the residues display a blue-shifted emission.

#### 16.4.1. Tyrosine to Tryptophan Energy Transfer in Interferon- $\gamma$

The most commonly observed resonance energy transfer in proteins is from tyrosine to tryptophan. This is because most proteins contain both of these amino acids, and both are readily excited at 275 nm. One example of tyr-to-trp transfer is human interferon- $\gamma$ , whose emission spectrum depends on the extent of self-association. Interferon- $\gamma$  is produced by activated lymphocytes and displays antiviral and immunoregulator activity. Its activity depends on the extent of association to dimers. The intrinsic fluorescence of interferon- $\gamma$  was used to study its dissociation into monomers.

Interferon- $\gamma$  is usually a dimer of two identical 17, kDa polypeptides, each containing one tryptophan residue at position 36 and four tyrosine residues (Figure 16.17).<sup>90</sup> The emission spectrum of the interferon- $\gamma$  dimer (Figure 16.18, top) displays emission from both tyrosine and tryptophan when excited at 270 nm. Only tryptophan emission is seen for 295-nm excitation. To compare the relative intensities of tyrosine and tryptophan the spectra were normalized at long emission wavelengths where only tryptophan emits, followed by subtraction of the spectrum with 295-nm excitation from the spectrum with 270-nm excitation. This difference spectrum is seen to be that expected for tyrosine. When incubated under the appropriate conditions, interferon- $\gamma$  dissociates into monomers. The relative intensity of the tyrosine increases in the monomeric state (Figure 16.18, lower panel). In the monomeric state the relative tyrosine intensity is about half that of tryptophan. In the dimer the

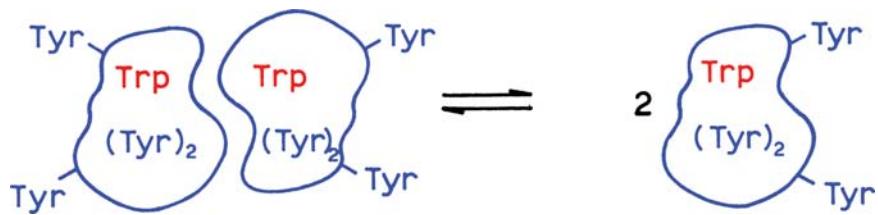


**Figure 16.17.** Schematic of the interferon- $\gamma$  dimer. Each monomer contains one tryptophan and four tyrosines.

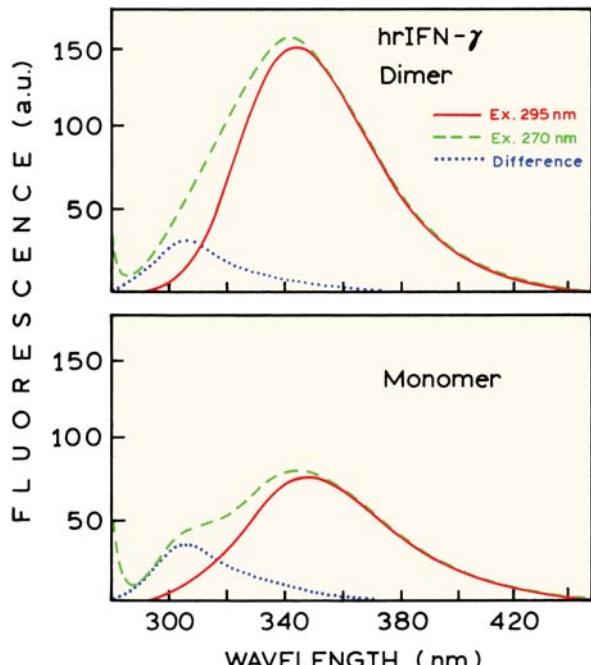


**Figure 16.18.** Emission spectra of human recombinant interferon- $\gamma$  (hrIFN- $\gamma$ ), 10 mM tris, pH 7.7. Revised from [90].

relative tyrosine intensity is about 20%. The relative increase in tyrosine fluorescence in the monomeric state occurs because the four tyrosines are more distant from the tryptophan acceptors that are on the dissociated subunit. This result shows that RET can occur between the subunits; otherwise, the extent of tyr-to-trp energy transfer would be independent of association.

#### 16.4.2. Quantitation of RET Efficiencies in Proteins

In the previous paragraph we explained the emission spectra of interferon- $\gamma$  in terms of energy transfer, but we did not consider the effect of dimer dissociation on the fluorescence intensity of the tryptophan residue. In fact, the tryptophan emission intensity decreases approximately twofold

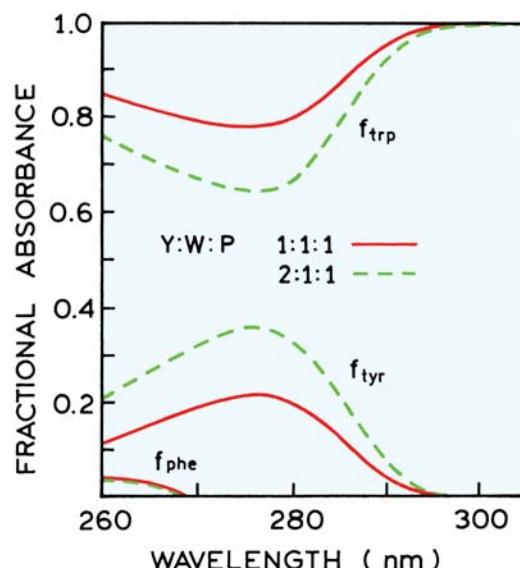


**Figure 16.19.** Fractional absorption of tyrosine, tryptophan and phenylalanine in a mixture of amino acids. The molar ratio of Tyr:Trp: Phe (Y:W:P) are 1:1:1 (solid) and 2:1:1 (dashed). Revised from [85].

on dissociation.<sup>90</sup> Fortunately, there is a means to measure the efficiency of tyrosine-to-tryptophan energy transfer that is independent of the tryptophan quantum yield. This approach depends on the relative absorbance of the aromatic amino acids at various wavelengths<sup>85</sup> (Figure 16.19). The fraction of total absorbance due to each type of amino acid can be calculated from the extinction coefficients in Figure 16.1. Above 295 nm only tryptophan absorbs, and its fractional absorbance is 1.0. This is the basis for selective excitation of tryptophan for wavelengths of 295 nm and longer. As the wavelength decreases the fractional absorption of tryptophan decreases and the fractional absorption of tyrosine increases. At a higher relative concentration of tyrosine its fractional absorbance is larger.

The extent of tyr-to-trp energy transfer can be found by measuring the relative tryptophan quantum yield for various excitation wavelengths. The relative quantum yield is deter-

mined from the intensity observed with a given excitation wavelength, divided by the absorbance at the excitation wavelength. If energy transfer is 100% efficient, then the tryptophan emits irrespective of whether tyrosine or tryptophan is excited. In this case the relative quantum yield  $Q(\lambda)$  is independent of excitation wavelength. If there is no tyro-to-trp energy transfer then the relative tryptophan quantum yield decreases at shorter wavelengths. This decrease occurs because light absorbed by the tyrosine does not result in emission from the tryptophan. This can be understood by recognizing that the absorbance is below 290 nm due to both tyrosine and tryptophan. In the absence of energy transfer only absorption by tryptophan results in tryptophan emission.

The fractional absorbance of each type of amino acid can be calculated from the absorbance due to each amino acid. The fractional absorbance due to tryptophan is given as follows:

$$f_{\text{trp}}(\lambda) = \frac{a_{\text{trp}}(\lambda)}{a_{\text{trp}}(\lambda) + a_{\text{tyr}}(\lambda)} \quad (16.1)$$

where  $\varepsilon_i(\lambda)$  is the absorbance of the individual residues at wavelength  $\lambda$ . For simplicity we deleted from this expression the minor term due to absorption by phenylalanine. Figure 16.19 shows that only tryptophan absorbs at wavelengths longer than 295 nm. The relative quantum yield at 295-nm excitation is taken as a reference point at which all the light is absorbed by tryptophan. The fluorescence is monitored at 350 nm or longer to avoid tyrosine emission. The relative quantum yield at any excitation wavelength is given by

$$Q(\lambda) = \frac{a_{\text{trp}}(\lambda) + Ea_{\text{tyr}}(\lambda)}{a_{\text{trp}}(\lambda) + a_{\text{tyr}}(\lambda)} \quad (16.2)$$

If  $E$  is 100% then the relative quantum yield of tryptophan fluorescence is independent of excitation wavelength. If  $E$  is zero then the relative quantum yield is given by the fractional absorption due to tryptophan.

Equation 16.1 is written in terms of absorbance due to each type of residues. If the number of tyrosine and tryptophan residues is known the fractional absorbance of tryptophan can be approximated from

$$f_{\text{trp}}(\lambda) = \frac{n\varepsilon_{\text{trp}}(\lambda)}{n\varepsilon_{\text{trp}}(\lambda) + m\varepsilon_{\text{tyr}}(\lambda)} \quad (16.3)$$

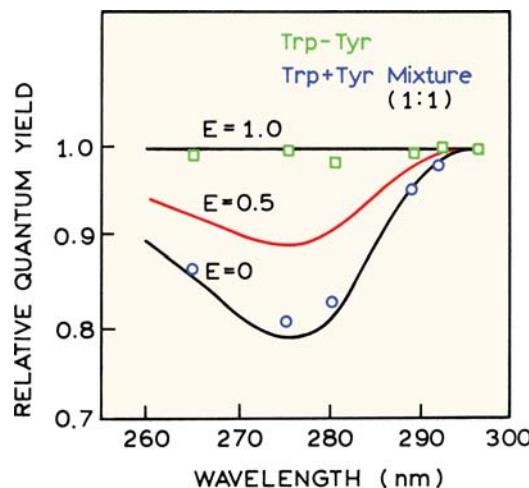


**Figure 16.20.** Excitation wavelength dependence of the relative quantum yield of the dipeptide tryptophanyltyrosine and an equimolar mixture of tyrosine and tryptophan. The lines correspond to transfer efficiencies of 0, 50, and 100%. Reprinted with permission from [85]. Copyright © 1969, American Chemical Society.

where  $\varepsilon_i(\lambda)$  are the extinction coefficients,  $n$  is the number of tryptophan residues per protein, and  $m$  is the number of tyrosine residues per protein. This expression can be slightly in error due to shifts in the absorption of the residues in different environments.

The use of the relative quantum yield to determine the energy transfer efficiency is illustrated by data for a dipeptide—tyr-trp—and for an equimolar mixture of tyrosine and tryptophan (Figure 16.20). In the dipeptide the donor and acceptor are well within the Förster distance and the transfer efficiency is expected to be near 100%. This prediction is confirmed by the independence of the tryptophan quantum yield from the excitation wavelength. All the energy absorbed by tyrosine or tryptophan appears as tryptophan fluorescence. For the mixture of unlinked tyrosine and tryptophan the relative quantum yield closely follows the fractional absorbance due to tryptophan ( $E = 0$ ), indicating the absence of significant energy transfer.

Such data can be used to estimate the efficiency of tyrosine–tryptophan energy transfer in proteins. The excitation wavelength-dependent tryptophan quantum yields are shown for interferon- $\gamma$  in Figure 16.21. These values are measured relative to the quantum yield at 295 nm, where only tryptophan absorbs. The relative quantum yield decreases with shorter excitation wavelengths in both the monomeric and dimeric states. The quenching efficiency ( $E$ ) is estimated by comparison with curves calculated for various transfer efficiencies. Using this approach the trans-

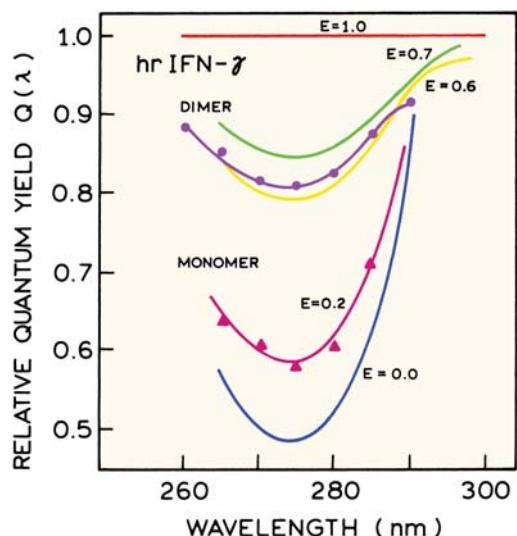


**Figure 16.21.** Wavelength-dependence of the relative quantum yield  $Q(\lambda)$  of  $1 \mu\text{M}$  hrIFN- $\gamma$  in the monomer and dimer states. All theoretical and experimental data are normalized to absorbance at 295 nm. Revised and reprinted with permission from [90]. Copyright © 1996, American Chemical Society.

fer efficiency is estimated to be 20 and 60% in the monomer and dimer, respectively. The decrease in relative quantum yield is less in the dimeric state, indicating more efficient tyr-to-trp energy transfer in the dimer. This implies that the tyrosine residues in one subunit transfer to the tryptophan residue in the other subunit. The larger decrease in relative quantum yield for the monomer at 270 nm can be understood as due to the lower transfer efficiency, so that fewer of the photons absorbed by tyrosine appear as tryptophan emission.

#### 16.4.3. Tyrosine-to-Tryptophan RET in a Membrane-Bound Protein

Tyrosine-to-tryptophan RET was used to study folding of the M13 procoat protein when bound to membranes. The final M13 coat protein is inserted into the inner membrane of *E. coli* prior to assembly of the M13 phage particle. The procoat protein is thought to form two closely spaced  $\alpha$ -helices when bound to membranes (Figure 16.22). In order to use tyr-to-trp RET the two natural tyrosine residues and one tryptophan residue were mutated to phenylalanines. Tyr and trp were then inserted at desired locations in the sequence near the ends of the  $\alpha$ -helical segments. The residues are numbered relative to a residue above the left-hand helix, which is taken as zero.

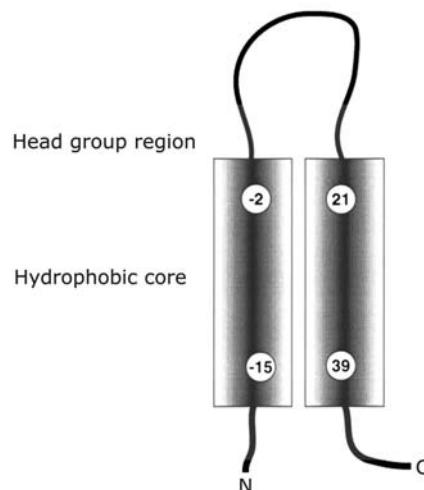


**Figure 16.22.** Schematic structure of membrane-bound M13 procoat protein. The numbers refer to the positions in the sequence related to residue 0 near the top of the left-side helix. Reprinted with permission from [91]. Copyright © 2001, American Chemical Society.

Emission spectra of three mutants are shown in Figure 16.23 for excitation at 280 and 295 nm.<sup>91</sup> In the W21Y24 mutant, where the tyrosine and tryptophan are located only three residues apart, there is no detectable tyrosine emission. For the W21Y(-15) mutant a tyrosine component is seen on the short-wavelength side of the tryptophan emission. The W39Y(-15) mutant shows a smaller tyrosine component.

It is difficult to use the emission spectra to determine the tyr-to-trp RET efficiencies. The RET efficiencies were determined from the excitation spectra (Figure 16.24). These spectra (top panel) show higher amplitude at 280 nm for the peptide that showed the lowest tyrosine emission (W21Y24), and a lower intensity for 280-nm excitation for the W21Y(-15) mutant. The transfer efficiencies can be determined by comparison with normalized intensities (lower panel). These results show the RET efficiency varies from 0 to 100% depending on the location of the tyrosine and tryptophan residues. The results of this analysis are shown in Figure 16.25. The 0% transfer efficiency for W21Y(-15) and the 50% transfer efficiency for W39Y(-15) shows that this protein binds to membranes as a pair of helices. Otherwise there would have been less efficient transfer between W39 and Y(-15).

#### 16.4.4. Phenylalanine to Tyrosine Energy Transfer

Resonance energy transfer can also occur from phenylalanine to tyrosine. Such transfer is rarely reported because

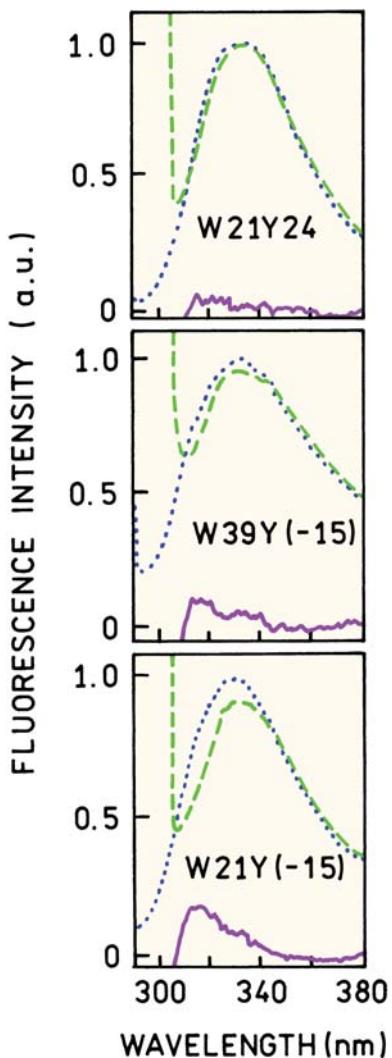


**Figure 16.23.** Emission spectra of the M13 procoat protein. The positions of the tyrosine and tryptophan residues are shown on the figure. Excitation at 280 (dashed) or 295 nm (dotted). The difference spectra are shown as solid lines. Revised from [91].

tyrosine and tryptophan dominate the emission of most proteins, and proteins are usually not excited at 260 nm where phenylalanine absorbs. Phenylalanine emission was detected from an unusual histone-like protein, HTa, from the thermophilic archaeabacterium *Thermoplasma acidophilum*.<sup>82</sup> HTa associates strongly with DNA to protect it from thermal degradation. This highly unusual protein is a tetramer, with five phenylalanine residues and one tyrosine residue in each monomer, and no tryptophan residues (Figure 16.26). In this class of organisms the more thermophilic variants have higher phenylalanine contents in their histone-like proteins. An experimentally useful property of this protein is the ability to remove the tyrosine residues, located at the

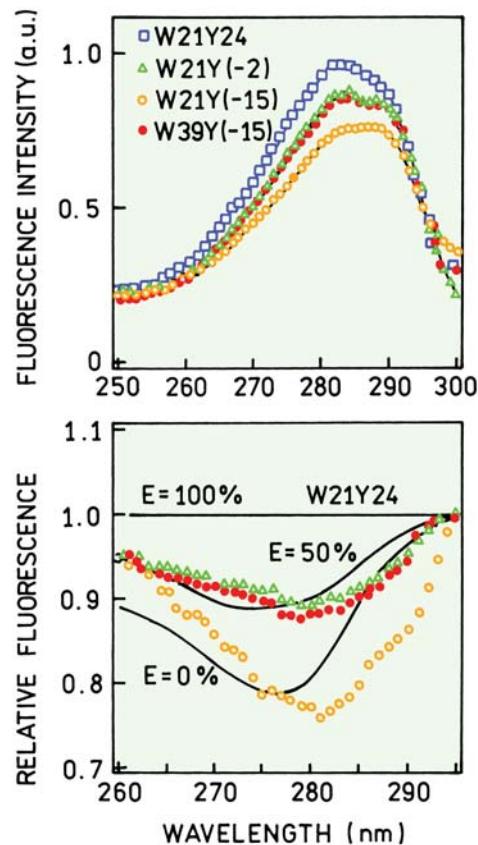


**Figure 16.24.** Excitation spectra of mutant M13 procoat proteins. The lower panel shows the quantum yields normalized according to eq. 16.2. Revised from [91].

third position from the carboxy terminus, by digestion with carboxypeptidase A.

The emission spectrum of HTa excited at 252 nm is shown in Figure 16.26 (solid, top panel). The emission

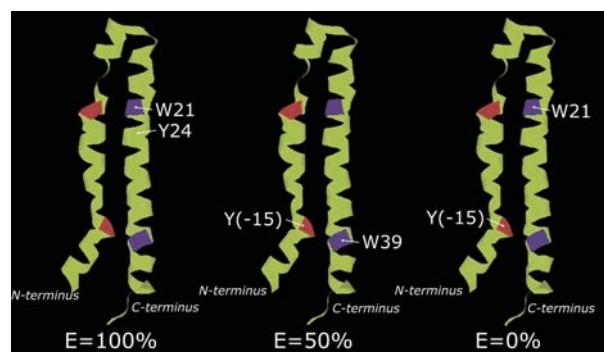


**Figure 16.25.** Structure and RET efficiencies for the mutant M13 procoat proteins. Data reprinted with permission from [91]. Copyright © 2001, American Chemical Society.

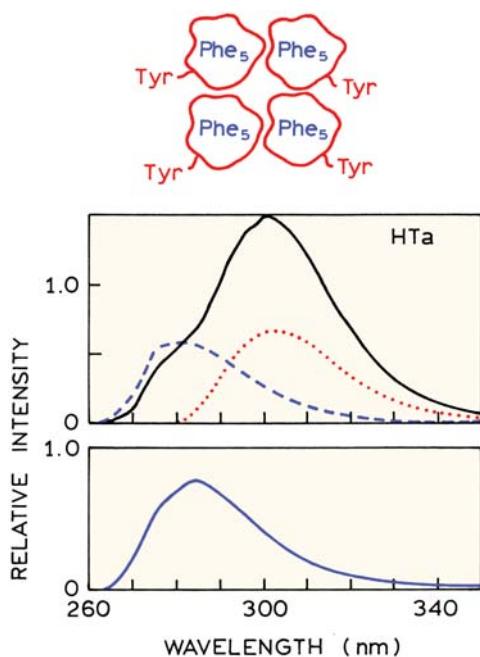


**Figure 16.26.** Top: Emission spectra of archaeabacterial histone-like protein (HTa) excited at 252 nm (solid). Also shown are the emission spectra of equivalent concentrations of phenylalanine (dashed) or tyrosine (dotted). Bottom: Emission of HTa following removal of the tyrosine by carboxypeptidase A digestion. Revised from [82].

appears to be similar to that of tyrosine with an emission maximum near 300 nm. However, the spectrum also shows a shoulder at 280 nm that is too blue-shifted to be due to tyrosine. The origin of the dual emission was determined by a comparison with the emission from tyrosine (dotted) and phenylalanine (dashed) at equivalent concentrations. These spectra show that the emission spectrum of HTa is due to contributions from both the phe and tyr residues. Assignment of the 280-nm emission to phenylalanine was also accomplished by removal of the tyrosine residue by digestion with carboxypeptidase A. This emission spectrum (Figure 16.23, lower panel) is identical to that found for phenylalanine, identifying the emission at 280 nm as due to phenylalanine.

The presence of phe-to-tyr energy transfer in HTa was detected from the excitation spectra. Figure 16.27 shows the corrected excitation spectrum of HTa, which was superimposed on the absorption spectra of tyrosine alone and a 5-to-1 mixture of phenylalanine and tyrosine. The emission was measured at 330 nm, where only tyrosine emits. If there were no phe-to-tyr energy transfer the excitation spectrum would be the same as the absorption spectrum of tyrosine. If phe-to-tyr RET was 100% efficient then the excitation spectrum would be the same as the 5-to-1 phe-tyr mix-

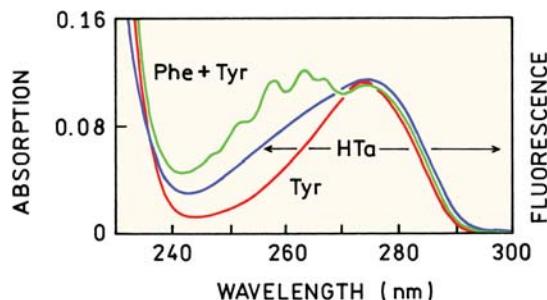


**Figure 16.27.** Corrected fluorescence excitation spectrum of HTa superimposed upon the ultraviolet absorbance spectra of a mixture of phenylalanine and tyrosine (5 to 1) or of tyrosine alone. Fluorescence emission was measured at 330 nm. Revised from [82].

ture. Hence the transfer efficiency is near 50%. Given  $R_0 = 13.5 \text{ \AA}$  for phe-to-tyr energy transfer,<sup>82</sup> and the diameter expected for a protein with a molecular weight of 9934 daltons, which is near 28 Å, it is not surprising that phenylalanine fluorescence is partially quenched in HTa. While most proteins are larger, they may also contain multiple phenylalanine and tyrosine residues. Phenylalanine-to-tyrosine energy transfer is probably a common occurrence in proteins when excited at 260 nm.

Removal of tyrosine from HTa provided a protein without tyrosine or tryptophan and an opportunity to study the emission of phenylalanine in a protein. The lifetime of phenylalanine was near 22 ns, which is considerably longer than the 2- to 5-ns values typical of tyrosine and tryptophan. This lifetime of 22 ns is comparable to a measured value of 20 ns for a constrained analogue of phenylalanine.<sup>92</sup> In HTa and in the presence of tyrosine the lifetime of phenylalanine is decreased to near 12 ns. This value is consistent with 50% energy transfer from phenylalanine to tyrosine. It is interesting to notice that the 12-ns decay time is observed at all emission wavelengths, even those where only tyrosine is expected to emit.<sup>82</sup> Such long decay times are unlikely for directly excited tyrosine. In this protein the excited phenylalanines continue to transfer to tyrosine during their decay, resulting in an apparent 12-ns tyrosine lifetime. This phenomenon was described in Chapter 7 on excited-state reactions.

## 16.5. CALCIUM BINDING TO CALMODULIN USING PHENYLALANINE AND TYROSINE EMISSION

Calmodulin functions as a calcium sensor in all vertebrate cells and regulates a large number of target enzymes. Calmodulin consists of a single polypeptide chain folded into

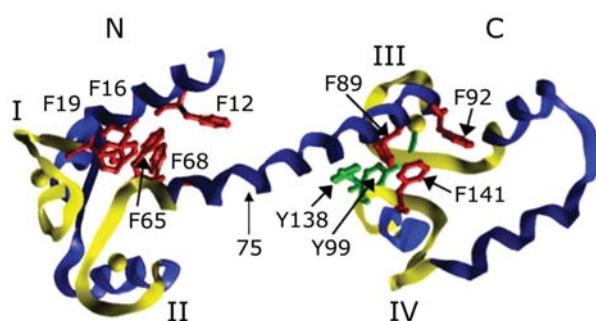


**Figure 16.28.** Ribbon structure for rat calmodulin saturated with calcium. The phenylalanine residues are shown in red and the tyrosine residues in green. Figure from [94] provided by Dr. Madeline A. Shea from the University of Iowa.

two domains connected by a flexible  $\alpha$ -helical linker (Figure 16.28). Each domain contains two calcium-binding sites (I-IV). Most calmodulins lack tryptophan residues. Rat calmodulin contains five phenylalanines in the N-terminal domain (N) and three in the C domain, which also contains two tyrosine residues. When calmodulin is excited at 250 nm, in the absence of calcium, emission from both phe and tyr is observed (Figure 16.29, bottom panel). This emission

spectrum shows components similar to that observed for a mixture of these two amino acids (top panel). Addition of calcium to calmodulin (1–145) results in disappearance of the phe emission and an increase in the tyr emission.<sup>93,94</sup> At first glance it appears that energy transfer is increased in the presence of calcium, which is expected to decrease the phe emission and increase the tyr emission. However, an increase in RET was not expected because calmodulin is more elongated in the presence of calcium than in the absence of calcium. The middle panel shows studies of the individual domain. The N domain consisting of residues 1–75 shows only phe emission, which is quenched upon addition of calcium. The C domain consists of residues 76–145 and showed an increase in tyrosine emission upon binding calcium but no phe emission. Hence the intensity changes seen for the entire molecule CaM 1–145 are probably not due to changes in RET. This is not a disappointment, but in fact an advantage, because calcium binding to each domain can be studied independently using the intrinsic phe and tyr emission of calmodulin.

#### 16.6. QUENCHING OF TRYPTOPHAN RESIDUES IN PROTEINS

Collisional quenching of proteins is used to determine the extent of tryptophan exposure to the aqueous phase.<sup>95–102</sup> The basic idea is shown in Figure 16.30, which depicts quenching by a water-soluble quencher that does not easily penetrate the protein matrix. Collisional quenching is essentially a contact phenomenon, so that the fluorophore and quencher need to be in molecular contact for quenching to occur. Consequently, if the tryptophan residue is buried inside the protein ( $W_1$ ), quenching is not expected to occur. If the tryptophan residue is on the protein surface ( $W_2$ ), then quenching is expected.

One example of selective quenching is shown for apoazurin Ade, which is azurin lacking copper. Apoazurin Ade has two tryptophan residues: one surface residue and one buried residue.<sup>101</sup> The emission spectra of this protein, along with those of its single-tryptophan variants, are shown in Figure 16.16. For our present purposes the properties of the protein with or without (apo) copper are the same.

Emission spectra were recorded in the absence and presence of 0.45 M iodide, which is a collisional quencher (Figure 16.31). The intensity decreases in the presence of iodide. The emission spectrum changes in the presence of iodide, and resembles the structured emission seen from the

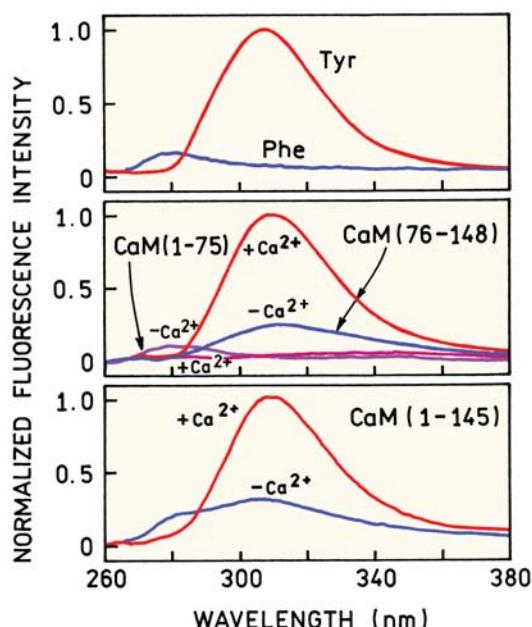


**Figure 16.29.** Emission spectra for excitation at 250 nm. Top: phe or tyr. Middle and bottom: rat calmodulin (CaM) with and without calcium. The numbers indicate the amino-acid residues in the calmodulin fragments. Revised from [94].

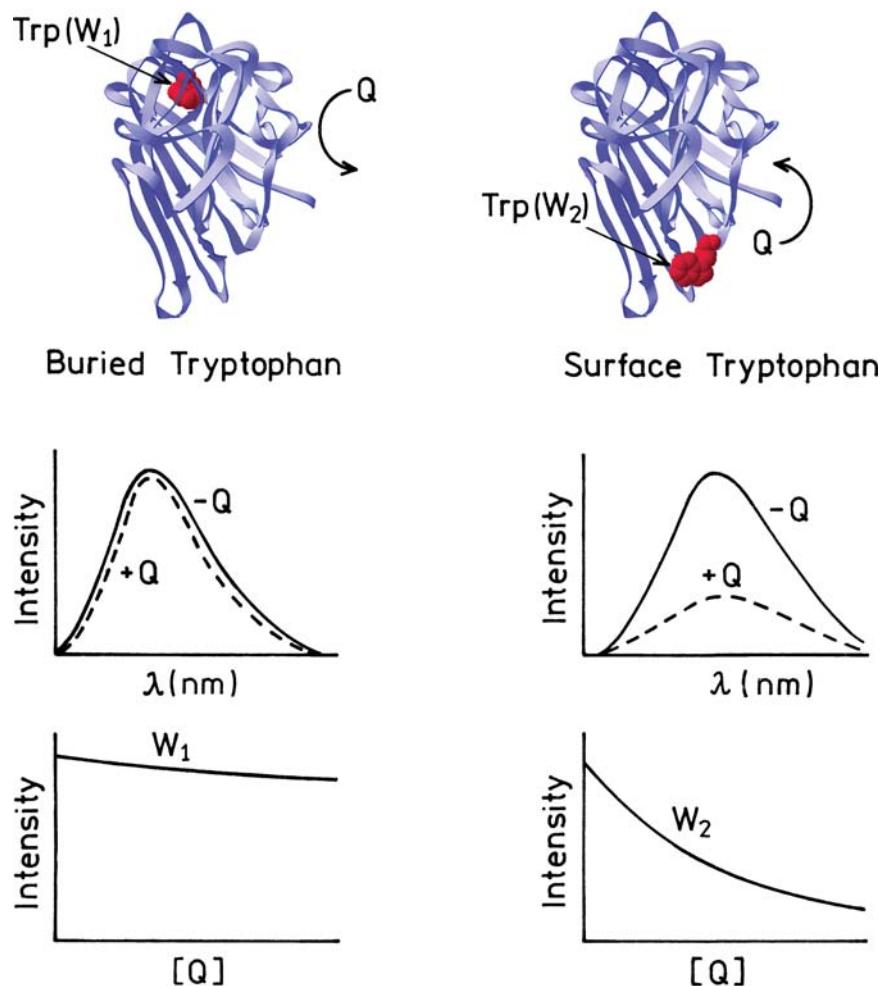


**Figure 16.30.** Collisional quenching of buried ( $W_1$ ) and surface accessible ( $W_2$ ) tryptophan residues in proteins.

single-tryptophan azurin Pae. The spectrum of the quenched tryptophan residue can be seen from the difference spectrum, and is characteristic of an exposed residue in a partially hydrophobic environment. In this favorable case, one residue is quenched and the other is not, providing resolution of the two emission spectra.

#### 16.6.1. Effect of Emission Maximum on Quenching

Water-soluble quenchers, including iodide and acrylamide, do not readily penetrate the hydrophobic regions of proteins. There is a strong correlation between the emission maximum and quenching constant.<sup>101–102</sup> Blue-shifted tryptophan residues are mostly inaccessible to quenching by acrylamide, and red-shifted residues are nearly as accessible as tryptophan in water. This correlation can be seen in the acrylamide quenching of several proteins (Figure

16.32). The emission of azurin is essentially unchanged in up to 0.8 M acrylamide. In contrast, the exposed tryptophan residue in adrenocorticotropin hormone (ACTH) is almost completely quenched at 0.4 M acrylamide (Figure 16.32, left panel).

Quenching data are typically presented as Stern-Volmer plots, which are shown for several single-tryptophan proteins (Figure 16.32, right panel). In these plots the larger slopes indicate larger amounts of quenching and can be used to calculate the bimolecular quenching constant ( $k_q$ ). The buried single-tryptophan residue in azurin Pae is not affected by acrylamide. In contrast, the fully exposed residue in ACTH is easily quenched by acrylamide. ACTH is quenched nearly as effectively as NATA. A plot of the bimolecular quenching constant ( $k_q$ ) for acrylamide versus emission maximum for a group of single-tryptophan proteins is shown in Figure 16.33. These data show that  $k_q$

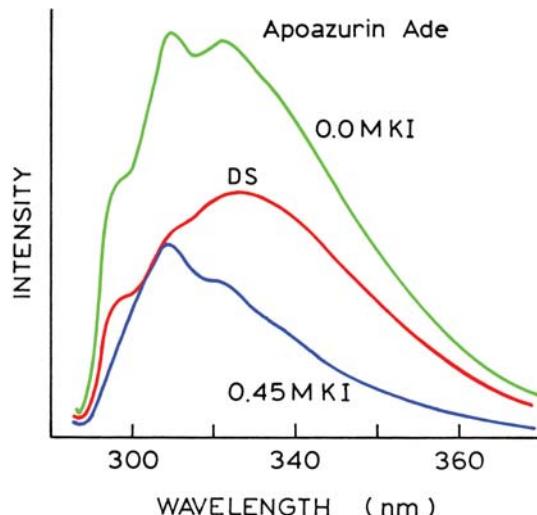


**Figure 16.31.** Fluorescence emission spectra of apoazurin Ade from *Alcaligenes denitrificans* in the absence (top curve) and presence (bottom curve) of 0.45 M KI. The middle line is the difference spectrum (DS) and is due to the easily quenched emission (presumably from Trp-118). The buffer was 0.05 M sodium acetate, pH 5.0. Revised from [101].

varies from almost completely inaccessible for azurin and asparaginase to completely accessible for glucagon. Glucagon is a relatively small peptide with 29 amino acids that opposes the action of insulin. Glucagon has a random structure in solution.<sup>103–105</sup> Hence, there is little opportunity for the protein to shield the single trp-25 residue from acrylamide quenching.

The extent of collisional quenching can also be dependent on protein conformation and/or the extent of subunit association. This effect has been observed for mel-

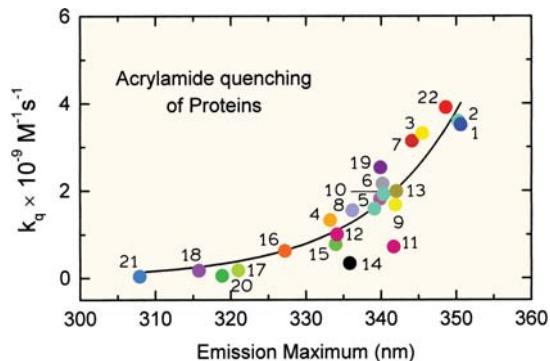


**Figure 16.33.** Dependence of the apparent acrylamide bimolecular quenching constant ( $k_q$ ) on the emission maximum for single-tryptophan proteins: 1, glucagon; 2, adrenocorticotropin; 3, melittin monomer; 4, melittin tetramer; 5, gonadotropin; 6, phospholipase A<sub>2</sub>; 7, human luteinizing hormone; 8, 9, monellin; 10, gonadotropin; 11, human serum albumin, N form; 12, human serum albumin, F form; 13, myelin basic protein; 14, elongation factor Tu-GDP; 15, nuclease; 16, fd phage; 17, ribonuclease T<sub>1</sub>; 18, parvalbumin; 19, calcium-depleted parvalbumin; 20, asparaginase; 21, apoazurin Pae; 22, mastopartan X. Revised from [101].

tin, which is a small peptide of 26 amino acids containing a single-tryptophan residue at position 19. Depending on ionic strength, melittin can exist as a monomer or tetramer. In the tetramer, the four tryptophan residues, one per monomer, are located in a hydrophobic pocket between the helices.<sup>106</sup> The tryptophan residues in melittin are more easily quenched when melittin is in the monomer state (Figure 16.33).

Acrylamide and iodide are polar molecules, and do not readily penetrate the nonpolar regions of proteins. However, small nonpolar oxygen molecules readily penetrate all

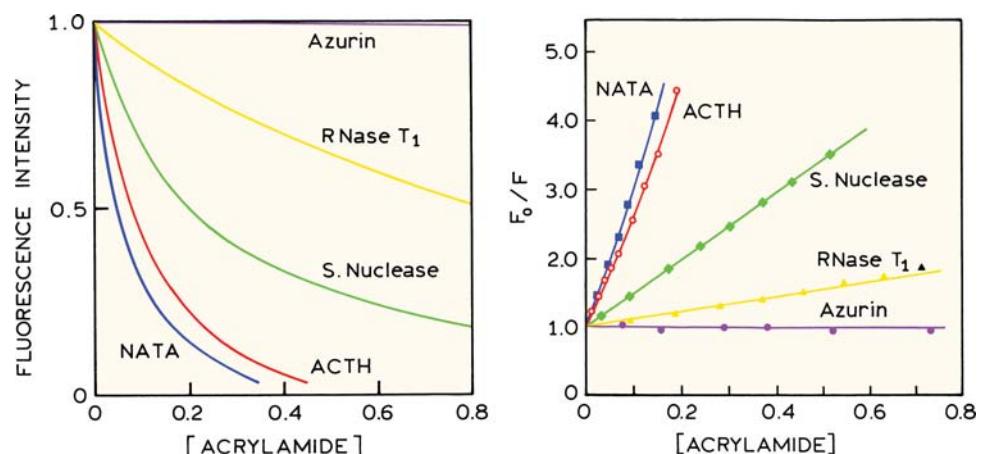


**Figure 16.32.** Acrylamide quenching of representative single-tryptophan proteins and NATA. Left: intensity versus acrylamide concentration. Right: Stern-Volmer plots. Data from [80], [86], and [99].

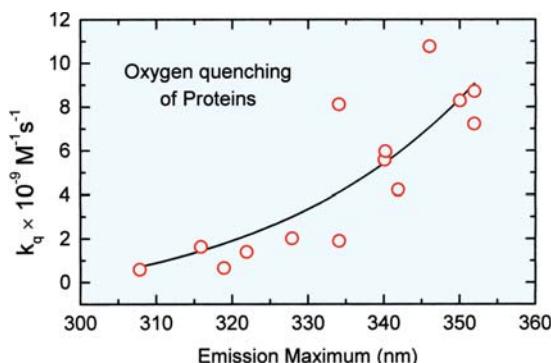


**Figure 16.34.** Correlation of emission maxima of multi-tryptophan proteins with the oxygen bimolecular quenching constants. Data from [107].

regions of proteins. The oxygen bimolecular quenching constants for a number of proteins show weaker correlation with the emission maxima (Figure 16.34). It is known from the x-ray structures of proteins that the interiors are densely packed, similar to crystals of organic molecules, so that there is little room for oxygen within the center of most proteins. Surprisingly, the bimolecular quenching constants for oxygen are 20 to 50% of the value for tryptophan in water (near  $1 \times 10^{10} M^{-1} s^{-1}$ ). These results indicate that proteins undergo rapid structural fluctuations that allow the oxygen

molecules to penetrate during the ns excited-state lifetime.<sup>107–109</sup> Structural fluctuations on the ns timescale are consistent with the anisotropy decays of most proteins, which typically show ns or subnanosecond components.<sup>110–111</sup> Acrylamide and iodide are less effective quenchers than oxygen because it is energetically unfavorable for them to enter nonpolar regions of proteins. Also, acrylamide is larger than oxygen or iodide, which also plays a role in its more selective quenching.

### 16.6.2. Fractional Accessibility to Quenching in Multi-Tryptophan Proteins

The selective quenching of surface tryptophan residues suggests the use of quenching to resolve the contributions of surface and buried tryptophans to the total fluorescence of a protein.<sup>112–113</sup> One example is apomyoglobin, which contains two tryptophan residues (Figure 16.35). Apomyoglobin refers to myoglobin without the heme group, which quenches tryptophan fluorescence by RET. In this protein W7 appears to be exposed to the aqueous phase, and W14 appears to be buried among the helices. The Stern-Volmer plots for quenching by iodide or trichloroethanol (TCE) both show downward curvature, indicating that some fraction of the total emission may be inaccessible to quenching (Figure 16.36).

The fraction of accessible fluorescence ( $f_a$ ) can be obtained from a modified Stern-Volmer plot, in which  $F_0/\Delta F$  is plotted versus reciprocal quencher concentration (Section 8.8). The y-intercept represents extrapolation to infinite quencher concentration. Complete quenching is expected for an accessible fluorophore, so the extrapolated value of  $F_0/\Delta F$  is unity. If a portion of the fluorescence is not accessible,  $\Delta F$  is smaller than  $F_0$ , and the intercept ( $f_a^{-1}$ ) is greater than unity. Figure 16.36 shows an intercept near 2, so that about half of the total fluorescence is assessable to quenching.

The fractional accessibility to quenchers can be measured for each emission wavelength (Figure 16.37, lower panel). The fractional accessibility is higher on the long-wavelength side of the emission spectrum. These fractions, when multiplied by the total intensity at each wavelength, yield the emission spectra of the quenched and unquenched components from apomyoglobin (top panel). The higher accessibility at longer wavelengths results in a red-shifted spectrum for the accessible fraction. It seems probable that the accessible and inaccessible components are from W7 and W14, respectively.

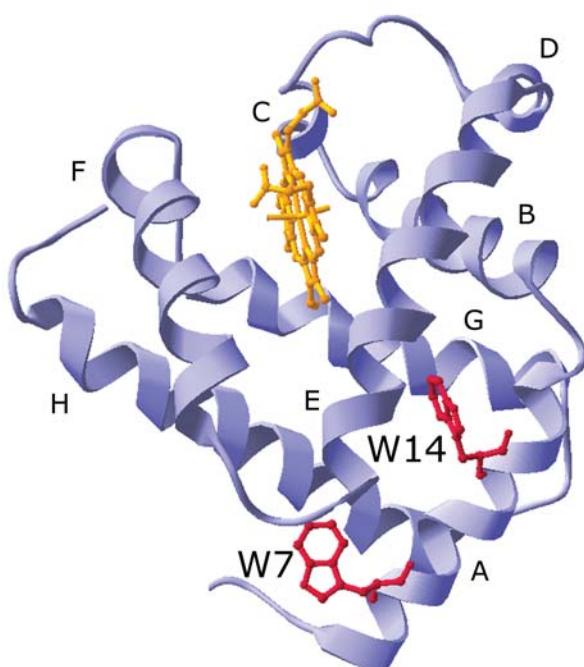


**Figure 16.35.** Ribbon structure of horse myoglobin showing the location of tryptophans 7 and 14. The letters denote the helices.

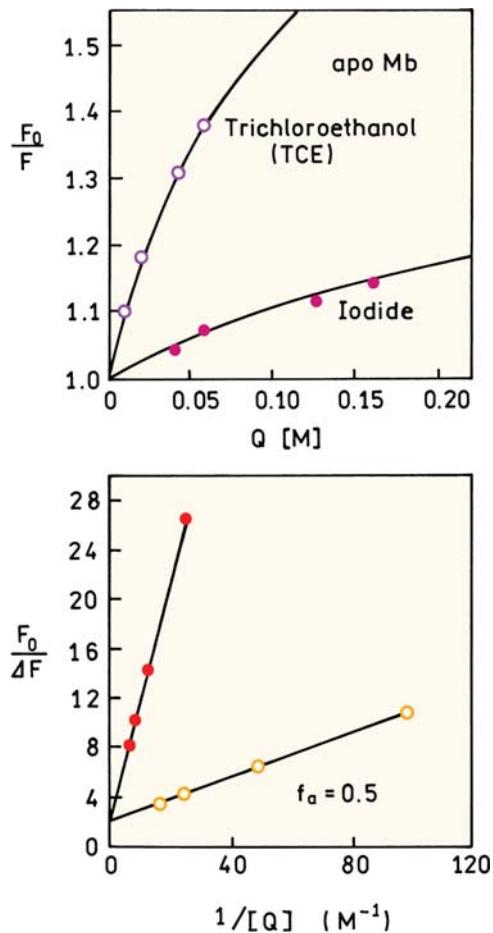


**Figure 16.36.** Stern-Volmer and modified Stern-Volmer plots for apomyoglobin quenching by iodide or trichloroethanol (TCE). The data in the upper panel was reconstructed from the data in the lower panel. Data from [113].

### 16.6.3. Resolution of Emission Spectra by Quenching

Selective quenching of tryptophan residues allows resolution of the emission spectra of the quenched and unquenched components. For apomyoglobin we assumed that some fraction of the emission was completely inaccessible to quenching. A more general procedure allows the emission spectra to be resolved even when both residues are partially accessible to quenching.<sup>114–116</sup> The basic approach is to perform a least-squares fit to the quenching data to recover the quenching constant and fractional intensity at each wavelength ( $\lambda$ ):

$$\frac{F(\lambda)}{F_0} = \sum_i \frac{f_i(\lambda)}{1 + K_i(\lambda)[Q]} \quad (16.4)$$

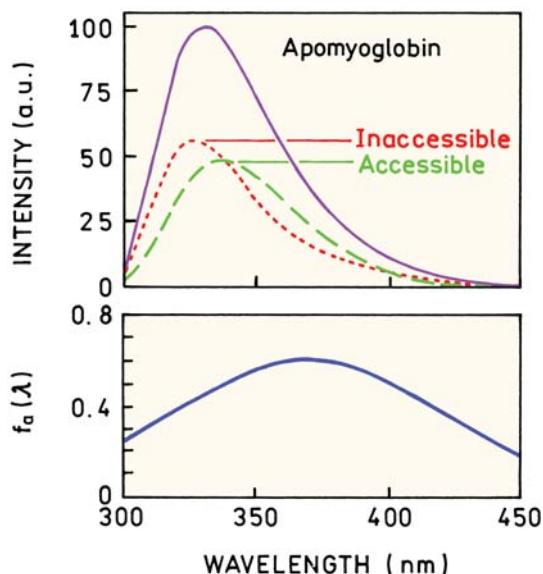


**Figure 16.37.** Emission spectra of apomyoglobin and of the accessible and inaccessible components. The lower panel shows the wavelength-dependent fractional accessibility to quenching. Revised from [113].

In this expression the values of  $f_i(\lambda)$  represent the fraction of the total emission quenchable at wavelength  $\lambda$  with a value  $K_i(\lambda)$  (Section 8.8).

This procedure was applied to a metalloprotease from *S. aureus* that contains two tryptophan residues.<sup>116</sup> For all emission wavelengths the Stern-Volmer plot is curved due to the different accessibilities of each residue (Figure 16.38). The data are fit by least-squares methods to obtain the values of  $K_i(\lambda)$  and  $f_i(\lambda)$ . Similar data are collected for a range of emission wavelengths. These data can be used to calculate the emission spectra of each component:

$$F_i(\lambda) = F_0(\lambda)f_i(\lambda) \quad (16.5)$$

where  $F_0(\lambda)$  is the unquenched emission spectrum. For metalloprotease this procedure yielded two well-resolved emission spectra (Figure 16.39).

The use of quenching-resolved spectra may not always be successful. One possible reason for failure would be if a tryptophan residue was not in a unique environment. In this case each tryptophan residue may display more than one emission spectrum, each of which would be quenched to a different extent. Quenching-resolved spectra have been obtained for proteins that contain a single-tryptophan residue.<sup>116–117</sup> These results have been interpreted as due to the protein being present in more than a single conformational

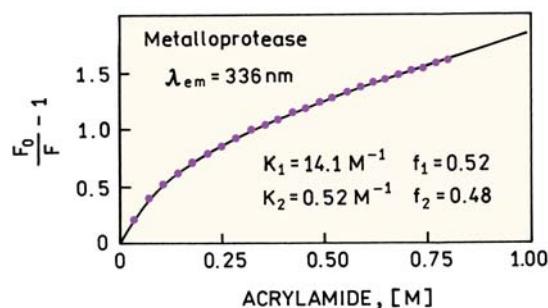


**Figure 16.38.** Stern-Volmer plot for acrylamide quenching of *S. aureus* metalloprotease (dotted). Excitation wavelength was 297 nm and emission was observed at 336 nm. The solid line shows the least-squares fit with parameters  $K_1 = 14.1 \text{ M}^{-1}$ ,  $K_2 = 0.52 \text{ M}^{-1}$ ,  $f_1 = 0.52$ , and  $f_2 = 0.48$ . Revised from [116].

state. A single-tryptophan residue can display a multi-exponential decay, and the decays can depend on wavelength. Hence, there is no a priori reason to assume the residue is quenched with the same quenching constants at all emission wavelengths.

## 16.7. ASSOCIATION REACTION OF PROTEINS

An important use of intrinsic protein fluorescence is to study binding interactions of proteins.<sup>118–120</sup> Such measurements take advantage of the high sensitivity of fluorescence

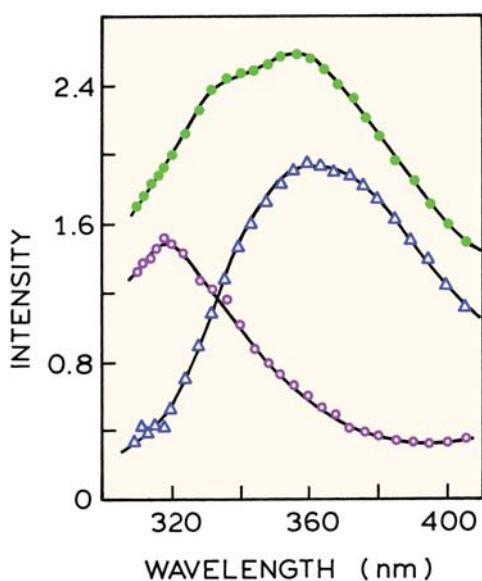


**Figure 16.39.** Resolution of the two tryptophan emission spectra from *S. aureus* metalloprotease. ○, component with  $K_1 = 0.52 \text{ M}^{-1}$ ; Δ, component with  $K_2 = 14.1 \text{ M}^{-1}$ ; ●, steady-state spectrum. Revised from [116].

and the ability to perform measurements on dilute protein solutions. Detection of protein association reactions by fluorescence is made possible by the high sensitivity of tryptophan to its local environment. A change in exposure to solvent or a change in proximity to a quenching group can often change the emission maximum or quantum yield of tryptophan residues.

### 16.7.1. Binding of Calmodulin to a Target Protein

Intrinsic protein fluorescence was used to study binding of calmodulin to a target protein. The target protein was a peptide fragment from a glutamate receptor. Glutamate is the dominant neurotransmitter in the human brain. The neuronal receptor peptide (NRP) contains a single-tryptophan residue. Calmodulin does not contain tryptophan, which allowed emission from the NRP to be observed selectively using 297-nm excitation. The intrinsic tryptophan emission of the NRP was used to study its binding to calmodulin in the absence and presence of calcium. It is frequently assumed that calmodulin does not interact with target proteins until it binds calcium. However, the absence of any interaction in the absence of calcium could result in a slow cellular response to calcium because of the time needed for diffusive encounters to occur. Pre-association of target proteins with calmodulin could increase the response speed to calcium transients.

Emission spectra of the NRP are shown in Figure 16.40. Upon addition of calcium and calmodulin to the NRP there was an increase in intensity and a blue shift of its tryptophan emission,<sup>120</sup> showing that calcium-saturated calmodulin binds to the NRP (lower left). Surprisingly, there was also an increase in intensity and blue shift of the NRP emission with calmodulin in the absence of calcium (upper left), showing that binding occurs without calcium. This result indicated that calmodulin pre-associates with the receptor, presumably to provide a more rapid response to calcium transients.

If calmodulin binds to the receptor without calcium then how does calcium trigger the receptor? This question was partially answered by studies of the N and C domains of calmodulin. The C domain alone was found to interact with the NRP in the absence of calcium (Figure 16.40, upper right). Interaction between the C domain and calmodulin was increased by calcium. The N domain was found to interact with the NRP only in the presence of calcium (middle panels). These results suggest that the C domain is responsible for pre-association and the N domain for signal-

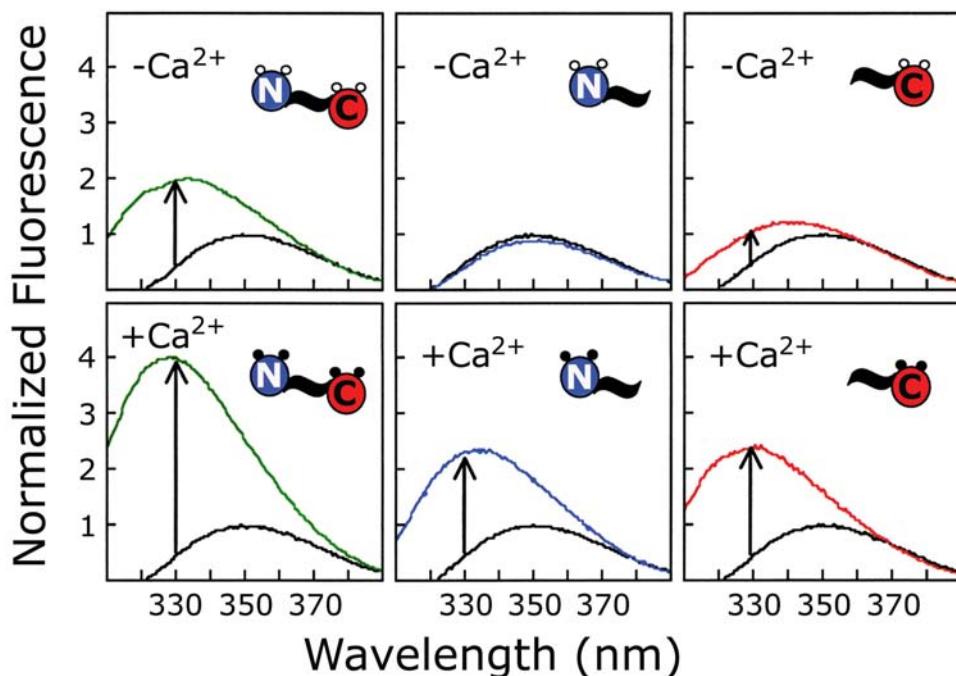


**Figure 16.40.** Emission spectra of a neuronal receptor peptide NRP in the presence of calmodulin and the N and C domains of calmodulin. Excitation was at 297 nm. Revised from [120].

ing. The high sensitivity of tryptophan emission to its local environment can provide detailed information on protein–protein interactions.

#### 16.7.2. Calmodulin: Resolution of the Four Calcium-Binding Sites Using Tryptophan-Containing Mutants

Site-directed mutagenesis allows single-tryptophan residues to be placed at desired locations in the protein. This approach was applied to calmodulin and resulted in an ability to detect binding of calcium to each of the four binding sites. Calmodulin has four binding sites for calcium, but little was known about the sequence of binding and possibility of cooperativity between the four binding sites. Other studies of calcium binding were not adequate to distinguish between various models for  $\text{Ca}^{2+}$  binding. Bulk measurements of binding can reveal only the total amount of bound calcium and do not indicate the sequence of calcium binding.

This problem was solved by the creation of single-tryptophan mutants.<sup>121</sup> Calmodulin contains several tyrosine residues, but it does not contain tryptophan. This allowed the insertion of tryptophan residues into the sequence to

probe various regions of the protein, and the use of these residues to probe local regions of the calmodulin structure. The tryptophan residues were inserted near each of the four  $\text{Ca}^{2+}$  binding sites, one trp residue per mutant. The normalized intensity changes for each tryptophan residue are shown in Figure 16.41. These measurements revealed the sequence of calcium binding to calmodulin, and revealed interactions between the various binding sites. Protein engineering and fluorescence spectroscopy can provide detailed information on the solution behavior of a protein. Similar tryptophan-containing calmodulin mutants were used to study binding of peptides to calmodulin.<sup>122</sup>

#### 16.7.3. Interactions of DNA with Proteins

Intrinsic protein fluorescence can be used to study binding of DNA to proteins.<sup>123–129</sup> These studies typically rely on quenching of intrinsic tryptophan fluorescence by the DNA bases. One example is the single-stranded DNA binding protein (SSB) from *E. coli* (Figure 16.42). This protein is a member of a class of proteins that bind ssDNA with high affinity but low specificity. Proteins that destabilize double-helical DNA are required for DNA replication and repair. SSB is a homotetramer that binds about 70 nucleotides.

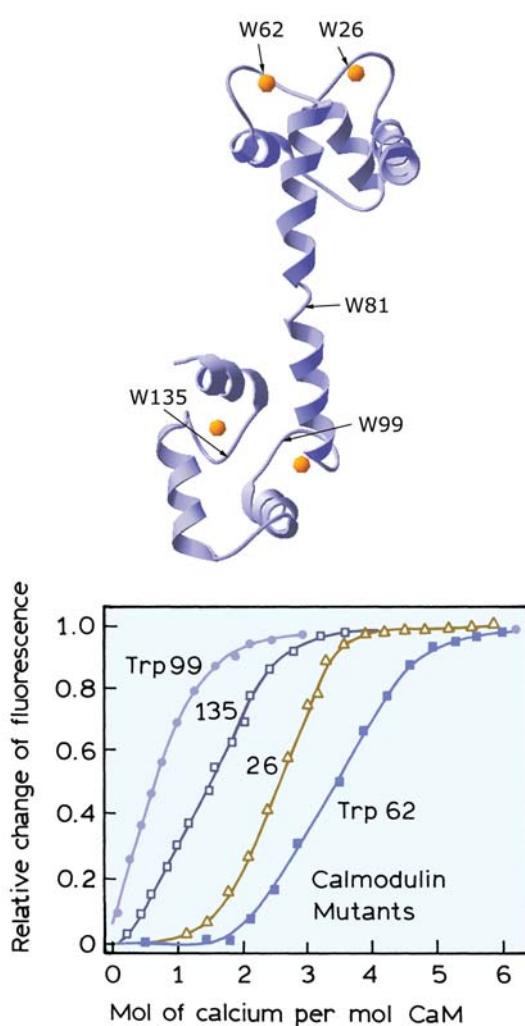


**Figure 16.41.** Relative changes in the fluorescence intensity of Trp 99 (●), Trp 135 (□), Trp 26 (△), and Trp 62 (■) in single-tryptophan mutants of calmodulin with changes in the amount of bound calcium. The arrows show the location of the tryptophan residues and the orange dots are calcium atoms. Reprinted with permission from [121]. Copyright © 1992, American Chemical Society.

DNA is tightly packed in chromatin, but DNA replication occurs rapidly nonetheless. Hence it is of interest to determine the rates of DNA folding around the SSB. This can be accomplished using rapid mixing stopped-flow measurements, while monitoring the intrinsic tryptophan fluorescence of SSB (Figure 16.43). Upon mixing with  $(dT)_{70}$  there is a rapid decrease in the tryptophan emission.<sup>128</sup> By studies with various concentrations of DNA and different lengths of DNA it was possible to determine the rate constants for initial DNA binding and subsequent folding of DNA around the protein. The rates of DNA folding

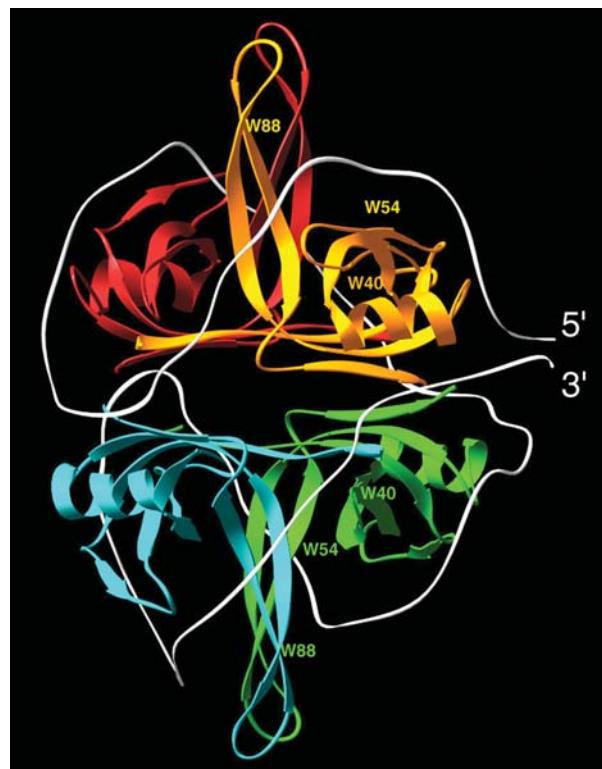


**Figure 16.42.** Ribbon structure for the *E. coli* single-stranded binding protein (SSB) with a bound 70-mer. Figure from [128] and provided by Dr. Alexander Kozlov and Dr. T. Lohman, Washington University, MO.

around the protein were also measured using RET between DNA oligomers labeled with Cy5 and Cy3 at the 5' and 3' ends, respectively. These probes were brought into closer contact when DNA wrapped around SSB (not shown). The changes in RET and intrinsic protein fluorescence occurred on the same timescale, indicating that wrapping of DNA around the protein proceeds very rapidly after binding occurs.

The intensity changes can be used to determine the fraction of the total emission that is quenched by DNA. The Myb oncogene is associated with chromatin and appears to function as a regulator of gene expression. The N-terminal region of this protein, which contains the DNA binding region, consists of three domains:  $R_1$ ,  $R_2$ , and  $R_3$ . The subscripts refer to the domain number, not the number of domains. Each domain contains three highly conserved tryptophan residues, which suggests these residues are involved in binding to DNA.

The intrinsic protein fluorescence of the  $R_2R_3$  fragment of the Myb oncogene is partially quenched by DNA.<sup>129</sup>

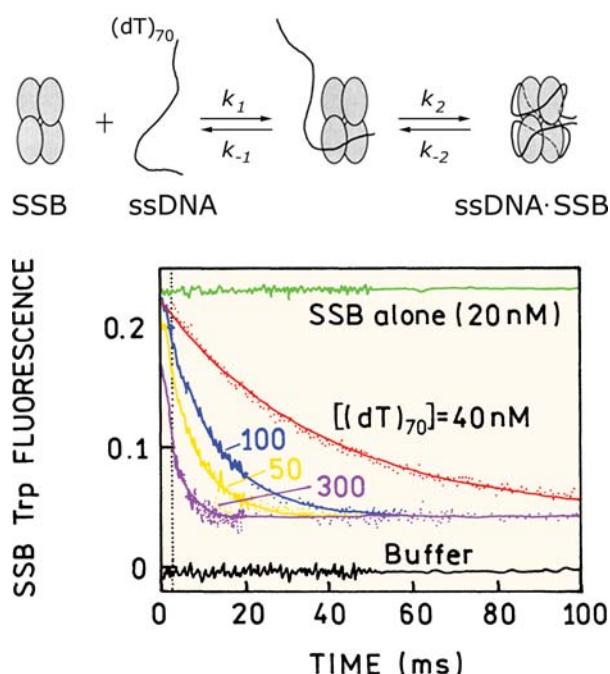


**Figure 16.43.** Stopped-flow intrinsic tryptophan emission of SSB upon mixing with  $(dT)_{70}$ . Revised from [128].

This fragment contains six tyr residues, three in each domain. Addition of a 16-mer results in quenching of the emission of  $R_2R_3$  and a small blue shift in the emission (Figure 16.44). The tryptophan intensities were measured for a number of 16-mer concentrations, and plotted in modified Stern-Volmer format. Extrapolation to high DNA concentrations shows that a fraction of 0.67 of the total intensity was quenched by DNA. Assuming all the tryptophans have the same quantum yield, this result indicates that 2 of the 3 trp residues in each domain are quenched by contact with DNA.

#### 16.8. SPECTRAL PROPERTIES OF GENETICALLY ENGINEERED PROTEINS

Interpretation of intrinsic protein fluorescence is complicated by the presence of multiple-tryptophan residues. When the intrinsic fluorescence of a multi-tryptophan protein is first measured it is not known whether all the trp contributes equally to the emission and the emission maxima of the emitting residues. Site-directed mutagenesis provides an approach to determining the spectral properties of each trp residue. For example, suppose the protein of interest contains two tryptophan residues in the wild-type sequence. One can attempt to use quenching or time-resolved methods

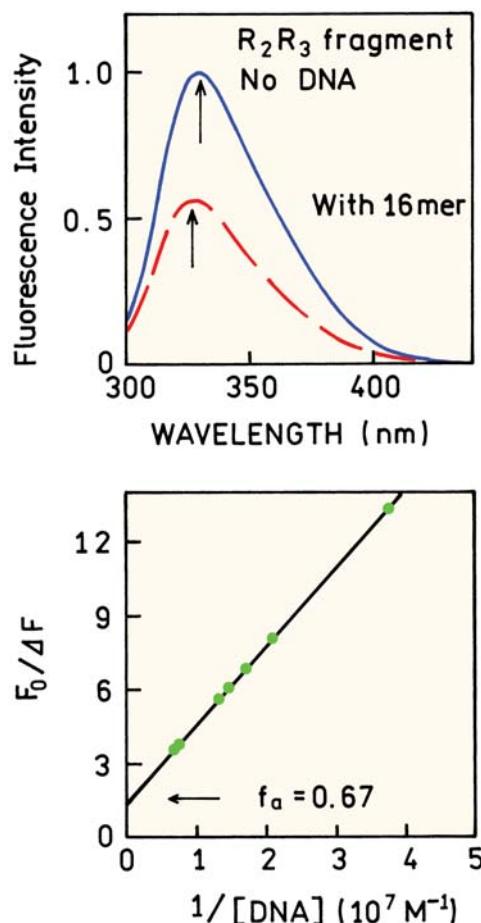


**Figure 16.44.** Emission spectra and modified Stern-Volmer plot for quenching of the tryptophan emission of the  $R_2R_3$  domain of the Myb oncogene by DNA. Revised from [129].

with the wild-type protein to resolve the emission spectra of the two residues. However, success requires that the residues have very different lifetimes or accessibilities to quenchers. Even if the resolution appears to be successful it may not reveal interactions between the two residues. That is, the emission from the wild-type protein may not be the same as the sum of the emission from the two single-tryptophan mutants.

A powerful approach to resolving the contributions of each tryptophan, and the interactions between the tryptophans, is by examination of the two single-tryptophan mutants. Each tryptophan residue is replaced in turn by a similar residue, typically phenylalanine. This approach to resolving protein fluorescence has been used in many laboratories.<sup>130–137</sup> It is not practical to describe all these results. Rather, we have chosen a few representative cases. These examples show simple non-interactive tryptophans and the

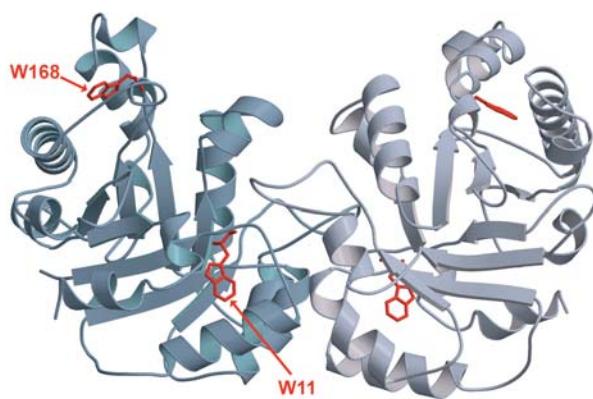


**Figure 16.45.** Structure of triosephosphate isomerase. Courtesy of Dr. Hema Balaram from the Jawaharlal Nehru Center for Advanced Scientific Research, India.

more complex cases in which there is trp-to-trp energy transfer.

#### 16.8.1. Single-Tryptophan Mutants of Triosephosphate Isomerase

Triosephosphate isomerase (TPI) is a protein that catalyzes isomerization of dihydroxyacetone phosphate and glyceraldehyde phosphate. The enzyme from the malarial parasite *Plasmodium falciparum* contains two tryptophan residues, at positions 11 and 168. The enzyme exists as a homodimer with each monomer containing W11 and W168 (Figure 16.45). The monomer structure consists of a central  $\beta$ -sheet surrounded by  $\alpha$ -helices, which is a common structural feature in this class of enzymes. It is difficult to judge the degree of exposure of each residue to water. Depending on the viewing angle, W168 appears to be either exposed to water (left monomer) or shielded from water (right monomer).

The contributions of each tryptophan emission to the total emission of TPI were determined by construction of the single-tryptophan mutants.<sup>138</sup> In each mutant one of the tryptophans was replaced with phenylalanine (F). The W168F mutant contains only W11 and the W11F mutant contains only W168. Emission spectra of the wild-type and mutant proteins are shown in Figure 16.46 (top panel). The emission from W168 is strongly blue shifted with an emission maximum at 321 nm, and the emission maximum of W11 is 332 nm. In this example the emission of the wild-type protein appears to be the sum of the emission from the two single-tryptophan mutants. This result indicates the

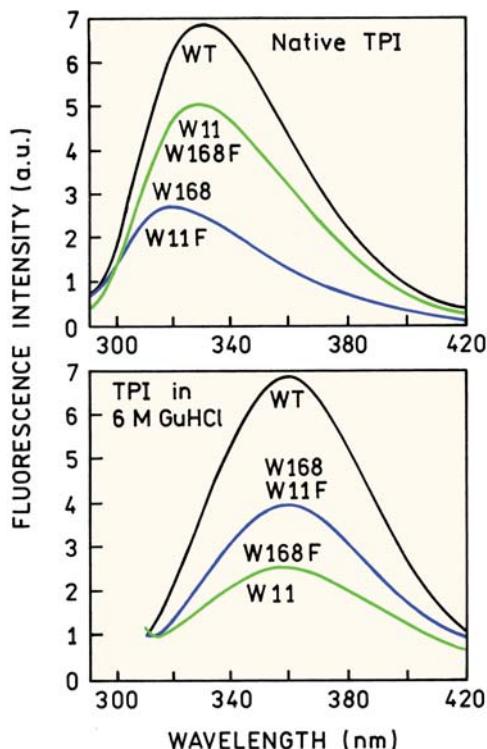


**Figure 16.46.** Emission spectra of wild-type triosephosphate isomerase and the two single-tryptophan mutants. Revised from [138].

tryptophan residues do not interact with each other. Denaturation of the protein in 6 M GuHCl equalized the emission maxima of both tryptophan residues to 357 nm (lower panel). The red shifts upon unfolding show that both residues are shielded from water to some extent in the native protein structure.

The emission spectra of the TPI mutants showed that both tryptophans are sensitive to the protein structure, and that these residues do not interact in the native protein. This result suggests that each tryptophan residue could be used to detect the effects of the trp-to-phe mutation on stability of TPI. Figure 16.47 shows the effects of the denaturant guanidine hydrochloride (GuHCl) on the emission maxima of the wild-type TPI and the two single-tryptophan mutants. The W168F mutant with W11 has the same stability as TPI. In contrast, the W11F mutant with W168 denatures more rapidly in GuHCl, which indicates lower protein stability. Hence, substitution of W11 with a phenylalanine destabilizes the protein. This is a surprising result because the emission spectra (Figure 16.46) showed that W168 is buried more deeply in the protein. One may have expected the buried residue to contribute more to the protein stability.

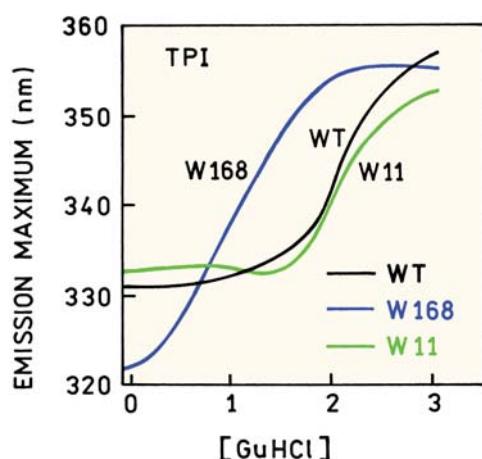


**Figure 16.47.** Effect of guanidium hydrochloride on the wild-type triosephosphate isomerase and the two single-tryptophan mutants. Revised from [138].

### 16.8.2. Barnase: A Three-Tryptophan Protein

Barnase is an extracellular ribonuclease that is often used as a model for protein folding. It is a relatively small protein: 110 amino acids, 12.4 kDa. The wild-type protein contains three tryptophan residues (Figure 16.48), one of which is located close to histidine 18 (H18). Examination of the three single-tryptophan mutants of barnase provides an example of energy transfer between tryptophan residues and the quenching effects of the nearby histidine.<sup>139</sup>

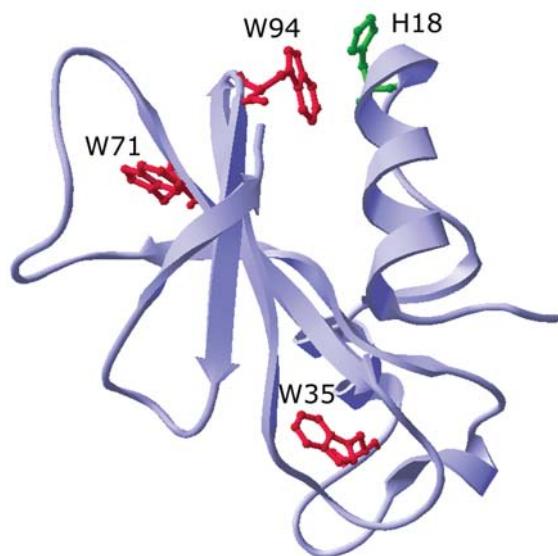


**Figure 16.48.** Structure of barnase showing the positions of the three tryptophan residues and histidine 18.

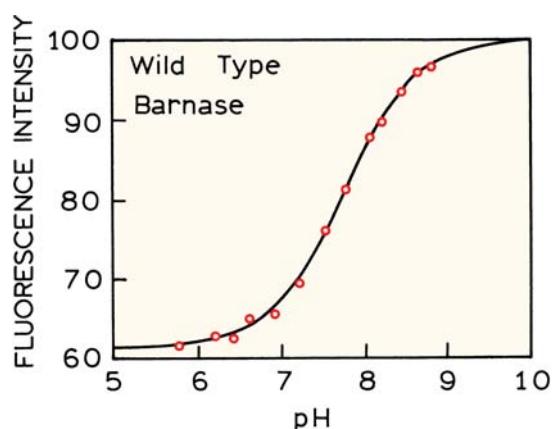


**Figure 16.49.** pH-dependent intensity of the tryptophan emission of wild-type barnase. Excitation, 295 nm; emission, 340 nm. Revised and reprinted with permission from [139]. Copyright © 1991, American Chemical Society.

The emission intensity of wild-type barnase, which contains all three tryptophan residues, increases nearly twofold as the pH is increased from 7 to 8.5 (Figure 16.49). This increase in fluorescence is due to the presence of W94 and the histidine. Only mutants containing both his-18 and trp-94 showed pH dependent intensities. Tryptophan residues are known to be quenched by the protonated form of histidine.<sup>140–141</sup> This is not surprising given the sensitivity of indole to electron deficient molecules.

Emission spectra of barnase and its mutants at pH 5.5 and 9.4 are shown in Figure 16.50. At first glance these spectra appear complex. First consider the contribution of W71. Substitution of W71 with tyrosine (W71Y) has little effect on the spectra. Hence, W71 is weakly fluorescent. It appears that weakly fluorescent or nonfluorescent trp residues is a common occurrence in proteins. Such effects may contribute to the frequent observation of longer-than-expected lifetimes of proteins that display low quantum yields and long apparent natural lifetimes (Figure 16.12).

The effect of H18 is immediately apparent from the glycine mutant H18G. The intensity at pH 5.5 increases 2.6-fold over that for the wild-type protein (Figure 16.50), and the intensity at pH 9.4 increases by about 70%. This result indicates that both the protonated and neutral forms of histidine quenched W94, but that quenching by the electron-deficient protonated form present at pH 5.5 is more efficient quencher.

Surprising results were found when W94 was replaced with leucine in W94L. The intensity of the protein increased even though the number of tryptophan residues decreased. These effects were not due to a structural change

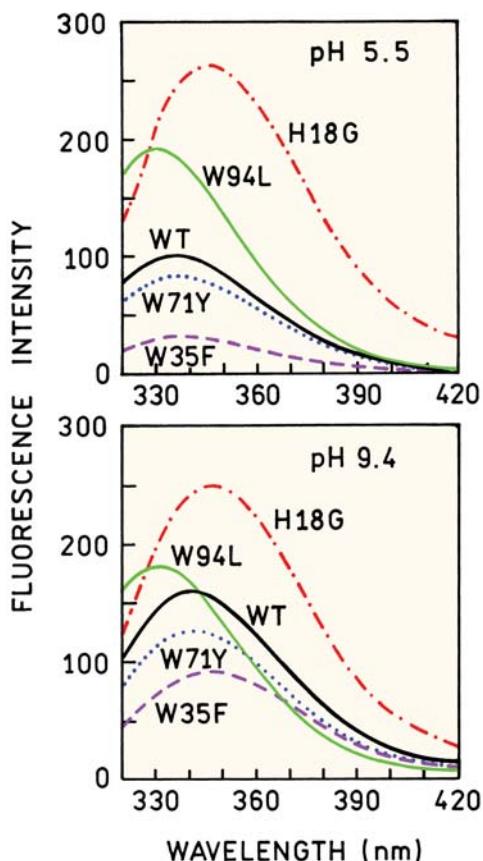


**Figure 16.50.** Fluorescence emission spectra of the wild-type (WT) barnase and its mutants in buffer at pH 5.5 (top), where histidine 18 is protonated and at pH 9.4 where histidine is neutral (bottom). Also shown are the emission spectra of the single-tryptophan mutants at these pH values. Revised and reprinted with permission from [139]. Copyright © 1991, American Chemical Society.

in the protein.<sup>139</sup> The increase in intensity upon removal of W94 is due to energy transfer from the other trp residues to W94. Tryptophan 94 serves as an energy trap for the other trp residues. The emission spectrum of trp94 is red shifted relative to W35 and W71, as seen in the H18G mutants. When W94 is removed (W94L), the blue-shifted emission from the other residues increases since they no longer transfer energy to the quenched residue W94. Examination of the structure (Figure 16.48) suggests that W94 is located on the surface of barnase, whereas W71 and W35 appear to be buried. Tryptophan 94 is red shifted and serves as an acceptor for the other two tryptophan residues. Trp-94 is also quenched by the presence of a nearby histidine residue. Hence, the overall quantum yield of barnase is strongly influenced by just one tryptophan residue. These results for barnase illustrate the complex spectral properties of multi-

tryptophan proteins, and how these properties can be understood by site-directed mutagenesis.

### 16.8.3. Site-Directed Mutagenesis of Tyrosine Proteins

The concept of engineered proteins has also been applied to tyrosine-only proteins.<sup>142-143</sup> One example is  $\Delta^5$ -3-ketosteroid isomerase (KSI), which catalyzes the isomerization of steroids. The protein is a dimer and each subunit contains three tyrosine residues (Y14, Y55, and Y88). The three double tyrosine deletion mutants were prepared by substitution with phenylalanine.<sup>143</sup> One of the residues—Y14—displayed a normal tyrosine emission (Figure 16.51) and a good quantum yield (0.16). The other two mutants (Y55 and Y88) displayed lower quantum yields (0.06 and 0.03, respectively) and long-wavelength tails on the tyrosine spectra. These spectra were interpreted as quenching due to hydrogen-bonding interactions with nearby groups. In this protein, the emission is dominated by one of the tyrosine residues.

## 16.9. PROTEIN FOLDING

The intrinsic tryptophan emission of proteins has proved to be particularly valuable in studies of protein folding.<sup>144-157</sup> It is widely recognized that proteins must fold by a particular pathway because the process is too fast to be explained by a random conformational search. The sensitivity of tryptophan to its local environment usually results in changes in intensity or anisotropy during the folding process. One example (not shown) are kinetic studies of the refolding of

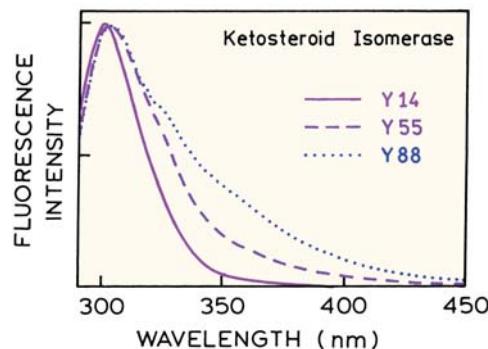


**Figure 16.51.** Normalized emission spectra of the single-tyrosine mutants of  $\Delta^5$ -3-ketosteroid isomerase. The wild-type enzyme has three tyrosine residues per subunit. Y14, Y55F/Y88F (solid); Y55, Y14F/Y88F (dashed); Y88, Y14F/Y55F (dotted). Revised from [143].

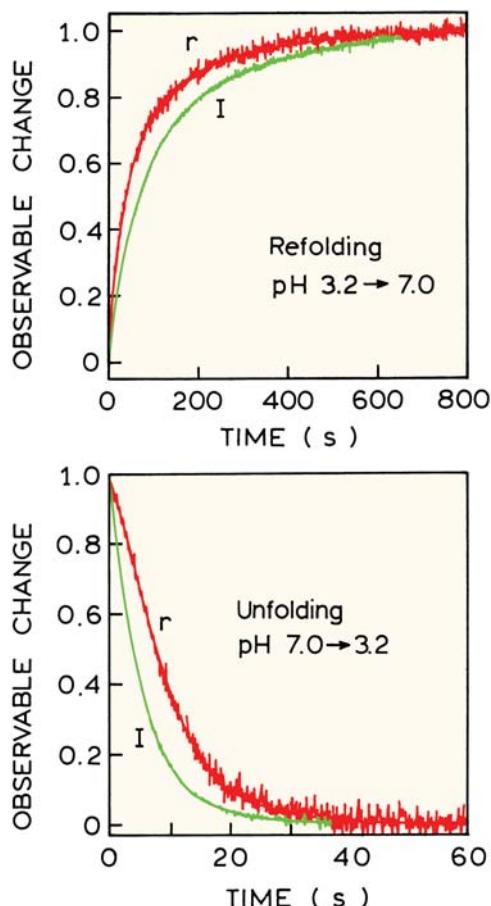


**Figure 16.52.** Time-dependent intensity (*I*) and anisotropy (*r*) of the single tryptophan in staphylococcal nuclease following a pH jump from 3.2 to 7.0 (top) or 7.0 to 3.2 (bottom). Revised from [150].

apo-myoglobin.<sup>151–152</sup> In this case one of the tryptophan residues is quenched as two helices of myoglobin come into contact. This quenching is due to contact of tryptophan 14 on one helix with methionine 131 on another helix. Methionine is known to quench tryptophan fluorescence.<sup>141</sup>

Figure 16.52 shows stopped-flow measurements for a mutant nuclease from *Staphylococcal aureus*. This nuclease contains a single-tryptophan residue at position 140 near the carboxy terminus. This residue is mostly on the surface of the protein, but its intensity and anisotropy are sensitive to protein folding. Folding and unfolding reactions were initiated by jumps in pH from 3.2 to 7.0, and from 7.0 to 3.2, respectively. For a pH jump to 7.0 the intensity increases over several minutes, indicating the intensity is larger in the folded state. A time-dependent decrease was observed for unfolding following a pH jump from 7.0 to 3.2, showing that unfolding proceeds more rapidly than folding.

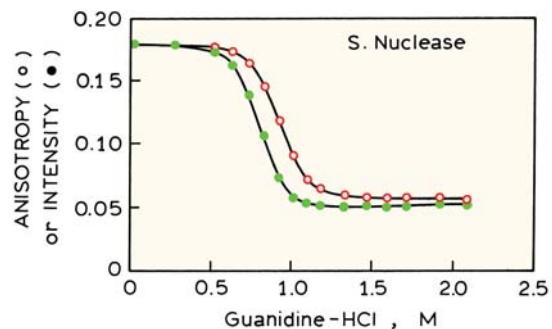


**Figure 16.53.** Unfolding of staphylococcal nuclease as observed by the steady-state intensity (●) or anisotropy (○). From [150].

Protein folding can be followed using fluorescence intensities, anisotropies, or lifetimes. It is important to recognize that the percent completion of the unfolding transitions may not be accurately represented by the percentage change in the lifetimes or anisotropies.<sup>153</sup> Suppose that the intensity and anisotropy both decrease when the protein is unfolded by denaturant. Then the folding transition seen by the anisotropy data will be weighted more toward the folded state than the unfolded state (Figure 16.53). A decrease in intensity was seen for unfolding of the staphylococcal nuclease. When the intensity decrease indicates unfolding is half complete, the anisotropy change is less than 50% because of the larger contribution of the folded state to the steady-state anisotropy. This is why the folding transition observed from the anisotropy data precedes that observed from the intensities (Figure 16.52, top). When performing measurements of protein folding it is important to remember that the anisotropy and mean lifetime are intensity-weighted parameters. For an intensity-weighted parameter the measured value depends on the relative fluorescence intensity of each state, as well as the fraction of the protein present in each state.

### 16.9.1. Protein Engineering of Mutant Ribonuclease for Folding Experiments

Since the classic refolding experiments of Christian Anfinsen on ribonuclease A (RNase A), this protein has been a favorite model for studies of protein folding. RNase A normally contains only tyrosine residues and no tryptophan. In order to create a unique probe to study folding,<sup>158</sup> a single-tryptophan residue was inserted at position 92. This position was chosen because, in the wild-type protein, the tyrosine residue at position 92 is hydrogen bonded to aspartate 38 (D38). This suggested the possibility that a tryptophan

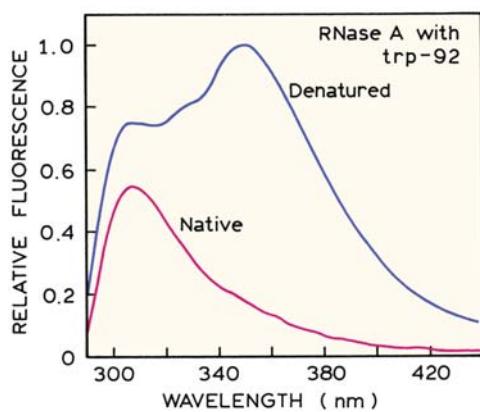


**Figure 16.54.** Emission spectra of the trp-92 mutant of RNase A in the native and denatured state at pH 5. Excitation at 280 nm. Revised from [158].

residue inserted at position 92 would be quenched by the nearby carboxyl group in the folded state.

Emission spectra of RNase A with the W92 insertion are shown in Figure 16.54. The excitation wavelength was 280 nm, so that both tyrosine and tryptophan are excited. The surprising feature of these spectra is that the relative tyrosine contribution is highest in the native protein. This is

the opposite of what is observed for most proteins. This unusual result occurs because W92 is quenched in the folded state by the nearby aspartate residue. The large amount of quenching by D38 suggests the carboxyl group is in the protonated form, which is known to quench tryptophan.

### 16.9.2. Folding of Lactate Dehydrogenase

In order to determine the folding pathway it is important to examine multiple positions in a protein.<sup>149,159</sup> This is possible using mutant proteins. One example is the folding-unfolding transition of lactate dehydrogenase from *Bacillus stearothermophilus*. This protein typically contains three tryptophans that were replaced by tyrosines. Nine single-tryptophan mutants were produced with the residues dispersed throughout the protein matrix (Figure 16.55). These mutant proteins were studied in increasing concentrations of guanidium hydrochloride. Three of the nine unfolding curves are shown (Figure 16.56). The unfolding transitions occur at different denaturant concentrations for each of the

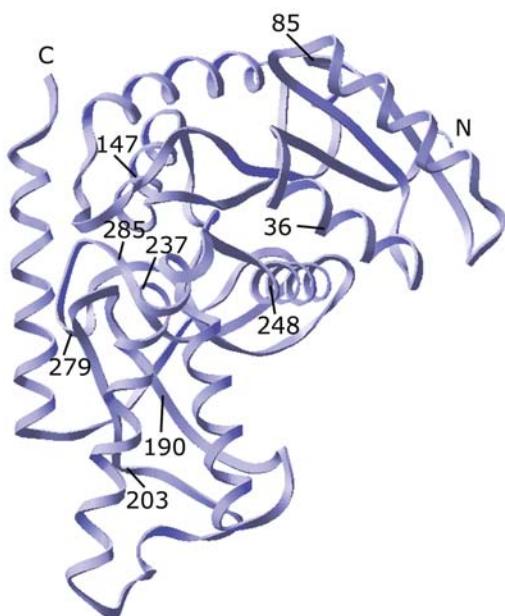


**Figure 16.55.** Positions of tryptophan probes in the lactate dehydrogenase subunit from *B. stearothermophilus*. The backbone of the protein is shown as a ribbon, and the positions of each single change of tyrosine to tryptophan are indicated by the residue number. Reprinted with permission from [149]. Copyright © 1991, American Chemical Society.

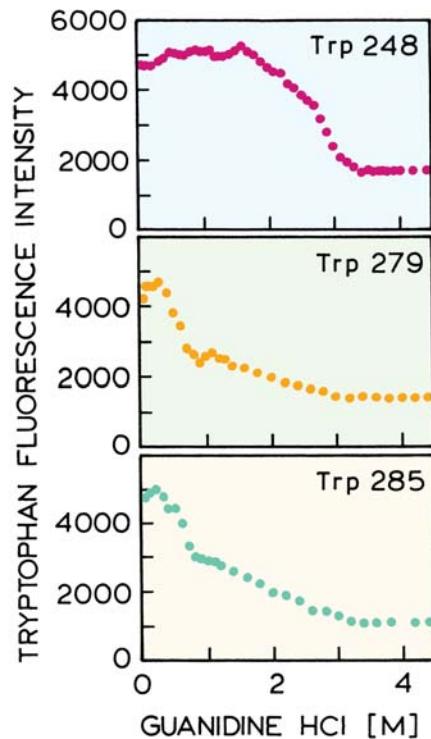


**Figure 16.56.** Equilibrium unfolding of a single-tryptophan mutants of lactate dehydrogenase monitored by tryptophan fluorescence intensity. Tryptophan fluorescence was excited at 295 nm and measured at 345 nm. Revised and reprinted with permission from [149]. Copyright © 1991, American Chemical Society.

three residues. For instance, the structure surrounding W248 persists to higher guanidium concentrations than the structure around residues W279 and W285. From such data it is possible to reconstruct which regions of the protein are more stable, and which are first disrupted during protein unfolding.

### 16.9.3. Folding Pathway of CRABPI

The folding pathway and kinetics can be studied using mutant proteins.<sup>160–161</sup> This was accomplished using cellular retinoic acid binding protein I (CRABPI). This protein has three tryptophan residues at positions 7, 87, and 109 (Figure 16.57). In the native state the emission spectra are strongly dependent on the excitation wavelength (not shown). This occurs because each of the tryptophan

residues are present in different environments, and the absorption and emission spectra of the residues depend on the local environment. When the protein is denatured, the emission spectra becomes independent of the excitation wavelength because the three tryptophan residues are all in a similar environment.

CRABPI mutants were used to study refolding of the denatured protein. This was accomplished by initially denaturing the protein in urea. The urea was then rapidly diluted in a stopped-flow instrument, followed by measurement of the tryptophan emission (Figure 16.57). These traces show that the region surrounding W7 folds most rapidly, followed by folding of the regions around W87 and W109, which occurs several-fold more slowly.

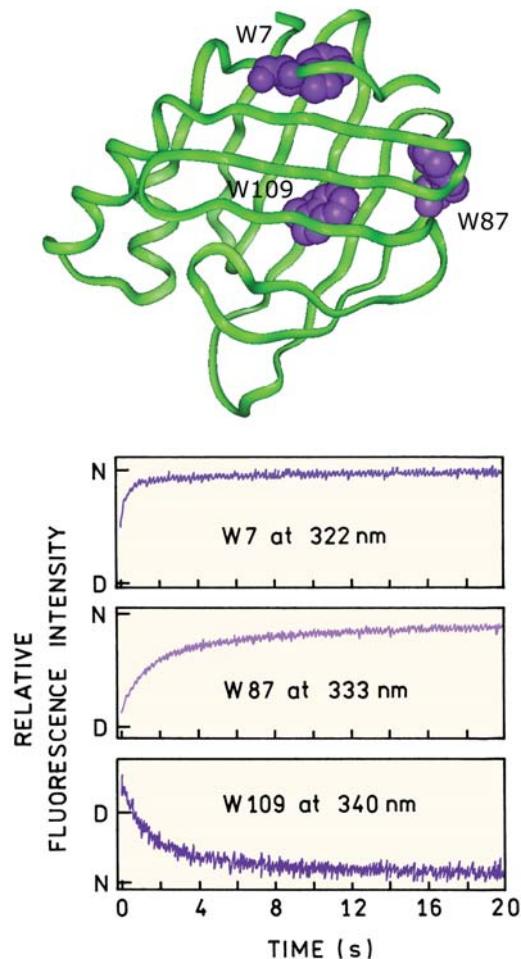


**Figure 16.57.** Structure (top) and refolding kinetics (bottom) of the three single-tryptophan mutants of CRABPI. Courtesy of Dr. Lila M. Giersch from the University of Massachusetts.

### 16.10. PROTEIN STRUCTURE AND TRYPTOPHAN EMISSION

Numerous protein structures are known and it is now becoming possible to correlate the environment around the tryptophan residues with their spectral properties. One example is human antithrombin (Figure 16.58). Human antithrombin (AT) responds to heparin with a 200- to 300-fold increase in the rate of inhibition of clotting factor Xa. Wild-type AT contains four tryptophan residues. The contri-

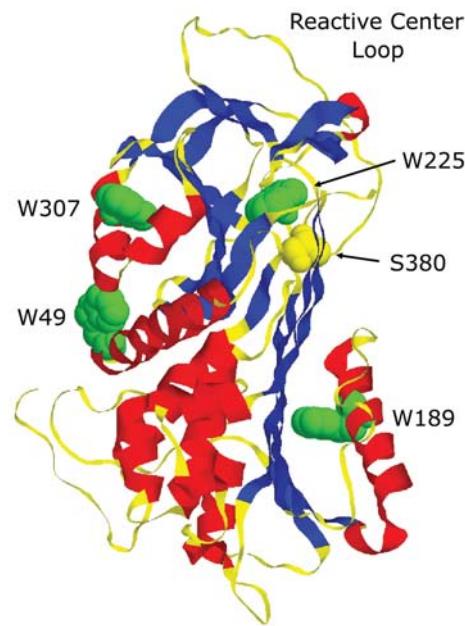


**Figure 16.58.** Structure of human antithrombin showing the four tryptophan residues and serine residue present in the wild-type protein. Courtesy of Dr. Peter G. W. Gettins from the University of Illinois.

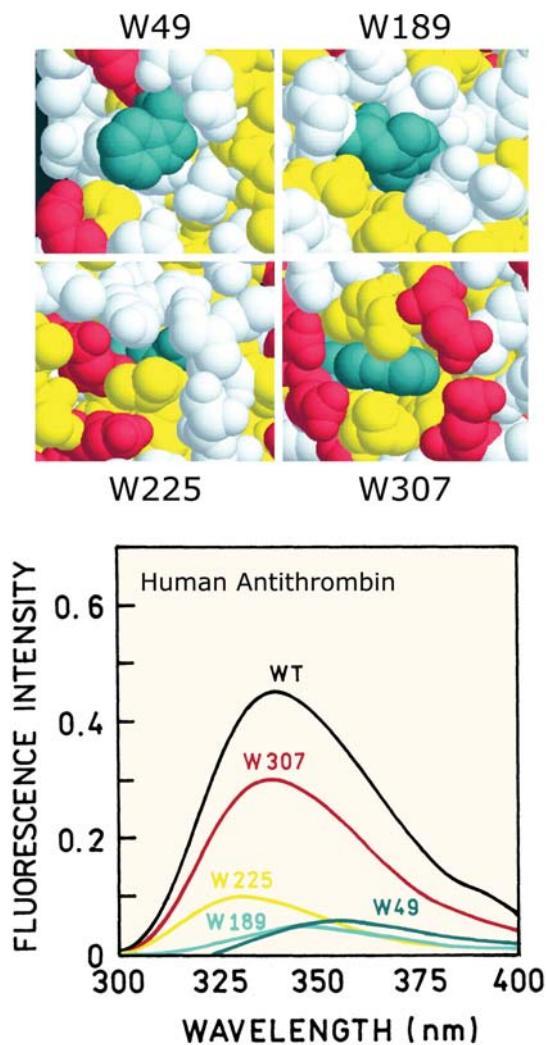


**Figure 16.59.** Emission spectra and local environment of each tryptophan residue in human antithrombin. Tryptophan is blue, acidic residues are red, hydrophobic residues are yellow and other residues are white. Revised from [162].

butions of each tryptophan to the total emission was determined indirectly using mutants, with a single tryptophan being substituted with phenylalanine.<sup>162</sup> Hence, each mutant protein contained three tryptophan residues. Since only a single mutation occurred in each protein it was more likely that AT retained its native structure than if more of the tryptophan residues were removed.

Figure 16.59 show the emission spectra recovered for each tryptophan residue in AT. These were not recorded directly but were calculated from the spectra of the mutants with three tryptophan residues. Also shown is a closeup image of each tryptophan residue as seen from outside the

protein. The most exposed residue W49 has the longest-wavelength emission maximum, and the most buried residue W225 has the most blue-shifted emission. While this result may seem obvious it is only recently that such correlations of a detailed three-dimensional structure with emission spectra have been published.

Another example of correlating the structure and solvent exposure to the tryptophan emission maxima is shown in Figure 16.60. Adrenodoxin (Adx) is a 14-kD single-chain protein that plays a role in electron transport. Wild-type Adx does not contain any tryptophan residues, but contains one tyrosine and four phenylalanine residues (Figure 16.60). These aromatic residues were substituted one by one with tryptophan.<sup>163</sup> The closeup view of W11 shows it is buried in the protein and the closeup view of W82 shows it is on the surface of the protein. The emission spectra of these two mutants (Figure 16.61) correlate with the visual degree of exposure of each residue. The acrylamide quenching constants also correlate with the degree of exposure seen in Figure 16.60.

### 16.10.1. Tryptophan Spectral Properties and Structural Motifs

Intrinsic protein fluorescence with site-directed mutagenesis provides an opportunity to correlate the spectral properties of tryptophan with its location in a structural motif.<sup>164–167</sup> Such experiments can also provide a test of the similarity of a protein structure in solution and in a crystal. This type of experiment was performed using tear lipocalin (TL). This protein is found in tears. TL binds a wide range of hydrophobic molecules such as fatty acids, cholesterol, and phospholipids. The structure of lipocalin shows regions of  $\alpha$ -helix and  $\beta$ -sheet, and regions of undefined structure (Figure 16.62). Wild-type lipocalin contains a single-tryptophan residue that was removed by making the W17Y mutant. Then about 150 mutant proteins were made with a single-tryptophan residue inserted sequentially along the sequence.<sup>166–167</sup>

Figure 16.63 shows the emission spectra of the mutants with tryptophan at positions 99 to 105. The emission maxima shift from shorter to longer wavelengths as the tryptophan is moved by one position along the peptide chain. Such an oscillating behavior is expected for a  $\beta$ -sheet structure. Lipocalin contains a  $\beta$ -sheet in this region. These mutant proteins were also analyzed using acrylamide quenching. The extents of quenching also oscillated with

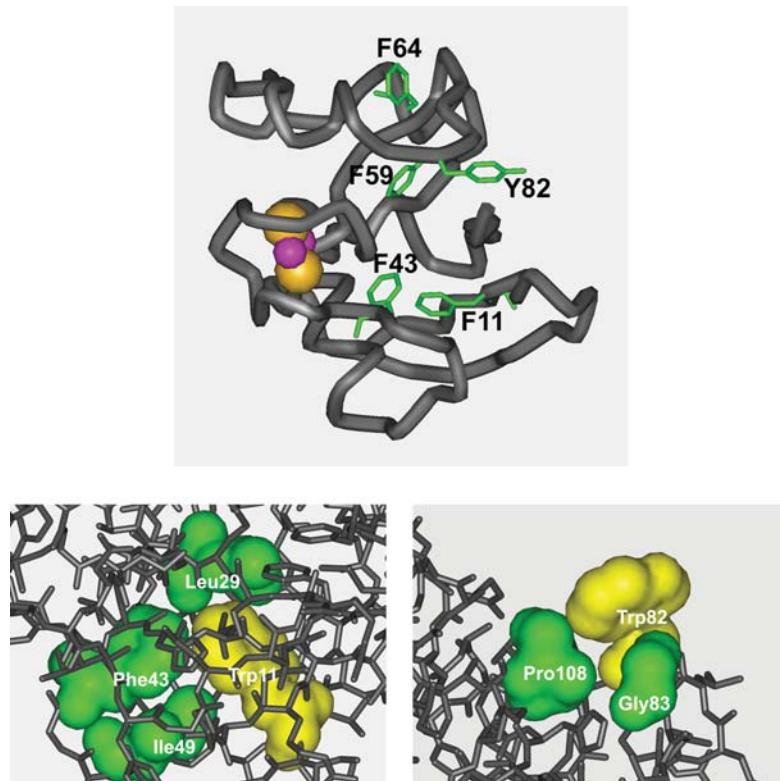


**Figure 16.60.** Structure of bovine adrenodoxin (top) and closeup views of W11 and W82 in the mutant proteins. Courtesy of Dr. Rita Bernhardt from Saarlandes University, Germany.

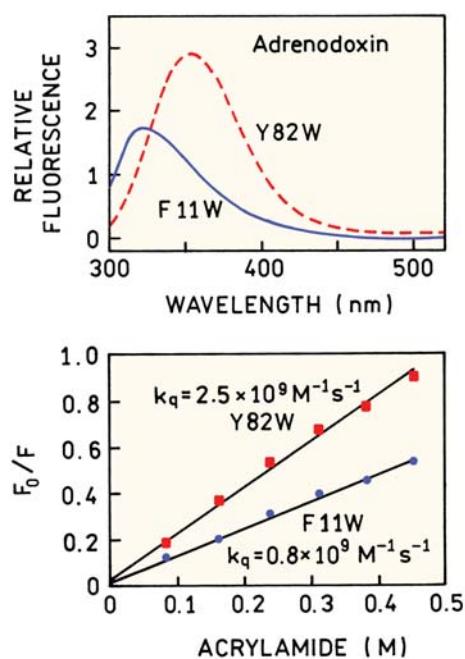


**Figure 16.61.** Emission spectra and acrylamide Stern-Volmer plots for adrenodoxin mutants F11W and Y82W. Revised from [163].

each step along the sequence (Figure 16.64). Hence, residues from positions 94 to 105 are alternately exposed or shielded from the solvent.

Figure 16.65 shows a summary of the tryptophan emission maxima for about 150 mutants. Also indicated are regions of  $\alpha$ -helical and  $\beta$ -sheet structure. In  $\beta$ -sheet regions the emission maxima oscillate with each step along the sequence. For the  $\alpha$ -helical region the emission maxima oscillates with a periodicity of about 3.6 residues per cycle. These data showed a close correlation between tryptophan emission and the x-ray structures of lipocalin.

### 16.11. TRYPTOPHAN ANALOGUES

**Advanced Topic**

For calmodulin and other tyrosine-only proteins a genetically inserted tryptophan residue can serve as a useful probe. However, most proteins contain several tryptophan residues that must all be removed to selectively observe the inserted tryptophan. It is useful to have tryptophan analogues that could be selectively observed in the presence of tryptophan-containing proteins. This can be accomplished



**Figure 16.62.** Structure of tear lipocalin. Red indicates  $\alpha$ -helical structure, green is  $\beta$ -sheet and grey is undefined structure. Courtesy of Dr. Ben J. Glasgow from the University of California, Los Angeles.

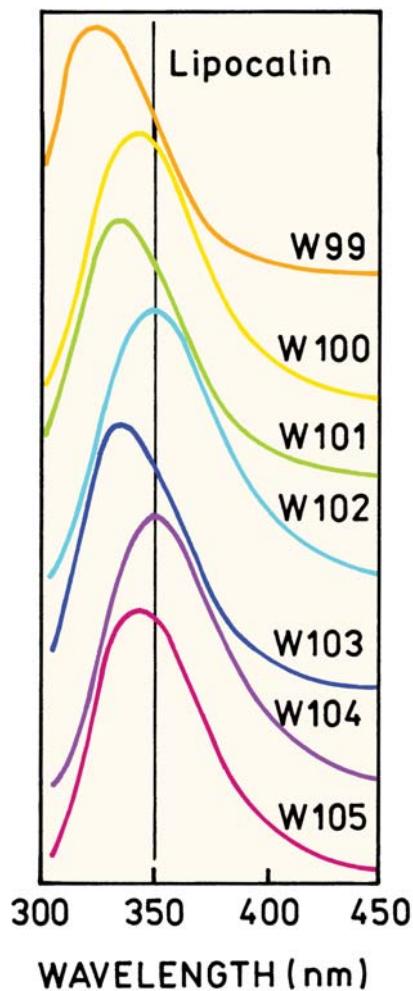


**Figure 16.63.** Emission spectra of tear lipocalin with single-tryptophan insertions. Revised from [166].

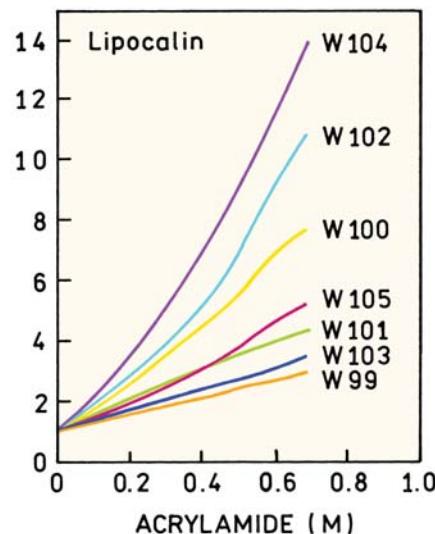


**Figure 16.64.** Acrylamide quenching of lipocalin with single-tryptophan insertions. Revised from [166].

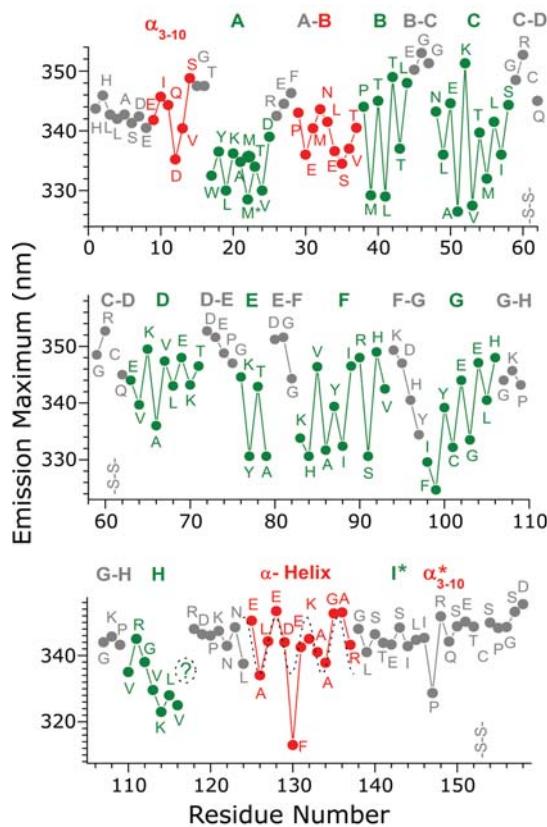


**Figure 16.65.** Emission maxima of lipocalin with single-tryptophan insertions. The letters indicate the amino acid in the wild-type protein. Red indicates  $\alpha$ -helix, green indicates  $\beta$ -sheet, and grey indicates undefined structure. Courtesy of Dr. Ben J. Glasgow from the University of California, Los Angeles.

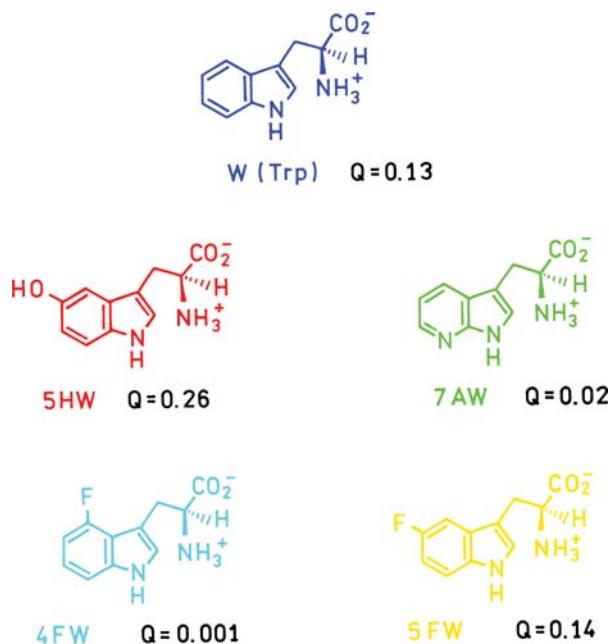


**Figure 16.66.** Structures of tryptophan analogues. The numbers under the structures are the quantum yields in neutral buffer [168].

using tryptophan or amino-acid analogues that absorb at longer wavelengths than tryptophan. These analogues must be inserted into the protein sequence. This can be accomplished in three ways. The entire protein can be synthesized

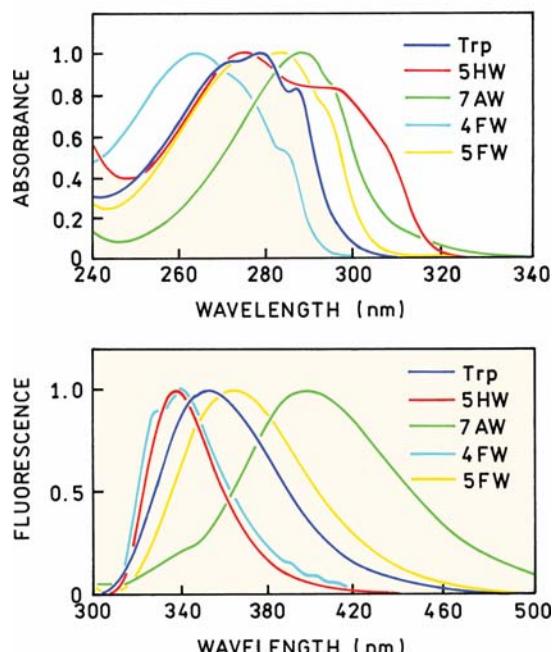


**Figure 16.67.** Absorption (top) and emission spectra (bottom) of tryptophan analogues. Revised from [168].

de novo. However, this approach is limited to small peptides and proteins that will fold spontaneously after synthesis. The second approach is by incorporation into protein grown in bacteria or a cell-free system. This is typically done using tryptophan auxotrophs, which cannot synthesize their own tryptophan. The amino-acid analogue is chemically attached to the tRNA, which is then added to the sample during protein synthesis. The inserted amino acids are typically selected to have a structure similar to tryptophan. The third and most elegant approach is modification of the genetic code and protein synthesis machinery to include a new amino acid.

### 16.11.1. Tryptophan Analogues

A group of tryptophan analogues have been synthesized and incorporated into proteins using tryptophan auxotrophs<sup>168–181</sup> (Figure 16.66). These analogues were designed to retain a size close to tryptophan itself. Except for 4-fluorotryptophan (4FW) these analogues absorb at longer wavelengths than tryptophan (Figure 16.67).

The spectral properties of 5HW and 7AW are different from tryptophan.<sup>178</sup> In water, 5HW displays a higher quantum yield than tryptophan (0.275 for 5HW versus 0.13 for W). 5HW is less sensitive to solvent polarity than tryptophan, and displays an emission maximum near 339 nm (Figure 16.67). The quantum yield of 7AW is highly dependent on solvent polarity and decreases upon contact with water.<sup>182</sup> In water its quantum yield is low, near 0.017, with an emission maximum near 403 nm. This property of 7AW is somewhat problematic. The use of 7AW was originally proposed as an alternative to tryptophan because 7AW was thought to display a simple single exponential decay.<sup>183–184</sup> Unfortunately, 7AW and azaindole display complex decay kinetics due to the presence of several solvated states.<sup>185–187</sup> A non-exponential decay has also been observed for an octapeptide that contains a 7AW residue.<sup>188</sup> 7AW is a useful tryptophan analogue, but it can display complex decay kinetics.

These tryptophan analogues have been incorporated into a number of proteins. One example is substitution of 5HW and 7AW for the single-tryptophan residue in staphylococcal nuclease (Figure 16.68). In this case the emission maxima of tryptophan and 5HW are similar. The advantages of 5HW and 7AW can be seen by their use in studies of more complex biochemical mixtures. 5HW was used to replace the tyrosine residue in insulin. This allowed the fluorescence of 5HW-insulin to be used to study its binding to

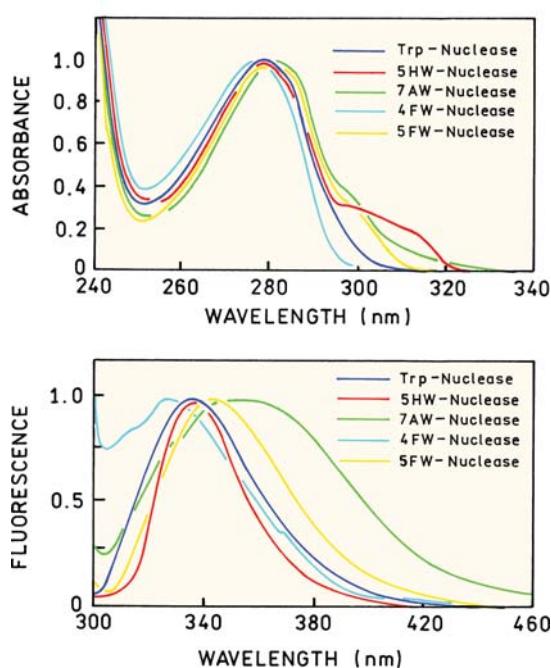


**Figure 16.68.** Absorption and emission spectra of wild-type staphylococcal nuclease (W140) and mutant proteins when W140 is replaced with a tryptophan analogue. Revised from [168].

the insulin receptor.<sup>179</sup> Such studies would not be possible using the tyrosine fluorescence of insulin because this emission is masked by the tryptophan emission of the insulin receptor protein. 5HW has proven valuable in measuring an antigen–antibody association.<sup>173</sup> 5HW was incorporated into the calcium-binding protein oncomodulin. Binding of

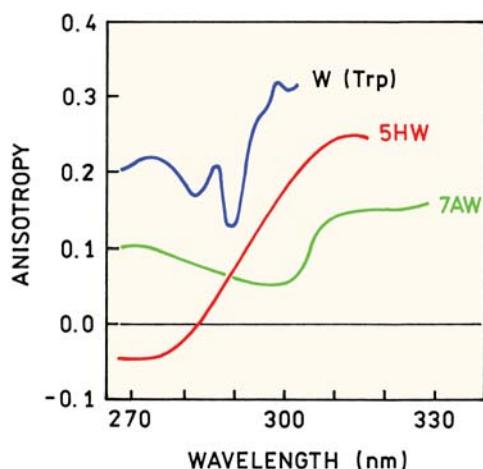


**Figure 16.69.** Low-temperature excitation anisotropy spectra of tryptophan, 5HW, and 7AW in 50% glycerol-phosphate buffer, 77°K. Revised and reprinted with permission from [178]. Copyright © 1997, Cambridge University Press.

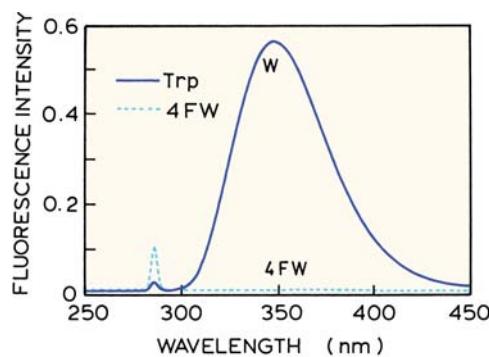


**Figure 16.70.** Relative fluorescence spectra in aqueous solution of tryptophan (solid) and 4-fluorotryptophan (dashed) at 25°C and 285-nm excitation. Revised from [189].

this protein to antibodies could be detected even though the antibody possessed numerous tryptophan residues.

These tryptophan analogues can be used to study protein association reactions, which are often studied using anisotropy measurements. For these purposes it is valuable to know the excitation anisotropy spectra. The anisotropy of both analogues is lower than that of tryptophan itself (Figure 16.69). The low anisotropy of 7AW is another indication of its complex spectral properties.

Another useful tryptophan analogue is 4-fluorotryptophan (4FW). This analogue is useful because it has a similar size and shape as tryptophan, but is almost nonfluorescent (Figure 16.70).<sup>189</sup> This analogue provides a means to eliminate the emission from a tryptophan while retaining almost the same size and shape.

### 16.11.2. Genetically Inserted Amino-Acid Analogues

During the past several years, a new method appeared to incorporating non-natural amino acids into proteins. This is accomplished by identifying a unique tRNA and aminoacyl-tRNA synthetase that will act independently of the other tRNAs and other enzymes.<sup>190–195</sup> In some cases an unused three-base codon is used, and in other cases a unique four-base codon is used.<sup>196–198</sup> This approach is general and can introduce a variety of amino-acid analogues, some of which are shown in Figure 16.71.

This approach was used to introduce amino-acid analogues into streptavidin.<sup>199–200</sup> Figure 16.72 shows the structure of a single subunit of streptavidin showing the portion of the mchAla or the 2,6-dnsAF analogues. These amino-acid analogues can be excited at wavelengths longer than

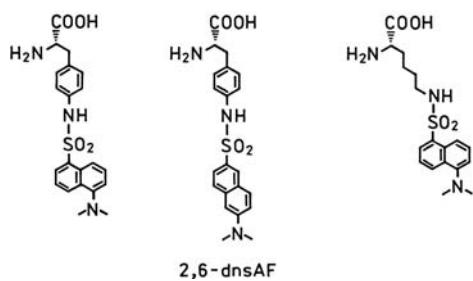
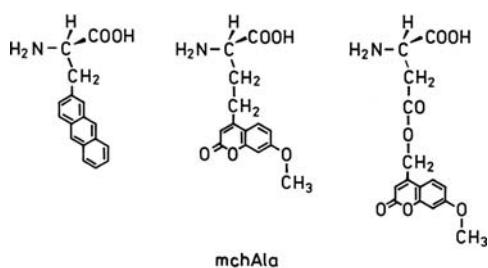


**Figure 16.71.** Amino-acid analogues inserted using a modified genetic code. From [196–200].

320 nm so that intrinsic tryptophans do not interfere with this probe. The mutant streptavidin with mchAla showed a change in emission intensity upon binding biotin (Figure 16.73). Streptavidin was also synthesized with the anthracene-like amino acid, yielding an unusual protein with the emission of anthracene. It seems probable that these methods for synthesis of labeled proteins will become more widely used as the methodology becomes more available.

### 16.12. THE CHALLENGE OF PROTEIN FLUORESCENCE

The intrinsic fluorescence of proteins represents a complex spectroscopic challenge. At the initial level one has to deal with multiple fluorophores with overlapping absorption and emission spectra. The presence of multiple fluorophores is itself a significant challenge. However, the actual situation is still more complex. The dominant fluorophore tryptophan displays complex spectral properties due to the presence of two overlapping electronic states. It is now accepted that

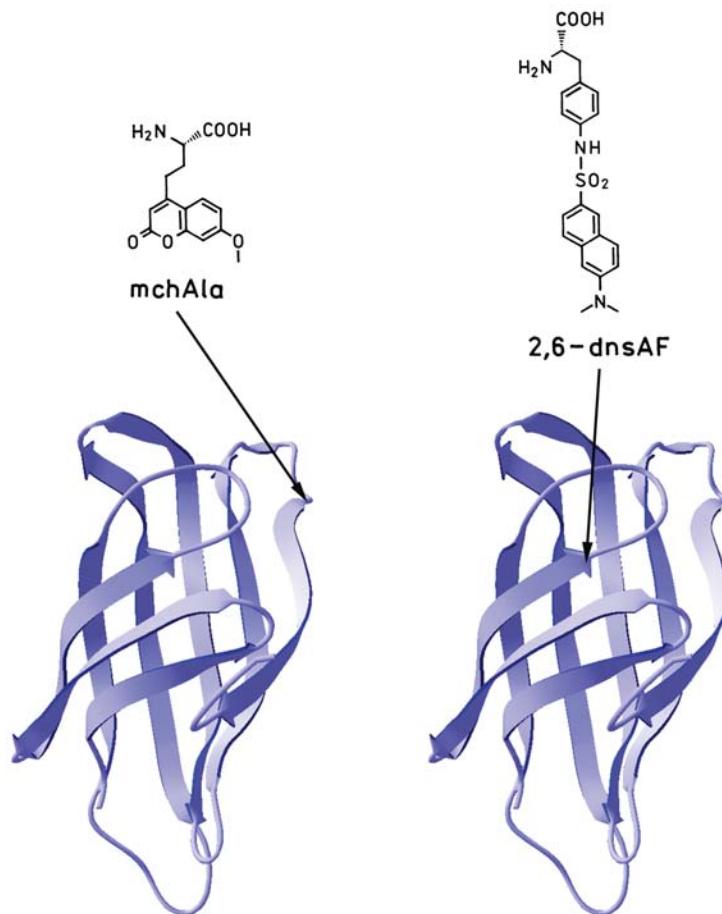


**Figure 16.72.** Structures of streptavidin containing mchAla at position 120 or streptavidin with 2,6-dnsAF at position 44. From [199–200].

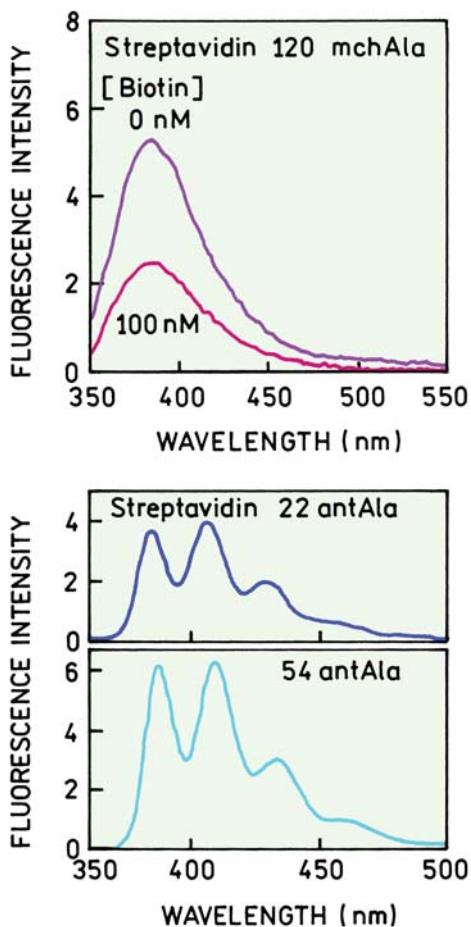


**Figure 16.73.** Emission spectra of streptavidin containing amino-acid analogue. Revised from [199]. Insert shows structure of streptavidin containing mchAla (red) with bound biotin (purple).

even for single-tryptophan proteins the emission often contains multiple spectral contributions due to either multiple conformations or the intrinsic heterogeneity of tryptophan itself. Tryptophan is uniquely sensitive to a variety of quenchers, many of which are present in proteins. Tryptophan is also sensitive to quenching by nearby peptide bonds. Small motions of the amino-acid side chains or backbone can apparently result in changes in tryptophan emission, and some of these motions may occur during the excited-state lifetime. And, finally, the fluorescent amino acids in proteins can interact by energy transfer. In some cases a quenched tryptophan residue can serve as a trap for normally fluorescent residues. Such effects will be highly sensitive to the conformation of the proteins and relative orientation of the fluorescent amino acids.

Given the complexity of tryptophan fluorescence, it is not surprising that the details remained elusive from studies

of multi-tryptophan proteins. It was recognized that tryptophan could be quenched by nearby groups and that energy transfer could occur. However, it was not until the availability of engineered proteins of known structure that we were able to identify convincing examples of these phenomena.

## REFERENCES

- Brand L, Johnson ML, eds. 1997. *Methods in enzymology*, Vol. 278: *Fluorescence spectroscopy*. Academic Press, San Diego.
- Ladokhin AS. 2000. Fluorescence spectroscopy in peptide and protein analysis. In *Encyclopedia of analytical chemistry*, pp. 5762–5779. Ed RA Meyers. John Wiley & Sons, New York.
- Engelborghs Y. 2001. The analysis of time-resolved protein fluorescence in multi-tryptophan proteins. *Spectrochim Acta, Part A* **57**: 2255–2270.
- Ladokhin AS, Jayasinghe S, White SH. 2000. How to measure and analyze tryptophan fluorescence in membranes properly, and why bother. *Anal Biochem* **285**:235–245.
- Weinryb I, Steiner RF. 1971. The luminescence of the aromatic amino acids. In *Excited states of proteins and nucleic acids*, pp. 277–318. Ed RF Steiner, I Weinryb. Plenum Press, New York.
- Demchenko AP. 1981. *Ultraviolet spectroscopy of proteins*. Springer-Verlag, New York.
- Konev SV. 1967. *Fluorescence and phosphorescence of proteins and nucleic acids*. Plenum Press, New York.
- Permyakov EA. 1993. *Luminescent spectroscopy of proteins*. CRC Press, Boca Raton, FL.
- Longworth JW. 1983. Intrinsic fluorescence of proteins. In *Time-resolved fluorescence spectroscopy in biochemistry and biology*, pp. 651–778. Ed RB Cundall, RE Dale. Plenum Press, New York.
- Chen RF. 1967. Fluorescence quantum yields of tryptophan and tyrosine. *Anal Lett* **1**(1):35–42.
- Lakowicz JR, Maliwal BP. 1983. Oxygen quenching and fluorescence depolarization of tyrosine residues in proteins. *J Biol Chem* **258**(8):4794–4801.
- Weber G. 1960. Fluorescence polarization spectrum and electronic-energy transfer in tyrosine, tryptophan, and related compounds. *Biochem J* **75**:335–345.
- Weber G. 1966. Polarization of the fluorescence of solutions. In *Fluorescence and phosphorescence analysis*, pp. 217–240. Ed DM Hercules. Wiley Interscience, New York.
- Norohna M, Lima JC, Lamosa P, Santos H, Maycock C, Ventura R, Macanita AL. 2004. Intramolecular fluorescence quenching of tyrosine by the peptide  $\alpha$ -carbonyl group revisited. *J Phys Chem A* **108**: 2155–2166.
- Guzow K, Ganzykowicz R, Rzeska A, Mrozek J, Szabelski M, Karolczak J, Liwo A, Wiczek W. 2004. Photophysical properties of tyrosine and its simple derivatives studied by time-resolved fluorescence spectroscopy, global analysis, and theoretical calculations. *J Phys Chem B* **108**:3879–3889.
- Ross JBA, Laws WR, Rousslang KW, Wyssbrod HR. 1992. Tyrosine fluorescence and phosphorescence from proteins and polypeptides. In *Topics in fluorescence spectroscopy*, Vol. 3: *Biochemical applications*, pp. 1–63. Ed JR Lakowicz. Plenum Press, New York.

17. Lakowicz JR, Maliwal BP, Cherek H, Balter A. 1983. Rotational freedom of tryptophan residues in proteins and peptides. *Biochemistry* **22**:1741–1752.
18. Eftink MR, Selvidge LA, Callis PR, Rehms AA. 1990. Photophysics of indole derivatives: experimental resolution of  ${}^1L_a$  and  ${}^1L_b$  transitions and comparison with theory. *J Phys Chem* **94**:3469–3479.
19. Yamamoto Y, Tanaka J. 1972. Polarized absorption spectra of crystals of indole and its related compounds. *Bull Chem Soc Jpn* **45**: 1362–1366.
20. Song P-S, Kurtin WE. 1969. A spectroscopic study of the polarized luminescence of indole. *J Am Chem Soc* **91**:4892–4906.
21. Albinsson B, Kubista M, Norden B, Thulstrup EW. 1989. Near-ultraviolet electronic transitions of the tryptophan chromophore: linear dichroism, fluorescence anisotropy, and magnetic circular dichroism spectra of some indole derivatives. *J Phys Chem* **93**:6646–6655.
22. Albinsson B, Norden B. 1992. Excited-state properties of the indole chromophore: electronic transition moment directions from linear dichroism measurements—effect of methyl and methoxy substituents. *J Phys Chem* **96**:6204–6212.
23. Callis PR. 1997.  ${}^1L_a$  and  ${}^1L_b$  transitions of tryptophan: applications of theory and experimental observations to fluorescence of proteins. *Methods Enzymol* **278**:113–150.
24. Valeur B, Weber G. 1977. Resolution of the fluorescence excitation spectrum of indole into the  ${}^1L_a$  and  ${}^1L_b$  excitation bands. *Photochem Photobiol* **25**:441–444.
25. Rayner DM, Szabo AG. 1977. Time-resolved fluorescence of aqueous tryptophan. *Can J Chem* **56**:743–745.
26. Petrich JW, Chang MC, McDonald DB, Fleming GR. 1983. On the origin of nonexponential fluorescence decay in tryptophan and its derivatives. *J Am Chem Soc* **105**:3824–3832.
27. Creed D. 1984. The photophysics and photochemistry of the near-UV absorbing amino acids, I: tryptophan and its simple derivatives. *Photochem Photobiol* **39**(4):537–562.
28. Fleming GR, Morris JM, Robbins RJ, Woolfe GJ, Thistlewaite PJ, Robinson GW. 1978. Nonexponential fluorescence decay of aqueous tryptophan and two related peptides by picosecond spectroscopy. *Proc Natl Acad Sci USA* **75**:4652–4656.
29. Gryczynski I, Wiczk W, Johnson ML, Lakowicz JR. 1988. Lifetime distributions and anisotropy decays of indole fluorescence in cyclohexane/ethanol mixtures by frequency-domain fluorometry. *Biophys Chem* **32**:173–185.
30. Walker MS, Bednar TW, Lumry R. 1966. Exciplex formation in the excited state. *J Chem Phys* **45**:3455–3456.
31. Hershberger MV, Lumry R, Verral R. 1981. The 3-methylindole/n-butanol exciplex: evidence for two exciplex sites in indole compounds. *Photochem Photobiol* **33**:609–617.
32. Strickland EH, Horwitz J, Billups C. 1970. Near-ultraviolet absorption bands of tryptophan: studies using indole and 3-methylindole as models. *Biochemistry* **9**(25):4914–4920.
33. Lasser N, Feitelson J, Lumry R. 1977. Exciplex formation between indole derivatives and polar solutes. *Isr J Chem* **16**:330–334.
34. Sun M, Song P-S. 1977. Solvent effects on the fluorescent states of indole derivatives-dipole moments. *Photochem Photobiol* **25**:3–9.
35. Lami H, Glasser N. 1986. Indole's solvatochromism revisited. *J Chem Phys* **84**(2):597–604.
36. Pierce DW, Boxer SG. 1995. Stark effect spectroscopy of tryptophan. *Biophys J* **68**:1583–1591.
37. Callis PR, Burgess BK. 1997. Tryptophan fluorescence shifts in proteins from hybrid simulations: an electrostatic approach. *J Phys Chem B* **101**:9429–9432.
38. Strickland EH, Billups C, Kay E. 1972. Effects of hydrogen bonding and solvents upon the tryptophanyl  ${}^1L_a$  absorption band: studies using 2,3-dimethylindole. *Biochemistry* **11**(19):3657–3662.
39. Van Duuren BL. 1961. Solvent effects in the fluorescence of indole and substituted indoles. *J Org Chem* **26**:2954–2960.
40. Willis KJ, Szabo AG. 1991. Fluorescence decay kinetics of tyrosinate and tyrosine hydrogen-bonded complexes. *J Phys Chem* **95**:1585–1589.
41. Willis KJ, Szabo AG, Krajcarski DT. 1990. The use of Stokes Raman scattering in time correlated single photon counting: application to the fluorescence lifetime of tyrosinate. *Photochem Photobiol* **51**: 375–377.
42. Rayner DM, Krajcarski DT, Szabo AG. 1978. Excited-state acid-base equilibrium of tyrosine. *Can J Chem* **56**:1238–1245.
43. Pal H, Palit DK, Mukherjee T, Mittal JP. 1990. Some aspects of steady state and time-resolved fluorescence of tyrosine and related compounds. *J Photochem Photobiol A: Chem* **52**:391–409.
44. Shimizu O, Imakubo K. 1977. New emission band of tyrosine induced by interaction with phosphate ion. *Photochem Photobiol* **26**: 541–543.
45. Dietze EC, Wang RW, Lu AYH, Atkins WM. 1996. Ligand effects on the fluorescence properties of tyrosine-9 in alpha 1-1 glutathione S-transferase. *Biochemistry* **35**:6745–6753.
46. Behmaaraai TA, Toulme JJ, Helene C. 1979. Quenching of tyrosine fluorescence by phosphate ions: a model study for protein-nucleic acid complexes. *Photochem Photobiol* **30**:533–539.
47. Schnarr M, Helene C. 1982. Effects of excited-state proton transfer on the phosphorescence of tyrosine-phosphate complexes. *Photochem Photobiol* **36**:91–93.
48. Szabo A, Lynn KR, Krajcarski DT, Rayner DM. 1978. Tyrosinate fluorescence maxima at 345 nm in proteins lacking tryptophan at pH 7. *FEBS Lett* **94**:249–252.
49. Prendergast FG, Hampton PD, Jones B. 1984. Characteristics of tyrosinate fluorescence emission in  $\alpha$ - and  $\beta$ -purothionins. *Biochemistry* **23**:6690–6697.
50. Libertini LJ, Small EW. 1985. The intrinsic tyrosine fluorescence of histone H1. *Biophys J* **47**:765–772.
51. Ruan K, Li J, Liang R, Xu C, Yu Y, Lange R, Balny C. 2002. A rare protein fluorescence behavior where the emission is dominated by tyrosine: case of the 33-kDa protein from spinach photosystem II. *Biochem Biophys Res Commun* **293**:593–597.
52. Pundak S, Roche RS. 1984. Tyrosine and tyrosinate fluorescence of bovine testes calmodulin calcium and pH dependence. *Biochemistry* **23**:1549–1555.
53. Longworth JW. 1971. Luminescence of polypeptides and proteins. In *Excited states of proteins and nucleic acids*, pp. 319–484. Ed RF Steiner, I Weinryb. Plenum Press, New York.
54. Kronman MJ, Holmes LG. 1971. The fluorescence of native, denatured and reduced denatured proteins. *Photochem Photobiol* **14**:113–134.
55. Burstein EA, Vedenkina NS, Ivkova MN. 1974. Fluorescence and the location of tryptophan residues in protein molecules. *Photochem Photobiol* **18**:263–279.

56. Burstein EA, Abornev SM, Reshetnyak YK. 2001. Decomposition of protein tryptophan fluorescence spectra into log-normal components, I: decomposition algorithms. *Biophys J* **81**:1699–1709.
57. Reshetnyak YK, Burstein EA. 2001. Decomposition of protein tryptophan fluorescence spectra into log-normal components, II: the statistical proof of discreteness of tryptophan classes in proteins. *Biophys J* **81**:1710–1734.
58. Reshetnyak YK, Koshevnik Y, Burstein EA. 2001. Decomposition of protein tryptophan fluorescence spectra into log-normal components, III: correlation between fluorescence and microenvironment parameters of individual tryptophan residues. *Biophys J* **81**:1735–1758.
59. Eftink MR. 1990. Fluorescence techniques for studying protein structure. *Methods Biochem Anal* **35**:117–129.
60. Burstein EA. 1976. Luminescence of protein chromophores. In *Model studies: science and technology results*, Vol. 6: *Biophysics*, VINITI, Moscow.
61. Vivian JT, Callis P. 2001. Mechanisms of tryptophan fluorescence shifts in proteins. *Biophys J* **80**:2093–2109.
62. Callis FR, Liu T. 2004. Quantitative prediction of fluorescence quantum yields for tryptophan in proteins. *J Phys Chem B* **108**:4248–4259.
63. Callis PR, Vivian JT. 2003. Understanding the variable fluorescence quantum yield of tryptophan in proteins using QM-MM simulations: quenching by charge transfer to the peptide backbone. *Chem Phys Lett* **369**:409–414.
64. Ababou A, Bombarda E. 2001. On the involvement of electron transfer reactions in the fluorescence decay kinetics heterogeneity of proteins. *Protein Sci* **10**:2102–2113.
65. Adams PD, Chen Y, Ma K, Zagorski M, Sonnichsen FD, McLaughlin ML, Barkley MD. 2002. Intramolecular quenching of tryptophan fluorescence by the peptide bond in cyclic hexapeptides. *J Am Chem Soc* **124**:9278–9286.
66. Chen Y, Barkley MD. 1998. Toward understanding tryptophan fluorescence in proteins. *Biochemistry* **37**:9976–9982.
67. Chen Y, Liu B, Yu H-T, Barkley MD. 1996. The peptide bond quenches indole fluorescence. *J Am Chem Soc* **118**:9271–9278.
68. Eftink MR, Ghiron CA. 1984. Indole fluorescence quenching studies on proteins and model systems: use of the inefficient quencher succinimide. *Biochemistry* **23**:3891–3899.
69. Froehlich PM, Gantt D, Paramasigamani V. 1977. Fluorescence quenching of indoles by *N,N*-dimethylformamide. *Photochem Photobiol* **26**:639–642.
70. Froehlich PM, Nelson K. 1978. Fluorescence quenching of indoles by amides. *J Phys Chem* **82**(22):2401–2403.
71. Finazzi-Agro A, Rotilio G, Avigliano L, Guerreri P, Boffi V, Mondovi B. 1970. Environment of copper in *Pseudomonas fluorescens* azurin: fluorometric approach. *Biochemistry* **9**(9):2009–2014.
72. Burstein EA, Permyakov EA, Yashin VA, Burkhanov SA, Agro AF. 1977. The fine structure of luminescence spectra of azurin. *Biochim Biophys Acta* **491**:155–159.
73. Szabo AG, Stepanik TM, Wayner DM, Young NM. 1983. Conformational heterogeneity of the copper binding site in azurin. *Biophys J* **41**:233–244.
74. Fuentes L, Oyola J, Fernández M, Quiñones E. 2004. Conformational changes in azurin from *Pseudomonas aeruginosa* induced through chemical and physical protocols. *Biophys J* **87**: 1873–1880.
75. Adman ET, Jensen LH. 1981. Structural features of azurin at 2.7 Å resolution. *Isr J Chem* **21**:8–12.
76. Aueuhel FM, Brent R, Kingston RE, Moore DD, Seidman JG, Smith JA, Struhl K, eds. 1987. *Current protocols in molecular biology*. John Wiley & Sons, New York, (see chapter 8).
77. Sambrook J, Fritsch EF, Maniatis T. 1989. *Molecular cloning*, chap. 15. Cold Spring Harbor Laboratory Press, Plainview, NY.
78. Gilardi G, Mei G, Rosato N, Canters GW, Finazzi-Agro A. 1994. Unique environment of Trp48 in *Pseudomonas aeruginosa* azurin as probed by site-directed mutagenesis and dynamic fluorescence anisotropy. *Biochemistry* **33**:1425–1432.
79. Petrich JW, Longworth JW, Fleming GR. 1987. Internal motion and electron transfer in proteins: a picosecond fluorescence study of three homologous azurins. *Biochemistry* **26**:2711–2722.
80. Lakowicz JR, Cherek H, Gryczynski I, Joshi N, Johnson ML. 1987. Enhanced resolution of fluorescence anisotropy decays by simultaneous analysis of progressively quenched samples. *Biophys J* **51**: 755–768.
81. Georghiou S, Thompson M, Mukhopadhyay AK. 1982. Melittin-phospholipid interaction studied by employing the single-tryptophan residue as an intrinsic fluorescent probe. *Biochim Biophys Acta* **688**: 441–452.
82. Searcy DG, Montenay-Garestier T, Helene C. 1989. Phenylalanine-to-tyrosine singlet energy transfer in the archaeabacterial histone-like protein HTa. *Biochemistry* **28**:9058–9065.
83. Kupryszecka M, Gryczynski I, Kawski A. 1982. Intramolecular donor-acceptor separations in methionine- and leucine-enkephalin estimated by long-range radiationless transfer of singlet excitation energy. *Photochem Photobiol* **36**:499–502.
84. Gryczynski I, Kawski A, Darlak K, Grzonka Z. 1985. Intramolecular electronic excitation energy transfer in morphine and its analogues. *J Photochem* **30**:371–377.
85. Eisinger J. 1969. Intramolecular energy transfer in adrenocorticotropin. *Biochemistry* **8**:3902–3908.
86. Moreno MJ, Prieto M. 1993. Interaction of the peptide hormone adrenocorticotropin, ACTH(1-24), with a membrane model system: a fluorescence study. *Photochem Photobiol* **57**(3):431–437.
87. Pearce SF, Hawrot E. 1990. Intrinsic fluorescence of binding-site fragments of the nicotinic acetylcholine receptor: perturbations produced upon binding  $\alpha$ -bungarotoxin. *Biochemistry* **29**:10649–10659.
88. Schiller PW. 1983. Fluorescence study on the conformation of a cyclic enkephalin analogue in aqueous solution. *Biochim Biophys Res Commun* **114**(1):268–274.
89. Al'fimova EYa, Likhtenstein GI. 1976. Fluorescence study of energy transfer as method of study of protein structure. *Mol Biol (Moscow)* **8**(2):127–179.
90. Boteva R, Zlateva T, Dorovska-Taran V, Visser AJWG, Tsanev R, Salvato B. 1996. Dissociation equilibrium of human recombinant interferon  $\gamma$ . *Biochemistry* **35**:14825–14830.
91. Eisenhawer M, Cattarinussi S, Kuhn A, Vogel H. 2001. Fluorescence resonance energy transfer shows a close helix–helix distance in the transmembrane M13 procoat protein. *Biochemistry* **40**:12321–12328.
92. Lankiewicz L, Stachowiak K, Rzeska A, Wiczk W. 1999. Photophysics of sterically constrained phenylalanines. In *Peptide science—present and future*, pp. 168–170. Ed Y Shimonishi. Kluwer, New York.

93. Vanscycoc WS, Shea MA. 2001. Phenylalanine fluorescence studies of calcium binding to N-domain fragments of *paramecium* calmodulin mutants show increased calcium affinity correlates with increased disorder. *Protein Sci* **10**:1758–1768.
94. VanScyoc WS, Sorensen BR, Rusinova E, Laws WR, Ross JBA, Shea MA. 2002. Calcium binding to calmodulin mutants monitored by domain-specific intrinsic phenylalanine and tyrosine fluorescence. *Biophys J* **83**:2767–2780.
95. Burshtein EA. 1996. Resolution of the fluorescence spectra by the degree of accessibility to quenchers. *Biophysics* **41**(1):235–239.
96. Raja SM, Rawat SS, Chattopadhyay A, Lata AK. 1999. Localization and environment of tryptophans in soluble and membrane-bound states of a pore-forming toxin from *Staphylococcus aureus*. *Biophys J* **76**:1469–1479.
97. Rausell C, Munoz-Garay C, Miranda-Casso Luengo R, Gomez I, Rudino-Pinera E, Soberon M, Bravo A. 2004. Tryptophan spectroscopy studies and black lipid bilayer analysis indicate that the oligomeric structure of Cry1Ab toxin from *bacillus thuringiensis* is the membrane-insertion intermediate. *Biochemistry* **43**:166–174.
98. Weber J, Senior AE. 2000. Features of F<sub>1</sub>-ATPase catalytic and non-catalytic sites revealed by fluorescence lifetimes and acrylamide quenching of specifically inserted tryptophan residues. *Biochemistry* **39**:5287–5294.
99. Eftink MR, Ghiron CA. 1977. Exposure of tryptophanyl residues and protein dynamics. *Biochemistry* **16**(25):5546–5551.
100. Eftink MR, Ghiron CA. 1981. Fluorescence quenching studies with proteins. *Anal Biochem* **114**:199–227.
101. Eftink MR. 1991. Fluorescence quenching: theory and applications. In *Topics in fluorescence spectroscopy*, Vol. 2: *Principles*, pp. 53–126. Ed JR Lakowicz. Plenum Press, New York.
102. Vazquez-Ibar JL, Guan L, Svrakic M, Kaback HR. 2003. Exploiting luminescence spectroscopy to elucidate the interaction between sugar and a tryptophan residue in the lactose permease of *Escherichia coli*. *Proc Natl Acad Sci USA* **100**(22):12706–12711.
103. Wu C-SC, Yang JT. 1980. Helical conformation of glucagon in surfactant solutions. *Biochemistry* **19**:2117–2122.
104. Boesch C, Bundi A, Oppliger M, Wüthrich K. 1978. <sup>1</sup>H nuclear-magnetic-resonance studies of the molecular conformation of monomeric glucagon in aqueous solution. *Eur J Biochem* **91**:209–214.
105. Edelhoch H, Lippoldt RE. 1969. Structural studies on polypeptide hormones. *J Biol Chem* **244**:3876–3883.
106. Terwilliger TC, Eisenberg D. 1982. The structure of melittin. *J Biol Chem* **257**:6016–6022.
107. Lakowicz JR, Weber G. 1973. Quenching of protein fluorescence by oxygen: detection of structural fluctuations in proteins on the nanosecond timescale. *Biochemistry* **12**:4171–4179.
108. Calhoun DB, Vanderkooi JM, Englander SW. 1983. Penetration of small molecules into proteins studied by quenching of phosphorescence and fluorescence. *Biochemistry* **22**:1533–1539.
109. Calhoun DB, Englander SW, Wright WW, Vanderkooi JM. 1988. Quenching of room temperature protein phosphorescence by added small molecules. *Biochemistry* **27**:8466–8474.
110. Kouyama I, Kinoshita K, Ikegami A. 1989. Correlation between internal motion and emission kinetics of tryptophan residues in proteins. *Eur J Biochem* **182**:517–521.
111. Lakowicz JR, Gryczynski I, Cherek I, Szmacinski H, Joshi N. 1991. Anisotropy decays of single tryptophan proteins measured by GHz frequency-domain fluorometry with collisional quenching. *Eur Biophys J* **19**:125–140.
112. Avigliano L, Finazzi-Agro A, Mondovi B. 1974. Perturbation studies on some blue proteins. *FEBS Lett* **38**:205–208.
113. Glandieres J-M, Twist C, Haouz A, Zentz C, Alpert B. 2000. Resolved fluorescence of the two tryptophan residues in horse apomyoglobin. *Photochem Photobiol* **71**(4):382–386.
114. Wasylewski Z, Kaszycki P, Guz A, Stryjewski W. 1988. Fluorescence quenching resolved spectra of fluorophores in mixtures and micellar solutions. *Eur J Biochem* **178**:471–476.
115. Stryjewski W, Wasylewski Z. 1986. The resolution of heterogeneous fluorescence of multityptophan-containing proteins studied by a fluorescence-quenching method. *Eur J Biochem* **158**:547–553.
116. Wasylewski Z, Poloczek H, Wasniowska A. 1988. Fluorescence quenching resolved spectroscopy of proteins. *Eur J Biochem* **172**:719–724.
117. Wasylewski Z, Kaszycki P, Drwiega M. 1996. A fluorescence study of Tn10-encoded tet repressor. *J Protein Chem* **15**(1):45–52.
118. Eftink MR. 1997. Fluorescence methods for studying equilibrium macromolecule-ligand interactions. *Methods Enzymol* **278**:221–257.
119. Ulrich A, Schmitz AAP, Braun T, Yuan T, Vogel HJ, Vergères G. 2000. Mapping the interface between calmodulin and MARCKS-related protein by fluorescence spectroscopy. *Proc Natl Acad Sci USA* **97**(10):5191–5196.
120. Akyol Z, Bartos JA, Merrill MA, Faga LA, Jaren OR, Shea MA, Hell JW. 2004. Apo-calmodulin binds with its C-terminal domain to the N-methyl-D-aspartate receptor NR1 C0 region. *J Biol Chem* **279**(3):2166–2175.
121. Kilhoffer M-C, Kubina M, Travers F, Haiech J. 1992. Use of engineered proteins with internal tryptophan reporter groups and perturbation techniques to probe the mechanism of ligand-protein interactions: investigation of the mechanism of calcium binding to calmodulin. *Biochemistry* **31**:8098–8106.
122. Chabbert M, Lukas TJ, Watterson DM, Axelsen PH, Prendergast FG. 1991. Fluorescence analysis of calmodulin mutants containing tryptophan: conformational changes induced by calmodulin-binding peptides from myosin light chain kinase and protein kinase II. *Biochemistry* **30**:7615–7630.
123. Dong CZ, De Rocquigny H, Rémy E, Mellac S, Fournié-Zaluski MC, Roques BP. 1997. Synthesis and biological activities of fluorescent acridine-containing HIV-1 nucleocapsid proteins for investigation of nucleic acid-NCp7 interactions. *J Pept Res* **50**:269–278.
124. Rai SS, O'Handley D, Nakai H. 2001. Conformational dynamics of a transposition repressor in modulating DNA binding. *J Mol Biol* **312**:311–322.
125. Lorenz M, Diekmann S. 2001. Quantitative distance information on protein-DNA complexes determined in polyacrylamide gels by fluorescence resonance energy transfer. *Electrophoresis* **22**:990–998.
126. Boyer M, Poujol N, Margeat E, Royer CA. 2000. Quantitative characterization of the interaction between purified human estrogen receptor  $\alpha$  and DNA using fluorescence anisotropy. *Nucleic Acids Res* **28**(13):2494–2502.
127. Bombarda E, Ababou A, Vuilleumier C, Gerard D, Roques BP, Piemont E, Mely Y. 1999. Time-resolved fluorescence investigation of the human immunodeficiency virus type 1 nucleocapsid protein: influence of the binding of nucleic acids. *Biophys J* **76**:1561–1570.

128. Kozlov AG, Lohman TM. 2002. Stopped-flow studies of the kinetics of single-stranded DNA binding and wrapping around the *Escherichia coli* SSB tetramer. *Biochemistry* **41**:6032–6044.
129. Zargarian L, Le Tilly V, Jamin N, Chaffotte A, Gabrielsen OS, Toma F, Alpert B. 1999. Myb-DNA recognition: role of tryptophan residues and structural changes of the minimal DNA binding domain of c-Myb. *Biochemistry* **38**:1921–1929.
130. Pokalsky C, Wick P, Harms E, Lytle FE, Van Etten RL. 1995. Fluorescence resolution of the intrinsic tryptophan residues of bovine protein tyrosyl phosphatase. *J Biol Chem* **270**(8):3809–3815.
131. Ramos P, Coste T, Piemont E, Lessinger JM, Bousquest JA, Chapus C, Kerfelec B, Ferard G, Mely Y. 2003. Time-resolved fluorescence allows selective monitoring of Trp30 environmental changes in the seven-trp-containing human pancreatic lipase. *Biochemistry* **42**:12488–12496.
132. Cheung C-W, Mas MT. 1996. Substrate-induced conformational changes in yeast 3-phosphoglycerate kinase monitored by fluorescence of single tryptophan probes. *Protein Sci* **5**:1144–1149.
133. Pham AS, Reinhart GD. 2003. Quantification of allosteric influence of *escherichia coli* phosphofructokinase by frequency domain fluorescence. *Biophys J* **85**:656–666.
134. Takita T, Nakagoshi M, Inouye K, Tonomura B. 2003. Lysyl-tRNA synthetase from *bacillus stearothermophilus*: the Trp314 residue is shielded in a non-polar environment and is responsible for the fluorescence changes observed in the amino acid activation reaction. *J Mol Biol* **325**:677–695.
135. Tang L, van Merode AEJ, Spelberg JHL, Fraaije MW, Janssen DB. 2003. Steady-state kinetics and tryptophan fluorescence properties of halohydrin dehalogenase from *agrobacterium radiobacter*: roles of W139 and W249 in the active site and halide-induced conformational change. *Biochemistry* **42**:14057–14065.
136. Clark EH, East JM, Lee AG. 2003. The role of tryptophan residues in an integral membrane protein: diacylglycerol kinase. *Biochemistry* **42**:11065–11073.
137. Van Duffelen M, Chrin LR, Berger CL. 2004. Nucleotide dependent intrinsic fluorescence changes of W29 and W36 in smooth muscle myosin. *Biophys J* **87**:1767–1775.
138. Pattanaik P, Ravindra G, Sengupta C, Maithal K, Balaram P, Balaram H. 2003. Unusual fluorescence of W168 in *plasmodium falciparum* triosephosphate isomerase, probed by single-tryptophan mutants. *Eur J Biochem* **270**:745–756.
139. Loewenthal R, Sancho J, Fersht AR. 1991. Fluorescence spectrum of barnase: contributions of three tryptophan residues and a histidine-related pH dependence. *Biochemistry* **30**:6775–6779.
140. Shopova M, Genov N. 1983. Protonated form of histidine 238 quenches the fluorescence of tryptophan 241 in subtilisin novo. *Int J Pept Res* **21**:475–478.
141. Eftink MR. 1991. Fluorescence quenching reactions. In *Biophysical and biochemical aspects of fluorescence spectroscopy*, pp. 1–41. Ed TG Dewey. Plenum Press, New York.
142. Lux B, Baudier J, Gerard D. 1985. Tyrosyl fluorescence spectra of proteins lacking tryptophan: effects of intramolecular interactions. *Photochem Photobiol* **42**(3):245–251.
143. Wu P, Li Y-K, Talalay P, Brand L. 1994. Characterization of the three tyrosine residues of  $\Delta^5$ -3-ketosteroid isomerase by time-resolved fluorescence and circular dichroism. *Biochemistry* **33**:7415–7422.
144. Canet D, Doering K, Dobson CM, Dupont Y. 2001. High-sensitivity fluorescence anisotropy detection of protein-folding events: application to  $\alpha$ -lactalbumin. *Biophys J* **80**:1996–2003.
145. Ghaemmaghami S, Word JM, Burton RE, Richardson JS, Oas TG. 1998. Folding kinetics of a fluorescent variant of monomeric  $\lambda$  repressor. *Biochemistry* **37**:9179–9185.
146. Tcherkasskaya O, Uversky VN. 2001. Denatured collapsed states in protein folding: example of apomyoglobin. *Proteins: Struct Funct Genet* **44**:244–254.
147. Gilmanish R, Gulotta M, Dyer RB, Callender RH. 2001. Structures of apomyoglobin's various acid-destabilized forms. *Biochemistry* **40**: 5127–5136.
148. Jones BE, Beechem JM, Matthews CR. 1995. Local and global dynamics during the folding of *Escherichia coli* dihydrofolate reductase by time-resolved fluorescence spectroscopy. *Biochemistry* **34**: 1867–1877.
149. Smith CJ, Clarke AR, Chia WN, Irons LI, Atkinson T, Holbrook JJ. 1991. Detection and characterization of intermediates in the folding of large proteins by the use of genetically inserted tryptophan probes. *Biochemistry* **30**:1028–1036.
150. Otto MR, Lillo MP, Beechem JM. 1994. Resolution of multiphasic reactions by the combination of fluorescence total-intensity and anisotropy stopped-flow kinetic experiments. *Biophys J* **67**:2511–2521.
151. Ballew RM, Sabelko J, Gruebele M. 1996. Direct observation of fast protein folding: the initial collapse of apomyoglobin. *Proc Natl Acad Sci USA* **93**:5759–5764.
152. Service RF. 1996. Folding proteins caught in the act. *Science* **273**: 29–30.
153. Eftink MR. 1994. The use of fluorescence methods to monitor unfolding transitions in proteins. *Biophys J* **66**:482–501.
154. Eftink MR, Ionescu R, Ramsay GD, Wong C-Y, Wu JQ, Maki AH. 1996. Thermodynamics of the unfolding and spectroscopic properties of the V66W mutant of staphylococcal nuclease and its 1-136 fragment. *Biochemistry* **35**:8084–8094.
155. Ropson IJ, Dalessio PM. 1997. Fluorescence spectral changes during the folding of intestinal fatty acid binding protein. *Biochemistry* **36**:8594–8601.
156. Royer CA, Mann CJ, Matthews CR. 1993. Resolution of the fluorescence equilibrium unfolding profile of trp aporepressor using single tryptophan mutants. *Protein Sci* **2**:1844–1852.
157. Szpikowska BK, Beechem JM, Sherman MA, Mas MT. 1994. Equilibrium unfolding of yeast phosphoglycerate kinase and its mutants lacking one or both native tryptophans: a circular dichroism and steady-state and time-resolved fluorescence study. *Biochemistry* **33**:2217–2225.
158. Sendak RA, Rothwarf DM, Wedemeyer WJ, Houry WA, Scheraga HA. 1996. Kinetic and thermodynamic studies of the folding/unfolding of a tryptophan-containing mutant of ribonuclease A. *Biochemistry* **35**:12978–12992.
159. Steer BA, Merrill AR. 1995. Guanidine hydrochloride-induced denaturation of the colicin E1 channel peptide: unfolding of local segments using genetically substituted tryptophan residues. *Biochemistry* **34**:7225–7234.
160. Clark PL, Liu Z-P, Zhang J, Giersch LM. 1996. Intrinsic tryptophans of CRABPI as probes of structure and folding. *Protein Sci* **5**: 1108–1117.

161. Clark PL, Weston BF, Giersch LM. 1998. Probing the folding pathway of a  $\beta$ -clam protein with single-tryptophan constructs. *Folding Des* **3**:401–412.
162. Meagher JL, Beechem JM, Olson ST, Gettins PGW. 1998. Deconvolution of the fluorescence emission spectrum of human antithrombin and identification of the tryptophan residues that are responsive to heparin binding. *J Biol Chem* **273**(36):23283–23289.
163. Hannemann F, Bera AK, Fischer B, Lisurek B, Lisurek M, Teuchner K, Bernhardt R. 2002. Unfolding and conformational studies on bovine adrenodoxin probed by engineered intrinsic tryptophan fluorescence. *Biochemistry* **41**:11008–11016.
164. Mansoor SE, Mchaourab HS, Farrens DL. 1999. Determination of protein secondary structure and solvent accessibility using site-directed fluorescence labeling: studies of T4 lysozyme using the fluorescent probe monobromobimane. *Biochemistry* **38**:16383–16393.
165. Kintrup M, Schubert P, Kunz M, Chabbert M, Alberti P, Bombarda E, Schneider S, Hillen W. 2000. Trp scanning analysis of tet repressor reveals conformational changes associated with operator and anhydrotetracycline binding. *Eur J Biochem* **267**:821–829.
166. Gasymov OK, Abduragimov AR, Yusifov TN, Glasgow BJ. 1997. Solution structure by site directed tryptophan fluorescence in tear lipocalin. *Biochem Biophys Res Commun* **239**:191–196.
167. Gasymov OK, Abduragimov AR, Yusifov TN, Glasgow BJ. 2001. Site-directed tryptophan fluorescence reveals the solution structure of tear lipocalin: evidence for features that confer promiscuity in ligand binding. *Biochemistry* **40**:14754–14762.
168. Wong C-Y, Eftink MR. 1998. Incorporation of tryptophan analogues into staphylococcal nuclease, its V66W mutant, and  $\Delta$ 137-149 fragment: spectroscopic studies. *Biochemistry* **37**:8938–8946.
169. Mohammadi F, Prentice GA, Merrill AR. 2001. Protein–protein interaction using tryptophan analogues: novel spectroscopic probes for toxin-elongation factor-2 interactions. *Biochemistry* **40**:10273–10283.
170. Li Q, Du H-N, Hu H-Y. 2003. Study of protein–protein interactions by fluorescence of tryptophan analogs: application to immunoglobulin G binding domain of streptococcal protein G. *Biopolymers* **72**:116–122.
171. Accione M, Guillemette JG, Twine SM, Hogue CWV, Rajendran B, Szabo AG. 2003. Fluorescence-based structural analysis of tryptophan analogue–AMP formation in single tryptophan mutants of *B. stearothermophilus* tryptophanyl-tRNA synthetase. *Biochemistry* **42**:14994–15002.
172. Das K, Ashby KD, Smirnov AV, Reinach FC, Petrich JW, Farah CS. 1999. Fluorescence properties of recombinant tropomyosin containing tryptophan 5-hydroxytryptophan and 7-azatryptophan. *Photochem Photobiol* **70**(5):719–730.
173. Hogue CWV, Rasquinha I, Szabo AG, MacManus JP. 1992. A new intrinsic fluorescent probe for proteins. *FEBS Lett* **310**:269–272.
174. Twine SM, Szabo AG. 2003. Fluorescent amino acid analogues. *Methods Enzymol* **360**:104–127.
175. Heyduk E, Heyduk T. 1993. Physical studies on interaction of transcription activator and RNA-polymerase: fluorescent derivatives of CRP and RNA polymerase. *Cell Mol Biol Res* **39**:401–407.
176. Laue TM, Senechal DF, Eaton S, Ross JBA. 1993. 5-hydroxytryptophan as a new intrinsic probe for investigating protein-DNA interactions by analytical ultracentrifugation: study of the effect of DNA on self-assembly of the bacteriophage  $\lambda$  cI repressor. *Biochemistry* **32**:2469–2472.
177. Soumillion P, Jespers L, Vervoort J, Fastrez J. 1995. Biosynthetic incorporation of 7-azatryptophan into the phage lambda lysozyme: estimation of tryptophan accessibility, effect on enzymatic activity and protein stability. *Protein Eng* **8**:451–456.
178. Wong C-Y, Eftink MR. 1997. Biosynthetic incorporation of tryptophan analogues into staphylococcal nuclease: effect of 5-hydroxytryptophan and 7-azatryptophan on structure and stability. *Protein Sci* **6**:689–697.
179. Laws WR, Schwartz GP, Rusinova E, Burke GT, Chu Y-C, Katsoyannis PG, Ross JBA. 1995. 5-hydroxytryptophan: an absorption and fluorescence probe which is a conservative replacement for [A14 tyrosine] in insulin. *J Protein Chem* **14**:225–232.
180. Hogue CWV, Szabo AG. 1993. Characterization of aminoacyl-adenylates in *B. subtilis* tryptophanyl-tRNA synthetase, by the fluorescence of tryptophan analogs 5-hydroxytryptophan and 7-azatryptophan. *Biophys Chem* **48**:159–169.
181. Broos J, Gabellieri E, Biemans-Oldehinkel E, Strambini GB. 2003. Efficient biosynthetic incorporation of tryptophan and indole analogs in an integral membrane protein. *Protein Sci* **12**:1991–2000.
182. Guharay J, Sengupta PK. 1996. Characterization of the fluorescence emission properties of 7-azatryptophan in reverse micellar environments. *Biochem Biophys Res Commun* **219**:388–392.
183. Negrerie M, Gai F, Bellefeuille SM, Petrich JW. 1991. Photophysics of a novel optical probe: 7-azaindole. *J Phys Chem* **95**:8663–8670.
184. Rich RL, Negrerie M, Li J, Elliott S, Thornburg RW, Petrich JW. 1993. The photophysical probe, 7-azatryptophan, in synthetic peptides. *Photochem Photobiol* **58**(1):28–30.
185. Chen Y, Gai F, Petrich JW. 1994. Solvation and excited state proton transfer of 7-azindole in alcohols. *Chem Phys Lett* **222**:329–334.
186. Chen Y, Gai F, Petrich JW. 1994. Single-exponential fluorescence decay of the nonnatural amino acid 7-azatryptophan and the nonexponential fluorescence decay of tryptophan in water. *J Phys Chem* **98**:2203–2209.
187. Chen Y, Rich RL, Gai F, Petrich JW. 1993. Fluorescent species of 7-azindole and 7-azatryptophan in water. *J Phys Chem* **97**:1770–1780.
188. English DS, Rich RL, Petrich JW. 1998. Nonexponential fluorescence decay of 7-azatryptophan induced in a peptide environment. *Photochem Photobiol* **67**(1):76–83.
189. Hott JL, Borkman RF. 1989. The non-fluorescence of 4-fluorotryptophan. *Biochem J* **264**:297–299.
190. England PM. 2004. Unnatural amino acid mutagenesis: a precise tool for probing protein structure and function. *Biochemistry* **43**(37):11623–11629.
191. Noren CJ, Anthony-Cahill SJ, Griffith MC, Schultz PG. 1989. A general method for site-specific incorporation of unnatural amino acids into proteins. *Science* **244**:182–188.
192. Bain JD, Glabe CG, Dix TA, Chamberlin AR. 1989. Biosynthetic site-specific incorporation of a non-natural amino acid into a polypeptide. *J Am Chem Soc* **111**:8013–8014.
193. Heckler TG, Chang L-H, Zama Y, Naka T, Chorghade MS, Hecht SM. 1984. T4 RNA ligase mediated preparation of novel "chemically misacylated" tRNA<sup>Phes</sup>. *Biochemistry* **23**:1468–1473.
194. Taki M, Hohsaka T, Murakami H, Taira K, Sisido M. 2002. Position-specific incorporation of a fluorophore–quencher pair into single

- streptavidin orthogonal four-base codon–anticodon pairs. *J Am Chem Soc* **124**:14586–14590.
195. Hohsaka T, Ashizuka Y, Taira H, Murakami H, Sisido M. 2001. Incorporation of nonnatural amino acids into proteins by using various four-base codons in an *Escherichia coli* in vitro translation systems. *Biochemistry* **40**:11060–11064.
196. Wang L, Brock A, Schultz PG. 2002. Adding L-3-(2-naphthyl)alanine to the genetic code of *E. coli*. *J Am Chem Soc* **124**:1836–1837.
197. Anderson RD, Zhou J, Hecht SM. 2002. Fluorescence resonance energy transfer between unnatural amino acids in a structurally modified dihydrofolate reductase. *J Am Chem Soc* **124**:9674–9675.
198. Wang L, Brock A, Herberich B, Schultz PG. 2001. Expanding the genetic code of *Escherichia coli*. *Science* **292**(5516):498–500.
199. Murakami H, Hohsaka T, Ashizuka Y, Hashimoto K, Sisido M. 2000. Site-directed incorporation of fluorescent nonnatural amino acids into streptavidin for highly sensitive detection of biotin. *Biomacromolecules* **1**:118–125.
200. Hohsaka T, Muranaka N, Komiyama C, Matsui K, Takaura S, Abe R, Murakami H, Sisido M. 2004. Position-specific incorporation of dansylated non-natural amino acids into streptavidin by using a four-base codon. *FEBS Lett* **560**:173–177.
201. Strasser F, Dey J, Eftink MR, Plapp BV. 1998. Activation of horse liver alcohol dehydrogenase upon substitution of tryptophan 314 at the dimer interface. *Arch Biochem Biophys* **358**(2):369–376. (The original data were courtesy of Dr. BU Plopp.)

---

## PROBLEMS

P16.1. *Determination of Protein Association and Unfolding by Fluorescence:* Suppose you have a protein that consists of a single subunit with a molecular weight of 25,000 daltons. The protein contains a single-tryptophan residue near the central core of the protein and several tyrosine residues. The protein also contains a single reactive sulphydryl residue on the surface.

- Assume that the monomeric protein can be unfolded by the addition of denaturant. Explain how the fluorescence spectral properties of the unmodified protein could be used to follow the unfolding process.
- Describe the use of collisional quenchers to probe the accessibility of the tryptophan residue to the solvent.
- Assume that the unmodified protein self-associates with another subunit to form a dimer. How could fluorescence spectroscopy be used to follow the association process?
- Describe how you would use fluorescence spectroscopy to measure the distance from the tryptophan residue to the reactive sulphydryl group.

Be specific with regard to the experiments that you would perform and how the data would be interpreted.

- Describe how you would use energy transfer to measure self-association of the protein after the protein has been modified on the sulphydryl groups with dansyl chloride.

P16.2. *Detection of Protein Dimerization:* Suppose you have a small protein with a single-tryptophan residue that displays  $r_0 = 0.30$ , and that the protein associates to a dimer. The correlation times of the monomer and dimer are  $\theta_M = 1.25$  and  $\theta_D = 2.5$  ns, respectively. Upon dimer formation the lifetime increases from  $\tau_M = 2.5$  to  $\tau_D = 5.0$  ns, and the relative quantum yield increases twofold. Describe how you would detect dimer formation using the:

- steady-state intensity,
  - intensity decay,
  - steady-state anisotropy, or
  - anisotropy decay.
- What fraction of the emission is due to the monomers and dimers when 50% of the monomers have formed dimers? What is the steady-state anisotropy? What are the intensity and anisotropy decays?

P16.3. *Effect of Excitation Wavelength on Protein Fluorescence:* Section 16.9.3 described kinetic studies of the refolding of cellular retinoic acid binding protein I (CRABPI). The wild-type protein contains three tryptophan residues (Figure 16.57). Figure 16.74 shows emission spectra of the native and denatured forms of CRABPI for various excitation wavelengths. The emission spectra of native CRABPI shift to longer wavelengths with increasing excitation wavelength. The emission spectra of denatured CRABPI do not depend on excitation wavelength. Explain these emission spectra. There may be more than one explanation.

P16.4. *Binding Between Calmodulin and a Protein Kinase C:* Myristoylated protein kinase (MRP) is a kinase that binds to calmodulin. MRP and CaM both lack tryptophan with wild-type sequence MRP. Emission spectra of wild-type and single-tryptophan mutants of MRP are shown in Figure 16.75. Explain these spectra.

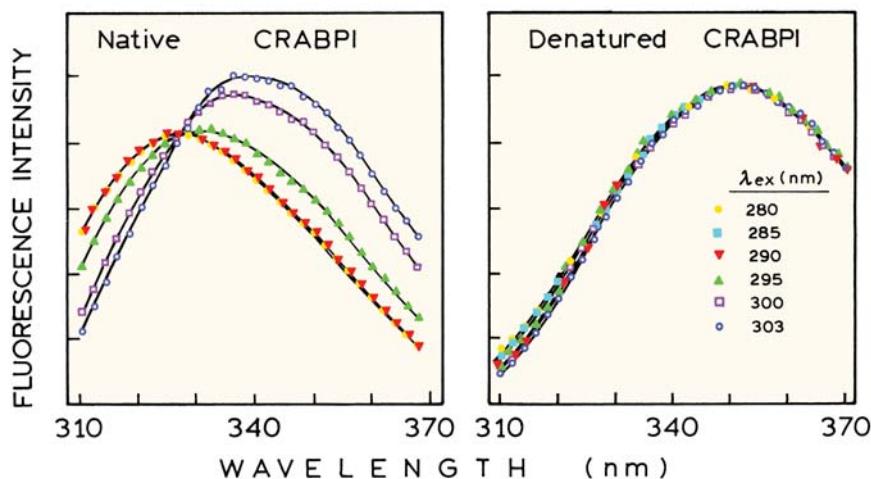


**Figure 16.74.** Emission spectra of cellular retinoic acid binding protein I (CRABPI) for various excitation wavelengths. Revised from [160].

P16.5. *Quenching of LADH and Its Mutants:* Liver alcohol dehydrogenase (LADH) contains two tryptophan residues at positions 15 and 314. Table 16.2 lists steady-state intensity quenching data for wild-type LADH and the mutant W314L containing only

W15. Interpret these data in terms of the accessibility of each tryptophan residue to quenching, the Stern-Volmer quenching constants, and fractional accessibilities to quenching.

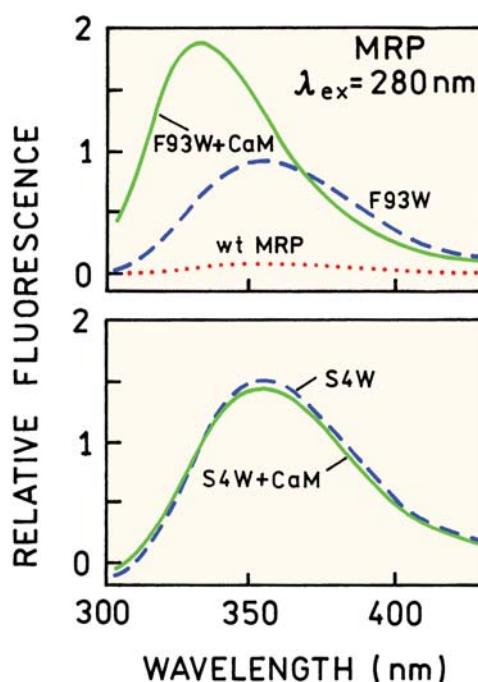


**Figure 16.75.** Emission spectra of wild-type myristoylated protein kinase C and single-tryptophan containing mutants, in the absence and presence of calmodulin. Revised from [119].

**Table 16.2.** Acrylamide and Iodide Quenching Data for the Wild-Type LADH and the W314F Mutant

[Acrylamide]	Wild-type LADH				
	$F/F_0$	$\Delta F/F_0$	[I <sup>-</sup> ]	$F/F_0$	$\Delta F/F_0$
0	1.00	0	0	1.00	0
0.025	0.86	0.14	0.061	0.96	0.04
0.050	0.77	0.23	0.122	0.93	0.07
0.074	0.71	0.29	0.181	0.89	0.11
0.098	0.67	0.33	0.238	0.863	0.137
0.120	0.63	0.36	0.294	0.856	0.144
0.146	0.60	0.40	0.349	0.84	0.16
0.170	0.57	0.43	0.402	0.83	0.17
0.190	0.55	0.45	0.455	0.82	0.18
0.238	0.51	0.49	0.506	0.80	0.20
0.280	0.49	0.51	0.556	0.77	0.23
0.370	0.45	0.54	0.604	0.76	0.23
0.450	0.42	0.58	0.652	0.75	0.25
0.550	0.40	0.60	0.700	0.74	0.26
0.650	0.38	0.62	0.745	0.73	0.27
0.745	0.34	0.66	0.790	0.72	0.28
0.830	0.33	0.67	0.833	0.71	0.29
1.000	0.31	0.69	0.876	0.70	0.296
			0.918	0.69	0.30
			0.960	0.69	0.31
			1.000	0.68	0.32
W314F LADH					
[Acrylamide]	$F/F_0$	$\Delta F/F_0$	[I <sup>-</sup> ]	$F/F_0$	$\Delta F/F_0$
0	1	0	0	1	0
0.025	0.85	0.15	0.063	0.94	0.058
0.050	0.70	0.29	0.124	0.88	0.115
0.075	0.62	0.38	0.184	0.83	0.17
0.098	0.54	0.45	0.243	0.79	0.21
0.122	0.50	0.50	0.300	0.75	0.25
0.146	0.45	0.54	0.355	0.71	0.29
0.170	0.41	0.59	0.410	0.70	0.31
0.190	0.38	0.62	0.463	0.67	0.33
0.215	0.33	0.67	0.515	0.63	0.37
0.240	0.32	0.68	0.566	0.61	0.39
0.260	0.27	0.73	0.615	0.60	0.40
0.280	0.27	0.73	0.664	0.58	0.42
0.305	0.26	0.74	0.711	0.56	0.44
0.327	0.24	0.76	0.756	0.55	0.45
0.370	0.21	0.79	0.803	0.54	0.46
0.410	0.18	0.81	0.847	0.52	0.48
0.450	0.17	0.83	1.016	0.46	0.54
0.500	0.15	0.85			
0.540	0.14	0.86			
0.570	0.13	0.87			
0.650	0.11	0.89			
0.745	0.09	0.90			
0.833	0.08	0.92			
0.920	0.07	0.93			
1.080	0.05	0.95			

<sup>a</sup>From [201].

# 17

# Time-Resolved Protein Fluorescence

The previous chapter described the general features of intrinsic protein fluorescence. We described the spectral properties of the aromatic amino acids and how these properties are influenced by the surrounding protein structure. We now describe time-resolved measurements of protein fluorescence. Such measurements have become increasingly common because of the increased availability of time-domain (TD) and frequency-domain (FD) instrumentation.<sup>1,2</sup> However, time-resolved studies of intrinsic protein fluorescence are made challenging by the lack of simple pulsed light sources. Pulsed laser diodes are not yet available for excitation of protein fluorescence. Pulsed LEDs for excitation of protein fluorescence have just been announced, but the pulse widths are over one nanosecond. Single-photon excitation of protein fluorescence requires wavelengths in the range from 280 to 305 nm. Prior to about 2000, the dominant pulsed light source for this range of wavelengths was a synchronously pumped cavity-dumped dye laser, typically rhodamine 6G, which was doubled to obtain the UV wavelengths. The synchronously pumped dye lasers require an actively mode-locked pump laser, typically an argon ion or Nd:YAG laser. At present the actively mode-locked lasers are becoming less available because of the widespread use of Ti:sapphire lasers. These lasers spontaneously mode lock and may not use an active mode locker. Wavelengths suitable for excitation of protein fluorescence can be obtained by frequency tripling the long-wavelength output of a Ti:sapphire laser. Tripling the output at 840 nm yields 280 nm. The femtosecond pulse widths from Ti:sapphire lasers make it practical to generate such harmonics. Excitation of intrinsic protein fluorescence can also be accomplished with synchrotron radiation. Many of the recent studies of time-resolved intrinsic protein fluorescence used the frequency-tripled output of a pulsed Ti:sapphire laser or synchrotron radiation.

Even with the best available instrumentation it is challenging to interpret the time-dependent data from proteins.

The intensity decays of proteins are usually complex and often depend on observation wavelength. The complexity is due to both the presence of multiple-tryptophan residues in a single protein and the complex decay kinetics displayed by even single-tryptophan residues in proteins. High time resolution and high signal-to-noise measurements are needed to resolve the multiple components in these decays. Once the multi-exponential intensity decays are resolved, it is tempting to assign the various components to the individual tryptophan residues in multi-tryptophan proteins. However, even proteins with a single tryptophan residue typically display two or more decay times.<sup>3,4</sup> Hence, there is no reason to believe that the individual decay times represent individual trp residues, until this fact is demonstrated by additional experiments. In some cases, where the decay times are very different, it has been possible to assign decay times to individual tryptophan residues. This assignment typically relies on the use of mutant proteins containing one tryptophan or a fewer number of tryptophans than are present in the wild-type protein.

An additional complication is that tryptophan itself in solution at neutral pH displays a multi-exponential or non-exponential decay. The heterogeneity is moderately weak. Most of the emission from tryptophan occurs with a decay time near 3.1 ns. There is also a second component with a decay time near 0.5 ns. For some time the origin of this component was not known. It appears that most of heterogeneity of the tryptophan decay is due to the presence of conformational isomers, called rotamers, which display distinct decay times. However, there may be additional factors that contribute to the complex decay kinetics of tryptophan.

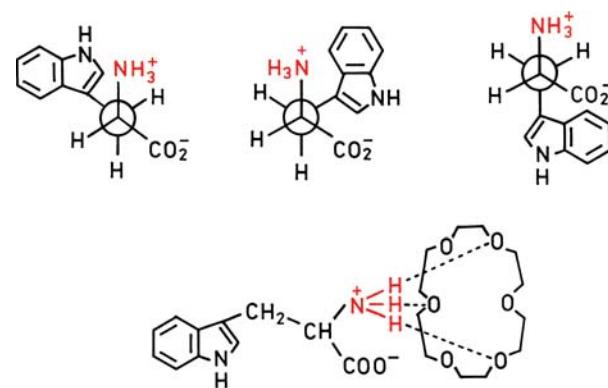
Interpretation of the intensity decays becomes more complicated because of additional processes that may not occur for the isolated amino acids. Energy transfer can occur from tyrosine to tryptophan, or between tryptophan residues themselves. Following excitation the tryptophan emission can display time-dependent spectral shifts due to

relaxation of the solvent or the protein matrix around the excited-state dipole moment. Proteins may exist in several conformations, each of which displays different intensity decay. Another source of complexity is the possibility of transient effects in collisional quenching, due to either added quenchers or the presence of nearby quenching groups in the protein. In principle, all these phenomena can be studied using time-resolved measurements. In practice, it is difficult to determine the contributions of each phenomenon to the intensity decay. The use of engineered proteins is critical to resolving these complex interactions.

While the interpretation of time-resolved protein fluorescence is not always simple, the time-resolved data provide opportunities for a more detailed understanding of protein structure and function. In favorable cases it is possible to resolve the emission spectra of individual tryptophan residues based on the time-dependent decays measured at various emission wavelengths. The time-resolved decays can sometimes be interpreted in terms of the location of the tryptophan residues in proteins, and the interactions of these residues with nearby amino-acid residues in the protein. Conformation changes in proteins often result in changes in the intensity decay due to altered interactions with nearby groups. The time-dependent anisotropy decays are invariably informative about the extent of local protein flexibility and the interactions of a protein with other macromolecules. Also, fluorescence quenching is best studied by time-resolved measurements, which can distinguish between static and dynamic processes. And, finally, it is now known that proteins can be phosphorescent at room temperature. The phosphorescence decay times are sensitive to exposure to the aqueous phase as well as the presence of nearby quenchers. In this chapter we present an overview of time-resolved protein fluorescence, with examples that illustrate the range of behavior seen in proteins.

### 17.1. INTENSITY DECAYS OF TRYPTOPHAN: THE ROTAMER MODEL

One difficulty in interpreting the time-resolved intensity decays of proteins has been a lack of understanding of the intensity decay of tryptophan itself. In neutral aqueous solution the intensity decay of tryptophan is known to be a double exponential, with decay times near 3.1 and 0.5 ns (Table 17.1).<sup>4–12</sup> The dominant origin of a bi-exponential decay of tryptophan is the presence of rotational isomers (Figure 17.1). In solution the side chain of tryptophan can adopt various conformational states, which appear to interchange slowly on the ns timescale. A tryptophan solution can be regarded as a mixture of these rotational isomers, called rotamers. In neutral aqueous solution, tryptophan is present in the zwitterionic form in which the amino group



Trp – 18 – Crown – 6

**Figure 17.1.** Rotational isomers of tryptophan rotamers. The rotamer on the left is thought to be responsible for the 0.5-ns decay time. The lower section shows tryptophan complexed with 18-Crown-6, which prevents quenching by the ammonium group. Revised from [12,27].

**Table 17.1.** Intensity Decays of the Aromatic Amino Acids and Related Compounds at 20°C, pH 7

Compound	$\tau_1$ (ns)	$\tau_2$ (ns)	$\alpha_1$	$\alpha_2$	$\lambda_{em}$ (nm)	Ref.
Indole	4.4	–	1.0	–	350	–
Tryptophan	3.1	0.53	0.67	0.33	330	6
NATA	3.0	–	1.0	–	330	6
Phenol	3.16	–	1.0	–	300	32, 34
Tyrosine (pH 6)	3.27	–	1.0	–	300	32, 34
Tyrosine (pH 5.5)	3.40	0.98	0.41	0.58	350	43
O-Methyl tyrosine (pH 5.5)	4.84	–	1.0	–	310	34
NATyrA	1.66	0.11	0.65	0.35	300	32, 34

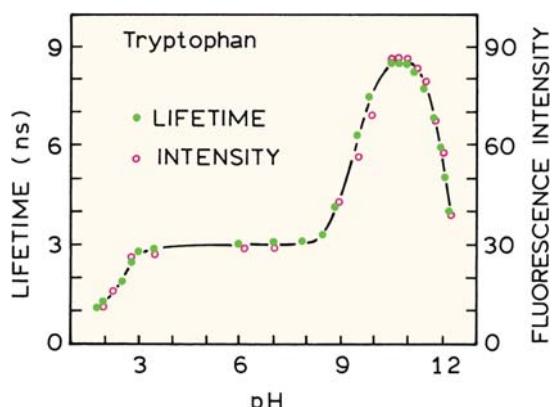


**Figure 17.2.** Relative fluorescence intensity and mean lifetime of tryptophan as a function of pH. Excitation was 280 nm, and emission through a Corning 0-52 filter. Mean lifetimes were measured from the phase angle at 10 MHz. Revised and reprinted with permission from [25]. Copyright © 1981, American Chemical Society.

is protonated ( $-\text{NH}_3^+$ ) and the carboxy group is ionized ( $-\text{CO}_2^-$ ). In solution the emission of tryptophan can be self-quenched by an intramolecular process involving the indole ring and the positively charged ammonium group. Recall that indole is uniquely sensitive to quenching, particularly by electron-deficient species. Reported quenchers of indole include acrylamide, amides, imidazolium, ammonium, methionine, tyrosine, disulfides, peptide bonds, trifluoroethanol, and electron scavengers.<sup>13–23</sup> Tryptophan can also be quenched by the amino-acid side chains, including glutamine, asparagine, protonated carboxyl groups on glutamate and aspartate, cysteine, and histidine.<sup>24</sup>

Quenching by the ammonium group is seen from the dependence of the tryptophan quantum yield on pH (Figure 17.2). As the pH is increased from 8 to 10 the amino group undergoes dissociation to the neutral form, and the quantum yield and mean lifetime increase approximately three-fold.<sup>7,25</sup> This increase in quantum yield and lifetime occurs because the neutral amino group does not quench the indole moiety. The quenching effect of a protonated amino group on tryptophan is general and occurs for a number of tryptophan-containing peptides.<sup>26</sup> Tryptophan analogues lacking the amino group, such as 3-methyl indole<sup>12</sup> or constrained tryptophan derivatives that prevent contact of the amino group with the indole ring,<sup>11</sup> do not show the pH-dependent increase in quantum yield between pH 8 and 10. Complexation of the amino group to a crown ether results in a several-fold increase in fluorescence intensity because the amino group can no longer come in contact with the indole ring.<sup>27</sup> Examination of the pH-dependent intensities of tryptophan

indicates that the intensity decreases further below pH 3 and above pH 11. The decrease in intensity below pH 3 is due to intramolecular quenching of indole by the neutral carboxyl group, which serves as an electron acceptor. At high pH indole is quenched by hydroxyl groups, which may be due to collisional quenching by  $\text{OH}^\bullet$  or by excited-state deprotonation of the proton on the indole nitrogen group.

How does quenching by the amino group explain the bi-exponential decay of tryptophan at pH 7? The quenching process is thought to be most efficient in one of the rotamers, and this species displays the shorter 0.5-ns decay time (Figure 17.1, left). The complete explanation is probably somewhat more complex. For instance, more than three conformations are possible if one considers the possible orientations of the indole ring.<sup>11</sup> Also, it is known that quenching is usually accompanied by transient effects that appear as short components in the intensity decay. Because of the complexity introduced by the amino and carboxyl groups, experiments are frequently performed on uncharged tryptophan analogues (Figure 17.3). In the neutral tryptophan analogue NATA the amino group is acetylated and the carboxyl group converted to an amide. Unchanged tyrosine derivatives are also used (NATyrA). These forms of the amino acids mimic the structures found when these amino acids are contained in a polypeptide chain.

The presence of rotamers is probably the dominant reason for the multi-exponential decay of tryptophan at neutral pH. However, there may be other factors that also contribute to the complex decays of tryptophan and proteins. One of these factors is quenching by peptide bonds.<sup>28</sup> The

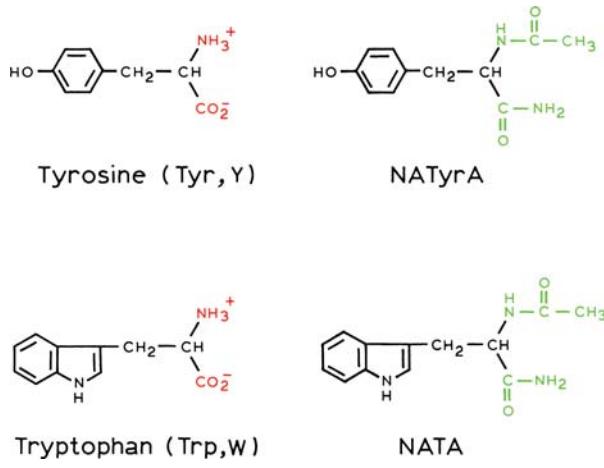


**Figure 17.3.** Structures of tyrosine and tryptophan and their neutral analogues, N-acetyl-L-tryptophanamide (NATA) and N-acetyl-L-tyrosinamide (NATyrA).

quantum yield of NATA in water is 0.14 and the quantum yield of 3-methyl indole (3-MI) in water is 0.34. The lower quantum yield of NATA is thought to be due to quenching by one or both of the amide groups on NATA (Figure 17.3). If this is true then it is surprising that the rotamer populations of NATA do not result in a multi-exponential decay as occurs in tryptophan. The extent of quenching by amides depends strongly on distance, polarity, and charge distribution surrounding the indole ring and the amide groups. The charge distribution around the tryptophan can either increase or decrease charge separation and quenching by amides. Hence, a variety of effects contribute to the complex intensity decays of proteins.

## 17.2. TIME-RESOLVED INTENSITY DECAYS OF TRYPTOPHAN AND TYROSINE

Controversy over the intensity decay of tryptophan persisted for many years, and one may wonder why the problem took so long to solve. At that time the measurements pushed the limits of the available instrumentation and methods of data analysis. Many of the early time-resolved decays of tryptophan were measured using flashlamps with nanosecond pulse widths. The low intensities and repetition rates of the flashlamps resulted in data just adequate to detect the short component, but not to reliably resolve its decay time and amplitude. Long data acquisition times were used to obtain the number of photon counts needed to recover the decay components. During this time the flashlamp profiles could change and introduce artifacts. Additionally, it is now known that the 0.5- and 3.1-ns decay components display different emission spectra. Some of the earlier measurements observed only the long-wavelength emission above 360 nm, where the emission from the 0.5-ns component is weak.

The difficulty in resolving the two intensity decay components is illustrated by the intensity decay of tryptophan at pH 7 (Figure 17.4). The light source was a cavity-dumped rhodamine 6G dye laser that was frequency doubled to 295 nm, which provided pulses about 7 ps wide. The detector was a microchannel plate (MCP) PMT detector. The data were fit to the single- and double-exponential models:

$$I(t) = \sum_i \alpha_i \exp(-t/\tau_i) \quad (17.1)$$

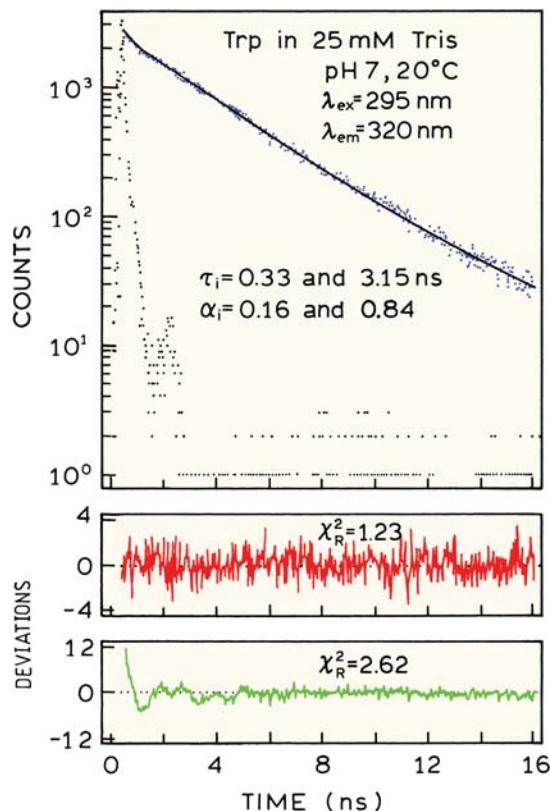


**Figure 17.4.** Time-domain intensity decay of tryptophan at pH 7. Excitation was at 295 nm, and the emission through a Corning WG 320 filter. The deviations are for the single- ( $\chi_R^2 = 2.62$ ) and double-exponential fit ( $\chi_R^2 = 1.23$ ). From [29].

where  $\alpha_i$  are the amplitudes of the components with decay times  $\tau_i$ . The fitted curves for both the single- and double-exponential models are visually superimposable on the measured data. Deviations of the data from the single-exponential fit are barely visible in the deviations (Figure 17.4, lower panels), and the decrease in  $\chi_R^2$  is only from 2.62 to 1.23 for the single- and double-exponential fits, respectively. Even with modern TCSCP instrumentation it remains difficult to resolve the two decay times of tryptophan.

The multi-exponential decay of tryptophan can also be observed using the frequency-domain method (Figure 17.5). The data were obtained using the same dye laser light source, a MCP PMT detector, and the harmonic content method (Chapter 5). The deviations from the single-exponential model are clearly non-random (lower panels). The 50-fold decrease in  $\chi_R^2$  for the double-exponential fit from 58.9 to 0.9 is convincing evidence for the non-single-exponential decay of tryptophan.

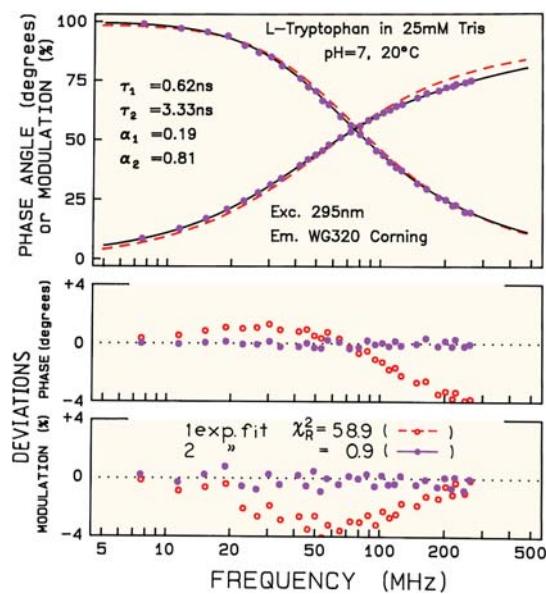


**Figure 17.5.** Frequency-domain intensity decay of tryptophan in  $\text{H}_2\text{O}$  at  $20^\circ\text{C}$  and pH 7. Excitation at 295 nm. The emission was collected through a long pass Corning WG 320 filter. From [2].

### 17.2.1. Decay-Associated Emission Spectra of Tryptophan

Suppose a sample displays a multi-exponential decay, and that the decay is different at different emission wavelengths. The intensity decay is then described by

$$I(\lambda, t) = I(t) = \sum_i \alpha_i(\lambda) \exp(-t/\tau_i) \quad (17.2)$$

where  $\alpha_i(\lambda)$  are the wavelength-dependent pre-exponential factors and  $\tau_i$  the decay times. This expression assumes the decay times are independent of wavelength. The emission spectrum due to each component can be calculated using

$$I_i(\lambda) = \frac{\alpha_i(\lambda) \tau_i I(\lambda)}{\sum_j \alpha_j(\lambda) \tau_j} \quad (17.3)$$

In this expression  $I(\lambda)$  is the steady-state emission spectrum. The product  $\alpha_i(\lambda) \tau_i$  appears in the numerator because the steady-state intensity is proportional to this product. The sum in the denominator is proportional to the total intensity at this wavelength. These spectra  $I_i(\lambda)$  are called decay-associated spectra (DAS) because they represent the emission spectrum of the component emitting with lifetime  $\tau_i$ .

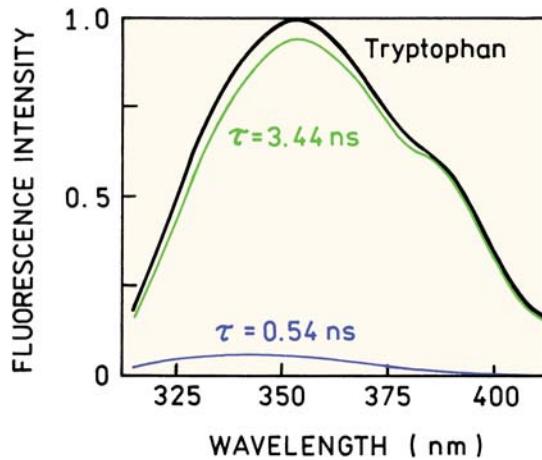


**Figure 17.6.** Spectral resolution of the short and long ns decay components of tryptophan. Similar results were reported in [5–6]. From [30].

The multi-exponential decays recovered for each emission wavelength are used to construct the emission spectra associated with each decay time. To calculate the decay-associated spectra one has to recall that the fractional contribution ( $f_i$ ) of each species to the steady-state intensity is proportional to the product  $\alpha_i \tau_i$ . The contribution of a short-decay-time component to the steady-state intensity is lower than the relative amplitude ( $\alpha_i$ ) of the short-decay-time component in the intensity decay. In the case of tryptophan the short component contributes only about 4% to the total emission of tryptophan at neutral pH (Figure 17.6). Emission from the short component is centered near 335 nm and occurs at slightly shorter wavelengths than for the overall emission. This blue shift of the emission is consistent with the expected effect of a nearby positive charge on the polar  ${}^1\text{L}_a$  state of indole. Little contribution from the  ${}^1\text{L}_b$  state is expected, as conversion of  ${}^1\text{L}_b$  to  ${}^1\text{L}_a$  occurs in less than 2 ps.<sup>31</sup>

### 17.2.2. Intensity Decays of Neutral Tryptophan Derivatives

In proteins the amino and carboxyl groups of tryptophan are converted into neutral groups by the formation of peptide bonds. The quenching effect of the  $\alpha$ -amino group is no longer present. Neutral tryptophan analogues typically display simpler decay kinetics than tryptophan itself. The most commonly used analogue is N-acetyl-L-tryptophanamide, which has essentially the same structure as a tryptophan residue in proteins (Figure 17.3). The intensity decay of

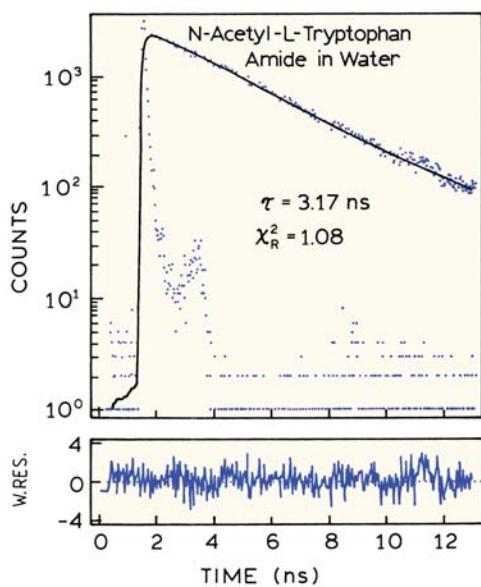


**Figure 17.7.** Time-domain intensity decay of N-acetyl-L-tryptophanamide (NATA) at pH 7. From [29].

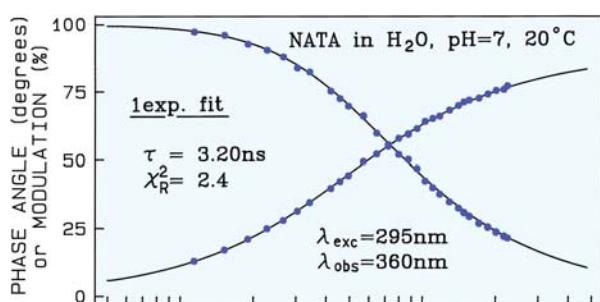


**Figure 17.8.** Frequency-domain intensity decay of NATA at pH 7, 20°C. The solid curves are for the single-exponential fit,  $\tau = 3.20\text{ ns}$ ,  $\chi^2_R = 2.4$ . The double-exponential fit yielded  $\tau_1 = 1.04\text{ ns}$ ,  $\tau_2 = 3.28\text{ ns}$ ,  $\alpha_1 = 0.05$  and  $\alpha_2 = 0.95$ , with  $\chi^2_R = 1.3$ . From [29].

NATA (Figure 17.7) is essentially a single exponential.<sup>6,12,32</sup> Comparable frequency-domain data for NATA also revealed a dominant single-exponential decay (Figure 17.8). There is some decrease in  $\chi^2_R$  for the double-exponential fit, so that the decay of NATA may display a weak second component. However, for all practical purposes NATA displays a single decay time (Table 17.1).

### 17.2.3. Intensity Decays of Tyrosine and Its Neutral Derivatives

Tyrosine can also display complex decay kinetics, but its properties are opposite to that of tryptophan. Frequency-

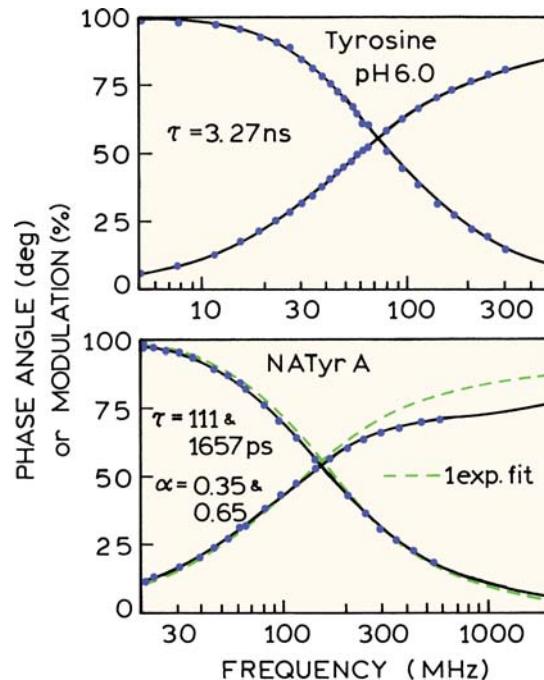


**Figure 17.9.** Frequency-domain intensity decays of tyrosine and NATyrA. Data reprinted with permission from [33]. Copyright © 1987, American Chemical Society.

domain intensity decays of tyrosine and its neutral analogue N-acetyl-L-tyrosinamide (NATyrA) are shown in Figure 17.9. Tyrosine itself displays a single-exponential decay,<sup>33–34</sup> whereas NATyrA displays a bi-exponential decay (Table 17.1). The molecular origin of the double-exponential decay of NATyrA is not clear but may be due to the presence of ground state rotamers.<sup>35–37</sup> The peptide bonds or carbonyl groups may quench the phenol emission by an electron-transfer mechanism.<sup>38–39</sup> Considerably less information is available on the intensity decays of phenylalanine.<sup>40–42</sup> pH-dependent lifetimes have not been reported.

The intensity decay of tyrosine in water is usually a single exponential, but different results can be obtained at different observation wavelengths (Figure 17.10). These intensity decays were measured using 277-nm excitation from a frequency-tripled Ti:sapphire laser and a microchannel plate PMT detector. For the peak tyrosine emission at 310 nm the intensity decay is a single exponential.<sup>43</sup> As the observation wavelength increases the plots become curved, showing the presence of additional components. The component with a decay time of 0.98 ns is due to tyrosinate, which forms during the excited-state lifetime. This component from tyrosine is seen as the rapidly decaying species at

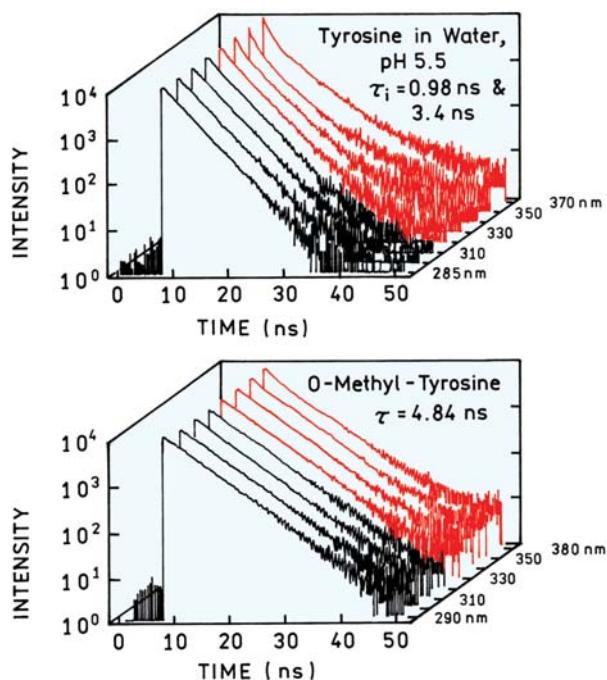


**Figure 17.10.** Wavelength-dependent intensity decays of tyrosine and o-methyl-tyrosine in water at pH 5.5. For tyrosine the upward curvature at long times and long wavelengths is thought to be due to impurities. Revised and reprinted with permission from [43]. Copyright © 2004, American Chemical Society.

short times and long wavelengths. Ionization of the hydroxyl group occurs because its  $pK_a$  decreases to about 4 in the excited state. The assignment of this component to ionized tyrosine is supported by the intensity decays of O-methyl-tyrosine (Figure 17.10, lower panel), which do not show this component. The DAS for the two main components in the tyrosine decay are shown in Figure 17.11. The dominant emission centered at 310 nm is associated with the 3.40-ns component. The 0.98-ns component is due to a longer-wavelength emission centered near 360 nm, which is emission from tyrosinate.

### 17.3. INTENSITY AND ANISOTROPY DECAYS OF PROTEINS

We now consider the intensity decays of tryptophan residues in proteins. Since NATA displays a single decay time, we can expect single-tryptophan proteins to display single-exponential decays. However, this is not the case. In a survey of eight single-tryptophan proteins, only one protein (apo-azurin) was found to display a single decay time.<sup>3</sup> This early report was confirmed by many subsequent studies showing that most single-tryptophan proteins display

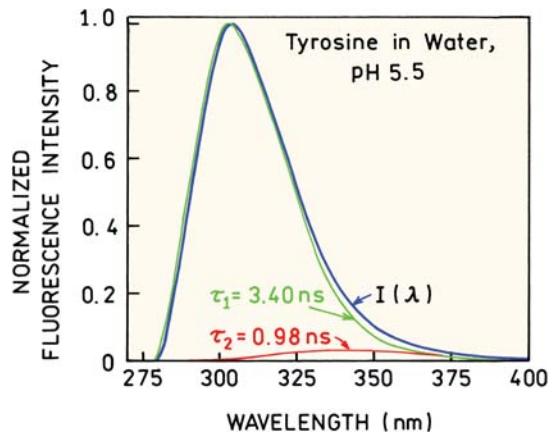


**Figure 17.11.** Decay-associated spectra of tyrosine in water at pH 5.5. From [43].

double or triple-exponential decays (Table 17.2), and of course multi-tryptophan proteins invariably display multi-exponential decays (Table 17.3).

What are the general features of protein intensity decays? The variability of the intensity decays is a result of protein structure. The intensity decays and mean decay times are more variable for native proteins than for denatured proteins. The decay times for denatured proteins can be grouped into two classes, with decay times near 1.5 and 4.0 ns, with the latter displaying a longer emission wavelength.<sup>3</sup> This tendency is enhanced in native proteins, and many of them show lifetimes as long as 7 ns, typically on the red side of the emission. Surprisingly, buried tryptophan residues seem to display shorter lifetimes. The longer lifetimes of exposed tryptophan residues have been puzzling because exposure to water is expected to result in shorter lifetimes. It is now known that peptide bonds can quench tryptophan emission.<sup>28</sup> Hence, the shorter lifetimes of

**Table 17.2.** Intensity Decays of Single-Tryptophan Proteins<sup>a</sup>

Protein	$\tau_1$ (ns)	$\tau_2$ (ns)	$\tau_3$ (ns)	Ref.
Azurin	4.8	0.18	—	4
Apoazurin	4.9	—	—	4
Staph. nuclease	5.7	2.0	—	3
RNase T <sub>1</sub> (pH 5.5)	3.87	—	—	—
RNase T <sub>1</sub> (pH 7.5)	3.57	0.98	—	—
Glucagon	3.6	1.1	—	4
Human serum albumin	7.8	3.3	—	4
Phospholipase A2	7.2	2.9	0.96	4
Subtilisin	3.82	0.83	0.17	44

<sup>a</sup>Additional intensity decays of single-tryptophan proteins can be found in [45].

**Table 17.3.** Intensity Decays of Multi-Tryptophan Proteins<sup>a</sup>

Protein	# of Trps	$\tau_1$ (ns)	$\tau_2$ (ns)	$\tau_3$ (ns)
Bovine serum albumin	2	7.1	2.7	—
Liver alcohol dehydrogenase	2	7.0	3.8	—
Ferredoxin	2	6.9	0.5	—
Sperm whale myoglobin	2	2.7	0.1	0.01
Papain	5	7.1	3.7	1.1
Lactate dehydrogenase	6	8.0	4.0	1.0

<sup>a</sup>From [4].

buried residues may be because the buried tryptophan residues have more contact with peptide bonds than the exposed residues. However, there is little correlation between the mean lifetime and emission maximum of proteins (see Figure 16.12). In proteins that contain chromophoric groups (ferredoxin and myoglobin), the tryptophan residues are often quenched by resonance energy transfer, resulting in subnanosecond decay times (Table 17.3).

Multi-exponential decays are not surprising for multi-tryptophan proteins. However, the origin of multi-exponen-

tial decays in single-tryptophan proteins is less clear. Given that NATA displays a single decay time, it seems that a single-tryptophan residue in a single unique protein environment should result in a single decay time. One possible origin of multi-exponential decays is the existence of multiple protein conformations. Since nearby amino-acid residues can act as quenchers, it seems logical that slightly different conformations can result in different decay times for native proteins. However, multi-exponential decays can be observed even when the proteins are thought to exist in a single conformation.<sup>46–47</sup> As shown in the following section, unfolding of a protein can change a single-exponential decay into a multi-exponential decay, which seems to be consistent with the presence of multiple conformations for a random coil peptide. It appears that multi-exponential decays of single-tryptophan proteins can result in part from dynamic processes occurring during the excited-state lifetime.<sup>48–49</sup> These dynamic processes can include nearby motion of quenchers, spectral relaxation, and/or resonance energy transfer.

### 17.3.1. Single-Exponential Intensity and Anisotropy Decay of Ribonuclease T<sub>1</sub>

In the previous section we saw that most single-tryptophan proteins display multi-exponential decays. However, there are two known exceptions—apoazurin and ribonuclease T<sub>1</sub> from *Aspergillus oryzae*. Most ribonucleases do not contain tryptophan. Ribonuclease T<sub>1</sub> is unusual in that it contains a single-tryptophan residue, and under some conditions displays a single-exponential decay. RNase T<sub>1</sub> consists of a single polypeptide chain of 104 amino acids (Figure 17.12). RNase T<sub>1</sub> has four phenylalanines, nine tyrosines, and a single-tryptophan residue at position 59. This tryptophan residue is near the active site. The emission maximum is near 323 nm, suggesting that this residue is buried in the protein matrix and not exposed to the aqueous phase. Quenching studies have confirmed that this residue is not easily accessible to quenchers in the aqueous phase.<sup>50–53</sup> Ribonuclease is also unusual in that its intensity decay is a single exponential at pH 5.5<sup>54–57</sup> (Figure 17.13, top). The decay becomes a double exponential at pH 7. A single-exponential decay is convenient because changes in the protein structure can be expected to result in more complex decay kinetics. It is easier to detect a single-exponential decay becoming a multi-exponential decay than it is to detect a change in a multi-exponential decay.

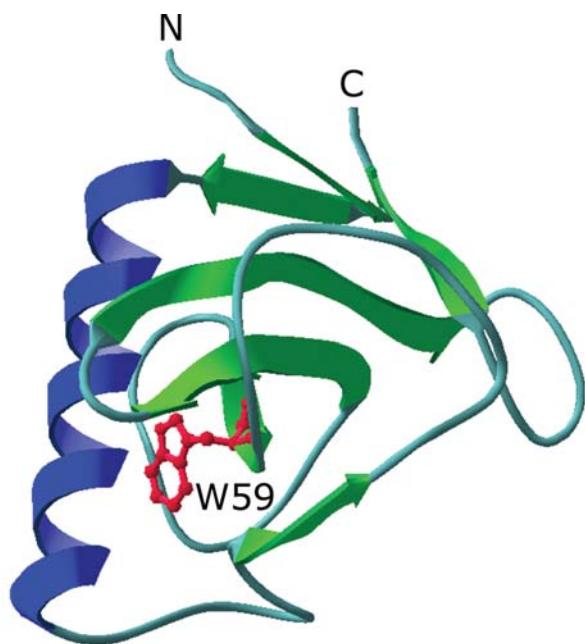


**Figure 17.12.** Structure of ribonuclease T<sub>1</sub> in the presence of 2'-GMP (2'-GMP removed). Trp 59 is located between the  $\alpha$ -helix and  $\beta$ -sheet structure.

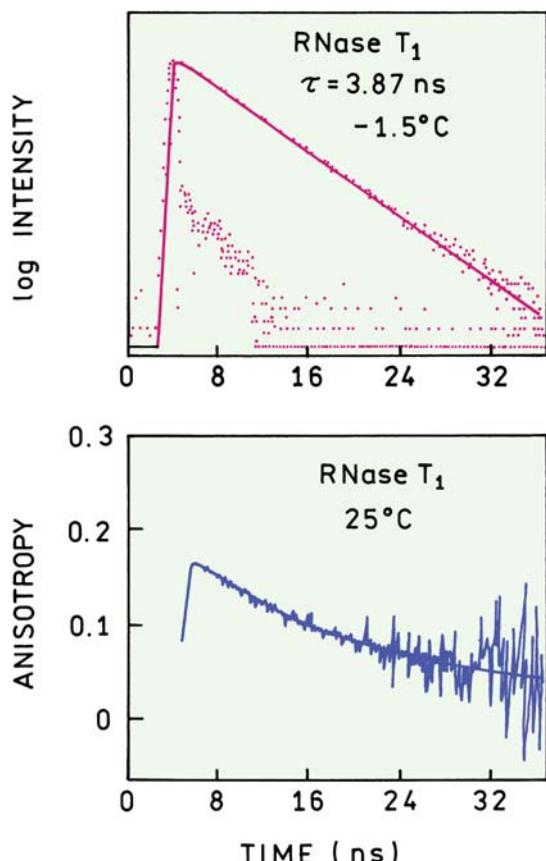
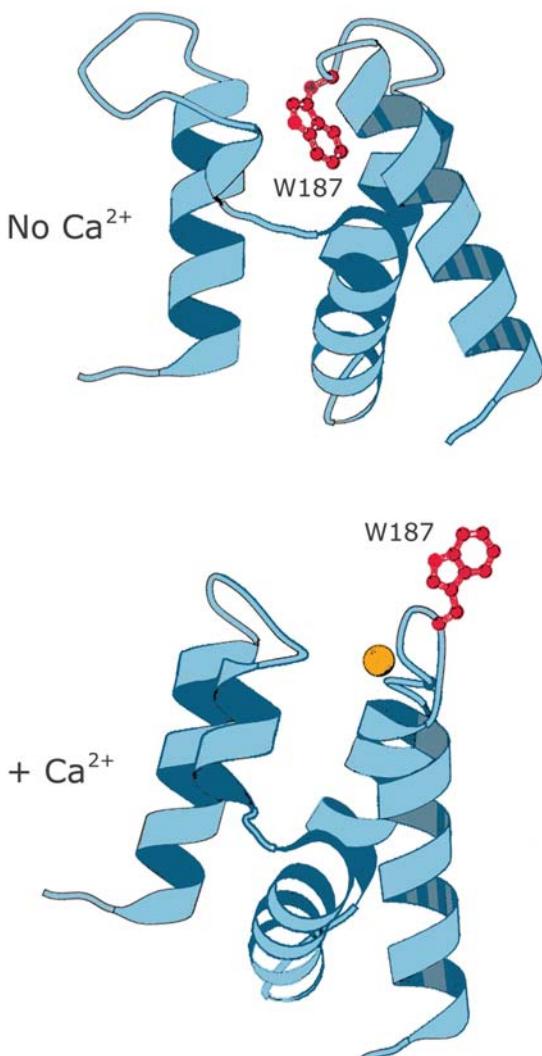


**Figure 17.13.** Time-resolved fluorescence intensity and anisotropy decay of RNase T<sub>1</sub> in buffered aqueous solution pH 5.5. Excitation at 295 nm. Data from [54].

### 17.3.2. Annexin V: A Calcium-Sensitive Single-Tryptophan Protein

Ribonuclease T<sub>1</sub> provided an example of a single-tryptophan protein that displayed single-exponential intensity and anisotropy decays (Figure 17.13, bottom). For most proteins, even with a single-tryptophan residue, the intensity and anisotropy decay are more complex. One example is annexin V, which possesses a single-tryptophan residue (Figure 17.14). Annexins are a class of homologous proteins that bind to cell membranes in a calcium-dependent manner. The crystal structure is known to be different with and without bound calcium.<sup>58</sup> The emission from the single-tryptophan residue is sensitive to calcium.<sup>59</sup> Addition of calcium results in shift of the emission maximum from 324 to 348 nm (Figure 17.15).

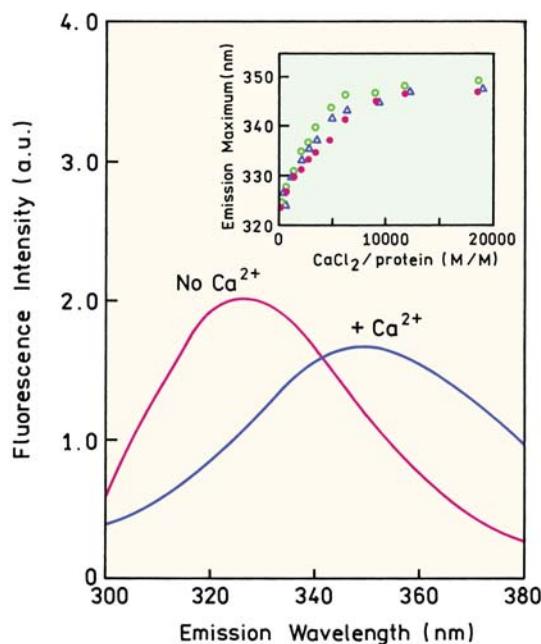
In the absence of calcium the intensity decay is highly non-exponential (Figure 17.16). Addition of calcium causes the intensity decay to become more like a single expo-



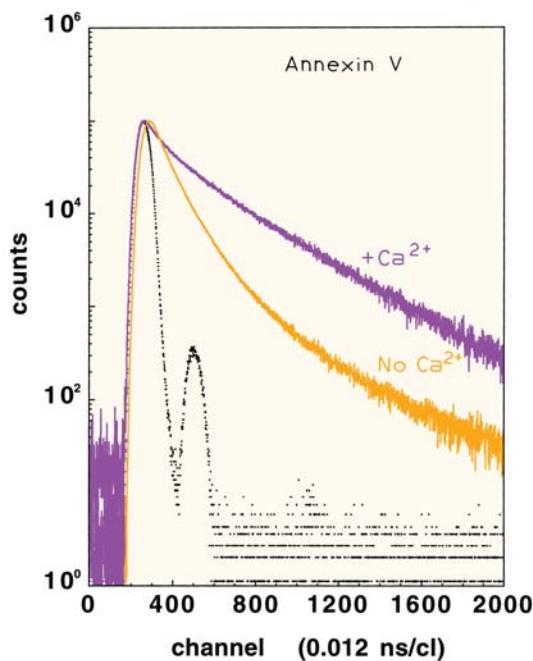
**Figure 17.14.** Structure of Annexin V in the absence (top) and presence (bottom) of Ca<sup>2+</sup>. The calcium atom is shown in red. Revised and reprinted with permission from [60]. Copyright © 1994, American Chemical Society.

nential. This dramatic change in calcium suggests the presence of a nearby quenching group in the calcium-free form. The crystal structures of annexin V are consistent with this suggestion because the tryptophan residue moves away from the protein in the presence of calcium (Figure 17.14).

As was described in Chapter 4 the multi-exponential model can be used to fit almost any intensity decay, even if the actual decay has some other functional form. When examining tables of multi-exponential decay parameters it is difficult to obtain an intuitive vision of the decays from the numerical values. The forms of complex intensity decays can be visualized from the lifetime distributions.



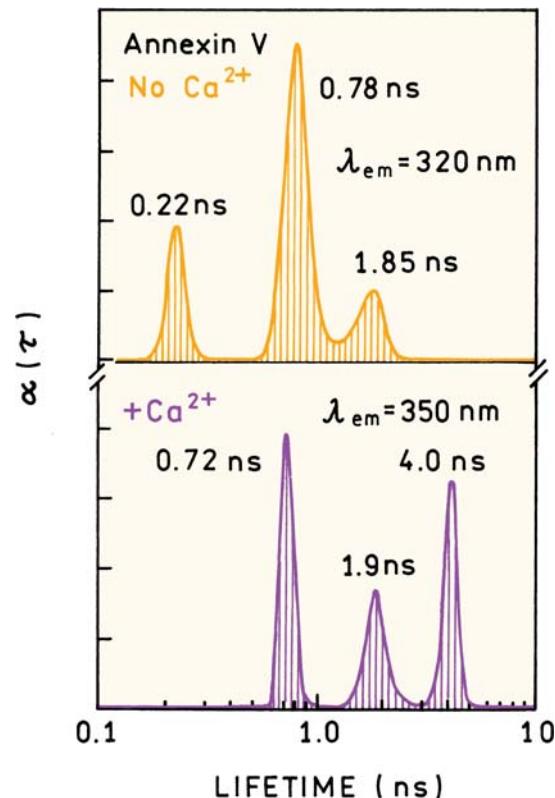
**Figure 17.15.** Fluorescence emission spectrum of trp 187 in annexin V with and without calcium-bound protein. The insert shows the dependence of the emission maximum of annexin V on the calcium-to-protein molar ratio under several conditions. Revised and reprinted with permission from [59]. Copyright © 1994, American Chemical Society.



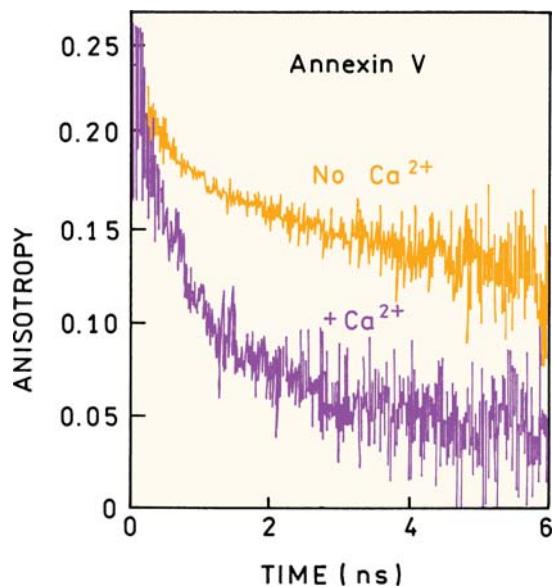
**Figure 17.16.** Fluorescence intensity decays of trp 187 in annexin V in the absence and presence of calcium. The intensity decays were measured at 320 nm without calcium and 350 nm with calcium. Revised and reprinted with permission from [59]. Copyright © 1994, American Chemical Society.

Figure 17.17 show the lifetime distributions of annexin V in the absence and presence of calcium. These plots shows the amplitude of the intensity decay for each decay time. The lifetime axis is logarithmic, as is common with maximum entropy analyses. The more rapid intensity decay in the absence of calcium can be understood from the decay component near 0.2 ns seen in the lifetime distribution. Binding of calcium to annexin V results in the appearance of a larger decay time component near 4 ns.

The calcium-dependent change in tryptophan exposure is expected to affect the anisotropy decay. As expected for a surface-exposed residue, the anisotropy decay also becomes more rapid in the presence of calcium (Figure 17.18). Once again it is helpful to visualize these decays as distributions, in this case distributions of correlation times. In the absence of calcium the anisotropy decay of annexin V is mostly due to overall rotational diffusion with a correlation time near 12 ns. In the presence of  $\text{Ca}^{2+}$  the anisotropy decay shows three correlation times near 80 ps, 1.2 ns, and 12 ns (Figure 17.19). Taken together these results are consistent with the



**Figure 17.17.** Lifetime distributions for the tryptophan emission from Annexin V in the absence and presence of calcium. The distributions were recovered using the maximum entropy method. Data from [60].



**Figure 17.18.** Time-resolved anisotropy decay of Annexin V in the absence and presence of calcium. Data from [59]; figure provided by Dr. Jacques Gallay from the Paris-Sud University, France.

known structural change induced by  $\text{Ca}^{2+}$ , which results in displacement of the trp 187 from a buried environment to an exposed environment in which the side chain is extended into the aqueous phase (Figure 17.14). It is apparent that the time-resolved intensity and anisotropy decays are highly sensitive to protein conformation.

### 17.3.3. Anisotropy Decay of a Protein with Two Tryptophans

From the previous examples we saw that in different proteins the tryptophan residues can be rigidly held by the protein or display segmental motions independent of overall rotational diffusion. In a multi-tryptophan protein residues, each residue may be rigid or mobile. This type of behavior is seen for single-tryptophan mutants of the IIA<sup>Glc</sup> protein.<sup>61</sup> This protein from *E. coli* is involved in transfer of phosphate groups, so we will call it the phosphoryl-transfer protein (PTP).

X-ray diffraction of the PTP shows a well-defined structure from residues 19 to 168. Residues 1 to 18 are not seen in the x-ray structure and are thus mobile in the crystal, and probably also in solution. Wild-type PTP does not contain any tryptophan residues. Single-tryptophan mutants were prepared with residues at positions 3 and 21, which were expected to be in the mobile and rigid regions, respectively. Time-resolved anisotropy decay of these mutant pro-

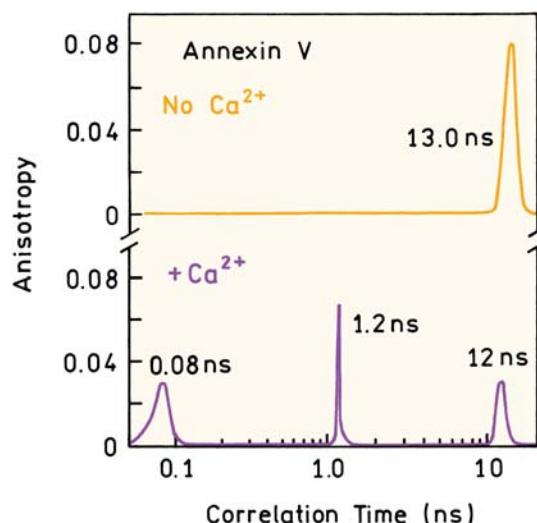


**Figure 17.19.** MEM-reconstituted correlation time distribution of trp 187 in annexin V. Data from [59].

teins are shown in Figure 17.20. At times longer than 3 ns both mutants display long correlation ( $\theta_L$ ) times near 40 ns. This correlation time is larger than expected for a protein with a molecular weight near 21 kDa (Table 10.4), which may be due to the flexible chain. The mutants show very different behavior at times below 3 ns, where the F3W mutants display short correlation times ( $\theta_s$ ) near 1 ns. The short correlation time is due to motion of residues 1–18,

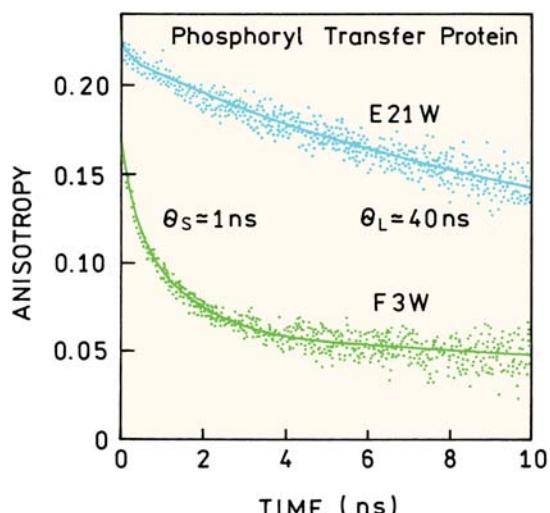


**Figure 17.20.** Time-resolved anisotropy decays of single-tryptophan mutants of the phosphoryl transfer protein. 296-nm excitation was obtained from a cavity-dumped frequency-doubled dye laser. Revised from [61].

**Table 17.4.** Anisotropy Decays of NATA and Single-Tryptophan Peptides and Proteins<sup>a</sup>

Proteins	$\theta_1$ (ps)	$\theta_2$ (ps)	$r_{01}$	$r_{02}$
RNase T <sub>1</sub> , 20°C	6520	—	0.310	—
Staph. nuclease	10160	91	0.303	0.018
Monellin	6000	360	0.242	0.073
ACTH	1800	200	0.119	0.189
Gly-trp-gly	135	39	0.105	0.220
NATA	56	—	0.323	—
Melittin monomer	1730	160	0.136	0.187
Melittin tetramer	3400	60	0.208	0.118

<sup>a</sup>20°C, excitation at 300 nm. From [77] and [78].

which are independent of the compact domain of the protein. These results show how tryptophan residues at different locations within the same protein can have different motions and different anisotropy decays.

#### 17.4. PROTEIN UNFOLDING EXPOSES THE TRYPTOPHAN RESIDUE TO WATER

The spectral properties of proteins are dependent upon their three-dimensional structure. This dependence can be seen by measuring the emission of native and denatured proteins. The effects of denaturation are easy to observe for ribonuclease T<sub>1</sub> (Figure 17.12), which displays single-exponential intensity and anisotropy decays in the native conformation (Figure 17.13). Emission spectra of ribonuclease T<sub>1</sub> (RNase T<sub>1</sub>) are shown in Figure 17.21. An excitation wavelength of 295 nm was chosen to avoid excitation of the tyrosine residues. For the native protein the emission maximum is at 323 nm, which indicates the indole group in a nonpolar

environment. Although not evident in Figure 17.21, others have reported the presence of weak vibrational structure in the emission spectrum,<sup>54</sup> as was seen for indole in cyclohexane and for azurin.

Proteins can be unfolded at high temperature or by the addition of denaturants such as urea or guanidine hydrochloride. These conditions result in a dramatic shift in the emission spectra of RNase T<sub>1</sub> to longer wavelengths. In the presence of 7.0 M guanidine hydrochloride, or at 65°C, the emission spectrum of RNase T<sub>1</sub> shifts to longer wavelength to become characteristic of a tryptophan residue that is fully exposed to water (Figure 17.21). These results show that protein structure determines the emission maximum of proteins or, conversely, that protein folding can be studied by changes in the intensity or emission spectra of proteins.

#### 17.4.1. Conformational Heterogeneity Can Result in Complex Intensity and Anisotropy Decays

Frequency-domain measurements were used to study the intensity decays of native and denatured RNase T<sub>1</sub> (Figure 17.22). In the native state at pH 5.5 the frequency-domain data reveal a single-exponential decay with  $\tau = 3.92$  ns. When the protein is denatured by heat the intensity decay becomes strongly heterogeneous.

Protein unfolding also affects the anisotropy decays of RNase T<sub>1</sub>. The frequency-domain data for RNase T<sub>1</sub> at 5°C is characteristic of a single correlation time (Figure 17.23). If the temperature is increased, or if one adds denaturant, there is an increase in the high-frequency differential phase angles and a decrease in the modulated anisotropy. These effects in the frequency-domain anisotropy data are charac-

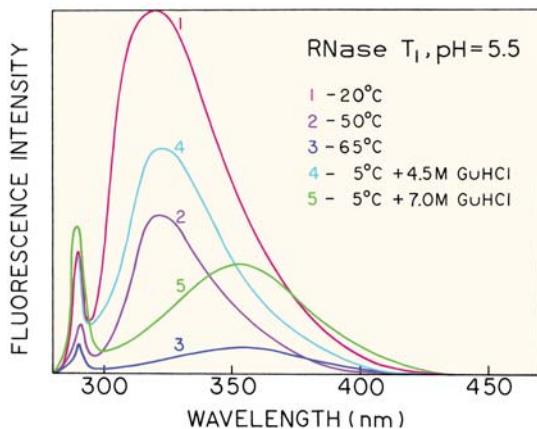


**Figure 17.21.** Emission spectra of ribonuclease T<sub>1</sub> (RNase T<sub>1</sub>),  $\lambda_{ex} = 295$  nm. From [62].

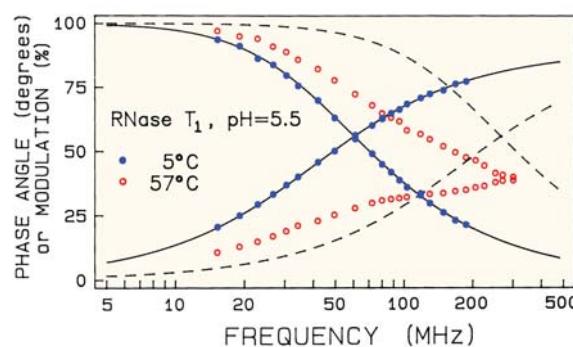


**Figure 17.22.** Frequency response of RNase T<sub>1</sub> at 5 (●) and 57°C (○). The solid and dashed lines show the best single component fits to the data at 5 and 57°C, respectively. The  $\chi_R^2$  values were 1.3 at 5°C and 2082 at 57°C. From [55].

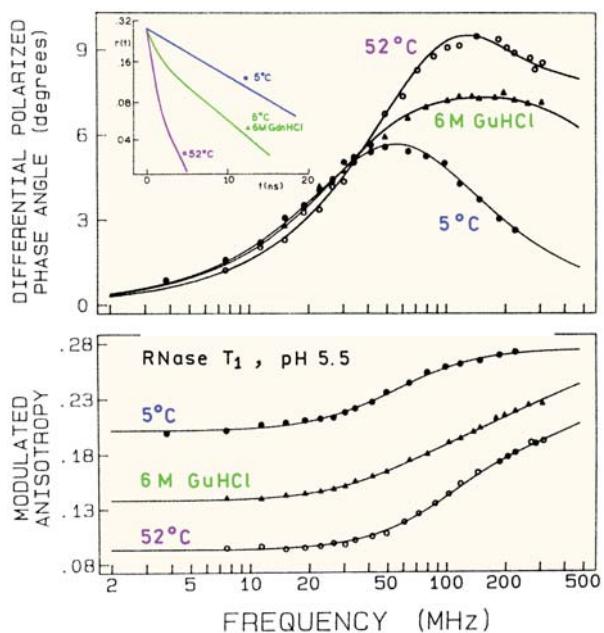


**Figure 17.23.** Frequency-domain anisotropy decays of RNase T<sub>1</sub> (pH 5.5) at 5°C (●) and 52°C (○) and at 5°C with 6 M guanidine hydrochloride (▲). The insert shows equivalent time-dependent anisotropies reconstructed from the FD data. Similar data were reported in [63]. From [2].

teristic of rapid motions of the residue in addition to slower overall rotational diffusion. At low frequency the modulated anisotropies are equal to the steady-state anisotropies. At high frequencies the modulated anisotropies approach the fundamental anisotropy ( $r_0$ ). The FD anisotropy data can be used to reconstruct the time-dependent anisotropy decays (insert). In the native state the anisotropy decay is a single exponential. When unfolded by either guanidine hydrochloride or high temperature, the anisotropy decay displays a fast component due to segmental motions of the tryptophan residue. Hence, rapid components in the anisotropy decay can be expected for random coil peptides, or for tryptophan residues on the surfaces of proteins that are not constrained by the three-dimensional structure.

## 17.5. ANISOTROPY DECAYS OF PROTEINS

Proteins display a variety of anisotropy decays. Most proteins show fast components in the decays at early times.<sup>63–78</sup> Typical anisotropy decays are shown in Figure 17.24. The single tryptophan in the lumazine protein shows a high degree of segmental flexibility. The long component near 17 ns is assigned to overall rotational diffusion of the protein. The short component near 0.45 ns is assigned to rapid

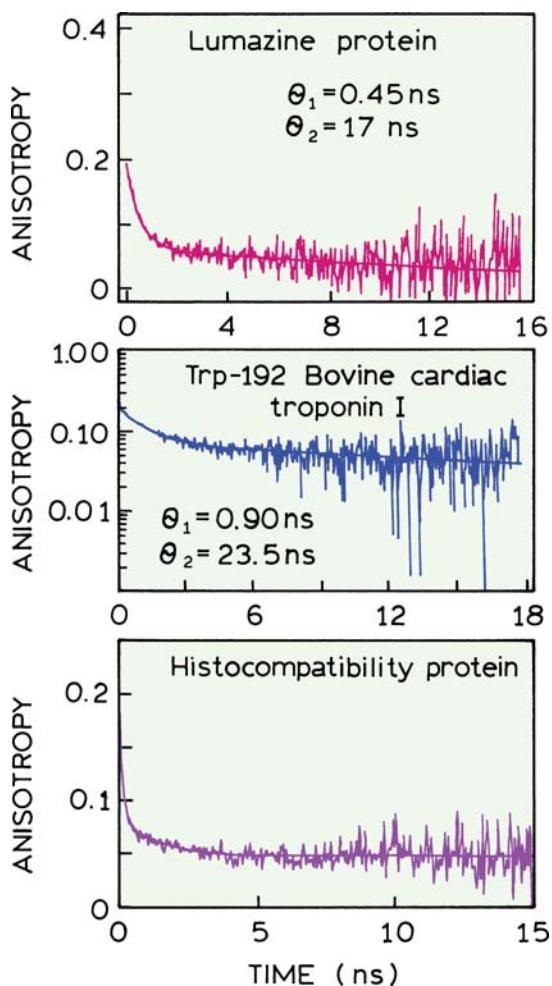


**Figure 17.24.** Anisotropy decay for the single-tryptophan residue in the lumazine protein (top), for trp-192 in bovine cardiac troponin I (middle) and for a histocompatibility protein (bottom). Revised from [74], [75], and [76].

motions of the tryptophan residue independent of overall rotational diffusion. Another example is the tryptophan residue in bovine troponin I, which shows a shorter correlation time near 0.90 ns and a correlation time of 23.5 ns due to overall rotational diffusion. In many cases the rapid components in the anisotropy decay are too fast to be measured, as shown for a histocompatibility complex protein. In this case about 75% of the anisotropy is lost due to rapid motions. The short correlation time observed in proteins is variable and ranges from 50 to 500 ps, with the values being determined in part by the time resolution of the instrument. The shorter correlation time is approximately equal to that observed for NATA in water or for small peptides (Table 17.4). These shorter correlation times are typically insensi-

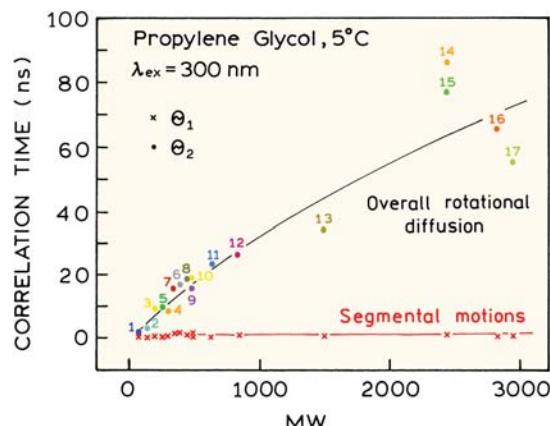


**Figure 17.25.** Short and long rotational correlation times for indole, tryptophan, and peptides in propylene glycol at 5°C. 1, indole; 2, 3-methylindole; 3, trp; 4, NATA; 5, gly-trp; 6, trp-trp; 7, gly-trp-gly; 8, leu-trp-leu; 9, glu-trp-glu; 10, lys-trp-lys; 11, gastrin; 12, pentagastrin; 13, [tyr<sup>4</sup>-bombesin]; 14, dynorphin; 15, [asn<sup>15</sup>]-dynorphin; 16, cosintropin; 17, melittin. From [79].

tive to protein folding and are not greatly affected by the viscosity of the solution.

The picosecond component in the anisotropy decays of proteins display some characteristic features. Their fraction of the total anisotropy is typically larger for small unstructured peptides than for tryptophan residues buried in a protein matrix. Unfolding of a protein usually increases the amplitude of the fast motions. The magnitude of the short correlation time seems to be mostly independent of the size of the protein or peptide. This is shown in Figure 17.25, which shows the two correlation times recovered for molecules ranging from indole, to tryptophan, to the tripeptide lys-trp-lys, to melittin.<sup>79</sup> The molecules were dissolved in propylene glycol, so the overall correlation times are longer than those found with water. The longer correlation time increases with molecular weight. However, the rapid correlation time is independent of molecular weight and is near 0.5 ns for all peptides.

### 17.5.1. Effects of Association Reactions on Anisotropy Decays: Melittin

The single-tryptophan peptide melittin provides a good example of how a protein anisotropy decay depends on the association with other biomolecules. In the presence of high salt concentration, melittin self-associates from monomers to tetramers. During this process the single-tryptophan residue on each chain is buried in the center of the four-

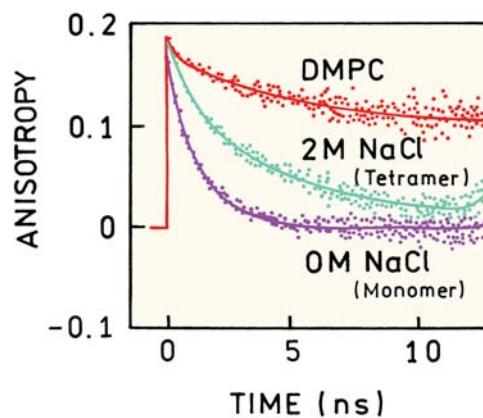


**Figure 17.26.** Anisotropy decays of monomeric and tetrameric melittin, in water and 2 M NaCl, respectively. Also shown is the anisotropy decay when bound to DMPC lipid vesicles. Excitation at 300 nm. Data from [80].

helix bundle. The anisotropy decay changes due to the larger overall size and restriction of segmental motions. Anisotropy decays for melittin have been reported by several laboratories.<sup>80–82</sup> Typical data for the monomer and tetramer are shown in Figure 17.26. The anisotropy decay was multi-exponential in both cases, with a 20–40-ps component in either state. The anisotropy decays more slowly in 2 M NaCl, where melittin forms a homotetramer. The longer global correlation time was 1.4 ns for the monomer and 5.5 ns for the tetramer, which are consistent with overall rotational diffusion.

Melittin binds to lipid vesicles because one side of the protein has nonpolar surface in the  $\alpha$ -helical state.<sup>83–85</sup> This binding results in a dramatic change in the anisotropy decay (Figure 17.26), which now shows a correlation time near 12 ns, but with uncertainty in the actual value.<sup>80</sup> It is difficult to obtain much information after 10 ns, or three times the mean lifetime, due to the low remaining intensity. In general one should select probes whose decay times are longer than the process being measured.

The data in Figure 17.26 illustrate a difficulty frequently encountered when measuring protein anisotropy decays. The measured time-zero anisotropy,  $r(0)$ , is less than the fundamental anisotropy ( $r_0 = 0.3$ ) for the 300-nm excitation wavelength. A low apparent time-zero anisotropy can be due to the limited time resolution of the instrumentation. If the correlation time is too short, the anisotropy decays within the instrument response function and the apparent time-zero anisotropy is less than the actual value.<sup>86</sup>

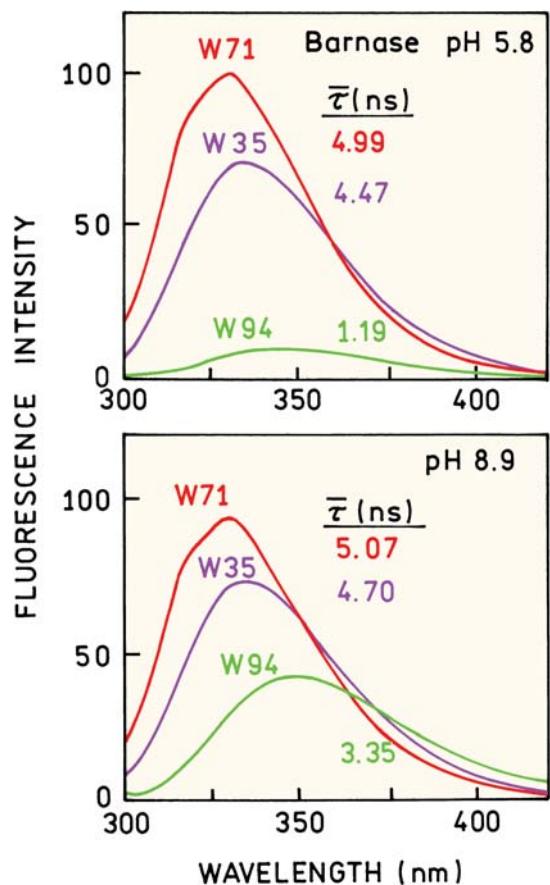


**Figure 17.27.** Emission spectra and mean decay time of the three single-tryptophan mutants of barnase at pH 5.8 and 8.9. The mean lifetimes are different than in [87] and were calculated using  $\bar{\tau} = 3f_i\tau_i$ . Data from [87].

## 17.6. BIOCHEMICAL EXAMPLES USING TIME-RESOLVED PROTEIN FLUORESCENCE

### 17.6.1. Decay-Associated Spectra of Barnase

In Section 16.8.2 we described the spectral properties of barnase. The wild-type protein contains three tryptophan residues: W35, W71, and W94 (Figure 16.48). Barnase displays a pH-dependent change in intensity that was attributed to quenching of W94 by the side chain of a protonated histidine residue H18. Time-resolved measurements and site-directed mutagenesis were used to determine the lifetimes of W94 when the histidine is positively charged or in the neutral state. This was accomplished by constructing three double mutants, each containing a single-tryptophan residue.<sup>87</sup> The intensity decays of all the single-tryptophan mutants were multi-exponential. The emission spectra and

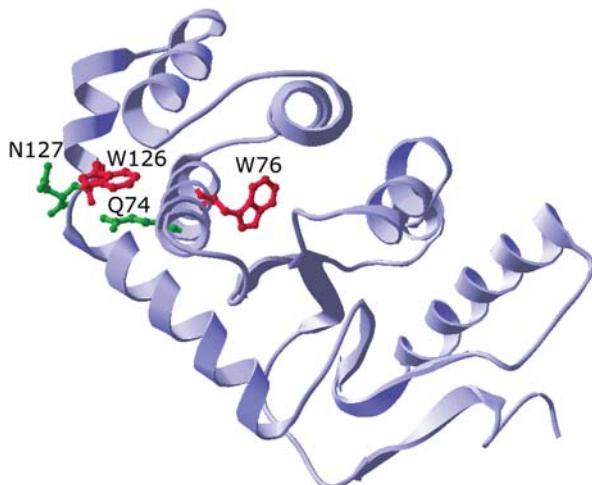


**Figure 17.28.** Structure of disulfide oxidoreductase DsbA from *E. coli*.

mean lifetimes are shown in Figure 17.27. The mean lifetimes of W71 and W35 are essentially independent of pH. The mean lifetime of W94 changes dramatically with pH, from 1.19 ns at pH 5.8 to 3.35 ns at pH 8.9. This effect is due to H18, which quenches W94 when in the protonated form. These results confirm the conclusions obtained using the mutants that contained two tryptophan residues (Section 16.8.2).

### 17.6.2. Disulfide Oxidoreductase DsbA

The emission of tryptophan residues in proteins is frequently affected by nearby groups in proteins. Such effects were seen in the disulfide oxidoreductase DsbA from *E. coli*.<sup>88-89</sup> The wild-type DsbA contains two tryptophan residues: W76 and W126 (Figure 17.28). W76 is sensitive to the redox state of DsbA. W126 was found to be essentially non-fluorescent irrespective of the redox state of the protein. The reason for quenching of W126 in DsbA was studied using site-directed mutagenesis. The mutant protein W76F was constructed to obtain a protein that contained only W126. The origin of the quenching was studied using W76F by mutating amino-acid residues close to W126. Since amides are known to be possible quenchers of tryptophan, glutamine 74 and asparagine 127 were replaced with alanine.

The time-resolved intensity decays of the DsbA mutants were measured for various wavelengths across the emission spectra. The recovered multi-exponential decays

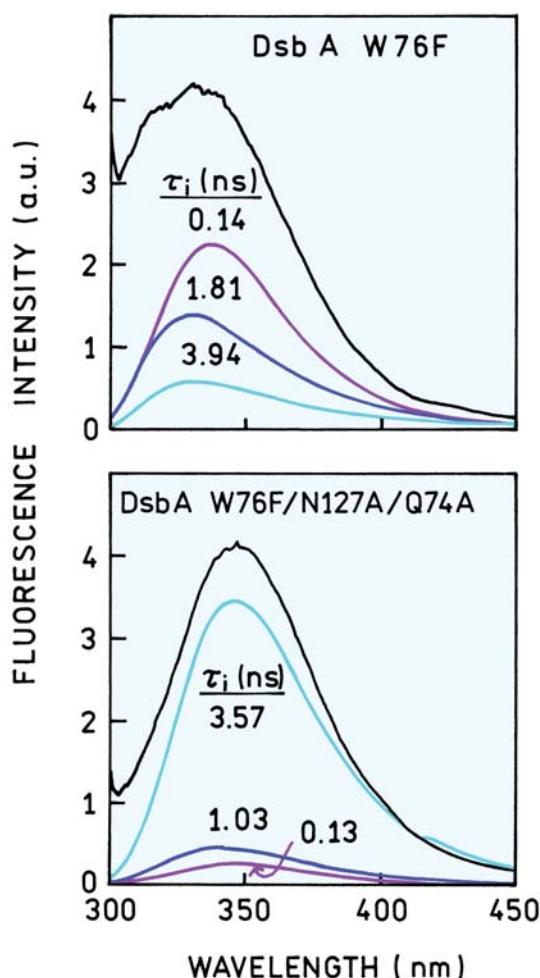


**Figure 17.29.** Steady-state emission and decay-associated spectra of W126 in DsbA mutants. Data from [88].

were used to calculate the decay-associated spectra (Figure 17.29). As is usually seen with single-tryptophan proteins, the intensity decays were multi-exponential. The DAS show that Q74 and N127 were responsible for quenching of W126. For the protein containing these residues, W76F, the largest component in the DAS is for a decay time of 0.14 ns. For the protein lacking residues N127 and Q74 (Figure 17.28, lower panel) the DAS are dominated by a component with a lifetime of 3.57 ns. In examining these data it is important to notice that the individual lifetimes were not assigned to a quenched or unquenched residue. In the quenched mutant protein (Figure 17.29 top) and in the unquenched mutant proteins (bottom) the tryptophan residue displays at least three decay times. The effects of Q74 and N127 were determined by considering which decay times were dominant in the total emission.

### 17.6.3. Immunophilin FKBP59-I: Quenching of Tryptophan Fluorescence by Phenylalanine

Immunophilin FKBP59-I provides another example of quenching of tryptophan by a nearby amino-acid side chain.<sup>90</sup> In this case the quencher is phenylalanine, which is not usually considered a quencher. Immunophilins are receptors for immunosuppressant drugs such as cyclosporin. The immunophilin domain FKBP59-I contains two tryptophan residues at positions 59 and 89 (Figure 17.30). In general it would be difficult to separate the contributions of the two tryptophan residues using data for just FKBP59-I. An analogous protein FKBP12 was available that contained just W89. The intensity of these two proteins is markedly different, with W89 showing a much lower quantum yield (0.025 versus 0.19 for FKBP59). Trp-89 in FKBP12 shows more rapid intensity decay than FKBP59-I, with two tryptophan residues (Figure 17.31). For the protein with two tryptophan residues, one of which is highly-fluorescent, the lifetime distribution analysis shows a dominant decay time near 6.16 ns. For the single-tryptophan protein the intensity decay is dominated by the more weakly emitting residue, which displays a more heterogeneous intensity decay with a dominant decay time near 0.21 ns.

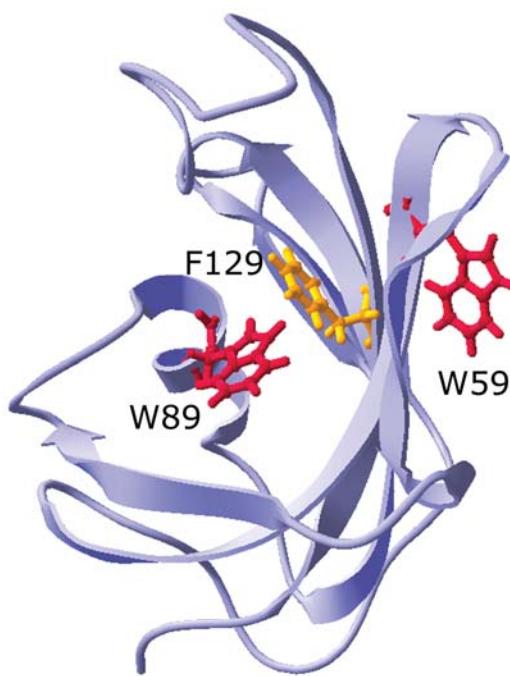


**Figure 17.30.** Location of the two tryptophan residues in FKBP59-I. FKBP12 has only trp-89.

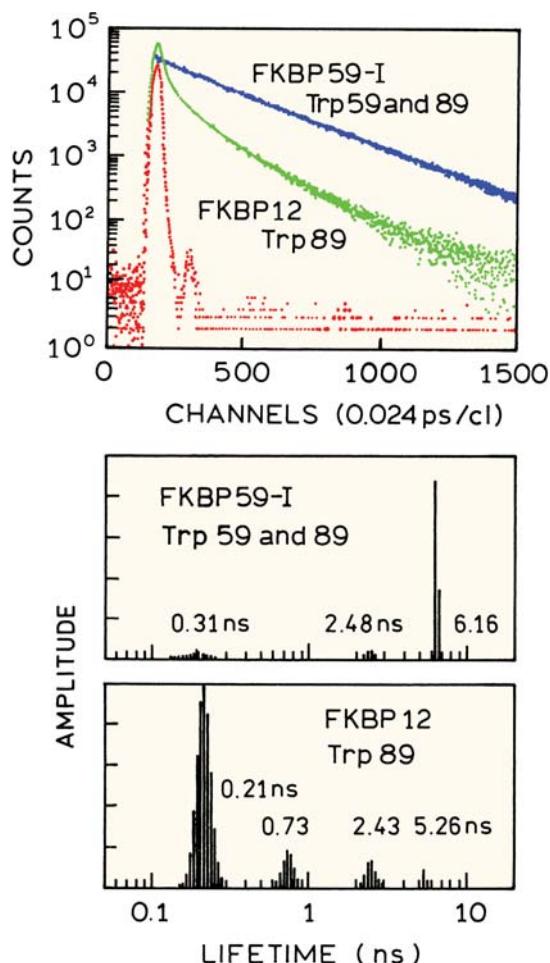


**Figure 17.31.** Top: Time-resolved intensity decay of FKBP59-I and FKBP12. Bottom: Lifetime distribution recovered using the maximum entropy method. Excitation at 295 nm. Emission at 340 nm, 20°C. Reprinted with permission from [90]. Copyright © 1997, American Chemical Society.

(Figure 17.31, lower panel). These results revealed an unexpected origin for quenching of W89. Apparently this tryptophan residue is quenched due to a nearby phenylalanine residue. Benzene is known to decrease the decay times of indole.<sup>91</sup> Although not reported, one would expect denaturation of the protein to decrease the extent of quenching and normalize the fluorescence of W89, which would support the conclusion that F129 is responsible for quenching of W89.

#### 17.6.4. Trp Repressor: Resolution of the Two Interacting Tryptophans

Site-directed mutagenesis and frequency-domain measurements were used to study the two tryptophan residues in the

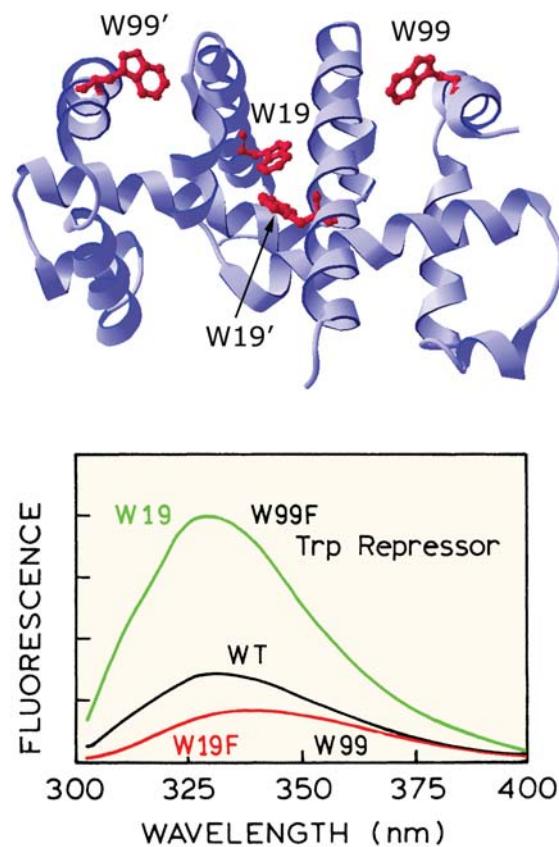


**Figure 17.32.** Emission spectra of the wild-type *E. coli* trp repressor (WT) and its two single-tryptophan mutants. Revised from [92].

tryptophan repressor from *E. coli*.<sup>92–93</sup> The wild-type protein is a symmetrical dimer and contains two tryptophans at positions 19 and 99 in each subunit. The W99F mutant contains only tryptophan 19 (W19) and the W19F mutant contains only tryptophan 99 (W99). Emission spectra of the three proteins show that the protein with W19 has a higher quantum yield than the protein with W99, or even the wild-type protein with two tryptophan residues (Figure 17.32).

Frequency-domain intensity decays of the three repressor proteins show that each displays a distinct intensity decay (Figure 17.33). The longest decay time is shown by the mutant with W19, as can be judged by the larger phase angles at lower frequencies. The mean decay time of W19 is even longer than that of the wild-type protein. These results indicate that W99 acts as a quencher in the wild-type protein, presumably by RET from W19 to W99. This is reasonable because W19 has a shorter emission maximum than W99.

The difficulties in resolving the emission from each residue using only the wild-type protein is illustrated by the

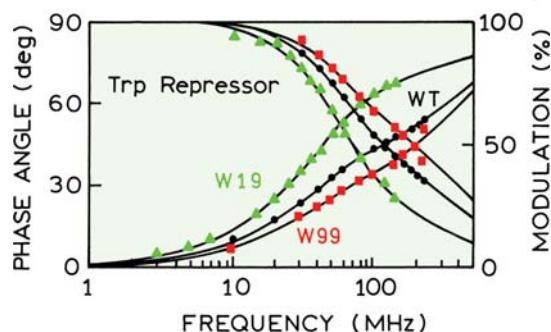


**Figure 17.33.** Frequency-domain intensity decay of the trp repressor (●) and its two single-tryptophan mutants with W19 (▲) or W99 (■). Revised and reprinted with permission from [92]. Copyright © 1993, American Chemical Society.

intensity decays (Table 17.5). Both the wild-type protein and the single-tryptophan mutants display a double-exponential decay. The decay times overlap for all three proteins. Also, the interactions between the tryptophan residues imply that the intensity decay of the wild-type protein is not a result of adding the intensity decays of the two single-tryptophan mutants. The emission of the wild-type protein is not the sum of the emission of the two single-tryptophan mutants.

### 17.6.5. Thermophilic $\beta$ -Glycosidase: A Multi-Tryptophan Protein

In the preceding sections we saw studies of proteins with a limited number of tryptophan residues. As the number of tryptophan residues increases, it becomes impractical to resolve the individual residues. Even if single-tryptophan mutants can be made it is unlikely that the protein will remain stable after substitution of a large number of tryptophan residues. In such cases it can be informative to examine the lifetime distributions of the wild-type protein. *S. sol-*

**Table 17.5.** Intensity Decays of the Trp Repressor, and Its Single-Tryptophan Mutants<sup>a</sup>

Protein	$\tau_i$ (ns)	$\alpha_i$	$f_i$	$\bar{\tau}$ (ns) <sup>b</sup>
WT (W19 and W99)	0.57 3.36	0.70 0.30	0.28 0.72	1.41
W19F (W99)	0.58 3.14	0.83 0.17	0.47 0.53	1.01
W99F (W19)	0.40 3.94	0.28 0.72	0.04 0.96	2.95

<sup>a</sup>From [92].

<sup>b</sup>Calculated using  $\bar{\tau} = \sum_i f_i \tau_i$ .

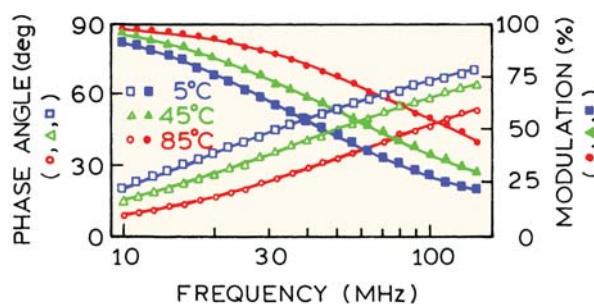
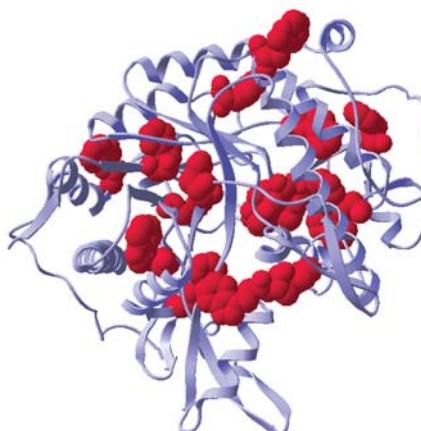


**Figure 17.34.** Frequency dependence of the phase shift and demodulation factors of *S. solfataricus*  $\beta$ -glycosidase fluorescence emission at neutral pH at 5, 45, and 85°C. The structure is one monomer from the tetramer; tryptophans are in red. Revised from [94].

*solfataricus* is an extreme thermophile growing at 87°C. Its  $\beta$ -glycosidase is a 240-kDa tetramer that contains 68 tryptophan residues, 17 per subunit (Figure 17.34). The  $\beta$ -glycosidase remains native and active to above 85°C. It is impractical to attempt to resolve the individual emission spectra, and equally impractical to prepare single-tryptophan mutants. One can nonetheless measure the intensity decays of the protein, which in this case were measured using the frequency-domain method. The decays are highly heterogeneous and were interpreted in terms of a bimodal lifetime distribution (Figure 17.35). As the temperature is increased the two components shift progressively towards shorter lifetimes.<sup>94</sup>

### 17.6.6. Heme Proteins Display Useful Intrinsic Fluorescence

For many years it was assumed that heme proteins were nonfluorescent. This was a reasonable assumption given that the intense Soret absorption band of the heme groups is expected to result in Förster distances ( $R_0$ ) for trp to heme

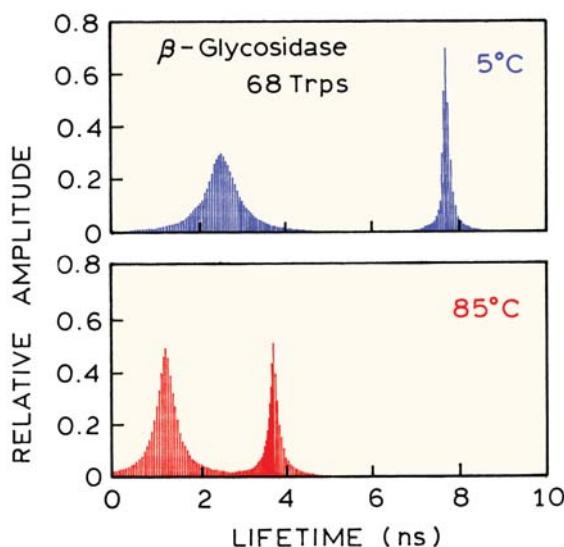


**Figure 17.35.** Tryptophanyl-lifetime-distribution of *S. solfataricus*  $\beta$ -glycosidase at the indicated temperatures. Revised from [94].

transfer near 32–34 Å. Since this distance is larger than the 20-Å radius of a myoglobin molecule, RET is expected to be nearly complete.

Detection of tryptophan emission from heme proteins is experimentally difficult. Suppose RET quenching is 99% efficient, and suppose that your protein solution contains a 1% impurity of the apoprotein or some non-heme protein. The signal from the impurity will be approximately equal to that from the heme protein. For this reason it is difficult to prove if the observed weak emission is due to heme proteins, to impurities, or to the apoproteins. In spite of these difficulties, some groups were successful in detecting heme protein emission from the steady-state data.<sup>95–98</sup> Subsequent time-resolved experiments confirmed that heme proteins do display weak intrinsic fluorescence, and the ps decay times found in heme proteins can be correlated with their structure.<sup>99–106</sup>

An example of intrinsic fluorescence from a heme protein is provided by seed-coat soybean peroxidase (SBP).<sup>105</sup> This protein contains 326 amino acids and a single-tryptophan residue, W117 (Figure 17.36). The intensity decay of W117 is highly heterogeneous, showing at least four decay times (Figure 17.37). The lifetime distribution recovered from the intensity decay is informative in showing that 97% of the steady-state intensity is due to the 36-ps component. This result illustrates the difficulty in studies of heme protein fluorescence. It is difficult to know if the minor longer lifetime components are due to the heme protein itself, or

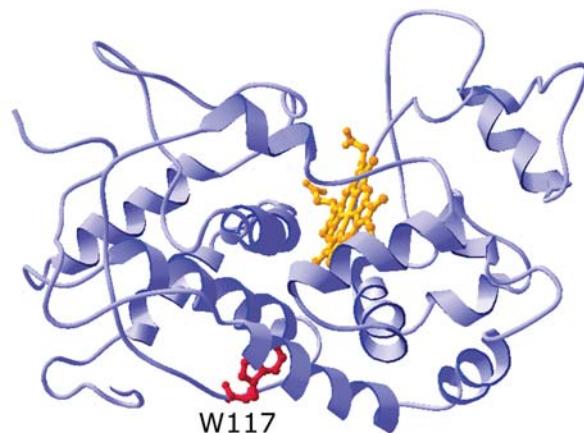


**Figure 17.36.** Structure of seed-coat soybean peroxidase.

impurities, apoprotein, or unusual conformations of the heme protein that do not allow efficient energy transfer.

The emission of heme proteins has also been studied using the frequency-domain method.<sup>106</sup> Representative intensity decays for hemoglobin are shown in Figure 17.38.

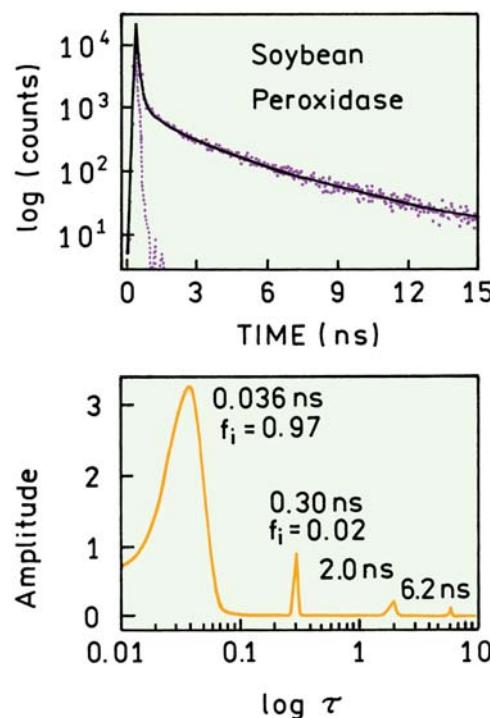


**Figure 17.37.** Intensity decays of the intrinsic tryptophan emission from soybean peroxidase. The fractional intensities of the 2.0- and 6.2-ns components are near 0.008 and 0.002, respectively. Data from [105].

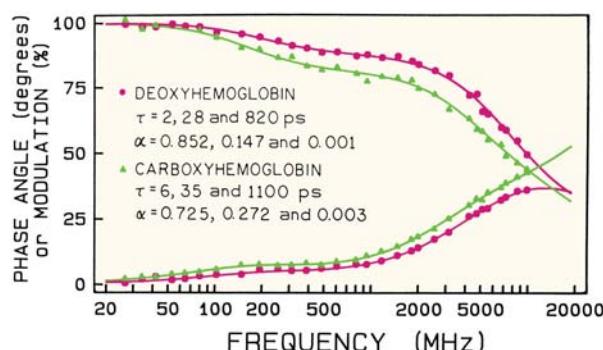


**Figure 17.38.** Frequency-domain intensity decays of the intrinsic tryptophan fluorescence from hemoglobin. From [106].

The frequency-domain data revealed both ps and ns decay times. Long-lifetime ns components were also found for myoglobin. These long-lived components are thought to be due to conformational isomers of the proteins in which the heme on the tryptophan residue is positioned so that energy transfer cannot occur. The time-resolved data can provide useful information under conditions where the steady-state data are ambiguous.

### 17.7. TIME-DEPENDENT SPECTRAL RELAXATION OF TRYPTOPHAN Advanced Topic

We have seen many examples of resolving the emission from individual tryptophan residues in multi-tryptophan proteins. During this analysis we assumed that each tryptophan residue displayed the same lifetime at all emission wavelengths. However, the lifetimes of a single-tryptophan

residue may not be the same at all emission wavelengths. Many examples are known where the intensity decays are different at different wavelengths. If the intensity decay of indole in water is measured the decays will be essentially the same at all emission wavelengths. However, the decays become strongly dependent on emission wavelength in more viscous solvents. Figure 17.39 shows intensity decay of indole in glycerol at 20°C. The intensity decays were measured for various wavelengths across the emission spectrum.<sup>107</sup> The intensity decay at 310 nm, which is on the blue side of the emission, is more rapid than the decay at 390 nm, which is on the long-wavelength side of the emission. This difference is due to solvent relaxation around the excited state, which is occurring on a timescale comparable to the decay time (Chapter 7). The intensity decay at 380 nm shows a rise time that is proof of an excited-state process.

The intensity decays at each wavelength can be analyzed by the multi-exponential model. In this global analysis the lifetimes  $\tau_i$  were assumed to be independent of wavelength and the amplitude  $\alpha_i(\lambda)$  was assumed to depend on wavelength. These are the same assumptions that are commonly used when analyzing wavelength-dependent data from proteins. The wavelength-dependent decays allow calculation of the decay-associated spectra (Figure 17.40, top). The results are presented in wavenumber units. The DAS for shorter decay times show shorter wavelength emission maxima, and the amplitudes are negative at some wavelengths.

For indole in glycerol we do not expect unique emitting species, so the DAS in Figure 17.40 give the misleading impression of discrete emitting states. The recovered decays can also be used to calculate the time-resolved emission spectra (Figure 17.40, bottom). The TRES show a gradual shift to longer wavelengths and probably provide a more reasonable description of indole in glycerol. Time-dependent spectral relaxation can result in DAS that are not due to unique emitting species.

Tryptophan residues in a protein are in a viscous environment, probably comparable to glycerol. A large amount of data suggest that spectral relaxation occurs in many proteins,<sup>108–119</sup> but there may also be proteins where relaxation does not occur. When wavelength-dependent intensity decays are measured for a protein it is not always clear whether to use DAS or TRES. For a multi-tryptophan protein one is tempted to use DAS and to associate the DAS with the individual tryptophan residues. This association may not always be correct. Similarly, for a single-tryptophan protein there is a tendency to associate the DAS with

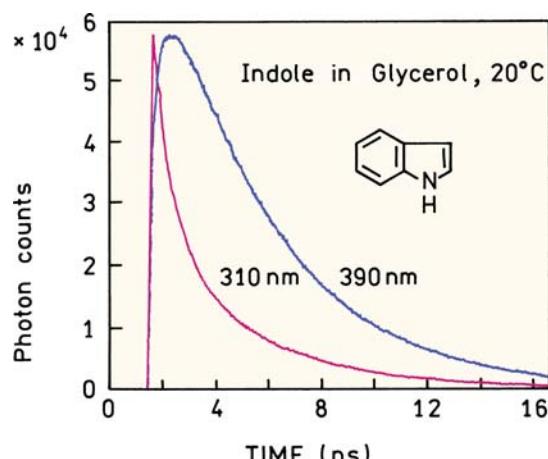


**Figure 17.39.** Intensity decays of indole in glycerol at 20°C. Revised from [107].

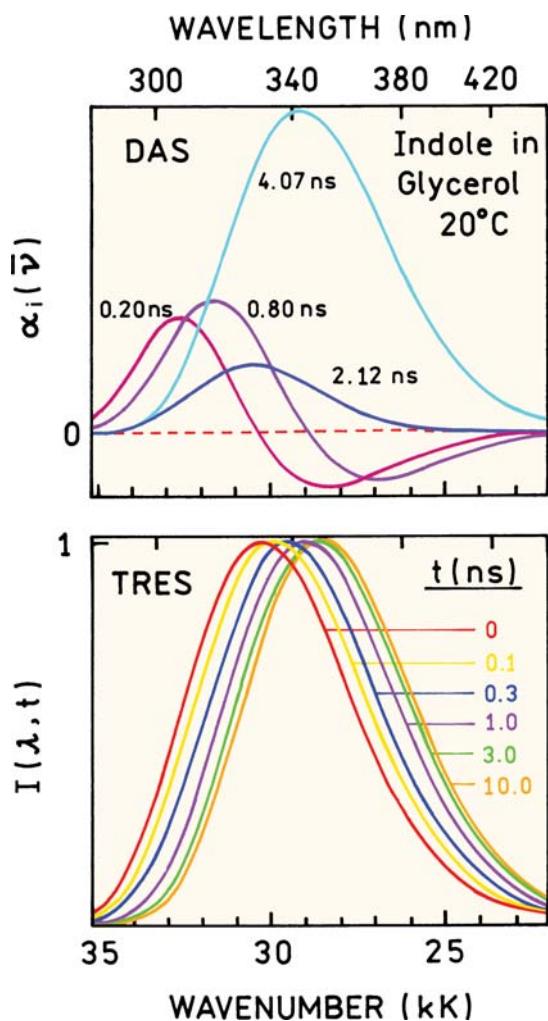


**Figure 17.40.** Decay-associated spectra (top) and time-resolved emission spectra (bottom). The DAS and TRES were calculated from the same time-resolved decays of indole in glycerol at 20°C. Revised from [107].

multiple conformations. However, it is important to remember that the DAS and TRES are representations of the data, and not of the protein. Most time-resolved data are not adequate to distinguish between discrete DAS or continuous relaxation.

Evidence for time-dependent relaxation of tryptophan residues is pervasive but not specific. One characteristic of spectral relaxation is an increase of the mean decay time with increasing observation wavelength. Since there seems to be no correlation between the emission maxima of proteins and their mean lifetimes (see Figure 16.12), there should be equal numbers of proteins that display increases or decreases in lifetime with increasing wavelength. However, for almost all proteins the mean lifetime increases

with increasing emission wavelength, which is characteristic of spectral relaxation. Even single-tryptophan proteins display lifetimes that increase with increasing wavelength. An unambiguous characteristic of an excited-state process is a negative pre-exponential factor in the intensity decay. Such components have only been rarely observed in proteins, one example being chicken pepsinogen.<sup>115</sup> The absence of negative pre-exponential factors does not prove the absence of spectral relaxation because these terms are easily eliminated by spectral overlap. However, the correlation between shorter emission wavelengths and shorter lifetimes could also be due to quenching by peptide bonds.

The difficulty in interpreting the data in terms of DAS or spectral relaxation is illustrated by studies of myelin basic protein (MBP),<sup>119</sup> which contains a single-tryptophan residue. This protein is found in the central nervous system associated with myelin. In solution in the absence of membranes, MBP is thought to be mostly unstructured. Time-resolved decays were collected across the emission spectrum and used to calculate the DAS and TRES (Figure 17.41). The DAS seem to imply multiple conformations and the TRES suggest a continuous relaxation process. The time-resolved data usually do not indicate whether the decays are due to discrete emitting species or a continuously changing population. Most papers on protein fluorescence select either the DAS or TRES for presentation, depending on the preferred interpretation of the data.

Under favorable conditions ground-state heterogeneity or spectral relaxation can be distinguished by detection of a negative pre-exponential factor on the long-wavelength side of the emission. Such a factor is rarely observed for proteins.<sup>115</sup> The typical absence of negative pre-exponential factors in proteins is probably due to the modest spectral shift during the excited-state lifetimes and spectral overlap between the initially excited and relaxed states (Chapter 7). Negative pre-exponential factors can be seen from indole derivatives under conditions that may mimic the interior of proteins.<sup>120–121</sup> Figure 17.42 shows the lifetime distributions for tryptophan octyl ester (TOE) in micelles of an uncharged detergent. On the short-wavelength side (305 nm) the amplitudes are all positive. The amplitudes become negative on the long-wavelength (375 nm) side of the emission, which proves that spectral relaxation has occurred. In proteins the time-dependent spectral shifts are usually smaller, and the multiple-tryptophan residues emit at different wavelengths. These factors probably prevent the appearance of negative pre-exponential factors. For most proteins it is probably safe to assume that multiple-tryptophan

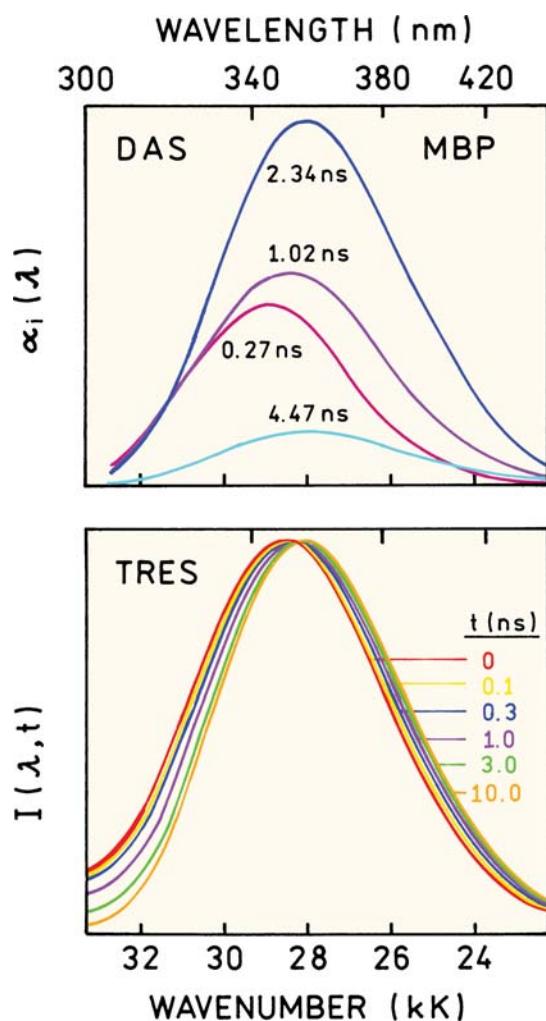


**Figure 17.41.** Decay-associated spectra and time-resolved emission spectra from myelin basic protein at 30°C, 289-nm excitation. Revised from [119].

residues, multiple conformations, and spectral relaxation all affect the intensity decays.

## 17.8. PHOSPHORESCENCE OF PROTEINS

### Advanced Topic

Phosphorescence is usually observed at low temperature and/or in the complete absence of quenchers.<sup>122–124</sup> These conditions are needed because phosphorescence lifetimes are typically long—milliseconds to seconds—and thus quenched by low concentrations of oxygen or impurities. Low temperatures are also needed to decrease the rates of non-radiative decay to be comparable with the phosphorescence emission rates. Otherwise, the quantum yield of phosphorescence will be very small.

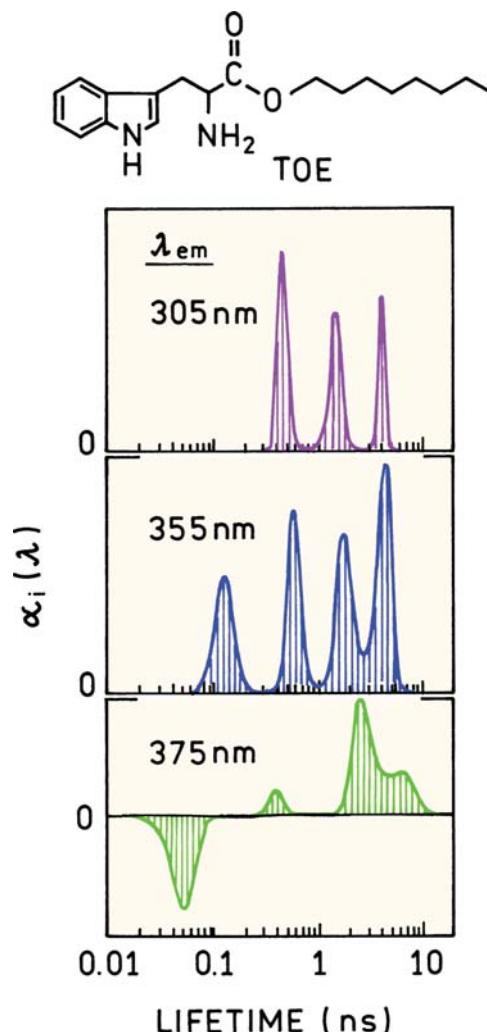


**Figure 17.42.** Lifetime distributions for tryptophan octyl ester (TOE) in dodecylmaltoside (DM) micelles, 20°C. Revised from [121].

Figure 17.43 shows the fluorescence and phosphorescence of tryptophan in a glass at low temperatures.<sup>125</sup> Phosphorescence occurs at longer wavelengths than fluorescence, and phosphorescence spectra are typically more structured. The phosphorescence is shown as a separate spectrum from the fluorescence. A separate phosphorescence spectrum is only observed if detection of the phosphorescence is gated to remove the fast decay fluorescence. More typical spectra are shown in Figure 17.44 for NATA in a glass-forming solvent at various temperatures.<sup>126</sup> At low temperature (100 to 190°K) the phosphorescence appears on the long-wavelength side of the fluorescence spectrum. Without gated detection both emissions are observed. The wavelength resolution of the phosphorescence is lower in Figure 17.44 than in Figure 17.43. The

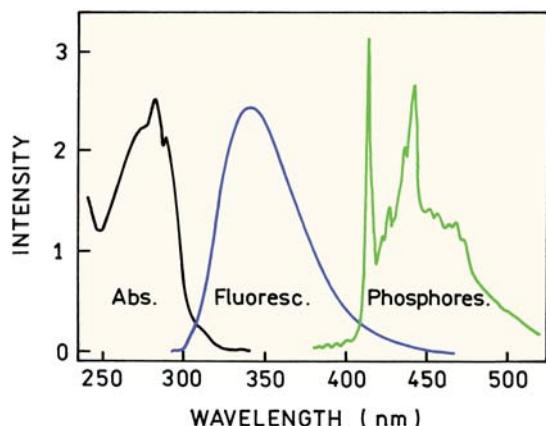


**Figure 17.43.** Absorption, fluorescence, and phosphorescence spectra of tryptophan in a low-temperature glass. Revised from [125].

spectra in 17.44 are more typical because a bandpass near 5 nm is typically used in recording fluorescence spectra. If the decay times were measured at 350 and 450 nm, the 450-nm emission would show a millisecond decay time and the 350-nm emission the usual nanosecond decay time.

In the 1980 reports there appeared an observation of tryptophan phosphorescence from proteins at room temperature,<sup>127–129</sup> in some cases in the presence of oxygen.<sup>130</sup> This was surprising given the long lifetimes for phosphorescence. Some of the early reports were in error due to depletion of oxygen with intense excitation intensities.<sup>131</sup> In

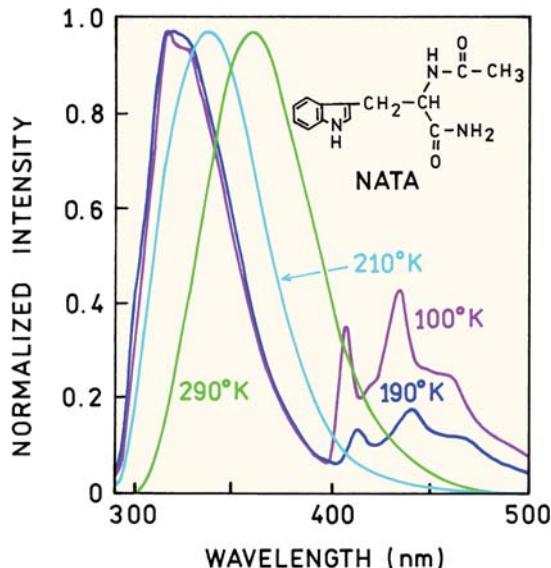


**Figure 17.44.** Emission spectra of NATA in a glycerol–water mixture. Revised from [126].

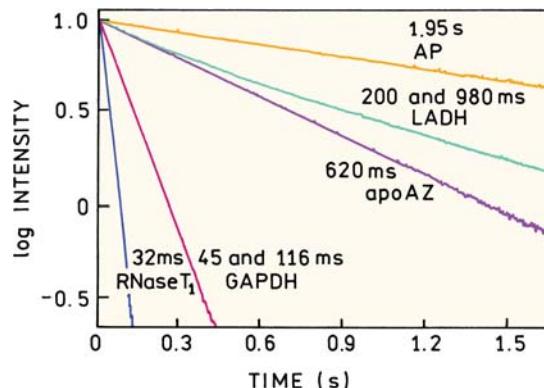


**Figure 17.45.** Phosphorescence intensity decays of proteins in aqueous solution at room temperature. Revised from [140].

spite of this initial confusion it is now accepted that some proteins display phosphorescence in solution at room temperature.<sup>132–140</sup> Observation of useful phosphorescence requires the complete exclusion of oxygen, but some studies have been performed with oxygen concentrations up to about 80  $\mu\text{M}$ .

The phosphorescence decay times of proteins at room temperature can be surprisingly long (Figure 17.45).<sup>140</sup> In contrast to fluorescence decays the decays of phosphorescence seem to be more like single exponentials. Buried tryptophans with short emission wavelength tend to have longer phosphorescence decay times than exposed residues (Table 17.6).<sup>141</sup> The nearly single-exponential decays of phosphorescence and the large range of phosphorescence decay times suggest the possibility of resolving the emission of several tryptophans in a multi-tryptophan protein.

The highly structured emission of tryptophan phosphorescence can allow the resolution of two tryptophan residues in a single protein.<sup>92</sup> This possibility is shown for the tryptophan repressor and its single-tryptophan mutants

**Table 17.6.** Correlation of Fluorescence Emission Maximum and Phosphorescence Lifetime in Single-Tryptophan Proteins<sup>a</sup>

Protein	Fluorescence maximum (nm)	Phosphorescence lifetime (ms)
Azurin	305	400
Parvalbumin (calcium)	320	5
Ribonuclease T <sub>1</sub>	325	14
Melittin	340	<0.5
Monellin	345	<0.5
Parvalbumin (no calcium)	350	<0.5

<sup>a</sup>From [141].

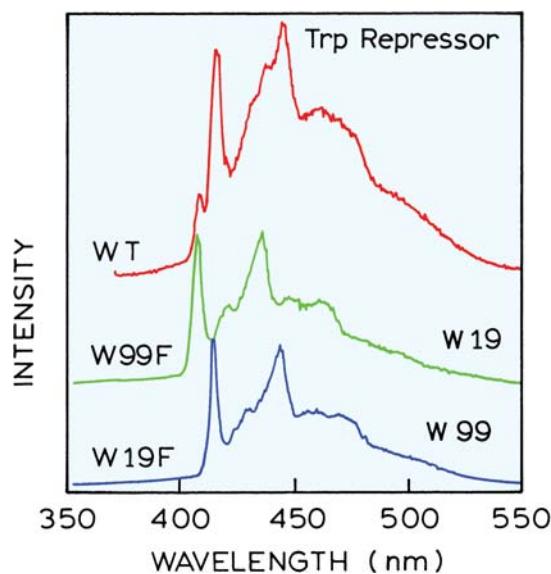


**Figure 17.46.** Low-temperature phosphorescence spectra of wild-type (WT) trp repressor and its two single-tryptophan mutants at liquid nitrogen temperature. The spectra are offset for visualization. Revised from [92].

(Figure 17.46). The wild-type protein shows two sharp peaks near 400 nm, and each of the single-tryptophan mutants shows a single peak near this wavelength. Each of these peaks is thus due to a single-tryptophan residue.

Multiple phosphorescence peaks have been observed for other proteins with two tryptophan residues.<sup>142–145</sup> Site-directed mutagenesis has been used to identify amino-acid side chains that quench tryptophan phosphorescence.<sup>146</sup> Figure 17.47 shows the phosphorescence emission spectra of glyceraldehyde-3-phosphate dehydrogenase (GPD) from *Bacillus stearothermophilus*. The wild-type protein contains two tryptophan residues: W84 and W310. The emission spectrum of the W84F mutant allows assignment of the peaks near 400 nm to each tryptophan residue. The lower panel shows the phosphorescence decays at 0°C. The mutant containing W310 shows a very short phosphorescence decay time. This short decay time is due to a tyrosine residue at position 283 (Y283). Replacement of this tyrosine with a valine (V) results in a 50-fold increase in the decay time of W310.

## 17.9. PERSPECTIVES ON PROTEIN FLUORESCENCE

Our understanding of protein fluorescence has increased dramatically in the past five years. The availability of a

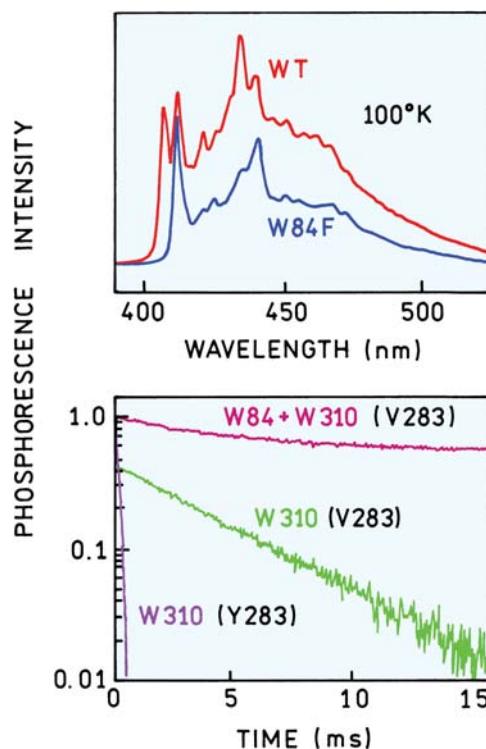


**Figure 17.47.** **Top:** Phosphorescence emission spectra of wild-type glyceraldehyde-3-phosphate dehydrogenase (GPD) and its W84F mutant at 100°K. **Bottom:** Phosphorescence intensity decays of mutants of GPD at 0°C. The letters and numbers in parentheses refer to the residues present in the mutant protein. Revised from [146].

large number of protein structures allows correlation between structural features of the proteins and their spectral properties. General trends are beginning to emerge, such as which side chains are most likely to quench tryptophan. Energy transfer from short- to long-wavelength tryptophans has been seen for several proteins. Emission maxima can be correlated with exposure to solvent, as seen from the protein structure. This improved understanding of protein fluorescence will allow its use to answer more specific questions about protein function and protein interactions with other biomolecules.

## REFERENCES

1. Birch DJS, Imhof RE. 1991. Time-domain fluorescence spectroscopy using time-correlated single-photon counting. In *Topics in fluorescence spectroscopy*, Vol. 1: *Techniques*, pp. 1–95. Ed JR Lakowicz. Plenum Press, New York.
2. Lakowicz JR, Gryczynski I. 1991. Frequency-domain fluorescence spectroscopy. In *Topics in fluorescence spectroscopy*, Vol 1: *Techniques*, pp. 293–355. Ed JR Lakowicz. Plenum Press, New York.

3. Grinvald A, Steinberg IZ. 1976. The fluorescence decay of tryptophan residues in native and denatured proteins. *Biochim Biophys Acta* **427**:663–678.
4. Beechem JM, Brand L. 1985. Time-resolved fluorescence of proteins. *Annu Rev Biochem* **54**:43–71.
5. Rayner DM, Szabo AG. 1978. Time-resolved fluorescence of aqueous tryptophan. *Can J Chem* **56**:743–745.
6. Szabo AG, Rayner DM. 1980. Fluorescence decay of tryptophan conformers in aqueous solution. *J Am Chem Soc* **102**:554–563.
7. Gudgin E, Lopez-Delgado R, Ware WR. 1981. The tryptophan fluorescence lifetime puzzle: a study of decay times in aqueous solution as a function of pH and buffer composition. *Can J Chem* **59**:1037–1044.
8. McLaughlin ML, Barkley MD. 1997. Time-resolved fluorescence of constrained tryptophan derivatives: implications for protein fluorescence. *Methods Enzymol* **278**:190–202.
9. Schiller PW. 1985. Application of fluorescence techniques in studies of peptide conformations and interactions. *Peptides* **7**:115–164.
10. Robbins RJ, Fleming GR, Beddard GS, Robinson GW, Thistletonwaite PJ, Woolfe GJ. 1980. Photophysics of aqueous tryptophan: pH and temperature effects. *J Am Chem Soc* **102**:6271–6280.
11. Eftink MR, Jia Y, Hu D, Ghiron CA. 1995. Fluorescence studies with tryptophan analogues: excited state interactions involving the side chain amino group. *J Phys Chem* **99**:5713–5723.
12. Petrich JW, Chang MC, McDonald DB, Fleming GR. 1983. On the origin of nonexponential fluorescence decay in tryptophan and its derivatives. *J Am Chem Soc* **105**:3824–3832.
13. Chen Y, Liu B, Yu H-T, Barkley MD. 1996. The peptide bond quenches indole fluorescence. *J Am Chem Soc* **118**(39):9271–9278.
14. Chen Y, Liu B, Barkley MD. 1995. Trifluoroethanol quenches indole fluorescence by excited-state proton transfer. *J Am Chem Soc* **117**:5608–5609.
15. Steiner RF, Kirby EP. 1969. The interaction of the ground and excited states of indole derivatives with electron scavengers. *J Phys Chem* **73**:4130–4135.
16. Froehlich PM, Gantt D, Paramasigamani V. 1977. Fluorescence quenching of indoles by N,N-dimethylformamide. *Photochem Photobiol* **26**:639–642.
17. Ricci RW, Nesta JM. 1976. Inter- and intramolecular quenching of indole fluorescence by carbonyl compounds. *J Phys Chem* **80**(9): 974–980.
18. Shopova M, Genov N. 1983. Protonated form of histidine 238 quenches the fluorescence of tryptophan 241 in subtilisin *novo*. *Int J Pept Protein Res* **21**:475–478.
19. Butler J, Land EJ, Prutz WA, Swallow AJ. 1982. Charge transfer between tryptophan and tyrosine in proteins. *Biochim Biophys Acta* **705**:150–162.
20. Prutz WA, Siebert F, Butler J, Land EJ, Menez A, Montenay-Garestier T. 1982. Intramolecular radical transformations involving methionine, tryptophan and tyrosine. *Biochim Biophys Acta* **705**:139–149.
21. Sanyal G, Kim E, Thompson FM, Brady EK. 1989. Static quenching of tryptophan fluorescence by oxidized dithiothreitol. *Biochem Biophys Res Commun* **165**(2):772–781.
22. Eftink MR. 1991. Fluorescence quenching reactions. In *Biophysical and biochemical aspects of fluorescence spectroscopy*, pp. 1–41. Ed TG Dewey. Plenum Press, New York.
23. Adams P, Chen Y, Ma K, Zagorski M, Sonnichsen FD, McLaughlin ML. 2002. Intramolecular quenching of tryptophan fluorescence by the peptide bond in cyclic hexapeptides. *J Am Chem Soc* **124**:9278–9286.
24. Chen Y, Barkley MD. 1998. Toward understanding tryptophan fluorescence in proteins. *Biochemistry* **37**:9976–9982.
25. Jameson DM, Weber G. 1981. Resolution of the pH-dependent heterogeneous fluorescence decay of tryptophan by phase and modulation measurements. *J Phys Chem* **85**:953–958.
26. Chen RF, Knutson JR, Ziffer H, Porter D. 1991. Fluorescence of tryptophan dipeptides: correlations with the rotamer model. *Biochemistry* **30**:5184–5195.
27. Shizuka H, Serizawa M, Shimo T, Saito I, Matsuura T. 1988. Fluorescence-quenching mechanism of tryptophan: remarkably efficient internal proton-induced quenching and charge-transfer quenching. *J Am Chem Soc* **110**:1930–1934.
28. Callis PR, Liu T. 2004. Quantitative prediction of fluorescence quantum yields for tryptophan in proteins. *J Phys Chem B* **108**:4248–4259.
29. Malak H, Gryczynski I, Lakowicz JR. Unpublished observations.
30. Lakowicz JR, Jayaweera R, Szmacinski H, Wiczk W. 1989. Resolution of two emission spectra for tryptophan using frequency-domain phase-modulation spectra. *Photochem Photobiol* **50**(4): 541–546.
31. Ruggiero AJ, Todd DC, Fleming GR. 1990. Subpicosecond fluorescence anisotropy studies of tryptophan in water. *J Am Chem Soc* **112**: 1003–1014.
32. Döring K, Konermann L, Surrey T, Jähnig F. 1995. A long lifetime component in the tryptophan fluorescence of some proteins. *Eur Biophys J* **23**:423–432.
33. Lakowicz JR, Laczko G, Gryczynski I. 1987. Picosecond resolution of tyrosine fluorescence and anisotropy decays by 2-GHz frequency-domain fluorometry. *Biochemistry* **26**:82–90.
34. Ross JBA, Laws WR, Rousslang KW, Wyssbrod HR. 1992. Tyrosine fluorescence and phosphorescence from proteins and polypeptides. In *Topics in fluorescence spectroscopy*, Vol. 3: *Biochemical applications*, pp. 1–63. Ed JR Lakowicz. Plenum Press, New York.
35. Laws WR, Ross JBA, Wyssbrod HR, Beechem JM, Brand L, Sutherland JC. 1986. Time-resolved fluorescence and <sup>1</sup>H NMR studies of tyrosine and tyrosine analogues: correlation of NMR-determined rotamer populations and fluorescence kinetics. *Biochemistry* **25**:599–607.
36. Ross JBA, Laws WR, Sutherland JC, Buku A, Katsoyannis PG, Schwartz IL, Wyssbrod HR. 1986. Linked-function analysis of fluorescence decay functions: resolution of side-chain rotamer populations of a single aromatic amino acid in small polypeptides. *Photochem Photobiol* **44**:365–370.
37. Contino PB, Laws WR. 1991. Rotamer-specific fluorescence quenching in tyrosinamide: dynamic and static interactions. *J Fluoresc* **1**(1):5–13.
38. Noronha M, Lima JC, Lamosa P, Santos H, Maycock C, Ventura R, Maçanita AL. 2004. Intramolecular fluorescence quenching of tyrosine by the peptide  $\alpha$ -carbonyl group revisited. *J Phys Chem A* **108**: 2155–2166.
39. Seidel C, Orth A, Greulich K-O. 1993. Electronic effects on the fluorescence of tyrosine in small peptides. *Photochem Photobiol* **58**(2): 178–184.

40. Leroy E, Lami H, Laustriat G. 1971. Fluorescence lifetime and quantum yield of phenylalanine aqueous solutions: temperature and concentration effects. *Photochem Photobiol* **13**:411–421.
41. Sudhakar K, Wright WW, Williams SA, Phillips CM, Vanderkooi JM. 1993. Phenylalanine fluorescence and phosphorescence used as a probe of conformation for cod parvalbumin. *J Fluoresc* **3**(2):57–64.
42. Lankiewicz L, Stachowiak K, Rzeska A, Wiczek W. 1999. Photophysics of sterically constrained peptides. In *Peptide science—present and future*, pp. 168–170. Ed Y Shimonishi. Kluwer, London.
43. Guzow K, Ganzynkowicz R, Rzeska A, Mrozek J, Szabelski M, Karolczak J, Liwo A, Wiczek W. 2004. Photophysical properties of tyrosine and its simple derivatives studied by time-resolved fluorescence spectroscopy, global analysis, and theoretical calculations. *J Phys Chem B* **108**:3879–3889.
44. Tanaka F, Tamai N, Mataga N, Tonomura B, Hiromi K. 1994. Analysis of internal motion of single tryptophan in *Streptomyces* subtilisin inhibitor from its picosecond time-resolved fluorescence. *Biophys J* **67**:874–880.
45. Tanaka F, Mataga N. 1992. Non-exponential decay of fluorescence of tryptophan and its motion in proteins. In *Dynamics and mechanisms of photoinduced electron transfer and related phenomena*, pp. 501–512. Ed N Mataga, T Okada, H Masuhara. North-Holland, Amsterdam.
46. Eftink MR, Ghiron CA, Kautz RA, Fox RO. 1989. Fluorescence lifetime studies with staphylococcal nuclease and its site-directed mutant: test of the hypothesis that proline isomerism is the basis for nonexponential decays. *Biophys J* **55**:575–579.
47. Dahms TES, Willis KJ, Szabo AG. 1995. Conformational heterogeneity of tryptophan in a protein crystal. *J Am Chem Soc* **117**: 2321–2326.
48. Tanaka F, Mataga N. 1987. Fluorescence quenching dynamics of tryptophan in proteins. *Biophys J* **51**:487–495.
49. Alcala JR. 1994. The effect of harmonic conformational trajectories on protein fluorescence and lifetime distributions. *J Chem Phys* **101**(6):4578–4584.
50. Eftink MR, Ghiron CA. 1975. Dynamics of a protein matrix as revealed by fluorescence quenching. *Proc Natl Acad Sci USA* **72**: 3290–3294.
51. Eftink MR, Ghiron CA. 1977. Exposure of tryptophanyl residues and protein dynamics. *Biochemistry* **16**:5546–5551.
52. Eftink MR, Hagaman KA. 1986. The viscosity dependence of the acrylamide quenching of the buried tryptophan residue in parvalbumin and ribonuclease T<sub>1</sub>. *Biophys Chem* **25**:277–282.
53. Longworth JW. 1968. Excited state interactions in macromolecules. *Photochem Photobiol* **7**:587–594.
54. James DR, Demmer DR, Steer RP, Verrall RE. 1985. Fluorescence lifetime quenching and anisotropy studies of ribonuclease T<sub>1</sub>. *Biochemistry* **24**:5517–5526.
55. Gryczynski I, Eftink M, Lakowicz JR. 1988. Conformation heterogeneity in proteins as an origin of heterogeneous fluorescence decays, illustrated by native and denatured ribonuclease T<sub>1</sub>. *Biochim Biophys Acta* **954**:244–252.
56. Eftink MR, Ghiron CA. 1987. Frequency domain measurements of the fluorescence lifetime of ribonuclease T<sub>1</sub>. *Biophys J* **52**:467–473.
57. Chen LX-Q, Longworth JW, Fleming GR. 1987. Picosecond time-resolved fluorescence of ribonuclease T<sub>1</sub>. *Biophys J* **51**:865–873.
58. Concha NO, Head JF, Kaetzel MA, Dedman JR, Seaton BA. 1993. Rat annexin V crystal structure: Ca<sup>2+</sup>-induced conformational changes. *Science* **261**:1321–1324.
59. Sopkova J, Gallay J, Vincent M, Pancoska P, Lewit-Bentley A. 1994. The dynamic behavior of Annexin V as a function of calcium ion binding: a circular dichroism, UV absorption, and steady state and time-resolved fluorescence study. *Biochemistry* **33**(15):4490–4499.
60. Sopkova J, Vincent M, Takahashi M, Lewit-Bentley A, Gallay J. 1998. Conformational flexibility of domain III of annexin V studied by fluorescence of tryptophan 187 and circular dichroism: the effect of pH. *Biochemistry* **37**:11962–11970.
61. Toptygin D, Savtchenko RS, Meadow ND, Brand L. 2001. Homogeneous spectrally- and time-resolved fluorescence emission from single-tryptophan mutants of IIA<sup>Glc</sup> protein. *J Phys Chem B* **105**:2043–2055.
62. Gryczynski I, Lakowicz JR. Unpublished observations.
63. Nishimoto E, Yamashita S, Szabo AG, Imoto T. 1998. Internal motion of lysozyme studied by time-resolved fluorescence depolarization of tryptophan residues. *Biochemistry* **37**:5599–5607.
64. Poveda JA, Prieto M, Encinar JA, Gonzalez-Ros JM, Mateo CR. 2003. Intrinsic tyrosine fluorescence as a tool to study the interaction of the shaker B "ball" peptide with anionic membranes. *Biochemistry* **42**:7124–7132.
65. Damberg P, Jarvet J, Allard P, Mets U, Rigler R, Gräslund A. 2002. <sup>13</sup>C-<sup>1</sup>H NMR relaxation and fluorescence anisotropy decay study of tyrosine dynamics in motilin. *Biophys J* **83**:2812–2825.
66. Kroes SJ, Canters GW, Gilardi G, van Hoek A, Visser AJWG. 1998. Time-resolved fluorescence study of azurin variants: conformational heterogeneity and tryptophan mobility. *Biophys J* **75**:2441–2450.
67. Tcherkasskaya O, Ptitsyn OB, Knutson JR. 2000. Nanosecond dynamics of tryptophans in different conformational states of apomyoglobin proteins. *Biochemistry* **39**:1879–1889.
68. Lakshmikanth GS, Krishnamoorthy G. 1999. Solvent-exposed tryptophans probe the dynamics at protein surfaces. *Biophys J* **77**:1100–1106.
69. Kouyama I, Kinoshita K, Ikegami A. 1989. Correlation between internal motion and emission kinetics of tryptophan residues in proteins. *Eur J Biochem* **182**:517–521.
70. Hansen JE, Rosenthal SJ, Fleming GR. 1992. Subpicosecond fluorescence depolarization studies of tryptophan and tryptophanyl residues of proteins. *J Phys Chem* **96**:3034–3040.
71. Ross JBA, Rousslang KW, Brand L. 1981. Time-resolved fluorescence and anisotropy decay of the tryptophan in adrenocorticotropin-(1–24). *Biochemistry* **20**:4361–4369.
72. Nordlund TM, Podolski DA. 1983. Streak camera measurement of tryptophan and rhodamine motions with picosecond time resolution. *Photochem Photobiol* **38**(6):665–669.
73. Nordlund TM, Liu X-Y, Sommer JH. 1986. Fluorescence polarization decay of tyrosine in lima bean trypsin inhibitor. *Proc Natl Acad Sci USA* **83**:8977–8981.
74. Data courtesy of Dr. John Lee, University of Georgia.
75. Liao R, Wang C-K, Cheung HC. 1992. Time-resolved tryptophan emission study of cardiac troponin I. *Biophys J* **63**:986–995.
76. Dittes K, Gakamsky DM, Haran G, Haas E, Ojcius DM, Kourilsky P, Pecht I. 1994. Picosecond fluorescence spectroscopy of a single-chain class I major histocompatibility complex encoded protein in its peptide loaded and unloaded states. *Immunol Lett* **40**:125–132.

77. Lakowicz JR, Gryczynski I, Szmacinski H, Cherek H, Joshi N. 1991. Anisotropy decays of single tryptophan proteins measured by GHz frequency-domain fluorometry with collisional quenching. *Eur Biophys J* **19**:125–140.
78. Lakowicz JR, Cherek H, Gryczynski I, Joshi N, Johnson ML. 1987. Enhanced resolution of fluorescence anisotropy decays by simultaneous analysis of progressively quenched samples. *Biophys J* **51**:755–768.
79. Gryczynski I, Lakowicz JR. Unpublished observations.
80. John E, Jähnig F. 1988. Dynamics of melittin in water and membranes as determined by fluorescence anisotropy decay. *Biophys J* **54**:817–827.
81. Lakowicz JR, Gryczynski I, Cherek H, Laczko G. 1991. Anisotropy decays of indole, melittin monomer and melittin tetramer by frequency-domain fluorometry and multi-wavelength global analysis. *Biophys Chem* **39**:241–251.
82. Georghiou S, Thompson M, Mukhopadhyay AK. 1981. Melittin-phospholipid interaction evidence for melittin aggregation. *Biochim Biophys Acta* **642**:429–432.
83. Dufourcq J, Faucon J-F. 1977. Intrinsic fluorescence study of lipid–protein interactions in membrane models. *Biochim Biophys Acta* **467**:1–11.
84. Faucon JF, Dufourcq J, Lussan C. 1979. The self-association of melittin and its binding to lipids. *FEBS Lett* **102**(1):187–190.
85. Kaszycki P, Wasylewski Z. 1990. Fluorescence-quenching-resolved spectra of melittin in lipid bilayers. *Biochim Biophys Acta* **1040**:337–345.
86. Papenhuijzen J, Visser AJWG. 1983. Simulation of convoluted and exact emission anisotropy decay profiles. *Biophys Chem* **17**:57–65.
87. De Beuckeleer K, Volckaert G, Engelborghs Y. 1999. Time resolved fluorescence and phosphorescence properties of the individual tryptophan residues of barnase: evidence for protein–protein interactions. *Proteins: Struct Funct Genet* **36**:42–53.
88. Sillen A, Hennecke J, Roethlisberger D, Glockshuber R, Engelborghs Y. 1999. Fluorescence quenching in the DsbA protein from *Escherichia coli*: complete picture of the excited-state energy pathway and evidence for the reshuffling dynamics of the microstates of tryptophan. *Proteins: Struct Funct Genet* **37**:253–263.
89. Hennecke J, Sillen A, Huber-Wunderlich M, Engelborghs Y, Glockshuber R. 1997. Quenching of tryptophan fluorescence by the active-site disulfide bridge in the DsbA protein from *Escherichia coli*. *Biochemistry* **36**:6391–6400.
90. Rouviere N, Vincent M, Craescu CT, Gallay J. 1997. Immunosuppressor binding to the immunophilin FKBP59 affects the local structural dynamics of a surface  $\beta$ -strand: time-resolved fluorescence study. *Biochemistry* **36**:7339–7352.
91. Suwaliyan A, Klein UKA. 1989. Picosecond study of solute–solvent interaction of the excited state of indole. *Chem Phys Lett* **159**(2–3):244–250.
92. Eftink MR, Ramsay GD, Burns L, Maki AH, Mann CJ, Matthews CR, Ghiron CA. 1993. Luminescence studies of trp repressor and its single-tryptophan mutants. *Biochemistry* **32**:9189–9198.
93. Royer CA. 1992. Investigation of the structural determinants of the intrinsic fluorescence emission of the trp repressor using single tryptophan mutants. *Biophys J* **63**:741–750.
94. Bismuto E, Irace G, D'Auria S, Rossi M, Nucci R. 1997. Multitryptophan-fluorescence emission decay of  $\beta$ -glycosidase from the extremely thermophilic archaeon *Sulfolobus solfataricus*. *Eur J Biochem* **244**:53–58.
95. Hirsch RE, Nagel RL. 1981. Conformational studies of hemoglobins using intrinsic fluorescence measurements. *J Biol Chem* **256**(3):1080–1083.
96. Hirsch RE, Peisach J. 1986. A comparison of the intrinsic fluorescence of red kangaroo, horse and sperm whale metmyoglobins. *Biochim Biophys Acta* **872**:147–153.
97. Hirsch RE, Noble RW. 1987. Intrinsic fluorescence of carp hemoglobin: a study of the R6T transition. *Biochim Biophys Acta* **914**:213–219.
98. Sebban P, Coppey M, Alpert B, Lindqvist L, Jameson DM. 1980. Fluorescence properties of porphyrin-globin from human hemoglobin. *Photochem Photobiol* **32**:727–731.
99. Hochstrasser RM, Negus DK. 1984. Picosecond fluorescence decay of tryptophans in myoglobin. *Proc Natl Acad Sci USA* **81**:4399–4403.
100. Bismuto E, Irace G, Gratton E. 1989. Multiple conformational states in myoglobin revealed by frequency domain fluorometry. *Biochemistry* **28**:1508–1512.
101. Willis KJ, Szabo AG, Zuker M, Ridgeway JM, Alpert B. 1990. Fluorescence decay kinetics of the tryptophyl residues of myoglobin: effect of heme ligation and evidence for discrete lifetime components. *Biochemistry* **29**:5270–5275.
102. Gryczynski Z, Lubkowski J, Bucci E. 1995. Heme–protein interactions in horse heart myoglobin at neutral pH and exposed to acid investigated by time-resolved fluorescence in the pico- to nanosecond time range. *J Biol Chem* **270**(33):19232–19237.
103. Janes SM, Holtom G, Ascenzi P, Brundri M, Hochstrasser RM. 1987. Fluorescence and energy transfer of tryptophans in *Aplysia* myoglobin. *Biophys J* **51**:653–660.
104. Szabo AG, Krajcik D, Zuker M, Alpert B. 1984. Conformational heterogeneity in hemoglobin as determined by picosecond fluorescence decay measurements of the tryptophan residues. *Chem Phys Lett* **108**:145–149.
105. Kamal JKA, Behere DV. 2001. Steady-state and picosecond time-resolved fluorescence studies on native and apo seed coat soybean peroxidase. *Biochim Biophys Res Comm* **289**:427–433.
106. Bucci E, Gryczynski Z, Fronticelli C, Gryczynski I, Lakowicz JR. 1992. Fluorescence intensity and anisotropy decays of the intrinsic tryptophan emission of hemoglobin measured with a 10-GHz fluorometer using front-face geometry on a free liquid surface. *J Fluoresc* **2**(1):29–36.
107. Toptygin D, Brand L. 2000. Spectrally- and time-resolved fluorescence emission of indole during solvent relaxation: a quantitative model. *Chem Phys Lett* **322**:496–502.
108. Lakowicz JR. 2000. On spectral relaxation in proteins. *Photochem Photobiol* **72**(4):421–437.
109. Vincent M, Gilles AM, Li de la Sierra IM, Briozzo P, Barzu O, Gallay J. 2000. Nanosecond fluorescence dynamic Stokes shift of tryptophan in a protein matrix. *J Phys Chem B* **104**:11286–11295.
110. Zhong D, Pal SK, Zhang D, Chan SI, Zewail AH. 2002. Femtosecond dynamics of rubredoxin: tryptophan solvation and resonance energy transfer in the protein. *Proc Natl Acad Sci USA* **99**(1):13–18.
111. Petushkov VN, van Stokkum IHM, Gobets B, van Mourik F, Lee J, van Grondelle R, Visser AJWG. 2003. Ultrafast fluorescence relaxation spectroscopy of 6,7-dimethyl-(8-ribityl)-lumazine and

- riboflavin, free and bound to antenna proteins from bioluminescent bacteria. *J Phys Chem B* **107**:10934–10939.
112. Kamal JKA, Zhao L, Zewail AH. 2004. Ultrafast hydration dynamics in protein unfolding: human serum albumin. *Proc Natl Acad Sci USA* **101**(37):13411–13416.
  113. Lakowicz JR, Cherek H. 1980. Nanosecond dipolar relaxation in proteins observed by wavelength-resolved lifetimes of tryptophan fluorescence. *J Biol Chem* **255**:831–834.
  114. Demchenko AP, Gryczynski I, Gryczynski Z, Wiczek W, Malak H, Fishman M. 1993. Intramolecular dynamics in the environment of the single tryptophan residue in staphylococcal nuclease. *Biophys Chem* **48**:39–48.
  115. Grinvald A, Steinberg IZ. 1974. Fast relaxation process in a protein revealed by the decay kinetics of tryptophan fluorescence. *Biochemistry* **25**(13):5170–5178.
  116. Georghiou S, Thompson M, Mukhopadhyay AK. 1982. Melittin–phospholipid interaction studied by employing the single tryptophan residue as an intrinsic fluorescent probe. *Biochim Biophys Acta* **688**:441–452.
  117. Szmacinski H, Lakowicz JR, Johnson M. 1988. Time-resolved emission spectra of tryptophan and proteins from frequency-domain fluorescence spectroscopy. *SPIE Proc* **909**:293–298.
  118. Buzady A, Erostyak J, Somogyi B. 2000. Phase-fluorimetry study on dielectric relaxation of human serum albumin. *Biophys Chem* **88**: 153–163.
  119. Russo AT, Brand L. 1999. A nanosecond time-resolved fluorescence study of recombinant human myelin basic protein. *J Fluoresc* **9**(4): 333–342.
  120. Vincent M, Gallay J, Demchenko AP. 1995. Solvent relaxation around the excited state of indole: analysis of fluorescence lifetime distributions and time-dependence spectral shifts. *J Phys Chem* **99**: 14931–14941.
  121. De Foresta B, Gallay J, Sopkova J, Champeil P, Vincent M. 1999. Tryptophan octyl ester in detergent micelles of dodecylmaltoside: fluorescence properties and quenching by brominated detergent analogs. *Biophys J* **77**:3071–3084.
  122. Steiner RF, Kolinski R. 1968. The phosphorescence of oligopeptides containing tryptophan and tyrosine. *Biochemistry* **7**:1014–1018.
  123. Purkey RM, Galley WC. 1970. Phosphorescence studies of environmental heterogeneity for tryptophyl residues in proteins. *Biochemistry* **9**:3569–3575.
  124. Strambini GB, Gonnelli M. 1985. The indole nucleus triplet-state lifetime and its dependence on solvent microviscosity. *Chem Phys Lett* **115**(2):196–200.
  125. Cioni P, Strambini GB. 2002. Tryptophan phosphorescence and pressure effects on protein structure. *Biochim Biophys Acta* **1595**: 116–130.
  126. Wright WW, Guffanti GT, Vanderkooi JM. 2003. Protein in sugar films and in glycerol/water as examined by infrared spectroscopy and by the fluorescence and phosphorescence of tryptophan. *Biophys J* **85**:1980–1995.
  127. Kai Y, Imakubo K. 1979. Temperature dependence of the phosphorescence lifetimes of heterogeneous tryptophan residues in globular proteins between 293 and 77 K. *Photochem Photobiol* **29**:261–265.
  128. Domanus J, Strambini GB, Galley WC. 1980. Heterogeneity in the thermally-induced quenching of the phosphorescence of multi-tryptophan proteins. *Photochem Photobiol* **31**:15–21.
  129. Barboy N, Feitelson J. 1985. Quenching of tryptophan phosphorescence in alcohol dehydrogenase from horse liver and its temperature dependence. *Photochem Photobiol* **41**(1):9–13.
  130. Saviotti ML, Galley WC. 1974. Room temperature phosphorescence and the dynamic aspects of protein structure. *Proc Natl Acad Sci USA* **71**(10):4154–4158.
  131. Strambini GB. 1983. Singular oxygen effects on the room-temperature phosphorescence of alcohol dehydrogenase from horse liver. *Biophys J* **43**:127–130.
  132. Papp S, Vanderkooi JM. 1989. Tryptophan phosphorescence at room temperature as a tool to study protein structure and dynamics. *Photochem Photobiol* **49**:775–784.
  133. Vanderkooi JM, Berger JW. 1989. Excited triplet states used to study biological macromolecules at room temperature. *Biochim Biophys Acta* **976**:1–27.
  134. Schauerte JA, Steel DG, Gafni A. 1997. Time-resolved room temperature tryptophan phosphorescence in proteins. *Methods Enzymol* **278**:49–71.
  135. Strambini GB, Cioni P. 1999. Pressure-temperature effects on oxygen quenching of protein phosphorescence. *J Am Chem Soc* **121**: 8337–8344.
  136. Bodis E, Strambini GB, Gonnelli M, Malnasi-Csizmadia A, Somogyi B. 2004. Characterization of f-actin tryptophan phosphorescence in the presence and absence of tryptophan-free myosin motor domain. *Biophys J* **87**:1146–1154.
  137. Mazhul VM, Zaitseva EM, Shavlovsky MM, Stepanenko OV, Kuznetsova IM, Turoverov KK. 2003. Monitoring of actin unfolding by room temperature tryptophan phosphorescence. *Biochemistry* **42**: 13551–13557.
  138. Gershenson A, Schauerte JA, Giver L, Arnold FH. 2000. Tryptophan phosphorescence study of enzyme flexibility and unfolding in laboratory-evolved thermostable esterases. *Biochemistry* **39**:4658–4665.
  139. Cioni P. 2000. Oxygen and acrylamide quenching of protein phosphorescence: correlation and protein dynamics. *Biophys Chem* **87**: 15–24.
  140. Gonnelli M, Strambini GB. 1997. Time-resolved protein phosphorescence in the stopped-flow: denaturation of horse liver alcohol dehydrogenase by urea and guanidine hydrochloride. *Biochemistry* **36**: 16212–16220.
  141. Vanderkooi JM, Calhoun DB, Englander SW. 1987. On the prevalence of room-temperature protein phosphorescence. *Science* **230**: 568–569.
  142. Strambini GB, Gonnelli M. 1990. Tryptophan luminescence from liver alcohol dehydrogenase in its complexes with coenzyme: a comparative study of protein conformation in solution. *Biochemistry* **29**: 196–203.
  143. Strambini GB, Gabellieri E. 1989. Phosphorescence properties and protein structure surrounding tryptophan residues in yeast, pig, and rabbit glyceraldehyde-3-phosphate dehydrogenase. *Biochemistry* **28**: 160–166.
  144. Strambini GB, Cioni P, Cook PF. 1996. Tryptophan luminescence as a probe of enzyme conformation along the O-acetylserine sulfhydrylase reaction pathway. *Biochemistry* **35**:8392–8400.

145. Burns LE, Maki AH, Spotts R, Matthews KS. 1993. Characterization of the two tryptophan residues of the lactose repressor from *Escherichia coli* by phosphorescence and optical detection of magnetic resonance. *Biochemistry* **32**:12821–12829.
146. Strambini GB, Gabellieri E, Gonnelli M, Rahuel-Clermont S, Branlant G. 1998. Tyrosine quenching of tryptophan phosphorescence in glyceraldehyde-3-phosphate dehydrogenase from *Bacillus stearothermophilus*. *Biophys J* **74**:3165–3172.
147. Brochon JC, Wahl Ph, Charlier M, Maurizot JC, Helene C. 1977. Time-resolved spectroscopy of the tryptophyl fluorescence of the *E. coli* lac repressor. *Biochem Biophys Res Commun* **79**:1261–1271.
148. Eisenberg D, Crothers D. 1979. *Physical chemistry with applications to the life sciences*. Addison-Wesley, Reading, MA. (See page 240.)
149. MacKerell AD, Rigler R, Nilsson L, Hahn U, Saenger W. 1987. A time-resolved fluorescence, energetic and molecular dynamics study of ribonuclease T<sub>1</sub>. *Biophys Chem* **26**:247–261.

## PROBLEMS

- P17.1. *Rotational Diffusion of Proteins:* Use the data in Table 17.7 to calculate the activation energy for rotational diffusion of RNase T<sub>1</sub> in aqueous solution. Also, predict the steady-state anisotropy of RNase T<sub>1</sub> at each temperature from the time-resolved data.

**Table 17.7.** Rotational Correlation Times ( $\lambda$ ), and Time-Zero Anisotropies,  $r(0)$ , for RNase T<sub>1</sub> at Various Temperatures<sup>a</sup>

T (°C)	$\eta/T$ ( $\times 10^{-3}$ kg) ( $m^{-1} s^{-1} K^{-1}$ )	$\tau$ (ns)	$r_0$	$\lambda$ (ns)
-1.5	6.63	4.50	$0.183 \pm 0.007$	$20.9 \pm 1.1$
1.5	6.18	4.45	$0.176 \pm 0.003$	$15.6 \pm 0.8$
15.4	3.92	4.19	$0.184 \pm 0.004$	$9.6 \pm 0.6$
29.9	2.63	3.83	$0.187 \pm 0.004$	$6.0 \pm 0.4$
44.4	1.89	3.33	$0.197 \pm 0.003$	$3.7 \pm 0.2$

<sup>a</sup>Also listed are the calculated values of  $\eta/T$ , where  $\eta$  is the solution viscosity. From [54].

P17.2. *Rotational Freedom of Tryptophan Residues in Proteins:* Use the data in Table 17.4 to calculate the cone angle for tryptophan motion, independent of overall rotational diffusion. Assume the fundamental anisotropy is 0.31. Perform the calculation for RNase T<sub>1</sub>, staph. nuclease, monellin, melittin monomer, and melittin tetramer.

- P17.3. *Apparent Time-Zero Anisotropies of Proteins:* The time-zero anisotropies from RNase T<sub>1</sub> are different in Tables 17.4 and 17.7. Describe possible reasons for these differences.
- P17.4. *Calculation of Decay Associated Spectra:* The lac repressor from *E. coli* is a tetrameric protein with two tryptophan residues per subunit. The intensity decays and emission spectra are shown in Figure 17.48, and the intensity decays are given in Table 17.8.

- Explain the intensity decays (Figure 17.48, left) in terms of the mean lifetime at each wavelength.
- Calculate the decay-associated spectra and interpret the results.

**Table 17.8.** Intensity Decays of the *E. coli* lac Repressor<sup>a</sup>

$\lambda_{em}$ (nm)	$\tau_1 = 3.8$ ns $\alpha_1(\lambda)$	$\tau_2 = 9.8$ ns $\alpha_2(\lambda)$
315	0.72	0.28
320	0.64	0.36
330	0.48	0.52
340	0.35	0.65
350	0.28	0.72
360	0.18	0.82
370	0.08	0.92
380	—	1.00

<sup>a</sup>From [147].

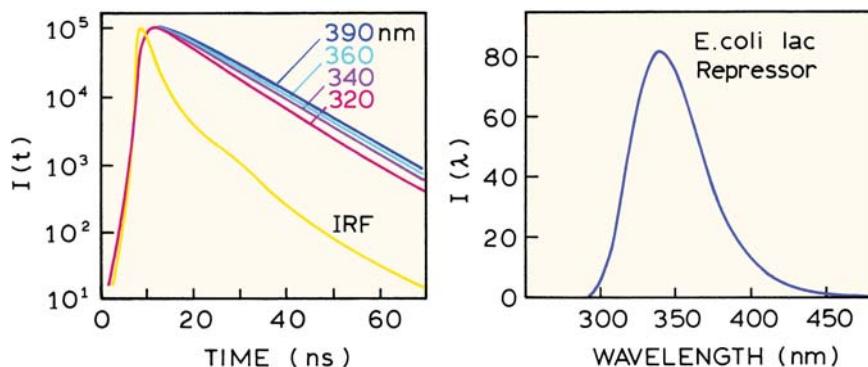


**Figure 17.48.** Intensity decays at the indicated emission wavelength (left) and emission spectrum (right) of the *E. coli* lac repressor. IRF is the instrument response function. Revised from [147].

- C. How could you confirm this assignment of the DAS to each tryptophan residue?

P17.5. *Calculation of a Tryptophan-to-Heme Distance:* Figure 17.36 shows the crystal structure of soybean peroxidase. The dominant component in the tryptophan intensity decay is 35 ps, which accounts for 97% of the emission. Assume the other components are due to

impurities or apoprotein, so that the transfer efficiency is up to 97%. Calculate the tryptophan-to-heme distance using the overlap integral of  $J(\lambda) = 9.1 \times 10^{-14} \text{ M}^{-1} \text{ cm}^3$  or the Förster distance of 35.1 Å for  $\kappa^2 = 2/3$ . The crystal structure indicates  $\kappa^2 = 2$ . Assume a quantum yield of 0.1 in the absence of energy transfer and a refractive index of 1.3.

# 18

# Multiphoton Excitation and Microscopy

In the previous chapters of this book we described the emission resulting from one-photon excitation (1PE). By 1PE we mean that an excited fluorophore has reached the excited state by absorption of a single photon. We now consider two-photon (2PE) and three-photon (3PE) excitation. The term 2PE indicates that the fluorophore has reached the excited state by absorption of two photons. We will only consider simultaneous absorption of two or more photons. We will not consider sequential absorption where there is a well-defined intermediate state.

Until 1990 multiphoton spectroscopy was considered to be an exotic phenomenon that was used primarily in chemical physics and optical spectroscopy. Two-photon absorbance or excitation requires high peak powers to increase the probability that two photons are simultaneously available for absorption. Because of the interaction of two photons with the fluorophore, the selection rules for light absorption are, in principle, different from those for one-photon spectroscopy. Because of the different selection rules, two-photon spectroscopy can be used as a tool to study the excited-state symmetry of organic chromophores.<sup>1–3</sup> Multiphoton experiments require complex lasers and high optical powers. It did not seem possible to use multiphoton excitation (MPE) in optical microscopy because the high power would damage the biological samples. Surprisingly, MPE is now widely used in fluorescence microscopy. Multiphoton microscopy (MPM) is possible because of the favorable properties of titanium–sapphire (Ti:sapphire) lasers and the development of laser-scanning microscopes. Multiphoton excitation is usually less damaging to biological samples than in one-photon excitation. Multiphoton microscopy was introduced in 1990<sup>4</sup> and is now used extensively in cell imaging.<sup>5–9</sup>

## 18.1. INTRODUCTION TO MULTIPHOTON EXCITATION

The phenomenon of multiphoton excitation can be depicted in a Jablonski diagram (Figure 18.1). For one-photon absorption a single photon elevates the fluorophore to the excited state. Depending upon the absorption spectrum and the excitation wavelength the fluorophore may be excited to higher vibration levels of the  $S_1$  state or even to the  $S_2$  state. Irrespective of the excitation wavelength the fluorophore has reached the excited state by absorption of a single photon. Almost all fluorophores emit from the lowest energy level of the relaxed  $S_1$  state.

MPE is accomplished using longer-wavelength excitation to avoid the much stronger single-photon absorption of the fluorophore (Figure 18.1), so that 2 or 3 photons are needed to reach the same energy level due to one-photon absorption. This diagram can give the impression that a fluorophore absorbs the photons sequentially. However, MPE is due to simultaneous absorption of multiple photons, which is why no intermediate states are shown in Figure 18.1. High illumination intensities must be used for MPE because two or more photons must interact simultaneously with the fluorophore. MPE is a nonlinear process. The extents of 2PE and 3PE are proportional to the intensity raised to the second or third power, respectively. To date all fluorophores examined with MPE have displayed the same emission spectra and lifetimes as if they were excited by one-photon absorption. Since the selection rules for optical excitation are different for 1PE, 2PE, and 3PE, the fluorophores may be placed into different excited states with different modes of excitation. However, the fluorophores emit from the same excited state, independent of one- or

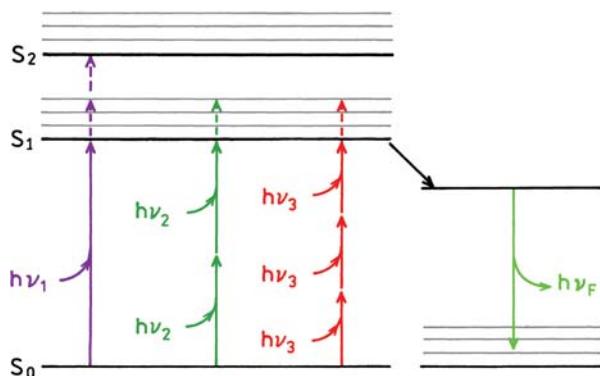


**Figure 18.1.** Jablonski diagram for one-, two-, and three-photon excitation.

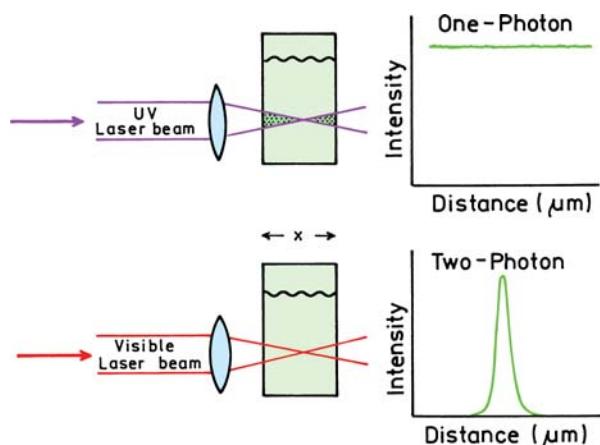


**Figure 18.2.** Schematic comparison of one- and two-photon excitation.

multiphoton absorption. Hence we can still use a Jablonski diagram with  $S_1$  emission to describe multiphoton excitation.

The quadratic or higher-order dependence of MPE on the incident intensity is a favorable property for optical imaging. Assume a wavelength for 1PE is incident on a

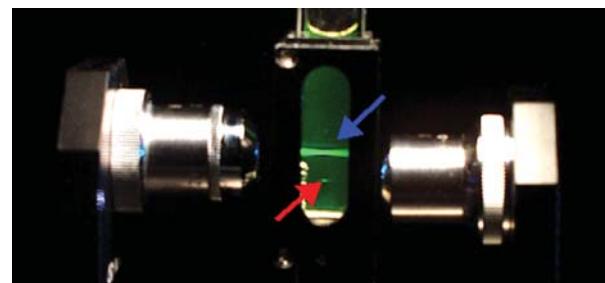


**Figure 18.3.** Comparison of one-photon excitation (blue arrow) and two-photon excitation (red arrow) of a fluorescein solution. Courtesy of Dr. Peter T. C. So from the Massachusetts Institute of Technology.

cuvette (Figure 18.2). The amount of light absorbed in any plane at a distance is proportional to the incident intensity at this plane. Focusing a beam on the center of a cuvette changes the size of the beam but does not change the total amount of light passing through a plane at a position  $x$ . The emission intensity is constant at all positions  $x$  across the cuvette, assuming the absence of inner-filter effects (top).

Now consider 2PE with a longer wavelength. The amount of light absorbed is proportional to the square of the intensity. Focusing the beam decreases its size but increases its intensity. As a result the amount of light absorbed is not constant across the cuvette, but shows a maximum at the focal point where the incident intensity is highest (Figure 18.2, bottom). This effect can result in strongly localized excitation. Figure 18.3 shows a fluorescein solution illuminated with wavelengths for 1PE and 2PE. For 1PE the fluorescein is excited across the cuvette. For 2PE the fluorescein is only excited in a small spot at the focal point of the laser beam.

Most fluorophores photobleach rapidly in fluorescence microscopy. Localized excitation is an advantage under these conditions. If a biological sample undergoes 1PE the light is absorbed at all depths in the sample, not just in the focal plane.<sup>11–12</sup> As a result the entire thickness of the sample undergoes photobleaching (Figure 18.4, left) and photo-damage occurs across the entire thickness of the sample.

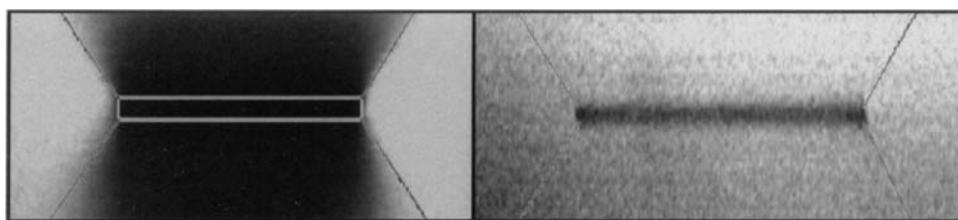


**Figure 18.4.** Photobleaching of rhodamine in a Formvar layer with one- (left) and two-photon excitation (right). From [12].

For three-dimensional reconstruction of the cell image it is necessary to obtain images from multiple focal planes. This is difficult with 1PE because all planes are bleached irrespective of the position of the focal plane.

The right side of Figure 18.4 shows photobleaching with 2PE, which is now strongly localized in the focal plane. The fluorophores are still photobleached, but it is possible to image above and below the focal plane because the fluorophores in these regions are not photobleached. The adverse effects due to absorption are localized to the focal plane, which may be less damaging to the specimen than when photobleaching occurs across the entire thickness. MPE is usually performed using wavelengths from 720 to 950 nm, where there is minimal absorption by water and intrinsic chromophores (see Figure 19.4).

## 18.2. CROSS-SECTIONS FOR MULTIPHOTON ABSORPTION

We are all familiar with the absorption coefficients for one-photon absorption, which are usually expressed as the molar extinction coefficients in units of  $M^{-1} \text{ cm}^{-1}$ . For a single molecule the absorption can be described in units of  $\text{cm}^2$ , which is the effective area over which a single molecule absorbs the incident light. For 1PE the optical cross-sections  $\sigma_1$  range from  $10^{-15}$  to  $10^{-17} \text{ cm}^2$ . Cross-sections of  $10^{-15}$ ,  $10^{-16}$ , and  $10^{-17} \text{ cm}^2$  correspond to squares with sides of 3, 1, and 0.3 Å, respectively. One-photon cross-sections are thus comparable to the size of fluorophores and can be understood intuitively.

It is more difficult to have an instructive understanding of cross-sections for multiphoton absorption. For 2PE the cross-sections are in units of  $\text{cm}^4 \text{ s}/\text{photon}$ . The values of the 2PE cross-sections are reported in terms of GM (Goppert-Mayer) units, where  $1 \text{ GM} = 10^{-50} \text{ cm}^4 \text{ s}/\text{photon}$ . The units are named after Maria Goppert-Mayer, who developed the theory for two-photon absorption processes.<sup>13–14</sup> These units for the 2PE cross-sections are more difficult to understand than the cross-sections for 1PE in units of area.

The physical origin of the 2PE cross-sections can be understood by some simple considerations. For one-photon absorption the number of photons absorbed per second ( $NA_1$ ) is given by

$$NA_1 (\text{photons/s}) = \sigma_1 (\text{cm}^2) I(\text{photon/cm}^2\text{s}) \quad (18.1)$$

where  $I$  is the intensity and  $\sigma_1$  is the cross-section for one-photon absorption. The units are given within the parentheses.

The cross-section in  $\text{cm}^2$  is multiplied by the number of photons passing near the molecule per second to yield the number of photons absorbed per second. To obtain  $NA_1$  in photons per second the cross-section must be in units of  $\text{cm}^2$ .

Now consider two-photon absorption. The number of photons absorbed per second by 2PE ( $NA_2$ ) is given by

$$NA_2 (\text{photons/s}) = \sigma_2 I^2 (\text{photons/cm}^2\text{s})^2 \quad (18.2)$$

In order for the units to match on both sides of eq. 18.2 the units of  $\sigma_2$  must be  $\text{cm}^4\text{s}/\text{photon}$ . Similarly, for 3PE,

$$NA_3 (\text{photons/s}) = \sigma_3 I^3 (\text{photons/cm}^2\text{s})^3 \quad (18.3)$$

and the units of a three-photon cross-section are  $\text{cm}^6 \text{ s}^2/\text{photon}^2$ .

## 18.3. TWO-PHOTON ABSORPTION SPECTRA

Since selection rules for one- and two-photon optical transitions are different there is no reason to expect the one- and two-photon absorption spectra to be the same.<sup>15–17</sup> Figure 18.5 shows these spectra for some commonly used fluorophores. Note that the  $y$ -axis is a logarithmic scale and the one-photon spectra are plotted on an arbitrary scale. For visual comparison the spectra are usually plotted on the same wavelength scale where the one-photon spectrum is plotted using twofold longer wavelengths. The  $x$ -axis is usually the wavelengths used for two-photon absorption measurements. Occasionally the data are plotted on the one-photon wavelength scale. The correct scale is usually apparent from the known one-photon absorption spectra of the fluorophores.

The one- and two-photon absorption spectra are different for the three fluorophores shown in Figure 18.5, which has been found for most fluorophores.<sup>15–17</sup> An important feature of the two-photon absorption is that, on a relative scale, the absorption is stronger at wavelengths below twice the long-wavelength absorption. For example, the one-photon absorption of RhB is much weaker at 400 nm than at 500 nm (middle panel). The two-photon absorption is stronger for RhB at 800 nm than at 1000 nm. This is convenient because two-photon microscopy is almost exclusively done using Ti:sapphire lasers, which have an output from 720 to 1000 nm. Additionally, the shape of the two-photon absorption spectra often allows simultaneous excitation of several fluorophores using a single wavelength.

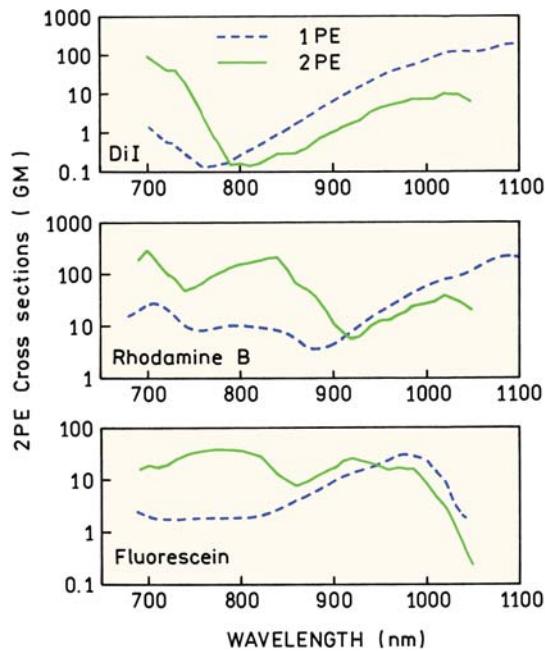


**Figure 18.5.** One- and two-photon absorption spectra of three commonly used fluorophores. The one-photon spectra are plotted on an arbitrary scale. From [17].

Additional two-photon absorption spectra are shown in Figure 18.6. It is difficult to measure their spectra because the amount of light absorbed depends strongly on the exact spatial and temporal profile of the pulses.<sup>18–19</sup> For this reason two-photon cross-sections are usually measured relative to a standard, typically bis-MSB, which appears to be the best characterized two-photon standard.<sup>20</sup> Fortunately, fluoresceins have large cross-sections at Ti:sapphire wavelengths. The cross-sections of UV-absorbing fluorophores such as indo-1 (IC) or fura-2 with calcium (FC) are small—above 700 nm—because two photons at wavelengths above about 700 nm do not contain enough energy to reach the S<sub>1</sub> state.

One-photon absorption spectra often show regions of low absorption at wavelengths below the long-wavelength absorption. For instance, see the absorption spectra of fluorescein (Figure 3.9) or dyes used for DNA sequencing. The low absorption at wavelengths below the S<sub>0</sub> ⊗ S<sub>1</sub> transition makes it difficult to excite more than one dye at a time using a laser source. The larger width of the two-photon absorption spectra makes it easier to excite multiple fluorophores using one wavelength. This possibility is shown in Figure 18.7 for five fluorophores that were all excited using 800 nm from a Ti:sapphire laser.

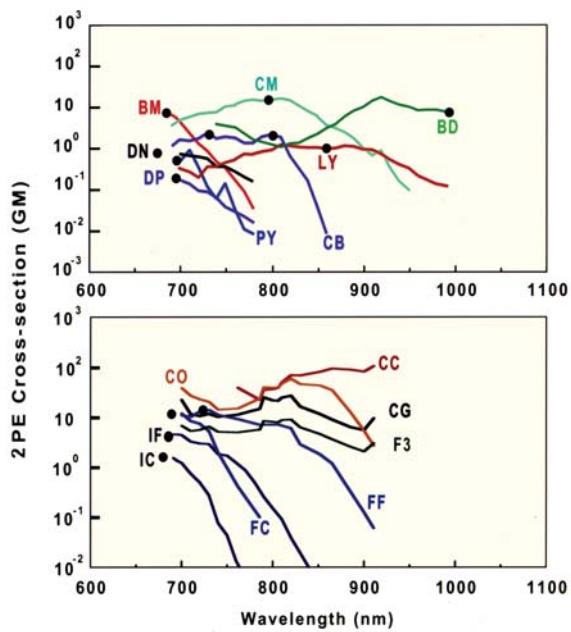


**Figure 18.6.** Two-photon fluorescence excitation spectra of fluorophores. For BM (Bis-MSB), data represent two-photon absorption cross-sections. For all the other fluorophores, data represent two-photon action cross-sections—i.e., the product of the fluorescence emission quantum efficiencies and the two-photon absorption cross-sections. Units are Goppert-Mayer (GM); 1 GM = 10<sup>-50</sup> cm<sup>4</sup> s/photon. Spectra are excited with linearly polarized light using a mode-locked Ti:sapphire laser. The black dot indicates twice the wavelength of the one-photon absorption maximum of the fluorophore. The fluorophores illustrated in *a* are as follows: BM, *p*-bis(*o*-methylstyryl)-benzene; CB, Cascade Blue hydrazine trisodium salt; LY, Lucifer Yellow CH ammonium salt; BD (BODIPY), 4,4-difluoro-1,3,5,7,8-pentamethyl-4-bora-3,4-a-diazaindacene-2,6-disulfonic acid disodium salt; DP (DAPI not DNA bound), 4',6-diamidino-2-phenylindole dihydrochloride; DN (dansyl), 5-dimethylaminonaphthalene-1-sulfonyl hydrazine; PY, 1,2-bis-(1-pyrenedecanoyl)-sn-glycero-3-phosphocholine; and CM, coumarin 307. The fluorophores illustrated in *b* are as follows: IC, indo-1 with Ca<sup>2+</sup>; IF, indo-1 without Ca<sup>2+</sup>; FC, fura-2 with Ca<sup>2+</sup>; FF, fura-2 without Ca<sup>2+</sup>; CG, calcium green-1 with Ca<sup>2+</sup>; CO, calcium orange with Ca<sup>2+</sup>; CC, calcium crimson Ca<sup>2+</sup>; and F3, fluo-3 with Ca<sup>2+</sup>. From [17].

#### 18.4. TWO-PHOTON EXCITATION OF A DNA-BOUND FLUOROPHORE

At present MPE is used primarily for cellular imaging or for fluorescence correlation spectroscopy (Chapter 24). Both of these applications make use of the small excited volumes obtained using MPE with a focused laser beam. Prior to describing MPE microscopy it is informative to see the effects of MPE on the fluorophores themselves.<sup>22</sup> Figure 18.8 shows emission spectra of DAPI bound to DNA when

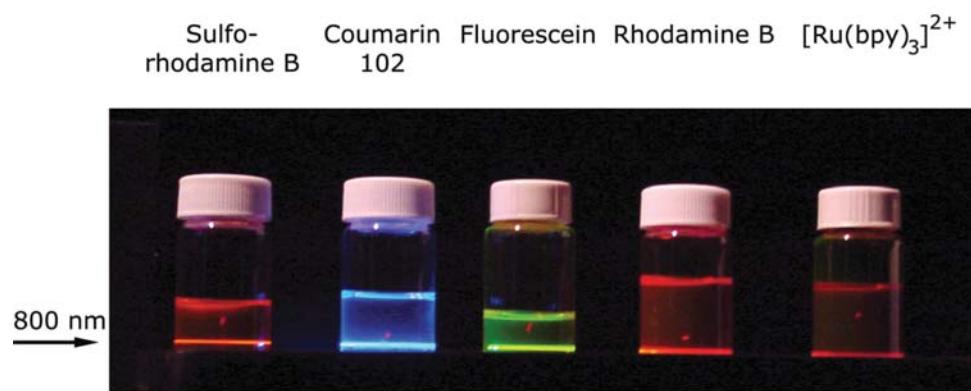


**Figure 18.7.** Simultaneous excitation of several fluorophores using the 800-nm output of a regeneratively amplified Ti:sapphire laser. The laser is incident near the bottom of the bottles. The upper lines are reflections off the surface. From [21].

excited at 360, 830, and 885 nm.<sup>23–25</sup> The emission spectra are the same at each excitation wavelength, showing that emission occurs from the lowest singlet state irrespective of the mode of excitation (Section 18.1). Although not shown, the intensity decays are the same for these excitation wavelengths.<sup>24</sup> When excited at 360 nm a twofold decrease in the incident intensity results in a twofold decrease in fluorescence intensity, as expected for a one-photon process. When excited at 830 and 885 nm, the emission intensity decreases four- and eight-fold, respectively. This indicates that 2PE occurs at 830 nm and 3PE occurs at 885 nm.

The mode of excitation can be determined by the dependence of the emission intensity on incident power

(Figure 18.9). For excitation at 830 and 885 nm a plot of DAPI emission intensity versus incident power yields slopes of 2.01 and 2.85, respectively. The mode of excitation switches from 2PE to 3PE between these wavelengths. The reason for this switch can be found in the DAPI absorption spectrum (top). The long-wavelength absorption ends near 420 nm. Above 840 nm 2PE can no longer occur because the energy of the combined photons is not adequate

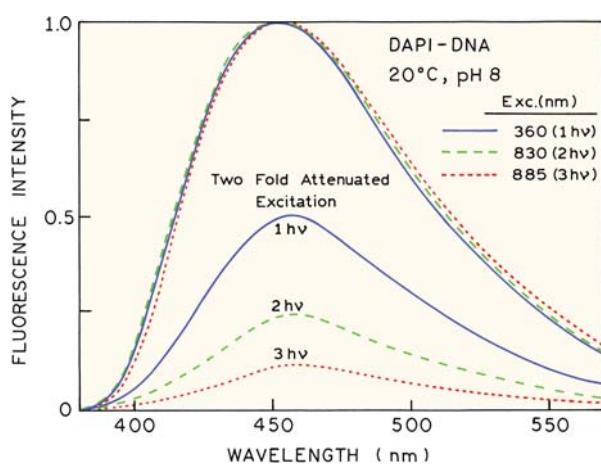


**Figure 18.8.** Normalized emission spectra of DAPI-DNA for excitation at 360, 830, and 885 nm. Also shown are the emission spectra with a twofold attenuation of the excitation. The excitation source at 830 and 885 nm was a femtosecond Ti:sapphire laser; 80 MHz repetition rate with a pulse width near 80 fs.

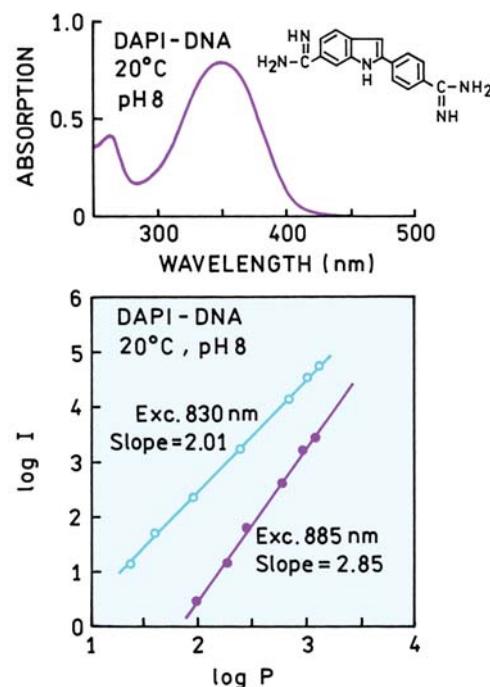


**Figure 18.9.** Absorption spectra and power-dependent intensities of DAPI-DNA. The laser power is in milliwatts. From [24].

to reach the  $S_1$  state. As a result the mode of excitation changes to 3PE. The 2PE-to-3PE transition occurs on the long-wavelength edge of the DAPI absorption. This is a result of the 2PE cross-section being much larger than the 3PE cross-section, so that 2PE dominates wherever possible. It was initially surprising that 3PE could be observed without detectable damage to the sample.

### 18.5. ANISOTROPIES WITH MULTIPHOTON EXCITATION

In the previous section we saw that the emission spectra of DAPI are the same for one, two, and three-photon excitations. In contrast, the anisotropies can be very different for each mode of excitation.<sup>26–32</sup> There are two reasons for the different anisotropies. Fundamental anisotropies can be different for each mode of excitation. This is a complex topic that we will not describe. The second reason is because excitation photocorrelation is different depending on the mode of excitation. More specifically, two-photon excitation results in a more strongly aligned population because this process depends on  $\cos^4 \theta$  photoselection, rather than  $\cos^2 \theta$  for one-photon excitation.

To avoid confusion we note that there are two types of polarization experiments in multiphoton spectroscopy. The experiments described in this book use only linearly polarized light, and the emission anisotropy value is determined by the motions of fluorophores in the excited state. A different type of polarization experiment is performed in chemical physics. These experiments compare the absorption of linearly and circularly polarized light, which provides information about the symmetry of the excited states.<sup>33–35</sup>

#### 18.5.1. Excitation Photoselection for Two-Photon Excitation

In section 10.2 we showed that an anisotropy is related to the average value of  $\cos^2 \theta$ . The fundamental anisotropy value of 0.4 for one-photon excitation is a consequence of  $\cos^2 \theta$  photoselection. For two-photon excitation the fluorophore interacts simultaneously with two photons, and each interaction is proportional to  $\cos^2 \theta$ . Hence, the photoselection function becomes<sup>29</sup>

$$f_2(\theta) = \cos^4 \theta \sin \theta d\theta \quad (18.4)$$

Introduction of this function into the calculation of  $\langle \cos^2 \theta \rangle$  (eq. 10.21) allows calculation of the anisotropies expect-

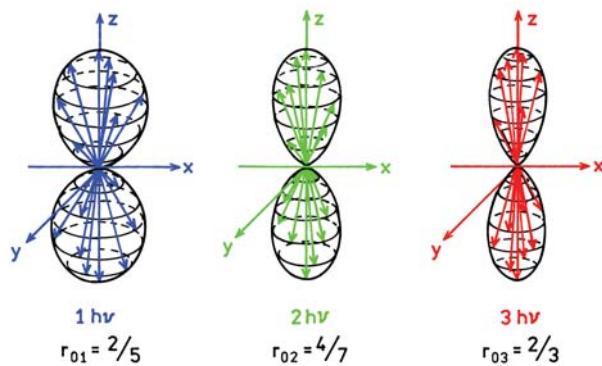


**Figure 18.10.** Excited-state distributions for  $r_0 = 0.40$  with one-, two-, and three-photon excitation.

ed for collinear transitions (Table 10.1). For  $\beta = 0$  the fundamental anisotropy for two-photon excitation is 0.57, rather than 0.4. For three-photon excitation the fundamental anisotropy can be as large as 0.66 (Figure 18.10 and Table 18.1).

It is important to recognize the meaning of these anisotropy values. A value of 0.4 for one-photon excitation and a value of 0.57 for two-photon excitation both mean the absorption and emission transition moments are parallel. There is no new information in the higher anisotropy value for two-photon excitation, except for confirming the transition moments are still parallel. In some cases the anisotropies do not follow the predictions based on  $\cos^2 \theta$  or  $\cos^4 \theta$  photoselection. One example is tryptophan and indole, which display lower anisotropies with two-photon excitation (Section 18.7).

#### 18.5.2. Two-Photon Anisotropy of DPH

It is instructive to see how the anisotropy depends on the mode of excitation. Figure 18.11 shows the excitation anisotropy spectra of DPH. For one-photon excitation (340–380 nm), the anisotropy in frozen solution is always

**Table 18.1.** Fundamental Anisotropies for One-, Two-, and Three-Photon Excitation<sup>a</sup>

$\beta$ (deg)	One-photon $r_{01}$	Two-photon $r_{02}$	Three-photon $r_{03}$
0	0.40	0.57	0.66
45	0.10	0.41	0.17
54.7	0.00	0.00	0.00
90	-0.20	-0.29	-0.33

<sup>a</sup>Data from [35].

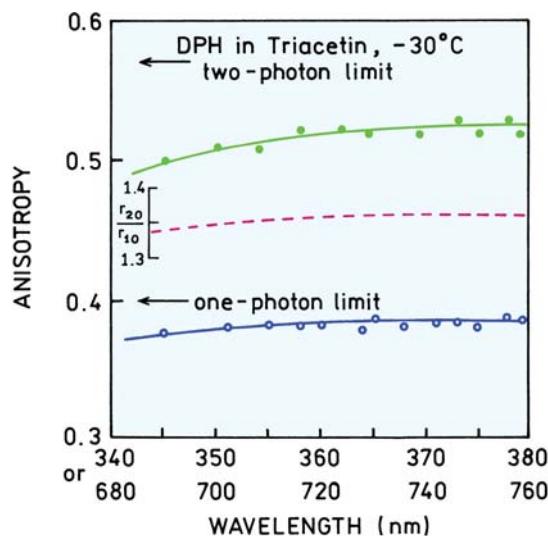


**Figure 18.11.** Excitation anisotropy spectra of DPH in frozen solution for one- and two-photon excitation. Revised with permission from [36]. Copyright © 1994, American Institute of Physics.

below the one-photon limit of 0.40. For two-photon excitation the anisotropy is near 0.5, well above the one-photon limit. The larger anisotropy for two-photon excitation is mostly due to  $\cos^4 \theta$  photoselection. This can be seen from the ratio of the one- and two-photon anisotropies. This ratio is near 1.35, which is close to the predicted ratio of 1.425 (Table 18.1). These data indicate that the value of  $\beta$  for DPH is nearly the same for one- and two-photon excitation. Anisotropy values larger than 0.57 have been observed with three-photon excitation.<sup>32</sup>

#### 18.6. MPE FOR A MEMBRANE-BOUND FLUOROPHORE

Multiphoton excitation requires high local light intensities, which is obtained from focused laser beams. Hence, it is natural to ask whether these conditions are compatible with studies of biological molecules. Remarkably, multiphoton excitation is possible without significant heating or damage of many samples. Figure 18.12 shows emission spectra of DPH in DPPG vesicles, and Figure 18.13 shows the intensity decays for the same sample.<sup>36–38</sup> The same emission spectra and nearly the same intensity decay were observed with 1PE and 2PE, suggesting the membrane is not damaged by the locally intense excitation. The anisotropy decay of DPH is more sensitive to the temperature of the membrane than the intensity decay. The anisotropy decay of DPH in DPPG was essentially the same for 1PE and 2PE,

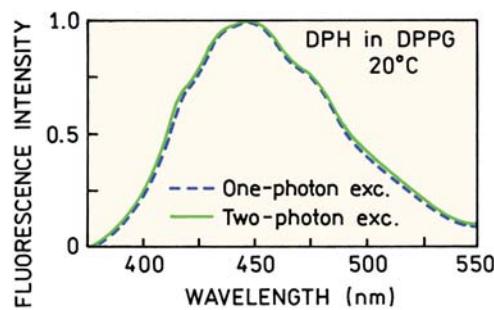


**Figure 18.12.** Fluorescence emission spectra of DPH in DPPG bilayers for excitation at 358 nm (dashed) and 716 nm (solid). From [36].

except for the photoselection factor (Figure 18.14). This result indicates that the membrane is not heated during 2PE of DPH. Remarkably, even three-photon excitation did not seem to elevate the temperature of the membranes (Figure 18.15). The steady-state anisotropies with 1PE and 3PE show phase transitions at the same temperature. The minimal effect of MPE on biomolecules has been demonstrated by continued viability of hamster embryos even after extensive multiphoton imaging.<sup>39</sup>

#### 18.7. MPE OF INTRINSIC PROTEIN FLUORESCENCE

Fluorescence microscopy is rarely performed using intrinsic protein fluorescence because of the difficulty in trans-

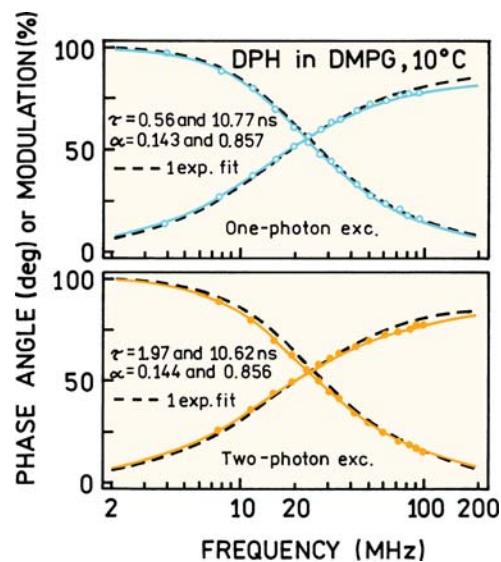


**Figure 18.13.** Frequency-domain intensity decay for DPH in DMPG vesicles, 10°C, for one-photon excitation at 358 nm (top) and two-photon excitation at 716 nm (bottom). From [36].

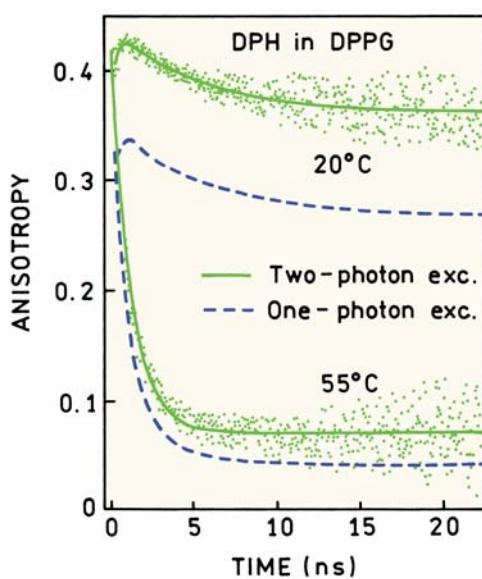


**Figure 18.14.** Time-domain anisotropy decay of DPH in DPPG bilayers for one- and two-photon excitation. From [37].

mitting UV light through the optical components. This problem can be avoided using two-photon excitation because the required wavelength near 560–600 nm is easily transmitted. Several reports have appeared on 2PE of proteins in solution.<sup>40–45</sup> Ti:sapphire lasers do not provide output at the wavelengths needed for 2PE of proteins, and Ti:sapphire lasers are presently the optimal choice for multiphoton microscopy.

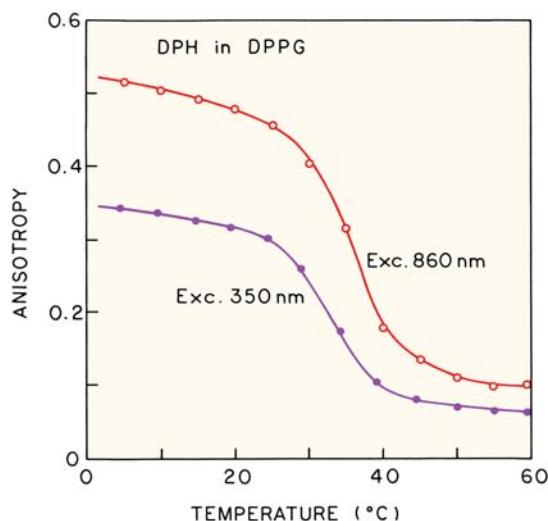


**Figure 18.15.** Temperature-dependent anisotropies of DPH in DPPG for three-photon excitation at 860 nm and one-photon excitation at 350 nm. From [38].

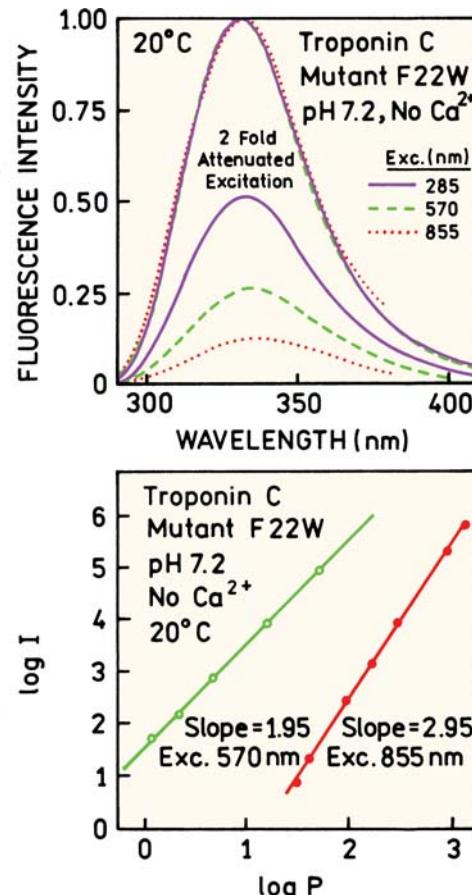


**Figure 18.16.** Emission spectra of troponin C F22W with one-, two-, and three-photon excitation. 570 nm was obtained from a cavity-dumped dye laser. The lower panel shows the dependence of the emission intensity on incident power, in mW. From [47].

The problem of exciting tyrosine and tryptophan fluorescence with a Ti:sapphire laser was solved by using three-photon excitation. Wavelengths near 850 nm can be used for three-photon excitation of tryptophan.<sup>46–47</sup> Multiphoton excitation of proteins is illustrated in Figure 18.16 for a mutant of troponin C (TnC). This protein from muscle typically contains only tyrosine residues. The TnC mutant contains a single tryptophan residue replacing a phenylalanine residue at position 22 (F22W). Emission spectra are shown for excitation at 285 nm, and at the unusual wavelengths of 570 and 855 nm. The same emission spectra were observed for all three excitation wavelengths. Since 570 and 855 nm are much longer than the last absorption band of tryptophan, the emission observed with these excitation wavelengths cannot be due to the unusual process of one-photon excitation.

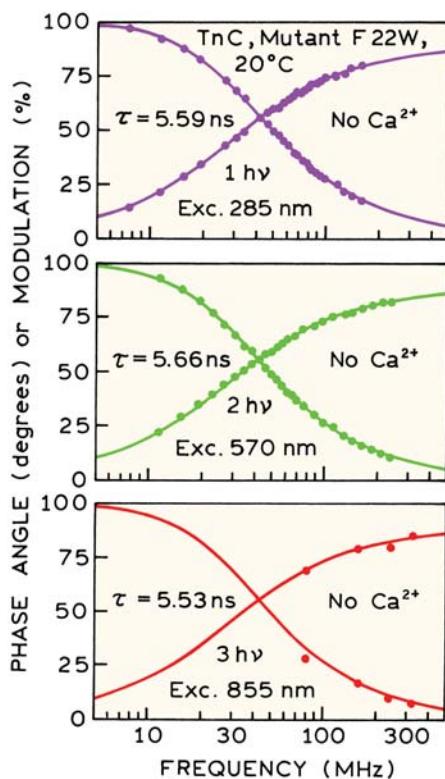


**Figure 18.17.** Frequency-domain intensity decays of TnC F22W without  $\text{Ca}^{2+}$  for one-, two-, and three-photon excitation. From [47].

The nature of the excitation process is revealed by the effects of attenuating the intensity of the incident light. At 285 nm a twofold decrease in the incident light results in a twofold decrease in the emission intensity, which is the usual result for one-photon excitation where the intensity of the emitted light is directly proportional to the excitation intensity. For excitation at 570 nm, twofold attenuation of the incident light results in a fourfold decrease in emission intensity. At 855 nm the same twofold decrease in incident intensity results in an eight-fold decrease in emission intensity. The emission intensity depends on the square of the incident intensity at 570 nm, and on the cube of the incident intensity at 855 nm (Figure 18.16). This data indicates that the emission with 570-nm excitation is due to two-photon excitation, and the emission with 855-nm excitation is due to three-photon excitation. The tryptophan intensity decay is the same for each excitation wavelength (Figure 18.17), which suggests the protein was not adversely affected by the intense 855 nm excitation.

Another feature for multiphoton excitation is the opportunity for new spectroscopic information. This is illus-

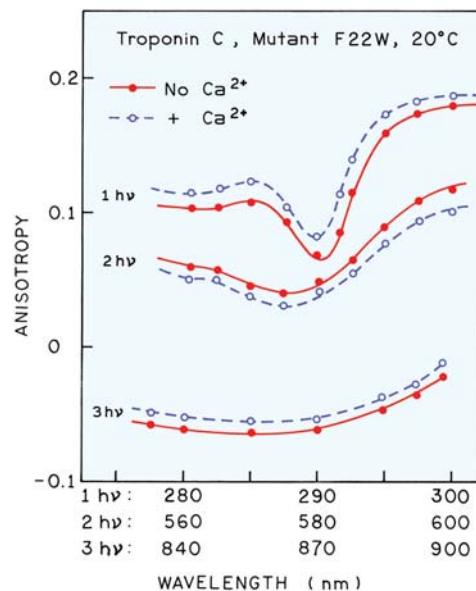


**Figure 18.18.** Excitation anisotropy spectrum of TnC mutant F22W for one-, two-, and three-photon excitation. From [47].

trated by the unusual anisotropies displayed by tryptophan with two- or three-photon excitation. Surprisingly, the anisotropies of the tryptophan residue in TnC F22W are lower for two-photon excitation (560–600 nm) than for one-photon excitation (280–300 nm, Figure 18.18). The anisotropies are still lower for three-photon excitation (840–900 nm). Multiphoton excitation is expected to result in higher anisotropies due to  $\cos^4 \theta$  or  $\cos^6 \theta$  photoselection. The lower anisotropies for tryptophan observed for MPE suggest that MPE is occurring primarily to the  ${}^1\text{L}_b$  state of tryptophan, with emission as usual from the  ${}^1\text{L}_a$  state. Apparently, MPE to the  ${}^1\text{L}_b$  state displays a higher MPE cross-section than does the  ${}^1\text{L}_a$  state, but a full explanation may require more complex analysis.<sup>48–49</sup>

It is of interest to understand how multiphoton excitation is accomplished. The 570-nm excitation was obtained from the cavity-dumped pulses from a rhodamine 6G dye laser. These pulses are about 7 ps wide. Excitation at 855 nm was accomplished using pulses from a Ti:sapphire laser, which are about 70 fs wide. Pulsed excitation is used because it is necessary to have a high instantaneous density of photons in order to have a significant probability of MPE.

At present we are not aware of 3PE of intrinsic protein fluorescence using optical microscopy. However, 3PE of serotonin (5-hydroxytryptamine) has been used in microscopy to image granules of this neurotransmitter in

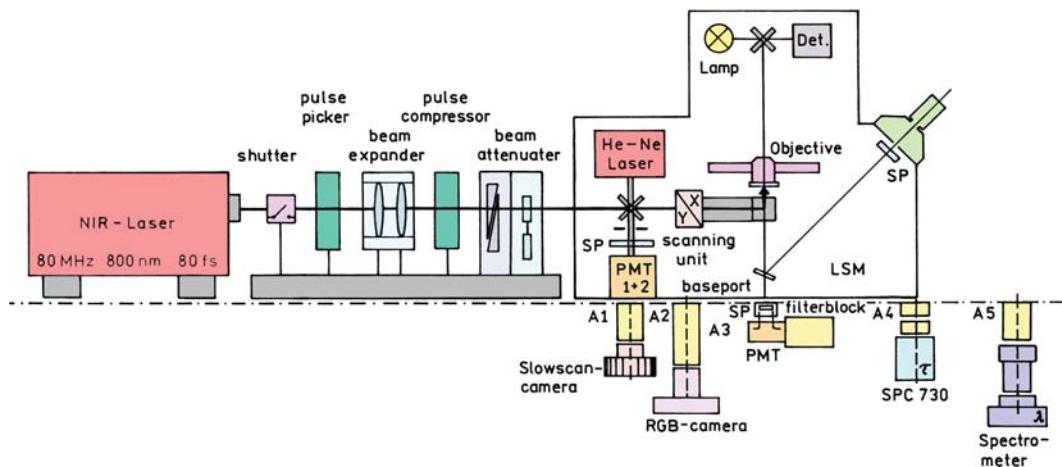


**Figure 18.19.** Schematic of a multiphoton microscope. Revised from [52].

intact cells,<sup>50</sup> but serotonin may undergo complex photochemistry with MPE.<sup>51</sup>

### 18.8. MULTIPHOTON MICROSCOPY

At present the dominant use of MPE is for optical imaging. Multiphoton microscopy (MPM) requires complex instruments that are often maintained by dedicated personnel. Most MPMs use a Ti:sapphire laser source (Figure 18.19). There may be a pulse picker to decrease the repetition rate. The optical path contains components for focusing the beam and for adjusting its intensity. In order to obtain an

image the focused laser beam is raster scanned across the sample by the scanning unit. In this instrument there is also a CW He-Ne laser for conventional confocal laser-scanning microscopy (CLSM) with one-photon excitation. When using MPE all the emitted light comes from the focal spot, and there is minimal out-of-plane fluorescence. For this reason the multiphoton-induced fluorescence is usually measured using a PMT behind the objective, which provides higher sensitivity than passing the emission back through the scanning unit as is done with CLSM.

Several detectors are shown below the baseplate of the microscope. Prior to reaching the detector the signal is passed through a short-pass (SP) filter to remove the longer-wavelength excitation from the emission. Separate detectors are available for measuring lifetimes or emission spectra.

#### 18.8.1. Calcium Imaging

Multiphoton microscopes have been used extensively for cellular imaging. We present just a few examples. MPM can be used for calcium imaging. Figure 18.20 shows neonatal rat cells labeled with a lipid conjugate of Calcium Green (left) or the lipid conjugate Indo-1 (right).<sup>53–54</sup> The two probes show different intracellular distributions. The different distributions occur because CG-C18 localizes on the outside of the cell and Indo-1-C18 was internalized and distributed throughout the cell except for the nucleus.

Multiphoton excitation microscopy is used to measure rapid signaling events in cells.<sup>55</sup> HeLa cells were transfected with the cDNA for a cameleon calcium sensor (Figure

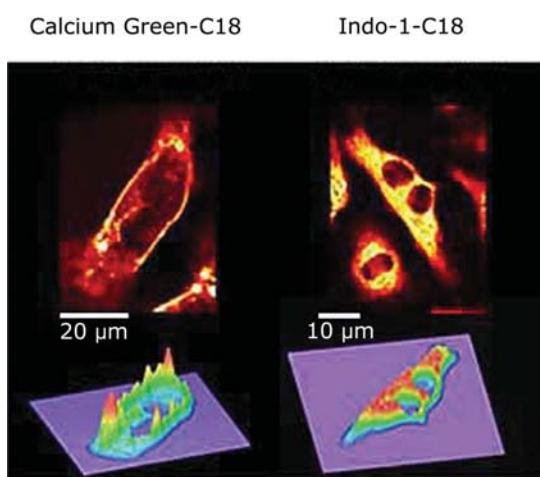


**Figure 18.20.** Multiphoton microscopy images of neonatal rat cells labeled with lipid conjugate of Calcium Green (CG-C18) or Indo-1 (Indo-1-C18). From [54].

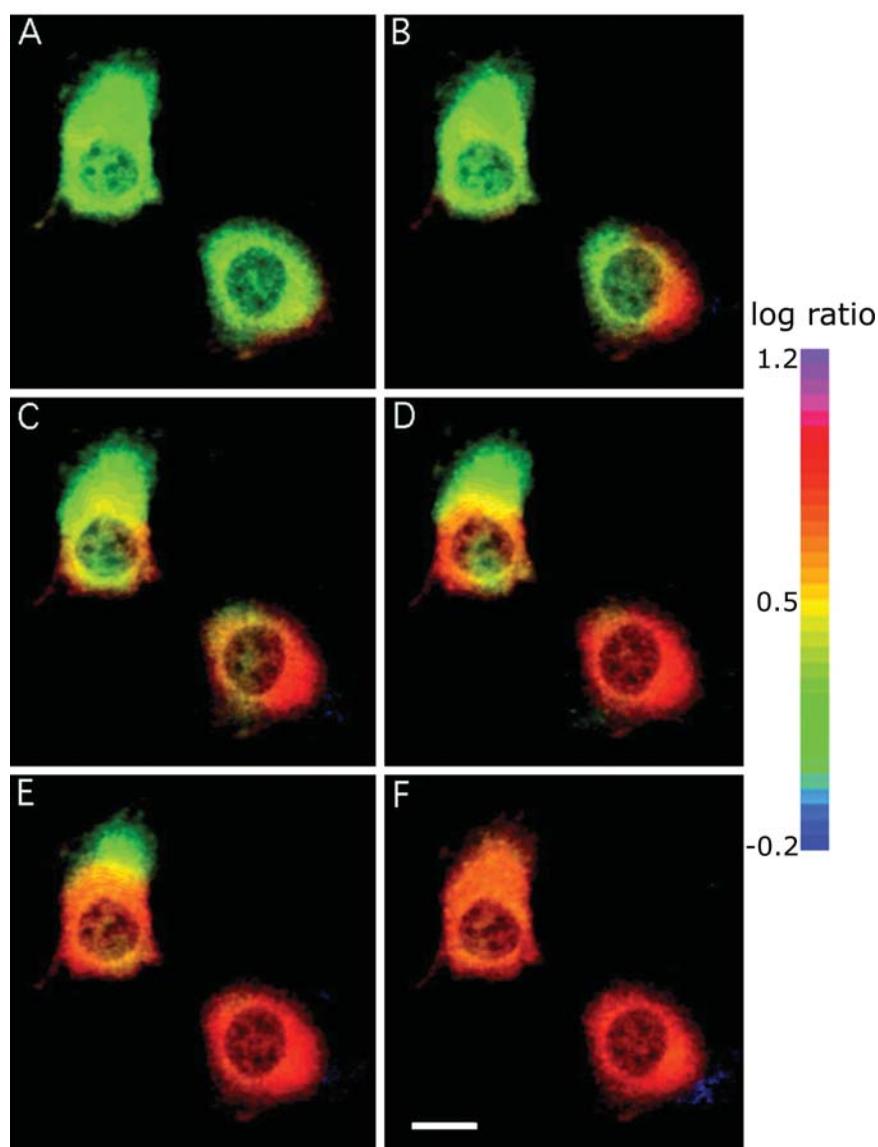


**Figure 18.21.** Fluorescence intensity ratios from a cameleon calcium sensor for HeLa cells locally exposed to histamine. The images were recorded at 1 second intervals starting 1 second before exposure to histamine. The intensity ratio is 535 nm/480 nm. Scale bar is 10  $\mu$ m. Reprinted with permission from [55].

18.21). These sensors are composed of a donor–acceptor GFP pair connected by a calcium-sensitive linker.<sup>56</sup> The linker consists of calmodulin and the M13 peptide. In the presence of calcium the peptide binds to calmodulin, bringing the donor and acceptor closer together and increasing the extent of energy transfer. The first image was taken 1 second before local exposure to histamine. Exposure to histamine results in a calcium wave that travels across the cell in about 4 seconds.

### 18.8.2. Imaging of NAD(P)H and FAD

The intracellular concentrations of NAD(P)H and FAD reflect the energy metabolism of cells. Figure 18.22 shows fluorescence images of an isolated cardiac myocyte with excitation at 750 nm.<sup>57</sup> The images were recorded in two wavelength regions. The image is brighter at shorter wavelengths, where the NADH emission is expected to be dominant, and weaker at wavelengths where FAD emits. There can be numerous reasons for the difference in intensity in

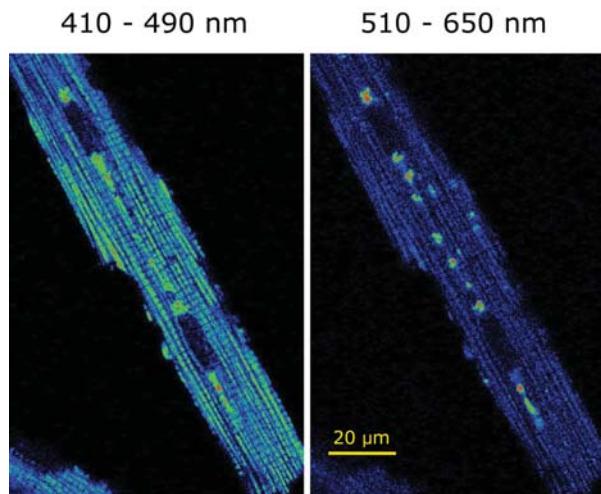


**Figure 18.22.** Two-photon induced fluorescence images of a cardiac myocyte observed at 410–490 nm (left) and 510–650 nm (right). Excitation at 750 nm. From [57].

these wavelength regions, such as the concentrations and quantum yields of these cofactors in the cells. Part of the explanation lies in the two-photon cross-sections of NADH and FAD (Figure 18.23). At 750 nm the cross-section of NADH is smaller than that of FAD. If a longer excitation wavelength were used the FAD emission may dominate the emission.

### 18.8.3. Excitation of Multiple Fluorophores

In Section 18.2 we described the two-photon absorption spectra of fluorophores. These spectra indicated that multiple fluorophores could be excited by MPE at a single wave-

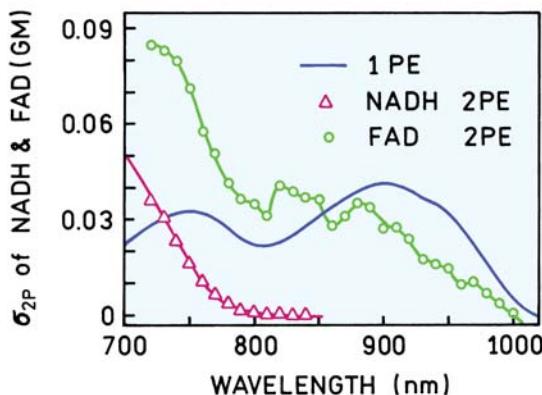


**Figure 18.23.** One-photon absorption spectra of FAD (—) and NADH (—Δ—). Also shown are the two-photon cross-sections for FAD (○) and NADH (Δ). Revised from [57].

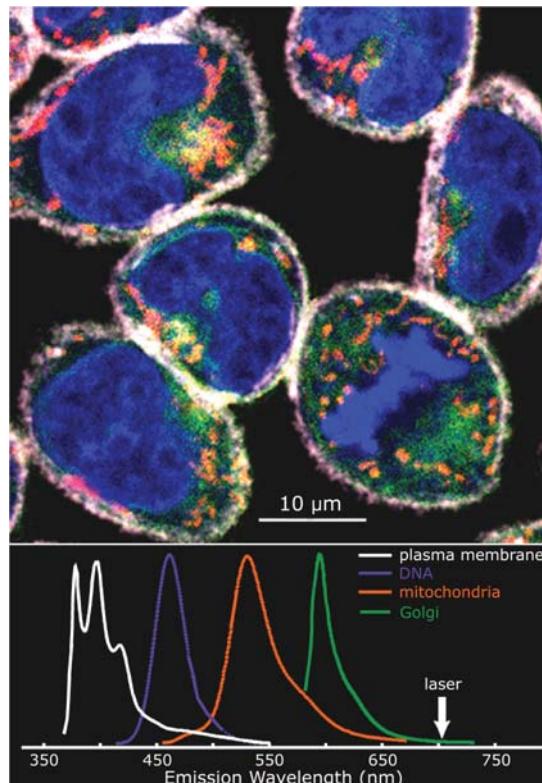


**Figure 18.24.** Multiphoton excitation images of rat basophilic leukemia (RBL) cells labeled with four probes: a plasma membrane label (pyrene lysophosphatidylcholine), a nuclear stain (DAPI), a Golgi label (Bodipy sphingomyelin), and a mitochondrial stain (rhodamine 123). From [17] and courtesy of Dr. Watt Webb from Cornell University, N.Y.

length. This possibility is demonstrated in Figure 18.24 for RBL cells labeled with four different fluorophores, each specific for a different region of the cell. All four fluorophores could be excited using a single wavelength. Given the one-photon absorption spectra of these probes, and the autofluorescence with UV excitation, it is very unlikely that such images could be obtained using one-photon excitation.

### 18.8.4. Three-Dimensional Imaging of Cells

A longstanding goal of multiphoton microscopy has been to obtain three-dimensional cellular images.<sup>58–59</sup> This is possible because the localized excitation allows collection of images at various focal planes in the cell (Figure 18.25, left). Using these 2D images it is possible to reconstruct a 3D image. Figure 18.26 shows a 3D reconstruction of a live PC12 cell stained with acridine orange. This probe emits in the green when bound to nuclear DNA and red when present in acidic organelles.

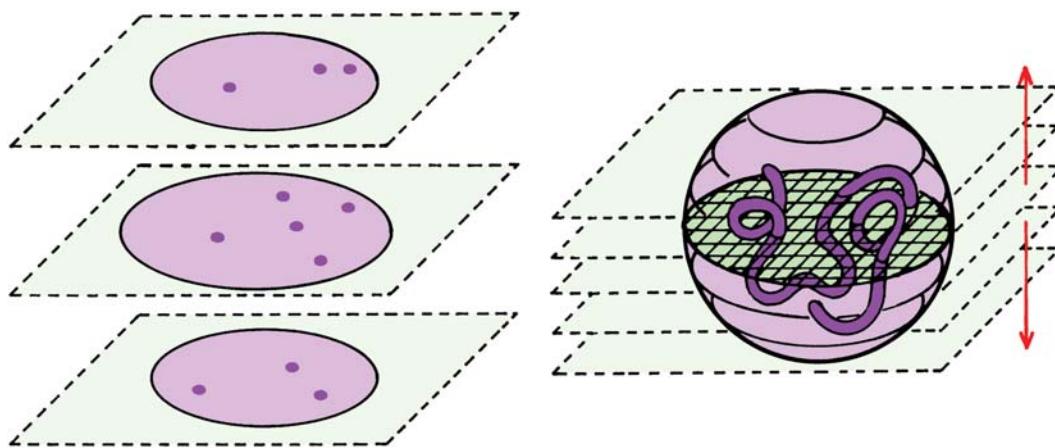


**Figure 18.25.** Three-dimensional cell imaging using confocal or multiphoton microscopy.

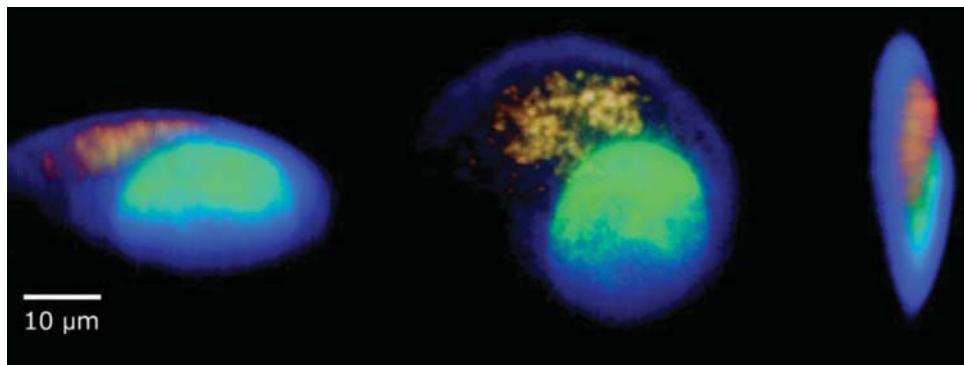


**Figure 18.26.** Three-dimensional reconstruction of a live PC cell stained with acridine orange, which emits green (525 nm) when bound to DNA and red (650 nm) when present in acidic organelles. The perspective on the left is rotated 60° from the cells around the horizontal axis. The perspective on the right is rotated 90° around the vertical axis. Figure courtesy of Dr. Stefan Hall, Max-Planck Institute for Physical Chemistry, Göttingen, Germany.

## REFERENCES

1. Friedrich DM, McClain WM. 1980. Two-photon molecular electronic spectroscopy. *Annu Rev Phys Chem* **31**:559–577.
2. Wirth MJ, Koskelo A, Sanders MJ. 1981. Molecular symmetry and two-photon spectroscopy. *Appl Spectrosc* **35**:14–21.
3. Birge RR. 1983. One- and two-photon excitation spectroscopy. In *Ultrasensitive laser spectroscopy*, pp. 109–174. Ed DS Kliger. Academic Press, New York.
4. Denk W, Strickler JH, Webb WW. 1990. Two-photon laser scanning fluorescence microscopy. *Science* **248**:73–76.
5. Masters BR, ed. 2003. *Selected papers on multiphoton excitation microscopy. SPIE milestone series*, SPIE Optical Engineering Press, Bellingham, WA.
6. Diaspro A, ed. 2002. *Confocal and two-photon microscopy foundations, applications, and advances*. Wiley-Liss, New York, 56.
7. Hell SW, ed. 1996. *Bioimaging special issue on nonlinear optical microscopy*, pp. 121–224. Institute of Physics Publishing, New York.
8. Diaspro A. 1999. Introduction to two-photon microscopy. *Microsc Res Technol* **47**:163–164.
9. Lakowicz JR, ed. 1997. *Topics in fluorescence spectroscopy*, Vol. 5: *Nonlinear and two-photon-induced fluorescence*, Plenum Press, New York.
10. So PTC, Dong CY, Masters BR, Berland KM. 2000. Two-photon excitation fluorescence microscopy. *Annu Rev Biomed Eng* **2**:399–429.
11. Williams RM, Piston DW, Webb WW. 1994. Two-photon molecular excitation provides intrinsic 3-dimensional resolution for laser-based microscopy and microphotochemistry. *FASEB J* **8**:804–813.
12. Denk W, Piston DW, Webb WW. 1995. Two-photon molecular excitation in laser-scanning microscopy. In *Handbook of biological confocal microscopy*, pp. 445–448. Ed JB Pawley. Plenum Press, New York.

13. Goppert-Mayer M. 1931. Über elementarakte mit zwei quantensprungen. *Ann Phys Leipzig* **9**:273–294.
14. Masters BR, So PTC. 2004. Antecedents of two-photon excitation laser scanning microscopy. *Microsc Res Technol* **63**:3–11.
15. Xu C, Webb WW. 1997. Multiphoton excitation of molecular fluorophores and nonlinear laser microscopy. In *Topics in fluorescence spectroscopy*, Vol. 5: *Nonlinear and two-photon-induced fluorescence*, pp. 471–540. Ed JR Lakowicz. Plenum Press, New York.
16. Xu C, Williams RM, Zipfel W, Webb WW. 1996. Multiphoton excitation cross-sections of molecular fluorophores. *Bioimaging* **4**: 198–207.
17. Xu C, Zipfel W, Shear JB, Williams RM, Webb WW. 1996. Multiphoton fluorescence excitation: new spectral windows for biological nonlinear microscopy. *Proc Natl Acad Sci USA* **93**:10763–10768.
18. Xu C, Webb WW. 1996. Measurement of two-photon excitation cross sections of molecular fluorophores with data from 690 to 1050 nm. *J Opt Soc Am B* **13**(3):481–490.
19. Xu C, Guild J, Webb WW. 1995. Determination of absolute two-photon excitation cross-sections by *in situ* second-order autocorrelation. *Opt Lett* **20**:2372–2374.
20. Kennedy SM, Lytle FE. 1986. P-bis(o-methylstyryl)benzene as a power-squared sensor for two-photon absorption measurements between 537 and 694 nm. *Anal Chem* **58**:2643–2647.
21. Courtesy of Drs. Zygmunt Gryczynski and Ignacy Gryczynski.
22. Birch DJS. 2001. Multiphoton excited fluorescence spectroscopy of biomolecular systems. *Spectrochim Acta, Part A* **57**:2313–2336.
23. Gryczynski I, Malak H, Lakowicz JR. 1996. Multiphoton excitation of the DNA stains DAPI and Hoechst. *Bioimaging* **4**:138–148.
24. Lakowicz JR, Gryczynski I, Malak H, Schrader M, Engelhardt P, Kano H, Hell SW. 1997. Time-resolved fluorescence spectroscopy and imaging of DNA labeled with DAPI and Hoechst 33342 using three-photon excitation. *Biophys J* **72**:567–578.
25. Lakowicz JR, Gryczynski I. 1992. Fluorescence intensity and anisotropy decay of the 4',6-diamidino-2-phenylindole–DNA complex resulting from one-photon and two-photon excitation. *J Fluoresc* **2**(2):117–122.
26. Callis PR. 1997. The theory of two-photon induced fluorescence anisotropy. In *Topics in fluorescence spectroscopy*, Vol. 5: *Nonlinear and two-photon induced fluorescence*, pp. 1–42. Ed JR Lakowicz. Plenum Press, New York.
27. Johnson CK, Wan C. 1997. Anisotropy decays induced by two-photon excitation. In *Topics in fluorescence spectroscopy*, Vol. 5: *Nonlinear and two-photon induced fluorescence*, pp. 43–85. Ed JR Lakowicz. Plenum Press, New York.
28. Callis PR. 1997. Two-photon induced fluorescence. *Annu Rev Phys Chem* **48**:271–297.
29. Lakowicz JR, Gryczynski I, Gryczynski Z, Danielson E, Wirth MJ. 1992. Time-resolved fluorescence intensity and anisotropy decays of 2,5-diphenyloxazole by two-photon excitation and frequency-domain fluorometry. *J Phys Chem* **96**:3000–3006.
30. Wan C, Johnson CK. 1994. Time-resolved two-photon induced anisotropy decay: the rotational diffusion regime. *J Chem Phys* **101**: 10283–10291.
31. Chen SY, Van Der Meer BW. 1993. Theory of two-photon induced fluorescence anisotropy decay in membranes. *Biophys J* **64**:1567–1575.
32. Gryczynski I, Malak H, Lakowicz JR. 1995. Three-photon induced fluorescence of 2,5-diphenyloxazole with a femtosecond Ti:Sapphire laser. *Chem Phys Lett* **245**:30–35.
33. Monson PR, McClain WM. 1970. Polarization dependence of the two-photon absorption of tumbling molecules with application to liquid 1-chloronaphthalene and benzene. *J Chem Phys* **53**(1):29–37.
34. Aleksandrov AP, Bredikhin VI, Genkin VN. 1971. Two-photon absorption by centrally symmetric organic molecules. *Soviet Phys JETP* **33**(6):1078–1082.
35. Mohler CE, Wirth MJ. 1988. Solvent perturbations on the excited state symmetry of randomly oriented molecules by two-photon absorption. *J Chem Phys* **88**(12):7369–7375.
36. Lakowicz JR, Gryczynski I, Kusba J, Danielson E. 1992. Two photon-induced fluorescence intensity and anisotropy decays of diphenylhexatriene in solvents and lipid bilayers. *J Fluoresc* **2**(4): 247–258.
37. Lakowicz JR, Gryczynski I. 1997. Multiphoton excitation of biochemical fluorophores. In *Topics in fluorescence spectroscopy*, Vol. 5: *Nonlinear and two-photon induced fluorescence*, pp. 84–144. Ed JR Lakowicz. Plenum Press, New York.
38. Malak H, Gryczynski I, Dattelbaum JD, Lakowicz JR. 1997. Three-photon-induced fluorescence of diphenylhexatriene in solvents and lipid bilayers. *J Fluoresc* **7**(2):99–106.
39. Squirrell JM, Wokosin DL, White JG, Bavister BD. 1999. Long-term two-photon fluorescence imaging of mammalian embryos without compromising viability. *Nature Biotechnol* **17**:763–767.
40. Lakowicz JR, Gryczynski I. 1992. Tryptophan fluorescence intensity and anisotropy decays of human serum albumin resulting from one-photon and two-photon excitation. *Biophys Chem* **45**:1–6.
41. Kierdaszuk B, Gryczynski I, Modrak-Wojciech A, Bzowska A, Shugar D, Lakowicz JR. 1995. Fluorescence of tyrosine and tryptophan in proteins using one- and two-photon excitation. *Photochem Photobiol* **61**(4):319–324.
42. Lakowicz JR, Kierdaszuk B, Gryczynski I, Malak H. 1996. Fluorescence of horse liver alcohol dehydrogenase using one- and two-photon excitation. *J Fluoresc* **6**(1):51–59.
43. Lakowicz JR, Gryczynski I, Danielson E, Frisoli J. 1992. Anisotropy spectra of indole and N-acetyl-L-tryptophanamide observed for two-photon excitation of fluorescence. *Chem Phys Lett* **194**(4,5,6):282–287.
44. Cramb DT, Wallace SC. 1998. The adsorption of L-tryptophan to the  $H_2O-CCL_4$  interface, monitored by red-edge two photon-induced polarized fluorescence. *J Fluoresc* **8**(3):243–252.
45. Lippitz M, Erker W, Decker H, van Holde KE, Basche T. 2002. Two-photon excitation microscopy of tryptophan-containing proteins. *Proc Natl Acad Sci USA* **99**(5):2772–2777.
46. Gryczynski I, Malak H, Lakowicz JR. 1996. Three-photon excitation of a tryptophan derivative using an fs-Ti:Sapphire laser. *Biospectroscopy* **2**:9–15.
47. Gryczynski I, Malak H, Lakowicz JR, Cheung HC, Robinson J, Umeda PK. 1996. Fluorescence spectral properties of troponin c mutant F22W with one-, two-, and three-photon excitation. *Biophys J* **71**:3448–3453.
48. Callis P. 1993. On the theory of two-photon induced fluorescence anisotropy with application to indoles. *J Chem Phys* **99**(1):27–37.
49. Rehms AA, Callis PR. 1993. Two-photon fluorescence excitation spectra of aromatic amino acids. *Chem Phys Lett* **208**(3,4):276–282.

50. Maiti S, Shear JB, Williams RM, Zipfel WR, Webb WW. 1997. Measuring serotonin distribution in live cells with three-photon excitation. *Science* **275**:530–532.
51. Gostkowski ML, Allen R, Plenert ML, Okerberg E, Gordon MJ, Shear JB. 2004. Multiphoton-excited serotonin photochemistry. *Biophys J* **86**:3223–3229.
52. Konig K. 2000. Multiphoton microscopy in life sciences. *J Microsc* **200**(2):83–104.
53. Blatter LA, Niggli E. 1998. Confocal near-membrane detection of calcium in cardiac myocytes. *Cell Calcium* **23**(5):269–279.
54. Niggli E, Egger M. 2004. Applications of multi-photon microscopy in cell physiology. *Front Biosci* **9**:1598–1610.
55. Fan GY, Fujisaki H, Miyawaki A, Tsay RK, Tsien RY, Ellisman MH. 1999. Video-rate scanning two-photon excitation fluorescence microscopy and ratio imaging with cameleons. *Biophys J* **76**:2412–2420.
56. Miyawaki A, Llopis J, Heim R, McCaffery JM, Adams JA, Ikura M, Tsien RY. 1997. Fluorescent indicators for  $\text{Ca}^{2+}$  based on green fluorescent proteins and calmodulin. *Nature* **388**:882–887.
57. Huang S, Heikal AA, Webb WW. 2002. Two-photon fluorescence spectroscopy and microscopy of NAD(P)H and flavoprotein. *Biophys J* **82**:2811–2825.
58. Konig K, Riemann I. 2003. High-resolution multiphoton tomography of human skin with subcellular spatial resolution and picosecond time resolution. *J Biomed Opt* **8**(3):432–439.
59. Bewersdorf J, Hell SW. 1998. Picosecond pulsed two-photon imaging with repetition rates of 200 and 400 MHz. *J Microsc* **191**(1): 28–38.
60. Courtesy of Dr. Ignacy Gryczynski.

## PROBLEMS

- P18.1. *Anisotropies of a Styrene Derivative:* Figure 18.26 shows the steady-state anisotropies of 4-Dimethylamino- $\omega$ -diphenylphosphinyl-*trans*-styrene (DPPS) in n-butanol. The anisotropies are higher for two-photon excitation than for one-photon excitation. In both cases the anisotropies are independent of temperature. Explain both results. The difference in anisotropy has been explained in the text, but not the reason for a constant anisotropy at all temperatures.
- P18.2. In Figure 18.17 the density of datapoints is less with Ti:sapphire excitation (855 nm) than with dye-laser (570 nm) or frequency-doubled dye-laser (285 nm) excitation. Suggest reasons why this is the case.
- P18.3. Explain the direction of the intensity ratio change shown in Figure 18.21.

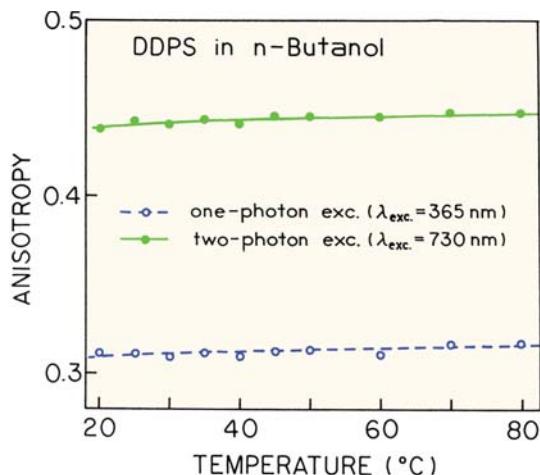


Figure 18.27. Steady-state anisotropies of DPPS. From [60].

# 19

# Fluorescence Sensing

Fluorescence sensing of chemical and biochemical analytes is an active area of research.<sup>1–8</sup> These efforts are driven by the desire to eliminate the use of radioactive tracers, which are costly to use and dispose of. There is also a need for rapid and low-cost testing methods for a wide range of clinical, bioprocess, and environmental applications. During the past decade numerous methods based on high-sensitivity fluorescence detection have been introduced, including DNA sequencing, DNA fragment analysis, fluorescence staining of gels following electrophoretic separation, and a variety of fluorescence immunoassays. Many of these analytical applications can be traced to the early reports by Udenfriend and coworkers,<sup>9</sup> which anticipated many of today's applications of fluorescence. The more recent monographs<sup>6–8</sup> have summarized the numerous analytical applications of fluorescence.

Why is fluorescence rather than absorption used for high-sensitivity detection? Fluorescence is more sensitive because of the different ways of measuring absorbance and fluorescence. Light absorbance is measured as the difference in intensity between light passing through the reference and the sample. In fluorescence the intensity is measured directly, without comparison with a reference beam. Consider a  $10^{-10}$  M solution of a substance with a molar extinction coefficient of  $10^5$  M<sup>-1</sup> cm<sup>-1</sup>. The absorbance will be  $10^{-5}$  per cm, which is equivalent to a percentage transmission of 99.9977%. Even with exceptional optics and electronics, it will be very difficult to detect the small percentage of absorbed light, 0.0023%. Even if the electronics allow measurement of such a low optical density, the cuvettes will show some variability in transmission and surface reflection, which will probably exceed the intensity difference due to an absorbance of  $10^{-5}$ . In contrast, fluorescence detection at  $10^{-10}$  M is readily accomplished with most fluorometers. This advantage is due to measurement of the fluorescence relative to a dark background, as compared to the bright reference beam in an absorbance mea-

urement. It is relatively easy to detect low levels of light, and the electronic impulses due to single photons are measurable with most photomultiplier tubes.

In this chapter we describe the various approaches to fluorescence sensing, which include essentially all the phenomenon discussed in previous chapters. Fluorescence sensing is described mostly within the framework of the medical applications, but it is clear that fluorescence detection is also widely used in biochemical, chemical, environmental and forensic analysis.

## 19.1. OPTICAL CLINICAL CHEMISTRY AND SPECTRAL OBSERVABLE

One long-range goal of fluorescence sensing is noninvasive monitoring of clinically relevant species and physiological parameters (Figure 19.1). A suitable portable device would measure the clinical values of interest, then store and/or transmit them to the physician. At present we are rather distant from the ultimate goal of noninvasive testing with devices similar to cell phones. The limitation is not in optics or electronics, but rather due to the lack of stable and biocompatible methods of in-vivo sensing. It is already possible to measure fluorescence through skin, and the measurements can accurately return pH and ion concentrations. In the near term we are likely to see devices similar to PDAs (Figure 19.2) that contain the chemistry and optics needed to perform clinical assays using body fluid samples. Such portable devices would find widespread usefulness, especially in emergency situations. The sensor array could be exposed to blood, and the results would be immediately available. This concept of rapid point-of-care clinical chemistry is driving the rapid development of numerous fluorescence sensing devices. In the following sections we describe the principles of fluorescence sensing, and illustrate how such devices can provide analytical data.

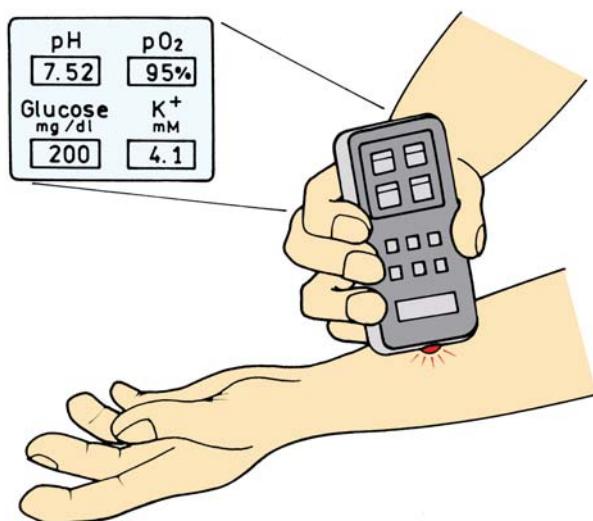


**Figure 19.1.** Optical clinical chemistry and noninvasive monitoring of physiological parameters.

## 19.2. SPECTRAL OBSERVABLES FOR FLUORESCENCE SENSING

The fluorescence intensity can be used to measure the concentration of the fluorescent species. In the present chapter sensing is understood in a different context. The goal is to measure the concentration of some analyte, not the amount of fluorophore. In the case of blood gases these analytes are pH,  $\text{pCO}_2$ , and  $\text{pO}_2$ . Blood electrolytes include  $\text{Na}^+$ ,  $\text{K}^+$ ,  $\text{Ca}^{2+}$ ,  $\text{Mg}^{2+}$  and  $\text{Cl}^-$ , and many additional analytes that are measured in the clinical laboratory.<sup>10,11</sup> Fluorescence sensing requires a change in a spectral property response to the analyte. Changes can occur in the intensity, excitation spec-

trum, emission spectrum, anisotropy, or lifetime of the sensing probe.

The most direct sensing method is when the fluorescence intensity of the probe changes in response to the analyte (Figure 19.3, left). Such changes often occur for fluorophores that are subject to collisional quenching by a relevant species, such as oxygen. While conceptually simple, collisional quenching is only useful with a few clinically relevant analytes. It is often inconvenient or unreliable to use intensity changes, which can occur for a wide variety of reasons. For instance, the use of fiber optics is desirable as a means to locate the sensor at the site of interest, and to have the light source and detector remotely located.<sup>12</sup> However, it is difficult to perform quantitation intensity measurements through fibers. Fluorescence microscopy is another instance where intensity measurements are difficult. It is not possible to control the fluorophore concentration at each location in the cell, and the local probe concentration changes continually due to diffusion and/or photobleaching. For such applications it is important to use measurements which are independent of fluorophore concentration. This can be accomplished using wavelength-ratiometric probes (Figure 19.3), which display shifts in the absorption or emission spectra upon binding of the analyte. Wavelength-ratiometric probes are desirable because the ratios are independent of the probe concentration. The analyte concentration can then be determined from the ratio of fluorescent intensities measured at two excitation or emission wavelengths.

Another ratiometric method is fluorescence polarization or anisotropy. In this case the analyte causes a change in the anisotropy of the label. Anisotropy measurements are

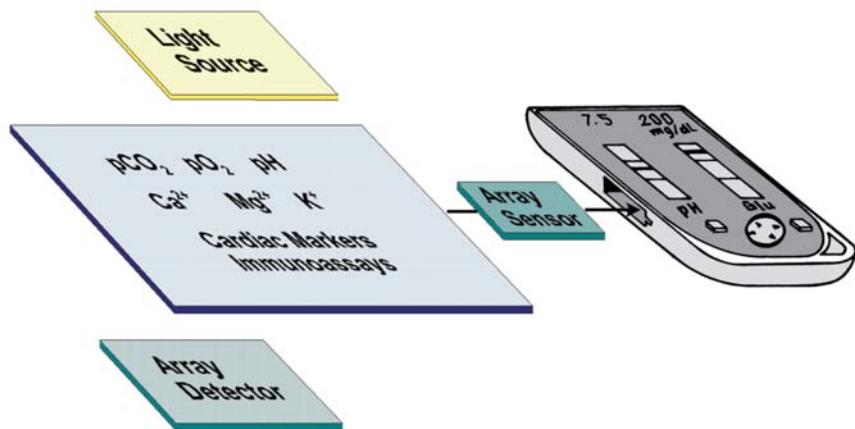


**Figure 19.2.** Fluorescence sensor for point-of-care testing.

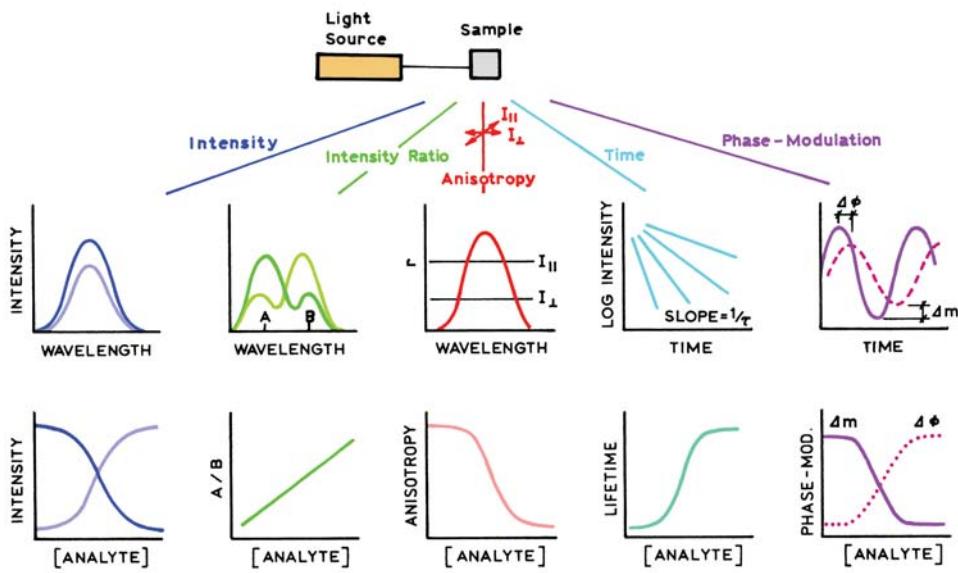


**Figure 19.3.** Spectral observables for fluorescence sensing. From left to right, sensing is performed using intensities, intensity ratios, anisotropies, time-domain lifetimes, and phase-modulation measurements.

frequently used in competitive immunoassays, in which the actual analyte displaces labeled analyte that is bound to specific antibody. This results in a decrease in the anisotropy. Anisotropy values are calculated using the ratio of polarized intensity measurements. The use of an intensity ratio makes the anisotropy measurements independent of fluorophore concentration as long as the measurements are not distorted by autofluorescence or poor signal-to-noise.

Fluorescence lifetimes can also be used for sensing (Figure 19.3). The lifetimes can be measured using either time-domain (TD) or frequency-domain (FD) methods. A few years ago lifetime measurements were regarded as too complex for sensing applications. However, advances in electrooptics technology now make it feasible to perform nanosecond decay time measurements using small inexpensive instruments. The use of lifetimes for sensing may be the next step in making sensors that display the long-term stability needed in real-world applications.<sup>13–16</sup>

#### 19.2.1. Optical Properties of Tissues

The design of fluorescence probes for clinical applications is determined in part by the optical properties of water and tissues.<sup>17</sup> In general, the autofluorescence from tissues or any biological sample is lower for longer excitation wavelengths. The use of longer wavelengths also avoids light

absorption by hemoglobin and melanin (Figure 19.4). In the past there has been a limited number of fluorophores that emit at long wavelengths. At present there is a growing number of fluorophores that emit between 700 and 1000 nm. This range is useful because water absorption increases above 1000 nm. The region of low absorption from 600 to 1000 nm is sometimes called the therapeutic range. Fortunately, a variety of lasers and solid-state lasers are available for excitation in this range of wavelengths.

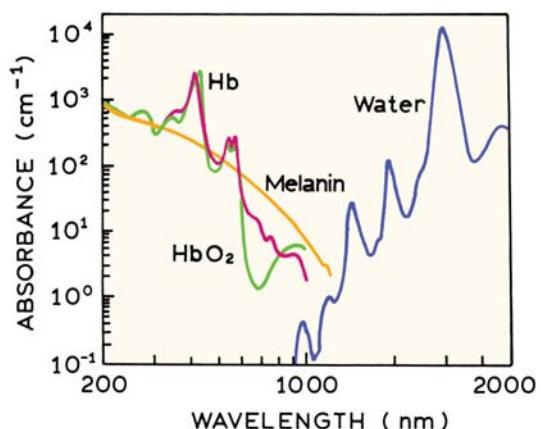


**Figure 19.4.** Optical absorbance of tissues and water. Hb, hemoglobin. Revised and reprinted with permission from [17]. Copyright © 1996, Annual Reviews.

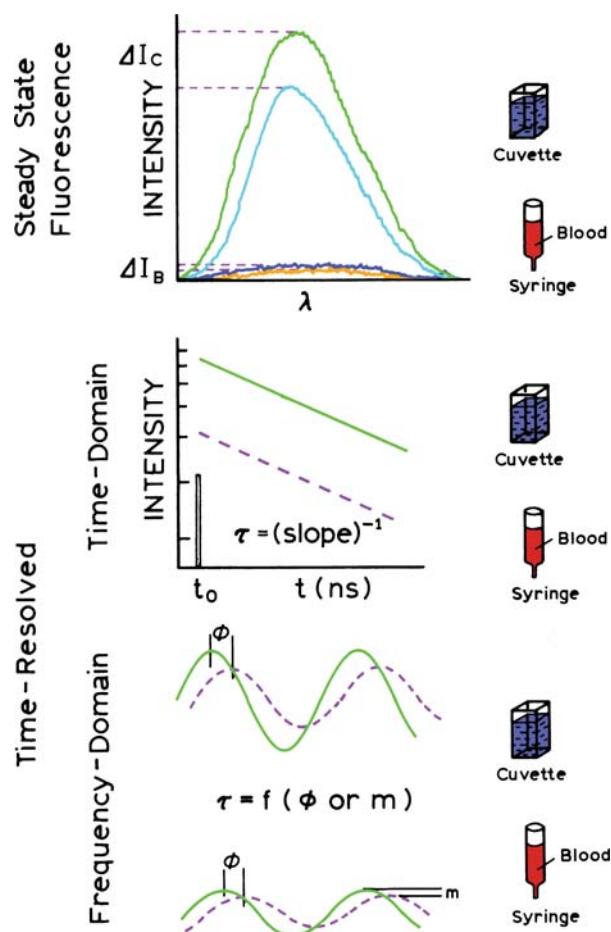


**Figure 19.5.** Intensity, time-domain, and frequency-domain sensing. In the top panel  $\Delta I_B$  is that obtained from measurements of blood in a syringe and  $\Delta I_C$  the value observed from a cuvette.

### 19.2.2. Lifetime-Based Sensing

Prior to describing the various mechanisms of sensing, it is useful to expand on the use of decay-time measurements for sensing (Figure 19.5). In the research laboratory, where clean cuvettes and optical surfaces are easy to maintain, intensity measurements can be accurate and reproducible (top panel in Figure 19.5). However, suppose that the sample is blood, which is contained in a translucent syringe. The intensity will be decreased by the absorbance of the blood and by the scattering properties of the syringe, and it may be difficult to obtain a reliable intensity-based calibration. Now consider lifetime instead of intensity measurements (middle panel in Figure 19.5). If the intensity is large enough to measure, the intensity decay is the same independent of attenuation of the signal. Similarly, if the life-

time is measured by phase or modulation (bottom panel), the values are expected to be independent of intensity.

Lifetime-based sensing is a means to avoid the difficulties of quantitative intensity measurements. Consider a sensing fluorophore placed on the end of an optical fiber that is used for oceanographic studies. The fiber will be flexing while being towed by the ship, resulting in intensity fluctuations. Additionally, the probe may be leaking from the tip, resulting in decreases in intensity. Quantitative intensity measurements would clearly be difficult under these conditions. Lifetime measurements have already been used for an oceanographic fiber optic oxygen sensor.<sup>18</sup>

### 19.3. MECHANISMS OF SENSING

Any phenomenon that results in a change of fluorescence intensity, wavelength, anisotropy, or lifetime can be used for sensing. The simplest mechanism to understand is collisional quenching, where the fluorophore is quenched by the analyte (Figure 19.6). Collisional quenching results in a decrease in the intensity or lifetime of the fluorophore, either of which can be used to determine the analyte concentration. Static quenching can also be used for sensing, but the lifetime would not change.

Resonance energy transfer (RET) is perhaps the most general and valuable phenomenon for fluorescence sensors (Figure 19.6, right). Any process that brings the donor and acceptor into close proximity will result in a decrease in the donor intensity and/or decay time. Since energy transfer acts over macromolecular distances, it can be used to detect association of proteins as occurs in immunoassays. However, the applications of RET are not limited to detection of protein association. RET has also been used as the basis for pH and cation sensors. Sensors were developed that contain acceptors whose absorption spectra are dependent on pH. A change in pH results in a change in absorbance of the acceptor, which in turn alters the donor intensity.

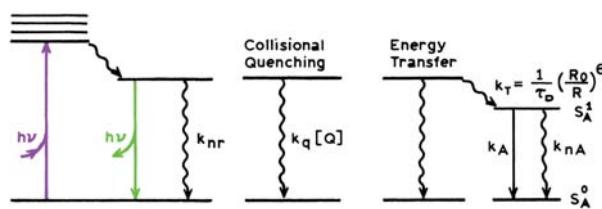


**Figure 19.6.** Modified Jablonski diagram for the processes of absorption and fluorescence emission (left), dynamic quenching (middle), and resonance energy transfer (RET) (right).

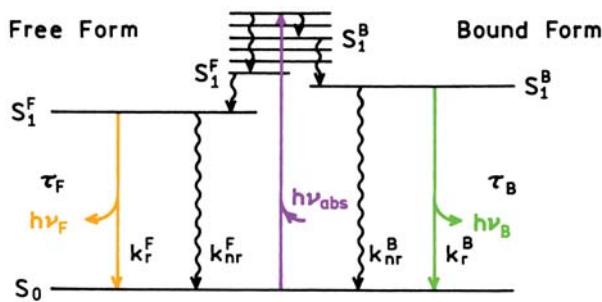


**Figure 19.7.** Jablonski diagram for the free (F) and bound (B) forms of a sensing probe. From [13].

Another mechanism for sensing is available when the fluorophore can exist in two states, if the fractions in each state depend on the analyte concentration (Figure 19.7). Typically there is equilibrium between the fluorophore free in solution and the fluorophore bound to analyte. One form can be nonfluorescent, in which case emission is only seen in the absence or presence of analyte, depending on which form is fluorescent. Probes that act in this manner are not wavelength-ratiometric or lifetime probes. Alternatively, both forms may be fluorescent but display different quantum yields or emission spectra. This type of behavior is often seen for pH probes, where ionization of the probe results in distinct absorption and/or emission spectra. Spectral shifts are also seen for probes that bind specific cations such as calcium. Such probes allow wavelength-ratiometric measurements. In this case the change in intensity or shift in the emission spectrum is used to determine the analyte concentration. Probes that bind specific analytes are often referred to as probes of analyte recognition.<sup>19</sup>

There are many mechanisms that can be used to design probes that exhibit changes in fluorescence in response to analytes. Fluorescence probes can form twisted intramolecular charge-transfer (TICT) states.<sup>20</sup> Another mechanism is photoinduced electron transfer (PET), which has been used to develop sensors for metal ions.<sup>21–23</sup> These sensors often rely on the well known quenching by amines due to PET. Figure 19.8 shows a PET-based zinc sensor. In the absence of zinc the anthracene is quenched by exciplex formation with the amino groups. Upon binding of zinc, the nitrogen lone pair of electrons is no longer available for PET. As a result charge transfer no longer occurs, and the anthracene becomes fluorescent.<sup>21</sup> While the mechanism of this particular sensor is understood, this is not true of all sensors. In many cases spectral changes are seen but the mechanism is not certain. In the following sections we describe examples

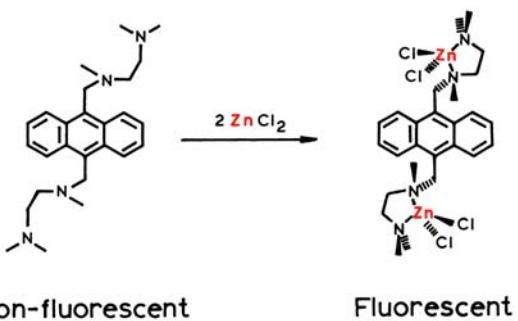


**Figure 19.8.** A zinc probe based on photoinduced electron transfer. Revised from [21].

of each type of sensor (collisional, RET or analyte recognition).

## 19.4. SENSING BY COLLISIONAL QUENCHING

### 19.4.1. Oxygen Sensing

Use of collisional quenching as the sensing mechanism requires the fluorescent probe to be sensitive to quenching by the desired analyte. Collisional quenching results in a decrease in intensity and lifetime, which is described by the Stern-Volmer equation:

$$\frac{F_0}{F} = \frac{\tau_0}{\tau} = 1 + k_q \tau_0 [Q] = 1 + K [Q] \quad (19.1)$$

In this equation  $F_0(\tau_0)$  and  $F(\tau)$  are the intensities (lifetimes) in the absence and presence of the quencher, respectively,  $K$  is the Stern-Volmer quenching constant, and  $k_q$  is the bimolecular quenching constant. The most obvious application of collisional quenching is oxygen sensing. In order to obtain sensitivity to low concentrations of oxygen, fluorophores are typically chosen that have long lifetimes in the absence of oxygen ( $\tau_0$ ). Long lifetimes are a property of transition metal complexes<sup>24</sup> (Chapter 20), and such complexes have been frequently used in oxygen sensors.<sup>25–31</sup> For use as an oxygen sensor the metal-ligand complexes (MLCs) are usually dissolved in silicone, in which oxygen is rather soluble and freely diffusing. The silicone also serves as a barrier to prevent other interfering molecules from interactions with the fluorophores and affect the intensity or lifetime.

The high sensitivity of the long-lifetime MLCs to oxygen is shown by the Stern-Volmer plots (Figure 19.9). The compound  $[\text{Ru}(\text{Ph}_2\text{phen})_3]^{2+}$  is more strongly quenched

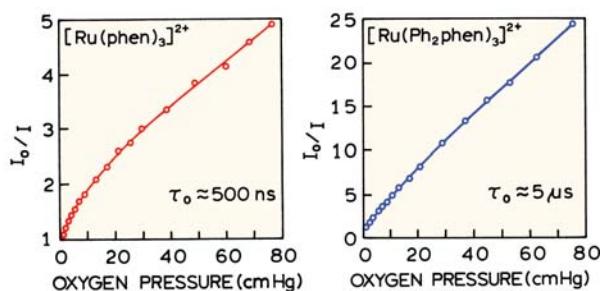


**Figure 19.9.** Stern-Volmer plots for oxygen quenching of  $[\text{Ru}(\text{phen})_3]^{2+}$  and  $[\text{Ru}(\text{Ph}_2\text{phen})_3]^{2+}$  in GE RTV 118 silicon. Phen is 1,10-phenanthroline; ph<sub>2</sub>phen is 4,7-diphenyl-1,10-phenanthroline. Revised from [24].

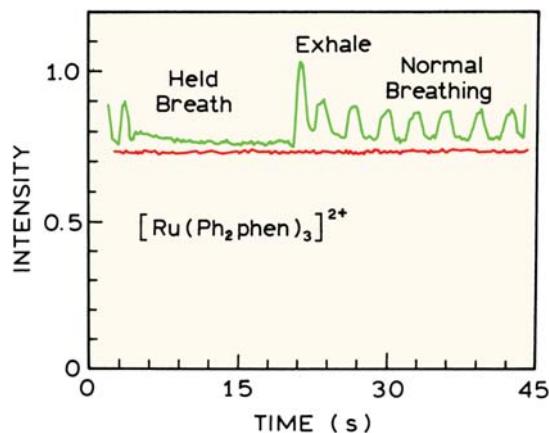


**Figure 19.10.** Luminescence intensity of an oxygen sensor with  $[\text{Ru}(\text{Ph}_2\text{phen})_3]^{2+}$  as the probe, when exposed to breathing. Revised from [24].

than  $[\text{Ru}(\text{phen})_3]^{2+}$ . The difference in sensitivity is due to the longer unquenched lifetime ( $\tau_0$ ) of the diphenyl derivative, and thus the larger Stern-Volmer quenching constant (eq. 19.1). These long-lifetime probes have been used in real-time oxygen sensors. For example, Figure 19.10 shows the intensity of  $[\text{Ru}(\text{Ph}_2\text{phen})_3]^{2+}$  in silicone while exposed to exhaled air. The intensity increases with each exhale because of the lower  $\text{O}_2$  and higher  $\text{CO}_2$  content of the exhaled air. The higher intensity on the first exhale after the breath was held is due to the lower  $\text{O}_2$  content in the air that was retained longer in the lungs. The oxygen sensitivity of the sensor can be adjusted by selecting probes with different lifetimes or by modifying the chemical composition of the supporting media. The sensitivity to oxygen can be increased by using MLCs with longer lifetimes, some of which are as long as  $50 \mu\text{s}$ .<sup>32</sup>

#### 19.4.2. Lifetime-Based Sensing of Oxygen

For practical sensing applications the device must be simple and inexpensive, which is possible using the long-lifetime MLCs. The oxygen-sensitive MLCs in Figure 19.9 absorb near 450 nm, and are thus easily excited with blue light-emitting diodes (LEDs). One simple oxygen sensor device is shown in Figure 19.11. Because of the long decay times and simple instrumentation, oxygen sensors were used to demonstrate the stability of phase-angle sensing in the presence of large-amplitude intensity fluctuations.<sup>33</sup> The intensity was varied by waving fingers in the light path, resulting in fivefold changes in intensity (Figure 19.11). In contrast to the measured intensities measurements, the phase angles remained constant.

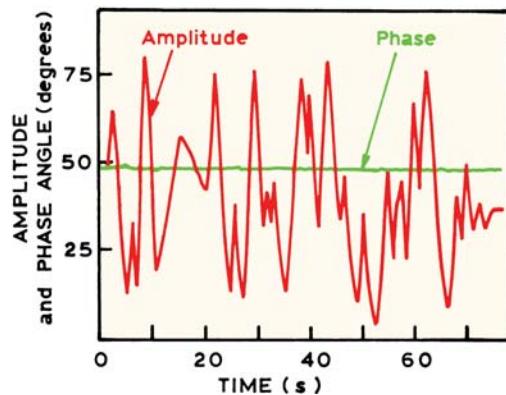
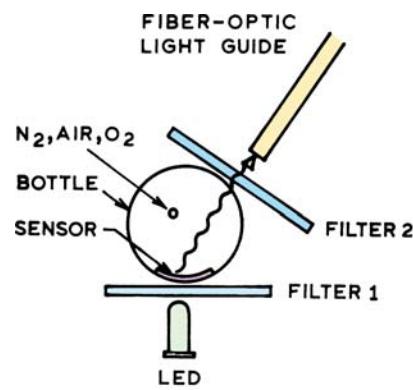


**Figure 19.11.** Phase-angle stability with intensity fluctuations measured with an oxygen-sensing device. The amplitude of the incident light was varied by waving fingers between the LED and the sensor. Revised from [33].

Lifetime-based sensing is valuable for probes that are subject to collisional quenching and do not display wavelength-ratiometric behavior. The capability for ratiometric measurements can be designed into oxygen sensors by including a nanosecond-lifetime fluorophore in the supporting media. This fluorophore can provide a reference that is not sensitive to the oxygen concentration. For in-vivo applications MLCs are known to have longer absorption and emission wavelengths.<sup>34</sup> These MLCs have been used to measure lifetimes and oxygen concentrations through skin.<sup>35</sup>

#### 19.4.3. Mechanism of Oxygen Selectivity

An important consideration for any sensor is selectivity. For oxygen, the selectivity is provided by a unique combination of the fluorophore and the supporting media. Almost all fluorophores are collisionally quenched by oxygen, so that no fluorophore is completely specific for oxygen. However, the extent of quenching is proportional to the unquenched lifetime  $\tau_0$  (eq. 19.1). For fluorophores in aqueous solution with decay times under 5 ns, the extent of quenching by dissolved oxygen from the atmosphere is negligible. Hence, one reason for the apparent oxygen selectivity of  $[\text{Ru}(\text{Ph}_2\text{phen})_3]^{2+}$  is its long lifetime near 5  $\mu\text{s}$ , which results in extensive quenching by atmospheric oxygen.

Selectivity of the MLC oxygen sensor is also due to the silicone support. Silicone is impermeable to most polar species, so most possible interferants cannot penetrate the silicon to interact with the probe. Fortunately, oxygen dissolves readily in silicon, so that the support is uniquely permeable to the desired analyte. Finally, there are no other substances in air which act as collisional quenchers. NO is also a quencher but is not usually found in the air. Hence, the sensor is selective for  $\text{O}_2$  because of a combination of the long lifetime of the MLC probe and the exclusion of potential interferants from the nonpolar silicone support.

#### 19.4.4. Other Oxygen Sensors

While  $[\text{Ru}(\text{Ph}_2\text{phen})_3]^{2+}$  is the most commonly used fluorophore in oxygen sensors, other probes are available. Almost any long-lived fluorophore can be used as an oxygen sensor, particularly when dissolved in an organic solvent. Because of the long decay times, phosphorescence can be used to detect oxygen. For many applications, such as oxygen sensing in blood or through skin, it is useful to have probes that can be excited with red or NIR wavelengths. Several porphyrin derivatives are known that dis-

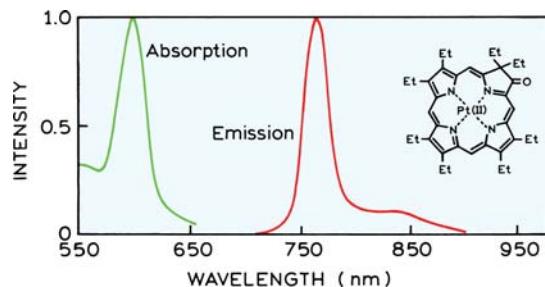


**Figure 19.12.** Absorption and emission spectra of a phosphorescent porphyrin ketone. Revised and reprinted with permission from [36]. Copyright © 1995, American Chemical Society.

play oxygen-sensitive phosphorescence.<sup>36–37</sup> One example is platinum (II) octaethylporphyrin ketone (Figure 19.12), which can be excited at 600 nm. This molecule shows a surprisingly large Stokes shift, with the emission maximum at 758 nm. The lifetime of 61.4  $\mu\text{s}$  results in oxygen-sensitive emission even when the probe is embedded in polystyrene.

Simple instrumentation can be constructed for lifetime-based sensing with long-lifetime emitters. Figure 19.13 (top) shows a schematic for a simple device for lifetime-based sensing of oxygen.<sup>38</sup> The fluorophore is platinum (II)

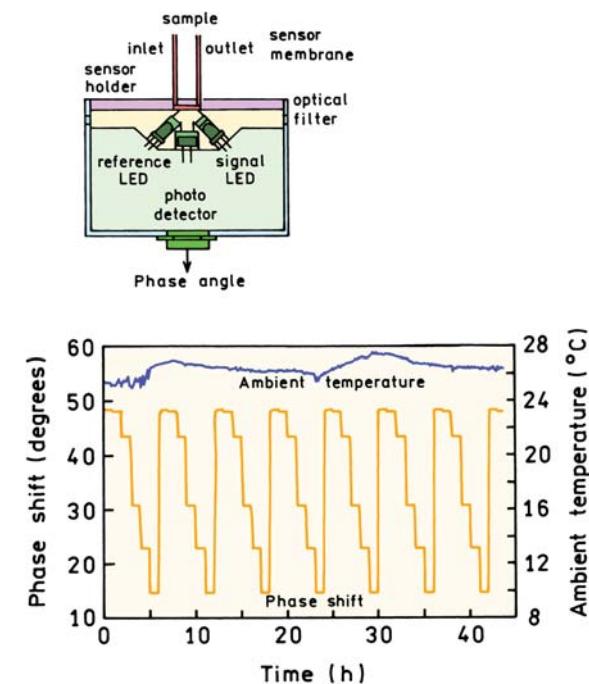


**Figure 19.13.** Lifetime-based sensing of oxygen using platinum (II) octaethylporphyrin ketone in a polymer membrane. The light modulation frequency is 3907 Hz. The gaseous oxygen concentrations were 0, 0.1, 5.1, 9.96, and 20.55%. Revised from [39].

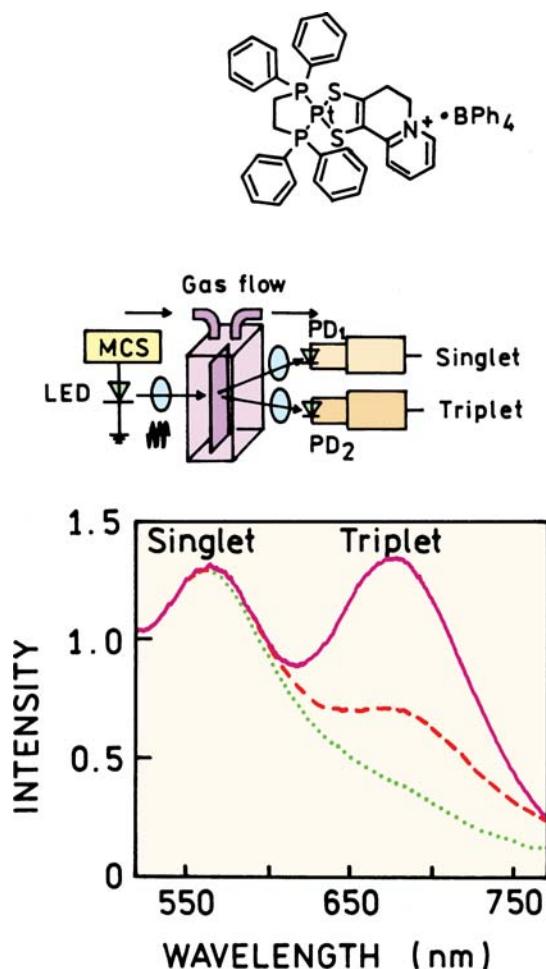


**Figure 19.14.** Oxygen sensing using a platinum complex in a polymeric film. Revised from [39].

octaethylporphyrin ketone in a polymer film, which displays an unquenched lifetime in the range of 40–60  $\mu$ s. The excitation source is an amplitude-modulated LED. The electronics measures the phase angle of the emission relative to the excitation, using separate detectors for the excitation and emission. The phase angles are highly sensitive to the oxygen concentration, and are stable over long periods of time. Reasonable amounts of photobleaching or continuity drifts would not affect the phase angle measurements.

Wavelength-ratiometric measurements are usually not possible with collisionally quenched probes. One interesting exception is the platinum complex shown in Figure 19.14. This compound displays both a singlet emission near 560 nm and a triplet emission near 670 nm, with lifetimes of 0.5 ns and 14  $\mu$ s, respectively.<sup>39</sup> The emission intensity of the long-lived emission is sensitive to oxygen and the short life-

time emission is not sensitive to oxygen (lower panel). A simple solid-state device can be used to measure the ratios of emission intensities at 560 and 670 nm, and thus the oxygen concentration.

#### 19.4.5. Lifetime Imaging of Oxygen

Molecules that display dual emission (Figure 19.14) are highly unusual, and there are not many opportunities for wavelength-ratiometric oxygen sensing. One method to make measurements that are mostly independent of intensity is to use fluorescence lifetime imaging microscopy (FLIM),<sup>40–41</sup> which is described in Chapter 22. In FLIM the contrast in the image is based on the lifetime at each point in the sample and not on the emission intensity. Figure 19.15 shows images of bronchial epithelial cells labeled with  $[\text{Ru}(\text{bpy})_3]^{2+}$ , which in the oxygen-free samples displays a lifetime near 600 ns.<sup>42–43</sup> The intensity image on the left reveals the local concentration and/or quantum yield of the probe in the cells. The image on the right shows the lifetimes in each region of the sample. The lifetimes are essentially constant which indicates the oxygen concentration is constant throughout the cells. These lifetime images were calculated from images taken with a gated image intensifier and CCD camera.

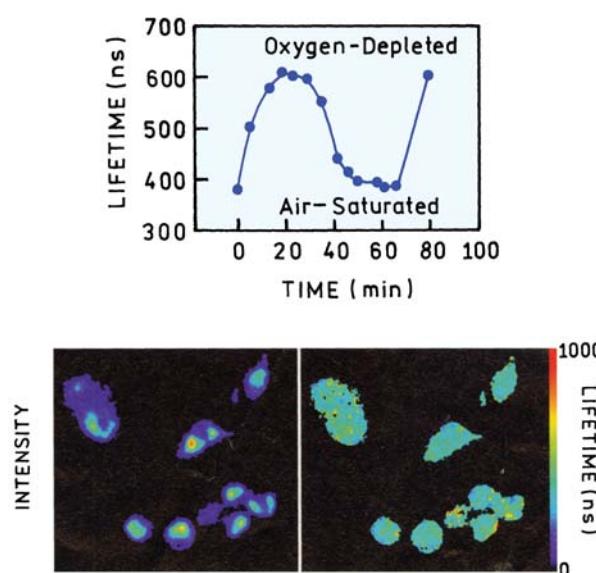


**Figure 19.15.** Fluorescence intensity and lifetime images of human bronchial epithelia cells labeled with  $[\text{Ru}(\text{bpy})_3]\text{Cl}_2$ . Lifetime images were obtained using a gated image intensifier and a CCD camera. From [43].

**Table 19.1.** Spectral Properties of Representative Chloride Probes<sup>a</sup>

Compound <sup>b</sup>	$\lambda_{\text{abs}}$ (nm)	$\lambda_{\text{em}}$ (nm)	Quantum yield	$K$ ( $M^{-1}$ )
SPQ <sup>c</sup>	318/345	450	0.69	118 <sup>d</sup>
SPA	—	—	—	5
Lucigenin	368/955	506	0.67	390
MACA	364/422	500	0.64	225
MAMC	366/424	517	0.24	160

<sup>a</sup>From [49].<sup>b</sup>Abbreviations: lucigenin, N,N,N-dimethyl-9,9'-bisacridinium nitrate; SPQ, 6-methoxy-N-(3-sulfopropyl)quinolinium; SPA, N-sulfopropyl-acridium; MACA, N-methylacridium-9-carboxamide; MAMC, N-methylacridium-9-methylcarboxylate.<sup>c</sup>The unquenched lifetime of SPQ is 26 ns.<sup>d</sup>The Stern-Volmer constant in cells is 13  $M^{-1}$ . From [51].

#### 19.4.6. Chloride Sensors

It is well known that heavy atoms like bromine and iodine act as collisional quenchers. For sensing applications chloride is more important because it is prevalent in biological systems. However, chloride is a less effective quencher, and relatively few fluorophores are quenched by chloride. A hint for developing chloride-sensitive probes was available from the knowledge that quinine is quenched by chloride. Quinine contains a quinolinium ring, which can be used to make a variety of chloride-sensitive probes.<sup>44–48</sup> Representative structures are shown in Figure 19.16. It is evident from the Stern-Volmer plots in Figure 19.17 that the quinolines are not equally sensitive to chloride, and that the quenching constant depends on the chemical structure (Table 19.1).

These chloride-sensitive probes can be used to measure chloride transport across cell membranes (Figure 19.18). Erythrocyte ghosts are the membranes from red blood cells



**Figure 19.16.** Representative chloride probes. These probes are collisionally quenched by chloride (Table 19.1). Revised and reprinted with permission from [49]. Copyright © 1994, Academic Press Inc.

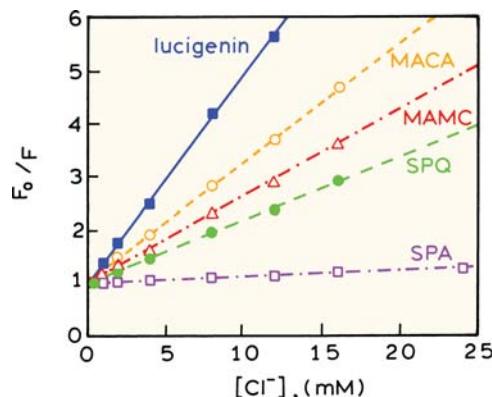


**Figure 19.17.** Stern-Volmer plots for chloride quenching of SPQ, SPA, lucigenin, MACA, and MAMC. See Table 19.1. Revised and reprinted with permission from [49]. Copyright © 1994, Academic Press Inc.

following removal of the intracellular contents. The ghosts were loaded with SPQ and 100 mM chloride. The ghosts were then diluted into a solution of 66 mM  $K_2SO_4$ . Sulfate does not quench SPQ. When diluted into sulfate-containing buffer the intensity of SPQ increased due to efflux of the chloride. This transport is due to an anion exchange pathway. Chloride transport could be blocked by dihydro-4,4'-diisothiocyanostilbene-2,2'-disulfonic acid ( $H_2DIDS$ ), which is an inhibitor of anion transport. Hence, the chloride probes can be used for physiological studies of ion transport.

The chloride probes are subject to interference. They are also quenched by bromide, iodide, and thiocyanate.<sup>50</sup>

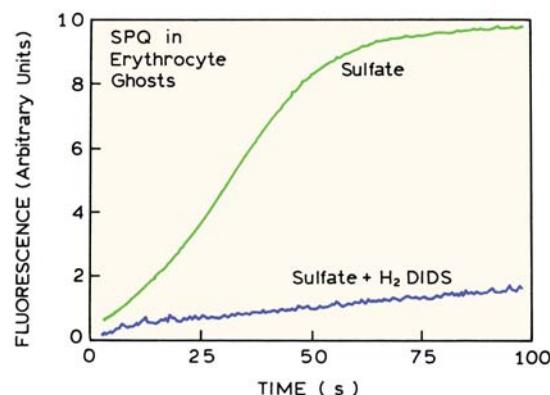


**Figure 19.18.** Fluorescence intensity of SPQ in erythrocyte ghosts as a function of time, reflecting chloride transport from the erythrocyte ghosts. The two curves are for SPQ-containing erythrocyte ghosts diluted into sulfate-containing buffer in the absence and in the presence of an anion-transport inhibitor ( $H_2DIDS$ ). Revised and reprinted with permission from [46]. Copyright © 1987, American Chemical Society.

Perhaps more importantly, SPQ is quenched by free amines, which can distort measurements in amine-containing buffers. In fact, the Stern-Volmer quenching constant of SPQ in aqueous solution is  $118 \text{ M}^{-1}$ , whereas in cells the quenching constant is near  $13 \text{ M}^{-1}$ . This decrease has been attributed to quenching of SPQ by non-chloride anions and proteins in cells.<sup>51</sup> Quenching of SPQ by amines was turned into an opportunity, by using the quenching caused by the amine buffers as an indicator of pH.<sup>50</sup> As the pH increases, more of the buffer is in the free amine form, resulting in a decrease in the intensity of SPQ. A disadvantage of the chlorine probes is that they are not ratiometric probes. Some of the probes leak out of cells, decreasing the intensity and preventing accurate measurements of the chloride concentration. The quinoline probes have been made into wavelength-ratiometric probes by linking them to a chloride-insensitive fluorophore using dextran or a flexible chain.<sup>52-53</sup>

#### 19.4.7. Lifetime Imaging of Chloride Concentrations

The need for covalently linked chloride-sensitive and -insensitive probes can be avoided by lifetime imaging. Since chloride is a collisional quencher, the decreases in lifetime are proportional to the decreases in intensity (Figure 19.17). FLIM of the chloride probe 6-methoxy-quinolyl acetoethyl ester (MQAE) was used to determine the concentrations of chloride in olfactory epithelium.<sup>54</sup> In this tissue the olfactory sensory neurons penetrate through supporting epithelial cells, terminating in dendritic knobs (Figure 19.19). The transduction mechanism for olfactory signal transduction involves an influx of calcium and an efflux of chloride. For this to occur the olfactory dendrites must accumulate higher concentrations of chloride than the surrounding tissue. Lifetime measurements of MQAE in this tissue revealed a shorter lifetime of MQAE in the dendrite knob than in the supporting cells, which indicates a higher chloride concentration in the knobs. Lifetime images were obtained using laser scanning microscopy and two-photon excitation (Chapter 18). Intensity decays were recorded by TCSPC at each point in the image. A calibration curve for the lifetime at various chloride concentrations was determined using a similar tissue and ionophore to control the intracellular chloride concentrations. Using this calibration it was possible to use the lifetime image to create a chloride concentration image in the olfactory tissue. This image shows higher chloride concentrations in the dendrites than

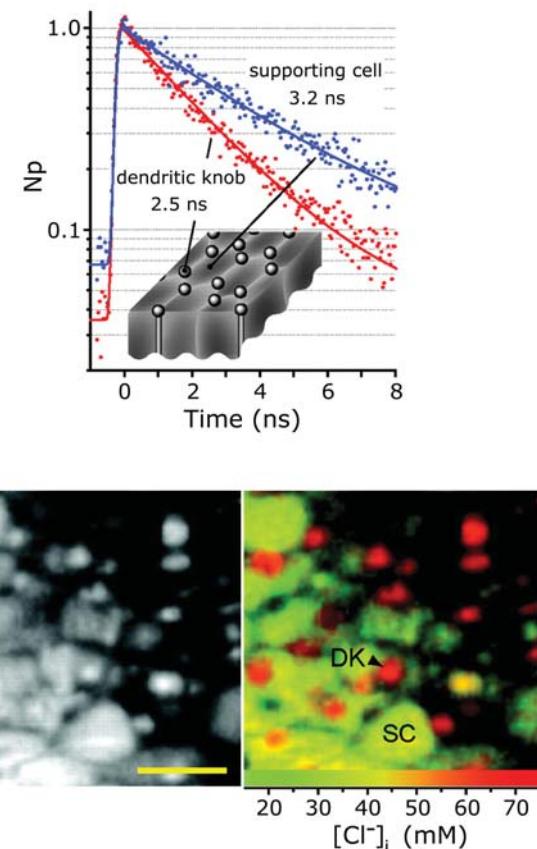


**Figure 19.19.** **Top:** Intensity decays of MQAE in the ends of the neuronal sensing cells (dendritic knob) or in the epithelial supporting cells. **Bottom:** The lower panels show the intensity (left) and chloride concentration image (right) of the olfactory epithelium. Reprinted with permission from [54]. Copyright © 2004, Journal of Neuroscience.

in the surrounding tissue. This experiment was made possible by the advances in TCSPC (Chapter 4) and multiphoton microscopy.

#### 19.4.8. Other Collisional Quenchers

A wide variety of molecules can act as quenchers (Chapter 8), and they permit developments of sensors based on collisional quenching. Benzo(b)fluoranthene was found to be highly sensitive to sulfur dioxide.<sup>55</sup> Oxygen interfered with the measurements but was 26-fold less efficient as a quencher than  $\text{SO}_2$ . Halogenated anesthetics are known to quench protein fluorescence and can be detected by collisional quenching of anthracene and perylene.<sup>56</sup> Carbazole is quenched by a wide variety of chlorinated hydrocarbons.<sup>57</sup> NO, which serves as a signal for blood vessel dilation, is

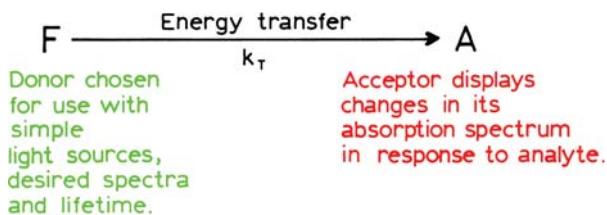


Figure 19.20. Principle of energy-transfer sensing.

also a collisional quencher.<sup>58–59</sup> However, physiologically relevant concentrations of NO are too low for significant collisional quenching. Fluorescent probes of NO usually react chemically with NO.<sup>60–62</sup>

## 19.5. ENERGY-TRANSFER SENSING

Resonance energy transfer (RET) offers many opportunities and advantages for fluorescence sensing. Energy transfer occurs whenever the donor and acceptor are within the Förster distance. Changes in energy transfer can occur due to changes in analyte proximity, or due to analyte-dependent changes in the absorption spectrum of acceptor (Figure 19.20). A significant advantage of RET-based sensing is that it simplifies the design of the fluorophore. For collisional quenching, or analyte recognition probes (Section 19.8), the probe must be specifically sensitive to these analytes. It is frequently difficult to obtain the desired sensitivity and fluorescence spectral properties in the same molecule. However, if RET is used, the donor and acceptor can be separate molecules (Figure 19.20). The donor can be selected for use with the desired light source, and need not be intrinsically sensitive to the analyte. The acceptor can be chosen to display a change in absorption in response to the analyte. Alternatively, an affinity sensor can be based on a changing concentration of acceptor around the donor due to the association reaction.

### 19.5.1. pH and pCO<sub>2</sub> Sensing by Energy Transfer

A wide variety of pH indicators are available from analytical chemistry. Since indicators are intended for visual observation, they display pH-dependent absorption spectra with absorption at visible wavelengths. These indicators have formed the basis for a number of RET-pH/pCO<sub>2</sub> sensors. One of the earliest reports used eosin as the donor and phenol red as the acceptor.<sup>63</sup> Phenol red was selected because it displays a pK<sub>a</sub> near 7, and the basic forms absorb

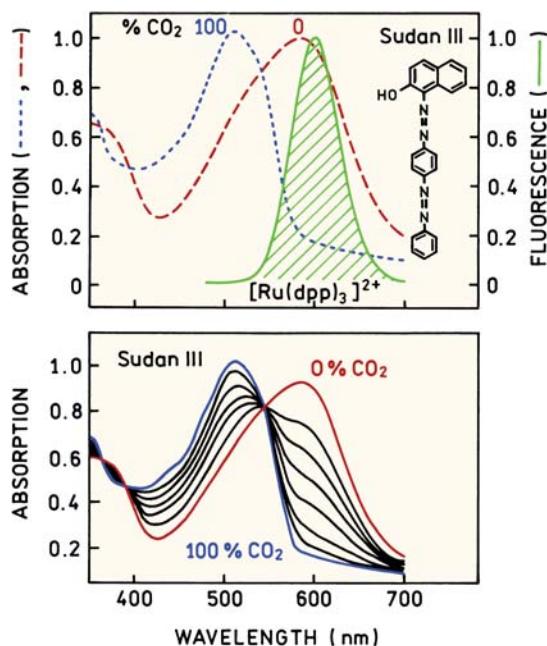
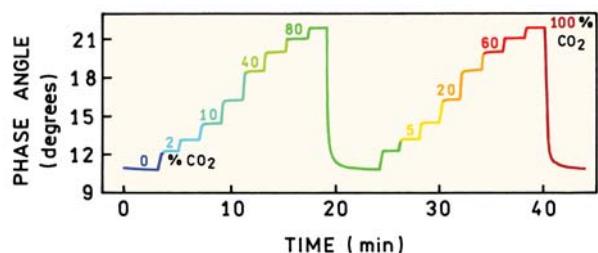


Figure 19.21. Top: Absorption spectra of Sudan III in the sensing matrix in the absence (0%) and presence (100%) of CO<sub>2</sub>. The emission spectrum is for [Ru(dpp)<sub>3</sub>]<sup>2+</sup>. Bottom: CO<sub>2</sub>-dependent absorption spectra of Sudan III. Revised from [69].

at 546 nm where eosin emits. Consequently, the eosin intensity decreased as the pH increased. In the case of this particular sensor it was not certain whether the decreased intensity was due to RET or to an inner filter effect, but it is clear that RET is a useful mechanism as the basis for designing sensors.

This same basic idea was used to create lifetime-based sensors for pH, pCO<sub>2</sub>,<sup>64–69</sup> and ammonia.<sup>70–73</sup> Spectra for a representative sensor are shown in Figure 19.21. The donor was [Ru(dpp)<sub>3</sub>]<sup>2+</sup>, where dpp is 4,7-diphenyl-1,10-phenanthroline.<sup>69</sup> This donor was chosen for its long decay time, allowing lifetime measurements with an amplitude-modulated LED at 20 kHz. The acceptor was Sudan III, which displayed a CO<sub>2</sub>-dependent absorption spectrum. This dependence on CO<sub>2</sub> was due to changes in pH in the polymeric media that contained the donor, acceptor, and buffering components. At low partial pressure of CO<sub>2</sub> the pH is high and Sudan III absorbs at the emission wavelength of the donor. As the partial pressure of CO<sub>2</sub> increases the long-wavelength absorption of Sudan III decreases.

This RET sensor could be used to measure the partial pressure of CO<sub>2</sub> (Figure 19.22). The apparent lifetime was measured from the phase angle of the [Ru(dpp)<sub>3</sub>]<sup>2+</sup> emission. As the partial pressure of CO<sub>2</sub> increased the phase



**Figure 19.22.**  $\text{CO}_2$ -dependent phase angles of  $[\text{Ru}(\text{dpp})_3]^{2+}$  in the sensor matrix containing Sudan III. The output of the LED was modulated at 20 kHz. Revised from [69].

angle increased, indicating an increase in the mean lifetime of  $[\text{Ru}(\text{dpp})_3]^{2+}$ . The change in phase angle or lifetime showed that the partial pressure of  $\text{CO}_2$  affected the extent of RET because inner filter effects are not expected to alter the lifetimes.

A critical point in sensor design is the support containing the probes. For the  $\text{pCO}_2$  sensor, the support consisted of silica gel and ethylcellulose (EC). The EC contained tetraoctylammonium hydroxide (TOAH) which served as a phase transfer agent for the  $\text{CO}_2$ . These details are mentioned to show that careful consideration of the support and actual use of the sensor is needed to result in a useful device. Depending on the support and analyte it may be necessary to use phase transfer agents to facilitate uptake of the analyte into the supporting media.<sup>74</sup> Another important technique for fabricating sensors is the use of sol gels. The basic idea is the hydrolysis of tetraethylorthosilicate (TEOS,  $\text{Si}(\text{OC}_2\text{H}_5)_4$ ) in a mixture of water and ethanol. As TEOS is hydrolyzed, it forms silica ( $\text{SiO}_2$ ). Monoliths and glass films of silica can be formed at low temperatures with mild conditions. The porosity of the sol gels can be controlled, and fluorophores or even enzymes can be trapped within the sol gel matrix.<sup>75–76</sup> The result is a solid sensor which contains the trapped molecules.

### 19.5.2. Glucose Sensing by Energy Transfer

Control of blood glucose is crucial for the long-term health of diabetics.<sup>77</sup> Present methods to measure glucose require fresh blood, which is obtained by a finger stick. This procedure is painful and inconvenient, making it difficult to determine the blood glucose as frequently as is needed. Erratic blood glucose levels due to diabetes are responsible for adverse long-term problems of blindness and heart disease. These effects are thought to be due to glycosylation of protein in blood vessels. Consequently, there have been

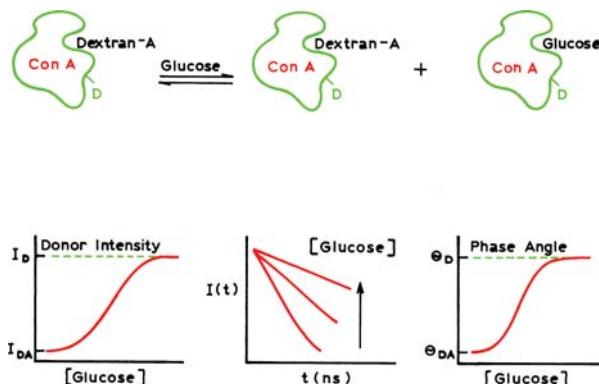


**Figure 19.23.** Glucose sensing by resonance energy transfer. Revised from [78].

numerous efforts to develop noninvasive methods to measure blood glucose.

Because of the medical need there have been continued efforts to develop a noninvasive means to measure blood glucose and to develop fluorescence methods to detect glucose. These have often been based on the glucose-binding protein concanavalin A (ConA) and a polysaccharide, typically dextran, which serves as a competitive ligand for glucose (Figure 19.23).<sup>78–79</sup> Typically, the ConA is labeled with

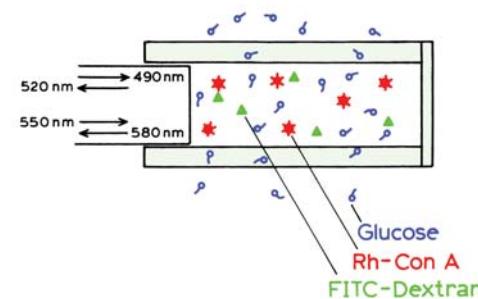
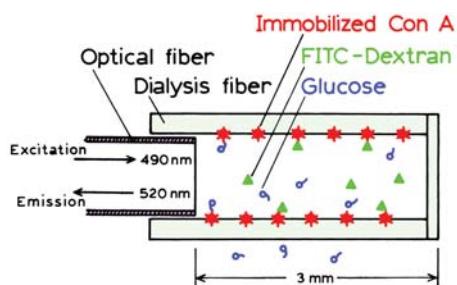


**Figure 19.24.** Resonance energy transfer sensor for glucose. Revised from [80].

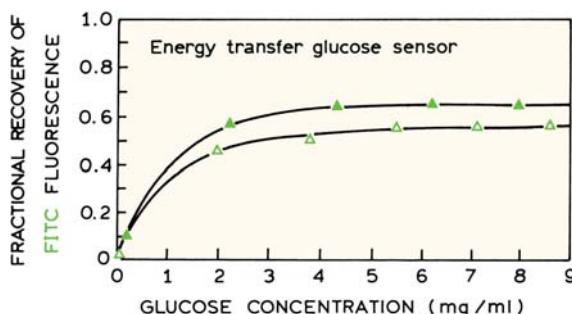


**Figure 19.25.** Recovery of FITC fluorescence during glucose titration for two weight ratios of Rh-ConA/FITC-dextran, 217 ( $\blacktriangle$ ) and 870 w/w ( $\triangle$ ). Revised from [81].

a donor (D) and the dextran with an acceptor (A), but the labels can be reversed. Binding of D-ConA to A-dextran results in a decrease in donor intensity or lifetime. The glucose in the sample competes for the glucose binding sites on D-ConA, releasing D-ConA from the acceptor. The intensity decay time and phase angles of the donor are thus expected to increase with increasing glucose concentration.

This principle was used in the first reports of glucose sensing by fluorescence intensities.<sup>79–81</sup> A fiber-optic glucose sensor was made using FITC-labeled dextran and rhodamine-labeled ConA (Figure 19.24). The acceptor could be directly excited as a control measurement to determine the amount of Rh-ConA. The response of this glucose sensor is shown in Figure 19.25. The donor and acceptor were placed on the dextran and ConA, respectively. The donor fluorescence was not completely recovered at high concentrations of glucose. This lack of complete reversibility is a problem that plagues ConA-based glucose sensors to the present day. It is hoped that these problems can be solved using alternative glucose binding proteins, especially those that have a single glucose binding site and may be less prone to irreversible associations. It seems probable that site-directed mutagenesis will be used to modify the glucose-binding proteins to obtain the desired glucose affinity and specificity.

As might be expected, lifetime-based sensing has been applied to glucose, and has been accomplished using nanosecond probes,<sup>82</sup> long-lifetimes probes,<sup>83</sup> and laser-diode-excitible probes.<sup>84</sup> The problem of reversibility has been addressed by using sugar-labeled proteins in an attempt to minimize crosslinking and aggregation of the multivalent ConA. Such glucose sensors are occasionally fully reversible,<sup>84</sup> but there is reluctance to depend on a system where reversibility is difficult to obtain.

### 19.5.3. Ion Sensing by Energy Transfer

Wavelength-ratiometric probes are available for  $\text{Ca}^{2+}$  and  $\text{Mg}^{2+}$ , but the performance of similar probes for  $\text{Na}^+$  and  $\text{K}^+$  is inadequate (Section 19.8.3). It is difficult to design probes for  $\text{K}^+$  and  $\text{Na}^+$  with the desired binding constant and selectivity, and that also display adequate spectral changes. These difficulties can be understood by considering a sensor for  $\text{K}^+$ . In blood the concentrations of  $\text{K}^+$  and  $\text{Na}^+$  are near 4.5 and 120 mM, respectively. A probe for  $\text{K}^+$  must be able to bind  $\text{K}^+$  selectively, and not be saturated by a 25-fold excess of  $\text{Na}^+$ . Given the similar chemical properties of  $\text{Na}^+$  and  $\text{K}^+$ , and the smaller size of  $\text{Na}^+$ , such selectivity is difficult to achieve. These problems can be alleviated to some extent by making use of ionophores like valinomycin that display high selectivity for  $\text{K}^+$ . Valinomycin is a cyclic molecule that unfortunately does not contain any useful chromophoric groups. Consequently, one has to develop a sensor that transduces the binding of  $\text{K}^+$  to result in a fluorescence spectral change.

One method to develop a  $\text{K}^+$  sensor is to use a dye that displays a change in its absorption spectrum on ionization.<sup>85</sup> The sensor was fabricated using polyvinyl chloride, valinomycin, plus fluorescent beads (FluoSpheresJ, Molecular Probes, Eugene, OR). The acceptor is shown in Figure 19.26. When  $\text{K}^+$  enters the membrane, KFU-111 loses a proton resulting in an increase in absorbance at 650 nm. This absorbance overlaps with the emission spectra of the FluoSpheresJ, resulting in a decreased intensity (Figure 19.27). As the  $\text{K}^+$  concentration is increased the FluoSphere intensity is progressively decreased (Figure 19.28).

Examination of Figure 19.27 reveals that the emission spectrum is distorted at higher concentrations of  $\text{K}^+$ . This indicates that the mechanism of  $\text{K}^+$  sensing is not energy transfer, but rather is an inner filter effect due to KFU-111, as was stated by the authors.<sup>85</sup> In this particular sensor there was no opportunity for the fluorophore and absorption dye to interact, as the fluorophores were in the beads, and thus distant from the absorber. The important point is that spectral overlap does not imply that the mechanism is resonance energy transfer. Potassium sensors using valinomycin but other donors such as rhodamine and cyanine dyes have also been reported.<sup>86–87</sup> For the cyanine donor 1,1'-dioctadecyl-3,3',3'-tetramethylindodicarbocyanine perchlorate [DiIC<sub>18</sub>(5)], lifetime measurements demonstrated that RET was the dominant mechanism for  $\text{K}^+$  sensing.<sup>87</sup> One difficulty with RET sensing is that the extent of energy transfer depends strongly on acceptor concentration, so that the sensors require frequent calibration. This problem can poten-

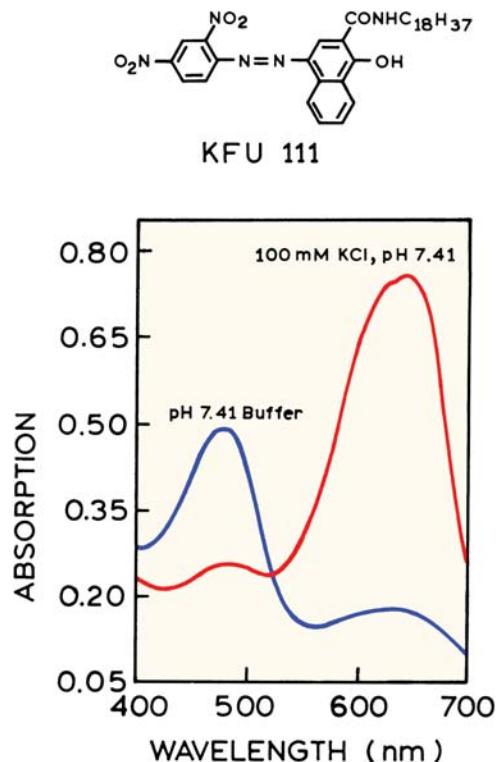


**Figure 19.26.** Absorption spectra of 4-((2',4'-dinitrophenyl)azo)-2-((octadecylamino)carbon-yl-l-naphthol (KFU 111) in a plasticized PVC membrane containing potassium tetrakis(4-chlorophenyl)borate (PTCB) and valinomycin, in contact with a 100 mM aqueous solution of KCl at pH 7.41, and with potassium-free buffer at pH 7.41. Revised and reprinted with permission from [85]. Copyright © 1993, American Chemical Society.

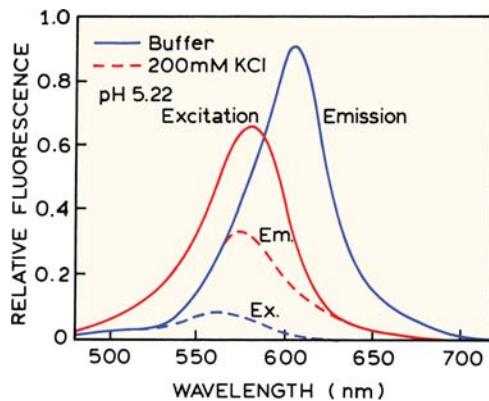


**Figure 19.27.** Excitation and emission spectra of FluoSphereJ particles contained in the plasticized PVC membrane containing PTCB, valinomycin, and KFU 111 contacted with a 200 mM KCl solution at pH 5.22 (dashed) and with plain buffer of pH 5.22 (solid). The emission spectrum of the FluoSpheres in the presence of K<sup>+</sup> is distorted due to the inner filter effect caused by the blue form of the absorber dye. Revised and reprinted with permission from [85]. Copyright © 1993, American Chemical Society.

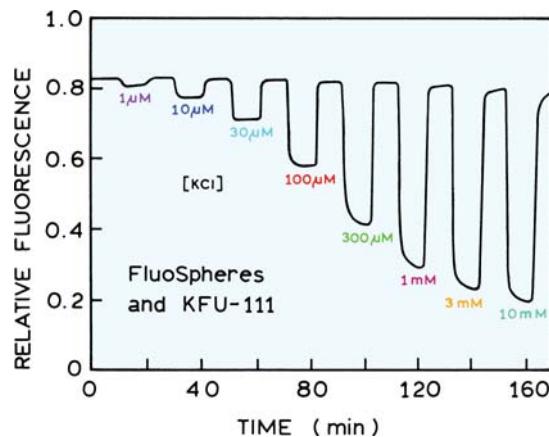


**Figure 19.28.** Response time, relative signal change, and reversibility of the potassium sensor in the presence of dye KFU 111 in the membrane; pH 5.82, excitation/emission wavelengths set to 560/605 nm. The sensor did not respond to potassium without KFU 11. Revised and reprinted with permission from [85]. Copyright © 1993, American Chemical Society.

tially be circumvented by using covalently linked donors and acceptors.

#### 19.5.4. Theory for Energy Transfer Sensing

The theory for sensing by energy transfer is complex and depends on the nature of the sensor. There are two limiting cases—unlinked donors and acceptors distributed randomly in space, and covalently linked donor-acceptor pairs. Suppose the donor–acceptor pair is not linked and that the acceptor can exist in two forms with different absorption spectra and Förster distances ( $R_{01}$  and  $R_{02}$ ). The intensity decay is given by

$$I_{DA}(t) = I_0 \exp\left[-\frac{t}{\tau_D} - 2(\gamma_1 + \gamma_2)\sqrt{\frac{t}{\tau_D}}\right] \quad (19.2)$$

where  $\tau_D$  is the donor decay time and  $\gamma_1$  and  $\alpha_2$  are functions of the acceptor concentration, and are related to  $R_{01}$  and  $R_{02}$ , as described in Chapter 15 (eqs. 15.1–15.3). Alternatively, the donor and acceptor may be covalently linked. In this the intensity decay is given by

$$I_{DA}(t) = I_D \left[ g_1 \int_0^\infty P(r) \exp\left(\frac{t}{\tau_{DA1}}\right) dr \right. \\ \left. + (1 - g_1) \int_0^\infty P(r) \exp\left(\frac{t}{\tau_{DA2}}\right) dr \right] \quad (19.3)$$

where

$$\frac{1}{\tau_{DAi}} = \frac{1}{\tau_D} + \frac{1}{\tau_D} \left( \frac{R_{0i}}{r} \right)^6 \quad (19.4)$$

$P(r)$  is the distance distribution, and  $g_1$  and  $(1 - g_1)$  are the fractional intensities of each form at  $t = 0$ . The transfer efficiency ( $E$ ) can be calculated by

$$E = 1 - \frac{F_{DA}}{F_D} = 1 - \frac{\int_0^\infty I_{DA}(t) dt}{\int_0^\infty I_D(t) dt} \quad (19.5)$$

where  $I_D(t)$  is an intensity decay of the donor with no acceptors;  $F_D$  and  $F_{DA}$  are the relative intensities of the donor in the absence and presence of acceptor. These general expressions can be used to simulate the expected performance of an energy-transfer sensor using known or estimated parameter values.<sup>13</sup>

## 19.6. TWO-STATE pH SENSORS

### 19.6.1. Optical Detection of Blood Gases

The phrase "blood gases" refers to the measurement of pH,  $pCO_2$ , and  $pO_2$  in arterial blood. Optical detection of blood gases is a longstanding goal of optical sensing. Blood-gas measurements are frequently performed on patients in the intensive care unit, premature infants, and trauma victims. Since the status of such patients changes rapidly, it is important to obtain the blood gas results as quickly as possible. While the status of optical detection of blood gases is evolving rapidly, many of the currently used methods do not satisfy the needs of intensive care and emergency health care situations where the blood gases are changing rapidly.<sup>88–89</sup>

Determination of blood gases is difficult, time-consuming, and expensive. Measuring a blood gas requires taking a sample of arterial blood, placing it on ice, and transporting it to a central laboratory. At the central laboratory the pH is measured using an electrode, and  $O_2$  and  $CO_2$  by the Clark and Severinghaus electrodes, respectively. Even for a stat request, it is difficult to obtain the blood-gas report in less than 30 minutes, by which time the patient's status is often quite different. Additionally, handling of blood by health-care workers is undesirable with regard to the risk of acquired immunodeficiency syndrome (AIDS) and other infectious diseases.

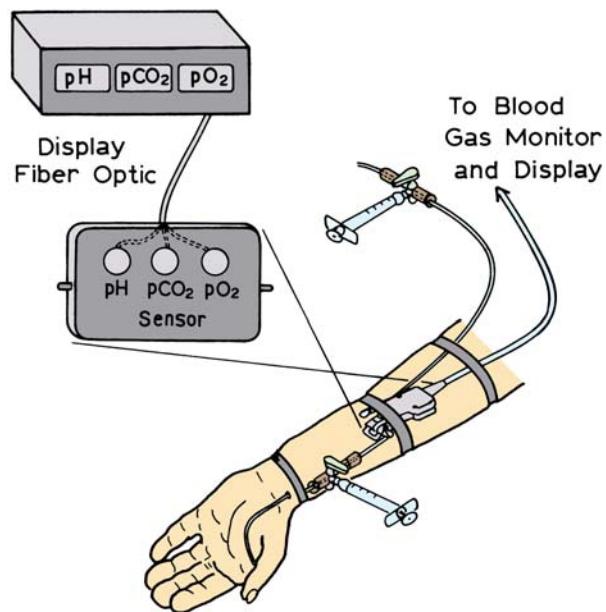
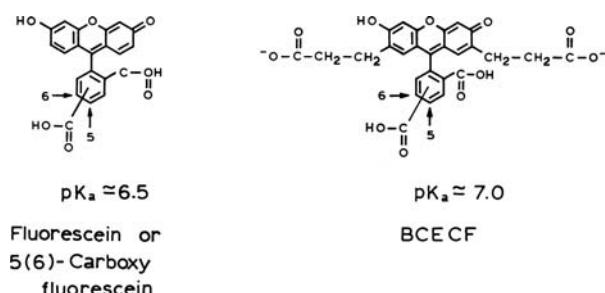


Figure 19.29. Arterial blood-gas sensor. Revised from [89].

How can optical sensing of blood gases improve on this situation? One approach is shown in Figure 19.29.<sup>89</sup> The sensor chemistry is a cassette that is attached to an arterial line. When needed, blood is drawn into the cassette, and the blood gases are determined by appropriate fluorescent sensors. Oxygen could be determined using  $[Ru(Ph_2phen)_3]^{2+}$ , and pH can be measured using HPTS or other pH-sensitive fluorophores (Section 19.6.2).<sup>90</sup> The ability to measure pH also allows  $pCO_2$  to be measured using the bicarbonate couple.<sup>91</sup> This is accomplished by measuring the pH of a bicarbonate solution that is exposed to the  $CO_2$ . The concentration of dissolved  $CO_2$  alters the extent of bicarbonate dissociation and hence the pH. With the use of such a device the blood-gas measurements could be made without loss or handling of blood and the results can be available immediately. Such instruments have been developed,<sup>92–93</sup> but improvements in performance are desirable. This idea of clinical chemistry using fiber optics originates with the early work of D. W. Lubbers and colleagues.<sup>94</sup> In the long term it is hoped that blood gases can be determined noninvasively, as shown in Figure 19.1, or with a simple point-of-care device (Figure 19.2).

### 19.6.2. pH Sensors

**Fluoresceins:** Fluorescein was one of the earliest pH sensors.<sup>95–96</sup> Fluorescein and other pH-sensitive probes have



**Figure 19.30.** Fluorescein-type pH probes.

also been used to measure  $pCO_2$  by the bicarbonate couple.<sup>97–98</sup> One early use of fluorescein was to determine intracellular pH values. However, fluorescein leaks rapidly from cells, so highly charged derivatives are often used, such as 5(6)-carboxyfluorescein or 2',7'-bis(2-carboxyethyl)-5(6)-carboxyfluorescein (BCECF) (Figure 19.30). Fluorescein displays a complex pH-dependent equilibrium, and emission from the various ionic forms<sup>99–102</sup> (Figure 19.31). The lactone form is usually found in organic solvents and is not formed in aqueous solutions above pH 5. Only the two high-pH anionic forms are fluorescent (Figure 19.31).

Fluorescein is a moderately useful excitation wavelength-ratiometric probe. The absorption spectrum shifts to higher wavelengths with a  $pK_a$  near 6.5 (Figure 19.32). These absorption and emission spectral changes are due to the equilibrium between the two fluorescent forms of fluorescein—the monoanion and dianion forms (Figure 19.31). These spectral changes allow wavelength-ratiometric pH measurements with two excitation wavelengths near 450 and 495 nm. The intensity ratio increases with increasing pH (Figure 19.33). The data in Figure 19.33 are for fluores-

cein linked to dextran, which was used to prevent the fluorescein from leaking out of the cells.

One disadvantage of fluorescein is that its  $pK_a$  is near 6.5, whereas the cytosolic pH of cells is in the range of 6.8 to 7.4. Hence, it is desirable to have a higher  $pK_a$  for accurate pH measurement. BCECF (Figure 19.30) was developed<sup>103</sup> to have spectral properties similar to those of fluo-

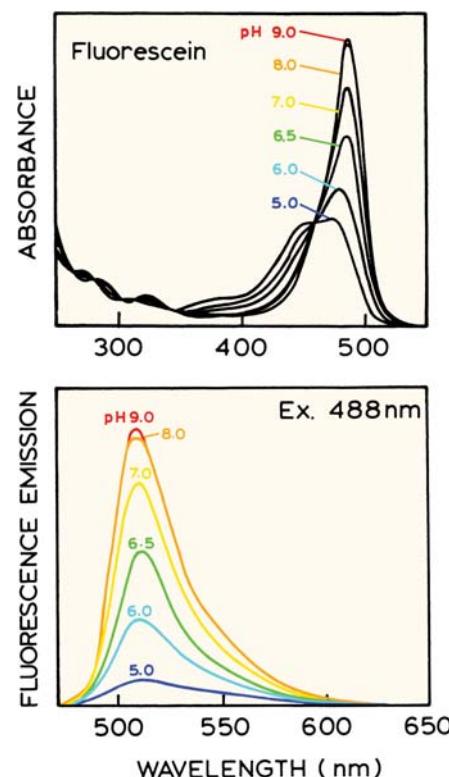


**Figure 19.32.** Absorption and emission spectra of fluorescein. Data from [100].

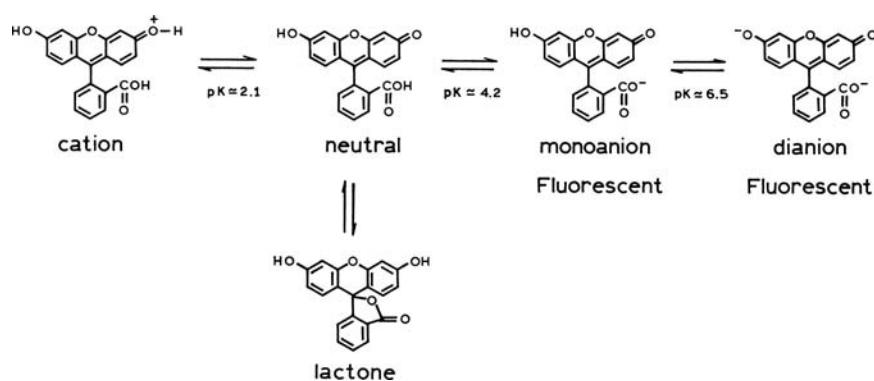


**Figure 19.31.** pH-dependent ionization of fluorescein. Only the monoanion and dianion forms of fluorescein are fluorescent.

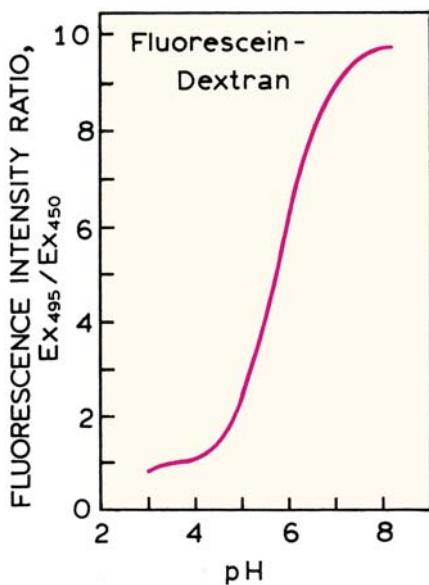


**Figure 19.33.** Wavelength-ratiometric pH calibration for fluorescein linked to dextran. Revised from [95].

rescein, but to have a higher  $pK_a$  near 7.0 (Table 19.2). This illustrates an important aspect of all sensing probes: the  $pK_a$  value or the analyte dissociation constant must be comparable to the concentration of the analyte to be measured. However, it can be difficult to adjust a  $pK_a$  value or dissoci-

ation constant. Additionally, the affinities observed in solution may be quite different from the values needed in a sensor, where the probe may bind to proteins or membranes or the probe may be present in a polymeric support. Significant development is often needed to adapt a sensor for use in a clinical application.

**HPTS, A Wavelength-Ratiometric pH Sensor:** A disadvantage of fluorescein as a sensor is that it is difficult to use as a wavelength-ratiometric probe. This is because the absorption and emission intensity is low for 450-nm excitation (Figure 19.32). The pH probe 8-hydroxypyrene-1,3,6-trisulfonate (HPTS)<sup>104–107</sup> displays more favorable properties as a wavelength-ratiometric probe. The sulfonate groups are for solubility in water and the hydroxyl group provides sensitivity to pH. Excitation and emission spectra of HPTS show a strong dependence on pH (Figure 19.34). As the pH is increased HPTS shows an increase in absorbance at 450 nm, and a decrease in absorbance below 420 nm. These changes are due to the pH-dependent ionization of the hydroxyl group. The emission spectrum is independent of pH, suggesting that emission occurs only from the ionized form of HPTS. Conveniently, the apparent  $pK_a$  of HPTS is near 7.5, making it useful for clinical measurements that need to be most accurate from 7.3 to 7.5 (Table 19.2). HPTS has also been used as a  $\text{CO}_2$  sensor when dissolved in the appropriate bicarbonate solution.<sup>108</sup>

**Table 19.2.** Spectral and Lifetime Properties of pH Probes

Probe <sup>b</sup>	Excitation $\lambda_B(\lambda_A)$ [nm]	Emission $\lambda_B(\lambda_A)$ [nm]	$Q_B(Q_A)$	Lifetime (ns) <sup>a</sup> $\bar{\tau}_B(\bar{\tau}_A)$	$pK_A$
BCECF	503 (484)	528 (514)	~0.7	4.49 (3.17)	7.0
SNAFL-1	539 (510)	616 (542)	0.093 (0.33)	1.19 (3.74)	7.7
C. SNAFL-1	540 (508)	623 (543)	0.075 (0.32)	1.11 (3.67)	7.8
C. SNAFL-2	547 (514)	623 (545)	0.054 (0.43)	0.94 (4.60)	7.7
C. SNARF-1	576 (549)	638 (585)	0.091 (0.047)	1.51 (0.52)	7.5
C. SNARF-2	579 (552)	633 (583)	0.110 (0.022)	1.55 (0.33)	7.7
C. SNARF-6	557 (524)	635 (559)	0.053 (0.42)	1.03 (4.51)	7.6
C. SNARF-X	575 (570)	630 (600)	0.160 (0.07)	2.59 (1.79)	7.9
Resorufin	571 (484)	528 (514)	NA <sup>c</sup>	2.92 (0.45)	~5.7
HPTS	454 (403)	511	NA	N/A	7.3
[Ru(deabpy)(bpy) <sub>2</sub> ] <sup>2+</sup>	450 (452)	615 (650)	NA	380 (235)	7.5
Oregon-Green	489 (506)	526	0.65 (0.22)	4.37 (2.47)	1.8
DM-Nerf	497 (510)	527 (536)	0.88 (0.37)	3.98 (2.50)	1.6
Cl-Nerf	504 (514)	540	0.78 (0.19)	4.00 (1.71)	2.3

<sup>a</sup> $\bar{\tau}_A$  and  $\bar{\tau}_B$  refer to the mean lifetimes of the acid and base forms, respectively.

<sup>b</sup>Abbreviations: BCECF, 2',7'-bis(2-carboxyethyl)-5(6)-carboxyfluorescein; bpy, 2,2'-bipyridine; HPTS, 8-hydroxypyrene-1,3,6-trisulfonate; deabpy, 4,4'-diethylaminomethyl-2,2'-bipyridine; bpy, 2,2'-bipyridine.

<sup>c</sup>NA: Not available.

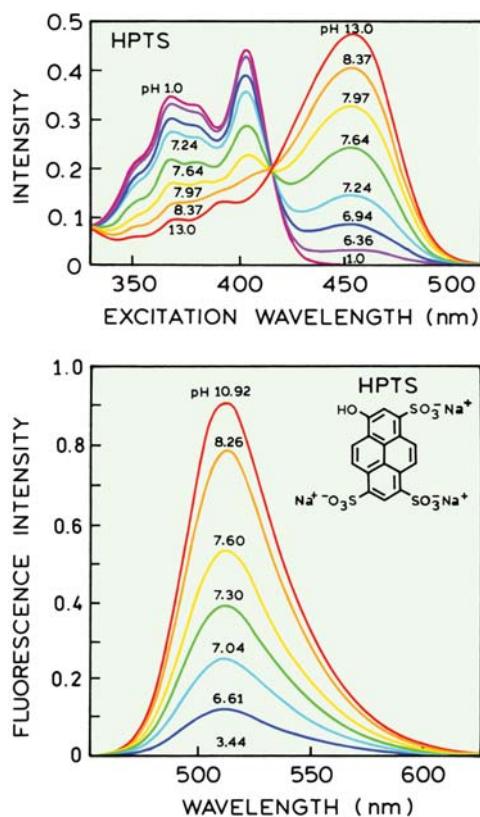


**Figure 19.34.** Top: Excitation spectra of the pH probe 1-hydroxypyrene-3,6,8-trisulfonate (HPTS) in 0.07 M phosphate buffer at various pH values. Bottom: Emission spectra of HPTS when excited at 454 nm. Revised from [105].

One possible disadvantage of HPTS is that it undergoes ionization in the excited state, rather than at ground-state equilibrium. The fact that HPTS undergoes an excited-state reaction can be recognized by noting that the excitation spectra are comparable to the absorption spectra of both the phenol and phenolate forms, but that there is only a single long-wavelength emission spectrum (Figure 19.34). The phenol form emits at shorter wavelengths and is only seen in highly acidic media. The presence of excited-state ionization is also indicated by a higher apparent  $pK_A$  in pure water than in buffers.<sup>105</sup> It is known that the  $pK_A$  values of the hydroxyl group for the ground- and excited-state HPTS are 7.3 and 1.4, respectively,<sup>106</sup> so that HPTS molecules in the protonated state will tend to undergo ionization upon excitation. It seems that any excited-state process will be dependent on the details of the local probe environment. Under most conditions excited-state ionization of HPTS is complete prior to emission, so that only the phenolate emission is observed. Nonetheless, for sensing purposes we pre-

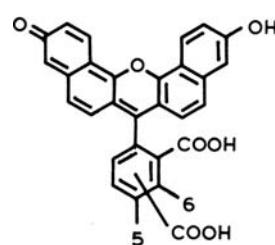
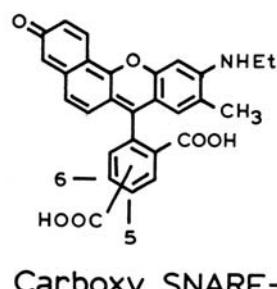
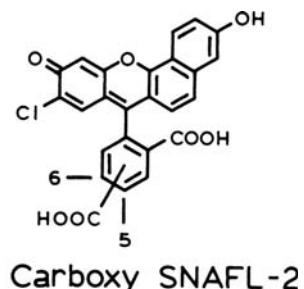


**Figure 19.35.** Wavelength-ratiometric pH sensors. Carboxy SNAFL-2 is a seminaphthofluorescein, carboxy SNARF-6 is a seminaphthorhodafluor, and CNF is 5-(and 6-)carboxy-naphthofluorescein.

fer probes that display a ground-state  $pK_A$  near 7.5. One disadvantage of HPTS has been the relatively short excitation wavelength, particularly for the acid form. However, availability of blue light-emitting diodes (Chapter 2) may result in increased use of HPTS.

**SNAFL and SNARF pH Probes:** A family of improved pH probes became available in 1991.<sup>109</sup> These dyes are referred to as seminaphthofluoresceins (SNAFLs) or seminaphthorhodafluors (SNARFs). Representative structures are shown in Figure 19.35. A favorable feature of these probes is that they display shifts in both their absorption and emission spectra with a  $pK_A$  from 7.6 to 7.9 (Figure 19.36). Also, the absorption and emission wavelengths are reasonably long, so that both forms of the probes can be excited with visible wavelengths near 540 nm (Table 19.2).

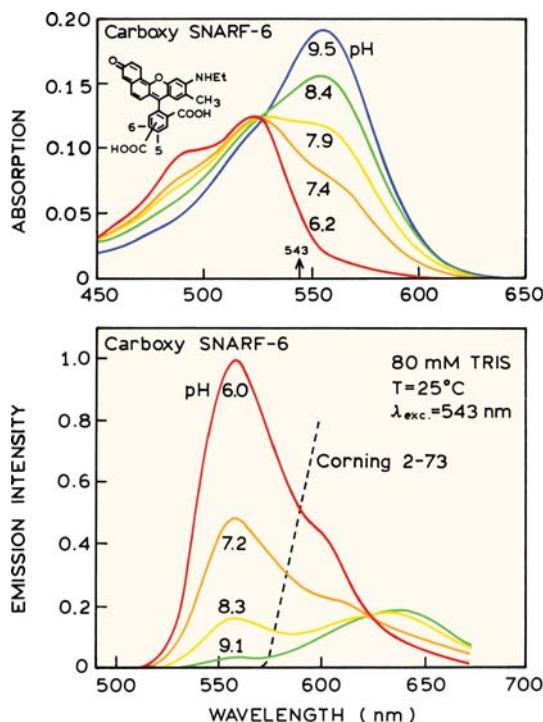


**Figure 19.36.** pH-dependent absorption (top) and emission spectra (bottom) of carboxy SNARF-6. The dashed line shows the transmission cutoff of the long-pass filter used for the phase and modulation measurements. Revised and reprinted with permission from [110]. Copyright © 1993, American Chemical Society.

The spectral shifts (Figure 19.36) allow the SNAFLs and SNARFs to be used as either excitation or emission wavelength-ratiometric probes.

The fact that both the acid and base forms of the probe are fluorescent allows their use as lifetime probes. If only one form was fluorescent then the lifetime would not change with pH. The pH-dependent phase and modulation data of carboxy SNARF-6 shows a strong dependence on pH (Figure 19.37). The decay time of the base form is less than that of the acid form. The decay times at pH 4.9 and 9.3 are 4.51 and 0.95 ns, respectively.<sup>110</sup> pH sensing based on lifetimes can provide stable measurements for extended periods of time. However, it is important to recognize that lifetime measurements, like intensity ratio measurements, can be affected by interactions of the probes with biological macromolecules. The intensity decays of carboxy SNARF-1 were found to be sensitive to the presence of serum albumin, or intracellular proteins.<sup>111</sup>

There is continued development of new pH probes<sup>112–113</sup> and sensors.<sup>114–116</sup> For clinical applications, longer wavelengths are usually preferable. This was accom-

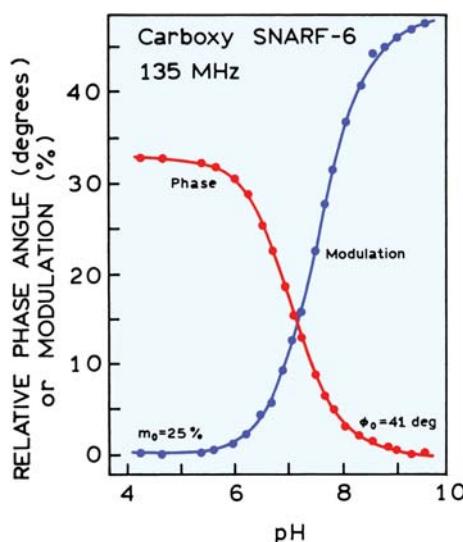


**Figure 19.37.** pH-dependent phase and modulation of carboxy SNARF-6 when excited at 543 nm with a green He-Ne laser. The phase values are relative to the value at high pH,  $\phi_0 = 41^\circ$ . The modulation values are relative to the value at low pH,  $m_0 = 0.25$ . Revised and reprinted with permission from [110]. Copyright © 1993, American Chemical Society.

plished with the SNAFL probes by introduction of an additional benzyl ring into the parent structure (Figure 19.35). This carboxynaphthofluorescein (CNF)<sup>118</sup> shows shifts in the absorption and emission spectra with pH (Figure 19.38). pH probes have been developed using cyanine dyes<sup>119</sup> and a pH sensor excitable at 795 nm has been described.<sup>120–121</sup> This carboxy carbocyanine dye shows a decrease in intensity near pH 8.5, but does not display spectral shifts, except at short wavelengths near 435 nm. UV-excitatable pH probes with multiple  $pK_A$  values from 1.7 to 9.0 have also been described.<sup>122</sup> For clinical applications with simple instruments it can be valuable to have long-lifetime pH probes. A pH-sensitive ruthenium metal–ligand complex with a decay time near 300 ns has been reported with a  $pK_A$  value near 7.5.<sup>123</sup> Additionally, a pH-dependent lanthanide has also been reported.<sup>124</sup> Given the continuing need for pH measurements, additional advances in practical pH sensors can be expected.

## 19.7. PHOTOINDUCED ELECTRON TRANSFER (PET) PROBES FOR METAL IONS AND ANION SENSORS

In the previous section we saw how probes could be designed based on reversible ionization of a group in conjugation

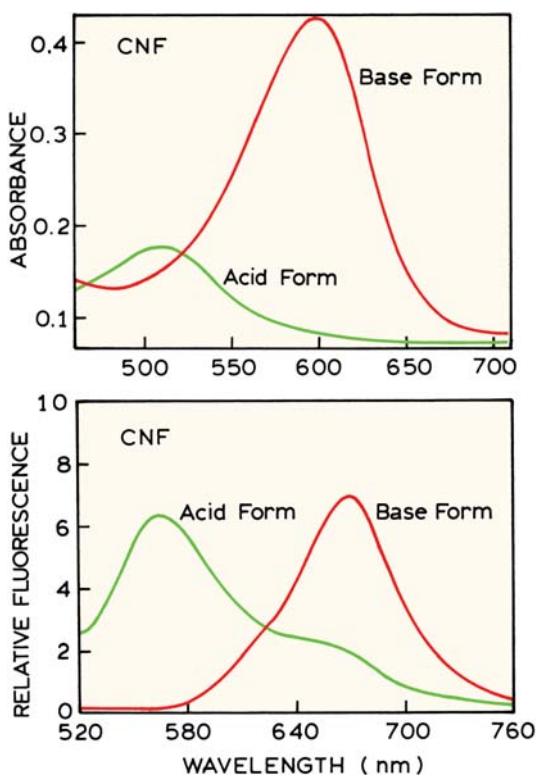


**Figure 19.38.** Absorption (top) and emission spectra (bottom) of the acid and base form of carboxynaphthofluorescein (CNF). Revised and reprinted with permission from [117]. Copyright © 2001, American Chemical Society.

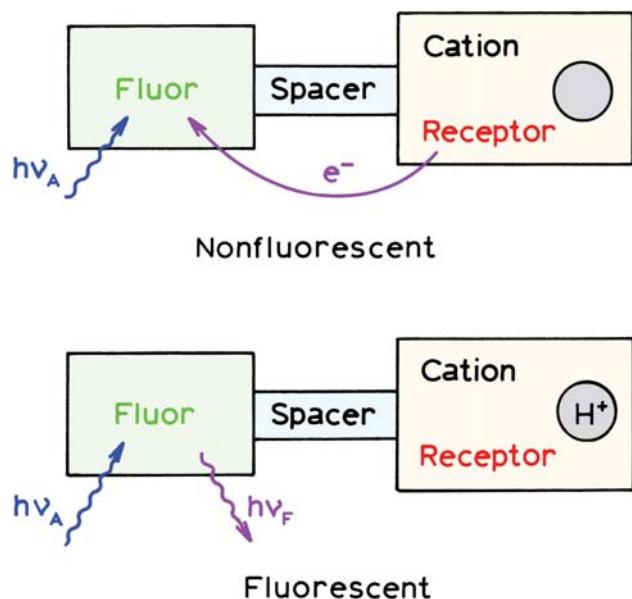


**Figure 19.39.** Chemical sensing based on photoinduced electron transfer.

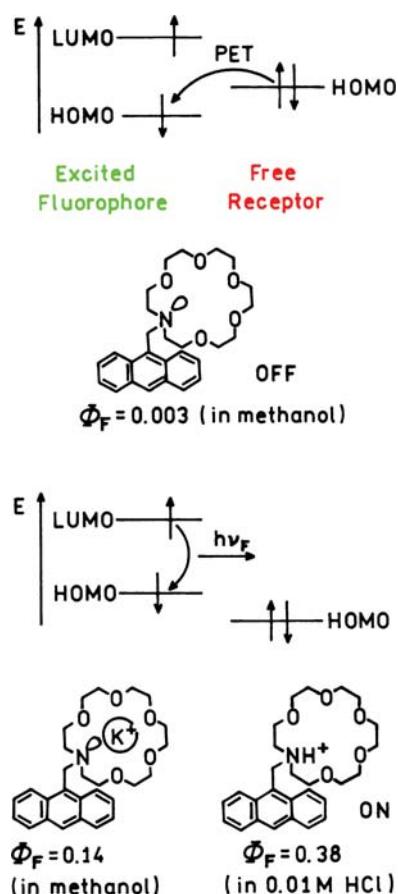


**Figure 19.40.** Molecular orbital energy and a typical structure for a PET sensor. Revised from [128].

tion with the aromatic ring (Figure 19.39). Another mechanism for sensors is the quenching interaction of a linked side chain with the fluorophore. The origin of these probes can be traced to the early studies of exciplex formation of amines with aromatic hydrocarbons. This phenomenon has been exploited to develop sensors based on quenching of fluorophores by amines.<sup>125–128</sup> The basic idea is that quenching by amines requires the lone pair of electrons localized on the nitrogen (Figure 19.40). When the fluorophore is in the excited state these lone pair electrons are in a higher-energy orbital (HOMO, top) than the energy of the vacancy left by the excited electron. Hence, an electron from the nitrogen enters this lower-energy orbital, effectively quenching the fluorescence. If the lone electron pair binds a proton or a cation the energy of this pair is lowered (bottom). Electron transfer is then inhibited and the fluorophore is not quenched. Such probes are said to undergo

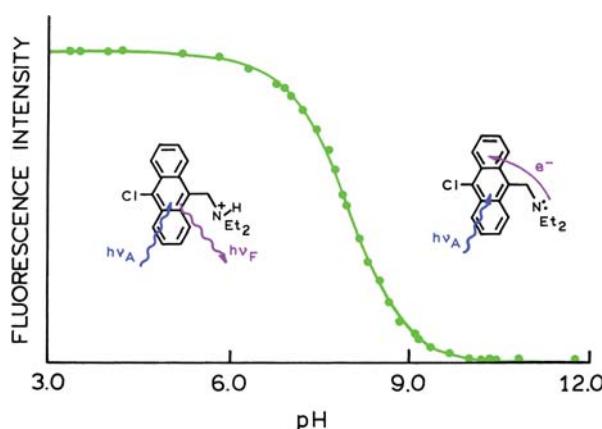


**Figure 19.41.** pH-dependent fluorescence of 9-chloro-10-(diethylaminomethyl)anthracene. Revised and reprinted with permission from [126]. Copyright © 1989, American Chemical Society.

photoinduced electron transfer (PET), which is the light-induced transfer of electrons from the nitrogen into the aromatic ring. A simple example of a PET sensor is the alkylamino anthracene shown in Figure 19.41. At low pH the amino group is protonated and does not quench the anthracene. As the pH is increased, the amino group becomes unprotonated, and the fluorescence decreases due to PET.

This use of PET has been extended to create sensors for metal ions<sup>129–131</sup> and for nonmetal anions.<sup>132–136</sup> As an example, Figure 19.42 shows an anthracene derivative with an aminoalkyl side chain which binds phosphate. Hydrogen bonding of phosphate to the amino groups results in increased anthracene fluorescence. A similar approach was used to create an anthracene derivative that displays

increased fluorescence when bound to citrate (Figure 19.43). The structures of these phosphate and citrate probes illustrate the rational design of fluorophores based on known principles. Unfortunately, PET mechanism may not be extendable to long-wavelength probes because quenching by amines becomes inefficient at long wavelengths.

## 19.8. PROBES OF ANALYTE RECOGNITION

Extensive efforts have been directed toward the design and synthesis of fluorescent probes for cations:  $\text{Na}^+$ ,  $\text{K}^+$ ,  $\text{Mg}^{2+}$  and especially  $\text{Ca}^{2+}$ . These efforts can be traced to the discovery of crown ethers and their ability to form complexes with metal ions,<sup>137–139</sup> and subsequent work to create more complex structures to bind a variety of small molecules. The greatest effort has been in synthesis of probes for cal-

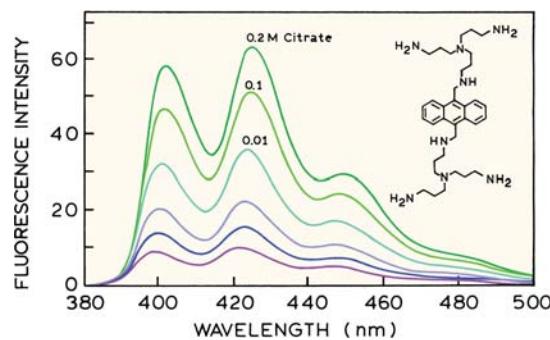


**Figure 19.43.** Emission spectra of an alkylaminoanthracene derivative in the presence of various amounts of citrate at pH 6. From bottom to top,  $[\text{Citrate}] = 0, 0.1, 1, 10 \text{ mM}, 0.1 \text{ M}, 0.2 \text{ M}$ . Revised from [134].

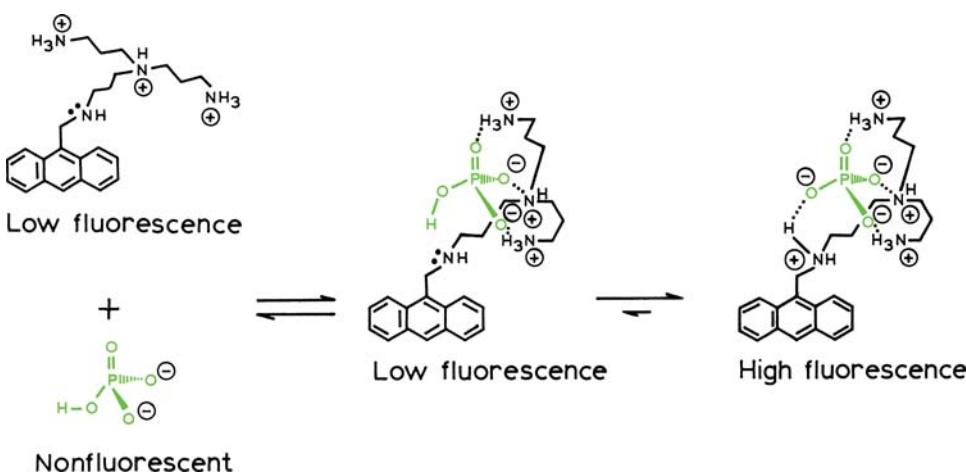


**Figure 19.42.** Phosphate sensing with an alkylamino anthracene derivative. Revised and reprinted with permission from [134]. Copyright © 1989, American Chemical Society.

**Table 19.3.** Typical Analyte Concentrations in Blood Serum and in Resting Cells

Analyte	In blood serum (mM)	In resting cells (mM)
H <sup>+</sup>	34–45 nM	10–1000 nM
(pH)	(7.35–7.46)	(6–8)
Na <sup>+</sup>	135–148	4–10
K <sup>+</sup>	3.5–5.3	100–140
Li <sup>+</sup>	0–2	—
Mg <sup>2+</sup>	—	0.5–2
Ca <sup>2+</sup>	4.5–5.5	50–200 nM
Cl <sup>-</sup>	95–110	5–100
HCO <sub>3</sub> <sup>-</sup>	23–30	—
CO <sub>2</sub>	4–7 (% Atm)	—
O <sub>2</sub>	8–16 (% Atm)	—

cium, and entire books have been devoted to calcium probes.<sup>140</sup> Much of this work can be traced to the development of intracellular cation probes by Tsien and colleagues.<sup>141–143</sup> Since these initial publications many additional cation probes have been developed. It is not possible to completely describe this extensive area of research. Instead we describe the most commonly used cation sensors, and the strength and weaknesses of existing probes.

### 19.8.1. Specificity of Cation Probes

A survey of the literature reveals that a large number of diverse structures can chelate cations. However, a dominant use of these probes is imaging of intracellular cations. In this case the indicators have to be sensitive to the intracellular concentrations of cations or anions (Table 19.3). These concentrations define the affinity needed by the chelators for the cation and the degree of discrimination required

against other cations. For example, a probe for K<sup>+</sup> in blood is not useful unless it does not bind Na<sup>+</sup> at its physiological concentration of 140 mM. Also, it is desirable to have a means for trapping the probes within cells. These criteria suggest a group of chelators that are useful for intracellular probes. The azacrown ethers have suitable affinity constants for Na<sup>+</sup> and K<sup>+</sup>, APTRA is a chelator for Mg<sup>2+</sup>, and BAPTA is a suitable chelator for Ca<sup>2+</sup> (Figure 19.44). These are the dominant chelation groups used in intracellular cation probes.

### 19.8.2. Theory of Analyte Recognition Sensing

Suppose the probe can exist in two states, free (P<sub>F</sub>) and bound (P<sub>B</sub>) to the analyte (A). If the binding stoichiometry is 1 to 1, the dissociation reaction is given by



and the dissociation constant is defined as

$$K_D = \frac{[P_F]}{[AP_B]} [A] \quad (19.7)$$

The relative concentrations of the free and bound form of the probes are given by

$$K_D = \frac{[P_F]}{[AP_B]} [A] \quad (19.8)$$

$$\frac{[AP_B]}{[P]} = \frac{[A]}{K_D + [A]} \quad (19.9)$$

where [P] is the total concentrations of indicator ([P] = [P<sub>F</sub>] + [AP<sub>B</sub>]).

These equations can be used to calculate the relative amounts of free and bound probes as the analyte concentration is increased (Figure 19.45). The range of analyte concentrations that can be measured are those for which there exist significant amounts of each form of the probe. The analyte concentration range over which a probe can be used is determined by the dissociation constant, K<sub>D</sub> (Figure 19.45). This is a critical factor in using probes that bind specific analytes. The binding constant of the probe must be comparable to analyte concentration. The useful range of analyte concentrations is typically restricted to  $0.1K_D < [A] < 10K_D$ . Concentrations lower than  $0.1K_D$  and higher than

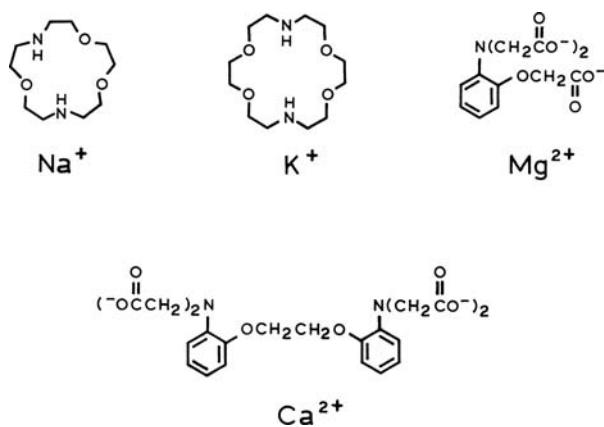


**Figure 19.44.** Chelating groups for Na<sup>+</sup>, K<sup>+</sup>, Mg<sup>2+</sup>, and Ca<sup>2+</sup>.

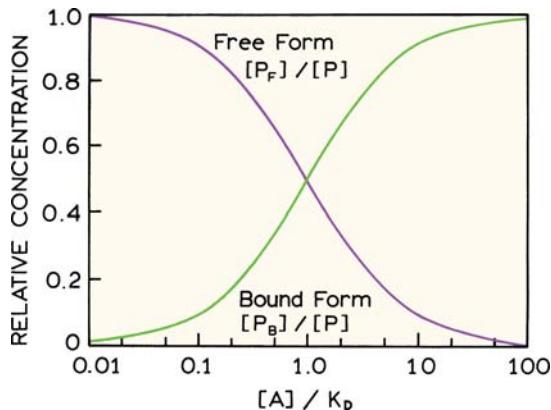


**Figure 19.45.** Relations between analyte concentration ( $[A]$ ), dissociation constant ( $K_D$ ) of the analyte-probe complex, and relative concentrations of the free ( $P_F$ ) and bound ( $P_B$ ) forms of the probe.

$10K_D$  will produce little change in the observed signal. In the use of fluorescence sensing probes, and eqs. 19.6–19.9, we are assuming that the analyte is present in much greater concentration than the probe. Otherwise, the probe itself becomes a buffer for the analyte and distorts the analyte concentration.

**Intensity-Based Sensing:** There are a number of probes that display changes in intensity but do not display spectral shifts. Such probes include the calcium probes Calcium Green<sup>1</sup>, Fluro-3, and Rhod-2. In these cases the analyte concentration can be obtained from

$$[A] = K_D \frac{F - F_{\min}}{F_{\max} - F} \quad (19.10)$$

where  $F_{\min}$  is the fluorescence intensity when indicator is in the free form,  $F_{\max}$  is the intensity when the indicator is totally complexed, and  $F$  is the intensity when indicator is partially complexed by analyte. Changes in the fluorescence intensity are typically due to different quantum yields of the free and complexed forms, rather than differences in the absorption spectrum. The changes in quantum yield have been explained as due to formation of twisted internal charge-transfer (TICT) states or to changes in the extent of PET.

In order to determine the analyte concentration using eq. 19.10, all intensities must be determined with the same instrumental configuration, the same optical path length, and the same probe concentration. These requirements are often hard to satisfy, especially in microscopy when observing cells. Measurement of  $F_{\max}$  and  $F_{\min}$  requires lysing the

cells and titrating the released indicator, or using ionophores to saturate the indicator. These calibration methods do not compensate for dye loss due to photo-bleaching or leakage during the experiment, and can also alter the spatial distribution of the probe. For this reason it is desirable to have methods that are independent of probe concentration. This is possible using wavelength-ratiometric probes or lifetime-based sensing.

**Wavelength-Ratiometric Probes:** Many probes display spectral shifts in their absorption or emission spectra upon binding analytes. In these cases the analyte concentrations can be determined from a ratio of intensities, independent of the overall probe concentration. For excitation-ratiometric probes the analyte concentration can be determined by<sup>143</sup>

$$[A] = K_D \left( \frac{R - R_{\min}}{R_{\max} - R} \right) \left( \frac{S_F(\lambda_2)}{S_B(\lambda_2)} \right) \quad (19.11)$$

where  $R = F(\lambda_1)/F(\lambda_2)$  is the ratio of intensities for the two excitation wavelengths  $\lambda_1$  and  $\lambda_2$ .  $R_{\min}$  and  $R_{\max}$  are the ratios for the free and the complexed probe, respectively. For an excitation wavelength-ratiometric probe the value of  $S_F(\lambda_2)$  and  $S_B(\lambda_2)$  are related to the extinction coefficients and quantum yields of the probe excited at  $\lambda_2$ :

$$\left( \frac{S_F(\lambda_2)}{S_B(\lambda_2)} \right) = \frac{\varepsilon_F \Phi_F}{\varepsilon_B \Phi_B} \quad (19.12)$$

For an emission wavelength-ratiometric probe one can use eq. 19.11 with the values of  $S_F(\lambda_2)$  and  $S_B(\lambda_2)$ . They are related to the relative intensities of the free and bound forms of the probe:

$$\frac{S_F(\lambda_2)}{S_B(\lambda_2)} = \frac{F_F}{F_B} \quad (19.13)$$

Unlike intensity-based measurements, use of wavelength-ratiometric probes and eq. 19.11 makes the measurements independent of probe concentration.

### 19.8.3. Sodium and Potassium Probes

Typical  $\text{Na}^+$  and  $\text{K}^+$  probes are shown in Figure 19.46, and all of these contain azacrown groups or a closely related structure. The first reported probes<sup>141</sup> were sodium-binding benzofuran isophthalate (SBFI) for  $\text{Na}^+$  and potassium-

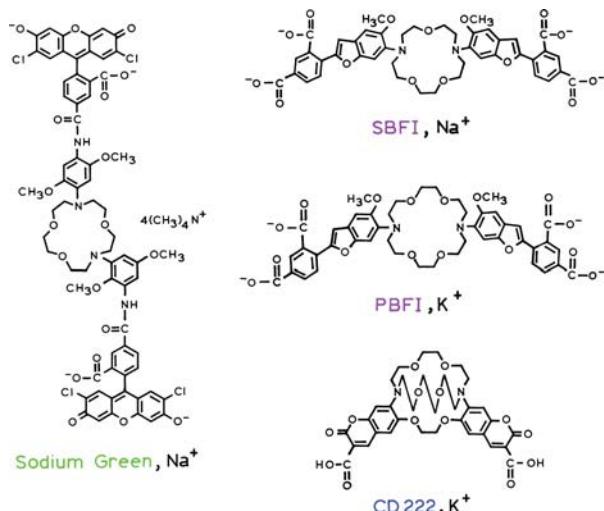
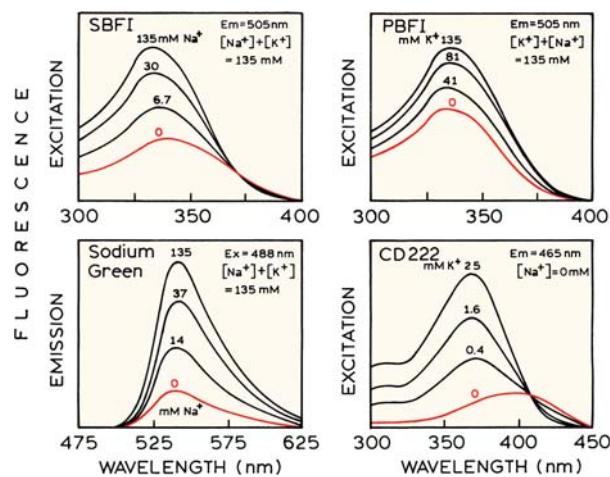
**Table 19.4.** Spectral and Lifetime Properties of Mg<sup>2+</sup>, Na<sup>+</sup>, and K<sup>+</sup> Probes

Probe <sup>b</sup>	Excitation <sup>a</sup> $\lambda_F (\lambda_B)$ [nm]	Emission $\lambda_F (\lambda_B)$ [nm]	$Q_F (Q_B)$	Lifetime (ns) <sup>a</sup> $\tau_F (\tau_B)$	$K_D$ (mM)
<b>Mg<sup>2+</sup> Probes</b>					
Mag-Quin-1	348 (335)	499 (490)	0.0015 (0.009)	0.57 (10.3)	6.7
Mag-Quin-2	353 (337)	487 (493)	0.003 (0.07)	0.84 (8.16)	0.8
Mag-Fura-2	369 (330)	511 (491)	0.24 (0.30)	1.64 (1.72)	1.9
Mag-Fura-5	369 (332)	505 (482)	NA <sup>c</sup>	2.52 (2.39)	2.3
Mag-Indo-1	349 (330)	480 (417)	0.36 (0.59)	1.71 (1.90)	2.7
Mag-Fura-Red	483 (427)	659 (631)	0.012 (0.007)	0.38 (0.35)	2.5
Mg Green	506	532	0.04 (0.42)	0.98 (3.63)	1.0
Mg Orange	550	575	0.13 (0.34)	1.06 (2.15)	3.9
<b>Na<sup>+</sup> Probes</b>					
SBFI	348 (335)	499 (490)	0.045 (0.083)	0.27 (0.47)	3.8
SBFO	354 (343)	515 (500)	0.14 (0.44)	1.45 (2.09)	31.0
Na Green	506	535	7-fold <sup>d</sup>	1.14 (2.38)	6.0
<b>K<sup>+</sup> Probes</b>					
PBFI	336 (338)	557 (507)	0.24 (0.72)	0.47 (0.72)	5.1
CD 222	396 (363)	480 (467)	3.7-fold	0.17 (0.71)	0.9

<sup>a</sup>F and B refer to the free and cation-bound forms of the probes, respectively.<sup>b</sup>Abbreviations: SBFI, sodium-binding benzofuran isophthalate; SBFO, sodium-binding benzofuran oxazole; PBFI, potassium-binding benzofuran isophthalate.<sup>c</sup>NA: not available.<sup>d</sup> $Q_B/Q_F = 7$ .

binding benzofuran isophthalate (PBFI) for K<sup>+</sup> (Table 19.4). While designed to be excitation wavelength-ratiometric probes, these probes suffer several disadvantages. They require UV excitation, which results in substantial

amounts of autofluorescence from cells. The excitation spectra show only minor changes in shape upon binding of Na<sup>+</sup> and K<sup>+</sup> to these probes (Figure 19.47). Apparently, the charge densities of these singly charged cations are not suf-

**Figure 19.46.** Representative Na<sup>+</sup> and K<sup>+</sup> probes. Sodium Green is a trademark of Molecular Probes Inc.**Figure 19.47.** Excitation (SBFI, PBFI and CD 222) and emission (Sodium Green) spectra of Na<sup>+</sup> and K<sup>+</sup> probes in the presence of various concentrations of the ions. Sodium Green is a trademark of Molecular Probes Inc. Data from [144].

ficient to result in substantial spectral shifts. In support of this hypothesis, one notices that PBFI, which binds the larger  $K^+$  ion, shows a smaller spectral shift than that seen for binding for  $Na^+$  and SBFI.

A coumarin-based probe is available for  $K^+$ : CD222. This probe has a more complex chelating group (Figure 19.46) that is directly connected to the coumarin fluorophore.<sup>145–146</sup> This probe can be excited at longer wavelengths than SBFI and PBFI, and displays larger spectral shifts (Figure 19.47). The dissociation constant for  $K^+$  binding to CD222 is near 1 mM (Table 19.4). This probe is useful for measurements of extracellular  $K^+$ , but the binding is too strong for measurements of intracellular  $K^+$  (Table 19.3). The apparent  $K_D$  of CD222 for  $K^+$  is increased in the presence of  $Na^+$ . As a result, CD222 may be useful for measurements of extracellular  $K^+$  in blood in the concentration range 3–6 mM.<sup>147</sup> Several other probes with a coumarin fluorophore and a chelator for  $K^+$  have been described.<sup>148–150</sup> Given the availability of blue and UV LEDs, these probes may soon find use in simple clinical devices.

In an effort to avoid cellular autofluorescence, several  $Na^+$  and  $K^+$  probes have been developed for longer excitation wavelength. One of these probes is Sodium Green<sup>TM</sup>, which is a sodium-specific azacrown conjugated on both nitrogens to a dichlorofluorescein (Figure 19.46). Sodium Green can be excited at 488 nm, and displays increasing intensity in the presence of increasing concentrations of  $Na^+$  (Figure 19.47). Unfortunately, Sodium Green does not display any spectral shifts, so that wavelength-ratiometric measurements are not possible. Furthermore, the analogous probe for potassium has not been reported, so that  $K^+$  probes are limited in number.

The inability to develop wavelength-ratiometric probes for  $Na^+$  and  $K^+$ , particularly with long excitation and emission wavelengths, illustrates an advantage of lifetime-based sensing. Sodium Green was found to display a multi-exponential decay, with lifetimes of 1.1 and 2.4 ns in the absence and presence of  $Na^+$ , respectively.<sup>151</sup> The phase and modulation values (Figure 19.48) are independent of total intensity, allowing the concentration of  $Na^+$  to be determined even if the probe concentration is unknown. Cation-dependent decay times of SBFI and PBFI have been reported. Unfortunately, SBFI, PBFI, and similar probes display only modest changes in lifetime,<sup>152–154</sup> so that these probes do not seem suitable for lifetime-based sensing of  $Na^+$  or  $K^+$ . CD222 does display useful changes in lifetime in response to  $K^+$ , even in the presence of large amounts of  $Na^+$ . In this case, lifetime-based sensing of  $K^+$  using CD222 at the con-

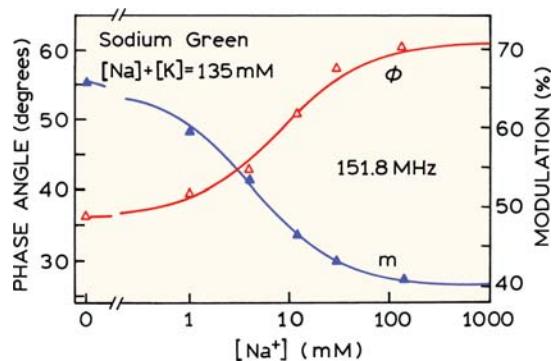


**Figure 19.48.** Sodium-dependent phase ( $\phi$ ) and modulation ( $m$ ) of Sodium Green. Excitation was at 514 nm, and emission was observed above 530 nm. Data from [151].

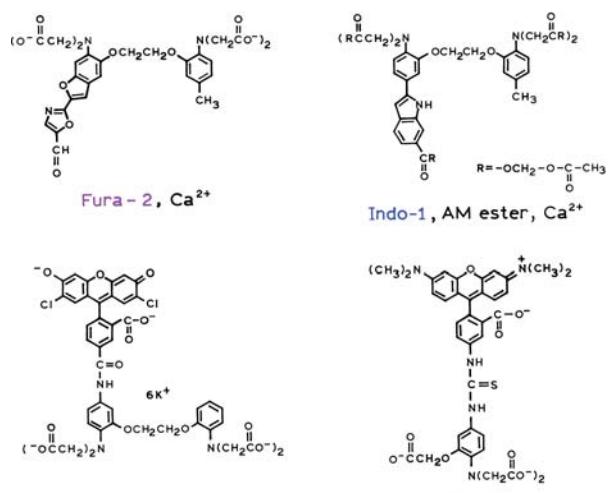


**Figure 19.49.** Representative  $Ca^{2+}$  and  $Mg^{2+}$  probes.

centration present in blood appears to be possible. In contrast, CD222 does not allow wavelength-ratiometric measurements of  $K^+$  in the presence of 100 mM sodium.<sup>147</sup>

#### 19.8.4. Calcium and Magnesium Probes

Calcium probes are perhaps the most widely used intracellular indicators (Figure 19.49). These indicators are based on the BAPTA chelator, which binds  $Ca^{2+}$  with affinities near 100 nM (Table 19.5). These probes are suitable for measurements of intracellular  $Ca^{2+}$ , but bind  $Ca^{2+}$  too tightly for measurement of  $Ca^{2+}$  in blood or serum, which is near 5 mM (Table 19.3). These probes are often used in fluorescence microscopy, where the local probe concentration is

**Table 19.5.** Spectral and Lifetime Properties of  $\text{Ca}^{2+}$  Probes

Probe	Excitation <sup>a</sup> $\lambda_F(\lambda_B)$ [nm]	Emission $\lambda_F(\lambda_B)$ [nm]	$Q_F(Q_B)$	Lifetime (ns) <sup>a</sup> $\tau_F(\tau_B)$	$K_D$ (nM)
Quin-2	356 (336)	500 (503)	0.03 (0.14)	1.35 (11.6)	60.0
Fura-2	362 (335)	518 (510)	0.23 (0.49)	1.09 (1.68)	145.0
Indo-1	349 (331)	482 (398)	0.38 (0.56)	1.40 (1.66)	230.0
Fura Red	472 (436)	657 (637)	Low QY <sup>b</sup>	0.12 (0.11)	140.0
BTC <sup>c</sup>	464 (401)	531	NA <sup>d</sup>	0.71 (1.38)	
Fluo-3	504	526	40-fold	0.04 (1.28)	390
Rhod-2	550	581	100-fold	NA	570
Ca Green	506	534	0.06 (0.75)	0.92 (3.60)	190
Ca Orange	555	576	0.11 (0.33)	1.20 (2.31)	185
Ca Crimson	588	611	0.18 (0.53)	2.55 (4.11)	185
Ca Green-2	505	536	~100-fold <sup>e</sup>	NA	550
Ca Green-5N	506	536	~30-fold	NA	14,000
Ca Orange-5N	549	582	~5-fold	NA	20,000
Oregon Green					
BAPTA-1	494	523	~14-fold	0.73 (4.0)	170
BAPTA-2	494	523	35-fold	NA	580
BAPTA-5N	494	521	NA	NA	20,000

<sup>a</sup>F and B refer to the  $\text{Ca}^{2+}$  free and  $\text{Ca}^{2+}$ -bound forms of the probes, respectively.

<sup>b</sup>Low quantum yield.

<sup>c</sup>BTC, coumarin benzothiazole-based indicator.

<sup>d</sup>NA: not available.

<sup>e</sup>The term x-fold refers to the relative increase in fluorescence upon cation binding.

unknown. The salt forms of these dyes (Figure 19.49) do not diffuse across cell membranes, so that the cells need to be labeled by microinjection or electrophoration. BAPTA-based probes are also available with esterified carboxy groups, the so-called acetoxymethyl esters (AM esters). Figure 19.49 shows the AM ester of Indo-1. In this form the dyes are less polar and passively diffuse across cell membranes. Once inside the cell the AM esters are cleaved by intracellular esterases, and the negatively charged probe is trapped in the cells.

Fura-2 and Indo-1 are both wavelength-ratiometric probes. Fura-2 displays a large shift in its absorption spectrum upon binding  $\text{Ca}^{2+}$ , and is thus used with two excitation wavelengths (Figure 19.50).<sup>155</sup> Indo-1 displays a shift in its emission spectrum upon binding  $\text{Ca}^{2+}$ . Indo-1 can be used with two emission wavelengths, and a single excitation wavelength. Thus Indo-1 is preferred when using laser excitation sources, such as in a laser scanning microscope, where it is difficult to get two different excitation wavelengths.

Like the  $\text{Na}^+$  and  $\text{K}^+$  probes, Fura-2 and Indo-1 absorb in the UV. This is a disadvantage because of cellular auto-

fluorescence and because it is difficult to obtain microscope optics with high-UV transmission. Hence it is desirable to develop calcium probes with longer excitation and emission wavelengths. Coumarin<sup>156</sup> and styryl-based<sup>157</sup> calcium probes have been developed but have not yet been widely used. The excitation spectra of one such probe are shown in Figure 19.51. These probes allow excitation up to 520 nm, but wavelength-ratiometric measurements require a second excitation wavelength below 430 nm.

Calcium probes based on fluoresceins and rhodamines are also available.<sup>158–159</sup> These probes typically have a BAPTA group linked to the fluorophore, rather than being part of the fluorophore. We refer to such probes as conjugate probes. One example is Calcium Green-1<sup>J</sup> (Figure 19.49), which shows an approximately eight-fold increase in fluorescence upon binding calcium (Figure 19.50). Calcium Green-1<sup>J</sup> is just one member of a series of conjugate probes for  $\text{Ca}^{2+}$  that display a range of emission wavelengths. Because Calcium Green-1 does not display a spectral shift it cannot be used for wavelength-ratiometric measurements. However, the lifetimes of the Calcium Green<sup>J</sup> series all increase on  $\text{Ca}^{2+}$  binding, allowing the calcium

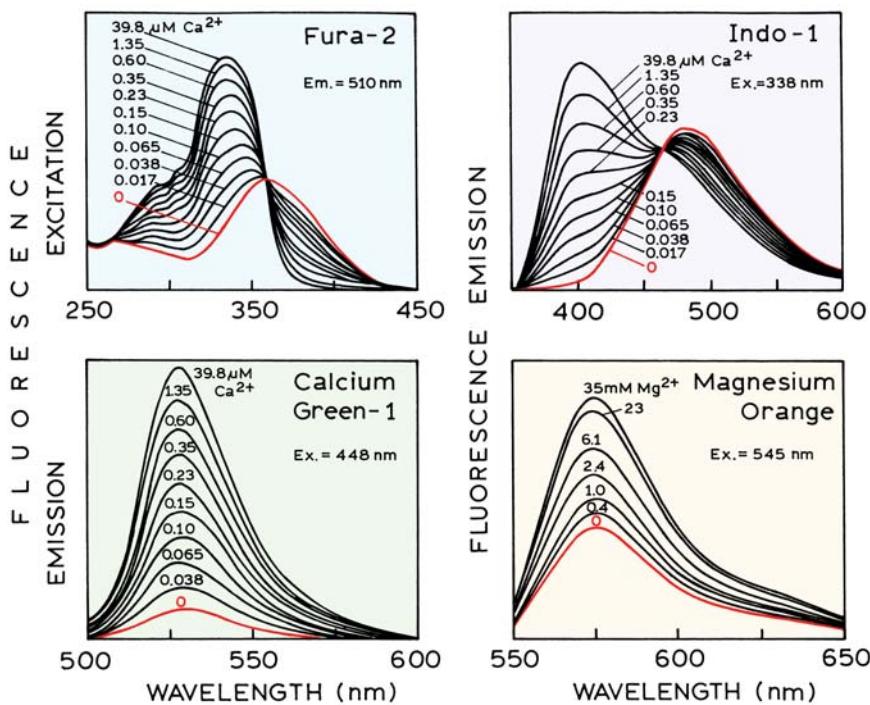


**Figure 19.50.** Excitation (Fura-2) and emission spectra (Indo-1, Calcium Green-1 and Magnesium Orange) of  $\text{Ca}^{2+}$  and  $\text{Mg}^{2+}$  probes in the presence of various concentrations of the ion. Revised from [142] and [144].

concentration to be determined from the lifetimes.<sup>160–161</sup> One of the first calcium probes, Quin-2, displays a tenfold increase in lifetime when bound to calcium.<sup>162–163</sup> However, Quin-2 requires UV excitation and displays a low quantum

yield, so that it is now used less frequently. Recently,  $\text{Ca}^{2+}$  probes based on squaraines have been reported, allowing excitation wavelengths as long as 635 nm.<sup>164–165</sup>

While the use of the calcium probes seems straightforward, calibration is difficult when such probes are located within cells.<sup>166–170</sup> When used as intracellular indicators, the calcium probes are typically calibrated in the presence of other intracellular ions at their expected concentrations.<sup>171</sup> It is difficult to maintain nanomolar  $\text{Ca}^{2+}$  concentrations in the calibration solutions, and the probes themselves can alter the overall  $\text{Ca}^{2+}$  concentration. For this reason, calcium buffers have been developed and are commercially available. And, finally, the probe may interact with intracellular macromolecules, or by phototransformation during illumination in the microscope, resulting in altered behavior compared to the calibration data.<sup>166,172</sup>

Calcium probes have also been developed using azacrown ethers as the chelator rather than BAPTA.<sup>173–177</sup> However, these probes have been mostly studied in organic solvents and used to study the effects of  $\text{Ca}^{2+}$  on electron transfer. Magnesium-sensitive probes are available (Table 19.4),<sup>176–184</sup> and some have been characterized as lifetime probes.<sup>184</sup> These probes typically have the APTRA chelator, rather than BAPTA, as can be seen for the calcium probe

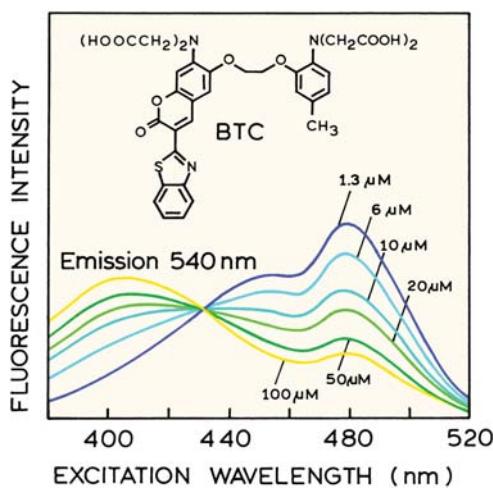


**Figure 19.51.** Excitation spectra of the coumarin benzothiazole-based indicator (BTC) lithium salt in  $\text{Ca}^{2+}$  solutions with concentrations ranging from 1.3 to 100  $\mu\text{M}$   $\text{CaCl}_2$ . Revised from [156].

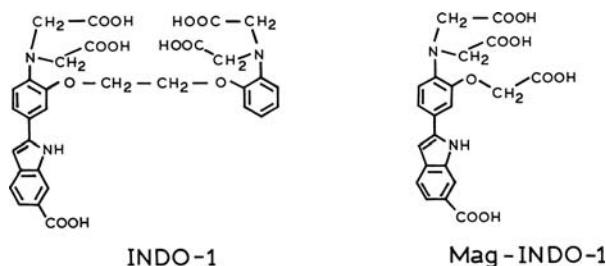


**Figure 19.52.** Chemical structures of the calcium probe of Indo-1 and the magnesium probe Mag-Indo-1. Data from [181].

Indo-1, and the analogous magnesium probe Mag-Indo-1 (Figure 19.52).

#### 19.8.5. Probes for Intracellular Zinc

In recent years there has been increased interest in zinc. It is well known that zinc if bound to a number of enzymes and plays a structural role in zinc finger proteins. At present there is interest in the possible rate of zinc in plaque formation in Alzheimer's disease, post-ischemic toxicity, and as a neurotransmitter.<sup>185</sup> A number of zinc-sensitive fluorophores are now available.<sup>186–189</sup> Most of these probes contain the chelating group shown for Zinpyr-1 (Figure 19.53). These probes show increases in fluorescence in the presence of zinc, which is probably due to a decrease in the amount of PET quenching in the zinc-bound form. The dissociation constants of these probes are near 1 to 3 nM. The

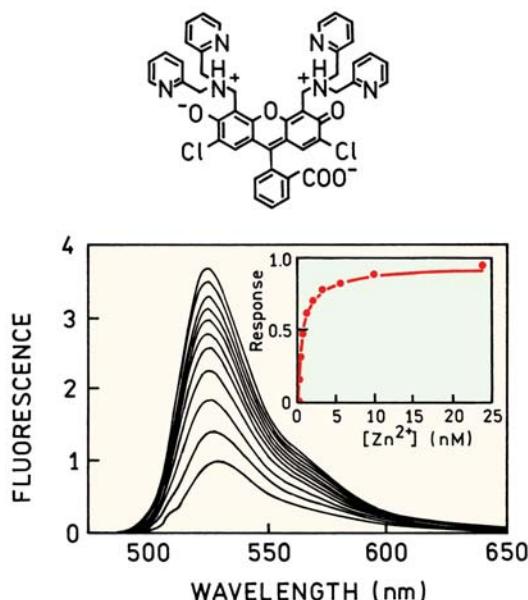


**Figure 19.53.** Chemical structure and emission spectra of Zinpyr-1. Reprinted with permission from [186]. Copyright © 2000, American Chemical Society.

levels of free zinc in cells may be in the picomolar range, so that zinc probes with higher affinity are needed.<sup>190–191</sup>

#### 19.9. GLUCOSE-SENSITIVE FLUOROPHORES

The principles of analyte recognition have been used to develop fluorophores that are sensitive to glucose. There is

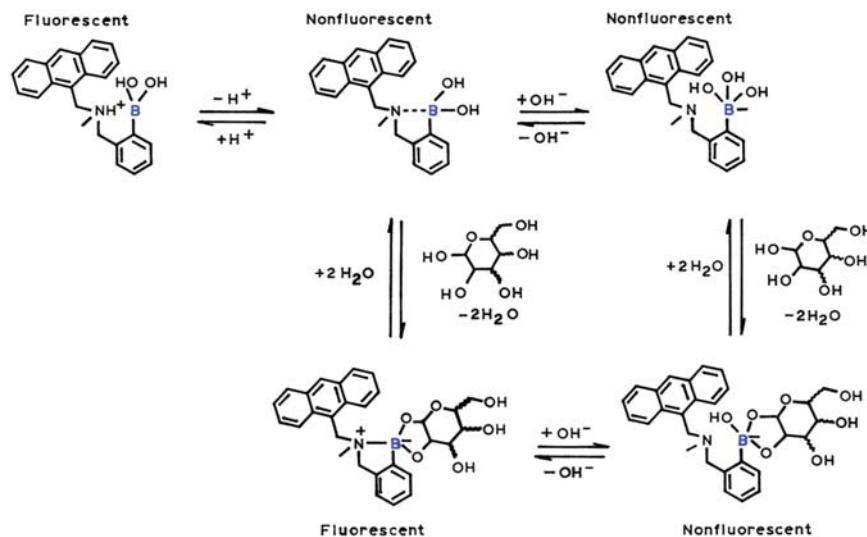


**Figure 19.54.** Glucose sensor based on photoinduced electron transfer. Revised from [194].

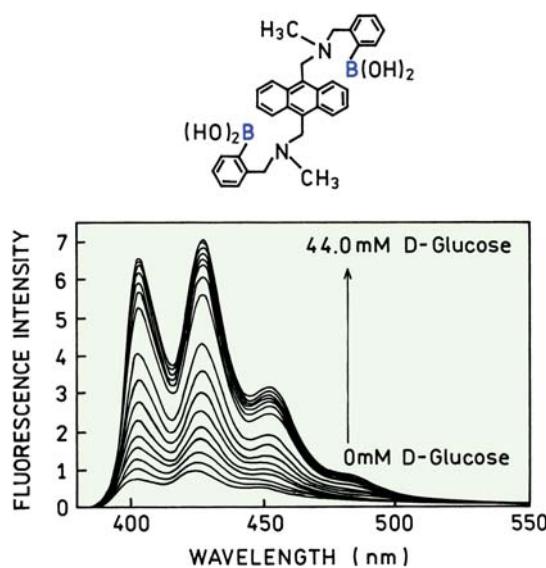


**Figure 19.55.** Glucose-dependent emission spectra of the shown structure. From [196].

vast literature on this topic,<sup>192–193</sup> from which we have selected several examples. These probes use boronic acid as part of the fluorophore. Boron forms complexes with diols, which has been used for decades for oxidation of sugars. Complexation of sugars to boron-containing fluorophores can result in changes in the emission intensity.<sup>194–195</sup> For the probe shown in Figure 19.54 complexation of sugars to the boron influences the extent of photoinduced electron transfer from the amino group. Depending on pH and sugar concentration, the anthracene group is either fluorescent or nonfluorescent. Figure 19.55 shows emission spectra of a similar probe. Addition of glucose results in an eight-fold increase in intensity.

A disadvantage of the probe shown in Figure 19.55 is that it is not wavelength ratiometric. Wavelength-ratiometric probes for glucose are now known.<sup>197–200</sup> One example is shown in Figure 19.56. This probe does not display PET quenching. Instead, complexation with glucose affects the extent of charge transfer from the amino group to the boronic acid. Upon binding of sugar there is more electron density on the boron, which decreases the extent of charge transfer and results in a blue shift in the emission spectra. Fructose usually gives the largest spectral change with such probes because it is the most reducing sugar. A difficulty with boronic acid fluorophores (BAFs) is to obtain a sugar-dependent spectral change at physiological pH. Many BAFs show sugar-dependent spectral changes only at pH 8 or higher. Several BAFs are now known that are sensitive at pH 7.5.<sup>201–202</sup>

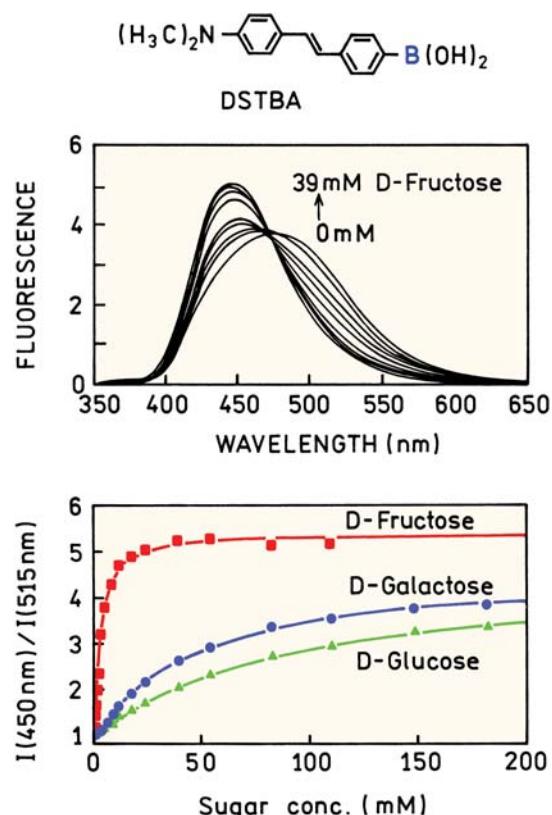
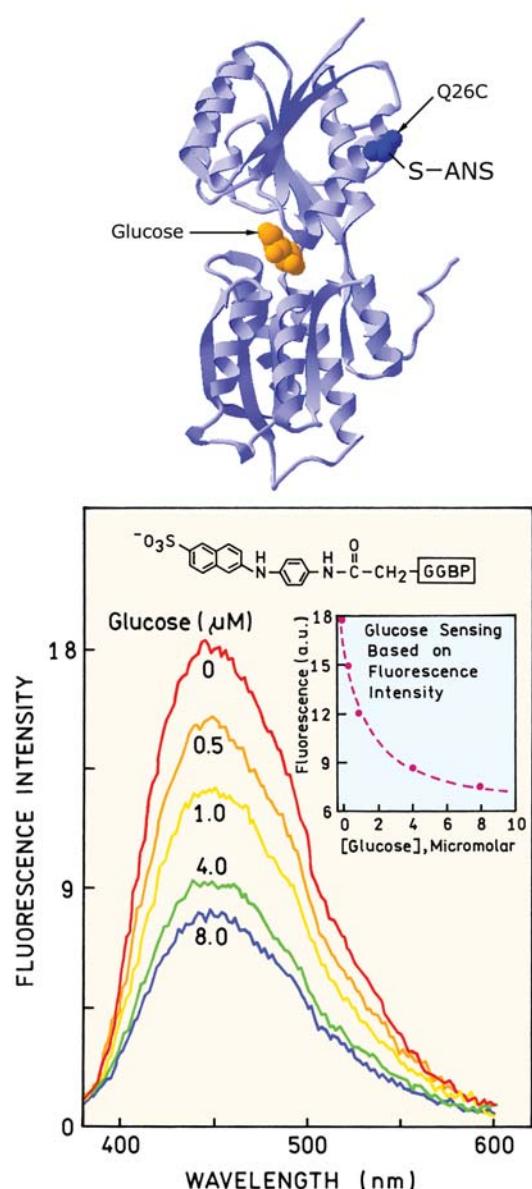


**Figure 19.56.** Emission spectra and wavelength ratios of the saccharide-sensitive probe DSTBA. Reprinted with permission from [200]. Copyright © 2001, American Chemical Society.

## 19.10. PROTEIN SENSORS

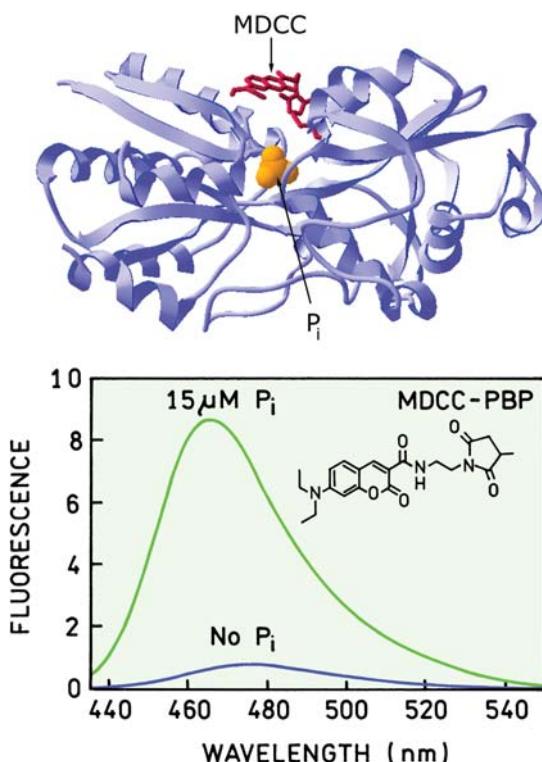
Another approach to sensing is to use proteins that bind the analyte of interest.<sup>203–209</sup> The usual approach is to express the recombinant protein with a single-cysteine residue for labeling. The probe is usually selected to be sensitive to solvent polarity, and the cysteine residue is positioned close to the binding site. Binding of the analyte to the protein may result in a change in the environment around the probe and a change in its fluorescence intensity. Protein sensors have been made for glucose,<sup>210–212</sup> maltose,<sup>213–214</sup> and other analytes.<sup>215–218</sup> Protein sensors are frequently based on the periplasmic protein from *E. coli*. These proteins provide the chemotactic signals needed by the bacterium to move toward nutrients. These signaling proteins have two domains.<sup>219</sup> The binding site is located between the domains that usually move closer together upon ligand binding.

Figure 19.57 shows an example of an engineered protein for glucose sensing. This protein sensor is based on the



**Figure 19.57.** Protein sensor for glucose based on the glucose–galactose binding protein from *E. coli*. From [212].

glucose-galactose binding protein (GGBP) from *E. coli*. The wild-type protein contains no cysteine residues. GGBP was mutated by insertion of a single-cysteine residue at position 26, which was labeled with a sulfhydryl-reactive analogue of ANS. Upon addition of glucose the ANS intensity decreases about twofold. This decrease probably occurs because glucose binding brings the two domains closer together. The ANS is distant from the glucose-binding site and probably becomes more exposed to water when the domains move closer together.



**Figure 19.58.** Emission spectra (bottom) of a coumarin-labeled phosphate binding protein from *E. coli* (top) in the absence and presence of 15  $\mu\text{M}$  phosphate. Revised and reprinted with permission from [214]. Copyright © 1998, American Chemical Society.

A different periplasmic protein from *E. coli* was used to make a protein sensor for phosphate.<sup>214–215</sup> In one of these sensors a cysteine residue was inserted at residue 197 and labeled with a coumarin derivative (Figure 19.58). In this case binding of the phosphate ligand resulted in a dramatic increase in fluorescence intensity that is probably the result of shielding the fluorophore from water.

### 19.10.1. Protein Sensors Based on RET

The large intensity change displayed by the phosphate sensor (Figure 19.58) is exceptional. Most protein sensors display smaller changes of 1.5- to 2-fold, comparable to that shown for the glucose sensor in Figure 19.57. The scientific literature does not contain many reports of experiments which did not work, but it is likely that many laboratories attempted to make protein sensors using the periplasmic proteins and RET. It was logical to speculate that the changing distance between the domains would result in a change in RET between donors and acceptors positioned on opposite domains. Few such reports have appeared, probably

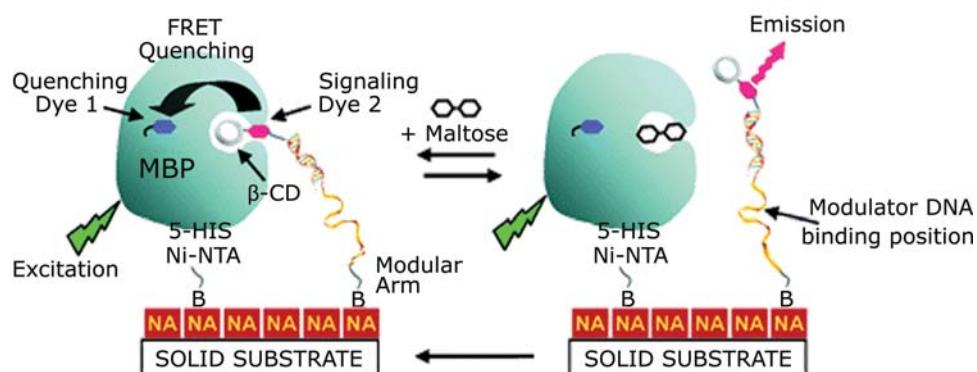


**Figure 19.59.** Schematic of a surface-bound maltose sensor based on the maltose-binding protein from *E. coli* and RET. Reprinted with permission from [220]. Copyright © 2004, American Chemical Society.

because the changes in distance have not been large enough to result in large changes in the transfer efficiency.

This problem of a limited change in intensity was solved by the use of RET between surface-bound reagents (Figure 19.59). This example also illustrates the increasingly sophisticated chemistry of sensors. This maltose sensor is based on the maltose-binding protein (MBP) from *E. coli*. The protein is bound to a NeutrAvidin surface by a biotinylated linker. MBP is labeled with a nonfluorescent acceptor

QSY7. The donor is Cy3.5, which is also bound to the surface by a specialized linker (Figure 19.60). This linker contains a cyclodextrin that binds to MBP as well as the Cy3.5 donor. These components are bound to the surface by a biotinylated DNA linker arm that contains regions of single- and double-stranded DNA. The single-stranded region is present to allow changes in rigidity of the DNA by binding of a complementary sequence called modulator DNA. When both MBP and the linker are bound to the surface the

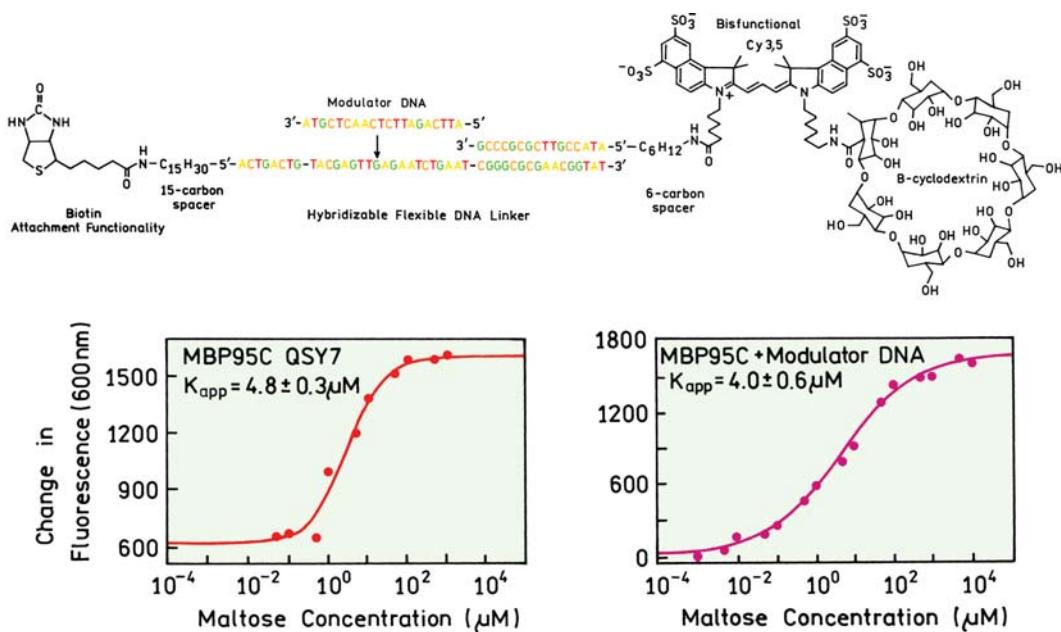


**Figure 19.60.** Linker arm containing the Cy3.5 donor and the cyclodextrin ligand. The fluorophore is bound to the surface via a biotinylated DNA oligomer with a single stranded region for binding of modulator DNA. The lower panels show the change in donor intensity of the sensor (Figure 19.58) in response to maltose. Revised and reprinted with permission from [220]. Copyright © 2004, American Chemical Society.

donor is quenched because the cyclodextrin binds to the protein that brings the Cy3.5 in close proximity to the QSY7 acceptor. Since QSY7 is nonfluorescent it is also called a quencher. Addition of maltose displaces cyclodextrin from MBP, resulting in an increased donor intensity (Figure 19.59). The extent of binding and, more importantly, the extent of RET could be increased by binding of the modulator DNA. These results describe a general strategy for surface-bound sensors that are adjustable and yield large changes in intensity. This approach is likely to be used in sensors for a wide variety of analytes.

### 19.11. GFP SENSORS

In Chapter 3 we described the ability of GFP to undergo internal reactions to create its own chromophore. This chromophore is contained within a  $\beta$ -barrel structure and is usually not sensitive to the surrounding solution conditions. GFP, its mutants, and the red coral proteins can be expressed in a wide variety of cells and organisms.<sup>221</sup> Hence, it would be useful if these proteins could be engineered to become sensitive to desired analytes. This has been accomplished in several ways, including the use of RET and modification of the protein structure so that the chromophore becomes sensitive to the analyte.

#### 19.11.1. GFP Sensors Using RET

Since RET is a through-space phenomenon it can be used to modify the spectral properties of the GFP chromophore. GFP sensors based on RET have been developed for several analytes, such as calcium,<sup>222–225</sup> protein phosphorylation,<sup>225–226</sup> histone methylation,<sup>227</sup> and others.<sup>228–230</sup> The basic idea for these sensors is to make linked donor–acceptor GFP pairs where the conformation of the linker changes in response to the analyte.

Figure 13.22 in Chapter 13 shows a GFP-RET sensor for protein phosphorylation.<sup>225</sup> Cyan fluorescent protein (CFP) and yellow fluorescent protein (YFP) are used as the donor–acceptor pair. CFP and YFP are linked by a peptide that is a substrate for protein kinase. The linker also contains a phosphorylation recognition domain that binds the phosphorylated peptide. Binding of the phosphopeptide to the recognition domain is expected to bring the GFPs closer together, resulting in an increase in energy transfer. The lower panel shows fluorescence ratio images of CHO cells that express the sensor. When the cells are treated with insulin the donor intensity at 480 nm decreases relative to

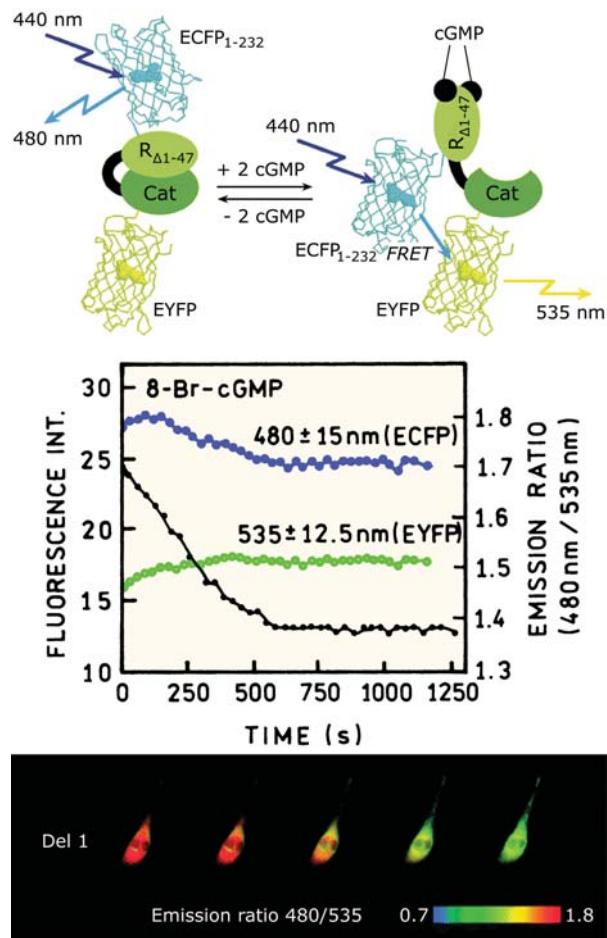


**Figure 19.61.** GFP-RET sensor for cGMP. Top: Schematic of sensor. Middle: Spectral response of sensor. Bottom: Ratio images of CHO cells expressing the GFP sensor. Revised and reprinted with permission from [230]. Copyright © 2000, American Chemical Society.

the acceptor emission at 535 nm. This result shows that cells can be grown and express protein sensors designed to detect a specific analyte or enzymatic activity.

Another example of a GFP-RET sensor is shown in Figure 19.61. The donor is enhanced cyan fluorescent protein (ECFP) and the acceptor enhanced yellow fluorescent protein (EYFP). The donor and acceptor are linked by the catalytic and regulating domains of cGMP-dependent protein kinase (PK). The PK was modified by removal of residues 1 to 47 ( $\Delta 1-47$ ), which are responsible for dimerization of this PK, insuring that the sensor is a monomer within the cell. This sensor was expressed in CHO cells. The cells were treated with 8-Br-cGMP, which is a phosphodiesterase-resistant analogue of cGMP. This treatment results in a decrease in donor emission at 480 nm and a

slight increase in acceptor emission at 535 nm (middle panel). The ratio of donor-to-acceptor emission of the intracellular protein shows that the extent of RET increases in response to 8-Br-cGMP. Apparently, binding of cGMP or 8-Br-cGMP brings the donor and acceptor closer together.

### 19.11.2. Intrinsic GFP Sensors

In the previous two examples RET was used as the transducer mechanism. RET was used because the chromophore in GFP is usually shielded from the solvent. RET was also used to obtain a wavelength-ratiometric sensor that is needed to provide a quantitative interpretation of intracellular fluorescence. Mutant GFPs have been identified that are sensitive to chloride (Section 8.14.3) and pH. These proteins typically do not display shifts in their emission spectra<sup>231–234</sup> and cannot be used as emission-ratiometric probes. Some of the pH-sensitive GFP mutants display changes in absorption with pH, but excitation-ratiometric probes are less convenient than emission-ratiometric probes in fluorescence microscopy.

An emission wavelength-ratiometric pH-sensitive GFP is now available.<sup>235</sup> The absorption spectrum is sensitive to pH; more importantly, the emission spectra are also sensitive to pH (Figure 19.62). This sensitivity is not due to RET, but to ionization of a tyrosine side chain. As might be expected the longer-wavelength absorption and emission occurs at higher pH where the tyrosine is ionized. This protein can be used for estimation of intracellular pH. Figure 19.63 shows images of fibroblasts transfected with the gene for this GFP. The transfected cells show emission from the blue emission near 460 nm (top panel) and the green emission near 515 nm (middle panel). These two emissions are seen to be co-localized from the overlay with the light image (lower panel).

In summary, it is now possible to grow cells, and probably organisms, that express GFPs with sensitivity to a wide variety of ions and biomolecules.

## 19.12. NEW APPROACHES TO SENSING

### 19.12.1. Pebble Sensors and Lipobeads

A wide variety of fluorophores are available for sensing cations and anions. These fluorophores are frequently used for measurement of intracellular ion concentration. However, these fluorophores can bind to intracellular biomolecules, which can alter the calibration curves by changing the binding constants or causing shifts in the absorption or

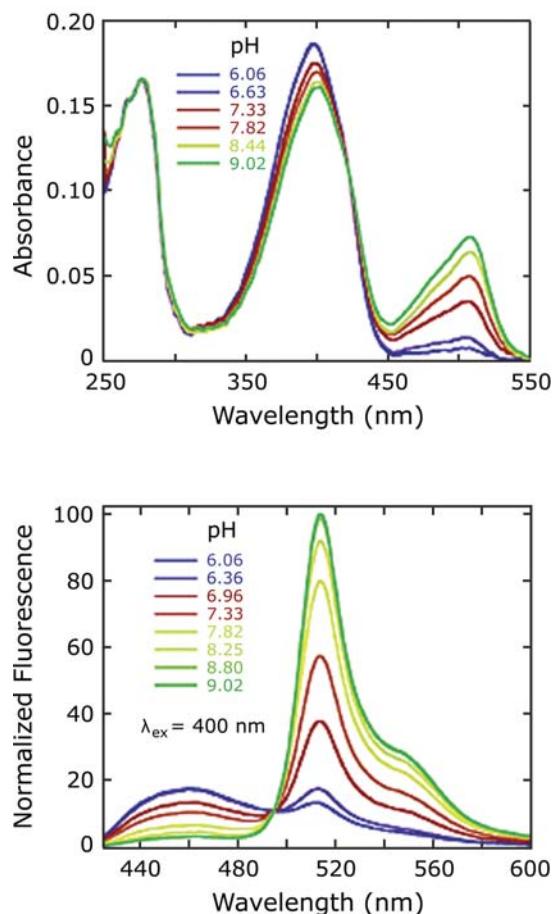


**Figure 19.62.** Absorption and emission spectra of a pH-sensitive GFP. Reprinted with permission from [235]. Copyright © 2000, American Chemical Society.

emission spectra. The so-called Pebble sensors were developed to avoid interference due to binding of the probes to biomolecules.

Pebble sensors consist of one or more fluorophores embedded in polymer beads, typically made from polyacrylamide. The polymer is highly crosslinked and formed in the presence of the desired fluorophores, which are then trapped within the beads.<sup>236–240</sup> The high degree of crosslinking prevents proteins from entering the beads, so that the calibration curve is the same inside and outside the cells.

Pebble sensors have been developed for several analytes. Since the sensors are intended for intracellular use with fluorescence microscopy it is important to have ratiometric data. Figure 19.64 shows a Pebble sensor for pH. The beads were dense polymers made with 27% acrylamide and 3% N,N-methylene-bis(acrylamide). The pH indicator

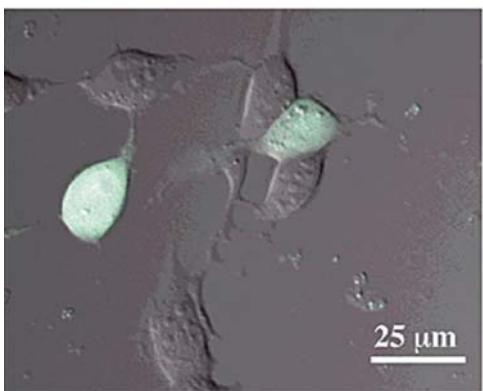
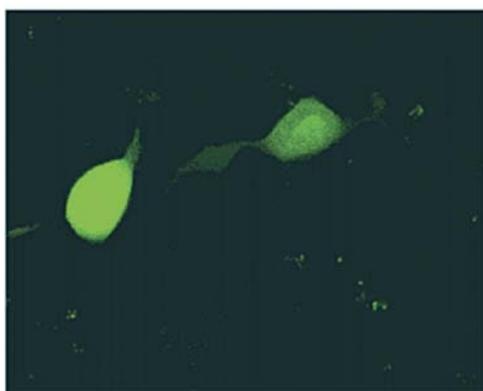
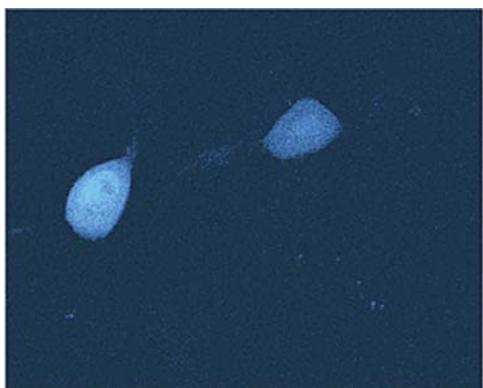


**Figure 19.63.** Fluorescence and light images of fibroblast cells which transiently express a pH-sensitive GFP. Top: Image at 435–485 nm. Middle: Image at 490–685 nm. Bottom: Overlay of the fluorescence images onto a light image. Reprinted with permission from [235]. Copyright © 2000, American Chemical Society.

was fluorescein, which is not practical for wavelength-ratiometric measurements. Wavelength-ratiometric measurements were made possible by inclusion of sulforhodamine, which is not sensitive to pH. Ratios of the intensi-

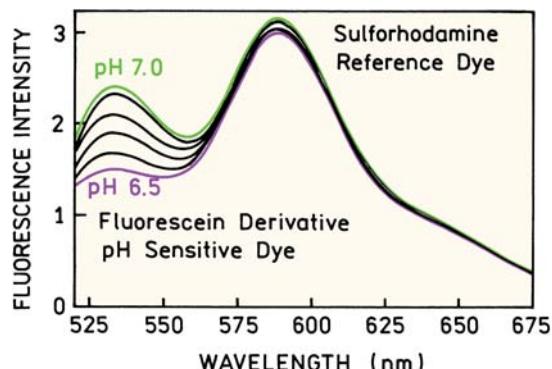


**Figure 19.64.** Emission spectra of a Pebble sensor, a polyacrylamide bead containing fluorescein as a pH-sensitive dye, and sulforhodamine as a pH-insensitive reference dye. Reprinted with permission from [238]. Copyright © 1999, American Chemical Society.

ties at 530 and 590 nm can be used to determine the pH without interference from biomolecules.

The intracellular use of Pebble sensors is shown in Figure 19.65. In this case the Pebbles were made by encapsulating Calcium Green and sulforhodamine in polyacrylamide beads.<sup>239</sup> Sulforhodamine served as a calcium-insensitive reference fluorophore. The laser scanning confocal images of human SY5Y neuroblastoma cells are shown in Figure 19.65. Images were recorded using filters that transmitted the emission of sulforhodamine (right) or calcium green (left). The cells were treated with m-dinitrobenzene, which caused the release of calcium from the mitochondria, which resulted in an increase in the emission from Calcium Green but no change in the emission from sulforhodamine.

Sensors using polymer beads have also been made by coating the outer surface of polystyrene particles.<sup>241–245</sup> This has been accomplished by covalent attachment of probes to the outer surface. Bead sensors have also been made by coating polystyrene beads with lipids which bind the sensing fluorophores. These particles are called Lipobeads.

### 19.13. IN-VIVO IMAGING

In-vivo imaging is an emerging futuristic application of fluorescence technology. By in-vivo imaging we mean the creation of three-dimensional fluorescence images of the internal structures of humans or small animals. In-vivo imaging can be traced to the suggestion by Chance and coworkers that images could be obtained from the diffusive migration of photons in scattering tissues.<sup>246–248</sup> Tissues are strongly absorbing and strongly scattering at wavelengths below 600 nm (Figure 19.66). Tissue absorption and scattering is much

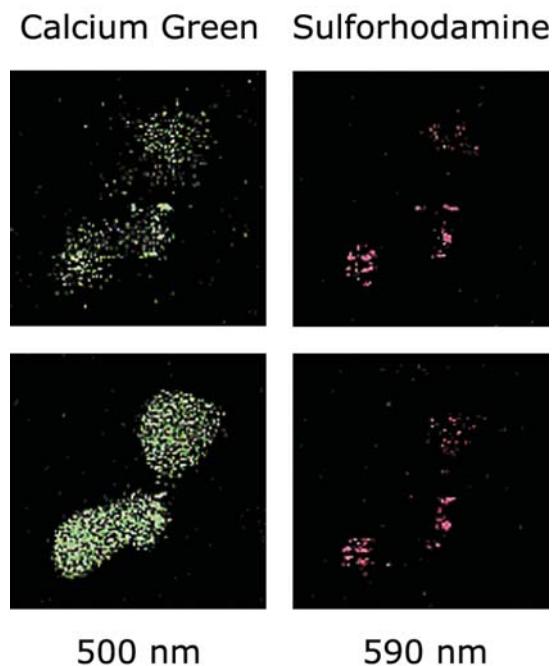


**Figure 19.65.** Laser scanning confocal microscopy images of human SYSY neuroblastoma C6 glioma cells containing Pebble sensors for calcium. The sensors contained Calcium Green and sulforhodamine as a reference dye. Images were recorded before (top) and after (bottom) treatment with m-dinitrobenzene. Revised and reprinted with permission from [239]. Copyright © 1999, American Chemical Society.

weaker above 650 nm, where tissues become somewhat translucent. This can be seen from the red light at 670 nm upon transillumination of a mouse.<sup>249</sup> When long-wavelength light passes through tissues the light migrates in a diffusive manner, similar to molecules in the gas phase. The photons move in a straight line until they are scattered, which results in a change in direction. The extent of scattering is described by a scattering coefficient  $\mu_s$  that is expressed in units of reciprocal distance. Light passing through the tissue can also be absorbed, which is expressed as the absorption coefficient  $\mu_a$ . Different tissues and different regions of tissues have different values of  $\mu_s$  and  $\mu_a$ , which affect the rate and distance over which photons can migrate in the tissue. The concept of photon migration imaging (PMI) is to measure spatially dependent transport of photons in tissues and to use the information to construct an image of the internal structure of the tissue.<sup>246–248</sup> This problem is much more difficult than x-ray computerized tomography because essentially none of the photons pass through the tissue without undergoing numerous scattering events.

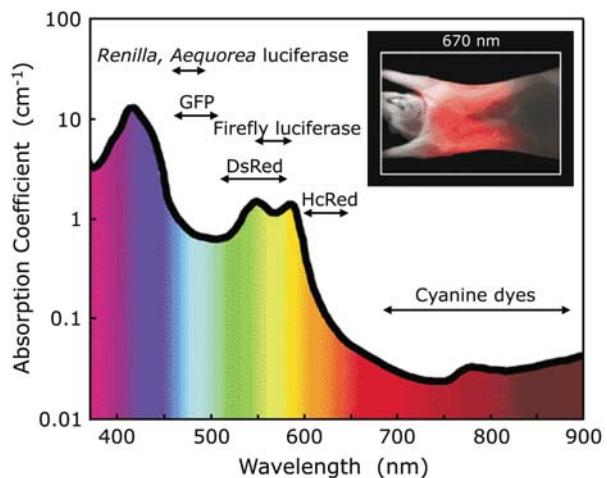


**Figure 19.66.** Absorption coefficient of typical tissue. The insert shows the transillumination of a mouse at 670 nm. Revised from [249].

One difficulty in PMI is the limited contrast in  $\mu_s$  and  $\mu_a$  between different regions of tissues. As a result there are attempts to increase the contrast by using injected dyes such as indocyanine green.<sup>250–251</sup> The instrumentation and algorithms developed for PMI are directly applicable to fluorescence in-vivo imaging. Figure 19.67 shows a relatively straightforward approach to in-vivo imaging. The mouse contained a tumor that overexpresses receptors for the peptide hormone somatostatin. The mouse was injected with an analogue to somatostatin labeled with a tricarbocyanine dye. The mouse was illuminated at 740 nm and imaged from the same side with a CCD camera. The location of the tumor is clearly seen from its long-wavelength emission. This tumor visualization was possible because of the weak light absorption of tissues and the absence of significant tissue autofluorescence at these long wavelengths.

Fluorescence is also being used for three-dimensional imaging of tissues.<sup>254–255</sup> This is accomplished by measuring the intensities or lifetimes with the light source and detector placed at a large number of locations around the animal<sup>256–258</sup> (Figure 19.68). Sophisticated algorithms are used to reconstruct the image from the data. An important development for in-vivo imaging is the fluorogenic probes for specific enzymes or tumors.<sup>259–261</sup> The image in Figure 19.68 was obtained with a peptide–polymer conjugate that was heavily labeled with Cy5.5. The fluorescence of the closely spaced Cy5.5 molecules was self-quenched due to the degree of labeling. The sequence of the peptide provided a cleavage site for a cathepsin. These enzymes degrade

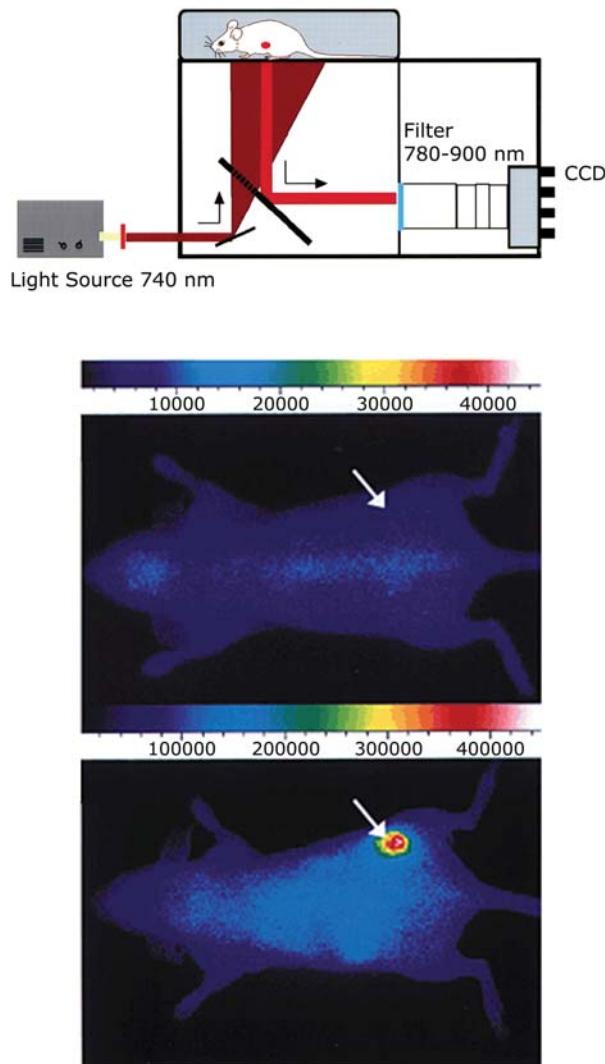


**Figure 19.67.** Fluorescence imaging of a labeled somatostatin analogue in a mouse tumor. The images were taken before (middle) and after (bottom) injection with the labeled peptide. The upper panel shows a schematic of the instrument. Revised from [252–253].

the extracellular matrix, and are often present at elevated levels in cancerous tissues and for other disease states.<sup>262–264</sup> The mouse in Figure 19.68 had a gliosarcoma surgically implanted in the brain.

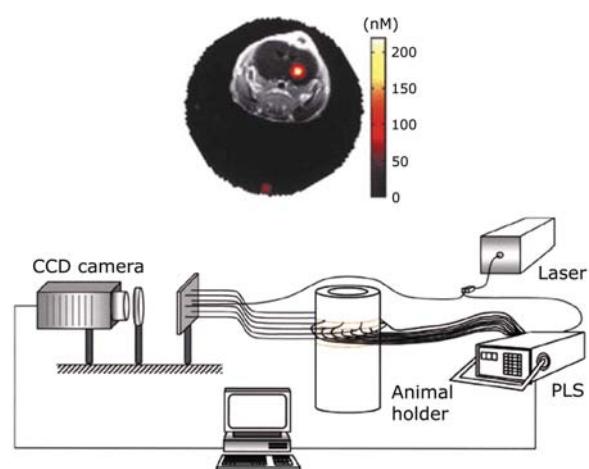


**Figure 19.68.** Schematic of an instrument for three-dimensional small animal imaging. PLS, programmable light switch. The image shows a sagittal section of a combined MRI and fluorescence image of a mouse injected with a cathepsin B-sensitive molecular beacon. From [258].

The labeled peptide was cleaved by a cathepsin in the tumor, resulting in increased intensity from Cy5.5 (color spot in Figure 19.68). The spot was superimposed on the MRI image of the same mouse. It is unlikely that in-vivo fluorescence imaging will provide the high spatial resolution available with MRI or CT. However, one can imagine a wide variety of labeled molecules that will localize in desired locations and be sensitive to specific enzymes. Fluorescence in-vivo imaging can add functional or physiological information to the images obtained using other modalities.

#### 19.14. IMMUNOASSAYS

Immunoassays constitute a large and diverse family of assays that are based on many of the principles described in this book. The basic idea is to couple the association of antibody (Ab) with antigen (Ag) to some other event that yields an observable spectral change. Various mechanisms are possible, including energy transfer, anisotropy, delayed lan-

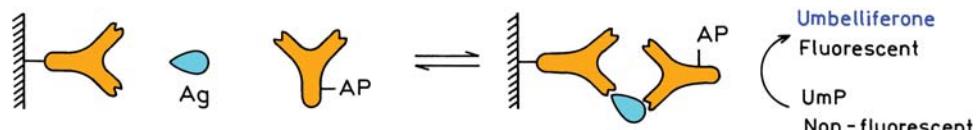


**Figure 19.69.** Schematic of an enzyme-linked immunosorbent assay (ELISA). AP is alkaline phosphatase. Ag is an antigen, and UmP is umbelliferyl phosphate.

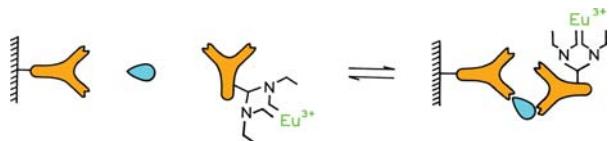


**Figure 19.70.** Time-resolved immunoassay based on the long-lived emission of europium.

thanide emission, or the use of enzymes to amplify the signal from a limited number of antigens.<sup>265–270</sup> The use of antibodies as analytical tools can be traced to the development of radioimmunoassays by Benson and Yalow,<sup>271</sup> which resulted in a Nobel prize. Since then immunoassays have been widely used, but are now based mainly on fluorescence detection.

#### 19.14.1. Enzyme-Linked Immunosorbent Assays (ELISA)

The ELISA method is perhaps the most commonly used immunoassay format owing to its high sensitivity, applicability to a wide range of antigens, and the ability to remove background by washing steps. This method relies on the specific interaction between antigen and antibody. A surface is coated with an antibody specific for the antigen of interest. The sample is incubated with the surface-bound antibody, to allow the antibody to capture the antigen (Figure 19.69). The sample is then exposed to a second antibody that is covalently bound to an enzyme, typically alkaline phosphatase (AP), horseradish peroxidase, or  $\beta$ -galactosidase. Hence, the antigen must have more than a single antigenic site, and the second antibody must be different from the first antibody. Following adequate time for binding, the surface is washed to remove unbound enzyme-labeled antibody and the enzyme substrate is added. In the case shown in Figure 19.69 the enzyme alkaline phosphatase cleaves nonfluorescent umbelliferyl phosphate (UmP), yielding to the highly fluorescent umbelliferone. A signal is observed only when the antigen is present.

ELISA assays exist in a number of formats. In some cases the reaction product absorbs light, and in other cases the product is strongly fluorescent. The second antibody is not always labeled with enzyme but can be detected with yet another antibody that contains the bound enzyme. This procedure eliminates the need to attach probe or enzyme to a specific antibody that may be in short supply.

#### 19.14.2. Time-Resolved Immunoassays

A variant of the ELISA method is the so-called "time-resolved immunoassay."<sup>272–277</sup> This type of assay also uses a polymeric support containing the capture antibody. The second labeled antibody has a covalently bound chelating group that contains a lanthanide such as europium (Figure 19.70). Detection is accomplished by addition of a so-called enhancer solution, which chelates the Eu<sup>3+</sup> and has the necessary chromophore for excitation of the lanthanide by energy transfer (Figure 19.71). The enhancer solution is needed because the lanthanides absorb light very weakly, and are rarely excited directly. With the enhancer solution light is absorbed by chelators, which then transfer the excitation to the lanthanide. The chelating group is typically an EDTA derivative that strongly binds the Eu<sup>3+</sup>. The Eu<sup>3+</sup> can be released from the chelator at low pH. The "time-resolved immunoassays" can be performed by direct detection or in a competitive format. Direct detection is usually used for proteins which contain multiple antigenic sites.

These assays are called "time-resolved" because the sample is excited with a pulse of light, and the detector is

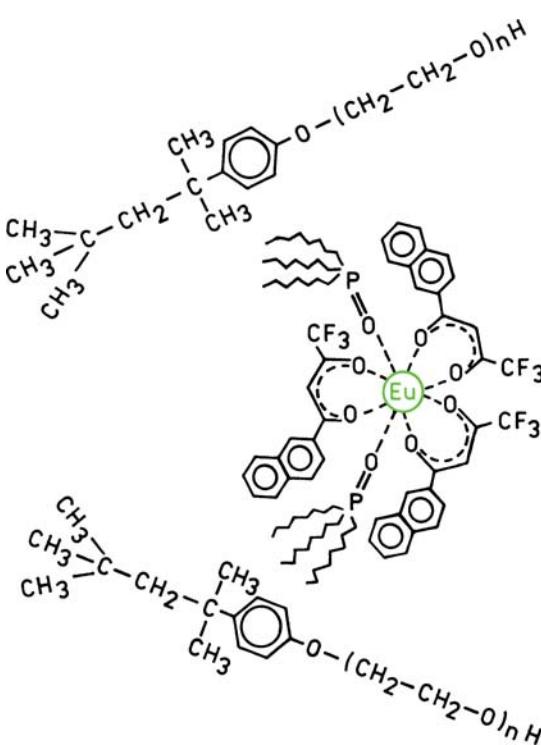


**Figure 19.71.** Europium in a fluorescent state following addition of enhancer solution. Structures from [274]. Copyright © 1990, CRC Press.

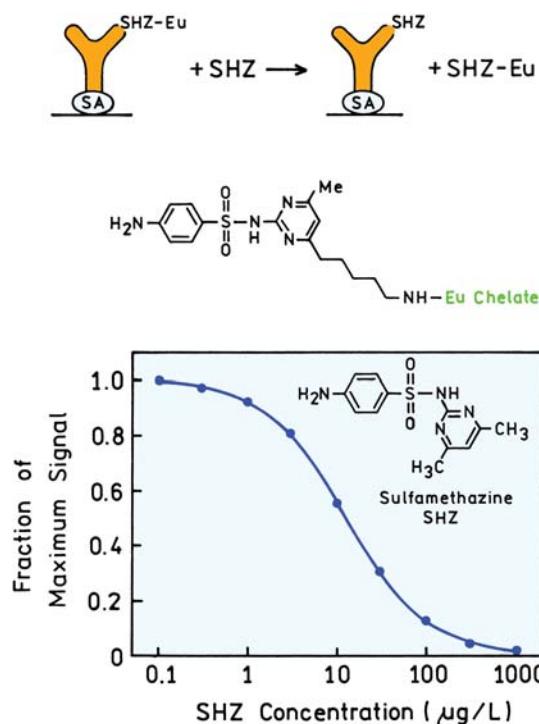


**Figure 19.72.** Competitive time-resolved immunoassay for sulfamethazine (SMZ). Reprinted with permission from [280]. Copyright © 2004, American Chemical Society.

gated on following decay of the prompt autofluorescence. Because the lanthanides display millisecond lifetimes, they continue to emit long after the ns interferences have decayed. The signal is integrated for a period of time, and the assay is based on measurement of integrated intensity, not a decay time. Hence, the phrase "time-resolved" should not be confused with a lifetime measurement.

Time-resolved immunoassays continue to be developed for a variety of analytes.<sup>277–281</sup> One example is a competitive immunoassay for the sulfa antibiotic sulfamethazine (SHZ) in food. The presence of residual antibiotics in food is of concern because of the potential health risk to humans and the development of antibiotic resistance in bacteria. This immunoassay is based on antibodies against SHZ. These antibodies are bound to streptavidin-coated microwell plates (Figure 19.72). These antibodies bind an analogue of SHZ that contains a covalently bound europium chelate (SHZ-Eu). This analogue is allowed to bind to the antibodies. The assay is performed by adding the sample to the well, allowing time for binding, washing the plate, then adding the enhanced solution and measuring the time-delayed emission. The intensity decreases as the SHZ increases because SHZ displays SHZ-Eu, and the SHZ-Eu

is washed out of the well prior to addition of the enhanced solution.

#### 19.14.3. Energy-Transfer Immunoassays

Resonance energy transfer provides an obvious approach to measuring antigen–antibody association, and was suggested for immunoassays in 1976.<sup>282</sup> Such an assay would typically be performed in a competitive format, and can be homogeneous (Figure 19.73). Suppose the analyte is the triazine herbicide simazine (SZ), which is shown as the open shape in Figure 19.73. An antibody against SZ is labeled with the donor Cy5 and bound to the bottom of the well.<sup>283</sup> The acceptor Cy5.5 is bound to BSA, which also contains a covalently bound analogue of SZ. The assay is then per-

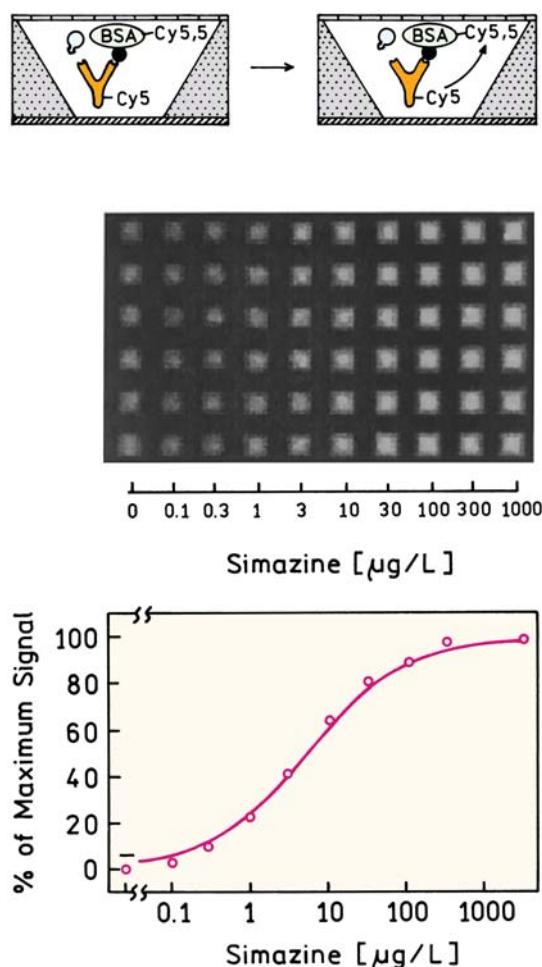


**Figure 19.73.** Competitive RET immunoassay for the herbicide simazine. Revised and reprinted with permission from [283]. Copyright © 2001, American Chemical Society.

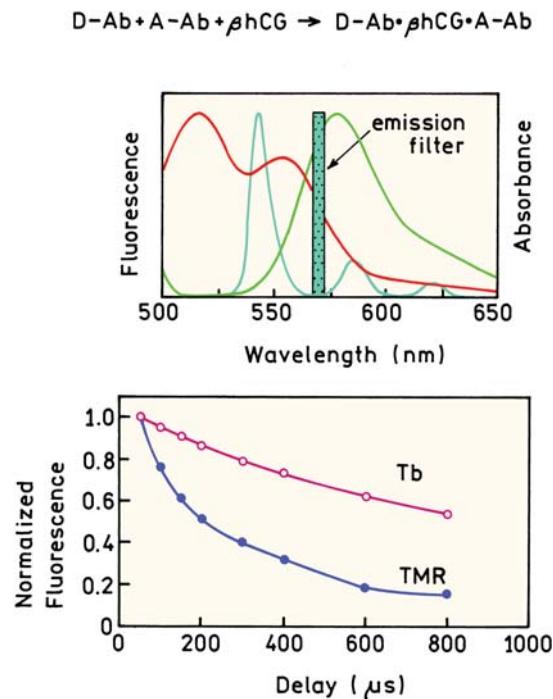


**Figure 19.74.** Time-resolved RET immunoassay for  $\beta\text{hCG}$ . The lower panel shows the intensity decay of the Tb donor and the TMR acceptor in a solution containing the complex shown in the top right. Revised from [289].

formed by adding the sample that contains SZ. As SZ increases the intensity of the surface-bound Cy5 donor increases, because the Cy5.5-BSA is displaced by SZ. This RET assay was facilitated by the large  $R_0$  for the Cy5-Cy5.5 donor-acceptor pair,<sup>284</sup> which is near 75 Å. However, there is overlap in the emission spectra of Cy5 and Cy5.5. This overlap could be tolerated in this case because the unbound acceptor was washed away. Some background from Cy5.5 is acceptable because the Cy5 emission could be measured on the blue side of its emission spectrum. It is usually easier to separately measure the donor emission because the short-wavelength sides of emission spectra often drop sharply to zero, but there are almost always tails at long wavelengths. Energy-transfer immunoassays have been described for other analytes,<sup>285–288</sup> but it can be difficult to obtain adequate energy transfer due to the size of the proteins.

The difficulties of overlapping emission spectra of the donors and acceptors can be minimized to some extent using lanthanide donors and measurement of the sensitized acceptor emission. Figure 19.74 shows an immunoassay for the  $\beta$  subunit of human chorionic gonadotropin ( $\beta\text{hCG}$ ).

Two antibodies were used and directed against different epitopes of  $\beta\text{hCG}$ .<sup>289</sup> One of the antibodies was labeled with a terbium chelate as the donor, and the second antibody was labeled with TMR as the acceptor. Binding of these two antibodies to  $\beta\text{hCG}$  resulted in long-lived sensitized emission of the acceptor, which could be observed selectively using a 570-nm emission filter. This wavelength is near the peak of the rhodamine emission but is between peaks of the structured terbium emission.

The lower panel shows time-resolved decays of the Tb and TMR in a mixture containing the immune complex. The decay of the Tb is slower than that of TMR because of the presence of Tb-labeled antibodies that are free in solution or not near an acceptor. The intensity decay of TMR is more rapid because the long-lived acceptor emission is due to RET, so that the acceptor decay is the same as the decay of the Tb bound near the acceptor. The use of sensitized acceptor emission made it unnecessary to wash away excess reagents, so that the assay could be performed in a homogeneous format.

#### 19.14.4. Fluorescence Polarization Immunoassays

The final type of immunoassay is the fluorescence polarization immunoassay (FPI). Assays of this type are based on anisotropy measurements of labeled antigens.<sup>290–291</sup> The use of the term "polarization" instead of anisotropy is historical, and now entrenched in the literature. The anisotropy of a mixture ( $r$ ) is determined by the anisotropies of the free (F) and bound (B) species ( $r_F$  and  $r_B$ ) and their relative fluorescence intensities ( $f_F$  and  $f_B$ ):

$$r = r_F f_F + r_B f_B \quad (19.14)$$

An FPI is a competitive assay that can be performed in a homogeneous format. Suppose that the antigen is the hormone cortisol (Cor).<sup>292</sup> The assay mixture would contain labeled cortisol, in this case labeled with fluorescein (Fl), and antibody specific for cortisol (Figure 19.75). Prior to addition of cortisol from the sample, the anisotropy will be

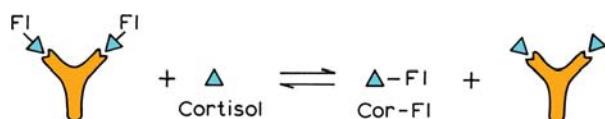


**Figure 19.75.** Homogeneous fluorescence polarization immunoassay for cortisol (Cor). Fl, fluorescein.

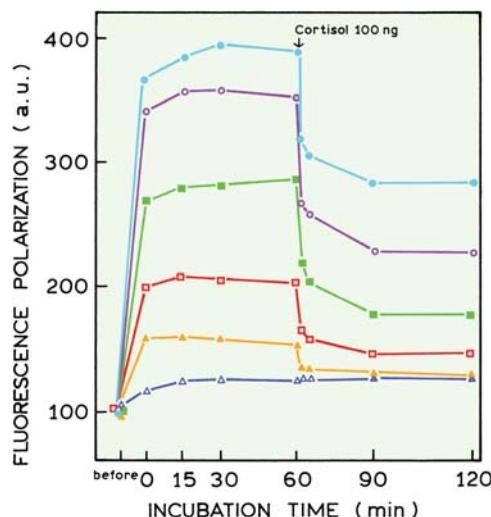


**Figure 19.76.** Time-dependent changes in polarization upon mixing of antibody to cortisol or nonspecific antibody ( $\Delta$ ) and fluorescein-labeled cortisol and upon addition, at 60 minutes, of 100 ng of unlabeled cortisol. The antibody is more dilute from top to bottom. Revised from [292].

the highest due to binding of antibody to Cor-Fl. Free cortisol from the sample will displace Cor-Fl from the antibody. The Co4Fl is now free to rotate, and the anisotropy decreases.

Typical data for a cortisol FPI are shown in Figures 19.76 and 19.77. Cor-Fl was prepared by reaction of cortisol-21-amine with fluorescein isothiocyanate (FITC). Upon mixing anti-Cor antibody (Ab) to cortisol with Cor-Fl the polarization increased, which was presumed due to specific

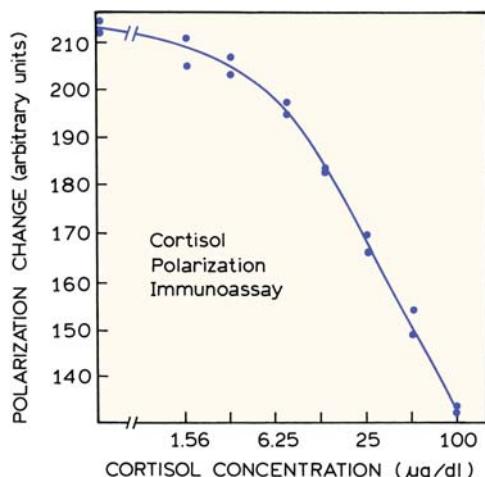


**Figure 19.77.** Cortisol fluorescence polarization immunoassay. Revised from [292].

binding of Ab to Cor-Fl. The specificity of the reaction was confirmed by adding unlabeled cortisol, which resulted in a decrease in polarization, and also by the absence of a change in polarization due to nonspecific antibody ( $\Delta$ ).

To perform the cortisol assay one uses a mixture of Ab and Cor-Fl, to which is added the serum sample. As the concentration of serum cortisol is increased, the polarization decreases (Figure 19.77). The polarization values are used to determine the cortisol concentration. Similar FPIs have been developed for a wide range of low-molecular-weight analytes, including antibiotics,<sup>293–294</sup> cocaine metabolites,<sup>295–296</sup> therapeutic drugs,<sup>297–298</sup> the immunosuppressant cyclosporin,<sup>299–300</sup> and phosphorylated proteins.<sup>301–303</sup> Numerous FPIs are routinely performed on automatic clinical analyzers.<sup>304</sup>

FPIs have advantages and disadvantages. FPIs do not require multiple antigenic sites, as is needed with heterogeneous capture immunoassays or RET immunoassays. FPIs can be performed in a homogeneous format, and may not require separation steps. However, because FPIs are usually performed with fluorescein, they are generally limited to low-molecular-weight analytes. This is because the emission must be depolarized in the unbound state, which would not occur for higher-molecular-weight fluorescein-labeled proteins.

The limitation of FPIs to low-molecular-weight analyte is illustrated by the FPI for creatine kinase-BB. Creatine kinase is a dimer, and the subunits can be from muscle (M) or brain (B). Creatine kinase MB is used as a marker for cardiac damage, and the presence of CK-BB in the blood may reflect a number of disease states, including brain trauma.<sup>305–307</sup> Figure 19.78 shows an FPI for CK-BB.<sup>307</sup> In this particular case the protein was labeled with dansylaziridine (DANZA), instead of fluorescein. The immunoassay was also performed with other probes (Table 19.6). One notices

**Table 19.6.** Fluorescein Polarization Immunoassay of Creatine Kinase BB<sup>a</sup>

Fluorophore-CK	$\tau$ (ns)	Polarization	
		No antibody	With antibody
CPM-CK <sup>b</sup>	~5	0.337	0.342
IAF-CK	~5	0.333	0.339
DNS-CK	~15	0.181	0.224
DANZA-CK	~15	0.170	0.242

<sup>a</sup>From [307].

<sup>b</sup>CPM, 3-(4-maleimidylphenyl)-7-diethylamino-4-methyl coumarin; IAF, 5'-iodo-acetamido-fluorescein; DNS, dansyl chloride; DANZA, dansylaziridine.

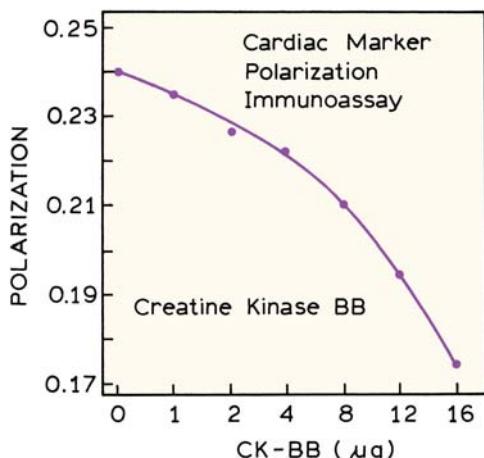


**Figure 19.78.** Fluorescence polarization immunoassay of creatine kinase BB. Revised from [307].

that the polarization changes are smaller with the other probes. This is because the lifetimes of these probes, the fluorescein derivative IAF, and coumarin derivative CPM are near 5 ns, while the lifetime of DANZA is near 15 ns. The longer lifetime of the dansyl-labeled protein (DNS or DANZA) allows more time for the protein to undergo rotational diffusion. This limitation of FPIs to low-molecular-weight substances can be overcome by the use of long-lifetime metal ligand probes, which is described in the following chapter.

## REFERENCES

- Wolfbeis OS. 2004. Fiber-optic chemical sensors and biosensors. *Anal Chem* **76**:3269–3284.
- Cammann K. 2003. Sensors and analytical chemistry. *Phys Chem Chem Phys* **5**:5159–5168.
- Rich RL, Myszka DG. 2002. Survey of the year 2001 commercial optical biosensor literature. *J Mol Recognit* **15**:352–376.
- de Silva AP, Fox DB, Moody TS, Weir SM. 2001. The development of molecular fluorescent switches. *Trends Biotechnol* **19**(1):29–34.
- Badugu R. 2005. Fluorescence sensor design for transition metal ions: the role of the PIET interaction efficiency. *J Fluoresc* **15**(1): 71–83.
- Geddes CD, Lakowicz JR, eds. 2005. *Topics in fluorescence spectroscopy*, Vol. 9: Advanced concepts in fluorescence sensing: macromolecular sensing. Springer-Verlag, New York. In press.
- Geddes CD, Lakowicz JR, eds. 2005. *Topics in fluorescence spectroscopy*, Vol. 10: Advanced concepts in fluorescence sensing: small molecule sensing. Springer-Verlag, New York. In press.
- Lakowicz JR, ed. 1994. *Topics in fluorescence spectroscopy*, Vol. 4: Probe design and chemical sensing. Plenum Press, New York.
- Underfriend S. 1969. *Fluorescence assay in biology and medicine*, Vol 2. Academic Press, New York. (See also Vol. 1. 1962.)
- Kricka LJ, Skogerboe KJ, Hage DA, Schoeff L, Wang J, Sokol LJ, Chan DW, Ward KM, Davis KA. 1997. Clinical chemistry. *Anal Chem* **69**:165R–229R.
- Burtis CA, Ashwood ER. 1999. *Tietz textbook of clinical chemistry*. W.B. Saunders, Philadelphia.
- Wolfbeis OS. 1991. Biomedical applications of fiber optic chemical sensors. In *Fiber optic chemical sensors and biosensors*, Vol. 2, pp. 267–300. Ed OS Wolfbeis. CRC Press, Boca Raton, FL.
- Szmacinski H, Lakowicz JR. 1994. Lifetime-based sensing. In *Topics in fluorescence spectroscopy*, Vol. 4: Probe design and chemical sensing, pp. 295–334. Ed JR Lakowicz. Plenum Press, New York.
- Kieslinger D, Draxler S, Trznadel K, Lippitsch ME. 1997. Lifetime-based capillary waveguide sensor instrumentation. *Sens Actuators B* **38–39**:300–304.
- Lippitsch ME, Draxler S, Kieslinger D. 1997. Luminescence lifetime-based sensing: new materials, new devices. *Sens Actuators B* **38–39**:96–102.
- Draxler S. 2005. Lifetime based sensors/sensing. In *Topics in fluorescence spectroscopy*, Vol. 10: Advanced concepts in fluorescence sensing: small molecule sensing, pp. 241–274. Ed CD Geddes, JR Lakowicz. Springer-Verlag, New York.
- Richards-Kortum R, Sevick-Muraca E. 1996. Quantitative optical spectroscopy for tissue diagnosis. *Annu Rev Phys Chem* **47**:555–606.
- Gouin JF, Baros F, Birot D, Andre JC. 1997. A fibre-optic oxygen sensor for oceanography. *Sens Actuators B* **38–39**:401–406.
- Valeur B. 1994. Principles of fluorescent probe design for ion recognition. In *Topics in fluorescence spectroscopy*, Vol. 4: Probe design and chemical sensing, pp. 21–48. Ed JR Lakowicz. Plenum Press, New York.
- Rettig W, Lapouyade R. 1994. Fluorescence probes based on twisted intramolecular charge transfer (TICT) states and other adiabatic photoreactions. In *Topics in fluorescence spectroscopy*, Vol. 4: Probe design and chemical sensing, pp. 109–149. Ed JR Lakowicz. Plenum Press, New York.
- Czarnik AW. 1994. Fluorescent chemosensors for cations, anions, and neutral analytes. In *Topics in fluorescence spectroscopy*, Vol. 4: Probe design and chemical sensing, pp. 49–70. Ed JR Lakowicz. Plenum Press, New York.
- Fabbrizzi L, Poggi A. 1995. Sensors and switches from supramolecular chemistry. *Chem Soc Rev* **24**:197–202.
- Bryan AJ, Prasanna de Silva A, de Silva SA, Dayasiri Rupasinghe AD, Samankumara Sandanayake KRA. 1989. Photo-induced electron transfer as a general design logic for fluorescent molecular sensors for cations. *Biosensors* **4**:169–179.
- Demas JN, DeGraff BA. 1994. Design and applications of highly luminescent transition metal complexes. In *Topics in fluorescence spectroscopy*, Vol. 4: Probe design and chemical sensing, pp. 71–107. Ed JR Lakowicz. Plenum Press, New York.
- Klimant I, Belser P, Wolfbeis OS. 1994. Novel metal-organic ruthenium (II) diimine complexes for use as longwave excitable luminescent oxygen probes. *Talanta* **41**(6):985–991.
- Demas JN, DeGraff BA, Coleman PB. 1999. Oxygen sensors based on luminescence quenching. *Anal Chem News Feat* 793A–800A.
- Bacon JR, Demas JN. 1987. Determination of oxygen concentrations by luminescence quenching of a polymer immobilized transition metal complex. *Anal Chem* **59**:2780–2785.

28. Wolfbeis OS. 1991. Oxygen sensors. In *Fiber optic chemical sensors and biosensors*, Vol. II, pp. 19–53. Ed OS Wolfbeis. CRC Press, Boca Raton, FL.
29. Mills A, Williams FC. 1997. Chemical influences on the luminescence of ruthenium diimine complexes and its response to oxygen. *Thin Solid Films* **306**:163–170.
30. Lippitsch ME, Pusterhofer J, Leiner MJP, Wolfbeis OS. 1988. Fibre-optic oxygen sensor with the fluorescence decay time as the information carrier. *Anal Chim Acta* **205**:1–6.
31. Draxler S, Lippitsch ME, Klimant I, Kraus H, Wolfbeis OS. 1995. Effects of polymer matrices on the time-resolved luminescence of a ruthenium complex quenched by oxygen. *J Phys Chem* **99**:3162–3167.
32. Simon JA, Curry SL, Schmehl RH, Schatz TR, Piotrowiak P, Jin X, Thummel RP. 1997. Intramolecular electronic energy transfer in ruthenium(II) diimine donor/pyrene acceptor complexes linked by a single C–C bond. *J Am Chem Soc* **119**:11012–11022.
33. Lakowicz JR, Johnson ML, Lederer WJ, Szmacinski H, Nowaczyk K, Malak H, Berndt KW. 1992. Fluorescence lifetime sensing generates cellular images. *Laser Focus World* **28**(5):60–80.
34. Xu W, Kneas KA, Demas JN, DeGraff BA. 1996. Oxygen sensors based on luminescence quenching of metal complexes: osmium complexes suitable for laser diode excitation. *Anal Chem* **68**:2605–2609.
35. Bambot SB, Rao G, Romauld M, Carter GM, Sipior J, Terpetschnig E, Lakowicz JR. 1995. Sensing oxygen through skin using a red diode laser and fluorescence lifetimes. *Biosens Bioelectron* **10**(6/7):643–652.
36. Papkovsky DB, Ponomarev GV, Trettnak W, O'Leary P. 1995. Phosphorescent complexes of porphyrin ketones: optical properties and applications to oxygen sensing. *Anal Chem* **67**:4112–4117.
37. Lu X, Han BH, Winnik MA. 2003. Characterizing the quenching process for phosphorescent dyes in poly[((n-butylamino)thionyl)-phosphazene] films. *J Phys Chem B* **107**:13349–13356.
38. Trettnak W, Kolle C, Reininger F, Dolezal C, O'Leary P. 1996. Miniaturized luminescence lifetime-based oxygen sensor instrumentation utilizing a phase modulation technique. *Sens Actuators B* **35**:36:506–512.
39. Kostov Y, Van Houten KA, Harms P, Pilato RS, Rao G. 2000. Unique oxygen analyzer combining a dual emission probe and a low-cost solid-state ratiometric fluorometer. *Appl Spectrosc* **54**(6):864–868.
40. Lakowicz JR, Szmacinski H, Nowaczyk K, Johnson ML. 1992. Fluorescence lifetime imaging of free and protein-bound NADH. *Proc Natl Acad Sci USA* **89**:1271–1275.
41. Lakowicz JR, Szmacinski H, Nowaczyk K, Berndt K, Johnson ML. 1992. Fluorescence lifetime imaging. *Anal Biochem* **202**:316–330.
42. Zhong W, Urayama P, Mycek MA. 2003. Imaging fluorescence lifetime modulation of a ruthenium-based dye in living cells: the potential for oxygen sensing. *J Phys D App. Phys* **36**:1689–1695.
43. Boas G. 2003. FLIM system measures long-lived, oxygen-sensitive probes. *Biophotonics Int*, September, pp. 59–60.
44. Geddes C. 2001. Optical halide sensing using fluorescence quenching: theory, simulations and applications—a review. *Meas Sci Technol* **12**:R53–R88.
45. Geddes CD. 2001. Halide sensing using the SPQ molecule. *Sens Actuators B* **72**:188–195.
46. Illsley NP, Verkman AS. 1987. Membrane chloride transport measured using a chloride-sensitive fluorescent probe. *Biochemistry* **26**:1215–1219.
47. Verkman AS. 1990. Development and biological applications of chloride-sensitive fluorescent indicators. *Am J Physiol* **253**:C375–C388.
48. Verkman AS, Sellers MC, Chao AC, Leung T, Ketcham R. 1989. Synthesis and characterization of improved chloride-sensitive fluorescent indicators for biological applications. *Anal Biochem* **178**:355–361.
49. Biwersi J, Tulk B, Verkman AS. 1994. Long-wavelength chloride-sensitive fluorescent indicators. *Anal Biochem* **219**:139–143.
50. Orosz DE, Carlid KD. 1992. A sensitive new fluorescence assay for measuring proton transport across liposomal membranes. *Anal Biochem* **210**:7–15.
51. Chao AC, Dix JA, Sellers MC, Verkman AS. 1989. Fluorescence measurement of chloride transport in monolayer cultured cells: mechanisms of chloride transport in fibroblasts. *Biophys J* **56**:1071–1081.
52. Sonawane ND, Thiagarajah JR, Verkman AS. 2002. Chloride concentration in endosomes measured using a ratioable fluorescent Cl<sup>-</sup> indicator. *J Biol Chem* **277**(7):5506–5513.
53. Jayaraman S, Biwersi J, Verkman AS. 1999. Synthesis and characterization of dual-wavelength Cl<sup>-</sup> sensitive fluorescent indicators for ration imaging. *Am J Physiol* **276**:C747–C751.
54. Kaneko H, Putzier I, Frings S, Kaupp UB, Gensch T. 2004. Chloride accumulation in mammalian olfactory sensory neurons. *J Neurosci* **24**(36):7931–7938.
55. Wolfbeis OS, Sharma A. 1988. Fibre-optic fluorosensor for sulphur dioxide. *Anal Chim Acta* **208**:53–58.
56. Sharma A, Draxler S, Lippitsch ME. 1992. Time-resolved spectroscopy of the fluorescence quenching of a donor–acceptor pair by halothane. *Appl Phys* **B54**:309–312.
57. Omann GM, Lakowicz JR. 1982. Interactions of chlorinated hydrocarbons insecticides with membranes. *Biochem Biophys Acta* **684**:83–95.
58. Vanderkooi JM, Wright WW, Erecinska M. 1994. Nitric oxide diffusion coefficients in solutions, proteins and membranes determined by phosphorescence. *Biochim Biophys Acta* **1207**:249–254.
59. Denicola A, Souza JM, Radi R, Lissi E. 1996. Nitric oxide diffusion in membranes determined by fluorescence quenching. *Arch Biochem Biophys* **328**(1):208–212.
60. Franz KJ, Singh N, Lippard SJ. 2000. Metal-based NO sensing by selective ligand dissociation. *Angew Chem, Int Ed* **39**(12):2120–2122.
61. Kojima H, Nagano T. 2000. Fluorescent indicators for nitric oxide. *Adv Mater* **12**(10):763–765.
62. Kojima H, Hirotani M, Urano Y, Kikuchi K, Higuchi T, Nagano T. 2000. Fluorescent indicators for nitric oxide based on rhodamine chromophore. *Tetrahedron Lett* **41**:69–72.
63. Jordan DM, Walt DR, Milanovich FP. 1987. Physiological pH fiber-optic chemical sensor based on energy transfer. *Anal Chem* **59**:437–439.
64. Lakowicz JR, Szmacinski H, Karakelle M. 1993. Optical sensing of pH and pCO<sub>2</sub> using phase-modulation fluorimetry and resonance energy transfer. *Anal Chim Acta* **272**:179–186.

65. Sipior J, Bambot S, Romauld M, Carter GM, Lakowicz JR, Rao G. 1995. A lifetime-based optical CO<sub>2</sub> gas sensor with blue or red excitation and Stokes or anti-Stokes detection. *Anal Biochem* **227**: 309–318.
66. Chang Q, Randers-Eichhorn L, Lakowicz JR, Rao G. 1998. Steam-sterilizable, fluorescence lifetime-based sensing film for dissolved carbon dioxide. *Biotechnol Prog* **14**:326–331.
67. Neurauter G, Klimant I, Wolfbeis OS. 1999. Microsecond lifetime-based optical carbon dioxide sensor using luminescence resonance energy transfer. *Anal Chim Acta* **382**:67–75.
68. Marazuela MD, Moreno-bondi MC, Orellana G. 1998. Luminescence lifetime quenching of a ruthenium(II) polypyridyl dye for optical sensing of carbon dioxide. *Appl Spectrosc* **52**(10): 1314–1320.
69. von Bultzingslowen C, McEvoy AK, McDonagh C, MacCraith BD. 2003. Lifetime-based optical sensor for high-level pCO<sub>2</sub> detection employing fluorescence resonance energy transfer. *Anal Chim Acta* **480**:275–283.
70. Preininger C, Ludwig M, Mohr GJ. 1998. Effect of the sol-gel matrix on the performance of ammonia fluorosensors based on energy transfer. *J Fluoresc* **8**(3):199–205.
71. Mohr GJ, Draxler S, Trznadel K, Lehmann F, Lippitsch ME. 1998. Synthesis and characterization of fluorophore-absorber pairs for sensing of ammonia based on fluorescence. *Anal Chim Acta* **360**:119–128.
72. Chang Q, Sipior J, Lakowicz JR, Rao G. 1995. A lifetime-based fluorescence resonance energy transfer sensor for ammonia. *Anal Biochem* **232**:92–97.
73. Wolfbeis OS, Klimant I, Werner T, Huber C, Kosch U, Krause C, Neurauter G, Durkop A. 1998. Set of luminescence decay time based chemical sensors for clinical appointments. *Sens Actuators* **B51**: 17–24.
74. Mills A, Chang Q, McMurray N. 1992. Equilibrium studies on colorimetric plastic film sensors for carbon dioxide. *Anal Chem* **64**: 1383–1389.
75. Wolfbeis OS, Reisfeld R, Oehme I. 1996. Sol-gels and chemical sensors. *Struct Bonding* **85**:51–98.
76. Avnir D, Braun S, Ottolenghi M. 1992. A review of novel photoactive, optical, sensing and bioactive materials. *ACS Symp Ser* **499**: 384–404.
77. The Diabetes Control and Complications Trial Research Group. 1993. The effect of intensive treatment of diabetes on the development and progression of long-term complications in insulin-dependent diabetes mellitus. *New Engl J Med* **329**(14):977–986.
78. Lakowicz JR. 1994. Emerging biomedical applications of time-resolved fluorescence spectroscopy. In *Topics in fluorescence spectroscopy, Vol. 4: Probe design and chemical sensing*, pp. 1–9. Ed JR Lakowicz. Plenum Press, New York.
79. Schultz JS, Sims G. 1979. Affinity sensors for individual metabolites. *Biotechnol Bioeng Symp* **9**:65–71.
80. Schultz J, Mansouri S, Goldstein IJ. 1982. Affinity sensor: a new technique for developing implantable sensors for glucose and other metabolites. *Diabetes Care* **5**(3):245–253.
81. Meadows D, Schultz JS. 1988. Fiber-optic biosensors based on fluorescence energy transfer. *Talanta* **35**(2):145–150.
82. Lakowicz JR, Maliwal BP. 1993. Optical sensing of glucose using phase-modulation fluorometry. *Anal Chim Acta* **271**:155–164.
83. Tolosa L, Szmacinski H, Rao G, Lakowicz JR. 1997. Lifetime-based sensing of glucose using energy transfer with a long lifetime donor. *Anal Biochem* **250**:102–108.
84. Tolosa L, Malak H, Rao G, Lakowicz JR. 1997. Optical assay for glucose based on the luminescence decay time of the long wavelength dye Cy5™. *Sens Actuators B* **45**:93–99.
85. He H, Li H, Mohr G, Kovacs B, Werner T, Wolfbeis OS. 1993. Novel type of ion-selective fluorosensor based on the inner filter effect: an optrode for potassium. *Anal Chem* **65**:123–127.
86. Roe JN, Szoka FC, Verkman AS. 1989. Optical measurement of aqueous potassium concentration by a hydrophobic indicator in lipid vesicles. *Biophys Chem* **33**:295–302.
87. Roe JN, Szoka FC, Verkman AS. 1990. Fibre optic sensor for the detection of potassium using fluorescence energy transfer. *Analyst* **115**:353–368.
88. Mahutte CK. 1994. Continuous intra-arterial blood gas monitoring. *Intensive Care Med* **20**:85–86.
89. Shapiro BA, Mahutte CK, Cane RD, Gilmour IJ. 1993. Clinical performance of a blood gas monitor: a prospective, multicenter trial. *Crit Care Med* **21**(4):487–494.
90. Yafuso M, Arick SA, Hansmann D, Holody M, Miller WW, Yan CF, Mahutte K. 1989. Optical pH measurements in blood. *Proc SPIE* **1067**:37–43.
91. Vurek GG, Feustel PJ, Severinghaus JW. 1983. A fiber optic pCO<sub>2</sub> sensor. *Ann Biomed Eng* **11**:499–510.
92. Mahutte CK, Holody M, Maxwell TP, Chen PA, Sasse SA. 1994. Development of a patient-dedicated, on-demand, blood gas monitor. *Am J Respir Crit Care Med* **149**:852–859.
93. Mahutte CK, Sasse SA, Chen PA, Holody M. 1994. Performance of a patient-dedicated, on-demand blood gas monitor in medical ICU patients. *Am J Respir Crit Care Med* **150**:865–869.
94. Opitz N, Lubbers DW. 1987. Theory and development of fluorescence-based optochemical oxygen sensors: oxygen optodes. *Int Anesthesiol Clin* **25**(3):177–197.
95. Ohkuma S, Poole B. 1978. Fluorescence probe measurement of the intralysosomal pH in living cells and the perturbation of pH by various agents. *Proc Natl Acad Sci USA* **5**(7):3327–3331.
96. Thomas JA, Buchsbaum RN, Zimniak A, Racker E. 1979. Intracellular pH measurements in Ehrlich ascites tumor cells utilizing spectroscopic probes generated *in situ*. *Biochemistry* **18**:2210–2218.
97. Munkholm C, Walt DR, Milanovich FP. 1988. A fiber-optic sensor for CO<sub>2</sub> measurement. *Talanta* **35**(2):109–112.
98. Kawabata Y, Kamichika T, Imasaka T, Ishibashi N. 1989. Fiber-optic sensor for carbon dioxide with a pH indicator dispersed in a poly(ethylene glycol) membrane. *Anal Chim Acta* **219**:223–229.
99. Yguerabide J, Talavera E, Alvarez JM, Quintero B. 1994. Steady-state fluorescence method for evaluating excited state proton reactions: application to fluorescein. *Photochem Photobiol* **60**(5): 435–441.
100. Haugland RP. 1996. *Handbook of fluorescent probes and research chemicals*. Molecular Probes Inc., Eugene, OR. (See Chapter 23, pp. 551–561.)

101. Sjoback R, Nygren J, Kubista M. 1995. Absorption and fluorescence properties of fluorescein. *Spectrochim Acta Part A* **51**:L7–L21.
102. Choi MMF. 1998. Spectroscopic behavior and proteolytic equilibrium of fluorescein immobilized in ethyl cellulose. *J Photochem Photobiol A: Chem* **114**:235–239.
103. Rink TJ, Tsien RY, Pozzan T. 1982. Cytoplasmic pH and free Mg<sup>2+</sup> in lymphocytes. *J Cell Biol* **95**:189–196.
104. Clement NR, Gould JM. 1981. Pyranine (8-hydroxy-1,3,6-pyrenetrisulfonate) as a probe of internal aqueous hydrogen ion concentration in phospholipid vesicles. *Biochemistry* **20**:1534–1538.
105. Wolfbeis OS, Fürlinger E, Kroneis H, Marsoner H. 1983. Fluorimetric analysis, I: a study on fluorescent indicators for measuring near neutral ("Physiological") pH-values. *Fresenius Z Anal Chem* **314**:119–124.
106. Schulman SG, Chen S, Bai F, Leiner MJP, Weis L, Wolfbeis OS. 1995. Dependence of the fluorescence of immobilized 1-hydroxypyrene-3,6,8-trisulfonate on sodium pH: extension of the range of applicability of a pH fluorosensor. *Anal Chim Acta* **304**:165–170.
107. Zhujun H, Seitz WR. 1984. A fluorescence sensor for quantifying pH in the range from 6.5 to 8.5. *Anal Chim Acta* **160**:47–55.
108. Uttamal M, Walt DR. 1995. A fiber-optic carbon dioxide sensor for fermentation monitoring. *BioTechnology* **13**:597–601.
109. Whitaker JE, Haugland RP, Prendergast FG. 1991. Spectral and photophysical studies of benzo[c]xanthene dyes: dual emission pH sensors. *Anal Biochem* **194**:330–344.
110. Szmacinski H, Lakowicz JR. 1993. Optical measurements of pH using fluorescence lifetimes and phase-modulation fluorometry. *Anal Chem* **65**:1668–1674.
111. Srivastava A, Krishnamoorthy G. 1997. Time-resolved fluorescence microscopy could correct for probe binding while estimating intracellular pH. *Anal Biochem* **249**:140–146.
112. Liu J, Diwu Z, Leung WY. 2001. Synthesis and photophysical properties of new fluorinated benzo[c]xanthene dyes as intracellular pH indicators. *Bioorgan Med Chem Lett* **11**:2903–2905.
113. Adamczyk M, Grote J. 2003. Synthesis of probes with broad pH range fluorescence. *Bioorgan Med Chem Lett* **13**:2327–2330.
114. Budisa N, Rubini M, Bae JH, Weyher E, Wenger W, Golbik R, Huber R, Moroder L. 2002. Global replacement of tryptophan with amino-tryptophans generates non-invasive protein-based optical pH sensors. *Angew Chem, Int Ed* **41**(21):4066–4069.
115. Kermis HR, Kostov Y, Harms P, Rao G. 2002. Dual excitation ratio-metric fluorescent pH sensor for noninvasive bioprocess monitoring: development and application. *Biotechnol Prog* **18**:1047–1053.
116. Bernhard DD, Mall S, Pantano P. 2001. Fabrication and characterization of microwell array chemical sensors. *Anal Chem* **73**:2484–2490.
117. Liebsch G, Klimant I, Krause C, Wolfbeis OS. 2001. Fluorescent imaging of pH with optical sensors using time domain dual lifetime referencing. *Anal Chem* **73**:4354–4363.
118. Wolfbeis OS, Rodriguez NV, Werner T. 1992. LED-compatible fluorosensor for measurement of near-neutral pH values. *Mikrochim Acta* **108**:133–141.
119. Briggs MS, Burns DD, Cooper ME, Gregory SJ. 2000. A pH-sensitive fluorescent cyanine dye for biological application. *Chem Commun* 2323–2324.
120. Zen J-M, Patonay G. 1991. Near-infrared fluorescence probe for pH determination. *Anal Chem* **63**:2934–2938.
121. Boyer AE, Devanathan S, Hamilton D, Patonay G. 1992. Spectroscopic studies of a near-infrared absorbing pH-sensitive carbocyanine dye. *Talanta* **39**(5):505–510.
122. Wolfbeis OS, Marhold H. 1987. A new group of fluorescent pH-indicators for an extended pH-range. *Anal Chem* **327**:347–350.
123. Murtaza Z, Chang Q, Rao G, Lin H, Lakowicz JR. 1997. Long-life-time metal-ligand pH probes. *Anal Biochem* **247**:216–222.
124. deSilva AP, Nimal Gunaratne HQ, Rice TE. 1996. Proton-controlled switching of luminescence in lanthanide complexes in aqueous solution: pH sensors based on long-lived emission. *Angew Chem, Int Ed Engl* **35**:2116–2118.
125. Kubo K, Sakurai T. 2000. Molecular recognition of PET fluorophores. *Heterocycles* **52**(2):945–976.
126. Bryan AJ, de Silva P, de Silva SA, Rupasinghe RADD, Sandanayake KRAS. 1989. Photo-induced electron transfer as a general design logic for fluorescent molecular sensors for cations. *Biosensors* **4**:169–179.
127. de Silva AP, Gunaratne HQN, Habib-Jiwan J-L, McCoy CP, Rice TE, Soumillion J-P. 1995. New fluorescent model compounds for the study of photoinduced electron transfer: the influence of a molecular electric field in the excited state. *Angew Chem, Int Ed Engl* **34**:1728–1731.
128. Kubo K. 2005. PET sensors. In *Topics in fluorescence spectroscopy, Vol. 9: Advanced concepts in fluorescence sensing: macromolecular sensing*, pp. 219–247. Ed CD Geddes, JR Lakowicz. Plenum Press, New York.
129. Akkaya EU, Huston ME, Czarnik AW. 1990. Chelation-enhanced fluorescence of anthrylazamacrocyclic conjugate probes in aqueous solution. *J Am Chem Soc* **112**:3590–3593.
130. Fages F, Desvergne JP, Bouas-Laurent H, Marsau P, Lehn J-M, Kotzyba-Hibert F, Albrecht-Gary A-M, Al-Joubbeh M. 1989. Anthraceno-cryptands: A new class of cation-complexing macrobicyclic fluorophores. *J Am Chem Soc* **111**:8672–8680.
131. de Silva AP, de Silva SA. 1986. Fluorescent signalling crown ethers; "switching on" of fluorescence by alkali metal ion recognition and binding in situ. *J Chem Soc Chem Commun* 1709–1710.
132. Gunnlaugsson T, Davis AP, Glynn M. 2001. Fluorescent photoinduced electron transfer (PET) sensing of anions using charge neutral chemosensors. *Chem Commun* 2556–2557.
133. Snowden TS, Anslyn EV. 1999. Anion recognition: synthetic receptors for anions and their application in sensors. *Curr Opin Chem Biol* **3**:740–746.
134. Huston ME, Akkaya EU, Czarnik AW. 1989. Chelation enhanced fluorescence detection of non-metal ions. *J Am Chem Soc* **111**:8735–8737.
135. Beer PD, Gale PA. 2001. Anion recognition and sensing: the state of the art and future perspectives. *Angew Chem, Int Ed* **40**:487–516.
136. Metzger A, Anslyn EV. 1998. A chemosensor for citrate in beverages. *Angew Chem, Int Ed* **37**(5):649–652.
137. Pederson CJ. 1967. Cyclic polyethers and their complexes with metal salts. *J Am Chem Soc* **89**:7017–7036.
138. Cram DJ. 1988. The design of molecular hosts, guests, and their complexes. *Science* **240**:760–767.
139. Pederson CJ. 1988. The discovery of crown ethers. *Science* **241**:536–540.

140. Nuccitelli R, ed. 1994. *Methods in cell biology*, Vol. 40: *A practical guide to the study of calcium in living cells*. Academic Press, New York.
141. Minta A, Tsien RY. 1989. Fluorescent indicators for cytosolic sodium. *J Biol Chem* **264**(32):19449–19457.
142. Grynkiewicz G, Poenie M, Tsien RY. 1985. A new generation of  $\text{Ca}^{2+}$  indicators with greatly improved fluorescence properties. *J Biol Chem* **260**(6):3440–3450.
143. Tsien RY. 1989. Fluorescent indicators of ion concentrations. *Methods Cell Biol* **30**:127–156.
144. Haugland RP. 1996. *Handbook of Fluorescent Probes and Research Chemicals*, 6th ed., pp. 503–584. Molecular Probes Inc., Eugene, OR.
145. Crossley R, Goolamali Z, Sammes PG. 1994. Synthesis and properties of a potential extracellular fluorescent probe for potassium. *J Chem Soc Perkin Trans 2*:1615–1623.
146. Buet P, Gersch B, Grell E. 2001. Spectral properties, cation selectivity, and dynamic efficiency of fluorescent alkali ion indicators in aqueous solution around neutral pH. *J Fluoresc* **11**(2):79–87.
147. Szmacinski H, Lakowicz JR. 1999. Potassium and sodium measurements in blood using phase-modulation fluorometry. *Sens Actuators B* **60**:8–18.
148. Leray I, Habib-Jiwan JL, Branger C, Soumillion JPh, Valeur B. 2000. Ion-responsive fluorescent compounds, VI: coumarin 153 linked to rigid crowns for improvement of selectivity. *J Photochem Photobiol A: Chem* **135**:163–169.
149. Crossley R, Goolamali Z, Gosper JJ, Sammes PG. 1994. Synthesis and spectral properties of new fluorescent probes for potassium. *J Chem Soc Perkin Trans 2*:513–520.
150. Golchini K, Mackovic-Basic M, Gharib SA, Masilamani D, Lucas ME, Kurtz I. 1990. Synthesis and characterization of a new fluorescent probe for measuring potassium. *Am J Physiol*, **258**:F438–F443.
151. Szmacinski H, Lakowicz JR. 1997. Sodium Green as a probe for intracellular sodium imaging based on fluorescence lifetime. *Anal Biochem* **250**:131–138.
152. Lakowicz JR, Szmacinski H. 1992. Fluorescence lifetime-based sensing of pH,  $\text{Ca}^{2+}$ ,  $\text{K}^+$  and glucose. *Sens Actuators B* **11**:133–143.
153. Meuwis K, Boens N, De Schryver FC, Gallay J, Vincent M. 1995. Photophysics of the fluorescent  $\text{K}^+$  indicator PBFI. *Biophys J* **68**:2469–2473.
154. Valeur B, Bourson J, Pouget J. 1993. Ion recognition detected by changes in photoinduced charge or energy transfer. *ACS Symp Ser* **538**:25–44.
155. Tsien RY, Rink TJ, Poenie M. 1985. Measurement of cytosolic free  $\text{Ca}^{2+}$  in individual small cells using fluorescence microscopy with dual excitation wavelengths. *Cell Calcium* **6**:145–157.
156. Iatridou H, Foukaraki E, Kuhn MA, Marcus EM, Haugland RP, Katerinopoulos HE. 1994. The development of a new family of intracellular calcium probes. *Cell Calcium* **15**:190–198.
157. Akkaya EU, Lakowicz JR. 1993. Styryl-based wavelength ratiometric probes: a new class of fluorescent calcium probes with long wavelength emission and a large Stokes shift. *Anal Biochem* **213**:285–289.
158. Minta A, Kao JPY, Tsien RY. 1989. Fluorescent indicators for cytosolic calcium based on rhodamine and fluorescein chromophores. *J Biol Chem* **264**(14):8171–8178.
159. Eberhard M, Erne P. 1991. Calcium binding to fluorescent calcium indicators: calcium green, calcium orange and calcium crimson. *Biochem Biophys Res Comm* **180**(1):209–215.
160. Lakowicz JR, Szmacinski H, Johnson ML. 1992. Calcium concentration imaging using fluorescence lifetimes and long-wavelength probes. *J Fluoresc* **2**(1):47–62.
161. Hirshfield KM, Toptygin D, Packard BS, Brand L. 1993. Dynamic fluorescence measurements of two-state systems: applications to calcium-chelating probes. *Anal Biochem* **209**:209–218.
162. Miyoshi N, Hara K, Kimura S, Nakanishi K, Fukuda M. 1991. A new method of determining intracellular free  $\text{Ca}^{2+}$  concentration using Quin-2 fluorescence. *Photochem Photobiol* **53**(3):415–418.
163. Lakowicz JR, Szmacinski H, Nowaczyk K, Johnson ML. 1992. Fluorescence lifetime imaging of calcium using Quin-2. *Cell Calcium* **13**:131–147.
164. Oguz U, Akkaya EU. 1997. One-pot synthesis of a red-fluorescent chemosensor from an azacrown, phloroglucinol and squaric acid: a simple in-solution construction of a functional molecular device. *Tetrahedron Lett* **38**(25):4509–4512.
165. Akkaya EU, Turkyilmaz S. 1997. A squaraine-based near IR fluorescent chemosensor for calcium. *Tetrahedron Lett* **38**(25):4513–4516.
166. Wahl M, Lucherini MJ, Gruenstein E. 1990. Intracellular  $\text{Ca}^{2+}$  measurement with Indo-1 in substrate-attached cells: advantages and special considerations. *Cell Calcium* **11**:487–500.
167. Groden DL, Guan Z, Stokes BT. 1991. Determination of Fura-2 dissociation constants following adjustment of the apparent  $\text{Ca}$ -EGTA association constant for temperature and ionic strength. *Cell Calcium* **12**:279–287.
168. David-Dufilho M, Montenay-Garestier T, Devynck M-A. 1989. Fluorescence measurements of free  $\text{Ca}^{2+}$  concentration in human erythrocytes using the  $\text{Ca}^{2+}$  indicator Fura-2. *Cell Calcium* **9**:167–179.
169. Hirshfield KM, Toptygin D, Grandhighe G, Kim H, Packard BZ, Brand L. 1996. Steady-state and time-resolved fluorescence measurements for studying molecular interactions: interaction of a calcium-binding probe with proteins. *Biophys Chem* **62**:25–38.
170. Kao JPY. 1994. Practical aspects of measuring  $[\text{Ca}^{2+}]$  with fluorescent indicators. *Methods Cell Biol* **40**:155–181.
171. Morris SJ, Wiegmann TB, Welling LW, Chronwall BM. 1994. Rapid simultaneous estimation of intracellular calcium and pH. *Methods Cell Biol* **40**:183–220.
172. Scanlon M, Williams DA, Fay FS. 1987. A  $\text{Ca}^{2+}$ -insensitive form of fura-2 associated with polymorphonuclear leukocytes. *J Biol Chem* **262**(13):6308–6312.
173. Bourson J, Pouget J, Valeur B. 1993. Ion-responsive fluorescent compounds, 4: effect of cation bonding on the photophysical properties of a coumarin linked to monoaza- and diaza-crown ethers. *J Phys Chem* **97**:4552–4557.
174. Dumon P, Jonusauskas G, Dupuy F, Pee P, Rulliere C, Letard JF, Lapouyade R. 1994. Picosecond dynamics of cation-macrocycle interactions in the excited state of an intrinsic fluorescence probe: the calcium complex of 4-(N-monoaza-15-crown-5)-4'-phenylstilbene. *J Phys Chem* **98**:10391–10396.
175. Letard J-F, Lapouyade R, Rettig W. 1993. Chemical engineering of fluorescence dyes. *Mol Cryst Liq Cryst* **236**:41–46.

176. Suzuki Y, Komatsu H, Ikeda T, Saito N, Araki S, Citterio D, Hisamoto H, Kitamura Y, Kubota T, Nakagawa J, Oka K, Suzuki K. 2002. Design and synthesis of  $Mg^{2+}$  selective fluoroionophores based on a coumarin derivative and application for  $Mg^{2+}$  measurement in a living cell. *Anal Chem* **74**:1423–1428.
177. Watanabe S, Ikishima S, Matsuo T, Yoshida K. 2001. A luminescent metalloreceptor exhibiting remarkably high selectivity for  $Mg^{2+}$  over  $Ca^{2+}$ . *J Am Chem Soc* **123**:8402–8403.
178. de Silva AP, Nimal Qunaratne HQ, Maguire GEM. 1994. Off-on fluorescent sensors for physiological levels of magnesium ions based on photoinduced electron transfer (PET), which also behave as photoionic OR logic gates. *J Chem Soc Chem Commun* 1213–1214.
179. Pesco J, Salmon JM, Vigo J, Viallet P. 2001. Mag-indo1 affinity for  $Ca^{2+}$ , compartmentalization and binding to proteins: the challenge of measuring  $Mg^{2+}$  concentrations in living cells. *Anal Biochem* **290**: 221–231.
180. Illner H, McGuigan JAS, Luthi D. 1992. Evaluation of mag-fura-5: the new fluorescent indicator for free magnesium measurements. *Eur J Physiol* **422**:179–184.
181. Morelle B, Salmon J-M, Vigo J, Viallet P. 1993. Proton,  $Mg^{2+}$  and protein as competing ligands for the fluorescent probe, mag-indo-1: a first step to the quantification of intracellular  $Mg^{2+}$  concentration. *Photochem Photobiol* **58**(6):795–802.
182. Otten PA, London RE, Levy LA. 2001. A new approach to the synthesis of APTRA indicators. *Bioconjugate Chem* **12**:76–83.
183. Shoda T, Kikuchi K, Kojima H, Urano Y, Komatsu H, Suzuki K, Nagano T. 2003. Development of selective, visible light-excitable, fluorescent magnesium ion probes with a novel fluorescence switching mechanism. *Analyst* **128**(6):719–723.
184. Szmacinski H, Lakowicz JR. 1996. Fluorescence lifetime characterization of magnesium probes: Improvement of  $Mg^{2+}$  dynamic range and sensitivity using phase-modulation fluorometry. *J Fluoresc* **6**(2): 83–95.
185. Thompson RB, Peterson D, Mahoney W, Cramer M, Maliwal BP, Suh SW, Frederickson C, Fierke C, Herman P. 2002. Fluorescent zinc indicators for neurobiology. *J Neurosci Methods* **118**:63–75.
186. Walkup GK, Burdette SC, Lippard SJ, Tsien RY. 2000. A new cell-permeable fluorescent probe for  $Zn^{2+}$ . *J Am Chem Soc* **122**:5644–5645.
187. Burdette SC, Frederickson CJ, Bu W, Lippard SJ. 2003. ZP4: an improved neuronal  $Zn^{2+}$  sensor of the zinpyr family. *J Am Chem Soc* **125**:1778–1787.
188. Burdette SC, Walkup GK, Spingler B, Tsien RY, Lippard SJ. 2001. Fluorescent sensors for  $Zn^{2+}$  based on a fluorescein platform: synthesis, properties and intracellular distribution. *J Am Chem Soc* **123**: 7831–7841.
189. Nolan EM, Burdette SC, Harvey JH, Hilderbrand SA, Lippard SJ. 2004. Synthesis and characterization of zinc sensors based on a monosubstituted fluorescein platform. *Inorg Chem* **43**:2624–2635.
190. Thompson RB, Maliwal BP, Feliccia VL, Fierke CA, McCall K. 1998. Determination of picomolar concentrations of metal ions using fluorescence anisotropy: biosensing with a "reagentless" enzyme transducer. *Anal Chem* **70**:4717–4723.
191. Thompson RB, Cramer ML, Bozym R, Fierke CA. 2002. Excitation ratiometric fluorescent biosensor for zinc ion at picomolar levels. *J Biomed Opt* **7**(4):555–560.
192. Kawanishi T, Romey MA, Zhu PC, Holody MZ, Shinkai S. 2004. A study of boronic acid based fluorescence glucose sensors. *J Fluoresc* **14**(5):499–512.
193. Cao H, Heagy MD. 2004. Fluorescent chemosensors for carbohydrates: a decade's worth of bright spies for saccharides in review. *J Fluoresc* **14**(5):569–584.
194. James TD, Sandanayake KRAS, Shinkai S. 1994. Novel photoinduced electron-transfer sensor for saccharides based on the interaction of boronic acid and amine. *J Chem Soc Chem Commun* 2:477–478.
195. Yoon J, Czarnik AW. 1992. Fluorescent chemosensors of carbohydrates: a means of chemically communicating the binding of polyols in water based on chelation-enhanced quenching. *J Am Chem Soc* **114**:5874–5875.
196. DiCesare N, Lakowicz JR. 2001. Evaluation of two synthetic glucose probes for fluorescence-lifetime-based sensing. *Anal Biochem* **294**: 154–160.
197. DiCesare N, Lakowicz JR. 2001. Wavelength-ratiometric probes for saccharides based on donor-acceptor diphenylpolyenes. *J Photochem Photobiol A: Chem* **143**:39–47.
198. DiCesare N, Lakowicz JR. 2001. A new highly fluorescent probe for monosaccharides based on a donor-acceptor diphenyloxazole. *Chem Commun* **19**:2022–2023.
199. DiCesare N, Lakowicz JR. 2002. Charge transfer fluorescent probes using boronic acids for monosaccharide signaling. *J Biomed Opt* **7**(4):538–545.
200. DiCesare N, Lakowicz JR. 2001. Spectral properties of fluorophores combining the boronic acid group with electron donor or withdrawing groups: implication in the development of fluorescence probes for saccharides. *J Phys Chem A* **105**:6834–6840.
201. Badugu R, Lakowicz JR, Geddes CD. 2005. Boronic acid fluorescent sensors for monosaccharide signaling based on the 6-methoxyquinolinium heterocyclic nucleus: progress toward noninvasive and continuous glucose monitoring. *Bioorg Med Chem* **13**:113–119.
202. Badugu R, Lakowicz JR, Geddes CD. 2005. Fluorescence sensors for monosaccharides based on the 6-methylquinolinium nucleus and boronic acid moiety: potential application to ophthalmic diagnostics. *Talanta* **65**:762–768.
203. Hellinga HW, Marvin JS. 1998. Protein engineering and the development of generic biosensors. *Trends Biotechnol* **16**:183–189.
204. Sloan DJ, Hellinga HW. 1998. Structure-based engineering of environmentally sensitive fluorophores for monitoring protein-protein interactions. *Protein Eng* **11**(9):819–823.
205. Thompson RB, Maliwal BP, Fierke CA. 1999. Selectivity and sensitivity of fluorescence lifetime-based metal ion biosensing using a carbonic anhydrase transducer. *Anal Biochem* **267**:185–195.
206. Brennan JD. 1999. Preparation and entrapment of fluorescently labeled proteins for the development of reagentless optical biosensors. *J Fluoresc* **9**(4):295–312.
207. Giuliano KA, Taylor DL. 1998. Fluorescent-protein biosensors: new tools for drug discovery. *Trends Biotechnol* **16**:135–140.
208. Shrestha S, Salins LLE, Ensor CM, Daunert S. 2002. Rationally designed fluorescently labeled sulfate-binding protein mutants: evaluation in the development of a sensing system for sulfate. *Biotechnol Bioeng* **78**(5):517–526.

209. Nguyen T, Rosenzweig Z. 2002. Calcium ion fluorescence detection using liposomes containing alexa-labeled calmodulin. *Anal Bioanal Chem* **374**:69–74.
210. Marvin JS, Hellinga HW. 1998. Engineering biosensors by introducing fluorescent allosteric signal transducers: construction of a novel glucose sensor. *J Am Chem Soc* **120**:7–11.
211. Gilardi G, Zhou LQ, Hibbert L, Cass AEG. 1994. Engineering the maltose binding protein for reagentless fluorescence sensing. *Anal Chem* **66**:3840–3847.
212. Tolosa L, Gryczynski I, Eichhorn LR, Dattelbaum JD, Castellano FN, Rao G, Lakowicz JR. 1999. Glucose sensor for low-cost lifetime-based sensing using a genetically engineered protein. *Anal Biochem* **267**:114–120.
213. Marvin JS, Corcoran EE, Hattangadi NA, Zhang JV, Gere SA, Hellinga HW. 1997. The rational design of allosteric interactions in a monomeric protein and its applications to the construction of biosensors. *Proc Natl Acad Sci USA* **94**:4366–4371.
214. Brune M, Hunter JL, Howell SA, Martin SR, Hazlett TL, Corrie JET, Webb MR. 1998. Mechanism of inorganic phosphate interaction with phosphate binding protein from *Escherichia coli*. *Biochemistry* **37**:10370–10380.
215. Lundgren JS, Salins LLE, Kaneva I, Daunert S. 1999. A dynamical investigation of acrylodan-labeled mutant phosphate binding protein. *Anal Chem* **71**:589–595.
216. Wada A, Mie M, Aizawa M, Lahoud P, Cass AEG, Kobatake E. 2003. Design and construction of glutamine binding proteins with a self-adhering capability to unmodified hydrophobic surfaces as reagentless fluorescence sensing devices. *J Am Chem Soc* **125**:16228–16234.
217. Looger LL, Dwyer MA, Smith JJ, Hellinga HW. 2003. Computational design of receptor and sensor proteins with novel functions. *Nature* **423**:185–190.
218. Morii T, Sugimoto K, Makino K, Otsuka M, Imoto K, Mori Y. 2002. A new fluorescent biosensor for inositol trisphosphate. *J Am Chem Soc* **124**(7):1138–1139.
219. Quijano FA, Ledvina PS. 1996. Atomic structure and specificity of bacterial periplasmic receptors for active transport and chemotaxis: variation of common themes. *Mol Microbiol* **20**(1):17–25.
220. Medintz IL, Anderson GP, Lassman ME, Goldman ER, Bettencourt LA, Mauro JM. 2004. General strategy for biosensor design and construction employing multifunctional surface-tethered components. *Anal Chem* **76**:5620–5629.
221. Wenck A, Pugieux C, Turner M, Dunn M, Stacy C, Tiozzo A, Dunder E, van Grinsven E, Khan R, Sigareva M, Wang WC, Reed J, Drayton P, Oliver D, Trafford H, Legris G, Rushton H, Tayab S, Launis K, Chang YF, Chen DF, Melchers L. 2003. Reef-coral proteins as visual, non-destructive reporters for plant transformation. *Plant Cell Rep* **22**:244–251.
222. Romoser VA, Hinkle PM, Persechini A. 1997. Detection in living cells of  $\text{Ca}^{2+}$ -dependent changes in the fluorescence emission of an indicator composed of two green fluorescent protein variants linked by a calmodulin-binding sequence: a new class of fluorescent indicators. *J Biol Chem* **272**(20):13270–13274.
223. Miyawaki A, Llopis J, Heim R, McCaffery JM, Adams JA, Ikura M, Tsien RY. 1997. Fluorescent indicators for  $\text{Ca}^{2+}$  based on green fluorescent proteins and calmodulin. *Nature* **388**:882–887.
224. Nagai T, Yamada S, Tominaga T, Ichikawa M, Miyawaki A. 2004. Expanded dynamic range of fluorescent indicators for  $\text{Ca}^{2+}$  by circularly permuted yellow fluorescent proteins. *Proc Natl Acad Sci USA* **101**(29):10554–10559.
225. Sato M, Ozawa T, Inukai K, Asano T, Umezawa Y. 2002. Fluorescent indicators for imaging protein phosphorylation in single living cells. *Nature Biotechnol* **20**:287–294.
226. Kawai Y, Sato M, Umezawa Y. 2004. Single color fluorescent indicators of protein phosphorylation for multicolor imaging of intracellular signal flow dynamics. *Anal Chem* **76**:6144–6149.
227. Lin CW, Jao CY, Ting AY. 2004. Genetically encoded fluorescent reporters of histone methylation in living cells. *J Am Chem Soc* **126**:5982–5983.
228. Kalab P, Weis K, Heald R. 2002. Visualization of a ran-GTP gradient in interphase and mitotic *xenopus* egg extracts. *Science* **295**:2452–2456.
229. Schleifenbaum A, Stier G, Gasch A, Sattler R, Schultz C. 2004. Genetically encoded FRET probe for PKC activity based on pleckstrin. *J Am Chem Soc* **126**:11786–11787.
230. Sato M, Hida N, Ozawa T, Umezawa Y. 2000. Fluorescent indicators for cyclic GMP based on cyclic GMP-dependent protein kinase I $\alpha$  and green fluorescent proteins. *Anal Chem* **72**:5918–5924.
231. Cano Abad MF, Di Benedetto G, Magalhaes PJ, Filippini L, Pozzan T. 2004. Mitochondrial pH monitored by a new engineered green fluorescent protein mutant. *Biol Chem* **279**(12):11521–11529.
232. Llopis J, McCaffery JM, Miyawaki A, Farquhar MG, Tsien RY. 1998. Measurement of cytosolic, mitochondrial, and golgi pH in single living cells with green fluorescent proteins. *Proc Natl Acad Sci USA* **95**:6803–6808.
233. Kneen M, Farinas J, Li Y, Verkman AS. 1998. Green fluorescent protein as a noninvasive intracellular pH indicator. *Biophys J* **74**:1591–1599.
234. Elsliger MA, Wachter RM, Hanson GT, Kallio K, Remington SJ. 1999. Structural and spectral response of green fluorescent protein variants to changes in pH. *Biochemistry* **38**:5296–5301.
235. Hanson GT, McAnaney TB, Park ES, Rendell MEP, Yarbrough DK, Chu S, Xi L, Boxer SG, Montrose MH, Remington SJ. 2002. Green fluorescent protein variants as ratiometric dual emission pH sensors, 1: structural characterization and preliminary application. *Biochemistry* **41**:15477–15488.
236. Park EJ, Brasuel M, Behrend C, Philbert MA, Kopelman R. 2003. Ratiometric optical PEBBLE nanosensors for real-time magnesium ion concentrations inside viable cells. *Anal Chem* **75**:3784–3791.
237. Brasuel M, Kopelman R, Miller TJ, Tjalkens R, Philbert MA. 2001. Fluorescent nanosensors for intracellular chemical analysis: decyl methacrylate liquid polymer matrix and ion-exchange-based potassium PEBBLE sensors with real-time application to viable rat C6 glioma cells. *Anal Chem* **73**:2221–2228.
238. Clark HA, Hoyer M, Philbert MA, Kopelman R. 1999. Optical nanosensors for chemical analysis inside single living cells, 1: fabrication, characterization, and methods for intracellular delivery of PEBBLE sensors. *Anal Chem* **71**:4831–4836.
239. Clark HA, Kopelman R, Tjalkens R, Philbert MA. 1999. Optical nanosensors for chemical analysis inside single living cells, 2: sensors for pH and calcium and the intracellular application of PEBBLE sensors. *Anal Chem* **71**:4837–4843.

240. Tsagkatakis I, Peper S, Retter R, Bell M, Bakker E. 2001. Monodisperse plasticized poly(vinyl chloride) fluorescent microspheres for selective ionophore-based sensing and extraction. *Anal Chem* **73**:6083–6087.
241. Ji J, Rosenzweig N, Jones I, Rosenzweig Z. 2001. Molecular oxygen-sensitive fluorescent lipobeads for intracellular oxygen measurements in murine macrophages. *Anal Chem* **73**:3521–3527.
242. Ma A, Rosenzweig Z. 2004. Submicrometric lipobead-based fluorescence sensors for chloride ion measurements in aqueous solution. *Anal Chem* **76**:569–575.
243. Tsagkatakis I, Peper S, Bakker E. 2001. Spatial and spectral imaging of single micrometer-sized solvent cast fluorescent plasticized poly(vinyl chloride) sensing particles. *Anal Chem* **73**:315–320.
244. McNamara KP, Nguyen T, Dumitrescu G, Ji J, Rosenzweig N, Rosenzweig Z. 2001. Synthesis, characterization, and application of fluorescence sensing lipobeads for intracellular pH measurements. *Anal Chem* **73**:3240–3246.
245. Ji J, Rosenzweig N, Griffin C, Rosenzweig Z. 2000. Synthesis and application of submicrometer fluorescence sensing particles for lysosomal pH measurements in murine macrophages. *Anal Chem* **72**:3497–3503.
246. Chance B, Leigh JS, Miyake H, Smith DS, Nioka S, Greenfeld R, Finander M, Kaufmann K, Levy W, Young M, Cohen P, Yoshioka H, Boretsky R. 1988. Comparison of time-resolved and –unresolved measurements of deoxyhemoglobin in brain. *Proc Natl Acad Sci USA* **85**:4971–4975.
247. Franceschini MA, Moesta KT, Fantini S, Gaida G, Gratton E, Jess H, Mantulin WW, Seeber M, Schlag PM, Kaschke M. 1997. Frequency-domain techniques enhance optical mammography: initial clinical results. *Proc Natl Acad Sci USA* **94**:6468–6473.
248. Wu J, Perelman L, Dasari RR, Feld MS. 1997. Fluorescence tomographic imaging in turbid media using early-arriving photons and Laplace transforms. *Proc Natl Acad Sci USA* **94**:8783–8788.
249. Weissleder R, Ntziachristos V. 2003. Shedding light onto live molecular targets. *Nature Med* **9**(1):123–128.
250. Godavarty A, Thompson AB, Roy R, Gurfinkel M, Eppstein MJ, Zhang C, Sevick-Muraca EM. 2004. Diagnostic imaging of breast cancer using fluorescence-enhanced optical tomography: phantom studies. *J Biomed Opt* **9**(3):488–496.
251. Kuwana E, Sevick-Muraca E. 2002. Fluorescence lifetime spectroscopy in multiply scattering media with dyes exhibiting multiexponential decay kinetics. *Biophys J* **83**:1165–1176.
252. Mahmood U, Tung CH, Bogdanov A, Weissleder R. 1999. Near-infrared optical imaging of protease activity for tumor detection. *Radiology* **213**:866–870.
253. Becker A, Hessnerius C, Licha K, Ebert B, Sukowski U, Semmler W, Wiedenmann B, Grotzinger C. 2001. Receptor-targeted optical imaging of tumors with near-infrared fluorescent ligands. *Nature Biotechnol* **19**:327–331.
254. Ntziachristos V, Schellenberger EA, Ripoll J, Yessayan D, Graves E, Bogdanov A, Josephson L, Weissleder R. 2004. Visualization of anti-tumor treatment by means of fluorescence molecular tomography with an annexin V-Cy5.5 conjugate. *Proc Natl Acad Sci USA* **101**(33):12294–12299.
255. Bremer C, Tung CH, Weissleder R. 2001. In vivo molecular target assessment of matrix metalloproteinase inhibition. *Nature Med* **7**(6):743–748.
256. Chen J, Tung CH, Mahmood U, Ntziachristos V, Gyurko R, Fishman MC, Huang PL, Weissleder R. 2002. In vivo imaging of proteolytic activity in atherosclerosis. *Circulation* **105**:2766–2771.
257. Graves EE, Ripoll J, Weissleder R, Ntziachristos V. 2003. A submillimeter resolution fluorescence molecular imaging system for small animal imaging. *Med Phys* **30**(5):901–911.
258. Ntziachristos V, Tung C-T, Bremer C, Weissleder R. 2002. Fluorescence molecular tomography resolves protease activity *in vivo*. *Nature Med* **8**(7):757–760.
259. Tung C-H, Bredow S, Mahmood U, Weissleder R. 1999. Preparation of a cathepsin D sensitive near-infrared fluorescence probe for imaging. *Bioconjugate Chem* **10**:892–896.
260. Tung C-H, Gerszten RE, Jaffer FA, Weissleder R. 2002. A novel near-infrared fluorescence sensor for detection of thrombin activation in blood. *Chem Biochem* **3**:207–211.
261. Weissleder R, Tung C-H, Mahmood U, Bogdanov A. 1999. In vivo imaging of tumors with proteas-activated near-infrared fluorescent probes. *Nature Biotechnol* **17**:375–378.
262. Hou W-S, Li Z, Gordon RE, Chan K, Klein MJ, Levy R, Keysser M, Keyszer G, Bromme D. 2001. Cathepsin K is a critical protease in synovial fibroblast-mediated collagen degradation. *Am J Pathol* **159**(6):2167–2177.
263. Suzumori N, Ozaki Y, Ogasawara M, Suzumori K. 2001. Increased concentrations of cathepsin D in peritoneal fluid from women with endometriosis. *Mol Human Reprod* **7**(5):459–462.
264. Oksjoki S, Soderstrom M, Vuorio E, Anttila L. 2001. Differential expression patterns of cathepsins B, H, K, L, and S in the mouse ovary. *Mol Human Reprod* **7**(1):27–34.
265. Hemmila IA. 1992. *Applications of fluorescence in immunoassays*. John Wiley & Sons, New York.
266. Van Dyke K, Van Dyke R., eds. 1990. *Luminescence immunoassay and molecular applications*. CRC Press, Boca Raton, FL.
267. Ozinskas AJ. 1994. Principles of fluorescence immunoassay. In *Topics in fluorescence spectroscopy*, Vol. 4: *Probe design and chemical sensing*, pp. 449–496. Ed JR Lakowicz. Plenum Press, New York.
268. Gosling JP. 1990. A decade of development in immunoassay methodology. *Clin Chem* **36**(8):1408–1427.
269. Davidson RS, Hilchenbach MM. 1990. The use of fluorescent probes in immunochemistry. *Photochem Photobiol* **52**(2):431–438.
270. Vo-Dinh T, Sepaniak MJ, Griffin GD, Alarie JP. 1993. Immuno-sensors: principles and applications. *Immunomethods* **3**:85–92.
271. Berson S, Yalow R. 1959. Quantitative aspects of the reaction between insulin and insulin-binding antibody. *J Clin Invest* **38**:1996–2016.
272. Lovgren T, Hemmila I, Pettersson K, Halonen P. 1985. Time-resolved fluorometry in immunoassay. In *Alternative immunoassays*, pp. 203–217. Ed WP Collins. John Wiley & Sons, New York.
273. Diamandis EP. 1988. Immunoassays with time-resolved fluorescence spectroscopy: principles and applications. *Clin Biochem* **21**:139–150.

274. Lövgren T, Pettersson K. 1990. Time-resolved fluoroimmunoassay, advantages and limitations. In *Luminescence immunoassay and molecular applications*, pp. 234–250. Ed K Van Dyke, R Van Dyke. CRC Press, Boca Raton, FL.
275. Khosravi M, Diamandis EP. 1987. Immunofluorometry of choriogonadotropin by time-resolved fluorescence spectroscopy, a new europium chelate as label. *Clin Chem* **33**(11):1994–1999.
276. Soini E. 1984. Pulsed light, time-resolved fluorometric immunoassay. In *Monoclonal antibodies and new trends in immunoassays*, pp. 197–208. Ed ChA Bizollon. Elsevier Science Publishers, New York.
277. Fiet J, Giton F, Auzerie J, Galons H. 2002. Development of a new sensitive and specific time-resolved fluoroimmunoassay (TR-FIA) of chlormadinone acetate in the serum of treated menopausal women. *Steroids* **67**:1045–1055.
278. Wu F-B, He Y-F, Han S-Q. 2001. Matrix interference in serum total thyroxin (T4) time-resolved fluorescence immunoassay (TRFIA) and its elimination with the use of streptavidin–biotin separation technique. *Clin Chim Acta* **308**:117–126.
279. Ohmura N, Tsukidate Y, Shinozaki H, Lackie SJ, Saiki H. 2003. Combinational use of antibody affinities in an immunoassay for extension of dynamic range and detection of multiple analytes. *Anal Chem* **75**:104–110.
280. Korpimaki T, Hagren V, Brockmann E-C, Tuomola M. 2004. Generic lanthanide fluoroimmunoassay for the simultaneous screening of 18 sulfonamides using an engineered antibody. *Anal Chem* **76**:3091–3098.
281. Korpimaki T, Brockmann E-C, Kuronen O, Saraste M, Lamminmaki U, Tuomola M. 2004. Engineering of a broad specificity antibody for simultaneous detection of 13 sulfonamides at the maximum residue level. *J Agric Food Chem* **52**:40–47.
282. Ullman EF, Schwarzberg M, Rubenstein KE. 1976. Fluorescent excitation transfer immunoassay: A general method for determination of antigens. *J Biol Chem* **251**(14):4172–4178.
283. Schobel U, Coille I, Brecht A, Steinwand M, Gauglitz G. 2001. Miniaturization of a homogeneous fluorescence immunoassay based on energy transfer using nanotiter plates as high-density sample carriers. *Anal Chem* **73**:5172–5179.
284. Schobel U, Egelhaaf H-J, Brecht A, Oelkrug D, Gauglitz G. 1999. New donor–acceptor pair for fluorescent immunoassays by energy transfer. *Bioconjugate Chem* **10**:1107–1114.
285. Qin Q-P, Peltola O, Pettersson K. 2003. Time-resolved fluorescence resonance energy transfer assay for point-of-care testing of urinary albumin. *Clin Chem* **49**(7):1105–1113.
286. Ohiro Y, Arai R, Ueda H, Nagamune T. 2002. A homogeneous and noncompetitive immunoassay based on the enhanced fluorescence resonance energy transfer by leucine zipper interaction. *Anal Chem* **74**:5786–5792.
287. Lee M, Walt DR, Nugent P. 1999. Fluorescent excitation transfer immunoassay for the determination of spinosyn A in water. *J Agric Food Chem* **47**:2766–2770.
288. Oswald B, Lehmann F, Simon L, Terpetschnig E, Wolfbeis OS. 2000. Red laser-induced fluorescence energy transfer in an immunoassay. *Anal Biochem* **280**:272–277.
289. Blomberg K, Hurskainen P, Hemmila I. 1999. Terbium and rhodamine as labels in a homogeneous time-resolved fluorometric energy transfer assay of the  $\beta$  subunit of human chorionic gonadotropin in serum. *Clin Chem* **45**(6):855–861.
290. Dandliker WB, de Saussure VA. 1970. Fluorescence polarization in immunochemistry. *Immunochemistry* **7**:799–828.
291. Spencer RD, Toledo FB, Williams BT, Yoss NL. 1973. Design, construction, and two applications for an automated flow-cell polarization fluorometer with digital read out: enzyme-inhibitor (antitrypsin) assay and antigen–antibody (insulin–insulin antiserum) assay. *Clin Chem* **19**(8):838–844.
292. Kobayashi Y, Amitani K, Watanabe F, Miyai K. 1979. Fluorescence polarization immunoassay for cortisol. *Clin Chim Acta* **92**:241–247.
293. Cox H, Whitby M, Nimmo G, Williams G. 1993. Evaluation of a novel fluorescence polarization immunoassay for teicoplanin. *Antimicrob Agents Chemother* **37**:1924–1926.
294. Mastin SH, Buck RL, Mueggler PA. 1993. Performance of a fluorescence polarization immunoassay for teicoplanin in serum. *Diagn Microbiol Infect Dis* **16**:17–24.
295. Ripple MG, Goldberger BA, Caplan YH, Blitzer MG, Schwartz S. 1992. Detection of cocaine and its metabolites in human amniotic fluid. *J Anal Toxicol* **16**:328–331.
296. de Kanel J, Dunlap L, Hall TD. 1989. Extending the detection limit of the TDx fluorescence polarization immunoassay for benzoylecgonine in urine. *Clin Chem* **35**(10):2110–2112.
297. Uber-Bucek E, Hamon M, Huy CP, Dadoun H. 1992. Determination of thevetin B in serum by fluorescence polarization immunoassay. *J Pharm Biomed Anal* **10**(6):413–419.
298. Klein C, Batz H-G, Draeger B, Guder H-J, Herrmann R, Josel H-P, Nagele U, Schenk R, Bogt B. 1993. Fluorescence polarization immunoassay. In *Fluorescence spectroscopy: new methods and applications*, pp. 245–258. Ed OS Wolfbeis. Springer-Verlag, Berlin.
299. Wang PP, Simpson E, Meucci V, Morrison M, Lunetta S, Zajac M, Boeckx R. 1991. Cyclosporine monitoring by fluorescence polarization immunoassay. *Clin Biochem* **24**:55–58.
300. Winkler M, Schumann G, Petersen D, Oellerich M, Wonigeit K. 1992. Monoclonal fluorescence polarization immunoassay evaluated for monitoring cyclosporine in whole blood after kidney, heart, and liver transplantation. *Clin Chem* **38**(1):123–126.
301. Turek TC, Small EC, Bryant RW, Hill WAG. 2001. Development and validation of a competitive AKT serine/threonine kinase fluorescence polarization assay using a product-specific anti-phospho-serine antibody. *Anal Biochem* **299**:45–53.
302. Martin K, Steinberg TH, Cooley LA, Gee KR, Beechem JM, Patton WF. 2003. Quantitative analysis of protein phosphorylation status and protein kinase activity on microarrays using a novel fluorescent phosphorylation sensor dye. *Proteomics* **3**:1244–1255.
303. Gaudet EA, Huang K-S, Zhang Y, Huang W, Mark D, Sportsman JR. 2003. A homogeneous fluorescence polarization assay adaptable for a range of protein serine/threonine and tyrosine kinase. *J Biomol Screening* **8**(2):164–175.
304. Fiore M, Mitchell J, Doan T, Nelson R, Winter G, Grandone C, Zeng K, Haraden R, Smith J, Harris K, Leszczynski J, Berry D, Safford S, Barnes G, Scholnick A, Ludington K. 1988. The Abbott IMx™ automated benchtop immunochemistry analyzer system. *Clin Chem* **34**:1726–1732.
305. Lang H, Wurzburg U. 1982. Creatine kinase, an enzyme of many forms. *Clin Chem* **28**:1439–1447.
306. Brayne CEG, Calloway SP, Dow L. 1982. Blood creatine kinase isoenzymes BB in boxers. *Lancet* **ii**:1308–1309.

307. Grossman SH. 1984. Fluorescence polarization immunoassay applied to macromolecules: creatine kinase-BB. *J Clin Immunol* 7:96–100.
308. Charlesworth JM. 1994. Optical sensing of oxygen by fluorescence quenching. *Sens Actuators B* 22:1–5.

## PROBLEMS

P19.1. *Calculation of Lifetimes:* Use the data in Figure 19.13 to calculate the lifetimes of the porphyrin probe at 0 and 20.55% oxygen. The light modulation frequency is 3907 Hz.

P19.2. *Oxygen Diffusion in a Polymer:* Long-lived phosphorescent species can be used as oxygen sensors. Figures 19.79 and 19.80 show emission spectra and intensity decays of camphorquinone in poly(vinyl chloride) and poly(methyl methacrylate) (PMMA). Use the data in these figures to calculate the oxygen bimolecular quenching constant of camphorquinone. Compare this value with that expected for a fluorophore in water, which is near  $1 \times 10^{10} \text{ M}^{-1} \text{ s}^{-1}$ . Also calculate the diffusion coefficient of oxygen in poly(methyl methacrylate). How does this compare with the value in water,  $2.5 \times 10^{-5} \text{ cm}^2/\text{s}$ ? Assume that the solubility of oxygen in poly(methyl methacrylate) is the same as in water, 0.001275 M/atm.

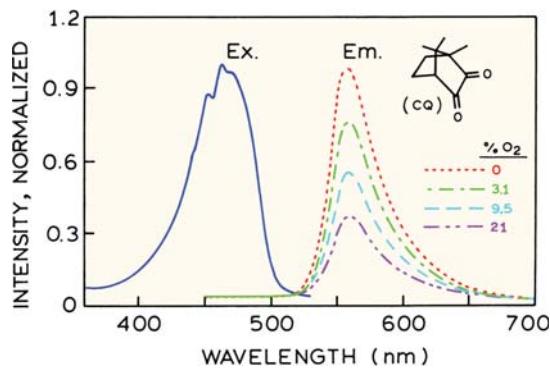


**Figure 19.79.** Normalized excitation and emission spectra of camphorquinone in poly(vinyl chloride) (PVC) illustrating the effect of oxygen concentration on phosphorescence intensity. Revised and reprinted from [308]. Copyright © 1994 with permission from Elsevier Science.

P19.3. *Lifetimes and Oxygen Quenching:* In Section 19.4.2, we stated that a short-lifetime probe can serve as an intensity reference in an oxygen sensor. Assume that the lifetime of the  $[\text{Ru}(\text{Ph}_2\text{phen})_3]^{2+}$  oxygen sensor is 5

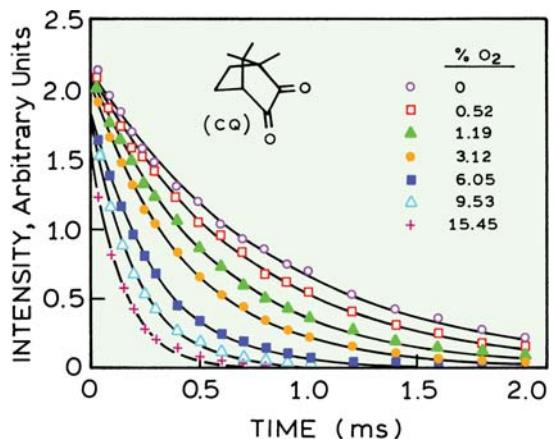


**Figure 19.80.** Phosphorescence lifetime measurements for camphorquinone in poly(methyl methacrylate) (PMMA), illustrating the influence of oxygen concentration on the triplet decay. The polymeric supports are different in Figures 19.79 and 19.80. Revised and reprinted from [308]. Copyright © 1994 with permission from Elsevier Science.

$\mu\text{s}$  and that the lifetime of the reference fluorophore is 5 ns. Using Figure 19.9 describe the relative extents of quenching for each probe?

P19.4. *Mechanism of Sensing:* Figures 19.81 and 19.82 show data for a  $\text{CO}_2$  sensor based on RET. Explain the changes in phase angle in response to  $\text{CO}_2$ . What are the apparent lifetimes of SR101 at 0% and 2%  $\text{CO}_2$ .

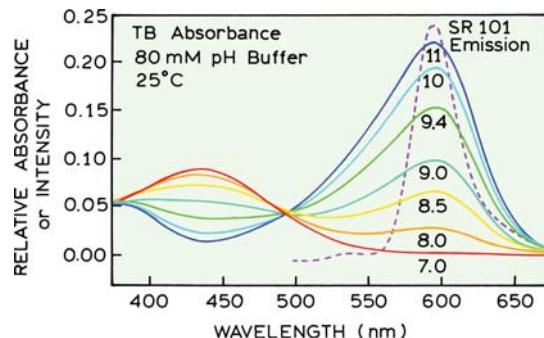


**Figure 19.81.** Spectral characteristics of the donor and acceptor employed in an RET  $\text{pCO}_2$  sensor. The solid curves show the absorption spectra of the Thymol Blue (TB) acceptor at different pH values (labeled on the curves), demonstrating overlap with the emission spectrum of the SR101 donor (dashed). SR101 and TB are present in a polymer matrix, which is weakly buffered and allows penetration of  $\text{CO}_2$ . From [65].

P19.5. *Fluorescence Polarization Immunoassays and Effects of Resonance Energy Transfer:* Suppose that you are

performing a fluorescence polarization immunoassay for a small peptide with a rotational correlation time ( $\Theta$ ) of 1 ns, and that the peptide (P) is labeled with fluorescein (Fl) for which,  $\tau = 4$  ns and  $r_0 = 0.40$ .

- A. What is the range of anisotropy values possible? Assume the antibody (Ab) to the peptide has a rotational correlation time of 100 ns.

- B. Assume that your starting assay contains Fl-P bound to Ab, and that upon mixing with the sample 10% of the Fl-P is displaced. What is the anisotropy?
- C. Now assume that the antibody is labeled with rhodamine (Rh) so that Fl-P is 90% quenched by RET. What is the anisotropy when 10% of the Fl-P is displaced?

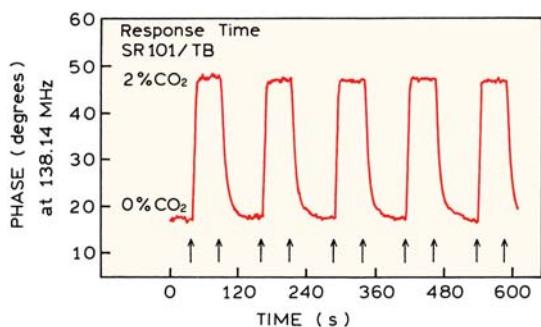


**Figure 19.82.** Response of an RET pCO<sub>2</sub> sensor employing SR 101 as donor and TB as acceptor to changes in the percentage of CO<sub>2</sub> between 0 and 2%. The phase-angle measurements were made at a light modulation frequency of 138.14 MHz. From [65].

# 20

# Novel Fluorophores

In the previous chapters we discussed small organic fluorophores typified by the Dansyl, fluorescein, rhodamine, and cyanine dyes. Numerous probes of this type have been characterized and are commercially available. The majority of these probes have extinction coefficients ranging from 10,000 to 100,000 M<sup>-1</sup> cm<sup>-1</sup> and decay times ranging from 1 to 10 ns. Some of these probes are photostable, but all the organic fluorophores display some photobleaching, especially in fluorescence microscopy with high illumination intensities. We now describe different types of lumino-phores that are mostly inorganic or display unusually long lifetimes. These classes of probes are semiconductor nanoparticles, lanthanides, and transition metal–ligand complexes (MLCs). We occasionally use the term lumino-phore, especially with the MLCs, because it is not clear if the emission occurs from a singlet or triplet state, but we will mostly use the term fluorescent to describe the emission from any of these species.

## 20.1. SEMICONDUCTOR NANOPARTICLES

Starting in 1998<sup>1</sup> there has been rapid development of fluorescent semiconductors nanoparticles. The main component of these particles is usually cadmium selenide (CdSe), but other semiconductors are also used. Particles of CdS, CdSe, InP, and InAs with diameters ranging from 3 to 6 nm can display intense fluorescence. Perhaps the best way to introduce the semiconductor nanoparticles (NPs) or quantum dots (QDots) is by their visual appearance. Figure 20.1 shows a color photograph of suspensions of NPs with different sizes.<sup>2</sup> These are core–shell NPs where the core is CdSe and the shell is ZnS. Another photograph of NPs with different sizes can be found in Figure 21.47. A wide range of emission wavelengths is available by changing the size or chemical composition of the NPs (Figure 20.2). The range of emission wavelengths has been extended to 4 μm using

PbSe particles.<sup>3</sup> PbSe QDots with emission wavelengths near 2 μm display quantum yields as high as 25%.

Studies of luminescent NPs first appeared in the early 1980s.<sup>4–7</sup> At that time the quantum yields were low. The NPs were chemically and photochemically unstable and had a heterogeneous size distribution. Since that time there have been many advances in synthesis of homogeneous and stable NPs.<sup>8–11</sup> The chemical and optical properties of NPs have been described in many reviews.<sup>12–16</sup> Figure 20.3 shows a schematic of a typical QDot. Chemical and photochemical stability are improved by coating the CdSe core with a material that has a higher bandgap. The bandgap of a semiconductor is the energy of the longest-wavelength absorption. ZnS has a higher bandgap than CdSe, which means the long-wavelength absorption of ZnS is at a shorter wavelength than CdSe.

The optical properties of NPs are similar to a quantum mechanical particle in a box. Absorption of light results in creation of an electron–hole pair. Recombination of the pair can result in emission. The energy of the excited state decreases as the particle size increases. The energy of the excited state also depends on the material. The use of a higher bandgap shell confines the excited state to the center of the particle. This prevents interactions with the surface that decrease the quantum yield and chemical stability. In order to use the NPs in biological systems they need to be water soluble, which is accomplished with a polymer or silica layer. This layer is then used to attach proteins or nucleic acids.

Several different methods are used to make the NPs biocompatible and to introduce binding specificity.<sup>17–20</sup> The surfaces can be coated with sulfhydryl groups using molecules like mercaptoacetic acid or dihydrolipoic acid, followed by crosslinking to amino groups on the biomolecules (Figure 20.4). NPs have also been coated with silica, for which the surface chemistry is well known. Biomolecules

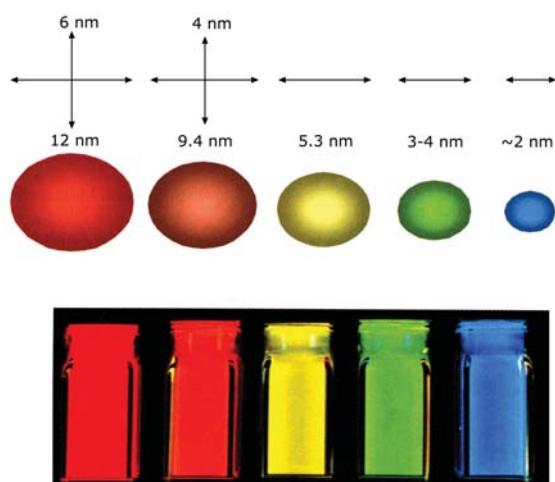


**Figure 20.1.** Color photographs of cadmium selenide nanoparticles illuminated with a long-wave UV lamp. Revised from [2].

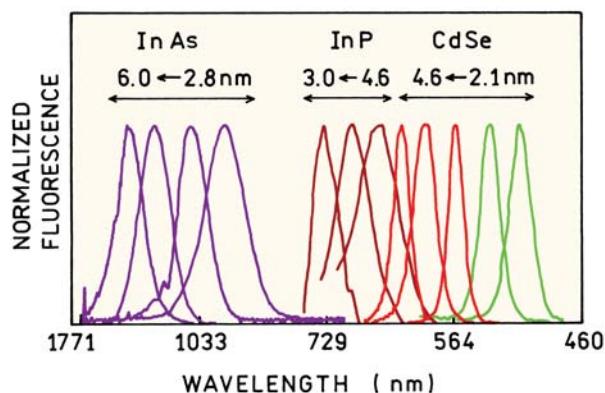


**Figure 20.2.** Emission spectra of semiconductor nanoparticles. The approximate diameters are labeled on the figure. These are core–shell particles. For CdSe the shell is ZnS or CdS. Revised from [1].

can also be bound to the surface by hydrophobic or electrostatic interactions. Using these procedures NPs have been coated with avidin and antibodies. Avidin, which is positively charged, binds spontaneously to negatively charged QDots.<sup>18</sup> When using NPs as probes it is useful to visualize their size.<sup>21</sup> NPs are comparable in size to modest size proteins (Figure 20.5), larger than GFP and smaller than IgG. NPs are much larger than standard fluorophores.

### 20.1.1. Spectral Properties of QDots

QDots display several favorable spectral features. The emission spectra of homogeneously sized QDots are about

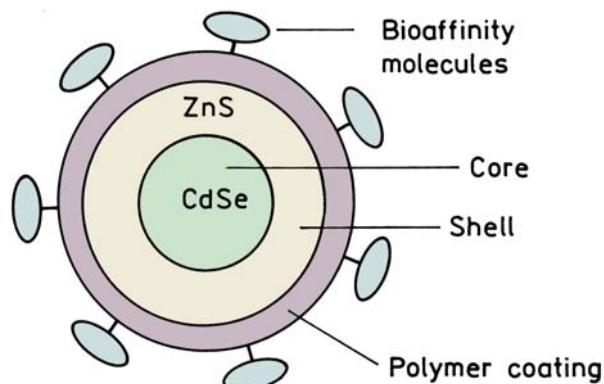


**Figure 20.3.** Schematic of a core–shell NPs with a biologically compatible surface.

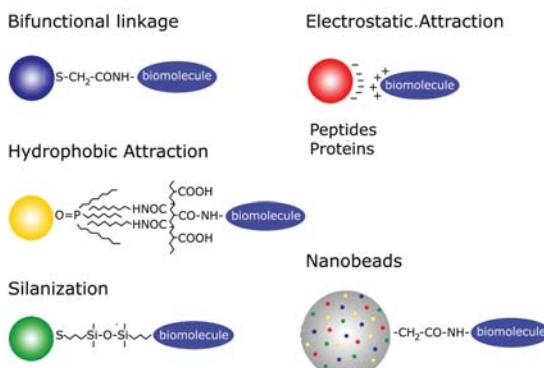


**Figure 20.4.** Methods used to attach biomolecules to NPs. Revised from [20].

twofold more narrow than typical fluorophores.<sup>22</sup> This feature can be seen by comparing the emission spectra of cyanine dyes with QDots (Figure 20.6). Additionally, the QDots do not display the long-wavelength tail common to all fluorophores. These tails interfere with the use of multiple fluorophores for imaging or multi-analyte measurements. The emission spectra of the QDots are roughly symmetrical on the wavelength scale and do not display such tails. For this reason the QDots are being used for optical bar codes for multiplexed assays.<sup>23–24</sup> This approach is shown in Figure 20.4 (lower right), which shows a polymer bead containing QDots with different emission wavelengths. See also Section 21.6.

An important spectral property of the QDots is their absorption at all wavelengths shorter than the onset of the absorption.<sup>22</sup> Many of the commonly used organic fluorophores display strong long-wavelength absorption, but

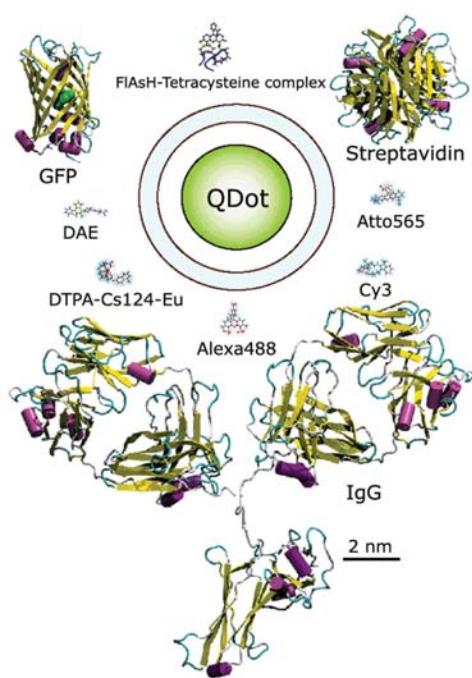


**Figure 20.5.** Relative sizes of luminescent probes and some biomolecules. Revised from [21].

much less absorption at shorter wavelengths. For example, Cy3 and Cy5 are essentially non-absorbing at 400 nm (Figure 20.6). In contrast, the QDots absorb at these shorter wavelengths. This spectral property allows excitation of a range of NP sizes using a single light source, which is needed for practical multiplex assays. The wide absorption spectra also allow excitation with a spectrally wide light source.

The QDots also have large extinction coefficients ( $\epsilon$ ) that on a molar basis can be up to tenfold larger than rhodamine.<sup>25–26</sup> Small QDots have  $\epsilon$  values similar to that of R6G, near  $200,000 \text{ M}^{-1} \text{ cm}^{-1}$ . Larger QDots can have  $\epsilon$  values as large as  $2 \times 10^6 \text{ M}^{-1} \text{ cm}^{-1}$ . And, finally, QDots can be highly photostable (below), making them useful probes for fluorescence microscopy.

### 20.1.2. Labeling Cells With QDots

Quantum dots are relatively large, and cadmium is toxic, so it was not known if they would be useful for cell labeling. QDots can be cytotoxic under some conditions,<sup>27–28</sup> but it seems that the core–shell particles are nontoxic. Quantum dots covered with mixtures of n-poly(ethylene glyco)phosphatidylethanolamine (PEG-PE) and phosphatidylcholine

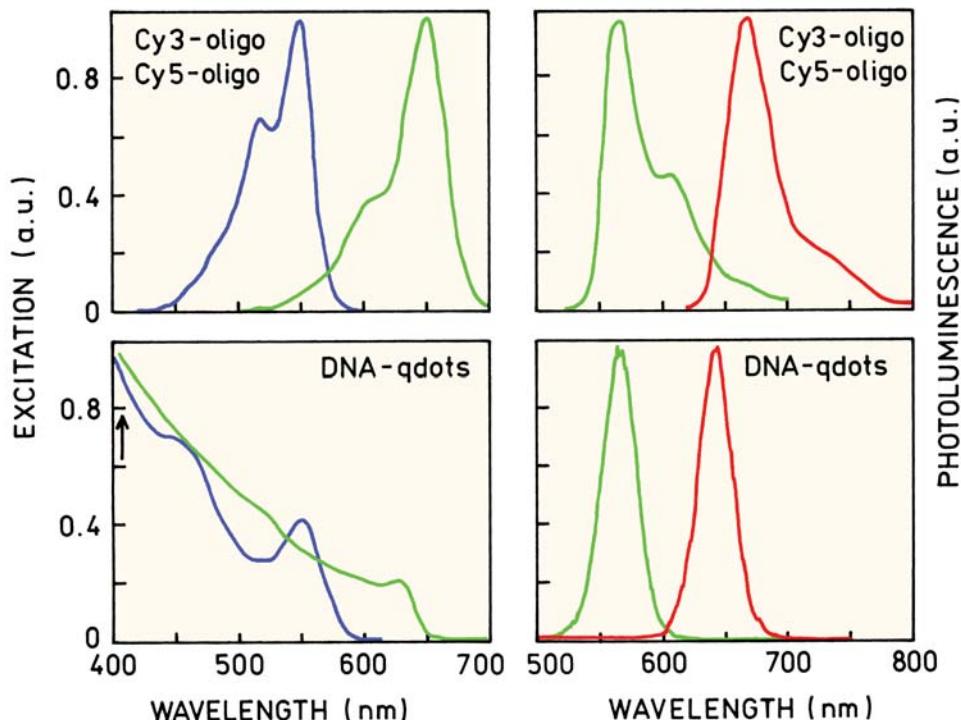


**Figure 20.6.** Absorption and emission spectra of Cy3- and Cy5-labeled oligomers and QDots with bound oligomers. Reprinted with permission from [22]. Copyright © 2003, American Chemical Society.

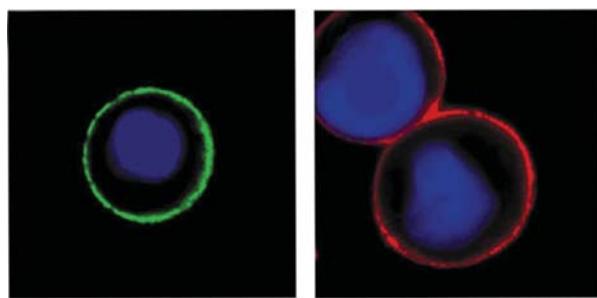


**Figure 20.7.** Labeling of the Her2 marker on breast cancer cells using QDots emitting at 535 (left) or 630 nm (right). From [30].

(PC) were injected into *Xenopus* embryos, with no effect on their development.<sup>29</sup>

QDots can be used for specific labeling of fixed and live cells.<sup>30–31</sup> Her2 is a cancer marker that is overexpressed on the surface of some breast cancer cells. Fixed cells were incubated with monoclonal antibodies against the external domain of Her2. QDots emitting at 535 nm or 630 nm were conjugated to anti-IgG antibodies. These protein-coated antibodies bound specifically to the Her2 markers (Figure 20.7).

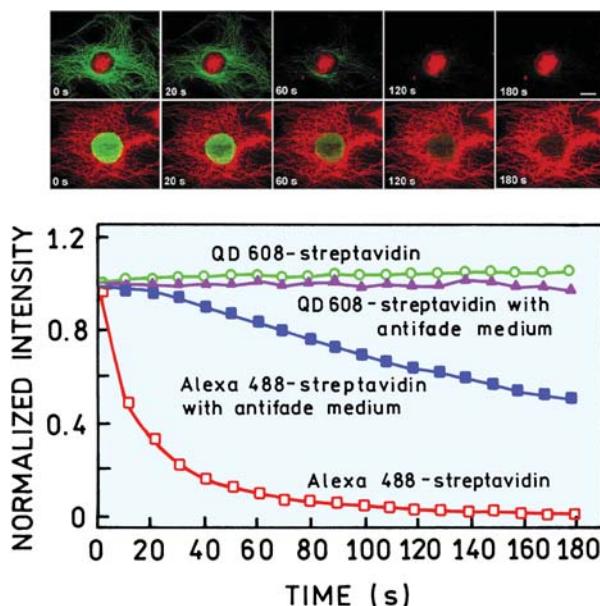


**Figure 20.8.** Photostability comparison between QDots and Alexa 488. Top row: the nuclear antigens were labeled with 630-nm QDots and the microtubules with Alexa 488. Second row: the microtubules were labeled with 630-nm QDots and the nuclear antigens with Alexa 488. The graph shows the intensities with continuous illumination. From [30].

An important property of the QDots is their photostability. Figure 20.8 shows cells labeled with both QDots and the photostable fluorophore Alexa 488. In the top row of images the QDots were localized in the nucleus. In the bottom row of images the QDots were bound to the microtubules in the cytoplasm. These images show that the signal from Alexa 488 is quickly bleached but the QDots remain fluorescent. These results also show that it is possible to label internal cellular structures with QDots and that the intracellular QDots can be highly photostable.

### 20.1.3. QDots and Resonance Energy Transfer

QDots appear to behave like any other fluorophore with regard to energy transfer. RET occurs between QDots.<sup>32–39</sup> The schematic in Figure 20.9 shows a system used to test for RET from a CdSe QDot to a rhodamine acceptor. The QDot surface was coated with biotinylated BSA. Addition of streptavidin labeled with tetramethylrhodamine (SAv-TMR) resulted in quenching of the QDot emission.

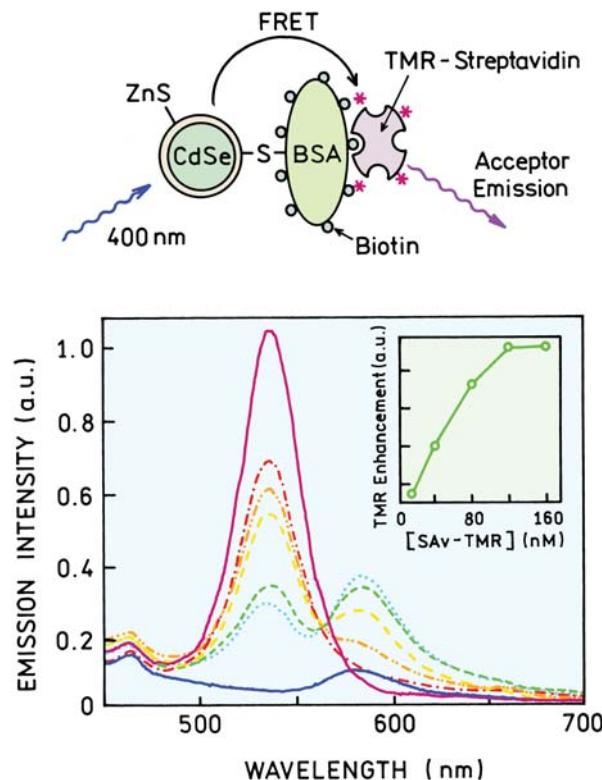


**Figure 20.9.** RET from CdSe QDots to tetramethylrhodamine. The QDot donor intensity decreased (top to bottom at 540 nm) as the concentration of TRM-streptavidin increased. Reprinted with permission from [39]. Copyright © 2001, American Chemical Society.

## 20.2. LANTHANIDES

The lanthanides europium ( $\text{Eu}^{3+}$ ) and terbium ( $\text{Tb}^{3+}$ ) are unique fluorescent probes. In contrast to all fluorophores described so far these lanthanides display line spectra from the individual atoms. The emission lifetimes of  $\text{Eu}^{3+}$  and  $\text{Tb}^{3+}$  are on the millisecond timescale and arise from transitions between the  $f$  orbitals. The emission rates are low because the transitions are formally forbidden. The inner shell  $f$  orbital electrons are shielded from the environment, so that lanthanides do not display polarity-dependent spectral shifts and are not quenched by oxygen.

The use of lanthanides in biochemistry originated with their use as a luminescent substitute for calcium.<sup>40–42</sup> Fluorescent probes are usually sensitive to the surrounding environment. The lanthanides can be sensitive to their environment, but in ways different from typical fluorophores. The decay times of the lanthanides depend on the number of coordinated water molecules.<sup>43–45</sup> The number of bound water molecules ( $n$ ) is given by

$$n = q \left( \frac{1}{\tau_{\text{H}_2\text{O}}} - \frac{1}{\tau_{\text{D}_2\text{O}}} \right) \quad (20.1)$$

where the lifetimes are measured in  $\text{H}_2\text{O}$  and  $\text{D}_2\text{O}$ . The values of  $q$  are 1.05 and 4.2 for  $\text{Eu}^{3+}$  and  $\text{Tb}^{3+}$ , respectively. The lanthanides can bind to proteins in place of calcium and the lifetimes can be used to determine the hydration of the protein-bound ions. The lanthanide decay times can also be affected by RET. Since the lanthanides have low extinction coefficients they are not useful as acceptors. However, the lanthanides can have high quantum yields and can serve as donors. At present most applications of the lanthanides are based on their use as RET donors.

Because of their low extinction coefficients the lanthanides are not usually excited directly. The ions are at first bound to chelators that contain a fluorophore (Figure 20.10). The energy from the fluorophore can be efficiently transferred to the lanthanide. The energy of the excited fluorophore must be adequate to excite the lanthanide. The chelators serve two other purposes. The chelator increases the quantum yield of the lanthanide by displacing the bound water molecules that act as quenchers. The chelator also provides a means to bind the lanthanide to a biomolecule using standard coupling chemistry. A large number of chelators have been described.<sup>46–48</sup> The more recent papers often describe chelators that are conjugatable or otherwise designed for biological applications.<sup>49–54</sup> However, many of

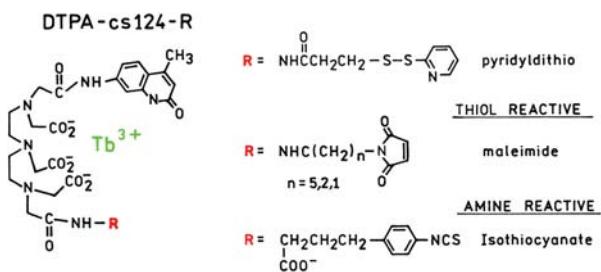


**Figure 20.10.** Conjugatable chelators for lanthanides. Reprinted with permission from [46]. Copyright © 1999. With kind permission of Springer Science and Business Media.

these chelators are not commercially available. The need to synthesize suitable chelators appears to limit the use of lanthanides in biochemical research.

Figure 20.11 shows the emission spectra and intensity decays of  $\text{Tb}^{3+}$  and  $\text{Eu}^{3+}$  when complexed with DTPA-cs124. These emission spectra show no component from the carbostyryl 124, which is part of the chelator. These spectra were recorded using a light chopper with a 145- $\mu\text{s}$  delay to suppress the prompt fluorescence from carbostyryl 124. It is possible to use such long time delays because of the 0.61- and 1.54-ms lifetimes of the  $\text{Eu}^{3+}$  and  $\text{Tb}^{3+}$  chelates, respectively. If the spectra were recorded without time-delayed

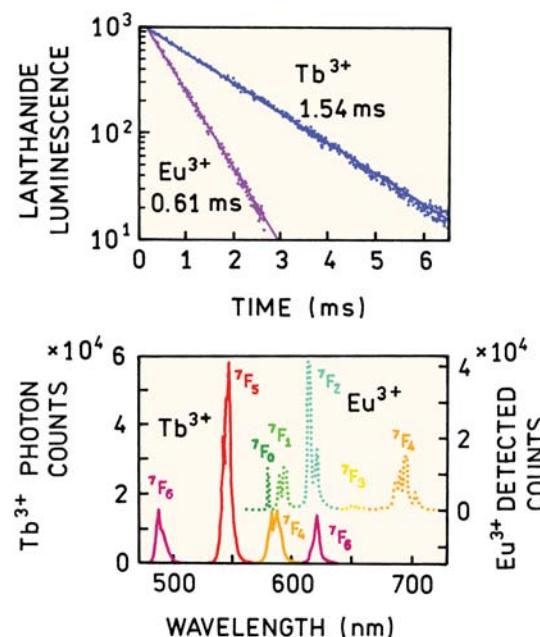


**Figure 20.11.** Emission spectra and intensity decays of  $\text{Tb}^{3+}$  and  $\text{Eu}^{3+}$  complexed with DTPA-cs124. Emission from  $\text{Tb}^{3+}$  in  $^5\text{D}_4 \rightarrow ^7\text{F}_j$  and from  $\text{Eu}^{3+}$  in  $^5\text{D}_0 \rightarrow ^7\text{F}_j$ . Reprinted with permission from [46]. Copyright © 1999. With kind permission of Springer Science and Business Media.

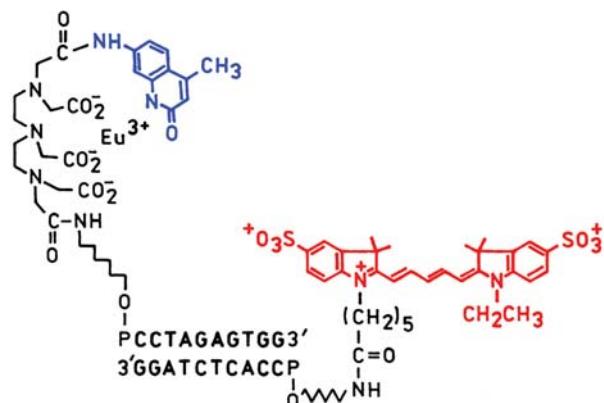


**Figure 20.12.** Lanthanide–cyanine donor–acceptor pair linked by a DNA oligomer. Revised and reprinted with permission from [57]. Copyright © 1994, American Chemical Society.

detection there would probably be a large contribution from carbostyryl 124, which would be due to DTPA-cs124 without bound lanthanide.

### 20.2.1. RET with Lanthanide

Lanthanides have a number of favorable properties as RET donors.<sup>46,55–57</sup> The value of  $R_0$  are typically 50–70 Å for transfer from chelated lanthanides. The Förster distances can be as large as 90 Å for transfer to allophycocyanine. The quantum yields of lanthanide chelates depend on the concentration of water, so that the quantum yield and the value of  $R_0$  can be adjusted to some degree using the H<sub>2</sub>O/D<sub>2</sub>O mixture. The emission from lanthanides is unpolarized so there is less concern with  $\kappa^2$ , which must be between 1/3 and 4/3 for the most extreme cases. This range of  $\kappa^2$  values can result in a maximum error in the distance of only 12%. The long decay times make it possible to measure the decays with high precision and with suppression of background. And, finally, use of the long-lived acceptor emission allows selective observation of only the D–A pairs without observing free donor or free acceptor.

Figure 20.12 shows an example of RET from a chelated lanthanide to a Cy5 acceptor. The donor and acceptor are linked to opposite ends of a DNA oligomer.<sup>55–56</sup> The emission spectrum for the D–A pair shows the expected europium emission spectrum and emission from Cy5 centered near 668 nm (Figure 20.13). This component was not due to directly excited Cy5 because the emission spectra were collected with a time delay of 90 µs and the decay time of directly excited Cy5 is close to 1 ns. The intensity decay of the donor alone is a single exponential. The donor decay in

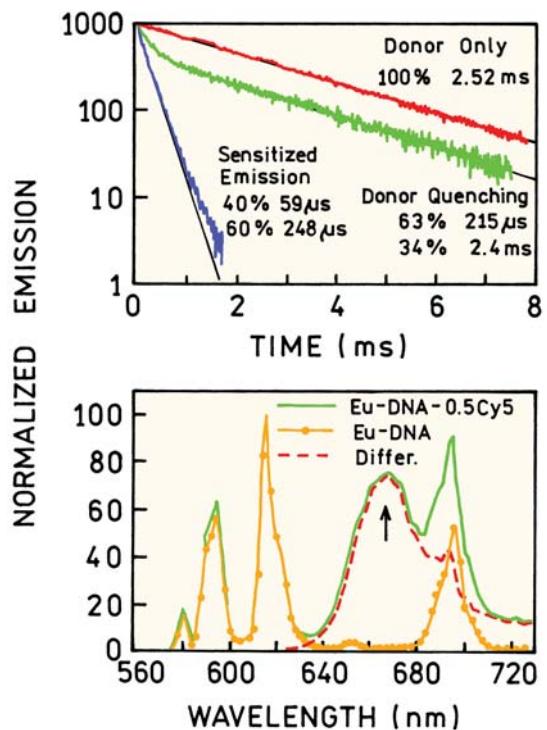


**Figure 20.13.** Emission spectra and intensity decays of the donor–acceptor pair shown in Figure 20.12. The emission spectra were collected with a time delay of 90 µs. The intensity decays were measured for the donor at 617 nm and for the sensitized acceptor emission at 668 nm. Reprinted with permission from [46]. Copyright © 1999. With kind permission of Springer Science and Business Media.

the D–A pair shows two decay times: 0.22 and 2.40 ms. The 2.40-ms component is the same decay time as the donor alone and the component is due to donor strands of DNA that are not hybridized with acceptor strands.

A valuable property of lanthanide donor–acceptor pairs is the ability to selectively observe the pairs in the presence of unpaired donors and acceptors. The rapidly decaying component in Figure 20.13 is for the sensitized acceptor emission measured at 668 nm. This acceptor emission is due to energy transfer from the donor, and it decays with the same rate as the donor. Hence the decay time of this component (0.22 ms) represents the decay time of the donor in D–A pairs. Selective observation of this component is possible because of the structured emission of the donor that does not emit at the maximum of the acceptor emission. The 59-µs component in the sensitized acceptor emission is due to an artifact in the detector.

There are several aspects of RET with lanthanide donors that are worthy of mention. RET occurs due to dipolar

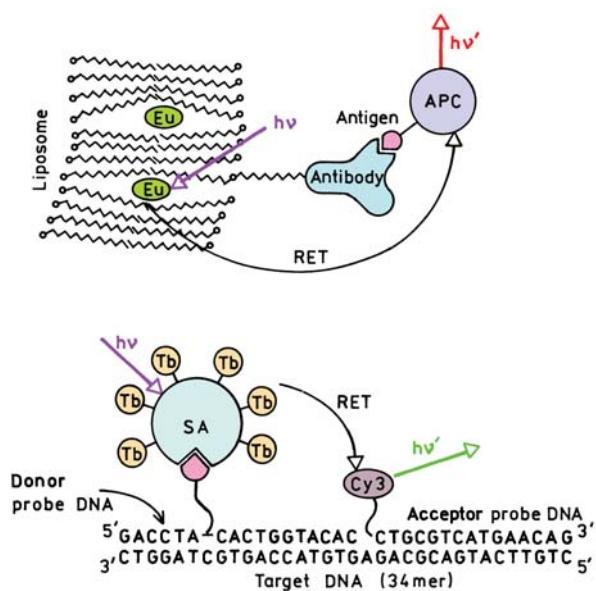


**Figure 20.14.** Schematic of an immunoassay and a DNA assay using RET with a lanthanide donor. APC, allophycocyanine; B, biotin; SA, streptavidin. The chelators are not shown. Revised from [58–59].

interactions. The two shorter wavelengths transitions around 590–600 nm for europium are thought to be magnetic dipoles and are not included in calculation of the overlap integrals. The intensity decay of the sensitized acceptor, and thus also that of the donor, are single exponentials. This is somewhat surprising because the flexibility of the linkers (Figure 20.12) is expected to result in a distribution of donor-to-acceptor distances. Any effect of a distance distribution is probably eliminated due to diffusive motions during the donor lifetime (Sections 15.5 and 15.6). It is also interesting to notice that RET from a lanthanide donor occurs on a millisecond timescale, whereas RET from a nanosecond donor occurs on a nanosecond timescale. This dependence on the decay time of the donor is because the transfer rate is proportional to the radiative decay rate of the donor (Section 13.2).

In Section 3.9.1 we described the use of lanthanides with gated detection for high-sensitivity assays. The detector is gated on after the prompt autofluorescence has decayed. With gated detection the goal is not to measure distances but rather to obtain the highest possible sensitivity. Figure 20.14 shows examples of DNA hybridization assays and immunoassays using lanthanides and RET.<sup>58–59</sup> In both cases the signal levels are increased by the use of multiple-lanthanide donors. The immunoassay uses allophycocyanine as the acceptor, which results in large Förster

distances due to the high extinction coefficients of the phycoobiliproteins. The DNA hybridization assay uses Cy3 as the acceptor.

RET with lanthanides can also be used for structural studies of proteins.<sup>60</sup> One example is tropomyosin that was labeled with a terbium donor and a TMR acceptor on cysteine residues at positions 56 and 100, respectively (Figure 20.15). The shortest component of 0.03 ms is due to a ringing artifact in the gated detector. The decrease in lifetime from 1.37 to 0.61 ms indicates a transfer efficiency of 56%. Based on the Förster distance of  $R_0 = 57 \text{ \AA}$ , this efficiency indicates a distance of 55 Å. This distance is shorter than the value of 65 Å obtained from the x-ray structure. The smaller recovered distance is probably due to flexing of tropomyosin during the millisecond donor lifetime.

## 20.2.2. Lanthanide Sensors

Because of the shielded *f* orbitals the lanthanides are rather insensitive to their local environment. This makes it difficult to develop analyte-sensitive probes like those available for calcium and other ions (Chapter 19). However, lanthanide-based sensors have been developed using different principles. Lanthanide-based sensors can depend on

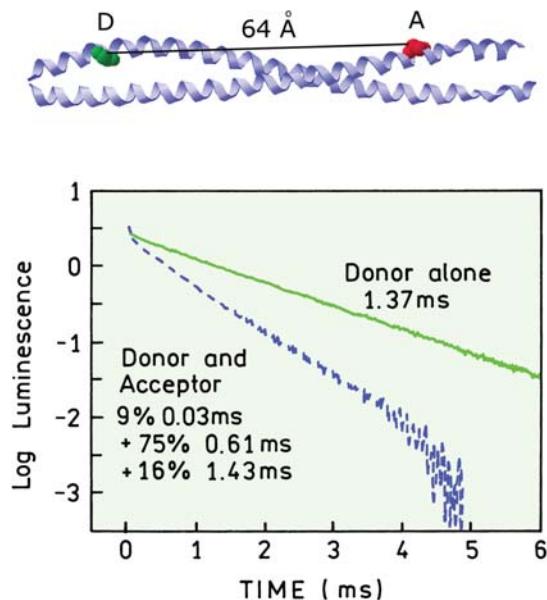


**Figure 20.15.** Intensity decays of tropomyosin labeled with a Tb<sup>3+</sup> donor, or with both the donor and a TMR acceptor. The chelator was a sulphydryl-reactive version of DPTA-cs124. Revised and reprinted with permission from [60]. Copyright © 2004, American Chemical Society.

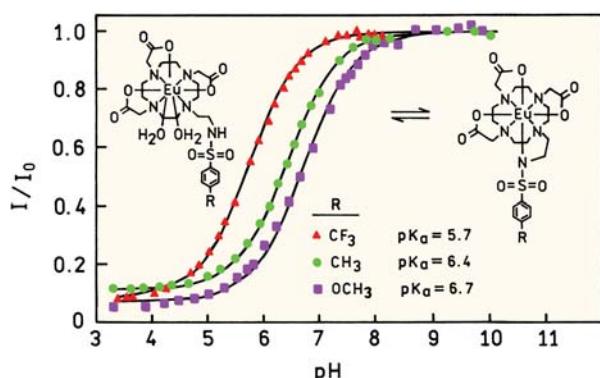


Figure 20.16. Lanthanide-based pH sensor. From [66].

changes in hydration or changes in RET from the chelator.<sup>61–67</sup> The lanthanide chelate shown in Figure 20.16 displays an increased intensity at higher pH values. This increase in intensity is due to removal of a bound water molecule that is displaced by the sulfonamide at high pH. Figure 20.17 shows excitation spectra of a cyclodextran terbium complex with increasing concentrations of naphthalene. The increased emission intensity of terbium at 544 nm is due to energy transfer from naphthalene as it binds in the cyclodextran cavity.

### 20.2.3. Lanthanide Nanoparticles

The long lifetime and large Stokes shift of the lanthanides make them useful in high-sensitivity assays. The sensitivity

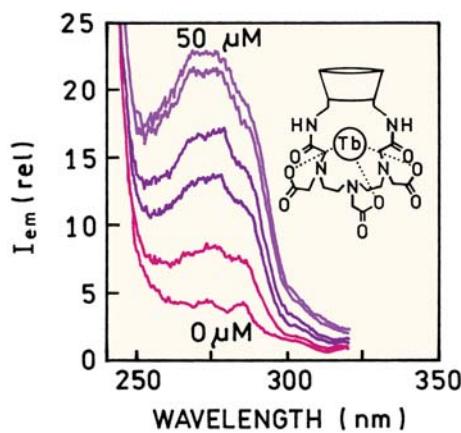


Figure 20.17. Excitation spectra of a cyclodextran terbium complex with increasing concentrations of naphthalene. Excitation at 275 nm and emission at 544 nm. Revised and reprinted with permission from [67]. Copyright © 1996, American Chemical Society.

can be increased using nanoparticles that contain a large number of lanthanide chelates.<sup>68–71</sup> These nanoparticles are just becoming available, and the compositions are likely to evolve. Some of the particles are polystyrene and contain the lanthanide and a hydrophobic chelator. Other preparations are based on silica-coated particles of the chelated lanthanide (Figure 20.18). In both cases the surfaces are derivatized to contain reactive groups for binding to biomolecules.

### 20.2.4. Near-Infrared Emitting Lanthanides

Red-emitting or near-infrared (NIR) emitting fluorophores can be useful for high-sensitivity detection because of the decreased autofluorescence at longer wavelengths. NIR-emitting lanthanides are also known. Erbium (Er), neodymium (Nd), and ytterbium (Yb) emit at wavelengths ranging from 900 to 1500 nm (Figure 20.19).<sup>72–74</sup> Because of their longer-wavelength absorption spectra these lanthanides can be sensitized by longer-wavelength fluorophores like fluorescein and eosin,<sup>73</sup> and even by an NIR fluorophore absorbing at 980 nm.<sup>75</sup> The spectra shown in Figure 20.19 were recorded with excitation at 488 nm, where these fluorophores absorb. At present, the quantum yield of the NIR lanthanides are low. However, there are ongoing efforts to synthesize chelators that result in higher quantum yields from the NIR lanthanides.<sup>76–77</sup> The NIR lanthanides are beginning to find a use in immunoassays.<sup>78</sup>

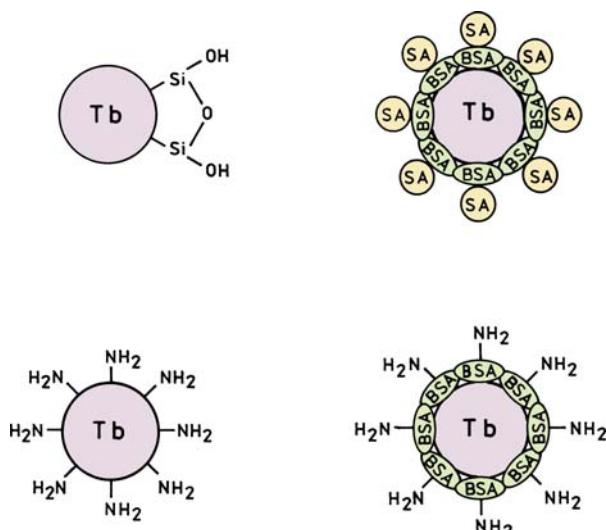
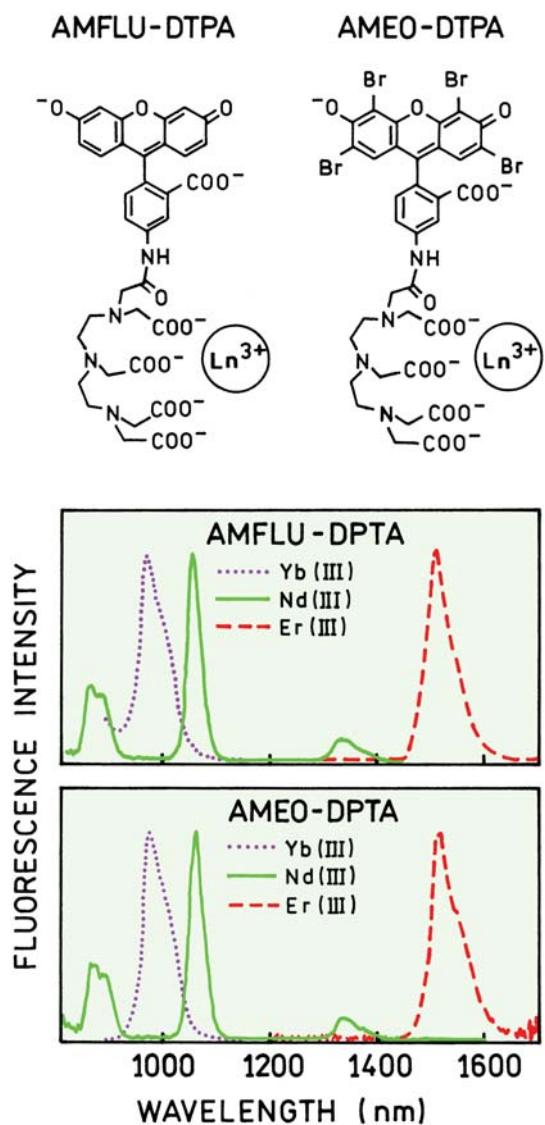


Figure 20.18. Lanthanide-containing nanoparticles. The particles are about 42 nm in diameter. Revised and reprinted with permission from [71]. Copyright © 2004, American Chemical Society.



**Figure 20.19.** Emission spectra of NIR-emitting lanthanide chelators. Excitation at 488 nm. Revised from [72].

### 20.2.5. Lanthanides and Fingerprint Detection

Detection and imaging of fingerprints is often performed in a crime-scene investigation (CSI). Fingerprints are often detected with colorimetric or fluorogenic reagents that react with amino groups.<sup>79–80</sup> Lanthanides can also be used for visualization of fingerprints.<sup>81–83</sup> Detection is based on the quenching of lanthanides by water. Fingerprints are often treated with cyanoacrylate, which reacts with molecules in the prints. These treated prints can be sprayed by a lanthanide chelate that has several bound water molecules. The chelator is usually hydrophobic. The chelator with its bound

lanthanide partitions into the polymer and/or fingerprints. When this occurs the water is left behind and the lanthanides become more brightly fluorescent. The large Stokes shift and narrow emission spectra of the lanthanides allows for effective use of filters to remove the incident light and unwanted background fluorescence.

### 20.3. LONG-LIFETIME METAL-LIGAND COMPLEXES

Organic fluorophores have decay times ranging from 1 to 20 ns and lanthanides have millisecond decay times. These timescales are useful for many biophysical measurements, but there are numerous instances where intermediate decay times are desirable. For instance, one may wish to measure rotational motions of large proteins or membrane-bound proteins. In such cases the overall rotational correlation times can be near 200 ns, and can exceed 1  $\mu\text{s}$  for larger macromolecular assemblies. Rotational motions on this timescale are not measurable using fluorophores that display ns lifetimes. Processes on the  $\mu\text{s}$  or even the ms timescale have occasionally been measured using phosphorescence.<sup>84–86</sup> However, relatively few probes display useful phosphorescence in room temperature aqueous solutions. Also, it is usually necessary to perform phosphorescence measurements in the complete absence of oxygen. The lanthanides are not quenched by oxygen, but their emission is not polarized so they are not useful for measurements of rotational diffusion. Also, the millisecond lanthanide lifetimes are too long for measurements of many dynamic processes. Hence, there is a clear need for probes that display microsecond lifetimes. In this section we describe a family of metal-ligand probes that display decay times ranging from 100 ns to 10  $\mu\text{s}$ . The long lifetimes of the metal-ligand probes allow the use of gated detection, which can be used to suppress interfering autofluorescence from biological samples and thus provide increased sensitivity.<sup>87</sup> And, finally, the metal-ligand probes display high chemical and photochemical stability and are reasonably soluble in water. Because of these favorable properties, metal-ligand probes can have numerous applications in biophysical chemistry, clinical chemistry, and DNA diagnostics.

#### 20.3.1. Introduction to Metal-Ligand Probes

The term metal-ligand complex (MLC) refers to transition metal complexes containing one or more diimine ligands. This class of probes is typified by  $[\text{Ru}(\text{bpy})_3]^{2+}$ , where bpy

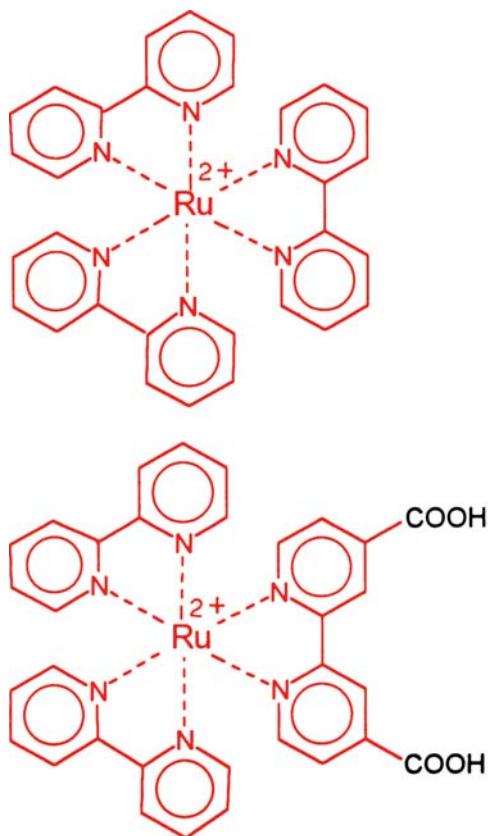
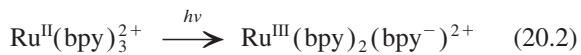


**Figure 20.20.** Chemical structure of  $[\text{Ru}(\text{bpy})_3]^{2+}$  and of  $[\text{Ru}(\text{bpy})_2(\text{dcbpy})]^{2+}$ . The latter compound is conjugatable and displays strongly polarized emission.

is 2,2'-bipyridine (Figure 20.20). This class of compounds was originally developed for use in solar energy conversion and has become widely used as model compounds to study excited-state charge transfer. Upon absorption of light  $[\text{Ru}(\text{bpy})_3]^{2+}$  becomes a metal-to-ligand charge-transfer species, in which one of the bpy ligands is reduced and ruthenium is oxidized:



where  $\text{Ru}^{\text{III}}$  is a strong oxidant and  $\text{bpy}^-$  a strong reductant. It was hoped that this charge separation could be used to split water to hydrogen and oxygen. A wide variety of luminescent MLCs are now known, some of which are strongly luminescent and some of which display little or no emission. The metals are typically rhenium (Re), ruthenium (Ru), osmium (Os), or iridium (Ir). A number of extensive reviews of their spectral properties is available.<sup>88–96</sup>

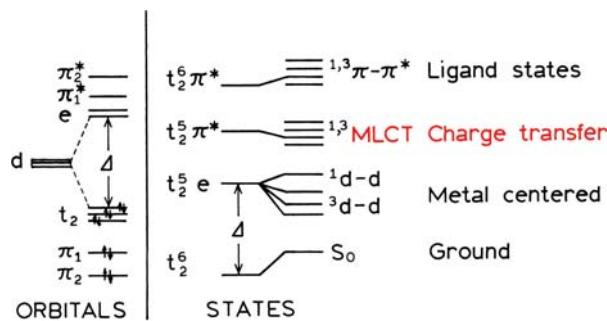


**Figure 20.21.** Orbital and electronic states of metal–ligand complexes. The  $d$  orbitals are associated with the metal, and are split by energy  $\Delta$  due to the crystal field created by the ligands. The  $\pi$  orbitals are associated with the organic ligands and the  $d$  orbitals are associated with the metal. All the transition metal complexes we will discuss have six  $d$  electrons. The presence of ligands splits the  $d$ -orbital energy levels into three lower ( $t$ ) and two higher ( $e$ ) orbitals. The extent of splitting is determined by the crystal field strength  $\Delta$ . The three lower energy  $d$  orbitals are filled by the six  $d$  electrons. Transitions between the orbitals ( $t \otimes e$ ) are formally forbidden. Hence, even if  $d$ - $d$  absorption occurs the radiative rate is low and the emission is quenched. Additionally, electrons in the  $e$  orbitals are antibonding with respect to the metal–ligand bonds, so excited  $d$ - $d$  states are usually unstable.

Prior to discussing the spectral properties of the MLCs, it is useful to have an understanding of their unique electronic states (Figure 20.21). The  $\pi$  orbitals are associated with the organic ligands and the  $d$  orbitals are associated with the metal. All the transition metal complexes we will discuss have six  $d$  electrons. The presence of ligands splits the  $d$ -orbital energy levels into three lower ( $t$ ) and two higher ( $e$ ) orbitals. The extent of splitting is determined by the crystal field strength  $\Delta$ . The three lower energy  $d$  orbitals are filled by the six  $d$  electrons. Transitions between the orbitals ( $t \otimes e$ ) are formally forbidden. Hence, even if  $d$ - $d$  absorption occurs the radiative rate is low and the emission is quenched. Additionally, electrons in the  $e$  orbitals are antibonding with respect to the metal–ligand bonds, so excited  $d$ - $d$  states are usually unstable.

The appropriate combination of metal and ligand results in a new transition involving charge transfer between the metal and ligands (Figure 20.22). For the complexes described in this chapter the electrons are promoted from the metal to the ligand, the so-called metal-to-ligand charge

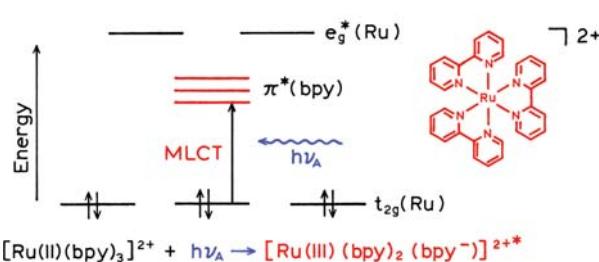


**Figure 20.22.** Metal-to-ligand charge transfer (MLCT) transition in  $[\text{Ru}(\text{bpy})_3]^{2+}$ . From [98].

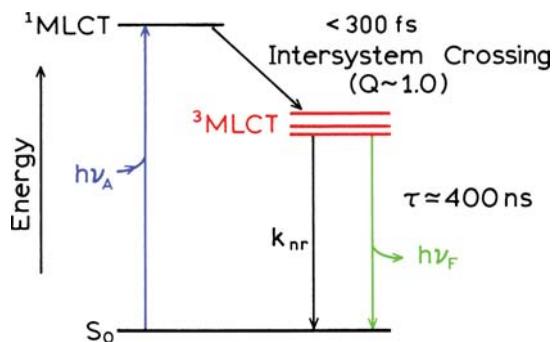


**Figure 20.23.** Jablonski diagram for a metal–ligand complex  $[\text{Ru}(\text{bpy})_3]^{2+}$ . The decay time is near 400 ns.

transfer (MLCT) transition. The MLCT transition is the origin of the absorbance of the ruthenium MLCs near 450 nm. Emission from these states is formally phosphorescence. However, these states are shorter lived (microseconds) than normal phosphorescent states, and thus can emit prior to quenching. The luminescence of MLCs is thought to be short lived due to spin–orbit coupling with the heavy metal atom, which increases the allowedness of the normally forbidden transition to the ground state.

A Jablonski diagram for the metal–ligand complexes is shown in Figure 20.23. Following absorption the complex undergoes intersystem crossing to the triplet MLCT state. This occurs rapidly:<sup>99–102</sup> in less than 300 fs and with high efficiency. Once in the MLCT state the excited-state complex decays by the usual radiative ( $\Gamma$ ) and non-radiative ( $k_{\text{nr}}$ ) decay pathways. In general the values of  $k_{\text{nr}}$  are larger

than  $\Gamma$ , and the decay times are determined mostly by the non-radiative decay rates.

For an MLC to be luminescent several criteria must be satisfied. The crystal field must be strong enough to raise the  $d$ – $d$  state above the MLCT state. Hence, iron MLCs  $[\text{Fe}(\text{L-L})_3]^{2+}$  are non-luminescent due to the low lying  $d$ – $d$  state (Figure 20.24). In contrast  $[\text{Ru}(\text{L-L})_3]^{2+}$  is luminescent because the  $d$ – $d$  states are above the MLCT state and do not serve as a major route of radiationless decay.  $[\text{Os}(\text{L-L})_3]^{2+}$  has still higher  $d$ – $d$  energies. Since the  $d$ – $d$  levels are not accessible, osmium complexes are highly photostable. However, osmium MLCs are usually weakly luminescent. This is a result of the energy gap law. As the energy of the excited state becomes closer to the ground state, the rate of radiationless decay increases due to the energy gap law. Smaller energy gaps result in more rapid radiationless decay (Section 20.3.4). Osmium MLCs typically have long-wavelength emission, a low-energy MLCT state, and a rapid rate of radiationless decay.

The relative levels of MLCT and  $d$ – $d$  states determine the sensitivity of the MLC decay times to temperature. If the  $d$ – $d$  levels are close to the MLCT level, then the  $d$ – $d$  states are thermally accessible. In such cases increasing temperature results in decreased lifetimes due to thermal population of the  $d$ – $d$  states, followed by rapid radiationless decay. Osmium complexes with thermally inaccessible  $d$ – $d$  levels are less sensitive to temperature.<sup>103–104</sup>

### 20.3.2. Anisotropy Properties of Metal–Ligand Complexes

The interest in MLCs as biophysical probes was stimulated by the observation that some MLCs display strongly polarized emission. The structure of  $[\text{Ru}(\text{bpy})_3]^{2+}$  is highly symmetrical with three identical ligands. Hence, one does not expect the excited state to be localized on any particular ligand, and the emission is expected to display low or zero anisotropy. However, it was found that Ru MLCs that contained nonidentical diimine ligands displayed high anisotropy. The first such compound studied<sup>105</sup> was the dicarboxy derivative  $[\text{Ru}(\text{bpy})_2(\text{dc bpy})]^{2+}$ , where dc bpy is 4,4'-dicarboxy-2,2'-bipyridyl (Figure 20.20, right). The excitation anisotropy spectrum of this MLC is shown in Figure 20.25, along with that of several similar RuMLCs. The dicarboxy ligand was conjugated to human serum albumin (HSA) via the carboxyl groups. Higher fundamental anisotropies ( $r_0$ ) were observed for the dicarboxy derivative than for  $[\text{Ru}(\text{bpy})_3]^{2+}$ . Also, usefully high anisotropies were

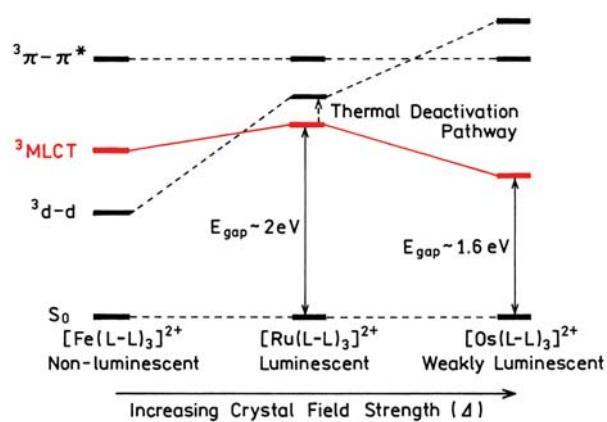


**Figure 20.24.** Lowest energy triplet states for metal–ligand complexes with increasing crystal field strength. Revised and reprinted with permission from [103]. Copyright © 1991, American Chemical Society.

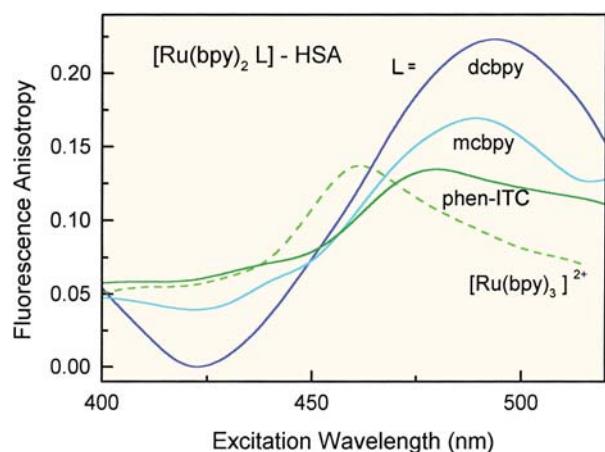


**Figure 20.25.** Excitation anisotropy spectra of  $[\text{Ru}(\text{dcbpy})(\text{bpy})_2]^{2+}$ ,  $[\text{Ru}(\text{mcbpy})(\text{bpy})_2]^{2+}$  and  $[\text{Ru}(\text{phen-ITC})(\text{bpy})_2]^{2+}$ , conjugated to HSA.  $[\text{Ru}(\text{bpy})_2\text{L}-\text{HSA}$  in 6:4 (V/V) glycerol/water,  $T = -55^\circ\text{C}$ . Also shown is the anisotropy spectrum of  $[\text{Ru}(\text{bpy})_3]^{2+}$  in 9:1 (V/V) glycerol/water,  $-55^\circ\text{C}$  (dashed).

observed for a number of MLCs (Figure 20.26). A variety of bioconjugatable MLCs have now been described,<sup>106–112</sup> including a biotin-containing MLC.<sup>113</sup> MLC-labeled nucleotides have also been reported.<sup>114–118</sup>

The potential of the MLCs as biophysical probes is illustrated by the range of decay times and quantum yields available with this diverse class of compounds. The chemi-

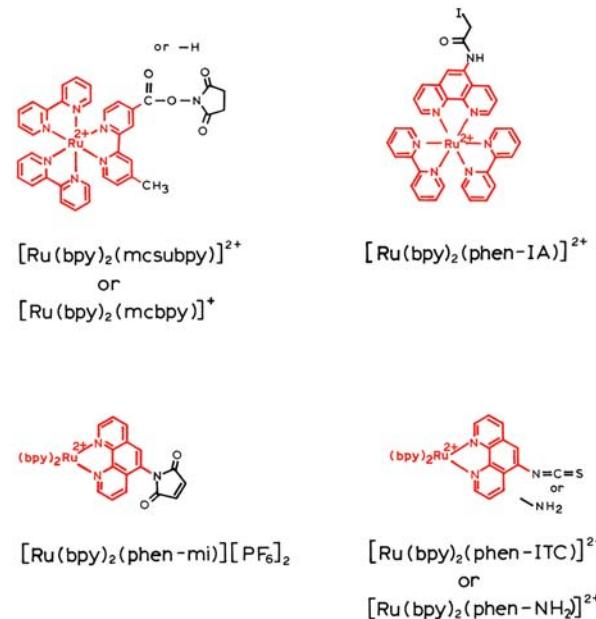


**Figure 20.26.** Conjugatable metal-ligand complexes.

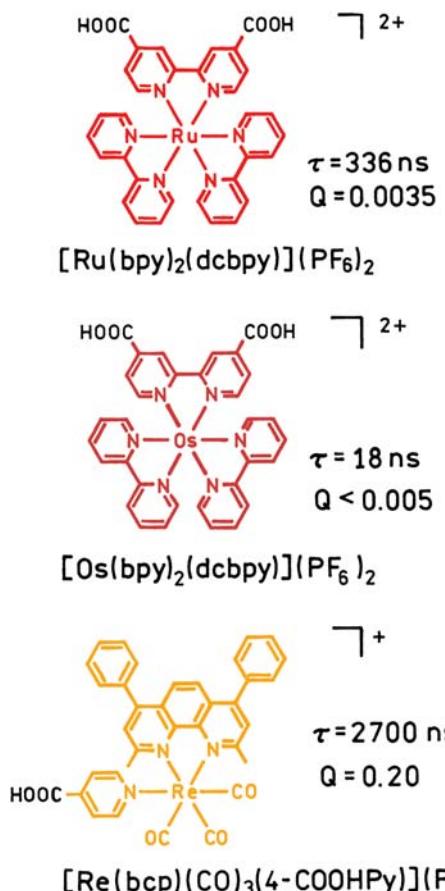


**Figure 20.27.** Chemical structures of ruthenium (II), osmium (II), and rhenium (I) metal-ligand complexes. The decay times and quantum yields are for these compounds covalently linked to human serum albumin. The decays are multi-exponential.

cal structures of useful rhenium (Re), ruthenium (Ru), and osmium (Os) complexes are shown in Figure 20.27. When conjugated to HSA in oxygenated aqueous solution at room temperature, the rhenium MLC display lifetimes as long as  $2.7 \mu\text{s}$ , and up to  $4 \mu\text{s}$  in the absence of oxygen.<sup>119</sup> The osmium complex displays a much shorter lifetime and lower quantum yield,<sup>120</sup> but can be excited at  $680 \text{ nm}$ . The possibility of long-wavelength excitation and long decay times shows that the MLCs have significant potential as biophysical probes.<sup>121–123</sup>

### 20.3.3. Spectral Properties of MLC Probes

The metal-ligand complexes have favorable absorption and emission spectra. Absorption and emission spectra of three conjugatable MLCs are shown in Figure 20.28. The long-wavelength absorption of the Ru MLCs is not due to

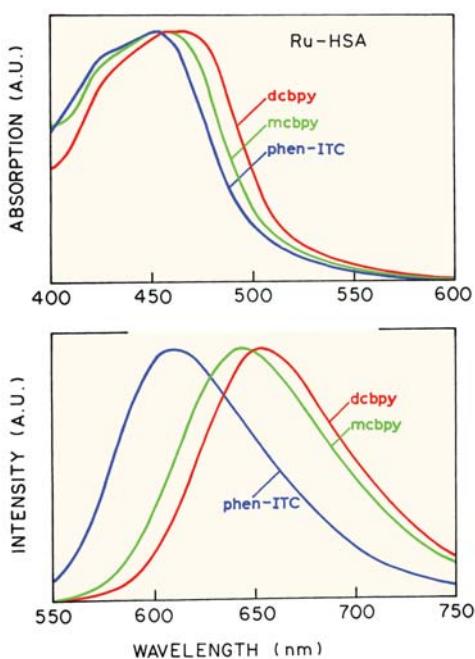


**Figure 20.28.** Absorption and emission spectra of  $[\text{Ru}(\text{bpy})_2(\text{dcbpy})]^{2+}$ ,  $[\text{Ru}(\text{bpy})_2(\text{mcbpy})]^+$ , and  $[\text{Ru}(\text{bpy})_2\text{phen-ITC}]^{2+}$  conjugated to HSA. Excitation wavelength 460 nm, at 20°C. Structures are shown in Figures 20.26 and 20.27. Revised from [110]. Copyright © 1996, with permission from Elsevier Science.

absorption of the metal alone or the ligand alone. Localized absorption by the ligand, referred to as ligand centered (LC) absorption, occurs at shorter wavelengths near 300 nm. Absorption by the  $d-d$  transitions of the metal is forbidden and the extinction coefficients are very low ( $1$  to  $200 \text{ M}^{-1} \text{ cm}^{-1}$ ). The broad absorption band at 450 nm is due to the metal-to-ligand charge transfer (MLCT) transition (eq. 20.2). The MLCT transitions display extinction coefficients of  $10,000$  to  $30,000 \text{ M}^{-1} \text{ cm}^{-1}$ . These values are not as large as fluorescein or cyanine dyes, but these extinction coefficients are comparable to those found for many fluorophores, and are adequate for some applications.

The emission of the metal–ligand complexes is also dominated by the MLCT transition, which is centered near 650 nm (Figure 20.28) for the Ru(II) complexes. The MLCs behave like a single chromophoric unit. In contrast to the lanthanides, the absorption and emission are not due to the atom, but rather to the entire complex. Also, the metal–ligand bonds are covalent bonds, and the ligands and metal do not dissociate under any conditions that are remotely physiological.

Examination of Figure 20.28 reveals another favorable spectral property of the MLCs, namely a large Stokes shift,

which makes it relatively easy to separate the excitation and emission. This large shift results in minimal probe–probe interaction. In contrast to fluorescein, which has a small Stokes shift, the MLCs do not appear to self-quench when multiple MLCs are attached to a protein molecule. Additionally, the MLCs do not appear to be prone to self-association.

For the ruthenium complexes, comparison of Figures 20.25 and 20.28 reveals that the MLCs with the longest emission wavelengths display the highest anisotropy. This behavior seems to correlate with the electron-withdrawing properties of the ligand, which are highest for dcbpy and lowest for phenanthroline isothiocyanate. In general it seems that having one ligand to preferentially accept the electron in the MLC transition results in high fundamental anisotropies. This suggests that MLCs with a single chromophoric ligand will have high anisotropies, which has been observed for Re(I) complexes.<sup>119</sup>

#### 20.3.4. The Energy Gap Law

One factor that affects the decay times of the metal–ligand complexes is the energy gap law. This law states that the non-radiative decay rate of a metal–ligand complex increases exponentially as the energy gap or emission energy decreases.<sup>124–130</sup> One example of the energy gap law is shown in Table 20.1 for Re(I) complexes. The structure of these complexes is similar to the lowest structure in Figure 20.27, except that the chromophoric ligand is bpy. In this complex the emission maximum is sensitive to the structure of the non-chromophoric ligand. The radiative decay rates ( $\Gamma$ ) are relatively independent of the ligand but the non-radiative decay rate ( $k_{nr}$ ) is strongly dependent on the ligand and emission maximum. The dependence of  $k_{nr}$  on emission energy for a larger number of Re(I) complexes is shown in Figure 20.29. The value of  $k_{nr}$  increases as the emission energy decreases. Because  $k_{nr}$  is much larger than  $\Gamma$ , the

**Table 20.1.** Spectral properties of the Rhenium MLC  $\text{fac-}\text{Re}(\text{bpy})(\text{CO})_3\text{L}^{\text{a}}$

L	$\lambda_{em}$ (nm)	Q	$\tau$ (ns)	$\Gamma$ (s $^{-1}$ )	$k_{nr}$ (s $^{-1}$ )
Cl <sup>-</sup>	622	0.005	51	$9.79 \times 10^4$	$1.95 \times 10^7$
4-NH <sub>2</sub> Py	597	0.052	129	$4.06 \times 10^5$	$7.34 \times 10^6$
Py	558	0.16	669	$2.36 \times 10^5$	$1.26 \times 10^6$
CH <sub>3</sub> CN	536	0.41	1201	$3.43 \times 10^5$	$4.90 \times 10^5$

<sup>a</sup>Data from [124].

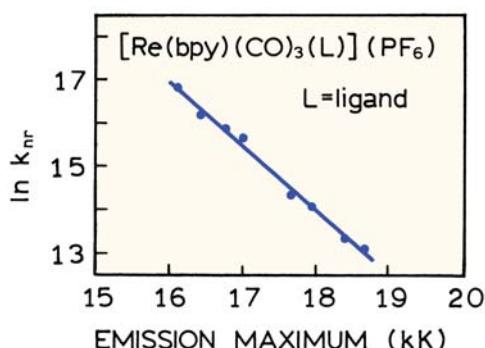


**Figure 20.29.** Dependence of the non-radiative decay rate of Re(I) complexes on the emission maxima. Revised and reprinted with permission from [124]. Copyright © 1983, American Chemical Society.

decay times of these complexes are determined mostly by the value of  $k_{nr}$ .

Another example of the energy gap law is shown in Figure 20.30 and Table 20.2 for osmium complexes. In this case the shortest-wavelength (highest energy) emission was found for the osmium complex with two phosphine (dppene) ligands. When the dppene ligands are replaced with phenanthroline ligands (phen) the emission maximum occurs at longer wavelengths. When this occurs the quantum yield ( $Q$ ) and lifetime decreases in agreement with the

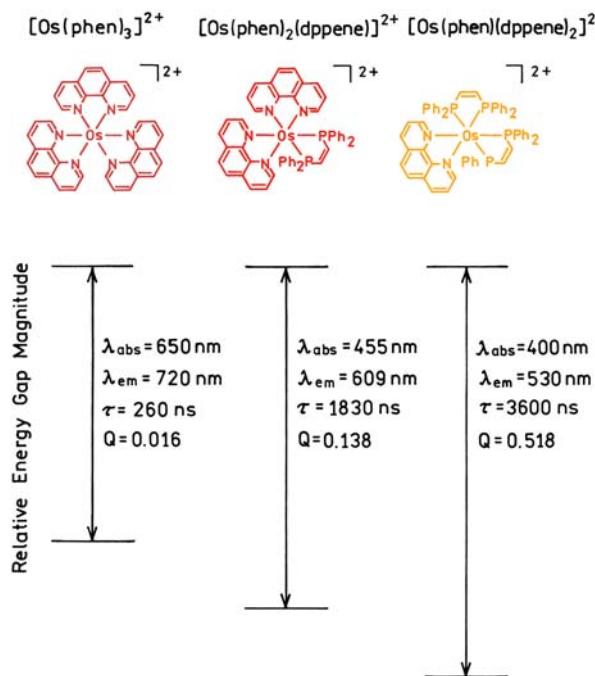


**Figure 20.30.** Osmium MLCs with different lifetimes and quantum yields. See Table 20.2.

**Table 20.2.** Spectral Properties of Osmium MLCs<sup>a</sup>

Compound	$\lambda_{em}$ (nm)	$Q$	$\tau$ (ns)	$\Gamma$ (s <sup>-1</sup> )	$k_{nr}$ (s <sup>-1</sup> )
[Os(phen) <sub>3</sub> ] <sup>2+</sup>	720	0.016	260	$6.15 \times 10^4$	$3.79 \times 10^6$
[Os(phen) <sub>2</sub> (dppene)] <sup>2+</sup>	609	0.138	1830	$7.54 \times 10^4$	$4.71 \times 10^5$
[Os(phen)(dppene) <sub>2</sub> ] <sup>2+</sup>	530	0.518	3600	$1.44 \times 10^5$	$1.37 \times 10^5$

<sup>a</sup>Data from [125].

energy gap law. These decreases are due to an increase in the non-radiative decay rate. The energy gap law is useful in understanding how the quantum yield and lifetime are related to the emission maxima, but it cannot be used to compare different types of complexes. The energy gap law works well within one homologous series of complexes, but is less useful when comparing different types of complexes.

### 20.3.5. Biophysical Applications of Metal–Ligand Probes

The MLCs can be used as biophysical probes. We present three representative applications: studies of DNA dynamics, measurement of domain-to-domain motions in proteins, and examples of metal-ligand lipid probes.

**DNA Dynamics with Metal–Ligand Probes:** Some metal–ligand complexes bind spontaneously to DNA. The strength of binding depends on the ligands and stereochemistry of the complexes. The MLCs have been used to probe DNA,<sup>131–138</sup> and some MLCs are quenched by nearby guanine residues.<sup>139–141</sup> One application is to study DNA dynamics using the polarized emission.<sup>142–145</sup> A spherical molecule will display a single correlation time, and, in general, globular proteins display closely spaced correlation times due to overall rotational diffusion. In contrast, DNA is highly elongated and expected to display motions on a wide range of timescales: from ns to  $\mu$ s (Section 12.8). Most experimental studies of DNA dynamics have been performed using ethidium bromide (EB), which displays a decay time for the DNA-bound state near 30 ns, or acridine derivatives that display shorter decay times. The short decay times of most DNA-bound dyes is a serious limitation because DNA is expected to display a wide range of relaxation times, and only the ns motions will affect the anisotropy of ns probes. In fact, most studies of DNA dynamics report only the torsional motions of DNA, which are detectable on the ns timescale. The slower bending motions of DNA are often ignored when using ns probes. These slower binding motions may be important for packaging of DNA into chromosomes.

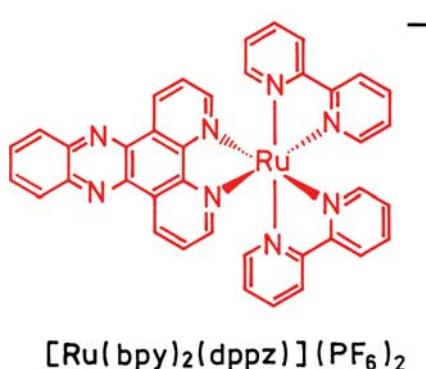


**Figure 20.31.** Chemical structure of a DNA anisotropy probe,  $[Ru(bpy)_2(dppz)]^{2+}$ .

An MLC probe that intercalates into double-helical DNA is shown in Figure 20.31. This probe is quenched in water and is highly luminescent when bound to DNA. The emission spectrum of  $[Ru(bpy)_2(dppz)]^{2+}$  bound to calf thymus DNA is shown in Figure 20.32. In aqueous solution the probe luminescence is nearly undetectable. In the presence of DNA the luminescence of  $[Ru(bpy)_2(dppz)]^{2+}$  is dramatically enhanced,<sup>146–147</sup> an effect attributed to intercalation of the dppz ligand into double-helical DNA. This MLC is highly luminescent in aprotic solvents but is dynamically quenched by water or alcohols.<sup>148–149</sup> The increase in fluorescence upon binding to DNA is due to shielding of the nitrogens on the dppz ligand from the solvent. This enhancement of emission upon binding to DNA means that the probe emission is observed from only the DNA-bound forms, without contributions from free probe in solution. In this respect  $[Ru(bpy)_2(dppz)]^{2+}$  is analogous to ethidium bromide, which also displays significant emission from only the DNA-bound form.

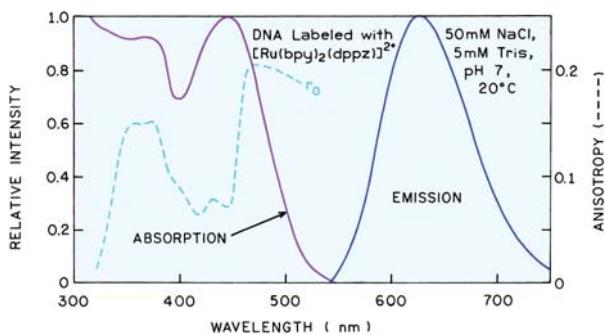


**Figure 20.32.** Absorption, emission, and excitation anisotropy spectra (dashed) of  $[Ru(bpy)_2(dppz)]^{2+}$  bound to calf thymus DNA. The excitation anisotropy spectrum is in 100% glycerol at  $-60^{\circ}\text{C}$ . From [144].

In order to be useful for anisotropy measurements, a probe must display a large fundamental anisotropy ( $r_0$ ). The excitation anisotropy spectrum of  $[Ru(bpy)_2(dppz)]^{2+}$  in vitrified solution (glycerol,  $-60^{\circ}\text{C}$ ) displays maxima at 365 and 490 nm (Figure 20.32). The high value of the anisotropy indicates that the excitation is localized on one of the organic ligands, not randomized among the ligands. It seems reasonable to conclude that the excitation is localized on the dppz ligand because shielding of the dppz ligand results in an increased quantum yield. The time-resolved intensity decay of  $[Ru(bpy)_2(dppz)]^{2+}$  bound to calf thymus DNA is shown in Figure 20.33. The intensity decay is best fit by a triple-exponential decay with a mean decay time near 110 ns. Anisotropy decay can typically be measured to about three times the lifetime, suggesting that  $[Ru(bpy)_2(dppz)]^{2+}$  can be used to study DNA dynamics to 300 ns or longer.

The time-resolved anisotropy decay of DNA-bound  $[Ru(bpy)_2(dppz)]^{2+}$  is shown in Figure 20.34. The anisotropy decay could be observed to 250 ns, several-fold longer than possible with EB. The anisotropy decay appears to be a triple exponential, with apparent correlation times as long as 189.9 ns. Future intercalative MLC probes may display

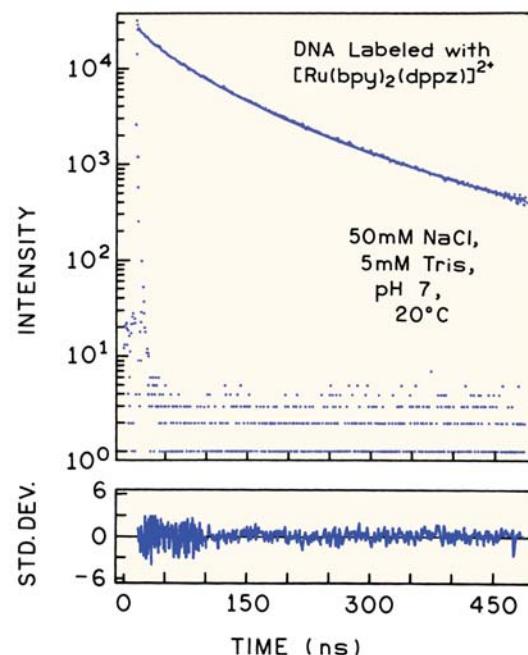


**Figure 20.33.** Time-dependent intensity decay of DNA labeled with  $[Ru(bpy)_2(dppz)]^{2+}$ . The data are shown as dots. The solid line and deviations (lower panel) are for the best three decay time fit, with decay times of 12.4, 46.6, and 126 ns. From [144].

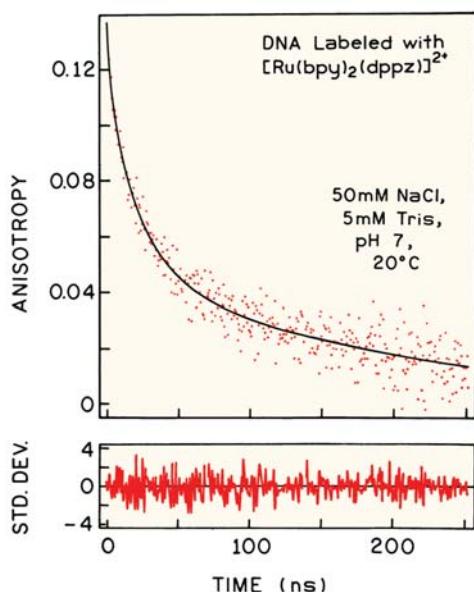


**Figure 20.34.** Time-dependent anisotropy decay of DNA labeled with  $[\text{Ru}(\text{bpy})_2(\text{dppz})]^{2+}$ . The data are shown as dots. The solid line and deviations (lower panel) are for the best three correlation time fits with correlation times of 3.1, 22.2, and 189.9 ns. From [144].

longer decay times. Studies of DNA-bound MLC probes offers the opportunity to increase the information content of the time-resolved measurements of nucleic acids by extending the observations to the microsecond timescale.

**Domain-to-Domain Motions in Proteins:** There is presently considerable interest in measuring the rates of domain flexing in multi-domain proteins. Domain motions in proteins occur in signaling proteins such as calmodulin and sugar receptors. Domain motions are thought to occur in proteins such as hexokinase,<sup>150</sup> creatine kinase,<sup>151–152</sup> protein kinase C, phosphoglycerate kinase,<sup>153</sup> and immunoglobulin.<sup>153–155</sup> As described in Section 14.7, such motions can be detected by the effects of donor-to-acceptor diffusion on the extent of resonance energy transfer. These measurements have not been successful to date, primarily because the decay time of most fluorophores is too short for significant motion during the excited state lifetime.<sup>153</sup> This fact is illustrated in Figure 20.35, which considers the effect of D-to-A diffusion on the donor decay, as measured in the frequency domain. For domain-to-domain motions the mutual diffusion coefficients are expected to be  $10^{-7} \text{ cm}^2/\text{s}$ , or smaller. If the donor decay time is 5 ns, then diffusion has essentially no effect on the extent of energy transfer (top). For this reason the donor decay contains no information on the diffusion coefficient and cannot be used to

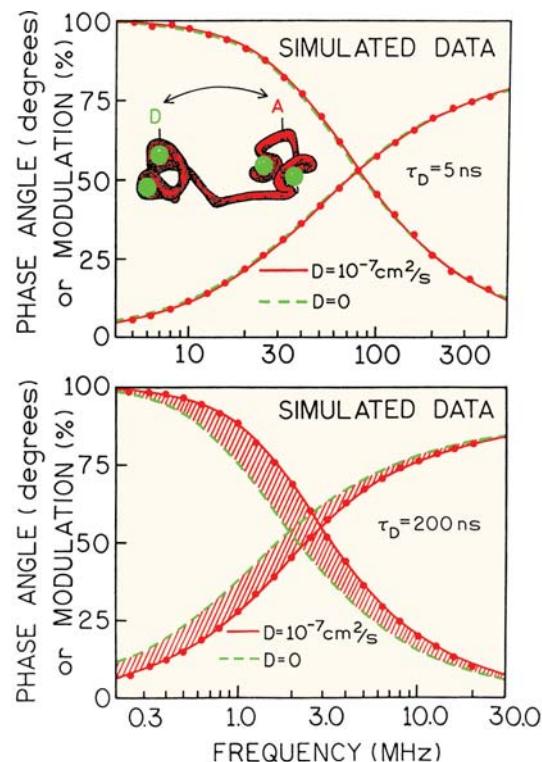


**Figure 20.35.** Simulated data illustrating effect of donor lifetime on the contribution of interdomain diffusion to the frequency-domain donor decays. For the simulations we assumed a D–A distance distribution with  $R_0 = 30 \text{ \AA}$  and  $hw = 20 \text{ \AA}$ . The insert shows a schematic donor (D) and acceptor (A) labeled domains for calmodulin. Top: for a donor decay time of 5 ns. Bottom: for a donor decay time of 200 ns.

recover the diffusion coefficient. Suppose now the donor decay time is increased to 200 ns. Then a diffusion coefficient of  $10^{-7} \text{ cm}^2/\text{s}$  has a significant effect on the extent of resonance energy transfer (RET), as shown by the shaded area in the bottom panel of Figure 20.35. To date, RET with MLCs has not been used to measure domain flexing in proteins. However, the potential seems clear, especially in light of the long decay times possible with rhenium MLCs. Decay times as long as 4  $\mu\text{s}$  have been found in aqueous solution,<sup>119</sup> suggesting that domain flexing will be measurable with D values smaller than  $10^{-8} \text{ cm}^2/\text{s}$ .

**MLC Lipid Probes:** Long-lifetime probes are expected to be especially valuable in membrane biophysics. Long-lifetime MLC probes could be used to study rotational motions of entire lipid vesicles, or to measure diffusion by its effect on resonance energy transfer. Several MLC lipids have been described (Figure 20.36), all of which show polarized emission.<sup>156–157</sup> The Ru MLC lipids display life-

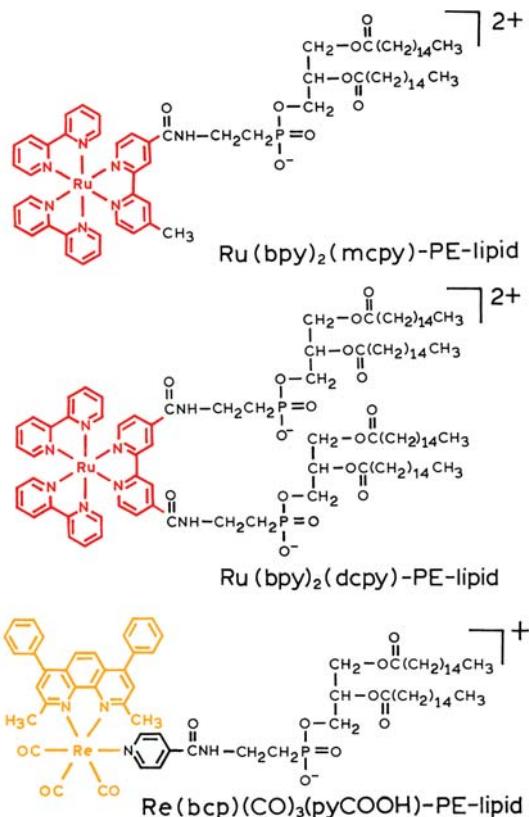


Figure 20.36. MLC lipid probes.

times near 400 ns, and the Re MLC lipid a lifetime near 4  $\mu$ s in dipalmitoyl-L- $\alpha$ -phosphatidylglycerol (DPPG) vesicles, in the presence of dissolved oxygen. Such long-lifetime probes can be used to measure microsecond correlation times in membranes, or even the rotational correlation times of lipid vesicles (Section 11.10.2).

### 20.3.6. MLC Immunoassays

Fluorescence-polarization immunoassays (FPIs) can be performed using MLCs.<sup>158–162</sup> FPIs are based on the changes in polarization (or anisotropy) that occur when a labeled drug analogue binds to an antibody specific for that drug. The anisotropy of the labeled drug can be estimated from the Perrin equation:

$$r = \frac{r_0}{1 + \tau/\Theta} \quad (20.3)$$

where  $r_0$  is the anisotropy observed in the absence of rotational diffusion and  $\Theta$  is the rotational correlation time.

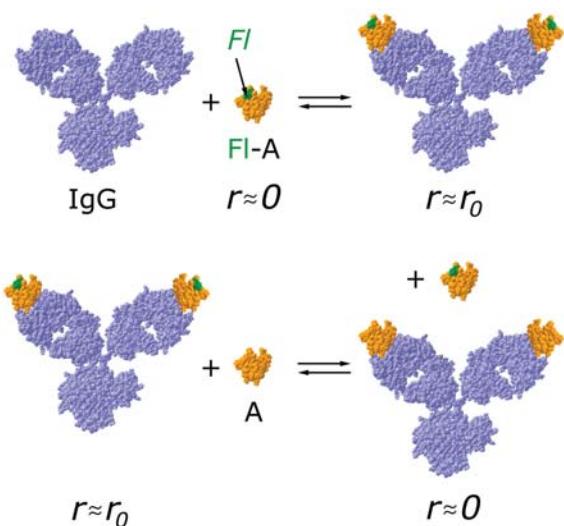
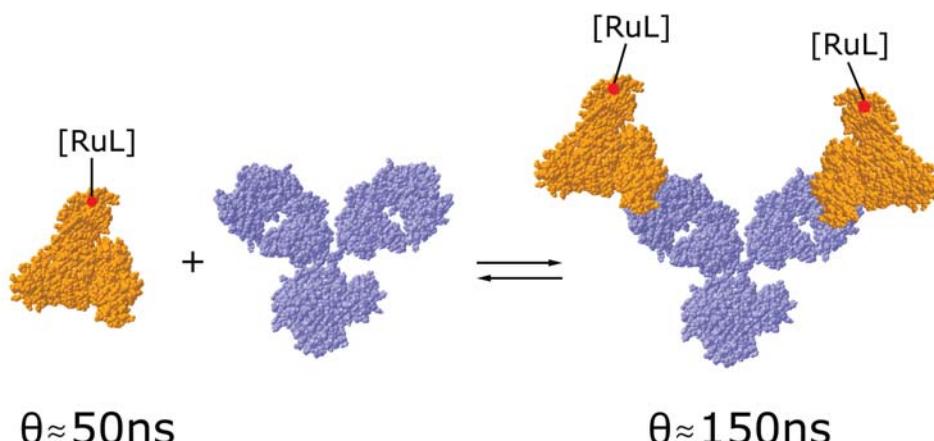


Figure 20.37. Schematic of a fluorescence polarization immunoassay.

Suppose the fluorophore is fluorescein (Fl) with a lifetime near 4 ns and the analyte (A) is a small molecule with a rotational correlation time near 100 ps (Figure 20.37, top). The assay is performed using a covalent adduct of fluorescein and the analyte (Fl-A). When free in solution, the anisotropy of Fl-A is expected to be near zero. The correlation time of an antibody is near 100 ns and the anisotropy of the Fl-A-IgG complex is expected to be near  $r_0$ . FPIs are typically performed in a competitive format. The sample is incubated with a solution containing the labeled drug (Fl-A) and antibody (Figure 20.37, bottom). The larger the amount of unlabeled drug, the more Fl-A is displaced from the antibody, and the lower the polarization. For an FPI to be useful there needs to be a substantial difference in the anisotropy between the free and bound forms of the labeled drug.

The usefulness of MLCs in clinical FPIs is illustrated by consideration of an FPI for a higher-molecular-weight species (Figure 20.38). Suppose that the antigen is HSA, with a molecular weight near 66 kD and a rotational correlation time near 50 ns. This correlation time is already much longer than the lifetime of fluorescein, so that the anisotropy is expected to be near  $r_0$ . For this reason, FPIs are typically used to measure only low-molecular-weight substances.

The use of MLC probes can circumvent these limitations of FPIs to low-molecular-weight antigens. The dependence of the anisotropy on the probe lifetime and the molecular weight of the antigen is shown in Figure 20.39.



**Figure 20.38.** Fluorescence polarization immunoassay of a high-molecular-weight species using an Ru(II) metal–ligand complex.

For typical probes with lifetimes near 4 ns (fluorescein or rhodamine) the anisotropy of low-molecular-weight antigens ( $MW < 1000$ ) can be estimated from Figure 20.39 to be near 0.05. An antibody has a molecular weight near 160,000, resulting in an anisotropy near 0.29 for the antigen–antibody complex. Hence a large change in anisotropy is expected upon binding of low-molecular-weight species to larger proteins or antibodies. However, if the molecular weight of the labeled antigen is larger—above 20,000 Daltons—then the anisotropy changes only slightly upon binding of the labeled antigen to a larger protein. For example, consider an association reaction that changes the molecular weight from 65,000 to 1 million daltons. Such a change could occur for an immunoassay of HSA using polyclonal

antibodies, for which the effective molecular weight of the immune complexes could be 1 million or higher. In this case the anisotropy of a 4-ns probe would change from 0.278 to 0.298, which is too small of a change for quantitative purposes. In contrast, by use of a 400-ns probe, which is near the value found for our metal–ligand complex, the anisotropy value of the labeled protein with a molecular weight of 65,000 is expected to increase from 0.033 to 0.198 when the molecular weight is increased from 65,000 to 1 million daltons (Figure 20.39).

FPIs of the high-molecular-weight antigen HSA have been performed using the Ru and Re MLCs.<sup>160–161</sup> The Re MLC shown in Figure 20.27 displays a quantum yield of 0.2 and a lifetime over 2700 ns.<sup>162</sup> Absorption, emission,

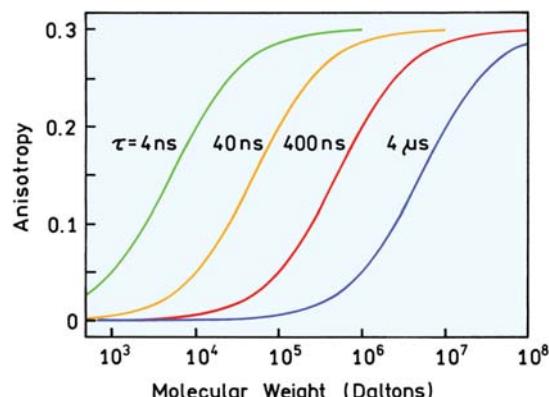


**Figure 20.39.** Molecular-weight-dependent anisotropies for probe lifetimes from 4 ns to 4  $\mu$ s. The curves are based on eq. 20.3 assuming  $v + h = 1.9$  ml/g for the proteins,  $r_0 = 0.30$ , in aqueous solution at 20°C with a viscosity of 1 cP.

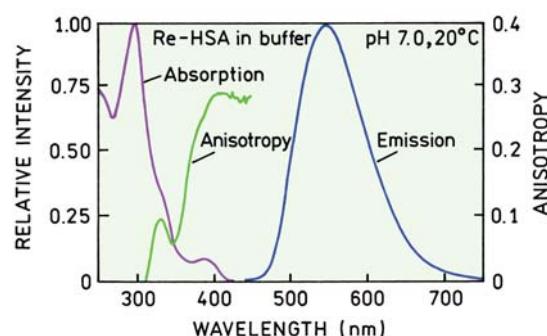


**Figure 20.40.** Absorption and emission spectra of  $[Re(bcp)(CO)_3(4-COOHPy)]^+$  (RE) conjugated to HSA in 0.1 M phosphate-buffered saline (PBS) buffer, pH 7.0. Excitation wavelength was 400 nm. The excitation anisotropy spectrum in 100% glycerol at -60°C was measured with an emission wavelength of 550 nm. Reprinted with permission from [162]. Copyright © 1998, American Chemical Society.

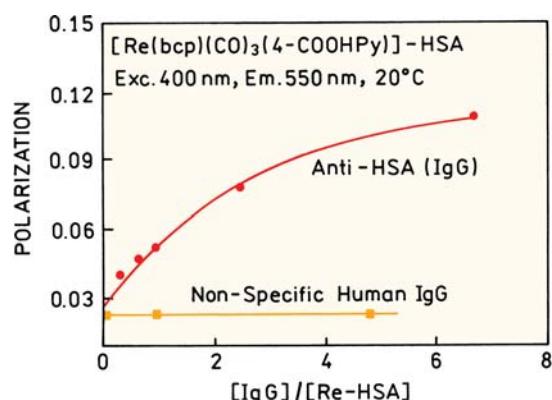


**Figure 20.41.** Steady-state fluorescence polarization of  $[\text{Re}(\text{bcp})(\text{CO})_3(4\text{-COOHPy})]\text{-HSA}$  at various concentrations of IgG specific for HSA (anti-HSA, circles) or nonspecific IgG (squares). Revised and reprinted with permission from [162]. Copyright © 1998, American Chemical Society.

and anisotropy spectra of this probe are shown in Figure 20.40. The Re complex can be excited near 400 nm, which is due in part to the long-wavelength absorption of the 4,7-dimethyl-1,10-phenanthroline (bcp) ligand. These wavelengths can be obtained from LEDs. The large Stokes shift from 350 to 520 nm makes it easy to isolate the MLC emission. Importantly, the Re MLC displays a high fundamental anisotropy near 0.3 for excitation at 400 nm.<sup>162–163</sup> This is probably due to the presence of just one chromophoric ligand, so there is no possible randomization of the excitation to other ligands.

The high-quantum-yield rhenium MLC was covalently bound to HSA used to detect binding of an antibody against human serum albumin (Figure 20.41). The steady-state anisotropy was found to increase nearly fourfold upon binding of IgG, and there was no effect from nonspecific IgG. These results demonstrated that long-lifetime MLCs are useful for immunoassays of high molecular weight antigens. It is important to note that the sensitivity of most fluorescence assays is limited not by the ability to detect the emission but rather by the presence of interfering autofluorescence that occurs on the 1- to 10-ns timescale. The availability of probes with longer decay times should also allow increased sensitivity by the use of gated detection following decay of the unwanted autofluorescence.

For many applications it is preferable to use the longest possible wavelength for excitation. At longer wavelengths there is less sample absorbance, less autofluorescence, and the light sources are less expensive. However, the quantum yields of long-wavelength MLCs are usually low. It is a challenge to obtain long-wavelength excitable MLCs that

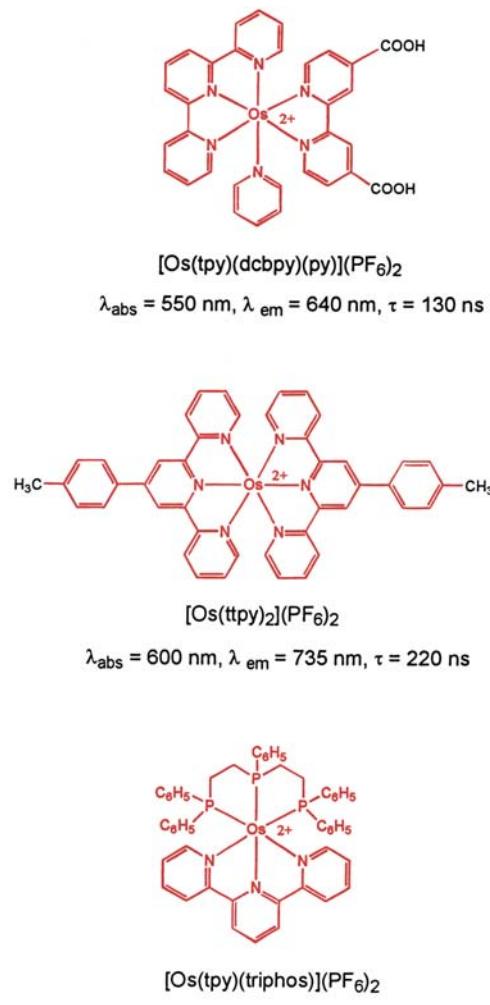


**Figure 20.42.** Long-wavelength long-lifetime osmium (II) complexes.

display long lifetimes and high quantum yields. Some progress has been made toward developing long-wavelength long-lifetime MLCs. It is known that the decay times of Os MLCs can be increased by the use of tridentate ligands in place of bidentate ligands.<sup>164–166</sup> Several such compounds have been synthesized (Figure 20.42). These Os complexes display long-wavelength absorption and decay times longer than 100 ns. Another approach to increasing the quantum yield and decay times of Os MLCs is by the use of arsine and phosphine ligands.<sup>167</sup> Using this approach it is possible to obtain high quantum yields. Unfortunately, the absorption spectra shift to shorter wavelengths, and the 450 nm absorption is weak. Some Ru MLCs display emission wavelengths as long as 715 nm and lifetimes over 100 ns.

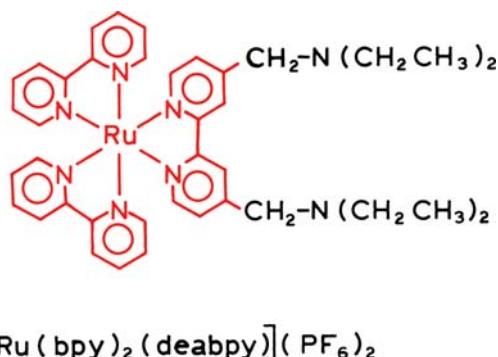


**Figure 20.43.** Structure of  $[\text{Ru}(\text{bpy})_2(\text{deabpy})]^{2+}$ , a long-lifetime MLC pH sensor. From [181].

### 20.3.7. Metal–Ligand Complex Sensors

Another area of interest is the use of MLCs in ion sensing. MLCs that are sensitive to ions<sup>168–175</sup> or pH<sup>176–181</sup> have recently become available. One example is the pH-sensitive MLC  $[\text{Ru}(\text{bpy})_2(\text{deabpy})]^{2+}$ , where deabpy is 4,4'-diethylaminomethyl-2,2'-bipyridine (Figure 20.43). The emission spectra of  $[\text{Ru}(\text{deabpy})(\text{bpy})_2]^{2+}$  at pH values ranging from 2 to 12 are shown in Figure 20.44. The emission intensity increases about threefold as the pH increases from 2.23 to 11.75. The pH-dependent intensity changes show a  $\text{pK}_A$  value near 7.5. This  $\text{pK}_A$  value is ideally suited for measurements of blood pH, for which the clinically relevant range is from 7.35 to 7.46, with a central value near 7.40. In addition, much cell culture work is performed near pH 7.0–7.2. The changes in emission with a change in pH are believed to be due to deprotonation of the amino

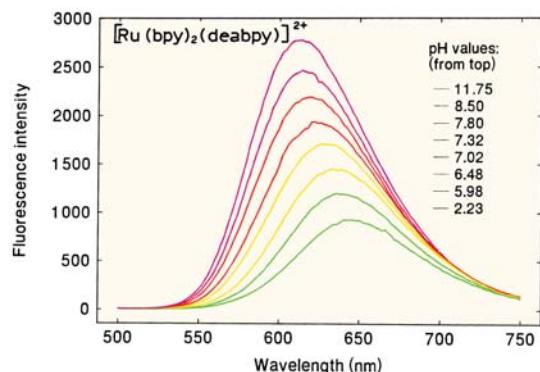


**Figure 20.44.** pH-dependent emission spectra of  $[\text{Ru}(\text{bpy})_2(\text{deabpy})](\text{PF}_6)_2$ . Excitation at 414 nm. Revised from [181].

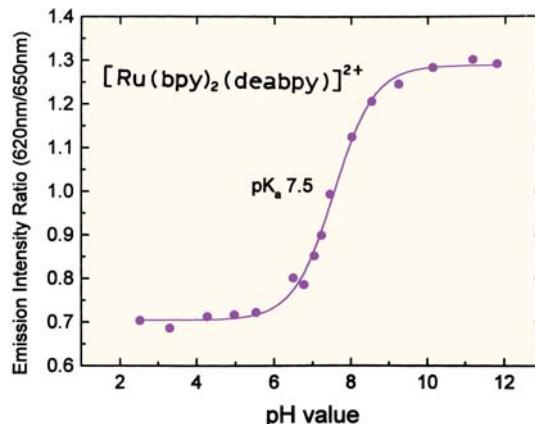


**Figure 20.45.** Wavelength-ratiometric measurements of pH using the emission intensities of  $[\text{Ru}(\text{bpy})_2(\text{deabpy})]^{2+}$  at 620 and 650 nm. From [181].

groups of  $[\text{Ru}(\text{bpy})_2(\text{deabpy})]^{2+}$ . The emission spectrum of the MLC pH probe shifts to longer wavelengths as the amino groups are protonated at low pH (Figure 20.44). This suggests the use of  $[\text{Ru}(\text{bpy})_2(\text{deabpy})]^{2+}$  as a wavelength-ratiometric probe (Figure 20.45). Such ratiometric probes are already in widespread use for measurement of  $\text{Ca}^{2+}$  and pH (Chapter 19), but these display ns decay times.

The emission shift to longer wavelengths at low pH (Figure 20.44) seems to be generally understandable in terms of the electronic properties of the excited MLCs. The long-wavelength emission is from a metal-to-ligand charge transfer (MLCT) state in which an electron is transferred from Ru to the ligand. The protonated form of deabpy is probably a better electron acceptor, lowering the energy of the MLCT state, shifting the emission to longer wavelengths, and thereby decreasing the lifetime. These results suggest a general approach to designing wavelength-ratiometric MLC probes based on cation-dependent changes in the electron affinity of the ligand. Changes in the emission spectra can be expected to cause changes in lifetime in accordance with the energy gap law (Section 20.3.4). The emission spectra (Figure 20.44) reveal that the probe is luminescent in both the protonated and unprotonated forms. This suggests that it can be useful as a lifetime probe because each form is luminescent and may display distinct decay times. At present there is an understandable interest in detection of dangerous substances. A cyanide-sensitive MLC has been reported (Figure 20.46). The emission intensity decreases as the cyanide concentration increases.

And, finally, the MLCs appear to be highly photo-stable.  $[\text{Ru}(\text{bpy})_2(\text{dcbpy})]^{3+}$  and fluorescein were illuminat-

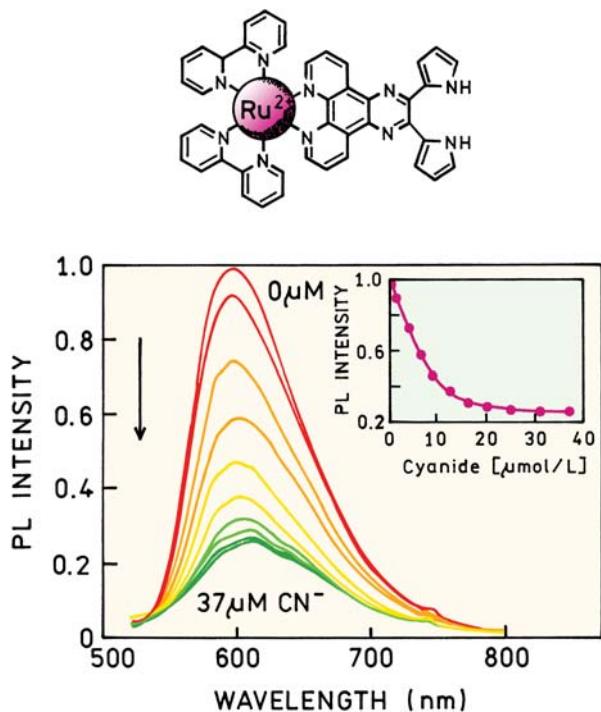


**Figure 20.46.** Structure and emission spectra of a cyanide-sensitive MLC. Revised and reprinted with permission from [175]. Copyright © 2002, American Chemical Society.

ed with the 488-nm output of an argon ion laser (Figure 20.47). The MLC was stable for extended periods of time, under conditions where fluorescein was rapidly bleached. The initial decrease in the MLC intensity is thought to be due to heating. The long-term photostability of MLCs should make them useful for high-sensitivity detection in fluorescence microscopy, fluorescence in-situ hybridization, and similar applications.

#### 20.4. LONG-WAVELENGTH LONG-LIFETIME FLUOROPHORES

Red- and NIR-emitting probes are desirable for many applications of fluorescence. However, the red–NIR probes with high extinction coefficients and high quantum yields also display short lifetimes. For MLCs the quantum yields decrease as the emission wavelength increases, and none of the MLCs have high extinction coefficients. Some of these disadvantages of MLCs can be circumvented using MLCs as donor to high quantum-yield long-wavelength acceptors.<sup>182–184</sup>

A tandem MLC–red fluorophore can be used to obtain a fluorophore that has both a long emission wavelength and

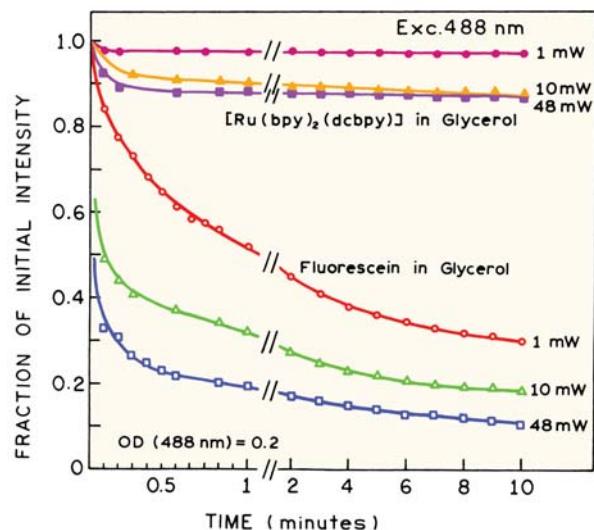


**Figure 20.47.** Photostability of  $[\text{Ru}(\text{bpy})_2(\text{dcbpy})]^{2+}$  and fluorescein.

a long lifetime. Assume the donor is an MLC with a 1000-ns decay time and that the distance between the donor and acceptor is  $r = 0.7R_0$ . An acceptor at this distance will reduce the lifetime of the MLC to about 100 ns. Because the acceptor lifetime is short ( $\tau_A = 1$  ns), the acceptor intensity will closely follow the donor intensity. The acceptor will display essentially the same decay time(s) as the donor. Most acceptors will display some absorption at the donor excitation wavelength. In this case the acceptor emission will typically display an ns component as a result of a directly excited acceptor, and a long decay time near 100 ns resulting from RET from the donor. The long-lifetime emission acceptor can be readily isolated with gated detection.

An important advantage of such an RET probe is an increase in the effective quantum yield of the long-lifetime D–A pairs. This increase in quantum yield occurs because the transfer efficiency can approach unity even though the donor quantum yield is low. The result of efficient RET from the donor is that the wavelength integrated intensity of the D–A pair can be larger than that of the donor or acceptor alone (Figure 20.48). Thus tandem RET probes with MLC donors can be used to create long-lifetime probes, with red–NIR emission, with the added advantage of an increased quantum yield for the D–A pair. The modular design of these probes allows adjustment of the spectral properties, including the excitation and emission wavelengths and the decay times.

At first glance an increase in the overall quantum yield due to RET is a surprising result, but some simple consid-

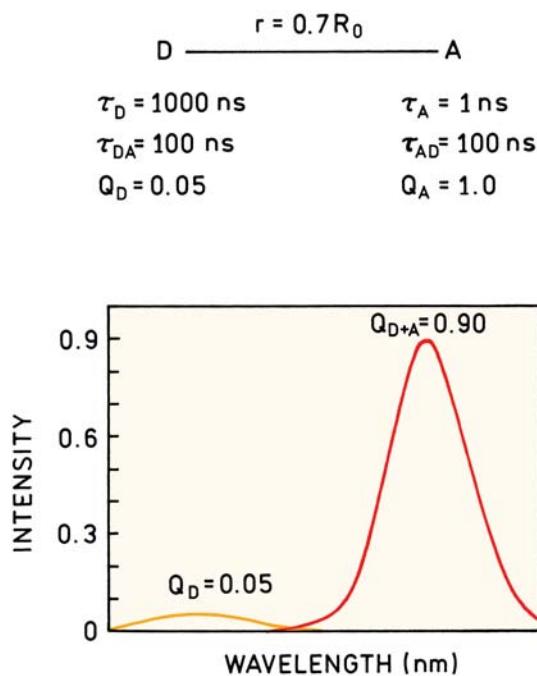


**Figure 20.48.** Schematic of a long-lifetime probe based on RET. For the simulated spectra we assumed the acceptor does not absorb at the donor excitation wavelength.

erations explain why this occurs. Consider a mixture of donor and acceptor where RET does not occur. The total emission of both the donor and acceptor is given by the sum of the two emissions. This total intensity is given by

$$F_T^0 = F_D^0 + F_A^0 = Q_D^0 \varepsilon_D + Q_A^0 \varepsilon_A \quad (20.4)$$

where  $Q_D^0$  and  $Q_A^0$  are the quantum yields of the donor and acceptor in the absence of RET, and  $\varepsilon_D$  and  $\varepsilon_A$  are the extinction coefficients of the donor and acceptor, respectively. Now assume RET occurs with efficiency  $E$ . The total emission is now given by

$$F_T = F_D + F_A = Q_D^0 \varepsilon_D (1 - E) + Q_A^0 (\varepsilon_A + E \varepsilon_D) \quad (20.5)$$

If the transfer efficiency is high the total intensity becomes

$$F_T = Q_A (\varepsilon_A + \varepsilon_D) \quad (20.6)$$

so that the total quantum yield is determined by the quantum yield of the acceptor, and not the donor.

If the acceptor does not absorb at the donor excitation wavelength, then

$$F_T = Q_A \varepsilon_D \quad (20.7)$$

so that the total quantum yield is determined by the quantum yield of the acceptor, and not the donor.

If the energy transfer is too efficient then the donor lifetime will be too short. However, it is possible to find conditions where the quantum yield is substantially increased and the acceptor lifetime is still acceptably long. An Ru MLC donor and a high-quantum-yield acceptor were linked by an polyproline linker (Figure 20.49). The acceptor emission is considerably more intense from the D-A pair than from the

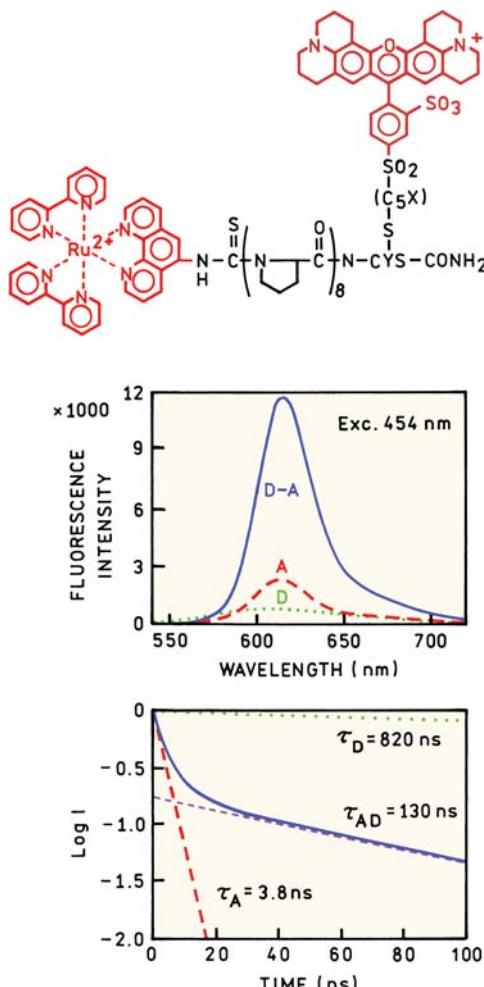


**Figure 20.49.** Structure of a tandem MLC-acceptor pair emission spectra, and intensity decays reconstructed from the frequency-domain data. Revised and reprinted with permission from [184]. Copyright © 2001, American Chemical Society.

donor or acceptor alone. In the absence of RET the donor lifetime is 820 ns. In the D–A pair the long component in the acceptor lifetime is 130 ns, which is long enough to use with gated detection. These results show a general approach to obtain the desired emission wavelengths and lifetime using MLCs as donors in tandem probes.

## REFERENCES

- Bruchez M, Moronne M, Gin P, Weiss S, Alivisatos AP. 1998. Semiconductor nanocrystals as fluorescent biological labels. *Science* **281**: 2013–2016.
- Watson A, Wu X, Bruchez M. 2003. Lighting up cells with quantum dots. *Biotechnology* **34**:296–303.
- Pietryga JM, Schaller RD, Werder D, Stewart MH, Klimov VI, Hollingsworth JA. 2004. Pushing the band gap envelope: mid-infrared emitting colloidal PbSe quantum dots. *J Am Chem Soc* **126**: 11752–11753.
- Kuczynski JP, Milosavljevic BH, Thomas JK. 1983. Effect of the synthetic preparation on the photochemical behavior of colloidal CdS. *J Phys Chem* **87**:3368–3370.
- Rossetti R, Nakahara S, Brus LE. 1983. Quantum size effects in the redox potentials, resonance Raman spectra, and electronic spectra of CdS crystallites in aqueous solution. *J Chem Phys* **79**(2):1086–1088.
- Weller H, Koch U, Gutierrez M, Henglein A. 1984. Photochemistry of colloidal metal sulfides: absorption and fluorescence of extremely small ZnS particles (the world of the neglected dimensions). *Ber Bunsenges Phys Chem* **88**:649–656.
- Ramsden JJ, Gratzel M. 1984. Photoluminescence of small cadmium sulphide particles. *J Chem Soc Faraday Trans* **80**:919–933.
- Murray CB, Kagan CR, Bawendi MG. 2000. Synthesis and characterization of monodisperse nanocrystals and close-packed nanocrystal assemblies. *Annu Rev Mater Sci* **30**:545–610.
- Gerion D, Pinaud F, Williams SC, Parak WJ, Zanchet D, Weiss S, Alivisatos AP. 2001. Synthesis and properties of biocompatible water-soluble silica-coated CdSe/ZnS semiconductor quantum dots. *J Phys Chem B* **105**:8861–8871.
- Kortan AR, Hull R, Opila RL, Bawendi MG, Steigerwald ML, Carroll PJ, Brus LE. 1990. Nucleation and growth of CdSe on ZnS quantum crystallite seeds, and vice versa, in inverse micelle media. *J Am Chem Soc* **112**:1327–1332.
- Dabbousi BO, Rodriguez-Viejo J, Mikulec FV, Heine JR, Mattoussi H, Ober R, Jensen KF, Bawendi MG. 1997. (CdSe)ZnS core-shell quantum dots: synthesis and characterization of a size series of highly luminescent nanocrystallites. *J Phys Chem B* **101**:9463–9475.
- Alivisatos AP. 1996. Perspectives on the physical chemistry of semiconductor nanocrystals. *J Phys Chem* **100**:13226–13239.
- Murphy CJ, Coffer JL. 2002. Quantum dots: a primer. *Appl Spectrosc* **56**:16A–27A.
- Parak WJ, Gerion D, Pellegrino T, Zanchet D, Micheel C, Williams SC, Boudreau R, Le Gros MA, Larabell CA, Alivisatos AP. 2003. Biological applications of colloidal nanocrystals. *Nanotechnology* **14**:R15–R27.
- Bawendi MG, Steigerwald ML, Brus LE. 1990. The quantum mechanics of larger semiconductor clusters ("quantum dots"). *Annu Rev Phys Chem* **41**:477–496.
- Weller H. 1993. Colloidal semiconductor Q-particles: chemistry in the transition region between solid state and molecules. *Angew Chem, Int Ed* **32**(1):41–53.
- Goldman ER, Anderson GP, Tran PT, Mattoussi H, Charles PT, Mauro JM. 2002. Conjugation of luminescent quantum dots with antibodies using an engineered adaptor protein to provide new reagents for fluoroimmunoassays. *Anal Chem* **74**:841–847.
- Goldman ER, Balighian ED, Mattoussi H, Kuno MK, Mauro JM, Tran PT, Anderson GP. 2002. Avidin: a natural bridge for quantum dot-antibody conjugates. *J Am Chem Soc* **124**:6378–6382.
- Jovin TM. 2003. Quantum dots finally come of age. *Nature Biotechnol* **21**:32–33.
- Chan WCW, Maxwell DJ, Gao X, Bailey RE, Han M, Nie S. 2002. Luminescent quantum dots for multiplexed biological detection and imaging. *Curr Opin Biotechnol* **13**:40–46.
- Jares-Erijman E, Jovin TM. 2003. FRET imaging. *Nature Biotechnol* **21**(11):1387–1395.
- Gerion D, Chen F, Kannan B, Fu A, Parak WJ, Chen DJ, Majumdar A, Alivisatos AP. 2003. Room-temperature single-nucleotide polymorphism and multiallele DNA detection using fluorescent nanocrystals and microarrays. *Anal Chem* **75**:4766–4772.
- Goldman ER, Clapp AR, Anderson GP, Uyeda HT, Mauro JM, Medintz IL, Mattoussi H. 2004. Multiplexed toxin analysis using four colors of quantum dot fluororeagents. *Anal Chem* **76**:684–688.
- Gao X, Chan WCW, Nie S. 2002. Quantum-dot nanocrystals for ultrasensitive biological labeling and multicolor optical encoding. *J Biomed Optics* **7**(4):532–537.
- Leatherdale CA, Woo WK, Mikulec FV, Bawendi MG. 2002. On the absorption cross-section of CdSe nanocrystal quantum dots. *J Phys Chem B* **106**:7619–7622.
- Schmelz O, Mews A, Basche T, Herrmann A, Mullen K. 2001. Supramolecular complexes from CdSe nanocrystals and organic fluorophors. *Langmuir* **17**:2861–2865.
- Derfus AM, Chan WCW, Bhatia SN. 2004. Probing the cytotoxicity of semiconductor quantum dots. *Nanotechnol Lett* **4**(1):11–18.
- Hoshino A, Fujioka K, Oku T, Suga M, Sasaki YF, Ohta T, Yasuhara M, Suzuki K, Yamamoto K. 2004. Physicochemical properties and cellular toxicity of nanocrystal quantum dots depend on their surface modification. *Nanotechnol Lett* **4**(11):2163–2169.
- Dubertret B, Skourides P, Norris DJ, Noireaux V, Brivanlou AH, Libchaber A. 2002. In vivo imaging of quantum dots encapsulated in phospholipid micelles. *Science* **298**(5599):1759–1762.
- Wu X, Liu H, Liu J, Haley KN, Treadway JA, Larson JP, Ge N, Peale F, Bruchez M. 2003. Immunofluorescent labeling of cancer marker Her2 and other cellular targets with semiconductor quantum dots. *Nature Biotechnol* **21**:41–46.
- Jaiswal JK, Mattoussi H, Mauro JM, Simon SM. 2003. Long-term multiple color imaging of live cells using quantum dot bioconjugates. *Nature Biotechnol* **21**:47–51.
- Wargnier R, Baranov AV, Maslov VG, Stsiapura V, Artemyev M, Pluot M, Sukhanova A, Nabiev I. 2004. Energy transfer in aqueous solutions of oppositely charged CdSe/ZnS core-shell quantum dots and in quantum dot-nanogold assemblies. *Nanotechnol Lett* **4**(3): 451–457.

33. Achermann M, Petruska MA, Crooker SA, Klimov VI. 2003. Picosecond energy transfer in quantum dot Langmuir-Blodgett nanoassemblies. *J Phys Chem B* **107**:13782–13787.
34. Kagan CR, Murray CB, Nirmal M, Bawendi MG. 1996. Electronic energy transfer in CdSe quantum dot solids. *Phys Rev Lett* **76**(9): 1517–1520.
35. Kagan CR, Murray CB, Bawendi MG. 1996. Long-range resonance transfer of electronic excitations in close-packed CdSe quantum-dot solids. *Phys Rev B* **54**(12):8633–8643.
36. Mamedova NN, Kotov NA, Rogach AL, Studer J. 2001. Albumin-CdTe nanoparticle bioconjugates: preparation, structure, and interunit energy transfer with antenna effect. *Nanotechnol Lett* **1**(6):281–286.
37. Javier A, Yun CS, Sorena J, Strouse GF. 2003. Energy transfer in CdSe nanocrystals assembled with molecular wires. *J Phys Chem B* **107**:435–442.
38. Kloepfer JA, Cohen N, Nadeau JL. 2004. FRET between CdSe quantum dots in lipid vesicles and water- and lipid-soluble dyes. *J Phys Chem B* **108**:17042–17049.
39. Willard DM, Carillo LL, Jung J, Van Orden A. 2001. CdSe-ZnS quantum dots as resonance energy transfer donors in a model protein–protein binding assay. *Nanotechnol Lett* **1**(9):469–474.
40. Martin RB, Richardson FS. 1979. Lanthanides as probes for calcium in biological systems. *Q Rev Biophys* **12**(2):181–209.
41. Horrocks WD, Albin M. 1984. Lanthanide ion luminescence in coordination chemistry and biochemistry. *Prog Inorg Chem* **31**:1–104.
42. Turro C, Fu PKL, Bradley PM. 2003. Lanthanide ions and luminescent probes of proteins and nucleic acids. In *The lanthanides and their interrelations with biosystems*, pp. 323–353. Ed A Sigel, H Sigel. Marcel Dekker, New York.
43. Lis S. 1992. Luminescence lifetime measurements of lanthanide aquo ions and their complexes: hydration study of Eu(III) systems. *Mater Sci.* **18**(2–4):51–60.
44. Choppin GR, Peterman DR. 1998. Applications of lanthanide luminescence spectroscopy to solution studies of coordination chemistry. *Coord Chem Rev* **174**:283–299.
45. Sabbatini N, Guardigli M, Manet I. 1997. Lanthanide complexes of encapsulating ligands as luminescent devices. In *Advances in photochemistry*, Vol. 23, pp. 213–278. Ed DC Neckers, DH Volman, G von Bünau. John Wiley & Sons, New York.
46. Selvin PR. 1999. Luminescent lanthanide chelates for improved resonance energy transfer and application to biology. In *Applied fluorescence in chemistry, biology and medicine*, pp. 457–487. Ed W Rettig, B Strehmel, S Schrader, H Seifert. Springer, New York.
47. de Sa GF, Malta OL, de Mello Donega C, Simas AM, Longo RL, Santa-Cruz PA, de Silva EF. 2000. Spectroscopic properties and design of highly luminescent lanthanide coordination complexes. *Coord Chem Rev* **196**:165–195.
48. Bakker BH, Goes M, Hoebe N, van Ramesdonk HJ, Verhoeven JW, Werts MHV, Hofstraat JW. 2000. Luminescent materials and devices: lanthanide azatriphenylene complexes and electroluminescent charge transfer systems. *Coord Chem Rev* **208**:3–16.
49. Heyduk E, Heyduk T. 1997. Thiol-reactive, luminescent europium chelates: luminescence probes for resonance energy transfer distance measurements in biomolecules. *Anal Biochem* **248**:216–227.
50. Ge P, Selvin PR. 2003. Thiol-reactive luminescent lanthanide chelates, part 2. *Bioconjugate Chem* **14**:870–876.
51. Yuan J, Wang G, Majima K, Matsumoto K. 2001. Synthesis of a terbium fluorescent chelate and its application to time-resolved fluorimmunoassay. *Anal Chem* **73**:1869–1876.
52. Roy BC, Santos M, Mallik S, Campiglia AD. 2003. Synthesis of metal-chelating lipids to sensitive lanthanide ions. *J Org Chem* **68**: 3999–4007.
53. Wu FB, Zhang C. 2002. A new europium  $\beta$ -diketone chelate for ultrasensitive time-resolved fluorescence immunoassays. *Anal Biochem* **311**:57–67.
54. Hemmila I, Mukkala VM, Takalo H. 1997. Development of luminescent lanthanide chelate labels for diagnostic assays. *J Alloys Compd* **249**:158–162.
55. Selvin PR, Hearst JE. 1994. Luminescence energy transfer using a terbium chelate: improvements on fluorescence energy transfer. *Proc Natl Acad Sci USA* **91**:10024–10028.
56. Chen J, Selvin PR. 2000. Lifetime- and color-tailored fluorophores in the micro- to millisecond time regime. *J Am Chem Soc* **122**: 657–660.
57. Selvin PR, Rana TM, Hearst JE. 1994. Luminescence resonance energy transfer. *J Am Chem Soc* **116**:6029–6030.
58. Sueda S, Yuan J, Matsumoto K. 2002. A homogeneous DNA hybridization system by using a new luminescence terbium chelate. *Bioconjugate Chem* **13**:200–205.
59. Okabayashi Y, Ikeuchi I. 1998. Liposome immunoassay by long-lived fluorescence detection. *Analyst* **123**:1329–1332.
60. Chen Y, Lehrer SS. 2004. Distances between tropomyosin sites across the muscle thin filament using luminescence resonance energy transfer: evidence for tropomyosin flexibility. *Biochemistry* **43**: 11491–11499.
61. Kessler MA. 1999. Probing the dissociation state of acid-base indicators by time-resolved lanthanide luminescence: a convenient transduction scheme for optical chemical sensors. *Anal Chem* **71**: 1540–1543.
62. Gunnlaugsson T, Mac Donaill D, Parker D. 2001. Lanthanide macrocyclic quinolyl conjugates as luminescent molecular-level devices. *J Am Chem Soc* **123**:12866–12876.
63. Lowe MP, Parker D, Reany O, Aime S, Botta M, Castellano G, Gianolio E, Pagliarin R. 2001. pH-dependent modulation of relaxivity and luminescence in macrocyclic gadolinium and europium complexes based on reversible intramolecular sulfonamide ligation. *J Am Chem Soc* **123**:7601–7609.
64. Hanaoka K, Kikuchi K, Kojima H, Urano Y, Nagano T. 2004. Development of a zinc ion-selective luminescent lanthanide chemosensor for biological applications. *J Am Chem Soc* **126**: 12470–12476.
65. Blair S, Lowe MP, Mathieu CE, Parker D, Senanayake PK, Kataky R. 2001. Narrow-range optical pH sensors based on luminescent europium and terbium complexes immobilized in a sol gel glass. *Inorg Chem* **40**:5860–5867.
66. Lowe MP, Parker D. 2000. Controllable pH modulation of lanthanide luminescence by intramolecular switching of the hydration state. *Chem Commun* **8**:707–708.
67. Mortellaro MA, Nocera DG. 1996. A supramolecular chemosensor for aromatic hydrocarbons. *J Am Chem Soc* **118**:7414–7415.
68. Harma H, Soukka T, Lovgren T. 2001. Europium nanoparticles and time-resolved fluorescence for ultrasensitive detection of prostate-specific antigen. *Clin Chem* **47**(3):561–568.

69. Soukka T, Paukkunen J, Harma H, Lonnberg S, Lindroos H, Lovgren T. 2001. Supersensitive time-resolved immunofluorometric assay of free prostate-specific antigen with nanoparticle label technology. *Clin Chem* **47**(7):1269–1278.
70. Riwotzki K, Meyssamy H, Kornowski A, Haase M. 2000. Liquid-phase synthesis of doped nanoparticles: colloids of luminescing LaPO<sub>4</sub>:Eu and CePO<sub>4</sub>:Tb particles with a narrow particle size distribution. *J Phys Chem B* **104**:2824–2828.
71. Ye Z, Tan M, Wang G, Yuan J. 2004. Preparation, characterization, and time-resolved fluorometric application of silica-coated terbium (III) fluorescence nanoparticles. *Anal Chem* **76**:513–518.
72. Werts MHV, Hofstraat JW, Geurts FAJ, Verhoeven JW. 1997. Fluorescein and eosin as sensitizing chromophores in near-infrared luminescent ytterbium (III), neodymium (III) and erbium (III) chelates. *Chem Phys Lett* **276**:196–201.
73. Hebbink GA, Grave L, Woldering LA, Reinhoudt DN, van Veggel FCJM. 2003. Unexpected sensitization efficiency of the near-infrared Nd<sup>3+</sup>, Er<sup>3+</sup>, and Yb<sup>3+</sup> emission by fluorescein compared to eosin and erythrosin. *J Phys Chem A* **107**:2483–2491.
74. Werts MHV, Verhoeven JW, Hofstraat JW. 2000. Efficient visible light sensitisation of water-soluble near-infrared luminescent lanthanide complexes. *J Chem Soc Perkin Trans 2* **2**:433–439.
75. Wang H, Qian G, Wang M, Zhang J, Luo Y. (2004). Enhanced luminescence of an erbium (III) ion-association ternary complex with a near-infrared dye. *J Phys Chem B* **108**:8084–8088.
76. Hebbink G. A. Reinhoudt, DN, van Veggel FCJM. 2001. Increased luminescent lifetimes of Ln<sup>3+</sup> complexes emitting in the near-infrared as a result of deuteration. *Eur J Org Chem* **4101**–4106.
77. Hasegawa Y, Kimura Y, Murakoshi K, Wada Y, Kim JH, Nakashima N, Yamanaka T, Yanagida S. 1996. Enhanced emission of deuterated tris(hexafluoroacetylacetoneato) neodymium (III) complex in solution by suppression of radiationless transition via vibrational excitation. *J Phys Chem* **100**:10201–10205.
78. Werts MHV, Woudenberg RH, Emmerink PG, van Gassel R, Hofstraat JW, Verhoeven JW. 2000. A near-infrared luminescent label based on Yb<sup>III</sup> ions and its application in a fluoroimmunoassay. *Angew Chem, Int Ed* **39**(24):4542–4544.
79. Gardner SJ, Hewlett DF. 2003. Optimization and initial evaluation of 1,2-indandione as a reagent for fingerprint detection. *J Forensic Sci* **48**(6):1–5.
80. Almog J, Cohen Y, Azoury M, Hahn TR. 2004. Genipin—a novel fingerprint reagent with colorimetric and fluorogenic activity. *J Forensic Sci* **49**(2):255–257.
81. Caldwell JP, Henderson W, Kim ND. 2001. Luminescent visualization of latent fingerprints by direct reaction with a lanthanide shift reagent. *J Forensic Sci* **46**(6):1332–1341.
82. Allred CE, Menzel ER. 1997. A novel europium-bioconjugate method for latent fingerprint detection. *Forensic Sci Int* **85**:83–94.
83. Wilkinson D. 1999. A one-step fluorescent detection method for lipid fingerprints; Eu(TTA)<sub>3</sub> 2TOPO. *Forensic Sci Int* **99**:5–23.
84. Vanderkooi JM. 1992. Tryptophan phosphorescence from proteins at room temperature. In *Topics in fluorescence spectroscopy*, Vol. 3: *Biochemical applications*, pp. 113–136. Ed JR Lakowicz. Plenum Press, New York.
85. Barthold M, Barrantes FJ, Jovin TM. 1981. Rotational molecular dynamics of the membrane-bound acetylcholine receptor revealed by phosphorescence spectroscopy. *Eur J Biochem* **120**:389–397.
86. Che A, Cherry RJ. 1995. Loss of rotational mobility of band 3 proteins in human erythrocyte membranes induced by antibodies to glycophorin A. *Biophys J* **68**:1881–1887.
87. Haugen GR, Lytle FE. 1981. Quantitation of fluorophores in solution by pulsed laser excitation and time-filtered detection. *Anal Chem* **53**:1554–1559.
88. Brewer KJ. 1999. Tridentate-bridged polyazine complexes of ruthenium (III) and osmium (III) and their application to the development of photochemical molecular devices. *Comments Inorg Chem* **21**(4–6):201–224.
89. Chen P, Meyer TJ. 1998. Medium effects on charge transfer in metal complexes. *Chem Rev* **98**:1439–1477.
90. Stufkens DJ, Vlèek Jr A. 1998. Ligand-dependent excited state behaviour of Re(I) and Ru(II) carbonyl-diimine complexes. *Coord Chem Rev* **177**:127–179.
91. Shan B-Z, Zhao Q, Goswami N, Eichhorn DM, Rillema DP. 2001. Structure, NMR and other physical and photophysical properties of ruthenium (II) complexes containing the 3,3'-dicarboxyl-2,2'-bipyridine ligand. *Coord Chem Rev* **211**:117–144.
92. Balzani V, Juris A. 2001. Photochemistry and photophysics of Ru(II)-polypyridine complexes in the bologna group: from early studies to recent developments. *Coord Chem Rev* **211**:97–115.
93. Sun S-S, Lees AJ. 2002. Transition metal based supramolecular systems: synthesis, photophysics, photochemistry and their potential applications as luminescent anion chemosensors. *Coord Chem Rev* **230**:171–192.
94. Balzani V, Sabbatini N. 1986. "Second-sphere" photochemistry and photophysics of coordination compounds. *Chem Rev* **86**:319–337.
95. Chen P, Meyer TJ. 1998. Medium effects on charge transfer in metal complexes. *Chem Rev* **98**:1439–1477.
96. Juris A, Balzani V, Barigelli F, Campagna S, Belser P, Von Zelewsky A. 1988. Ru(II) polypyridine complexes: photophysics, photochemistry, electrochemistry and chemiluminescence. *Coord Chem Rev* **84**:85–277.
97. Demas JN, DeGraff BA. 1994. Design and applications of highly luminescent transition metal complexes. In *Topics in fluorescence spectroscopy*, Vol. 4: *Probe design and chemical sensing*, pp. 71–107. Ed JR Lakowicz. Plenum Press, New York.
98. Castellano FN. Personal communication.
99. McCusker JK. 2003. Femtosecond absorption spectroscopy of transition metal charge-transfer complexes. *Acc Chem Res* **36**:876–887.
100. Yeh AT, Shank CV, McCusker JK. 2000. Ultrafast electron localization dynamics following photo-induced charge transfer. *Science* **289**:935–938.
101. Bhasikuttan AC, Suzuki M, Nakashima S, Okada T. 2002. Ultrafast fluorescence detection in tris(2,2'-bipyridine)ruthenium(II) complex in solution: relaxation dynamics involving higher excited states. *J Am Chem Soc* **124**:8398–8405.
102. Damrauer NH, Cerullo G, Yeh A, Boussie TR, Sharnk CV, McCusker JK. 1997. Femtosecond dynamics of excited state evolution in [Ru(bpy)<sub>3</sub>]<sup>2+</sup>. *Science* **275**:54–57.

103. Demas JN, DeGraff BA. 1991. Design and applications of highly luminescent transition metal complexes. *Anal Chem* **63**:829A–837A.
104. Kalayanasundaram K. 1992. *Photochemistry of polypyridine and porphyrin complexes*. Academic Press, New York.
105. Terpetschnig E, Szmacinski H, Malak H, Lakowicz JR. 1995. Metal-ligand complexes as a new class of long-lived fluorophores for protein hydrodynamics. *Biophys J* **68**:342–350.
106. Kise KJ, Bowler BE. 2002. A ruthenium (II) tris(bipyridyl) amino acid: synthesis and direct incorporation into an  $\alpha$ -helical peptide by solid-phase synthesis. *Inorg Chem* **41**(2):379–386.
107. Lo KK-W, Hui W-K, Ng DC-M, Cheung K-K. 2002. Synthesis, characterization, photophysical properties, and biological labeling studies of a series of luminescent rhenium (I) polypyridine maleimide complexes. *Inorg Chem* **41**(1):40–46.
108. Muheim A, Todd RJ, Casimiro DR, Gray HB, Arnold FH. 1993. Ruthenium-mediated protein cross-linking and stabilization. *J Am Chem Soc* **115**:5312–5313.
109. Rau HK, DeJonge N, Haehnel W. 1998. Modular synthesis of *de novo*-designed metalloproteins for light-induced electron transfer. *Proc Natl Acad Sci USA* **95**:11526–11531.
110. Szmacinski H, Terpetschnig E, Lakowicz JR. 1996. Synthesis and evaluation of Ru-complexes as anisotropy probes for protein hydrodynamics and immunoassays of high-molecular-weight antigens. *Biophys Chem* **62**:109–120.
111. Castellano FN, Dattelbaum JD, Lakowicz JR. 1998. Long-lifetime Ru(II) complexes as labeling reagents for sulphydryl groups. *Anal Biochem* **255**:165–170.
112. Terpetschnig E, Dattelbaum JD, Szmacinski H, Lakowicz JR. 1997. Synthesis and spectral characterization of a thiol-reactive long-life-time Ru(II) complex. *Anal Biochem* **251**:241–245.
113. Slim M, Sleiman HF. 2004. Ruthenium(II)-phenanthroline-biotin complexes: synthesis and luminescence enhancement upon binding to avidin. *Bioconjugate Chem* **15**(5):949–953.
114. Hu X, Smith GD, Sykora M, Lee SJ, Grinstaff MW. 2000. Automated solid-phase synthesis and photophysical properties of oligodeoxynucleotides labeled at 5'-aminothymidine with Ru(bpy)<sub>2</sub>-(4-m-4'-cam-bpy)<sup>2+</sup>. *Inorg Chem* **39**:2500–2504.
115. Khan SI, Beilstein AE, Tierney MT, Sykora M, Grinstaff MW. 1999. Solid-phase synthesis and photophysical properties of DNA labeled at the nucleobase with Ru(bpy)<sub>2</sub>(4-m-4'-pa-bpy)<sup>2+</sup>. *Inorg Chem* **38**:5999–6002.
116. Khan SI, Beilstein AE, Smith GD, Sykora M, Grinstaff MW. 1999. Synthesis and excited-state properties of a novel ruthenium nucleoside: 5[Ru(bpy)<sub>2</sub>(4-m-4'-pa-bpy)]<sup>2+</sup>-2'-deoxyuridine. *Inorg Chem* **38**:2411–2415.
117. Khan SI, Beilstein AE, Grinstaff MW. 1999. Automated solid-phase synthesis of site-specifically labeled ruthenium-oligonucleotides. *Inorg Chem* **38**:418–419.
118. Hurley DJ, Tor Y. 1998. Metal-containing oligonucleotides: solid-phase synthesis and luminescence properties. *J Am Chem Soc* **120**:2194–2195.
119. Guo X, Li L, Castellano FN, Szmacinski H, Lakowicz JR. 1997. A long-lived, highly luminescent rhenium (I) metal-ligand complex as a bimolecular probe. *Anal Biochem* **254**:179–186.
120. Terpetschnig E, Szmacinski H, Lakowicz JR. 1996. Fluorescence polarization immunoassay of a high molecular weight antigen using a long wavelength absorbing and laser diode-excitible metal-ligand complex. *Anal Biochem* **240**:54–59.
121. Lakowicz JR, Terpetschnig E, Murtaza Z, Szmacinski H. 1997. Development of long-lifetime metal-ligand probes for biophysics and cellular imaging. *J Fluoresc* **7**(1):17–25.
122. Demas JN, DeGraff BA. 1992. Applications of highly luminescent transition metal complexes in polymer systems. *Macromol Chem, Macromol Symp* **59**:35–51.
123. Demas JN, DeGraff BA. 1997. Applications of luminescent transition metal complexes to sensor technology and molecular probes. *J Chem Educ* **74**(6):690–695.
124. Caspar J, Meyer TJ. 1983. Application of the energy gap law to non-radiative, excited-state decay. *J Phys Chem* **87**:952–957.
125. Kober EM, Marshall JL, Dressick WJ, Sullivan BP, Caspar JV, Meyer TJ. 1985. Synthetic control of excited states: nonchromophoric ligands and variations in polypyridyl complexes of osmium (II). *Inorg Chem* **24**:2755–2763.
126. Kober EM, Sullivan BP, Dressick WJ, Caspar JV, Meyer TJ. 1980. Highly luminescent polypyridyl complexes of osmium (II). *J Am Chem Soc* **102**:1383–1385.
127. Caspar JV, Meyer TJ. 1983. Photochemistry of Ru(bpy)<sub>3</sub><sup>2+</sup>: solvent effects. *J Am Chem Soc* **105**:5583–5590.
128. Caspar JV, Kober EM, Sullivan BP, Meyer TJ. 1982. Application of the energy gap law to the decay of charge-transfer excited states. *J Am Chem Soc* **104**:630–632.
129. Bixon M, Jortner J. 1968. Intramolecular radiationless transitions. *J Chem Phys* **48**(2):715–726.
130. Freed KF, Jortner J. 1970. Multiphonon processes in the nonradiative decay of large molecules. *J Chem Phys* **52**(12):6272–6291.
131. Nuñez ME, Barton JK. 2000. Probing DNA charge transport with metallointercalators. *Curr Opin Chem Biol* **4**:199–206.
132. Grimm GN, Boutorine AS, Lincoln P, Nordén B, Hélène C. 2002. Formation of DNA triple helices by an oligonucleotide conjugated to a fluorescent ruthenium complex. *ChemBioChem* **3**:324–331.
133. Turro C, Bossmann SH, Jenkins Y, Barton JK, Turro NJ. 1995. Proton transfer quenching of the MLCT excited state of Ru(phen)<sub>2</sub>-dppz<sup>2+</sup> in homogeneous solution and bound to DNA. *J Am Chem Soc* **117**:9026–9032.
134. Nair RB, Cullum BM, Murphy CJ. 1997. Optical properties of [Ru(phen)<sub>2</sub>dppz]<sup>2+</sup> as a function of nonaqueous environment. *Inorg Chem* **36**:962–965.
135. Nair RB, Murphy CJ. 1998. On the interaction of [Ru(phen)<sub>2</sub>dppz]<sup>2+</sup> (dppz=dipyrro[3,2-*a*:2',3'-*c*]phenazine) with different oligonucleotides. *J Inorg Biochem* **69**:129–133.
136. Coates CG, McGarvey JJ, Callaghan PL, Coletti M, Hamilton JG. 2001. Probing the interaction of [Ru(phen)<sub>2</sub>(dppz)]<sup>2+</sup> with single-stranded DNA—what degree of protection is required for operation of the "light-switch effect"? *J Phys Chem* **105**:730–735.
137. Önfelt B, Lincoln P, Nordén B. 2001. Enantioselective DNA threading dynamics by phenazine-linked [Ru(phen)<sub>2</sub>dppz]<sup>2+</sup> dimers. *J Am Chem Soc* **123**:3630–3637.
138. Friedman AE, Chambron JC, Sauvage J-P, Turro NJ, Barton JK. 1990. Molecular light switch for DNA Ru(bpy)<sub>2</sub>(dppz)<sup>2+</sup>. *J Am Chem Soc* **112**:4960–4962.
139. Del Guerzo A, Mesmaeker AK-D. 2002. Novel DNA sensor for guanine content. *Inorg Chem* **41**(4):938–945.

140. Garcia-Fresnadillo D, Boutonnet N, Schumm S, Moucheron C, Mesmaeker AK-D, Defrancq E, Constant JF, Lhomme J. 2002. Luminescence quenching of Ru-labeled oligonucleotides by targeted complementary strands. *Biophys J* **82**:978–987.
141. Del Guerzo A, Mesmaeker AK-D, Demeunynck M, Lhomme J. 1997. Photophysics of bifunctional Ru(II) complexes bearing an aminoquinoline organic unit: potential new photoprobes and photoreagents of DNA. *J Phys Chem B* **101**:7012–7021.
142. Kang JS, Abugo OO, Lakowicz JR. 2002. Dynamics of supercoiled and relaxed pTZ18U plasmids probed with a long-lifetime metal–ligand complex. *J Biochem Mol Biol* **35**(4):389–394.
143. Kang JS, Abugo OO, Lakowicz JR. 2002. Dynamics of supercoiled and linear pTZ18U plasmids observed with a long-lifetime metal–ligand complex. *Biopolymers* **67**:121–128.
144. Lakowicz JR, Malak H, Gryczynski I, Castellano FN, Meyer GJ. 1995. DNA dynamics observed with long lifetime metal–ligand complexes. *Biospectroscopy* **1**:163–168.
145. Malak H, Gryczynski I, Lakowicz JR, Meyer GJ, Castellano FN. 1997. Long-lifetime metal–ligand complexes as luminescent probes for DNA. *J Fluoresc* **7**(2):107–112.
146. Jenkins Y, Friedman AE, Turro NJ, Barton JK. 1992. Characterization of dipyridophenazine complexes of ruthenium (II): the light switch effect as a function of nucleic acid sequence and conformation. *Biochemistry* **31**:10809–10816.
147. Holmlin RE, Stemp EDA, Barton JK. 1998. Ru(phen)<sub>2</sub>dppz<sup>2+</sup> luminescence: dependence on DNA sequences and groove-binding agents. *Inorg Chem* **37**:29–34.
148. Chang Q, Murtaza Z, Lakowicz JR, Rao G. 1997. A fluorescence lifetime-based solid sensor for water. *Anal Chim Acta* **350**:97–104.
149. Guo X-Q, Castellano FN, Li L, Lakowicz JR. 1998. A long-lifetime Ru(II) metal–ligand complex as a membrane probe. *Biophys Chem* **71**:51–62.
150. Anderson CM, Zucker FH, Steitz TA. 1979. Space-filling models of kinase clefts and conformation changes. *Science* **204**:375–380.
151. Grossman SH. 1990. Resonance energy transfer between the active sites of creatine kinase from rabbit brain. *Biochim Biophys Acta* **1040**:276–280.
152. Grossman SH. 1989. Resonance energy transfer between the active sites of rabbit muscle creatine kinase: analysis by steady-state and time-resolved fluorescence. *Biochemistry* **28**:5902–5908.
153. Haran G, Haas E, Szpikowska BK, Mas MT. 1992. Domain motions in phosphoglycerate kinase: Determination of interdomain distance-distributions by site-specific labeling and time-resolved fluorescence energy transfer. *Proc Natl Acad Sci USA* **89**:11764–11768.
154. Holowka D, Wensel T, Baird B. 1990. A nanosecond fluorescence depolarization study on the segmental flexibility of receptor-bound immunoglobulin E. *Biochemistry* **29**:4607–4612.
155. Zheng Y, Shopes B, Holowka D, Biard B. 1991. Conformations of IgE bound to its receptor Fc epsilon RI and in solution. *Biochemistry* **30**:9125–9132.
156. Li L, Szmacinski H, Lakowicz JR. 1997. Long-lifetime lipid probe containing a luminescent metal–ligand complex. *Biospectroscopy* **3**(2):155–159.
157. Li L, Szmacinski H, Lakowicz JR. 1997. Synthesis and luminescence spectral characterization of long-lifetime lipid metal–ligand probes. *Anal Biochem* **244**:80–85.
158. Urios P, Cittanova N. 1990. Adaptation of fluorescence polarization immunoassays to the assay of macromolecules. *Anal Biochem* **185**:308–312.
159. Thompson RB, Vallarino LM. 1988. Novel fluorescent label for time-resolved fluorescence immunoassay. *SPIE Proc* **909**:426–433.
160. Terpetschnig E, Szmacinski H, Lakowicz JR. 1995. Fluorescence polarization immunoassay of a high molecular weight antigen based on a long-lifetime Ru–ligand complex. *Anal Biochem* **227**:140–147.
161. Youn HJ, Terpetschnig E, Szmacinski H, Lakowicz JR. 1995. Fluorescence energy transfer immunoassay based on a long-lifetime luminescence metal–ligand complex. *Anal Biochem* **232**:24–30.
162. Guo X-Q, Castellano FN, Li L, Lakowicz JR. 1998. Use of a long-lifetime Re(I) complex in fluorescence polarization immunoassays of high-molecular-weight analytes. *Anal Chem* **70**:632–637.
163. Lakowicz JR, Murtaza Z, Jones WE, Kim K, Szmacinski H. 1996. Polarized emission from a rhenium metal–ligand complex. *J Fluoresc* **6**(4):245–249.
164. Brewer RG, Jensen GE, Brewer KJ. 1994. Long-lived osmium (II) chromophores containing 2,3,5,6-tetrakis(2-pyridyl)pyrazine. *Inorg Chem* **33**:124–129.
165. Murtaza Z, Herman P, Lakowicz JR. 1999. Synthesis and spectral characterization of a long-lifetime osmium (II) metal–ligand complex: a conjugatable red dye for applications in biophysics. *Biophys Chem* **80**:143–151.
166. Murtaza Z, Lakowicz JR. 1999. Long-lifetime and long-wavelength osmium (II) metal complexes containing polypyridine ligands: excellent red fluorescent dyes for biophysics and for sensors. *SPIE Proc* **3602**:309–315.
167. Shen Y, Maliwal BP, Lakowicz JR. 2003. Red-emitting Ru(II) metal–ligand complexes. *J Fluoresc* **13**(2):163–168.
168. Sun S-S, Lees AJ, Zavalij PY. 2003. Highly sensitive luminescent metal-complex receptors for anions through charge-assisted amide hydrogen bonding. *Inorg Chem* **42**(11):3445–3455.
169. Duff T, Grubing A, Thomas J-L, Duati M, Vos JG. 2003. Luminescent anion recognition: probing the interaction between dihydrogenphosphate anions and Ru(II) polypyridyl complexes in organic and aqueous media. *Polyhedron* **22**:775–780.
170. Rowe HM, Xu W, Demas JN, DeGraf BA. 2002. Metal ion sensors based on a luminescent ruthenium (II) complex: the role of polymer support in sensing properties. *Appl Spectrosc* **56**(2):167–173.
171. Uppadine LH, Redman JE, Dent SW, Drew MGB, Beer PD. 2001. Ion pair cooperative binding of potassium salts by new rhenium (I) bipyridine crown ether receptors. *Inorg Chem* **40**:2860–2869.
172. Wolfbeis OS, Klimant I, Werner T, Huber C, Kosch U, Krause C, Neurauter G, Dürkop A. 1998. Set of luminescence decay time based chemical sensors for clinical applications. *Sens Actuators B* **51**:17–24.
173. Sun S-S, Lees AJ. 2000. Anion recognition through hydrogen bonding: a simple, yet highly sensitive, luminescent metal–complex receptor. *Chem Commun* **17**:1687–1688.
174. deSilva AP, Fox DB, Huxley AJM, McClenaghan WM, Roigor J. 1999. Metal complexes as components of luminescent signalling systems. *Coord Chem Rev* **185–186**:297–306.
175. Anzenbacher P, Tyson DS, Jursiková K, Castellano FN. 2002. Luminescence lifetime-based sensor for cyanide and related anions. *J Am Chem Soc* **124**:6332–6233.

176. Montalti M, Wadhwa S, Kim WY, Kipp RA, Schmehl RH. 2000. Luminescent ruthenium (II) bipyridyl-phosphonic acid complexes: pH dependent photophysical behavior and quenching with divalent metal ions. *Inorg Chem* **39**:76–84.
177. Wang K-Z, Gao L-H, Bai G-Y, Jin L-P. 2002. First protein-induced near-infrared fluorescent switch at room temperature of a novel Ru(II) complex. *Inorg Chem Commun* **5**:841–843.
178. Grigg R, Norbert WDJA. 1992. Luminescent pH sensors based on di(2,2'-bipyridyl)(5,5-diaminomethyl-2,2'-bipyridyl)-ruthenium(II) complexes. *J Chem Soc Chem Commun*, pp 1300–1302.
179. Mack NH, Bare WD, Xu W, Demas JN, DeGraff BA. 2001. An automated approach to luminescence lifetime and intensity titrations. *J Fluoresc* **11**(2):113–118.
180. Licini M, Williams JAG. 1999. Iridium (III) bis-terpyridine complexes displaying long-lived pH sensitive luminescence. *Chem Commun* **18**:1943–1944.
181. Murtaza Z, Chang Q, Rao G, Lin H, Lakowicz JR. 1997. Long-lifetime metal-ligand pH probe. *Anal Biochem* **247**:216–222.
182. Kang JS, Piszczek G, Lakowicz JR. 2002. Enhanced emission induced by FRET from a long-lifetime, low quantum yield donor to a long-wavelength, high quantum yield acceptor. *J Fluoresc* **12**(1):97–103.
183. Lakowicz JR, Piszczek G, Kang JS. 2001. On the possibility of long-wavelength long-lifetime high-quantum yield luminophores. *Anal Biochem* **288**:62–75.
184. Maliwal BP, Gryczynski Z, Lakowicz JR. 2001. Long-wavelength long-lifetime luminophores. *Anal Chem* **73**:4277–4285.
185. Castellano FN, Lakowicz JR. 1998. A water-soluble luminescence oxygen sensor. *Photochem Photobiol* **67**(2):179–183.

## PROBLEMS

P20.1. *Effect of Off-Gating on the Background Level:* Figure 20.50 shows the intensity decay of a long-lifetime sensing probe ( $\tau_2$ ) with an interfering autofluorescence of  $\tau_1 = 7$  ns.

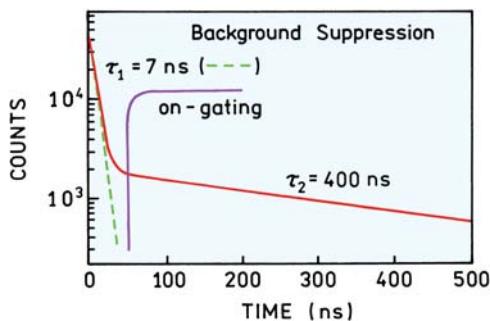


**Figure 20.50.** Intensity decay of a long-lifetime probe having a decay time of 400 ns, with an interfering autofluorescence of 7 ns.

- The decay time of the long-lifetime component is 400 ns. Confirm this by your own calculations.
- What are the values of  $\alpha_i$  in the intensity decay law? That is, describe  $I(t)$  in terms of  $\alpha_1 \exp(-t/\tau_1) + \alpha_2 \exp(-t/\tau_2)$ .
- What are the fractional intensities ( $f_i$ ) of the two components in the steady-state intensity measurements?
- Suppose the detector was gated on at 50 ns, and that the turn-on time is essentially instantaneous in Figure 20.50. Assume that the intensities are integrated to 5  $\mu$ s, much longer than  $\tau_2$ . What are the fractional intensities of each component? Explain the significance of this result for clinical and environmental sensing applications. It is recommended that the integrated fractional intensities be calculated using standard computer programs.

P20.2. *Oxygen Bimolecular Quenching Constant for a Metal-Ligand Complex:* The complex of ruthenium with three diphenylphenanthrolines  $[\text{Ru}(\text{dpp})_3]^{2+}$  displays a long lifetime near 5  $\mu$ s and has found widespread use as an oxygen sensor. Recently a water-soluble version of the sensor has been synthesized (Figure 20.51).<sup>185</sup> Frequency-domain intensi-

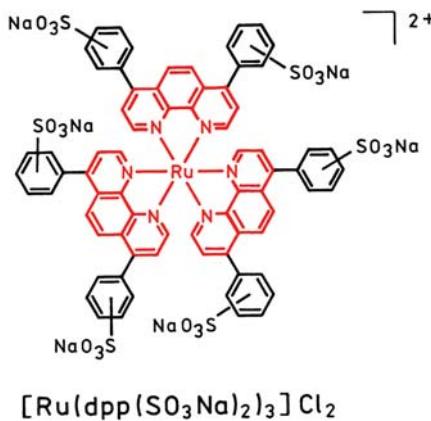


**Figure 20.51.** Structure of a water-soluble MLC used as an oxygen sensor.

ty data for  $[\text{Ru}(\text{dpp})(\text{SO}_3\text{Na})_2]_{\text{Cl}_2}$  are shown in Figure 20.52. Calculate the oxygen bimolecular

quenching constant for this complex. Assume the solubility of oxygen in water is 0.001275 M/atm.

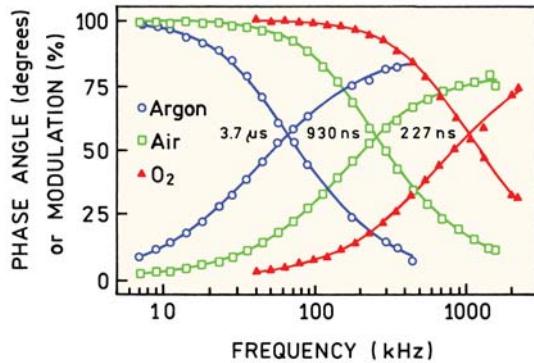


**Figure 20.52.** Frequency-domain intensity decay of  $[\text{Ru}(\text{dpp})(\text{SO}_3\text{Na})_2]_{\text{Cl}_2}$  in water, under an atmosphere of argon (o), air (□), or oxygen (▼).

# 21

# DNA Technology

During the past 20 years there have been remarkable advances in the use of fluorescence to study DNA. Fluorescence methods are now used for DNA sequencing, detection of DNA hybridization, restriction enzyme fragment analysis, and fluorescence in-situ hybridization (FISH), and to detect polymerase chain reaction products. Molecular beacons can be used to detect messenger RNA within cells. DNA arrays can be used to monitor the expression of thousands of genes using a single microscope slide. Fluorescence was used to sequence the human genome that was reported in 2000.<sup>1–2</sup> Given these advances it is surprising to realize that DNA sequencing by fluorescence was first reported in 1986. It is not practical to describe the many specialized methods used to study DNA in molecular biology, genetics, and medical diagnostics. In this chapter we provide an overview of the dominant users of fluorescence in DNA analysis.

## 21.1. DNA SEQUENCING

DNA sequencing first became practical in 1977.<sup>3–4</sup> The original method involved chemical degradation of the DNA using conditions that were partially selective for one of the four bases. The DNA fragments were then separated by chromatography and the fragments detected using  $^{32}\text{P}$  autoradiography. In the same year a method became available for generating fragments terminating in each of the four bases.<sup>5</sup> This method used termination of enzymatic DNA synthesis using dideoxynucleotides. The fragments were again detected using radioactivity. An overview of the history of DNA sequencing methods can be found in the informative text by Watson et al.<sup>6</sup>

The use of radioactive tracers is problematic with regards to cost, safety, and disposal. Also the use of radioactivity was not amenable to the degree of automation needed to sequence long DNA chains, chromosomes or an entire genome. DNA sequencing using fluorescence was first

reported in 1986.<sup>7–12</sup> At present essentially all sequencing is done using fluorescence detection. It is unlikely that the human genome would have been sequenced without the use of fluorescence. DNA sequencing is now highly automated<sup>11</sup> and performed in numerous laboratories around the world.

### 21.1.1. Principle of DNA Sequencing

A number of slightly different methods are used for DNA sequencing, but all methods rely on the use of dideoxynucleotide triphosphate (ddNTP) to terminate DNA synthesis. The basic idea of sequencing using ddNTP terminators is shown in Figures 21.1 and 21.2. In DNA the nucleotides are linked in a continuous strand via the 5' and 3' hydroxyl groups of the pentose sugar. DNA is replicated by adding nucleotides to the 3' hydroxyl group. For sequencing a DNA strand with an unknown sequence is replicated using DNA polymerase. Replication is started from a primer location with a known sequence. The most commonly used primer is the M13 sequence, which is 17 nucleotides long. In the example shown in Figure 21.2 a single fluorescent primer is used to initiate the reaction. The sample contains DNA polymerase and the four deoxynucleotide triphosphates.

Within a short period of time the DNA polymerase molecules are randomly distributed along the unknown sequence. The strands being synthesized have a sequence complementary to the unknown strand. The reaction mixture is split into four parts, one part for each of the four bases. The DNA polymerase reaction is randomly terminated by adding one of the ddNTPs to each of the four parts of the reaction. The ddNTPs are added along the growing chain. The absence of a 3' hydroxyl group on the ddNTPs prevents further elongation and terminates the reaction. This results in a mixture of oligonucleotides of varying length. The different size oligomers are separated by poly-

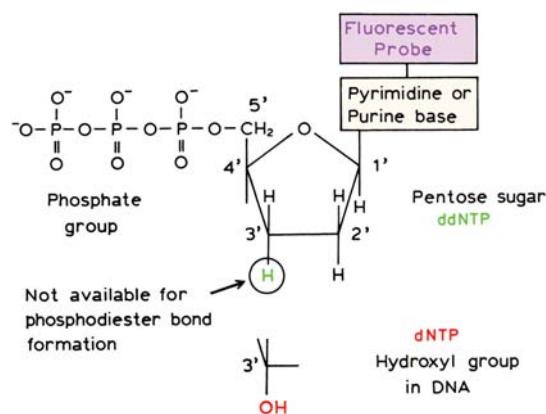


**Figure 21.1.** Schematic of a dideoxynucleotide triphosphate (ddNTP). Fluorescent and nonfluorescent ddNTPs are used for DNA sequencing, depending on the method. The 2' group is hydrogen in DNA, and is a hydroxyl group in RNA. In a ddNTP the 3'hydroxyl group is not present so the DNA chain cannot be continued.

acrylamide gel electrophoresis. Remarkably, numerous fragments differing by just one base pair can be resolved: up to several hundred bases. Each reaction mixture is electrophoresed in a separate lane. Each lane of the reaction mixture contains oligomers which are terminated with only

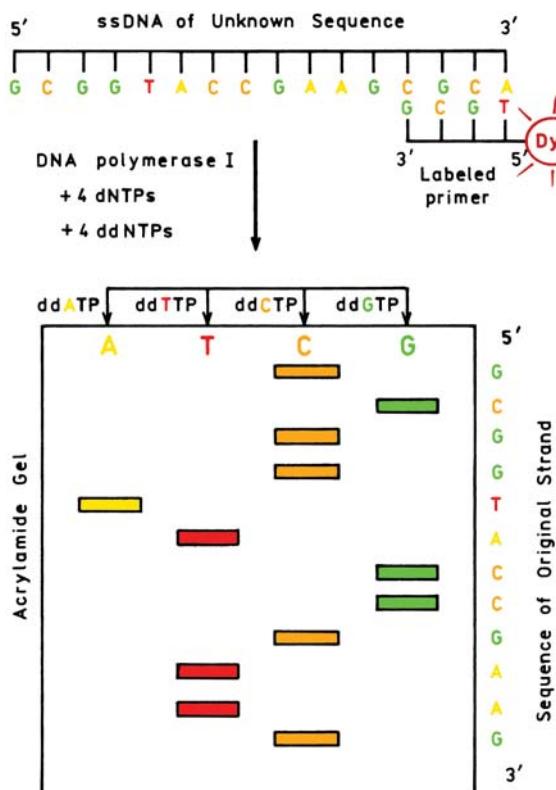


**Figure 21.2.** Four-lane DNA sequencing using nonfluorescent ddNTPs and a fluorescent primer for DNA synthesis.

one of the ddNTPs. The gels separate the DNA fragments according to size, so that the sequence can be determined from the fluorescence of the separated DNA fragments.

Because of the large number of sequences that need to be determined it is desirable to have the highest possible throughput. The throughput can be increased fourfold if the four DNA bases can be identified in a single lane of the chromatography gel. This can be accomplished using four fluorescent ddNTPs if each ddNTP contains a different fluorophore (Figure 21.3). In this case the reaction is initialized using a nonfluorescent primer. The reaction is terminated by addition to the four labeled ddNTPs. This inserts a labeled fluorophore that identifies the base at the 3' end of the terminated chains. The mixture can be analyzed in a single lane and the emission spectra used to identify the bases. Single- and four-lane sequencing represent the limiting cases, and many hybrid methods are also in use.

### 21.1.2. Examples of DNA Sequencing

A variety of fluorophores have been used for DNA sequencing: typically a set of four fluorophores, one for each base—A, C, G, or T. The fluorophores are typically select-

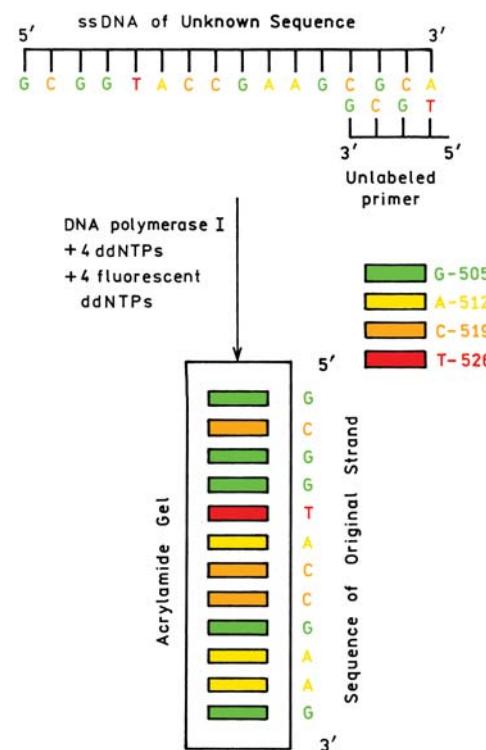


**Figure 21.3.** Single-lane DNA sequencing using a nonfluorescent primer and four fluorescent ddNTPs.

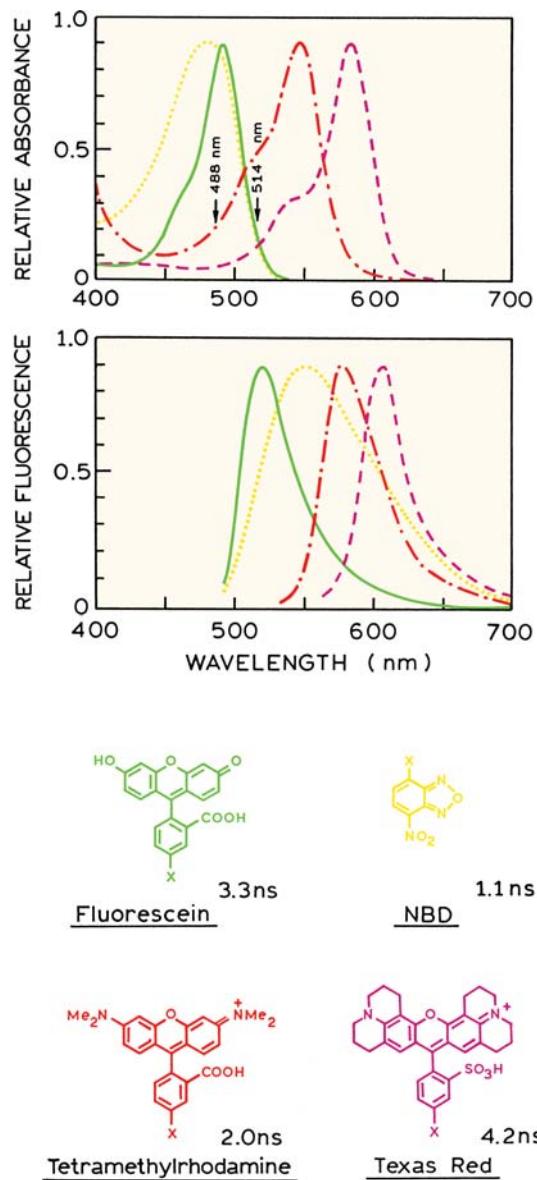


**Figure 21.4.** Fluorophores used for DNA sequencing with fluorescent primers. Top, absorption spectra; middle, emission spectra; bottom, probe structures. The X was linked to the 5' end of the DNA using an aliphatic amino group on the 5' terminus. Revised from [8]. Decay times are from [42] below.

ed so that all can be excited using the 488 nm line from an argon ion laser. The first set of fluorophores<sup>8</sup> used for DNA sequencing is shown in Figure 21.4. These fluorophores were attached to primers, which is different from the approaches shown in Figures 21.2 and 21.3. The four dyes could be excited at 488 nm, but the absorption of Texas Red and tetramethylrhodamine is obviously weak at 488 nm.

For this reason it was necessary to use 514-nm excitation in order to obtain relatively equal intensities for all four probes. Another difficulty with these four dyes is the overlapping emission spectra. It was necessary to record intensities at more than one excitation and emission wavelength in order to identify the fluorophore. In spite of these difficulties the use of four fluorophores allowed use of a single gel column containing the mixture of labeled DNA fragments.

An improved series of dyes for use as fluorescent dideoxy terminators is shown in Figure 21.5. A hydroxyl group is not present on the 3' portion of the sugar, so that these nucleotide analogues are unable to elongate the DNA chain. These dyes displayed similar extinction coefficients at 488 nm, allowing the use of a single excitation wavelength (Figure 21.6). The fluorescence intensities of these fluorophores differ by less than a factor of two. The letters SF indicate succinylfluorescein, which was linked to the base. The numbers refer to the emission maximum of each fluorescein derivative. In the lower panel the letter refers to the base to which the fluorescein is attached.

The emission spectra in Figure 21.6 show that there is substantial overlap of the emission spectra at all useful wavelengths. While the overlap can be decreased using different dyes there is always some spectral overlap. These dyes were identified by measuring the emission intensities through filters (Figure 21.6, lower panel). The fluorescent intensities at each location in the gel are measured with a laser scanning instrument (Figure 21.7). The laser beam is scanned across the gel and the intensity ratios are measured using two filters and two detectors. The intensity ratios are used to identify the base.

### 21.1.3. Nucleotide Labeling Methods

A wide variety of chemical structures have been used to covalently label DNA.<sup>13–14</sup> One typical linkage was shown in Figure 21.5, which showed acetylene linkages between the fluorophores and the nucleotide bases. Other typical structures are shown in Figure 21.8. Probes can be attached to the 5' end of DNA via a sulphydryl group linked to the terminal phosphate. Amino groups can also be placed on the terminal phosphate. The 5' phosphate can be made reactive with iodoacetamide probes by attaching a terminal —PO<sub>3</sub>S residue. Alternatively, fluorophores have been linked to the bases themselves, typically opposite to the base recognition hydrogen bonding side of the base. This type of attachment is used to label the internal DNA bases.

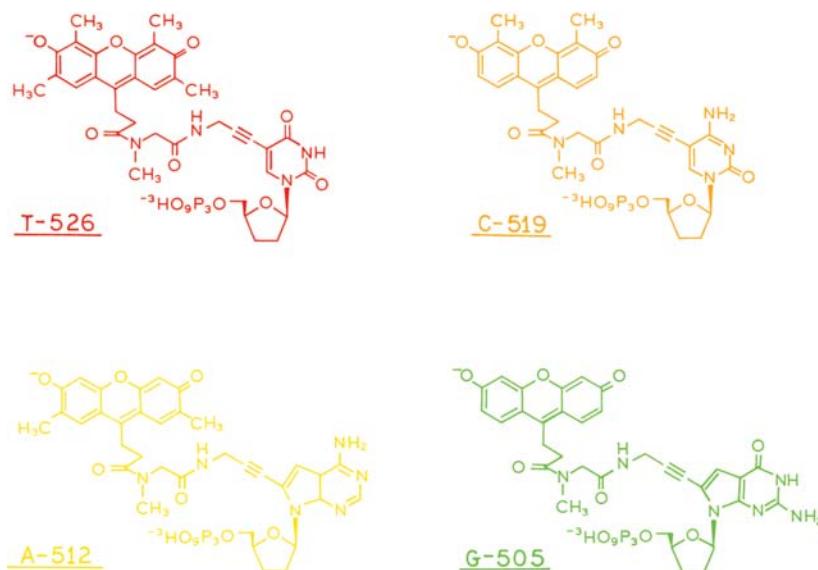


**Figure 21.5.** Fluorescent chain-terminating dideoxynucleotides. The letters refer to the DNA base, and the numbers refer to the emission maximum. Reprinted with permission from Prober JM, Trainor GL, Dam RJ, Hobbs FW, Robertson CW, Zagursky RJ, Cocuzza AJ, Jensen MA, Baumeister K. 1987. A system for rapid DNA sequencing with fluorescent chain-terminating dideoxynucleotides. *Science* **238**:336–343 [9]. Copyright © 1987, American Association for the Advancement of Science.

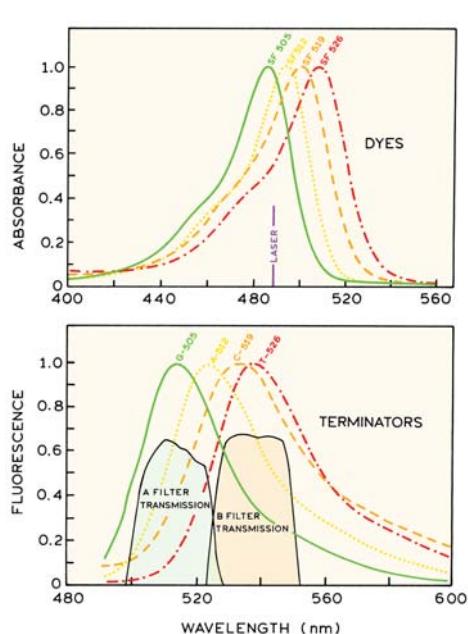


**Figure 21.6.** Absorption (top) and emission spectra (bottom) of the fluorescent chain terminating dideoxynucleotides in Figure 21.5. The absorption spectra are of the succinyl fluorescein (SF) dyes, prior to coupling to the amine reactive ddNTPs. Reprinted with permission from Prober JM, Trainor GL, Dam RJ, Hobbs FW, Robertson CW, Zagursky RJ, Cocuzza AJ, Jensen MA, Baumeister K. 1987. A system for rapid DNA sequencing with fluorescent chain-terminating dideoxynucleotides. *Science* **238**:336–343 [9]. Copyright © 1987, American Association for the Advancement of Science.

#### 21.1.4. Example of DNA Sequencing

It is informative to see some actual data from DNA sequencing,<sup>15–16</sup> which was accomplished using the fluorophores shown in Figure 21.9. These probes show moderately distinct emission spectra (Figure 21.10), so that single-lane sequencing should be possible. However, it is difficult to excite these four fluorophores using a single excitation wavelength.<sup>17</sup> Two laser sources were used at 488 and

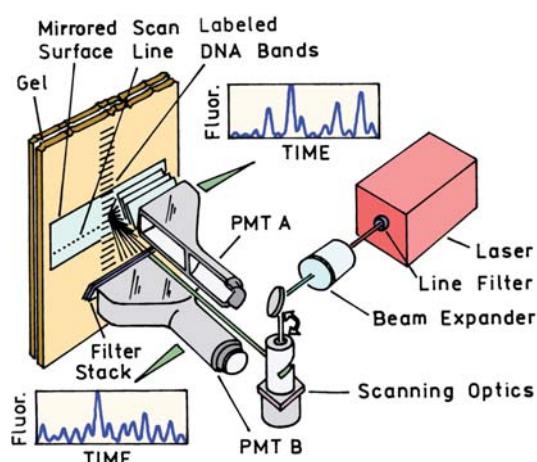


**Figure 21.7.** Apparatus for wavelength ratio intensity measurements from DNA gels. From [9].

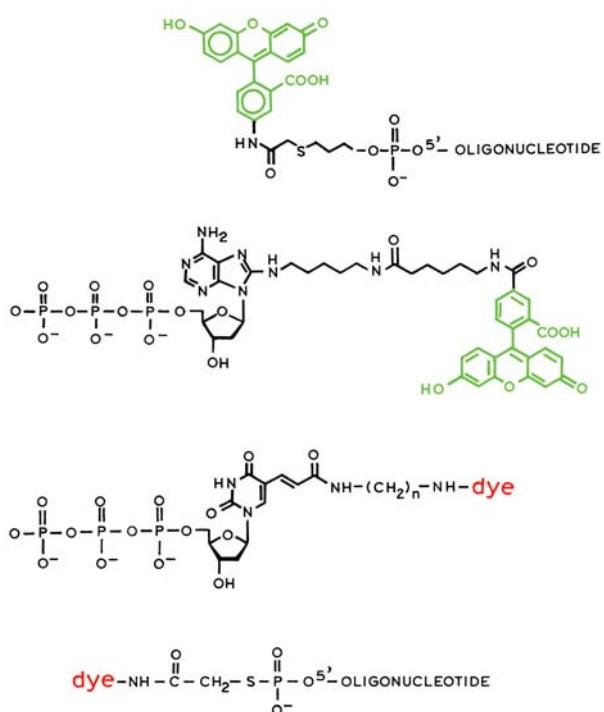


**Figure 21.8.** Methods to label DNA. In the top structure DNA is labeled with a fluorescent primer. The two structures in the middle show labeling of DNA using labeled nucleotide triphosphates. In the bottom structure DNA can also be labeled on the 5' end via a thiophosphate linkage (bottom). Revised from [13] and [14].

543.5 nm (Figure 21.11), and the emission was observed at four wavelengths. The excitation wavelength was selected using a spatial filter or sector wheel. The emission was observed using four emission filters. The primers were labeled with the fluorophores and sequencing was accomplished using a single capillary tube. The lower panel shows the intensity tracers for each combination of excitation and emission wavelength that uniquely identifies each fluorophore and base.

### 21.1.5. Energy-Transfer Dyes for DNA Sequencing

In the previous example it was necessary to use two laser wavelengths to obtain comparable intensities from the four dyes. For sequencing it is desirable to have dyes that display distinct emission spectra and similar intensities with a single excitation wavelength. This is difficult to accomplish using a single fluorophore. Donor–acceptor pairs have been designed to fulfill these requirements.<sup>18–25</sup> One set of energy-transfer primers for sequencing was constructed using

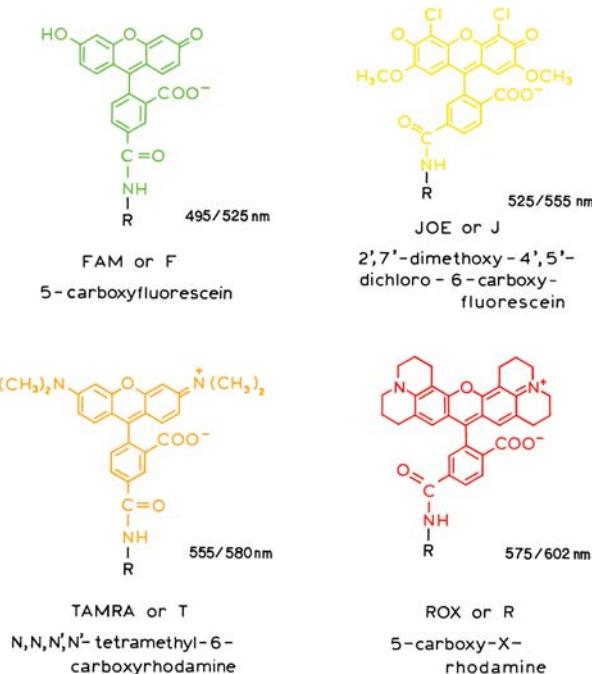


**Figure 21.9.** Fluorophores used as energy-transfer DNA sequencing probes. The two wavelengths are the excitation and emission maxima. Revised from [15].

the fluorophores shown in Figure 21.9. The emission spectra of these four probes are moderately distinct (Figure 21.10), suggesting allowance of sequencing in a single lane. However, the intensities are unequal when excited at a single wavelength of 488 nm, which is why two excitation wavelengths are used in Figure 21.11. The donors and acceptors were covalently linked within the Förster distance

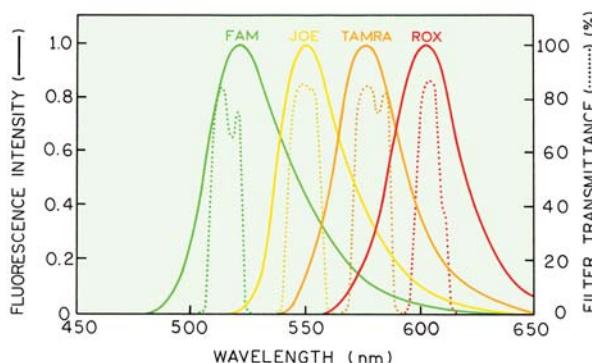


**Figure 21.10.** Emission spectra of the four probes used for construction of the energy-transfer primers. Reprinted with permission from [16]. Copyright © 1994, American Chemical Society.

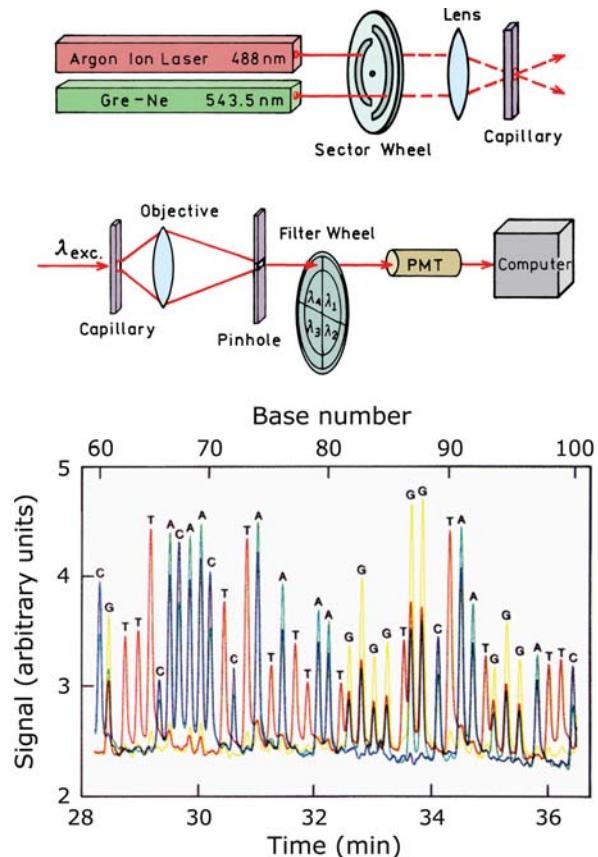


**Figure 21.11.** DNA sequencing using two excitation wavelengths and the fluorophores shown in Figure 21.10. Revised and reprinted with permission from [17]. Copyright © 1991, American Chemical Society.

( $R_0$ ) using reactive oligonucleotides (Figure 21.12 top) or DNA-like sugar polymers without the nucleotide bases (bottom). The lengths of the oligonucleotide linkers were adjusted to obtain the amount of energy transfer so that the acceptor intensities are comparable to excitation at 488 nm.

The energy-transfer cassettes displayed nearly equal intensities when excited at 488 nm (Figure 21.13). The emission spectra are moderately well separated, which is easier to see in the normalized emission spectra (Figure 21.14). The bases can be readily identified by measurement at the four emission wavelengths, which allows DNA sequencing with capillary electrophoresis using a single 488 nm excitation wavelength. However, Figure 21.14 shows that the emission spectra overlap, and that there is residual emission from the donors which contributes to the intensities at shorter wavelengths. Hence, there is still a need for improved dyes for DNA sequencing. Another set of energy-transfer primers has been reported based on the Bodipy fluorophore.<sup>25</sup> These primers are claimed to show

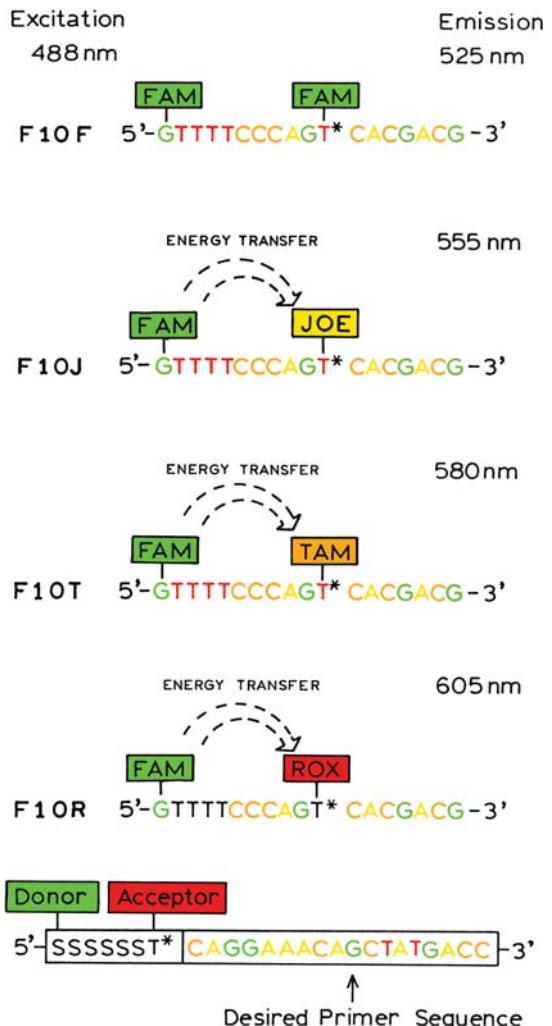


**Figure 21.12.** Energy-transfer primers used for DNA sequencing. F10F, F10J, F10T, and F10R are energy-transfer primers in which the donor and acceptor (see Figure 21.9 for the structures of F, J, T, and R) have been covalently linked using reactive oligonucleotides. Excitation is at 488 nm, and the emission wavelengths are indicated on the right-hand side of the figure. As shown at the bottom of the figure, donor–acceptor pairs can also be placed on sugar polymers (—SSS—) prior to the primer sequence. Revised from [15] and [16].

more distinct emission spectra than shown in Figure 21.13, but the Bodipy fluorophores are thought to be less photo-stable. Given the need for sequencing, there will be continued development of probes with improved spectral properties.

### 21.1.6. DNA Sequencing with NIR Probes

The genomes of many organisms are being sequenced, which must be accomplished as rapidly and inexpensively

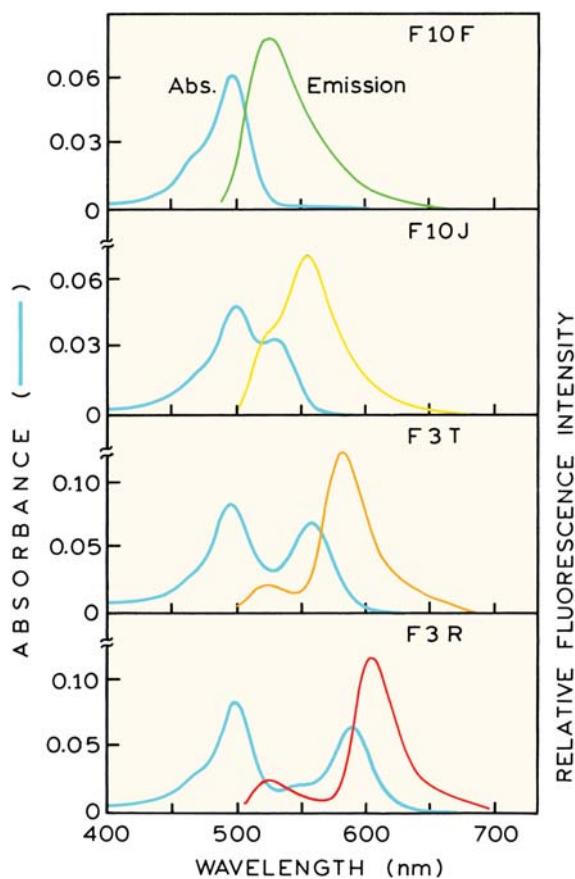


**Figure 21.13.** Absorption and emission spectra of the four energy-transfer primers showing the relative fluorescence intensity excitation at 488 nm. See Figure 21.9 for the structures of F, J, T, and R. The emission spectrum for each primer pair was determined in solutions having the same absorbance at 260 nm. From [15].

as possible. One method to decrease the cost is to use semiconductor laser diodes, which are now available for many wavelengths. These lasers consume little power and can operate for up to 100,000 hours between failures.<sup>26</sup> An additional advantage of red and NIR excitation is the lower autofluorescence from biological samples, gels, solvents, and optical components. Several groups have described NIR dyes for DNA sequencing.<sup>27–31</sup> One such DNA primer is shown in Figure 21.15. Excitation can be accomplished in the NIR at 785 nm, and emission occurs at 810 nm. Such dyes often display small Stokes shifts, which can result in difficulties in rejecting scattered excitation. The Stokes shift can be increased using donor–acceptor pairs, as shown in Section 21.1.5. The quantum yield of the NIR probe shown in Figure 21.15 is low (0.07), and considerably less than that of fluorescein (0.90). Nonetheless, the detection limit

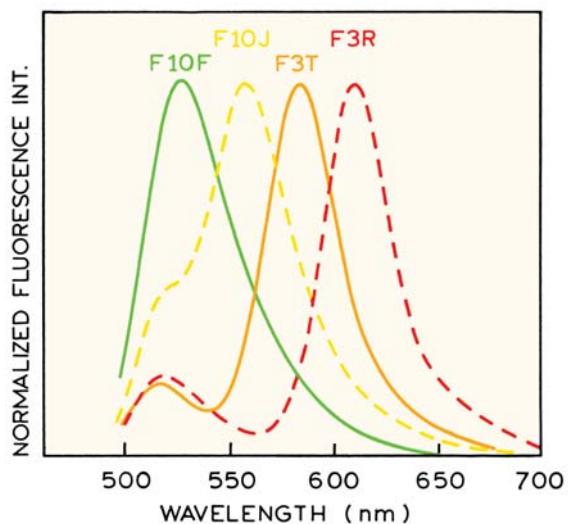


**Figure 21.14.** Normalized emission spectra of the energy-transfer DNA probes in Figure 21.12. From [15].

was 40-fold lower for this NIR probe, primarily because of the decreased background signal.<sup>27</sup>

Most sequencing instruments have been designed around the spectral properties of available probes. However, there are significant advantages in designing the probes prior to the instrumentation. For instance, the probes shown in Figure 21.4 require an argon ion laser at 488- and 514-nm excitation. Synthesis of the NIR DNA primer allowed design of a sensitive and reliable sequencer (Figure 21.16). The long-wavelength absorption maximum allowed use of a 785-nm laser diode as the excitation source.<sup>27</sup> The long-wavelength emission could be efficiently detected with an avalanche photodiode. The excitation beam is incident on the glass plate at the Brewster angle to minimize scattered light. This sequencer illustrates the effectiveness of including probe design as an integral part of the instrument design process. Because only a single fluorophore is used the NIR sequencing is done using four lanes.

At present a set of four NIR probes for single-lane DNA sequencing does not seem to be available, but the spectral properties of many NIR dyes are known.<sup>32–33</sup> Most NIR probes are used as primers with nonfluorescent dideoxy terminators. It is difficult and challenging to develop probes for use in DNA sequencing. The dyes must display similar intensities at a single excitation wavelength, and must not alter too greatly the electrophoretic mobility of the labeled DNA fragments. While it seems possible to have four distinct red-NIR dyes for DNA sequencing, this has not yet been accomplished.

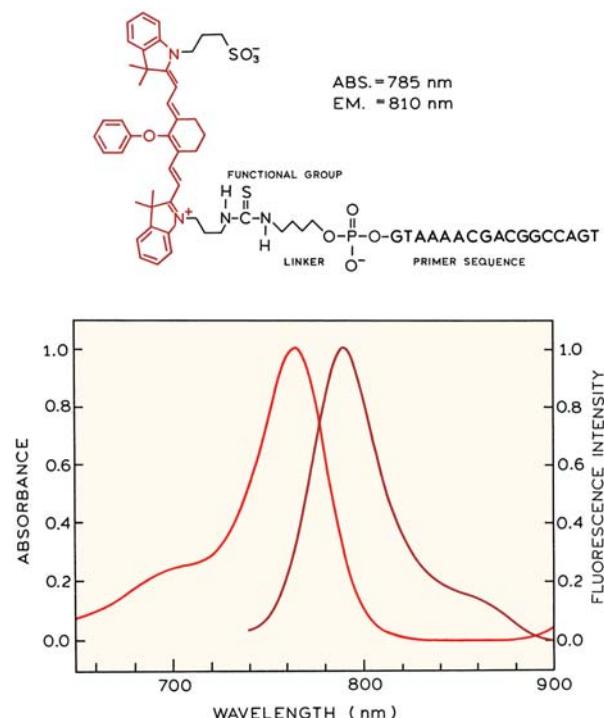


**Figure 21.15.** Structure, absorption, and emission spectra of an NIR DNA primer. Revised from [27].

#### 21.1.7. DNA Sequencing Based on Lifetimes

It is difficult to obtain four dyes with similar absorption spectra and different emission spectra, which allows determination of all four bases on a single gel column. The use of decay times, instead of emission maxima, offers an alternative method to identify the bases. An additional advantage of lifetime-based sequencing is that the decay times are mostly independent of intensity. If decay times are used to identify the bases, the emission spectra can overlap, possibly making it easier to identify suitable fluorophores. Furthermore, the instrumentation for time-resolved measurements has become simpler, less expensive, and more reliable (Chapter 4), so that rapid and continuous lifetime measurements is relatively simple to implement. Progress has been made on lifetime-based sequencing.<sup>34–41</sup> The decay times for the initially used DNA sequencing dyes have been measured in polyacrylamide gels under sequencing conditions.<sup>42</sup> These decay times are listed on Figure 21.4. While the decay times are different for each dye, pulsed light sources at 488 and 514 nm were not available at that time. Hence the efforts on lifetime-based sequencing were focused on longer wavelength dyes. A set of lifetime

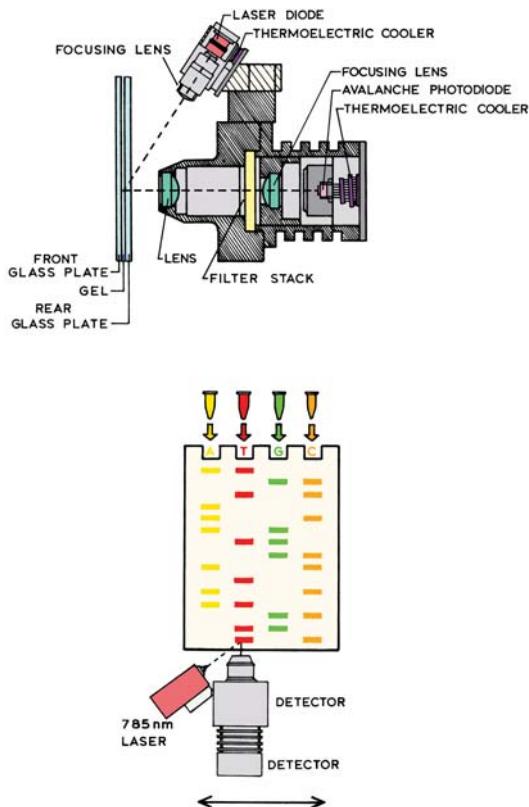


**Figure 21.16.** NIR DNA sequencer. Redrawn with permission from LiCor Inc.

DNA dyes excitable at 636 nm has been developed (Figure 21.17).<sup>43</sup> The decay times are seen to range from 3.6 to 0.7 ns. Methods have been described for "on-the-fly" lifetime measurements of labeled DNA primers in capillary electrophoresis,<sup>44–46</sup> and there is continuing progress on the instrumentation<sup>47–48</sup> and probes<sup>49–50</sup> for lifetime-based sequencing. Capillary gel electrophoresis is being used in place of slab gels, providing more rapid separations with improved resolution.<sup>51</sup> It is now possible to identify up to one thousand bases in a single separation,<sup>52–53</sup> and there is continuing development of new formats and instruments for high throughput DNA sequencing.<sup>54–58</sup>

#### 21.2. HIGH-SENSITIVITY DNA STAINS

There are numerous applications that require detection of DNA and DNA fragments. One example is analysis of DNA fragments following digestion with restriction enzymes. Frequently one wishes to know whether a DNA sample is from a particular individual, or whether an individual car-

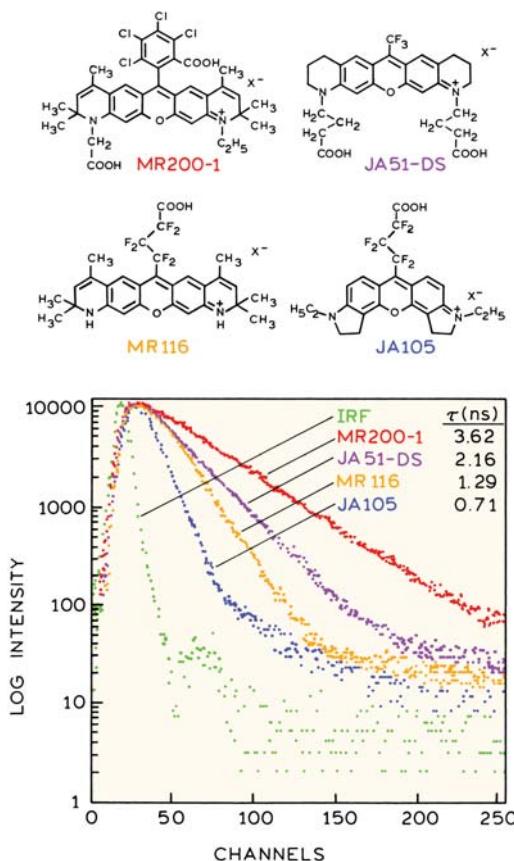


**Figure 21.17.** Structure and intensity decays of dyes for lifetime-based sequencing. Excitation was with a pulsed laser diode at 636 nm. IRF, instrument response function. Revised from [43].

ries a particular gene. This determination does not require sequencing and can be accomplished by examination of the DNA fragments formed by enzymatic degradation of DNA by restriction enzymes. A large number of restriction enzymes are known, each of which is specific for a particular base sequence, but they sometimes recognize more than one sequence. Generally, the enzymes are specific for relatively long sequences of four to nine base pairs, so that relatively small numbers of DNA fragments are formed. A schematic of a restriction fragment analysis is shown in Figure 21.18. The normal DNA has three restriction enzyme sites, and the mutant is missing one of these sites. Following digestion and electrophoresis, the mutant DNA shows one larger DNA fragment, whereas the normal DNA showed two smaller DNA fragments.

Typically samples of DNA are examined using one or more restriction enzymes. The fragments are different for each individual due to sequence polymorphism occurring in

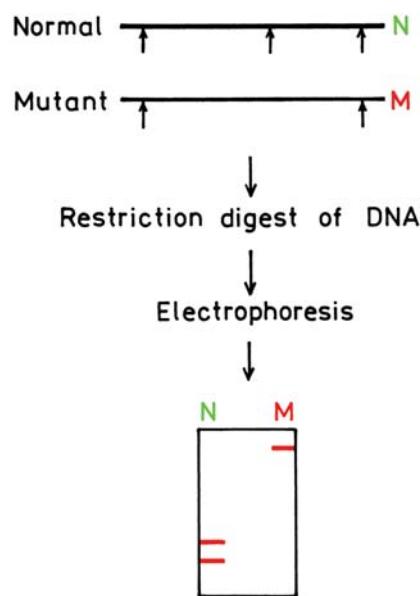


**Figure 21.18.** Analysis of DNA restriction fragments. The arrows indicate three cleavage sites in normal DNA (N), one of which is missing in the mutant DNA (M). The smaller fragments at the end were not detected.

the population. These different size fragments are referred to as restriction fragment length polymorphisms (RFLPs), which do not represent mutations but rather the usual diversity in the gene pool. Following enzymatic digestion the fragments are separated on agarose gels. Originally the DNA was detected using  $^{32}\text{P}$  and autoradiography. Today detection is accomplished mostly by fluorescence.

Detection of DNA using stains has a long history, starting with staining of chromatin with acridine dyes. The situation was improved by the introduction of dyes such as ethidium bromide and propidium iodide, which fluoresce weakly in water and more strongly when bound to DNA.<sup>59</sup> DNA on gels is detected by exposing the gels to ethidium bromide (EB). When using EB the gel typically contains micromolar concentrations of EB to ensure that the DNA binds significant amounts of EB. Because of the micromolar binding constants, sensitivity can be low because of background from the free dyes.

### 21.2.1. High-Affinity Bis DNA Stains

There are now a number of greatly improved dyes which have high affinity for DNA and almost no fluorescence in water. Some of these dyes are dimers of acridine or ethidi-

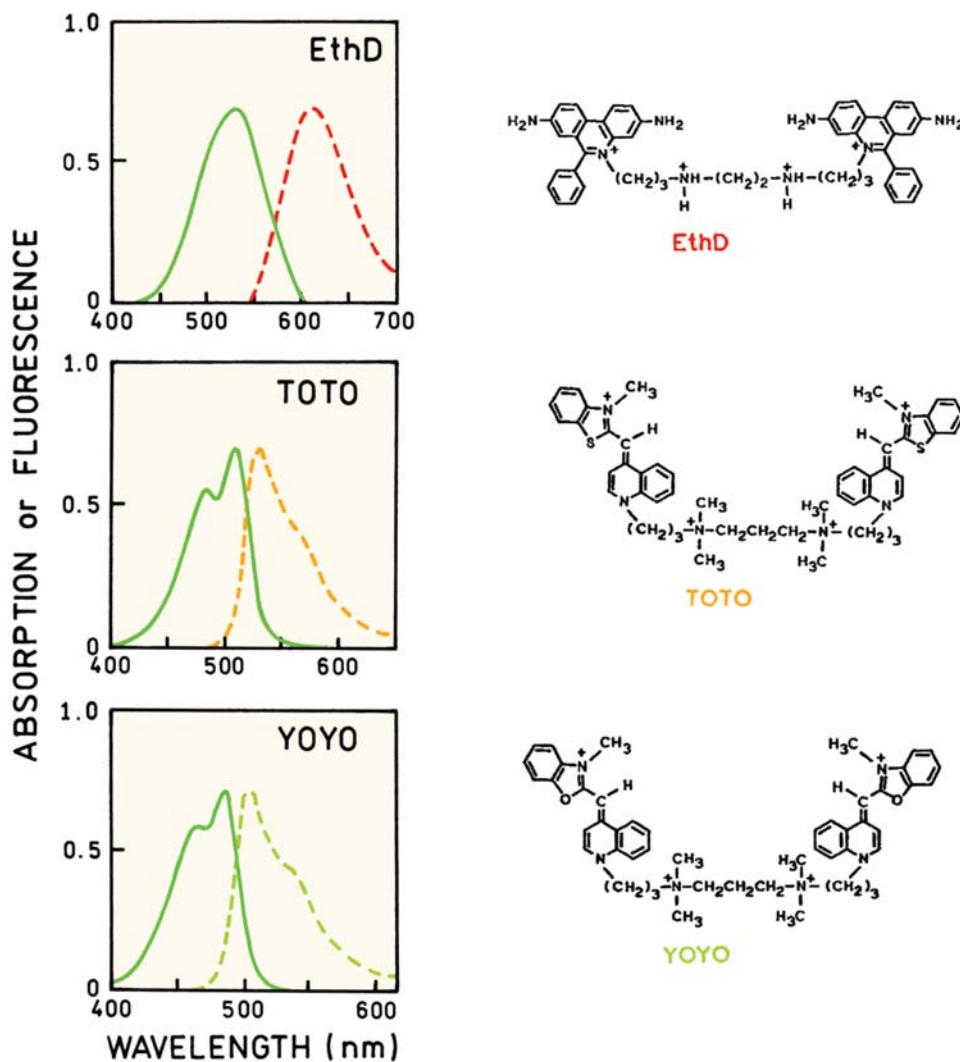


**Figure 21.19.** Chemical structures of high-affinity DNA dyes: absorption (dashed) and emission (solid) spectra of the dyes bound to DNA. The relative enhancements of the fluorescence of the dyes on binding to DNA are (top to bottom) 35, 1,100, and 3,200. Data from [68].

um bromide.<sup>60–61</sup> The ethidium dimer was found to bind DNA  $10^3$  to  $10^4$  more strongly than the monomer.<sup>62</sup> The homodimer of ethidium bromide (Figure 21.19) was found to remain bound to DNA during electrophoresis. This result is surprising because the positively charged dye is expected to migrate in the opposite direction from the DNA. This result suggests the dyes do not dissociate from DNA on the timescale of electrophoresis. The DNA fragments can be stained prior to electrophoresis and it is not necessary to maintain a micromolar concentration of free dye. The DNA gels display little background fluorescence, and the DNA fragments can be detected with high sensitivity.

The usefulness of the EB homodimer resulted in further development of DNA dyes with high affinity for DNA.<sup>63–70</sup> The structures of several high-affinity dyes are shown in Figure 21.19. These dyes are positively charged and display large enhancements in fluorescence upon binding to DNA. The EB homodimer displays an enhancement of 35-fold, and TOTO-1 displays an enhancement of 1,100-fold. The name TOTO is used to describe thiazole homodimers. The use of these dyes with pre-stain DNA fragments provided a 500-fold increase in sensitivity as compared with gels stained with ethidium bromide after electrophoresis.<sup>68</sup> These dyes are widely used as DNA stains, and ana-

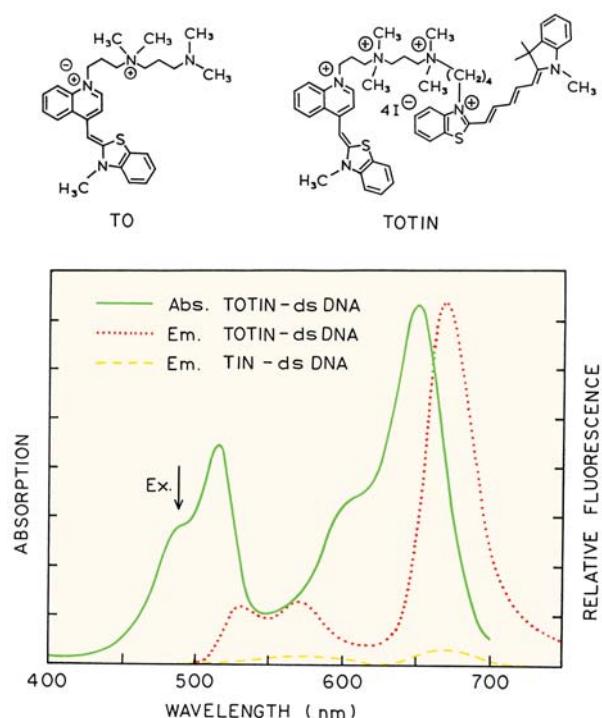


**Figure 21.20.** Top: Structures of thiazole orange (TO) and the thiazole orange-thiazole-indolenine-heterodimer TOTIN, an energy-transfer dye for staining of DNA. Bottom: Absorption (solid) and emission (dotted) spectra of TOTIN and emission spectrum of TIN (dashed); the structure on the right side of TOTIN, bound to double-stranded DNA. Excitation was at 488 nm. Reprinted with permission from [72]. Copyright © 1995, Academic Press Inc.

logues with slightly longer excitation and emission wavelengths are also available. Different DNA samples can be stained with different dyes prior to electrophoresis. The dyes do not exchange between the DNA strands, allowing the samples to be identified from the spectral properties. This allows molecular weight standards to be electrophoresed in one lane on the gel with the unknown sample.

### 21.2.2. Energy-Transfer DNA Stains

The bis dyes shown in Figure 21.19 display favorable properties, but it is desirable to have dyes excitable at 488 nm with larger Stokes shifts. Such dyes were created using donor–acceptor pairs.<sup>71–72</sup> One such dye is shown in Figure 21.20. The thiazole dye on the left (TO) serves as the donor for the thiazole–indolenine acceptor (TIN) on the right. TOTIN remains bound to DNA during electrophoresis. The half-time for dissociation is 317 min.<sup>71</sup> TOTIN can be excit-

ed at 488 nm, and displays emission from the TIN moiety near 670 nm. For excitation at 488 nm the emission from TIN alone is much weaker (dashed). TOTIN also allows red excitation at 630 nm with laser diode or HeNe sources.

### 21.2.3. DNA Fragment Sizing by Flow Cytometry

DNA fragment sizing is usually performed almost exclusively on slab or capillary gels. These methods are typically limited to fragment sizes up to 50 kb in length, and the size resolution is highly nonlinear. Flow cytometry is a method in which cells flow one by one through an area illuminated by a laser beam. Information about the cells is obtained using fluorescent labels. The development of high-affinity DNA stains allows DNA fragment sizing using flow technology.<sup>73–81</sup> The amount of dye bound by the DNA fragments is proportional to the fragment length. Longer DNA fragments bind more dye. The DNA fragments are analyzed in a flow system similar to that used for flow cytometry. This approach allows measurement of the size and number of DNA fragments, without physical separation of the fragments by chromatography or electrophoresis.

An example of DNA fragment sizing by flow cytometry is shown in Figure 21.21. The DNA was from bacteriophage  $\lambda$ , which was digested with the HindIII restriction enzyme.<sup>80</sup> The DNA was stained with TOTO-1, and excited by an argon ion laser at 514 nm. As the TOTO-1 stained DNA passes through the laser beams the instrument records a histogram based on the size of the photon bursts (Figure 21.21, top). For this combination of DNA and restriction enzyme the size of the DNA fragments was known. The photon burst size correlated precisely with fragment size (Figure 21.21, bottom). The photon burst size was found linear with fragment size up to 167 kb.<sup>79</sup> Given the expense and complexity of DNA gels, it seems probable that DNA analysis by flow cytometry will become more widely used in the near future. Flow analysis of DNA has already been used to measure DNA damage<sup>73</sup> and for rapid identification of photogens.<sup>74</sup>

### 21.3. DNA HYBRIDIZATION

Detection of DNA hybridization is widely useful in molecular biology, genetics, and forensics. Hybridization occurs during polymerase chain reaction (PCR) and fluorescence in-situ hybridization. A variety of methods have been used to detect DNA hybridization by fluorescence. Several possible methods are shown schematically in Figure 21.22.

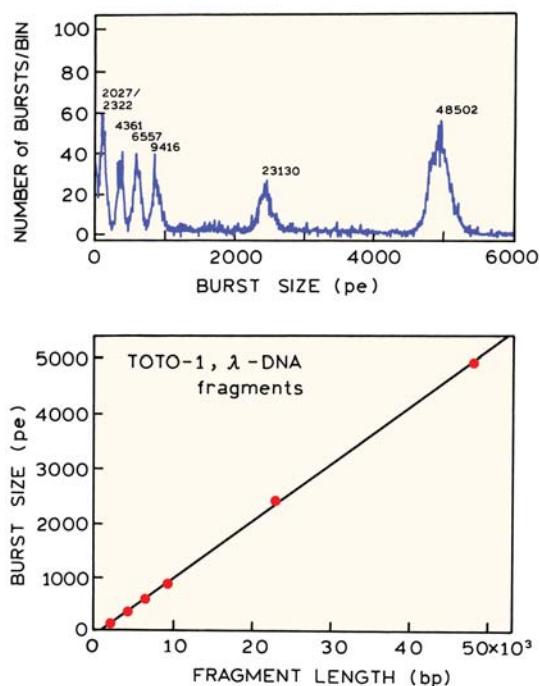


**Figure 21.21.** **Top:** Histogram of photon burst sizes of TOTO-1 stained DNA from a HindIII digest of  $\lambda$ -DNA. **Bottom:** Correlation of the photon burst size with DNA fragment length. Excitation was at 514 nm from an argon ion laser, and emission was observed through a 550-nm interference filter. Modified and reprinted from [80]. Copyright © 1995, American Chemical Society.

One commonly used method is to detect an increase in RET when complementary donor and acceptor labels hybridize (upper left). The presence of complementary DNA sequences can be detected by increased energy transfer when these sequences are brought into proximity by hybridization.<sup>82-89</sup> This can occur if the complementary strands are labeled with donors and acceptors. An example of this approach was shown in Figure 1.27. Energy transfer can also occur if the donor- and acceptor-labeled oligonucleotides bind to adjacent regions of a longer DNA sequence (Figure 21.22). An example of this approach is shown below in Figure 21.36. Hybridization can be detected if a donor intercalates into the double-helical DNA, and transfers to an acceptor-labeled oligonucleotide. The use of an intercalating dye has been extended to include a covalently attached intercalators, whose fluorescence increases in the presence of double-stranded DNA (d).<sup>90-91</sup> One example is shown in Figure 21.23, in which the acridine dye is covalently linked to the 3' phosphate of an oligothymidylate. Upon binding to a complementary adenine oligonucleotide the acridine fluorescence increases about twofold. Hybridization can be competitive where the presence of increased amounts of target DNA competes with formation of donor–acceptor pairs.<sup>92</sup> The acceptor can be fluorescent, or it can be nonfluorescent, in which case the donor appears to be quenched. A competitive assay (Figure 21.22) was

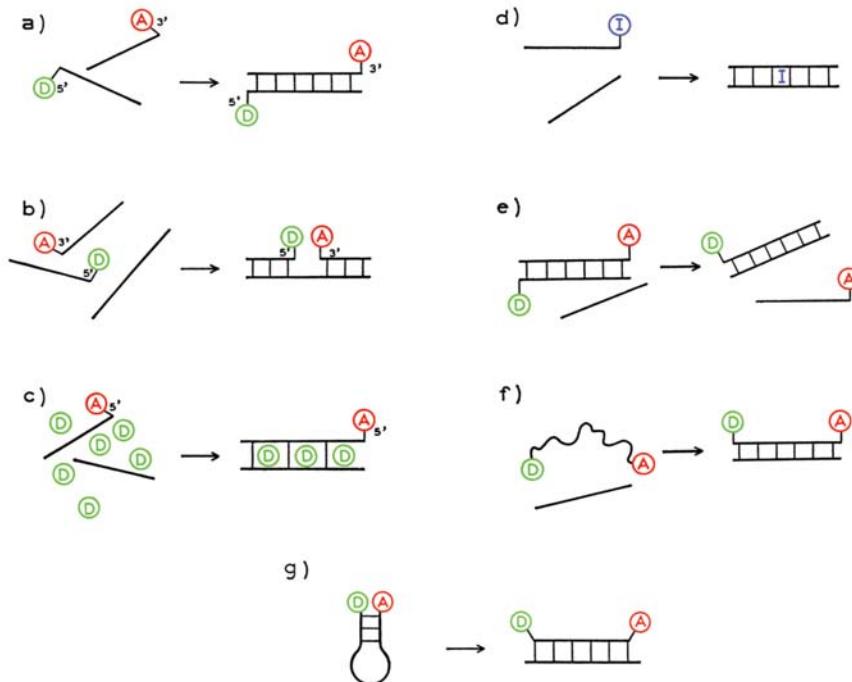


**Figure 21.22.** Methods to detect DNA hybridization by energy transfer. D, donor; A, acceptor or quencher; I, intercalating dye.

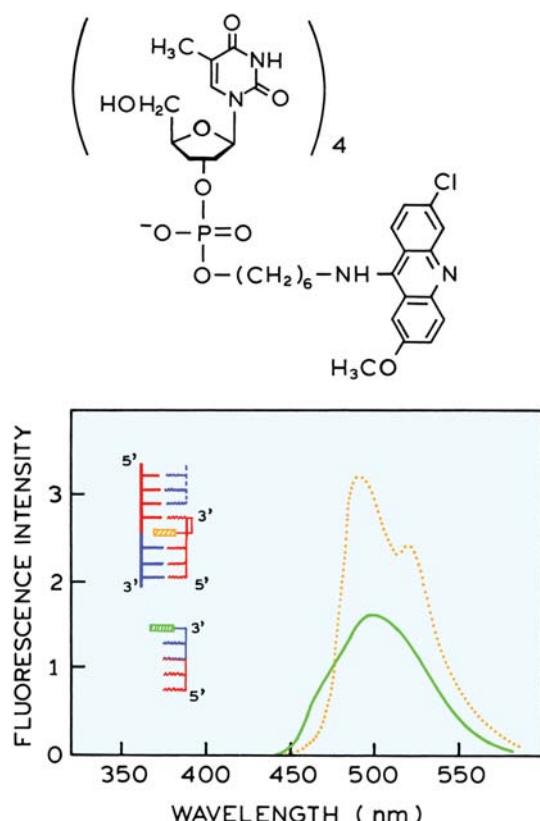


**Figure 21.23.** DNA hybridization detected by a covalently bound intercalating probe. Fluorescence intensity of the probe, an acridine dye covalently linked to the 3'-phosphate of an oligothymidylate (dashed); fluorescence intensity of the probe upon binding to a complementary adenine oligonucleotide (dotted). From [91].

performed with complementary DNA strands in which the opposite strands were labeled with fluorescein and rhodamine.<sup>93</sup> Hybridization of the strands resulted in quenching of the donor fluorescence. Increasing amounts of unlabeled DNA, complementary to one of the labeled strands, resulted in displacement of the acceptor and increased donor fluorescence. Such arrays can be useful in amplification reactions in which the DNA is thermally denatured during each cycle.

### 21.3.1. DNA Hybridization Measured with One-Donor- and Acceptor-Labeled DNA Probe

Most DNA hybridization methods (Figure 21.22) require two probe DNA molecules, one labeled with donor and the other with acceptor. Assays can be based on a single donor- and acceptor-labeled probe DNA.<sup>93</sup> One example is shown in Figure 21.24, in which single-stranded DNA is labeled on opposite ends with a donor and acceptor, respectively. In

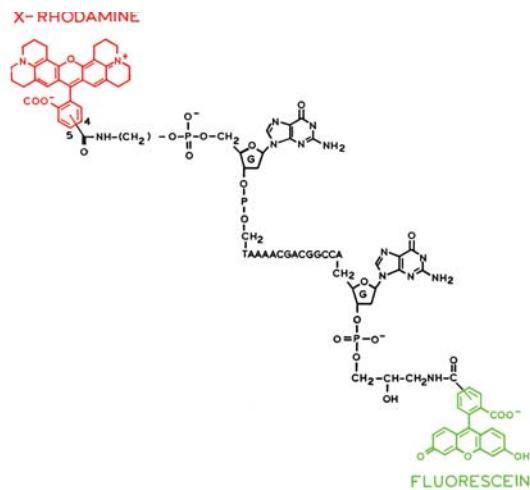


**Figure 21.24.** Detection of DNA hybridization with a single donor-and acceptor-labeled oligonucleotide. The increase in donor emission and decrease in acceptor emission occurred upon binding of the oligonucleotide to its complementary strand is shown. From [93].

the absence of the complementary strand the single-stranded probe DNA is flexible. This allows the donor- and acceptor-labeled ends to approach closely, resulting in a high FRET efficiency. Upon binding of the single-stranded probe DNA to its complementary strand, the donor and acceptor become more distant due to the greater rigidity of double-stranded DNA. Hybridization can be detected by an increase in donor emission and a decrease in acceptor emission. There are many circumstances where an FRET assay would be simplified by the use of only a single probe molecule. The donor and acceptor concentrations are forced to remain the same, independent of sample manipulations, because they are covalently linked. This allows the extent of

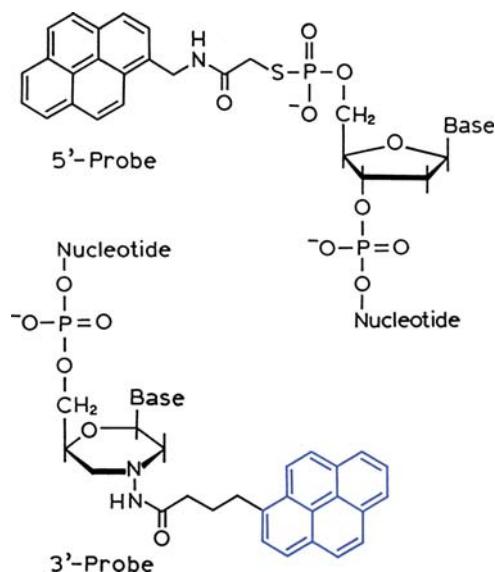


**Figure 21.25.** Pyrene-labeled oligonucleotide probes. Modified from [96].

hybridization to be determined using wavelength-ratiometric measurements.

### 21.3.2. DNA Hybridization Measured by Excimer Formation

DNA hybridization can also be detected by pyrene excimer formation.<sup>94–96</sup> DNA probes were synthesized with pyrene attached to the 5' and 3' ends (Figure 21.25). It is well known that one excited pyrene molecule can form an excit-

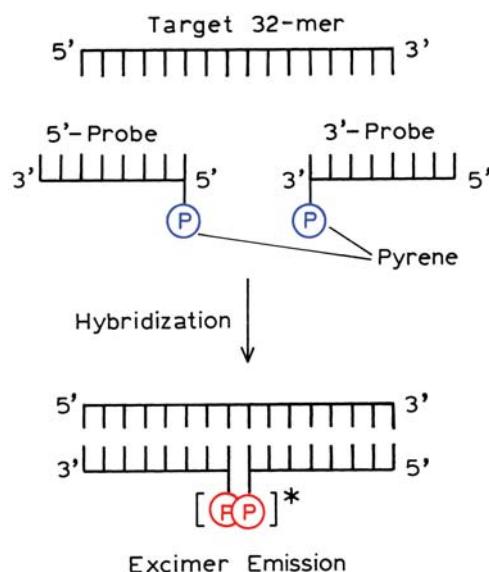


**Figure 21.26.** Principle of the excimer-forming DNA hybridization array. Modified from [96].

ed-state complex with another ground-state pyrene, forming an excimer. This complex displays an unstructured emission near 500 nm as compared to the structured emission of pyrene monomer near 400 nm. The use of excimer formation to detect DNA hybridization is shown in Figure 21.26. The assay requires two DNA probes that bind to adjacent sequences on the target DNA. In this example the correct target DNA is a 32-mer oligonucleotide. If both the 5'- and 3'-pyrene probe bind to target DNA, the pyrene

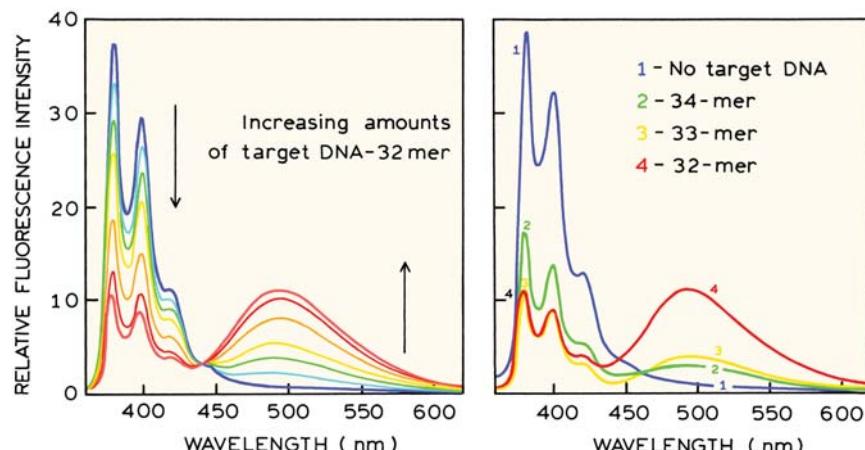


**Figure 21.27.** Effect of target DNA (32-mer) and mismatched target DNA (33- and 34-mer) on the emission from DNA probes labeled with pyrene at the 3' and 5' ends. The target DNA 32-mer and the mismatched target DNA have the sequence 5'-AGAGGGCACGGATACC\*GCGAGGTGGAGC-GAAT-3', where the asterisk denotes the location of one or two extra thymine residues in the 33- and 34-mer, respectively. Modified from [96].

monomers will be in close proximity, resulting in excimer emission. Emission spectra of a mixture of the 3' and 5' probes are shown in Figure 21.27. In the absence of target DNA the emission is near 400 nm and characteristic of a pyrene monomer. Titration with increasing amounts of target DNA results in increasing emission from the excimer near 500 nm.

This hybridization assay based on excimer formation is sensitive to precise matching of the target sequence with the probe sequence. Just one extra thymine residue in the target DNA, between the pyrene sites on the probe DNA, eliminates most of the excimer emission. This property of the assay is distinct from a hybridization assay based on FRET. In the case of FRET the donor–acceptor interaction occurs over long distances, so that the additional distance of one base would not abolish FRET. In contrast, excimer formation is a short range interaction that requires molecular contact between the pyrene monomers. For this reason it is sensitive to small changes in the pyrene-to-pyrene distance.

### 21.3.3. Polarization Hybridization Arrays

DNA hybridization has also been detected using fluorescence anisotropy.<sup>97–99</sup> Hybridization is detected by the increase in anisotropy when labeled DNA binds to its complementary strand. These assays are analogous to the fluorescence polarization immunoassays. Polarization or anisotropy measurements have the favorable property of being independent of the intensity of the signal and dependent on the molecular weight of the labeled molecule. Also polarization measurements do not require separation steps.

DNA hybridization arrays based on polarization have been reported using the fluorescein probes,<sup>100–101</sup> as well as a more novel NIR dye.<sup>99</sup> The structure of an NIR dye, LaJolla Blue<sup>TM</sup>, is shown in Figure 21.28. The central chromophore is a phthalocyanine, which displays the favorable property of absorbing in the NIR, and in this case was excited by a pulsed laser diode at 685 nm. The phthalocyanines are poorly soluble in water, and hence the central silicon atom was conjugated to polar groups to increase the water solubility and prevent aggregation.

Polarization values of the LaJolla Blue<sup>TM</sup> oligonucleotide are shown in Figure 21.29. The dye-DNA probe was mixed with either complementary (●) or non-complementary DNA (▲, ■). The polarization increases upon mixing with the complementary strand, but not with the non-complementary oligomers. This result suggests that polarization measurements can be used to monitor the production of

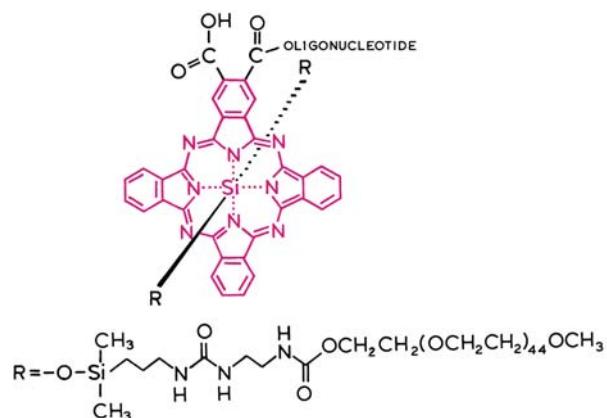


**Figure 21.28.** Structure of the LaJolla Blue<sup>TM</sup>-oligonucleotide. Revised and reprinted with permission from [99]. Copyright © 1993, American Association for Clinical Chemistry.

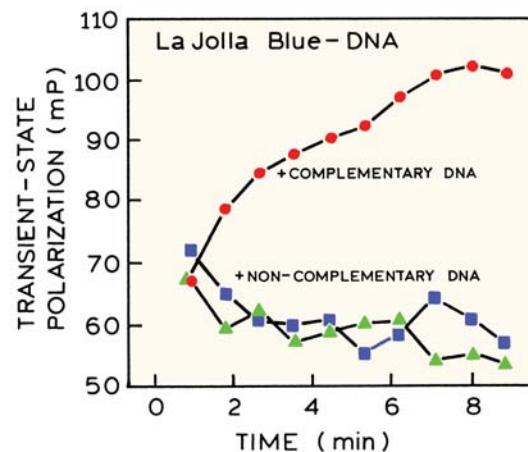


**Figure 21.29.** Fluorescence polarization DNA hybridization array. One mP is equivalent to 0.001 polarization units. The probe DNA was mixed with complementary (●) or non-complementary DNA (▲, ■). The excitation source was a pulsed laser diode at 685 nm. The emission at 705 nm was detected after the excitation pulse. Modified from [99].

complementary DNA by PCR and related amplification methods. However, the change in polarization is not large, which is probably because the fluorophores have substantial motional freedom when present in both single-stranded and double-stranded DNA. A unique aspect of the data in Figure 21.29 is the use of pulsed excitation and gated detection after the excitation pulse. This was done to avoid detection of scattered light and/or background fluorescence from the sample.

### 21.3.4. Polymerase Chain Reaction

Polymerase chain reaction (PCR) is an important advance for DNA technology.<sup>102–105</sup> PCR allows almost unlimited amplification of DNA. Small amounts of DNA isolated from forensic evidence, DNA libraries, or archaeological sites can be replicated many times to obtain useful amounts for further studies. The progress of a PCR reaction can be followed by any probe that detects the presence of double-helical DNA. These methods include probes like Syber Green, which are only fluorescent in the presence of double-stranded DNA or molecular beacons (Section 21.4) that bind to the amplified DNA and become fluorescent. The most widely used approach is based on energy transfer and is called Taqman. This name refers to the use of Taq DNA polymerase, which is stable at the high temperatures needed to denature the double-stranded DNA prior to each round of amplification. The sample initially contains a D–A oligonucleotide, in which the donor fluorescence is quenched.<sup>103–104</sup> During the PCR reaction this D–A strand is displaced and cleaved by DNA polymerase, which displays some nuclease activity as well as polymerase activity. Upon cleavage of the D–A pair, the donor becomes distant from the acceptor and thus more fluorescent (Figure 21.30). PCR assays based on fluorogenic donor–acceptor pairs are presently used in commercial instruments. The oligonucleotide sequence in the D–A pair is complementary to a

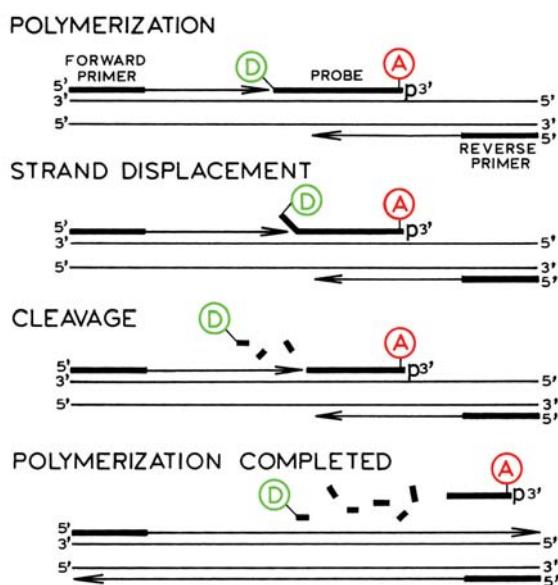


**Figure 21.30.** Release of donor quenching during polymerase chain reaction. From [103].

portion of the DNA to be amplified. This type of assay is an extension of the concept of fluorogenic probes described in Chapter 3, wherein the molecule becomes more fluorescent as the result of enzymatic cleavage.

## 21.4. MOLECULAR BEACONS

### 21.4.1. Molecular Beacons with Nonfluorescent Acceptors

In DNA or genetic analysis it is frequently necessary to detect the presence of a single gene in a sample containing the entire genome. This can be accomplished by identifying and detecting a base sequence that is unique for a particular gene. Detection of such sequences in a mixture of DNA can be accomplished using molecular beacons.

Molecular beacons were introduced in 1996<sup>106–107</sup> and have become widely used in biotechnology and the biosciences. A schematic of a typical molecular beacon is shown in Figure 21.31. A molecular beacon contains a fluorophore (donor)–quencher (acceptor) pair, a loop region, and a stem region that contains two short complementary sequences. The loop region contains a base sequence that is complementary to a target sequence. In the absence of target DNA the complementary sequences on each end hybridize, bringing the fluorophore and quencher in close contact. Binding to target DNA results in extension of the beacon and increased fluorescence.

Molecular beacons possess a number of characteristics that are favorable for their use in biotechnology, diagnostics and genetic analysis. Molecular beacons allow detection of the target sequence without any separation steps. It was found that hybridization of beacons to target sequences is

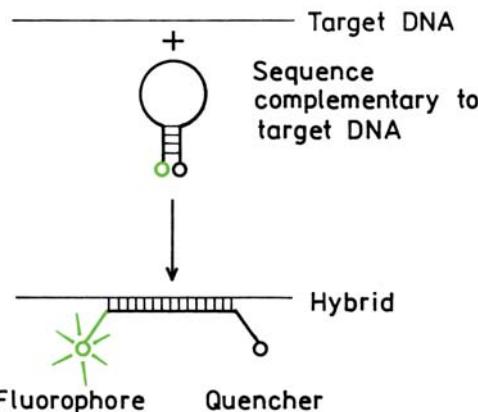


**Figure 21.31.** Schematic of a typical molecular beacon.

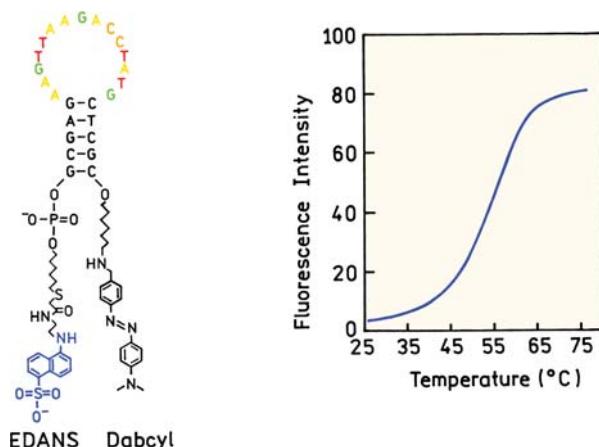


**Figure 21.32.** Structure and thermal unfolding of a molecular beacon. From [106].

more specific than hybridization of linear DNA to a similar size sequence. The beacon can be almost completely specific for a target sequence and discriminate against sequences with a single base mismatch. The beacons rapidly unfold and fold as the temperature is increased and decreased,

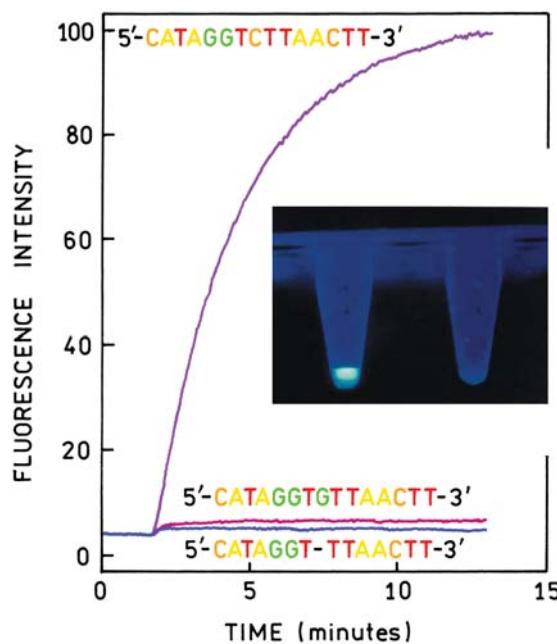


**Figure 21.33.** Fluorescence intensity of the molecular beacon in Figure 21.32 upon addition of the complementary oligo, or oligos with a one-base mismatch or deletion. The photo shows the UV-illuminated molecular beacon in the presence (left) and absence (right) of the complementary oligomer. Revised from [106].

allowing their use with real-time detection in polymerase chain reaction (PCR). Molecular beacons can also be used as intracellular probes for DNA or mRNA.

Figure 21.32 shows the sequence and structure of a molecular beacon.<sup>106</sup> The stem region contains five base pairs and the loop is complementary to a 15-base sequence in the target DNA. The fluorophore EDANS is a dansyl derivative. The quencher is Dabcyl, which is an RET acceptor. At low temperatures the beacon is hybridized and almost nonfluorescent. Upon heating the beacon unfolds and the EDANS emission increases 25-fold. Figure 21.33 shows the fluorescence intensities of a molecular beacon upon addition of the complementary sequence, and sequences with a single base mismatch or deletion. The intensity increases significantly for the perfectly matched sequence. The photograph of the UV-illuminated beacon shows a bright visible emission in the presence of the target and no visible emission in the absence of target DNA. Molecular beacons display a high on-off contrast ratio as well as high specificity.

Molecular beacons are used to follow PCR amplification (Figure 21.34). In this example the beacon contained a loop sequence that is complementary to a middle segment of an 84-base long amplicon. The intensities are measured after the reaction mixture is cooled to the annealing temperature at 50°C. At higher temperatures all the beacons are unfolded and not hybridized, so the intensity represents the total number of beacons in the sample. When the sample is annealed the intensity depends on the number of target sequences. This number increases with each PCR cycle, resulting in a higher intensity at the annealing temperature.

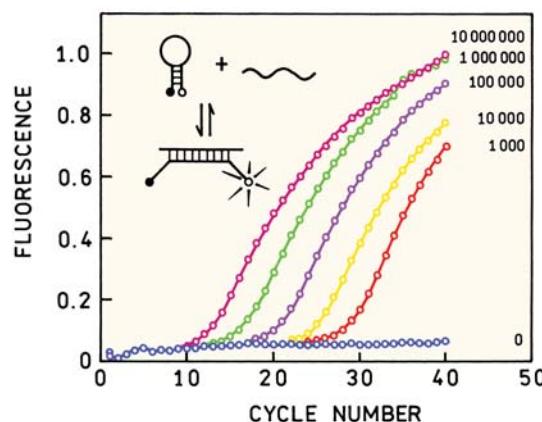


**Figure 21.34.** Use of a fluorescein-dabcyl molecular beacon to follow PCR amplification. The numbers on the right are the initial number of template molecules. Revised from [107].

The cycle at which the fluorescence becomes detectable depends on the number of amplicons at the start of the amplification.

A somewhat surprising result with molecular beacons is that dabcyll quenches fluorophores with emission from blue to red wavelengths.<sup>107</sup> This quenching appears to be independent of spectral overlap between the emission and the dabcyll absorption. Quenching occurs even when there is no obvious spectral overlap. This is a favorable result because a single type of quencher can be used with a wide variety of fluorophores. The reasons for universal quenching by dabcyll are not completely known and may be the result of complex formation between the fluorophore and quencher.<sup>108</sup> Dabcyll is not the only quencher used in molecular beacons. Molecular beacons have been reported which use a variety of quenchers including pyrene.<sup>109</sup> Molecular beacons have also been based on intercalation into the double helix.<sup>110</sup>

#### 21.4.2. Molecular Beacons with Fluorescent Acceptors

The previous section described molecular beacons with a single emitting species. Molecular beacons can also be made using fluorescent acceptors.<sup>111–115</sup> The beacon shown in Figure 21.35 has a Cy3 donor and a Cy5 acceptor. In this beacon one of the probes is located within the oligomer rather than at one of the ends. Upon addition of the target sequence the extent of energy transfer decreased, resulting in an increase in the donor emission and a decrease in the acceptor emission. For a molecular beacon with two fluorophores the intensity ratio is independent of the total molecular beacon concentration. Additionally, the ratio can be used to determine the concentration of the target sequence, if the concentration of the beacon is known.

Molecular beacons with a quencher or fluorescent acceptor serve different purposes. A molecular beacon of the type shown in Figure 21.35 may not be useful for detection of a small quantity of target in a sample containing other DNA. A small amount of target DNA will result in a small change in the intensity ratio, which may not be detectable. In contrast, a molecular beacon of the type shown in Figure 21.31 displays emission against a dark background, allowing low concentrations of target to be detected. However, the intensity data alone do not reveal the concentration of target DNA.

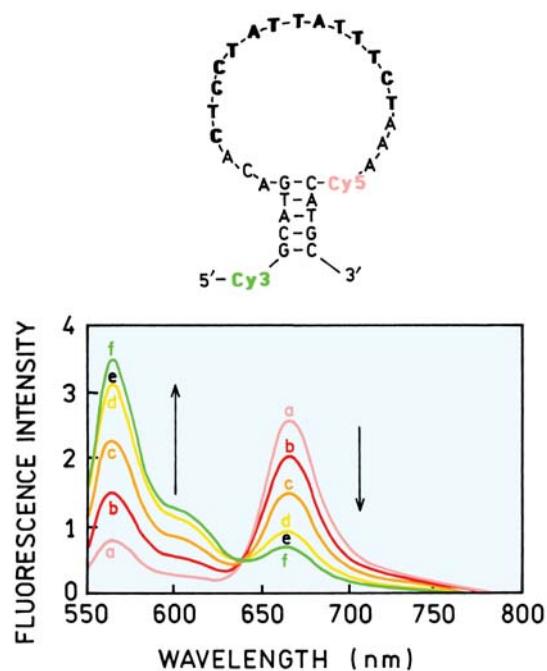


**Figure 21.35.** Molecular beacon based on RET between a Cy3 donor and a Cy5 acceptor. The arrows indicate increasing concentrations of the target sequence. Revised and reprinted with permission from [113]. Copyright © 2004, American Chemical Society.

#### 21.4.3. Hybridization Proximity Beacons

Molecular beacons can be highly specific, but it can be important to decrease the number of false positives. This can be accomplished by using molecular beacons which hybridize close to each other on the target sequence (Figure 21.36). The beacons are designed so that RET occurs between a donor on one beacon and an acceptor on the other beacon.<sup>116</sup> Both beacons are quenched in the absence of target DNA. Specificity is increased because RET will only occur when both beacons are bound. Binding of the donor beacon alone or the acceptor beacon alone will increase the donor or acceptor intensities, but it will not increase the extent of RET.

Figure 21.37 shows emission spectra of the donor and acceptor beacons. In the absence of target DNA both the donor and acceptor are quenched and the signal is close to zero. If only the donor beacon binds to the target the donor emission is high. The acceptor emission remains low, even in the presence of target DNA, because the acceptor absorbs weakly at the excitation wavelength. When both beacons are bound to the target the acceptor emission increases due to RET. The donor is partially quenched by RET to the

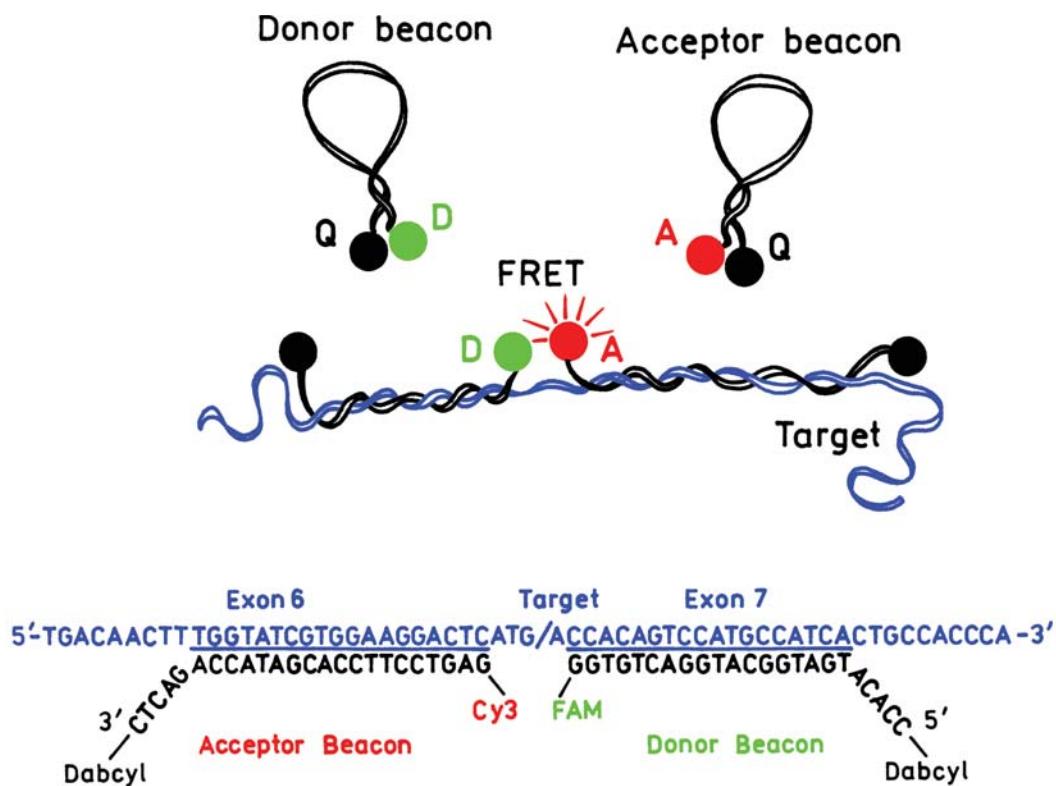


**Figure 21.36.** Donor and acceptor molecular beacons for a hybridization proximity array. Reprinted with permission from [116]. Copyright © 2003, American Chemical Society.

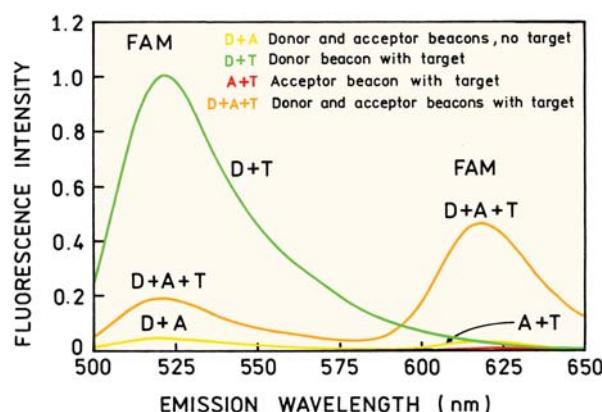


**Figure 21.37.** Emission spectra of the donor and acceptor beacons in Figure 21.36 in the absence and presence of target DNA. Revised and reprinted with permission from [116]. Copyright © 2003, American Chemical Society.

nearby acceptor. Emission from both the donor and acceptor is only seen when both beacons bind to the same target sequence. This type of beacon could be made even more

specific using a lanthanide donor and detection of the sensitized acceptor emission

#### 21.4.4. Molecular Beacons Based on Quenching by Gold

Gold surfaces and colloids are becoming more widely used in bioassays because of the well-developed chemistry for linkage to the surface, the ease of colloid preparation, and the chemical stability of the surfaces. Gold is an highly effective quencher of fluorescence.<sup>117–119</sup> Quenching probably occurs by RET to the gold surface, but other mechanisms may also be present. Because of the strong quenching gold can provide a large on-off ratio for molecular beacons.<sup>120–121</sup> A molecular beacon on a gold surface is made by binding a labeled oligomer to the surface by a sulphydryl group.<sup>121</sup> In the absence of target DNA the rhodamine label is quenched (Figure 21.38). In the presence of target DNA the rhodamine moves away from the gold surface and becomes fluorescent. Surface-bound molecular beacons could have a different sequence at each position on an array,

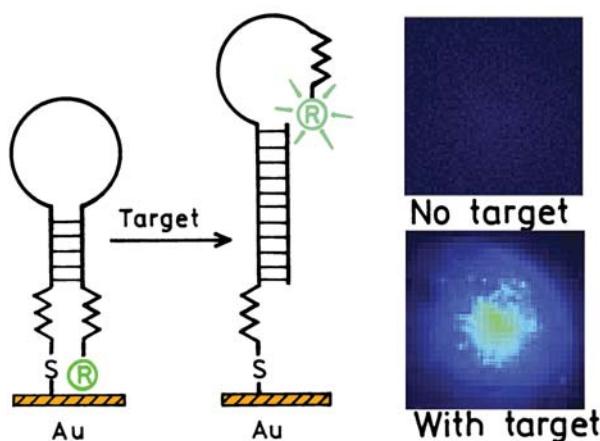


**Figure 21.38.** Surface-bound molecular beacon with quenching by a gold surface. The CCD photons shows epifluorescence confocal microscope image of the surface-bound beacon in the absence (top) and presence (bottom) of the target sequence. Reprinted with permission from [121]. Copyright © 2003, American Chemical Society.

allowing detection of a good number of sequences by the spatial localization of complementary sequences on the array.

#### 21.4.5. Intracellular Detection of mRNA Using Molecular Beacons

An ability to monitor gene expression in a single cell would be of great value in cell biology. However, detection of specific messenger RNAs within a cell is a challenging task. Staining with nucleic acid probes will label both DNA and RNA. Even if a stain is specific for RNA, it will stain all the RNA, not just the desired gene product. Molecular beacons can be used to monitor specific mRNAs in living cells.<sup>122–124</sup>

Figure 21.39 shows light and fluorescence images of mammalian kidney cells.<sup>124</sup> The light image shows a cluster of five cells. One cell was microinjected with a molecular beacon specific for  $\beta$ -actin mRNA. The fluorophore was TAMRA and the quencher dabcyll. The images were recorded with an intensified CCD camera so the different colors represent different intensities. The fluorescence images taken at 3-minute intervals show a progressive increase in fluorescence intensity. Only the single microinjected cell showed this emission. Control experiments showed that a nonspecific molecular beacon did not display a time-dependent increase in intensity. This control experiment indicates that the increase in intensity is due to the mRNA for  $\beta$ -actin and not the result of hydrolysis of the molecular

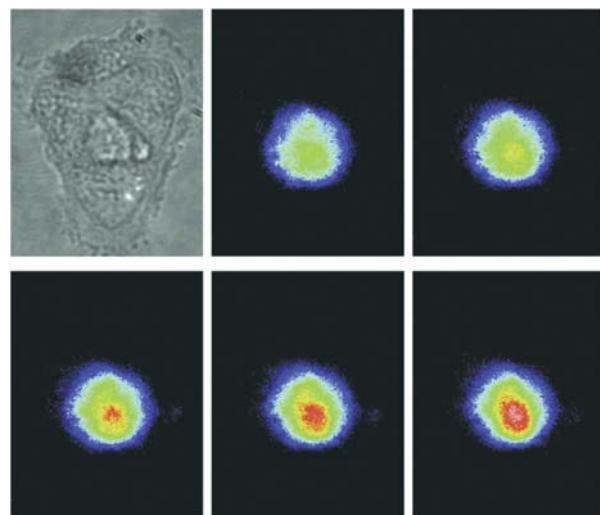


**Figure 21.39.** Light and fluorescence images of kangaroo rat kidney cells. The fluorescence images are taken at 3-minute intervals following microinjection of a molecular beacon specific for  $\beta$ -actin mRNA. The molecular beacon contained TAMRA and a dabcyll acceptor. Revised and reprinted with permission from [124]. Copyright © 2001, American Chemical Society.

beacon. This result shows that molecular beacons can be used to study gene expression in living cells.

#### 21.5. APTAMERS

Molecular beacons are used to detect the presence of specific sequences in biological samples. Specially designed sequences of DNA can also be used to detect other molecules that are not nucleic acids. These nucleic-acid sequences that bind to specific molecules are called aptamers. Specific detection by aptamers depends on specific interactions with the analyte as well as base pairing between different parts of the aptamer.

The concept of an aptamer is best illustrated by a specific example.<sup>125–126</sup> Figure 21.40 shows an aptamer that binds cocaine. This aptamer contains a fluorescein donor and a dabcyll acceptor. Cocaine binds to a central region of the aptamer, which then forms additional base pairs between the two ends of the aptamer. This folding brings the donor and acceptor closer together and results in quenching of fluorescein by the dabcyll acceptor (Figure 21.41). Addition of closely related molecules does not result in donor quenching.

Aptamers provide a general approach to the design of reagents with high affinity for the desired species.<sup>127–131</sup> Aptamers can be made from DNA or RNA. The specificity

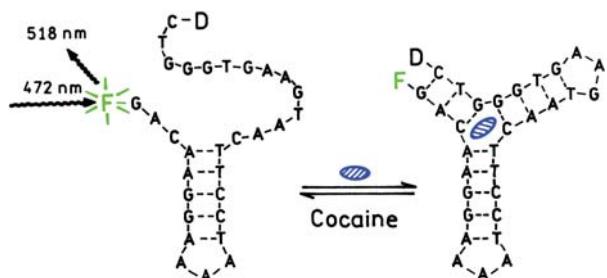


**Figure 21.40.** Structure of DNA aptamer that binds cocaine; F is fluorescein and D is dabcyl. Reprinted with permission from [126]. Copyright © 2001, American Chemical Society.

of aptamers can be as high as that obtained with antibodies. The base sequence of an aptamer determines its binding specificity. The sequence is determined by a procedure called Selex: selective enrichment of ligands by exponential enrichment. The procedure starts with a library of random DNA or RNA sequences that are flanked by the primer sequences used for polymerase chain reaction (PCR). The library is enriched for the molecule of interest, typically by binding to a chromatography column that contains this molecule. The oligomers that bind to the column are eluted, and amplified by PCR, followed by additional rounds of enrichment and selection. Finally the enriched library is cloned and sequenced, followed by selection of those sequences with the optimal binding affinity for the molecule of interest. Aptamers have been designed for a variety of molecules including cAMP,<sup>132</sup> adenosine,<sup>133</sup> steroids,<sup>134</sup> carbohydrates,<sup>135</sup> and the protein HIV reverse transcriptase.<sup>136-137</sup> Aptamers can contain more than one oligonucleotide, as shown for the aptamer that binds rATP (Figure 21.42). The aptamer consists of two oligonucleotides, one labeled with

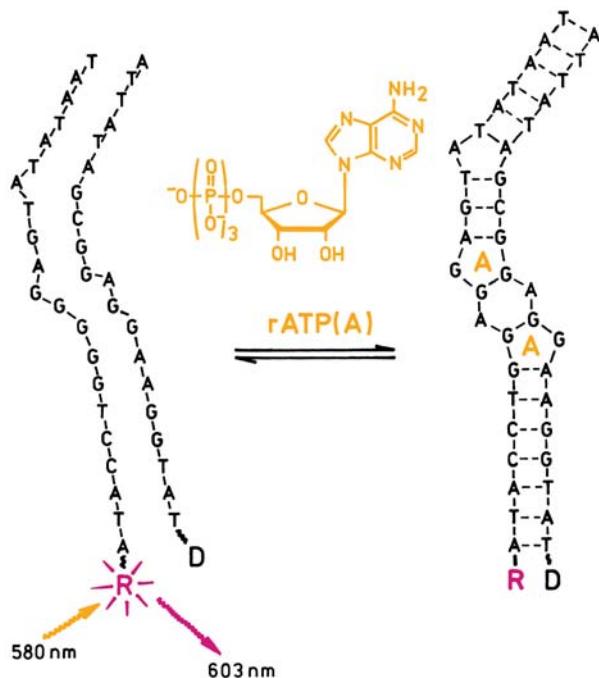


**Figure 21.42.** DNA aptamer specific for rATP; R is rhodamine and D is dabcyll. Reprinted with permission from [125]. Copyright © 2000, American Chemical Society.

a rhodamine donor and the other with a dabcyl acceptor.<sup>125</sup> Addition of rATP results in binding of the two oligonucleotides to two rATP molecules. This binding results in quenching of the rhodamine donor, which only occurs in the presence of rATP and not the other ribonucleotides (Figure 21.43).

Aptamers can be designed for proteins as well as for small molecules. Platelet-derived growth factor (PDGF) stimulates cell division and cell proliferation, and is a

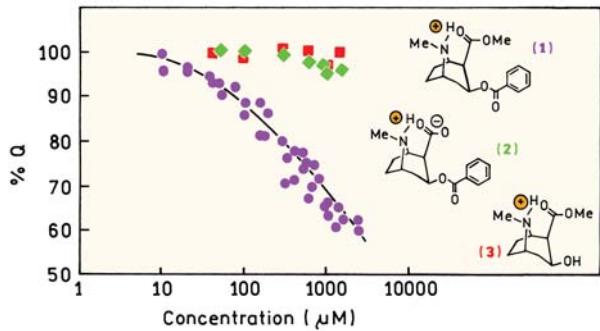


**Figure 21.41.** Donor intensity of the cocaine-binding aptamer in the presence of cocaine (1, ●), benzoyl-ecgonine (2, ♦) and ecgonine methyl ester (3, ▀). Reprinted with permission from [126]. Copyright © 2001, American Chemical Society.

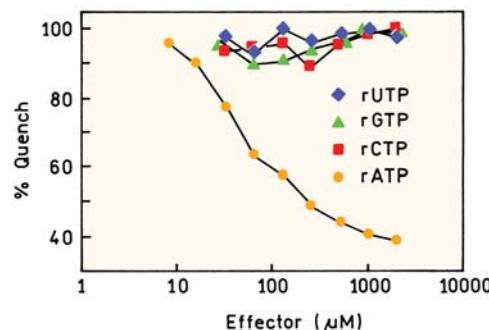


**Figure 21.43.** Rhodamine donor intensities of the aptamer shown in Figure 21.42 in the presence of ribonucleotides. Reprinted with permission from [125]. Copyright © 2000, American Chemical Society.

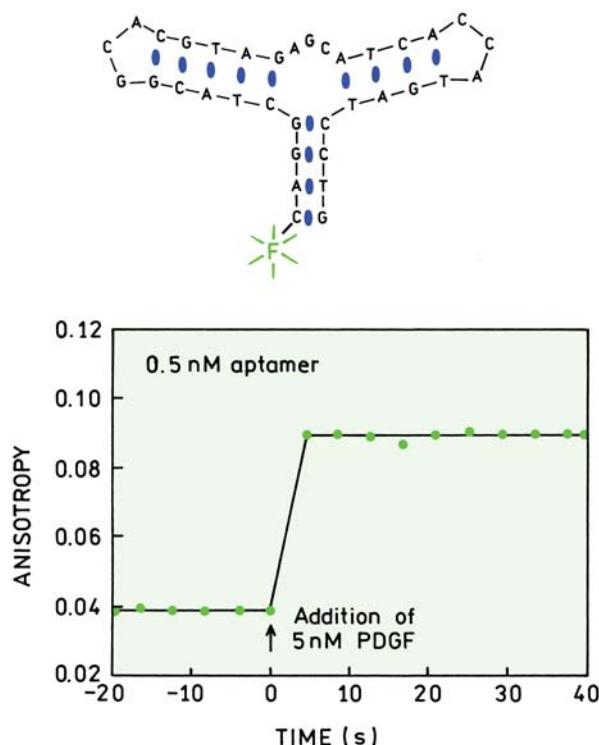


**Figure 21.44.** Structure of a fluorescein-labeled aptamer specific for PDGF. The lower panel shows the fluorescein anisotropy. Revised and reprinted with permission from [138]. Copyright © 2001, American Chemical Society.

potential protein marker for cancer diagnosis. PDGF is typically detected using ELISA or radiotracer methods. Figure 21.44 shows a fluorophore-labeled aptamer specific for PDGF. Upon addition of PDGF the anisotropy increases more than twofold.<sup>138</sup> This result shows that other fluorescence parameters can be used with an aptamer, not just RET. The twofold increase in anisotropy is probably larger than could be obtained with a fluorescein-labeled antibody. The molecular weight of IgG is near 150,000, and an Fab fragment has a molecular weight near 50,000. For proteins of this size the fluorescein anisotropy would be near its maximal value before binding to PDGF. The smaller size of the aptamers and their high degree of flexibility in the absence of ligand should result in similar anisotropy changes in other aptamers.

### 21.5.1. DNAzymes

The uses of aptamers have been extended to include DNA sequences that have enzymatic activity,<sup>139–140</sup> analogous to the activity displayed by ribozymes. A combination apta-

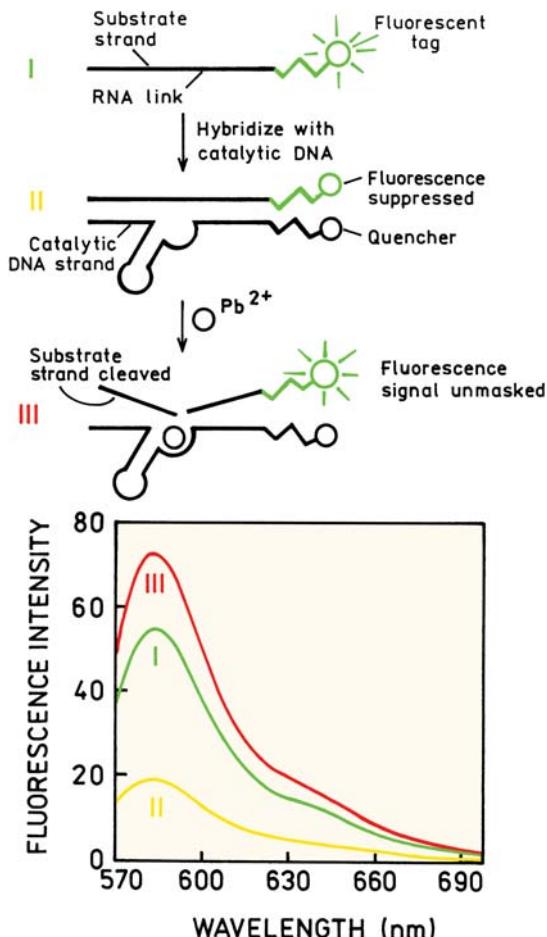


**Figure 21.45.** Detection of Pb<sup>2+</sup> using a DNAzyme. The fluorophore is TAMRA and the quencher is dabyl. From [142].

mer-DNAzyme was developed for detection of lead ions.<sup>141–142</sup> The aptamer contained two parts that were labeled with a TAMRA donor or a dabyl acceptor. These two oligomers spontaneously hybridized, which resulted in quenching of TAMRA by RET (Figure 21.45). Upon addition of Pb<sup>2+</sup> the DNAzyme undergoes autocatalytic cleavage to release the fragments of the cleaved oligomer. The donor intensity increases when the quencher oligomer is released, which can be used to perform assays for lead. Aptamer technology may evolve to create a new class of sensors with high specificity and enzymatic activity.

## 21.6. MULTIPLEXED MICROBEAD ARRAYS: SUSPENSION ARRAYS

In Section 21.9 we will describe detection of DNA sequences using two-dimensional arrays of capture oligomers

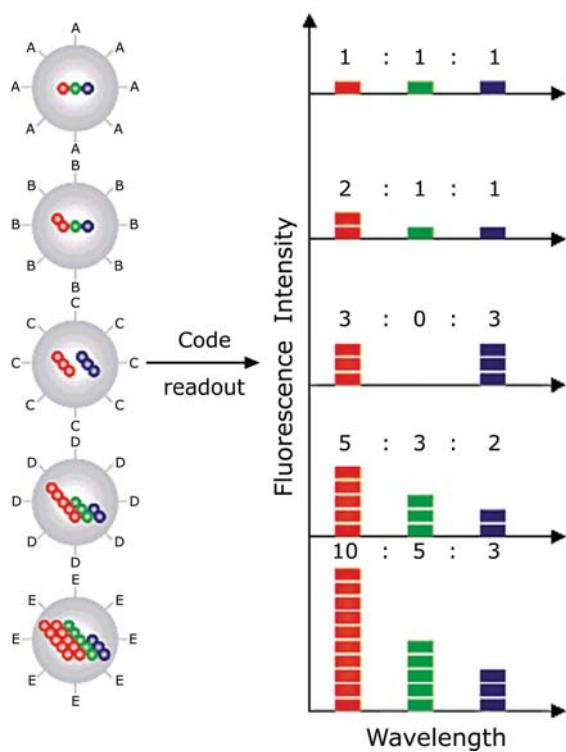


**Figure 21.46.** Optical coding of microbeads based on emission intensity and wavelengths. From [147].

on a glass support. These arrays are expensive to produce and the surface-localized molecules require long times to reach equilibrium binding. An alternative for multiplex assays is the use of optically coded beads or suspension arrays.<sup>143–147</sup> This approach is based on beads with unique optical signatures. The surface of each bead contains molecules that bind to a single analyte or single DNA oligomer.

The concept of a suspension array is shown in Figure 21.46. In this example the polymer beads contain varying amounts of semiconductor nanoparticles or quantum dots (QDs) with different emission wavelengths. QDs are described in Chapter 20. If it is possible to distinguish ten different intensity levels and six wavelengths then one million unique codes can be created. In practice the number of detectable unique codes is likely to be less. Suspension arrays can also be created using different types of fluorophores.<sup>146</sup> However, the width of emission spectra usually limits the number of unique wavelengths. Quantum dots are well suited for multiplex assays.<sup>148</sup> The narrow emission spectra allows a reasonable number of different emission wavelengths, as is shown by a photograph of QD suspensions illuminated with a UV lamp (Figure 21.47). The pho-



**Figure 21.47.** Real-color photograph of ZnS-capped CdSe quantum dots excited with a near-UV lamp. From [148].

tostability of QDs is also important for a multiplex assays because the relative intensities as well as the wavelengths are used to identify the beads.

Suspension arrays can be used to rapidly detect the presence of DNA sequences in a mixture.<sup>148</sup> This is accomplished by attaching a different capture oligomer to each type of bead (Figure 21.48). The beads are mixed with the DNA sample. Each type of bead and hence each sequence is identified by its emission spectrum. If a labeled oligomer binds to a particular bead then an additional emission peak is seen from this bead. The mixture of oligomers can all be labeled with the same fluorophore because the bead identifies the sequence and the fluorophore emission indicates the presence or absence of the sequence in the sample.

Figure 21.49 shows emission spectra of several types of microbeads. The top panels show the bead with a 1:1:1 intensity ratio before and after incubation with the target sequence labeled with Cascade Blue. Emission from the target sequence is seen near 440 nm. The lower panels show detection of different target sequences with different microbeads. In practice it would be necessary to collect such data from a larger number of beads. This can be accomplished using flow analysis similar to that used in flow cytometry or DNA fragment size analysis (Section 21.2.3).

## 21.7. FLUORESCENCE IN-SITU HYBRIDIZATION

Fluorescence in-situ hybridization (FISH) is a widely used method in cell biology, medical testing, and genomics.<sup>149–152</sup> The concept of FISH is shown in Figure 21.50. The DNA to be tested, typically metaphase chromosomes, is exposed to fluorescently labeled probe DNA. The exposure conditions result in denaturation of the chromosomes and hybridization of the chromosomes with the probe DNA. The probe DNA has a base sequence directed toward one or

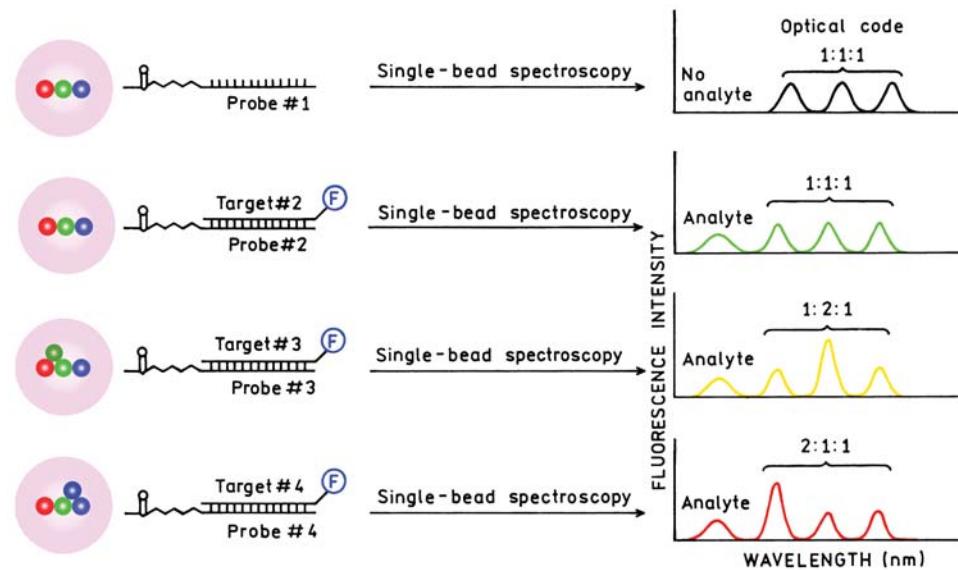


**Figure 21.48.** Schematic of a DNA hybridization array using QD-labeled microbeads. From [148].

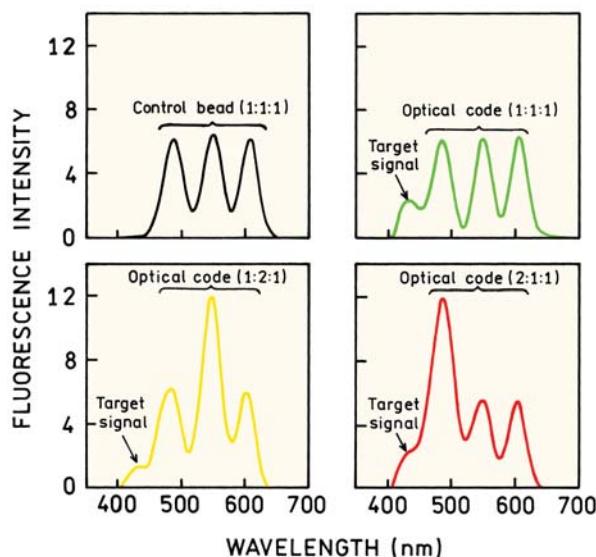


**Figure 21.49.** Emission spectra of a single type of microbead after equilibration with its target sequence. The target oligomer was labeled with Cascade Blue emitting near 440 nm using biotin-streptavidin chemistry. From [148].

more chromosomes. The probe DNA is labeled with one or more fluorophores. Following exposure to the probe DNA, one or more of the chromosomes become fluorescent. Alternatively, the probe DNA can be specific for the centromeric or telomeric region of chromosomes, in which case only the ends of the chromosomes become fluorescent.

DNA probes can also be specific for small regions of DNA representing one or several genes. FISH can also be used with dispersed DNA in interphase cells, typically to detect individual genes. When first introduced in-situ hybridization was performed using radioactive tracers and radiography. At present in-situ hybridization is performed almost exclusively using fluorescence.

### 21.7.1. Preparation of FISH Probe DNA

Preparation of probe DNA to identify individual genes is relatively straightforward. A DNA oligomer with the gene sequence and appropriate primer sequences is synthesized. This task was aided by completion of the human genome in

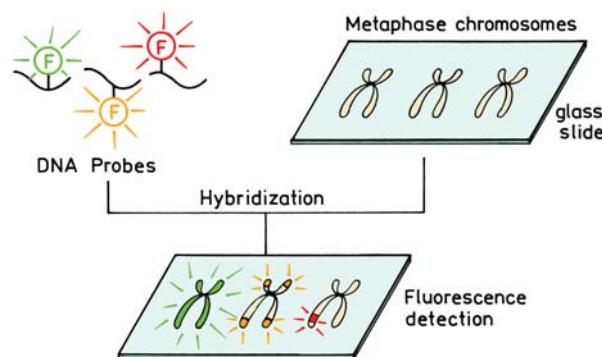


**Figure 21.50.** Schematic of fluorescence in-situ hybridization (FISH).

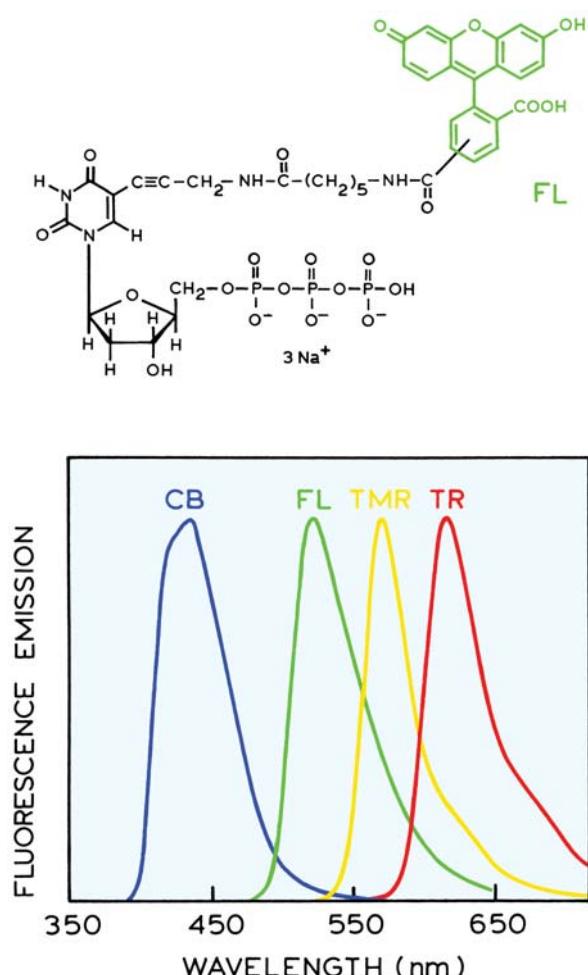


**Figure 21.51.** Emission spectra of fluorescent deoxynucleotide for incorporation into DNA FISH probes. The fluorophore can be fluorescein (FL), or one of a variety of other fluorophores such as tetramethyl rhodamine (TMR), Texas red (TR), or cascade blue (CB). From Molecular Probes literature.

2001. The DNA can be amplified using DNA polymerase and/or PCR. Fortunately, it is possible to incorporate a high density of fluorophores into the probe DNA. This is accomplished using labeled deoxynucleotide triphosphates (dNTPs). Several labeled dNTPs are shown in Figure 21.51. Note that these labeled bases contain the 3' hydroxyl group so that the DNA strand can be continued, in contrast to the ddNTPs shown in Figure 21.1. These nucleotides can be incorporated at reasonable densities without interfering with hybridization or base pairing. A wide variety of fluorophores can be used. The highest sensitivity has typically been found using rhodamines,<sup>152</sup> which are more photostable than fluorescein. These probes can be used to identify regions of a chromosome or the location of a gene within a chromosome (Figure 21.50).

More complex procedures are needed to prepare probe DNA to entirely label or paint a selected chromosome. This requires that the probe DNA contains a large number of different sequences so that the entire chromosome is labeled. At the same time the probe DNA cannot contain sequences that bind to the other chromosomes. This task is made more complex by the presence of repetitive sequences that are present in all the chromosomes. The preparation of probe DNA to paint individual chromosomes starts with isolation of the individual chromosomes using flow cytometry. The chromosomal DNA is then amplified using PCR in the presence of the labeled nucleotide. The DNA can also be labeled using nick-translation. In this procedure the DNA is incubated with DNase I, DNA polymerase, as well as labeled and unlabeled nucleotides. The enzymes partially cleave the DNA, remove nucleotides, and replace the nucleotides with labeled nucleotides from the reaction mixture. This procedure also reduces the average size of the DNA fragments, which improves the rate of hybridization. Because of the repetitive sequences that appear in all the chromosomes, the probe DNA described above will bind to these regions in all the chromosomes. These sequences are removed by incubation with a competitor DNA sample that contains these sequences, forming double-helical DNA that contains the unwanted sequences. An excess amount of the competitive DNA is used to prevent binding of these sequences to the chromosomes.

FISH is usually performed on fixed cells on microscope slides. Prior to fixation the cells can be trapped in the metaphase by colchicine, which interferes with mitosis. Following fixation unwanted cellular components are removed with enzymes and/or solvents. Considerable experimentation and testing is needed to identify the detailed treatments needed to prepare useful samples.<sup>150</sup> The fixed preparations are then incubated with various solvents and at elevated temperatures to allow the probe DNA to hybridize with the chromosomes.

### 21.7.2. Applications of FISH

FISH has numerous applications in cell biology and genetic testing.<sup>153–154</sup> Some examples include studies of gene expression,<sup>155</sup> detection of the gene for Duchenne muscular dystrophy,<sup>156</sup> detection of the human papillomavirus thought responsible for cervical cancer,<sup>157</sup> and fetal sex determination from amniotic fluid.<sup>158</sup> The power of FISH

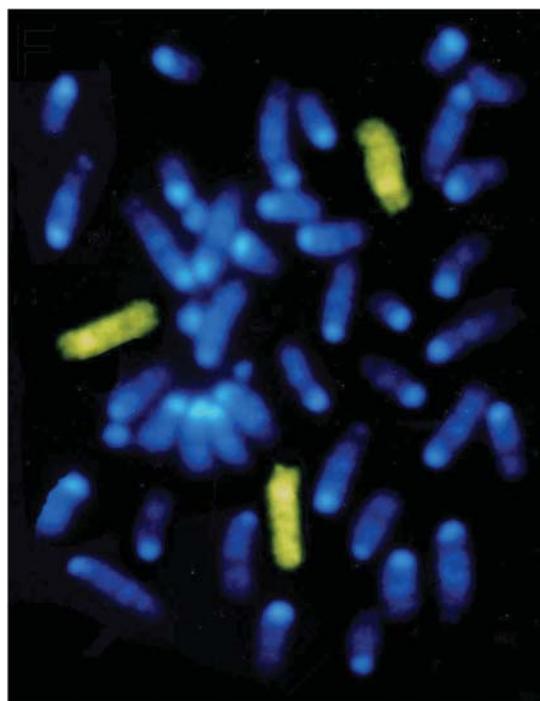


**Figure 21.52.** FISH of a human-hamster hybrid cell. All the chromosomes are stained uniformly using a nonspecific probe like DAPI. Three copies of human chromosome 4 were identified by a probe (yellow) specific for this chromosome. From [150]. Courtesy of Dr. Thomas Ried from the Center for Cancer Research (NCI/NIH).

can be illustrated by several examples. Figure 21.52 shows metaphase chromosomes from a human-hamster hybrid cell line.<sup>150</sup> All the chromosomes were stained with a nonspecific probe with blue emission. The chromosomes were exposed to a FISH probe specific for human chromosome 4. The yellow emission from this probe shows the cell contains three copies of this chromosome.

FISH can be used to locate individual genes instead of painting entire chromosomes (Figure 21.53). Metaphase mouse tumor chromosomes were stained with DNA probes specific for the immunoglobulin heavy-chain locus (red) or for the c-myc gene (green). In this case only small regions of the chromosome are labeled.<sup>150</sup> The interphase nucleus in the lower right released some of its DNA during sample preparation. FISH can also be applied to interphase nuclei when the DNA is not condensed into chromosomes. An interphase cell was stained with three gene-specific probes, one with green emission and two with red emission (Figure 21.54). The image shows that the gene labeled with the green probe is localized between the two other genes.

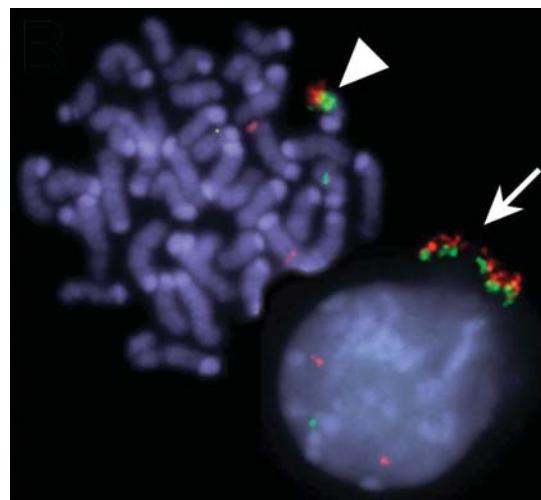


**Figure 21.53.** Mouse tumor metaphase chromosomes stained for the immunoglobulin heavy chain locus (red) and the c-myc gene (green). All the DNA was stained with a nonspecific blue fluorophore. Image courtesy of Dr. Thomas Ried from the Center for Cancer Research (NCI/NIH).

## 21.8. MULTICOLOR FISH AND SPECTRAL KARYOTYPING

Suppose it is necessary to identify each of the chromosomes by staining with FISH probes. Because of the width of the emission from most fluorophores it is not possible to visually identify more than about five fluorophores. Identifica-

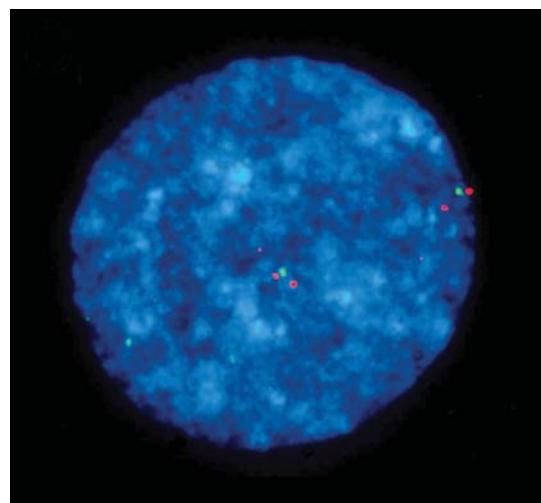


**Figure 21.54.** Labeling of an interphase nucleus with three gene-specific probes. Images courtesy of Dr. Thomas Ried from the Center for Cancer Research (NCI/NIH).

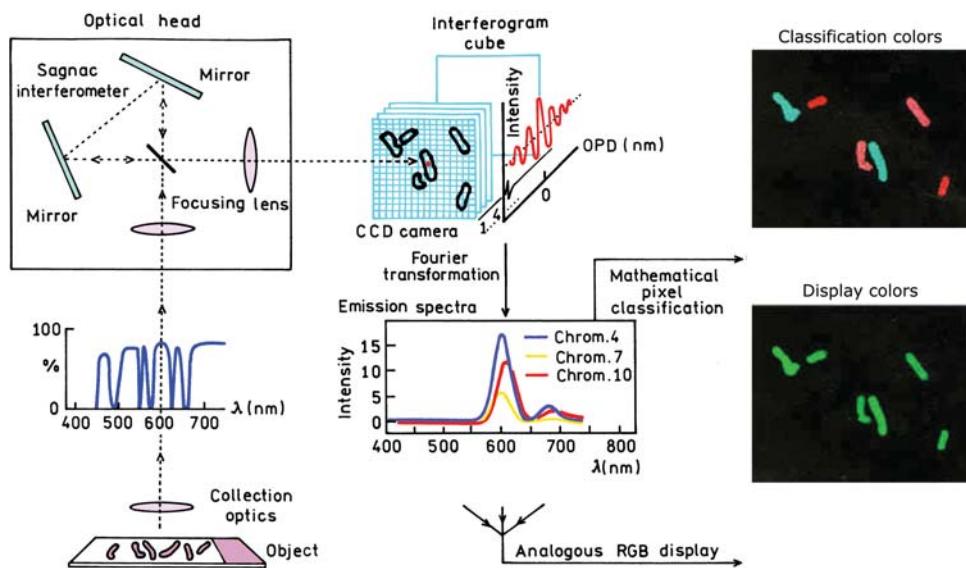


**Figure 21.55.** Principle of spectral imaging and karyotyping. The wavelength distribution of the emission is determined with an interferometer. The results can be displayed as true colors (display color) or pseudocolor (clarification color). From [165].

tion of all 24 chromosomes could be accomplished by sequential staining with different DNA probes, but this is impractical. This problem of chromosome identification was solved using mixtures of fluorophores in each DNA probe. The fluorophore mixtures are designed so that the emission spectrum of each mixture can be uniquely identified and assigned a pseudocolor. The DNA probe is now a complex mixture containing different sequences to label the entire chromosome and different fluorophore ratios to yield 24 individually identifiable emission spectra. The fluorophores are usually attached to the DNA in two different ways. Some fluorophores are attached directly, as shown in Figure 21.51. Some fluorophores are attached indirectly using protein linkers. This is accomplished using biotin or digoxigenin-labeled nucleotides. These nucleotides are then labeled with avidin or antibodies that have covalently linked fluorophores.

Two approaches are used to record the spectral information, multicolor FISH (m-FISH),<sup>159–161</sup> and spectral karyotyping (SKY).<sup>162–165</sup> In m-FISH the emission is imaged through several filters. These images are used to identify the mixture which stained each chromosome. In SKY the emission is imaged through an interferometer that is scanned to obtain the spectral information (Figure 21.55). The value of spectral labeling of the chromosomes is shown by the images on the right side of Figure 21.55. The display colors, which approximate the true colors, are essentially

the same for all six chromosomes. However, three of the chromosomes are labeled with Cy3 and three with Texas Red. Use of the emission spectra allowed the identity of the chromosomes to be determined, and each type was assigned a different pseudocolor.

Spectral karyotyping has been extended to allow for identification of all 24 chromosomes (Figure 21.56). The display colors approximate the visual appearance of the painted chromosomes. The spectral distribution is used to identify each chromosome based on the known spectral distribution of the painting probes.<sup>165</sup> Each spectral distribution is assigned a pseudocolor that allows visual discrimination. The chromosomes can then be easily paired and analyzed.

Spectral karyotyping and m-FISH provide an approach to the study of abnormal cells.<sup>162</sup> Figure 21.57 shows a chromosomal image from an ovarian cancer. The image on the left is an inverted DAPI image, which is used because it approximates the Giemsa stains familiar to cell biologists. The middle panel is an RGB image created from separate images taken through three different emission filters which is intended to represent the visual image. The device shown in Figure 21.55 was used to identify the spectral signatures. The SKY images show that there have been many chromosomal rearrangements, which can be seen from chromosomes that are assigned multiple pseudocolors. SKY and m-FISH provide a means to detect chromosome abnormalities.

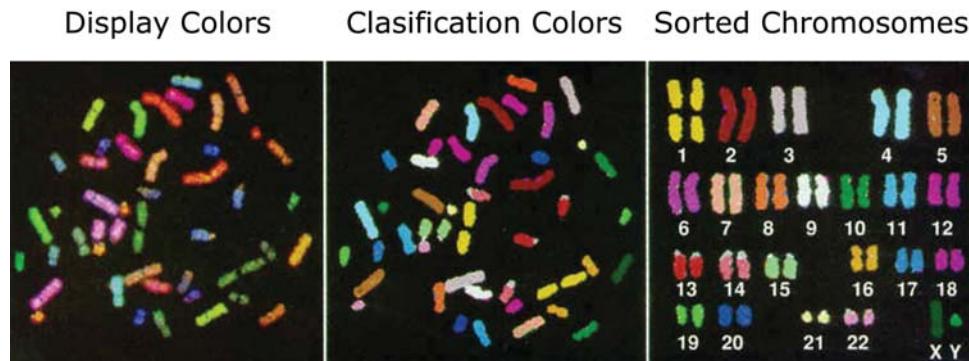


**Figure 21.56.** Spectral karyotyping of 24 human chromosomes using 24 pointing probes. From [165].

ties and rearrangements, as well as monitoring bone marrow cells following transplantation and cancer therapy.<sup>166–172</sup> The use of FISH relies on methods for labeling DNA, computerized imaging, and high, sensitivity CCD detection. FISH technology represents a combination of modern optics, molecular biology, and fluorescence spectroscopy, and promises to become a central tool in molecular medicine.

## 21.9. DNA ARRAYS

DNA arrays provide a method for parallel high-throughput analysis of gene expression. This capability has resulted in a paradigm shift in biological research. Traditional experiments in gene expression studied one or a few genes in an organism. Presently it is possible to simultaneously study the expression of thousands of genes in a single experiment.<sup>173–180</sup>

DNA arrays consist of regular arrays of DNA fragments or oligomers on a solid support, usually glass microscope slides. These slides can contain more than 20,000 different sequences or more in only a few square centimeters of area. There are two general methods to prepare arrays, by mechanical spotting of DNA solutions on slides or by light-generated arrays. Spotted arrays are now being produced in individual laboratories and in core facilities. Light-generated arrays are more expensive to produce and are usually manufactured commercially.

### 21.9.1. Spotted DNA Microarrays

Preparation of a DNA array is somewhat expensive and complex (Figure 21.58). DNA clones are prepared by one of several available methods.<sup>180</sup> Usually mRNA is isolated from the desired sample and used to create cDNA using reverse transcriptase. The use of mRNA or cDNA results in DNA fragments that represent the expressed genes. The use of mRNA or cDNA is generally preferable to using the entire genome, which contains many regions that are repetitive or not converted into gene products. The DNA clones are then spotted onto microscope slides. Prior to spotting, the slides are treated with polylysine or an aminosilane reagent to cover the surface with positive charges, which results in DNA binding to the surface. After drying, the slides are illuminated with UV light, which probably crosslinks the DNA to the surface. The surface is then treated with succinic anhydride to remove the positive charges on the surface, which would result in nonspecific binding. Spotting of the slides is accomplished using automated instruments designed for this purpose.<sup>181</sup> Spotting is usually done using small capillaries that make contact with the

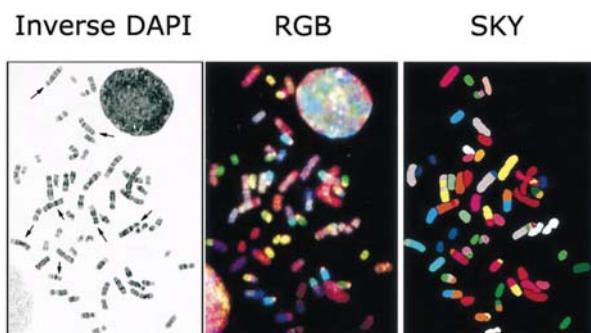


**Figure 21.57.** Chromosome images of an ovarian carcinoma. Left, inverted DAPI image. Middle, RGB image. Right, SKY classification image. From [162].

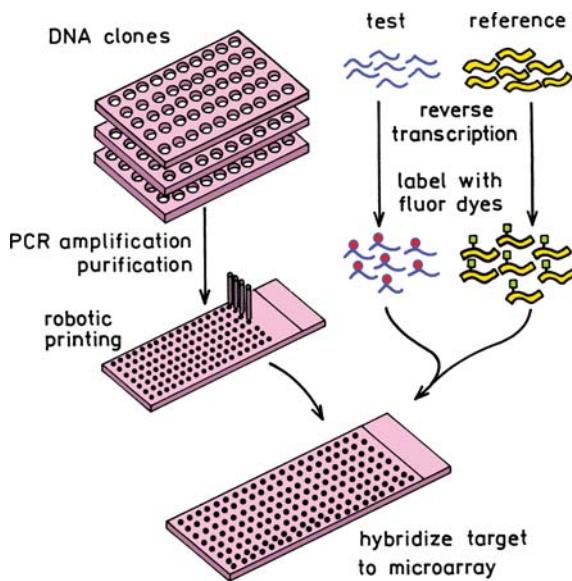


**Figure 21.58.** Use of DNA arrays for gene expression profiling. From [178].

slide (Figure 21.59). The microarrays can also be spotted using ink jet or bubble jet technology.<sup>182–184</sup>

DNA microarrays with a modest number of spots can be used for specific diagnostic tests or bioassays. Microarrays with a larger number of surface-bound oligomers are often used to measure profiles of gene expression.<sup>185</sup> A schematic of these experiments is shown in Figure 21.60. Messenger RNA is isolated from two samples that originate

with the same organism or cell line, but which have been treated differently. One sample serves as the control. The other sample is stimulated to divide or is treated in a way that affects the cell. The mRNA is isolated from both samples and converted to cDNA. During synthesis the cDNA is labeled using fluorescent oligonucleotides, typically containing Cy3 and Cy5. These two samples of cDNA are then coated over all the spots and allowed to hybridize. The concentrations of cDNA are adjusted so that the amounts are less than that bound to the surface. Under these conditions the amount of labeled cDNA bound is roughly proportional to the amount in the samples.

The relative level of each cDNA is determined from the relative intensities of the two fluorophores on each spot of the array. Figure 21.61 shows a portion of an array. The color image is usually constructed from the relative intensities of the green Cy3 emission and the red Cy5 emission. In this experiment the CDKN1A gene is overexpressed in the sample relative to the control, and the MYC gene is underexpressed. These expression levels are seen from the red spot for CDKN1A and a green spot for MYC, or from the intensity traces for this row of spots (lower panel). The other spots are yellow, which indicates that the expression levels of these genes are the same in the control and the sample.

DNA arrays can contain large numbers of genes. The array in Figure 21.62 contains more than 9000 genes from the plant *Arabidopsis*. The color of each spot indicates the relative expression level of each gene. By using such arrays

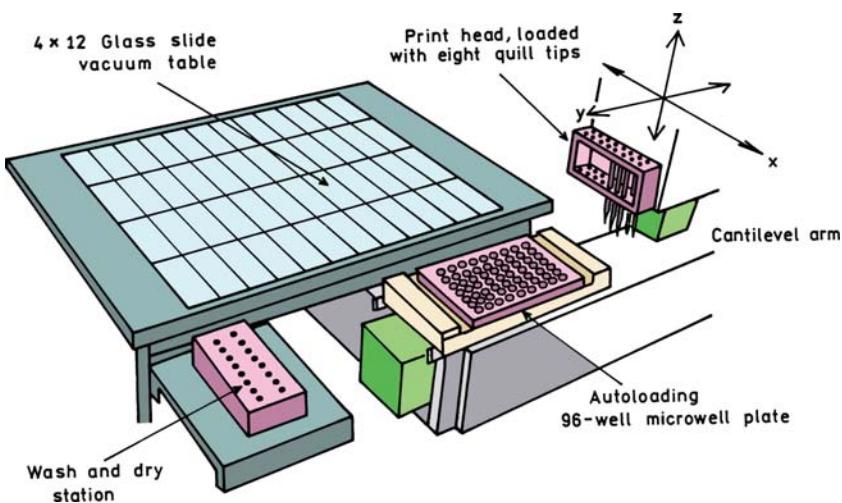


**Figure 21.59.** Apparatus for making spotted DNA microarrays. From [175].

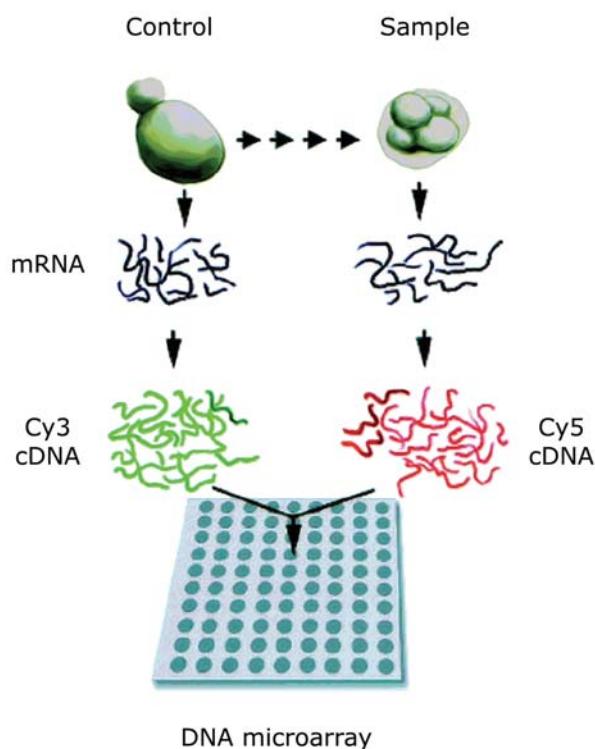


**Figure 21.60.** Analysis of gene expression using a spotted DNA microarray. Revised from [185].

it is possible to study how families of genes are activated in response to stimuli or at different phases of the growth cycle.

### 21.9.2. Light-Generated DNA Arrays

DNA arrays can also be made using a combination of photochemistry and photolithography.<sup>187–189</sup> This approach is shown in Figure 21.63. The surface is coated with a protected hydroxyl groups. Regions of the surface are deprotected by light and coupled to a nucleotide. Another region of the surface is then deprotected and another nucleotide is added. This process is repeated until the oligomers are 15 to 25 bases long. Up to 300,000 oligonucleotides can be synthesized and located in a 1.28 x 1.28 cm array. Typically a single gene is represented by about 20 oligomers. These light-generated arrays are manufactured by Affymetrix Inc. Gene chips are available for a number of organisms. It appears that the expression levels are determined by intensities at a single wavelength rather than by intensity ratios for different wavelengths. Light-generated arrays can also be made using micromirror arrays or digital light processors.<sup>190–191</sup>

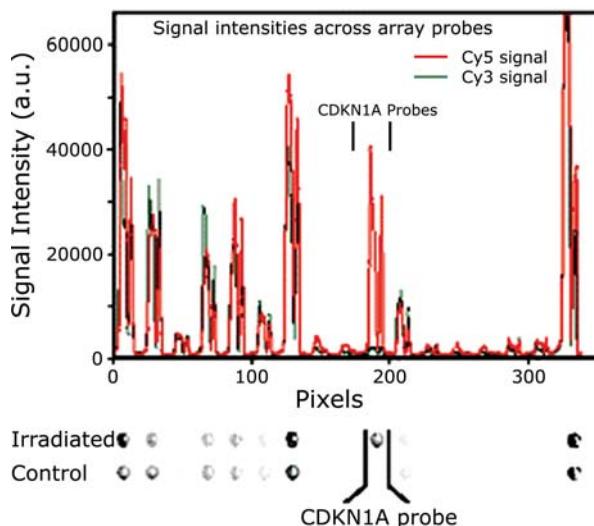
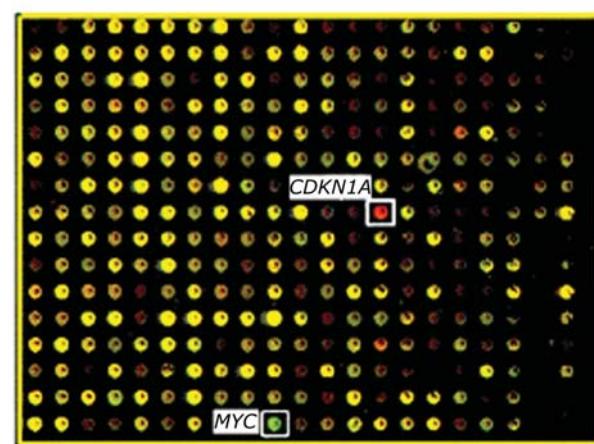


**Figure 21.61.** Color image of portion of a DNA array. The lower panel shows the intensity profiles of Cy3 (green) and Cy5 (red) across one row of the array. From [178].

### REFERENCES

- International Human Genome Sequencing Consortium. 2001. Initial sequencing and analysis of the human genome. *Nature* **409**:860–921.
- Venter JC, et al. 2001. The sequence of the human genome. *Science* **291**:1304–1351.
- Maxam AM, Gilbert W. 1977. A new method for sequencing DNA. *Proc Natl Acad Sci USA* **74**:560–564.
- Maxam AM, Gilbert W. 1980. Sequencing end-labeled DNA with base-specific chemical cleavage. *Methods Enzymol* **65**:499–560.
- Sanger F, Nicklen S, Coulson AR. 1977. DNA sequencing with chain-terminating inhibitors. *Proc Natl Acad Sci USA* **74**:5463–5467.
- Watson JD, Gilman M, Witkowski J, Zoller M. 1992. *Recombinant DNA*, 2nd ed. Scientific American Books, New York.

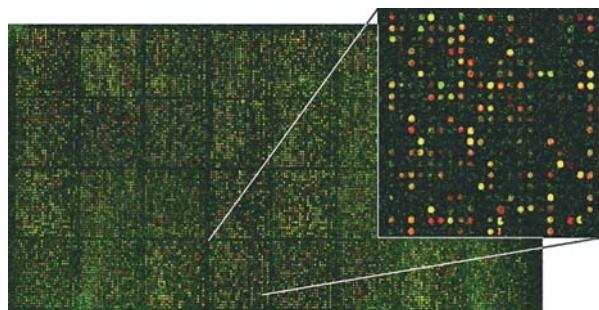


**Figure 21.62.** Gene expression by *Arabidopsis* plants using an 18,000-element DNA microarray. The control DNA was labeled with Cy5 and the sample was labeled with Cy3. From [186].

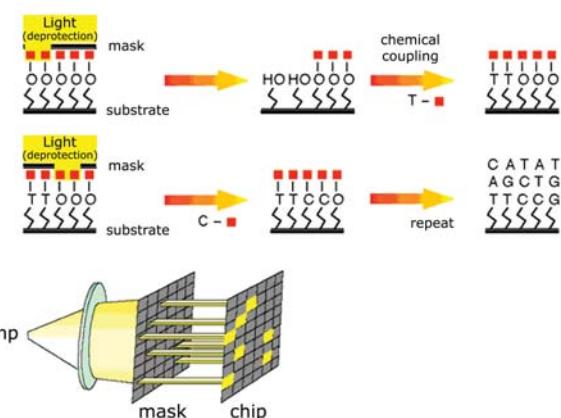


**Figure 21.63.** Light-directed synthesis of oligonucleotide arrays. From [189].

7. Lipshutz RJ, Morris D, Chee M, Hubbell E, Kozal MJ, Shah N, Shen N, Yang R, Foder SPA. 1995. Using oligonucleotide probe arrays to access genetic diversity. *Biotechniques* **19**:442–447.
8. Smith LM, Sanders JZ, Kaiser RJ, Hughes P, Dodd C, Connell CR, Heiner C, Kent SBH, Hood, LE 1986. Fluorescence detection in automated DNA sequence analysis. *Nature* **321**:674–679.
9. Prober JM, Trainor GL, Dam RJ, Hobbs FW, Robertson CW, Zagursky RJ, Cocuzza AJ, Jensen MA, Baumeister K. 1987. A system for rapid DNA sequencing with fluorescent chain-terminating dideoxynucleotides. *Science* **238**:336–343.
10. Ansorge W, Sproat BS, Stegemann J, Schwager C. 1986. A non-radioactive automated method for DNA sequence determination. *J Biochem Biophys Methods* **13**:315–323.
11. Griffin HG, Griffin AM. 1993. *DNA sequencing protocols: Methods in molecular biology*. Humana Press, Totowa, NJ.
12. Soper SA, Owens C, Lassiter S, Xu Y, Waddell E. DNA Sequencing using fluorescence detection. In *Topics in fluorescence spectroscopy*, Vol. 7: *DNA technology*, pp. 1–68. Ed JR Lakowicz. Kluwer Academic/Plenum Publishers, New York.
13. Ansorge W, Sproat B, Stegemann J, Schwager C, Zenke M. 1987. Automated DNA sequencing: ultrasensitive detection of fluorescent bands during electrophoresis. *Nucleic Acids Res* **15**(11):4593–4602.
14. Brumbaugh JA, Middendorf LR, Grone DL, Ruth JL. 1988. Continuous on-line DNA sequencing using oligodeoxynucleotide primers with multiple fluorophores. *Proc Natl Acad Sci USA* **85**:5610–5614.
15. Ju J, Ruan C, Fuller CW, Glazer AN, Mathies RA. 1995. Fluorescence energy transfer dye-labeled primers for DNA sequencing and analysis. *Proc Natl Acad Sci USA* **92**:4347–4351.
16. Takahashi S, Murakami K, Anazawa T, Kambara H. 1994. Multiple sheath-flow gel capillary-array electrophoresis for multicolor fluorescent DNA detection. *Anal Chem* **66**:1021–1026.
17. Swerdlow H, Zhang JZ, Chen DY, Harke HR, Grey R, Wu S, Dovichi NJ. 1991. Three DNA sequencing methods using capillary gel electrophoresis and laser-induced fluorescence. *Anal Chem* **63**:2835–2841.
18. Hung SC, Mathies RA, Glazer AN. 1997. Optimization of spectroscopic and electrophoretic properties of energy transfer primers. *Anal Biochem* **252**:78–88.
19. Tong AK, Li Z, Ju J. 2002. Combinational fluorescence energy transfer tags: new molecular tools for genomics applications. *IEEE J Quantum Electron* **38**(2):110–121.
20. Li A, Glazer AN. 1999. Design, synthesis, and spectroscopic properties of peptide-bridged fluorescence energy-transfer cassettes. *Bioconjugate Chem* **10**:241–245.
21. Hung SC, Mathies RA, Glazer AN. 1998. Comparison of fluorescence energy transfer primers with different donor–acceptor dye combinations. *Anal Biochem* **255**:32–38.
22. Jiao GS, Thoresen LH, Burgess K. 2003. Fluorescent, through-bond energy transfer cassettes for labeling multiple biological molecules in one experiment. *J Am Chem Soc* **125**:14668–14669.
23. Ju J, Glazer AN, Mathies RA. 1996. Energy transfer primers: A new fluorescence labeling paradigm for DNA sequencing and analysis. *Nature Med* **2**(2):246–249.
24. Ju J, Kheterpal I, Scherer JR, Ruan C, Fuller CW, Glazer AN, Mathies RA. 1995. Design and synthesis of fluorescence energy transfer dye-labeled primers and their application for DNA sequencing and analysis. *Anal Biochem* **231**:131–140.
25. Metzker ML, Lu J, Gibbs RA. 1996. Electrophoretically uniform fluorescent dyes for automated DNA sequencing. *Science* **271**:1420–1422.
26. Middendorf LR, Bruce JC, Bruce RC, Eckles RD, Roemer SC, Sloniker GD. 1993. A versatile infrared laser scanner/electrophoresis apparatus. *SPIE Proc* **1885**:423–434.
27. Soper SA, Flanagan JH, Legendre BL, Williams DC, Hammer RP. 1996. Near-infrared, laser-induced fluorescence detection for DNA sequencing applications. *IEEE J Sel Top Quantum Electron* **2**(4):1–11.
28. Shealy DB, Lipowska M, Lipowski J, Narayanan N, Sutter S, Strekowski L, Patonay G. 1995. Synthesis, chromatographic separation, and characterization of near-infrared labeled DNA oligomers for use in DNA sequencing. *Anal Chem* **67**:247–251.
29. Williams DC, Soper SA. 1995. Ultrasensitive near-IR fluorescence detection for capillary gel electrophoresis and DNA sequencing applications. *Anal Chem* **67**:3427–3432.

30. Middendorf L, Amen J, Bruce B, Draney D, DeGraff D, Gewecke J, Grone D, Humphrey P, Little G, Lugade A, Narayanan N, Oommen A, Osterman H, Peterson R, Rada J, Raghavachari R, Roemer S. 1998. Near-infrared fluorescence instrumentation for dna analysis. In *Near-infrared dyes for high-technology applications*, pp. 21–54. Ed S. Daehne, U Resch-Genger, O Wolfbeis. Kluwer Academic Publishers, Dordrecht.
31. Middendorf LR, Bruce JC, Bruce RC, Eckles RD, Grone DL, Roemer SC, Sloniker GD, Steffens DL, Sutter SL, Brumbaugh JA, Patonay G. 1992. Continuous, on-line DNA sequencing using a versatile infrared laser scanner/electrophoresis apparatus. *Electrophoresis* **13**:487–494.
32. Middendorf L, Bruce R, Brumbaugh J, Grone D, Jang G, Richterich P, Holtke HJ, Williams RJ, Peralta JM. 1995. A two-dimensional infrared fluorescence scanner used for DNA analysis. *SPIE Proc* **2388**:44–54.
33. Daehne S, Resch-Genger U, Wolfbeis OS, eds. 1998. *Near-infrared dyes for high technology applications*. Kluwer Academic Publishers, Dordrecht.
34. Zhu L, Stryjewski W, Lassiter S, Soper SA. 2003. Fluorescence multiplexing with time-resolved and spectral discrimination using a near-IR detector. *Anal Chem* **75**:2280–2291.
35. McIntosh SL, Nunnally BK, Nesbit AR, Deligeorgiev TG, Gadjev NI, McGown LB. 2000. Fluorescence lifetime for on-the-fly multiplex detection of DNA restriction fragments in capillary electrophoresis. *Anal Chem* **72**:5444–5449.
36. Llopis SD, Stryjewski W, Soper SA. 2004. Near-infrared time-resolved fluorescence lifetime determinations in poly (methyl-methacrylate) microchip electrophoresis devices. *Electrophoresis* **25**(21–22):3810–3819.
37. He H, McGown LB. 2000. DNA sequencing by capillary electrophoresis with four-decay fluorescence detection. *Anal Chem* **72**: 5865–5873.
38. Mihindukulasuriya SH, Morcone TK, McGown LB. 2003. Characterization of acridone dyes for use in four-decay detection in DNA sequencing. *Electrophoresis* **24**:20–25.
39. Lieberwirth U, Arden-Jacob J, Drexhage KH, Herten DP, Muller R, Neumann M, Schulz A, Siebert S, Sagner G, Klingel S, Sauer M, Wolfrum J. 1998. Multiplex dye DNA sequencing in capillary gel electrophoresis by diode laser-based time-resolved fluorescence detection. *Anal Chem* **70**:4771–4779.
40. Han K-T, Sauer M, Schulz A, Seeger S, Wolfrum J. 1993. Time-resolved fluorescence studies of labelled nucleosides. *Ber Bunsenges Phys Chem* **97**:1728–1730.
41. Legendre BL, Williams DC, Soper SA, Erdmann R, Ortmann U, Enderlein J. 1996. An all solid-state near-infrared time-correlated single photon counting instrument for dynamic lifetime measurements in DNA sequencing applications. *Rev Sci Instrum* **67**(11): 3984–3989.
42. Chang K, Force RK. 1993. Time-resolved laser-induced fluorescence study on dyes used in DNA sequencing. *Appl Spectrosc* **47**(1):24–29.
43. Sauer M, Han K-T, Ebert V, Müller R, Schulz A, Seeger S, Wolfrum J. 1994. Design of multiplex dyes for the detection of different biomolecules. *Proc SPIE* **2137**:762–774.
44. Li L-C, He H, Nunnally BK, McGown LB. 1997. On-the-fly fluorescence lifetime detection of labeled DNA primers. *J Chromatogr* **695**: 85–92.
45. McGown LB. 2003. On-the-fly fluorescence lifetime detection in capillary electrophoresis for dna analysis. In *Topics in fluorescence spectroscopy*, Vol. 7: *DNA technology*, pp. 129–149. Ed JR Lakowicz. Kluwer Academic/Plenum Publishers, New York.
46. Li L-C, McGown LB. 1996. On-the-fly frequency-domain fluorescence lifetime detection in capillary electrophoresis. *Anal Chem* **68**: 2737–2743.
47. Waddell E, Wang Y, Stryjewski W, McWhorter S, Henry AC, Evans D, McCarley RL, Soper S. 2000. High-resolution near-infrared imaging of DNA microarrays with time-resolved acquisition of fluorescence lifetimes. *Anal Chem* **72**:5907–5917.
48. Lassiter SJ, Stryjewski W, Legendre BL, Erdmann R, Wahl M, Wurm J, Peterson R, Middendorf L, Soper SA. 2000. Time-resolved fluorescence imaging of slab gels for lifetime base-calling in DNA sequencing applications. *Anal Chem* **72**:5373–5382.
49. Flanagan JH, Owens CV, Romero SE, Waddell E, Kahn SH, Hammer RP, Soper SA. 1998. Near-infrared heavy-atom-modified fluorescent dyes for base-calling in DNA sequencing applications using temporal discrimination. *Anal Chem* **70**:2676–2684.
50. Zhu L, Stryjewski WJ, Soper SA. 2004. Multiplexed fluorescence detection in microfabricated devices with both time-resolved and spectral-discrimination capabilities using near-infrared fluorescence. *Anal Biochem* **330**:206–218.
51. Flick PK. 1995. DNA sequencing by nonisotopic methods. In *Nonisotopic probing, blotting, and sequencing*, pp. 475–511. Ed JJ Kricka. Academic Press, New York.
52. Hunkapiller T, Kaiser RJ, Koop BF, Hood L. 1991. Large-scale and automated DNA sequence determination. *Science* **254**:59–67.
53. Zimmermann J, Wiemann S, Voss H, Schwager C, Ansorge W. 1994. Improved fluorescent cycle sequencing protocol allows reading nearly 1000 bases. *Biotechniques* **17**(2):302–307.
54. O'Brien KM, Wren J, Dave VK, Bai D, Anderson RD, Rayner S, Evans GA, Dabiri AE, Garner HR. 1998. ASTRAL, a hyperspectral imaging DNA sequencer. *Rev Sci Instrum* **69**(5):2141–2146.
55. Liu S, Ren H, Gao Q, Roach DJ, Loder RT, Armstrong TM, Mao Q, Blaga L, Barker DL, Jovanovich K. 2000. Automated parallel DNA sequencing on multiple channel microchips. *Proc Natl Acad Sci USA* **97**(10):5369–5374.
56. Paegel BM, Emrich CA, Wedemayer GJ, Scherer JR, Mathies RA. 2002. High-throughput DNA sequencing with a microfabricated 96-lane capillary array electrophoresis bioprocessor. *Proc Natl Acad Sci USA* **99**(2):574–579.
57. Paegel BM, Yeung SHI, Mathies RA. 2002. Microchip bioprocessor for integrated nanovolume sample purification and DNA sequencing. *Anal Chem* **74**:5092–5098.
58. Emrich CA, Tian H, Medintz IL, Mathies RA. 2002. Microfabricated 384-lane capillary array electrophoresis bioanalyzer for ultrahigh-throughput genetic analysis. *Anal Chem* **74**:5076–5083.
59. Le Pecq J-B, Paoletti C. 1967. A fluorescent complex between ethidium bromide and nucleic acids. *J Mol Biol* **27**:87–106.
60. Le Pecq J-B, Le Bret M, Barbet J, Roques B. 1975. DNA polyintercalating drugs: DNA binding of diacridine derivatives. *Proc Natl Acad Sci USA* **72**(8):2915–2919.
61. Markovits J, Roques BP, Le Pecq J. 1979. Ethidium dimer: a new reagent for the fluorimetric determination of nucleic acids. *Anal Biochem* **94**:259–264.

62. Glazer AN, Peck K, Mathies RA. 1990. A stable double-stranded DNA ethidium homodimer complex: application to picogram fluorescence detection of DNA in agarose gels. *Proc Natl Acad Sci USA* **87**:3851–3855.
63. Ueyama H, Takagi M, Takenaka S. 2002. Tetrakis-acridinyl peptide: a novel fluorometric reagent for nucleic acid analysis based on the fluorescence quenching upon DNA binding. *Analyst* **127**:886–888.
64. Privat E, Melvin T, Merola F, Schweizer G, Prodhomme S, Asseline U, Vigny P. 2002. Fluorescent properties of oligonucleotide-conjugated thiazole orange probes. *Photochem Photobiol* **75**(3):201–210.
65. Timtcheva I, Maximova V, Deligeorgiev T, Gadjev N, Drexhage KH, Petkova I. 2000. Homodimeric monomethine cyanine dyes as fluorescent probes of biopolymers. *J Photochem Photobiol B: Biol* **58**:130–135.
66. Cosa G, Focsaneanu KS, McLean JRN, McNamee JP, Scaiano JC. 2001. Photophysical properties of fluorescent DNA-dyes bound to single- and double-stranded DNA in aqueous buffered solution. *Photochem Photobiol* **73**(6):585–599.
67. Tarasov SG, Casas-Finet JR, Cholody WM, Kosakowska-Cholody T, Gryczynski Z, Michejda CJ. 2003. Bisimidazoacridones, 2: steady-state and time-resolved fluorescence studies of their diverse interactions with DNA. *Photochem Photobiol* **78**(4):313–322.
68. Rye HS, Yue S, Wemmer DE, Quesada MA, Haugland RP, Mathies RA, Glazer AN. 1992. Stable fluorescent complexes of double-stranded DNA with bis-intercalating asymmetric cyanine dyes: properties and applications. *Nucleic Acids Res* **20**(11):2803–2812.
69. Abramo KH, Pitner JB, McGown LB. 1997. Spectroscopic studies of single-stranded DNA ligands and oxazole yellow dyes. *Biospectroscopy* **4**:27–35.
70. Nygren J, Svanvik N, Kubista M. 1998. The interactions between the fluorescent dye thiazole orange and DNA. *Biopolymers* **46**:39–51.
71. Benson SC, Mathies RA, Glazer AN. 1993. Heterodimeric DNA-binding dyes designed for energy transfer: stability and applications of the DNA complexes. *Nucleic Acids Res* **21**:5720–5726.
72. Benson SC, Zeng Z, Glazer AN. 1995. Fluorescence energy-transfer cyanine heterodimers with high affinity for double-stranded DNA. *Anal Biochem* **231**:247–255.
73. Filippova EM, Monteleone DC, Trunk JG, Sutherland BM, Quake SR, Sutherland JC. 2003. Quantifying double-strand breaks and clustered damages in DNA by single-molecule laser fluorescence sizing. *Biophys J* **84**:1281–1290.
74. Larson EJ, Hakovirta JR, Cai H, Jett JH, Burde S, Keller RA, Marrone BL. 2000. Rapid DNA fingerprinting of pathogens by flow cytometry. *Cytometry* **41**:203–208.
75. Foquet M, Korlach J, Zipfel W, Webb WW, Craighead HG. 2002. DNA fragment sizing by single molecule detection in submicrometer-sized closed fluidic channels. *Anal Chem* **74**:1415–1422.
76. Van Orden A, Machara NP, Goodwin PM, Keller RA. 1998. Single-molecule identification in flowing sample streams by fluorescence burst size and intraburst fluorescence decay rate. *Anal Chem* **70**:1444–1451.
77. Van Orden A, Keller RA, Ambrose WP. 2000. High-throughput flow cytometric DNA fragment sizing. *Anal Chem* **72**:37–41.
78. Goodwin PM, Johnson ME, Martin JC, Ambrose WP, Marrone BL, Jett JH, Keller RA. 1993. Rapid sizing of individual fluorescently stained DNA fragments by flow cytometry. *Nucleic Acids Res* **21**(4):803–806.
79. Huang Z, Petty JT, O'Quinn B, Longmire JL, Brown NC, Jett JH, Keller RA. 1996. Large DNA fragment sizing by flow cytometry: application to the characterization of P1 artificial chromosome (PAC) clones. *Nucleic Acids Res* **24**(21):4202–4209.
80. Petty JT, Johnson ME, Goodwin PM, Martin JC, Jett JH, Keller RA. 1995. Characterization of DNA size determination of small fragments by flow cytometry. *Anal Chem* **67**:1755–1761.
81. Ambrose WP, Cai H, Goodwin PM, Jett JH, Habbersett RC, Larson EJ, Grace WK, Werner JH, Keller RA. 2003. Flow cytometric sizing of DNA fragments. In *Topics in fluorescence spectroscopy*, Vol. 7: *DNA technology*, pp. 239–270. Ed JR Lakowicz. Kluwer Academic/Plenum Publishers, New York.
82. Morrison LE. 2003. Fluorescence in nucleic acid hybridization assays. In *Topics in fluorescence spectroscopy*, Vol. 7: *DNA technology*, pp. 69–103. Ed JR Lakowicz. Kluwer Academic/Plenum Publishers, New York.
83. Masuko M, Ohuchi S, Sode K, Ohtani H, Shimadzu A. 2000. Fluorescence resonance energy transfer from pyrene to perylene labels for nucleic acid hybridization assays under homogeneous solution conditions. *Nucleic Acids Res* **28**(8):e34.
84. Cardullo RA, Agrawal S, Flores C, Zamecnik PC, Wolf DE. 1988. Detection of nucleic acid hybridization by nonradiative fluorescence resonance energy transfer. *Proc Natl Acad Sci USA* **85**:8790–8794.
85. Morrison LE, Stols LM. 1993. Sensitive fluorescence-based thermodynamic and kinetic measurements of DNA hybridization in solution. *Biochemistry* **32**:3095–3104.
86. Morrison LE. 1995. Detection of energy transfer and fluorescence quenching. In *Nonisotopic probing, blotting, and sequencing*, pp. 429–471. Ed LJ Kricka. Academic Press, New York.
87. Okamura Y, Kondo S, Sase I, Suga T, Mise K, Furusawa I, Kawakami S, Watanabe Y. 2000. Double-labeled donor probe can enhance the signal of fluorescence resonance energy transfer (FRET) in detection of nucleic acid hybridization. *Nucleic Acids Res* **28**(24):e107.
88. Sueda S, Yuan J, Matsumoto K. 2002. A homogeneous DNA hybridization system by using a new luminescence terbium chelate. *Bioconjugate Chem* **13**:200–205.
89. Templeton EFG, Wong HE, Evangelista RA, Granger T, Pollack A. 1991. Time-resolved fluorescence detection of enzyme-amplified lanthanide luminescence for nucleic acid hybridization assays. *Clin Chem* **37**(9):1506–1512.
90. Asseline U, Delarue M, Lancelot G, Toulme F, Thuong NT, Montenay-Garestier T, Helene C. 1984. Nucleic acid-binding molecules with high affinity and base sequence specificity: intercalating agents covalently linked to oligodeoxynucleotides. *Proc Natl Acad Sci USA* **81**:3297–3301.
91. Hélène C, Montenay-Garestier T, Saison T, Takasugi M, Asseline U, Lancelot G, Maurizot JC, Tolumé F, Thuong NT. 1985. Oligodeoxynucleotides covalently linked to intercalating agents: a new class of gene regulatory substances. *Biochemistry* **67**:777–783.
92. Morrison LE, Halder TC, Stols LM. 1989. Solution-phase detection of polynucleotides using interacting fluorescent labels and competitive hybridization. *Anal Biochem* **188**:231–244.
93. Parkhurst KM, Parkhurst LJ. 1996. Detection of point mutations in DNA by fluorescence energy transfer. *J Biomed Opt* **1**(4):435–441.
94. Paris PL, Langenan JM, Kool ET. 1998. Probing DNA sequences in solution with a monomer-excimer fluorescence color change. *Nucleic Acids Res* **26**(16):2789–2793.

95. Okamoto A, Kanatani K, Saito I. 2004. Pyrene-labeled base-discriminating fluorescent DNA probes for homogeneous SNP typing. *J Am Chem Soc* **126**:4820–4827.
96. Ebata K, Masuko M, Ohtani H, Kashiwasake-Jibu M. 1995. Nucleic acid hybridization accompanied with excimer formation from two pyrene-labeled probes. *Photochem Photobiol* **62**(5):836–839.
97. Yan Y, Myrick ML. 2001. Quantitative measurement and discrimination of isochromatic fluorophores based on micelle-enhanced steady-state fluorescence polarization in fluid solution. *Anal Chim Acta* **441**: 87–93.
98. Yan Y, Myrick ML. 2001. Identification of nucleotides with identical fluorescent labels based on fluorescence polarization in surfactant solutions. *Anal Chem* **73**:4508–4513.
99. Devlin R, Studholme RM, Dandliker WB, Fahy E, Blumeyer K, Ghosh SS. 1993. Homogeneous detection of nucleic acids by transient state polarized fluorescence. *Clin Chem* **39**(9):1939–1943.
100. Murakami A, Nakaura M, Nakatsuji Y, Nagahara S, Tran-Cong Q, Makino K. 1991. Fluorescent-labeled oligonucleotide probes: detection of hybrid formation in solution by fluorescence polarization spectroscopy. *Nucleic Acids Res* **19**(15):4097–4102.
101. Kumke MU, Shu L, McGown LB, Walker GT, Pitner JB, Linn CP. 1997. Temperature and quenching studies of fluorescence polarization detection of DNA hybridization. *Anal Chem* **69**:500–506.
102. Walker NJ. 2002. A technique whose time has come. *Science* **296**: 557–559.
103. Livak KJ, Flood SJA, Marmaro J, Giusti W, Deetz K. 1995. Oligonucleotides with fluorescent dyes at opposite ends provide a quenched probe system useful for detecting PCR product and nucleic acid hybridization. *PCR Methods Appl* **4**:357–362.
104. Gibson UEM, Heid CA, Williams PM. 1996. A novel method for real time quantitative RT-PCR. *Genome Res* **6**:995–1001.
105. Wittwer CT, Herrmann MG, Moss AA, Rasmussen RP. 1997. Continuous fluorescence monitoring of rapid cycle DNA amplification. *BioTechniques* **22**(1):130–138.
106. Tyagi S, Kramer FR. 1996. Molecular beacons: probes that fluoresce upon hybridization. *Nature Biotechnol* **14**:303–308.
107. Tyagi S, Bratu DP, Kramer FR. 1998. Multicolor molecular beacons for allele discrimination. *Nature Biotechnol* **16**:49–53.
108. Marras SAE, Kramer FR, Tyagi S. 2002. Efficiencies of fluorescence resonance energy transfer and contact-mediated quenching in oligonucleotide probes. *Nucleic Acids Res* **30**(21):e122. 1–8.
109. Yamane A. 2002. MagiProbe: a novel fluorescence quenching-based oligonucleotide probe carrying a fluorophore and an intercalator. *Nucleic Acids Res* **30**(19):e97. 1–8.
110. Hwang GT, Seo YJ, Kim BH. 2004. A highly discriminating quencher-free molecular beacon for probing DNA. *J Am Chem Soc* **126**:6528–6529.
111. Tyagi S, Marras SAE, Kramer FR. 2000. Wavelength-shifting molecular beacons. *Nature Biotechnol* **18**:1191–1196.
112. Zhang P, Beck T, Tan W. 2001. Design of a molecular beacon DNA probe with two fluorophores. *Angew Chem, Int Ed* **40**(2):402–405.
113. Ueberfeld J, Walt DR. 2004. Reversible ratiometric probe for quantitative DNA measurements. *Anal Chem* **76**:947–952.
114. Root DD, Vaccaro C, Zhang Z, Castro M. 2004. Detection of single nucleotide variations by a hybridization proximity assay based on molecular beacons and luminescence resonance energy transfer. *Biopolymers* **75**:60–70.
115. Ohya Y, Yabuki K, Hashimoto M, Nakajima A, Ouchi T. 2003. Multistep fluorescence resonance energy transfer in sequential chromophore array constructed on oligo-DNA assemblies. *Bioconjugate Chem* **14**(6):1057–1066.
116. Tsourkas A, Behlke MA, Xu Y, Bao G. 2003. Spectroscopic features of dual fluorescence/luminescence resonance energy-transfer molecular beacons. *Anal Chem* **75**:3697–3703.
117. Aslan K, Perez-Luna VH. 2004. Quenched emission of fluorescence by ligand functionalized gold nanoparticles. *J Fluoresc* **14**(4):401–405.
118. Rant U, Arinaga K, Fujita S, Yokoyama N, Abstreiter G, Tornow M. 2004. Structural properties of oligonucleotide monolayers on gold surfaces probed by fluorescence investigations. *Langmuir* **20**(23): 10086–10092.
119. Li H, Rothberg LJ. 2004. DNA sequence detection using selective fluorescence quenching of tagged oligonucleotide probes by gold nanoparticles. *Anal Chem* **76**(18):5414–5417.
120. Dubertret B, Calame M, Libchaber AJ. 2001. Single-mismatch detection using gold-quenched fluorescent oligonucleotides. *Nature Biotechnol* **19**:365–370.
121. Du H, Disney MD, Miller BL, Krauss TD. 2003. Hybridization-based unquenching of DNA hairpins on Au surfaces: prototypical "molecular beacon" biosensors. *J Am Chem Soc* **125**:4012–4013.
122. Sokol DL, Zhang X, Lu P, Gewirtz AM. 1998. Real time detection of DNA-RNA hybridization in living cells. *Proc Natl Acad Sci USA* **95**:11538–11543.
123. Fang X, Mi Y, Li JJ, Beck T, Schuster S, Tan W. 2002. Molecular beacons: fluorogenic probes for living cell study. *Cell Biochem Biophys* **37**:71–81.
124. Perlette J, Tan W. 2001. Real-time monitoring of intracellular mRNA hybridization inside single living cells. *Anal Chem* **73**:5544–5550.
125. Stojanovic MN, de Prada P, Landry DW. 2000. Fluorescent sensors based on aptamer self-assembly. *J Am Chem Soc* **122**:11547–11548.
126. Stojanovic MN, de Prada P, Landry DW. 2001. Aptamer-based folding fluorescent sensor for cocaine. *J Am Chem Soc* **123**:4928–4931.
127. Hermann T, Patel DJ. 2000. Adaptive recognition by nucleic acid aptamers. *Science* **287**:820–825.
128. Hoppe-Seyler F, Butz K. 2000. Peptide aptamers: powerful new tools for molecular medicine. *J Molec Med* **78**:466–470.
129. Jayasena SD. 1999. Aptamers: an emerging class of molecules that rival antibodies as diagnostics. *Clin Chem* **45**(9):1628–1650.
130. Fang X, Sen A, Vicens M, Tan W. 2003. Synthetic DNA aptamers to detect protein molecular variants in a high-throughput fluorescence quenching assay. *ChemBioChem* **4**:829–834.
131. Brody EN, Gold L. 2000. Aptamers as therapeutic and diagnostic agents. *Rev Mol Biotechnol* **74**:5–13.
132. Koizumi M, Breaker RR. 2000. Molecular recognition of cAMP by an DNA aptamer. *Biochemistry* **39**:8983–8992.
133. Jhaveri SD, Kirby R, Conrad R, Maglott EJ, Bowser M, Kennedy RT, Glick G, Ellington AD. 2000. Designed signaling aptamers that transducer molecular recognition to changes in fluorescence intensity. *J Am Chem Soc* **122**:2469–2473.

134. Stojanovic MN, Green EG, Semova S, Nikic DB, Landry DW. 2003. Cross-reactive arrays based on three-way functions. *J Am Chem Soc* **125**:6085–6089.
135. Yang Q, Goldstein IJ, Mei H-Y, Engelke DR. 1998. DNA ligands that bind tightly and selectively to cellobiose. *Proc Natl Acad Sci USA* **95**:5462–5467.
136. Pavski V, Le XC. 2001. Detection of human immunodeficiency virus type 1 reverse transcriptase using aptamers as probes in affinity capillary electrophoresis. *Anal Chem* **73**:6070–6076.
137. Yamamoto R, Kumar PKR. 2000. Molecular beacon aptamer fluoresces in the presence of Tat protein of HIV-1. *Genes Cells* **5**: 389–396.
138. Fang X, Cao Z, Beck T, Tan W. 2001. Molecular aptamer for real-time oncoprotein platelet-derived growth factor monitoring by fluorescence anisotropy. *Anal Chem* **73**:5752–5757.
139. Sen D, Geyer CR. 1998. DNA enzymes. *Curr Opin Chem Biol* **2**:680–687.
140. Breaker RR. 1997. DNA enzymes. *Nature Biotechnol* **15**:427–431.
141. Liu J, Lu Y. 2003. Improving fluorescent DNAzyme biosensors by combining inter- and intramolecular quenchers. *Anal Chem* **75**:6666–6672.
142. Lu Y, Liu J, Li J, Bruesehoff PJ, Pavot CM-B, Brown AK. 2003. New highly sensitive and selective catalytic DNA biosensors for metal ions. *Biosens Bioelectron* **18**:529–540.
143. Nolan JP, Sklar LA. 2002. Suspension array technology: evolution of the flat-array paradigm. *Trends Biotechnol* **20**(1):9–12.
144. Braeckmans K, De Smedt SC, Leblans M, Pauwels R, Demeester J. 2002. Encoding microcarriers: present and future technologies. *Nature Rev* **1**:447–456.
145. Ferguson JA, Steemers FJ, Walt DR. 2000. High-density fiber-optic DNA random microsphere array. *Anal Chem* **72**:5618–5624.
146. Battersby BJ, Bryant D, Meutermans W, Matthews D, Smythe ML, Trau M. 2000. Toward larger chemical libraries: encoding with fluorescent colloids in combinatorial chemistry. *J Am Chem Soc* **122**:2138–2139.
147. Steemers FJ, Ferguson JA, Walt DR. 2000. Screening unlabeled DNA targets with randomly ordered fiber-optic gene arrays. *Nature Biotechnol* **18**:91–94.
148. Han M, Gao X, Su JZ, Nie S. 2001. Quantum-dot-tagged microbeads for multiplexed optical coding of biomolecules. *Nature Biotechnol* **19**:631–635.
149. Levsky JM, Singer RH. 2003. Fluorescence in situ hybridization: past, present, and future. *J Cell Sci* **116**:2833–2838.
150. Difilippantonio MJ, Reid T. 2003. Technicolor genome analysis. In *Topics in fluorescence spectroscopy*, Vol. 7: DNA technology, pp. 291–316. Ed JR Lakowicz. Kluwer Academic/Plenum Publishers, New York.
151. Lichter P, Boyle AL, Cremer T, Ward DC. 1991. Analysis of genes and chromosomes by nonisotropic in situ hybridization. *Genet Anal Technol Appl* **8**(1):24–35.
152. Polak JM, McGee JOD. 1990. *In situ hybridization, principles and practice*. Oxford University Press, New York.
153. Denijn M, Schuurman H-J, Jacobse KC, De Weger RA. 1992. In situ hybridization: a valuable tool in diagnostic pathology. *APMIS* **100**:669–681.
154. Fuller CE, Perry A. 2002. Fluorescence in situ hybridization (FISH) in diagnostic and investigative neuropathology. *Brain Pathol* **12**:67–86.
155. Levsky JM, Shenoy SM, Pezo RC, Singer RH. 2002. Single-cell gene expression profiling. *Science* **297**(5582):836–840.
156. Voskova-Goldman A, Peier A, Caskey CT, Richards CS, Shaffner LG. 1997. DMD-specific FISH probes are diagnostically useful in the detection of female carriers of DMD gene deletions. *Neurology* **48**:1633–1638.
157. Siadat-Pajouh M, Periasamy A, Ayscue AH, Moscicki AB, Palefsky JM, Walton L, DeMars LR, Power JD, Herman B, Lockett SJ. 1994. Detection of human papillomavirus type 16/18 DNA in cervicovaginal cells by fluorescence based in situ hybridization and automated image cytometry. *Cytometry* **15**:245–257.
158. Pandya PP, Cardy DLN, Jauniaux E, Campbell S, Nicolaides KH. 1994. Rapid determination of fetal sex in coelomic and amniotic fluid by fluorescence in situ hybridization. *Fetal Diagn Ther* **10**:66–70.
159. Saracoglu K, Brown J, Kearney L, Uhrig S, Azofeifa J, Fauth C, Speicher MR, Eils R. 2001. New concepts to improve resolution and sensitivity of molecular cytogenetic diagnostics by multicolor fluorescence in situ hybridization. *Cytometry* **44**:7–15.
160. Wiegant J, Bezrookove V, Rosenberg C, Tanke HJ, Raap AK, Zhang H, Bittner M, Trent JM, Meltzer P. 2000. Differentially painting human chromosome arms with combined binary ratio-labeling fluorescence in situ hybridization. *Genome Res* **10**:861–865.
161. Jentsch I, Geigl J, Klein CA, Speicher MR. 2003. Seven-fluorochrome mouse M-FISH for high-resolution analysis of interchromosomal rearrangements. *Cytogenetic Genome Res* **103**:84–88.
162. Bayani J, Squire JA. 2001. Advances in the detection of chromosomal aberrations using spectral karyotyping. *Clin Genet* **59**:65–73.
163. Macville M, Veldman T, Padilla-Nash H, Wangsa D, O'Brien P, Schrock E, Ried T. 1997. Spectral karyotyping, a 24-colour FISH technique for the identification of chromosomal rearrangements. *Histochem Cell Biol* **108**:299–305.
164. Buwe A, Steinlein C, Koehler MR, Bar-Am I, Katzin N, Schmid M. 2003. Multicolor spectral karyotyping of rat chromosomes. *Cytogenetic Genome Res* **103**:163–168.
165. Schrock E, du Manoir S, Veldman T, Schoell B, Wienberg J, Ferguson-Smith MA, Ning Y, Ledbetter DH, Bar-Am I, Soenksen D, Garini Y, Ried T. 1996. Multicolor spectral karyotyping of human chromosomes. *Science* **273**(5274):494–497.
166. Le Beau MM. 1996. One FISH, two FISH, red FISH, blue FISH. *Nature Genet* **12**:341–344.
167. Speicher MR, Ward DC. 1996. The coloring of cytogenetics. *Nature Med* **2**(9):1046–1048.
168. Bentz M, Döhner H, Cabot G, Lichter P. 1994. Fluorescence in situ hybridization in leukemias: the FISH are spawning. *Leukemia* **8**(9):1447–1452.
169. Fox JL, Hsu P-H, Legator MS, Morrison LE, Seelig SA. 1995. Fluorescence in situ hybridization: Powerful molecular tool for cancer prognosis. *Clin Chem* **41**(11):1554–1559.
170. Popescu NC, Zimonjic DB. 1997. Molecular cytogenetic characterization of cancer cell alterations. *Cancer Genet Cytogenet* **93**:10–21.
171. Swiger RR, Tucker JD. 1996. Fluorescence in situ hybridization. *Environ Mol Mutagen* **27**:245–254.

172. Kallioniemi A, Kallioniemi OP, Sudar D, Rutovitz D, Gray JW, Waldman F, Pinkel D. 1992. Comparative genomic hybridization for molecular cytogenetic analysis of solid tumors. *Science* **258**:818–821.
173. Meldrum D. 2000. Automation for genomics, part two: sequencers, microarrays, and future trends. *Genome Res* **10**:1288–1303.
174. Harrington CA, Rosenow C, Retief J. 2000. Monitoring gene expression using DNA microassays. *Curr Opin Microbiol* **3**:285–291.
175. Khan J, Saal LH, Bittner ML, Chen Y, Trent JM, Meltzer PS. 1999. Expression profiling in cancer using cDNA microarrays. *Electrophoresis* **20**:223–229.
176. Ferea TL, Brown PO. 1999. Observing the living genome. *Curr Opin Genet Dev* **9**:715–722.
177. Lipshutz RJ, Morris D, Chee M, Hubbell E, Kozal MJ, Shah N, Shen N, Yang R, Fodor SPA. 1995. Using oligonucleotide probe arrays to access genetic diversity. *Biotechniques* **19**:442–447.
178. Duggan DJ, Bittner M, Chen Y, Melter P, Trent JM. 1999. Expression profiling using cDNA microarrays. *Nature Genet Suppl* **21**:10–14.
179. Schena M, Heller RA, Theriault TP, Konrad K, Lachenmeier E, Davis RW. 1998. Microarrays: biotechnology's discovery platform for functional genomics. *Trends Biotechnol* **16**:301–306.
180. D'Auria S, Rossi M, Malicka J, Gryczynski Z, Gryczynski I. 2003. DNA arrays for genetic analyses and medical diagnostics. In *Topics in fluorescence spectroscopy*, Vol. 7: *DNA technology*, pp. 213–237. Ed JR Lakowicz. Kluwer Academic/Plenum Publishers, New York.
- 180A. Alberts B, Johnson A, Lewis J, Raff M, Roberts K, Walter P. 2002. *The molecular biology of the cell*, 4th ed. Garland Science, New York.
181. *The MGuide*. Version 2.0. <http://cmgm.stanford.edu/pbrown/mguide/>
182. Cheung VG, Morley M, Aguilar F, Massimi A, Kucherlapati R, Childs G. 1999. Making and reading microarrays. *Nature Genet Suppl* **21**:15–19.
183. Blanchard AP, Kaiser RJ, Hood LE. 1996. High-density oligonucleotide arrays. *Biosens Bioelectron* **11**(6/7):687–690.
184. Okamoto T, Suzuki T, Yamamoto N. 2000. Microarray fabrication with covalent attachment of DNA using bubble jet technology. *Nature Biotechnol* **18**:438–441.
185. Brown PO, Botstein D. 1999. Exploring the new world of genome with DNA microarrays. *Nature Genet Suppl* **21**:33–37.
186. Deyholos MK, Galbraith DW. 2001. High-density microarrays for gene expression analysis. *Cytometry* **43**:229–238.
187. Pease AC, Solas D, Sullivan EJ, Cronin MT, Holmes CP, Fodor SPA. 1994. Light-generated oligonucleotide arrays for rapid DNA sequence analysis. *Proc Natl Acad Sci USA* **91**:5022–5026.
188. McGall G, Labadie J, Brock P, Wallraff G, Nguyen T, Hinsberg W. 1996. Light-directed synthesis of high-density oligonucleotide arrays using semiconductor photoresists. *Proc Natl Acad Sci USA* **93**:13555–13560.
189. Lipshutz RJ, Fodor SPA, Gingras TR, Lockhart DJ. 1999. High-density synthetic oligonucleotide arrays. *Nature Genet Suppl* **21**:20–24.
190. Nuwaysir EF, Huang W, Albert TJ, Singh J, Nuwaysir K, Pitas A, Richmond T, Gorski T, Berg JP, Ballin J, McCormick M, Norton J, Pollock T, Sumwalt T, Butcher L, Porter D, Molla M, Hall C, Blattner F, Sussman MR, Wallace RL, Cerrina F, Green RD. 2002. Gene expression analysis using oligonucleotide arrays produced by maskless photolithography. *Genome Res* **12**:1749–1755.
191. Singh-Gasson S, Green RD, Yue Y, Nelson C, Blattner F, Sussman MR, Cerrina F. 1999. Maskless fabrication of light-directed oligonucleotide microarrays using a digital micromirror array. *Nature Biotechnol* **17**:974–978.

---

## PROBLEM

- P21.1. *Spectra Observables Useful for DNA Sequencing:* Intensity, intensity-ratio, and lifetime measurements have been used for DNA sequencing. Suggest reasons why anisotropy and collisional quenching have not been used for DNA sequencing.

# 22

# Fluorescence-Lifetime Imaging Microscopy

Fluorescence microscopy is one of the most widely used tools in the biological sciences. There has been a rapid growth in the use of microscopy due to advances in several technologies, including probe chemistry, confocal optics, multiphoton excitation, detectors, computers, and genetically expressed fluorophores such as GFP. Perhaps the most limiting aspect of fluorescence microscopy is knowledge of the local probe concentrations within the cell. These concentrations are usually variable based on the affinity of the fluorophore for various biomolecules within the cell. For example, probes such as DAPI and Hoechst have affinity for nucleic acids and are primarily nuclear stains. Probes such as rhodamine 123 have affinity for mitochondria. The known affinities of probes for specific biomolecules is a basic tool of optical microscopy, histology, and fluorescence microscopy. However, in general, the concentrations of the probes in each region of the cell are not known.

In the 1980s the use of fluorescence microscopy expanded from staining biomolecules within cells to studies of the intracellular concentrations of ions and to detection of association of reactions within the cells. This emphasis on intracellular physiology required different types of fluorophores, ones which changed their spectral properties in response to the ion or in response to the binding reaction of interest. The best-known examples of such probes are the wavelength-ratiometric probes for cell calcium (Chapter 19). Wavelength-ratiometric probes were needed because the local concentrations of fluorophores within cells are not known. These concentrations are unknown because the probes diffuse rapidly, undergo photobleaching, and can be washed out of the cells. Also, the quantum yields of probes can change due to the local environment. Even if the local intensity of a fluorophore is measured it is difficult to use the intensity to determine the local concentration. Without knowledge of the probe concentration it is not possible to make quantitative use of intensity measurements within the cells.

Wavelength-ratiometric probes provide a way to make measurements that are independent of the local probe concentrations. Suppose the emission spectrum of a fluorophore changes in response to calcium. The ratio of the emission intensities at two wavelengths will depend on the calcium concentration, but the ratio will be independent of the probe concentration. This ratiometric measurement allows quantitative information to be obtained from the images without precise knowledge of the probe concentrations in each region of the cell.

Fluorescence-lifetime imaging microscopy (FLIM) provides measurements that are independent of probe concentration. The intensity of a fluorophore depends on its concentration. However, the lifetime of a fluorophore is mostly independent of its concentration. Suppose the lifetime of a probe changes in response to pH, calcium, or some other analyte. If the lifetime is measured this value can be used to determine the analyte concentration, and the determination will be independent of the probe concentration.

The concept of fluorescence-lifetime imaging is illustrated in Figure 22.1. Suppose that the cell has two regions, each with an equal steady-state fluorescence intensity. Assume further that the lifetime of the probe in the central region of the cell ( $\tau_2$ ) is several-fold longer than that in the outer region ( $\tau_1$ ). The longer lifetime in the central region could be due to the presence of an ionic species such as calcium, binding of the probe to a macromolecule, or other environmental factors. The quantum yields of the probe in the central and outer regions could be the same or different due to interactions of the probe with biomolecules. The concentrations of the probe could be different due to partial exclusion of the probe from some region of the cell. The intensity image will not reveal the different environments in regions 1 and 2 (lower left). However, if the lifetimes were measured in regions 1 and 2 then the distinct environments would be detected. FLIM allows image contrast to be based

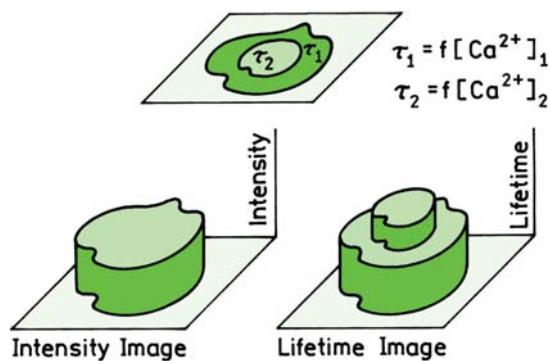


**Figure 22.1.** Intuitive presentation of the concept of fluorescence-lifetime imaging (FLIM). The object is assumed to have two regions that display the same fluorescence intensity but different decay times,  $\tau_2 > \tau_1$ .

on the lifetimes in each region of the cell, which can be presented on a color scale or as a 3D surface in which the height represents the local decay times.

The concept of FLIM is an optical analogue of magnetic resonance imaging (MRI). In MRI the proton relaxation times at each location in the patient are measured. The numerical value of the relaxation time is used to determine the contrast in the calculated image. The MRI images are presented as grayscale images because they are familiar to radiologists. The local chemical composition of the tissue determines the proton relaxation times. MIR image contrast is not based on signal intensity or proton concentration. The contrast in FLIM is determined by similar principles. The local environment determines the fluorescent lifetime, which is then used to calculate an image that is independent of probe concentration.

It is more difficult to measure lifetimes than intensities. So what is the value of FLIM? The advantages of lifetime imaging frequently justify the effort. There are a relatively small number of wavelength-ratiometric probes useful for intracellular use. Most of the available wavelength-ratiometric probes are for the divalent ions calcium and magnesium. There are fewer wavelength-ratiometric probes for the monovalent ions sodium and potassium, and these probes are more difficult to use. The wavelength-ratiometric probes for sodium absorb in the UV and display only small spectral changes. There are a larger number of probes that display changes in lifetime in response to ions or the environment, without displaying spectra shifts. For example, there are several long-wavelength probes for sodium that change intensity but not wavelength (Chapter 19). Probes for chloride are based on collisional quenching,

which decreases the lifetimes but does not cause a spectral shift. In general, there are more lifetime probes for ions than there are wavelength-ratiometric probes.

Another advantage of lifetime imaging is that intracellular measurements of FRET using the donor lifetimes can be more reliable than intensity measurements of the donor and/or acceptor. Suppose the cell contains two proteins that associate with each other in response to a stimulus, and that the proteins are labeled each with a donor or acceptor. In principle the extent of association can be determined from the decrease in donor intensity. However, since the local donor concentration is not known the extent of quenching cannot be determined from the donor intensity alone. The intensity of the donor in the absence of acceptor must also be known. Such control measurements are difficult to perform when using cells. Why not use the donor-to-acceptor intensity ratio? This ratio is difficult to use because the local acceptor concentration is also unknown and the donor and acceptor labeled proteins may not be present at equal concentrations within the cell. The intensity ratio can be different due to different donor and acceptor concentrations as well as differences in the RET efficiency. Determination of the extent of binding is more straightforward using the donor lifetime. The donor lifetime will be decreased by FRET to a bound acceptor. The donor lifetime will not be affected by an acceptor-labeled protein that is not bound to the donor-labeled protein. If the donor intensity is well above the background intensity the donor lifetime will be independent of its concentration.

Creation of a lifetime image with reasonable spatial resolution requires measurement of 256 x 256 or more individual lifetime measurements, or even more lifetimes if higher spatial resolution is required. Additionally, the lifetimes have to be measured using a microscope. There are two general approaches to FLIM. The FLIM images can be measured using scanning methods when the lifetime is measured at discrete locations. Lifetime images can also be measured by wide-field methods even in solution when a time-resolved imaging detector is used. Because of the difficulty of measuring a single lifetime the concept of lifetime imaging seemed impractical with the technology available in the 1980s and early 1990s. Even if such measurements could be performed, the data acquisition times would be excessively long, precluding studies of live cells. At present the situation is completely different. Because of advances in technology FLIM studies of cells are now practical, and are becoming almost routine. FLIM can be performed using time-domain or frequency-domain methods, and by variants

of these methods, and the use of FLIM is increasing in the biosciences.

## 22.1. EARLY METHODS FOR FLUORESCENCE-LIFETIME IMAGING

In Chapter 4 we mentioned that the first lifetimes were measured by the phase method. Similarly, the first lifetime images were obtained using a phase method. In the late 1980s it was not practical to create a lifetime image using pixel scanning, and a wide-field method was needed. CCD cameras were available for wide-field steady-state imaging. However, CCDs are slow accumulating detectors which do not provide an opportunity for the nanosecond time resolution needed for FLIM. This problem was solved by using a gain-modulated image intensifier as an optical phase-sensitive detector.<sup>1-4</sup>

In Section 5.12 we described phase-sensitive detection. The phase angle of the detector is set at a known value relative to the phase of the incident light and the phase-sensitive intensity is measured. The phase-sensitive intensity is a steady-state signal that is proportional to  $\cos(\theta - \theta_D)$  where  $\theta_D$  is the phase angle of the detector and  $\theta$  is the phase angle of the emission. If the phase-sensitive intensity is measured using several detector phase angles then the phase angle or lifetime of the emission can be determined. Phase-sensitive detection can be used to measure lifetime images using an image intensifier instead of a PMT (Figure 22.2). In this figure

the sample consists of four cuvettes, each containing a fluorophore with a different lifetime or a calcium-sensitive fluorophore. These cuvettes are illuminated with the same laser beam. The phase and modulation of the emission from each cuvette is different due to the different decay times.

Lifetime imaging was accomplished by measuring the images using a frequency-modulated image intensifier. The gain or voltage across the intensifier is modulated at the same frequency as the frequency of the modulated excitation, and the signals are phase locked so there is no drift between them. This measurement results in a constant image where the intensity at each location in the image is proportional to  $\cos(\theta(r) - \theta_D)$  where  $\theta(r)$  is the phase angle of the emission at position  $r$ . The image intensifier contains a phosphor screen where the brightness is proportional to the intensity, and the intensity is recorded with a CCD camera. The result is a steady signal from each cuvette, which is the phase-sensitive intensity. This configuration results in an optical phase-sensitive detector operating at the same frequency as the light modulation. This approach is analogous to using a PMT as a high-frequency phase-sensitive detection.<sup>5</sup>

Measurement of a single phase-sensitive intensity is not adequate to determine the lifetime. The phase angle and modulation of the emission can be determined by collection of a series of phase-sensitive images using different detector phase angles. At any position in the sample the phase-sensitive intensity is given by

$$I(\theta_D, r) = kC(r) \left( 1 + \frac{1}{2}m_D m(r) \cos\{\theta(r) - \theta_D\} \right) \quad (22.1)$$

In this expression  $m_D$  is the modulation of the detector,  $m(r)$  is the modulation of the emission at position  $r$ ,  $k$  is a constant, and  $C(r)$  is the concentration or steady-state intensity of the fluorophore at position  $r$ . The detector is in phase with a zero lifetime when the detector angle  $\theta_D = 0$ .

Measurement of lifetimes from the phase-sensitive intensities is illustrated in Figure 22.3. The cell is illuminated with light modulated at 80 MHz. The phase angle and modulation of the emission is different in these two regions because of the different lifetimes. The phase-sensitive intensities and modulations are different in each region of the cell due to the different lifetimes. The phase angles and modulations in each region are determined by fitting the phase-sensitive intensities to a cosine function. The phase angle or modulation image is then used to calculate the lifetime image.

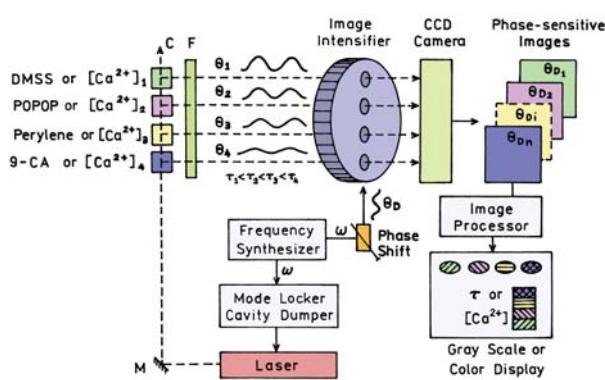


**Figure 22.2.** Schematic diagram of an FLIM experiment. The "object" consists of a row of four cuvettes each with a different fluorophore or a calcium-sensitive fluorophore with different calcium concentrations. The lifetime of the four samples are different. These cuvettes are illuminated with intensity-modulated light. The emission is detected with a phase-sensitive image intensifier, which is imaged onto a CCD camera. The light source is a pulsed laser.

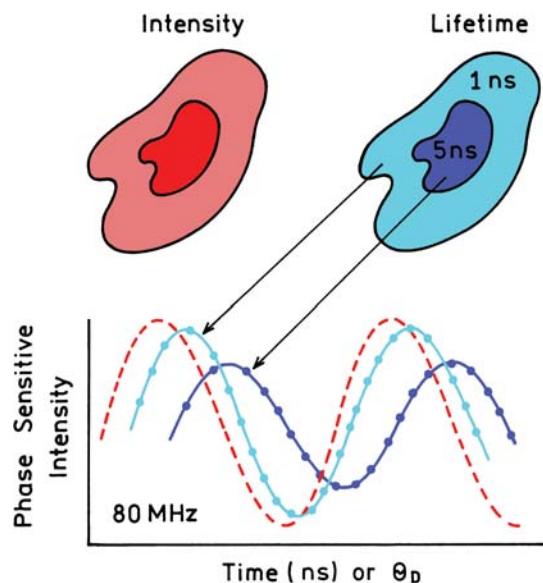


**Figure 22.3.** Schematic of lifetime imaging using phase-sensitive images.

### 22.1.1. FLIM Using Known Fluorophores

The actual use of phase-sensitive images to measure lifetime images is shown in Figure 22.4. The excitation is passed through four cuvettes, each containing a fluorophore with a different lifetime. DMSS has the shortest lifetime, smallest phase angle, and highest modulation. 9-Cyanoanthracene has the longest lifetime, largest phase angle, and smallest modulation. The phase-sensitive intensities at the various detector phase angles can be fit to determine the phase angle and modulation of the emission. Since the phase-sensitive intensities were measured using an imaging detector, the data can be used to create an image when the contrast or color is based on phase angle, modulation or apparent lifetime.

## 22.2. LIFETIME IMAGING OF CALCIUM USING QUIN-2

### 22.2.1. Determination of Calcium Concentration from Lifetime

Lifetime imaging depends on the use of a probe that changes lifetime in response to a change in conditions. Imaging of calcium concentrations requires a probe that displays calcium-dependent lifetimes. Figure 22.5 shows non-imaging frequency-domain data for the calcium probe Quin-2 with various concentrations of calcium.<sup>6</sup> The frequency response shifts dramatically to lower frequencies at

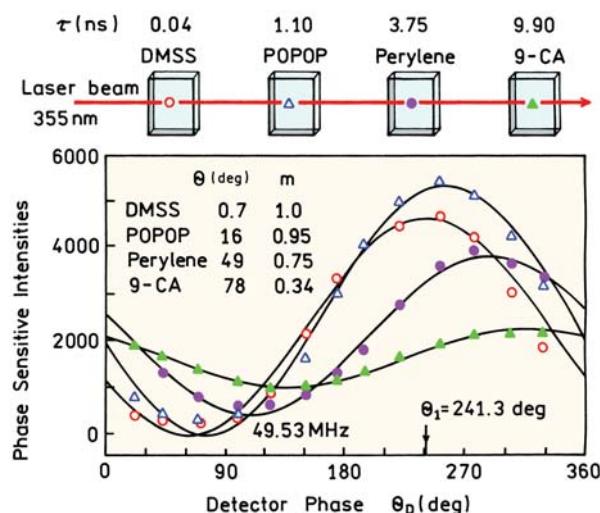


**Figure 22.4.** Phase-sensitive intensities of standard fluorophores at various detector phase angles. The decay times from left to right are 0.04 (○), 1.10 (Δ), 3.75 (●), and 9.90 ns (▲). The modulation frequency was 49.53 MHz. DMSS, 4-dimethylamino- $\omega$ -methylsulfonyl-*trans*-styrene; 9-CA, 9-cyanoanthracene; POPOP, *p*-bis[2-(5-phenyl-oxazolyl)]benzene.  $\theta_1$  is the arbitrary phase angle of the incident light.

higher concentrations of calcium. At intermediate calcium concentrations near 8 nM the decays are multi-exponential, as can be seen from the shape of the frequency response. The data were fit globally to two lifetimes:  $\tau_1 = 1.38$  ns and  $\tau_2 = 11.58$  ns, with amplitudes that depend on the calcium concentration.

The data in Figure 22.5 can be used to create a calibration curve for calcium (Figure 22.6). These curves can be used to determine the concentration of calcium from the phase or modulation of the emission. It is important to rec-

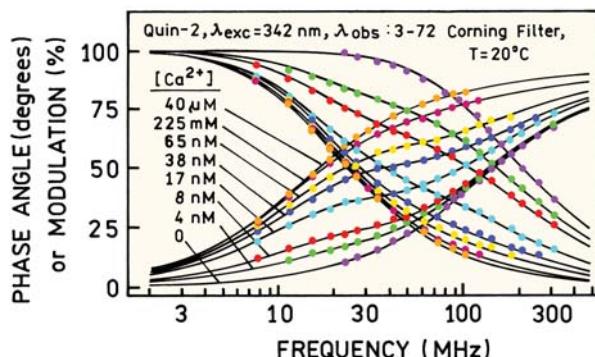


**Figure 22.5.** Frequency-domain intensity decays for Quin-2 with varying concentrations of calcium. The data were fit globally with two lifetimes  $\tau_1 = 1.38$  ns and  $\tau_2 = 11.58$  ns.

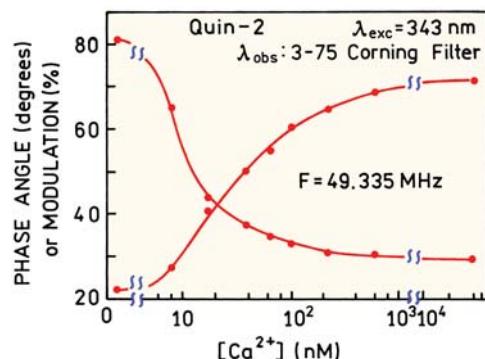


**Figure 22.6.** Dependence of the phase angle and modulation of Quin-2 on the calcium concentration. Revised from [7].

ognize that the calcium concentrations can be determined using measurements at a single modulation frequency without resolution of the multi-exponential decay. This is because there is always a single phase angle and modulation of the emission irrespective of the complexity of the decay. Of course, a different calibration curve would be obtained using different modulation frequencies.

### 22.2.2. Lifetime Images of Cos Cells

Once a calibration curve is known the phase and modulation values can be used to determine calcium concentrations in cells. Fluorescence intensity images for Quin-2 in three Cos cells are shown in Figure 22.7. The intensity of Quin-2 is highly variable in different regions of the cells (top). The intensity images alone do not indicate if the intensity differences are due to differences in Quin-2 concentrations or to different calcium concentrations. Phase-sensitive images were obtained using the apparatus shown in Figure 22.2 and the phase angles determined at each location in the image. In contrast to the intensities the phase angles are more constant throughout the cells (Figure 22.7, middle). The phase angle image can be converted to a calcium concentration image (bottom) using a calibration curve like that in Figure 22.6. The calcium concentration appears higher in the periphery of the cells than near the center. The regions of lower calcium concentration correspond to regions of lower phase angles. The calcium concentration images are more constant than are the intensity images. This result indicates that most of the intensity variations seen in Figure 22.7 are due to differences in Quin-2 concentrations rather than locally different calcium concentrations. The use of FLIM allowed the calcium concentrations to be determined with-

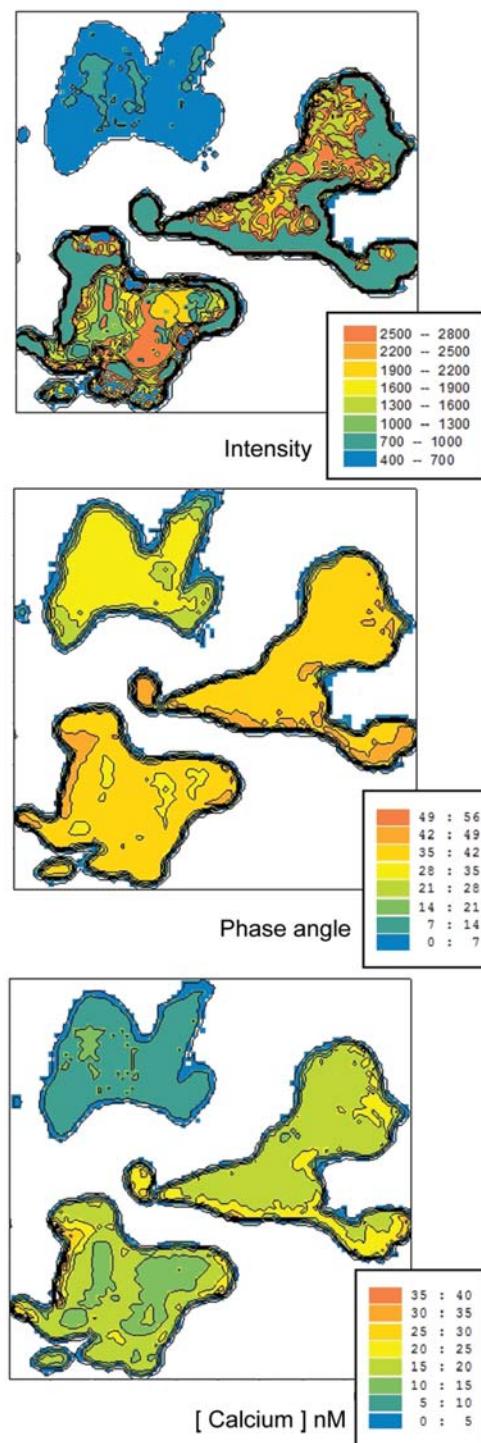


**Figure 22.7.** Fluorescence imaging of Cos cells labeled with Quin-2. Top, intensity. Middle, phase angle image at 45.53 MHz. Bottom, calcium concentration image. The calibration curve used to calculate the calcium concentration is different from Figure 22.6, and included a photobleaching correction. Reprinted with permission from [7].

out knowledge of the local probe concentrations within the cell.

### 22.3. EXAMPLES OF WIDE-FIELD FREQUENCY-DOMAIN FLIM

Since the early use of FLIM for calcium imaging there has been a dramatic increase in the use of FLIM.<sup>8–13</sup> Several methods can be used to create lifetime images, including time-domain, frequency-domain, and gated methods. A number of laboratories have constructed wide-field frequency-domain FLIM instruments.<sup>14–19</sup> Additional references on FLIM methods and applications are listed in the section entitled Additional Reading on Fluorescence-Lifetime Imaging Microscopy near the end of the chapter.

#### 22.3.1. Resonance Energy-Transfer FLIM of Protein Kinase C Activation

Wide-field frequency-domain FLIM can be used to study the activation of intracellular proteins. One example is the

use of FLIM to study protein phosphorylation in response to stimuli.<sup>20–22</sup> Figure 22.8 shows images of Cos7 cells that expressed GFP-labeled protein kinase C (PKC). The intensity images in the top panels show the locations of GFP-labeled PKC. This protein is phosphorylated upon activation by the tumor-producing substance phorbol myristoyl acetate (PMA). The cells were microinjected with Cy3.5-labeled IgG that is specific for the phosphorylated epitope of PKC. Binding of the labeled antibody to PKC is expected to reduce the lifetime of the GFP label by resonance energy transfer to the acceptor Cy3.5.

The lower panels in Figure 22.8 show the lifetime images of the three cells at various times. Initially the GFP lifetimes are the same in all the cells and constant within the cells. At later times the GFP lifetime in the central cell decreases. All the cells were treated with PMA, and only the central cell was injected with Cy3.5-labeled IgG specific for phosphorylated PKC. The lifetime of GFP-PKC in the central cell decreases because of energy transfer to the Cy 3.5-labeled antibody. These images are not confocal so it is difficult to know if phosphorylated PKC appears uniformly throughout the cell or is localized near the membrane.

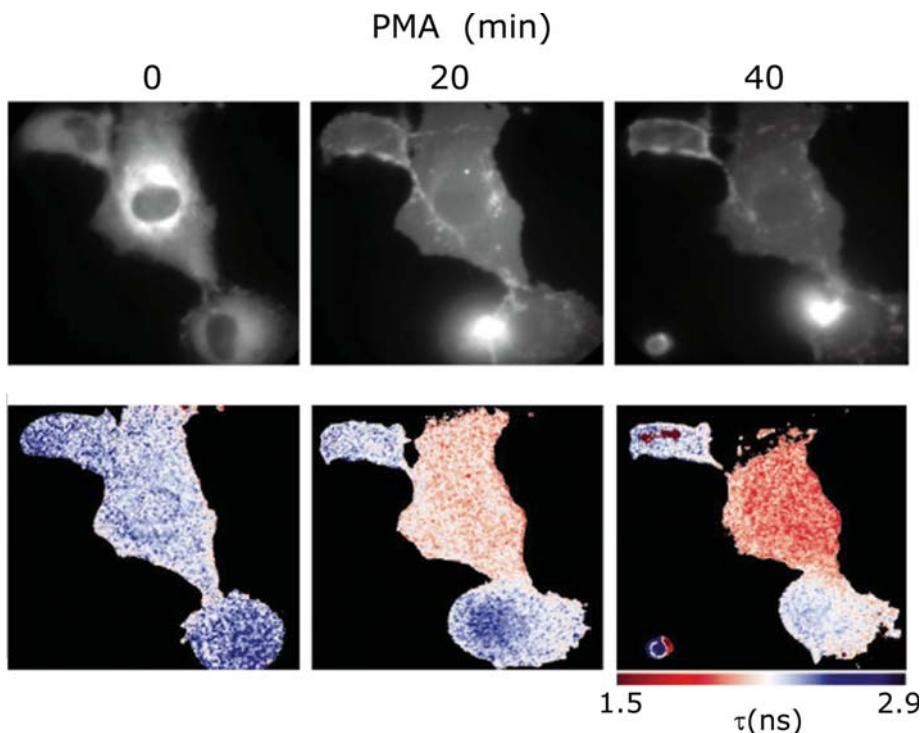


**Figure 22.8.** Activation of lipid/calcium-dependent protein kinase C (PKC) in Cos7 cells. The top panels show the intensity images of GFP-tagged PKC. All the cells were treated with phorbol myristoyl acetate (PMA). The lower panels show the GFP-lifetime images the central cell was injected with Cy3.5-IgG specific for the phosphorylated epitope of PKC. Reprinted with permission from [22].

The images in Figure 22.8 show an advantage of using lifetime images as compared to intensity images. In principle RET from GFP to Cy3.5 could have been measured using intensity ratios of GFP to Cy 3.5. However, the ratios would not allow the extent of RET to be calculated without knowledge of the local concentrations of unbound acceptor. The donor lifetime is not affected by unbound acceptor and thus reflects the extent of acceptor binding to GFP-PKC and the extent of its phosphorylation. The donor-to-acceptor intensity ratio would be dependent on the concentration of unbound acceptor.

### 22.3.2. Lifetime Imaging of Cells Containing Two GFPs

GFP-labeled proteins are widely used in cellular imaging. Because of the need to monitor more than a single intracellular protein a number of GFP mutants have been developed with different absorption and emission wavelengths. However, the wide absorption and emission spectra of the GFPs

limit the number that can be observed in a single experiment. One approach to distinguishing more GFPs is to use lifetimes instead of or in addition to wavelength to identify the GFP.<sup>23</sup>

The possibility of resolving multiple GFPs using lifetimes is shown in Figure 22.9. These panels show Vero cells that are expressing more than one type of GFP. All the cells express YFP5 in the cytoplasm that displays a lifetime near 3.4 ns. The cells also express GFP5 that displays a lifetime near 2.2 ns. In the upper left GFP5 is located near the golgi. In the other three cells GFP5 is localized in the nucleus. The presence and location of GFP5 can be seen as a decrease in lifetime in these regions of the cell. This effect is most obvious for the cell in case YFP5 was not present in the nucleus (lower right), so that the emission is mostly due to GFP5, which has a shorter lifetime. These results show how FLIM can be used to resolved similar molecules in cells if the lifetimes are different.

### 22.4. WIDE-FIELD FLIM USING A GATED-IMAGE INTENSIFIER

Another approach to lifetime imaging is analogous to the pulse sampling method described in Section 4.8.1. Instead of sinusoidally modulating the gain of the image intensifier, the intensifier is gated on for short periods of time (Figure 22.10). The intensity images collected at various time delays are used to calculate the lifetime at each pixel.<sup>24–35</sup> The time intervals can be non-overlapping, as shown in Figure 22.10, or overlapping to provide a larger signal in each image. Gated-image intensifiers are commercially available

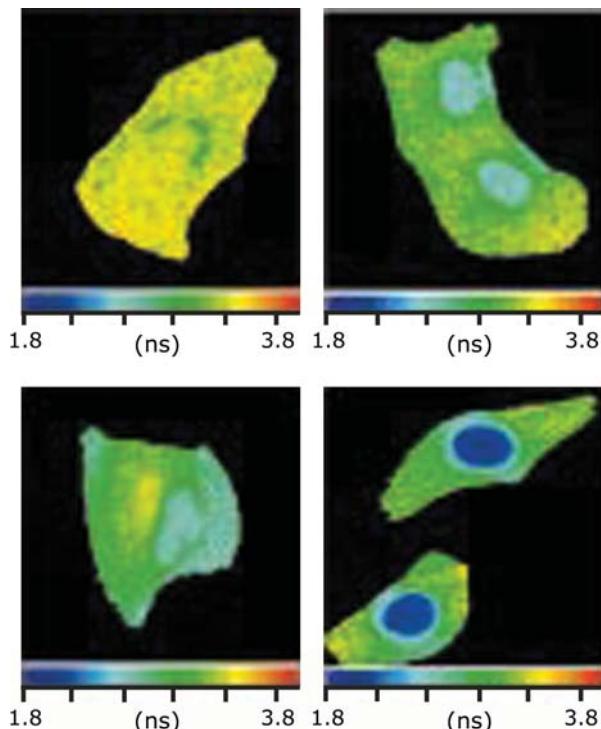


**Figure 22.9.** Lifetime images of Vero cells expressing two GFPs. All cells express YFP5 ( $\tau = 3.4$  ns) in the cytoplasm. The cells in the upper right and lower left express GFP5 localized in the nucleus. The cell in the lower right does not have YFP5 in the nucleus so that only the shorter lifetime GFP5 contributes to the signal. Reprinted with permission from [23].

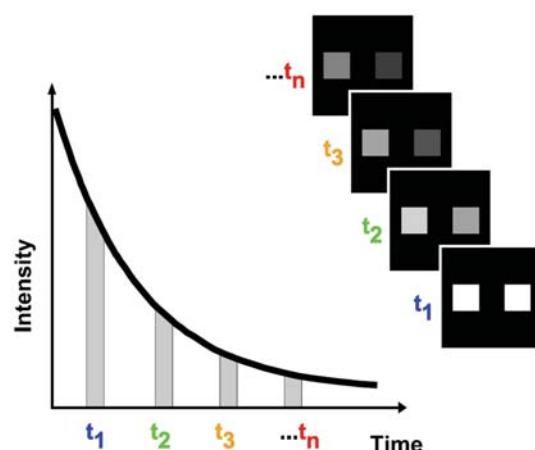


**Figure 22.10.** Schematic of FLIM using a gated-image intensifier. Reprinted with permission from [35].

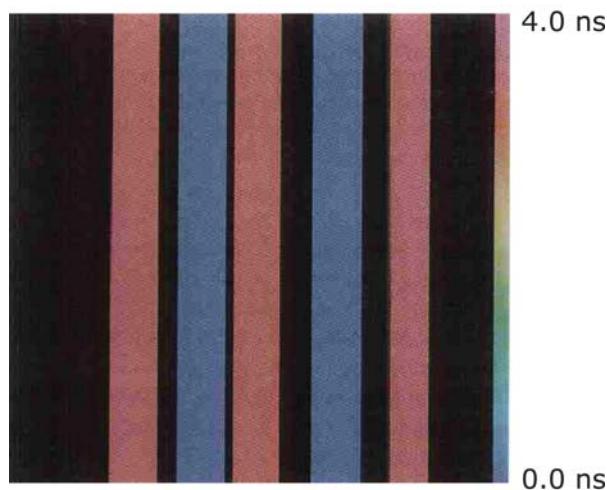


**Figure 22.11.** FLIM of small containers of Coumarin-314 ( $\tau = 3.46$  ns) and 2-(*p*-dimethylamino-styryl)-pyridylmethyl iodide (DASPI,  $\tau = 143$  ps) in a 50:50 mixture of water and glycerol. Reprinted with permission from [35].

and in the past several years have become fast enough for nanosecond FLIM.<sup>36–38</sup>

The lifetime images obtained using a gated-image intensifier can be relatively free of noise. Figure 22.11 shows lifetime images of small samples of Coumarin-314 ( $\tau = 3.46$  ns) and of DASPI ( $\tau = 143$  ps). The images clearly distinguish the two lifetimes, and the lifetime is constant in each solution. FLIM with a gated intensifier has also been applied to cellular imaging. In this case the time windows for gating were 2 ns wide and spaced 1 ns apart.<sup>28</sup> The gated time intervals were overlapped in time. Figure 22.12 shows lifetime images of protein dimerization in mouse pituitary cells. These cells expressed the transcription factor EBP $\Delta$ 224, which was fused with GFP. Two fusion proteins of this transcription factor were expressed, one with CFP and another with YFP, which served as a donor–acceptor pair. The presence of dimers of EBP $\Delta$ 224 is seen around the periphery of the cell as a decreased lifetime for the donor.

## 22.5. LASER SCANNING TCSPC FLIM

An alternative to wide-field microscopy is laser scanning microscopy (LSM). When using LSM the images are created by sequentially measuring all the pixels in an image.<sup>39</sup> This is accomplished by scanning a focused laser beam across the sample and measuring the intensities at each position. LSM is usually performed using confocal optics to reject out-of-focus fluorescence. LSM is also performed

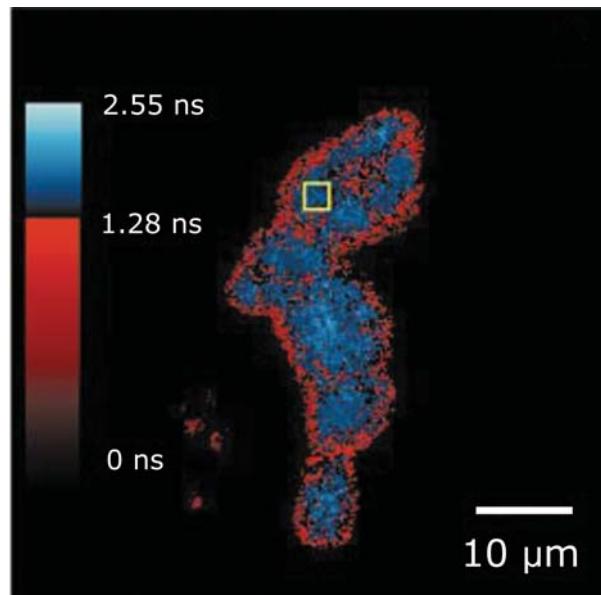


**Figure 22.12.** FLIM of small containers of Coumarin-314 ( $\tau = 3.46$  ns) and 2-(*p*-dimethylamino-styryl)-pyridylmethyl iodide (DASPI,  $\tau = 143$  ps) in a 50:50 mixture of water and glycerol. Reprinted with permission from [35].

using multiphoton excitation, in which case out-of-plane fluorescence is not excited and the confocal pinholes are not needed. LSM offers many opportunities for lifetime imaging because of the well-developed technology for time-resolved measurements using point detectors such as PMTs and APDs.

Figure 22.13 shows a schematic for TCSPC when using a laser scanning microscope. The basic idea is to perform the TCSPC measurements while the laser scans across the sample. At each point in the image the instrument measures a decay curve. This is possible because the repetition rate of the laser is usually high enough that many excitation pulses arrive during the dwell time at each pixel. For example, if the dwell time is 20  $\mu$ s and the laser repetition rate is 80 MHz, then 1600 pulses arrive at each pixel while scanning a single image. The data are then stored in a three-dimensional matrix. The *x*- and *y*-axes indicate the position in the sample (Figure 12.13). The third dimension represents the arrival times of the photons associated with each pixel in the image.

The principle of TCSPC FLIM is straightforward but its implementation is complex.<sup>41–52</sup> Specialized hardware and software is needed to keep track of the time between the laser pulses and detected photons, and the position of the laser beam on the sample. Fortunately, these capabilities are

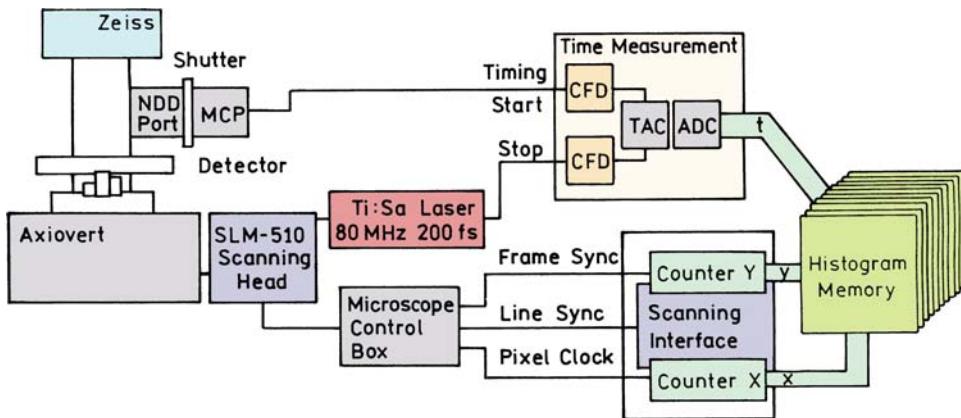


Figure 22.13. Schematic for FLIM using TCSPC. Revised from [40].

available commercially and can be added to laser scanning microscopes. TCSPC appears to have many advantages for FLIM. Since individual photons are counted the measurements provide high efficiency. TCSPC makes use of all the photons reaching the detector. FLIM using a gated-image intensifier only makes use of a small fraction of the photons that arrive while the gate is open. Frequency-domain FLIM uses more of the available photons than gating, but the duty cycle is 50% or less. Using all the available photons is an important feature in fluorescence microscopy because the fluorophores are being photobleached during observation.

The total time to acquire a lifetime image depends on the photon count rate and the desired accuracy in the decay times. A single-exponential lifetime can be estimated with 10% accuracy with 185 photons.<sup>51</sup> At a count rate of  $10^6$

photons/s acquisition of 200 photons requires 0.2 ms and data for a  $128 \times 128$  lifetime image can be acquired in 3.3 s. It is easily possible to collect 200 photons with a dwell time of 0.2 ms because there will be 16,000 excitation pulses. The time needed to acquire an FLIM image increases dramatically if it is necessary to resolve a double exponential decay at each pixel. Resolution of a double-exponential decay to an accuracy of 10% requires 10,000 to 100,000 photons.<sup>51</sup> Hence the time to acquire the data can become longer than practical with biological samples.

Presently available technology for TCSPC imaging goes beyond that shown in Figure 22.14. Many laser scanning microscopes have multiple detectors for emission at different wavelengths. Multiple detectors are useful because cells are often labeled with more than one fluo-

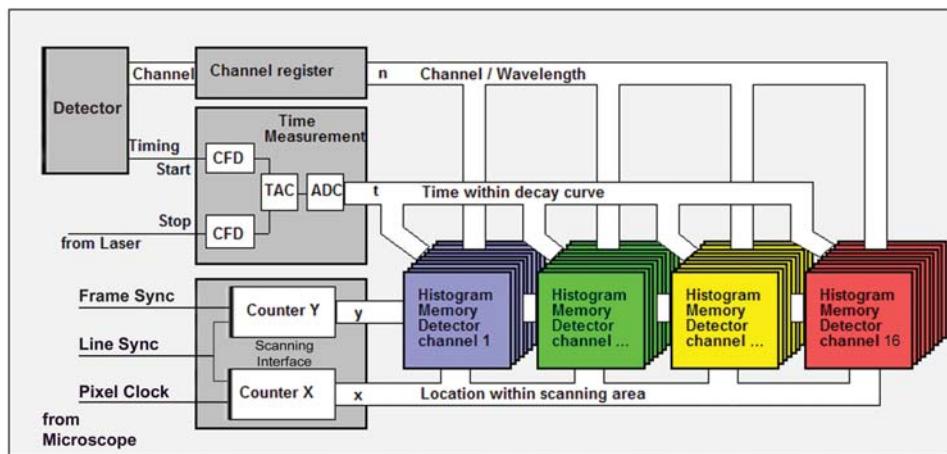
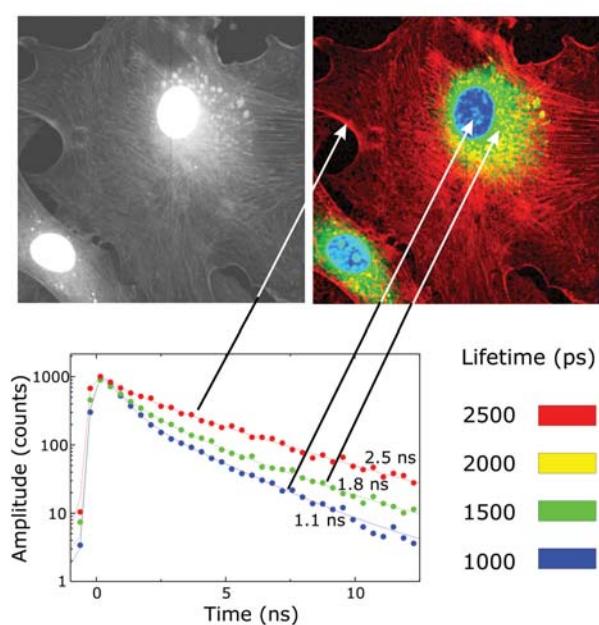


Figure 22.14. Schematic for multi-wavelength TCSPC lifetime imaging. Reprinted with permission from [49].



**Figure 22.15.** Intensity (left) and lifetime image (right) of bovine artery endothelial cells. The nuclei were stained with DAPI for DNA (blue), F-actin was stained with Bodipy FL-phallacidin (red), and the mitochondria were stained with MitoTracker Red CMX Ros (green). Two-photon excitation of 800 nm. Courtesy of Dr. Axel Bergman, Becker & Hickl GmbH.

rophores, some ion indicators are wavelength-ratiometric, and donor and acceptor intensities can be measured simultaneously.

### 22.5.1. Lifetime Imaging of Cellular Biomolecules

FLIM can yield dramatic images showing the locations of different biomolecules within cells. Figure 22.15 shows intensity and lifetime images of bovine artery endothelial cells stained with three fluorophores. Nucleic acids were stained with DAPI, F-actin was stained with Bodipy FL-phallacidin, and the mitochondria were stained with Mito-Tracker Red CMX Ros. The intensity image shows regions of the cell with different brightness but does not distinguish between the three fluorophores. TCSPC measurements in each region of the cell showed that DAPI decayed with a lifetime of 1.1 ns, Bodipy-FL displayed a lifetime of 2.5 ns, and MitoTracker CMX Ros displayed a lifetime of 1.8 ns. These lifetimes were used to assign pseudocolors to each of the fluorophores. The lifetime image clearly resolved the locations of the probes based on their lifetimes.

### 22.5.2. Lifetime Images of Amyloid Plaques

Alzheimer's disease is associated with the accumulation of plaques composed primarily of an amyloid peptide that forms  $\beta$ -sheets. Formation of the plaques depends on the presence of presenilin 1 (PS1), which contains part of the enzymatic activity needed for plaque formation. Lifetime imaging was used to determine the location of PS1 in Chinese hamster ovary (CHO) cells that expressed this protein. The cells were stained with fluorescein-labeled antibodies that bound closely to PS1. The lifetime of these antibodies was mostly constant throughout the cell (Figure 22.16). The cells were then exposed to Cy3-labeled antibodies that also bound closely to PS1 and serve as an acceptor for FITC. The presence of the Cy3 acceptor resulted in a decrease in the lifetime of the FITC donor.<sup>53</sup> The mean lifetime of FITC changed from about 2.6 ns in the absence of acceptor to about 1.6 ns in the presence of acceptor. These results show that RET and laser scanning FLIM can be used to detect local proximity of proteins within cells.

### 22.6. FREQUENCY-DOMAIN LASER SCANNING MICROSCOPY

Laser scanning microscopy can also be used with frequency-domain measurements for lifetime imaging.<sup>54–57</sup> The instrumentation is similar to that shown in Figure 22.13

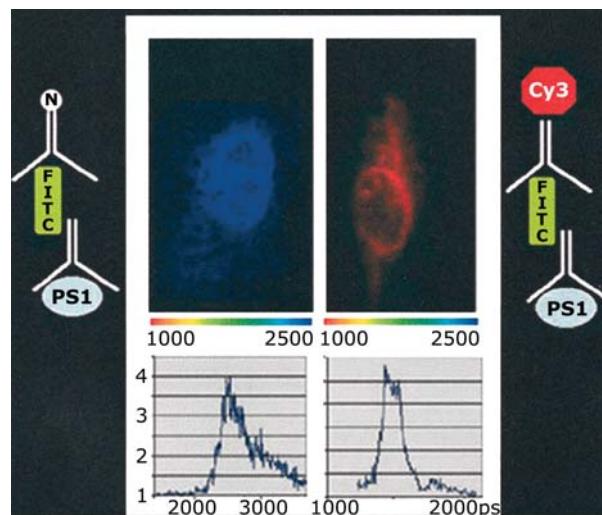


**Figure 22.16.** TCSPC lifetime images of CHO cells that express presenilin 1. The cell on the left was exposed to FITC-labeled antibody that bound near PS1. The cell on the right contained both FITC and Cy3-labeled antibodies near PS1. Revised from [53].

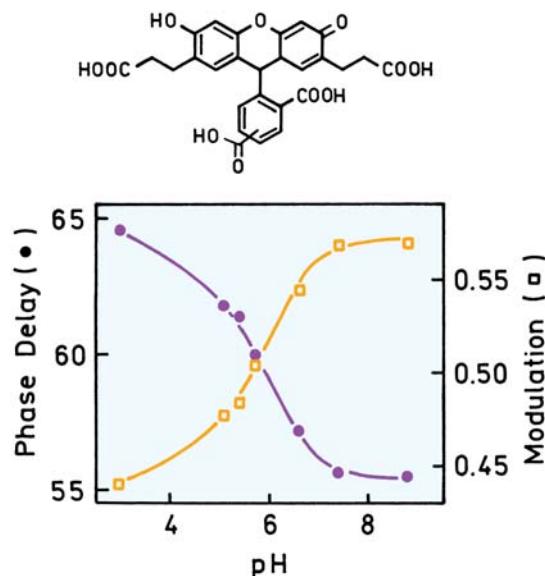


**Figure 22.17.** pH-dependent phase and modulation values of BCECF for 820 nm excitation with a Ti:sapphire laser, 80 MHz. Revised from [57].

except that the phase and modulation of the emission is measured rather than using TCSPC. An example of such measurements is lifetime imaging of the stratum corneum, which is the outermost layer of the skin. The lifetime probe was BCECF,<sup>57</sup> which displays a pH-dependent change in lifetime. This change was used to obtain a calibration curve of phase and modulation versus pH (Figure 22.17). The stratum corneum was imaged using two-photon excitation of BCECF at 820 nm. It was possible to obtain images at various depths in the stratum corneum because the long wavelength used for two-photon excitation can penetrate tissues and two-photon excitation is intrinsically confocal due to localized excitation at the focal point of the laser. The images of BCECF at a depth of 6.8 microns in the stratum corneum are shown in Figure 22.18. The intensity image shows that BCECF is present in the cells and in the interstitial spaces. The modulation is higher and the lifetime is lower in the interstitial spaces. These data allow the pH to be imaged within and around the keratinocytes. This result shows the ability of FLIM to provide quantitative molecular imaging using minimal perturbation of tissues.

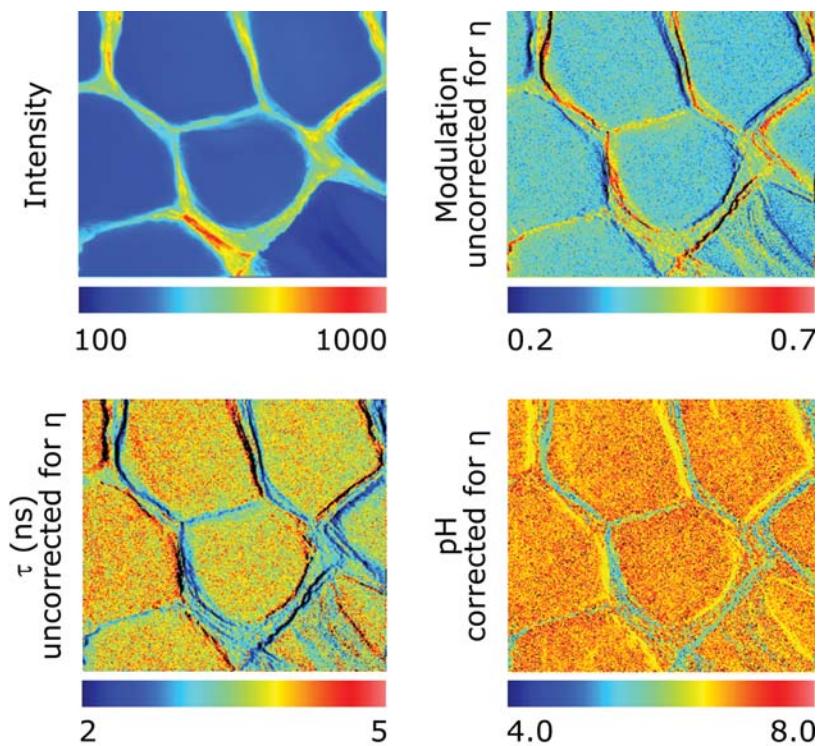


**Figure 22.18.** pH lifetime imaging of the skin stratum corneum at a depth of 6.8 microns using BCECF. See Figure 22.17.  $\eta$  is refractive index of the surrounding environment. Reprinted with permission from [57]. Images courtesy of Dr. Kerry M. Hanson from the University of Illinois at Urbana-Champaign.

## 22.7. CONCLUSIONS

FLIM is a robust method for molecular imaging that can be accomplished using several approaches, some of which are listed in the section entitled Additional Reading on Fluorescence-Lifetime Imaging Microscopy near the end of this chapter. FLIM can be used for imaging of ions, biomolecule proximity, and conditions that result in a change in the lifetime of the fluorophore. The instrumentation of FLIM is becoming simpler and less expensive, and can be created using modest modifications of existing instruments. The use of FLIM and the range of its applications is likely to expand greatly with the near future.

## REFERENCES

1. Lakowicz JR, Berndt KW. 1991. Lifetime-selective fluorescence imaging using an rf phase-sensitive camera. *Rev Sci Instrum* **62**(7): 1727–1734.
2. Lakowicz JR, Szmacinski H, Nowaczyk K, Berndt BW, Johnson ML. 1992. Fluorescence lifetime imaging. *Anal Biochem* **202**:316–330.
3. Szmacinski H, Lakowicz JR, Johnson ML. 1994. Fluorescence lifetime imaging microscopy: homodyne technique using high-speed gated image intensifier. *Methods Enzymol* **240**:723–748.
4. Lakowicz JR, Szmacinski H, Nowaczyk K, Berndt KW, Johnson ML. 1993. Fluorescence lifetime imaging and application to Ca<sup>2+</sup> imaging. In *Fluorescence spectroscopy: new methods and applications*, chap. 10. Ed OS Wolfbeis. Springer-Verlag, New York.
5. Veselova TV, Cherkasov AS, Shirokov VI. 1970. Fluorometric method for individual recording of spectra in systems containing two types of luminescent centers. *Opt Spectrosc* **29**:617–618.
6. Lakowicz JR, Szmacinski H, Nowaczyk K, Johnson ML. 1992. Fluorescence lifetime imaging of calcium using Quin-2. *Cell Calcium* **13**:131–147.
7. Lakowicz JR, Szmacinski H, Nowaczyk K, Johnson ML. 1994. Fluorescence lifetime imaging of intracellular calcium in COS cells using Quin-2. *Cell Calcium* **15**:7–27.
8. Gerritsen H, Draaijer A, Lakowicz JR. 1997. Introduction, second international lifetime imaging meeting, Utrecht, the Netherlands, June 14, 1996. *J Fluoresc* **7**(1):1–98.
9. Draaijer A, Sanders R, Gerritsen HC. 1995. Fluorescence lifetime imaging, a new tool in confocal microscopy. In *Handbook of biological confocal microscopy*, pp. 491–505. Ed JB Pawley. Plenum Press, New York.
10. Herman B, Wang XF, Wodnicki P, Periasamy A, Mahajan N, Berry G, Gordon G. 1999. Fluorescence lifetime imaging microscopy. In *Applied fluorescence in chemistry, biology and medicine*, pp. 491–507. Ed W Rettig, B Strehmel, S Schrader, H Seifert. Springer, Berlin.
11. Clegg RM, Holub O, Gohlke C. 2003. Fluorescence lifetime-resolved imaging: measuring lifetimes in an image. *Methods Enzymol* **360**:509–542.
12. Centonze VE, Sun M, Masuda A, Gerritsen H, Herman B. 2003. *Methods Enzymol* **360**:542–560.
13. Chen Y, Mills JD, Periasamy A. 2003. Protein localization in living cells and tissues using FRET and FLIM. *Differentiation* **71**:528–541.
14. Gadella TWJ, Jovin TM, Clegg RM. 1993. Fluorescence lifetime imaging microscopy (FLIM): spatial resolution of microstructures on the nanosecond time scale. *Biophys Chem* **48**:221–239.
15. Gadella TWJ, van Hoek A, Visser AJWG. 1997. Construction and characterization of a frequency-domain fluorescence lifetime imaging microscopy system. *J Fluoresc* **7**(1):35–43.
16. Birmingham JJ. 1997. Frequency-domain lifetime imaging methods at unilever research. *J Fluoresc* **7**(1):45–54.
17. Squire A, Verveer PJ, Bastiaens PIH. 2000. Multiple frequency fluorescence lifetime imaging microscopy. *J Microsc* **197**(pt.2):136–149.
18. Clayton AHA, Hanley QS, Arndt-Jovin DJ, Subramaniam V, Jovin TM. 2002. Dynamic fluorescence anisotropy imaging microscopy in the frequency domain (rFLIM). *Biophys J* **83**(3):1631–1649.
19. Clegg RM, Feddersen B, Gratton E, Jovin TM. 1992. Time-resolved imaging fluorescence microscopy. *Proc SPIE* **1640**:448–460.
20. Wouters FS, Bastiaens PIH. 1999. Fluorescence lifetime imaging of receptor tyrosine kinase activity in cells. *Curr Biol* **9**:1127–1130.
21. Verveer PJ, Squire A, Bastiaens PIH. 2001. Improved spatial discrimination of protein reaction states in cells by global analysis and deconvolution of fluorescence lifetime imaging microscopy data. *J Microsc* **202**(3):451–456.
22. Bastiaens PIH, Squire A. 1999. Fluorescence lifetime imaging microscopy: spatial resolution of biochemical processes in the cell. *Trends Cell Biol* **9**:48–52.
23. Pepperkok R, Squire A, Geley S, Bastiaens PIH. 1999. Simultaneous detection of multiple green fluorescent proteins in live cells by fluorescence lifetime imaging microscopy. *Curr Biol* **9**:269–272.
24. Dowling K, Hyde SCW, Dainty JC, French PMW, Hares JD. 1997. 2-D fluorescence lifetime imaging using a time-gated image intensifier. *Opt Commun* **135**:27–31.
25. Oida T, Sako Y, Kusumi A. 1993. Fluorescence lifetime imaging microscopy (flimscopy). *Biophys J* **64**:676–685.
26. Schneckenburger H, Konig K, Dienersberger T, Hahn R. 1994. Time-gated microscopic imaging and spectroscopy in medical diagnosis and photobiology. *Opt Eng* **33**(8):2600–2605.
27. Straub M, Hell SW. 1998. Fluorescence lifetime three-dimensional microscopy with picosecond precision using a multifocal multiphoton microscope. *Appl Phys Lett* **73**(13):1769–1771.
28. Elangovan M, Day RN, Periasamy A. 2002. Nanosecond fluorescence resonance energy transfer-fluorescence lifetime imaging microscopy to localize the protein interactions in a single living cell. *J Microsc* **205**(1):3–14.
29. Sharman KK, Periasamy A, Ashworth H, Demas JN, Snow NH. 1999. Error analysis of the rapid lifetime determination method for double-exponential decays and new windowing schemes. *Anal Chem* **71**:947–952.
30. Vereb G, Jares-Erijman E, Selvin PR, Jovin TM. 1998. Temporally and spectrally resolved imaging microscopy of lanthanide chelates. *Biophys J* **74**:2210–2222.
31. Herman B, Wodnicki P, Kwon S, Periasamy A, Gordon GW, Mahajan N, Wang XF. 1997. Recent developments in monitoring cal-

- cium and protein interactions in cells using fluorescence lifetime microscopy. *J Fluoresc* **7**(1):85–91.
32. Schneckenburger H, Gschwend MH, Strauss WSL, Sailer R, Steiner R. 1997. Time-gated microscopic energy transfer measurements for probing mitochondrial metabolism. *J Fluoresc* **7**(1):3–10.
  33. Webb SED, Gu Y, Lévéque-Fort S, Siegel J, Cole MJ, Dowling K, Jones R, French PMW, Neil MAA, Juskaitis R, Sucharov LOD, Wilson T, Lever MJ. 2002. A wide-field time-domain fluorescence lifetime imaging microscopy with optical sectioning. *Rev Sci Instrum* **73**(4):1898–1907.
  34. Dowling K, Dayel MJ, Hyde SCW, French PMW, Lever MJ, Hares JD, Dymoke-Bradshaw AKL. 1999. High resolution time-domain fluorescence lifetime imaging for biomedical applications. *J Mod Opt* **46**(2):199–209.
  35. Cole MJ, Siegel J, Webb SED, Jones R, Dowling K, Dayel MJ, Parsons-Karavassis D, French PMW, Lever MJ, Sucharov LOD, Neil MAA, Juskaitis R, Wilson T. 2001. Time-domain whole-field fluorescence lifetime imaging with optical sectioning. *J Microsc* **203**(3):246–257.
  36. Kentech Instruments Ltd., Oxfordshire, UK. <http://www.kentech.co.uk>.
  37. LaVision Inc., Ypsilanti, Michigan. <http://www.lavision.de/products/cameras/picostar/picostar.htm>.
  38. Hamamatsu Corp. <http://usa.hamamatsu.com>.
  39. Diaspro A. 2002. *Confocal and two-photon microscopy foundations, applications, and advances*. Wiley-Liss, New Jersey, 56.
  40. Duncan RR, Bergmann A, Cousin MA, Apps DK, Shipston MJ. 2004. Multi-dimensional time-correlated single photon counting (TCSPC) fluorescence lifetime imaging microscopy (FLIM) to detect FRET in cells. *J Microsc* **215**(1):1–12.
  41. Becker & Hickl GmbH, Berlin. <http://www.becker-hickl.de>.
  42. Becker W, Hickl H, Zander C, Drexhage KH, Sauer M, Siebert S, Wolfrum J. 1999. Time-resolved detection and identification of single analyte molecules in microcapillaries by time-correlated single-photon counting (TCSPC). *Rev Sci Instrum* **70**(3):1835–1841.
  43. Becker W, Bergmann A. 2004. Multi-dimensional time-correlated single photon counting. In *Review in fluorescence 2005*. Ed CD Geddes, JR Lakowicz. Springer, New York.
  44. Becker W, Bergmann A, Hink MA, Konig K, Benndorf K, Biskup C. 2004. Fluorescence lifetime imaging by time-correlated single-photon counting. *Microsc Res Technol* **63**:58–66.
  45. Becker W, Bergmann A, Weiss G. 2002. Lifetime imaging with the Zeiss LSM-510. *Proc. SPIE* **4620**:30–35.
  46. Becker W, Bergmann A, Biscotti G, Koenig K, Riemann I, Kelbauskas L, Biskup C. 2004. High-speed FLIM data acquisition by time-correlated single photon counting. *Proc SPIE* **5323**:27–35.
  47. Becker W, Bergmann A, Biscotti G, Ruck A. 2004. Advanced time-correlated single photon counting technique for spectroscopy and imaging in biomedical systems. *Proc SPIE* **5340**:104–112.
  48. van der Oord CJR, de Grauw CJ, Gerritsen HC. 2001. Fluorescence lifetime imaging module LIMO for CLSM. *Proc SPIE* **4252**:119–123.
  49. Becker W, Bergmann A. 2002. Multi-wavelength TCSPC lifetime imaging. *Proc SPIE* **4620**:79–84.
  50. Becker W, Bergmann A, Konig K, Tirlapur U. 2001. Picosecond fluorescence lifetime microscopy by TCSPC imaging. *Proc SPIE* **4262**:414–419.
  51. Köllner M, Wolfrum J. 1992. How many photons are necessary for fluorescence-lifetime measurements? *Chem Phys Lett* **200**:199–204.
  52. Becker & Hickl GmbH, Berlin, Germany, <http://www.becker-hickl.de>, 2000. TCSPC adds a new dimension to 3D laser scanning microscopy. *Photonik* **3**:16–19.
  53. Berezhovska O, Ramdy P, Skich J, Wolfe MS, Bacska BJ, Hyman BT. 2003. Amyloid precursor protein associates with a nicastrin-dependent docking site on the presenilin 1- $\gamma$ -secretase complex in cells demonstrated by fluorescence lifetime imaging. *J Neurosci* **23**(11):4560–4566.
  54. Carlsson K, Liljeborg A. 1998. Simultaneous confocal lifetime imaging of multiple fluorophores using the intensity-modulated multiple-wavelength scanning (IMS) technique. *J Microsc* **191**(pt.2):119–127.
  55. Gratton E, Breusegem S, Sutin J, Ruan Q, Barry N. 2003. Fluorescence lifetime imaging for the two-photon microscope: time-domain and frequency-domain methods. *J Biomed Opt* **8**(3):381–390.
  56. Carlsson K, Liljeborg A, Andersson RM, Brismar H. 2000. Confocal pH imaging of microscopic specimens using fluorescence lifetimes and phase fluorometry: influence of parameter choice on system performance. *J Microsc* **119**(pt.2):106–114.
  57. Hanson KM, Behne MJ, Barry NP, Mauro TM, Gratton E, Clegg RM. 2002. Two photon fluorescence lifetime imaging of the skin stratum corneum pH gradient. *Biophys J* **83**:1682–1690.
  58. Molecular Probes product information FluoCels #1. <http://www.probes.com/servlets/product?item=14780>.

## ADDITIONAL READING ON FLUORESCENCE-LIFETIME IMAGING MICROSCOPY

### Applications of FLIM

- Calleja V, Ameer-Beg SM, Vojnovic B, Woscholski R, Downward J, Larijani B. 2003. Monitoring conformational changes of proteins in cells by fluorescence lifetime imaging microscopy. *Biochem J* **372**:33–40.
- Eliceiri KW, Fan C-H, Lyons GE, White JG. 2003. Analysis of histology specimens using lifetime multiphoton microscopy. *J Biomed Opt* **8**(3):376–380.
- Harpur AG, Wouters FS, Bastiaens PIH. 2001. Imaging FRET between spectrally similar GFP molecules in single cells. *Biotechnology* **19**: 167–169.
- Marriott G, Clegg RM, Arndt-Jovin DJ, Jovin TM. 1991. Time resolved imaging microscopy, phosphorescence and delayed fluorescence imaging. *Biophys J* **60**:1374–1387.
- Tadrous PJ, Siegel J, French PMW, Shousha S, Lalani E-N, Stamp GWH. 2003. Fluorescence lifetime imaging of unstained tissues: early results in human breast cancer. *J Pathol* **199**:309–317.
- van Zandvoort MAMJ, de Grauw CJ, Gerritsen HC, Broers JLV, oude Egbrink MGA, Ramaekers FCS, Slaaf DW. 2002. Discrimination of DNA and RNA in cells by a vital fluorescent probe: lifetime imaging of SYTO13 in healthy and apoptotic cells. *Cytometry* **47**:226–235.
- Vermeer JEM, Van Munster EB, Vischer NO, Gadella TWJ. 2004. Probing plasma membrane microdomains in cowpea protoplasts using lipidated GFP-fusion proteins and multimode FRET microscopy. *J Microsc* **214**(2):190–200.

### Frequency-Domain FLIM

- Clayton AHA, Hanley QS, Verveer PJ. 2004. Graphical representation and multicomponent analysis of single-frequency fluorescence lifetime imaging microscopy data. *J Microsc* **213**(1):1–5.
- Gadella TWJ, van Hoek A, Visser AJWG. 1997. Construction and characterization of a frequency-domain fluorescence lifetime imaging microscopy system. *J Fluoresc* **7**(1):35–43.
- Schneider PC, Clegg RM. 1997. Rapid acquisition, analysis, and display of fluorescence lifetime-resolved images for real-time applications. *Rev Sci Instrum* **68**(11):4107–4119.
- Squire A, Bastiaens PIH. 1998. Three-dimensional image restoration in fluorescence lifetime imaging microscopy. *J Microsc* **193**(1):36–49.
- Van Munster EB, Gadella TWJ. 2004. φFLIM: a new method to avoid aliasing in frequency-domain fluorescence lifetime imaging microscopy. *J Microsc* **213**(1):29–38.
- Verveer PJ, Squire A, Bastiaens PIH. 2000. Global analysis of fluorescence lifetime imaging microscopy data. *Biophys J* **78**:2127–2137.
- Wagnieres G, Mizeret J, Studzinski A, van den Bergh H. 1997. Frequency-domain fluorescence lifetime imaging for endoscopic clinical cancer photodetection: apparatus design and preliminary results. *J Fluoresc* **7**(1):75–83.

### Gated CCD FLIM

- Hartmann P, Ziegler W. 1996. Lifetime imaging of luminescent oxygen sensors based on all-solid-state technology. *Anal Chem* **68**:4512–4514.
- Mitchell AC, Wall JE, Murray JG, Morgan CG. 2002. Direct modulation of the effective sensitivity of a CCD detector: a new approach to time-resolved fluorescence imaging. *J Microsc* **206**(3):225–232.
- Mitchell AC, Wall JE, Murray JG, Morgan CG. 2002. Measurement of nanosecond time-resolved fluorescence with a directly gated interline CCD camera. *J Microsc* **206**(3):233–238.
- Morgan CG, Mitchell AC, Murray JG, Wall EJ. 1997. New approaches to lifetime-resolved luminescence imaging. *J Fluoresc* **7**(1):65–73.

### Novel FLIM Methods

- Dong CY, So PTC, French T, Gratton E. 1995. Fluorescence lifetime imaging by asynchronous pump-probe microscopy. *Biophys J* **69**:2234–2242.

### Oxygen Imaging

- Gerritsen HC, Sanders R, Draaijer A, Ince C, Levine YK. 1997. Fluorescence lifetime imaging of oxygen in living cells. *J Fluoresc* **7**(1):11–15.
- Holst G, Franke U, Grunwald B. 2002. Transparent oxygen optodes in environmental applications at fine scale as measured by luminescence lifetime imaging. *Proc SPIE* **4576**:138–148.
- Vinogradov SA, Lo L-W, Jenkins WT, Evans SM, Koch C, Wilson DF. 1996. Noninvasive imaging of the distribution in oxygen in tissue *in vivo* using near-infrared phosphors. *Biophys J* **70**:1609–1617.

### pH Imaging

- Lin H-J, Herman P, Lakowicz JR. 2003. Fluorescence lifetime-resolved pH imaging of living cells. *Cytometry* **52A**:77–89.

- Sanders R, Draaijer A, Gerritsen HC, Houpt PM, Levine YK. 1995. Quantitative pH imaging in cells using confocal fluorescence lifetime imaging microscopy. *Anal Biochem* **227**:302–308.

### Position Sensitive Detection

- Charbonneau S, Allard LB, Young JF, Dyck YG, Kyle BJ. 1992. Two-dimensional time-resolved imaging with 100-ps resolution using a resistive anode photomultiplier tube. *Rev Sci Instrum* **63**(11):5315–5319.
- Emiliani V, Sanvitto D, Tramier M, Piolot T, Petrasek Z, Kemnitz K, Durieux C, Coppey-Moisan M. 2003. Low-intensity two-dimensional imaging of fluorescence lifetimes in living cells. *Appl Phys Lett* **83**(12):2471–2473.
- Kemnitz K, Pfeifer L, Paul R, Coppey-Moisan M. 1997. Novel detectors for fluorescence lifetime imaging on the picosecond time scale. *J Fluoresc* **7**(1):93–98.
- Suhling K, Hungerford G, Airey RW, Morgan BL. 2001. A position-sensitive photon event counting detector applied to fluorescence imaging of dyes in sol-gel matrices. *Meas Sci Technol* **12**:131–141.
- Tramier M, Gautier I, Piolot T, Ravalet S, Kemnitz K, Coppey J, Durieux C, Mignotte V, Coppey-Moisan M. 2002. Picosecond-hetero-FRET microscopy to probe protein–protein interactions in live cells. *Biophys J* **83**:3570–3577.

### Reviews

- Cubeddu R, Comelli D, D'Andrea C, Taroni P, Valentini G. 2002. Time-resolved fluorescence imaging in biology and medicine. *J Phys D: Appl Phys* **35**:R61–R76.
- Gratton E, vandeVen MJ. 1995. Laser sources for confocal microscopy. In *Handbook of biological confocal microscopy*, pp. 61–97. Ed JB Pawley. Plenum Press, New York.
- Periasamy A, Wang XF, Wodnicki P, Gordon GW. 1995. High-speed fluorescence microscopy: lifetime imaging in the biomedical sciences. *J Microsc Soc Am* **1**(1):13–23.
- Wang XF, Periasamy A, Wodnicki P, Gordon GW, Herman B. 1996. Time-resolved fluorescence lifetime imaging microscopy: instrumentation and biomedical applications. In *Fluorescence imaging spectroscopy and microscopy*, Chemical Analysis Series, Vol. 137, pp. 313–350. Ed XF Wang, B Herman. John Wiley & Sons, New York.

### Streak Camera FLIM

- Krishnan RV, Saitoh H, Terada H, Centonze VE, Herman B. 2003. Development of a multiphoton fluorescence lifetime imaging microscopy system using a streak camera. *Rev Sci Instrum* **74**(5):2714–2721.
- Krishnan RV, Masuda A, Centonze VE, Herman B. 2003. Quantitative imaging of protein–protein interactions by multiphoton fluorescence lifetime imaging microscopy using a streak camera. *J Biomed Opt* **8**(3):362–367.

### TCSPC FLIM

- Ameer-Beg SM, Barber PR, Hodgkiss RJ, Locke RJ, Newman RG, Tozer GM, Vojnovic B, Wilson J. 2002. Application of multiphoton steady

- state and lifetime imaging to mapping of tumor vascular architecture *in vivo*. *Proc SPIE* **4620**:85–95.
- Biskup C, Kelbauskas L, Zimmer T, Benndorf K, Bergmann A, Becker W, Ruppersberg JP, Stockklauser C, Klocker N. 2004. Interaction of PSD-95 with potassium channels visualized by fluorescence lifetime-based resonance energy transfer imaging. *J Biomed Opt* **9**(4):753–759.
- Eliceiri KW, Fan C-H, Lyons GE, White JG. 2003. Analysis of histology specimens using lifetime multiphoton microscopy. *J Biomed Opt* **8**(3):376–380.
- Jakobs S, Subramaniam V, Schonle A, Jovin TM, Hell SW. 2000. EGFP and DsRed expressing cultures of *Escherichia coli* imaged by confocal, two-photon and fluorescence lifetime microscopy. *FEBS Lett* **479**:131–135.
- Konig K, Riemann I. 2003. High-resolution multiphoton tomography of human skin with subcellular spatial resolution and picosecond time resolution. *J Biomed Opt* **8**(3):432–439.
- Philip J, Carlsson K. 2003. Theoretical investigation of the signal-to-noise ratio in fluorescence lifetime imaging. *J Opt Soc Am A* **20**(2):368–379.
- Soloviev VY, Wilson DF, Vinogradov SA. 2004. Phosphorescence lifetime imaging in turbid media: the inverse problem and experimental image reconstruction. *Appl Opt* **43**(3):564–574.

### Time-Gated FLIM

- De Grauw CJ, Gerritsen HC. 2001. Multiple time-gated module for fluorescence lifetime imaging. *Appl Spectrosc* **55**(6):670–678.
- Gerritsen HC, Asselbergs MAH, Agronskaia AV, Van Sark WGJHM. 2002. Fluorescence lifetime imaging scanning microscopes: acquisition speed, photon economy and lifetime resolution. *J Microsc* **206**(3):218–224.
- Sytsma J, Vroom JM, De Grauw CJ, Gerritsen HC. 1998. Time-gated fluorescence lifetime imaging and microvolume spectroscopy using two-photon excitation. *J Microsc* **191**(1):39–51.

### Theory

- Carlsson K, Philip J. 2002. Theoretical investigation of the signal-to-noise ratio for different fluorescence lifetime imaging techniques. *Proc SPIE* **4622**: 70–73.
- Hanley QS, Subramaniam V, Arndt-Jovin DJ, Jovin TM. 2001. Fluorescence lifetime imaging: multi-point calibration, minimum resolvable differences, and artifact suppression. *Cytometry* **43**:248–260.

### PROBLEMS

- P22.1. Figures 22.15 and 22.19 show images of the same type of cells stained with the same three fluorophores. Explain the different colors of the images. Do the legends correctly identify each fluorophore?

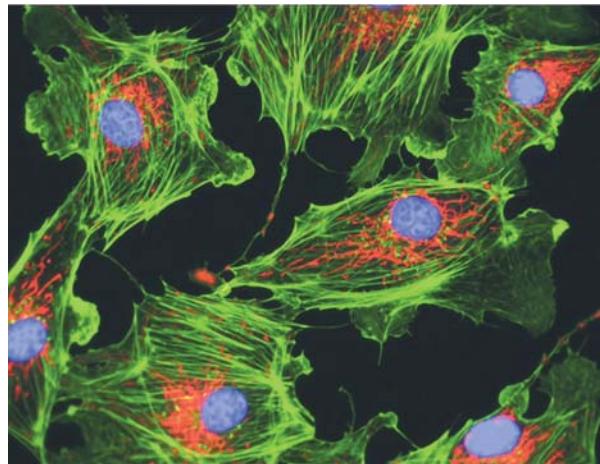


**Figure 22.19.** Fluorescence intensity images of bovine pulmonary artery endothelial cells stained with DAPI, Bodipy FL-phallacidin, and MitoTracker Red CMXRos. Multi-exposure image obtained with DAPI, fluorescein, and Texas Red filter sets. From [58].

# 23

# Single-Molecule Detection

Detection of single molecules represents the ultimate level of sensitivity and has been a longstanding goal of analytical methods. Because of its high sensitivity, and because a bright signal appears against a dark background, fluorescence is one obvious choice for single-molecule detection (SMD). However, SMD using fluorescence is technically difficult. The first report on SMD using fluorescence with a single fluorophore at room temperature appeared just 15 years ago in 1990.<sup>1</sup> In that report SMD was accomplished under flow conditions to minimize the observed volume. Pulsed laser excitation was used to allow off-gating of the scattered light, which otherwise obscured the signal. Even with careful optical filtering and solvent purification the detected signal was only about 50 photons per molecule of rhodamine 6G in water, with background counts of up to 20 photons. This work<sup>1</sup> demonstrated that SMD would be a difficult task, particularly in less pure biological samples. The literature contains earlier reports of SMD. These include the report by Hirshfeld in 1976<sup>2</sup> and reports by Keller, Mathies, and coworkers in 1989.<sup>3–4</sup> However, these experiments were performed with large molecules, each of which contained multiple fluorophores. In Hirshfeld's work the protein–polymer complex contained about 100 fluorescein molecules.<sup>2</sup> In other studies SMD was accomplished with phycobiliproteins.<sup>3–4</sup> Single-molecule detection was reported in the late 1980s at liquid helium temperature<sup>5</sup> or for trapped atoms,<sup>6–7</sup> which are conditions not suitable for biochemical experiments. In this chapter we will focus mainly on SMD of single fluorophore molecules or a larger molecule containing a single bound fluorophore under typical conditions used for biochemical experiments.

There are several methods for detection of single or small numbers of fluorophores. Fluorescence correlation spectroscopy (FCS) measures fluctuations in the small number of molecules in a focused laser beam. FCS will be described in the following chapter. FCS is useful with freely diffusing molecules. Other methods for SMD are based on

optical imaging using various forms of microscopy. Using these methods a molecule can only be imaged if it stays in one place during observation. Hence spectroscopic studies of single molecules are almost invariably performed on immobilized molecules. This can be accomplished with highly viscous or rigid polymers or with molecules tethered to a surface.

SMD is an exciting methodology for several reasons. From a fluorescence point of view we begin to deal with absolute quantities rather than relative intensity values. When performing anisotropy measurements on single molecules the theory changes because the classic equations for anisotropy (Chapter 10) were derived based on averaging of the signal from a large number of randomly oriented molecules. Perhaps the dominant reason for using SMD is to avoid ensemble averaging. For instance, suppose a solution contains two types of fluorophores. The emission spectra of a single molecule in the mixture will be representative of just one type of molecule, and not an average spectrum. Single-molecule studies of enzymes can reveal the time course of the enzymatic reaction, without the use of high-speed mixing or other synchronization methods that are needed when studying a large number (ensemble) of molecules. Structural fluctuations of macromolecules may be seen directly, which is not possible with ensemble-averaged measurements.

The usefulness of avoiding ensemble averaging is shown in Figure 23.1. Consider a molecular beacon that can exist in a closed state that is quenched or an open state that is fluorescent. Assume that the temperature is adjusted so that half the molecules are closed and half are open. The ensemble spectrum from a solution containing many molecular beacons would have an intensity 50% of the maximum unquenched intensity (lower panel). This ensemble spectrum would not reveal if half of the beacons are open or closed, or if all the beacons are 50% quenched. Emission spectra of the single molecules would provide this informa-

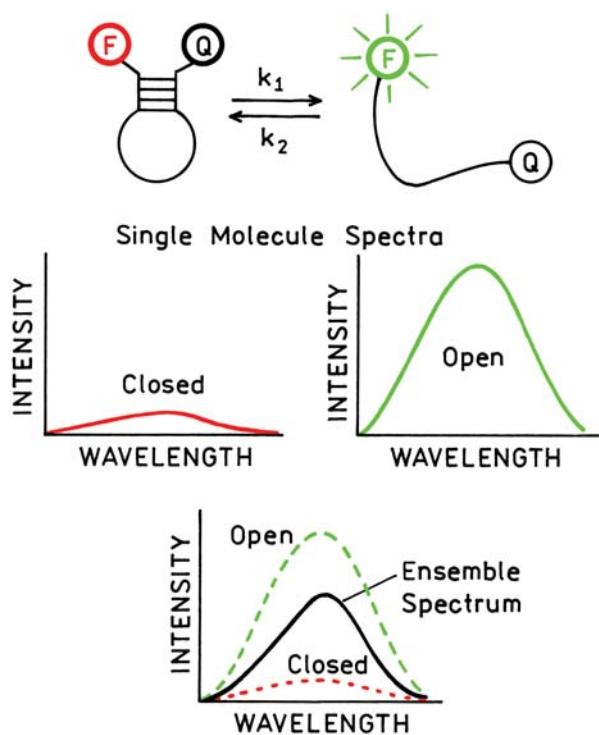


**Figure 23.1.** Comparison of single-molecule and ensemble emission spectra for a molecular beacon.

If the observed single-molecular beacon were open the single-molecule spectrum would have the intensity expected for a single fluorophore. If the observed molecular beacon were closed, it would display a lower intensity or would not be observable. Intermediate intensities would be observed if the beacon was partially quenched. If the molecular beacon folds and unfolds on the timescale of the measurements then the signal would fluctuate. This example shows how observation of single molecules can reveal information about the conformation of biomolecules which is not available when observing many molecules.

Another opportunity using SMD is to study reaction kinetics without synchronization of the reaction. Consider an enzyme catalyzed reaction where the substrate is nonfluorescent and the product is fluorescent. The reaction is usually started by addition of the substrate (Figure 23.2, top panel) and the progress of the reaction followed by the change in fluorescence intensity. These data would not reveal any intermediate steps in the reaction. Now consider an experimental design where a single enzyme molecule is bound to a surface. In this case the enzyme (E) is labeled with a fluorophore (F) and the substrate contains a quencher. When the substrate (S–Q) binds to the enzyme

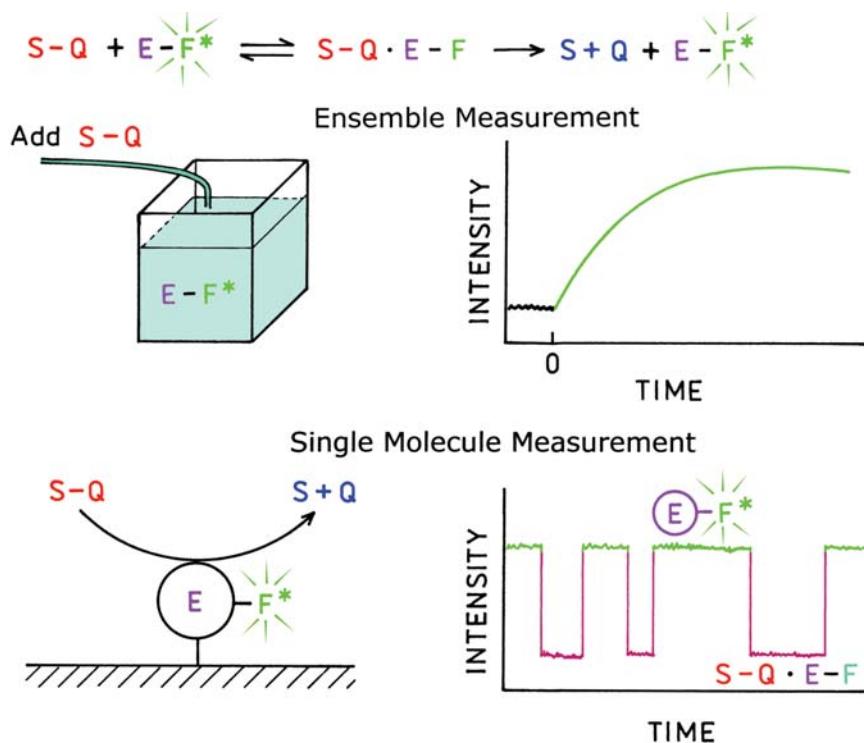


**Figure 23.2.** Comparison of ensemble and single-molecule enzyme kinetics. The enzyme is labeled with a fluorophore (F). The substrate contains a group (Q) that quenches the fluorophore.

the intensity of F decreases (lower panel). When the product dissociates the intensity will return to the initial value. If intermediate states are present they might be observed by intermediate intensities. The time intervals when the intensities are high or low can be used to determine the rate constants for the reaction. In the case of the single molecule it is not necessary to consider the starting time for the reaction. The reaction can be studied in a stationary experiment, assuming the substrate concentration is not changing. Measurements on different single enzyme molecules would reveal if there were subpopulations with different kinetic constants. These two examples (Figure 23.1 and 23.2) show that a wealth of new information is available when observing single molecules.

Perhaps surprisingly, SMD is not presently used for high-sensitivity detection. Single molecules are observed but not usually counted. At present it is considerably easier to find and measure single immobilized molecules than to count the number of molecules in a sample. However, single-molecule counting is likely to be used more frequently in the future, as shown by attempts to determine the sequence of single strands of DNA.<sup>8–9</sup> The field of SMD is growing rapidly. We have attempted to provide a snapshot of this changing technology. More detail about SMD can be found in recent reviews and monographs.<sup>10–18</sup>

### 23.1. DETECTABILITY OF SINGLE MOLECULES

It is informative to consider the samples and instrumental requirements needed to detect the emission from a single molecule above the background signal from the system. In any real system there will be background signal due to impurities in the sample, emission from optical components, scattered light at the incident wavelength, and dark counts (dark current) from the detector. Assume for the moment that the instrument is perfect without signal from these sources. Surprisingly, even a perfect instrument does not guarantee that a single fluorophore can be detected. If one examines the literature on SMD one finds that SMD is almost always performed in a restricted volume, that is, by observing a small region of the sample. This restriction is a consequence of intrinsic Raman scattering, which cannot be avoided.

Rhodamine 6G (R6G) is frequently used for SMD. Figure 23.3 shows the emission spectrum of R6G along with the Raman spectrum of the solvent ethylene glycol.<sup>19</sup> The optical cross-section of a chromophore ( $\sigma$ ) can be calculated from its molar extinction coefficient ( $\epsilon$ ) using<sup>16</sup>

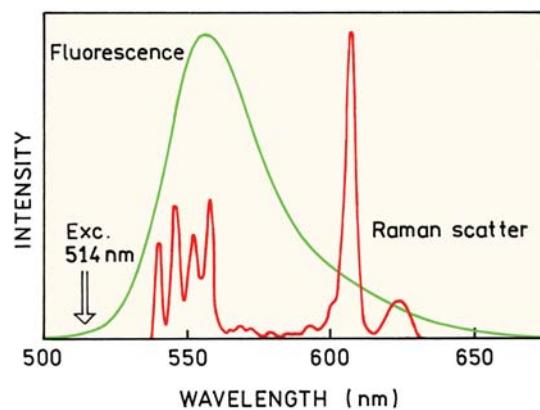


**Figure 23.3.** Emission spectrum of rhodamine 6G in ethylene glycol. Also shown is the Raman spectrum for ethylene glycol. Revised from [19].

$$\sigma_A = 2.303 \epsilon / N \quad (23.1)$$

where  $N$  is Avogadro's number. The electronic transition of R6G is strongly allowed and the cross-section for absorption ( $\sigma_A$ ) is essentially equal to its geometric cross-section, about  $4 \times 10^{-16} \text{ cm}^2$ , or  $4 \text{ \AA}^2$ . For a single molecule of ethylene glycol (EG) the cross-section for Raman scattering is about  $3 \times 10^{-28} \text{ cm}^2$ , or  $3 \times 10^{-12} \text{ \AA}^2$ .<sup>19</sup> Since the Raman signal appears in the same wavelength range of R6G fluorescence, the contribution of Raman scatter cannot be completely eliminated by emission filters. The Raman scatter from the ethylene glycol solvent will equal the emission from R6G when one R6G molecule is dissolved in  $1.3 \times 10^{12}$  molecules of EG. Since one mole of EG occupies about 56 ml, this number of molecules occupies a volume of  $1.2 \times 10^{-10} \text{ ml}$  or  $120 \mu\text{m}^3$ . In order to obtain a signal from R6G equal to the Raman scatter the molecule must be in a square less than  $4.9 \mu\text{m}$  on each side. Raman scatter, from the solvent limits the detectability of signal fluorophores to volumes of less than about 100 fl. Single-molecule experiments are usually designed so that the observed volume surrounding a single fluorophore is about 1 femtoliter ( $10^{-15} \text{ l}$ ), which is the volume of a cube  $1 \mu\text{m}$  on each side.

The difficulty of SMD can be seen by considering a single R6G molecule in 1 ml of water (Figure 23.4). Assume that the quantum yield of R6G is unity and that the spatial distribution of the emission and scattered light is similar. The signal observed for each molecule will be proportional to its cross-section and the number of molecules.

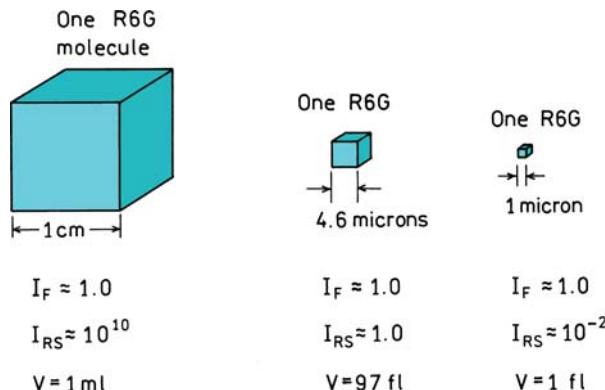


Figure 23.4. Intensities of Raman scattering from water relative to a single R6G fluorophore.

Assume the Raman cross-section for water is  $10^{-28} \text{ cm}^2$ . One ml of water contains  $3.3 \times 10^{22}$  molecules, so that the Raman scatter from 1 ml of water is the product of the Raman cross-section ( $\sigma_S$ ) and the number of molecules, or about  $3 \times 10^{-6} \text{ cm}^2$ . The Raman scatter from 1 ml of water is  $10^{10}$ -fold greater than the signal from one R6G molecule. Without some breakthrough in technology a single fluorophore in a milliliter volume cannot be detected.

While SMD is difficult, the situation is not hopeless. In order to obtain signal from the fluorophore, comparable to or greater than from the solvent, the size of the observed sample has to be restricted. For example, in order to make the emission of one R6G equal to that of the solvent water the volume has to be reduced by a factor of  $10^{10}$  to  $10^{-10} \text{ cm}^3$ . This volume corresponds to a box  $4.6 \mu\text{m}$  on each side (Figure 23.4). Of course, for a useful experiment the signal has to be larger than the scatter. To make the emission 100-fold larger than the scatter the volume has to be reduced to  $10^{-12} \text{ cm}^3$ , which corresponds to a box 1 micron on each side, which is  $10^{-15} \text{ l} = 1 \text{ fL}$ . Modern microscope objectives easily focus light to wavelength dimensions, which for 600 nm light would be about 0.22 fL. Hence, based on consideration of only Raman scatter, it should be possible to detect single fluorophores using microscope objectives. In reality the situation is far less favorable because all the molecules in the light path of the microscope contribute to the signal. Confocal optics are needed to reduce the observed volume by rejecting signal from above and below the focal plane. The solvent or sample may contain fluorescent impurities; the detectors always have dark counts. Additionally, single molecules often photobleach while they are being observed. SMD is still a technological challenge.

## 23.2. TOTAL INTERNAL REFLECTION AND CONFOCAL OPTICS

### 23.2.1. Total Internal Reflection

Prior to describing the optical methods needed for SMD it is necessary to understand the principles used to restrict the observed volume. One commonly used method is total internal reflection (TIR). TIR occurs when a beam of light encounters an interface with a lower refractive index on the distal side, and the angle of incidence exceeds the critical angle ( $\theta_C$ ). The underlying physics of TIR is somewhat complex<sup>20–23</sup> but the end result is simple. Consider a hemicylindrical prism ( $n_2$ ) optically coupled to a slide with the same refractive index  $n_2$  (Figure 23.5), and assume light is incident at an angle  $\theta_I$ . Assume the sample has a lower refractive index  $n_1$ . The values of  $n_2 = 1.5$  and  $n_1 = 1.3$  are typical of glass and water, respectively. If one examines the intensity of the transmitted light one finds most of the light is transmitted at low angles of incidence. The reflectance is above zero when values of  $\theta_I$  are less than  $60^\circ$  (lower panel). For angles greater than the critical angle  $\theta_C$ , the transmission drops to zero and the reflectivity increases to 100%. For  $\theta_I > \theta_C$  the beam is said to be totally internally reflected. The critical angle can be calculated from  $n_1$  and  $n_2$  using

$$\theta_C = \sin^{-1}\left(\frac{n_1}{n_2}\right) \quad (23.2)$$

For  $\theta_I > \theta_C$  the beam is completely reflected at the interface, but the incident beam can still interact with the sample at the glass–water interface. This is because when TIR occurs the intensity penetrates a short distance into the sample. The intensity of the light along the  $z$ -axis, the square of the electric field, is given by

$$I(z) = I(0) \exp(-z/d) \quad (23.3)$$

where  $I(0)$  is the intensity at the interface. The decay constant is given by

$$d = \frac{\lambda_0}{4\pi} (n_2^2 \sin \theta_2 - n_1^2)^{-1/2} \quad (23.4)$$

where  $\lambda_0$  is the wavelength of the incident light in a vacuum. For 600-nm light with the parameters in Figure 23.5

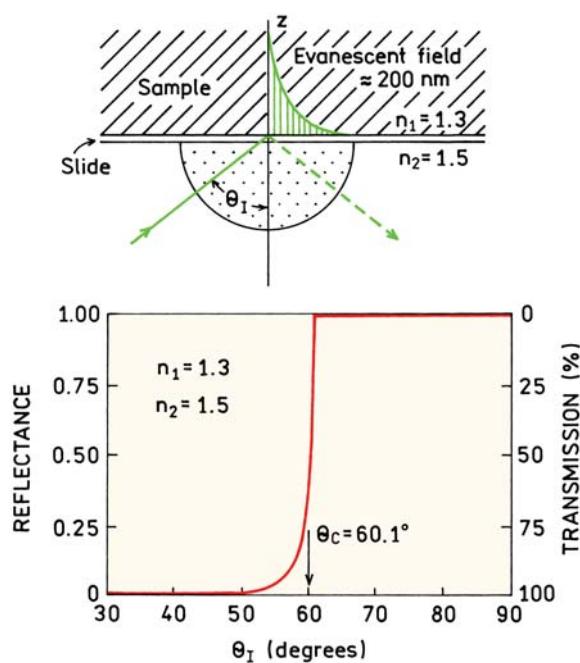


**Figure 23.5.** Top: Optical geometry for total internal reflection (TIR). Bottom: Calculated reflectance and transmittance for  $n_2 = 1.5$  and  $n_1 = 1.3$ .

and an incidence angle of  $70^\circ$  one finds  $d = 73.3$  nm. The values of  $d$  are typically a fraction of the wavelength. Equation 23.4 is sometimes defined incorrectly in various publications, and describes the distance-dependent decreases in intensity. Equation 23.4 is sometimes presented with a factor of  $2\pi$  in the denominator rather than  $4\pi$ . The expression with  $2\pi$  in the denominator represents the distance-dependent decrease in the electric field, not the intensity.

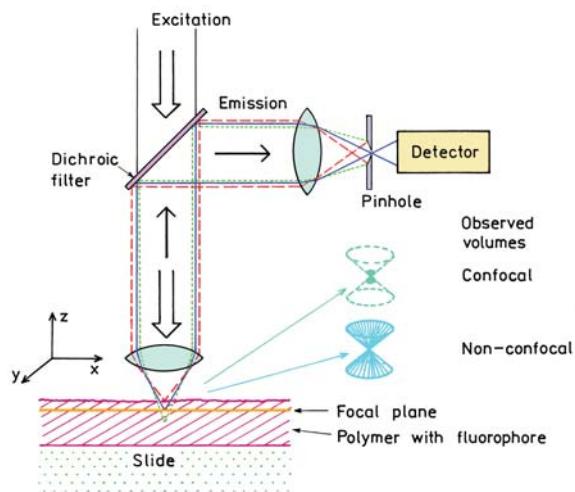
Total internal reflection is valuable in SMD because it provides a way to limit the volumes. When using TIR only fluorophores within the evanescent field are excited. Instead of a long illuminated path through the sample, the effective illuminated path is sub-wavelength in size. The restricted illuminated distance along the  $z$ -axis reduces the effective volume and makes it possible to detect single molecules. This can be seen by calculating the volume of a spot illuminated using TIR conditions. Suppose the spot size is  $20 \mu\text{m}$  in diameter and the penetration depth is  $100 \text{ nm}$ . The effective volume of the illuminated region is about  $30 \mu\text{m}^3 = 30 \text{ fl}$ . Hence a single molecule of R6G should be detectable using these conditions, with a signal-to-noise ratio (S/N) near 3 when observing the entire volume. If the observed volume is reduced further the S/N ratio will be improved.

### 23.2.2. Confocal Detection Optics

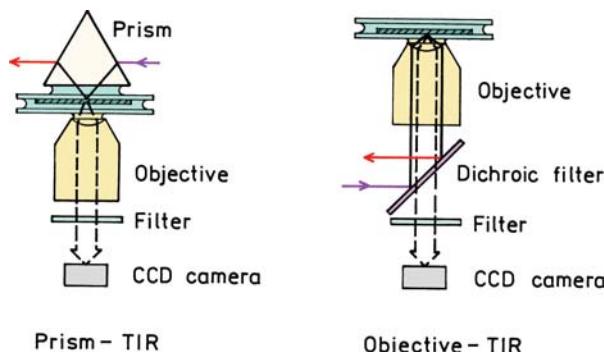
Figure 23.4 demonstrated the need to decrease the effective sample size in order to detect a fluorophore above intrinsic scatter from the sample. It would be difficult to prepare such a nano-sized structure containing a single fluorophore. Even if one could prepare a small volume with a single fluorophore this would not be useful because the goal is usually to select and observe a region from homogeneous solutions or heterogeneous biological samples. Fortunately, confocal fluorescence microscopy provides an optical method to limit the observed volume.

Figure 23.6 shows a schematic of confocal optics. The principles have been described in more detail in many reports.<sup>24–27</sup> Suppose the sample is thicker than a single layer of fluorophores, such as a polymer film containing a low concentration of fluorophores. Illumination through the objective is called epi-illumination. The incident light excites all the fluorophores within the illuminated cone. Emission is collected back through the objective, which is called the epifluorescence configuration. Emission is separated from light at the incident wavelength by a dichroic filter that reflects wavelengths longer than the incident light to a detector. A dichroic filter is a device that transmits some wavelengths and reflects others. In this case the dichroic filter transmits the excitation and reflects the emission wavelengths.

When using single-photon excitation the incident light excites the entire thickness of the sample with a cone-like



**Figure 23.6.** Principle of epifluorescence with confocal detection.



**Figure 23.7.** Optics for SMD imaging based on total internal reflection. Revised from [16].

pattern (Figure 23.6). The objective will collect the light from this cone, which includes the signal from the fluorophore, Raman scatter from the solvent, and emission from impurities in the solvent. If a single fluorophore is present in the illuminated cone its emission can be overwhelmed by the background from the solvent because the observed volume is too large. Suppose the laser beam is focused to a diameter of 500 nm and the sample is 100  $\mu\text{m}$  thick. Then the observed volume is about 20 fL, which is borderline for single-molecule detection.

The difficulty due to unwanted signal from the solvent can be solved to some extent using confocal optics. This means that a small pinhole aperture is placed at a focal point in the light path. By ray tracing of the light path one can see that light from above or below the focal plane is not focused on the pinhole, and does not reach the detector. Using this approach the effective depth of the sample can be reduced to about twice the incident wavelength. The  $z$ -axis resolution is typically several-fold less than the resolution in the  $x$ - $y$  focal plane. Suppose the effective observed volume is a cylinder 500 nm in diameter and 1000 nm long. The volume of the cylinder is about 0.2 fL. Using Figure 23.4 one sees that the signal from a single fluorophore can be about 500-fold larger than the Raman scatter. This is a very optimistic estimate of the S/N ratio, which does not include a number of factors, including impurities, nonideal properties of the lenses and filters, photobleaching, and saturation of the fluorophore.

### 23.3. OPTICAL CONFIGURATIONS FOR SMD

Essentially all SMD instruments use an optical configuration which limits the observed volume. Different approaches are used for wide-field observations and point-by-point

observations. For wide-field observations the most common approach is to use TIR. Two commonly used wide-field approaches<sup>16,28</sup> are shown in Figure 23.7. Both configurations are based on an inverted microscope. The most direct approach (left) is to excite the sample through a prism so that the excitation undergoes TIR. Fluorophores in the sample, which are also within about 200 nm of the interface, are excited by the evanescent field. The emission is collected by an objective, filtered to remove unwanted light, and imaged on a low-noise CCD camera. When using this approach it is necessary to aim the incident light at the focal point of the objective.

A somewhat more convenient approach to TIR illumination is shown on the right side of Figure 23.7. In this case illumination occurs around the sides of the objective, causing the light to be incident on the glass–water interface at an angle above the critical angle. This creates an evanescent field that excites a thin plane of the sample next to the interface. With this configuration the excitation light is always aligned with the collection optics because the excitation and emission pass through the same objective.

It is informative to examine a single-molecule image. Figure 23.8 shows an image of a mutant T203Y of green fluorescent protein (GFP).<sup>16</sup> This image was obtained using the prism and TIR configuration with a CCD detector. The GFP molecules were immobilized in dense poly(acrylamide) to prevent translational diffusion during the 100 ms exposure time. If the molecules were not immobilized they would diffuse several microns during this time and not be seen in the image. The single-molecule intensities are not all the same, which is due in part to the decaying evanescent

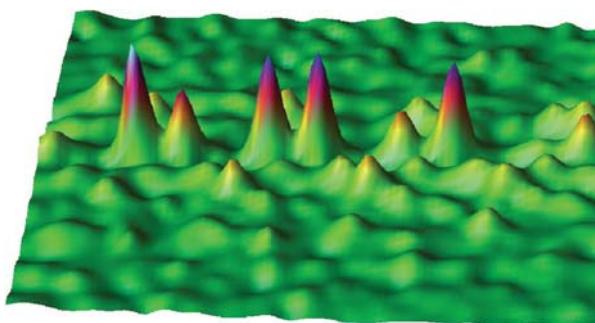


**Figure 23.8.** Single-molecule image of GFP mutant T203Y. The image was obtained using TIR illumination and a CCD camera. The GFP mutant was immobilized in poly(acrylamide). The image is 2.4  $\times$  2.4  $\mu\text{m}$ . Images courtesy of Dr. W. C. Moerner from Stanford University.

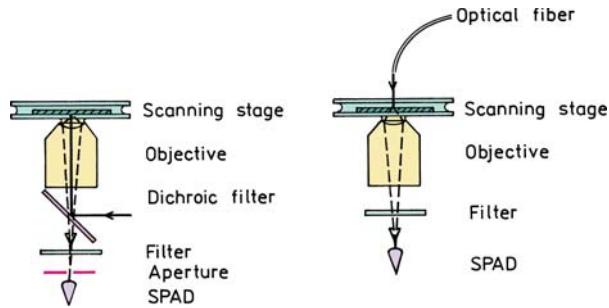


**Figure 23.9.** Optics for SMD using point-by-point measurements. Revised and reprinted with permission from [16], Copyright © 2003, American Institute of Physics.

field and different distances of the GFP molecules from the glass–polymer interface. As we will describe below, single molecules often show blinking behavior. Blinking is not seen in the images because the CCD is an integrating detector that measures total intensity during the data collection time. The diameter of each single-molecule image is about 200 nm, which is much larger than the size of the GFP or its chromophore. The size of the spots is determined by the resolution of the optics.

Another approach to limiting the observed volume for SMD is to use confocal optics<sup>29–31</sup> and point-by-point detection, rather than imaging. Two configurations for point-by-point SMD measurements are shown in Figure 23.9.<sup>16</sup> The left side shows a confocal configuration with objective illumination. There is a single-point detector so the sample is not directly imaged. Instead, a single point is observed at one time. The sample stage is raster scanned to create an image. Fortunately, highly accurate motorized stages are available that provide resolution down to molecular sizes, or even less. For SMD the present detector of choice is a single-photon-counting avalanche photodiode (SPAD).

Figure 23.10 shows single-molecule images of a GFP mutant—10C—collected using confocal optics and stage scanning.<sup>32</sup> The size of the spots are about 500 nm in diameter, which is determined by the optical resolution and not the size of the molecules. The appearance of the images is dramatically different from the GFP images in Figure 23.8. These images were obtained by raster scanning so the same GFP molecule is illuminated several times. Some of the GFP molecules disappear completely on subsequent scans, and some molecules disappear in some scans but reappear in later scans. This occurs because the GFP molecules are blinking and/or photobleaching during the observation.

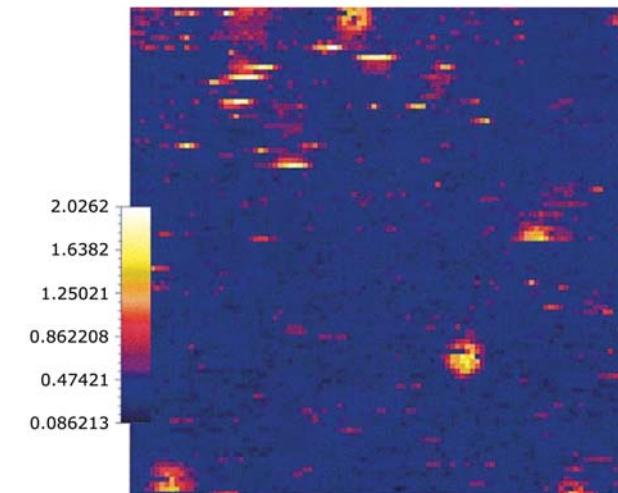


**Figure 23.10.** Confocal fluorescent images of single molecules of GFP mutant 10C in poly(acrylamide) measured by stage scanning. Image size 10 x 10  $\mu\text{m}$ . Reprinted with permission from [32].

Blinking occurs when the molecules undergo intersystem crossing to the triplet state. These molecules remain dark until they return to the ground singlet state. Blinking was not seen in Figure 23.8 because the CCD integrated all the emission occurring during the exposure time.

Another single-point approach to SMD and/or imaging is based on near-field scanning optical microscopy (NSOM). NSOM is based on a simple principle<sup>33–35</sup> but in practice is difficult. Highly localized excitation is obtained using an optical fiber (Figure 23.9 right). The end of the fiber is drawn to be very thin: typically 80 nm in diameter. The sides of the fiber are then coated with aluminum. Laser light is focused to enter the larger distal end of the fiber. A very small fraction of the light is transmitted from the tip of the fiber. Alternatively, the light in the fiber can be imagined as creating an evanescent field at the tip of the fiber, analogous to TIR. The tip is then positioned near the sample, typically with in 20 nm using components similar to an atomic force microscope (AFM). The fibers are fragile and the stage is usually scanned to create an image, while the fiber is held at a known distance above the sample. Because only a small region of the sample is excited, there is no need for a confocal aperture to eliminate scattered light from a larger volume of the sample.

Figure 23.11 shows a single-molecule NSOM image of the dye oxazine 720 in poly(methylmethacrylate) (PMMA). This image was obtained by scanning a metal-coated fiber above the surface, with illumination through the fiber. The

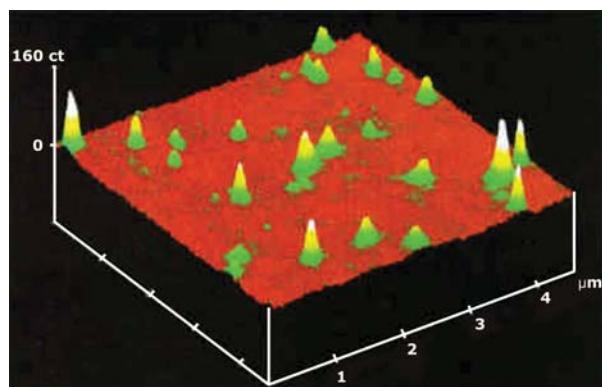


**Figure 23.11.** Single-molecule images of oxazine 720 in poly(methyl methacrylate) obtained using NSOM. Image size  $4.5 \times 4.5 \mu\text{m}$ . Revised from [13].

spatial resolution is not limited to optical resolution and is determined by the diameter of the fiber. In this image the spots are below 100 nm in diameter.

SMD imaging is also measured using laser scanning confocal microscopy (LSCM). LSCM is accomplished using optics similar to Figure 23.6. Instead of observing a single spot in the image, the laser excitation is raster scanned so that the focused light is scanned across the sample.<sup>29–31</sup> The light collected by the objective is focused on the pinhole to pass light from the desired volume element and reject light from outside the focal volume. A single-point detector, usually an SPAD, is used to measure the light returning from each point in the image.

Single-molecule imaging has been accomplished using standard epifluorescence and a high-quality CCD detector. This is possible if the sample is thin, where there is little or no signal from molecules outside of the focal plane. Figure 23.12 shows an epifluorescence image of a tetramethylrhodamine-labeled lipid (TMR-POPE) in a monolayer of POPC prepared as a Langmuir-Blodgett film.<sup>36</sup> Single molecules were observable because the sample was only the thickness of a phospholipid monolayer. This image illustrates the need for extremely low fluorophore concentrations for SMD. The mole fraction of TMR-POPE has to be below about  $10^{-6}$  for single molecules to be observed because two fluorophores closer than the optical resolution of the microscope appear as a single spot.

#### 23.4. INSTRUMENTATION FOR SMD

Prior to showing additional experimental results it is valuable to examine a typical instrument used for these meas-

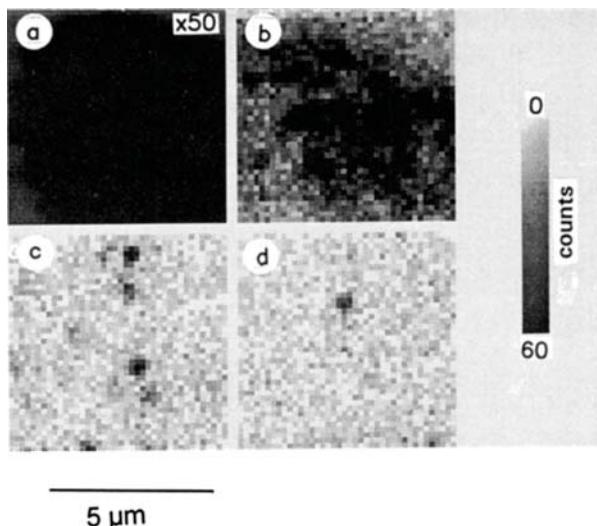


**Figure 23.12.** Epifluorescence images of TMR-POPE in a monolayer of POPC. The mole fractions of labeled lipid are (a)  $6.5 \times 10^{-3}$ , (b)  $6.5 \times 10^{-6}$ , (c)  $6.5 \times 10^{-8}$ , and (d)  $6.5 \times 10^{-9}$  mole/mole. In (a) the intensity was divided by 50. Exposure time was 5 ms. Reprinted with permission from [36]. Copyright © 1995, American Chemical Society.

urements. Figure 23.13 shows the schematic for a confocal SMD instrument.<sup>37</sup> Laser light is brought to the sample by reflection off the dichroic filter. If needed, the polarization of the incident light is adjusted with polarizers and/or wave plates. Emission is selected by the same dichroic filter and then passes to the detectors. In order to find and/or image the fluorophores the stage is scanned in the *xy* direction,

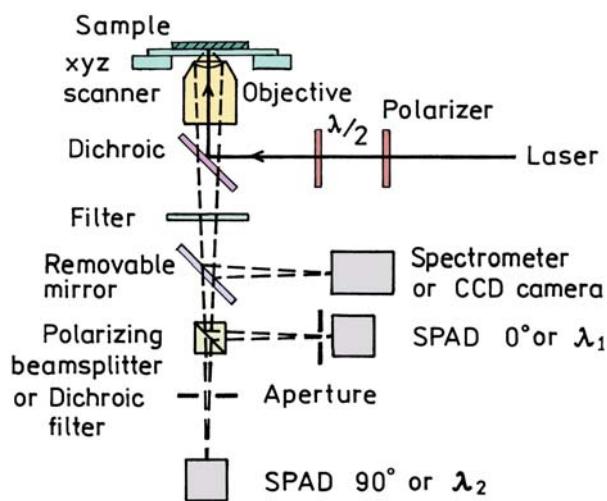


**Figure 23.13.** Schematic for stage-scanning confocal SMD. Revised and reprinted with permission from [37]. Copyright © 1998, American Chemical Society.

with  $z$  scanning if needed for focusing. The presence of a fluorophore is seen as a burst of photons when the fluorophore is in the incident beam. The most commonly used detector is the single-photon-counting avalanche photodiode (SPAD). The emission can pass through an aperture to provide confocality, or may just be focused on the SPAD allowing the small active area to serve as the aperture. In many measurements two SPADs are used, which allows measurements through different polarizer orientations or different wavelengths. If needed the emission can be directed toward a CCD camera for imaging, or a spectrometer for collecting emission spectra.

The instrumentation for single-molecule detection using NSOM is similar except that the excitation is delivered to the sample via a tapered metal-coated optical fiber (Figure 23.14). The fiber tips are fragile so there are usually feedback mechanisms to keep the fiber at a known distance above the sample. Because the sample is only excited near the fiber top there is no need for a confocal aperture to reduce background from out-of-focus regions of the sample.

### 23.4.1. Detectors for Single-Molecule Detection

For single-point measurements on single molecules the presently preferred detector is the SPAD. At first glance it seems surprising to use an SPAD rather than a photomultiplier tube (PMT). PMTs are able to multiply single-photoelectron events by a million-fold. In contrast, a typical SPAD provides an amplification near 100-fold.<sup>39</sup> Essentially all single-point SMD experiments are performed using some type of single-photon counting (SPC) rather than analog detection. This is because the photon arrival rate is typically low so that individual photoelectron pulses are detectable. The use of SPC allows the lower threshold to be adjusted to neglect smaller noise pulses. It is possible to observe single-photon events with an SPAD, and there is no need for further amplification if the photon can be counted.

Single-photon counting can be accomplished using either a PMT or an SPAD. SPADs have several advantages over PMTs. One issue is that of simplicity. SPADs along with the electronics to count single-photon events are available in small packages that require only a 5-volt source. The higher voltages near 20 volts needed to drive the SPAD are obtained from internal circuits. In contrast, a PMT requires a much higher voltage—typically over 1000 volts for SPC. While small PMT high-voltage supplies are available, it is more difficult to create and shield these higher voltages.

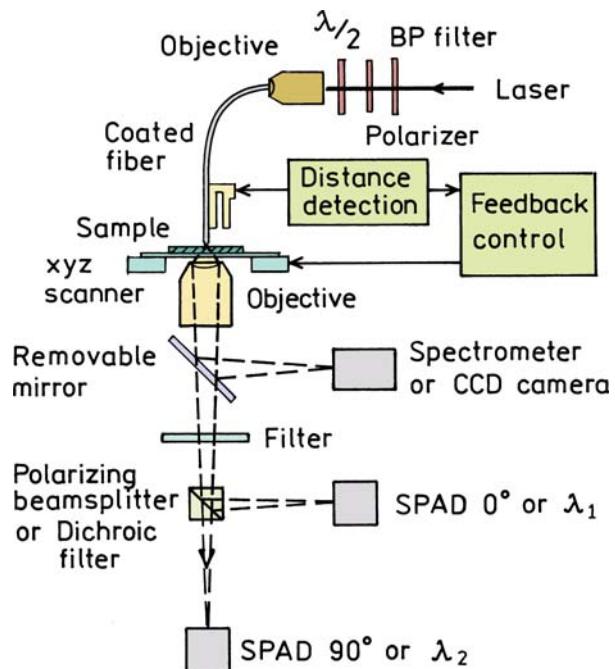


**Figure 23.14.** Schematic of a stage-scanning NSOM instrument for SMD. Revised and reprinted with permission from [38].

Perhaps the main advantage of SPADs over PMTs is their quantum efficiency. As is described below, a single fluorophore can only emit a limited number of photons prior to photodestruction. This fact, and the limited total collection efficiency with a confocal microscope, makes it important to detect the incident photons with the highest possible efficiency. PMTs typically have quantum efficiencies near 20%. SPADs have efficiencies near 60% in the visible and up to 90% in the NIR. The quantum efficiencies of PMTs typically decrease at longer wavelengths. SMD is usually performed using red dyes because they have high extinction coefficients and because autofluorescence from the sample and apparatus is lower at the longer wavelengths. Hence SPADs provide a considerable quantum efficiency advantage over PMTs for SMD. SPADs also have a low rate of background count—25 to 100 counts per second—which is comparable to the best-cooled PMTs.

If SPADs are such efficient detectors, why are PMTs still the dominant detectors in fluorescence spectroscopy? An important advantage of PMTs is the large active area of the photocathode, which can be a square centimeter or more. As a result the emission does not need to be tightly focused to obtain efficient detection. Additionally, the high amplification of a PMT is an advantage in non-photon-counting applications. In contrast to PMTs, SPADs have

small active areas: typically near 200  $\mu\text{m}$  in diameter. Such a small detection area would be inconvenient in a typical fluorometer, and most of the photons collected by the optics would fall on inactive regions of the SPAD. However, SMD is performed using confocal optics, so the emission is already focused to a small area, which can be on the active area of the SPAD. In fact, the SPAD itself can act like a pinhole because only the focal point of the optics falls in the active area.

For single-molecule imaging the detector of choice is the charged coupled device (CCD). A CCD contains an array of pixels, each of which acts like an individual detector.<sup>40</sup> A CCD is not a photon-counting detector, but it is an integrating detector. The signal in each pixel is proportional to the number of incident photons for as long as the CCD is active. Importantly, the noise in each pixel does not increase significantly with integration time, at least not with cooled scientific CCDs. There is a certain amount of noise associated with reading out the signal in each pixel, so that longer integration times are an advantage. Like SPADs, CCDs have a high quantum efficiency, especially at long wavelengths. The most detailed information on the performance of CCDs is usually provided by the camera companies.

### 23.4.2. Optical Filters for SMD

In single-molecule detection it is essential to reject scattered light at the excitation wavelength. Fortunately, high-quality optical filters are available for this purpose. Depending on their method of production they may be called holographic notch filters or Rugate notch filters.<sup>41–42</sup> Figure 23.15 shows the absorption spectra of typical notch filters. These filters transmit all wavelengths except a narrow band at the wavelength that needs to be rejected. The optical densities at these wavelengths can be very high—4 to 6—with half-widths of 10 to 20 nm.

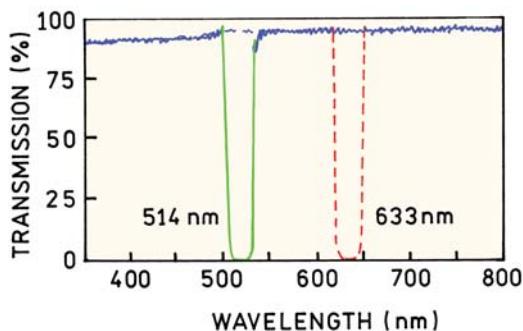


Figure 23.15. Transmission profiles of laser notch filters.

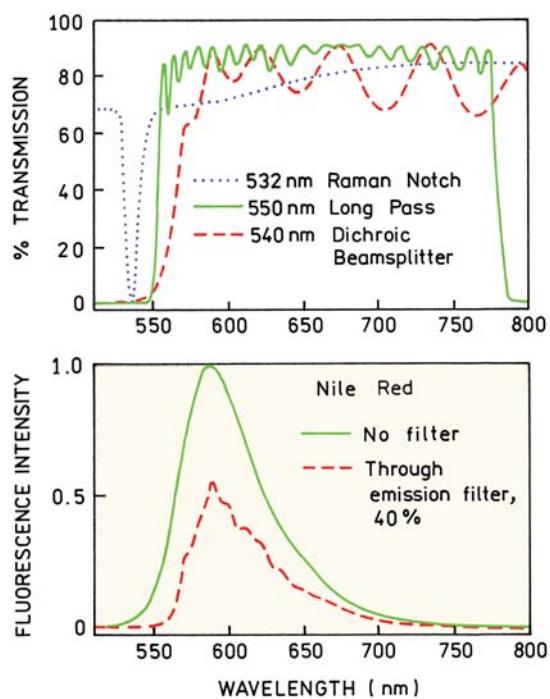
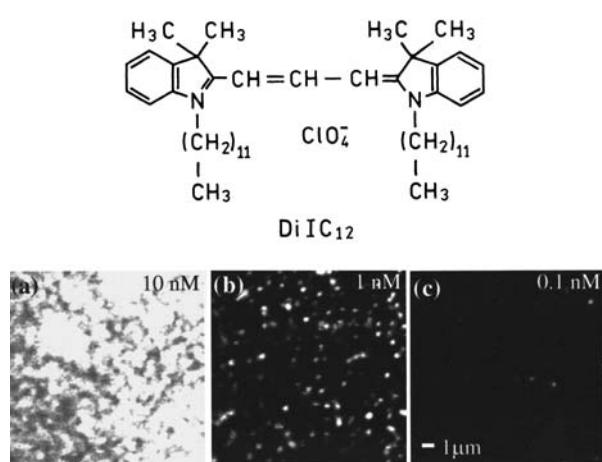


Figure 23.16. Emission filters and emission spectra of Nile Red in methanol. Revised from [16]. Revised and reprinted with permission from [16], Copyright © 2003, American Institute of Physics.

row band at the wavelength that needs to be rejected. The optical densities at these wavelengths can be very high—4 to 6—with half-widths of 10 to 20 nm.

In single-molecule experiments extreme care is needed to eliminate scattered light, so that selection of emission filters is critical. Because of the intense illumination used for SMD the Rayleigh scattered excitation needs to be attenuated by a factor of  $10^7$  to  $10^8$ -fold. Figure 23.16 (top panel) shows a combination of filters selected to observe Nile Red using 532-nm excitation. The Rayleigh scatter is rejected by a combination of three filters: a notch filter, a dichroic filter, and a longpass filter.<sup>16</sup> By careful selection of the filters the desired emission was attenuated only twofold (lower panel).

Figure 23.17 shows images of the fluorophore DiIC<sub>12</sub> that was spin coated on glass from a toluene solution.<sup>43</sup> If the initial solution is too concentrated the signals from the molecules overlap, resulting in a spatially continuous intensity (left). At a lower initial concentration, individual DiIC<sub>12</sub> molecules can be seen (middle), and at lower concentrations only few molecules are seen (right). The spots for a single molecule are about 300 nm across, reflecting the limited resolution available with light microscopy. The bright spots were assigned to single molecules based on the pro-



**Figure 23.17.** Single-molecule images of DiIC<sub>12</sub> on glass obtained using the stage-scanning configuration shown in Figure 23.13. Revised and reprinted with permission from [43], Copyright © 1998, American Institute of Physics.

portionality of number density to concentration and observation of single-step photobleaching. The different intensities for the various single molecules are thought to be due to different orientations of the fluorophore relative to the polarized incident light.

Close examination of the middle panel in Figure 23.17 shows that some of the single-molecule spots are half-circles rather than circular. This result shows an important aspect of SMD, all the fluorophores display blinking. Examples of the blinking are shown in Figure 23.18 for three different DiIC<sub>12</sub> molecules. In each case the intensity fluctuates dramatically, and eventually the emission stops when the molecule undergoes permanent photodestruction. The middle panel is the most typical blinking profile: a relatively constant intensity, followed by a rapid drop in intensity, followed by a return of the intensity. This blinking phenomenon explains the half-circles in Figure 23.17. Recall that the stage is scanned in the *x* and *y* directions to create the image. A single molecule is illuminated several times as the sample is raster scanned through the laser beam. If the fluorophore undergoes blinking or destruction during this somewhat continuous illumination it is not seen in the subsequent line scans, resulting in the partial circles. This illustrates an important advantage of stage scanning with SPADs. One can follow a single molecule in time to obtain a more detailed view of its photophysical behavior.

An important feature of SMD is the ability to examine the behavior of a single molecule rather than the average

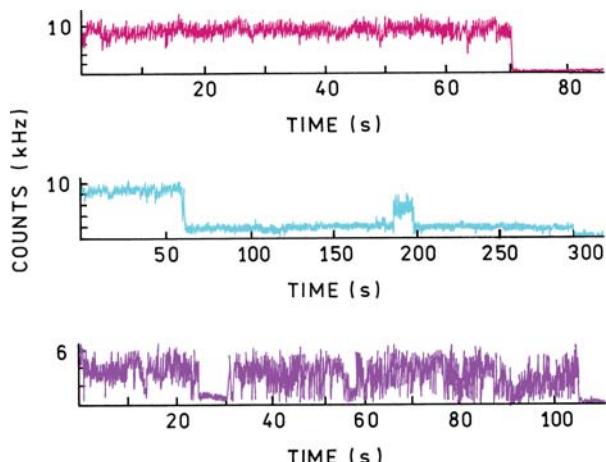


**Figure 23.18.** Time-dependent intensities of DiIC<sub>12</sub> on glass. Revised and reprinted with permission from [43], Copyright © 1998, American Institute of Physics.

behavior of numerous molecules. This property is revealed by the emission spectra for individual molecules of DiIC<sub>12</sub> (Figure 23.19). These spectra are not for the same molecules used for Figure 23.18. Different emission spectra were found for different molecules. Often the single-molecule spectra were the same as the bulk phase spectra (lower left and dashed). However, the spectra of single molecules can also be dramatically different (right panels). These spectral changes can be the result of a number of mechanisms, such as different local environments on the glass. The behavior of the molecules depends upon the composition of the sample. The blinking and spectral changes are usually different for fluorophores on glass or embedded in a polymer. In the case of DiIC<sub>12</sub> in PMMA, different emission spectra were observed for the same fluorophore at different times,<sup>16</sup> a phenomenon called spectral diffusion. The important point is that SMD can provide resolution of underlying molecular heterogeneity, which can be due to either the local environment of the fluorophore or the conformational heterogeneity in macromolecules.

Single-molecule images of DiI-C<sub>18</sub> embedded in poly(methylmethacrylate) were also observed using NSOM.<sup>44</sup> The excitation was circularly polarized to provide equal excitation of each fluorophore irrespective of the dipole orientation around the *z*-axis. The emission was passed through a polarizing beamsplitter to separate the polarized components and sent to separate SPAD detectors. The spots are color coded to show the dipole orientation, which was determined by the relative intensities of each polarized component (Figure 23.20). It is interesting to notice that single molecules display polarized emission, even if the

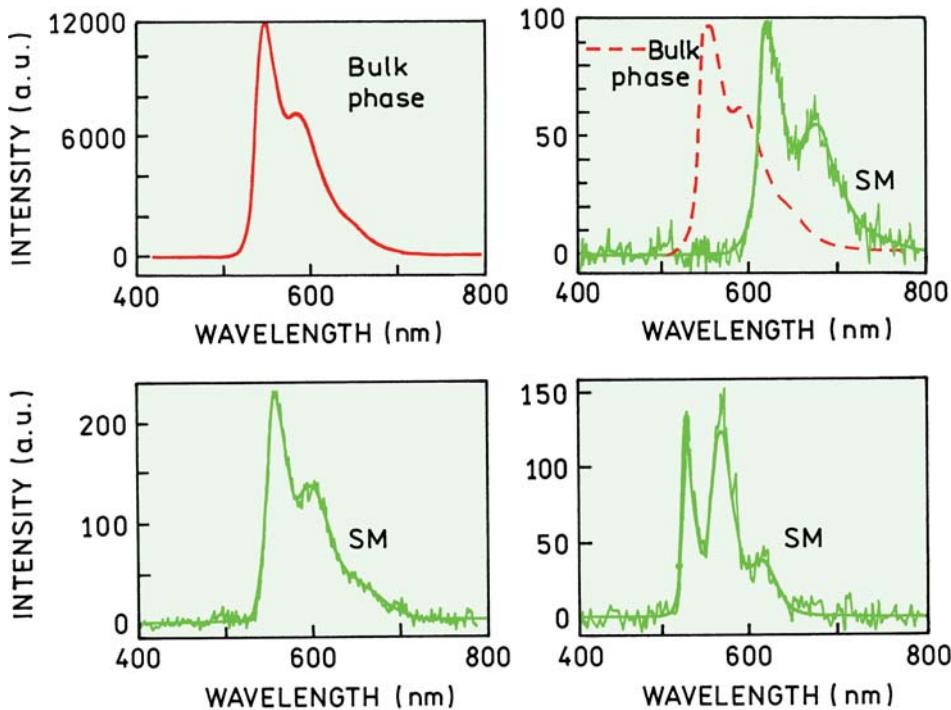


**Figure 23.19.** Emission spectra of single molecules of DiIC<sub>12</sub> on glass. These spectra are not from the same molecules used for the time-dependent traces in Figure 23.18. The spectrum in the upper left is from a bulk phase solution. SM, single molecule. The dashed line in the upper right is the bulk phase emission, normalized with the SM emission. Revised and reprinted with permission from [43], Copyright © 1998, American Institute of Physics.

excitation along the  $z$ -axis is unpolarized. This occurs because the dipole in the rigid polymer has a unique orientation. If a fluorophore is excited it will emit according to its orientation, and not the polarization of the incident beam. Additionally, the polarization can be greater than 0.5, or the anisotropy greater than 0.4, because the maximum polarization or anisotropy of a single dipole along an axis is 1.0 (Chapter 10). The extent of excitation is complex because the near field at the fiber top is more complex than simple linear polarization.<sup>45–46</sup>

### 23.5. SINGLE-MOLECULE PHOTOPHYSICS

When observed with high illumination intensities almost all fluorophores display blinking. This blinking by single fluorophores can be explained by a simple photophysical model.<sup>47–50</sup> The dominant origin of fluorophore blinking is thought to be intersystem crossing (isc) to the triplet state (Figure 23.21). In this Jablonski diagram the wide arrows are intended to represent high rates of excitation and emission, which is typically the case when detecting single mol-

ecules. The incident intensity has to be high enough to result in a rate of detected photons that is higher than the dark count of the detector. Increased incident intensities will not increase the signal-to-noise ratio if the background signal is due to autofluorescence from the sample, because this component will also increase with increases in incident intensity.

The origin of fluorophore blinking can be understood from the kinetic equations describing the population of the S state. The steady-state solution of these equations yields the dependence of S<sub>1</sub> on the rate constants in Figure 23.21. The number of molecules in the first singlet state is given by

$$S_1 = \frac{\sigma I_e S_T}{\tau^{-1} + \sigma I_e (1 + k_{\text{isc}}/k_{\text{ph}})} = \frac{\tau \sigma I_e S_T}{1 + I_e/I_s} \quad (23.5)$$

The rate of excitation is proportional to the excitation intensity  $I_e$  and the cross-section for absorption  $\sigma$ .  $S_T$  is the total number of fluorophores and  $\tau$  is the lifetime. The S<sub>1</sub> population will show a hyperbolic dependence on the incident

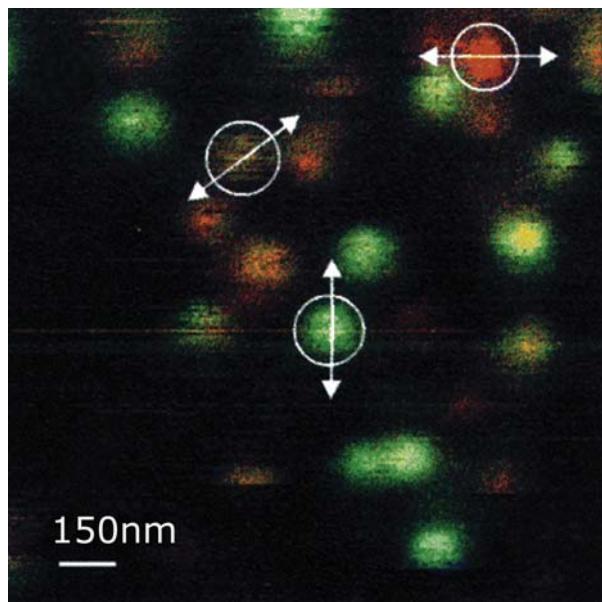


**Figure 23.20.** NSOM single-molecule imaging of DiI-C<sub>18</sub>. The colors represent the emission dipole orientation, red horizontal 0°, green vertical 90°, yellow equal signals in both channels. Reprinted with permission from [44].

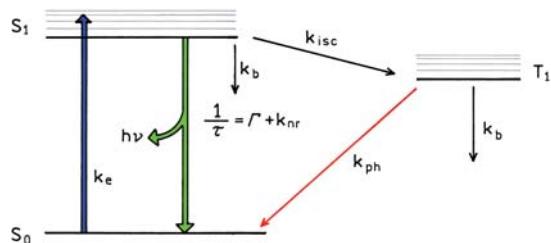


**Figure 23.21.** Jablonski diagram for single-molecule blinking. The wider arrows are intended to show high rates of excitation and return to the ground state.

intensity  $I_c$ . Equation 23.5 describes the entire population. If individual molecules are examined those in the triplet state are dark. The blinking properties of the fluorophore are determined primarily by the rate constants for crossing to the triplet state ( $k_{isc}$ ) and for return from  $T_1$  to the ground state ( $k_{ph}$ ). It is likely that photobleaching ( $k_b$ ) occurs from either the  $S_1$  or  $T_1$  state.

Figure 23.22 shows the photon count rate observed for a tetramethylrhodamine (TMR)-labeled lipid.<sup>36</sup> The numbers of photons per second initially increases linearly with incident intensity, but quickly reaches a saturating value. The laser intensities for SMD are typically rather high,

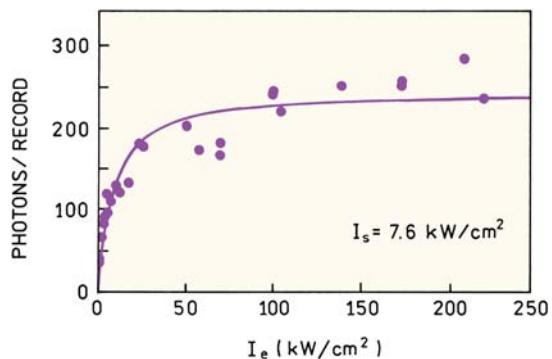


**Figure 23.22.** Laser intensity-dependent emission for a single lipid molecule labeled with TMR. Revised and reprinted with permission from [36]. Copyright © 1995, American Chemical Society.

which is needed to partially saturate the fluorophores and obtain a high photon emission rate. These conditions result in blinking and photodestruction photophysics of fluorophores. The general conclusion is that good fluorophores such as rhodamine can emit  $10^5$  to  $10^6$  photons prior to destruction. Many fluorophores are much less stable and may emit less than 1000 photons prior to bleaching. There is an interesting dilemma with regard to the effect of oxygen on photobleaching. On one hand it appears likely that oxygen can react with the excited states to destroy the fluorophore.<sup>51–52</sup> On the other oxygen quenching of  $T_1$  should decrease the  $T_1$  population, so the fluorophores will return more quickly to the ground state. Brighter single-molecule emission has been observed in the presence of oxygen, relative to an oxygen-free sample,<sup>53</sup> which was interpreted as due to the shorter lived  $T_1$  state.

In addition to blinking the fluorophores also display irreversible photobleaching. The resistance of a fluorophore to photobleaching determines the average number of photons a fluorophore can emit prior to its destruction. The photostability of a fluorophore is described by its photobleaching quantum yield ( $\phi_B$ ) or the inverse ( $\mu = \phi_B^{-1}$ ). The value of  $\mu$  is the average number of excitation-relaxation cycles a fluorophore can undergo before photobleaching. When multiplied by the quantum yield, the product represents the average number of photons emitted by a fluorophore. Typical values of  $\phi_B$  and  $\mu$  are listed in Table 23.1 for representative fluorophores. These values are only rough estimates obtained by collecting data from several reports.<sup>47–48</sup> The number of cycles varies widely from 700 to 3 million depending on the fluorophore. These numbers are only guidelines because the actual number of cycles will

**Table 23.1.** Photostability of Representative Fluorophores<sup>a</sup>

Fluorophore	$\phi_B$	$\mu$
Carbostyryl 124	$1.4 \times 10^{-3}$	700
Coumarin 139	$1.2 \times 10^{-3}$	800
Coumarin 120	$4.3 \times 10^{-4}$	2300
Cy5	$5 \times 10^{-6}$	200,000
EGFP	$8 \times 10^{-6}$	125,000
Fluorescein	$3.8 \times 10^{-5}$	26,000
B-Phycoerythrin	$8.8 \times 10^{-6}$	114,000
Rhodamine 6G	$8.9 \times 10^{-6}$	112,000
Rhodamine 123	$6.4 \times 10^{-7}$	1,600,000
TMR	$2.6 \times 10^{-6}$	380,000
Texas Red	$5.5 \times 10^{-5}$	18,200
TRITC	$5.6 \times 10^{-6}$	179,000

<sup>a</sup>Representative values obtained from [47–48].  $\phi_B$  is the photo-bleaching quantum yield and  $\mu = 1/\phi_B$ . For some probes the averaged values are given.

vary widely depending upon the precise conditions of the samples such as the polymers and the presence or absence of oxygen.

## 23.6. BIOCHEMICAL APPLICATIONS OF SMD

### 23.6.1. Single-Molecule Enzyme Kinetics

Single-molecule detection provides an opportunity to follow a single enzyme molecule during its catalytic cycle. Suppose an enzyme molecule E is bound to the surface and labeled with a green-emitting fluorophore G (Figure 23.23), and that the substrate is labeled with a red-emitting fluorophore R. If one images the sample through a green filter there will be spots due to the immobilized enzyme. Except for blinking the green intensity will be constant. If the sample is imaged through a red filter there will be few if any red spots because the red fluorophores are rapidly diffusing. Occasionally the labeled substrate molecule will bind to the immobilized enzyme molecule. The immobilized red fluorophore will appear as a transient red spot. The duration of the red spot will depend on the time it takes for the substrate to bind, be cleaved, and then dissociate from the enzyme molecule. If a substrate analogue binds irreversibly the red spots will remain indefinitely until the fluorophore photo-bleaches. If the color images are overlaid the enzyme molecules with bound substrate will appear as yellow spots. The enzyme molecules without substrate will appear as green spots. Free substrates will not be seen as images due to their rapid diffusion.

Suppose the enzyme undergoes a conformational change upon binding substrate that increases the quantum

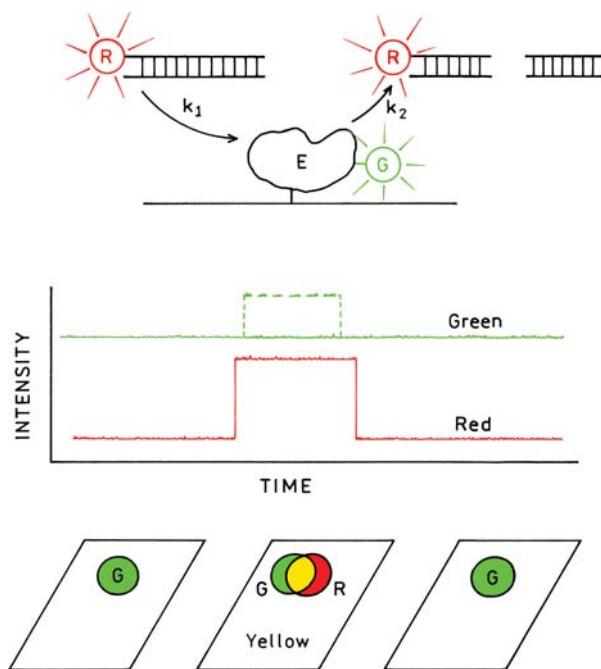


**Figure 23.23.** Schematic of a single-molecule enzyme-catalyzed reaction. The dotted line represents the case where the quantum yield of the green fluorophore increases upon substrate binding.

yield of the green fluorophore. In this case there will be an increase in the green intensity when the substrate binds (Figure 23.23, dashed line) and a return to the initial level when the substrate dissociates. The change in green intensity may correlate with the red intensity, or may exist for a shorter duration if a conformational change occurs after binding and before release of the substrate. Such a result would indicate the enzyme returns to its initial conformation before the products dissociate from the enzyme. Such a transient increase in green intensity would be difficult to observe in an ensemble measurement because only a small fraction of the enzyme molecules would be in the high-quantum-yield state at any given time. This description shows that considerable information can be obtained from measurements on single enzyme molecules.

### 23.6.2. Single-Molecule ATPase Activity

An example of single-molecule enzymatic activity is shown in Figure 23.24.<sup>54</sup> The S1 subfragment of myosin was bound to a glass surface using an albumin–biotin–avidin coating. The S1 subfragment possesses ATPase activity that cleaves the Cy3-labeled ATP. The protein was also labeled with Cy3, which allowed the single enzyme molecules to be located on the slide. After localization of the labeled

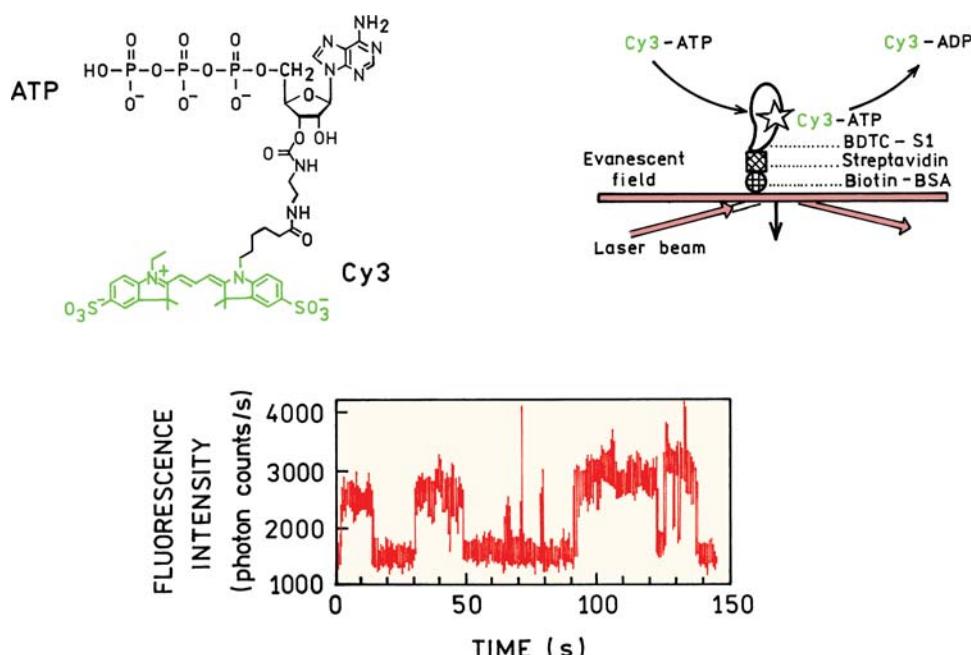


**Figure 23.24.** Single-molecule enzyme kinetics of ATPase activity. The enzyme was myosin subfragment 1 (S1). The measurements were performed using objective-type TIR. Reprinted with permission from [54].

ATPase the Cy3 bound to S1 was photobleached to eliminate its emission. This location was then observed after addition of Cy3-ATP. The intensity shows transient increases when Cy3-ATP/ADP is immobilized on the enzyme. The intensity returns to background when the Cy3-ADP dissociates from the protein. This experiment was performed using objective-type TIR. The small thickness of the illuminated area was important to reduce the background intensity from freely diffusing Cy3-ATP.

### 23.6.3. Single-Molecule Studies of a Chaperonin Protein

The concept shown in Figure 23.23 can be used to study any association reaction. Suppose the surface contains a green capture protein that binds to a red protein. Green dots will be seen whenever there is a capture protein. Red dots will only appear when this protein binds to the capture protein. Co-localization of green and red spots will indicate the presence of a complex on the surface. This concept has been applied to the study of chaperonin GroEL.

Chaperonins are a class of proteins that promote folding reactions in cells. They can facilitate folding of newly synthesized proteins or the refolding of denatured proteins. A well-known chaperonin is GroEL from *(Escherichia coli)*.

GroEL is a large cylindrical protein containing 12 subunits (Figure 23.25). GroEL was labeled with an indocyanine dye IC5 and bound to a glass surface.<sup>55</sup> Bovine (BSA) and human serum albumin (HSA) spontaneously

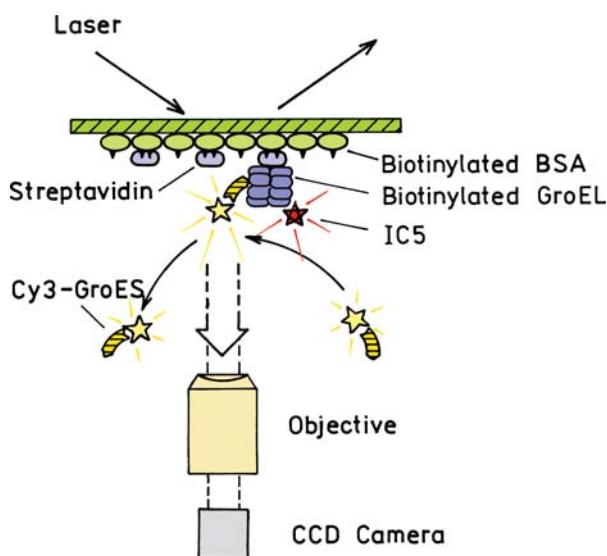


**Figure 23.25.** Chaperonin GroEL and GroES. GroEL is labeled with IC5 and GroES is labeled with Cy3. Reprinted with permission from [55].

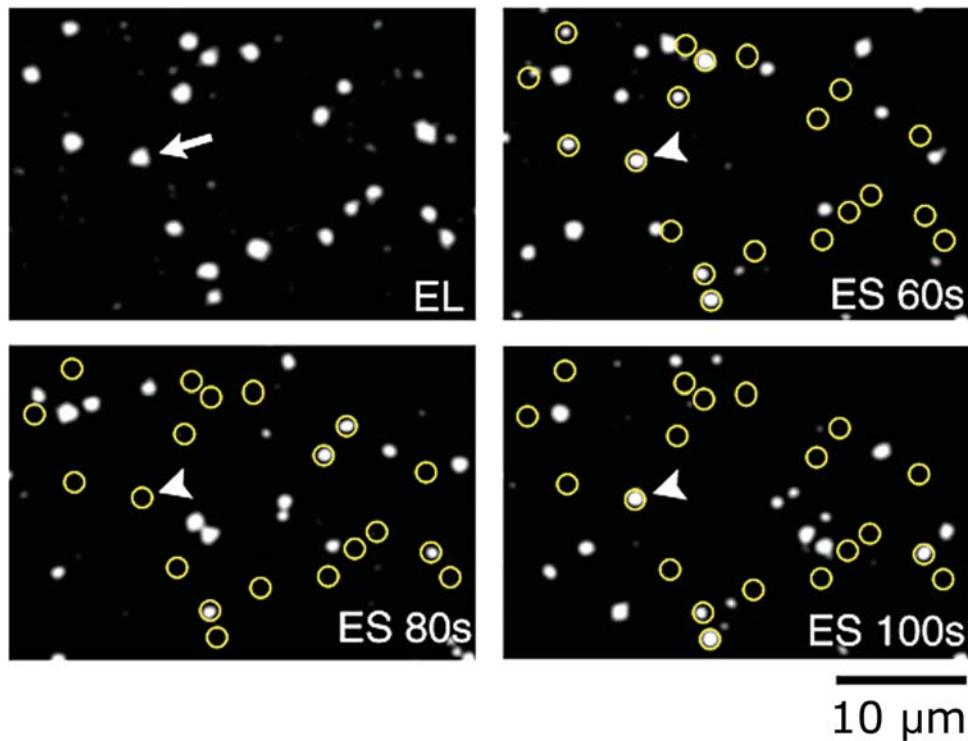


**Figure 23.26.** Single-molecule images from IC5-labeled GroEL (EL) and Cy3-labeled GroES (ES) at the indicated times. The images were obtained using TIR and an intensified CCD camera. The circles show the positions of GroEL. Reprinted with permission from [55].

bind to glass surfaces. If the BSA is biotinylated then avidin or streptavidin binds strongly to the surface. Streptavidin contains four biotin binding sites, providing residual binding sites for biotinylated GroEL. This method of attachment is frequently used to attach biomolecules to surfaces.

This system was examined using TIR excitation and an intensified CCD camera for imaging. The upper left panel in Figure 23.26 shows the locations of GroEL, as determined by emission from IC5. The remaining three panels show images of Cy3-GroES. In the presence of ATP GroES binds to GroEL and the complex acts to refold proteins. At first the images of GroES are confusing. Some appear where GroEL is also located and other GroES molecules appear where there appeared to be no GroEL. In either case the GroES has to be immobilized to see its emission. The different positions of GroES binding can be understood as due to molecular heterogeneity. The surface contains GroEL molecules that are labeled with IC5 and GroEL molecules that are not labeled with IC5. This shows how different types of reasoning are needed to interpret single-molecule and ensemble measurements.

The arrows in Figure 23.26 point to one GroEL molecule where a GroES molecule also binds. The GroES molecule appears in 2 of the 3 frames. In this case the absence of GroES in the 80-second frame is not due to blinking, but rather to dissociation from GroEL. The process of GroES binding to GroEL can be followed with time (Figure 23.27). The Cy3-GroES emission appears and disappears as it binds to and dissociates from GroEL. This observation of single-molecule binding kinetics provides a unique way to measure association and dissociation rates for the reaction. The times when GroES is observed and when it is missing provides a statistical measure of the rate constants. If a suitably large number of events are studied the fluctuations in Cy3-GroES emission can be used to determine the on and off rates for the reaction.

Histograms of the on and off times are shown in Figure 23.28. The top panel of Figure 23.28 shows a histogram of the off time, the time duration when emission from Cy3-labeled GroES is not observed. A large number of short-duration events were observed. A smaller number of events were observed for longer durations. This type of data can be

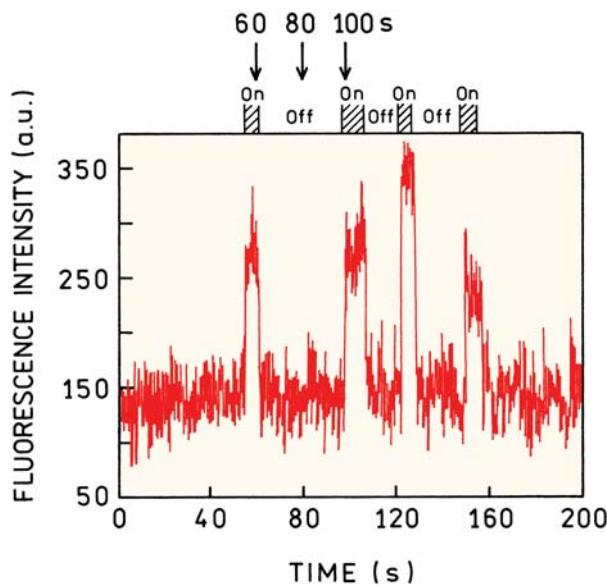


**Figure 23.27.** Time-dependent intensities of Cy3-labeled GroES for the spot indicated by the arrows on Figure 23.26. Reprinted with permission from [55].

used to calculate the rate constant for binding. Consider a single GroEL molecule that does not contain GroES. At short times there is a high probability that GroES is not bound. At longer times there is a smaller probability that GroES has not bound to GroEL. The histogram of the times needed for binding reveals the binding rate constant, just like the histogram in TCSPC reveals the lifetimes.

In a similar way the on times can be used to obtain the rate of GroES dissociation. Assume the starting point is the GroEL–GroES complex. We know the complex is present because of the emission from Cy3. The complex dissociates spontaneously, as seen by the disappearance of Cy3 emission (Figure 23.28, lower panel). This decay of the complex is just like the decay of an excited state, and the histogram of decay times yields the decay rate. In the case of GroEL there appears to be a time lag prior to dissociation, as seen by the rise time at short times. The authors attribute this time decay to an intermediate state of the complex that has not been identified.<sup>55</sup>

### 23.7. SINGLE-MOLECULE RESONANCE ENERGY TRANSFER

Single-molecule detection becomes an even more powerful tool when combined with resonance energy transfer (RET). Figure 23.29 shows a typical experiment in which emission

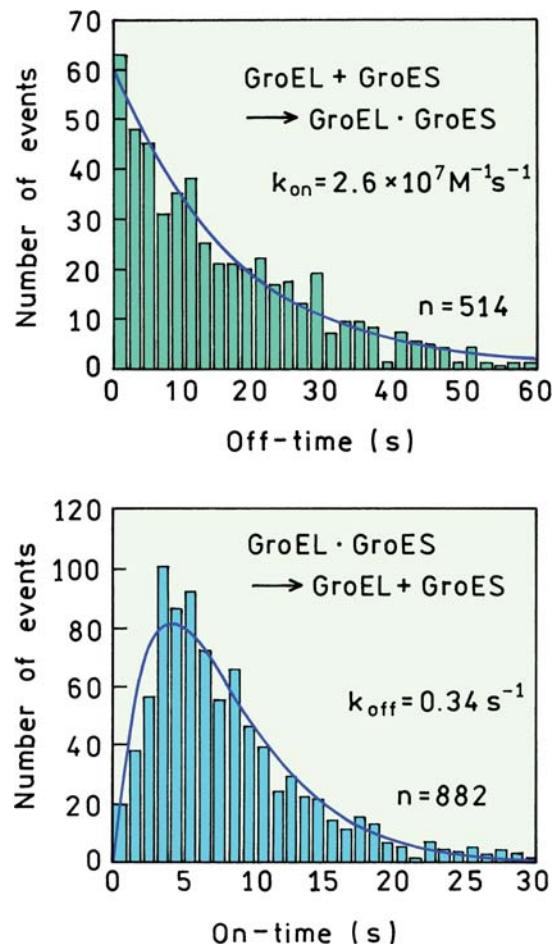


**Figure 23.28.** Histogram of the off (top) and on time durations (bottom) of GroES binding to GroEL.  $N$  is the number of events. The on and off times refer to the time duration when GroES contains, or does not contain, GroEL, respectively.  $k_{on}$  is the rate constant for the association reaction,  $k_{off}$  is the rate constant for the dissociation reaction. Revised from [55].

spectra and lifetimes are measured for a mixture of protein molecules each labeled with a donor D. The solution also contains a fluorescent acceptor A that binds to some of the donor-labeled protein. The emission spectrum of the solution will show the presence of both the donor and acceptor. The situation is complicated because the acceptor emission will be due to two subpopulations: acceptor free in solution and acceptor bound to donor. Similarly, the donor emission spectrum will be due to two components—D and DA. Even if the intensity decays of the donor or DA pair alone are single exponentials the donor decay for the mixture would be multi-exponential because there would be two species—D and DA.

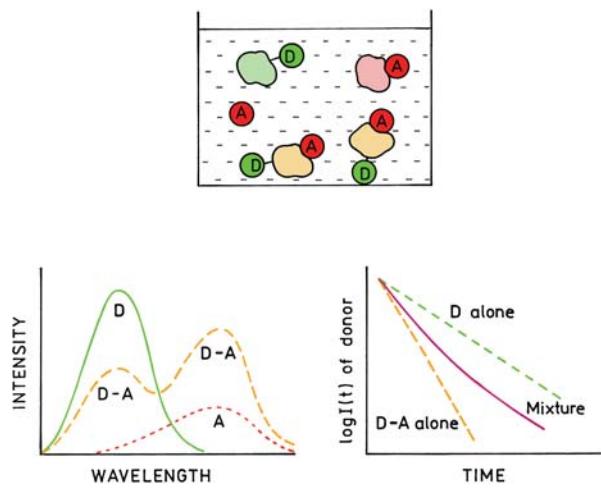


**Figure 23.29.** Emission spectra and intensity decay for a mixture of donor-alone (D) and donor–acceptor (D–A) pairs, and acceptor alone, as seen in an ensemble-averaged measurement.

Observations on single molecules can resolve such heterogeneity and bypass ensemble averaging. Suppose the donor-labeled protein is immobilized on a glass surface (Figure 23.30) and that single protein molecules could be separately observed. Then the signal due to any single molecule would be due to either a donor-alone molecule (left) or a protein molecule that contains bound acceptor (right).

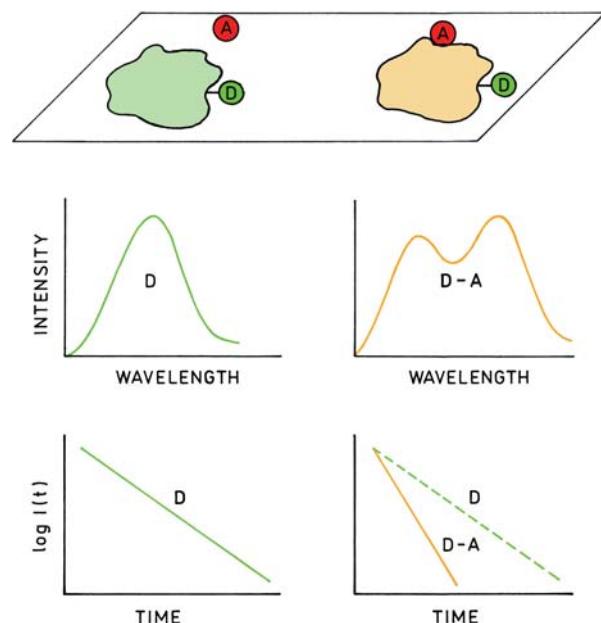


**Figure 23.30.** Emission spectra and intensity decays for single-molecule measurements for a mixture of donor-alone and donor–acceptor pairs immobilized on a surface.

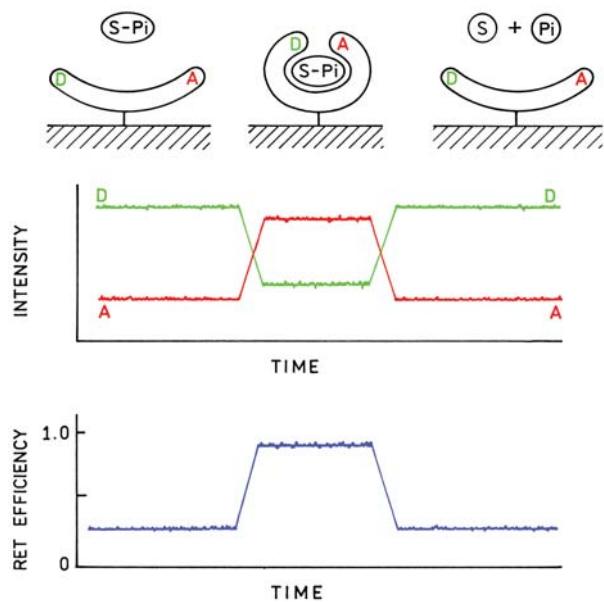


**Figure 23.31.** Schematic of enzyme-catalyzed hydrolysis of a substrate–phosphate (S–Pi) as seen by SMD.

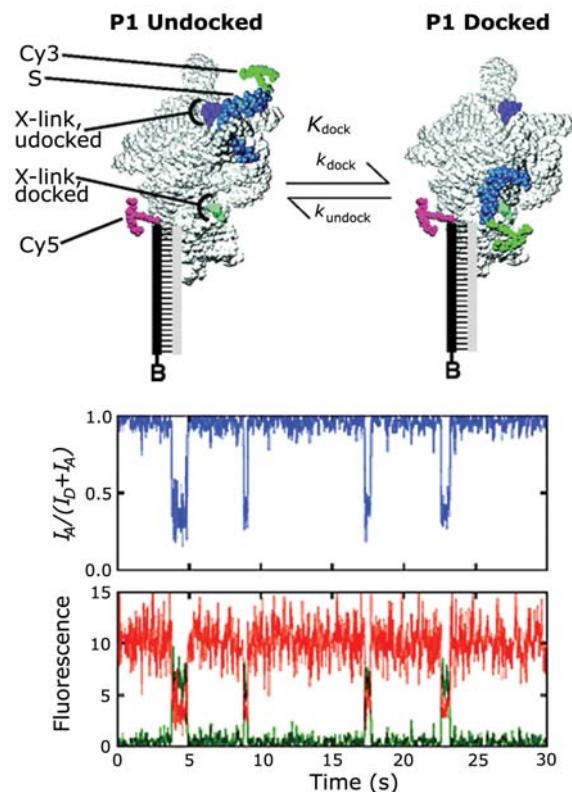


**Figure 23.32.** Single-molecule RET of a ribozyme molecule. The lower panels show the time-dependent donor (green) and acceptor (red) intensity and RET efficiency. Reprinted with permission from [56], [58].

As a result the emission spectrum would be that of the donor alone or of a donor–acceptor pair. Similarly, the intensity decay would be a single exponential, a longer lifetime for the donor-alone and a shorter lifetime for the DA pair. Hence observation of the single protein molecules allows the properties of each species (D and DA) to be measured.

Single-molecule RET can also be used to detect conformational changes in macromolecules. Assume the macromolecule is labeled with both a donor and an acceptor. Suppose the donor and acceptor are initially too far apart for RET but closer together when a complex is formed (Figure 23.31). Complex formation will result in a decrease in donor intensity and increased acceptor intensity. These intensity changes can be used to calculate the efficiency of energy transfer at any point in time. This coupling of changes in the donor and acceptor intensities provides a direct approach to study the dynamics of macromolecules.

Single-molecule RET has been used to follow conformational changes in a single ribozyme molecule.<sup>56</sup> Figure 23.32 shows a ribozyme from *Tetrahymena thermophila*. The ribozyme was linked to the surface by extending the 3' end of the ribozyme. An oligonucleotide complementary to the extension was bound to the surface by biotin–streptavidin chemistry. This tethering oligo was also labeled with a Cy5, providing the acceptor labeling on the ribozyme. The substrate of the reaction, which is another short oligonucleotide, was labeled with Cy3 as the donor. The labeled molecules were observed using TIR microscopy.

The lower panel in Figure 23.32 shows the time traces of the Cy3-donor and Cy5-acceptor emission. These signals are clearly anticorrelated, when the donor intensity drops the acceptor intensity increases, and vice versa. These signals were used to calculate the time traces for RET, showing oscillations from about 35 to 100%, indicating a change in D–A distance from about 70 to 15 Å. These data thus revealed the time-dependent motions of the labeled substrate on the ribozyme, which is shown schematically in the figure. It is clear from these examples that single-molecule studies of biomolecules can provide unique insights into the function and dynamics of biomolecules.

### 23.8. SINGLE-MOLECULE ORIENTATION AND ROTATIONAL MOTIONS

Since single molecules can now be detected, laboratories have started performing more detailed spectroscopic measurements.<sup>57–60</sup> Studies of polarized emission from single

fluorophores provides some unique opportunities. At first glance the experimental results are counterintuitive when viewed from the perspective of ensemble-averaged measurements (Chapters 10–12). It is easier to understand the single-molecule results following an intuitive description of the unique features of single-molecule polarized emission. We are using both the terms polarization and anisotropy because there is presently no standardized formalism for SMD. Both the polarization and anisotropy are useful under different experimental conditions.

Figure 23.33 (top panel) shows a schematic optical configuration and results for a single fluorophore with collinear absorption (A) and emission (E) dipoles, where  $\beta = 0$ , and  $\beta$  is the angle between the transition moments. In such experiments the excitation is frequently delivered to the sample by an optical fiber. Assume there is a single immobilized fluorophore with its transition moment oriented along the  $x$ -axis, and that the emission is observed without a polarizer. Recall that the probability of absorption is proportional to  $\cos^2 \theta$ , where  $\theta$  is the angle between the absorption transition moment  $A$  and the incident electric field. As the electric vector of the incident light is varied the intensity changes as  $\cos^2 \theta$  (top panel). The maximum intensity occurs at  $\theta = 0$ , where the incident field is parallel to  $A$ .

Now consider excitation with unpolarized light (Figure 23.33, lower panel) with observation through a polarizer. Rotating the emission polarizer will yield the same result, with the intensity changing as  $\cos^2 \theta$ . In fact, polarization of the incident light does not affect the result, except at  $\theta = 90^\circ$  when the fluorophore is not excited. The emission always displays  $\cos^2 \theta$  dependence centered at  $\theta = 0$  because the single molecule radiates as a dipole oriented along the  $z$ -axis. Assume in the lower panel the intensity along the  $x$ -axis is  $I_{\parallel}$ , and  $I_{\perp}$  along the  $y$ -axis. Both the polarization and anisotropy are 1.0. Recall that the highest anisotropy of a solution is 0.4, which is the result of  $\cos^2 \theta$  photoselection with ensemble averaging. Recall that a fluorophore always emits from the lowest singlet state. As a result the polarization of a single molecule is the same independent of the polarization of the excitation. SMD avoids averaging, returning the value of 1.0 expected for a single fluorophore (Chapter 10).

Now consider similar measurements for a fluorophore with perpendicular absorption and emission dipoles, where  $\beta = 90^\circ$  (Figure 23.34, top). Assume the angle of the incident field is rotated, and the emission is observed without an emission polarizer (top). One obtains the same  $\cos^2 \theta$  dependence as for  $\beta = 0$ . Notice the maximum is again at  $\theta$

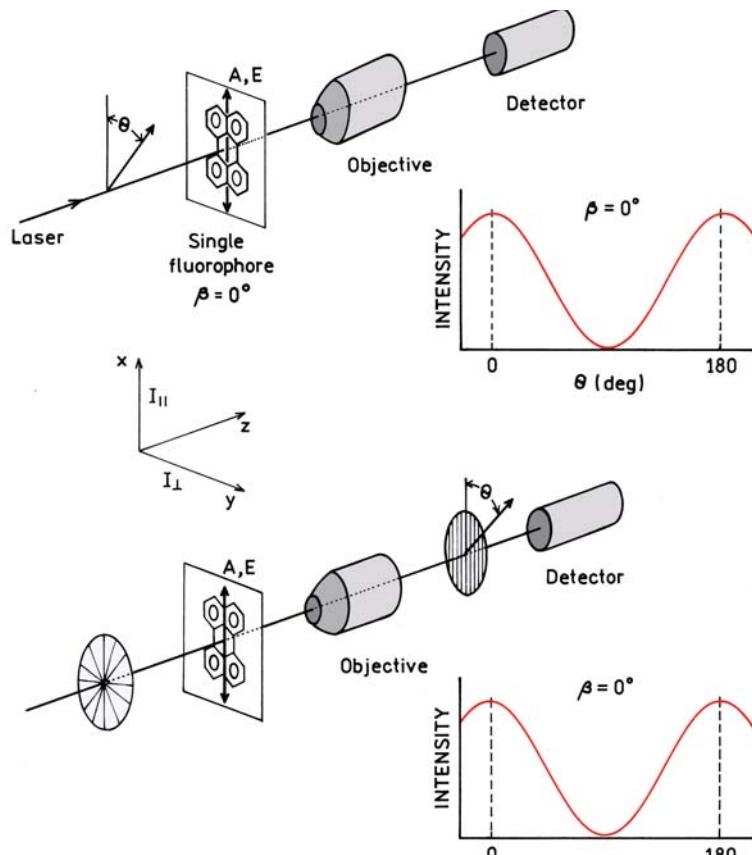


**Figure 23.33.** Polarization properties of a single fluorophore with colinear ( $\beta = 0^\circ$ ) absorption (A) and emission (E) dipoles.

$= 0^\circ$ , even though  $\beta = 90^\circ$ . This surprising result can be understood as the result of the  $\cos^2 \theta$  dependence on absorption. Since the fluorophore is observed without an emission polarizer the maximum signal is seen when the excitation rate is the highest, at  $\theta = 0$ . A different result is obtained if the fluorophore is excited with unpolarized light and observed through an emission polarizer (Figure 23.34, bottom panel). Now the  $\cos^2 \theta$  dependence is shifted  $90^\circ$  due to  $\theta = 90^\circ$ . The same dependence on  $\cos^2 \theta$  would be observed for any polarization of the incident light because the emission intensity through the polarizer is determined by the position of the emission dipole. The polarization of the emission is  $-1.0$  because the emission is polarized along the  $y$ -axis.

In a typical ensemble anisotropy measurement one usually rotates the emission polarizer to perform the measurement (Chapter 10). However, in Figure 23.33 and 23.34 (top panels) the excitation polarization was rotated. This is frequently done in polarized fluorescence microscopy because of the depolarizing effects of the microscope objec-

tive. If linearly polarized light is passed through the aperture and focused on the sample or molecule, the field is partially depolarized.<sup>61</sup> This effect is a result of the large numerical aperture and the different angles of incidence for light, passing through the center or the outer region of the objective. Light can be brought to the sample without this effect if the light is not passed through the objective, but instead directly to the sample (Figure 23.35). The larger aperture of the objective does not affect the emission measurements because the objective simply collects the emission which depends only on the orientation of the incident polarization and the fluorophore. The orientation of the incident polarization defines the parallel component ( $I_{\parallel}$ ). This component can be rotated to be at any angle in the focal plane. Of course, the single molecule will only be excited if its absorption dipole has a component along the incident electric field. The emission is collected by an objective and passed through a filter to remove the scattered light.

In single-molecule experiments every photon is valuable. The molecule may display blinking and will be

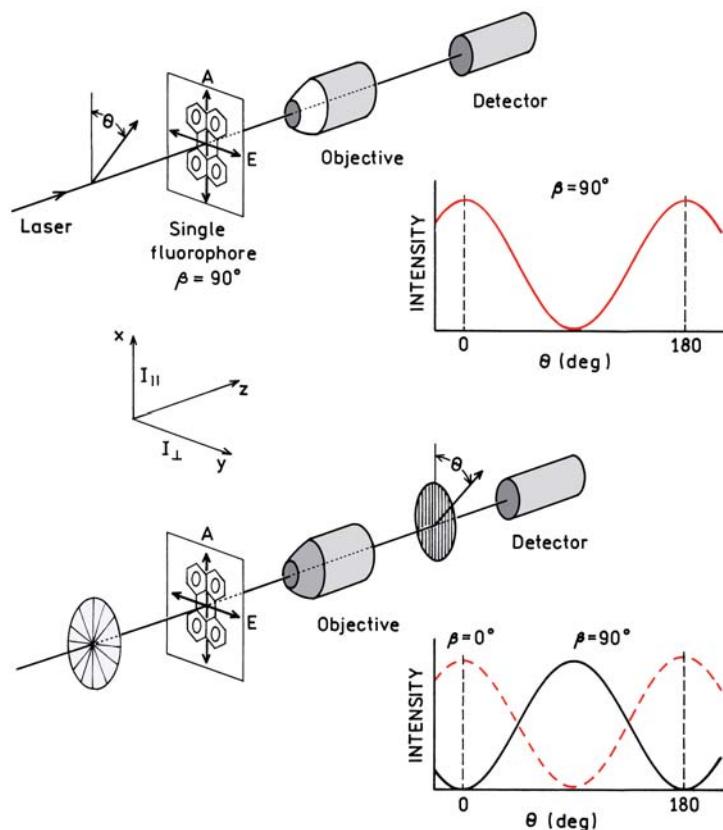


Figure 23.34. Polarization properties of a single fluorophore with perpendicular absorption (A) and emission (E) dipoles.

destroyed after a short period of observation. For these reasons it is not practical to rotate an emission polarizer to separately measure the two polarized components of the emission. These polarized components are easily separated with a polarizing beamsplitter (Figure 23.35). With this device the p-component relative to the reflective surface of the beamsplitter is p-polarized. The s-polarized component is not reflected and passes through the device.<sup>62</sup> See Chapter 2 for a definition of p and s polarization. One can see that the p-polarized intensity ( $I_p$ ) corresponds to the parallel intensity ( $I_{\parallel}$ ), and the s-polarized component ( $I_s$ ) corresponds to the perpendicular intensity ( $I_{\perp}$ ). The relative detection efficiencies of the two channels (G-factor) can be measured with solution of fluorophores which displays an anisotropy of zero. It is important to remember that the objective will depolarize the emission to some extent due to its large collection angle.<sup>61,63</sup>

In this discussion of single-molecule polarization we assumed that the dipoles were perpendicular to the optical axis. In reality the transition moments will also have com-

ponents along the optical axis that are out of the sample plane. Rather than present the somewhat complex mathematical expression to describe these cases, then intuitive concepts in Figures 23.33 and 23.34 will provide an understanding of the experimental results for single molecules.

### 23.8.1. Orientation Imaging of R6G and GFP

The optical configuration shown in Figure 23.35 was used to study R6G molecules in a polymer.<sup>64-65</sup> A number of R6G molecules were imaged by scanning the sample stage. The images (Figure 23.36) were obtained by simultaneous measurement of the s and p components. The left and middle images show these polarized components. During the scan the signal in each image transiently disappears which looks like blinking. However, the summed image (right) does not show the dark vertical line which indicates the fluorophores are not blinking under these experimental conditions. These results indicate that the R6G molecules displayed rotational diffusion or jumps in the polymer. This is

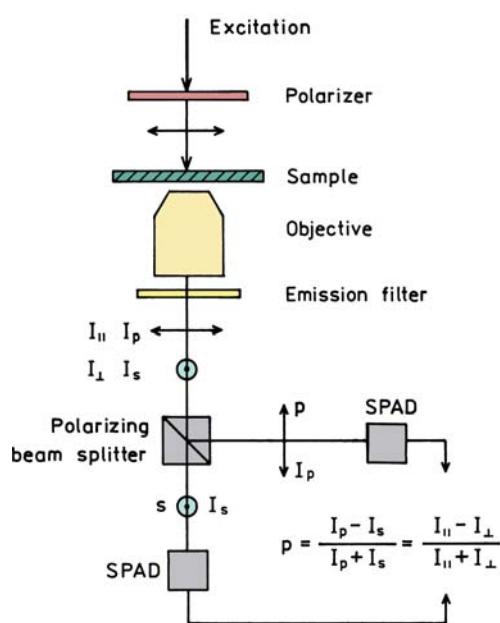


**Figure 23.35.** Typical configuration for single-molecule polarization measurements.

reasonable when one recalls it takes considerable time to scan the sample stage, so the molecule can rotate before the stage returns to that molecule for a second illumination.

Another approach to single-molecule orientation imaging is to use polarized excitation. As shown in Figure 23.33 the emission will show the same polarization independent of the polarization of the incident light. Polarized excitation was used with NSOM to image GFP in poly(acrylamide) (Figure 23.37). Excitation was accomplished with an aluminum-coated fiber optic with a 70-nm aperture using 488-nm laser light.<sup>66</sup> The relative intensities in the two polarized channels were used to calculate the orientation of the trans-

sition dipoles on the slide. Since the emission remained polarized during the scan, the GFP molecules were immobilized by the poly(acrylamide) gel. The images show that the individual GFP molecules each have different photostabilities. Molecules 2 and 3 are stable and did not blink. Molecules 4 and 5 displayed blinking. Molecule 1 appears to have been photobleached during the scan.

Single-molecule orientations can also be determined using NSOM and the shape of the single-molecule image.<sup>67–69</sup> Figure 23.38 shows a focused-ion-beam (FIB) image of the NSOM probe. The probe is coated with aluminum, except for the small dark ring in the center (a). The sample was DiIC<sub>12</sub> in PMMA. Image b shows the NSOM images when the excitation is circularly polarized. The images are not simple circles because of the sharp electric-field gradients that exist near the tip of the metal-coated fiber. Because of these field gradients the interactions of the fluorophore with the NSOM tip depend on its location and the orientation of the transition moments.

The orientation of the fluorophore can be determined from the shapes, but the theory is rather complex. The lower two images were obtained using linearly polarized light, as shown by the arrows. All the images are color coded according to the detected polarization. One of the circular images in panel b becomes a double-labeled image with linearly polarized excitation in panels c and d. These polarized NSOM images provide remarkable detail on fluorophore orientation.

### 23.8.2. Imaging of Dipole Radiation Patterns Advanced Topic

The previous results on single-molecule polarization imaging were obtained using point-by-point measurements and a

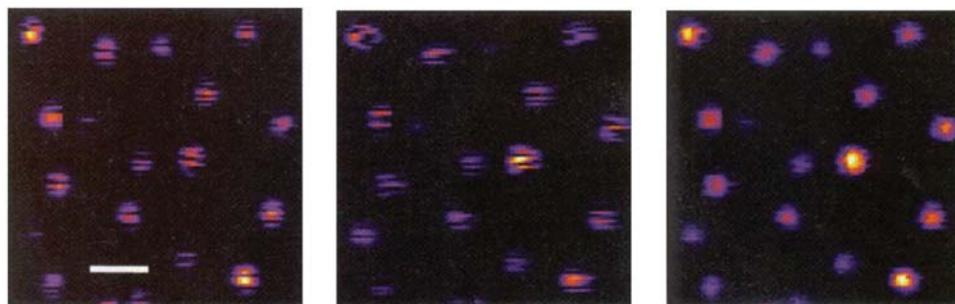


**Figure 23.36.** Polarized emission images of R6G molecules in poly(methylmethacrylate). The PMMA had a glass temperature of 8°C. The two orthogonal polarization images (left and center) were used to construct the summed image (right). The white bar is 1 μm. Reprinted with permission from [64].

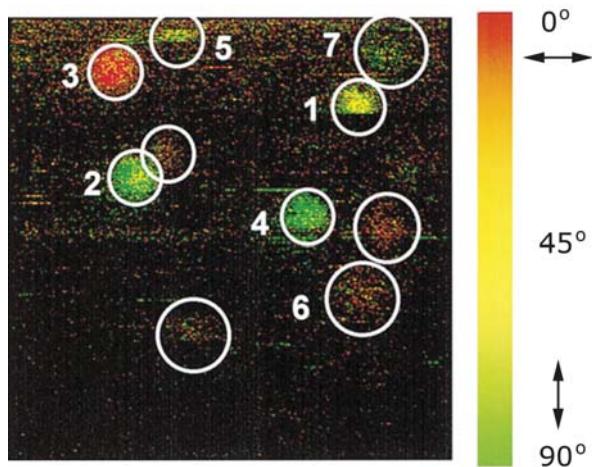


**Figure 23.37.** NSOM orientation imaging of GFP in poly(acrylamide). Image size  $1.8 \times 1.8 \mu\text{m}$ . Reprinted with permission from [66].

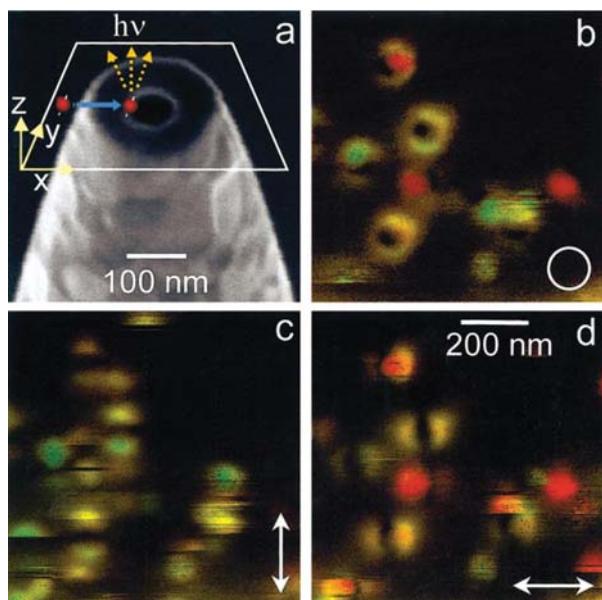


**Figure 23.38.** Imaging of dipole orientation using NSOM. The sample was DiIC<sub>12</sub> in PMMA. The circle and arrows represent the incident polarization. The green-to-red scale indicates the polarization of the emission. Reprinted with permission from [68].

scanning sample stage. It is also possible to determine fluorophore orientations by a direct imaging method.<sup>70-74</sup> The theory is rather complex, but the result is intuitively simple. If the light collection optics are perfect each fluorophore will appear as a diffraction limited spot, irrespective of its orientation. However, if there is a slight mismatch in the immersion fluid then light entering the objective at different

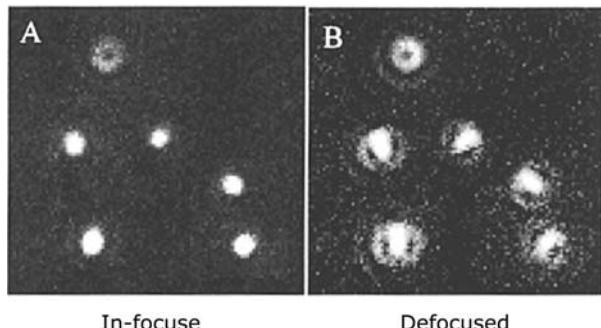
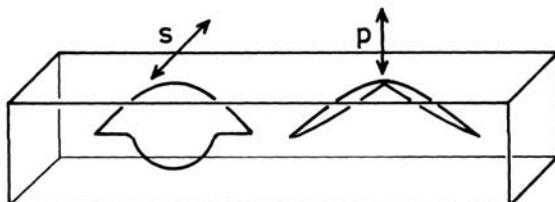


**Figure 23.39.** Imaging of single molecule DiIC<sub>12</sub> in PMMA. Upper panel shows radiation pattern for a dipole near a dielectric interface. Reprinted with permission from [70].

angles is not focused at the same point. Figure 23.39 shows such images. The spatial emission patterns are dots, circles, or a more complex distorted circle with a central dot. These images can be understood by the angle-dependent radiation patterns for a dipole near a dielectric interface (top schematic). These patterns can be calculated from classical electrodynamics. The image on the left was obtained with the fluorophores in the focal plane and the image on the right was obtained with slight defocusing. In this latter image the transition moments perpendicular to the interface (p) result in a doughnut-like image. This can be understood from the strong angular dependence of the p-dipole coupling into the glass substrate. Transition moments parallel to the interface (s) yield filled circles. If the image is slightly defocused (right) additional information becomes available. The images become distorted along the direction of the dipole orientation. Remarkably, it is now possible to image not only single molecules, but to image their orientations as well.

### 23.9. TIME-RESOLVED STUDIES OF SINGLE MOLECULES

Time-resolved ensemble measurements frequently reveal multi-exponential decays for seemingly homogeneous sam-

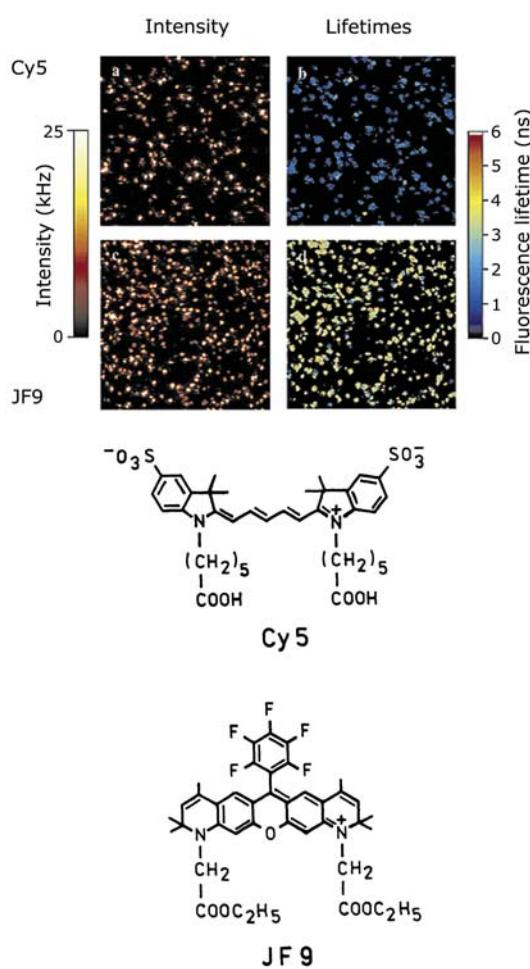


**Figure 23.40.** Single-molecule intensities (left) and lifetimes (right) for Cy5 (top) and JF9 (bottom) on a glass surface. Images were obtained using confocal laser scanning microscopy. The lifetimes of Cy5 and JF9 are near 2 and 4 ns, respectively. Reprinted with permission from [78].

ples, particularly for biomolecules. Such results are frequently explained as the result of some underlying heterogeneity, such as the rotamer conformations for tryptophan (Chapter 16). Hence it is natural to use time-resolved detection with single molecules to observe the properties of each subspecies. Several reports have appeared on time-resolved SMD. To date essentially all such studies have been performed using TCSPC at a defined position in the sample.<sup>75–78</sup> Typically the sample is raster scanned to find the locations of the molecules. The stage is then repositioned on the molecule of interest, which is excited with a pulsed laser. The repetition rate of the laser is typically 1 MHz or higher and the dwell time at each location is about 1 ms.

There is time for a number of pulses to arrive at the sample during the dwell time. The time intervals between the start and stop pulses are recorded along with an identifier for the location of the molecule on the slide.

An example of single-molecule lifetime imaging is shown in Figure 23.40 for Cy5 and JF9. The two left panels are the intensity images. The dyes cannot be distinguished based on the intensities. The two right images show the lifetime for Cy5 (top) and JF9 (bottom). The two fluorophores can be distinguished from the lifetimes, even at the single-molecule level. The measurements were then extended to a mixture of Cy5 and JF9 (Figure 23.41). The two fluorophores cannot be distinguished in the intensity image (left). However, the individual fluorophores can be identified from the fluorescence lifetime (right). Since lifetimes are independent of the total intensity, and since the fluorophores photobleach, we can expect to see more uses of single-molecule lifetime imaging. These applications will be facilitated by the increasing ease of lifetime measurements using pulsed laser diodes and modern electronics.

## 23.10. BIOCHEMICAL APPLICATIONS

### 23.10.1. Turnover of Single Enzyme Molecules

Single-molecule detection has been used to image the activity of individual enzyme molecules. The protein cholesterol oxidase (Cox) was immobilized in an agarose gel.<sup>79</sup> Polarization studies showed that the protein displayed rotational diffusion, but the gel prevented translational diffusion. Cox catalyzes the oxidation of cholesterol, as shown in the top panel of Figure 23.42. The cofactor FAD is tightly bound to the enzyme and is not expected to dissociate. The slide containing immobilized enzyme was imaged by scanning a 442-nm HeCd laser beam across the sample. Recall that the oxidized form of FAD is fluorescent (Chapter 3). Hence the reaction results in transient emission from the FAD until it is reduced by the enzymatic reaction. The on-off fluorescence from the protein results in bright spots due to single Cox molecules (Figure 23.43). The spots display a range of intensities. This is because photon counts are accumulated for the entire time the oxidized form is present on the protein. FAD itself did not display blinking under these conditions. If a single spot is examined with higher time resolution it displays a blinking intensity, which indicates reduction or oxidation of the cofactor (Figure 23.42, lower panel). Accumulation of a longer time trace and examination of multiple enzyme molecules allowed the Michaelis-

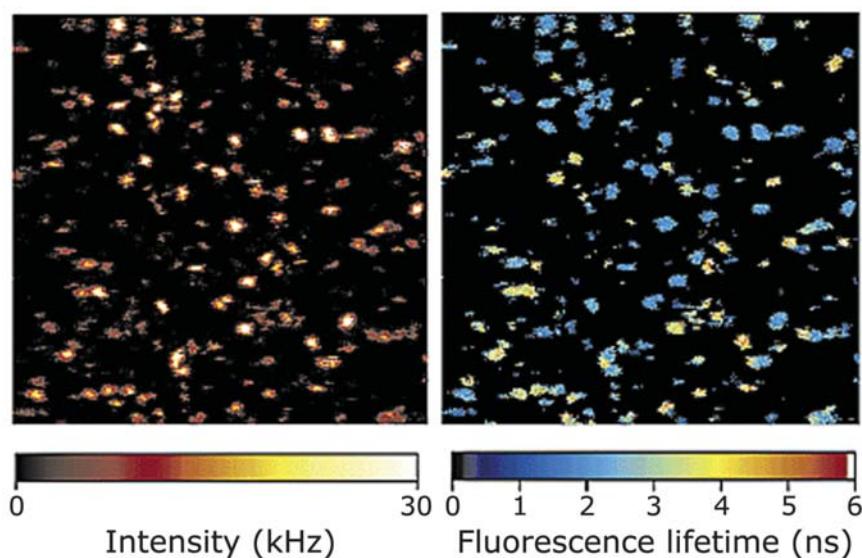


**Figure 23.41.** Single-molecule intensity and lifetime images for a mixture of Cy5 and JF9 on a glass surface. Reprinted with permission from [78]. Copyright © 2002, American Chemical Society.

Menten rate constants to be determined from the reaction-induced blinking.<sup>79</sup>

Another example of single-molecule enzyme kinetics is shown in Figure 23.44. The enzyme dihydroorotate dehydrogenase (DHOD) catalyses a reaction in the first step of de-novo pyrimidine synthesis. In this reaction cycle FMN is reduced and oxidized. Unfortunately, the flavin is quenched by a tyrosine residue in the wild-type *E. coli* protein (Figure

23.44). To obtain a useful signal the nearby tyrosine residue responsible for the quenching was mutated to a leucine.<sup>80</sup> The enzyme molecules were immobilized in a 1% agarose gel and localized by the flavin emission. However, the emission quickly disappeared (Figure 23.45), and the disappearing signal was due to dissociation of FMN from the protein and not photobleaching. Because the rate of disappearance was not dependent on incident power, in the presence of substrates the FMN displayed rapid blinking in addition to disappearance that was the result of the oxidation-reduction cycles occurring prior to dissociation (Figure 23.45). The distribution of on and off times could be used to determine kinetic constants for the reaction.

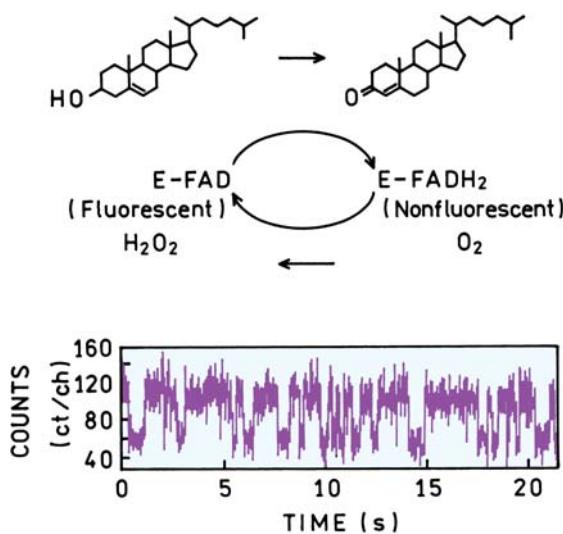


**Figure 23.42.** Blinking of FAD emission during oxidation of cholesterol by Cox. The top panel shows the chemical reaction. Revised from [79].

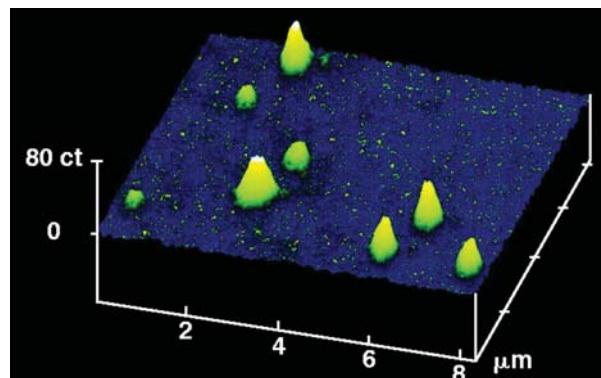


**Figure 23.43.** Single-molecule images of cholesterol oxidase as seen from the emission of FAD. Reprinted from [79].

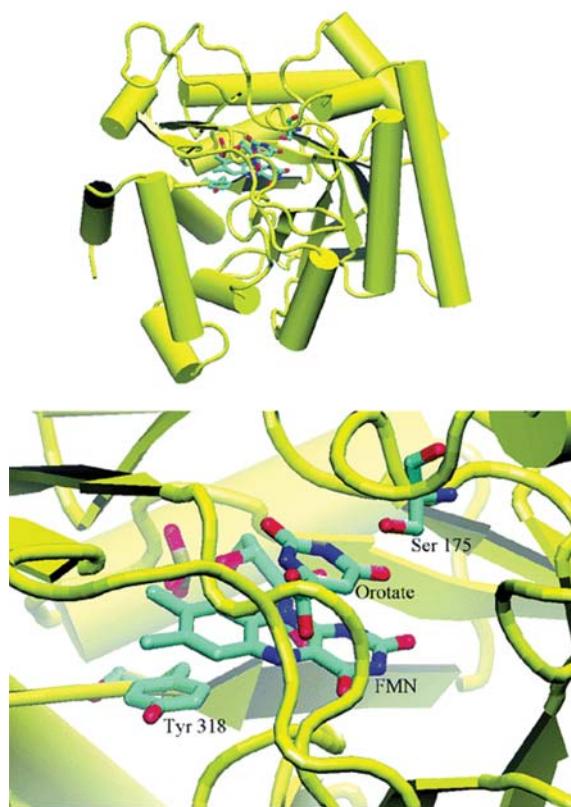


**Figure 23.44.** Top: Structure of wild-type DHOD from *E. coli*. Bottom: Environment of FMN in the catalytic site. Reprinted with permission from [80]. Copyright © 2004, American Chemical Society.

### 23.10.2. Single-Molecule Molecular Beacons

We started this chapter with a schematic of a single-molecule molecular beacon (Figure 23.1). In fact, such an experiment has been reported.<sup>81</sup> Figure 23.46 shows a surface-bound molecular beacon. This sequence has a biotin on one end and the fluorophore MR121 at the opposite end. The sequence is designed so that a guanine residue is next to MR121 when the beacon is in the hairpin conformation. In solution this beacon displays a sixfold increase in intensity when hybridized with the complementary oligo.

The lower panels in Figure 23.46 show confocal images of surface-bound beacons in the absence (left) and presence (right) of the complementary oligo. Hybridization with the complementary oligo results in an increase in the number of observable spots. The actual increase in intensity is larger than it appears because the scale on the left image is four times smaller than the right image. This approach allows detection of single hybridization events.

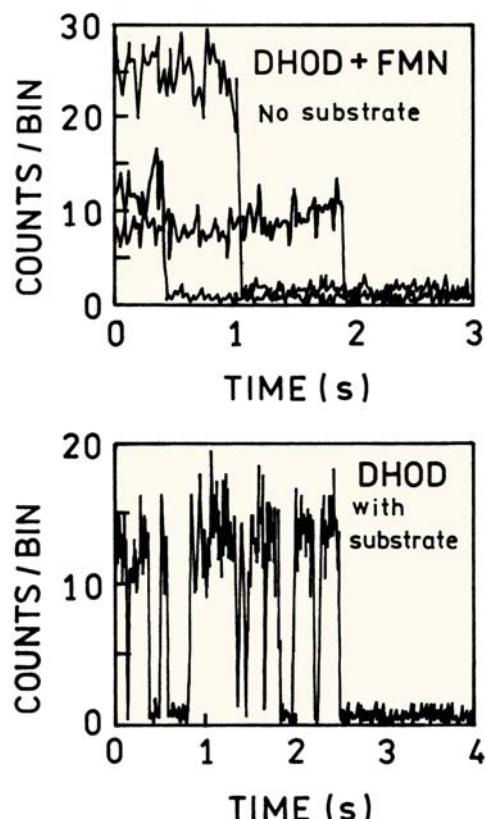
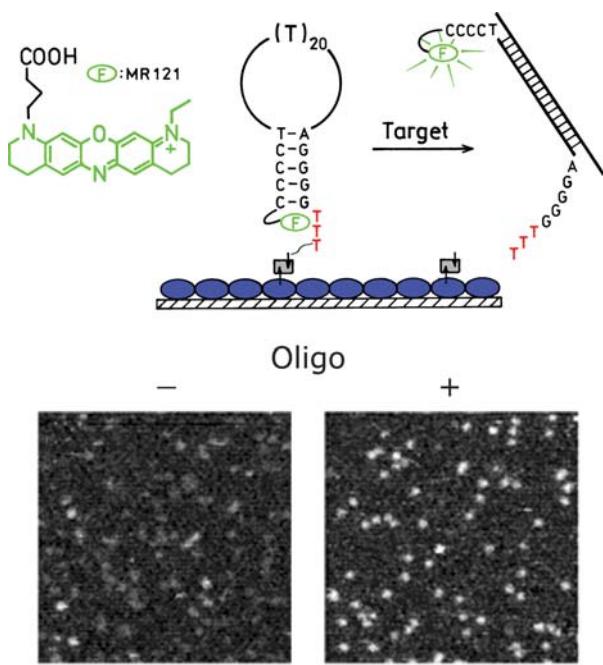


**Figure 23.45.** Emission intensities of FMN bound to dihydroorotate dehydrogenase in the absence (top) and presence (bottom) of substrates. The top panel shows traces for three different molecules. The protein was immobilized in an agarose gel. Reprinted with permission from [80]. Copyright © 2004, American Chemical Society.

### 23.10.3. Conformational Dynamics of a Holliday Junction

Single-molecule FRET has been extensively useful in studies of the conformational dynamics of DNA and RNA.<sup>82–88</sup> One example is a study of the structural dynamics of a Holliday junction.<sup>83</sup> Genetic recombination is an important component of genetic diversity and evolution. Recombination occurs when sections of DNA are exchanged between chromosomes. This recombination occurs at sites that are called Holliday junctions. These junctions or sections of DNA form a four-way cross (Figure 23.47). These junctions are formed and break when DNA strands are exchanged.

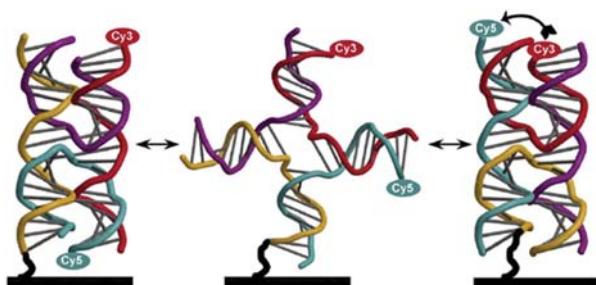
The Holliday junction in Figure 24.47 contains four DNA oligomers. One oligomer was synthesized with a donor (Cy3) and a second oligomer was synthesized with an acceptor (Cy5) both on the 5' ends of the DNA strands. A third strand was labeled with biotin for surface immobilization. The four-way junction was expected to change its con-



**Figure 23.46.** Confocal images of an immobilized beacon, with and without the complementary oligo, respectively. The left and right intensity scales are 0–4 and 0–16, respectively. Reprinted with permission from [81]. Copyright © 2003, American Chemical Society.

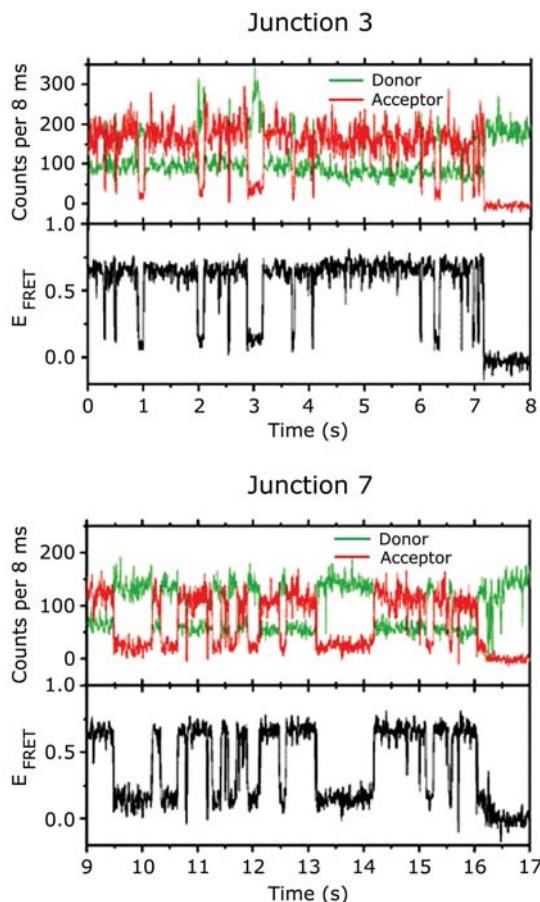
formation to position the Cy3 and Cy5 close to each other, or more distant, resulting in changes in energy transfer.

Figure 23.48 shows the single-molecule time traces of two different junctions, each with a different sequence. In both junctions the donor and acceptor intensities fluctuate. The intensity changes are anticorrelated, showing that the fluctuations are due to energy transfer between Cy3 and Cy5. In single-molecule studies the extent of energy transfer is presented as  $E_{\text{FRET}} = I_A/(I_A + I_D)$ , rather than an actu-



**Figure 23.47.** Structural flexibility in a DNA four-way Holliday junction. Reproduced with permission from [82]. Copyright © 2003, American Chemical Society.

Junction 3	Junction 7
C G	C G
G C	G C
<b>G C</b>	<b>C G</b>
A <b>G G</b> T G A	A G C C G A
T C C <b>A C T</b>	T C G G C T
<b>T A</b> G C	<b>C G</b> G C
A T	A T



**Figure 23.48.** Single-molecule conformational changes in two Holliday junctions. Junctions 3 and 7 refer to different sequences;  $E_{\text{FRET}} = I_A/(I_A + I_D)$ . Reprinted with permission from [83].

al transfer efficiency. The extent of energy transfer fluctuates between two levels. This indicates that there is no significant population of the intermediate state shown in the center of Figure 23.47. These junctions exist in only two conformations. The single-molecule RET data also show that the sequence affects the preferred conformation. Junction 3 remains mostly in the form with high-energy transfer. Junction 7 is equally distributed between the two states (Figure 23.48).

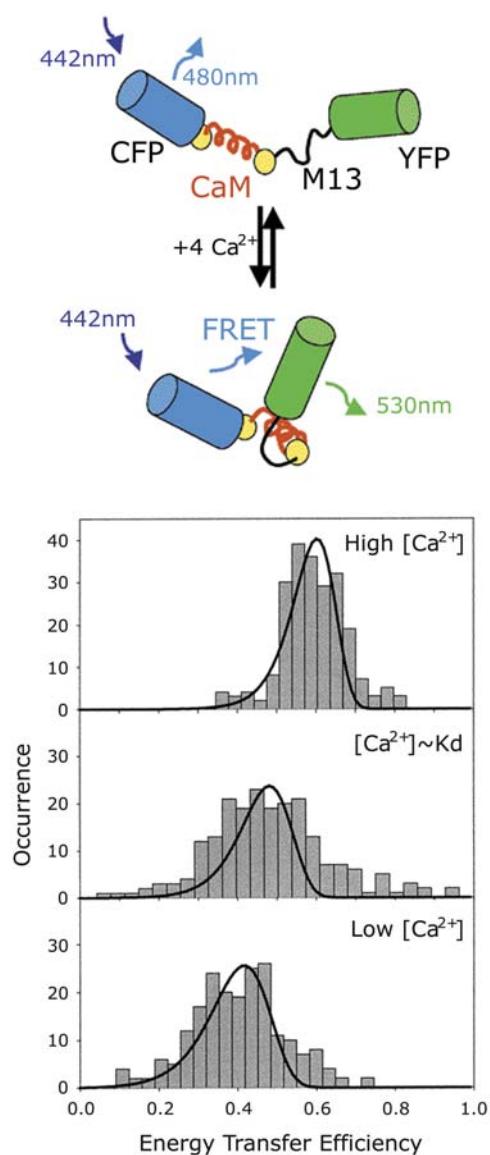


**Figure 23.49.** Calcium sensor based on a GFP donor–acceptor pair linked by calmodulin (CaM) and the M13 peptide. The panels show the single-molecule RET efficiency. Reprinted with permission from [10, 89].

#### 23.10.4. Single-Molecule Calcium Sensor

Single-molecule detection has been extended to single-molecule sensors.<sup>89</sup> A single-molecule sensor was designed according using two GFPs as a donor–acceptor pair, linked by calcium-sensitive proteins (Figure 23.49). The linker consisted of calmodulin (CaM) and the M13 peptide. In the presence of calcium CaM expresses a hydrophobic region that binds the M13 peptide, bringing the GFPs closer together.<sup>90</sup> Single molecules of a similar sensor were ob-

served using a confocal scanning microscope. The individual molecules were examined at various concentrations of calcium. Histograms were constructed showing the number of times a particular transfer efficiency was observed. These histograms show the closer average distance of the donor and acceptor in the presence of calcium. In this case the distributions are rather wide, with overlap of the high- and low-calcium histograms. This suggests that this sensor adopts more than two conformations in the presence of calcium.

#### 23.10.5. Motions of Molecular Motors

Motion occurs constantly in cells and tissues, and are due to a variety of proteins. Intracellular transport of organelles, mRNA, and other molecules is due in part to kinesin. Kinesin is a dimeric protein that moves along actin filaments while it consumes ATP. Single-molecule imaging has been used to follow the motion of kinesin<sup>91</sup> and other proteins.<sup>92–95</sup> For kinesin there were two possible modes of motion: hand-over-hand and inchworm motion (Figure 23.50). Previous studies had shown that the central stalk in kinesin does not rotate during motion, so this mechanism was not considered.

To study kinesin motions one of the actin-binding domains was labeled with Cy3 and the other left unlabeled.<sup>91</sup> Actin filaments were immobilized on the slides to provide a binding site for kinesin. Upon addition of ATP the Cy3 spot was found to move in discrete steps (Figure 23.50, lower panel). Several different kinesin mutants were labeled and studied, and all displayed similar step sizes. The size of the steps allowed selection of the hand-over-hand model for kinesin motion. The average step size of 17 nm was consistent with the size of two actin molecules. The inchworm mode of motion would have resulted in a smaller 8.3-nm step size.

### 23.11. ADVANCED TOPICS IN SMD

#### 23.11.1. Signal-to-Noise Ratio in Single-Molecule Detection

We have now seen examples of SMD. These experiments all had one feature in common, which is careful design of the sample and optical system to achieve an adequate S/N ratio. In order to detect a single molecule the signal from the molecule must be larger than the fluctuations in the background signal. Additionally, all single-molecule exper-

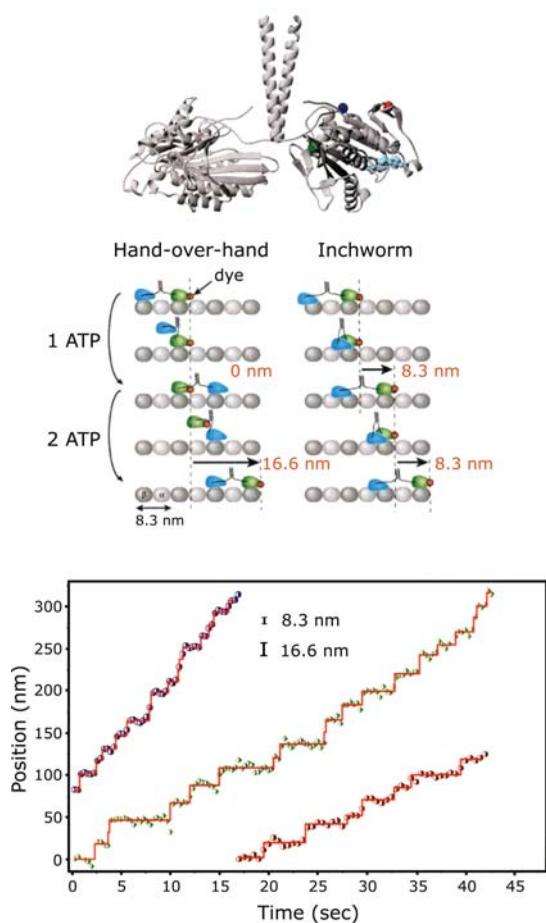


**Figure 23.50.** Possible mechanisms for movement of kinesin on actin filaments. The lower panel shows the time-dependent motion and the distance for each step. Reprinted with permission from [91]. Copyright © 2000, American Chemical Society.

iments are performed over a limited range of incident intensities, concentrations, and dye characteristics. At present it is only possible to observe single molecules above the background under certain conditions. For SMD the S/N ratio is given by<sup>16</sup>

$$S/N = \frac{DQ \left( \frac{\sigma}{A} \right) \left( \frac{P_0}{hv} \right) T}{\sqrt{\left( \frac{DQ\sigma_p P_0 T}{Ahv} \right) + C_B P_0 T + N_D T}} \quad (23.6)$$

In this expression  $D$  is the instrument detection efficiency,  $Q$  is the quantum yield of the fluorophore,  $\sigma$  is its absorption cross-section,  $A$  is the illuminated area,  $P_0/hv$  is the number of incident photons per second, and  $T$  is the data

collection time. In the denominator  $C_B$  is the number of background counts per watt of incident power and  $N_D$  the number of dark counts per second. At first glance this expression appears complex but its meaning becomes clear upon examination. The term in the numerator represents the signal from the fluorophore. The three terms in the denominator are the signals from the fluorophore, autofluorescence from the sample and instrument, and the number of dark counts recorded by the detector. The denominator is raised to one-half power because it represents the fluctuations or noise in the intensity rather than the intensity itself.

Figure 23.51 shows calculations of the S/N ratio for assumed parameter values that roughly describe R6G in water. The surfaces show the dependence of S/N on the incident power and observed area. The middle panel assumes there is no photobleaching, and the lower panel assumes a photobleaching quantum yield of  $10^{-5}$ . This sur-

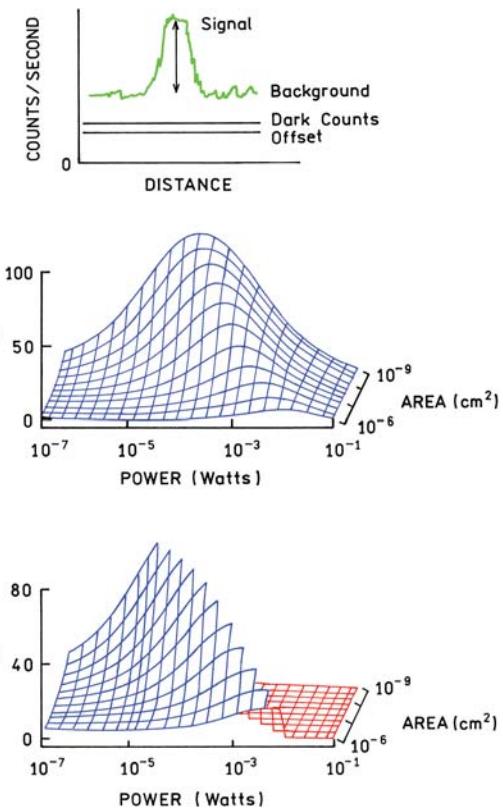


**Figure 23.51.** Calculations of the signal-to-noise (S/N) ratio in single-molecule detection using eq. 23.6; 532 nm,  $5.6 \times 10^3 \text{ W/cm}^2$ ,  $Q = 0.28$ ,  $\sigma = 4 \times 10^{-16} \text{ cm}^2$ ,  $D = 0.072$ ,  $N_D = 100 \text{ cts/s}$ ,  $C_B = 2 \times 10^8 \text{ counts/W}$ ,  $T = 0.1 \text{ s}$ . For the lower panel the photobleaching quantum yield was taken as  $10^{-5}$ . Revised and reprinted with permission from [16], Copyright © 2003, American Institute of Physics.

face shows that even under good conditions S/N is unlikely to exceed 100. Also, S/N is adequate over a limited range of incident intensities and sample sizes. S/N initially increases with incident power, but decreases at higher power due to increased contributions from the background. The useful range of conditions is even more limited if photobleaching is considered (lower panel) because the fluorophore disappears after emitting some average number of photons. The surfaces in Figure 23.51 shows that SMD is possible because of several favorable conditions, including high photon detection efficiency, high photostability, and low dark counts. An unfavorable change in any of these parameters can make it impossible to detect the emission from a single fluorophore.

### 23.11.2. Polarization of Single Immobilized Fluorophores

In Figures 23.33 and 23.34 we described the polarization of single molecules when excited with polarized light. These concepts are clarified by a mathematical description of this system. Consider a fluorophore on a glass slide, with colinear absorption and emission dipoles (Figure 23.52). The

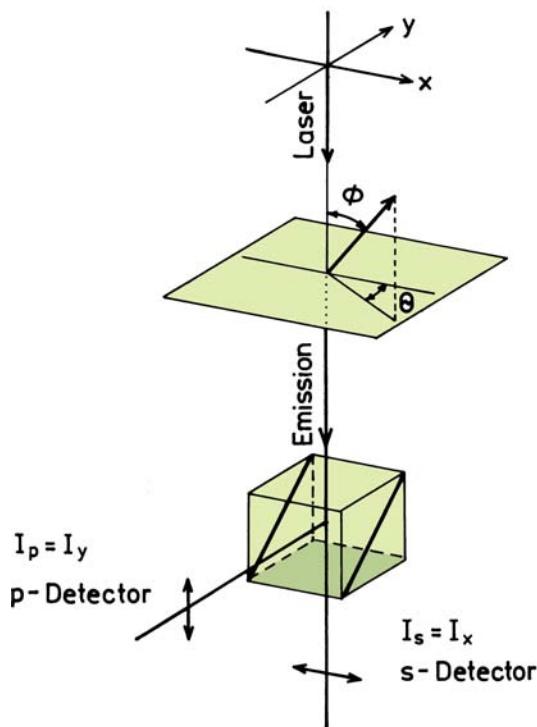


**Figure 23.52.** Polarized intensities for a single immobilized fluorophore.

transition moment is oriented at an angle  $\theta$  from the  $x$ -axis and an angle  $\phi$  from the optical  $z$ -axis. The polarized components of the emission are separated with a polarizing beamsplitter. The intensity of each polarized component is given by the square of the electric field projected onto the axis. Hence,

$$I_s = I_x = k \sin^2\phi \cos^2\theta \quad (23.7)$$

$$I_p = I_y = k \sin^2\phi \sin^2\theta \quad (23.8)$$

where  $k$  is an instrument constant assumed to be the same for both channels. Notice that it was not necessary to consider the polarization of the incident light. The intensity a fluorophore emits along the  $x$ - and  $y$ -axes depends only on the orientation of the emission dipole, regardless of how the molecule was excited. The polarization of the emission is given by

$$P = \frac{I_p - I_s}{I_p + I_s} = 1 - 2 \cos^2\theta \quad (23.9)$$

Perhaps surprisingly, the polarization does not depend on the angle  $\phi$  because the intensity is proportional to the same factor  $\sin^2\phi$  in both channels.

### 23.11.3. Polarization Measurements and Mobility of Surface-Bound Fluorophores

The ability to measure the polarization of single molecules makes it possible to measure their mobility. Because only a limited number of photons per fluorophore can be detected it may be difficult to determine the correlation time from the polarized intensity decays. An alternative approach to mobility measurements is to measure the polarized emission interaction when the excitation polarization is rotated.<sup>96</sup> Figure 23.53 shows such measurements of Texas Red using an electrooptic device to repetitively rotate the excitation polarization. The intensity of this single Texas Red molecule changes from nearly zero to a maximum value with rotation of the polarization. The insert shows the averaged intensities at various angles of incident polarization. There is an angle near  $60^\circ$  where the intensity is near zero. Recall that excitation of a single molecule is proportional to  $\cos^2\theta$ , so that the intensity minimum occurs where the absorption transition is perpendicular to the excitation polarization. Such a high contrast ratio is not seen for

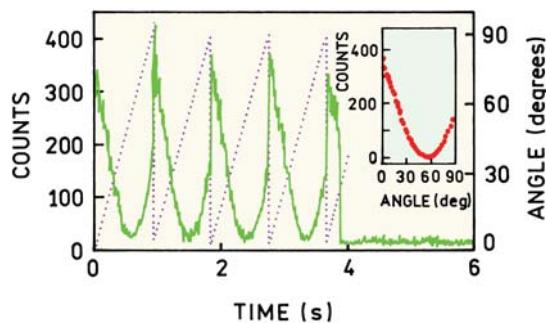


**Figure 23.53.** Single-molecule emission intensity of Texas Red on glass using a confocal microscope. The excitation polarization was rotated as shown. The insert shows the intensity for different excitation polarizing angles, averaged from the first four cycles. Reprinted with permission from [96].

ensemble measurements in random media because some of the fluorophores are always aligned with the incident polarization.

Single-molecule polarization measurements can provide a direct measurement of the angle between the absorption and emission dipoles.<sup>58</sup> Figure 23.54 shows the intensities of an immobilized Cy5 molecule. For rotation of the excitation or emission polarizer. As described in Figure 23.33 and 23.34, the angle-dependent intensities will overlap for parallel transitions and be shifted when the absorption and emission dipoles are displaced by an angle  $\beta$ . In the case of Cy5 the angle-dependent intensities nearly overlap. The small offset is consistent with a small angle of  $\beta = 5^\circ$ .

The concepts shown in Figures 23.53 and 23.54 were applied to a labeled DNA oligomer that was bound to APS-

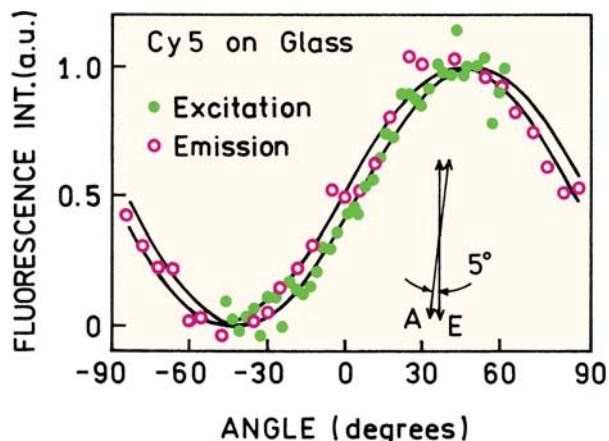


**Figure 23.54.** Dependence of the emission intensity of an immobilized Cy5 molecule on the angle of the excitation (●) and emission (○) polarization. The data represent an average from 15 molecules. Reprinted with permission from [58].

treated glass.<sup>97</sup> The sample was immersed in water to allow the possibility of probe rotation, but the oligomers did not migrate on the slide. The intensities of the polarized components of a single molecule were excited with different polarizations (Figure 23.55). The polarized components are completely out of phase. This is because when the fluorophore is parallel to one detection channel it is perpendicular to the other detection channel. Additionally, the correlation time of the probe must be much longer than the excited-state lifetime. Otherwise the emission in both channels would be the same. Using these considerations, molecules a, b, and e in Figure 23.55 are mobile. Molecule c must be immobilized because the intensities are in phase. The pattern seen for molecule d is characteristic of hindered rotational motion.

#### 23.11.4. Single-Molecule Lifetime Estimation

Calculation of the lifetimes using single-molecule data requires a different algorithm from that described for

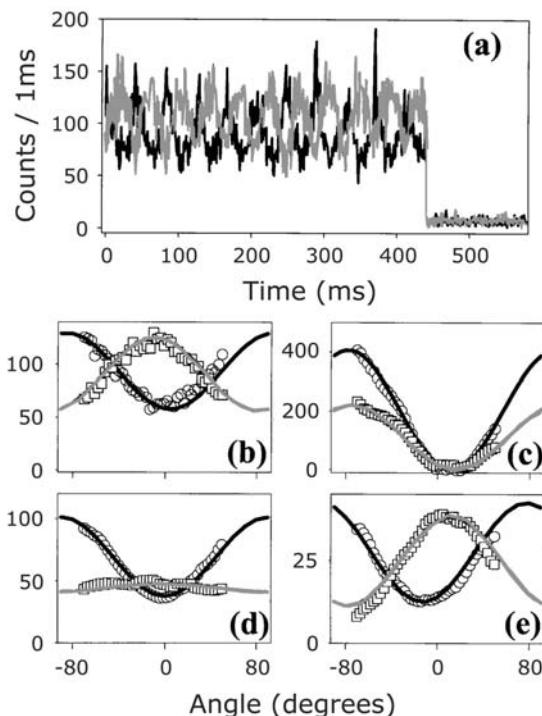


**Figure 23.55.** Time traces of the polarized intensities of a single labeled DNA oligomer bound to APS-treated glass. In a, b, and e the fluorophore is freely rotating. In c the fluorophore is immobile. The data in panel b are for the same molecule observed for panel a. The pattern in panel d is said to be characteristic of a hindered motion. Reprinted with permission from [97].

TCSPC. For TCSPC there is usually a large number of photons in each time interval, and the measurements are accurately described as Gaussian distributions around the true value. It should be remembered that the use of nonlinear least squares is based on the assumption that measurements have Gaussian properties. For the single-molecule data there is usually a small number of counts in each time interval. As a result the number of counts in each bin is distributed according to Poisson probability function. Nonlinear least squares is not the correct approach for such data.<sup>98</sup>

Methods have been developed to recover single-molecule lifetimes from sparse data.<sup>99–100</sup> In many single-molecule experiments the goal is not to resolve multi-exponential decays, but rather to obtain the best estimate of the decay time, the decay time which has the maximum likelihood of being the correct value. For this simple case there is an analytical expression for the estimated lifetime.<sup>100</sup> Assume the time width of each bin is  $\Delta t$  and that there are  $m$  bins, so the total time width of the data is  $m\Delta t = T$ . Then the lifetime can be found from

$$A - B = \frac{1}{N} \sum_{i=1}^m i\Delta t \frac{N_i}{N} \quad (23.10)$$

where  $N_i$  is the number of counts in the  $i$ th bin and  $N$  is the total number of counts. The best estimate lifetime can be found using

$$A = \Delta t [1 - \exp(-\Delta t/\tau)] \quad (23.11)$$

$$B = T [\exp(T/\tau) - 1] \quad (23.12)$$

These expressions are solved interactively to recover the lifetime  $\tau$ . Different expressions are needed to estimate multiple parameters by the maximum-likelihood method. The important point is that nonlinear least squares should not be used with sparse data.

### 23.12. ADDITIONAL LITERATURE ON SMD

The technology and applications for SMD have expanded dramatically during the past several years. It was not practical in this chapter to describe the many elegant results published on SMD. To assist the reader in finding reports of interest we have included, after the main references, a compilation of additional references on single-molecule detec-

tion that summarizes many of these reports according to their main emphasis.

In closing, SMD is a powerful technology that bypasses ensemble averaging and provides direct information on the behavior and/or kinetics of single molecules. While many papers have been published, the majority are still proof-of-principle experiments that are always necessary to systematize a new technology. The reader may notice the absence of examples on single-molecule diffusion or intracellular single-molecule detection. Several reports on these topics have appeared but were not selected as teaching examples because the results are not as clear as those shown above. It appears likely that there will be considerable difficulty performing SMD experiments on freely diffusing or intracellular species.

### REFERENCES

1. Shera EB, Seitzinger NK, Davis LM, Keller RA, Soper SA. 1990. Detection of single fluorescent molecules. *Chem Phys Lett* **174**(6): 553–557.
2. Hirschfeld T. 1976. Optical microscopic observation of single small molecules. *Appl Opt* **15**(12):2965–2966.
3. Nguyen DC, Keller RA, Jett JH, Martin JC. 1987. Detection of single molecules of phycoerythrin in hydrodynamically focused flows by laser-induced fluorescence. *Anal Chem* **59**:2158–2161.
4. Peck K, Stryer L, Glazer AN, Mathies RA. 1989. Single-molecule fluorescence detection: autocorrelation criterion and experimental realization with phycoerythrin. *Proc Natl Acad Sci USA* **89**:4087–4091.
5. Moerner WE, Kador L. 1989. Optical detection and spectroscopy of single molecules in a solid. *Phys Rev Lett* **62**(21):2535–2538.
6. Bergquist JC, Hulet RG, Itano WM, Wineland DJ. 1986. Observation of quantum jumps in a single atom. *Phys Rev Lett* **57**(14):1699–1702.
7. Diedrich F, Walther H. 1987. Nonclassical radiation of a single stored ion. *Phys Rev Lett* **58**(3):203–206.
8. Jett JH, Keller RA, Martin JC, Marrone BL, Moyzis RK, Ratliff RL, Seitzinger NK, Shera EB, Stewart CC. 1989. High-speed DNA sequencing: an approach based upon fluorescence detection of single molecules. *J Biomol Struct Dyn* **7**(2):301–309.
9. Werner JH, Cai H, Jett JJ, Reha-Krantz L, Keller RA, Goodwin PM. 2003. Progress towards single-molecule DNA sequencing: a one color demonstration. *J Biotechnol* **102**:1–14.
10. Moerner WE. 2002. A dozen years of single-molecule spectroscopy in physics, chemistry, and biophysics. *J Phys Chem B* **106**:910–927.
11. Erdmann R, Enderlein J, Seidel C, eds. 1999. Single molecule detection and ultrasensitive analysis in the life sciences. *Cytometry* **36**(3):161–264.
12. Weiss S. 1999. Fluorescence spectroscopy of single biomolecules. *Science* **283**:1676–1683.
13. Moerner WE, Orrit M. 1999. Illuminating single molecules in condensed matter. *Science* **283**:1670–1676.

14. Tamarat PH, Maali A, Lounis B, Orrit M. 2000. Ten years of single-molecule spectroscopy. *J Phys Chem A* **104**(1):1–16.
15. Ambrose WP, Goodwin PM, Jett JH, Orden AV, Werner JH, Keller RA. 1999. Single molecule fluorescence spectroscopy at ambient temperature. *Chem Rev.* **99**(10):2929–2956.
16. Moerner WE, Fromm DP. 2003. Methods of single-molecule fluorescence spectroscopy and microscopy. *Rev Sci Instrum* **74**(8):3597–3619.
17. García-Parajó M, Veerman J-A, Bouwhuis R, Vallée M, van Hulst NF. 2001. Optical probing of single fluorescent molecules and proteins. *Chem Phys Chem* **2**:347–360.
18. Zander C, Enderlein J, Keller RA, eds. 2002. *Single molecule detection in solution: methods and applications*. Wiley-VCH, Darmstadt, Germany.
19. Enderlein J, Zander C. 2002. Theoretical foundations of single molecule detection in solution. In *Single molecule detection in solution: methods and applications*, pp. 288–324. Ed Ch Zander, J Enderlein, RA Keller. Wiley-VCH, Darmstadt, Germany.
20. Born M, Wolf E. 2002. *Principles of optics: electromagnetic theory of propagation, interference and diffraction of light*. Cambridge UP, Cambridge.
21. Halliday D, Resnick R, Krane KS. 1992. *Physics*, Vol. 2, 4th ed. John Wiley & Sons, New York.
22. Axelrod D, Hellen EH, Fulbright RM. 1992. Total internal reflection fluorescence. In *Topics in fluorescence spectroscopy*, Vol. 3: *Probe design and chemical sensing*, pp. 289–343. Ed JR Lakowicz. Plenum Press, New York.
23. Axelrod D. 1989. Total internal reflection fluorescence microscopy. *Methods Cell Biol* **30**:245–270.
24. Wilson T, ed. 1990. *Confocal microscopy*. Academic Press, New York.
25. Inoué S. 1995. Foundations of confocal scanned imaging in light microscopy. In *Handbook of biological confocal microscopy*, pp. 1–17. Ed JB Pawley (Ed.). Plenum Press, New York.
26. Lemasters JJ, Chacon E, Zahrebelski G, Reece JR, Nieminen AL. 1993. Laser scanning confocal microscopy of living cells. In *Optical microscopy: emerging methods and applications*, pp. 339–354. Ed G Herman, JJ Lemasters. Academic Press, New York.
27. Webb WW, Wells KS, Sandison DR, Strickler J. 1990. Criteria for quantitative dynamical confocal fluorescence imaging. In *Optical microscopy for biology*, pp. 73–108. Ed B Herman, K Jacobson. Wiley-Liss, New York.
28. Ambrose WP, Goodwin PM, Nolan JP. 1999. Single-molecule detection with total internal reflection excitation: comparing signal-to-background and total signals in different geometries. *Cytometry* **36**: 224–231.
29. Pawley JB, ed. 1995. *Handbook of biological confocal microscopy*. Plenum Press, New York.
30. Matsumoto B, ed. 1993. *Methods in cell biology: cell biological applications of confocal microscopy*. Academic Press, New York.
31. Diaspro A, ed. 2002. *Confocal and two-photon microscopy foundations: applications, and advances*. Wiley-Liss, New York, 56.
32. Moerner WE, Peterman EJG, Braaselet S, Kummer S, Dickson RM. 1999. Optical methods for exploring dynamics of single copies of green fluorescent protein. *Cytometry* **36**:232–238.
33. Shubeita GT, Sekatskii SK, Dietler G, Letokhov VS. 2002. Local fluorescent probes for the fluorescence resonance energy transfer scanning near-field optical microscopy. *Appl Phys Lett* **80**(15): 2625–2627.
34. Muramatsu H, Kim JM, Sugiyama S, Ohtani T. 2003. Simultaneous multicolor fluorescence imaging by scanning near-field optical/atomic force microscopy. *Rev Sci Instrum* **74**(1):100–103.
35. Vickery SA, Dunn RC. 1999. Scanning near-field fluorescence resonance energy transfer microscopy. *Biophys J* **76**:1812–1818.
36. Schmidt TH, Schutz GJ, Baumgartner W, Gruber HJ, Schindler H. 1995. Characterization of photophysics and mobility of single molecules in fluid lipid membrane. *J Phys Chem* **99**:17662–17668.
37. Weston KD, Buratto SK. 1998. Millisecond intensity fluctuations of single molecules at room temperature. *J Phys Chem A* **102**(21): 3635–3638.
38. Weber MA, Stracke F, Meixner AJ. 1999. Dynamics of single dye molecules observed by confocal imaging and spectroscopy. *Cytometry* **36**:217–223.
39. www.perkinelmer.com/optoelectronics.
40. Christenson M. 2000. Advances in detector systems for imaging single molecule fluorescence. *Single Mol* **1**(2):177–179.
41. Edmund Optics Catalogue. 2004. (See p. 79.)
42. Kaiser Optical Systems, Ann Arbor, Michigan.
43. Weston KD, Carson PJ, Metiu H, Buratto SK. 1998. Room-temperature fluorescence characteristics of single dye molecules adsorbed on a glass surface. *J Chem Phys* **109**(17):7474–7485.
44. Garcia-Parajo MF, Veerman JA, van Noort SJT, de Groot BG, Greve J, van Hulst NF. 1998. Near-field optical microscopy for DNA studies at the single molecular level. *Bioimaging* **6**:43–53.
45. Bian RX, Dunn RC, Xie XS. 1995. Single molecule emission characteristics in near-field microscopy. *Phys Rev Lett* **75**(26): 4772–4775.
46. Chang R, Wei PK, Fann WS, Hayashi MT, Lin SH. 1997. Theoretical investigation of near-field optical properties of tapered fiber tips and single molecule fluorescence. *J Appl Phys* **81**(8):3369–3376.
47. Soper SA, Nutter HL, Keller RA, Davis LM, Shera EB. 1993. The photophysical constants of several fluorescent dyes pertaining to ultrasensitive fluorescence spectroscopy. *Photochem Photobiol* **57**(6):972–977.
48. Eggeling C, Widengren J, Rigler R, Seidel CAM. 1999. Photostability of fluorescent dyes for single-molecule spectroscopy: mechanisms and experimental methods for estimating photobleaching in aqueous solution. In *Applied fluorescence in chemistry, biology and medicine*, pp. 193–240. Ed W Rettig, B Strehmel, S Schrader, H Seifert. Springer-Verlag, New York.
49. Eggeling C, Widengren J, Rigler R, Seidel CAM. 1998. Photobleaching of fluorescent dyes under conditions used for single-molecule detection: evidence of two-step photolysis. *Anal Chem* **70**:2651–2659.
50. Peterman EJG, Brasselet S, Moerner WE. 1999. The fluorescence dynamics of single molecules of green fluorescent protein. *J Phys Chem A* **103**:10553–10560.
51. English DS, Furube A, Barbara PF. 2000. Single-molecule spectroscopy in oxygen-depleted polymer films. *Chem Phys Lett* **324**: 15–19.
52. Deschenes LA, Vanden Bout DA. 2002. Single molecule photobleaching: increasing photon yield and survival time through suppression of two-step photolysis. *Chem Phys Lett* **365**:387–395.

53. Hubner CG, Renn A, Renge I, Wild UP. 2001. Direct observation of the triplet lifetime quenching of single dye molecules by molecular oxygen. *J Chem Phys* **115**(21):9619–9622.
54. Tokunaga M, Kitamura K, Saito K, Iwane AH, Yanagida T. 1997. Single molecule imaging of fluorophores and enzymatic reactions achieved by objective-type total internal reflection fluorescence microscopy. *Biochem Biophys Res Commun* **235**:47–53.
55. Taguchi H, Ueno T, Tadakuma H, Yoshida M, Funatsu T. 2001. Single-molecule observation of protein-protein interactions in the chaperonin system. *Nature Biotechnol* **19**:861–865.
56. Zhuang X, Bartley LE, Babcock HP, Russell R, Ha T, Herschlag D, Chu S. 2000. A single-molecule study of RNA catalysis and folding. *Science* **288**:2048–2051.
57. Ha T, Laurence TA, Chemla DS, Weiss S. 1999. Polarization spectroscopy of single fluorescent molecules. *J Phys Chem B* **103**: 6839–6850.
58. Weiss S. 2000. Measuring conformational dynamics of biomolecules by single molecule fluorescence spectroscopy. *Nature Struct Biol* **7**(9):724–729.
59. Ha T, Glass J, Enderle TH, Chemla DS, Weiss S. 1998. Hindered rotational diffusion and rotational jumps of single molecules. *Phys Rev Lett* **80**(10):2093–2096.
60. Gensch T, Hofkens J, Kohn F, Vosch T, Herrmann A, Mullen K, De Schryver FC. 2001. Polarization sensitive single molecule fluorescence detection with linear polarized excitation light and modulated polarization direction applied to multichromophoric entities. *Single Mol* **2**(1):35–44.
61. Axelrod D. 1989. Fluorescence polarization microscopy. *Methods Cell Biol* **30**:333–352.
62. Bennet JM, Bennet HE. 1978. Polarization, In *Handbook of optics*, pp. 10-1–10-164. Ed WG Driscoll. McGraw-Hill, New York.
63. Forkey JN, Quinlan ME, Goldman YE. 2000. Protein structural dynamics by single-molecule fluorescence polarization. *Prog Biophys Mol Biol* **74**:1–35.
64. Deschenes LA, Venden Bout DA. 2001. Single-molecule studies of heterogeneous dynamics in polymer melts near the glass transition. *Science* **292**:255–258.
65. Deschenes LA, Venden Bout DA. 2001. Molecular motions in polymer films near the glass transition: a single molecule study of rotational dynamics. *J Phys Chem B* **105**:11978–11985.
66. Garcia-Parajo MF, Veerman JA, Segers-Nolten GMJ, de Groot BG, Greve J, van Hulst NF. 1999. Visualizing individual green fluorescent proteins with a near field optical microscope. *Cytometry* **36**:239–246.
67. Betzig E, Chichester RJ. 1993. Single molecules observed by near-field scanning optical microscopy. *Science* **262**(5138):1422–1425.
68. van Hulst NF, Veerman J-A, Garcia-Parajo MF, Kuipers L. 2000. Analysis of individual (macro)molecules and proteins using near-field optics. *J Chem Phys* **112**(18):7799–7810.
69. Veerman JA, Garcia-Parajo MF, Kuipers L, van Hulst NF. 1999. Single molecule mapping of the optical field distribution of probes for near-field microscopy. *J Microsc* **194**(part 2/3):477–482.
70. Bartko AP, Dickson RM. 1999. Imaging three-dimensional single molecule orientations. *J Phys Chem B* **103**:11237–11241.
71. Dickson RM, Norris DJ, Moerner WE. 1998. Simultaneous imaging of individual molecules aligned both parallel and perpendicular to the optic axis. *Phys Rev Lett* **81**(24):5322–5325.
72. Bohmer M, Enderlein J. 2003. Orientation imaging of single molecules by wide-field epifluorescence microscopy. *J Opt Soc Am B* **20**(3):554–559.
73. Bartko AP, Dickson RM. 1999. Three-dimensional orientations of polymer-bound single molecules. *J Phys Chem B* **103**(16):3053–3056.
74. Bartko AP, Peyser LA, Dickson RM, Mehta A, Thundat T, Bhargava R, Barnes MD. 2002. Observation of dipolar emission patterns from isolated Eu<sup>3+</sup>:Y<sub>2</sub>O<sub>3</sub> doped nanocrystals: new evidence from single ion luminescence. *Chem Phys Lett* **358**:459–465.
75. Tinnefeld P, Herten D-P, Sauer M. 2001. Photophysical dynamics of single molecules studied by spectrally-resolved fluorescence lifetime imaging microscopy (SFLIM). *J Phys Chem A* **105**:7989–8003.
76. Trautman JK, Macklin JJ. 1996. Time-resolved spectroscopy of single molecules using near-field and far-field optics. *Chem Phys* **205**: 221–229.
77. Bohmer M, Pampaloni F, Wahl M, Rahn H-J, Erdmann R, Enderlein J. 2001. Time-resolved confocal scanning device for ultrasensitive fluorescence detection. *Rev Sci Instrum* **72**(11):4145–4152.
78. Heilemann M, Herten DP, Heintzmann R, Cremer C, Muller C, Tinnefeld P, Weston KD, Wolfrum J, Sauer M. 2002. High-resolution colocalization of single dye molecules by fluorescence lifetime imaging microscopy. *Anal Chem* **74**:3511–3517.
79. Lu P, Xun L, Xie XS. 1998. Single-molecule enzymatic dynamics. *Science* **282**:1877–1882.
80. Shi J, Palley BA, Dertouzos J, Jensen KF, Gafni A, Steel D. 2004. Multiple states of the Tyr318Leu mutant of dihydroorotate dehydrogenase revealed by single-molecule kinetics. *J Am Chem Soc* **126**: 6914–6922.
81. Piestert O, Barsch H, Buschmann V, Heinlein T, Knemeyer J-P, Weston KD, Sauer M. 2003. A single-molecule sensitive DNA hairpin system based on intramolecular electron transfer. *Nanotechnol Lett* **3**(7):979–982.
82. Chruchill MEA. 2003. Watching flipping junctions. *Nature Struct Biol* **10**(2):73–75.
83. McKinney SE Declais A-C, Lilley DMJ, Ha T. 2003. Structural dynamics of individual Holliday junctions. *Nature Struct Biol* **10**(2): 9397.
84. Tan E, Wilson TJ, Nahas MK, Clegg RM, Lilley DMJ, Ha T. 2003 A four-way junction accelerates hairpin ribozyme folding via a discrete intermediate. *Proc Natl Acad Sci USA* **100**(16):9308–9313.
85. Zhuang X, Kim H, Pereira MJB, Babcock HP, Walter NG, Chu S. 2002. Correlating structural dynamics and function in single ribozyme molecules. *Science* **296**:1473–1476.
86. Ha T, Zhuang X, Kim HD, Orr JW, Williamson JR, Chu S. 1999. Ligand-induced conformational changes observed in single RNA molecules. *Proc Natl Acad Sci USA* **96**:9077–9082.
87. Kim HD, Nienhaus GU, Ha T, Orr JW, Williamson JR, Chu S. 2002. Mg<sup>2+</sup>-dependent conformational change of RNA studied by fluorescence correlation and FRET on immobilized single molecules. *Proc Natl Acad Sci USA* **99**(7):4284–4289.
88. Ha T. 2004. Structural dynamics and processing of nucleic acids revealed by single-molecule spectroscopy. *Biochemistry* **43**(14): 4056–4063.
89. Brasselet S, Peterman EJG, Miyawaki A, Moerner WE. 2000. Single-molecule fluorescence resonant energy transfer in calcium concentration dependent cameleon. *J Phys Chem B* **104**:3676–3682.

90. Miyawaki A, Llopis J, Heim R, McCaffery JM, Adams JA, Ikura M, Tsien RY. 1997. Fluorescent indicators for  $\text{Ca}^{2+}$  based on green fluorescent proteins and calmodulin. *Nature* **388**:882–887.
91. Yildiz A, Tomishige M, Vale RD, Selvin PR. 2004. Kinesin walks hand-over-hand. *Science* **303**:676–678.
92. Yildiz A, Forkey JN, McKinney SA, Ha T, Goldman YE, Selvin PR. 2003. Myosin V walks hand-over-hand: single fluorophore imaging with 1.5-nm localization. *Science* **300**:2061–2065.
93. Kitamura K, Tokunaga M, Iwane AH, Yanagida T. 1999. A single myosin head moves along an actin filament with regular steps of 5.3 nanometers. *Nature* **397**:129–134.
94. Ishii Y, Iwane AH, Yokota HY, Inoue Y, Wazawa T, Nishiyama M, Tanaka H, Kitamura K, Yanagida T. 2002. Studying molecular motors on the single molecule level. In *Single molecule detection in solution: methods and applications*, pp. 273–292. Ed Ch Zander, J Enderlein, RA Keller. Wiley-VCH, Darmstadt, Germany.
95. Sase E, Miyata H, Corrie JET, Craik JS, Kinoshita Jr, K. 1995. Real time imaging of single fluorophores on moving actin with an epifluorescence microscope. *Biophys J* **69**:323–328.
96. Ha T, Enderle Th, Chemla DS, Selvin P, Weiss S. 1996. Single molecule dynamics studied by polarization modulation. *Phys Rev Lett* **77**(19):3979–3982.
97. Ha T, Glass J, Enderle Th, Chemla DS, Weiss S. 1998. Hindered rotational diffusion and rotational jumps of single molecules. *Phys Rev Lett* **80**(10):2093–2096.
98. Bevington PR, Robinson DK. 1992. *Data reduction and error analysis for the physical sciences*, 2nd ed. McGraw-Hill, New York.
99. Enderlein J, Sauer M. 2001. Optimal algorithm for single-molecule identification with time-correlated single-photon counting. *J Phys Chem A* **105**:48–53.
100. Tellinghuisen J, Wilkerson Jr CW. 1993. Bias and precision in the estimation of exponential decay parameters from sparse data. *Anal Chem* **65**:1240–1246.

## ADDITIONAL REFERENCES ON SINGLE-MOLECULE DETECTION

### Analytical Chemistry and Single Molecules

- Dörre K, Stephan J, Lapeczyna M, Stuke M, Dunkel H, Eigen M. 2001. Highly efficient single molecule detection in microstructures. *J Biotechnol* **86**:225–236.
- Enderlein J. 1999. Single molecule fluorescence in ultrathin capillaries: an electrodynamic study. *Chem Phys Lett* **301**:430–434.
- Fisher BR, Eisler HJ, Stott NE, Bawendi MG. 2004. Emission intensity dependence and single-exponential behavior in single colloidal quantum dot fluorescence lifetimes. *J Phys Chem B* **108**:143–148.
- Hanley DC, Harris JM. 2001. Quantitative dosing of surfaces with fluorescent molecules: characterization of fractional monolayer coverages by counting single molecules. *Anal Chem* **73**:5030–5037.
- Kang SH, Yeung ES. 2002. Dynamics of single-protein molecules at a liquid/solid interface: implications in capillary electrophoresis and chromatography. *Anal Chem* **74**:6334–6339.
- Ludes MD, Wirth MJ. 2002. Single-molecule resolution and fluorescence imaging of mixed-mode sorption of a dye at the interface of  $\text{C}_{18}$  and acetonitrile/water. *Anal Chem* **74**:386–393.

- Ma Y, Shortreed MR, Yeung ES. 2000. High-throughput single molecule spectroscopy in free solution. *Anal Chem* **72**:4640–4645.
- Schutz GJ, Gruber HJ, Schindler H, Schmidt TH. 1997. Fluorophores for single molecule microscopy. *J Luminesc* **72–74**:18–21.
- Yeung ES. 2001. High-throughput single molecule screening of DNA proteins. *Chem Rec* **1**:123–139.

### Co-Localization of Molecules

- Lacoste TD, Michalet X, Pinaud F, Chemla DS, Alivisatos AP, Weiss S. 2000. Ultrahigh-resolution multicolor colocalization of single fluorophores. *Proc Natl Acad Sci USA* **97**(17):9461–9466.
- Osborne MA, Barnes CL, Balasubramanian S, Klenerman D. 2001. Probing DNA surface attachment and local environment using single molecule spectroscopy. *J Phys Chem B* **105**:3120–3126.
- Thompson RE, Larson DR, Webb WW. 2002. Precise nanometer localization analysis for individual fluorescent probes. *Phys J* **82**:2775–2783.
- Trabesinger W, Hecht B, Wild UP, Schutz GJ, Schindler H, Schmidt TH. 2001. Statistical analysis of single-molecule colocalization assays. *Anal Chem* **73**:1100–1105.

### Data Analysis of Single-Molecule Emission

- Novikov E, Hofkens J, Cotlet M, Maus M, De Schryver FC, Boens N. 2001. A new analysis method of single molecule fluorescence using series of photon arrival times: theory and experiment. *Spectrochim Acta, Part A* **57**:2109–2133.
- Turton DA, Reid GD, Beddard GS. 2003. Accurate analysis of fluorescence decays from single molecules in photon counting experiments. *Anal Chem* **75**:4182–4187.

### Dendrimers and Polymers

- Bowden NB, Willets KA, Moerner WE, Waymouth RM. 2002. Synthesis of fluorescently labeled polymers and their use in single-molecule imaging. *Macromolecules* **35**:8122–8125.
- Gensch T, Hofkens J, Heermann A, Tsuda K, Verheijen W, Vosch T, Christ T, Basché T, Müllen K, De Schryver FC. 1999. Fluorescence detection from single dendrimers with multiple chromophores. *Angew Chem, Int Ed* **38**(24):3752–3756.
- Gronheid R, Hofkens J, Köhn F, Weil T, Reuther E, Müllen K, De Schryver FC. 2002. Intramolecular Förster energy transfer in a dendritic system at the single molecule level. *J Am Chem Soc* **124**(11):2418–2419.

### Diffusion or Tracking of Single Molecules

- Cao J. 2001. Single molecule tracking of heterogeneous diffusion. *Phys Rev E* **63**:041101-1–041101-7.
- Ghosh RN, Webb WW. 1994. Automated detection and tracking of individual and clustered cell surface low density lipoprotein receptor molecules. *Biophys J* **66**:1301–1318.
- Hashimoto F, Tsukahara S, Watari H. 2003. Lateral diffusion dynamics for single molecules of fluorescent cyanine dye at the free and surfactant-modified dodecane–water interface. *Langmuir* **19**:4197–4204.

- Ke PC, Naumann CA. 2001. Single molecule fluorescence imaging of phospholipid monolayers at the air–water interface. *Langmuir* **17**: 3727–3733.
- Schmidt TH, Schutz GJ, Baumgartner W, Gruber HJ, Schindler H. 1996. Imaging of single molecule diffusion. *Proc Natl Acad Sci USA* **93**: 2926–2929.
- Simpson R, Sheets ED, Jacobson K. 1995. Detection of temporary lateral confinement of membrane proteins using single-particle tracking analysis. *Biophys J* **69**:989–993.
- Swinton DJ, Wirth MJ. 2001. Single molecule study of the lateral transport of four homooligonucleotides at the interface of water and chemically modified silica. *J Phys Chem B* **105**:8679–8684.
- Swinton DJ, Wirth MJ. 2001. Single-molecule study of an adsorbed oligonucleotide undergoing both lateral diffusion and strong adsorption. *J Phys Chem B* **105**:1472–1477.
- Tadakuma H, Yamaguchi J, Ishihama Y, Funatsu T. 2001. Imaging of single fluorescent molecules using video-rate confocal microscopy. *Biochem Biophys Res Commun* **287**:323–327.
- Xu XH, Yeung ES. 1997. Direct measurement of single-molecule diffusion and photodecomposition in free solution. *Science* **275**:1106–1109.
- Xu XH, Yeung ES. 1998. Long-range electrostatic trapping of single-protein molecules at a liquid–solid interface. *Science* **281**:1650–1653.
- Hirose T, Ohtani T, Muramatsu H, Tanaka A. 2002. Direct visualization of abasic sites on a single DNA molecule using fluorescence microscopy. *Photochem Photobiol* **76**(2):123–126.
- Kang SO, Shortreed MR, Yeung ES. 2001. Real-time dynamics of single-DNA molecules undergoing adsorption and desorption at liquid–solid interfaces. *Anal Chem* **73**:1091–1099.
- Knemeyer JP, Marne N, Sauer M. 2000. Probes for detection of specific DNA sequences at the single-molecule level. *Anal Chem* **72**: 3717–3724.
- Osborne MA, Furey WS, Klenerman D, Balasubramanian S. 2000. Single-molecule analysis of DNA immobilized on microspheres. *Anal Chem* **72**:3678–3681.
- Schäfer B, Gemeinhardt H, Uhl V, Greulich KO. 2000. Single molecule DNA restriction analysis in the light microscope. *Single Mol* **1**:33–40.
- Tachi-iri Y, Ishikawa M, Hirano K. 2000. Investigation of the hydrolysis of single DNA molecules using fluorescence video microscopy. *Anal Chem* **72**:1649–1656.
- Werner JH, Cai H, Jett JH, Reha-Krantz L, Keller RA, Goodwin PM. 2003. Progress towards single-molecule DNA sequencing: a one color demonstration. *J Biotechnol* **102**:1–14.

### DNA Applications Using SMD

- Anazawa T, Matsunaga H, Yeung ES. 2002. Electrophoretic quantitation of nucleic acids without amplification by single-molecule imaging. *Anal Chem* **74**:5033–5038.
- Deniz AA, Dahan M, Grunwell JR, Ha T, Faulhaber AE, Chemla DS, Weiss S, Schultz PG. 1999. Single-pair fluorescence resonance energy transfer on freely diffusing molecules: observation of Förster distance dependence and subpopulations. *Proc Natl Acad Sci USA* **96**: 3670–3675.
- Edman L, Mets Ü, Rigler R. 1996. Conformational transitions monitored for single molecules in solution. *Proc Natl Acad Sci USA* **93**: 6710–6715.
- Eggeling C, Fries JR, Brand L, Günther R, Seidel CAM. 1998. Monitoring conformational dynamics of a single molecule by selective fluorescence spectroscopy. *Proc Natl Acad Sci USA* **95**:1556–1561.
- Gueroui Z, Freyssingea E, Place B, Berge B. 2003. Transverse fluctuation analysis of single extended DNA molecules. *Eur Phys J E* **11**: 105–108.
- Gueroui Z, Place E, Freyssingea E, Berge B. 2002. Observation by fluorescence microscopy of transcription on single combed DNA. *Proc Natl Acad Sci USA* **99**(9):6005–6010.
- Ha T. 2001. Single-molecule fluorescence methods for the study of nucleic acids. *Curr Opin Struct Biol* **11**:287–292.
- Ha T, Rasnik I, Cheng W, Babcock HP, Gauss GH, Lohman TM, Chu S. 2002. Initiation and re-initiation of DNA unwinding by the *Escherichia coli* rep helicase. *Nature* **419**:638–641.
- Harada Y, Funatsu T, Murakami K, Nonoyama Y, Ishihama A, Yanagida T. 1999. Single-molecule imaging of RNA polymerase–DNA interactions in real time. *Biophys J* **76**:709–715.
- Herrick J, Bensimon A. 1999. Imaging of single DNA molecule: Applications to high-resolution genomic studies. *Chromosome Res* **7**:409–423.

### General Papers on SMD

- Bloess A, Durand Y, Matsushita M, Van Dermeer HV, Brakenhoff GJ, Schmidt J. 2002. Optical far-field microscopy of single molecules with 3.4 nm lateral resolution. *J Microsc* **205**(1):76–85.
- Harbron EJ, Barbara PF. 2002. The Poisson distribution and single-molecule spectroscopy. *J Chem Educ* **79**(2):211–213.
- Nie S, Chiu DT, Zare RN. 1994. Probing individual molecules with confocal fluorescence microscopy. *Science* **266**:1018–1021.

### Green Fluorescent Protein and Its Mutants

- Bowen B, Woodbury N. 2003. Single-molecule fluorescence lifetime and anisotropy measurements of the red fluorescent protein, DsRed, in solution. *Photochem Photobiol* **77**(4):362–369.
- Cotlet M, Hofkens J, Habuchi S, Dirix G, Van Guyse M, Michiels J, Vanderleyden J, De Schryver FC. 2001. Identification of different emitting species in the red fluorescent protein DsRed by means of ensemble and single-molecule spectroscopy. *Proc Natl Acad Sci USA* **98**(25):14398–14403.
- Dickson RM, Cubitt AB, Tsien RY, Moerner WE. 1997. On/off blinking and switching behaviour of single molecules of green fluorescent protein. *Nature* **388**(6640):355–358.
- Garcia-Parajo MF, Koopman M, van Dijk EMHP, Subramaniam V, van Hulst NF. 2001. The nature of fluorescence emission in the red fluorescent protein DsRed, revealed by single-molecule detection. *Proc Natl Acad Sci USA* **98**(25):14392–14397.
- Harms GS, Cognet L, Lommelse PHM, Blab GA, Schmidt T. 2001. Autofluorescent proteins in single-molecule research: applications to live cell imaging microscopy. *Biophys J* **80**:2396–2408.

### Identification of Single Molecules

- Dahan M, Deniz AA, Ha T, Chemla DS, Schultz PG, Weiss S. 1999. Ratiometric measurement and identification of single diffusing molecules. *Chem Phys* **247**:85–106.

Knemeyer J-P, Herten D-P, Sauer M. 2003. Detection and identification of single molecules in living cells using spectrally resolved fluorescence lifetime imaging microscopy. *Anal Chem* **75**:2147–2153.

### Intracellular SMD

- Byassee TA, Chan WCW, Nie S. 2000. Probing single molecules in single living cells. *Anal Chem* **72**:5606–5611.
- Iino R, Koyama I, Kusumi A. 2001. Single molecule imaging of green fluorescent proteins in living cells: e-cadherin forms oligomers on the free cell surface. *Biophys J* **80**:2667–2677.
- Iino R, Kusumi A. 2001. Single-fluorophore dynamic imaging in living cells. *J Fluoresc* **11**(3):187–195.
- Murakoshi H, Iino R, Kobayashi T, Fujiwara T, Ohshima C, Yoshimura A, Kusumi A. 2004. Single-molecule imaging analysis of Ras activation in living cells. *Proc Natl Acad Sci USA* **101**(19):7317–7322.
- Sako Y, Minoguchi S, Yanagida T. 2000. Single-molecule imaging of EGFP signaling on the surface of living cells. *Nat Cell Biol* **2**:168–172.
- Sako Y, Uyemura T. 2002. Total internal reflection fluorescence microscopy for single-molecule imaging in living cells. *Cell Struct Funct* **27**:357–365.
- Seisenberger G, Ried MU, Endress T, Buning H, Hallek M, Brauchle C. 2001. Real-time single-molecule imaging of the infection pathway of an adeno-associated virus. *Science* **294**:1929–1932.
- van Hulst NF, Garcia-Parajo MF, Moers MHP, Veerman JA, Ruiter AGT. 1997. Near-field fluorescence imaging of genetic material: toward the molecular limit. *J Struct Biol* **119**:222–231.

### Low-Temperature Single-Molecule Studies

- Moerner WE, Dickson RM, Norris DJ. 1997. Single-molecule spectroscopy and quantum optics in solids. *Adv At, Mol, Opt Phys* **38**:193–236.
- Orrit M, Bernard J, Personov RI. 1993. High-resolution spectroscopy of organic molecules in solids: from fluorescence line narrowing and hole burning to single molecule spectroscopy. *J Phys Chem* **97**:10256–10268.
- Orrit M, Bernard J. 1990. Single pentacene molecules detected by fluorescence excitation in a *p*-terphenyl crystal. *Phys Rev Lett* **65**(21):2716–2719.
- Osad'ko IS. 2003. *Selective spectroscopy of single molecules*. Springer, New York.

### Near-Field Scanning Optical Microscopy and Single Molecules

- Ambrose WP, Goodwin PM, Martin JC, Keller RA. 1994. Single molecule detection and photochemistry on a surface using near-field optical excitation. *Phys Rev Lett* **72**:(1):160–163.
- Azoulay J, Debarre A, Richard A, Tchenio P. 1999. Field enhancement and apertureless near-field optical spectroscopy of single molecules. *J Microsc* **194**(2/3):486–490.
- Colas des Francs G, Girard C. 2002. Theory of near-field optical imaging with a single fluorescent molecule used as a point-like detector. *Chem Phys* **282**:277–287.

Gimzewski JK, Joachim C. 1999. Nanoscale science of single molecules using local probes. *Science* **283**:1683–1688.

Hamann HF, Gallagher A, Nesbitt DJ. 2000. Near-field fluorescence imaging by localized field enhancement near a sharp probe tip. *Appl Phys Lett* **76**:1953–1955.

Kramer A, Trabesinger W, Hecht B, Wild UP. 2002. Optical near-field enhancement at a metal tip probed by a single fluorophore. *Appl Phys Lett* **80**(9):1652–1654.

Ruiter AGT, Veerman JA, Garcia-Parajo MF, van Hulst NF. 1997. Single molecule rotational and translational diffusion observed by near-field scanning optical microscopy. *J Phys Chem A* **101**:7381–7323.

Sick B, Hect B, Wild UP, Novotny L. 2001. Probing confined fields with single molecules and vice versa. *J Microsc* **202**(2):365–373.

Veerman JA, Levi SA, van Veggel FCJM, Reinhoudt DN, van Hulst NF. 1999. Near-field scanning optical microscopy of single fluorescent dendritic molecules. *J Phys Chem A* **103**:11264–11270.

Xie XS, Dunn RC. 1994. Probing single molecule dynamics. *Science* **265**: 361–364.

Zhang Z, Rajagopalan PTR, Selzer T, Benkovic SJ, Hammes GG. 2004. Single-molecule and transient kinetics investigation of the interaction of dihydrofolate reductase with NADPH and dihydrofolate. *Proc Natl Acad Sci USA* **101**(9):2764–2769.

### Photobleaching

Gordon MP, Ha T, Selvin PR. 2004. Single-molecule high-resolution imaging with photobleaching. *Proc Natl Acad Sci USA* **101**(17): 6462–6465.

Ko D-S. 2004. Photobleaching time distribution of a single tetramethylrhodamine molecule in agarose gel. *J Chem Phys* **120**(5):2530–2531.

Tsien RY, Waggoner A. 1995. Fluorophores for confocal microscopy: photophysics and photochemistry. In *Handbook of biological confocal microscopy pawley*, pp. 267–279. Ed JB Pawley. Plenum Press, New York.

van Dijk MA, Kapitein LC, van Mameren J, Schmidt CF, Peterman EJG. 2004. Combining optical trapping and single-molecule fluorescence spectroscopy: enhanced photobleaching of fluorophores. *J Phys Chem B* **108**:6479–6484.

Zondervan R, Kulzer F, Kol'chenko MA, Orrit M. 2004. Photobleaching of rhodamine 6G in (polyvinyl alcohol) at the ensemble and single-molecule levels. *J Phys Chem A* **108**:1657–1665.

### Photobleaching of Single Molecules

Basche TH, Kummer S, Brauchle C. 1995. Direct spectroscopic observation of quantum jumps of a single molecule. *Nature* **373**:132–134.

Ha T, Enderle TH, Chemla DS, Selvin PR, Weiss S. 1997. Quantum jumps of single molecules at room temperature. *Chem Phys Lett* **271**:1–5.

Kohn F, Hofkens J, Gronheid R, Van der Auweraer M, De Schryver FCD. 2002. Parameters influencing the on- and off-times in the fluorescence intensity traces of single cyanine dye molecules. *J Phys Chem A* **106**:4808–4814.

Lu HP, Xie XS. 1997. Single-molecule spectral fluctuations at room temperature. *Nature* **385**(6612):143–146.

Wennmalm S, Rigler R. 1999. On death numbers and survival times of single dye molecules. *J Phys Chem* **103**:2516–2519.

### Polarization and Orientation of Single Molecules

- Bopp MA, Jia Y, Haran G, Morlino EA, Hochstrasser RM. 1998. Single-molecule spectroscopy with 27 fs pulses: time-resolved experiments and direct imaging of orientational distributions. *Appl Phys Lett* **73**(1):7–9.
- Güttler F, Croci M, Renn A, Wild UP. 1996. Single molecule polarization spectroscopy: pentacene in p-terphenyl. *Chem Phys* **211**:421–430.
- Güttler F, Sepiol J, Plakhotnik T, Mitterdorfer A, Renn A, Wild UP. 1993. Single molecule spectroscopy: fluorescence excitation spectra with polarized light. *J Luminesc* **56**:29–38.
- Harms GS, Sonnleitner M, Schutz GJ, Gruber HJ, Schmidt TH. 1999. Single-molecule anisotropy imaging. *Biophys J* **77**:2864–2870.
- Hu D, Lu PH. 2003. Single-molecule nanosecond anisotropy dynamics of tethered protein motions. *J Phys Chem B* **107**:618–626.
- Kreiter M, Prummer M, Hecht B, Wild UP. 2002. Orientation dependence of fluorescence lifetimes near an interface. *J Chem Phys* **117**(20): 9430–9433.
- Lieb MA, Zavislán JM, Novotny L. 2004. Single-molecule orientations determined by direct emission pattern imaging. *J Opt Soc Am B* **21**: 1210–1215.
- Sick B, Hecht B, Novotny L. 2000. Orientational imaging of single molecules by annular illumination. *Phys Rev Lett* **85**(21):4482–4485.
- Weston K, Goldner LS. 2001. Orientation imaging and reorientation dynamics of single dye molecules. *J Phys Chem B* **105**:3453–3462.

### Proteins

- Chen Y, Hu D, Vorpagel ER, Lu HP. 2003. Probing single molecule T4 lysozyme conformational dynamics by intramolecular fluorescence energy transfer. *J Phys Chem B* **107**:7947–7956.
- Fix M, Melia TJ, Jaiswal JK, Rappoport JZ, You D, Sollner TH, Rothman JE, Simon SM. 2004. Imaging single membrane fusion events mediated by SNARE proteins. *Proc Natl Acad Sci USA* **101**(19):7311–7316.
- Funatsu T, Harada Y, Tokunaga M, Saito K, Yanagida T. 1995. Imaging of single fluorescent molecules and individual ATP turnovers by single myosin molecules in aqueous solution. *Nature* **374**(6522):555–559.
- Ha T, Ting AY, Liang J, Caldwell WB, Deniz AA, Chemla DS, Schultz PG, Weiss S. 1999. Single-molecule fluorescence spectroscopy of enzyme conformational dynamics and cleavage mechanism. *Proc Natl Acad Sci USA* **96**:893–898.
- Isshii Y, Yoshida T, Funatsu T, Wazawa T, Yanagida T. 1999. Fluorescence resonance energy transfer between single fluorophores attached to a coiled-coil protein in aqueous solution. *Chem Phys* **247**:163–173.
- Margittai M, Widengren J, Schweinberger E, Schroder GF, Felekyan S, Haustein E, Konig M, Fasshauer D, Grubmuller H, Jahn R, Seidel CAM. 2003. Single-molecule fluorescence resonance energy transfer reveals a dynamic equilibrium between closed and open conformations of syntaxin 1. *Proc Natl Acad Sci USA* **100**(26):15516–15521.
- Rutkauskas D, Novoderezhkin V, Cogdell RJ, van Grondelle R. 2004. Fluorescence spectral fluctuation of single LH2 complexes from *Rhodopseudomonas acidiphila* strain 10050. *Biochemistry* **43**:4431–4438.
- Yang H, Luo G, Karnchanaphanurach P, Louie T-M, Rech I, Cova S, Xun L, Xie XS. 2003. Protein conformational dynamics probed by single-molecule electron transfer. *Science* **302**:262–266.

### Resonance Energy Transfer in Single Molecules

- Allen MW, Bieber Urbauer RJ, Johnson CK. 2004. Single-molecule assays of calmodulin target binding detected with a calmodulin energy-transfer construct. *Anal Chem* **76**:3630–3637.
- Deniz AA, Laurence TA, Beligere GS, Dahan M, Martin AB, Chemla DS, Dawson PE, Schultz PG, Weiss S. 2000. Single-molecule protein folding: diffusion fluorescence resonance energy transfer studies of the denaturation of chymotrypsin inhibitor 2. *Proc Natl Acad Sci USA* **97**(10):5179–5184.
- Ha T, Ting AY, Liang J, Deniz AA, Chemla DS, Schultz PG, Weiss S. 1999. Temporal fluctuations of fluorescence resonance energy transfer between two dyes conjugated to a single protein. *Chem Phys* **247**: 107–118.
- Heilemann M, Tinnefeld P, Mosteiro GS, Parajo MG, Van Hulst NF, Sauer M. 2004. Multistep energy transfer in single molecular photonic wires. *J Am Chem Soc* **126**:6514–6515.
- Kapanidis AN, Lee NK, Laurence TA, Doose S, Margeat E, Weiss S. 2004. Fluorescence-aided molecule sorting: analysis of structure and interactions by alternating-laser excitation of single molecules. *Proc Natl Acad Sci USA* **101**(24):8936–8941.
- Lee M, Tang J, Hochstrasser RM. 2001. Fluorescence lifetime distribution of single molecules undergoing Förster energy transfer. *Chem Phys Lett* **344**:501–508.
- Lipman EA, Schuler B, Bakajin O, Eaton WA. 2003. Single molecule measurement of protein folding kinetics. *Science* **301**:1233–1235.
- Rothwell PJ, Berger S, Kensch O, Felekyan S, Antonik M, Wohr BM, Restle T, Goody RS, Seidel CAM. 2003. Multiparameter single-molecule fluorescence spectroscopy reveals heterogeneity of HIV-1 reverse transcriptase:primer/template complexes. *Proc Natl Acad Sci USA* **100**(4):1655–1660.
- Tinnefeld P, Buschmann V, Weston KD, Sauer M. 2003. Direct observation of collective blinking and energy transfer in a bichromophoric system. *J Phys Chem A* **107**(3):323–327.
- Yasuda R, Masaike T, Adachi K, Noji H, Itoh H, Kinoshita K. 2003. The ATP-waiting conformation of rotating F<sub>1</sub>-ATPase revealed by single-pair fluorescence resonance energy transfer. *Proc Natl Acad Sci USA* **100**(16):9314–9318.

### Reviews and Monographs on Single-Molecule Detection

- Dietrich A, Buschmann V, Müller C, Sauer M. 2002. Fluorescence resonance energy transfer (FRET) and competing processes in donor–acceptor substituted DNA strands: a comparative study of ensemble and single-molecule data. *Rev Mol Biotechnol* **82**:211–231.
- Isshii Y, Yanagida T. 2000. Single molecule detection in life science. *Single Mol* **1**:5–16.
- Moerner WE, Basché T. 1993. Optical spectroscopy of single impurity molecules in solids. *Angew Chem, Int Ed* **32**:457–476.
- Rigler R, Orrit M, Basche T. 2001. *Single molecule spectroscopy*. Springer, New York.
- Xie XS, Trautman JK. 1998. Optical studies of single molecules at room temperature. *Annu Rev Phys Chem* **49**:441–480.

## Sensing

Boldt FM, Heinze J, Diez M, Petersen J, Borsch M. 2004. Real-time pH microscopy down to the molecular level by combined scanning electrochemical microscopy/single-molecule fluorescence spectroscopy. *Anal Chem* **76**:3473–3481.

## Single-Molecule Detection

Bohmer M, Enderlein J. 2003. Fluorescence spectroscopy of single molecules under ambient conditions: methodology and technology. *ChemPhysChem* **4**:792–808.

Enderlein J. 1999. New approach to fluorescence spectroscopy of individual molecules on surfaces. *Phys Rev Lett* **83**(19):3804–3807.

## Spectroscopy of Single Molecules

Basche TH, Moerner WE. 1992. Photon antibunching in the fluorescence of a single dye molecule trapped in a solid. *Phys Rev Lett* **69**(10): 1516–1519.

Deperasinska I, Kozankiewicz B, Bikhtantaev I, Sepiol J. 2001. Anomalous fluorescence of terrylene in neon matrix. *J Phys Chem* **105**:810–814.

Donley E, Plakhotnik T. 2001. Luminescence lifetimes of single molecules in disordered media. *J Chem Phys* **114**(22):9993–9997.

Fleury L, Sick B, Zumofen G, Hecht B, Wild UP. 1998. High photo-stability of single molecules in an organic crystal at room temperature observed by scanning confocal optical microscopy. *Mol Phys* **95**(6):1333–1338.

Kador L, Horne DE, Moerner WE. 1990. Optical detection and probing of single dopant molecules of pentacene in a *p*-terphenyl host crystal by means of absorption spectroscopy. *J Phys Chem* **94**:1237–1248.

Kreiter M, Prummer M, Hecht B, Wild UP. 2002. Orientation dependence of fluorescence lifetimes near an interface. *J Chem Phys* **117**(20): 9430–9433.

Hernando J, van der Schaaf M, van Dijk EMHP, Sauer M, Garcia-Parajo MF, van Hulst NF. 2003. Excitonic behavior of rhodamine dimers: a single-molecule study. *J Phys Chem A* **107**:43–52.

Hou Y, Higgins DA. 2002. Single molecule studies of dynamics in polymer thin films and at surfaces: effect of ambient relative humidity. *J Phys Chem B* **106**:10306–10315.

Sanchez EJ, Novotny L, Holtom GR, Xie XS. 1997. Room-temperature fluorescence imaging and spectroscopy of single molecules by two-photon excitation. *Phys Chem A* **101**(38):7019–7023.

Viteri CR, Gilliland JW, Yip WT. 2003. Probing the dynamic guest-host interactions in sol-gel films using single molecule spectroscopy. *J Am Chem Soc* **125**:1980–1987.

## Theory of Single-Molecule Fluorescence

Barsegov V, Mukamel S. 2002. Multidimensional spectroscopic probes of single molecule fluctuations. *J Chem Phys* **117**(20):9465–9477.

Berezhkovskii AM, Szabo A, Weiss GH. 1999. Theory of single-molecule fluorescence spectroscopy of two-state systems. *J Chem Phys* **110**(18):9145–9150.

Berezhkovskii AM, Szabo A, Weiss GH. 2000. Theory of fluorescence of single molecules undergoing multistate conformational dynamics. *J Phys Chem B* **104**:3776–3780.

Enderlein J. 2000. Theoretical study of detection of a dipole emitter through an objective with high numerical aperture. *Opt Lett* **25**(9): 634–636.

Enderlein J. 1997. Statistics of single-molecule detection. *J Phys Chem B* **101**:3626–3632.

Schenter GK, Lu HP, Xie XS. 1999. Statistical analyses and theoretical models of single-molecule enzymatic dynamics. *J Phys Chem* **103**: 10477–10488.

Weston KD, Dyck M, Tinnefeld P, Muller C, Herten DP, Sauer M. 2002. Measuring the number of independent emitters in single-molecule fluorescence images and trajectories using coincident photons. *Anal Chem* **74**:5342–5349.

Zheng Y, Brown FLH. 2003. Photon emission from driven single molecules. *J Chem Phys* **119**(22):11814–11828.

## Time-Resolved Studies of Single Molecules

De Schryver FC. 1998. Time, space and spectrally resolved photochemistry from ensembles to single molecules. *Pure Appl Chem* **70**(11): 2147–2156.

Fries JR, Brand L, Eggeling C, Kollner M, and Seidel CAM. 1998. Quantitative identification of different single molecules by selective time-resolved confocal fluorescence spectroscopy. *J Phys Chem A* **102**:6601–6613.

Lee M, Kim J, Tang J, Hochstrasser RM. 2002. Fluorescence quenching and lifetime distributions of single molecules on glass surfaces. *Chem Phys Lett* **359**:412–419.

Molski A, Hofkens J, Gensch T, Boens N, De Schryver FC. 2000. Theory of time-resolved single-molecule fluorescence spectroscopy. *Chem Phys Lett* **318**:325–332.

Sauer M, Wolfrum J. 1999. Single-molecule detection in biology with multiplex dyes and pulsed semiconductor lasers. In *Applied Fluorescence in Chemistry, Biology and Medicine*, pp. 39–58. Ed W Rettig, B Strehmel, S Schrader, H Seifert. Springer, New York.

Vallee RAL, Cotlet M, Hofkens J, De Schryver FC. 2003. Spatially heterogeneous dynamics in polymer glasses at room temperature probed by single molecule lifetime fluctuations. *Macromolecules* **36**:7752–7758.

## PROBLEMS

- P23.1. Suppose you have a fluorophore with a molar extinction of  $104,000 \text{ M}^{-1} \text{ cm}^{-1}$  at 600 nm, and a lifetime of 4 ns. Assume there is no intersystem crossing or blinking. Calculate the light intensity in watts/cm<sup>2</sup> needed to result in half of the molecule in the excited state. If the illuminated area is 1  $\mu\text{m}^2$  what is the needed power? Assume the objective transmits 100% of the light.

# 24

# Fluorescence Correlation Spectroscopy

In the previous chapter we described fluorescence imaging and spectroscopy on single molecules. Individual fluorophores can be studied if the observed volume is restricted and the fluorophores are immobilized on a surface. With present technology it is difficult to track freely diffusing single molecules. Single-molecule detection (SMD) on surfaces is a powerful technique because it avoids ensemble averaging and allows single events to be observed. If a dynamic process such as a chemical reaction is being studied, there is no need to synchronize the population because the individual kinetic events can be observed. However, SMD has its limitations. The most stable fluorophores typically emit  $10^5$  to  $10^6$  photons prior to irreversible photodestruction. Because of the modest detection efficiency of optical systems, and the need for high emissive rates for detection of the emission over background, single molecules can only be observed for a brief period of time—1 second or less—which may be too short to observe many biochemical processes. When the fluorophore is bleached the experiment must be started again with a different molecule. Additionally, SMD requires immobilization on a surface, which can affect the functioning of the molecule and slow its access to substrates and/or ligands because of unstirred boundary layers near the surface.

Fluorescence correlation spectroscopy (FCS) is also a method based on observation of a single molecule or several molecules. In contrast to SMD, FCS does not require surface immobilization and can be performed on molecules in solution. The observed molecules are continuously replenished by diffusion into a small observed volume. FCS thus allows continuous observation for longer periods of time and does not require selection of specific molecules for observation. FCS is based on the analysis of time-dependent intensity fluctuations that are the result of some dynamic process, typically translation diffusion into and out of a small volume defined by a focused laser beam and a confocal aperture. When the fluorophore diffuses into a focused

light beam, there is a burst of emitted photons due to multiple excitation-emission cycles from the same fluorophore. If the fluorophore diffuses rapidly out of the volume the photon burst is short lived. If the fluorophore diffuses more slowly the photon burst displays a longer duration. Under typical conditions the fluorophore does not undergo photo-bleaching during the time it remains in the illuminated volume, but transitions to the triplet state frequently occur. By correlation analysis of the time-dependent emission, one can determine the diffusion coefficient of the fluorophore. In this case "time-dependent" refers to the actual time and not to a time delay or time-dependent decay following pulsed excitation.

FCS has many applications because a wide variety of processes can result in intensity fluctuations. In addition to translation diffusion, intensity fluctuations can occur due to ligand–macromolecule binding, rotational diffusion, internal macromolecule dynamics, intersystem crossing, and excited-state reactions. The data are interpreted in terms of correlation functions. Different equations are needed to describe each process, and usually two or more processes affect the data at the same time. It is also necessary to account for the size and shape of the observed volume. As a result the theory and equations for FCS are rather complex.

FCS was first described in the early 1970s in a series of classic papers.<sup>1–4</sup> An extensive description of FCS and its applications can be found in a recent monograph.<sup>5</sup> These papers describe the theory for FCS and recognize its potential for measurement of diffusion and reaction kinetics. The theory showed that FCS would allow measurement of kinetic constants even when the system was in equilibrium, if the reversible process caused spectral changes. The FCS data will contain information on the reaction rates because a reaction at equilibrium still proceeds in both directions, so that the spectral properties will continue to fluctuate. However, the early FCS measurements were plagued by low sig-

nal-to-noise (S/N) ratios for a variety of reasons, including a large number of observed molecules, intensity changes in the laser light sources, low-quantum-yield fluorophores, and low-efficiency detectors.<sup>6</sup> In contrast to fluorescence intensity measurements, where it is easier to measure solutions with higher fluorophore concentrations, FCS measurements are best performed when observing a small number of fluorophores (<10). In order to detect a small number of fluorophores with a focused laser beam the sample needed to be dilute, typically near 1 nM. Since the samples are diluted, the unwanted background due to fluorescent impurities and scatter needed to be suppressed by confocal optics and effective filtering. Because of all these requirements FCS was not widely used for 20 years. By the early 1990s a number of technical advances made FCS a practical technology, including confocal optics, high-efficiency avalanche photodiode (APD) detectors, stable lasers, and multiphoton excitation and commercially available instruments.<sup>6</sup> As a result there has been a rapid increase in the applications of FCS to biochemical analysis.<sup>7–16</sup> FCS is now being used to detect protein association reactions, DNA hybridization, immunoassays, binding to membrane receptors, gene expression, and diffusion of labeled intracellular proteins, to name a few.

#### 24.1. PRINCIPLES OF FLUORESCENCE CORRELATION SPECTROSCOPY

FCS is typically performed using freely diffusing molecules. Excitation is usually accomplished with a laser focused to a diffraction-limited spot. A confocal pinhole is used to reject signal from outside the desired volume. Using these optical conditions, the observed volume is an ellipsoid that is elongated along the optical axis. The concentration of the fluorophores needs to be in a range where just a few molecules are present in the observed volume.

To illustrate the principle of FCS consider a cylindrical volume 0.08 μm in diameter and 2 μm in length (Figure 24.1) that is slightly larger than for a typical FCS instrument. The volume of this cylinder is 1 fl = 10<sup>-15</sup> liters. If the fluorophore concentration is 1 nM, then the observed volume contains an average of 0.6 molecules. The average number of fluorophores in the volume is determined by the bulk concentration and remains constant in a stationary experiment. However, random diffusion of the fluorophores results in time-dependent changes, called fluctuations, in the number of fluorophores in the volume. Fluctuations in occupancy number in this small volume result in intensity

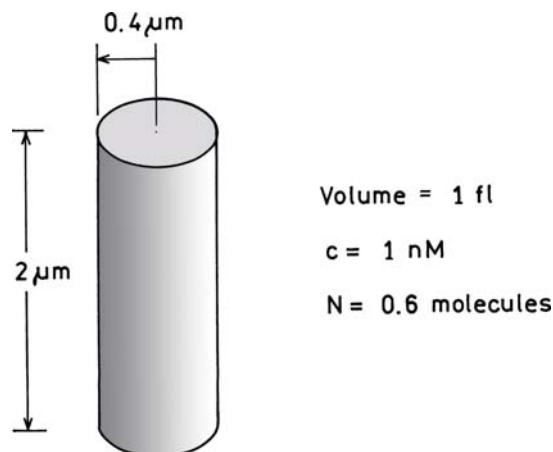


**Figure 24.1.** Typical volume in an FCS experiment.

fluctuations in the fluorescence intensity. The theory for FCS provides the basis for extracting molecular information from the molecules by analysis of the rates and amplitudes of the intensity fluctuations.

The theory of FCS is based on Poisson statistics. For random discrete events the number of fluorophores in the volume can be described by the Poisson distribution

$$P(n,N) = \frac{N^n}{n!} e^{-N} \quad (24.1)$$

In this expression  $P(n,N)$  is the probability of  $n$  fluorophores being present in the volume when the average number of molecules in the volume is  $N$ . Using eq. 24.1 one can calculate that for  $N = 0.6$  there is a 55% probability that the volume contains no fluorophores, a 33% probability that the volume contains 1 fluorophore, and a 10% probability that the volume contains 2 fluorophores (Figure 24.2). The fluorescence intensity from this volume will fluctuate as the fluorophores diffuse into and out of the volume.

The changes in occupation number of the volume will result in changes in the intensity (Figure 24.3). If the diffusion is slow the fluorophores will move slowly into and out of the volume. If the diffusion is faster the occupation number and intensity will change more rapidly. This time-dependent intensity is analyzed statistically to determine the amplitude and frequency distribution of fluctuations. The intensity at a given time  $F(t)$  is compared with the intensity at a slightly later time  $F(t + \tau)$ . If diffusion is slow,  $F(t)$  and  $F(t + \tau)$  are likely to be similar (top panel). If diffusion is fast,  $F(t)$  and  $F(t + \tau)$  are likely to be different (lower

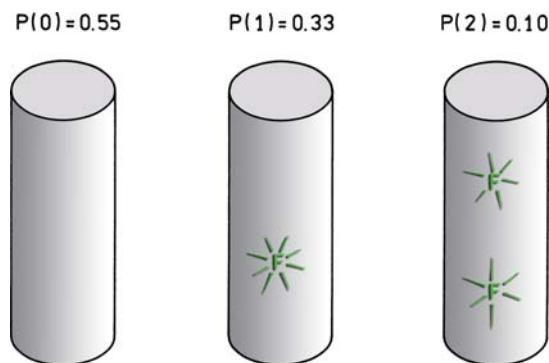


**Figure 24.2.** Poisson distribution of a 1-nM fluorophore solution in a 1-fl volume,  $N = 0.6$ .

panel). In an FCS instrument a dedicated correlation board is usually used to calculate the correlation between  $F(t)$  and  $F(t + \tau)$  for a range of delay times  $\tau$ . This results in an autocorrelation function  $G(\tau)$  that contains information on the diffusion coefficient and occupation number of the observed volume. The dependence of the correlation function on the rate of diffusion makes FCS valuable for measuring a wide range of binding interactions, such as protein–ligand binding and DNA hybridization. Note that the correlation time  $\tau$  in an FCS measurement is not related to the lifetime of the fluorophore.

An important feature of FCS is a measurement of the number of diffusing species in the observed volume. In principle, this measurement does not rely on an external calibration or the quantum yields of the fluorophores. In practice, calibrations are performed using known solutions. The important point is the amplitude of the autocorrelation function at  $\tau = 0$  reveals the average number of molecules being observed. Sometimes a proportionality constant is used to adjust this number. FCS can thus be used to detect changes in particle density due to association or cleavage reactions. In contrast to single molecule detection, the observed molecules are continually replaced by diffusion, so that photobleaching is less of a problem. Additionally, since only a few molecules are observed, FCS provides high sensitivity. Intensity fluctuations can also occur due to blinking of the fluorophores upon transition to the triplet state, structural changes in biomolecules, and the rate of lateral translation in flowing samples. There are also more advanced types of FCS, such as dual-color cross-correlation FCS, which selectively detects species that contain two fluorophores, such as DNA oligomers labeled with two different fluorophores.

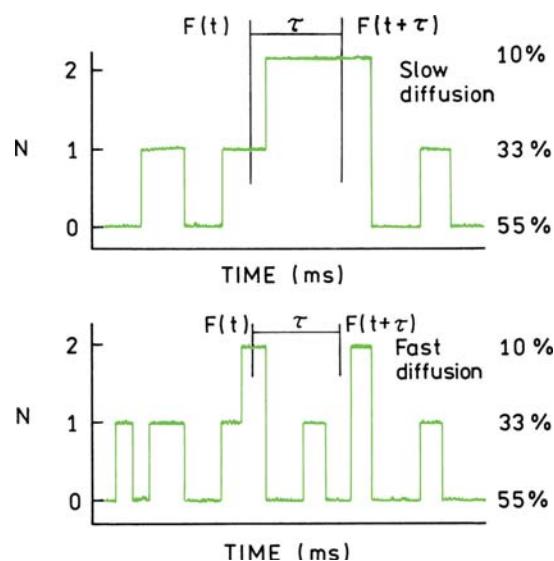


**Figure 24.3.** Fluctuations in the number of fluorophores ( $N$ ) in the observed volume of 1 fl with  $c = 1$  nM. The intensity axis is in units of the intensity from a single fluorophore.

FCS can provide information about reaction kinetics even when the reaction is in equilibrium. Consider a simple reaction  $F + M \rightleftharpoons F^*M$ , where  $F$  is a fluorophore that is nonfluorescent in solution but fluorescent ( $F^*$ ) when bound to a macromolecule ( $M$ ). The reaction kinetics would usually be studied by starting the reaction from a nonequilibrium condition, such as mixing separate solutions of  $F$  and  $M$  in a stopped-flow instrument. Upon mixing the intensity would change as the reaction approached equilibrium. When the reaction reaches equilibrium the fluorescence intensity will remain constant and no additional information is obtained by continuing to measure the intensity. In contrast, FCS can measure the reaction kinetics under equilibrium conditions. If a small number of molecules are observed the intensity will fluctuate as the fluorophore binds to and dissociates from the macromolecules. The rate of intensity fluctuations contains information on the sum of the forward and reverse reaction rates.

Because of the ability of FCS to determine the number of observed particles, and to determine the rates of diffusion, and other dynamic processes, there has been a rapid expansion of FCS technology into a wide range of applications, including high-throughput screening, DNA analysis, and detection of small numbers of intracellular species. In the following section we describe the theory and practice of FCS with examples to illustrate the potential of this technology.

## 24.2. THEORY OF FCS

The equations for FCS are moderately complex, and there are many subtle points that result from the unique aspects of the measurements. Different authors use slightly different terminology for FCS. Hence it is valuable to review the theory to provide a basis for understanding the data and the factors that influence the measured correlation functions.

The autocorrelation function of the fluorescence intensity is given by the product of the intensity at time  $t$ ,  $F(t)$ , with the intensity after a delay time  $\tau$ ,  $F(t + \tau)$ , averaged over a large number of measurements.<sup>17–21</sup> The time  $t$  refers to the actual time as the intensities are observed. Data collection times range from seconds to minutes. The delay time  $\tau$  is the difference in real time between measurement of  $F(t)$  and  $F(t + \tau)$ , typically in the range from  $10^{-2}$  to  $10^2$  ms. If the intensity fluctuations are slow compared to  $\tau$ , then  $F(t)$  and  $F(t + \tau)$  will be similar in magnitude. That is, if  $F(t)$  is larger than the average intensity  $\langle F \rangle$ , then  $F(t + \tau)$  is likely to be larger than  $\langle F \rangle$ . If the intensity fluctuations are fast relative to  $\tau$ , then the value of  $F(t)$  and  $F(t + \tau)$  will not be related. The value of the autocorrelation for a time delay  $\tau$  is given by the average value of the products

$$\begin{aligned} R(\tau) &= \langle F(t)F(t + \tau) \rangle \\ &= \frac{1}{T} \int_0^T F(t)F(t + \tau) dt \end{aligned} \quad (24.2)$$

where  $T$  is the data accumulation time. The factor  $1/T$  normalizes the value of the products  $F(t)F(t + \tau)$  for the data accumulation time. This mathematical process is typically performed using dedicated correlation boards that perform the needed operations in real time as the fluctuating intensity is observed. With modern electronics it is now also possible to record the time ( $t$ )-dependent intensities for the duration of the data collection ( $T$ ) and then perform the calculations. Additional information can be obtained from the complete list of time-dependent intensities, so it seems likely that this approach will eventually be standard in FCS experiments.

The quantities of interest are the fluctuations in  $F(t)$  around the mean value

$$\delta F(t) = \langle F \rangle - F(t) \quad (24.3)$$

The autocorrelation function for the fluorescence intensities, normalized by average intensity squared, is given by

$$\begin{aligned} G(\tau) &= \frac{\langle F(t)F(t + \tau) \rangle}{\langle F \rangle \langle F \rangle} \\ &= 1 + \frac{\langle \delta F(0)\delta F(\tau) \rangle}{\langle F \rangle^2} \end{aligned} \quad (24.4)$$

In this expression we have replaced  $t$  with 0. The delay time  $\tau$  is always relative to a datapoint at an earlier time so that only the difference  $\tau$  is relevant. It is important to remember the meaning of  $t$  and  $\tau$  in FCS, which is different from their meaning in time-resolved fluorescence. In time-resolved fluorescence  $t$  refers to the time after the excitation pulse and  $\tau$  refers to the decay time. In FCS  $t$  refers to real time and  $\tau$  refers to a time difference between two intensity measurements. In the FCS literature there are occasional inaccuracies in the words used to describe the correlation functions in eqs. 24.2 and 24.4. Equation 24.2 is the autocorrelation function of the fluorescence intensities. The term  $\delta F(t)$  in eq. 24.3 is the variance, so that the last term on the right side of eq. 24.4 is actually the autocovariance of  $F(t)$ , but is conventionally referred to as the "autocorrelation function." A more accurate term is "the autocorrelation function of the fluorescence fluctuations."<sup>17</sup> Another confusing point is the definition of the autocorrelation function. Some authors use eq. 24.4 and other authors use

$$G(\tau) = \frac{\langle \delta F(0)\delta F(\tau) \rangle}{\langle F \rangle^2} \quad (24.5)$$

which is the autocorrelation function of fluorescence fluctuations. We will use eq. 24.5 since this avoids inclusion of one (1) in all the subsequent equations. For simplicity we will refer to eq. 24.5 as the correlation or autocorrelation function.

In order to interpret the FCS data we need a theoretical model to describe the fluctuations. The data are typically the number of photon counts in a given time interval, typically about a microsecond, which are due to a small number of fluorophores. The intensity is dependent on the number of photons detected from each fluorophore in a given period of time. For FCS it is convenient to use a parameter called the brightness, which is given by

$$B = q\sigma Q \quad (24.6)$$

where  $q$  is the quantum efficiency for detection of the emitted photons,  $\sigma$  is the cross-section for absorption, and  $Q$  is the quantum yield for emission of the fluorophore. The brightness is the number of photons per second for a single fluorophore observed for a given set of optical conditions. Unlike the quantum yield, the brightness is not a molecular property of the fluorophore, but depends on the precise optical conditions including the light intensity, light collection efficiency of the instrument, and the counting efficiency of the detector. The measured intensity from the sample, typically in kHz, is given by the integral of the fluorophore concentration over the observed volume:

$$F(t) = B \int CEF(r)I(r)C(r,t)dV \quad (24.7)$$

In this expression  $CEF(r)$  is the collection efficiency function of the instrument as a function of position ( $r$ ). The integral extends over the entire observed space. The position  $r$  is more properly described as a vector ( $\vec{r}$ ) but for simplicity we assume  $r$  is a vector. The excited fluorophores will be distributed in a three-dimensional volume, in the  $x$ - $y$  plane and along the optical  $z$ -axis.  $I(r)$  is the excitation intensity at each position  $r$ , and  $C(r,t)$  is the distribution of fluorophores. Equation 24.7 looks complex, but it has a simple meaning. The intensity depends on the concentration and spatial distribution of the excitation and detection efficiency, and the brightness of the fluorophores. The observed intensity also depends on the excited and observed volumes, which is accounted for by the integral. It is usually not necessary to consider these factors separately, so that the instrument is described as having a detection profile:

$$p(r) = CEF(r)I(r) = MDE(r) \quad (24.8)$$

which is also referred to as the molecular detection efficiency  $MDE(r)$ .

Figure 24.4 shows a typical FCS instrument. A laser is focused on the sample. The emission is selected with a dichroic filter. The out-of-focus light is rejected with a pinhole, which is typically large enough to pass all light from a region slightly larger than the illuminated spot.<sup>10</sup> The intensity profile of the focused laser is assumed to be Gaussian. For this configuration, the brightness profile can be approximated by a three-dimensional Gaussian (Figure 24.5):

$$p(r) = I_0 \exp[-2(x^2 + y^2)/s^2] \exp(-2z^2/u^2) \quad (24.9)$$

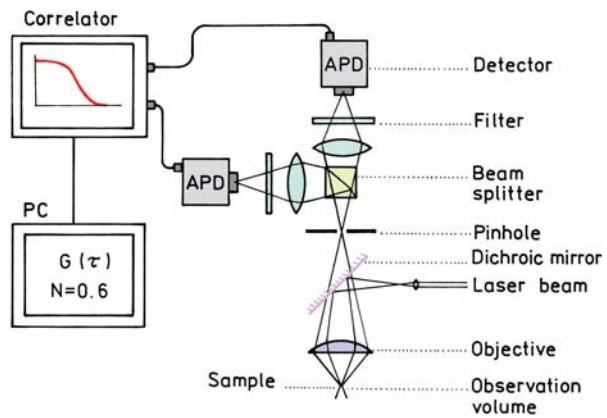


Figure 24.4. Typical instrumentation for FCS. Revised from [17].

The surface of the volume is not sharply defined. The radius  $s$  and half-length  $u$  refer to distances at which the profile decreases to  $e^{-2}$  of its maximal value  $I_0$ .

Equation 24.7 gives the time-dependent intensity. We now need to calculate the autocorrelation function due to concentration fluctuations throughout the observed volume. This function is more complex than for a fluorophore diffusing in and out of a volume with a sharp boundary (Figure 24.1). As the fluorophore diffuses it enters regions where the count rate per fluorophore is higher or lower

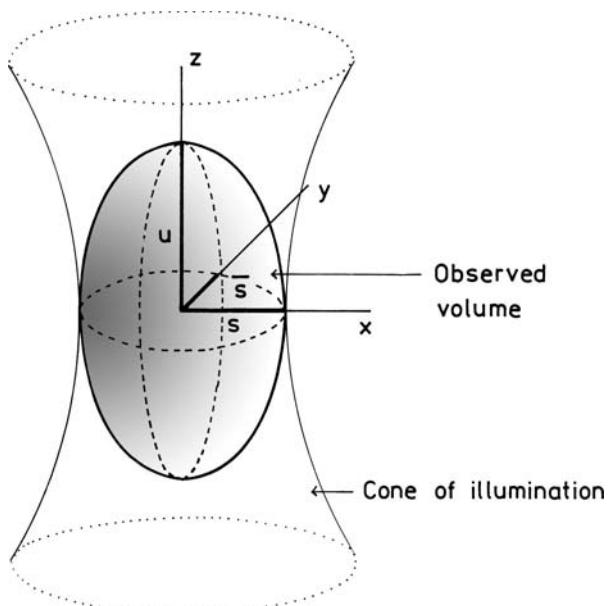


Figure 24.5. Ellipsoidal observed volume with focused single photon excitation and confocal detection.

based on the detection profile  $p(r)$ . The autocorrelation function for the intensity fluctuation is given by

$$G(\tau) = \frac{B^2 \int \int p(r)p(r') \langle \delta C(r,0)\delta C(r',\tau) \rangle dVd'V}{[BC \int p(r)dV]^2} \quad (24.10)$$

where  $r$  is the position of the fluorophore at  $t = 0$  and  $r'$  is its position at  $t = \tau$ . This formidable expression can be understood as follows. The denominator contains the average intensity, which is given by the product of the brightness  $B$ , mean concentration  $C$ , and the detection profile of the instrument integrated over the observed volume. The concentration term and brightness appear outside the integral because  $Q$  is independent of position, and only the average concentration is needed to calculate the average intensity. The detection profile  $p(r)$  accounts for the excitation and detection efficiency. The numerator calculates the intensity fluctuations from the concentration fluctuations at each point in the sample, which is then integrated over the observed volume. When the fluorophore moves from  $r$  to a new location  $r'$ , its brightness becomes proportional to the detection profile at this position  $p(r')$ . The integral extends over the observed volume for all the fluorophores present in the volume. The term  $B^2$  is again outside the integral because the intrinsic brightness of the fluorophore does not depend on position. Remarkably, the correlation function (but not the S/N ratio) is independent of fluorophore brightness, which cancels in eq. 24.10. This makes sense because we are measuring the correlation between fluorophore locations, which should not depend on the brightness of the fluorophore.

It is instructive to consider the number of fluorophores in a typical FCS experiment. A diffraction-limited volume will typically have a diameter of  $0.5 \mu\text{m}$  and a total length of  $2 \mu\text{m}$ . For this size and shape the effective volume is  $0.35 \text{ fL}$ . The effective volume is not equal to the geometric volume of an ellipsoid because the detection profile does not have sharp boundaries. Figure 24.6 shows calculations of the number of fluorophores in this volume. Occupation numbers of 2 to 20 are expected for fluorophore concentrations from  $9.6 \text{ nM}$  to  $96 \text{ nM}$ . The width of the distribution is given by  $\sqrt{N}$  and increases with the occupation number, as characteristic for a Poisson distribution.

Equation 24.10 is not limited to diffusion and can be used to derive a correlation function for any process that results in the intensity fluctuations. Chemical or photochemical processes that change the brightness of a flu-

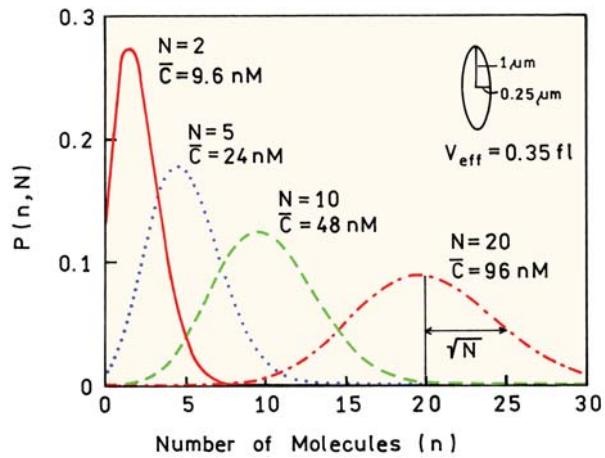


**Figure 24.6.** Poisson distribution in an ellipsoidal volume for various fluorophore concentrations. The volume of a geometric ellipsoid with  $s = 0.25 \mu\text{m}$  and  $u = 1.0 \mu\text{m}$  is  $0.26 \text{ fL}$ .

rophore can also be studied. In place of  $\delta C(r,\tau)$  eq. 24.10 is then used with a different  $r'$  model to derive the expected autocorrelation function.

### 24.2.1. Translational Diffusion and FCS

Perhaps the most common application of FCS is to measure translational diffusion. The rate of diffusion depends on the size of the molecule and its interactions with other molecules. The correlation function for diffusion in three dimensions is given by<sup>18</sup>

$$\langle \delta C(r,0)\delta C(r',\tau) \rangle$$

$$= \bar{C} (4\pi D\tau)^{3/2} \exp[-|r - r'|^2/4D\tau] \quad (24.11)$$

where  $D$  is the diffusion coefficient. Insertion of eq. 24.11 in 24.10, using the Gaussian detection profile (eq. 24.9) and some complex mathematics, yields the correlation function for three-dimensional diffusion:

$$G(\tau) = G(0) \left( 1 + \frac{4D\tau}{s^2} \right)^{-1} \left( 1 + \frac{4D\tau}{u^2} \right)^{-1/2} \\ = G(0)D(\tau) \quad (24.12)$$

where  $G(0)$  is the amplitude at  $\tau = 0$ . For future convenience we define  $D(\tau)$  as the portion of the correlation function

which contains the diffusion coefficient. This expression is also written as

$$\begin{aligned} G(\tau) &= G(0) \left(1 + \frac{\tau}{\tau_D}\right)^{-1} \left(1 + \left(\frac{s}{u}\right)^2 \frac{\tau}{\tau_D}\right)^{-1/2} \\ &= G(0) D(\tau) \end{aligned} \quad (24.13)$$

where the diffusion time is

$$\tau_D = s^2/4D \quad (24.14)$$

The origin of eq. 24.14 is understood by recalling that the mean distance a molecule diffuses in a time  $\tau$  is proportional to  $\sqrt{D\tau}$ . The form of eq. 24.12 is a result of the shape of the detection profile (eq. 24.9) being integrated with the concentration correlation function. Different detection profiles will result in different forms of eq. 24.12.

Figure 24.7 shows the correlation functions expected for a single freely diffusing species, that is, a homogeneous population, with diffusion coefficients ranging from  $10^{-5}$  to  $10^{-7} \text{ cm}^2/\text{s}$ . We assumed the observed volume was an ellipsoid with radius  $s = 0.25 \mu\text{m}$  and half-length  $u = 1 \mu\text{m}$ . The correlation function  $G(\tau)$  is usually plotted using a logarithmic  $\tau$  axis. The amplitude of  $G(\tau)$  decreases as  $\tau$  increases.  $G(\tau)$  approaches zero because at long times the fluorophores have no memory of their initial position. The value of  $\tau_D$  is usually determined by least-squares fitting of the simulated curve with the measured data. A diffusion coefficient of  $10^{-6} \text{ cm}^2/\text{s}$  results in  $\tau_D = 0.156 \text{ ms}$ . As the diffusion coefficient decreases the correlation function shifts to longer  $\tau$  values, which reflects slower intensity fluctuations as the fluorophores diffuse more slowly into and out of the observed volume. As we will discuss below, a 100-fold change in diffusion coefficient would require a 10,000-fold change in molecular weight, so that the curves in Figure 24.7 are more shifted than is typical in an FCS experiment. The autocorrelation function is also expected to depend on the fluorophore concentration.

The autocorrelation function is that it provides a measurement of the average number of molecules  $N$  in the observed volume, even if the bulk concentration is not known. The number of molecules is given by the inverse of the intercept at  $\tau = 0$ ,  $G(0) = 1/N$ . Hence the amplitude of the correlation function is larger for a smaller number of molecules. This is the reason why FCS was relatively unused in the 1970s and 1980s. Without confocal optics to

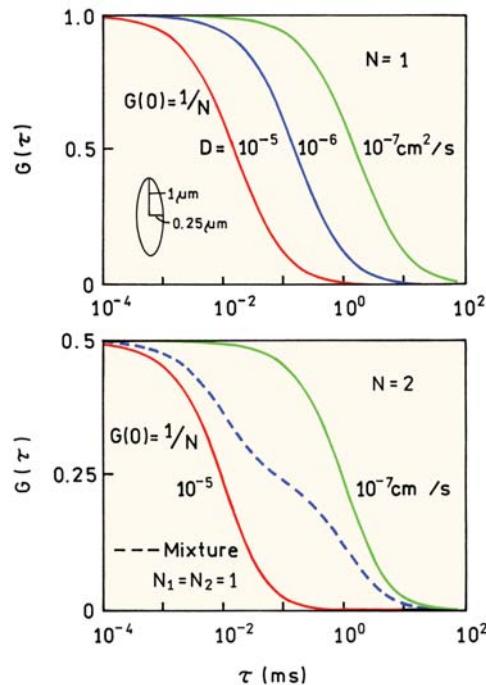


**Figure 24.7.** Simulated autocorrelation functions for diffusion in three dimensions (eq. 24.12) for diffusion coefficients of  $10^{-5}$  to  $10^{-7} \text{ cm}^2/\text{s}$  (top) and for a mixture of two diffusing species (bottom). The observed volume was assumed to be an ellipsoid with  $s = 0.25 \mu\text{m}$  and  $u = 1 \mu\text{m}$ .

reduce the observed volume the number of molecules was large and the amplitudes of the correlation functions were too small for reliable measurements, even with long data acquisition times. Another important feature of  $G(\tau)$  for a single species is that  $G(\tau)$  does not depend on the brightness of the fluorophore. The brightness  $B$  affects the S/N of the measurement and the ability to see the fluorophore over the background. However, the correlation function itself is independent of the brightness and  $G(0)$  depends only on the average number of observed fluorophores.

At first glance it is difficult to see from eqs. 24.5 and 24.10 why the value of  $G(0)$  is equal to  $1/N$ . Since  $N$  is proportional to  $\bar{c}$  the denominator contains a factor  $N^2$ . The numerator also has two concentration terms as a product, suggesting a factor of  $N^2$  in the numerator. However, for a Poisson distribution the variance is proportional to the square root of the mean, so that  $\delta C$  is proportional to  $\sqrt{N}$ . Hence the numerator contains a factor  $N$ , and the ratio gives  $G(0) = 1/N$ .

One might think that if  $G(\tau)$  reveals the number of fluorophores then it should be possible to determine the fluorophore concentration. This is only partially correct. The

number of fluorophores in the effective volume observed by the instrument is given by

$$N = \bar{C} V_{\text{eff}} \quad (24.15)$$

If  $V_{\text{eff}}$  was precisely known then  $\bar{C}$  could be calculated. In FCS we have an estimate of  $V_{\text{eff}}$ , but we do not know an exact volume. The effective volume is dependent on the exact shape of the detection function  $p(r)$ . If the observed volume is described by 24.9 then

$$V_{\text{eff}} = \pi^{3/2} s^2 u \quad (24.16)$$

This effective volume is different from the geometric volume of an ellipsoid, which is given by  $(4/3)\pi s^2 u$ . For the ellipsoid shown in Figure 24.7 the effective volume is  $V_{\text{eff}} = 0.35$  fl and the geometric volume is 0.26 fl. The effective volume is different for other shapes, such as for a flat cylinder, a highly elongated volume, or when using two-photon excitation. While the shape of  $V_{\text{eff}}$  is not known precisely the number of observed fluorophores is known. For this reason volume is defined in an unusual way. The value of  $V_{\text{eff}}$  is that volume which contains  $N$  fluorophores at a known concentration.

It is also important to understand the meaning of  $\tau_D$  obtained from the autocorrelation function. The diffusion coefficient  $D$  is a molecular property with a defined value that is independent of any instrumental parameters. Since  $\tau_D$  depends on  $D$  one is inclined to think that  $\tau_D$  is also a molecular parameter and independent of the instrument. However,  $\tau_D$  depends on the radius of the observed volume. This means that the recovered value of  $D$  depends on accurate knowledge of the shape of  $V_{\text{eff}}$ . For this reason FCS instruments are frequently calibrated with fluorophores with known diffusion coefficients. The width and length of the volume are adjusted until the known diffusion coefficient is recovered and the measured correlation function matches the calculated correlation function. In principle, there is no need to calibrate the concentration or instrument sensitivity because the value of  $N = G(0)^{-1}$  is determined without any assumptions, except that the solution contains only a single type of fluorophore with the same spectral and diffusive properties. Solutions with known concentrations are used for calibration procedures. Since FCS measurements are often used to measure relative diffusion coefficients of two species, the results can be useful even if the absolute values of the diffusion coefficients are somewhat inaccurate.

## 24.2.2. Occupation Numbers and Volumes in FCS

### Advanced Topic

There are some differences in how authors use the  $G(0)$  intercept to calculate  $N$ . Instead of  $G(0) = 1/N$ , some authors use  $G(0) = \gamma/N$ , where  $\gamma$  is a geometric factor that depends on the detection profile. For a Gaussian volume,  $\gamma$  is sometimes set equal to  $1/\sqrt{8} = 0.35$ . For a volume with a Gaussian profile for the width and a Lorentzian profile for the length, the factor is  $\gamma = 0.076$ . This difference arises from how the sample volume is defined. The volume of a Gaussian-shaped sample is obtained by integration of eq. 24.9 to yield  $V_G = \pi^{3/2} s^2 u / \sqrt{8}$ . The  $\gamma$  factor for a Gaussian-Lorentzian shape is obtained in a similar way. The  $\gamma$  factor is used if the sample volume is taken as the integrated volume. If the effective volume of a Gaussian shape is defined by eqs. 24.15 and 24.16 then  $G(0) = 1/N$ . For this chapter we will use  $V_{\text{eff}} = \pi^{3/2} s^2 u$  and  $G(0) = 1/N$ .

## 24.2.3. FCS for Multiple Diffusing Species

The use of FCS to measure binding reactions depends on the shape of the autocorrelation function for a sample with two diffusion coefficients. Assume the ligand is labeled with the fluorophore and that the labeled ligand binds to a protein. In solution the ligand has a diffusion coefficient  $D_1$ , and the protein-bound ligand has a diffusion coefficient  $D_2$ . If the free and bound fluorophores have equal brightness, that is, the absorption spectra and quantum yield of the labeled ligand do not change upon binding, the autocorrelation function is given by

$$G(\tau) = \frac{1}{N^2} [N_1 D_1(\tau) + N_2 D_2(\tau)] \quad (24.17)$$

where  $N_1$  and  $N_2$  are the number of free and bound fluorophores and  $N = N_1 + N_2$  is the total number of fluorophores. The diffusive parts of the autocorrelation function are given by eq. 24.12 with diffusion coefficients  $D_1$  and  $D_2$ . Note that  $D_i$  refers to a diffusion coefficient and  $D_i(\tau)$  refers to the part of the autocorrelation function that contains the diffusion coefficients.

The lower panel in Figure 24.7 shows simulated autocorrelation functions for a mixture of diffusing fluorophores with  $D_1 = 10^{-5}$  cm<sup>2</sup>/s and  $D_2 = 10^{-7}$  cm<sup>2</sup>/s. In this case we assumed the total number of diffusing fluorophores to be  $N = 2$ . When both species are present the heterogeneity in the diffusion coefficients can be seen in the shape of

the autocorrelation function (dashed line). This change in shape serves as the basis for measuring association reactions between biomolecules. Autocorrelation functions are calculated for various assumed diffusion coefficients and functional amplitudes until the calculated function matches the measured function. This procedure is analogous to that used to resolve multi-exponential decays from time-resolved measurements. Note that the value of  $G(0)$  is 0.5 because we assumed an average of two fluorophores are in the effective volume for these simulations. Equation 24.17 only applies if the two species do not exchange between the free and bound forms during the timescale of the experiment, which is the diffusion time  $\tau_D$ . If the ligand binds and dissociates within the time it is in the observed volume, only a single diffusion coefficient will be observed. If the ligand moves from the free to bound form on a timescale comparable to the diffusion time, the correlation function cannot be written as a sum of two correlation functions with different diffusion coefficients.

Fluorophores frequently display changes in quantum yield or brightness (eq. 24.6) upon binding to a biomolecule. In this case the two species still contribute to the autocorrelation function, but do not contribute in direct proportion to their relative concentrations or quantum yields. For a sample with two different quantum yields,  $Q_1$  and  $Q_2$ , with brightness  $B_1$  and  $B_2$ , and diffusion coefficients  $D_1$  and  $D_2$ , the correlation function is given by

$$G(\tau) = \frac{N_1 B_1^2 D_1(\tau) + N_2 B_2^2 D_2(\tau)}{(N_1 B_1 + N_2 B_2)^2} \quad (24.18)$$

with  $D_i(\tau)$  defined as in eq. 24.12. For several different species this expression becomes

$$G(\tau) = \frac{\sum N_i B_i^2 D_i(\tau)}{(\sum N_i B_i)^2} \quad (24.19)$$

Notice that each species contributes to the autocorrelation function proportional to the square of its quantum yield or brightness. This means that the autocorrelation function is strongly weighted by the brightest species in the sample. For instance, suppose the sample contains one molecule with  $Q_1 = 1.0$  and one molecule with  $Q_2 = 0.1$ . The fraction of the signal due to  $Q_1$  will be about 99%.

The presence of two or more species with different brightness complicates interpretation of  $G(0)$ . The  $\tau = 0$

intercept reflects an apparent number of observed molecules according to

$$N_{\text{app}} = \frac{(\sum N_i B_i)^2}{\sum N_i B_i^2} \quad (24.20)$$

For the sample containing one molecule with  $Q_1 = 1$  and one molecule with  $Q_2 = 0.1$ , the apparent number of molecules will not be 2, but will be 1.20.

## 24.3. EXAMPLES OF FCS EXPERIMENTS

### 24.3.1. Effect of Fluorophore Concentration

Figure 24.8 shows autocorrelation functions for rhodamine 6G (R6G) in 70% sucrose.<sup>22</sup> The sucrose was used to decrease the diffusion coefficient of R6G and shift the curves to longer values of  $\tau$ . The amplitudes of  $G(\tau)$  are strongly dependent on the concentration of R6G. These data illustrate the effect of occupation number on the autocorrelation functions. As the R6G concentration increases the  $G(\tau)$  amplitude decreases. At an R6G concentration of 0.62 nM the  $G(0)$  intercept shows there are an average of 5 molecules in the observed volume. At an R6G concentration of 20 nM about 150 molecules contribute to the autocorrelation function, which results in the low amplitude. Notice that the number of R6G molecules is known even if the effective volume is not known. By comparison with Figure

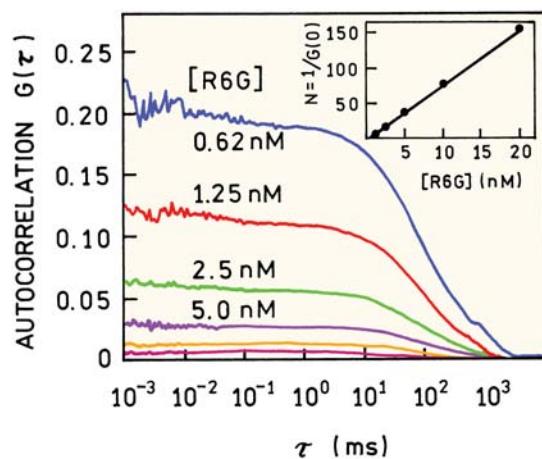


**Figure 24.8.** Fluorescence autocorrelation function for rhodamine 6G (R6G) in 70% sucrose. From top to bottom the R6G concentrations were 0.62, 1.25, 2.5, 5, 10, and 20 nM. The insert shows the measured average number of molecules. Redrawn from [22].

24.6 one can determine that the effective volume was probably larger than 0.35 fl.

While the amplitude of  $G(\tau)$  depends on the R6G concentration, the curves all display the same correlation time. This is expected because the diffusion coefficient of R6G should not depend on its concentration, at least at low concentrations used for FCS. By fitting these curves to eq. 24.12 one can recover the diffusion time without any assumptions. The diffusion time can be used to calculate the R6G diffusion coefficient (eq. 24.14), but this requires knowledge of the dimensions of the ellipsoid. This dependence shows that the value of  $\tau_D$  is not a molecular parameter and that assumptions are needed to calculate the diffusion coefficient.

#### 24.3.2. Effect of Molecular Weight on Diffusion Coefficients

Since the autocorrelation function depends on the rate of diffusion, it seems natural to use FCS to determine molecular weights. It is known that the translational diffusion coefficient of a molecule is related to its size by

$$D = \frac{kT}{6\pi\eta r} \quad (24.21)$$

where  $k$  is Boltzmann's constant,  $T$  is the temperature,  $\eta$  is the viscosity of the solvent, and  $R$  is the hydrodynamic radius. The radius is related to the molecular weight MW of the molecule with a specific gravity  $\bar{v}$  by

$$V = MW\bar{v} = \frac{4}{3}\pi R^3 \quad (24.22)$$

$$R = \left( \frac{3MW\bar{v}}{4\pi} \right)^{1/3} \quad (24.23)$$

where  $V$  is the volume. These equations show that the radius and diffusion coefficient are weakly dependent on the molecular weight. For instance, a 10-fold increase in the molecular weight will only result in a  $(10)^{1/3} = 2.15$ -fold change in the diffusion coefficient. The association of two proteins of equal size will double the molecular weight and cause only a 1.26-fold or 26% increase in the diffusion coefficient. For this reason it is difficult to measure the association of two similar size proteins by FCS. In many

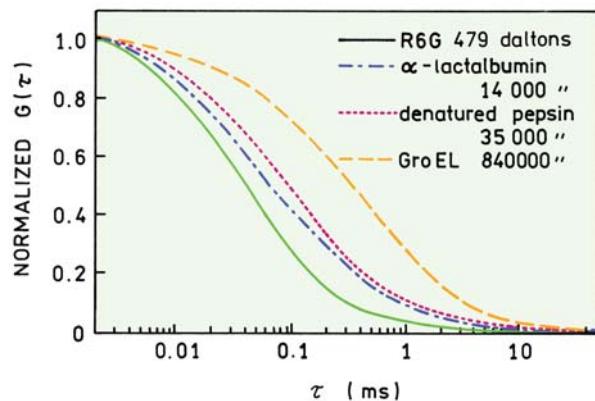


**Figure 24.9.** Effect of molecular weight on the autocorrelation functions of proteins labeled with tetramethylrhodamine-5-isothiocyanate (TRITC). The effective volume was determined by assuming the diffusion coefficient of R6G was  $2.8 \times 10^{-6} \text{ cm}^2/\text{s}$ . Revised from [23].

applications of FCS a system is selected because it provides a large change in effective molecular weight of the diffusing species.

Figure 24.9 shows experimental curves for R6G and three proteins with very different molecular weights.<sup>23</sup> This figure also contains the autocorrelation function for R6G. The data for R6G were used to determine the effective volume using a known diffusion coefficient of  $2.8 \times 10^{-6} \text{ cm}^2/\text{s}$  for R6G (MW = 479). Autocorrelation functions are shown for three proteins:  $\alpha$ -lactalbumin (MW = 14,000), denatured pepsin (MW = 35,000), and the chaperonin GroEL (MW = 840,000). The midpoint of the curves shifts 2.5-fold from 0.08 to 0.2 ms. The molecular weight increases from 14,000 to 840,000, which predicts a  $(60)^{1/3}$ -, or approximately fourfold increase in the diffusion coefficient. These curves show that the autocorrelation functions are dependent on molecular weight, but that substantial changes in molecular weight are needed to result in detectable changes in the diffusion time. In the case of binding interactions it is possible to couple one of the reactants to polymeric nanoparticles so as to increase the change in molecular weight upon binding, as has been done for FCS immunoassays.<sup>24</sup>

It is interesting to recall that the rotational correlation time ( $\theta$ ) of a molecule is directly proportional to the volume ( $V$ ) or molecular weight of a molecule:

$$\theta = \frac{\eta V}{kT} = \frac{\eta MW\bar{v}}{kT} = \frac{1}{6D_R} \quad (24.24)$$

where  $D_R$  is the rotational diffusion coefficient. Anisotropy measurements are preferred when the binding reaction results in a modest change in molecular weight.

#### 24.4. APPLICATIONS OF FCS TO BIOAFFINITY REACTIONS

The dependence of the autocorrelation functions on the diffusion coefficients has resulted in the use of FCS to measure binding reactions, including binding of small ligands to proteins,<sup>25–26</sup> protein–protein interactions,<sup>27–28</sup> DNA hybridization,<sup>29–30</sup> polymerase chain reactions,<sup>31–33</sup> DNA–protein interactions,<sup>34–35</sup> and interactions with receptors.<sup>36–38</sup> Additional references are listed following the main reference section.

##### 24.4.1. Protein Binding to the Chaperonin GroEL

The use of FCS to measure binding reactions is illustrated by studies of protein binding to GroEL. Chaperonin GroEL is a large multi-subunit protein (MW = 840,000) that promotes folding of denatured proteins or folding of peptide chains as they are extended during protein synthesis. The subunits form a cylindrical cavity that appears to interact with the hydrophobic regions of unfolded proteins. FCS was used to study the interactions of partially denatured  $\alpha$ -lactalbumin ( $\alpha$ -LA) with GroEL.<sup>23</sup> The partially denatured protein was obtained by reducing the four disulfide bonds of  $\alpha$ -LA, followed by labeling with TRITC. Upon addition of GroEL the autocorrelation functions of labeled  $\alpha$ -LA shifted to longer times (Figure 24.10). This shift is readily detectable because of the relative sizes of  $\alpha$ -LA (14,000) and GroEL (840,000). Titration of  $\alpha$ -LA with GroEL resulted in dilution of the sample, which caused an increase in amplitude for the more dilute solutions of  $\alpha$ -LA (insert). For these experiments the concentration of  $\alpha$ -LA was about 100 nM, which resulted in the low amplitudes of the autocorrelation curves (not shown).

Data of the type shown in Figure 24.10 can be used to recover the fractional binding of  $\alpha$ -LA to GroEL. If the brightness of labeled  $\alpha$ -LA does not change upon binding to GroEL the autocorrelation function is given by

$$G(\tau) = \frac{1}{N}[(1 - y)D_F(\tau) + yD_B(\tau)] \quad (24.25)$$

where the subscripts refer to  $\alpha$ -LA free (F) in solution or bound (B) to GroEL.  $D_F(\tau)$  and  $D_B(\tau)$  are diffusive parts of

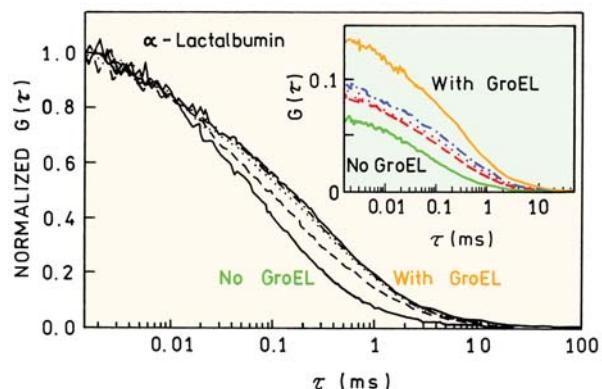


**Figure 24.10.** Normalized autocorrelation curves for reduced TRITC-labeled  $\alpha$ -lactalbumin ( $\alpha$ -LA) upon titration with GroEL. The insert shows the un-normalized curves. Revised from [23].

the autocorrelation function (eq. 24.12) with diffusion coefficients  $D_F$  and  $D_B$ . The fraction of total  $\alpha$ -LA bound to GroEL is given by  $y$ . This fraction can be used to calculate the binding constant for the reaction. However, there are several parameters to be recovered from the data: the two diffusion times, the fraction bound, and possibly the  $\tau = 0$  intercept. For this analysis the diffusion times of the individual proteins were measured for  $\alpha$ -LA or GroEL (Figure 24.9), and these values used as fixed parameters. This allowed analysis of the data in terms of just two parameters: the fraction bound and the total number of diffusing molecules (eq. 24.17).

##### 24.4.2. Association of Tubulin Subunits

FCS can be used to study the self-assembly or aggregation of proteins. One example is the association of tubulin to form microtubules that are important components in the mitotic machinery of cells. A variety of natural products are known that interact with tubulin to disrupt cell division. Such natural products apparently evolved as part of the competition between organisms for survival. These compounds are often small peptides or depsipeptides and are of interest for use as antineoplastic drugs. These compounds interact with the  $\alpha,\beta$ -dimer of tubulin, which is referred to as tubulin. In some cases the compounds depolymerize the microtubules, and in other cases they prevent depolymerization or cause formation of unique aggregates. FCS was used to study the sizes of tubulin aggregates induced by these compounds.<sup>38</sup> The TAMRA-labeled tubulin dimer was observed upon addition of cryptophycin (Figure 24.11). This addition resulted in an approximate 2.5-fold

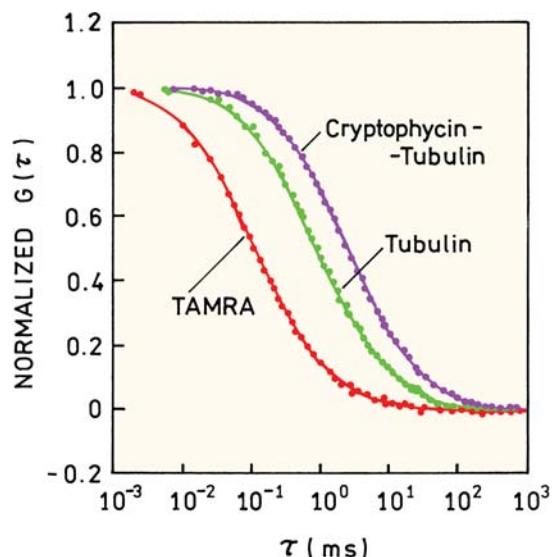


**Figure 24.11.** Effect of cryptophycin on the normalized autocorrelation function of TAMRA-labeled tubulin dimer. Revised and reprinted with permission from [38]. Copyright © 2003, American Chemical Society.

increase in the diffusion time of tubulin. Such a large increase in  $\tau_D$  indicates that tubulin must aggregate into larger particles than dimers. This increase in  $\tau_D$  was roughly consistent with the increase in hydrodynamic radius expected for self-association to an octamer.<sup>38</sup>

#### 24.4.3. DNA Applications of FCS

As might be expected, FCS has been applied to DNA analysis. Surprisingly, a relatively small number of papers have appeared on hybridization of oligomers of similar size.<sup>30</sup> A large number of papers have appeared where one of the DNA strands was much larger than the other or using dual-color FCS, which is discussed later in this chapter. FCS has also been used to study the interaction of DNA with proteins,<sup>39–42</sup> DNA condensation,<sup>43–44</sup> or binding of DNA oligomers to larger RNA targets.<sup>45</sup>

FCS can be effectively used to monitor DNA hybridization when there is a large change in diffusion coefficient.<sup>46–48</sup> Figure 24.12 shows the normalized autocorrelation functions for a rhodamine-labeled 18-mer during hybridization with M13 DNA, which contains about 7250 base pairs (specifically M13mp18). Because of the large change in effective molecular weight the shift in  $G(\tau)$  is dramatic. There was no change in brightness of the labeled oligomer upon binding to M13, so that the fractions bound and free could be calculated using eq. 24.17.

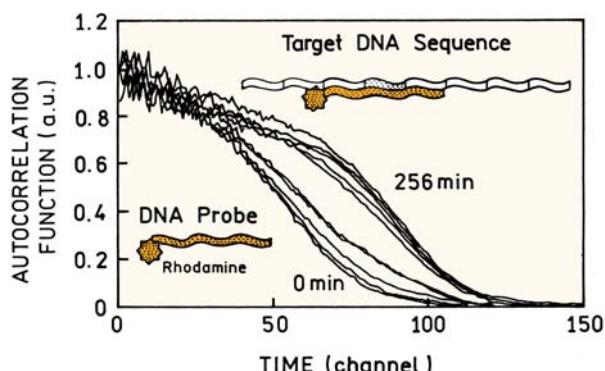


**Figure 24.12.** Hybridization of a rhodamine-labeled 18-mer to M13 DNA containing the appropriate complementary sequence. M13 DNA has about 7250 bases. Revised from [47].

FCS has also been used to study degradation of DNA by enzymes. One example is shown in Figure 24.13 for double-stranded DNA with a 500-base-pair oligomer.<sup>47–48</sup> The 500-mer was randomly labeled at low density with a tetramethylrhodamine-labeled nucleotide, TMR-dUTP. The oligomer was progressively digested from the 3' end by T7 exonuclease. As the reaction proceeds the amplitude of  $G(\tau)$  decreases, reflecting the increased number of diffusing species. Examination of the normalized curves (insert) shows a progressive shift to shorter diffusion times as the DNA is progressively degraded. This shift is expected given the small size of a labeled nucleotide relative to a 500-base-pair oligomer. In principle the  $\tau = 0$  intercepts of  $G(\tau)$  can be used to recover the number of diffusing species. However, for such an analysis it is necessary to know the relative brightness of each species (eq. 24.20). For the case shown in Figure 24.13 there are two dominant species: free TMR-dUTP and the residual section of the 500-mer. The relative brightness of the species will be approximately proportional to the number of fluorophores per particle. In the initial stages of the reaction one could probably assume just two species: a dim monomer that contains one TMR and a bright oligomer that contains many TMRs. As the reaction proceeds it will become progressively more difficult to resolve the population of the various sized DNA fragments.

FCS was also used to measure the appearance of labeled DNA fragments during polymerase chain reaction (PCR) and to characterize the size of the fragments.<sup>31</sup> The fluorophore TMR-dUTP was incorporated into the PCR products. FCS analysis was performed following removal of the free TMR-dUTP, which otherwise would decrease the amplitude of  $G(\tau)$ . Incorporation of TMR-dUTP into a 217-mer was easily observed from the shift in  $G(\tau)$  (Figure

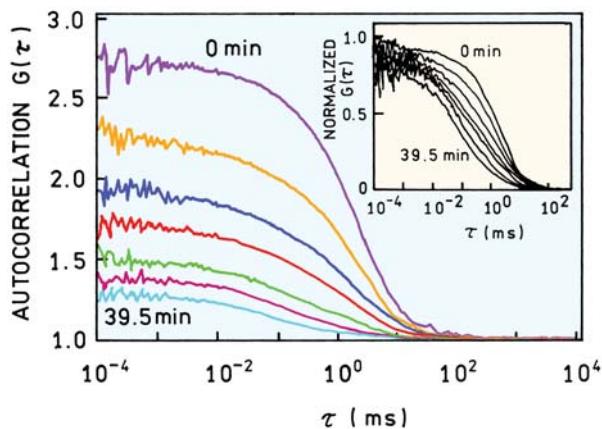


**Figure 24.13.** Autocorrelation functions for double-stranded DNA, 500 base pairs long, randomly labeled with tetramethylrhodamine-4-dUTP in the presence of T7 DNA polymerase, acting as an exonuclease. Revised from [47].

24.14). The PCR reaction was used to synthesize labeled DNA with different lengths. In the case of DNA fragments it is possible to obtain information on their length from the diffusion times (Figure 24.15). This was possible because increasing the molecular weight of DNA results in elongating a relatively stiff rod in one dimension, rather than filling a three-dimensional volume. For such molecules the diffusion time increases nearly linearly with length ( $L$ ) according to<sup>49–50</sup>

$$\tau_D = \frac{3\pi\eta s^2}{4kT} \frac{L}{\ln p + \gamma} \quad (24.26)$$

where  $L$  is the length of the rod,  $p$  is the length/diameter ratio, and  $\gamma$  is an end-group correction. The important point

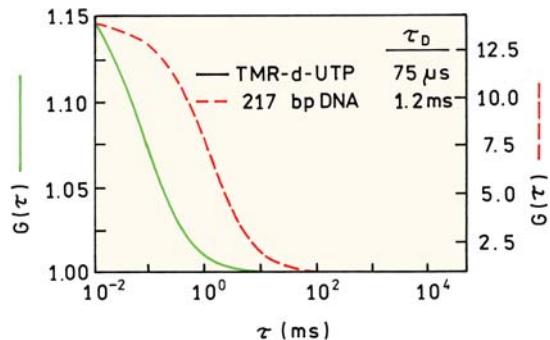


**Figure 24.14.** Normalized autocorrelation curves for TMR-dUTP and when incorporated into a 217-mer by PCR. Revised and reprinted with permission from [31]. Copyright © 1998, American Chemical Society.

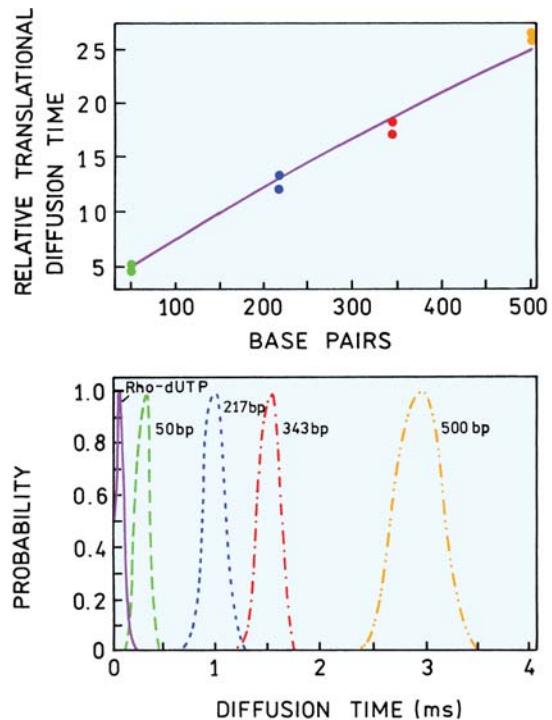


**Figure 24.15.** Effect of DNA length on FCS diffusion times. Revised and reprinted with permission from [31]. Copyright © 1998, American Chemical Society.

is that  $\tau_D$  should increase roughly in proportion to the number of bases in the oligomer.

DNA oligomers of known length were used to create a calibration curve of diffusion time versus the number of base pairs. The autocorrelation curves for the fragments (Figure 24.14) were used to recover the distribution of diffusion times for the oligomers. This was accomplished by fitting the data to

$$G(\tau) = \frac{1}{N} \int_0^\infty P(\tau_D) G(\tau_D) d\tau_D \quad (24.27)$$

where  $G(\tau)$  is given by eq. 24.12 and  $P(\tau_D)$  is the normalized probability for value of  $\tau_D$ . The meaning of this integral is that the observed correlation function is the sum of a large number of such functions, weighted by the relative probability of  $\tau_D$  in the sample. This analysis is similar to the analysis of intensity decays in terms of lifetime distributions. The recovered correlation times for these fragments increase significantly with the number of base pairs. The distribution (Figure 24.15, lower panel) shows good resolution of  $\tau_D$ , but it would be difficult to recover more than sev-

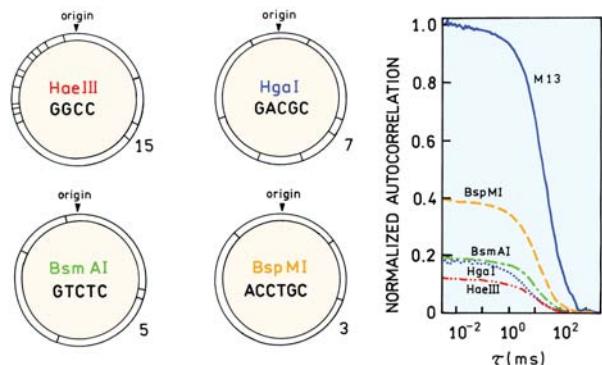


**Figure 24.16.** Cleavage of rhodamine-labeled M13 DNA by four restriction enzymes. The number of cleavage sites is shown under each circle. Revised from [51].

eral  $\tau_D$  values in a mixed sample if the lengths were more similar. The distributions were obtained from measurements on a single species, with a single brightness, so that resolution of multiple  $\tau_D$  values can be expected to be more difficult for a mixture of species with different brightness.

In addition to monitoring the length of DNA oligomers, FCS can be used to roughly estimate the number of fragments formed during DNA cleavage.<sup>51</sup> Figure 24.16 shows the  $G(\tau)$  curves for M13 DNA (7250 base pairs) after cleavage by several restriction enzymes. From the known sequence and enzyme specificity one can predict the number of fragments formed by each enzyme. The  $G(0)$  values from autocorrelation curves are largest for BspMI, which generates only 3 fragments, and smallest for HaeIII, which generates 15 fragments. Of course, the  $G(0)$  values give only an apparent number of diffusing species since the fragments are of unequal length and their contributions to  $G(\tau)$  are weighted according to eq. 24.18.

#### 24.5. FCS IN TWO DIMENSIONS: MEMBRANES

FCS is not limited to three-dimensional samples, but can also be used to study cell membranes.<sup>52–61</sup> FCS is especially useful for studies of membranes because diffusion is limited to two dimensions. Also, the typically viscous nature of membranes result in a wide range of diffusion times for membrane-localized fluorophores. The wide range of diffusion times possible with cells or cell membranes is shown in Figure 24.17. The correlation curves are for rhodamine derivatives in solution (S), in the cytoplasm (C), and bound to the membranes of a rat leukemia cell (M). Also shown is the curve for Cy3-labeled IgE bound to the IgE receptor. The diffusion times span four orders of magnitude. Hence

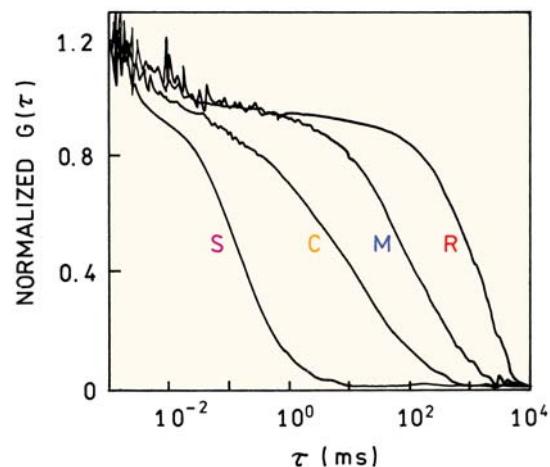


**Figure 24.17.** Autocorrelation curves for rhodamine derivatives in solution (S), in the cytoplasm (C), and bound to the membranes (M) of rat basophilic leukemia cells (RBL). A lipophilic rhodamine derivative was used to bind to the membranes. Also shown is the curve for Cy3-labeled IgE bound to the IgE receptor on the membrane (R). The pinhole was 100  $\mu\text{m}$  in diameter. Revised from [62].

we expect the autocorrelation curves to contain information about diffusive transport in membranes. To obtain a similar change in diffusion times for a three-dimensional solution the molecular weight would need to change by a factor of  $10^{12}$ .

Recall that the correlation function eq. 24.12 was derived assuming a three-dimensional Gaussian volume (eq. 24.9). In a membrane the fluorophores are constrained in a two-dimensional plane. In this case the observed volume can be described by a planar two-dimensional Gaussian distribution:

$$p(r) = I_0 \exp[-2(x^2 + y^2)/s^2] \quad (24.28)$$

For this geometry the correlation function for a freely diffusing species is

$$G(\tau) = G(0)(1 + \tau/\tau_D)^{-1} = G(0) \left( 1 + \frac{4D\tau}{s^2} \right)^{-1} \quad (24.29)$$

where  $s$  is the radius of the disk and the diffusion time is given by  $\tau_D = s^2/4D$  (eq. 24.14). Intuitively this expression is similar to eq. 24.12, except that the exit pathway out of the plane is no longer available to the molecule, and the square-root term is no longer present.

It is informative to examine the properties of the correlation function in two and three dimensions:  $G_{2D}(\tau)$  and

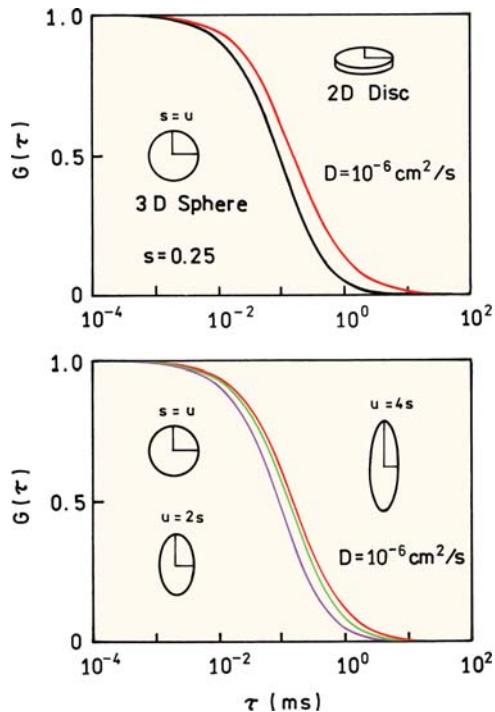


**Figure 24.18.** Simulated autocorrelation functions for a sphere in three dimensions and a disk in two dimensions (top), and for spherical and elongated 3-dimensional shapes (bottom).  $D = 10^{-6} \text{ cm}^2/\text{s}$  and  $s = 0.25 \mu\text{m}$ .

$G_{3D}(\tau)$ , respectively. Figure 24.18 (top) shows the correlation function for a sphere and a disk, plotted for the same diffusion coefficient of  $10^{-6} \text{ cm}^2/\text{s}$ . The disk shows a modest shift to longer times due to the restricted diffusion path. In this model it is assumed the fluorophore cannot diffuse out of the plane. Frequently in the FCS literature one finds that  $G_{2D}(\tau)$  is used when  $G_{3D}(\tau)$  seems appropriate and vice versa. This occurs because there are only minor differences between the correlation functions once the shape of the volume is considered. The lower panel shows simulated autocorrelation functions for a sphere and two progressively elongated shapes. When the ellipsoid has an aspect ratio of 4 the autocorrelation is virtually indistinguishable from  $G_{2D}(\tau)$ . This result is due to the elongated volume in  $G_{3D}(\tau)$  and the modest contribution of the last term on the right in eq. 24.12.<sup>21</sup> Note also that these curves were drawn with a fixed diffusion coefficient. If the value of  $D$  is allowed to vary, as in the case when analyzing experimental data, then the curves would shift along the  $\tau$  axis to the position of maximum overlap. In this case it would become even more difficult to distinguish between  $G_{2D}(\tau)$  and  $G_{3D}(\tau)$ .

While the shapes of the autocorrelation functions are not strongly dependent on two versus three dimensions, the

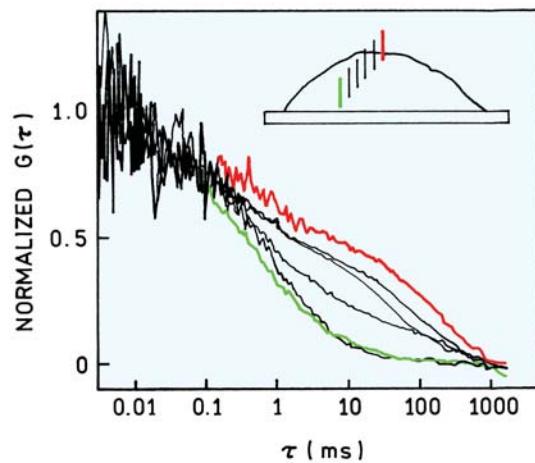


**Figure 24.19.** Diffusion of a lipid-containing GFP at various positions with an RBL cell as indicated on the insert. Revised from [62].

autocorrelation function for membranes can be dramatically different from free diffusion in solution. The effect of a cell membrane on diffusion of a lipophilic GFP derivative is shown in Figure 24.19.<sup>62</sup> This GFP molecule contained a bound palmitoyl chain to provide binding affinity for the membranes. As the focal volume was moved up from the cytoplasm to the cell membrane the autocorrelation function showed increased amplitude at long times. The  $G(\tau)$  curves could be modeled using two diffusion times according to

$$G(\tau) = \frac{\bar{C}_{2D}D_{2D}(\tau) + \bar{C}_{3D}D_{3D}\tau}{V_{\text{eff}}(\bar{C}_{2D} + \bar{C}_{3D})^2} \quad (24.30)$$

$$D_{2D}(\tau) = \left(1 + \frac{4D_B(\tau)}{s^2}\right)^{-1} \quad (24.31)$$

$$D_{3D}(\tau) = \left(1 + \frac{4D_F\tau}{s^2}\right)^{-1} \left(1 + \frac{4D_F\tau}{u^2}\right)^{-1/2} \quad (24.32)$$

where  $D_B$  and  $D_F$  are the diffusion coefficients of membrane-bound and free GFP, respectively. Equation 24.30 can be obtained from eq. 24.18 by noting  $N_i = C_i V_{\text{eff}}$ . Notice that this expression has different diffusion coefficients for the free and bound forms of the fluorophore. These different diffusion coefficients account for the shape of  $G(\tau)$  in Figure 24.19 as compared to the simulations in Figure 24.18, where the shapes of  $G_{2D}(\tau)$  and  $G_{3D}(\tau)$  are similar. The long timescale of FCS measurements, extending to seconds, has

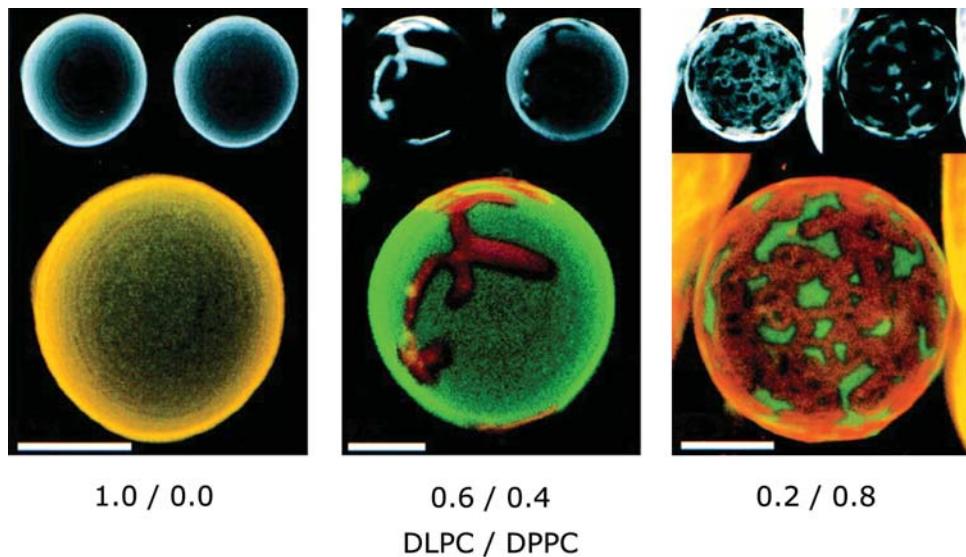


**Figure 24.20.** Confocal fluorescence images of giant unilamellar vesicles (GUVs) labeled with a cyanine (DiI-C<sub>20</sub>) or a Bodipy (Bodipy-PC)-labeled lipid. The lipid compositions are shown under the images. In the upper black and white images DiI-C<sub>20</sub> is on the left and Bodipy-PC on the right. The bars indicate 10 μm. Revised from [67].

revealed the phenomenon of anomalous subdiffusion of membrane-bound proteins where the  $G(\tau)$  curve is spread out over a larger range of  $\tau$  values.<sup>63–66</sup>

#### 24.5.1. Biophysical Studies of Lateral Diffusion in Membranes

The ability of FCS to measure widely different diffusion coefficients has been useful in studies of lateral diffusion in membranes. Giant unilamellar vesicles (GUVs) about 35 μm in diameter were used to allow observation of specific regions of the membranes. Figure 24.20 shows confocal fluorescence microscopy images of GUVs that were labeled with two lipophilic dyes: DiI-C<sub>20</sub> and Bodipy-PC.<sup>67</sup> For these images the GUVs were composed of two phospholipids: dilauroyl phosphatidylcholine (DLPC) and dipalmitoyl phosphatidylcholine (DPPC). At room temperature DLPC bilayers are in the fluid state and DPPC bilayers in the solid state. Because of the difference in length of the acyl side chain, C12 for lauroyl and C16 for palmitoyl, bilayers containing both lipids show lateral phase separation. This does not mean that each phase is composed only of DLPC or DPPC but rather that two phases exist: a fluid phase rich in DLPC and a solid phase rich in DPPC.

The images in Figure 24.20 were taken through two different emission filters to select for the shorter-wavelength emission of Bodipy-PC (shown as green) or the

longer-wavelength emission of DiI-C<sub>20</sub> (shown as red). To obtain the confocal images the GUVs were labeled with both probes at relatively high concentrations. When the GUV contains only DLPC both probes are distributed homogeneously (left). When the GUVs contain a mixture of DLPC and DPPC one finds liquid domains rich in Bodipy-PC and solid domains rich in DiI-C<sub>20</sub>. As the mole fraction of DPPC increases the extent of the solid phase containing DiI-C<sub>20</sub> increases (middle and right). GUVs similar to those shown in Figure 24.20 were studied by FCS. For FCS the GUVs were labeled with only one probe DiI-C<sub>20</sub> at a lower concentration to allow observation of only a few probe molecules. For this system we expect the diffusion to be two dimensional with different diffusion coefficients in each phase. Assuming the probe brightness is the same in both phases the autocorrelation function becomes

$$G(\tau) = \frac{\bar{C}_F D_F(\tau) + \bar{C}_S D_S(\tau)}{V_{\text{eff}} (\bar{C}_F + \bar{C}_S)^2} \quad (24.33)$$

where *F* and *S* refer to the fluid and solid phases, respectively, and the diffusion correlation function in each phase is given by

$$D_i(\tau) = \left( 1 + \frac{4D_i\tau}{s^2} \right)^{-1} \quad (24.34)$$

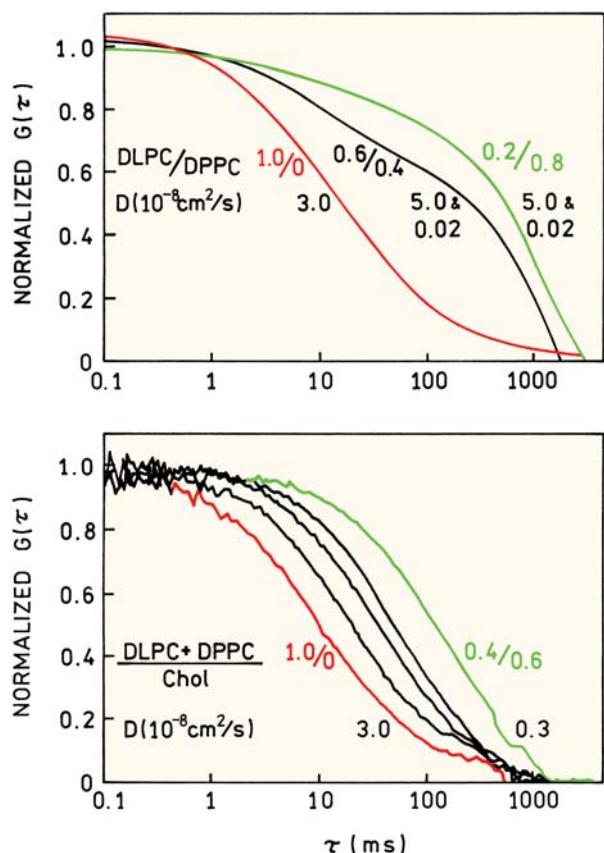


**Figure 24.21.** Autocorrelation functions of DiI- $C_{20}$  in GUVs with the indicated molar ratios of DLPC to DPPC (top) and phospholipid (DLPC + DPPC) to cholesterol (bottom). The observed volume is about 1  $\mu\text{m}$  in diameter. Revised from [67].

Figure 24.21 (top) shows the autocorrelation function for DiI- $C_{20}$  in GUVs with different amounts of DLPC and DPPC. In GUVs containing only DLPC, fitting to eq. 24.23 yielded a single diffusion coefficient of  $3 \times 10^{-8} \text{ cm}^2/\text{s}$ .

The autocorrelation functions become more complex for GUVs containing both DLPC and DPPC. For a DLPC/DPPC ratio between 0.6 to 0.4 it is easy to see the contribution of more than one diffusion coefficient to the shape of the autocorrelation function. As the amount of DPPC increases the diffusion appears to be more homogeneous, but fitting the data still required two diffusion coefficients. The measurements on GUVs containing both DLPC and DPPC were repeated several times and averaged, so that the correlation function contains contributions from both phases. If the observation volume is focused on one phase then one expects to see only the diffusion coefficient(s) characteristic of that phase. The effect of cholesterol on the GUVs

is shown in the lower panel. As the mole fraction of cholesterol increases the diffusion coefficient decreases (Figure 24.21, bottom). The autocorrelation function shifts aggressively to longer diffusion times without a dramatic change in shape. This result indicates that only a single phase state is present in the bilayers that contain cholesterol.

#### 24.5.2. Binding to Membrane-Bound Receptors

Cell membranes contain receptors for a wide variety of molecules. Since FCS provides information on long timescales, it is logical to use FCS to measure the slow diffusion of membrane-bound proteins. One example is the receptor for the C-peptide of insulin, which is now known to have physiological activity. Insulin is composed of two peptide chains that are linked by two disulfide bonds. When insulin is first synthesized it appears as a single longer inactive peptide called proinsulin.<sup>68</sup> Insulin is activated by cleaving off a small peptide called the C-peptide. The released C-peptide is physiologically active and causes increased glomerular filtration rates.<sup>69–70</sup> This suggests there is a cell surface receptor for the C-peptide.

FCS was used to detect specific binding of the C-peptide to human renal tubular cells.<sup>71–73</sup> This was accomplished using rhodamine-labeled C-peptide and by focusing the observed volume on the cell membrane (Figure 24.22, insert). The upper panel shows the intensity fluctuations for the labeled peptide when free in solution (left) and when bound to the cell membrane (right). The rate of fluctuation is much faster for the free as compared to the membrane-bound peptide. The autocorrelation functions show that the diffusion time increased nearly 1000-fold when bound to the membranes. The specificity of binding was shown by adding unlabeled C-peptide, which shifted the curve back to that typical of the free peptide (dashed line).

The data can be analyzed in two ways. One approach is to use a mixture of the correlation functions for 2D and 3D diffusion. In this case the fitting function is

$$G(\tau) = \frac{1}{N}[(1 - y)G_{3D}(\tau) + yG_{2D}(\tau)] \quad (24.35)$$

where the  $G(\tau)$  function for 2D and 3D are defined in eqs. 24.31 and 24.32, respectively. The terms  $(1 - y)$  and  $y$  represent the fractions of labeled peptide that are free and bound, respectively. Another approach is to recover the probability distribution for the diffusion times  $\tau_D$ :

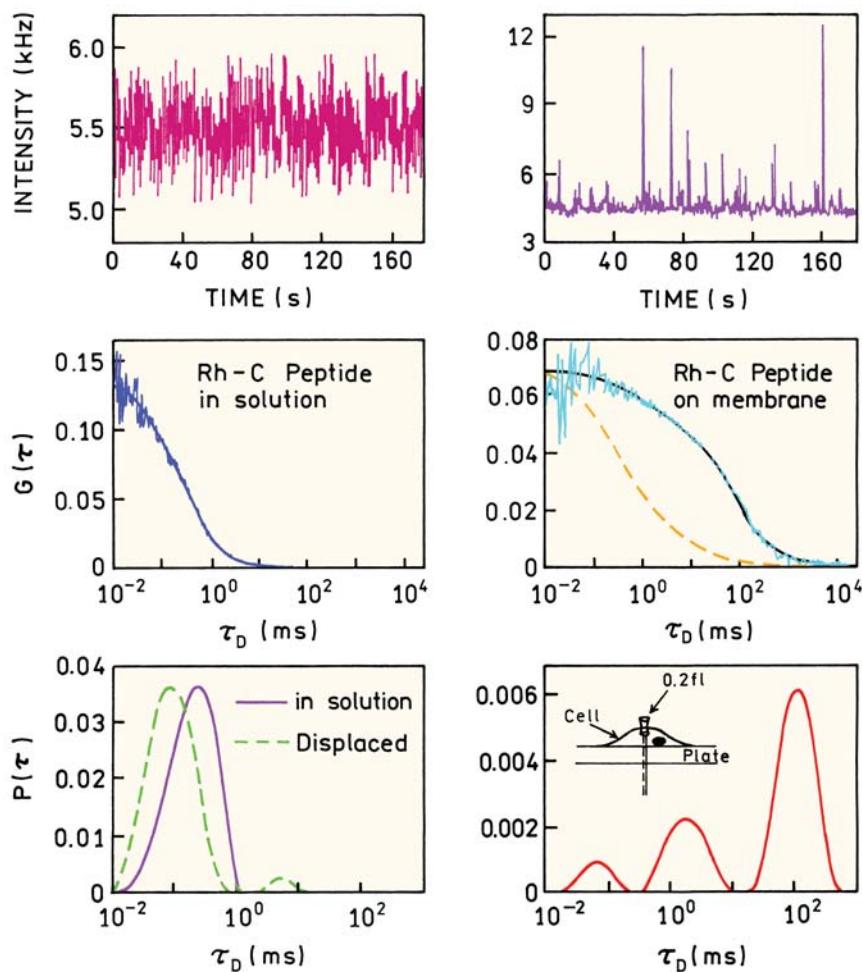


**Figure 24.22.** FCS studies of insulin C-peptide binding to human renal tubular cells using rhodamine-labeled (Rh) C-peptide. The dashed lines show  $G(\tau)$  and  $P(\tau)$  after addition of a 1000-fold excess of unlabeled C-peptide. Revised from [71].

$$G(\tau) = \frac{1}{N} \int_0^\infty \frac{P(\tau_D)}{(1 + \tau/\tau_D)} d\tau_D \quad (24.36)$$

In the absence of the receptor the diffusion time is near 0.5 ms (lower left panel). In the presence of the receptor there is a dramatic increase in  $\tau_D$  to 100 ms, with some fraction of the peptide diffusing more rapidly (lower right panel). There is nearly complete reversal of binding upon addition of an excess of unlabeled C-peptide, showing the specificity of C-peptide binding (dashed line, lower left).

FCS measurements of membranes provides information that is different from fluorescence measurements in bulk solution or fluorescence microscopy. It would not be possible to detect lateral diffusion of the insulin receptor

using steady-state measurements because the nanosecond decay times are short relative to the long times needed for diffusion. Receptor diffusion would also be undetectable by fluorescence microscopy because the system is roughly stationary. The receptors are diffusing but the average distribution is constant. FCS can detect receptor motion because diffusion affects the number of fluorophores in the observed volume, even under conditions when the average distribution of receptors is not changing. The results shown in Figure 24.22 also indicate that the rate at which labeled C-peptide dissociates from its receptor is slow relative to the longest time, near one second, in the autocorrelation function.

It is instructive to compare FCS and fluorescence recovery after photobleaching (FRAP) for studies of mobil-

ity in membranes. When performing FRAP a laser is focused on the region of interest in the membrane.<sup>74–76</sup> The laser is transiently brought to high intensity to photobleach the fluorophores in the focal region. The laser intensity is then decreased to allow continuous monitoring of the emission from this same region of the membrane. The intensity increases as the unbleached probes diffuse into the bleached area, and the rate of recovery is used to determine the diffusion coefficients. In this FRAP measurement the experimental system was synchronized with the bleaching pulse and the system studied as it returned to equilibrium. The system is not stationary during the experiment. In contrast to FRAP, FCS measurements are performed under stationary conditions. The system is hopefully not perturbed by the illumination needed for FCS. Information about mobility in the membrane is obtained by diffusion of the probe molecules under equilibrium conditions.

#### 24.6. EFFECTS OF INTERSYSTEM CROSSING

In the preceding sections we described the effects of translational diffusion on the autocorrelation functions of labeled molecules. Diffusion is just one of several mechanisms that can cause intensity fluctuations, and such processes can be studied by FCS. Because of the high illumination intensities in FCS, intersystem crossing from the first excited singlet state ( $S_1$ ) to the triplet state (T) is frequently observed. A Jablonski diagram for intersystem crossing is shown in Figure 24.23. The excitation intensities used in FCS can result in a significant fraction of the fluorophores in the triplet state. The fluorophores in the triplet state are not observed, resulting in an apparent decrease in

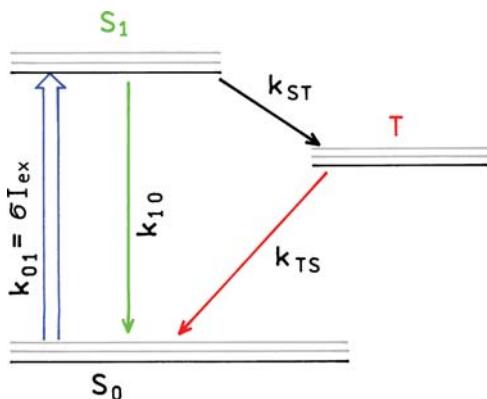


**Figure 24.23.** Jablonski diagram with intersystem crossing from the singlet (S) to the triplet (T) state.  $k_{10}$  is the sum of the radiative and non-radiative decay rates.

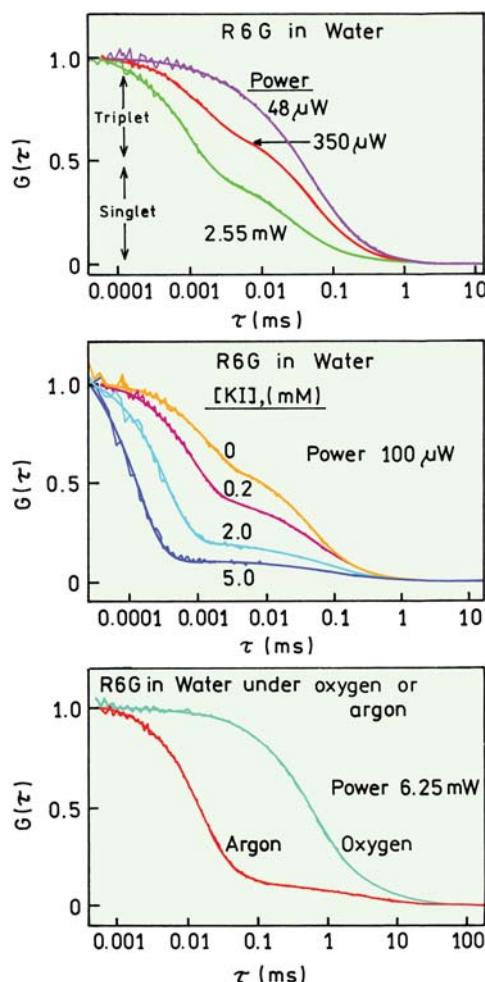


**Figure 24.24.** Effect of illumination intensity, iodide, and oxygen on the normalized autocorrelation function of rhodamine 6G in water. Revised and reprinted with permission from [78]. Copyright © 1995, American Chemical Society.

the number of fluorophores in the effective volume. If the fluorophores do not return to  $S_0$  within the diffusion time then only the amplitude of the correlation function will be changed. If the triplet fluorophores can return to  $S_0$  within the diffusion time then this is a mechanism that can cause fluctuations or blinking of the fluorophores,<sup>77–80</sup> as is also observed in single-molecule experiments.

Prior to describing the theory for blinking in FCS it is informative to examine some examples. The top panel in Figure 24.24 shows autocorrelation functions for rhodamine 6G (R6G) in water, using different illumination intensities. At low incident power of 48  $\mu\text{W}$ ,  $G(\tau)$  appears normal with a diffusion time near 0.03 ms (top panel). As the incident power increases a new component appears in

$G(\tau)$  with a new characteristic time ( $\tau_T$ ), which, depending on intensity, ranged from 0.5 to 1  $\mu\text{s}$ . We do not call this a diffusion time since the origin of the component is not diffusion, but rather the rate of transition and return from the triplet state. The relative amplitude of the short  $\tau_T$  component represents the fraction of the fluorophore in the triplet state.

#### 24.6.1. Theory for FCS and Intersystem Crossing

The presence of an additional fluctuation mechanism requires a different correlation function. In general the theory for such systems can be complex. Some simplification is possible if the reaction is faster than the diffusion time and if there is no change in diffusion coefficient due to the reaction.<sup>17</sup> In this case the overall correlation function can be written as the product

$$G(\tau) = G_D(\tau)G_T(\tau) \quad (24.37)$$

where  $G_D(\tau)$  is the term due to translational diffusion and  $G_T(\tau)$  is the term due to the additional mechanism, in this case transition to the triplet state. For the system shown in Figure 24.23 the correlation function is given by<sup>81</sup>

$$G_T(\tau) = \left[ 1 + \frac{\bar{T}}{1 - \bar{T}} \exp(-\tau/\tau_T) \right] \quad (24.38)$$

where  $T$  is the fraction of the molecules in the triplet state and  $\tau_T$  is the relaxation time for the singlet-triplet relaxation. This equation accounts for the decrease in the average number of singlet molecules in the observed volume by increasing the amplitude of  $\tau = 0$ . Increased amplitudes are not seen in Figure 24.24 because the autocorrelation functions are normalized. The relaxation time for the triplet path shown in Figure 24.23 is given by

$$\frac{1}{\tau_T} = k_{TS} + \frac{\sigma I_{ex} k_{ST}}{\sigma I_{ex} + k_{10}} \quad (24.39)$$

where  $\sigma$  is the cross-section for absorption,  $I_{ex}$  is the illumination intensity,  $k_{ST}$  is the rate of intersystem crossing, and  $k_{10}$  is the rate of return to the ground state from the excited singlet state. The fraction of fluorophores present in the triplet state is given by

$$\bar{T} = \frac{\sigma I_{ex} k_{ST}}{\sigma I_{ex}(k_{ST} + k_{TS}) + k_{TS}(k_{ST} + k_{10})} \quad (24.40)$$

Fitting the data in Figure 24.24 to the full correlation function allows determination of the value of  $T$  and  $\tau_T$ . These values then need to be interpreted with consideration of the system being studied, because other chemical mechanisms can yield similar effects.

This theory can be used to account for the effects of different solution conditions on the autocorrelation function for R6G. The middle panel in Figure 24.24 shows the effect of iodide on the autocorrelation. As the iodide concentration increases the amplitude of the triplet portion of  $G(\tau)$  increases. This is the result of iodide increasing the rate of intersystem crossing so that  $k_{ST}$  becomes

$$k_{ST} = k_{ST}^0 + k[\text{KI}] \quad (24.41)$$

where  $k_{ST}^0$  is the rate in the absence of iodide and  $k$  is the bimolecular rate constant for intersystem crossing due to iodide. By examination of eq. 24.40 one can see that an increase in  $k_{ST}$  will result in an increase in the fraction of fluorophores in the triplet state.

It is surprising to find that the effect of oxygen was opposite of the effect of iodide. To study this effect the sample was strongly illuminated to obtain a large fractional population in the triplet state (Figure 24.24, lower panel). For this 6.25-mW intensity, in the absence of oxygen, most of the fluorophores are in the triplet state. Equilibration of the water solution with oxygen resulted in almost complete recovery of the correlation function due to diffusion alone. This effect occurred because oxygen increased the rate of return to the singlet state ( $k_{TS}$ ) more than it increased the rate of crossing to the triplet ( $k_{ST}$ ). The net result was a decrease in the triplet population.

#### 24.7. EFFECTS OF CHEMICAL REACTIONS

Kinetics processes other than intersystem crossing can be detectable by FCS. FCS has been used to study conformational transitions of fluorophores,<sup>82</sup> association reactions of fluorescent indicators,<sup>83</sup> and kinetic processes in GFP.<sup>84-86</sup> One example is shown in Figure 24.25 for EGFP. In this case the  $G(\tau)$  function shows an increasing amplitude of a short-time component as the pH is decreased.<sup>86</sup> The longer characteristic time is due to translational diffusion of EGFP. It is known that the emission intensity of EGFP is strongly quenched at low pH (insert). This quenching is due to protonation of an ionized hydroxyl group, because EGFP is only fluorescent when the tyrosine is ionized. As the pH is decreased a new short-time component appears in  $G(\tau)$ ,

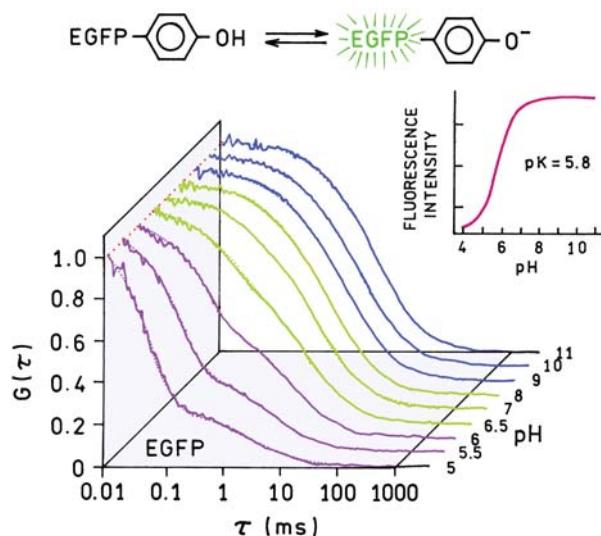


**Figure 24.25.** Normalized autocorrelation function for EGFP at various pH values. Revised from [86].

which is assigned to pH-dependent protonation of the tyrosine residue. The rate of protonation increases at lower pH values, resulting in the increased amplitude at short times. The proton may come from the bulk solution or from the protein itself.

#### 24.8. FLUORESCENCE INTENSITY DISTRIBUTION ANALYSIS

In the preceding sections we considered processes that result in intensity and/or concentration fluctuations in the observed volume. The relative contributions of different brightness fluorophores to the correlation function was given in eq. 24.19, but we did not describe any approach to resolve the different fluorophores from each other. The presence of different brightness fluorophores changes the apparent number of observed molecules (eq. 24.20), but the information about their individual brightness values is lost during collection of  $G(\tau)$ , as can be seen by examining eq. 24.10. The amplitude of the correlation function is due to the same fluorophore emitting more than a single photon during the binning time. During a particular time interval the signal from the same dim fluorophores correlate with each other, as will the signal from the bright fluorophores. When the diffusion coefficients are the same the brightness of each fluorophore cannot be resolved and the correlation function will have the usual shape for a single diffusion species.

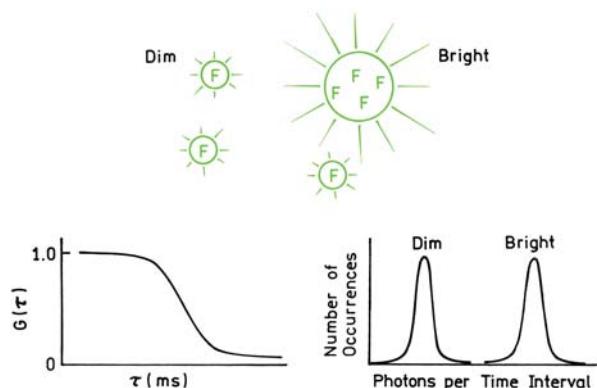


**Figure 24.26.** Comparison of correlation function and photon-count histogram for a mixture of dim and bright particles.

Suppose the sample contains two types of molecules with the same diffusion coefficient (Figure 24.26). This could be the same protein labeled with one or several fluorophores. If  $G(\tau)$  were measured for this mixture one would see the usual correlation function for a single diffusion coefficient (lower left). Suppose now that the entire time course of intensities was available instead of the correlation functions. There would be lower and higher intensity fluctuations due to the dimmer and brighter particles, respectively. One can count the number of times a fluctuation has a dim or bright amplitude, and create a histogram of the results (lower right). For the mixture there will be two populations of fluorophores, which will be seen from the intensity distributions. If the particles display very different brightness it is possible to count the number of times dim and bright particles pass through the observed volume. One example is shown in Figure 24.27 for coumarin-labeled

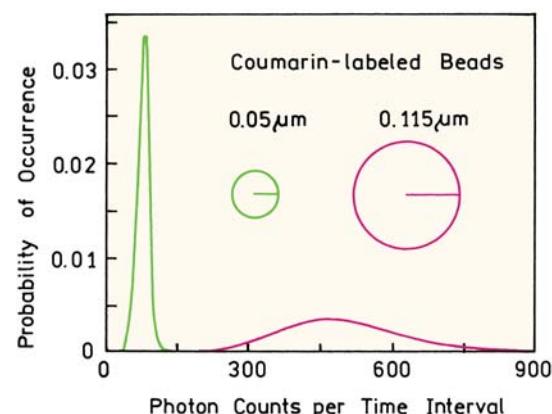


**Figure 24.27.** Photon-count histogram for a mixture of 0.05 and 0.115  $\mu\text{m}$  coumarin-labeled beads. Revised from [87].

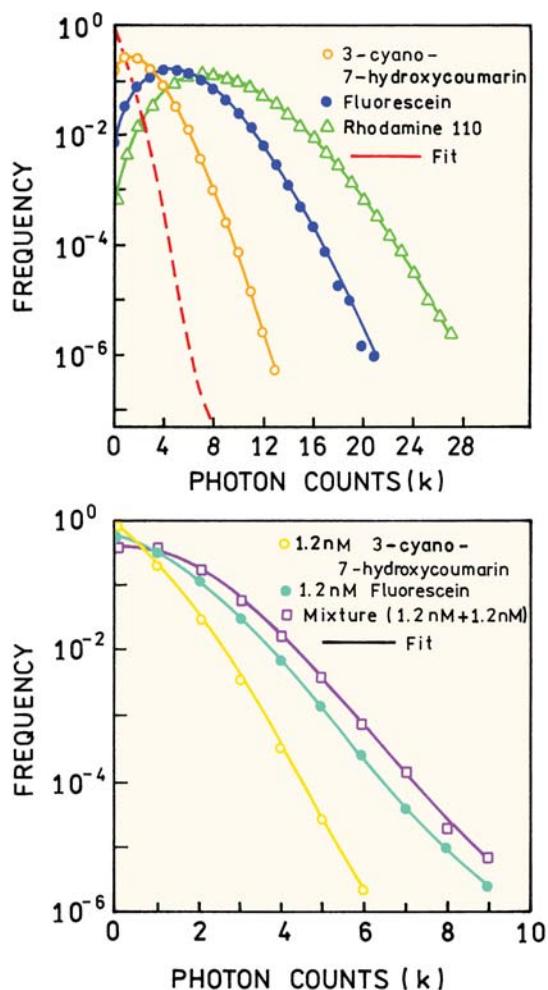


**Figure 24.28.** Photon counting histogram for three fluorophores (top) and for a fluorophore mixture. Also shown as a dashed line is the distribution for fluorescein at a lower concentration. Revised from [91].

beads with radii of 0.05 and 0.115  $\mu\text{m}$ .<sup>87</sup> Two populations are already visible in the photon-count histogram.

Until recently the correlation functions were obtained with dedicated circuit boards that calculate  $G(\tau)$  in real time. This was necessary because of the need to rapidly sample the fluctuating signal on a timescale short enough to characterize the process of interest. With modern electronics and computers it is possible to record the intensities for each time interval during the measurement. This allows the data to be analyzed in a different way, which is called fluorescence intensity distribution analysis (FIDA) or photon-counting histograms (PCH) by different authors.<sup>88–97</sup>

Unfortunately, actual use of this concept with fluorophores rather than beads is not as clear as in Figures 24.26

and 24.27. This is because there are multiple Poisson distributions that need to be considered.<sup>91–92</sup> The number of photons observed during a given time interval shows a Poisson distribution, as does the number of fluorophores in the volume. Additionally, a given fluorophore will display a different brightness in each region of the observed volume. As a result the distribution of the number of photon counts is broad even for a single fluorophore. These effects were less important in Figure 24.27 because of the brightness of the labeled beads and/or the mutual exclusion of the beads from being in the laser beams at the same time. The theory of FIDA/PCH is complex and not yet used in a standardized way. Hence we will present just a few examples to illustrate the nature of the data and the possible resolution.

Figure 24.28 (top) shows an example of FIDA data.<sup>91</sup> The top panel shows the photon-count histograms for three individual fluorophores. The data represent the probability a bin contained  $k$  photon counts. A different distribution was observed for each fluorophore. While the histograms appear distinct for each fluorophore this appearance is somewhat misleading because the shapes of the distributions depend on fluorophore concentration, as shown for a lower concentration of fluorescein (dashed line). The lower panel shows the use of these histograms to resolve a mixture of fluorophores. Curves are shown for fluorescein, a coumarin derivative, and a mixture of both fluorophores, 1.2 nM each. The PCH for the mixture was different from each fluorophore alone, but the difference is due in part to the overall higher photon counts when the two fluorophores are present in the solution. The relative concentration and brightness of each fluorophore to the PCH are determined by fitting the data to simulated histograms. In this example the difference in brightness was about twofold. It may be difficult to use this approach if there is only a modest difference in fluorophore brightness.

The resolution of FIDA increases as the fluorophores display larger differences in brightness. Figure 24.29 shows the photon-count histograms for TMR and R6G, and for a mixture (top).<sup>89</sup> These data were used to recover two populations of particles: one with a brightness of 36.6 kHz per molecule (TMR) and the second about threefold brighter—107 kHz per molecule (R6G). In this case the two populations are well resolved. The dashed lines show the distributions observed for the individual fluorophores, which are already wide. This intrinsic width must be taken into account when using the measured distributions to resolve the underlying populations.

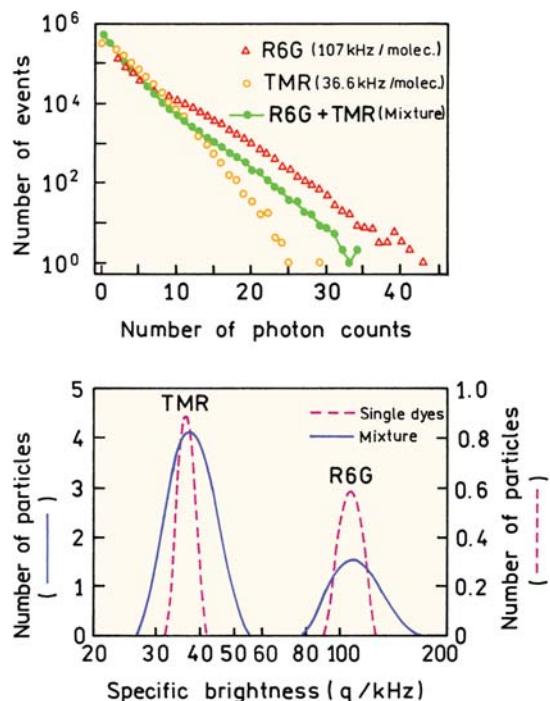


**Figure 24.29.** Fluorescence-intensity distribution and analysis for a mixture of TMR and R6G. The dashed line shows the results for separate solutions of each fluorophore. Revised from [89].

## 24.9. TIME-RESOLVED FCS

### Advanced Topic

Nanosecond time-resolved measurements are now being combined with FCS.<sup>98–100</sup> This is accomplished using high-repetition-rate pulse lasers and time-domain detection. It is possible to recover correlation data using a pulse train because the fluorophore in the observed volume can be excited by many light pulses during the millisecond timescale diffusion times. Lifetimes on the nanosecond timescale are also shorter than the diffusion time. For example, suppose the laser repetition rate is 40 MHz, so the pulses are 25 ns apart. This time interval is  $4 \times 10^3$ -fold shorter than a diffusion time of 0.1 ms. Hence there is time for the same fluorophore to be excited many times while in the laser beam, which allows the correlation curves to be measured.

Time-resolved methods can use off gating at short times to suppress unwanted autofluorescence from the samples.<sup>98</sup> Figure 24.30 shows the correlation curves for a pure solution of 10-nM TMR (top curve) and for 10-nM TMR containing ANS as the mock impurity (lower 3 curves). The presence of ANS decreases the amplitude of the autocorre-

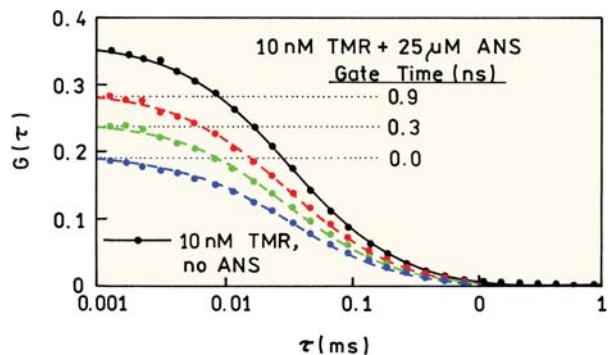


**Figure 24.30.** Background suppression in FCS using gated detection. The top line shows 10-nM TMR with no ANS. Two-photon excitation at 790 nm. Revised from [98].

lation curves and increases the apparent number of observed molecules. The lifetimes of TMR and ANS were 2.2 ns and less than 100 ps, respectively. Because of the short lifetimes the emission from ANS could be suppressed by off gating the detection during the excitation pulse and turning the detector on after a time delay. The correlation curves were measured with three delay times: 0.0, 0.3, and 0.9 ns. As the delay time increased the amplitude of the curves increased, demonstrating a decreased contribution from the short-lived ANS impurity. For a delay time of 1.4 ns the correlation curves become almost the same as for TMR alone (not shown). Gating is likely to become useful for FCS because the small number of observed molecules makes FCS sensitive to impurities, particularly in studies of intracellular fluorophores.

As described above, FIDA can be used to determine the presence and brightness of two or more species in an FCS sample. Another approach is to resolve the FCS data from a mixture using the decay times of the two species.<sup>100</sup> Figure 24.31 (top) shows autocorrelation curves for pure Cy5, pure FR662, and a mixture of both fluorophores. Apparently these fluorophores have somewhat different diffusion coefficients even though their molecular weights are similar. The lifetime of FR662 near 3.5 ns is almost threefold longer than that of Cy5, which is near 1 ns. This difference was used with a fast-fitting algorithm<sup>101</sup> to determine the amplitude of each decay time and to resolve the autocorrelation function for each fluorophore (lower panel). Since probe lifetimes frequently change upon binding to macromolecules it seems likely that time-resolved measurements will become widely used in FCS.

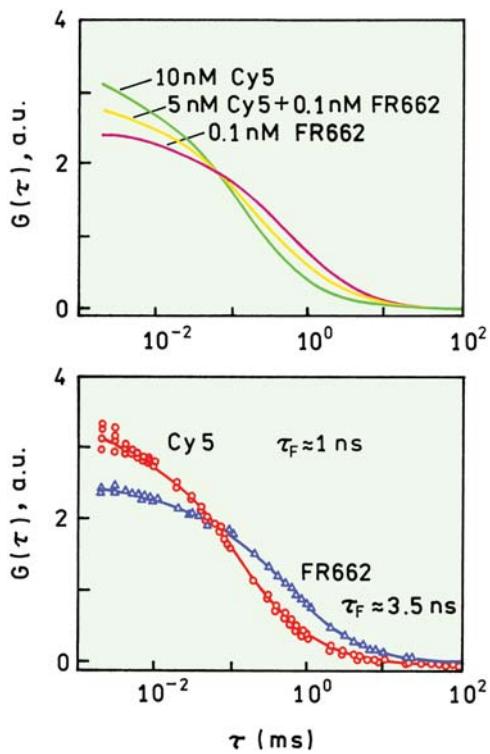


**Figure 24.31.** Top: Autocorrelation curves for pure Cy5, pure FR662, and a mixture. Bottom:  $G(\tau)$  resolved from the mixture using the time-resolved decays. Revised from [100].

#### 24.10. DETECTION OF CONFORMATIONAL DYNAMICS IN MACROMOLECULES

Since FCS can detect blinking and chemical reactions that change the intensity, it seems natural to use FCS to study the conformational dynamics of macromolecules.<sup>102–108</sup> Given the ms timescale of FCS, and the possibility of increasing the diffusion time by increasing the size of the volume, FCS should be able to detect conformational changes that occur during the diffusion time. Since the observed volume is limited by background emission, the observed volume cannot be made too large, so the events will probably need to occur on the microsecond timescale or faster to be detectable by FCS. One example of measuring macromolecular dynamics is shown in Figure 24.32. This shows a molecular beacon that is opening and closing with rate constants  $k_1$  and  $k_2$ . The open state is fluorescent and the closed state is quenched.

The correlation functions were measured for the beacon  $G_B(\tau)$  and for a control oligonucleotide  $G_C(\tau)$  that did not have the quencher (Figure 24.32, middle panel). While

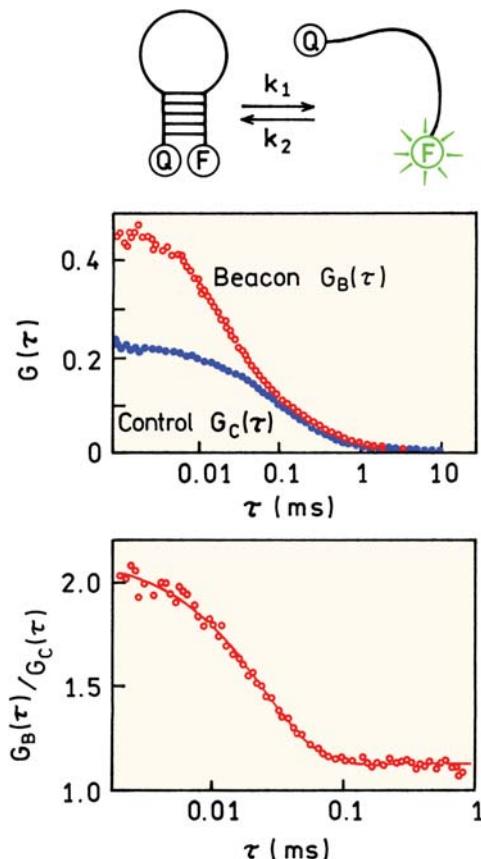


**Figure 24.32.** Folding kinetics of a molecular beacon at 45°C. Revised from [108].

the difference between  $G_B(\tau)$  and  $G_C(\tau)$  seems substantial, the difference in amplitude may be the result of about 65% the beacon being in the closed state at the experimental temperature of 45°C, thus reducing the effective fluorophore concentration. If the timescales are very different, the overall correlation function is the product of the functions due to the different processes. In this case the control molecule reveals the portion of  $G(\tau)$  due to translational diffusion:

$$G_C(\tau) = \frac{1}{N} \left( 1 + \frac{\tau}{\tau_D} \right)^{-1} \quad (24.42)$$

The overall correlation function is given by

$$G_B(\tau) = G_C(\tau) \left[ 1 + \frac{1-p}{p} \exp\left(-\frac{\tau}{\tau_R}\right) \right] \quad (24.43)$$

where  $p$  is the fraction of the beacons in the open conformation and  $1/\tau_R = k_1 + k_2$  is the relaxation time for the reaction. The functional form of eq. 24.43 is the same as eq. 24.38 because both equations account for fluorophore blinking, but due to different mechanisms. Division of  $G_B(\tau)$  by  $G_C(\tau)$  reveals the part of the correlation function that is due to opening and closing of the molecular beacon (lower panel). Note the time axes on the panels are different, and the ratio is greater than unity only for delay times less than 0.1 ms. This ratio of correlation function is consistent with a relaxation time near 24  $\mu$ s. By examination of a range of DNA sequences the authors were able to show that the opening rate  $k_1$  was mostly independent of sequence, but the closing rate  $k_2$  was strongly dependent on sequence.<sup>108</sup>

The FCS measurements provided a measure of the sum of the forward and reverse reaction rates for the molecular beacon. Additional information is needed to determine both rates individually. The equilibrium constant  $K$  for folding of the beacon is given by  $K = k_1/k_2$  and can be measured in a steady-state experiment. One can show that the forward and reverse reaction rates are related to the equilibrium constant by

$$k_1 = \frac{1}{\tau_R 1 + K} \quad (24.44)$$

$$k_2 = \frac{1}{\tau_R 1 + K} \quad (24.45)$$

The FCS measurements only provide information on the reaction rates if the relaxation time is comparable to the correlation time, irrespective of the fraction of the fluorophore in either form. This can be seen by examination of eq. 24.43. The exponential term approaches unity when  $\tau_R > \tau$ .

#### 24.11. FCS WITH TOTAL INTERNAL REFLECTION

Measurement of the correlation functions requires observation of a small number of fluorophores in a restricted volume. This can be accomplished by focused illumination and confocal detection. Another approach to FCS is to obtain the small volume using total internal reflection (TIR). Recall from Chapter 23 on Single-Molecule Fluorescence that TIR occurs from light incident on an interface when the index of refraction is lower in the distal region and the angle of incidence, measured from the normal, exceeds the criti-

cal angle  $\theta_C$ . Under these conditions there is an evanescent field in the distal region. The intensity of this field decays according to

$$I(z) = I(0) \exp(-z/d) \quad (24.46)$$

where  $I(0)$  is the intensity at the interface and  $z$  is the distance above the interface. The decay constant for the intensity of the evanescent field is given by

$$d = \frac{\lambda_0}{4\pi} (n_2^2 \sin\theta_C - n_1^2)^{-1/2} \quad (24.47)$$

where  $\lambda_0$  is the wavelength in a vacuum, and  $n_1$  and  $n_2$  are the refractive indices of the distal (water) and local (glass) regions, respectively. The evanescent field typically penetrates a distance  $d = 200$  nm. As a result the volume can be restricted by localized excitation of fluorophores near the interface.

Figure 24.33 shows a typical configuration of FCS using TIR. The observed volume is a thin circle or elliptical disk 100–200 nm thick and about 5  $\mu$ m in diameter. In this configuration fluorophores that are free in solution can enter or exit the volume by diffusion to and away from the glass surface. Diffusion out of the observed volume along

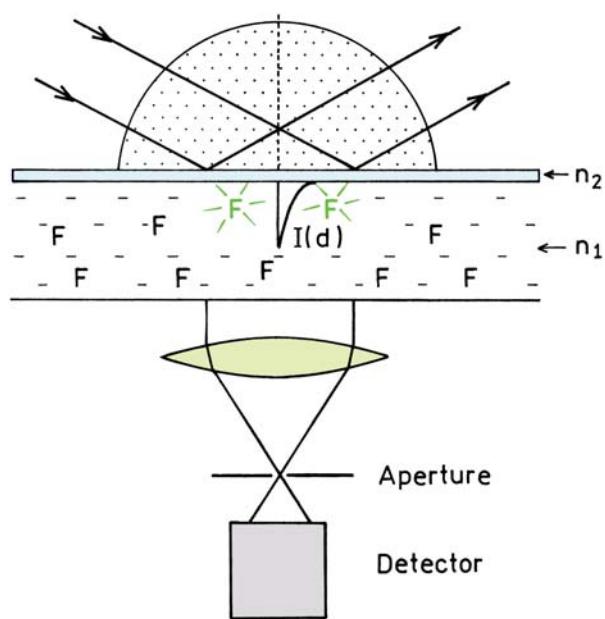


**Figure 24.33.** Experimental configuration for FCS using total internal reflection.

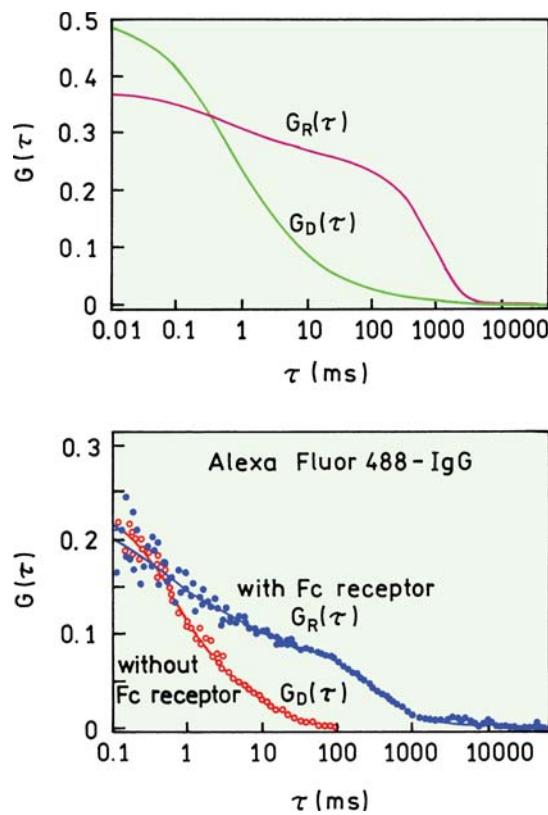


**Figure 24.34.** FCS with TIR. **Top:** Simulated correlation functions near a planar surface, without ( $G_D(\tau)$ ) and with ( $G_R(\tau)$ ) binding sites for the diffusing species. **Bottom:** Experimental data for labeled IgG near a lipid surface, without and with receptors for the Fc region. Revised from [111].

the interface is slow due to the large diameter of the spot. If the fluorophores are bound to the surface then they can only leave the volume by lateral diffusion along the surface or dissociation from the surface. Because of the difference in geometry and diffusion paths the correlation functions have a different functional form. This theory has been developed<sup>109–111</sup> and TIR-FCS has been used to study diffusion and binding near glass or membrane interfaces. The equations are rather complex and can be found elsewhere.<sup>112–115</sup> However, we will present an experimental example.

The correlation function for diffusion with TIR geometry has a characteristic shape (Figure 24.34). The shape depends strongly on whether the labeled molecules simply diffuse near the surface  $G_D(\tau)$  or, if there are receptor sites on the surface,  $G_R(\tau)$ . The presence of binding sites results in a long time component in the correlation function that can be used to detect binding to the surface. The lower panel in Figure 24.34 shows experimental data for Alexa Fluor 488-labeled IgG. The correlation function was mea-

ured near a lipid-coated surface, or near a lipid-coated surface that contained a receptor for the Fc region. The presence of binding sites results in a dramatic shift in  $G(\tau)$ . One can imagine such measurements being used to measure binding to cells to screen for drug–receptor interactions.

## 24.12. FCS WITH TWO-PHOTON EXCITATION

Two-photon (TPE) or multiphoton excitation (MPE) is very useful in FCS. When using MPE the excited volume is small because of the quadratic dependence on light intensity. Importantly, the  $z$ -axis resolution is improved because the excited volume is less elongated. Sensitivity is also improved because the emission can be observed without a confocal aperture. The theory for FCS using MPE is very similar to that for one-photon excitation. The molecules can still enter and exit the observed volume from three directions. However, the shape of the volume is changed due to the quadratic dependence on intensity. For two-photon excitation diffusion time is related to the volume diameter:

$$\tau_D = \frac{s^2}{8D} \quad (24.48)$$

where  $s$  is the distance at which the intensity is  $1/e^2$  of its maximum value. Equation 24.48 for two-photon excitation is different than eq. 24.14 because the intensity profile is squared to provide the two-photon excitation profile.<sup>62</sup> That is, the dimensions of the excited volume are described in terms of the original long-wavelength intensity profile rather than the square of the intensity profile. For two-photon excitation the correlation function for diffusion becomes<sup>116–117</sup>

$$G_D(\tau) = G(0) \left(1 + \frac{8D\tau}{s^2}\right)^{-1} \left(1 + \frac{8D\tau}{u^2}\right)^{-1/2} \quad (24.49)$$

For the same diameter beam the diffusion times are smaller with TPE even if the diffusion coefficient is not changed because of the quadratic dependence on intensity and the smaller excited volume. Some authors assume the excitation intensity is Gaussian in the focal plane and Lorentzian along the  $z$ -axis. This assumption results in an expression for  $G_D(\tau)$  that is different from eq. 24.49 and more complex, but the visual shape of  $G_D(\tau)$  is similar. A significant fraction of the publications on FCS<sup>118–121</sup> use two-photon excitation because of its experimental advantages. When using

two-photon excitation there is no need for a confocal aperture and the beam profile is shorter along the  $z$ -axis.

#### 24.12.1. Diffusion of an Intracellular Kinase Using FCS with Two-Photon Excitation

Localized excitation using TPE has made it possible to study labeled intracellular proteins in selected regions of a cell. One example is studies of the ubiquitous enzyme adenylate kinase in HeLa cells.<sup>122</sup> Adenylate kinase (AK) occurs in two forms: a cytoplasmic form AKC and a membrane-bound form AKM. The membrane-bound form contains an additional 18-amino-acid chain that appears to bind AKM to membranes. These two forms of AK from murine cells were fused with EGFP and expressed in HeLa cells. Figure 24.35 shows a microscope image of cells expressing these proteins. The cells containing AKC-EGFP are bright in the cytoplasm and the cells containing AKM-EGFP show a line of fluorescence at the plasma membrane, showing that the two forms of AK are localized differently in the cells. The bottom panel shows the correlation functions recovered for both proteins. The autocorrelation functions for the cytoplasmic form ( $\circ$ ) shows the protein diffuses freely, as can be seen by comparison with the autocorrelation function for EGFP alone in the cells ( $\blacktriangle$ ). The membrane-bound protein shows a large long  $\tau$  component centered near 100 ms. The middle panel in Figure 24.35 shows the diffusion coefficients of AKM-EGFP on or near the plasma membrane. At the plasma membrane two diffusion coefficients are found, one being about tenfold smaller than in the cytoplasm. This component is thought to be due to membrane-bound AKM. These separate measurements on each form of AK were facilitated by the use of localized two-photon excitation.

#### 24.13. DUAL-COLOR FLUORESCENCE CROSS-CORRELATION SPECTROSCOPY

We have seen that the fluorescent fluctuation autocorrelation functions are sensitive to the rate of diffusion and to chemical or photophysical processes that occur during observation. The weak dependence of the diffusion coefficients on molecular weight makes it difficult to use FCS to measure binding reactions unless there is a large change in molecular weight. Formation of dimers is near the resolution limit for FCS using the diffusion time to distinguish two species. The addition of two-color excitation and detection to FCS changes the form of the correlation functions

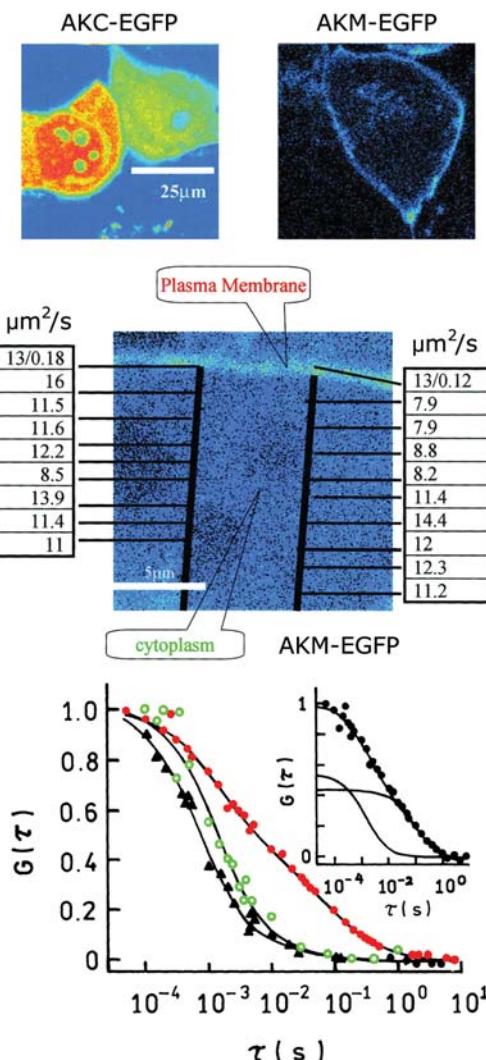


**Figure 24.35.** Top: Image of an HeLa cell containing AKC-EGFP (left) or AKM-EGFP (right). Middle: Image of the cell membrane with AKM-EGFP with the recovered diffusion coefficients. Bottom: Normalized autocorrelation function for cytoplasmic AKC-EGFP ( $\circ$ ), membrane-bound AKM-EGFP ( $\bullet$ ), and EGFP in the cytoplasm ( $\blacktriangle$ ). The solid lines in the insert show the components due to each diffusion coefficient. Revised from [122].

and provides new applications of FCS. Figure 24.36 shows a schematic of a dual-color FCS experiment. Suppose the sample contains three types of molecules, labeled with green (G), red (R), or both green and red (RG) fluorophores. Such a sample could be observed with an FCS instrument configured for two-color measurements and separate detectors for the R and G signals. Different time-dependent fluctuations will be observed in each channel (Figure 24.36). If a G fluorophore diffuses into the volume

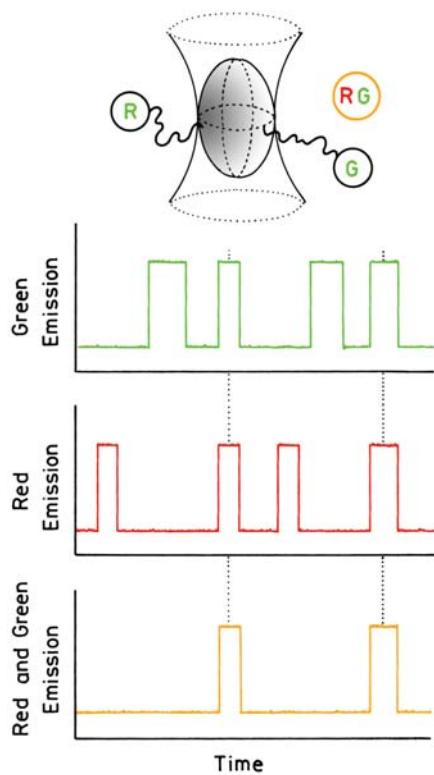


**Figure 24.36.** Dual-color fluorescence cross-correlation spectroscopy.

there is a burst of photons in the G channel, and similarly for an R fluorophore. If the RG fluorophore diffuses into the volume then a burst of photons is observed in both channels. This shows that doubly labeled molecule can be detected by cross-correlation between the two channels. The method is called fluorescence cross-correlation spectroscopy (FCCS).

#### 24.13.1. Instrumentation for Dual-Color FCCS

Before describing the theory for FCCS it is instructive to examine the instrumentation (Figure 24.37). We have assumed a red and a green channel since these wavelengths have been used in FCCS.<sup>123–131</sup> Two lasers are used typically: an argon laser for 488 nm and an HeNe laser for 633 nm. Additionally, a single laser has been used with two-photon excitation to excite two fluorophores.<sup>132</sup> In order to obtain a cross-correlation signal the observed volumes for both colors must overlap in space. For this reason it is convenient to bring the excitation to the microscope using an optical fiber, which provides the same point source for both wavelengths and overlap the excitation volumes, assuming the objective

is corrected for color aberration. The emission wavelengths are separated by a dichroic filter and sent to separate detectors.

The optics used to separate the green and red signals are sophisticated. The emission spectra of rhodamine green (RhG) and Cy5 are shown in Figure 24.38. It is necessary to excite both fluorophores and to separate their emissions. The double dichroic filter is a specialized component. It reflects both 488 and 633 nm and transmits the emission from both RhG and Cy5. The emission from these fluorophores is then sent to different detectors using additional dichroic filters. There is always some overlap or crosstalk between the channels. Excitation at 488 nm excites mostly RhG but will weakly excite Cy5. The emission of RhG extends to the region of Cy5 emission. Excitation at 633 nm excites only Cy5. Analysis of the cross-correlation signals requires correction for crosstalk. The actual equation becomes complex, so we will only describe the theory assuming no crosstalk between the channels.

#### 24.13.2. Theory of Dual-Color FCCS

The theory of dual-color FCCS has been described in detail.<sup>123–124</sup> The sample will contain some average concentrations of each species— $C_B$ ,  $C_R$ , and  $C_{GR}$ —and each species will have an autocorrelation function— $G_G(\tau)$ ,  $G_R(\tau)$ , and  $G_{GR}(\tau)$ . The observed autocorrelation or cross-correlation function will depend on which detector is observed and the crosstalk between the detectors, which we assume to be zero. The green fluorophore is excited with the green excitation source, and the red fluorophore with the red source. For simplicity we assume the brightness of all species are the same. In this case the correlation functions for the three species are given by

$$G_G(\tau) = \frac{\bar{C}_G D_G(\tau) + \bar{C}_{GR} D_{GR}(\tau)}{V_{\text{eff}} (\bar{C}_G + \bar{C}_{GR})^2} \quad (24.50)$$

$$G_R(\tau) = \frac{\bar{C}_R D_R(\tau) + \bar{C}_{GR} D_{GR}(\tau)}{V_{\text{eff}} (\bar{C}_R + \bar{C}_{GR})^2} \quad (24.51)$$

$$G_{GR}(\tau) = \frac{\bar{C}_{GR} D_{GR}(\tau)}{V_{\text{eff}} (\bar{C}_G + \bar{C}_{GR})(\bar{C}_R + \bar{C}_{GR})} \quad (24.52)$$

where  $D_i(\tau)$  are the portion of the correlation functions that contain the diffusion coefficients. These expressions can be

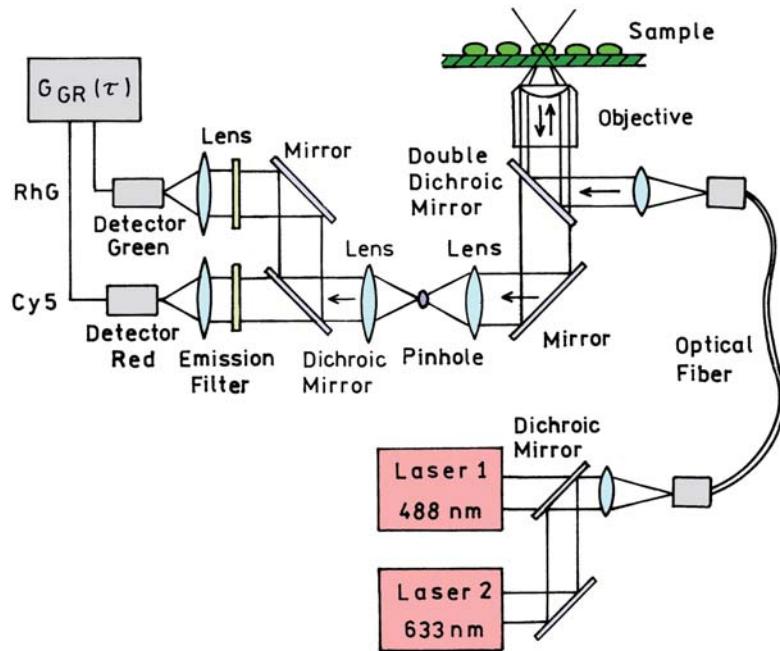


Figure 24.37. Instrumentation for dual-color FCS. Revised from [125].

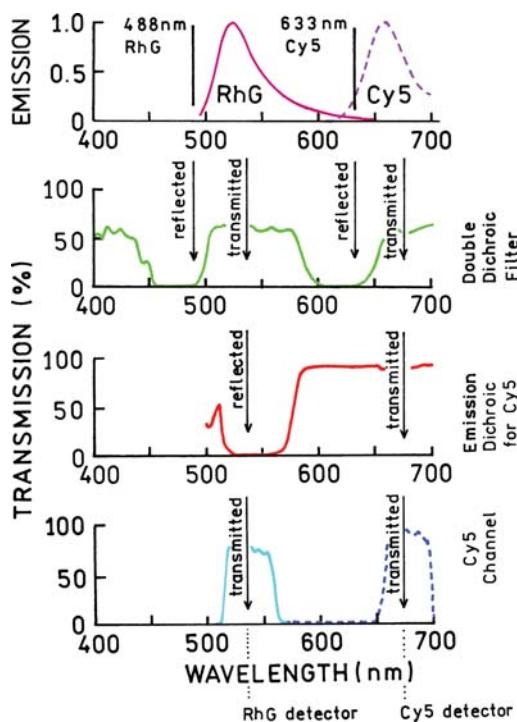


Figure 24.38. Optical filters for FCCS using RhG and Cy5. In the bottom panel the solid line is the dichroic mirror and the dashed line is the emission filter. Revised from [125].

understood as each autocorrelation function being the weighted sum for each species (G and R) as seen through one of the channels. For instance, the G fluorophore is detected in the G channel if it is present on the G or GR particle. It is important to notice that the amplitude of the cross-correlation function is proportional to the concentration of the doubly labeled species  $C_{GR}$ .

Because of the different excitation wavelengths the dimension of the observed volume will be different for each color, and different for the cross-correlation function. For each channel

$$V_{\text{eff}}^G = \pi^{3/2} s_G^2 u_G, \quad \tau_D^G = \frac{s_G^2}{4D} \quad (24.53)$$

$$V_{\text{eff}}^R = \pi^{3/2} s_R^2 u_R, \quad \tau_D^R = \frac{s_R^2}{4D} \quad (24.54)$$

For the cross-correlation measurement

$$V_{\text{eff}}^{GR} = \frac{\pi^{3/2}}{2^{3/2}} [(s_G^2 + s_R^2)(u_G^2 + u_R^2)]^{1/2} \quad (24.55)$$

$$\tau_{GR} = \frac{s_G^2 + s_R^2}{8D} \quad (24.56)$$

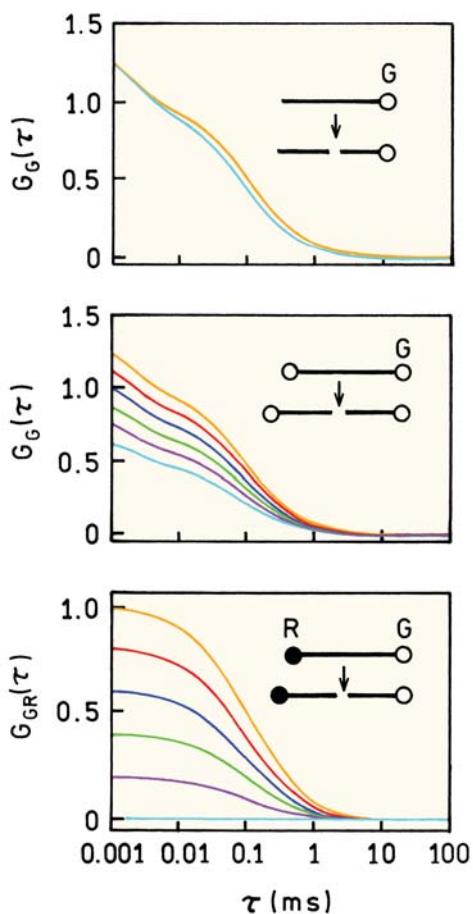


**Figure 24.39.** Autocorrelation and cross-correlation function for cleaving of labeled DNA. Revised from [125].

It is informative to visualize how the cross-correlation function is different from autocorrelation functions. Assume a DNA strand is labeled and cleaved by an enzyme (Figure 24.39). If the strand contains one green fluorophore and the strand is cut in half, then  $G_G(\tau)$  shifts slightly to shorter diffusion times due to slightly faster diffusion:  $2^{1/3} = 1.26$ -fold. The intercept  $G_G(0)$  is not changed because the number of diffusing fluorophores remains the same. Now assume the DNA contains two green fluorophores, one on each end. Cleavage of the strand again results in an increase in the diffusion coefficient, but also a decrease in  $G_G(0)$  because the number of independent diffusing species is doubled. In practice it may be difficult to quantify the  $G(0)$  value since it depends on the bulk concentration and the extent of triplet formation.

A remarkably different and useful result is obtained if the fluorophore is labeled on each end, but with a different-

color fluorophore (Figure 24.39 bottom). In the intact strand the G and R fluorophores diffuse together and yield a cross-correlation function  $G_{GR}(\tau)$  that is proportional to the concentration of the intact strand. As the DNA is cleaved the amplitude of the cross-correlation function decreases dramatically to zero when all the DNA is cleaved. The cross-correlation measurement detects only the doubly labeled species. Notice that the amplitude of  $G_{GR}(\tau)$  is proportional to  $C_{GR}$ , rather than the inverse,  $C_G^{-1}$  or  $C_R^{-1}$ , as for the autocorrelation functions.

While dual-color FCCS is very powerful it does have some intrinsic limitations. Examination of eq. 24.52 reveals that the cross-correlation amplitude is inversely proportional to the concentration of the singly labeled species. Hence FCCS is not useful for detection of trace amounts of doubly labeled species in the presence of excess amounts of singly labeled species.

#### 24.13.3. DNA Cleavage by a Restriction Enzyme

The unique information provided by FCCS is illustrated by the cleavage of a 66-bp long double-stranded DNA oligomer.<sup>125</sup> This DNA is labeled on one end with rhodamine green (RhG) and on the other end Cy5. The cleavage site for the restrictive enzyme EcoRI is near the middle of the strand (Figure 24.40). The cross-correlation was measured for various times following addition of EcoRI, and its amplitude decreased progressively to near zero. The residual amplitude at long times is probably due to crosstalk between the channels.

At first glance one may think that the cross-correlation signal is dependent on RET between RhG and Cy5 (Figure 24.38), since these probes would be a good donor–acceptor pair for Förster transfer. However, the distance between RhG and Cy5 in the 66-mer is too long for RET. The appearance of cross-correlation does not depend on energy transfer, but instead on the two probes being linked so both appear in the observed volume at the same time.

#### 24.13.4. Applications of Dual-Color FCCS

Applications of FCCS have already been published.<sup>133–142</sup> One example is the stoichiometry of binding of RNA oligomers to transcription activator protein NtrC.<sup>136</sup> This protein controls part of the nitrogen metabolism pathway in bacteria. It was thought that the octameric NtrC complex may bind two DNA oligomers, which could be tested by dual-color FCS. The oligomers were labeled with either

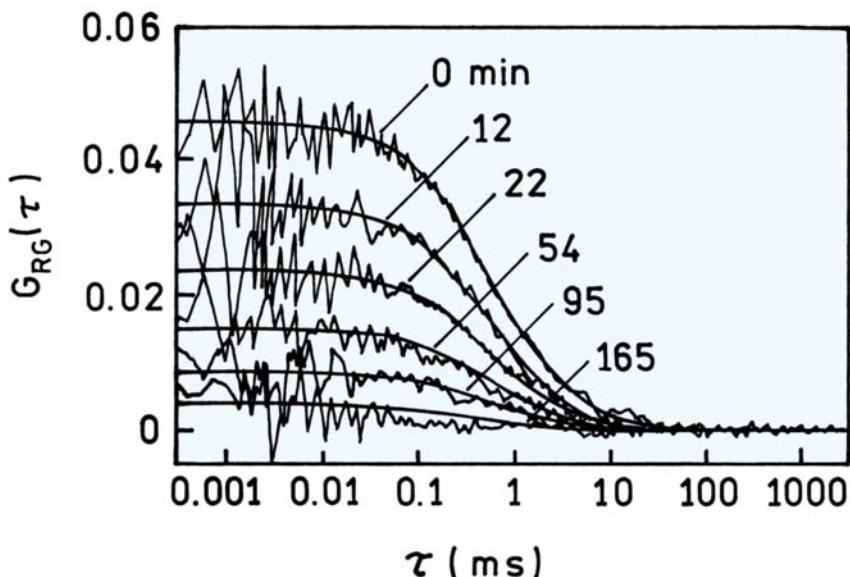
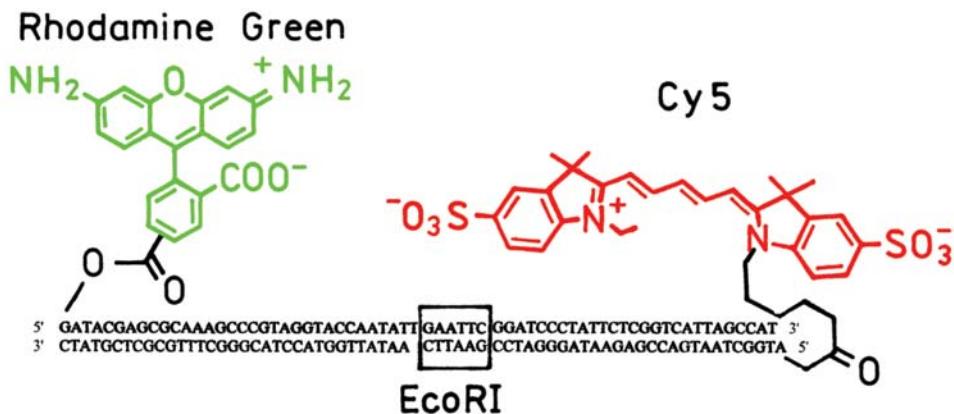


**Figure 24.40.** Sequence of DNA labeled with both RhG and Cy5. The lower panel shows the cross-correlation function during incubation of the labeled DNA with the restriction enzyme EcoRI. Revised from [125].

FAM or ROX (Figure 24.41). Detection of binding of both labeled oligomers was demonstrated by the cross-correlation signal. If NtrC bound only one oligomer then the cross-correlation amplitude would be zero.

Dual-color FCCS is likely to find widespread use in studies of gene expression. This can be accomplished by synthesis of two oligonucleotides, each labeled with a different fluorophore and each specific for a different region of the same gene. The concept of the experiment is shown in Figure 24.42.<sup>137</sup> The RNA from the cells of interest is extracted and converted to cDNA using reverse transcriptase. The cDNA is then mixed with the two labeled probes,

which are specific for nearby regions of the same gene. If the gene is present the G and R probes bind near to each other and create a cross-correlation signal. If the probes are mixed with cDNA that was depleted of this gene the cross-correlation signal is near zero.

Dual-color FCS can be used to measure protein association. Aggregation of amyloid proteins appears to be an important component of Alzheimer's disease, and aggregation of prion proteins occurs in bovine spongiform encephalopathy and Creutzfeldt-Jakob disease.<sup>138</sup> Dual-color FCS has been used to study aggregation of prion proteins (PrP). The isolated proteins were labeled either with

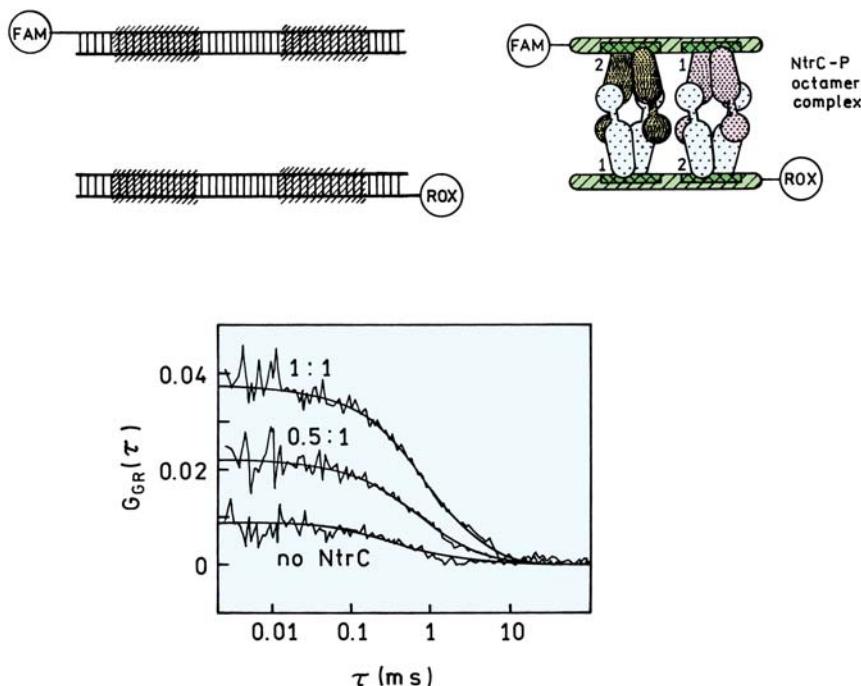


**Figure 24.41.** Detection of binding of two DNA oligomers to the regulatory protein NtrC by dual-color FCCS. Revised and reprinted with permission from [136]. Copyright © 2000, American Chemical Society.

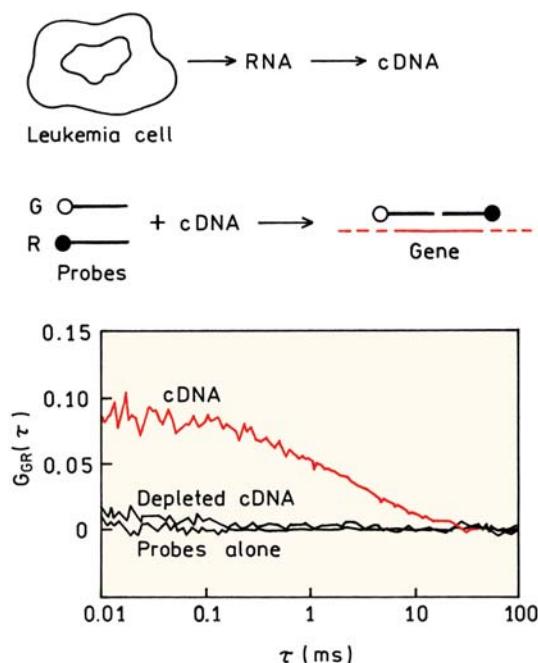


**Figure 24.42.** Detection of gene expression using dual-color FCCS. Revised from [137].

Cy5 or Oregon Green.<sup>139</sup> A cross-correlation signal appeared immediately upon mixing (Figure 24.43), showing the formation of aggregates. The use of FCCS allows kinetics to be studied, and to see if aggregate formation is spontaneous or requires seeds of aggregated proteins.

In the previous examples the needed information was contained in the amplitude of the cross-correlation function. The diffusion coefficients were not needed, and hence there was no need to calculate the cross-correlation function. Instead, the data can be analyzed by coincidence analysis.<sup>143–147</sup> The oligonucleotides with the desired requirements are labeled with two different probes (Figure 24.44). Instead of the correlation function one records the time-dependent intensities from each channel. The data are analyzed to count the number of events where signals appear in both channels.

#### 24.14. ROTATIONAL DIFFUSION AND PHOTON ANTIBUNCHING

**Advanced Topic**

Since FCS is sensitive to translational diffusion it seems logical to use FCS to measure rotational diffusion. Such measurements would be useful because rotational correlation times are directly proportional to the molecular weight, but translational diffusion coefficients are proportional to

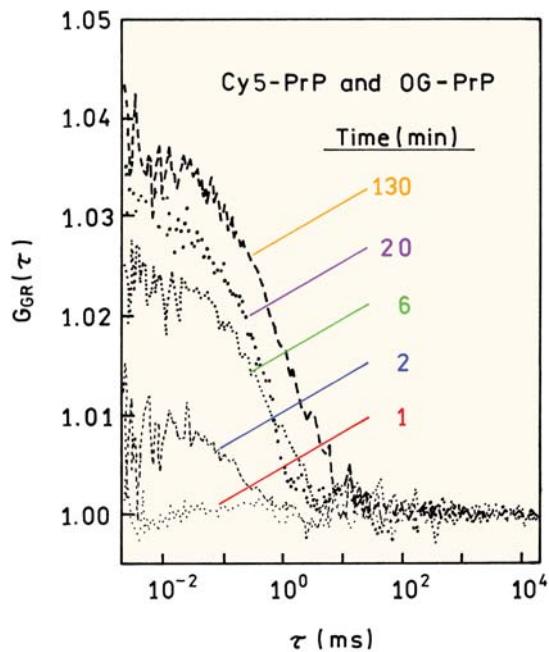


**Figure 24.43.** Association of prion proteins (PrP) by dual wavelength cross-correlation FCS. PrP were labeled with either Cy5 or Oregon Green (OG). Revised from [139].

$(\text{MW})^{1/3}$ . The use of FCS to measure the hydrodynamics and internal dynamics of macromolecules is promising because the timescale is not limited by fluorescence lifetimes. However, there have been relatively few publications on rotational diffusion<sup>148–152</sup> because there are a number of physical limitations and technical challenges. To measure rotational motions using FCS it is necessary to account for photon antibunching and triplet formation, which can occur on the same timescale as rotational diffusion.

In a typical FCS experiment the timescale of interest is the diffusion time  $\tau_D$ , which is usually much longer than the fluorescence lifetime  $\tau_F$ . Hence there is time for the fluorophore to return to the ground state to be excited again while still in the observed volume. However, rotational correlation times  $\theta$  are usually comparable to the lifetimes and much shorter than the diffusion times. In order to observe a correlation it is necessary to detect more than a single photon from the molecule before its orientation is randomized by rotational diffusion. While the fluorophore is in the excited state it cannot be excited again. As a result there is always some time delay, comparable to the fluorescence lifetime, between detection of two photons from the same fluorophore. This delay is called photon antibunching, to

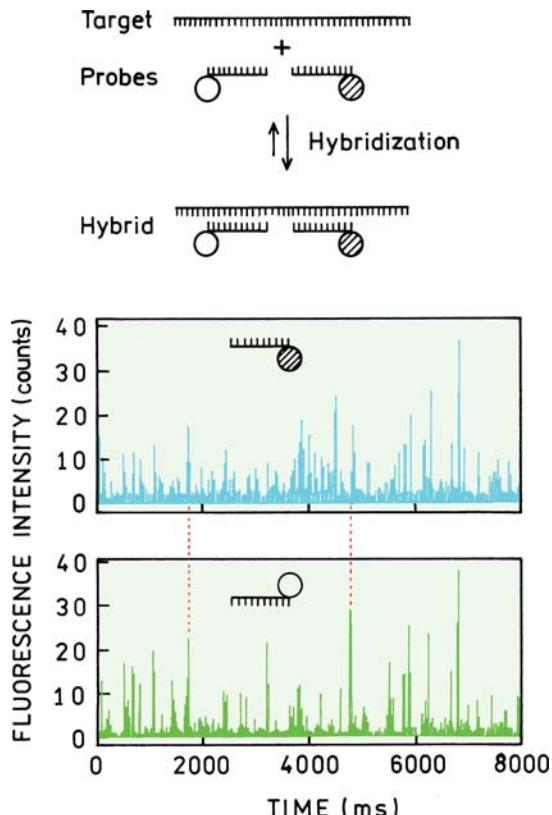


**Figure 24.44.** Coincidence analysis to detect  $\lambda$  phage DNA. Coincidence events are shown by the vertical dashed lines. Revised and reprinted with permission from [143]. Copyright © 1997, American Chemical Society.

indicate that detection of a second photon is statistically less probable as the time delay becomes smaller.<sup>153–155</sup>

An optical configuration for anisotropy FCS (AFCS) is shown in Figure 24.45. The sample is excited with polarized light. The emission is observed using two detectors. The emission is split by a beamsplitter that randomly transmits or reflects the photons. The detection electronics is similar to that used for TCSPC. The difference in arrival times of the emitted photons is measured with the time-domain electronics. Because the photons are randomly distributed the first photon can arrive in either channel, so the correlation function will appear to be symmetrical around  $\tau = 0$ . Figure 24.45 shows polarizers in the emission light paths, but they are not necessary because photoselection occurs upon excitation.

The theory for AFCS can be complex,<sup>148–149</sup> so we will present the simplest case. Assume that the lifetime  $\tau_F$  is much shorter than the rotational correlation time  $\theta$ , and that

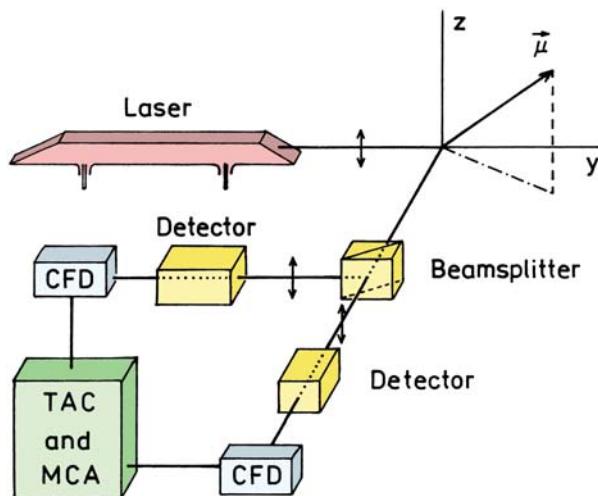


**Figure 24.45.** Measurement of photon antibunching and rotational diffusion by FCS. CFD, constant fraction discriminator. TAC, time-to-amplitude converter. MCA, multichannel analyses. Revised from [150].

both of these are shorter than the diffusion time. Also assume that the absorption and emission dipoles are parallel, and that the excitation is polarized in the  $z$  direction and the emission is observed without polarizers, the observed volume is long along the  $z$ -axis. The correlation function is then given by

$$G(\tau) = G(0) \left[ \frac{1}{1 + \tau/\tau_D} + \frac{4}{5} \exp\left(-\frac{\tau}{\theta}\right) - \frac{9}{5} \exp\left(-\frac{\tau}{\tau_F}\right) \right] \quad (24.57)$$

The correlation time information is available without polarizers because the probability of excitation depends on the orientation of the fluorophore relative to the incident polarization. This separation of correlation time from lifetime can be seen in the middle term of eq. 24.57, where the exponential relationship depends on the ratio of the experimental correlation time  $\tau$  to the rotational correlation time  $\theta$ . This is different from time-resolved anisotropy decays, where the lifetime must be comparable to the rotational correlation time to obtain useful information. The last term in eq. 24.57 represents the photon antibunching, which decreases exponentially with the ratio of the experimental correlation time to the lifetime  $\tau_F$ .

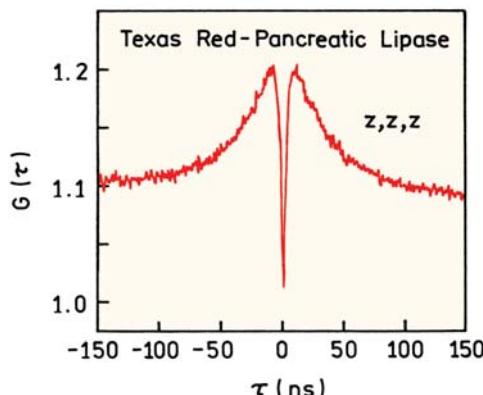


**Figure 24.46.** Measurement of rotational diffusion of Texas Red-labeled pancreatic lipase using FCS. Revised from [151].

It is interesting to notice that eq. 24.57 contains two exponential terms plus the diffusion term. Recall that the concentration autocorrelation function is also exponential in  $\tau$  (eq. 24.11). The averaging over a Gaussian volume results in the dependence shown in eq. 24.57. The photon antibunching term and the rotational diffusion terms still show the exponential dependence because they do not depend on the position of the fluorophore in the volume.

Figure 24.46 shows an AFCS experiment, in this case for pancreatic lipase labeled with Texas Red.<sup>151</sup> The data were collected using three parallel polarizers (Figure 24.45), so that eq. 24.57 is not appropriate for these data but requires additional geometric factors.  $G(\tau)$  is symmetrical because of the random distribution of photons by the beam-splitter. Notice that the timescale is ns rather than ms because rotational diffusion occurs on this timescale. The dip in the middle is due to photon antibunching and is several ns wide, comparable to the lifetime  $\tau_F$ . The decays on either side are due, at least in part, to rotational diffusion of the protein.

## 24.15. FLOW MEASUREMENTS USING FCS

As a final application of FCS we will describe how it can be used to detect the velocity in flowing samples. This is not a trivial problem, especially in microfluidic structures where the velocity will vary across the channel and will be different in branches of a channel. The theory of FCS with flow has been described,<sup>156</sup> and the interest in such measurements appears to be growing rapidly.<sup>157–162</sup> A typical

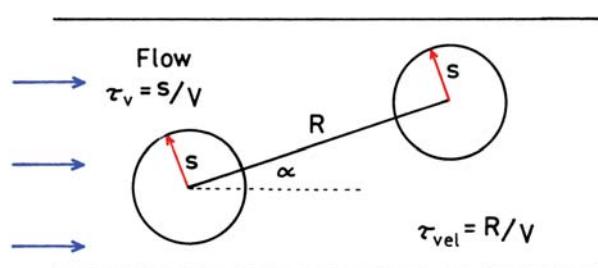


Figure 24.47. Flow velocity measurements using FCS.

arrangement for flow measurements is shown in Figure 24.47. The flowing sample is illuminated with one laser beam or with two spatially separated laser beams. Flow velocities can be measured using either the autocorrelation function from one volume or the cross-correlation signal from two spatially separated volumes.

When a single volume is observed the time a fluorophore remains in the laser beam is reduced in a flowing sample.  $G(\tau)$  is expected to decay more quickly as the velocity increases. In the presence of flow, if diffusion can be neglected, the single volume autocorrelation function is given by

$$G(\tau) = \frac{1}{N} \exp\left[-\left(\frac{\tau}{\tau_v}\right)^2\right] \quad (24.58)$$

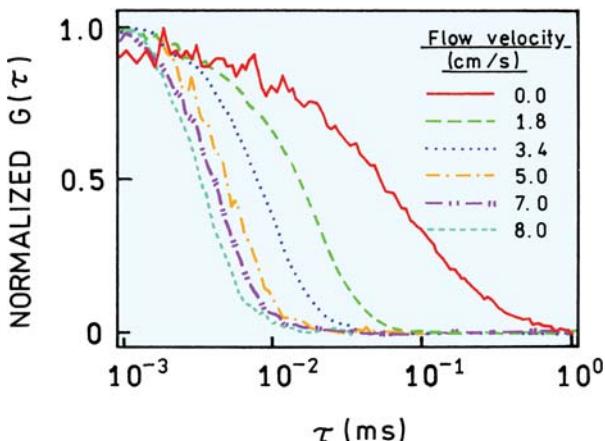


Figure 24.48. Normalized autocorrelation curves for 5-nM rhodamine green flowing in a capillary. Revised and reprinted with permission from [161]. Copyright © 2002, American Chemical Society.

where  $\tau_v$  is the time for a fluorophore to be swept through the volume at a velocity  $V$ :

$$\tau_v = s/V \quad (24.59)$$

The effect of flow is shown in Figure 24.48 for rhodamine green in water.<sup>161</sup> In the absence of flow the usual autocorrelation function is observed. As the flow rate increases the curves shift progressively to shorter times, and begin to take on the exponential shape given by eq. 24.58. This shift is the result of the fluorophores being removed from the observed volume prior to being excited multiple times.

Another approach to measuring flow is to use cross-correlation between two spatially separate volumes (Figure 24.49). In this case the cross-correlation curves show a peak at the time needed for a fluorophore to flow from one volume to the next volume.<sup>162</sup> The increased amplitude below 0.1 ms is due to crosstalk between the channels. The expression for cross-correlation due to flow, neglecting diffusion, is given by

$$G(\tau) = \frac{1}{N} \exp\left[\frac{-R^2}{s^2}\left(\frac{\tau^2}{\tau_{vel}V^2} + 1 - 2\frac{\tau^2}{\tau_{vel}^2} \cos\alpha\right)\right] \quad (24.60)$$

where  $\tau_{vel} = R/V$ . This last expression is complex, but the result is simple. The cross-correlation curves show a peak at

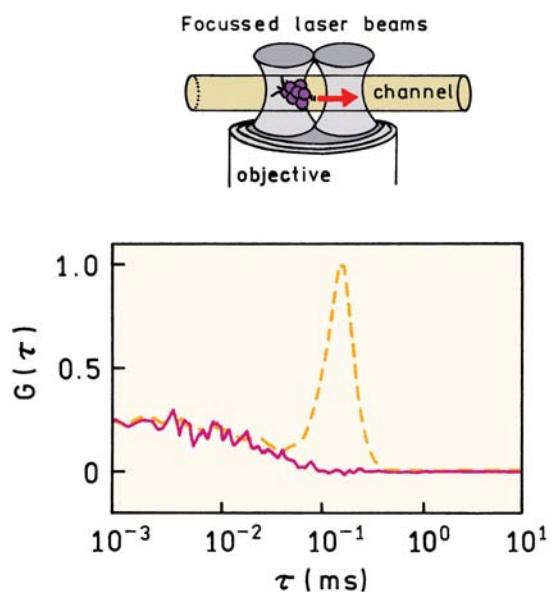


Figure 24.49. Measurement of the flow of TMR in water using cross-correlation between spatially separated channels. Revised and reprinted with permission from [162]. Copyright © 2002, American Chemical Society.

a time that corresponds to the transit time between the two volumes.

#### 24.16. ADDITIONAL REFERENCES ON FCS

FCS is in a stage of rapid development. Additional references on various aspects of FCS are listed after the main reference section.

#### REFERENCES

- Magde D, Elson E, Webb WW. 1972. Thermodynamic fluctuations in a reacting system—measurement by fluorescence correlation spectroscopy. *Phys Rev Lett* **29**(11):705–708.
- Elson E, Magde D. 1974. Fluorescence correlation spectroscopy: conceptual basis and theory. *Biopolymers* **13**:1–27.
- Magde D, Elson E, Webb WW. 1974. Fluorescence correlation spectroscopy. *Biopolymers* **13**:29–61.
- Aragon SR, Pecora R. 1975. Fluorescence correlation spectroscopy and brownian rotational diffusion. *Biopolymers* **14**:119–138.
- Rigler R, Elson ES, eds. 2001. *Fluorescence correlation spectroscopy: theory and applications*. Springer, New York.
- Webb WW. 2001. Fluorescence correlation spectroscopy: genesis, evolution, maturation and prognosis. In *Fluorescence correlation spectroscopy: theory and applications*, pp. 305–330. Ed R Rigler, ES Elson. Springer, New York.
- Eigen M, Rigler R. 1994. Sorting single molecules: application to diagnostics and evolutionary biotechnology. *Proc Natl Acad Sci USA* **91**:5740–5747.
- Haustein E, Schwille P. 2003. Ultrasensitive investigations of biological systems by fluorescence correlation spectroscopy. *Methods* **29**: 153–166.
- Visser AJWG, Hink MA. 1999. New perspectives of fluorescence correlation spectroscopy. *J Fluoresc* **9**(1):81–87.
- Thompson NL, Lieto AM, Allen NW. 2002. Recent advances in fluorescence correlation spectroscopy. *Struct Biol* **12**:634–641.
- Hess ST, Huang S, Heikal AA, Webb WW. 2002. Biological and chemical applications of fluorescence correlation spectroscopy: a review. *Biochemistry* **41**(3):647–708.
- Brock R, Jovin TM. 2001. Fluorescence correlation microscopy (FCM): fluorescence correlation spectroscopy (FCS) in cell biology. In *Fluorescence correlation spectroscopy: theory and applications*, pp. 133–161. Ed R Rigler, ES Elson. Springer, New York.
- Rigler R. 1995. Fluorescence correlations, single molecule detection and large number screening: applications in biotechnology. *J Biotechnol* **41**:177–186.
- Földes-Papp Z, Demel U, Domej W, Tilz GP. 2002. A new dimension for the development of fluorescence-based assays in solution: from physical principles of FCS detection to biological applications. *Exp Biol Med* **227**(5):291–300.
- Sterer S, Henco K. 1997. Fluorescence correlation spectroscopy (FCS)—a highly sensitive method to analyze drug/target interactions. *J Recept Signal Transduction Res* **17**(1–3):511–520.
- Kim SA, Schwille P. 2003. Intracellular applications of fluorescence correlation spectroscopy: prospects for neuroscience. *Curr Opin Neurobiol* **13**:583–590.
- Widengren J, Mets Ü. 2002. Conceptual basis of fluorescence correlation spectroscopy and related techniques as tools in bioscience. In *Single molecule detection in solution*, pp. 69–120. Ed CH Zander, J Enderlein, RA Keller. Wiley-VCH, Darmstadt, Germany.
- Thompson NL. 1991. Fluorescence correlation spectroscopy. In *Topics in fluorescence spectroscopy*, Vol. 1: *Techniques*, pp. 337–378. Ed JR Lakowicz. Plenum Press, New York.
- Rigler R, Mets Ü, Widengren J, Kask P. 1993. Fluorescence correlation spectroscopy with high count rate and low background: analysis of translational diffusion. *Eur Biophys J* **22**:169–175.
- Rigler R, Widengren J, Mets Ü. 1993. Interactions and kinetics of single molecules as observed by fluorescence correlation spectroscopy. In *Fluorescence spectroscopy*, pp. 14–24. Ed O Wolfbeis. Springer-Verlag, New York.
- Müller JD, Chen Y, Gratton E. 2003. Fluorescence correlation spectroscopy. *Methods Enzymol* **361**:69–92.
- Maiti S, Haupt U, Webb WW. 1997. Fluorescence correlation spectroscopy: diagnostics for sparse molecules. *Proc Natl Acad Sci USA* **94**:11753–11757.
- Pack CG, Nishimura G, Tamura M, Aoki K, Taguchi H, Yoshida M, Kinjo M. 1999. Analysis of interaction between chaperonin GroEL and its substrate using fluorescence correlation spectroscopy. *Cytometry* **36**:247–253.
- Meyer-Almes FJ. 2001. Nanoparticle immunoassays: a new method for use in molecular diagnostics and high throughput pharmaceutical screening based on fluorescence correlation spectroscopy. In *Fluorescence correlation spectroscopy: theory and applications*, pp. 379–395. Ed R Rigler, ES Elson. Springer, New York.
- Wohland T, Friedrich K, Hovius R, Vogel H. 1999. Study of ligand-receptor interactions by fluorescence correlation spectroscopy with different fluorophores: evidence that the homopentameric 5-hydroxytryptamine type 3<sub>As</sub> receptor binds only one ligand. *Biochemistry* **38**:8671–8681.
- Van Craenenbroeck E, Engelborghs Y. 1999. Quantitative characterization of the binding of fluorescently labeled colchicine to tubulin in vitro using fluorescence correlation spectroscopy. *Biochemistry* **38**: 5082–5088.
- Larson DR, Ma YM, Vogt VM, Webb WW. 2003. Direct measurement of gag–gag interaction during retrovirus assembly with FRET and fluorescence correlation spectroscopy. *J Cell Biol* **162**(7):1233–1244.
- Pitschke M, Prior R, Haupt M, Riesner D. 1999. Detection of single amyloid β-protein aggregates in the cerebrospinal fluid of Alzheimer's patients by fluorescence correlation spectroscopy. *Nature Med* **4**(7):832–834.
- Schwille P, Bieschke J, Oehlenschläger F. 1997. Kinetic investigations by fluorescence correlation spectroscopy: the analytical and diagnostic potential of diffusion studies. *Biophys Chem* **66**:211–228.
- Schwille P, Oehlenschläger F, Walter NG. 1996. Quantitative hybridization kinetics of DNA probes to RNA in solution followed by diffusional fluorescence correlation analysis. *Biochemistry* **35**: 10182–10193.

31. Bjorling S, Kinjo M, Foldes-Papp Z, Hagman E, Thyberg P, Rigler R. 1998. Fluorescence correlation spectroscopy of enzymatic DNA polymerization. *Biochemistry* **37**:12971–12978.
32. Rigler R, Foldes-Papp Z, Meyer-Almes FJ, Sammet C, Volcker M, Schnetz A. 1998. Fluorescence cross-correlation: a new concept for polymerase chain reaction. *Biotechnology* **63**:97–109.
33. Kinjo M. 1998. Detection of asymmetric PCR products in homogeneous solution by fluorescence correlation spectroscopy. *Biotechnology* **25**:706–715.
34. Schubert F, Zettl H, Hafner W, Krauss G, Krausch G. 2003. Comparative thermodynamic analysis of DNA–protein interactions using surface plasmon resonance and fluorescence correlation spectroscopy. *Biochemistry* **42**:10288–10294.
35. Wohland T, Friedrich-Benet K, Pick H, Preuss A, Hovius R, Vogel H. 2001. The characterization of a transmembrane receptor protein by fluorescence correlation spectroscopy. In *Single molecule spectroscopy*, pp. 195–210. Ed R Rigler, M Orrit, T Basche. Springer, New York.
36. Schuler J, Frank J, Trier U, Schäfer-Korting M, Saenger W. 1999. Interaction kinetics of tetramethylrhodamine transferrin with human transferrin receptor studied by fluorescence correlation spectroscopy. *Biochemistry* **38**:8402–8408.
37. Pick H, Preuss AK, Mayer M, Wohland T, Hovius R, Vogel H. 2003. Monitoring expression and clustering of the ionotropic 5HT<sub>3</sub> receptor in plasma membranes of live biological cells. *Biochemistry* **42**: 877–884.
38. Boukari H, Nossal R, Sackett DL. 2003. Stability of drug-induced tubulin rings by fluorescence correlation spectroscopy. *Biochemistry* **42**:1292–1300.
39. Sevenich FW, Langowski J, Weiss V, Rippe K. 1998. DNA binding and oligomerization of ntrC studied by fluorescence anisotropy and fluorescence correlation spectroscopy. *Nucleic Acids Res* **26**(6): 1373–1381.
40. Auer M, Moore KJ, Meyer-Almes FJ, Guenther R, Pope AJ, Stoeckli KA. 1998. Fluorescence correlation spectroscopy: lead discovery by miniaturized HTS. *Drug Discovery Today* **3**(10):457–465.
41. Xu H, Frank J, Trier U, Hammer S, Schroder W, Behlke J, Schafer-Korting M, Holzwarth JF, Saenger W. 2001. Interaction of fluorescence labeled single-stranded DNA with hexameric DNA-helicase repA: a photon and fluorescence correlation spectroscopy study. *Biochemistry* **40**:7211–7218.
42. Daniel DC, Thompson M, Woodbury NW. 2002. DNA-binding interactions and conformational fluctuations of tc3 transposase DNA binding domain examined with single molecule fluorescence spectroscopy. *Biophys J* **82**:1654–1666.
43. Kral T, Langner M, Benes M, Baczyńska D, Ugorski M, Hof M. 2002. The application of fluorescence correlation spectroscopy in detecting DNA condensation. *Biophys Chem* **95**:135–144.
44. Kral T, Hof M, Langner M. 2002. The effect of spermine on plasmid condensation and dye release observed by fluorescence correlation spectroscopy. *Biol Chem* **383**:331–335.
45. Schwille P, Oehlenschläger F, Walter NG. 1996. Quantitative hybridization kinetics of DNA probes to RNA in solution followed by diffusional fluorescence correlation analysis. *Biochemistry* **35**: 10182–10193.
46. Kinjo M, Rigler R. 1995. Ultrasensitive hybridization analysis using fluorescence correlation spectroscopy. *Nucleic Acids Res* **23**:1795–1799.
47. Foldes-Papp Z, Kinjo M. 2001. Fluorescence correlation spectroscopy in nucleic acid analysis. In *Fluorescence correlation spectroscopy: theory and applications*, pp. 25–64. Ed R Rigler, ES Elson. Springer, New York.
48. Nishimura G, Rigler R, Kinjo M. 1997. Number analysis of fluorescence correlation spectroscopy for the cleaving process of fluorescence labeled DNA. *Bioimaging* **5**:129–133.
49. Kovacic RT, van Holde KE. 1977. Sedimentation of homogeneous double-strand DNA molecules. *Biochemistry* **16**(7):1490–1498.
50. Eisenberg D, Crothers D, eds. 1979. *Physical chemistry with applications to the life sciences*, Benjamin Cummings, Melno Park, CA.
51. Kinjo M, Nishimura G, Koyama T, Mets Ü, Rigler R. 1998. Single-molecule analysis of restriction DNA fragments using fluorescence correlation spectroscopy. *Anal Biochem* **260**:166–172.
52. Fradin C, Abu-Arish A, Granek R, Elbaum M. 2003. Fluorescence correlation spectroscopy close to a fluctuating membrane. *Biophys J* **84**:2005–2020.
53. Benda A, Benes M, Marecek V, Lhotsky A, Hermens WTh, Hof M. 2003. How to determine diffusion coefficients in planar phospholipid systems by confocal fluorescence spectroscopy. *Langmuir* **19**:4120–4126.
54. Palmer III AG, Thompson NL. 1989. Fluorescence correlation spectroscopy for detecting submicroscopic clusters of fluorescent molecules in membranes. *Chem Phys Lipids* **50**:253–270.
55. Hegener O, Jordan R, Haberlein H. 2002. Benzodiazepine binding studies on living cells: application of small ligands for fluorescence correlation spectroscopy. *Biol Chem* **383**:1801–1807.
56. Briddon SJ, Middleton RJ, Yates AS, George MW, Kellam B, Hill SJ. 2004. Application of fluorescence correlation spectroscopy to the measurement of agonist binding to a G-protein coupled receptor at the single cell level. *Faraday Discuss* **126**:197–207.
57. Hink MA, van Hoek A, Visser AJWG. 1999. Dynamics of phospholipid molecules in micelles: characterization with fluorescence correlation spectroscopy and time-resolved fluorescence anisotropy. *Langmuir* **15**:992–997.
58. Gennerich A, Schild D. 2002. Anisotropic diffusion in mitral cell dendrites revealed by fluorescence correlation spectroscopy. *Biophys J* **83**:510–522.
59. Meissner O, Häberlein H. 2003. Lateral mobility and specific binding to GABA<sub>A</sub> receptors on hippocampal neurons monitored by fluorescence correlation spectroscopy. *Biochemistry* **42**:1667–1672.
60. Pramanik A, Thyberg P, Rigler R. 2000. Molecular interactions of peptides with phospholipid vesicle membranes as studied by fluorescence correlation spectroscopy. *Chem Phys Lipids* **104**:35–47.
61. Kahya N, Scherfeld D, Bacia K, Poolman B, Schwille P. 2003. Probing lipid mobility of raft-exhibiting model membranes by fluorescence correlation spectroscopy. *J Biol Chem* **278**(30):28109–28115.
62. Schwille P, Haupt U, Maiti S, Webb WW. 1999. Molecular dynamics in living cells observed by fluorescence correlation spectroscopy with one- and two- photon excitation. *Biophys J*, **77**:2251–2265.

63. Schwille P, Korlach J, Webb WW. 1999. Fluorescence correlation spectroscopy with single-molecule sensitivity on cell and model membranes. *Cytometry* **36**:176–182.
64. Weiss M, Hashimoto H, Nilsson T. 2003. Anomalous protein diffusion in living cells as seen by fluorescence correlation spectroscopy. *Biophys J* **84**:4043–4052.
65. Wachsmuth M, Waldeck W, Langowski J. 2000. Anomalous diffusion of fluorescent probes inside living cell nuclei investigated by spatially-resolved fluorescence correlation spectroscopy. *J Mol Biol* **298**:677–689.
66. Milon S, Hovius R, Vogel H, Wohland T. 2003. Factors influencing fluorescence correlation spectroscopy measurements on membranes: simulations and experiments. *Chem Phys* **288**:171–186.
67. Korlach J, Schwille P, Webb WW, Feigenson GW. 1999. Characterization of lipid bilayer phases by confocal microscopy and fluorescence correlation spectroscopy. *Proc Natl Acad Sci USA* **96**:8461–8466.
68. Steiner DF, Cunningham D, Spigelman L, Aten B. 1967. Insulin biosynthesis: evidence for a precursor. *Science* **157**:697–700.
69. Wahren J, Johansson B-L, Wallberg-Henriksson H. 1994. Does C-peptide have a physiological role? *Diabetologia* **37**(2):S99–S107.
70. Wahren J, Ekberg K, Johansson J, Henriksson M, Pramanik A, Johansson B-L, Rigler R, Jörnvall H. 2000. Role of C-peptide in human physiology. *Am J Physiol Endocrinol Metab* **278**:E759–E768.
71. Rigler R, Pramanik A, Jonasson P, Kratz G, Jansson OT, Nygren PD, Stahl S, Ekberg K, Johansson B-L, Uhlén S, Uhlén M, Jörnvall H, Wahren J. 1999. Specific binding of proinsulin C-peptide to human cell membranes. *Proc Natl Acad Sci USA* **96**(23):13318–13323.
72. Zhong Z-H, Pramanik A, Ekberg K, Jansson OT, Jörnvall H, Wahren J, Rigler R. 2001. Insulin binding monitored by fluorescence correlation spectroscopy. *Diabetologia* **44**:1184–1188.
73. Pramanik A, Rigler R. 2001. FCS-analysis of ligand-receptor interactions in living cells. In *Fluorescence correlation spectroscopy: theory and applications*, pp. 101–131. Ed R Rigler, ES Elson. Springer, New York.
74. Wolf DE. 1992. Theory of fluorescence recovery after photobleaching measurements on cylindrical surfaces. *Biophys J* **61**:487–493.
75. Braeckmans K, Peeters L, Sanders NN, DeSmedt SC, Demeester J. 2003. Three-dimensional fluorescence recovery after photobleaching with the confocal scanning laser microscope. *Biophys J* **85**:2240–2252.
76. Lopez A, Dupou L, Altibelli A, Trotard J, Tocanne JF. 1988. Fluorescence recovery after photobleaching (FRAP) experiments under conditions of uniform disk illumination: critical comparison of analytical solutions, and a new mathematical method for calculation of diffusion coefficient D. *Biophys J* **53**:963–970.
77. Widengren J, Rigler R, Mets Ü. 1994. Triplet-state monitoring by fluorescence correlation spectroscopy. *J Fluoresc* **4**(3):255–258.
78. Widengren J, Mets Ü, Rigler R. 1995. Fluorescence correlation spectroscopy of triplet states in solution: a theoretical and experimental study. *J Phys Chem* **99**:13368–13379.
79. Widengren J. 2001. Photophysical aspects of FCS measurements. In *Fluorescence correlation spectroscopy: theory and applications*, pp. 177–301. Ed R Rigler, ES Elson. Springer, New York.
80. Hegerfeldt GC, Seidel D. 2003. Blinking molecules: determination of photophysical parameters from the intensity correlation function. *J Chem Phys* **118**(17):7741–7746.
81. Widengren J, Mets Ü, Rigler R. 1999. Photodynamic properties of green fluorescent proteins investigated by fluorescence correlation spectroscopy. *Chem Phys* **250**:171–186.
82. Widengren J, Schwille P. 2000. Characterization of photoinduced isomerization and back-isomerization of the cyanine dye Cy5 by fluorescence correlation spectroscopy. *J Phys Chem A* **104**:6416–6428.
83. Widengren J, Rigler R. 1997. An alternative way of monitoring ion concentrations and their regulation using fluorescence correlation spectroscopy. *J Fluoresc* **7**(1):2118–2135.
84. Malvezzi-Campeggi F, Jahnz M, Heinze KG, Dittrich P, Schwille P. 2001. Light-induced flickering of DsRed provides evidence for distinct and interconvertible fluorescent states. *Biophys J* **81**:1776–1785.
85. Jung G, Mais S, Zumbusch A, Bräuchle C. 2000. The role of dark states in the photodynamics of the green fluorescent protein examined with two-color fluorescence excitation spectroscopy. *J Phys Chem* **104**(5):873–877.
86. Haupt U, Maiti S, Schwille P, Webb WW. 1998. Dynamics of fluorescence fluctuations in green fluorescent protein observed by fluorescence correlation spectroscopy. *Proc Natl Acad Sci USA* **95**:13573–13578.
87. Qian H, Elson EL. 1990. Distribution of molecular aggregation by analysis of fluctuation moments. *Proc Natl Acad Sci USA* **87**:5479–5483.
88. Müller JD, Chen Y, Gratton E. 2001. Photon counting histogram statistics. In *Fluorescence correlation spectroscopy: theory and applications*, pp. 410–437. Ed R Rigler, ES Elson. Springer, New York.
89. Kask P, Palo K, Ullmann D, Gall K. 1999. Fluorescence-intensity distribution analysis and its application in biomolecular detection technology. *Proc Natl Acad Sci USA* **96**:13756–13761.
90. Kask P, Palo K, Fay N, Brand L, Mets Ü, Ullmann D, Jungmann J, Pschorr J, Gall K. 2000. Two-dimensional fluorescence intensity distribution analysis: theory and application. *Biophys J* **78**:1703–1713.
91. Chen Y, Müller J, So PTC, Gratton E. 1999. The photon counting histogram in fluorescence fluctuation spectroscopy. *Biophys J* **77**:553–567.
92. Müller JD, Chen Y, Gratton E. 2000. Resolving heterogeneity on the single molecule level with the photon-counting histogram. *Biophys J* **78**:474–486.
93. Haupt U, Rüdiger M, Ashman S, Turconi S, Bingham R, Wharton C, Hutchinson J, Carey C, Moore KJ, Pope AJ. 2003. Single-molecule detection technologies in miniaturized high-throughput screening: fluorescence intensity distribution analysis. *J Biomol Screening* **8**(1):19–33.
94. Chen Y, Müller JD, Ruan Q-Q, Gratton E. 2002. Molecular brightness characterization of EGFP in vivo by fluorescence fluctuation spectroscopy. *Biophys J* **82**:133–144.
95. Laurence TA, Kapanidis AN, Kong X, Chemia DS, Weiss S. 2004. Photon arrival-time interval distribution (PAID): a novel tool for analyzing molecular interactions. *J Phys Chem B* **108**:3051–3067.
96. Chen Y, Wei L-N, Müller JD. 2003. Probing protein oligomerization in living cells with fluorescence fluctuation spectroscopy. *Proc Natl Acad Sci USA* **100**(26):15492–15497.
97. Kask P, Egeling C, Palo K, Mets Ü, Cole M, Gall K. 2002. Fluorescence intensity distribution analysis (FIDA) and related fluorescence fluctuation techniques: theory and practice. In *Fluorescence spectroscopy, imaging and probes. New tools in chemical, physical*

- and life sciences*, pp. 152–181. Ed R Kraayenhof, AJWG Visser, HC Gerritsen. Springer, New York.
98. Lamb DC, Schenk A, Rocker C, Scalfi-Happ C, Nienhaus GU. 2000. Sensitivity enhancement in fluorescence correlation spectroscopy of multiple species using time-gated detection. *Biophys J* **79**:1129–1138.
  99. Palo K, Brand L, Eggeling C, Jager S, Kask P, Gall K. 2002. Fluorescence intensity and lifetime distribution analysis: toward higher accuracy in fluorescence fluctuation spectroscopy. *Biophys J* **83**: 605–618.
  100. Bohmer M, Wahl M, Rahn HJ, Erdmann R, Enderlein J. 2002. Time-resolved fluorescence correlation spectroscopy. *Chem Phys Lett* **353**: 439–445.
  101. Enderlein J, Erdmann R. 1997. Fast fitting of multi-exponential decay curves. *Opt Commun* **134**:371–378.
  102. Chattopadhyay K, Saffarian S, Elson EL, Frieden C. 2002. Measurement of microsecond dynamic motion in the intestinal fatty acid binding protein by using fluorescence correlation spectroscopy. *Proc Natl Acad Sci USA* **99**(22):14171–14176.
  103. Lumma D, Keller S, Vilgis T, Rädler JO. 2003. Dynamics of large semiflexible chains probed by fluorescence correlation spectroscopy. *Phys Rev Lett* **90**(21):218301-1–218301-4.
  104. Borejdo J, Putnam S, Morales MF. 1979. Fluctuations in polarized fluorescence: evidence that muscle cross bridges rotate repetitively during contraction. *Proc Natl Acad Sci USA* **76**(12):6346–6350.
  105. Altan-Bonnet G, Libchaber A, Krichevsky O. 2003. Bubble dynamics in double-stranded DNA. *Phys Rev Lett* **90**(13):138101-1–138101-4
  106. Edman L, Rigler R. 2000. Memory landscapes of single-enzyme molecules. *Proc Natl Acad Sci USA* **97**(15):8266–8271.
  107. Wallace MI, Ying L, Balasubramanian S, Klenerman D. 2000. FRET fluctuation spectroscopy: exploring the conformational dynamics of a DNA hairpin loop. *J Phys Chem B* **104**:11551–11555.
  108. Bonnet G, Krichevsky O, Libchaber A. 1998. Kinetics of conformational fluctuations in DNA hairpin-loops. *Proc Natl Acad Sci USA* **95**:8602–8606.
  109. Thompson NL, Burghardt TP, Axelrod D. 1981. Measuring surface dynamics of biomolecules by total internal reflection fluorescence with photobleaching recovery or correlation spectroscopy. *Biophys J* **33**:435–455.
  110. Starr TE, Thompson NL. 2001. Total internal reflection with fluorescence correlation spectroscopy combined surface reaction and solution diffusion. *Biophys J* **80**:1575–1584.
  111. Lieto AM, Cush RC, Thompson NL. 2003. Ligand-receptor kinetics measured by total internal reflection with fluorescence correlation spectroscopy. *Biophys J* **85**:3294–3302.
  112. Starr TE, Thompson NL. 2002. Local diffusion and concentration of IgG near planar membranes: Measurement by total internal reflection with fluorescence correlation spectroscopy. *J Phys Chem B* **106**:2365–2371.
  113. Hansen RL, Harris JM. 1998. Total internal reflection fluorescence correlation spectroscopy for counting molecules at solid/liquid interfaces. *Anal Chem* **70**:2565–2575.
  114. Hansen RL, Harris JM. 1998. Measuring reversible adsorption kinetics of small molecules at solid/liquid interfaces by total internal reflection fluorescence correlation spectroscopy. *Anal Chem* **70**: 4247–4256.
  115. McCain KS, Harris JM. 2003. Total internal reflection fluorescence-correlation spectroscopy study of molecular transport in thin sol-gel films. *Anal Chem* **75**:3616–3624.
  116. Guiot E, Enescu M, Arrio B, Johannin G, Roger G, Tosti S, Tfibel F, Mérola F, Brun A, Georges P, Fontaine-Aupart MP. 2000. Molecular dynamics of biological probes by fluorescence correlation microscopy with two-photon excitation. *J Fluoresc* **10**(4):413–419.
  117. Chen Y, Müller JD, Eid JS, Gratton E. 2001. Two-photon fluorescence fluctuation spectroscopy. In *New trends in fluorescence spectroscopy: applications to chemical and life sciences*, pp. 277–296. Ed B Valeur, JC Brochon. Springer, New York.
  118. Chirico G, Fumagalli C, Baldini G. 2002. Trapped brownian motion in single- and two-photon excitation fluorescence correlation experiments. *J Phys Chem B* **106**:2508–2519.
  119. Heinze KG, Koltermann A, Schwille P. 2000. Simultaneous two-photon excitation of distinct labels for dual-color fluorescence cross-correlation analysis. *Proc Natl Acad Sci USA* **97**(19):10377–10382.
  120. Alexandrakis G, Brown EB, Tong RT, McKee TD, Campbell RB, Boucher Y, Jain RK. 2004. Two-photon fluorescence correlation microscopy reveals the two-phase nature of transport in tumors. *Nature Med* **10**(2):203–207.
  121. Clamme JP, Azoulay J, Mely Y. 2003. Monitoring of the formation and dissociation of polyethylenimine/DNA complexes by two photon fluorescence correlation spectroscopy. *Biophys J* **84**:1960–1968.
  122. Ruan Q, Chen Y, Gratton E, Glaser M, Mantulin WM. 2002. Cellular characterization of adenylate kinase and its isoform: Two-photon excitation fluorescence imaging and fluorescence correlation spectroscopy. *Biophys J* **83**:3177–3187.
  123. Rigler R, Foldes-Papp Z, Franz-Josef MA, Sammet C, Volcker M, Schnetz A. 1998. Fluorescence cross-correlation: a new concept for polymerase chain reaction. *J Biotechnol* **63**:97–109.
  124. Schwille P, Franz-Josef MA, Rigler R. 1997. Dual-color fluorescence cross-correlation spectroscopy for multicomponent diffusional analysis in solution. *Biophys J* **72**:1878–1886.
  125. Rabach M, Kettling U, Koltermann A, Eigen M. 2001. Dual-color fluorescence cross-correlation spectroscopy for monitoring the kinetics of enzyme-catalyzed reactions. *Methods* **24**:104–116.
  126. Kettling U, Koltermann A, Schwille P, Eigen M. 1998. Real-time enzyme kinetics monitored by dual-color fluorescence cross-correlation spectroscopy. *Proc Natl Acad Sci USA* **95**:1416–1420.
  127. Koltermann A, Kettling U, Stephan J, Winkler T, Eigen M. 2001. Dual-color confocal fluorescence spectroscopy and its application in biotechnology. In *Fluorescence correlation spectroscopy: theory and applications*, pp. 187–203. Ed R Rigler, ES Elson. Springer, New York.
  128. Bacia K, Schwille P. 2003. A dynamic view of cellular processes by *in vivo* fluorescence auto- and cross-correlation spectroscopy. *Methods* **29**:74–85.
  129. Jankowski T, Janka R. 2001. ConfoCor 2—the second generation of fluorescence correlation microscopes. In *Fluorescence correlation spectroscopy: theory and applications*, pp. 331–345. Ed R Rigler, ES Elson. Springer, New York.

130. Qian H, Elson EL. 2004. Fluorescence correlation spectroscopy with high-order and dual color correlation to probe nonequilibrium steady states. *Proc Natl Acad Sci USA* **101**(9):2828–2833.
131. Schwille P. 2001. Cross-correlation analysis in FCS. In *Fluorescence correlation spectroscopy: theory and applications*, pp. 360–378. Ed R Rigler, ES Elson. Springer, New York.
132. Heinze KG, Koltermann A, Schwille P. 2000. Simultaneous two-photon excitation of distinct labels for dual-color fluorescence cross-correlation analysis. *Proc Natl Acad Sci USA* **97**(19):10377–10382.
133. Koltermann A, Kettling U, Bieschke J, Winkler T, Eigen M. 1998. Rapid assay processing by integration of dual-color fluorescence cross-correlation spectroscopy: high-throughput screening for enzyme activity. *Proc Natl Acad Sci USA* **95**:1421–1426.
134. Lucas B, Van Rompaey E, De Smedt SC, Demeester J. 2002. Dual-color fluorescence fluctuation spectroscopy to study the complexation between poly-L-lysine and oligonucleotides. *Macromolecules* **35**:8152–8160.
135. Bieschke J, Schwille P. 1998. Aggregation of prion protein investigated by dual-color fluorescence cross-correlation spectroscopy. In *Fluorescence microscopy and fluorescent probes*, Vol. 2, pp. 81–86. Ed J Slavik. Plenum Press, New York.
136. Rippe K. 2000. Simultaneous binding of two DNA duplexes to the NtrC-enhancer complex studied by two-color fluorescence cross-correlation spectroscopy. *Biochemistry* **39**(9):2131–2139.
137. Korn K, Gardellin P, Liao B, Amacker M, Bergstrom A, Bjorkman H, Camacho A, Dorhofer S, Dorre K, Enstrom J, Ericson T, Favez T, Gosch M, Honegger A, Jaccoud S, Lapczyna M, Litborn E, Thyberg P, Winter H, Rigler R. 2003. Gene expression analysis using single molecule detection. *Nucleic Acids Res* **31**(16):e89.
138. Riesner D. 2001. Protein aggregation associated with Alzheimer and prion diseases. In *Fluorescence correlation spectroscopy: theory and applications*, pp. 225–247. Ed R Rigler, ES Elson. Springer, New York.
139. Bieschke J, Schwille P. 1998. Aggregation of prion protein investigated by dual-color fluorescence cross-correlation spectroscopy. In *Fluorescence microscopy and fluorescent probes*, Vol. 2. Ed J Slavik. Plenum Press, New York, 27.
140. Berland KM. 2004. Detection of specific DNA sequences using dual-color two-photon fluorescence correlation spectroscopy. *J Biotechnol* **108**(2):127–136.
141. Winter H, Korn K, Rigler R. 2004. Direct gene expression analysis. *Curr Pharm Biotechnol* **5**(2):191–197.
142. Foldes-Papp Z, Kinjo M, Saito K, Kii H, Takagi T, Tamura M, Costa JM, Birch-Hirschfeld E, Demel U, Thyberg P, Tilz GP. 2003. C677T single nucleotide polymorphisms of the human methylene tetrahydrofolate reductase and specific identification: a novel strategy using two-color cross-correlation fluorescence spectroscopy. *Mol Diagn* **7**(2):99–111.
143. Castro A, Williams JGK. 1997. Single-molecule detection of specific nucleic acid sequences in unamplified genomic DNA. *Anal Chem* **69**:3915–3920.
144. Winkler T, Kettling U, Koltermann A, Eigen M. 1999. Confocal fluorescence coincidence analysis: an approach to ultra high-throughput screening. *Proc Natl Acad Sci USA* **96**:1375–1378.
145. Heinze KG, Rabach M, Jahnz M, Schwille P. 2002. Two-photon fluorescence coincidence analysis: rapid measurements of enzyme kinetics. *Biophys J* **83**:1671–1681.
146. Li H, Ying L, Green JJ, Balasubramanian S, Kleinerman D. 2003. Ultrasensitive coincidence fluorescence detection of single DNA molecules. *Anal Chem* **75**:1664–1670.
147. Weston KD, Dyck M, Tinnefeld P, Müller C, Herten DP, Sauer M. 2002. Measuring the number of independent emitters in single-molecule fluorescence images and trajectories using coincident photons. *Anal Chem* **74**:5342–5349.
148. Ehrenberg M, Rigler R. 1974. Rotational brownian motion and fluorescence intensity fluctuations. *Chem Phys* **4**:390–401.
149. Kask P, Piksarv P, Pooga M, Mets Ü, Lippmaa E. 1989. Separation of the rotational contribution in fluorescence correlation experiments. *Biophys J* **55**:213–220.
150. Ehrenberg M, Rigler R. 1976. Fluorescence correlation spectroscopy applied to rotational diffusion of macromolecules. *Q Rev Biophys* **9**(1):69–81.
151. Mets Ü. 2001. Antibunching and rotational diffusion in FCS. In *Fluorescence correlation spectroscopy: theory and applications*, pp. 346–359. Ed R Rigler, ES Elson. Springer, New York.
152. Kask P, Piksarv P, Mets Ü, Pooga M, Lippmaa E. 1987. Fluorescence correlation spectroscopy in the nanosecond time range: rotational diffusion of bovine carbonic anhydrase B. *Eur Biophys J* **14**:257–261.
153. Davidovich L. 1996. Sub-poissonian processes in quantum optics. *Rev Mod Phys* **68**(1):127–173.
154. Kask P, Piksarv P, Mets Ü. 1985. Fluorescence correlation spectroscopy in the nanosecond time range: photon antibunching in dye fluorescence. *Eur Biophys J* **12**:163–166.
155. Basché Th, Moerner WE. 1992. Photon antibunching in the fluorescence of a single dye molecule trapped in a solid. *Phys Rev Lett* **69**(10):1516–1519.
156. Magde D, Webb WW, Elson EL. 1978. Fluorescence correlation spectroscopy: uniform translation and laminar flow. *Biopolymers* **17**:361–376.
157. Van Orden A, Keller RA. 1998. Fluorescence correlation spectroscopy for rapid multicomponent analysis in a capillary electrophoresis system. *Anal Chem* **70**(21):4463–4471.
158. Brinkmeier M, Dorre K, Stephan J, Eigen M. 1999. Two-beam cross-correlation: a method to characterize transport phenomena in micrometer-sized structures. *Anal Chem* **71**:609–616.
159. Gosch M, Blom H, Holm J, Heino T, Rigler R. 2000. Hydrodynamic flow profiling in microchannel structures by single molecule fluorescence correlation spectroscopy. *Anal Chem* **72**:3260–3265.
160. Lenne PF, Colombo D, Giovannini H, Rigneault H. 2002. Flow profiles and directionality in microcapillaries measured by fluorescence correlation spectroscopy. *Single Mol* **3**:194–200.
161. Kunst BH, Schots A, Visser AJWG. 2002. Detection of flowing fluorescent particles in a microcapillary using fluorescence correlation spectroscopy. *Anal Chem* **74**:5350–5357.
162. Dittrich PS, Schwille P. 2002. Spatial two-photon fluorescence cross-correlation spectroscopy for controlling molecular transport in microfluidic structures. *Anal Chem* **74**:4472–4479.

## ADDITIONAL REFERENCES TO FCS AND ITS APPLICATIONS

### Binding Reactions

- Daniel DC, Thompson M, Woodbury NW. 2002. DNA-binding interactions and conformational fluctuations with single molecule fluorescence spectroscopy. *Biophys J* **82**:1654–1666.
- Foldes-Papp Z, Demel U, Tilz GP. 2002. Detection of single molecules: solution-phase single-molecule fluorescence correlation spectroscopy as an ultrasensitive, rapid and reliable system for immunological investigation. *J Immunol Methods* **260**:117–124.
- Kral T, Langner M, Benes M, Baczyńska D, Ugorski M, Hof M. 2002. The application of fluorescence correlation spectroscopy in detecting DNA condensation. *Biophys Chem* **95**:135–144.
- Krouglova T, Amayed P, Engelborghs Y, Carlier M-F. 2003. Fluorescence correlation spectroscopy analysis of the dynamics of tubulin interaction with RB3, a stathmin family protein. *FEBS Lett* **546**:365–368.
- Nishimura G, Kinjo M. 2004. Systematic error in fluorescence correlation measurements identified by a simple saturation model of fluorescence. *Anal Chem* **76**:1963–1970.
- Sanchez SA, Brunet JE, Jameson DM, Lagos R, Monasterio O. 2004. Tubulin equilibrium unfolding followed by time-resolved fluorescence correlation spectroscopy. *Protein Sci* **13**:81–88.
- Schubert F, Zettl H, Hafner W, Krauss G, Krausch G. 2003. Comparative thermodynamic analysis of DNA-protein interactions using surface plasmon resonance and fluorescence correlation spectroscopy. *Biochemistry* **42**:10288–10294.
- Vercammen J, Maertens G, Gerard M, Clercq ED, Debyser Z, Endelborghs Y. 2002. DNA-induced polymerization of HIV-1 integrase analyzed with fluorescence fluctuation spectroscopy. *J Biol Chem* **277**(41):38045–38052.
- Wolcke J, Reimann M, Klumpp M, Gohler T, Kim E, Deppert W. 2003. Analysis of p53 "latency" and "activation" by fluorescence correlation spectroscopy. *J Biol Chem* **278**(35):32587–32595.
- Zettl H, Hafner W, Boker A, Schmalz H, Lanzendorfer M, Muller AHE, Krausch G. 2004. Fluorescence correlation spectroscopy of single dye-labeled polymers in organic solvents. *Macromolecules* **37**:1917–1920.

### Classics

- Aragón SR, Pecora R. 1976. Fluorescence correlation spectroscopy as a probe of molecular dynamics. *J Chem Phys* **64**:1791–1803.
- Koppel DE, Axelrod D, Schléssinger J, Elson EL, Webb WW. 1976. Dynamics of fluorescence marker concentration as a probe of mobility. *Biophys J* **16**:1315–1329.

### Data Analysis

- Brock R, Hink MA, Jovin TM. 1998. Fluorescence correlation microscopy of cells in the presence of autofluorescence. *Biophys J* **75**:2547–2557.
- Koppel DE. 1974. Statistical accuracy in fluorescence correlation spectroscopy. *Phys Rev A* **10**(6):1938–1945.
- Meseth U, Wohland T, Rigler R, Vogel H. 1999. Resolution of fluorescence correlation measurements. *Biophys J* **76**:1619–1631.

- Nishimura G, Kinjo M. 2004. Systematic error in fluorescence correlation measurements identified by a simple saturation model of fluorescence. *Anal Chem* **76**:1963–1970.
- Perroud TD, Huang B, Wallace MI, Zare RN. 2003. Photon counting histogram for one-photon excitation. *ChemPhysChem* **4**:1121–1123.
- Saffarian S, Elson EL. 2003. Statistical analysis of fluorescence correlation spectroscopy: the standard deviation and bias. *Biophys J* **84**:2030–2042.
- Sengupta P, Garai K, Balaji J, Periasamy N, Maiti S. 2003. Measuring size distribution in highly heterogeneous systems with fluorescence correlation spectroscopy. *Biophys J* **84**:1977–1984.
- Van Craenenbroeck E, Matthys G, Beirlant J, Engelborghs Y. 1999. A statistical analysis of fluorescence correlation data. *J Fluoresc* **9**(4):325–331.
- Wahl M, Gregor I, Patting M, Enderlein J. 2003. Fast calculation of fluorescence correlation data with asynchronous time-correlated single-photon counting. *Opt Express* **11**(26):3583–3591

### DNA Applications

- Scalettar BA, Hearst JE, Klein MP. 1989. FRAP and FCS studies of self-diffusion and mutual diffusion in entangled DNA solutions. *Macromolecules* **22**:4550–4559.
- Lucas B, Remaut K, Braeckmans K, Haustraete J, Smedt SC, Demeester J. 2004. Studying pegylated DNA complexes by dual color fluorescence fluctuation spectroscopy. *Macromolecules* **37**:3832–3840.

### Dual Color

- Berland KM. 2004. Detection of specific DNA sequences using dual-color two-photon fluorescence correlation spectroscopy. *J Biotechnol* **108**:127–136.
- Koltermann A, Kettling U, Stephan J, Rarbach M, Winkler T, Eigen M. 2001. Applications of dual-color confocal fluorescence spectroscopy in biotechnology. In *Single molecule spectroscopy*. Ed R Rigler, M Orrit, T Basché. Springer, New York.

### Image Correlation Spectroscopy

- Huang Z, Thompson NL. 1996. Imaging fluorescence correlation spectroscopy: nonuniform IgE distributions on planar membranes. *Biophys J* **70**:2001–2007.
- Palmer AG, Thompson NL. 1989. Optical spatial intensity profiles for high order autocorrelation in fluorescence spectroscopy. *Appl Opt* **28**(6):1214–1220.
- Petersen NO, Brown C, Kaminski A, Rocheleau J, Srivastava M, Wiseman PW. 1998. Analysis of membrane protein cluster densities and sizes in situ by image correlation spectroscopy. *Faraday Discuss* **111**:289–305.
- Petersen NO, Hoddelius PL, Wiseman PW, Seger O, Magnusson KE. 1993. Quantitation of membrane receptor distributions by image correlation spectroscopy: concept and application. *Biophys J* **65**:1135–1146.
- Vanden Broek W, Huang Z, Thompson NL. 1999. High-order autocorrelation with imaging fluorescence correlation spectroscopy: application to IgE on supported planar membranes. *J Fluoresc* **9**(4):313–324.
- Wiseman PW, Petersen NO. 1999. Image correlation spectroscopy: optimization for ultrasensitive detection of preexisting platelet-derived

growth factor- $\beta$  receptor oligomers on intact cells. *Biophys J* **76**: 963–977.

### Instrumentation

- Lamb DC, Schenk A, Rocker C, Scalfi-Happ C, Nienhaus GU. 2000. Sensitivity enhancement in fluorescence correlation spectroscopy of multiple species using time-gated detection. *Biophys J* **79**:1129–1138.
- Mukhopadhyay A, Zhao J, Bae SC, Granick S. 2003. An integrated platform for surface forces measurements and fluorescence correlation spectroscopy. *Rev Sci Instrum* **74**(6):3067–3072.
- Ruckstuhl T, Seeger S. 2004. Attoliter detection volumes by confocal total-internal-reflection fluorescence microscopy. *Opt Lett* **29**(6):569–571.
- Sorscher SM, Klein MP. 1980. Profile of a focused collimated laser beam near the focal minimum characterized by fluorescence correlation spectroscopy. *Rev Sci Instrum* **51**(1):98–102.

### Intracellular

- Braun K, Peschke P, Pipkorn R, Lampel S, Wachsmuth M, Waldeck W, Friedrich E, Debus J. 2002. A biological transporter for the delivery of peptide nucleic acids (PNAs) to the nuclear compartment of living cells. *J Mol Biol* **318**:237–343.
- Brock R, Jovin TM. 1998. Fluorescence correlation microscopy (FCM)–fluorescence correlation spectroscopy (FCS) taken into the cell. *Cell Mol Biol* **44**(5):847–856.
- Brock R, Vamosi G, Vereb G, Jovin TM. 1999. Rapid characterization of green fluorescent protein fusion proteins on the molecular and cellular level by fluorescence correlation spectroscopy. *Proc Natl Acad Sci USA* **96**:10123–10128.
- Politz JC, Browne ES, Wolf DE, Pederson T. 1998. Intranuclear diffusion and hybridization state of oligonucleotides measured by fluorescence correlation spectroscopy. *Proc Natl Acad Sci USA* **95**:6043–6048.
- Wachsmuth M, Weidemann T, Muller G, Hoffmann-Rohrer UW, Knoch TA, Waldeck W, Langowski J. 2003. Analyzing intracellular binding and diffusion with continuous fluorescence photobleaching. *Biophys J* **84**:3353–3363.
- Wang Z, Shah JV, Chen Z, Sun C, Berns MW. 2004. Fluorescence correlation spectroscopy investigation of a GFP mutant-enhanced cyan fluorescent protein and its tubulin fusion in living cells with two-photon excitation. *J Biomed Opt* **9**(2):395–403.

### Kinetics

- Bismuto E, Gratton E, Lamb DC. 2001. Dynamics of ANS binding to tuna apomyoglobin measured with fluorescence correlation spectroscopy. *Biophys J* **81**:3510–3521.
- Rigler R, Edman L, Földes-Papp Z, Wennmalm S. 2001. Fluorescence correlation spectroscopy in single-molecule analysis: enzymatic catalysis at the single molecule level in *Single molecule spectroscopy*. Ed R Rigler, M Orrit, T Basché. Springer, New York.
- Widengren J, Dapprich J, Rigler R. 1997. Fast interactions between Rh6G and dGTP in water studied by fluorescence correlation spectroscopy. *Chem Phys* **216**:417–426.

### Membranes

- Briddon SJ, Middleton RJ, Yates AS, George MW, Kellam B, Hill SJ. 2004. Application of fluorescence correlation spectroscopy to the measurement of agonist binding to a G-protein coupled receptor at the single cell level. *Faraday Discuss* **126**:197–207.
- Fahey PF, Koppel DE, Barak LS, Wolf DE, Elson EL, Webb WW. 1977. Lateral diffusion in planar lipid bilayers. *Science* **195**:305–306.
- Fahey PF, Webb WW. 1978. Lateral diffusion in phospholipid bilayer membranes and multilamellar liquid crystals. *Biochemistry* **17**: 3046–3053.
- Palmer III AG, Thompson NL. 1989. Fluorescence correlation spectroscopy for detecting submicroscopic clusters of fluorescent molecules in membranes. *Chem Phys Lipids* **50**:253–270.

### Moments and Higher Orders

- Palmer III AG, Thompson NL. 1987. Molecular aggregation characterized by high order autocorrelation in fluorescence correlation spectroscopy. *Biophys J* **52**:257–270.
- Palmer III AG, Thompson NL. 1989. Optical spatial intensity profiles for high-order autocorrelation in fluorescence spectroscopy. *Appl Opt* **28**(6):1214–1220.
- Palmer III AG, Thompson NL. 1989. High-order fluorescence fluctuation analysis of model protein clusters. *Proc Natl Acad Sci USA* **86**: 6148–6152.
- Palmer III AG, Thompson NL. 1989. Intensity dependence of high-order autocorrelation functions in fluorescence correlation spectroscopy. *Rev Sci Instrum* **60**(4):624–633.
- Qian H, Elson EL. 2004. Fluorescence correlation spectroscopy with high-order and dual-color correlation to probe nonequilibrium steady states. *Proc Natl Acad Sci USA* **101**(9):2828–2833.
- Qian H, Elson EL. 1990. On the analysis of high order moments of fluorescence fluctuations. *Biophys J* **57**:375–380.

### Novel Methods

- Eggeling C, Berger S, Brand L, Fries JR, Schaffer J, Volkmer A, Seidel CAM. 2001. Data registration and selective single-molecule analysis using multi-parameter fluorescence detection. *J Biotechnol* **86**:163–180.
- Hansen RL, Zhu XR, Harris JM. 1998. Fluorescence correlation spectroscopy with patterned photoexcitation for measuring solution diffusion coefficients of robust fluorophores. *Anal Chem* **70**:1281–1287.
- Lenne P-F, Etienne E, Rigneault H. 2003. Subwavelength patterns and high detection efficiency in fluorescence correlation spectroscopy using photonic structures. *Appl Phys Lett* **80**(22):4106–4108.
- Levene MJ, Korlach J, Turner SW, Foquet M, Craighead HG, Webb WW. 2003. Zero-mode waveguides for single-molecule analysis at high concentrations. *Science* **299**:682–686.
- Muller JD, Gratton E. 2003. High-pressure fluorescence spectroscopy. *Biophys J* **85**:2711–2719.
- Rigneault H, Lenne P-F. 2003. Fluorescence correlation spectroscopy on a mirror. *J Opt Soc Am B* **20**(10):2203–2214.

Sonehara T, Kojima K, Irie T. 2002. Fluorescence correlation spectroscopy excited with a stationary interference pattern for capillary electrophoresis. *Anal Chem* **74**:5121–5131.

### Photon Counting Histograms

- Chirico G, Olivini F, Beretta S. 2000. Fluorescence excitation volume in two-photon microscopy by autocorrelation spectroscopy and photon counting histogram. *Appl Spectrosc* **54**(7):1084–1090.
- Hillesheim LN, Müller JD. 2003. The photon counting histogram in fluorescence fluctuation spectroscopy with non-ideal photodetectors. *Biophys J* **85**:1948–1958.

### Proteins and FCS

- Chattopadhyay K, Saffarian S, Elson EL, Frieden C. 2002. Measurement of microsecond dynamic motion in the intestinal fatty acid binding protein by using fluorescence correlation spectroscopy. *Proc Natl Acad Sci USA* **99**(22):14171–14176.
- Lippitz M, Erker W, Decker H, Van Holde KE, Basché T. 2002. Two-photon excitation microscopy of tryptophan-containing proteins. *Proc Natl Acad Sci USA* **99**:2772–2777.

### Polymers and FCS

- Sukhishvili SA, Chen Y, Müller JD, Gratton E, Schweizer KS, Granick S. 2000. Diffusion of a polymer "pancake." *Nature* **406**:146.

### Resonance Energy Transfer

- Hom EFY, Verkman AS. 2002. Analysis of coupled bimolecular reaction kinetics and diffusion by two-color fluorescence correlation spectroscopy: enhanced resolution of kinetics by resonance energy transfer. *Biophys J* **83**:533–545.
- Katiliene Z, Katilius E, Woodbury NW. 2003. Single molecule detection of DNA looping by *NgoMIV* restriction endonuclease. *Biophys J* **84**:4053–4061.
- Margittai M, Widengren J, Schweinberger E, Schroder GF, Felekyan S, Haustein E, Konig M, Fasshauer D, Grubmuller H, Jahn R, Seidel CAM. 2003. Single-molecule fluorescence resonance energy transfer reveals a dynamic equilibrium between closed and open conformations of syntaxin. *Proc Natl Acad Sci USA* **100**(26):15516–15521.
- Talaga DS, Leung Lau W, Roder H, Tang J, Jia Y, DeGrado WF, Hochstrasser RM. 2000. Dynamics and folding of single two-stranded coiled-coil peptides studied by fluorescent energy transfer confocal microscopy. *Proc Natl Acad Sci USA* **97**(24):13021–13026.
- Widengren J, Schweinberger E, Berger S, Seidel CAM. 2001. Two new concepts to measure fluorescence resonance energy transfer via fluorescence correlation spectroscopy: theory and experimental realizations. *J Phys Chem A* **105**:6851–6866.

### Scanning FCS

- Koppel DE, Morgan F, Cowan AE, Carson JH. 1994. Scanning concentration correlation spectroscopy using the confocal laser microscope. *Biophys J* **66**:502–507.

Palmer III AG, Thompson NL. 1987. Theory of sample translation in fluorescence correlation spectroscopy. *Biophys J* **51**:339–343.

Petersen NO. 1986. Scanning fluorescence correlation spectroscopy: theory and simulation of aggregation measurements. *Biophys J* **49**:809–815.

Petersen NO, Johnson DC, Schlesinger MJ. 1986. Scanning fluorescence correlation spectroscopy: application to virus glycoprotein aggregation. *Biophys J* **49**:817–820.

### Reviews

- Valeur B, Brochon J-C., ed. 2001. *New trends in fluorescence spectroscopy: applications to chemical and life sciences*. Springer, New York.
- Webb WW. 2001. Fluorescence correlation spectroscopy: inception, biophysical experimentations, and prospectus. *Appl Opt* **40**(24):3969–3983.

### Theory of FCS

- Edman L. 2000. Theory of fluorescence correlation spectroscopy on single molecules. *J Phys Chem A* **104**:6165–6170.
- Enderlein J. 1996. Path integral approach to fluorescence correlation experiments. *Phys Lett A* **221**:427–433.
- Enderlein J, Gregor I, Patra D, Fitter J. 2004. Art and artifacts of fluorescence correlation spectroscopy. *Curr Pharm Biotechnol* **5**:155–161.
- Generich A, Schild D. 2000. Fluorescence correlation spectroscopy in small cytosolic compartments depends critically on the diffusion model used. *Biophys J* **79**:3294–3306.
- Hess ST, Webb WW. 2002. Focal volume optics and experimental artifacts in confocal fluorescence correlation spectroscopy. *Biophys J* **83**:2300–2317.
- Hoshikawa H, Asai H. 1985. On the rotational Brownian motion of a bacterial idle motor, II: theory of fluorescence correlation spectroscopy. *Biophys Chem* **22**:167–172.
- Qian H, Elson EL. 1991. Analysis of confocal laser-microscopy optics for 3-D fluorescence correlation spectroscopy. *Appl Opt* **30**(10):1185–1195.
- Scalettar BA, Klein MP, Hearst JE. 1987. A theoretical study of the effects of driven motion on rotational correlations of biological systems. *Biopolymers* **26**:1287–1299.
- Starchev K, Zhang J, Buffle J. 1998. Applications of fluorescence correlation spectroscopy-particle size effect. *J Colloid Interface Sci* **203**:189–196.

### Total Internal Reflection

- Thompson NL, Axelrod D. 1983. Immunoglobulin surface-binding kinetics studied by total internal reflection with fluorescence correlation spectroscopy. *Biophys J* **43**:103–114.
- Thompson NL, Pearce KH, Hsieh HV. 1993. Total internal reflection fluorescence microscopy: application to substrate-supported planar membranes. *Eur Biophys J* **22**:367–378.
- Thompson NL, Lagerholm BC. 1997. Total internal reflection fluorescence: applications in cellular biophysics. *Curr Opin Biotechnol* **8**:58–64.

## PROBLEMS

- P24.1. Figure 24.8 shows autocorrelation curves for several concentrations of R6G. Assume these concentrations are correct. What is the effective volume ( $V_{\text{eff}}$ ) of the sample? Assume the ratio for the ellipsoidal volume is  $\mu/\text{s} = 4.0$ . What are the dimensions of the ellipsoid?
- P24.2. Figure 24.10 shows the autocorrelation function for labeled  $\alpha$ -lactalbumin (14,000 daltons) in the absence and presence of GroEL (840,000 daltons). Is the change in diffusion time consistent with complete binding of  $\alpha$ -lactalbumin to GroEL?
- P24.3. Figure 24.21 shows autocorrelation functions for GUVs composed of DLPC or DLPC/DPFC (0.2/0.8). Assume the laser beam diameter is 1  $\mu\text{m}$ . Using the same diffusion coefficient, calculate the time it takes a Dil-C<sub>20</sub> molecule to diffuse 10  $\mu\text{m}$ . Suppose the beam diameter is increased to 2  $\mu\text{m}$ . How long does it take the molecule to diffuse 10  $\mu\text{m}$ ?
- P24.4. Figure 24.32 shows a correlation function for the opening and closing of a molecular beacon. Assume you have access to a steady-state fluorometer with control of the sample temperature. Suggest a way to separately determine the values of  $k_1$  and  $k_2$ .
- P24.5. Figure 24.33 shows a typical configuration for FCS using TIR. Suppose you wanted to measure diffusion coefficients near the interface, and the illuminated spot had a diameter of 5.0  $\mu\text{m}$ . Calculate the volume of the observed solution assuming  $d = 100$  nm. What concentration of fluorophore is needed to

obtain approximately 10 fluorophores in the volume?

Assume the volume contains a single phospholipid bilayer that contains all the probe molecules. What fraction of the lipids need to be labeled to obtain 10 fluorophores in the volume? The area occupied by a single phospholipid molecule is about 70  $\text{\AA}^2$ .

- P24.6. Figure 24.50 shows autocorrelation curves for tubulin with cryptophycin as the sample was diluted. Explain how these data can be used to determine if the complex dissociates upon dilution. Assume all the tubulin substrates contain the TMR label.

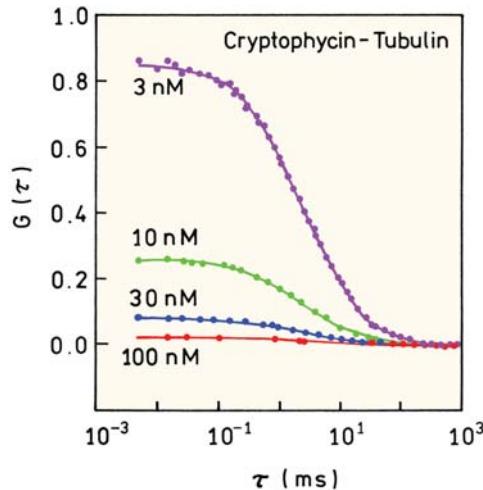


**Figure 24.50.** Effect of increasing concentrations of cryptophycin on labeled tubulin dimers. Revised and reprinted with permission from [38]. Copyright © 2003, American Chemical Society.

# 25

# Radiative Decay Engineering: Metal-Enhanced Fluorescence

In the preceding chapters we described the wide-ranging applications of fluorescence. All these applications relied upon the spontaneous emission of fluorophores in free space. By free space we mean optically transparent nonconducting media. In these final chapters we describe a new topic called radiative decay engineering (RDE). The term RDE is used because the environment around the fluorophore is modified or engineered to change the radiative decay rate of the fluorophore. In Chapter 1 we showed that the radiative decay rate ( $\Gamma$ ) is determined by the extinction coefficient of the fluorophore. Extinction coefficients do not change substantially in different environments. Similarly, the radiative rates remain nearly the same under most conditions. The changes in quantum yield or lifetime displayed by fluorophores in different environments are due to changes in the non-radiative decay rates.

In this chapter we describe the effects of conducting metallic silver particles on fluorescence. A fluorophore in the excited state has the properties of an oscillating dipole. The excited fluorophore can induce oscillations of the electrons in the metal. The electric field created by the metal can interact with the excited fluorophore and alter its emission. This interaction is almost certainly bidirectional so that light-induced oscillations in the metal can affect the fluorophore. The interactions of fluorophores with metallic surfaces can have a number of useful effects, including increased quantum yields, increased photostability, increased distances for resonance energy transfer, and decreased lifetimes. These changes can result in increased sensitivity, increased photostability, and decreased interference from unwanted background emission. These effects are called metal-enhanced fluorescence (MEF).

The mechanisms of metal-enhanced fluorescence are not yet completely understood, and the applications of MEF

are just beginning. Because of the potential importance of RDE and MEF we decided to include chapters on these topics. This is a new topic and the field is changing very rapidly. Hence this chapter represents a summary of the current knowledge in this field. RDE and MEF were developed in this laboratory, and as a result many of the examples are from our own work.

## 25.1. RADIATIVE DECAY ENGINEERING

Prior to describing the unusual effects of metal surfaces on fluorescence it is valuable to describe what we mean by RDE and in particular spectral changes expected for increased radiative decay rates.

### 25.1.1. Introduction to RDE

We typically perform fluorescence measurements in macroscopic solutions, or at least macroscopic in comparison with the size of a fluorophore. The solutions are typically transparent to the emitted radiation. There may be modest changes in refractive index, such as for a fluorophore in a membrane, but such changes have a relatively minor effect on the fluorescence spectral properties.<sup>1-2</sup> In such nearly homogeneous solutions, the fluorophores emit into free space and are observed in the far field. Local effects due to surfaces are not usually observed because of the small size of fluorophores relative to the experimental chamber. The spectral properties of a fluorophore in the excited state are well described by Maxwell's equations for an oscillating dipole radiating into free space and we detect the far-field radiation as light.

For clarity we note that we are not considering reflection of the emitted photons from the metal surfaces. Reflection occurs after emission. We are considering the effects of the nearby surface on altering the "free space" condition, and modifying Maxwell's equation from their free space counterparts.<sup>3-4</sup> Like a radiating antenna, a fluorophore is an oscillating dipole, but one that oscillates at high frequency and radiates short wavelengths. Nearby metal surfaces can respond to the oscillating dipole and modify the rate of emission and the spatial distribution of the radiated energy. The electric field felt by a fluorophore is affected by interactions of the incident light with the nearby metal surface and also by interaction of the fluorophore oscillating dipole with the metal surface. Additionally, the fluorophores oscillating dipole induces a field in the metal. These interactions can increase or decrease the field incident on the fluorophore and increase or decrease the radiative decay rate.

For simplicity we will refer to metallic particles as metals. At first glance it seems unusual to consider using metallic surfaces to enhance fluorescence. Metals are known to quench fluorescence. For example, silver surfaces 50 Å thick are used in microscopy to quench emission from regions near the metal.<sup>5</sup> We now know that metals can also enhance fluorescence by several mechanisms. The metal particles can cause increased rates of excitation due to a more concentrated electric field around the particle. Metals also appear to increase the rates of radiative decay ( $\Gamma$ ). We will describe the effects of metallic particles on fluorescence as if an increase in  $\Gamma$  is a known fact. However, the physics is complex and it is not always clear what is emitting the light: the fluorophore or the metal.

Prior to describing RDE in more detail it is informative to see a result. Figure 25.1 shows a photograph of a microscope slide that is coated with fluorescein-labeled human serum albumin. The left side of the slide has no metal. The right side of the slide is covered with silver particles. The fluorescein molecules near the metal particles are remarkably brighter. Similar effects have now been observed for many different fluorophores, showing that MEF is a general effect.

### 25.1.2. Jablonski Diagram for Metal-Enhanced Fluorescence

An increase in the radiative decay rate can have unusual effects on fluorophores.<sup>6</sup> These effects can be understood by considering a Jablonski diagram that includes MEF (Figure 25.2). For simplicity we will only consider radiative

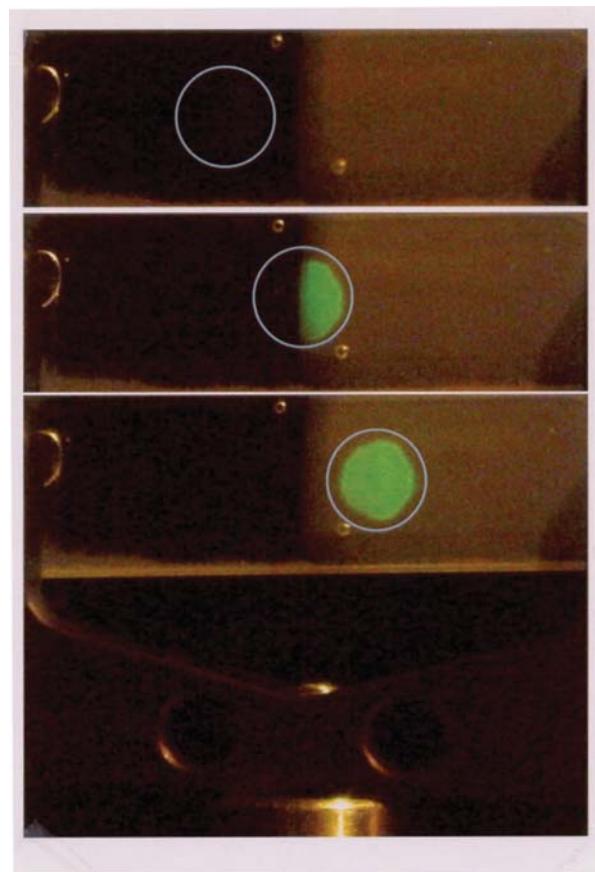


**Figure 25.1.** Effect of metallic silver particles on surface-bound fluorescein-labeled human serum albumin. Left, no silver; right, with silver particles.

decay ( $\Gamma$ ) and non-radiative decay ( $k_{nr}$ ). In the absence of metals the quantum yield and lifetimes are given by

$$Q_0 = \Gamma / (\Gamma + k_{nr}) \quad (25.1)$$

$$\tau_0 = (\Gamma + k_{nr})^{-1} \quad (25.2)$$

Since the radiative decay rate is nearly constant for any fluorophore the quantum yield can only be increased by decreasing the value of  $k_{nr}$ .

Now consider the effect of a metal. If the metal results in an increased rate of excitation ( $E + E_m$ ) this will result in increased brightness without changing the quantum yield or lifetime. This is a useful effect that can allow decreased incident intensities and decreased background. Metal-enhanced excitation can also result in selective excitation of fluorophores near the metal. Another possible effect is an increase in the radiative decay rate. In this case the quantum

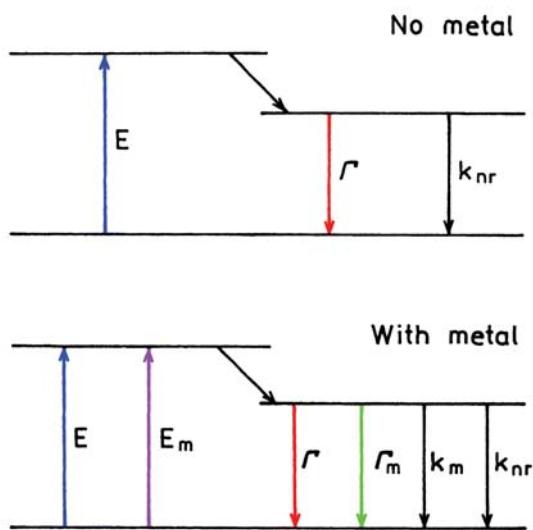


**Figure 25.2.** Jablonski diagram without (top) and with (bottom) the effects of near metal surfaces.  $E$  is the rate of excitation without metal.  $E_m$  is the additional excitation in the presence of metal [6].

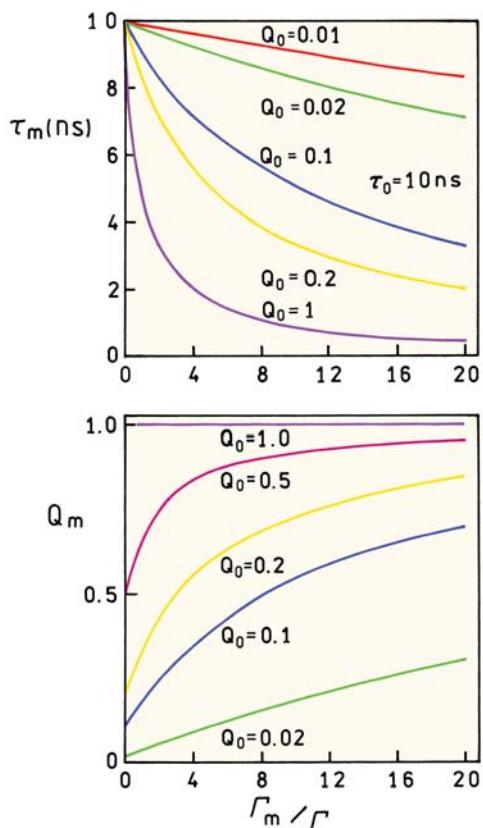


**Figure 25.3.** Effect of an increase in the metal-induced radiative rate on the lifetime and quantum yields of fluorophores. For  $Q = 0.5$ ,  $\Gamma = 5 \times 10^7/\text{s}$  and  $k_{\text{nr}} = 5 \times 10^7/\text{s}$ . For  $Q = 0.1$ ,  $\Gamma = 1 \times 10^7/\text{s}$  and  $k_{\text{nr}} = 9 \times 10^7/\text{s}$ . From [6].

yield and lifetime of the fluorophore near the metal surface are given by

$$Q_m = \frac{\Gamma + \Gamma_m}{\Gamma + \Gamma_m + k_{\text{nr}}} \quad (25.3)$$

$$\tau_m = (\Gamma + \Gamma_m + k_{\text{nr}})^{-1} \quad (25.4)$$

These equations result in unusual predictions for a fluorophore near a metal surface. As the value of  $\Gamma_m$  increases the quantum yield increases while the lifetime decreases.

The effects of increasing  $\Gamma_m$  are shown in Figure 25.3. The  $x$ -axis is the relative value between the radiative decay rate due to the metal ( $\Gamma_m$ ) and the rate in the absence of metal ( $\Gamma$ ). As  $\Gamma_m$  increases the lifetime decreases. A decrease in lifetime is usually associated with a decrease in quantum yield. However, this is because a decrease in lifetime is usually due to an increase in  $k_{\text{nr}}$ . When the total decay rate,  $\Gamma_T = \Gamma + \Gamma_m$ , increases the quantum yield increases. This increase occurs because more of the fluorophores emit before they can decay through the non-radiative pathway. The effect is larger for fluorophores with low quantum yields because increasing  $\Gamma_m$  has no effect on  $Q$  if it is already unity.

## 25.2. REVIEW OF METAL EFFECTS ON FLUORESCENCE

There is extensive physics literature on the interaction of fluorophores with metal surfaces and particles, much of it theoretical.<sup>7–12</sup> The possibility of altering the radiative decay rates was experimentally demonstrated by measurements of the decay times of a europium ( $\text{Eu}^{3+}$ ) complex positioned at various distances from a planar silver mirror.<sup>13–16</sup> In a mirror the metal layer is continuous and thicker than the optical wavelength. The lifetimes oscillate with distance but remain a single exponential at each distance (Figure 25.4). This effect can be explained by changes in the phase of the reflected field with distance and the effects of this reflected near-field on the fluorophore. The changes in lifetime with distance are not due to interactions of the fluorophore with emitted photons. A decrease in lifetime is found when the reflected field is in phase with the fluorophore's oscillating dipole. An increase in the lifetime is found if the reflected field is out of phase with the oscillating dipole. As the distance increases the amplitude of the oscillations decreases. The effects of a plane mirror occurs

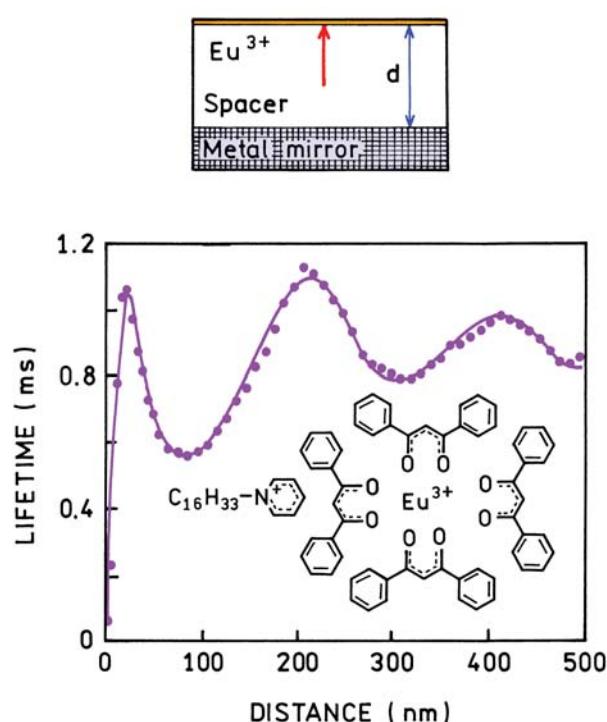


**Figure 25.4.** Lifetime of  $\text{Eu}^{3+}$  ions in front of an Ag mirror as a function of separation between the  $\text{Eu}^{3+}$  ions and the mirror. The solid curve is a theoretical fit. From [6].

over distances comparable to the excitation and emission wavelengths. At short distances below 20 nm the emission is quenched. The oscillations in lifetime with distance from the metal surface are rather modest. These effects have been of theoretical interest but have not found use in the applications of fluorescence.

The effects of metallic surfaces on optical spectra are strongly dependent on the nature of the metal surface and/or metal particles. In general more dramatic effects are observed for metal colloids than planar mirrored surfaces. The experiment that led to our interest in RDE is shown in Figure 25.5. A glass slide was coated with silver island films (SIFs). These films are a partial coating of the surface with sub-wavelength size silver particles, which are formed by chemical reduction. The surface was coated with  $\text{Eu}(\text{ETA})_3$ . The intensity decays were measured in the absence and presence of an SIF. The lifetime of  $\text{Eu}(\text{ETA})_3$  decreased more than 100-fold on the SIF.<sup>17</sup> At first this decrease in lifetime did not seem interesting to us because we thought it could be due to quenching or scattered light giving the appearance of a shorter lifetime. However, the intensity increased fivefold even though the lifetime was decreased 100-fold. To the best of our knowledge these

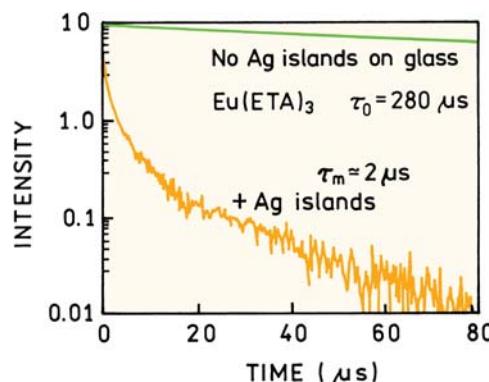


**Figure 25.5.** Fluorescence decay of  $\text{Eu}(\text{ETA})_3$  on silver-island films.  $\text{Eu}^{3+}$  was complexed with thenoyltrifluoroacetone (ETA). From [6].

results can only be explained by an increase in the radiative decay rate. This increase in  $\Gamma$  must be 100-fold or greater. This result suggested the metal particles could be used to modify or control the radiative rates of fluorophores. The magnitude of the effect was large, which suggested the use of metal particles to increase the sensitivity of fluorescence detection.

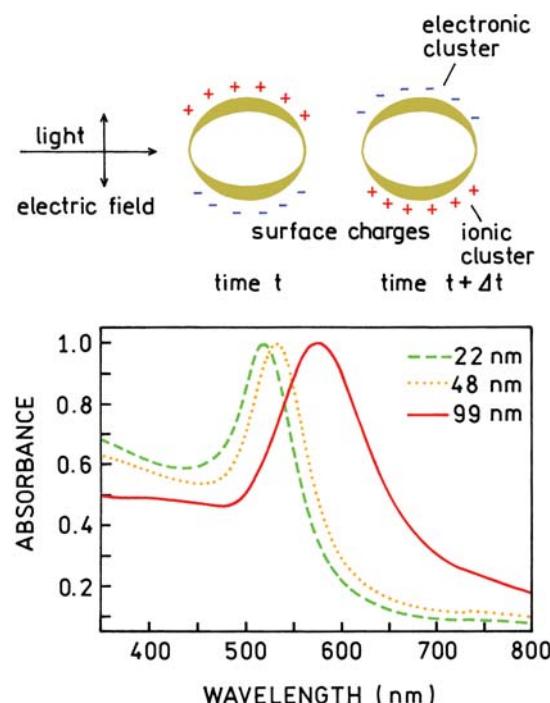


**Figure 25.6.** Electron oscillations in a metal colloid induced by incident light. Revised and reprinted with permission from [22]. Copyright © 1999, American Chemical Society.

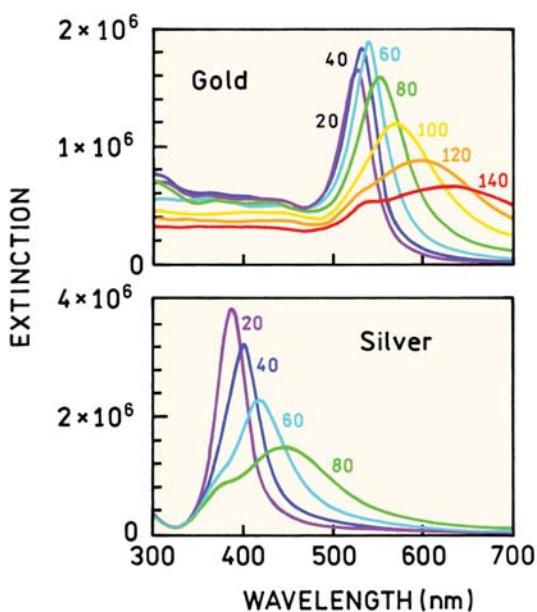


**Figure 25.7.** Extinction spectra of gold and silver colloids. Revised and reprinted with permission from [22]. Copyright © 1999, American Chemical Society.

### 25.3. OPTICAL PROPERTIES OF METAL COLLOIDS

Metal colloids have been used for centuries to make some colored glasses.<sup>18</sup> However, the origin of the colors was not understood until 1857, when Faraday discovered that the colors were due to finely divided silver or gold particles.<sup>19</sup> Incident light interacts with small metal particles and induces electron oscillations (Figure 25.6).<sup>20–22</sup> The oscil-

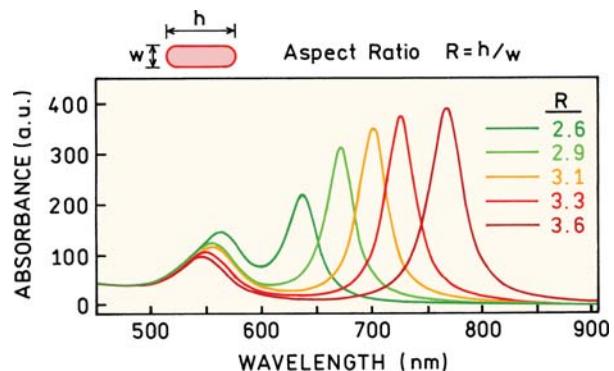


**Figure 25.8.** Absorption spectra of gold rods with different aspect ratios. From [22].

lating field can generate far-field radiation at the same wavelength. The result is that the incident light is scattered by the colloids, so the glass appears the color of the unscattered light. The actual situation is a little more complex in that colloids can also absorb light.

Extinction spectra of silver and gold colloids are shown in Figure 25.7. The term extinction refers to attenuation of the light as it goes through the sample. The extinction is due to both absorption and scattering. We will occasionally use the term "absorption" to refer to extinction. The extinction shifts to longer wavelengths as the size of the colloids increases.<sup>23–27</sup> Gold colloids absorb at longer wavelengths than silver colloids. The absorption depends strongly on colloid shape. This effect is seen by the shift in the absorption spectrum of gold colloids as they become elongated (Figure 25.8).

The unusual spectral properties of colloids can be seen by visual observation. Figure 25.9 shows absorption spectra

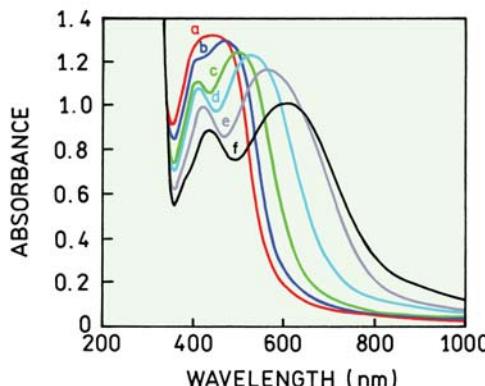


**Figure 25.9.** Extinction spectra and photograph of suspensions of silver colloids. The aspect ratios increase from left to right. Reprinted with permission from [23].

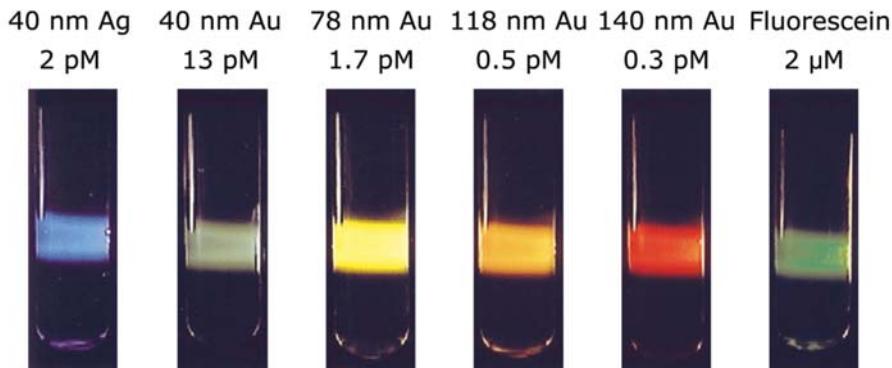


**Figure 25.10.** Photographs of colloid suspensions when illuminated from the side with white light. The rows of numbers indicate the diameter and concentration of the colloids. The rightmost sample is fluorescein. Reprinted with permission from [24-25].

and a backlit photo of silver colloid suspensions.<sup>23</sup> The aspect ratio increases from left to right and the perceived color changes with aspect ratio. A different result is seen if the samples are illuminated from the side without a backlight (Figure 25.10). These samples give the appearance of being fluorescent. The rightmost sample is fluorescent but the others are not. These samples are illuminated with a beam of white light. The perceived color is the color that is scattered by the colloids. The smallest silver colloids scatter blue light and the largest gold colloids scatter red light.

Samples that scatter light usually have a turbid appearance. However, the colloid suspensions in Figure 25.9 and 25.10 are clear. This occurs because the colloids are extremely dilute. Colloids have a large cross-section for interacting with light and extinction coefficients on the order of  $10^{10}$  or  $10^{11} \text{ M}^{-1} \text{ cm}^{-1}$ . The cross-section for a strongly absorbing chromophore like fluorescein is  $2.0 \times 10^{-15} \text{ cm}^2$  or  $4.5 \text{ \AA}$  across, which is about the size of the molecule. The cross-section for a 60-nm silver colloid is  $1.4 \times 10^{-10} \text{ cm}^2$  or  $1000 \text{ \AA}$  across. Only a low density of colloids is needed to cause enough scattering to change the color. Because of this high optical cross-sections colloids are being used to develop a number of bioaffinity assays.<sup>26-33</sup>

#### 25.4. THEORY FOR FLUOROPHORE-COLLOID INTERACTIONS

A complete explanation of fluorophore–colloid interactions would require extensive electrodynamic theory, and the description would probably still be incomplete. We will describe an overview of those results that are relevant to MEF. The details are not known with certainty, but there probably are three dominant interactions of fluorophores with metals (Figure 25.11). Fluorophores may be quenched

at short distances from the metal ( $k_m$ ), but there may be ways to recover this energy as useful emission (Chapter 26). There can be an increased rate of excitation ( $E_m$ ), which is called the lightening-rod effect, and there can be an increased rate of radiative decay ( $\Gamma_m$ ). The distance of the interactions probably increases, in order, with quenching, increased excitation, and increased radiative rate. However, additional experimental results are needed to better determine the distance dependence of these interactions.

The interactions between fluorophores and metal colloids have been considered theoretically.<sup>7-12</sup> A typical model is shown in Figure 25.12 for a prolate spheroid with an aspect ratio of  $a/b$ . The particle is assumed to be a metal-

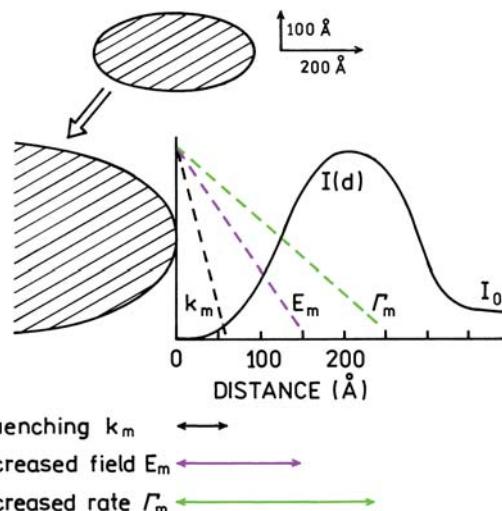


**Figure 25.11.** Effects of a metallic particle on transitions of a fluorophore. Metallic particles can cause quenching ( $k_m$ ), can concentrate the incident light field ( $E_m$ ), and can increase the radiative decay rate ( $\Gamma_m$ ). From [6].

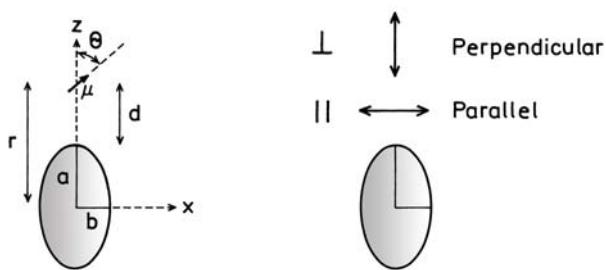


Figure 25.12. Fluorophore near a metallic spheroid.

lic ellipsoid with a fluorophore positioned near the particle. The fluorophore is located outside the particle at a distance  $r$  from the center of the spheroid and a distance  $d$  from the surface. The fluorophore is located on the major axis and can be oriented parallel or perpendicular to the metallic surface.

The theory can be used to calculate the effect of the metal particle on a nearby fluorophore. Figure 25.13 shows the radiative rates expected for a fluorophore at various distances from the surface of a silver particle and for different orientations of the fluorophore transition moment. The

most remarkable effect is for a fluorophore aligned along the long axis and perpendicular to the surface of a spheroid with an aspect ratio of  $a/b = 1.75$ . In this case the radiative rate can be enhanced by a factor of 1000-fold or greater. The effect is much smaller for a sphere ( $a/b = 1.0$ ) and for a more elongated spheroid ( $a/b = 3.0$ ). For this elongated particle the optical transition is not in resonance with the fluorophore. In this case the radiative decay rate can be decreased by over 100-fold. If the fluorophore displays a high quantum yield or a small value of  $k_{nr}$ , this effect could result in longer lifetimes. The magnitude of these effects depends on the location of the fluorophore around the particle and the orientation of its dipole moment relative to the metallic surface. The dominant effect of the perpendicular orientation is thought to be due to an enhancement of the local field along the long axis of the particle.

Colloids can also affect the extent of resonance energy transfer.<sup>34–35</sup> Suppose the donor and acceptor are located along the long axis of an ellipsoid with the dipoles also oriented along this axis. Figure 25.14 shows enhancement of the rate of energy transfer due to the metal particle, that is, the ratio of the rates of transfer in the presence ( $k_T^m$ ) and absence ( $k_T^0$ ) of the metal. Enhancements of  $10^4$  are possible. The enhancement depends on the transition energy that is in resonance with the particle. A smaller but still significant enhancement is found for a less resonant particle (lower curve). The enhanced rate of energy transfer persists for distances much larger than typical Förster distances. These simulations are for dipoles on the long axis and oriented along that axis, but the enhancements are still large

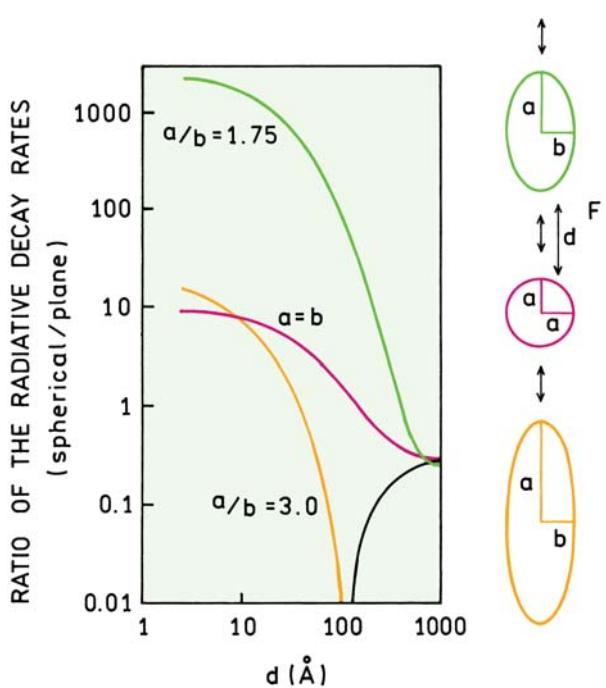


Figure 25.13. Effect of a metallic spheroid on the radiative rate of a fluorophore. The resonant frequency of the dye is assumed to be  $25,600 \text{ cm}^{-1}$ , approximately equal to 391 nm. The volume of the spheroids is equal to that of a sphere with a radius of  $200 \text{ \AA}$ .

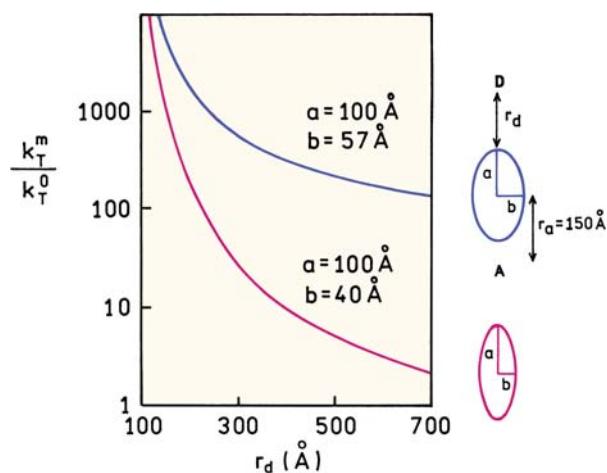
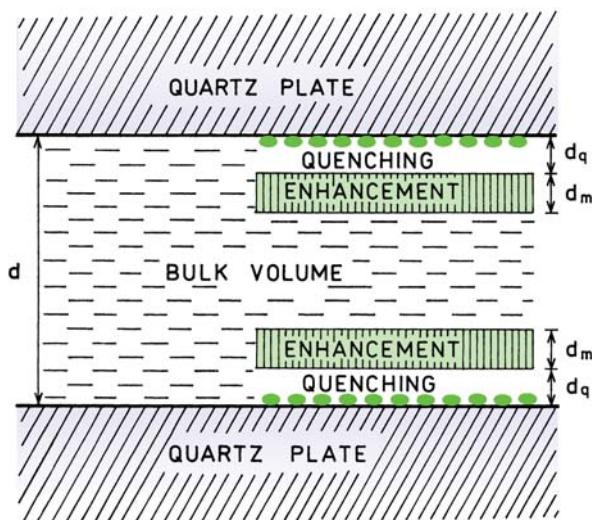


Figure 25.14. Enhancements in the rate of energy transfer in the presence of a silver particle.



**Figure 25.15.** Schematic for a fluorophore solution between two silver island films. The solid ellipsoids represent the silver island films.

when the donors and acceptors have different orientations and locations around the particle.

## 25.5. EXPERIMENTAL RESULTS ON METAL-ENHANCED FLUORESCENCE

Prior to describing biochemical applications of MEF it is informative to see the effects of silver particles on standard fluorophores. Silver island films are deposited on glass or quartz plates. Two plates are put together with water in between, yielding a sample about  $1\text{ }\mu\text{m}$  thick (Figure 25.15). With this sample most of the volume is distant from the silver and thus not affected by the silver. Fluorophores with high and low quantum yields were placed between the SIFs.<sup>36</sup> As shown in Figure 25.3, an increase in the radiative decay rate increases the intensity when the quantum yield is low but will not affect the intensity of a high-quantum-yield fluorophore. For this reason we examined two fluorophores, with high or low quantum yields. The intensity of rhodamine B (RhB) with a quantum yield of 0.48 is (Figure 25.16) almost unchanged by the SIFs. In contrast, the intensity of rose bengal (RB) with a quantum yield of 0.02 is increased about fivefold by proximity to the silver island films. In this sample the fluorophores are not attached to the silver and most of the fluorophores are too distant from the silver to be affected. Hence the intensity increase of those RB molecules near the metal film is significantly greater than fivefold.

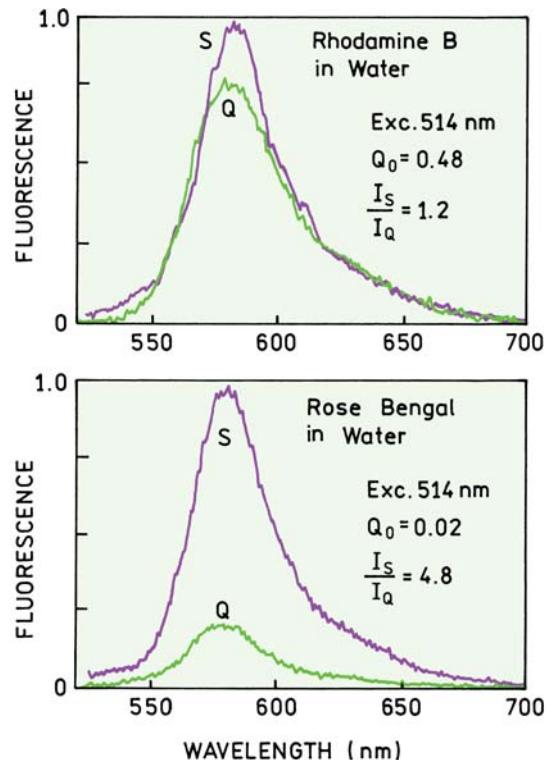


**Figure 25.16.** Emission spectra of rhodamine B (top) and rose bengal (bottom) between silver island films (S) or unsilvered quartz plates (Q). From [36].

Metal-enhanced fluorescence by SIFs is a general phenomenon that appears to occur with most if not all fluorophores. Figure 25.17 shows the relative intensities in the presence ( $I_S$ ) and absence ( $I_Q$ ) of metal for the fluorophores. If the quantum yield is above 0.5 the intensity is not significantly increased between the SIFs. As the quantum yield decreases the intensity ratio  $I_S/I_Q$  increases. This result is consistent with an increase in the radiative decay rate near the SIFs. Fluorophores with a variety of structures were examined so that the effect is unlikely to be the result of some specific interactions of a fluorophore with the silver.

### 25.5.1. Application of MEF to DNA Analysis

DNA analysis is a widely used application of fluorescence, and MEF can be used to obtain increased intensities from labeled DNA.<sup>36–40</sup> Figure 25.18 shows the chemical structures of DNA oligomers labeled with Cy3 or Cy5. These fluorophores are frequently used on DNA arrays. The glass or quartz substrate from these arrays is often treated with 3-aminopropyltriethoxysilane (APS), which makes the sur-

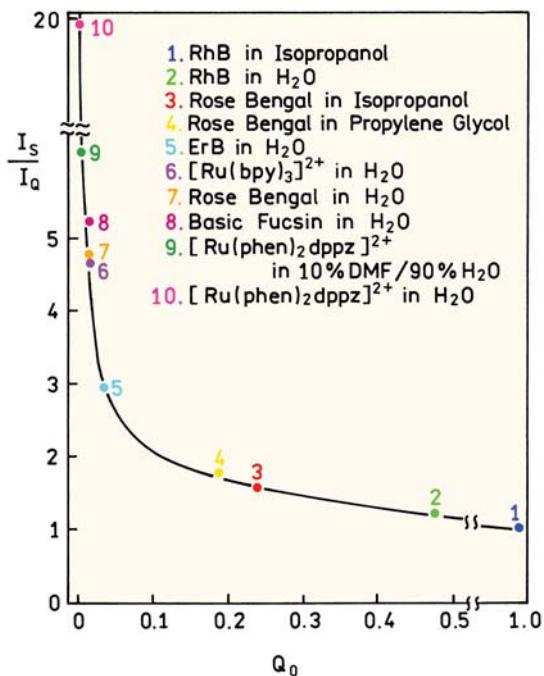


Figure 25.17. Enhancement of the emission of fluorophores with different quantum yields. From [36].

face positively charged for DNA binding. The emission intensity of both oligomers is increased about fourfold when bound to the SIFs as compared to quartz (Figure 25.19).

The previous figures showed that the intensities of fluorophores increased when near SIFs. However, fluorescence intensities can change for many reasons, and it would not be surprising if surface-bound fluorophores in a rigid environment displayed higher intensities than in solution. As shown in Figure 25.3, an increase in the radiative decay rate will decrease the lifetime, as will increasing quantum yield. This is an unusual effect so that lifetime measurements can be used to determine if the radiative decay rate is increased near the metal. Figure 25.20 shows frequency-domain (FD) intensity decays of the labeled oligomers when bound to quartz and SIFs. The mean lifetimes of Cy3 and Cy5 are decreased dramatically on the SIFs. The decreased lifetimes and increased intensities show that the radiative decay rate increased near the SIFs. The right-hand panels show the intensity decays reconstructed from the FD data. These curves show an initial rapid decay followed by a slower decay comparable to that found for the labeled DNA on glass. In this case the more slowly decaying components are probably due to labeled DNA bound to the glass but distant from the metal particles.

A decrease in lifetime should result in increased photo-stability of a fluorophore. Photochemical reactions occur while the fluorophore is in the excited state. If the lifetime is shorter, it is more probable that the fluorophore emits before it undergoes decomposition. This means that the fluorophore can undergo more excitation-relaxation cycles prior to permanent photobleaching. This reasoning assumes

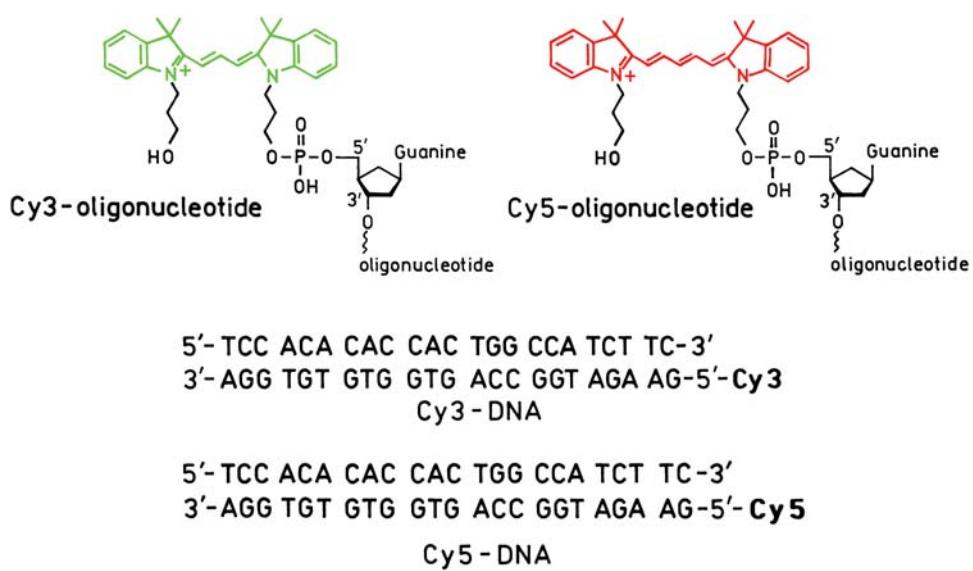
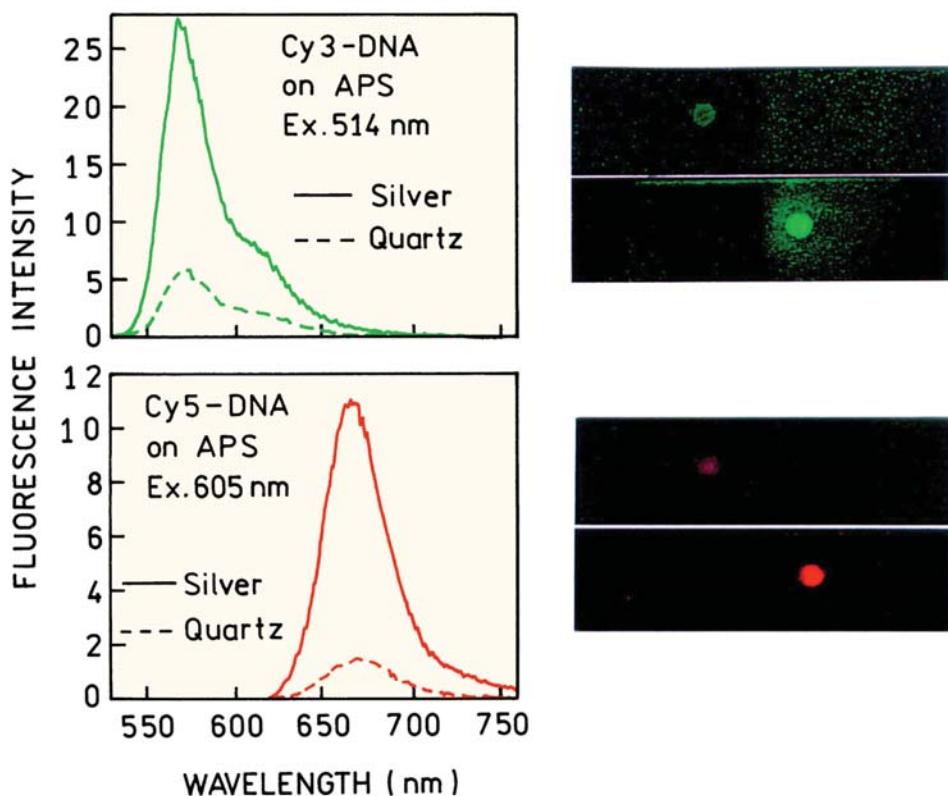


Figure 25.18. Structure of DNA oligomers labeled with Cy3 or Cy5. From [37].



**Figure 25.19.** Emission spectra and photographs of the labeled DNA oligomer on quartz and SIFs. The quartz was treated with APS. From [40].

that the metal does not introduce a new pathway for photodecomposition. The photostability of a fluorophore can be studied by measuring the intensity with continuous excitation (Figure 25.21). These photostability curves for Cy3- and Cy5-labeled DNA were measured with the same inci-

dent light intensity, so that the initial intensities are higher on the SIFs. The total number of photons emitted by a fluorophore prior to photobleaching is proportional to the area under the intensity-versus-time curves. These non-normalized curves (left) show that considerably more photons per fluorophore can be observed on the SIFs. If the curves are normalized at time zero (right) the fluorophores on the SIFs are seen to bleach somewhat more slowly. Results similar to those in Figure 25.21 have been observed for a number of fluorophores,<sup>41–43</sup> but it is too early to know if increased photostability will be observed with most fluorophores.

Detection of DNA using fluorescence is almost always performed using extrinsic probes. The intrinsic fluorescence of the DNA bases is very weak. Silver particles were found to increase the intrinsic fluorescence of unlabeled DNA. Figure 25.22 shows emission spectra of calf thymus DNA in solution when placed between quartz plates and when between SIFs.<sup>44</sup> The intensity is increased manyfold between the SIFs. In this experiment the DNA was not bound to the glass, so that most of the DNA is distant from the silver particles. This suggests that the intensity of the DNA near the silver particles is dramatically increased.

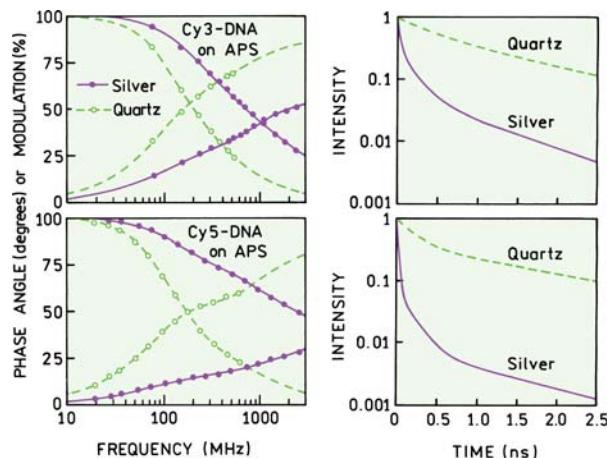


**Figure 25.20.** Time-dependent intensity decays of Cy3- and Cy5-labeled DNA oligomers on quartz and SIFs. From [40].

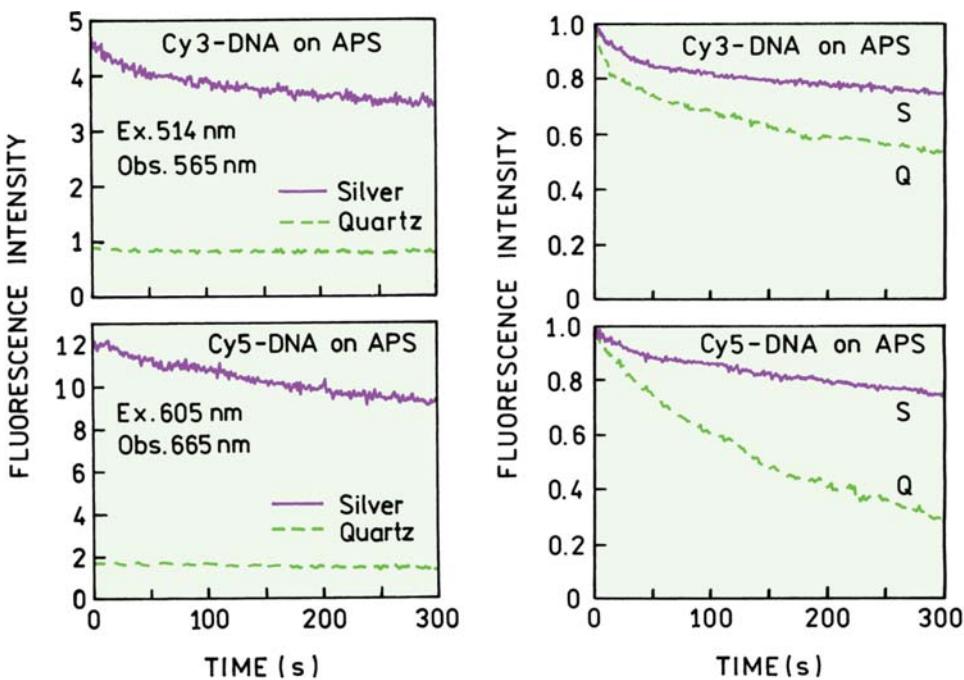


**Figure 25.21.** Photostability of Cy3- and Cy5-labeled DNA oligomers on quartz and SIFs. From [40].

## 25.6. DISTANCE-DEPENDENCE OF METAL-ENHANCED FLUORESCENCE

The use of MEF requires an understanding of the optimal distance between the fluorophore and the silver surface for enhanced fluorescence. This dependence was studied using protein layers to separate labeled DNA oligomers from the SIF.<sup>45</sup> The glass or SIF surface is first incubated with biotinylated bovine serum albumin (BSA). BSA adsorbs to most surfaces and forms a monolayer. The surface is then treated with avidin, which forms a layer on the biotinylated

BSA (Figure 25.23). This process can be repeated many times, adding a thickness of about 90 Å for each layer of BSA and avidin. After the desired thickness is achieved the surface is treated with a biotinylated DNA oligomer that also contains a fluorophore (Figure 25.24).

Figure 25.25 shows the intensity of Cy3- and Cy5-labeled DNA oligomers on SIFs. The oligomers were separated from the SIF by one or more layers of BSA-avidin. The highest intensity was found with a single layer of BSA-avidin. Hence a distance of about 90 Å from a metal appears to yield the largest increases in intensity. This result is only an initial attempt to identify the optimal distances, and additional studies are needed to determine the range of distances that can be used for MEF. It should be recognized that the experimental studies of MEF shown above were performed using fluorophores that were distributed evenly across the surfaces and not localized exclusively on the metal.

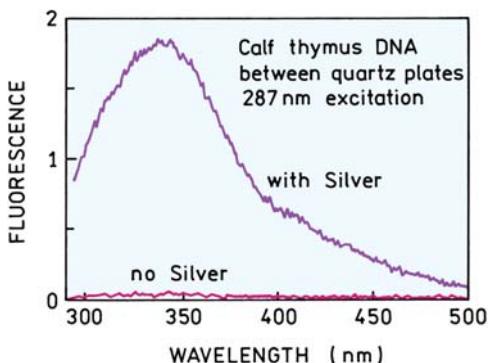


**Figure 25.22.** Emission spectra of calf thymus DNA between quartz plates and between SIFs.

## 25.7. APPLICATIONS OF METAL-ENHANCED FLUORESCENCE

Metal-enhanced fluorescence is a new technology, and the applications are now being developed.<sup>46-49</sup> We will describe a few initial results indicating the types of applications that can be expected in the near future.

- BSA - biotin
  - avidin

💡 DNA(Cy3)-biotin or DNA(Cy5)-biotin

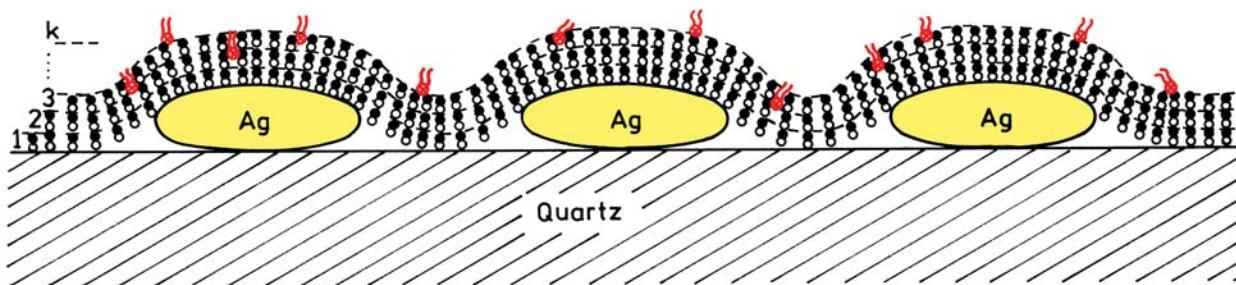


**Figure 25.23.** Schematic of SIFs with layers of biotinylated BSA, avidin and a top layer of labeled DNA oligomers. From [45].

5'-GAA GAT GGC CAG TGG TGT GTG GA-3'-biotin  
3'-CTT CTA CCG GTC ACC ACA CAC CT-5'-Cy3

### DNA(Cy3)-biotin

5'-TCC ACA CAC CAC TGG CCA TCT TC-3'-biotin  
3'-AGG TGT GTG GTG ACC GGT AGA AG-5'-C<sub>5</sub>

### DNA(Cy5)-biotin

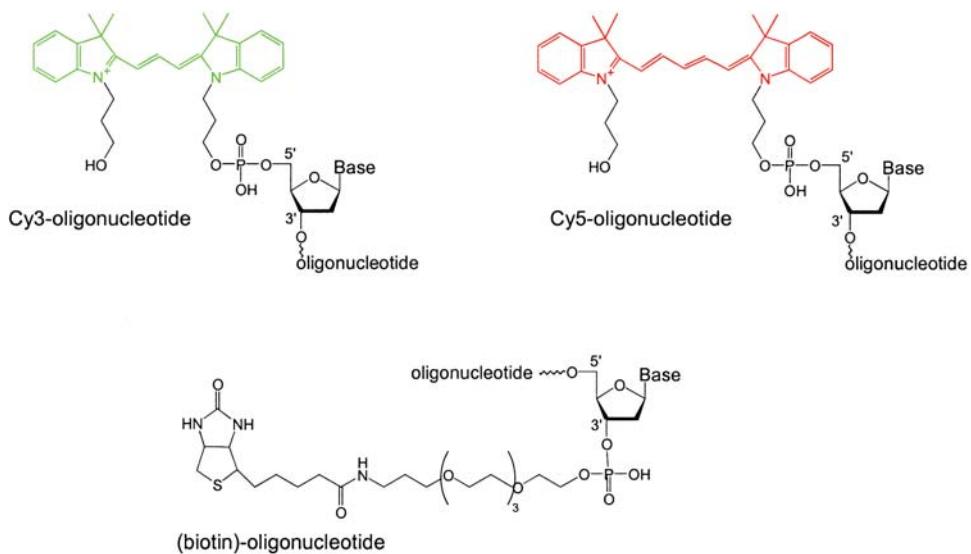


**Figure 25.24.** Structure of labeled and biotinylated DNA oligomers. From [45].

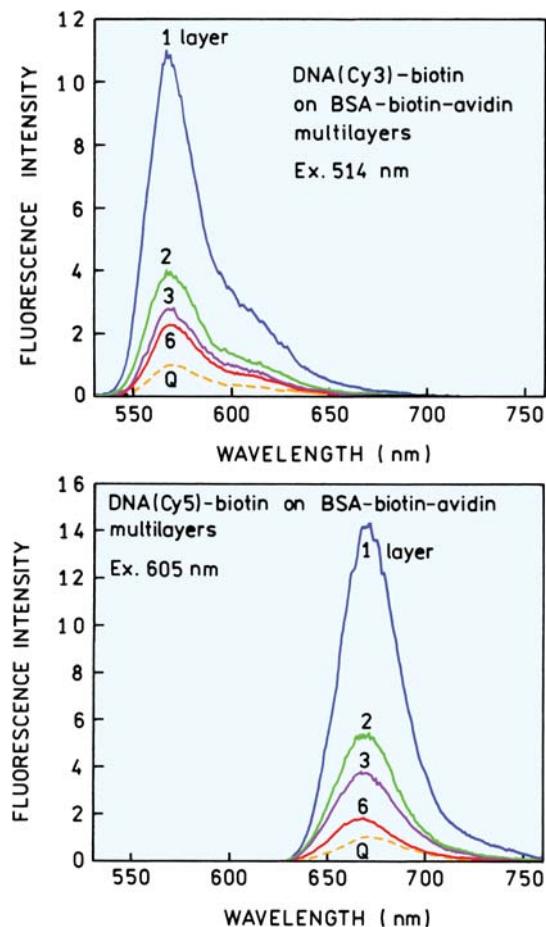


**Figure 25.25.** Effect of distance from the SIFs on the intensities of labeled DNA oligomers. From [45].

### 25.7.1. DNA Hybridization Using MEF

DNA hybridization is frequently measured using fluorophores that display increased intensity when bound to double-helical DNA. MEF allows hybridization to be measured using fluorophores for which the quantum yield, in the absence of metal, does not change upon DNA hybridization.<sup>50</sup> This possibility is shown for a fluorescein-labeled oligomer (Figure 25.26). A complementary DNA oligomer was bound to an SIF. Upon addition of the labeled oligomer the fluorescein intensity showed a time-dependent increase in intensity. The intensity of fluorescein increased about 10-fold upon hybridization. The effect of the SIF on the intensity is seen in the real-color photographs of the hybridized DNA before and after hybridization (Figure 25.27). It is important to understand that the increase in intensity is not due to the effect of hybridization on quantum yield of the probe. The increase in intensity is due to the localization of the probe near the SIF. This result shows that MEF can be used to detect any binding reaction that brings a fluorophore close to an SIF. A change in intensity due to the binding event is not necessary.

### 25.7.2. Release of Self-Quenching

Labeled immunoglobulins are frequently used in immunoassays. When performing such assays it is desirable to have the brightest possible labeled proteins. One approach to obtaining bright reagents is to label the protein with multiple fluorophores. Unfortunately, this approach is usually not successful. When proteins are labeled with flu-

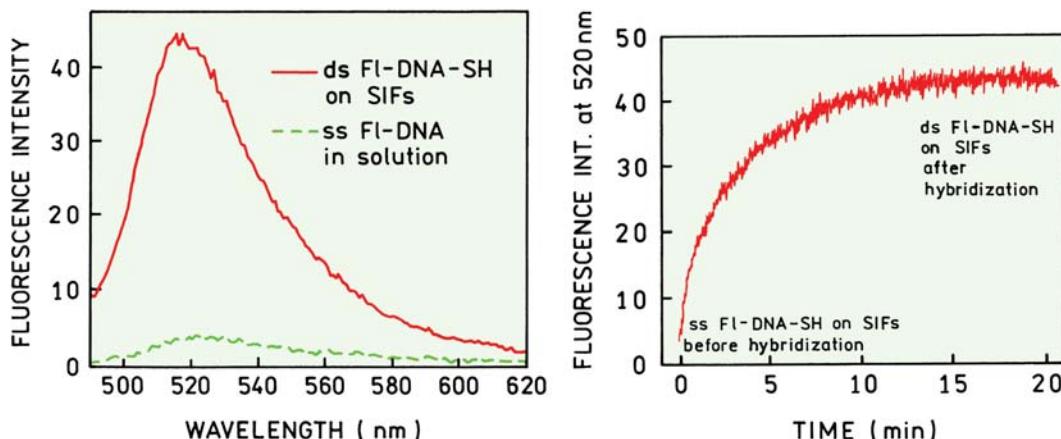


**Figure 25.26.** Emission spectra and time-dependent intensity of a fluorescein-labeled oligomer upon binding to a complementary oligomer bound exclusively to an SIF. From [50].

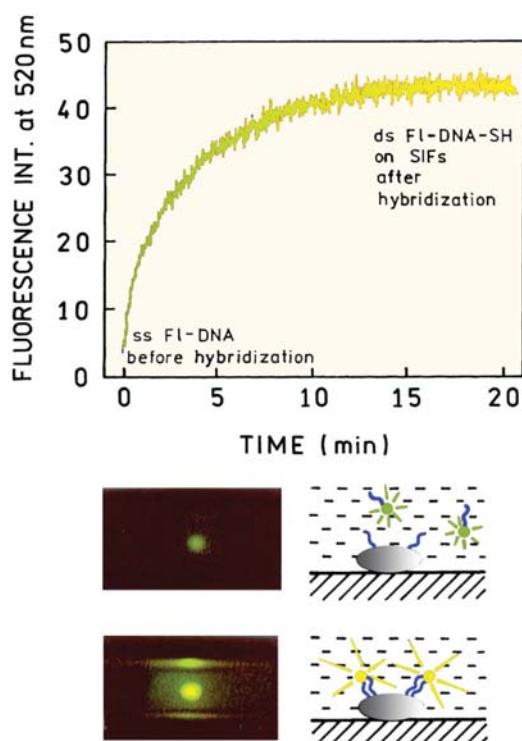


**Figure 25.27.** Photograph of a fluorescein-labeled DNA oligomer before (top) and after (bottom) hybridization. From [50].

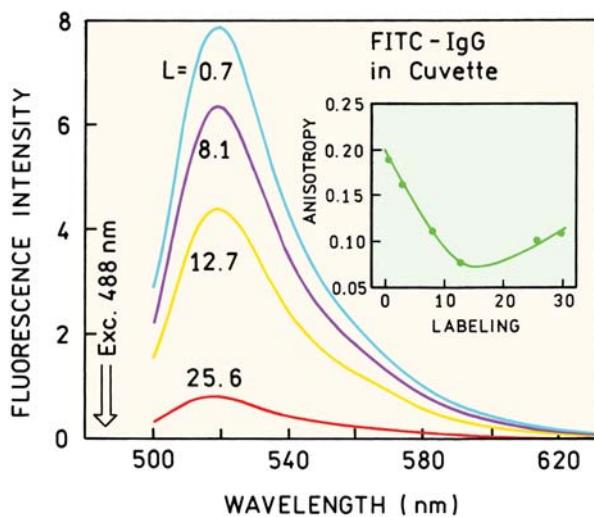


**Figure 25.28.** Emission spectra of fluorescein-labeled IgG. The numbers indicate the molar ratio of fluorescein to IgG. The intensities were measured for solutions with the same optical density for fluorescein. From [53].

orophores with a small Stokes shift the intensity does not increase in proportion to the number of bound fluorophores, and sometimes the intensity decreases. This effect is due to homo RET between the fluorophores, which decreases the quantum yield. Proximity of heavily labeled biomolecules to SIFs can result in increased intensities and apparently less quenching due to homo RET.<sup>51–53</sup> One example is shown in Figure 25.28 for immunoglobulin G (IgG) labeled with fluorescein.<sup>53</sup> As the labeling ratio is increased the intensity per fluorescein molecule decreases. This effect is due to homo RET between the fluoresceins, which decreases the quantum yield. The anisotropy values (insert) also decrease with increasing labeling ratio, which indicates that RET has occurred. Figure 25.29 shows that the intensity per fluorescein residue can increase as much as 40-fold for heavily labeled samples near SIFs. The release of self-quenching appears to be a general result<sup>51–53</sup> that suggests its use with any surface-bound assay.

### 25.7.3. Effect of Silver Particles on RET

Resonance energy transfer occurs over relatively large distances up to 100 Å. This distance is comparable to the size of large proteins and some protein assemblies. However, there are instances where RET over larger distances is

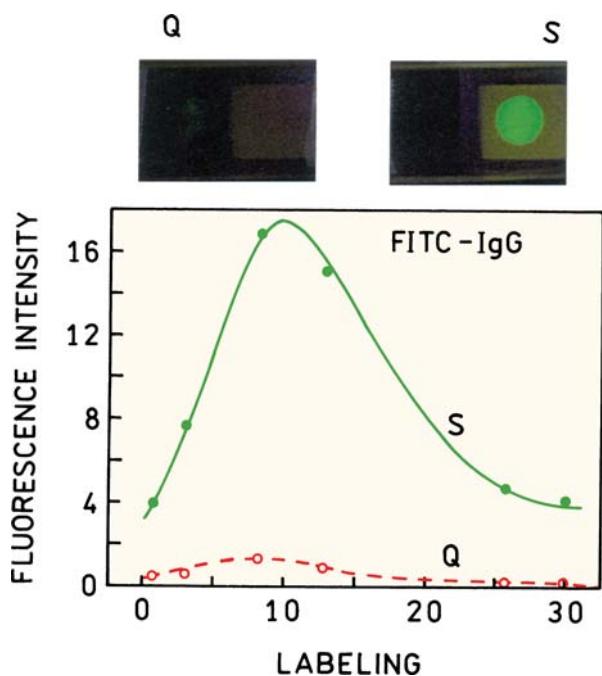


**Figure 25.29.** Photograph and relative intensities of fluorescein-labeled IgG on glass (Q) and SIFs (S). From [53].

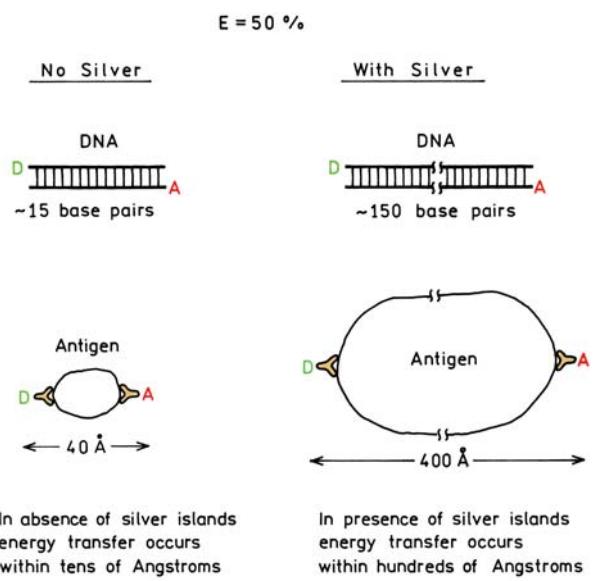


Figure 25.30. RET in the presence and absence of metallic particles.

desirable. One example is RET immunoassays (Figure 25.30). Fluorescence immunoassays are widely used, typically polarization as ELISA assays. Immunoassays are not usually performed using RET. This absence is probably due to the fact that in a sandwich assay the sizes of the antigen and antibodies are too large for RET to occur. Similarly, RET can be used to measure DNA hybridization if the donor and acceptor are within about 15 base pairs, but will not occur if the donor and acceptor are spaced by a much larger number of base pairs.

A small number of experiments have indicated that proximity to metal particles can increase the extent of energy transfer.<sup>54–56</sup> The effect of SIFs on RET was studied using a double-stranded DNA oligomer labeled with AMCA as the donor and Cy3 as the acceptor (Figure 25.31). The distance between the donor and acceptor was chosen so that the extent of energy transfer was small in the absence of single particles. The DNA oligomers labeled with both donor and acceptor were placed either near a single island film or between two SIFs. The RET efficiency was not affected by a single SIF, but was increased when the D-A pair was between two SIFs. The increase in RET can be seen from the increase in acceptor intensity near 570 nm. This result suggests that RET can be used to measure association reactions between large molecules or assemblies by passing the molecules between two layers of silver particles.

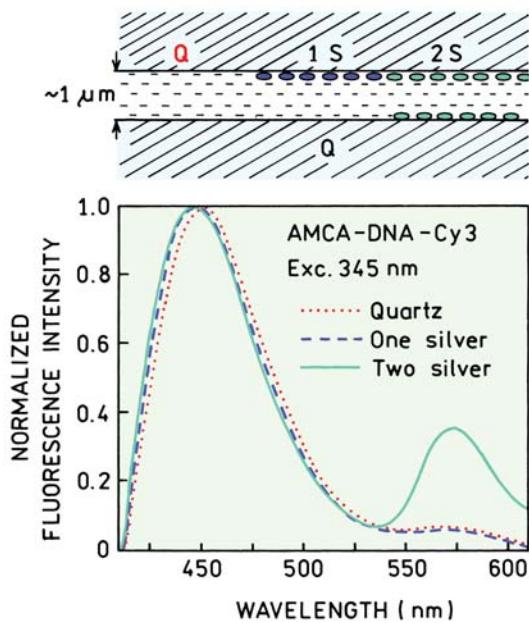
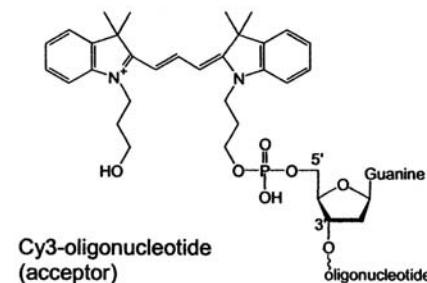
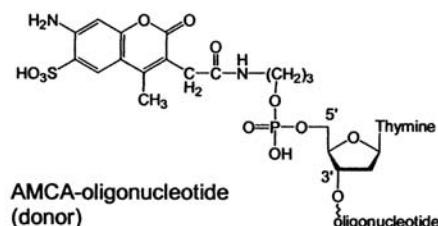


Figure 25.31. Effect of one or two SIFs on RET between AMCA and Cy3 bound to DNA. From [56].

## 25.8. MECHANISM OF MEF

In the preceding sections we described experiments that were all consistent with an increase in the radiative decay rate. However, some preparations of metal particles do not result in enhanced fluorescence. It is important to know

what types of particles are most effective for MEF and the properties of these particles that result in metal-enhanced fluorescence. We have developed a conceptually simple model that we hope has predictive value for MEF.<sup>57</sup> Mie theory can be used to calculate the optical properties of metal colloids when the colloids are smaller than the incident wavelength. These calculations show that the extinction of colloids is due to both light absorption and light scattering. The relative contribution of absorption and scattering depends on the size and shape of the colloids. In general, larger particles and non-spherical particles show larger relative contributions of scatter to the total extinction. At present we believe the scattering contribution of the total extinction is the origin of MEF. The scattering component represents far-field radiation from the induced oscillating dipole. In a sense this effect is similar to emission. This similarity can be seen in Figure 25.10, where the scattered light appears to be visually similar to fluorescence. It seems logical that the excited fluorophore and nearby metal particle cooperate in producing far-field radiation at the emission wavelength. We refer to this concept as the radiating plasmon (RP) model.<sup>57</sup> If correct, the RP model provides a rational approach for the design of metal particles for MEF. The particle or structure should be selected for a high cross-section for scattering and for a scattering component that is dominant over the absorption.

## 25.9. PERSPECTIVE ON RET

At present relatively few laboratories are performing studies on MEF.<sup>58–65</sup> The early results are confirming the results from our laboratory. If this trend continues MEF will become widely used in sensing, biotechnology, and forensics. The studies described in this chapter were performed using SIFs, which have a heterogeneous distribution of particle sizes. In the future we can expect MEF to use better-defined particles. Silver and gold colloids can be made with a variety of shapes,<sup>66–79</sup> some of which may be more useful for MEF. And, finally, it seems likely that MEF will be performed using regular particulate surfaces of a type prepared using nanosphere lithography,<sup>80–82</sup> dip-pen lithography,<sup>83</sup> microcontact printing,<sup>84</sup> and other emerging methods for nanolithography.

Our vision for the future of RDE is shown in Figure 25.32. At present almost all fluorescence experiments are performed using the free-space emission. This emission is mostly isotropic and the radiative decay rates are mostly constant (top). The use of RDE will allow the design of

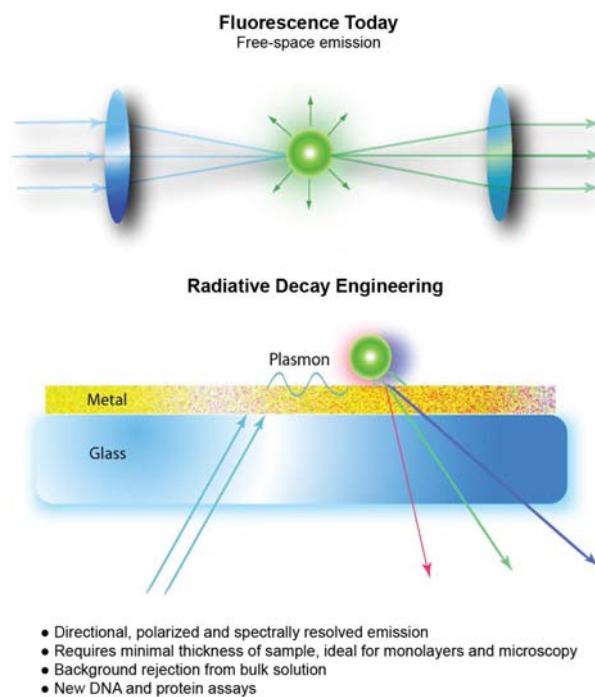


**Figure 25.32.** Comparison of free-space fluorescence emission with emission modified and directed by metallic structures.

metallic structures that interact with the excited fluorophore. These interactions can result in modified spectral properties and directional emission (bottom). In some cases the directionality will be the result of the excited fluorophores creating plasmons in the metal, which in turn result in far-field radiation. The ability to control the emission process represents a paradigm shift for the field of fluorescence spectroscopy.

## REFERENCES

- Strickler SJ, Berg RA. 1962. Relationship between absorption intensity and fluorescence lifetimes of molecules. *J Chem Phys* **37**:814–822.
- Toptygin D, Savchenko RS, Meadow ND, Roseman S, Brand L. 2002. Effect of the solvent refractive index on the excited state lifetime of a single tryptophan residue in a protein. *J Phys Chem B* **106**(14):3724–3734.
- Ford GW, Weber WH. 1984. Electromagnetic interactions of molecules with metal surfaces. *Phys Rep* **113**:195–287.
- Chance RR, Pock A, Silbey R. 1978. Molecular fluorescence and energy transfer near interfaces. *Adv Chem Phys* **37**:1–65.
- Axelrod D, Hellen EH, Fulbright RM. 1992. Total internal reflection fluorescence. In *Topics in Fluorescence Spectroscopy*, Vol. 3: *Biochemical applications*, pp. 289–343. Ed JR Lakowicz. Plenum Press, New York.

6. Lakowicz JR. 2001. Radiative decay engineering: biophysical and biomedical applications. *Anal Biochem* **298**:1–24.
7. Das P, Metju H. 1985. Enhancement of molecular fluorescence and photochemistry by small metal particles. *J Phys Chem* **89**:4680–4687.
8. Gersten J, Nitzan A. 1981. Spectroscopic properties of molecules interacting with small dielectric particles. *J Chem Phys* **75**(3):1139–1152.
9. Weitz DA, Garoff S, Gersten JI, Nitzan A. 1983. The enhancement of Raman scattering, resonance Raman scattering, and fluorescence from molecules absorbed on a rough silver surface. *J Chem Phys* **78**(9):5324–5338.
10. Chew H. 1987. Transition rates of atoms near spherical surfaces. *J Chem Phys* **87**(2):1355–1360.
11. Kummerlen J, Leitner A, Brunner H, Ausseneegg FR, Wokaun A. 1993. Enhanced dye fluorescence over silver island films: analysis of the distance dependence. *Mol Phys* **80**(5):1031–1046.
12. Philpott MR. 1975. Effect of surface plasmons on transitions in molecules. *J Chem Phys* **62**(5):1812–1817.
13. Amos RM, Barnes WL. 1997. Modification of the spontaneous emission rate of Eu<sup>3+</sup> ions close to a thin metal mirror. *Phys Rev B* **55**(11):7249–7254.
14. Barnes WL. 1998. Fluorescence near interfaces: the role of photonic mode density. *J Mod Opt* **45**(4):661–699.
15. Amos RM, Barnes WL. 1999. Modification of spontaneous emission lifetimes in the presence of corrugated metallic surfaces. *Phys Rev B* **59**(11):7708–7714.
16. Drexhage KH. 1974. Interaction of light with monomolecular dye lasers. In *Progress in optics*, pp. 161–232. Ed E Wolfe. North-Holland Publishing, Amsterdam.
17. Weitz DA, Garoff S, Hanson CD, Gramila TJ. 1982. Fluorescent lifetimes of molecules on silver-island films. *Opt Lett* **7**(2):89–91.
18. Kerker M. 1985. The optics of colloidal silver: something old and something new. *J Colloid Interface Sci* **105**:297–314.
19. Faraday M. 1857. The Bakerian Lecture: experimental relations of gold (and other metals) to light. *Philos Trans* **147**:145–181.
20. Link S, El-Sayed MA. 2000. Shape and size dependence of radiative, non-radiative and photothermal properties of gold nanocrystals. *Int Rev Phys Chem* **19**:409–453.
21. Kreibig U, Vollmer M. 1995. *Optical properties of metal clusters*. Springer, New York.
22. Link S, El-Sayed MA. 1999. Spectral properties and relaxation dynamics of surface plasmon electronic oscillations in gold and silver nanodots and nanorods. *J Phys Chem B* **103**:8410–8426.
23. Murphy CJ, Jana NR. 2002. Controlling the aspect ratio of inorganic nanorods and nanowires. *Adv Mater* **14**(1):80–83.
24. Yguerabide J, Yguerabide EE. 1998. Light scattering submicroscopic particles as highly fluorescent analogs and their use as tracer labels in clinical and biological applications, I: theory. *Anal Biochem* **262**(2):137–156.
25. Yguerabide J, Yguerabide EE. 1998. Light scattering submicroscopic particles as highly fluorescent analogs and their use as tracer labels in clinical and biological applications, II: experimental characterization. *Anal Biochem* **262**(2):157–176.
26. Yguerabide J, Yguerabide EE. 2001. Resonance light scattering particles as ultrasensitive labels for detection of analytes in a wide range of applications. *J Cell Biochem Suppl* **37**:71–81.
27. Schultz S, Mock J, Smith DR, Schultz DA. 1999. Nanoparticle based biological assays. *J Clin Ligand Assay* **22**(2):214–216.
28. Bauer G, Voinov S, Sontag G, Leitner A, Ausseneegg FR, Pittner F, Schalkhammer T. 1999. Optical nanocluster microchips for human diagnostics. *SPIE Proc* **3606**:40–45.
29. Bauer G, Pittner F, Schalkhammer Th. 1999. Metal nano-cluster biosensors. *Mikrochim Acta* **131**:107–114.
30. Stich N, Gandhum A, Matushin V, Mayer C, Bauer G, Schalkhammer T. 2001. Nanofilms and nanoclusters: energy courses driving fluorophores of biochip bound labels. *J Nanosci Nanotechnol* **1**(4):397–405.
31. Taton TA, Mirkin CA, Letsinger RL. 2000. Scanometric DNA array detection with nanoparticle probes. *Science* **289**:1757–1760.
32. Reichert J, Csáki A, Köhler M, Fritzsche W. 2000. Chip-based optical detection of DNA hybridization by means of nanobead labeling. *Anal Chem* **72**:6025–6029.
33. Nam J-M, Thaxton CS, Mirkin CA. 2003. Nanoparticle-based bio-bar codes for the ultrasensitive detection of proteins. *Science* **301**:1884–1886.
34. Gersten JI, Nitzan A. 1984. Accelerated energy transfer between molecules near a solid particle. *Chem Phys Lett* **104**(1):31–37.
35. Hua XM, Gersten JI, Nitzan A. 1985. Theory of energy transfer between molecules near solid state particles. *J Chem Phys* **83**:3650–3659.
36. Lakowicz JR, Shen Y, D'Auria S, Malicka J, Fang J, Gryczynski Z, Gryczynski I. 2002. Radiative decay engineering, 2: effects of silver island films on fluorescence intensity, lifetimes and resonance energy transfer. *Anal Biochem* **301**:261–277.
37. Malicka J, Gryczynski I, Maliwal BP, Fang J, Lakowicz JR. 2003. Fluorescence spectral properties of cyanine dye labeled DNA near metallic silver particles. *Biopolymers* **72**:96–104.
38. Malicka J, Gryczynski I, Fang J, Lakowicz JR. 2003. Fluorescence spectral properties of cyanine dye-labeled DNA oligomers on surfaces coated with silver particles. *Anal Biochem* **317**:136–146.
39. Lakowicz JR, Malicka J, Gryczynski I. 2003. Increased intensities of YOYO-1-labeled DNA oligomers near silver particles. *Photochem Photobiol* **77**(6):604–607.
40. Lakowicz JR, Malicka J, Gryczynski I. 2003. Silver particles enhance emission of fluorescent DNA oligomers. *BioTechniques* **34**(1):62–66.
41. Malicka J, Gryczynski I, Geddes CD, Lakowicz JR. 2003. Metal-enhanced emission from indocyanine green: a new approach to *in vivo* imaging. *J Biomed Opt* **8**(3):472–478.
42. Parfenov A, Gryczynski I, Malicka J, Geddes CD, Lakowicz JR. 2003. Enhanced fluorescence from fluorophores on fractal silver surfaces. *J Phys Chem* **107**:8829–8833.
43. Geddes CD, Cao H, Gryczynski I, Gryczynski Z, Fang J, Lakowicz JR. 2003. Metal-enhanced fluorescence (MEF) due to silver colloids on a planar surface: potential applications of indocyanine green to *in vivo* imaging. *J Phys Chem A* **107**:3443–3449.
44. Lakowicz JR, Shen B, Gryczynski Z, D'Auria S, Gryczynski I. 2001. Intrinsic fluorescence from DNA can be enhanced by metallic particles. *Biochem Biophys Res Commun* **286**:875–879.
45. Malicka J, Gryczynski I, Gryczynski Z, Lakowicz JR. 2003. Effects of fluorophore-to-silver distance on the emission of cyanine-dye labeled oligonucleotides. *Anal Biochem* **315**:57–66.

46. Stich N, Mayer C, Bauer G, Schalkhammer T. 2001. DNA biochips based on surface-enhanced fluorescence (SEF) for high-throughput interaction studies. *SPIE Proc* **4434**:128–137.
47. Mayer C, Stich N, Schalkhammer T. 2001. Surface-enhanced fluorescence biochips using industrial standard slide format and scanners. *SPIE Proc* **4252**:37–46.
48. Lochner N, Lobmaier C, Wirth M, Leitner A, Pittner F, Gabor F. 2003. Silver nanoparticle enhanced immunoassays: one step real time kinetic assay for insulin in serum. *Eur J Pharm Biopharm* **56**: 469–477.
49. Lobmaier Ch, Hawa G, Götzinger M, Wirth M, Pittner F, Gabor F. 2001. Direct monitoring of molecular recognition processes using fluorescence enhancement at colloid-coated microplates. *J Mol Recognit* **14**:215–222.
50. Malicka J, Gryczynski I, Lakowicz JR. 2003. DNA hybridization assays using metal-enhanced fluorescence. *Biochem Biophys Res Commun* **306**:213–218.
51. Lakowicz JR, Malicka J, D'Auria S, Gryczynski I. 2003. Release of the self-quenching of fluorescence near silver metallic surfaces. *Anal Biochem* **320**:13–20.
52. Malicka J, Gryczynski I, Lakowicz JR. 2003. Enhanced emission of highly labeled DNA oligomers near silver metallic surfaces. *Anal Chem* **75**:4408–4414.
53. Lakowicz JR, Malicka J, Huang J, Gryczynski Z, Gryczynski I. 2004. Ultrabright fluorescein-labeled antibodies near silver metallic surfaces. *Biopolymers* **74**:467–475.
54. Lakowicz JR, Kusba J, Shen Y, Malicka J, D'Auria S, Gryczynski Z, Gryczynski I. 2003. Effects of metallic silver particles on resonance energy transfer between fluorophores bound to DNA. *J Fluoresc* **13**(1):69–77.
55. Malicka J, Gryczynski I, Kusba J, Lakowicz JR. 2003. Effects of metallic silver island films on resonance energy transfer between N,N'-dipropyl-tetramethyl-indocarbocyanine (Cy3)- and N,N'-dipropyl-tetramethyl-indodicarbocyanine (Cy5)-labeled DNA. *Biopolymers* **70**:595–603.
56. Malicka J, Gryczynski I, Fang J, Kusba J, Lakowicz JR. 2003. Increased resonance energy transfer between fluorophores bound to DNA in proximity to metallic silver particles. *Anal Biochem* **315**:160–169.
57. Lakowicz JR. 2004. Radiative decay engineering, 5: metal-enhanced fluorescence and plasmon emission. *Anal Biochem* **337**:171–194.
58. Sokolov K, Chumanov G, Cotton TM. 1998. Enhancement of molecular fluorescence near the surface of colloidal metal films. *Anal Chem* **70**:3898–3905.
59. Hayakawa T, Selvan ST, Nogami M. 1999. Field enhancement effect of small Ag particles on the fluorescence from Eu<sup>3+</sup>-doped SiO<sub>2</sub> glass. *Appl Phys Lett* **74**(11):1513–1515.
60. Selvan ST, Hayakawa T, Nogami M. 1999. Remarkable influence of silver islands on the enhancement of fluorescence from Eu<sup>3+</sup> ion-doped silica gels. *J Phys Chem B* **103**:7064–7067.
61. Vasilev K, Stefani FD, Jacobsen V, Knoll W. 2004. Reduced photo-bleaching of chromophores close to a metal surface. *J Chem Phys* **120**(14):6701–6704.
62. Aussenegg FR, Leitner A, Lippitsch ME, Reinisch H, Reigler M. 1987. Novel aspects of fluorescence lifetime for molecules positioned close to metal surfaces. *Surface Sci* **139**:935–945.
63. DeSaja-Gonzalez J, Aroca R, Nagao Y, DeSaja JA. 1997. Surface-enhanced fluorescence and SERRS spectra of *N*-octadecyl-3,4:9,10-perylenetetracarboxylic monoanhydride on silver island films. *Spectrochim Acta* **53**:173–181.
64. Wiederrecht GP, Wurtz GA, Im JS, Hranisavljevic J. 2004. J-aggregates on metal nanoparticles characterized through ultrafast spectroscopy and near-field optics. *Scanning* **26**(I):I-2/I-9.
65. Wiederrecht GP, Wurtz GA, Hranisavljevic J. 2004. Coherent coupling of molecular excitons to electronic polarizations of noble metal nanoparticles. *Nanotechnol Lett* **4**(11):2121–2125.
66. Sosa IO, Noguez C, Barrera RG. 2003. Optical properties of metal nanoparticles with arbitrary shapes. *J Phys Chem B* **107**:6269–6275.
67. Zhang J, Han B, Liu M, Liu D, Dong Z, Liu J, Li D. 2003. Ultrasonication-induced formation of silver nanofibers in reverse micelles and small-angle x-ray scattering studies. *J Phys Chem B* **107**:3679–3683.
68. Kim F, Song JH, Yang P. 2002. Photochemical synthesis of gold nanorods. *J Am Chem Soc* **124**:14316–14317.
69. Taub N, Krichevski O, Markovich G. 2003. Growth of gold nanorods on surfaces. *J Phys Chem B* **107**:11579–11582.
70. Jana NR, Gearheart L, Murphy CJ. 2001. Wet chemical synthesis of high aspect ratio cylindrical gold nanorods. *J Phys Chem B* **105**:40656–40667.
71. Chen S, Carroll DL. 2002. Synthesis and characterization of truncated triangular silver nanoplates. *Nanotechnol Lett* **2**(9):1003–1007.
72. Pham T, Jackson JB, Halas NJ, Lee TR. 2002. Preparation and characterization of gold nanoshells coated with self-assembled monolayers. *Langmuir* **18**:4915–4920.
73. Maillard M, Giorgio S, Pileni MP. 2003. Tuning the size of silver nanodisks with similar aspect ratios: synthesis and optical properties. *J Phys Chem B* **107**:2466–2470.
74. Wei G, Zhou HL, Liu ZG, Song YH, Wang L, Sun LL, Li Z. 2005. One-step synthesis of silver nanoparticles, nanorods, and nanowires on the surface of DNA network. *J Phys Chem B* **109**(18):8738–8743.
75. Ni CY, Hassan PA, Kaler EW. 2005. Structural characteristics and growth of pentagonal silver nanorods prepared by a surfactant method. *Langmuir* **21**(8):3334–3337.
76. Liu FK, Chang YC, Huang PW, Ko FH, Chu TC. 2004. Preparation of silver nanorods by rapid microwave heating. *Chem Lett* **33**(8): 1050–1051.
77. Lee GJ, Shin SI, Kim YC, Oh SG. 2004. Preparation of silver nanorods through the control of temperature and pH of reaction medium. *Mater Chem Phys* **84**(2–3):197–204.
78. Sharma J, Chaki NK, Mahima S, Gonnade RG, Mulla IS, Vijayamohanan K. 2004. Tuning the aspect ratio of silver nanostructures: the effect of solvent mole fraction and 4-aminothiophenol concentration. *J Mater Chem* **14**(6):970–975.
79. Hu JQ, Chen Q, Xie ZX, Han GB, Wang RH, Ren B, Zhang Y, Yang ZL, Tan ZW. 2004. A simple and effective route for the synthesis of crystalline silver nanorods and nanowires. *Adv Funct Mater* **14**(2): 183–189.
80. Whitney AV, Myers BD, Van Duyne RP. 2004. Sub-100 nm triangular nanopores fabricated with the reactive ion etching variant of nanosphere lithography and angle-resolved nanosphere lithography. *Nanotechnol Lett* **4**(8):1507–1511.

81. Haynes CL, McFarland AD, Smith MT, Hulteen JC, Van Duyne RP. 2002. Angle-resolved nanosphere lithography: manipulation of nanoparticle size, shape, and interparticle spacing. *J Phys Chem B* **106**(8):1898–2002.
82. Jensen TR, Malinsky MD, Haynes CL, Van Duyne RP. 2000. Nanosphere lithography: tunable localized surface plasmon resonance spectra of silver nanoparticles. *J Phys Chem B* **104**(45): 10549–10556.
83. Choi D-G, Kim S, Lee E, Yang S-M. 2005. Particle arrays with patterned pores by nanomatching with colloidal masks. *J Am Chem Soc* **127**:1636–1637.
84. Ormonde AD, Hicks ECM, Castillo J, Van Duyne RP. 2004. Nanosphere lithography: fabrication of large-area Ag nanoparticle arrays by convective self-assembly and their characterization by scanning UV-visible extinction spectroscopy. *Langmuir* **20**:6927–6931.

---

**PROBLEM**

P25.1. *Calculation of the Quantum Yield and Increase in Radiative Rate Near an SIF.* Figure 25.16 shows the emission spectra of rose bengal (RB) in solution and between SIFs. Assume all the molecules are affected equally by the SIF. What is the relative increase in the radiative decay rate ( $\Gamma$ ) due to the SIF? Assume the natural radiative lifetime in the absence of metals is 4 ns. Also assume the excitation rate and the non-radiative decay rates are the same in the presence and absence of the SIF.

Now assume that only 10% of the RB molecules are affected by the SIF. What are the quantum yield and relative increased in  $\Gamma$  due to the SIF?

# 26

# Radiative-Decay Engineering: Surface Plasmon- Coupled Emission

In the preceding chapter we described the use of metallic particles to modify emission. This was accomplished by interaction of the excited dipoles of the fluorophore with oscillating electrons in a nearby metallic surface. We used the term "metal" to describe such surfaces. We described how a fluorophore near a metal can have a different radiative-decay rate. This is an unusual effect because this rate does not change substantially when a fluorophore is in different environments.

In this chapter we describe another phenomenon that occurs when a fluorophore is near a metal. Under certain circumstances a fluorophore can couple with a continuous metallic surface to create groups of oscillating electrons called surface plasmons. If the metal film is thin and on an appropriate substrate the plasmons radiate their energy into the substrate. We call this phenomenon surface plasmon-coupled emission (SPCE).<sup>1</sup> There are numerous potential applications for this phenomenon that efficiently collects the emission and transforms it into directional radiation.

## 26.1. PHENOMENON OF SPCE

Prior to describing the theory for SPCE it is informative to describe this phenomenon (Figure 26.1). Suppose an excited fluorophore is positioned above a thin silver film, where the metal film is continuous and about 50 nm thick. Such films are visually opaque. Remarkably, the emission from the fluorophore is not reflected but is efficiently transferred through the film. The spatial distribution of fluorescence is isotropic or nearly isotropic. However, the emission seen through the film occurs only at a unique angle  $\theta_F$  measured from the normal. Since the sample is symmetric about the normal  $z$ -axis the emission occurs as a cone around the axis. This cone is not due to selective transmission of emission

through the film. A large fraction of the total emission appears in the cone. About half of the emission appears in the cone and about half is free-space emission away from the film. The emission in the cone has the same emission spectrum as the fluorophore.

The light from the excited fluorophore appearing in the cone is called surface plasmon-coupled emission (SPCE).<sup>1</sup> This name reflects our current understanding of the phenomenon. We believe the excited fluorophore creates surface plasmons in the metal. These plasmons do not appear to be the result of RET to the surface because the distances over which SPCE occurs are too large for RET. SPCE occurs over distances up to 200 nm or 2000 Å, which are much larger than Förster distances near 50 Å. The plasmons radiate into the substrate at an angle determined by the optical properties of the metal and substrate. Since the wavelength distribution of SPCE is the same as the fluorophore emission it is tempting to assume it originates from the fluorophore. However, the emission is 100% p-polarized, even if the fluorophores are randomly oriented and excited with unpolarized light. See Chapter 2 for a definition of p-polarization. This polarization indicates the surface plasmons are radiating and not the fluorophores.

## 26.2. SURFACE-PLASMON RESONANCE

The phenomenon of SPCE appears to be closely related to surface-plasmon resonance (SPR). SPR is now widely used in the biosciences and provides a generic approach to measurement of biomolecule interactions on surfaces.<sup>2-6</sup> A schematic description of SPR is shown in Figure 26.2. The measurement is based on the interaction of light with thin metal films on a glass substrate. The film is typically made of gold 40–50 nm thick. The surface contains a capture bio-

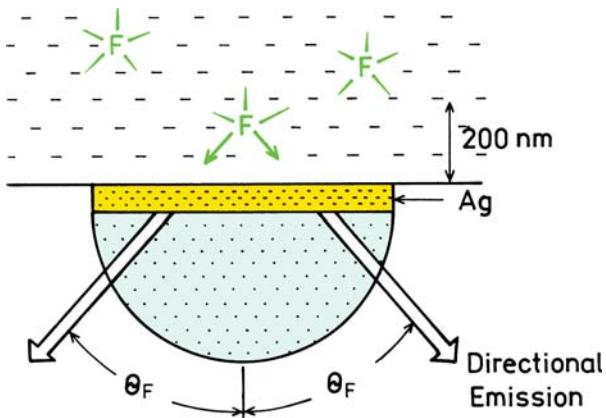


Figure 26.1. Surface plasmon-coupled emission. F is a fluorophore.

molecule that has affinity for the analyte of interest. The capture biomolecule is typically covalently bound to the gold surface. This sample is optically coupled to a hemispherical or hemicylindrical prism by an index-matching fluid. Light impinges on the gold film through the prism, which is called the Kretschmann configuration. The instrument measures the reflectivity of the gold film at various angles of incidence ( $\theta$ ), with the same angle used for observation ( $\theta$ ).

The usefulness of SPR is due to the dependence of the reflectivity of the gold film on the refractive index of the solution immediately above the gold film. The angle-dependent reflectivity of the gold surface is dependent on the refractive index of the solution because there is an evanescent field extending from the gold surface into the solution. Binding of macromolecules above the gold film

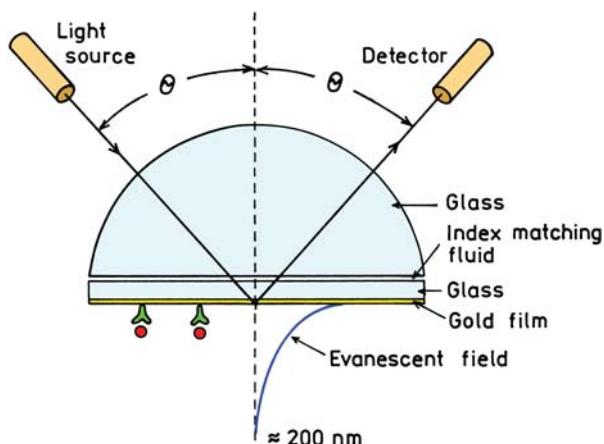


Figure 26.2. Typical configuration for surface-plasmon resonance analysis. The incident beam is p-polarized.

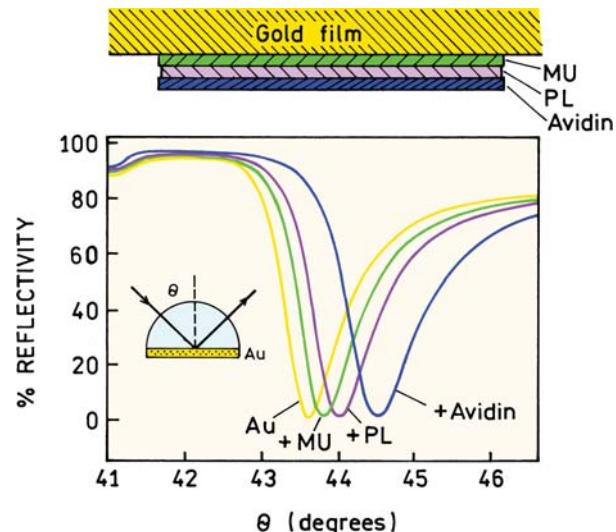
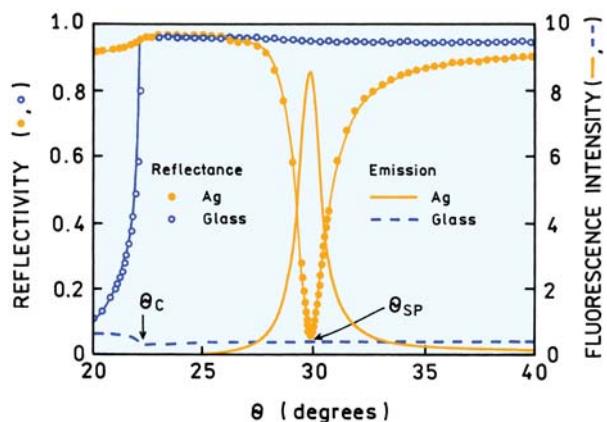


Figure 26.3. SPR reflectivity curves for a 47-nm gold film on BK-7 glass. Illumination was at 633 nm. The gold film was progressively coated with 11-mercaptopundecanoic acid (MU), followed by biotinylated polylysine (PL), and then avidin. Adapted from [7–9].

causes small changes in the refractive index, which result in changes in reflectivity. Figure 26.3 shows typical SPR data: a plot of reflectivity versus the angle of incidence for a 47-nm gold film.<sup>7–9</sup> The reflectivity minimum occurs at the SPR angle. The SPR angles change as the gold surface is coated with 11-mercaptopundecanoic acid (MU), then biotinylated polylysine (PL), and finally avidin. The changes in SPR angle are due to changes in the refractive index near the gold surface due to the adsorbed layers.

The decrease in reflectivity at the SPR angle ( $\theta_{SP}$ ) is due to absorption of the incident light at this particular angle of incidence. At this angle the incident light is absorbed and excites electron oscillations on the metal surface. The reflectivity is sensitive to the refractive index because of the evanescent field that penetrates approximately 200 nm into the solution (Figure 26.2). The evanescent field appears whenever there is resonance between the incident beam and the gold surface. An evanescent field is not present when there is no plasmon resonance, that is, when the reflectivity is high.

The existence of an evanescent field is reminiscent of total internal reflectance (TIR), which occurs between a glass–water interface when the angle of incidence from the glass slide exceeds the critical angle.<sup>10</sup> There can be confusion about the relationship between the critical angle in TIR ( $\theta_C$ ) and the SPR angle ( $\theta_{SP}$ ). The physical origins of  $\theta_C$  and  $\theta_{SP}$  are similar, in that both are dependent on wavevector



**Figure 26.4.** Reflectivity curves for a bare glass and silver-coated glass, both spin coated with a fluorophore in polyvinyl alcohol. The prism is LaSFN9 glass, 633 nm. Also shown is the fluorescence from the labeled PVA film on the glass and silver surfaces. Adapted from [11].

matching at the sample–glass or metal interface. However, these angles are different and not directly related. This difference between  $\theta_C$  and  $\theta_{SP}$  is illustrated in Figure 26.4, which compares glass and silver-coated glass surfaces.<sup>11–12</sup> The silver-coated surface shows high reflectivity at all angles except around the plasmon angle near 30°. The reflectivity of a glass surface is quite different. The reflectivity is low below the critical angle  $\theta_C$ , increases sharply to nearly 100% at  $\theta_C$ , and remains high for all angles above  $\theta_C$ . For the glass surface and angles above  $\theta_C$  there exists an evanescent field from the totally internally reflected light. For the silver-coated glass there is no evanescent field in the aqueous phase unless the angle of incidence is near the SPR angle. The reflectivity of the silver film is high at angles significantly larger or smaller than  $\theta_{SP}$ .

The evanescent wave due to SPR is much more intense than that due to TIR.<sup>11–17</sup> The relative strengths of the fields can be measured by the fluorescence from fluorophores near the surface. For the sample shown in Figure 26.4 fluorophores were localized within the evanescent field by coating with a polyvinyl alcohol (PVA) film that contained a fluorophore. The dependence of the emission on the incident angle indicates the relative intensity of the evanescent wave felt by the fluorophores. For the glass surface the emission intensity is low for  $\theta < \theta_C$ . This low value is essentially the same as seen in a typical fluorescence measurement where the fluorophore is excited in a glass or quartz cuvette. As the incident angle exceeds  $\theta_C$  the intensity drops about twofold because the incident light undergoes TIR

rather than passing into the sample. Above the critical angle the remaining intensity represents the amount of excitation due to the TIR evanescent wave. This result indicates that the field strength for TIR is roughly the same for the incident light and the evanescent wave.

Different results are seen for the labeled film on the silver surface. The emission intensity is near zero for angles above and below  $\theta_C$  because of the high reflectivity of the metal film. In contrast to uncoated glass, the light does not penetrate the sample even though  $\theta < \theta_C$ . There is a dramatic increase in the emission intensity of the film near the plasmon angle: about 15-fold. This effect is due to a 10- to 40-fold increase in the intensity of the evanescent field above silver as compared to above glass with TIR.<sup>18–21</sup> This increase in field strength above a metal film is one origin of the increased sensitivity possible with plasmon-coupled emission.

An important characteristic of the SPR angles is that they are strongly dependent on wavelength. Figure 26.5 shows the reflectivity curves of a gold film for several wavelengths.<sup>22</sup> The surface plasmon angle decreases as the wavelength decreases. The dependence on wavelength can be understood in terms of the optical constants of the metals, which depend upon wavelength (frequency) and the dielectric constant of the adjacent prism. This dependence of  $\theta_{SP}$  on wavelength is the origin of intrinsic spectral resolution when observing surface plasmon-coupled emission.

### 26.2.1. Theory for Surface-Plasmon Resonance

An understanding of SPR is useful for understanding surface plasmon-coupled emission. The theory to describe the reflectivity of metal-coated surfaces is complex. It can be difficult to understand the underlying physical interactions that are responsible for angle-dependent absorption. We will not describe the detailed equations needed to calculate the reflectivity.

The phenomenon of SPR can be understood by considering the propagation constant of the incident electromagnetic wave across the surface of the metal, along the  $x$ -axis. An electromagnetic wave propagating in space can be described by

$$\bar{E}(\bar{r},t) = \bar{E}_0 \exp(i\omega t - i\bar{k} \cdot \bar{r}) \quad (26.1)$$

where the bars indicate vector quantities,  $\bar{r}$  is a unit vector in the direction of propagation,  $\omega$  is the frequency in radians/s,  $i = -1^{1/2}$ , and  $\cdot$  indicates the dot product. The term  $k$

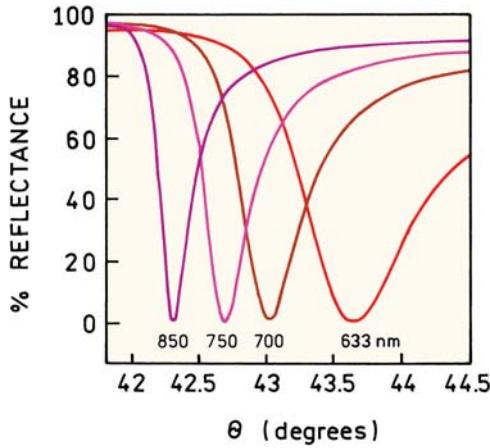


**Figure 26.5.** Calculated wavelength-dependent reflectivity for a 47-nm-thick gold film. From [22].

is the propagation constant, which is sometimes called the wavevector. This value is given by

$$k = \frac{2\pi}{\lambda} = \frac{n\omega}{c} = nk_0 \quad (26.2)$$

where  $\lambda = \lambda_0/n$  is the wavelength,  $\lambda_0$  is the wavelength in a vacuum,  $n$  is the refractive index of the medium, and  $k_0$  is the propagation constant of the wave in a vacuum. It is understood that the physical values are given by the real part of eq. 26.1. Hence the electric field is described by

$$\bar{E}(\bar{r},t) = \bar{E}_0 \exp(\cos \omega t - \bar{k} \cdot \bar{r}) \quad (26.3)$$

For SPR we need to consider the electric field along the  $x$ -axis at the metal–water interface. This component is given by

$$E(x,t) = E_{0x} \exp(\cos \omega t - k_x x) \quad (26.4)$$

To satisfy Maxwell's equations the electric fields have to be continuous across the interface, which requires  $k_x$  to be equal in both media.

The phenomenon of SPR can be understood by considering the propagation constant of the electromagnetic wave in the metal along the  $x$ -axis. In the metal film the field is described by eqs. 26.3 and 26.4 with  $k_x = k_r + ik_{im}$  being the complex wavevector along the  $x$ -axis. For a metal the propagation constant for the surface plasmon is given by

$$k_{SP} = \frac{\omega}{c} \left( \frac{\epsilon_m \epsilon_s}{\epsilon_m + \epsilon_s} \right)^{1/2} = k_0 \left( \frac{\epsilon_m \epsilon_s}{\epsilon_m + \epsilon_s} \right)^{1/2} \quad (26.5)$$

where  $\epsilon_m$  and  $\epsilon_s$  are the dielectric constant of the metal ( $m$ ) and sample ( $s$ ), respectively.  $\epsilon_s$  refers to the effective dielectric constant in the region of the evanescent field (Figure 26.2). Because the real part of  $\epsilon_m$  is larger than the imaginary part the propagation constant can be approximated by

$$k_{SP} = k_0 \left( \frac{\epsilon_r \epsilon_s}{\epsilon_r + \epsilon_s} \right)^{1/2} \quad (26.6)$$

The incident light can excite a surface plasmon when its  $x$ -axis component equals the propagation constant for the surface plasmon (Figure 26.6). The propagation constant for the incident light in the prism (p) is given by

$$k_p = k_0 n_p \quad (26.7)$$

and the component along the  $x$ -axis is equal to

$$k_x = k_0 n_p \sin \theta_p \quad (26.8)$$

where  $\theta_p$  is the incidence angle in the prism. Hence the conditions for SPR absorption is satisfied when

$$k_{SP} = k_x = k_0 n_p \sin \theta_{sp} \quad (26.9)$$

where  $\theta_{sp}$  is the angle of incidence in the metal for surface-plasmon resonance to occur. These considerations show

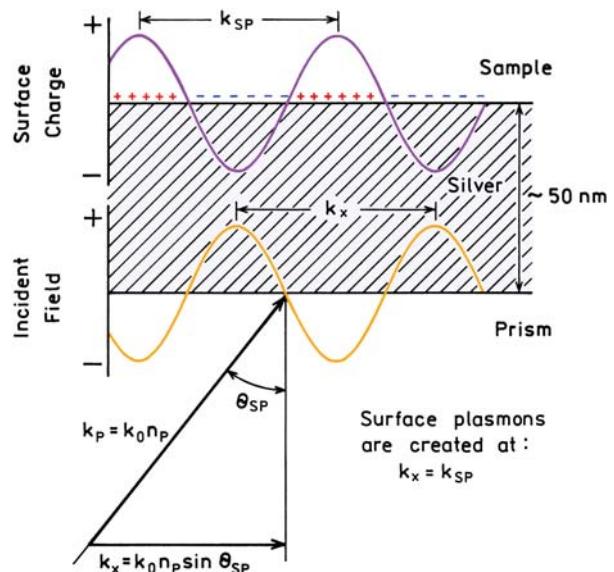


**Figure 26.6.** Schematic showing propagation constants in a prism and a thin film.

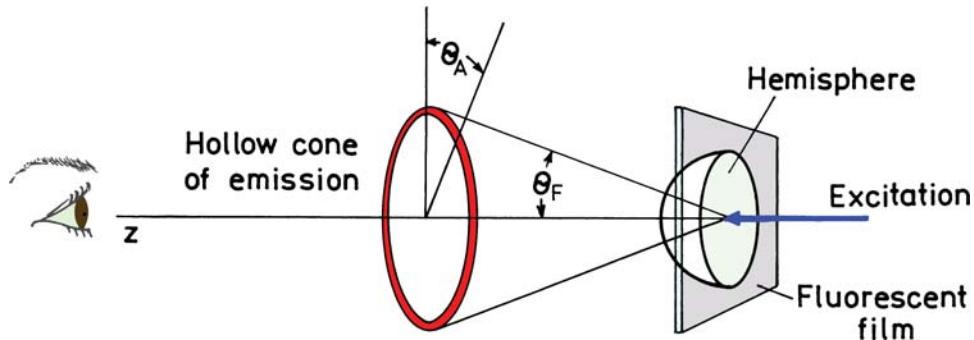


**Figure 26.7.** Surface plasmon-coupled cone of emission for fluorophores near a metallic film.

that the surface-plasmon resonance occurs whenever the  $x$ -axis component of the incident field equals that obtained from eq. 26.5.

A mental picture of SPR can be found by considering the wavelength of the incident light in the prism and the projection of this distance onto the interface (Figure 26.6). SPR occurs when this projected distance matches the wavelength of the surface plasmon. This visualization of SPR explains the increase in  $\theta_p$  needed for resonance at shorter wavelengths.

### 26.3. EXPECTED PROPERTIES OF SPCE

The previous explanation of SPR allows us to make several predictions for the properties of SPCE. The fluorophores are randomly distributed and the sample can be excited with unpolarized light. There is no preferential direction around the  $z$ -axis. Hence the SPCE is expected to appear as a cone around the  $z$ -axis (Figure 26.7). Figure 26.5 shows that SPR occurred at different angles of incidence for different wavelengths. The analogy with SPR suggests different emission wavelengths will appear at different angles (Figure 26.8). Hence the SPCE is expected to appear as a circular rainbow with the range of colors determined by the emission wavelength range of the fluorophore. In SPR only p-polarized incident light is absorbed. This suggests the SPCE will also be p-polarized around the  $z$ -axis. The polarization is expected to point radially away from the  $z$ -axis at all positions about the  $z$ -axis.

### 26.4. EXPERIMENTAL DEMONSTRATION OF SPCE

It was important to have an experimental demonstration of SPCE. The sample was sulforhodamine 101 (S101) in a 15-

nm-thick PVA film.<sup>23</sup> The film was on a 50-nm-thick layer of silver. Figure 26.9 shows the angular distribution of the emission which is distributed sharply at  $\pm 47^\circ$  from the normal. Integration of the angle-dependent emission, and the free-space emission away from the hemispherical prism, indicated that about half of the emission is contained in the directional component exiting through the prism.

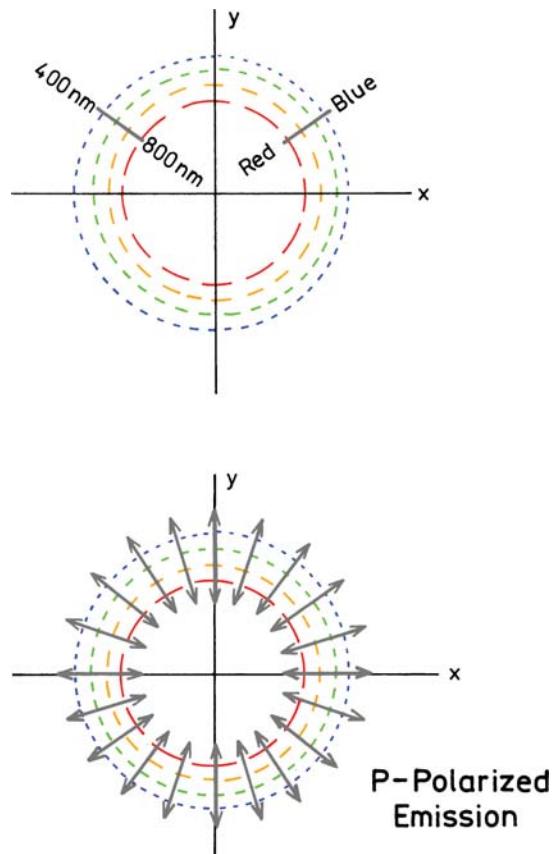


**Figure 26.8.** Color distribution and polarization expected for SPCE.

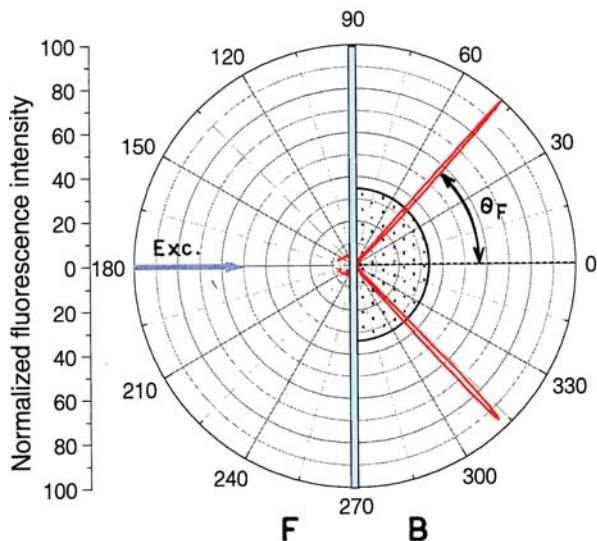


**Figure 26.9.** Angular distribution of the SPCE from sulforhodamine 101 (S101) in a 15-nm PVA film using the reverse Kretschmann configuration. From [23].

We also tested if the wavelength dependence seen for SPR (Figure 26.5) occurred for SPCE. A mixture of three fluorophores was used to obtain a wider range of wavelengths. The SPCE was found to be dispersed at different angles according to the wavelength (Figure 26.10) in the same direction as the SPR absorption. This result shows that a simple metal film can be used to efficiently collect the emission from nearby fluorophores, convert the emission to directional emission, and disperse the emission according to wavelength.

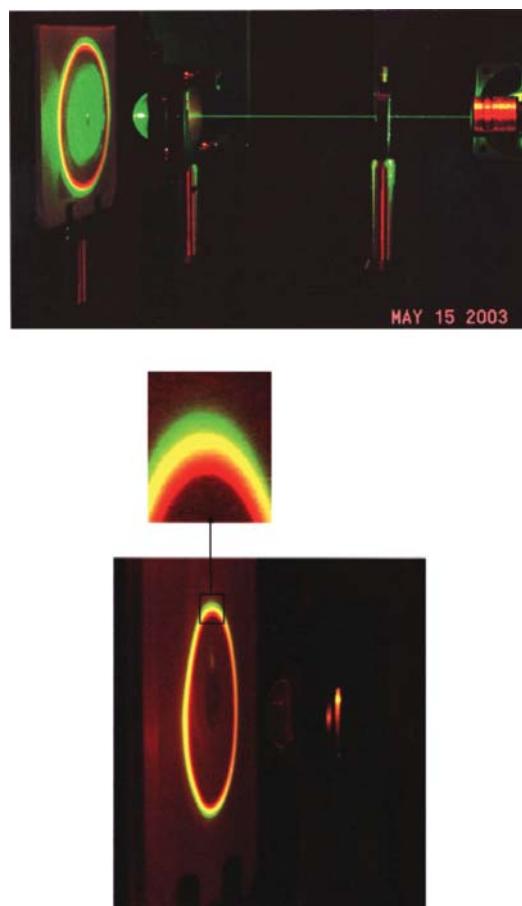


**Figure 26.10.** Photograph of SPCE from the mixture of fluorophores using RK excitation and a hemispherical prism, 532 nm excitation. From [23].

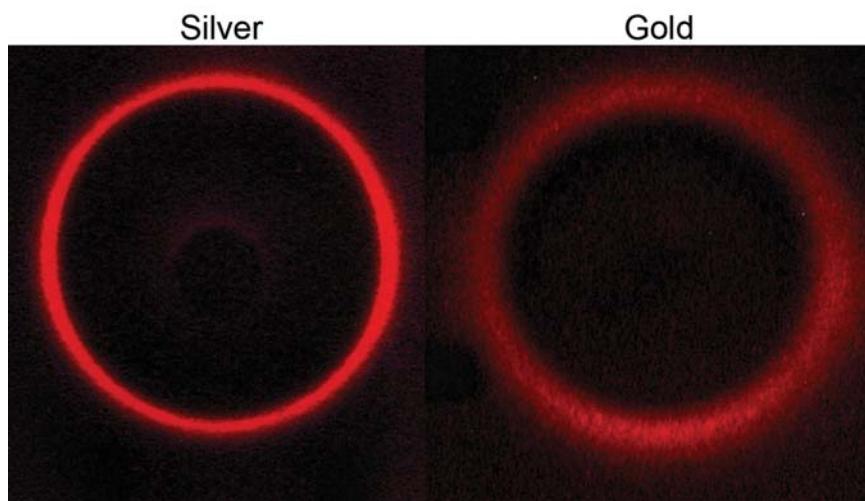


**Figure 26.11.** Cone of emission for S101 in PVA on silver and gold films.

In the application of SPCE it would be an advantage to use gold rather than silver surfaces. Gold does not tarnish and the chemistry for coating the surface with organic molecules is more highly developed for gold than silver. However, in contrast to silver, gold is known to quench fluorescence.<sup>24–26</sup> Fortunately, gold can be used for SPCE (Figure 26.11).<sup>27</sup> The angular distribution is slightly wider on gold than on silver, which is a result of its different optical properties. The reason gold does not quench in SPCE is because of the longer distances for SPCE as compared to Förster transfer, which is probably the mechanism by which gold quenches fluorescence.

SPCE is due mostly to fluorophores within about 200 nm of the surface. This suggests the possibility of selective observation of fluorophores localized near the metal surface. We tested this possibility by adding a "background" fluorophore more distant from the metal. This was accomplished by making the coated silver film part of a 1-mm-thick demountable cuvette. The cuvette was filled with a solution of rhodamine 6G in ethanol. PVA is weakly soluble in ethanol and the dyes remained separate for the course of the experiments. The free-space emission was observed at 149° and the SPCE at 77°. The concentrations were chosen so that the free-space emission was dominated by the R6G background (Figure 26.12). Even with this large background signal the SPCE was dominated by S101, which is closer to the metal film. The PVA thickness was only 30 nm, so that some R6G was present within the distance for SPCE, accounting for the remaining intensity of R6G at 550 nm. More effective background suppression can be

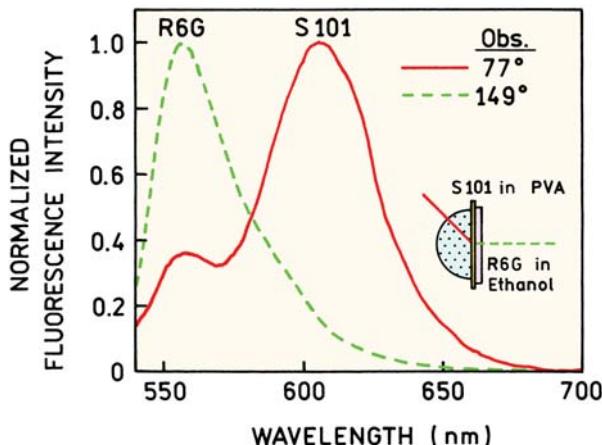
expected with a thicker PVA or sample film to keep this impurity more distant from the metal film.

## 26.5. APPLICATIONS OF SPCE

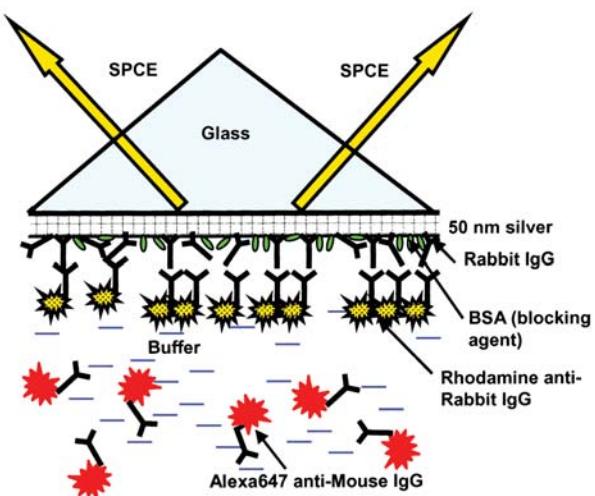
Since SPCE occurs for fluorophores near surfaces it will most likely be used with surface-based assays. One expected advantage of SPCE is the suppression of unwanted background because fluorophores distant from the metal surface will not create surface plasmons and SPCE. For this assay the surface-bound antibody was rabbit IgG (Figure 26.13). This surface was incubated with rhodamine-labeled anti-rabbit IgG and Alexa 647-labeled anti-mouse IgG. The later antibody does not bind to the surface and serves as the unwanted background.

Figure 26.14 shows the emission spectra of the free-space and surface-plasmon coupled emission. The free-space emission is dominated by the Alexa 647 background. In contrast, the SPCE is due mostly to the surface-bound antibody. This result shows that SPCE can be used to selectively observe fluorophores near the metal surface and to effectively decrease the amount of background emission. SPCE provides a potentially simple approach for improved performance in a wide variety of surface-bound arrays.

Intrinsic biochemical fluorophores such as tryptophan emit at ultraviolet wavelengths. It is possible to imagine many biochemical applications of SPCE occurring at shorter wavelengths. SPCE of UV-emitting fluorophores has



**Figure 26.12.** Emission spectra of S101 in PVA with simulated background emission from rhodamine 6G (R6G). The concentration of S101 in the PVA film was about 10 mM and the concentration of R6G in ethanol about 5 μM. From [23].



**Figure 26.13.** SPCE immunoassay. Anti-rabbit antibodies (labeled with Rhodamine Red-X) bind to rabbit IgG immobilized on the silver surface. Non-binding anti-mouse antibodies labeled with Alexa Fluor 647 remain in solution. From [28].

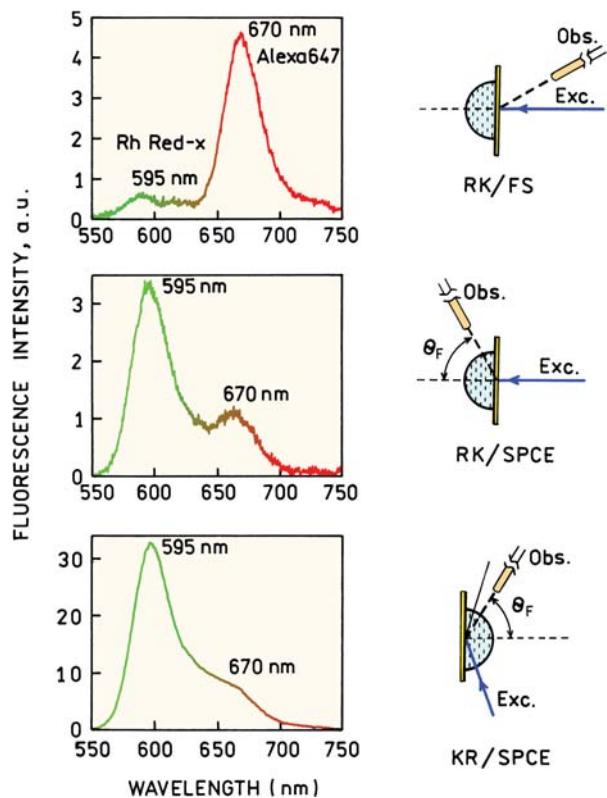


**Figure 26.14.** Emission spectra of the rhodamine red-X labeled anti-rabbit antibodies bound to rabbit IgG immobilized on a 50-nm silver mirror surface in the presence of a fluorescent background (anti-mouse antibodies labeled with Alexa Fluor 647). Top, free-space emission. Bottom, SPCE. From [28].

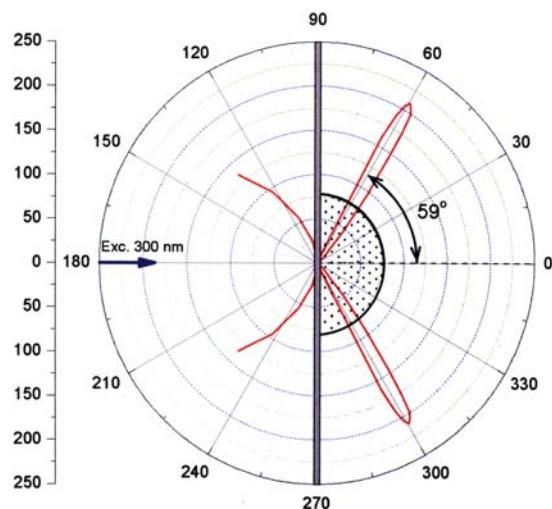


**Figure 26.15.** Angle-dependent SPCE of 2-aminopurine (2-AP) at 380 nm with reverse Kretschmann excitation. 2-AP is in a PVA film. Revised and reprinted with permission from [39]. Copyright © 2004, American Chemical Society.

been observed with aluminum films.<sup>29–31</sup> Figure 26.15 shows the angle-dependent emission of 2-aminopurine in PVA on a 20-nm-thick aluminum film. Once again SPCE occurs over a narrow angular distribution, but the distribution is wider than that found for silver (Figure 26.9). This wider angular distribution is a result of the optical properties of aluminum and appears to result in a greater angular dispersion of different wavelengths (Figure 26.16). The apparent emission spectra of 2-AP are strongly dependent on the observation angle.

## 26.6. FUTURE DEVELOPMENTS IN SPCE

SPCE offers numerous opportunities for new types of assays and sample configurations. A guiding concept may be the radiating plasmon (RP) model.<sup>32</sup> This model suggests that the optical and geometric properties of the sample can be chosen so that plasmons can radiate effectively and in the desired direction. An example of this approach is for a thin silver grating.

Excited fluorophores near such a grating display plasmon-coupled emission through the grating, with different wavelengths appearing at different angles. Plasmon-coupled emission through the grating provides opportunities for novel fluorescence-sensing configurations. Figure 26.17 shows an example where a sensing layer is positioned above the thin film grating. Emission from the sensing layer will couple through the grating and could be observed with

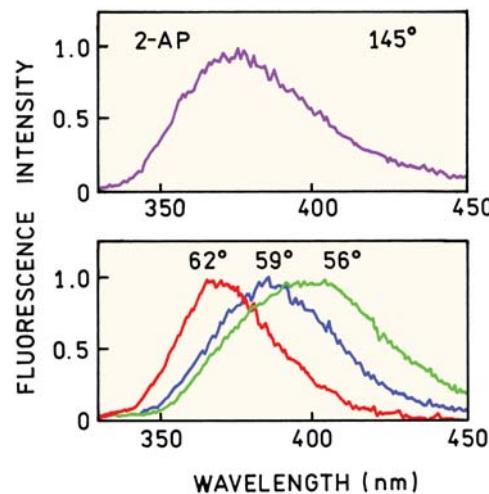


**Figure 26.16.** Free-space (top) and SPCE (bottom) of 2-AP. The emission spectra were recorded at different observation angles. Revised and reprinted with permission from [30]. Copyright © 2004, American Chemical Society.

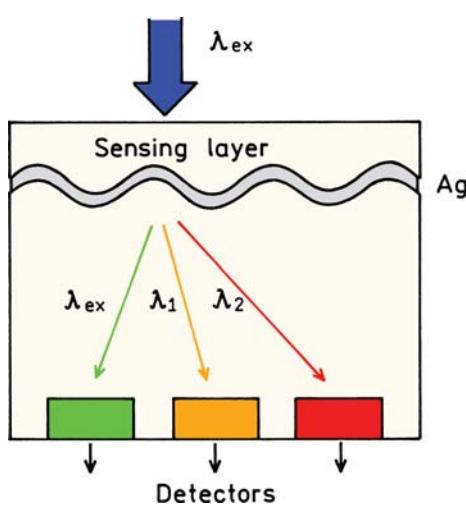


**Figure 26.17.** Fluorescence-sensing module based on grating-coupled plasmon emission.

closely spaced and/or proximity focused detectors. Ratio-metric sensing should be possible using the wavelength separation provided by the grating. The application of SPCE will be guided by theory that is becoming more refined.<sup>32–33</sup>

In 1998 a report appeared which showed that thick metal films with a regular array of sub-wavelength-size holes can display extraordinary optical transmission greatly in excess of the transmission expected based on the open area of the holes.<sup>34</sup> This effect is shown schematically in Figure 26.18. The silver film was 300 nm thick, which is opaque in the absence of holes. If the films contained nanoholes there was efficient transmission through the films, much more efficient than would be expected from the size of the holes. The transmitted wavelength depended on

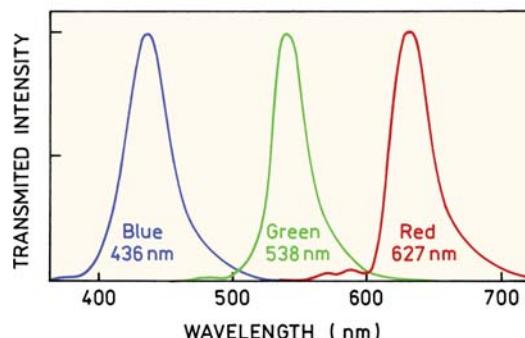
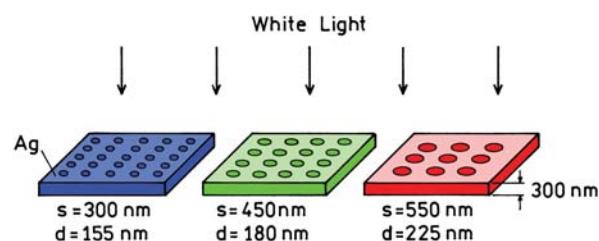


**Figure 26.18.** Light transmission through perforated but otherwise opaque silver films.  $s$  and  $d$  refer to the interhole spacing and diameter, respectively. Figure drawn from results in and reprinted with permission from [34]. Copyright © 2004, American Chemical Society.

the size and spacing of the holes. This observation resulted in theoretical studies to explain this effect.<sup>35–37</sup> It is now thought that the transmission is due to the creation of surface plasmons on one surface, migration of the plasmons through the holes, and subsequent radiation of the plasmons from the distal side of that metal. Such films should be useful in fluorescence devices. The transmitted radiation is strongly dependent on wavelength, so that the films may be used as both an excitation filter and/or for the creation of far-field radiation (Figure 26.19). For example, the hole

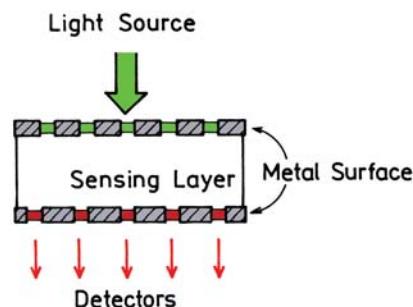
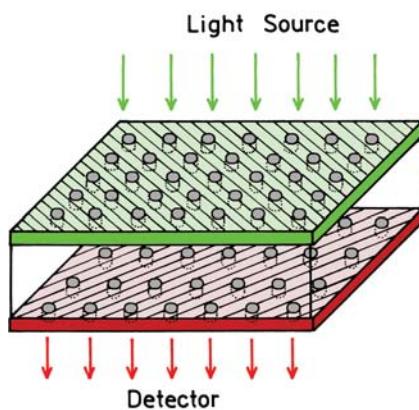


**Figure 26.19.** Fluorescence-sensing device base on plasmon transport through a metal surface with a regular array of holes.

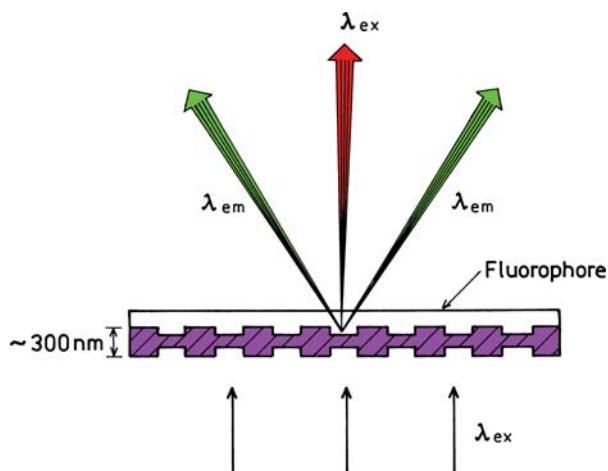


**Figure 26.20.** Directional and diffracted emission from a fluorophore on a metal film with linear opening. Adapted from [38].

spacing of the top metal layer could be selected to transmit the excitation wavelength, and the spacing in the lower layer selected to transmit the emission wavelength.

Even more elegant configurations are possible by combining plasmon engineering with nanoengineering, which can be used to obtain strongly directional emission. One example is shown in Figure 26.20 for an array of parallel lines etched through the metal.<sup>38–40</sup> This structure serves as a type of monochromator in that light near 600 nm is transmitted most efficiently. Importantly, the transmitted light

radiates only at defined directions into the far field on the distal side of the metal and the various wavelengths radiate in different directions. An even more remarkable result is shown in Figure 26.21 for a metal film with open concentric rings. In addition to being wavelength selective, the transmitted light migrates as a narrow beam into the far field.

These optical transmission phenomenon can be used with the properties of radiating plasmons to design novel fluorescence devices which serve as both the excitation filter and, more importantly, to focus the emission in the desired direction and pattern. Using the concept that if a plasmon can radiate it will, fluorophores could be placed on either side of the films shown in Figures 26.20 and 26.21. Depending on the geometry of the film and the optical constants of all the materials, fluorophores on or near the metal will transfer to the plasmons, which in turn will radiate according to electromagnetic theory.

In closing, we believe the rational design of metallic structures that couple with fluorophores and efficiently radiate the energy will provide the basis for a new generation of nanooptical sensing devices.

## REFERENCES

1. Lakowicz JR. 2004. Radiative decay engineering, 3: surface plasmon-coupled directional emission. *Anal Biochem* **324**:153–169.
2. Salamon Z, Macleod HA, Tollin G. 1997. Surface plasmon resonance spectroscopy as a tool for investigating the biochemical and biophysical properties of membrane protein systems, I: theoretical principles. *Biochim Biophys Acta* **1331**:117–129.
3. Melendez J, Carr R, Bartholomew DU, Kukanskis K, Elkind J, Yee S, Furlong C, Woodbury R. 1996. A commercial solution for surface plasmon sensing. *Sens Actuators B* **35–36**:212–216.
4. Liedberg B, Lundstrom I. 1993. Principles of biosensing with an extended coupling matrix and surface plasmon resonance. *Sens Actuators B* **11**:63–72.
5. Cooper MA. 2002. Optical biosensors in drug discovery. *Nature Rev* **1**:515–528.
6. Wegner GJ, Lee HJ, Corn RM. 2002. Characterization and optimization of peptide arrays for the study of epitope–antibody interactions using surface plasmon resonance imaging. *Anal Chem* **74**:5161–5168.
7. Frutos AG, Corn RM. 1998. SPR of ultrathin organic films. *Anal Chem* **70**:449A–455A.
8. Jordan CE, Frey BL, Kornguth S, Corn RM. 1994. Characterization of Poly-L-lysine adsorption onto alkanethiol-modified gold surfaces with polarization-modulation fourier transform infrared spectroscopy and surface plasmon resonance measurements. *Langmuir* **10**:3642–3648.
9. Frey BL, Jordan CE, Kornguth S, Corn RM. 1995. Control of the specific adsorption of proteins onto gold surfaces with poly(L-lysine) monolayers. *Anal Chem* **67**:4452–4457.

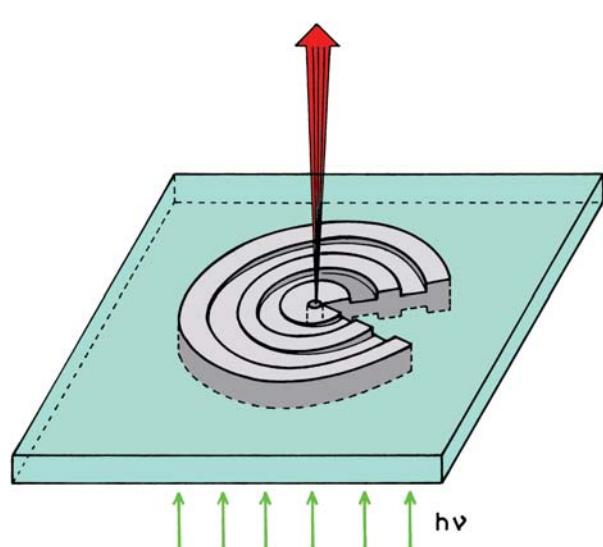


**Figure 26.21.** Directional emission from a fluorophore on a metal film with open concentric rings. Adapted from [38].

10. Axelrod D, Hellen EH, Fulbright RM. 1992. Total internal reflection fluorescence. In *Topics in fluorescence spectroscopy*, Vol 3: *Biochemical applications*, pp. 289–343. Ed JR Lakowicz. Plenum Press, New York.
11. Neumann T, Johansson ML, Kambhampati D, Knoll W. 2002. Surface-plasmon fluorescence spectroscopy. *Adv Funct Mater* **12**: 9–575–586.
12. Liebermann T, Knoll W. 2000. Surface-plasmon field-enhanced fluorescence spectroscopy. *Colloids Surf* **171**:115–130.
13. Ekgasit S, Stengel G, Knoll W. 2004. Concentration of dye-labeled nucleotides incorporated into DNA determined by surface plasmon resonance-surface plasmon fluorescence spectroscopy. *Anal Chem* **76**:4747–4755.
14. Ekgasit S, Thammacharoen C, Yu F, Knoll W. 2004. Evanescent field in surface plasmon resonance and surface plasmon field-enhanced fluorescence spectroscopies. *Anal Chem* **76**:2210–2219.
15. Roy S, Kim J-H, Kellis JT, Poulose AJ, Robertson CR, Gast AP. 2002. Surface plasmon resonance/surface plasmon enhanced fluorescence: an optical technique for the detection of multicomponent macromolecular adsorption at the solid/liquid interface. *Langmuir* **18**:6319–6323.
16. Yokota H, Saito K, Yanagida T. 1998. Single molecule imaging of fluorescently labeled proteins on metal by surface plasmons in aqueous solution. *Phys Rev Lett* **80**(20):4606–4609.
17. Yu F, Persson B, Löfås S, Knoll W. 2004. Attomolar sensitivity in bioassays based on surface plasmon fluorescence spectroscopy. *J Am Chem Soc* **126**:8902–8903.
18. Attridge JW, Daniels PB, Deacon JK, Robinson GA, Davidson GP. 1991. Sensitivity enhancement of optical immunosensors by the use of a surface plasmon resonance fluoroimmunoassay. *Biosens Bioelectron* **6**:201–214.
19. Liebermann T, Knoll W, Sluka P, Herrmann R. 2000. Complement hybridization from solution to surface-attached probe-oligonucleotides observed by surface-plasmon-field-enhanced fluorescence spectroscopy. *Colloids Surf* **169**:337–350.
20. Fukuda N, Mitsuishi M, Aoki A, Miyashita T. 2002. Photocurrent enhancement for polymer Langmuir–Blodgett monolayers containing ruthenium complex by surface plasmon resonance. *J Phys Chem B* **106**:7048–7052.
21. Stengel G, Knoll W. 2005. Surface plasmon field-enhanced fluorescence spectroscopy studies of primer extension reactions. *Nucleic Acids Res* **33**(7):e69.
22. Natan MJ, Lyon LA. 2002. Surface plasmon resonance biosensing with colloidal Au amplification. In *Metal nanoparticles: synthesis, characterization, and applications*, pp. 183–205. Ed DL Feldheim, CA Foss. Marcel Dekker, New York.
23. Gryczynski I, Malicka J, Gryczynski Z, Lakowicz JR. 2004. Radiative decay engineering, 4: experimental studies of surface plasmon-coupled directional emission. *Anal Biochem* **324**:170–182.
24. Thomas KG, Kamat PV. 2003. Chromophore-functionalized gold nanoparticles. *Acc Chem Res* **36**:888–898.
25. Kamat PV. 2002. Photophysical, photochemical, and photocatalytic aspects of metal nanoparticles. *J Phys Chem B* **106**(32):7729–7744.
26. Du H, Disney MD, Miller BL, Krauss TD. 2003. Hybridization-based unquenching of DNA hairpins on Au surfaces: prototypical ‘molecular beacon’ biosensors. *J Am Chem Soc* **125**:4012–4013.
27. Gryczynski I, Malicka J, Gryczynski Z, Lakowicz JR. 2004. Surface plasmon-coupled emission with gold films. *J Phys Chem* **108**: 12568–12574.
28. Matveeva E, Gryczynski Z, Gryczynski I, Lakowicz JR. 2004. Immunoassays based on directional surface plasmon coupled emission. *J Immunol Methods* **286**:130–140.
29. Malicka J, Gryczynski I, Gryczynski Z, Lakowicz JR. 2004. Surface plasmon-coupled ultraviolet emission of 2,5-diphenyl-1,3,4-oxadiazole. *J Phys Chem B* **108**:19114–19118.
30. Gryczynski I, Malicka J, Gryczynski Z, Nowaczyk K, Lakowicz JR. 2004. Ultraviolet surface plasmon-coupled emission using thin aluminum films. *Anal Chem* **76**:4076–4081.
31. Gryczynski I, Malicka J, Lukomska J, Gryczynski Z, Lakowicz JR. 2004. Surface plasmon-coupled polarized emission of N-acetyl-L-tryptophanamide. *Photochem Photobiol* **80**(3):482–485.
32. Calander N. 2004. Theory and simulation of surface plasmon-coupled directional emission from fluorophores at planar structures. *Anal Chem* **76**:2168–2173.
33. Lakowicz JR. 2004. Radiative decay engineering, 5: metal-enhanced fluorescence and plasmon emission. *Anal Biochem* **337**:171–194.
34. Ebbesen TW, Lezec HJ, Ghaemi HF, Thio T, Wolff PA. 1998. Extraordinary optical transmission through sub-wavelength hole arrays. *Nature* **381**:667–669.
35. Bonod N, Enoch S, Li L, Popov E, Neviere M. 2003. Resonant optical transmission through thin metallic films with and without holes. *Optics Express* **11**(5):482–490.
36. Zayats AV, Salomon L, De Fornel F. 2003. How light gets through periodically nanostructured metal films: a role of surface polaritonic crystals. *J Microsc* **210**(3):344–349.
37. Thio T, Lezec HJ, Ebbesen TW, Pellerin KM, Lewen GD, Nahata A, Linke RA. 2002. Giant optical transmission of sub-wavelength apertures: physics and applications. *Nanotechnology* **13**:429–432.
38. Martin-Moreno L, Garcia-Vidal FJ, Lezec HJ, Degiron A, Ebbesen TW. 2003. Theory of highly directional emission from a single sub-wavelength aperture surrounded by surface corrugations. *Phys Rev Lett* **90**(16):167401-1–167401-4.
39. Garcia-Vidal FJ, Lezec HJ, Ebbesen TW, Martin-Moreno L. 2003. Multiple paths to enhance optical transmission through a single sub-wavelength slit. *Phys Rev Lett* **90**(21):213901-1–213901-4.
40. Lezec HJ, Degiron A, Devaux E, Linke RA, Martin-Moreno L, Garcia-Vidal FJ, Ebbesen TW. 2002. Beaming light from a subwavelength aperture. *Science* **297**:820–822.

# Appendix I

## Corrected Emission Spectra

A relatively limited number of corrected emission spectra are available. In this Appendix we include the well-documented corrected spectra. It is not possible to state which are the "most correct." Corrected spectra can be interchanged from photons per wavenumber interval  $I(\bar{v})$  to photons per wavelength interval  $I(\lambda)$  using  $I(\lambda) = I(\bar{v})\lambda^{-2}$ , followed by normalization of the peak intensity to unity. Most of the compounds listed below satisfy the suggested criteria for emission spectral standards, which are as follows:

1. Broad wavelength emission with no fine structure
2. Chemically stable, easily available and purified
3. High quantum yield
4. Emission spectrum independent of excitation wavelength
5. Completely depolarized emission.

### I. EMISSION SPECTRA STANDARDS FROM 300 TO 800 NM

Corrected emission spectra on the wavelength scale were reported for six readily available fluorophores in neat solvents (Table I.1). The emission spectra of these standards overlap, providing complete coverage from 300 to 800 nm. For convenience the numerical values of the emission spectra are given in Table I.2. The values are plotted in Figure I.1, and the chemical structures are given in Figure I.2. These correct spectra cover almost all needed wavelengths. It is recommended that these spectra be adopted as the accepted standards for determination of instrument

corrections factors and for calculation of corrected emission spectra.

### 2. $\beta$ -CARBOLINE DERIVATIVES AS FLUORESCENCE STANDARDS

Corrected emission spectra of the carboline derivatives shown in Figure I.3 and I.4 were published.<sup>2</sup> All compounds were measured in 0.1 N H<sub>2</sub>SO<sub>4</sub>, except for 2-methyl-harmine, which was measured in 0.01 N H<sub>2</sub>SO<sub>4</sub>, 25°C. Corrected emission spectra were reported in graphical form (Figure I.3) and in numerical form (Table I.3). Quantum yields and lifetimes were also reported (Table I.4). Quantum yields were determined relative to quinine sulfate in 1.0

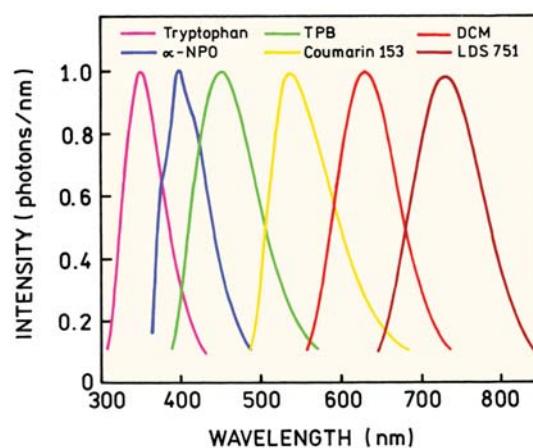


**Figure I.1.** Corrected emission spectra of six standards from [1]. From left to right the spectra are for tryptophan,  $\alpha$ -NPO, TPB, coumarin 153, DCM, and LDS 751.

**Table I.1.** Properties of the Emission Intensity Standards\*

Probe	CAS	Solvent	Excitation	Emission range
Tryptophan	54-12-6	Water	265	310–428
α-NPO	846-63-9	Methanol	315	364–486
TPB	1450-63-1	Cyclohexane	340	390–570
Coumarin 153	53518-18-6	Methanol	400	486–678
DCM	51325-91-8	Methanol	460	556–736
LDS 751	N/A	Methanol	550	646–844

\*CAS number (Chemical Abstract Service registry number) provides a unique identification for each fluorophore. The excitation wavelength and emission range is reported in nm. LDS-751 is a proprietary material of Exciton Inc. (Dayton, OH) and is similar to Styrl 8. Coumarin 153 is also referred to as Coumarin 540A (Exciton). From [1].

**Table I.2.** Normalized Emission Intensities for Each Emission Standard  
(emission wavelength is reported in nm and intensity given in photons/nm)

Tryptophan		NPO		TPB		Coumarine 153		DCM		LDS 751	
nm	int.	nm	int.	nm	int.	nm	int.	nm	int.	nm	int.
310	0.111	364	0.162	390	0.11	486	0.118	556	0.1	646	0.101
312	0.149	366	0.247	392	0.137	488	0.142	558	0.115	648	0.114
314	0.194	368	0.342	394	0.167	490	0.169	560	0.132	650	0.128
316	0.242	370	0.433	396	0.199	492	0.2	562	0.148	652	0.143
318	0.299	372	0.509	398	0.235	494	0.235	564	0.168	654	0.159
320	0.357	374	0.571	400	0.271	496	0.274	566	0.19	656	0.177
322	0.417	376	0.618	402	0.31	498	0.315	568	0.214	658	0.196
324	0.485	378	0.656	404	0.35	500	0.36	570	0.238	660	0.216
326	0.547	380	0.69	406	0.393	502	0.407	572	0.266	662	0.238
328	0.611	382	0.725	408	0.436	504	0.458	574	0.303	664	0.26
330	0.675	384	0.764	410	0.478	506	0.509	576	0.331	666	0.284
332	0.727	386	0.813	412	0.525	508	0.56	578	0.353	668	0.308
334	0.771	388	0.864	414	0.571	510	0.613	580	0.38	670	0.334
336	0.814	390	0.915	416	0.62	512	0.665	582	0.412	672	0.361
338	0.86	392	0.959	418	0.663	514	0.715	584	0.444	674	0.388
340	0.906	394	0.988	420	0.699	516	0.762	586	0.478	676	0.416
342	0.928	396	0.999	422	0.735	518	0.806	588	0.513	678	0.445
344	0.957	398	1	424	0.773	520	0.847	590	0.548	680	0.474
346	0.972	400	0.991	426	0.805	522	0.882	592	0.584	682	0.504
348	0.996	402	0.978	428	0.834	524	0.914	594	0.62	684	0.534
350	1	404	0.959	430	0.864	526	0.941	596	0.659	686	0.564
352	0.999	406	0.94	432	0.887	528	0.962	598	0.696	688	0.594
354	0.987	408	0.921	434	0.91	530	0.979	600	0.732	690	0.624
356	0.972	410	0.901	436	0.931	532	0.99	602	0.763	692	0.653
358	0.946	412	0.886	438	0.951	534	0.997	604	0.79	694	0.682
360	0.922	414	0.87	440	0.963	536	1	606	0.818	696	0.711
362	0.892	416	0.855	442	0.976	538	1	608	0.842	698	0.738
364	0.866	418	0.835	444	0.985	540	0.996	610	0.869	700	0.765
366	0.837	420	0.803	446	0.991	542	0.991	612	0.893	702	0.791
368	0.798	422	0.773	448	0.998	544	0.981	614	0.915	704	0.815
370	0.768	424	0.743	450	0.999	546	0.97	616	0.934	706	0.839
372	0.728	426	0.708	452	1	548	0.958	618	0.953	708	0.86
374	0.697	428	0.676	454	0.993	550	0.944	620	0.968	710	0.881
376	0.663	430	0.644	456	0.987	552	0.929	622	0.98	712	0.899
378	0.627	432	0.611	458	0.981	554	0.914	624	0.989	714	0.916
380	0.592	434	0.58	460	0.969	556	0.898	626	0.995	716	0.931
382	0.558	436	0.55	462	0.957	558	0.884	628	0.999	718	0.946
384	0.523	438	0.521	464	0.944	560	0.867	630	1	720	0.956
386	0.492	440	0.494	466	0.931	562	0.852	632	0.998	722	0.965

[continued]

Table I.2, cont'd

388	0.461	442	0.467	468	0.915	564	0.835	634	0.994	724	0.973
390	0.43	444	0.441	470	0.896	566	0.818	636	0.986	726	0.978
392	0.404	446	0.418	472	0.879	568	0.801	638	0.978	728	0.982
394	0.375	448	0.394	474	0.856	570	0.785	640	0.964	730	0.984
396	0.348	450	0.371	476	0.835	572	0.768	642	0.952	732	0.983
398	0.323	452	0.349	478	0.816	574	0.75	644	0.938	734	0.982
400	0.299	454	0.326	480	0.796	576	0.729	646	0.923	736	0.977
402	0.279	456	0.306	482	0.775	578	0.712	648	0.904	738	0.971
404	0.259	458	0.285	484	0.752	580	0.69	650	0.886	740	0.963
406	0.239	460	0.266	486	0.727	582	0.672	652	0.867	742	0.954
408	0.222	462	0.248	488	0.706	584	0.653	654	0.843	744	0.943
410	0.204	464	0.232	490	0.68	586	0.634	656	0.821	746	0.931
412	0.19	466	0.216	492	0.657	588	0.615	658	0.795	748	0.917
414	0.176	468	0.201	494	0.633	590	0.596	660	0.771	750	0.902
416	0.163	470	0.187	496	0.609	592	0.576	662	0.745	752	0.885
418	0.151	472	0.174	498	0.586	594	0.557	664	0.718	754	0.868
420	0.139	474	0.162	500	0.564	596	0.538	666	0.694	756	0.849
422	0.128	476	0.151	502	0.542	598	0.518	668	0.666	758	0.83
424	0.118	478	0.14	504	0.521	600	0.501	670	0.639	760	0.81
426	0.109	480	0.131	506	0.499	602	0.483	672	0.613	762	0.789
428	0.101	482	0.122	508	0.476	604	0.465	674	0.586	764	0.767
		484	0.113	510	0.456	606	0.447	676	0.559	766	0.745
		486	0.105	512	0.437	608	0.43	678	0.534	768	0.722
				514	0.419	610	0.414	680	0.509	770	0.699
				516	0.4	612	0.398	682	0.485	772	0.676
				518	0.382	614	0.383	684	0.46	774	0.653
				520	0.364	616	0.368	686	0.431	776	0.63
				522	0.348	618	0.355	688	0.407	778	0.606
				524	0.332	620	0.341	690	0.391	780	0.583
				526	0.318	622	0.328	692	0.371	782	0.56
				528	0.302	624	0.315	694	0.355	784	0.537
				530	0.289	626	0.303	696	0.336	786	0.514
				532	0.274	628	0.292	698	0.319	788	0.492
				534	0.261	630	0.28	700	0.302	790	0.47
				536	0.249	632	0.269	702	0.284	792	0.449
				538	0.237	634	0.258	704	0.268	794	0.428
				540	0.226	636	0.248	706	0.254	796	0.407
				542	0.215	638	0.239	708	0.239	798	0.387
				544	0.205	640	0.229	710	0.225	800	0.368
				546	0.194	642	0.219	712	0.212	802	0.349
				548	0.184	644	0.211	714	0.199	804	0.331
				550	0.175	646	0.204	716	0.188	806	0.313
				552	0.166	648	0.195	718	0.177	808	0.296
				554	0.158	650	0.188	720	0.166	810	0.28
				556	0.15	652	0.18	722	0.156	812	0.264
				558	0.143	654	0.173	724	0.147	814	0.249
				560	0-135	656	0.166	726	0.138	816	0.234
				562	0.129	658	0.159	728	0.131	818	0.221
				564	0.122	660	0.152	730	0.123	820	0.207
				566	0.116	662	0.146	732	0.116	822	0.195
				568	0.11	664	0.14	734	0.109	824	0.183
				570	0.105	666	0.134	736	0.103	826	0.171
						668	0.129			828	0.16
						670	0.124			830	0.15
						672	0.118			832	0.14
						674	0.113			834	0.131
						676	0.108			836	0.122
						678	0.104			838	0.114
										840	0.106
										842	0.099
										844	0.092

**Table I.3.** Normalized and Corrected Fluorescence Spectra for Nor-harmane, Harmane, Harmine, 2-Methyl Harmine, and Harmaline in  $H_2SO_4$  Aqueous Solutions (0.1 N  $H_2SO_4$  for nor-harmane, harmane, harmine and 2-methyl harmine and 0.01 N for harmaline)\*

Wave length (nm)	Nor-harmane or $\beta$ -carboline	Harmane	Harmine	2-Methyl harmine	Harmaline
400			0.63		
405			0.76	0.53	
410			0.87	0.68	
415		0.56	0.93	0.78	
420		0.70	0.98	0.89	
425	0.54	0.81	1.00	0.95	
430	0.67	0.90	0.99	0.98	
433				1.00	
435	0.79	0.97	0.94	0.99	
440	0.90	1.00	0.97**	0.97	
445	0.96	0.98	0.80	0.90	
450	0.99	0.94	0.73	0.84	
454	1.00				
455	0.99	0.88	0.64	0.76	
460	0.98	0.82	0.54	0.66	0.48
465	0.96	0.76	0.48	0.58	0.59
470	0.93	0.69		0.52	0.69
475	0.87	0.61		0.44	0.78
480	0.83	0.56			0.86
485	0.78	0.50			0.92
490	0.73				0.96
495	0.67				0.98
498					1.00
500	0.61				0.99
505	0.54				0.97
510					0.96
515					0.92
520					0.89
525					0.83
530					0.77
535					0.74
540					0.71
550					0.59
560					0.49

\*From [2].

\*\*This number is in question.

**Table I.4.** Quantum Yields and Lifetimes of the  $\beta$ -Carboline Standards<sup>a</sup> (from [2])

Compound	Quantum yield	Lifetime (ns)
Nor-harmane	$0.58 \pm 0.02$	21.2
Harmane	$0.83 \pm 0.03$	$20.0 \pm 0.5$
Harmine	$0.45 \pm 0.03$	$6.6 \pm 0.2$
2-Methylharmine	$0.45 \pm 0.03$	$6.5 \pm 0.2$
Harmaline	$0.32 \pm 0.02$	$5.3 \pm 0.2$

<sup>a</sup>Same conditions as in Table I.3.

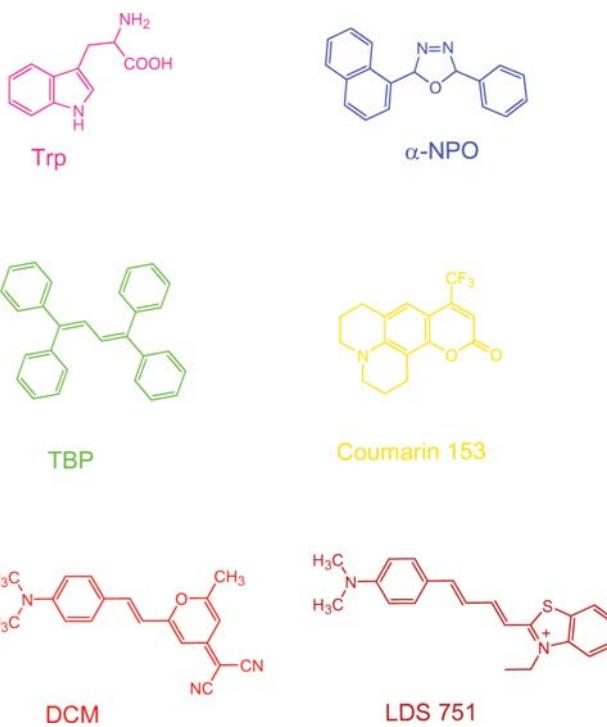


**Figure I.2.** Chemical structure of the emission spectra standards.

$N H_2SO_4$ , with  $Q = 0.546$ . Corrected spectra are in relative quanta per wavelength interval. A second corrected emission spectrum of nor-harmane ( $\beta$ -carboline) was also reported (Table I.5).<sup>3</sup> The spectral properties of  $\beta$ -carboline are similar to quinine sulfate. While the polarization of the  $\beta$ -carboline standards was not measured, these values are likely to be near zero given the lifetimes near 20 ns (Table I.4).

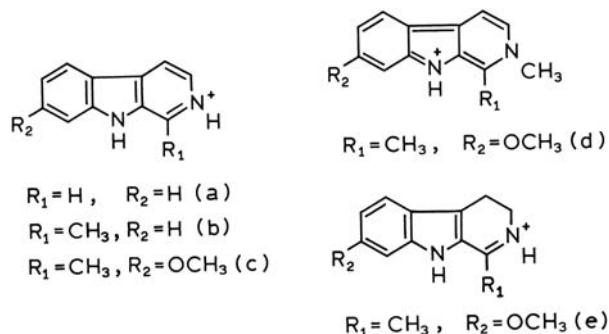


**Figure I.3.**  $\beta$ -Carboline standards. Cationic species structures: (a)  $\beta$ -carboline or nor-harmane, (b) harmane, (c) harmine, (d) 2-methyl harmine, and (e) harmaline. Revised from [2]. Copyright © 1992, with permission from Elsevier Science.

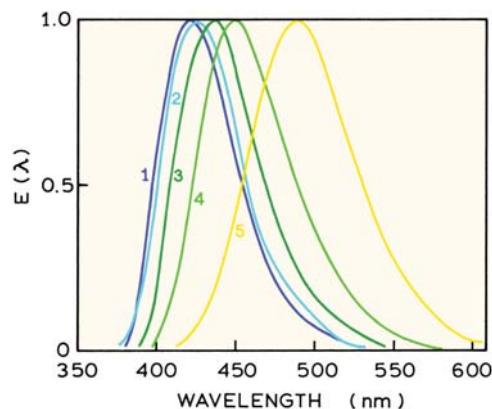


**Figure I.4.** Corrected and normalized fluorescence spectra for some  $\beta$ -carboline derivatives: (1) harmine 0.1 N  $H_2SO_4$ ; (2) 2-methyl harmine 0.1 N  $H_2SO_4$ ; (3) harmane 0.1 N  $H_2SO_4$ ; (4) nor-harmane 0.1 N  $H_2SO_4$ ; (5) harmaline 0.01 N  $H_2SO_4$ . Revised from [2]. Copyright © 1992, with permission from Elsevier Science.

### 3. CORRECTED EMISSION SPECTRA OF 9,10-DIPHENYLANTHRACENE, QUININE, AND FLUORESCIN

Corrected spectra in quanta per wavelength interval  $I(\lambda)$  were published for these three compounds<sup>4</sup> (Figure I.5 and Table I.6). The emission spectrum for quinine was found to be at somewhat shorter wavelengths than that published by Melhuish.<sup>5</sup>

### 4. LONG-WAVELENGTH STANDARDS

Corrected emission spectra in relative quanta per wavelength interval were reported<sup>4</sup> for quinine sulfate (QS), 3-

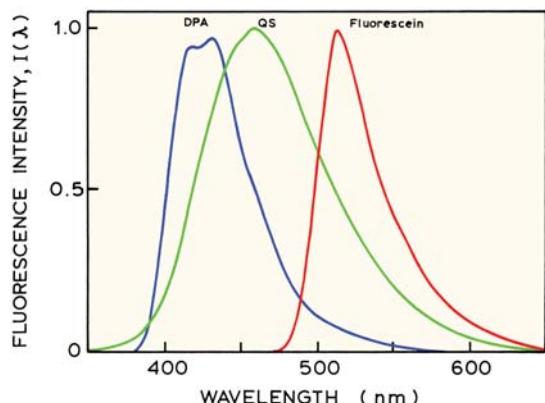


**Figure I.5.** Corrected emission spectra in relative photons per wavelength interval ( $I(\lambda)$ ) for 9,10-diphenylanthracene, quinine sulfate, and fluorescein. From [4].

**Table I.5.** Corrected Emission Intensities for  $\beta$ -Carboline in 1.0 N  $H_2SO_4$  at 25°C<sup>a</sup>

Wave-length (nm)	Corrected intensity	Wave-length (nm)	Corrected intensity
380	0.001	510	0.417
390	0.010	520	0.327
400	0.068	530	0.255
410	0.243	540	0.193
420	0.509	550	0.143
430	0.795	560	0.107
440	0.971	570	0.082
450	1.000	580	0.059
460	0.977	590	0.044
470	0.912	600	0.034
480	0.810	610	0.025
490	0.687	620	0.019
500	0.540	630	0.011

<sup>a</sup>Excitation at 360 nm. From [3].

aminophthalimide (3-APT), and N,N-dimethylamino-m-nitrobenzene (N,N-DMAMB). Chemical structures are shown in Figure I.6. These standards are useful because they extend the wavelength range to 750 nm (Figure I.7).

**Table I.6.** Corrected Emission Spectra in Relative Quanta per Wavelength Interval (from [4])

Quinine sulfate <sup>a</sup> λ (nm)	$I(\lambda)$	Fluorescein <sup>b</sup> λ (nm)	$I(\lambda)$	DPA <sup>c</sup> λ (nm)	$I(\lambda)$
310	0	470	0	380	0
350	4	480	7	390	39
380	18	490	151	400	423
400	151	495	360	412	993
410	316	500	567	422	914
420	538	505	795	432	1000
430	735	510	950	440	882
440	888	512	1000	450	607
445	935	515	985	460	489
450	965	520	933	470	346
455	990	525	833	480	222
457.2	1000	530	733	490	150
400	998	540	533	500	103
465	979	550	417	550	4
470	951	560	333	600	0
475	916	570	233		
480	871	580	167		
490	733	600	83		
500	616	620	42		
520	408	640	17		
550	171	650	8		
600	19	670	0		
650	3				
700	0				

<sup>a</sup>Quinine sulfate was in 1.0 N  $H_2SO_4$ , excitation at 346.5.

<sup>b</sup>Fluorescein (Uranine) was in 0.1 N NaOH, excitation at 322 nm.

<sup>c</sup>9,10-diphenylanthracene (DPA) was in benzene, excitation at 385 nm.

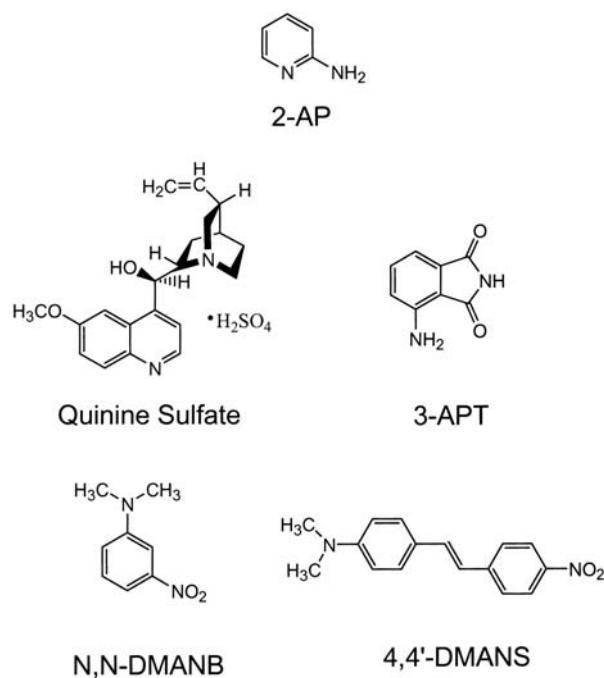


**Figure I.6.** Chemical structure of fluorophores used as spectral standards.

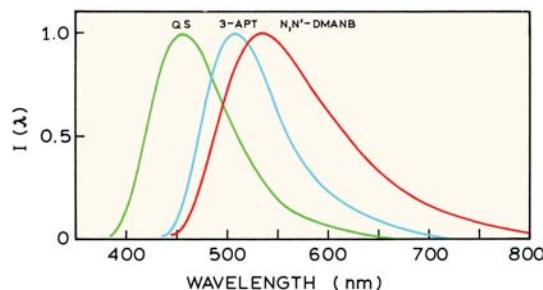


**Figure I.7.** Corrected emission spectra in relative quanta per wavelength interval ( $I(\lambda)$ ). The quinine sulfate (QS) was in 0.1 N  $H_2SO_4$ . 3-aminophthalimide (3-APT) was in 0.1 N  $H_2SO_4$ . N,N-dimethylamino-m-nitrobenzene (N,N'-DMANB) was in 70% n-hexane, 30% benzene. Modified from [4].

The data were not reported in numerical form. These corrected emission spectra  $I(\lambda)$  were in agreement with that reported earlier<sup>6</sup> in relative quanta per wavenumber ( $I(\bar{v})$ ), following the appropriate transformation.

A more complete set of corrected spectra,<sup>6,7</sup> in  $I(\bar{v})$  per wavenumber interval, are summarized numerically in Figure I.8 and Table I.7. These data contain an additional standard, 4-dimethylamino-4'-nitrostilbene (4,4'-DMANS), which extends the wavelength range to 940 nm. These spectra are plotted on the wavenumber scale in Figure I.8. For

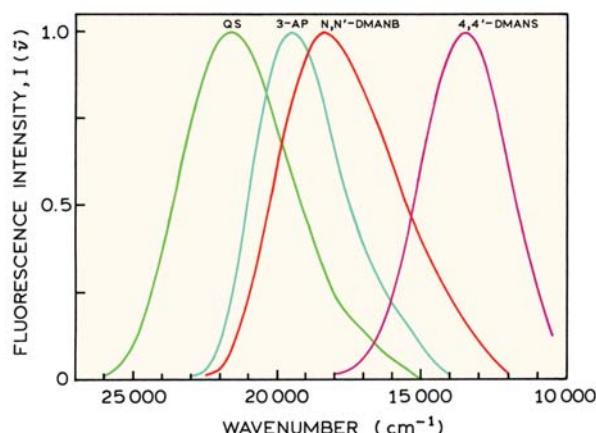


**Figure I.8.** Corrected emission spectra in relative quanta per wavenumber interval  $I(\bar{v})$ . See Table I.6 for additional details. Data from [6] and [7].

convenience the data were transformed to the wavelength scale, and are shown in Figure I.9 and Table I.8. In summarizing these corrected spectra we omitted  $\beta$ -naphthol, whose emission spectrum depends on pH and buffer concentration. Because these factors change its spectral shape, naphthol is not a good standard.

## 5. ULTRAVIOLET STANDARDS

2-aminopyridine (Figure I.10) has been suggested as a standard from 315 to 480 nm,<sup>8,9</sup> which covers most but not all of the wavelengths needed for tryptophan fluorescence

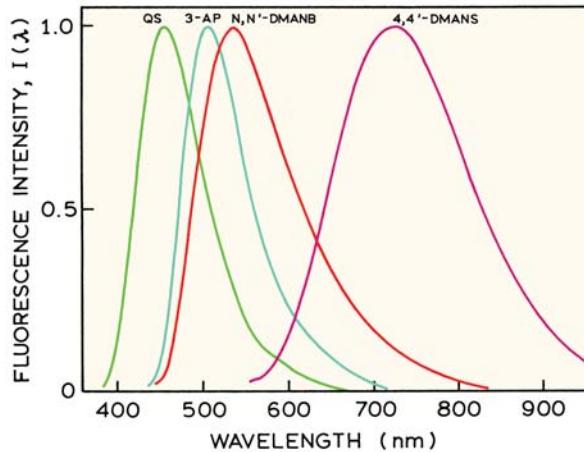


**Figure I.9.** Corrected emission spectra in relative quanta per wavelength interval  $I(\lambda)$ . See Table I.5 for additional details. Data from [6] and [7].

**Table I.7.** Corrected Emission Spectra in Relative Quanta per Wavenumber Interval

Quinine sulfate <sup>b</sup> $\bar{v}$ (cm <sup>-1</sup> )	$I(\bar{v})$	3-APTC $\bar{v}$ (cm <sup>-1</sup> )	$I(\bar{v})$	N,N'-DMANB <sup>d</sup> $\bar{v}$ (cm <sup>-1</sup> )	$I(\bar{v})$	4,4'-DMANS <sup>e</sup> $\bar{v}$ (cm <sup>-1</sup> )	$I(\bar{v})$
15.0	0	14.0	1.5	12.0	2.0	10.5	12.5
15.25	1.5	14.25	3.0	12.25	4.0	10.75	18.5
15.5	3.0	14.5	5.0	12.5	6.0	11.0	24.5
15.75	4.5	14.75	7.5	12.75	8.5	11.25	32.5
16.0	6.0	15.0	10.0	13.0	11.0	11.5	41.5
16.25	7.5	15.25	13.0	13.25	13.5	11.75	50.5
16.5	9.5	15.5	16.0	13.5	17.0	12.0	60.0
16.75	11.5	15.75	19.0	13.75	20.0	12.25	70.5
17.0	14.0	16.0	22.0	14.0	23.5	12.5	80.5
17.25	16.0	16.25	25.5	14.25	27.5	12.75	89.0
17.5	18.0	16.5	29.5	14.5	31.0	13.0	95.0
17.75	20.5	16.75	33.5	14.75	35.5	13.25	98.5
18.0	24.0	17.0	38.5	15.0	40.5	13.5	100.0
18.25	28.5	17.25	44.0	15.25	45.0	13.75	98.0
18.5	34.5	17.5	50.0	15.5	50.0	14.0	94.0
18.75	40.5	17.75	56.5	15.75	55.5	14.25	88.0
19.0	46.0	18.0	65.0	16.0	61.5	14.5	81.0
19.25	52.5	18.25	73.0	16.25	68.0	14.75	72.0
19.5	58.5	18.5	82.5	16.5	73.0	15.0	61.5
19.75	65.0	18.75	90.0	16.75	78.0	15.25	51.0
20.0	71.5	19.0	95.0	17.0	82.5	15.5	41.0
20.25	78.5	19.25	98.5	17.25	87.0	15.75	32.0
20.5	84.5	19.5	100.0	17.5	91.5	16.0	24.0
20.75	90.0	19.75	98.5	17.75	95.0	16.25	17.5
21.0	95.0	20.0	94.5	18.0	97.5	16.5	13.0
21.25	98.5	20.25	87.5	18.25	99.5	16.75	9.0
21.5	100.0	20.5	77.5	18.5	99.5	17.0	6.0
21.75	99.5	20.75	66.0	18.75	97.5	17.25	4.0
22.0	98.0	21.0	53.0	19.0	93.5	17.5	2.5
22.25	94.5	21.25	39.5	19.25	87.0	17.75	2.0
22.5	89.0	21.5	28.0	19.5	80.0	18.0	1.5
22.75	82.5	21.75	17.5	19.75	71.5		
23.0	74.0	22.0	11.0	20.0	61.0		
23.25	65.5	22.25	6.0	20.25	51.0		
23.5	55.5	22.5	3.0	20.5	41.5		
23.75	46.0	22.75	1.5	20.75	32.5		
24.0	37.5	23.0	1.0	21.0	23.5		
24.25	29.5			21.25	16.0		
24.5	21.0			21.5	10.5		
24.75	15.0			21.75	6.0		
25.0	10.5			22.0	3.0		
25.25	6.5			22.25	2.0		
25.5	4.0			22.5	1.5		
25.75	2.5						
26.0	1.0						
Max.		Max.		Max.		Max.	
21.6	100.0	19.5	100.0	18.4	100.0	13.5	100.0

<sup>a</sup>All listings are in 10<sup>3</sup> cm<sup>-1</sup>, that is, 13.5 is 13,500 cm<sup>-1</sup>.<sup>b</sup>Quinine sulfate (10<sup>-3</sup> M) in 0.1 N H<sub>2</sub>SO<sub>4</sub>, 20°C.<sup>c</sup>3-aminophthalimide (5 x 10<sup>-4</sup> M) in 0.1 N H<sub>2</sub>SO<sub>4</sub>, 20°C.<sup>d</sup>N,N-dimethylamino-m-nitrobenzene (10<sup>-4</sup> M) in 30% benzene, 70% n-hexane, 20°C.<sup>e</sup>4-dimethylamino-4'-nitrostilbene in o-dichlorobenzene, 20°C.

**Table I.8.** Corrected Emission Spectra in Relative Quanta per Wavelength Interval<sup>f</sup>

Quinine sulfate <sup>b</sup> λ (nm) <sup>a</sup>	I(λ)	3-APT <sup>c</sup> λ (nm)	I(λ)	N,N-DMANB <sup>d</sup> λ (nm)	I(λ)	4,4'-DMANS <sup>e</sup> λ (nm)	I(λ)
384.6	1.4	434.8	1.4	444.4	2.2	555.6	2.6
388.3	3.5	439.6	2.0	449.4	2.9	563.4	3.4
392.2	5.5	444.4	4.0	454.5	4.2	571.4	4.1
396.0	8.7	449.4	7.7	459.8	8.3	579.7	6.4
400.0	13.8	454.5	13.9	465.1	14.2	588.2	9.4
404.0	19.4	459.8	21.5	470.6	21.1	597.0	13.6
408.2	26.6	465.1	33.7	476.2	30.2	606.1	19.1
412.4	36.6	470.6	46.4	481.9	40.8	615.4	24.9
416.7	45.5	476.2	60.8	487.8	50.9	625.0	33.2
421.1	54.7	481.9	74.0	493.8	61.0	634.9	42.8
425.5	64.6	487.8	84.8	500.0	71.2	645.2	53.2
430.1	74.6	493.8	93.4	506.3	81.4	655.7	64.0
434.8	82.5	500.0	98.4	512.8	88.7	666.7	74.7
439.6	90.0	506.3	100.0	519.5	94.1	678.0	84.5
444.4	95.0	512.8	99.0	526.3	98.5	689.7	91.9
449.4	98.6	519.5	95.0	533.3	100.0	701.8	96.4
454.5	100.0	526.3	89.2	540.5	99.3	714.3	99.4
459.8	99.2	533.3	82.3	547.9	96.7	727.3	100.0
465.1	97.5	540.5	73.5	555.6	92.2	740.7	98.4
470.6	93.8	547.9	63.3	563.4	87.3	754.7	93.3
476.2	88.3	555.6	54.8	571.4	81.8	769.2	86.7
481.9	81.7	563.4	46.3	579.7	75.5	784.3	78.1
487.8	74.9	571.4	39.9	588.2	69.6	800.0	67.9
493.8	67.9	579.7	34.1	597.0	63.8	816.3	57.1
500.0	60.3	588.2	29.0	606.1	58.0	833.3	46.6
506.3	53.4	597.0	24.5	615.4	52.4	851.1	37.6
512.8	46.9	606.1	20.9	625.0	45.9	869.6	29.6
519.5	41.0	615.4	17.5	634.9	40.2	888.9	22.2
526.3	35.0	625.0	14.7	645.2	35.0	909.1	16.0
533.3	30.0	634.9	12.3	655.7	30.5	930.2	11.5
540.5	24.9	645.2	10.0	666.7	26.6	952.4	7.4
547.9	20.0	655.7	7.9	678.0	22.5		
555.6	16.4	666.7	5.9	689.7	19.0		
563.4	13.6	678.0	4.2	701.8	16.3		
571.4	11.6	689.7	2.7	714.3	13.4		
579.7	10.0	701.8	1.6	727.3	11.0		
588.2	8.5	714.3	0.8	740.7	9.0		
597.0	6.8			754.7	6.9		
606.1	5.5			769.2	5.4		
615.4	4.2			784.3	4.0		
625.0	3.2			800.0	2.7		
634.9	2.4			816.3	1.8		
645.2	1.5			833.3	0.8		
655.7	0.7						
666.7	0.0						

<sup>a</sup> Calculated from Table I.7.<sup>b</sup> Quinine sulfate ( $10^{-3}$  M) in 0.1 N H<sub>2</sub>SO<sub>4</sub>, 20°C.<sup>c</sup> 3-aminophthalimide ( $5 \times 10^{-4}$  M) in 0.1 N H<sub>2</sub>SO<sub>4</sub>, 20°C.<sup>d</sup> N,N'-dimethylamino-m-nitrobenzene ( $10^{-4}$  M) in 30% benzene, 70% m-heptane, 20°C<sup>e</sup> 4-dimethylamino-4'-nitrostilbene in o-dichlorobenzene, 20°C.<sup>f</sup> Calculated from Table I.7 using  $I(\lambda) = \lambda^{-2} I(v)$ , followed by normalization of the peak intensity to 100.

**Table I.9.** Corrected Emission Spectrum of 2-Aminopyridine<sup>a</sup>

$\bar{v}$ (cm <sup>-1</sup> )	$I(\bar{v})$	$\lambda$ (nm)	$I(\lambda)^b$
20,800	0.010	480.8	0.006
21,500	0.038	465.1	0.024
22,200	0.073	450.5	0.049
23,000	0.133	434.8	0.095
23,800	0.264	420.2	0.202
24,700	0.450	404.9	0.371
25,600	0.745	390.6	0.660
26,600	0.960	375.9	0.918
27,200	1.00	367.7	1.00
27,800	0.939	359.7	0.981
28,900	0.587	346.0	0.663
30,150	0.121	331.7	0.149
31,000	0.033	322.6	0.049

<sup>a</sup>10<sup>-5</sup> M in 0.1 N<sub>2</sub>SO<sub>4</sub>. From [10] and [11].<sup>b</sup>Calculated using  $I(\lambda) = I(\bar{v})\lambda^{-2}$  followed by normalization of the maximum to unity.

(Table I.9 and Figure I.10). Corrected emission spectra have been reported<sup>10</sup> for phenol and the aromatic amino acids, phenylalanine, tyrosine and tryptophan (Figure I.11).

## 6. ADDITIONAL CORRECTED EMISSION SPECTRA

Corrected spectra as  $I(\bar{v})$  versus  $\bar{v}$  can be found in the compendium by Berlman.<sup>11</sup> Included in that volume are a number of UV-emitting species including indole and phenol, which can be used to obtain corrected emission spectra of proteins. For convenience Berlman's spectra for phenol and

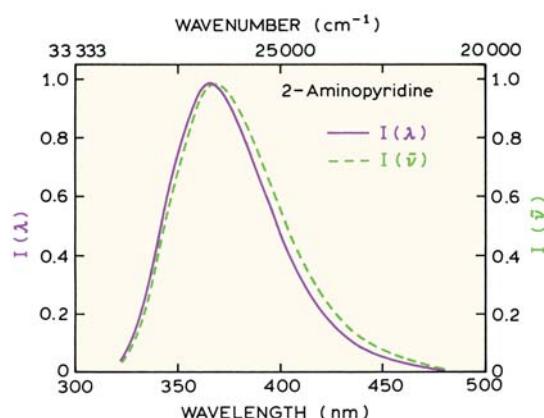


**Figure I.10.** Corrected emission spectra of 2-aminopyridine in relative quanta per wavenumber interval  $I(\bar{v})$  and per wavelength interval  $I(\lambda)$ . See Table I.8 for additional details. From [8] and [9].

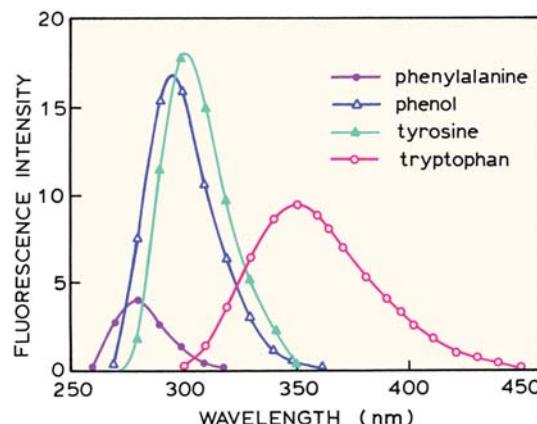


**Figure I.11.** Corrected emission spectrum ( $I(\lambda)$ ) for phenylalanine (●), phenol (△), tyrosine (▲), and tryptophan (○). The areas underneath the curves are proportional to the quantum yields. Data from [10].

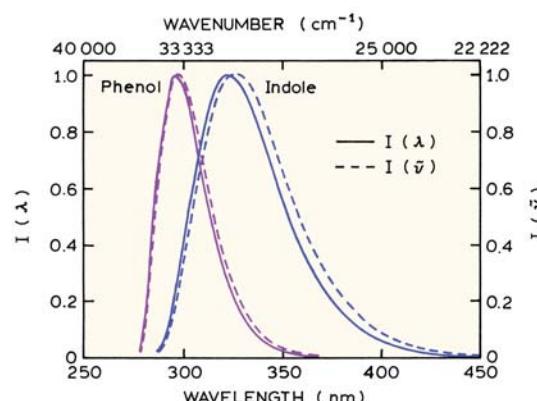


**Figure I.12.** Corrected emission spectra of phenol in methanol and indole in ethanol. From [11].

indole are provided as Figure I.12. Cresyl violet in methanol has been proposed as a quantum yield and emission spectral standard for red wavelengths.<sup>12</sup> In methanol at 22°C the quantum yield of cresyl violet is reported to be 0.54, with an emission maximum near 614 nm. The use of quinine as a standard has occasionally been questioned.<sup>13–16</sup> Additional discussion about corrected emission spectra can be found in [17–20].

## REFERENCES

1. Gardecki JA, Maroncelli M. 1998. Set of secondary emission standards for calibration of the spectral responsibility in emission spectroscopy. *Appl Spectrosc* 52:1179–1189.

2. Pardo A, Reyman D, Poyato JML, Medina F. 1992. Some  $\beta$ -carboline derivatives as fluorescence standards. *J Luminesc* **51**:269–274.
3. Ghiggino KP, Skilton PF, Thistletonwaite PJ. 1985.  $\beta$ -Carboline as a fluorescence standard. *J Photochem* **31**:113–121.
4. Heller CA, Henry RA, McLaughlin BA, Bliss DE. 1974. Fluorescence spectra and quantum yields: quinine, uranine, 9,10-diphenylanthracene, and 9,10-bis(phenylethynyl) anthracenes. *J Chem Eng Data* **19**(3):214–219.
5. Melhuish WH. 1960. A standard fluorescence spectrum for calibrating spectro-fluorophotometers. *J Phys Chem* **64**:762–764.
6. Lippert EN, Nägele W, Seibold-Blankenstein I, Staiger W, Voss W. 1959. Messung von fluoreszenzspektren mit hilfe von spektralphotometern und vergleichsstandards. *Z Anal Chem* **170**:1–18.
7. Schmillen A, Legler R. 1967. *Landolt-Börnstein*, Vol. 3: *Lumineszenz Organischer Substanzen*. Springer-Verlag, New York, pp. 228–229.
8. Testa AC. 1969. Fluorescence quantum yields and standards. *Am Instrum Co, Newslett Luminesc* **4**(4):1–3.
9. Rusakowicz R, Testa AC. 1968. 2-aminopyridine as a standard for low wavelength spectrofluorimetry. *J Phys Chem* **72**:2680–2681.
10. Chen RF. 1967. Fluorescence quantum yields of tryptophan and tyrosine. *Anal Lett* **1**:35–42.
11. Berlman IB. 1971. *Handbook of fluorescence spectra of aromatic molecules*, 2nd ed, Academic Press, New York.
12. Magde D, Brannon JH, Cremers TL, Olmsted J. 1979. Absolute luminescence yield of cresyl violet: a standard for the red. *J Phys Chem* **83**(6):696–699.
13. Chen RF. 1967. Some characteristics of the fluorescence of quinine. *Anal Biochem* **19**:374–387.
14. Fletcher AN. 1968. Fluorescence emission band shift with wavelength of excitation. *J Phys Chem* **72**:2742–2749.
15. Itoh K, Azumi T. 1973. Shift of emission band upon excitation at the long wavelength absorption edge: a preliminary survey for quinine and related compounds. *Chem Phys Lett* **22**(2):395–399.
16. Gill JE. 1969. The fluorescence excitation spectrum of quinine bisulfate. *Photochem Photobiol* **9**:313–322.
17. Melhuish WH. 1972. Absolute spectrofluorometry. *J Res Natl Bur Stand* **76A**:547–560.
18. Credi A, Prodi L. 1996. Correction of luminescence intensity measurements in solution: a simple method to standard spectrofluorimeters. *EPA Newslett* **58**:50–59.
19. Eaton DF. 1988. Reference materials for fluorescence measurement. *Pure Appl Chem* **60**(7):1107–1114.
20. Zwinkels JC, Gauthier F. 1999. Instrumentation, standards, and procedures used at the National Research Council of Canada for high-accuracy fluorescence measurements. *Anal Chimica Acta* **380**:193–209.

## Appendix II

# Fluorescence Lifetime Standards

It is valuable to have fluorophores of known lifetimes for use as lifetime standards in time-domain or frequency-domain measurements. Perhaps more important than the actual lifetime is knowledge that the fluorophore displays single-exponential decays. Such fluorophores are useful for testing the time-resolved instruments for systematic errors. We summarized the results from several laboratories on lifetime standards. There is no attempt to compare the values, or to evaluate that values are more reliable. Much of the data is from this laboratory because it was readily available with all the experimental details.

### I. NANOSECOND LIFETIME STANDARDS

A series of scintillator fluorophores were characterized as standards for correcting timing errors in photomultiplier

tubes.<sup>1</sup> While the decay times were only measured at one or two frequencies, these compounds are thought to display single-exponential decays in ethanol. The decay times are in equilibrium with air, and are not significantly sensitive to temperature (Table II.1). These excitation wavelengths range from 280 to 360 nm, and the emission wavelengths range from 300 to 500 nm (Figure II.1).

One of our most carefully characterized intensity decays is for PPD in ethanol at 20°C, in equilibrium with air.<sup>2</sup> The frequency response was measured with a GHz frequency-domain instrument. No deviations from a single-exponential decay were detected over the entire range of frequencies (Figure II.2).

**Table II.1.** Nanosecond Reference Fluorophores

Compound <sup>a</sup>	Emission wavelength range	$\tau$ (ns) <sup>b</sup>
p-Terphenyl	310–412	1.05
PPD	310–440	1.20
PPO	330–480	1.40
POPOP	370–540	1.35
(Me) <sub>2</sub> POPOP	390–560	1.45

<sup>a</sup>The abbreviations are: PPD, 2,5-diphenyl-1,3,4-oxadiazole; PPO, 2,5-diphenyloxazole; POPOP, *p*-bis[2-(5-phenyloxazolyl)]benzene; dimethyl or (Me)<sub>2</sub>POPOP, 1,4-bis-2-(4-methyl-5-phenyloxazolyl)-benzene.

<sup>b</sup>These values are judged to be accurate to  $\pm 0.2$  ns at 10 and 30 MHz. From [1].

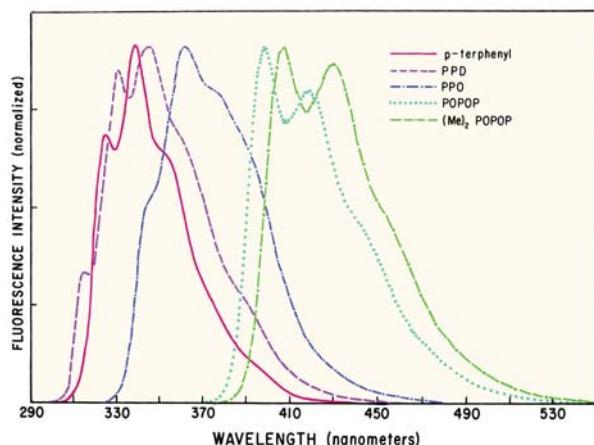


**Figure II.1.** Emission spectra of nanosecond lifetime reference fluorophores. Reprinted from [1]. Copyright © 1981, with permission from Elsevier Science.

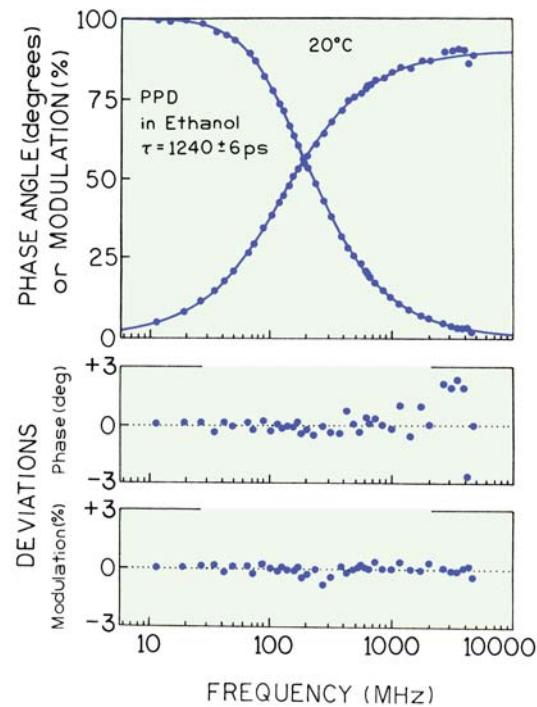


**Figure II.2.** PPD in ethanol as a single-decay-time standard, in ethanol in equilibrium with air. Reprinted with permission from [2]. Copyright © 1990, American Institute of Physics.

## 2. PICOSECOND LIFETIME STANDARDS

Derivatives of dimethylamino-stilbene were characterized as lifetime standards with subnanosecond lifetimes<sup>3</sup> (Figure II.3). Excitation wavelengths range up to 420 nm, and emission wavelengths from 340 to over 500 nm (Figure II.4).

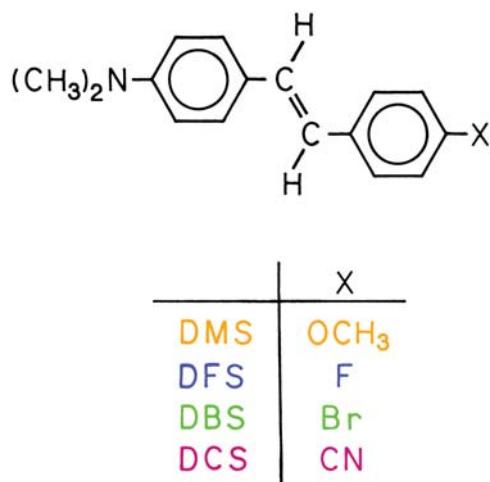


**Figure II.3.** Picosecond lifetime standard fluorophores. From [3].

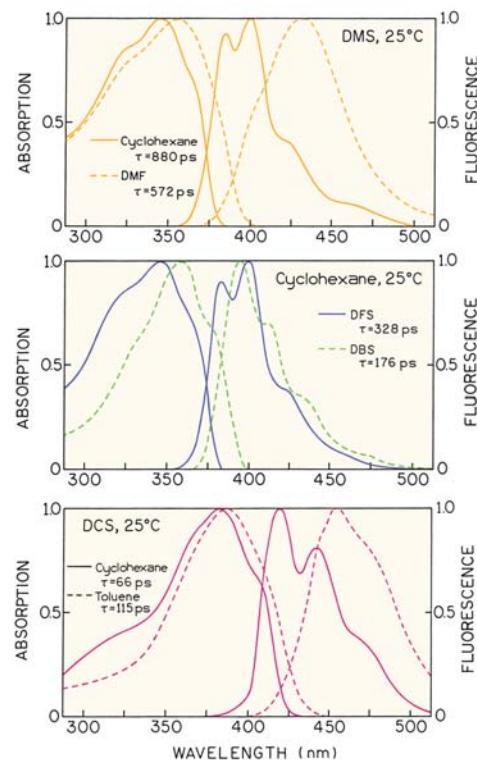


**Figure II.4.** Top: Absorption and fluorescence spectra of DMS in cyclohexane (solid) and N,N'-dimethylformamide (dashed) at 25°C. Middle: Absorption and fluorescence spectra of DFS (solid) and DBS (dashed) in cyclohexane at 25°C. Bottom: Absorption and fluorescence spectra of DCS in cyclohexane (solid) and toluene (dashed) at 25°C. Revised from [3].

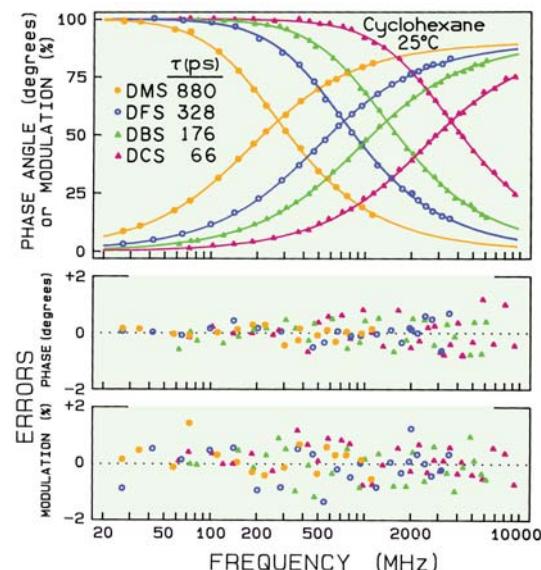


**Figure II.5.** Representative frequency response of the picosecond lifetime standards. From [3].

**Table II.2.** Picosecond Lifetime Standards<sup>a</sup>

Compound	No. <sup>a</sup>	Solvent <sup>b</sup>	Q <sup>c</sup>	T (°C)	τ (ps)
DMS	1	C	0.59	25	880
	2	C	—	37	771
	3	T	0.32	25	740
	4	T	—	5	921
	5	DMF	0.27	25	572
	6	EA	0.15	25	429
DFS	7	C	—	25	328
	8	C	—	37	252
	9	T	0.16	25	305
	10	T	—	5	433
DBS	11	C	0.11	25	176
	12	C	—	37	133
	13	T	0.12	25	168
	14	T	—	5	248
DCS	15	C	0.06	25	66
	16	C	—	37	57
	17	T	0.06	25	115
	18	T	—	5	186

<sup>a</sup>From [3]. Numbers refer to Figure II.6. These results were obtained from frequency-domain measurements.

<sup>b</sup>C, cyclohexane; T, toluene; DMF, dimethylformamide; EA, ethyl acetate. The excitation wavelength was 365 nm.

<sup>c</sup>Quantum yields.

Representative frequency responses show that the intensity decays are all single exponentials (Figure II.5). The solutions are all in equilibrium with air. The decay times range from 57 to 921 ps (Table II.2 and Figure II.6).

Rose Bengal can serve as a picosecond lifetime standard at longer wavelengths (Figure II.7). Rose Bengal can

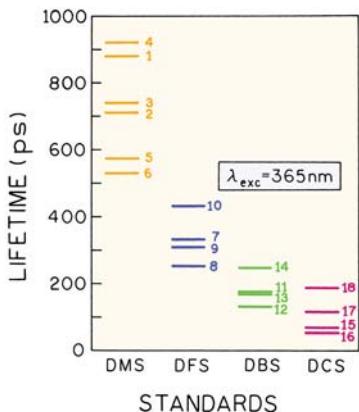


**Figure II.6.** Lifetimes of the picosecond standards. From [3].

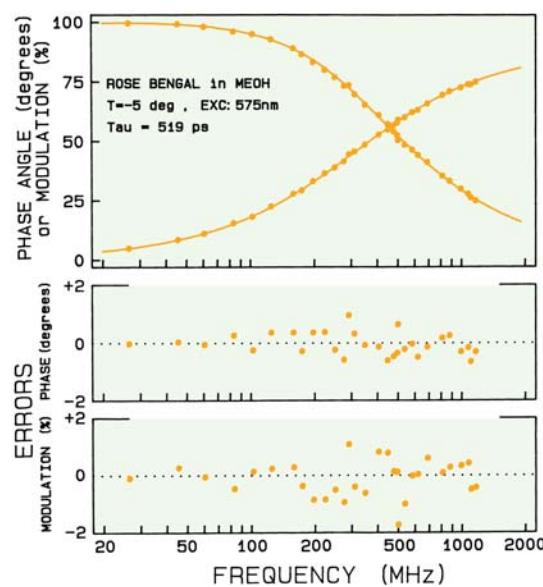


**Figure II.7.** Rose Bengal as long-wavelength picosecond lifetime standard. For additional lifetime data on Rose Bengal see [4].

also be used as a standard for a short rotational correlation time (Figure II.8).

### 3. REPRESENTATIVE FREQUENCY-DOMAIN INTENSITY DECAYS

It can be useful to have access to the actual lifetime data. Representative frequency-domain data for single-exponen-

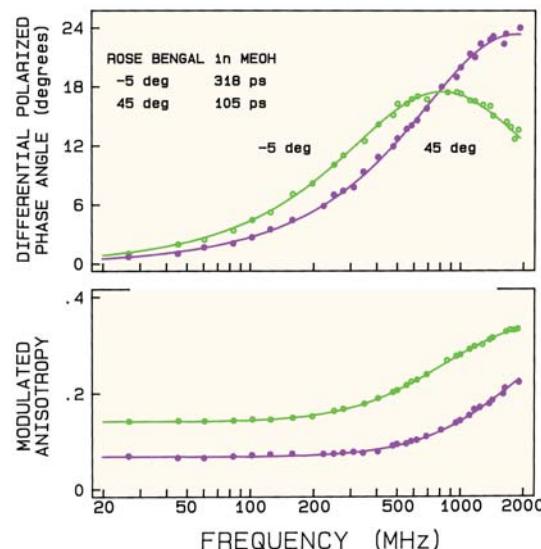


**Figure II.8.** Rose Bengal as a picosecond correlation time standard. For additional data on Rose Bengal see [4].

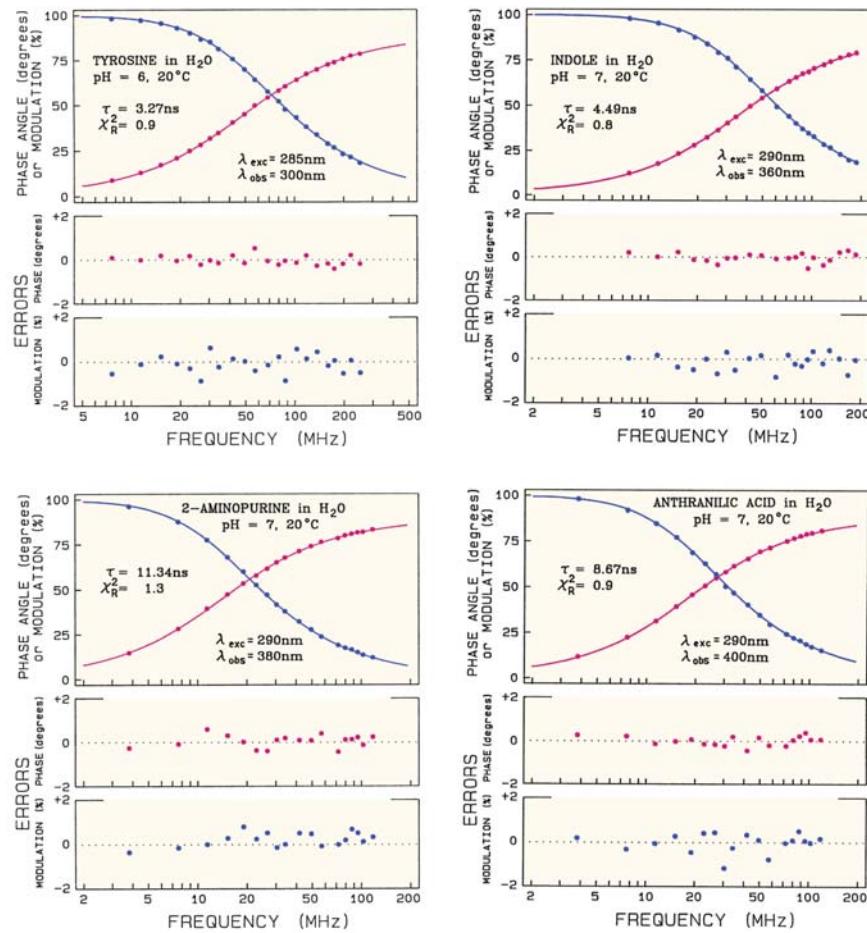


Figure II.9. Representative frequency-domain intensity decays. From [5].

**Table II.3.** Time-Domain Single Lifetime Standards<sup>a</sup>

Compound	Solvent, 20°C	Emission (nm)	$\tau$ (ns)
PPO	cyclohexane (D)	440	1.42
PPO	cyclohexane (U)	440	1.28
Anthracene	cyclohexane (D)	405	5.23
Anthracene	cyclohexane (U)	405	4.10
1-cyanonaphthalene	hexane (D)	345	18.23
1-methylindole	cyclohexane (D)	330	6.24
3-methylindole	cyclohexane (D)	330	4.36
3-methylindole	ethanol (D)	330	8.17
1,2-dimethylindole	ethanol (D)	330	5.71

<sup>a</sup>From [13]. These results were obtained using time-correlated single-photon counting.

<sup>b</sup>D = degassed; U = undegassed.

tial decays as shown in Figure II.9. All samples are in equilibrium with air.<sup>5</sup> Additional frequency-domain data on sin-

gle-decay-time fluorophores are available in the literature,<sup>6–10</sup> and a cooperative report between several laboratories on lifetime standards is in preparation.<sup>11</sup>

#### 4. TIME-DOMAIN LIFETIME STANDARDS

The need for lifetime standards for time-domain measurements has been recognized for some time.<sup>12</sup> A number of laboratories have suggested samples as single-decay-time standards.<sup>13–17</sup> The data are typically reported only in tables (Tables II.3 to II.5), so representative figures are not available. The use of collisional quenching to obtain different lifetimes<sup>17–18</sup> is no longer recommended for lifetime standards due to the possibility of transient effects and non-exponential decays. Quinine is not recommended as a lifetime standard due to the presence of a multi-exponential decay.<sup>19–20</sup>

**Table II.4.** Single-Exponential Lifetime Standards

Sample <sup>a</sup>	$\lambda_{\text{em}}$ (nm)	$\tau$ (ns <sup>a</sup> )
Anthracene	380	5.47
PPO	400	1.60
POPOP	400	1.38
9-cyanoanthracene	440	14.76

<sup>a</sup>All samples in ethanol. The lifetimes were measured by time-correlated single-photon counting. From [14]. The paper is unclear on purging, but the values seem consistent with digassed samples.

**Table II.5.** Single-Exponential Standards<sup>a</sup>

Fluorophore	$\tau$ (ns)
POPOP in cyclohexane	$1.14 \pm 0.01$
POPOP in EtOH	$1.32 \pm 0.01$
POPOP in aq EtOH	$0.87 \pm 0.01$
Anthracene in EtOH	$4.21 \pm 0.02$
9-Cyanoanthracene in EtOH	$11.85 \pm 0.03$

<sup>a</sup>All measurements were at 25°C, in equilibrium with air, by time-correlated single photon counting. From [17].

## Appendix III

# Additional Reading

It is not possible in a single volume to completely describe the molecular photophysics and the application of fluorescence spectroscopy. The following books are recommended for additional details on specialized topics. This listing is not intended to be inclusive, and the author apologizes for absence of important citations.

### I. TIME-RESOLVED MEASUREMENTS

- Chemical applications of ultrafast spectroscopy* 1986. Fleming, GR. Oxford University Press, New York.
- Excited state lifetime measurements* 1983. Demas JN. Academic Press, New York, pp. 267.
- Time-correlated single photon counting* 1984. O'Connor DV, Phillips D. Academic Press, New York.
- Topics in fluorescence spectroscopy*. Vol 1. 1991. Lakowicz JR, ed. Plenum Press, New York.

### 2. SPECTRA PROPERTIES OF FLUOROPHORES

- Energy transfer parameters of aromatic compounds*. 1973. Berlman IB. Academic Press, New York.
- Biological techniques: fluorescent and luminescent probes for biological activity*. 1999. Mason WT. Academic Press, New York.
- Handbook of fluorescence spectra of aromatic molecules*, 2nd ed. 1971. Berlman IB. Academic Press, New York.
- Handbook of fluorescent probes and research chemicals*, 9th ed. 2003. Haugland RP, ed. Molecular Probes Inc.
- Landolt-Börnstein: zahlenwerte und funktionen aus naturwissenschaften und technik*. 1967. Serie N. Springer-Verlag, Berlin.
- Molecular luminescence spectroscopy: methods and applications: part 1*. 1985. Schulman SG, ed. John Wiley & Sons, New York.
- Molecular luminescence spectroscopy: methods and applications: part 2*. 1988. Schulman SG, ed. John Wiley & Sons, New York.
- Molecular luminescence spectroscopy: methods and applications: part 3*. 1993. Schulman SG, ed. John Wiley & Sons, New York.

*Organic luminescent materials*. 1984. Krasovitskii BM, Bolotin BM (Vopian VG, transl). VCH Publishers, Germany.

*Practical fluorescence*, 2nd ed. 1990. Guilbault GG, ed. Marcel Dekker, New York.

### 3. THEORY OF FLUORESCENCE AND PHOTOPHYSICS

*Photophysics of aromatic molecules*. 1970. Birks JB. Wiley Interscience, New York.

*Organic molecular photophysics*, Vol 1. 1973. Birks JB, ed. John Wiley & Sons, New York.

*Organic molecular photophysics*, Vol 2. 1975. Birks JB, ed. John Wiley & Sons, New York.

*Fotoluminescencja roztworow*. 1992. Kawski A. Wydawnictwo Naukowe PWN, Warszawa.

The 1970 and 1973 books by Birks are classic works that summarize organic molecular photophysics. These books start by describing fluorescence from a quantum mechanical perspective, and contain valuable detailed tables and figures that summarize spectral properties and photophysical parameters. Unfortunately, these books are no longer in print, but they may be found in some libraries.

### 4. REVIEWS OF FLUORESCENCE SPECTROSCOPY

*Methods in enzymology*, Vol. 278: *Fluorescence spectroscopy*. 1997. Brand L, Johnson ML. Academic Press, New York.

*Molecular fluorescence, phosphorescence, and chemiluminescence spectrometry*. 2004. Powe AM, Fletcher KA, St. Luce NN, Lowry M, Neal S, McCarroll ME, Oldham PB, McGown LB, Warner IM. *Anal Chem* **76**:4614–4634. This review is published about every two years.

- Resonance energy transfer: theory and data.* 1991. Wieb Van Der Meer B, Coker G, Chen S-Y. Wiley-VCH, New York.
- Topics in fluorescence spectroscopy, Vol 2: Principles.* 1991. Lakowicz JR, ed. Plenum Press, New York. Provides information on the biochemical applications of anisotropy, quenching, energy transfer, least-square analysis, and oriented systems.
- Topics in fluorescence spectroscopy, Vol 3: Biochemical applications.* 1992. Lakowicz JR, ed. Plenum Press, New York. Describes the spectral properties of intrinsic biological fluorophores and labeled macromolecules. There are chapters on proteins, membranes and nucleic acids.
- Topics in fluorescence spectroscopy, Vol 7: DNA technology 2003.* Lakowicz JR, ed. Kluwer Academic/Plenum Publishers, New York.

## 5. BIOCHEMICAL FLUORESCENCE

- Analytical use of fluorescent probes in oncology.* 1996. Kohen E, Hirschberg JG, eds. Plenum Press, New York.
- Applications of fluorescence in the biomedical sciences.* 1986. Taylor DL, Waggoner AS, Murphy RF, Lanni F, Birge RR, eds. Alan R. Liss, New York.
- Biophysical and biochemical aspects of fluorescence spectroscopy.* 1991. Dewey TG, ed. Plenum Press, New York.
- Biotechnology applications of microinjection, microscopic imaging, and fluorescence.* 1993. Bach PH, Reynolds CH, Clark JM, Mottley J, Poole PL, eds. Plenum Press, New York.
- Fluorescent and luminescent probes for biological activity: a practical guide to technology for quantitative real-time analysis,* 2nd ed. 1999. Mason WT, ed. Academic Press, San Diego.
- Fluorometric analysis in biomedical chemistry.* 1987. Ichinose N, Schwedt G, Schneppel FM, Adachi K. John Wiley & Sons.
- Fluorescence spectroscopy.* 1997. Brand L, Johnson ML, eds. Academic Press, New York.
- Methods in cell biology, Vol 58: Green fluorescent proteins.* 1999. Sullivan KF, Kay SA, eds. Academic Press, San Diego.
- Spectroscopic membrane probes, Vol 1.* 1988. Loew LM, ed. CRC Press, Boca Raton, FL.
- Spectroscopic membrane probes, Vol 2.* 1988. Loew LM, ed. CRC Press, Boca Raton, FL.
- Spectroscopic membrane probes, Vol 3.* 1988. Loew LM, ed. CRC Press, Boca Raton, FL.

## 6. PROTEIN FLUORESCENCE

- Fluorescence and phosphorescence of proteins and nucleic acids.* 1967. Konev SV. (Udenfriend S, transl). Plenum Press, New York.
- Luminescence of polypeptides and proteins.* 1971. Longworth JW. In *Excited states of proteins and nucleic acids*, pp. 319–484. Steiner RF, Weinryb I, eds. Plenum Press, New York.
- Luminescent spectroscopy of proteins.* 1993. Permyakov EA. CRC Press, Boca Raton, FL.
- Ultraviolet spectroscopy of proteins.* 1981. Demchenko AP. Springer-Verlag, New York.

## 7. DATA ANALYSIS AND NONLINEAR LEAST SQUARES

- Data reduction and error analysis for the physical sciences,* 2nd ed. 1992. Bevington PR, Robinson DK. McGraw-Hill, Boston.
- Evaluation and propagation of confidence intervals in nonlinear, asymmetrical variance spaces: analysis of ligand binding data. 1983. Johnson ML. *Biophys J* 44:101–106.
- An introduction to error analysis.* 1982. Taylor JR. University Science Books, California.
- Methods in enzymology, Vol 240: Numerical computer methods.* 1994. Johnson ML, Brand L, eds. Academic Press, New York.
- Methods in enzymology, Vol 210: Numerical computer methods.* 1992. Brand L, Johnson ML, eds. Academic Press, New York.
- Statistics in spectroscopy.* 1991. Mark H, Workman J. Academic Press, New York.

## 8. PHOTOCHEMISTRY

- Essentials of molecular photochemistry.* 1991. Gilbert A, Baggott J. CRC Press, Boca Raton, FL.
- Fundamentals of photoinduced electron transfer.* 1993. Kavarnos GJ. VCH Publishers, New York.
- Modern molecular photochemistry.* 1978. Turro NJ. Benjamin/Cummings Publishing, San Francisco.
- Photochemistry and photophysics, Vol 1.* 1990. Rabek JF. CRC Press, Boca Raton, FL.
- Photochemistry and photophysics, Vol 2.* 1990. Rabek JF. CRC Press, Boca Raton, FL.
- Photochemistry and photophysics, Vol 3.* 1991. Rabek JF. CRC Press, Boca Raton, FL.
- Principles and applications of photochemistry.* 1988. Wayne RP. Oxford University Press, New York.

For most applications of fluorescence, photochemical effects are to be avoided. However, it can be valuable to understand that chemical reactions occur in the excited state.

## 9. FLOW CYTOMETRY

- Flow cytometry.* 1992. Givan AL. Wiley-Liss, New York.
- Practical flow cytometry.* 2nd ed. 1988. Shapiro HM. Alan R. Liss, New York.

## 10. PHOSPHORESCENCE

- Phosphorimetry: theory, instrumentation, and applications.* 1990. Hurtubise RJ. VCH Publishers, New York.

## 11. FLUORESCENCE SENSING

- Chemical sensors and biosensors for medical and biological applications.* 1998. Spichiger-Keller UE. Wiley-VCH, Weinheim.

*Sensors and actuators B.* 1996. Part 1: Plenary and Parallel Sessions; Part 2: Poster Sessions. Kunz RE, ed. Proceedings of the Third European Conference on Optical Chemical Sensors and Biosensors. Europt(R)ode III. Elsevier Publishers, New York.

*Topics in fluorescence spectroscopy, Vol 4: Probe design and chemical sensing.* 1994. Lakowicz JR, ed. Plenum Press, New York.

*Biosensors in the body—continuous in vivo monitoring.* 1997. Fraser DM, ed. Biomaterials Science and Engineering Series, Wiley, New York.

## 12. IMMUNOASSAYS

*Applications of fluorescence in immunoassays.* 1991. Hemmila IA. John Wiley & Sons, New York.

*Luminescence immunoassay and molecular applications.* 1990. Van Dyke K, Van Dyke R. CRC Press, Boca Raton, FL.

## 13. APPLICATIONS OF FLUORESCENCE

*Analytical use of fluorescent probes in oncology.* 1996. Kohen E, Hirschberg JG, eds. Plenum Press, New York.

*Fluorescent chemosensors for ion and molecule recognition.* 1992. Czarnik AW, ed. ACS Symposium Series, Vol 538.

*Fluorescent probes in cellular and molecular biology.* 1994. Slavik J. CRC Press, Boca Raton, FL.

*Fluorescence microscopy and fluorescent probes.* 1996. Slavik J, ed. Plenum Press, New York.

*Fluorescence spectroscopy.* 1993. Wolfbeis OS, ed. Springer-Verlag, New York.

*Sensors and actuators B: chemical.* 1994. Baldini F, ed. Elsevier Press. Vol B2.(1–3).

*Applied fluorescence in chemistry, biology and medicine.* 1999. Rettig W, Strehmel B, Schrader S, Seifert H. Springer, New York.

*New trends in fluorescence spectroscopy.* 2001. Valeur B, Brochon J-C, eds. Springer, New York.

*Fluorescence spectroscopy, imaging, and probes.* 2002. Kraayenhof R, Visser AJWG, Gerritsen HC, eds. Springer, New York.

## 14. MULTIPHOTON EXCITATION

*Topics in fluorescence spectroscopy, Vol 5: Non-linear and two-photon induced fluorescence.* 1997. Lakowicz JR, ed. Plenum Press, New York.

*Fluorescence microscopy and fluorescent probes, Vol 2.* 1998. Slavik J, ed. Plenum Press, New York.

## 15. INFRARED AND NIR FLUORESCENCE

*Infrared absorbing dyes.* 1990. Matsuoka M. Plenum Press, New York.

*Phthalocyanines: properties and applications.* 1989. Leznoff CC, Lever ABP, eds. VCH Publishers, New York.

*Near-infrared dyes for high technology applications.* 1998. Daehne S, Resch-Genger U, and Wolfbeis OS, eds. Kluwer Academic Publishers, Boston.

## 16. LASERS

*Fundamentals of laser optics.* 1994. Iga K. (Miles RB, tech ed). Plenum Press, New York.

*Principles of lasers,* 4th ed. 1998. Svelto O. (Hanna DC, ed, transl) Plenum Press, New York.

*An introduction to laser spectroscopy.* 2002. Andrews DL, Deminov AA, eds. Kluwer Academic/Plenum Publishers, New York.

*Laser spectroscopy: basic concepts and instrumentation,* 3rd ed. 2003. Demtroder W. Springer, New York.

## 17. FLUORESCENCE MICROSCOPY

*Chemical analysis: a series of monographs on analytical chemistry and its applications.* 1996. Fluorescence Imaging Spectroscopy and Microscopy, Vol 137. Wang XF, and Herman B, eds. John Wiley & Sons, New York.

*Fluorescence imaging spectroscopy and microscopy.* 1996. Wang XF, Herman B. John Wiley & Sons, New York.

*Handbook of confocal microscopy,* 2nd ed. 1995. Pawley JB, ed. Plenum Press, New York. See also the First Edition, 1990.

*Methods in cell biology,* Vol 38: *Cell biological applications of confocal microscopy.* 1993. Matsumoto B, ed. Academic Press, New York.

*Methods in cell biology,* Vol 40: *A practical guide to the study of calcium in living cells.* 1994. Nuccitelli R, ed. Academic Press, New York.

*Optical microscopy, emerging methods and applications.* 1993. Herman B, Lemasters JJ. Academic Press, New York.

*Optical microscopy for biology.* 1990. Herman B, Jacobson K, eds. Wiley-Liss, New York.

*Fluorescent microscopy and fluorescent probes, Vol 2.* 1998. Slavik J, ed. Plenum, New York.

## 18. METAL-LIGAND COMPLEXES AND UNUSUAL LUMOPHORES

*Molecular level artificial photosynthetic materials.* 1997. Meyer GJ, ed. John Wiley & Sons, New York.

*Photochemistry of polypyridine and porphyrin complexes.* 1992. Kalyanasundaram K. Academic Press, New York.

*Ru(II) polypyridine complexes: photophysics, photochemistry, electrochemistry, and chemiluminescence.* 1988. Juris A, Balzani V, Barigelletti F, Campagna S, Belser P, Von Zelewsky A. *Coord Chem Rev* 84:85–277.

## 19. SINGLE-MOLECULE DETECTION

*Selective spectroscopy of single molecules.* 2003. Osad'ko IS. Springer, New York.

*Single molecule detection in solution methods and applications.* 2002. Zander Ch, Enderlein J, Keller RA, eds. Wiley-Vch, Darmstadt, Germany.

*Single molecule spectroscopy: Nobel conference letters.* 2001. Rigler R, Orrit M, and Basche T. Springer, New York.

---

**20. FLUORESCENCE CORRELATION SPECTROSCOPY**

*Fluorescence correlation spectroscopy theory and applications.* 2001. Rigler R, Elson ES. Springer, New York.

---

**21. BIOPHOTONICS**

*Methods in enzymology*, Vol. 360: *Biophotonics, part a* 2003. Marriott G, Parker I, eds. Academic Press, New York.

*Methods in Enzymology*, Vol. 361: *Biophotonics part b* 2003. Marriott G, Parker I, eds. Academic Press, New York.

*Introduction to biophotonics.* 2003. Prasad PN, Wiley-Interscience, New York.

---

**22. NANOPARTICLES**

*Nanoparticles.* 2004. Rotello V, ed. Kluwer Academic/Plenum Publishers, New York.

*Optical properties of semiconductor nanocrystals.* 1998. Gaponenko SV. Cambridge University Press, New York.

---

**23. METALLIC PARTICLES**

*Electronic excitations at metal surfaces.* 1997. Liebsch A. Plenum Press, New York.

*Metal nanoparticles synthesis, characterization, and applications.* 2002. Feldheim DL, Foss CA, eds. Marcel Dekker, New York.

---

**24. BOOKS ON FLUORESCENCE**

*Introduction to fluorescence spectroscopy.* 1999. Sharma A, Schulman SG, eds. Wiley-Interscience, New York.

*Molecular fluorescence principles and applications.* 2002. Valeur B. Wiley-VCH, New York.

*Who's who in fluorescence 2004.* 2004. Geddes CD, Lakowicz JR, eds. Kluwer Academic/Plenum Publishers, New York.

# Answers to Problems

---

## CHAPTER I

- A1.1. A. The natural lifetimes and radiative decay rates can be calculated from the quantum yields and experimental lifetimes:

$$\tau_N(\text{eosin}) = \tau/Q = \frac{3.1}{0.65} = 4.77 \text{ ns} \quad (1.18)$$

$$\tau_N(\text{EB}) = \tau Q = \frac{0.61}{0.12} = 5.08 \text{ ns} \quad (1.19)$$

Hence eosin and erythrosin B have similar natural lifetimes and radiative decay rates (eq. 1.3). This is because both molecules have similar absorption and emission wavelengths and extinction coefficients (eq. 1.4).

The non-radiative decay rates can be calculated from eq. 1.2, which can be rearranged to

$$\frac{1}{\tau} - \frac{1}{\tau_N} = k_{nr} \quad (1.20)$$

For eosin and erythrosin B the non-radiative decay rates are  $1.1 \times 10^8 \text{ s}^{-1}$  and  $1.44 \times 10^9 \text{ s}^{-1}$ , respectively. The larger non-radiative decay rate of erythrosin B is the reason for its shorter lifetime and lower quantum yield than eosin.

- B. The phosphorescence quantum yield ( $Q_p$ ) can be estimated from an expression analogous to eq 1.1:

$$Q_p = \frac{\Gamma_p}{\Gamma_p + k_{nr}} \quad (1.21)$$

Using the assumed natural lifetime of 10 ms, and  $k_{nr} = 1 \times 10^8 \text{ s}^{-1}$ ,  $Q_p = 10^{-6}$ . If  $k_{nr}$  is larger,  $Q_p$  is still smaller, so that  $Q_p < 10^{-7}$  for ErB. This explains why it is difficult to observe phosphorescence at room temperature: most of the molecules that undergo intersystem crossing return to the ground state by non-radiative paths prior to emission.

- A1.2. The quantum yield ( $Q_2$ ) of  $S_2$  can be estimated from

$$Q_2 = \frac{\Gamma}{\Gamma + k_{nr}} \quad (1.22)$$

The value of  $k_{nr}$  is given by the rate of internal conversion to  $S_1$ ,  $10^{13} \text{ s}^{-1}$ . Using  $\Gamma = 2.1 \times 10^8$ , one can estimate  $Q_2 = 2 \times 10^{-5}$ . Observation of emission from  $S_2$  is unlikely because the molecules relax to  $S_1$  prior to emission from  $S_2$ .

- A1.3. The energy spacing between the various vibrational energy levels is revealed by the emission spectrum of perylene (Figure 1.3). The individual emission maxima (and hence vibrational energy levels) are about  $1500 \text{ cm}^{-1}$  apart. The Boltzmann distribution describes the relative number of perylene molecules in the 0 and 1 vibrational states. The ratio ( $R$ ) of molecules in each state is given by

$$R = e^{-\Delta E/kT} \quad (1.23)$$

where  $\Delta E$  is the energy difference,  $k$  is the Boltzmann constant, and  $T$  is the temperature in degrees kelvin (K). Assuming a room temperature of 300 K, this ratio is about 0.01. Hence most molecules will be present in the lowest vibrational state, and light absorption results mainly from molecules in this energy level. Because of the larger energy difference between  $S_0$  and  $S_1$ , essentially no fluorophores can populate  $S_1$  as a result of thermal energy.

- A1.4. A. The anisotropy of the DENS-labeled protein is given by eq. 1.10. Using  $\tau = \theta$ , the steady-state anisotropy is expected to be 0.15.
- B. If the protein binds to the larger antibody, its rotational correlation time will increase to 100 ns or longer. Hence the anisotropy will be 0.23 or higher. Such increases in anisotropy upon antigen–antibody binding are the basis of the fluorescence polarization immunoassays, which are used to detect drugs, peptides, and small proteins in clinical samples.
- A1.5. The dependence of transfer efficiency on distance ( $r$ ) between a donor and acceptor can be calculated using eq. 1.12 (Figure 1.41). At  $r = R_0$  the efficiency is 50%; at  $r = 0.5R_0$ ,  $E = 0.98$ ; and at  $r = 2R_0$ ,  $E = 0.02$ .

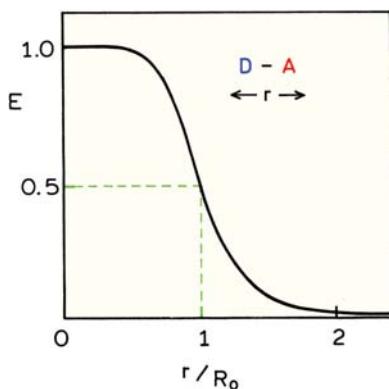


**Figure 1.41.** Effect of donor-to-acceptor distance on transfer efficiency.

- A1.6. The distance can be calculated for the relative quantum yield of the donor in the presence or absence of the acceptor. The data in Figure 1.37 reveal a relative tryptophan intensity of 0.37, assuming the anthraniloyl group does not contribute at 340 nm. A transfer efficiency of 63% corresponds (see eq. 1.12) to a distance of  $r = 0.92R_0 = 27.7 \text{ \AA}$ .

In reality the actual calculation is more complex, and the tryptophan intensity needs to be corrected for anthraniloyl emission.<sup>42</sup> When this is done the transfer efficiency is found to be about 63%, and the distance near 31.9 Å.

- A1.7. The changes in  $\lambda_{\max}$ ,  $K$ , and  $r$  shown in Figure 1.38 are the result of the tryptophan residue being exposed to or shielded from the water. Increases in

$\lambda_{\max}$  and  $K$  indicate increased exposure to water, and decreases in  $\lambda_{\max}$  and  $K$  indicate decreases in exposure to water. Increases and decreases in  $r$  indicate a less mobile and more mobile tryptophan residue, respectively. The three parameter values show a cyclical behavior with a period of about 3.5 amino acid residues per cycle. This suggests that the MLCK peptide is in an  $\alpha$ -helical state when bound to calmodulin (Figure 1.42). The spectral changes seen in Figure 1.38 are the result of the tryptophan residue being alternately exposed to water or shielded between the MLCK peptide and calmodulin as its position is shifted along the peptide chain.

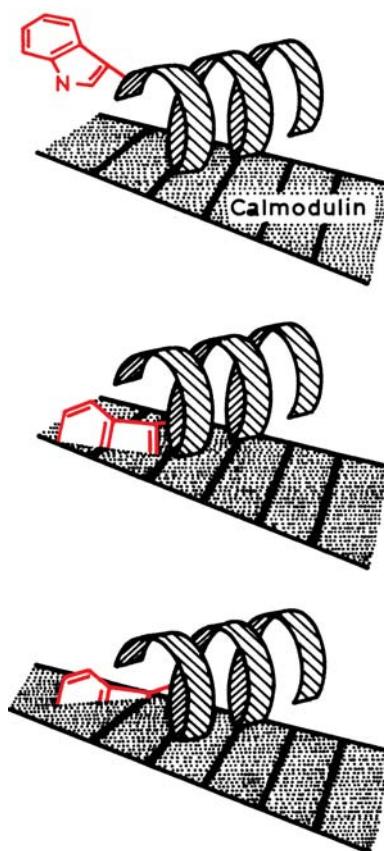


**Figure 1.42.** Schematic of the interactions of the O-helical MLCK peptide with calmodulin. The position of the single tryptophan residue is moved along the helix in 16 synthetic peptides. Reprinted with permission from [40]. (O'Neil KT, Wolfe HR, Erickson-Vitanen S, DeGrado WF. 1987. Fluorescence properties of calmodulin-binding peptides reflect O-helical periodicity. *Science* **236**:1454–1456, Copyright © 1987, American Association for the Advancement of Science.)

- A1.8. Figure 1.40 shows that the donor intensity increases and the acceptor intensity decreases upon addition of cAMP and PKI. These spectral changes indicate a decrease in RET. The donor and acceptor must move further apart when the protein binds cAMP, but change this relative conformation (Figure 1.43). PKI was said to dissociate the subunit.

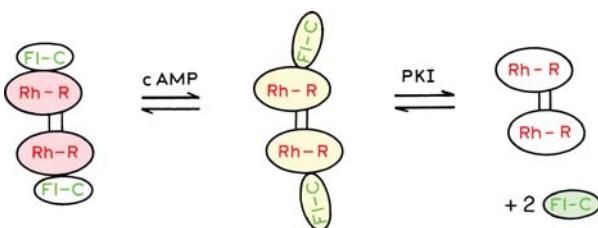


**Figure 1.43.** Effect of cAMP and protein kinase inhibitor (PKI) on the structure and association of cAMP-dependent protein kinase. The holoenzyme consists of two catalytic and two regulatory subunits.

## CHAPTER 2

- A2.1. The true optical density is 10. Because of stray light the lowest percent transmission ( $\%T$ ) you can measure is 0.01%. The  $\%T$  of the rhodamine solution is much less than 0.01%. In fact  $I/I_0 = 10^{-10}$  and  $\%T = 10^{-8}\%$ . Hence your instrument will report an optical density of 4.0. The calculated concentration of rhodamine B would be  $4 \times 10^{-5} \text{ M}$ , 2.5-fold less than the true concentration.
- A2.2. The concentrations of solutions are  $10^{-5}$  and  $10^{-7} \text{ M}$ , respectively. A 1% error in  $\%T$  means the OD can be

$$\text{OD} = \log \frac{I_0}{I} = \log \frac{1}{0.51} \text{ or } \log \frac{1}{0.49} \quad (2.13)$$

Hence the concentration can be from  $0.97 \times 10^{-5}$  to  $1.03 \times 10^{-5} \text{ M}$ .

For the more dilute solution, the 1% error results in a large error in the concentration:

$$\text{OD} = \log \frac{I_0}{I} = \log \frac{1.00}{1.00} \text{ or } \log \frac{1.0}{0.98} \quad (2.14)$$

The measured OD ranges from 0 to 0.009, so the calculated concentration ranges from 0 to  $2.9 \times 10^{-7} \text{ M}$ . This shows that it is difficult to determine the concentration from low optical densities. In contrast, it is easy to obtain emission spectra with optical densities near 0.003.

## CHAPTER 3

- A3.1. Binding of the protein to membranes or nucleic acids could be detected by several types of measurements. The most obvious experiment would be to look for changes in the intrinsic tryptophan fluorescence upon mixing with lipid bilayers or nucleic acids. In the case of membranes one might expect the tryptophan emission to shift to shorter wavelengths due to shielding of the indole moiety from water. The blue shift of the emission is also likely to be accompanied by an increase in the tryptophan emission intensity. In the case of nucleic acids, tryptophan residues are typically quenched when bound to DNA, so that a decrease in the emission intensity is expected.

Anisotropy measurements of the tryptophan emission could also be used to detect binding. In this case it is difficult to predict the direction of the changes. In general one expects binding to result in a longer correlation time and higher anisotropy (see eq. 1.10), and an increase of the tryptophan anisotropy is likely upon binding to proteins. However, the anisotropy increase may be smaller than expected if the tryptophan lifetime increases on binding to the membranes (eq. 1.10).

In the case of protein binding to nucleic acids, it is difficult to predict the anisotropy change. The tryptophan residues would now be in two states, free (F) and bound (B), and the anisotropy given by

$$r = r_F f_F + r_B f_B, \quad (3.2)$$

where  $f_F$  and  $f_B$  represent the fraction of the total fluorescence from the protein in each state. If the protein is completely quenched on binding to DNA, then the anisotropy will not change because  $f_B = 0$ . If the protein is partially quenched the anisotropy will probably increase, but less than expected due to the small contribution of the DNA-bound protein by the total fluorescence.

Energy transfer can also be used to detect protein binding. Neither DNA nor model membranes possess chromophores that can serve as acceptors for the tryptophan fluorescence. Hence it is necessary to add extrinsic probes. Suitable acceptors would be probes that absorb near 350 nm, the emission maximum of most proteins. Numerous membranes and nucleic-acid probes absorb near 350 nm. The membranes could be labeled with DPH (Figure 1.18), which absorbs near 350 nm. If the protein is bound to DPH-labeled membranes, its emission would be quenched by resonance energy transfer to DPH. Similarly, DNA could be labeled with DAPI (Figure 3.23). An advantage of using RET is that through-space quenching occurs irrespective of the details of the binding interactions. Even if there were no change in the intrinsic tryptophan emission upon binding to lipids or nucleic acids, one still expects quenching of the tryptophan when bound to acceptor-labeled membranes or nucleic acids.

- A3.2. A. The data in Figure 3.48 can be used to determine the value of  $F_0/F$  at each  $[Cl^-]$ , where  $F_0 = 1.0$  is the SPQ fluorescence intensity in the absence of  $Cl^-$ , and  $F$  is the intensity at each  $Cl^-$  concentration. These values are plotted in Figure 3.49. Using Stern-Volmer eq. 1.6, one obtains  $K = 124 M^{-1}$ , which is in good agreement with the literature value<sup>182</sup> of  $118 M^{-1}$ .  
 B. The value of  $F_0/F$  and  $\tau_0/\tau$  for  $0.103 M Cl^-$  can be found from eq. 1.6. Using  $K = 118 M^{-1}$ , one obtains  $F_0/F = \tau_0/\tau = 13.15$ . Hence the intensity of SPQ is  $F = 0.076$ , relative to the intensity in the absence of  $Cl^-$ ,  $F_0 = 1.0$ . The

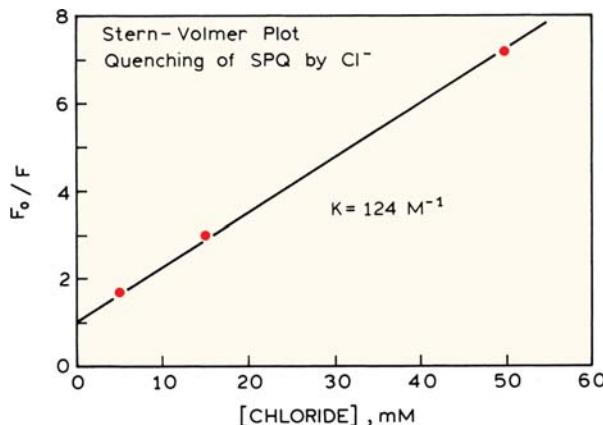


Figure 3.49. Stern-Volmer plot for the quenching of SPQ by chloride.

lifetime is expected to be  $\tau = 26.3/13.15 = 2.0$  ns.

- C. At  $[Cl^-] = 0.075 M$ ,  $F = 0.102$  and  $\tau = 2.67$ .  
 D. The Stern-Volmer quenching constant of SPQ was determined in the absence of macromolecules. It is possible that SPQ binds to proteins or membranes in blood serum. This could change the Stern-Volmer quenching constant by protecting SPQ from collisional quenching. Also, binding to macromolecules could alter  $\tau_0$ , the unquenched lifetime. Hence it is necessary to determine whether the quenching constant of SPQ is the same in blood serum as in protein-free solutions.

- A3.3. A. The dissociation reaction of the probe ( $P_B$ ) and analyte ( $A$ ) is given by

$$P_B = A + P_B, \quad (3.3)$$

where B and F refer to the free and bound forms of the probe. The fraction of free and bound probe is related to the dissociation constant by

$$K_D = \frac{[P_F]}{[P_B]}[A] \quad (3.4)$$

For the non-ratiometric probe Calcium Green, the fluorescein intensity is given by

$$F = q_F C_F + q_B C_B, \quad (3.5)$$

where  $q_i$  are the relative quantum yields,  $C_i$  the molecular fraction in each form, and  $C_F + C_B = 1.0$ . The fluorescent intensities when all the probe is free is  $F_{\min} = kq_F C$ , and then all the probe is bound in  $F_{\max} = kq_B C$ , where  $k$  is an instrumental constant.

Equation 3.5 can be used to derive expressions for  $C_B$  and  $C_F$  in terms of the relative intensities:

$$F_B = \frac{F - F_{\min}}{F_{\max} - F_{\min}} \quad (3.6)$$

$$F_F = \frac{F_{\max} - F}{F_{\max} - F_{\min}} \quad (3.7)$$

The fractions  $C_B$  and  $C_F$  can be substituted for the probe concentration in (3.4), yielding

$$[A] = [\text{Ca}^{2+}] = K_D \frac{F - F_{\max}}{F_{\max} - F} \quad (3.8)$$

- B. The fluorescence intensity ( $F_1$  or  $F_2$ ) observed with each excitation wavelength (1 or 2) depends on the intensity and the concentrations ( $C_F$  and  $C_B$ ) of the free ( $S_{f1}$  or  $S_{f2}$ ), or bound ( $S_{b1}$  or  $S_{b2}$ ), forms at each excitation wavelength:

$$F_1 = S_{f1}C_F + S_{b1}C_B, \quad (3.9)$$

$$F_2 = S_{f2}C_F + S_{b2}C_B. \quad (3.10)$$

The term  $S_i$  depends on the absorption coefficient and relative quantum yield of Fura-2 at each wavelength.

Let  $R = F_1/F_2$  be the ratio of intensities. In the absence and presence of saturating  $\text{Ca}^{2+}$ ,

$$R_{\min} = S_{f1}/S_{f2}, \quad (3.11)$$

$$R_{\max} = S_{b1}/S_{b2}. \quad (3.12)$$

Using the definition of the dissociate constant,

$$[\text{Ca}^{2+}] = \frac{C_B}{C_F} K_D \quad (3.13)$$

one obtains

$$[\text{Ca}^{2+}] = K_D \frac{R - R_{\max}}{R_{\min} - R} \left( \frac{S_{f2}}{f_{b2}} \right) \quad (3.14)$$

Hence one can measure the  $[\text{Ca}^{2+}]$  from these ratios of the emission intensities at two excitation wavelengths. However, one needs control measurements, which are the ratio of the intensities of the free and bound forms measured at one excitation wavelength, as well as measurements of  $R_{\min}$  and  $R_{\max}$ .<sup>183</sup>

## CHAPTER 4

- A4.1. Calculation of the lifetimes from intensity decay is straightforward. The initial intensity decreases to 0.37 (=1/3) of the initial value at  $t = 5$  ns. Hence, the lifetime is 5 ns.

From Figure 4.2 the phase angle is seen to be about 60 degrees. Using  $\omega = 2\pi \cdot 80$  MHz and  $\tau_\phi = \omega^{-1} [\tan \phi]$  one finds  $\tau = 3.4$  ns. The modulation of the emission relative to the excitation is near 0.37. Using eq. 4.6 one finds  $\tau_m = 5.0$  ns. Since the phase and modulation lifetimes are not equal, and since  $\tau_m > \tau_\phi$ , the intensity decay is heterogeneous. Of course, it is difficult to read precise values from Figure 4.2.

- A4.2. The fractional intensity of the 0.62-ns component can be calculated using eq. 4.28, and is found to be 0.042 or 4%.
- A4.3. The short lifetime was assigned to the stacked conformation of FAD. For the open form the lifetime of the flavin is reduced from  $\tau_0 = 4.89$  ns to  $\tau = 3.38$  ns due to collisions with the adenine. The collision frequency is given by  $k = \tau^{-1} - \tau_0^{-1} = 9 \times 10^7/\text{s}$ .
- A4.4. In the presence of quencher the intensity decay is given by

$$I(t) = 0.5 \exp(-t/0.5) + 0.5 \exp(-t/5) \quad (4.42)$$

The  $\alpha_1$  and  $\alpha_2$  values remain the same. The fact that the first tryptophan is quenched tenfold is accounted for by the  $\alpha_i \tau_i$  products,  $\alpha_1 \tau_1 = 0.25$  and  $\alpha_2 \tau_2 = 2.5$ . Using eq. 4.29 one can calculate  $\bar{\tau} = 4.59$  ns and  $\langle \tau \rangle = 2.75$  ns. The average lifetime is close to the unquenched value because the quenched residue ( $\tau_1 = 0.5$  ns) contributes only  $f_1 = 0.091$  to the steady-state or integrated intensity. If the sample contained two tryptophan residues with equal steady-state intensities, and lifetimes of 5.0 and 0.5 ns then  $\bar{\tau} = 0.5(\tau_1) + 0.5(\tau_2) = 2.75$  ns. The fact that  $\langle \tau \rangle$  reflects the relative quantum yield can be seen from noting that  $\langle \tau \rangle / \tau_0 = 2.75/5.0 = 0.55$ , which is the quantum yield of the quenched sample relative to the unquenched sample.

- A4.5. The DAS can be calculated by multiplying the fractional intensities ( $f_i(\lambda)$ ) by the steady-state intensity at each wavelength ( $I(\lambda)$ ). For the global analysis these values (Figure 4.65) match the emission spectra of the individual components. However, for the single-wavelength data the DAS are poorly matched to the individual spectra. This is because the  $\alpha_i(\lambda)$  values are not well determined by the data at a single wavelength.
- A4.6. The total number of counts in Figure 4.45 can be calculated from the  $\alpha \tau$  product. The value of  $\alpha$  is the number of counts in the time zero channel or  $10^4$  counts. The total number of photons counted is thus 4

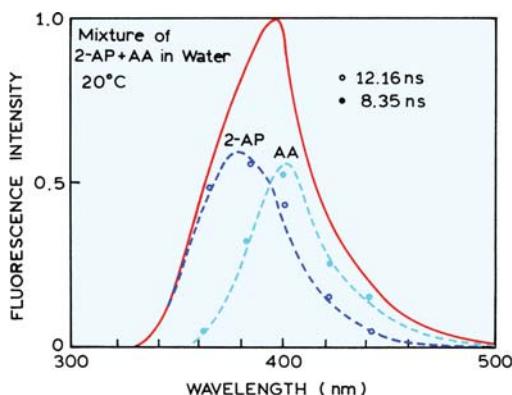


**Figure 4.65.** Emission spectra of a two-component mixture of antranilic acid (AA) and 2-aminopurine (2-AP). The data show the fractional amplitudes associated with each decay time recovered from the global analysis. From [187].

$\times 10^6$ . Assuming 1 photon is counted each  $10^{-5}$  seconds the data acquisition time is 400 s or 6.7 minutes. If the data were collected by TCSPC with a 1% count rate the data acquisition time would be 670 minutes.

- A4.7. For a 4-ns lifetime the excitation pulses should be at least 16 ns apart, which corresponds to a pulse rate of 62.5 MHz. Using a 1% count rate yields a photon detection rate of 0.625 MHz. At this rate the time needed to count  $4 \times 10^6$  photons is 6.4 seconds. Can the TAC convert photons at this rate? The 0.625 MHz count rate corresponds to 1.6 microsecond to store the data. Using a TAC with a 120-ns deadtime the TAC should be able to accept all the photons. A TAC with a 2  $\mu$ s deadtime would be unable to accept the data and the counting would be inefficient.
- A4.8. The fractional intensity is proportional to the  $\alpha\tau$  products. Using eq. 4.28,  $f_1 = 0.9990$  and  $f_2 = 0.001$ .

## CHAPTER 5

- A5.1. The decay times can be calculated from either the phase or modulation data at any frequency, using eqs. 5.3 and 5.4. These values are listed in Table 5.7. Since the decay times are approximately equal from phase and modulation, the decay is nearly a single exponential. One expects the decay to become non-exponential at high chloride concentrations due to transient effects in quenching. This effect is not yet visible in the FD data for SPQ.

**Table 5.7.** Apparent Phase and Modulation Lifetimes for the Chloride Probe SPQ

Chloride concentration	Frequency (MHz)	Apparent phase lifetime ( $\tau_\phi$ ) (ns)	Apparent modulation lifetime ( $\tau_m$ ) (ns)
0	10	24.90	24.94
	100	24.62	26.49
10 mM	10	11.19	11.07
	100	11.62	11.18
30 mM	10	5.17	5.00
	100	5.24	5.36
70 mM	10	2.64	2.49
	100	2.66	2.27

A5.2. The chloride concentration can be determined from the phase or modulation values of SPQ at any frequency where these values are sensitive to chloride concentration. Examination of Figure 5.15 indicates that this is a rather wide range from 5 to 100 MHz. One can prepare calibration curves of phase or modulation of SPQ versus chloride, as shown in Figure 5.56. An uncertainty of  $\pm 0.2^\circ$  in phase or  $\pm 0.5\%$  in modulation

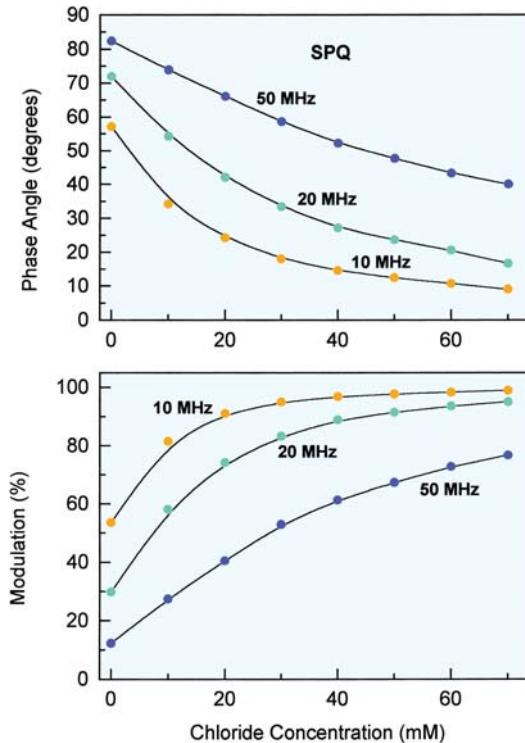


**Figure 5.56.** Dependence of the phase and modulation of SPQ on chloride concentration.

**Table 5.8.** Phase-Modulation Apparent Lifetimes for a Double-Exponential Decay<sup>a</sup>

Frequency (MHz)	$\phi$ (deg)	$m$	$\tau_\phi$ (ns)	$\tau_m$ (ns)
50 ( $\alpha_1 = \alpha_2$ )	50.5	0.552	3.86	4.81
50 ( $f_1 = f_2$ )	25.6	0.702	1.53	3.23
100 ( $\alpha_1 = \alpha_2$ )	60.1	0.333	2.76	4.51
100 ( $f_1 = f_2$ )	29.8	0.578	0.91	3.17

<sup>a</sup>For both decay laws the lifetimes are 0.5 and 5.0 ns.

results in chloride concentrations accurate to approximately  $\pm 0.2$  and 0.3 mM respectively, from 0 to 25 mM.

- A5.3. A list of the phase and modulation values for the two decay laws, as well as the apparent phase and modulation lifetimes, is given in Table 5.8. As expected,  $\tau_{\phi}^{\text{app}} < \tau_m^{\text{app}}$ . Both values decrease with higher modulation frequency. The phase angles are smaller, and the modulation is higher, when  $f_1 = f_2$  than when  $\alpha_1 = \alpha_2$ . When  $f_1 = f_2$ , the  $\alpha_i$  values are  $\alpha_1 = 0.909$  and  $\alpha_2 = 0.091$ . The fractional contribution of the short-lifetime component is larger when  $f_1 = f_2$ .
- A5.4. The Raman peak at 410 nm is equivalent to 24,390  $\text{cm}^{-1}$ . The Raman peak of water is typically shifted 3,600  $\text{cm}^{-1}$ . Hence the excitation wavelength is at 27,990  $\text{cm}^{-1}$ , or 357 nm.
- A5.5. The scattered light has an effective lifetime of zero. Hence the scattered light can be suppressed with  $\phi_D = 90^\circ$ . The phase angle of quinine sulfate at 10 MHz can be calculated from  $\phi = \tan(\omega\tau) = 51.5^\circ$ . The maximum phase-sensitive intensity for quinine sulfate would be observed with  $\phi_D = 51.5^\circ$ . The scattered light is suppressed with  $\phi_D = 90^\circ$ . At this phase angle the phase-sensitive intensity is attenuated by a factor of  $\cos(\phi_D - \phi) = \cos(90 - 51.5) = 0.78$  relative to the phase-sensitive intensity with  $\phi_D = 51.5^\circ$ .
- A5.6. The detector phases of  $17.4 + 90^\circ$  and  $32.1 - 90^\circ$  are out of phase with DNS-BSA and DNS, respectively. This is known because at  $\phi_D = 32.1 - 90^\circ$  only free DNS is detected. In the equimolar DNS-BSA mixture the phase-sensitive intensity of DNS is decreased by 50%. Hence 50% of the DNS is bound to BSA. Similarly, at  $\phi_D = 17.4 + 90^\circ$  only the fluorescence of the DNS-BSA complex is detected. Relative to the solution in which DNS is completely bound, the intensity is 50%. Hence 50% of the DNS is bound. The phase-sensitive intensities of the first two solutions may be

rationalized as follows. Upon addition of a saturating amount of BSA all the DNS is bound. Therefore its contribution to the signal at  $\phi_D = 32.1 - 90^\circ$  is eliminated. The intensity increases twofold, and now is observed with  $\phi_D = 17.4 + 90^\circ$ . However, a twofold increase in intensity is not observed because the signal from the bound DNS is more demodulated than that of the free DNS. Specifically, these values are 0.954 and 0.847 for 5 and 10 ns, respectively. Hence the expected twofold increase in fluorescence intensity is decreased by a factor of  $0.847/0.954 = 0.888$ .

- A5.7. The viscosity of propylene glycol changes dramatically with temperature, which affects the rate of solvent relaxation. At an intermediate temperature of  $-10^\circ\text{C}$  the relaxation time is comparable to the lifetime. Under these conditions the emission spectrum contains components of the unrelaxed initially excited state (F) and the relaxed excited state (R). Suppression on the red side of the emission (410 nm) results in recording the emission spectrum of the F state. Suppression of the blue side of the emission (310 nm) results in recording of the emission spectrum of the R state. Of course, these are only the approximate spectra of these states, but the phase-sensitive spectra appear to show the positions of the unrelaxed and relaxed emission spectra. At very low temperatures ( $-60^\circ\text{C}$ ) all the emission is from the unrelaxed state, and at high temperatures ( $40^\circ\text{C}$ ) all the emission is from the relaxed state. Since there is only one lifetime across the emission spectra, suppression on either side of the emission suppresses the entire emission spectrum.

## CHAPTER 6

- A6.1. The Stokes shift in  $\text{cm}^{-1}$  can be calculated from the Lippert equation (eq. 6.17). Because it is easy to confuse the units, this calculation is shown explicitly:

$$\nu_A - \nu_F = \frac{2(0.3098)}{(6.6256 \times 10^{-27})(2.9979 \times 10^{10})} \frac{(14 \times 10^{-18})^2}{(4.0 \times 10^{-8})^3}$$

$$\bar{\nu}_A - \bar{\nu}_F = 9554 \text{ cm}^{-1} \quad (6.23)$$

The emission maximum in the absence of solvent effects is assumed to be 350 nm, which is 28,571  $\text{cm}^{-1}$ . The orientation polarizability of methanol is

expected to decrease the excited state energy by  $9554 \text{ cm}^{-1}$ , to  $19,017 \text{ cm}^{-1}$ , which corresponds to  $525.8 \text{ nm}$ .

The units for  $\bar{\nu}_A - \bar{\nu}_F$  are as follows:

$$\frac{(\text{esu cm})^2}{(\text{ergs})(\text{cm/s(cm}^3))} \quad (6.24)$$

Recalling that  $\text{erg} = g \text{ cm}^2/\text{s}^2$  and  $\text{esu} = g^{1/2} \text{ cm}^{3/2}/\text{s}$ , one obtains  $\bar{\nu}_A - \bar{\nu}_F$  in  $\text{cm}^{-1}$ .

- A6.2. The change in dipole moment can be estimated from the Lippert plot (Figure 6.53). This plot shows biphasic behavior. In low-polarity solvents the emission is probably due to the LE state, and in higher-polarity solvents the emission is due to the ICT state. The slopes for each region of the Lippert plot are

$$\begin{aligned} \text{slope (LE)} &= 7000 \text{ cm}^{-1} \\ \text{slope (ICT)} &= 33,000 \text{ cm}^{-1} \end{aligned}$$

The slope is equal to  $2(\mu_E - \mu_G)^2/hca^3$ . Assuming a radius of  $4.2 \text{ \AA}$  used previously,<sup>42</sup>

$$(\mu_E - \mu_G)^2 = \frac{7000}{2} hca^3 \quad (6.25)$$

$$= \frac{7000}{2} (6.626 \times 10^{-27}) (3 \times 10^{10}) (4.2 \times 10^{-8})^3 = 5.15 \times 10^{-35}$$

The units of  $(\mu_E - \mu_G)^2$  are  $(\text{cm}^{-1}) (\text{erg s})(\text{cm/s})(\text{cm}^3)$ . Using  $\text{erg} = g \text{ cm}^2/\text{s}^2$ , one obtains the units  $(g \text{ cm}^{3/2}/\text{s}^2)(\text{cm}^2)$ . Taking the square root yields

$$\frac{g^{1/2} \text{ cm}^{3/2}}{\text{s}} \text{ cm} \quad (6.26)$$

Since  $\text{esu} = g^{1/2} \text{ cm}^{3/2}/\text{s}$ , the result  $(\mu_E - \mu_G)$  is in esu/cm. This yields  $(\mu_E - \mu_G) = 7.1 \times 10^{-18} \text{ esu cm} = 7.1 \text{ D}$ . The dipole moment of Prodan is estimated to change by 7.1 Debye units upon excitation. An electron separated from a unit positive charge by  $1 \text{ \AA}$  has a dipole moment of  $4.8 \text{ D}$ . Hence there is only partial charge separation in the LE state. It should be noted that this value is smaller than initially reported<sup>42</sup> due to a trivial error during the calculations.<sup>58</sup>

For the ICT state a similar calculation yields  $(\mu_E - \mu_G)^2 = 2.42 \times 10^{-34}$  and  $\Delta\mu = 1.56 \times 10^{-17} \text{ esu cm} =$

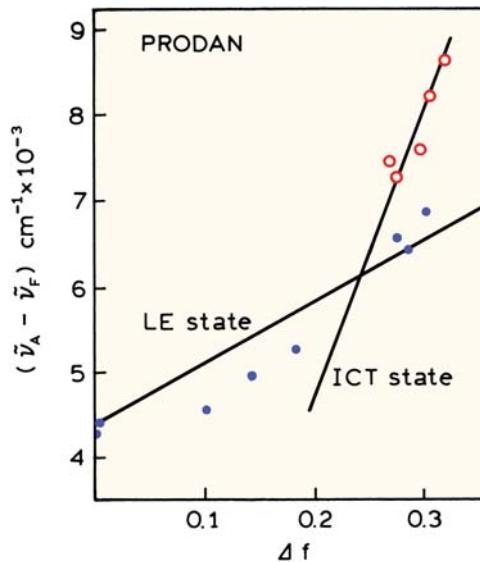


Figure 6.53. Lippert plot of the Stokes shift of Pordan. Data from [42].

15.6D. This change in dipole moment is equivalent to separation of a unit change by  $3.2 \text{ \AA}$ , which suggests nearly complete charge separation in the ICT state of Prodan.

## CHAPTER 7

- A7.1. Assume the decay is a single exponential. Then the time where the intensity has decayed to  $37\%$  of its original intensity is the fluorescence lifetime. These values are  $\tau_F = 1 \text{ ns}$  at  $390 \text{ nm}$  and  $\tau = 5 \text{ ns}$  at  $435 \text{ nm}$ . The decay time of  $5 \text{ ns}$  at  $435 \text{ nm}$  is the decay time the F-state would display in the absence of relaxation. The lifetime of the F-state at  $390 \text{ nm}$  is given by  $1/\tau_F = 1/\tau + 1/\tau_S$ . This is equivalent to stating the decay time of the F-state ( $\gamma_F$ ) is equal to the sum of the rates that depopulate the F-state,  $\gamma_F = 1/\tau + k_S$ . Hence  $\tau_S = 1.25 \text{ ns}$ .

- A7.2. In the fluid solvents ethanol or dioxane the apparent lifetimes of TNS are independent of wavelength, indicating spectral relaxation is complete in these solvents. In glycerol or DOPC vesicles the apparent lifetimes increase with wavelength, suggesting time-dependent spectral relaxation. The observation of  $\tau^\phi > \tau^m$  at long wavelength is equivalent to observing a negative pre-exponential factor, and proves that relax-

- ation is occurring at a rate comparable to the intensity decay rate.
- A7.3. The lifetime of the R state ( $\tau_{OR}$ ) can be calculated from the phase angle difference  $\Delta\phi = \phi_R - \phi_F$ . At 100 MHz this difference is  $58^\circ$ , which corresponds to a lifetime of 16 ns.
- A7.4. A. Acridine and acridinium may be reasonably expected to display distinct absorption spectra. The emission spectrum in 0.2 M  $\text{NH}_4\text{NO}_3$  (Figure 7.49) shows evidence for emission from both acridine and acridinium. Hence if both species were present in ground state, the absorption spectrum should be a composite of the absorption spectra of acridine and acridinium. In contrast, if the acridinium is formed only in the excited state, then the absorption spectrum in 0.2 M  $\text{NH}_4\text{NO}_3$  should be almost identical to that of neutral acridine.
- B. Examination of the data (Table 7.6) reveals two decay times that are independent of emission wavelength. This indicates that there are two emitting species and that their decay rates are independent of emission wavelength. On the short-wavelength side of the emission the decay is a single exponential. This result indicates the reaction is irreversible and that the measured decay times at other wavelengths contain contributions from both acridine and acridinium. Proof of an excited-state reaction is provided by observation of negative pre-exponential factors. As the observation wavelength is increased this term becomes more predominant. At the longest observation wavelengths one finds that the pre-exponential factors are nearly equal in magnitude and opposite in sign. This near equality of the pre-exponential factors indicates that at 560 nm the emission is predominantly from the relaxed species. The fact that  $\alpha_2$  is slightly larger than  $\alpha_1$  indicates that there is still some emission from neutral acridine at 560 nm.
- A7.5. Red-edge excitation selects for fluorophores that are most strongly interacting with the solvent. The solvent configuration around these selected fluorophores is similar to that in a solvent-relaxed state. The TRES with 416-nm excitation do not show a time-dependent

shift because the fluorophore is already in the relaxed state.

## CHAPTER 8

- A8.1. The apparent bimolecular quenching of 2-AP by  $\text{Cu}^{2+}$  can be found by noting that  $F_0/F = 1.10$  at  $2 \times 10^{-6}$  M  $\text{Cu}^{2+}$ . Hence  $K = 50,000 \text{ M}^{-1}$  and  $k_q = 5 \times 10^{12} \text{ M}^{-1} \text{ s}^{-1}$ . Similarly,  $F_0/F = 1.7$  at 0.001 M DMA, yielding  $K = 700 \text{ M}^{-1}$  and  $k_q = 7 \times 10^{10} \text{ M}^{-1} \text{ s}^{-1}$ . Both values are larger than the maximum value possible for diffusive quenching in water, near  $1 \times 10^{10} \text{ M}^{-1} \text{ s}^{-1}$ . This implies some binding or localization of the quenchers near the fluorophores.
- A8.2. The data in Figure 8.72 can be used to calculate the lifetimes of pyrene, which are 200, 119, and 56 ns in the presence of  $N_2$ , air or  $O_2$ , respectively. Assuming the oxygen solubility in DMPC vesicles is fivefold larger than in water (0.001275 M/atm in water), the oxygen bimolecular quenching constant is  $k_q = 2 \times 10^9 \text{ M}^{-1} \text{ s}^{-1}$ . This value is about 20% of the value expected for a fluorophore dissolved in water.
- A8.3. The data in the absence of benzyl alcohol (Figure 8.73) can be used to calculate a bimolecular quenching constant of  $6 \times 10^9 \text{ M}^{-1} \text{ s}^{-1}$ . This indicates that the naphthalene is mostly accessible to iodide and probably not bound to the cyclodextrin. This conclusion is supported by the data in the presence of benzyl alcohol. In the presence of benzyl alcohol the Stern-Volmer plots curve downward in the presence of  $\beta$ -CD (Figure 8.74). This suggests the presence of two naphthalene populations, one of which is less accessible to iodide quenching. In the presence of benzyl alcohol and 5.1 mM  $\beta$ -CD the Stern-Volmer plot is still curved, and the apparent value of  $k_q$  decreases, which indicates shielding from iodide quenching. Under these conditions it seems that naphthalene binds to  $\beta$ -CD only in the presence of benzyl alcohol.
- A8.4. Figure 8.77 shows a plot of  $F_0/F$  versus  $[I^-]$ . From the upward curvature of this plot it is apparent that both static and dynamic quenching occur for the same population of fluorophores. The dynamic ( $K_D$ ) and static ( $K_S$ ) quenching constants can be calculated by a plot of the apparent quenching constant ( $K_{app}$ ) versus the

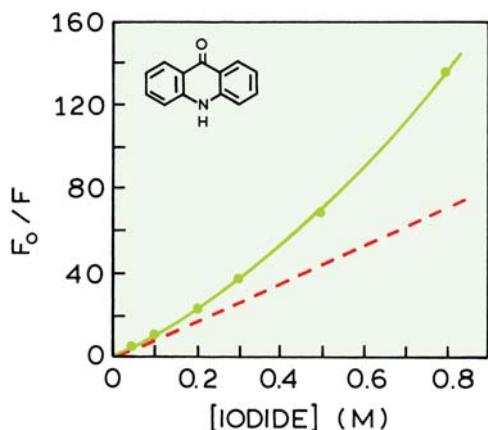


**Figure 8.77.** Iodide quenching of acridone. Data from [175].

concentration of quencher  $[I^-]$ . The apparent quenching constant is given by  $(F_0/F - 1)/[I^-] = K_{app}$ .

M KI	$K_{app}$
0	—
0.04	91.0
0.10	96.0
0.20	110.0
0.30	121.0
0.5	135.0
0.8	170.0

These results are plotted in Figure 8.78. In the plot the y-intercept is  $K_D + K_S = 89 \text{ M}^{-1}$ , and the slope is  $K_D K_S = 101 \text{ M}^{-2}$ . The quadratic equation can be solved to find  $K_D$  and  $K_S$ . Assuming the larger value is  $K_D$  we obtain  $K_D = 87.8 \text{ M}^{-1}$  and  $K_S = 1.15 \text{ M}^{-1}$ . The bimolecular quenching constant is given by  $K_D/\tau_0 = k_q = 4.99 \times 10^9 \text{ M}^{-1} \text{ s}^{-1}$ . The collisional frequency can be calculated independently from the Smoluchowski equation. Assuming a collision radius of 4 Å, and the diffusion of the quencher to be dominant, one obtains

$$\begin{aligned} k_0 &= 4\pi RDN/10^3 \\ &= [(4\pi(4 \times 10^{-8} \text{ cm})(2.065 \times 10^{-5} \text{ cm}^2/\text{sec}) \\ &\quad (6.02 \times 10^{23} \text{ mole}^{-1})]/(10^3 \text{ cm}^3 \text{l}^{-1}) \\ &= 0.625 \times 10^{10} \text{ M}^{-1} \text{ sec}^{-1} \end{aligned} \quad (8.51)$$

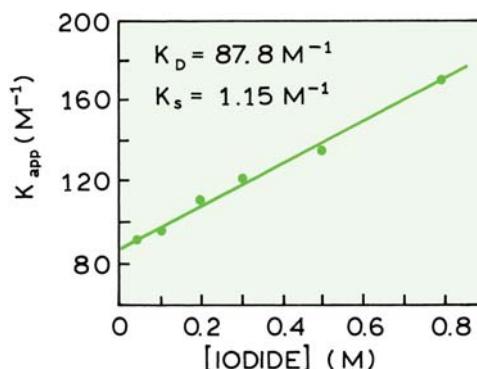


**Figure 8.78.** Static and dynamic quenching constants of acridone. Data from [175].

This value describes the quenching constant expected if 100% of the collisional encounters are effective in quenching. Hence the quenching efficiency  $\gamma = k_q/k_0 = 0.80$ .

The radius of the sphere of action can be calculated using any of the  $F_0/F$  values for which there is excess quenching. At 0.8 M iodide the expected value of  $F_0/F$  due only to dynamic quenching is

$$\left(\frac{F_0}{F}\right)_D = 1 + 87.8(0.8) = 71.24 \quad (8.52)$$

This is indicated by the dashed line in Figure 8.77. The observed value of  $F_0/F$  is 137. Using

$$F_0/F = (1 + K_D[Q]) \exp([Q]NV/1000) \quad (8.53)$$

we obtain  $\exp([Q]NV/1000) = 1.92$  or  $[Q]NV/1000 = 0.653$ . From these results one can calculate that the volume of the sphere of action is  $V = 1.36 \times 10^{-21} \text{ cm}^3$ . Using  $V = 4/3 \pi r^3$ , where  $r$  is the radius, one finds  $r = 6.9 \text{ \AA}$ . According to this calculation, whenever an iodide ion is within 6.9 Å of an excited acridone molecule the probability of quenching is unity.

The static quenching constant is quite small, as is the radius of the sphere of action. It seems that no actual complex is formed in this case. Rather, the static component is due simply to the probability that a fluorophore is adjacent to a quencher at the moment of excitation.

- A8.5. Using the data in Problem 8.5 one may calculate the following:

[AMP] (mM)	$\tau_0/\tau$	$F_0/F$	$(F_0/F)/(\tau_0/\tau)$
0.0	1.0	1.0	1.0
1.75	1.265	1.40	1.107
3.50	1.502	1.80	1.198
5.25	1.741	2.35	1.35
7.0	1.935	3.00	1.55

The collisional or dynamic quenching constant can be calculated from a plot of  $\tau_0/\tau$  versus [AMP] (Figure 8.79). The dynamic quenching constant is  $136 \text{ M}^{-1}$ . Using the lifetime in the absence of quencher one finds  $k_q = K_D/\tau_0 = 4.1 \times 10^9 \text{ M}^{-1} \text{ s}^{-1}$ , which is typical for a diffusion-controlled reaction which occurs with high efficiency.

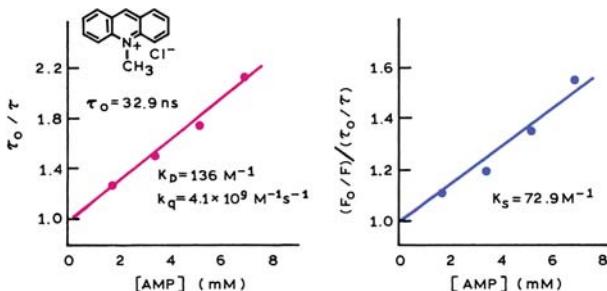


Figure 8.79. Quenching of methylacridinium chloride by AMP. From [18].

In the previous problem we obtained  $K_S$  and  $K_D$  from a plot of the apparent quenching constant versus quencher concentration (Figure 8.78). In this case both the lifetime and yield data are given, and a simpler procedure is possible. We calculated the quantity  $(F_0/F)/(\tau_0/\tau)$ . From eqs. 8.8, and 8.19 this quantity is seen to reflect only the static component of the quenching:

$$\frac{F_0/F}{\tau_0/\tau} = 1 + K_S[\text{AMP}] \quad (8.54)$$

A plot of  $(F_0/F)/(\tau_0/\tau)$  versus [AMP] yields the association constant as the slope (Figure 8.79).

In contrast to the apparent association constant for the "acridone–iodide complex," this value ( $72.9 \text{ M}^{-1}$ ) is much larger. An actual ground-state complex is likely in this case. This was demonstrated experimentally by examination of the absorption spectrum of MAC, which was found to be changed in the presence of AMP. If the MAC–AMP complex is nonfluorescent, then the only emission observed is that from the

### A8.6.

uncomplexed MAC. Since these molecules are not complexed, the excitation spectrum of MAC in the presence of AMP will be that of MAC alone.

The susceptibility of a fluorophore to quenching is proportional to its fluorescence lifetime. Fluorophores with longer lifetimes are more susceptible to quenching. To decide on the upper limit of lifetimes, above which oxygen quenching is significant, we need to consider dissolved oxygen from the air. Based on the assumed accuracy of 3% we can use  $F_0/F = \tau_0/\tau = 1.03$ . Since the atmosphere is 20% oxygen, the oxygen concentrations due to atmospheric oxygen are one-fifth the total solubility. For aqueous solutions

$$\frac{F_0}{F} = \frac{\tau_0}{\tau} = 1.03 = 1 + k_q \tau_0 [O_2] \quad (8.55)$$

Using the information provided for aqueous solutions

$$\tau_0 = \frac{0.03}{k_q [O_2]} = \frac{0.03(5)}{(1 \times 10^{10})(.001275)} = 11.8 \text{ ns} \quad (8.56)$$

For the ethanol solution

$$\tau_0 = \frac{0.03(5)}{(2 \times 10^{10})(.001275)(5)} = 1.2 \text{ ns} \quad (8.57)$$

If the unquenched lifetimes are longer than 1.2 ns in ethanol, or 11.8 ns in water, then dissolved oxygen from the air can result in significant quenching (greater than 3%). If desired this quenching can be minimized by purging with an inert gas, such as nitrogen or argon.

### A8.7.

The rate of collisional deactivation can be calculated from the decrease in lifetime due to collisions with the adenine ring. The lifetimes in the absence ( $\tau_0$ ) and presence of ( $\tau$ ) of the adenine moiety are  $\tau_0 = \gamma^{-1}$  and  $\tau = (\gamma + k)^{-1}$ . Therefore,

$$k = \frac{1}{\tau} - \frac{1}{\tau_0} = 2.0 \times 10^8 \text{ s}^{-1} \quad (8.58)$$

The quantum yield of FAD is decreased by both static and dynamic quenching:

$$\frac{F}{F_0} = \frac{Q(\text{FAD})}{Q(\text{FMN})} = f \frac{\tau}{\tau_0} \quad (8.59)$$

where  $f$  is the fraction not complexed. Hence

$$f = \frac{\tau_0 Q(\text{FAD})}{\tau Q(\text{FMN})} = \frac{(4.6)(0.09)}{(2.4)(1.0)} = 0.17 \quad (8.60)$$

83% of the FAD exists as a nonfluorescent complex.

- A8.8. Using the data provided one can calculate the following quantities needed for the Stern-Volmer plots:

$[I^-]$ , M	$F_0/F$	$\Delta F$	$F_0/\Delta F$	$[I^-]^{-1}$ , M $^{-1}$
0.0	1.000	0	—	—
0.01	1.080	0.074	13.51	100
0.03	1.208	0.172	5.814	33.3
0.05	1.304	0.233	4.292	20.0
0.10	1.466	0.318	3.145	10.0
0.20	1.637	0.389	2.571	5.0
0.40	1.776	0.437	2.288	2.5

The downward curvature of the Stern-Volmer plot indicates an inaccessible fraction (Figure 8.80). From the intercept on the modified Stern-Volmer plot one finds  $f_a = 0.5$ . Hence one tryptophan residue per subunit is accessible to iodide quenching. The slope on the modified Stern-Volmer plot is equal to  $(f_a K)^{-1}$ . Thus  $K = 17.4 \text{ M}^{-1}$ . By assumption, the quenching constant of the inaccessible fraction is zero using these results one can predict the quenching plots for each tryptophan residue.

$[I^-]$ , M	$[I^-]^{-1}$ , M $^{-1}$	$(F_0/F)_b$	$(F_0/F)_a^+$	$(F_0/F)_b$	$(F_0/\Delta F)_a^{++}$
0.0	0	1.0	1.0	—	—
0.01	100	"	1.174	"	6.747
0.03	33.3	"	1.522	"	2.916
0.05	20.0	"	1.870	"	2.149
0.10	10.0	"	2.740	"	1.575
0.20	5.0	"	4.480	"	1.287
0.40	2.5	"	7.96	"	1.144

<sup>a</sup>Calculated from  $F_0/F = 1 + 17.4 [I^-]$ .

<sup>b</sup>Calculated from  $F_0/\Delta F = 1/K[Q] + 1$ .

For the accessible fraction the Stern-Volmer plot is linear and the apparent value of  $f_a = 1$  (Figure 8.81). Hence if the quenching data were obtained using 300-nm excitation, where only the accessible residue was excited, all the fluorescence would appear to be accessible. Since the inaccessible fraction is not quenched,  $F_0/F = 1$  for this fraction. One cannot construct a modified Stern-Volmer plot since  $\Delta F = 0$  for this fraction. The bimolecular quenching constant can be calculated using  $K = 17.4 \text{ M}^{-1}$  and  $\tau = 5 \text{ ns}$ , yielding a bimolecular quenching constant  $k_q = 0.35 \times 10^{10} \text{ M}^{-1} \text{ s}^{-1}$ .

- A8.9. Quenching of Endo III by poly(dAdT) displays saturation near 20  $\mu\text{M}$ , which indicates specific binding of

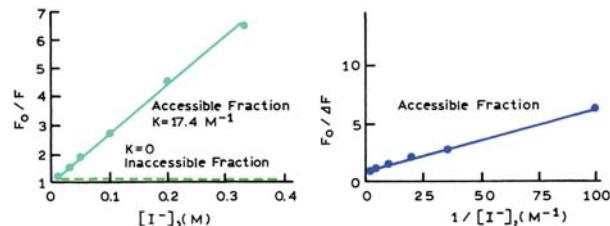


Figure 8.80. Predicted Stern-Volmer plots for the accessible and inaccessible tryptophan residues.

poly(dAdT) to Endo III. Assume the quenching is dynamic. Then  $K_D$  is near  $10^5 \text{ M}^{-1}$ , resulting in an apparent value of  $k_q = 2 \times 10^{13} \text{ M}^{-1} \text{ s}^{-1}$ . This is much larger than the diffusion controlled limit, so there must be some specific binding.

About 50% of the fluorescence is quenched. In Section 8.9.1 we saw that both residues were equally fluorescent. Hence the titration data (Figure 8.75) suggests that one residue, probably 132, is completely quenched when poly(dAdT) binds to Endo III.

- A8.10. The structure of wild-type tet repressor is shown in Figure 8.39. The W75F mutant contains a phenylalanine in place of Trp 75, and thus only one Trp at position 43. This tryptophan is immediately adjacent to bound DNA, which quenches the Trp 43 emission. The extent of quenching is over 50% because there is only one type of tryptophan. The wild-type protein would be expected to show less quenching because Trp 75 will probably not be quenched by DNA.
- A8.11. The relative intensities can be calculated from the Stern-Volmer equation:

$$\frac{F_0}{F} = \frac{\tau_0}{\tau} = 1 + k_q \tau_0 \quad (8.61)$$

For DBO with a lifetime of 120 ns, and  $k_q = 9 \times 10^6 \text{ s}^{-1}$ , the relative intensity is  $F/F_0 = 0.48$ . The DBO is about 50% quenched. For  $\tau_0 = 2 \text{ ns}$ ,  $F/F_0 = 0.98$  and the quenching would probably not be detectable. For  $\tau_0 = 2 \text{ ms}$ ,  $F/F_0 = 5.6 \times 10^{-5}$  and the fluorophore would be completely quenched.

## CHAPTER 9

- A9.1. In order for PET to occur  $\Delta G < 0$ . We can use the Rehm-Weller equation to estimate the oxidation

potential of donor fluorophore if the other quantities are known. The  $S_0 \otimes S_1$  wavelength of 365 nm corresponds to 3.4 eV (eqs. 9.11 and 9.12). Using  $\Delta G < 0$  and eq. 9.10 yields  $E(D^+/D) \otimes 3$  V. Hence it requires more than 69.2 kcal/mole to oxidize the fluorophore. If more than 3 volts were required to remove an electron from the fluorophore then PET would not occur. It is difficult to intuitively understand the sign of  $E(D^+/D)$  because of the convention that  $\Delta E > 0$  corresponds to  $\Delta G < 0$ .

- A9.2. Methylation of the pyridine results in a greater affinity for electrons. Hence PET from the fluorophore occurs to the pyridinium group but not to the more electron-rich pyridine group.

## CHAPTER 10

- A10.1. At 430, 290, and 270 nm the  $r_0$  values of perylene are near 0.38, 0.10, and 0.0, respectively. The angle  $\beta$  between the absorption and emission moments can be calculated using eq. 10.22. These calculations yield  $\beta = 16.8^\circ$ ,  $45^\circ$ , and  $54.7^\circ$ , respectively.
- A10.2. If the sample is weakly scattering, the scattered component will be completely polarized ( $r = 1.0$ ). The measured anisotropy can be obtained using eq. 10.6

$$r_{\text{obs}} = 0.30(0.80) + 1.0(0.20) = 0.44 \quad (10.53)$$

The anisotropy above 0.40 should be an immediate warning that the measured value was not due only to fluorescence.

- A10.3. The corrected ratio,  $I_{\text{VV}}/I_{\text{HV}}$ , is given by  $1.33/0.45 = 2.96$ . Therefore  $r_0 = 0.395$  and  $P_0 = 0.495$ . The angle between the absorption and emission dipoles can be calculated using eq. 10.22. Substitution of  $r_0 = 0.395$  yields  $\beta = 5.2^\circ$ .
- A10.4. The denominator in eq. 10.43 is given by

$$\int_0^\infty I(t) dt = I_0 \int_0^\infty \exp(-t/\tau) dt = I_0 \tau \quad (10.54)$$

The numerator in eq. 10.43 is given by

$$\int_0^\infty I(t)r(t) dt = \int_0^\infty \exp\left[-t\left(\frac{1}{\tau} + \frac{1}{\theta}\right)\right] dt = I_0 r_0 \frac{\tau \theta}{\tau + \theta} \quad (10.55)$$

Division of eq. 10.55 by 10.54 yields eq. 10.44.

- A10.5. The rotational correlation time of perylene can be calculated using eq. 10.46:

$$\theta = \frac{\eta V}{RT} = \frac{(0.01194 P)(252 \text{ g/mole})(0.74 \text{ ml/g})}{(293^\circ\text{K})(8.314 \times 10^7 \text{ erg/mole } ^\circ\text{K})} \quad (10.56)$$

$$\theta = 91 \text{ ps} \quad (10.57)$$

The anisotropy can be calculated using eq. 10.44:

$$r = \frac{0.36}{1 + 6/0.091} = 0.005 \quad (10.58)$$

A similar calculation for propylene glycol at  $25^\circ\text{C}$  yields  $\theta = 2.4 \text{ ns}$  and  $r = 0.103$ .

- A10.6. Equation 10.51 can be derived by reasoning an expression for the average anisotropy. Suppose the quantum yield of the free and bound forms are  $q_F$  and  $q_B$ , respectively. Then the measured anisotropy is

$$r = \frac{f_F q_F r_F + f_B q_B r_B}{f_F q_F + f_B q_B} \quad (10.59)$$

- The correctness of this expression can be seen by noting the numerator is simply a revised form of the additivity law for anisotropies, and the products  $f_F q_F$  and  $f_B q_B$  represent the intensities of each form of the probe. The denominator normalizes these values to fractional fluorescence intensities. Equation 10.59 can be rearranged to eq. 10.51 by noting  $f_F + f_B = 1.0$  and  $R = q_B/q_F$ . Setting  $R = 1$  yields eq. 10.50.

- A10.7. A. The observed polarizations may be converted into anisotropies using  $r = 2P/(3 - P)$ . The latter are more convenient since

$$\bar{r} = f_F r_F + f_B r_B \quad (10.60)$$

where the subscripts F and B represent the free and bound forms of the fluorophore, and  $f_i$  is the fraction of fluorescence due to each form of the probe. When  $[\text{BSA}] = 0$  one observes  $r_F$ , and when  $[\text{BSA}] \gg K_d$  one observes  $r_B$ . These considerations are summarized below:

[BSA]	Observable	$r$
0	$r_F$	0.010
$2 \times 10^{-5}$ M	$r$	0.200
$\gg K_d$	$r_B$	0.300

Using eq. 10.59 one obtains

$$0.20 = f_F(0.01) + (1 - f_F)(0.30) \quad (10.61)$$

and hence  $f_F = 0.345$  and  $f_B = 0.655$ . Since the concentration of DNS is much less than that of BSA, we can assume that the concentration of unliganded BSA is not depleted by the binding of DNS. The ratio of free to bound DNS is given by  $0.345/0.655$ . Hence from eq. 10.52:

$$K_d = \frac{(2 \times 10^{-5} \text{ M})(0.345)}{(0.655)} = 1.05 \times 10^{-5} \text{ M} \quad (10.62)$$

- B. In the use of eq. 10.60 we assumed that the calculated fractional intensity of each species represented the fraction of the DNS which was bound and free. However, if the relative quantum yield of the bound probe is twofold larger than the free probe, then clearly the concentration of the bound form is twofold lower. Therefore:

$$K_d = \frac{(2 \times 10^{-5} \text{ M})(0.345)}{(0.655)/2} = 2.1 \times 10^{-5} \text{ M} \quad (10.63)$$

- C. A change in quantum yield could be readily detected by comparing the intensity of the DNS solution, with and without added BSA. Since the DNS concentrations are identical the relative intensities represent the relative quantum yields.
- D. Using the data provided, the calculated rotational correlation time of BSA is 20 ns. The anisotropy of free DNS will decay too rapidly for measurement with most currently available instruments. For the solution containing a concentration of BSA adequate to bind all the DNS one expects

$$r(t) = 0.20 e^{-t/20} \quad (10.64)$$

For the  $2 \times 10^{-5}$  M solution

$$r(t) = f_B r_0 e^{-t/20} = 0.131 e^{-t/20} \quad (10.65)$$

## CHAPTER 11

- A.11.1. The angle can be calculated using eq. 11.51. Using an apparent time of 0, an anisotropy of 0.22, as  $r_\infty$ , one finds  $\langle \cos^2 \theta \rangle = 0.924$  and  $\theta = 16^\circ$ .
- A.11.2. The most direct approach is to use the amplitudes from the intensity decay. The radiative rate of a fluorophore is usually not affected by its environment. Hence, the relative values of  $\alpha_i$  represent the fraction of the FMN free or bound to YFP. The dissociation constant is given by

$$K_d = \frac{[\text{FMN}][\text{YFP}]}{[\text{FMN} \cdot \text{YFP}]} \quad (11.52)$$

This equation can be rewritten in terms of the total YFP concentration and the fraction of FMN bound ( $f_B$ ):

$$K_d = \frac{[\text{YFP}]_\tau (1 - f_B)^2}{f_B} \quad (11.53)$$

where  $[\text{YFP}]_\tau = [\text{YFP}] + [\text{FMN} \cdot \text{YFP}]$  is the total concentration of YFP. This expression can be understood by noticing that the concentrations of free YFP and FMN are both given by  $[\text{YFP}]_\tau(1 - f_B)$ , and that the concentration of  $[\text{FMN} \cdot \text{YFP}] = [\text{YFP}]_\tau f_B$ . At  $[\text{YFP}] = 0.18 \mu\text{M}$  the fraction bound is given by

$$f_B = \frac{\alpha_2}{\alpha_1 + \alpha_2} = 0.31 \quad (11.54)$$

Hence,  $K_d = 0.28 \times 10^{-6} \text{ M}$ .

## CHAPTER 12

- A12.1. The anisotropy of any time can be calculated using eq. 12.1. These values are listed in Table 12.3. The

**Table 12.3.** Associated Anisotropy Decay

<i>t</i> (ns)	<i>f</i> <sub>1</sub> ( <i>t</i> )	<i>f</i> <sub>2</sub> ( <i>t</i> )	<i>r</i> <sub>1</sub> ( <i>t</i> )	<i>r</i> <sub>2</sub> ( <i>t</i> )	<i>r</i> ( <i>t</i> )
0	0.5	0.5	0.3	0.3	0.30
1	0.45	0.55	0.0	0.29	0.16
5	0.25	0.75	0.0	0.27	0.20

anisotropy values for the non-associated decay can be calculated using

$$r(t) = r_0[0.5 \exp(-t/0.05) + 0.5 \exp(-t/40)] \quad (12.51)$$

For *t* = 0, 1, and 5 ns these values are 0.30, 0.146, and 0.132, respectively.

The presence of an associated anisotropy decay can be seen from the increase in anisotropy at 5 ns as compared to 1 ns. For the non-associated decay the anisotropy decreases monotonically with time.

- A12.2. For a non-associative model the anisotropy decay is given by

$$r(t) = r_0[g_1 \exp(-t/\theta_1) + g_2 \exp(-t/\theta_2)] \quad (12.52)$$

where subscripts 1 and 2 refer to components in the decay, not the location of the fluorophore. From Figure 12.5 the time-zero anisotropy appears to be about 0.32. Using the parameter values in this figure,

$$r(t) = 0.32[0.7 \exp(-t/0.30) + 0.3 \exp(-t/685)] \quad (12.53)$$

A plot of *r*(*t*) would show a rapid decrease to 30% of the time-zero value followed by a long tail where the anisotropy does not decay during the lifetime of the fluorophore.

- A12.3. The anisotropy can be calculated using eqs. 10.6 and 10.22. The anisotropy from the three transitions can be calculated using  $\beta = 0^\circ$  and  $\pm 120^\circ$ . Hence,  $r = 0.33(0.40) + 0.33(-0.05) + 0.33(-0.05) = 0.10$ .
- A12.4. The apparent *r*(0) values of melittin are near 0.16, which is considerably less than  $r_0 = 0.26$ . This indicates that the tryptophan residue in melittin displays fast motions that are not resolved with the available range of lifetimes (0.6 to 2.4 ns).

The apparent correlation times from melittin can be calculated from the slopes in Figure 12.41. For example, in the absence of NaCl the slope is near  $5.8 \times 10^9$ ,

which is equal to  $(r(0)\theta)^{-1}$ . Hence the apparent correlation time is 1.08 ns.

## CHAPTER 13

- A13.1. The D–A distance can be calculated using eq. 13.12. The transfer efficiency is 90%. Hence the D–A distance is  $r = (0.11)^{1/6}R_0 = 0.69R_0 = 17.9 \text{ \AA}$ . The donor lifetime in the D–A pair can be calculated from eq. 13.14, which can be rearranged to  $\tau_{\text{DA}} = (1 - E)\tau_D = 0.68 \text{ ns}$ .
- A13.2. The equations relating the donor intensity to the transfer efficiency can be derived by recalling the expressions for relative quantum yields and lifetimes. The relative intensities and lifetimes are given by

$$F_D = \frac{\Gamma_D}{\Gamma_D + k_{\text{nr}}}, \quad \tau_D = \frac{1}{\Gamma_D + k_{\text{nr}}} \quad (13.34)$$

$$F_{\text{DA}} = \frac{\Gamma_D}{\Gamma_D + k_{\text{nr}} + k_T}, \quad \tau_{\text{DA}} = \frac{1}{\Gamma_D + k_{\text{nr}} + k_T} \quad (13.35)$$

where  $\Gamma_D$  is the emission rate of the donor and  $k_{\text{nr}}$  is the non-radiative decay rate. The ratio of intensities is given by

$$\frac{F_{\text{DA}}}{F_D} = \frac{\Gamma_D + k_{\text{nr}}}{\Gamma_D + k_{\text{nr}} + k_T} = \frac{\tau_D^{-1}}{\tau_D^{-1} + k_T} \quad (13.36)$$

Hence

$$1 - \frac{F_{\text{DA}}}{F_D} = \frac{k_T}{\tau_D^{-1} + k_T} = E \quad (13.37)$$

One can derive a similar expression for the transfer efficiency *E* based on lifetime using the right-hand side of eqs. 13.34 and 13.35.

It should be noted that  $k_T$  was assumed to be a single value, which is equivalent to assuming a single distance. We also assumed that the donor population was homogeneous, so that each donor had a nearby acceptor, that is, labeling by acceptor is 100%.

- A13.3. The excitation spectra reveal the efficiency of energy transfer by showing the extent to which the excitation of the naphthalyl donor at 290 nm results in dansyl

emission. The transfer efficiency can be calculated from the emission intensity at 450 nm for 290-nm excitation, which reflects acceptor emission due to excitation of the donor and direct excitation of the acceptor. Dansyl-L-propyl-hydrazide does not contain a donor, and hence this excitation spectrum defines that expected for 0% transfer. For dansyl-L-propyl- $\alpha$ -naphthyl, in which the donor and acceptor are closely spaced, energy transfer is 100% efficient. For this donor–acceptor pair the greatest sensitivity of the excitation spectrum to energy transfer is seen near 290 nm, the absorption maximum of the naphthyl donor. For the other derivatives the intensity is intermediate and dependent upon the length of the spacer. For 290-nm excitation the transfer efficiency can be calculated from the relative intensity between 0 and 100% transfer. The efficiency of energy transfer decreases as the length of the spacer is increased.

The object of these experiments was to determine the distance dependence of radiationless energy transfer. Hence we assume that the efficiency of energy transfer depends on distance according to

$$E = \frac{(R_0/r)^j}{(R_0/r)^j + 1} \quad (13.38)$$

where  $R_0$  and  $r$  have their usual meanings, and  $j$  is an exponent to be determined from the observed dependence of  $E$  on  $r$ . Rearrangement of eq. 13.38 yields

$$\ln(E^{-1} - 1) = j \ln r - j \ln R_0 \quad (13.39)$$

Hence a plot of  $\ln(E^{-1} - 1)$  versus  $\ln r$  has a slope of  $j$ . These data are shown in Figure 13.41. The slope was found to be  $5.9 \pm 0.3$ .<sup>18</sup> From this agreement with the

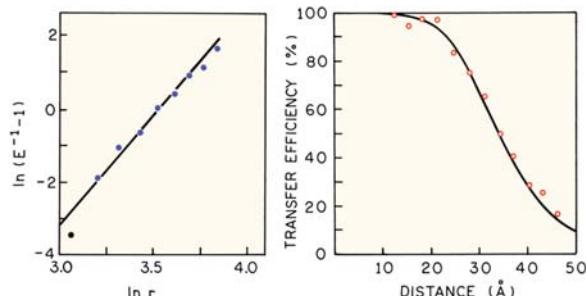


**Figure 13.41.** Distance dependence of the energy transfer efficiencies in dansyl-(L-propyl)<sub>n</sub>- $\alpha$ -naphthyl;  $n = 1\text{--}12$ . Revised from [18].

predicted value of  $j = 6$  these workers concluded that energy transfer followed the predictions of Förster. See [18] for additional details.

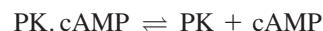
The value of  $R_0$  can be found from the distance at which the transfer efficiency is 50%. From Figure 13.41 (right)  $R_0$  is seen to be near 33 Å.

- A13.4. The lifetime of compound I is  $\tau_{\text{DA}}$  and the lifetime of compound II is  $\tau_{\text{D}}$ . Compound II serves as a control for the effect of solvent on the lifetime of the indole moiety, in the absence of energy transfer. The rate of energy transfer is given by  $k_{\text{T}} = \tau_{\text{DA}}^{-1} - \tau_{\text{D}}^{-1}$ .

$$k_{\text{T}} = CJ \quad (13.40)$$

where  $C$  is a constant. Hence a plot of  $k_{\text{T}}$  versus  $J$  should be linear. The plot of  $k_{\text{T}}$  vs.  $J$  is shown in Figure 13.42. The slope is 1.10. These data confirm the expected dependence of  $k_{\text{T}}$  on the overlap integral. See [20] for additional details.

- A13.5. If the wavelength ( $\lambda$ ) is expressed in nm, the overlap integral for Figure 13.9 can be calculated using eq. 13.3 and is found to be  $4.4 \times 10^{13} \text{ M}^{-1} \text{ cm}^{-1} (\text{nm})^4$ . Using eq. 13.5, with  $n = 1.33$  and  $Q_{\text{D}} = 0.21$ , one finds  $R_0 = 23.6 \text{ \AA}$ . If  $\lambda$  is expressed in cm then  $J(\lambda) = 4.4 \times 10^{-15} \text{ M}^{-1} \text{ cm}^3$ , and using eq. 13.8 yields  $R_0 = 23.6 \text{ \AA}$ .
- A13.6. The disassociation reaction of cAMP (A) from protein kinase (PK) is described by



$$B \rightleftharpoons F + A \quad (13.41)$$

where  $B$  represents PK with bound cAMP,  $F$  the PK without bound cAMP, and  $A$  the concentration of

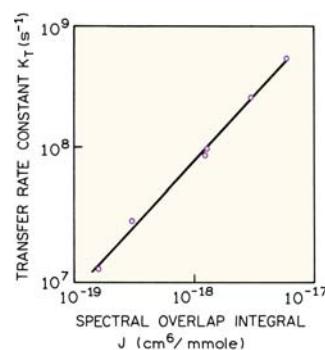


**Figure 13.42.** Dependence of the rate of energy transfer on the magnitude of the overlap integral. Revised from [20].

cAMP. The dissociation constant for cAMP is defined by

$$K_D = \frac{[F][A]}{[B]} \quad (13.42)$$

Using conservation of mass,  $[F] + [B] = [T]$  is the total protein kinase concentration, and one can show the bound and free fractions of PK are given by

$$f_B = \frac{[B]}{[T]} = \frac{[A]}{K_D + [A]}, \quad f_F = \frac{[F]}{[T]} = \frac{K_D}{K_D + [A]} \quad (13.43)$$

Let  $R_B$  and  $R_F$  represent the intensity ratio of each species. At any given cAMP concentration the observed ratio  $R$  is

$$R = f_B R_B + f_F R_F \quad (13.44)$$

Assuming that  $f_B + f_F = 1.0$ , one obtains

$$[A] = [\text{cAMP}] = K_D \left( \frac{R - R_F}{R_B - R} \right) \quad (13.45)$$

A ratio of intensities is independent of the total PK concentration, and independent of sample-to-sample variations in PK concentration. Hence intensity ratio-metric measurements are convenient and accurate. See [99] for additional details.

- A13.7. A. The efficiency of energy transfer can be calculated from eq. 13.13:

$$E = 1 - \frac{4.1}{20.5} = 0.80 \quad (13.46)$$

- B. The expected lifetime in the presence of DNP can be calculated using eq. 13.14 with  $\tau_D = 5.0$  ns and  $E = 0.8$ :

$$\tau_{DA} = \tau_D (1-E) = 1 \text{ ns} \quad (13.47)$$

- C. The rate of energy transfer ( $k_T$ ) can be calculated using eq. 13.11 with  $E = 0.8$  and  $\tau_D = 5$  ns:

$$k_T = \frac{E\tau_D^{-1}}{1-E} = 8 \times 10^8 \text{ s}^{-1} \quad (13.48)$$

- D. The distance can be calculated using eq. 13.12. Substitution and rearrangement yields,  $r^6 = 0.20 R_0^6$ , and therefore  $r = 38.2 \text{ \AA}$ .
- E. The efficiency can be calculated using eq. 13.12 with  $r = 20 \text{ \AA}$ . The efficiency is 0.9959. Once the efficiency is known the intensity can be calculated using eq. 13.13. The fluorescence intensity ( $F_{DA}$ ) is expected to be 0.0041  $F_D = 0.0841$ .
- F. The 1% impurity would contribute 1% of 20.5, or 0.205 to the total intensity. The contribution from this minor component would be  $(0.205/0.0841) = 2.44$ -fold more intense than the signal from the DNP-binding protein, and would invalidate any interpretation of the intensity in the presence of DNP.
- G. The lifetime of the sample would be dominated by the impurity and thus would be near 5 ns. Such a result is indicative of an impurity. Specifically, the yield is decreased to 0.0041 of the original value, but the lifetime is relatively unchanged. When this result is found one should consider the presence of a fluorescent impurity.

- A13.8. In order to calculate the possible effects of  $\kappa^2$  on distance we need to determine the depolarization factors due to segmental motion of the donor and acceptor. Knowledge of the rotational correlation time of the protein ( $\theta$ ) allows us to account for this component in the steady state anisotropy. The depolarization factors due to overall rotation ( $d_{pi}$ ) can be calculated from the Perrin equation. For the donor ( $\tau_D = 5 \text{ ns}$ ) and acceptor ( $\tau_A = 15 \text{ ns}$ ) these factors are

$$d_{PD} = \frac{1}{1 + \tau_D/\theta} = 0.5 \quad (13.49)$$

$$d_{PA} = \frac{1}{1 + \tau_A/\theta} = 0.25 \quad (13.50)$$

Recall that the overall depolarization is given by Soleillet's rule (Chapter 10),  $r = r_0 d_{pi} d_{si}$ , where  $d_{si}$  is the factor due to segmental motions of the donor or acceptor. Hence we can use the steady-state anisotropies and calculate the depolarization factors due to rapid segmental probe motions:

$$d_D^\kappa = \left( \frac{r_D}{r_0 d_{PD}} \right)^{1/2} = 0.71 \quad (13.51)$$

$$d_A^R = \left( \frac{r_A}{r_0 d_{PA}} \right)^{1/2} = 0.71 \quad (13.52)$$

Hence the maximum and minimum values of  $\kappa^2$  are 0.19 and 2.62 (eqs. 13.18 and 13.19). According to eqs. 13.23 and 13.24, the D–A distance can range from  $0.81R_0$  to  $1.26R_0$ , or from 20.3 to 31.5 Å.

- A13.9. If  $f_A = 1.0$  then the transfer efficiency is given by eq. 13.13:

$$E = 1 - \frac{0.5}{1.0} = 0.5 \quad (13.53)$$

and the D–A distance is thus equal to  $R_0$ . If  $f_A = 0.5$  the transfer efficiency is given by eq. 13.17:

$$E = 1 - \frac{0.5 - 1.0(0.5)}{1.0(0.5)} = 1.0 \quad (13.54)$$

If  $f_A = 0.5$  then the transfer efficiency for the actual D–A pair is 100%, and thus the D–A distance is less than  $0.5R_0$ . The presence of acceptor underlabeling results in a higher intensity for the presumed D–A pair and an overestimation of the true D–A distance.

- A13.10. Equation 13.25 can be easily derived by writing expression for the acceptor intensity. In the absence ( $F_A$ ) and presence of donor ( $F_{AD}$ ) the intensities are given by

$$F_A(\lambda_A^{em}) = \varepsilon_A(\lambda_D^{ex}) C_A(\lambda_A^{em}) \quad (13.55)$$

$$F_{AD}(\lambda_A^{em}) = [\varepsilon_A(\lambda_D^{ex}) + E\varepsilon_D(\lambda_D^{ex})]C_A(\lambda_A^{em}) \quad (13.56)$$

where excitation is at  $\lambda_D$ , intensities are measured at  $\lambda_A$ , and  $E$  is the transfer efficiency.  $C_A(\lambda_A^{em})$  is a constant relating the intensity at  $\lambda_A$  to the acceptor concentration. Dividing 13.55 by 13.56, followed by rearrangement, yields eq. 13.25.

If the extent of donor labeling is less than 1.0, then the acceptor intensities are given by

$$F_A(\lambda_A^{em}) = \varepsilon_A(\lambda_D^{ex}) C_A(\lambda_A^{em}) \quad (13.57)$$

$$F_A(\lambda_A^{em}) = [\varepsilon_A(\lambda_D^{ex}) + f_D E\varepsilon_D(\lambda_D^{ex})]C_A(\lambda_A^{em}) \quad (13.58)$$

where  $f_D$  is the fractional labeling with the donor. These expressions can be understood by recognizing that the directly excited acceptor intensity is independent of  $f_D$ , but the acceptor intensity due to energy transfer depends on  $f_D$ . Rearrangement of eqs. 13.57 and 13.58 yields 13.25.

- A13.11. Let  $C_A(\lambda_A)$  and  $C_D(\lambda_A)$  be the constants relating the intensities at  $\lambda_A$  to the acceptor and donor concentrations, respectively, when both are excited at  $\lambda_D$ . Since the donor is assumed to emit at  $\lambda_A$ , eqs. 13.55 and 13.56 become

$$F_A(\lambda_A) = \varepsilon_A(\lambda_D) C_A(\lambda_A) \quad (13.59)$$

$$\begin{aligned} F_{AD}(\lambda_A) &= [\varepsilon_A(\lambda_D) + E\varepsilon_D(\lambda_D)]C_A(\lambda_A) \\ &\quad + \varepsilon_D(\lambda_D) C_{DA}(\lambda_A) \end{aligned} \quad (13.60)$$

In eq. 13.58 we considered the contribution of the donor in the D–A pair to the intensity at  $\lambda_A$ . In general  $C_{DA}(\lambda_A)$  will be smaller than  $C_D(\lambda_A)$  due to FRET quenching of the donor. However,  $C_D(\lambda_A)$  can be measured with the donor-alone sample.  $C_{DA}(\lambda_A)$  can be estimated using the shape of the donor emission to estimate the donor contribution at  $\lambda_A$  in the doubly labeled sample. Eqs. 13.59 and 13.60 can be rearranged to

$$\frac{F_{AD}(\lambda_A)}{F_D(\lambda_D)} - 1 = \frac{E\varepsilon_D(\lambda_D)}{\varepsilon_A(\lambda_D)} + \frac{\varepsilon_D(\lambda_D)C_{DA}(\lambda_A)}{\varepsilon_A(\lambda_D)C_A(\lambda_A)} \quad (13.61)$$

The transfer efficiency as seen from the acceptor emission is given by eq. 13.25, which assumes that the donor does not emit at the acceptor wavelength. Hence the acceptor emission increases the apparent efficiency to

$$E_{app} = E + \frac{C_{DA}(\lambda_A)}{C_A(\lambda_A)} \quad (13.62)$$

and would thus be larger than the actual efficiency. If the donor does not contribute at  $\lambda_A$ , then  $C_{DA}(\lambda_A) = 0$

and  $E_{\text{app}}$  becomes the true efficiency. See [83] for additional details.

- A13.12. The true transfer efficiency is defined by the proportion of donors that transfer energy to the acceptor, and is given by

$$E = \frac{k_T}{\tau_D^{-1} + k_q + k_T} \quad (13.63)$$

The apparent efficiency seen for the donor fluorescence is given by

$$E_D = \frac{k_T + k_q}{\tau_D^{-1} + k_q + k_T} \quad (13.64)$$

The apparent efficiency ( $E_D$ ) is larger than the true efficiency ( $E$ ) because the additional quenching pathway decreases the donor emission more than would have occurred by FRET alone. See [56] for additional details.

## CHAPTER 14

- A14.1. The intensity decays of A and C would both be single exponential, but the intensity decay of B would be a triple exponential. For sample A the donors are at a unique distance from acceptors at 15, 20, and 25 Å. The transfer rate is given by

$$k_T = \frac{1}{\tau_D} \left( \frac{20}{15} \right)^6 + \frac{1}{\tau_D} \left( \frac{20}{20} \right)^6 + \frac{1}{\tau_D} \left( \frac{20}{25} \right)^6 \quad (14.27)$$

Calculation of the transfer rate yields  $k_T = 6.88\tau_D^{-1}$ . Hence the decay of sample A is given by eq. 14.1 and is a single exponential with

$$I_{DA}(t) = \exp \left[ -\frac{t}{\tau_D} - \frac{t6.88}{\tau_D} \right] = \exp \left( -\frac{t}{0.63} \right) \quad (14.28)$$

The intensity decay of sample C would be the same single exponential with the same decay time of 0.63 ns.

The intensity decay of sample B would be a triple exponential. There would be three different decay times, which can be calculated from the three transfer

rates in eq. 14.28. The decay times are 0.76, 2.5, and 3.96 ns.

- A14.2. Since the unquenched lifetime and quantum yields of the three proteins in sample B are the same, the radiative decay rates are the same and the relative amplitude of the three proteins would be the same. Hence the intensity decay would be given by

$$I(t) = \sum_i \alpha_i e^{-t/\tau_D} \quad (14.29)$$

with  $\alpha_1 = \alpha_2 = \alpha_3 = 0.33$  and  $\tau_1 = 0.76$ ,  $\tau_2 = 2.5$  and  $\tau_3 = 3.96$  ns.

In contrast to the  $\alpha_i$  values, the fractional intensities will be very different for each protein in sample B. These values are given by

$$f_i = \frac{\alpha_i \tau_i}{\sum_j \alpha_j \tau_j} \quad (14.30)$$

Hence the fractional intensities of the three proteins are 0.105, 0.346, and 0.549.

- A14.3. The presence of three acceptors could not be detected in sample A. This is because the only observable would be the decreased donor quantum yield or lifetime. The only way the three acceptors could be detected is from the absorption spectrum, assuming one knows the extinction coefficient for a single acceptor.
- A14.4. The apparent distance for an assumed single acceptor can be found from eq. 14.2. Numerically we found  $k_T = 6.88 \tau_D^{-1}$ , which can be equated to an apparent distance:

$$k_T = \frac{6.88}{\tau_D} = \frac{1}{\tau_D} \left( \frac{R_0}{r_{\text{app}}} \right)^6 \quad (14.31)$$

Solving for  $r_{\text{app}}$  yields  $R_0/r_{\text{app}} = 1.38$ , so  $r_{\text{app}} = 14.5$  Å. The extent of energy transfer is thus seen to be dominated by the closest acceptor at 15 Å. The presence of two more acceptors at 20 and 25 Å only decreases the apparent distance by 0.5 Å.

- A.14.5. A. One acceptor per 60-Å cube corresponds to an acceptor concentration of 8 mM. Use of eq. 13.33 with  $R_0 = 30$  Å yields a critical concentration of 17 mM.

- B. A covalently linked acceptor is somewhat equivalent to one acceptor per sphere of 30 Å, or  $8.84 \times 10^{18}$  acceptors/cm<sup>3</sup>. This is equivalent to an acceptor concentration of 15 mM. Covalent attachment of an acceptor results in a high effective acceptor concentration.

## CHAPTER 15

- A.15.1. Using the data provided in Figure 15.28 one can calculate the following values:

Mole% Rh-PE	Rh-PE/Å <sup>2</sup>	Rh-PE/R <sub>0</sub> <sup>2</sup>	F <sub>DA</sub> /F <sub>D</sub>
0.0	0.0	0.0	1.0
0.2	$2.8 \times 10^{-5}$	0.071	0.62
0.4	$5.7 \times 10^{-5}$	0.143	0.40
0.8	$11.4 \times 10^{-5}$	0.286	0.21
1.2	$17.1 \times 10^{-5}$	0.429	0.15

The distance of closest approach can be estimated by plotting the last two columns of this table on the simulations shown in Figure 15.17. The observed energy transfer quenching is greater than predicted for no excluded area,  $r_C = 0$ , or much less than  $R_0$ . This suggests that the donors and acceptors are fully accessible and probably clustered in the PE vesicles. The  $R_0$  value was not reported in [64].

- A15.2. The decay times can be used with eq. 15.20 to obtain the transfer rate  $k_T = 1.81 \times 10^3$  s<sup>-1</sup>. Dividing by the EB concentration (2.77 μM) yields  $k_T^b = 6.5 \times 10^8$  M<sup>-1</sup> s<sup>-1</sup>.

Using eq. 15.25 and the values of  $R_0$  and  $r_C$ , the maximum bimolecular rate constant is  $1.1 \times 10^6$  M<sup>-1</sup> s<sup>-1</sup>. The measured values could be larger than the theoretical values for two reasons. The positively charged donors may localize around the negatively charged DNA. This results in a larger apparent concentration of EB. Given the small value of  $r_C$  we cannot exclude the possibility of an exchange contribution to  $k_T^b$ .

- A15.3. To a first approximation the donor intensity is about 50% quenched when  $C/C_0 = 0.5$ . This value of  $C/C_0$  can be used to calculate the acceptor concentration in any desired units, as listed in Table 15.3.

Acceptor concentrations near 2 mM are needed in homogeneous solution. This is generally not practical for proteins because the absorbance due the acceptor would not allow excitation of the protein. Also, such high concentrations of acceptors are likely to perturb the protein structure.

**Table 15.3.** Approximate Concentrations for 50% Quenching in One, Two, and Three Dimensions

Equation	Concentrations for 50% energy transfer
$C_0 = (4/3\pi R_0^3)^{-1}$	$9.55 \times 10^{17}$ acceptors/cm <sup>3</sup> = 1.59 mM
$C_0 = (\pi R_0^2)^{-1}$	$6.4 \times 10^{11}$ acceptors/cm <sup>2</sup> = $4.5 \times 10^{-3}$ acceptors/lipid
$C_0 = (2R_0)^{-1}$	$5 \times 10^5$ acceptors/cm = $1.7 \times 10^{-2}$ acceptors/base pair

The situation is much better in proteins and nucleic acids. In this case the acceptors need only to be about one per 222 lipids or one per 59 base pairs. This favorable situation is the result of a locally high concentration of acceptors due to their localization in the lipid or nucleic acid. The bulk concentration of acceptors can be low and is determined by the bulk concentration of membrane or nucleic acid.

- A15.4. The simulations in Figure 15.31 determine the  $R_0$  value because the two-dimensional concentration of acceptors is known from the area/lipid and the fractional acceptor concentrations. Any point on these curves can be used to calculate  $R_0$ . For an acceptor density of 0.05 and  $t = \tau_D$  the value of  $I_{DA}(t)/I_D^0$  is about 0.003. The value of  $\beta$  can be found from eq. 15.9, yielding  $\beta = 2.41$ . For A/PL = 0.05 the area per acceptor molecule is  $C_0 = 1400$  Å/acceptor. Using eq. 15.10 and 15.11 yields  $R_0 = 39.8$  Å, which agrees with the value of 40 Å given in [50].

## CHAPTER 16

- A16.1. A. Without experimentation, it is not possible to predict how the fluorescence properties of the protein will vary when it is unfolded. In general, one can expect the extent of tyrosine fluorescence to increase when the protein is unfolded. This could be detected by excitation at 280 nm. The tyrosine emission would appear near 308 nm. It is also probable that the fluorescent intensity or the emission maxima of the single-tryptophan residue would change as the protein is unfolded. Once the spectral characteristics of the native and unfolded states are determined, the data can be used to quantify the unfolding process. It is important to remember that anisotropy or lifetime measurements may not

- accurately reflect the fractional populations of the folded and unfolded states. This is particularly true if the quantum yields of the fluorescent residues in the protein change upon unfolding.
- B. The extent of exposure to the aqueous phase could be studied by measuring the Stern-Volmer bimolecular quenching constant ( $k_q$ ) and comparison of the measured values with those observed for an N-acetyl-L-tryptophanamide in the same solvent. One should choose the neutral tryptophan analogue to avoid electrostatic effects on the quenching process. The extent of exposure to the aqueous phase can be estimated by comparing the measured quenching constant for the protein with that found for the model compounds.
  - C. If the protein associates to form a dimer, it is possible that the tryptophan residue becomes shielded from the aqueous phase. In this case one can expect a change in the intensity or emission maximum of the protein. If the tryptophan residue remains exposed to the aqueous phase upon dimer formation, then it is probable that the emission spectrum and intensity will remain the same. In this case the extent of the association should still be detectable by changes in the steady-state anisotropy.
  - D. In order to measure the distance of the tryptophan to the reactive site it is necessary to select an appropriate acceptor and to covalently label the protein. It is critical for the protein to be completely labeled with acceptor, because the unlabeled fraction will contribute a large amount to the measured intensity, resulting in an underestimation of the distance. Following calculation of the Förster distance,  $R_0$ , from the spectral properties of the donor and acceptor, the distance can be measured from the decrease in the donor quantum yield due to the presence of acceptor.
  - E. While not immediately obvious, the extent of energy transfer from a tryptophan donor to an acceptor is expected to change upon association of the acceptor-labeled monomers. This is because, upon dimerization, each tryptophan residue will be brought into proximity of the acceptor on the other subunit. Hence each tryptophan will transfer to two acceptors, resulting

- in a higher amount of energy transfer and a lower donor quantum yield in the dimeric state.
- A16.2. A. Dimerization could be detected from the steady-state intensity or the intensity decay. Upon dimer formation one will observe a twofold increase in the relative quantum yield. If the dimerization occurs due to a change in protein concentration, then it is necessary to normalize the measured intensities to the same protein concentration. If dimerization occurs as a result of a change in solution conditions, then the intensity change may be observed at a constant protein concentration.
- B. Dimer formation could be detected by an increase in the mean lifetime. When dimerization is partially complete one expects the decay to be a double exponential.
- C. Dimerization could not be detected from the steady-state anisotropy. The anisotropy ( $r$ ) of the monomer and dimer can be calculated using the Perrin equation:

$$r = \frac{r_0}{1 + \tau/\theta} \quad (16.6)$$

where  $\tau$  is the lifetime and  $\theta$  is the rotational correlation time. The steady-state anisotropy of the monomer ( $r_M$ ) and dimer ( $r_D$ ) are equal:  $r_M = r_D = 0.10$ .

- D. Dimerization could be detected by measuring the anisotropy decay, which will display a longer mean correlation time as dimers are formed.
- E. When 50% of the monomers have formed dimers, these dimers contribute twice as much as the monomers to steady-state intensity. Hence the fractional intensities are  $f_M = 0.33$  and  $f_D = 0.66$ . The steady-state anisotropy is given by

$$r = 0.33r_M + 0.66r_D = 0.10 \quad (16.7)$$

and is unchanged during dimerization.

For the intensity decay we need to calculate the values of  $\alpha_M$  and  $\alpha_D$ . The relative values are given by  $\alpha_M = 0.33/2.5 = 0.13$  and  $\alpha_D = 0.66/5.0 = 0.13$ . Hence the intensity decay is given by

$$I(t) = 0.5 \exp(t/\tau_M) + 0.5 \exp(-t/\tau_D) \quad (16.8)$$

The  $\alpha_i$  values are equivalent because we assumed that the intensities and lifetimes both increased by the same amount, meaning that the radiative decay rate stayed the same.

For a mixture of monomers and dimers the anisotropy decay follows the associated model, where each decay time is associated with one of the correlation times. At any time  $t$  the fractional intensity of the monomer or dimer is given by

$$f_M(t) = \frac{0.5e^{-t/\tau_M}}{I(t)} \quad (16.9)$$

$$f_D(t) = \frac{0.5e^{-t/\tau_D}}{I(t)} \quad (16.10)$$

where  $I(t)$  is given by eq. 16.8. The anisotropy decay is given by

$$r(t) = f_M(t)r_M(t) + f_D(t)r_D(t) \quad (16.11)$$

Hence this mixture of monomers and dimers displays an associated anisotropy decay.

- A16.3. There are two possible explanations for the CRABPI emission spectra in Figure 16.74. Figure 16.6 shows that the absorption spectra of indole shift to longer wavelengths with increasing solvent polarity and/or hydrogen bonding. CRABPI contains three tryptophan residues in different environments, which probably results in slightly different absorption spectra. An increase in excitation wavelength could result in selective excitation of the tryptophan residues in a more polar environment, which have longer-wavelength emission maxima.

A second possible explanation is a real-edge excitation shift (REES). A solution of indole or tryptophan in a viscous polar solution will show a shift to longer-wavelength emission as the excitation wavelength is increased. This effect is due to selective excitation of those fluorophores that are surrounded by solvent molecules that have orientations similar to the relaxed excited state. In the case of CRABPI the dominant cause of the emission spectral shifts is probably the different environments of the three tryptophan residues.

- A16.4. The emission spectra in Figure 16.75 show that the region of MRP near W93 binds to calmodulin. The N-terminal region of MRP does not appear to interact with calmodulin, or at least interaction does not result in a spectral shift. The presence or absence of interaction of W4 with calmodulin could be further studied by steady-state anisotropy measurements. If W4 does not interact with calmodulin, then there should be no change in the anisotropy of W4 upon addition of calmodulin.

- A16.5. Figure 16.76 shows the steady-state intensities of WT-LADH and the W314L mutant. For both acrylamide and iodide the amount of quenching is higher for W15 in the mutant protein than for the WT protein containing both W15 and W314. The Stern-Volmer plots in Figure 16.77 show a higher quenching constant for W15 in W314L than for the WT protein. The data in Figure 16.76 and 16.71 thus indicate that W15 in LADH is more accessible to water-soluble quenchers than is W314, which contributes part of the observed intensity in the WT protein. The modified Stern-

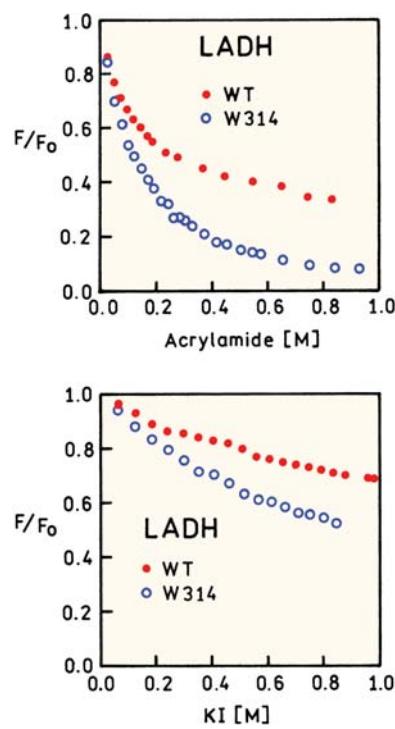


**Figure 16.76.** Fluorescence intensity of WT-LADH and the W314L tryptophan mutant in the presence of acrylamide and iodide. Revised from [201].

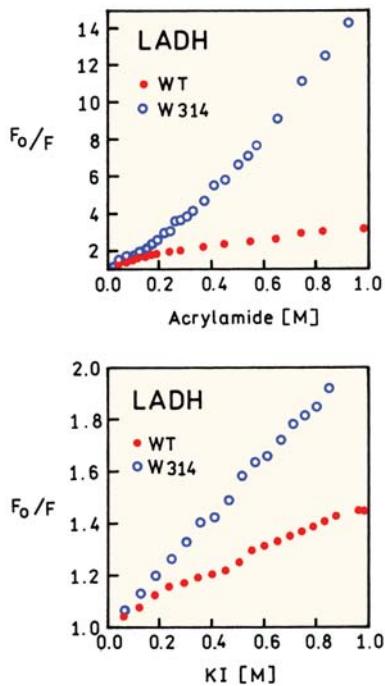


**Figure 16.77.** Stern-Volmer plots for acrylamide and iodide quenching of WT-LADH and the W314L tryptophan mutant.

Volmer plots in Figure 16.78 suggest a somewhat higher y-axis intercept for the WT protein than for W314L. A higher y-axis intercept indicates a larger fraction of fluorescence that is not accessible to quenchers, which in the case of the WT protein is W15.

## CHAPTER 17

- A17.1. The activation energy for any process can be calculated by plotting the logarithm of the rate constant ( $k$ ) versus the inverse of the temperature in degrees Kelvin. For an anisotropy decay the rotational rate ( $R$ ) is related to the rotational correlation time ( $\theta$ ) by  $\theta = (6R)^{-1}$ . The plot of  $\ln(6R)$  versus  $(EK)^{-1}$  is shown in Figure 17.49. The activation energy can be calculated from the Arrhenius equation:<sup>148</sup>

$$\ln(k) = \ln(6R) = -\frac{E_A}{R_g} + \ln A \quad (17.4)$$

where  $A$  is a constant of integration and  $R_g$  is the gas constant. This equation is simply an expression that

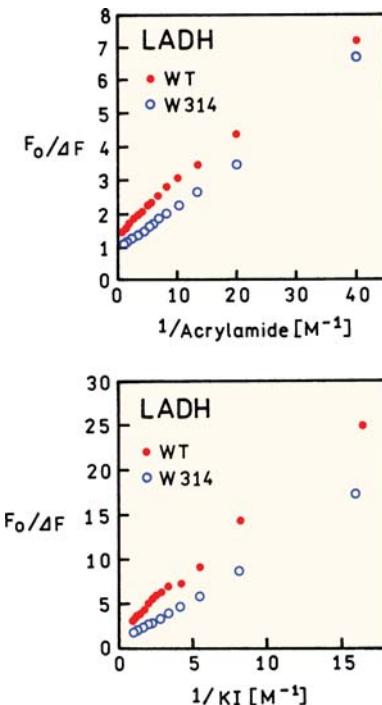


**Figure 16.78.** Modified Stern-Volmer plots for iodide and acrylamide quenching of WT-LADH and the W314L tryptophan mutant.

the rate of a process depends on a frequency factor and the energy needed to pass over an energy barrier:

$$k = A \exp(-E_A/RT) \quad (17.5)$$

From this analysis (Figure 17.49) one finds  $E_A = 6.178$  kcal/mole, which is typical for rotational diffusion of proteins in water. Also, this value is comparable to the activation energy for the temperature-dependent viscosity of water,  $E_A = 4.18$  kcal/mole.

The steady-state anisotropy for RNase T<sub>1</sub> at each temperature can be calculated from the Perrin equation

$$r = \frac{r_0}{1 + \tau/\theta} \quad (17.6)$$

Hence the values are expected to be 0.151, 0.137, 0.128, 0.114, and 0.104, in order of increasing temperature from -1.5 to 44.4°C in Table 17.7.

- A17.2. The cone angle for tryptophan rotational freedom can be calculated from the ratio of the anisotropy amplitude associated with the long correlation time, to the

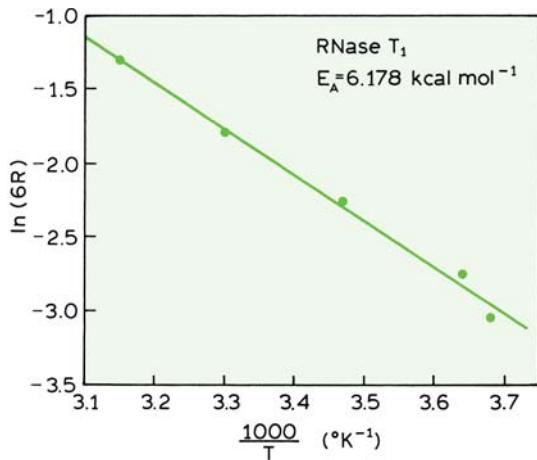


**Figure 17.49.** Arrhenius plot for the rotational correlation times of RNase T<sub>1</sub>. Data from [54].

total anisotropy. The fractional contribution of the long correlation time ( $t_L$ ) is given by

$$f_L = \frac{r_{01}}{r_{01} + r_{02}} \quad (17.7)$$

This fraction can be related to the displacement of the transition dipole according to the definition of anisotropy:

$$\cos^2 \beta = \frac{2f_L + 1}{3} \quad (17.8)$$

Alternatively, this fraction can be related to the angle ( $\theta_c$ ) through which the tryptophan rotates before striking an energy barrier:

$$f_L = \left[ \frac{1}{2} \cos \theta_c (1 + \cos \theta_c) \right]^2 \quad (17.9)$$

Application of these expressions to the data in Table 17.4 yields the following results in Table 17.9.

- A17.3. The time-zero anisotropy,  $r(0)$ , for RNase T<sub>1</sub> in Table 17.7 is derived from the time-domain data and is lower than from other reports. One possible origin of the difference is the shorter excitation wavelength (295 nm) for the time-domain data and the possibility of a small error in the reported excitation wavelength. Another difference is that  $r(0)$  was a variable parameter in the analysis of the time-domain data. It is possible that a short component in the anisotropy decay was missed by limited time resolution, as suggested by molecular dynamics simulations or RNase T<sub>1</sub>.<sup>149</sup>
- A17.4. A. The intensity decays more slowly at longer emission wavelengths. This indicates that the mean decay time is increasing. In this case the effect is due to an increasing fractional contribution of the long-lived component (9.8 ns).  
B. The decay-associated spectra are calculated using the data in Table 17.8 and eq. 17.3, resulting in the DAS shown in Figure 17.50. In order to interpret the DAS one has to assume that each decay time (3.8 or 9.8 ns) is associated with one of the tryptophan residues. Using this assumption the 3.8 ns decay time is associated with a blue-shifted emission and a lower quantum yield than the red-shifted 9.8 ns residue.  
C. The most rigorous way to confirm assignment of the DAS is to create the single tryptophan mutants. Each mutant should display one of the calculated DAS. One could also use quenching by iodide or acrylamide with the two tryptophan

**Table 17.9.** Angular Freedom of NATA and Tryptophan Residues in Single-Tryptophan Peptides and Proteins at 20°C

Proteins	$r_0 = r_{01} + r_{02}$	$f_L$	$\beta$ (deg)	$\theta_c$ (deg)
RNase T <sub>1</sub> , 20°C	0.310	1.00	0.0	0.0
Staph. nuclease	0.321	0.944	11.1	11.2
Monellin	0.315	0.768	23.2	23.8
ACTH	0.308	0.386	39.8	43.8
Gly-trp-gly	0.325	0.323	42.2	47.3
NATA	0.323	1.00	0.00	0.00
Melittin monomer	0.323	0.421	38.4	41.9
Melittin tetramer	0.326	0.638	29.4	30.8

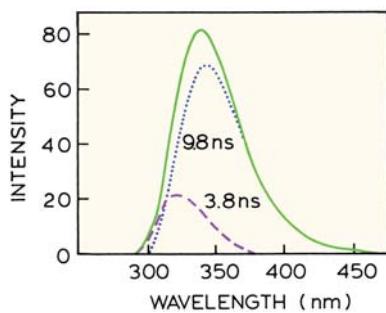


**Figure 17.50.** Decay-associated spectra calculated from Table 17.7. Data from [147].

wild type protein. In this case one expects the 9.8-ns emission to be more sensitive to quenching given its longer lifetime and higher exposure to the aqueous phase. The emission spectra could also be resolved by the quenching-resolved method.

- A17.5. The Förster distance for any given value of  $\kappa^2$  can be calculated using

$$R_0(\text{in } \text{\AA}) = 9.78 \times 10^3 [\kappa^2 n^{-4} Q_D J(\lambda)]^{1/6} \quad (17.10)$$

Using this expression the Förster distance is 35.1 Å for  $\kappa^2 = 2/3$  and 42.2 Å for  $\kappa^2 = 2$ . Since the crystal structure shows  $\kappa^2 = 2$ , the  $R_0$  value of 42.2 Å should be used to calculate the tryptophan-to-heme distance. This distance  $r$  can be calculated using the transfer efficiency ( $E$ ) and  $R_0$  values from

$$E = \frac{R_0^6}{R_0^6 + r^6} \quad (17.11)$$

For a transfer efficiency of 97% the distance is  $r = 23.6$  Å using  $R_0 = 42.2$  Å. If the value of  $R_0 = 35.1$  Å is used, then  $r = 19.7$  Å. The trp-to-heme distance<sup>106</sup> from the crystal structure is 17.2 Å. Even though the crystal structure shows  $\kappa^2 = 2$ , the calculated distance is in better agreement with the structure using  $\kappa^2 = 2/3$ .

## CHAPTER 18

- A18.1. The anisotropy of DPPS is higher for two-photon excitation because of  $\cos^4 \theta$  photoselection. The ratio of the two- to one-photon anisotropies is near 1.39,

which is close to the predicted values for parallel transitions: 1.425 (Section 18.5).

The anisotropy is independent of temperature because the lifetime decreases with increasing temperature. The decrease in lifetime offsets the decrease in correlation time, resulting in a constant anisotropy.

- A18.2. The output of mode-locked dye lasers is usually cavity dumped by a device inside the laser cavity. During the time periods between dumping, power builds up in the optical cavity and the average power does not decrease much as the repetition rate is decreased. The repetition rate of a Ti:sapphire laser is usually reduced using a pulse picker that is outside the cavity. The extra pulses are discarded and there is no buildup of power in the cavity between picking. The average power drop is proportional to the decreased repetition rate. For this reason Ti:sapphire lasers are usually used without pulse pickers with an 80-MHz repetition rate. The FD data in Figure 18.17 were obtained using the harmonic content of the 80-MHz pulse train so that only a limited number of frequencies were measured (Chapter 5).
- A18.3. Release of calcium in the cell results in increased energy transfer in the cameleon. When energy transfer increases the donor intensity at the shorter wavelength (480 nm) decreases relative to the acceptor intensity at 535 nm. Hence the ratio becomes larger, which is shown on the scale as the red color.

## CHAPTER 19

- A19.1. The lifetimes can be calculated using  $\tan \phi = \omega \tau$ . From Figure 19.13 the phase angles at 0 and 20.55% oxygen are 48 and 15°, respectively. Recalling the frequency  $\omega = 2\pi\nu$ , the respective lifetimes are 45.2 and 10.9 μs.
- A19.2. The data in Figure 19.80 can be used to determine the lifetimes of camphorquinone in PMMA at various partial pressures of oxygen. These values can be used to construct a lifetime Stern-Volmer plot (Figure 19.83). The oxygen bimolecular quenching constant is near  $2.8 \times 10^6 \text{ M}^{-1} \text{ s}^{-1}$ , which is nearly  $10^4$  smaller than that for oxygen in water. This suggests a low diffusion coefficient of oxygen in PMMA of about  $7 \times 10^{-9} \text{ cm}^2/\text{s}$ . Of course, the accuracy of these values depends on the assumed oxygen solubility in PMMA.
- A19.3. Careful examination of Figure 19.9 reveals that  $[\text{Ru}(\text{Ph}_2\text{phen})_3]^{2+}$  is quenched tenfold at 30 torr oxy-

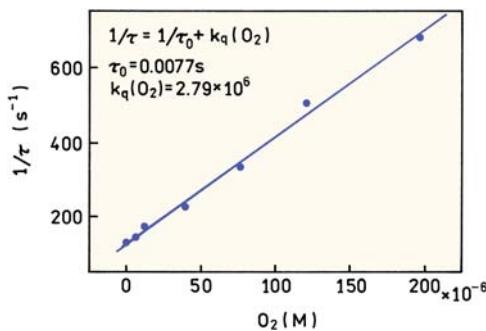


**Figure 19.83.** Stern-Volmer plot for oxygen quenching of camphorquinone in PMMA. Data from [308].

gen. The Stern-Volmer quenching constant is proportional to the lifetime, which is near 5  $\mu\text{s}$ . Hence for the 5-ns probe  $F_0/F = 1.009$  at this same oxygen pressure. At the highest oxygen pressure of 80 torr, the short-lifetime probe will be quenched less than 3%. This extent of quenching is negligible, so the 5-ns probe can serve as an intensity reference.

- A19.4. The spectra in Figure 19.81 show that the absorption of TB decreases with decreasing pH. The high-pH form of TB is the acceptor for SR101. As the percentage of  $\text{CO}_2$  increases the pH of the polymer matrix decreases. This results in a decreased absorbance of TB, less RET from SR101 to TB, and an increase in the apparent lifetime. The increases in apparent lifetime result in the larger phase angle with 2%  $\text{CO}_2$ . The apparent lifetimes of 0 and 2%  $\text{CO}_2$  are 0.35 and 1.24 ns, respectively.
- A19.5. A. The range of anisotropies can be calculated from the Perrin equation

$$r = \frac{r_0}{1 + (\tau/\theta)} \quad (19.15)$$

The anisotropy of the free peptide will be 0.080, and the anisotropy of Ab-Fl-P will be 0.385.

- B. The anisotropies are additive (e.g., 19.14). Hence the anisotropy with 10% free Fl-P is given by

$$r = 0.10(0.08) + 0.90(0.385) = 0.355 \quad (19.16)$$

- C. Displacement of Fl-P from Rh-Ab will result in a tenfold increase in the intensity of Fl-P due to elimination of RET. For such cases, the fraction-

al intensity of the free and bound forms are given by

$$f_F = \frac{m_F q_F}{m_F q_F + m_B q_B} \quad (19.17)$$

$$f_B = \frac{m_B q_B}{m_F q_F + m_B q_B} \quad (19.18)$$

where  $m_i$  are the molecular fractions in the free or bound state, and  $q_i$  are the quantum yields. If  $q_F = 10q_B$ , then

$$f_F = \frac{10m_F}{10m_F + m_B} \quad (19.19)$$

For a molecular fraction of 10%,  $f_F = 0.53$ . Hence 10% displacement of Fl-P results in over 50% of the emission from the free peptide. The anisotropy is

$$r = 0.53(0.08) + 0.47(0.40) = 0.230 \quad (19.20)$$

and is seen to decrease more rapidly with displacement of Fl-P. We used 0.40 for the anisotropy of the bound form because RET will decrease the lifetime of the fluorescein to 0.40 ns.

## CHAPTER 20

- A20.1. A. The decay time can be calculated from the slope of the long-lifetime component using any two points. For instance, extrapolating the long decay time to zero, the intensities of this component at  $t = 0$  and  $t = 500$  ns in Figure 20.50 are near 2000 and 600, respectively. For a single-exponential decay the intensities at two points in time are related by  $\ln I(t_1) - \ln I(t_2) = -t_1/\tau + t_2/\tau$ . Insertion of the values at  $t = 0$  and  $t = 500$  ns yields  $\tau = 415$  ns.
- B.  $\alpha_1 = 0.962$ ,  $\alpha_2 = 0.038$ . These values are from Figure 20.50, following normalization of  $\alpha_1$  and  $\alpha_2 = 1.0$ .
- C.  $f_1 = 0.296$ ,  $f_2 = 0.704$ .

- D.  $f_1 = 0.0004, f_2 = 0.9996$ . This result shows that off-gating essentially eliminates the short-lived component, decreasing its fractional contribution from 0.296 to 0.0004.
- A20.2. The oxygen bimolecular quenching constant can be calculated using the decay times in the absence and in the presence of 100% oxygen. The value of  $\tau_0/\tau = 16.3 = 1 + k_q \tau_0 [O_2]$ . Using  $[O_2] = 0.001275 \text{ M}$  and  $\tau_0 = 3.7 \mu\text{s}$  one obtains  $k_q = 3.24 \times 10^9 \text{ M}^{-1} \text{ s}^{-1}$ . This value is reasonably close to the diffusion-controlled limit and indicates that the quenching by oxygen is highly efficient.

## CHAPTER 21

- A21.1. To answer this question we need to design quenching or anisotropy measurements that could potentially be used for sequencing. Consider sequencing with four fluorescent ddNTPs. The Stern-Volmer quenching constants could be different due to either different lifetimes or different accessibilities to the collisional quencher. Then the sequence could be determined by the quenching constant for each fluorescent band on the gel. Determination of the quenching constant requires a minimum of two intensity measurements: in the absence of quencher and in the presence of a known concentration of quencher. Although such measurements are possible, the use of two samples to measure a single base is too complicated for large-scale sequencing of DNA.

Suppose that the sequencing reaction is performed with a single fluorescent primer. Because anisotropy measurements depend on molecular weight, in principle each oligonucleotide will display a different anisotropy. In practice the anisotropies for DNA oligomers, differing by a single base pair, are likely to be too similar in magnitude for useful distinction between oligomers. If the adjacent base pair changes the lifetime of the labeled oligomer, then the anisotropy measurements may be able to identify the base.

Consider the use of four fluorescent ddNTPs, each with a different lifetime. In this case the anisotropy would be different for each base pair, and the anisotropy measurement could be used to identify the base. This approach is more likely to succeed for longer oligomers, where the anisotropy will become

mostly independent of molecular weight. For shorter oligomers the anisotropy will depend on the fragment length.

---

## CHAPTER 22

- A22.1. In Figure 22.15 it is clear that the F-actin is red and the green color is where the mitochondria are expected to be localized. In Figure 22.19 the colors are reversed: F-actin is green and mitochondria are red. At first glance it appears that the legend for one of the figures is incorrect, or that the cells in Figure 22.15 were labeled with fluorophores that stained actin red and mitochondria green. The legends are correct. Both images are created using pseudocolors. Figure 22.19 was created by an overlay of three intensity images. The color of each image was assigned to be similar to the emission maxima of the probes: DAPI is blue, Bodipy-FL is green, and MitoTracker is red. These assignments give the impression that Figure 22.19 is a real color image. In Figure 22.15 the colors were assigned according to lifetime. The lifetime in the nucleus was assigned a blue color, which agrees with Figure 22.19. However, in Figure 22.15 the lifetime of F-actin was assigned to be red, and the lifetime of MitoTracker was assigned to be green. The pseudocolor assignments of the red- and green-emitting fluorophores are opposite in Figures 22.15 and 22.19.

---

## CHAPTER 23

- A23.1. The intensity needed to excite the fluorophore can be calculated using eq. 23.5. If there is no intersystem crossing than  $S_1 = \tau\sigma I_e S_T$ . The intensity required is given by  $S_1/S_T = 0.5 \tau\sigma I_e$ . The cross-section for absorption can be calculated using eq 23.1, yielding  $\sigma = 4 \times 10^{-16} = 4 \text{ \AA}^2$ . In performing this calculation it is important to use a conversion factor of  $10^3 \text{ cm}^2/\text{liter}$ .

The number of photons per  $\text{cm}^2$  per second can be calculated from  $I_e = 0.5 (\tau\sigma)^{-1} = 3.1 \times 10^{23}/\text{cm}^2 \text{ s}$ . The power can be calculated from the number of photons per second per  $\text{cm}^2$  and the energy per photon  $= h\nu/\lambda$ , yielding  $103 \text{ kW/cm}^2$ , and an area of  $1 \mu\text{m}^2 = 10^{-8} \text{ cm}^2$ , so the power needed to saturate the fluorophore is 0.001 watts/ $\text{cm}^2$ .

**CHAPTER 24**

- A24.1. Figure 24.8 gives the concentration of R6G and the inverses of the  $\tau = 0$  intercept give the apparent number of fluorophores. Using  $G(0) = 0.12$  at 1.25 nM yields  $N = 8.3$  molecules. The volume can be calculated from

$$V_{\text{eff}} = N/\bar{C}N_A$$

where  $N_A$  is Avogadro's number, yielding  $V_{\text{eff}} = 11.0$  fl. The effective volume is related to the dimensions by  $V_{\text{eff}} = \pi^{3/2} s^2 u$ , which becomes  $V_{\text{eff}} = 4\pi^{3/2} s^3$  for the assumed  $u/s$  ratio. Recalling that  $10^3$  liters = 1 cubic meter, one finds  $s = 0.79$   $\mu\text{m}$  and  $u = 3.16$   $\mu\text{m}$ .

- A24.2. The ratio of the diffusion times can be read off the graph. Taking the maximum difference near  $G(\tau) = 0.35$ , one finds  $\tau_D(\text{GroEL})/\tau_D(\alpha\text{-LA}) = 0.4/0.15 = 2.7$ , which indicates a  $3^3 = 19.7$ -fold increase in molecular weight. This is somewhat less than the expected value of 49.4 from the ratio of the molecular weight. One possible explanation is the diffusion coefficient of denatured  $\alpha\text{-LA}$  is lower than for the native protein, causing the  $\tau_D$  ratio to be lower than expected.

- 24.3. If we know the diffusion coefficient the time can be calculated without knowing the beam diameter. The time required to diffuse 10  $\mu\text{m}$  can be calculated using  $\Delta x^2 = 2\Delta\tau$ , where  $\Delta x$  is the distance. Using  $D = 3 \times 10^{-8}$   $\text{cm}^2/\text{s}$  and recalling that  $10^4 \text{ cm}^2 = 1 \text{ m}^2$ , one finds  $\tau = 16.7$  s. The time required to diffuse 10  $\mu\text{m}$  does not depend on the beam diameter, so  $\tau$  is the same for a 1- or 2- $\mu\text{m}$  diameter beam.

- A24.4. The autocorrelation function yields the relaxation time for the opening–closing reaction, which is  $\tau_R = (k_1 + k_2)^{-1}$ . The equilibrium constant is given by  $K = k_1/k_2$ . The values of  $K$  can be determined by examining the fluorescence intensity of the beacon as a function of temperature. The fractional intensity between the low- and high-temperature intensities yields the fraction of the beacon that is open at the temperature used to collect  $G(\tau)$ . This fraction yields the equilibrium constant  $K$ , allowing  $k_1$  and  $k_2$  to be calculated.

- A24.5. The volume in the TIR FCS experiment can be estimated using  $V = \pi s^2 d$ . The volume is 1.96 fl. The concentration needed is given by

$$\bar{C} = N/VN_A$$

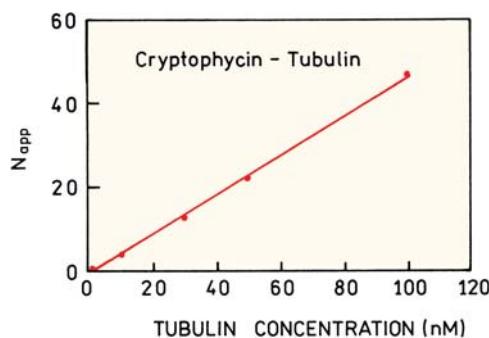


**Figure 24.51.** Effect of sample dilution on the apparent number of diffusing tubulin particles. Revised and reprinted with permission from [38]. Copyright © 2003, American Chemical Society.

where  $N_A$  is Avogadro's number, and

$$\bar{C} = 8.5 \text{ nM}$$

The area occupied by a single lipid molecule is 0.7  $\text{nm}^2$ . The area of the illuminated membrane is 19.6  $\mu\text{m}^2 = 19.6 \times 10^6 \text{ nm}^2$ . Hence to obtain 10 fluorophores in the illuminated area the fraction of labeled fluorophores should be  $7.3 \times 10^{-7}$ , or approximately 1 labeled lipid per 1,372,000 unlabeled lipid molecules.

- A24.6. The effect of dilution on the self-association of tubulin can be determined in two ways. If the tubulin complex dissociates upon dilution then the diffusion coefficient will decrease and the autocorrelation curves shift to shorter times. Because of the change in amplitude the presence or absence of a shift cannot be seen in Figure 24.50.

Another way to determine if the complex dissociates is from the apparent number of diffusing molecules. If all the substrates are labeled, dissociation will result in a higher value of  $N_{\text{app}}$ . Figure 24.51 shows a plot of  $N_{\text{app}}$  versus total tubulin concentration.  $N_{\text{app}}$  scales linearly with concentration, showing the complexes do not dissociate. This approach is only valid if all the tubulin is labeled. If there was only one labeled tubulin per complex then dissociation would not increase  $N_{\text{app}}$  but the diffusion coefficient would change.

**CHAPTER 25**

- A25.1. The radiative decay rate in the absence of SIF can be calculated from the quantum yield and natural lifetime

$\tau_N$ . Since  $\Gamma = \tau_N^{-1}$ , then  $\Gamma = 2.5 \times 10^8 \text{ s}^{-1}$ . Using the definition of the quantum yield in eq. 25.1 the non-radiative decay rate is given by

$$k_{nr} = \frac{\Gamma - Q_O \Gamma}{Q_O} = 122.5 \times 10^8 \text{ s}^{-1} \quad (25.5)$$

This value of  $k_{nr}$  is reasonable because  $k_{nr}$  must be significantly larger than  $\Gamma$  to account for the low value of  $Q_O = 0.02$ .

In the presence of SIF the quantum yield increases 4.8-fold to  $Q_m = 0.096$ . This quantum yield is related to the total decay rate by

$$Q_m = \frac{\Gamma_T}{\Gamma_T + k_{nr}} \quad (25.6)$$

so that

$$\Gamma_T = \frac{Q_m k_{nr}}{1 - Q_m} = 1.3 \times 10^9 \text{ s}^{-1} \quad (25.7)$$

The radiative decay rate due to the metal is given by  $\Gamma_m = \Gamma_T - \Gamma = 1.05 \times 10^9 \text{ s}$ . Hence  $\Gamma_m/\Gamma = 4.7$ .

If only 10% of the Rose Bengal is affected, then the apparent quantum yield ( $Q_A$ ) is related to the quantum yield near the SIF and in solution as

$$Q_A = 0.90Q_O + 0.10Q_m \quad (25.8)$$

Using  $Q_A = 0.096$ , then  $Q_m = 0.78$ . The value of  $\Gamma_T$  can be calculated from eq. 25.7, so that  $\Gamma_T = 4.34 \times 10^{10} \text{ s}^{-1}$ , and then  $\Gamma_m = 4.32 \times 10^{10} \text{ s}^{-1}$ . If only 10% of the RB population is affected by the SIF, then  $\Gamma_m/\Gamma = 173$ .

# Index

## A

- Absorption spectroscopy, 12  
Acetate quenching, 535  
Acetoxymethyl esters, 647, 648  
2-Acetylanthracene (2-AA), 214–215  
*N*-Acetyl-L-tryptophanamide. *See* NATA (*N*-acetyl-L-tryptophanamide)  
*N*-Acetyl-L-tyrosinamide (NATyrA). *See* NATyrA  
N-Acetyl tryptamine, 314  
Acoustooptic (AO) crystal, 110, 112  
Acoustooptic (AO) modulators, 165  
Acoustooptic deflector, laser, 111–112  
Acridine  
  DNA technology, 716–717  
  excited-state reactions, 260, 267–268  
Acridine orange, 2, 3, 514–515  
Acriflavine, 190, 191  
Acrylamide quenching, 278–279, 284–286, 287, 290, 292–293, 313, 336  
  absorption spectra, 301  
  bimolecular quenching constants, 281–282  
  covalent adduct formation, 314  
  intensity decays, 346  
  NATA, 285, 346, 347  
  proteins, 547  
    DNA  $\beta$  helicase hexamer, 313  
    metalloprotease, 550–551  
    single-tryptophan, 547, 548  
    tryptophan position and, 550  
  quenching efficiency, 281  
  quenching-resolved spectra, 302  
  structural motifs and tryptophan spectral properties, 561–562, 563  
  transient effects, 346–347  
Acrylodan, 70, 217, 226  
Actin, 784  
1-Adamantanol, 228  
Adduct formation, intramolecular quenching, 314  
Adenine and derivatives, 16, 278, 287–288  
  Förster distances, 468  
Adenosine monophosphate, 16  
Adenylate kinase, 823  
ADMAN, 230  
 $\epsilon$ -ADP, 313  
Adrenocorticotropin (ACTH), 536, 547  
Adrenodoxin (AD), 561  
*Aequores victoria*, 81, 82  
Aladan-GB1, 245  
Alcohol dehydrogenase, 395, 584  
Alcohols, dielectric relaxation times, 250–251  
Alexa 488  
Alexa 546, 459  
Alexa Fluor, 69, 70–71  
Alkaline phosphatase, 318  
Alkylaminoanthracene derivatives, phosphate sensors, 643  
N-Alkyl pyridinium, 278  
Allophycocyanin, 84, 468  
Alpha helices, 561–562, 563  
Aluminum, 868  
Alzheimer's disease, 827  
  aggregation of  $\beta$ -amyloid peptides, 515–516  
  fluorescence-lifetime imaging microscopy, 750  
  time-resolved RET imaging, 498  
Amines, 316  
  fluorogenic probes, 79  
  quenching, 278, 279, 314, 642  
Amino acids  
  genetically inserted, 565–566  
  phosphorescence quenching, 318  
  time-resolved emission spectra (TRES), 244–245  
9-Aminoacridine, 434  
Aminocetyl-tRNA synthetase, 565  
3-Aminofluoranthene (AFA), 190, 191  
3-Amino-N-methylphthalimide, 257  
4-Aminophthalimide (4-AP), 240  
2-Aminopurine, 75, 76  
  frequency-domain lifetime measurements, 180–185  
  mixture lifetime resolution, 138–141  
  time-domain lifetime measurements, 137–138  
Ammonium group, 579  
Amphiphilic starlike macromolecules (ASM), 253  
Amplifiers, 115  
Amplitude-weighted lifetime, 142  
 $\beta$ -Amyloid peptides, energy transfer, 515–516  
Amyloid plaques, fluorescence-lifetime imaging microscopy, 750  
Amyloid proteins, 827  
Analog-to-digital converter (ADC), 105, 115, 122  
Analyte recognition probes, 78–79, 643–650. *See also* specific elements  
  calcium and magnesium, 647–650  
  cation probe specificity, 644  
  intracellular zinc, 650  
  sodium and potassium, 645–647  
  theory of, 644–645  
2-Anilinonaphthalene (2-AN), 213–214, 216, 242  
1-Anilinonaphthalene-8-sulfonic acid. *See* ANS (1,8-anilinonaphthalene-8-sulfonic acid)  
8-Anilinonaphthalene-1-sulfonic acid (8-ANS). *See* 8,1-ANS  
Anion indicators, 16–17  
Anion sensors, 641–643. *See also* Chloride probes  
  chloride, 631–632  
  oxygen, 627–630

Anisotropy, 353–378  
 applications, 20–21  
 biochemical applications, 372–374  
 helicase-catalyzed DNA unwinding, 373–374  
 melittin association detected from homotransfer, 374  
 peptide binding to calmodulin, 372–373  
 trp repressor binding to DNA, 373  
 definition, 353–355  
 electronic state resolution from polarization spectra, 360–361  
 emission wavelength and, 437–438  
 energy transfer, 453  
 excitation anisotropy spectra, 358–361, 531–533  
 excitation photoselection of fluorophores, 357–358  
 instrumentation, 36–37  
 lifetime-resolved, 435–436  
 measurement, 361–366  
 comparison of methods, 363–364  
 depolarization, trivial causes, 365–366  
 factors affecting anisotropy, 366  
 L-format or single channel method, 361–363  
 magic-angle polarizer conditions, 364  
 polarizer alignment, 364  
 resonance energy-transfer effects, 364–365  
 T-format or two-channel method, 363–364  
 total intensity, 364  
 membranes and membrane-bound proteins, 374–377  
 distribution, 375–377  
 membrane microviscosity, 374–375  
 metal–ligand complexes, 685, 688–689  
 multiphoton excitation, 612–613, 615  
 excitation photoselection for two-photon excitation, 612  
 two-photon anisotropy for DPH, 612–613  
 Perrin equation, rotational diffusion effects, 366–370  
 examples of Perrin plots, 369–370  
 rotational motions of proteins, 367–369  
 Perrin plots  
 of proteins, 370–372  
 segmental motion effects, 436  
 photoselection, 357–358  
 polarization, molecular information from fluorescence, 19  
 principles, 12–13  
 proteins  
 association reactions, 372–374  
 Perrin plots, 370–372  
 rotational motion, 102–103  
 segmented motions, 436  
 single-molecule detection, 775–776  
 Soleillet's rule, depolarization factor multiplication, 436–437  
 theory, 355–358  
 transition moments, 377–378  
 tryptophan, 531–532  
 Anisotropy, advanced concepts, 413–438  
 associated anisotropy decay, 413–417  
 theory, 414–415  
 time-domain measurements, 415–417  
 biochemical examples, 417–419  
 frequency-domain measurements, 417–418  
 time-domain studies of DNA binding to Klenow fragment, 417  
 DNA, 432–433  
 ellipsoids, anisotropy decay, 419–420  
 ellipsoids of revolution, 420–425  
 oblate, intuitive description of, 422–423  
 rotational correction times, 423–425

simplified, 421–422  
 stick vs. slip rotational diffusion, 425  
 global anisotropy decay analysis, 429–432  
 with collisional quenching, 430–431  
 with multi-wavelength excitation, 429–430  
 quenching application to protein anisotropy decays, 431–432  
 planar fluorophores with high symmetry, 435  
 rotational diffusion  
 of ellipsoids, theory, 425–426  
 frequency-domain studies of, 427–429  
 of non-spherical molecules, 418–419  
 time-domain studies, 426–427  
 transition moments, 433–435  
 Anisotropy decay laws, 390–394  
 associated delays, 393  
 correlation time distributions, 393  
 hindered rotors, 391–392  
 non-spherical fluorophores, 391  
 segmental mobility of biopolymer-bound fluorophore, 392–393  
 Anisotropy decays, 14, 102–103, 413–417  
 energy transfer, 453  
 in frequency domain, 588–589  
 melittin, 590–591  
 proteins, 587–588, 589–591  
 ribonuclease T<sub>1</sub>, 584–585  
 Anisotropy decays, time-dependent, 383–409  
 analysis, 387–389  
 frequency-domain decays, 390  
 $r_0$  value, 389  
 time-domain decays, 387–389  
 correlation time imaging, 406–408  
 laws governing, 390–394  
 associated decays, 393  
 correlation time distributions, 393  
 decays of rhodamine green and rhodamine green-dextran, 394  
 hindered rotors, 391–392  
 non-spherical fluorophores, 391  
 segmental mobility of biopolymer-bound fluorophore, 392–393  
 membrane probe, characterization of, 401–402  
 membranes, hindered rotational diffusion in, 399–402  
 microsecond, 408–409  
 long-lifetime metal–ligand complexes, 408–409  
 phosphorescence, 408  
 nucleic acids, 402–406  
 DNA binding to HIV integrase, 404–406  
 DNA oligomer hydrodynamics, 403  
 intracellular DNA dynamics, 403–404  
 proteins, frequency-domain decays of, 383–387, 397–399  
 apomyoglobin, rigid rotor, 397–398  
 melittin, 398  
 oxytocin, picosecond rotational diffusion, 399  
 proteins, time-domain decays of, 383–387, 394–397  
 alcohol dehydrogenase, 395  
 domain motions of immunoglobulins, 396–397  
 free probe, effects of, 397  
 phospholipase A<sub>2</sub>, 395  
 Subtilisin Carlsberg, 395–396  
 Anisotropy fluorescence correlation spectroscopy, 829  
 Anisotropy polarization, 624–625  
 molecular information from fluorescence, 19  
 Anisotropy spectra, excitation, 358–361, 531–533  
 Annexins, 148  
 Annexin V, 148, 585–587

- ANS  
time-resolved fluorescence correlation spectroscopy, 819  
8,1-ANS (8-anilino-1-naphthalenesulfonate), 226–227, 258  
ANS (1-anilinonaphthalene-6-sulfonic acid), 71–72  
ANS (1-anilinonaphthalene-8-sulfonic acid)  
anisotropy decay, 417–418  
red-edge excitation, 258  
solvent effects, 212  
6-ANS (6-anilinonaphthalene-2-sulfonic acid), 230  
Förster distances, 468  
ANS derivatives, solvent effects, 212  
Anthracene, 3, 56, 59, 316, 632  
emission spectrum, 9, 199  
frequency-domain lifetime measurements, 170–171  
orientation factor, 465  
quenchers of, 278, 279  
TRES and DAS comparison, 255  
Anthranilic acid  
frequency-domain lifetime measurements, 180–185  
mixture lifetime resolution, 138–141  
time-domain lifetime measurements, 137–138  
9-Anthroycholine (9-AC), 226–227  
Anthroyl fatty acid, 72  
Anthroyloxy fatty acids, 279  
9-AS, 359–360  
12-AS, 360, 375  
Förster distances, 468  
solvent relaxation, 248–249  
TRES, 248–249  
12-Anthroyloxy stearate, 375  
9-Anthroyloxy stearic acid, 359–360, 369  
Anthroylxanthyl cations, quenchers of, 279  
Antibody labeling, 69  
APC (allophycocyanin)  
Förster distances, 468  
Apoazurin, 546–547, 583–584  
Apo E3, 454–455  
Apo E4, 454–455  
Apolipoproteins, 454  
Apomyoglobin, 17, 368, 417–418, 549  
anisotropy decay, 397–398  
protein folding, 560  
time-resolved emission spectra (TRES), 243–244  
Apoperoxidase, 368  
Apparent distance distributions, 478–480  
Apparent phase and modulation lifetimes, 191–192, 266–267  
Aptamers, 724–726  
APTRA, 644, 649  
Archaeabacterial histone-like protein (HTa), 544–545  
Arc lamps, 28, 31, 33  
Argon-hydrogen flashlamps, 113–114  
Argon-ion lasers, 39, 109, 110–111, 715–716  
Aromatic amino acids, 314. *See also* Phenylalanine; Tryptophan;  
Tyrosine  
fluorescence parameters of, 64  
intensity decays, 578  
quantum yield standards, 54  
spectral properties, 530–535  
Arrays  
DNA, 732–734  
multiplexed microbead:suspension, 726–728  
Arsine ligand, 693  
9-Arylxanthyl cations, 279  
9-AS, 359–360  
12-AS, 360, 375  
Asparaginase, 548  
Associated anisotropy decays, 393, 413–417  
Association constant, 282  
Association reactions  
anisotropy, 372–374  
helicase-catalyzed DNA unwinding, 373–374  
melittin association detected from homotransfer, 374  
peptide-calmodulin binding, 372–373  
Trp repressor-DNA binding, 373  
calmodulin, tryptophan mutants, calcium binding site resolution, 552  
energy transfer, 455–456  
literature references, 837  
orientation of bound peptide, 456–457  
Prodan effects on emission spectra, 217–219  
quenching, 304–305  
accessibility to quenchers, 312–313  
substrate binding to ribozymes, 311–312  
specific binding reactions, 304–305  
Asymptotic standard errors (ASEs), 134–135, 163, 180  
ATP, 455  
ATPase, single-molecule activity, 770–771  
Autocorrelation function, 132–133  
Autocorrelation function of fluorescence fluctuations, 800–802,  
804–805, 810–811, 813  
Avalanche photodiodes (APDs), 114  
Avidin, 450, 676  
7AW, 564, 565  
Azacrown, 79  
Azacrown ethers, 644  
Azide, 348  
Azurin, 536, 546, 547, 583, 588  
emission spectra of molecules with one or two tryptophan, 539  
fluorescence studies of, 538  
site-directed mutagenesis of single-tryptophan, 538–539
- B**
- BABAPH, 253–255  
BABP, 253–255  
Background signal, 366  
Bandpass filters, 39  
BAPTA, 79, 644, 647–648  
BAPTA-based probes, 648–649  
Barnase, 556–557  
decay-associated spectra, 591–592  
β-Barrel, 538  
BCECF, 751  
Bead sensors, 656  
Beam splitter, 29, 777  
Beer-Lambert law, deviation from, 58–59  
Beer's law, deviation from, 59  
Benzene, 230  
quenching of indole, 537  
Benzo(b)fluoranthene, 632  
Benzodiazepines, 23  
5,6-Benzoquinoline, 279  
Bialkali photocathode, 45–46  
Bilins, 84  
Bimolecular quenching, 281–282, 294, 304, 547–549  
Bimolecular quenching constant, 339  
Binding. *See* Association reactions

- Bioaffinity reactions, 807–810
- Biomembranes**
- fluorescence correlation spectroscopy, 810–815
  - binding to membrane-bound receptors, 813–815
  - lateral diffusion, 812–813
  - literature references, 838
- Biomolecules**
- anisotropy, 372–374
    - peptide binding to calmodulin, 372–373
  - co-localization of, literature references, 791
  - diffusion of, literature references, 791–792
  - energy transfer (*See* Energy transfer)
  - fluorophores, principles, 15–17, 20–21 (*See also* Fluorophores)
  - frequency-domain lifetime measurements, 177, 186–189
    - DNA, DAPI-labeled, 186–187
    - fluorescence microscopy with LED light source, 189
    - gigahertz data, 177–178
    - green fluorescent protein, one- and two-photon excitation, 171
    - Mag-Quin-2, magnesium probe, 187–188
    - melittin lifetime distributions, cross fitting of models, 188–189
    - NADH intensity decay, 172
    - recovery of lifetime distributions from data, 188
    - SPQ, collisional quenching, 171–172
    - staphylococcal nuclease and melittin multi-exponential decay, 171
  - laser scanning microscopy, 750
  - photoinduced electron transfer quenching, 341–342
  - polarization, literature references, 794
  - quenching
    - effects of quenchers on proteins, 292
    - ethenoadenine derivatives, 287–288
    - substrate binding to ribozymes, 311–312
  - Tet repressor, 302–304
  - single-molecule detection, 757–788
    - ATPase activity, 770–771
    - calcium sensor, 784
    - chaperonin protein, 771–773
    - conformational dynamics of Holliday junction, 782–783
    - enzyme kinetics, 770
    - molecular beacons, 782
    - motions of molecular motors, 784
    - turnover of single enzyme molecules, 780–782
  - single-molecule detection, time-resolved studies, 779–780
  - solvent effects on emission spectra
    - calmodulin, hydrophobic surface exposure, 226–227
    - cyclodextrin binding using dansyl probe, 227–228
    - membrane binding site polarity, 206–207
    - with Prodan, 217–219
    - with solvent-sensitive probes, 226–229
  - structural analogs as fluorophores, 80
  - time-domain lifetime measurements
    - chlorophyll, 146–147
    - FAD intensity decay, 147–148
    - multi-exponential or heterogeneous decays of, 101–103
    - single-tryptophan protein, 145
  - time-resolved emission spectra (TRES)
    - analysis, 246–248
    - apomyoglobin, 243–244
    - labeled membranes, 245–249
    - proteins, spectral relaxation in, 242–243
- Biopolymers**
- bound fluorophore segmental mobility, 392–393
  - diffusion in, 501
- Biotin, 310
- 2,2'-Bipyridine, 684
- Bis DNA stains, 713–715
- Bis-MSB, 610
- Blood gas sensors**
- energy-transfer mechanisms, 633–634
  - two-state, optical detection of, 637
- Blue-shifted spectra, 538–539, 551
- BODIPY, 69–70, 221
- DNA technology, 710
  - Förster distances, 468
  - homotransfer, 450
- Bodipy-PC, 812–813
- Bodipy TR, 24
- Bombesin, 590
- Boron-containing fluorophores, 651
- Boundary lipid, membranes, 298
- Bound fluorophore segmental mobility, 392–393
- Bovine cardiac troponin I, 589
- Bovine pancreatic trypsin inhibitor (BPTI), 482
- Bovine serum albumin, 71, 584, 589, 678
  - metal-enhanced fluorescence, 851–853
- Bovine spongiform encephalopathy, 827
- BPE ( $\beta$ -phycoerythrin), 468
- Förster distances, 468
- Brightness of fluorophores, 802–803, 817–819
- Bromate, quenching by, 278–279
- Bromide, 278, 295–296, 631
- Brominated phosphatidylcholines, 295
- Bromine, 5
- Bromobenzene, 278–279
- Bromo-phosphatidylcholine, 295–296, 298, 301
- Brownian rotation, 365
- Butanol, Stokes shift, 210
- C**
- Ca<sup>2+</sup>-ATPase
  - anisotropy decay, 408
  - boundary lipid quenching, 298
- Cadmium, 278
- Cadmium selenide, 675
- Caffeine, 304
- Calcite, 51
- Calcium
  - calmodulin binding using phenylalanine and tyrosine, 545–546
  - calmodulin binding using tryptophan-containing mutants, 552
  - concentration from lifetime, 744–745
  - induced changes in troponin C conformation, 490–493
  - intensity decay, 585–587
  - lanthanides, 679
  - multiphoton microscopy, 616–617
  - single-molecule sensor, 784
- Calcium-binding proteins, 679
- Calcium Green, 79, 616, 645, 648–649, 656
- Calcium sensors, 17, 617, 647–650
  - chelators, 644
  - green fluorescent protein mutant-based, 455–456, 654–655
  - QUIN-2, fluorescence lifetime imaging microscopy, 744–745
- Calibration of monochromators, 38
- Calmodulin, 20, 88–89
  - binding to target protein, 551–552
  - calcium binding site resolution, 552

- calcium binding using phenylalanine and tyrosine, 545–546
- calcium sensors, 617
- energy transfer
  - MLCK binding and, 456–457
  - melittin binding, 485
  - peptide binding anisotropy, 372–373
  - single-molecule calcium sensor, 784
  - solvent effects on emission spectra, 226–227
- Camphorquinones, 672
- Capillary gel electrophoresis, 712
- Carbazole, 632
  - quenchers of, 278–279
- Carbocyanine, 72
- $\beta$ -Carboline, 53
- Carbon dioxide
  - blood gas measurement, 637
  - energy-transfer mechanisms, 633–634
- Carbon disulfide, 279
- Carbonic anhydrase, 368
- Carboxyfluorescein, 638
- Carboxy groups, quenching by, 279
- Carboxynaphthofluorescein, 641
- Cascade Blue, 727–729
- Cascade Yellow, 70
- Cavity dumper, 111–112
- CCD detectors, 49
- CCVJ, 224
- CD 220, 174
- CD 222, 647
- CDKN1A gene, 733
- Cells
  - labeling with quantum dots, 677–678
  - three-dimensional imaging of, 618–619
- Cellular retinoic acid binding protein I (CRABPI), 560
- Cesium, 278, 279
- C-fos protein, 461
- Chaperonin, 771–773, 806
- Chaperonin GroEL, protein binding, 807
- Charged-coupled device (CCD), 766
- Charge effects, quenching, 286–288
- Charge transfer
  - quenching, 306
  - solvent effects, 219–221
- Charge-transfer complex, 9, 337
- Chelators, 644, 659
  - for lanthanides, 679
- Chemical sensing probes. *See Analyte recognition probes; specific ions*
- Chicken pepsinogen, 597
- Chloride
  - green fluorescent protein, 307–309
  - imaging of, 306–307
  - quenching by, 171–172, 279, 306
- Chloride probes, 17, 67, 306–307, 631–632
- Chlorinated compounds, quenching by, 278–279
- Chlorinated hydrocarbons, 632
- Chloroform, Stokes shift, 210
- Chlorophyll, intensity decay of, 146–147
- Cholesterol, 293–294, 297, 400
  - analogs, 80
- Cholesterol oxidase (Cox), 780, 781
- Chromatin, 403
- Chromophores, 84
- Chymotrypsin, 368
- Clinical chemistry, 19
  - sensors, 623–624
- Coaxial flashlamps, 112–113
- Cobalt, quenching by, 279
- Cocaine, 724
- Cofactors
  - intrinsic fluorescence, 63–64
  - protein binding of NADH, 65–66
  - time-domain lifetime measurement, 147
- Colicin E1 folding, 292–293
- Collection efficiency function, 801
- Collisional frequency, fluorophore-quencher, 281
- Collisional quenching, 11, 277–278, 546
  - anisotropy decay, time-dependent, 430–431
  - combined with static quenching, 282–283
  - DNA probes, 286
  - ethenoadenine–DNA- $\beta$  helicase hexamer, 313
  - examples, 283–284
  - frequency-domain lifetime measurements, 171
  - relaxation dynamics, 256
  - as sensor mechanisms, 306–309, 627–633
  - chloride, 306–309, 631–632
  - oxygen, 627–630
  - sensors, 626
  - simulated intensity decay, 101–102
  - theory of, 278–282
  - bimolecular quenching constant, interpretation of, 281–282
  - Stern-Volmer equation, derivation of, 280–281
- Colloids
  - interactions with fluorophores, 846–848
  - metal, 845–846
  - in metal-enhanced fluorescence, 856
- Colored-glass filters, 38–39
- Color effects
  - frequency-domain lifetime measurements, 168–169
  - in photomultiplier tubes, 47
  - time-domain lifetime measurements, 119–121
- Combination filters, 40
- Compact PMTs, 118
- Concanavalin A, 634–635
- Confidence intervals
  - frequency-domain lifetime measurements, 179–180
  - resolution of two closed spaced lifetimes, 182
  - time-domain lifetime measurements, 134–135, 136
  - of two widely spaced lifetimes, 179–180
- Confocal detection optics, 761–763
- Conformation, 436, 529
  - changes of, 291–293
  - heterogeneity
  - ribonuclease  $T_f$ , 584–585
  - rotational (*See* Rotamers)
- Conformational distance. *See Energy transfer, time-resolved*
- Conformational dynamics in macromolecules, 820–821
- Constant function discriminator (CFD), 104–106
- Continuous relaxation model, 237
- Continuous spectral relaxation, 237–241, 247–248
- Continuous wave, laser, 112
- Convolution integral, 106–107, 193, 487
- COPA, 401–402
- Copper, 278
- Coronene, 86, 287
- Corrected emissions spectra, 51–54

- Correlation time distributions, 386–387, 393  
 DNA binding to HIV integrase, 404–406
- Correlation time imaging, 406–408
- Correlation times, 353–354, 367–371, 422
- Cortisol, 661–662
- Cos cells  
 fluorescence-lifetime imaging microscopy, 745–746
- Cosyntropin, 590
- Coumarin, 57–58, 73  
 Förster distances, 468
- Coumarin 108, 151–152, 222
- Coumarin-based potassium probe, 646–648
- Coumarin derivatives  
 fluorescence-lifetime imaging microscopy, 748  
 photoinduced electron transfer quenching, 338–340  
 quenching, 284  
 solvent relaxation, 249–250, 253
- Coum-Eu, 189–190
- Covalent adduct formation, intramolecular quenching, 314
- C-peptide, 813–814
- CRABPI (retinal binding protein), 560
- Crambin, 535
- Cramer's rule, 198
- Creatine kinase, 662–663
- Cresyl violet, 54
- Creutzfeldt-Jakob disease, 827
- Critical concentration, 466
- Cross-correlation in flow measurements, 831
- Cross-correlation method, 164–167, 177, 194
- Crown ethers, 17, 643–645, 647, 649
- C-SnafI 2, 127–128
- Cy3, metal-enhanced fluorescence, 848–851
- Cy3.5, 746–747
- Cy5.5, 657–658, 660–661
- Cyan fluorescent protein (CFP), 458, 497, 654
- Cyanine dyes, 74–75, 512–513  
 immunoassays, 641  
 potassium sensors, 635
- 9-Cyanoanthracene, 185–186, 255, 279, 364, 744  
 frequency-domain lifetime measurements, 170–171
- 3-Cyanoperylene (PeCN), 129
- Cy5 (carboxymethylindocyanine-N-hydroxysuccinimidyl ester), 780, 787, 824  
 acceptor, 680  
 Förster distances, 468  
 metal-enhanced fluorescence, 848–851
- Cyclic AMP receptor protein (CRP), 291–292
- Cyclodextrins  
 phosphorescence of bound probes, 317  
 quenching, 286  
 solvent effects, 227–228
- Cyclohexane, indole emission spectra in cyclohexane-ethanol mixture, 533–534
- Cysteine, 278, 651
- Cytotoxin II, 535
- D**
- Dabcyl, 721–722
- Dabcyl acceptor, 724
- Danca, 243–244
- Dansylamide  
 RET in three dimensions, 509–510
- Dansyl chloride, 16–17
- Dansyl groups, 16, 67–68  
 anisotropy decay, 396–397  
 creatine kinase immunoassay, 663  
 energy transfer, 447–449, 451  
 ethylenediamine, 495  
 Förster distances, 447, 468  
 solvent effects, 227–228
- DANZA, 662–663
- DAPI, 15, 16, 41, 75, 186–187, 359  
 fluorescence-lifetime imaging microscopy, 750  
 multiphoton excitation, 610–612
- Dapoxyl probes, 229
- Dapoxyl SEDA, 229–230
- DAS. *See Decay-associated spectra (DAS)*
- Data analysis, 129–130  
 cross-fitting  
 distance distribution, 481–482  
 melittin lifetime distributions, 188–189  
 frequency-domain lifetime measurements, 162–163  
 literature references, 837  
 time-domain lifetime measurement, 129–133  
 maximum entropy method, 148–149
- DBO, 314
- DCM, 112
- DCVJ, 225
- d-d state, 685
- Dead time, 124  
 time-to-amplitude converter (TAC), 115
- Debye-Sears modulator, 163
- Decay, 170–173. *See also Intensity decay*
- Decay-associated spectra (DAS), 581, 596–598  
 barnase, 591  
 frequency-domain data for calculation of, 269–270  
 TRES and DAS comparison, 255  
 two-state model, 263
- Decay time. *See Lifetime (decay time)*
- Deconvolution, 131
- Dehydroergosterol, 80
- Delay lines, 116
- Demodulation, 98
- Denaturation, 588
- Denatured pepsin, 806
- Denatured proteins, emission spectra for, 538
- Dendrimers and polymers  
 literature references, 791
- DENS, 26. *See also Dansyl groups*
- Deoxycytidine quenching, 284
- Deoxynucleotide triphosphates (dNTPs), 729
- Depolarization, trivial causes, 365–366
- Depolarization factor multiplication, 436–437
- Depth-dependent quenching, 296–298
- Detection profile, 802–803
- Detectors  
 CCD, 49  
 charged-coupled device, 766  
 higher-frequency measurements, 176–177  
 laser scanning microscopy, 749–750  
 optical phase-sensitive, 743  
 for single-molecule detection, 765–766  
 single-photon-counting avalanche photodiode, 765  
 time-correlated single-photon counting, 117–121  
 color effects in, 119–121

- compact PMTs, 118
- DNA sequencing, 123–124
- dynode chain PMTs, 118
- microchannel plate PMTs, 117–118
- multi-detector and multidimensional, 121–124
- photodiodes as, 118–119
- time effects of monochromators, 121
- Deuterium pulse lamps, 113
- Dexter interaction, 335
- Dextran, 394, 634–635
- 1,2-bis(9,10-Dibromooleyl)phosphatidylcholine, 298
- Dicarboxy derivatives, 685
- Dichloroacetamide, 278
- Dichroic beam splitter, 41
- Dichroic filter, 761
- 4-(Dicyanomethylene)-2-methyl-6-(4-dimethylaminostyryl)-4H-pyran (DCM), 112
- Dideoxynucleotide triphosphate (ddNTP), 705, 706, 708
- Dielectric constant, 210, 211
- Dielectric properties of solvents, 250
- Dielectric relaxation times, 250–251
- 4,4'-Diethylaminomethyl-2,2'-bipyridine, 694
- Diethylaniline, 129, 196, 197, 199, 278
- Diffusion
  - of intracellular kinase, 823
  - lateral in membranes, 812–813
  - representative literature references, 504
  - rotational, 828–830
  - of single molecules, literature references, 791–792
  - translational, fluorescence correlation spectroscopy, 802–804
- Diffusion, rotational. *See* Rotational diffusion
- Diffusion coefficients, 277, 498–501, 803–804
  - effect of molecular weight, 806–807
- Diffusion effects
  - anisotropy decay, non-spherical molecules, 418–419
  - for linked D–A pairs, 498–501
    - apparent distance distributions, 478–480
    - experimental measurement, 500–501
    - RET and diffusive motions in biopolymers, 501
    - simulations of RET for flexible pair, 499–500
  - oxytocin, 399
  - RET in rapid-diffusion limit, 520–524
    - acceptor location in lipid vesicles, 521–522
    - retinal location in rhodopsin disk membranes, 522–524
  - RET with unlinked donors and acceptors, 508–509
- Diffusion-enhanced energy transfer in solution, 467
- Diffusion in membranes
  - lateral, 300–301
  - rotational, 399–402 (*See also* Rotational diffusion)
- Diffusion-limited quenching, 281–282
- Diffusive motions in biopolymers, 501
- Dihexadecyl phosphate, 514
- Dihydro-4,4-diisothiocyanostilbene-2,2-disulfonic acid (H2DIDS), 631
- Dihydroequilenin (DHE), 270, 284, 285–286
- Dihydrolipoic acid, 675
- Dihydronicotinamide, 278
- Dihydrorootate dehydrogenase (DHOD), 781–782
- Dihydroxyacetone phosphate, 555
- DiIC<sub>12</sub>, 766–767
- DiIC<sub>20</sub>, 812–813
- DiIC<sub>1</sub>, 512–513
- Dilauroyl phosphatidylcholine (DLPC), 812–813
- Dimensionality effect, experimental RET, 511–515
  - one dimension, 514–515
  - two dimensions, 512–514
- Dimethoxynaphthalene, 336
- 4-Dimethylamino-4'-bromostilbene, 177
- 7-(Dimethylamino)coumarin-4-acetate, 251
- 5-Dimethylamino-1-naphthalenesulfonic acid (Danysl). *See* Dansyl groups
- 4-Dimethylamino-4'-nitrostilbene (DNS), 206
- trans-4-Dimethylamino-4'-(1-oxobutyl) stilbene (DOS), 206–207
- Dimethylaniline (DMA), 336
- N,N-Dimethylaniline sulfonate (DMAS), 286
- 9,10-Dimethylanthracene (DMA), 426
- Dimethylazaperopyrenium (DMPP), 514, 515
- Dimethylformamide, 278–279
- Dimethylnaphthalene, 279
- Dimyristoyl-L- $\alpha$ -phosphatidylcholine. *See* DMPC (dimyristoyl-L- $\alpha$ -phosphatidylcholine)
- Dinitrobenzenesulfonyl (DNBS)
  - Förster distances, 468
- Dioleoyl-L- $\alpha$ -phosphatidylcholine. *See* DOPC
- Dipalmitoyl-L- $\alpha$ -phosphatidylcholine (DPPC), 207, 293–294, 812–813
- Dipalmitoyl-L- $\alpha$ -phosphatidylglycerol (DPPG)
  - metal–ligand complexes, 691
- Dipeptides, 542
- 9,10-Diphenylanthracene (DPA), 54, 172–173
- 1,6-Diphenyl-1,3,5-hexatriene. *See* DPH (1,6-diphenyl-1,3,5-hexatriene)
- 2,5-Diphenyl-1,3,4-oxadiazole (PPD), 105
- 2,5-Diphenyloxazole (DPO), 228–229
- Dipicolinate, 523
- Dipicolinic acid, 522
- Dipole moments, solvent effects in emission spectra, 210–211
- Dipoles
  - imaging of radiation patterns, 778–779
  - single-molecule detection, 776–777
- Dirac delta-function, 120
- Direct recording, TRES, 240–241
- Distance-dependent quenching (DDQ) model, 344–346
- Distance distribution functions, 487
- Distance distributions, 477–479. *See also* Energy transfer; time-resolved calcium-induced changes in troponin C conformation, 490–493
  - DNA, four-way Holliday junction in, 493–494
  - in glycopeptide, 495–496
  - in peptides, 479–481
    - concentration of D–A pairs and, 482
    - cross-fitting data to exclude alternative models, 481–482
    - donor decay with acceptor, 482
    - rigid vs. flexible hexapeptide, 479–481
  - in proteins, 485–489
    - distance distribution functions, 487
    - melittin, 483–485
    - from time-domain measurements, 487
  - of proteins
    - analysis with frequency domain data, 485–487
    - representative literature references, 504
    - unfolding of yeast phosphoglycerate kinase, 494–495
- Distance measurements, resonance energy transfer, 451–453
  - melittin,  $\alpha$  helical, 451–452
  - orientation factor effects on possible range of distances, 452–453
  - protein folding measured by RET, 453–454
- Disulfide oxidoreductase DsbA, 591–592
- Disulfides, quenching by, 279

- DM-Nerf, 639  
 DMPC (dimyristoyl-L- $\alpha$ -phosphatidylcholine), 18, 216, 400  
   cholesterol membranes, 256–257, 293–294  
 DMPP (dimethyldiazaperopyrenium), 514–515  
 DMQ (2,2'-dimethyl-p-quaterphenyl), 23  
 DMSS, 744  
 DNA  
   anisotropy decay  
     time-domain studies of DNA binding to Klenow fragment, 417  
   anisotropy decay, time-dependent, 402–406, 432–433  
     DNA binding to HIV integrase, 404–406  
     intracellular DNA dynamics, 403–404  
     oligomer hydrodynamics, 403  
   distance distributions  
     double-helical, 507–508  
     four-way Holliday junction in, 493–494  
   dynamics with metal-ligand probes, 688–690  
   energy transfer, 507  
     in one dimension, 514–515  
   frequency-domain lifetime measurements, 186–187  
   helicase-catalyzed unwinding, 373–374  
   hybridization, 20  
     using metal-enhanced fluorescence, 853  
   interaction with proteins, 552–554  
   metal-enhanced fluorescence, 848–851  
   quenching, 341–342  
     intramolecular, 314–315  
   representative literature references, 504  
   Trp repressor binding anisotropy, 373  
     two-photon excitation of DNA bound fluorophore, 610–612  
 DNA base analogs, 75–78  
 DNA- $\beta$  helicase, 313  
 DNA-bound probe accessibility, quenching, 286–287  
 DNA polymerase, 417  
 DNA probes, 75–80  
 DNA sequencing, 705–712  
 DNA technology, 705–734  
   aptamers, 724–726  
     DNAzymes, 726  
   cleavage, 810  
     by restriction enzyme, 826  
   conformational dynamics of Holliday junction, 782–783  
   distance-dependence of metal-enhanced fluorescence, 851–853  
 DNA arrays, 732–734  
   light-generated, 734  
   spotted microarrays, 732–734  
 fluorescence correlation spectroscopy  
   bioaffinity reactions, 808–810  
 fluorescence in-situ hybridization, 727–730  
   applications of, 729–730  
   preparation of probe DNA, 728–729  
 hybridization, 715–720  
   excimer formation, 225, 718–719  
   one donor- and acceptor-labeled probe, 717–718  
   polarization assays, 719  
   polymerase chain reaction, 720  
 lanthanides, 681  
 molecular beacons, 720–724  
   based on quenching by gold, 723–724  
   with fluorescent acceptors, 722  
   hybridization proximity beacons, 722–723  
   intracellular detection of mRNA, 724  
   with nonfluorescent acceptors, 720–722  
 multicolor FISH and spectral karyotyping, 730–732  
 multiplexed microbead arrays:suspension arrays, 726–728  
 oligomers, 809–810  
 RET applications, 493–494  
 sequencing, 705–712  
   energy-transfer dyes, 709–710  
   examples of, 706–707, 708–709  
   lifetime-based, 712  
   multidimensional time-correlated single-photon counting (TCSPC), 123–124  
   NIR probes, 710–711  
   nucleotide labeling methods, 707–708  
   principle of, 705–706  
 single-molecule detection  
   literature references, 792  
 stains, high-sensitivity, 712–715  
   energy-transfer stains, 715  
   fragment sizing by flow cytometry, 715  
   high-affinity bis, 713–715  
 DNAzymes, 726  
 DNBS (dinitrobenzenesulfonyl)  
   Förster distances, 468  
 Docking, energy transfer, 460  
 Domain motion, 396–397, 501  
 Domain-to-domain motions in proteins, 690  
 Donor–acceptor pairs. *See also* Energy transfer  
   acceptor decays, 489  
   and distance distributions in peptides, 477–478  
   DNA hybridization, one donor- and acceptor-labeled probe, 717–718  
   effect of concentration on, 482  
   energy-transfer mechanisms, 13–14  
   fluorescence-lifetime imaging microscopy, 742  
   Förster distance, 443–444, 468  
   linked, 340–341  
   linked, diffusion effects, 498–501  
     experimental measurement, 500–501  
     RET and diffusive motions in biopolymers, 501  
     simulations of RET for flexible pair, 499–500  
   molecular beacons, 720  
   single-molecule detection, 773–775  
   theory of, 445–448  
   unlinked, effect of diffusion, 508–509  
 Donor decay without acceptor in peptides, 482  
 DOPC (dioleoyl-L- $\alpha$ -phosphatidylcholine), 275  
   quenching, 294–295  
 DOS (trans-4-dimethylamino-4'-(1-oxybutyl)-stilbene), 206–207  
 DOTCI, 174  
 10-Doxynonadecane (10-DN), 295  
 5-Doxylstearate (5-NS), 299  
 DPA (diphenylanthracene), 54, 172–173, 301–302  
 DPH (1,6-diphenyl-1,3,5-hexatriene), 11, 15–16, 72, 355, 375  
   anisotropic rotational diffusion, 428  
   anisotropy decays, time-dependent, 399–401  
   ellipsoids of revolution, 421  
   in film, 433–434  
   Förster distances, 468  
   hindered rotors, 391  
   quenching-resolved spectra, 301–302  
   two-photon anisotropy of, 612–613  
 DPO (2,5-diphenyloxazole), 228–229  
 DPPC (dipalmityl-L-i-a-phosphatidylcholine) systems, 206–207, 293–294  
   energy transfer in two dimensions, 512–513  
   Patman-labeled, TRES, 245–247

DPPG vesicles, 408, 691  
 DsRed, 82  
 DTAC micelles, 286  
 Dual-color cross fluorescence correlation spectroscopy, 823–828  
 Dye lasers, 110–112  
 Dyes. *See also* specific dyes  
     energy-transfer, 709–710  
     red and near-IR, 74–75  
     solvent relaxation, 253  
 Dynamic quenching. *See* Collisional quenching; Quenching  
 Dynamics of relaxation. *See* Relaxation dynamics  
 Dynode chains, 44–45, 46–47  
 Dynorphin, 590

**E**

EcoRI, 826  
 EDANS, 721  
 Efficiency, quenching, 281, 333–334, 542  
 EGFP (excited green fluorescent protein)  
     fluorescence correlation spectroscopy, 816–817  
 EIA 5-(iodoacetamido)eosin  
     Förster distances, 468  
 Einstein equation, 12  
 Electrical bias, 166  
 Electron-exchange quenching, 335  
 Electronics  
     frequency-domain fluorometers, 164–165  
     photomultiplier tube, 44–45  
     time-correlated single-photon counting, 114–117  
 Electronic state resolution from polarization spectra, 360–361  
 Electronic states, 1, 5  
     of metal–ligand complexes, 684–685  
 Electron scavengers, quenching by, 278  
 Electron transfer  
     photoinduced (PET), 335–336, 627  
     quenching in flavoprotein, 315–317  
 Electrooptic modulators, 165–166  
 ELISA, 659  
 Ellipsoids, 418–419  
     anisotropy decay, 419–420  
     of revolution, 420–425  
     rotational diffusion of, 425–426  
 Elongation factor (Ta-GDP), 548  
 Emission center of gravity, 246–247  
 Emission filter, 41  
 Emission spectra, 3–4, 7–8  
     decay-associated, 591–592, 596–598  
     instrumentation, 27–31  
         distortions in, 30–31  
         for high throughput, 29–30  
         ideal spectrofluorometer, 30  
     molecular information from fluorescence, 17–18  
     phase-sensitive, 194–197  
     solvent effects, 219–221  
     through optical filters, 43–44  
     tryptophan decay-associated, 581  
 Emission spectra, corrected  
     instrumentation, 52–54  
         comparison with known emission spectra, 52–53  
         conversion between wavelength and wavenumber, 53–54  
         correction factors obtained with standard lamp, 53  
         quantum counter and scatterer use, 53

Emission spectra, quenching-resolved, 301–304  
     fluorophore mixtures, 301–302  
     Tet repressor, 302–304  
 Emission wavelength, and anisotropy, 437–438  
 Encounter complexes, 333–334  
 Endonuclease, 290–291  
 Energy gap law, 687–688  
 Energy transfer, 443–468  
     biochemical applications, 453–458  
         intracellular protein folding, 454–455  
         orientation of protein-bound peptide, 456–457  
         protein binding to semiconductor nanoparticles, 457–458  
         protein folding measured by RET, 453–454  
         RET and association reactions, 455–456  
     data analysis, 485–487  
     diffusion-enhanced, 467  
     distance distributions, 477–479  
     distance measurements  
         melittin,  $\alpha$  helical, 451–452  
     distance measurements using RET, 451–453  
         incomplete labeling effects, 452  
         orientation factor effects on possible range of distances, 448–449, 452–453  
     DNA hybridization, one donor- and acceptor-labeled probe, 717–718  
     effect of colloids, 847  
     energy-transfer efficiency from enhanced fluorescence, 461–462  
     Förster distances, 443–444, 445–446, 468  
     GFP sensors, 654–655  
     homotransfer, 450  
     incomplete labeling effects, 452  
     lanthanides, 680–681  
     long-wavelength long-lifetime fluorophores, 696  
     in membranes, 462–465  
         lipid distributions around Gramicidin, 463–465  
         membrane fusion and lipid exchange, 465  
     nucleic acids, 459–461  
         imaging of intracellular RNA, 460–461  
     orientation factor, 465  
     protein kinase C activation, fluorescence-lifetime imaging  
         microscopy, 746–747  
     proteins, 539–545  
         anisotropy decreases, detection of ET by, 531–532  
         interferon- $\gamma$ , tyrosine-to-tryptophan energy transfer in, 540–541  
         phenylalanine-to-tyrosine, 543–545  
         RET efficiency quantitation, 541–543  
     proteins as sensors, 652–654  
     quantum dots, 678  
     radiationless, anisotropy measurement, 365  
     red-edge excitation shifts, 259  
     representative  $R_0$  values, 467–468  
     RET sensors, 458–459  
         imaging of intracellular protein phosphorylation, 459  
         intracellular RET indicator for estrogens, 458  
         Rac activation in cells, 459  
     sensor mechanisms, 633–637  
         glucose, 634–635  
         ion, 635–636  
         pH and CO<sub>2</sub>, 633–634  
         theory for, 636–637  
     silver particles effect, 854–855  
     single-molecule detection, 773–775  
         literature references, 794  
     in solution, 466–467

- Energy transfer [cont'd]  
 theory of, 445–451  
   for donor–acceptor pair, 445–448  
   homotransfer and heterotransfer, 450–451  
   orientation factor, 448–449  
   transfer rate dependence on distance, overlap integral, and orientation factor, 449–450
- Energy transfer, time-resolved, 477–501  
 acceptor decays, 489  
 advanced topics  
   single-protein-molecule distance distribution, 496–497  
   biochemical applications of distance distributions, 490–496  
   calcium-induced changes in troponin C conformation, 490–493  
   DNA, four-way Holliday junction in, 493–494  
   hairpin ribozyme, 493  
   unfolding of yeast phosphoglycerate kinase, 494–495
- diffusion effects for linked D–A pairs, 498–501  
 experimental measurement, 500–501  
 RET and diffusive motions in biopolymers, 501  
 simulations of RET for flexible pair, 499–500
- distance distribution data analysis, 485–489  
 frequency-domain analysis, 485–487  
 time-domain analysis, 487
- distance distribution in proteins  
 analysis with frequency domain data, 485–487  
 distance distribution functions, 487  
 from time-domain measurements, 487
- distance distributions from steady-state data, 443  
 D–A pairs with different  $R_0$  values, 445–446  
 quenching, changing  $R_0$  by, 447
- distance distributions in glycopeptide, 495–496
- distance distributions in peptides, 479–482  
 concentration of D–A pairs and, 482  
 cross-fitting data to exclude alternative models, 481–482  
 donor decay without acceptor, 482  
 rigid vs. flexible hexapeptide, 479–481
- distance distributions in proteins, 482–485  
 domain motion in, 501  
 melittin, 483–485
- incomplete labeling effects, 487–489
- orientation factor effects, 489  
 representative literature references, 504  
 RET imaging, 497–498
- Energy-transfer efficiency from enhanced fluorescence, 461–462
- Energy-transfer immunoassay, 660–661
- Energy-transfer stains and dyes, DNA, 715
- Energy transfer to multiple acceptors in one, two, or three dimensions, 507–524  
 dimensionality effect on RET, 511–515  
   one dimension, 514–515  
   two dimensions, 512–514  
 with multiple acceptors, 515–516  
   aggregation of  $\beta$ -amyloid peptides, 515–516  
   RET imaging of fibronectin, 516
- in presence of diffusion, 519–524  
 restricted geometries, 516–519  
   effect of excluded area, 518–519
- RET in rapid-diffusion limit, 520–524  
 acceptor location in lipid vesicles, 521–522  
 retinal location in rhodopsin disk membranes, 522–524
- three dimensions, 507–511  
 diffusion effects on RET with unlinked donors and acceptors, 508–509  
 experimental studies, 509–511
- Enzyme cofactors  
 intrinsic fluorescence, 63–65  
 time-domain lifetime measurement, 147
- Enzyme kinetics, 770
- Enzymes  
 DNA, degradation, 808  
 turnover of, 780–781, 782
- Eosin, 10, 633  
 Eosin-labeled ethanolamine, 448  
 Eosin-labeled lipid, 447  
 Epifluorescence, 41  
 Epi-illumination, 761  
 Erbium, 682, 683  
 Erythrosin, 408  
 Erythrosin B, 10  
*Escherichia coli* maltose-binding protein, 653  
*Escherichia coli* Tet repressor, 302–304  
 Estradiol, 80  
 Estrogens, intracellular RET indicator for, 458  
 1,2-Ethanedithiol (EDT), 86
- Ethanol  
 indole emission spectra in cyclohexane-ethanol mixture, 533–534  
 indole lifetime in, 533–534  
 polarizability properties, 207  
 rotational diffusion in, 367  
 specific solvent effects, 213, 214  
 tryptophan anisotropy spectra in, 533
- Ethenoadenine derivatives, 287–288  
 Förster distances, 468
- Ethers, 209, 279
- Ethidium bromide, 75, 286  
 anisotropy decay, 402, 403–404, 432–433  
 DNA technology, 713, 714  
 energy transfer in one dimension, 514, 515  
 metal–ligand probes, 688
- Ethidium homodimer, 75
- Ethoxycoumarin, 230
- Ethyl acetate, 206–207
- Ethylaniline, 338
- Ethylcellulose, 634
- Ethylenediamine, dansylated, 229, 230
- 1-Ethylpyrene, 286
- Europium, 3  
 as fluorophores, 679  
 Förster distances, 468  
 immunoassays, 659  
 metal-enhanced fluorescence, 843, 844
- Excimers, 9, 269–270  
 DNA hybridization, 225, 718–719
- Exciplex formation, 9, 278
- Excitation, polarized, 778
- Excitation anisotropy, two-photon and multiphoton, 21–22, 612–613
- Excitation anisotropy spectra, 358–361, 531–533
- Excitation filter, 41
- Excitation photoselection of fluorophores, 357–358
- Excitation spectra  
 anisotropy, 358–360, 531–533  
 instrumentation, 27–31

corrected spectra, 51–52  
 distortions in, 30–31  
 ideal spectrofluorometer, 30  
 spectrofluorometer for high throughput, 29–30  
 polarization, tyrosine and tryptophan, 531–533  
 Excitation wavelength independence of fluorescence, 7–8  
 Excited charge-transfer complex (exciplex), 9, 278  
 Excited-state intramolecular photon transfer (ESIPT), 221–222  
 Excited-state reactions  
   analysis by phase-modulation fluorometry, 265–270  
   apparent phase and modulation lifetimes, effects on, 266–267  
   wavelength-dependent phase and modulation values, 267–269  
   differential wavelength methods, 264  
   frequency-domain measurement of excimer formation, 196–197  
   naphthol dissociation, time-domain studies of, 264–265  
   naphthol ionization, 260–262  
   overview, 237–240  
   phase modulation, 265–270  
   phase-sensitive detection, 196–197  
   relaxation dynamics, 259–262  
   reversible two-state model, 262–264  
   steady-state fluorescence, 262–263  
   time-resolved decays for, 263–264  
   two-photon, 822–823  
 Exponential decays, frequency-domain lifetime measurements, 170–171  
 Extinction coefficients, 677  
 Extrinsic fluorophores, 15, 67

**F**

FAD (flavin adenine dinucleotide), 64  
 imaging of, multiphoton microscopy, 617–618  
 quenching by adenine moiety, 278  
 time-domain lifetime measurement, 147–148  
 turnover of cholesterol oxidase, 780, 781  
 Fatty acid binding proteins, 226  
 Fatty acids. *See also* specific fatty acids  
   fluorenyl, 295–296  
   membrane probes, 72  
 FCVJ, 225  
 Femtosecond titanium:sapphire lasers, 108–109  
 Ferredoxin, 584  
 Fibronectin, 516  
 Film polarizers, 51, 366  
 Films, 433–434  
   laser scanning TCSPC film, 748–750  
   surface-plasmon resonance, 863  
   wide-field frequency-domain, 746–747  
 Filters. *See also* Optical filters  
   double dichroic, 824  
   holographic, 766  
   Rugate notch, 766  
   for single-molecule detection, 766–768  
 Fingerprint detection, 683  
 FITC. *See* Fluorescein isothiocyanate (FITC)  
 Fitted function, 106  
 FKBP5901, 149, 592–593  
 Flash-EDT<sub>2</sub>, 86  
 Flashlamps, 32  
   time-correlated single-photon counting, 112–114  
 Flavin adenine dinucleotide. *See* FAD  
 Flavin mononucleotide, 16, 64, 316, 317, 397, 398  
 Flavoprotein, electron transfer, 315–316, 317

Flavoproteins, 65  
 Flexible D–A pairs, 499–500  
 Flexible hexapeptide, distance distributions, 479–481  
 Flow cytometry, 85  
   DNA fragment sizing, 715  
 Flow measurements using fluorescence correlation spectroscopy, 830–832  
 Fluid flow, 225  
 Fluorenyl fatty acids, 295–296, 299  
 Fluorenyl-PC, 72  
 Fluorescein, 2, 3, 20, 69, 70, 122, 695  
   anisotropic rotational diffusion, 428  
   brightness, 818  
   DNA energy-transfer reaction, 454  
   DNA technology, 707, 717, 719, 726  
   filters, 38  
   melittin labeled with, 374  
   metal–ligand complexes, 691  
   methionyl-tRNA synthetase labeled with, 370–371  
   as pH sensor, 637–639  
   quantum yield standards, 52  
   quenching, 310–312  
   resonance energy transfer, 365  
   time-resolved RET imaging, 498  
 Fluorescein isothiocyanate (FITC), 16, 17, 68  
   FITC-dextran, 635  
   Förster distances, 468  
 Fluorescence  
   energy-transfer efficiency, 461–462  
   intensity fluctuations, 798–799, 800  
   metal-enhanced, 841  
 Fluorescence anisotropy. *See* Anisotropy  
 Fluorescence correlation spectroscopy, 22–23, 757, 797–832  
   applications to bioaffinity reactions, 807–810  
    association of tubulin subunits, 807–808  
    DNA applications, 808–810  
    protein binding to chaperonin GroEL, 807  
   detection of conformational dynamics in macromolecules, 820–821  
   dual-color, 823–828  
    applications of, 826–828  
    DNA cleavage by restriction enzyme, 826  
    instrumentation for, 824  
    literature references, 837  
    theory of, 824–826  
   effects of chemical reactions, 816–817  
   examples of experiments, 805–807  
    effect of fluorophore concentration, 805–806  
    effect of molecular weight on diffusion coefficients, 806–807  
   flow measurements, 830–832  
   fluorescence intensity distribution analysis, 817–819  
   intersystem crossing, 815–816  
    theory for, 816  
   literature references, 837–839  
   in membranes, 810–815  
    binding to membrane-bound receptors, 813–815  
    lateral diffusion, 812–813  
   principles of, 798–799  
   rotational diffusion and photon antibunching, 828–830  
   theory of, 800–805  
    multiple diffusing species, 804–805  
    occupation numbers and volumes, 804  
    translational diffusion, 802–804  
   time-resolved, 819–820

- Fluorescence correlation spectroscopy [cont'd]  
 total internal reflection, 821–822  
 with two-photon excitation, 822–823  
 diffusion of intracellular kinase, 823
- Fluorescence in-situ hybridization (FISH), 727–730  
 applications of, 729–730  
 preparation of probe DNA, 728–729  
 spectral karyotyping, 730–732
- Fluorescence intensity distribution analysis, 817–819
- Fluorescence lifetime imaging microscopy (FLM), 97–98, 630, 741–752  
 calcium concentration from lifetime, 744–745  
 cos cells images, 745–746  
 early methods for, 743–744  
 frequency-domain laser scanning microscopy, 750–751  
 literature references, 754
- laser scanning TCSPC film, 748–750  
 images of amyloid plaques, 750  
 literature references, 754
- literature references, 753–755
- using gated-image intensifier, 747–748
- wide-field frequency-domain film, 746–747  
 imaging cells containing GFPs, 747  
 laser scanning TCSPC film of cellular biomolecules, 750  
 protein kinase C activation, 746–747
- Fluorescence microscopy, filters for, 41
- Fluorescence polarization. *See* Polarization
- Fluorescence-polarization immunoassays (FPIs), 661–663, 691–692
- Fluorescence quenching. *See* Quenching
- Fluorescence recovery after photobleaching, 814–815
- Fluorescence resonance energy transfer (FRET), 443. *See also*  
 Energy transfer
- Fluorescence scanning spectroscopy  
 theory of, 839
- Fluorescence standards. *See* Standards
- Fluorogenic probes, 79–80
- Fluorophore blinking, 767, 768, 769
- Fluorophores, 1, 63–95  
 anisotropy decay, time-dependent, 391  
 anisotropy of planar fluorophores with high symmetry, 435  
 biochemical, 15–16  
 blinking of, 815  
 brightness, 817–819  
 chemical sensing probes, 78–79  
 colloid interactions, 846–848  
 concentration, 805–806  
 DNA probes, 15, 75–78  
 dual color, 824–826  
 excitation of multiple, 618  
 excitation photoselection of, 357–358  
 extrinsic, 15, 67–74  
 membrane potential probes, 72–74  
 membrane probes, 72  
 photostability, 70–71  
 protein labeling, role of Stokes shift in, 69–70  
 protein-labeling probes, non-covalent, 71–72  
 protein-labeling reagents, 67–69
- fluorescent proteins, 81–86  
 green fluorescent protein, 81–83  
 phycobiliproteins, 84–86  
 phytofluors, 83–84
- fluorescence-lifetime imaging microscopy, 744
- glucose-sensitive, 650–651
- intercalated, 432–433
- intracellular proteins  
 specific labeling of, 86
- intrinsic or natural, 15, 63–67  
 enzyme cofactors, 63–65  
 protein binding of NADH, 65–67
- lanthanides, 679–683  
 fingerprint detection, 683  
 nanoparticles, 682  
 near-infrared emitting, 682, 683  
 resonance energy transfer, 680–681  
 sensors, 681–682
- long-lifetime metal-ligand complexes, 683–695
- long-lifetime probes, 86–88  
 lanthanides, 87–88  
 transition metal-ligand complexes, 88
- long-wavelength long-lifetime, 695–697
- mixtures, quenching-resolved emission spectra, 301–302
- multiphoton excitation for membrane-bound, 613
- photobleaching, 769
- photostability, 769–770, 849–850
- polarization, surface-bound, 786–787
- polarization of single immobilized, 786
- probe–probe interactions, 225–226
- proteins as sensors, 88–89
- quenchers of, 278, 279
- red and near-IR dyes, 74–75
- semiconductor nanoparticles, 675–678  
 quantum dots, labeling cells with, 677–678  
 quantum dots, resonance energy transfer, 678  
 quantum dots, spectral properties, 676–677
- single-molecule detection, 23
- solvent effects on emission spectra, 226–228
- special probes  
 fluorogenic, 79–80  
 structural analogs of biomolecules, 80  
 viscosity probes, 80–81
- two-photon excitation of, 610–612
- 4-Fluorotryptophan (4FW), 565
- FluoSphereJ, 635–636
- Fluo-3, 645
- FMN, enzyme turnover, 781–782
- Focused-ion-beam (FIB), 778
- Folate receptor, 375–376
- Förster, Theodor, 448
- Förster cycle, 261–262
- Förster distance ( $R_0$ ), 14, 19, 332–333, 366, 468  
 anisotropy decay, time-dependent, 389  
 distance distribution from steady-state, 499, 500  
 donor–acceptor pairs, 443–444, 468  
 homotransfer, 450  
 indole acceptor pair, 500  
 proteins, 540  
 representative, 467–468  
 RET in three dimensions, 511
- Fractal dimensions, 514
- Fractional accessibility, 288–290, 290–291, 549
- Fractional intensity, 413
- Franck–Condon principle, 5, 8, 12, 211
- Franck–Condon state, 237
- Frequency-domain decays  
 anisotropy, time-dependent, 383–387, 390
- Frequency-domain films, wide-field, 746–747

- Frequency-domain lifetime measurements, 157–204  
 apparent phase and modulation lifetime, 191–192  
 background correction, 169–170  
 biochemical examples, 186–189  
 DNA, DAPI-labeled, 186–187  
 fluorescence microscopy with LED light source, 189  
 Mag-Quin-2, magnesium probe, 187–188  
 melittin lifetime distributions, cross fitting of models, 188–189  
 recovery of lifetime distributions from data, 188  
 color effects, 168–169  
 gigahertz fluorometry, 175–178  
 biochemical examples, 177–178  
 measurements, 177  
 instrumentation, 163–168  
 cross-correlation detection, 166  
 frequency synthesizers, 167  
 history, 163–164  
 light modulators, 165–166  
 200-MHz fluorometers, 164–165  
 photomultiplier tubes, 167–168  
 principles of measurement, 168  
 radio-frequency amplifiers, 167  
 multi-exponential data analysis, 178–186  
 global analysis of two-component mixture, 182–183  
 two closely spaced lifetimes, 180–182  
 two widely spaced lifetimes, 178–180  
 multi-exponential decay analysis  
 maximum entropy analysis, 185–186  
 three-component mixture, limits of resolution, 183–185  
 three-component mixture, resolution of 10-fold range of decay times, 185  
 phase angle and modulation spectra, 189–191  
 phase modulation fluorescence equations, derivation of, 192–194  
 cross-correlation detection, 194  
 lifetime relationship to phase angle and modulation, 192–194  
 phase-modulation resolution of emission spectra, 197–199  
 phase-sensitive emission spectra, 194–197  
 examples of PSDF and phase suppression, 196–197  
 representative decays, 170–173  
 collisional quenching of chloride sensor, 171–172  
 exponential, 170–171  
 green fluorescent protein, one- and two-photon excitation, 171  
 intensity decay of NADH, 172  
 multi-exponential decays of staphylococcal nuclease and melittin, 171  
 SPQ, collisional quenching, 171–172  
 scattered light, 172–173  
 simple frequency-domain instruments, 173–175  
 laser diode excitation, 174  
 LED excitation, 174–175  
 theory, 158–163  
 global analysis of data, 162–163  
 least-squares analysis of intensity decays, 161–162
- Frequency-domain measurements  
 anisotropy decay, 417–418, 428–429, 588–589  
 excimer formation, 269–270  
 laser scanning microscopy, 750–751  
 protein distance distributions from, 485–487  
 time-domain lifetime measurements, 98–100  
 lifetime or decay time, meaning of, 99  
 phase modulation lifetimes, 99–100
- Frequency doubling, 112
- Frequency response, 160
- Frequency synthesizers, 167
- FRET. *See* Energy transfer
- FR-GPI, 375–377
- Front-face illumination, 55
- FR-TM, 375–377
- Fructose, 651
- F-statistic, 133–134, 135, 136, 180
- Fumarate, 278
- Fura-2, 79, 648
- Fusion proteins, 86
- G**
- $\beta$ -Galactosidase, 79
- Gastrin, 590
- Gated detection, 124–125
- Gated-image intensifier, 747–748
- Gating, 819
- Gaussian distributions, 487  
 correlation time, 393
- Gaussian lifetime distributions, 143
- Gauss-Newton algorithms, 131
- Gaviola, 163
- GB1, 244–245
- Generalized polarization, 218
- Genetically engineered proteins  
 azurins, 538–539  
 for ribonuclease protein folding studies, 558–559  
 in sensors, 651–652  
 spectral properties, 554–557  
 barnase, 556–557  
 tyrosine proteins, 557
- G-factor, 36, 362, 389
- GFP, 86  
 anisotropy, 377–378  
 fluorescence-lifetime imaging microscopy, 747
- GFP5, 747
- GFP sensors, 654–655
- Giant unilamellar vesicles (GUVs), 219, 465, 466  
 fluorescence correlation spectroscopy, 812
- Gigahertz fluorometry, 175–178
- Glan-Thompson polarizer, 50, 51
- Global analysis  
 anisotropy decay  
 with multi-wavelength excitation, 429–430  
 frequency-domain lifetime measurements, 162–163, 182–183  
 time-domain lifetime measurements, 138, 144–145
- Glucagon, 547, 548, 583
- Glucose-galactose binding protein (GGBP), 652
- Glucose sensors, 650–651
- energy-transfer mechanisms, 634–635
- Glutamate, 551
- Glyceraldehyde phosphate, 555
- Glyceraldehyde-3-phosphate dehydrogenase (GPD), 292, 600
- Glycerol, 250, 359
- Glycopeptides, 495–496
- $\beta$ -Glycosidase, 594
- gly-trp-gly, 588
- Gold  
 quenching, 313–315  
 molecular beacons, 723–724  
 surface plasmon-coupled emission, 867
- Gold colloids, 845–846

- Gonadotropin, 548  
 Goodness of fit ( $\chi^2_R$ ), 134–135, 136  
   diffusion of D–A pairs, 500  
   frequency-domain lifetime measurements, 162, 179–182  
   mixture lifetime resolution, 140–141  
   three-decay time model, 183–184  
   time-domain lifetime measurements, 131–132, 133–134, 146
- Goppert-Mayer, Maria, 609  
 Goppert-Mayer units, 609  
 Gramicidin, 463–465  
 Gratings  
   in monochromators, 34–35, 36  
   in spectrofluorometer, 28, 29  
   surface plasmon-coupled emission, 868–869
- Green fluorescent protein, 307–309, 360  
   fluorescence correlation spectroscopy, 811  
   fluorophores, 81–83  
   frequency-domain lifetime measurements, 171  
   indicator for estrogens, 458  
   single-molecule detection, 762–763, 778  
   time-domain lifetime measurement, 145–146
- GroEL, 455–456, 771–773, 807  
 GroES, 455–456, 772–773
- Ground-state complex  
   quenching mechanisms, 278  
   tyrosine, 534–535
- Guanidine hydrochloride, 555, 556  
 Guanine, 311, 341, 342  
 Guanosine-containing substrate-binding strand (G-SBS), 312  
 Guanosine nucleotides, 311–312
- H**
- Hairpin ribozyme, 493  
 Half-wave voltage, 166  
 Halides, 335  
 Halocarbons, 335–336  
 Halogenated anesthetics, 632  
 Halogens, 11, 278, 279  
   quenching by, 334  
 Halothane, 304–305  
 Hand-over-hand motion, 784  
 Head-on photomultiplier tubes, 47  
 Heat filter, 32  
 $\alpha$ -Helical structure, 561–562, 563  
 Helicase, 313  
 Helicase-catalyzed DNA unwinding, 373–374  
 Helium-cadmium laser, 173  
 Heme proteins  
   Förster distances, 468  
   intrinsic fluorescence, 594–596  
   solvent relaxation, 243–244  
 Hemicyanine dyes, 254  
 Her2 marker, labeling of, 678  
 Herschel, John Frederick William, 2–3, 3  
 Heterogeneous decays, time-domain lifetime measurements, 101–103  
 Heterotransfer, 450–451  
 Hexane, 214  
   chlorophyll aggregates, 146–147  
   polarizability, 209  
   Stokes shift, 209, 210  
 Hexokinase, 690  
 High throughput, spectrofluorometer for, 29–30  
 Hindered rotational diffusion, membranes, 399–402  
 Hindered rotors, 391–392  
 Histidine, 341  
   quenching, 278, 279  
 Histocompatibility protein, 589  
 HITC, 52  
 HIV integrase, 78, 404–406  
 HIV protease, 80  
 Hoechst 33258, 286–287  
 Hoechst 33342, 75  
 Hoechst 33358, 75  
 Holliday junction  
   in distance distributions, 493–494  
   in single-molecule detection, 782–783  
 Holographic filters, 766  
 Holographic gratings, 37  
 Homotransfer, 374, 450–451  
 HPLC, 175  
 HPTS (8-hydroxypyrene-1,3,6,8-trisulfonate)  
   blood gas measurement, 637  
   mirror-image rule exceptions, 8  
   pH sensors, 639–640  
 HTa (histone-like protein), 544–545  
 Human antithrombin (AT), 560–561  
 $\beta$ -Human chorionic gonadotropin, 661  
 Human immunodeficiency virus integrase, 78  
 Human immunodeficiency virus protease, 80  
 Human luteinizing hormone, 435, 436  
 Human serum albumin, 13, 72, 304, 548  
   anisotropy decay, 413–414  
   intensity decay, 583, 584  
   laser diode excitation, measurement with, 71, 72  
 Hybridization, release of quenching, 310, 311  
 Hydration, 367  
 Hydrogen peroxide, 278, 279  
 Hydrogen pulse lamps, 113  
 Hydrophobic surface, calmodulin, 226–227  
 7-Hydroxycoumarin (umbelliferone), 79  
 8-Hydroxypyrene-1,3,6,8-trisulfonate. *See* HPTS  
 17 $\beta$ -Hydroxysteroid dehydrogenase, 66  
 5-Hydroxytryptophan (5HW), 564, 565
- I**
- IAEDANS  
   distance distributions, 490–493  
   Förster distances, 468  
   immunoglobulin fragment labeled with, 371–372  
   quenching-resolved spectra, 301–302
- IAF-CK, 662  
 IAF [5-(Iodoacetamido)fluorescein], 68  
   domain motion, 495  
   Förster distances, 468  
 ICT (internal charge transfer), 207, 220–221, 223–224, 229, 232  
 Image correlation spectroscopy  
   literature references, 837–838  
 Imaging  
   intracellular, 306–307  
   *in vivo*, 656–658  
 Imidazole and imidazolium, quenching by, 278  
 Imidazolium, 336, 341  
 Immunoassays, 658–663  
   ELISA, 659  
   energy-transfer, 660–661

- fluorescence polarization, 661–663
- metal-ligand complexes, 691–693
- surface plasmon-coupled emission, 867
- time-resolved, 659–660
- Immunoglobulin G, 854
- Immunoglobulins
  - anisotropy decay, 396–397
  - domain-to-domain motions in, 690
  - fragment, Perrin plot, 371–372
  - rotational correlation time, 367
- Immunophilin KFB59-1, 592–593
- Impulse response function, 106–107, 158, 246
- Inchworm motion, 784
- Incomplete labeling effects, energy-transfer studies, 452, 487–489
- Indicators, principles, 16–17
- Indo-1, 647, 648, 649, 650
- Indole
  - covalent adduct formation, 314
  - decay times, 489
  - electronic state resolution, 360–361
  - frequency-domain lifetime measurements, 178–180, 185
  - intensity decays, 579
  - mixture lifetime resolution, 138–141
  - quenching, 11, 278, 279, 341, 537
  - RET in three dimensions, 509–510
  - solvent effects, 533–534
  - spectral relaxation, 596
  - time-domain lifetime, multi-exponential decays, 133, 134
- Infrared and NIR fluorescence
  - dyes, 74–75
  - light sources, 32
- Inner filter effects, 55–56, 290
- In situ DNA hybridization, 715–717
- Instrumentation, 21–24
  - corrected emission spectra, 52–54
    - comparison with known emission spectra, 52–53
    - conversion between wavelength and wavenumber, 53–54
    - correction factors obtained with standard lamp, 53
    - quantum counter and scatterer use, 53
  - corrected excitation spectra, 51–52
  - dual-color fluorescence cross correlation spectroscopy, 824
  - excitation and emission spectra, 21–24, 27–31
    - distortions in, 30–31
    - ideal spectrofluorometer, 30
  - fluorescence correlation spectroscopy, 22–23
  - frequency-domain lifetime measurements, 163–168, 194–175
    - cross-correlation detection, 166
    - frequency synthesizers, 167
    - history, 163–164
    - laser diode excitation, 174
    - LED excitation, 174–175
    - light modulators, 165–166
    - 200-MHz fluorometers, 164–165
    - photomultiplier tubes, 167–168
    - principles of measurement, 168
    - radio-frequency amplifiers, 167
    - simple frequency-domain instruments, 173–175
  - light absorption and deviation from Beer-Lambert law, 58–59
  - light sources, 31–34
    - arc and incandescent lamps, 31–34
  - literature references, 838
  - monochromators, 34–38
    - calibration of, 38
- polarization characteristics of, 36
- second-order transmission in, 37
- stray light in, 36–37
- wavelength resolution and emission spectra, 35
- multiphoton excitation, 21–22
- optical filters, 38–41
  - bandpass, 39
  - combination, 40
  - for fluorescence microscopy, 41
  - neutral density, 40
  - signal purity and, 41–44
  - thin-film, 39–40
- photomultiplier tubes, 44–49
  - CCD detectors, 49
  - failure of, symptoms, 49
  - hybrid, 49
  - photon counting vs. analog detection of fluorescence, 48–49
  - PMT design and dynode chains, 46–47
  - polarizers, 49–51
  - spectral response, 45–46
  - time response of, 47
  - quantum counters, 51–52
  - quantum yield standards, 54–55
  - sample geometry effects, 55–57
  - sample preparation, common errors in, 57–58
  - single-molecule detection, 23–24, 764–768
  - time-correlated single-photon counting (*See* Time-correlated single-photon counting (TCSPC))
    - two-photon and multiphoton excitation, 21–22
- Instrument response function (IRF), 100, 105–106, 387, 487
- Insulin, 813
- Integrins, energy transfer, 518–519
- Intensity-based sensing, 645
- Intensity decay, 98, 577–578
  - aromatic amino acids, 578
  - correlation time imaging, 406–407
  - least-squares analysis, 161–162
  - microsecond luminescence decays, 129
  - multi-exponential model, 101–102
  - of NADH, 172
  - RET in three dimensions, 509–511
  - ribonuclease  $T_1$  and single-exponential intensity, 584, 585
  - time-domain lifetime measurements, 145–148
    - chlorophyll aggregates in hexane, 146–147
    - FAD, 147–148
    - green fluorescent protein, systematic data errors, 145–146
    - picosecond decay time, 146
    - single-tryptophan protein, 145
  - tryptophan, 580–583
    - decay-associated emission spectra, 581
    - neutral tryptophan derivatives, 581–582
    - rotamer model, 578–580
  - tyrosine, 580–583
    - neutral tyrosine derivatives, 582–583
- Intensity decay laws, 141–144
  - lifetime distributions, 143
  - multi-exponential decay, 141–143
  - stretched exponentials, 144
  - transient effects, 144–145
- Intensity fluctuations, 798–799, 800
- Interference filters, 39–40
- Interferon- $\gamma$ 
  - resonance energy transfer, 540–542

Internal charge transfer (ICT) state, 207, 220–221, 223–224, 229, 232  
 Internal conversion in fluorophores, 5  
 Intersystem crossing, 5–6, 334–335, 815–816  
 Intracellular protein folding, 454–455  
 Intramolecular quenching, 314–317  
 Intrinsic fluorophores, 15  
 Intrinsic/natural fluorescence, 15, 63–67  
   enzyme cofactors, 63–65  
   multiphoton excitation, 613–616  
   of proteins, 594–596  
 In-vivo imaging, sensors, 656–658  
 Iodide  
   absorption spectra, 303  
   autocorrelation function in fluorescence correlation spectroscopy, 816  
   quenching by, 18, 278, 279, 287, 288, 290, 303–304, 306  
     chloride probe, 631  
     proteins, 290, 546–547  
 Iodine, 5  
 Iodoacetamides, 68  
 Ionic quenchers, 290. *See also* specific ions  
 Ion indicators/probes/sensors. *See also* specific elements/ions  
   analyte recognition probes, 644–650  
     calcium and magnesium, 647–650  
     cation probe specificity, 644  
     sodium and potassium, 645–647  
   chloride, 631–632  
   energy-transfer mechanisms, 635–636  
   oxygen, 627–630  
   photoinduced electron-transfer (PET) probes, 316, 318, 335–336, 627, 641–643  
 Ionization  
   naphthol, 260–262  
   tyrosine, 534–535  
 IR-125, 74  
 IR-144, 174  
 Iridium metal–ligand complexes, 684  
 I7S, 539  
 Isomers, rotational, 253–255, 529, 578  
 Isoxanthopterin (IXP), 75, 76  
 Iterative deconvolution, 131

**J**

Jablonski, Alexander, 4–5  
 Jablonski diagram, 3–6  
   collisional quenching and resonance energy transfer, 11  
   lanthanide probe, 87  
   metal-enhanced fluorescence, 842–843  
   red-edge excitation, 257  
   solvent effects, 207  
   solvent relaxation, 206, 238  
 JF9, 780

**K**

Karyotyping, spectral, 730–732

Kasha's rule, 7, 359

Kerr lens mode locking, 109

$\Delta^5$ -3-Ketosteroid isomerase (KSI), 557

KFU 111, 635, 636

Kinase, intracellular, 823

Kinesin, 784

Kinetics, literature references, 838

Klenow fragment of DNA polymerase, 417  
 Kretschmann configuration, 862

**L**

Labeling, incomplete, energy-transfer studies, 452, 487–489

$\alpha$ -Lactalbumin, 806

Lactate dehydrogenase, 559–560, 584

Lactoglobulin, 368

LaJolla Blue, 719

Lamps. *See* Light sources

Lanthanide MLCs, 87–88

long-lifetime probes, 87–88

quenching, 523

retinal energy-transfer study, 523

Lanthanides, 3, 467

fingerprint detection, 683

as fluorophores, 679–683

nanoparticles, 682

near-infrared emitting, 682, 683

resonance energy transfer, 680–681

as sensors, 681–682

Laplace method, 130

Laser diodes, 21

DNA technology, 711

frequency-domain lifetime measurements, 174

human serum albumin measurement with, 71, 72

instrumentation, 33, 34

time-domain lifetime measurements, 107–108

Laser line filter, 39

Lasers

DNA technology, 711

dual-color fluorescence cross correlation spectroscopy, 824

frequency-domain lifetime measurements, 173–174

monochromators, 34

multiphoton excitation, 577

time-correlated single-photon counting

film, 748–750

picosecond dye devices, 105–107

solid-state devices, 107

time-resolved protein fluorescence, 577

Laser scanning confocal microscopy (LSCM), 764

Laser scanning microscopy (LSM), 748–750

frequency-domain, 750–751

imaging of cellular biomolecules, 750

Lateral diffusion in membranes, 300–301, 812–813

Laurdan, 219, 220, 221

Least-squares analysis, 160, 487

frequency-domain lifetime measurements, 161–162

Stern–Volmer plots, 304

time-domain lifetime measurements, 129–130

TRES, 254

Least-squares fitting, 103

Lecithin:cholesterol acyltransferase, 454

Lecithin vesicles, 248

LED. *See* Light-emitting diodes

Leucine, 294

L-format anisotropy measurement or single-channel method, 361–363

Lifetime-based probes and sensing, 626

DNA sequencing, 712

metal–ligand complexes, 88 (*See also* Metal–ligand complexes (MLCs))

oxygen, 628–629

- Lifetime (decay time), 5–6  
 antibodies, 498  
 collisional quenching and, 256–257  
 estimation, single-molecule detection, 787–788  
 fluorescence-lifetime imaging microscopy, 741–752  
 frequency-domain (*See* Frequency-domain lifetime measurements)  
 long-wavelength long-lifetime fluorophores, 695–697  
 meaning of, 99  
 metal-enhanced fluorescence, 842–843  
 metal–ligand complexes, 683–695  
 natural, 10, 537  
 phase-modulation  
   apparent lifetimes, 191–192  
   phase angle and modulation, 192–194  
 principles, 9–12  
   quenching, 12  
   timescale of molecular processes in  
     solution, 12  
 protein folding and, 558  
 quantum yield and, 537  
 solvent effects, 222–223  
 steady-state intensity and, 14  
 time-domain (*See* Time-domain lifetime measurements)
- Lifetime distributions, time-domain lifetime measurements, 143
- Lifetime imaging, 743
- Lifetime reference, 133
- Lifetime-resolved anisotropy, 435–436
- Lifetime-resolved emission spectra, relaxation dynamics, 255–257
- Lifetime standards, 169
- Lifetime-weighted quantum yield, 142
- Ligand analogs, 80
- Ligand-centered absorption, 687
- Light absorption and deviation from Beer-Lambert law, 59
- Light diffraction, 37
- Light-emitting diodes, 33  
 frequency-domain lifetime measurements, 174–175, 189  
 instrumentation, 33–34  
 time-domain lifetime measurements, 108
- Light-generated DNA arrays, 734
- Light-generated probe arrays, DNA hybridization, 734
- Light modulators  
 frequency-domain lifetime measurements, 165–166  
 monochromators, 34–35
- Light sources, 28  
 instrumentation, 31–34  
 lamps in corrected emission spectra, 34  
 time-correlated single-photon counting, 107–114  
   femtosecond titanium:sapphire lasers, 108–109  
   flashlamps, 112–114  
   picosecond dye lasers, 110–112  
   synchrotron radiation, 114
- Linear-focused dynode chain PMTs, 118
- Linearity, time-to-amplitude converter (TAC), 115–116
- Lipid probes, 690–691
- Lipids  
 energy transfer, 521–522  
 membrane (*See* Membranes)  
 metal–ligand complex probes, 690  
 pyrenyl-labeled, 72  
 pyrenyl-PC, 72
- Lipids, boundary  
 lipid-water partitioning effects, 298–300
- Lipids, membrane  
 boundary, 298  
 distributions around Gramicidin, 463–465  
 energy transfer, 513  
 exchange of, 465
- Lipobeads, 656
- Lipocalin, 561, 563
- Lippert equation, 208–213  
 application of, 212–213  
 derivation of, 210–212
- Lippert-Mataga equation, 208–210
- Lippert plots, solvent effects, 215–216
- Liquid crystals, 377
- Lissamine rhodamine B, 70
- Liver alcohol dehydrogenase (LADH), 395, 584
- Localized quenchers, membranes, 332
- Locally excited state, 220–221
- Longitudinal relaxation times, 250, 252
- Long-lifetime probes, 86–88
- Long-pass filters, 38, 39
- Long-wavelength long-lifetime fluorophores, 695–697
- Lorentzian distributions, 487  
 correlation time, 393
- Lorentzian lifetime distributions, 143
- Low-frequency polarization, 210
- Low-pressure mercury lamps, 33
- Lucigenin, 631
- Lumazine, 589
- Luminescence, defined, 1
- Luminescence decays, 129
- Lysozyme, 288

**M**

- MACA (N-methylacridinium-9-carboxamide), 631
- Macromolecules, detection of conformational dynamics, 820–821
- Magic-angle conditions, 43
- Magic-angle polarizer conditions, 364
- Mag-INDO-1, 646
- Magnesium indicators/probes/sensors, 17, 187–188, 647–650
- Magnesium Orange, 646, 649
- Magnesium oxide scatterer, 53
- Magnetic resonance imaging (MRI), 406, 742
- Mag-Quin-2, 187–188
- Malachite green, 514
- Maleimides, 68
- Maltose binding protein (MBP), 457–458, 653
- Manganese, 278
- Maximum entropy analysis (MEM), 185–186
- Maximum entropy method, 148–149
- Melittin, 20, 547, 548  
 anisotropy decay, 398, 453, 590–591  
 association reactions  
   detection from homotransfer, 374  
 distance distributions, 483–485  
 frequency-domain lifetime measurements, 171, 188–189  
 phosphorescence, 599  
 RET distance measurements, 451–452  
 rotational correlation time, 590
- Membrane binding site polarity, solvent effects on emission spectra, 206–207

- Membrane-bound fluorophore  
anisotropy, 353  
solvent effects on emission spectra, 215–216
- Membrane-bound receptors, 813–815
- Membrane fusion and lipid exchange, 465
- Membrane potential probes, 72–74
- Membrane probes, 72  
absorption and emission spectra, 16  
anisotropy decay, time-dependent, 401–402
- Membranes, 37  
acceptor location in lipid vesicles, 521–522  
affecting anisotropy, 366  
anisotropy, 374–377  
distribution of membrane-bound proteins, 375–376  
membrane microviscosity, 374–375
- anisotropy decay, hindered rotational diffusion in, 399–402  
diffusion in lateral, 300–301
- diffusive motions in biopolymers, 501
- energy transfer, 462–465  
lipid distributions around Gramicidin, 463–465  
membrane fusion and lipid exchange, 465  
relative donor quantum yields, 518  
tyrosine-to-tryptophan in membrane-bound protein, 543
- multiphoton excitation for membrane-bound fluorophore, 613
- phase transitions, 217–219
- quenching, 18  
boundary lipid, 298  
depth-dependent, 296, 297–298  
lipid–water partitioning effects, 298–300  
localization of tryptophan residues, 294–295  
localized quenchers, 295–296  
oxygen diffusion, 293–294  
parallax quenching in, 296–298  
red-edge excitation shifts, 258–259
- RET in rapid-diffusion limit  
retinal location in rhodopsin disk membranes, 522–524
- shear stress on viscosity, 225
- TNS spectrum, 17–18
- TRES, 245–249
- Mercaptoacetic acid, 675
- Mercury lamps, 33, 38
- Merocyanine, 72–73
- Metal colloids, optical properties, 845–846
- Metal-enhanced fluorescence, 841  
applications of, 851–855  
DNA hybridization, 853  
release of self-quenching, 853–854  
silver particles on resonance energy transfer, 854–855
- distance dependence of, 851–853  
experimental results, 848–851  
DNA analysis, 848–851
- Jablonski diagram, 842–843  
mechanism, 855–856  
perspective on, 856  
review of, 843–845  
theory for fluorophore–colloid interactions, 846–848
- Metal ion and anions sensors, 641–643
- Metal–ligand complexes (MLCs), 1  
energy transfer, 520  
frequency-domain lifetime measurements, 174  
long-lifetime, 683–695  
anisotropy properties, 685–686  
biomedical applications, 688–691
- energy gap law, 687–688  
immunoassays, 691–693  
introduction to, 683–685  
sensors, 694–695  
spectral properties of, 686–687
- long-wavelength long-lifetime fluorophores, 695–697
- microsecond anisotropy decay, 408–409
- oxygen sensors, 627–630
- Metalloprotease, 550–551
- Metals  
effects on fluorescence, 843–845  
excitation in metal-enhanced fluorescence, 842–843  
interactions with fluorophores, 846–848  
quenching by, 305  
radiative decay engineering, 842
- Metal-to-ligand charge transfer (MLCT), 684–685, 687, 694
- Metaphase chromosomes, 730
- Methanol, 230, 510  
dielectric properties, 250  
Stokes shift, 209
- Methionine, 278, 558
- Methionyl-tRNA synthetase, 370–371
- Method of moments (MEM), 124, 130
- 2-Methylanthracene, 293, 294
- 9-Methylanthracene, 185, 186
- N-Methylanthraniloyl amide (NMA), 398
- Methyl 8-(2-anthroyl)octanate, 215
- Methylindole, 590
- Methylmercuric chloride, 279
- N-Methylnicotinamide, 278
- N-Methylquinolinium iodide (MAI), 306
- O-Methyltyrosine, 583
- Methylviologen, 309–310, 336, 340, 341
- 200-MHz fluorometers, 164–165
- Micelles, 300
- Microbeads, 727, 728
- Microchannel plate photomultiplier tubes (PMT), 47, 117–118, 176
- Microplate readers, 29–30
- Microscopy  
fluorescence lifetime imaging, 741–752  
laser scanning, 748–750  
laser scanning confocal, 764  
with LED light source, 189
- Microsecond anisotropy decays, 408–409  
long-lifetime metal–ligand complexes, 408–409  
phosphorescence, 408
- Microsecond luminescence decays, 129
- Microviscosity, membrane, 374–375
- Mirror image rule, exceptions to, 8–9
- Mixtures  
fluorescence-lifetime imaging microscopy, 748  
quenching-resolved emission spectra, 301–302  
sample preparation errors, 57–58  
solvent, emission spectra effects, 229–231  
TRES and DAS comparison, 255
- MLC. *See* Metal–ligand complexes (MLCs)
- Mode locking, laser, 110
- Modulation lifetimes, 99–100  
apparent, 191–192  
phase-modulation fluorometry, 198, 266–267
- Modulation spectra, 189–191

- Molecular beacons, 311, 720–724  
 based on quenching by gold, 723–724  
 emission spectra, 757–758  
 with fluorescent acceptors, 722  
 hybridization proximity beacons, 722–723  
 intracellular detection of mRNA, 724  
 with nonfluorescent acceptors, 720–722  
 quenching by gold colloids, 313–314  
 quenching by gold surface, 314, 315  
 single-molecule detection, 782
- Molecular biology quenching applications, 310–313
- Molecular chaperonin cpn60 (GroEL), 371
- Molecular information from fluorescence, 17–19  
 emission spectra and Stokes shift, 17–18  
 fluorescence polarization of anisotropy, 19  
 quenching, 18–19  
 resonance energy transfer, 19
- Molecular weight effect on diffusion coefficients, 806–807
- Moments and higher orders  
 literature references, 838
- Monellin, 548  
 anisotropy decay, 432, 588  
 phosphorescence, 599
- Monochromators, 28, 34–35  
 instrumentation  
 calibration of, 38  
 polarization characteristics of, 36  
 second-order transmission in, 37  
 stray light in, 36–37  
 time-correlated single-photon counting, 121  
 wavelength resolution and emission spectra, 35
- Monte Carlo simulations  
 energy transfer, 517  
 parameter uncertainty, 135
- Motions of molecular motors, 784
- MQAE [N-(ethoxycarbonylmethyl)-6-methoxyquinolinium], 79, 632
- MR121, 311, 782
- mRNA  
 intracellular detection of by molecular beacons, 724
- M13 peptide, single-molecule calcium sensor, 784
- Multi-alkali photocathode, 46
- Multichannel analyzer (MCA), 116, 121
- Multicolor fluorescence in-situ hybridization (m-FISH), 731
- Multi-exponential decay  
 emission center of gravity, 583  
 frequency-domain lifetime measurements, 171, 178–186  
 global analysis of two-component mixture, 182–183  
 maximum entropy analysis, 185–186  
 melittin, 171  
 three-component mixture, resolution limits, 183–185  
 three-component mixture, resolution of 10-fold range of decay times, 185  
 two closely spaced lifetimes, 180–182  
 two widely spaced lifetimes, 178–180
- multi-tryptophan proteins, 584
- resolution, 103
- solvent effects, 229–231
- time-domain lifetime measurements, 133–141  
 anthranilic acid and 2-aminopurine, 137–138  
 global analysis, multi-wavelength measurements, 138  
 goodness of fit comparison, F-statistic, 133–134  
 intensity decay laws, 141–143  
 multi-exponential or heterogeneous decays of, 101–103
- number of photon counts, 135, 137  
 parameter uncertainty-confidence intervals, 134–135, 136  
 p-terphenyl and indole, 133  
 resolution of three closely spaced lifetimes, 138–141
- Multi-exponential phosphorescence, 599
- Multi-exponential relaxation  
 measurement, 252–253  
 in water, 251–252
- Multiphoton excitation, 607–619, 822  
 cross-sections for, 609  
 instrumentation, 21–22  
 of intrinsic protein fluorescence, 613–616  
 for membrane-bound fluorophore, 613  
 microscopy, 616–619  
 calcium imaging, 616–617  
 excitation of multiple fluorophores, 618  
 imaging of NAD(P)H and FAD, 617–618  
 three-dimensional imaging of cells, 618–619  
 two-photon absorption spectra, 609–610  
 two-photon excitation of fluorophore, 610–612
- Multiphoton excitation anisotropy, 612–613
- Multiphoton microscopy, 607, 616–619  
 calcium imaging, 616–617  
 excitation of multiple fluorophores, 618  
 imaging of NAD(P)H and FAD, 617–618  
 three-dimensional imaging of cells, 618–619
- Multiple decay time quenching, 291
- Multiple intensity decay, 122
- Multiplexed microbead arrays:suspension arrays, 726–727, 728
- Multiplex-FISH, 731
- Multiscalars, 129
- Multi-wavelength excitation, time-dependent anisotropy decay, 429–430
- Myb oncogene, 553–554
- Myelin basic protein, 548
- Myoglobin, 243, 584, 596
- Myosin light-chain kinase (MLCK), 372, 456–457
- Myosin S-1, 452
- Myosin S-1 subfragment, 770–771
- N**
- NADH, 16, 63–65  
 frequency-domain lifetime measurements, 172, 177, 178  
 imaging of, multiphoton microscopy, 617–618  
 protein binding, 65–67  
 quenching by adenine moiety, 278
- Nanoengineering, surface plasmon-coupled emission, 870
- Nanoparticles  
 lanthanides, 682  
 protein binding to, 457–458  
 semiconductor, 675–678
- Nanosecond flashlamp, 112–113
- Naphthalene, 279  
 Förster distances, 468  
 1,8-Naphthalimide, 340, 341
- Naphthalocyanines, 75
- Naphthol  
 dissociation, time-domain studies of, 264–265  
 excited-state reactions, 260–262
- Naphthyl-2-acetyl, 495
- Naphthylamine derivatives, 213

- Naphthylamines and sulfonic acids  
excited-state reactions, 610  
quenchers of, 279
- Naphthylamine sulfonic acids, 71. *See also* ANS; TNS  
(2-(*p*-toluidinyl)naphthalene-6-sulfonic acid)
- NATA (N-acetyl-L-tryptophanamide), 217  
anisotropy decay of, 588  
decay-associated spectra, 582  
intensity decay, 120, 579–580, 581–582  
lifetime reference, 100  
quenching, 285, 341, 547, 548  
rotational correlation times, 590  
structure, 579
- Natural fluorescence of proteins, 594–596
- Natural lifetime, 10, 537
- NATyrA (N-acetyl-L-tyrosinamide), 531–532  
intensity decay of, 582–583
- NBD derivatives  
Förster distances, 468  
lipids  
quenching, 279, 299, 300  
red-edge excitation shifts, 258–259
- NBD (7-nitrobenz-2-oxa-1,3-diazole)  
quenchers of, 279
- NBS (nitrobenzenesulfenyl)  
Förster distances, 468
- Nd:YAG lasers, 108, 109–111
- Near-field scanning optical microscopy (NFSOM),  
763–764, 765, 778  
literature references, 793
- Near-infrared emitting lanthanides, 682, 683
- Near-IR. *See* Light-emitting diodes
- Near-IR probes, DNA sequencing, 710–711
- Negative pre-exponential factor, 597
- Nelder-Mead algorithm, 131
- Neodymium, 682–683
- Neodymium:YAG lasers, 110
- Neuro-2a, 455
- Neuronal receptor peptide (NRP), 551–552
- Neutral density filters, 40
- Neutral Red (NR), 223, 338, 339
- N-Hydroxysuccinimide, 68
- Nickel, 278, 279
- Nicotinamide, 348
- Nicotinamide adenine dinucleotide. *See* NADH
- Nile Blue, 514–515
- Nitric oxide, 278, 279
- Nitrite, 348
- Nitrobenz-2-oxa-1,3-dioxol-4-yl. *See* NBD
- Nitrogen as flashlamp, 113
- Nitromethane, 279
- Nitrous oxide, 632–633
- Nitroxide-labeled 5-doxylstearate, 299
- Nitroxide-labeled phosphatidylcholines, 295, 296
- Nitroxide quenching, 278, 279, 295
- Nonlinear least-squares analysis. *See*  
Least-squares analysis
- Nonlinear least squares (NLLS), 124
- Non-radiative decay, 842–843
- Non-radiative decay rate, 222–223
- Non-spherical fluorophores, 391
- Notch filters, 39, 40
- Nuclease, 548
- Nucleic acids, 65  
anisotropy decay, time-dependent, 402–406  
DNA binding to HIV integrase, 404–406  
DNA oligomer hydrodynamics, 403  
intracellular DNA dynamics, 403–404  
aptamers, 724–726  
energy transfer, 459–461  
labeling methods, 707–708  
quenching, 284
- Nucleotides, 65  
quenching by, 341–342
- O
- Oblate ellipsoids of revolution, 422–423
- Occupation numbers, 804
- Octadecapentaenoic acid, 401–402
- Octadecyl rhodamine B (ORB), 512–513
- Octadecyl rhodamine (ODR), 519  
Förster distances, 468
- Octanol, 210, 215
- Off-center illumination, 55
- Olefins, 278, 279
- Oligonucleotides  
anisotropy decay, 416  
energy transfer, 710
- Oligosaccharides, distance distributions, 495–496
- One-photon excitation, 171, 608–609  
absorption spectra, 610  
cross-sections for, 609
- Optical bias, 166
- Optical density, 55
- Optical filters, 29, 766–768  
bandpass, 39  
colored, 38–39  
combination, 40  
for fluorescence microscopy, 41  
interference, 38–39  
neutral density, 40  
signal purity and, 41–44  
thin-film, 39–40
- Optical properties  
of metal colloids, 845–846  
of tissues, 625
- Optics  
confocal, 761–762, 763  
internal reflection, 760–761  
single-molecule detection, 762–764
- Oregon Green, 516, 639, 648
- Orientation factor ( $k^2$ ), 448–450  
energy transfer, 465, 489  
on possible range of distances, 448–449, 452–453
- Orientation imaging of R6G and GFP, 777–778
- Orientation polarizability, 209, 211
- Oriented fluorophores, transition moments,  
353, 377–378
- Oscillator strength, 59
- Osmium metal–ligand complexes, 684, 685, 686  
energy gap law, 688
- Osmium MLCs, 88
- Overlap integral, 445, 449–450
- Oxazine dyes, 74
- Oxonal, 73

Oxygen  
intersystem crossing, 816  
quenching by, 334

Oxygen imaging  
literature references, 754

Oxygen probes/sensors, 17  
blood gas measurement, 637  
camphorquinone, 672  
collisional quenching mechanism, 627–630  
lifetime-based, 628–629  
mechanism of oxygen selectivity, 529

Oxygen quenching, 277, 278, 279  
diffusion coefficient, 293–294  
DMPC/cholesterol vesicles, 256–257, 293–294  
DNA-probes, 286  
intensity decays, 346  
lifetime-resolved anisotropy, 435–436  
membrane lipids, 293–294  
monellin, 432  
of phosphorescence, 317–318  
of proteins, 548–549  
quenching efficiency, 281  
transient effects, 346  
of tryptophan, 283–284

Oxytocin, 178, 399

## P

Papain, 584

Parallel component, 776

Parallax quenching in membranes, 296–298

Parameter uncertainty, time-domain lifetime measurements, 134–135

Parinaric acid, 72, 415

Parvalbumin, 548, 599

Patman, 217, 218

membrane TRES, 245–246, 247, 248

Pebble sensors, 655–656

Pentagastrin, 590

Pepsinogen, chicken, 597

Peptides

calmodulin binding, 372–373

distance distributions, 479–481

concentrations of D–A pairs and, 482

cross-fitting data to exclude alternative models, 481–482

donor decay without acceptor, 482

energy transfer

aggregation of  $\beta$ -amyloid peptides, 515–516

membrane-spanning, 294–295

rigid vs. flexible hexapeptide, 479–481

Peroxides, quenching by, 279

Perrin equation, 13, 366–370

examples of Perrin plots, 369–370

Perrin plots, 369–370, 453

immunoglobulin fragment, 371–372

molecular chaperonin cpn60 (GroEL), 371

segmental motion effects, 436

tRNA binding to tRNA synthetase, 370–371

Perylene, 3, 4, 5, 10, 226, 391

anisotropy, 427–428, 429, 434, 435

rotational diffusion and, 422

anisotropy decay, 429–430

emission spectra, 7

energy transfer, 450

photoinduced electron energy transfer, 342–343  
quenchers of, 279

pH, indicators/probes/sensors, 17, 175  
blood gases, optical detection of, 637  
energy-transfer mechanisms, 633–634  
fluorescein, 637–639  
GFP sensors, 655  
HPTS, 639–640  
literature references, 754  
metal–ligand complexes, 694  
pH sensors, 637–641  
SNAFL and SNARF, 640–641  
two-state, 637–641

Phase angles, 99, 162

frequency-domain anisotropy decays, 385, 386–387  
frequency-domain lifetime measurements, 189–191  
lifetime relationship to, 192–194  
phase-modulation resolution of emission spectra, 198  
solvent relaxation, 246

Phase lifetimes, apparent, 191–192

Phase modulation

fluorescence equations, derivation of, 192–194  
lifetime relationship to, 192–194

Phase-modulation fluorometry, 265–270

apparent phase and modulation lifetimes, 266–267  
wavelength-dependent phase and modulation values,  
267–269

Phase-modulation lifetimes

HPLC, 175  
time-domain lifetime measurements, 98

Phase-modulation spectra

frequency-domain lifetime measurements, 194–196

Phase-sensitive and phase-resolved emission spectra, 194–197  
fluorescence-lifetime imaging microscopy, 743  
phase-modulation resolution of emission spectra, 197–199

from phase and modulation spectra, 198–199

phase angle and modulation-based, 198

phase or modulation lifetime-based, 198

theory of phase-sensitive detection, 195–196

examples of PSDF and phase suppression, 196–197

high-frequency or low-frequency, 197

Phase shift, 159

Phase transition in membranes, 217–219

Phenol

excited-state reactions, 259–260

intensity decays, 578

quantum yield standards, 54

Phenol red, 633

Phenylalanine, 63

calcium binding to calmodulin using phenylalanine and tyrosine, 545–546

mutants of triosephosphate isomerase, 555, 556

quantum yield standards, 54

quenching of indole, 537

resonance energy transfer in proteins,  
542, 543–545

spectral properties, 530, 531

tryptophan quenching of, 537, 592–593

2-Phenylindole, 269, 610

N-Phenyl-1-naphthylamine (NPN), 226, 227

Phorbol myristoyl acetate (PMA), 746

Phosphate, tyrosine absorption and emission, 534, 535

Phosphatidic acid, energy transfer, 463–464

- Phosphatidylcholine  
brominated, 295  
dansyl, energy transfer, 463–465  
parinaroyl, 415
- Phosphatidylethanolamine  
energy transfer, 522
- Phosphine ligand, 693
- Phosphoglycerate kinase, 494–495, 501, 690
- Phospholipase A<sub>2</sub>, 395, 548, 583
- Phospholipids, 295
- Phosphorescence  
defined, 1  
microsecond anisotropy decays, 408  
protein, 598–600  
quenching, 317–318
- Phosphoryl-transfer protein (PTP), 587
- Photobleaching, 34, 299, 523–524, 608–609, 769  
fluorescence recovery after, 814–815  
literature references, 793
- Photocathodes (PD), 44, 45–46, 765
- Photo-counting streak camera (PCSC), 126–127, 128
- Photodiodes (PD), 177  
amplification, 115  
fast, 176  
single-photon-counting avalanche, 755  
time-correlated single-photon counting, 118–119
- Photoinduced electron transfer (PET)  
energetics of, 336–341  
examples of, 338–340  
in linked donor–acceptor pairs, 340–341  
quenching  
in biomolecules, 341–342  
single-molecule, 342–343
- Photoinduced electron-transfer (PET) probes, 316, 318, 335–336, 627, 641–643
- Photomultiplier tubes (PMTs), 44–49  
amplification, 115  
constant fraction discriminators, 114–115  
frequency-domain lifetime measurements, 167–168  
instrumentation, 44–49  
CCD detectors, 49  
designs and dynode chains, 46–47  
failure of, symptoms, 49  
hybrid, 49  
photon counting vs. analog detection of fluorescence, 48–49  
spectral response, 45–46  
time response of, 47  
multi-anode, 122  
pulse pileup, 116–117  
single-molecule detection, 765  
time-correlated single-photon counting, 103–104  
dynode chain, 118  
microchannel plate, 117–118
- Photon antibunching, 829–830
- Photon burst, 715, 716
- Photon counting histograms, 818  
literature references, 839
- Photon counting rate, 124
- Photon migration imaging (PMI), 657
- Photophysics of single-molecule detection, 768–770
- Photoselection, 12, 357–358  
for two-photon excitation, 612–613
- Photostability of fluorophores, 70–71
- pH sensors. *See pH, indicators/probes/sensors*
- Phthalocyanines, 75
- Phycobiliproteins, 84–86
- Phycocyanine, 84
- Phycoerythrin, 84
- Phycoerythrobilin, 84
- Phytochromes, 83–84
- Phytofluors, 83–84
- Picolinium salts, quenching by, 278, 279
- Picosecond dye lasers, time-correlated single-photon counting, 110–112
- Picosecond intensity decays, 146
- Picosecond relaxation in solvents, 249–252  
multi-exponential relaxation in water, 251–252  
theory of time-dependent solvent relaxation, 250–251
- Picosecond rotational diffusion, oxytocin, 399
- Planar fluorophores with high symmetry, anisotropy, 435
- Plasma emission, 39
- Plasmons, 861, 869
- Platelet-derived growth factor (PDGF), 725, 726
- Platinum (II) octaethylporphyrin ketone, 629
- Point-by-point detection, 763
- Poisson distribution, 798
- Poisson noise, 103
- Polarity  
protein, 531, 533–534  
solvent effects on emission spectra, 206, 533–534  
Lippert equation, 210–211  
membrane-bound fluorophore, 206–207
- Polarization, 12–13. *See also Anisotropy*  
anisotropy measurement, 19, 354  
definition, 354–355  
fluorescence immunoassay, 661–663  
generalized, 218  
instrumentation, 36  
mobility of surface-bound fluorophores, 786–787  
monochromator characteristics, 36  
of single immobilized fluorophores, 786  
single-molecule detection, 775–777  
literature references, 794  
surface plasmon-coupled emission, 865
- Polarization assays, DNA hybridization, 719
- Polarization spectra  
electronic state resolution from, 360–361  
tyrosine and tryptophan, 531–533
- Polarized excitation, 778
- Polarizers, 29, 49–51, 364
- Polycyclic aromatic hydrocarbons, 279
- Poly-L-proline, 449
- Polymerase chain reaction (PCR), 720, 808
- Polymer beads, 656
- Polymer films, 433–434
- Polymers  
fluorescence correlation spectroscopy  
literature references, 839
- Poly(methylmethacrylate) (PMMA), 763
- Polynuclear aromatic hydrocarbons, 175
- Polyvinyl alcohol film, 359
- POPOP, 2, 3, 185, 186
- Porphyrin, 465
- Porphyrin ketone derivative, 629
- Position sensitive detection  
literature references, 754
- Potassium-binding benzofuran isophthalate (PBFI), 645–646, 647

- Potassium dehydrogen phosphate (KDP), 251  
 Potassium probes, 635–636, 645–647  
 PPD (2,5-diphenyl-1,3,4-oxadiazole), 105  
 PPO, 279  
 Presenilin I, 750  
 Primol 342, 369  
 Principles of fluorescence, 1–26
  - anisotropy, fluorescence, 12–13
  - biochemical fluorophores, 15–16
  - emission characteristics, 6–9
    - excitation wavelength independence, 7–8
    - mirror image rule, exceptions to, 8–9
    - Stokes shifts, 6–7
  - fluorescence sensing, 3
  - indicators, 16–17
  - Jablonski diagram, 3–6
  - lifetimes and quantum yields, 9–12
  - molecular information from fluorescence, 17–20
    - emission spectra and Stokes shift, 17–18
    - fluorescence polarization of anisotropy, 19
    - quenching, 18–19
    - resonance energy transfer, 19–20
  - phenomenon, 1–3
  - quenching, 11
  - resonance energy transfer, 13–14
  - steady-state and time-resolved fluorescence, 14–15- Prion proteins, 827  
*Probes. See Fluorophores*  
 Prodan, 70, 221
  - apo-myoglobin spectral relaxation, 244–245
  - solvent effects, 219
    - fatty acid binding proteins, 217
    - LE and ICT states, 221
    - phase transitions in membranes, 217–219
- Prodan derivatives, 217, 218  
 Proflavin, 286–287  
 Programmable gain amplifier (PGA), 105  
 Propanol, 210, 250, 252  
 Propidium iodide, 713  
 Propylene glycol, 346, 347, 510
  - anisotropic rotational diffusion, 428, 429
  - excitation anisotropy spectra, 359, 360
  - rotational correlation times in, 590
  - solvent relaxation, 217
  - tryptophan anisotropy spectra in, 532
- Protein binding and association reactions. *See Association reactions*  
 Protein fluorescence, 529–567
  - aromatic amino acids, spectral properties, 530–535
  - tryptophan, solvent effects on emission, 533–534
  - tyrosinate emission from proteins, 535
  - tyrosine, excited-state ionization, 534–535
  - tyrosine and tryptophan, excitation polarization of, 531–533
  - association reactions, 551–554
    - calmodulin, binding to target protein, 551–552
    - calmodulin, tryptophan mutants, calcium binding site resolution, 552
    - interactions of DNA with proteins, 552–554
    - calcium binding to calmodulin, 545–546
    - energy transfer, 539–545
      - interferon- $\gamma$ , tyrosine-to-tryptophan energy transfer in, 540–541
      - membrane-bound protein, tyrosine-to-tryptophan energy transfer in, 543
  - phenylalanine-to-tyrosine, 543–545
  - RET efficiency quantitation, 541–543
  - general features, 535–538
  - genetically engineered proteins, spectral properties, 554–557
    - barnase, 556–557
    - ribonuclease mutants for, 558–559
    - triosephosphate isomerase, 555, 556
    - tyrosine proteins, 557
  - indole, 531
  - phenylalanine, 545
  - protein folding, 557–560
    - cellular retinoic acid binding protein I (CRABPI), 560
    - lactate dehydrogenase, 559–560
  - protein structure and tryptophan emission, 560–562
  - tryptophan emission in apolar environment, 538–539
    - azurins, emission spectra of molecules with one or two tryptophan, 539
    - azurins, site-directed mutagenesis of single-tryptophan, 538–539
  - tryptophan quenching, 546–551
    - emission maximum, effects of, 547–549
    - emission spectra resolution by, 550–551
    - fractional accessibility in multi-tryptophan proteins, 549–550
  - Protein fluorescence, time-resolved, 577–600
    - anisotropy decays, 583–588
    - annexin V, 585–587
    - melittin, 590–591
    - protein with two tryptophans, 587–588
    - representative proteins, 589–591
      - ribonuclease T<sub>1</sub>, 584, 585
    - decay-associated spectra, 591
    - intensity decays, 578–580
    - perspectives, 600
    - phosphorescence, 598–600
    - protein folding, conformational heterogeneity, 588–589
    - protein unfolding, 588–589
      - conformational heterogeneity, 588–589
    - representative proteins
    - disulfide oxidoreductase DsbA, 591–592
    - heme proteins, intrinsic fluorescence, 594–596
    - immunophilin FKBP59-1, phenylalanine quenching of tryptophan fluorescence, 592–593
    - thermophilic  $\beta$ -glycosidase, 594
    - tryptophan repressor, site-directed mutagenesis, 593–594
    - spectral relaxation, 596–598
    - tryptophan, intensity decays, rotamer model, 578–580
    - tryptophan and tyrosine, intensity decays, 580–583
      - decay-associated tryptophan emission spectra, 581
      - neutral tryptophan derivatives, intensity decays, 581–582
      - neutral tyrosine derivatives, intensity decays, 582–583
    - Protein folding, 292–293, 453–455, 557–560  
 Protein kinase C, 654, 690, 746–747  
 Protein phosphorylation, 459  
 Proteins. *See also Fluorophores*
      - anisotropy
        - Perrin equation, 367–369
        - Perrin plots, 370–372
      - anisotropy of membranes and membrane-bound proteins, 374–377
      - association of tubulin subunits, 807–808
      - binding of NADH, 65–67
      - binding to chaperonin GroEL, 807
      - conformation (*See Conformation*)
      - diffusive motions in biopolymers, 501

- Proteins [cont'd]
- distance distributions, 482–485
  - analysis with frequency domain data, 479–482
  - melittin, 452, 483–485
  - representative literature references, 504
  - from time-domain measurements, 487
  - domain-to-domain motions, 690
  - energy transfer, 509, 681
    - orientation of protein-bound peptide, 456–457
    - protein binding to semiconductor nanoparticles, 457–458
    - RET and association reactions, 455–456
    - RET imaging of fibronectin, 516
    - single-protein-molecule distance distribution, 496–497
  - fluorescence correlation spectroscopy
    - literature references, 839
  - labeling
    - probes, non-covalent, 71–72
    - reagents, 67–69
    - Stokes shift in, 69–70
  - literature references, 794
  - metal-ligand complexes, domain-to-domain motions in, 690
  - protein kinase C activation, 746–747
  - quenching
    - distance dependent, 348
    - radiation boundary model, 344–346
    - substrate binding to ribozyme, 311–312
    - conformational changes and tryptophan accessibility, 291
    - effects of quenchers on proteins, 292
    - endonuclease III, 290–291
    - multiple decay time quenching, 291–292
  - as sensors, 88–89, 651–652
    - based on resonance energy transfer, 652–654
  - single-molecular resonance energy transfer, 773–775
  - specific labeling of intracellular, 86
  - time-resolved emission spectra (TRES)
    - apomyoglobin, 243–244
    - membranes, 245–249
    - spectral relaxation in, 242–243
- Proteins, anisotropy decay
- collisional quenching, analysis with, 431–432
  - frequency-domain, 397–399
    - apomyoglobin, rigid rotor, 397–398
    - melittin, 398
    - oxytocin, picosecond rotational diffusion, 399
  - time-domain, 394–397
    - alcohol dehydrogenase, 395
    - domain motions of immunoglobulins, 396–397
    - free probe, effects of, 397
    - phospholipase A<sub>2</sub>, 395
    - Subtilisin Carlsberg, 395–396
- Proteins, fluorescent, 81–86
- green fluorescent protein, 81–83, 307–309
  - phycoobiliproteins, 84–86
  - phytofluors, 83–84
- Protonation, 643
- Protons
- excited-state reactions, 259
  - quenching by, 279
- Pulsed laser diodes, 577
- Pulsed xenon lamps, 32
- Pulse lasers, 21
- Pulse picker, 110
- Pulse pileup, 116–117
- Pulse repetition rate, 124
- Pulse sampling or gated detection, time-resolved measurements, 124–125
- Purines, 278, 284
- Purothionines, 535
- PyDMA, 126
- Pyrene, 86, 126
  - DNA technology, 718
  - emission spectrum, 9
  - excited-state reactions, 610
  - Förster distances, 468
  - lipids labeled with, 86, 296, 297
    - pyrenyl-PC, 72
  - quenchers of, 279, 300
  - release of quenching upon hybridization, 310, 311
  - rotational diffusion, 371
- Pyrenedodecanoic acid (PDA), 293
- 1-Pyrenesulfonylchloride, 371
- Pyridine, 278, 279
- Pyridine-1, 2, 3
- Pyridine-2, 112
- Pyridinium, 336
- Pyridinium hydrochloride, 278
- Pyridoxal 5-phosphate, 64
- Pyridoxamine, 64
- Pyrimidines, 278, 284
- Pyrophosphate, 316

## Q

- Quantum counters
- corrected spectra, 52–53
  - instrumentation, 51–52
- Quantum dots, 457, 675
  - labeling cells, 677–678
  - multiplexed arrays, 727
  - resonance energy transfer, 678
  - spectral properties, 676–677
- Quantum yields, 9
  - and lifetime, 537
  - long-wavelength long-lifetime fluorophores, 695
  - in membranes, 518
  - principles, 9–12
  - quenching, 10
  - timescale of molecular processes in solution, 12
    - protein fluorescence, 536–537
  - resonance energy transfer in proteins, 541–542
- Quantum yield standards, 54–55
- Quartz-tungsten halogen (QTH) lamps, 33
- Quenchers, 278. *See also* specific agents
- Quenching, 11, 18, 277–318, 401–402
  - and association reactions, 304–305
  - accessibility to quenchers, 312–313
    - specific binding reactions, 304–305
  - bimolecular quenching constant, 281–282
  - collisional, 171–172
  - collisional, theory of, 278–282
    - bimolecular quenching constant, interpretation of, 281–282
    - Stern-Volmer equation, derivation of, 280–281

comparison with resonance energy transfer, 331–334  
 distance dependence, 332–333  
 encounter complexes and quenching efficiency, 333–334  
   by dabcyl, 722  
 energy transfer, 519  
 energy transfer,  $\chi_0$  changes from, 480  
 fractional accessibility, 288–290  
   experimental considerations, 289–290  
   Stern-Volmer plots, modified, 288–289  
 by gold, molecular beacons, 723–724  
 on gold surfaces, 313–314  
   molecular beacon by gold colloids, 313–314  
   molecular beacon by gold surface, 314  
 intramolecular, 314–317  
   DNA dynamics, 314–315  
   electron transfer in flavoprotein, 315–316  
   sensors based on photoinduced electron transfer, 316, 318  
 of lanthanides, 523  
 mechanisms of, 334–336  
   electron-exchange, 335  
   intersystem crossing, 334–335  
   photoinduced electron transfer, 335–336  
 molecular biology applications, 310–313  
   molecular beacons by guanine, 311  
   release of quenching upon hybridization, 310, 311  
   substrate binding to ribozymes, 311–312  
 molecular information from fluorescence, 18–19  
 of phosphorescence, 317–318  
 photoinduced electron transfer, 336–341  
   examples of, 338–340  
   in linked donor–acceptor pairs, 340–341  
 photoinduced electron transfer quenching in biomolecules, 341–342  
   DNA bases and nucleotides, 341–342  
   quenching of indole by imidazolium, 341  
 proteins  
   anisotropy decays, 431–432  
   tryptophan position and, 550  
 proteins, applications to, 290–300  
   colicin E1 folding, 292–293  
   conformational changes and tryptophan accessibility, 291  
   effects of quenchers on proteins, 292  
   endonuclease III, 290–291  
   multiple decay time quenching, 291–292  
 quenchers, 278  
 quenching-resolved emission spectra, 301–304  
   fluorophore mixtures, 301–302  
   Tet repressor, 302–304  
 self-, metal-enhanced fluorescence, 853–854  
 sensing applications, 305–310  
   amplified, 309–310  
   chloride-sensitive fluorophores, 306  
   chloride-sensitive green fluorescent protein, 307–309  
   intracellular chloride imaging, 306–307  
 simulated intensity decay, 101  
 single-molecule photoinduced electron transfer, 342–343  
 sphere of action, 285–286  
 static, theory of, 282  
 static and dynamic, 282–283  
   examples of, 283–284  
 steric shielding and charge effects, 286–288  
   DNA-bound probe accessibility, 286–287  
   ethenoadenine derivatives, 287–288  
 Stern-Volmer equation, deviations from, 284–285

transient effects, 343–348  
   experimental studies, 346–348  
   proteins, distance-dependent quenching in, 348  
   tryptophan fluorescence, by phenylalanine, 537  
 Quenching, advanced topics, 293–301  
   membranes, 293–300  
    boundary lipid, 298  
    lipid-water partitioning effects, 298–300  
    localization of membrane-bound tryptophan residues, 294–295  
    in micelles, 300  
    oxygen diffusion, 293–294  
    partitioning, 298–300  
   membranes, applications to  
    localized quenchers, 295–296  
    parallax and depth-dependent quenching, 296–298  
   membranes, diffusion in, 300–301  
    lateral, 300–301  
   probe accessibility to water- and lipid-soluble quenchers, 286–287  
   quenching efficiency, 281, 333, 543  
 Quenching constants, 309, 348, 548–549  
 Quenching efficiency, 281, 333, 542  
   encounter complexes, 333–334  
 Quin-2, 648, 649  
   fluorescence-lifetime imaging microscopy, 744–745  
 Quinine, 2, 7  
   chloride sensors, 631  
 Quinine sulfate, 51–52, 53, 56, 196, 197  
 Quinolinium, 279

**R**

$R_0$ . *See* Förster distance  
 Rac activation, 459, 460  
 Radiating plasmon model, 856, 868  
 Radiation boundary condition (RBC) model, 344–346  
 Radiation patterns, 778–779  
 Radiative decay, 842–843  
 Radiative decay engineering, 841–870  
   introduction, 841–843  
   Jablonski diagram, 842–843  
   optical properties of metal colloids, 845–846  
   surface plasmon-coupled emission, 861–870  
 Radiative decay rate, 223, 537  
 Radiative transfer, 366  
 Radio-frequency amplifiers, frequency-domain lifetime measurements, 167  
 Raman notch filter, 39  
 Raman scatter, 39, 42, 43, 289  
 Rapid diffusion limit, 467  
 Ras in single-molecule detection, 24  
 rATP, 725  
 Rayleigh scatter, 42, 59, 289, 766  
 Reaction coordinate, 238  
 Reaction kinetics, 758–759, 799  
 Receptors, membrane-bound, 813–815  
 Red and near-IR dyes, 74–75  
 Red-edge excitation shifts, 257–259  
   energy transfer, 259  
   membranes, 258–259  
 Red fluorescent protein, 81  
 Red shift, solvent effects on, 533–534  
 Reflectivity in surface-plasmon resonance, 862–863  
 Refractive index, 50, 208, 209

- Rehm-Weller equation, 337  
 Relaxation, 7, 12  
 Relaxation dynamics, 237–270
  - analysis of excited-state reactions, 265–270
  - continuous and two-state spectral relaxation, 237–239
    - phase modulation studies of solvent relaxation, 265–267
  - excited-state ionization of naphthalol, 260–262
  - excited-state processes, overview, 237–240
  - excited-state reactions, 259–262
    - lifetime-resolved emission spectra, 255–257
    - multi-exponential spectral relaxation, measurement, 252–253
    - picosecond relaxation in solvents, 249–252
      - multi-exponential relaxation in water, 251–252
      - theory of time-dependent solvent relaxation, 250–251
  - red-edge excitation shifts, 257–259
    - energy transfer, 259
    - membranes, 258–259
  - solvent relaxation vs. rotational isomer formation, 253–255
  - time-resolved emission spectra (TRES)
    - analysis, 246–248
    - anthroyloxy fatty acids, 248–249
    - labeled apomyoglobin, 243–244
    - measurement, 240–242
    - membranes, spectral relaxation in, 245–249
    - overview, 239–240
    - proteins, spectral relaxation in, 242–243
    - synthetic fluorescent amino acid, 244–245
  - time-resolved emission spectra (TRES) measurement
    - direct recording, 240–241
    - from wavelength-dependent decays, 241–242
  - TRES vs. DAS, 255- Resonance, surface-plasmon, 861–865
- Resonance energy transfer (RET), 13, 144, 375, 443. *See also*
  - Energy transfer
  - applications, 20–21, 490–496
  - characteristics of, 443–445
  - comparison with quenching, 331–334
    - distance dependence, 332–333
    - encounter complexes and quenching efficiency, 333–334
  - Dexter interaction, 335
  - and diffusive motions in biopolymers, 501
  - effects on anisotropy, 364–365
  - efficiency, 333
  - literature references, 839
  - molecular information from fluorescence, 19–20
  - principles, 13–14
  - sensors, 626
    - time-resolved RET imaging, 497–498
  - Restricted geometries, energy transfer, 516–519
  - Restriction enzymes, 712–713, 826
  - Restriction fragment length polymorphisms (RFLPs), 713
  - RET. *See* Resonance energy transfer (RET)
  - Retinal, 522–524
  - Reversible two-state model, 262–264
    - differential wavelength methods, 264
    - steady-state fluorescence of, 262–263
    - time-resolved decays for, 263–264
  - Rhenium complex, 520
  - Rhenium metal-ligand complexes, 88, 684, 686
    - immunoassays, 692–693
    - spectral properties, 687
  - Rhod-2, 645
  - Rhodamine, 2, 3, 20, 314, 315
    - anisotropy decay, 394, 416
    - DNA technology, 723, 725, 729
    - glucose sensor, 635
    - quantum yield standards, 54
    - time-resolved RET imaging, 498
  - Rhodamine 800, 74
  - Rhodamine B, 51, 279
    - metal-enhanced fluorescence, 848
  - Rhodamine derivatives, 74, 76
    - Förster distances, 468
      - structures of, 74–75
  - Rhodamine 6G, 122, 514
    - concentration in fluorescence correlation spectroscopy, 805–806
    - single-molecule detection, 759–760
  - Rhodamine 6G dye laser. *See* R6G laser
  - Rhodamine green (RhG), 824
  - Rhodamines, 68–69
  - Rhodopsin disk membranes, retinal in, 522–524
  - Riboflavin, 64
  - Ribonuclease A, 501, 558–559
  - Ribonuclease T<sub>i</sub>, 536, 548, 588–589
    - anisotropy decays, 584, 585
  - Ribozymes
    - energy transfer, 460
    - hairpin, 493
    - representative literature references, 505
      - in single-molecule detection, 23–24, 775
  - Ribozyme substrate binding, 311–312
  - Rigid rotor, 397–398
  - Rigid vs. flexible hexapeptide, distance distributions, 479–481
  - RNA
    - energy transfer, 459–461
    - imaging of intracellular RNA, 460–461
  - Room-temperature phosphorescence of proteins, 599
  - Rose bengal, 848
  - Rotamers (rotational isomers), 253–255, 529, 578–580
  - Rotational correlation time, 102–103, 353
    - ellipsoids, 423–425
  - Rotational diffusion, 12, 13, 102, 168, 365, 422–423, 828–830
    - anisotropy decay
      - ellipsoids, theory, 425–426
      - frequency-domain studies of, 427–429
      - non-spherical molecules, 418–419
      - time-domain studies of, 426–427
      - membranes, hindered, 399–402
      - oxytocin, 399
      - Perrin equation, 366–370
      - rotational motions of proteins, 367–369
        - stick vs. slip rotational diffusion, 425
    - Rotational isomer formation, 253–255, 529, 578–580
    - Rotational motion
      - measurement of, 102
      - single-molecule detection, 775–779
    - Rotors
      - hindered, 391–392
      - rigid, 397–398
    - R6G laser, 111, 112, 120
      - fluorescence intensity distribution analysis, 818, 819
      - single-molecule detection, 777–778
    - R3809U, 117

Ru(bpy)<sub>2</sub>phe-C<sub>12</sub>, 189, 190  
 Rugate notch filters, 766  
 Ruthenium metal-ligand complexes, 88, 684, 686

**S**

Sample geometry effects, 55–57  
 Sample preparation, common errors in, 57–58  
 SBFI (sodium-binding benzofuran isophthalate), 645–647  
 Scanning fluorescence correlation spectroscopy  
     literature references, 839  
 Scattered light, 366, 766  
     phase-sensitive detection, 196, 197  
 Scattered light effect, frequency-domain lifetime measurements, 172–173  
 Second-order transmission, monochromator, 37  
 Segmental mobility, biopolymer-bound fluorophore, 392–393  
 Selex, 725  
 Self-quenching, 69–70  
     metal-enhanced fluorescence, 853–854  
 Semiconductor nanoparticles, 675–678  
 Seminaphthofluoresceins (SNAFLS), 640–641  
 Seminaphthorhodofluors (SNARFS), 640–641  
 Senile plaques, 498  
 Sensing and sensors, 78–79, 623–663  
     analyte recognition probes, 643–650  
         calcium and magnesium, 647–650  
         cation probe specificity, 644  
         intracellular zinc, 650  
         sodium and potassium, 645–647  
         theory of, 644–645  
     calcium, 784  
     cardiac, 662  
     chloride, 631–632  
     clinical chemistry, 623–624  
     by collisional quenching, 627–633  
         chloride, 631–632  
         miscellaneous, 632  
         oxygen, 627–630  
     energy transfer  
         glucose, 634–635  
         ion, 635–636  
         pH and CO<sub>2</sub>, 633–634  
         theory for, 636–637  
     energy-transfer, 633–637  
 GFP sensors, 654–655  
     intrinsic, 655  
     using resonance energy transfer, 654–655  
 glucose-sensitive fluorophores, 650–651  
 immunoassays, 658–663  
     ELISA, 659  
     energy transfer, 660–661  
     fluorescence polarization, 661–663  
     time-resolved, 659–660  
 in-vivo imaging, 656–658  
 lanthanides, 659, 681–682  
 literature references, 795  
 mechanisms of sensing, 626–627  
 metal-ligand complexes (*See* Metal-ligand complexes (MLCs))  
 molecular information from fluorescence, 17–20  
 new approaches to, 655–656  
     pebble sensors and lipobeads, 655–656  
 pH, two-state sensors, 637–641  
     blood gases, optical detection of, 637  
     pH sensors, 637–641  
     phosphorescence, 629  
     photoinduced electron-transfer (PET), 316, 318  
     photoinduced electron-transfer (PET) probes for metal ions and anions, 641–643  
     probes, 79–81  
     proteins as sensors, 651–652  
         based on resonance energy transfer, 652–654  
     RET, 458–459  
     spectral observables, 624–626  
         lifetime-based sensing, 626  
         optical properties of tissues, 625  
 Serotonin, 615–616  
 Serum albumin, 13, 71, 72, 304, 584, 589, 678  
     anisotropy decay of, 413–414  
     intensity decay of, 583, 584  
     laser diode excitation, measurement with, 71, 72  
     metal-enhanced fluorescence, 851–853  
     rotational correlation time, 368  
 Shear stress on membrane viscosity, 225  
 β-Sheet structure, 561–562, 563  
 Side-window dynode chain PMTs, 118  
 Signaling, intracellular, 459  
 Signal-to-noise ratio in single-molecule detection, 784–786  
 Silicone, oxygen sensor support materials, 627, 628, 629  
 Silver, 278, 279  
     effect on resonance energy transfer, 854–855  
 Silver colloids, 845–846  
 Silver island films, 848  
 Simazine, 660  
 Simulated intensity decay, 101, 102  
 Single-channel anisotropy measurement method, 361–363  
 Single-exponential decay, 120, 121  
     spherical molecules, 367  
     time-dependent intensity, 198  
 Single-exponential decay law, 346  
 Single-exponential fit, FD intensity decay approximation, 479  
 Single-exponential intensity and anisotropy decay of ribonuclease T<sub>1</sub>, 584, 585  
 Single-molecule detection, 23–24, 757–788  
     advanced topics, 784–788  
         lifetime estimation, 787–788  
         polarization measurements and mobility of surface-bound fluorophores, 786–787  
         polarization of single immobilized fluorophores, 786  
         signal-to-noise ratio in single-molecule detection, 784–786  
     biochemical applications, 770–773, 780–784  
     chaperonin protein, 771–773  
     conformational dynamics of Holliday junction, 782–783  
     enzyme kinetics, 770  
     molecular beacons, 782  
         motions of molecular motors, 784  
         single-molecule ATPase activity, 770–771  
         single-molecule calcium sensor, 784  
         turnover of single enzyme molecules, 780–781, 782  
     detectability of single molecules, 759–761  
     instrumentation, 764–768  
         detectors, 765–766  
         optical filters, 766–768  
     internal reflection and confocal optics, 760–762  
         confocal detection optics, 761–762  
         total internal reflection, 760–761  
     literature references, 788, 791–795  
     optical configurations for, 762–764

- Single-molecule detection [cont'd]  
 photophysics, 768–770  
 resonance energy transfer, 773–775  
 single-molecule orientation and rotational motions, 775–779  
   imaging of dipole radiation patterns, 778–779  
   orientation imaging of R6G and GFP, 777–778  
   time-resolved studies of single molecules, 779–780
- Single-molecule detection (SMD), 342–343
- Single-particle detection, 85
- Single-photon counting, 103. *See also* Time-correlated single-photon counting
- Single-photon-counting avalanche photodiode (SPAD), 755, 763
- Single-photon excitation, green fluorescent protein, 171
- Single-stranded DNA binding protein, 552–554
- Singlet state, 334
- Site-directed mutagenesis, azurins, 538–539. *See also* Genetically engineered proteins
- Skeletal muscle troponin C, 490–492
- Skilling-Jaynes entropy function, 148
- Smoluchowski model, 281, 344, 345–346, 347
- SNAFL, 640–641
- SNARF, 640–641
- Sodium analyte recognition probes, 645–647
- Sodium-binding benzofuran isophthalate (SBFI), 645, 647
- Sodium Green, 16, 17, 646, 647
- Sodium probes, 17, 635–636, 643, 645–647
- Soleillet's rule, depolarization factor multiplication, 436–437
- Sol gels, 634
- Solvent effects on emission spectra, 205–235, 533–534  
   additional factors, 219–223  
     changes in non-radiative decay rates, 222–223  
     excited-state intramolecular photon transfer, 221–222  
     locally excited and internal charge transfer states, 219–221  
   biochemical examples  
     calmodulin, hydrophobic surface exposure, 226–227  
     cyclodextrin binding using dansyl probe, 227–228  
     fatty acid binding proteins, 226  
     with solvent-sensitive probes, 226–229  
   development of advanced solvent-sensitive probes, 228–229
- Lippert equation, 208–213  
   application of, 212–213  
   derivation of, 210–212
- Lippert-Mataga equation, 208–210
- Lippert plots, specific solvent effects, 215–216  
 mixtures, effects of, 229–231  
 overview, 205–208  
 polarity surrounding membrane-bound fluorophore, 206–207  
 probe–probe interactions, 225–226
- Prodan  
   phase transitions in membranes, 217–219  
 specific, 213–215  
 spectral shift mechanisms, 207–208  
 summary of, 231–232  
 temperature effects, 216–217  
 tryptophan, 533–534  
 viscosity effects, 223–225  
   shear stress on membrane viscosity, 225
- Solvent relaxation, 12. *See also* Relaxation dynamics; Solvent effects on emission spectra  
   vs. rotational isomer formation, 253–255
- Solvent-sensitive probes, 226–229
- Soybean peroxidase (SBP), 595
- SPA (N-sulfopropylacridinium), 631
- Species-associated spectra (SAS), 269–270
- Spectral diffusion in single-molecule detection, 767
- Spectral karyotyping, 730–732
- Spectral observables, sensors, 624–626
- Spectral overlap, two-state model, 661
- Spectral relaxation, 239, 596–598. *See also* Relaxation dynamics
- Spectral response, PMTs, 45–46
- Spectral shift mechanisms, solvent effects on emission spectra, 207–208
- Spectrofluorometer, 3, 27–29  
   for high throughput, 29–30  
   ideal, 30  
   schematics of, 28
- Spectroscopy  
   fluorescence correlation, 757, 797–832  
   general principles (*See* Principles of fluorescence)
- Sperm whale myoglobin, 584
- Sphere of action, 285–286
- Spin-labeled naphthalene derivative, 314
- Spin-labeled PC, 298
- Spin-orbit coupling, quenching, 278
- Spotted DNA microarrays, 732–734
- SPQ [6-methoxy-N-(3-sulfopropyl)quinolinium]  
   chloride sensors, 171–172, 631–632  
   quenching, 279
- Squirrel cage, 46
- Stains, DNA, 712–715  
   energy-transfer stains, 715  
   fragment sizing by flow cytometry, 715  
   high-affinity bis, 713–715
- Standard lamp, correction factors obtained with, 53
- Standards  
   corrected emission spectra, 52–53  
   emission spectra correction, 52–53  
   quantum yield, 54–55
- Staphylococcal nuclease, 346, 347, 536, 558, 560, 564–565  
 anisotropy, 588  
 frequency-domain lifetime measurements, 171  
 intensity decay of, 583
- Staphylococcus aureus* metalloprotease, 550–551
- Static quenching, 11, 65, 277. *See also* Quenching  
   combined with dynamic quenching, 282–283  
   examples, 283–284  
   theory of, 280, 282
- Steady-state and time-resolved fluorescence principles, 14–15
- Steady-state anisotropy  
   calculation of, 367  
   DPH in DPMC vesicles, 302  
   proteins, tryptophan position and, 551
- Steady-state intensity, 15
- Steady-state measurements  
   continuous relaxation model, 238  
   light sources, 31–34  
   vs. time-resolved measurements, 97
- Steric shielding, quenching, 281, 286–288
- Stern-Volmer equation, 278, 283–284  
   derivation of, 280–281  
   deviations from, 284–285
- Stern-Volmer plots, 549–550
- Stern-Volmer plots, modified, 288–289
- Stern-Volmer quenching, 11
- Stern-Volmer quenching constant, 18, 279
- Steroid analogs, 80
- Steroid binding protein (SBP), 286

- Steroids, quenching, 284, 286–287  
 Stilbene, 223–224, 309, 310  
 Stokes, G.G., 6, 7  
 Stokes-Einstein equation, 281  
 Stokes shift, 6–7, 119
  - advanced solvent-sensitive probes, 228–229
  - dielectric constant and refractive index effects, 207, 208
  - emission spectra and, 17–18
  - in protein labeling, 69–70
  - solvent effects, 208–210, 222
 Stratum corneum, 751  
 Stray light, 36–37  
 Streak camera fluorescence-lifetime imaging microscopy, literature references, 754  
 Streak cameras, 125–128  
*Streptavidin*, 565–566, 678  
 Streptococcal protein G, 244  
 Stretched exponentials, time-domain lifetime measurements, 144  
 Stroboscopic sampling, 124–125  
 Structural analogs of biomolecules, 80  
 Structural motifs
  - tryptophan spectral properties and, 561–562
 Structure
  - protein (*See* Conformation; Protein folding)
  - steric shielding and quenching, 286–288
 Stryryl, 72  
 Substrate binding to ribozymes, 311–312  
 Subtilisin, 583  
 Subtilisin Carlsberg, 395–396  
 Succinimide, 278, 279, 281  
 Succinyl fluorescein, 707, 708  
 Sudan III, 633  
 Sulfa antibiotic sulfamethazine (SHZ), 660  
 Sulfonyl chlorides, 68  
 Sulforhodamine, 656, 657  
 Sulforhodamine, 865, 866  
 Sulfur dioxide, 279, 632  
 Support materials, oxygen sensors, 627, 628, 629  
 Support plane analysis, 134  
 Surface-bound assays, 867  
 Surface plasmon-coupled emission (SPCE), 861–870
  - applications of, 867–868
  - expected properties, 865
  - experimental demonstration, 865–867
  - future developments, 868–870
  - phenomenon of, 861
  - surface-plasmon resonance, 861–865
  - theory, 863–865
 Surface-plasmon resonance (SPR), 861–865  
 Suspension arrays, multiplexed microbead, 726–727, 728  
 Syber Green, 720  
 Synchrotron radiation, 114  
 Syto 14, 189, 190
- T**
- TAMRA, 724, 726  
 Taqman, 720  
 Temperature effects
  - excited-state lifetime, 221
  - LE and ICT states of Prodan, 216–217
  - metal–ligand complexes, 685
  - room-temperature phosphorescence of proteins, 599
 rotational motions of proteins, 368, 369  
 solvent relaxation, 216–217  
 Terbium, 3, 87, 523–524
  - energy transfer, 467, 521
  - as fluorophores, 679
  - Förster distances, 468
 Terbium probes, 87  
*p-Terphenyl*, 120, 133, 134, 178
  - resolution of two widely spaced lifetimes, 178–180
 Tetraethylorthosilicate (TEOS), 634  
 Tetrahydrorhodamine, 454  
 Tetramethylrhodamine-labeled lipid (TMR-POPE), 764  
 Tetramethylrhodamine-labeled nucleotide, 808–809  
 Tetramethylrhodamine (TMR), 313, 314, 707, 729, 769
  - RET imaging of fibronectin, 516
 Tetraoctylammonium hydroxide (TOAH), 634  
 Tet repressor, 145, 302–304  
 Texas Red, 41, 69, 70, 72, 707  
 Texas Red-PE, 72  
 T-format anisotropy measurement, 29, 363–364  
 Thallium, 279  
 Theory
  - anisotropy, 355–358
  - anisotropy decay, 414–415
  - energy transfer
    - for donor–acceptor pair, 445–448
    - homotransfer and heterotransfer, 450–451
    - orientation factor, 448–449
    - transfer rate dependence on distance, overlap integral, and orientation factor, 449–450
  - energy-transfer sensing, 636–637
  - frequency-domain lifetime measurements, 161–163
    - global analysis of data, 162–163
    - least-squares analysis of intensity decays, 161–162
  - phase-sensitive detection, 195–197
    - examples of PSDF and phase suppression, 196–197
    - quenching, 278–282
    - relaxation dynamics, time-dependent, 250–251
    - representative literature references, 504- Thermophilic  $\beta$ -glycosidase, 594
- Thiazole dyes, DNA technology, 715  
 Thiazole orange, 74–75  
 Thin-film filters, 39–40  
 Thiocyanate, 279, 631  
 Three-decay time model, 178, 179  
 Three-dimensional imaging of cells, 618–619  
 Three-photon excitation, cross-sections for, 609  
 Thymidine kinase, 497  
 TICT (twisted internal charge transfer), 207, 220, 221, 627, 645  
 Time-correlated single-photon counting (TCSPC), 103–107, 241
  - convolution integral, 106–107
  - detectors
    - color effects in, 119–121
    - DNA sequencing, 123–124
    - dynode chain PMTs, 118
    - microchannel plate PMTs, 117–118
    - multi-detector and multidimensional, 121–124
    - timing effects of monochromators, 121
  - electronics, 114–117
    - amplifiers, 115
    - analyte-to-digital converter (ADC), 115
    - constant fraction discriminators, 114–115
    - delay lines, 116

- Time-correlated single-photon counting [cont'd]
- multichannel analyzer (MCA), 116
  - photodiodes as, 118–119
  - pulse pileup, 116–117
  - time-to-amplitude converter (TAC), 115–116
  - examples of data, 105–106
  - laser scanning microscopy, 748–750
  - light sources, 107–114
    - femtosecond titanium:sapphire lasers, 108–109
    - flashlamps, 112–114
    - laser diodes and light-emitting diodes, 107–108
    - picosecond dye lasers, 110–112
    - synchrotron radiation, 114
  - principles, 104–105
- Time-correlated single-photon counting (TCSPC) detectors, 117–121
- compact PMTs, 118
- Time-dependent anisotropy decays. *See* Anisotropy decays, time-dependent
- Time-dependent solvent relaxation, theory of, 250–251
- Time-domain decays
- anisotropy, time-dependent, 383–387
- Time-domain lifetime measurements, 97–155
- alternative methods for time-resolved measurements, 124–129
    - microsecond luminescence decays, 129
    - streak cameras, 125–128
    - transient recording, 124–125
    - upconversion methods, 128–129
  - applications of time-correlated single-photon counting (TCSPC)
    - chlorophyll aggregates in hexane, 146–147
    - FAD intensity decay, 147–148
    - green fluorescent protein, systematic data errors, 145–146
    - picosecond decay time, 146
  - applications of time-correlated single-photon counting (TSCPC), 145–148
    - single-tryptophan protein, 145
  - biopolymers, multi-exponential or heterogeneous decays of, 101–103
  - data analysis, 129–133
    - assumptions of nonlinear least-squares method, 130
    - autocorrelation function, 132–133
    - goodness of fit ( $\chi_R^2$ ), 131–132
    - least-square analysis, 129–131
    - maximum entropy method, 148–149
  - frequency-domain measurements, 98–100
    - examples of time-domain and frequency-domain lifetimes, 100
    - lifetime or decay time, meaning of, 99
    - phase modulation lifetimes, 99–100
  - global analysis, 144–145
  - intensity decay laws, 141–144
    - lifetime distributions, 143
    - multi-exponential decay, 141–143
    - stretched exponentials, 144
    - transient effects, 144–145
  - multi-exponential decays, analysis of, 133–141
    - anthranilic acid and 2-aminopurine, 137–138
    - global analysis, multi-wavelength measurements, 138
    - goodness of fit comparison, F-statistic, 133–134
    - number of photon counts, 135, 137
    - parameter uncertainty-confidence intervals, 134–135, 136
    - p-terphenyl and indole, 133
    - resolution of three closely spaced lifetimes, 138–141
  - vs. steady-state measurements, 97
    - time-correlated single-photon counting (TCSPC), 103–107
- convolution integral, 106–107
- examples of data, 105–106
- principles, 104–105
- time-correlated single-photon counting (TCSPC) detectors, 117–121
- color effects in, 119–121
  - compact PMTs, 118
  - DNA sequencing, 123–124
  - dynode chain PMTs, 118
  - microchannel plate PMTs, 117–118
  - multi-detector and multidimensional, 121–124
  - photodiodes as, 118–119
  - timing effects of monochromators, 121
- time-correlated single-photon counting (TCSPC) electronics, 114–117
- amplifiers, 115
  - analyte-to-digital converter (ADC), 115
  - constant fraction discriminators, 114–115
  - delay lines, 116
  - multichannel analyzer (MCA), 116
  - pulse pileup, 116–117
  - time-to-amplitude converter (TAC), 115–116
- time-correlated single-photon counting (TCSPC) light sources, 107–114
- femtosecond titanium:sapphire lasers, 108–109
  - flashlamps, 112–114
  - laser diodes and light-emitting diodes, 107–108
  - picosecond dye lasers, 110–112
  - synchrotron radiation, 114
- Time-domain measurements
- anisotropy decay, 394–397, 415–417
  - protein distance distributions from, 487
- Time-resolved emission spectra (TRES), 596–597, 598. *See also* Relaxation dynamics
- analysis, 246–248
  - vs. DAS, 255
  - frequency-domain data for calculation of, 264–265
  - labeled apomyoglobin, 243–244
  - membranes, spectral relaxation in, 245–249
  - overview, 239–240
  - synthetic fluorescent amino acid, 244–245
- Time-resolved emission spectra (TRES) measurement, 240–242
- Time-resolved energy transfer. *See* Energy transfer, time-resolved
- Time-resolved fluorescence
- anisotropy decay, 102, 367
  - Förster distance determination, 499
  - light sources, 31
  - principles, 14–15
  - protein (*See* Protein fluorescence, time-resolved)
  - reasons for, 14
  - reversible two-state model, 263–264
- Time-resolved fluorescence correlation spectroscopy, 819–820
- Time-resolved immunoassays, 659–660
- Time-resolved measurements, 779–780
- Time-to-amplitude converter (TAC), 104, 105, 115–116, 121, 122
- TIN, 715
- TIRF, 56
- Tissues
- in-vivo imaging, 656–658
  - optical properties of, 625
- Titanium:sapphire lasers, 108–109, 128, 577
- for multiphoton microscopy, 614
- TMA, 500–501
- TMA-DPH, 72

- TMR (tetramethylrhodamine), 468  
 fluorescence intensity distribution analysis, 818, 819  
 Förster distances, 468  
 time-resolved fluorescence correlation spectroscopy, 819
- TNB (trinitrophenyl)  
 Förster distances, 468
- TNS [6-(*p*-toluidinyl)naphthalene-2-sulfonate]  
 red-edge excitation, 256  
 vesicles, TRES, 256
- TNS [2-(*p*-toluidinyl)naphthalene-6-sulfonic acid], 71–72  
 anisotropy decay, 397–398
- TNS [6-(*p*-toluidinyl)naphthalene-2-sulfonic acid], 17–18
- TO, 715
- TO-8, 118  
 format of photomultiplier tubes, 46
- [2-(*p*-Toluidinyl)naphthalene-6-sulfonic acid] (TNS). *See* TNS  
 (2-(*p*-Toluidinyl)naphthalene-6-sulfonic acid)
- Total internal reflection (TIR), 56, 760–761, 762, 821–822, 862  
 literature references, 839
- TOTIN, 715
- TOTO, 75, 714, 715
- Transfer efficiency, 446, 447
- Transferrin, energy transfer, 521
- Transient effects, time-domain lifetime measurements, 143
- Transient recording, 124–125
- Transition metal–ligand complexes. *See* Metal–ligand complexes  
 (MLCs); specific elements
- Transition moments, anisotropy, 355, 356, 377–378, 433–435
- Transit time spreads (TTS), 47, 117–118, 119
- Translation diffusion and fluorescence correlation spectroscopy, 802–804
- TRES. *See* Time-resolved emission spectra (TRES)
- Trichloroethanol (TCE), 278, 292
- Trifluoperazine, 89
- Trifluoroacetamide (TFA), 288
- Trifluoroethanol (TFE), 304
- Triosephosphate isomerase, 555, 556
- tRNA binding to tRNA synthetase, 370–371
- Tropomyosin, 681
- Troponin C, 614  
 calcium-induced conformation changes, 490–493
- Troponin I, 589
- Trp repressor-DNA binding anisotropy, 373
- Trypsin, 368
- Tryptophan, 11, 15, 63, 490  
 absorption and emission spectra, 16, 17  
 acceptor decay, 489  
 challenge of, 566–567  
 conformational changes and accessibility, 288–289  
 decay-associated emission spectra, 581  
 emission, 536  
 emission and protein structure, 560–562  
 genetically inserted amino-acid analogues, 565–566  
 tryptophan spectral properties and structural motifs, 561–562  
 emission in apolar environment, 538–539  
 emission spectra, 44  
 energy transfer, 450, 451  
 excitation polarization spectra, 531–533  
 frequency-domain lifetime measurements, 188–189  
 intensity decays, 145, 580–583  
 multiphoton excitation of, 614  
 mutants, 552, 555, 556  
 pH and, 579
- phosphorescence of, 598–600  
 protein fluorescence, 529–530  
 quantum yield standards, 54  
 resonance energy transfer in proteins, 540–541, 542  
 rotamers, 578–579  
 rotational correlation times, 590  
 simulated intensity decay, 101–102  
 solvent effects on emission spectra, 533–534  
 spectral properties, 530, 531, 561–562  
 spectral relaxation, 596–598  
 structure, 579  
 tryptophan analogs, 562–567  
 unfolding and exposure to water, 588–589
- Tryptophan analogs, protein fluorescence, 562–567
- Tryptophan quenching, 279, 280, 283–284, 546–551. *See also*  
 specific proteins  
 accessibility of quencher, 18, 288, 291, 549–550  
 emission maxima, effects of, 547–549  
 emission spectra resolution by, 550–551  
 endonuclease III, 290–291  
 localization of membrane-bound residues, 294–295  
 by phenylalanine, 592–593  
 quenching constant, 281–282, 548–549
- Tryptophan repressor, site-directed mutagenesis, 593–594
- Tubulin subunits, 807–808
- TU2D, 500–501
- Turbidity, 365–366
- Twisted internal charge transfer (TICT) state, 207, 220, 221, 627, 645
- Two-channel method anisotropy measurement, 363–364
- Two-component mixture, global analysis, frequency-domain lifetime  
 measurements, 182–183
- Two-photon excitation, 171, 608, 822–823  
 absorption spectra, 609–610  
 cross-sections for, 609  
 diffusion of intracellular kinase, 823  
 excitation photoselection, 612–613  
 of fluorophore, 610–612  
 instrumentation, 21–22
- Two-state pH sensors, 637–641
- Two-state relaxation, 246, 262–263  
 model, 237
- Tyr-No<sub>2</sub>  
 Förster distances, 468
- Tyrosinate-like emissions, 535
- Tyrosine, 63, 316  
 calcium binding to calmodulin using phenylalanine and  
 tyrosine, 545–546  
 dipeptides, 542  
 emission from proteins, 535  
 emission spectra, 44  
 excitation polarization spectra, 531–533  
 excited-state ionization of, 534–535  
 intensity decays, 580–583  
 protein fluorescence, 529  
 quantum yield standards, 54  
 quenchers of, 279  
 resonance energy transfer in proteins, 540–541, 542, 543–545  
 spectral properties, 530, 531  
 structure, 579  
 vasopressin, 178
- Tyrosine kinase, 459
- Tyrosine proteins, genetically engineered, 557

**U**

- Umbelliferone (7-hydroxycoumarin), 79  
 Umbelliferyl phosphate (7-UmP), 79, 659  
 Underlabeling, 488–489  
 Upconversion methods, time-resolved measurements, 128–129  
 Uridine quenching, 284

**V**

- Valinomycin, 635  
 Vasopressin, 177, 178  
 Vesicles  
     giant unilamellar, 465, 466  
     Patman-labeled, TRES, 246–247, 248  
     Prodan, 219  
     red-edge excitation, 258–259  
     RET in rapid-diffusion limit, 521–522  
     TNS-labeled, TRES, 256  
 Vibrational structure of fluorophores, 5  
 Viscosity  
     and rotational diffusion, 366  
     rotational motion of proteins, 367–368  
     solvent effects, 223–225  
 Viscosity probes, 80–81  
 Voltage and fluorophores, 73–74  
 Volume calculation in fluorescence correlation spectroscopy, 804

**W**

- W71, 556  
 W92, 558–559  
 W94, 556–557  
 Water  
     dielectric properties, 251  
     multi-exponential relaxation in, 251–252

- phosphorescence quenching, 317  
 polarizability properties, 209  
 Wavelength, 27  
     dye lasers, 112  
     emission spectrum, 4  
     excitation, emission characteristics, 6–8  
 Wavelength-dependent decays, 239–240  
     TRES measurement from, 241–242  
 Wavelength-ratiometric probes, 79, 624, 645, 651, 741, 742  
 Wavelength-to-wavenumber conversion, 53–54  
 Wavenumber, 27  
 Weber, Gregorio, 68, 69  
 W168F mutant, 555  
 Wide-field frequency-domain film, 746–747  
 Window discriminator (WD), 105

**X**

- Xenon, 279  
 Xenon lamp, 28, 31–32  
     pulsed, 32

**Y**

- Y-base, 65  
 Yellow fluorescent protein (YFP), 81, 307–309, 397, 398, 458, 497, 654  
 YFP5, 747  
 Yt-base, 230–231  
     solvent relaxation, 251–252  
 Ytterbium, 682, 683

**Z**

- Z (collisional frequency, fluorophore-quencher), 281  
 Zener diode, 167  
 Zinc-finger peptide, 88, 89, 501